Alexander M. McKinney

Atlas of Normal Imaging Variations of the Brain, Skull, and Craniocervical Vasculature

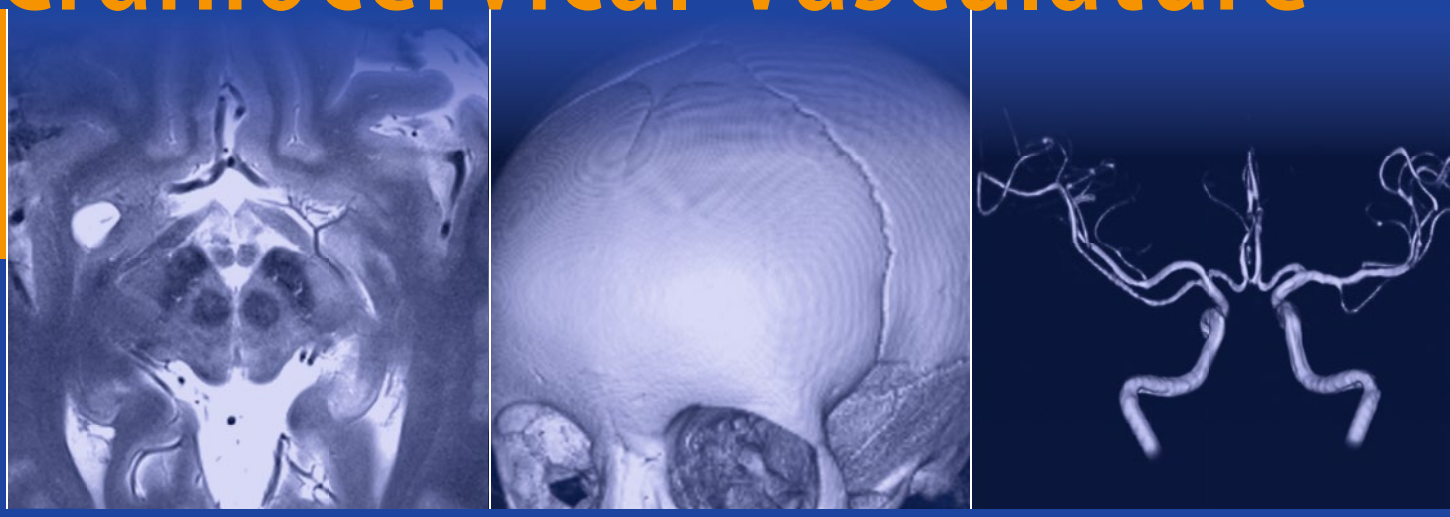

Springer

Atlas of Normal Imaging Variations of the Brain, Skull, and Craniocervical Vasculature

Alexander M. McKinney

Atlas of Normal Imaging Variations of the Brain, Skull, and Craniocervical Vasculature

Springer

Alexander M. McKinney, MD, CIIP
Professor, Peterson Chair of Neuroradiology
Neuroradiology Division
Department of Radiology
University of Minnesota
Minneapolis, MN
USA

ISBN 978-3-319-39789-4 ISBN 978-3-319-39790-0 (eBook)
DOI 10.1007/978-3-319-39790-0

Library of Congress Control Number: 2016961315

Printed on acid-free paper

This Springer imprint is published by Springer Nature
The registered company is Springer International Publishing AG
The registered company address is Gewerbestrasse 11, 6330 Cham, Switzerland

This is primarily dedicated to my family, who have been exceedingly patient and have attempted to keep me balanced, including Jennelle, Amina, Aliya, Zaki, and Nura. Also, to my parents Alex and Roni, and my brother Zeke, who have also helped me to stay focused on what is most important (i.e., family). My family has really supported me along the way in more ways than I could imagine.

Additionally, I would like to thank my radiology mentors: Drs. Chip Truwit, Stephen Kieffer, and Charles Dietz from whom I have not just learned about neuroradiology, but also about the importance of being an academician regardless of ever-changing environments. I also would like to acknowledge and express my appreciation for three colleagues (neuroradiologists) for contributing cases: Drs. Chris Palmer, Barbara Knoll, and David Nascene, who really did take the time out to save cases just for this book.

Finally, I dedicate this to my past, current, and future residents, fellows, medical students, and research assistants who I have learned from as much as they have learned from me. Without an academic environment and those individuals who are eager to learn, we would lose the initiative to improve.

Foreword

The distinction between normal variant, anomaly, and abnormality in the human nervous system is often subtle but carries profound clinical consequence. Imaging has become indispensable in diagnosis and patient management in modern clinical neuroscience. The clinician is barraged frequently with new imaging sequences labeled with clever acronyms and abbreviations. The result is an evolution in our understanding of what constitutes a normal variation and what is considered a pathological entity. The failure to distinguish what is normal and abnormal can lead to inappropriate decision making, ranging from unnecessary serial imaging to ill-fated surgical intervention. A repository of these normal variations is long overdue, and I congratulate Dr. McKinney on assuming such an arduous task.

Many neuroradiology texts are actually applied works that focus on pathological conditions with clinical correlates. These integrative works tend to appeal to a broad clinical audience including neuroradiologists, neurologists, psychiatrists, and neurosurgeons. Dr. McKinney's atlas could be classified as a work of pure neuroradiology, but its impact will be much broader. In many ways, this book carries the same significance as Krayenbühl and Yaşargil's *Cerebral Angiography* or Osborn's *Diagnostic Neuroradiology*. Like these classic texts, Dr. McKinney's current volume will have wide appeal and importance to the same audience of clinicians.

The length of this work should not intimidate the reader. However, its length requires us to contemplate the extensiveness of this subject. Our clinical focus often is directed towards pathology, and we often overlook the normal and its variants. We are passing this habit to our trainees, leading to the possibility of them not knowing the difference between normal and abnormal. This book, which is comprised mostly of images, represents an endeavor to halt this tendency. The accompanying text is purposefully brief but informative and reads easily. The reader will not need nearly as many years to review this work as was required to compose it. Like many atlases, it will serve as a valuable reference on our shelves. Even on a limited schedule, the determined student of clinical neuroscience can review all the material presented in this book in a short period.

As contemporaries in clinical neuroscience, Dr. McKinney and I have overlapped in our training and now in our respective practices. While a resident and fellow, he routinely collected cases for future reference and didactic material. I doubt he knew at the time that those cases would be the seed for this book. The absence of a single source about anatomic variations combined with Dr. McKinney's curiosity and indefatigability laid the foundations for this impressive atlas. I am confident that the reader will affirm the author's and my own notion that this atlas is a work of art.

Despite the exhaustive approach taken by Dr. McKinney, we must recognize that this volume is incomplete. As noted in the author's preface, there are neurological variations outside of the brain, skull, and vasculature that must be cataloged. Dr. McKinney may be reluctant to produce another volume to address these issues because of the time and energy necessary for such an endeavor. Based on the quality of the current work, let us all persuade him to reconsider.

Minneapolis, MN, USA — Ramachandra P. Tummala, MD

Preface

I would opine that "art can be work" and "work can be art," depending on how much someone enjoys their profession. I certainly feel this way about the field of neuroradiology. I must confess that this book has undergone evolution for several reasons since I agreed to undertake this topic during my third year as a staff neuroradiologist (and now in my 15th!). Most notable is that the book was originally intended to include three parts: *brain*, *spine*, and *head and neck*, but I found that I am so meticulous that it was impossible to ignore the topics of *craniocervical vasculature* and *skull*, as these structures are immediately adjacent to the *brain*. This work was also driven by my quest to be practical. For example, I feel strongly that in order to properly interpret a routine brain MRI, a working knowledge of vascular variants is necessary even if an MR angiogram was not performed. Similarly, variants of the skull may also simulate disease when interpreting a routine brain MRI. Thus, given size constraints, normal variations of the *spine* and *head and neck* were not included here, and are left for a possible, future book.

For the abovementioned reason that this might be akin to composing "art," this book is hands-down the hardest work I have completed, and took the longest; finding rare cases of variants compounded that difficulty. I find that composing journal articles, reviews, and chapters in a book is quicker and more straightforward, since there is a limited range of possibilities. In fact, what makes the subject of normal variations so difficult to address is that one may not realize the importance of a finding because either: (1) it is not seen or mentioned as it is of no consequence anyway; (2) it is seen but constantly called abnormal and never proven to be so, as it is not a surgical entity; (3) in the reverse of #1, it is thought to be abnormal, but dedicated imaging and attention to detail is sometimes necessary, which may require "putting one's shoulder against the ocean liner" of physicians ready to perform surgery or other unnecessary therapy. Certainly, #3 is the most clinically important scenario for normal variations, particularly with regards to the brain, where operating on a suspected finding that is actually a normal variant can have catastrophic consequences. To prevent situation #3 and to prevent expectation bias, I routinely urge the residents and fellows that, prior to looking at the clinical history, to first simply "say what they see" about an image (to borrow the words of our famous neuroradiology predecessor in Minnesota, *Harold O. Peterson*). Often times, what is suspected to be a normal variant by a radiologist is often just that; however, proof may be lacking. Thus, the goal of this book is to compile the most common and identifiable (or the most interesting) variants, and to provide the most facile methods or sequences to identify them expediently, as well as provide a range of appearances.

And yet another reason that this book evolved over several years to the point of being delayed is that I not only wanted to include the common, standard variants that most radiologists and neuroradiologists are already aware of (e.g., *cavum septum pellucidum*, *hyperostosis frontalis*, *etc.*) but I also sought to cover newly identified variants that can be proven or described further by newer techniques (e.g., *brain capillary telangiectasias* on susceptibility weighted imaging [SWI]). Regarding those techniques, such as SWI, diffusion-weighted imaging (DWI), and multidetector/multislice CT, I also sought to cover artifacts or appearances that simulate disease using those techniques, which I felt has not been covered well in prior texts, although there may have been online descriptions or literature references.

I also attempted to provide "Comparison Cases" for many normal variants. I opine that one way to cement the appearance of a normal variant in one's mind is to demonstrate the actual abnormality that the radiologist is worried about it being. In this fashion, I hope such cases in this text create a "spectrum of normal" in radiologists' minds for future and immediate comparison to cases they are considering being potential normal variations.

Further, I felt that one particular area required much experience that can be potentially quite difficult to discern normal from abnormal: the infant brain with determination of myelination and the presence or absence of *hypoxic-ischemic injury/encephalopathy* (*HII/HIE*). To me, this topic seemed vital for my experience level with, and continued exposure to, pediatric neuroradiology to grow before I compiled the segment on the Pediatric Brain. This necessitated that I followed numerous cases within the files for years, and intermittently rechecked their medical records to make sure that a patient's development remained normal. Hopefully, this arduous task will be rewarded, as I have also attempted to add some attributes and normal appearances of neonates, infants, and young children on MRI and CT that have not been described well in prior texts or within the literature. My development and (hopefully) capability as a pediatric neuroradiologist really has paralleled the evolution of this text.

Finally, regarding the length of text and references, I have chosen to reference and describe each particular subject in what I thought would be the briefest fashion possible while simultaneously attempting to do justice to each subject. My attempt to keep such descriptions under the length of 1–2 pages would have otherwise been rendered futile, and would have disrupted the intent of the publisher and myself for there to be "more pictures than text." I apologize ahead of time to those who would prefer a much more meticulous description of each subtopic. But I would submit that the purpose of the References, which are generally provided in the order that the topic is described, are for more detailed analyses at the reader's behest. I admit this book is not intended for an in-depth analysis or discussion-type of reference; rather, it could be for quick reference to a particular imaging appearance.

Hence, if mistakes are identified (which I am confident there will be), I am open to an email to improve the text. Please provide a reference, if possible, and if a future version is published, I plan to acknowledge that contribution. Additionally, any suggestion for future topics to include is welcome.

Minneapolis, MN, USA Alexander M. McKinney, MD

Acknowledgments

I personally thank and acknowledge the following individuals for their contributions to this text: Bibi Husain (*University of Minnesota, Minneapolis, MN*): Chief Editorial Assistant and Proofreading, Copying, Saving, and Correspondence

Contributions of images:
David Nascene, MD (*University of Minnesota, Minneapolis, MN*) contributed the following cases: Right-sided Arch (non-Mirror Image), Double Aortic Arch, Arch Origin of the External Carotid Artery, Azygous ACA/Bihemispheric ACA, Dorsal Ophthalmic artery, Duplicated MCA, Accessory MCA, Fenestrated MCA.

Charles ("Chip") Truwit, MD (*Hennepin County Medical Center, Minneapolis, MN*) contributed the following cases: Persistent Hypoglossal Artery, Persistent Proatlantal Intersegmental Artery.

Dr. Francis Hui, MD (*National Neuroscience Institute, Singapore*) contributed: Persistent Hypoglossal Artery.

Basar Sarikaya, MD (*Yeditepe University Hospital, Istanbul, Turkey*) contributed: Lateral Tentorial Sinus Prominence, Azygous/Bihemispheric ACA, Primitive Olfactory Artery/ Olfactory course of the ACA.

Phillipe Gailloud, MD (*Johns Hopkins University, Baltimore, MD*) contributed the following cases: Duplicated MCA, Accessory MCA, Fenestrated MCA.

Christopher Palmer, MD (*Hennepin County Medical Center, Minneapolis, MN*) contributed cases of: Arch origin of the External Carotid Artery and Superficial Middle Cerebral Vein Prominence.

Chang-Woo Ryu, MD (*Kyung Hee University Hospital at Gangdong, Seoul, Republic of Korea*) contributed cases of: Persistent Falcine Sinus.

Kirk M. Welker, MD (*Mayo Foundation for Medical Education and Research, Rochester, Minnesota*) contributed cases of: Arrested Pneumatization (Incomplete Aeration) of the Skull Base.

Jeffrey Brace, MD (*Suburban Radiologic Consultants, Edina, MN*) contributed a case of: Aberrant Arch origin of the Right Vertebral Artery.

Luke Kim and John Saali (representatives for *Philips Healthcare, Andover, MA*): aiding in demonstrating SENSE-related artifacts in MR Angiography.

Other contributions:
Offering knowledge and excellent teaching: Elisa Widjaja, MD; Manohar Shroff, MD; Charles Raybaud, MD; and Susan Blaser, MD (*The Hospital for Sick Children, Toronto, Ontario, CA*).

Contents

Part I Brain

Part I

Brain

Brain: Introduction

1

The *Brain* section of this book is the largest and covers a combination of normal variants, normal anatomy, and artifacts that can mimic disease. Although there is an attempt to organize such normal variations by region or anatomic structure, such a classification is inherently problematic because some normal variants can be in multiple locations (e.g., choroid plexus or dilated perivascular spaces), while some commonly encountered artifacts can occur anywhere in the brain (e.g., flow voids). Thus, this section of the book is generally organized starting from inferiorly at the skull base to more superiorly, while normal variants that can occur anywhere in the brain are generally placed in the middle. Also, artifacts or magnetic resonance related sequence phenomena that may simulate disease are placed toward the end of this section.

Some basic terminology and abbreviations regarding standard sequences is necessary, since magnetic resonance imaging (MRI) manufacturers unfortunately have not adopted one standard for sequences outside of the routine ones such as T1-weighted images, T2-weighted images, fluid-attenuated inversion recovery (FLAIR), and diffusion-weighted images. Thus, standard terminology used throughout this section and the remainder of the book is described below.

1.1 Terminology

1.5 T and 3 T	1.5 Tesla and 3.0 Tesla MRI magnet field strengths
3D	Three dimensional
BFFE	Balance FFE (similar to CISS)
CECT	Contrast-enhanced computed tomography (CT)
CISS	Constructive interference in steady state, similar to T2WI, emphasizes cerebrospinal fluid hyperintensity
DWI	Diffusion-weighted image
FFE	Fast field echo (either T1- or T2-weighted)
FLAIR	Fluid-attenuated inversion recovery imaging
GE	Gradient echo
GE T2*WI	Gradient echo T2*-weighted imaging
IR	Inversion recovery imaging
T1IR	T1-weighted IR imaging
T2IR	T2-weighted IR imaging
MiniP	Minimum intensity projection
MIP	Maximum intensity projection
MPR	Multiplanar reformat
MRA	MR angiography
TOF MRA	Time-of-flight MRA
NECT	Non-enhanced CT
SWI	Susceptibility-weighted imaging
T1WI	T1-weighted imaging
T2WI	T2-weighted imaging
T2*WI	GE T2*WI
US	Ultrasound

A.M. McKinney, *Atlas of Normal Imaging Variations of the Brain, Skull, and Craniocervical Vasculature*,
DOI 10.1007/978-3-319-39790-0_1

Cerebellar Tonsillar Ectopia

2

The *cerebellar tonsils* have a range of "normal positioning" relative to the *foramen magnum*, and the range of normal particularly depends on age, whereas the degree of descent/position (in millimeters) of the tonsils has a normal distribution relative to age. Traditionally defined, a *Chiari 1 malformation* was simply defined as a hindbrain and skull anomaly consisting of "tonsillar herniation" below the foramen magnum; however, it was later defined more by the neuroradiologic criteria of descent of the tonsils 5 mm or greater below the foramen magnum with symptoms of tussive headache (i.e., with coughing). In a seminal work by Barkovich and coworkers in 1986 that consisted of over 200 normal patients and 25 with Chiari 1 malformations, the mean position of the tonsils in the normal group was 1 mm above the foramen magnum (range of 8 mm above to 5 mm below). Meanwhile, in Chiari 1 patients, the mean tonsillar descent was 13 mm below the foramen magnum (range of 3–29 mm below). The authors found that a tonsillar position of 2 mm or greater below the foramen magnum had a sensitivity of 100 % and a specificity of 98.5 % for predicting symptomatic patients. Later, it was shown that the most consistent finding in Chiari 1 patients was tonsillar "herniation" (i.e., downward descent with mass effect) of 5 mm or more in adult patients, while patients with tonsils 3–5 mm below the foramen magnum might be asymptomatic but did not exclude that diagnosis. Notably, larger prospective studies of the asymptomatic general population have demonstrated that tonsillar "ectopia" (i.e., descent without clear mass effect) of less than 5 mm is present in 0.5–1.0 % of the adult population as an incidental finding; however, it is not certain whether such patients with less than 5 mm of tonsillar ectopia eventually develop symptoms, and the degree of compression of the cervicomedullary junction is not well described. Hence the need for correlation with the presence of clinical symptoms. Other factors that may affect the tonsillar position include possible normal or slight differences in the degree of ectopia from side to side and that the degree of ectopia may change slightly even with the cardiac cycle (up to 0.4–0.5 mm in controls and even to a greater degree in Chiari 1 patients).

To make it more challenging, the pediatric range of tonsillar ascent/descent may be wider, probably caused by variation in the pediatric skull base and upper cervical spine; this may be related to the variable size of the pediatric foramen magnum, the variable distance between the foramen magnum and the arches of C1 and C2, and variable patterns of ossification. Thus, a degree of tonsillar ectopia even greater than 5 mm may be tolerated without the patient developing true herniation (compression) or symptoms, and such descent can improve or resolve over time. Interestingly, following the neonatal period, the tonsils may descend further during childhood, typically reaching their lowest point between 5 and 15 years age; however, this author has noted that in some juvenile patients the tonsils may ascend as well, even leading to some cases of tonsillar ectopia (or herniation!) that spontaneously resolve.

Therefore, the current thinking varies by author, but a few simple rules may help to define symptomatic patients. First, the term "tonsillar herniation" in children should be considered only when the degree of descent is greater than 5 mm below the foramen magnum. In adults, neither *tonsillar herniation* nor *ectopia* should be considered if the degree of descent is less than 2 mm. The "mildly ectopic," "benign ectopia," or "borderline herniation" range is 3–5 mm of descent in adults. In such patients, appropriate clinical symptoms and potentially accessory imaging (such as a cerebrospinal fluid [CSF] flow study) may help to define associated abnormal flow around the tonsils. A common-sense rule that may help to identify potentially symptomatic patients in this borderline range is whether or not the cervicomedullary junction is truly compressed by the tonsils (i.e., truly fitting the definition of "herniation," in which the bright CSF on T2WI surrounding the junction is effaced).

A.M. McKinney, *Atlas of Normal Imaging Variations of the Brain, Skull, and Craniocervical Vasculature*,
DOI 10.1007/978-3-319-39790-0_2

Again, by definition, a Chiari 1 malformation is comprised of cerebellar tonsillar herniation below the foramen magnum of at least 5 mm, typically compressing the cervicomedullary junction if the patient is symptomatic. It is important to mention that a cervical or cervicomedullar *syrinx* (i.e., syringomyelia) may be present in 20–25 % of Chiari 1 patients. A related anomaly may be the so-called *Chiari 1.5 malformation* (brainstem herniation through the foramen magnum). A *Chiari 2 malformation* typically consists of a small posterior fossa, tonsillar herniation (with or without brainstem kinking or syrinx), and a spinal myelomeningocele; numerous other congenital brain malformations may be associated. A *Chiari III malformation* is quite rare and consists of a cervico-occipital encephalocele (Figs. 2.1, 2.2, 2.3, 2.4, 2.5, 2.6, 2.7, and 2.8).

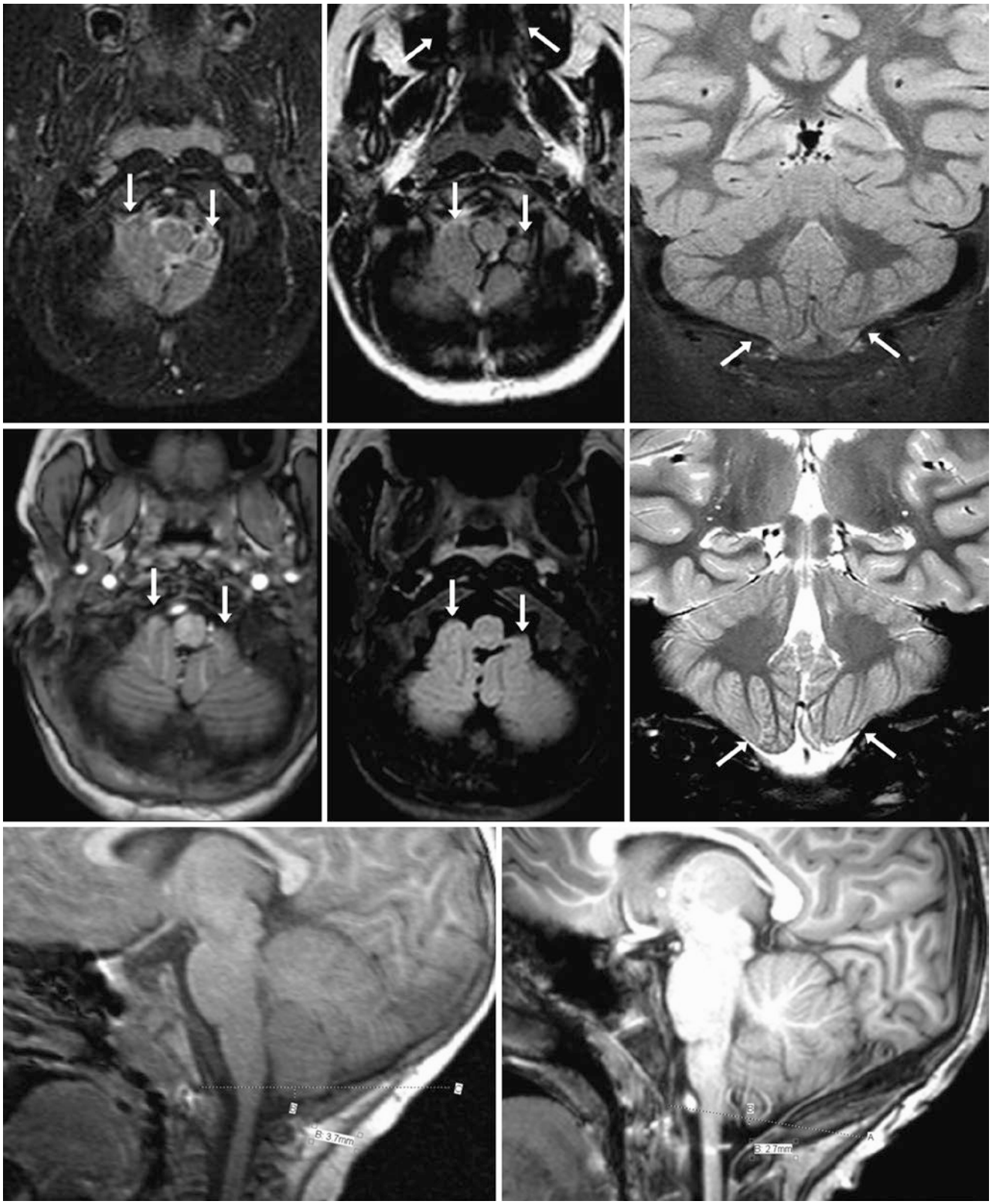

Fig. 2.1 A 4-year-old child with mild tonsillar ectopia (*arrows*) on an otherwise negative 1.5 T MRI for developmental delay. *Top row*: on axial T2WI (*left*), FLAIR (*middle*), and coronal IR T2WI (*right*) there was mild tonsillar ectopia but a lack of mass effect (i.e., herniation) on the cervicomedullary junction, with CSF clearly seen surrounding it. *Middle row*: a repeat MRI 10 years later demonstrates similar findings on axial T1WI (*left*), FLAIR (*middle*), and coronal T2WI (*right*). *Bottom row*: when comparing the degree of tonsillar ectopia on sagittal T1WI from the MRI at 4 years of age (*left*) with that at 14 years of age (*right*), there was little change from 3.7 to 2.7 mm, respectively

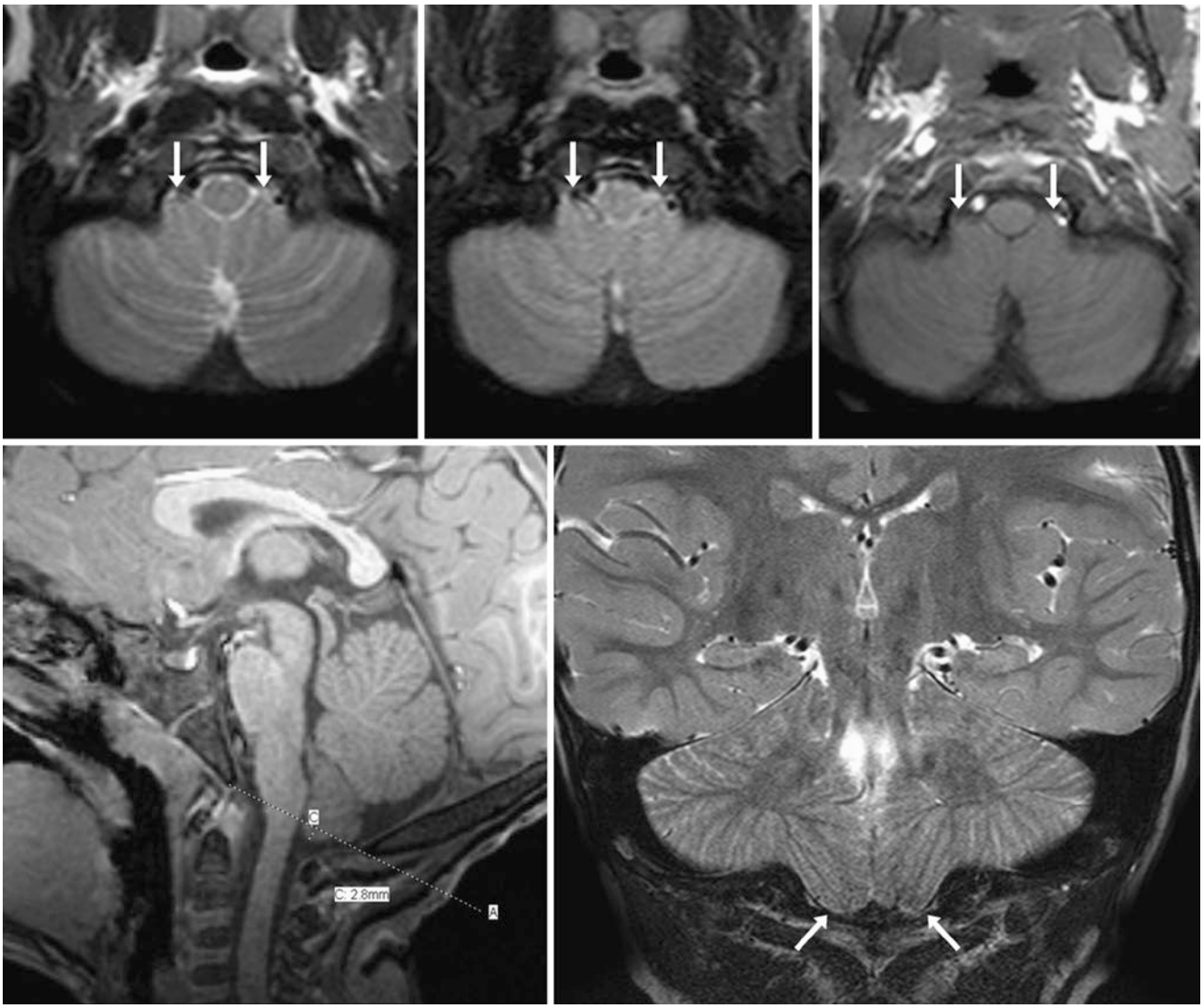

Fig. 2.2 A 2.5-year-old child had mild tonsillar ectopia (*arrows*) on an otherwise negative 1.5 T MRI for febrile seizures. On axial T2WI (*top left*), FLAIR (*top middle*), and T1WI (*top right*), there was mild tonsillar ectopia with narrowing but not complete effacement of the cerebrospinal signal surrounding the cervicomedullary junction at the level of the foramen magnum. Sagittal T1WI (*bottom left*) and coronal T2WI (*bottom right*) measured 2.8–3.0 mm of tonsillar descent

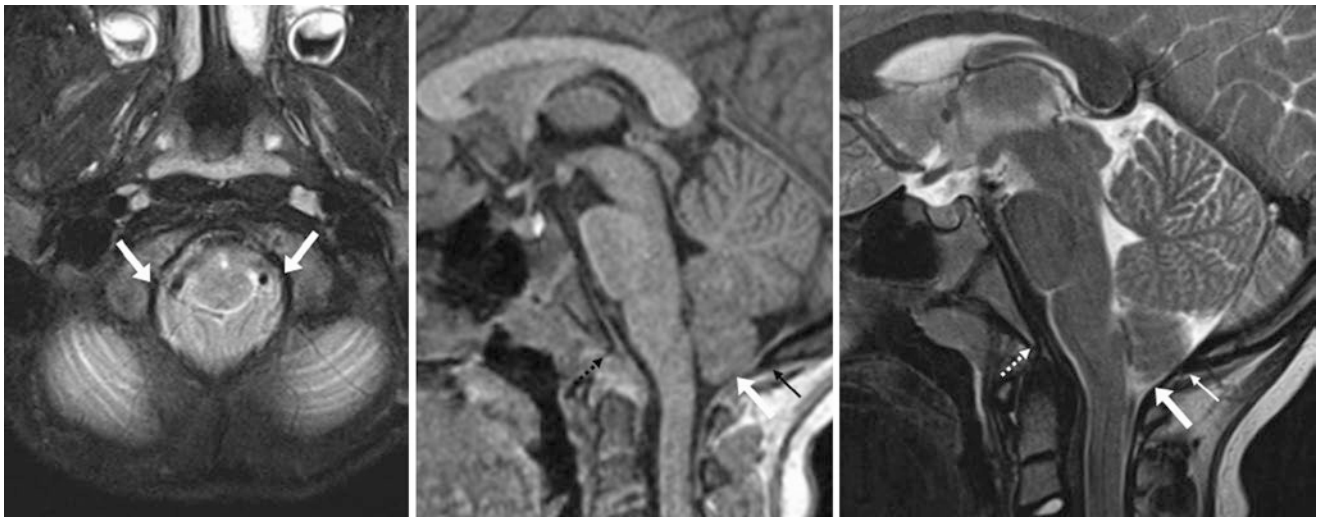

Fig. 2.3 A 7-year-old child with tonsillar ectopia (*arrows*) on an otherwise negative 1.5 T MRI for seizures. On axial T2WI (*left*), there was tonsillar ectopia, with narrowing of the cerebrospinal signal surrounding the cervicomedullary junction, but brainstem or cord compression was lacking. Sagittal T1WI (*middle*) and T2WI (*right*) measured 4.5–4.9 mm of tonsillar descent below the foramen magnum, as measured from the bottom of the basion (*dotted arrows*) to the opisthion (*thin arrows*)

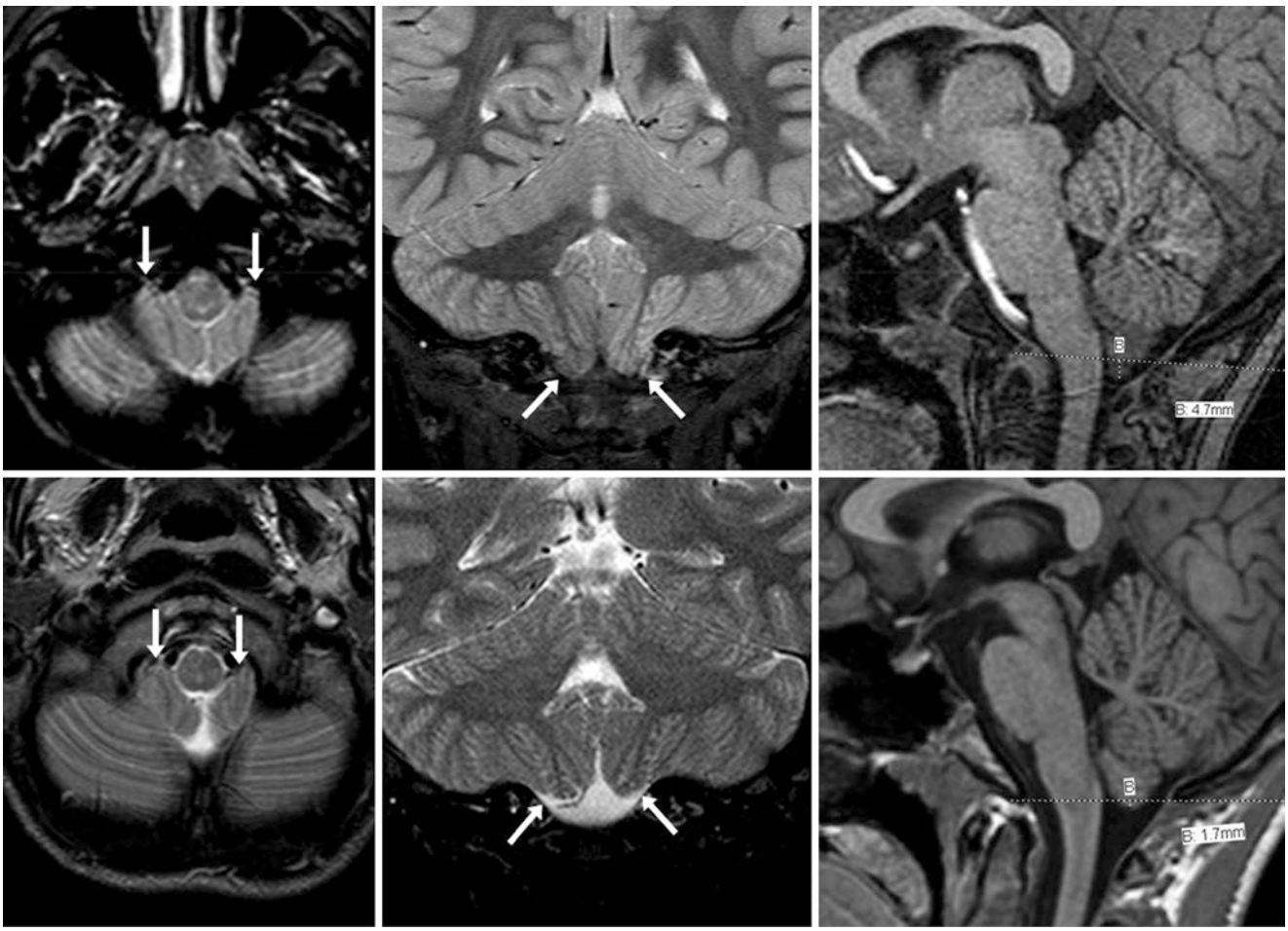

Fig. 2.4 A 6-year-old child with moderate tonsillar ectopia (*arrows*) on an otherwise negative 1.5 T MRI for febrile seizures. Axial (*top left*) and coronal T2WI (*top middle*) demonstrate decreased CSF surrounding the cervicomedullary junction at the level of the foramen magnum, without mass effect on the brainstem. On sagittal T1WI (*top right*), the tonsillar descent ranged from 4.7 to 5.3 mm on several measurements. At 17 years of age, on axial (*bottom left*) and coronal (*bottom middle*) T2WI, the tonsillar descent/ectopia had improved to only 1.7 mm on sagittal T1WI (*bottom right*)

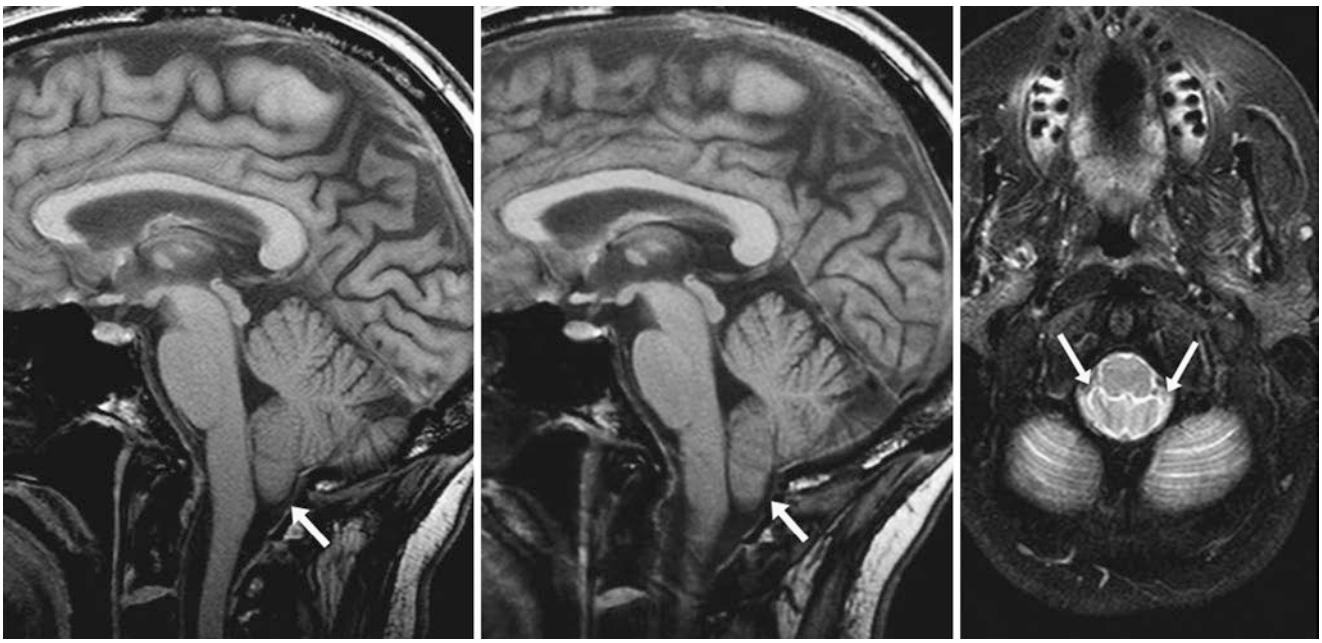

Fig. 2.5 A 49-year-old patient with a 1.5 T MRI performed for mild cognitive impairment noted mild 5.8 mm of tonsillar ectopia (*arrows*) on sagittal T1WI (*left*) and was unchanged 6 months later (*middle*). The patient did not have headaches. Axial T2WI (*right*) depicts decreased but present CSF surrounding the cervicomedullary junction without mass effect on the medulla. This illustrates how adults may occasionally have greater than 5 mm of asymptomatic tonsillar descent

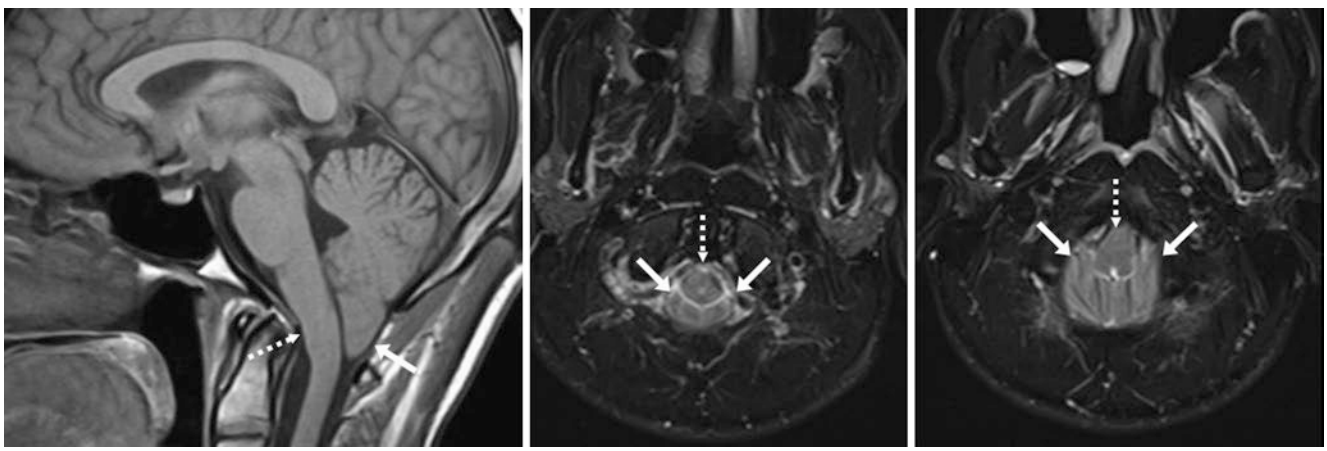

Fig. 2.6 Comparison case of Chiari 1 malformation without syrinx. A 26-year-old patient with tussive headaches had 11 mm of tonsillar herniation (*arrows*) on a 1.5 T MRI with sagittal T1WI (*left*) and axial T2WI's (*middle and right*). Note the mild compression of the cervicomedullary junction (*dotted arrows*) and the effacement of CSF fluid within the foramen magnum

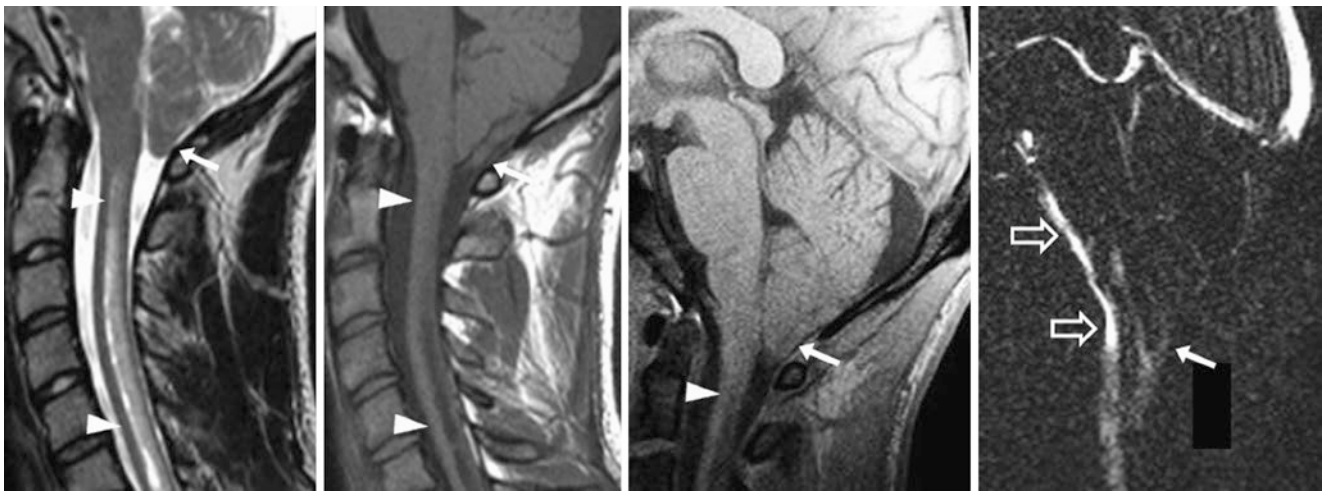

Fig. 2.7 Comparison case of Chiari 1 malformation with syrinx. An 18-year-old patient with upper extremity symptoms and headaches had 10 mm of tonsillar ectopia/herniation (*arrows*) on a 1.5 T MRI with sagittal T2WI (*left*) and T1WI (*left middle*) as well as a syrinx (*arrowheads*) extending down to the midthoracic region. A 3 T brain MRI with T1WI (*right middle*) and a cerebrospinal flow study (*right*) showed flow ventrally (*open arrows*) but not dorsally above the tonsils

Fig. 2.8 Comparison case of improved Chiari 1 malformation. A 5-month-old infant with speech delays had tonsillar herniation (*arrows*) on 1.5 T MRI axial T2WI (*left*) and sagittal T1WI (*middle*). The cerebrospinal fluid signal was effaced on T2WI at the foramen magnum, and the tonsillar descent measured 11.5–12 mm. By 13 years of age, sagittal T1WI (*right*) shows that the tonsillar herniation had improved to being only 7.8 mm, but the headaches persisted

Suggested Reading

Barkovich AJ, Wippold FJ, Sherman JL, Citrin CM. Significance of cerebellar tonsillar position on MR. Am J Neuroradiol. 1986;7:795–9.

Cousins J, Haughton V. Motion of the cerebellar tonsils in the foramen magnum during the cardiac cycle. Am J Neuroradiol. 2009;30:1587–8.

Christophe C, Dan B. Magnetic resonance imaging cranial and cerebral dimensions: is there a relationship with Chiari I malformation? A preliminary report in children. Eur J Paediatr Neurol. 1999;3:15–23.

Meadows J, Kraut M, Guarnieri M, Haroun RI, Carson BS. Asymptomatic Chiari Type I malformations identified on magnetic resonance imaging. J Neurosurg. 2000;92:920–6.

Milhorat TH, Chou MW, Trinidad EM, Kula RW, Mandell M, Wolpert C, Speer MC. Chiarai 1 malformation redefined: clinical and radiographic findings for 364 symptomatic patients. Neurosurgery. 1999;44:1005–17.

Smith BW, Strahle J, Bapuraj JR, Muraszko KM, Garton HJ, Maher CO. Distribution of cerebellar tonsil position: implications for understanding Chiari malformation. J Neurosurg. 2013;119:812–9.

Tubbs RS, Wellons 3rd JC, Oakes WJ. Asymmetry of tonsillar ectopia in Chiari I malformation. Pediatr Neurosurg. 2002;37:199–202.

Vernooij MW, Ikram MA, Tanghe HL, Vincent AJ, Hofman A, Krestin GP, et al. Incidental findings on brain MRI in the general population. N Engl J Med. 2007;357:1821–8.

Wu YW, Chin CT, Chan KM, Barkovich AJ, Ferriero DM. Pediatric Chiari I malformations: do clinical and radiologic features correlate? Neurology. 1999;53:1271–6.

Cerebellar Flocculus Pseudomass

3

The *cerebellar flocculus* is a well-known cause of a pseudomass in the *cerebellopontine angle* (CPA), particularly on nonenhanced CT (NECT) or occasionally on noncontrast MRI sequences. Since the flocculus juts out into the CPA and is surrounded by cerebrospinal fluid, asymmetry (from side to side), volume averaging (with normal adjacent cerebellar hemispheres or the middle cerebellar peduncle), and beam-hardening artifact (from adjacent quite dense petrous apices of the temporal bones) may combine to exacerbate the appearance of an extra-axial mass such as a *schwannoma*, a *meningioma*, a *glioma*, or rarely an *aneurysm*. Schwannomas and meningiomas typically compress the cerebellum, whereas nonenhancing gliomas typically expand it. Aneurysms ususally can be seen to connect with a parent artery (Figs. 3.1, 3.2, 3.3, 3.4, 3.5, 3.6, and 3.7).

A.M. McKinney, *Atlas of Normal Imaging Variations of the Brain, Skull, and Craniocervical Vasculature*,
DOI 10.1007/978-3-319-39790-0_3

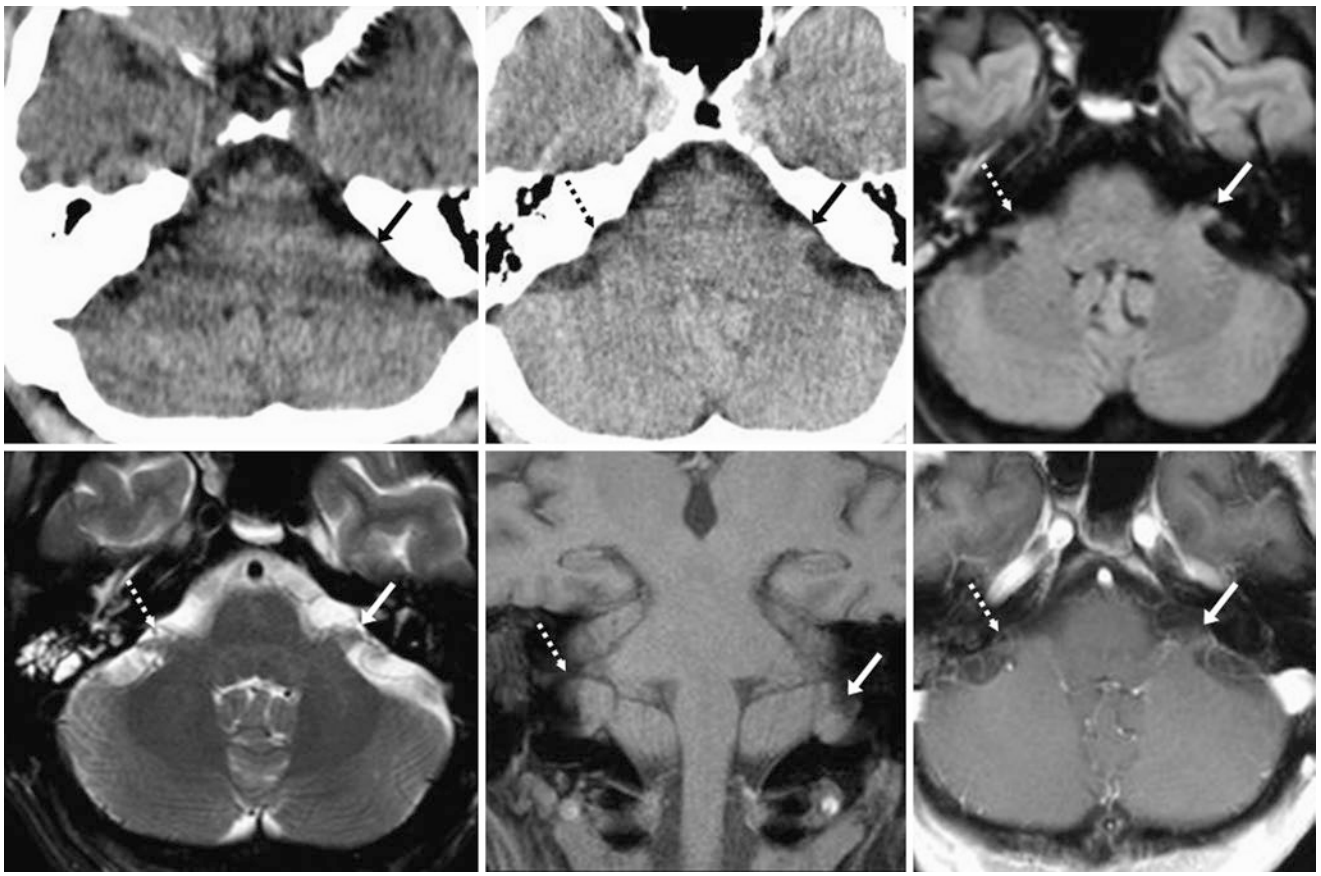

Fig. 3.1 A 55-year-old patient with headaches and balance problems (negative study). On NECT (*top left*), there was a prominent hyperdensity within the left CPA (*arrows*), unchanged from 5 years previously (*top middle*). A 1.5 T MRI axial FLAIR (*top right*), T2WI (*bottom left*), coronal T1WI (*bottom middle*), and postcontrast T1WI (*bottom right*) depict asymmetry of the left cerebellar flocculus (*arrows*) as compared to the right one (*dotted arrows*). The prominence of the left flocculus was attributable to normal asymmetry, and the CT appearance was exacerbated by beam-hardening artifact

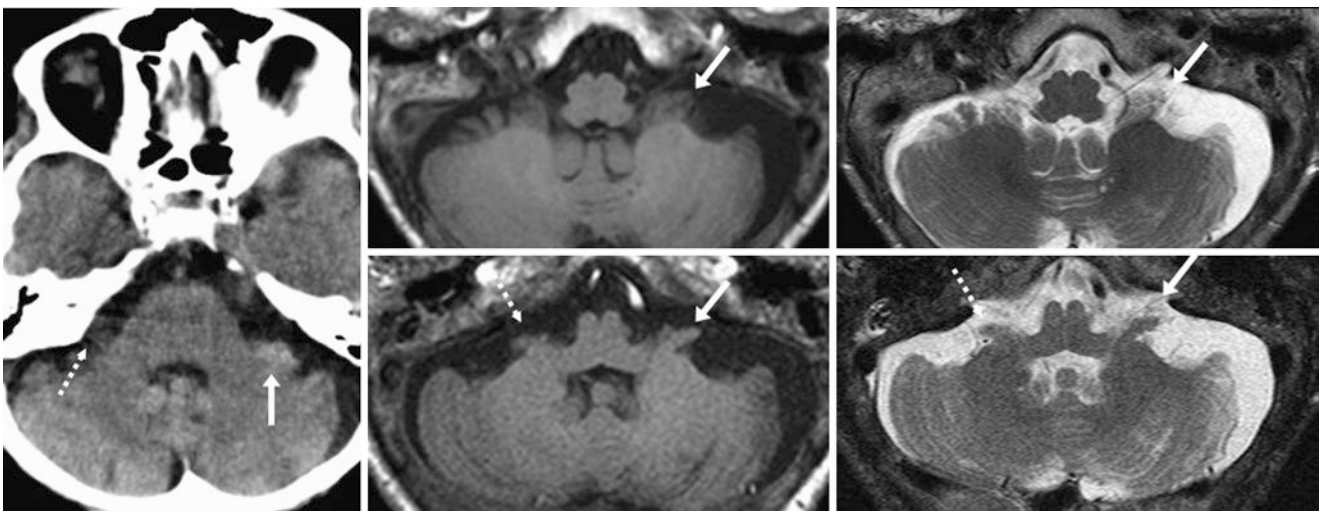

Fig. 3.2 The patient was a 70 year old with visual deficit (negative 1.5 T MRI). On NECT (*left*), there was a hyperdense pseudomass of the left CPA (*arrows*), which was shown to be the left cerebellar flocculus on T1WI (*middle images*) and T2WI (*right images*). Note the smaller right flocculus (*dotted arrows*). The flocculus appeared dense because of beam hardening

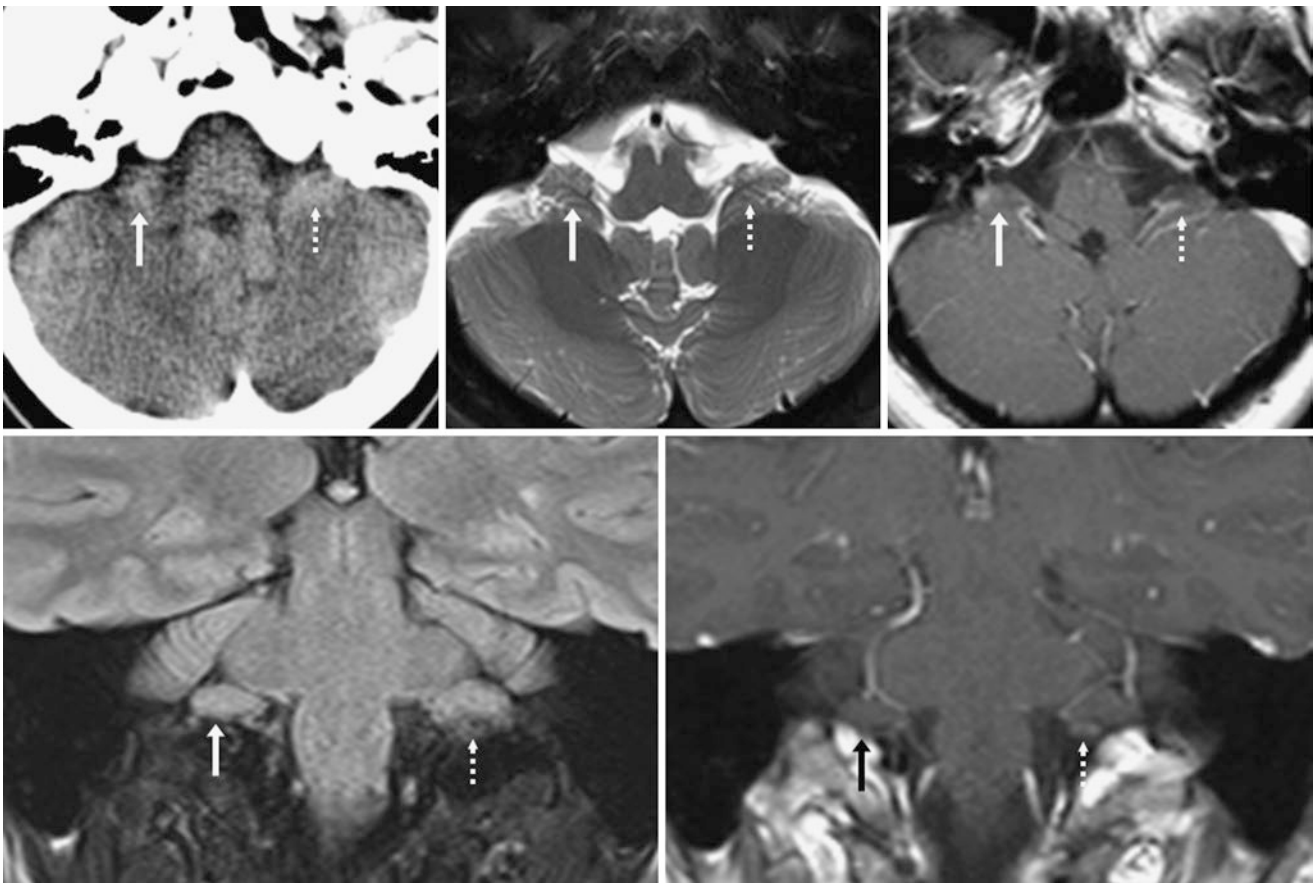

Fig. 3.3 A 39-year-old patient with a suspected stroke (negative 3 T MRI). On NECT (*top left*) a right CPA apparent pseudomas (*arrows*) was questioned but was found to be the flocculus on axial T2WI (*top middle*) and postcontrast T1WI (*top right*). Coronal FLAIR (*bottom left*) and postcontrast T1WI (*bottom right*) also depicted the left flocculus (*dotted arrows*)

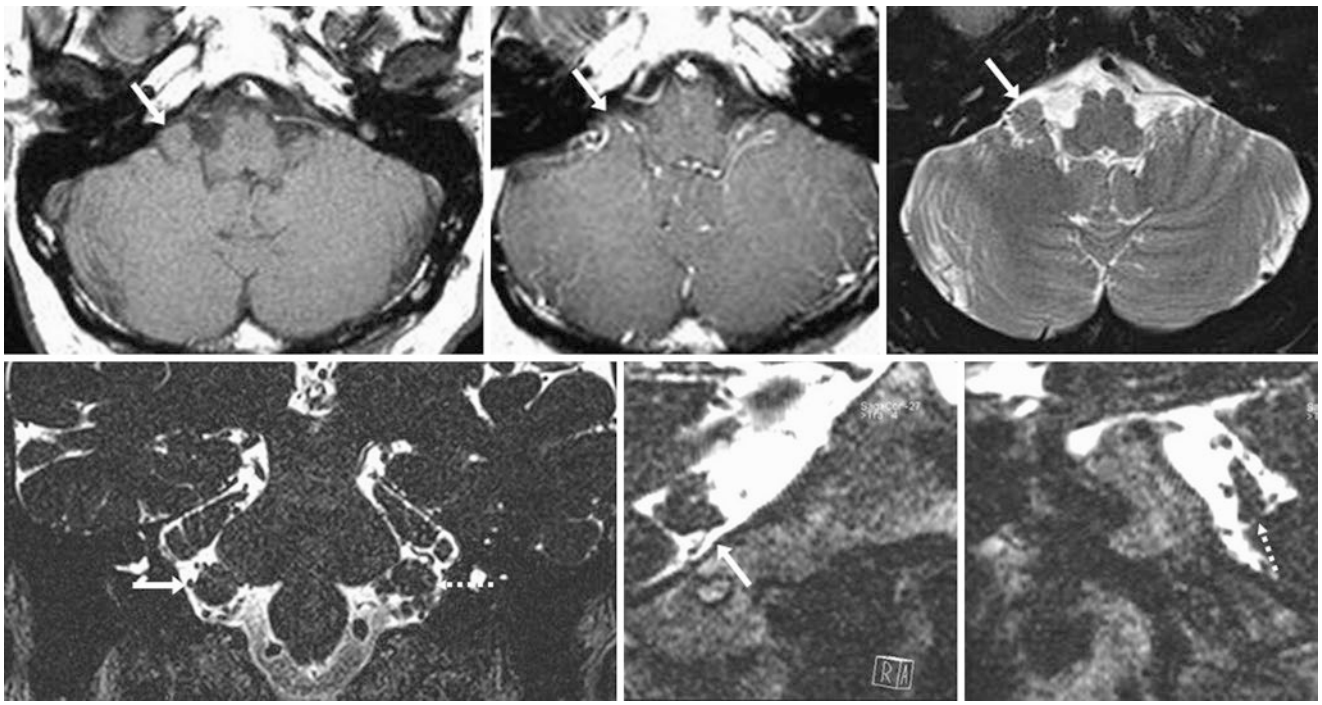

Fig. 3.4 A 57-year-old patient with hearing loss. On a negative 1.5 T MRI, noncontrast T1WI (*top left*) demonstrated a right CPA pseudomas (*arrows*) that did not enhance on postcontrast T1WI (*top middle*). Axial (*top right*) and three-dimensional-acquired "balanced" T2WIs reconstructed in coronal (*bottom left*) and sagittal (*bottom middle*: *right side*, *bottom right*: *left side*) planes confirmed asymmetry of the right cerebellar flocculus as compared with the left (*dotted arrows*)

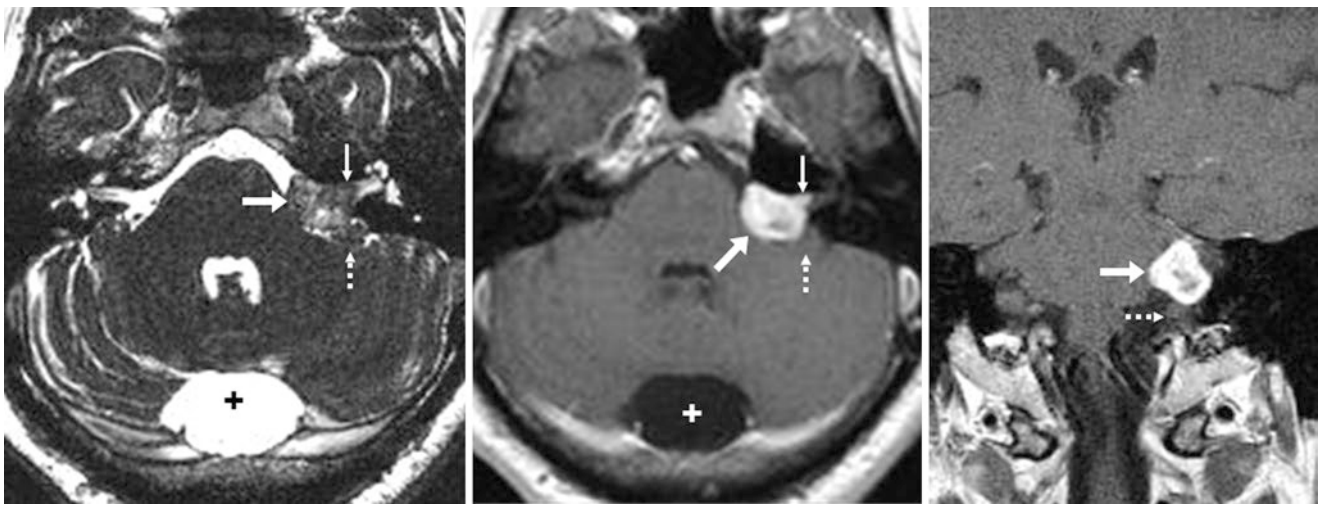

Fig. 3.5 Comparison case of a CPA schwannoma: a 50-year-old patient with left-sided hearing loss had a CPA extra-axial mass (*arrows*) on a 1.5 T 3D T2WI MRI (*left*), which enhanced on postcontrast axial (*middle*) and coronal (*right*) T1WIs. Note the compression of the flocculus inferolaterally (*dotted arrows*) and the extension of the tumor into the internal auditory canal via the porus acousticus (*thin arrows*). Also note a normal, incidental mega cisterna magna (+)

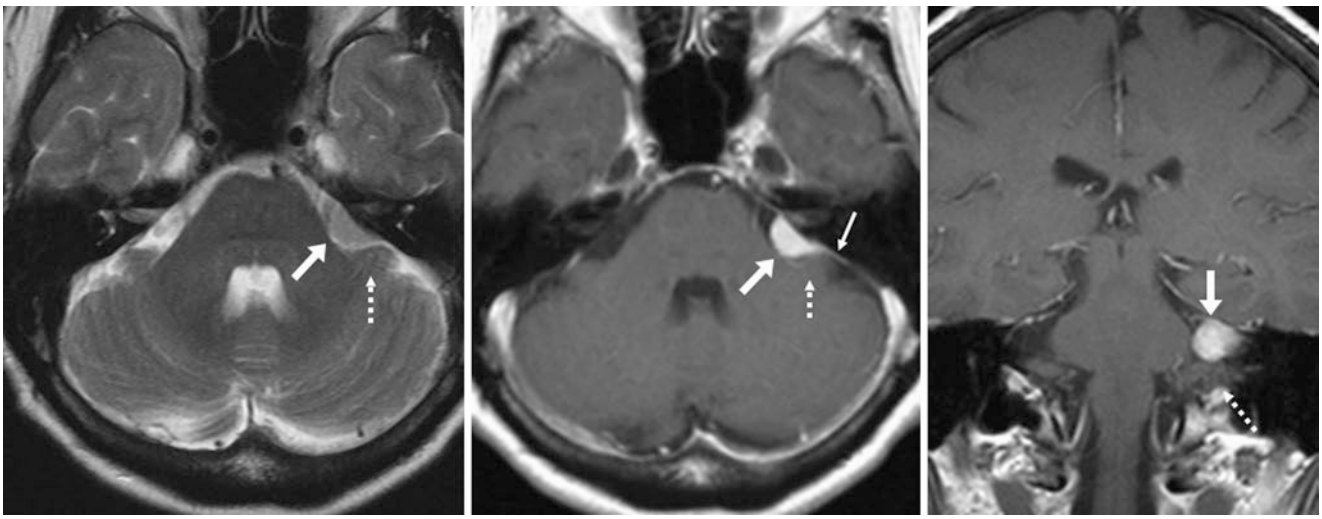

Fig. 3.6 Comparison case of a CPA meningioma: a 70 year old with left-sided hearing loss had an extra-axial mass (*arrows*) within the left CPA on a 1.5 T T2WI MRI (*left*), which enhanced on postcontrast axial (*middle*) and coronal (*right*) T1WIs. Note a normal cerebellar flocculus inferolaterally (*dotted arrows*) and the thin dural tail of enhancement (*thin arrows*) consistent with a meningioma rather than a schwannoma

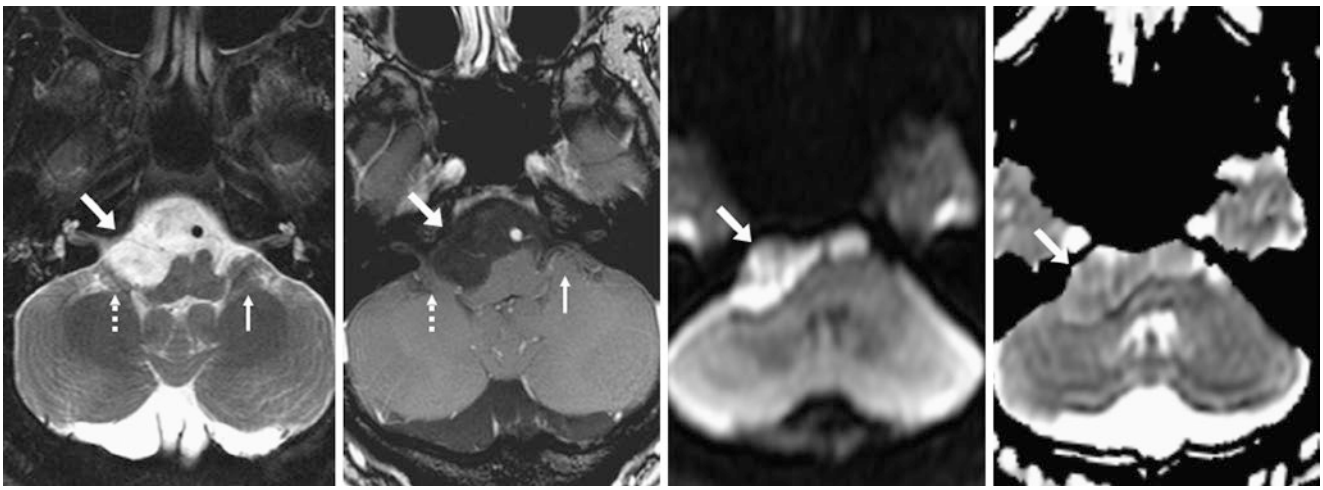

Fig. 3.7 Comparison case of a CPA epidermoid: a 27-year-old patient with headaches and hearing loss had an extra-axial cystic mass (*arrows*) on a 1.5 T T2WI MRI (*left*), which did not enhance on postcontrast T1WI (*left middle*). However, it had reduced diffusivity (bright) relative to cerebrospinal fluid on DWI (*right middle*) as confirmed on ADC maps (*right*). Note the compression of the right flocculus (*dotted arrows*) as compared to a normal contralateral flocculus (*thin arrows*)

Suggested Reading

Daniels DL, Haughton VM, Williams AL, Berns TF. The flocculus in computed tomography. Am J Neuroradiol. 1981;2:227–9.

Salzman KL, Davidson HC, Harnsberger HR, Glastonbury CM, Wiggins RH, Ellul S, et al. Dumbbell schwannomas of the internal auditory canal. Am J Neuroradiol. 2001;22:1368–76.

Mega Cisterna Magna and Retrocerebellar Arachnoid Cysts

4

There is debate as to whether *mega cisterna magna* (MCM) arises from a pathologic insult; recent evidence suggests that it may be on the mildest end of the Dandy-Walker continuum. However, it can be considered an asymptomatic normal variation in which the posterior fossa appears mildly enlarged on imaging, typically with prominence of the *subarachnoid space* (SAS) posterior to the cerebellum (retrocerebellar space). This prominence of the cerebellar-medullary cistern communicates freely with the SAS and does not result in CSF obstruction or hydrocephalus because the foramina of Magendie and Luschka are patent, by definition. The development of the cerebellar hemispheres and vermis are normal. The tentorium may appear slightly higher than normal but has a normal insertion. MCM is thought to result from evagination of the tela choroidea's posterior membranous area, possibly caused by delayed completion of the foramen of Magendie. Larger MCMs may simulate and be very difficult to distinguish from arachnoid cysts (which have a thin surrounding membrane) because of mild compression of the cerebellar vermis or hemispheres. They may have a split falx/dural fold, which can be seen in over half of the cases traversing the MCM and can distinguish MCM from arachnoid cysts.

Retrocerebellar arachnoid cysts (RACs) are distinct from MCMs but often are often quite difficult to distinguish from them on standard imaging. The posterior fossa is usually normal in size, although the inner table of the occipital bone may be scalloped; scalloping traditionally was considered a sign of RAC, but evidence suggests that it occurs with MCM as well. RACs arise from defects in the arachnoid membrane and are not a normal variant, although they are usually considered don't touch lesions because hydrocephalus does not occur in the vast majority. In addition, the vast majority have only a mild, asymptomatic mass effect on the cerebellar hemispheres. However, occasionally RACs can compress the cerebellum and displace the fourth ventricle anteriorly if they are large enough, but they rarely cause CSF obstruction. The thin membrane of a RAC can occasionally be visualized by thin-section, balance gradient echo T2WI technique or by utilizing cisternography to confirm a lack of communication with the CSF. However, some RACs may communicate with the CSF; therefore cisternography is not entirely confirmatory. Hence, mass effect or hydrocephalus may be better predictors of a RAC.

Other true abnormalities that should be distinguished from a MCM and RAC are developmental abnormalities of the posterior fossa, ranging from varying degrees of cerebellar *vermian hypoplasia* (CVH, at the milder end of the spectrum) to *Dandy-Walker malformations* (DWM, which is more severe) as well as the rare *Blake pouch cyst* (BPC). The cerebellum begins development around the fifth gestational week; around the ninth week midline fusion occurs, with completion of the vermis around the 18th week. Interruption of development during this timeline may result in varying degrees of cerebellar and even pontine hypoplasia (severe cases), with milder CVH occurring from later interruptions. It should be noted that fetal MRIs performed even after the completion of cerebellar development, such as during the late second or early third trimester, may depict a mild prominence of the cisterna magna or SAS around the cerebellum; this is normal and should not be mistaken for any form of cerebellar hypoplasia.

Subtle cases of inferior *cerebellar vermian hypoplasia* (ICVH) are the subject of debate, since in the past some classified this as part of the Dandy-Walker continuum (so-called Dandy-Walker variants). Such terminology should be avoided because it causes confusion, and most patients with ICVH are otherwise developmentally normal. However, a minority do have developmental delay, and they typically have a normal sized or slightly enlarged posterior fossa without a cyst or hydrocephalus. ICVH can be discerned from artifactual volume averaging (which causes incomplete visualization of a relatively small vermis, particularly on sagittal images), since with ICVH the posterior angle of the fourth ventricle appears incomplete on sagittal images. A true DWM consists of vermian agenesis or severe hypoplasia

A.M. McKinney, *Atlas of Normal Imaging Variations of the Brain, Skull, and Craniocervical Vasculature*,
DOI 10.1007/978-3-319-39790-0_4

with a significantly enlarged posterior fossa, a posterior fossa cyst (typically cystic enlargement of the fourth ventricle), and usually hydrocephalus (in about three quarters of cases). What was previously termed a *Dandy-Walker variant* (DWV) consists of varying degrees of CVH with a posterior fossa cyst but without an enlarged posterior fossa. Again this term should be avoided, and instead a description should be provided.

A persistent *Blake pouch cyst* (BPC) is a developmental anomaly that arises from a lack of regression of a temporary cyst (Blake pouch) during the embryonic formation of the fourth ventricle prior to the opening of the foramen of Magendie. This arises at the site of the area membranacea anterior within the tela choroidae of the developing fourth ventricle. This lack of regression leads to an imperforate foramen Magendie, with a cyst that variably can extend between the fourth ventricle, the foramen of Magendie, and even laterally into the foramina of Luschka. The clinical presentation is variable; there may be hydrocephalus caused by fourth ventricular obstruction, or patients may be otherwise normal and remain asymptomatic even into adulthood if the foramen of Luschka balances (although precariously) CSF flow equilibrium. Thin sections on MR sequences can detect the cyst's walls and can confirm that the vermis is intact, although mass effect from the cyst may simulate CVH or DWV. Notably, BPC could theoretically be considered on the milder edge of the spectrum of DWM-DWV, since DWM and DWV also arise from a lack of the area membranacea anterior's incorporation, resulting in cystic enlargement of the fourth ventricle. However, the foramen of Magendie is typically patent in both DWM and DWV (Figs. 4.1, 4.2, 4.3, 4.4, 4.5, 4.6, 4.7, 4.8, 4.9, 4.10, 4.11, 4.12, 4.13, 4.14, 4.15, 4.16, 4.17, and 4.18).

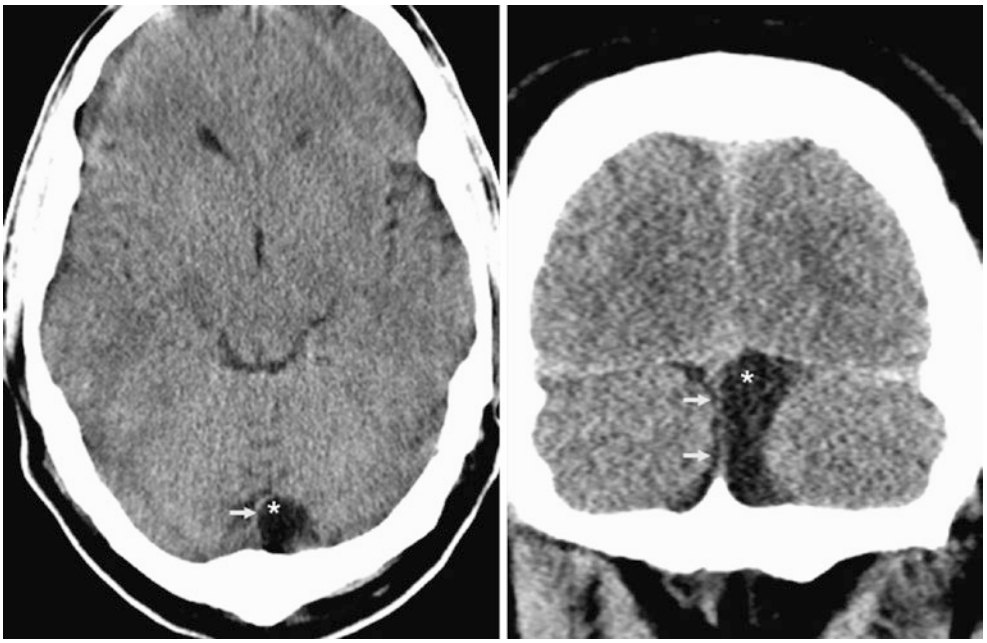

Fig. 4.1 A 45 year old was found to have a small cyst (*) posterior to the cerebellum and to the left of the midline and the falx (*arrows*) on axial (*left*) and coronal (*right*) NECT images. While asymmetric, this appearance would favor a MCM as the falx traverses it, although a RAC cannot be excluded

Fig. 4.2 A 54 year old was reported to have a tiny retrocerebellar cyst (*) and two small appendages of the falx (*arrows*) on NECT. The image favors a MCM since the falx traverses it, but a RAC cannot entirely be excluded

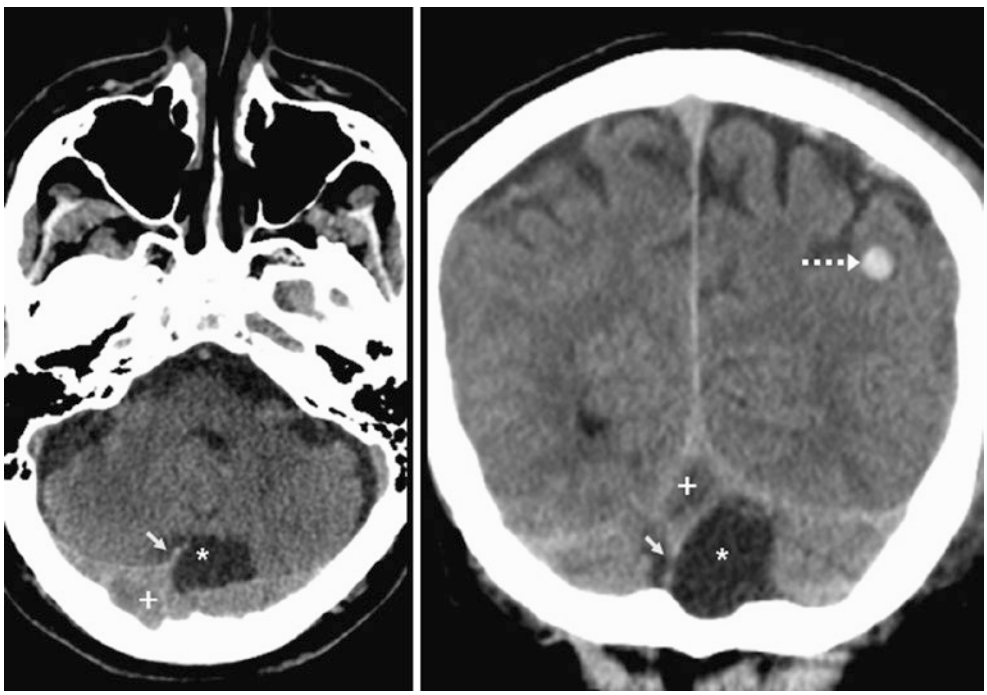

Fig. 4.3 A 35 year old had a small midline cyst (*) posteriorly on axial (*left*) and coronal (*right*) CECT images displacing the falx (*arrows*), lying anteroinferior to the torcular (+). The appearance favors a MCM as the falx traverses it, although it is asymmetric; a RAC cannot be excluded. Note an enhancing metastasis in the left parietal lobe (*dotted arrow*)

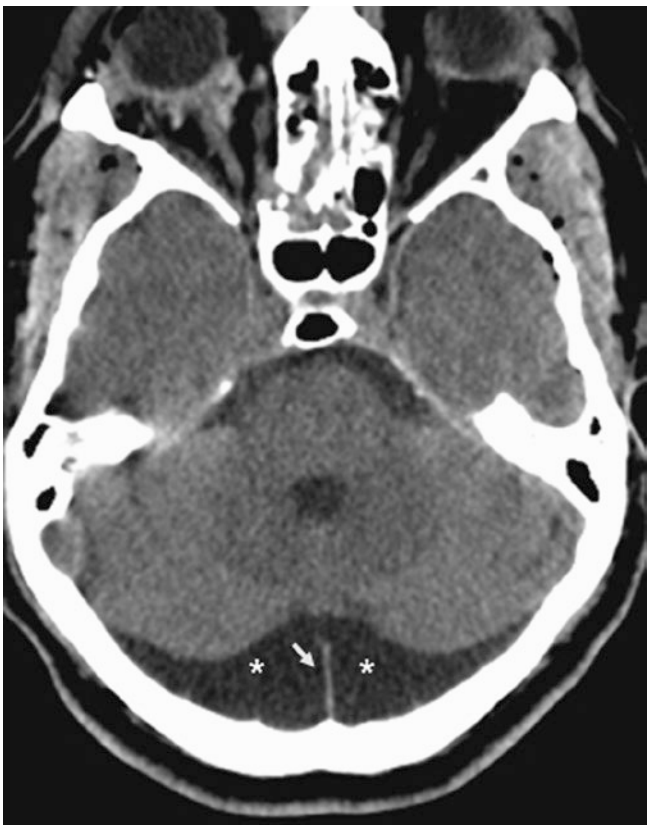

Fig. 4.4 A 47 year old was studied who had a retrocerebellar SAS prominence (*) and a midline falx (*arrow*) on NECT. The image heavily favors an MCM since the falx traverses the cyst

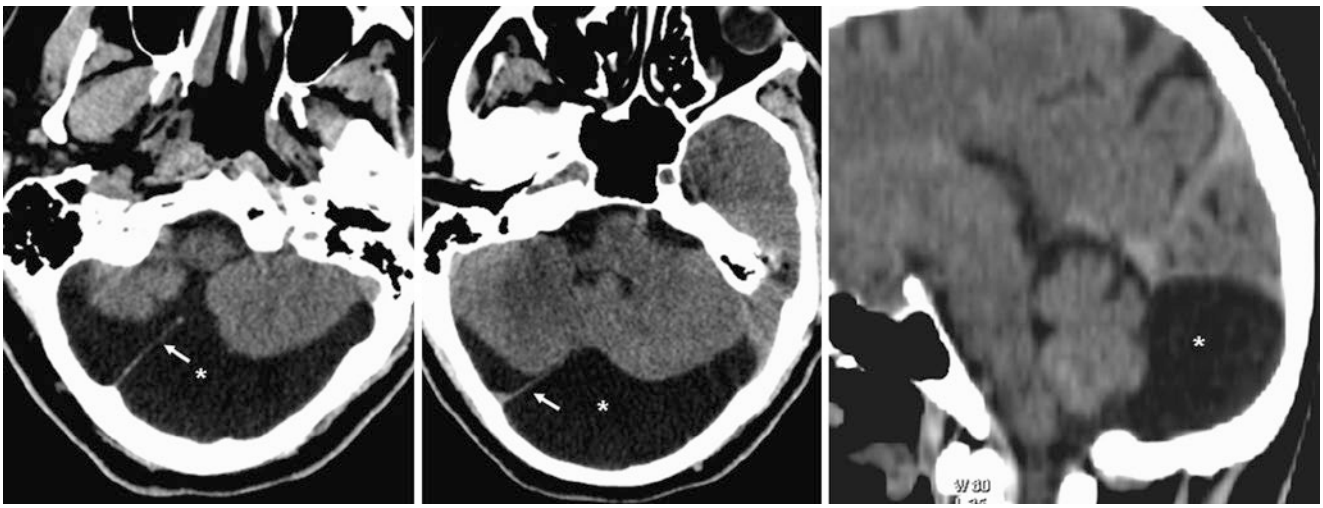

Fig. 4.5 A 34 year old was examined and a retrocerebellar cystic dilatation (*) was found with a mildly enlarged posterior fossa and prominence of the retrocerebellar SAS bilaterally. The cyst is traversed by the falx (*arrows*) on axial NECT images (*left two images*) and on a sagittal reconstruction (*right*). The appearance favors a MCM, particularly given the lack of mass effect on the cerebellum. Note that the falx is asymmetric to the right within the MCM. Thus, it does not have to be exactly at the midline within a MCM and there may be asymmetry in the SAS

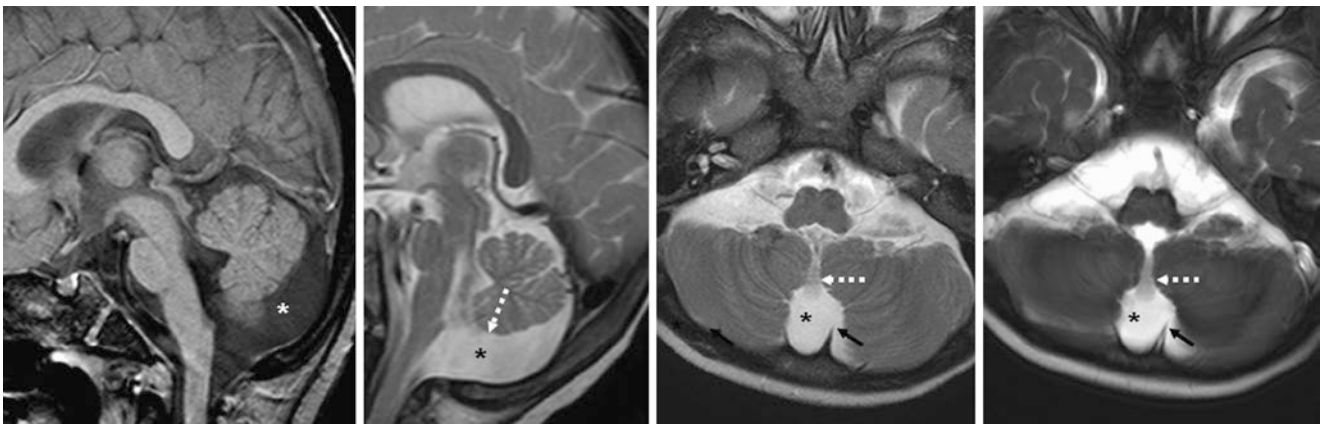

Fig. 4.6 A 2 year old was found to have a small, cystic dilatation (*) posteroinferior to the cerebellar midline and vermis with a slightly enlarged posterior fossa. The cyst is traversed by the falx (*arrows*) on sagittal T1WI (*left*), T2WI (*left middle*), axial thin 2-mm T2WI (*right middle*), and balanced echo T2WI (*right*) 3 T MR images. The appearance favors a MCM, given the lack of mass effect. T2-dark flow voids that extend through the foramen of Magendie (*dotted arrows*) confirm communication between the fourth ventricle and the cyst, confirming that this is not a RAC

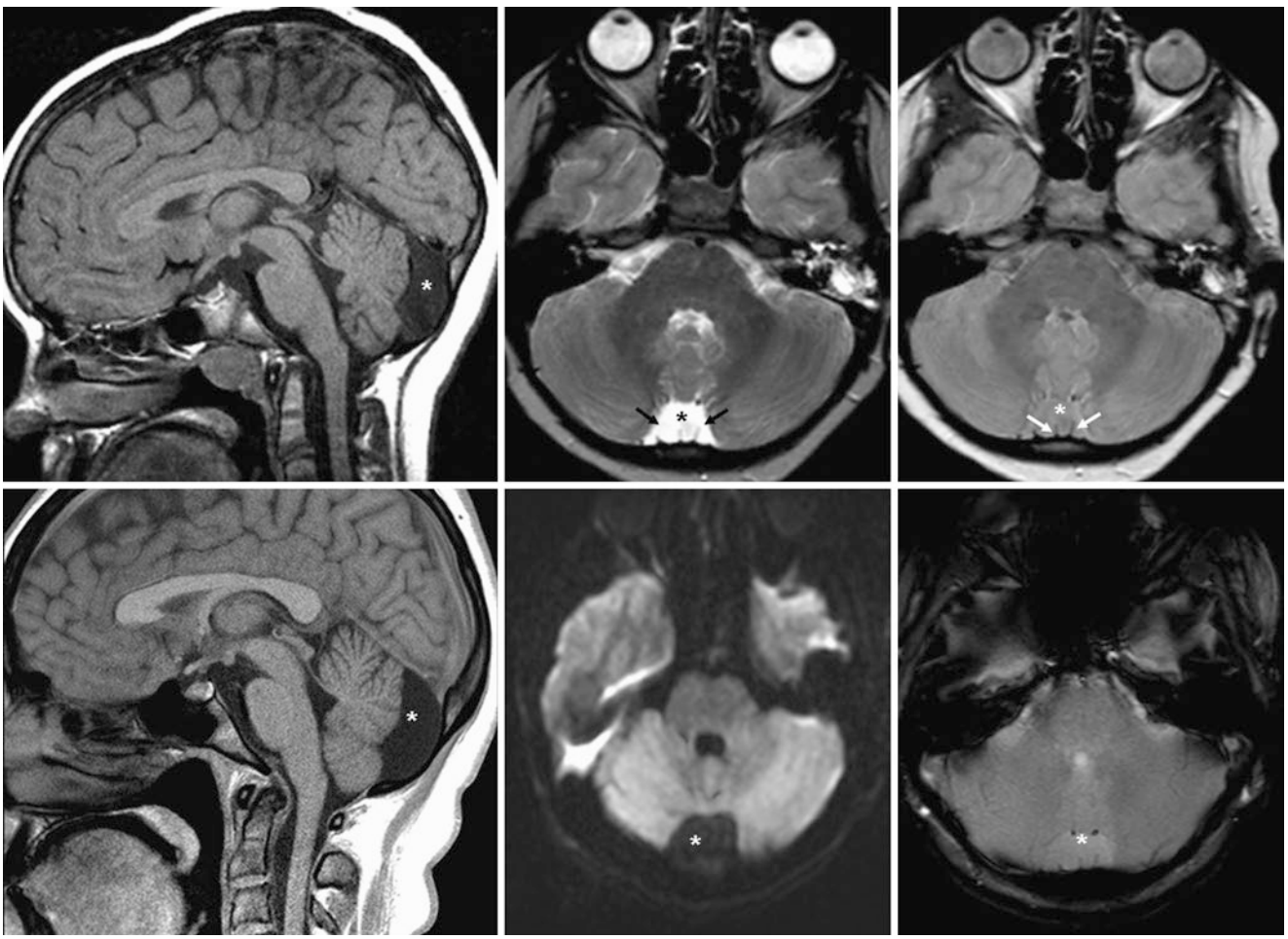

Fig. 4.7 An 8 year old with a prominent retrocerebellar cystic space (*) on sagittal T1WI MRI (*top left*) following CSF on T2WI (*top middle*) and proton density images (*top right*). An MRI 7 years later demonstrates no significant change on sagittal T1WI (*bottom left*) and confirms a CSF-like signal on DWI (*bottom middle*) and T2*WI (*bottom right*). It appears that the falx (*arrows*) at least partially traverses the cystic region, suggesting a MCM, although a RAC cannot entirely be excluded. The lack of mass effect is also suggestive of a MCM

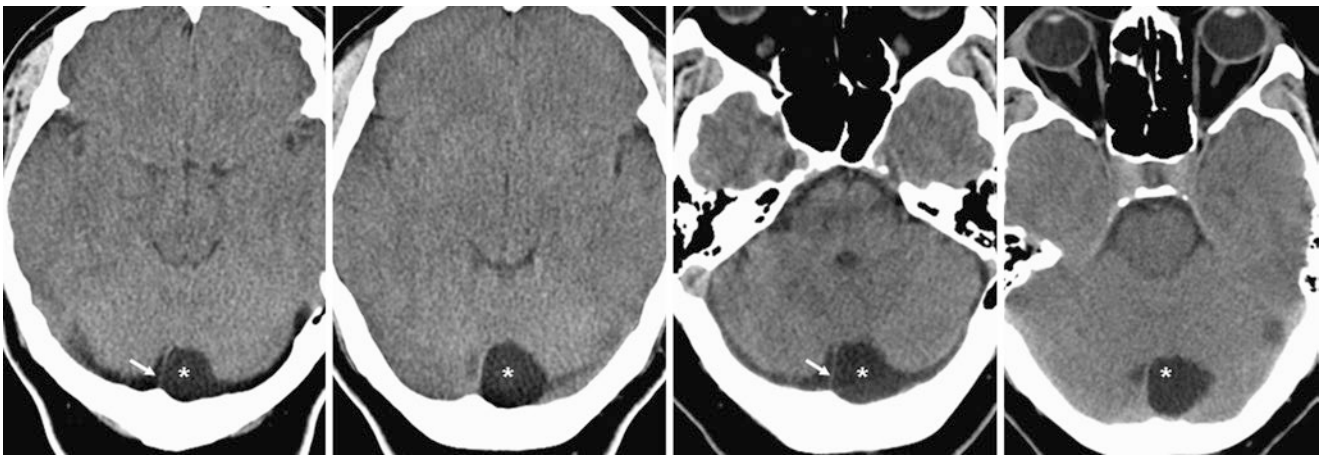

Fig. 4.8 A 40 year old had a prominent left retrocerebellar space (*) on axial NECT (*left two images*). The retrocerebellar SAS is also prominent to a lesser degree on the right side. The falx (*arrows*) partially traverses the cystic region. A NECT obtained 8 years later (*right two images*) showed no significant change in size or extent. The lack of mass effect, the appearance of the falx traversing the cyst, and the bilaterality all favored a MCM

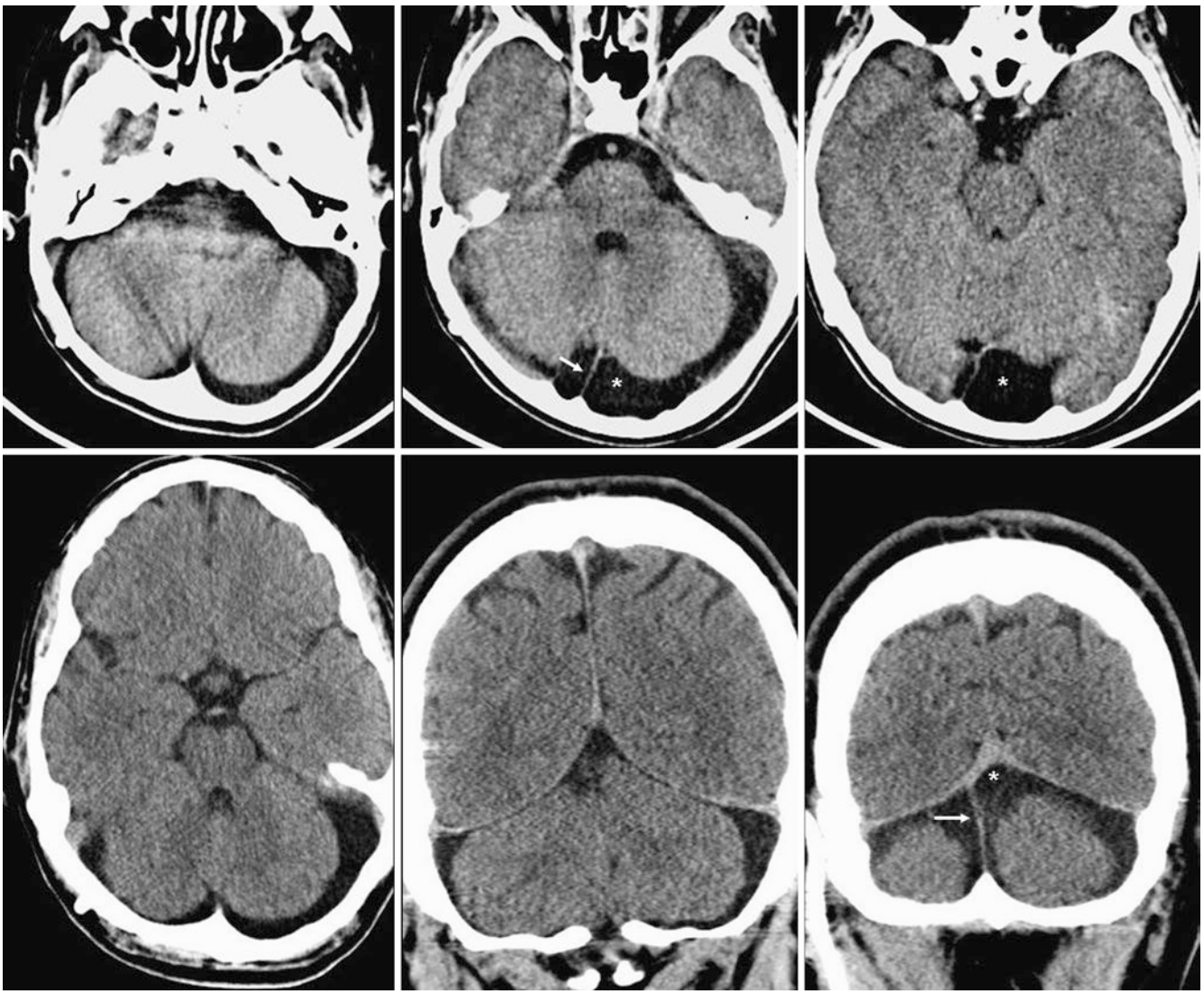

Fig. 4.9 A 19 year old wo had prominent retrocerebellar/paracerebellar subarachnoid spaces (*) seen on the NECT (*top row*). The falx (*arrows*) traverses the cystic region, suggesting an MCM. The lack of notable mass effect is also suggestive of a MCM. A NECT obtained 13 years later (*bottom row*) shows that there is no significant change, likely confirming this is a MCM. Coronal reformats (*bottom middle and right*) are also provided

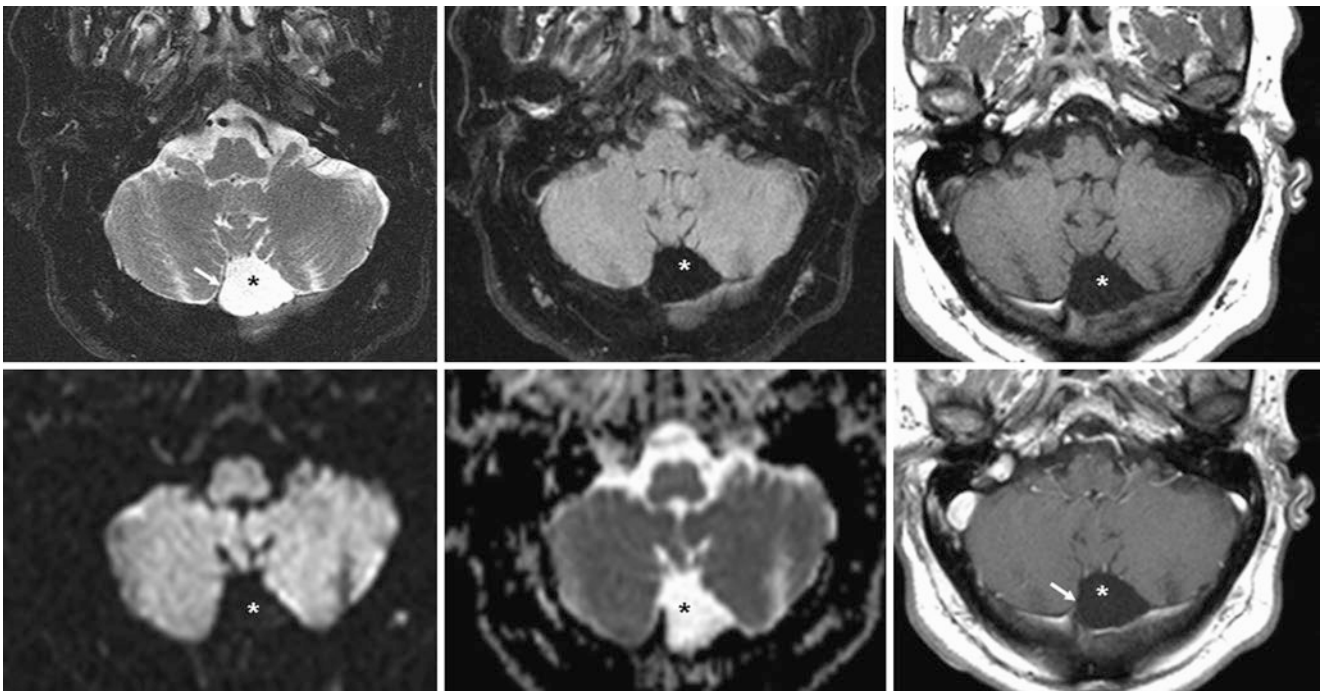

Fig. 4.10 A 65 year old with what was called a retrocerebellar cyst (*) on axial T2WI MRI (*top left*), FLAIR (*top middle*), and T1WI (*top right*), with high diffusivity akin to CSF on DWI (*bottom left*) and ADC map (*bottom middle*). There is likely falx (*arrows*) to the right of the cyst on axial T2WI and postcontrast T1WI (*bottom right*). The appearance favors a MCM, given a lack of mass effect on the cerebellum. Notice falx asymmetry to the right within the MCM

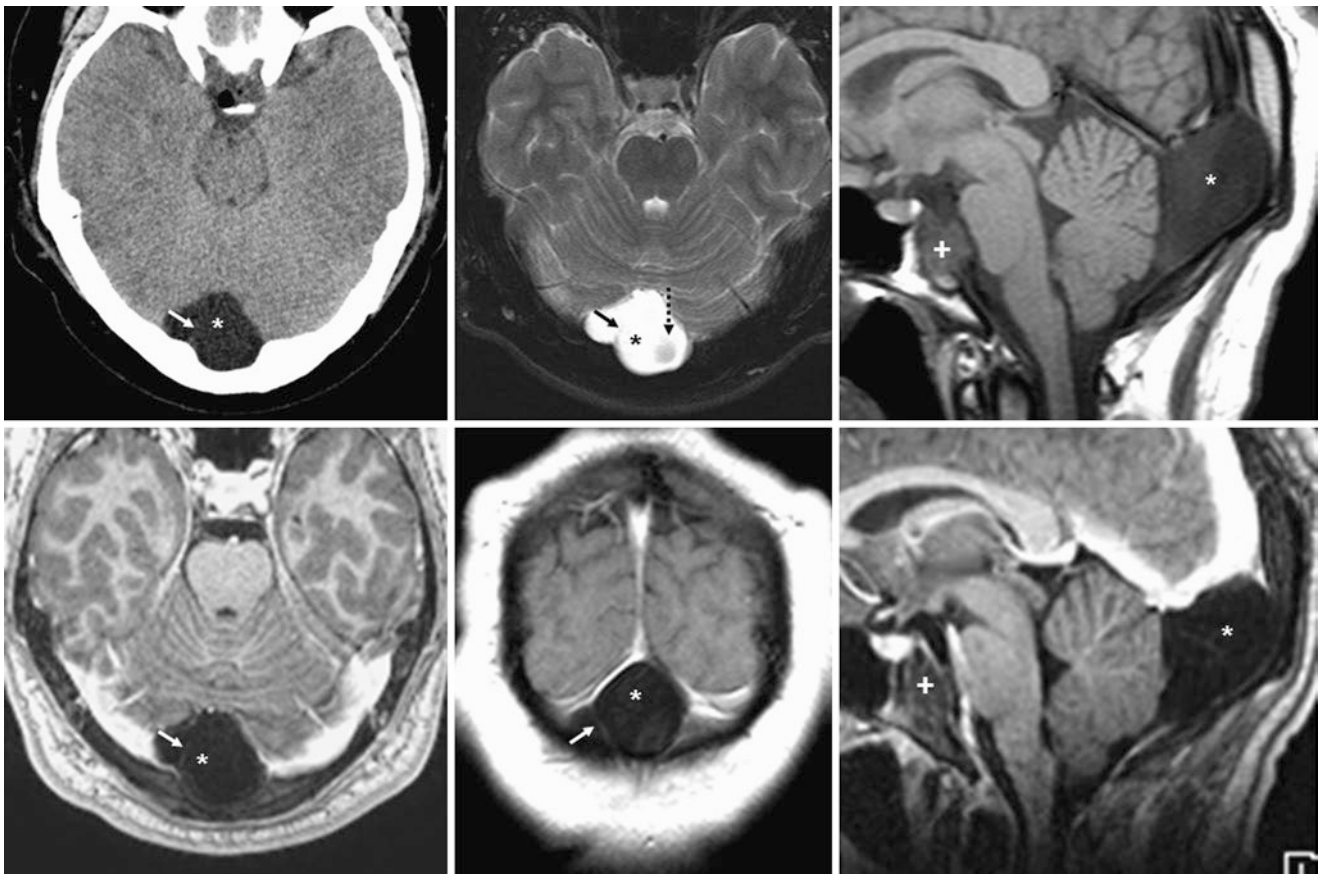

Fig. 4.11 A 21 year old was diagnosed with what was called a retrocerebellar cyst (*), with a prominent posterior fossa and scalloping of the occipital bone on axial NECT (*top left*), MRI T2WI (*top middle*), and sagittal T1WI (*top right*), lacking contrast enhancement on axial (*bottom left*), coronal (*bottom middle*), and sagittal (*bottom right*) T1WIs. There is a thin falx (*arrows*) on T2WI and postcontrast T1WI. Also, there may be a flow void (*dashed arrows*) within the cyst on T2WI. The overall appearance favors a MCM. Note a nonenhancing chordoma at the spheno-occipital junction (+)

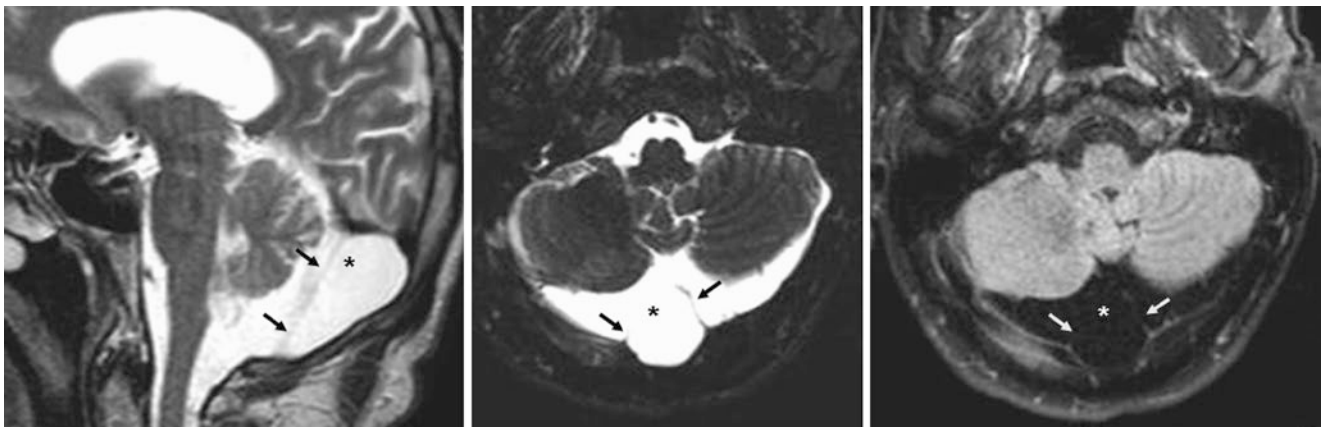

Fig. 4.12 A 65 year old was seen to have a cystic dilatation (*) posterior to the cerebellar midline and vermis, with a mildly enlarged SAS and posterior fossa. The cyst is traversed by the falx (*arrows*) on sagittal T2WI (*left*), axial thin 1 mm T2WI (*middle*), and FLAIR (*right*) MR images. The appearance would favor a MCM but a RAC cannot be excluded

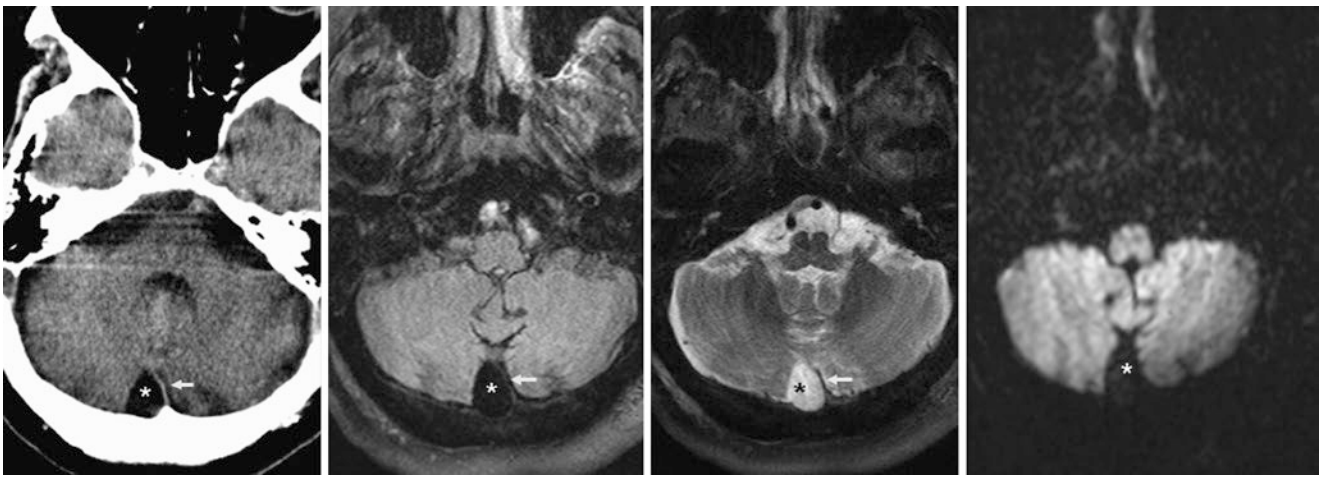

Fig. 4.13 A 59 year old with an incidental small cyst (*) posterior to the right hemicerebellum, lying to the right of midline and to the right of the falx (*arrows*) on axial NECT (*left*), and MRI FLAIR (*left middle*), T2WI (*right middle*) and DWI (*right*) images. This would favor a MCM since the falx traverses it, but a RAC cannot be excluded

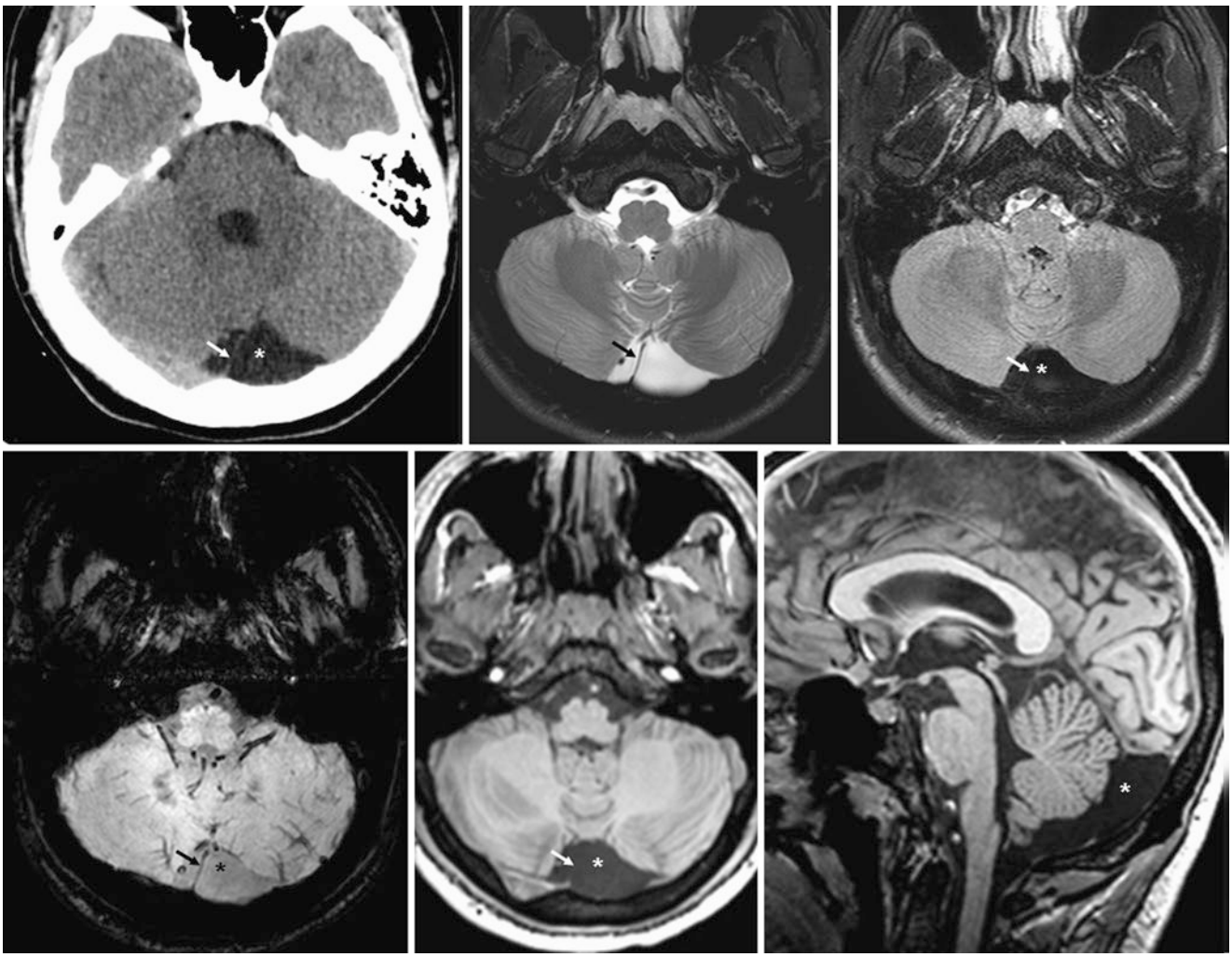

Fig. 4.14 An 18 year old had a prominent retrocerebellar space (*) shown on axial NECT (*top left*), 3 T MRI T2WI (*top middle*), FLAIR (*top right*), SWI (*bottom left*), T1WI (*bottom middle*), and sagittal T1WI (*bottom right*). This cyst-like space follows the CSF on all sequences. The falx (*arrows*) partially traverses the cystic region, and the posterior fossa appears slightly enlarged, suggesting a MCM. The lack of a significant mass effect also suggests a MCM

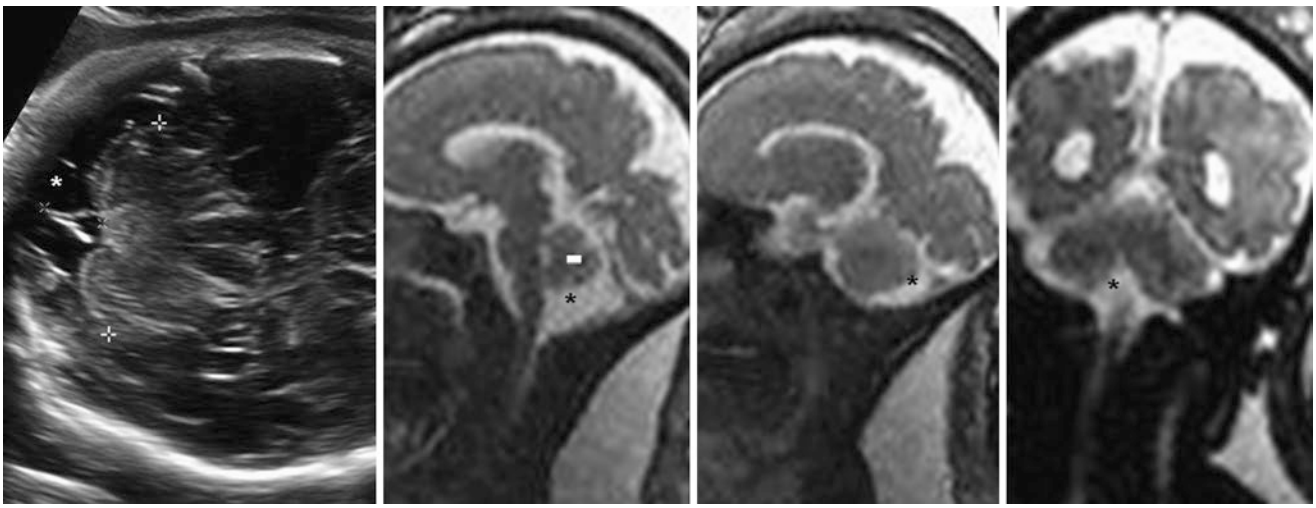

Fig. 4.15 A 34 week gestational age fetus was shown to have a prominent retrocerebellar space (*) on axial ultrasound (*left*, *face is at the right side of the image*); the cisterna magna measured 11.2 mm (10 mm is upper normal at ultrasound). A midline fetal MRI image in the sagittal plane on fast T2WI (*left middle*) confirmed isolated enlargement of the cisterna magna, with a normal cerebellar vermis present (−). The cerebellum was normal on images of the right side (*right middle*, *left side not shown*) and on coronal images (*right*). There is no mass effect on the cerebellum

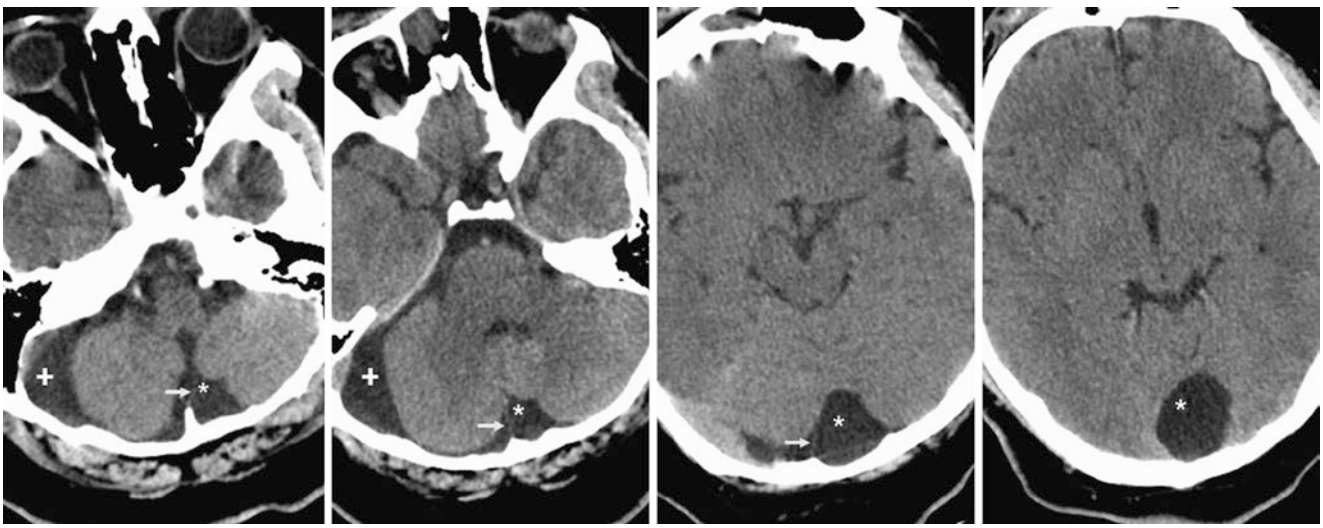

Fig. 4.16 A 17 year old had a cystic-appearing midline retrocerebellar cyst (*) that was traversed by the falx (*arrows*) on NECT. This would favor a MCM because the falx traverses it and because there is prominence of the SAS lateral to the right hemicerebellum (+). However, the uncommon possibility of two adjacent arachnoid cysts cannot be excluded

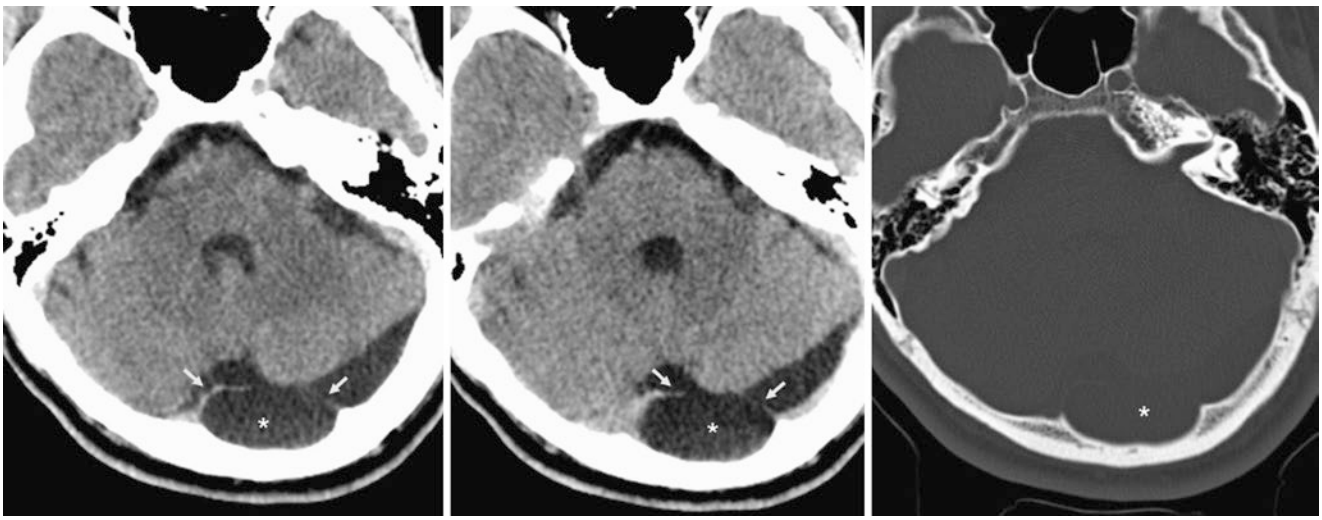

Fig. 4.17 A 21 year old was thought to have a possible cyst (*) on NECT posterior to the cerebellar midline, as shown on brain windows (*left and middle*) and bone window (*right*). The cyst displaces the falx (*arrows*) and seems to cause mild occipital scalloping. The appearance favors a RAC, since the falx does not traverse it. However, an MCM cannot be excluded

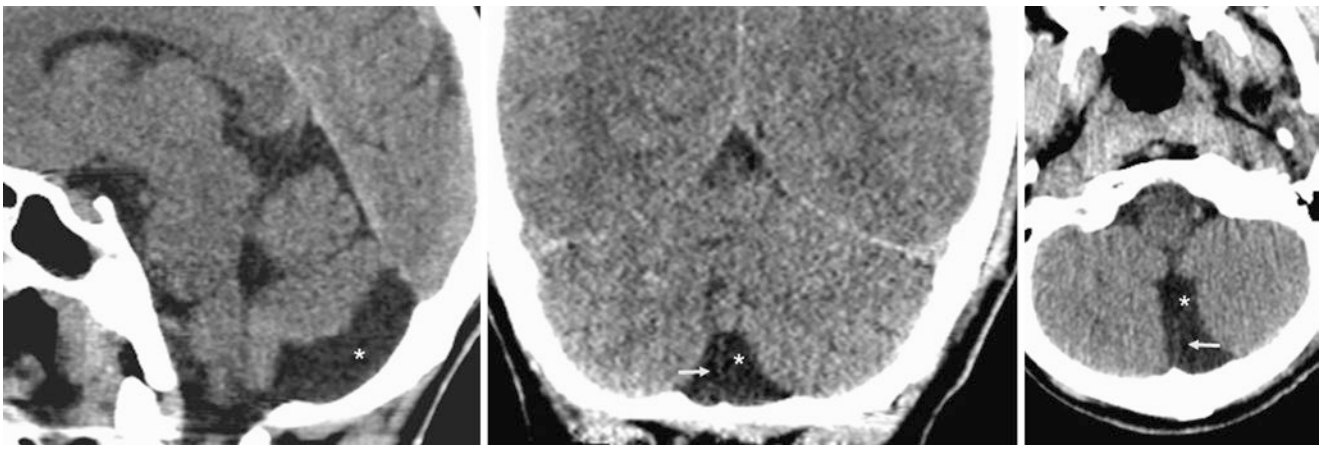

Fig. 4.18 A 20 year old who had a slightly enlarged cisterna magna with a retrocerebellar cyst-like focus (*) on sagittal (*left*) and coronal (*middle*) reformats from an axial NECT (*right*). The falx appears to partially traverse through the cyst (*arrows*) on an axial image (*right*). The appearance is indeterminate for an MCM versus a RAC

4.1 Retrocerebellar Arachnoid Cyst

Again, *retrocerebellar arachnoid cysts* (RACs) are different from MCMs but may be difficult to distinguish. The presence of a bulging or displaced thin membrane, mass effect or hydrocephalus may confirm a RAC. To visualize the thin membrane, heavily T2WI or balanced echo imaging (CISS, BFFE, FIESTA, depending on the vendor) is useful (Figs. 4.19, 4.20, 4.21, 4.22, and 4.23).

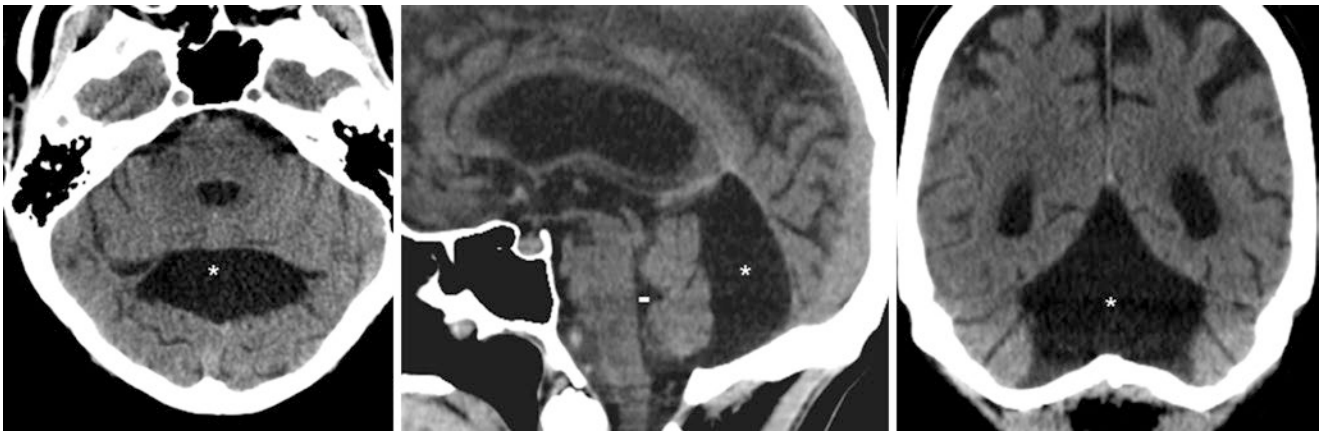

Fig. 4.19 A 40 year old who was found to have NECT axial (*left*) and sagittal (*middle*) images that demonstrate a RAC (*) that mildly compresses the cerebellum anteriorly to narrow the fourth ventricle (−). The falx is not identified as traversing the cyst. An MCM is unlikely given the lack of enlargement of the posterior fossa and the mass effect. Additionally, the cyst splays the cerebellar hemispheres apart laterally on the coronal image (*right*)

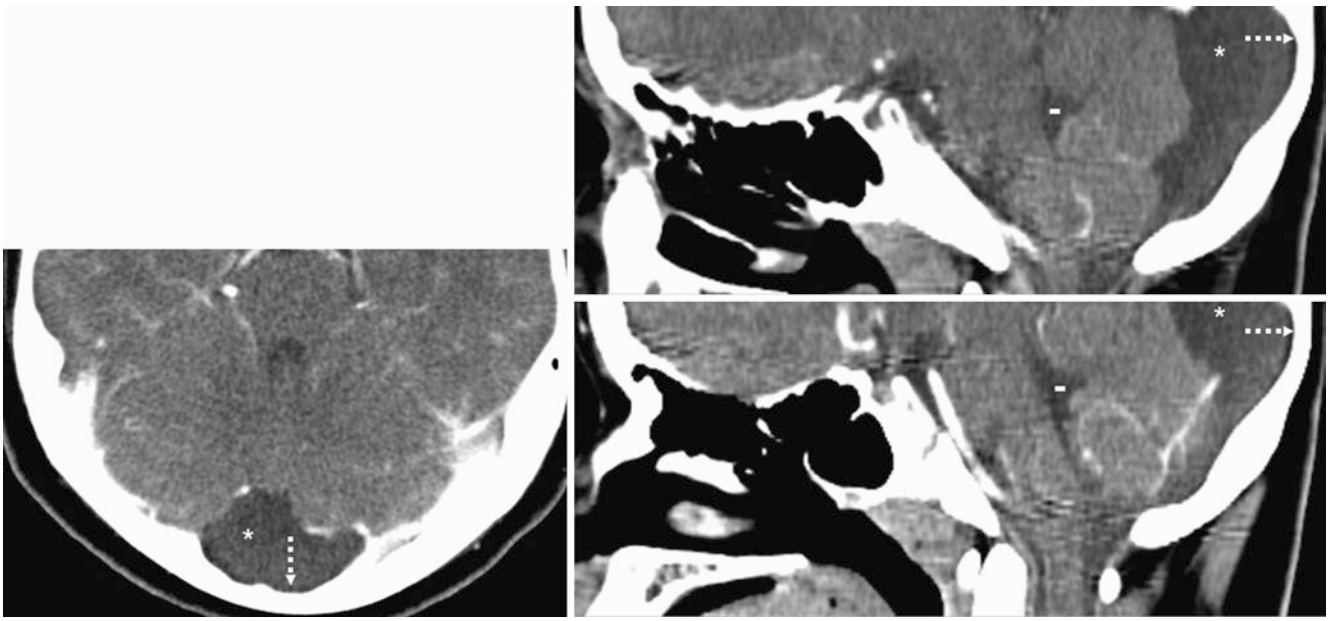

Fig. 4.20 An 11 year old with CECT images obtained from the top of a neck CT. Axial (*left*), and sagittal (*right*) reconstructions demonstrate a RAC (*) that mildly compresses the superior aspect of the cerebellum to narrow the fourth ventricle (−). The falx is not identified as traversing the cyst. There is scalloping of the inner table of the occipital bone (*dashed arrows*), falsely giving the posterior fossa a mildly enlarged appearance. No hydrocephalus is present

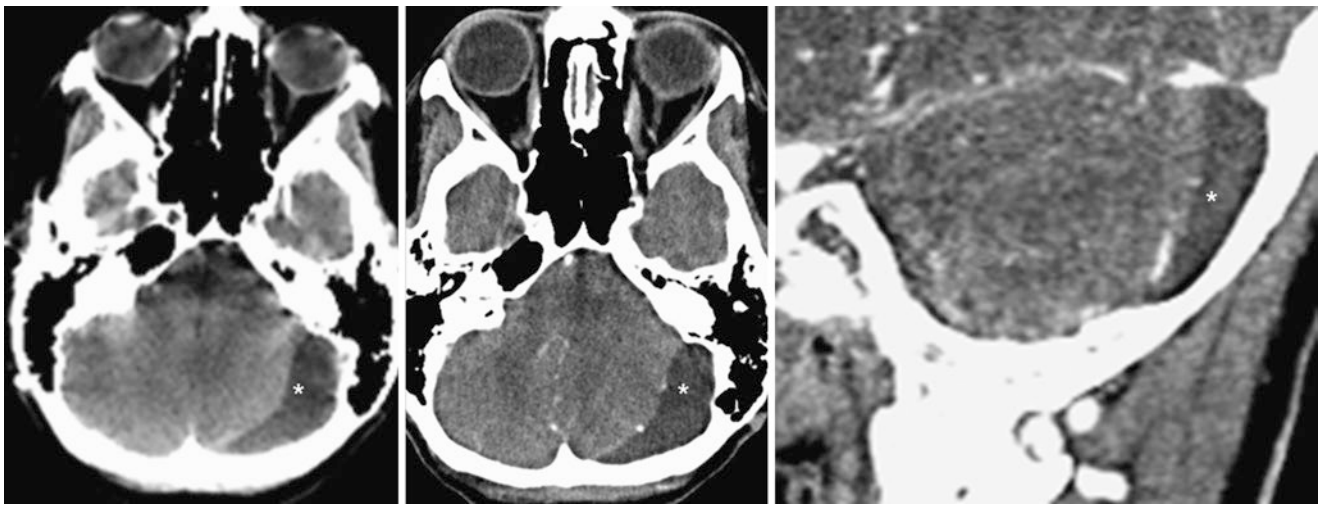

Fig. 4.21 A 24 year old with a moderate sized retrocerebellar cyst (*) posterior to and compressing the left hemicerebellum on an axial CECT image (*left*); this was not traversed by the falx. The posterior fossa did not appear enlarged. Four years later, axial (*middle*) and coronal (*right*) CECT images confirmed that there was no change in size but there was continued mass effect from the RAC

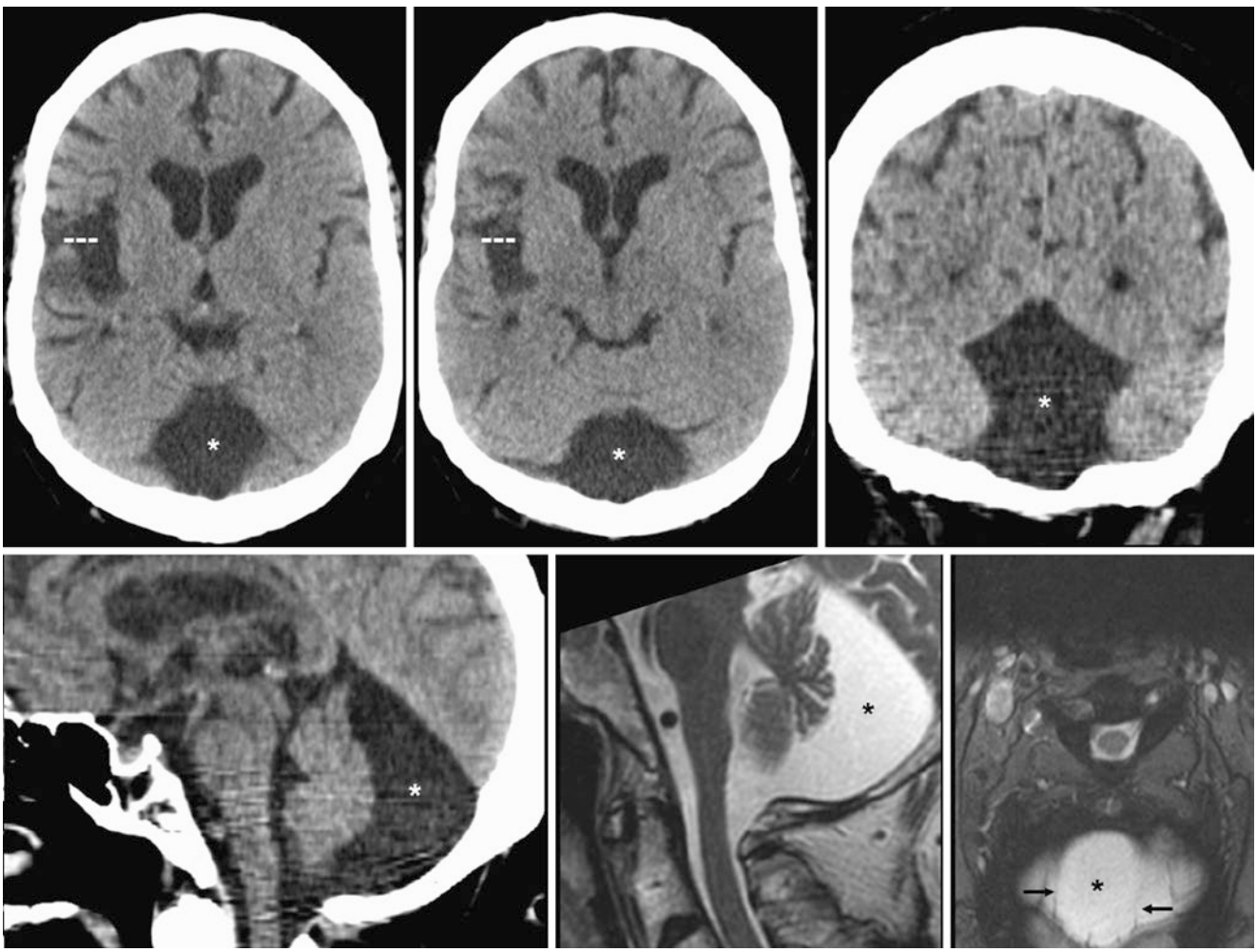

Fig. 4.22 A 59 year old had an axial NECT (*top left two images*) with coronal reformats (*top right*) performed to evaluate for a new stroke. Note encephalomalacia (−−−) of the right frontal and temporal opercular structures. A cyst-like structure was noted to mildly compress the cerebellum (*) from posteriorly on sagittal reformats (*bottom left*), suggesting a RAC. Images from a cervical MRI 5 years prior were then obtained, including sagittal T2WI (*bottom middle*) and axial GET2*WI (*bottom right*), which confirmed no change in the cyst. The walls of the RAC were subtle (*arrows*)

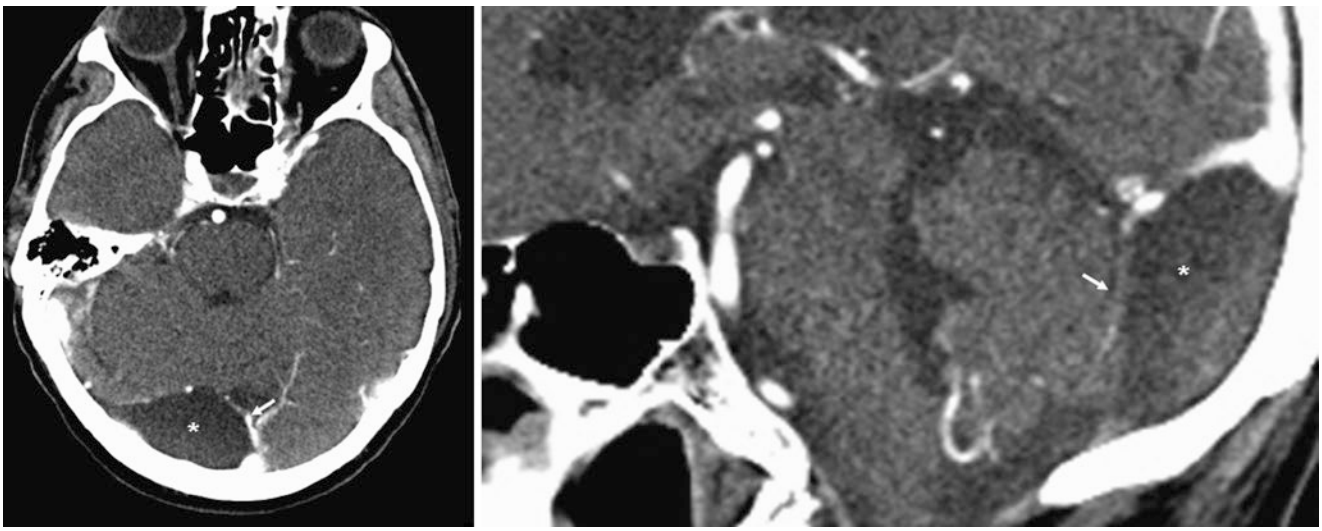

Fig. 4.23 A 66 year old had a cystic-like structure posterior to the cerebellum (*) on axial (*left*) and sagittal (*right*) NECT images, where the cyst was to the right of the falx (*arrows*), although the falx is nearly at the midline and is not clearly displaced. The posterior fossa and retrocerebellar subarachnoid spaces are mildly enlarged, with questionable mass effect from the cyst. Therefore, this cyst is indeterminate for being an MCM versus a RAC

4.2 Fetal MRI of the Normal Posterior Fossa Versus True Abnormalities

As the cerebellum begins development around the fifth gestational week, interruption of development during this time period until the 18th week may result in varying degrees of cerebello-pontine hypoplasia. Milder forms of cerebello-vermian hypoplasia can also occur from interruptions at later dates. Again, fetal MRIs performed even after the completion of cerebellar development, such as during the late second or early third trimester, may depict a mild *prominence of the cisterna magna or SAS around the cerebellum*; this is normal and should not be mistaken for any form of cerebellar hypoplasia (Figs. 4.24, 4.25, 4.26, 4.27, 4.28, 4.29, 4.30, 4.31, 4.32, 4.33, 4.34, 4.35, 4.36, 4.37, 4.38, 4.39, and 4.40).

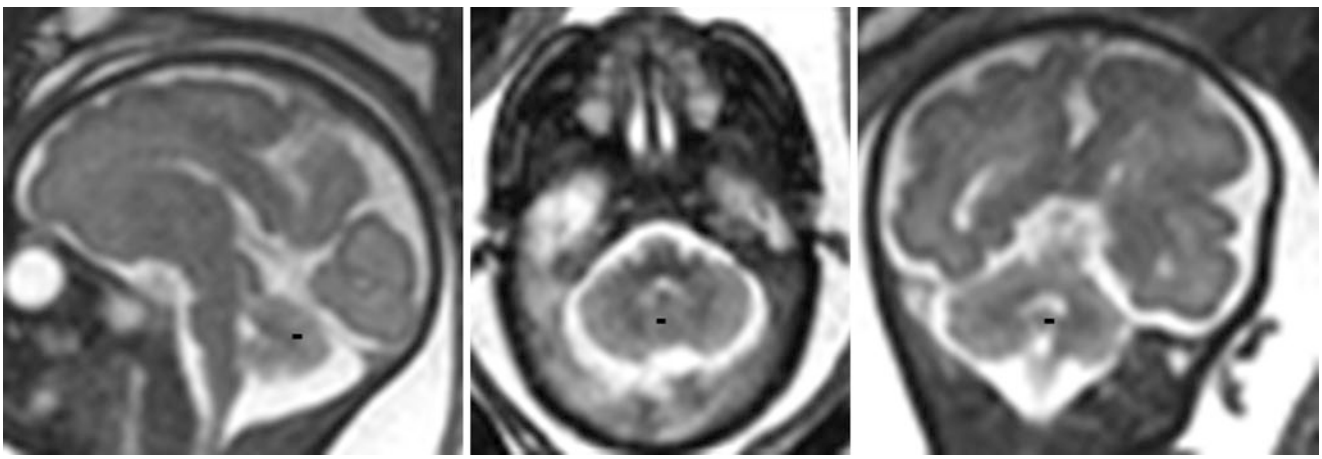

Fig. 4.24 A 29-week-old fetus underwent a fast sagittal T2WI fetal MRI for a possible brain abnormality (negative). On sagittal (*left*), axial (*middle*), and coronal (*right*) ultrafast T2WI, there is mild prominence of the SAS surrounding the cerebellum; the vermis (−) appears normal. This mild prominence of the SAS in the posterior fossa is normal and should not be mistaken for cerebellar hypoplasia or a cyst

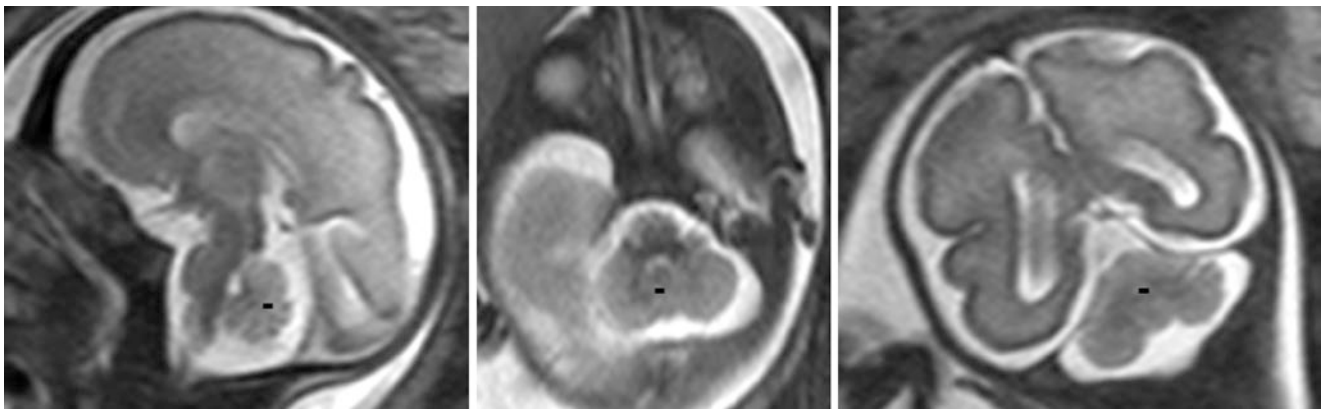

Fig. 4.25 A 28-week fetus underwent a fast T2WI fetal MRI for possible abdominal abnormality (negative). On sagittal (*left*), axial (*middle*), and coronal (*right*) fast T2WI, there is mild prominence of the SAS surrounding the cerebellum, while the vermis (−) appears normal. This mild prominence of the SAS in the posterior fossa is normal and should not be mistaken for cerebellar hypoplasia or a posterior fossa cyst

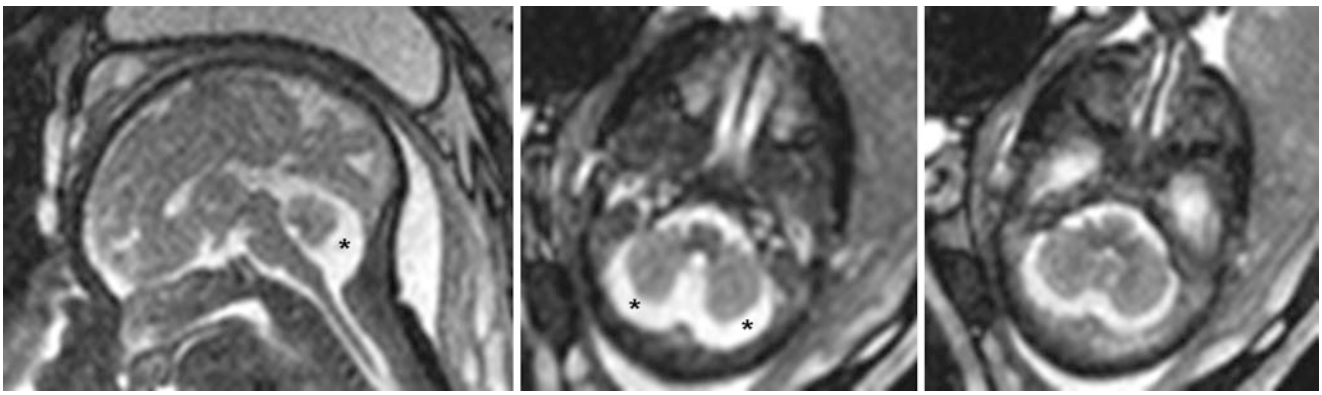

Fig. 4.26 A 29-week-old fetus underwent MRI for a possible posterior fossa abnormality. A retrocerebellar cystic dilatation (*) is noted bilaterally and symmetrically on ultrafast T2WIs in the sagittal (*left*) and axial (*right two images*) planes without enlargement of the posterior fossa. This could be considered either normal or an early MCM

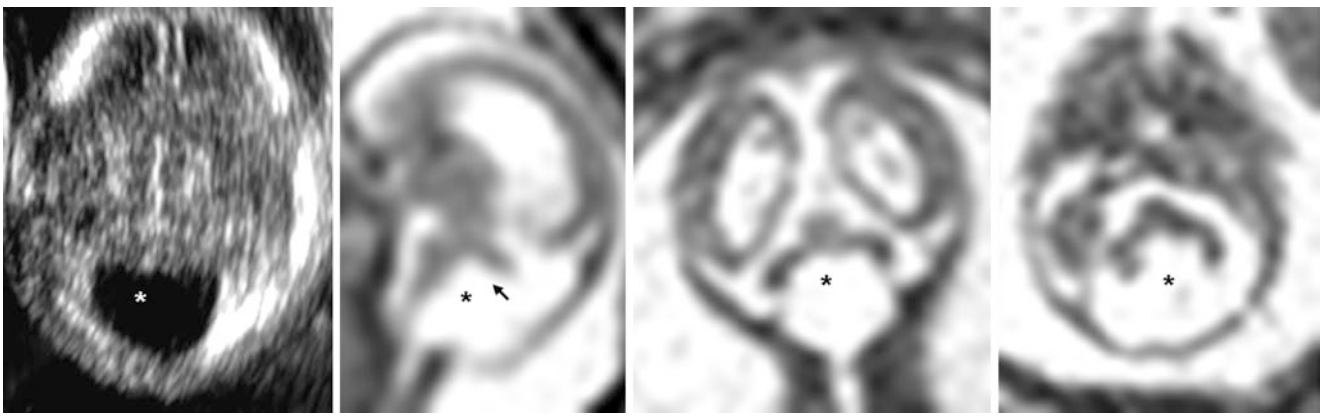

Fig. 4.27 Comparison case of Dandy-Walker malformation (DWM). A 19-week-old fetus had a cystic-appearing posterior fossa (*) on US (*left*), confirmed on fetal MRI fast T2WIs in sagittal (*left middle)*, coronal (*right middle*), and axial (*right*) planes. There was a mildly enlarged posterior fossa and lateral ventricular enlargement (hydrocephalus). The posterior angle of the fourth ventricle, i.e., the fastigium (*arrows*), is absent. Thus, the combination of findings indicates a DWM

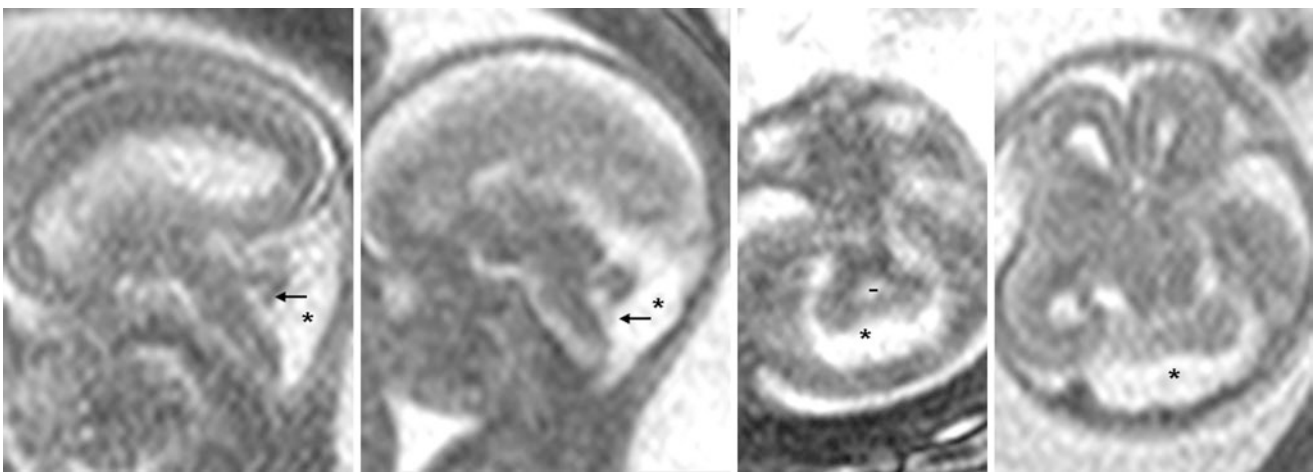

Fig. 4.28 Comparison case of cerebellar vermian hypoplasia (CVH). A 19-week-old fetus had a cystlike posterior fossa (*) on US. On MRI, ultrafast T2WIs in sagittal (*left and left middle)* and axial (*right and right middle*) planes depict a normal size posterior fossa without lateral ventricular enlargement. The posterior angle of the fourth ventricle (*arrows*) is curtailed and the vermis (–) is small, suggesting CVH. Caution must be exercised in the late second trimester, as the SAS in the posterior fossa can normally appear somewhat prominent relative to cerebellar size

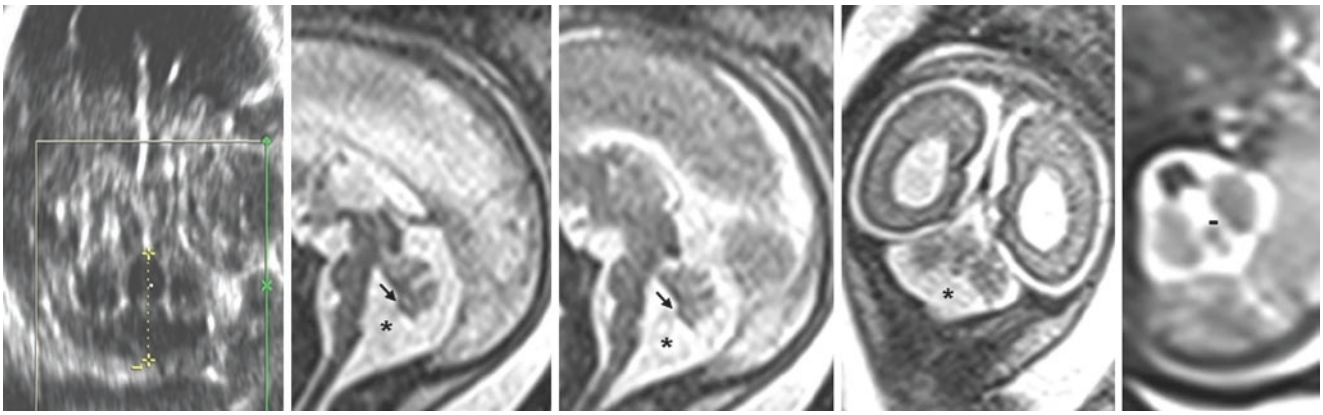

Fig. 4.29 Comparison case of inferior cerebellar vermian hypoplasia (ICVH). A 19-week-old fetus underwent an MRI for an abnormal posterior fossa on US (*left*). A retrocerebellar and infracerebellar cystic dilatation (*) was noted on T2WIs in the sagittal (*left middle and middle*), coronal (*right middle*), and axial (*right*) planes without enlargement of the posterior fossa. The posterior angle (fastigium) of the fourth ventricle (*arrows*) is curtailed, indicating ICVH

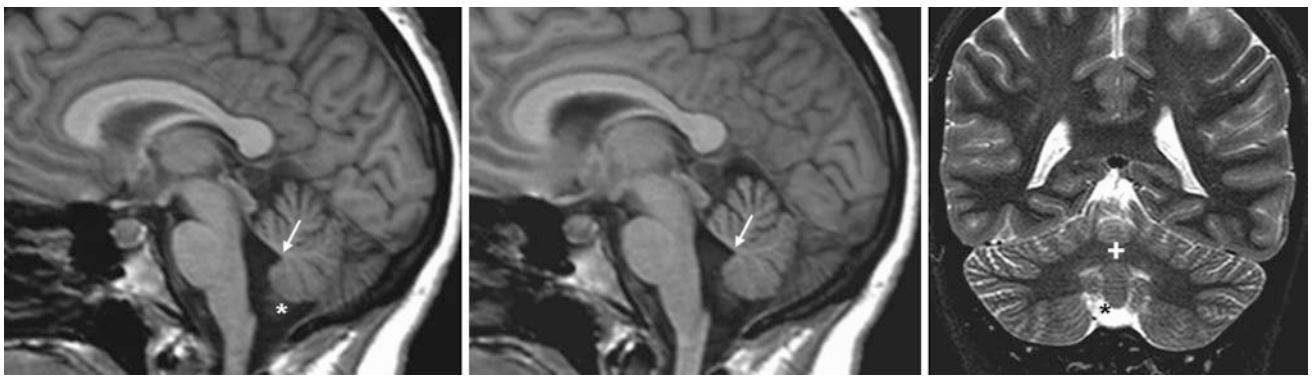

Fig. 4.30 Comparison case of minimal Inferior cerebellar vermian hypoplasia (ICVH). A 28-year- old asymptomatic patient underwent a 1.5 T MRI that depicted a slightly prominent SAS below the vermis (*), with mild enlargement of the caudal portion of the fourth ventricle and a normal posterior angle of the fourth ventricle (*arrows*) on sagittal T1WI MRI (*left two images*). The cerebellar vermis does not appear abnormal on coronal IR T2WI (*right*). As the inferior vermis is mildly foreshortened, this could represent a very mild ICVH, whereas others may consider it normal

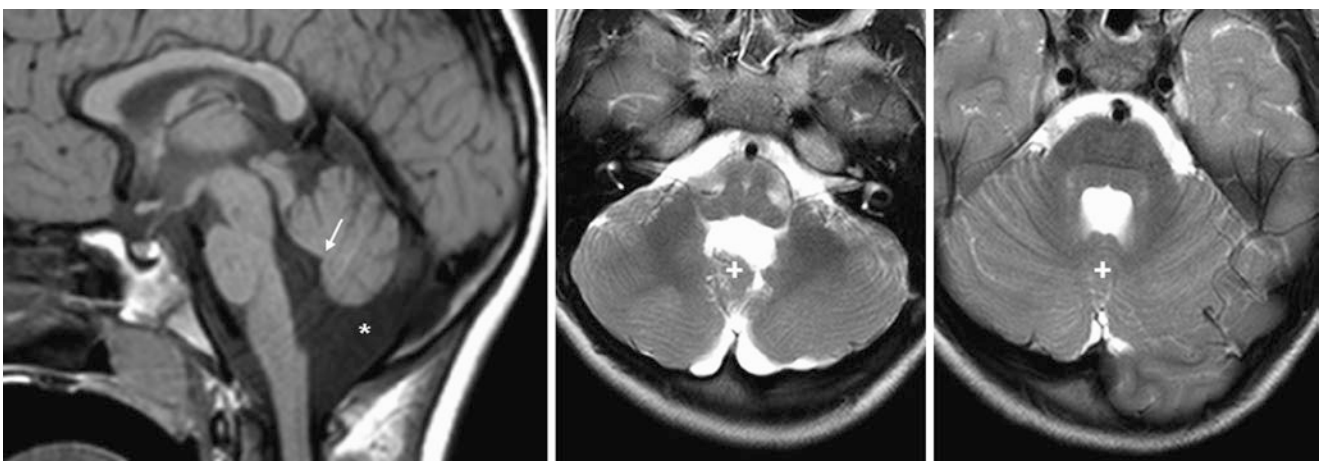

Fig. 4.31 Comparison case of mild Inferior cerebellar vermian hypoplasia (ICVH). A 6 year old underwent a 3 T MRI as part of a developmental delay evaluation. There was a prominent SAS below the vermis (*) with caudal fourth ventricular mild enlargement and an obtuse posterior angle of the fourth ventricle (*arrows*) on a sagittal T1WI MRI (*left*). The inferior segment of the vermis also appears small on axial T2WI (*middle*), while the superior segment appears more normal in size (*right*). Therefore, there is definitely at least a mild component of ICVH

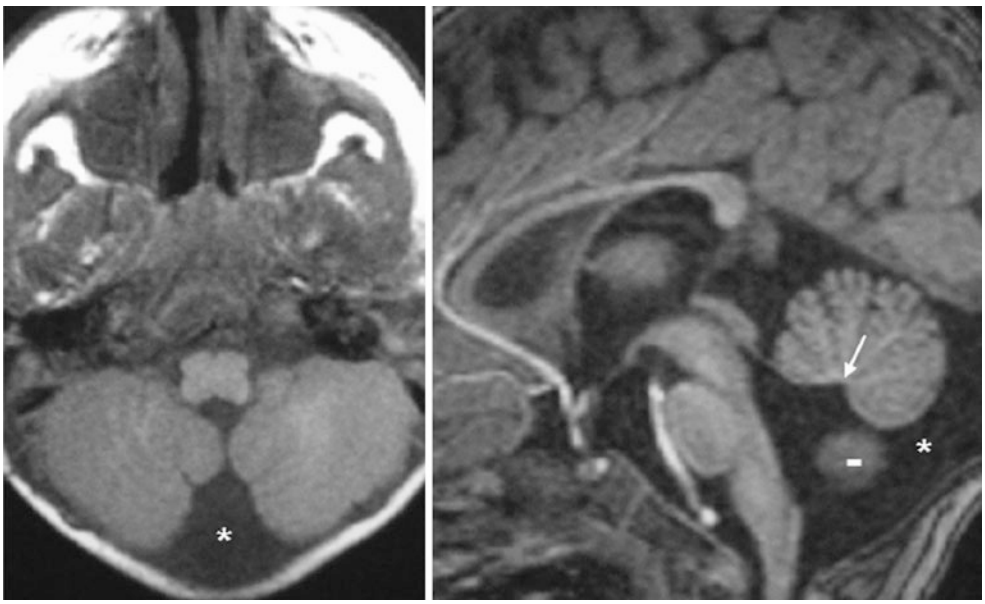

Fig. 4.32 Comparison case of moderate ICVH. A 33 year old with an MRI showing a mildly prominent SAS below the vermis (*) and an obtuse posterior angle of the fourth ventricle (*arrows*), which indicates moderate ICVH. Note a cerebellar hemisphere (−) at the midline on the sagittal image, which is not the vermis

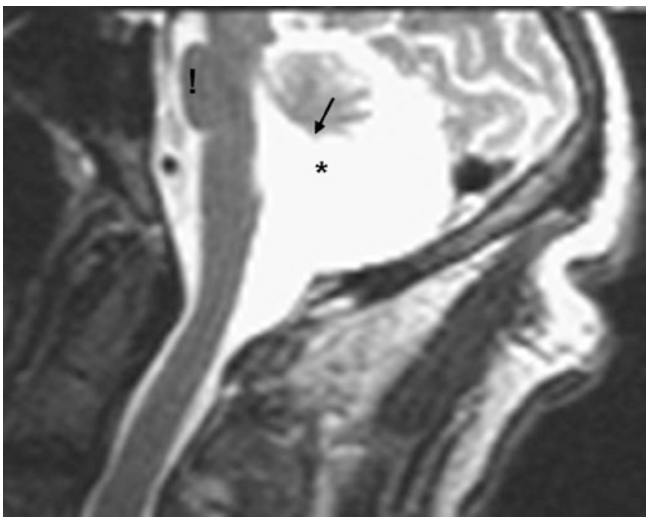

Fig. 4.33 Comparison case of severe CVH. A 35 year old underwent a cervical MRI to check for lymphoma, and the test showed prominent SAS below the vermis (*), an absent posterior angle (fastigium) of the fourth ventricle (*arrows*), and a hypoplastic pons (*!*), indicating severe CVH

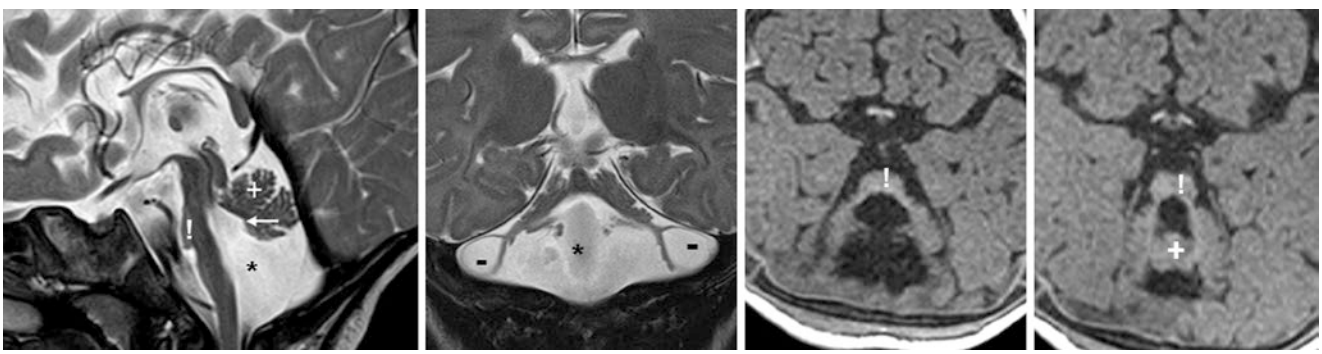

Fig. 4.34 Comparison case of olivopontocerebellar hypoplasia. In a 4 month old, a 3 T MRI showed a prominent SAS (*) below the vermis (+), fourth ventricular enlargement, an obtuse posterior angle (fastigium) of the fourth ventricle (*arrows*) on sagittal T2WI MRI (*left*), and cystic cerebellar hemispheres (−). The inferior vermis is small on coronal T2WI (*left middle*), while the superior segment is hypoplastic on axial T1WIs (*right two images*). The pons (*!*) is quite hypoplastic

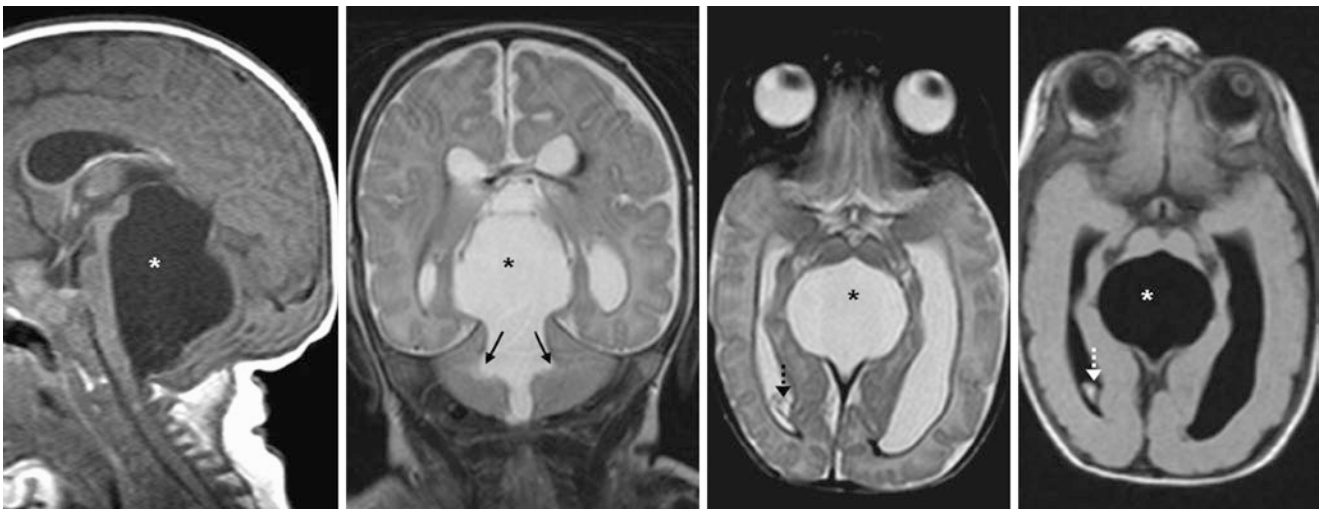

Fig. 4.35 Comparison case of Dandy-Walker syndrome with cerebellar vermian hypoplasia (ICVH). In a 3 month old with mild hydrocephalus, an MRI showed a large posterior fossa (or fourth ventricular) cyst (*) and an absent vermis on sagittal T1WI (*left*) and on coronal (*left middle*) and axial (*right middle*) T2WI. The cerebellar hemispheres (*arrows*) are displaced laterally by the cyst, which suppresses with CSF on FLAIR (*right*). T2-dark hemosiderin lines the lateral ventricles and choroid plexus (*dashed arrows*), which are sequelae of intraventricular hemorrhage

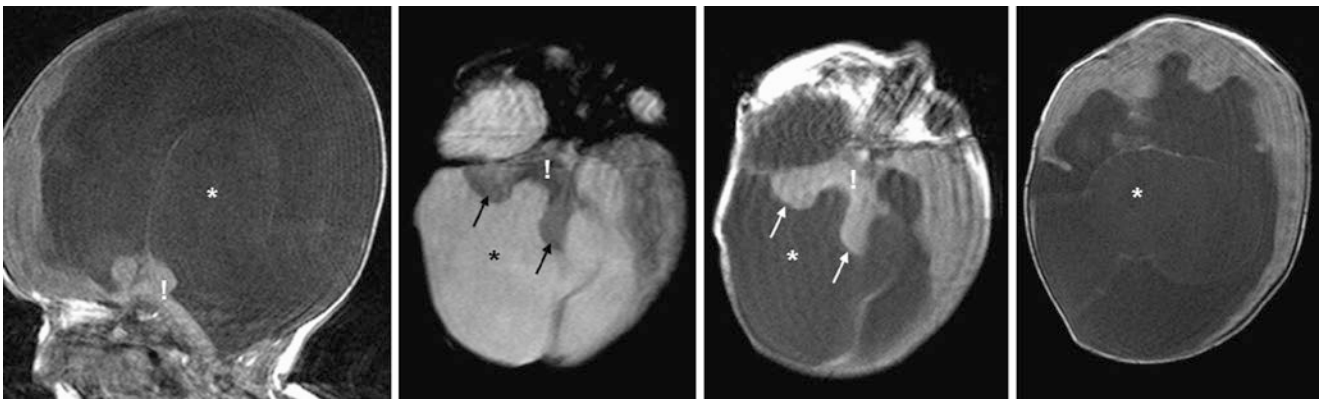

Fig. 4.36 Comparison case of Dandy-Walker syndrome. In a 10 day old with severe hydrocephalus, an MRI showed an enormous posterior fossa (or fourth ventricular) cyst (*) on sagittal T1WI (*left*), on T2WI (*left middle*), and on T1WI (*right middle and right*); the vermis is not visualized. The cerebellar hemispheres (*arrows*) are displaced laterally. The cyst extends far superiorly and anteriorly, severely compressing the brainstem (*!*) against the sphenoid bone

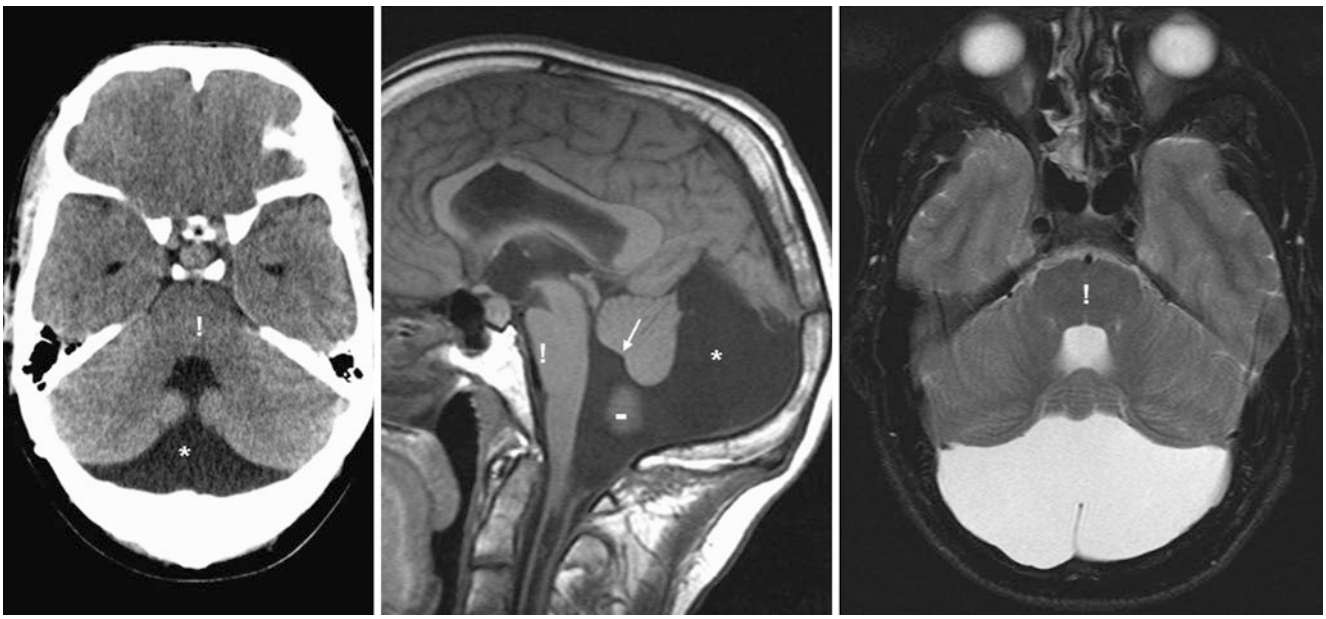

Fig. 4.37 Comparison case of Dandy-Walker syndrome in a chronically shunted patient. In a 31 year old with long-term ventriculostomy shunt catheters to treat hydrocephalus, an MRI demonstrated a mildly enlarged posterior fossa (or fourth ventricular) cyst (*) on axial NECT (*left*), sagittal T1WI (*middle*), and on an axial T2WI at a level slightly higher than the CT (*right*). The posterior angle of the fourth ventricle (*arrow*) is too obtuse on the sagittal T1WI, indicating moderate CVH. The pons (*!*) is compressed against the spheno-occipital junction and clivus

Fig. 4.38 Comparison case of Blake pouch cyst (BPC). On MRI, a 15 month old with hydrocephalus had a normal size posterior fossa but had cystic prominence (*) below the vermis on sagittal T1WI (*left*), axial FLAIR (*left middle*), and T2WI (*right middle*). The BPC expands the foramina of Magendie (+) and fourth ventricle by extending posterosuperiorly as well as scalloping the temporal bones (*arrowheads*). The posterior angle of the fourth ventricle (*arrows*) is widened, imitating ICVH, but this is probably from the cyst's mass effect. Note a widened optic recess of the third ventricle (*dotted arrow*, *left*) along with the temporal horns (−) on coronal T2WI (*right*), indicating hydrocephalus

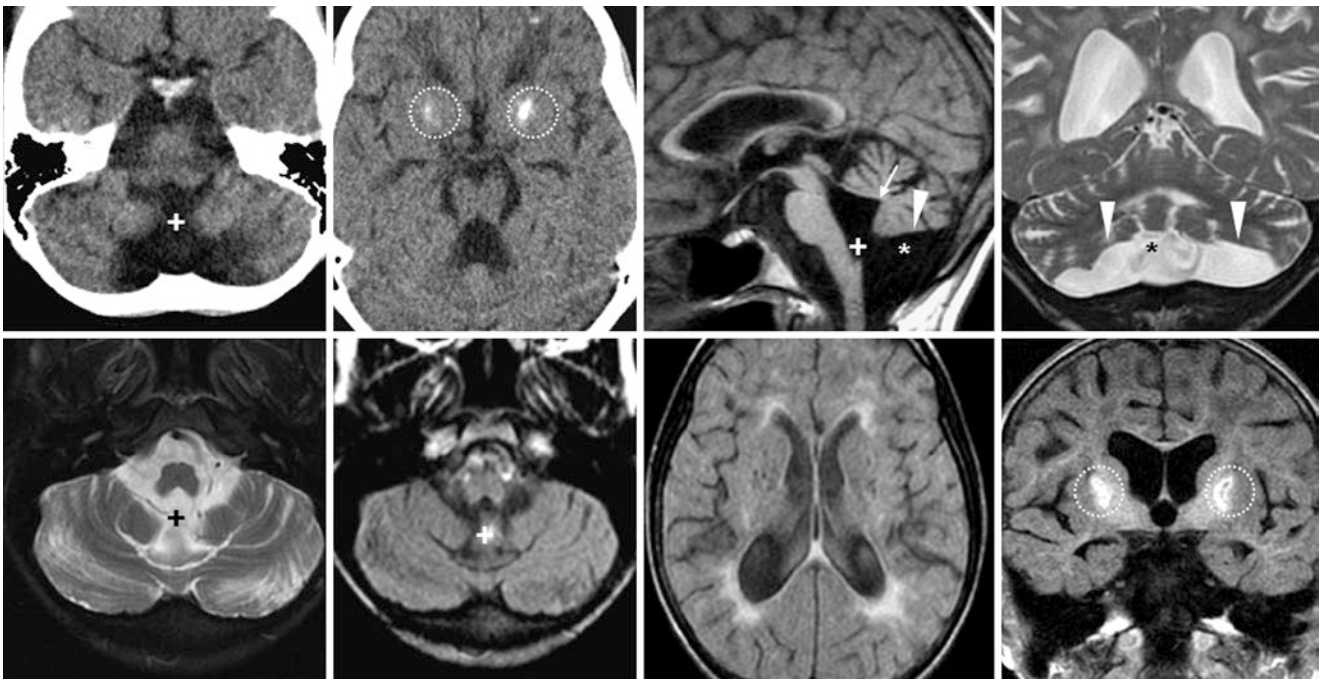

Fig. 4.39 Comparison case of BPC. In a 13 year old with Cockayne syndrome, NECT shows basal ganglia calcifications (*dotted circles*) abnormal for age (*top left*). Sagittal T1WI (*top*, *right middle*) and coronal T2WI (*top right*) depict a normal size posterior fossa with cystic prominence (*) below a formed vermis and a large foramen of Magendie (+), also seen on axial T2WI and FLAIR (*bottom left images*). The BPC displaces the inferior vermis (*arrowheads*). The posterior angle of the fourth ventricle (*arrows*) appears normal; thus, there is no CVH. At a higher level, FLAIR (*right middle*) illustrates white matter atrophy. Coronal T1-FLAIR (*bottom right*) confirms the basal ganglia findings

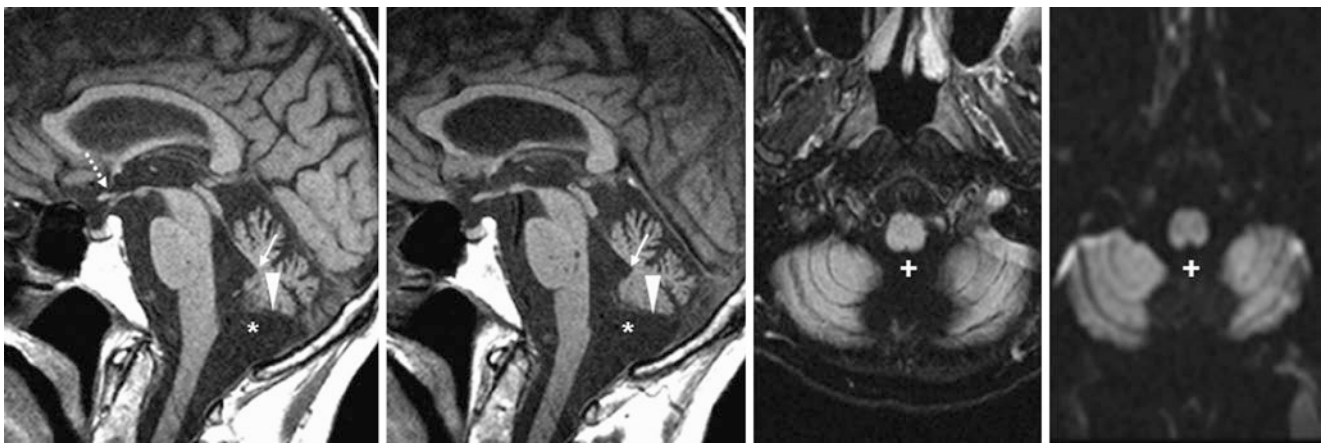

Fig. 4.40 Companion case of BPC. In a 70 year old given an MRI for a stroke work-up (negative), there was a normal size posterior fossa, but with cystic prominence (*) below a normally formed vermis on sagittal T1WI (*left images*), axial FLAIR (*right middle*), and DWI (*right*). The BPC enlarges the foramen of Magendie (+), displacing the inferior margin of the vermis superiorly (*arrowheads*). The posterior angle of the fourth ventricle (*arrows*) appears normal. There were no clinical signs of hydrocephalus; note the normal, thin optic recess (*dotted arrow*, *left*)

Suggested Reading

Barkovich AJ, Kjos BO, Norman D, Edwards MS. Revised classification of posterior fossa cysts and cystlike malformations based on the results of multiplanar MR imaging. Am J Radiol. 1989;153:1289–300.

Barkovich AJ, Wippold FJ, Sherman JL, Citrin CM. Significance of cerebellar tonsillar position on MR. Am J Neuroradiol. 1986;7:795–9.

Calabrò F, Arcuri T, Jinkins JR. Blake's pouch cyst: an entity within the Dandy-Walker continuum. Neuroradiology. 2000;42:290–5.

Christophe C, Dan B. Magnetic resonance imaging cranial and cerebral dimensions: is there a relationship with Chiari I malformation? A preliminary report in children. Eur J Paediatr Neurol. 1999;3:15–23.

Cousins J, Haughton V. Motion of the cerebellar tonsils in the foramen magnum during the cardiac cycle. Am J Neuroradiol. 2009;30:1587–8.

Daniels DL, Haughton VM, Williams AL, Berns TF. The flocculus in computed tomography. Am J Neuroradiol. 1981;2:227–9.

Garel C, Delezoide A. MRI of the fetal brain: normal development and cerebral pathologies. Secaucus: Springer; 2004. p. 228–30.

Limperopoulos C, Robertson RL, Estroff JA, Barnewolt C, Levine D, Bassan H, et al. Diagnosis of inferior vermian hypoplasia by fetal MRI: potential pitfalls and neurodevelopmental outcome. Am J Obstet Gynecol. 2006;194:1070–6.

Meadows J, Kraut M, Guarnieri M, Haroun RI, Carson BS. Asymptomatic Chiari type I malformations identified on magnetic resonance imaging. J Neurosurg. 2000;92:920–6.

Milhorat TH, Chou MW, Trinidad EM, Kula RW, Mandell M, Wolpert C, et al. Chiari 1 malformation redefined: clinical and radiographic findings for 364 symptomatic patients. Neurosurgery. 1999;44:1005–17.

Salzman KL, Davidson HC, Harnsberger HR, Glastonbury CM, Wiggins RH, Ellul S, et al. Dumbbell schwannomas of the internal auditory canal. Am J Neuroradiol. 2001;22:1368–76.

Smith BW, Strahle J, Bapuraj JR, Muraszko KM, Garton HJ, Maher CO. Distribution of cerebellar tonsil position: implications for understanding Chiari malformation. J Neurosurg. 2013;119:812–9.

Tortori-Donati P, Fondelli MP, Rossi A, Carini S. Cystic malformations of the posterior cranial fossa originating from a defect of the posterior membranous area. Mega cisterna magna and persisting Blake's pouch: two separate entities. Childs Nerv Syst. 1996;12:303–8.

Tubbs RS, Wellons 3rd JC, Oakes WJ. Asymmetry of tonsillar ectopia in Chiari I malformation. Pediatr Neurosurg. 2002;37:199–202.

Vernooij MW, Ikram MA, Tanghe HL, Vincent AJ, Hofman A, Krestin GP, et al. Incidental findings on brain MRI in the general population. N Engl J Med. 2007;357:1821–8.

Wu YW, Chin CT, Chan KM, Barkovich AJ, Ferriero DM. Pediatric Chiari I malformations: do clinical and radiologic features correlate? Neurology. 1999;53:1271–6.

Yock DH. Imaging of CNS disease: a CT and MR teaching file. 2nd ed. New York: Mosby; 1991. p. 89–93.

Cranial Nerve VII: Normal Contrast Enhancement on Magnetic Resonance Imaging

5

Cranial nerve VII (CN7) may have normal *contrast enhancement* in several locations. This is important to be aware of because MRI studies of the *internal auditory canal* (IAC) are quite common. Such MRI examinations typically employ postcontrast T1WI with fat suppression in order to augment visualization of an abnormally enhancing CN7 (e.g., Bell palsy, Ramsay Hunt syndrome, Lyme disease, leukemia, sarcoidosis) or CN8 (e.g., schwannoma, labyrinthitis) or to evaluate for a mass within the adjacent petrous bone (e.g., glomus tumor, cholesteatoma, metastasis) or cerebellopontine angle (CPA; e.g., schwannoma or meningioma). Thus, the following descriptions of normal and abnormal regions of enhancement refer to contrast-enhanced fat-suppressed spin echo T1WI (FS T1WI).

To understand the normal pattern of enhancement of the facial nerve, a brief review of the nerve's course is necessary. Overall, the motor component of CN7 originates from the brainstem and travels anterolaterally into the IAC and thereafter into the bony facial canal (also known as the fallopian canal); this is followed by its egress from the skull base via the stylomastoid foramen. Thus, the segments of CN7 serially may be considered to be the following, followed by the rate that they enhance in asymptomatic patients as based on several studies:

1. The *cisternal segment* (also known as the intracranial segment, within the CPA): typically does not enhance;
2. The *canalicular segment* (also known as the meatal segment, within the IAC): usually does not enhance but 15 % were documented to enhance in one study;
3. The *labyrinthine segment*: typically does not enhance, although was documented at 5 % in one study;
4. The *horizontal segment* (also known as the tympanic segment): 21–88 % enhance;
5. The *descending segment* (also known as the mastoid segment): 88–100 % enhance;
6. The *extratemporal segment* (also known as the extracranial segment): typically does not enhance.

Note that the intraparotid subsegments of the extracranial facial nerve are not discussed here. Also, the *geniculate ganglion* (also known as the *first genu*) is situated where the nerve turns to travel posteriorly, between the labyrinthine and horizontal segments, and the rate of enhancement in that location varies widely between studies from 21 to 100 %. The *second genu* is the point at which the nerve turns to travel inferiorly between the horizontal (tympanic) and descending (mastoid) segments; there are no definite numbers for the rate of enhancement at that point, but they are probably similar to those of the horizontal and descending segments.

Thus, most studies report that there should not be enhancement within the CPA, IAC, or labyrinthine segments, although in more recent reports faint enhancement within the IAC has been shown to occasionally occur, which this author suggests may represent a prominent perineural plexus, a prominent loop of the anterior inferior cerebellar artery (AICA), or one of its branches extending into the IAC. Interestingly, to demonstrate the degree of variation in facial nerve enhancement, early studies demonstrated that 76–98 % of asymptomatic patients had enhancement of at least one segment of the facial nerve and at least 69 % had asymmetric enhancement side-to-side. Notably, *cranial nerve VIII* (CN8) should not have enhancement at any point.

In clinically symptomatic patients, particularly those with *Bell palsy*, the enhancement is most commonly within the distal, lateral meatal (i.e., fundus of the IAC), and labyrinthine segments, visualized in some studies in up to nearly 100 % of symptomatic patients. There have been studies showing that even in patients with clinical abnormalities of the facial nerves the intensity of enhancement does not correlate with the degree of symptoms. Other etiologies that may present with CN7 enhancement on MRI include *Ramsay Hunt syndrome*, *Lyme disease*, bacterial or fungal *meningitis*, *leukemia*, *carcinomatosis*, *sarcoidosis*, *tuberculosis*, *schwannoma* (of CN7, particularly neurofibromatosis type 2), *polyneuritis*, *Wegener granulomatosis*, *radiation injury*, and of

A.M. McKinney, *Atlas of Normal Imaging Variations of the Brain, Skull, and Craniocervical Vasculature*,
DOI 10.1007/978-3-319-39790-0_5

course *perineural spread of contiguous tumor* (particularly adenoid cystic or squamous cell carcinoma).

Hence, an easy, practical rule to remember is that the facial nerve should not enhance outside of the facial canal or in the labyrinthine segment. In other words, the facial nerve may normally enhance within the geniculate, horizonal (tympanic), and descending (mastoid) segments but not within the cistern, IAC (meatal), or just after exiting from the stylomastoid foramen. Note that the labyrinthine segment is the exception to the concept that "CN7 enhancement within the facial canal is normal." The reason that it is best to exercise caution when calling CN7 enhancement of the labyrinthine segment by itself is that this segment is quite short (only 3–4 mm long, while the other segments are all at least 8 mm in length) and can often be volume-averaged with the geniculate segment and hard to discern with inadequate technique on thicker images or with motion. Also, it should be noted that these numbers may vary by sequence and field strength, where FS SET1WI may be more sensitive in visualizing enhancement of CN7 than spoiled gradient echo T1WI (GET1WI, also known as "FLASH," "SPGR," or "T1FFE," depending on the MRI manufacturer), and that contrast enhancement at 3 T may be easier to visualize than at 1.5 T.

For this section, all postcontrast images are FS SET1WI, at 2–3 mm thickness unless otherwise noted (Figs. 5.1, 5.2, 5.3, 5.4, 5.5, 5.6, 5.7, 5.8, 5.9, 5.10, 5.11, 5.12, 5.13, 5.14, 5.15, 5.16, 5.17, and 5.18).

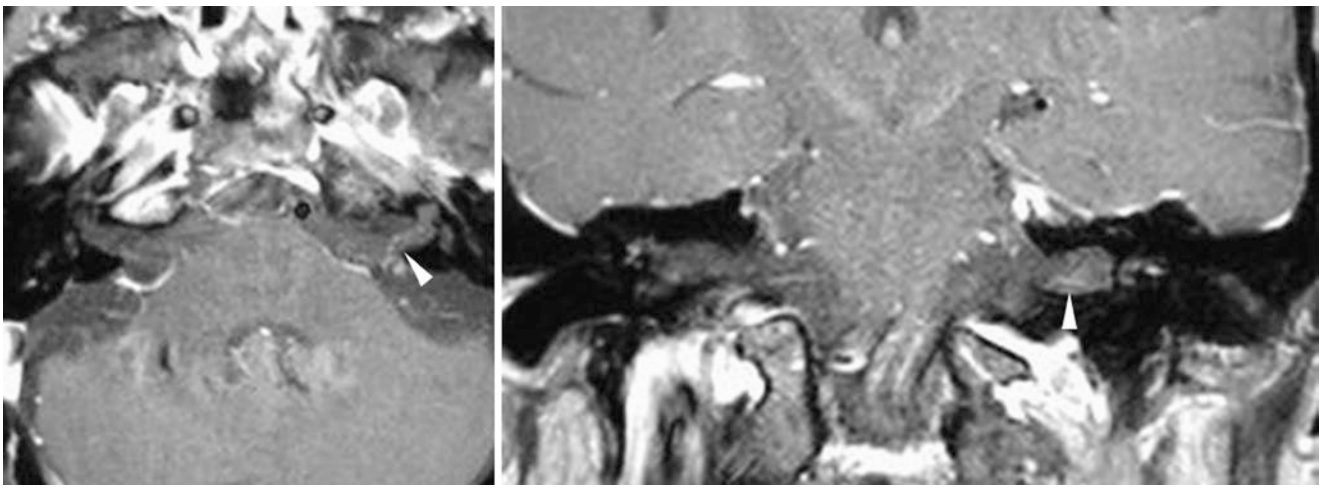

Fig. 5.1 A 65-year-old patient with bilateral hearing changes underwent an IAC protocol MRI at 3 T. Postcontrast FS SET1WIs in the axial (*left*) and coronal (*right*) planes depicted normal mild, wispy perineural enhancement (*arrowheads*) surrounding the intracanalicular portion of CN7. While enhancement in this segment of CN7 is typically abnormal, such cases usually involve the distal IAC segment of the nerve (e.g., Bell palsy), the nerve is enlarged, or avidly diffusely, or circumferentially enhancing (e.g., schwannoma, leukemia, Lyme disease)

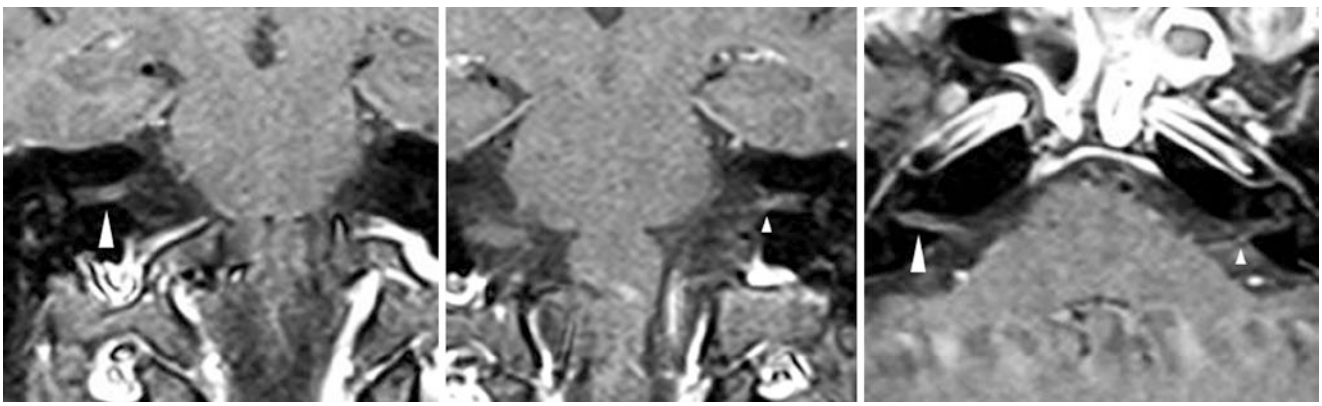

Fig. 5.2 A 58-year-old patient with an IAC protocol MRI at 1.5 T for dizziness and giddiness. Coronal postcontrast FS SET1WIs of the right (*left*) and left (*middle*) sides illustrate mild, wispy perineural enhancement of the intracanalicular portion of CN7 on the right (*arrowheads*), which mimics an intracanalicular schwannoma on coronal images (*left*) but is better defined to be a perineural plexus on axial images (*right*). Alternatively, this could represent looping of the AICA or one of its branches into the IAC. Note normal mild enhancement within the left IAC as well (*tiny arrowheads*)

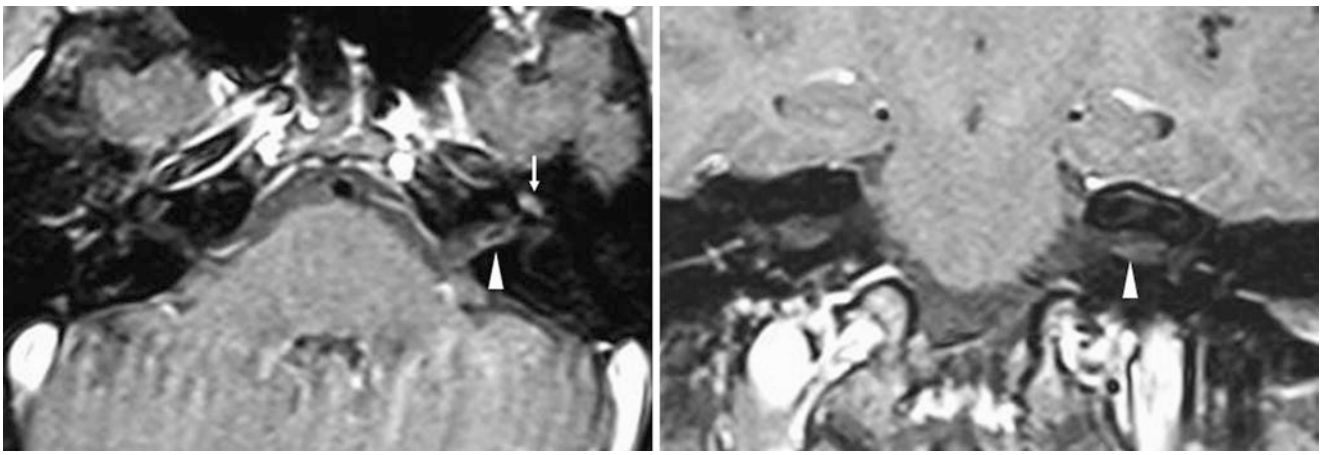

Fig. 5.3 A 50-year-old patient with a history of dizziness and giddiness underwent an IAC protocol MRI at 1.5 T. Postcontrast FS SET1WI in the axial (*left*) plane depicts normal mild, wispy perineural enhancement surrounding the intracanalicular portion of the left CN7 (*arrows*). This is not as well visualized on the coronal image (*right*). Note incidental, normal enhancement of the geniculate (GG) and horizontal (tympanic) segments of CN7 on the left as well (*thin arrow*)

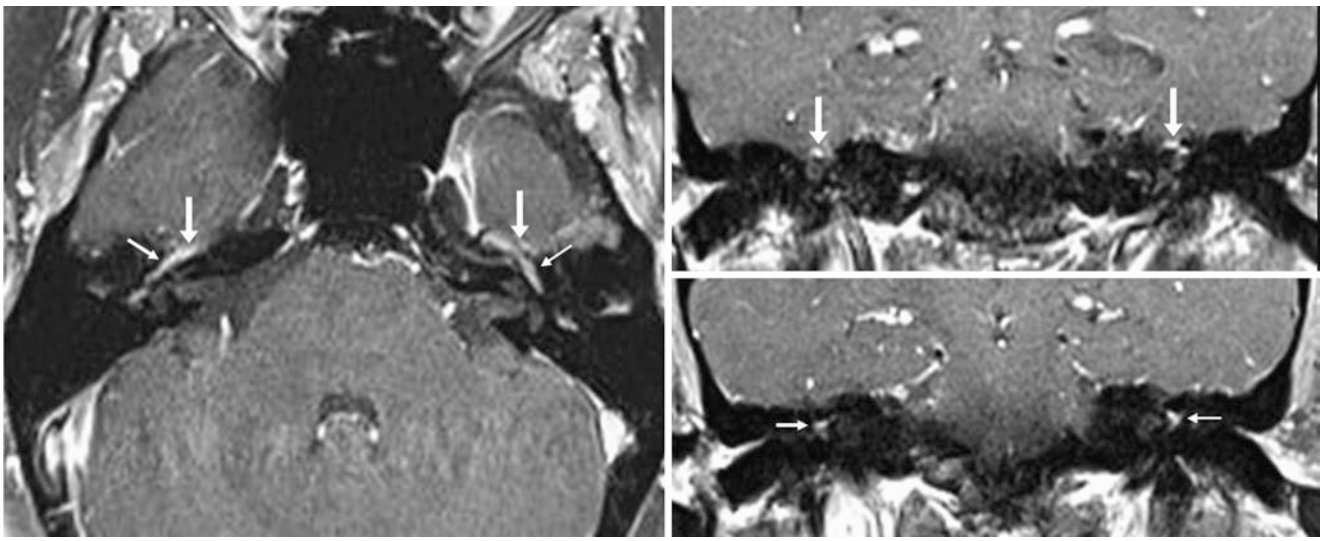

Fig. 5.4 A 38-year-old patient with an orbit protocol MRI at 3 T. Postcontrast FS SET1WIs in the axial (*left*) and coronal (*right*) planes depict avid, bilateral normal enhancement of the geniculate ganglia (*arrows*), the right greater than the left, as well as bilateral enhancement of the proximal portions of the horizonal/tympanic segments of CN7 (*thin arrows*)

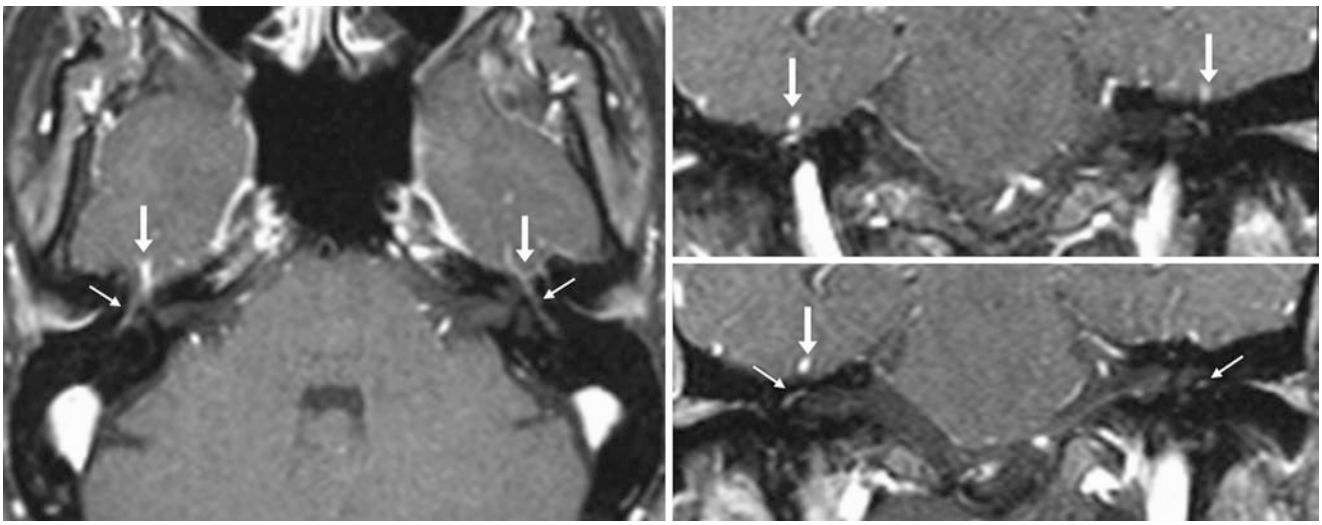

Fig. 5.5 A 46-year-old patient with a negative 1.5 T MRI IAC protocol for vertigo. Axial (*left*) and coronal (*right*) postcontrast FS SET1WIs demonstrate asymmetric, avid enhancement of the right geniculate ganglion (*arrows*) which is only mild on the left (*thin arrows*). There is also greater enhancement of the right horizontal segment of CN7 (*thin arrows*)

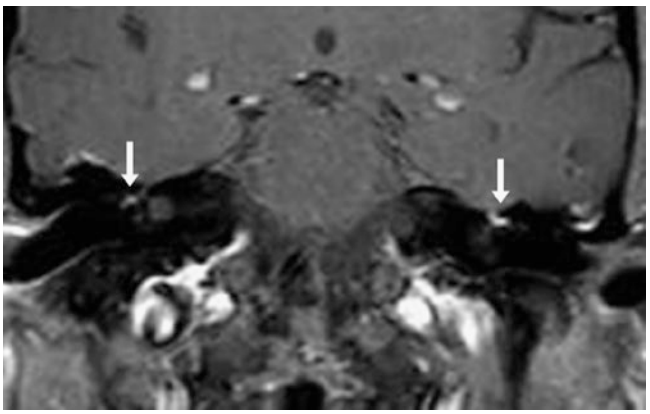

Fig. 5.6 A 62-year-old patient with a negative 3 T MRI for metastases. A coronal postcontrast FS SET1WI shows avid, asymmetric enhancement of the left geniculate ganglion (*arrows*); the enhancement on the right side is much milder

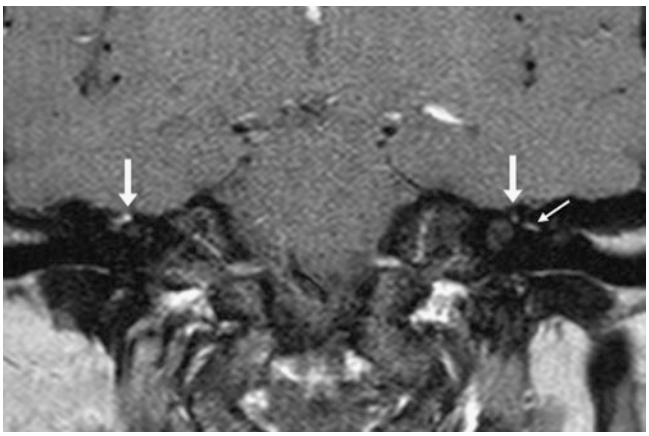

Fig. 5.7 A 60-year-old patient with a negative 1.5 T MRI for tinnitus. A coronal postcontrast FS SET1WI shows asymmetric, mild right geniculate ganglion enhancement (*arrows*) with left horizontal segment enhancement (*thin arrow*)

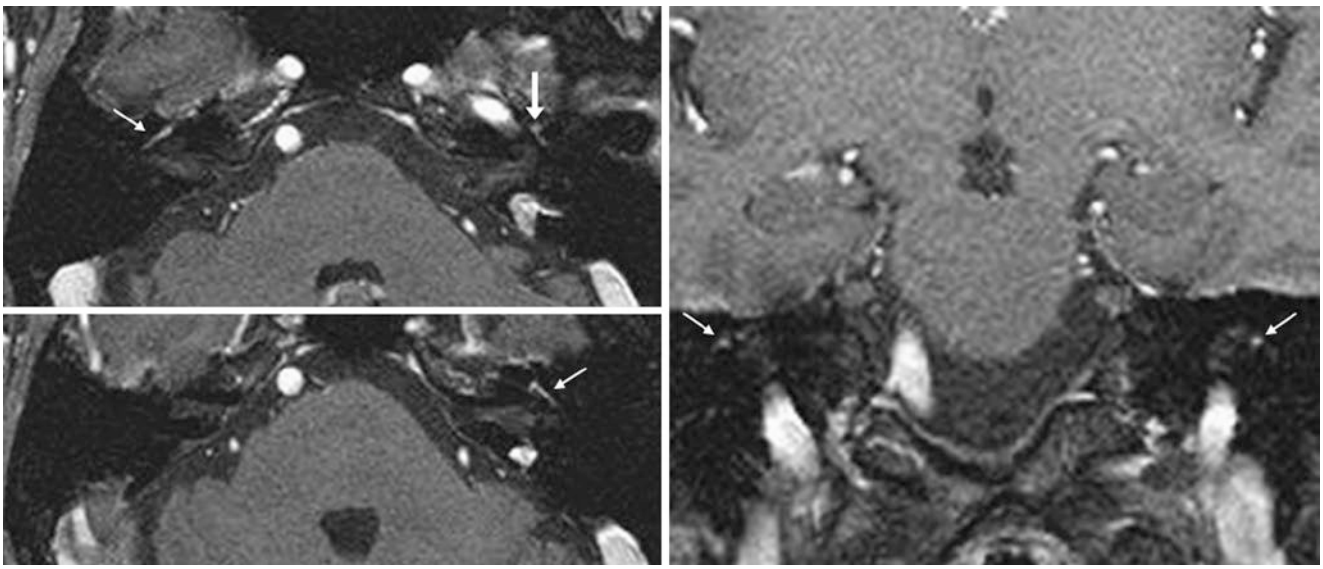

Fig. 5.8 A 41-year-old patient with an orbit protocol MRI at 1.5 T. Postcontrast FS spoiled GET1WIs (T1FFE) in the axial (*left images*) and coronal (*right*) planes depict normal mild enhancement of the left geniculate ganglion (*arrows*) as well as enhancement of the proximal portions of the left horizonal/tympanic segment of CN7 (*thin arrows*)

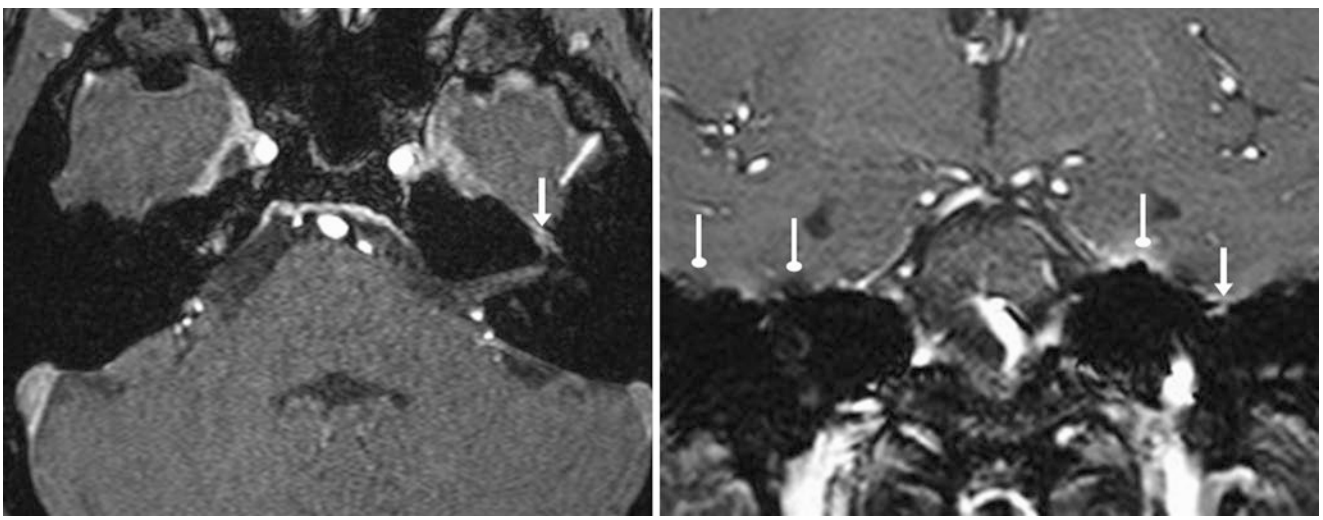

Fig. 5.9 A 55-year-old patient with a negative 1.5 T MRI for dizziness. On axial (*left*) and coronal (*right*) postcontrast FS spoiled GET1WI (T1FFE) there is mild left geniculate ganglion enhancement (*arrows*). Note that on this sequence there are more regions of susceptibility artifact (*circle tip arrows*) as compared with SET1WI. Such susceptibility artifacts (often from aerated mastoid air cells or petrous apices) may obscure regions of CN7 enhancement on GET1WI

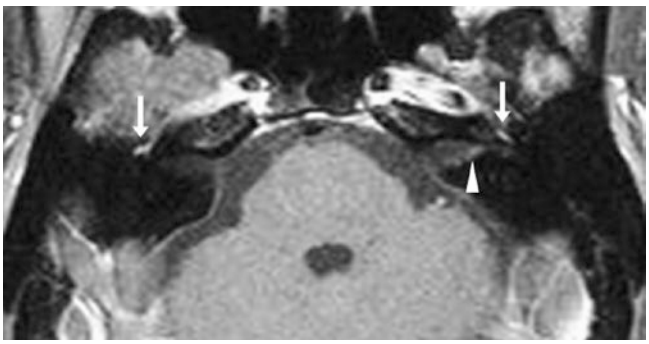

Fig. 5.10 A 55-year-old patient with a negative 1.5 T MRI for hearing loss. On postcontrast axial FS SET1WI there is mild normal bilateral geniculate ganglion enhancement (*arrows*), with incidental normal faint perineural enhancement (*arrowhead*) within the left IAC

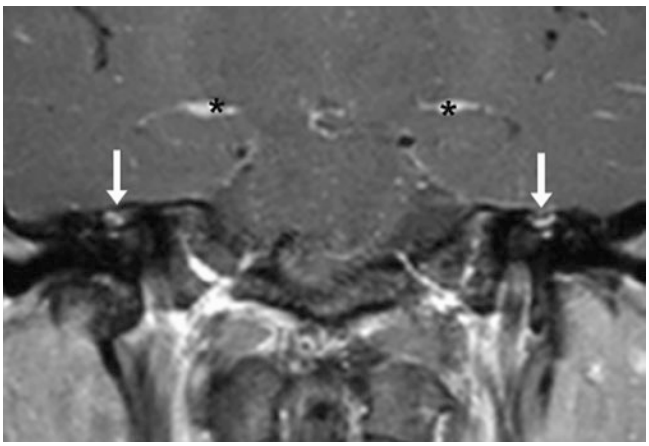

Fig. 5.11 A 31-year-old patient. A negative 1.5 T MRI postcontrast coronal FS SET1WI illustrates normal enhancement of both geniculate ganglia (*arrows*). Compare the degree of enhancement to the choroid plexi (*)

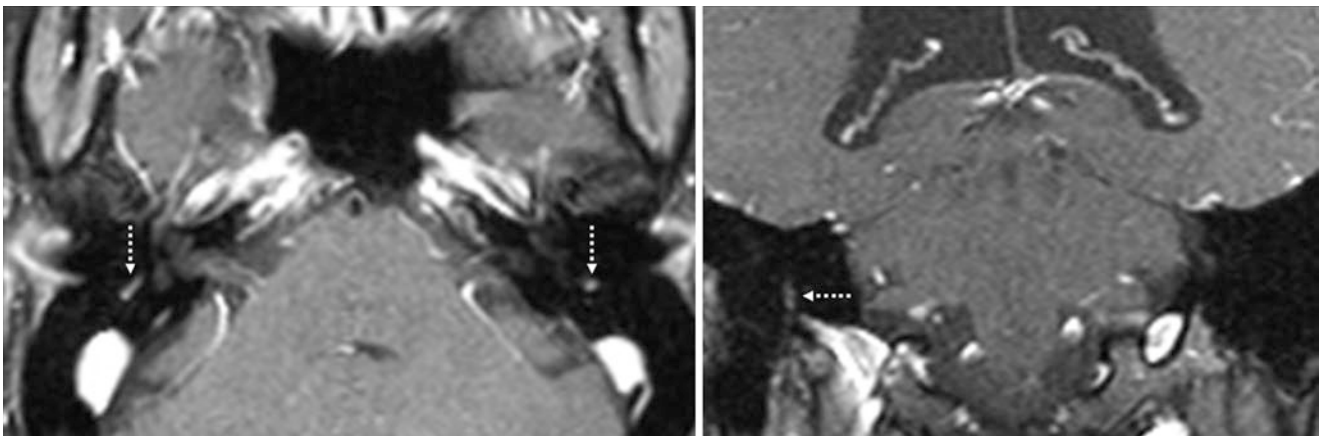

Fig. 5.12 A 46-year-old patient with a negative 1.5 T MRI IAC protocol for vertigo. Axial (*left*) postcontrast FS SET1WIs demonstrate bilateral, symmetric, avid enhancement of the descending (mastoid) segments of CN7 (*arrows*). On a coronal image (*right*), enhancement of the right descending segment is depicted

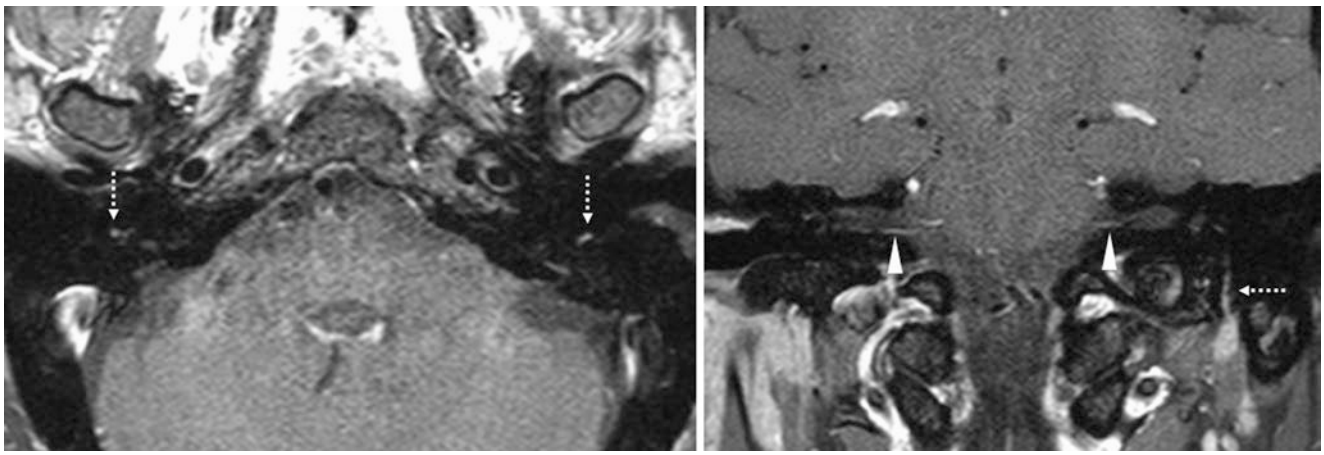

Fig. 5.13 A 60-year-old with a negative 1.5 T MRI for tinnitus. Axial (*left*) and coronal (*right*) postcontrast FS SET1WIs depict mild bilateral enhancement of the descending segments of CN7 (*dotted arrows*), which is greater on the left side. Also, note mild enhancement within the IAC bilaterally (*arrowheads*), likely from the AICAs looping into the IACs

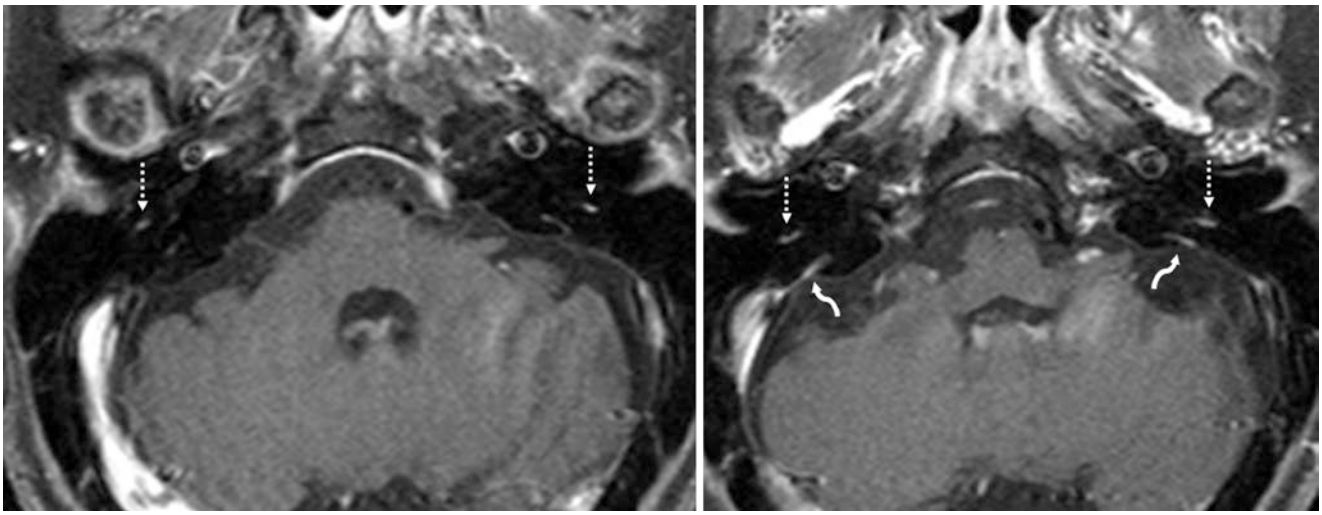

Fig. 5.14 A 55-year-old patient with a 1.5 T MRI for *chronic* hearing loss. There is normal bilateral enhancement of the descending (mastoid) segments of CN7 (*dotted arrows*). Also, note enhancement of both vestibular aqueducts (*curved arrows*), a finding that has debatedly been associated with *sudden* sensorineural hearing loss and is probably incidental in this case

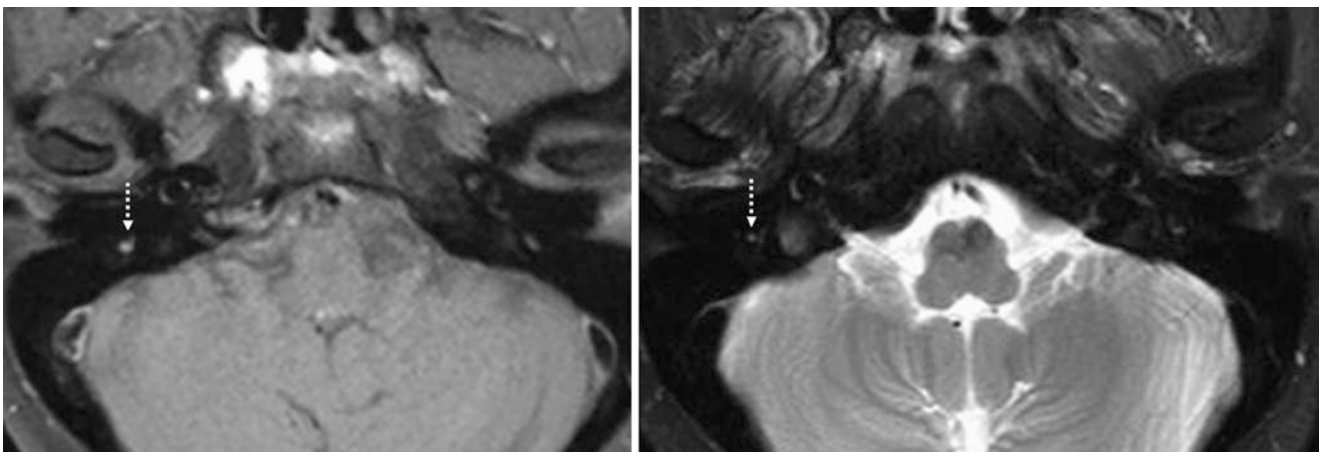

Fig. 5.15 A 58-year-old patient with a negative 3 T MRI IAC protocol for dizziness. An axial postcontrast FS SET1WI (*left*) depicts mild enhancement of the right descending (mastoid) segment of CN7 (*dotted arrows*). On a FS T2WI (*right*), there is only a faint signal with no edema or enlargement of the nerve, further confirming that this appearance is normal

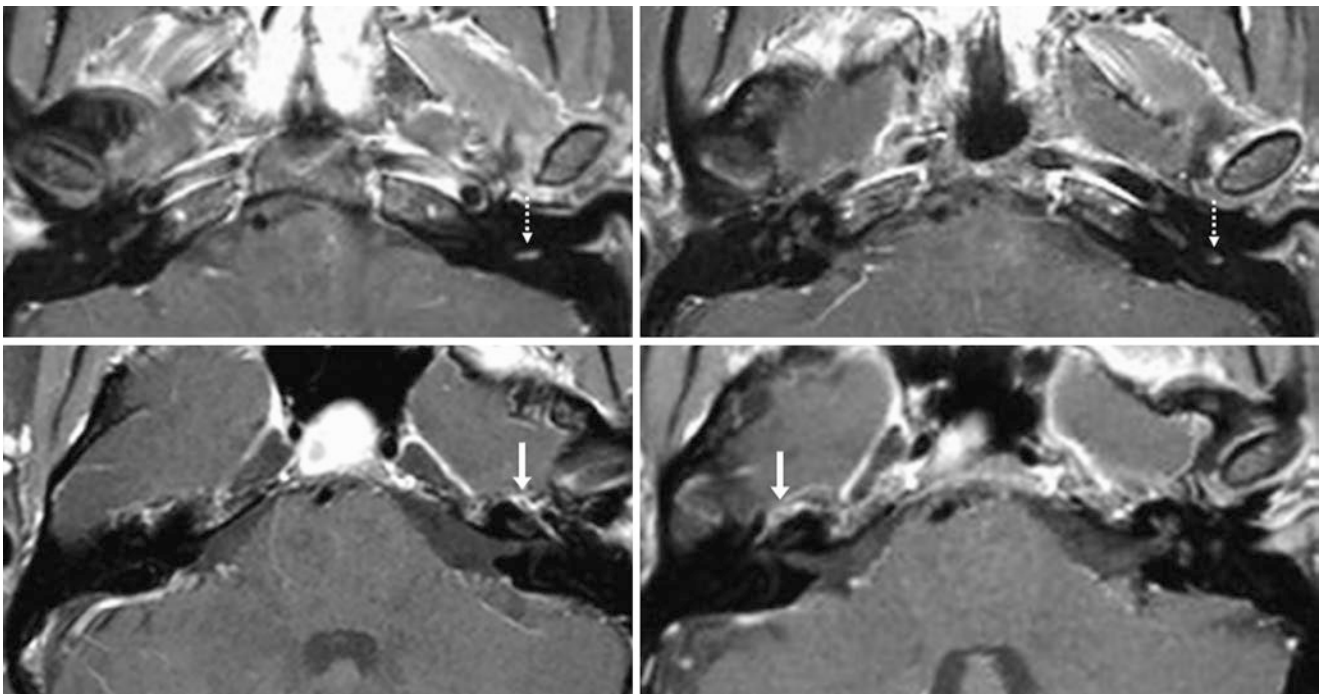

Fig. 5.16 A 31-year-old patient with a negative 3 T MRI for facial pain. There is asymmetric enhancement of only the left descending CN7 segment (*dotted arrows*) on axial FS SET1WIs (*top row*); the fat suppression was incomplete. On axial images more superiorly (*bottom row*), note normal, bilateral enhancement of the geniculate ganglia (*arrows*)

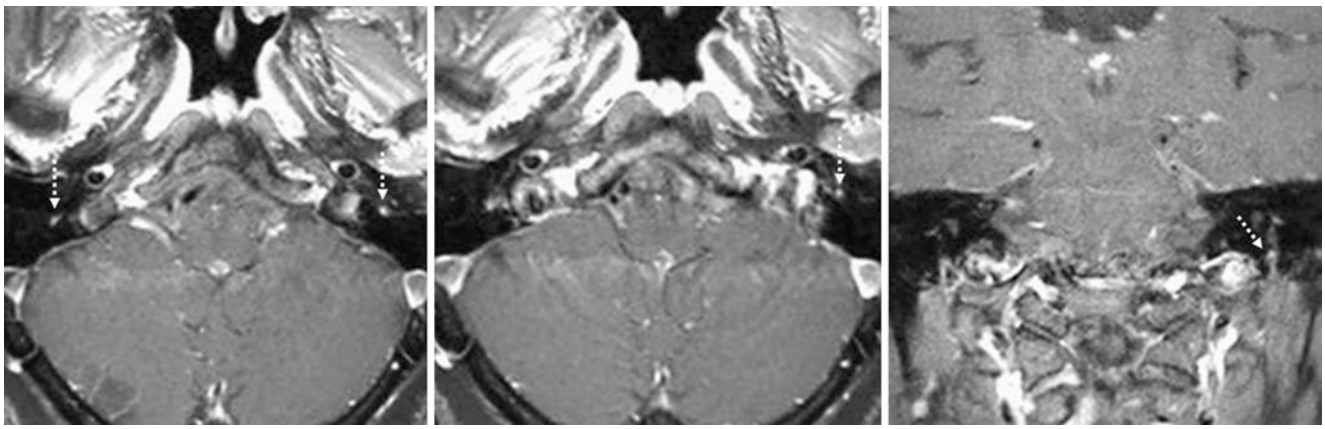

Fig. 5.17 A 79-year-old patient with a negative 3 T MRI IAC protocol for tinnitus. Axial postcontrast FS SET1WIs (*left and middle*) show bilateral but asymmetric enhancement of the descending (mastoid) segment of CN7 (*dotted arrows*), the left being greater than the right. On a coronal image (*right*), the enhancement is seen to stop just as CN7 exits the skull base

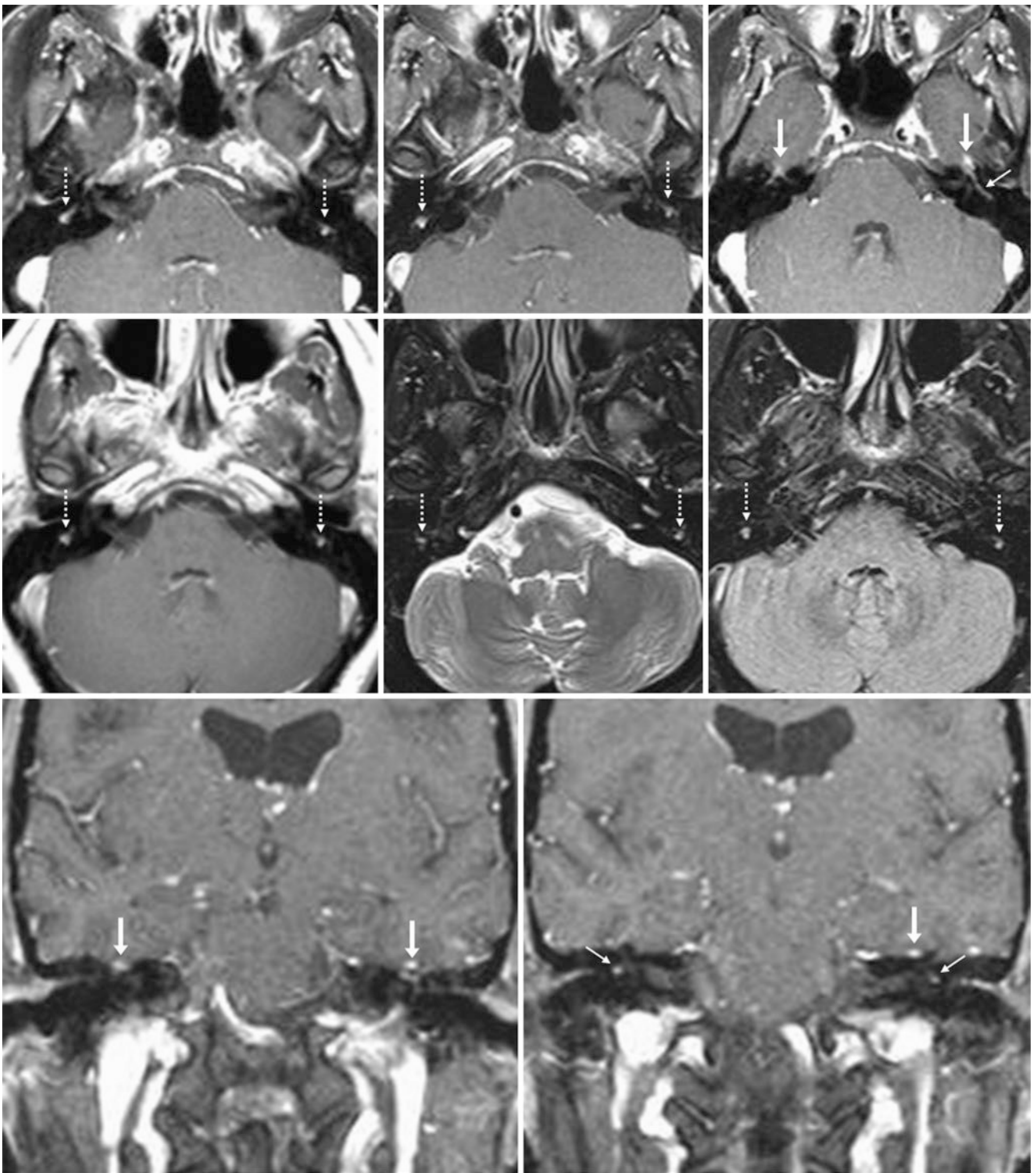

Fig. 5.18 Normal, multisegment CN7 enhancement in a patient with only orbital symptoms. A 50-year-old patient with a negative 1.5 T MRI orbit protocol for eye pain. *Top row*: axial postcontrast FS SET1WIs (*left*) show enhancement of both descending segments of CN7 (*dotted arrows*) unchanged 6 months later (*middle and right*). Also, note normal enhancement of both geniculate ganglia (*arrows*) and of the left tympanic segment (*thin arrow*). *Middle row*: on the initial postcontrast non–FS SEWI (*left*), enhancement was also visualized within the descending (mastoid) segments (*dotted arrows*) but with mild hyperintensity on T2WI (*middle*) and FLAIR (*right*). The lack of enhancement on that examination within the distal IAC (along with a lack of symptoms) confirmed that this enhancement was normal. *Bottom row*: Coronal postcontrast FS T1WIs further demonstrate these findings

5.1 Vestibular Aqueduct Enhancement

Vestibular aqueduct (VA) *enhancement* can be a normal finding in 20–30 % of asymptomatic patients on MRIs that cover the temporal bones (IACs). Some studies have noted that this enhancement may occur with a higher frequency in patients with sudden sensorineural hearing loss, which has not been definitively proved. Interestingly, many of these patients may also have VA enhancement on the opposite side. This should not be confused with the unrelated most common cause of pediatric sensorineural hearing loss, that is, VA enlargement, typically defined as greater than 1.5–2 mm diameter of the VA (on computed tomography) (Figs. 5.19, 5.20, 5.21, 5.22, 5.23, 5.24, 5.25, 5.26, 5.27, 5.28, 5.29, and 5.30).

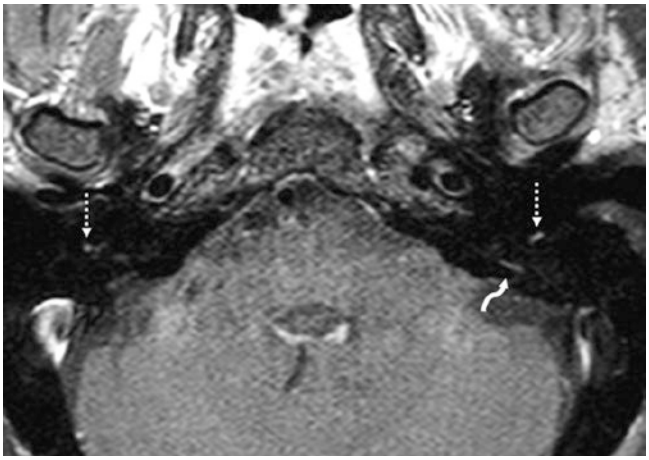

Fig. 5.19 A 31-year-old patient with dizziness; a 3 T MRI axial postcontrast FS SET1WI was negative, with faint left VA enhancement (*curved arrows*). Note CN7 enhancement (*dotted arrows*)

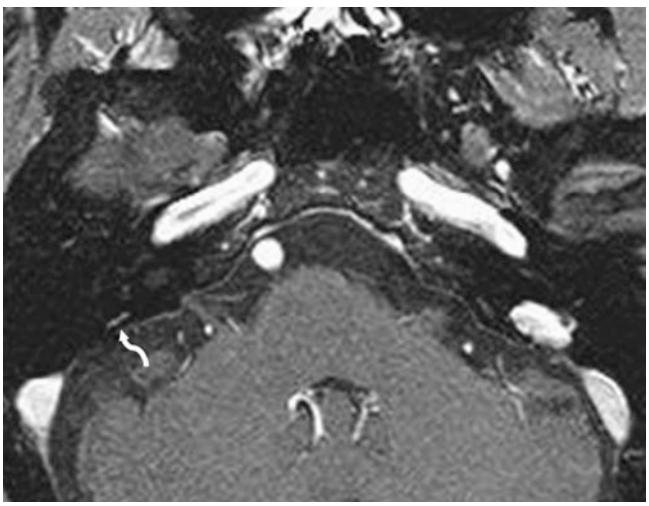

Fig. 5.20 A 53-year-old with facial pain; an otherwise negative 1.5 T MRI axial postcontrast FS SET1WI showed mild right VA enhancement (*curved arrows*)

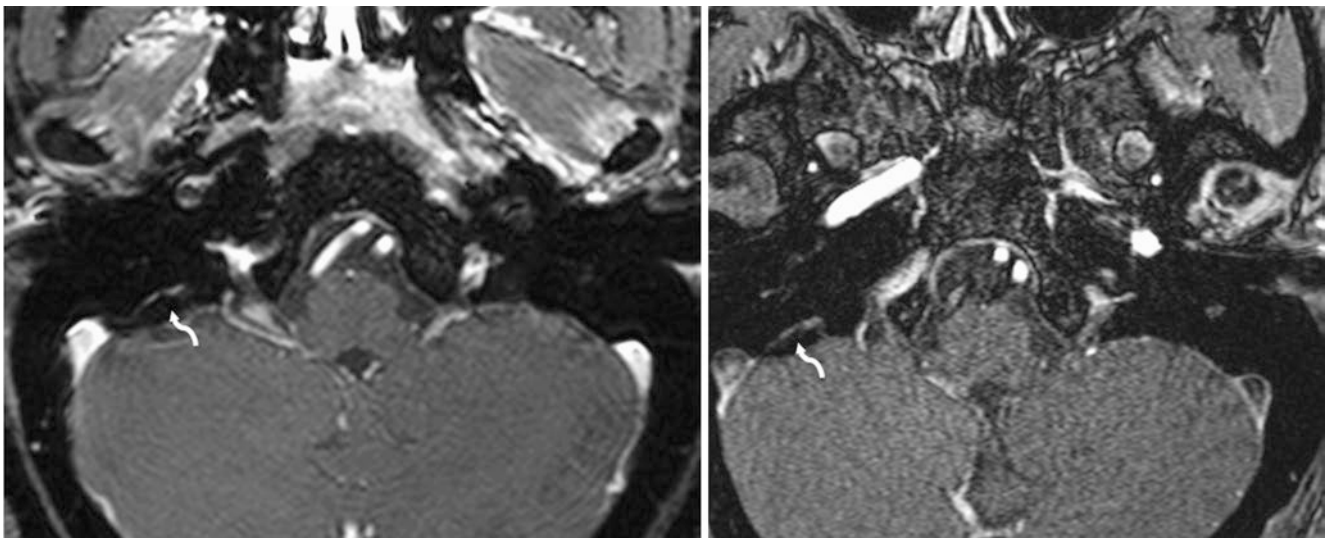

Fig. 5.21 A 55-year-old patient with a negative 3 T MRI for dizziness. On a 0.5-mm thickness postcontrast FS spoiled GET1WI (T1FFE, *left*) and on a postcontrast 3D TOF MRA source image (also a gradient echo image, *right*), there is right VA enhancement (*curved arrows*). Note a greater degree of susceptibility artifact on such gradient echo images

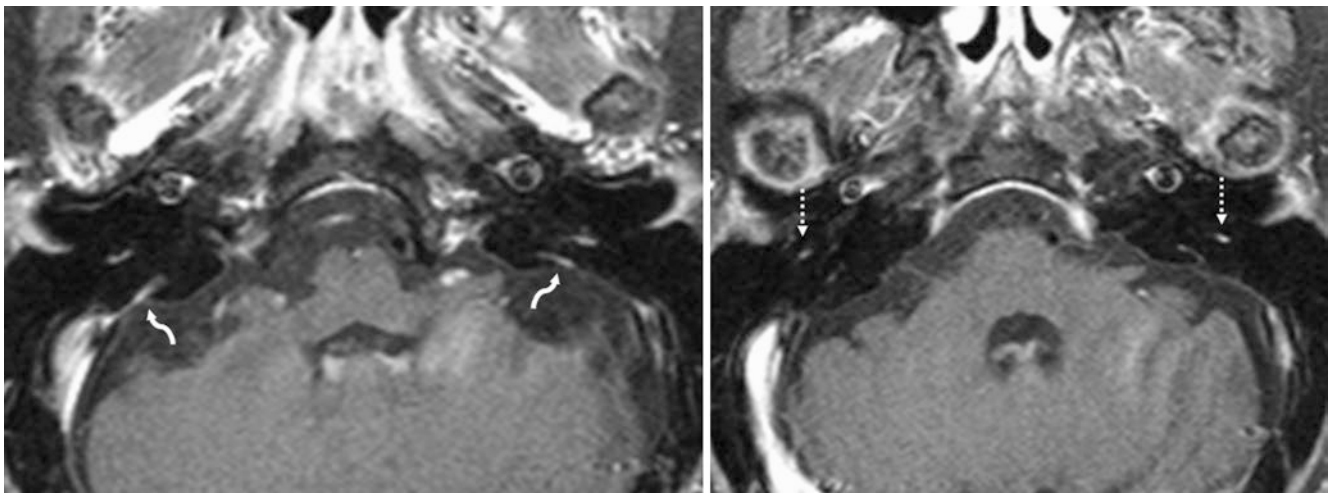

Fig. 5.22 Another 55 year old (different patient than the previous one) with a negative 1.5 T MRI for hearing loss. There is bilateral mild to moderate VA enhancement (*curved arrows*). Also, note enhancement of the descending (mastoid) segments of CN7 bilaterally (*dotted arrows*)

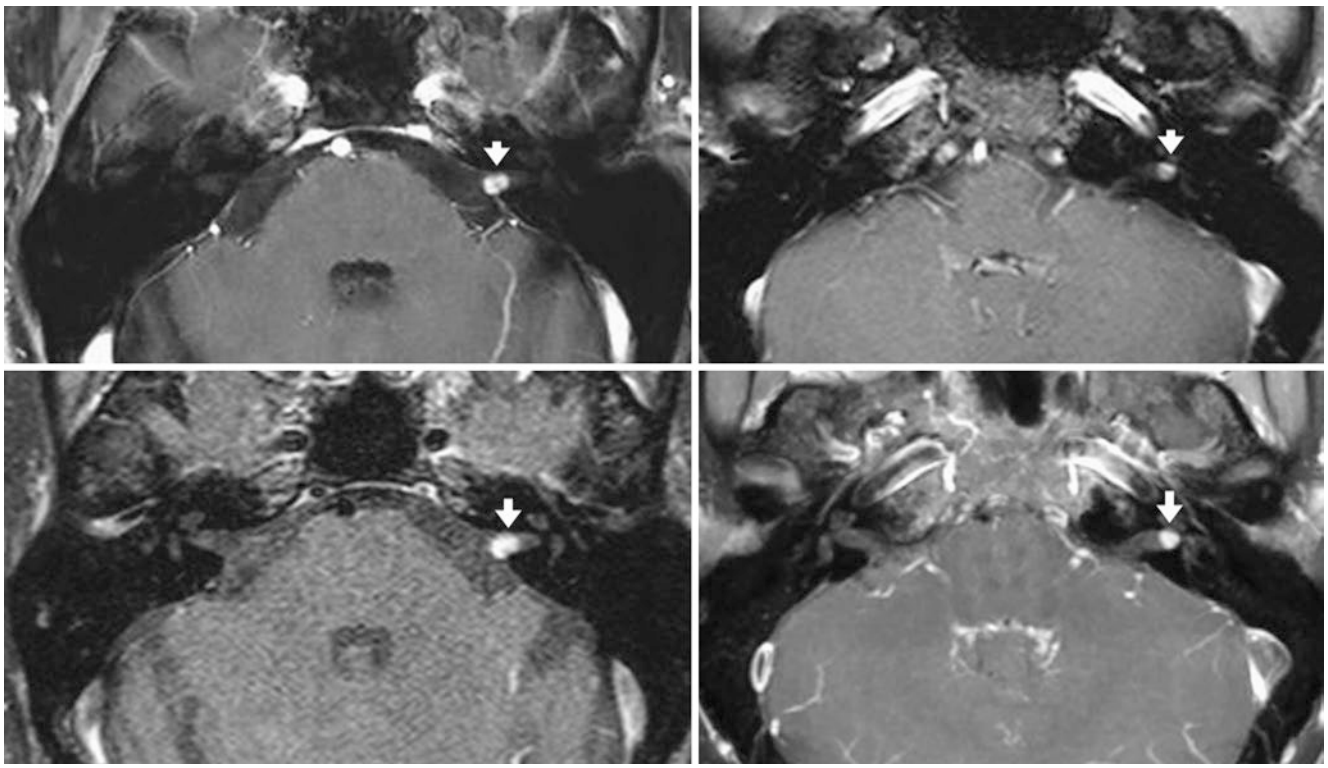

Fig. 5.23 Comparison case of schwannoma and FS SET1WI versus GET1WI. A 37-year-old patient with vertigo had an enhancing lesion (*wide arrows*) of the left porus acousticus (opening of the IAC), as demonstrated on 1.5 T 2-mm (*top left*) and 4-mm thick (*top right*) postcontrast FS spoiled GET1WI (T1FFE) and 2-mm (*bottom left*) and 4-mm thick (*bottom right*) FS SET1WI. Note the greater degree of susceptibility artifact on the GET1WI as compared to SET1WI, making it more difficult to visualize the tumor at the greater 4-mm thickness on GET1WI

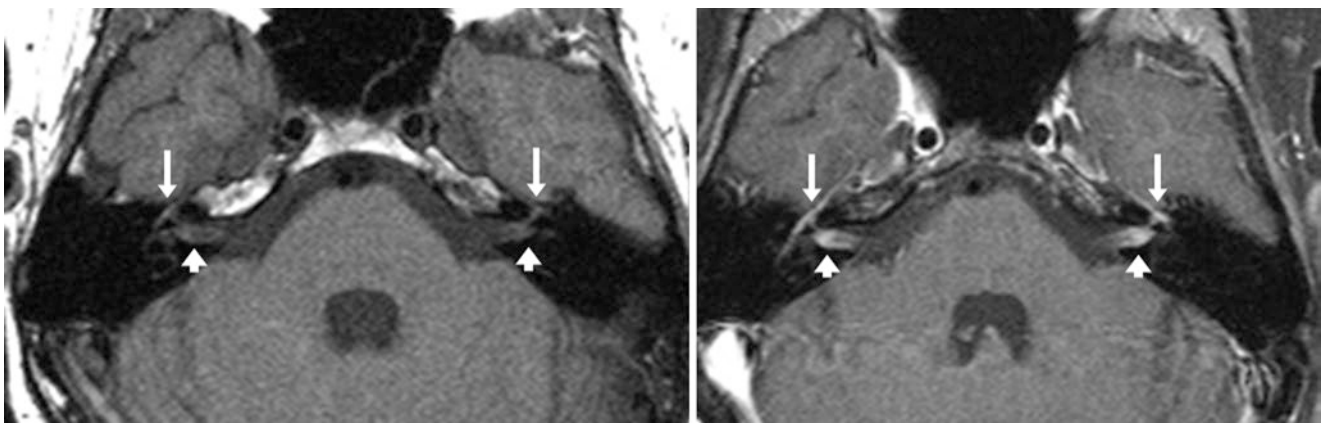

Fig. 5.24 Comparison case of leukemic infiltrates. An 18-year-old patient with leukemia had bilateral enhancing lesions (*wide arrows*) within the distal portions of the IACs, as shown on 1.5 T 3-mm precontrast non–FS (*left*) and postcontrast FS (*right*) SET1WIs. Note normal enhancement of the geniculate ganglia as well (*arrows*)

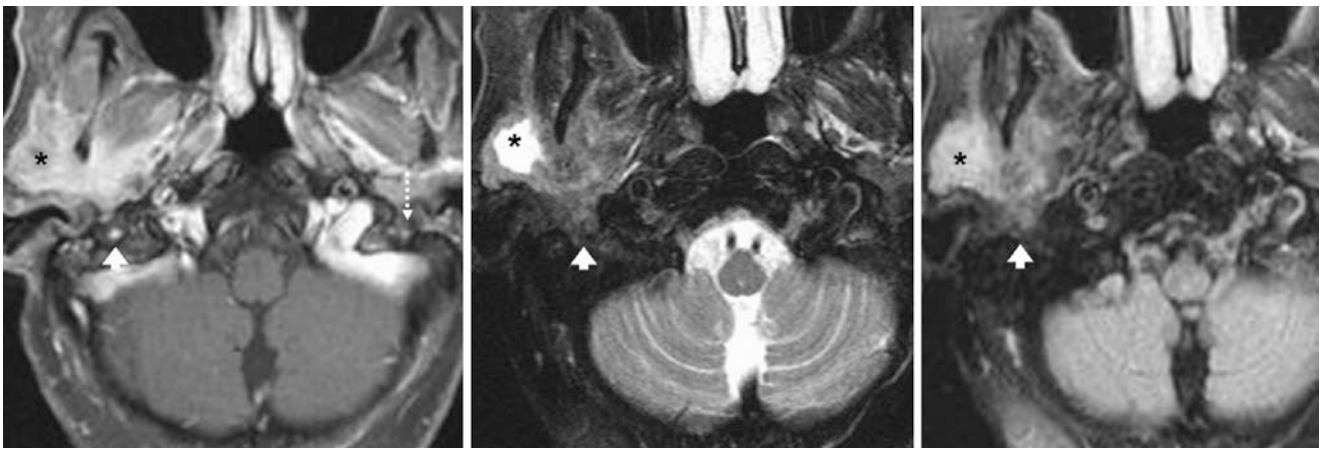

Fig. 5.25 Comparison case of parotid squamous cell cancer. A 75-year-old patient with a parotid malignancy (*) also had mild enlargement and enhancement of the right descending segment of CN7 (*wide arrows*) on 1.5 T 3-mm postcontrast FS SET1WI (*left*), which was more prominent than the same contralateral segment (*dotted arrows*). A lack of edema on T2WI (*middle*) or FLAIR (*right*) argues against but does not definitively exclude perineural invasion by tumor

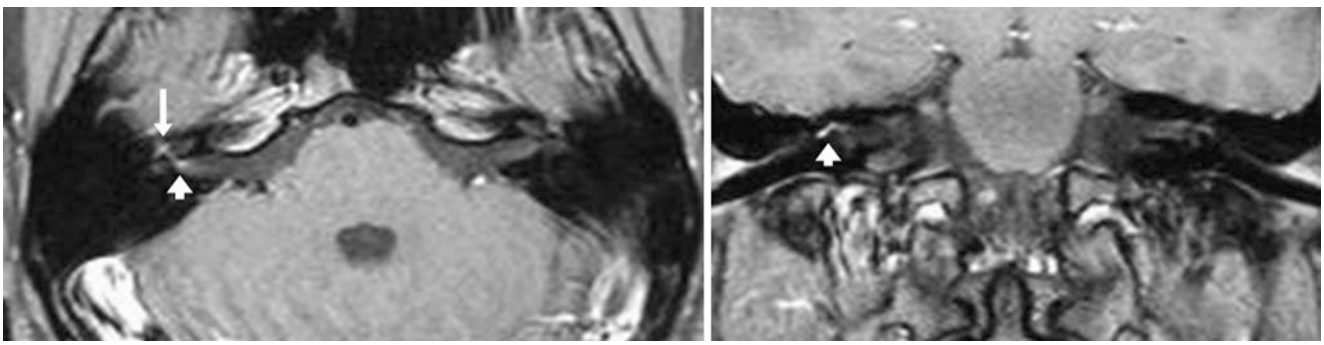

Fig. 5.26 Comparison case of Bell palsy. A 20-year-old patient with right facial weakness had abnormal enhancement of the fundus of the right IAC (*wide arrows*), as shown on 1.5 T 3-mm postcontrast FS SET1WIs in axial (*left*) and coronal (*right*) planes. Note the enhancement of the right geniculate ganglion as well (*arrow*), which can be normal

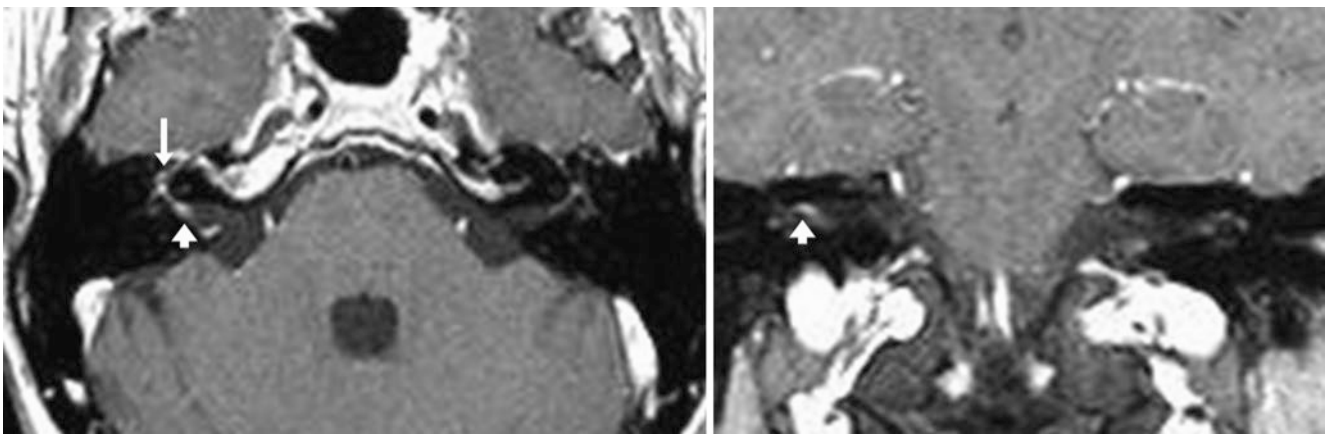

Fig. 5.27 Comparison case of Bell palsy. A 53-year-old patient with right facial weakness had abnormal enhancement of the fundus of the right IAC (*wide arrows*), as shown on 1.5 T 3-mm postcontrast non–FS SET1WIs in axial (*left*) and coronal (*right*) planes. Note the enhancement of the right geniculate ganglion as well (*arrow*), which can be normal

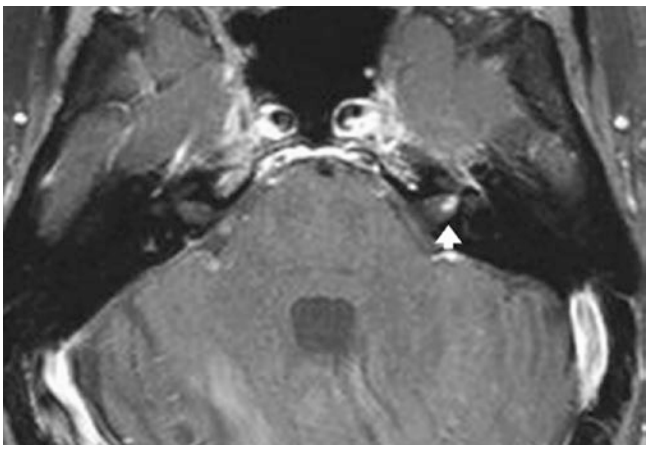

Fig. 5.28 Comparison case of Bell palsy. A 48-year-old with left facial weakness and enhancement of the distal IAC (*wide arrow*) on a 3 T postcontrast FS SET1WI

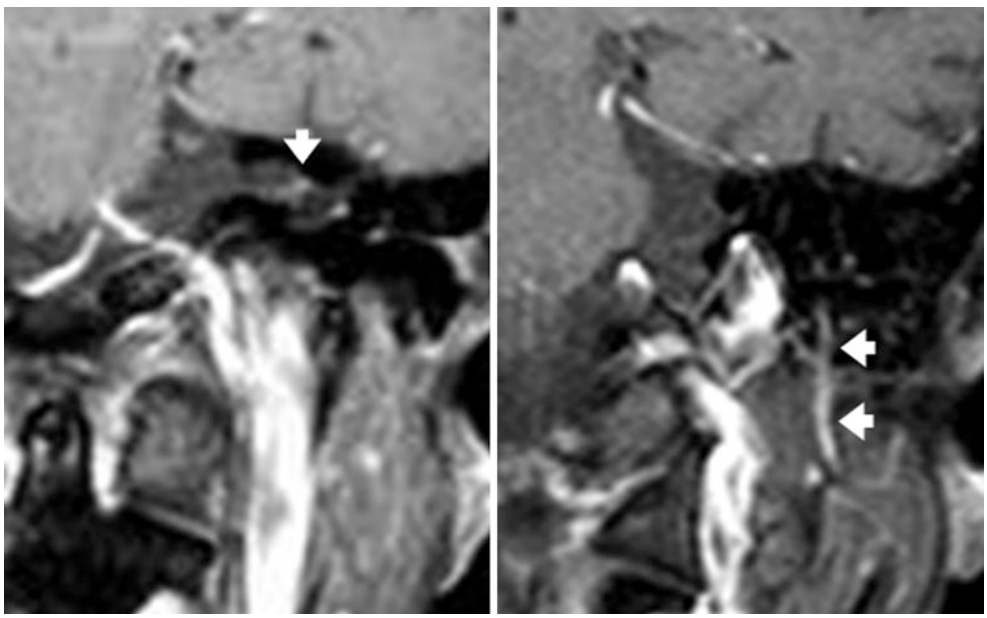

Fig. 5.29 Comparison case of Bell palsy. A 62-year-old with focal enhancement both at the IAC fundus and CN7 exit sites (*wide arrows*) on 3 T postcontrast coronal FS SET1WIs

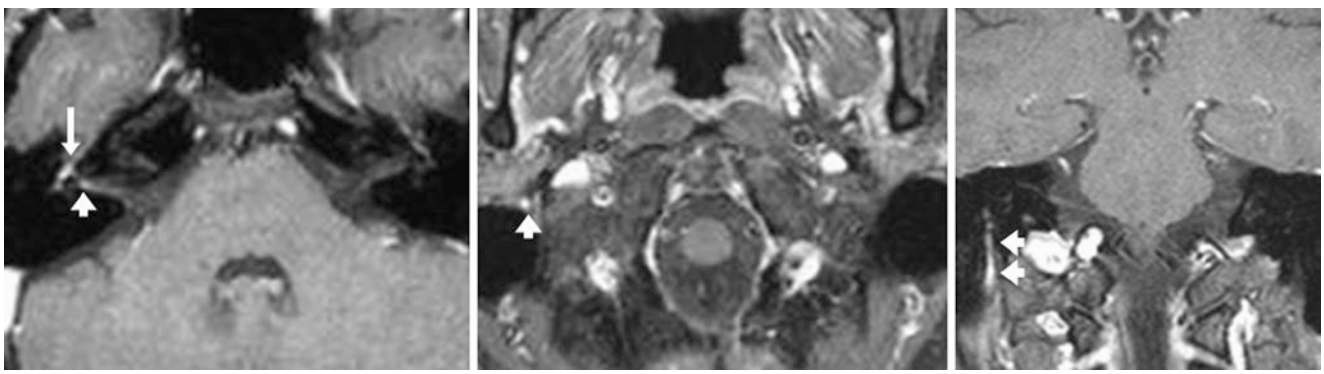

Fig. 5.30 Comparison case of Bell palsy. A 30-year-old with right facial weakness had enhancement of the fundus of the right IAC (*wide arrows*), as shown on 1.5 T 3-mm postcontrast axial FS SET1WIs (*left and middle*). Also, note right geniculate ganglion enhancement (*arrow*), which can be normal. On coronal images (*right*), CN7 enhances *below* where it has exited the stylomastoid foramen, which is also abnormal although less commonly seen

Suggested Reading

Brändle P, Satoretti-Schefer S, Böhmer A, Wichmann W, Fisch U. Correlation of MRI, clinical, and electroneuronographic findings in acute facial nerve palsy. Am J Otol. 1996;17:154–61.

Fitzgerald DC, Mark AS. Endolymphatic duct/sac enhancement on gadolinium magnetic resonance imaging of the inner ear: preliminary observations and case reports. Am J Otol. 1996;17:603–6.

Gebarski SS, Telian SA, Niparko JK. Enhancement along the normal facial nerve in the facial canal: MR imaging and anatomic correlation. Radiology. 1992;183:391–4.

Hong HS, Yi B-H, Cha J-G, Park SJ, Kim DH, Lee HK, Lee JD. Enhancement pattern of the normal facial nerve at 3.0 T temporal MRI. Br J Radiol. 2010;83:118–21.

Kinoshita T, Ishii K, Okitsu T, Okudera T, Ogawa T. Facial nerve palsy: evaluation by contrast-enhanced MR imaging. Clin Radiol. 2001;56:926–32.

Martin-Duverneuil N, Sola-Martínez MT, Miaux Y, Cognard C, Weil A, Mompoint D, Chiras J. Contrast enhancement of the facial nerve on MRI: normal or pathological? Neuroradiology. 1997;39:207–12.

Mowry S, Kirsch C. S127–Idiopathic facial nerve paralysis: analysis of 3 T MRI images. Otolaryngol Head Neck Surg. 2008;139(2 Suppl):119.

Naganawa S, Koshikawa T, Fukatsu H, Ishigaki T, Nakashima T, Ichinose N. Contrast-enhanced MR imaging of the endolymphatic sac in patients with sudden hearing loss. Eur Radiol. 2002;12:1 121–6.

Sartoretti-Schefer S, Brändle P, Wichmann W, Valavanis A. Intensity of MR contrast enhancement does not correspond to clinical and electroneurographic findings in acute inflammatory facial nerve palsy. Am J Neuroradiol. 1996;17:1229–36.

Sugiura M, Naganawa S, Ishida IM, Teranishi M, Nakata S, Yoshida T, Nakashima T. Vestibular aqueduct in sudden sensorineural hearing loss. J Laryngol Otol. 2008;122:887–92.

Sugiura M, Naganawa S, Nakashima T, Misawa H, Nakamura T. Magnetic resonance imaging of endolymphatic sac in acute low-tone sensorineural hearing loss without vertigo. J Otorhinolaryngol Relat Spec. 2003;65:254–60.

Sugita M, Sano M, Uchigata M, Aruga T, Matsuoka R. Facial nerve enhancement on gadolinium-DTPA in a case with neurosarcoidosis. Intern Med. 1997;36:825–8.

Tada Y, Aoyagi M, Tojima H, Inamura H, Saito O, Maeyama H, et al. Gd-DTPA enhanced MRI in Ramsay Hunt syndrome. Acta Otolaryngol Suppl. 1994;511:170–4.

Tien R, Dillon WP, Jackler RK. Contrast-enhanced MR imaging of the facial nerve in 11 patients with Bell's palsy. Am J Neuroradiol. 1990;11:735–41.

Vanzieleghem B, Lemmerling M, Carton D, Matthys E, Kunnen M. Lyme disease in a child presenting with bilateral facial nerve palsy: MRI findings and review of the literature. Neuroradiology. 1998;40:739–42.

Meckel Cave Prominence, Asymmetry, and Petrous Apex Cephaloceles

6

Meckel cave is the location of the gasserian ganglion of the *trigeminal cranial nerve V* (CNV), being situated in the medial portion of the middle cranial fossa and inferolateral to the cavernous sinus. Basically, the trigeminal fibers (using the sensory pathways as an example) from *V1* (ophthalmic), *V2* (maxillary), and *V3* (mandibular) combine in Meckel cave at the *gasserian ganglion* (also termed the *trigeminal ganglion* or *semilunar ganglion*). The nerves then pass through the porus trigeminus (the transit point between the middle cranial fossa into the posterior fossa) into the cisternal portion (prepontine cistern) to enter the brainstem at the *root entry zone* (REZ) and then to the appropriate nuclei.

The *mild prominence of Meckel cave* is a normal variation; the rates of this common occurrence are not well described but are increasingly encountered because of the increased use of neuroimaging, in particular MRI. This manifests as a cerebrospinal fluid (CSF) intensity bright signal that is bright on T2WI and suppresses on FLAIR. There may be mild peripheral enhancement after contrast administration caused by a *perivascular plexus;* the venous plexus surrounding the trigeminal ganglion may enhance (even asymmetrically), while a perineural plexus surrounding V2 or V3 peripherally may also enhance in a majority of patients. However, no enhancement should be seen surrounding the cisternal segment of the trigeminal nerve. Notably, after Meckel cave, V1 and V2 (arguably) are situated within the cavernous sinus, after which they exit through their corresponding foramina, while V3 immediately exits the skull base through the foramen ovale after the Meckel cave.

Thus, a differential exists regarding enlargement of the Meckel cave, whether symmetric or asymmetric, and regarding the degree of contrast enhancement. Disorders with an enlarged Meckel cave and nonenhancing T2-bright signal intensity may be seen with *petrous apex cephaloceles* (PACs, CSF-like signal intensity that may be symmetric in certain disorders), *arachnoid cysts* (often CSF-like signal intensity but asymmetric), or other diseases of the petrous apex, including *cholesterol granulomas* (T1-bright), *epidermoid cyst*, i.e., *cholesteatoma* (DWI-bright), or petrous apex effusions (usually have concomitant mastoiditis and are T2-bright). There is also a large differential for enhancing lesions in Meckel cave or the adjacent petrous apex or cavernous sinus that includes *meningioma, schwannoma, metastasis, pseudotumor,* and *aneurysm-pseudoaneurysm,* to name a few. If a mass is suspected, one should also assess the size and presence of expansion of the foramen ovale (transmits V3 through the skull base), although asymmetric enlargement of this foramen can also be a normal variant (in the Skull section of this text). Notably, PACs have been found incidentally, the majority of which are asymptomatic and appear as enlargement of the subarachnoid space (SAS) of Meckel cave extending into the petrous apex. These only present as a source of symptoms if there is compression of an adjacent structure such as a cranial nerve or if there is concomitant mastoiditis (Figs. 6.1, 6.2, 6.3, 6.4, 6.5, 6.6, 6.7, 6.8, 6.9, 6.10, 6.11, 6.12, 6.13, and 6.14).

A.M. McKinney, *Atlas of Normal Imaging Variations of the Brain, Skull, and Craniocervical Vasculature*,
DOI 10.1007/978-3-319-39790-0_6

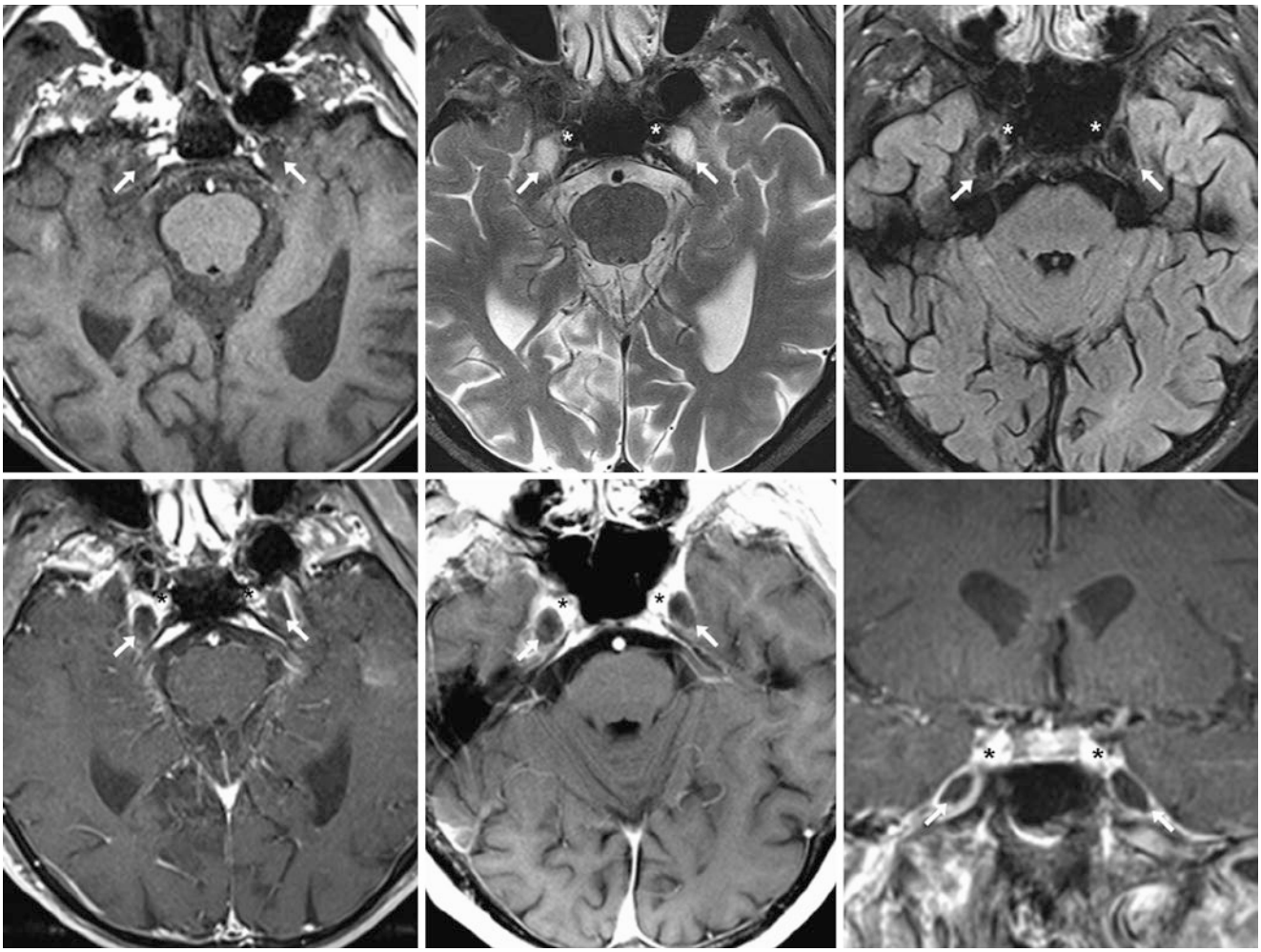

Fig. 6.1 A 78-year-old patient with normal but prominent Meckel caves (*arrows*) bilaterally on a 3 T MRI with axial T1WI (*top left*), T2WI (*top middle*), FLAIR (*top right*), and postcontrast axial fat suppressed T1WI (*bottom left*) as well as non–fat suppressed axial (*bottom middle*) and coronal (*bottom right*) T1WIs. Note that, on postcontrast T1WIs the trigeminal ganglion appears as a "filling defect." The ICAs are visualized anteromedially and superiorly (*)

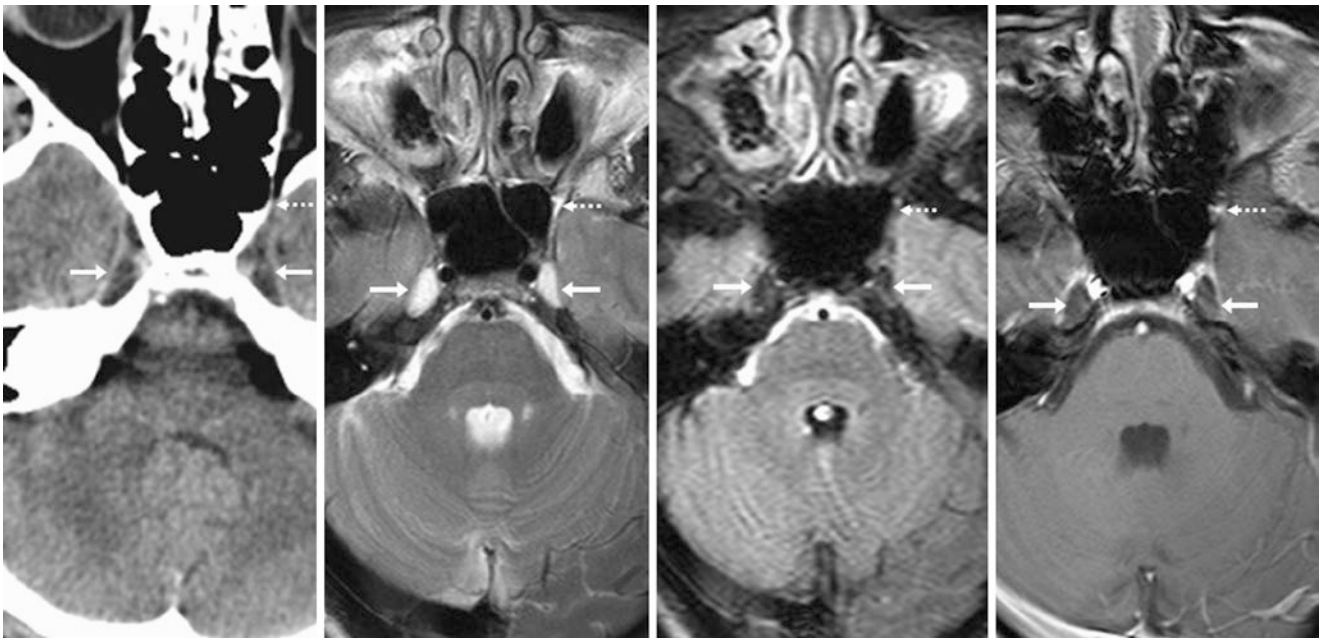

Fig. 6.2 A 57-year-old patient with a non-enhanced CT (NECT) (*left*) and 3 T MRI axial T2WI (*left middle*), FLAIR (*right middle*), and post-contrast T1WI (*right*) that demonstrate mildly prominent subarachnoid spaces in Meckel caves bilaterally surrounding the trigeminal ganglia (*arrows*). Note that the signal intensity follows the CSF on all sequences. The foramen rotundum (*dotted arrows*), transmitting V2, is visualized on the left side

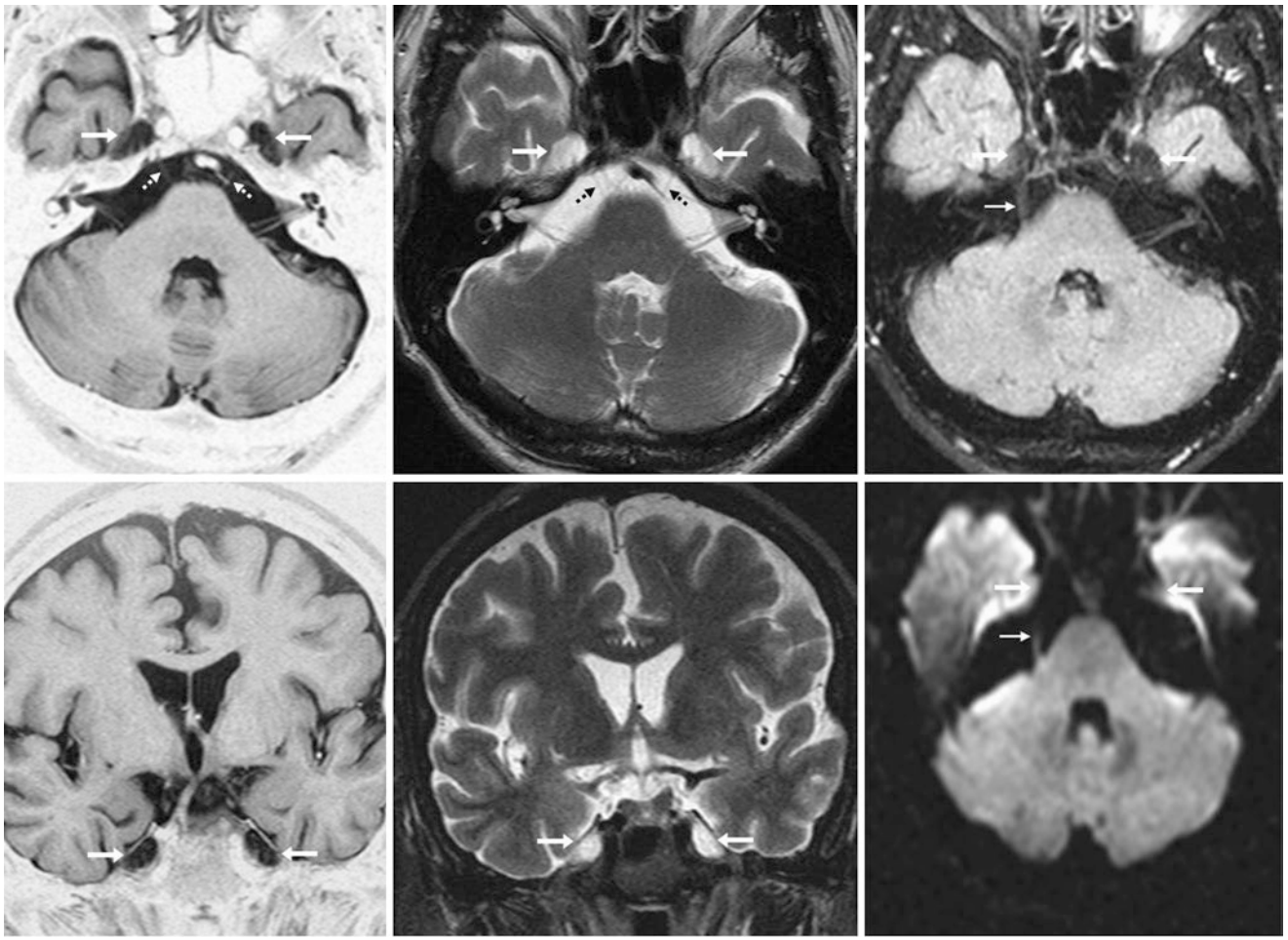

Fig. 6.3 A 69-year-old patient with moderately prominent Meckel caves (*arrows*) bilaterally on a 1.5 T MRI with axial T1WI-IR (*top left*), T2WI (*top middle*), FLAIR (*top right*), coronal T1WI-IR (*bottom left*), T2WI (*bottom middle*), and axial DWI (*bottom right*). Note the cisternal courses of the right cranial nerve V (*thin arrows*) and the bilateral cranial nerve VI (*dotted arrows*). On DWI, Meckel caves are usually dark due to CSF, but in this patient they are mildly heterogeneous as a result of artifact; this is probably from a combination of arterial pulsation (from the internal carotid arteries) and gas from the sphenoid sinus

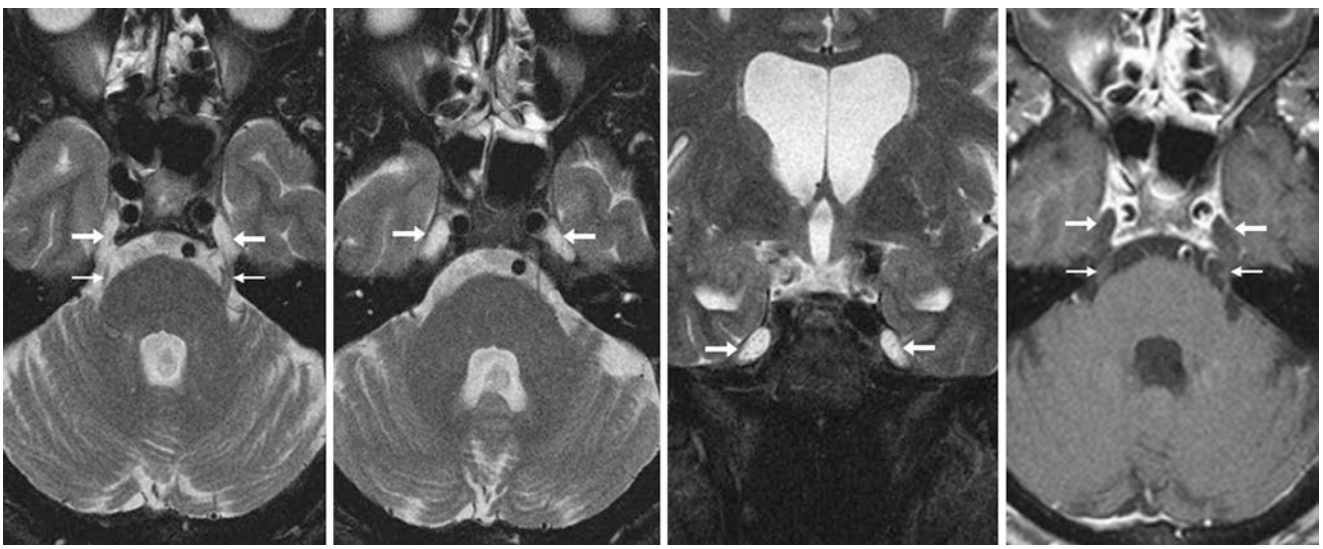

Fig. 6.4 A 62-year-old patient with migraines presented for MRI (negative). Axial T2WIs (*left and left middle*) demonstrate mildly prominent subarachnoid spaces extending into Meckel caves bilaterally (*arrows*). These appear normal on coronal T2WI (*right middle*) and postcontrast T1WI (*right*). They should not be mistaken for arachnoid cysts or petrous apex cephaloceles, since there is no mass effect and they do not extend into the petrous apices

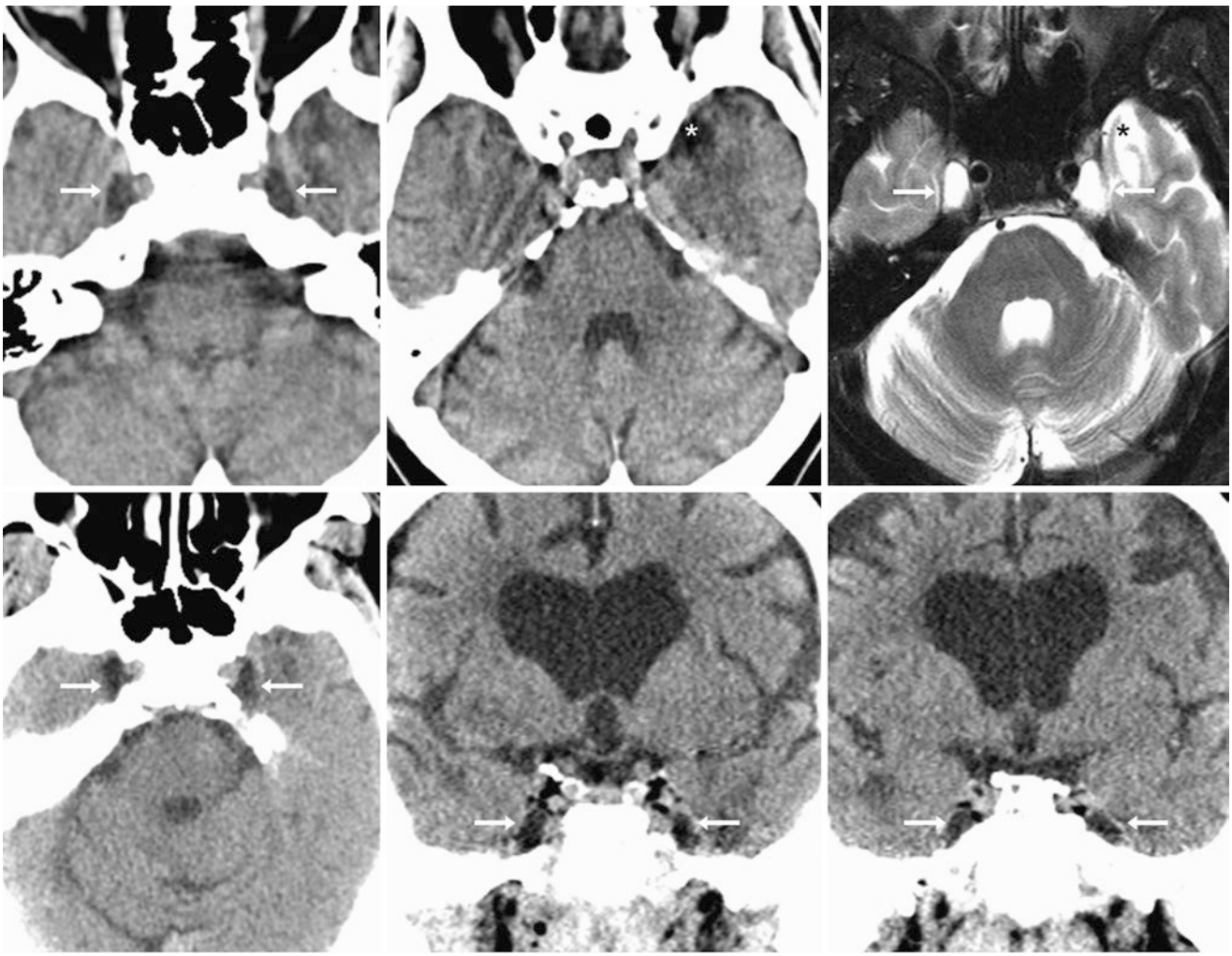

Fig. 6.5 A 69-year-old patient with trauma; there are moderately prominent Meckel caves (*arrows*) bilaterally on axial NECT (*top left and top middle*). Note the left anterior temporal encephalomalacia (*). On a 1.5 T MRI at that time with T2WI (*top right*), these are confirmed to be Meckel caves. A repeat NECT 10 year later (*bottom left*) with coronal reconstructions (*bottom middle and bottom right*) demonstrated no significant change in their size

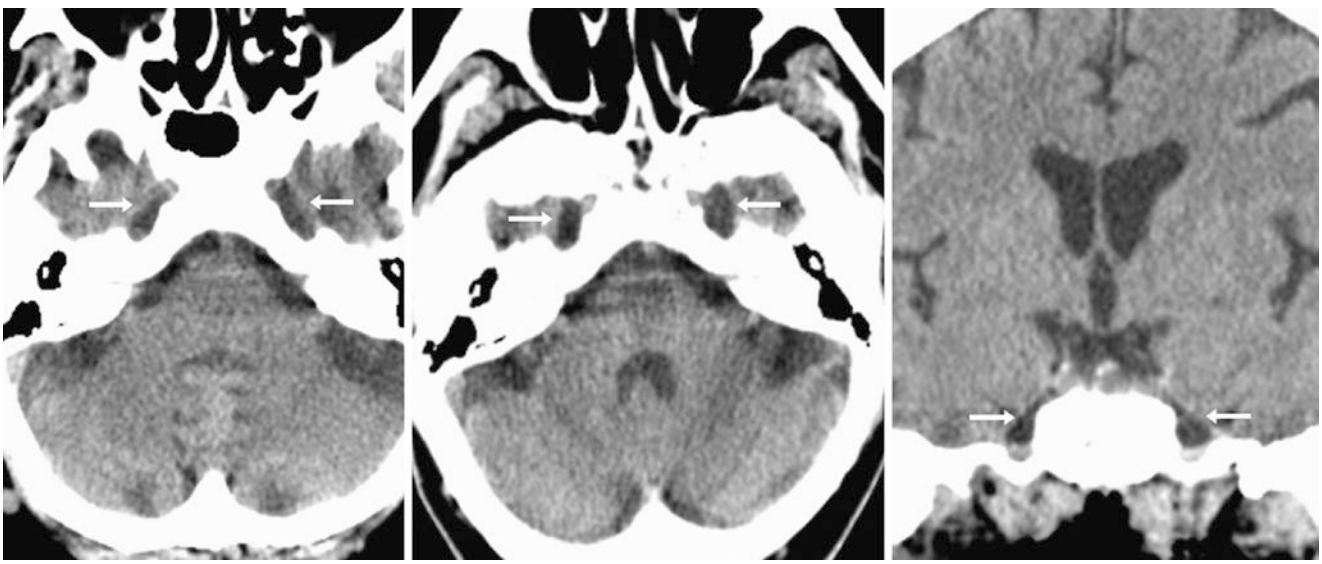

Fig. 6.6 A 55-year-old patient with headaches. There are bilateral moderately prominent Meckel caves (*arrows*) on axial NECT (*left*), which were unchanged 3 years later (*middle*). Their appearance is also shown on coronal reformats (*right*)

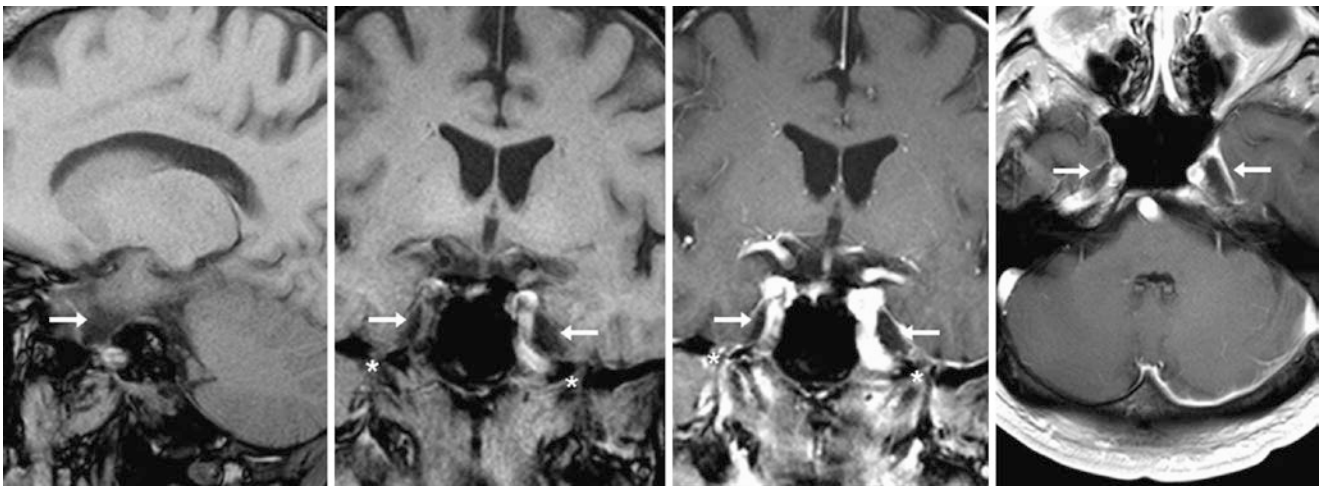

Fig. 6.7 A 56-year-old patient with 3 T MRI sagittal T1WI (*left*) of an asymmetric left Meckel cave (*arrows*), on coronal pre- (*left middle*) and postcontrast (*right middle*) T1WI and on axial T1WI (*right*). Note the foramina of ovale (*), which transmit V3. This could be confused with a cephalocele, but note that it does not extend below the skull base

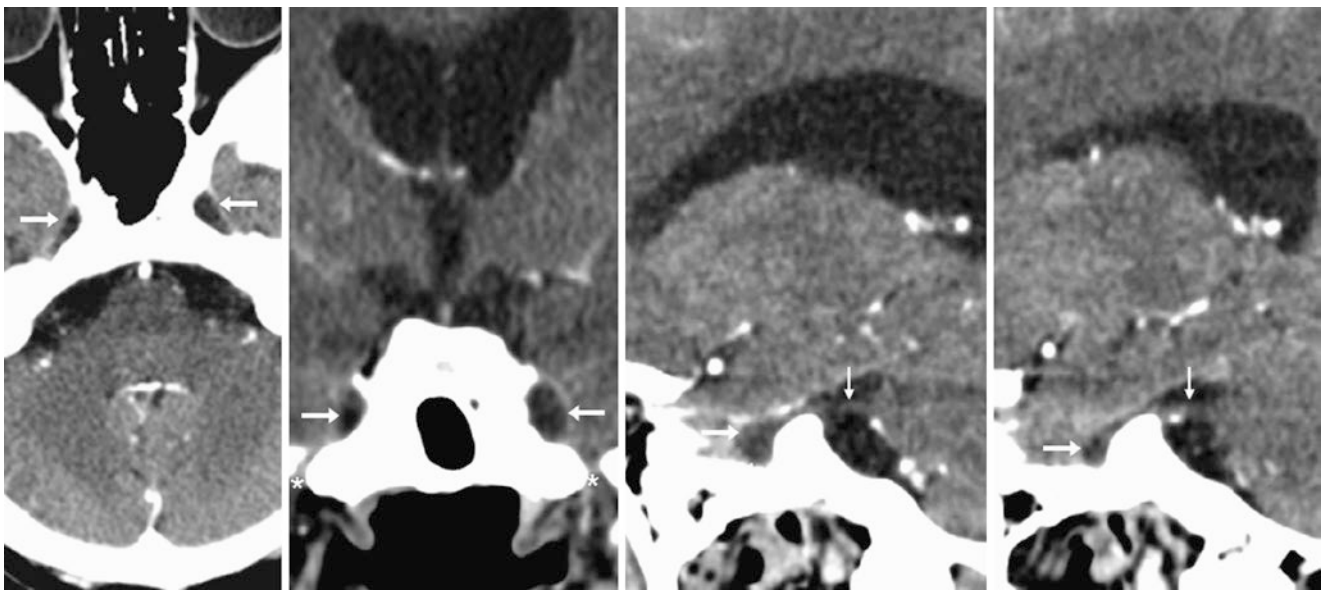

Fig. 6.8 A 63-year-old patient with a contrast-enchanced CT (CECT) axial image (*left*) reconstructed from a CT angiography, demonstrating asymmetric prominence of the right Meckel cave as compared to the left (*arrows*). This is more evident on coronal reformats (*left middle*) and on sagittal reformats of the left (*right middle*), and right (*right*) sides. Note the faintly visualized cisternal course of the trigeminal nerves (*thin arrows*) and the asymmetry in the size of the foramina of ovale (*)

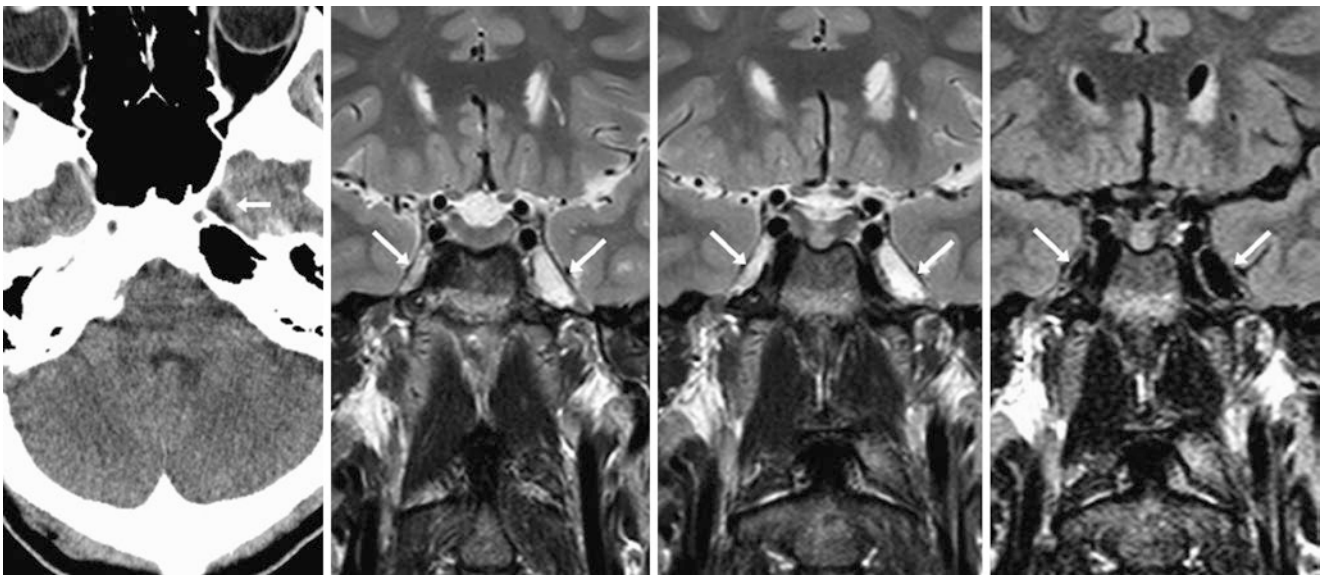

Fig. 6.9 A 25-year-old female patient with a unilaterally prominent left Meckel cave (*arrows*) on axial NECT (*left*) and on a 3 T MRI with coronal T2WI (*left and left middle*) and coronal FLAIR (*right*). The cause of the seizure was a cortical contusion. The prominent left Meckel cave had not changed on a follow-up MRI performed 6 months later (*not shown*)

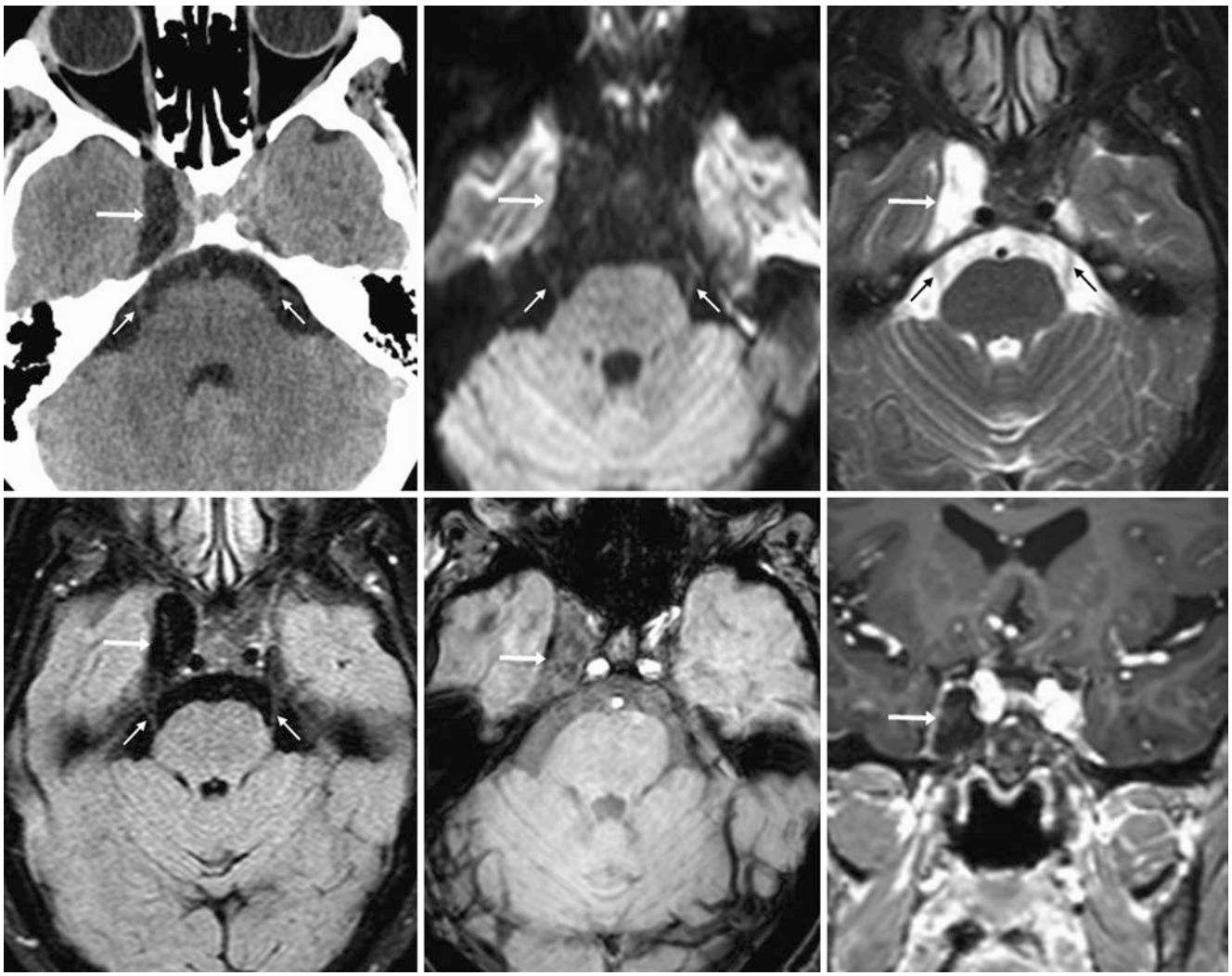

Fig. 6.10 Comparison case of arachnoid cyst (AC). A 60-year-old female patient with headaches had asymmetric enlargement of the right Meckel cave (*arrows*) on axial NECT (*top left*), which on 3 T MRI followed the CSF signal on DWI (*top middle*), T2WI (*top right*), FLAIR (*bottom left*), SWI (*bottom middle*), and on postcontrast coronal T1WI (*bottom right*). These findings were consistent with an AC. Note the cisternal segments of CNV (*thin arrows*)

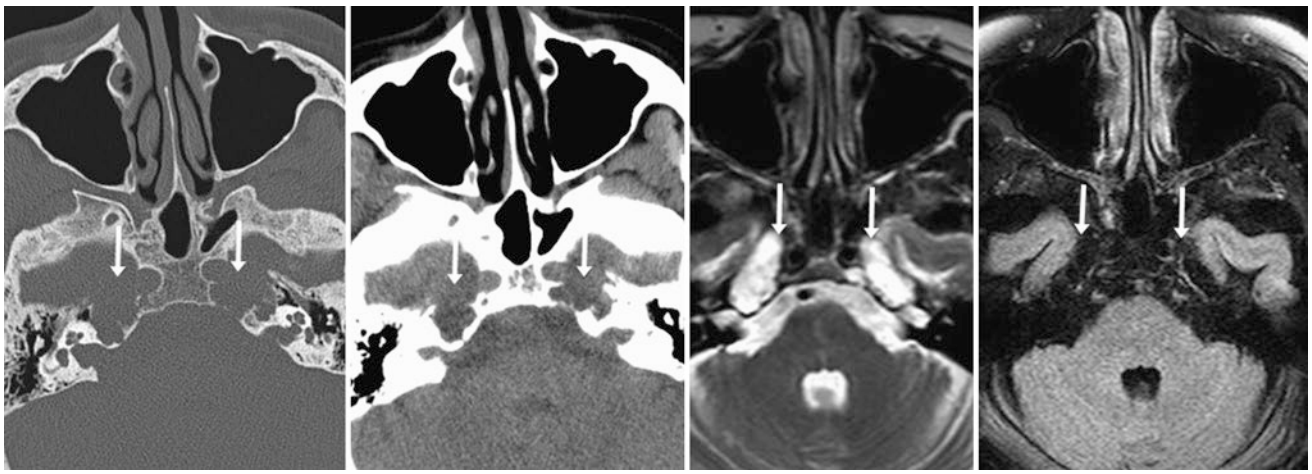

Fig. 6.11 Comparison case of petrous apex cephaloceles (PACs). A 58-year-old male with Usher syndrome had bilateral erosive lesions of the petrous apices contiguous with Meckel cave (*arrows*) on axial NECT bone (*left*) and brain (*left middle*) windows, with bright signal on 1.5 T MRI axial T2WI (*right middle*) while suppressing with CSF on FLAIR (*right*). Such PACs as well as diffusely dilated subarachnoid spaces can be seen with this syndrome

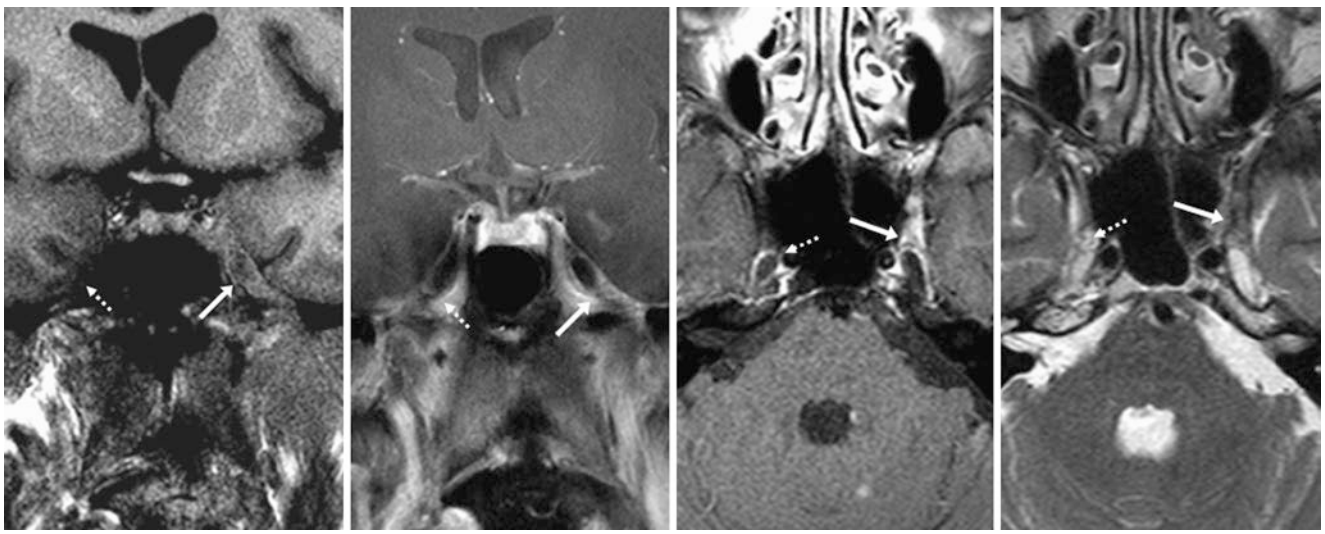

Fig. 6.12 Comparison case of lymphoma. A 64-year-old patient with lymphoma was shown to have an enlarged left Meckel cave on both pre- (*left*) and postcontrast (*left middle*) coronal 1.5 T T1WIs. Postcontrast axial T1WI (*right middle*) and T2WI (*right*) illustrate enlargement compared with the opposite side (*dashed arrows*) as a result of a tumor

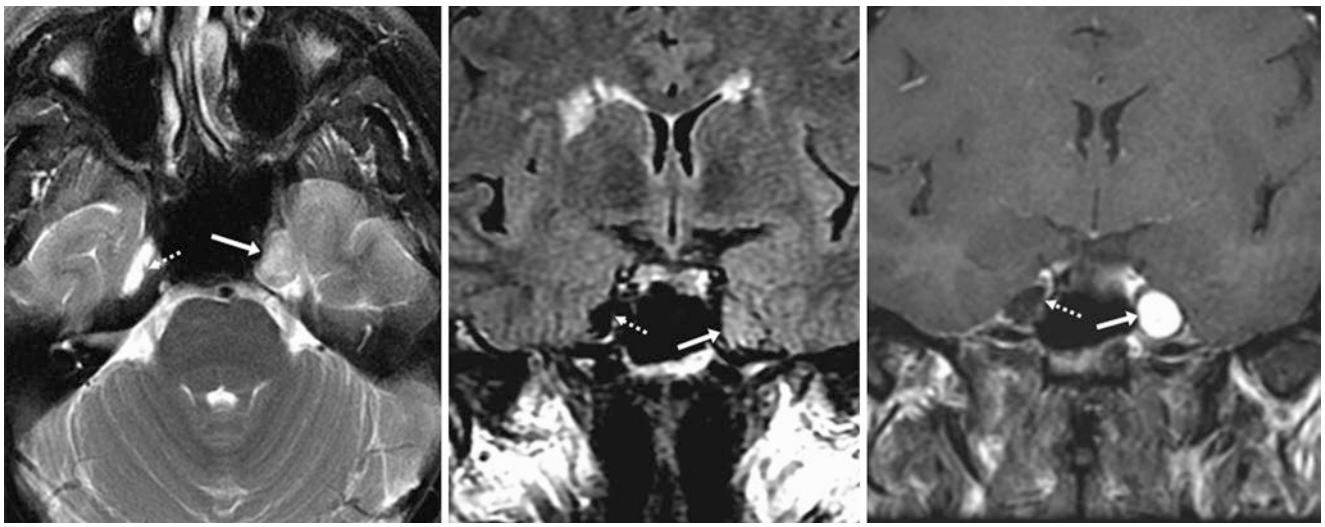

Fig. 6.13 Comparison case of meningioma. A 58-year-old patient had a left-sided enhancing mass within Meckel cave (*arrows*) on 1.5 T MRI axial T2WI (*left*), coronal FLAIR (*middle*), and coronal fat-suppressed postcontrast T1WI (*right*). Note the normal size and appearance of the right Meckel cave (*thin arrows*), which suppresses like CSF on FLAIR

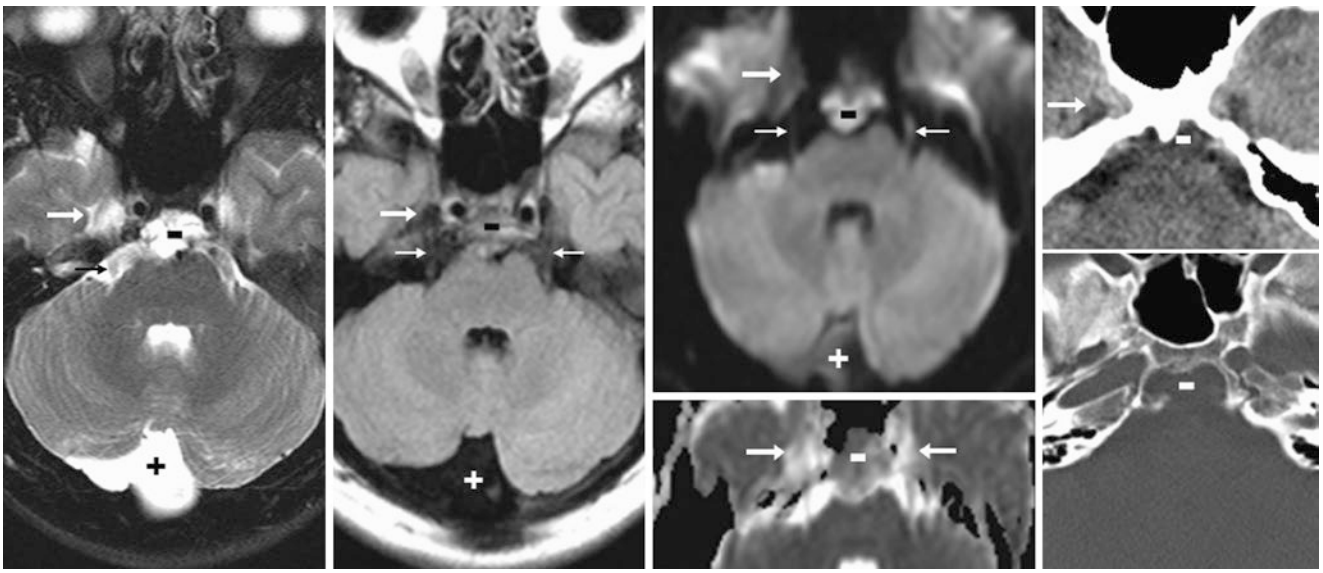

Fig. 6.14 Comparison case of epidermoid cyst. A 20-year-old patient with 1.5 T MRI axial T2WI (*left*) and FLAIR (*left middle*) had an normal incidental enlarged right Meckel cave (*arrows*). A T2- and FLAIR-bright lesion (−) was also noted within the clivus and prepontine cistern that did not enhance (*not shown*) that was bright on DWI (*right middle*) and later identified as an epidermoid cyst. Note that both the right Meckel cave and a normal mega cisterna magna (+) had isointense signals on DWI, probably from the CSF pulsation artifact. NECT (*far right*) confirmed bony clival erosions

Suggested Reading

Chapman PR, Shah R, Cure JK, Bag AK. Petrous apex lesions: pictorial review. Am J Roentgenol. 2011;196:WS26–37.

Kapila A, Chakeres DW, Blanco E. The Meckel cave: computed tomographic study. Part I: normal anatomy. Part II: pathology. Radiology. 1984;152:425–33.

Moore K, Fischbein N, Harnsberger H, Glastonbury CM, White DK, Dillon WP. Petrous apex cephaloceles. Am J Neuroradiol. 2001;22:1867–71.

VandeVyver V, Lemmerling M, Van Hecke W, Verstraete K. MRI findings of the normal and diseased trigeminal nerve ganglion and branches: a pictorial review. J Belge Radiol. 2007;90:272–7.

Williams LS, Schmalfuss IM, Sistrom CL, Inoue T, Tanaka R, Seoane ER, Mancuso A. MR imaging of the trigeminal ganglion, nerve, and the perineural vascular plexus: normal appearance and variants with correlation to cadaver specimens. Am J Neuroradiol. 2003;24:1317–23.

Cavernous Sinus Fat and Pseudomasses

7

Most *cavernous sinuses* (>90 %) have some degree of *fat* on autopsy, but on occasion fat can replace most of the cavernous sinus on computed tomography (CT) and may simulate air or gas. Without proper windowing the hypodensity on CT can lead to undue concern for *air emboli* or *gas* from a fracture involving the skull base (such as gas from the sphenoid sinus or petrous apices), for an arachnoid cyst, or it may even be windowed appropriately but considered a congenital anomaly such as a *lipoma* or *dermoid cyst*. This may occur bilaterally or unilaterally.

On CT, detectable/visible *cavernous sinus fat* can be visualized in 20–30 % of the population incidentally. If the cavernous sinus is divided into thirds (anterior, middle, and posterior), fat is present on CT in the anterior third in a majority of cases (about 70 %) and to a lesser degree in the middle and posterior thirds (30–56 %). Cavernous sinus fat can be contiguous with fat in adjacent locations, such as the superior orbital fissure and Meckel cave. Also, such fat within the cavernous sinus may surround the internal carotid artery (ICA). It occurs more frequently (≥25 %) in the population above 50 years age. Notably, fat occurs in the cavernous sinus to a much higher degree than the other dural sinuses, since less than 5 % of patients have fat within or along other dural sinuses (Figs. 7.1, 7.2, 7.3, 7.4, 7.5, 7.6, 7.7, 7.8, 7.9, 7.10, 7.11, 7.12, 7.13, 7.14, 7.15, 7.16, 7.17, 7.18, 7.19, and 7.20).

A.M. McKinney, *Atlas of Normal Imaging Variations of the Brain, Skull, and Craniocervical Vasculature*,
DOI 10.1007/978-3-319-39790-0_7

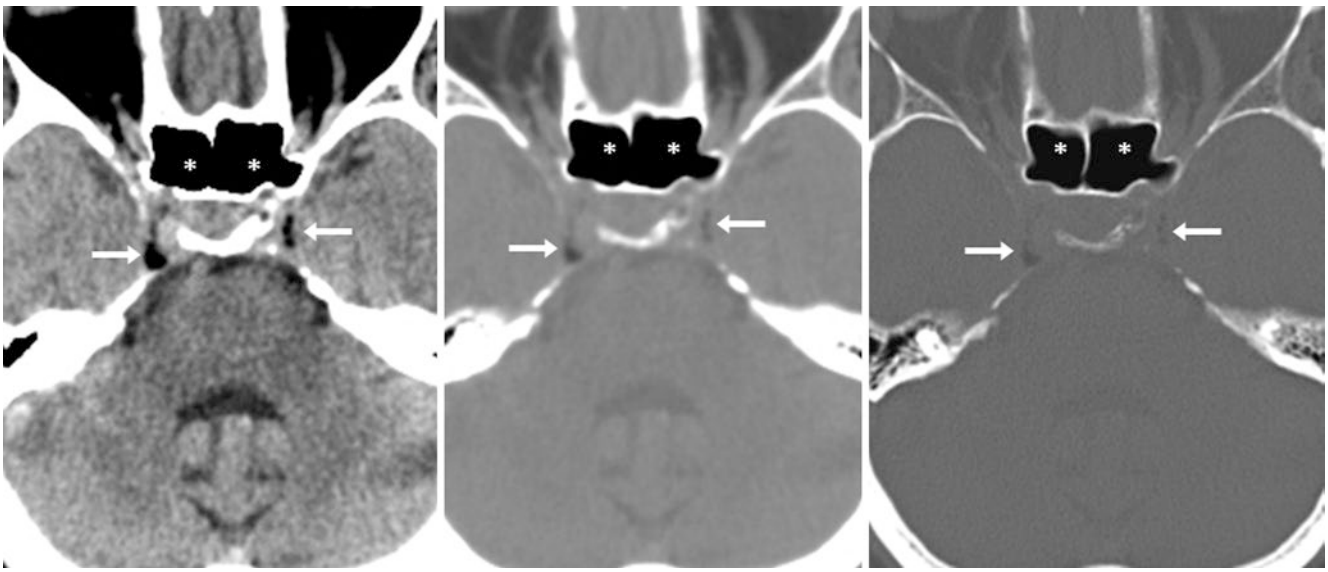

Fig. 7.1 A 51-year-old male with confusion and trauma who had normal cavernous sinus fat (*arrows*) bilaterally on the brain windows (*left*) simulating fracture-related gas. Note the similarity to sphenoid sinus gas (*). However, on soft tissue (*middle*) and bone windows (*right*), it is clear that this is not gas and also that there is no evidence of fracture

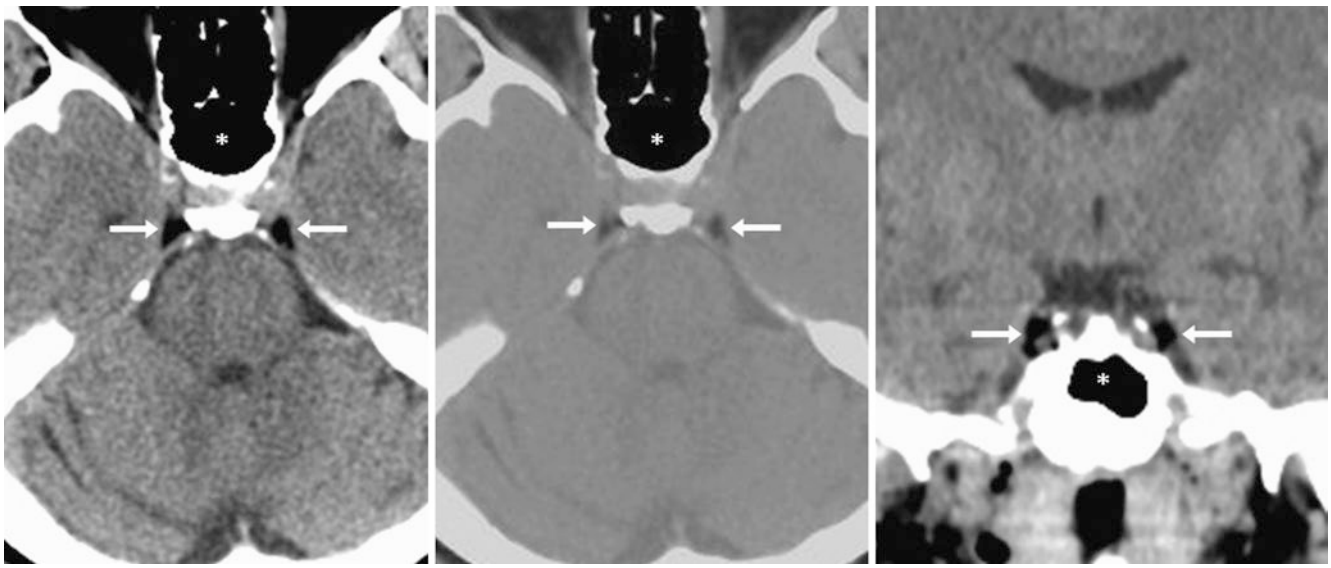

Fig. 7.2 A 60-year-old male with cognitive decline with normal cavernous sinus fat (*arrows*) bilaterally on brain windows (*left*). Note the similarity to sphenoid sinus gas (*), but on soft tissue windows (*middle*) it is clear that this is not gas and also that there is no evidence of fracture. Coronal brain windows (*right*) also depict the fat

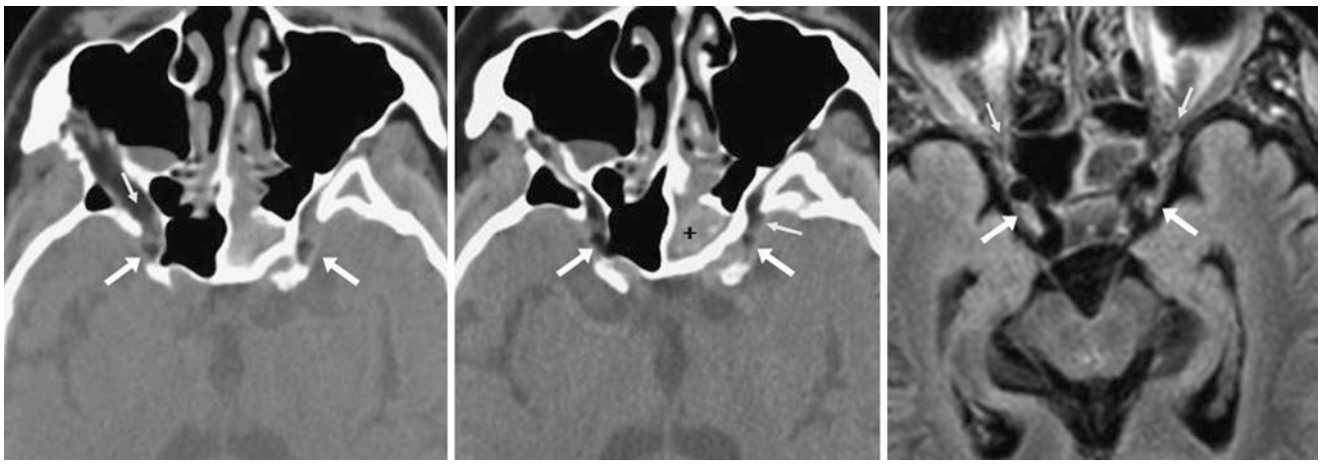

Fig. 7.3 An 83-year-old female with facial trauma and normal bilateral cavernous sinus fat (*arrows*); note hemorrhage (+) within the sphenoid sinus. This fat is contiguous with the fat of the superior orbital fissures (*thin arrows*) as demonstrated on axial soft tissue windows (*left*, *middle*), and on 1.5 T FLAIR MRI (*right*, no fat suppression)

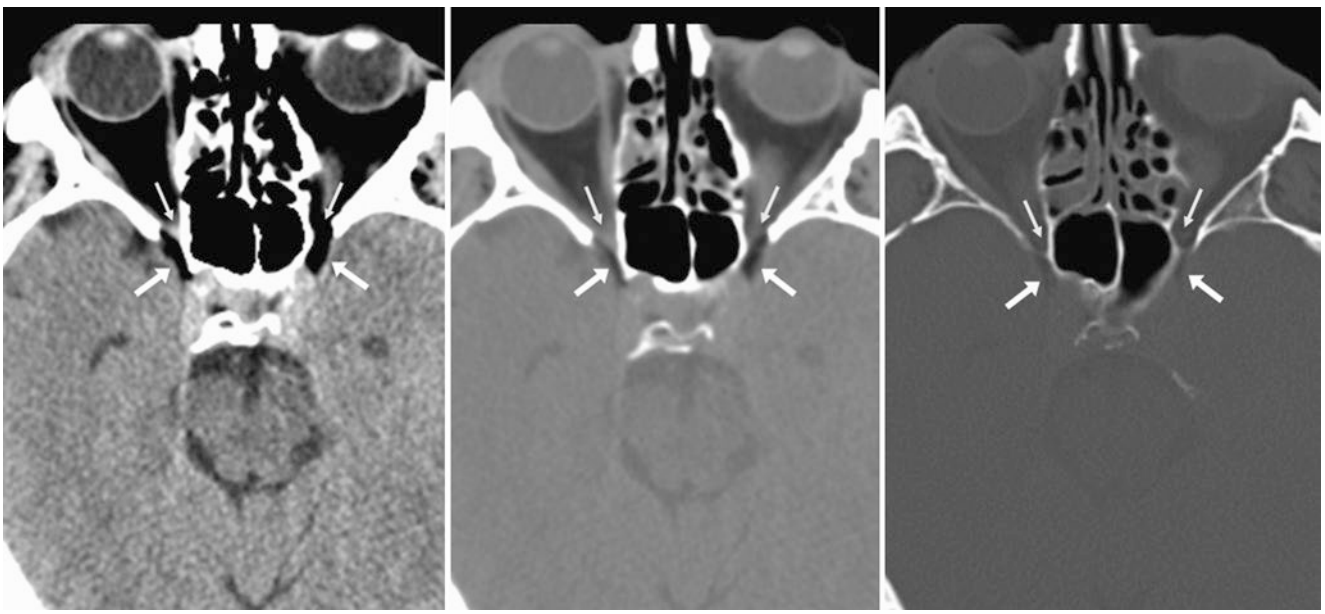

Fig. 7.4 A 57-year-old male with headache incidentally having normal cavernous sinus fat bilaterally (*arrows*). The cavernous sinus fat is contiguous with fat within the superior orbital fissures bilaterally (*thin arrows*), as demonstrated on brain windows (*left*), soft tissue windows (*middle*), and bone windows (*right*)

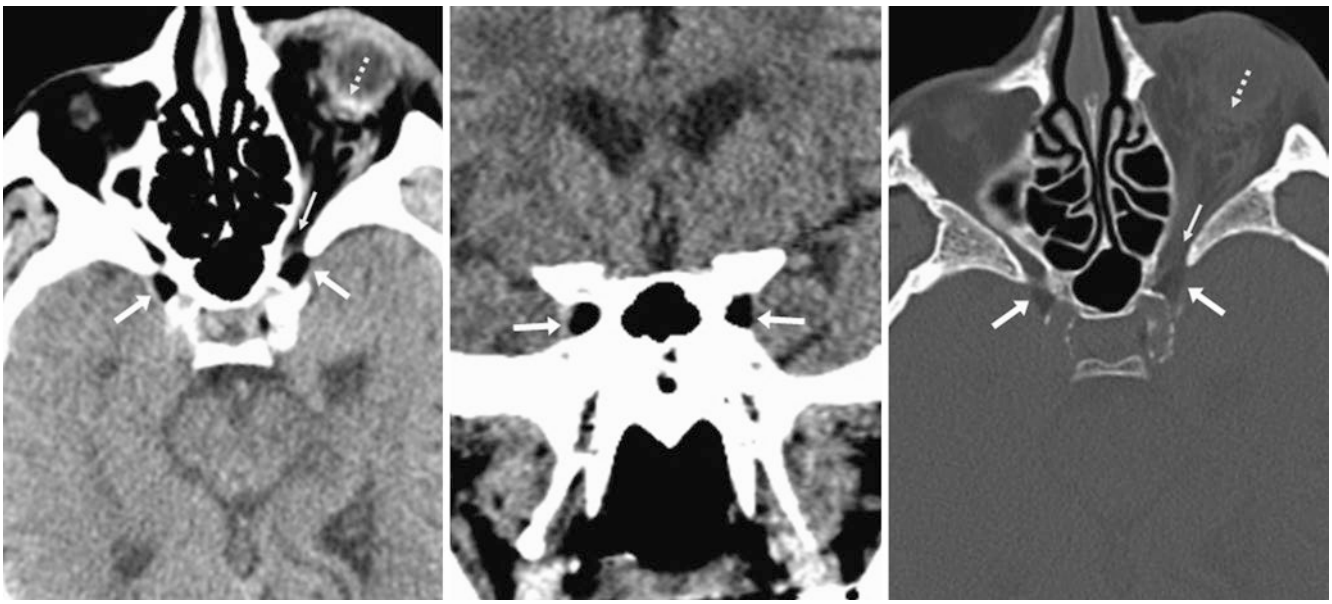

Fig. 7.5 An 83-year-old female with orbital trauma. *Dashed arrows* denote a retrobulbar hematoma with fat stranding posteriorly, as demonstrated on axial (*left*) and coronal (*middle*) brain windows and on bone windows (*right*). There is incidental normal cavernous sinus fat bilaterally (*arrows*), which is contiguous with the fat of the superior orbital fissures (*thin arrows*). No fracture of the bony orbital apex was noted on bone windows

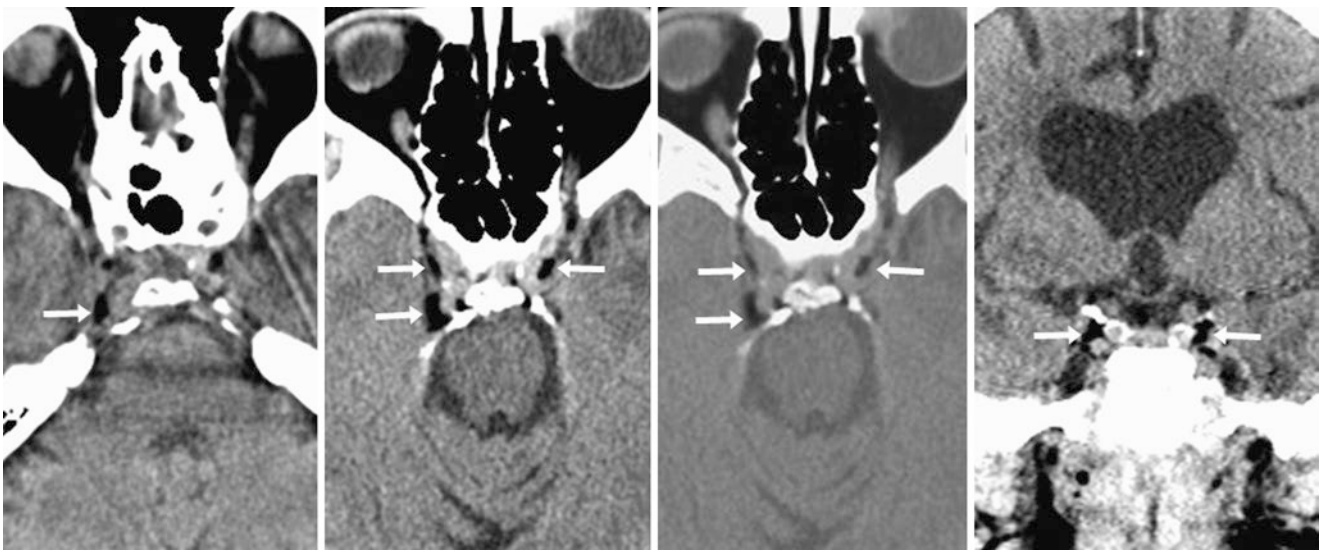

Fig. 7.6 A 39-year-old female post trauma with an otherwise negative head CT scan. There was normal cavernous sinus fat bilaterally (*arrows*) on the brain windows (*left*). A NECT 10 years later demonstrated that this finding had slightly progressed based on brain (*left middle*) and soft-tissue windows (*right middle*) and on coronal reformats (*right*)

Fig. 7.7 A 73-year-old female with a neck CT scan performed for a right parotid mass *(!),* having incidental, normal cavernous sinus fat bilaterally (*arrows*) on soft-tissue window coronal reformatted images. The right parotid mass was later biopsied and proved to be a rare, benign parotid oncocytoma

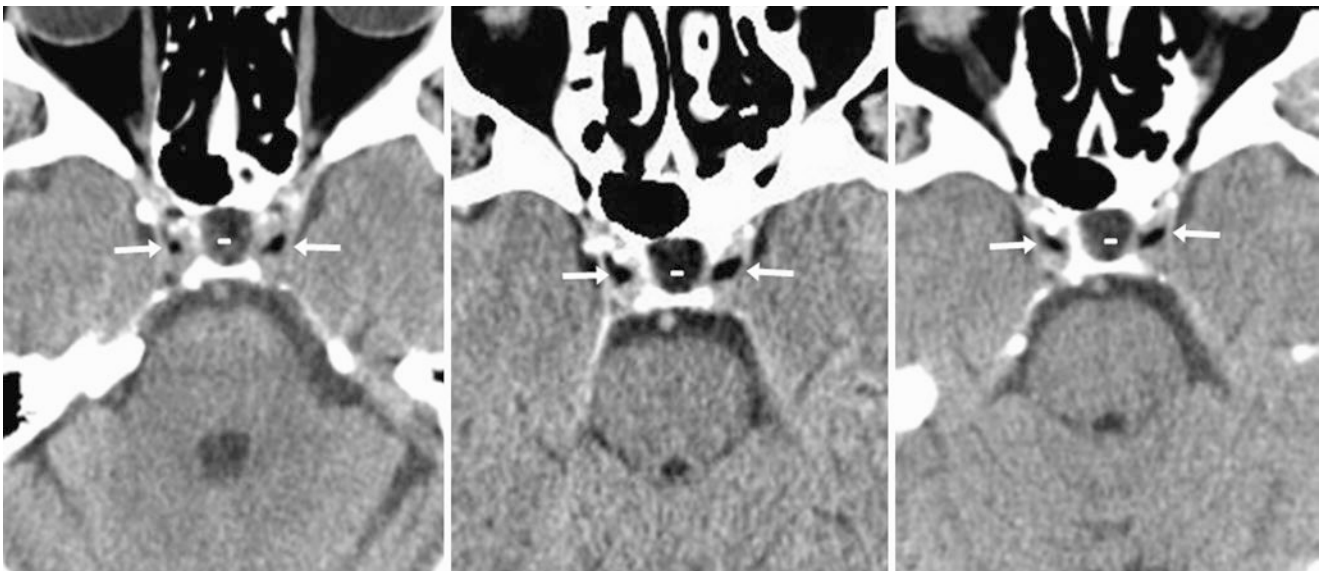

Fig. 7.8 A 55-year-old female with chronic headaches and an otherwise negative head CT scan with normal cavernous sinus fat bilaterally (*arrows*) on brain windows (*left*). Note an incidental primary empty sella as well (−). These findings were unchanged on repeat NECTs at 1 year (*middle*) and at 5 years later (*right*)

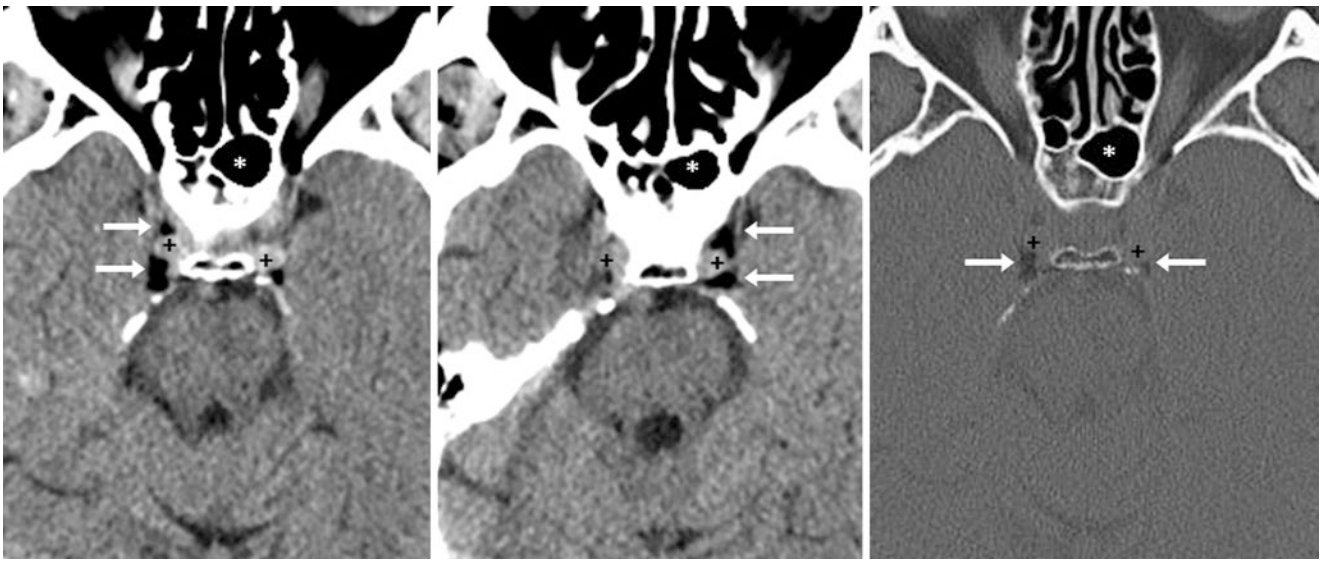

Fig. 7.9 A 61-year-old female with trauma and normal cavernous sinus fat bilaterally (*arrows*) on the brain windows (*left*, *middle*) that surround the ICAs (+). Note the dark density similar to sphenoid sinus gas (*) on the brain windows, while on the bone windows (*right*) it becomes clear that this is indeed not gas and that there is no fracture

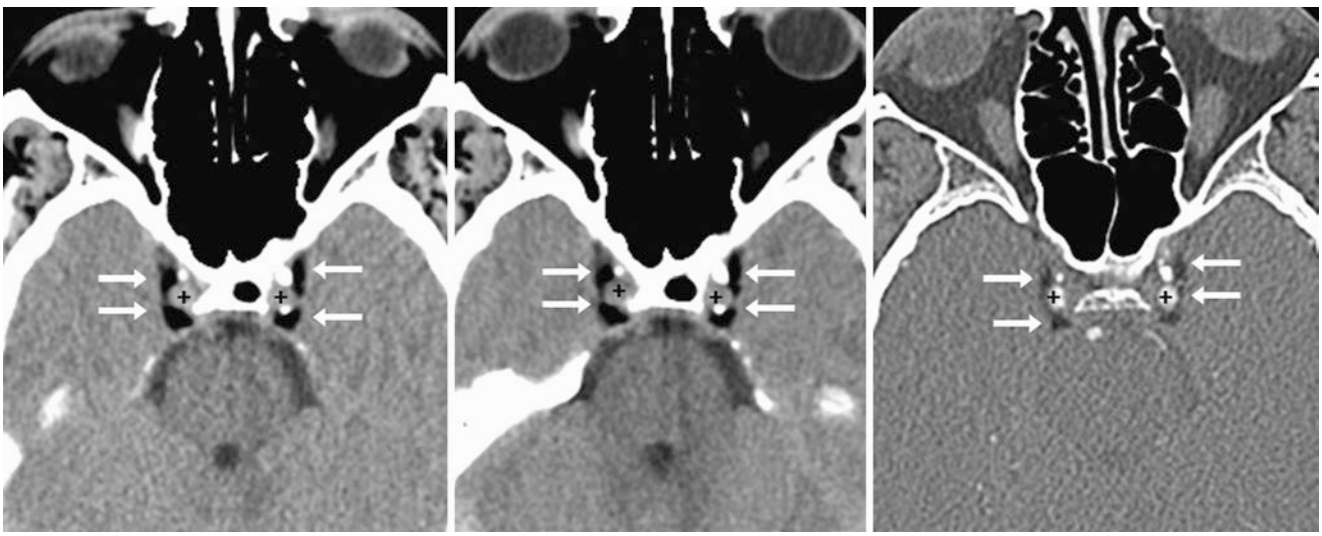

Fig. 7.10 A 45-year-old male with headaches with normal cavernous sinus fat bilaterally (*arrows*) that surrounds the ICAs (+), as demonstrated on the brain windows (*left*). This was unchanged 2 months later (*middle*), at which time computed tomography angiography (CTA) was performed; hybrid bone/soft-tissue windows (*right*) demonstrate the ICAs and the cavernous fat density

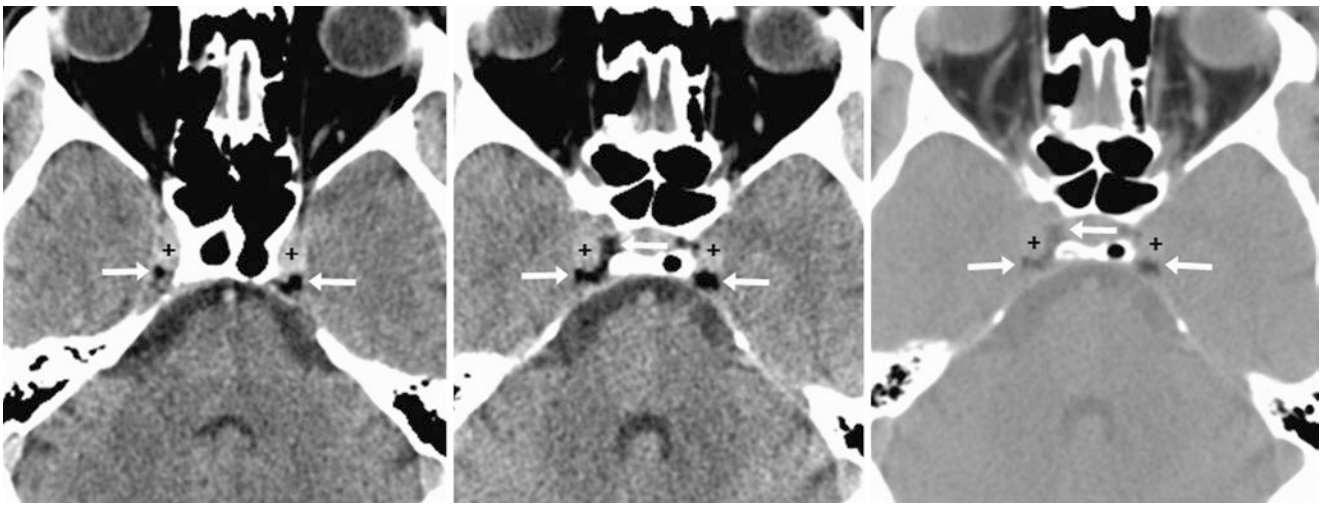

Fig. 7.11 A 38-year-old male with altered mental status and normal cavernous sinus fat bilaterally (*arrows*) that surrounds the ICAs (+), as demonstrated on the brain windows (*left and middle*) and on soft-tissue windows (*right*)

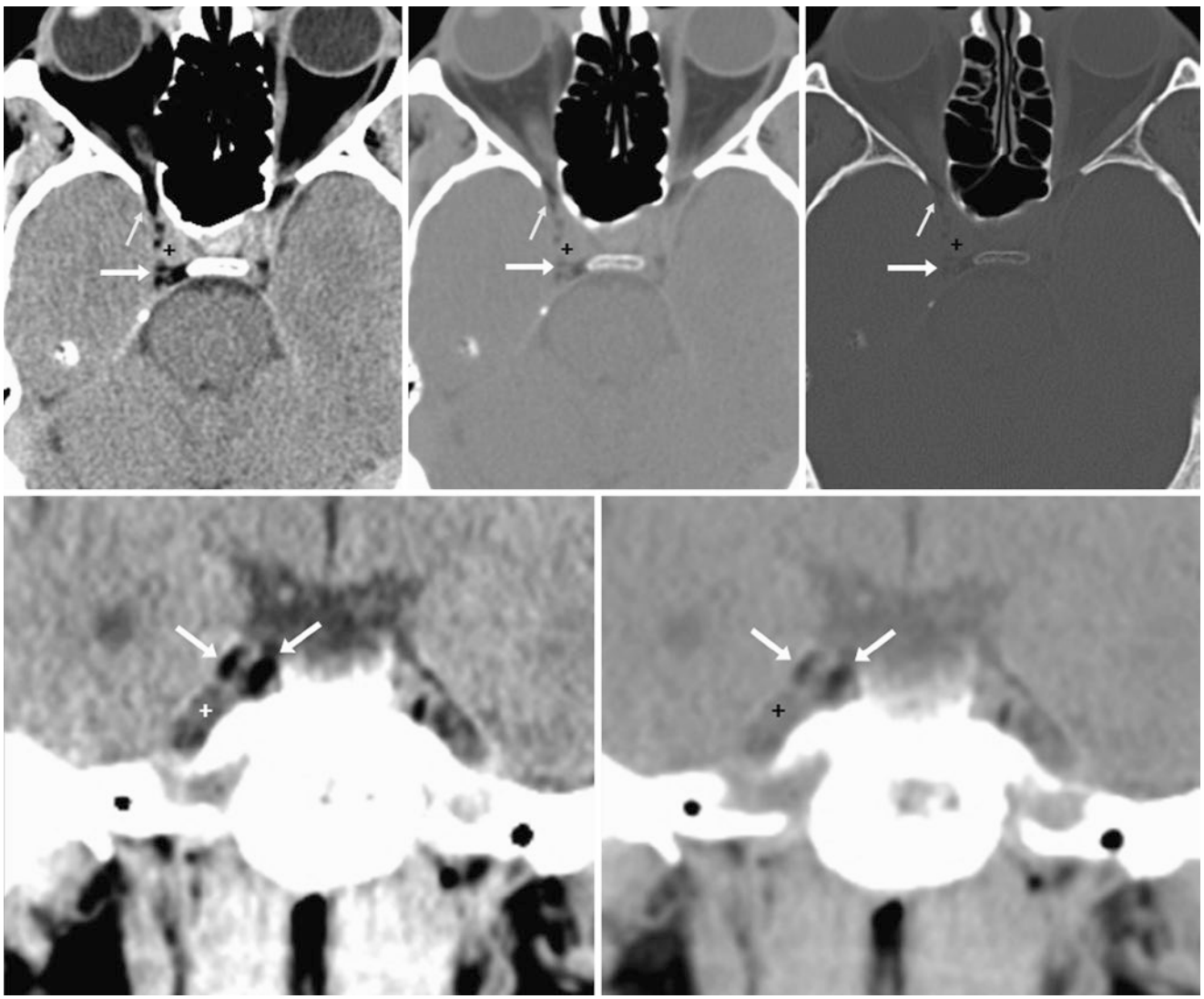

Fig. 7.12 A 55-year-old female with headaches and right-sided cavernous sinus fat (*arrows*) that is contiguous with the superior orbital fissure (*thin arrows*) and surrounds the ICA (+) on axial brain (*top left*), soft-tissue (*top middle*), and bone (*top right*) windows and on magnified coronal brain (*bottom left*) and soft-tissue (*bottom right*) windows

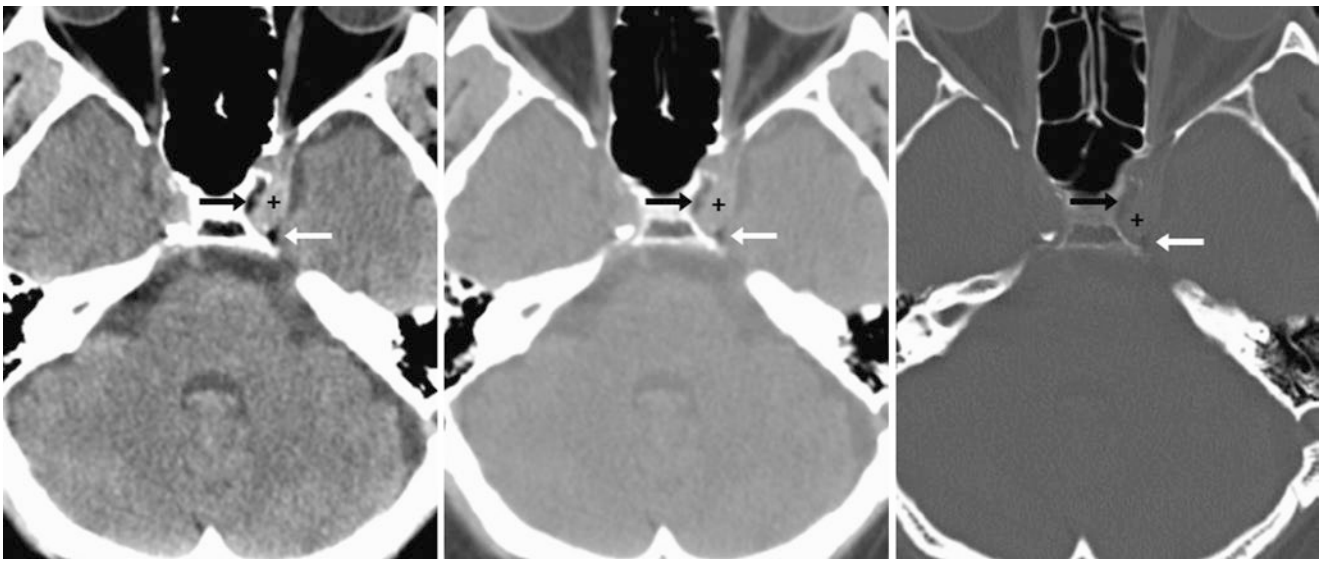

Fig. 7.13 A 54-year-old male with headaches following trauma. Left-sided cavernous sinus fat (*arrows*) partially surrounds the ICA (+) on the brain (*left*), soft tissue (*middle*), and on bone (*right*) windows. This could mimic fracture-related gas

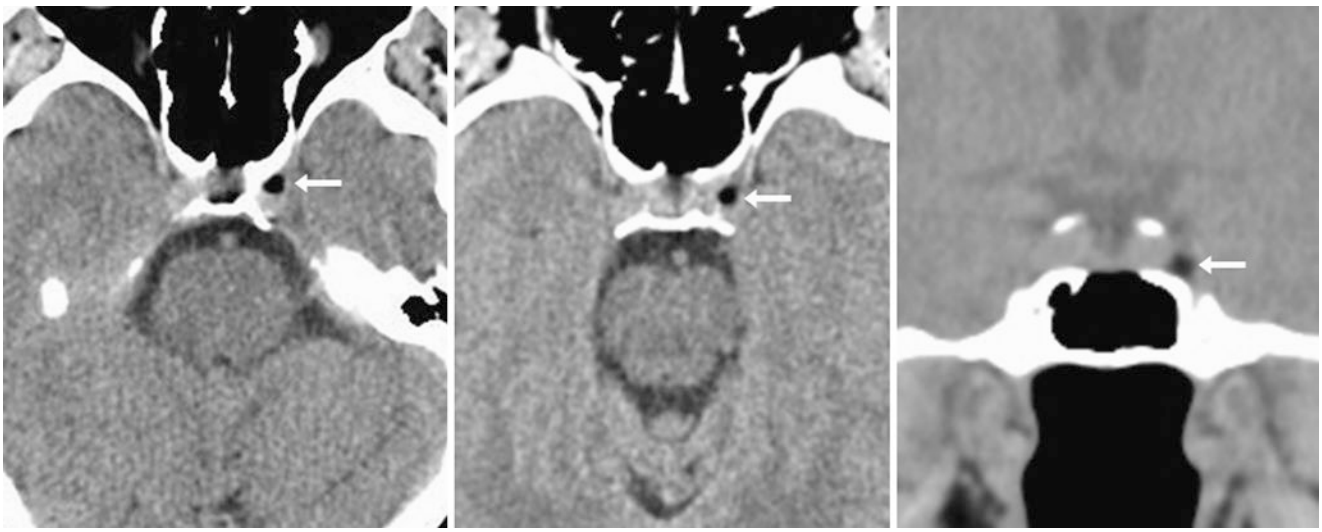

Fig. 7.14 A 73-year-old female with a small focus of left-sided cavernous sinus fat (*arrows*) on brain windows (*left*), which was unchanged 1 year later on axial brain windows (*middle*) and on coronal soft-tissue windows (*right*)

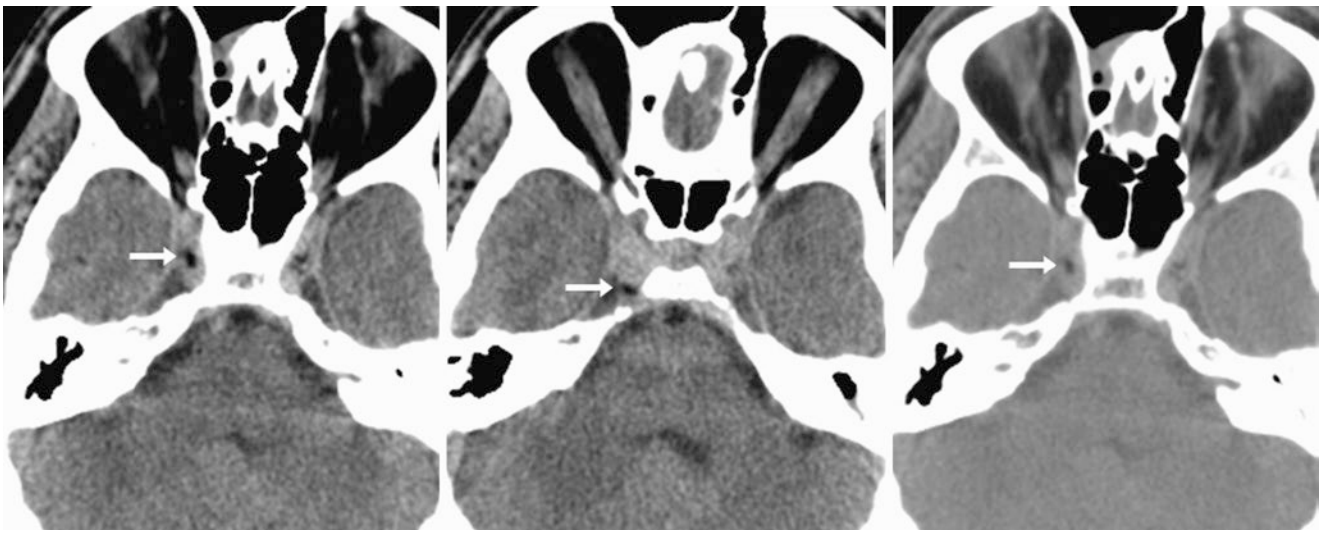

Fig. 7.15 A 45-year-old male with headaches. A tiny focus of right-sided cavernous sinus fat (*arrows*) is noted on brain windows (*left and middle*) and on soft-tissue windows (*right*). This can mimic gas from a fracture

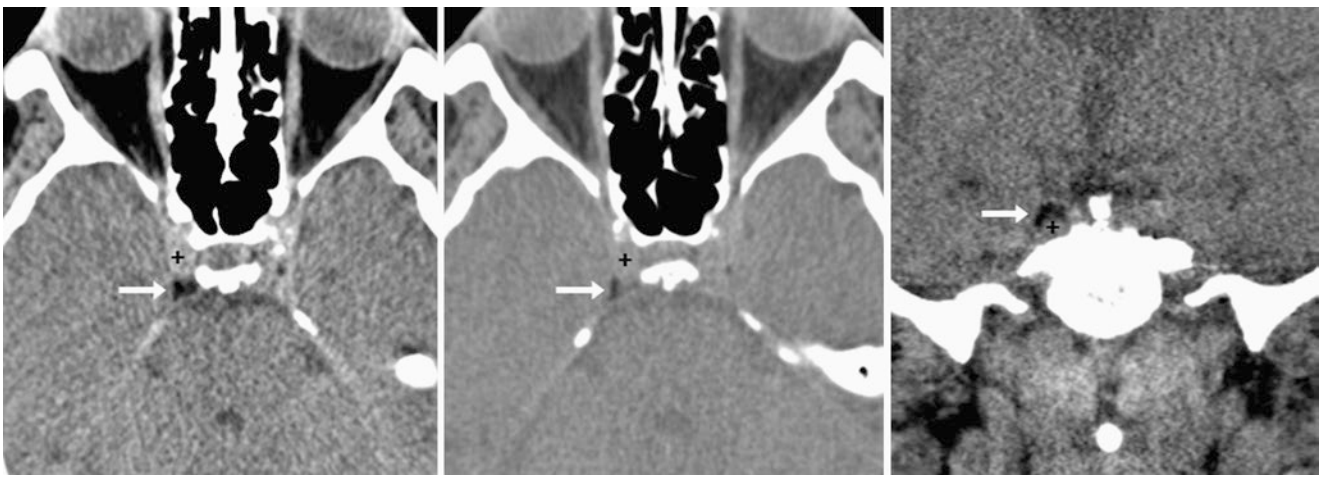

Fig. 7.16 A 69-year-old male with trauma; a CT of facial bones demonstrates right-sided cavernous sinus fat (*arrows*) posteriorly on brain windows (*left*), soft-tissue windows (*middle*), and coronal brain windows (*right*); these findings could mimic the condition of fracture-related gas. The coronal windows demonstrate that the fat partially surrounds the ICA (+)

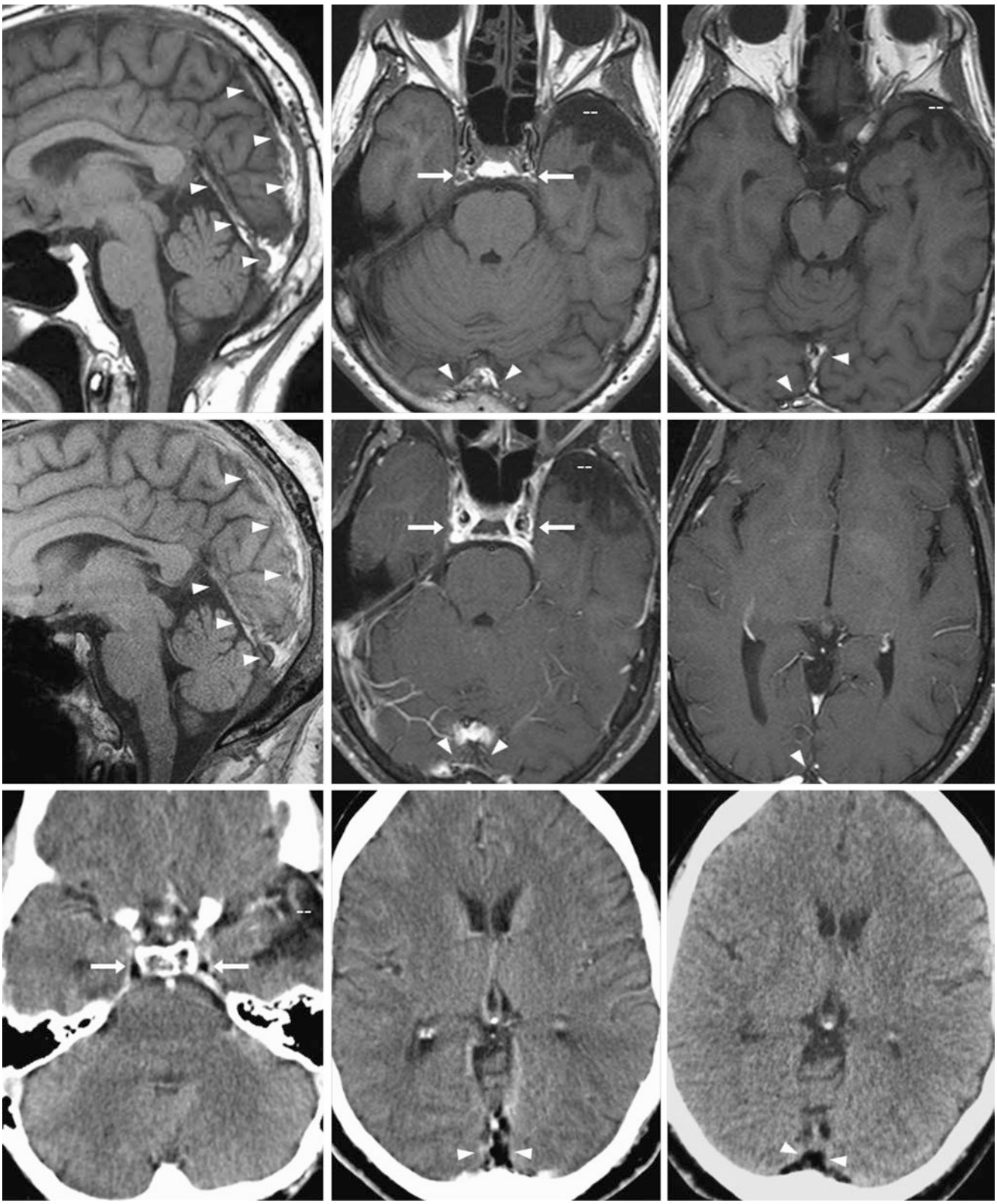

Fig. 7.17 A 37-year-old patient with seizures from remote trauma. *Top row:* Note left temporal atrophy (––) on 1.5 T MRI noncontrast sagittal (*top left*) and axial (*top middle and right*) T1WIs, with T1-bright fat diffusely along the dural (*arrowheads*), and cavernous sinuses (*arrows*). This was unchanged 2 years later on a 3 T sagittal T1WI (*middle row, left*). *Middle row:* Sagittal T1WI shows the findings described above, while fat-suppressed, postcontrast T1WI (*right and middle*) depicts enhancement of the cavernous sinuses (*arrows*) with suppression of dural sinus fat (*arrowheads*). *Bottom row:* contrast-enhanced computer tomography (CECT) (*left and middle*) shows similar findings, while a NECT 6 years later (*right*) shows no change

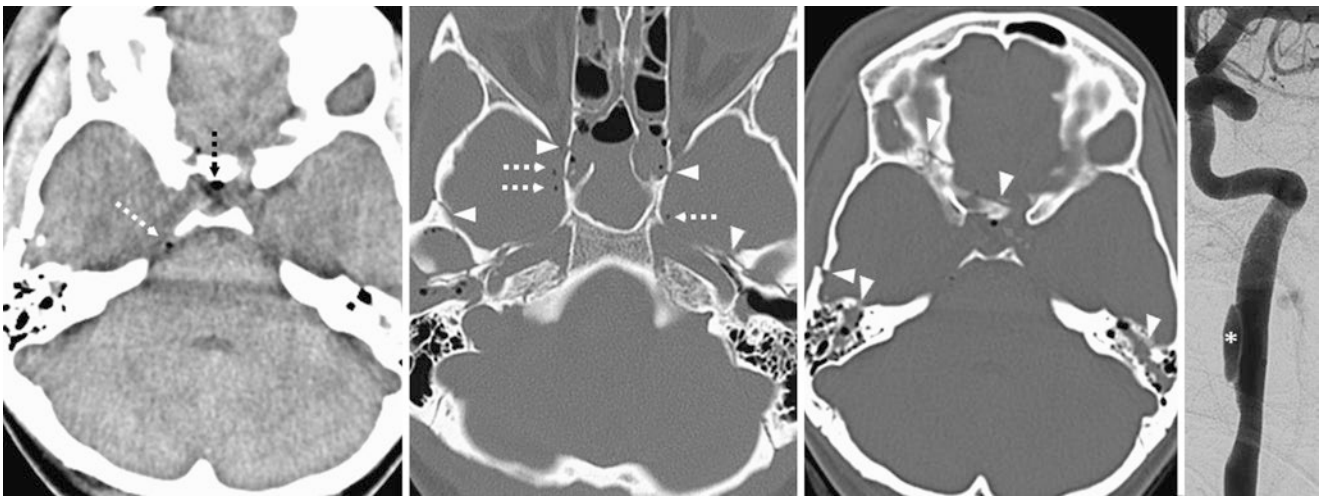

Fig. 7.18 Comparison case of traumatic gas. A 16-year-old patient with trauma having cavernous and intrasellar gas (*dashed arrows*) on NECT soft tissue (*left*) and bone (*middle*) windows from adjacent temporal (*thin arrows*) and sphenoid (*arrowheads*) fractures. Catheter angiography (oblique view, *right*) found a cervical left ICA pseudoaneurysm (*)

Fig. 7.19 Comparison case of iatrogenic gas. A 90-year-old patient without trauma and with cavernous and intrasellar gas (*dashed arrows*) on axial NECT (*left*). There was also gas in the location of the superior ophthalmic vein (*thick arrows*) on axial (*left middle*) and coronal (*right middle*) images. The patient had intravenous access via the jugular vein. The next day, a repeat NECT (*right*) showed resolution of the gas with a residual hyperdense varix

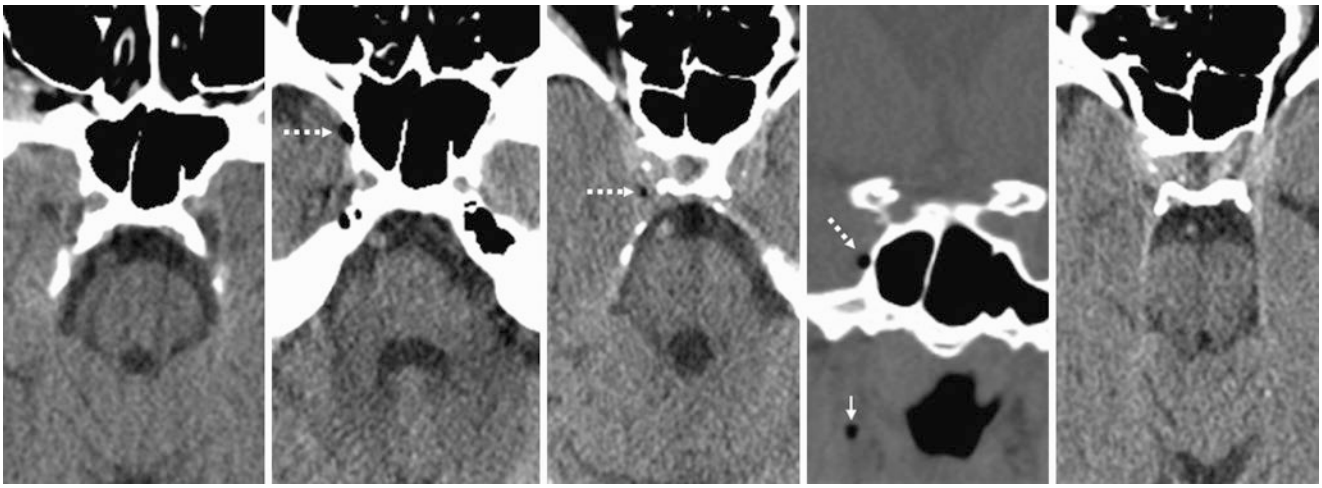

Fig. 7.20 Comparison case of iatrogenic gas from intravenous injection. A 46-year-old patient with altered mental status (soon resolved), had a comparison CT 3 weeks earlier (*left*) that was normal but the current axial NECT (*left middle and middle*) and coronal soft tissue window (*right middle*) demonstrated cavernous sinus gas (*dashed arrows*) and gas within the right pterygoid plexus (*small arrow*). This resolved 12 h later on axial NECT (*right*)

7.1 Cavernous Sinus Pseudomass on CT

Occasionally, the cavernous sinus or the ICA surrounded by the *cavernous sinus may appear asymmetric* and/or enlarged, particularly on axial non-enhanced CT (NECT) images. Most commonly this results from asymmetry in patient positioning with volume averaging, such as when a patient's head is obliquely positioned or tilted in the scanner, but occasionally it may occur as a result of tortuosity or dolichoectasia of the ICA. This may simulate various abnormalities such as a *neoplasm* (e.g., meningioma), an *inflammatory disorder* (e.g., pseudotumor also known as Tolosa-Hunt syndrome), or even an *aneurysm/pseudoaneurysm*. Multiplanar reformats of the NECT (particularly the coronal plane), CT angiography, MRI, or MR angiography may be necessary to exclude an abnormality (Figs. 7.21, 7.22, 7.23, 7.24, 7.25, 7.26, and 7.27).

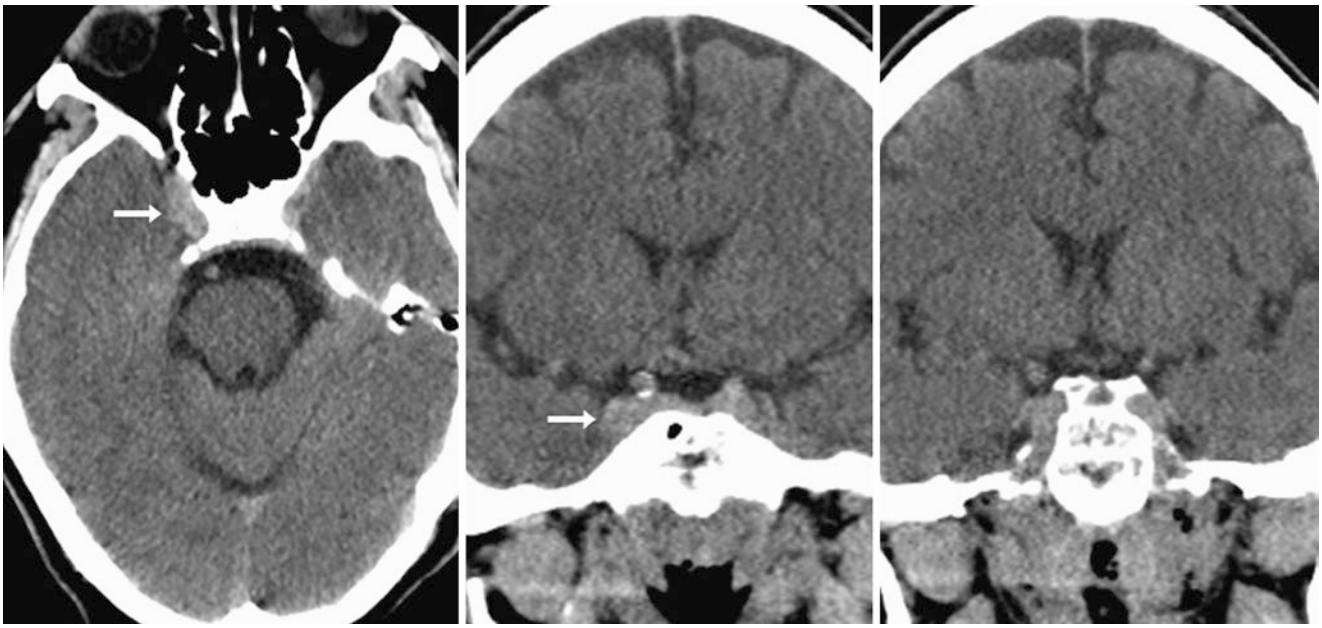

Fig. 7.21 A 51-year-old female with altered mental status with a mildly hyperdense prominence along the lateral aspect of the right cavernous sinus (*arrows*) on axial NECT (*left*) and on coronal reformats (*middle*). A coronal image just posteriorly reveals this to simply represent a mildly tortuous right ICA within the cavernous sinus (*right*)

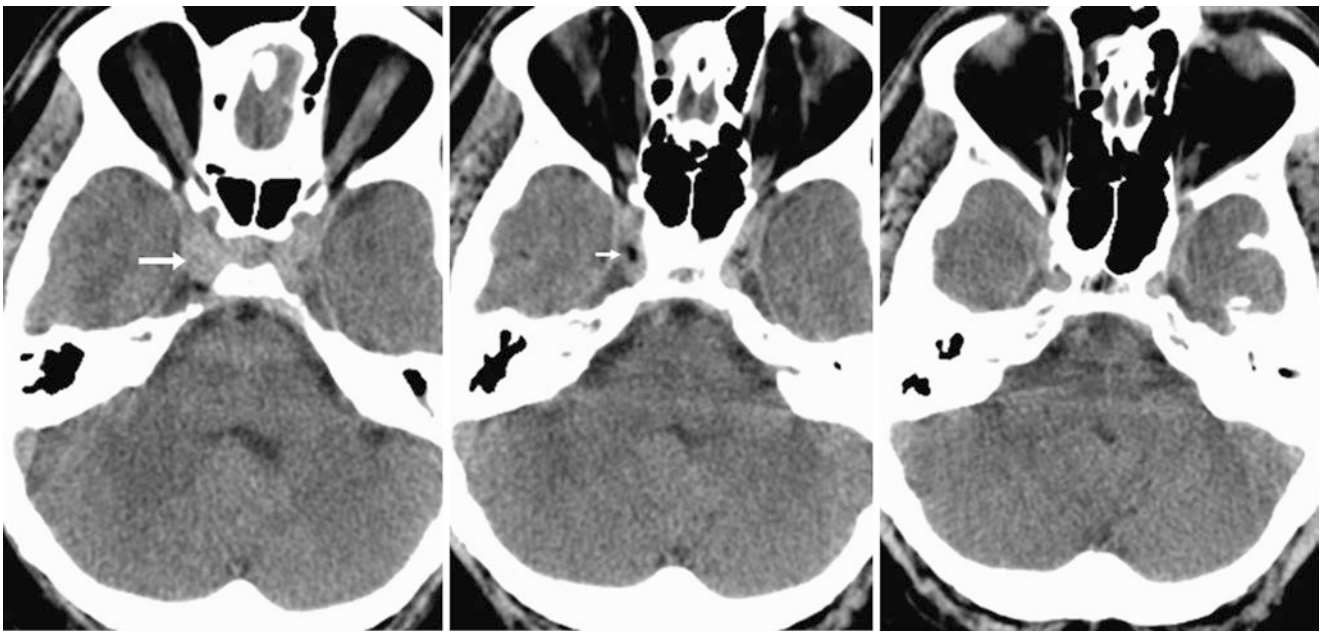

Fig. 7.22 A 45-year-old male with headaches with a mildly hyperdense prominence along the lateral aspect of the right cavernous sinus (*arrows*) on an axial NECT image (*left*). However, more inferior images (*middle and right*) confirmed this to be contiguous with a mildly tortuous right ICA, which appears normal. Note a tiny focus of normal fat (*tiny arrow*) within the right cavernous sinus as well

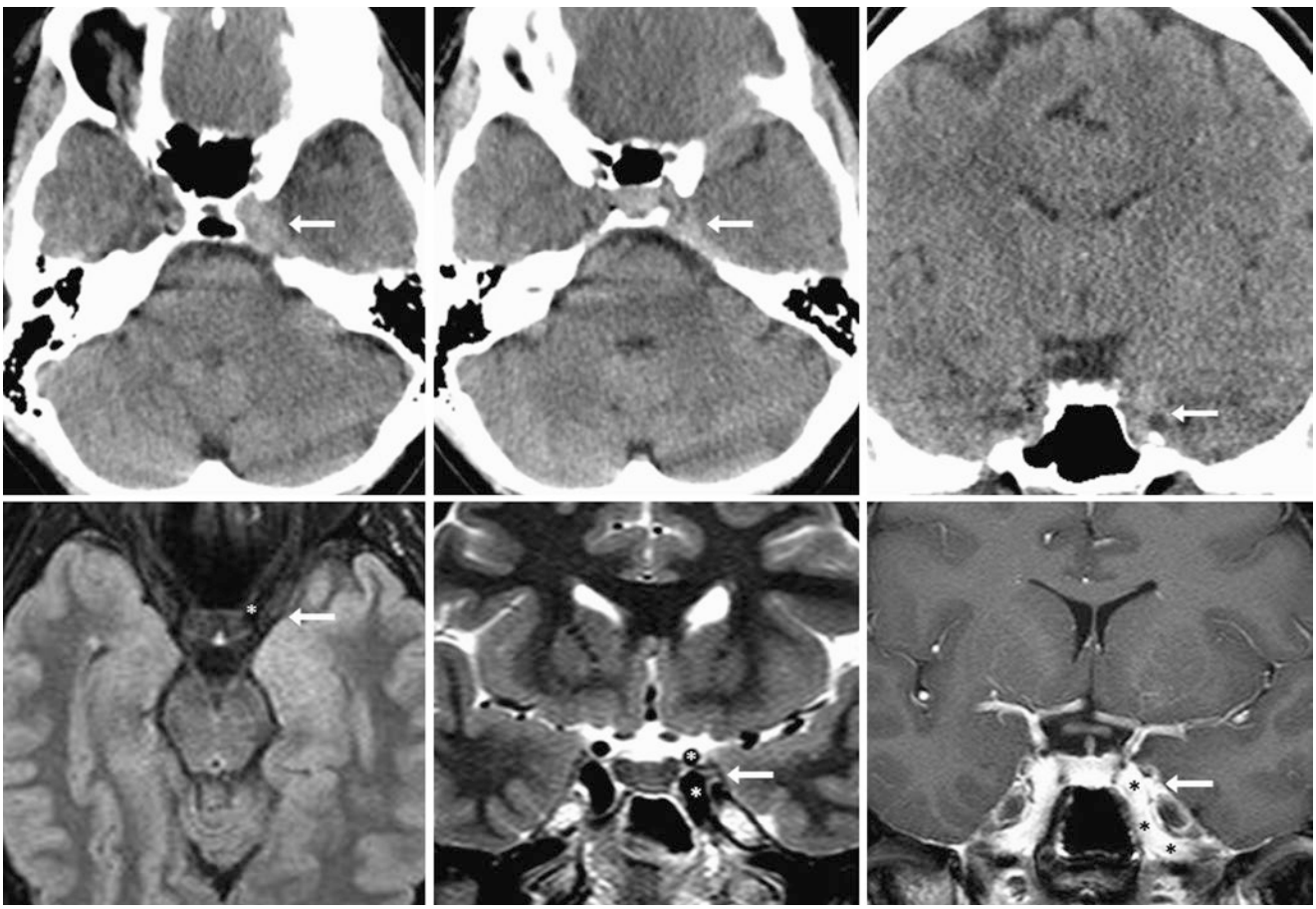

Fig. 7.23 A 38 year old male with seizure, having prominence of the left cavernous sinus (*arrow*) on axial NECT (*top left and top middle*); coronal reformats (*top right*) were indeterminate. On 1.5 T MRI, axial fat suppressed FLAIR (*bottom left*), coronal T2WI (*bottom middle*), and coronal postcontrast T1WI (*bottom right*) were normal. Note the left ICA (*)

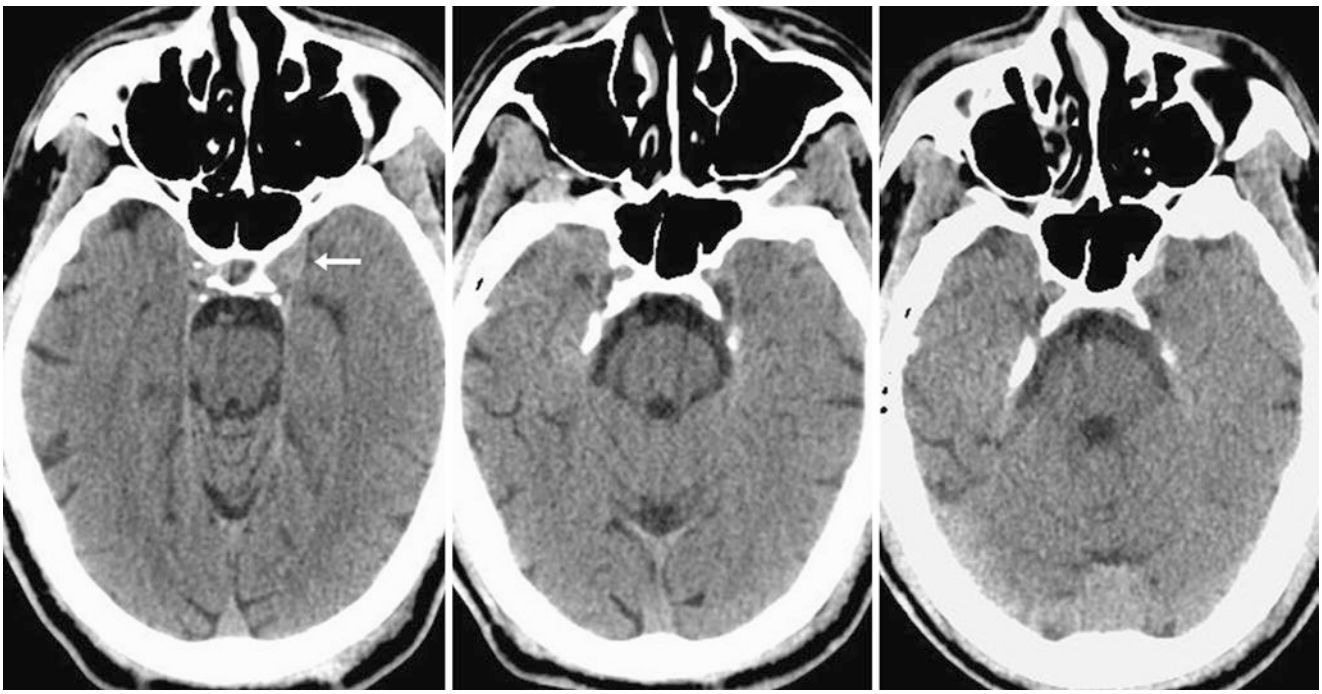

Fig. 7.24 A 46-year-old female with trauma with a mildly hyperdense prominence along the lateral aspect of the left cavernous sinus (*arrow*) on axial NECT (*left*). With slightly different positioning, this resolved on repeat NECTs both several weeks later (*middle*) and months later (*right*)

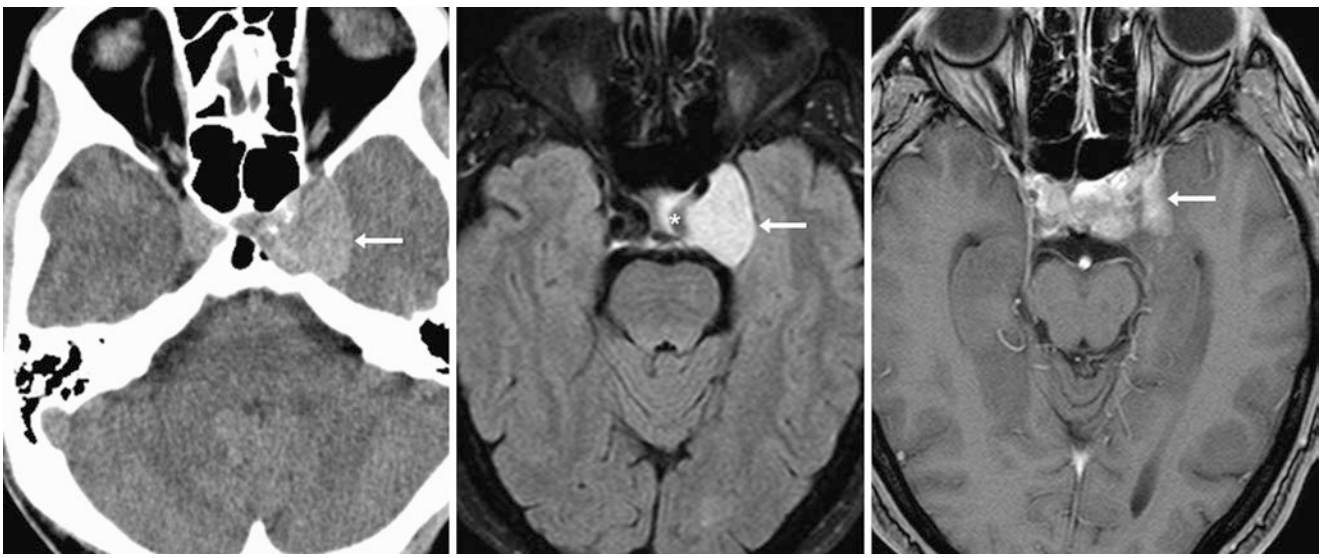

Fig. 7.25 Comparison case of meningioma. A 52-year-old male had a mass within the left cavernous sinus (*arrows*) that was isodense to the ICA and overall mildly hyperdense on axial NECT (*left*), on 1.5 T FLAIR MRI (*middle*), and on postcontrast T1WI (*right*). Note the left ICA (*) surrounded by the mass on FLAIR

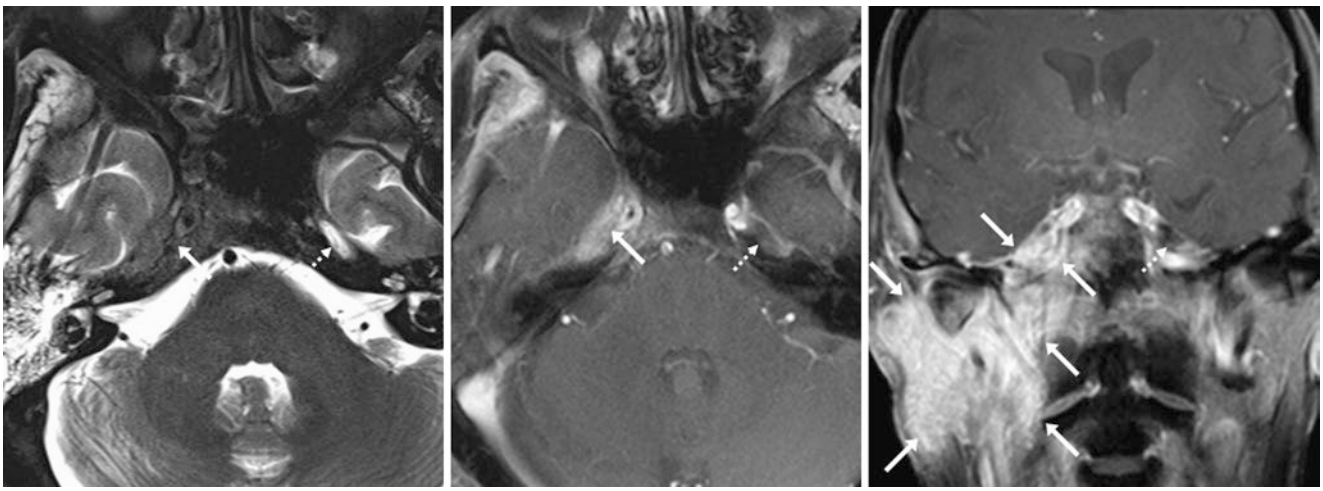

Fig. 7.26 Comparison case of squamous cell sarcinoma (SCCa). A 54-year-old with SCCa underwent 1.5 T MRI axial T2WI (*left*), postcontrast fat-suppressed axial (*middle*), and coronal (*right*) T1WIs, which depicted a replaced, T2-dark right cavernous sinus and Meckel cave (*arrows*), as compared with the left side (*dashed arrows*). The postcontrast images depict the extensive, enhancing mass as contiguous with the upper cervical region

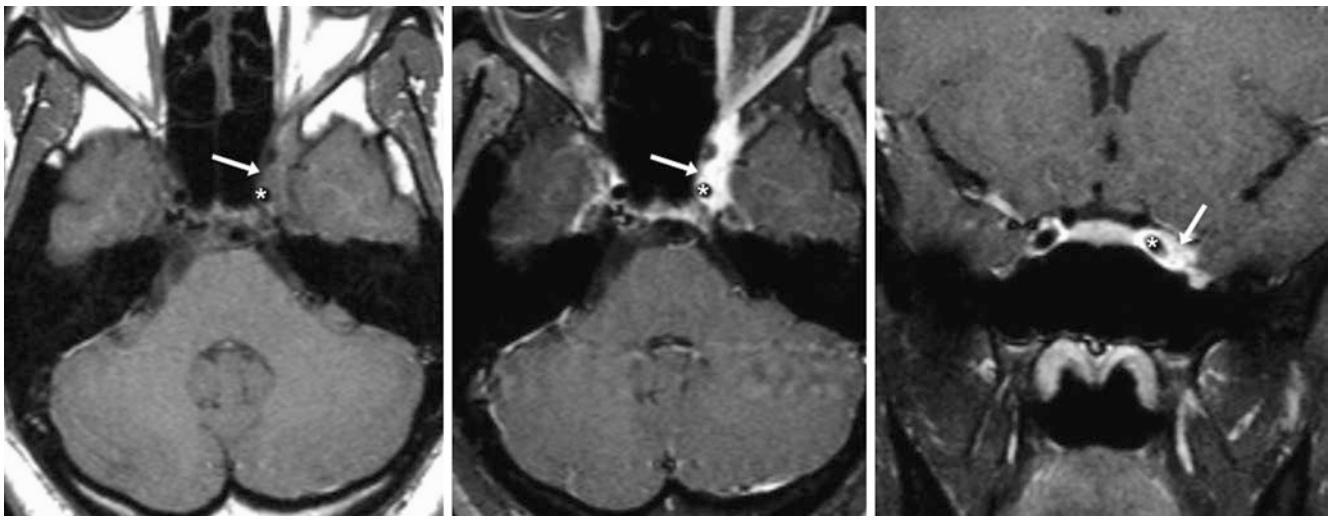

Fig. 7.27 Comparison case of Tolosa-Hunt (pseudotumor). A 29-year-old female with painful ophthalmoplegia had a left-sided mass within Meckel cave and the left cavernous sinus (*arrows*) surrounding the left ICA (**) on 1.5 T MRI axial T1WI pre- (*left*), and postcontrast (*middle*), and on postcontrast coronal fat-suppressed T1WI (*right*)

Suggested Reading

Bachow TB, Hesselink JR, Aaron JO, Davis KR, Taveras JM. Fat deposition in the cavemous sinus in Cushing disease. Radiology. 1984;153:135–6.

Hasso AN, Pop PM, Thompson JR, Hinshaw DB, Aubin ML, Bar D, et al. High resolution thin section computed tomography of the cavernous sinus. Radiographics. 1982;2:83–100.

Stricof DD, Gabrielsen TO, Latack JT, Gebarski SS, Chandler WF. CT demonstration of cavernous sinus fat. Am J Neuroradiol. 1989;10:1199–201.

Tokiguchi S. [Investigation of fat in the dural sinus.] article in Japanese. Nihon Igaku Hoshasen Gakkai Zasshi. 1991;51:871–82.

Pituitary Variations, Artifacts, Primary Empty Sella, and Incidentalomas

8

The *pituitary gland* arises from the ectoderm but has two separate components both embryologically and functionally: the *anterior lobe (adenohypophysis)* and the *posterior lobe (neurohypophysis)*. The adenohypophysis arises from the Rathke pouch, which represents an upward invagination of the oral ectoderm; the adenohypophysis is also called the anterior lobe and secretes a number of important endocrine hormones (under direction from the hypothalamus) for growth, fertility, lactation, and to respond to biological stress. The neurohypophysis represents a downward protrusion of the neural ectoderm from the diencephalon/hypothalamus; the neurohypophysis is also called the posterior lobe, which secretes hormones (also under direction from the hypothalamus) that regulate water absorption/resorption and uterine contractions. Between the anterior and posterior lobes lies the *pars intermedia* (the intermediate lobe), which is rudimentary and only vestigial in humans. Occasionally, *Rathke cleft cysts* (also known as *pars intermedia cysts*) form in this site as a result of incomplete regression of this lobe.

Imaging of the gland is optimally performed in all three standard imaging planes, but at a minimum, both sagittal and coronal 1–3-mm thickness sections are necessary for adequate depiction and diagnosis. Typically, both pre- and postcontrast T1WI and T2WI in these planes are necessary; an initial evaluation optimally implements both dynamic postcontrast T1WI (over the first 0–2 min after the intravenous gadolinium bolus) and a delayed postcontrast T1WI (at 2–5 min). Dynamic and delayed images allow for comparison of the normal gland (typically enhances in a fashion similar to that of the cavernous sinuseslocated laterally) relative to a microadenoma (<10 mm size) or macroadenoma (>10 mm size). In general, adenomas usually exhibit delayed enhancement and are darker than the remainder of the gland on both dynamic and delayed images. Other newer sequences that may be helpful include DWI, three-dimensional acquisition of FLAIR images, STIR, or balanced gradient echo (e.g., vendor-specifc CISS, BFFE, true FISP, or FIESTA).

Most of the variations in MRI appearance are related to the *differential contrast enhancement* between various portions of the gland or from side-to-side, termed by this author as the "lateral aspects of the anterior lobes," best seen on dynamic images. Because the posterior lobe lacks a blood–brain barrier (BBB), all structures of the adenohypophysis and neurohypophysis often enhance normally on postcontrast examinations, including the anterior and posterior lobes (which are outside of the BBB, since both must secrete substances into the circulation), the infundibulum/stalk, and the median eminence of the hypothalamus (MEH, upon which the stalk attaches, also outside the BBB because hormones secreted by the gland must collect there before being released into the blood). Typically, the stalk will enhance at the same time as the cavernous sinus by 30 s after the initiation of the contrast bolus, while on the delayed postcontrast MRI (usually at ≥1 min) the pituitary gland typically enhances with uniformly bright signal intensity.

There is a certain amount of variation in the size of the pituitary gland based on age, fertility status, and gender. Regarding age, the pituitary is uniformly bright at birth; after about 6 weeks of age the gland assumes the typical appearance of the isointense anterior lobe and the bright posterior lobe ("posterior bright spot" on nonconstrast Sagittal T1WI). The overall pituitary size varies with age; the height typically peaks in the 20–30-year-old age group and declines slowly thereafter. Regarding gender, the pituitary appears largest in female subjects in the 10–30-year-old age groups (fertile age) and can be even larger during pregnancy. The pituitary then decreases in size for the next two decades; there is debate as to whether it slightly increases or decreases in size in the 50–60-year-old age group. The average overall pituitary height ranges from 3–9 mm, but again this varies with gender; generally, this author considers 9–10 mm as the upper limit of normal. Physiologic *pituitary hypertrophy* can also occur (>9–10 mm height), which is effectively normal pituitary tissue with an enlarged gland; this can be difficult to discern from an adenoma that replaces the whole gland. A *macroadenoma* should not enhance in timing with the remainder of the normal gland and should enhance later after the infundibulum and cavernous sinus. In such patients with mild hypertrophy there can be mild

A.M. McKinney, *Atlas of Normal Imaging Variations of the Brain, Skull, and Craniocervical Vasculature*,
DOI 10.1007/978-3-319-39790-0_8

upward "tenting" of the pituitary gland (normally the superior aspect of the gland has a concave appearance), but the gland should not abut or displace the optic chiasm.

The pituitary infundibulum (i.e., stalk) may measure 1.5–3.5 mm and often tapers/decreases in size inferiorly toward its insertion on the pituitary gland. Notably, although a secondary criterion for diagnosing a *microadenoma* (defined as <10 mm in size) is stalk deviation away from the side of the lesion; however, this criterion should not be implemented by itself because a certain degree of deviation or "tilt" may be present in up to 30–45 % of the population. There can also be asymmetry regarding the size of the anterior lobe from side-to-side, where one side may be mildly larger. However, the signal intensity on both sides should be identical.

Notably, *three-dimensional FLAIR images* are becoming increasingly utilized because they eliminate problematic cerebrospinal fluid (CSF) flow voids in the suprasellar and other basal cisterns. A normal variant appearance on such noncontrast three-dimensional FLAIR images is that the infundibulum/stalk as well as the tuber cinereum may exhibit a normal bright signal, which becomes even more hyperintense following intravenous contrast administration because the stalk does not have a blood–brain barrier. The reason for the bright signal in these structures prior to contrast administration is unknown but could be related to a higher water/fluid level within the structures such as the stalk and certain portions of the hypothalamus (such as the tuber cinereum), perhaps caused by the presence of neurosecretory cells or granules.

Other variations in appearance in the pituitary may relate to *artifacts. Vascular-related flow voids* can project in the phase direction (most commonly the transverse direction) and may appear superimposed on the gland itself, possibly also simulating a pituitary lesion. These most commonly arise from the internal carotid arteries (ICAs), and the implementation of flow compensation or altering band width may improve the appearance. Another potential pitfall is that artifacts from *CSF-related flow voids* can project into the suprasellar cistern alongside the pituitary stalk, which can simulate a mass; this is most prominent on dual echo or fast spin echo images.

Other variations may occur in the amount of fluid within the sella relative to the size of the pituitary gland. Such appearances include the so-called *empty sella* and the *partially empty sella*, which may occur in the general adult population in about 5–10 % based on postmortem examinations and in the adult population scanned for nonpituitary reasons at a rate of approximately 15–16 % (partially or mostly empty sella) and/or 11–14 % (empty sella). Regarding the terminology, the term *primary empty sella* (PES) refers to the presumed pathophysiologic mechanism of this appearance; the concept involves the downward herniation/invagination of CSF subarachnoid space into the sella turcica, which compresses and flattens the pituitary gland. However, most PES literature that addresses the incidence or significance of symptoms does not separate a completely from a partially empty sella, thus causing confusion regarding the significance of PES in an otherwise asymptomatic patient. Of note, the term secondary empty sella is related to degeneration of the pituitary gland, whether caused by necrosis, hemorrhage, ischemia, infection, autoimmune disorder, surgery, medication, or other causes and is not discussed further here.

The PES entity is thought to be related to either a congenital defect in the diaphragm sella, intermittent increases in intracranial pressure, or intermittent changes in volume of the pituitary gland; a commonly proposed theory is that PES results from spontaneous regression or treatment of a pituitary tumor (a theory yet to be proved). Of note, intrasellar pressure measurements have been shown to be normal in most patients with PES, arguing against the theory of increased pressure. Interestingly, the incidence of PES has been shown to be much lower in children, estimated at 1–2 %; however if present, PES may be more likely to be symptomatic in pediatric patients. Regarding symptoms in adults, patients with PES may be either symptomatic or asymptomatic, but the majority are incidental and asymptomatic; the incidence of symptoms in patients with PES is approximately 20–40 %, and those symptoms may consist of hypo- or hyperpituitarism, headaches, visual disturbances, or other neurologic symptoms. PES occurs more commonly in women, which may be as high as a 4:1 or 5:1 ratio as compared to men, and defects in the diaphragm sella occur with a similar incidence. PES is also more common in women with multiple pregnancies, obese patients, and hypertensive patients. Thus, the current thinking is that while PES is an incidental finding in most patients scanned for nonpituitary reasons, it becomes of more concern the smaller the pituitary volume and the larger the contour of the bony sella, particularly in obese females or children. Thus, the finding should be reported, but the significance should be individualized to the patient based on age, gender, presenting symptoms, weight, and other clinical factors.

Another important point to note is that incidental but real pituitary lesions may exist in up to 6–10 % of the population based on large studies at autopsy (so-called incidentalomas). Of these, *Rathke cleft cysts* (RCCs) are the most common, occurring incidentally in 3–10 % of the population; next most common are *adenomas* (although some studies suggest microadenomas are the most common), occurring incidentally in 2–11 % of the general population based on large postmortem studies. Such incidental pituitary adenomas have also been termed silent adenomas; these cause some difficulty in interpretation, particularly on thicker (e.g., 5 mm or more) images that happen to cover the pituitary on routine brain MRI examinations. In addition, in such cases dedicated pituitary imaging may be necessary for confirmation, which should consist of dynamic postcontrast images. Also, *arachnoid cysts, intrasellar hemorrhages*, and *pituitary infarcts* are other rare incidental findings, occurring in less than 1 % of the population (Figs. 8.1, 8.2, 8.3, 8.4, 8.5, 8.6, 8.7, 8.8, 8.9, and 8.10).

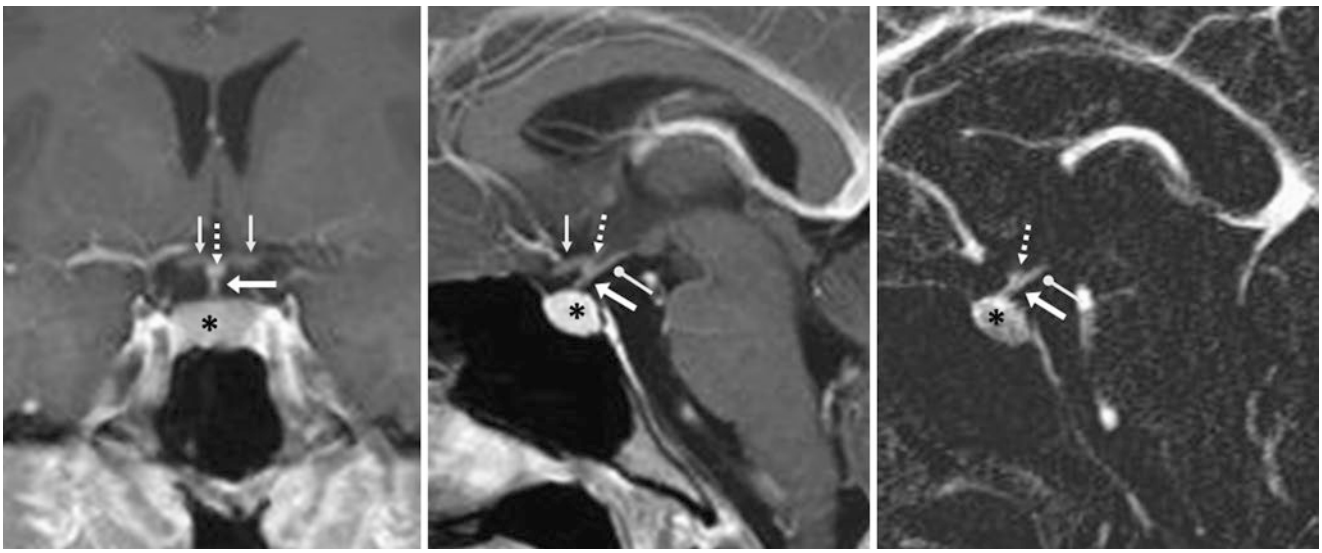

Fig. 8.1 A 16-year-old female patient had a 1.5 T MRI that demonstrated a normal, enhancing pituitary infundibulum (*arrows*) relative to the nonenhancing optic chiasm (*thin arrows*). The pituitary (*) was normal and borderline enlarged because the patient was of childbearing age, as shown on postcontrast coronal (*left*) and sagittal T1WI (*middle*) and on subtracted postcontrast T1WI (with precontrast images subtracted from the postcontrast images, *right*). Also note enhancement of the median eminence of the hypothalamus (*dashed arrows*) and of the tuber cinereum (*circle tip arrow*)

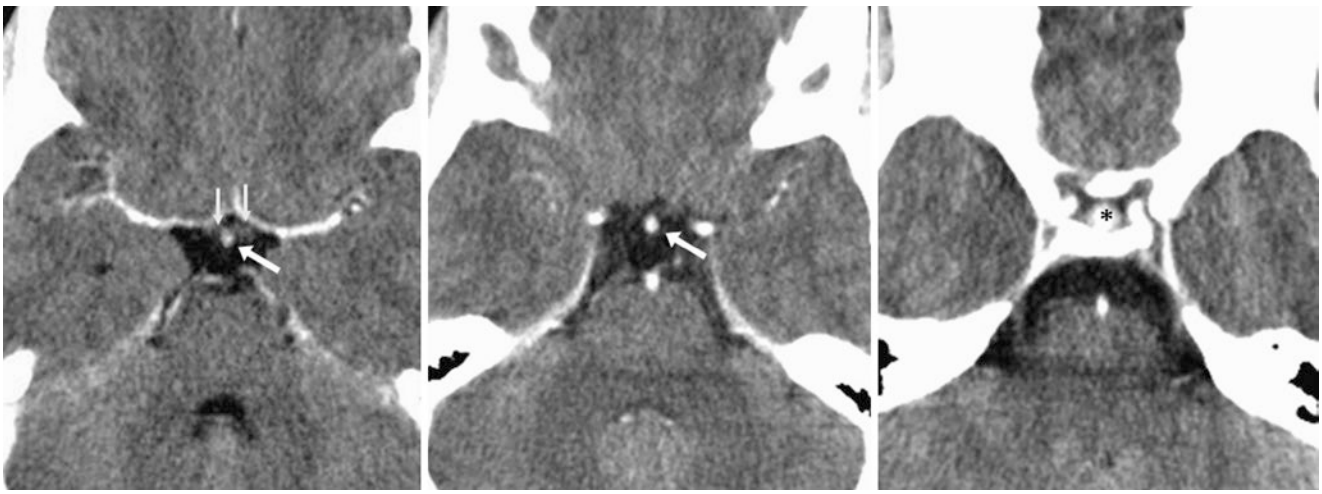

Fig. 8.2 A 15-year-old female patient with headaches. Axial contrast-enhanced computed tomography (CECT) images demonstrate a normal, enhancing pituitary infundibulum (*arrows*) relative to the nonenhancing optic chiasm (*thin arrows*). Note normal pituitary gland enhancement (*)

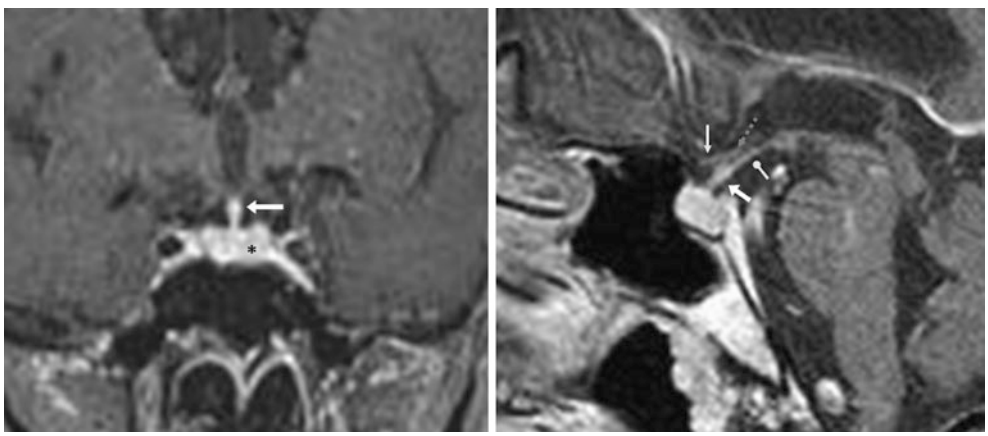

Fig. 8.3 A 53-year-old female patient with 1.5 T MRI postcontrast coronal (*left*) and sagittal (*right*) T1WIs that depict normal enhancement of the infundibulum (*arrows*) relative to the nonenhancing optic chiasm (*thin arrow*). The left side of the gland (*) is slightly larger than the right, a normal variation. Also note enhancement of the median eminence of the hypothalamus (*dashed arrow*) and minimal enhancement of the tuber cinereum (*circle tip arrow*)

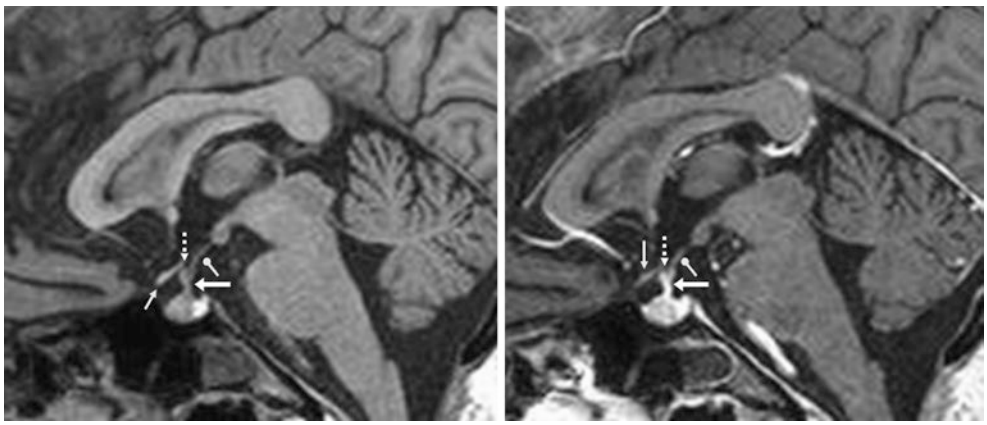

Fig. 8.4 An 18-year-old female patient with 1.5 T MRI sagittal pre- (*left*) and postcontrast (*right*) T1WIs. Note normal enhancement of the infundibulum (*arrows*) relative to the nonenhancing optic chiasm (*thin arrows*). Also, note the enhancement of the median eminence of the hypothalamus (*dashed arrows*) and of the tuber cinereum (*circle tip arrows*)

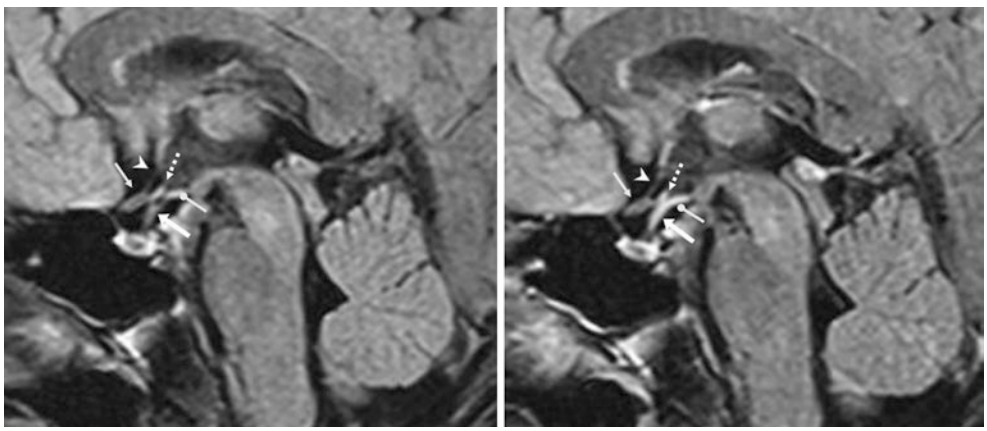

Fig. 8.5 A 35-year-old female patient; 1.5 T MRI sagittal pre- (*left*) and postcontrast (*right*) FLAIR images depict normal enhancement of the infundibulum (*arrows*), tuber cinereum (*circle tip arrows*), and median eminence (*dashed arrows*) relative to the nonenhancing optic chiasm (*thin arrows*). A faintly enhancing lamina terminalis (*arrowheads*) can be noted on the postcontrast image, since that structure also does not have a blood–brain barrier

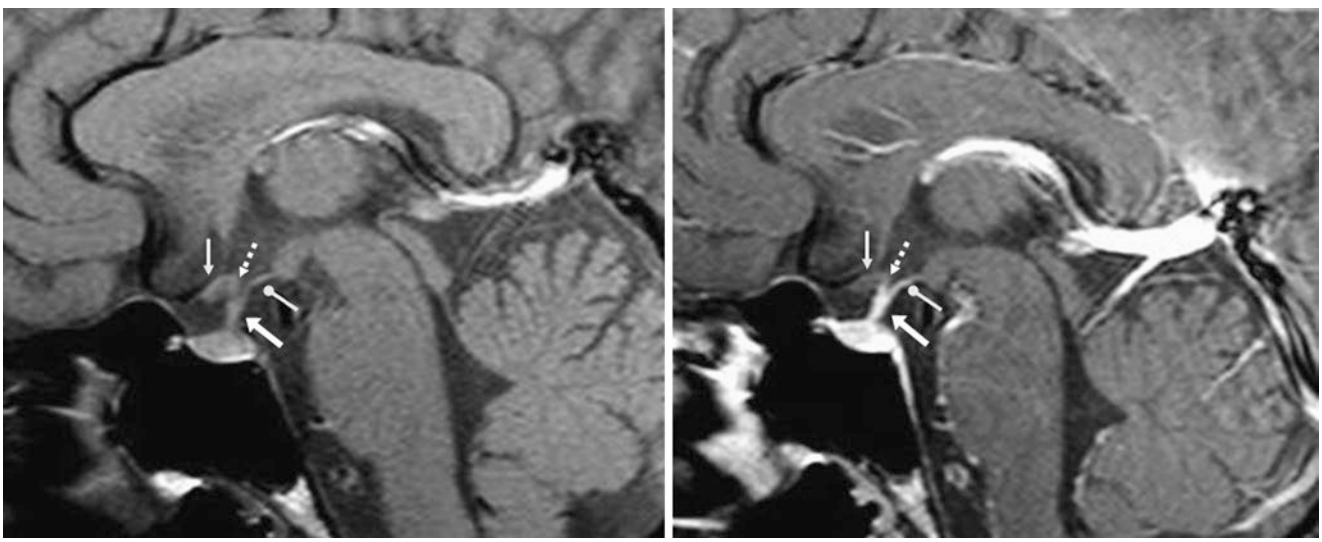

Fig. 8.6 A 22-year-old male patient with 3 T MRI sagittal pre- (*left*) and postcontrast (*right*) T1WIs demonstrating normal enhancement of the infundibulum (*arrows*) relative to the nonenhancing optic chiasm (*thin arrows*). Also, note the enhancement of the median eminence (*dashed arrows*) and of the tuber cinereum (*circle tip arrows*)

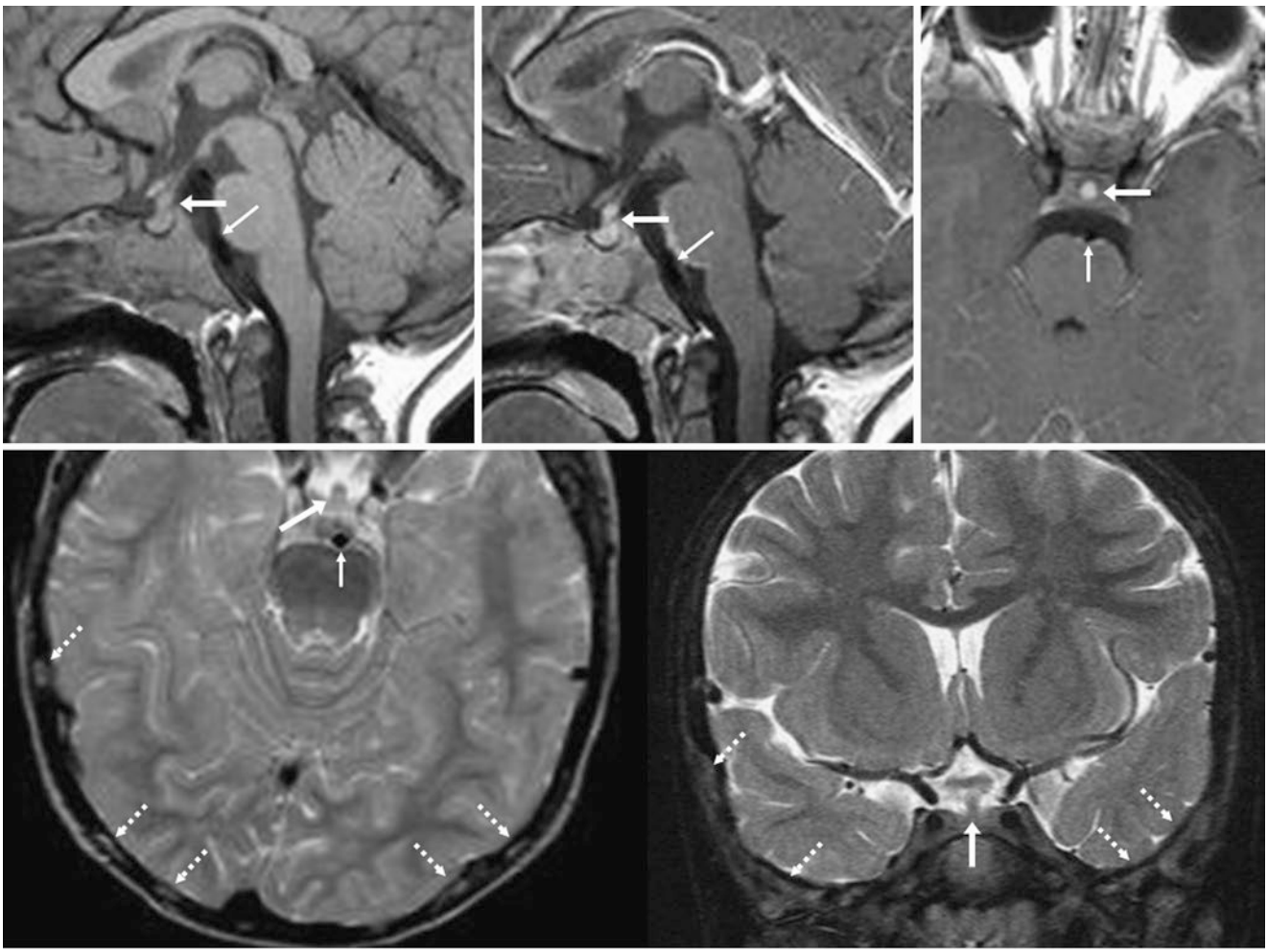

Fig. 8.7 Comparison case of Langerhans cell histiocytosis: A 3-year-old male patient with diabetes insipidus; a 3 T MRI demonstrates moderate thickening of the pituitary stalk (*arrows*), which is as thick as the basilar artery (*thin arrows*) on pre- (*left*) and postcontrast (*middle*) sagittal T1WIs and on axial postcontrast T1WI (*right*). Axial (*bottom left*) and coronal (*bottom right*) images depict the bone lesions typically associated with Langerhans cell histiocytosis (*dashed arrows*)

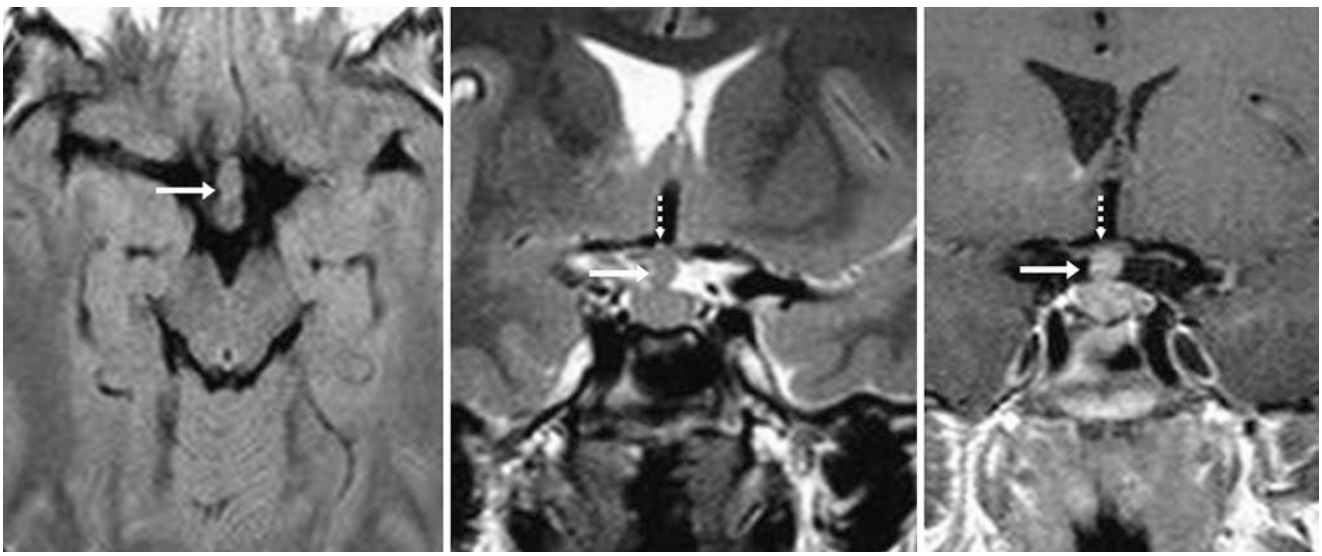

Fig. 8.8 Comparison case of lymphocytic hypophysitis (biopsy proven): A 16-year-old male with growth delay; a 1.5 T MRI depicts moderate enlargement of the stalk (*arrows*) on noncontrast axial FLAIR (*left*), coronal T2WI (*middle*), and coronal postcontrast T1WI (*right*). Note that the stalk indents the optic chiasm (*dashed arrows*)

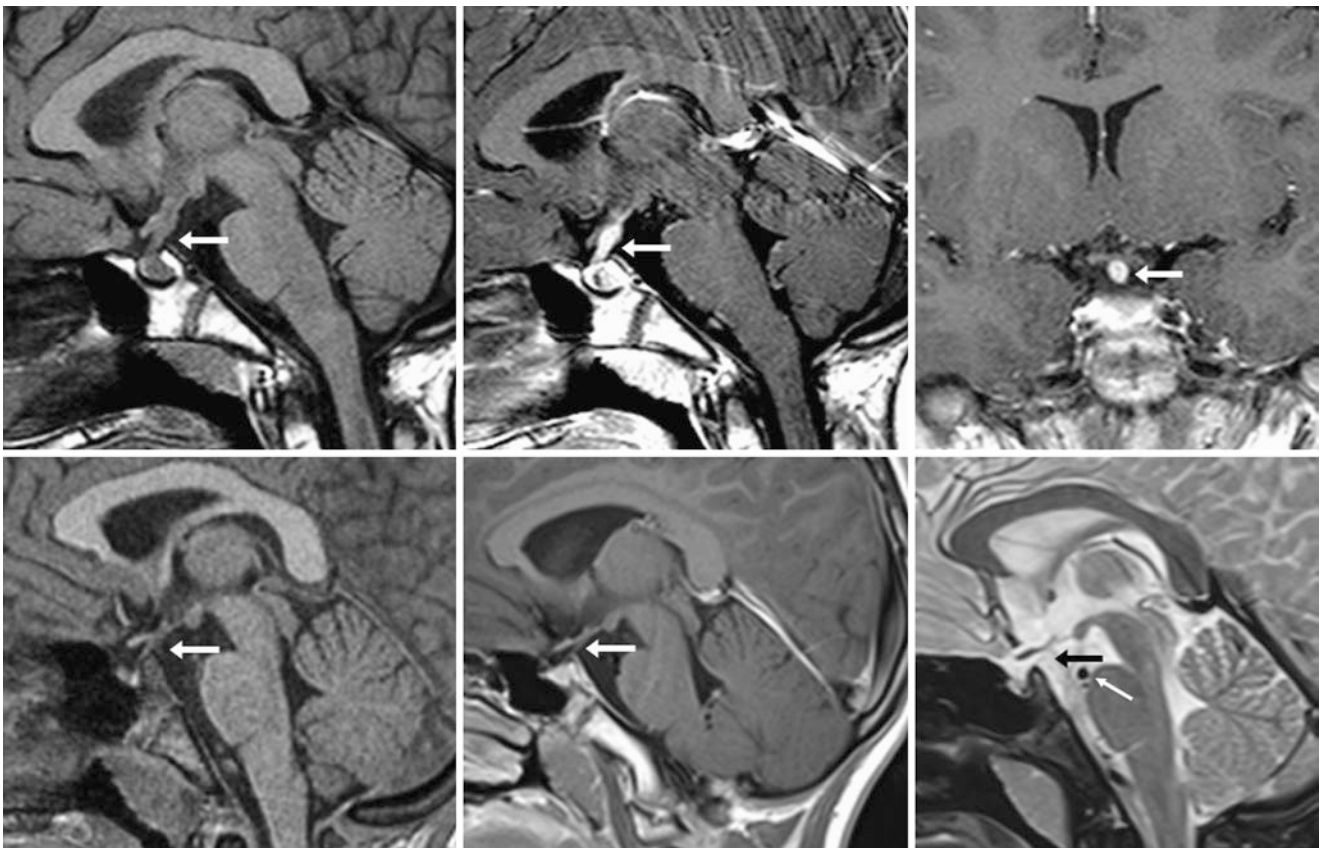

Fig. 8.9 Comparison case of germ cell tumor: A 7-year-old patient with a mild to moderately enlarged pituitary stalk (*arrows*) on 3 T MRI sagittal noncontrast (*top left*) and postcontrast (*top middle*) T1WI and on coronal postcontrast T1WI (*top right*). This had markedly improved after therapy, as demonstrated on an MRI 3 years later (*bottom row*), including sagittal precontrast (*bottom left*) and postcontrast (*bottom middle*) T1WI and sagittal T2WI (*bottom right*). Note that the stalk (*arrows*) was initially larger than the basilar artery (denoted by the *thin arrows*, *bottom right*)

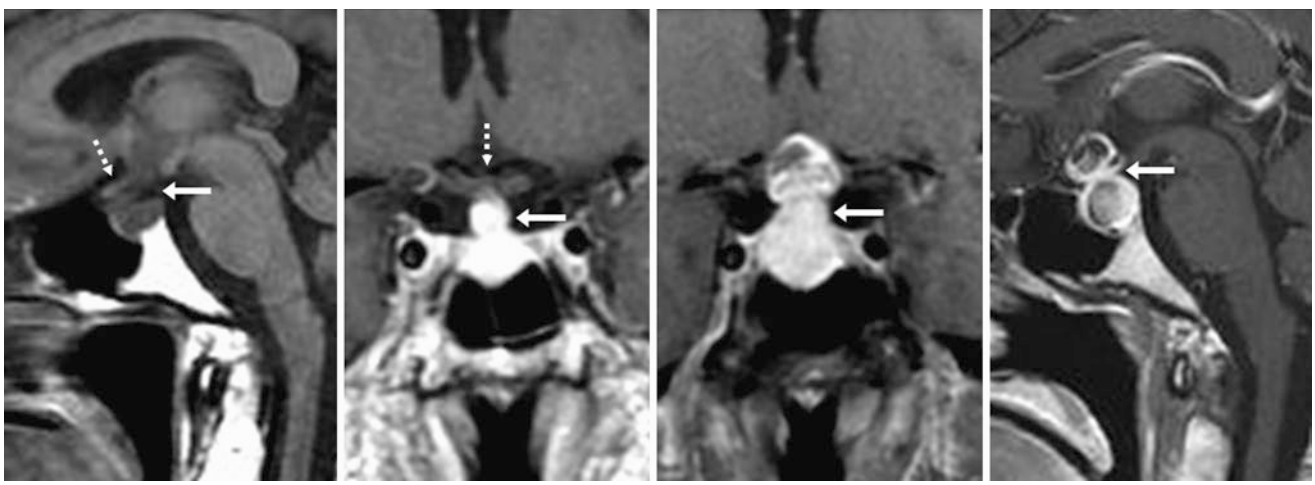

Fig. 8.10 Comparison case of metastasis to the pituitary stalk (biopsy proven): The patient was a 35-year-old male with lung cancer; a 1.5 T MRI depicts moderate enlargement of the stalk (*arrows*) on noncontrast sagittal T1WI (*left*) and postcontrast coronal T1WI (*left middle*). This was termed indeterminate for malignancy. However, 1 year later, postcontrast coronal (*right middle*) and sagittal (*right*) T1WIs demonstrated enlargement of the mass that became necrotic. Note that the stalk indented the optic chiasm (*dashed arrows*) initially and subsequently engulfed the chiasm

8.1 Lateral Anterior Lobe Pituitary Enhancement

The anterior lobe of the pituitary may have *differential enhancement* comparing medially to laterally. On the earliest images, enhancement around the base of the pituitary infundibulum *or* stalk at the midline should be noted (a tuft of enhancement representing the hypophyseal capillary bed, which is not constrained by the blood–brain barrier), along with enhancement of the posterior pituitary and cavernous sinus. This can occur less than 10 s following the presence of intravenous contrast medium within the ICAs. Uniform enhancement of the gland (i.e., extending peripherally and laterally) occurs sometime between 60 and 200 s after contrast administration. On the other hand, about two thirds of microadenomas exhibit slower enhancement, with their peak later than that of normal gland. Unfortunately, about one third of *adenomas* may enhance as early as the remainder of the gland, possibly because of an arterial supply (rather than the typical indirect pituitary portal supply). Identifying this minority of adenomas requires assessing both the dynamic and several minutes delayed postcontrast images (Figs. 8.11, 8.12, 8.13, 8.14, 8.15, 8.16, 8.17, 8.18, 8.19, and 8.20).

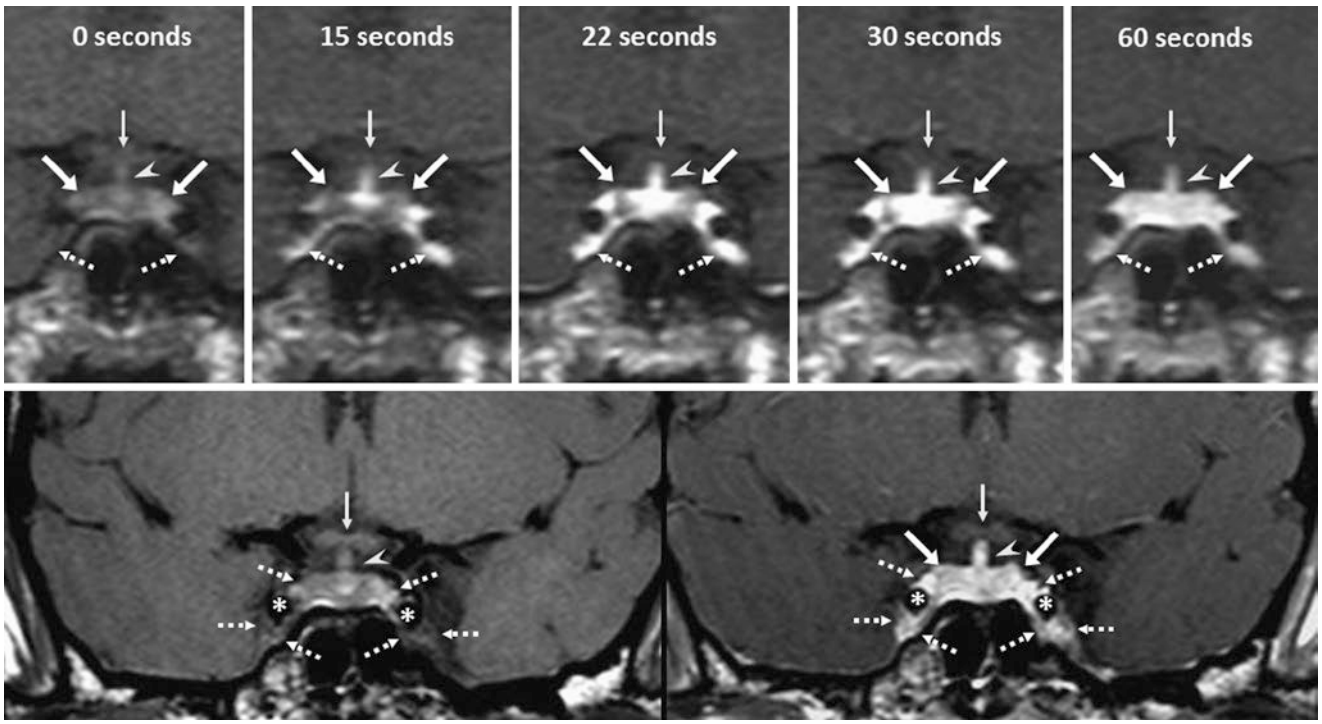

Fig. 8.11 Normal dynamic enhancement of the pituitary extending laterally. The patient was a 21-year-old female with hypopituitarism. On a 3 T MRI (interpreted as normal), dynamic contrast enhanced T1WIs (*top row*) from time 0 (noncontrast) to 60 s, the lateral aspects of the anterior lobes (*arrows*) filled with contrast more slowly than the stalk (*arrowheads*) and than the cavernous sinus (*dashed arrows*). On noncontrast (*bottom left*) and delayed postcontrast (5 min, *bottom right*) T1WI, the cavernous sinus is outlined by the *dashed arrows* surrounding the carotids (*)

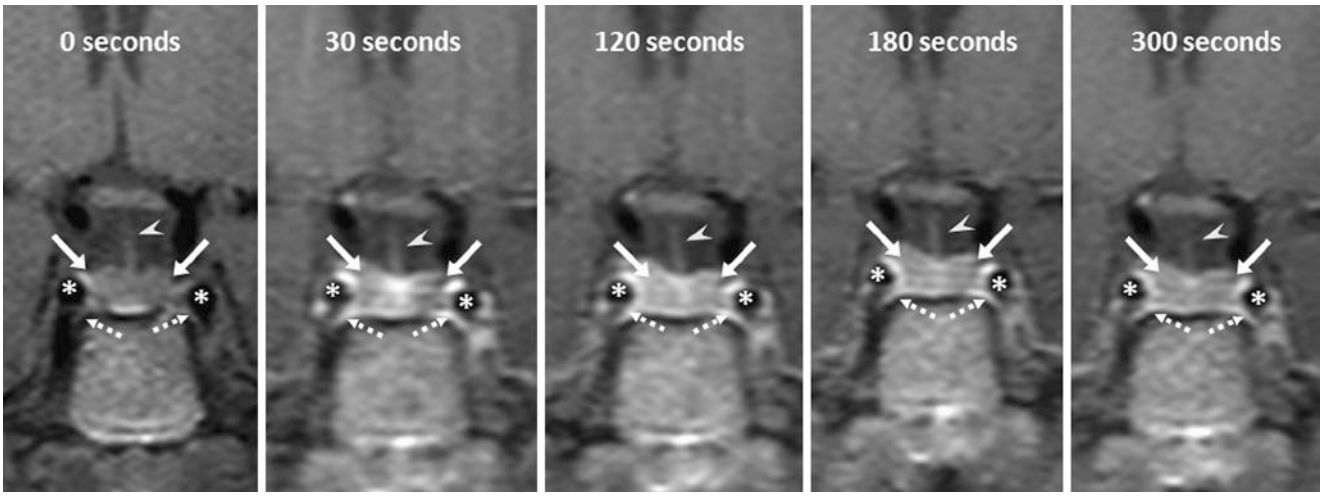

Fig. 8.12 Normal pituitary dynamic enhancement extending laterally. The patient was a 27-year- old female with hyperprolactinemia. On a 3 T MRI (interpreted as normal), dynamic contrast enhanced T1WIs from time 0 s (noncontrast) to 300 s depict the lateral anterior lobes (*arrows*) filling with contrast, where subtle hypointensity in these regions remains on the 300 s image. The stalk (*arrowheads*) enhances only minimally or does not enhance. Note early enhancement of the cavernous sinus (*dashed arrows*) surrounding the ICAs (*)

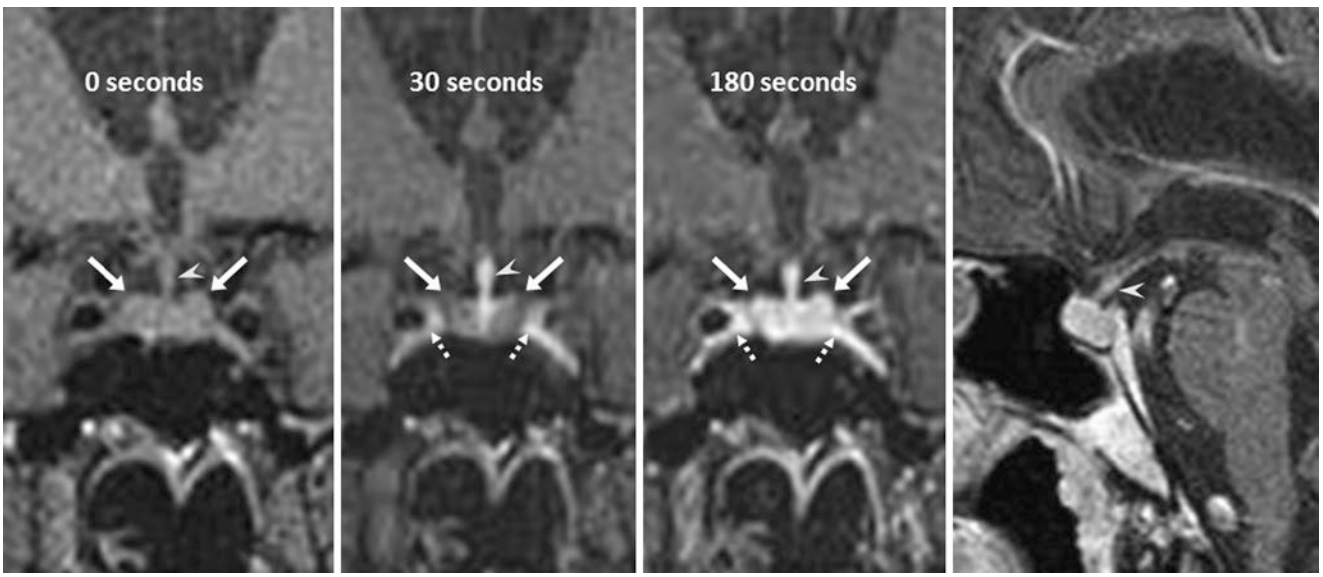

Fig. 8.13 Normal lateral anterior lobe delayed enhancement. In a 67-year-old female with a negative 1.5 T MRI, the gland is homogeneously isointense prior to the use of contrast on coronal T1WI (*left*). The lateral, peripheral portions of the anterior lobes (*arrows*) are mildly hypointense at 30 s (*left middle*) but fill in by 180 s (*right middle*). The sagittal T1WI (*right*) appears normal; thus, the examination was interpreted as normal. Note the simultaneous enhancement of the cavernous sinus (*dashed arrows*) and the stalk (*arrowheads*) on the 30-s dynamic image

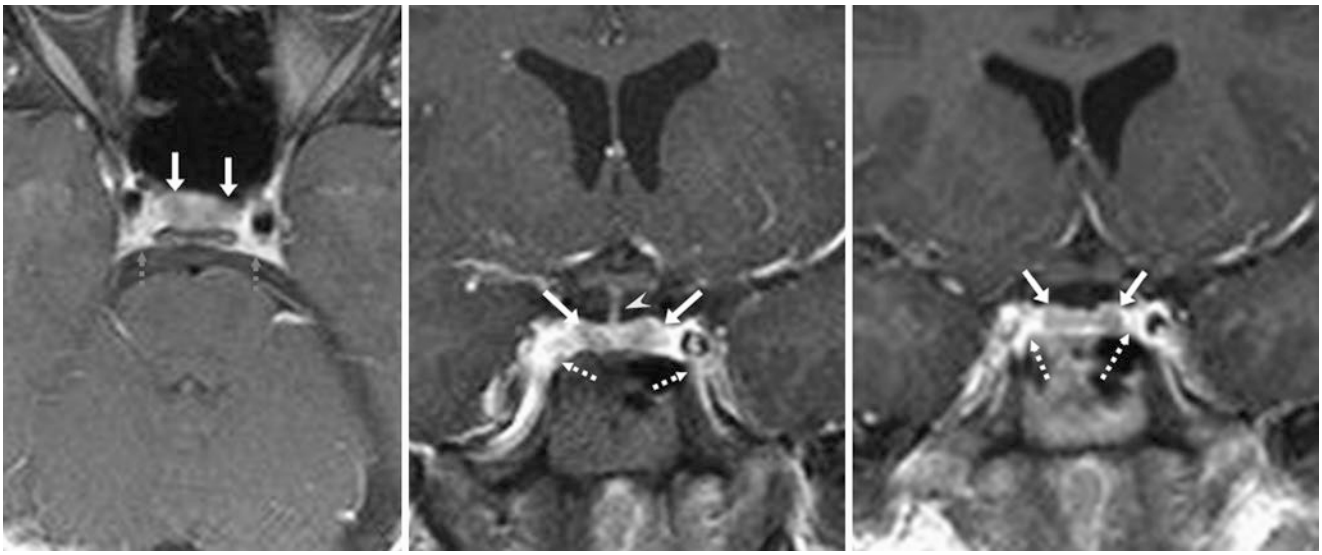

Fig. 8.14 Normal lateral anterior lobe delayed enhancement. In a 13-year-old female with hearing loss (negative 1.5 T MRI), the lateral, peripheral portions of the anterior lobes (*arrows*) remain mildly hypointense on axial (*left*) and coronal (*middle and right*) images. The stalk (*arrowhead*) appears normal in that it mildly enhances and is at midline. Note the mildly enhancing cavernous sinus (*dashed arrows*). Thus the examination was interpreted as normal

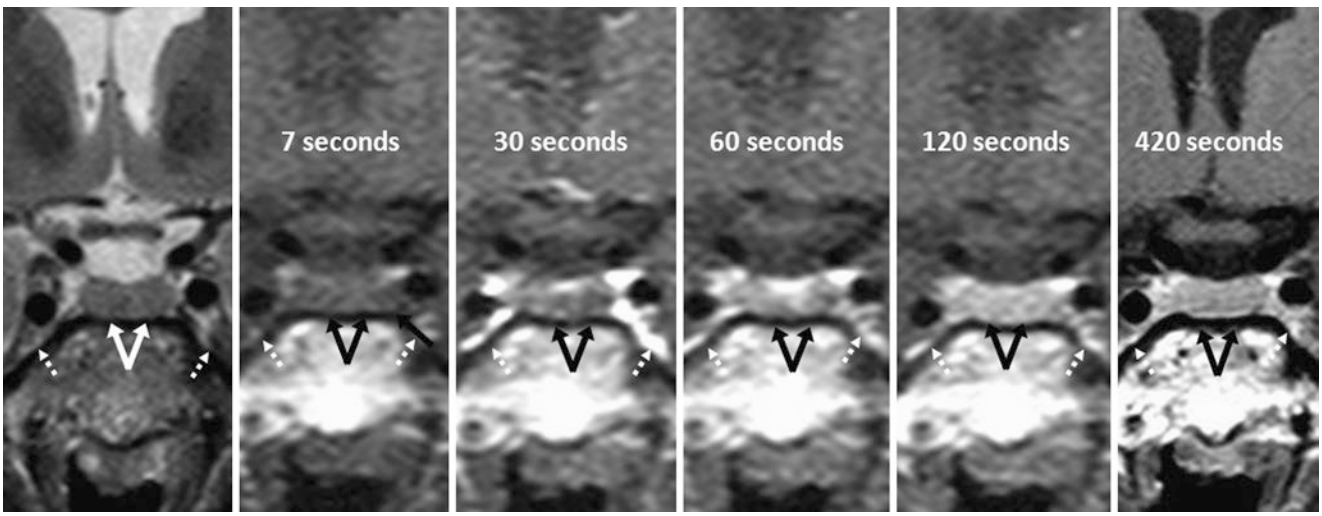

Fig. 8.15 Normal delayed enhancement peripherally. In a 35-year-old female with vision loss, 3 T MRI (interpreted as normal) coronal T2WI (*left*), and serial dynamic enhanced T1WIs from time 7–420 s postcontrast depict the lateral areas (*arrows*) filling with contrast, although more slowly than expected; mild hypointensity remains on delayed images. Note the enhancing cavernous sinus (*dashed arrows*). The findings were unchanged 1 year later (*not shown*)

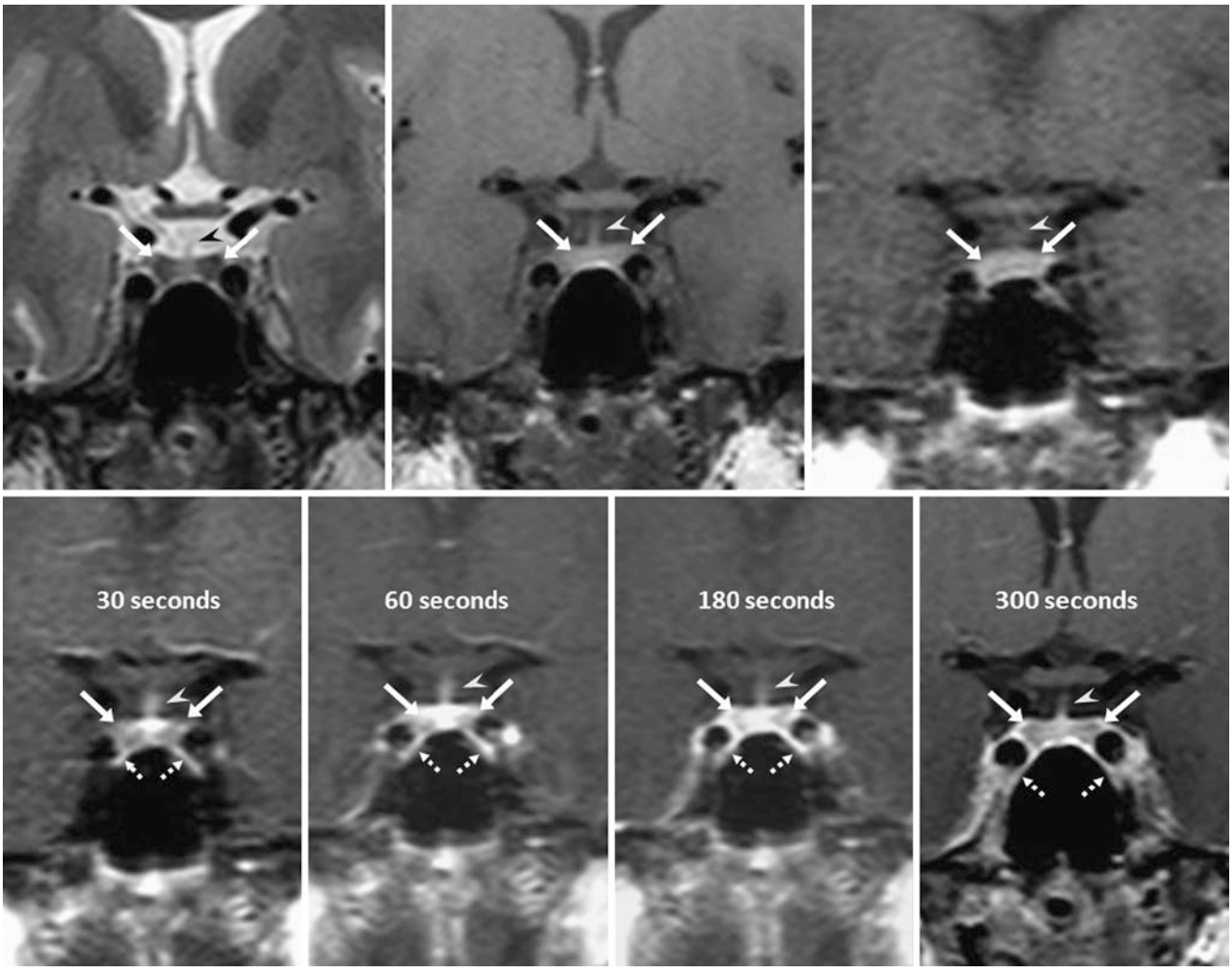

Fig. 8.16 Normal lateral anterior lobe enhancement with persistent hypointensity. In a 22-year- old hypernatremic male, the lateral aspects of the anterior lobes (*arrows*) are hypointense prior to contrast on 3 T MRI coronal T2WI (*top left*) and T1WI (*top middle*); the MRI was interpreted as normal. Dynamic enhanced images at 0 (*top right*) through 300 s (*bottom right*) depict normal persistence of the hypointense lateral anterior lobes, even on delayed images. The enhancing stalk (*arrowheads*) and cavernous sinus (*dashed arrows*) enhance earlier and more avidly

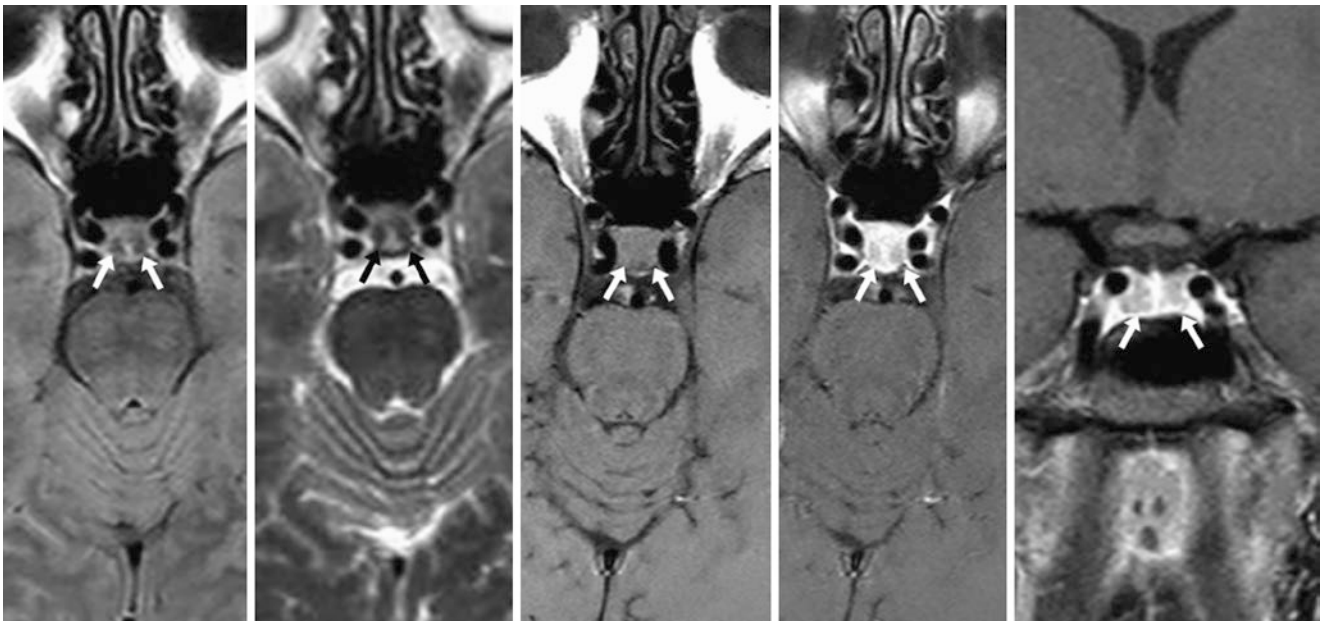

Fig. 8.17 Normal lateral anterior lobe enhancement on delayed images. In a 36-year-old female with vertigo, the lateral anterior lobes (*arrows*) are hypointense prior to contrast on 1.5 T MRI axial FLAIR (*left*) and T2WI (*left middle*) but not on T1WI (*middle*). Postcontrast axial (*right middle*) and coronal (*right*) T1WIs depict the hypointense lateral anterior lobes, which persist even on 5–7-min delayed postcontrast images. The examination was called normal

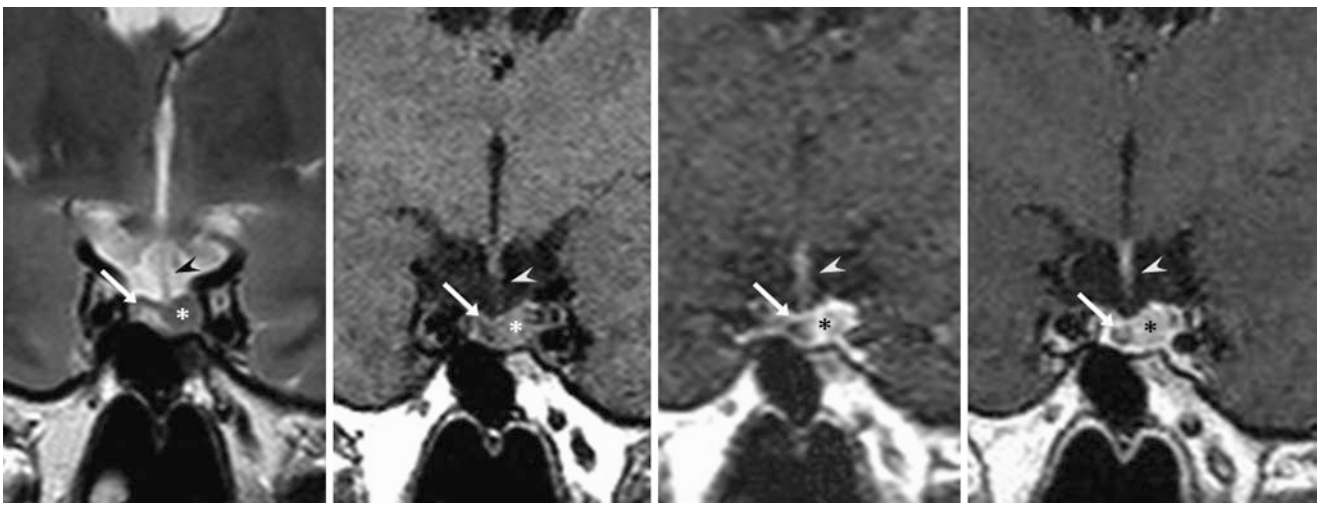

Fig. 8.18 Comparison case of microadenoma. A 31-year-old female with hyperprolactinemia in whom coronal T2WI (*left*) demonstrates a bright focus in the lateral right anterior lobe (*arrows*). Pre- (*left middle*) and postcontrast 60-s delay (*right middle*), and 5-min delayed (*right*) coronal T1WIs show that this 4-mm focus does not follow the enhancement pattern of the stalk (*arrowheads*) or the left side of the gland (*), which indicates an adenoma

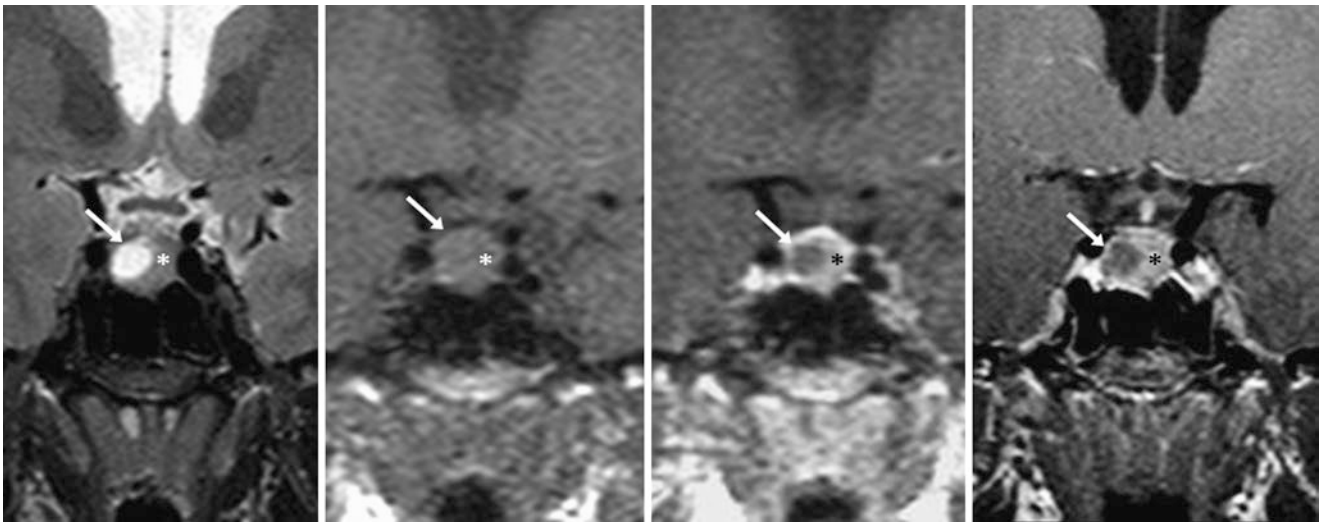

Fig. 8.19 Comparison case of microadenoma. A 22-year-old female with hyperprolactinemia in whom coronal T2WI (*left*) depicts a well-circumscribed bright focus (*arrows*) in the lateral aspect of the right anterior lobe. Precontrast (*left middle*), postcontrast 120-s delay (*right middle*), and 5-min delayed (*right*) coronal T1WIs show that this 7.5-mm lesion does not follow the enhancement of the left side of the gland (*), which indicates an adenoma

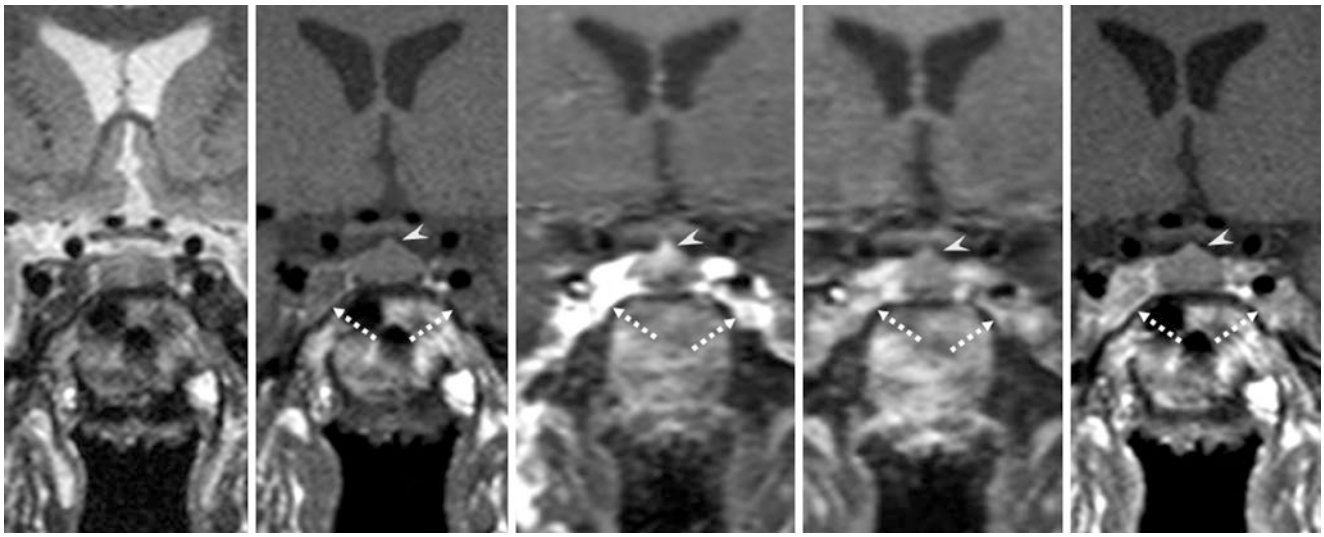

Fig. 8.20 Comparison case of a macroadenoma replacing the entire gland. A 22-year-old male patient with panhypopituitarism in whom coronal T2WI (*left*) depicts mild enlargement of the anterior lobe with upward tenting (*arrowheads*) at the midline near the stalk insertion site. Precontrast (*left middle*) and dynamic postcontrast 60- (*middle*), 300- (*right middle*), and 420-s (*right*) coronal T1WIs demonstrate that on the delayed images the gland remains uniformly hypointense relative to the enhancing cavernous sinus (*dashed arrows*), even as the contrast begins to leave by 5–7 min

8.2 Pituitary Hypertrophy and Tenting

As stated previously, the pituitary size varies with age, peaking at 20–30 years of age and is larger in females, particularly in the 10–30-year-old age group (fertile age); it can be larger in pregnancy. The average overall pituitary height should range from 3 to 9 mm and be less than 10 mm maximum height. Physiologic *pituitary hypertrophy* can occur when the height is slightly greater than 9–10 mm or when normal pituitary tissue is present in an enlarged gland, which can mimic *adenoma* that replaces the whole gland. However any mass effect on adjacent structures should raise the question of macroadenoma (Figs. 8.21, 8.22, 8.23, 8.24, 8.25, 8.26, 8.27, 8.28, 8.29, and 8.30).

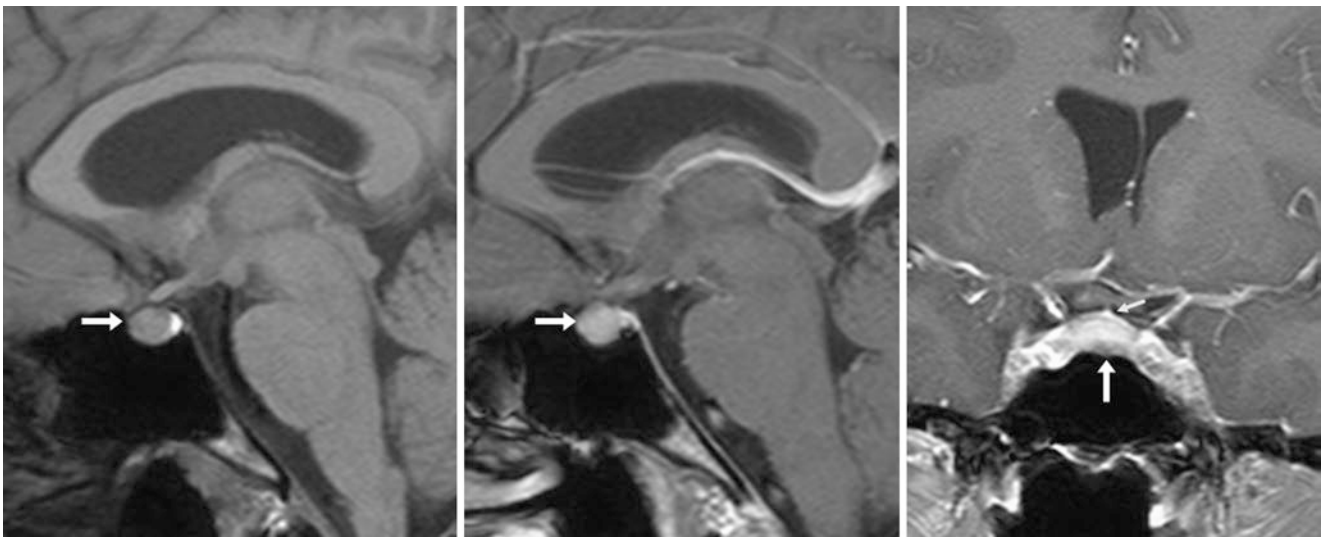

Fig. 8.21 A 38-year-old female patient with headaches and an otherwise normal MRI. The borderline enlarged pituitary (*arrows*) on a 1.5 T MRI measured 8.7 mm in height on sagittal noncontrast (*left*) and postcontrast (*middle*) T1WI at the midline. Note normal tenting (*thin arrow*) of the pituitary at the stalk's insertion site on a postcontrast coronal T1WI (*right*)

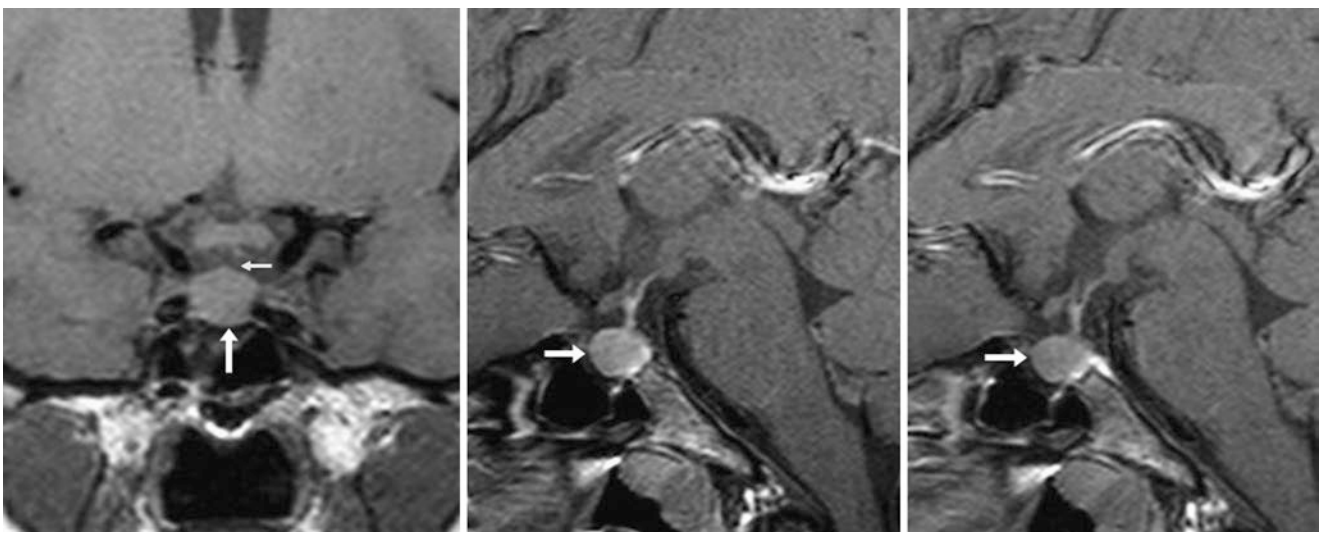

Fig. 8.22 An 18-year-old female with right-sided headaches but an otherwise normal MRI. The mildly enlarged pituitary (*arrows*) on a 3 T MRI measured 10.3 mm in height on coronal noncontrast T1WI (*left*); note the normal tenting (*thin arrow*) of the pituitary at the stalk's insertion site. Sagittal T1WIs were obtained both pre- (*middle*) and postcontrast (*right*)

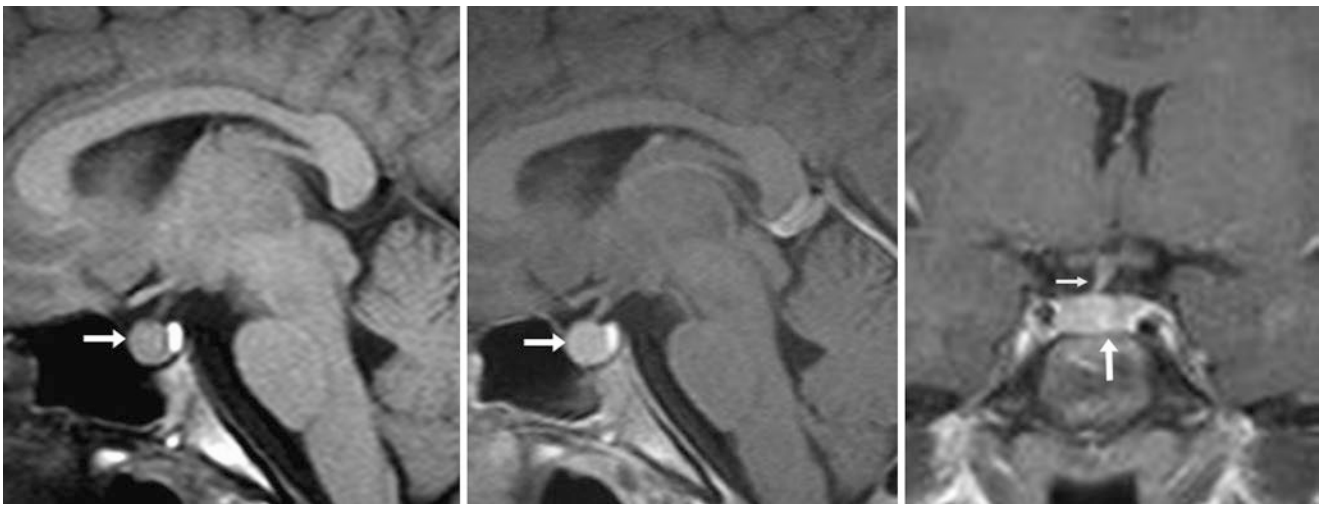

Fig. 8.23 The patient was a 12-year-old pubescent female with headaches but an otherwise normal MRI. The borderline enlarged pituitary (*arrows*) on a 1.5 T MRI measured 9.3 mm in height on sagittal T1WI both pre- (*left*) and postcontrast (*middle*). Note the mild shift of the stalk to the right (*thin arrow*) on postcontrast coronal T1WI (*right*), which is another normal variation

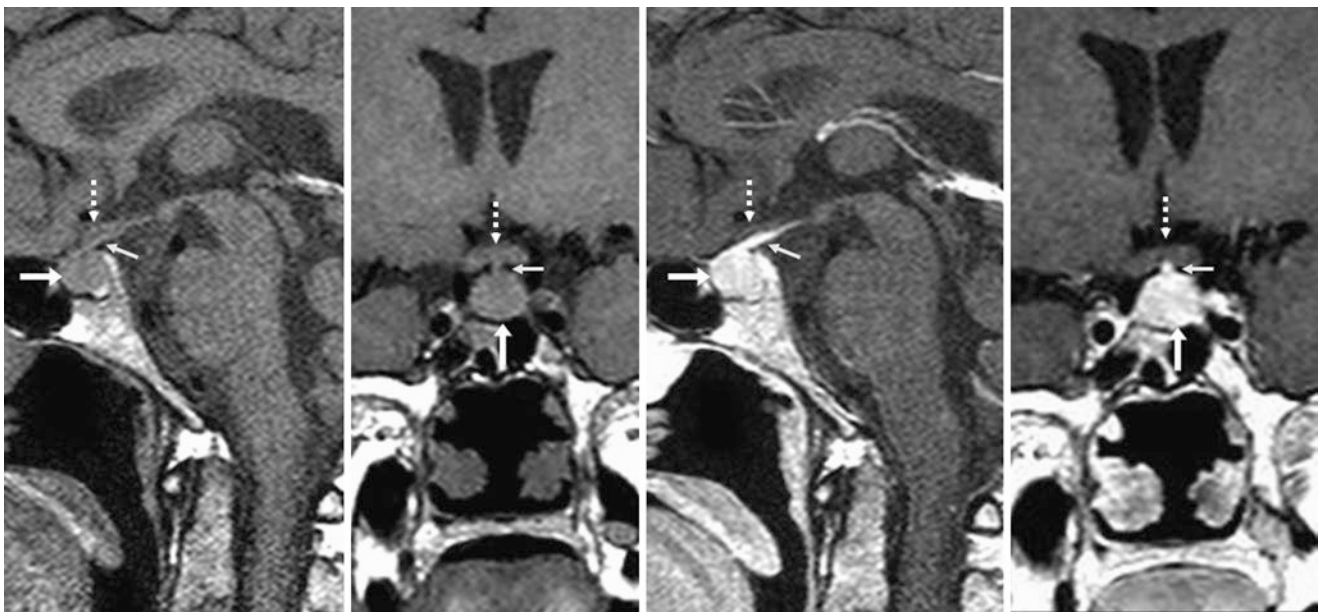

Fig. 8.24 The patient was a 42-year-old female with facial pain; the pituitary (*arrows*) was mildly enlarged (10.1 mm in height) on noncontrast sagittal (*left*) and coronal (*left middle*) T1WIs and on postcontrast sagittal (*right middle*) and coronal (*right*) T1WIs. The hypertrophy was unchanged 6 months later. The stalk is mildly displaced (*thin arrows*) upward toward the chiasm (*dashed arrows*), i.e., tenting. On dynamic images (*not shown*), the gland homogeneously enhanced

Fig. 8.25 The patient was a 27-year-old female with a borderline enlarged pituitary (*arrows*) at the top of an axial non-enhanced computed tomography (NECT) (*left*) performed for trauma as well as on an axial CECT (*middle*). The height was 9.0 mm on a coronal reconstruction (*right*)

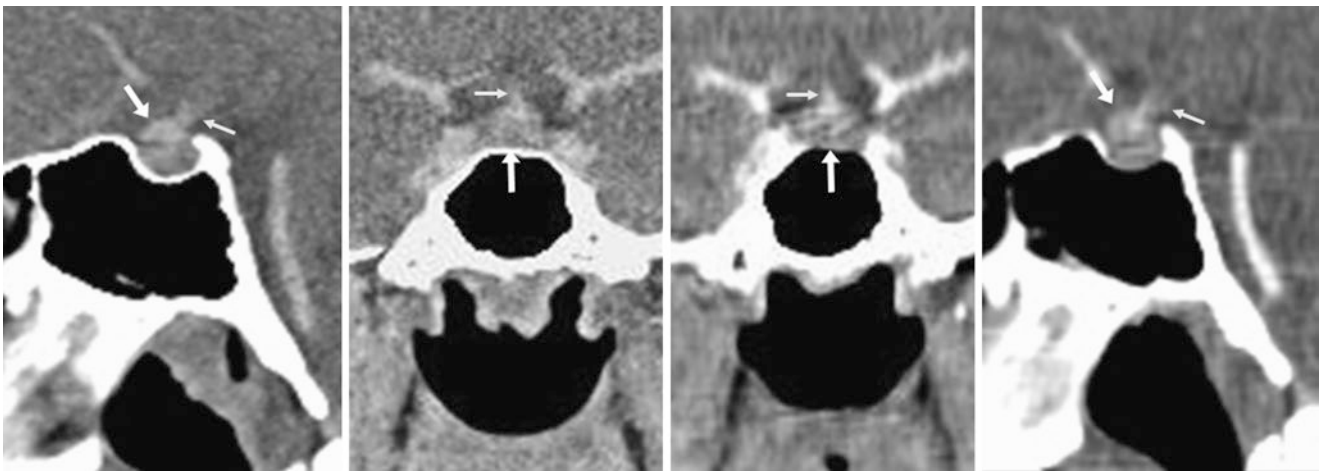

Fig. 8.26 A 20-year-old female with a borderline enlarged pituitary (*arrows*) at the top of a CECT of the neck (obtained to follow lymphadenopathy). The height was 9.3 mm on sagittal (*left*) and coronal (*left middle*) reconstructions. This was unchanged 1 year later on coronal (*right middle*) and sagittal (*right*) reformats. Note the stalk (*thin arrows*)

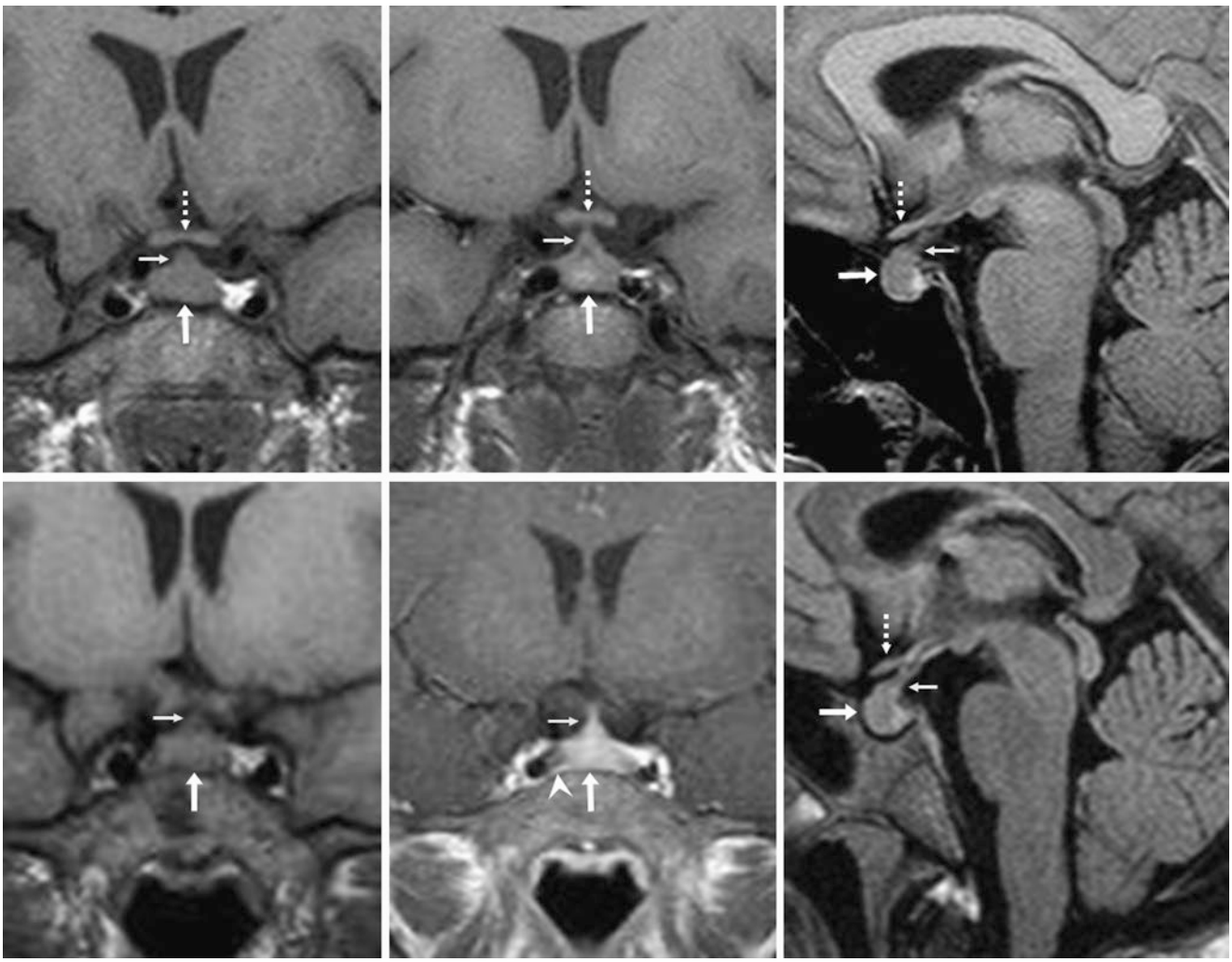

Fig. 8.27 A 21-year-old female with visual symptoms and pituitary hypertrophy (*arrows*) on 1.5 T MRI noncontrast coronal (*top left and middle*) and sagittal (*top right*) T1WIs. The ophthalmologist considered the symptoms to be unrelated. Seven years later, pre- (*bottom left*) and postcontrast (*bottom middle*) coronal T1WI and noncontrast sagittal FLAIR (*bottom right*) were unchanged. Note upward tenting (*thin arrows*), where the top of the gland comes close to but does not abut the optic chiasm (*dashed arrows*). Volume averaging artifact (*arrowhead*) simulates a microadenoma

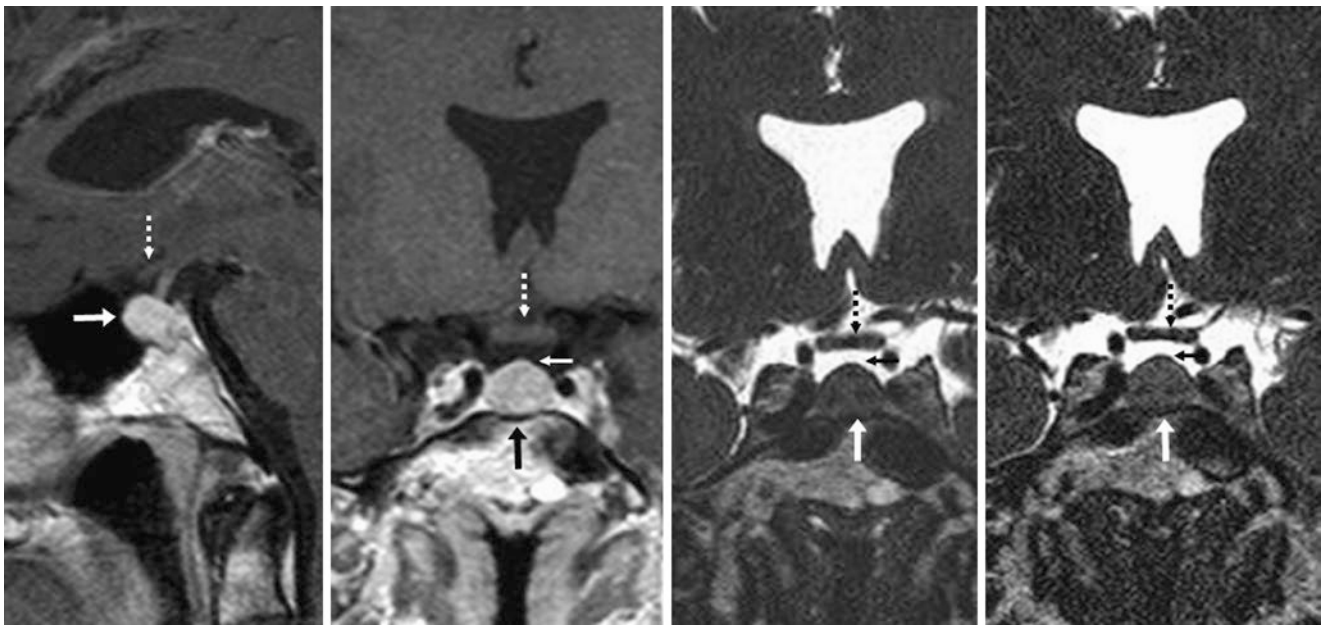

Fig. 8.28 The patient was a 50-year-old female with headaches who had a borderline enlarged pituitary (*arrows*) that measured 9.1 mm on sagittal (*left*) and coronal (*left middle*) postcontrast T1WIs; there was mild tenting of the gland upward (*thin arrows*) at the midline on the coronal image. Balanced echo coronal T2WI performed at that time (*right middle*) and 2 years later (*right*) showed no change. The pituitary did not abut the chiasm (*dashed arrows*)

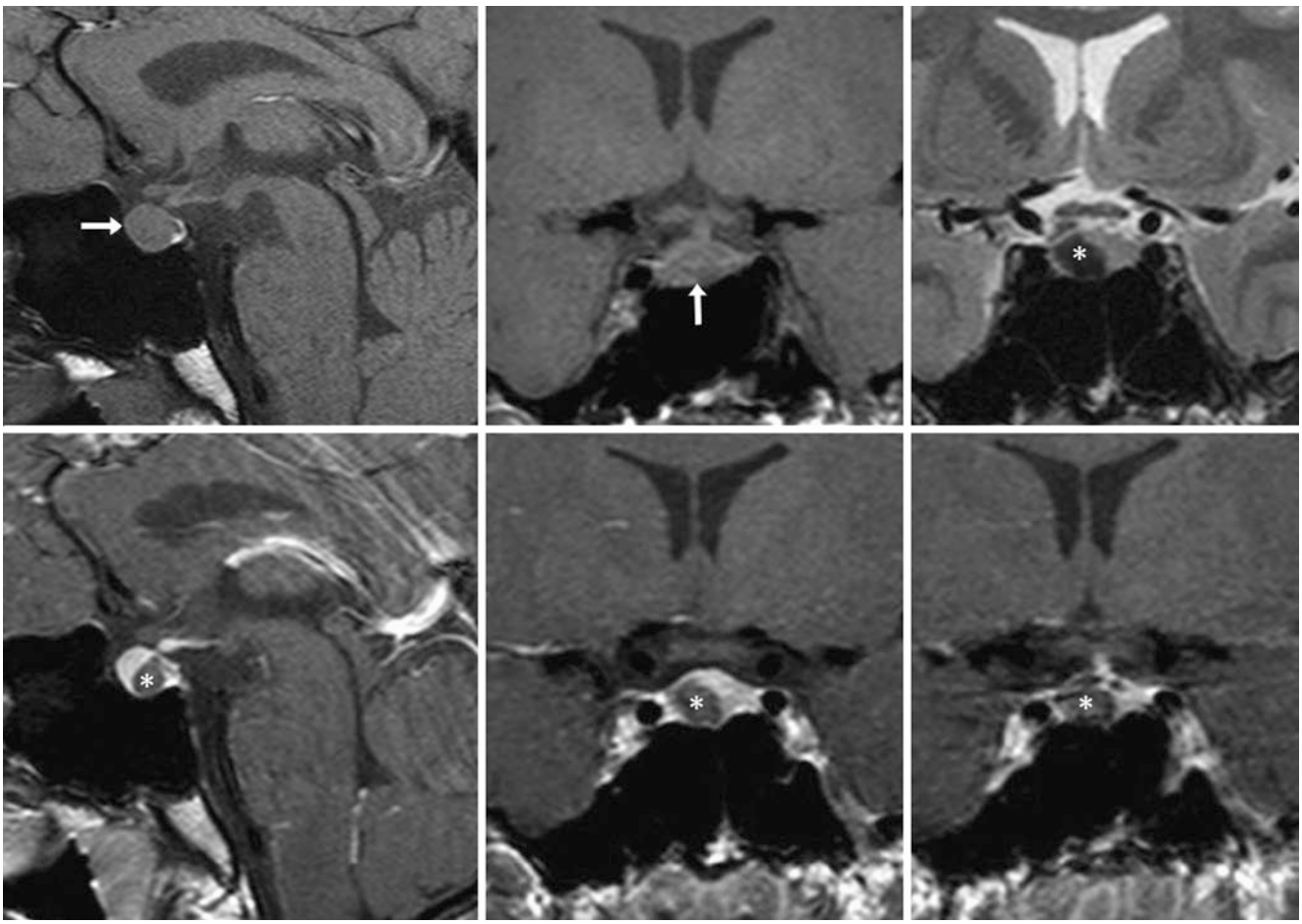

Fig. 8.29 Comparison case of macroadenoma enlarging the gland. The patient was a 23-year- old female with an incidental pituitary lesion in the midst of a mildly enlarged pituitary (*arrows*) that was 9.9 mm in height on noncontrast sagittal T1WI (*top left*) and coronal T1WI (*top middle*). On coronal T2WI (*top right*), a T2-dark focus measures just under 1 cm in size (*). Postcontrast sagittal (*bottom left*) and coronal (*bottom middle and right*) T1WIs confirm a nonenhancing adenoma. The adenoma's dark signal on T2WI is likely caused by the presence of either hemorrhage or proteinaceous debris

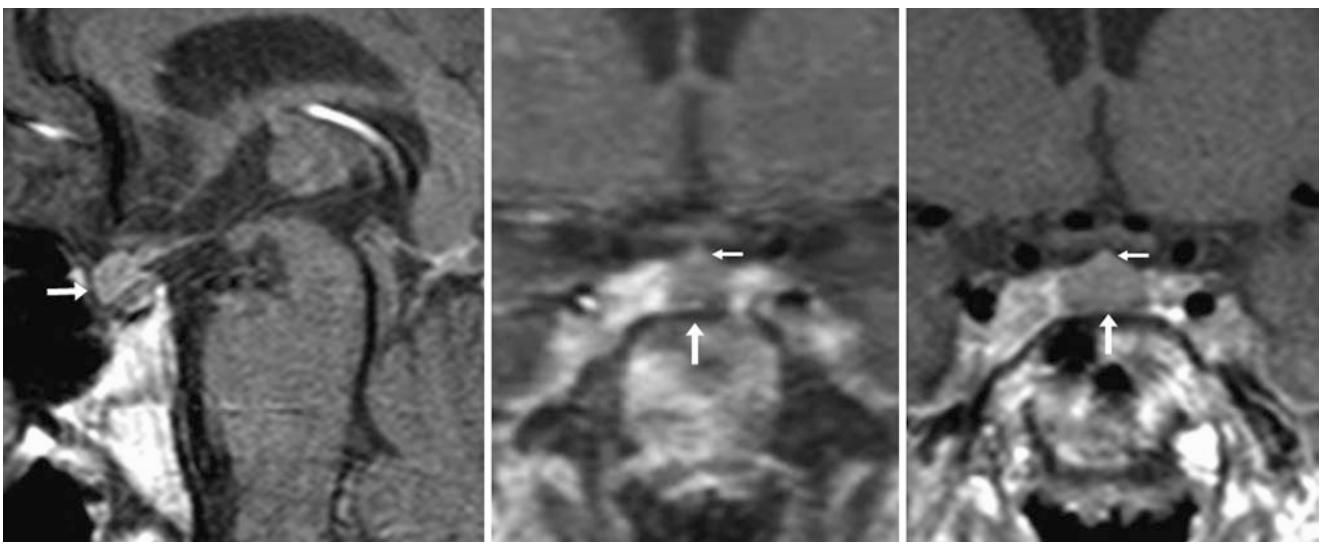

Fig. 8.30 Comparison case of macroadenoma enlarging the gland. The patient was a 22-year-old male with hypopituitarism and pituitary enlargement (*arrows*) measuring 10.1 mm on a delayed (10 min) sagittal postcontrast T1WI (*left*) that suffered from motion; note the tenting of the stalk insertion (*thin arrows*). Dynamic postcontrast coronal T1WIs both at 300 s (*middle*) and 420 s (*right*) showed little to no enhancement. This markedly delayed enhancement of the gland, indicating that it was mostly replaced by a macroadenoma

8.3 Infundibular Shift or Tilt and Pituitary Asymmetry

As mentioned earlier, while a secondary criterion for diagnosing a microadenoma (<10 mm in size) is *stalk deviation* away from the side of the lesion, this criterion should not be used solely by itself as a small amount of deviation or "tilt" may be present in up to 30–45 % of the population. When evaluating for a *microadenoma*, other factors such as differential enhancement (less than the remainder of the gland), expansion of the gland, and necrosis/cystic contents should also be looked for (Figs. 8.31, 8.32, 8.33, 8.34, 8.35, 8.36, 8.37, 8.38, 8.39, 8.40, and 8.41).

Also, another normal variation is that the pituitary lobes may appear mildly asymmetric from side-to-side. Sizes or heights <9-10mm can be normal. Again, asymmetric dynamic or delayed enhancement, mass effect, and expansion of the gland should be assessed for when determining whether or not there is a microadenoma.

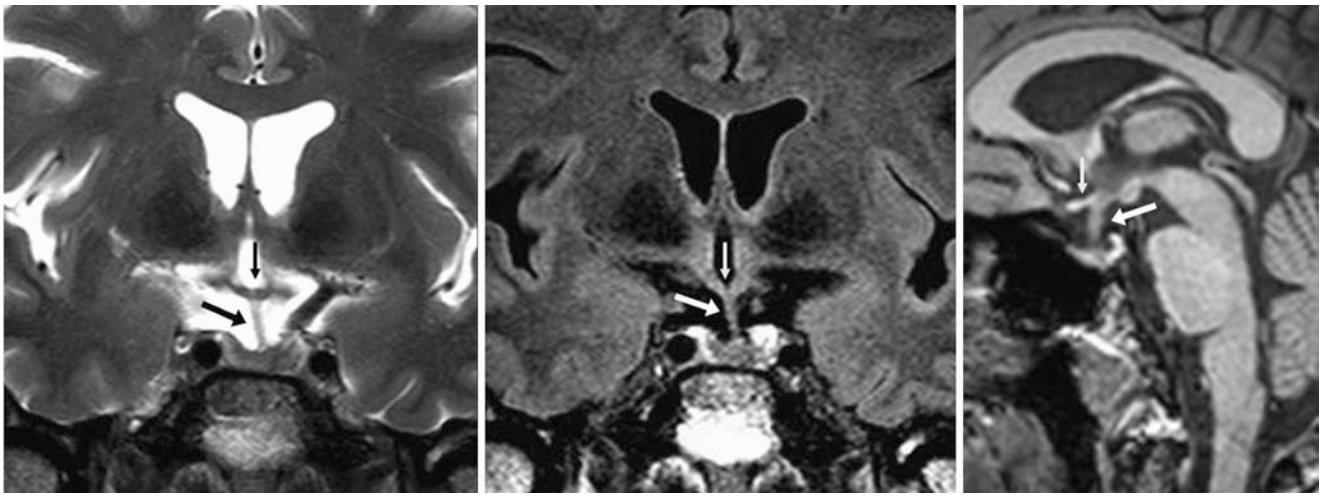

Fig. 8.31 A 55-year-old patient with a 3 T MRI that demonstrated normal mild infundibular/stalk shift to the left (*arrows*), incidentally noted on coronal T2WI (*left*) and FLAIR (*middle*). The stalk appears normal on noncontrast sagittal T1WI (*right*). The patient had symptoms (vertigo) that were not related to the pituitary. Note the optic chiasm (*thin arrows*)

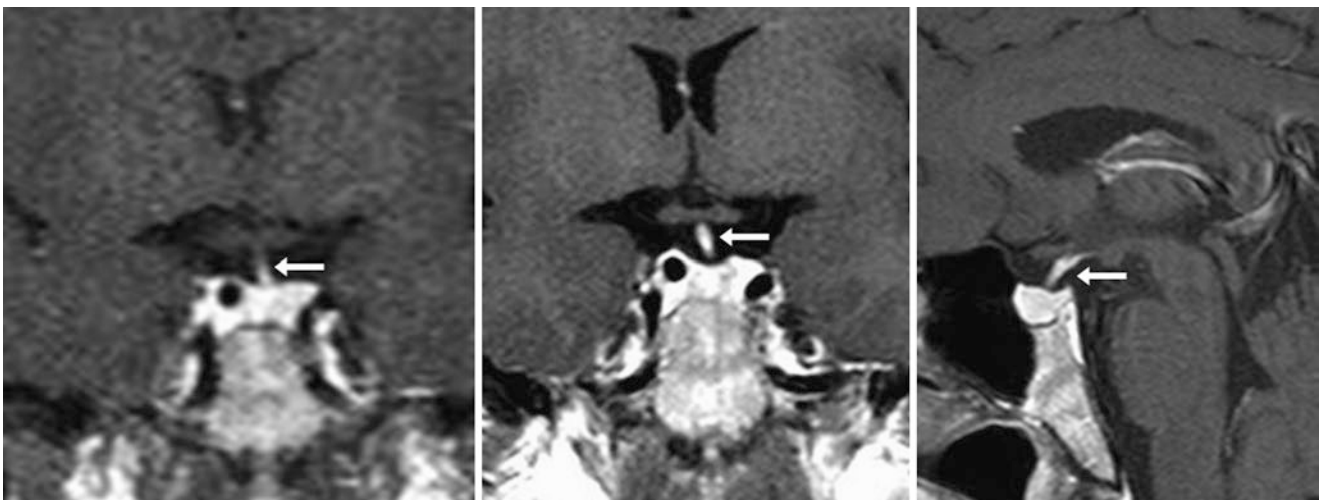

Fig. 8.32 The patient was a 53-year-old female with hypothyroid symptoms (negative MRI). A 1.5 T MRI noted normal, mild infundibular shift to the left (*arrows*) on the 1-min dynamic postcontrast T1WI (*left*) as well as on the 5-min delayed postcontrast coronal T1WI (*middle*). Postcontrast sagittal T1WI (*right*) also confirmed no abnormality

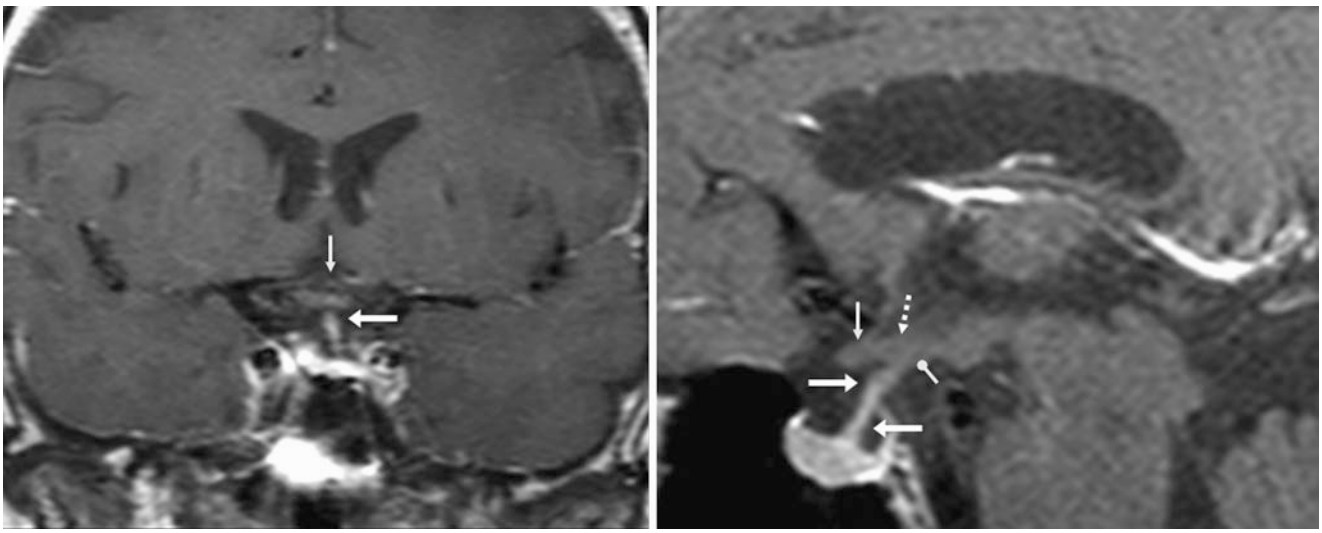

Fig. 8.33 A 59-year-old female with a 3 T MRI that demonstrated normal enhancement of the pituitary infundibulum (*arrows*) relative to the nonenhancing optic chiasm (*thin arrows*). The infundibulum has a normal shift to the left on coronal delayed 5-min postcontrast T1WI (*left*). On a magnified postcontrast sagittal T1WI (*right*) also note the median eminence of the hypothalamus (*dashed arrow*) and the tuber cinereum (*circle tip arrow*)

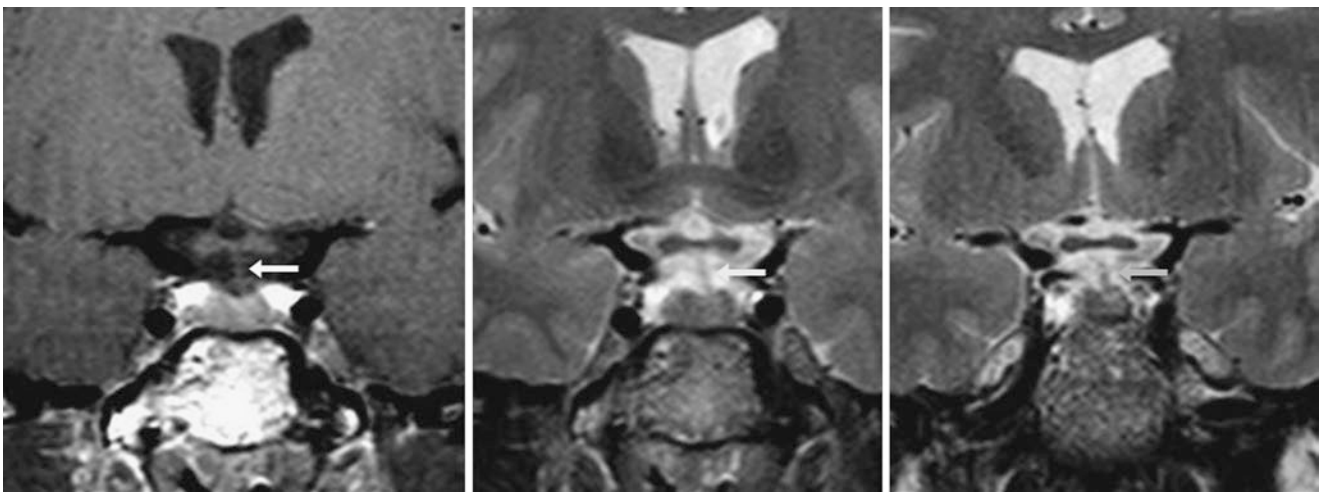

Fig. 8.34 The patient was a 34-year-old female with visual symptoms (thought related to demyelinating disease) with a 3 T MRI that demonstrated normal mild infundibular shift to the left (*arrows*). This was incidentally noted on noncontrast coronal T1WI (*left*) and T2WI (*middle*). The shift was not changed 1 year later on coronal T2WI (*right*)

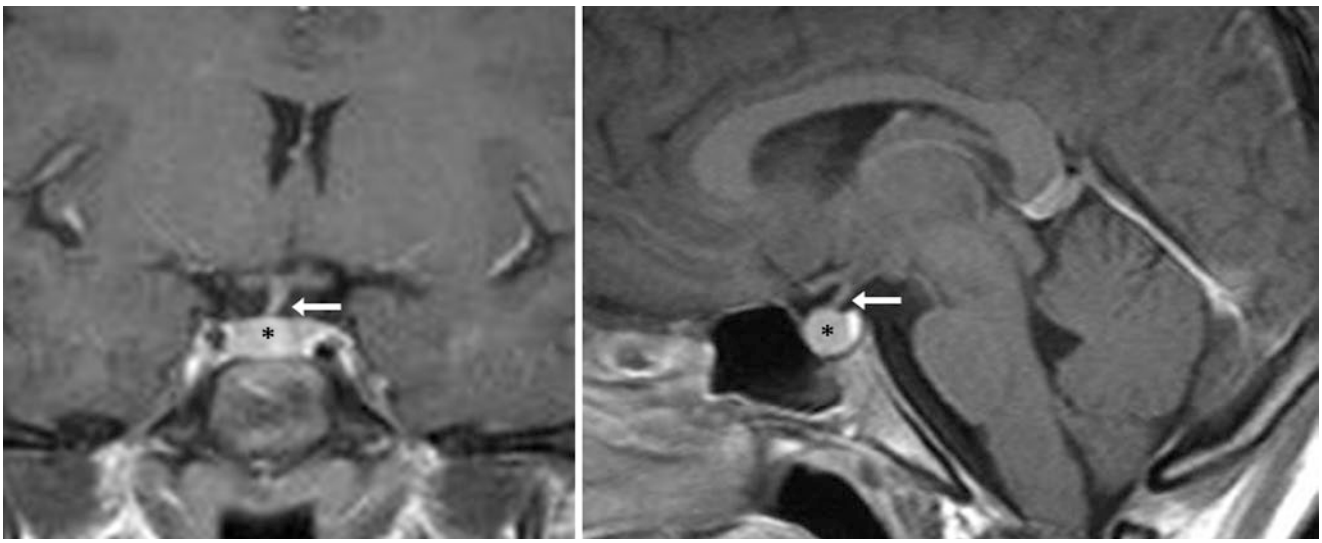

Fig. 8.35 The patient was a 12-year-old female with headaches (thought related to migraines), with a 1.5 T MRI that demonstrates normal mild infundibular shift to the right (*arrow*) on postcontrast coronal T1WI (*left*). There was borderline pituitary hypertrophy (*). The pituitary height measured 9.3 mm, also depicted on sagittal postcontrast T1WI (*right*)

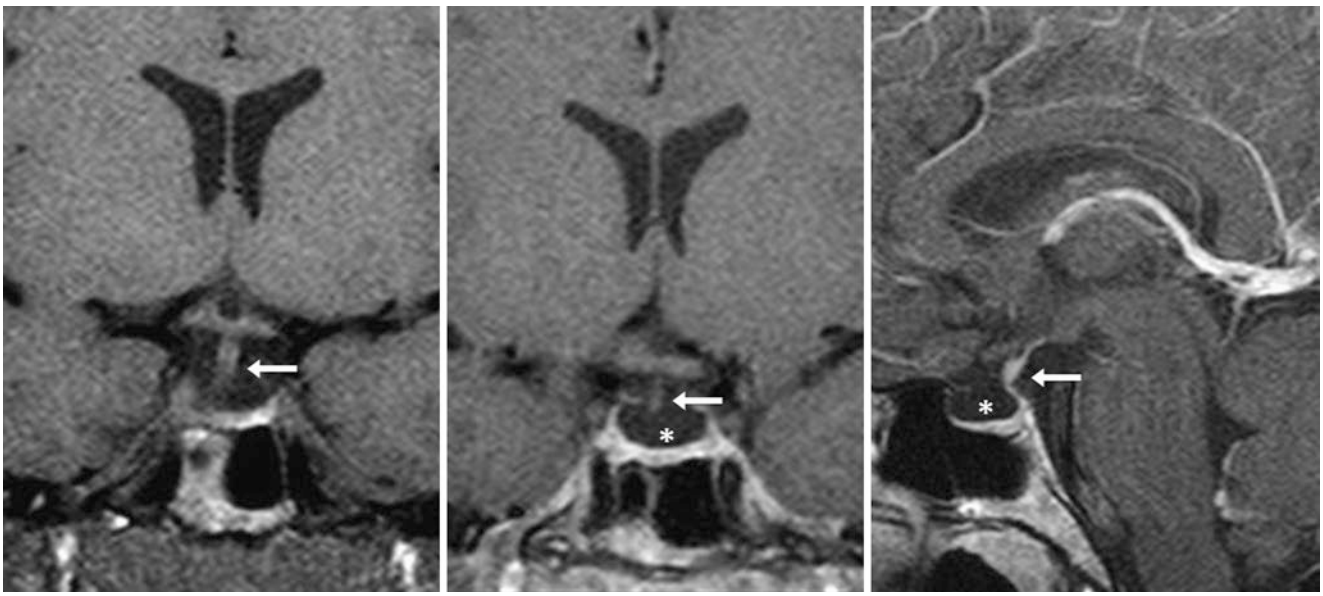

Fig. 8.36 A 34-year-old female soon after trauma (but no brain injury) with a 1.5 T MRI that depicts normal mild infundibular shift to the right (*arrow*) on noncontrast coronal T1WI (*left*) and on postcontrast coronal (*middle*) and sagittal (*right*) T1WI. There was a partially empty sella (*) with pituitary tissue along the floor of the sella, a normal variation

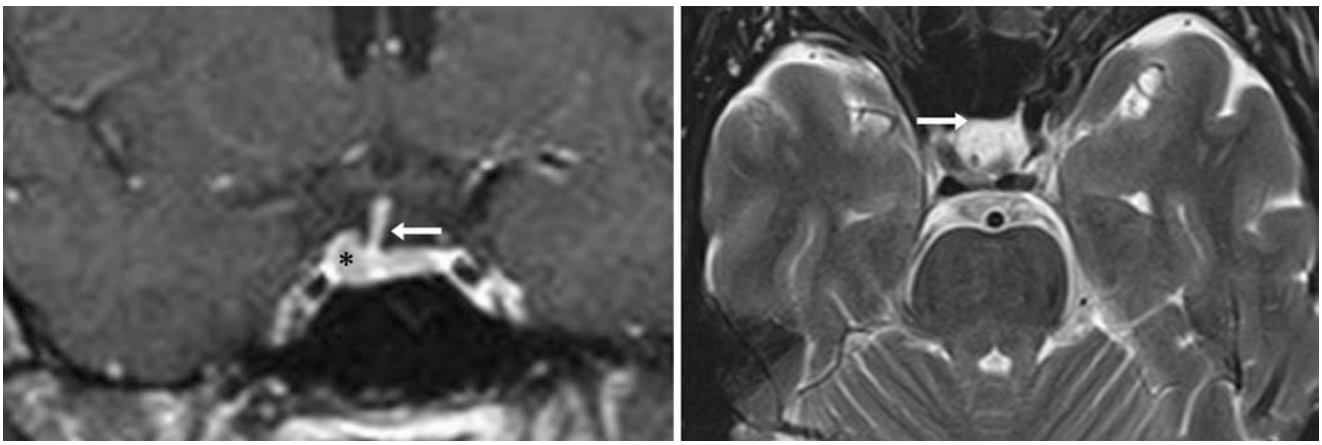

Fig. 8.37 A 57-year-old male patient with disequilibrium (from an inner ear abnormality) had a 1.5 T MRI that depicted moderate stalk shift to the right (*arrows*) as well as asymmetry of the lobes (*); the right lobe appears slightly larger than the left on postcontrast coronal T1WI (*left*) and axial T2WI (*right*). There was no history of a sellar tumor or prior surgery

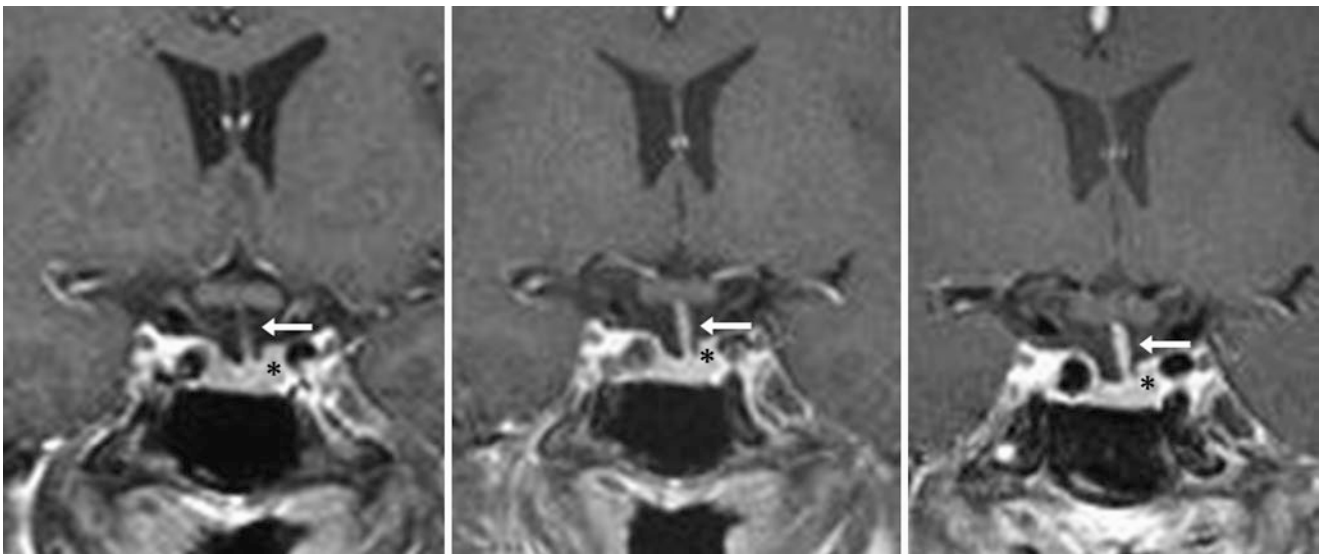

Fig. 8.38 The patient was a 54-year-old male who underwent an unrelated acoustic neuroma resection many years earlier. A 3 T MRI depicts incidental, leftward infundibular shift (*arrows*) as well as asymmetry of the lobes (*); the left lobe is slightly taller than the right on postcontrast coronal T1WI (*left*). The findings were not changed 1 (*middle*) or 2 years later (*right*)

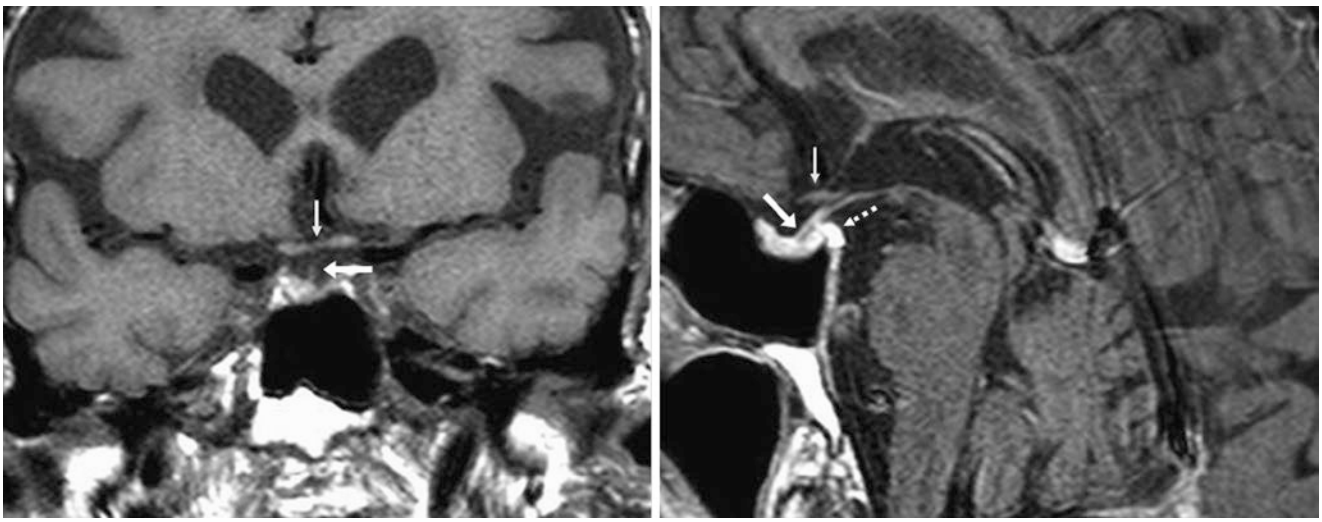

Fig. 8.39 The patient was a 78-year-old male with visual symptoms of unknown etiology. A 1.5 T MRI found normal mild asymmetry; the right lobe was slightly more prominent, along with infundibular shift to the right (*arrows*) on coronal T1WI (*left*). There was no history of prior sellar surgery. Postcontrast sagittal T1WI (*right*) showed the infundibulum and chiasm (*thin arrows*) to be normal. Note a T1-bright posterior clinoid process (*dashed arrow*), which can simulate a pituitary lesion on coronal images if close to the infundibulum, such as in this case

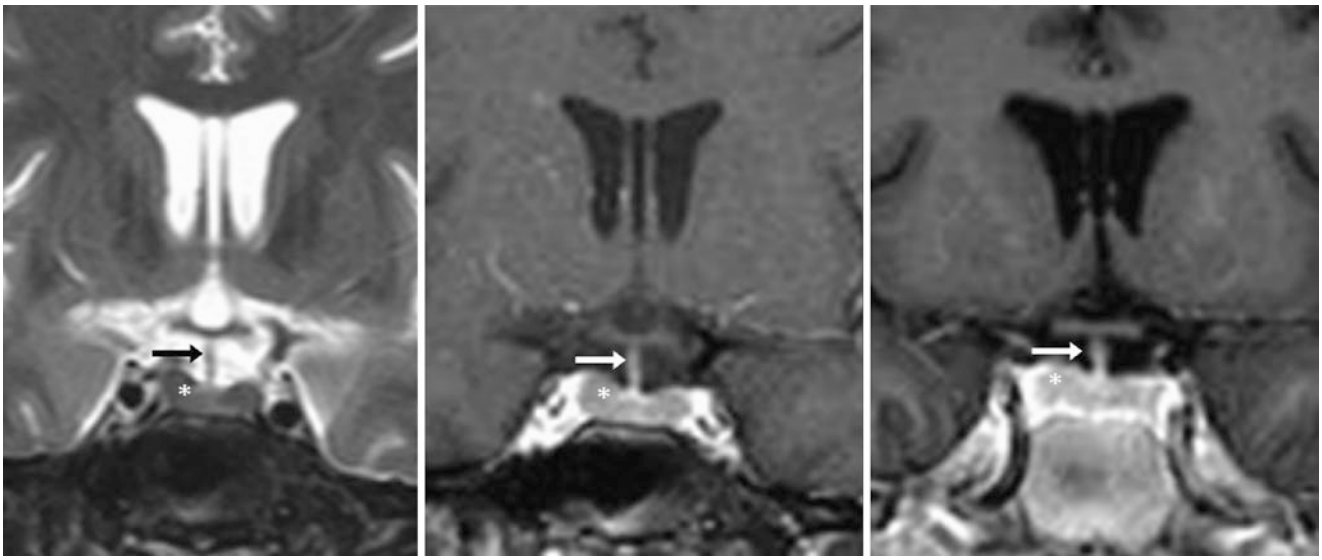

Fig. 8.40 The patient was a 20-year-old female with a history of vasculitis (no pituitary symptoms). A 1.5 T MRI depicted a midline infundibulum (*arrows*), but there was asymmetry of the lobes (*); the right lobe was slightly taller than the left on coronal T2WI (*left*) and on postcontrast T1WI (*middle*). This was unchanged 1 year later on postcontrast T1WI (*right*)

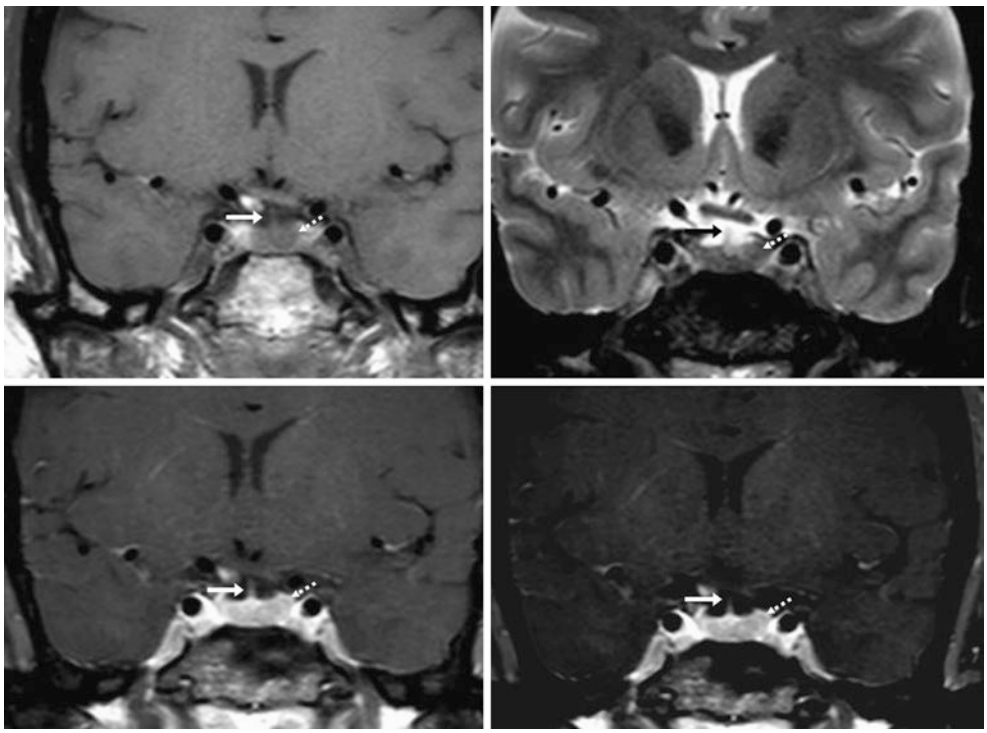

Fig. 8.41 Case of infundibular shift and pituitary asymmetry, indeterminate for a microadenoma. A 47-year-old female with vertigo underwent a 3 T MRI, which demonstrated incidental slight rightward infundibular shift (*arrows*) as well as asymmetry of the lobes (*dashed arrows*, the left is slightly larger than the right) on coronal noncontrast T1WI (*top left*), T2WI (*top right*), and postcontrast coronal T1WI (*bottom left*). Tightly windowed postcontrast T1WI (*bottom right*) raises the question of whether there is an incidental microadenoma; this study was considered indeterminate for the presence of tumor

8.4 Infundibular Hyperintensity on Three-Dimensional FLAIR

Three-dimensional FLAIR images eliminate CSF flow voids in the basal cisterns but can cause hyperintensity of the *pituitary infundibulum/stalk* and *tuber cinereum*; this becomes even more hyperintense following intravenous contrast administration, since the stalk does not have a blood–brain barrier. Again, the reason for the bright signal in these structures prior to contrast is unknown. Interestingly, this characteristic actually often aids visualization of the stalk on this noncontrast sequence (Figs. 8.42, 8.43, 8.44, 8.45, and 8.46).

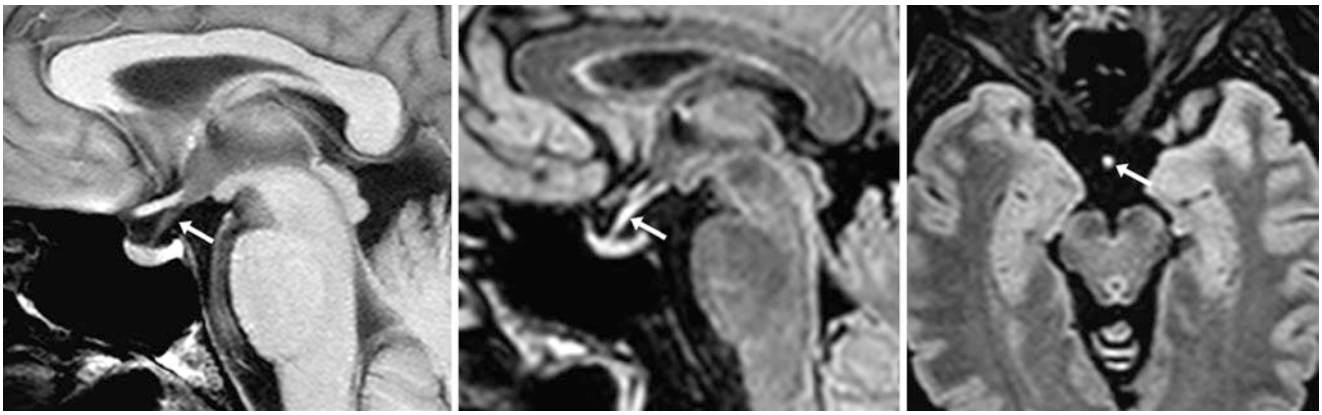

Fig. 8.42 Normal infundibular hyperintensity on noncontrast 3D FLAIR. In a 58-year-old female postconcussion (negative 1.5 T MRI) the infundibulum (*arrows*) appears normal on a sagittal T1WI (*left*) but appears hyperintense on sagittal (*middle*) and axial (*right*) reformats from a three-dimensional FLAIR acquisition

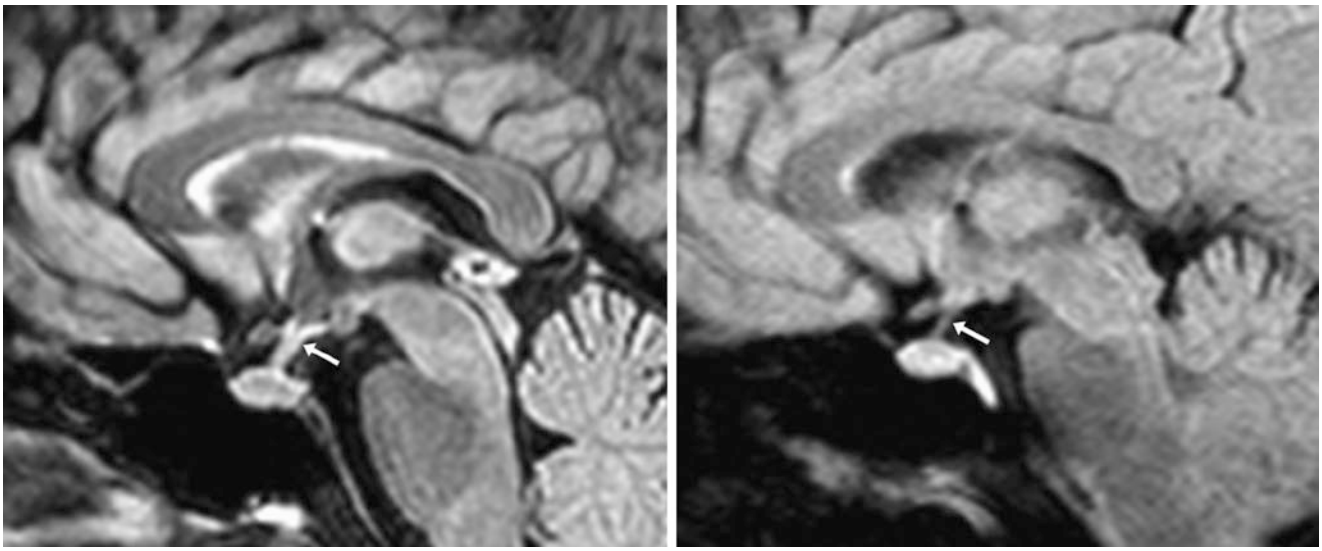

Fig. 8.43 Normal infundibular hyperintensity on noncontrast three-dimensional FLAIR. In a 57- year-old female with visual symptoms (negative 3 T MRI), the infundibulum (*arrows*) is hyperintense prior to contrast administration on sagittal reformats (*left*) from a three-dimensional FLAIR acquisition. Sagittal FLAIR two-dimensional images at 1.5 T from 5 years earlier (*right*) did not have the same appearance

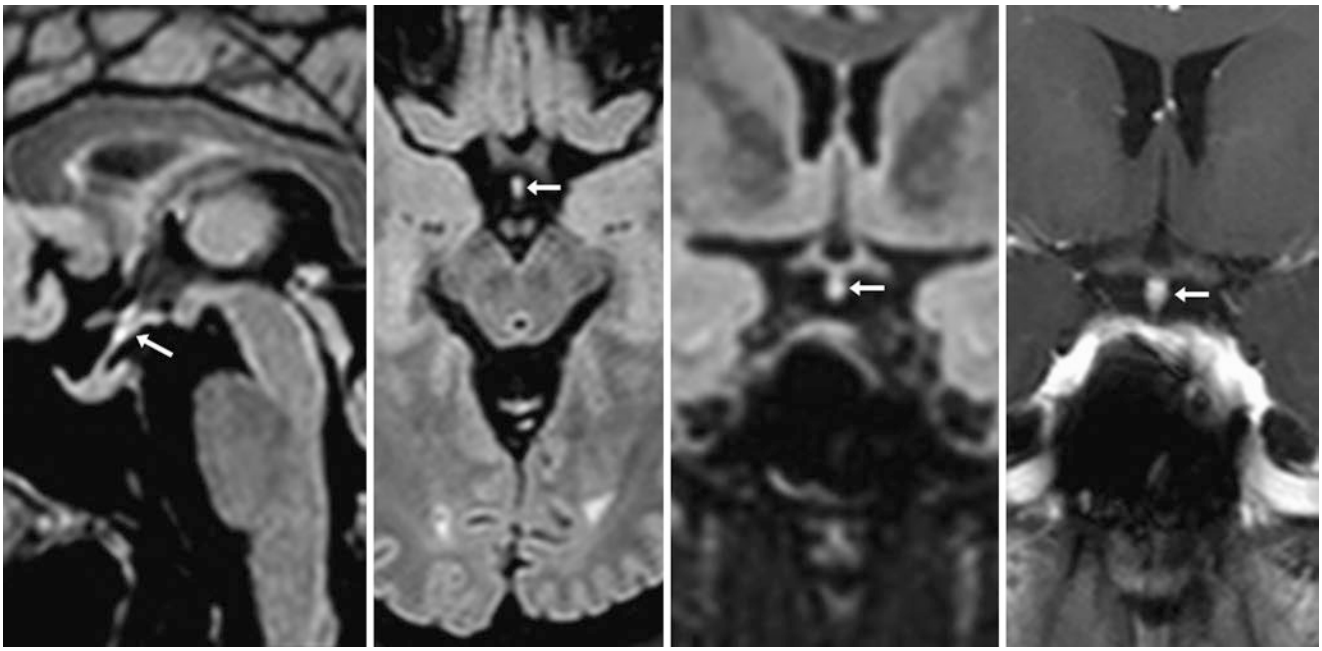

Fig. 8.44 Normal infundibular hyperintensity on three-dimensional FLAIR. In a 35-year-old female with hearing loss, the infundibulum (*arrows*) is hyperintense prior to contrast on a 1.5 T MRI three-dimensional FLAIR acquisition, with sagittal (*left*), axial (*left middle*), and coronal (*right middle*) reconstructions. A postcontrast coronal T1WI (*right*) depicts normal stalk enhancement

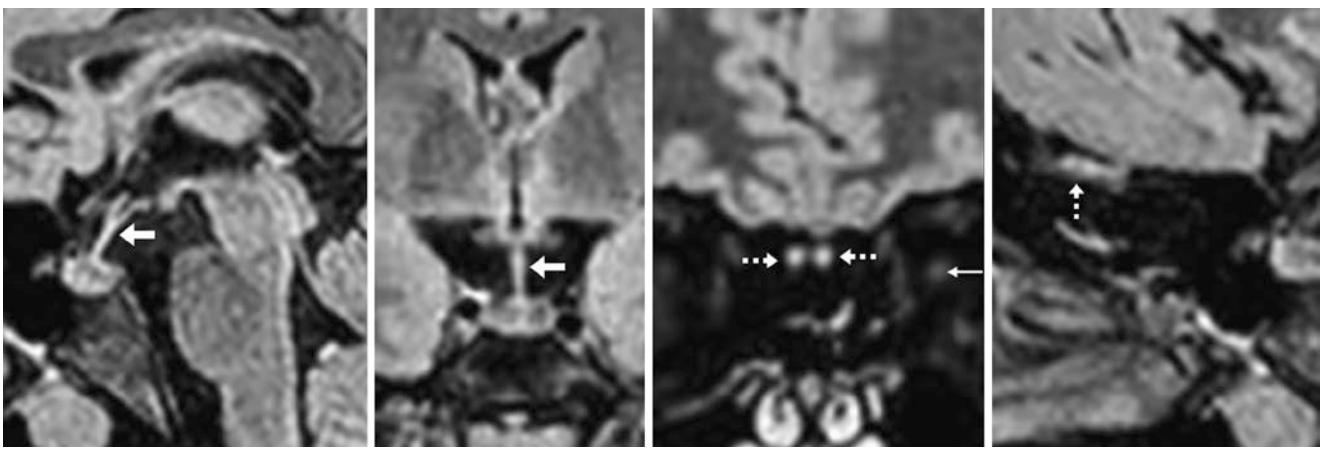

Fig. 8.45 Normal infundibular and olfactory nerve hyperintensity on three-dimensional FLAIR. In a 17-year-old patient female with a negative 1.5 T MRI for hearing loss, mild stalk hyperintensity (*arrows*) is depicted on sagittal (*left*) and coronal (*left middle*) reformats of a three-dimensional FLAIR acquisition. The olfactory nerves (*dashed arrows*) are also mildly bright on coronal (*right middle*) and sagittal (*right*) reformats. Note the normal left optic nerve signal for comparison (*thin arrow*)

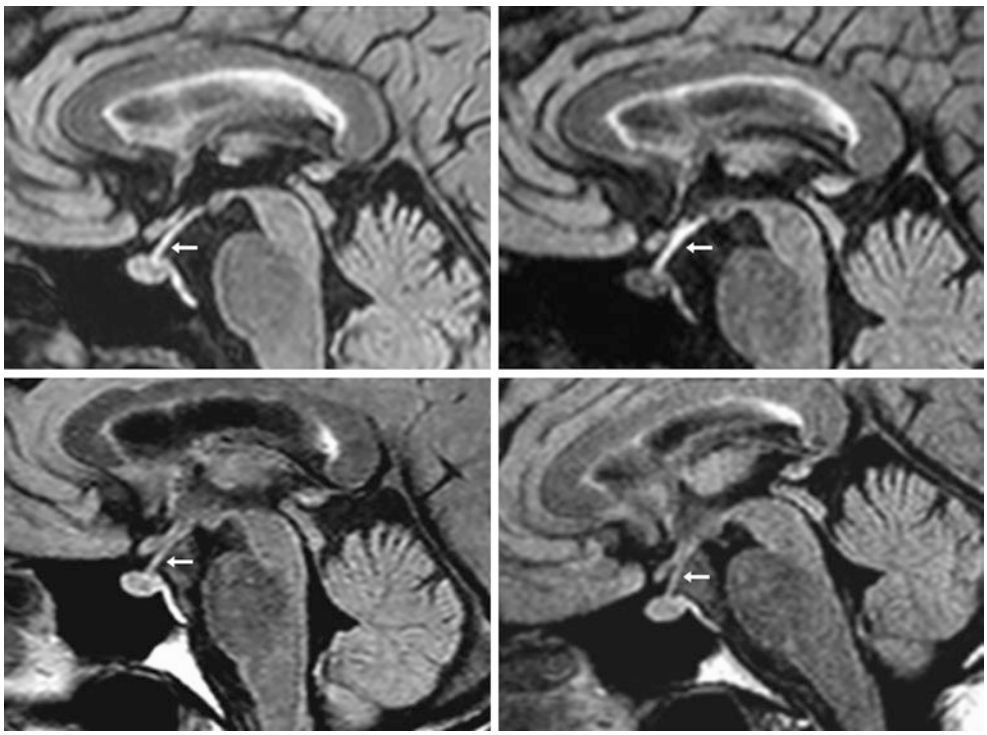

Fig. 8.46 Normal infundibular hyperintensity on three-dimensional FLAIR and enhancement. In a 65-year-old female patient (negative 1.5 T MRI), the stalk (*arrows*) is hyperintense on noncontrast sagittal reformats (*top left*) from a three-dimensional FLAIR acquisition. On postcontrast three-dimensional FLAIR (*top right*) the stalk enhances and becomes brighter, as expected. In contrast, 1.5 T two-dimensional FLAIR images at both 3 months (*bottom left*) and 8 years prior (*bottom right*) did not have the same appearance

8.5 Artifacts Simulating Pituitary Microadenomas

As stated previously, various *artifacts* within the pituitary or suprasellar regions may simulate a lesion such as a micro- or macroadenoma. This is most commonly related to *volume averaging* (particularly with the dorsal portion of the bony sella or with adjacent CSF), *flow voids* (from CSF pulsation), or *phase-related artifacts* from ICA pulsation (particularly when the transverse dimension is the phase encoding direction on coronal images). Flow compensation techniques or three-dimensional acquisitions with thin reformats can mitigate such pseudolesions (Figs. 8.47, 8.48, 8.49, 8.50, 8.51, 8.52, 8.53, and 8.54).

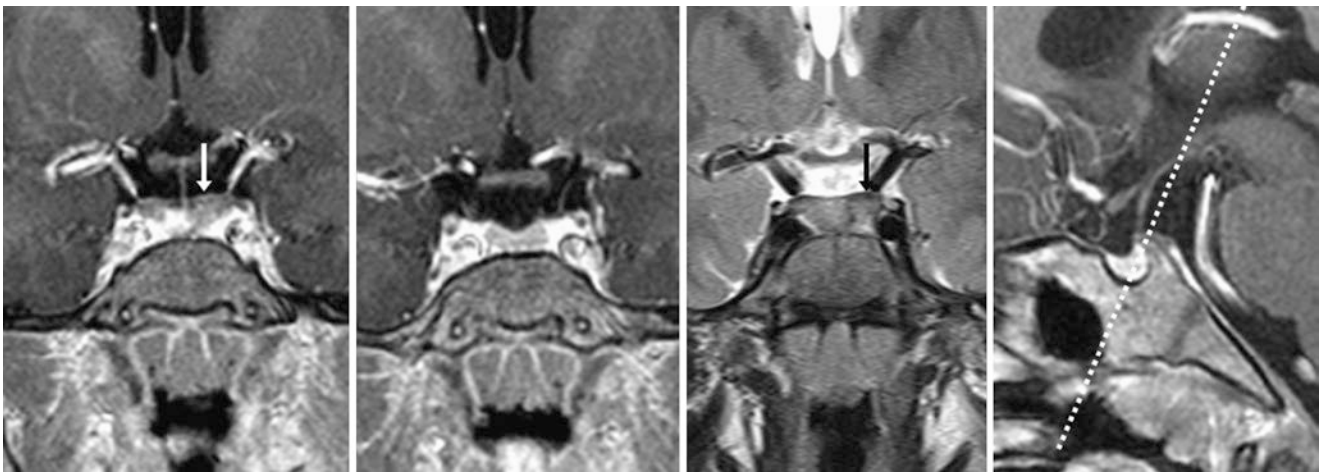

Fig. 8.47 Volume averaging simulating an adenoma. A 7-year-old male patient with short stature and an otherwise normal MRI had a hypointense focus (*arrows*) within the left side of the gland on postcontrast coronal T1WI (*left*) that was not present on a slice just anterior (*left middle*), thus simulating an adenoma. Coronal T2WI (*right middle*) confirmed that this focus had signal intensity similar to the rest of the sella. Sagittal T1WI (*right*) was normal; the oblique acquisition was found to average the bony dorsum sella with the pituitary (the *dotted line* depicts the imaging plane of acquisition)

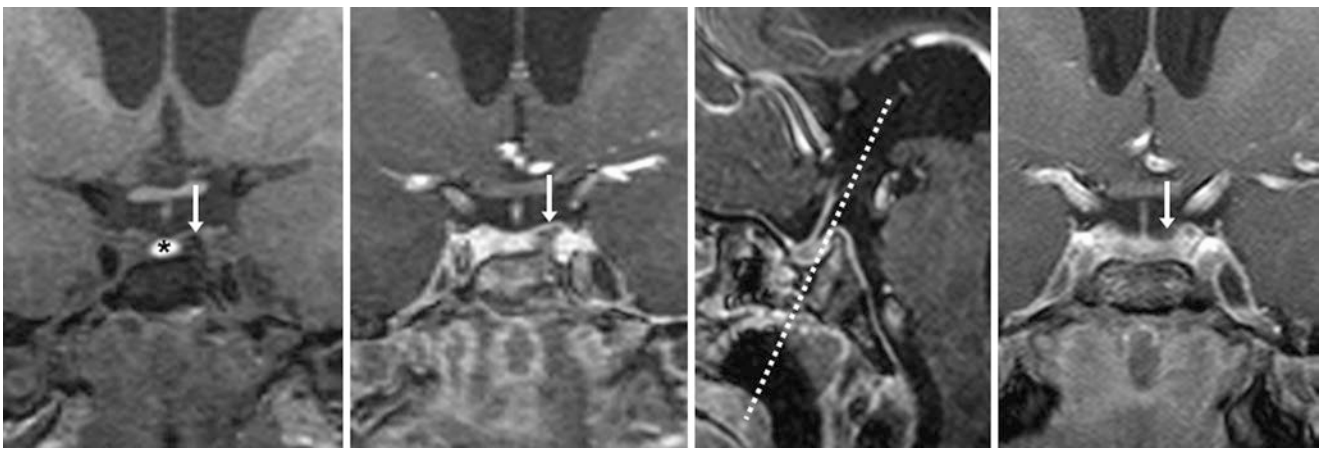

Fig. 8.48 Volume averaging simulating an adenoma. A 2-year-old male with developmental delay and a normal MRI had a hypointensity (*arrows*) within the left side of the gland on both noncontrast (*left*) and postcontrast (*middle*) coronal T1WIs, simulating an adenoma. However, sagittal images (*right middle*) showed that the oblique coronal acquisition averaged the posterior pituitary (* denotes the posterior pituitary bright spot) with the dorsum sella (the *dotted line* is the acquisition plane). The pseudolesion was not present on postcontrast T1WI 2 months later (*right*)

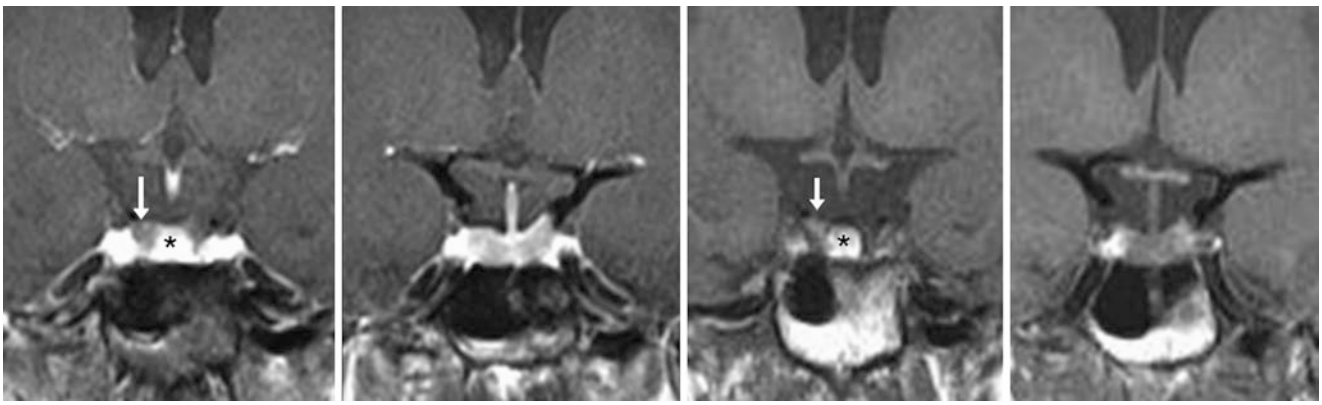

Fig. 8.49 Volume averaging simulating an adenoma. A 36-year-old patient had a hypointense focus (*arrows*) on postcontrast T1WI (*left two images*), simulating an adenoma. On noncontrast T1WI (*right two images*), this was found to be volume averaging of the gland with the bony dorsum sella. Note T1-bright fatty marrow medially (*)

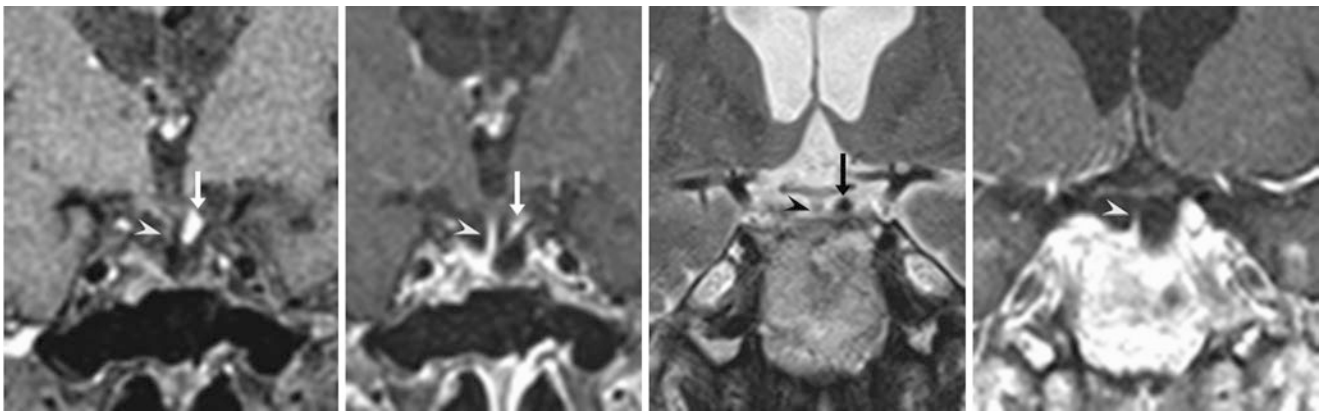

Fig. 8.50 Flow-related artifact simulating an adenoma. A 64-year-old patient with a history of a prior adenoma resection (and no recurrence for 5 years) had T1-bright signal (*arrows*) to the left of the stalk (*arrowheads*) on coronal T1WI performed both precontrast (*left*) and postcontrast (*left middle*) and on coronal T2WI (*right middle*). A repeat postcontrast T1WI was normal (*right*). This artifact was deemed likely related to CSF pulsation

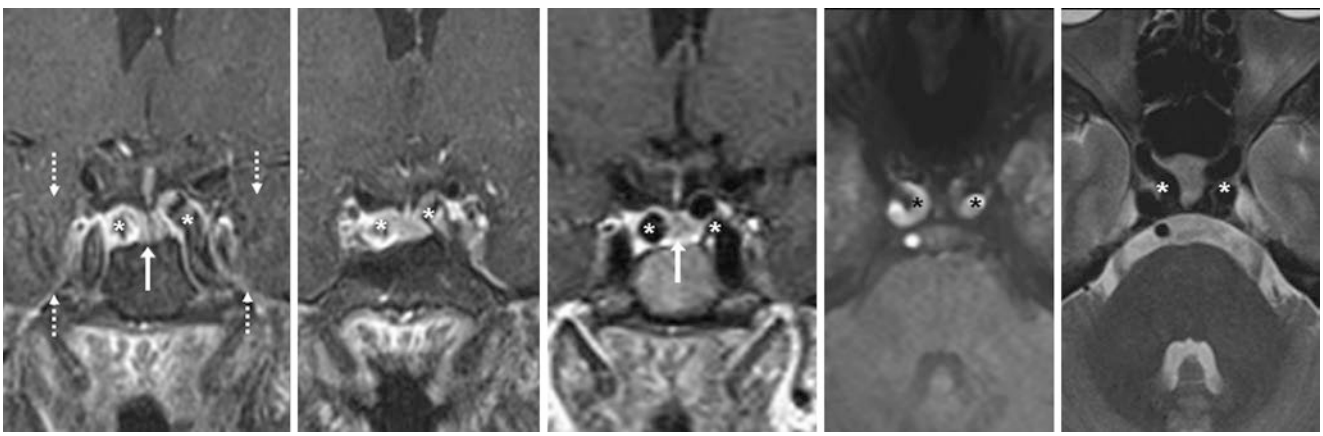

Fig. 8.51 Pulsation-related artifact. A 32-year-old patient had pulsation artifact in the phase direction (*dotted arrows*) that obscured the gland (*arrows*) on postcontrast coronal T1WI (*left and left middle*). The addition of a flow compensation technique removed the artifact (*middle*). Axial SWI (*right middle*) and T2WI (*right*) depict a normal variation: bilateral medially oriented cavernous segments of the internal carotid arteries (*), which were the source of the artifact

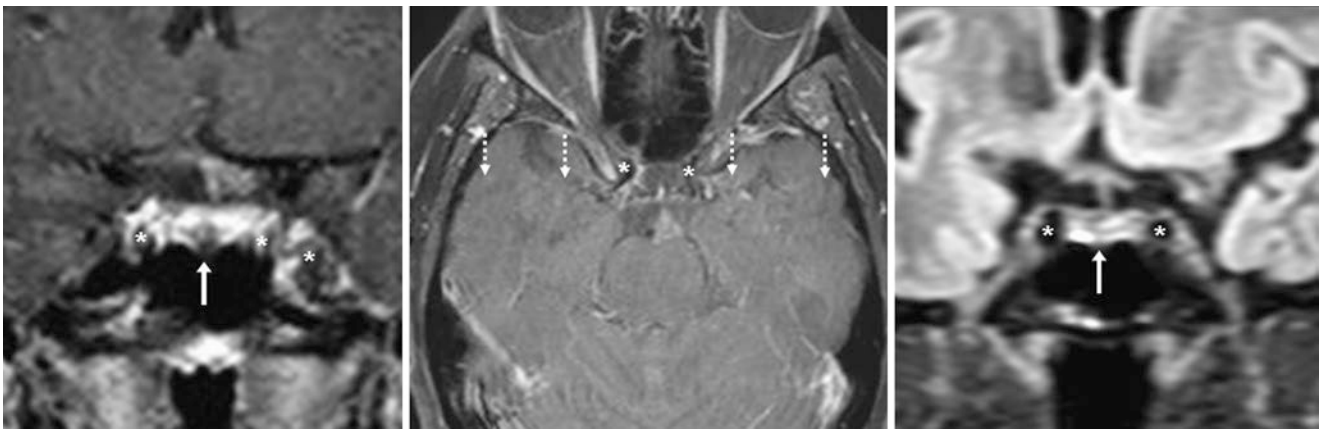

Fig. 8.52 Pulsation-related artifact. A 46-year-old patient had pulsation artifact in the phase direction (*dotted arrows*), mimicking a microadenoma (*arrows*) on postcontrast coronal T1WI (*left*); the extent of the artifact is better shown on axial T1WI (*middle*). A third-dimensional FLAIR sequence, which is relatively insensitive to flow or pulsation artifacts, was reconstructed in the coronal plane (*right*) and was negative. The ICAs (*) were the source of the artifact

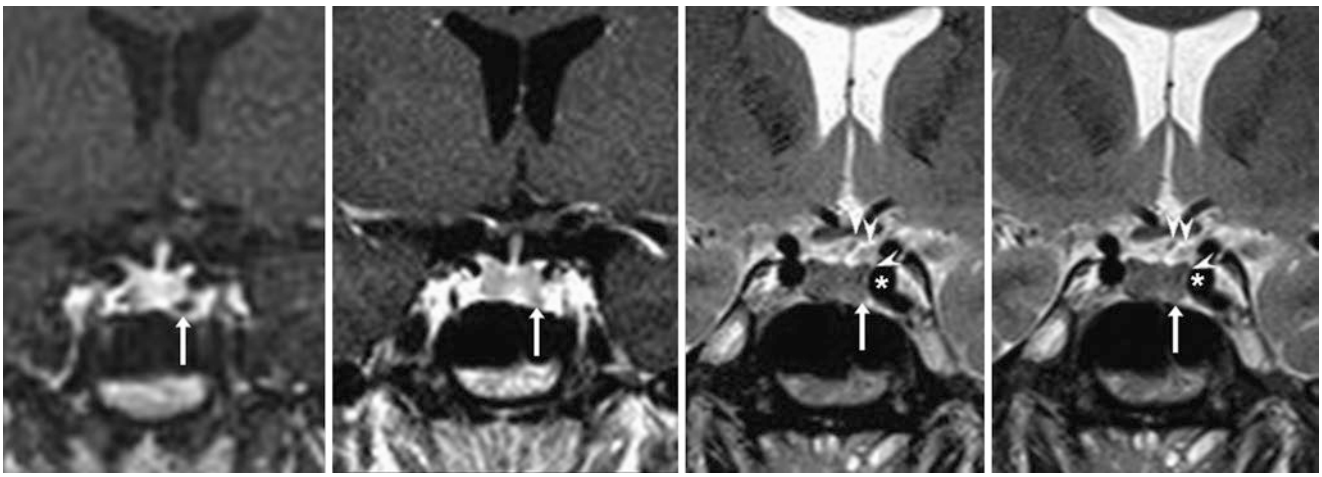

Fig. 8.53 Flow-related artifacts. The patient was a 41-year-old male with headaches (and an otherwise normal 3 T MRI). A subtle, hypointense focus (*arrows*) within the inferolateral left side of the gland was present on a 1-min dynamic postcontrast coronal T1WI (*left*), simulating an adenoma but not on a 3-min delayed images (*left middle*). Coronal T2WI (*right middle*) depicted multiple subtle flow voids around the pituitary gland, which were also present on repeat T2WI (*right*). The left ICA (*) may have been a source of these pseudolesions

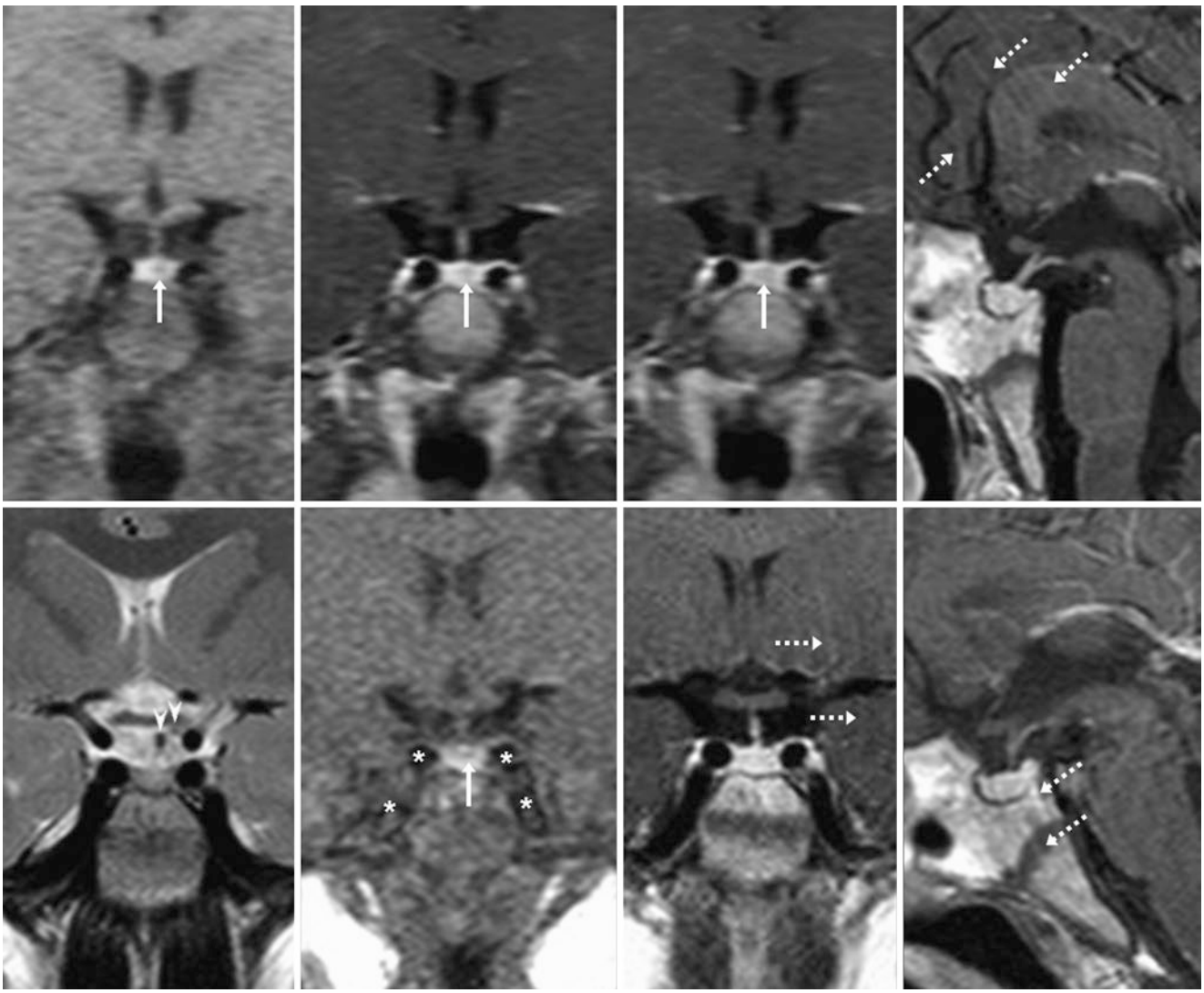

Fig. 8.54 Multiple artifacts from vasculature, CSF, and patient motion. An 8-year-old male with growth deficiency underwent a 1.5 T MRI (interpreted as normal), which depicted a subtle, hypointense (*arrows*) focus within the left side of the gland on coronal noncontrast (*top left*) and dynamic postcontrast 30-s (*top*, *left middle*) and 1-min delay (*top*, *right middle*) on coronal T1WIs, simulating an adenoma. However, sagittal postcontrast T1WIs revealed moderate patient motion (*dashed arrows*), suggesting that motion was the cause of the artifact. One year later, a coronal T2WI (*bottom left*) was affected by a CSF motion artifact (*arrowheads*), but the gland appeared normal. However, dynamic 30-s (*bottom*, *left middle*) images were affected by pulsatility of the ICAs (*) or the CSF, causing a lesion similar to the pseudolesion on the original MRI; this disappeared by 1-min delayed T1WI (*bottom*, *right middle*). A moderate amount of motion is also present on the sagittal postcontrast T1WI (*bottom right*)

8.6 Primary Empty Sella (PES): Partial Form

Again, *PES* is more common in women, obese patients, hypertensive patients, and patients with multiple pregnancies. It is more commonly incidental than symptomatic. The presence of PES becomes more of an issue with smaller pituitary volumes and enlarged bony sellar contours, particularly in obese females or children (Figs. 8.55, 8.56, 8.57, 8.58, 8.59, 8.60, 8.61, 8.62, 8.63, 8.64, 8.65, 8.66, 8.67, 8.68, 8.69, 8.70, 8.71, 8.72, 8.73, 8.74, 8.75, 8.76, and 8.77).

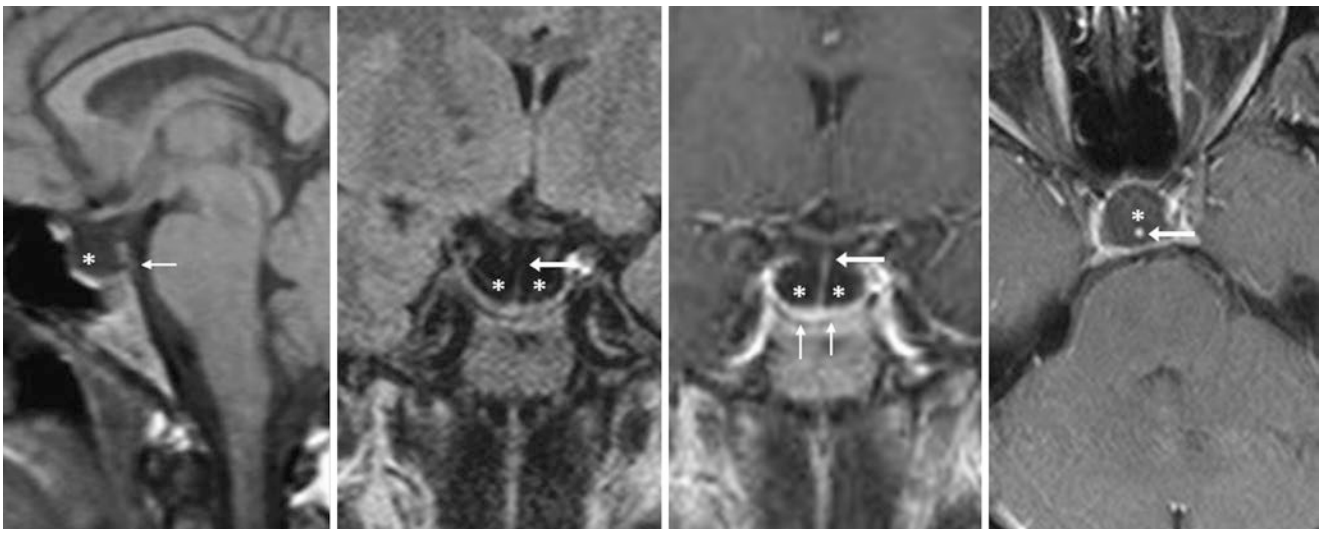

Fig. 8.55 A 46-year-old female patient with seizures and an otherwise negative 1.5 T MRI had a mildly enlarged, partial form of PES (*). Note a normal stalk (*arrows*) on noncontrast sagittal T1WI (*left*) and coronal FLAIR (*left middle*) and on postcontrast coronal (*right middle*) and axial (*right*) T1WI. Note normal pituitary tissue peripherally (*thin arrows*)

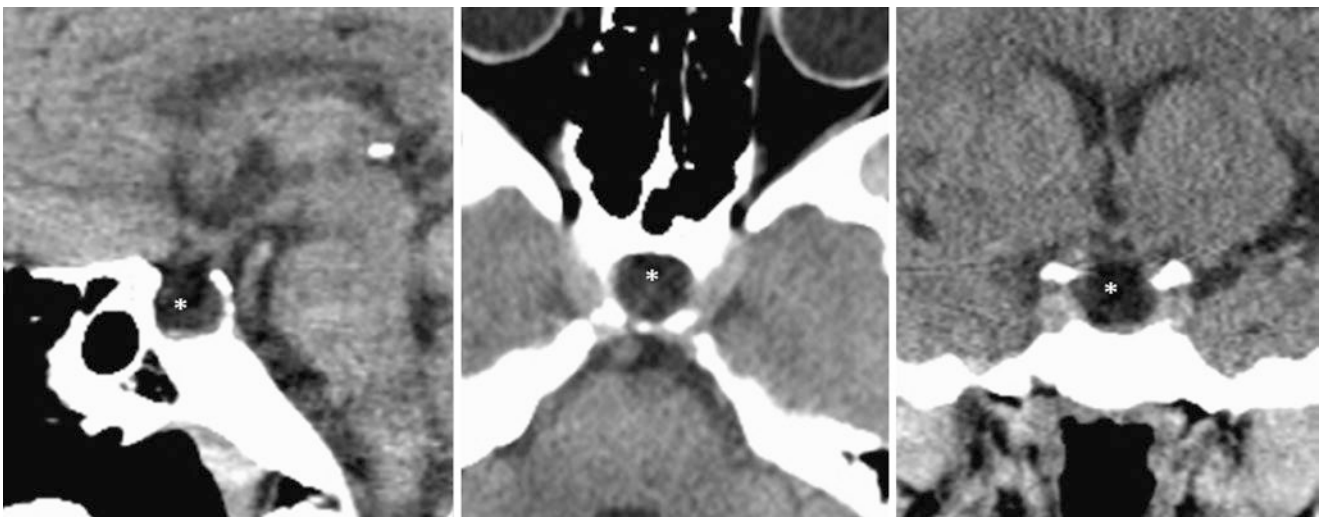

Fig. 8.56 A 70-year-old female with altered mental status had an incidental PES (*) on a 256-slice NECT, visualized on sagittal (*left*), axial (*middle*), and coronal (*right*) reconstructions. The stalk is not well visualized

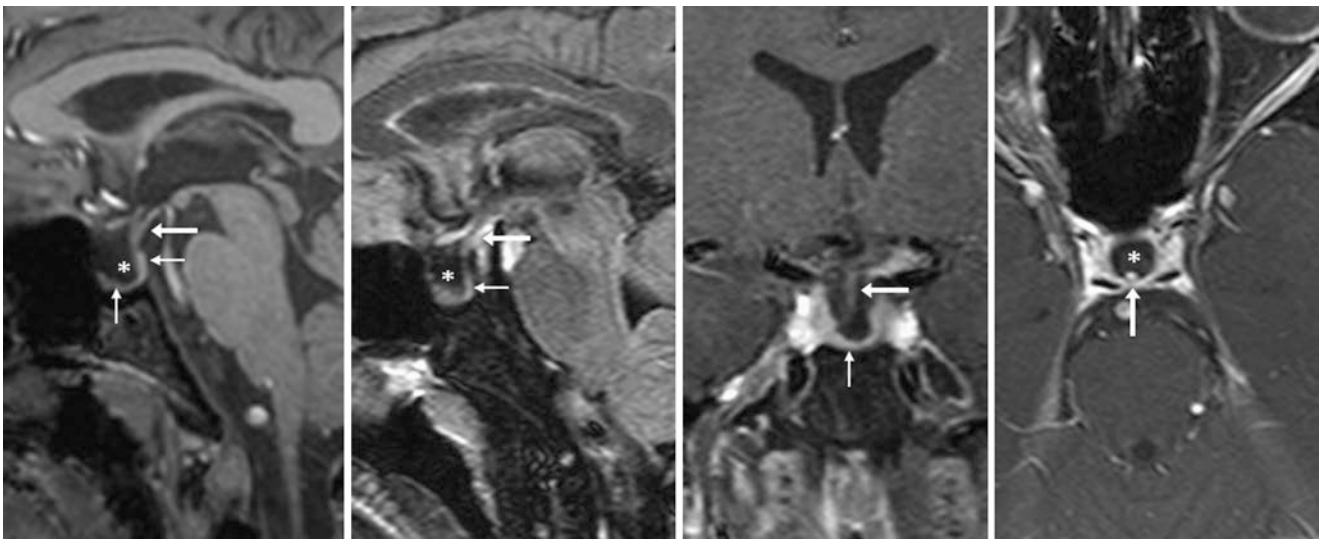

Fig. 8.57 A 57-year- old female patient had vision loss (from glaucoma) and an otherwise negative 3 T MRI but a partial PES (*). Note a normal stalk (*arrows*) on sagittal T1WI (*left*) that was mildly bright on a three-dimensional FLAIR sagittal reformat (*left middle*). On postcontrast coronal (*right middle*) and axial (*right*) T1WIs, note normal pituitary tissue (*thin arrows*)

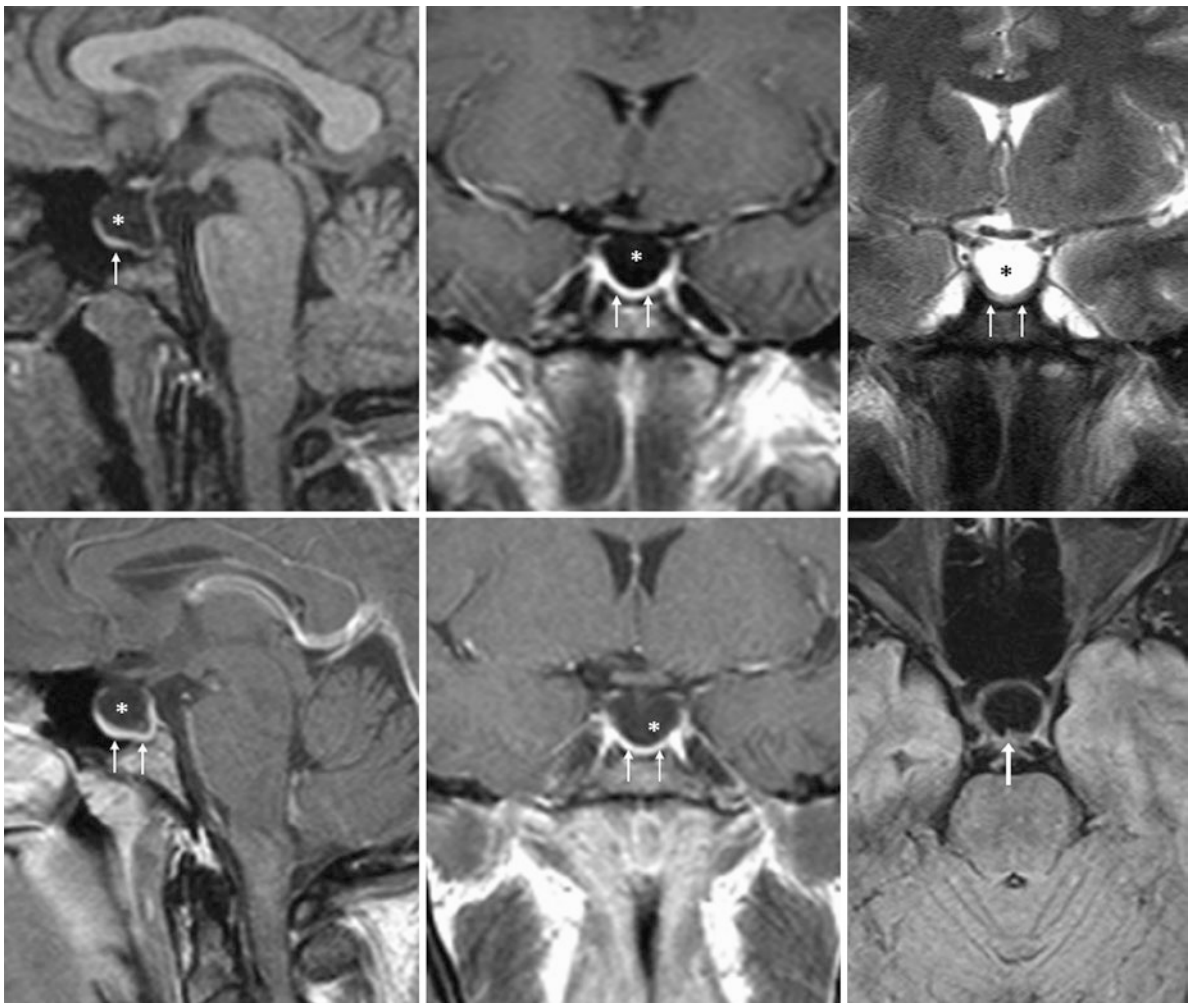

Fig. 8.58 A 40-year-old female patient had headaches and a partial PES (*) on an otherwise negative 1.5 T MRI; the stalk was not seen at that time. Note a thin rim of tissue (*thin arrows*) on sagittal noncontrast (*top left*) and coronal postcontrast (*top middle*) T1WIs and on coronal T2WI (*top right*). Seven years later there are unchanged postcontrast sagittal (*bottom left*) and coronal (*bottom middle*) T1WIs; axial FLAIR depicts the stalk posteriorly (*arrow*, *bottom right*)

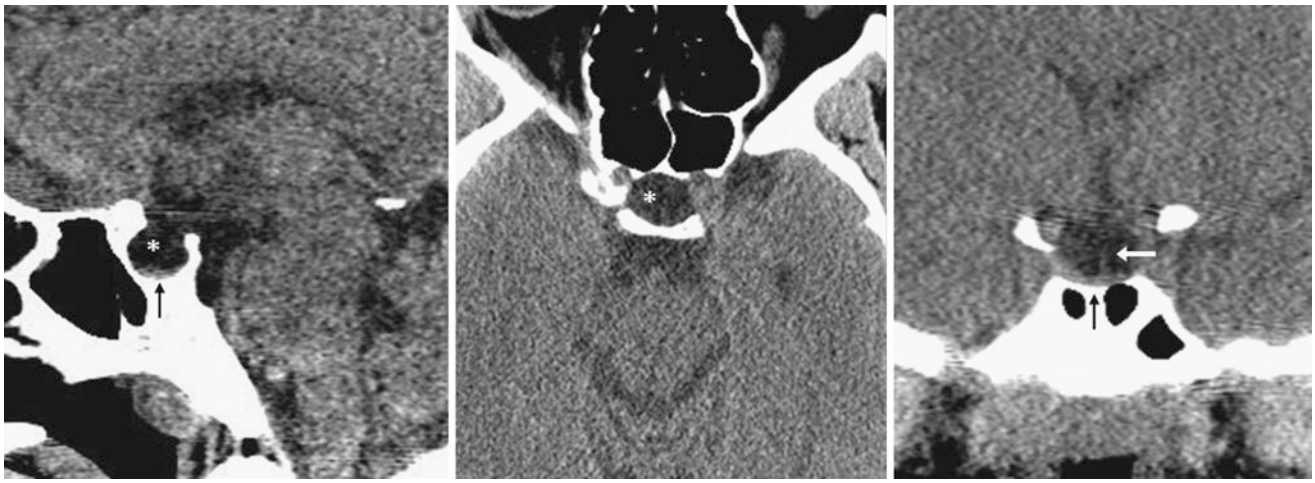

Fig. 8.59 A 49-year-old female patient had photophobia and an incidental partial PES (*) on a 16-slice NECT, visualized on sagittal (*left*), axial (*middle*), and coronal (*right*) reconstructions. The stalk (*arrows*) is barely visible on the coronal reformats. There is likely a thin rim of pituitary tissue (*thin arrows*) inferiorly within the sella

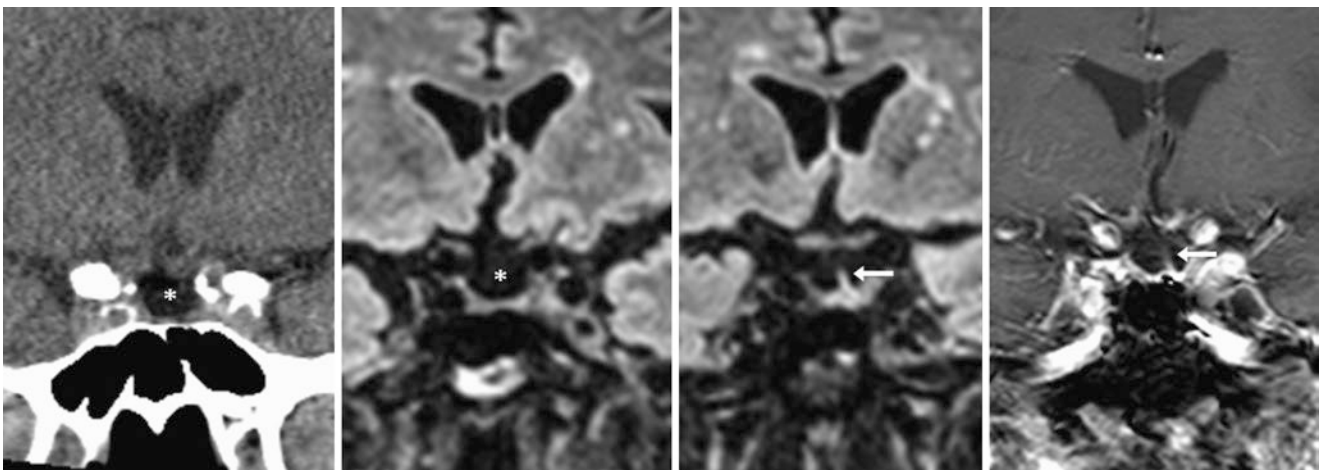

Fig. 8.60 An 80-year-old female had a 3 T MRI performed for stroke symptoms (interpreted as negative) and an incidental partial form of PES (*) on NECT coronal reformats (*left*) and on coronal FLAIR images reformatted from a three-dimensional acquisition (*left middle and right middle*). The stalk (*arrows*) enhances on postcontrast coronal T1WI (*right*)

Fig. 8.61 A 38-year-old female patient with headaches after trauma had an incidental partial form of PES (*) on CECT axial (*left*), sagittal (*left middle*), and coronal (*middle*) reformats, where a rim of pituitary tissue (*thin arrows*) was present along the floor of the sella. This was confirmed on 1.5 T MRI noncontrast sagittal (*right middle*) and postcontrast coronal (*right*) T1WIs. The stalk/infundibulum (*arrows*) is posteriorly located where it abuts the dorsum sella

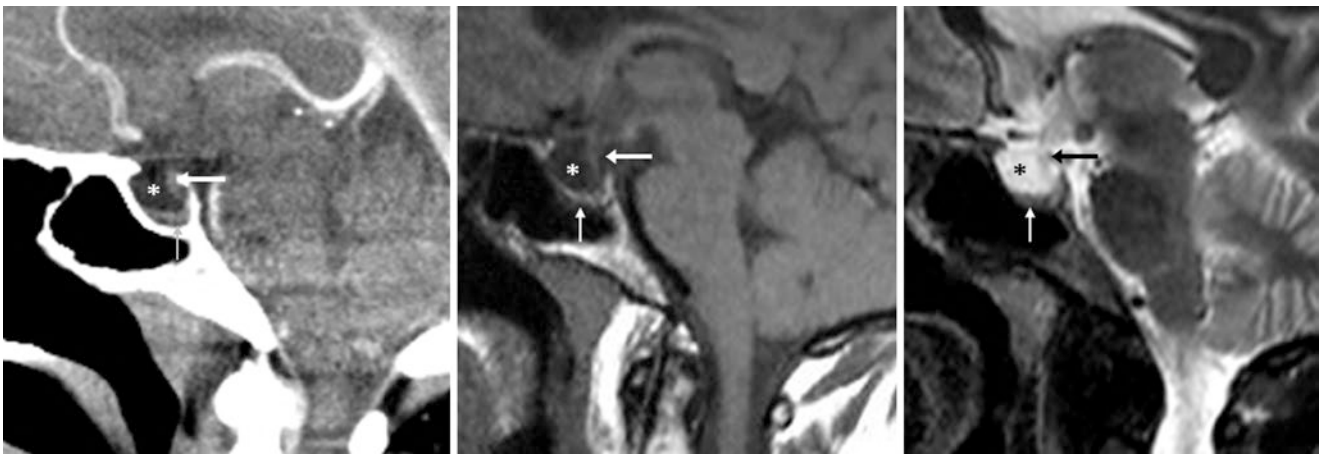

Fig. 8.62 A 54-year-old female patient with an incidental partial form of PES (*) on a CECT (*left*), where a rim of pituitary tissue (*thin arrows*) was present along the floor of the sella. This was confirmed on 1.5 T MRI sagittal T1WI (*middle*) and T2WI (*right*). The stalk/infundibulum (*arrows*) is posteriorly located, where it abuts the dorsum sella

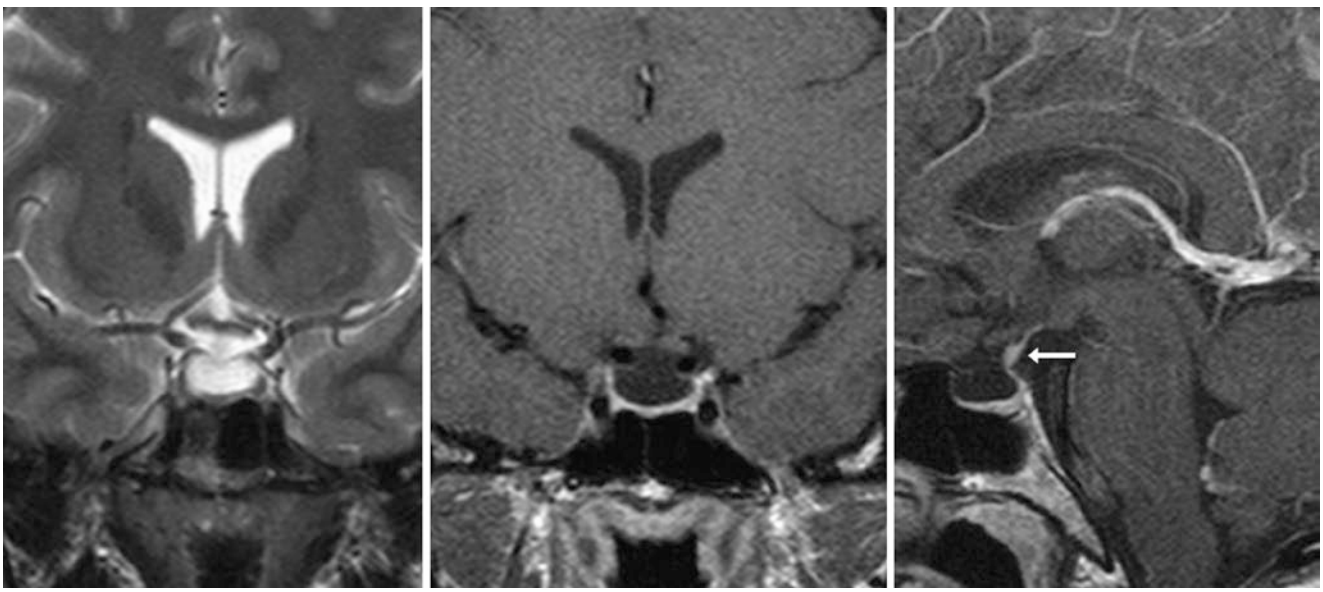

Fig. 8.63 A 34-year-old female patient had an incidental partial PES (*) on a 1.5 T MRI after a motor vehicle accident. The contour of the sella is moderately enlarged. The stalk (*arrows*) is not visible on non-contrast coronal T2WI (*left*) or on postcontrast coronal T1WI (*middle*) but is seen posteriorly within the sella on postcontrast sagittal T1WI (*right*)

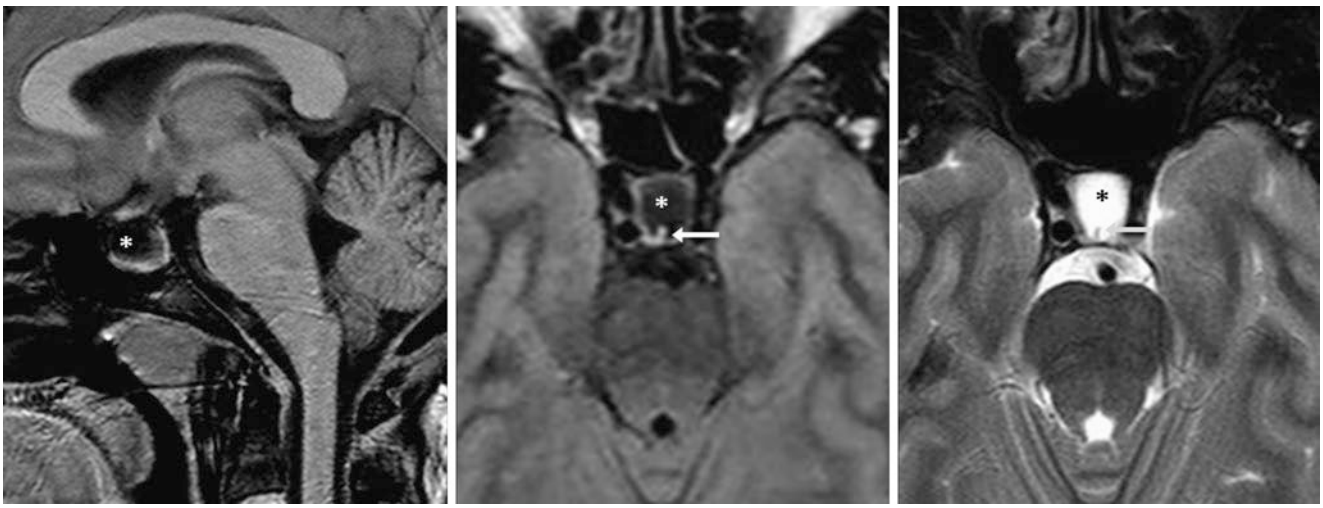

Fig. 8.64 A 35-year-old female patient had an incidental PES (*) on a 1.5 T MRI. The bony contour of the sella is slightly enlarged. The stalk (*arrows*) was not visible on noncontrast sagittal T1WI (*left*) but is clearly visualized as located posteriorly within the sella on axial FLAIR (*middle*) and T2WI (*right*)

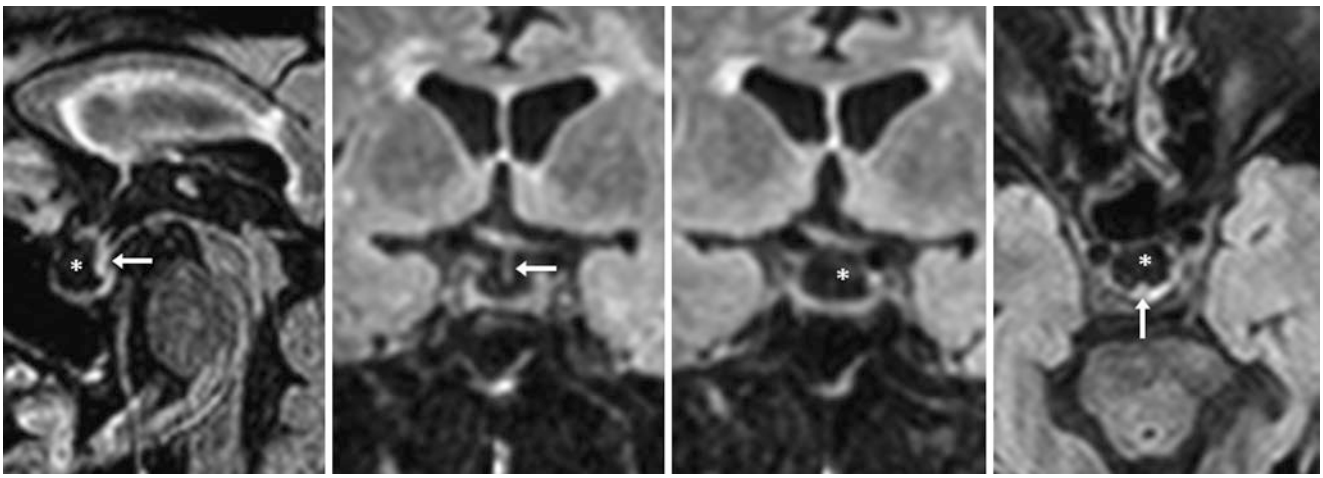

Fig. 8.65 A 66-year-old female patient had a 3 T MRI performed for stroke-like symptoms that was read as negative and an incidental near-complete form of PES (*) on noncontrast FLAIR images reconstructed from a three-dimensional acquisition in sagittal (*left*), coronal (*left middle*, *right middle*) and axial (*right*) planes. The stalk (*arrows*) is noted posteriorly within the sella

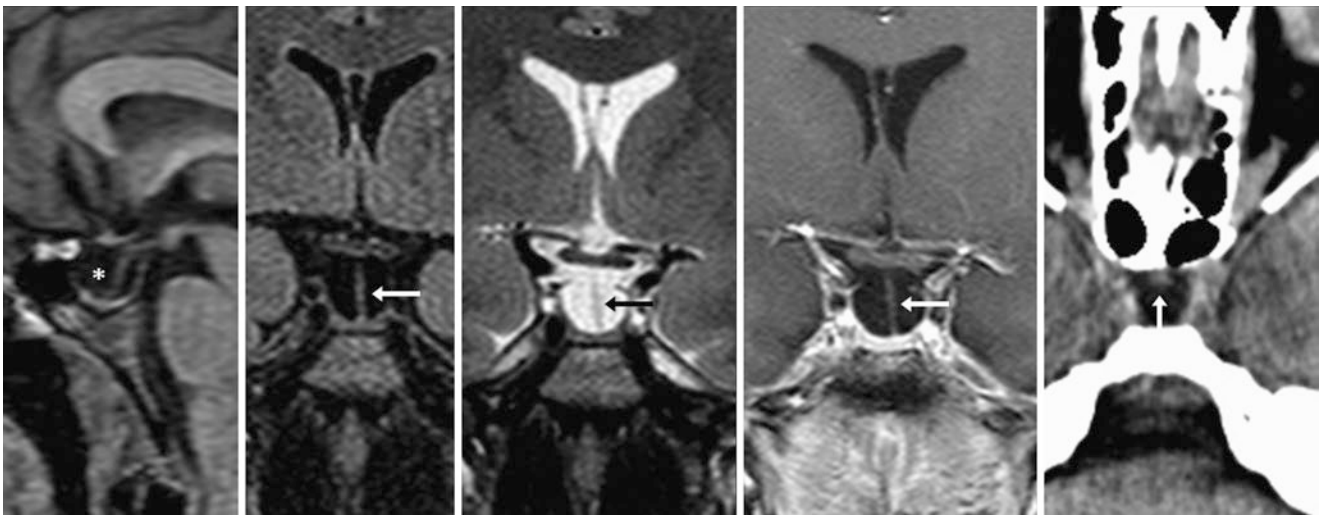

Fig. 8.66 A 52-year-old female with seizures had an incidental, near-complete PES (*) and a mildly enlarged bony sella on 1.5 T MRI noncontrast sagittal T1WI (*left*). The stalk (*arrows*) is shifted slightly to the left on coronal FLAIR (*left middle*), T2WI (*middle*), and postcontrast T1WI (*right middle*). A PES was noted on a NECT 10 years earlier (*right*)

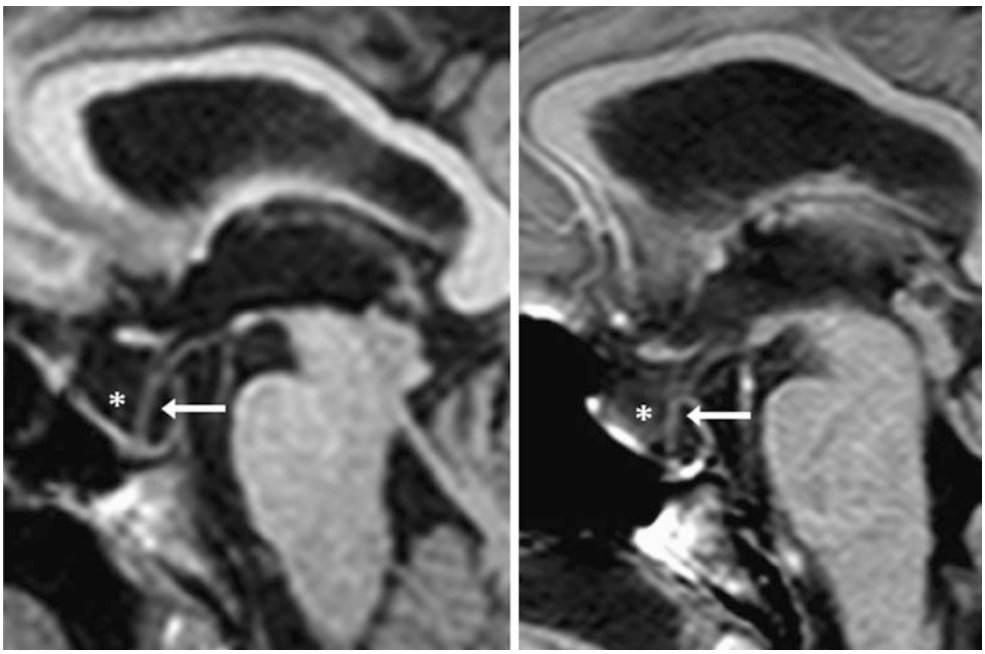

Fig. 8.67 A 62-year-old female patient was experiencing confusion. The stalk (*arrows*) of a near-complete PES (*) extended to the sellar floor on noncontrast sagittal T1WI (*left*) and was unchanged 3 years later (*right*)

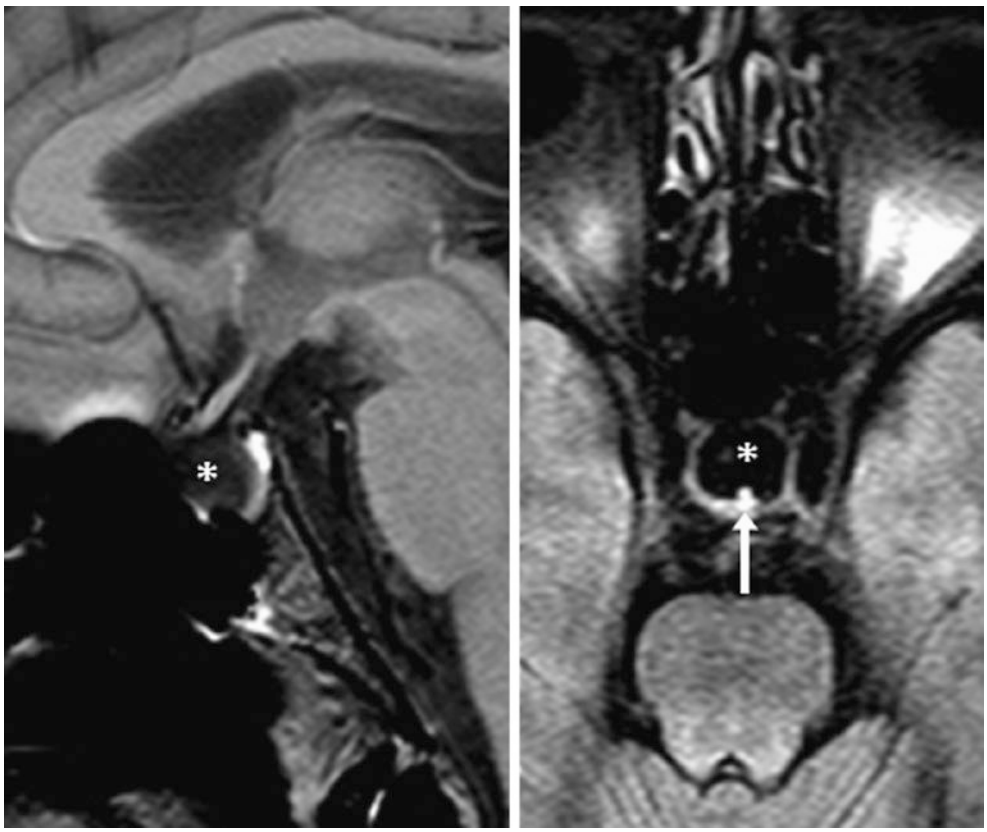

Fig. 8.68 A 54-year-old patient with headaches. The stalk (*arrows*) of a PES (*) is not seen on noncontrast sagittal T1WI (*left*) but is found on axial FLAIR (*right*)

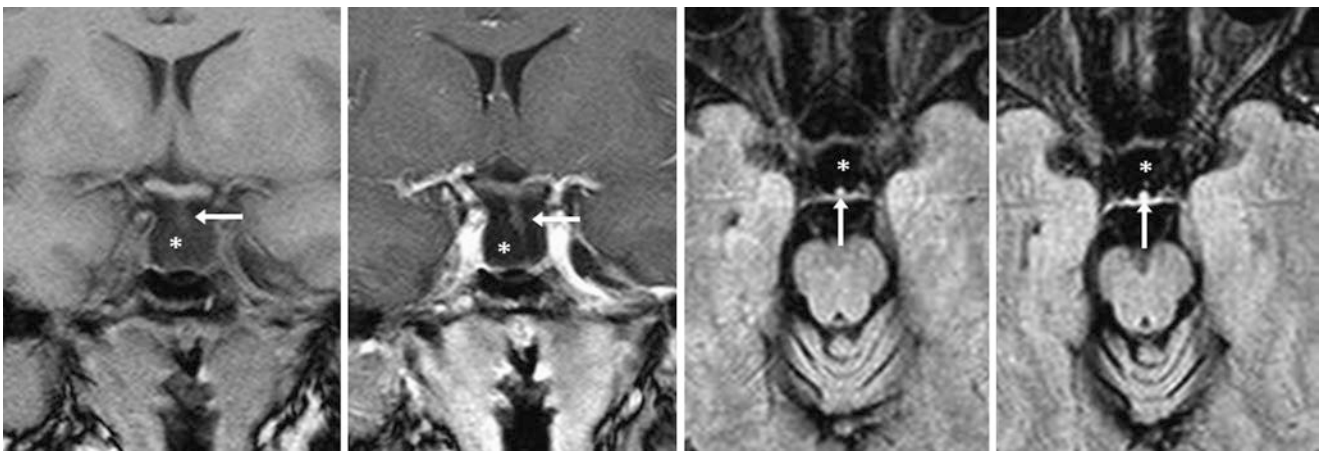

Fig. 8.69 **A** 41-year-old female with a 1.5 T MRI performed after a stroke had an incidental complete form of PES (*) on noncontrast (*left*) and postcontrast (*left middle*) coronal T1WIs and on noncontrast (*right middle*) and postcontrast (*right*) axial FLAIR images. The stalk (*arrows*) is posteriorly located as well as deviated to the left

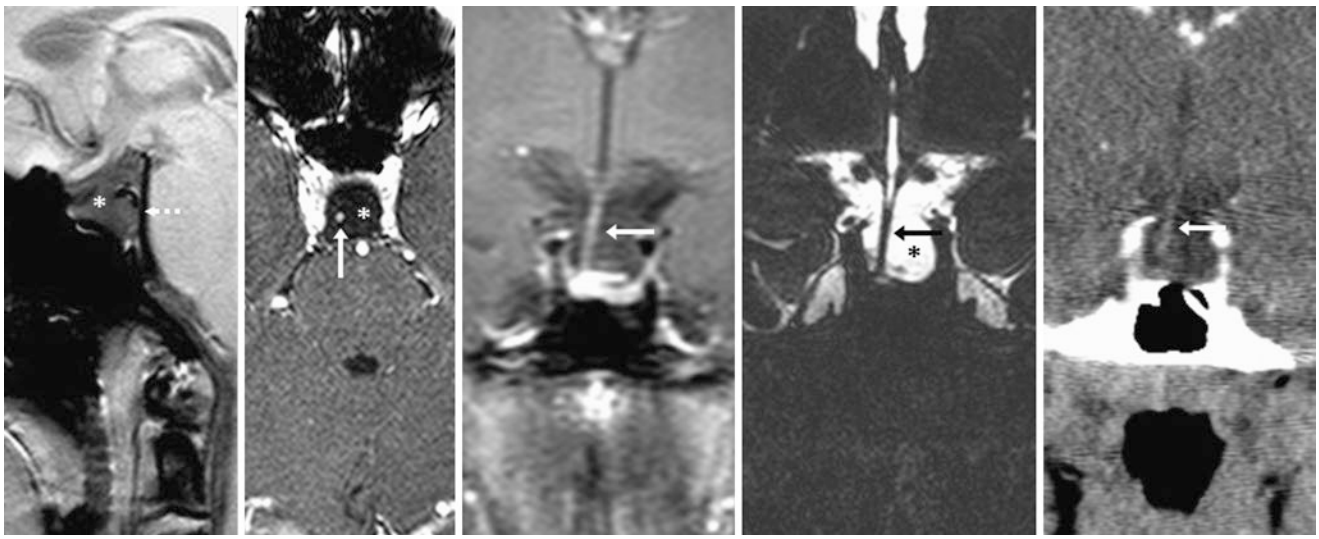

Fig. 8.70 A 45-year-old female patient was seen with otalgia and neck pain. A complete form of PES (*) was found incidentally with a moderately enlarged sella on a cervical 3 T MRI. Note the thin posterior wall of the sella (*dashed arrow*) on noncontrast sagittal T1WI (*left*). The stalk (*arrows*) is shifted to the right of midline on postcontrast axial (*left middle*) and coronal (*middle*) T1WI as well as on a coronal three-dimensional balanced T2WI (*right middle*) and a coronal CECT (*right*)

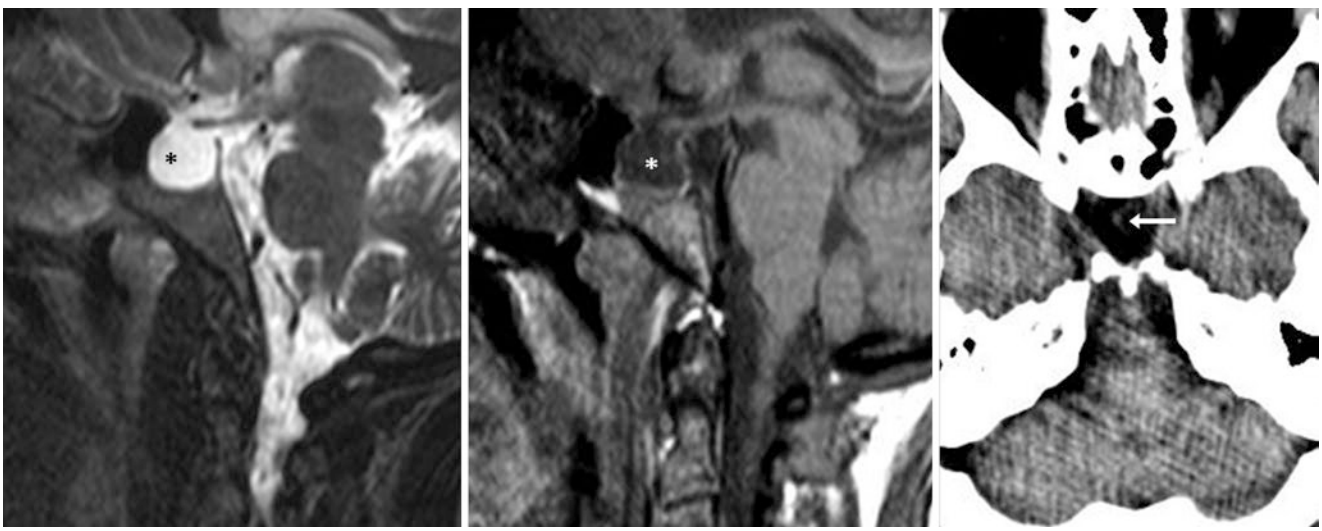

Fig. 8.71 A 47-year-old male patient was seen with neck pain; a complete PES (*) was noted incidentally on a cervical 3 T MRI. The bony contour of the sella is enlarged. The stalk (*arrows*) was not visible on noncontrast sagittal T2WI (*left*) and T1WI (*middle*) but had been present but barely visible (*arrows*) on an axial NECT 8 years earlier (*right*)

Fig. 8.72 A 38-year-old female patient with headache had an incidental complete form of PES (*) on a 64-slice NECT. The PES is visualized on axial (*left*), sagittal (*middle*), and coronal (*right*) reconstructions. The stalk (*arrows*) is not visualized on these images

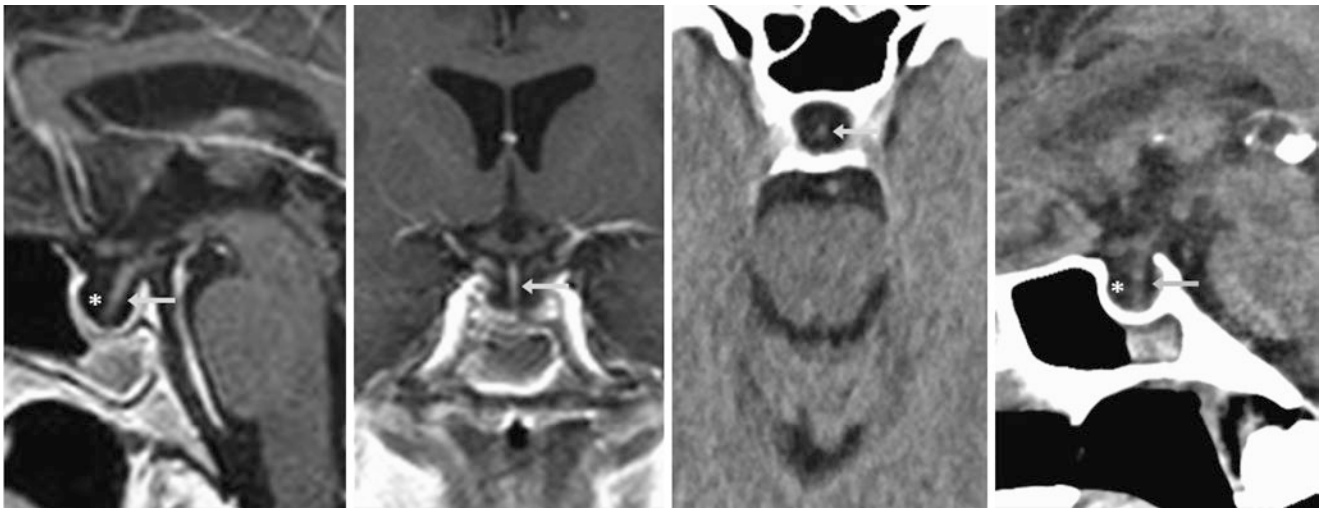

Fig. 8.73 A 56-year-old female patient with confusion and an otherwise negative 1.5 T MRI had a completely empty PES (*). Note a normal stalk (*arrows*) on postcontrast sagittal (*left*) and coronal (*left middle*) T1WI. On CECT axial (*right middle*) and sagittal (*right*) reformats, the stalk is also visualized. Note that normal pituitary tissue is difficult to visualize

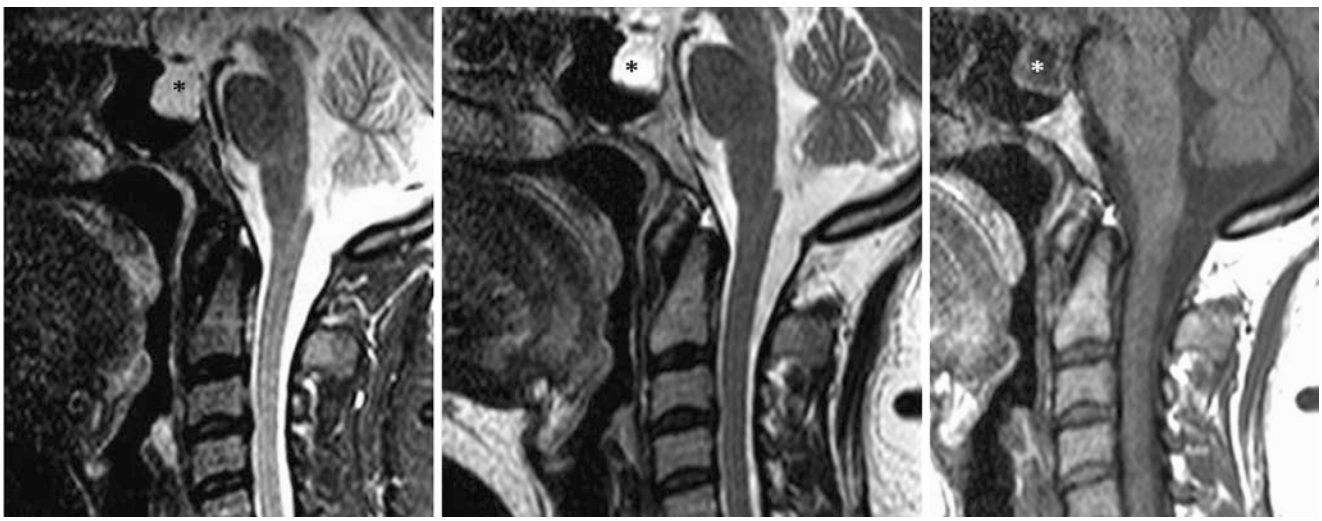

Fig. 8.74 A 44-year-old female patient with neck pain had a completely empty PES (*) noted incidentally at the top of a cervical 1.5 T MRI. The bony contour of the sella is mildly enlarged. The stalk was not visible on sagittal STIR (*left*), T2WI (*middle*), or on noncontrast T1WI (*right*)

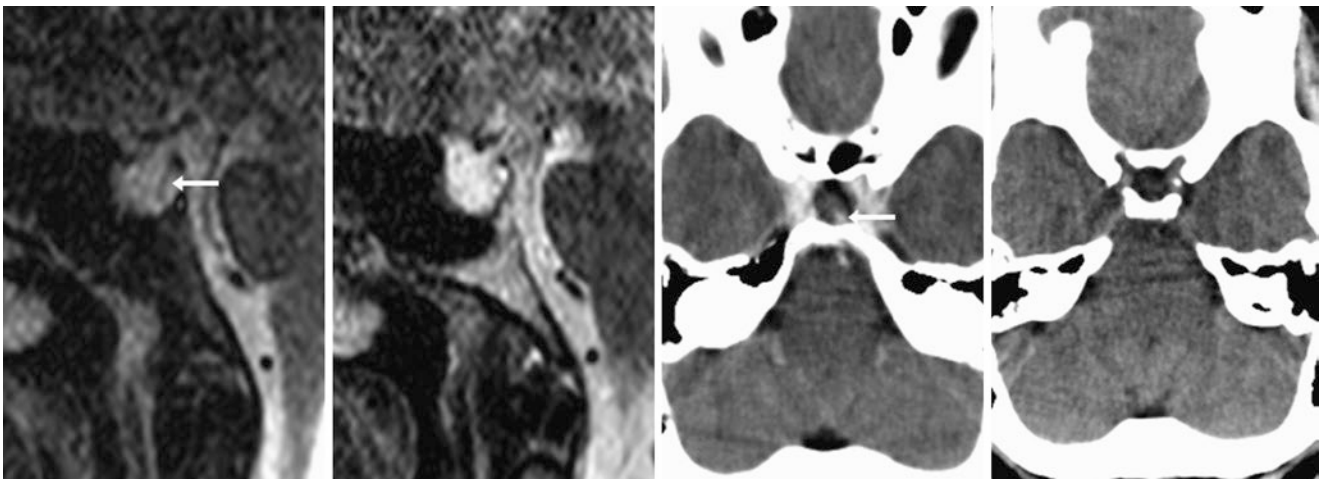

Fig. 8.75 A 53-year-old asymptomatic female had an incidental complete form of PES (*) on a 1.5 T MRI sagittal STIR (*left*) and T2WI (*left middle*). This was confirmed on CECT axial reformats (*right middle and right*). The stalk/infundibulum is present (*arrows*) but is somewhat difficult to visualize

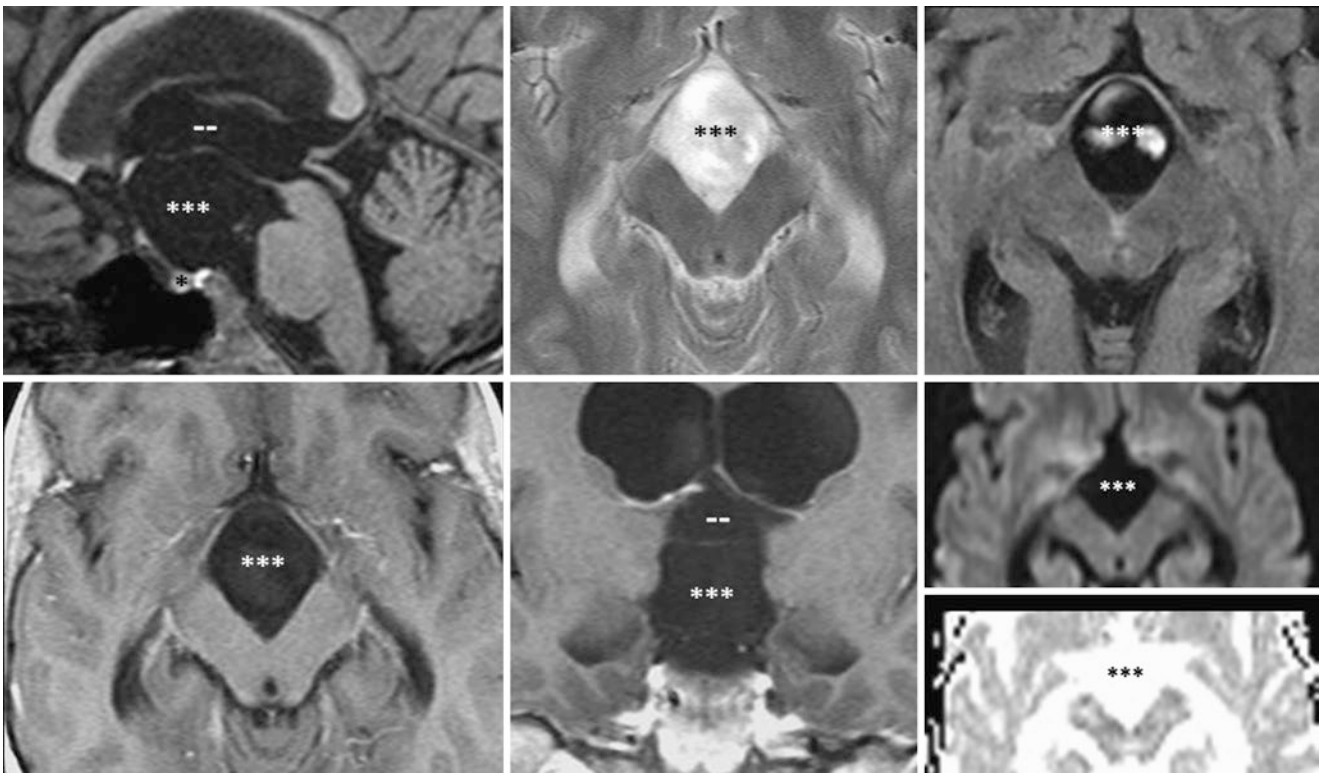

Fig. 8.76 Comparison case of suprasellar arachnoid cyst. A 43-year-old male with hydrocephalus and an enlarged suprasellar cistern (***) as compared to the sella (*) on 3 T MRI noncontrast sagittal T1WI (*top left*), axial T2WI (*top middle*), FLAIR (*top right*), and postcontrast axial (*bottom left*) and coronal (*bottom middle*) T1WI. The cyst does not have reduced diffusivity on DWI and ADC maps (*bottom right*). Note the displaced third ventricle (−−)

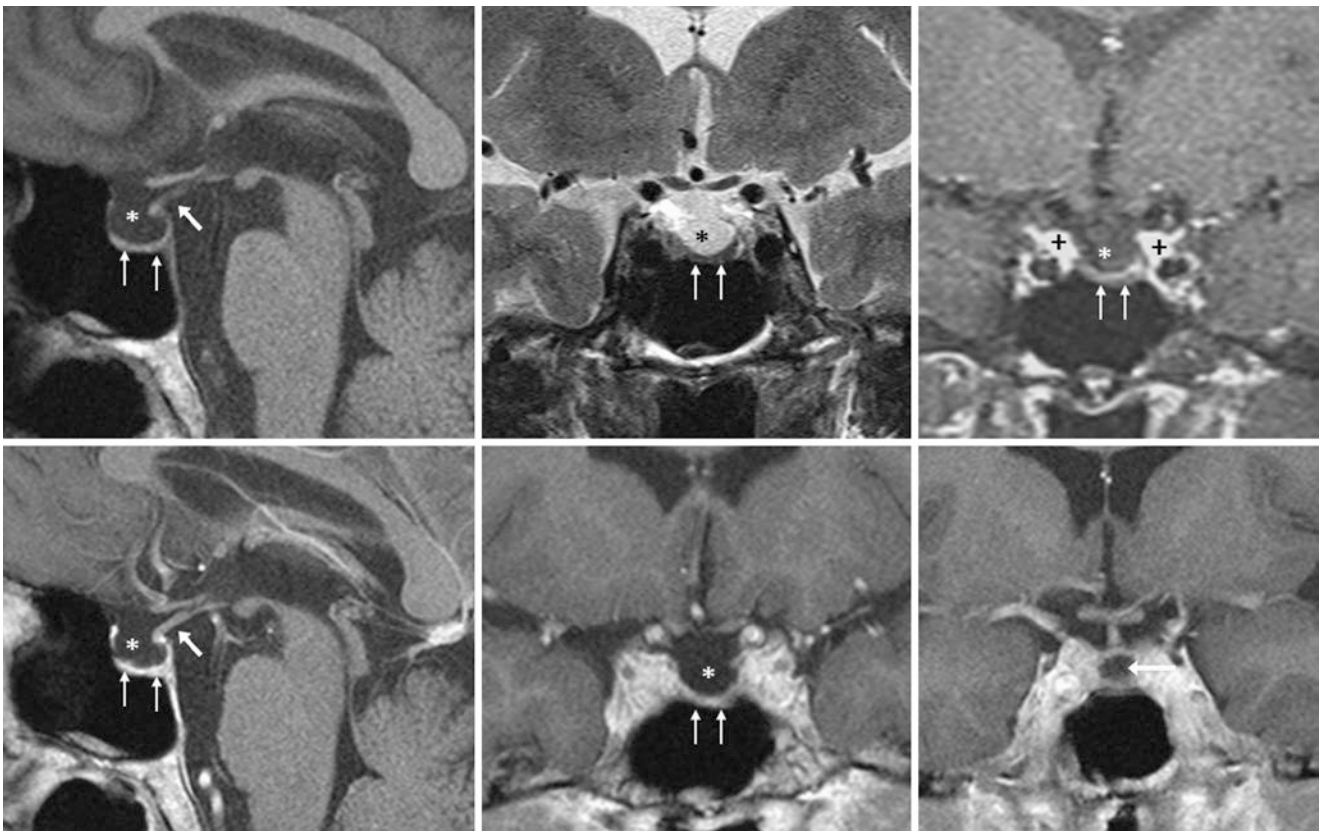

Fig. 8.77 Comparison case of panhypopituitarism associated with PES. The patient was a 71-year-old symptomatic male 20–30 years post-trauma with a near-complete form of PES (*) on 3 T MRI sagittal noncontrast T1WI (*top left*), coronal T2WI (*top middle*), and dynamic 1-min postcontrast T1WI (*top right*). A thin rim of residual pituitary tissue (*thin arrows*) showed enhancement immediately following the cavernous sinus (+). Sagittal (*bottom left*) and coronal (*bottom middle and bottom right*) postcontrast T1WIs demonstrated enhancement of the stalk/infundibulum (*arrows*) as well

8.7 Rathke Cleft and Pars Intermedia Cysts

Rathke cleft cysts (RCCs) represent a benign, cystic remnant lined by epithelial cells. They are situated within the anatomic separation between the anterior pituitary (i.e., the adenohypophysis or pars distalis) and the posterior pituitary (neurohypophysis, which mostly consists of the pars nervosa). Regarding the formation of RCCs, a brief understanding of the embryologic development of the pituitary is necessary. During the third to fourth weeks of gestation, a projection of the embryonic stomodeum, called the *Rathke pouch*, converges with an invagination of the floor of the third ventricle, the infundibulum/stalk, to form what will later be called the pituitary gland. Regarding the Rathke pouch, the anterior portion later forms the *anterior pituitary*, while the posterior portions has a residual lumen that typically narrows to form a cleft (Rathke cleft). Persistence of the pouch's posterior portion or cleft is termed the *pars intermedia*, which in some instances remains as a cyst. Thus, since the pars intermedia is typically entirely absent (i.e., has totally regressed) or is quite small in normal adults, RCCs are also called *pars intermedia cysts* owing to this failed regression of the posterior portion of the Rathke pouch.

An RCC is typically situated medially but may extend laterally or superiorly into the suprasellar cistern and may even appear to be predominately suprasellar. The RCC is the most common incidental finding (i.e., incidentaloma) of the pituitary gland, occurring in 3–10 % of asymptomatic patients at autopsy. This range of incidence is wide, and the range may be even be larger depending on whether one includes microscopic, less than 2 mm RCCs (the majority), versus greater than 2-mm cysts as well. The quite tiny RCCs, seen only microscopically and centrally located within the pars intermedia, may occur with a frequency as high as 13–22 % of the asymptomatic population! These numbers are in contrast to the second most common incidentalomas, the *asymptomatic microadenomas*, which occur in 2–11 % of the population at autopsy.

On imaging, the signal intensity of smaller RCCs (<4–5 mm) is often homogeneously T2-bright and T1-hypointense, similar to that of CSF. Technically, a RCC is considered the same entity as a pars intermedia cyst because an RCC arises from the pars intermedia. However some references separately term tiny, CSF-like cysts occurring centrally near the insertion of the stalk that are less than 3 mm in size pars intermedia cysts while calling larger, proteinaceous T1-bright cysts RCCs. One basis for this terminology is that as pars intermedia cysts enlarge, over 70 % of those greater than 5 mm in size will have T1-bright signal intensity, which is more typical of an RCC appearance. Surgically, the T1-bright signal has been shown to represent yellow and waxy but solid mucinoid material representing cholesterol and protein on biochemical testing. Regarding gadolinium contrast, RCCs typically do not enhance, although the surrounding anterior or posterior lobes may enhance; these can simulate an enhancing rim of the cyst.

The vast majority of RCCs are asymptomatic, but they may become symptomatic as they enlarge. Enlargement, based on studies of asymptomatic RCCs as incidentalomas, is estimated to occur in somewhere from 5–30 % over several years; this range likely depends on the criteria of what is classified as an RCC. Most commonly, such enlargement may cause symptoms of pituitary dysfunction, headaches, or visual loss. Another underreported phenomenon is that RCCs may actually undergo spontaneous involution, which early reports suggest may occur in up to 30 % of patients with asymptomatic RCCs.

Since mucinous material may collect within the cyst and enlarge it, thereby producing a T1-bright and/or T2-dark signal, RCCs may simulate a pituitary adenoma. In particular, larger RCCs may be difficult to discern from macroadenomas that are cystic, degenerated, or have undergone internal hemorrhage. When having such a complex appearance, RCCs can also be difficult to distinguish from *craniopharyngiomas*. They may also resemble suprasellar *arachnoid cysts*. Regarding macroadenomas, dynamic contrast images demonstrate a lack of filling of RCCs with contrast material in all phases, whereas macroadenomas eventually enhance unless there has been a large amount of internal hemorrhage or necrosis. Craniopharyngiomas are typically mostly suprasellar and are often cystic; even if entirely cystic, they typically have a rim of enhancement peripherally, while RCCs are uncommonly solely suprasellar (unless very large) and do not exhibit rim enhancement (although again, enhancement of adjacent pituitary tissue may simulate a rim). An arachnoid cyst in such a location may appear similar as both RCCs and arachnoid cysts can be T2-bright, but typically an RCC would not arise from or extend into the cleft between the anterior and posterior lobes (i.e., should not connect to the pars intermedia) (Figs. 8.78, 8.79, 8.80, 8.81, 8.82, 8.83, 8.84, 8.85, 8.86, 8.87, 8.88, 8.89, 8.90, 8.91, 8.92, 8.93, 8.94, 8.95, 8.96, 8.97, 8.98, 8.99, 8.100, and 8.101).

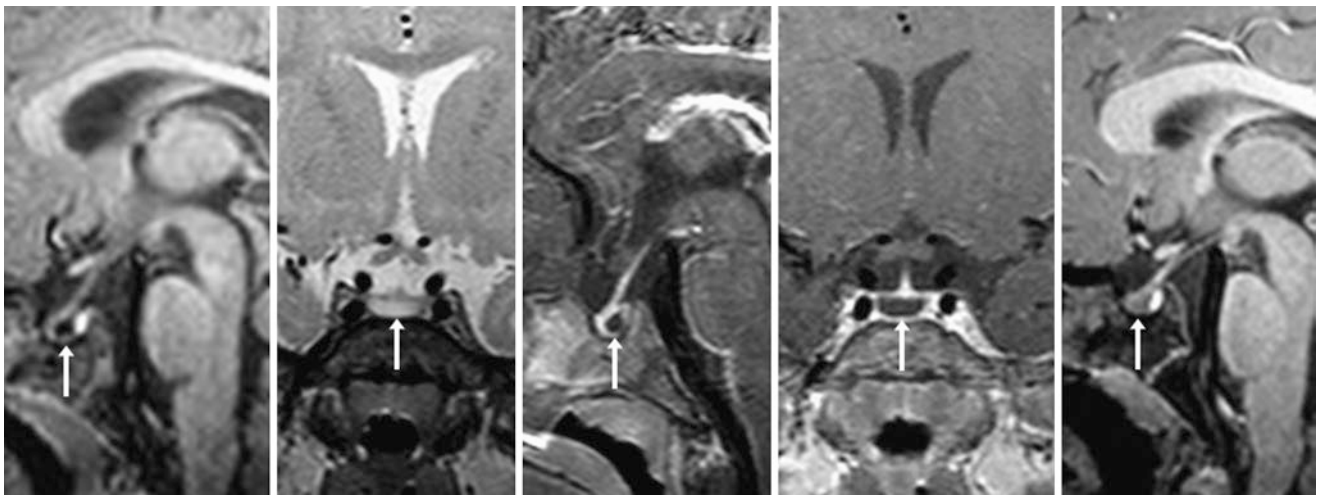

Fig. 8.78 The patient was a 9-month-old male infant with hypotonia (due to mild myelination delay). A 3 T MRI demonstrated a small, 3-mm size pars intermedia cyst (RCC) at the junction of the anterior and posterior lobes (*arrows*) on sagittal noncontrast T1WI (*left*), coronal T2WI (*left middle*), sagittal postcontrast T1WI (*middle*), and on postcontrast coronal T1WI (*right middle*). At 18 months age, the RCC is unchanged on a noncontrast sagittal T1WI (*right*)

Fig. 8.79 The patient was a 2-month-old male with a right retinoblastoma; on a 3 T MRI, the pituitary appeared normal on a sagittal noncontrast T1WI (*top left*). However, by 8 months age, a 3.5-mm pars intermedia/RCC (*arrows*) was noted on a repeat T1WI (*top right*), being hyperintense on coronal (*bottom left*) and axial (*bottom middle*) T2WI. On SWI (*bottom right*), the RCC does not exhibit the dark signal of hemorrhage. Note the calcified residual retinoblastoma (*arrowheads*)

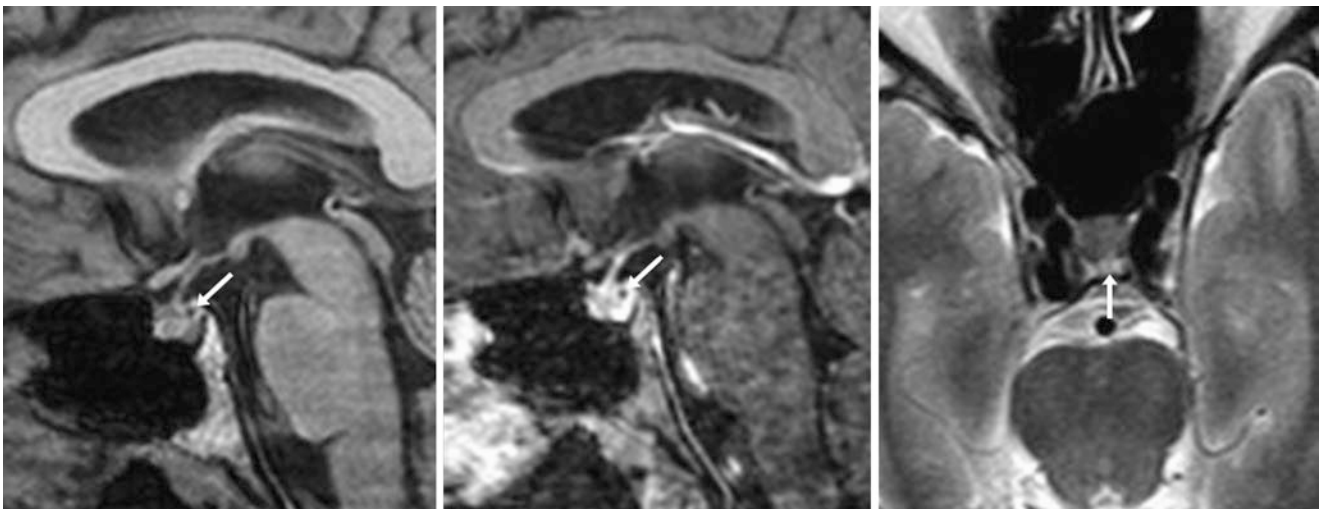

Fig. 8.80 The patient was a 51-year-old male with dizziness (no pituitary-related symptoms). A 1.5 T MRI demonstrated a tiny, 2-mm pars intermedia cyst (RCC) just posterior to the stalk and along the superior surface of the gland (*arrows*) on sagittal precontrast T1WI (*left*), postcontrast T1WI (*middle*), and an axial T2WI (*right*)

Fig. 8.81 The patient was a 49-year-old female with hearing loss (no pituitary-related symptoms). A 1.5 T MRI depicted a 3-mm RCC (*arrows*) located just posterior to the stalk on axial pre- (*top left*) and postcontrast (*top*, *left middle*) T1WI, on FLAIR (*top*, *right middle*), and on postcontrast sagittal T1WI (*top right*). On an MRI 1.5 years later, coronal T1WI pre- (*bottom left*) and postcontrast dynamic (*bottom*, *left middle*) and 120-s delayed (*bottom*, *right middle*) images confirmed a lack of enhancement and no definite change. A coronal T2WI (*bottom right*) confirmed bright signal akin to that produced by CSF

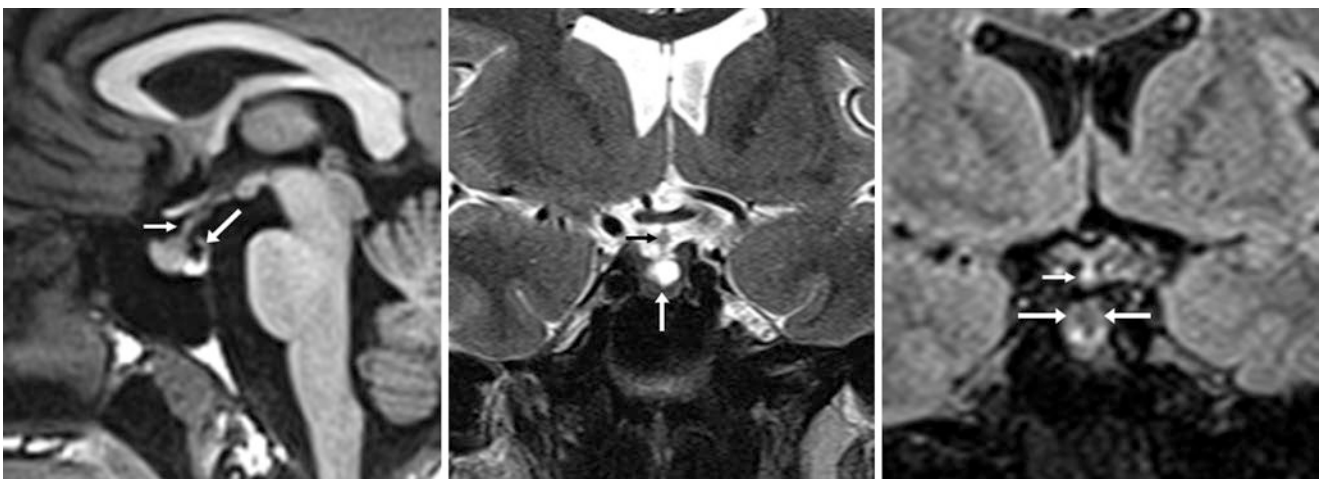

Fig. 8.82 The patient was an 18-year-old female with seizures (no pituitary-related symptoms). A 3 T MRI demonstrated a 4-mm RCC (*arrows*) located just posterior to the stalk (*thin arrows*) on sagittal non-contrast T1WI (*left*), on coronal T2WI (*middle*), and on coronal FLAIR (*right*). Note that the signal intensity is as bright as cerebrospinal fluid on T2WI but does not suppress as does the fluid on FLAIR

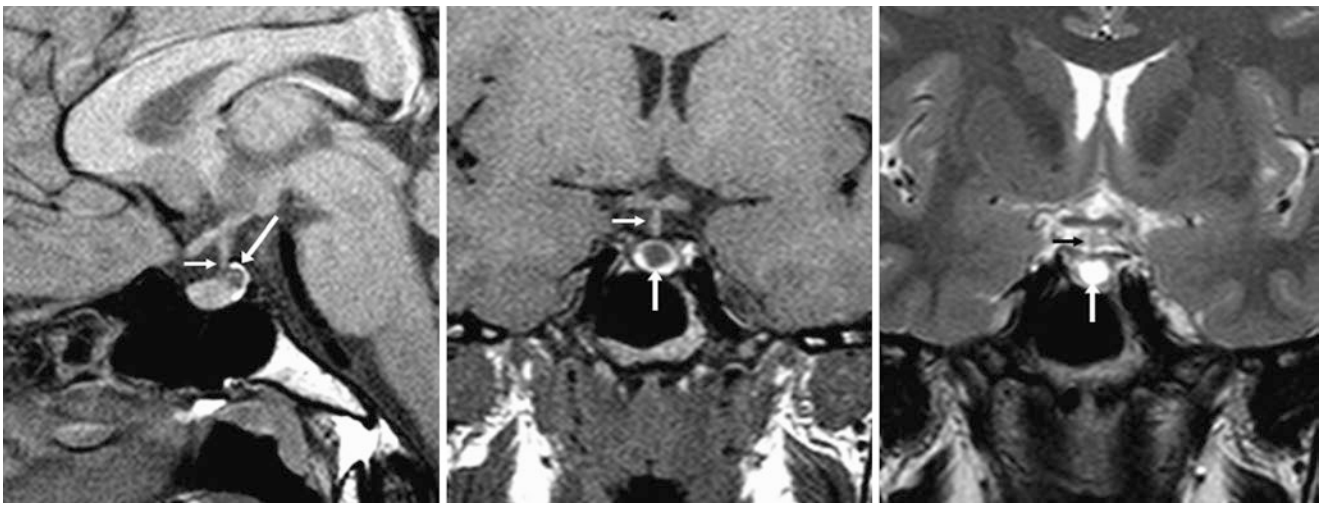

Fig. 8.83 The patient was a 25-year-old female with oligomenorrhea. A 1.5 T MRI demonstrated a 4–5-mm RCC (*arrows*) located just posterior to the stalk (*thin arrows*) that appeared hypointense on noncontrast sagittal T1WI (*left*) and coronal T1WI (*middle*). The RCC is bright on coronal T2WI (*right*). The symptoms were thought to be unrelated to the RCC

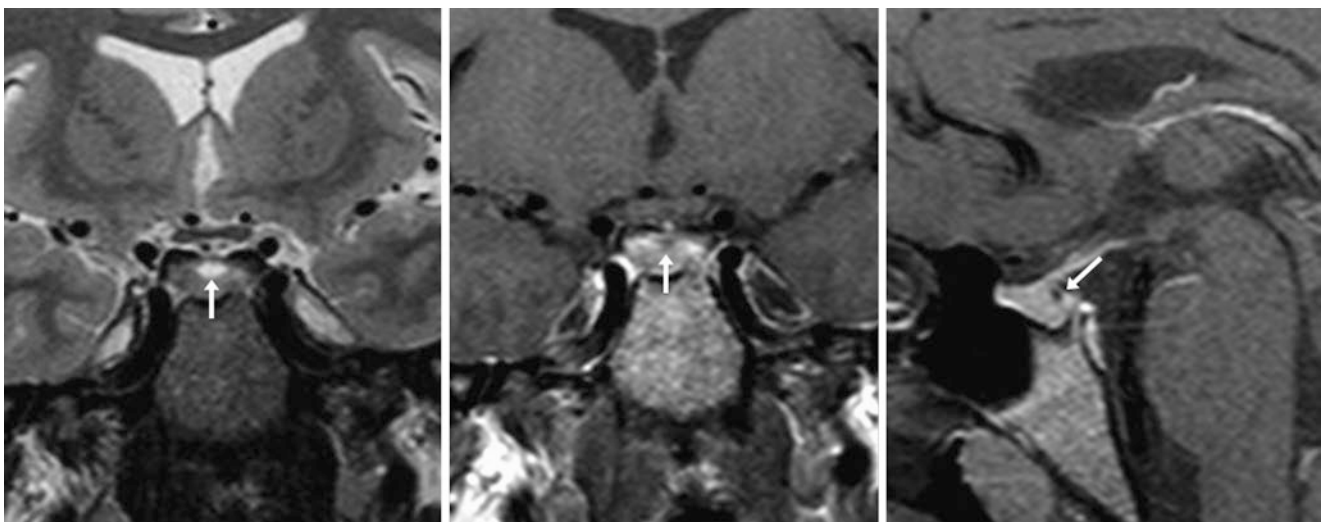

Fig. 8.84 The patient was a 23-year-old female with prolactinemia. A 1.5 T MRI depicted a tiny 1.5- to 2-mm pars intermedia cyst (RCC) just posterior to the stalk along the superior surface of the gland (*arrows*) on coronal T2WI (*left*), on postcontrast coronal T1WI (*middle*), and on postcontrast sagittal T1WI (*right*). The symptoms were considered unrelated to the RCC

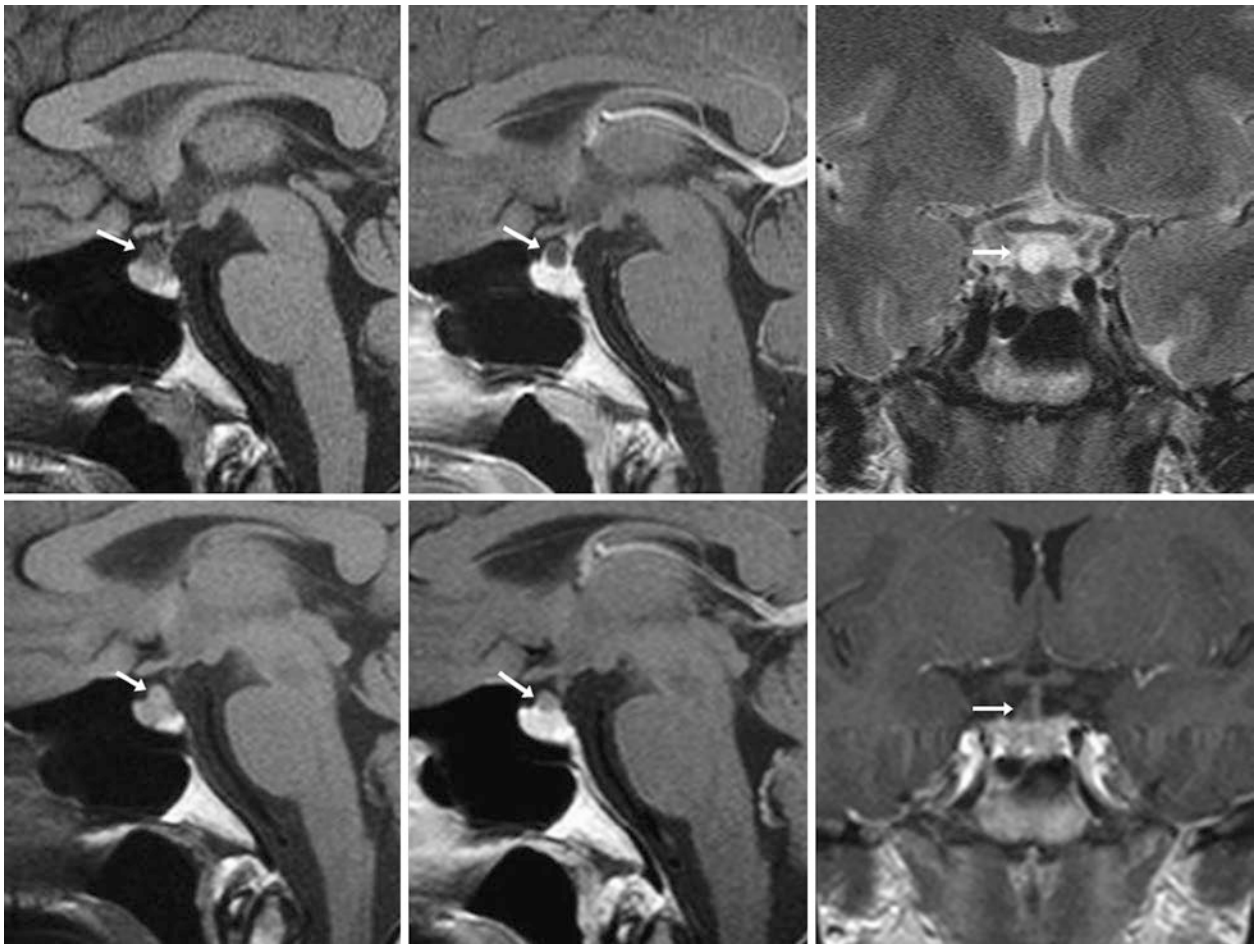

Fig. 8.85 The patient was a 27-year-old female without pituitary symptoms. A 1.5 T MRI delineated a small, 5-mm pars intermedia cyst (RCC) within the anterior pituitary (*arrows*) that was hypointense on both noncontrast sagittal T1WI (*top left*) and postcontrast sagittal T1WI (*top middle*), with signal intensity similar to that of CSF on T2WI (*top right*). A repeat MRI 3 years later showed that the cyst became T1-bright on pre- (*bottom left*) and on postcontrast (*bottom middle*) sagittal T1WIs and on coronal T1WI (*bottom right*), presumably due to an accumulation of mucinous products internally

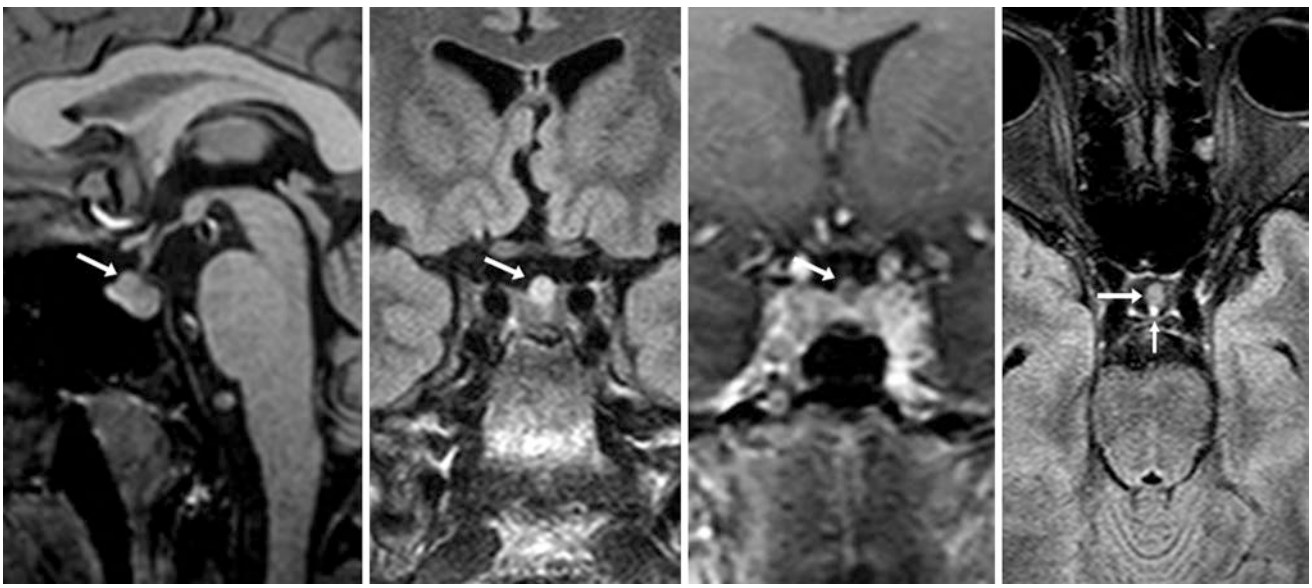

Fig. 8.86 The patient was a 33-year-old female with seizures lacking pituitary symptoms. On a 3 T MRI, a 4–5-mm T1-isointense RCC (*arrows*) is along the superior aspect of the gland on noncontrast sagittal T1WI (*left*), on coronal FLAIR (*left middle*), and on postcontrast coronal T1WI (*right middle*). Note stalk enhancement (*thin arrow*) on postcontrast axial FLAIR (*right*)

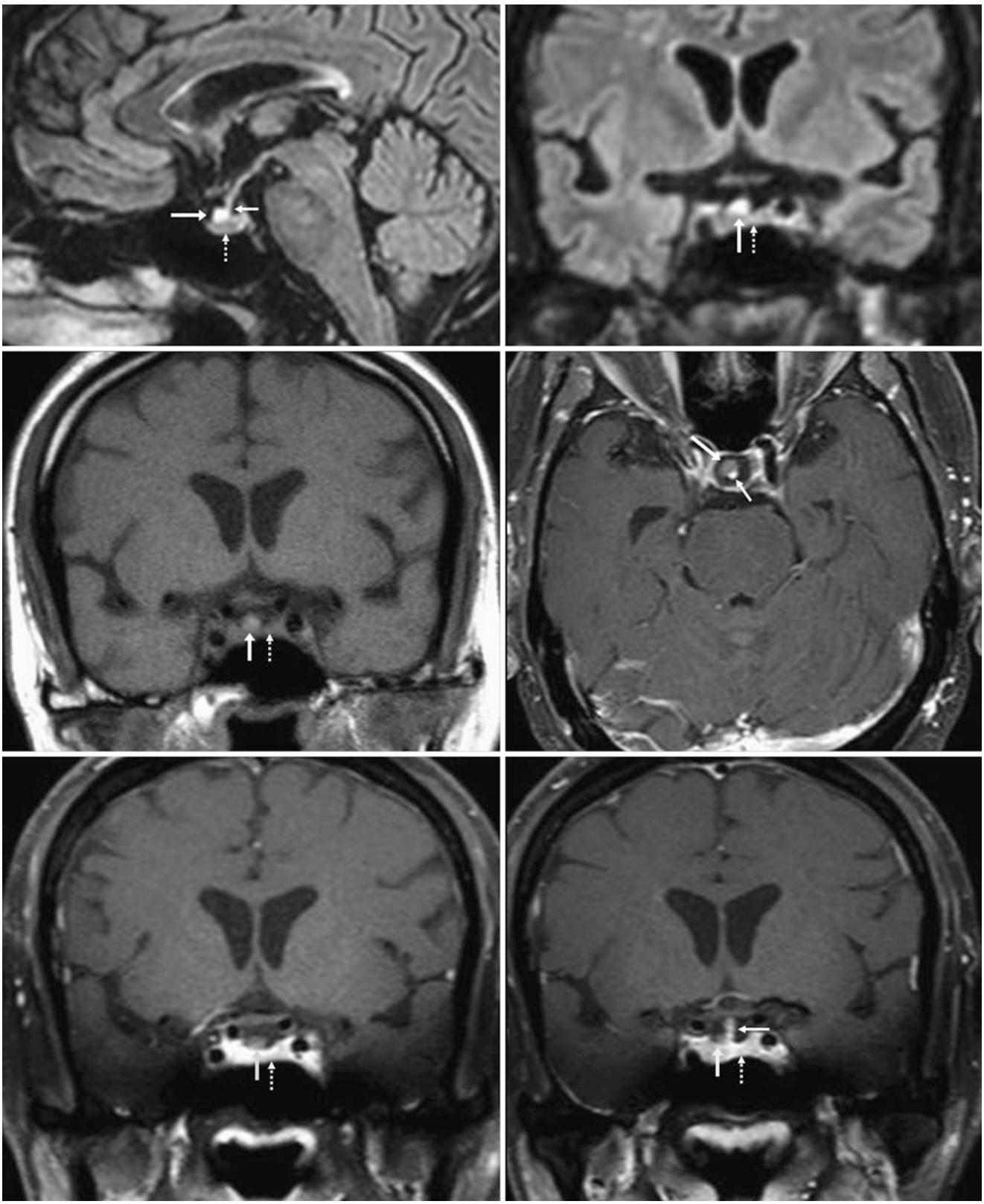

Fig. 8.87 The patient was a 57-year-old female without pituitary symptoms with an acute vision deficit and an otherwise negative MRI. *Top row*: a 3 T MRI depicted a small, 5-mm RCC (*arrows*) just anterior to the stalk (*thin arrows*) that was bright on sagittal (*left*) and coronal (*right*) reconstructions obtained from a noncontrast 3D FLAIR acquisition. *Middle row*: the RCC was isointense to the remainder of the gland (*dotted arrow*) on a noncontrast coronal T1WI (*left*). An axial postcontrast T1WI (*right*) showed that the RCC was clearly situated just anterior to the stalk and did not enhance. *Bottom row*: coronal postcontrast T1WIs with fat suppression confirm a lack of RCC enhancement

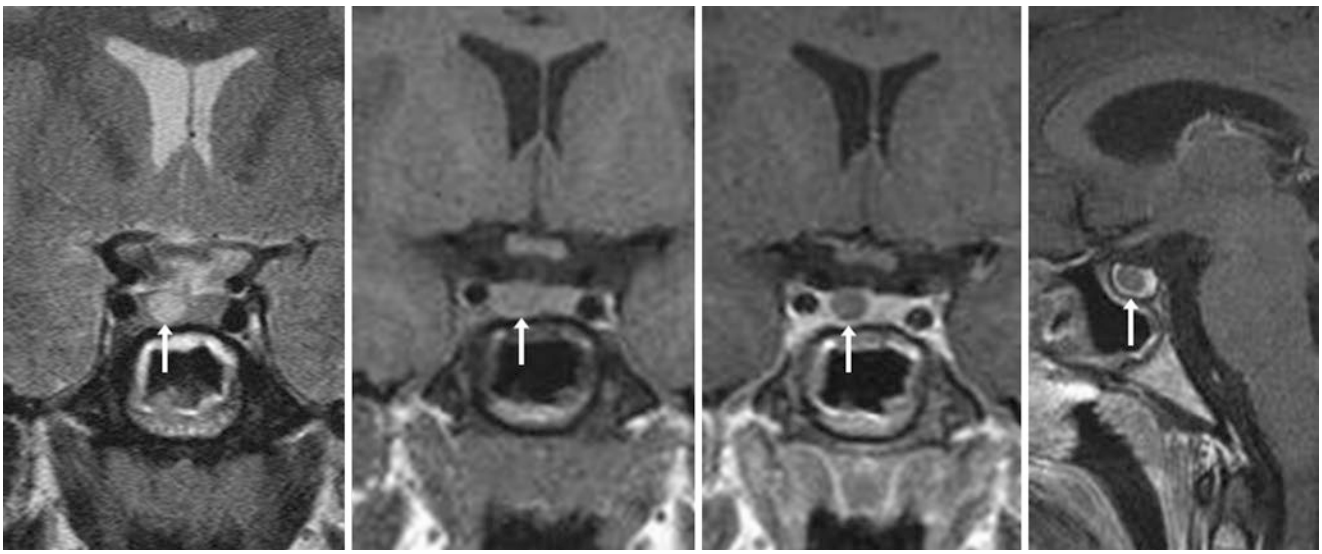

Fig. 8.88 The patient was a 21-year-old female with headaches and weight gain. A 1.5 T MRI noted a 6-mm T1-isointense (to gland) RCC (*arrows*) within the gland but lateral to the stalk on coronal T2WI (*left*), on precontrast T1WI (*left middle*), on postcontrast T1WI (*right middle*), and on sagittal postcontrast T1WI (*right*)

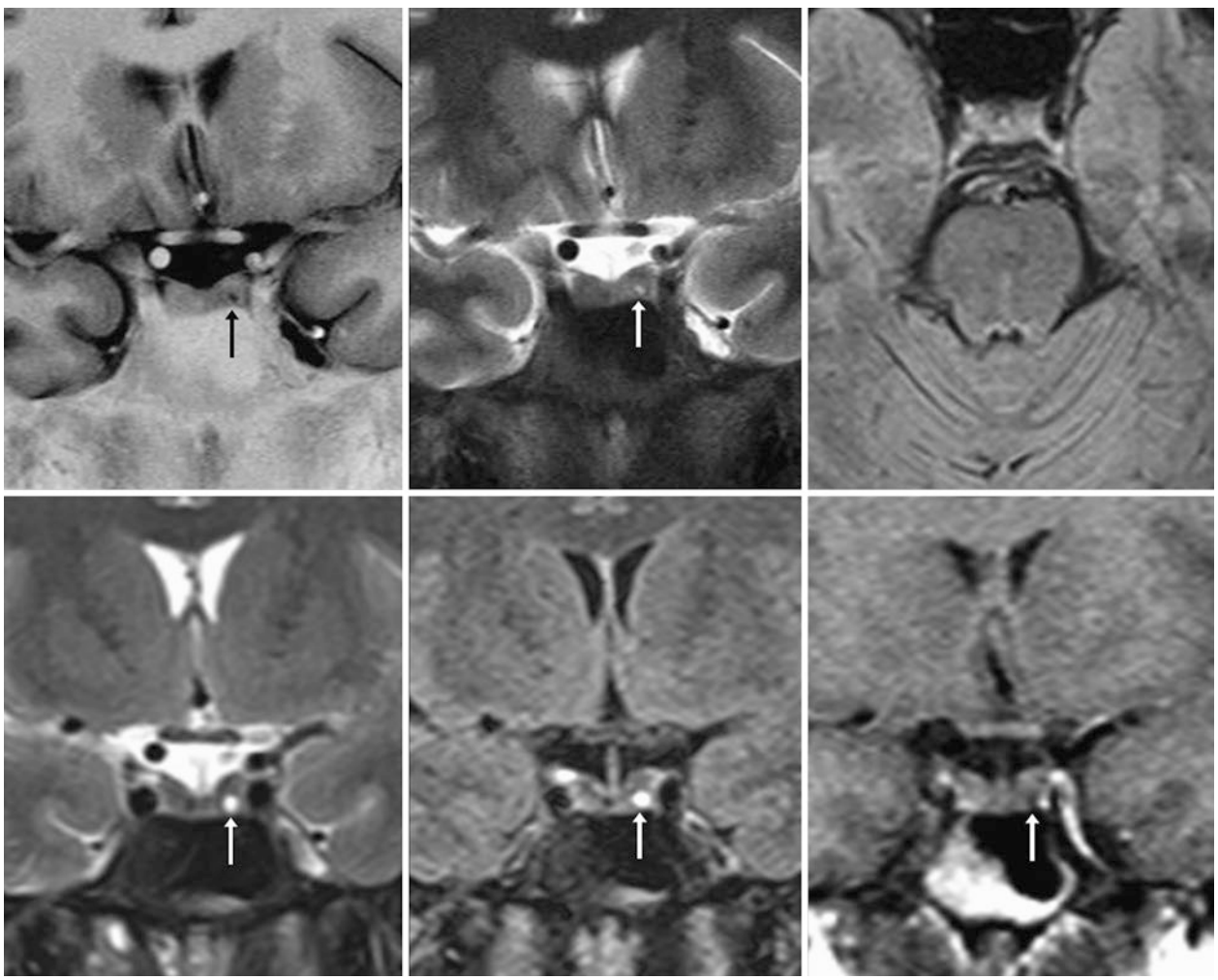

Fig. 8.89 The patient was a 33-year-old female with headaches but no pituitary-related symptoms. A 1.5 T MRI depicted a tiny, 2-mm pars intermedia cyst (RCC) within the left side of the pituitary (*arrows*) on coronal IR T1WI (*top left*) and T2WI (*top middle*) but not seen on axial FLAIR (*top right*) because of averaging with the normal gland. On a 1.5 T MRI 9 years later, there was no change on coronal T2WI (*bottom left*), FLAIR (*bottom middle*), or postcontrast T1WI (*bottom right*)

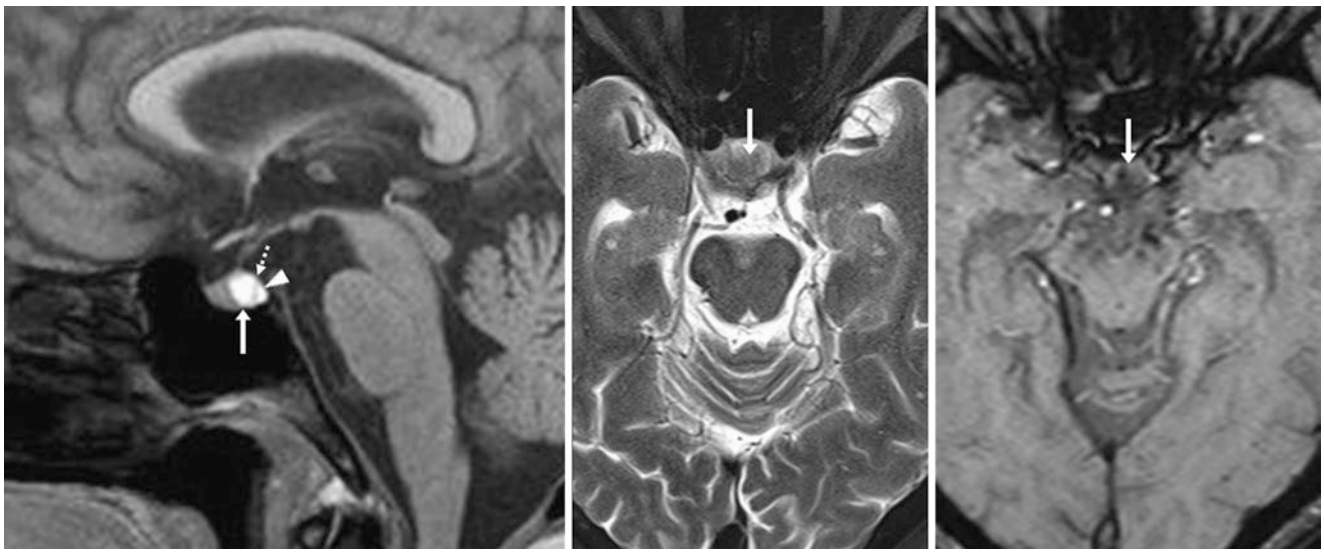

Fig. 8.90 The patient was a 59-year-old female with dementia; a 5-mm RCC (*arrow*) on noncontrast sagittal T1WI (*left*) was mildly hypointense on axial T2WI (*middle*) but not as dark as hemorrhage on SWI (*right*), excluding a hemorrhagic adenoma. There was a thin separation (*dotted arrow*) from the similarly T1-bright posterior lobe (*arrowhead*)

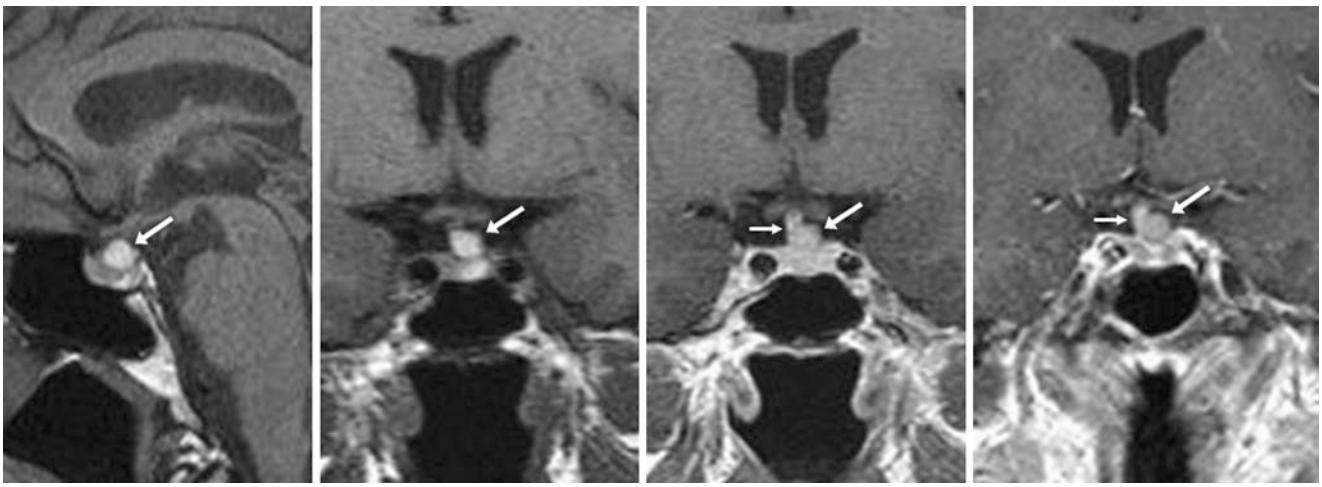

Fig. 8.91 The patient was a 61-year-old female with stroke-like symptoms lacking pituitary symptoms. A 1.5 T MRI demonstrated a 7-mm T1-bright RCC (*arrows*) superiorly along the gland and to the left of the stalk (*thin arrows*) on noncontrast sagittal T1WI (*left*) and coronal T1WI (*left middle*) with intensity similar to the rest of the gland postcontrast coronal T1WI (*right middle*). A repeat postcontrast T1WI (*right*) did not demonstrate any significant change several months later

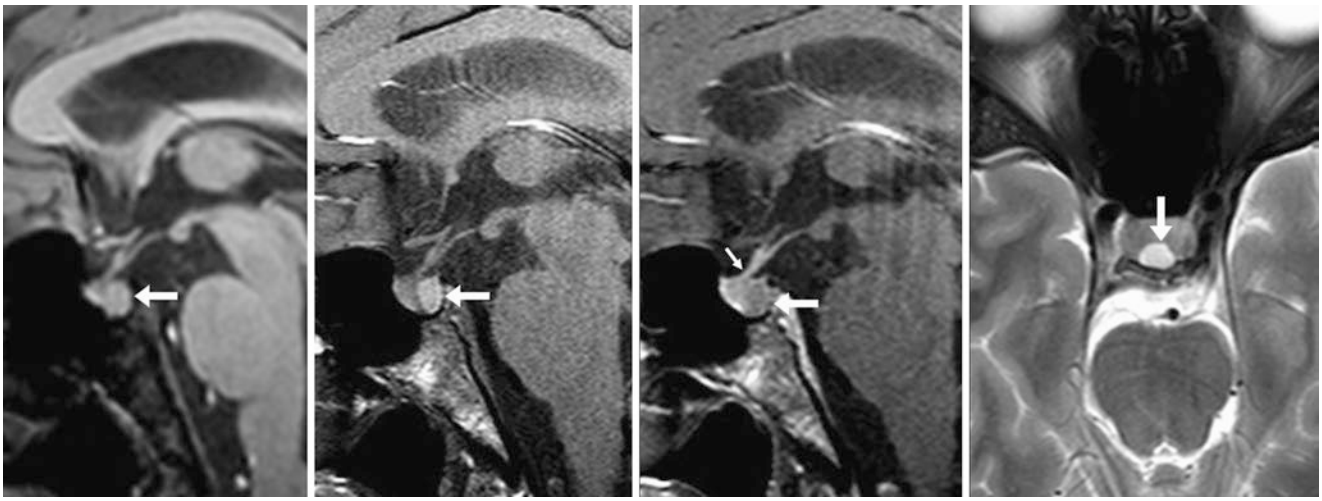

Fig. 8.92 The patient was a 42-year-old female with migraines with a 7-mm RCC (*arrows*) that was slightly bright on gradient-echo T1WI (*left*), brighter on spin-echo (SE) T1WI (*left middle*), and with no enhancement on postcontrast SET1WI (*right middle*), since it did not become as bright as the enhancing stalk (*thin arrow*). It was also bright on T2WI (*right*)

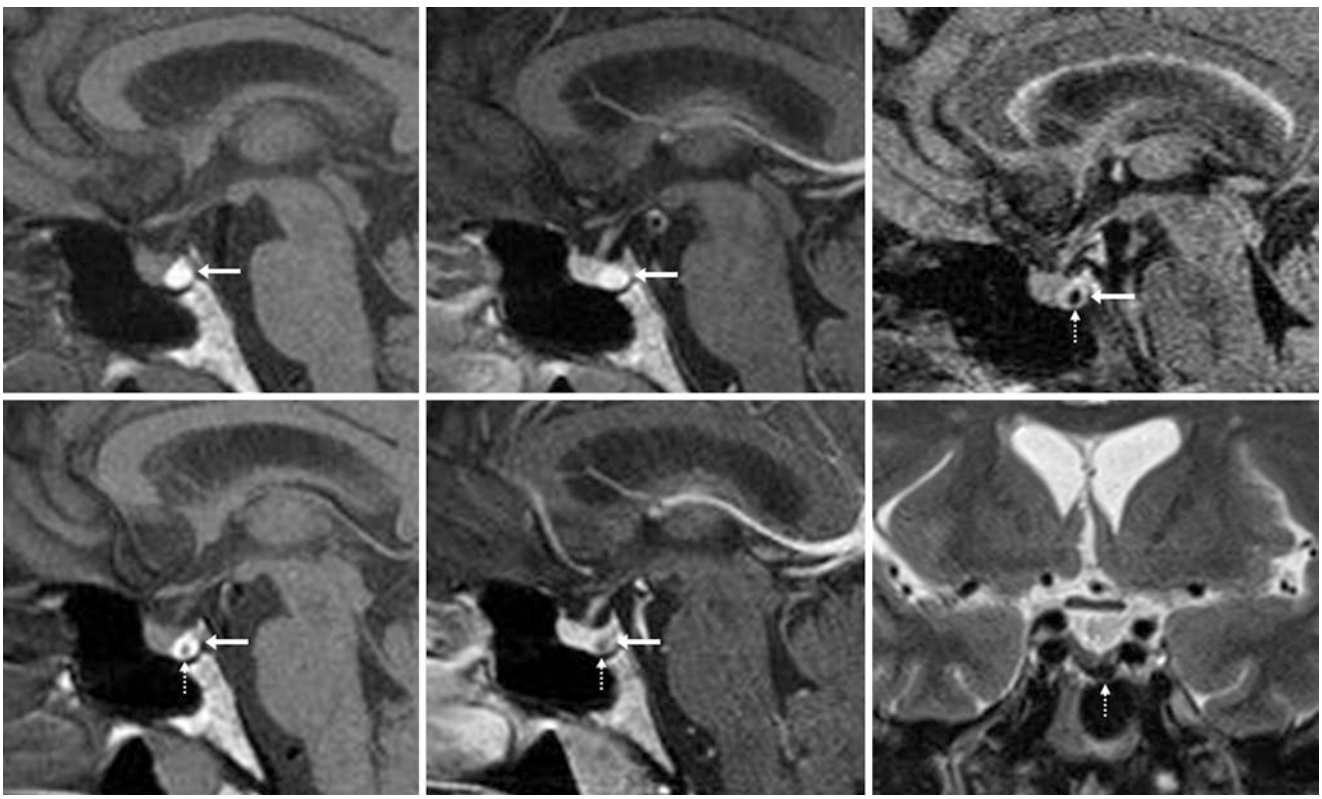

Fig. 8.93 The patient was a 43-year-old female with symptoms of stroke (negative pituitary serum tests). A 1.5 T MRI showed a 7-mm RCC (*arrows*) just posterior to the anterior lobe that was hyperintense on sagittal precontrast (*top left*) and postcontrast (*top middle*) T1WIs. On sagittal FLAIR (*top right*), a T2-dark focus (*dotted arrows*) was thought to be hemorrhage within the RCC. On an MRI 1.5 years later, precontrast (*bottom left*) and postcontrast (*bottom middle*) sagittal T1WIs demonstrated the hemorrhage within the RCC, which continues to be dark on coronal T2WI (*bottom right*)

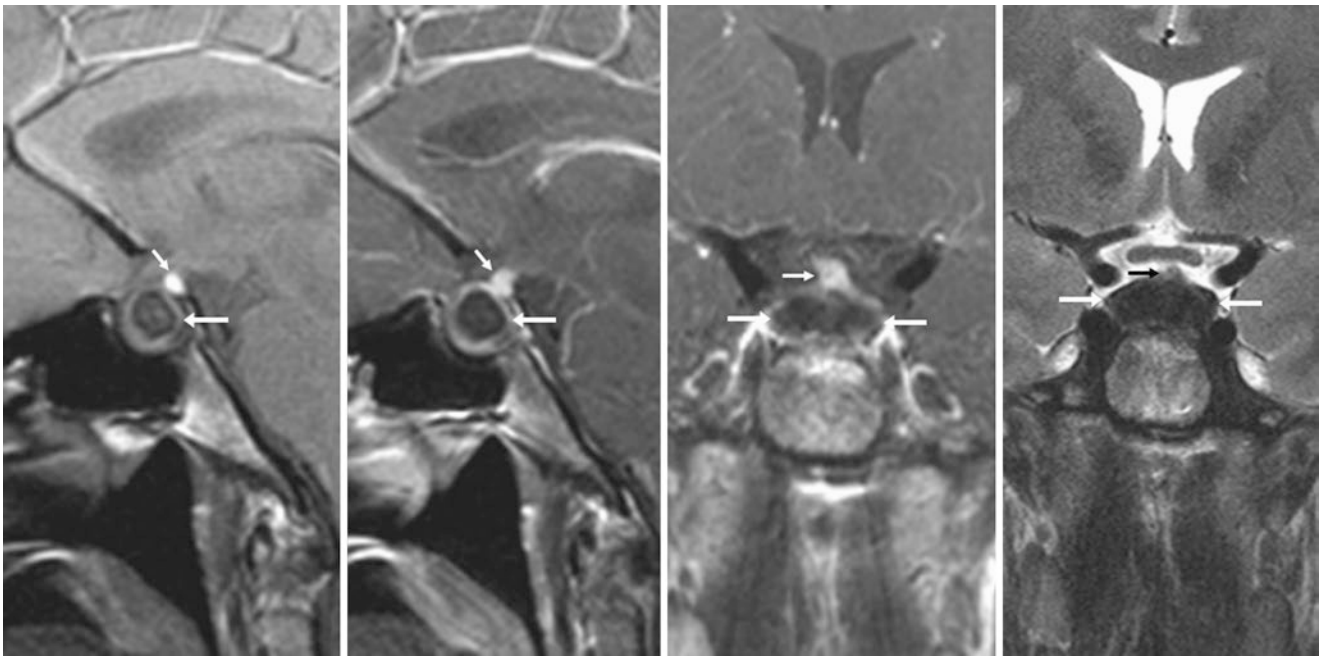

Fig. 8.94 The patient was a 39-year-old female with hypogonadism. A 3 T MRI demonstrated a 11×19 mm T1- and T2-dark RCC (*arrows*) that replaced most of the gland and compressed the stalk (*thin arrows*) superiorly on noncontrast sagittal T1WI (*left*), on postcontrast sagittal T1WI (*left middle*), on postcontrast coronal T1WI (*right middle*), and on coronal T2WI (*right*). A hemorrhagic macroadenoma was in the differential diagnosis but a hemorrhagic RCC was confirmed at biopsy

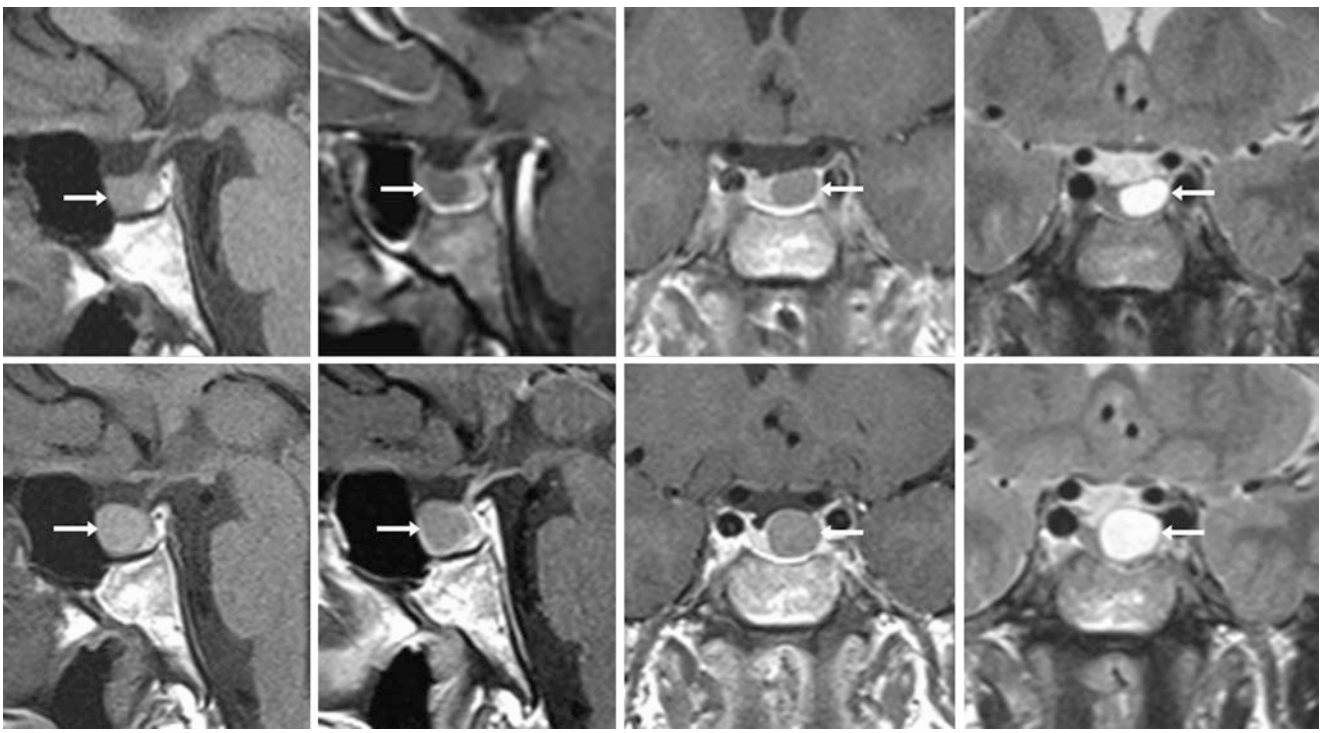

Fig. 8.95 The patient was a 27-year-old male with retro-orbital pain. A 1.5 T MRI noted a 10×9 mm RCC (*arrows*) on sagittal precontrast (*top left*) and postcontrast (*top*, *left middle*) T1WIs, on coronal postcontrast T1WI (*top*, *right middle*), and on T2WI (*top right*). An MRI 7 years later depicted mild enlargement to 13×11 mm on precontrast T1WI (*bottom left*) and postcontrast sagittal (*bottom*, *left middle*) and coronal (*bottom*, *right middle*) T1WIs and on coronal T2WI (*bottom right*)

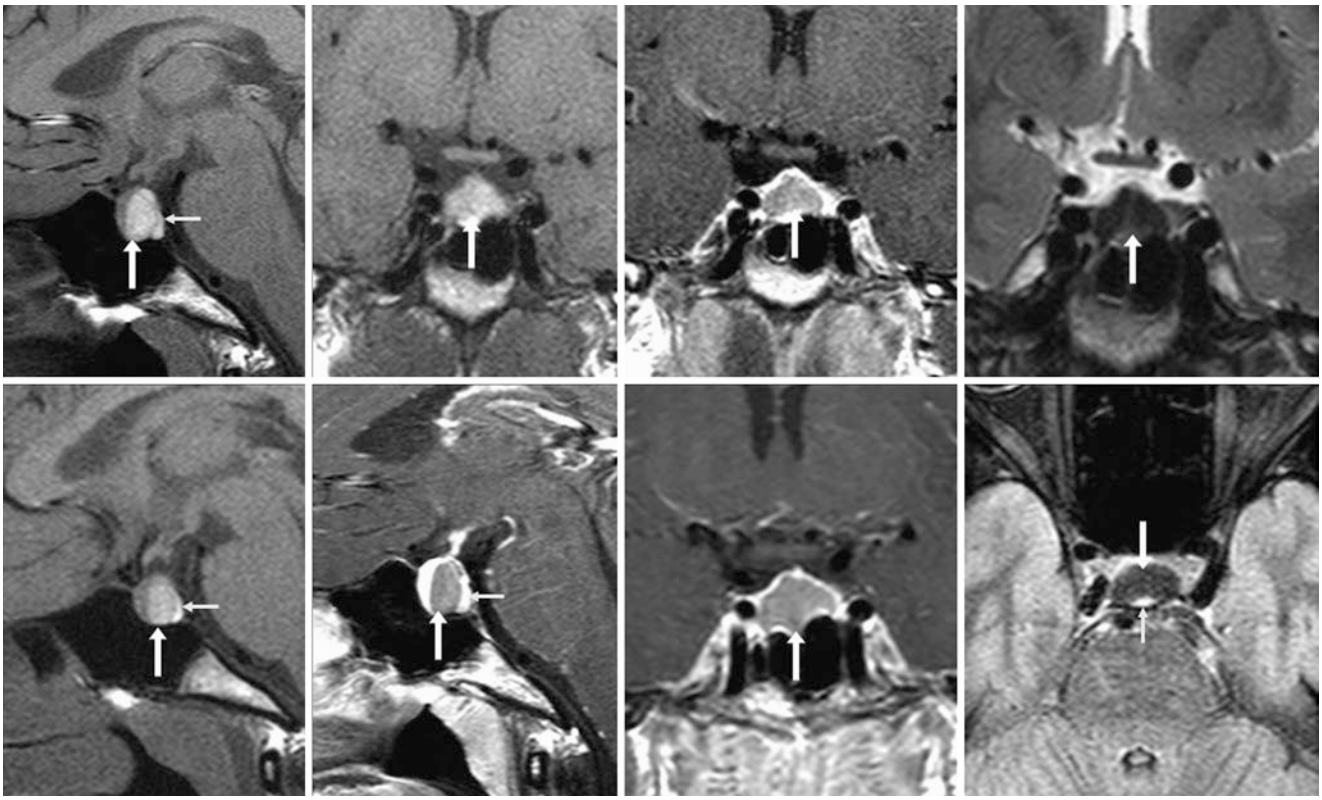

Fig. 8.96 The patient was a 16-year-old female with seizures (no pituitary-related symptoms). A 1.5 T MRI noted a T1-bright 11×9 mm RCC (*arrows*) on noncontrast sagittal (*top left*) and coronal (*top*, *left middle*) T1WIs and on postcontrast coronal T1WI (*top*, *right middle*) and T2WI (*top right*). An MRI 9 years later depicted slight enlargement to 13×10 mm on sagittal precontrast (*bottom left*) and postcontrast (*bottom*, *left middle*) T1WIs, coronal postcontrast T1WI (*bottom*, *right middle*) and on axial FLAIR (*bottom right*). Although it was enlarging, the patient was still not symptomatic from the RCC. The *thin arrows* denote the normal bright spot of the posterior pituitary gland, which is separate from the RCC

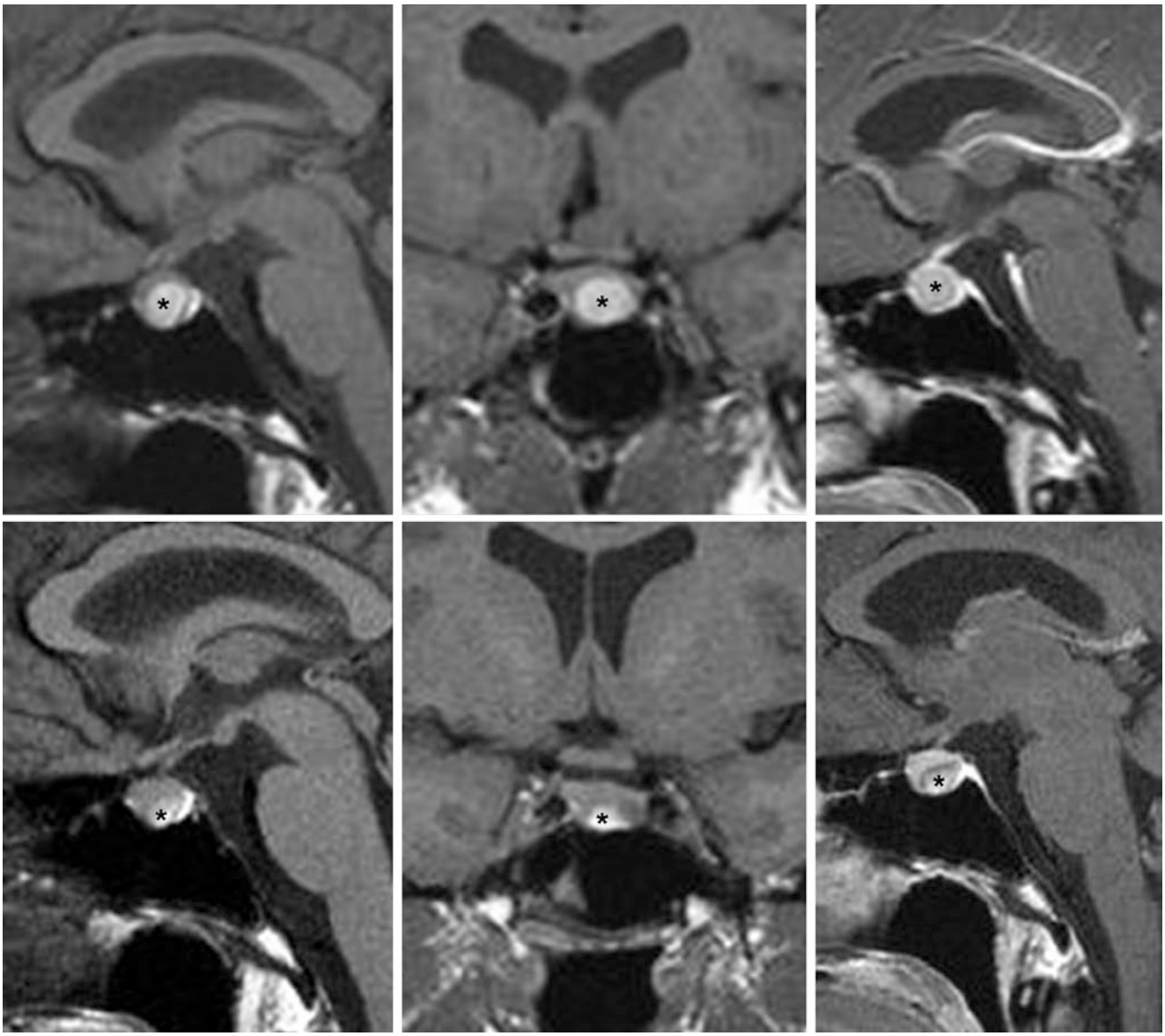

Fig. 8.97 Comparison case of macroadenoma with hemorrhage. A 23-year-old female patient with prolactinemia had an 11-mm T1-bright pituitary lesion on MRI (*), on noncontrast sagittal (*top left*) and coronal (*top middle*) T1WIs that was isointense to the surrounding glandular tissue on postcontrast sagittal T1WI (*top right*). The radiologist initially called this a macroadenoma. A 1.5 T MRI 3 years later depicted that the T1-bright portion of the lesion was smaller on noncontrast sagittal (*bottom left*) and coronal (*bottom middle*) T1WI. On postcontrast T1WI (*bottom right*), there was less enhancement at the tumor's periphery. Typically, a T1-bright RCC would continue to be T1-bright

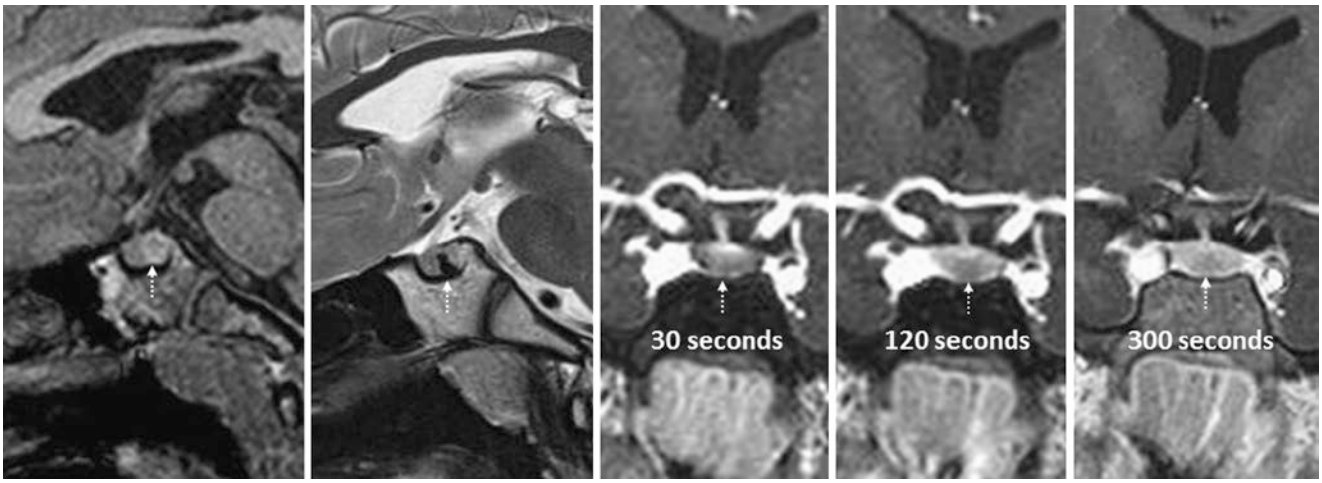

Fig. 8.98 Companion case of microadenoma with hemorrhage. The patient was a 12-year-old male with hypogonadism; 3 T MRI depicted a 6-mm T1-bright and T2-dark lesion simulating an RCC (*dotted arrows*) on noncontrast sagittal T1WI (*left*) and T2WI (*left middle*). However, dynamic postcontrast coronal T1WIs (*rightmost images*) illustrate that although the lesion was T1-bright, it progressively although slowly enhanced with contrast at 30, 120, and 300 s

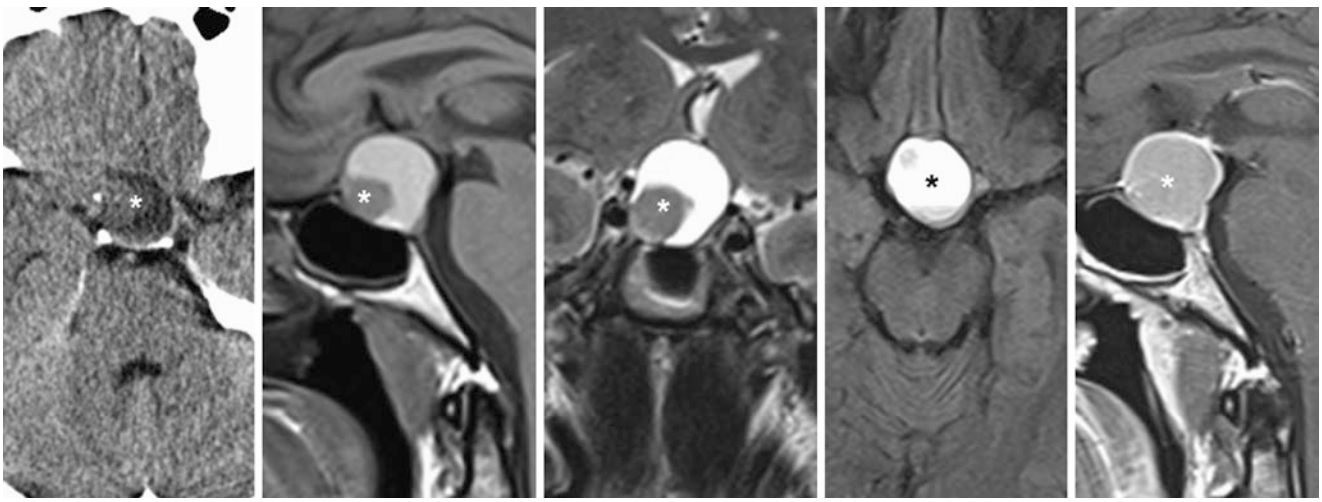

Fig. 8.99 Companion case of hemorrhagic adenoma. A 53-year-old male with visual symptoms underwent NECT (*left*), which demonstrated a 25×25 mm sellar and suprasellar mass (*). A 1.5 T MRI noncontrast sagittal T1WI (*left middle*), coronal T2WI (*middle*), axial FLAIR (*right middle*), and postcontrast sagittal T1WI (*right*) showed a T1-bright and T2-bright component peripheral to an isointense region. At resection, this was found to be an adenoma

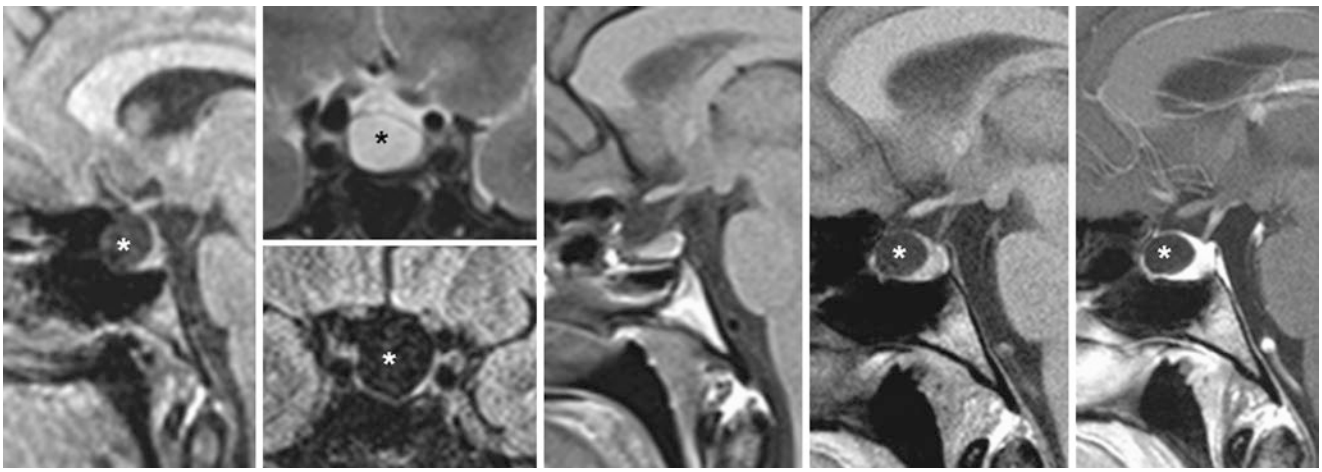

Fig. 8.100 Companion case of intrasellar arachnoid cyst. A 30-year-old female with seizures; a 3 T MRI depicted an incidental, 11-mm intrasellar cyst (*) on noncontrast sagittal T1WI (*left*) and on coronal T2WI/FLAIR (*left middle*); the cyst suppressed with CSF on FLAIR (*left middle and bottom*). It was resected and confirmed to be an arachnoid cyst. At 6 months postsurgery, a repeat sagittal T1WI (*middle*) showed no recurrence. However, 2 years later, the cyst was shown to have recurred on sagittal precontrast (*right middle*) and postcontrast (*right*) T1WIs

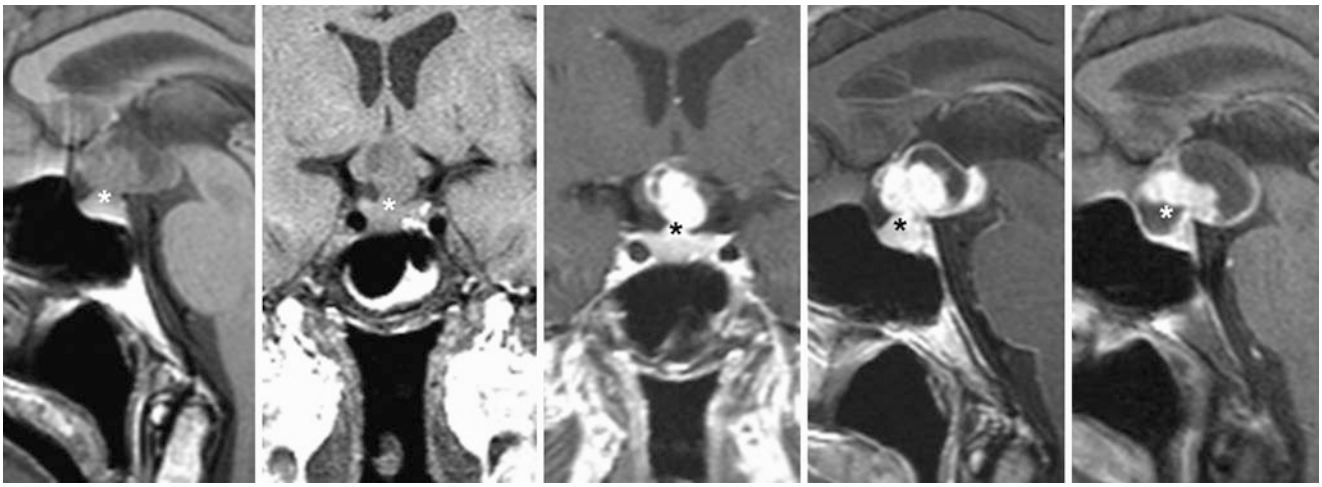

Fig. 8.101 Companion case of craniopharyngioma. A 60-year-old female with visual symptoms underwent a 1.5 T MRI, which demonstrated a suprasellar mass connected to a T1-bright lesion (*) within the sella. Noncontrast sagittal (*left*) and coronal (*left middle*) T1WIs and postcontrast coronal (*middle*) and sagittal (*right middle*) T1WIs showed small, cystic components. Four months later, postcontrast sagittal T1WI (*right*) showed enlarged cystic regions

Suggested Reading

Ahmadi H, Larsson EM, Jinkins JR. Normal pituitary gland: coronal MR imaging of infundibular tilt. Radiology. 1990;177:389–92.

Aho CJ, Liu C, Zelman V, Couldwell WT, Weiss MH. Surgical outcomes in 118 patients with Rathke cleft cysts. J Neurosurg. 2005;102:189–93.

Amhaz HH, Chamoun RB, Waguespack SG, Shah K, McCutcheon IE. Spontaneous involution of Rathke cleft cysts: is it rare or just underreported? J Neurosurg. 2010;112:1327–32.

Barrow DL, Spector RH, Yakei Y, Tindall GT. Symptomatic Rathke cleft cysts located entirely in the suprasellar region: review of diagnosis, management, and pathogenesis. Neurosurgery. 1985;16:766–72.

Bergland RM, Ray BS, Torack RN. Anatomical variations in the pituitary gland and adjacent structures in 225 human autopsy cases. J Neurosurg. 1968;28:93–9.

Bonneville JF, Cattin F, Moussa-Bacha K, Portha C. Dynamic computed tomography of the pituitary gland: the "tuft sign.". Radiology. 1983;149:145–8.

Bonneville JF, Cattin F, Gorczyca W, Hardy J. Pituitary microadenomas: early enhancement with dynamic CT—implications of arterial blood supply and potential importance. Radiology. 1993;187:857–61.

Brisman R. Endocrine studies with empty sella. J Neurosurg. 1973;38:537.

Busch W. Morphology of sella turcica and its relation to the pituitary gland. Virchows Arch. 1951;320:437–58.

Buchfelder M, Brockmeier S, Pichl J, Schrell U, Fahlbusch R. Results of dynamic endocrine testing of hypothalamic pituitary function in patients with a primary "empty" sella syndrome. Horm Metab Res. 1989;21:573–6.

Chanson P, Daujat F, Young J, Bellucci A, Kujas M, Doyon D, Schaison G. Normal pituitary hypertrophy as a frequent cause of pituitary incidentaloma: a follow-up study. J Clin Endocrinol Metab. 2001;86:3009–15.

De Marinis L, Bonadonna S, Bianchi A, Maira G, Giustina A. Primary empty sella. J Clin Endocrinol Metab. 2005;90:5471–7.

Dietrich RB, Lis LE, Greensite FS, Pitt D. Normal MR appearance of the pituitary gland in the first 2 years of life. Am J Neurolradiol. 1995;16:1413–9.

Dinc H, Esen F, Demirci A, Sari A, Resit Gümele H. Pituitary dimensions and volume measurements in pregnancy and post partum. MR Assessment. Acta Radiol. 1998;39:64–9.

Ezzat S, Asa SL, Couldwell WT, Barr CE, Dodge WE, Vance ML, McCutcheon IE. The prevalence of pituitary adenomas: a systematic review. Cancer. 2004;101:613–9.

Foresti M, Guidali A, Susanna P. Primary empty sella. Incidence in 500 asymptomatic subjects examined with magnetic resonance. Radiol Med. 1991;81:803–7.

Guitelman M, Garcia Basavilbaso N, Chervin A, Katz D, Miragaya K, et al. Primary empty sella (PES): a review of 175 cases. Pituitary. 2013;16:270–4.

Hayakawa K, Konishi Y, Matsuda T, Kuriyama M, Konishi K, Yamashita K, et al. Development and aging of brain midline structures: assessment with MR imaging. Radiology. 1989;172:171–7.

Hayashi Y, Tachibana O, Muramatsu N, Tsuchiya H, Tada M, Arakawa Y, et al. Rathke cleft cyst: MR and biomedical analysis of cyst content. J Comput Assist Tomogr. 1999;23:34–8.

Ishikawa S, Furuse M, Saito T, Okada K, Kuzuya T. Empty sella in control subjects and patients with hypopituitarism. Endocrinol Jpn. 1988;35:665–74.

Kucharczyk W, Peck WW, Kelly WM, Norman D, Newton TH. Rathke cleft cysts: CT, MR imaging, and pathologic features. Radiology. 1987;165:491–5.

Krzysiek J, Gregorczyk A. Hypophysis volume in computerized tomography and clinical grounds for diagnosing a primary completely empty sella turcica. Przegl Lek. 1990;47:637–41.

Lees PD, Fahlbusch R, Zrinzo A, Pickard JD. Intrasellar pituitary tissue pressure, tumour size and endocrine status – an international comparison in 107 patients. Br J Neurosurg. 1994;8:313–8.

Molitch ME. Pituitary tumours: pituitary incidentalomas. Best Pract Res Clin Endocrinol Metab. 2009;23:667–75.

Nemoto Y, Inoue Y, Fukuda T, Shakudo M, Katsuyama J, Hakuba A, et al. MR appearance of Rathke's cleft cysts. Neuroradiology. 1988;30:155–9.

Sanno N, Oyama K, Tahara S, Teramoto A, Kato Y. A survey of pituitary incidentaloma in Japan. Eur J Endocrinol. 2003;149:123–7.

Sakamoto Y, Takahashi M, Korogi Y, Bussaka H, Ushio Y. Normal and abnormal pituitary glands: gadopentetate dimeglumine-enhanced MR imaging. Radiology. 1991;178:441–5.

Shanklin WM. On the presence of cysts in the human pituitary. Anat Rec. 1949;104:399–407.

Simmons GE, Suchnicki JE, Rak KM, Damiano TR. MR imaging of the pituitary stalk: size, shape, and enhancement pattern. Am J Roentgenol. 1992;159:375–7.

Takanashi J, Suzuki H, Nagasawa K, Kobayashi K, Saeki N, Kohno Y. Empty sella in children as a key for diagnosis. Brain Dev. 2001;23:422–3.

Tsunoda A, Okuda O, Sato K. MR height of the pituitary gland as a function of age and sex: especially physiological hypertrophy in adolescence and in climacterium. Am J Neurolradiol. 1997;18:551–4.

Wolpert SM, Osborne M, Anderson M, Runge VM. The bright pituitary gland – a normal MR appearance in infancy. Am J Neurolradiol. 1988;9:1–3.

Zucchini S, Ambrosetto P, Carlà G, Tani G, Franzoni E, Cacciari E. Primary empty sella: differences and similarities between children and adults. Acta Paediatr. 1995;84:1382–5.

Liliequist Membrane

9

The *Liliequist membrane* (LM) is a distinct arachnoid structure within the basal cisterns that can be vital to identify during neurosurgical procedures, particularly during endoscopic third ventriculostomy. This membrane is generally located posterior to the pituitary infundibulum (stalk), anterior to the interpeduncular cistern of the midbrain, inferior to the third ventricular floor, superior to the prepontine cistern, and medial to the tip of the uncus at the tentorial edge. The membrane consists of a double or even triple fold of *arachnoid mater*, while it essentially contains three different "leafs" of membranes that converge within the above-mentioned location; these three leafs or segments have been variably named among authors. It is generally better to refer to them based on the site of attachment: the diencephalic segment attaches to the posterior edges of the mammillary bodies and is the more superior and posterior leaf; the mesencephalic segment attaches to the junction of the midbrain and pons and is the more inferior and posterior leaf, also called the anterior pontine membrane; and the sellar segment attaches to the dorsum sella and is the more anterior and inferior leaf. There is some controversy as to exactly where the LM attaches laterally with respect to the mesial temporal lobe/uncus (MTL), tentorium, or oculomotor nerve/cranial nerve III (CNIII). However, more recent evidence suggests that its lateral attachment is variable, that is, where there is direct attachment to the *tentorium* in the large majority, to the *uncus* of the MTL in greater than half of cases, and attachment to a membrane that lies underneath (and is likely attached to) the *oculomotor membrane* (OMM) in more than half of cases as well. It is important to note that the OMM can itself attach to the uncus but is separate from the LM because it is in close apposition to CNIII.

The most readily and consistently identified segment of the LM on brain imaging is the *sellar segment* of the LM, which can be confirmed in nearly 90 % of patients as attached to the dorsum sella on thin section imaging, particularly in the sagittal plane (*see* next paragraph). The *diencephalic segment* can be identified in about half of patients with proper thin section imaging, based on its attachment to the mammillary bodies. The *mesencephalic segment* can be more difficult to identify. Additionally, the lateral attachment of the LM to the OMM can be visualized in about a half of patients, although interestingly, the lateral attachment to the uncus and tentorium is less readily visualized on imaging compared with on histologic examination, leading some to posit that the lateral aspect of the LM can be a free edge.

Typically, the LM is not visualized on routine MRI sequences at 3 mm or greater in thickness. Most commonly, it is visualized on three-dimensional acquisition images reconstructed at 1 mm or less. The three-dimensional acquisition sequences that best depict the LM are constructive interference in the steady state (CISS), balanced echo T2-weighted sequences (i.e., vendor-specific sequences such as BFFE, FIESTA, True FISP, True SSFP, or BASG, depending on the manufacturer), or T2-weighted turbo field echo or balanced turbo field echo (TFE or BTFE, respectively). Newer three-dimensional acquisition FLAIR images may also identify the LM if the reconstructions are thin enough, since three-dimensional FLAIR acquisitions usually null the CSF pulsation relative to the older, two-dimensional acquisitions. If a two-dimensional acquisition of T2WI or FLAIR is utilized, it is uncommon (although not impossible) to visualize the LM, even with thinner sequences, since CSF flow-related artifacts will typically obscure the LM. As described above, although the LM can be visualized in any imaging plane, the sagittal plane is likely the best to discern the sellar and diencephalic segments and their attachments, while the lateral attachments are variably identified.

While knowledge of the appearance, location, and sites of attachment of the LM typically prevent this normal structure from being confused with disease, there is a potential that as sequences become more powerful with thinner and thinner reconstruction thicknesses, the LM can be confused with abnormal cysts such as *arachnoid cysts* (typically will expand the cisterns), *epidermoid cysts* (do not have CSF signal on FLAIR and are bright on DWI), or cysts of *neurocysticercosis*

A.M. McKinney, *Atlas of Normal Imaging Variations of the Brain, Skull, and Craniocervical Vasculature*,
DOI 10.1007/978-3-319-39790-0_9

(typically will have multiple lesions with non-CSF signal) within the basal cisterns. Also, the LM could be confused with *webs* or synechia, which can occur from a previous infection, hemorrhage, or ventriculostomy. Another helpful point is that the vast majority of LMs (about 90%) are less than one-half the thickness of the floor of the third ventricle; greater thicknesses may indicate lesions such as those described above, with the appropriate clinical scenario (Figs. 9.1, 9.2, 9.3, 9.4, 9.5, 9.6, 9.7, and 9.8).

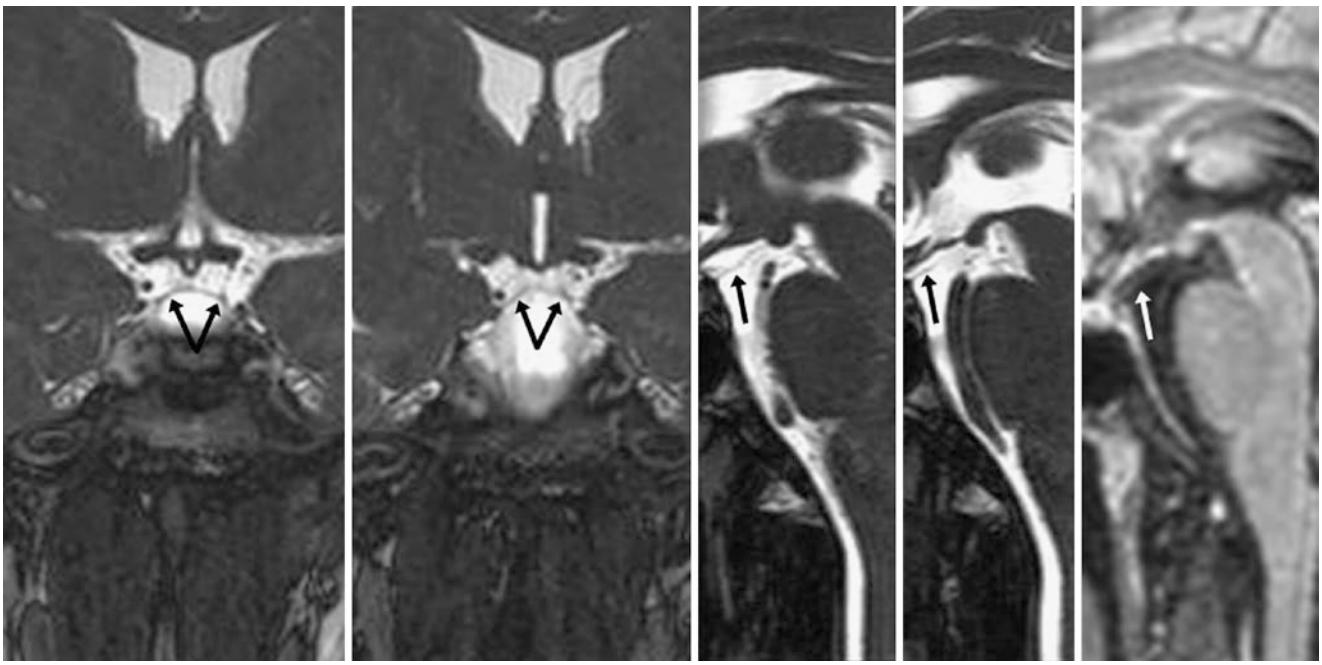

Fig. 9.1 A 29-year-old patient with an incidental LM (*arrows*) on a negative MRI obtained for ear infections. The LM attaches to the dorsum sella anteriorly, as delineated on three-dimensional reformatted 0.5-mm thickness BFFE images in the coronal (*left and left middle*) and sagittal (*middle and right middle*) planes. A sagittal FLAIR 1-mm thickness image is at midline (*right*)

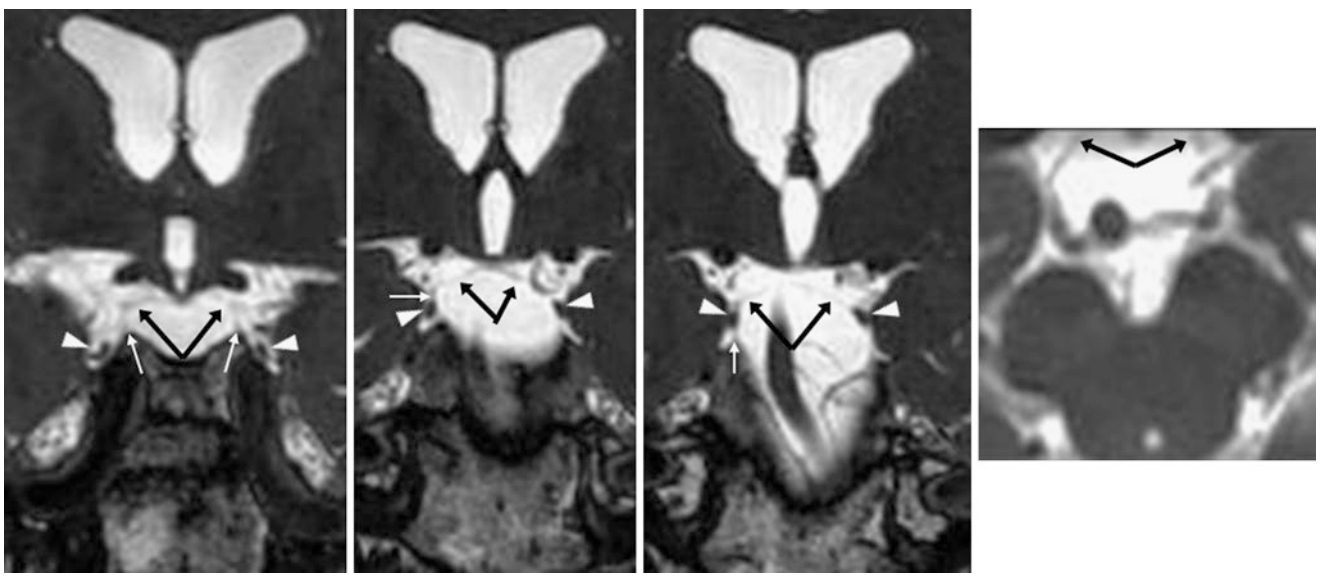

Fig. 9.2 A 63-year-old patient with an incidental LM (*arrows*) that attaches to the OMM laterally (*thin arrows*), as illustrated on three-dimensional reformatted coronal 0.5-mm thickness BFFE images (*left three images*), from a negative skull base MRI obtained for tinnitus. On a three-dimensional axial reconstruction at a similar thickness (*right*), the LM is also shown. Note CNIII (*arrowheads*)

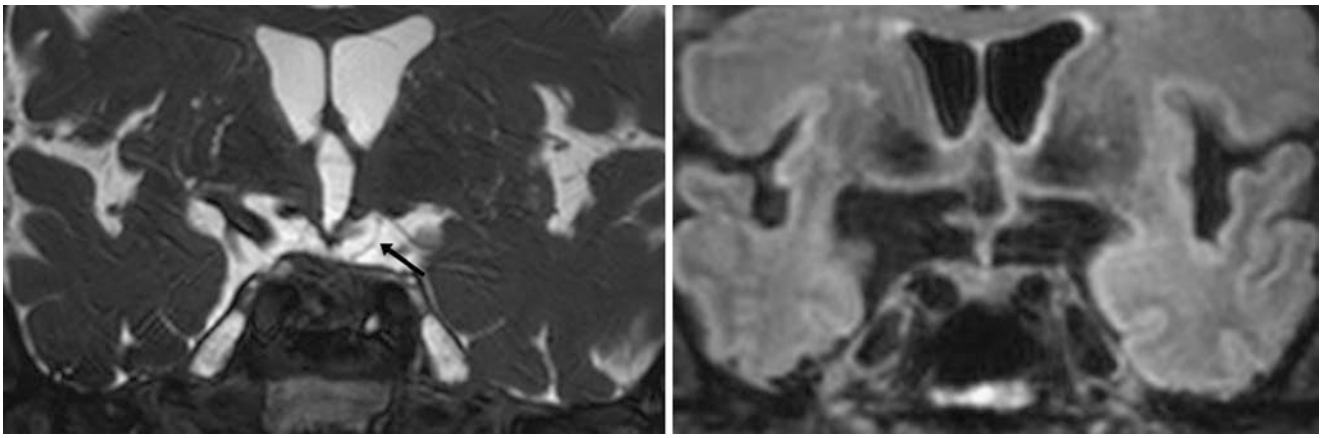

Fig. 9.3 A 65-year-old with an incidental LM seen clearly only on the left (*arrows*), which was demonstrated by coronal three-dimensional reconstruction 0.5-mm thickness BFFE images (*left*) on an otherwise negative skull base MRI for tinnitus. On a three-dimensional coronal FLAIR reconstruction at a similar thickness (*right*), the LM is not well visualized, probably due to mild motion

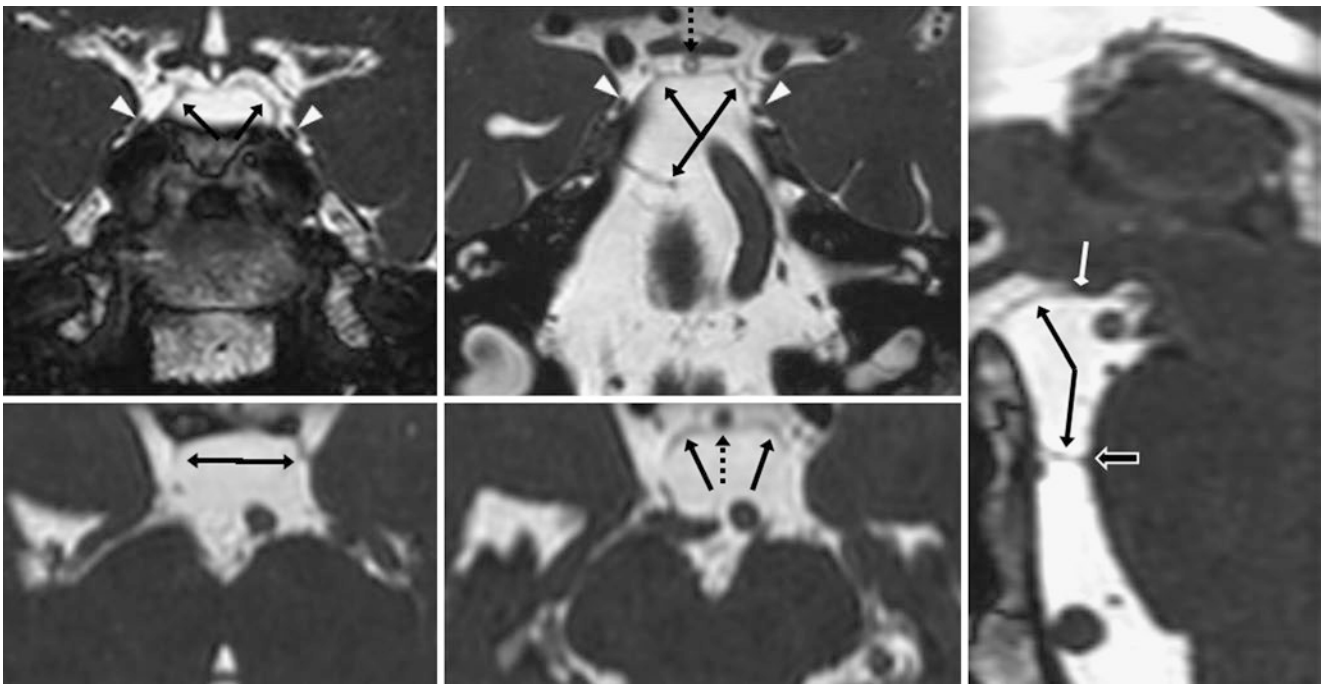

Fig. 9.4 A 55-year-old with hearing loss and an incidental LM (*arrows*) on three-dimensional Constructive Interference in the Steady State (CISS) T2WI with 0.5-mm thickness reformats in coronal (*top left and middle*) and axial (*bottom left and middle*) planes. Note CNIII (*arrowheads*) lateral to the LM and the pituitary stalk (*dotted arrows*) ventral to the LM. On a right of midline sagittal reformat (*right*), note that the LM attaches superiorly at the mammillary bodies (*diamond tip arrow*) and inferiorly at the superior pons (*open arrow*)

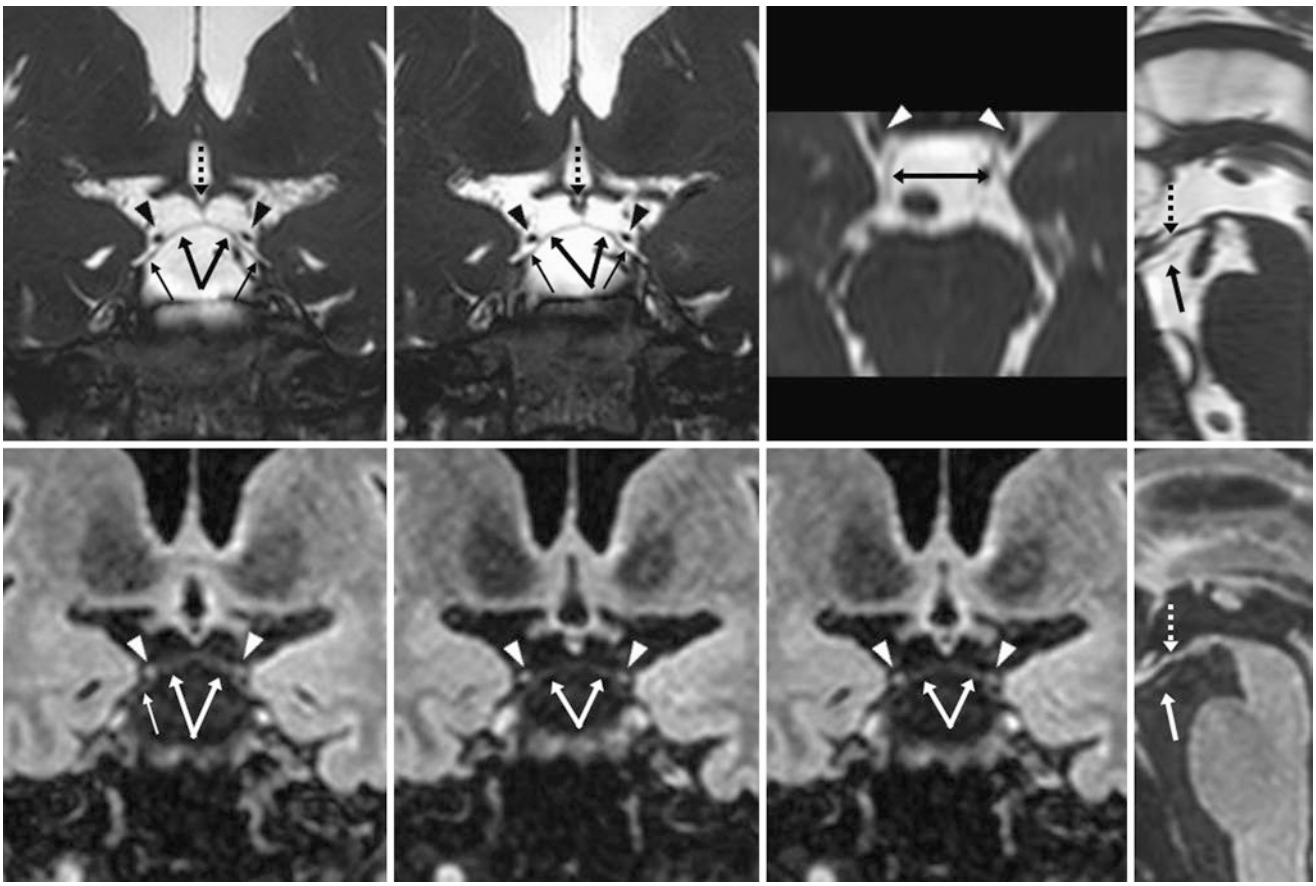

Fig. 9.5 A 49-year-old with an incidental LM (*arrows*) on three dimensional CISS T2WI with 1-mm thickness reconstructions in the coronal (*top*, *left*, *and left middle*), axial (*top*, *right middle*), and sagittal (*top right*) planes. The LM is also seen on coronal 1-mm three-dimensional FLAIR reformats (*bottom*, *left three images*). Note CNIII (*arrowheads*) coursing on top of the LM and the OMM (*thin arrows*). Sagittal reformats of FLAIR (*bottom right*) show the LM behind the pituitary stalk (*dotted arrows*)

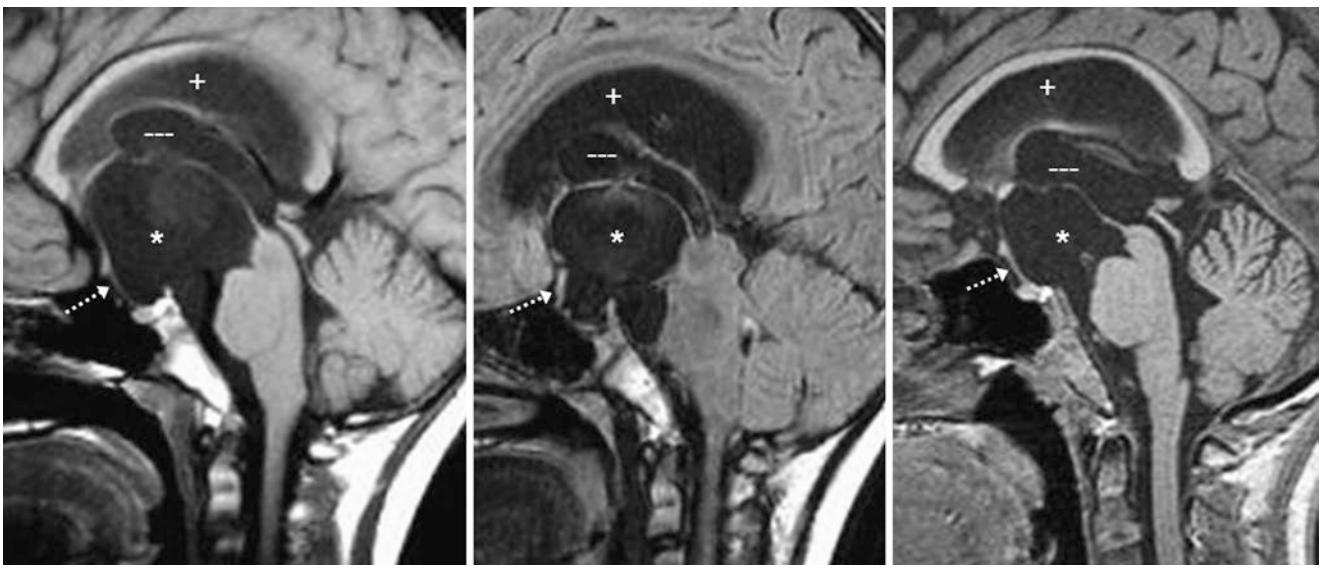

Fig. 9.6 Comparison case of arachnoid cyst (suprasellar). An 11-year-old with headaches had a cyst (*) that followed CSF signal, located within the suprasellar cistern on sagittal T1WI (*left*) and on FLAIR (*middle*, to left of midline); this is the cistern and caused hydrocephalus. Note enlargement of the third (−−−) and lateral ventricles (+), and the displaced pituitary stalk (*dotted arrows*). An endoscopic 3rd ventriculostomy confirmed an arachnoid cyst. On a followup MRI 2 years later, the cyst had slightly decreased in size, as shown on noncontrast T1WI (*right*)

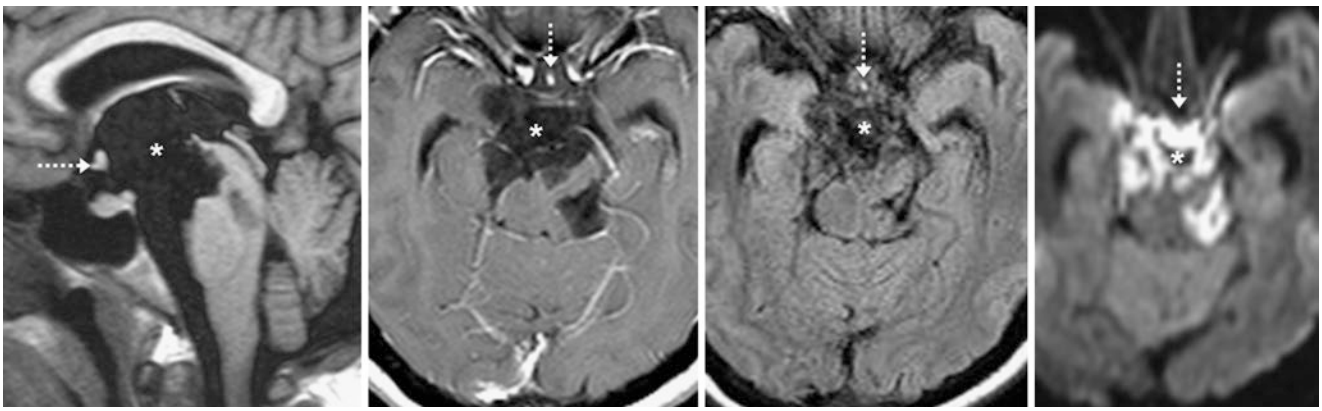

Fig. 9.7 Comparison case of epidermoid cyst. A 40-year-old with multiple cranial nerve symptoms had a cyst (*) within the suprasellar cistern on 1-mm thickness sagittal reconstructions from a three-dimensional T1WI (*left*), axial postcontrast T1WI (*left middle*), noncontrast axial FLAIR (*right middle*), and DWI (*right*). The complex, non-CSF signal on FLAIR and the bright signal on DWI, are consistent with an epidermoid. Note that the pituitary stalk is compressed ventrally against the optic chiasm (*dotted arrows*), and the cyst compresses and partially surrounds the brainstem

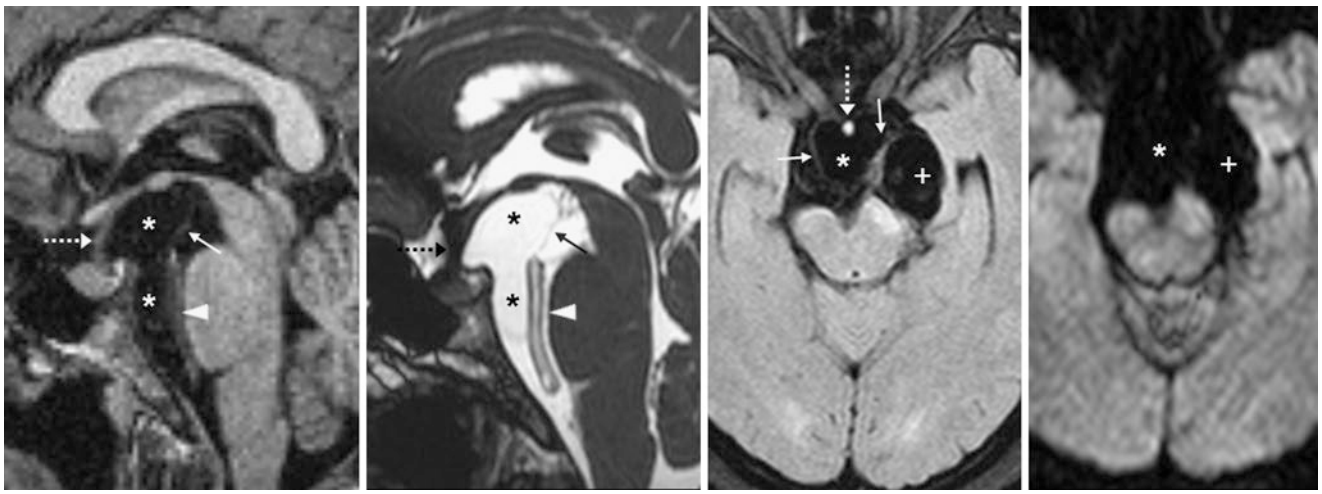

Fig. 9.8 Comparison case of neurocysticercosis (racemose). A 33-year-old with headaches had loculated cysts (*) in the basal cisterns and a frontal calcification on NECT (*not shown*). On three-dimensional T1WI (*left*) and CISS T2WI (*left middle*) with 0.5-mm thickness reformats, the pituitary stalk is noted anteriorly (*dotted arrows*) and the basilar artery posteriorly (*arrowheads*), in locations similar to the LM. However, note that one cyst expands the suprasellar cistern, while another cyst (+) compresses the left cerebral peduncle and uncus on axial FLAIR (*right middle*) and DWI (*right*). Note the thin walls of the multilocular cysts (*thin arrows*)

Suggested Reading

Brasil AV, Schneider FL. Anatomy of Liliequist's membrane. Neurosurgery. 1993;32:956–60.

Fushimi Y, Miki Y, Takahashi JA, Kikuta K, Hashimoto N, Hanakawa T, et al. MR imaging of Liliequist's membrane. Radiat Med. 2006;24:85–90.

Fushimi Y, Miki Y, Ueba T, Ademar Jr L, Luiz AFF, Nelson FPDF. Liliequist membrane: three-dimensional constructive interference in steady state MR imaging. Radiology. 2003;229:360–5.

Lü J, Zhu XI. Microsurgical anatomy of Liliequist's membrane. Minim Invasive Neurosurg. 2003;46:149–54.

Qi ST, Fan J, Zhang XA, Pan J. Reinvestigation of the ambient cistern and its related arachnoid membranes: an anatomical study. J Neurosurg. 2011;115:171–8.

Wang SS, Zheng HP, Zhang FH, Wang RM. Microsurgical anatomy of Liliequist's membrane demonstrating three-dimensional configuration. Acta Neurochir. 2011;153:191–200.

Zhang M, An PC. Liliequist's membrane is a fold of the arachnoid mater: study using sheet plastination and scanning electron microscopy. Neurosurgery. 2000;47:902–8.

Zhang XA, Qi ST, Huang GL, Long H, Fan J, Peng J. Anatomical and histological study of Liliequist's membrane: with emphasis on its nature and lateral attachments. Childs Nerv Syst. 2012;28:65–72.

Pineal Gland: Normal Size, Appearance, and Enhancement

10

At times, the *pineal gland* can appear prominent and simulate an enhancing lesion, with or without the presence of a cyst. The pineal gland increases in weight and volume with age and can even gradually increase in adulthood. Also, the degree of *calcification of* the pineal gland should not significantly increase after 30–40 years of age. The glands are typically not calcified in children younger than 5 years of age but may progressively calcify into adulthood. Pineal glands may appear partially cystic in up to 50–60 % of patients and may enhance inhomogeneously after administration of intravenous contrast (remember that the pineal gland enhances since it is outside the blood–brain barrier). However, the pineal gland should not cause mass effect on the adjacent midbrain tectum, which places the patient at risk for hydrocephalus as a result of aqueductal obstruction. Also, the margins of a normally enhancing pineal gland should be regular and rounded, although calcifications may cause the gland to appear to enhance inhomogeneously on MRI.

A practical measurement to use is that the pineal gland should measure less than 10 mm in each dimension, whether or not there are cysts or inhomogeneous enhancement. However, a simple-appearing pineal cyst may be slightly larger and still be considered normal (discussed separately in Sect. 10.2). Thus, a homogeneously enhancing gland up to 1-cm in size is usually entirely normal. Additionally, small cysts or calcifications are occasionally also present within a normal, asymptomatic gland, and these cysts or calcifications may cause the gland to appear as though it inhomogeneously (i.e., heterogeneously) enhances; correlation with computed tomography can help. On occasion, the anteroposterior diameter measures slightly larger, and histologically normal cases have been identified with dimensions slightly larger than 10 mm. However, using this 10-mm rule excludes most neoplasms. If slightly larger dimensions are measured and no other cranial lesions are identified, these can be followed serially over a period of 1–2 years to document stability.

DWI can be helpful in detecting malignant pineal lesions, since several of the uncommon primary *malignant pineal lesions* have reduced diffusivity, such as pineoblastoma, retinoblastoma, and other round, blue cell tumors (although germinomas exhibit less diffusion reduction). *Metastases* variably exhibit reduced diffusion. Traditionally, it is thought that pineal calcifications are dispersed by pineal tissue lesions (pineocytoma and pineoblastoma), while the other pineal tumors surround or engulf the calcifications.

A.M. McKinney, *Atlas of Normal Imaging Variations of the Brain, Skull, and Craniocervical Vasculature*,
DOI 10.1007/978-3-319-39790-0_10

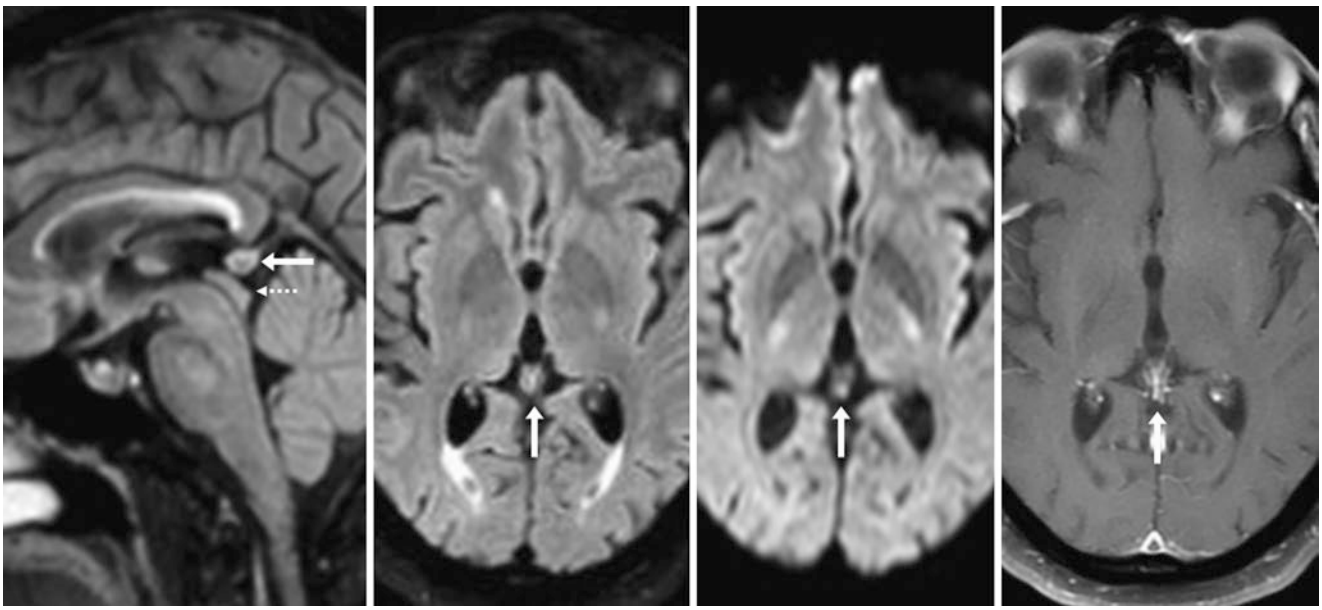

Fig. 10.1 A 57-year-old patient with an incidental upper limit of a normal sized pineal gland (*arrows*), measuring 9 mm on three dimensional sagittal (*left*) and axial (*left middle*) FLAIR, without reduced diffusion on DWI (*right middle*). There is normal enhancement on postcontrast axial T1WI (*right*). Note that the gland does not compress or abut the tectum (*dotted arrow*)

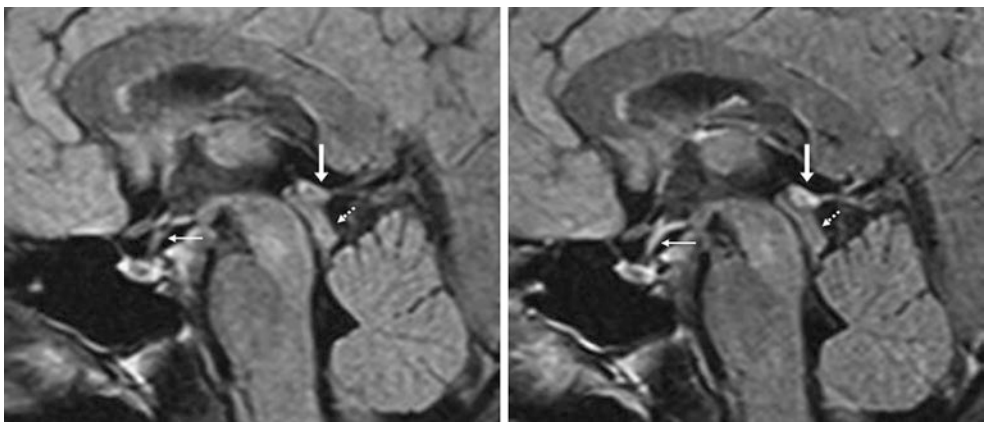

Fig. 10.2 A 35-year-old patient with a homogeneously enhancing 9-mm pineal gland (*arrows*) on pre- (*left*) and postcontrast (*right*) FLAIR at 1.5 T, which abuts but does not compress the top of the tectum (*dotted arrows*). Note the normal enhancement of the pituitary infundibulum (*thin arrows*), which likewise lacks a blood–brain barrier

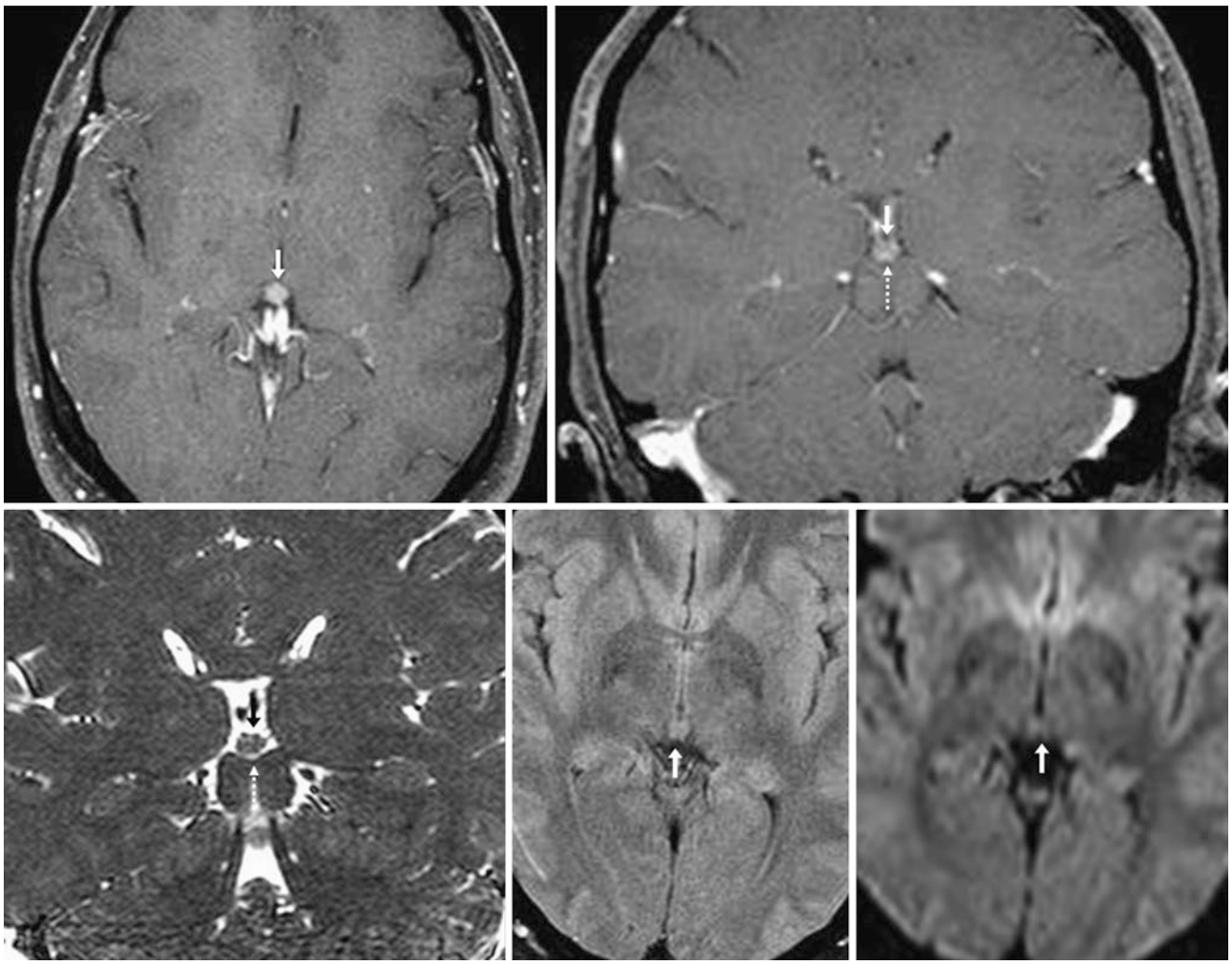

Fig. 10.3 A 27-year-old with a homogeneously enhancing 9-mm pineal gland (*arrows*) on postcontrast axial (*top left*) and coronal (*top right*) T1WI, on coronal balanced CISS/T2WI (*bottom left*), and on axial FLAIR (*bottom middle*). No reduced diffusion is noted (*bottom right*). It is adjacent to but does not compress the tectum (*dotted arrows*)

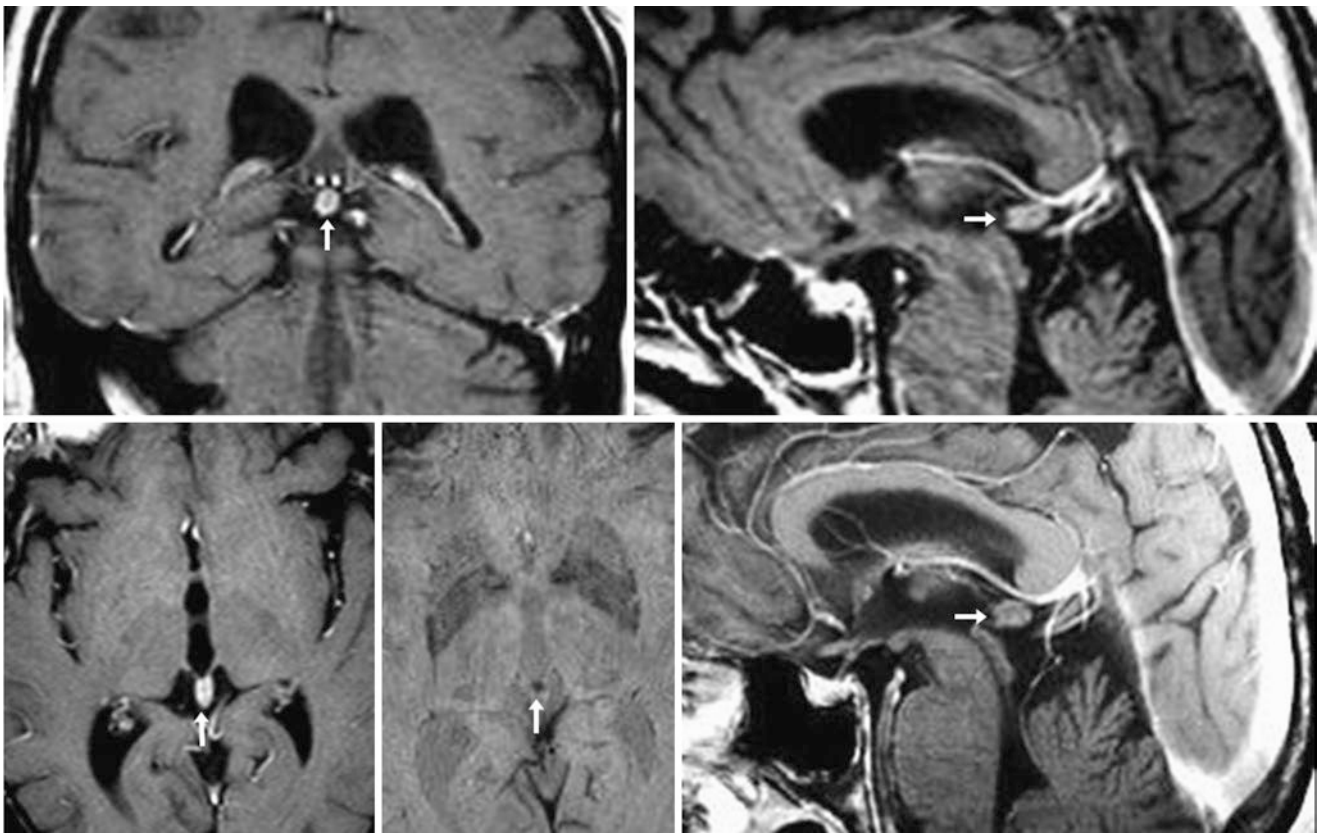

Fig. 10.4 A 68-year-old patient with a homogeneously enhancing 8-mm pineal gland (*arrows*) on postcontrast coronal (*top left*), sagittal (*top right*), and axial (*bottom left*) T1WI. On axial SWI (*bottom middle*), a small dark focus probably represents a tiny internal calcification. This is not changed from 3 years earlier on sagittal postcontrast T1WI (*bottom right*)

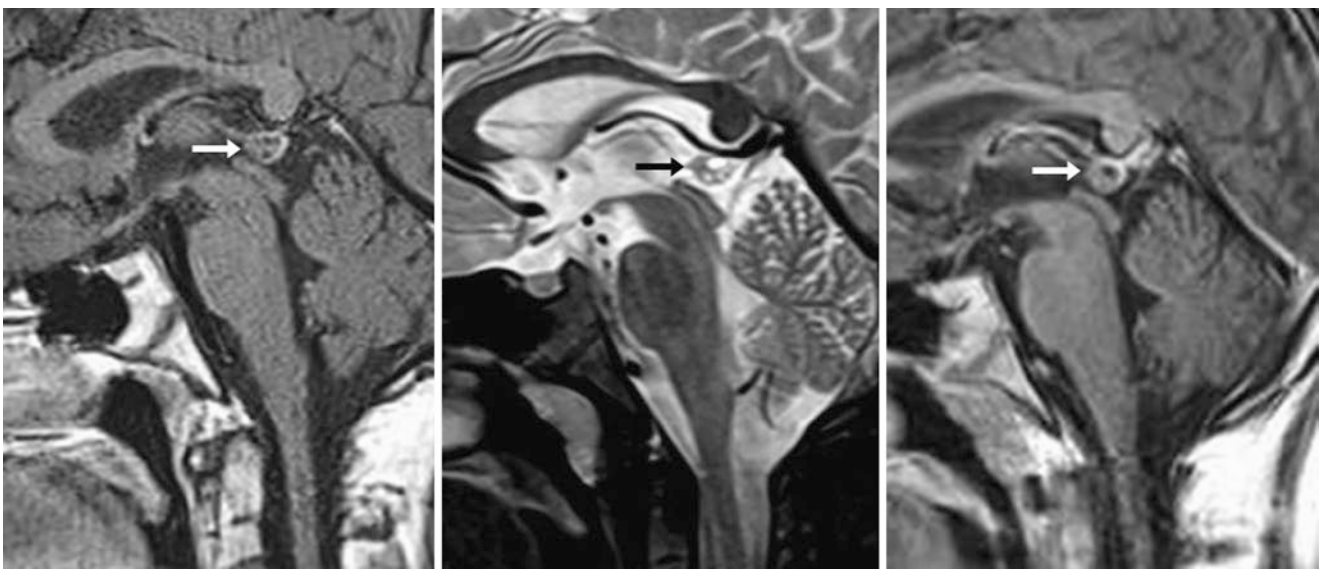

Fig. 10.5 A 14-year-old with a faintly enhancing but multicystic pineal gland (*arrows*) on postcontrast sagittal T1WI (*left*) and T2WI (*middle*). The gland was borderline enlarged, being 11 mm maximum in diameter, but it did not abut the tectum; thus, although a normal pineal gland was favored, it was elected to follow it at 1 and 2 years to exclude a mass. Postcontrast T1WI 2 years later (*right*) was unchanged, consistent with a normal albeit atypical pineal gland

10.1 The Pineal Gland: Normal Calcifications

Again, the pineal gland slightly increases in size and amount of calcification with age, but the degree of *calcification* should not significantly increase after 30–40 years of age. Calcifications are typically not present in children younger than 5 years of age but may progressively calcify into adulthood. Since pineal glands may appear partially cystic in up to 50–60 % of patients, it is not uncommon to note a partially calcified pineal gland with interspersed small cysts and mild contrast enhancement. However, the gland should not be enlarged (>10 mm size) and should not compress the aqueduct or cause hydrocephalus.

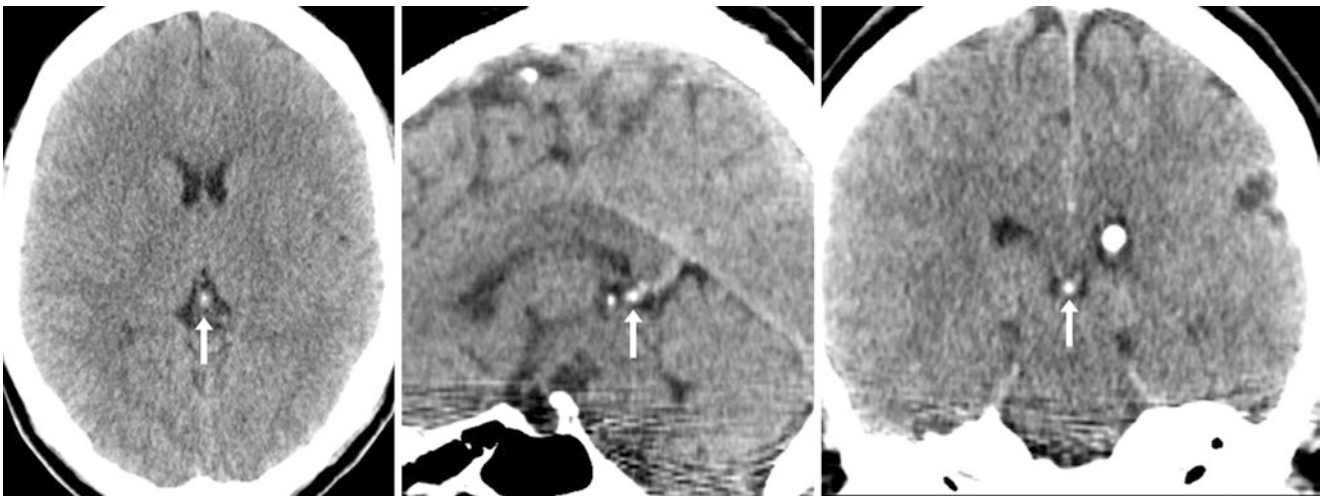

Fig. 10.6 A 31-year-old patient with mild calcifications of the pineal gland (*arrows*) on axial (*left*), sagittal (*middle*), and coronal (*right*) NECT images. This appearance is normal and should not change much after this age

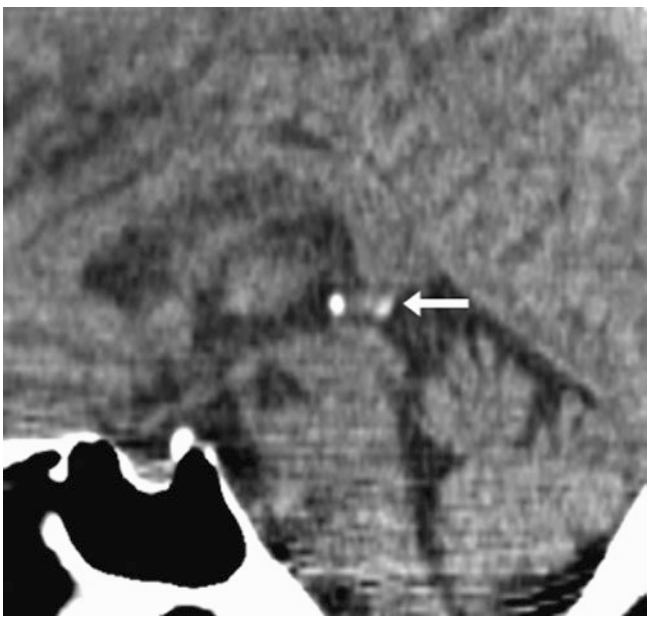

Fig. 10.7 A 62-year-old patient with a mildly calcified pineal gland (*arrows*) on sagittal NECT

Fig. 10.8 A 43-year-old with a normal, nearly completely calcified pineal gland (*arrows*) on axial (*left*) and sagittal (*right*) NECT

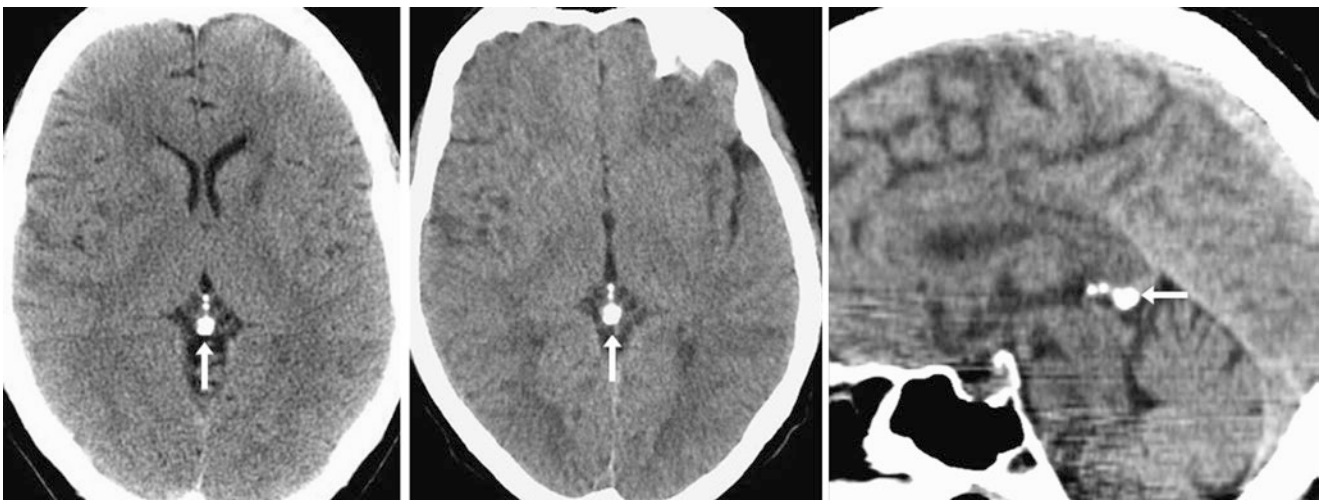

Fig. 10.9 A 75-year-old patient with calcification of most of the pineal gland (*arrows*) on axial NECT (*left*); 6 years later at 81 years of age (*middle*), the pineal gland's degree of calcification had not changed, consistent with the concept that the amount of calcification is stable after 30–40 years of age. Sagittal reconstructions (*right*) are also provided

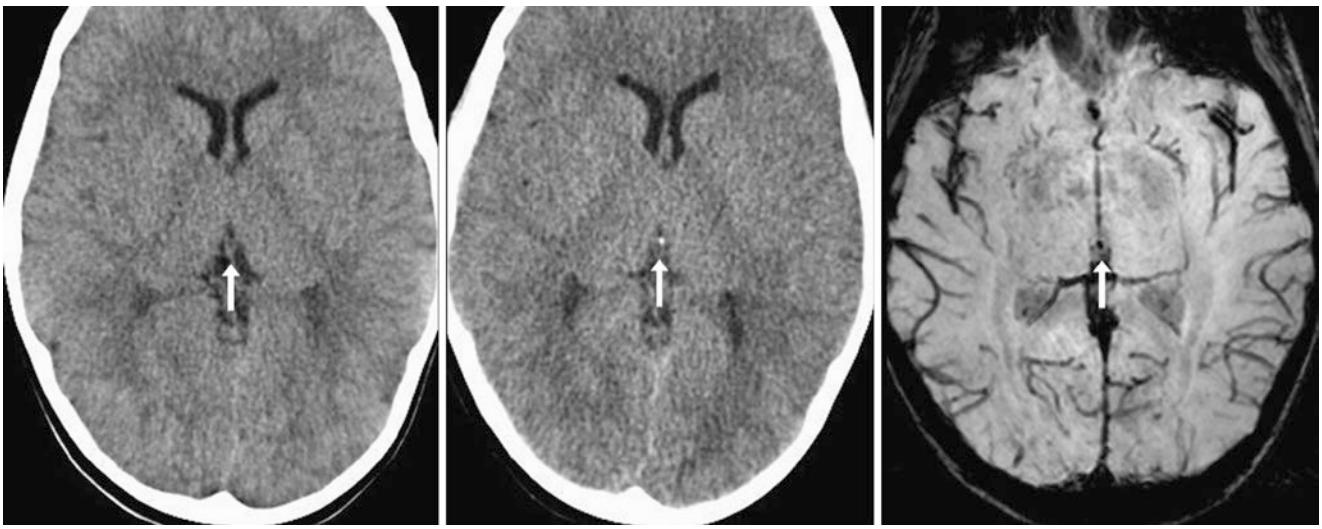

Fig. 10.10 A 2-year-old patient with no calcification noted of the pineal gland (*arrows*) on NECT at that age (*left*). Six years later at 8 years of age, there was a tiny, central calcification on NECT (*middle*), appearing as a punctate hypointensity on 3 T axial SWI (*right*). This is consistent with the concept that the pineal gland progressively calcifies from ages 5–40 years

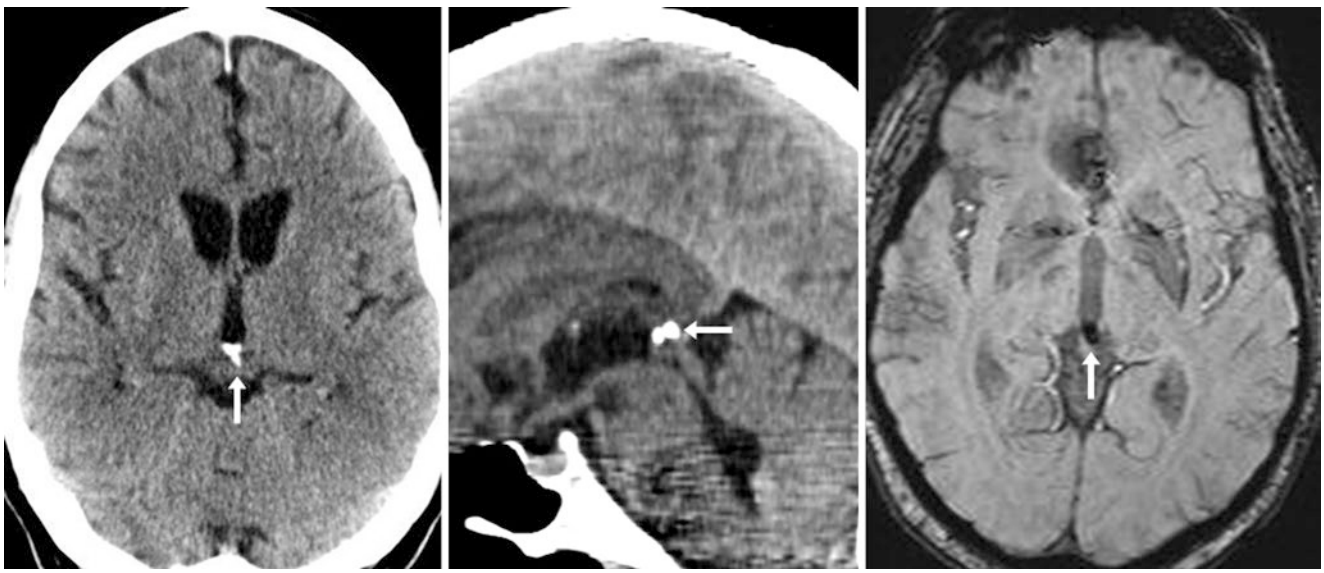

Fig. 10.11 A 67-year-old patient with calcification of the pineal gland (*arrows*) on axial (*left*) and sagittal (*middle*) NECT. This is manifested as a focal region of dark susceptibility artifact on 1.5 T axial SWI MRI (*right*)

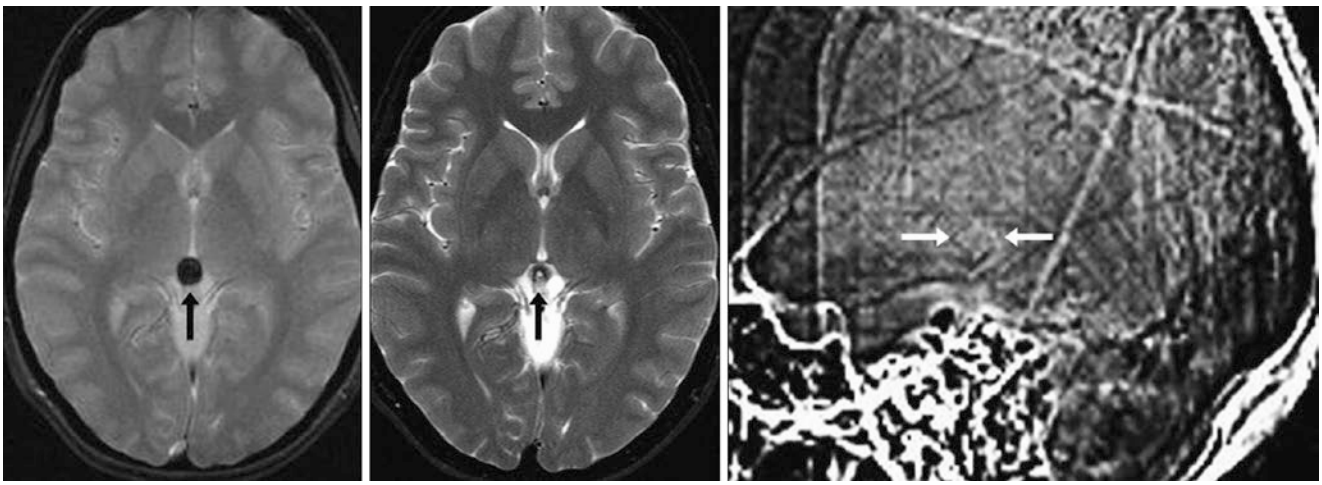

Fig. 10.12 A 31-year-old patient with a large focus of susceptibility effect (*arrows*) with dark blooming on gradient-echo T2*WI (GRET2*WI), with a less prominent dark signal on turbo spin echo T2WI (*middle*). A scout sagittal image from a cervical spine CT that did not cover the head (*right*) confirms that this is caused by a prominent pineal calcification

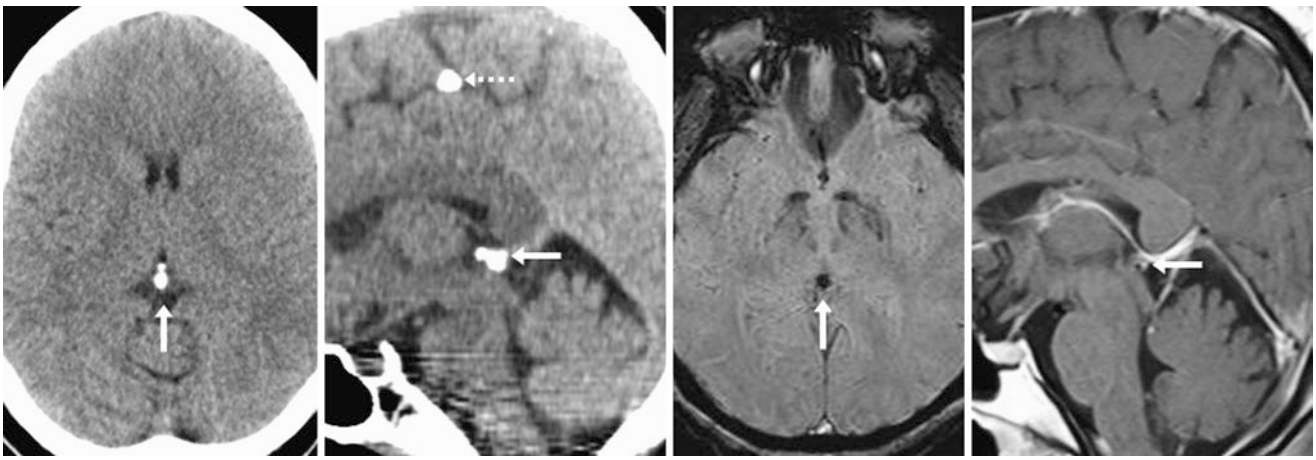

Fig. 10.13 A 52-year-old patient with a completely calcified pineal gland (*arrows*) on axial (*left*) and sagittal (*left middle*) NECT, with a focus of dark signal on SWI (*right middle*) from the susceptibility effects of calcium. A postcontrast sagittal T1WI (*right*) shows minimal enhancement, since it is largely calcified. Also, note an incidental dural calcification (*dotted arrow*)

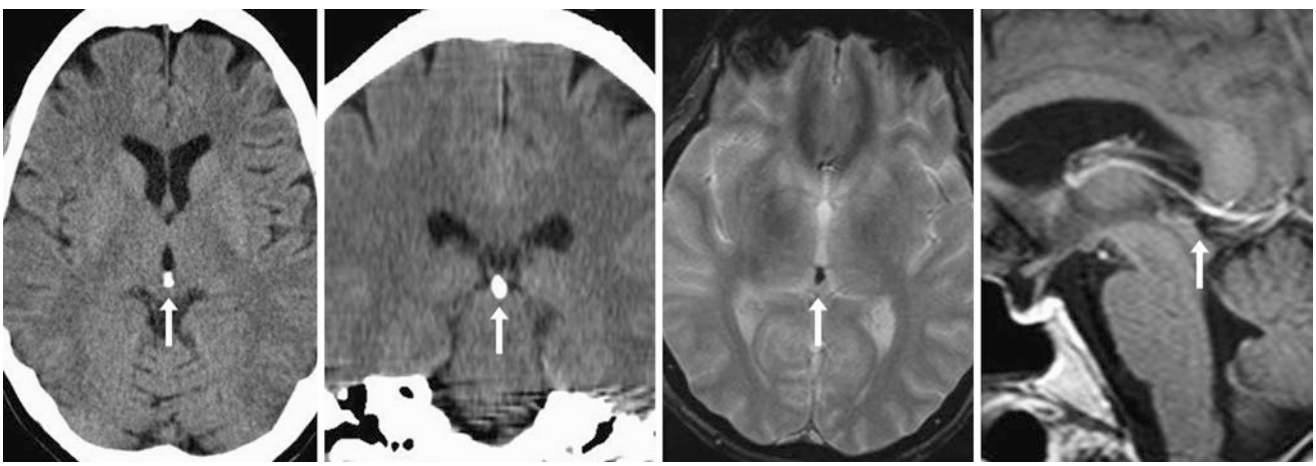

Fig. 10.14 A 55-year-old with a nearly completely calcified pineal gland (*arrows*) on axial (*left*) and coronal (*left middle*) NECT. There is dark signal on GRET2*WI (*right middle*) caused by the susceptibility effects of calcium. A postcontrast sagittal T1WI (*right*) does not demonstrate any enhancement, since the pineal gland is largely calcified

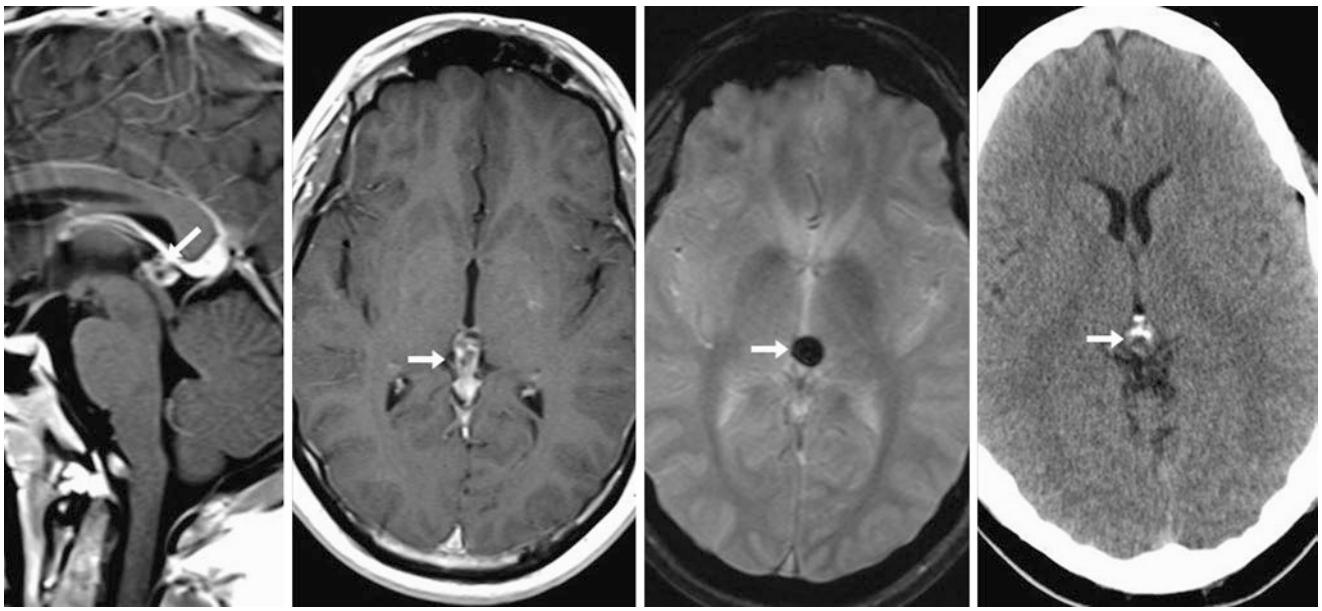

Fig. 10.15 A 33-year-old patient with an 11 mm partially cystic focus within the pineal gland (*arrows*) and on postcontrast sagittal (*left*) and axial (*left middle*) T1WIs with a focus of dark signal on GRET2*WI (*right middle*), thought to be calcium. A NECT (*right*) showed that calcium was interspersed throughout the gland. This was considered a normal, pineal gland that was partially cystic owing to the size. A follow-up MRI 1 year later was unchanged (*not shown*)

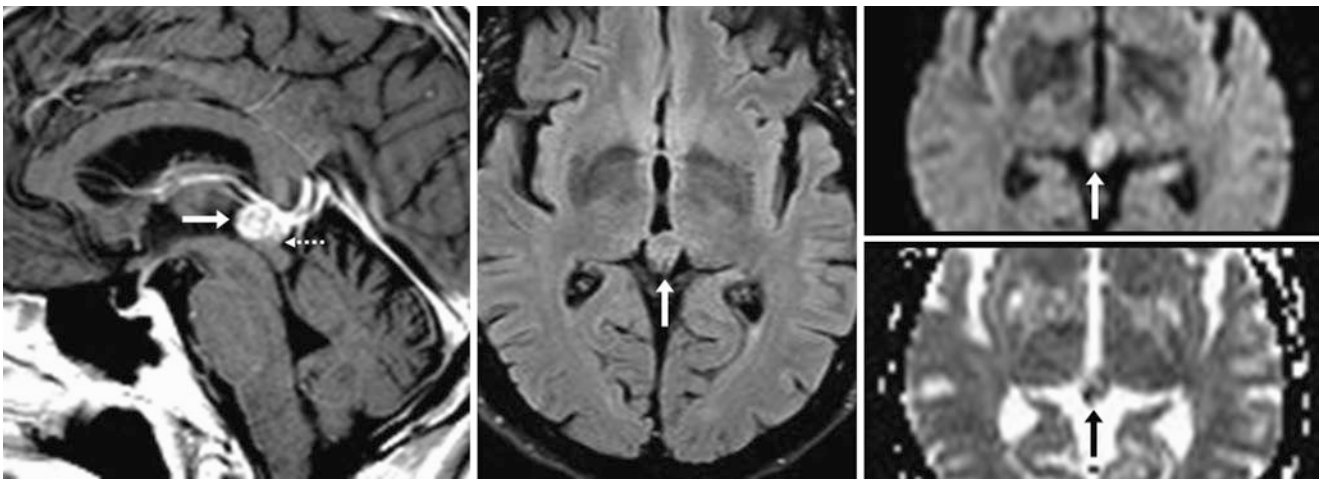

Fig. 10.16 Comparison case of pineal metastasis: a 57-year-old patient with known bronchial cancer and metastases elsewhere had a 13-mm homogeneously enhancing pineal lesion (*arrows*) on a postcontrast sagittal T1WI (*left*), which mildly indented the superior aspect of the midbrain tectum (*dashed arrow*). The lesion was isointense on FLAIR (*middle*) with mildly reduced diffusion on DWI (*right*, *top image*) and ADC map (*right*, *bottom image*)

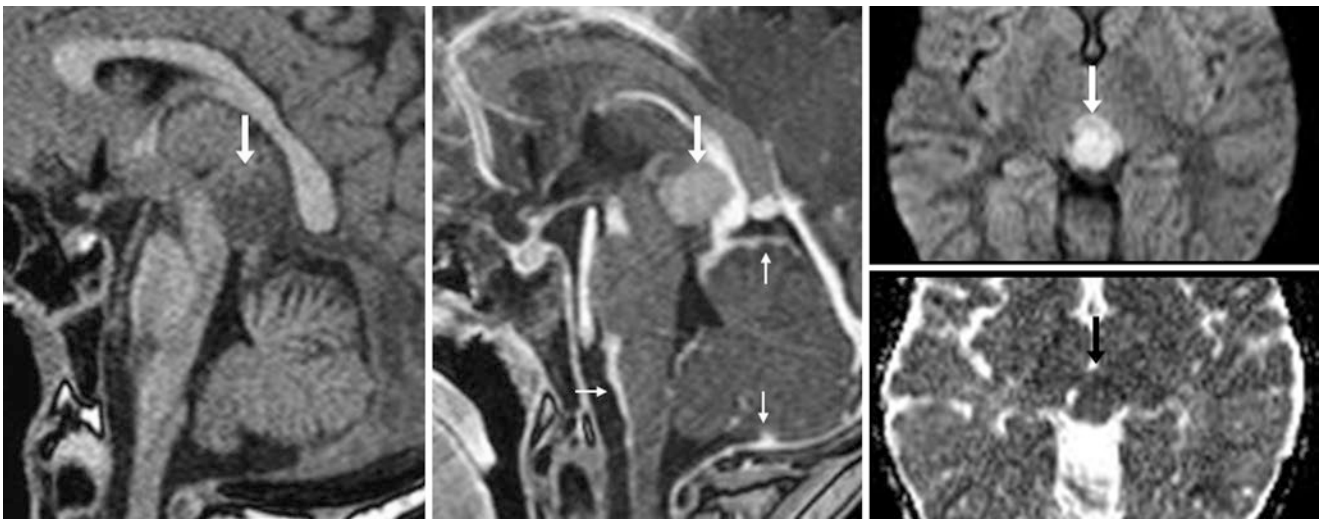

Fig. 10.17 Comparison case of pineoblastoma: a 2-year-old patient with a sizeable pineal mass (*arrows*) on precontrast (*left*) and postcontrast (*middle*) sagittal T1WIs that completely effaced the tectum. A ventriculostomy had already been placed for hydrocephalus. The mass had reduced diffusion on DWI (*right*, *top image*) and ADC map (*right*, *bottom image*). Note enhancing leptomeningeal metastases along the brainstem and cerebellum (*thin arrows*)

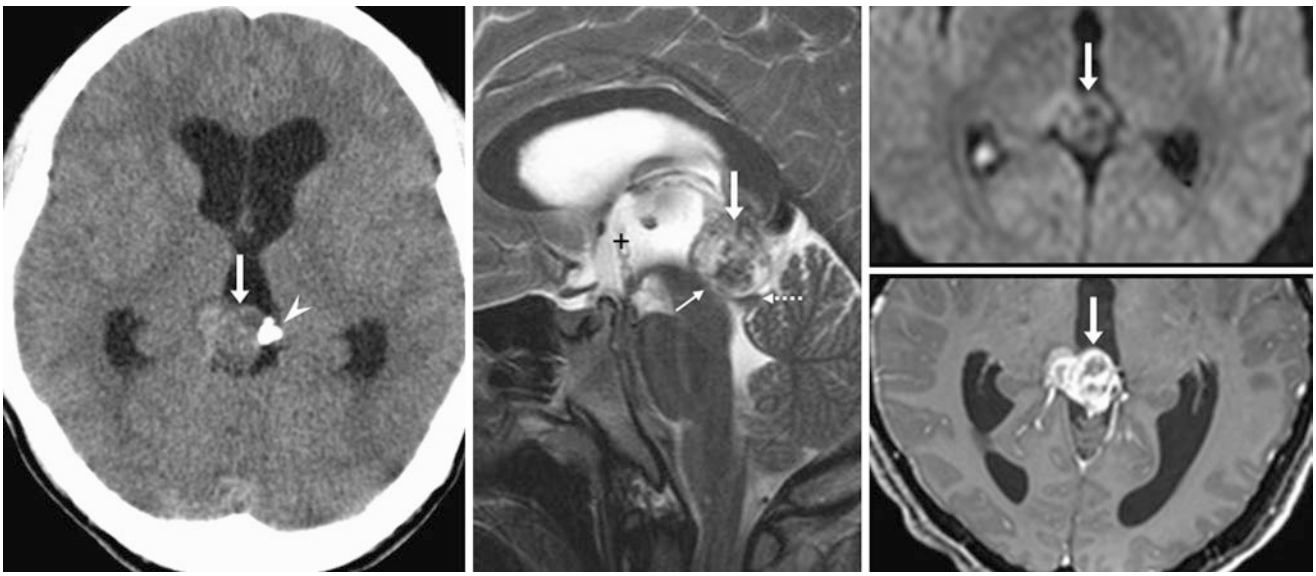

Fig. 10.18 Comparison case of germinoma: a 17-year-old patient with a sizeable pineal mass (*arrows*) on NECT (*left*), which displaced a calcification peripherally (*arrowhead*) and caused hydrocephalus by compressing the tectum (*thin arrows*) and subsequently the cerebral aqueduct, as depicted on a 3 T sagittal T2WI MRI (*middle*). Note a third ventriculostomy on T2WI (+), which is intended to decompress the third ventricle. Axial DWI (*right*, *top image*) and postcontrast T1WI (*right*, *bottom image*) show that the tumor does not appear to be high grade, while it enhances avidly

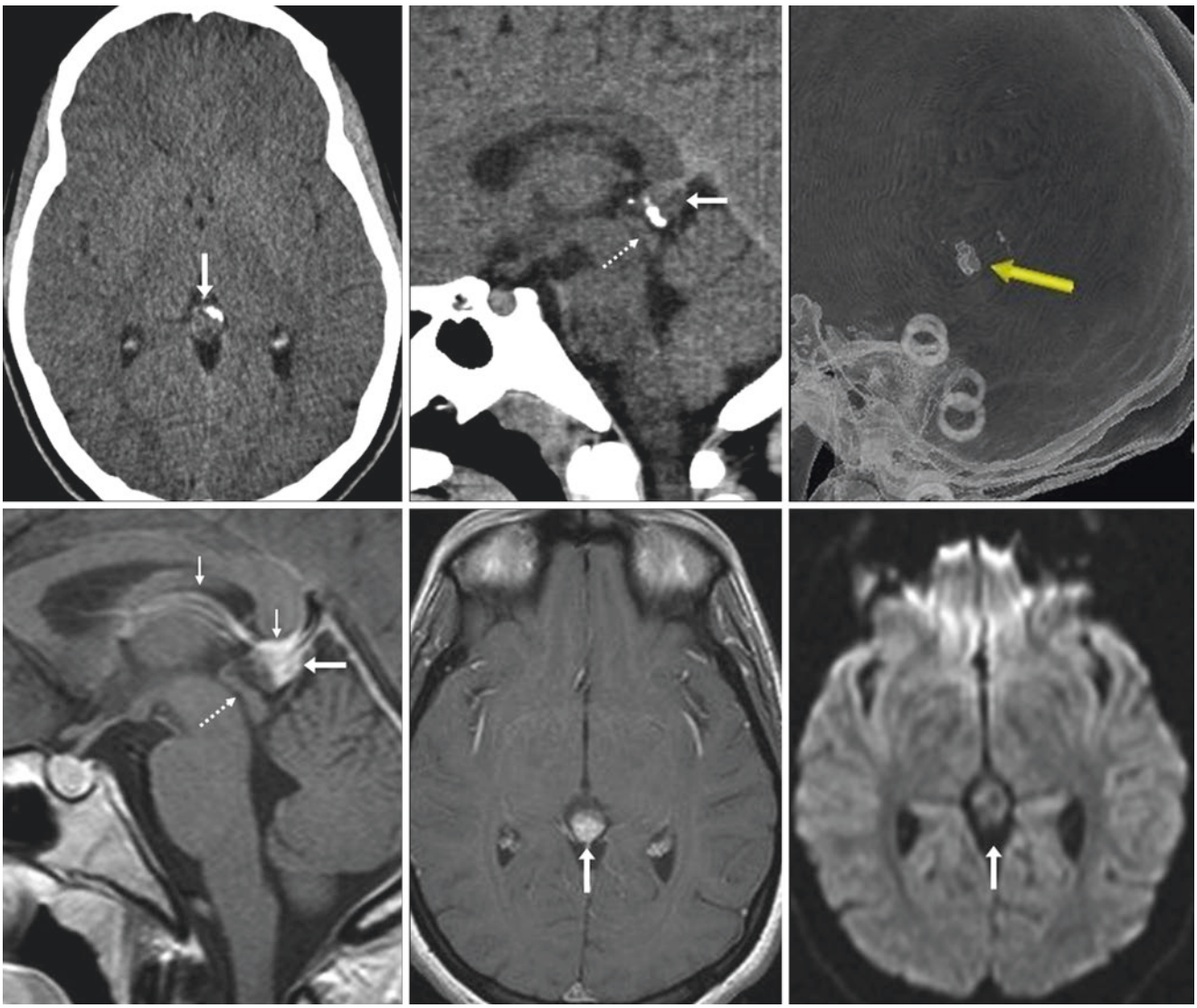

Fig. 10.19 Comparison case of pineocytoma (benign): a 19-year-old patient with a 15-mm pineal mass (*arrows*) on NECT (*above*). Calcifications were noted in its ventral aspect on axial (*top left*), sagittal (*top middle*), and sagittal three-dimensional reformats (*top right*). The mass abutted the tectum (*dotted arrows*), but the displacement of calcifications raised concern for a neoplasm. MRI showed homogeneous enhancement (except for the calcified portion) on sagittal (*bottom left*) and axial (*bottom middle*) postcontrast T1WIs; note normal internal cerebral veins (*thin arrows, bottom left*). On DWI (*bottom right*), there was no reduced diffusivity

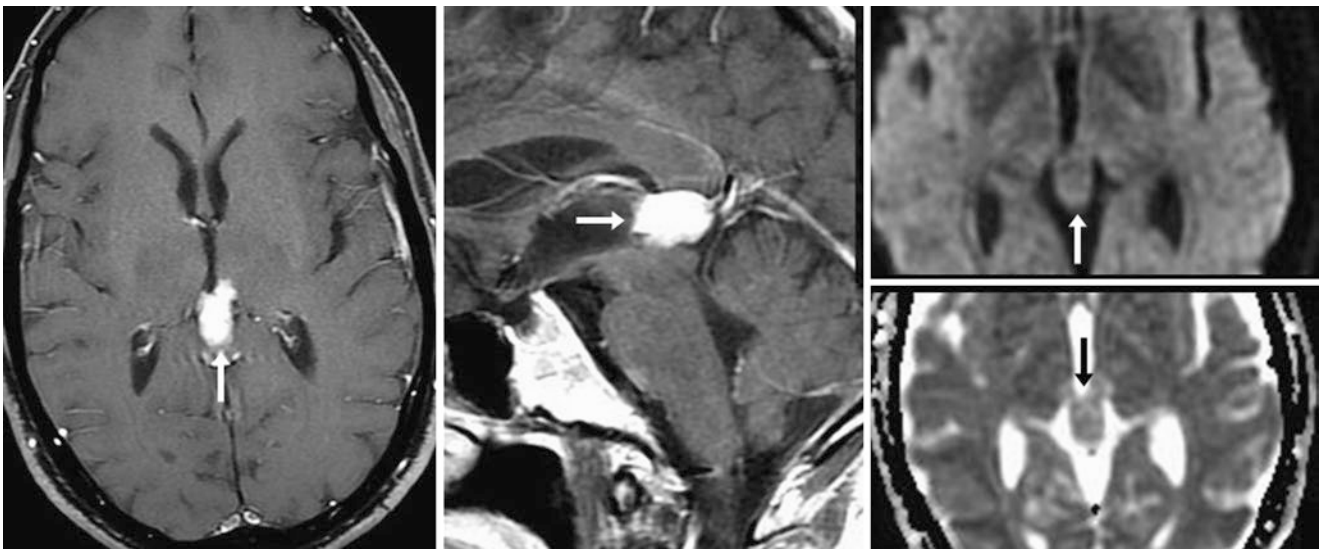

Fig. 10.20 Comparison case of pineal region meningioma (benign): a 52-year-old patient with a 20-mm pineal mass (*arrows*) on postcontrast axial (*left*) and sagittal (*middle*) T1WIs. The mass did not have reduced diffusivity on DWI (*right*, *top image*) or on ADC map (*right*, *bottom image*). A dural tail (which is typical of meningioma) was not visualized

10.2 Pineal Cysts

Benign, small, asymptomatic *cysts of the pineal gland* should be considered "don't touch" lesions and have been reported to occur incidentally in various age groups with a frequency of up to 40 % of the population according to autopsy-based studies and in up to 20 % based on MRI studies. Earlier MRI-based studies found a much lower frequency of cysts (in the range of 1–5 %), but this was probably related to the thicker sections and lower resolution of such preliminary studies. This observation has led to varying recommendations regarding their follow-up. Several studies have shown that the majority of smaller pineal cysts (<1.0 cm in size) either do not change in size or occasionally slightly decrease or increase by only a couple of millimeters; also they typically do not become symptomatic if the cyst is incidental (i.e., not the reason for presentation and without hydrocephalus) and if the cyst is not nodular or hemorrhagic. Other studies have shown no change in asymptomatic patients with cysts up to 1.5 cm in size even if there is mild contact of the tectum as long as there is no overt mass effect or compression of the aqueduct.

On imaging, pineal cysts are hypodense on CT, while on MRI they are T2-bright, T1-dark, and variably bright on FLAIR (unless hemorrhage has occurred). Calcifications may be present peripherally and even eccentrically relative to the cyst on CT, which confirms the cyst's pineal origin. However, calcifications that are eccentric to the cyst or gland may be worrisome, particularly if there is enhancing tissue or a nodular component of a cyst that is eccentric to the expected location of the gland. Contrast enhancement may be present in a crescentic or slightly thickened fashion; this is of no clinical significance unless the region of enhancement is either nodular or abuts the tectum. If they are large enough, the cysts may elevate and separate/splay the *internal cerebral veins* (ICVs). Again, care should be taken to ensure that there is no *hemorrhage* (e.g., fluid-hemorrhage level in a dependent fashion), *hydrocephalus*, or *compression* of the tectum/aqueduct and also that there is no evidence of nodular enhancement. Thus, this author recommends that cysts less than 1.5 cm without any of the aforementioned atypical features do not have to be followed by imaging, except in the unlikely development of clinical symptoms related to the cyst. Such symptoms could include headache, visual changes, vertigo, blurred vision/diplopia, nausea, vomiting, third or fourth cranial nerve paralysis, or Parinaud syndrome.

There are a few true abnormalities to be included in the differential diagnosis of pineal cysts. These include *arachnoid cysts* in the superior vermian cistern, *lesions of the tectum*, and *pineal or germ cell tumors* (which typically uniformly enhance with contrast). These can usually be discriminated from pineal cysts based on thin sections in various planes and the use of intravenous contrast material (Figs. 10.21, 10.22, 10.23, 10.24, 10.25, 10.26, 10.27, 10.28, 10.29, 10.30, 10.31, 10.32, 10.33, and 10.34).

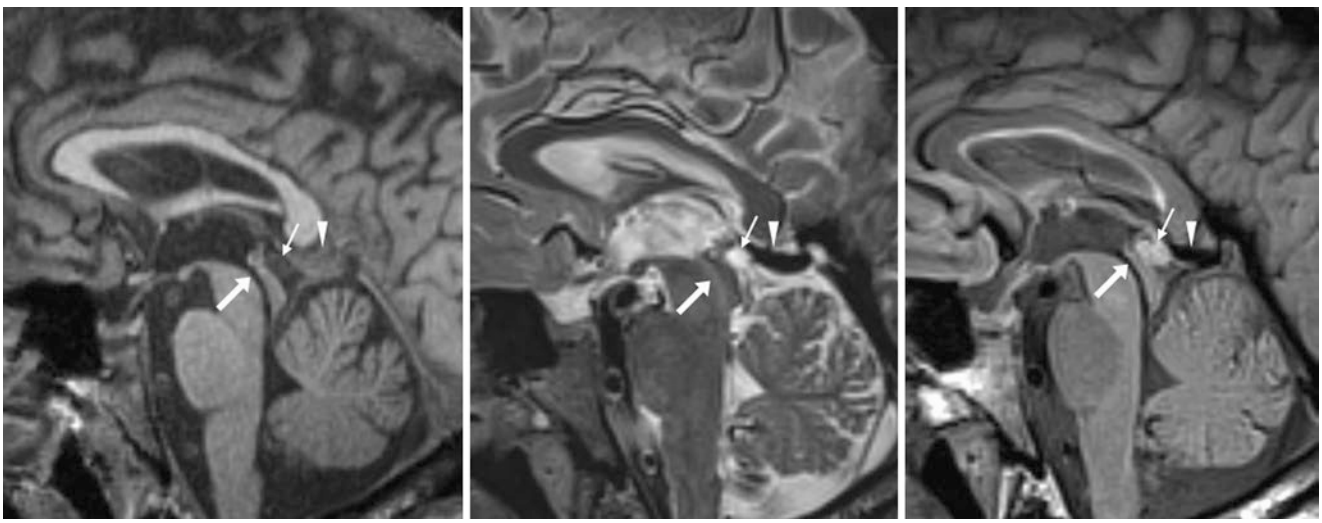

Fig. 10.21 A 13-year-old who was asymptomatic but underwent a 3 T MRI as part of a research study. There is a tiny, 7-mm pineal cyst (*thin arrows*) posterior to the tectum and aqueduct (*larger arrows*; *note the dark flow void indicating patency on FLAIR*), as shown on sagittal 1-mm thickness T1WI (*left*), T2WI (*middle*), and FLAIR (*right*) images, reconstructed from three-dimensional acquisitions. The cyst is bright on FLAIR. Note the ICVs (*arrowheads*) just superior to the cyst. Also, note how such a small cyst may be difficult to visualize on T1WI or T2WI

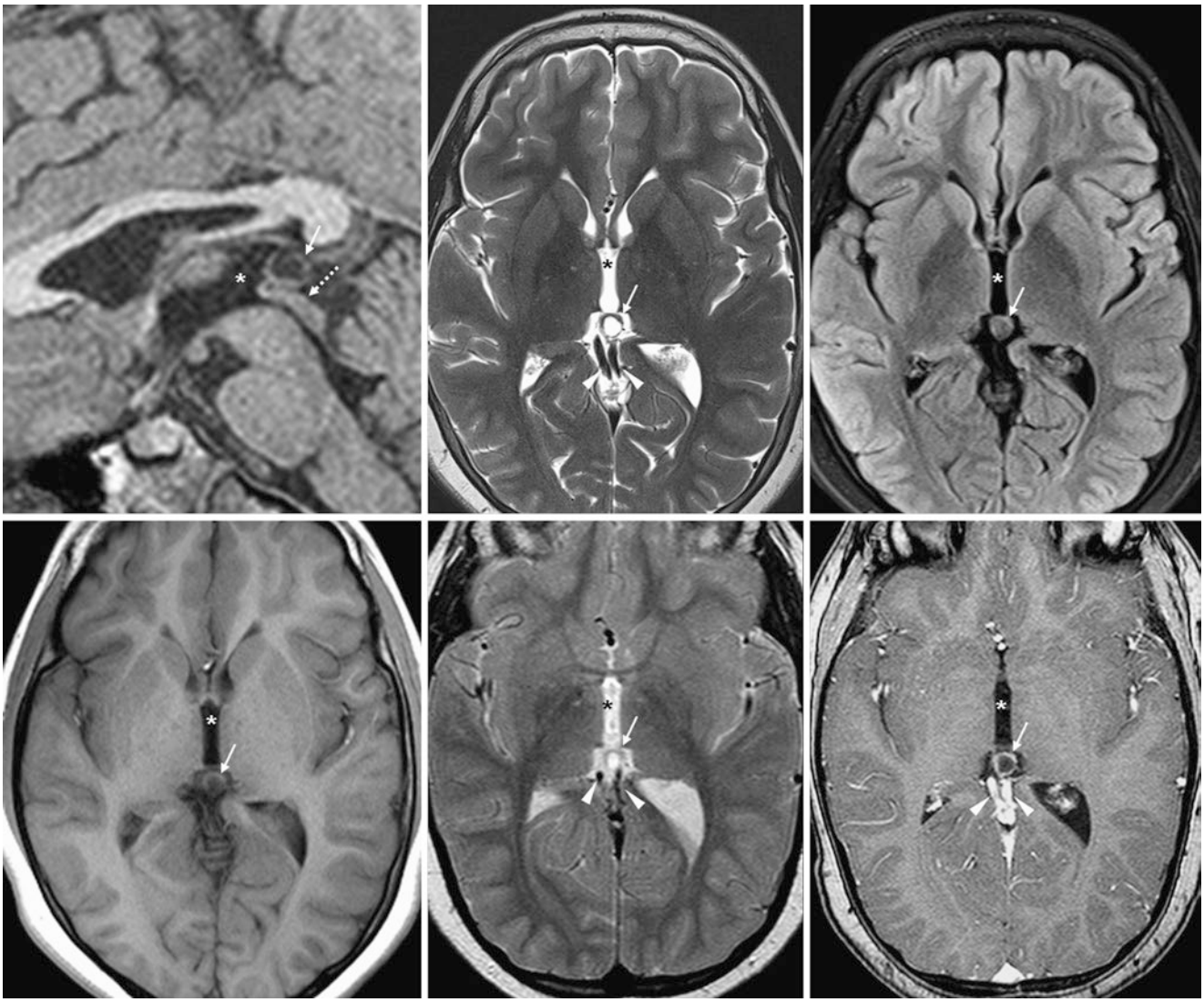

Fig. 10.22 An asymptomatic 12-year-old who was evaluated for developmental delay underwent a 3 T MRI. A 9-mm pineal cyst (*thin arrows*) is depicted on sagittal 1-mm thickness T1WI (*top left*), axial T2WI (*top middle*), FLAIR (*top right*), and axial T1WI (*bottom left*). This was unchanged from 5 years earlier (1.5 T) on T2WI (*bottom middle*) and on postcontrast T1WI (*bottom right*). Note that the cyst is isointense on FLAIR and comes close to the tectum (*dotted arrows*, *top left*). Also, note the ICVs (*arrowheads*) just posterior to the cyst. The third ventricle (*) is anterior to the pineal cyst

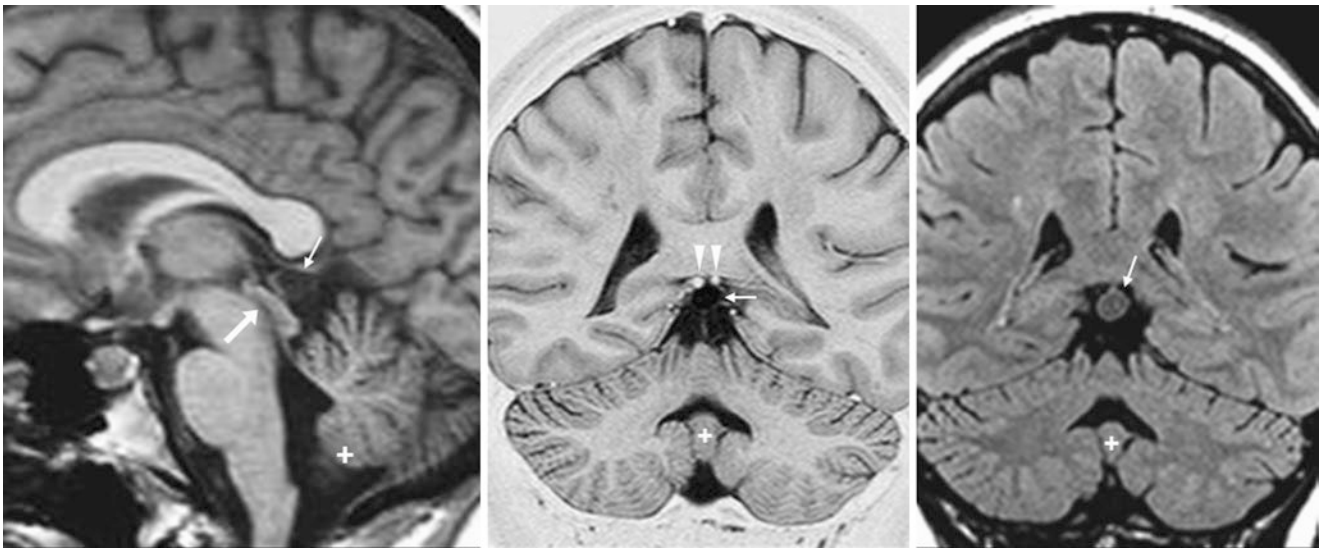

Fig. 10.23 A 28-year-old patient was evaluated for a first time seizure. Present was a small, 9-mm pineal cyst (*thin arrows*) posterior to the tectum and aqueduct (*larger arrows*) shown on 3-mm thickness sagittal T1WI (*left*), coronal T1WI-IR (*middle*), and coronal FLAIR (*right*) images. The cyst is isointense on FLAIR. Note the ICVs (*arrowheads*) coursing superior to the cyst. Subtle inferior cerebellar vermian hypoplasia (+) was questioned in this patient

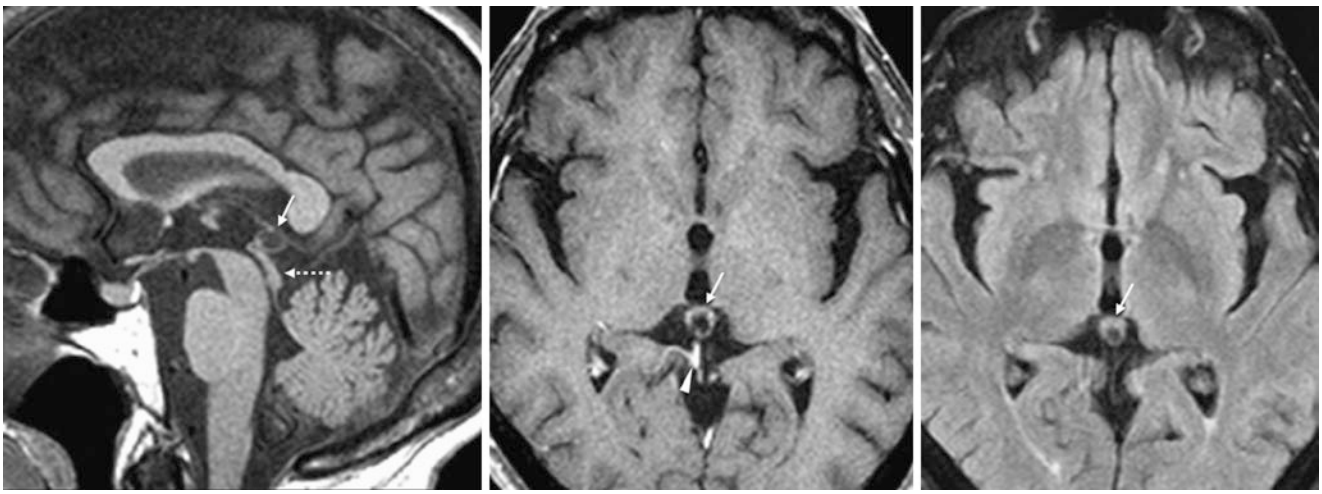

Fig. 10.24 A 64-year-old patient with a small, 9-mm pineal cyst (*thin arrows*) adjacent to but not compressing the tectum (*dotted arrows*) on a 5-mm thickness sagittal T1WI (*left*), axial postcontrast T1WI (*middle*), and axial FLAIR (*right*) images. The cyst has a slightly thickened and enhancing rim on postcontrast T1WI. The enhancing rim is isointense on FLAIR, while the cyst is centrally dark on FLAIR. Note an ICV (*arrowhead*, *middle*) just posterior to the cyst

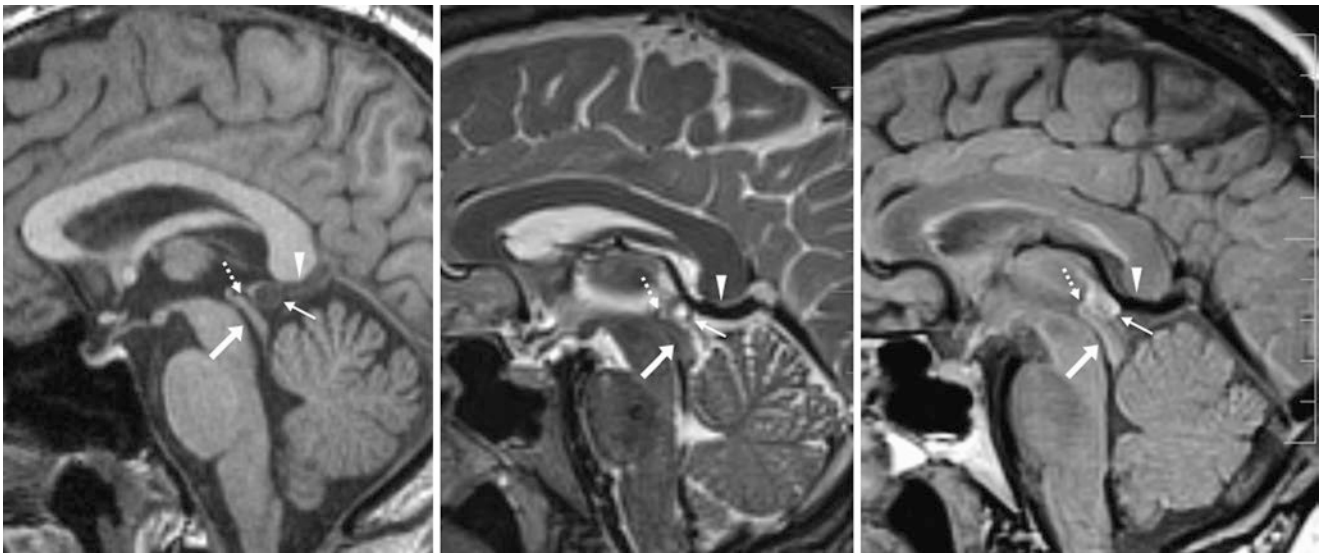

Fig. 10.25 A 54-year-old patient who was asymptomatic underwent a 3 T research MRI. The patient had a tiny, 6-mm pineal cyst (*thin arrows*) posterior to the tectum (*dotted arrows*) without compression of the tectum or aqueduct (*larger arrows*; *note the dark flow void indicating patency on T2WI and FLAIR*) as shown on sagittal 1-mm thickness T1WI (*left*), T2WI (*middle*) and FLAIR (*right*) images; all were reconstructed from three-dimensional volumetric acquisitions. Note that the cyst is bright on FLAIR. Also note the ICVs (*arrowheads*) coursing just superior to the cyst

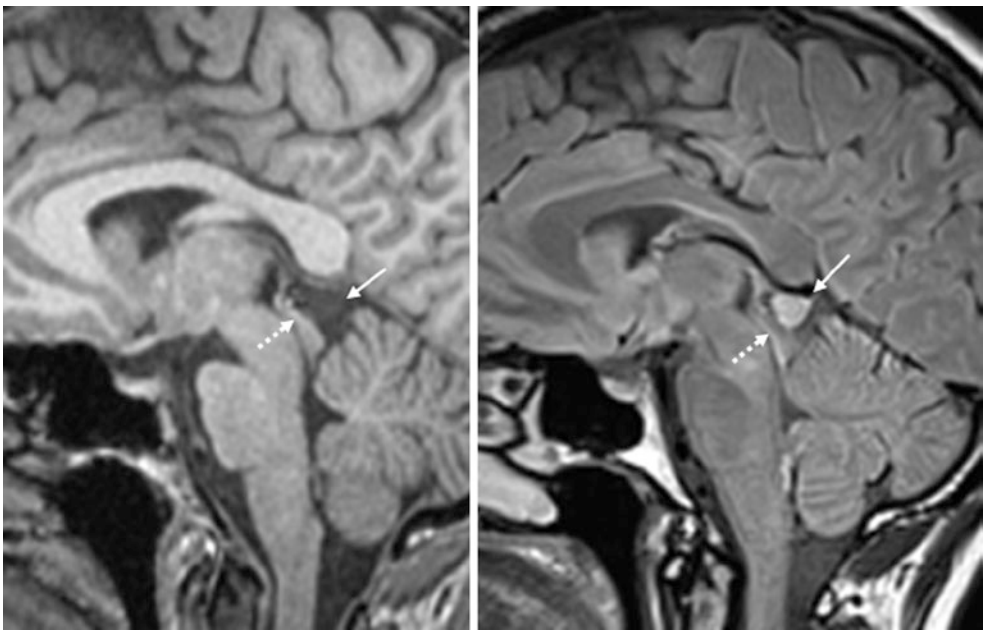

Fig. 10.26 A 55-year-old patient with a routine research 3 T MRI. An incidental 11 mm pineal cyst (*thin arrows*) slightly compressed the tectum (*dotted arrows*), as shown on 1-mm thickness sagittal T1WI (*left*) and FLAIR (*right*), obtained via three-dimensional acquisitions. The cyst is bright on FLAIR

Fig. 10.27 A 50-year-old patient; a research 3 T MRI showed a 10-mm pineal cyst (*thin arrow*) that abutted the tectum (*dotted arrow*), with heterogeneous signal on a sagittal T1WI

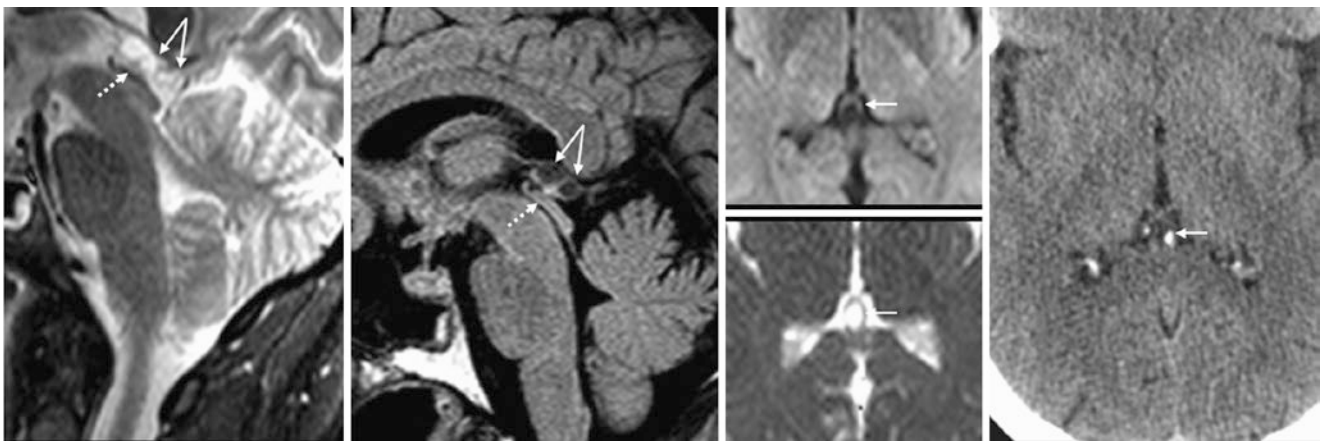

Fig. 10.28 A 33-year-old female patient was evaluated for multiple sclerosis, with an incidental bilobed 1.4-cm pineal cyst (*thin arrows*) noted on the top of a sagittal T2WI of the cervical spine (*left*), later confirmed by sagittal FLAIR (*left middle*). It came close to but did not compress the tectum (*dotted arrows*). The cyst had increased diffusion on DWI and ADC map (*right middle*). A NECT (*right*) performed later showed typical pineal calcifications peripheral to the cyst

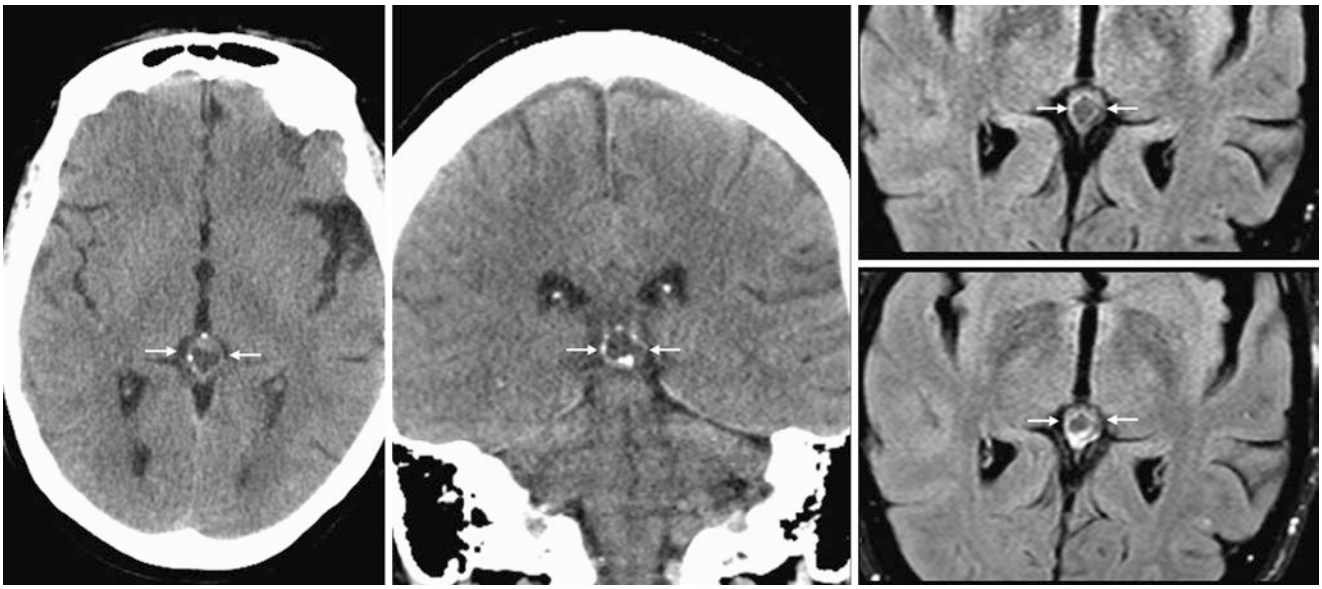

Fig. 10.29 A 65-year-old patient with an incidental 1.1-cm pineal cyst with peripheral calcifications and internal heterogeneous density (*thin arrows*) on NECT axial (*left*) and coronal (*middle*) reformats. This did not cause hydrocephalus. The cyst had a non-CSF signal on noncontrast FLAIR (*right*, *top*), while the rim mildly enhanced on postcontrast FLAIR (*right*). The recommendation was to follow this cyst in 1 year to exclude enlargement

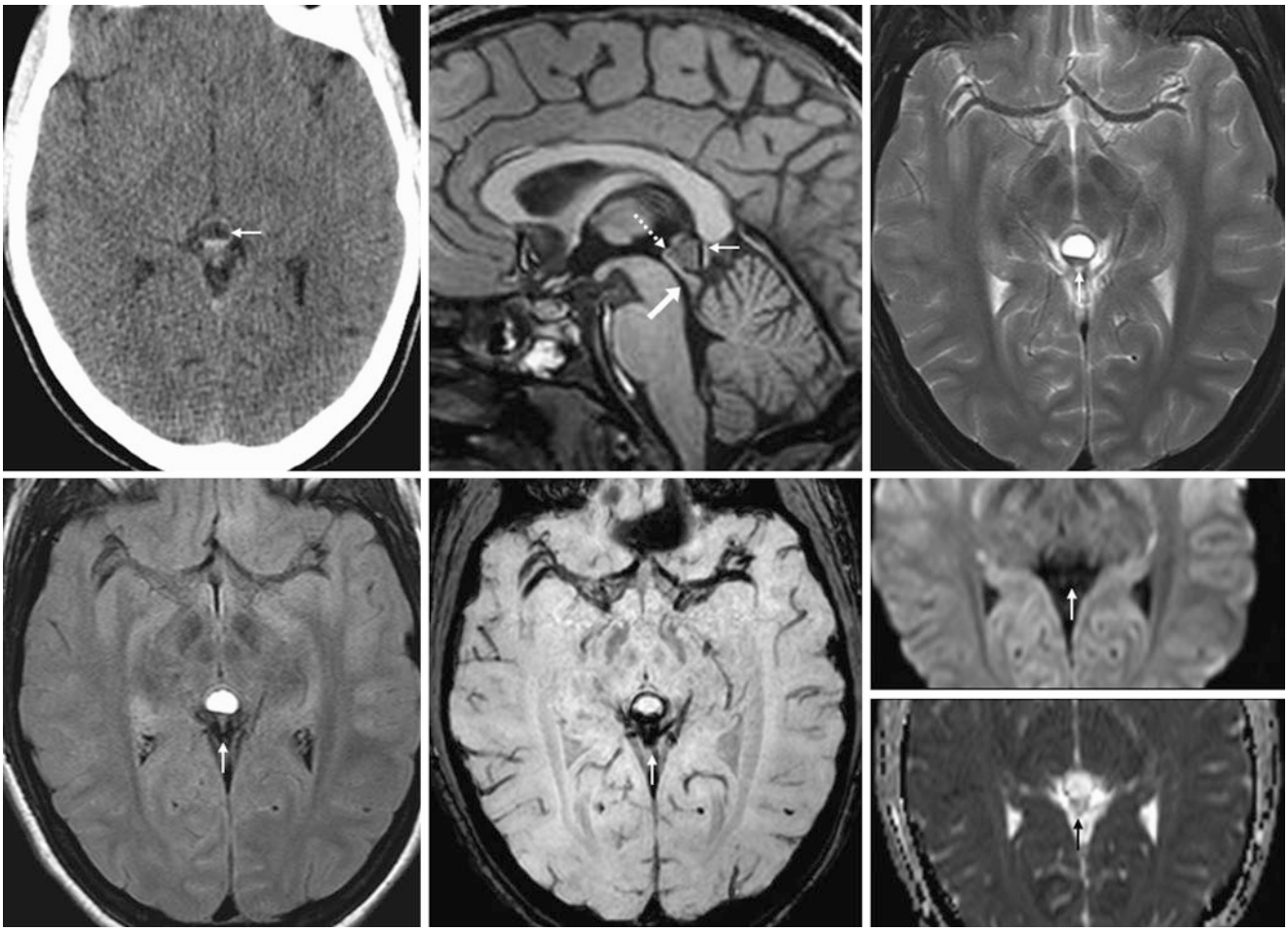

Fig. 10.30 Companion case of hemorrhagic pineal cyst. A 14-year-old patient was evaluated by NECT (*top left*) for hypoxic-ischemic encephalopathy (negative). The patient had a 13-mm pineal cyst (*thin arrows*) that contained a "blood-fluid" level, with dependent dense hemorrhage. A 3 T sagittal T1WI (*top middle*) showed that the cyst slightly compressed the tectum (*dotted arrows*) without obstructing the aqueduct (*larger arrows*) or causing hydrocephalus. Also, the dependent portion of the cyst was dark on axial T2WI (*top right*), FLAIR (*bottom left*), and SWI (*bottom middle*), consistent with acute hemorrhage. DWI and ADC map (*bottom right*) showed increased diffusion within the cyst. While the size was less than 1.5 cm, a follow-up MRI was recommended because of the presence of hemorrhage but was not performed

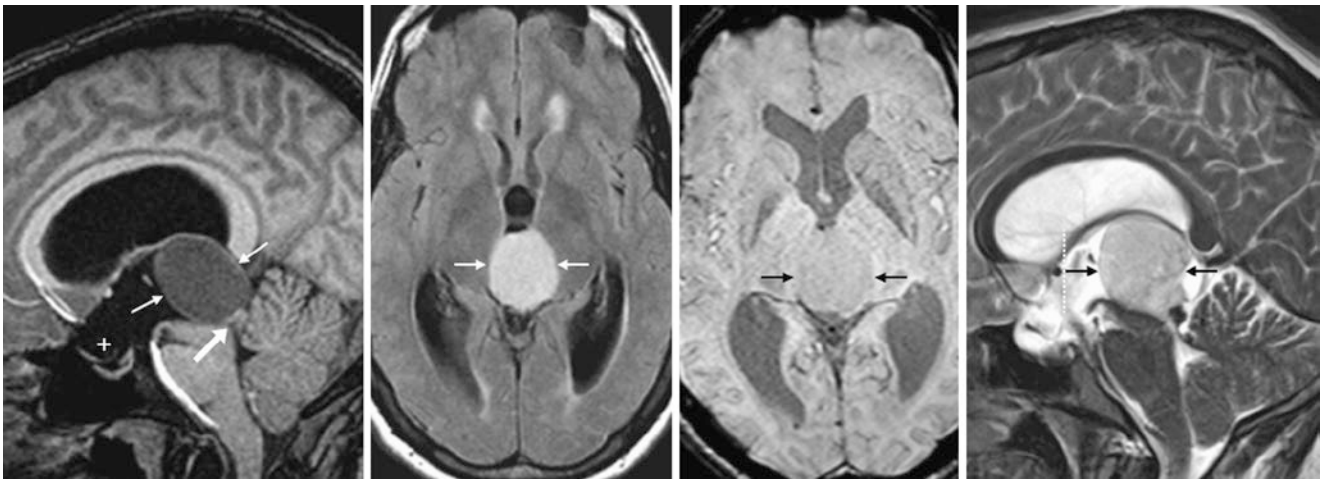

Fig. 10.31 Companion case of a complex pineal cyst. A 24-year-old patient had a nonenhancing 3-cm cyst (*thin arrows*) and hydrocephalus. Note the enlarged optic recess of the third ventricle (+) on sagittal T1WI (*left*) and axial FLAIR (*left middle*), indicating hydrocephalus. The cyst compressed the tectum and aqueduct (*larger arrows*). Four years later the cyst had mildly enlarged, as shown on axial SWI (*right middle*; note lack of hemorrhage within the cyst) and sagittal T2WI (*right*)

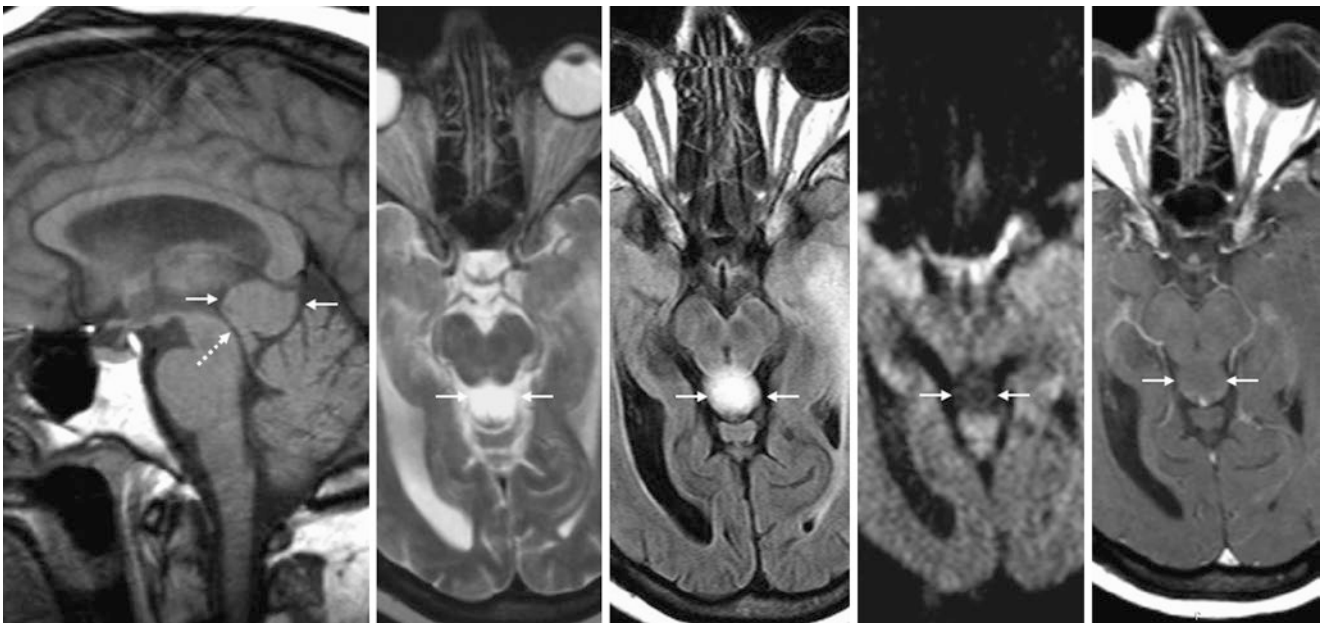

Fig. 10.32 Companion case of a complex pineal cyst. A 61-year-old patient with dizziness had an 18-mm pineal cyst (*thin arrows*) that was isointense on sagittal T1WI MRI (*left*) and bright on T2WI (*left middle*) and FLAIR (*middle*). It compressed the tectum (*dotted arrows*) and superior vermis without obstructing the aqueduct. It had increased diffusivity on DWI (*right middle*), and did not enhance on postcontrast T1WI (*right*), opposing the idea of a tumor. Thus, it was a complex pineal cyst, perhaps from a prior hemorrhage. A follow-up MRI was recommended but not performed

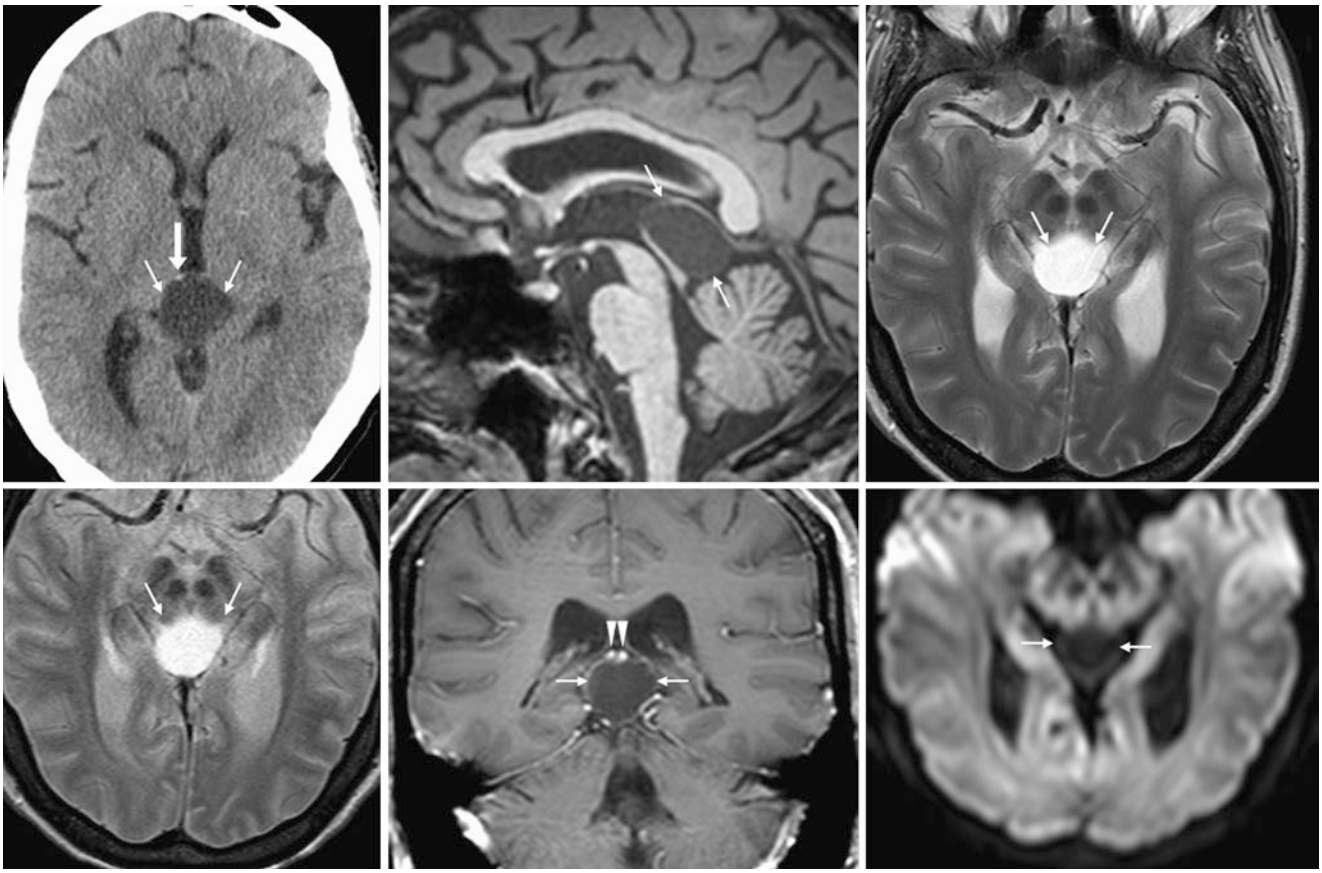

Fig. 10.33 Companion case of pineal cyst with mass effect. In a 36-year-old, a NECT (*top left*) 1 month post-trauma (no initial images obtained) found a 2.5-cm pineal cyst (*thin arrows*) that displaced calcifications peripherally (*larger arrow*). 3 T sagittal T1WI (*top middle*) showed that the cyst compressed the tectum but without hydrocephalus. The cyst was bright on T2WI (*top right*) and FLAIR (*bottom left*). It had a thin rim of enhancement on coronal T1WI (*bottom middle*) and was dark on DWI (*bottom right*). It was unchanged 5 months later, but a skull CT found from 2 years prior measured the cyst at 2.2 cm. A follow-up MRI was recommended at 1 year as a result of size, enlargement, and mass effect but was not performed. Note ICVs (*arrowheads*) above the cyst

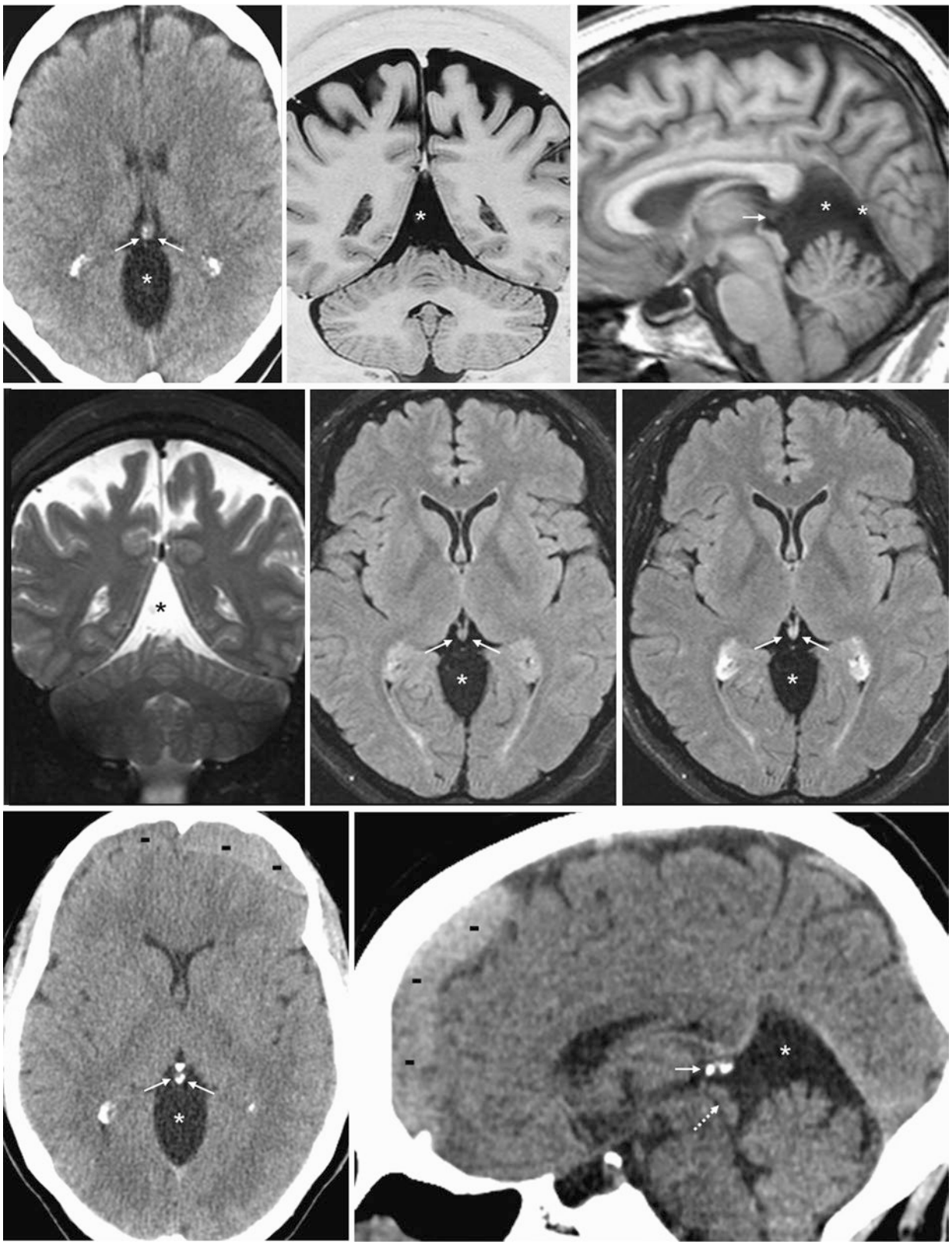

Fig. 10.34 Companion case of an arachnoid cyst. The patient was a 31-year-old post-trauma individual. *Top row*: a NECT (*left*) was negative for hemorrhage, but a pineal cyst was questioned because a cyst (*) was visible above the vermis. However, the cyst appeared to be posterior to the pineal calcifications (*thin arrows*). On a 1.5 T MRI, coronal T1WI (*middle*) and sagittal T1WI (*right*) confirmed the location of the lesion. *Middle row*: coronal T2WI (*left*) and axial precontrast FLAIR (*middle*) confirm CSF-like suppression of the cyst. Postcontrast FLAIR (*right*) confirms the pineal enhancement anteriorly. *Bottom row:* 6 years later after another traumatic injury, axial (*left*) and sagittal (*right*) reformats confirm unchanged findings in the pineal region, while new frontal subdural hematomas (--) had developed. Since the cyst abuts the vermis, rather than the tectum, it is likely a supravermian arachnoid cyst

Suggested Reading

Barboriak DP, Lee L, Provenzale JM. Serial MR imaging of pineal cysts: implications for natural history and follow-up. Am J Roentgenol. 2001;176:737–43.

Cauley KA, Linnell GJ, Braff SP, Filippi CG. Serial follow-up MRI of indeterminate cystic lesions of the pineal region: experience at a rural tertiary care referral center. Am J Roentgenol. 2009;193:533–7.

Cooper ER. The human pineal gland and pineal cysts. J Anat. 1932;67:28–46.

Deepak S, Jayakumar B. Intracranial calcifications. J Assos Physicians India. 2005;53:948.

Dumrongpisutikul N, Intrapiromkul J, Yousem DM. Distinguishing between germinomas and pineal cell tumors on MR imaging. Am J Neurol Radiology. 2012;33:550–5.

Engel U, Gottschalk S, Niehaus L, Lehmann R, May C, Vogel S, Jänisch W. Cystic lesions of the pineal region: MRI and pathology. Neuroradiology. 2000;42:399–402.

Inoue Y, Saiwai S, Miyamoto T, Katsuyama J. Enhanced high-resolution sagittal MRI of normal pineal glands. J Comput Assist Tomogr. 1994;18:182–6.

Hasegawa A, Ohtsubo K, Mori W. Pineal gland in old age: quantitative and qualitative morphological study of 168 human autopsy cases. Brain Res. 1987;409:343–9.

Kendall B, Cavanagh N. Intracranial calcification in paediatric computed tomography. Neuroradiology. 1986;28:324–30.

Kieffer SA, Gold LH. Intracranial physiologic calcifications. Semin Roentgenol. 1974;2:151–62.

Kıroğlu Y, Çalli C, Karabulut N, Oncel C. Intracranial calcifications on CT. Diagn Interv Radiol. 2010;16:263–9.

Sumida M, Barkovich AJ, Newton TH. Development of the pineal gland: measurement with MR. Am J Nuclear Radiol. 1996;17:233–6.

Tapp E, Huxley M. The weight and degree of calcification of the pineal gland. J Pathol. 1971;105:31–9.

Tapp E, Huxley M. The histological appearance of the human pineal gland from puberty to old age. J Pathol. 1972;108:137–44.

Yamamoto Y, Kageyama N. Microsurgical anatomy of the pineal region. J Neurosurg. 1980;53:205–21.

Zimmerman RA, Bilaniuk LT. Aged-related incidence of pineal calcification detected by computed tomography. Radiology. 1982;142:659–62.

Choroid Plexus: Normal Locations and Appearances

11

The *choroid plexus'* (CPs) rich blood supply and the lack of a blood–brain barrier often lead to avid enhancement after intravenous contrast administration. Such enhancement is typically normal, but it can occasionally appear asymmetric or mass-like, leading to a mistaken interpretation of tumors. *Metastasis*, *glioma*, *CP papilloma,* or *subependymal giant cell astrocytoma* (when near the foramen of Monro in a patient with tuberous sclerosis) are considerations in the differential diagnosis for tumors in such locations. Abnormal enhancement of the CP should be considered if it is large and mass-like with hydrocephalus, although the presence of the asymptomatic don't touch CP xanthogranuloma (see the following section) can appear mass-like as well. Volume averaging artifacts can exacerbate the mass-like appearance, which often occurs from a CP located anteriorly within the choroidal fissures or temporal horns of the lateral ventricles, especially on routine axial images. Linear or non-nodular CP enhancement can simulate abnormal leptomeningeal enhancement.

Alternatively, the CP can be entirely calcified and enlarged and lack enhancement. This appearance can simulate pathologic lesions, the differential diagnosis of which depends on the location. For example, an enlarged or mass-like CP within the fourth ventricle can simulate an infectious or postinfectious lesion such as a *tuberculoma* or *neurocysticercosis*, while calcified choroid within the cerebellopontine angle may simulate a calcified, nonenhancing *meningioma* (a so-called burnt-out meningioma) or a *schwannoma*.

Thus, normal a CP can range from being calcified and nonenhancing to being avidly enhancing. A CP can appear asymmetric in locations that are expected to be bilateral (such as the foramina of Luschka) and thus may simulate a mass. This can be particularly problematic when the choroid is noncalcified or only partially calcified, i.e., it appears mildly hyperdense and thus simulates *subarachnoid hemorrhage* (SAH); this can lead to unnecessary CT or MRI scans. Additionally, bright signal on FLAIR or T2WI within a noncalcified CP can simulate lesions in particular locations owing to the close apposition of the CP, such as simulating *mesial temporal lobe sclerosis* from adjacent choroid within the choroidal fissure. The normal CP is presented in the following pages caudally to cranially (inferior to superior).

Note that only a few examples of a normal CP within the trigones of the lateral ventricles are illustrated here, since a CP in that location is not usually mistaken for disease unless it is quite large. The exception is *xanthogranulomas*, which can have varying appearances and are covered separately herein (Figs. 11.1, 11.2, 11.3, 11.4, 11.5, 11.6, 11.7, 11.8, 11.9, 11.10, 11.11, 11.12, 11.13, 11.14, 11.15, 11.16, 11.17, 11.18, 11.19, 11.20, 11.21, 11.22, 11.23, 11.24, 11.25, 11.26, 11.27, 11.28, 11.29, 11.30, 11.31, 11.32, 11.33, 11.34, 11.35, 11.36, 11.37, 11.38, 11.39, 11.40, 11.41, 11.42, 11.43, 11.44, 11.45, 11.46, 11.47, 11.48, 11.49, 11.50, 11.51, 11.52, 11.53, 11.54, 11.55, 11.56, 11.57, 11.58, 11.59, 11.60, and 11.61).

A.M. McKinney, *Atlas of Normal Imaging Variations of the Brain, Skull, and Craniocervical Vasculature*,
DOI 10.1007/978-3-319-39790-0_11

Fig. 11.1 A 50-year-old patient with a CP calcification (*arrow*) in the foramen of Magendie (median aperture) on axial NECT

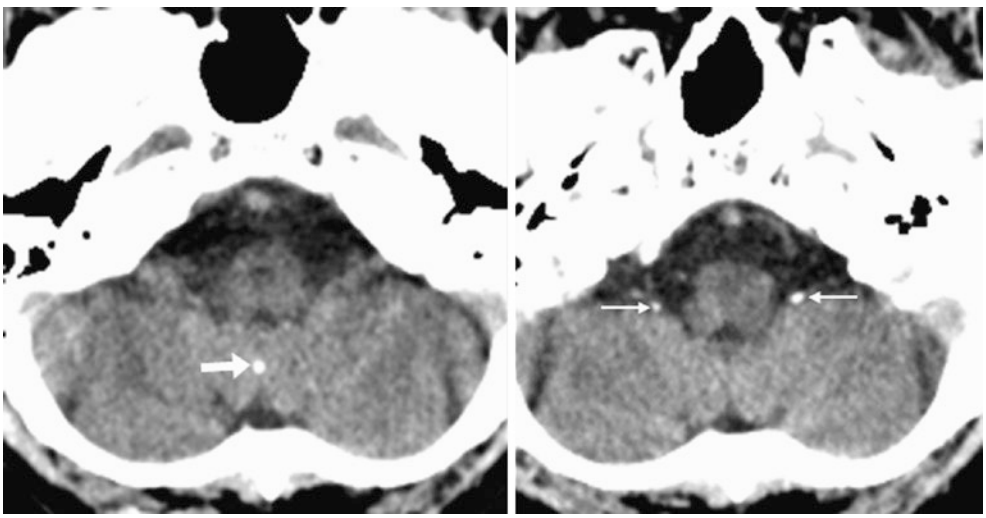

Fig. 11.2 A 52-year-old patient with a CP calcification (*arrow*) in the foramen of Magendie (median aperture) on axial NECT (*left*). On one slice below (*right*), CP calcifications are seen lateral to the foramina of Luschka (*thin arrows*)

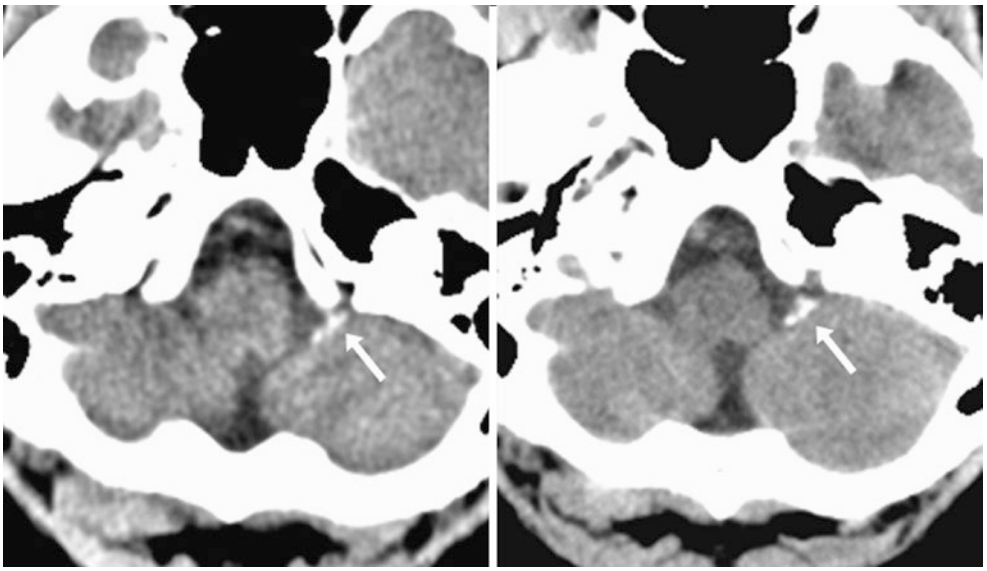

Fig. 11.3 A 50-year-old patient with an asymmetric CP calcification (*arrow*) in the foramen of Luschka on axial NECT (*left*). Seven years later (*right*), this is unchanged

Fig. 11.4 A 49-year-old patient with a unilateral CP calcification (*arrow*) within the left foramina of Luschka on axial NECT

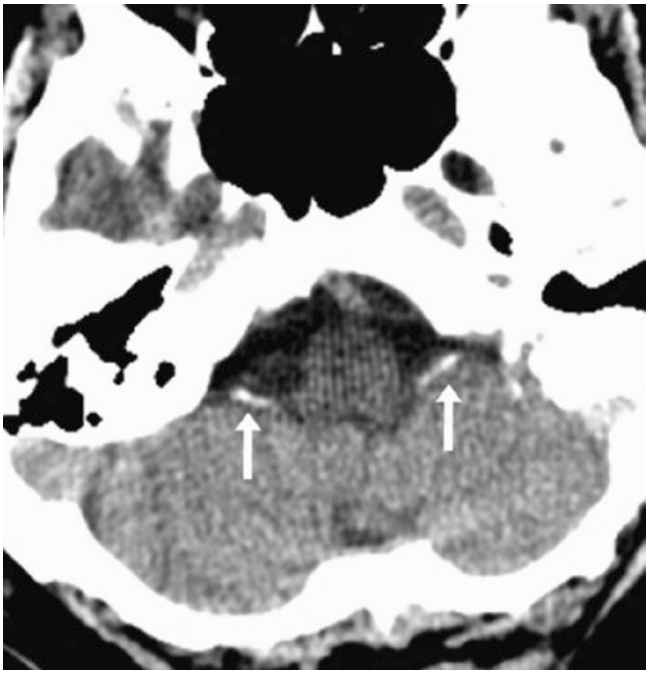

Fig. 11.5 An 82-year-old patient with bilateral calcifications of the CP (*arrows*) within the foramina of Luschka on axial NECT

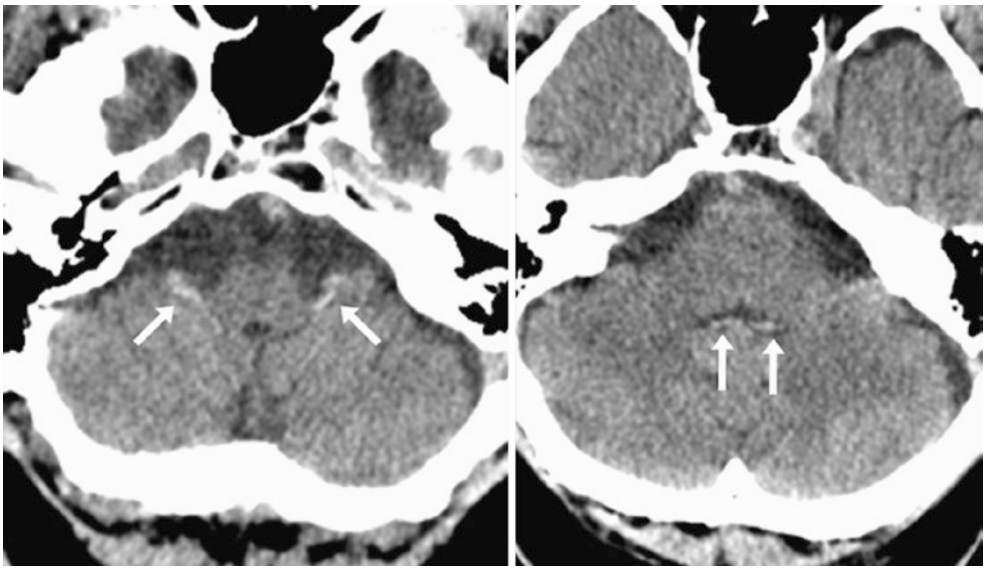

Fig. 11.6 A 54-year-old patient with mild to moderately calcified CP (*arrows*) within the foramina of Luschka bilaterally on NECT (*left*) and within the fourth ventricle (*right*), which simulated hemorrhage in a trauma patient

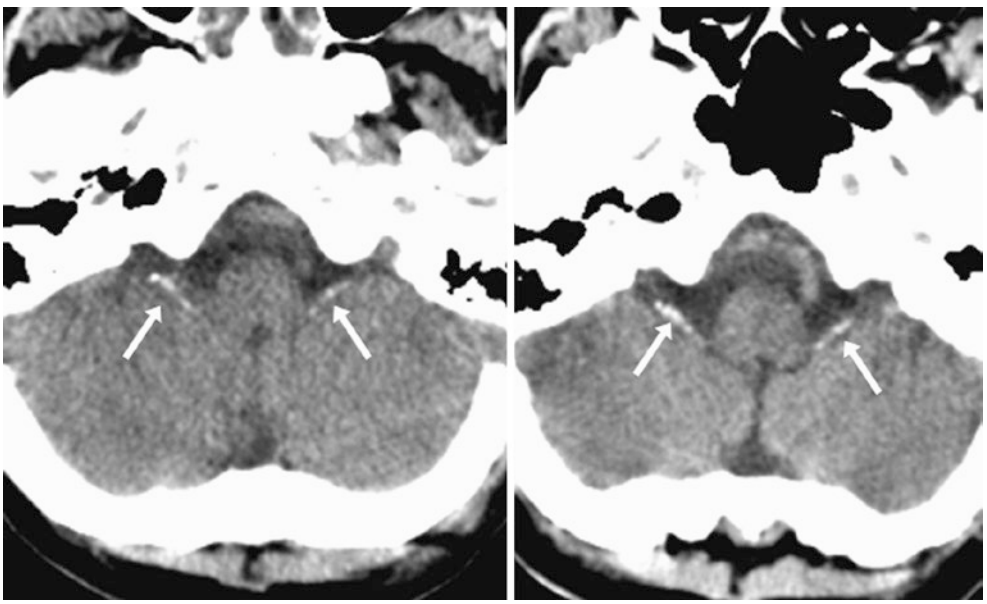

Fig. 11.7 A 58-year-old patient with moderately calcified CP (*arrows*) within the foramina of Luschka bilaterally on NECT

Fig. 11.8 An 82-year-old patient with bilateral CP calcifications (*arrows*) within the foramina of Luschka on NECT. Dense CP within the fourth ventricle (*thin arrow*) mimics hemorrhage

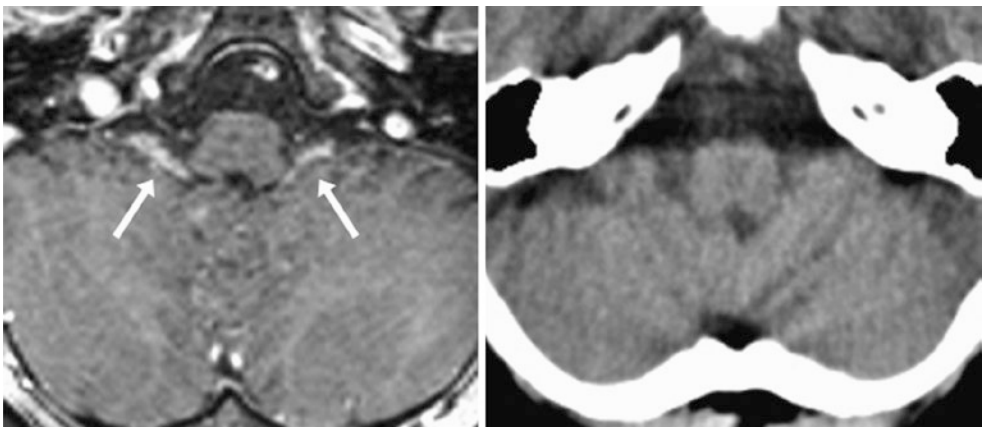

Fig. 11.9 A 6-year-old with headaches who underwent a negative 3TMRI. CP enhancement was noted (*arrows*) within the foramina of Luschka bilaterally on postcontrast T1WI (*left*) but is invisible on NECT (*right*) because it is noncalcified

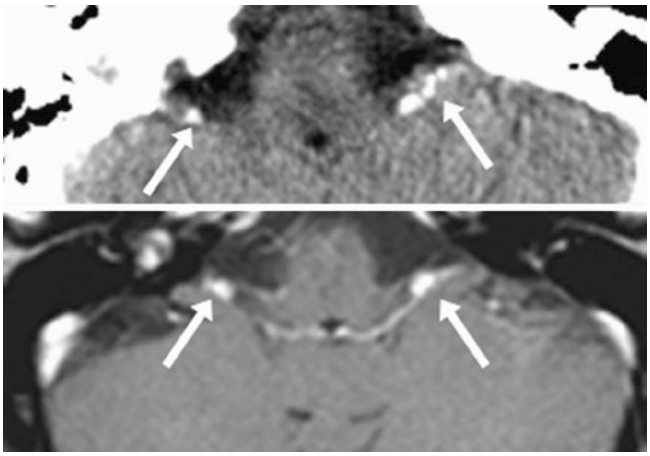

Fig. 11.10 A 52-year-old patient; CP on NECT (*top*) in the foramina of Luschka (*arrows*) enhance on postcontrast T1WI (*bottom*)

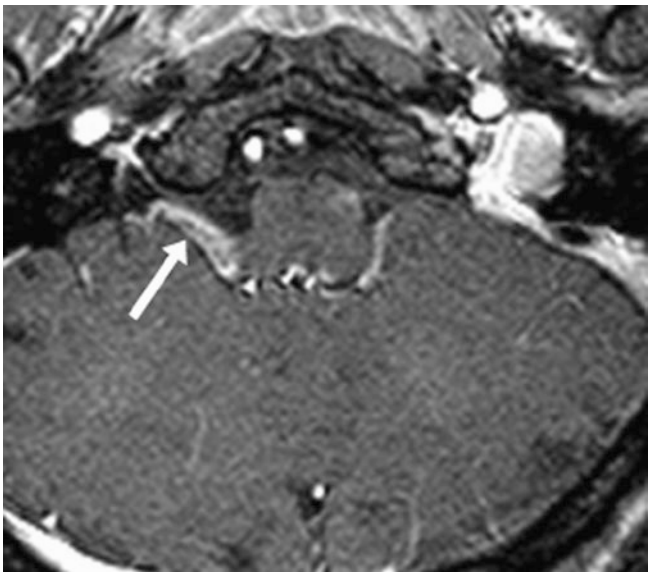

Fig. 11.11 A 34-year-old patient; postcontrast T1WI shows unilaterally prominent CP (*arrow*) in the right foramen of Luschka, simulating a cerebellopontine angle lesion

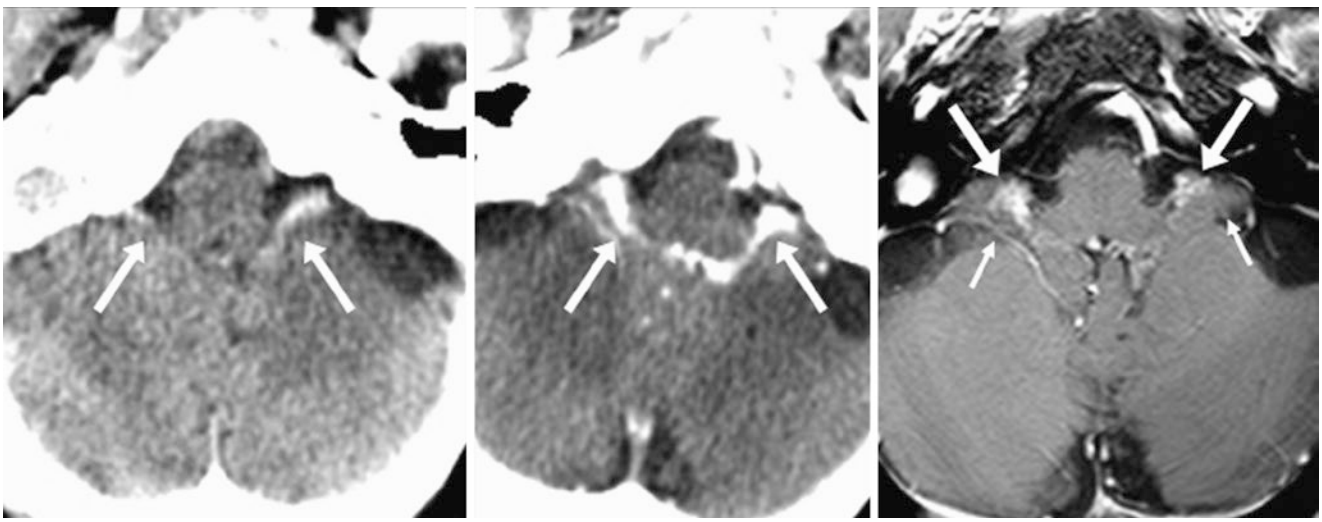

Fig. 11.12 A 49-year-old patient with mildly calcified CP (*arrows*) within the foramina of Luschka on NECT (*left*), which enhances avidly on CECT (*middle*) and on postcontrast T1WI (*right*). Note the flocculi of the cerebellum (*thin arrows*) lateral to the CP

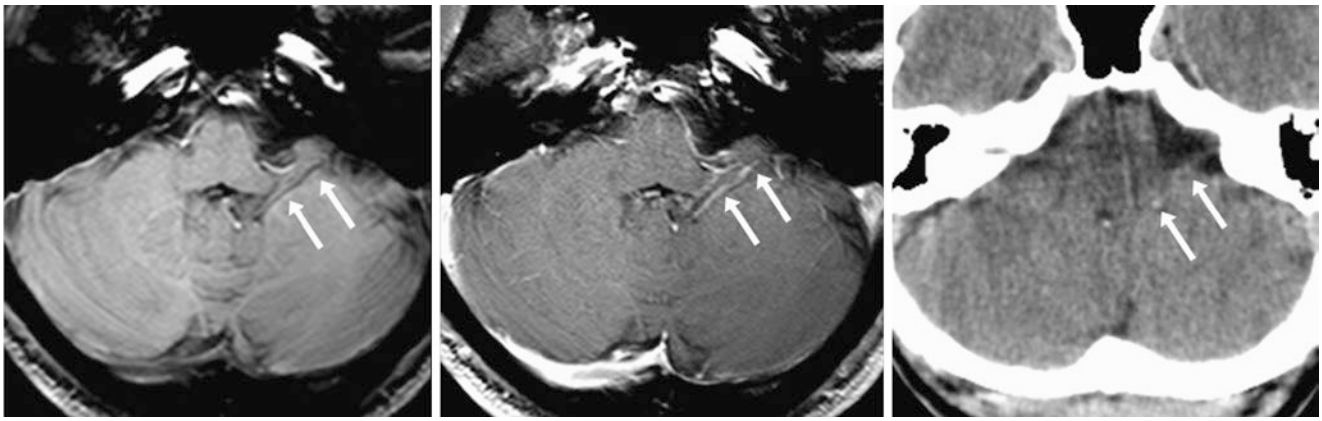

Fig. 11.13 A 49-year-old patient with CP (*arrow*) within the left foramen of Luschka simulating a cerebellopontine angle lesion on noncontrast T1WI (*left*), which mildly enhances after contrast administration on T1WI (*middle*) and is only slightly calcified on NECT (*right*). The asymmetry is also exacerbated by the fact that the patient's head is slightly tilted

Fig. 11.14 A 42-year-old patient with the CP within the right foramen of Luschka that is relatively invisible on noncontrast FLAIR (*left*). However there is moderate, linear enhancement within the right foramen of Luschka extending into the fourth ventricle on postcontrast FLAIR (*middle*) and T1WI (*right*). This CP enhancement simulates leptomeningeal inflammation

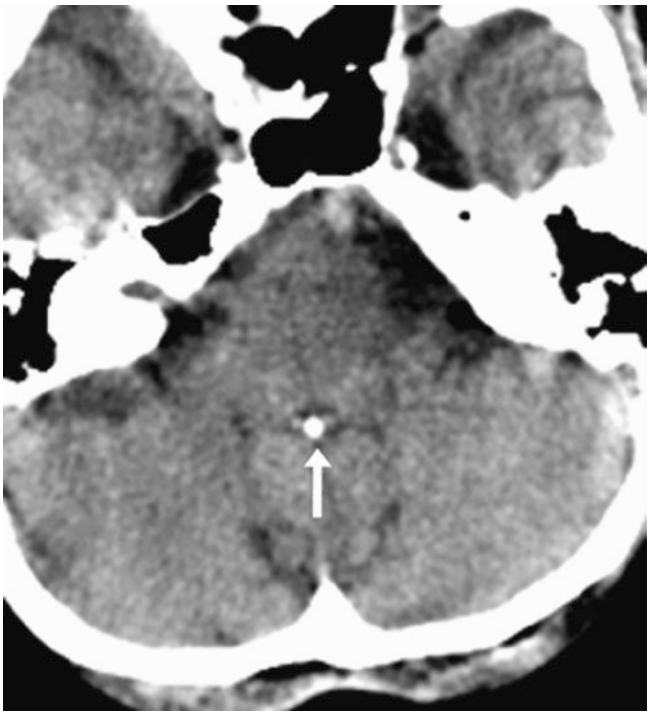

Fig. 11.15 An 87-year-old patient with calcified CP (*arrow*) located centrally within the fourth ventricle on NECT

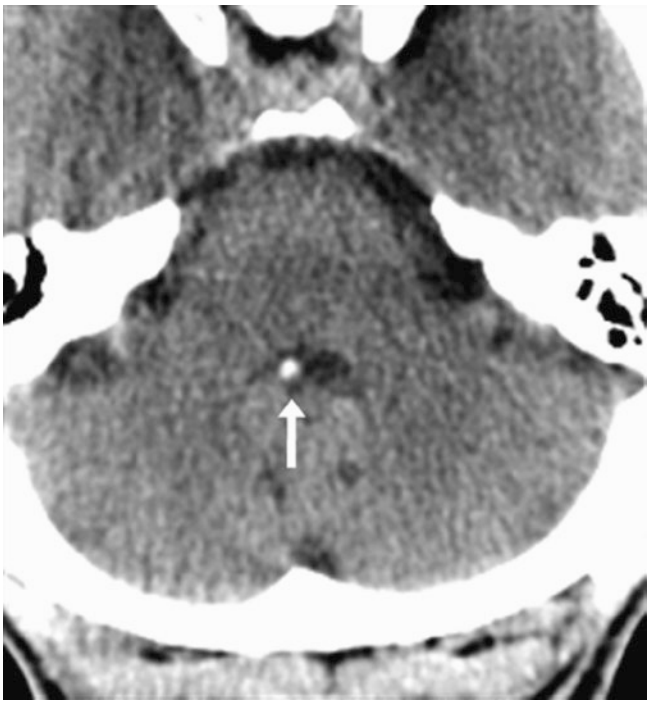

Fig. 11.17 A 36-year-old patient with calcified CP (*arrow*) situated just to the right of the midline of the fourth ventricle on NECT

Fig. 11.16 A 40-year-old patient with calcified CP (*arrow*) located centrally within the fourth ventricle on NECT

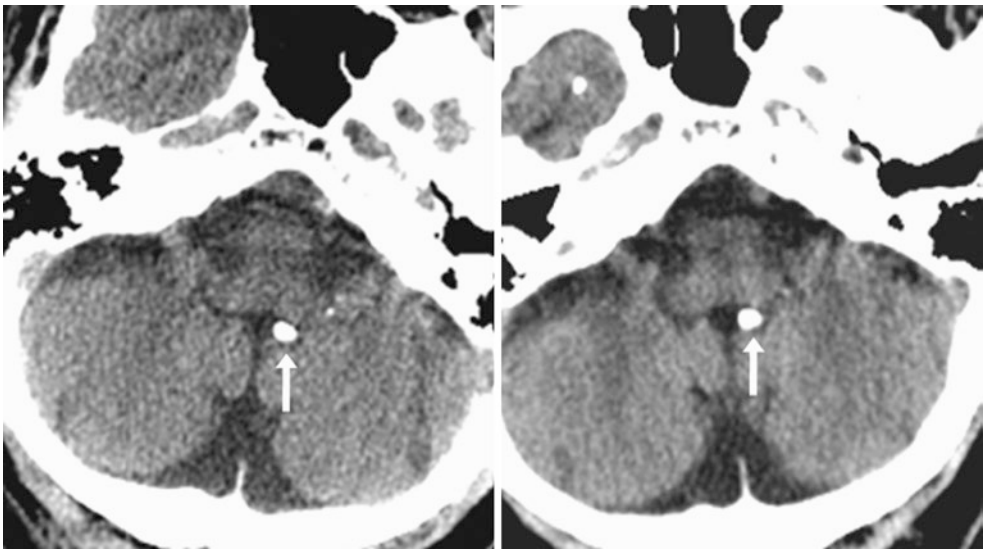

Fig. 11.18 A 74-year-old patient with calcified CP (*arrow*) located just left of the midline within the fourth ventricle on NECT (*left*). It was unchanged at 1 year (*right*)

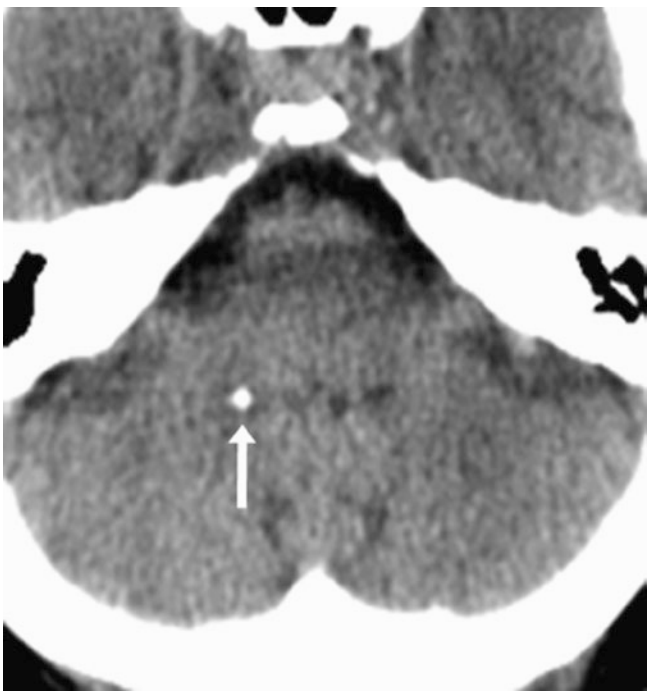

Fig. 11.19 A 45-year-old patient with calcified CP (*arrow*) of the lateral fourth ventricle on NECT

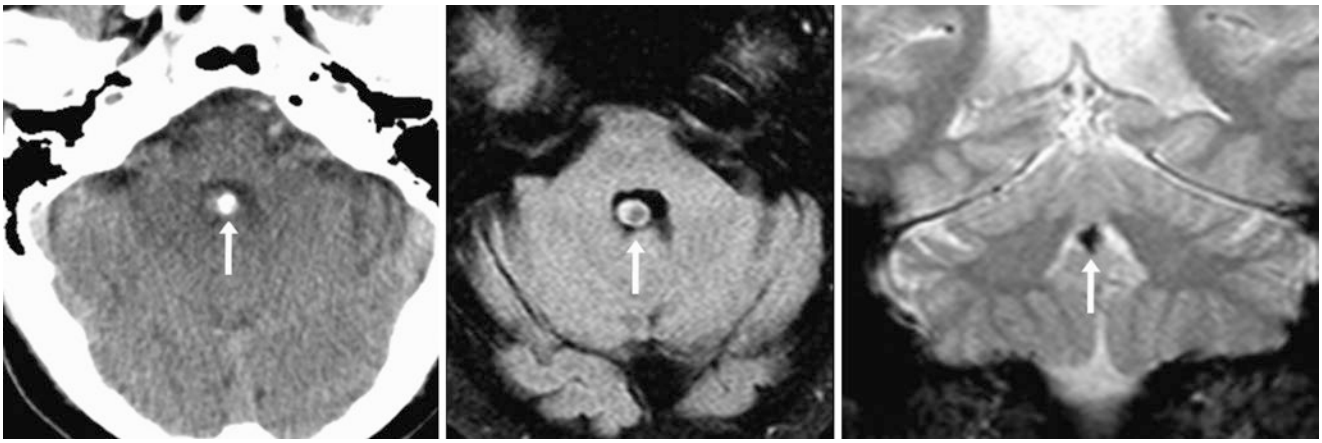

Fig. 11.20 A 36-year-old patient with calcified CP (*arrow*) within the fourth ventricle along the cerebellar nodulus on axial NECT (*left*). On a 1.5 T MRI, the CP produced focal susceptibility artifact on axial FLAIR images (*middle*) caused by calcium, which was confirmed on coronal T2*WI (*right*). Such focal calcium could simulate a postinfectious or post-traumatic lesion

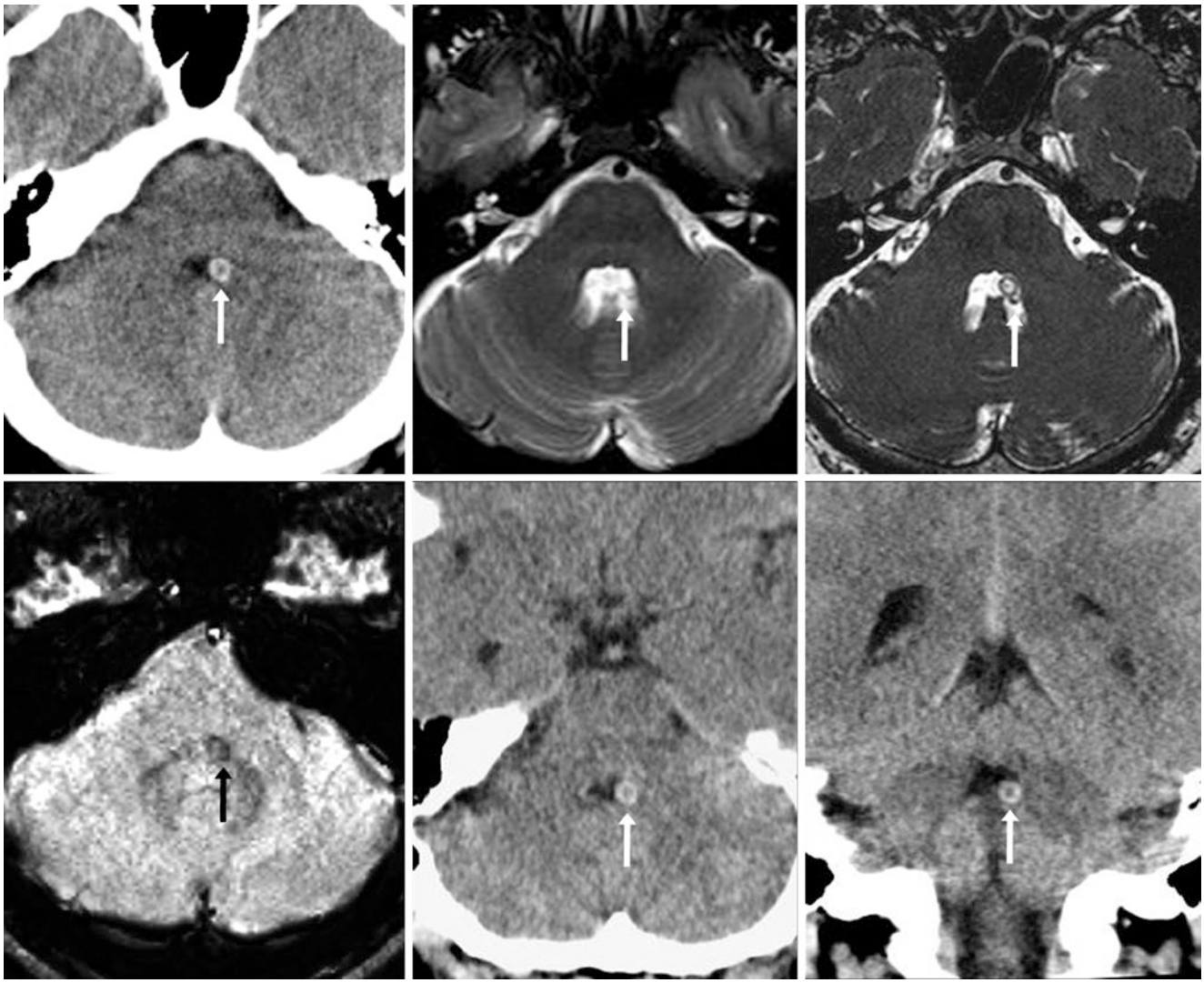

Fig. 11.21 A 44-year-old patient with headaches and calcified CP (*arrows*) within the fourth ventricle on NECT (*top left*). On a 1.5 T MRI the CP is seen not on spin-echo T2WI (*top middle*) but is visualized on a balanced three-dimensional T2WI (*top right*), a sequence that accentuates CSF signal intensity. The CP produces focal susceptibility artifact on SWI (*bottom left*). One month later, axial (*bottom middle*) and coronal (*bottom right*) reconstructions from a NECT show no change. This simulates a postinfectious lesion such as neurocysticercosis, although no other lesions were noted

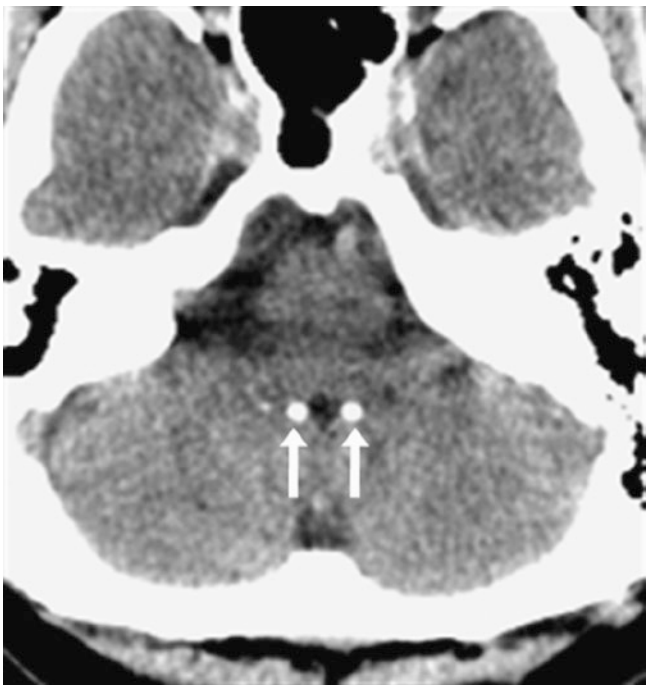

Fig. 11.22 A 36-year-old patient with bilaterally calcified CP (*arrows*) just lateral to the midline of the fourth ventricle on NECT

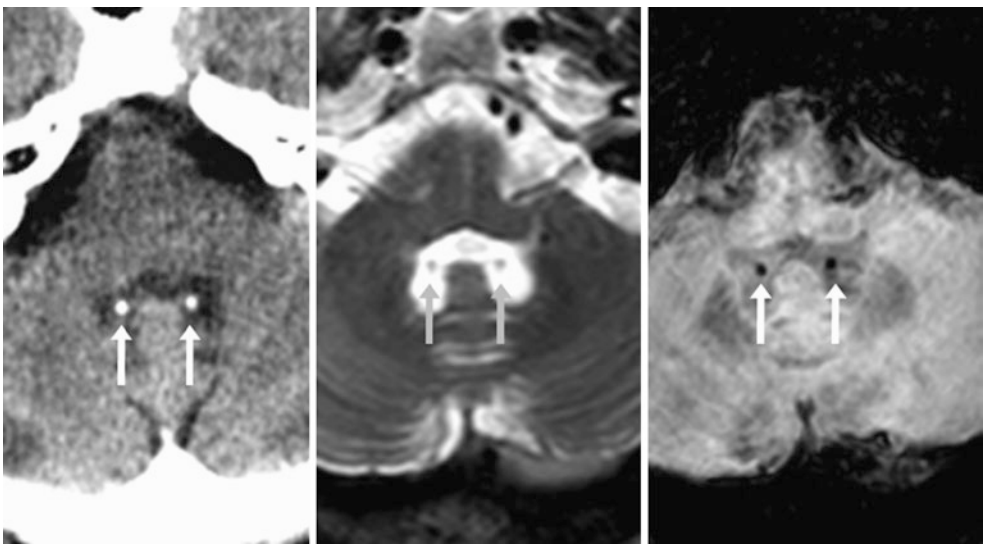

Fig. 11.23 A 53-year-old patient with bilaterally calcified CP (*arrows*) within the fourth ventricle on NECT (*left*), on 3 T T2WI (*middle*), and on SWI (*right*). The calcifications cause the susceptibility effect on SWI

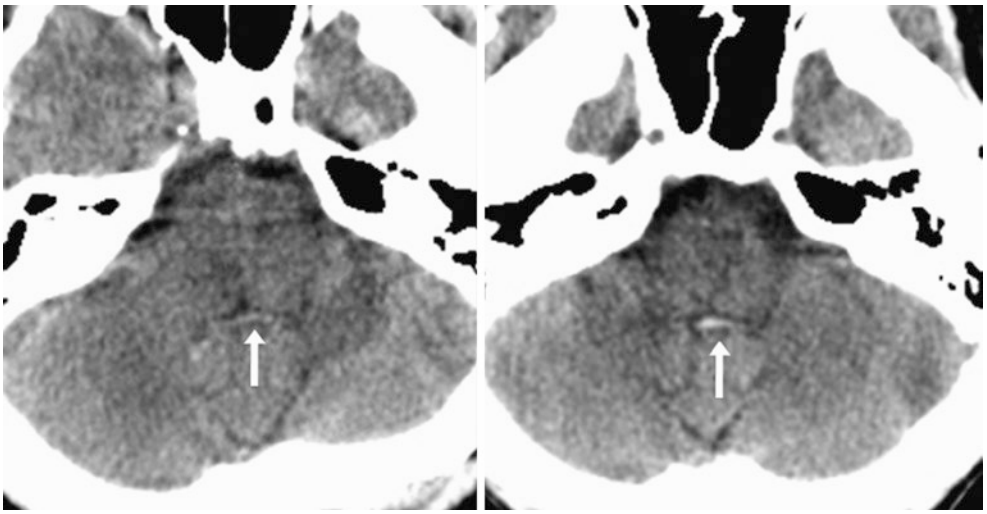

Fig. 11.24 A 35-year-old patient with trauma who had a partially calcified CP (*arrow*) of the fourth ventricle on NECT (*left*). Its location was unchanged 4 years later, but it became more hyperdense (*right*), which could simulate hemorrhage

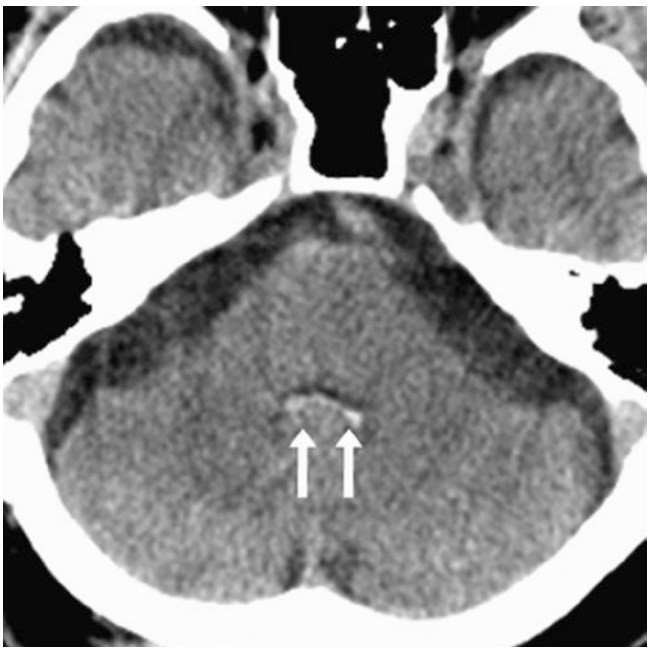

Fig. 11.25 A 61-year-old patient with altered mental status and partially calcified CP (*arrow*) of the fourth ventricle on NECT

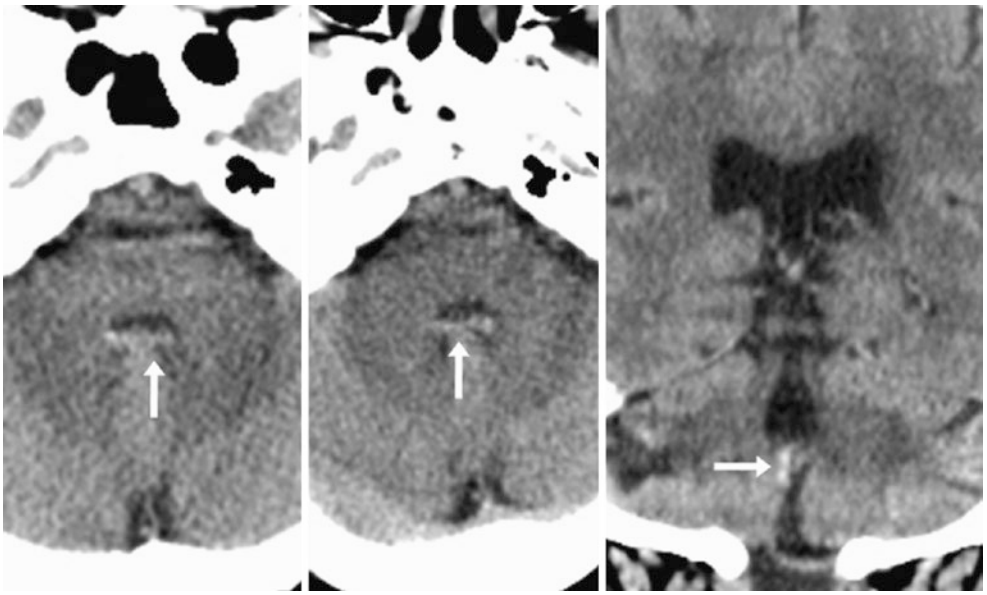

Fig. 11.26 A 66-year-old patient with trauma and a partially calcified CP (*arrow*) of the fourth ventricle on NECT (*left*) that simulated hemorrhage. Its location was unchanged 9 months later (*middle*). Coronal reformats (*right*) at that time more clearly demonstrate this to be CP

Fig. 11.27 An 80-year-old with acute weakness and a bilaterally calcified CP (*arrows*) just lateral to the midline of the fourth ventricle on NECT

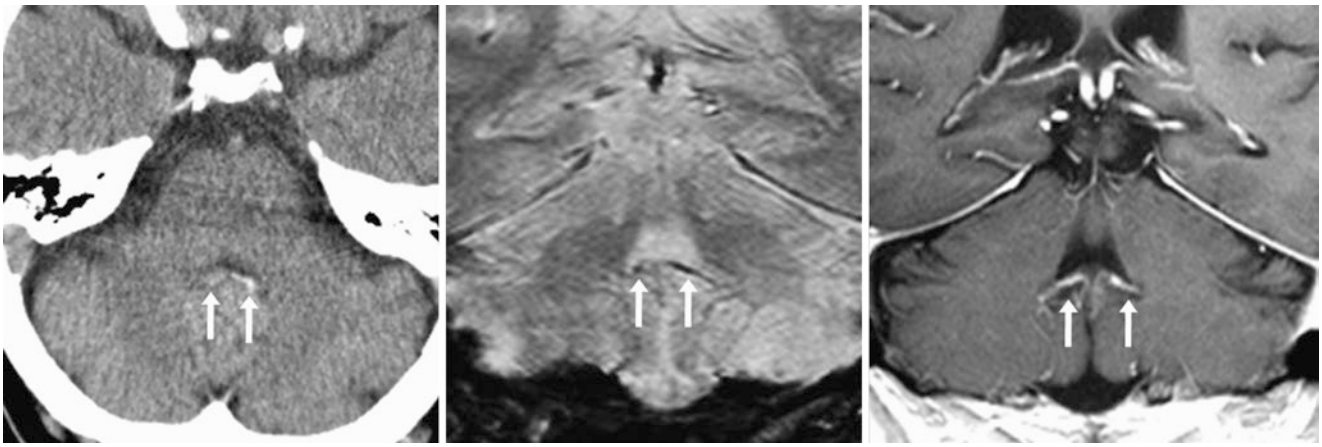

Fig. 11.28 A 67-year-old patient with partially calcified CP (*arrows*) of the fourth ventricle on axial NECT (*left*), mimicking subarachnoid hemorrhage (SAH). A 3 T MRI confirmed that this was CP since there was susceptibility effect from the calcium on coronal GE T2*WI (*middle*), and CP enhanced avidly on coronal postcontrast T1WI (*right*)

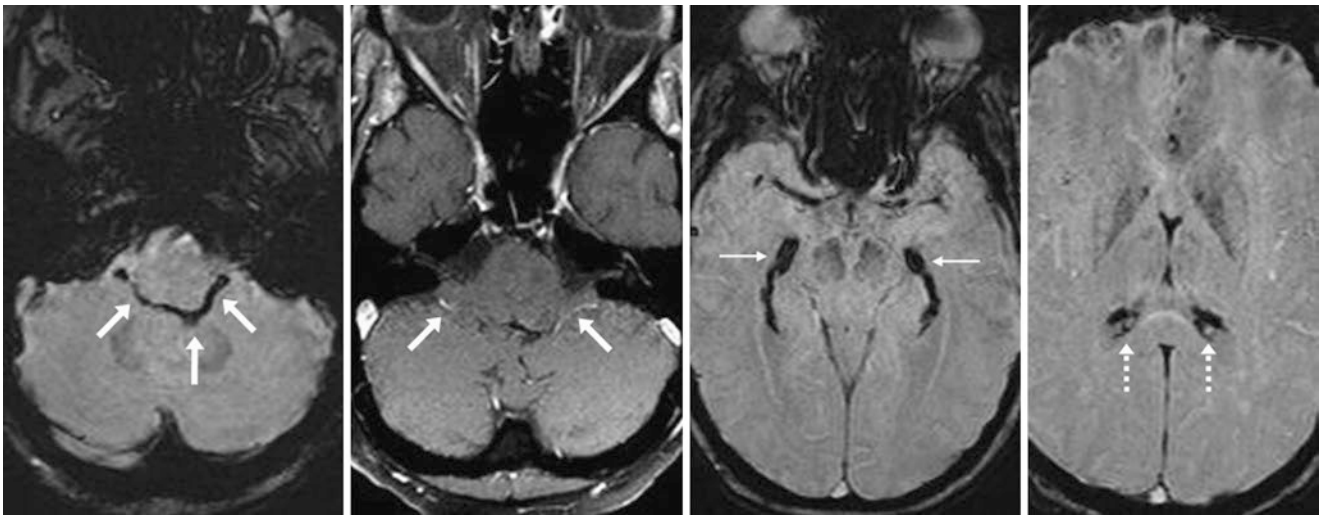

Fig. 11.29 A 53-year-old patient with weakness. There was calcified CP (*arrows*) throughout the fourth ventricle and foramina of Luschka on 1.5 T MRI axial SWI (*left*) simulating SAH, but the CP enhanced mildly on postcontrast T1WI (*left middle*). The CP is also prominent in the temporal horns of the lateral ventricles (*thin arrows*, *right middle*) and atria (*dotted arrows*, *right*)

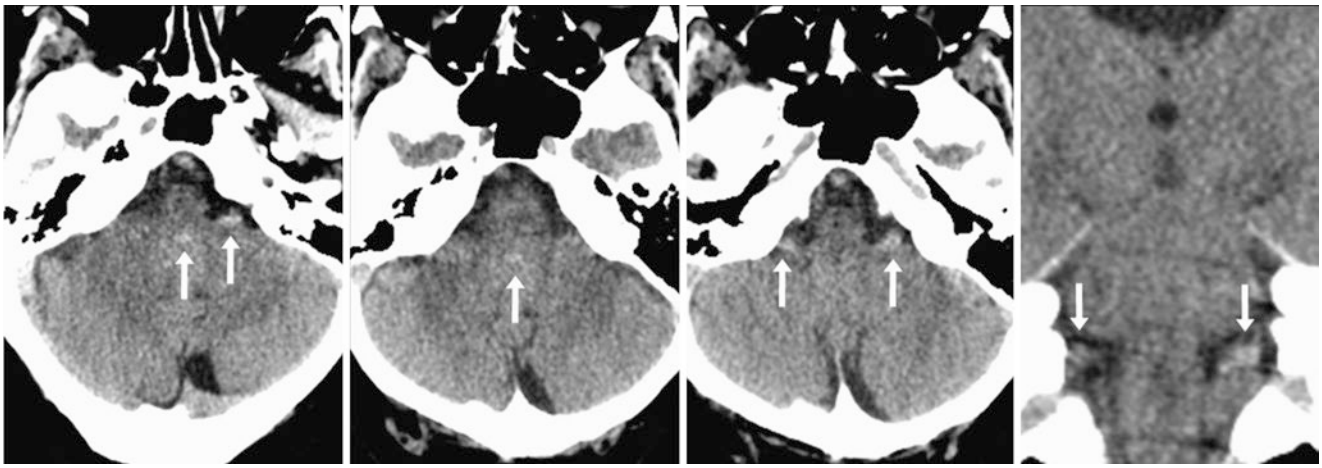

Fig. 11.30 A 67-year-old patient with headaches with mildly calcified CP (*arrows*) within the fourth ventricle and laterally along the left flocculus on axial NECT (*left*) that simulated SAH. Hemorrhage was not found elsewhere. Reangled images (*left middle and right middle*) showed that these were in nondependent locations and that the CP calcifications along the cerebellar flocculi were bilateral, as confirmed on coronal reformats (*right*)

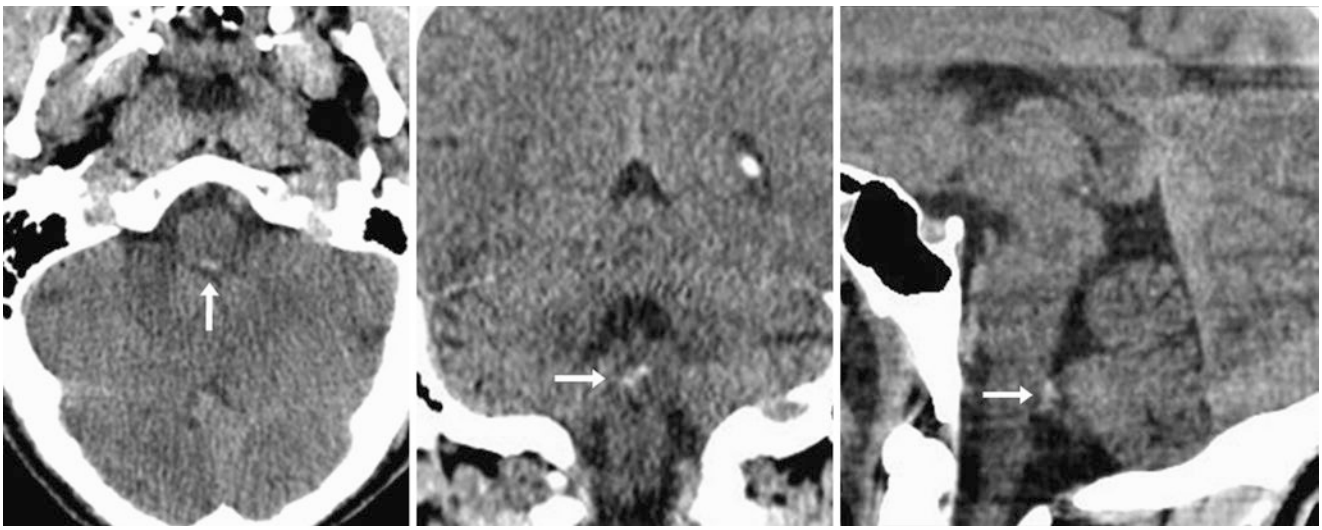

Fig. 11.31 A 30-year-old patient with altered mental status and with mildly calcified CP (*arrows*) within the fourth ventricle on axial NECT (*left*) that simulated SAH. Hemorrhage was not noted elsewhere intracranially. Note that the focus is not located in a dependent location on coronal (*middle*) and sagittal (*right*) reconstructions

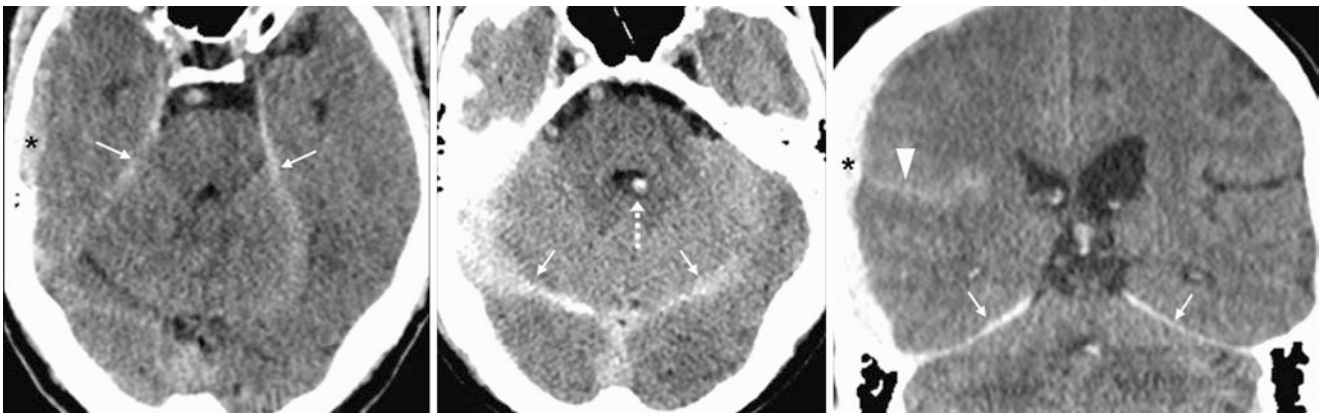

Fig. 11.32 Comparison case of fourth ventricular hemorrhage. The patient was a 48 year old with trauma; NECT (*left*) showed subdural hemorrhage along the temporal convexity (*) and tentoria (*thin arrows*). A NECT 6 h later (*middle*) found new fourth ventricular (*dotted arrow*) and sylvian fissure (*arrowhead*) subarachnoid hemorrhage on coronal views (*right*)

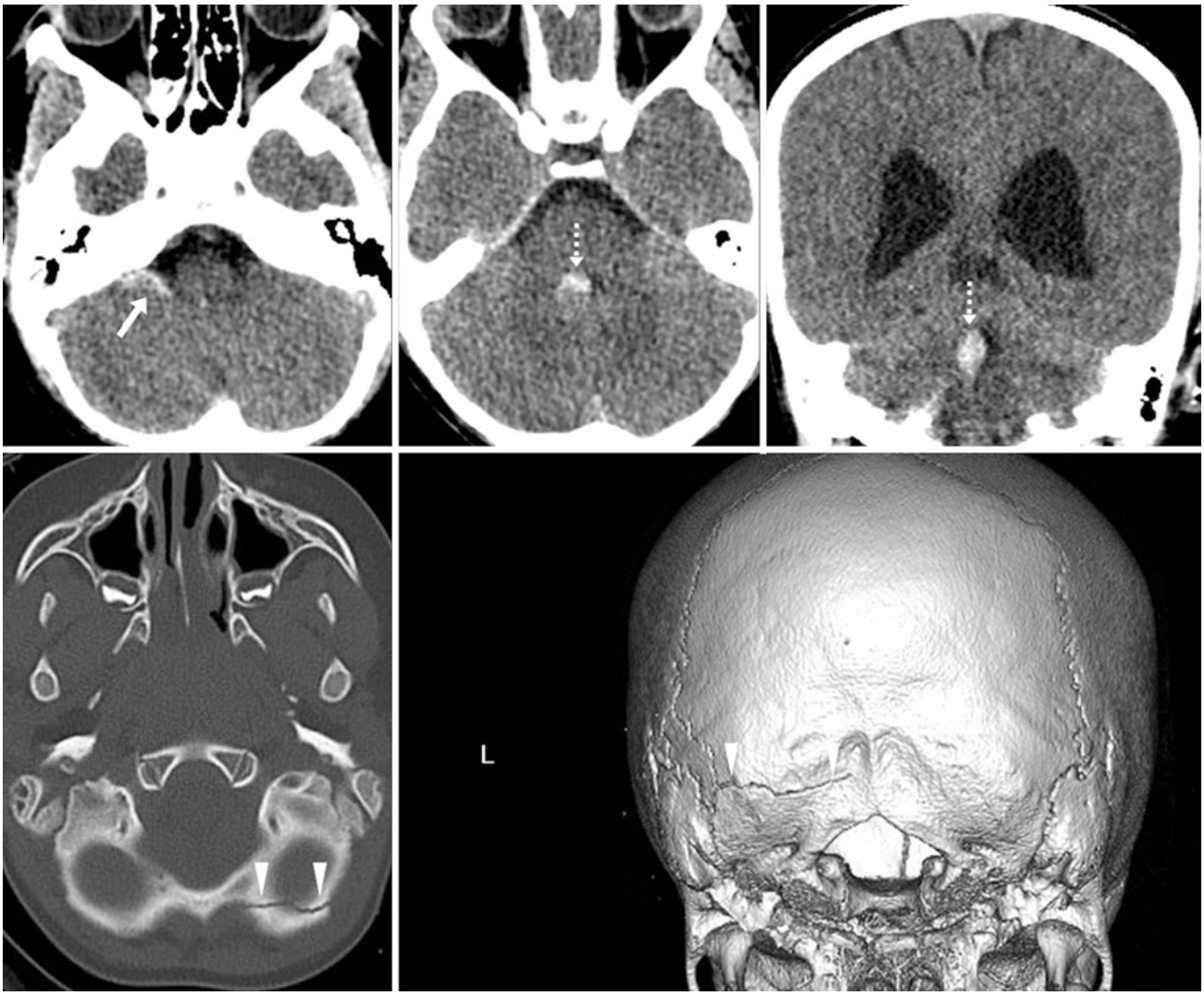

Fig. 11.33 Comparison case of traumatic hemorrhage. The patient was a 5-year-old child with trauma. An axial NECT (*top left and middle*) showed subarachnoid hemorrhage focally solely within the right foramen of Luschka (*arrows*) and the fourth ventricle (*dotted arrows*), also confirmed on coronal reformat (*top right*). Bone windows (*bottom left*) found a left occipital skull fracture (*arrowheads*). On a three-dimensional volume rendered posteroanterior view (i.e., view from posteriorly, *bottom right*), the fracture line is noted; it involves only the left occipital calvarium

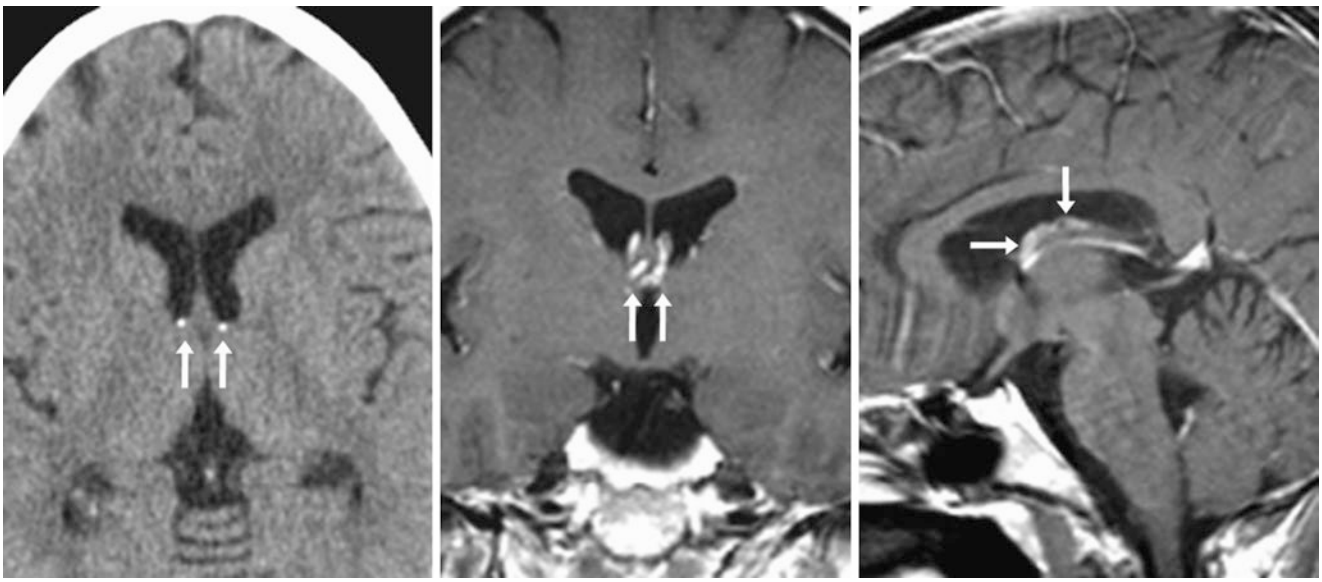

Fig. 11.34 A 34-year-old with altered mental status with bilateral, punctate CP calcifications (*arrows*) of the foramina of Monro on axial NECT (*left*). On postcontrast coronal T1WI MRI (*middle*), avid enhancement confirms CP in that location, as the extent of the enhancement on T1WI MRI is actually larger than the areas of calcified foci on NECT. Sagittal T1WI (*right*) illustrates enhancing CP of the right foramen of Monro and lateral ventricle

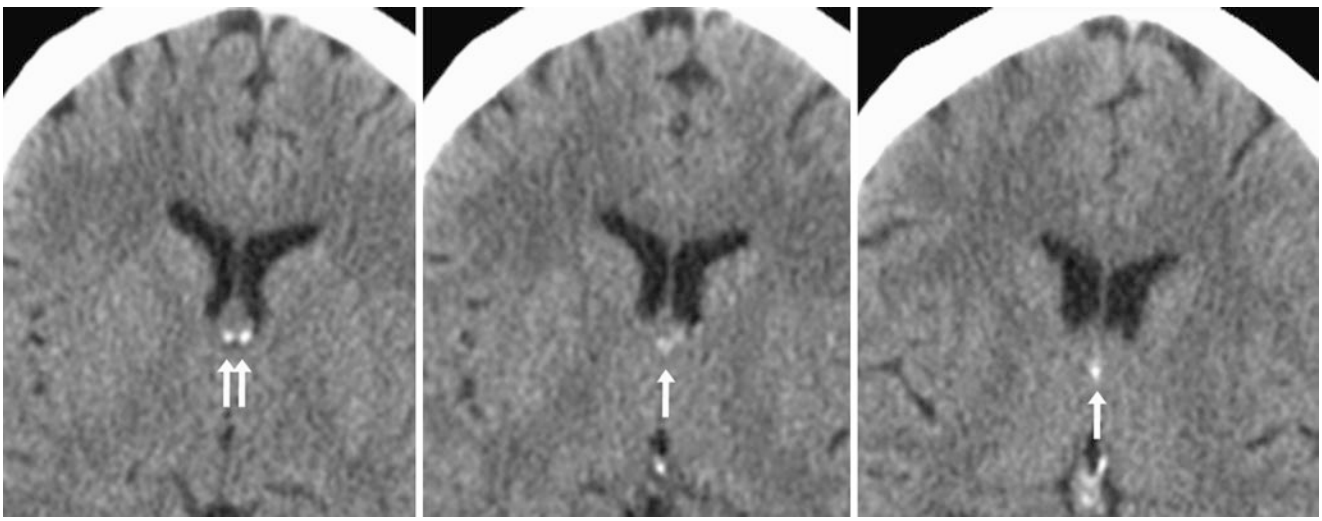

Fig. 11.35 A 36-year-old patient was given a NECT that depicts calcified CP bilaterally within the foramina of Monro (*arrows*) on NECT (*left*). There is also a partially calcified CP of the third ventricle on other images (*middle and right*), simulating hemorrhage. Note that the CP in this case is confluent through these locations and varies in the degree of calcification

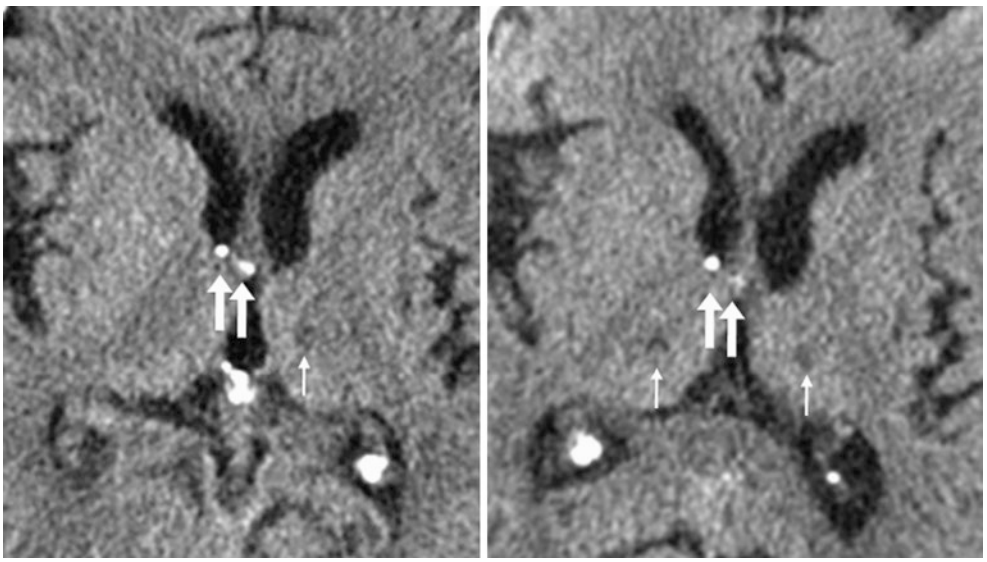

Fig. 11.36 A 57-year-old patient with asymmetric calcified CP (*arrows*) of the anterior third ventricle on NECT (*left*). This appearance was unchanged 2 years later on NECT (*right*). Note small infarcts within the thalami (*thin arrows*)

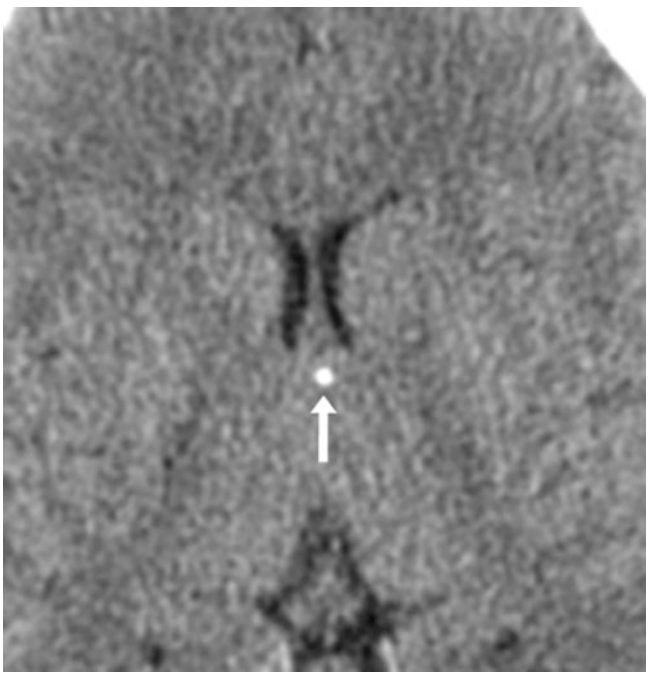

Fig. 11.37 A 29-year-old patient with a calcified CP (*arrow*) of the anterior third ventricle on NECT

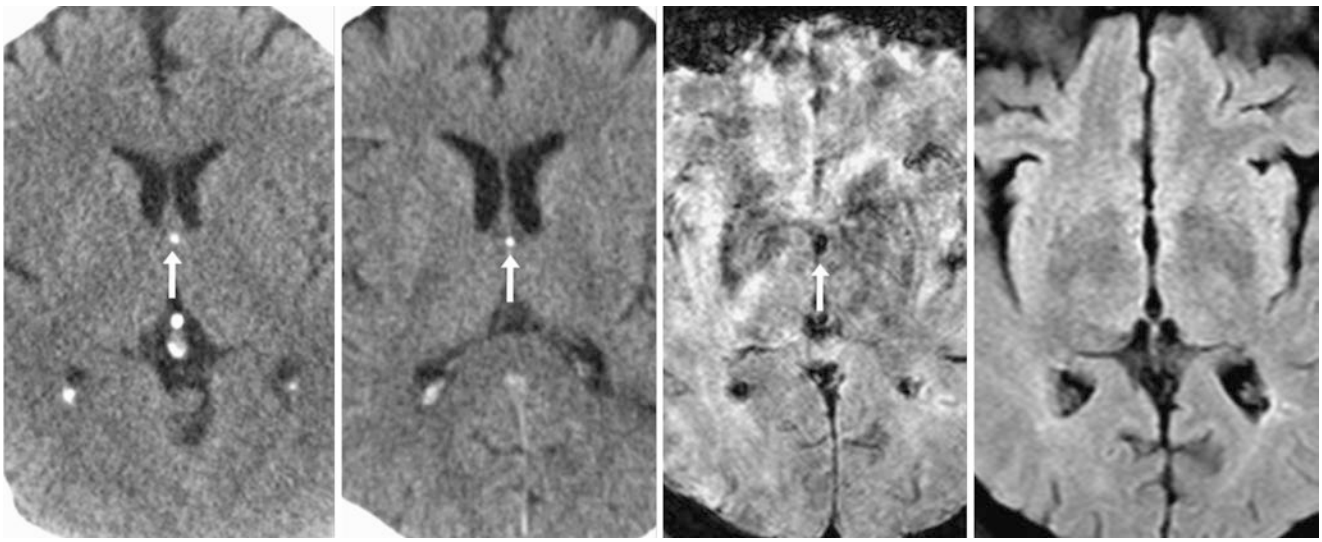

Fig. 11.38 A 53-year-old patient with a calcified CP (*arrow*) of the ventral third ventricle on NECT (*left*) simulating hemorrhage or a colloid cyst. Its location and appearance were unchanged 4 years later (*left middle*). SWI MRI at 1.5 T (*right middle*) depicted a focal susceptibility artifact in that location from calcification, whereas FLAIR (*right*) was normal

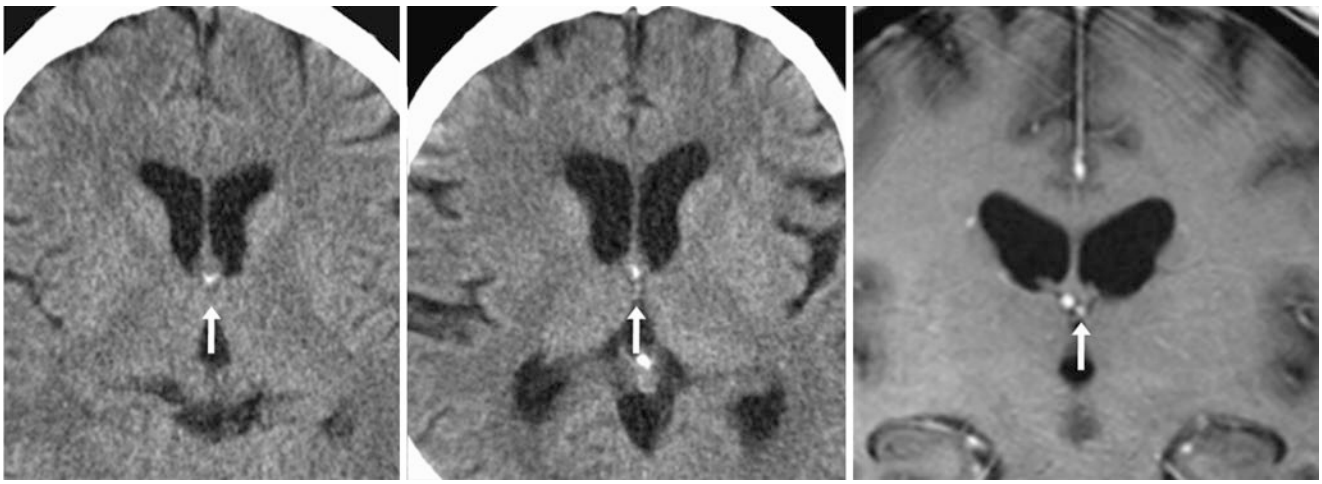

Fig. 11.39 A 62-year-old with a partially calcified lesion (*arrows*) on NECT (*left*) within the anterior third ventricle that did not change 9 months later (*middle*). On a 3 T MRI that included postcontrast coronal T1WI (*right*), this was found to be a CP that moderately enhanced with contrast

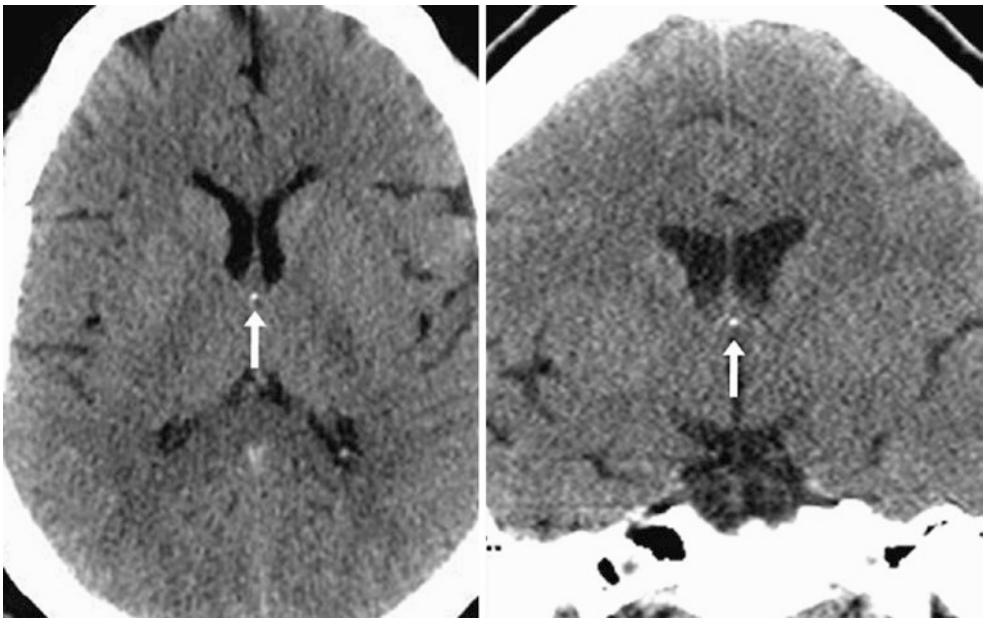

Fig. 11.40 A 46-year-old patient with a tiny calcified CP (*arrow*) of the ventral third ventricle on NECT axial (*left*) and on coronal (*right*) reconstructions

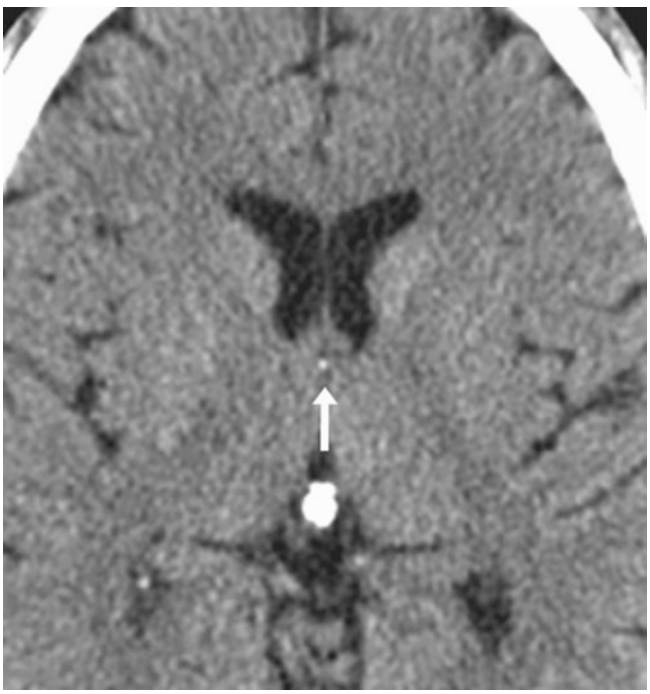

Fig. 11.41 A 46-year-old patient with a tiny, barely calcified CP (*arrow*) of the third ventricle on NECT

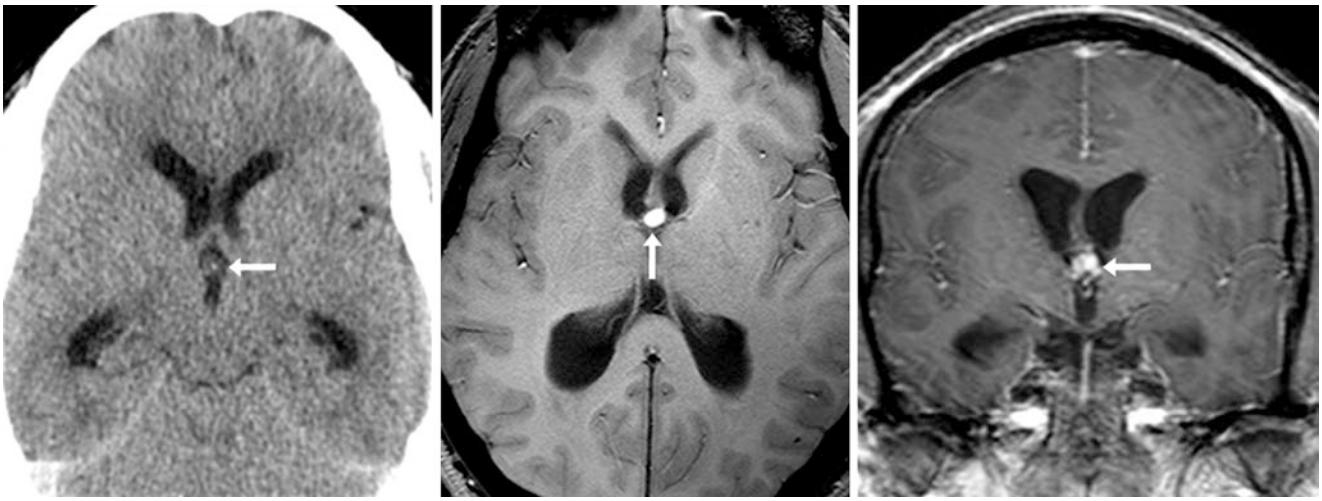

Fig. 11.42 Comparison case of neurocysticercosis (colloidal vesicular phase): a 27-year-old patient with hydrocephalus. An intermediate density lesion (*arrows*) in the third ventricle on NECT (*left*) was bright on noncontrast T1WI (*right*) and obstructed CSF flow. A colloid cyst may appear similar on MRI but is usually hyperdense on CT

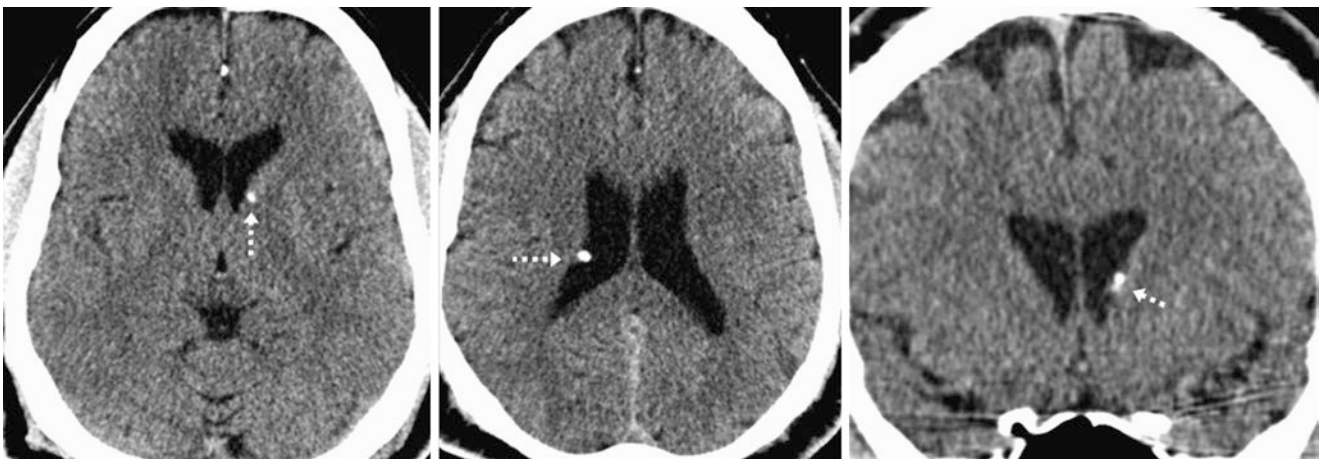

Fig. 11.43 Comparison case of tuberous sclerosis: a 33-year-old male patient with tuberous sclerosis had a subependymal calcified lesion just above the left foramen of Monro (*dotted arrows*) on axial (*left two images*) and coronal (*right*) reformats from a NECT. These may calcify over time and/or enhance with contrast medium

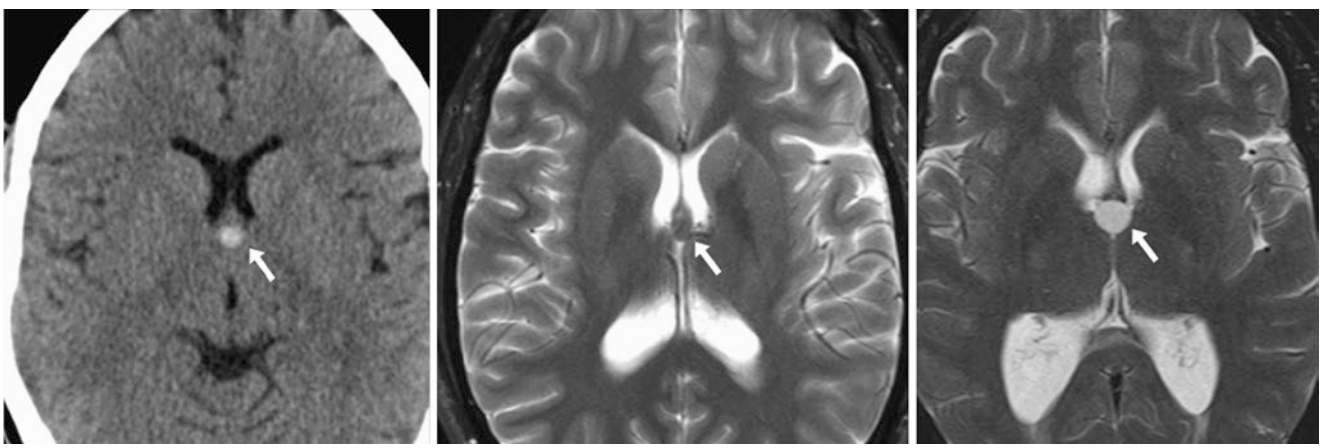

Fig. 11.44 Comparison case of colloid cyst: a 25-year-old patient had a hyperdense lesion (noncalcified) at the midline within the anterior third ventricle on NECT (*left*) and on T2WI MRI (*middle*) without hydrocephalus. The patient returned 5 years later with neurologic symptoms, as the cyst had enlarged on T2WI (*right*) with enlarging lateral ventricles. Note the characteristic location

Fig. 11.45 An 87-year-old patient with calcified CP (*arrow*) within the right choroidal fissure on NECT

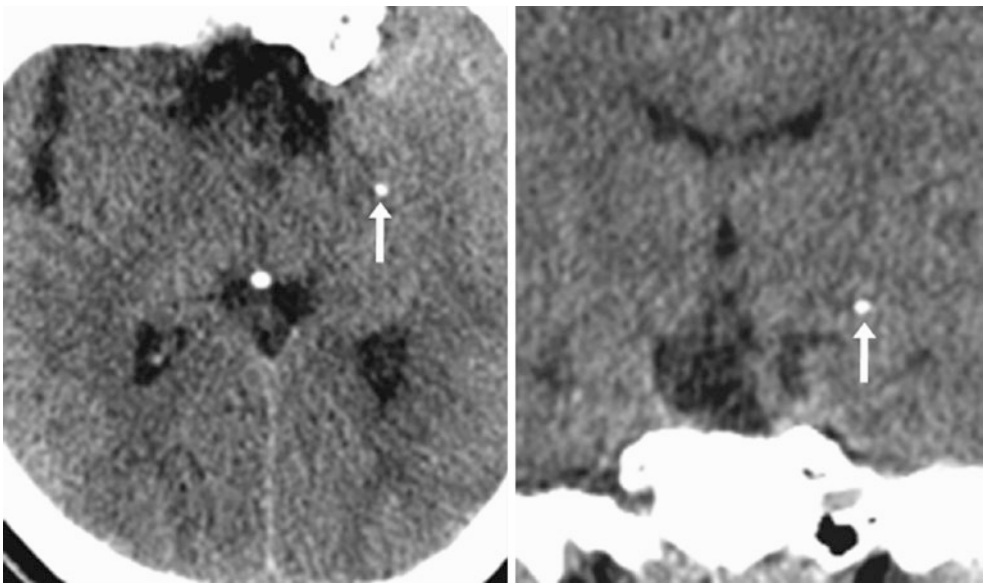

Fig. 11.46 A 53-year-old patient with NECT with calcified CP (*arrows*) within the left CF on NECT (*left*). A coronal reformat (*right*) further depicts the calcification

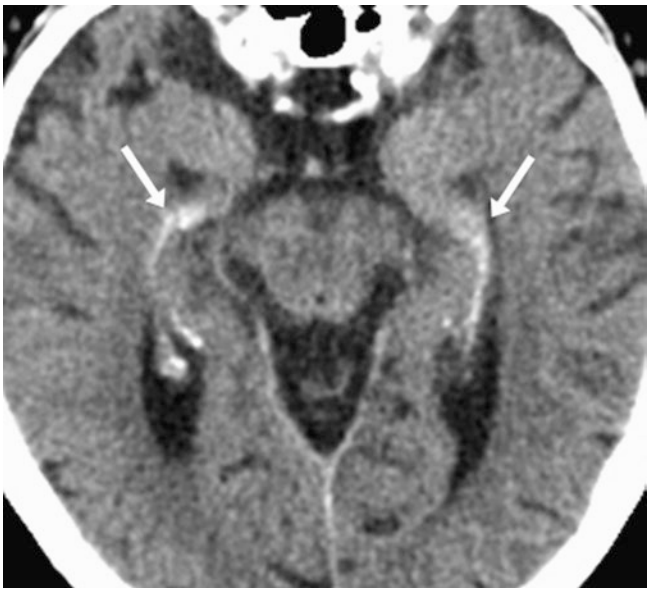

Fig. 11.47 A 65-year-old patient; NECT depicts bilateral partially calcified CP (*arrows*) in the temporal horns

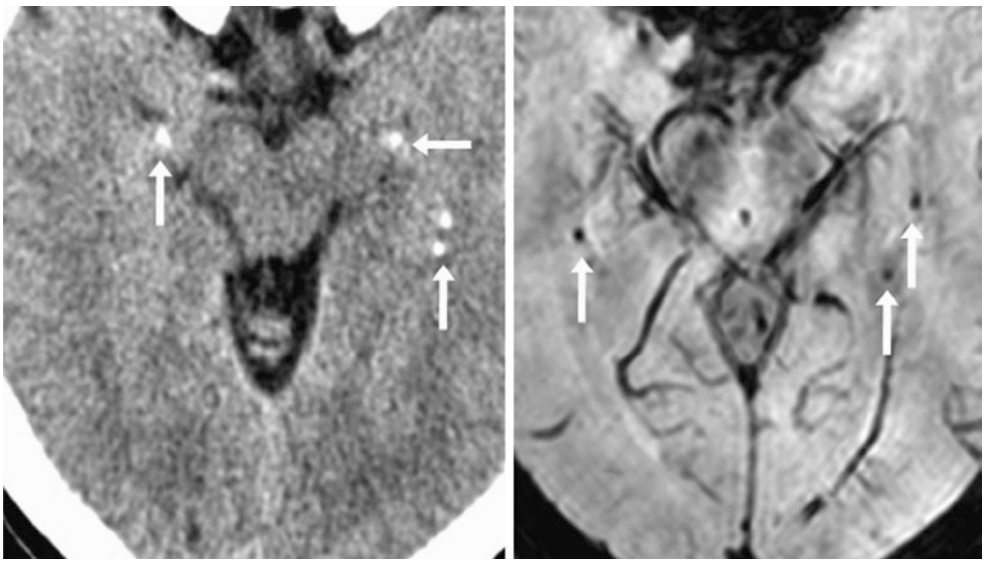

Fig. 11.48 A 61-year-old patient with bilateral CP (*arrows*) within the temporal horns on NECT (*left*). On SWI (*right*), some CP has a dark signal from calcium

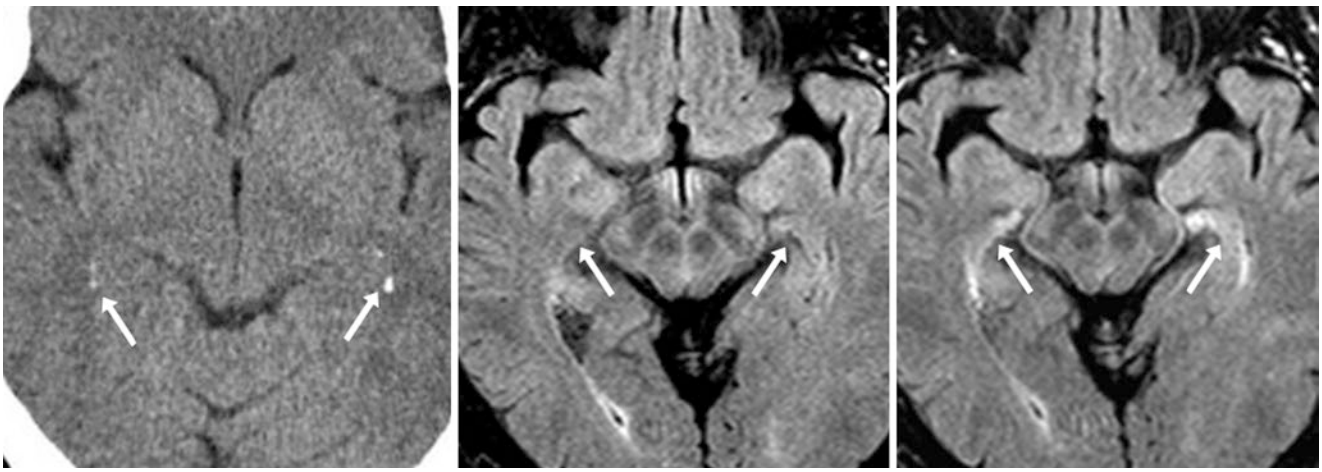

Fig. 11.49 A 57-year-old patient with NECT (*left*) that shows calcified CP with the temporal horns bilaterally (*arrows*). On noncontrast axial FLAIR MRI (*middle*), the CP is nearly invisible. However, on postcontrast FLAIR (*right*), the CP enhances moderately, illustrating how it is actually much larger than the calcified portions

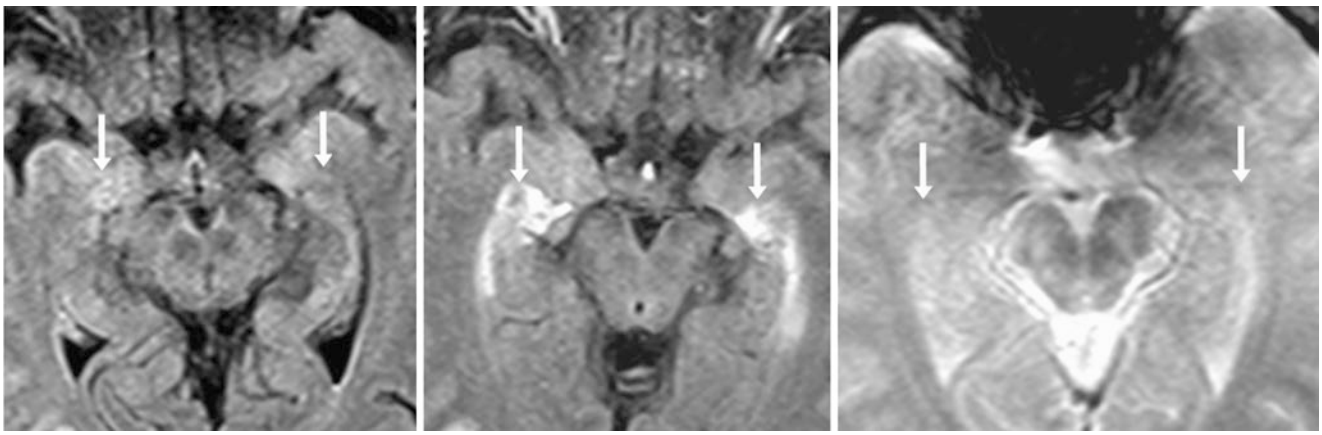

Fig. 11.50 A 61-year-old patient with CP visualized (*arrows*) on noncontrast FLAIR images (*left*) and with quite avid enhancement on postcontrast FLAIR images (*middle*), which occurs because the CP lacks a blood–brain barrier. GE T2*WI (*right*) does not depict any dark foci of susceptibility within the CP, suggesting a lack of calcium within the CP

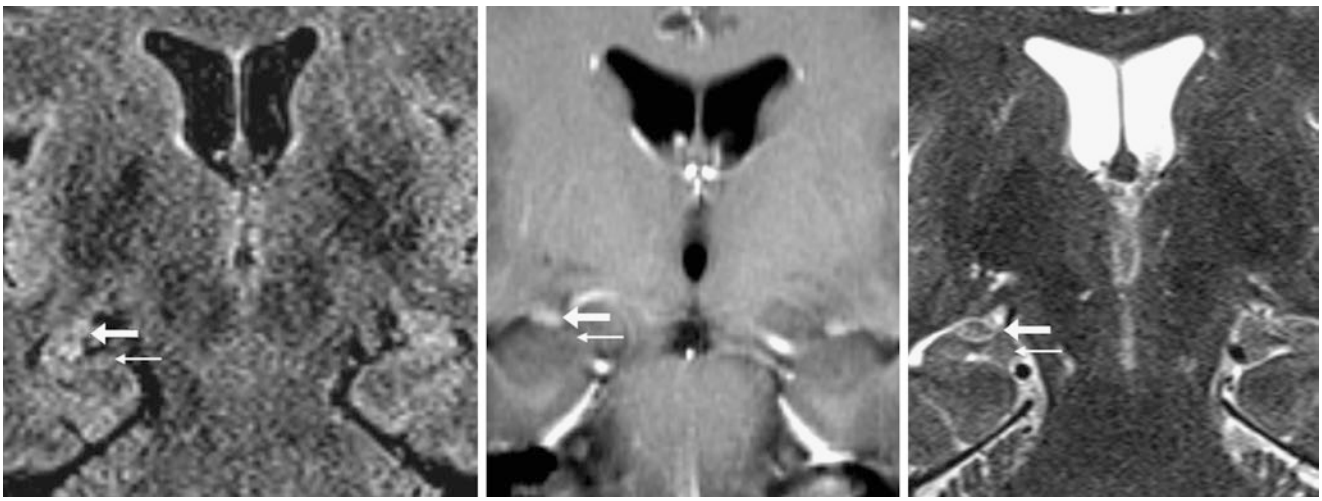

Fig. 11.51 A 59-year-old patient with a seizure. A 3 T MRI with coronal FLAIR images (*left*) demonstrated a bright signal (*arrows*) overlying the right hippocampus that initially simulated a hippocampal lesion such as mesial temporal sclerosis. However, this region enhanced on postcontrast T1WI (*middle*) and was found to be within the choroidal fissure on T2WI (*right*) consistent with CP. Note the normal hippocampus just inferior to the CP (*thin arrows*)

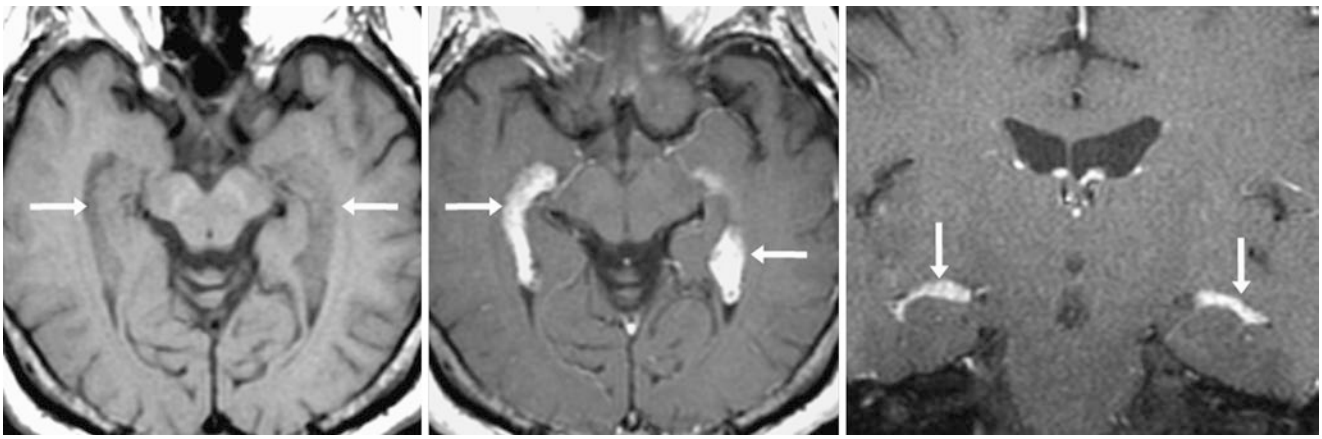

Fig. 11.52 A 57-year-old patient was given a 1.5 T MRI, including an axial T1WI (*left*) that demonstrated a prominent CP (*arrows*) within the trigones and temporal horns that avidly enhanced on postcontrast axial (*middle*) and coronal (*right*) T1WI. This was consistent with normal, prominent CP within the choroidal fissure. Note the normal hippocampus just inferior to that (*thin arrows*)

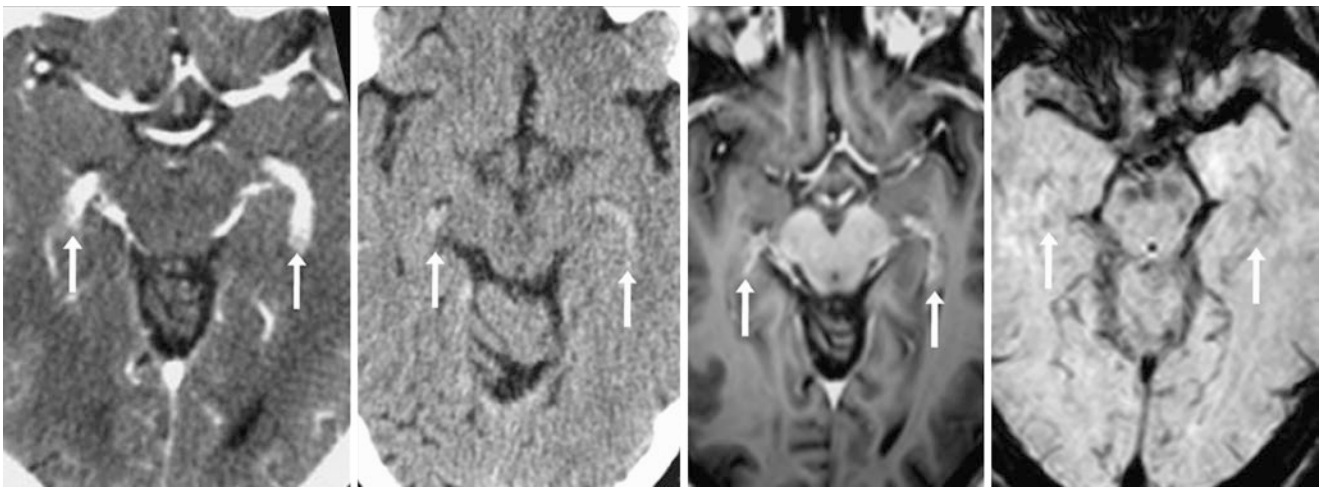

Fig. 11.53 A 49-year-old patient with a CECT (*left*) that shows avid enhancement of the CP with the temporal horns bilaterally (*arrows*); it was only mildly hyperdense on NECT (*left middle*). 3 T MRI axial post-contrast T1WI (*right middle*) depicts less enhancement and no dark signal on SWI (*right*) consistent with the finding that the CP is incompletely calcified

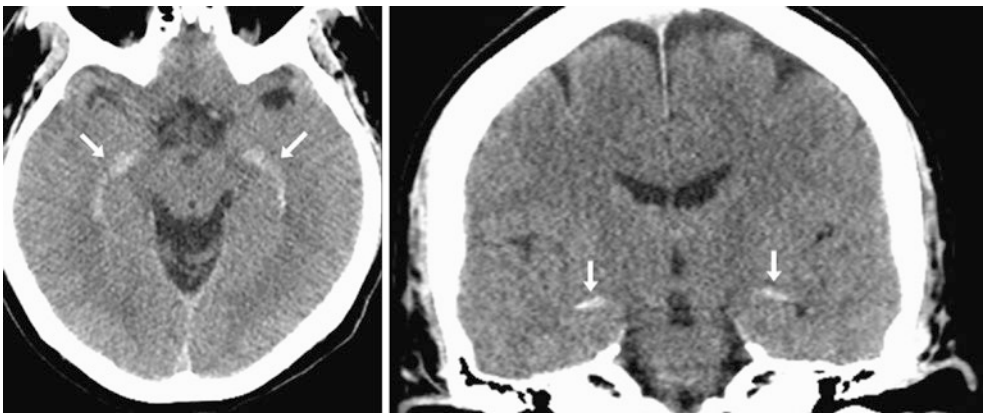

Fig. 11.54 A 50-year-old patient with an axial NECT (*left*) and coronal NECT (*right*) obtained post-trauma (negative examination). This examination demonstrated how the bilateral, incompletely calcified CP (*arrows*) may appear hyperdense within the choroidal fissures. The bilateral appearance makes it clear that this does not represent hemorrhage

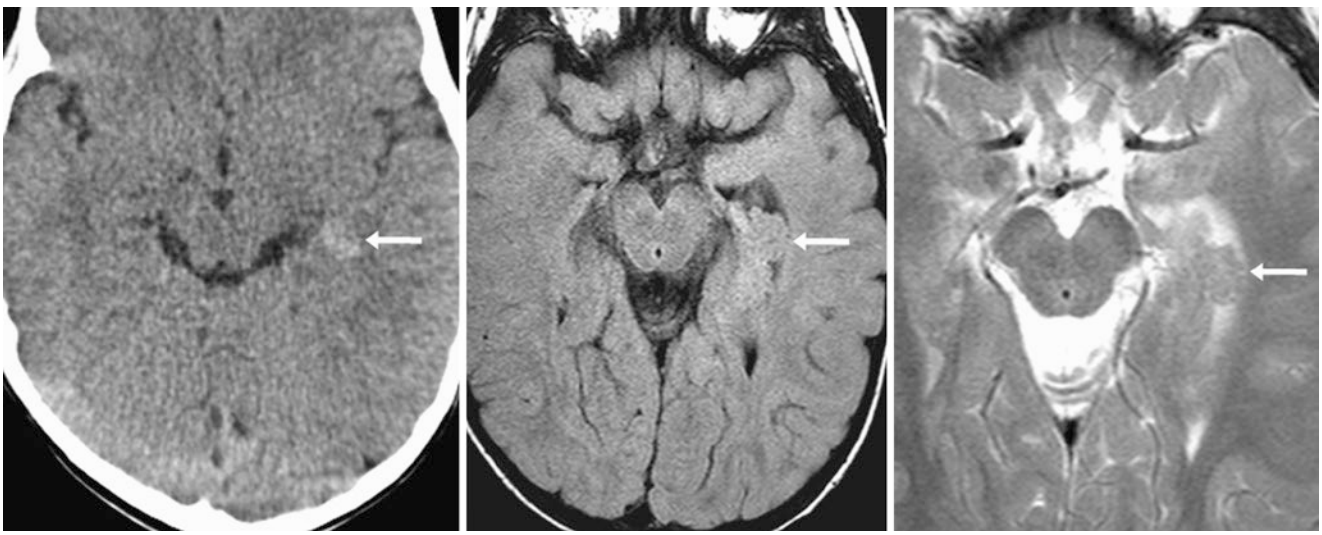

Fig. 11.55 A 3-year-old patient with a NECT (*left*) obtained post-trauma, which demonstrates how incompletely calcified CP (*arrows*) may appear hyperdense within the choroidal fissure. It was questioned by a radiology resident as representing hemorrhage. A 3 T MRI the next day depicted the asymmetric CP on axial FLAIR (*middle*) and T2WI (*right*)

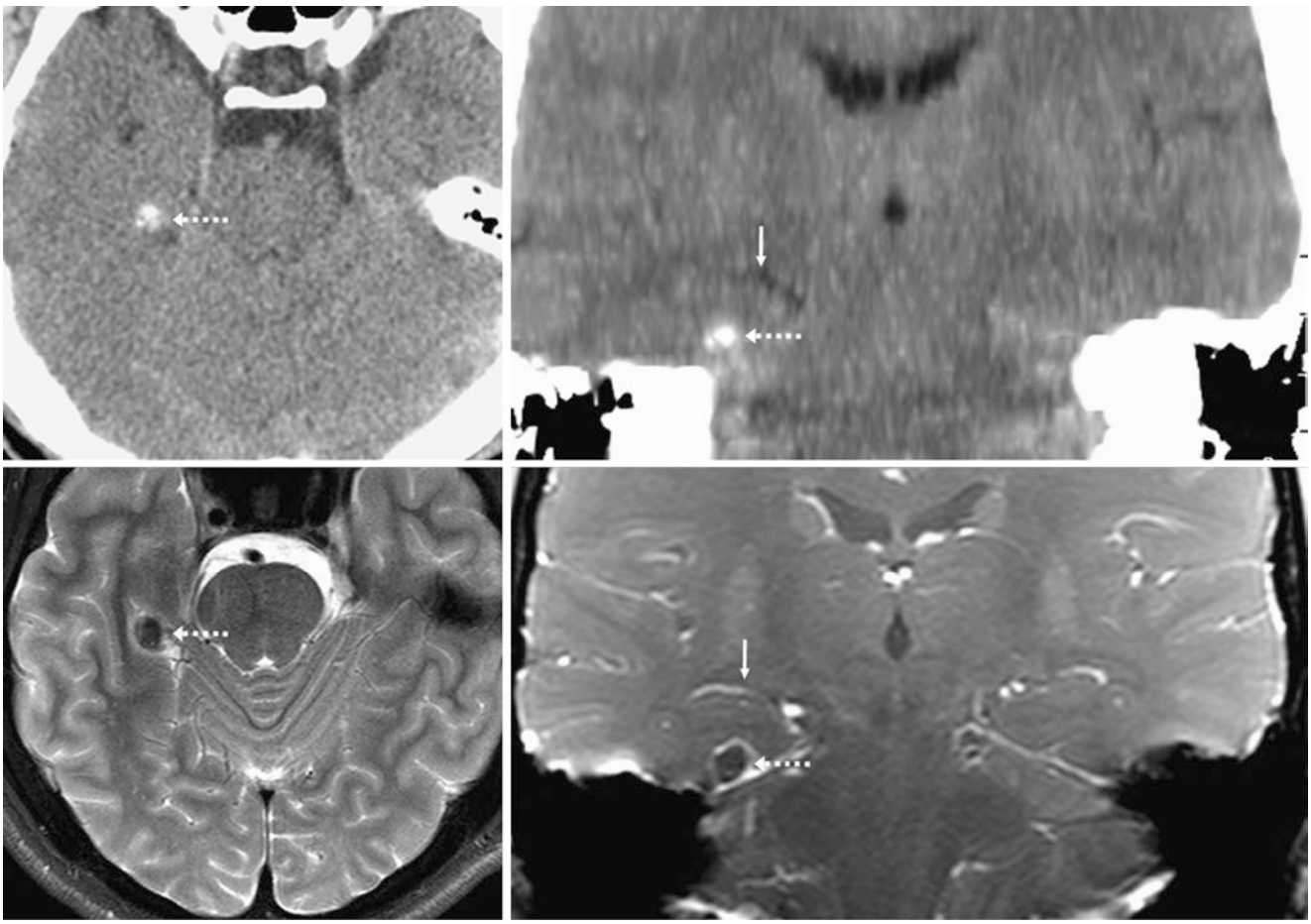

Fig. 11.56 Companion case of neurocysticercosis. A 29-year-old patient with seizures underwent an emergent NECT that demonstrated a calcified lesion (*dashed arrows*) on axial images (*top left*). However, the lesion was shown to be inferior to the choroidal fissure (*thin arrows*) on 1-cm-thick coronal reformats (*top right*) and was actually located within the right parahippocampal gyrus. A 3 T MRI axial T2WI (*bottom left*) and a coronal postcontrast T1WI (*bottom right*) depicted a dark signal within the calcified lesion and confirmed a lack of enhancement. The lesion represents an "inactive" (but still may cause seizures) sequela of desiccated material that was previously cystic

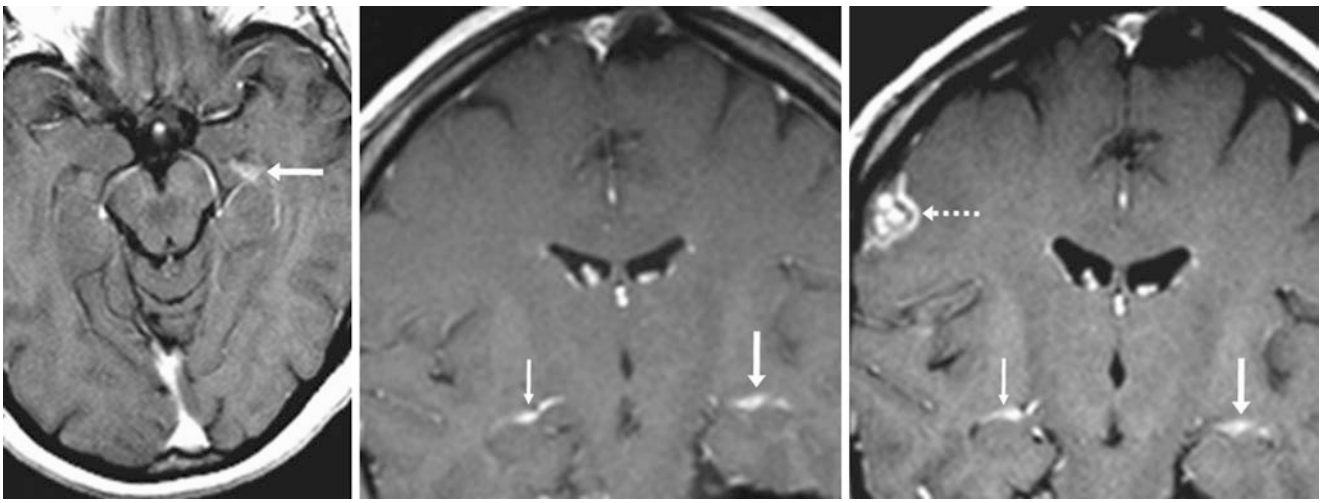

Fig. 11.57 Companion case of lung cancer metastasis. A 30-year-old patient with a prominent CP unilaterally that was initially thought to be an enhancing metastasis (*arrow*) based on postcontrast axial T1WI (*left*). However, on a postcontrast coronal T1WI (*middle*), it was confirmed to be within the choroidal fissure and was symmetric as compared to the opposite side (*thin arrows*). The asymmetry on axial images was caused by head tilting. Two years later on repeat postcontrast coronal T1WI (*right*) a true metastasis was noted (*dashed arrow*)

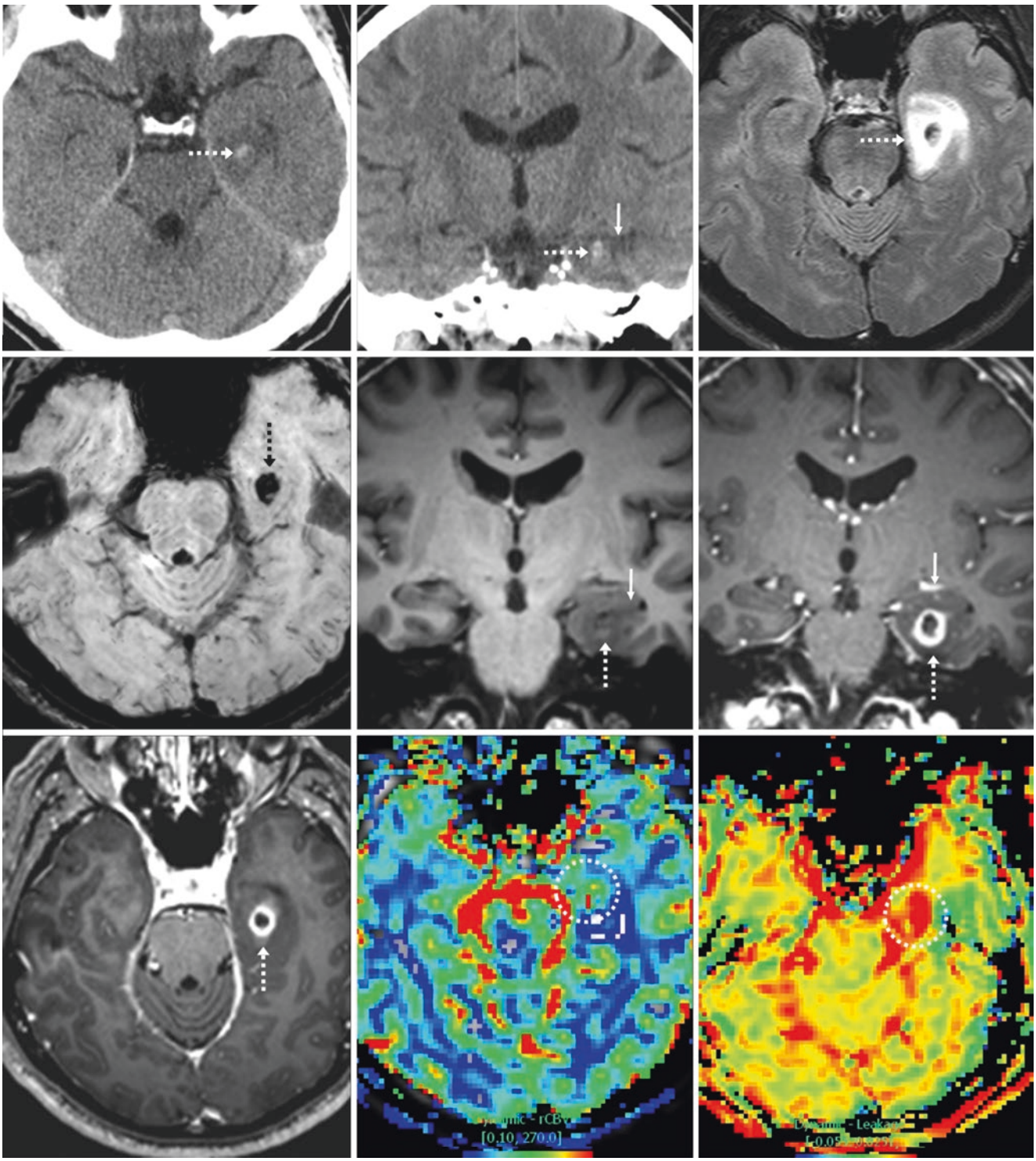

Fig. 11.58 Companion case of glioblastoma. A 50-year-old patient with seizures. *Top row*: an emergent NECT showed a mildly hyperdense lesion (*dashed arrows*) on axial (*left*) and coronal (*middle*) reformats. Note mild hypodense edema surrounding the lesion, also confirmed to have surrounding edema on 3 T FLAIR (*right*). *Middle row*: SWI (*left*) depicted T2-dark hemorrhage within, with edema on noncontrast axial T1WI (*middle*) and avid enhancement surrounding the hemorrhage on postcontrast coronal T1WI (*right*). *Bottom row*: using axial postcontrast T1WI (*left*), MR perfusion CBV (*middle*) was measured in the enhancing lesion, and the CBV was 2.7 times the non-affected white matter (>2 times is suggestive of a higher grade primary brain tumor). Dynamic leakage maps (*right*) confirmed blood–brain barrier dysfunction, also consistent with a high-grade primary brain tumor

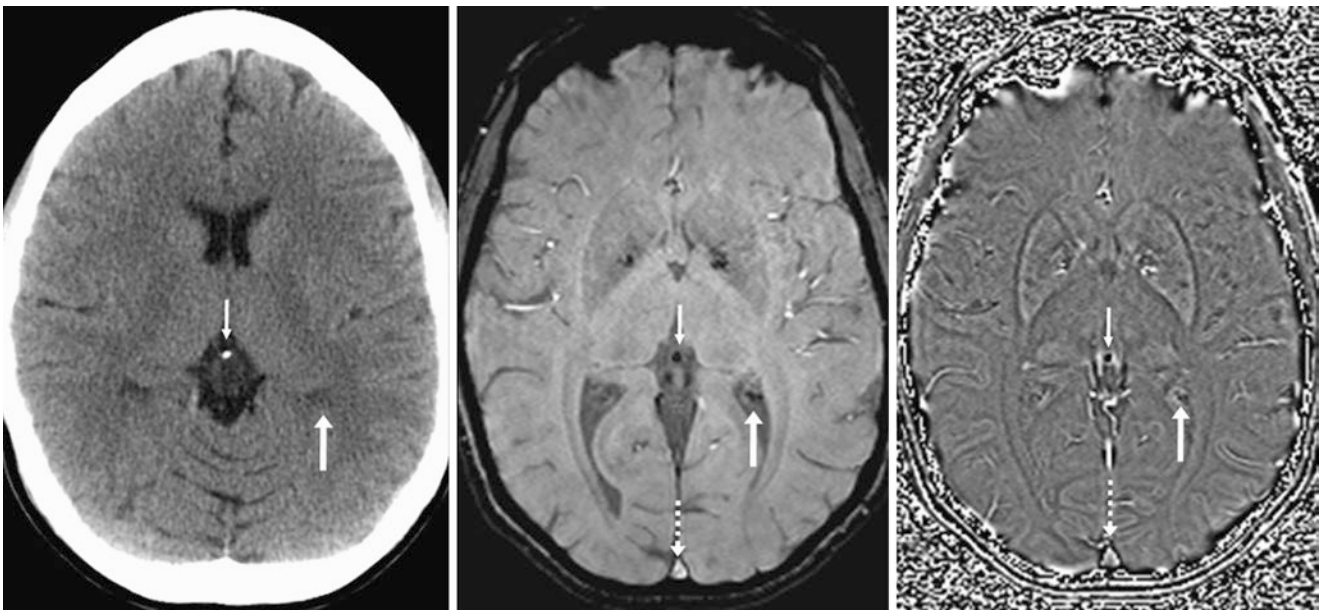

Fig. 11.59 A 35-year-old patient with a NECT (*left*) had a 3 T MRI (*middle*) with accompanying phase map (*right*) of a typical location of CP (*arrows*) within the trigones of the lateral ventricles. This is probably partially calcified although not visible on NECT, since the dark signal on SWI indicates that it is diamagnetic as it is also dark on phase map, while the superior sagittal sinus should have bright paramagentic signal (*dotted arrows*). Also note a normal pineal calcification (*thin arrows*), which is also diamagnetic because it is dark on both SWI and phase map

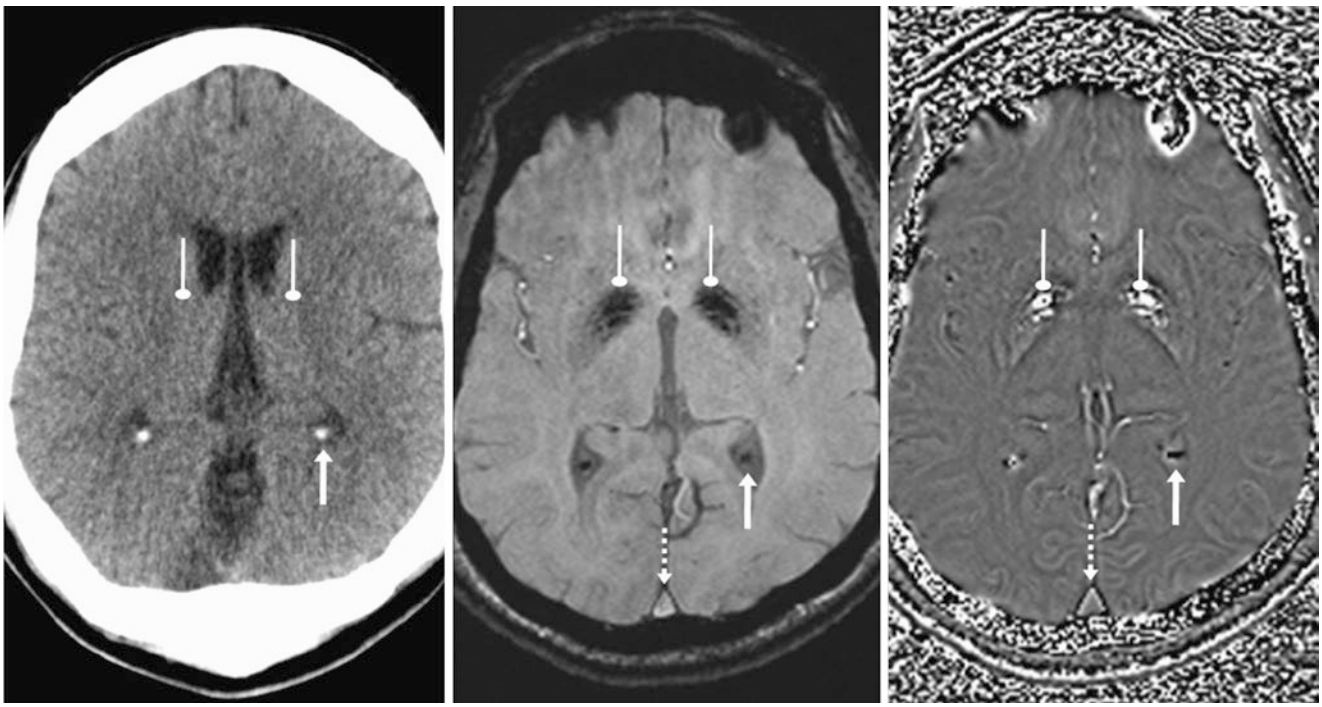

Fig. 11.60 A 51-year-old with a NECT (*left*) had a 3 T MRI (*middle*) with accompanying phase map (*right*) of a typical location of CP (*arrows*) within the trigones of the lateral ventricles. The CP is mostly calcified, such as on NECT, since the dark signal on SWI indicates that it is diamagnetic and it is also dark on the phase map, while the superior sagittal sinus has bright paramagentic signal (*dotted arrows*). Also note the normal iron of the noncalcified globi pallidi (*circle tip arrows*), which are paramagnetic since they are dark on SWI but bright on the phase map, akin to the dural sinuses

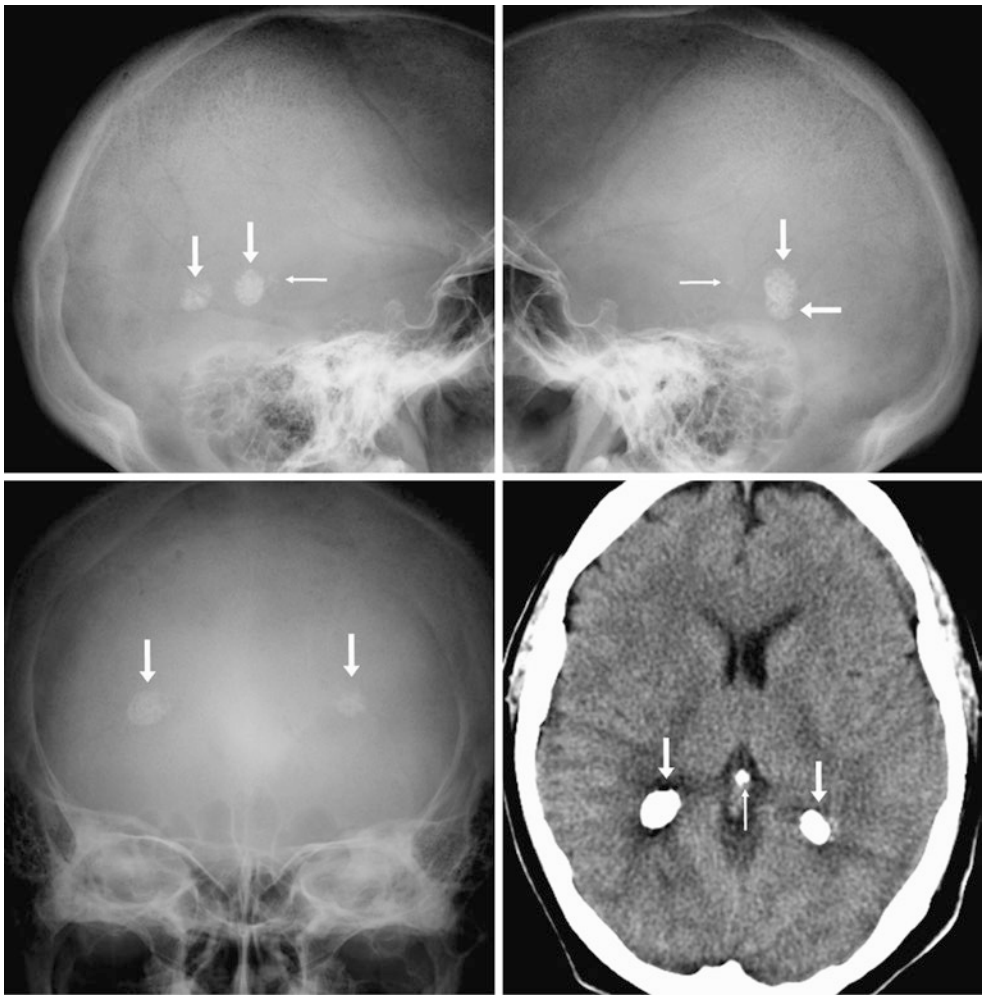

Fig. 11.61 A 55-year-old patient with prominent intracranial calcification on left lateral (*top left*), right lateral (*top right*) and anteroposterior view (*bottom left*) plain films. This is consistent with CP calcifications (*arrows*) within the trigones of the lateral ventricles and was confirmed by a NECT (*bottom right*). Note a normal pineal calcification as well (*thin arrows*)

11.1 Choroid Plexus Cysts

It should be noted at this point that there is some controversy and confusion as to exactly what *choroid plexus cysts* (CPCs) are histologically, how to classify them, and when the term choroid plexus cyst should be used. Traditionally, the term CPCs refers to benign cysts that are usually transitory/impermanent and are commonly encountered on second trimester ultrasound (US) examinations. Traditional sources consider that such transient cysts do not have an epithelial lining histologically. This is because they are thought to develop between the folds lined by the epithelium rather than being lined by epithelium themselves. They are also considered to exist only in the fetus or neonate, as opposed to the adult form of *choroidal fissure cysts* (a form of *neuroepithelial cyst*), which may exist in late childhood or even adulthood. Other sources group these two categories of neonates and adults together on more of a histologic basis and consider CPCs to consist of benign, clear-colored cysts of neuroepithelial origin caused by trapping or infolding of columnar epithelial lining, possibly persisting into childhood or rarely into adulthood. It is likely that most of the controversy in terminology and classification arises from the lack of literature following normal CPCs encountered prenatally and continuing into the juvenile period or into adulthood. For the purposes of this book, both fetal/neonatal and juvenile/adult CPCs are discussed based on location, using the traditional thinking but keeping in mind that there may be an overlap and perhaps an evolution of such cysts between prenatal to juvenile to adult age groups.

Conforming to the traditional understanding, CPCs typically develop around the fetal sixth gestational week, and the incidence on second trimester prenatal US examinations is estimated to be between 0.3 and 3.5 %. An incidence of around 1 % appears to be the most reproducible statistic based on many different studies over the past few decades. One reason that this statistic varies significantly is probably because the majority (over 90 %) are thought to resolve by the 28th gestational week. Thus, the measured incidence within such studies probably relates to the gestational age at which the US is performed, the transitory nature of these cysts, and the resolution of the US machine. Interestingly, a more recent study by Norton and colleagues found an incidence as high as 12 % in a noncongenital heart disease goup (nonsyndromic) as opposed to 26 % in the congenital heart disease group. The authors hypothesized that the difference was due to the utilization of newer equipment. Thus, the incidence of CPCs in normal neonates is probably higher than traditionally thought and indicates that these CPCs may persist into childhood and on rare occasion into adulthood.

Thus, such CPCs found during prenatal or neonatal US are most commonly a normal variation, since they are typically isolated and the vast majority are not associated with a syndrome or other congenital abnormality. However, in certain syndromes or genetic anomalies, such as *trisomy 18* (with CPCs in 40–70 %), *trisomy 21* (with CPCs in 17 %), and perhaps in *congenital heart disease* (possibly with CPCs in up to 26 %), the incidence is much higher than encountered in the general population. Currently, the literature suggests that if other congenital abnormalities are not detected on fetal US in a patient with incidental, small size (<1 cm) CPCs, the likelihood of finding such syndromes is less than 1 %.

This has led to much debate about the management and work-up for other congenital abnormalities in the scenario where a CPC is the only finding on routine prenatal US. Although they are overwhelmingly asymptomatic, severely enlarged CPCs found prenatally or in the neonate may rarely obstruct if they are present in atypical locations, such as near the foramen of Monro or Luschka. Thus, larger cysts (>1 cm) should likely be followed serially prenatally. However, following delivery, there are no good data to indicate whether such cysts should be followed.

If CPCs persist into neonatal or early childhood, their imaging is typically hypodensity on CT, while occasionally CPCs may occur within or adjacent to a calcified choroid plexus in adults. On MRI, the cysts are typically T1-dark, T2-bright, and suppress with CSF on FLAIR; on DWI, the cysts are typically dark, unless it is a *choroid plexus xanthogranuloma*, which is typically present only in adults (and covered in Sect. 11.3). Contrast enhancement of CPCs is typically absent, although they may be surrounded by a thin rim. In older children or adults, CPCs may occasionally be seen between calcifications. Again, there is controversy as to whether such prenatal/infantile CPCs can persist later into childhood or adulthood. Notably, CPCs have also been shown in some limited reports to regress or disappear between the neonatal period and later childhood (Figs. 11.62, 11.63, 11.64, 11.65, 11.66, 11.67, and 11.68).

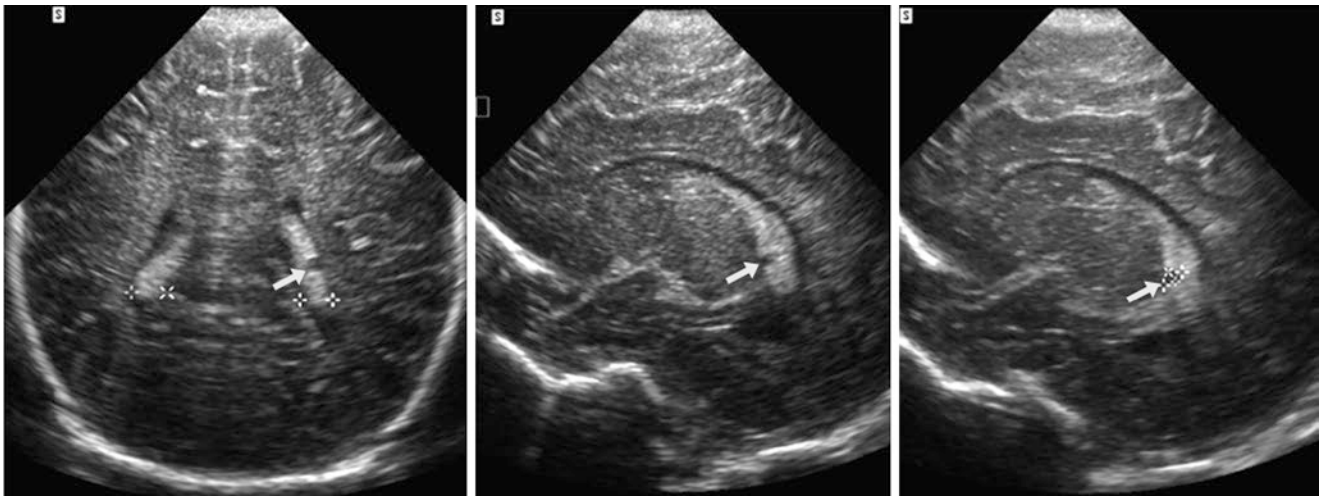

Fig. 11.62 A 2-day-old term infant had an incidental CPC (*arrows*) within the left lateral ventricle on coronal (*left*) and sagittal (*middle and right*) US images. No other significant findings were noted, and the patient did not have a history of syndromic abnormality. The cyst measured 2.4 mm

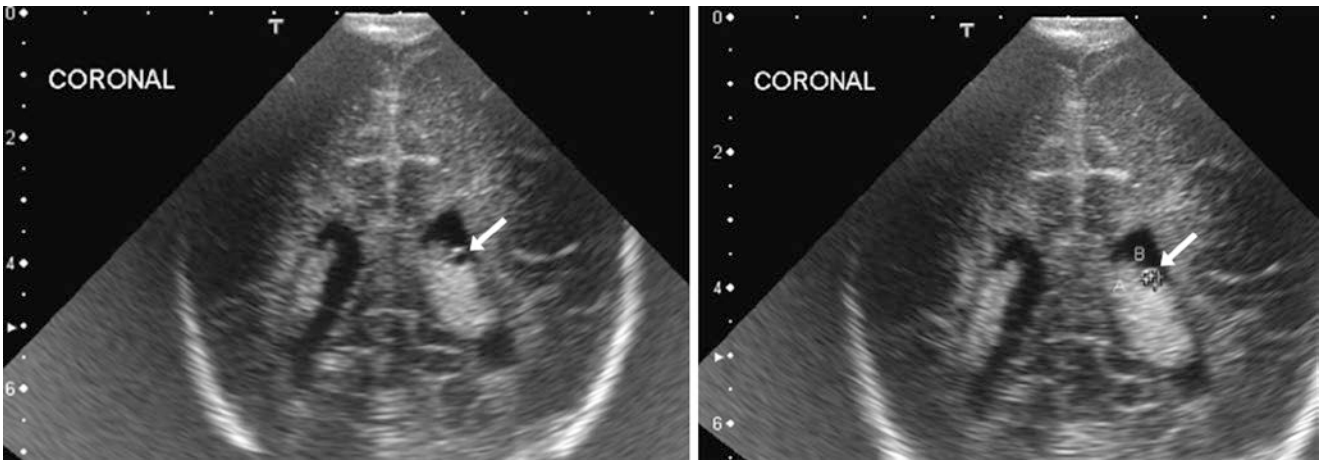

Fig. 11.63 A 6-day-old premature infant (born at 30+ weeks' gestational age) with a tiny, incidental CPC (*arrows*) within the left lateral ventricle on coronal US images. No other significant findings were noted, and the patient did not have a history of syndromic abnormality. This cyst measured 1.9 mm

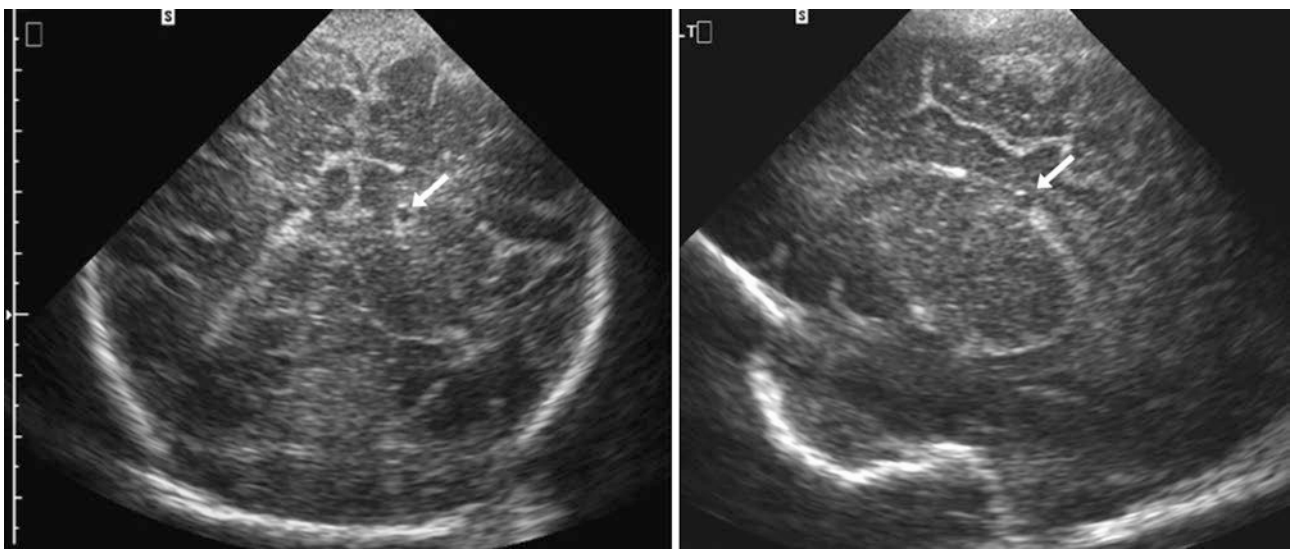

Fig. 11.64 A 2-day-old term infant with a small, incidental CPC (*arrows*) within the left lateral ventricle on coronal US images. No other findings were noted, and the patient did not have a syndromic abnormality. The CPC measured 3.4 mm

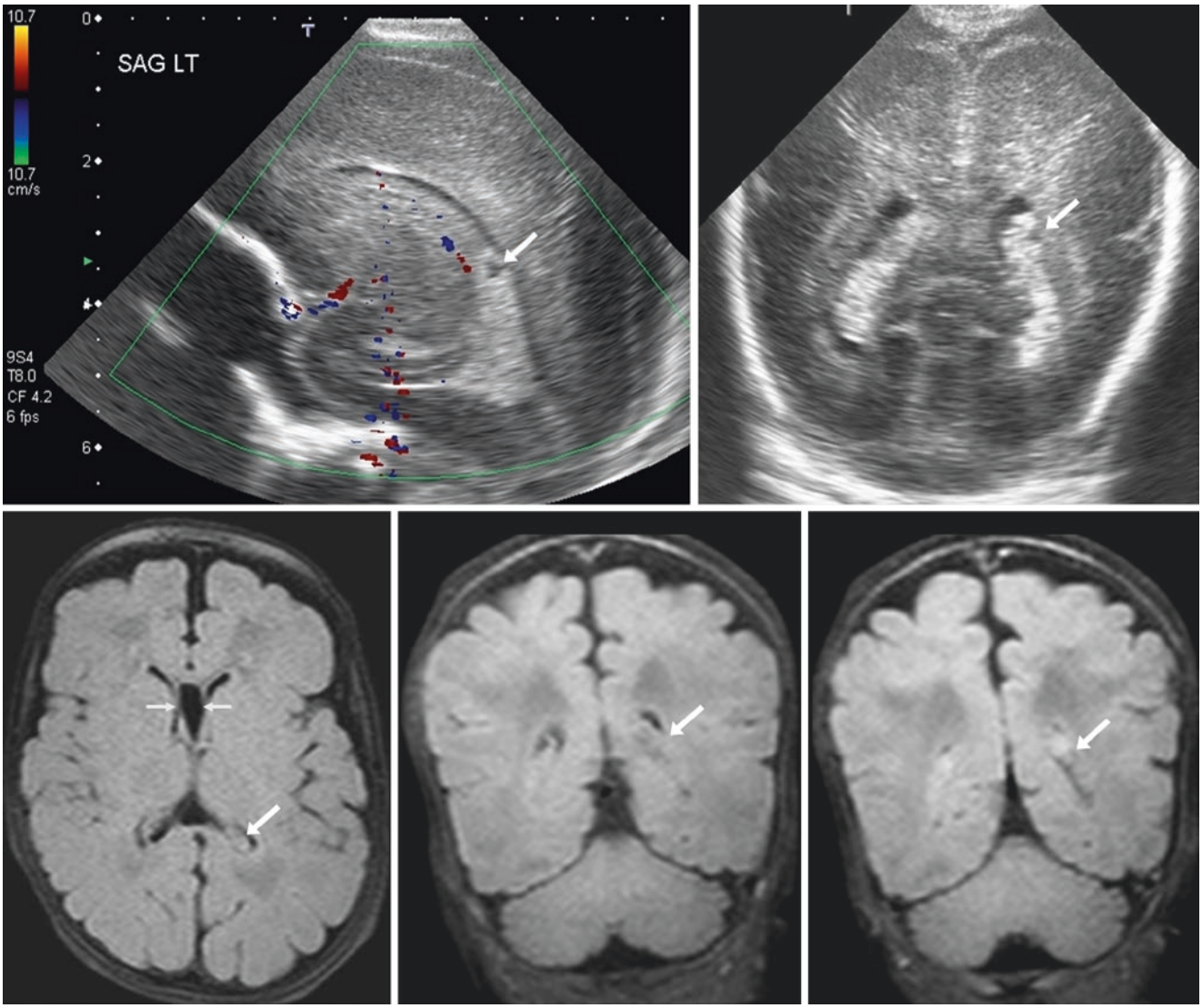

Fig. 11.65 A 10-day-old premature infant (26 weeks' gestational age at birth) with a 2.5-mm CPC (*arrows*) within the left lateral ventricle on sagittal (*top left*), and coronal (*top right*) US images. No other findings were noted; the patient did not have a syndromic abnormality. On a 3 T MRI at term-equivalent age (about 3 months postnatal), the cyst was not visualized on axial (*bottom left*) or coronal (*bottom middle and bottom right*) images. Therefore, the CPC was presumed to have regressed or was too small to visualize. Note a normal cavum septum pellucidum (*tiny arrows*)

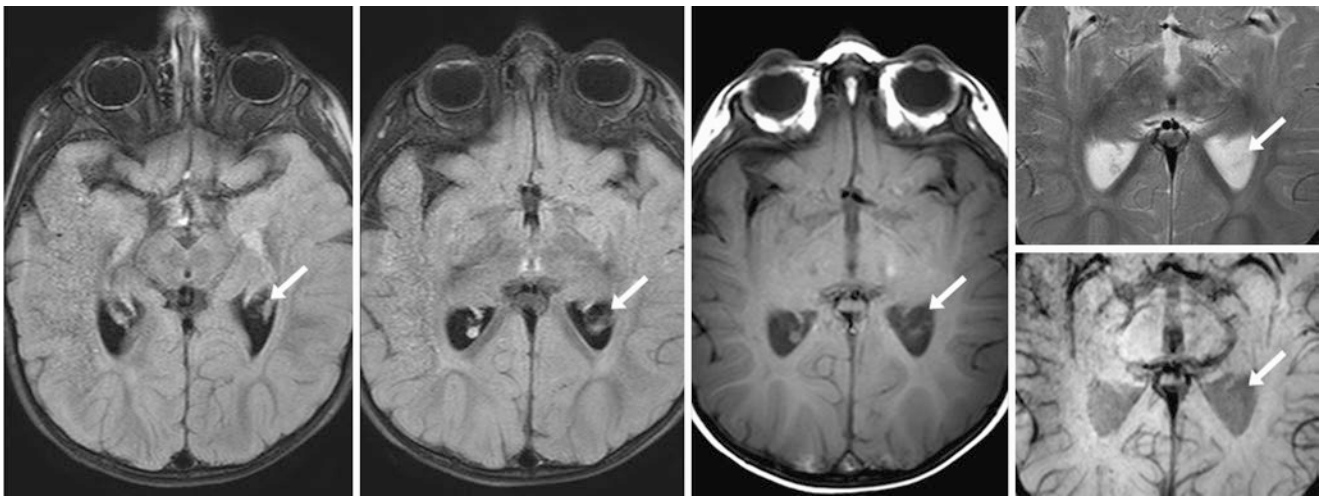

Fig. 11.66 A 13-month-old infant with a mild developmental delay but lacking evidence of syndromic or other abnormality on clinical examination and on a 3 T MRI. A CPC (*arrows*) was incidentally noted within the left lateral ventricle on axial FLAIR (*left and left middle*) and on axial T1WI (*right middle*). No other findings were noted, and the myelination pattern was normal for age. The CPC is nearly invisible on axial T2WI (*right*, *top image*) and SWI (*right*, *bottom image*)

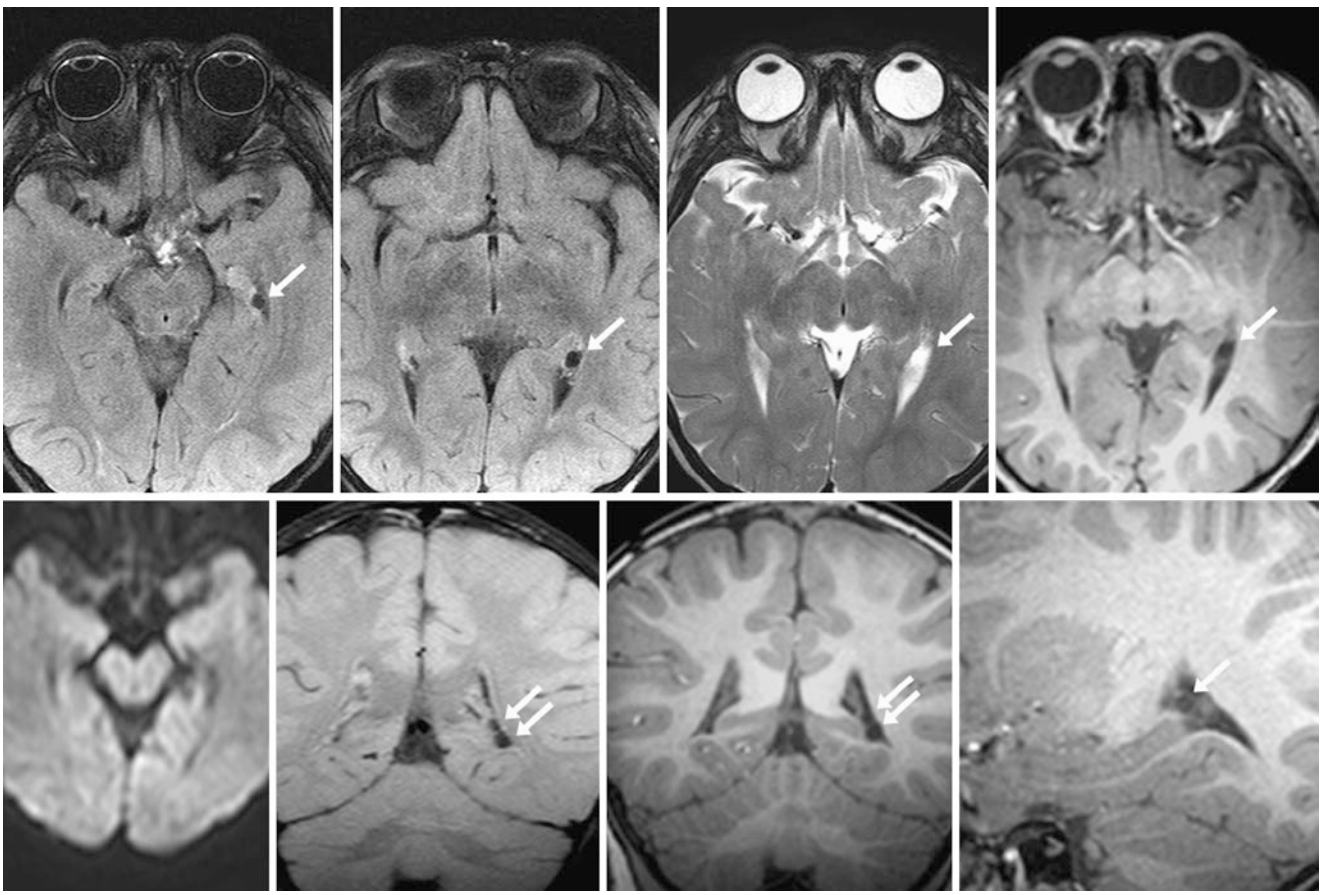

Fig. 11.67 An 18-month-old infant with developmental delay and trisomy 21 who underwent a 3 T MRI. Two CPCs (*arrows*) within the left lateral ventricle were depicted on axial FLAIR (*top*, *left*, *and left middle*), axial T2WI (*top*, *right middle*), and axial T1WI (*top right*). Note the difficulty in visualizing the CPCs on axial T2WI and DWI (*bottom left*). Coronal FLAIR (*bottom*, *left middle*), and coronal (*bottom*, *right middle*) and sagittal (*bottom right*) T1WIs also illustrate the cysts

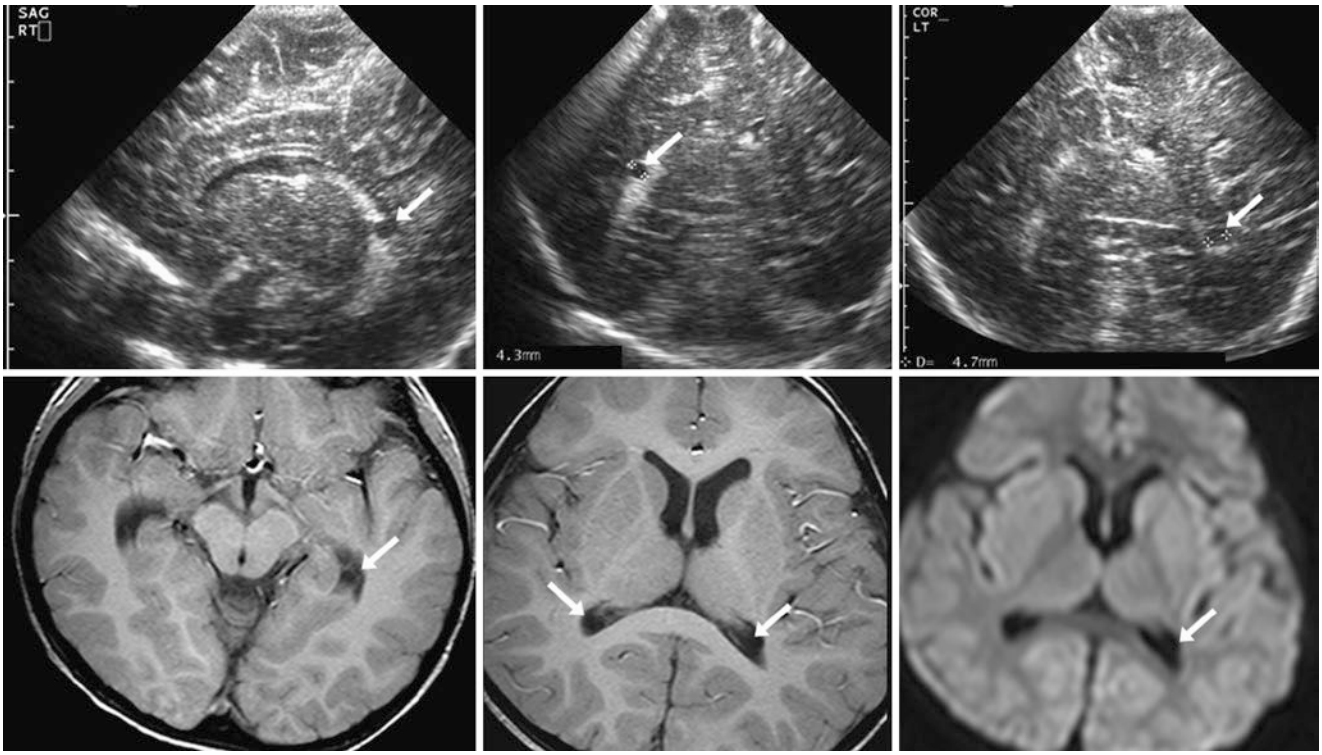

Fig. 11.68 A patient with trisomy 21 and developmental delay had bilateral CPCs (*arrows*) noted both within the right lateral ventricle on a sagittal US image at 3 months of age (*top left*) as well as within the lateral ventricles of both sides on coronal US images (*top middle*, *and right*). On a 3 T MRI at 2 years of age, axial T1WIs (*bottom left and middle*) showed the cysts, although they were not seen on DWI (*bottom right*). No other findings were noted, and the myelination was normal

11.2 Choroidal Fissure and Neuroepithelial Cysts

The *choroidal fissure* is a space between the fornix and hypothalamus that communicates medially with the ambient cistern and laterally with the temporal horn of the lateral ventricle on that side. The choroidal fissure is the site of attachment of the choroid plexus within the lateral ventricle and can have some degree of side-to-side asymmetry, a form of lateral ventricular asymmetry, which is discussed elsewhere in this book.

Within the choroidal fissure, benign, nonneoplastic cysts may be noted in childhood or adults that usually have CSF-like signal intensity on MRI sequences and are occasionally bilateral. In such a location, these can be considered *choroidal fissure cysts* (CFCs) or *neuroepithelial cysts* (NECs, also termed neuroglial or ependymal cysts); they are usually lined by either ependymal or choroid plexus cells. NECs are thought to be distinct, although this is not clearly established in relation to the fetal CPCs that are most commonly a transitory phenomenon on US and typically disappear by term neonatal age. Most commonly neuroepithelial-origin CFCs suppress in signal intensity along with CSF on FLAIR, although they are occasionally bright on FLAIR. Although the literature is sparse regarding long-term follow-up of such cysts, they are overwhelmingly asymptomatic when located in the choroidal fissure. They also do not change over time (unless trauma or iatrogenic injury ensues) and likely can be considered as normal variations if exhibiting CSF-like signal intensity on T2WI, T1WI, and FLAIR. They are less than 1 cm in size. They do not have significant enhancement with contrast medium, although a thin rim may be present (like CPCs). These cysts may mimic various *low-grade primary brain tumors* such as a dysembryoplastic neuroepithelial tumor (DNET) or a ganglioglioma, both of which may occur in the adjacent medial temporal lobe. Cysts that do not suppress on FLAIR are larger (>2 cm) or have an abnormal signal in the surrounding cerebral parenchyma. Such larger cysts should probably be followed for some time in order to exclude low-grade tumors. Also, *epidermoid cysts* may occasionally present as T2-bright, do not suppress on FLAIR, and have reduced diffusion (bright on DWI) relative to CSF. They are often present in an adjacent location near the skull base. Notably, CFCs/NECs only very rarely occur in the posterior fossa, and thus a cyst in that location is more likely to be an arachnoid cyst, an epidermoid cyst, a dermoid cyst, or a neurenteric cyst (very rare) in a young patient.

Again, there is often debate as to whether CSF-like cysts in the choroidal fissure truly represent neuroepithelial cysts versus *arachnoid cysts*, although the current prevailing opinion is that these are neuroepithelial in origin. This controversy probably arises because the numerous case reports of larger (>2 cm) cysts within the lateral ventricle with surgical confirmation have variably been ascribed to both neuroepithelial cysts and arachnoid cysts in nearly equal numbers. However, this could partly depend on location, since those cysts within the choroidal fissure (CFC) are usually less than 2 cm and are nearly always asymptomatic (i.e., likely being NECs), while larger cysts that may occur within the trigones of the lateral ventricles or within the third ventricle can occasionally cause symptoms, possibly caused by intermittent obstruction (i.e., likely being arachnoid cysts). Since such larger, trigonal cysts occasionally enlarge, some believe that such cysts are arachnoid cysts, while others have used the term simple intraventricular cysts. Hence, NECs can be indistinguishable from arachnoid cysts when they are located within trigones of the lateral ventricles.

Neither the NEC nor the arachnoid cyst should be confused with synechiae/webs that occasionally result from chronic ventricular shunting or after trauma or with cystic leukomalacia; these can occur as a sequela of hemorrhagic *periventricular leukomalacia* in premature infants. Therefore, intraventricular cysts should be correlated with the clinical history and followed appropriately unless they are quite small (<1 cm), particularly if they do not have CSF-like signal intensity on FLAIR or if hydrocephalus is present. Other rare causes of intraventricular cysts include *neurocysticercosis* (e.g., racemose form) and *hydatid* (echinococcal) *cysts*. Of note, *colloid cysts* are also neuroepithelial in origin (the term typically refers to those cysts occurring at the midline between the foramina of Monro), but they are considered abnormal because they may obstruct those foramina. They typically have some degree of hyperdensity on CT and some degree of either T1-bright or T2-dark signal internally. Interestingly, recent literature suggests that neuroglial cysts may arise from ependymocytes, while colloid cysts arise from endoderm, which could explain their difference in the rates of symptoms and of enlargement.

As noted previously, there could be overlap between the appearance of prenatal/neonatal CPCs (which typically regress), and CFCs/NECs encountered in childhood or, uncommonly, in adulthood. It is plausible that these two entities could be related and might represent a spectrum over time. However, this concept is speculative, and there is a lack of longitudinal studies that focus on the persistence or regression of these cysts from the neonatal to juvenile/adult ages (Figs. 11.69, 11.70, 11.71, 11.72, 11.73, 11.74, 11.75, 11.76, 11.77, 11.78, 11.79, 11.80, 11.81, 11.82, 11.83, 11.84, 11.85, and 11.86).

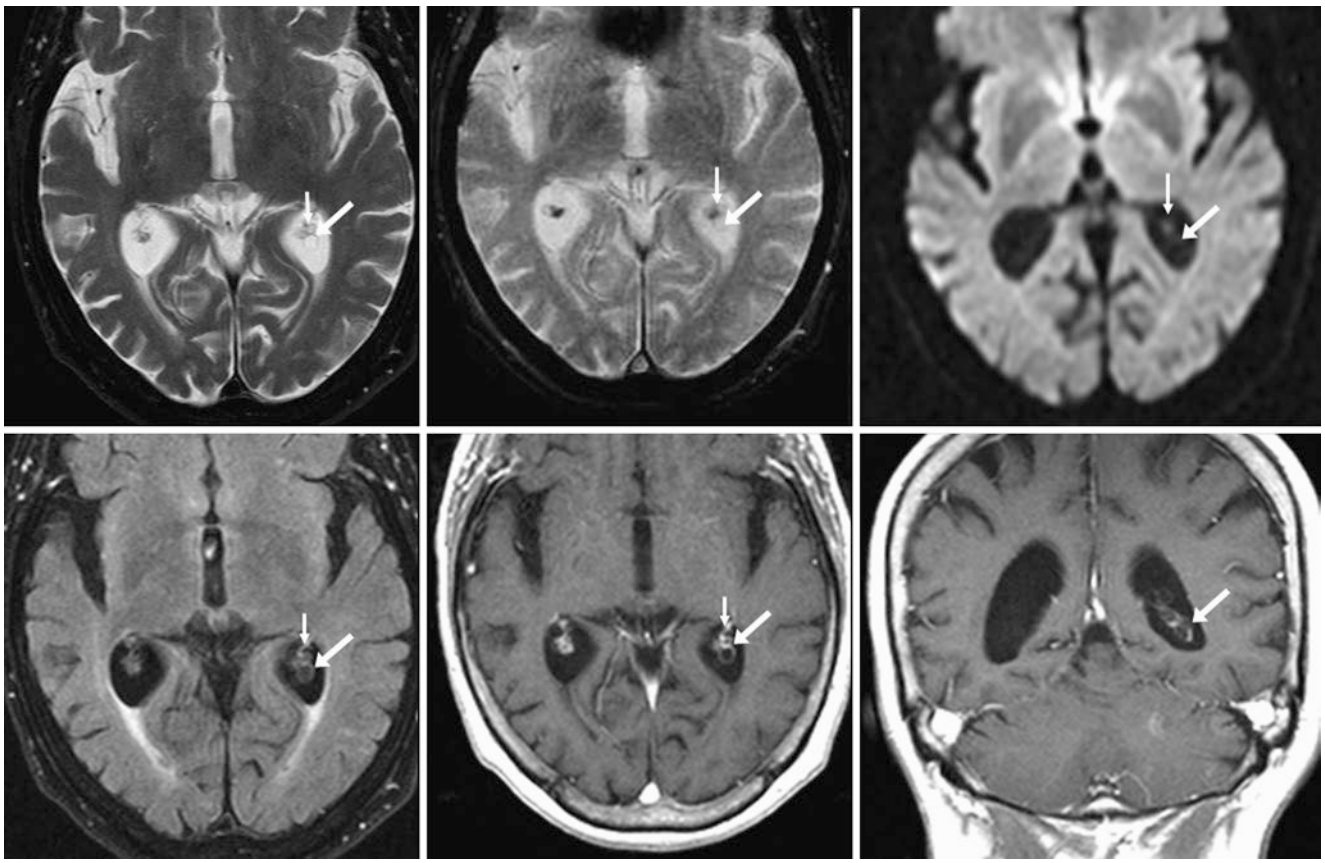

Fig. 11.69 A 71-year-old patient with a largely negative MRI performed for headaches. A single CPC (*arrows*) is located within the atria of the left lateral ventricle on axial T2WI (*top left*), T2*WI (*top middle*), DWI (*top right*), FLAIR (*bottom left*), and on postcontrast axial (*bottom middle*) and coronal (*bottom right*) T1WIs. Note a thin rim of enhancement on postcontrast T1WI, where choroid plexus enhancement is often noted owing to the lack of a blood–brain barrier. A smaller focus of reduced diffusivity just anteriorly (*thin arrows*) is likely an incidental xanthogranuloma

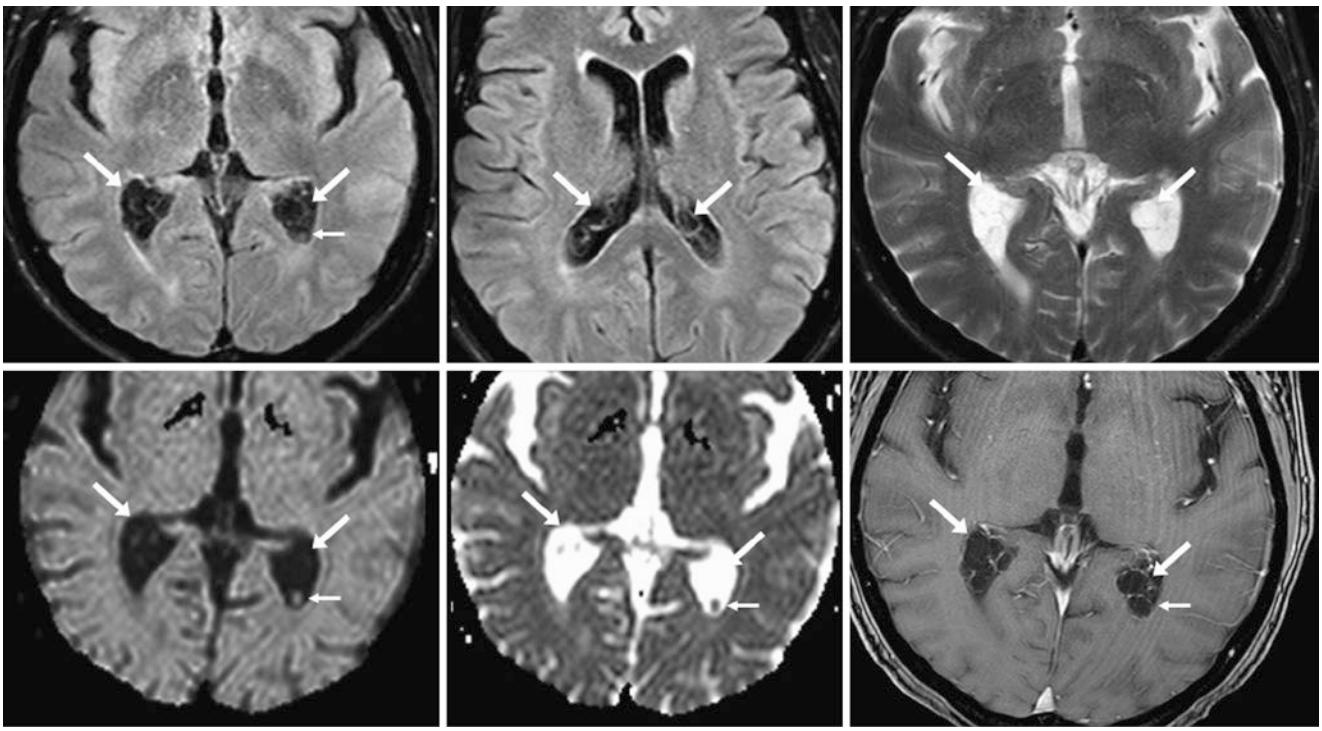

Fig. 11.70 A 72-year-old patient underwent an MRI for stroke work-up (negative). Multiple, loculated, bilateral CPCs (*arrows*) are present within the atria of the lateral ventricles on axial FLAIR (*top left and middle*), T2WI (*top right*), and DWI (*bottom left*) with ADC map (*bottom middle*). Note the thin, enhancing rims of fibrovascular stroma on postcontrast T1WI (*bottom right*), where choroid plexus enhancement is typically noted caused by the lack of a blood–brain barrier. One smaller cyst may be an incidental xanthogranuloma (*thin arrows*), since it exhibits a tiny focus of reduced diffusion

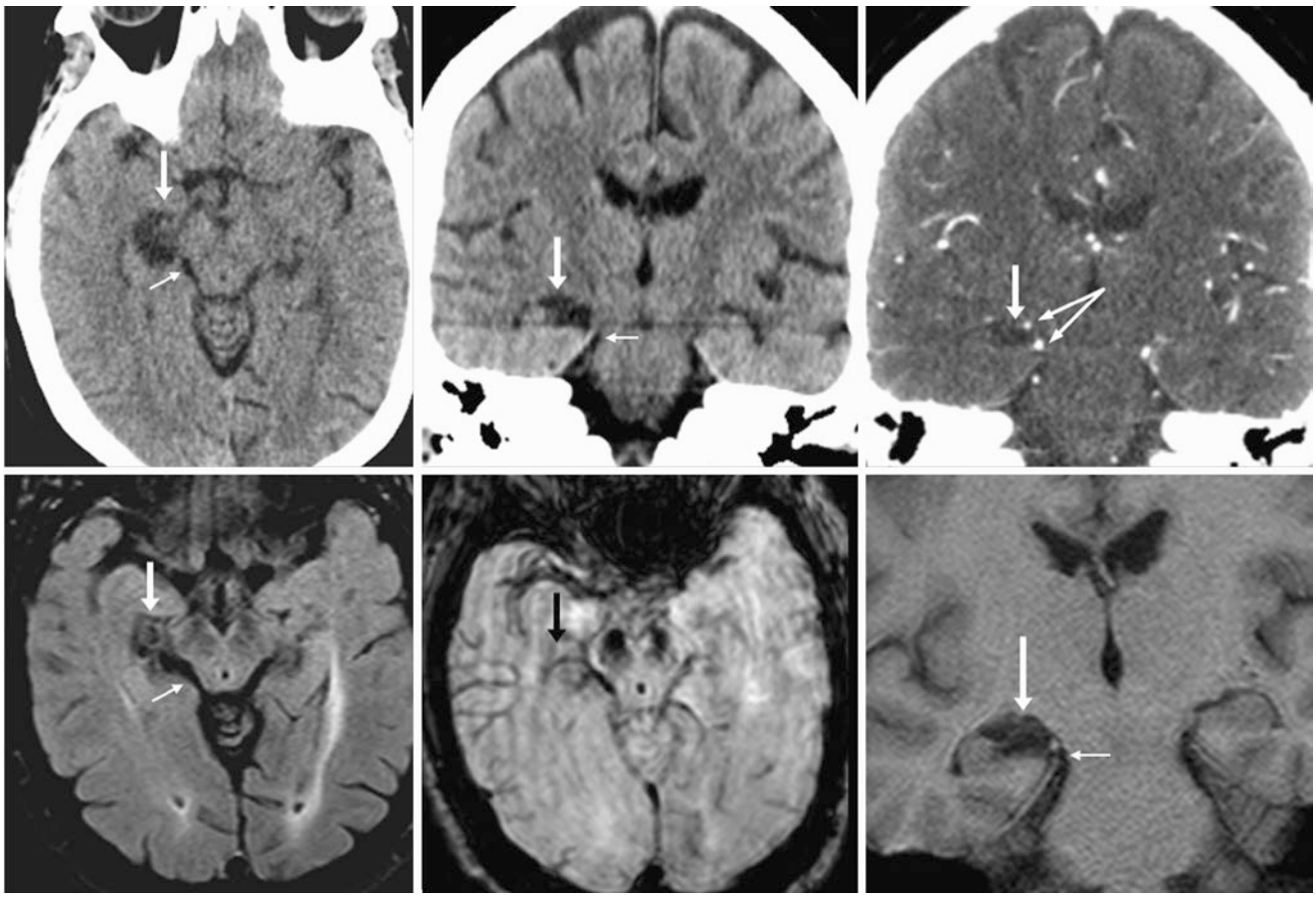

Fig. 11.71 A 54-year-old patient with axial (*left*) and coronal (*middle*) NECT images that depict right choroidal fissure prominence from a CFC (*arrows*). Note the ambient cistern (*thin arrows*), within which is the posterior cerebral artery and anterior choroidal artery (*double arrows*) on CTA coronal images (*right*). A 1.5 T MRI with axial FLAIR (*bottom left*), SWI (*bottom middle*), and magnified coronal T1WI (*bottom right*) images is also provided

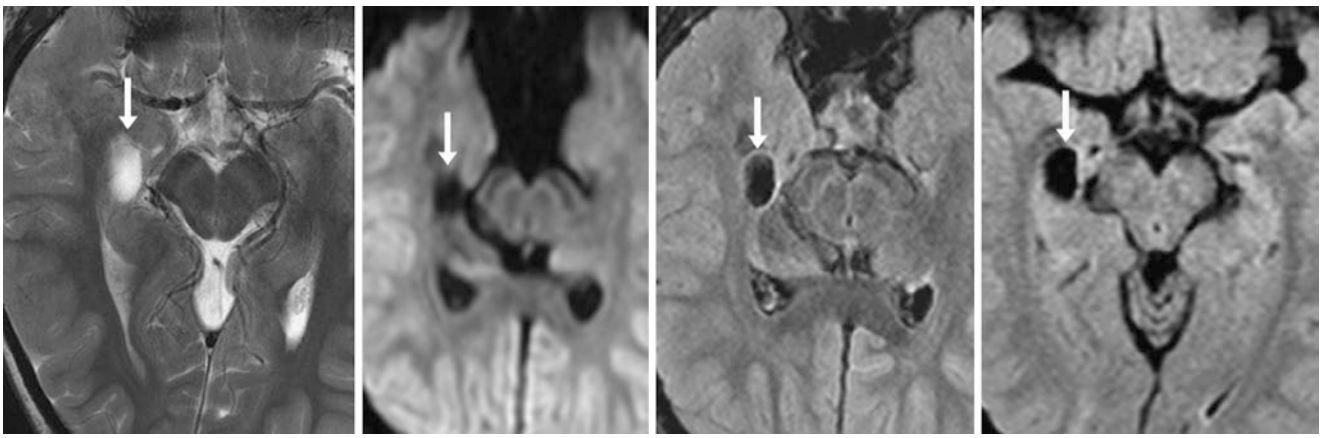

Fig. 11.72 A 6-year-old patient with a well-defined 1.5 cm right CFC (*arrows*) on a 3 T MRI with axial T2WI (*left*), having a CSF-like signal on DWI (*left middle*) and FLAIR (*right middle*). There was no change 1 year later on FLAIR (*right*). This could simulate a low-grade tumor on T2WI and FLAIR, but note the lack of surrounding bright T2 edema

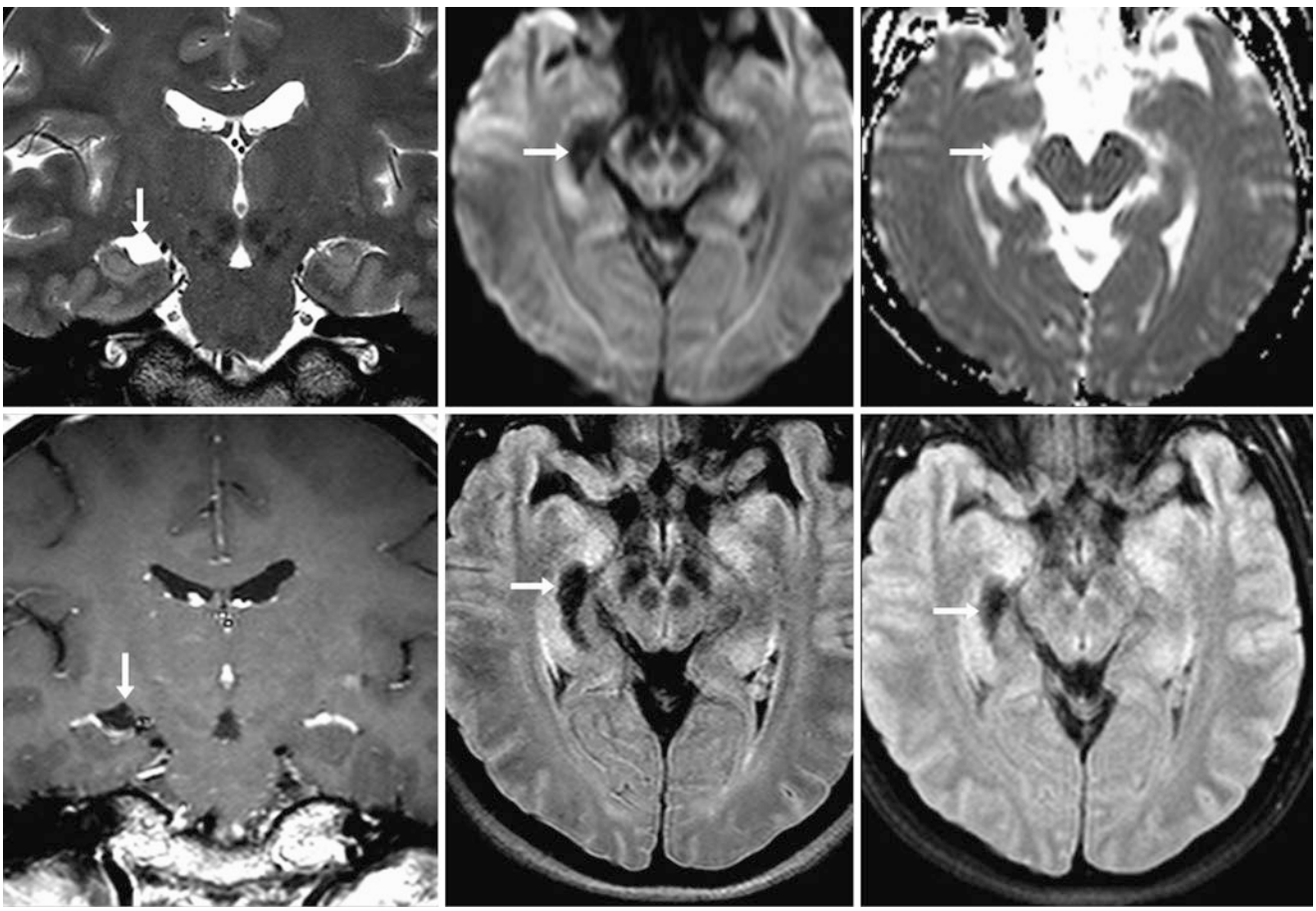

Fig. 11.73 A 46-year-old female underwent a 3 T MRI performed for seizures that shows prominence of the right choroidal fissure representing a CFC (*arrows*), as shown on a coronal T2WI (*left*), axial DWI (*top middle*), ADC maps (*top right*), and postcontrast coronal T1WI (*bottom left*). On FLAIR (*bottom middle*), the signal within the cyst suppresses similar to that of CSF. A 1.5 T FLAIR image from 3 years earlier (*bottom right*) confirms no significant change over time

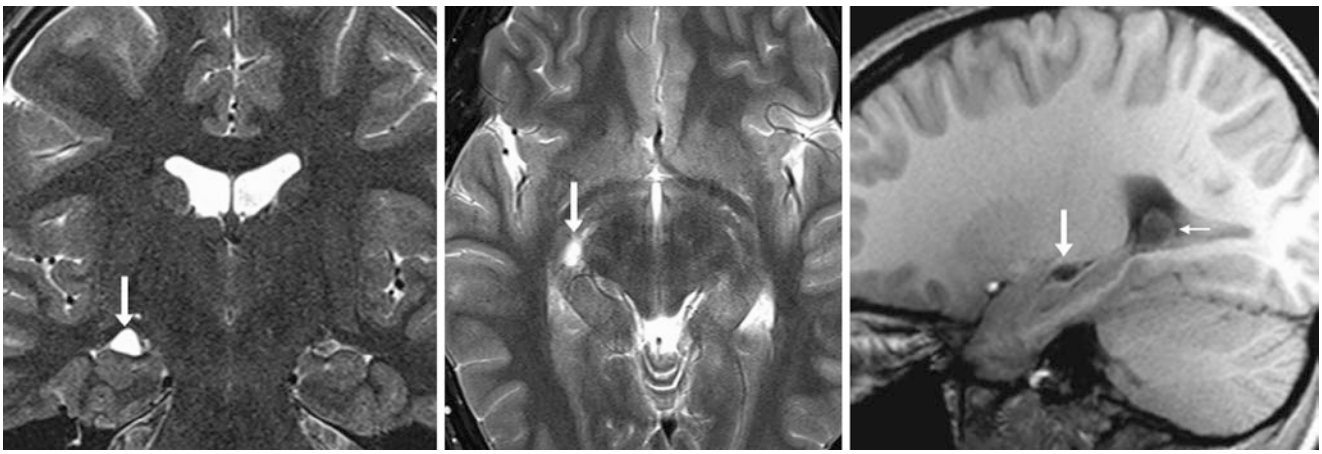

Fig. 11.74 A 12-year-old patient with a small CFC (*arrows*) on a 3 T MRI with coronal T2WI (*left*), axial T2WI (*middle*), and sagittal T1WI (*right*). The cyst can be localized to within the choroidal fissure on sagittal T1WI (*right*). Note a normal xanthogranuloma within the atrium of the right lateral ventricle (*tiny arrow*, *right*)

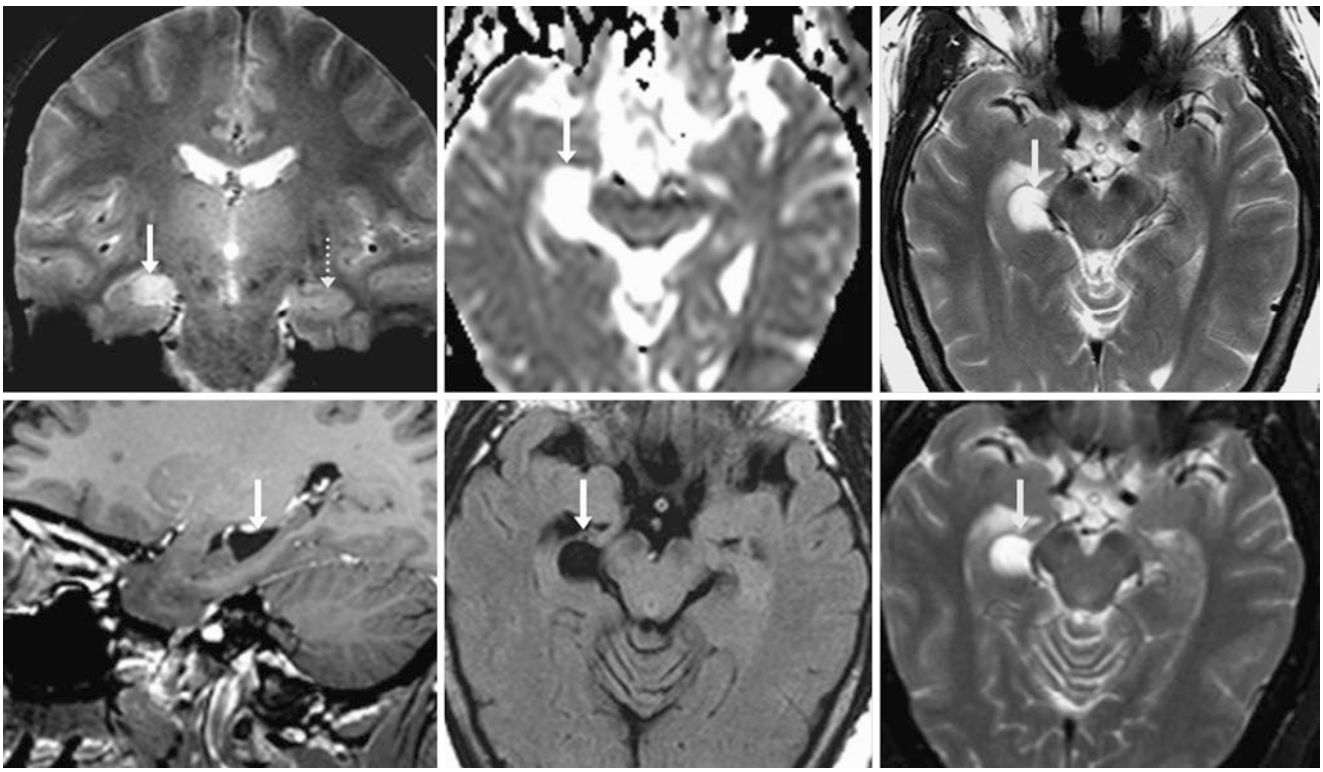

Fig. 11.75 A 59-year-old with a 3 T MRI of a CFC (*arrows*) that mimics edema from mesial temporal sclerosis on coronal T2*WI (*top left*). The cyst has high diffusivity on an ADC map (*top middle*) and is bright on T2WI (*top right*). A sagittal postcontrast T1WI (*bottom left*) depicts how the cyst mildly displaces adjacent structures. On a 1.5 T MRI from 10 years earlier, the cyst appeared the same on FLAIR (*bottom middle*) and T2WI (*bottom right*)

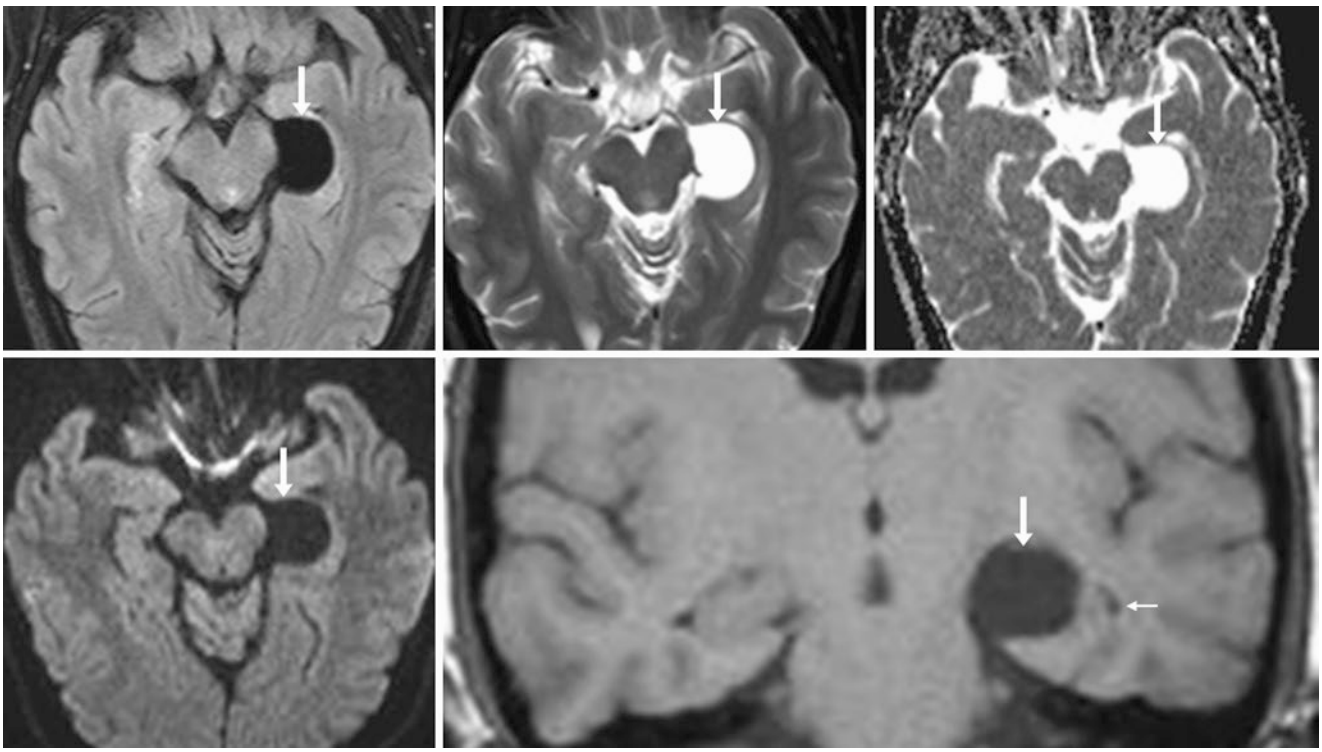

Fig. 11.76 A 19-year-old patient with hand numbness. A 3 T MRI demonstrated a 2-cm cyst (*arrows*) within the left ambient cistern and choroidal fissure that displaced the hippocampus laterally. The signal characteristics were that of a CFC on axial FLAIR (*top left*), T2WI (*top middle*), ADC map (*top right*), DWI (*bottom left*), and magnified coronal T1WI (*bottom right*). Note the temporal horn laterally (*thin arrow*). The displacement of adjacent structures could simulate a cystic low-grade tumor, but note the lack of adjacent parenchymal hyperintensity on FLAIR. This was unchanged several years later (*not shown*), and so was thought to be a CFC/NEC and less likely an arachnoid cyst

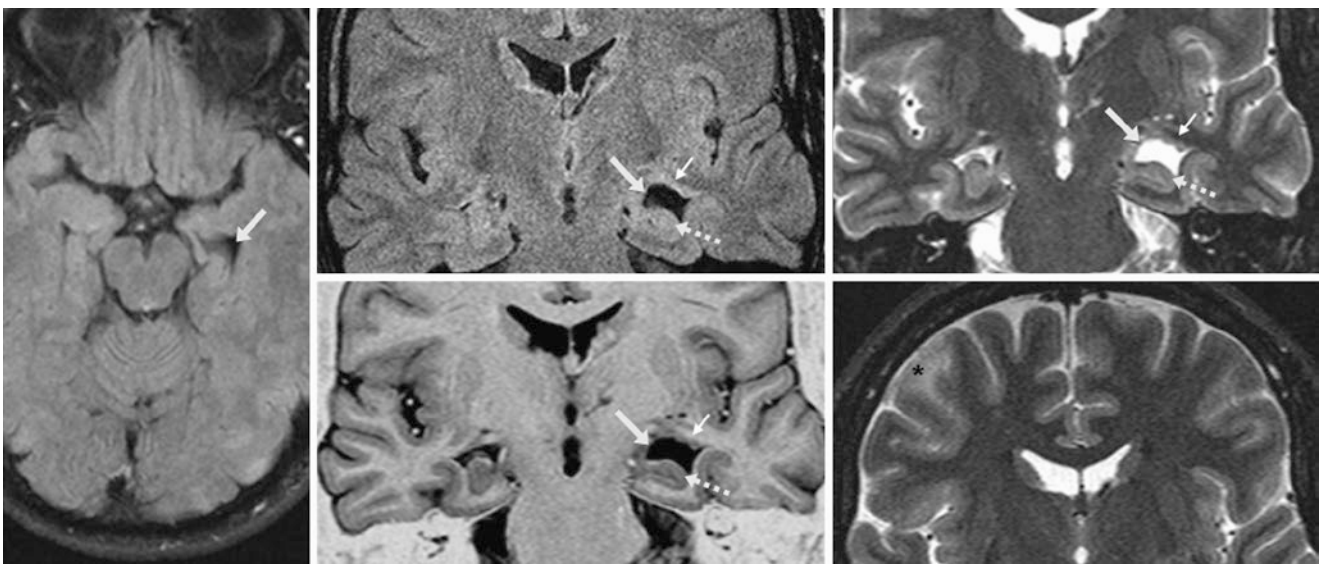

Fig. 11.77 Comparison case of tuberous sclerosis. A 33 year old with seizures had enlargement of the left temporal horn (*arrows*) on axial FLAIR MRI (*left*). Coronal FLAIR (*top middle*), coronal T1WI-IR (*bottom middle*), and coronal T2WI (*top right*) demonstrated abnormally thickened tissue (*tiny arrows*), indicating dysplastic tissue within and above the left hippocampus (*dashed arrows*). There was also a focus of dysplastic tissue/hamartoma in the right middle frontal gyrus (*) on T2WI (*bottom right*). This patient was later found to have tuberous sclerosis

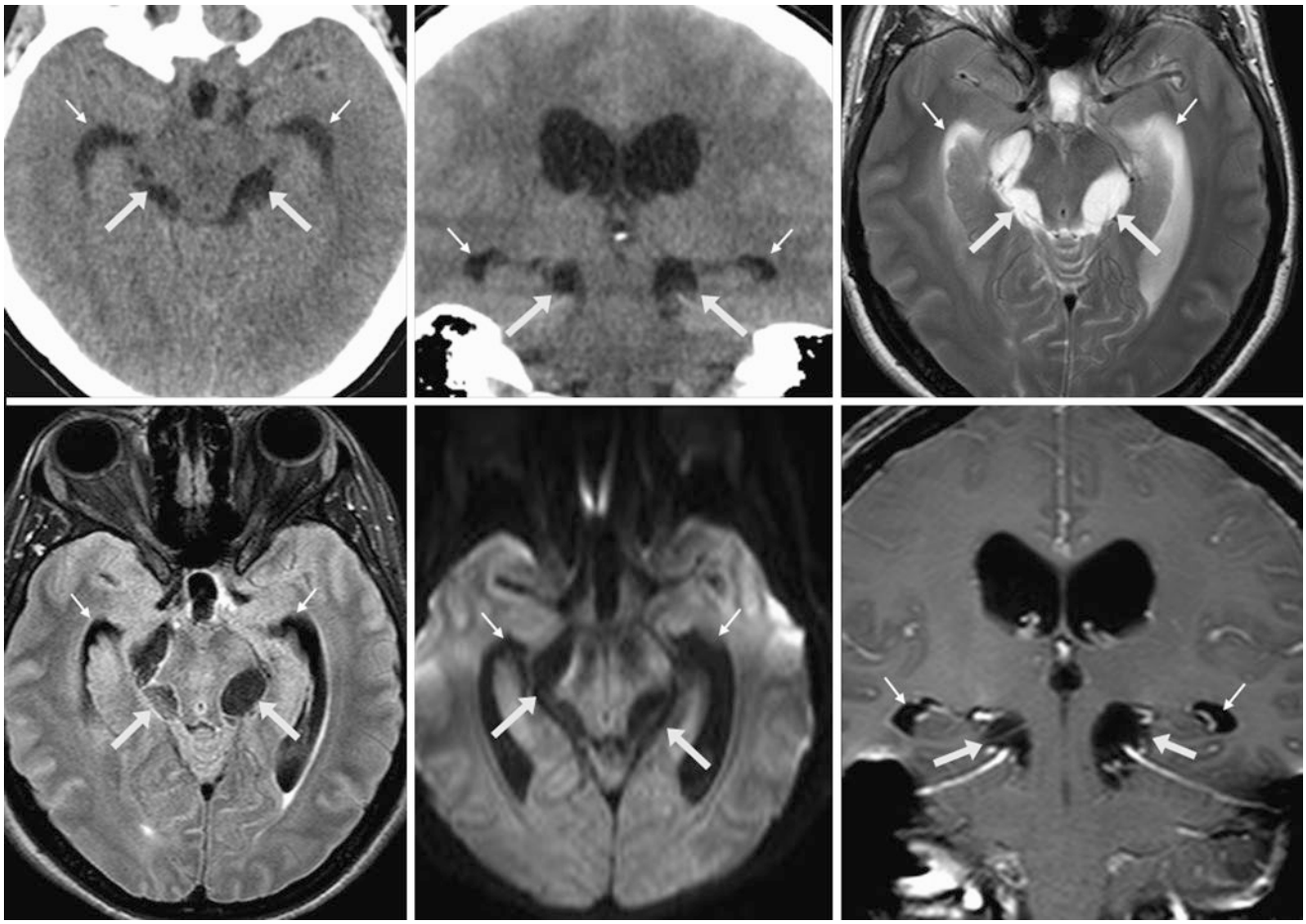

Fig. 11.78 Comparison case of racemose neurocysticercosis. On axial (*top left*) and coronal (*top middle*) NECT, a 33 year old had cystic enlargement of the perimesencephalic cisterns (*arrows*) and mild enlargement of the temporal horns (*tiny arrows*). Axial T2WI (*top right*), FLAIR (*bottom left*), DWI (*bottom middle*), and postcontrast coronal T1WI (bottom right) from a 3 T MRI demonstrated that the cysts' signal is slightly greater than that of CSF and does not enhance, which are characteristics often seen with racemose (i.e., grape-like clusters) neurocysticercosis

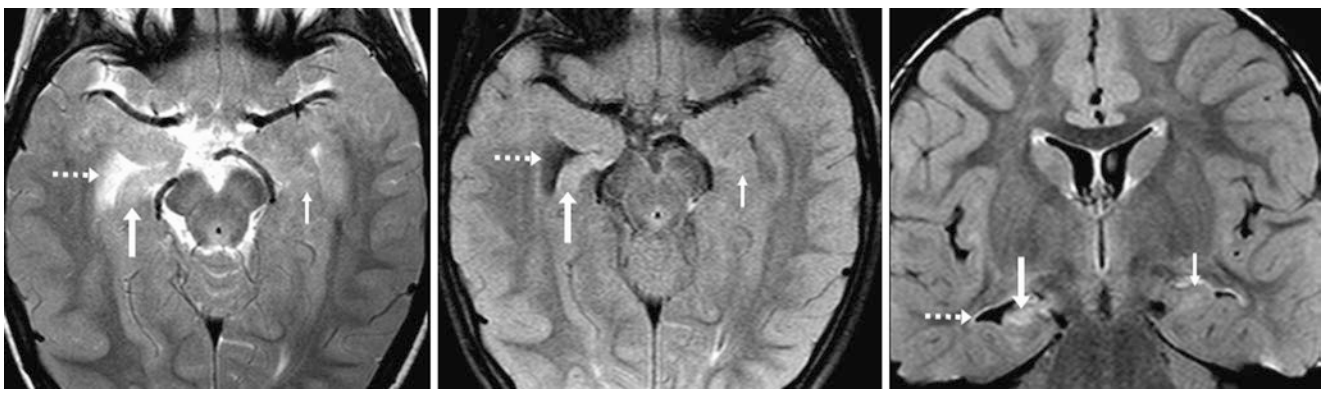

Fig. 11.79 Comparison case of mesial temporal sclerosis (MTS). In a 3-year-old patient with seizures, axial 3 T MRI T2WI (*left*), FLAIR (*middle*), and coronal FLAIR (*right*) images showed abnormal right hippocampal signal (*arrows*) as compared to the left (*tiny arrows*), with prominence of the right choroidal fissure and anterior temporal horn (*dashed arrows*). The asymmetric atrophy of the hippocampus and bright T2 signal confirmed MTS

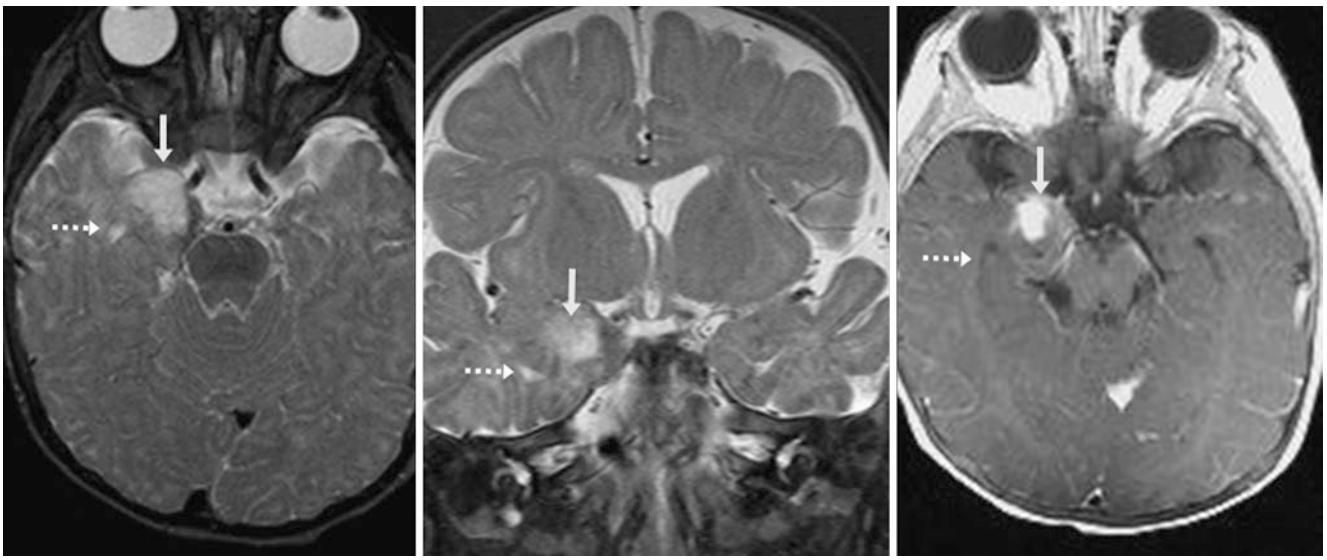

Fig. 11.80 Comparison case of ganglioglioma. In an 8 month old with seizures, a noncontrast 3 T MRI with axial (*left*) and coronal (*middle*) T2WIs depicted a potentially cystic lesion; the temporal horns (*dashed arrows*) were normal. However, the lesion's internal signal was less hyperintense than that of CSF. The patient returned for axial postcontrast T1WI (*right*), which confirmed a homogeneously enhancing mass rather than a simple CFC

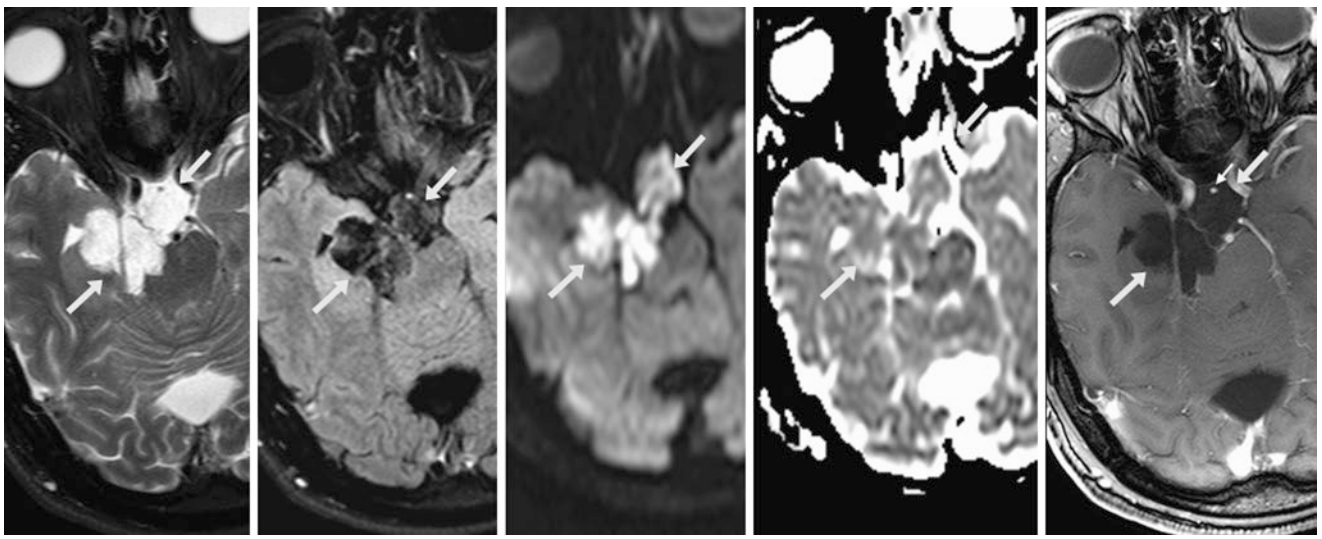

Fig. 11.81 Comparison case of epidermoid cyst. A 27 year old underwent a 1.5 T MRI, including axial T2WI (*left*), postcontrast FLAIR (*left middle*), DWI (*middle*), ADC map (*right middle*), and postcontrast T1WI (*right*), which showed a T2-bright cystic mass (*arrows*) within the right perimesencephalic cistern and the suprasellar cistern that causes a mass effect on the brainstem. Mild internal FLAIR signal is present, arguing against an NEC or arachnoid cyst. Note the bright signal on DWI, with ADC values lower than those of CSF on the ADC map as well as the lack of contrast enhancement

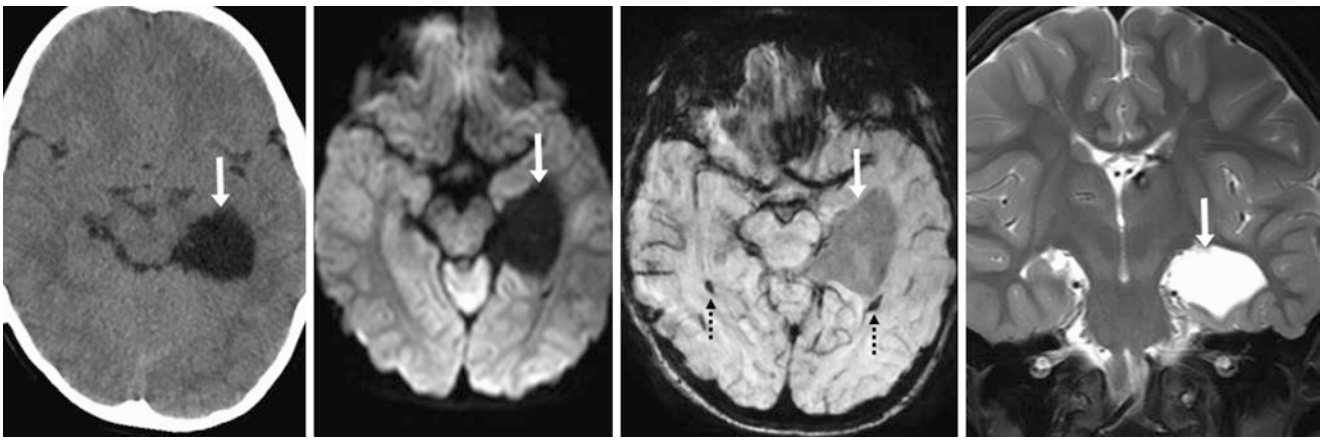

Fig. 11.82 Comparison case of a large choroid fissure cyst. A 7 year old with a remote perinatal insult had left choroidal fissure enlargement from a 3.5-cm cyst (*arrows*), without hydrocephalus, on NECT (*left*). The cyst had a CSF-like signal on DWI (*left middle*), FLAIR (*not shown*), SWI (*right middle*), and coronal T2WI (*right*). Note intraventricular hemosiderin on SWI from an old germinal matrix injury (*dotted arrows*), although the periventricular white matter was normal. It was thought to be a CFC, based on location, but was not followed because it was asymptomatic at that time

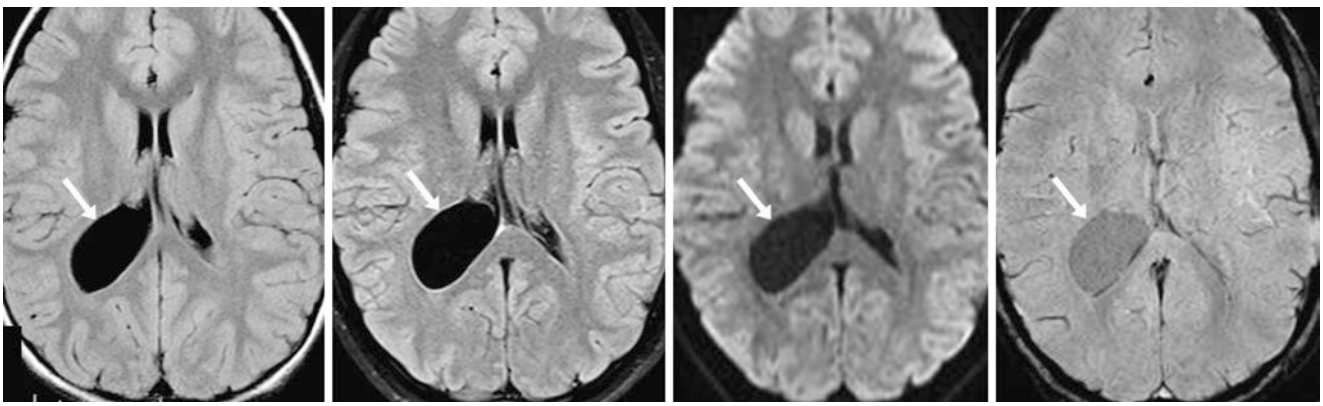

Fig. 11.83 Comparison case of a large intraventricular cyst. An 8 year old with headaches had an enlarged right lateral ventricle on FLAIR (*left*) caused by a 4.0-cm cyst (*arrows*); there was no hydrocephalus or parenchymal lesion. At 21 years of age (13 years later), with worsening headaches, FLAIR (*left middle*), DWI (*right middle*), and SWI (*right*) showed a CSF-like signal internally without hemorrhage; the cyst was minimally enlarged to 4.5 cm. It was indeterminate whether it was a NEC or an arachnoid cyst, and it was unsure (although unlikely) if the cyst was the cause of the symptoms

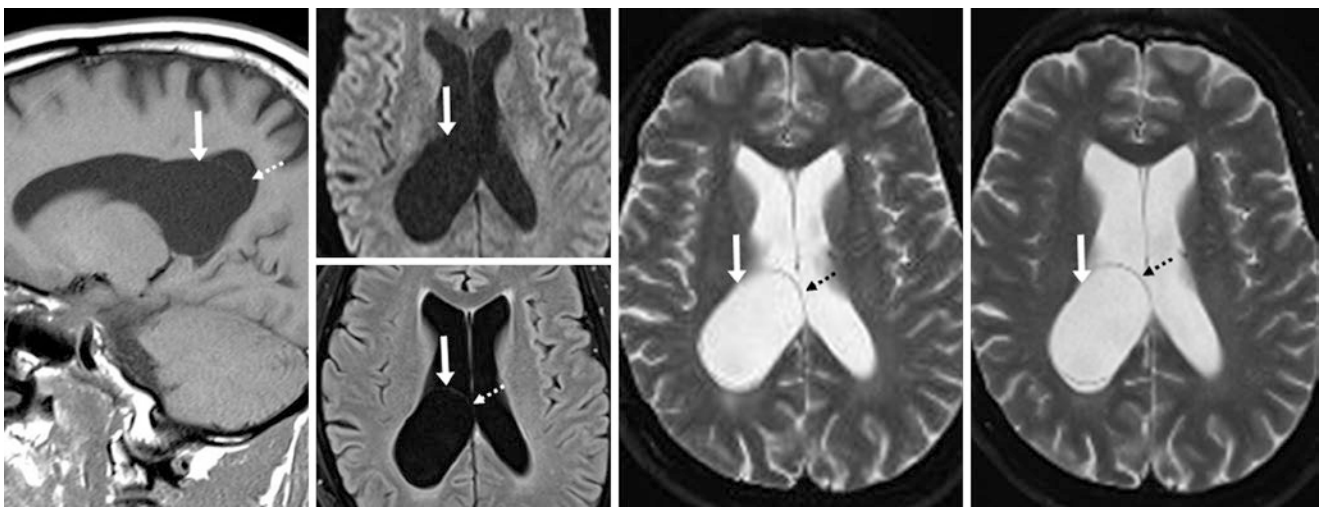

Fig. 11.84 Comparison case of a large intraventricular cyst. A 54-year-old patient with headaches had a 4.5-cm cyst (*arrows*) of the right lateral ventricle without hydrocephalus on sagittal T1WI MRI (*left*), with a CSF-like signal on DWI/FLAIR (*top and bottom*, *left middle*). T2WI (*right middle*) best delineated the walls of the cyst (*dotted arrows*), and 1 year later it was unchanged (*right*). This was considered indeterminate for an arachnoid cyst (favored) versus a CPC

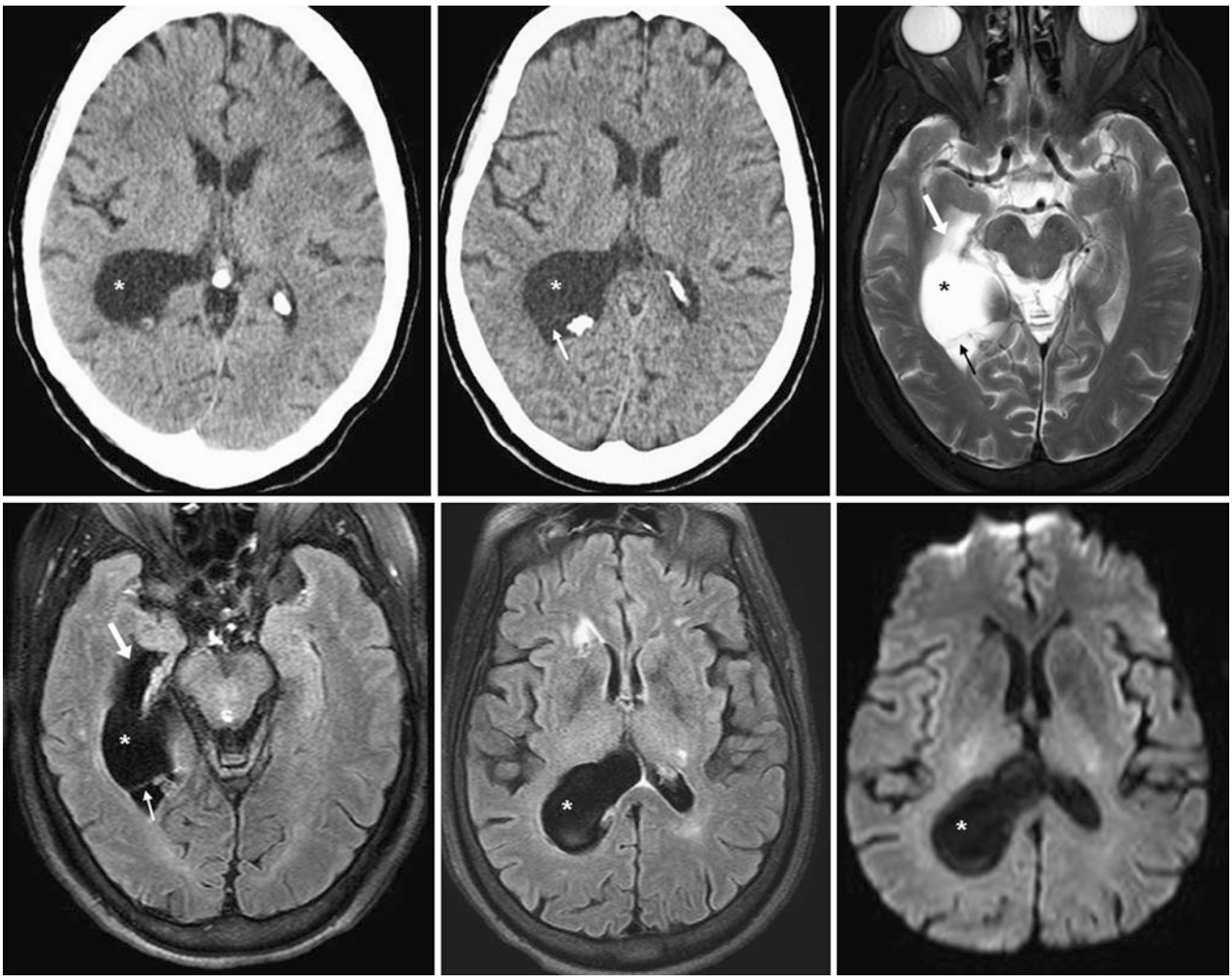

Fig. 11.85 Comparison case of an arachnoid cyst within a lateral ventricle. A 73-year-old patient with headaches had cyst-like enlargement (*) of the atrium of the right lateral ventricle on a NECT (*top left*) that was unchanged 2 years later (*top middle*). A 3 T MRI was performed at the time of the repeat NECT, which delineated the cyst (*) within the atrium of the right lateral ventricle on T2WI (*top right*); it had a signal intensity similar to that of CSF on FLAIR (*bottom left and middle*) and DWI (*bottom right*). The right temporal horn (*arrows*) was mildly dilated. A thin membrane (*thin arrows*) was noted on the second NECT and on some MR sequences, indicating that this was an arachnoid cyst

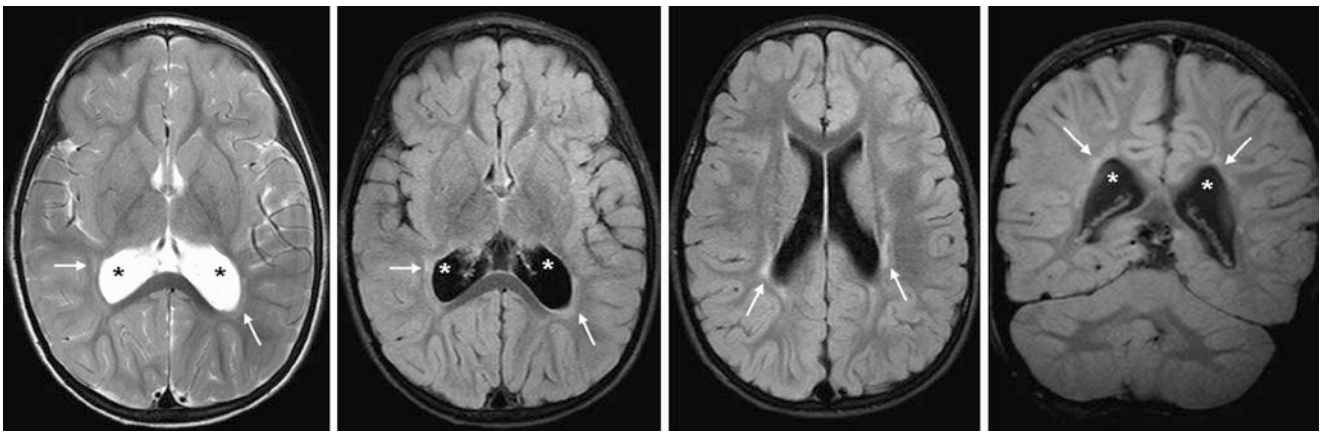

Fig. 11.86 Comparison case of periventricular leukomalacia (PVL)-related dilatation of the atria of the lateral ventricles. The patient was a 3 year old with developmental delay, abnormal gait, and spastic diplegia born premature at 29 weeks' gestational age. There is cyst-like enlargement (*) of the atria of the lateral ventricles on a 3 T MRI with axial T2WI (*left*), FLAIR (*left middle and right middle*), and coronal FLAIR (*right*) images. Findings that are indicative of PVL include T2 and FLAIR-bright signal in a periventricular distribution adjacent to focal areas of volume loss, where the cortices that overlie the parietal and occipital periventricular white matter come close to and nearly appose the ventricles (*thin arrows*)

11.3 Choroid Plexus Xanthogranulomas

Choroid plexus xanthogranulomas (CPXGs) are relatively common don't touch lesions occurring within the atria of the lateral ventricles. They are present in approximately 1.6–7.0 % of the population based on postmortem examinations. They are almost always incidental and asymptomatic, although in very rare instances they may spontaneously enlarge or hemorrhage; however, this has been described only anecdotally.

CPXGs are focal collections of a mixture of xanthomatous debris, macrophages or histiocytes, mixed lymphocytes, and occasionally hemosiderin. They range from a few millimeters in size to several centimeters. They can at times appear mass-like, although they usually only slightly expand the lateral ventricle (if at all) without causing hydrocephalus. Although there are a number of studies describing their appearance on histopathologic examination, there are only a few cases clearly documenting their appearance on MRI followed by histopathologic study and even less evidence using diffusion-weighted imaging (DWI) MRI. However, most evidence suggests that DWI-bright and T2-bright cyst-like lesions in the choroid plexus are CPXGs. Notably, they are variably bright on FLAIR and enhance only mildly or not at all; the variable slight enhancement may occur because the more normal choroid often enhances (lacks a blood–brain barrier) surrounding the cyst-like CPXG. Another important point is that although they are bright on DWI, being even brighter than gray or white matter, they do not truly have reduced diffusivity relative to the cerebral parenchyma and are isointense or even brighter than the parenchyma on ADC maps. This occurs because the DWI-bright signal intensity is a combination not only of reduced diffusivity but also of T2-brightness.

Since this author could not find a thorough article on the ADC values of suspected CPXGs, the values of the seven CPXGs shown in this chapter were obtained using ADC maps, from normal-appearing white matter (NAWM), and from CSF. Interestingly, the ADC values in CPXGs were an average of 192 % higher than the NAWM and were an average of 49 % less than that of the CSF. Thus, they must be have some component of reduced diffusion, combined with a bright T2 signal akin to that of CSF, which together causes their bright (light bulb) appearance on DWI. Another method to assess this characteristic visually is to utilize exponential DWI, which removes the T2 component from the DWI. Thus, a CPXG that is bright on the standard trace DWI will often become isointense or dark on exponential DWI.

Pathologic lesions in the differential diagnosis of CPXGs within the atria of the lateral ventricles include tumors that enhance avidly and expand the lateral ventricle, such as *choroid plexus papilloma/carcinoma* or *metastasis*; also, an *abscess* of the choroid plexus is a consideration (bright on DWI but avidly enhanced, with findings of meningitis or ventriculitis elsewhere). Tumors adjacent to the atria may also appear to be in the choroid plexus if they cause significant compression and/or displacement of the lateral ventricle (Figs. 11.87, 11.88, 11.89, 11.90, 11.91, 11.92, 11.93, 11.94, 11.95, and 11.96).

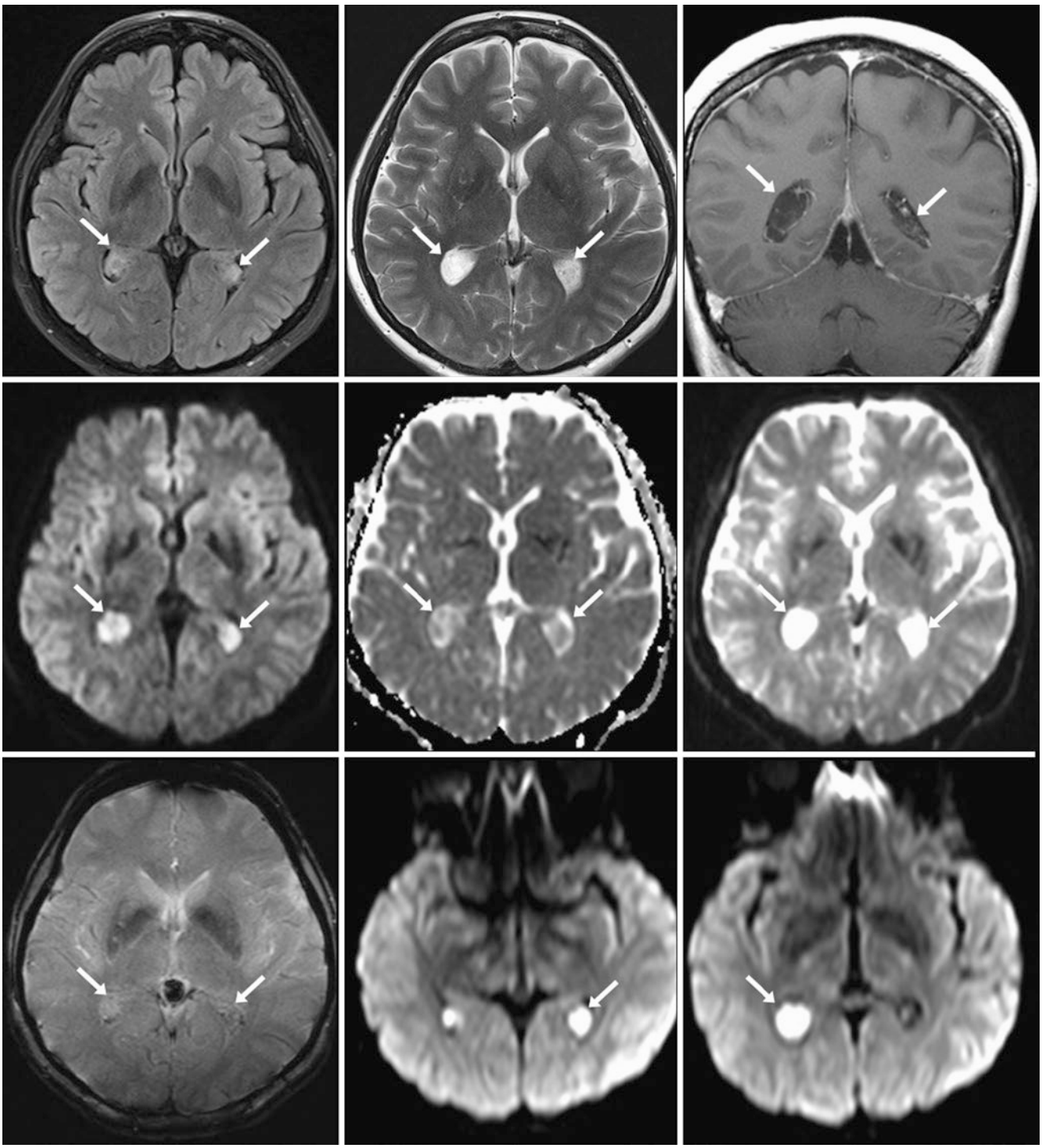

Fig. 11.87 Choroid plexus xanthogranuloma (CPXG). A 48 year old underwent a 3 T MRI to rule out stroke (negative examination). *Top row*: there are bilateral CPXGs (*arrows*) within the atria of the lateral ventricles on FLAIR (*left*), T2WI (*middle*), and coronal postcontrast T1WI (*right*). *Middle row*: axial DWI with corresponding ADC maps (*left and middle images*) demonstrate bright and mildly dark signal, respectively. But why are the CPXGs brighter than the periventricular white matter on DWI if they are not darker than the white matter on the ADC maps? *Middle row*: The answer lies in evaluation of the "b = 0" DWI (where the gradient strengths are set to the b-value of zero; a normal DWI typically uses b = 1000). On the "b = 0" image (*middle row*, *right*) the CPXGs are very bright, indicating that they have very high T2 signal; thus the combination of the mildly low ADC value and the extremely high T2 values cause quite bright signal on standard DWI. *Bottom row*: GE T2*WI (*left*) depicts only minimal calcification within the CPXGs. DWIs from 1 year earlier with the patient's head slightly tilted within the scanner (*middle and right images*) appeared quite similar and showed that these CPXGs are unchanged

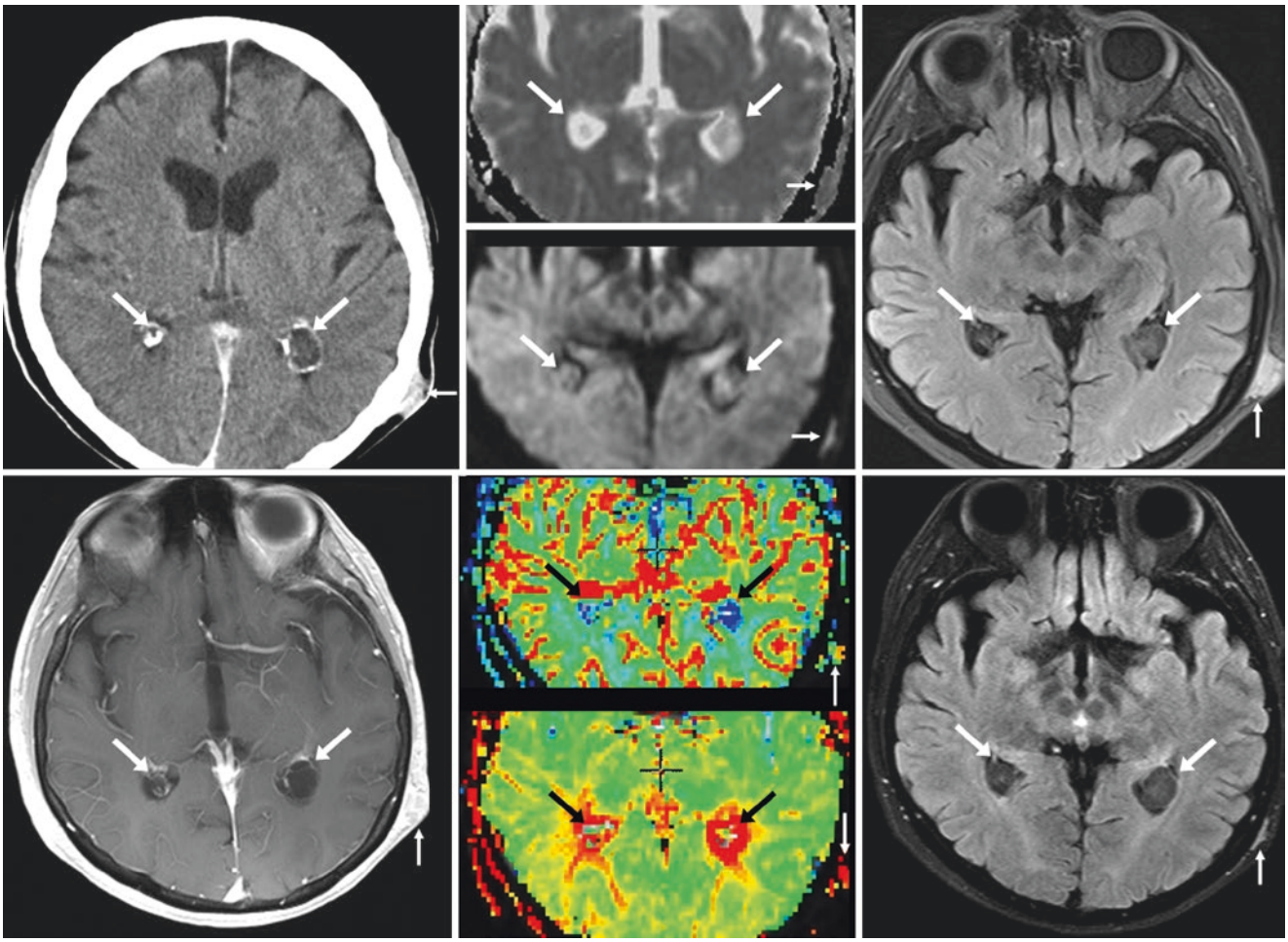

Fig. 11.88 A 70 year old had a NECT (*top left*) that showed bilateral CPXGs (*arrows*). A 3 T MRI performed to evaluate a left scalp malignancy (*thin arrows*) depicted the CPXGs within the atria of the lateral ventricles on axial DWI and their ADC maps (*top*, *middle images*), with intermediate signal on FLAIR (*top right*) and peripheral enhancement on T1WI postcontrast (*bottom left*). MR perfusion images depict that the CPXGs have a low CBV and elevated MTT (*bottom*, *middle images*, *respectively*) with a low CBF (*not shown*); the scalp lesion had elevations of both values. A 3 T MRI was found from 2 years prior that confirmed that the CPXGs did not change on FLAIR (*bottom right*)

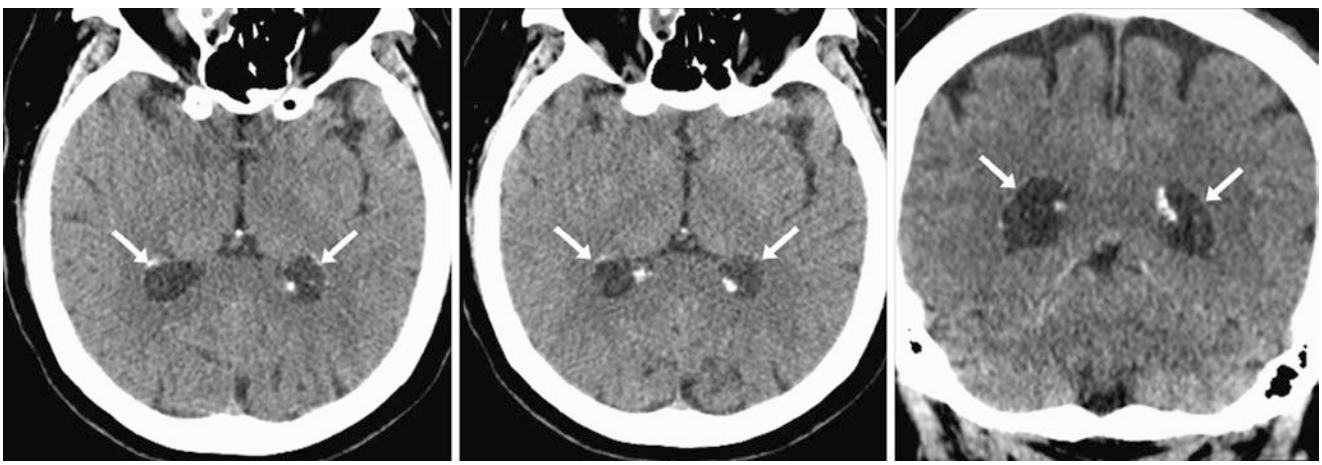

Fig. 11.89 A 65 year old had NECT axial (*left two images*) and coronal (*right*) images of bilateral CPXGs (*arrows*). Note that the cysts are similar to CSF density, while the calcifications of the choroid plexus are mostly peripheral within the cysts

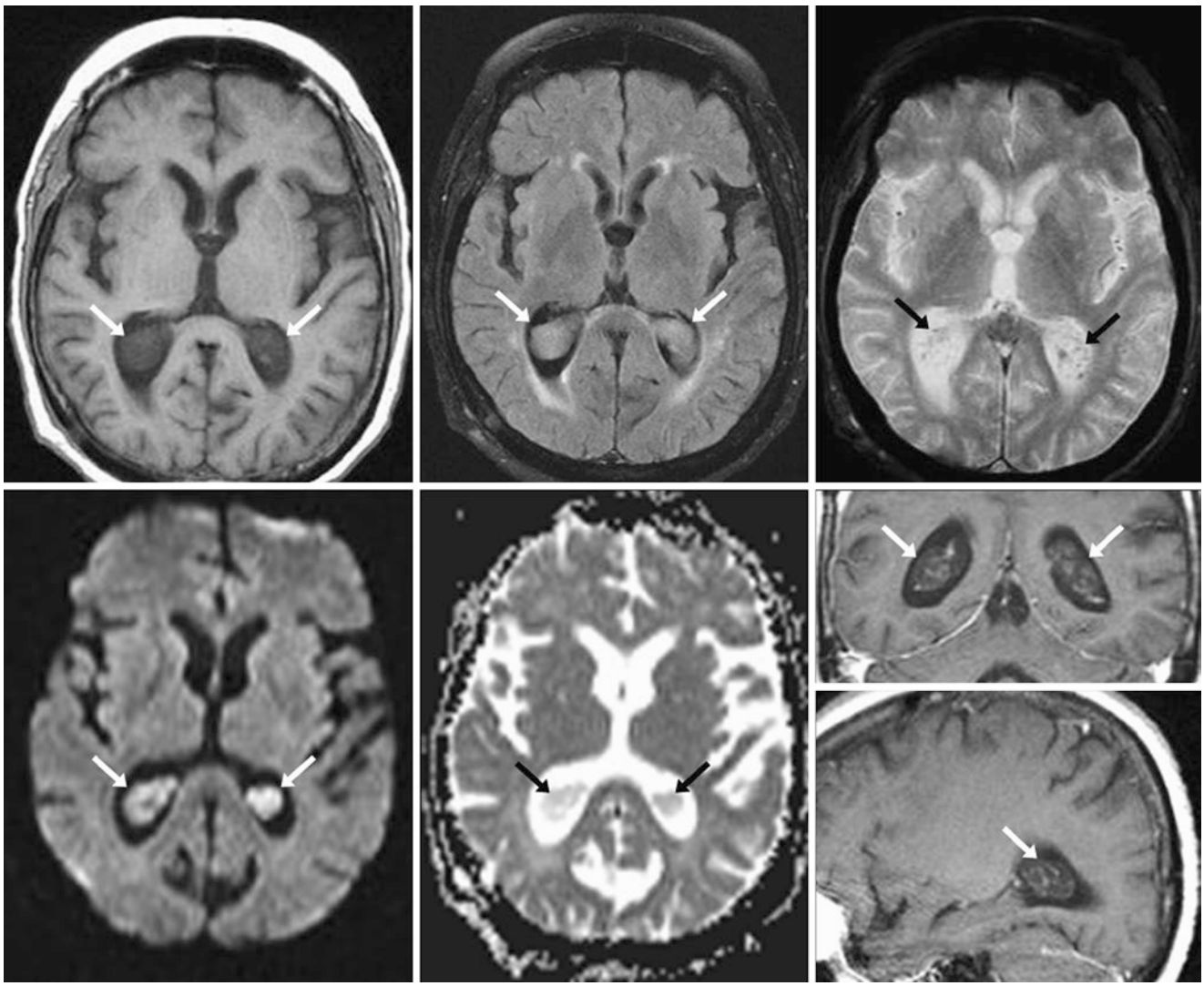

Fig. 11.90 A 68 year old with bilateral CPXGs (*arrows*) on a 1.5 T MRI with noncontrast axial T1WI (*top left*), FLAIR (*top middle*), GE T2*WI (*top right*), and DWI (*bottom left*) with associated ADC maps (*bottom middle*). Postcontrast coronal and sagittal T1WIs (*bottom right*, *top and bottom*, *respectively*) are also provided. Again, there is reduced diffusivity relative to CSF as the CPXGs are brighter than CSF on DWI, but they have greater diffusivity than deep white matter since they are not as dark as the periventricular white matter on ADC maps (*bottom right*)

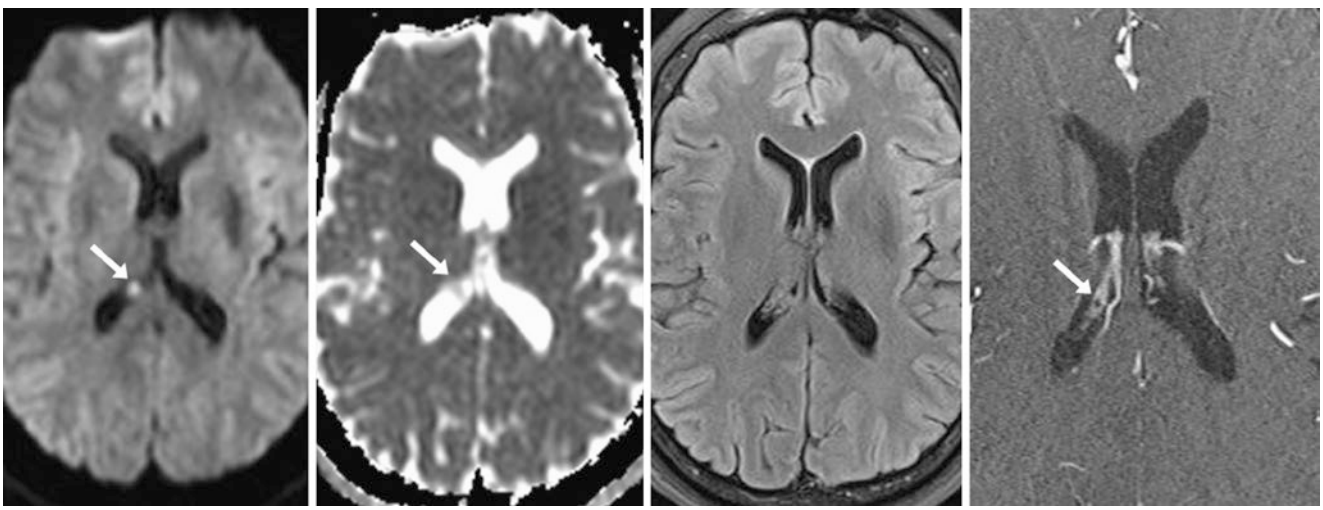

Fig. 11.91 A 50 year old with a tiny, unilateral right CPXG (*arrows*) on a 3 T MRI, measuring 2 mm as noted on axial DWI (*left*) and the corresponding ADC map (*left middle*). This focus was not seen on FLAIR (*right middle*). A three-dimensional TOF MRA (0.8-mm thickness) with magnified postcontrast axial images (*right*) happened to delineate this tiny CPXG

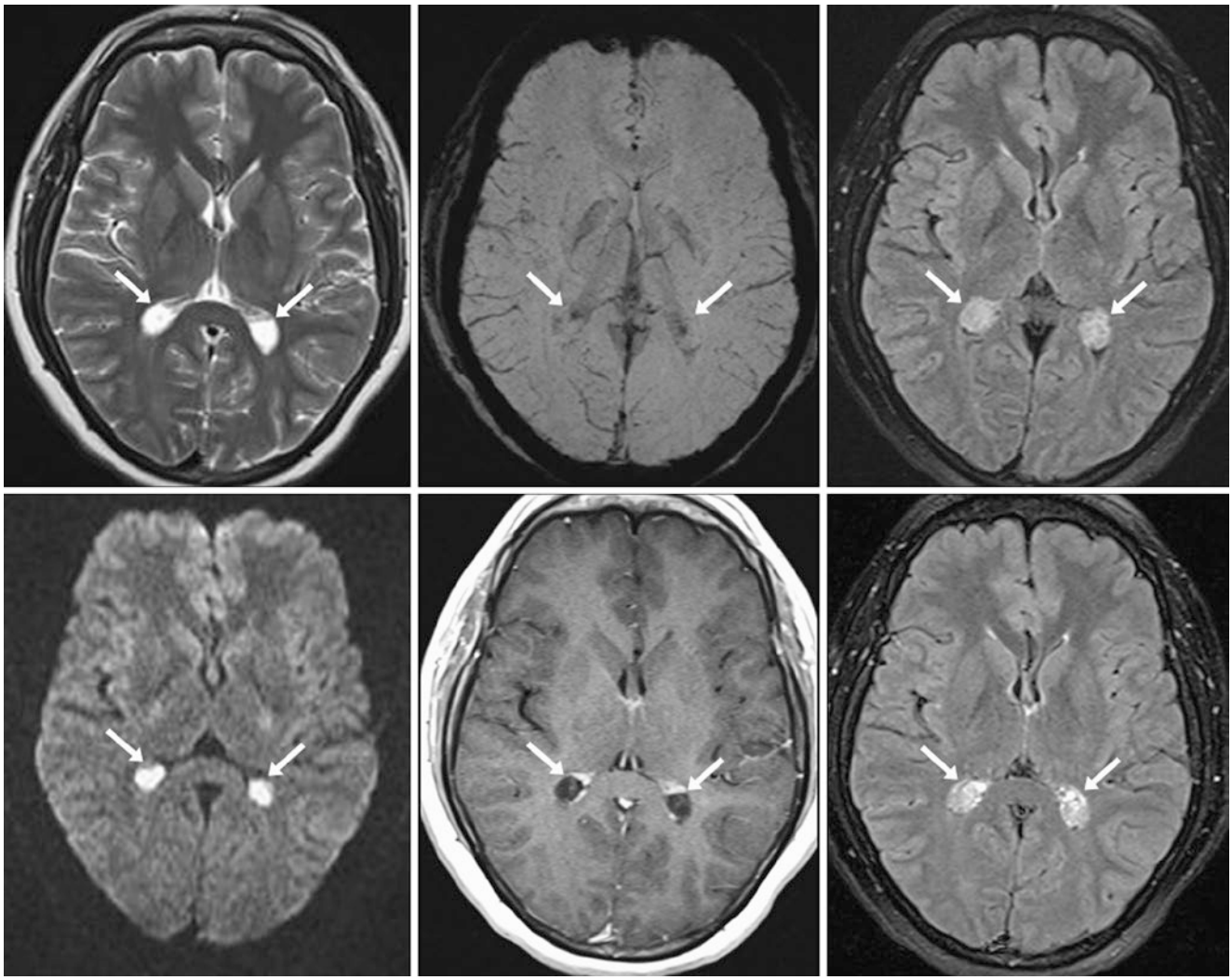

Fig. 11.92 A 38 year old with bilateral CPXGs (*arrows*) on a 1.5 T MRI with axial T2WI (*top left*), SWI (*top middle*), FLAIR (*top right*), and DWI (*bottom left*). Postcontrast axial T1WI (*bottom middle*) and FLAIR (*bottom right*) images depict slight internal enhancement and avid peripheral enhancement owing to the choroid plexus' lack of a blood–brain barrier

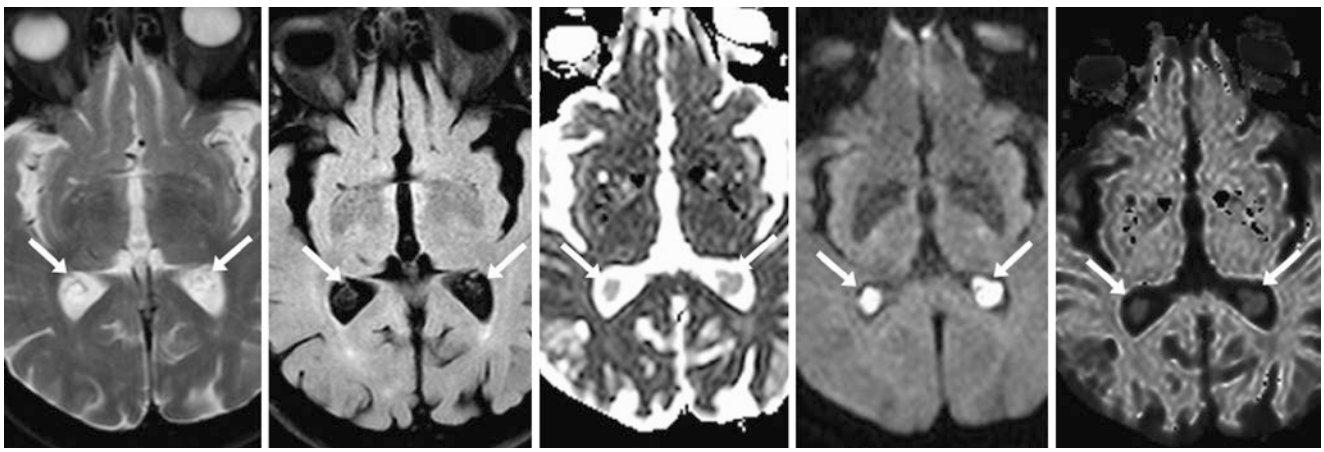

Fig. 11.93 A 79 year old with bilateral CPXGs (*arrows*). A 1.5 T MRI, axial T2WI (*left*), FLAIR (*left middle*), ADC (*middle*), DWI (*right of middle*), and "exponential" DWI (*right*, removes the T2 contribution from the DWI) show that the CPXGs suppress on FLAIR but have a darker signal on the ADC map relative to CSF while darkening on the exponential DWI. Thus most of the bright signal is related to the T2 contribution rather than to reduced diffusivity

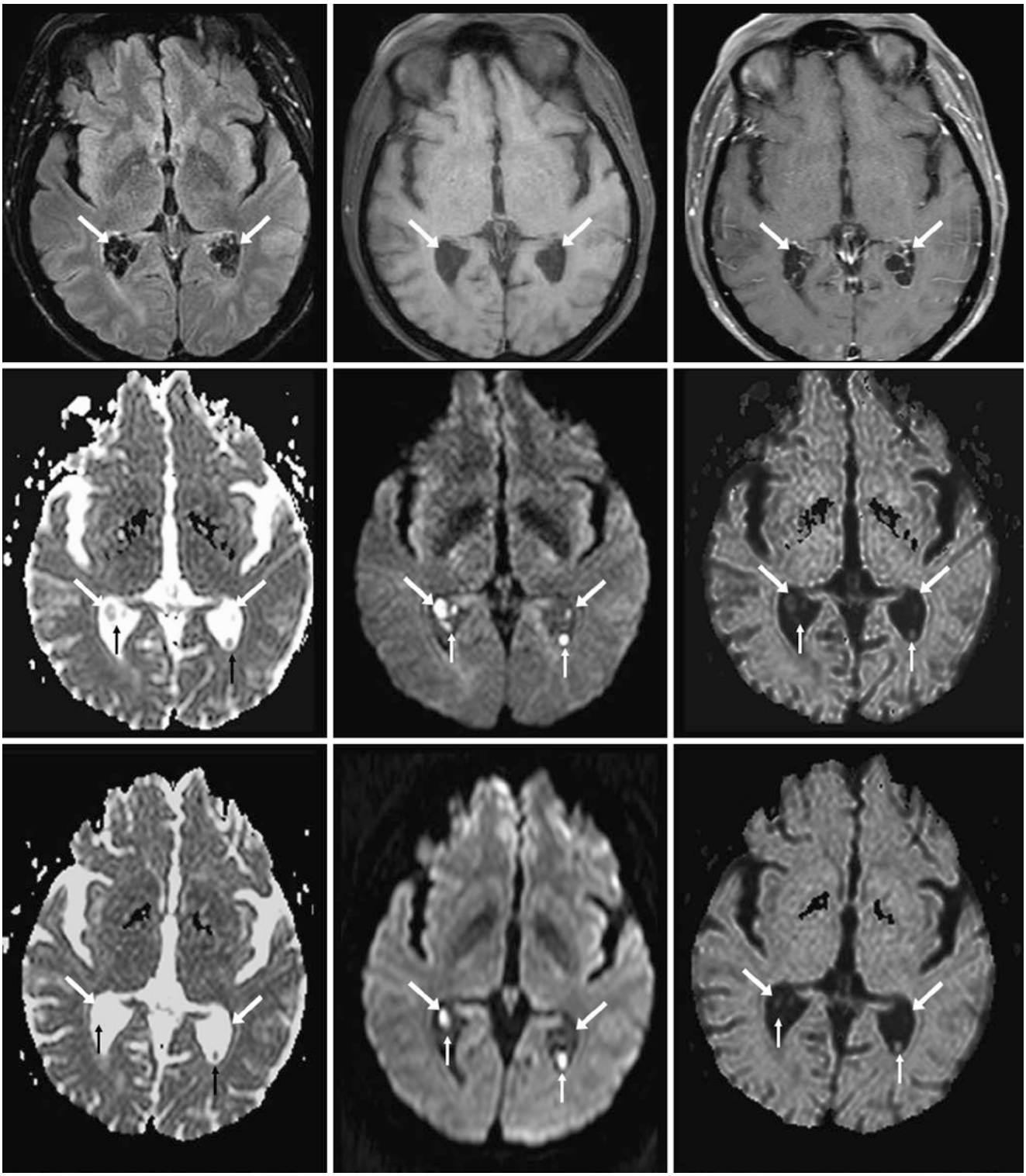

Fig. 11.94 Choroid plexus xanthogranuloma (CPXG). A 74 year old underwent a 1.5 T MRI to evaluate for infarct (negative examination). *Top row*: there were bilateral CPXGs (*arrows*) noted on axial postcontrast FLAIR (*left*; *note the enhancing septae of the CPXG*), noncontrast T1WI (*middle*), and postcontrast T1WI (*right*). *Middle row*: The reduced diffusivity is inhomogeneous on the ADC map (*left*) and DWI (*middle*) and appears spotty. An exponential DWI (*right*) shows several punctate foci (*tiny arrows*) within the CPXGs that were bright on DWI but not on exponential DWI, confirming that much of their DWI-brightness was from T2 contribution. *Bottom row*: 18 months later, the ADC map (*left*), DWI (*middle*), and exponential DWI (*right*) are unchanged

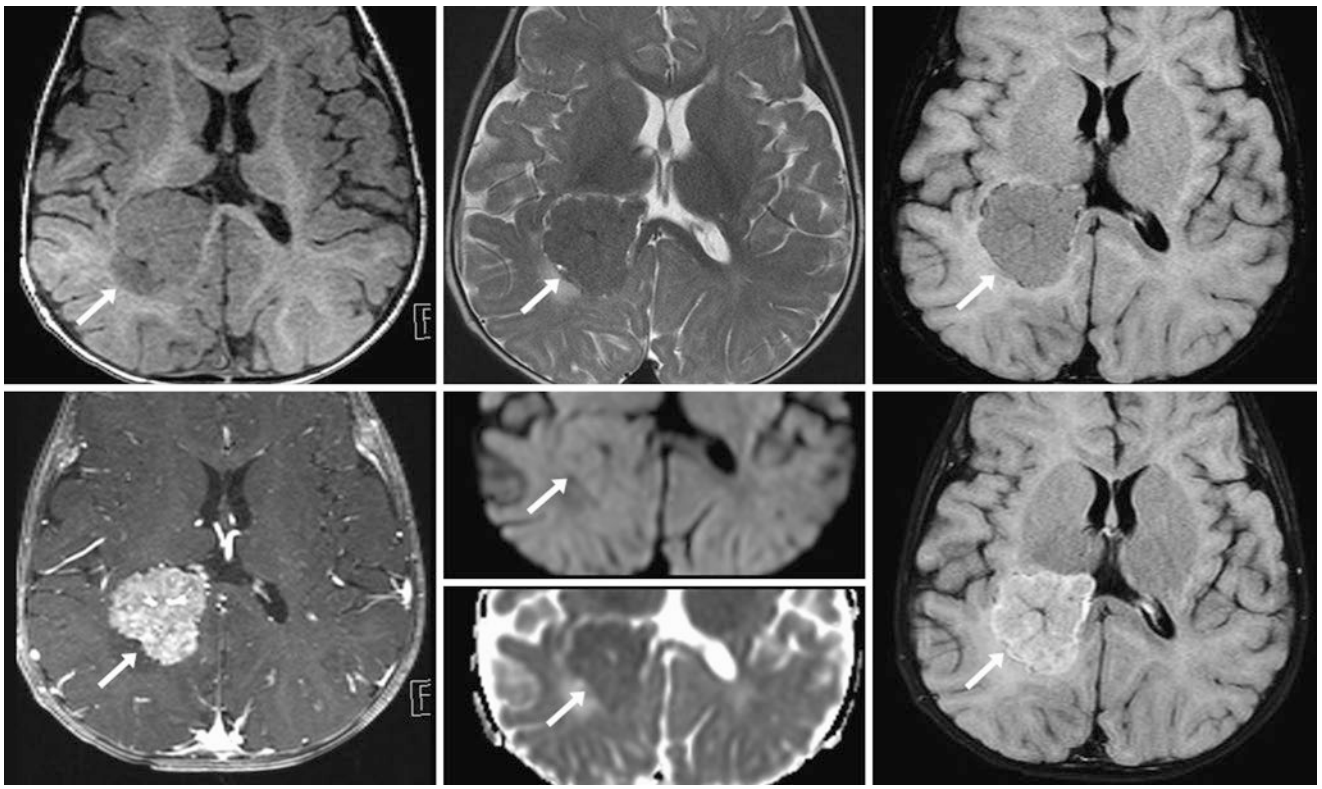

Fig. 11.95 Comparison case of choroid plexus papilloma. A 7 month old with a mass (*arrows*) within the atrium of the right lateral ventricle on MRI T1WI (*top left*), T2WI (*top middle*), and FLAIR (*top right*). It avidly enhances on postcontrast T1WI (*bottom left*) and FLAIR (*bottom right*). DWI and ADC map (*bottom middle*) are also shown

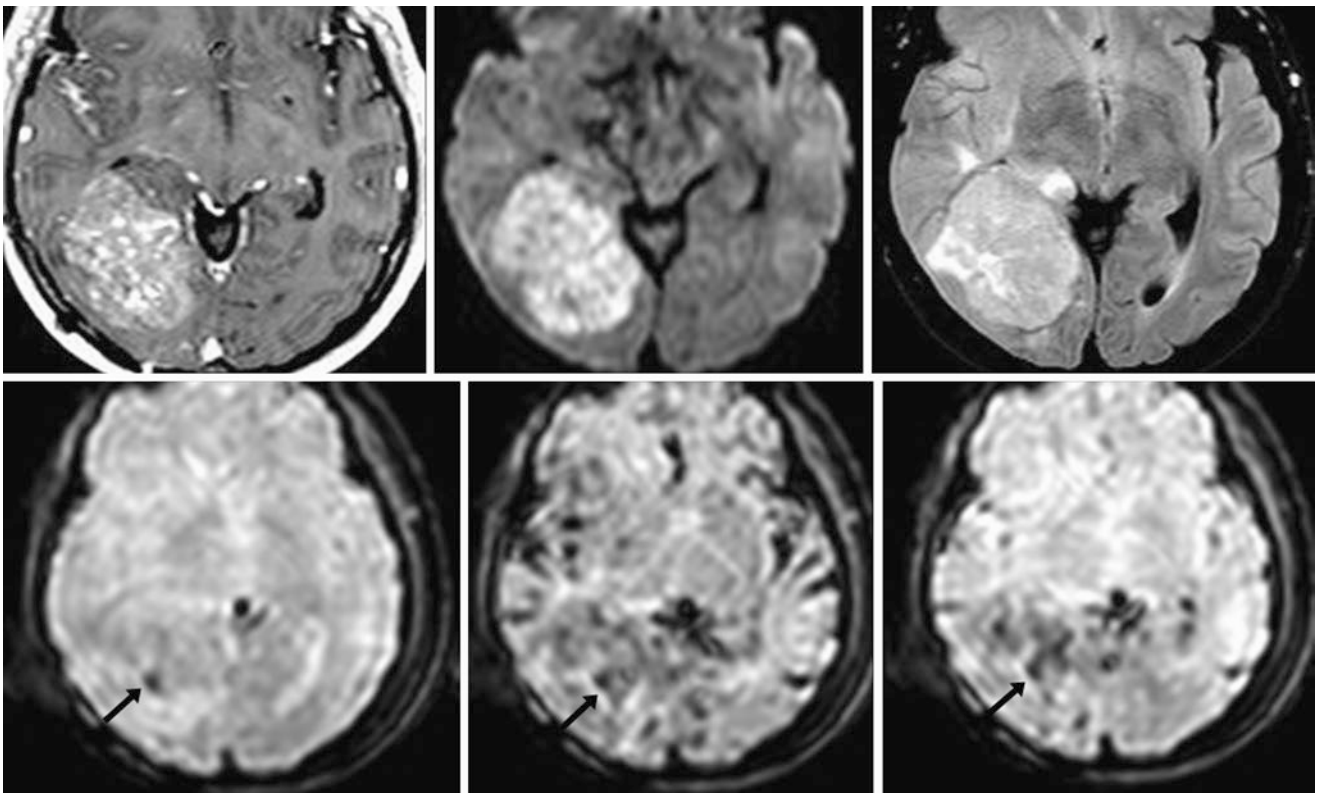

Fig. 11.96 Comparison case of anaplastic oligastrocytoma. A 39 year old with a mass adjacent to and compressing the atrium of the right lateral ventricle on MRI postcontrast T1WI (*top left*), DWI (*top middle*, the reduced diffusivity is suggestive of malignancy), and noncontrast FLAIR (*top right*). The *bottom row* images are dynamic MR perfusion images in the early, middle, and late phases, respectively. A small focus of susceptibility-dark hemorrhage is present (*arrows*), with increasingly susceptibility-dark contrast that persists into the late phase. This indicates a high-grade tumor, also confirmed by an elevated CBV two to three times greater than the unaffected deep white matter

11.4 Choroid Plexus and Pericallosal Lipomas

Choroid plexus lipomas (CPLs) are quite rare and are not considered a normal variant, since they are usually associated to some degree with callosal lipomas (termed *pericallosal lipomas*, or *interhemispheric lipomas* if the corpus callosum is not involved); callosal lipomas occur in less than 0.5% of the population and may be associated with *callosal dysgenesis*. However, CPLs are usually asymptomatic if they occur by themselves and are considered a don't touch lesion (Figs. 11.97 and 11.98).

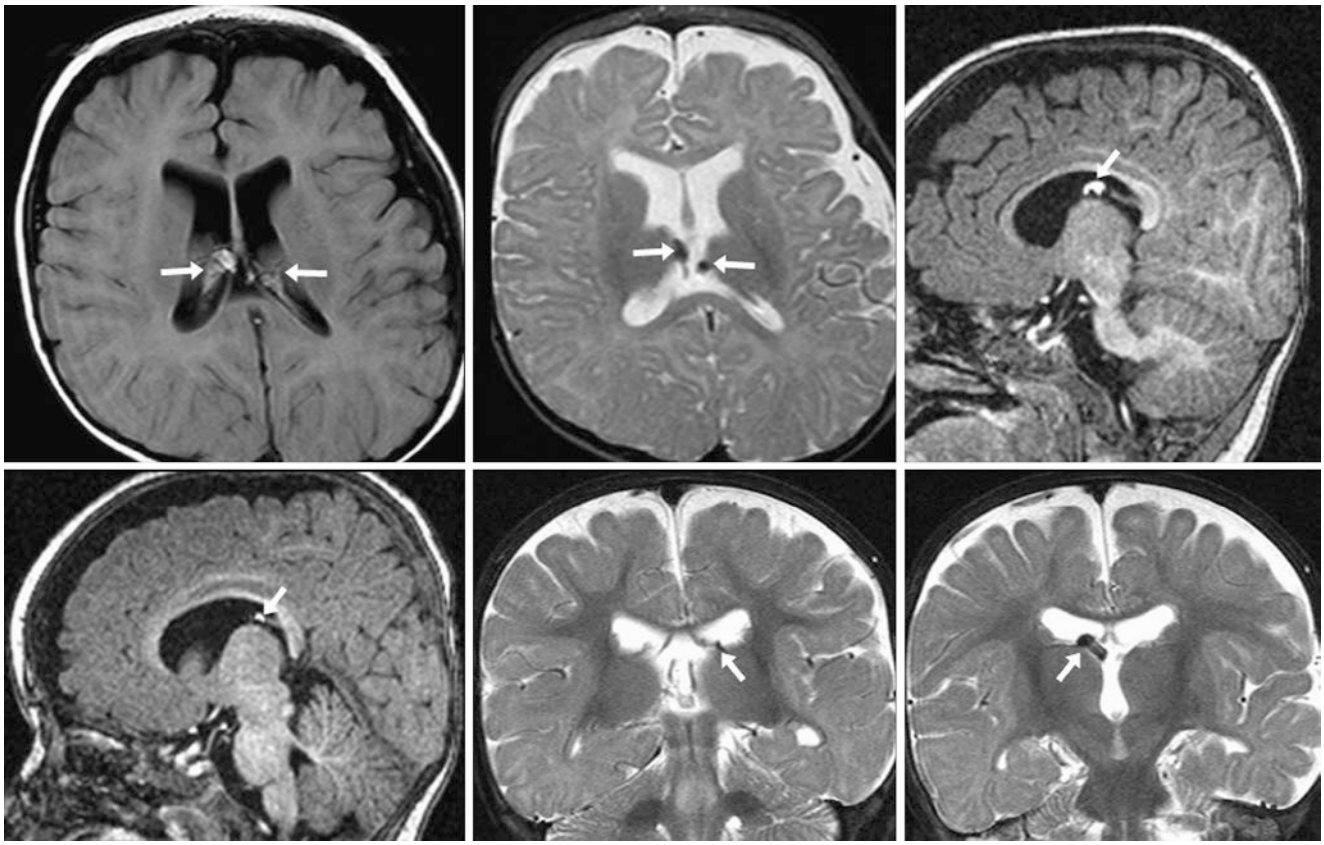

Fig. 11.97 A 5 month old had an MRI demonstrating a lipoma within the choroid plexus (*arrows*) on axial FLAIR (*top left*), axial T2WI (*top middle*), sagittal T1WI (*top right and bottom left*), and coronal T2WI (*bottom middle and right*). These are usually associated with and can be considered part of callosal/pericallosal lipomas, which may have a degree of callosal agenesis or dysgenesis (not present here). These should be distinguished from CPXGs, which are usually T1-isointense, T2-bright, and have some degree of bright signal on DWI

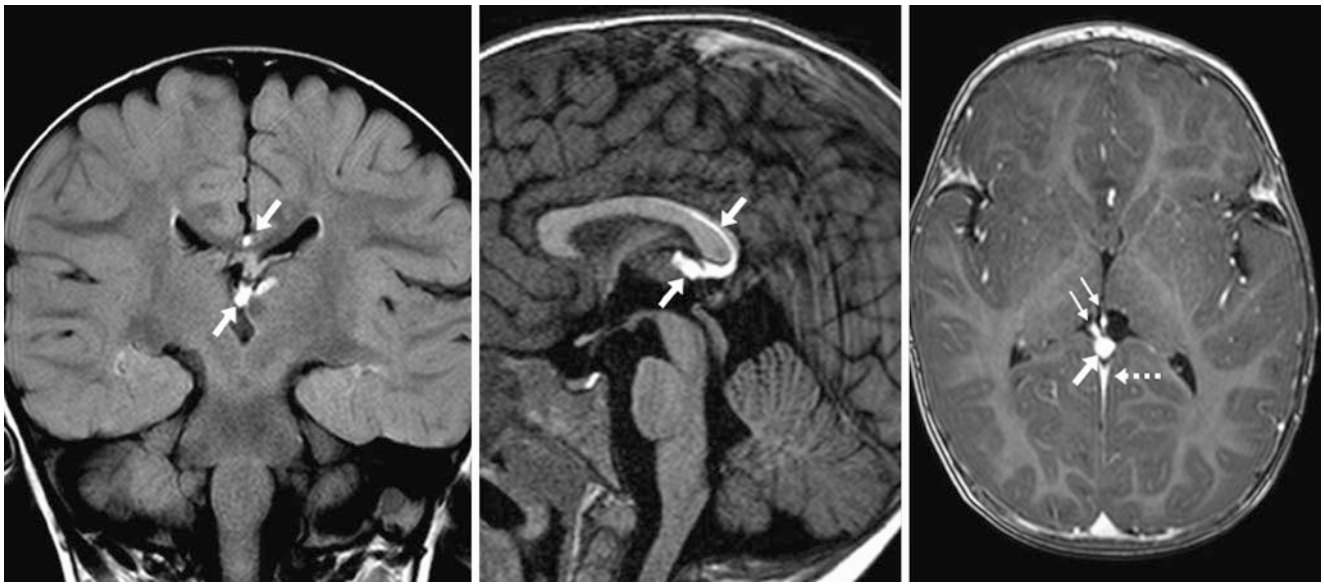

Fig. 11.98 A 17 month old had an MRI demonstrating a pericallosal lipoma (*arrows*) without callosal dysgenesis on coronal FLAIR (*left*), sagittal T1WI (*middle*), and postcontrast axial T1WI (*right*). On the postcontrast T1WI, the lipoma can be seen between the internal cerebral veins (*thin arrows*) and the great vein of Galen (*dashed arrow*)

11.5 Choroidal Fissure Asymmetry

The choroidal fissure is not uncommonly asymmetric, as can occur with normal variation lateral ventricular asymmetry. This is normal as long as there are no other findings of focal atrophy around the ventricles (such as from periventricular leukomalacia) or within the anterior temporal lobes (such as from prior traumatic brain injury), or evidence of mass obstructing the ventricles. Also, this is normal variant is distinct from the choroidal fissure cyst variant (Figs. 11.99, 11.100, 11.101, 11.102, and 11.103).

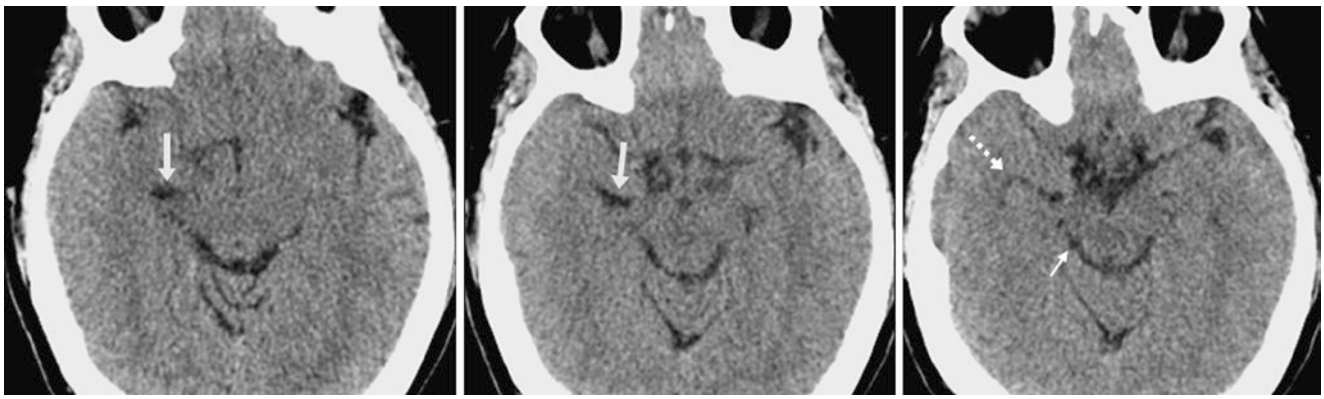

Fig. 11.99 A 48 year old who had multiple images from a routine head CT (which was negative) after a fall. There is asymmetric prominence of the right choroidal fissure (*arrow*). Note the location of the ambient cistern medially (*tiny arrow*, *right*) and the normal sized temporal horn of the right lateral ventricle laterally (*dashed arrow*, *right*)

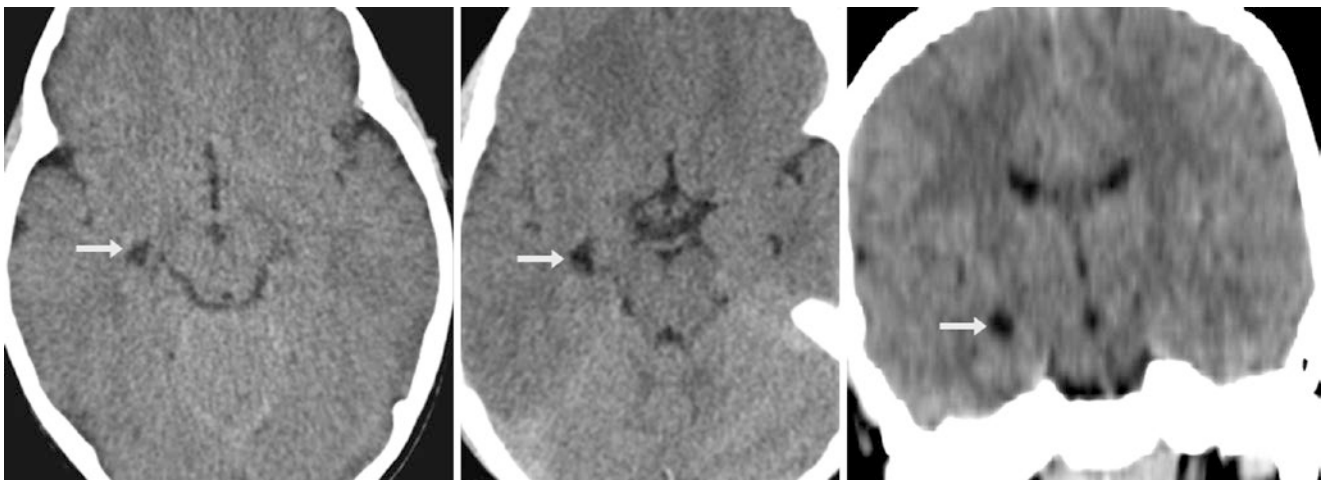

Fig. 11.100 A 2 year old had a negative NECT (*left images*) after a fall. Asymmetric prominence of the right choroidal fissure was noted (*arrows*) and was considered a normal variation. Seven years later, another CT was performed (*middle*), which was unchanged. A coronal reformat confirmed that this is normal asymmetry; a CFC/NEC is also a possibility

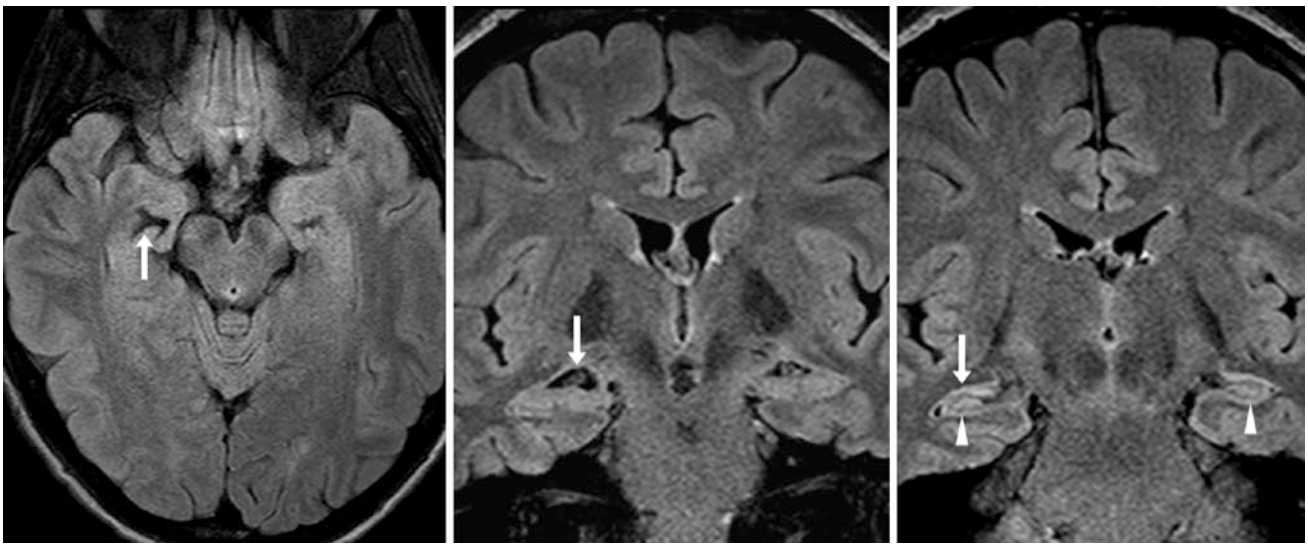

Fig. 11.101 A 22 year old had a 3 T MRI performed for seizures, which showed prominence of the right choroidal fissure near the tip of the temporal horn (*arrows*) on axial (*left*) and coronal (*middle and right*) FLAIR images. This mimics mesial temporal sclerosis, but the hippocampus is not atrophied; also, the choroidal fissure is normal in size posteriorly (*right*). Note bilateral mildly bright hippocampal signal on FLAIR (*arrowheads*), which is a normal variant at 3 T

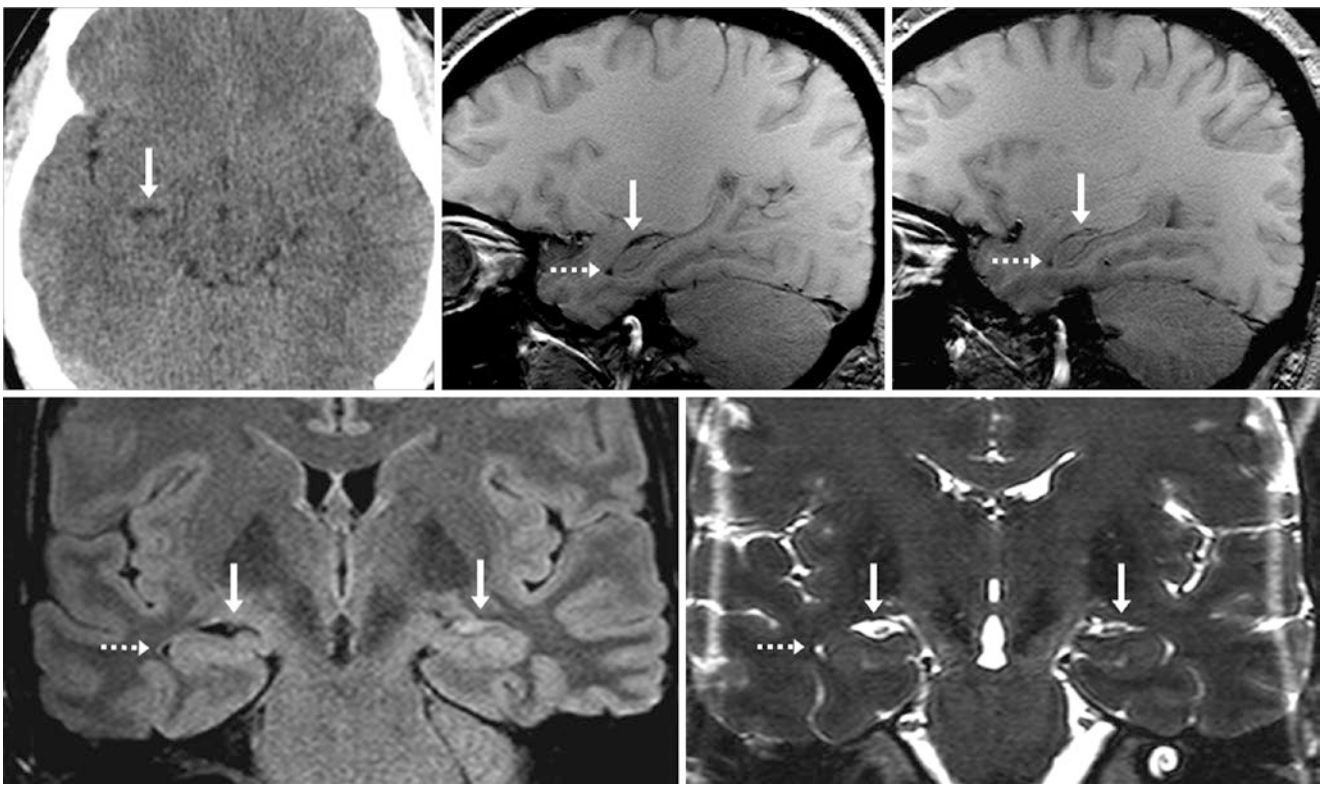

Fig. 11.102 A 31 year old had an axial NECT (*top left*) depicting prominence of the right choroidal fissure (*arrows*) near the temporal horn's anterior tip (*dashed arrows*), better seen on a 3 T MRI with sagittal T1WI of the right (*top middle*), as compared to the left side (*top right*). Coronal FLAIR (*bottom left*) and thin 3D T2WI (*bottom right*) depict this normal finding, simulating mesial temporal sclerosis; however, note a lack of hippocampal edema or atrophy

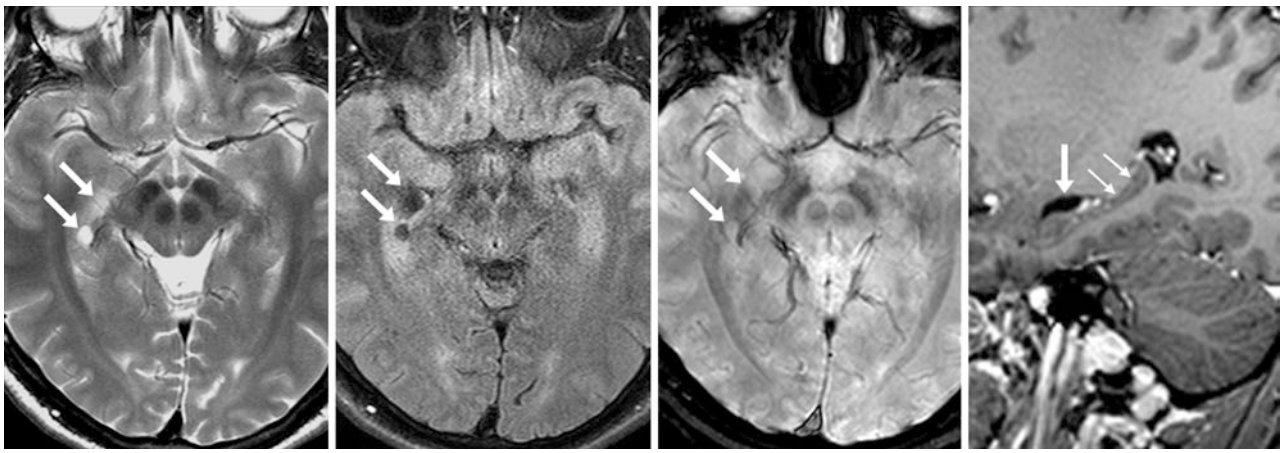

Fig. 11.103 A 36 year old was given a 3 T MRI, including axial T2WI (*left*), FLAIR (*left middle*), SWI (*right middle*), and postcontrast sagittal T1WI (*right*). The images showed asymmetry of the right choroidal fissure, probably from two cystic foci (*arrows*) without mass effect or internally bright FLAIR signal. Thus the location is suggestive of two CFCs/NECs. A more normal appearance of the choroidal fissure (*thin arrows*) is seen posteriorly on the sagittal T1WIs

Suggested Reading

Andrews BT, Halks-Miller M, Berger MS, Rosenblum ML, Wilson CB. Neuroepithelial cysts of the posterior fossa: pathogenesis and report of two cases. Neurosurgery. 1984;15:91–5.

Ayres WW, Haymaker W. Xanthoma and cholesterol granuloma of the choroid plexus. J Neuropathol Exp Neurol. 1960;9:280–95.

Czervionke LF, Daniels DL, Meyer GA, Pojunas KW, Williams AL, Haughton VM. Neuroepithelial cysts of the lateral ventricles: MR appearance. Am J Neuroradiol. 1987;8:609–13.

Chinn DH, Miller EI, Workty LM, Towers CV. Sonographically detected choroid plexus cysts: frequency and association with aneupolidy. J Ultrasound Med. 1991;10:255–8.

Clark SL, DeVore GR, Sabey PL. Prenatal diagnosis of cysts of the fetal choroid plexus. Obstet Gynecol. 1988;72:585–6.

Deepak S, Jayakumar B. Intracranial calcifications. J Assoc Physicians India. 2005;53:948.

Demasio K, Canterino J, Ananth C, Fernandez C, Smulian J, Vintzileos A. Isolated choroid plexus cyst in low-risk women less than 35 years old. Am J Obstet Gynecol. 2002;187:1246–9.

Donelan KJ, Randall BB, Newby PE. A 51-year-old man with sudden unexpected death. Brain Pathol. 2009;19:151–2.

Hinshaw Jr DB, Fahmy JL, Peckham N, Thompson JR, Hasso AN, Holshouser B, et al. The bright choroid plexus on MR: CT and pathologic correlation. Am J Neuroradiol. 1988;9:483–6.

Kieffer SA, Gold LH. Intracranial physiologic calcifications. Semin Roentgenol. 1974;2:151–62.

Kinoshita T, Moritani T, Hiwatashi A, Numaguchi Y, Wang HZ, Westesson PL, et al. Clinically silent choroid plexus cyst: evaluation by diffusion-weighted MRI. Neuroradiol. 2005;47:251–5.

Kıroğlu Y, Çalli C, Karabulut N, Oncel C. Intracranial calcifications on CT. Diagn Interv Radiol. 2010;16:263–9.

Kondziolka D, Bilbao JM. An immunohistochemical study of neuroepithelial (colloid) cysts. J Neurosurg. 1989;71:91–7.

Lopez JA, Reich D. Choroid plexus cysts. J Am Board Fam Med. 2006;19:422–5.

Modic MT, Weinstein MA, Rothner AD, Erenberg G, Duchesneau PM, Kaufman B. Calcification of the choroid plexus visualized by computed tomography. Radiology. 1980;135:369–72.

Nagata S, Rhoton Jr AL, Barry M. Microsurgical anatomy of the choroidal fissure. Surg Neurol. 1988;30:3–59.

Nakase H, Ishida Y, Tada T, Sakaki T, Goda K, Tunoda S, et al. Neuroepithelial cyst of the lateral ventricle. Clinical features and treatment. Surg Neurol. 1992;37:94–100.

New PF, Davis KR. Intraventricular noncolloid neuroepithelial cysts. Am J Neuroradiol. 1981;2:569–76.

Numaguchi Y, Foster RW, Gum GK. Large asymptomatic noncolloid neuroepithelial cysts in the lateral ventricle: CT and MR features. Neuroradiol. 1989;31:98–101.

Numaguchi Y, Kumra A, Schmidt RD, Martino C. Noncolloid neuroepithelial cysts in the lateral ventricle: magnetic resonance features. J Comput Tomogr. 1988;12:174–81.

Norton KI, Rai B, Desai H, Brown D, Cohen M. Prevalence of choroid plexus cysts in term and near-term infants with congenital heart disease. Am J Roentgenol. 2011;196:W326–9.

Osborn AG, Preece MT. Intracranial cysts: radiologic-pathologic correlation and imaging approach. Radiology. 2006;239:650–64.

Pear BL. Xanthogranuloma of the choroid plexus. Am J Roentgenol. 1984;143:401–2.

Radaideh MM, Leeds NE, Kumar AJ, Bruner JM, Sawaya R. Unusual small choroid plexus cyst obstructing the foramen of Monroe: case report. Am J Roentgenol. 2002;23:841–3.

Sherman JL, Camponovo E, Citrin CM. MR imaging of CSF-like choroidal fissure and parenchymal cysts of the brain. Am J Roentgenol. 1990;11:939–45.

Sener RN, Magalhães AC. Nonneoplastic, noninflammatory, cerebral intraventricular cysts. Rev Hosp Clin Fac Med Sao Paulo. 1995;50:195–9.

Tillich M, Ranner G, Trummer M, Kleinert R. Symptomatic neuroepithelial (ependymal) cyst of the fourth ventricle: MR appearance. Am J Roentgenol. 1999;172:553–4.

Wolf A, Cowen D, Graham S. Xanthomas of the choroid plexus in man. J Neuropathol Exp Neurol. 1950;9:286–97.

Zhou J, Weiguo L, Yongjiang D. Lateral ventricle neuroglial cysts: a clincopathological analysis of five cases. Chinese J Clin Exper Pathol. 2003;4:382–3.

Hippocampi, Caudate Tail, and Ependymal Variants

12

12.1 Hippocampal Cysts

Hippocampal cysts are considered incidental, normal variations that occur to varying degrees, and they are particularly dependent on patient age. They are seen in less than 15 % of patients under the age of 30 years but can be found in a majority of those over 70 years of age. Traditionally, such hippocampal cysts are thought to be related to incomplete involution of the *hippocampal sulcus*.

The hippocampal sulcus typically becomes invisible by 18–20 weeks' gestational age as a consequence of the normal development of the hippocampus; the increasing hippocampal infolding takes on an interlocking C shape as it becomes more medial within the temporal lobe. However, an alternative theory regarding the development of hippocampal cysts is that such cysts actually represent *perivascular spaces* (PVSs) that increase in prominence with age, occurring along transhippocampal arteries or veins within the sulcus. This alternative theory has been recently favored because there is an increased incidence of these cysts with increasing age, just as PVSs increase in number and size with increasing age. There is also an increased frequency of hippocampal cysts with the presence of Alzheimer disease or mild cognitive impairment relative to cognitively normal elderly patients. On the other hand, their occurrence has not been definitively associated with the presence or absence of hypertension, white matter hypertensities, ventricular size, or global cerebral sulcal prominence, which are factors that have been partially associated with the typical deep white matter, periventricular, subinsular, basal ganglia, or brainstem PVSs. Please note that the subject of dilated PVSs has a chapter dedicated to it in Chap. 14.

On imaging, these cysts are usually not readily detectable on CT because of their small size and volume averaging with parenchyma, but they may be readily noted on MRI owing to multiplanar capabilities, particularly at 3 T. These cysts do indeed follow the signal characteristics expected of PVSs; they have signal intensity similar to that of CSF on T2WI, suppress on FLAIR, and do not enhance after contrast administration. This author's experience is that hippocampal cysts are usually less than 1.5 cm in size and do not have a mass effect. However, a tumefactive appearance could theoretically occur if hippocampal cysts are indeed PVSs, as PVSs rarely become giant in size. Such cysts may partly mimic *cystic neoplasms* (e.g., gangliogliomas or pilocytic astrocytomas), *demyelinating lesions* (such as multiple sclerosis), or *post-traumatic lesions* (Figs. 12.1, 12.2, 12.3, 12.4, 12.5, 12.6, 12.7, 12.8, 12.9, 12.10, 12.11, 12.12, 12.13, 12.14, 12.15, 12.16, 12.17, 12.18, 12.19, 12.20, 12.21, 12.22, 12.23, 12.24 and 12.25).

A.M. McKinney, *Atlas of Normal Imaging Variations of the Brain, Skull, and Craniocervical Vasculature*,
DOI 10.1007/978-3-319-39790-0_12

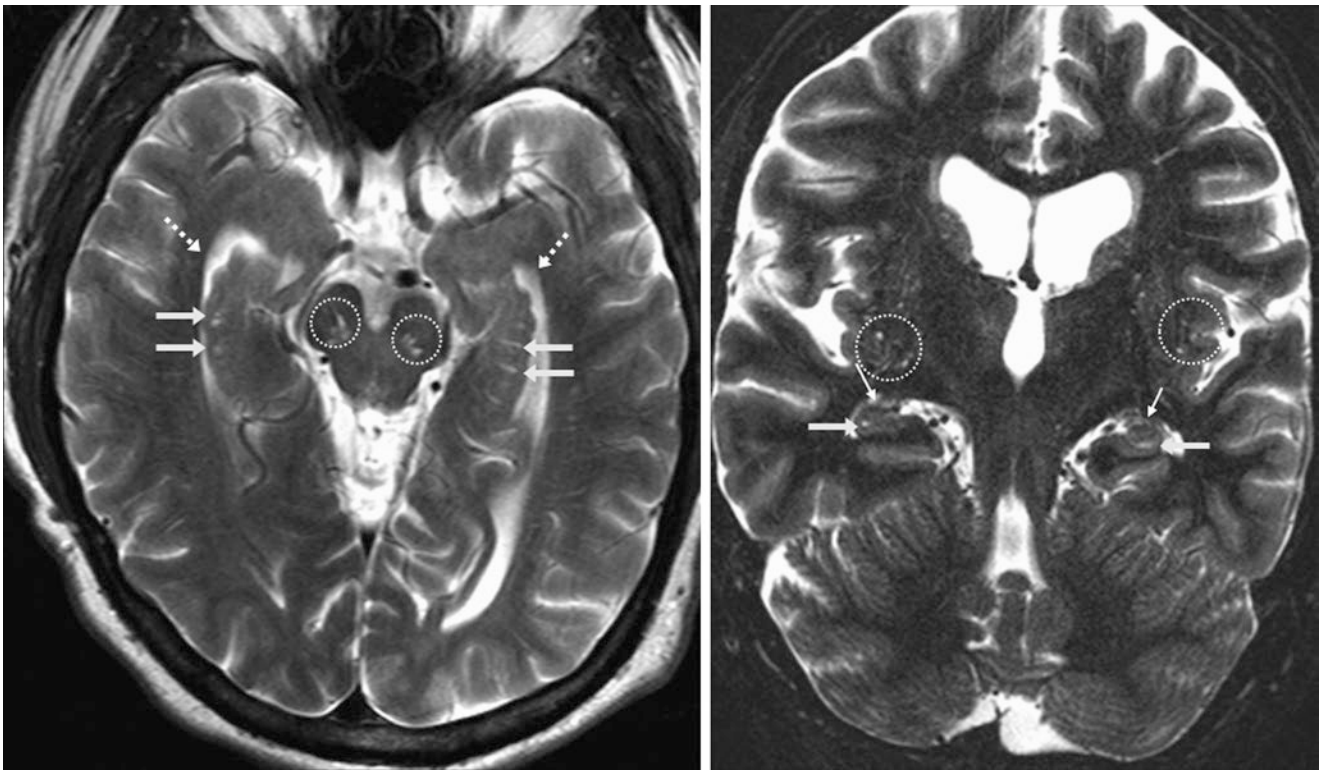

Fig. 12.1 A 60 year old underwent axial (*left*) and coronal (*right*) T2WIs from a 1.5 T MRI that demonstrated hippocampal cysts bilaterally (*arrows*), located medial to the lateral ventricles' temporal horns (*dashed arrows*). On the coronal image, note the choroidal fissures (*thin arrows*). There are also incidental slightly dilated PVSs within the subinsular white matter bilaterally, cerebral peduncles, and the anterior perforated substance (*dotted circles*)

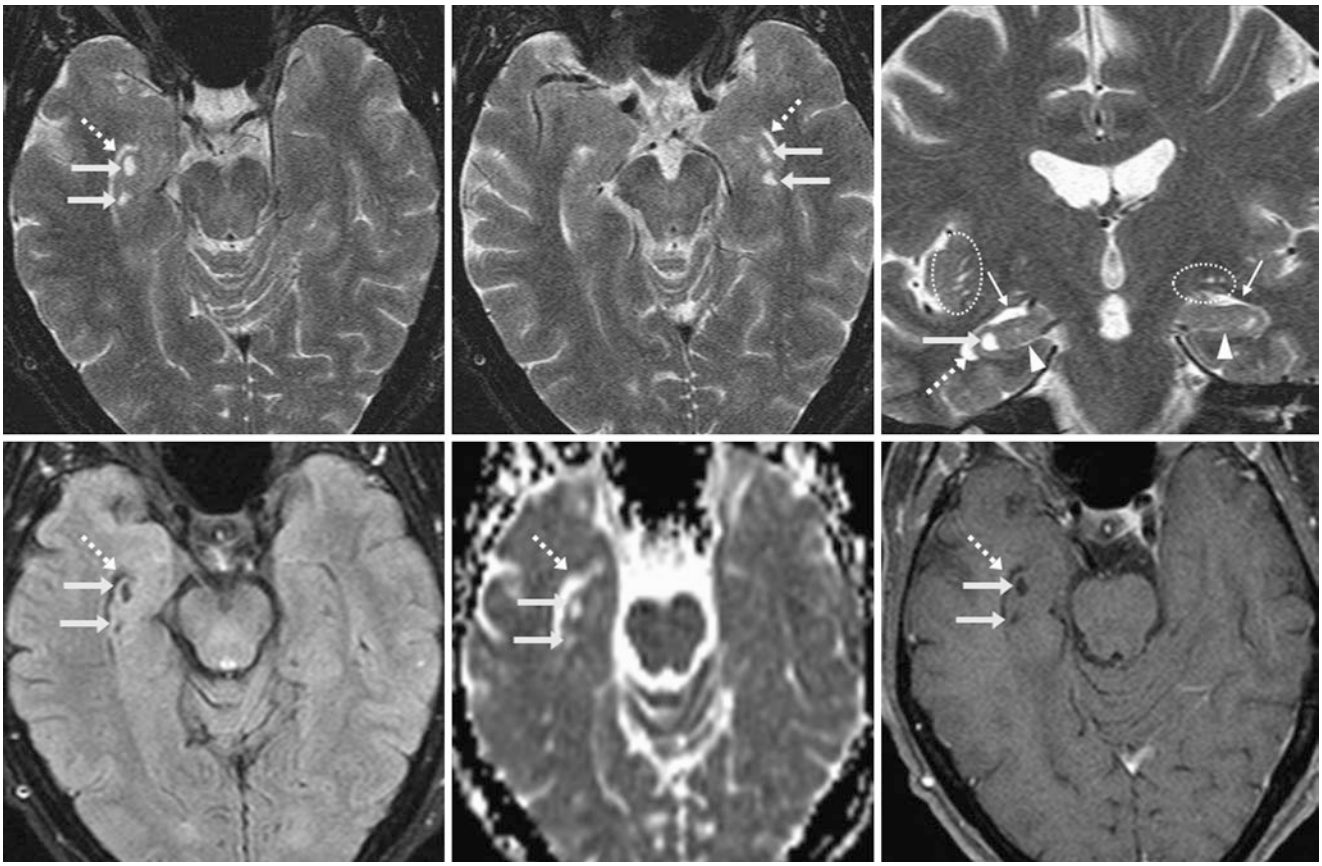

Fig. 12.2 A 62 year old had a 1.5 T MRI. On axial (*top left and middle*) and coronal (*top right*) T2WIs, there are hippocampal cysts bilaterally (*arrows*) medial to the lateral ventricles' temporal horns (*dashed arrows*). On the coronal image, note the asymmetry of the choroidal fissures (*thin arrows*), with mildly enlarged hippocampal fissures (*arrowheads*). There are also slightly dilated PVSs within the right subinsular white matter and within the left anterior perforated substance (*dotted ovals*). The hippocampal cysts suppress like CSF on FLAIR images (*bottom left*), have high diffusivity on ADC maps (*bottom middle*), and do not enhance on postcontrast T1WI (*bottom right*)

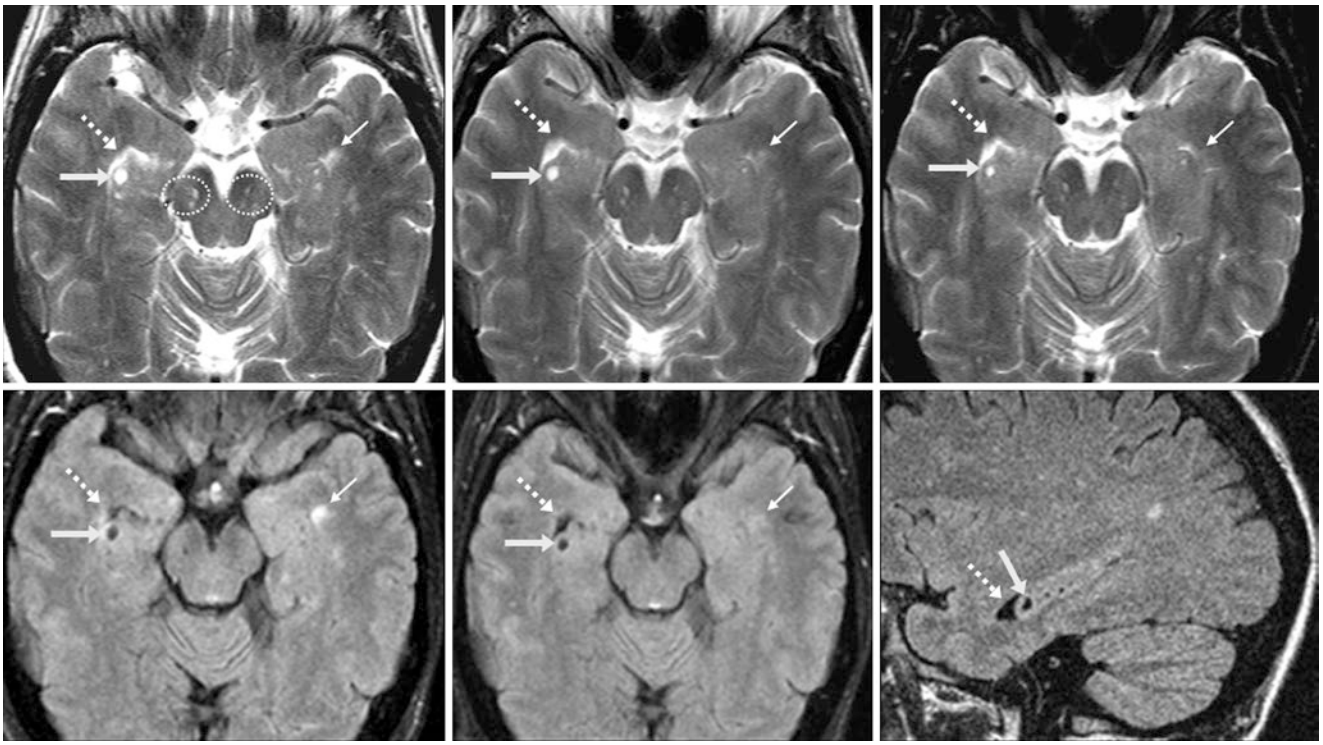

Fig. 12.3 A 47 year old underwent a 1.5 T MRI. A T2WI (*top left*) depicts a single prominent right hippocampal cyst (*arrows*), with other smaller cysts medial to the temporal horn (*dashed arrows*) as well as dilated PVSs within the cerebral peduncles (*dotted circles*). The cysts and PVSs were unchanged from MRIs both 3 years (*top middle*) and 6 years earlier (*top right*). The cysts suppressed on FLAIR (*bottom left*), as they did 3 years prior (*bottom middle*). Sagittal FLAIR (*bottom right*) delineates the cysts well. In comparison, note that a multiple sclerosis plaque (*thin arrows*) progressively worsened over that time, which was situated anterior to the left temporal horn

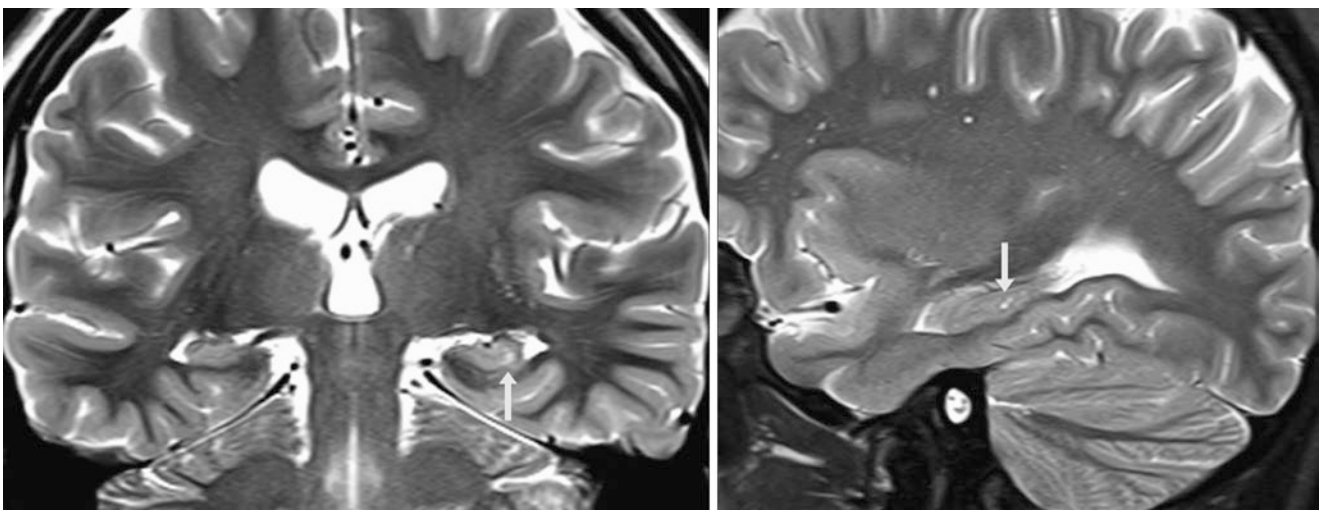

Fig. 12.4 A 16 year old was tested for headaches. Coronal T2WI MRI (*left*) depicted a tiny focus of a potentially abnormal signal (*arrows*) that simulated cortical loss, which can lead to mesial temporal sclerosis. However, on sagittal T2WI (*right*), this is within the expected site of the vestigial hippocampal fissure representing a hippocampal cyst/PVS

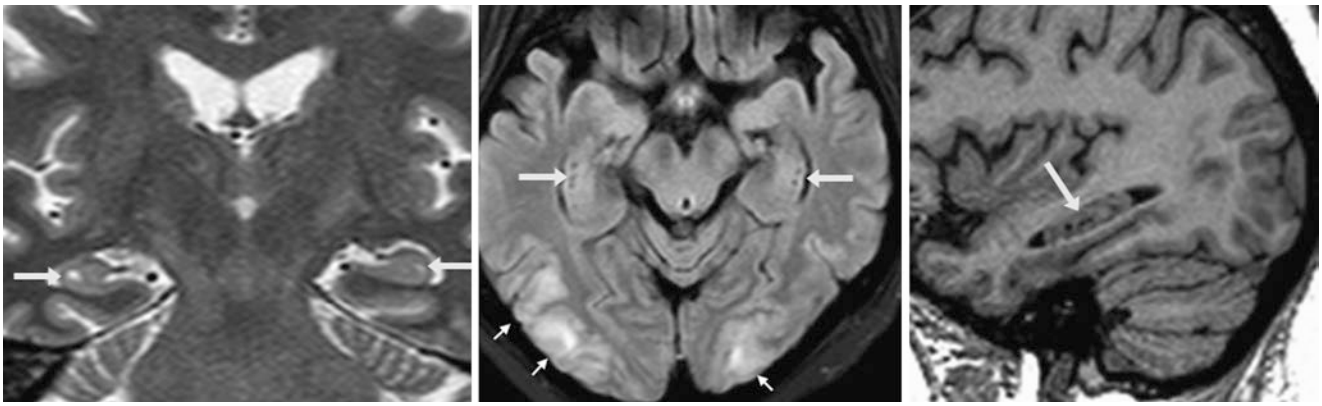

Fig. 12.5 A 52 year old was tested for seizures. Coronal T2WI MRI (*left*) demonstrated tiny, right hippocampal cysts (*arrows*), with a signal akin to that of CSF on FLAIR (*middle*) and sagittal T1WI (*right*). These are visualized on the opposite side to a lesser degree. This hypertensive patient had suffered a seizure with parieto-occipital cortical-subcortical edema (*thin arrows*) on FLAIR images; this is characteristic of posterior reversible encephalopathy syndrome (PRES)

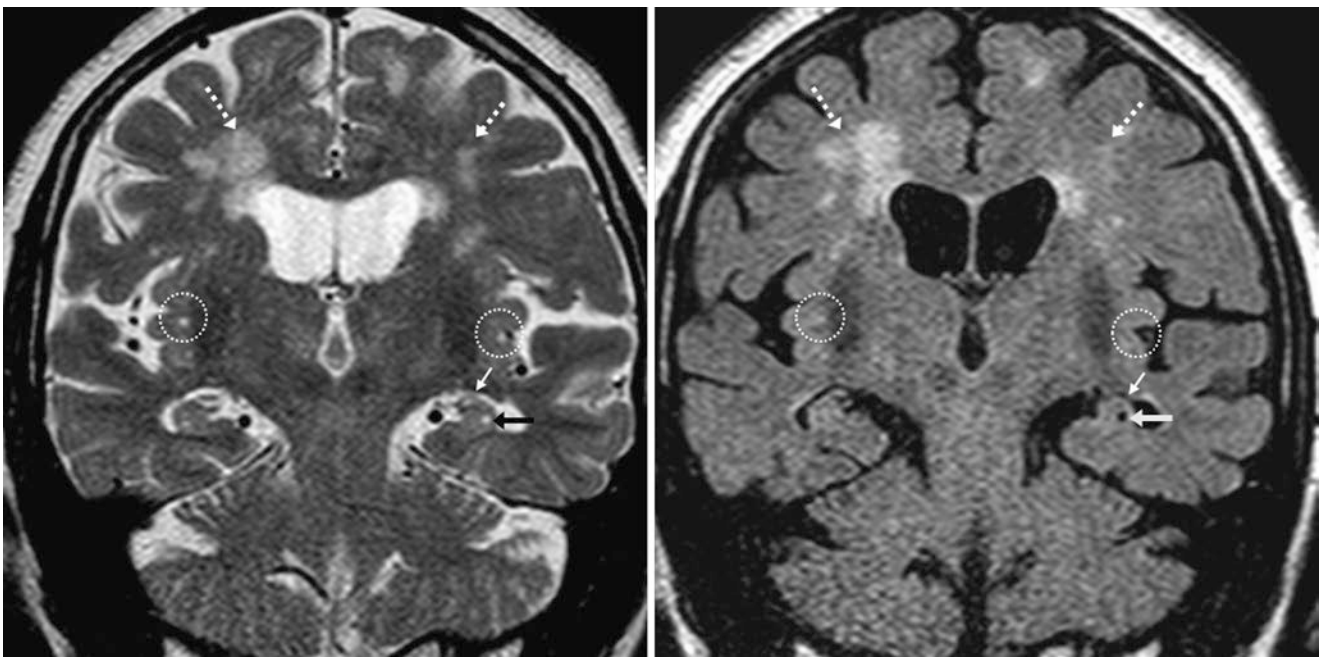

Fig. 12.6 Testing of a 71 year old with coronal T2WI (*left*) and FLAIR (*right*) MR images revealed a small left hippocampal cyst (*arrows*) just inferior to the choroidal fissure (*thin arrows*). There are also incidental slightly dilated PVSs within the subinsular white matter bilaterally (*dotted circles*), which also largely suppress with CSF on FLAIR. Note that patchy, chronic small vessel ischemic disease (*dashed arrows*) does not suppress on FLAIR images

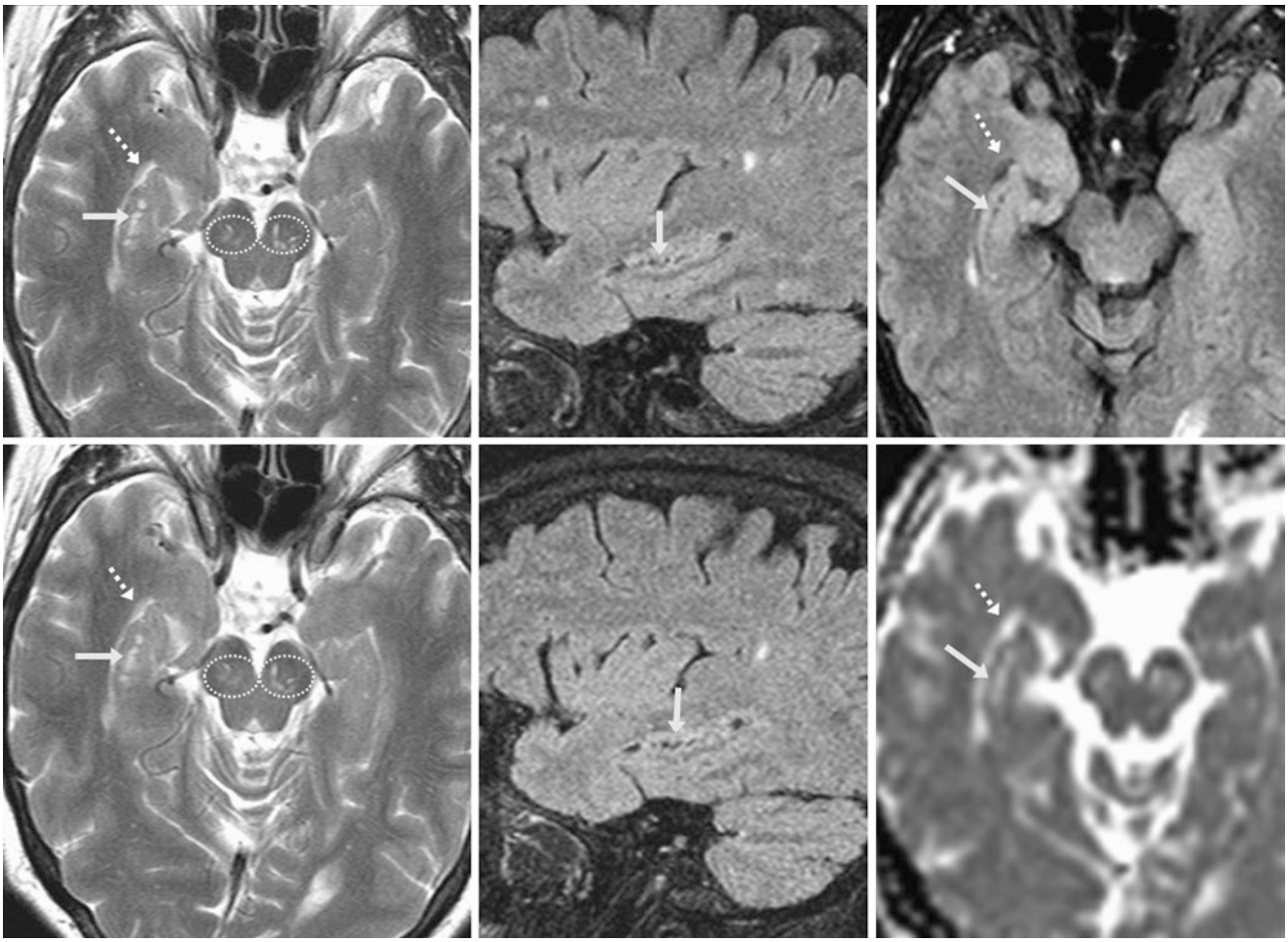

Fig. 12.7 A 54 year old underwent an axial T2WI MRI (*top left*) that depicted multiple small hippocampal cysts (*arrows*) on the right side medial to the temporal horn (*dashed arrows*). Their appearance in the sagittal (*top middle*) and axial (*top right*) planes on FLAIR is also shown. There are also incidental dilated PVSs within the cerebral peduncles bilaterally (*dotted circles*), which have signal characteristics that follow those of CSF. Neither the hippocampal cysts or the PVSs in the peduncles were changed in size from imaging 2 years earlier on axial T2WI (*bottom left*) or on sagittal FLAIR (*bottom middle*). Like CSF, the cysts have high diffusivity on ADC maps (*bottom right*)

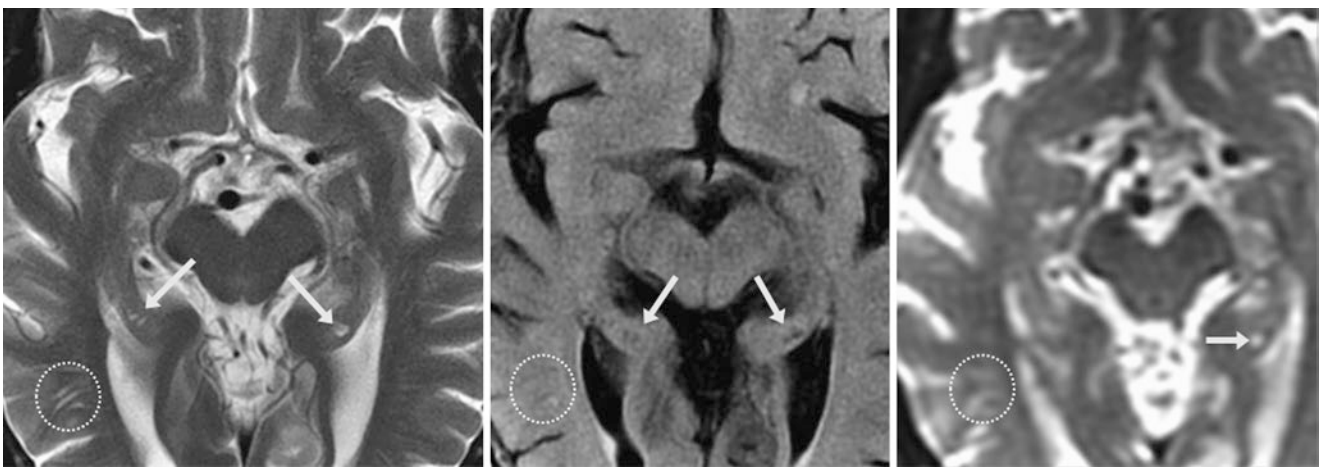

Fig. 12.8 A 73 year old was tested with an axial T2WI MRI (*left*) that demonstrated a small left hippocampal cyst and much smaller cysts on the right (*arrows*). These have a signal intensity of CSF on FLAIR (*middle*) and on the DWI b = 0 maps (*right*). Also, note the incidental dilated PVSs within the right temporal subcortical white matter (*dotted circles*)

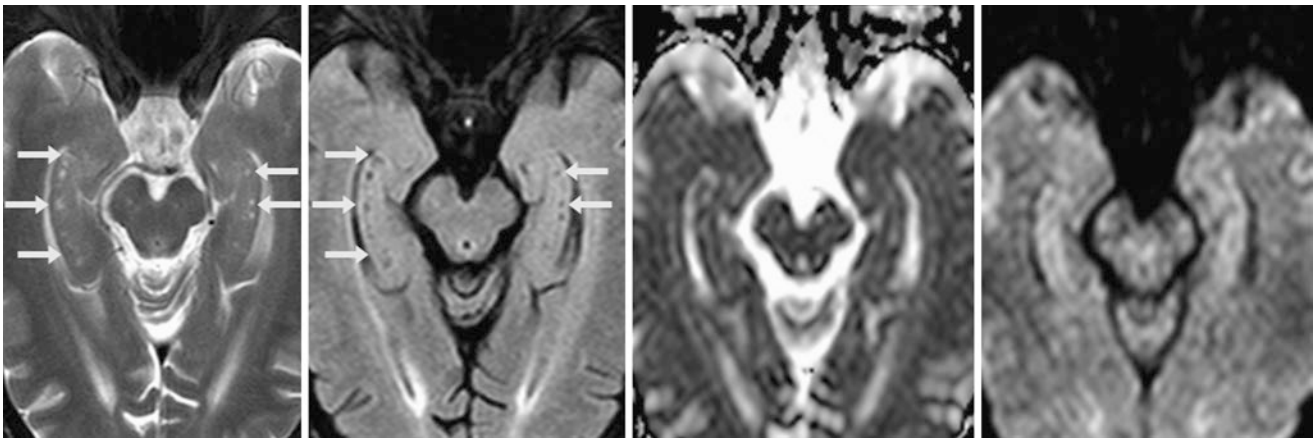

Fig. 12.9 A 40 year old underwent a 1.5 T MRI axial T2WI (*left*) that demonstrated multiple bilateral tiny hippocampal cysts (*arrows*), which have a signal intensity akin to that of CSF on FLAIR (*left middle*), on ADC maps (*right middle*), and on DWI (*right*)

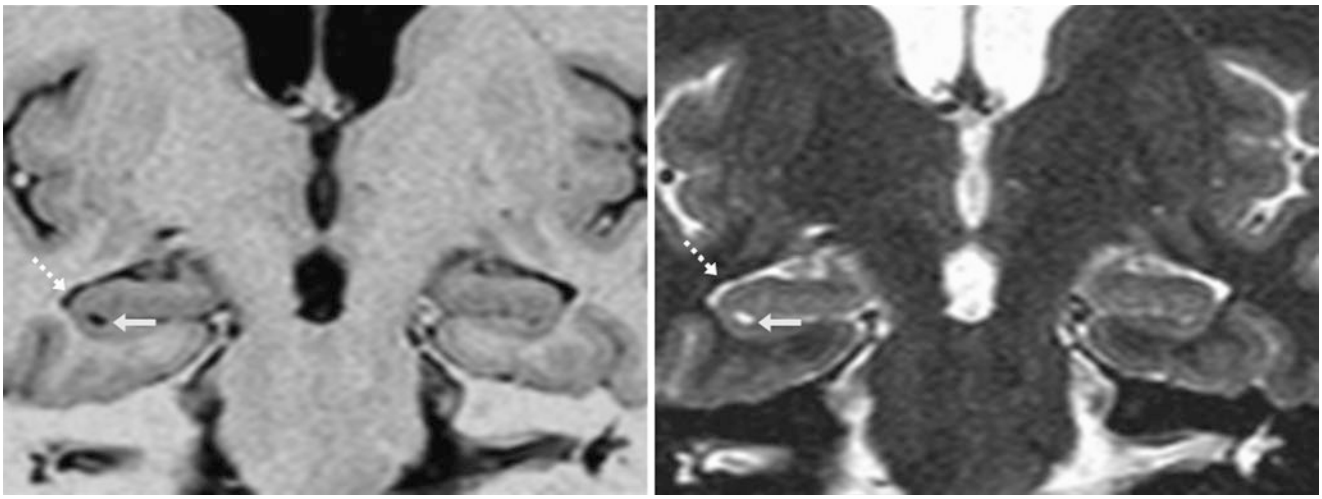

Fig. 12.10 A 27 year old was given a 1.5 T MRI that depicted a tiny right hippocampal cyst (*arrows*) with a signal intensity of CSF on thin coronal T1 IR (*left*) and T2 IR (*right*) images. Note the temporal horn of the lateral ventricle (*dashed arrows*)

Fig. 12.11 A 53 year old volunteer underwent a high-resolution 7 T MRI that demonstrated a right hippocampal cyst (*arrow*) at the depths of the hippocampal fissure (*thin arrow*) on a thin coronal T2WI (0.5-mm thickness). Note the adjacent temporal horn of the lateral ventricle (*dashed arrows*). On the contralateral side, a very tiny hippocampal cyst is also noted (*arrowhead*) that normally would not be visualized on lower resolution images

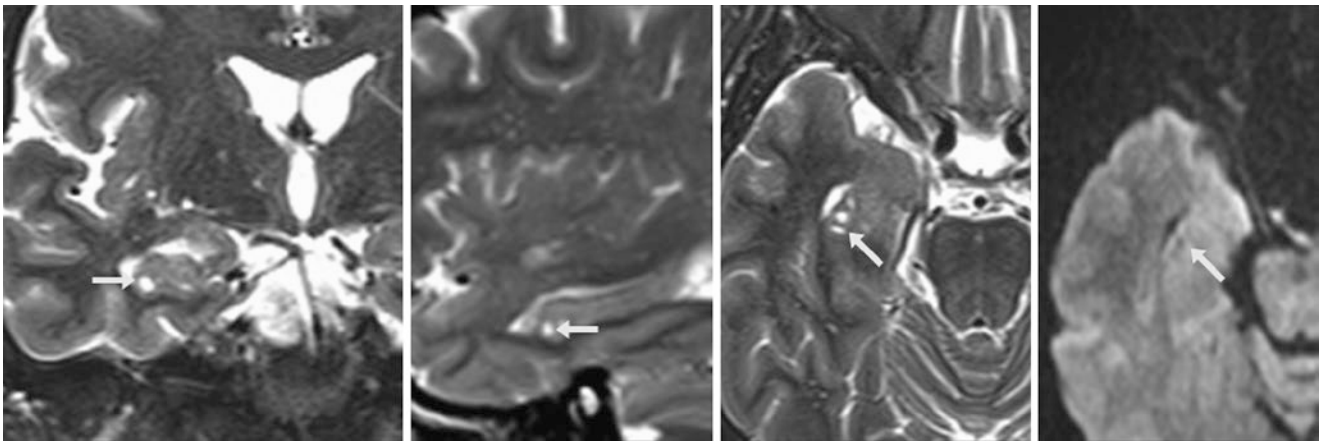

Fig. 12.12 A 61 year old with 1.5 T MRI coronal (*left*), sagittal (*left middle*), and axial (*right middle*) T2WIs showing multiple right hippocampal cysts (*arrows*) with a signal akin to CSF (i.e., increased diffusivity) on DWI (*right*)

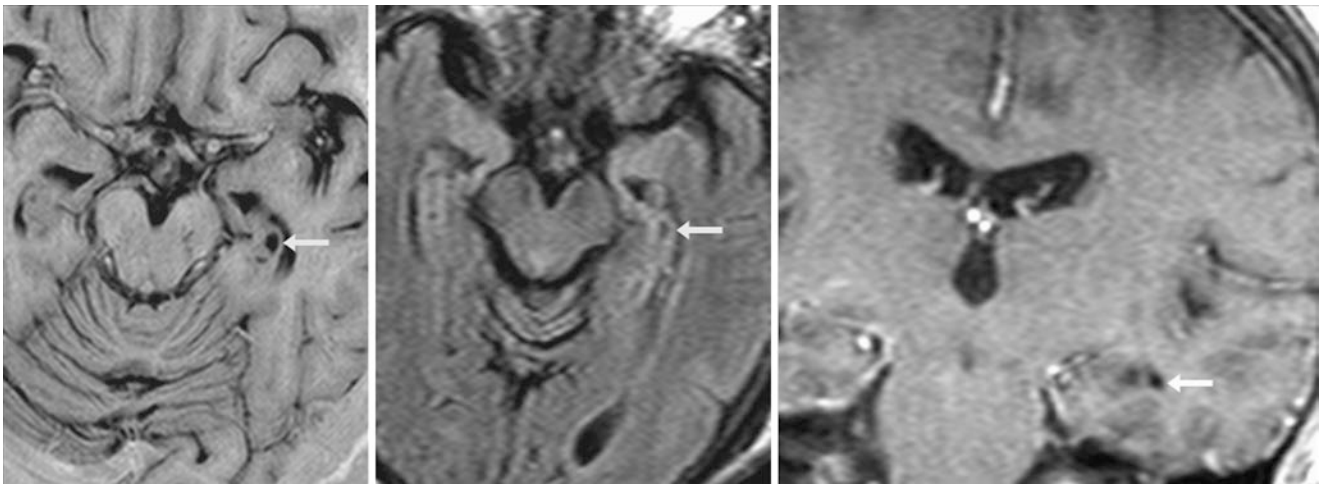

Fig. 12.13 A 70 year old was tested with a 1.5 T MRI that showed a prominent left hippocampal cyst (*arrows*) on a 1-mm-thick axial T1 IR (*left*). The cyst suppresses like CSF on FLAIR (*middle*) and lacks enhancement on coronal postcontrast T1WI (*right*)

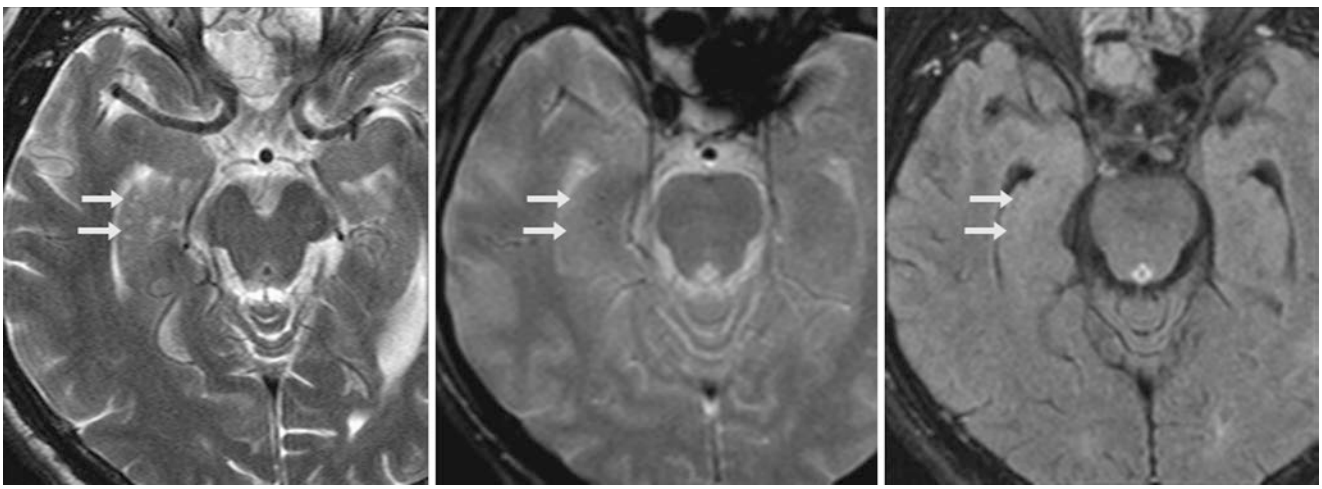

Fig. 12.14 A 50 year old had multiple tiny right hippocampal cysts (*arrows*) that were visualized on a 1.5 T axial T2WI (*left*) but are basically invisible at the same slice thickness on axial T2* GE (*middle*) and on FLAIR (*right*) MR images

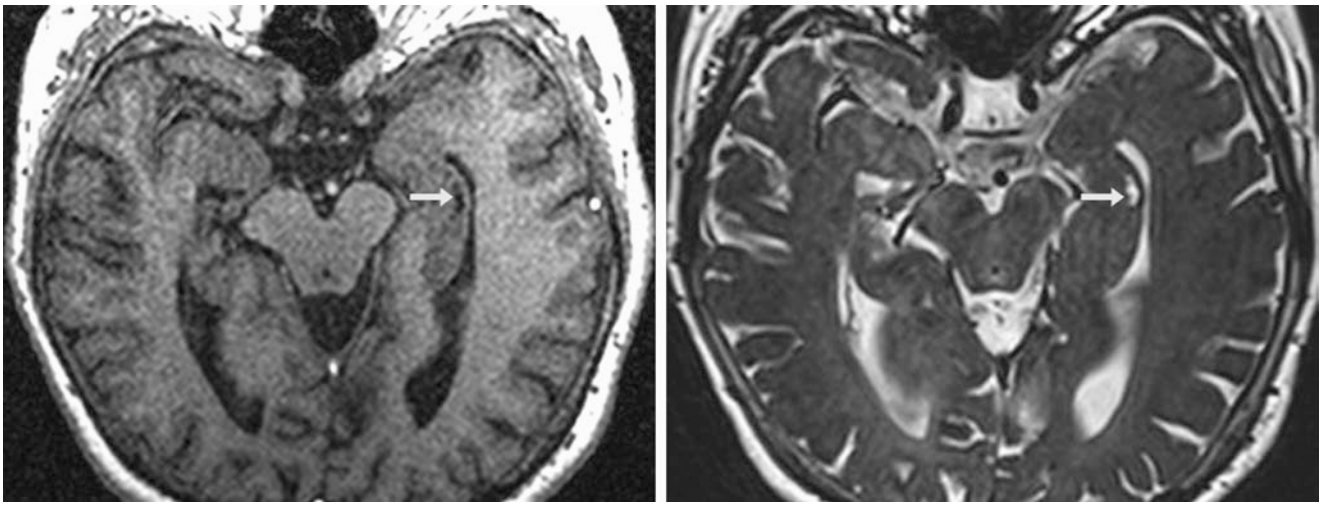

Fig. 12.15 A 78 year old had an incidental finding of a string of left hippocampal cysts (*arrows*) on thin 1-mm axial T1WI (*left*) and T2WI (*right*). The MRI was obtained as stereotactic planning for deep brain stimulator placement

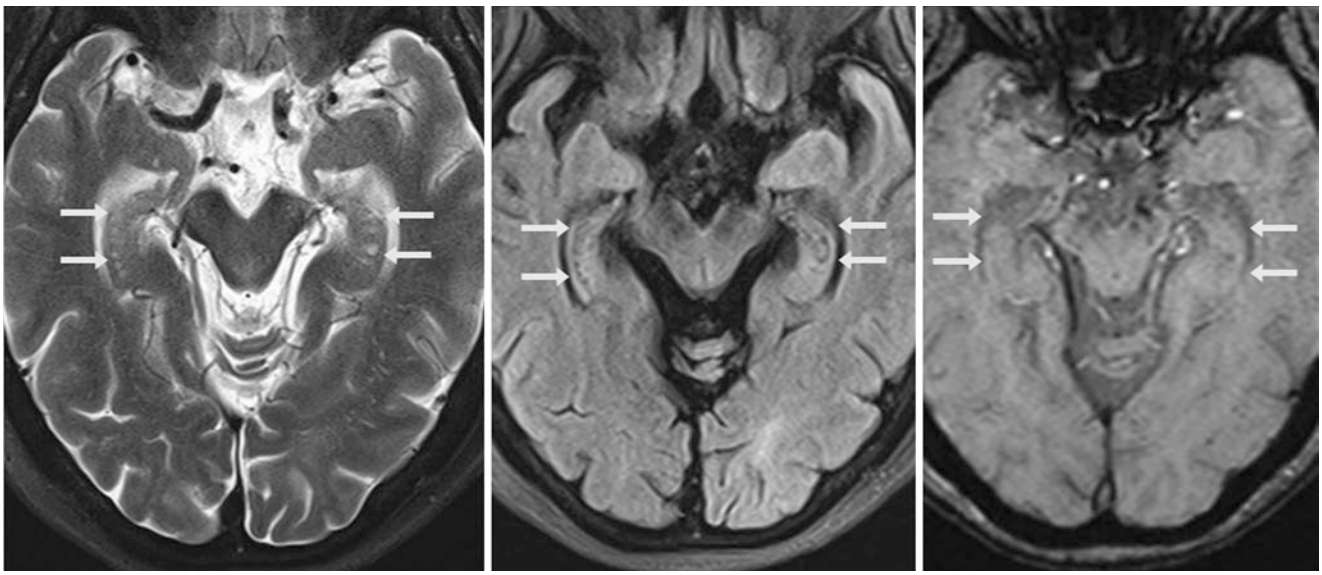

Fig. 12.16 A 59 year old who had a history of dementia had the incidental finding of a string of bilateral hippocampal cysts (*arrows*) on 1.5 T MRI axial T2WI (*left*), which suppress on FLAIR (*middle*) and are invisible on SWI (*right*)

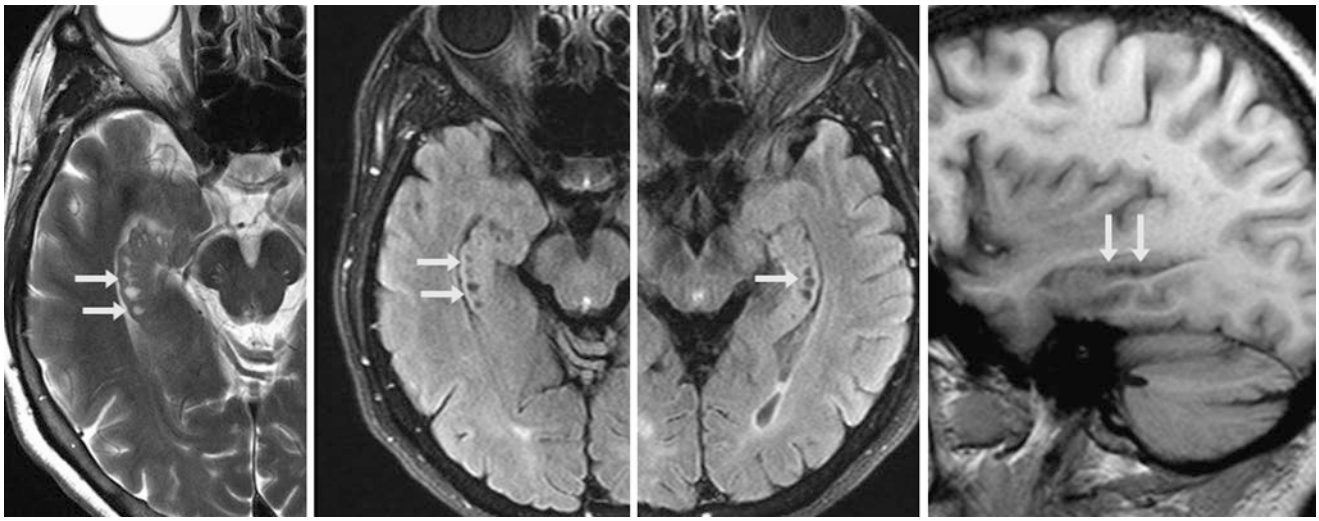

Fig. 12.17 A 69 year old with a 3 T MRI that shows multiple right hippocampal cysts (*arrows*) on axial T2WI (*left*) and on FLAIR (*left middle*). They are also noted on the left side on FLAIR (*right middle*) and on sagittal T1WI (*right*)

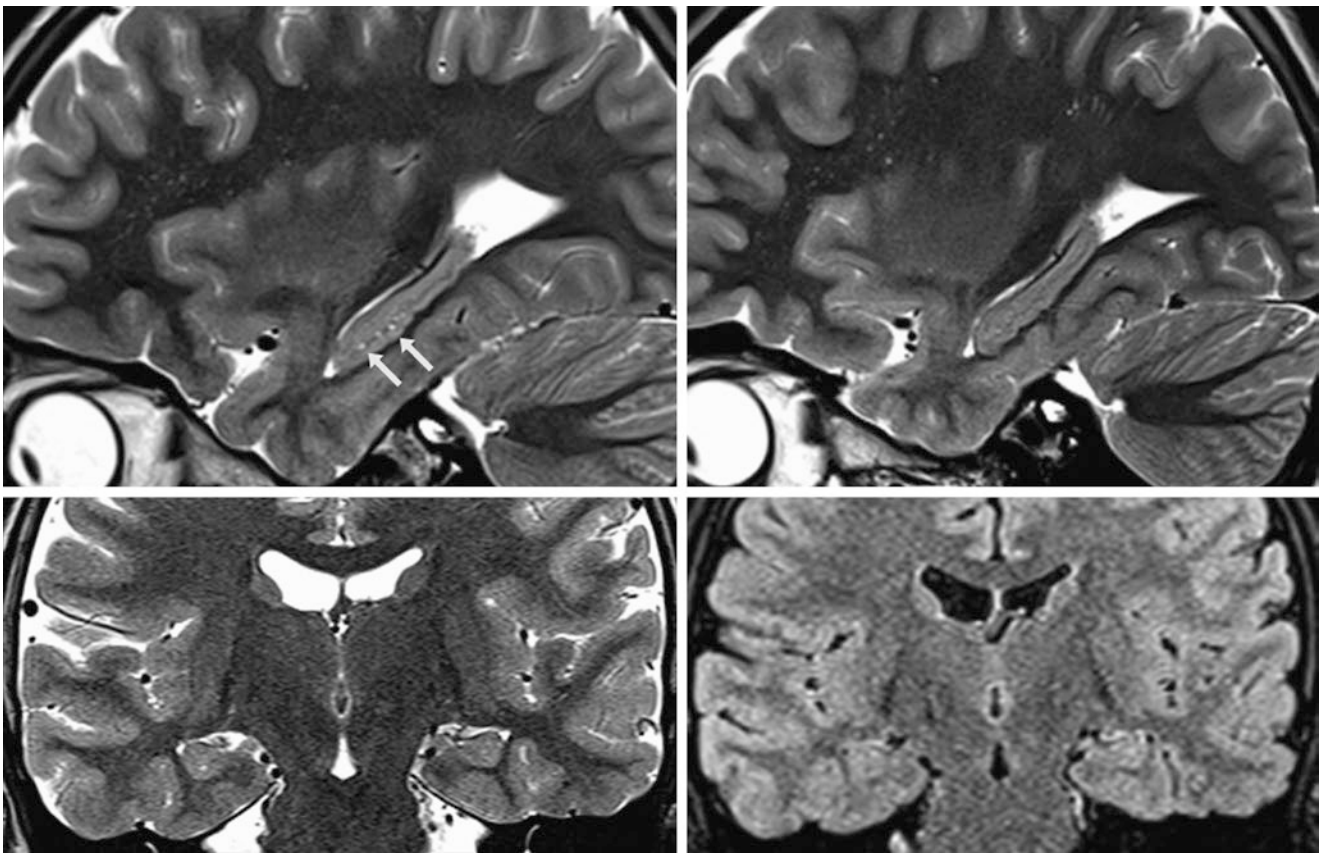

Fig. 12.18 A 10 year old had a 3 T MRI that depicted very tiny cysts within the right hippocampal sulcus (*arrows*) on sagittal T2WI of the right side (*top left*), not seen on the left side (*top right*). These may represent cavities of the residual hippocampal sulcus. On coronal T2WI (*bottom left*) and FLAIR (*bottom right*), the cysts are not seen

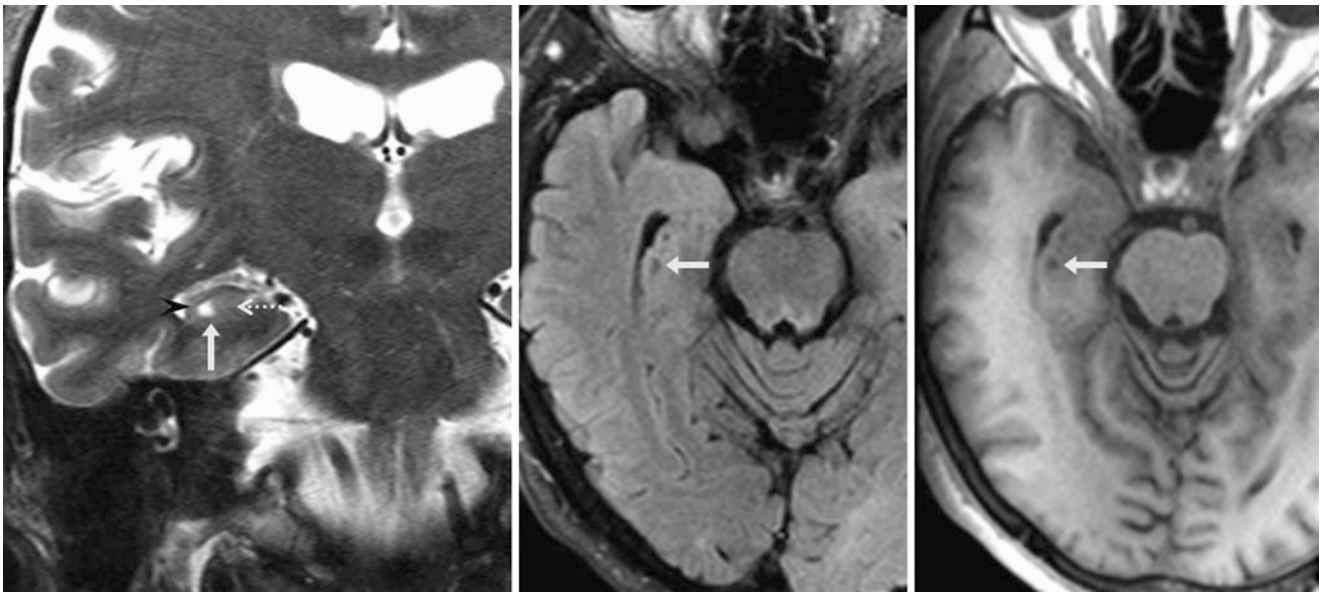

Fig. 12.19 A 68 year old had a 3 T MRI that showed a right hippocampal cyst (*arrows*), which may represent a remnant hippocampal sulcus. On coronal T2WI (*left*), note the hippocampus' cornu ammonis laterally (*black arrowhead*) and the dentate gyrus medially (*dotted arrow*). The cyst is similar to CSF on FLAIR (*middle*) and T1WI (*right*)

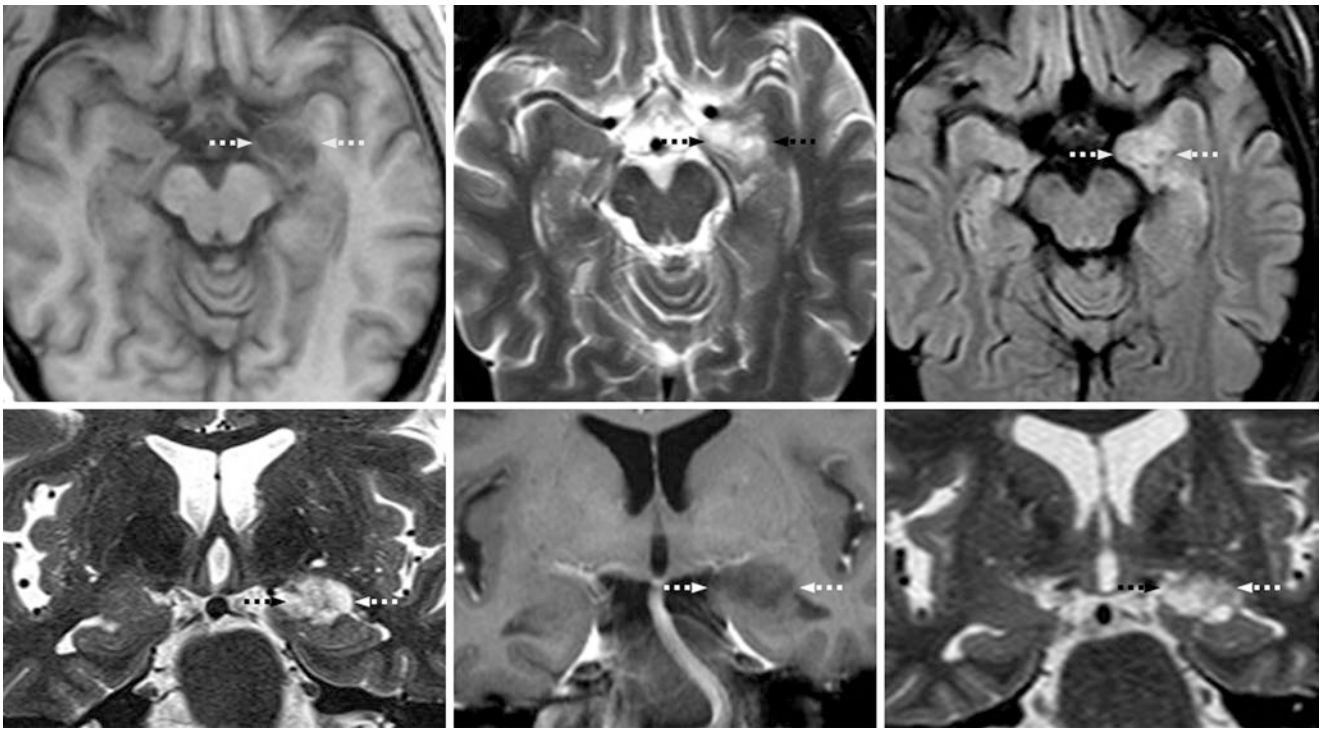

Fig. 12.20 Comparison case of low-grade astrocytoma. A 51 year old with seizures underwent a 1.5 T MRI with axial T1WI (*top left*), T2WI (*top middle*), FLAIR (*top right*), coronal T2WI (*bottom left*), and postcontrast coronal T1WI (*bottom middle*). All showed a medial left temporal lobe mass (*dotted arrows*) that was hyperintense on T2WI but not cystic on FLAIR. This was later proven to be a low-grade astrocytoma. It was unchanged 3 years later on coronal T2WI (*bottom right*)

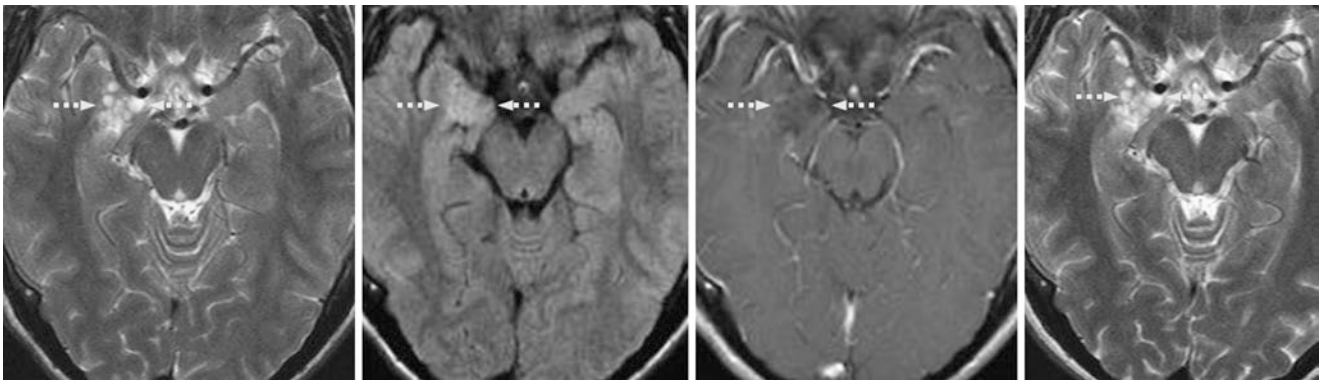

Fig. 12.21 Comparison case of cystic ganglioglioma. A 26 year old with seizures had a right medial temporal lobe mass that appeared multicystic on a 1.5 T MRI with axial T2WI (*left*); however, the lesion was entirely hyperintense on FLAIR (*left middle*). The mass did not enhance on postcontrast T1WI (*right middle*). It was later proven to be a low-grade ganglioglioma and was unchanged 3 years later on axial T2WI (*right*)

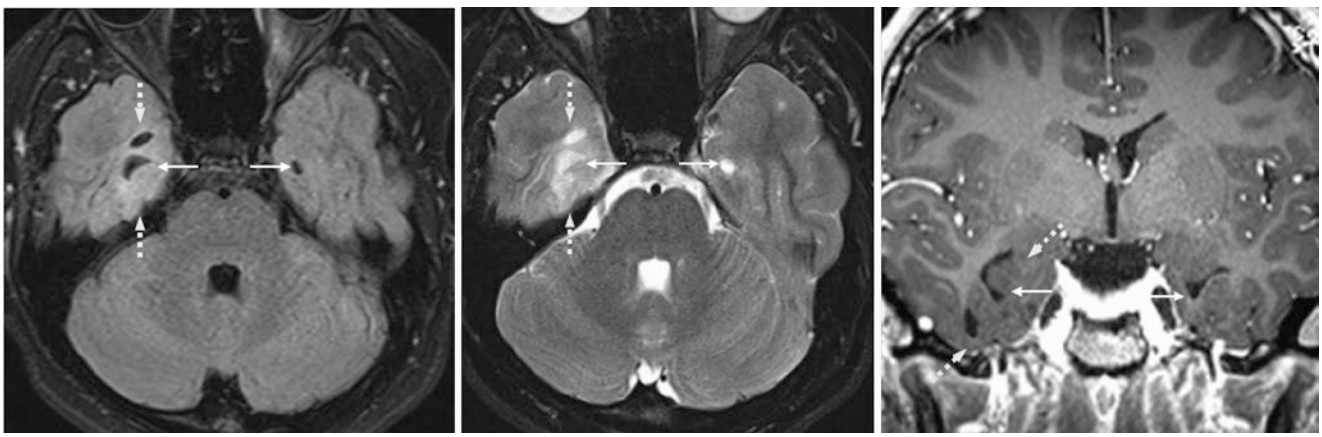

Fig. 12.22 Comparison case of presumed low-grade glioma. A 25 year old with seizures had a right medial temporal lobe mass on a 1.5 T MRI with axial T2WI (*left*) and FLAIR (*left middle*). The mass did not enhance on postcontrast T1WI (*right middle*) and was not biopsied but it was unchanged 4 years later on FLAIR (*right*). Note the normal temporal horn of the lateral ventricle (*thin arrows*) just posterior to the cystic portion of the mass on T2WI and FLAIR

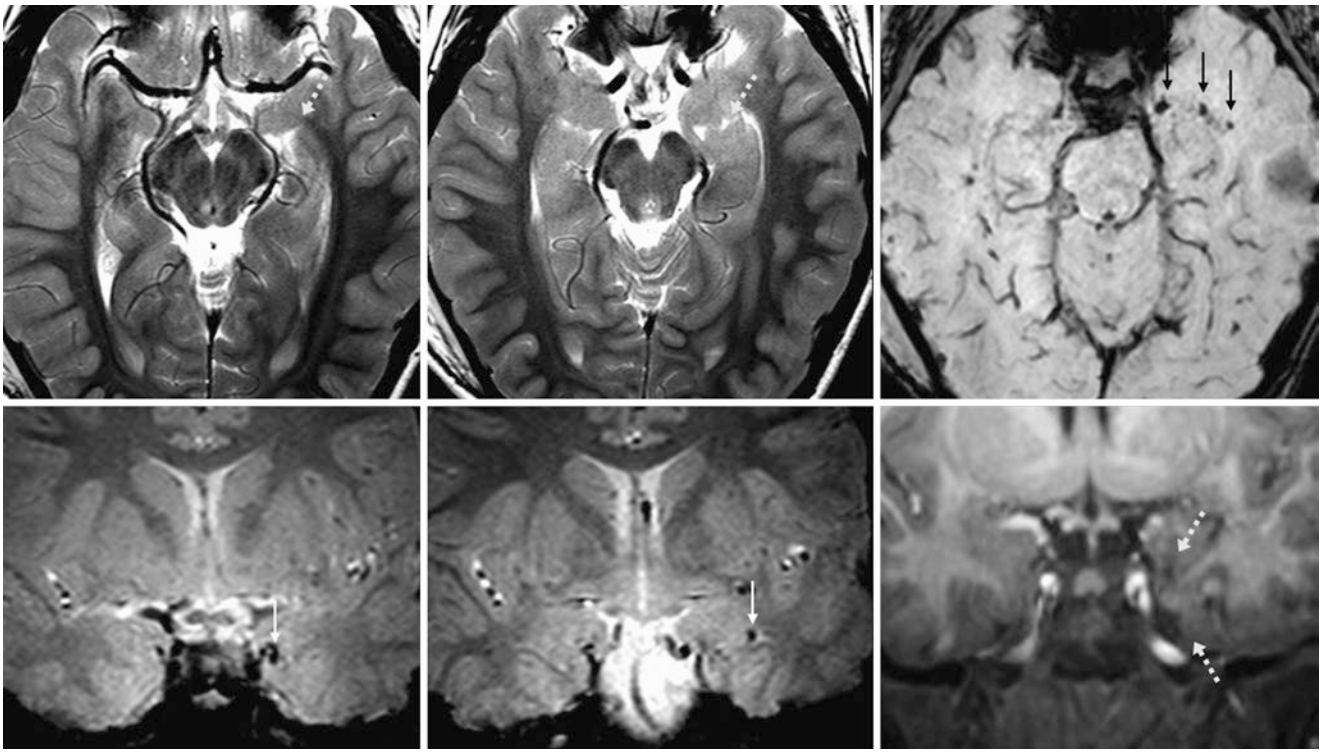

Fig. 12.23 Comparison case of diffuse axonal Injury (DAI). In an 8 year old who had seizures several months post-trauma the 3 T MRI depicted focal left temporal atrophy (*dotted arrows*) on T2WI (*top left and middle*), with microhemorrhages (*thin arrows*) on SWI (*top right*) and coronal T2*WI (*bottom left and middle*). A coronal T1WI (*bottom right*) also showed the focal atrophy

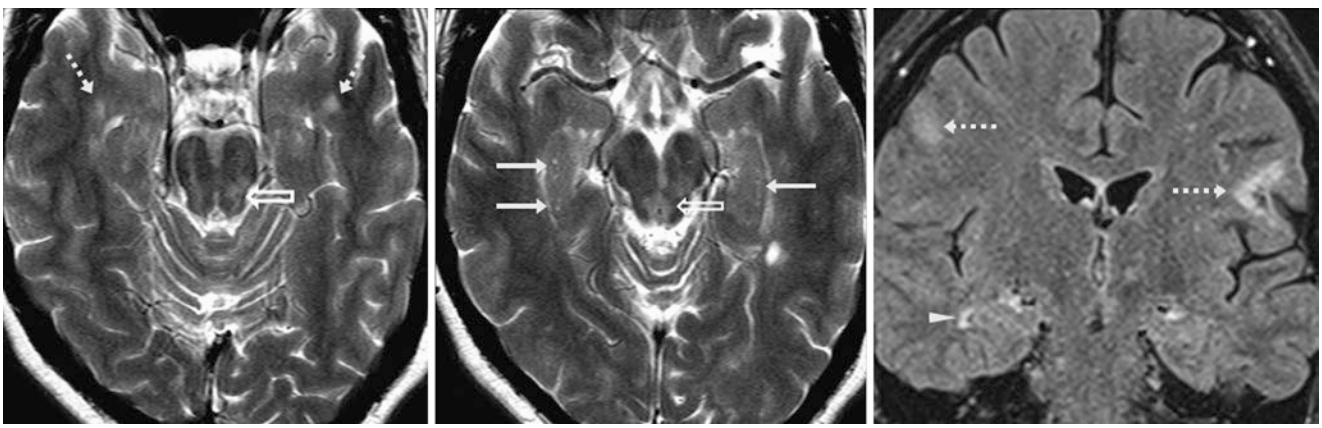

Fig. 12.24 Comparison case of multiple sclerosis. On axial T2WI (*left and middle*), a 32 year old had bilateral temporal plaques (*dotted arrows*). Note and compare to normal hippocampal cysts (*arrows*). Coronal FLAIR (*right*) shows other plaques, such as a right temporal plaque (*arrowhead*); also note midbrain lesions (*open arrows*)

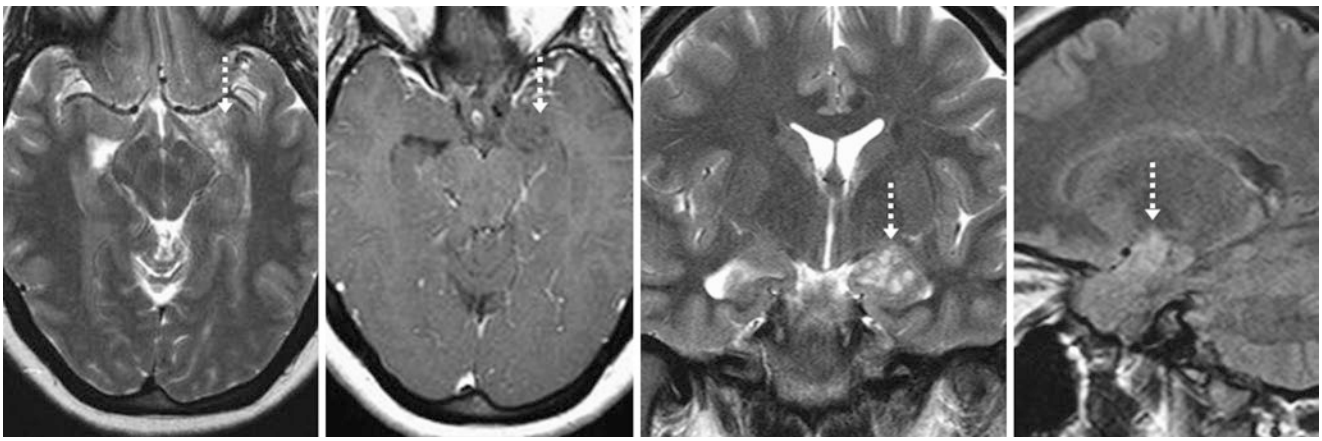

Fig. 12.25 Comparison case of dysembryoplastic neuroepithelial tumor (DNET). A 23 year old with seizures had a left temporal lesion (*dotted arrows*) on axial T2WI (*left*), which did not enhance on postcontrast T1WI (*left middle*). Coronal T2WI (*right middle*) and sagittal FLAIR (*right*) confirmed that the lesion was within the hippocampus

12.2 Caudate Tail Pseudolesion and Hippocampal Anatomy

The *caudate nucleus* is associated with learning, memory, and motor control. It has a head, body, and tail; some variably state that it also has a genu. The head and body are easily recognized on standard MRI and CT sequences. However, the *caudate tail* wraps around posteroanteriorly in the roof of the temporal horn of the lateral ventricle opposite the hippocampus. Most often, the caudate tail is not well discerned. However, it can occasionally appear slightly prominent or asymmetric as a pseudolesion, particularly mimicking periventricular *nodular heterotopia*, since both have gray matter signal. This may present a diagnostic dilemma in seizure MRI protocols that include oblique coronal images through the hippocampi. The tail's course and location can be distinguished most readily on oblique coronal T2WI (perpendicular to the long axis of the hippocampus) or on sagittal T1WI (parallel to the long axis of the hippocampus). The caudate tail is often relatively invisible on axial images and on coronal FLAIR images. Relevant, adjacent hippocampal anatomy is also provided in the following examples (Figs. 12.26, 12.27, 12.28, 12.29, 12.30, 12.31, 12.32, 12.33, 12.34, 12.35, 12.36, and 12.37).

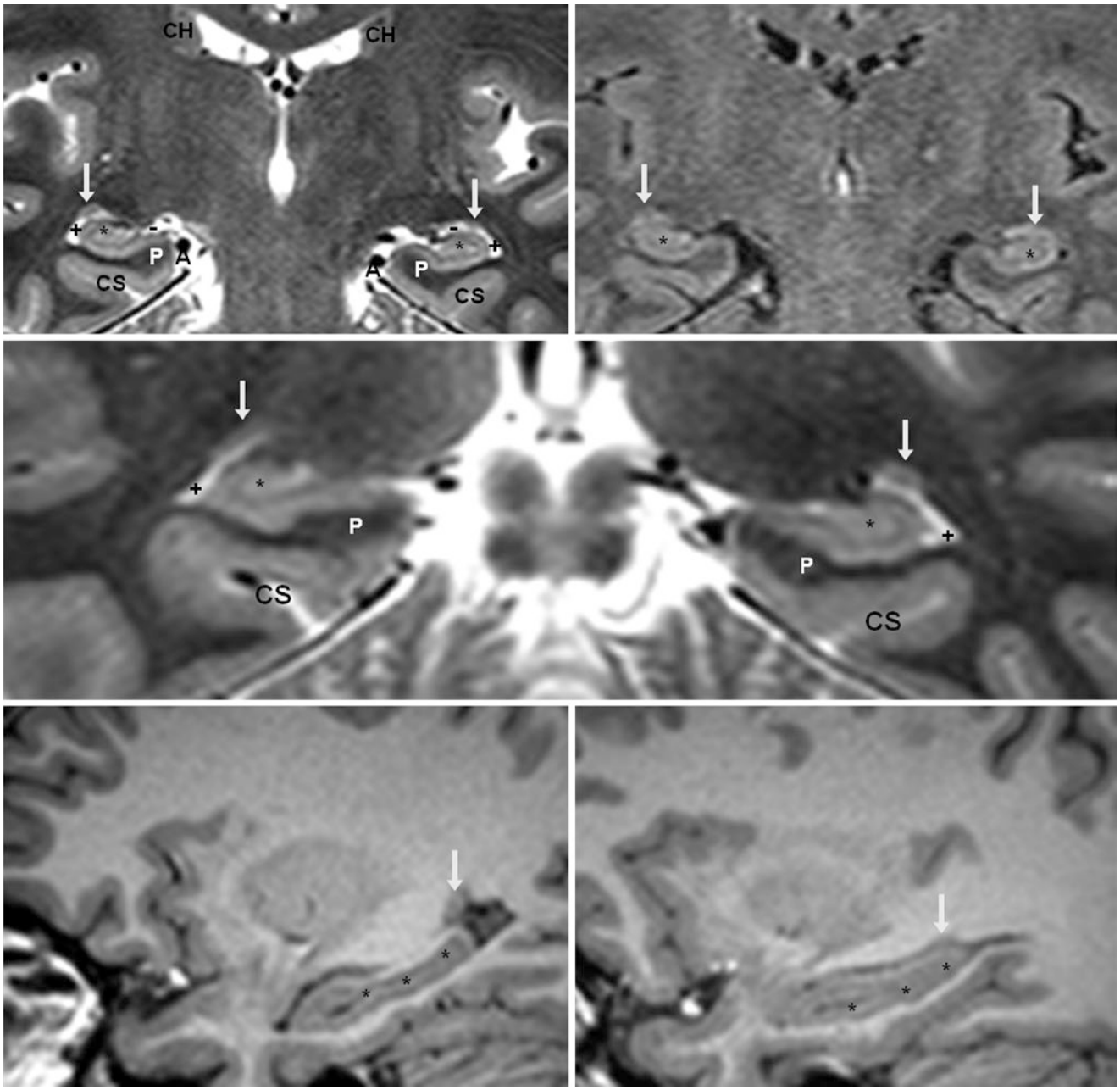

Fig. 12.26 A 31 year old with seizures had a negative 3 T MRI evaluation. On a coronal T2WI through the hippocampus (*top left*), a structure with gray matter signal intensity representing the caudate tail (*arrows*) is seen on the right side better than the left. It is not well visualized on coregistered coronal FLAIR (*top right*). A coronal T2WI located more posteriorly (*middle*) also depicts the caudate tails, which are more discernible on the left side. Sagittal T1WIs of the right (*bottom right*) and left (*bottom right*) sides through the hippocampi (*) further delineate the caudate tails. Also, note the ambient cistern (*A*), dentate gyri of the hippocampi (*), temporal horns (+), choroidal fissures (−), parahippocampal gyri (*P*), collateral sulci (*CS*), and the caudate heads (*CH*)

Fig. 12.27 A 38 year old with seizures who had a negative 3 T MRI evaluation. Coronal T2WI (*top*) and FLAIR (*bottom*) through the hippocampi denote the caudate tails (*arrows*). Adjacent (para-) hippocampal anatomy includes the ambient cistern (*AC*), alveus (*arrowheads*), fimbria (*dotted arrows*), hippocampal sulci (*tiny arrows*), cornu ammonis CA2 (^), CA4 underlying the dentate gyri (*), subiculum (*oval*), temporal horns (+), choroidal fissure (–), parahippocampal gyri (*P*), collateral sulci (*CS*), fusiform/occipitotemporal gyri (*FG*), and the caudate heads (*CH*). Note that T2WI better demonstrates the anatomic detail. Also, note the normal mildly bright signal of the hippocampi on FLAIR at 3 T

Fig. 12.28 A 7 year old with seizures had a negative 3 T MRI evaluation. On coronal T2WIs through the hippocampus from anterior (*top*) to posterior (*bottom*), the caudate tails are visualized (*arrows*), being more prominent on the left. Also note the ambient cistern (*AC*), alveus (*arrowhead*), hippocampal fimbria (*dotted arrows*), hippocampal sulci (*tiny arrows*), cornu ammonis CA2 (^), CA4 underlying the dentate gyri (*), temporal horns (+), choroidal fissures (−), subiculum (*ovals*), parahippocampal gyri (*P*), and the caudate heads adjacent to the frontal horns (*CH*)

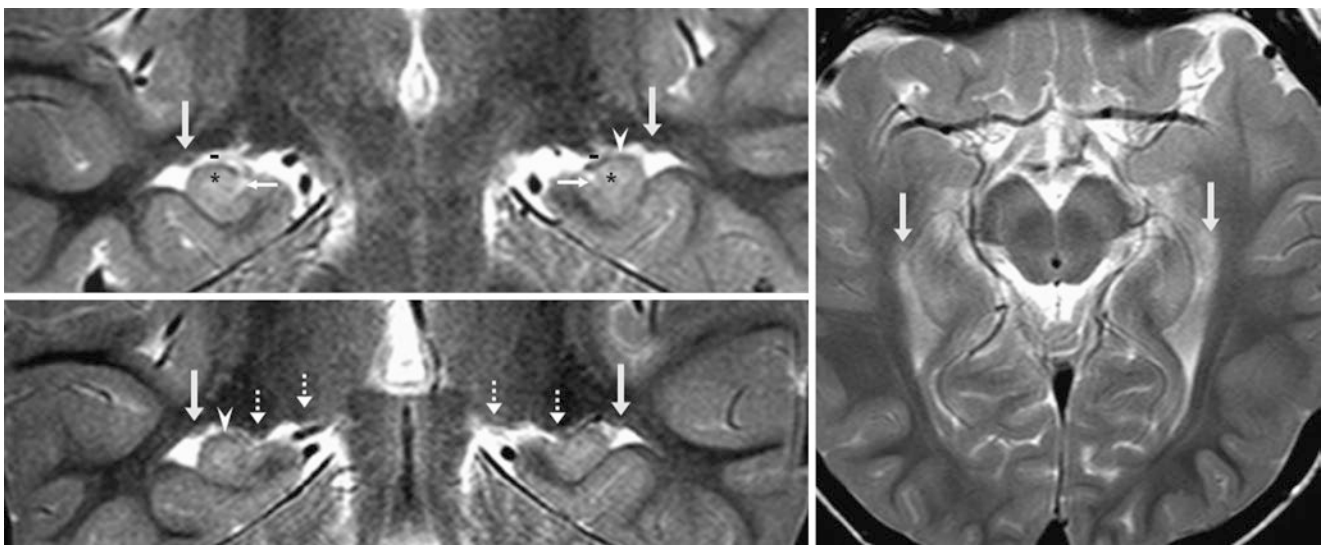

Fig. 12.29 A 2.5 year old with developmental delay had a negative 3 T MRI evaluation. On coronal T2WIs through the hippocampus anteriorly (*top left*) and more posteriorly (*bottom left*), the caudate tail (*arrows*) is defined bilaterally and is slightly more prominent on the right side. This could simulate nodular (subependymal) heterotopia. The medial and lateral geniculate nuclei (*dotted arrows*) are located medially, relative to the caudate tails. Also note the alveus (*arrowhead*), hippocampal sulci (*tiny arrows*), dentate gyri (*), and the choroidal fissures (−). Localizers were used to find the caudate tails on axial T2WI (*arrows*, *right*), but they still appear relatively invisible on axial images

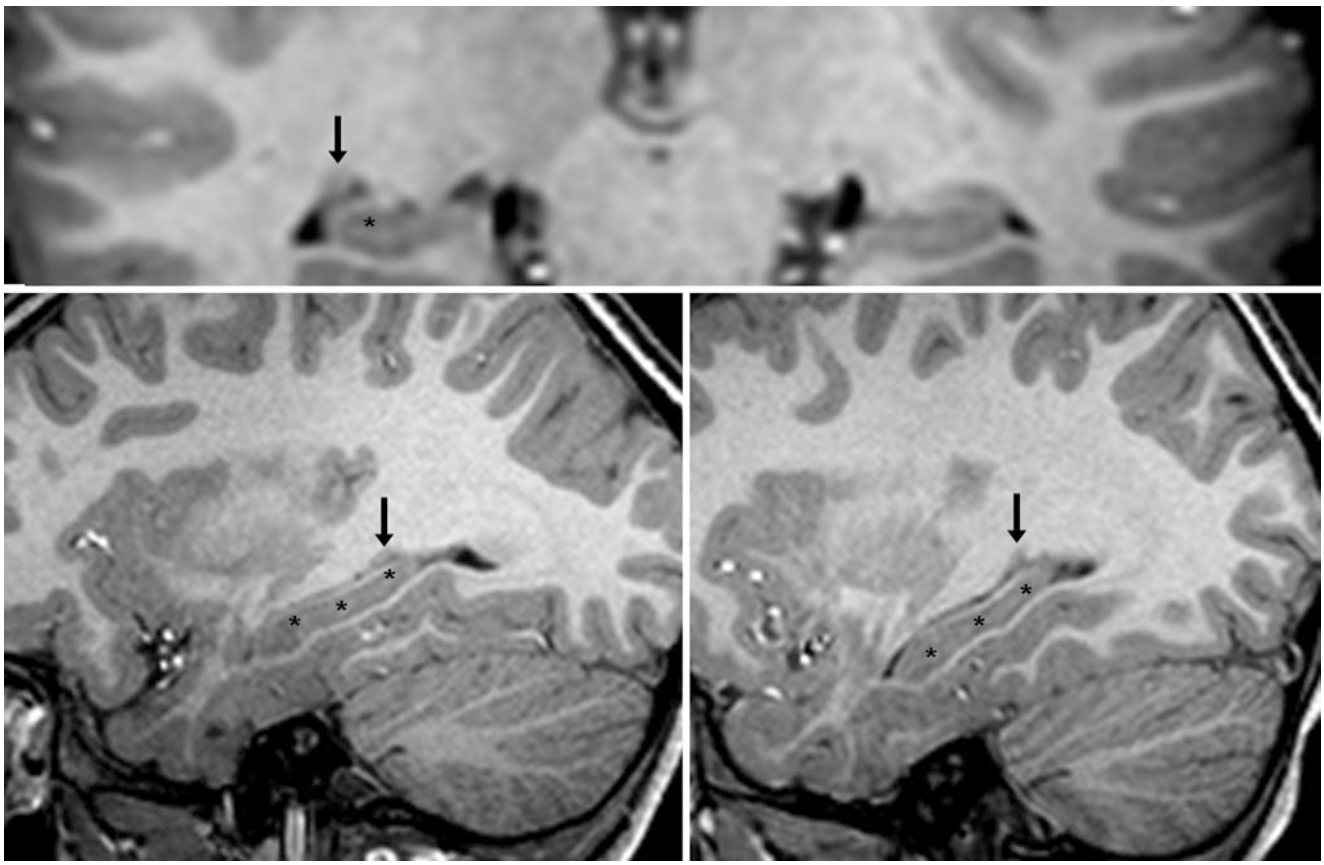

Fig. 12.30 A 6 year old with headaches had a negative 3 T MRI evaluation. On coronal T1WI (*top*), a nodular focus of gray matter signal (*arrows*) is noted just superior to the posterior portion of the hippocampus (* denotes the dentate gyrus within the center of the hippocampus). This could simulate nodular heterotopia. Sagittal T1WIs of the right (*bottom left*) and left (*bottom right*) sides confirmed that this is indeed the caudate tail, which is present bilaterally

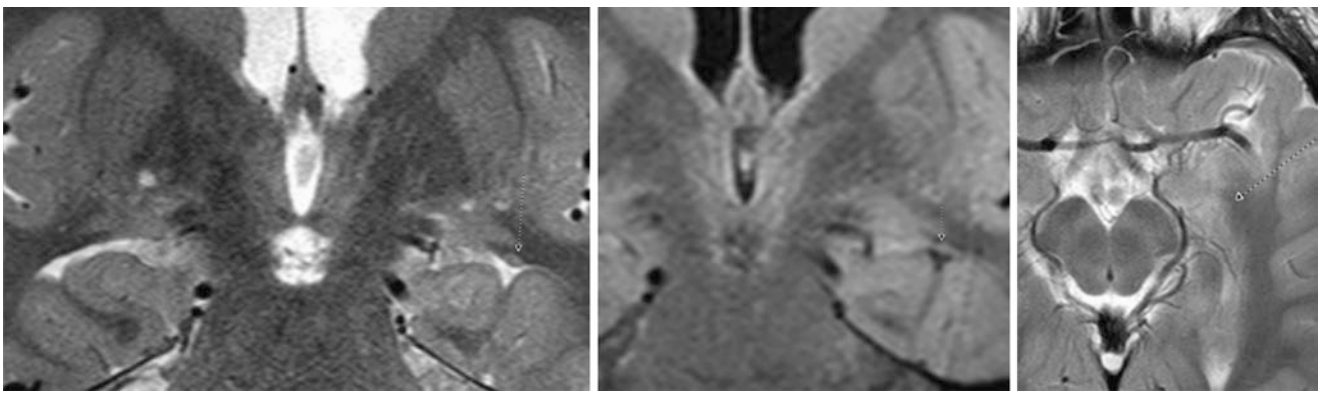

Fig. 12.31 The patient was a 7 year old with developmental delay. On a negative 3 T MRI, a coronal T2WI (*left*) depicts the left caudate tail. Localizer arrows (*tiny dotted arrows*) demonstrate how difficult it is to visualize the caudate tail on coronal FLAIR (*middle*) and axial T2WI (*top right*). In this patient, the asymmetry of the caudate tail could simulate nodular heterotopia

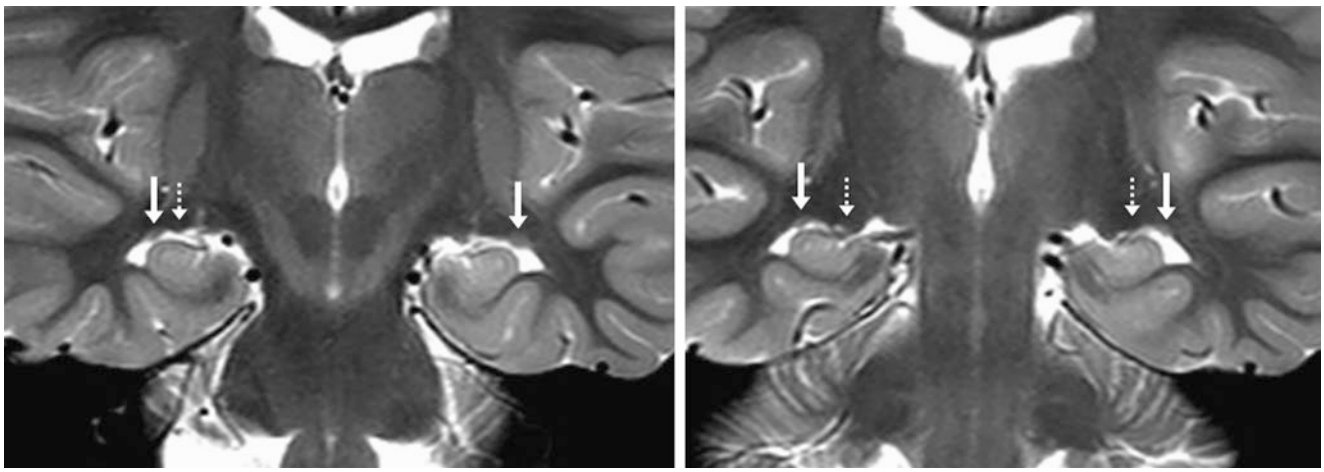

Fig. 12.32 A 4 year old with seizures had a negative study. On a 3 T MRI, serial coronal T2WIs demonstrate that the caudate tails may be mildly asymmetric in size (in this case, the left was slightly larger than the right). Thus, the asymmetric prominence of the left caudate tail may mimic nodular heterotopia. Note the lateral geniculate nuclei medially (*dotted arrows*)

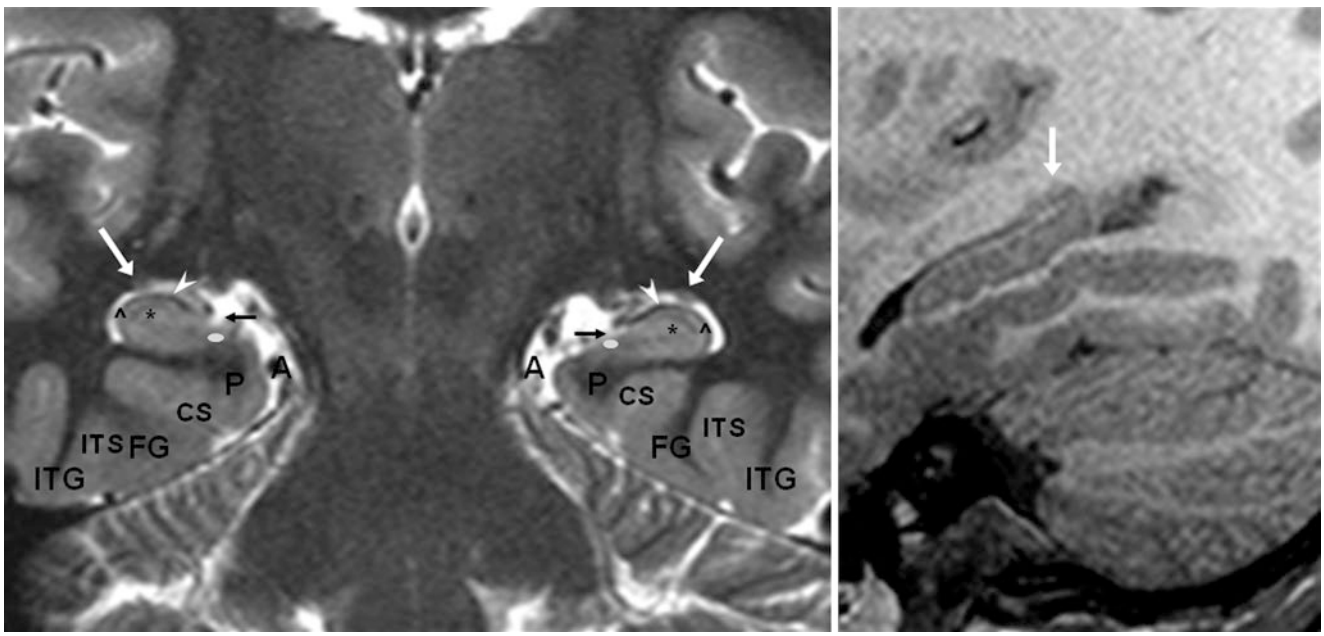

Fig. 12.33 A 10 year old with neurocognitive decline had a negative MRI. On a coronal T2WI through the hippocampus (*left*), the caudate tail (*arrows*) is seen on the left better than on the right; this is consistent with a sagittal T1WI (*right*). Note the white matter of the alveus (*arrowheads*), hippocampal sulci (*tiny arrows*), CA2 of the cornu ammonis (^), and the dentate gyri (*). Also note the subicula (*ovals*), ambient cisterns (*A*), parahippocampal gyri (*P*), collateral sulci (*CS*), fusiform gyri/occipitotemporal gyri (*FG*), inferior temporal sulci (ITS), and the inferior temporal gyri (*ITG*)

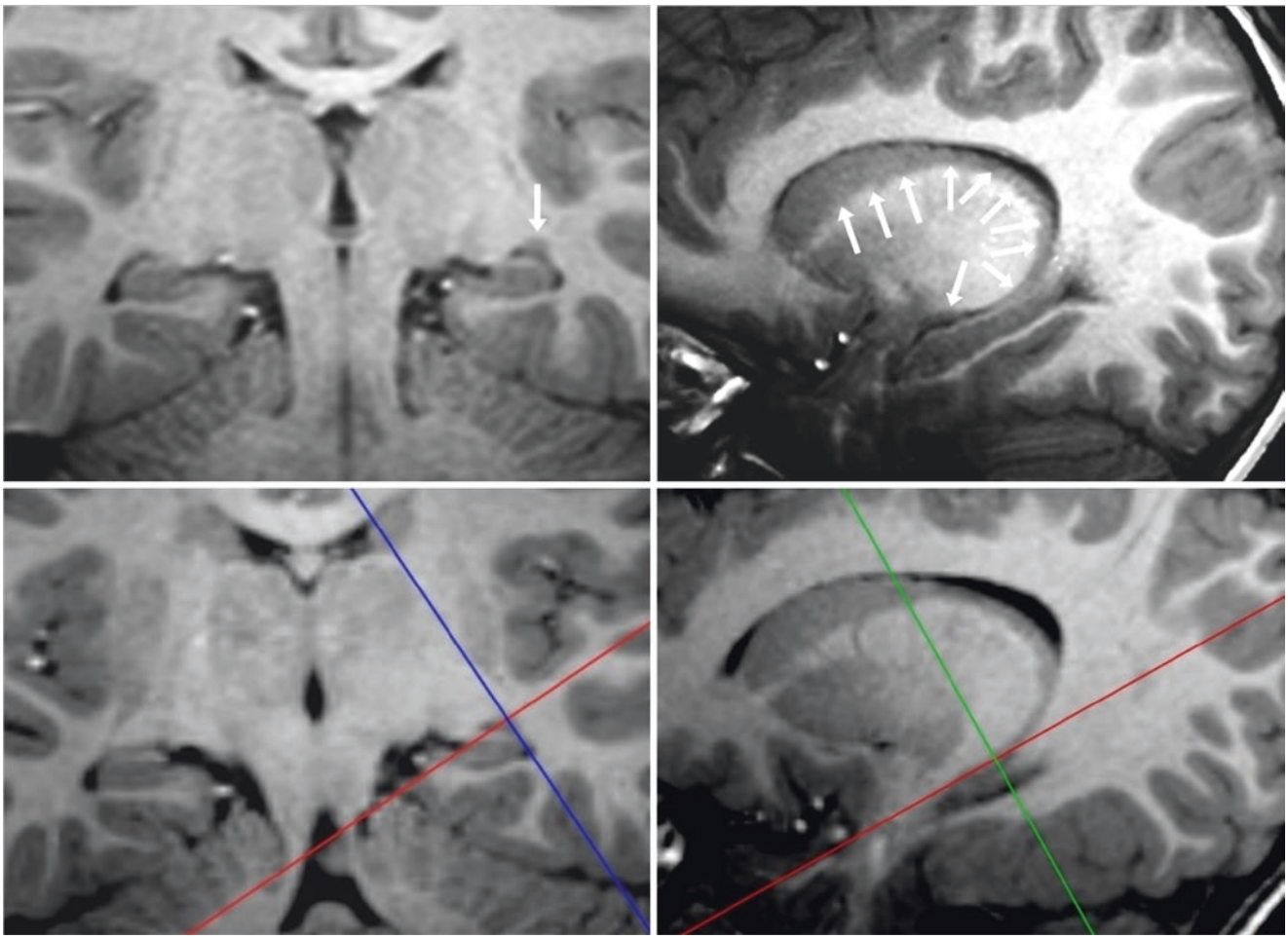

Fig. 12.34 A 3 year old with new seizures. On a negative 3 T MRI, a coronal T1WI (*top left*) demonstrates the left caudate tail. Reconstruction of a three-dimensional T1WI in a sagittal, oblique plane along the caudate nucleus (*top right*) shows the course of the nucleus by *arrows*, while images in similar planes with localizer cross-hairs (*bottom row*) confirm its location

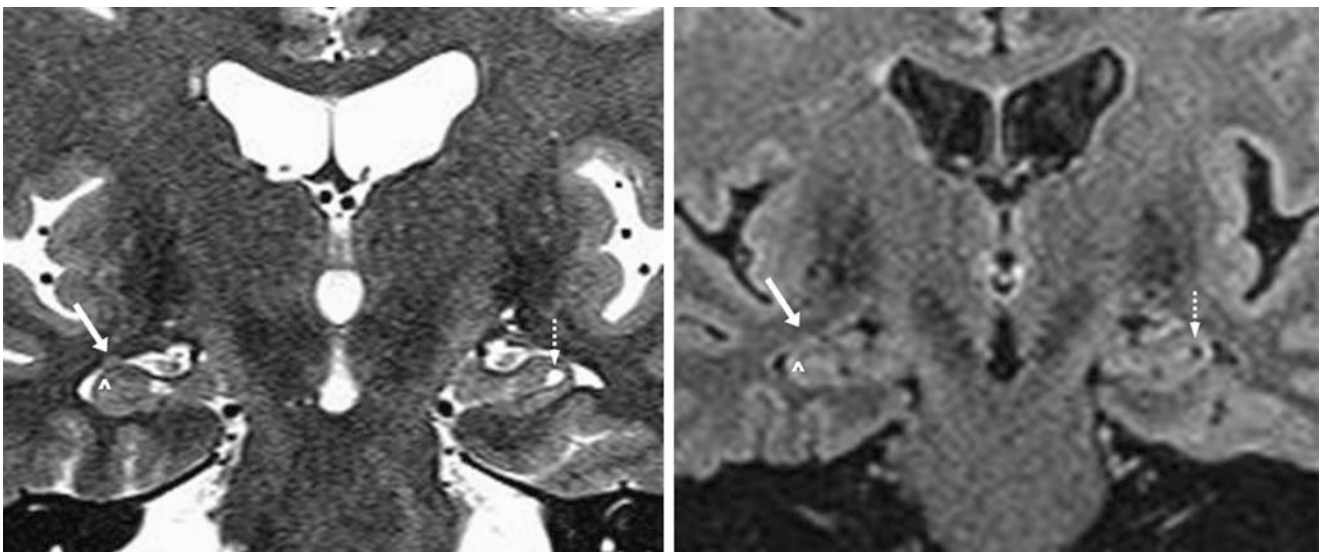

Fig. 12.35 A 54 year old with seizures; on a negative 3 T MRI, coronal T2WI (*left*) depicts the right caudate tail (*arrows*), which is not well visualized on coronal FLAIR (*right*). Note the hippocampus/CA2 inferiorly (^) as well as a contralateral hippocampal cyst (*dotted arrows*, *note suppression with CSF on FLAIR*), which is another normal variation

Fig. 12.36 A 30 year old with seizures; on a negative 3 T MRI, a coronal T2WI (*left*) delineates both caudate tails (*arrows*), which are also visualized on a coronal FLAIR image (*right*). Note the hippocampi/CA2s inferomedially bilaterally (^), the hippocampal sulci (*tiny arrows*), and the bright signal of the normal choroid plexus on FLAIR (*open arrows*)

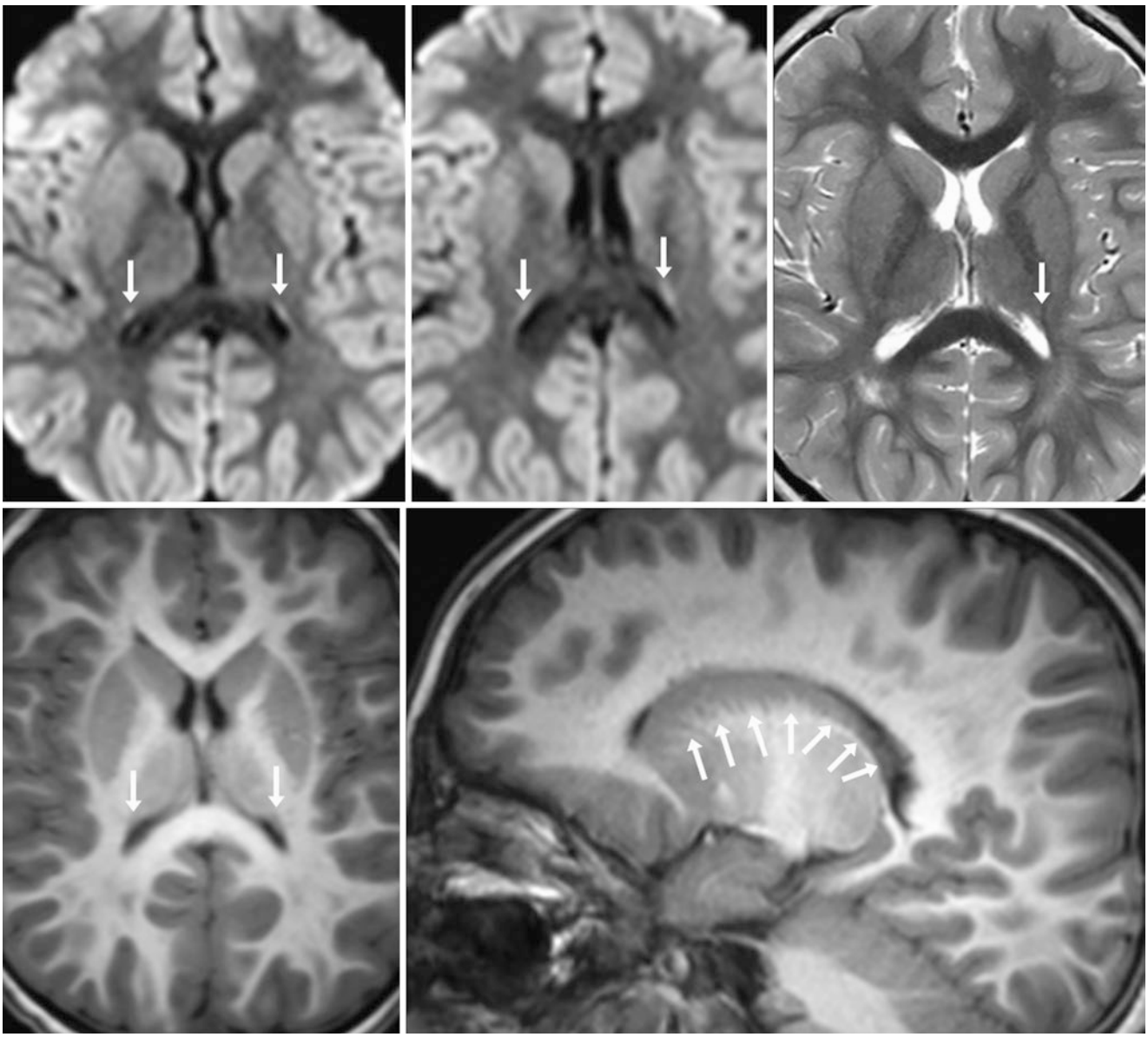

Fig. 12.37 A 3 year old with febrile seizures; on a negative 3 T MRI, axial DWIs (*top left and middle*) showed mild, linear bright signal within what was confirmed to be the caudate tail (*arrows*) on T2WI (*top right*). This was seen as well on three-dimensional T1WI that was reconstructed in the axial (*bottom left*) and sagittal (*bottom right*, *of the left side*) planes. The *arrows* in the bottom right images outline the entire caudate nucleus

12.3 Hippocampal Corrugated Appearance

The hippocampus may appear *corrugated* or have an *undulating appearance* in its middle to posterior portion on higher resolution T1WI only in the sagittal plane. It should appear normal in the other planes. The cause of this appearance is unknown. It may be mistaken for congenital abnormalities such as *polymicrogyria, heterotopia,* or *cortical dysplasia*. Interestingly, a loss of this appearance, or smoothing, could actually be an early sign of *mesial temporal sclerosis* (i.e., seizure-related atrophy) (Figs. 12.38, 12.39, 12.40, 12.41, 12.42, 12.43, 12.44, 12.45, 12.46, and 12.47).

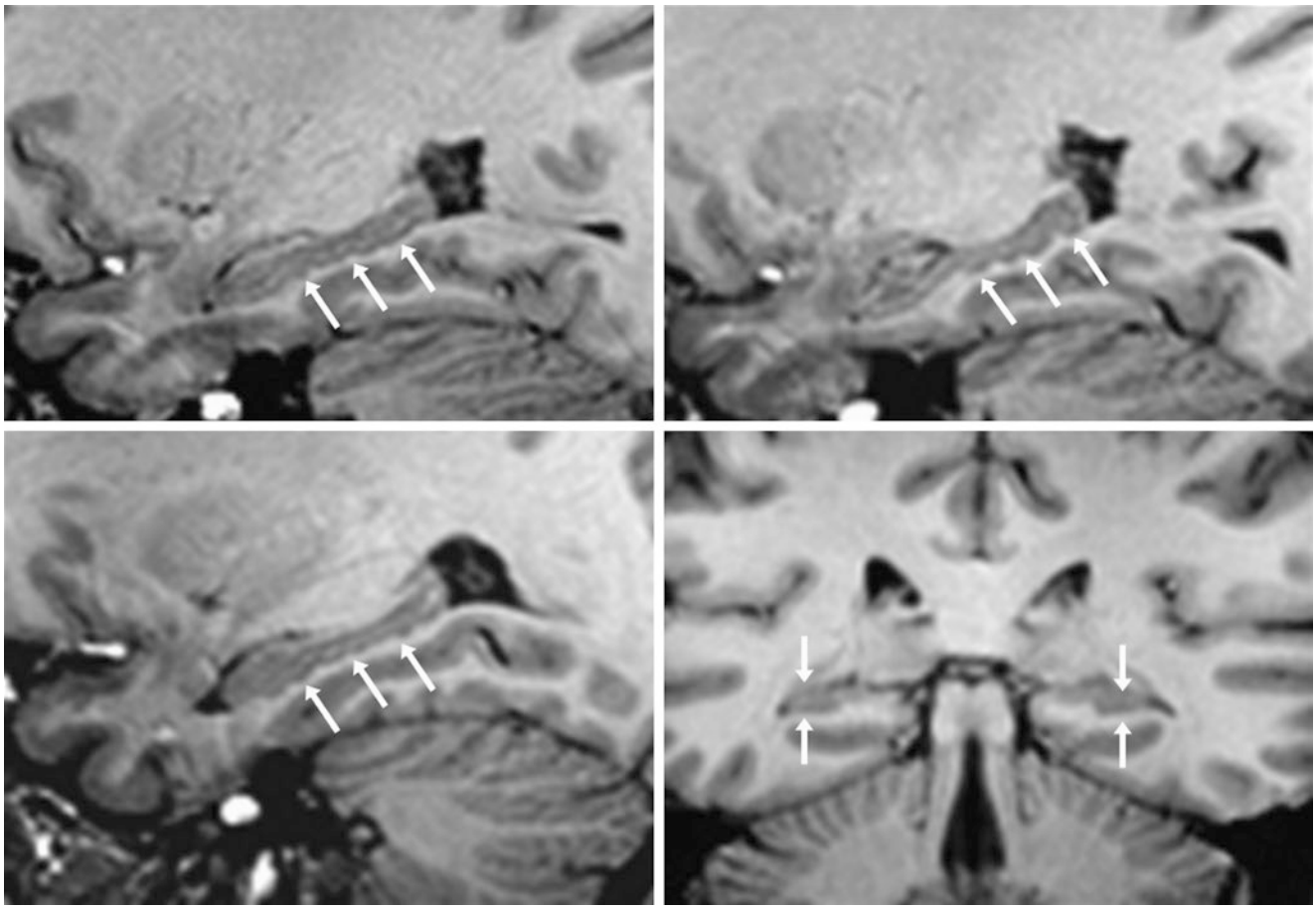

Fig. 12.38 A 39 year old who had a corrugated or undulating configuration of the hippocampi bilaterally (*arrows*) on a 3 T MRI, with 1-mm-thick sagittal T1WIs of the left (*top row*) and right (*bottom left*) sides. A coronal T1WI (*bottom right*) confirms that no abnormality is present within the hippocampi (*the hippocampi are located between the arrows*)

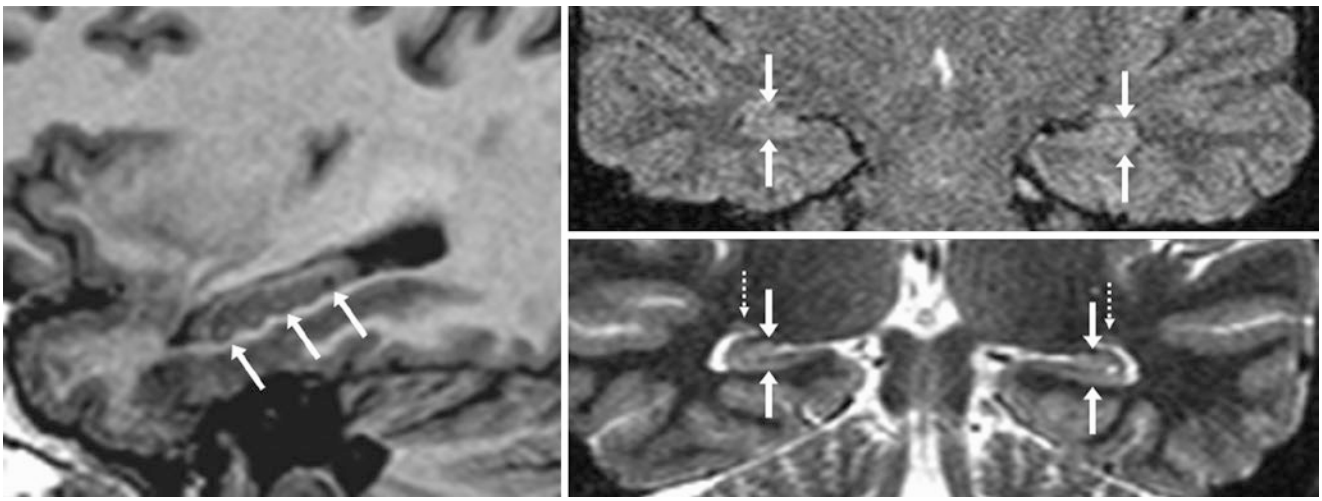

Fig. 12.39 A 37 year old with a corrugated or undulating configuration of the right hippocampus (*arrows*) on a 1.5 T MRI with a 1-mm-thickness sagittal T1WI (*left image*). Coronal FLAIR (*top right*) and coronal T2WI (*bottom right*) confirm that there is no abnormality present within the hippocampi (*the hippocampi are located between the arrows*). Also, note the normal caudate tails (*dotted arrows*) on the coronal T2WI (*bottom right*)

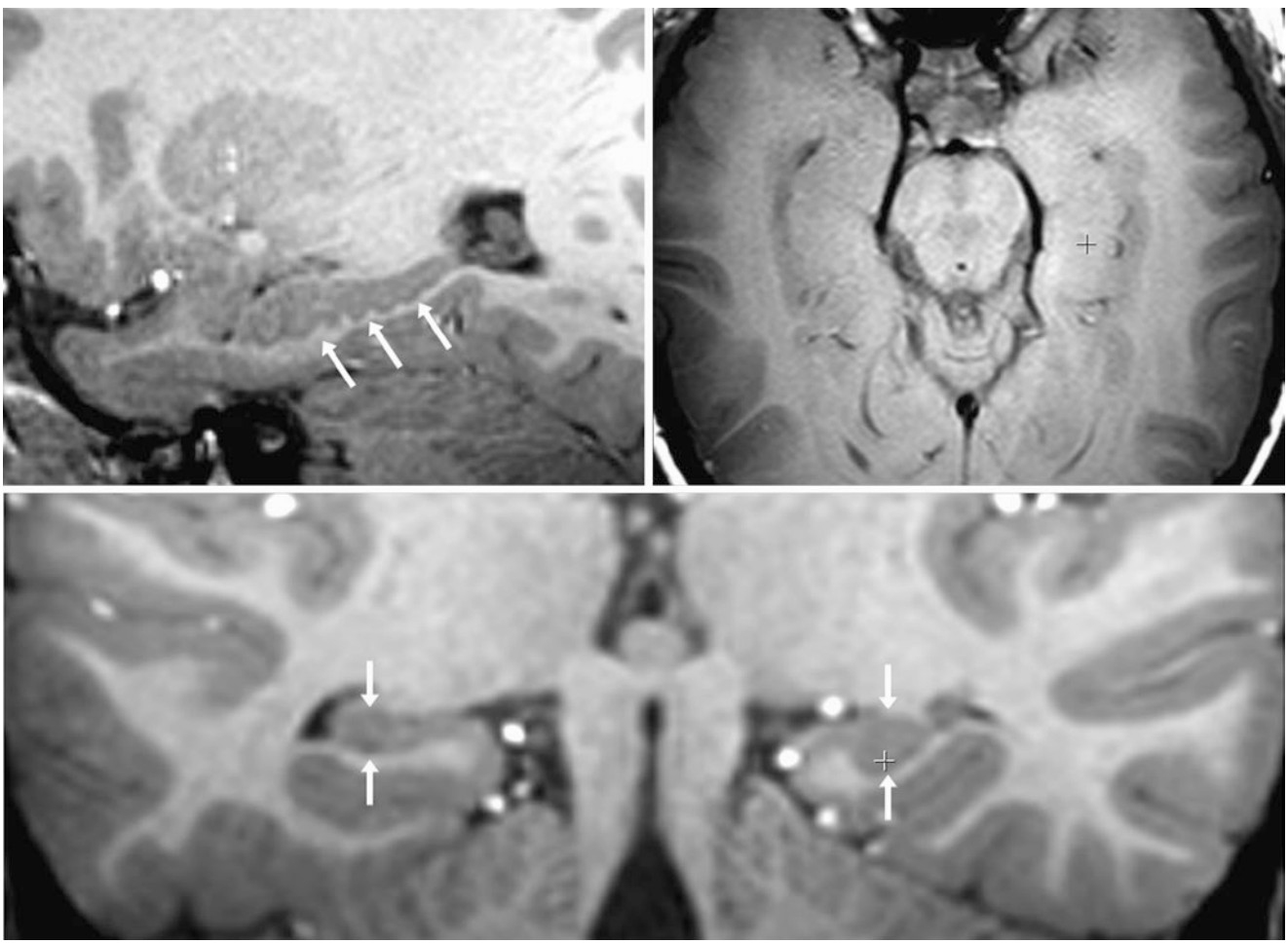

Fig. 12.40 A 7 year old whose images showed a corrugated appearance of the left hippocampus (*arrows*) on a 3 T MRI with a 1-mm thin sagittal T1WI of the left side (*top left*). Axial (*top right*) and coronal (*bottom*) T1WIs have scout cross-hairs on the left hippocampus. On the coronal T1WI, the hippocampi appear normal (*located between the arrows*)

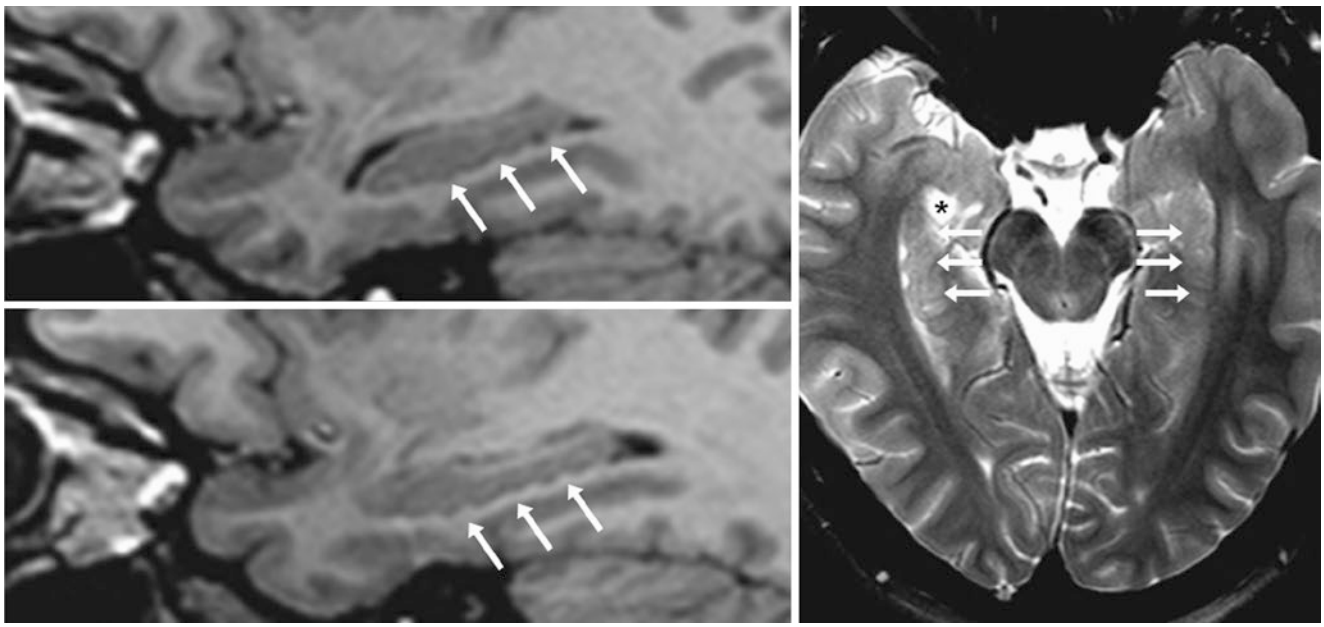

Fig. 12.41 A 48 year old with a corrugated appearance of the hippocampi bilaterally (*arrows*) on a 3 T MRI with thin sagittal T1WI of the left (*top left*) and right (*bottom left*) sides. On an axial T2WI (*right*), the hippocampi appear normal bilaterally (*arrows*). Also, note the incidental enlargement of the temporal horn (*) of the right lateral ventricle

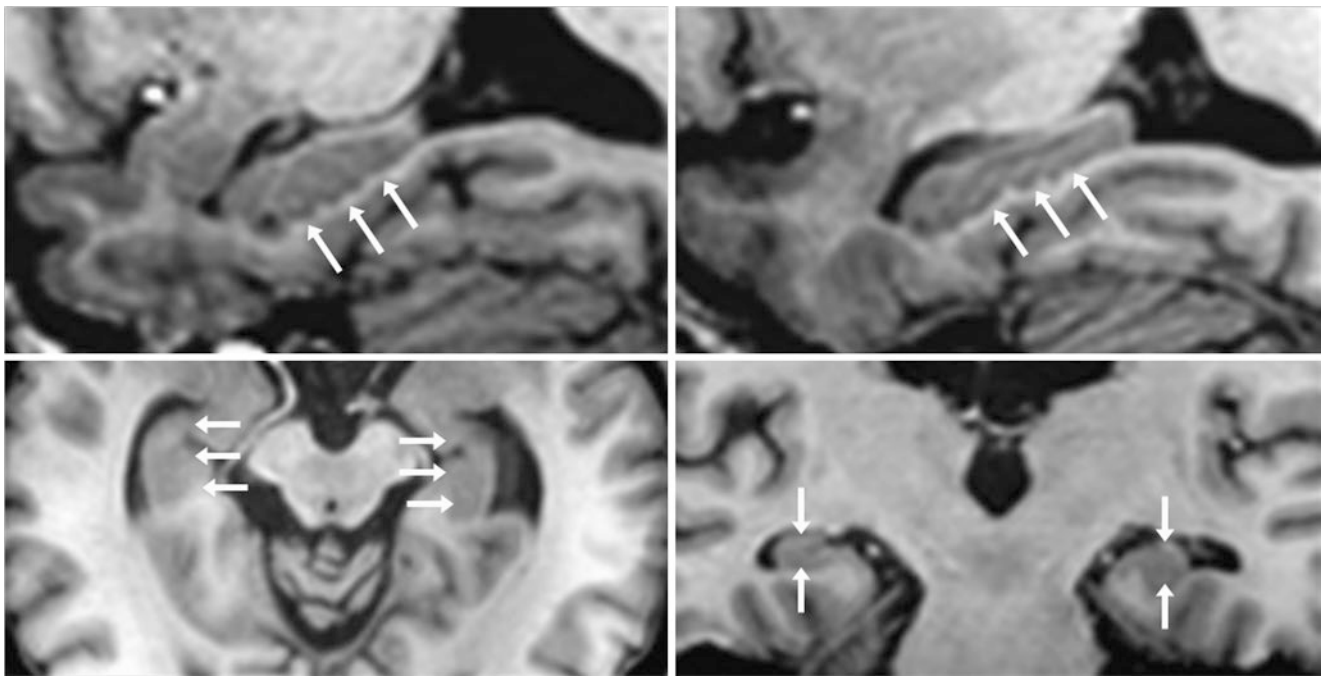

Fig. 12.42 A 53 year old whose testing showed a corrugated appearance of the hippocampi bilaterally (*arrows*) on a 3 T MRI with a thin sagittal T1WI of the left (*top left*) and right (*top right*) sides. On the thin axial T1WI (*bottom left*) and coronal T1WI (*right*), the hippocampi appear normal (*arrows*)

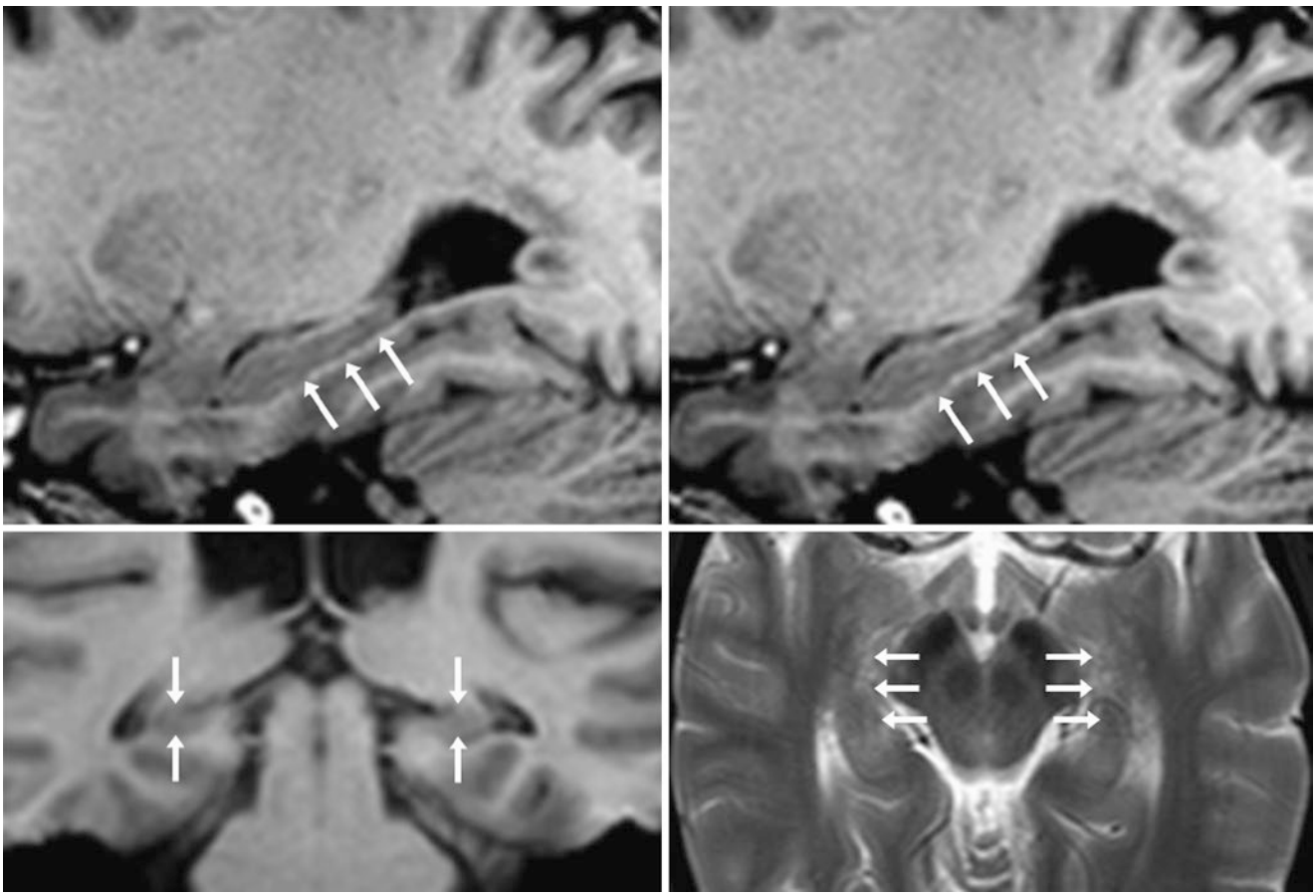

Fig. 12.43 A 58 year old whose images showed a relatively uniform and smooth but slightly corrugated appearance of the hippocampi bilaterally (*arrows*) on a 3 T MRI with thin (1-mm thickness) sagittal T1WI s of the left (*top left*) and right (*top right*) sides. On coronal T1WI (*bottom left*) and axial T2WI (*right*), the hippocampi appear normal (*arrows*)

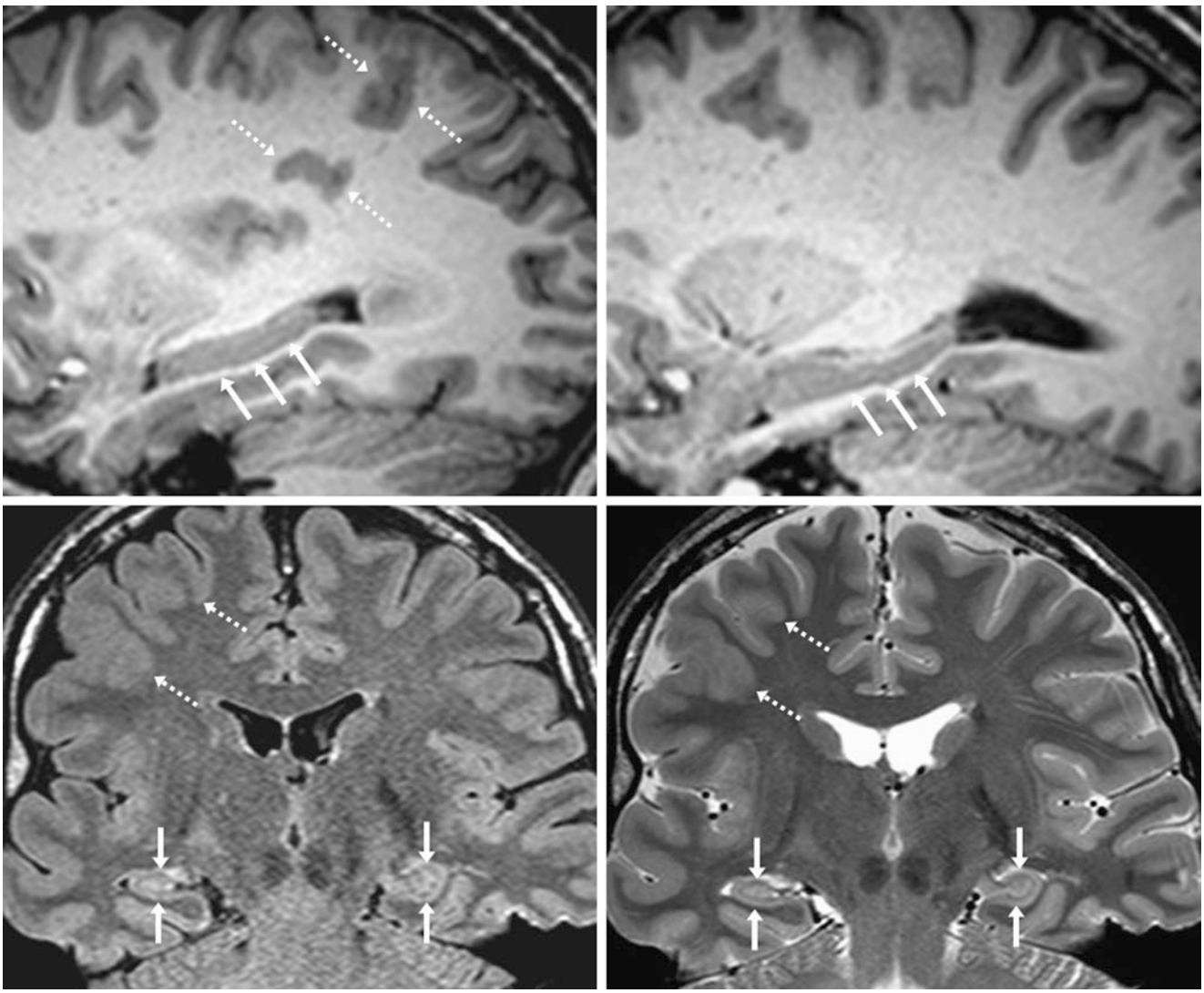

Fig. 12.44 Comparison case of polymicrogyria. A 24 year old with seizures had a normal, smooth left hippocampus (*arrows*, *top left*) and a slightly corrugated right hippocampus (*arrows*, *top right*) on 3 T sagittal T1WI. However, irregularity of the gray-white junction is noted along the edges of the right inferior frontal sulcus and the precentral sulcus (*dashed arrows*). On coronal FLAIR (*bottom left*) and T2WI (*right*), the hippocampi appear normal (*arrows*), while the abnormal gray-white junction of the right-sided polymicrogyria is further demonstrated

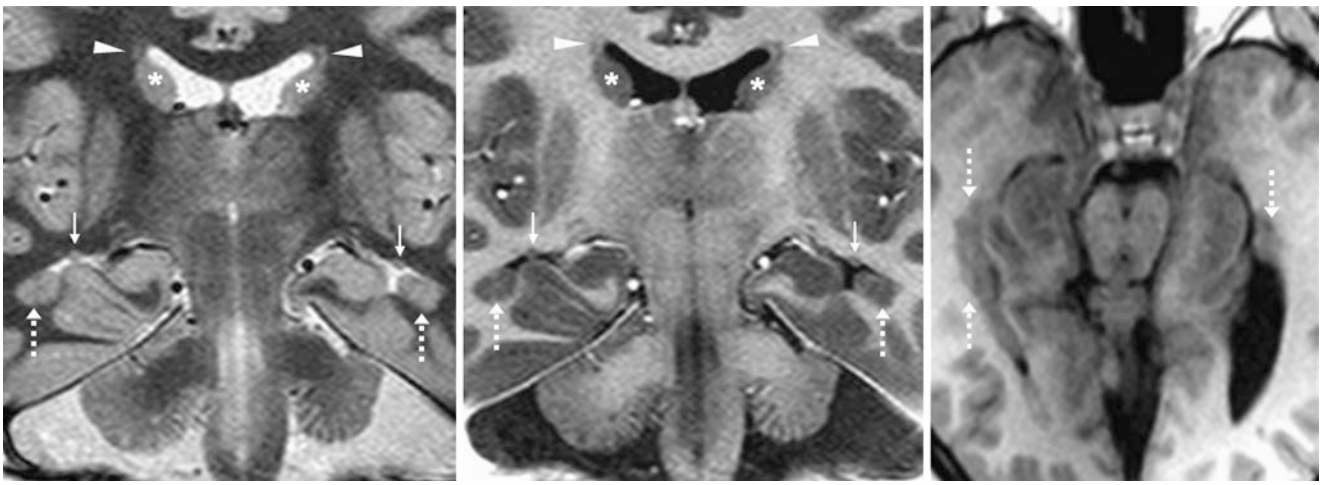

Fig. 12.45 Comparison case of periventricular nodular heterotopia (PVNH). A 14 year old with seizures had bilateral temporal PVNHs (*dashed arrows*) on coronal T2WI (*left*) and on coronal (*middle*) and axial (*right*) T1WI. The PVNHs are situated opposite the caudate tails (*tiny arrows*). Note the caudate heads (*) and the bilateral periventricular ependymal pseudolesions (PEPs, *arrowheads*), which may also mimic PVNHs

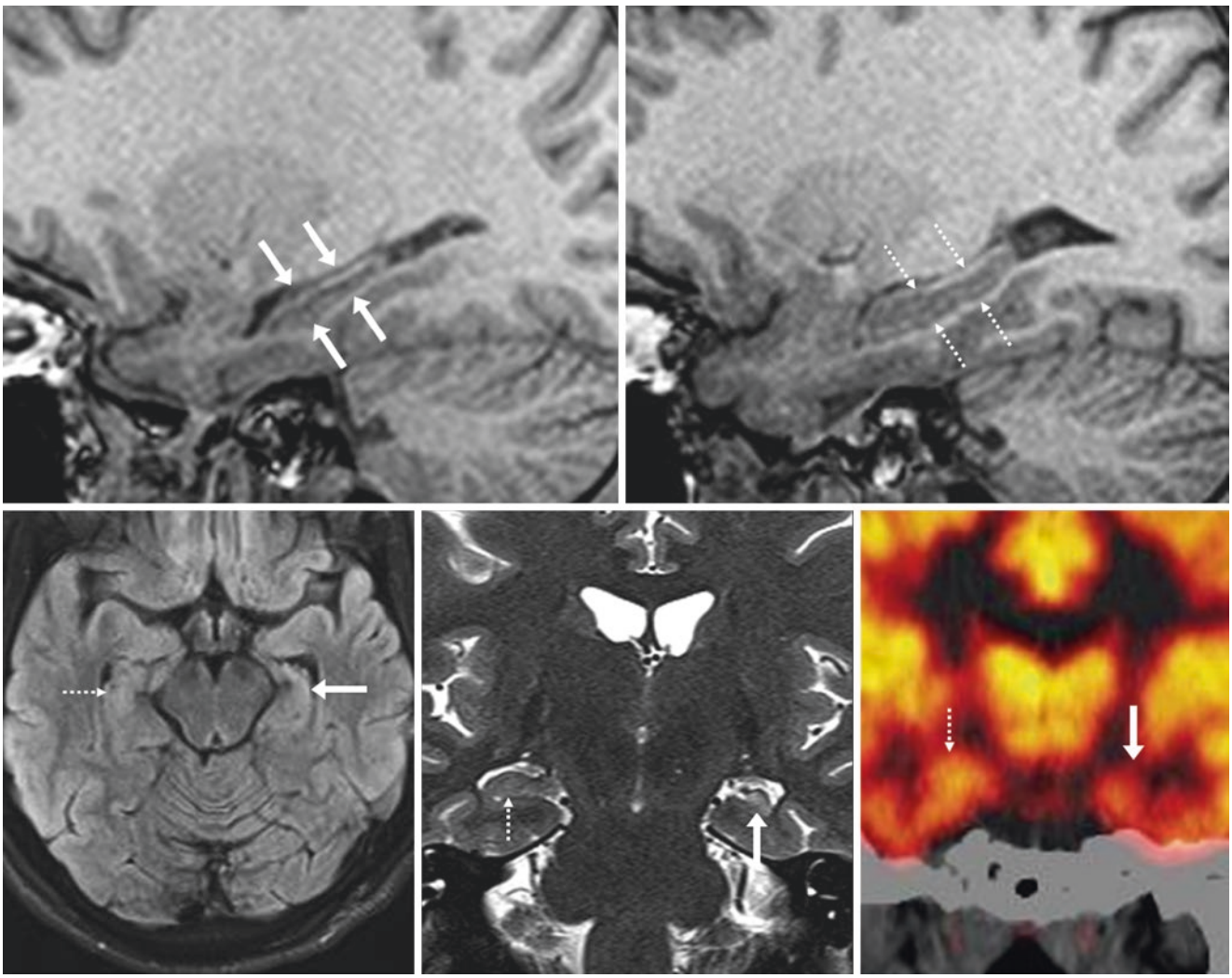

Fig. 12.46 Comparison case of mesial temporal sclerois (MTS). A 22 year old with seizures had left hippocampal MTS-atrophy (between *arrows*) when comparing sagittal T1WIs of the left (*top left*) and right (*top right*) sides and was also seen on axial FLAIR (*bottom left*) and coronal T2WI (*bottom middle*). *Dotted arrows* outline the normal right hippocampus, which has mild normal corrugation. ^{18}FDG-PET (*bottom right*) confirms decreased left medial temporal uptake

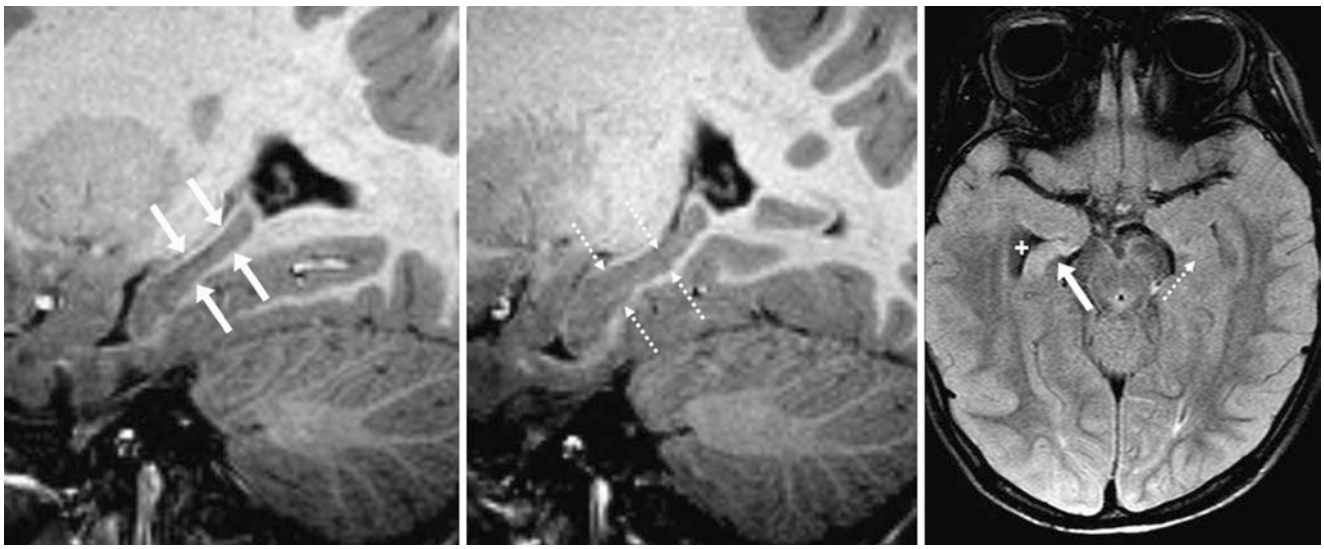

Fig. 12.47 Comparison case of mesial temporal sclerois (MTS). A 3 year old with seizures had right-sided hippocampal atrophy (between *arrows*) on comparing sagittal T1WIs of the right (*left*) and left (*middle*) sides and axial FLAIR (*right*). The *dotted arrows* denote the outline of the normal left hippocampus, which has mild normal corrugation

12.4 Periventricular Ependymal Pseudolesion, Ependymitis Granularis, and Connatal Cysts

A frequent *periventricular ependymal pseudolesion* (PEP) occurs along the ependymal surface of the frontal horns of the lateral ventricles and is seen immediately anterior to the head of the caudate nucleus (i.e., caudate head) on axial images, and immediately superior to the caudate head on coronal images. This is most notable on coronal T2WIs, since it simulates gray matter signal, but it is not actually gray matter at all. Thus, it may mimic abnormalities such as *periventricular nodular heterotopia* (PVNH, which is heterotopic gray matter), which frequently occurs in periventricular, supendymal locations.

Sze et al. [1] have described three different phenomena that may occur in this location and account for such signal, and they have provided histopathologic correlation. First, the density of white matter axons is normally less in this location, since it is less tightly packed relative to other deep periventricular white matter (PVWM) regions. Second, they have described that *ependymitis granularis* occurs in all specimens and in all age groups to varying degrees. Ependymitis granularis consists of ependymal structural loss with astrocytic gliosis. Therefore, most evidence suggests that ependymitis granularis should be considered normal in this location. Third, they have demonstrated an increased concentration of interstitial, extracellular fluid with bubble-like regions (a microscopic observation) separating the axons.

Thus, a PEP is considered normal but should not be confused with abnormal PVWM or ependymal lesions that occur in such disorders as *multiple sclerosis* (linear T2-/FLAIR-bright foci that are oriented perpendicular to the lateral ventricles), *mucopolysaccharidoses* (dilated perivascular spaces spread diffusely throughout the subcortical and PVWM that suppress in the manner of CSF on FLAIR), or *PVNH* (usually not symmetric and follows gray matter on all sequences). Although commonly seen on most coronal T2WI as similar to gray matter signal intensity or as slightly brighter on FLAIR/T2WI, PEP/ependymitis granularis may have variable signal on FLAIR and T1WI. Also, since it often occurs so close to and may have signal intensity similar to the caudate head (another reason it may be confused with heterotopia), it should not be considered part of the caudate nucleus. In addition, this author has noted that there may be faint, perivenular contrast enhancement paralleling the lateral ventricle in this location (on sagittal images) that corresponds to the location of the ependymitis granularis. This can further confirm that this is a PEP; notably, this phenomenon may be explained by a venous plexus that does exist in this location as well.

Normal *connatal cysts* may occur in the same locations as PEP on ultrasound (US) and can be visualized in up to fetal, preterm, or occasionally neonatal infants (about 0.7–1.5 % of those undergoing US). These are relatively rare and are asymptomatic, although initially they were thought to represent ischemic sequela. These tear-shaped cysts are now considered to be transient normal variations that are located just lateral to the tops of the angles of the lateral ventricles on coronal US images, and their appearance likely relates to a temporary developmental phenomenon (typically presenting at <33 weeks' gestational age and resolving by 1–2 months postnatally). They range from 2 to 11 mm in size although they can slightly enlarge before regressing. Their appearance on imaging follows that of the CSF (i.e., bright on T2WI and suppressed on FLAIR). They may be mistaken for *cystic periventricular leukomalacia* (PVL), which is typically accompanied by parenchymal white matter atrophy or periventricular hemorrhage. This author has noted that these connatal cysts appear to occur in the same location as PEP/ependymitis granularis, but it is unknown if there is any relation between these entities (Figs. 12.48, 12.49, 12.50, 12.51, 12.52, 12.53, 12.54, 12.55, 12.56, 12.57, 12.58, 12.59, 12.60, 12.61, and 12.62).

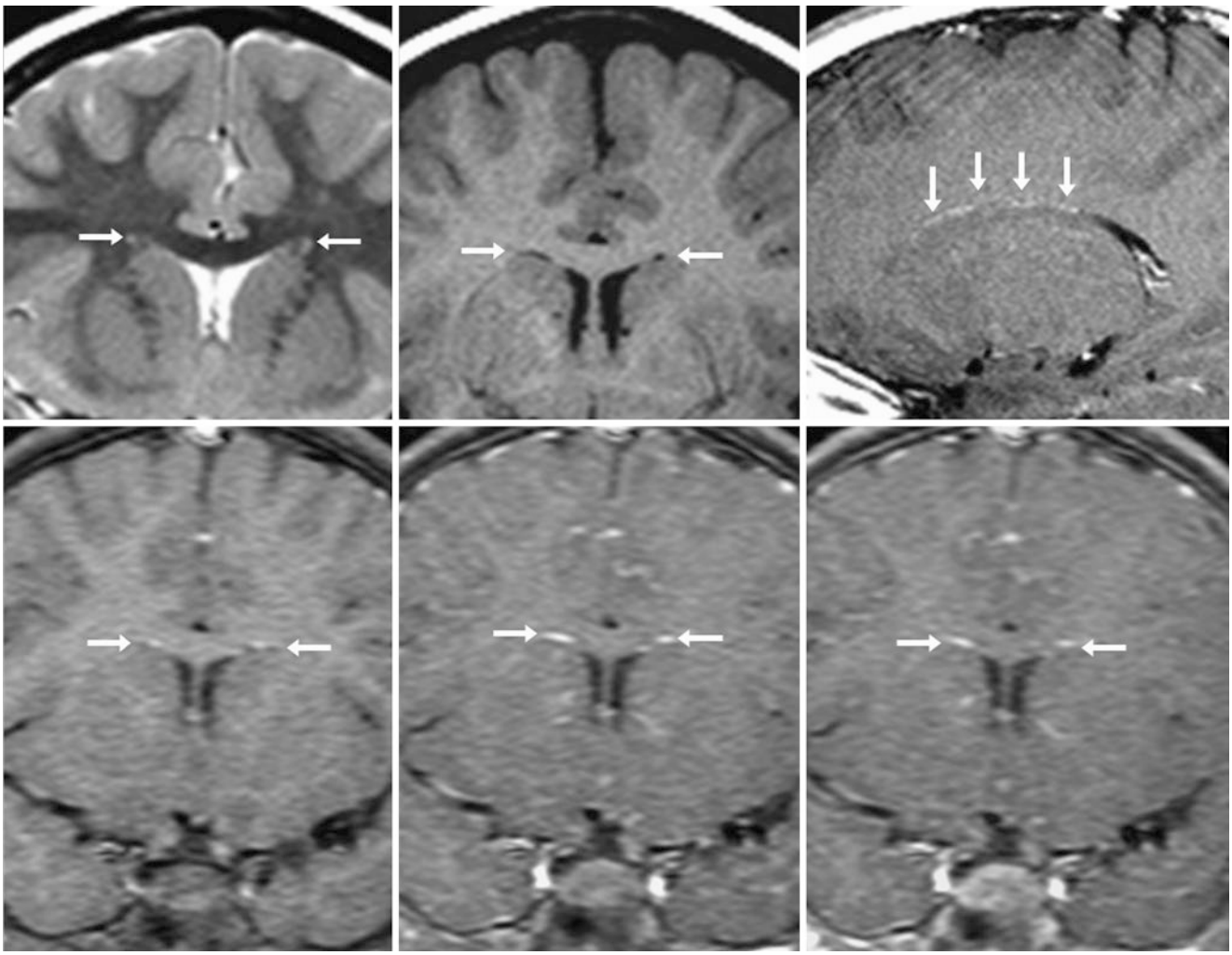

Fig. 12.48 A 5 year old with bilateral PEPs (*arrows*) just above the caudate heads on coronal T2WI (*top left*) and T1WI (*top middle*). Postcontrast sagittal T1WIs (*top right*) illustrate how PEPs/ependymitis granularis may exhibit subtle enhancement. On dynamic postcontrast T1WIs (*bottom row*, *20 s apart*), gradual enhancement occurs

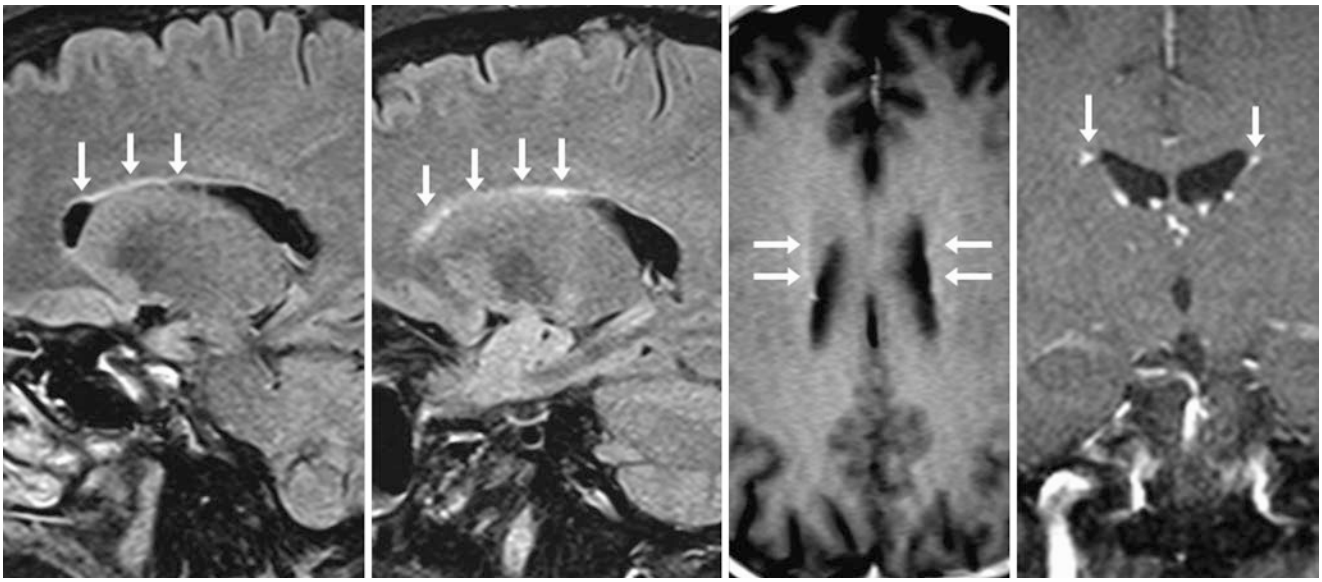

Fig. 12.49 A 53 year old showed mild hyperintense signal (*arrows*) in a parallel configuration to the lateral ventricles on sagittal FLAIR images of the left (*leftmost image*) and right (*left of middle*) sides, which is immediately superior to the caudate heads (*) on axial (*right of middle*) and coronal (*rightmost image*) postcontrast T1WIs. These areas also demonstrate mild, faint enhancement bilaterally along the frontal horns typical of PEP/ependymitis granularis. Demyelinating lesions typically have hyperintensities perpendicular to the lateral ventricles on FLAIR images

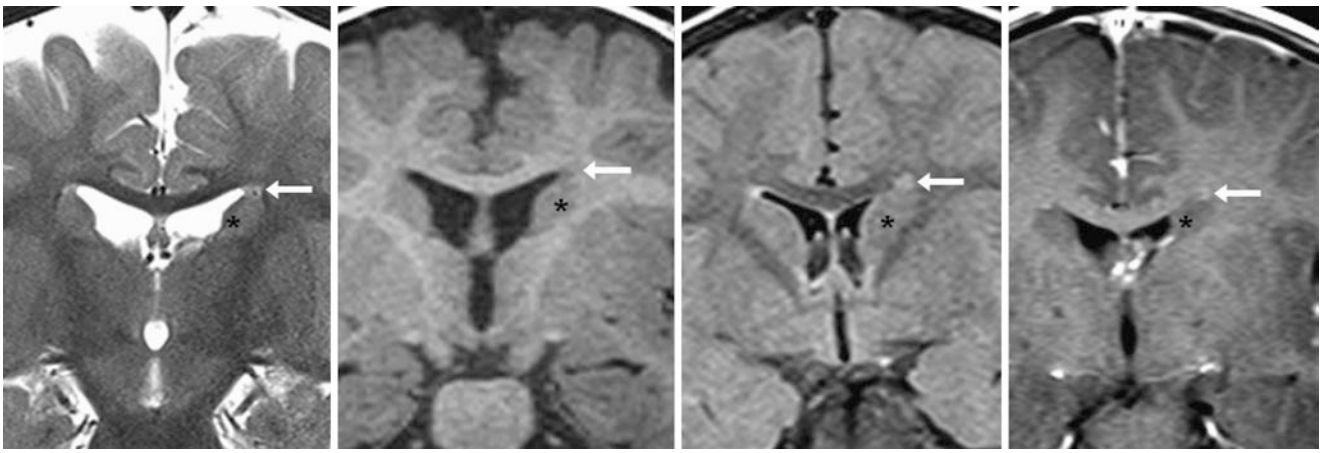

Fig. 12.50 A 9 month old with a left-sided PEP (*arrows*) on coronal T2WI MRI (*left*), not well seen on T1WI (*left middle*). One year later, FLAIR images (*right middle*) show that the PEP appears asymmetric and could be mistaken for a focus of demyelination, which this patient is too young for. Postcontrast T1WI (*right*) depictd faint enhancement, which can be seen in PEP/ependymitis granularis. Note the caudate head just inferior to the PEP (*)

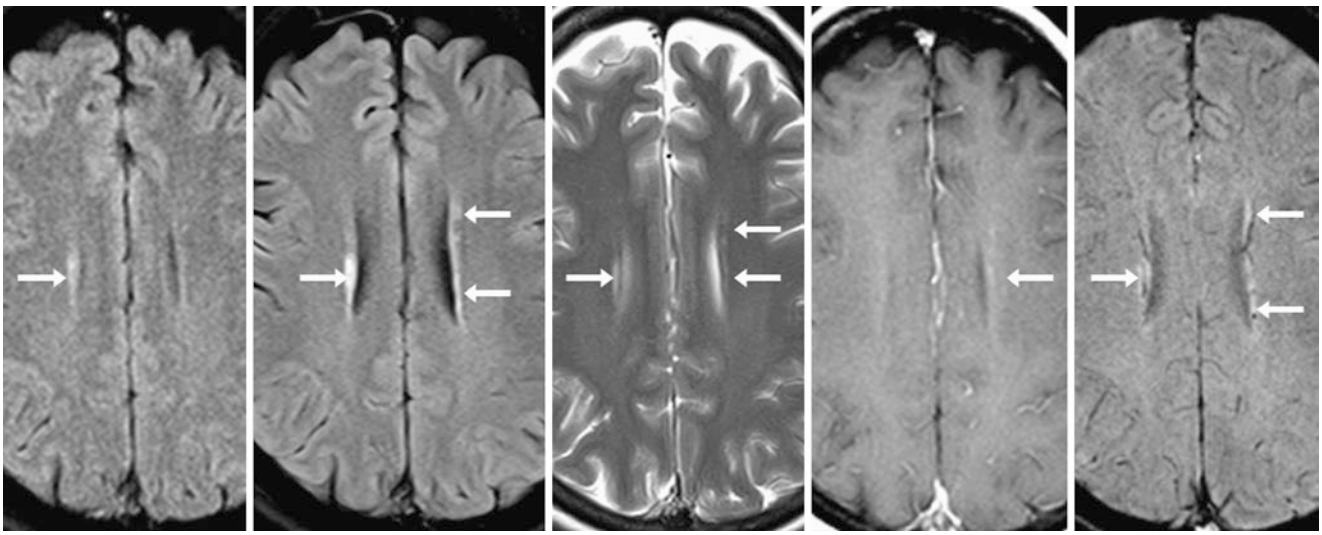

Fig. 12.51 A 52 year old with a right-sided PEP (*arrows*) seen on axial FLAIR MRI (*left*). It became more discernible and likely worsened because a left-sided PEP had developed as well on a FLAIR MRI 2 years later (*left middle*) and on T2WI (*middle*). Postcontrast T1WI (*right middle*) depicts faint enhancement, which can be seen in PEP/ependymitis granularis. SWI (*right*) demonstrates mild, linear hyperintensity in these regions of PEP bilaterally

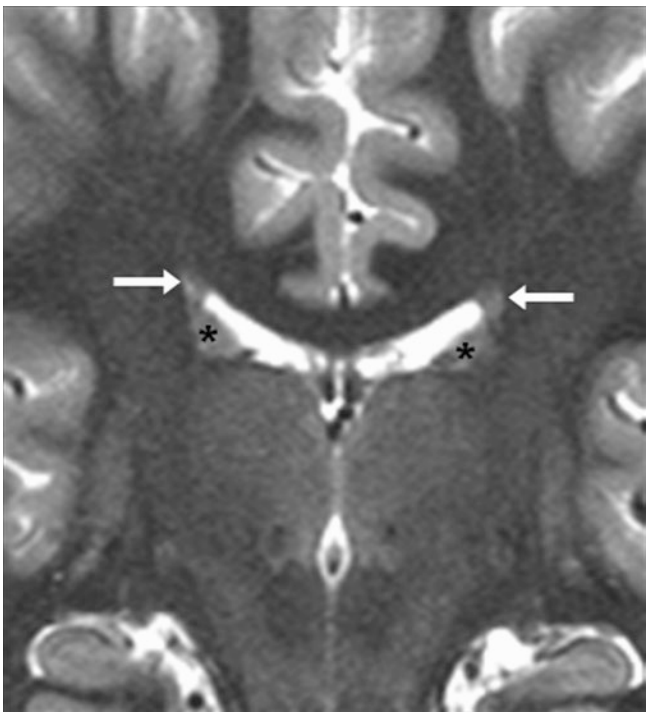

Fig. 12.52 A 10 year old whose 3 T MRI showed asymmetric PEPs (*arrow*), the left being slightly more prominent than the right. Note the caudate heads (*) inferiorly

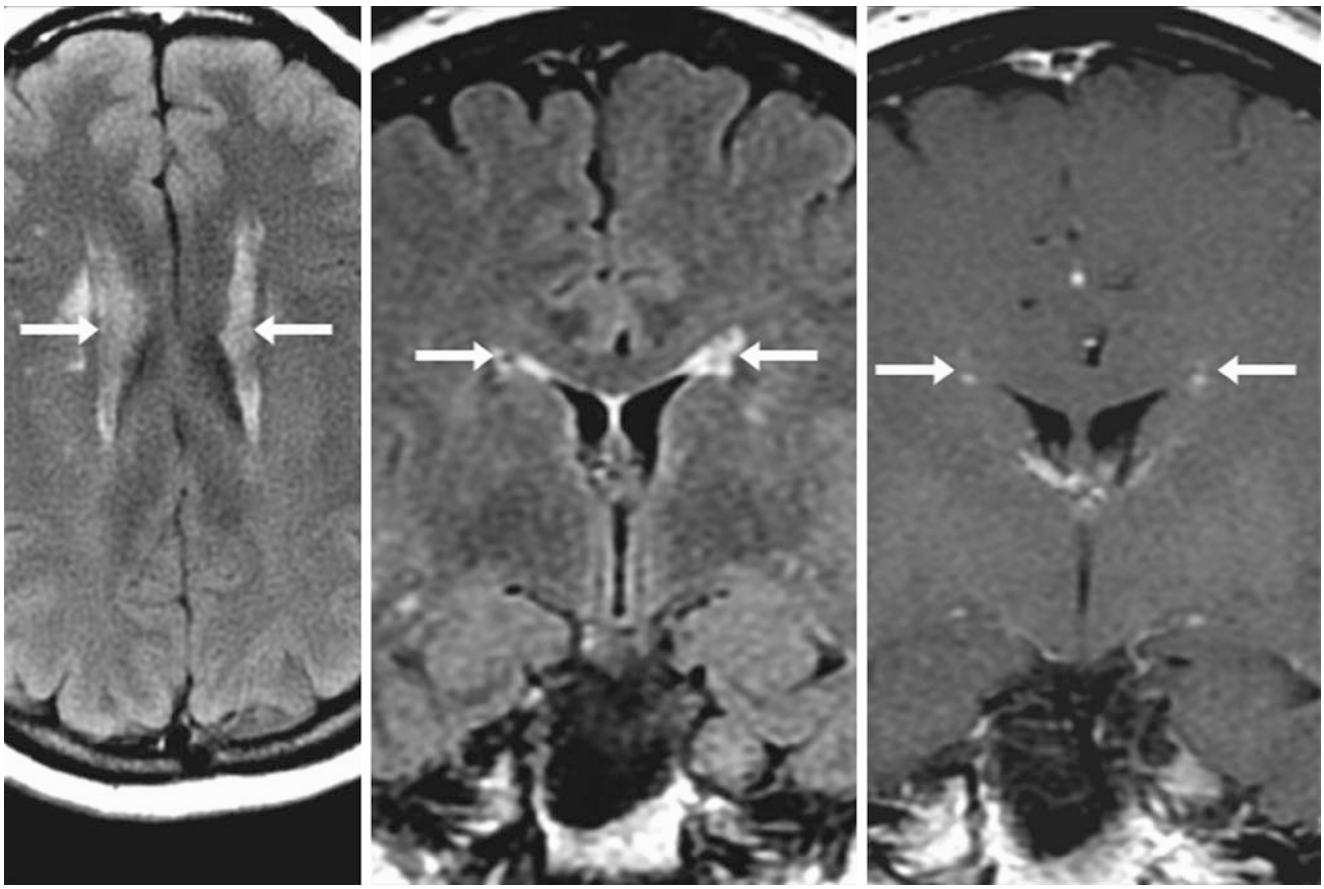

Fig. 12.53 A 56 year old whose images showed asymmetric PEPs (*arrows*), the left greater than the right on axial (*left*) and coronal (*middle*) FLAIR images. Note the mild underlying periventricular leukoariosis, which augments the appearance of the PEPs. The PEPs enhance mildly on coronal postcontrast T1WI (*right*)

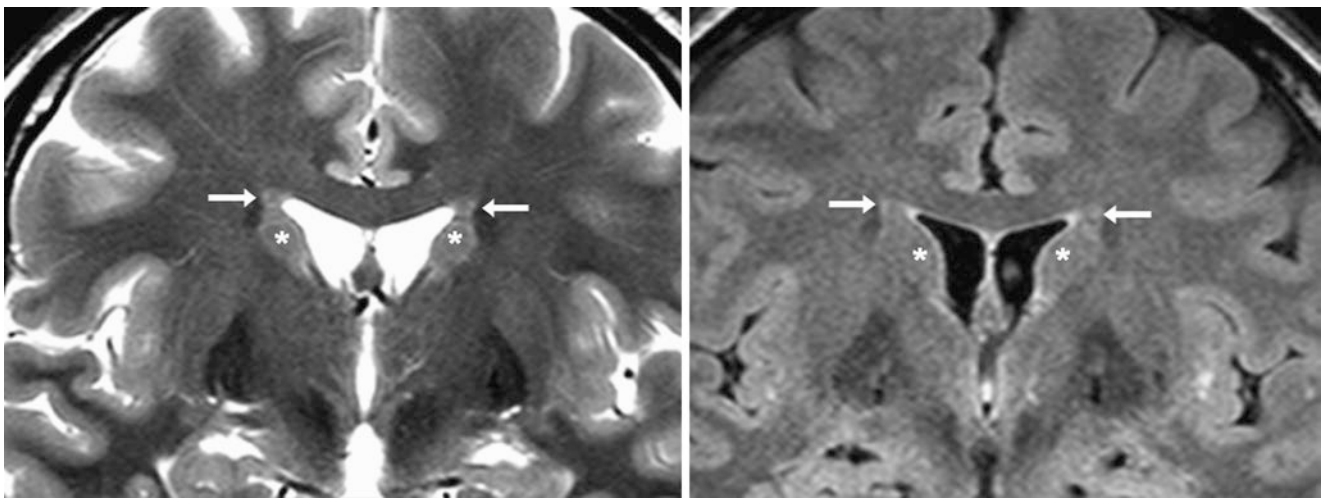

Fig. 12.54 A 27 year old volunteer whose tests showed coronal 3 T MRI T2WI (*left*) and FLAIR (*right*) images, which demonstrate bilateral PEPs (*arrows*) that have signal intensity similar to the caudate heads (*). This caused the radiologist to initially call the PEPs nodular heterotopia. However, these are not nodular and have slight hyperintensity along the ependymal surface on FLAIR, consistent with ependymitis granularis, which is seen in association with PEPs

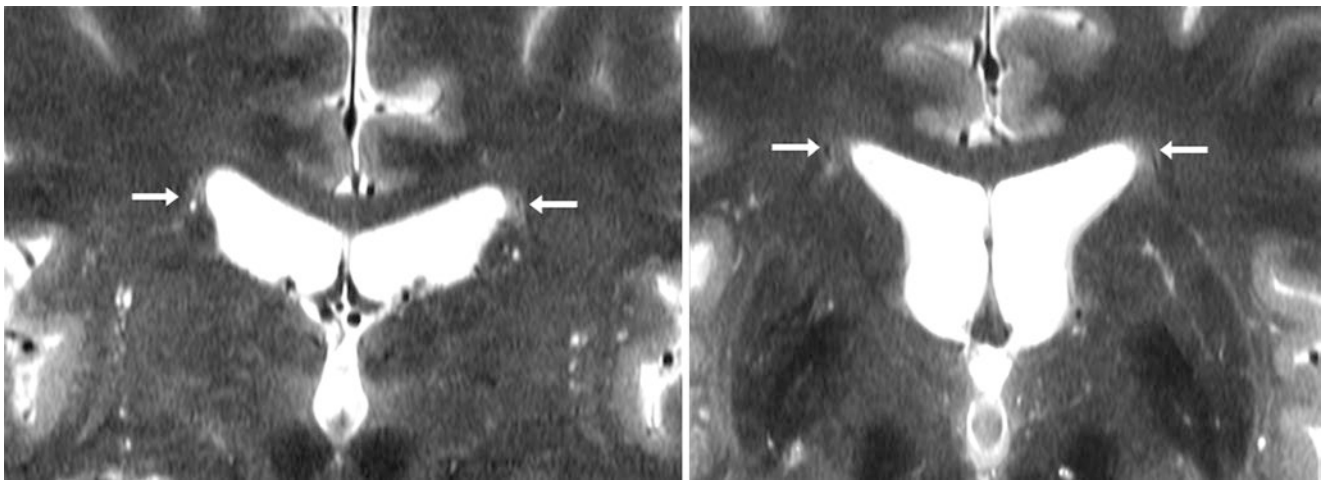

Fig. 12.55 A 50 year old volunteer with 7 T MRI coronal T2WIs showing a left PEP (*arrows*); similar periependymal hyperintensity is present to a lesser degree on the right side. Additionally, note the multiple, incidental, tiny dilated perivascular spaces located diffusely throughout the basal ganglia

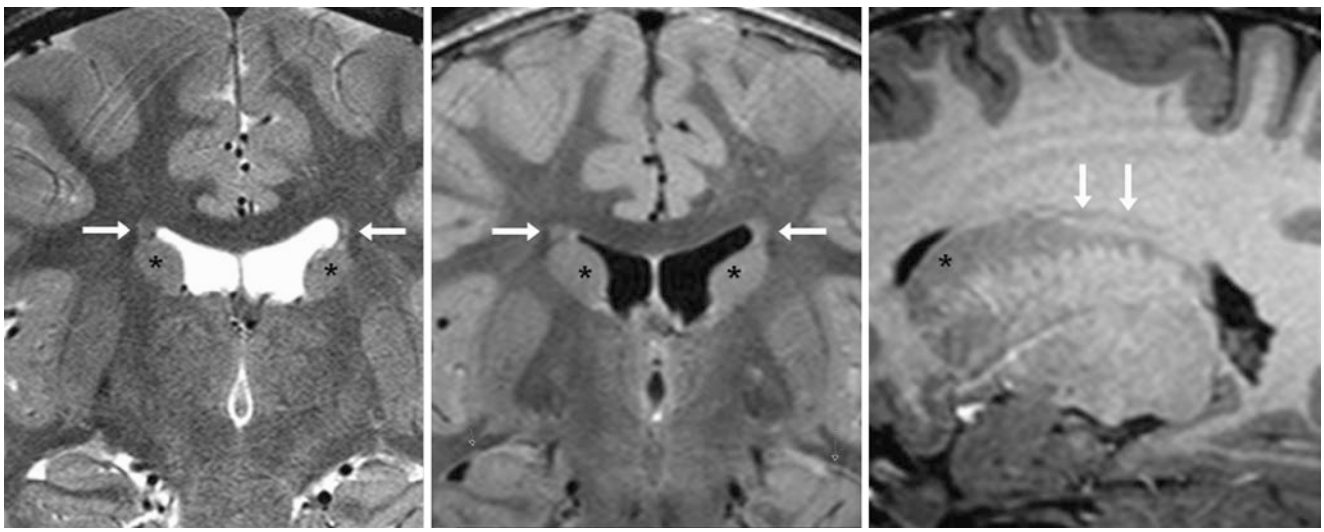

Fig. 12.56 A 7 year old had a 3 T MRI performed for seizures (negative study). Bilateral PEPs (*arrows*) are noted immediately superior to the caudate nuclei (*) on coronal T2WI (*left*) and FLAIR (*middle*), but they are not well visualized on sagittal T1WI (*right*). Their signal intensity is similar to the caudate nuclei and may be mistaken for nodular heterotopia

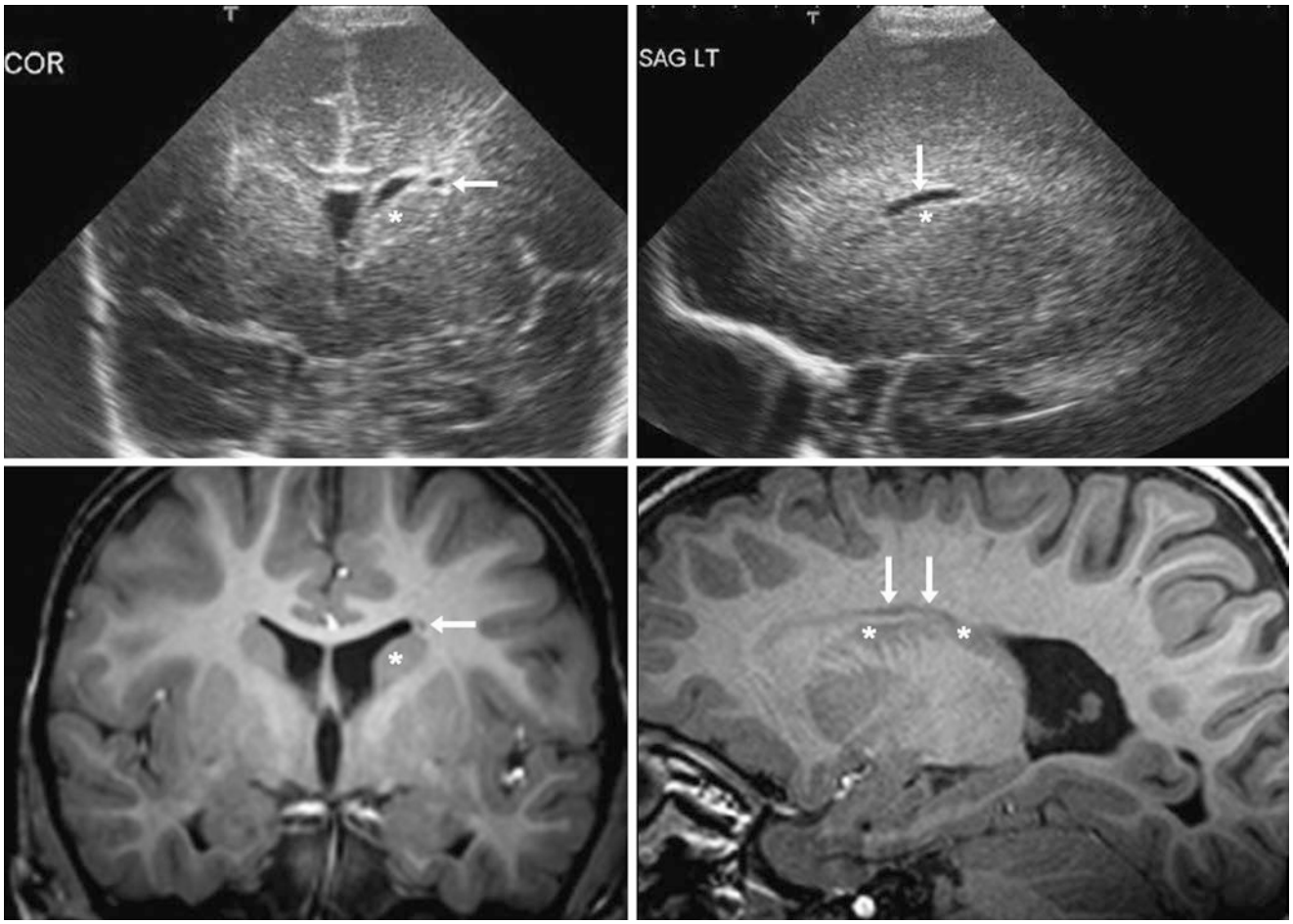

Fig. 12.57 In a 29-week-old premature infant, an US a few days after birth in coronal (*top left*) and sagittal (*top right*) planes demonstrates a left-sided connatal cyst, without white matter hemorrhage, atrophy, or hydrocephalus. A 3 T MRI performed at 2 years of age shows a PEP (*arrows*) in that location, with signal intensity similar to that of the caudate head (*) on coronal T1WI (*bottom left*) and on sagittal T1WI (*bottom right*), both reconstructed from a three-dimensional acquisition

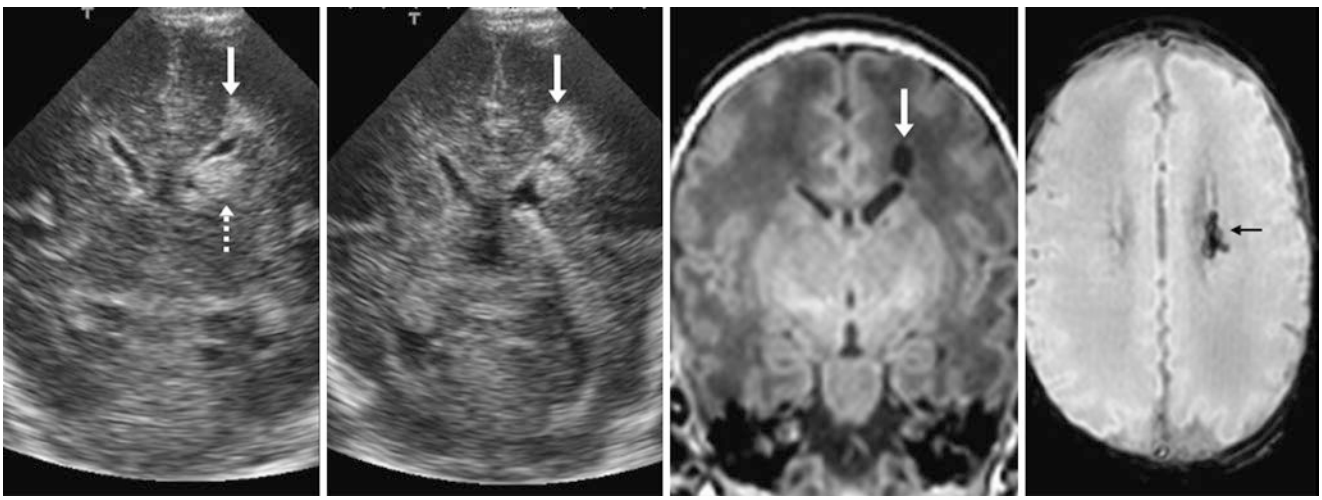

Fig. 12.58 Comparison case of hemorrhagic periventricular leukomalacia (PVL): In a 27 week old premature infant, an US the day after birth in the coronal plane (*left and left middle*) demonstrated hyperechogenicity in a periventricular location caused by hemorrhage (grade IV) as well as within the left caudothalamic groove (*dashed arrows*). On a follow-up MRI 3 months later at term equivalent age, coronal T1WI (*right middle*) shows resultant cystic PVL, with ex vacuo dilatation of the lateral ventricle. SWI (*right*) depicts hemorrhage (*thin arrow*) around the cystic PVL

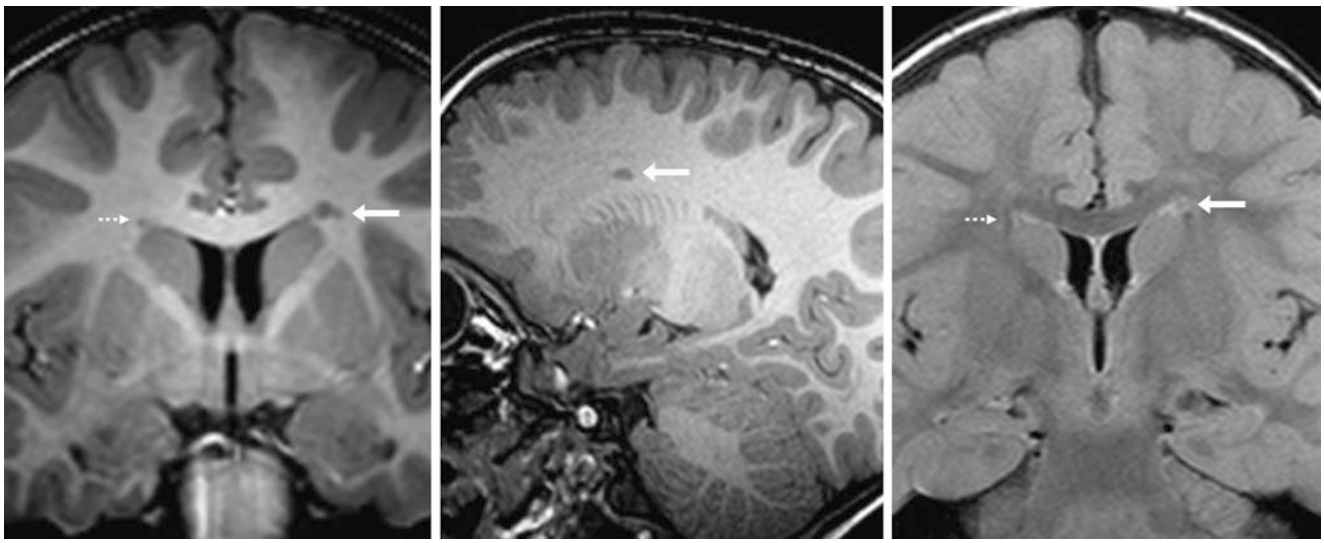

Fig. 12.59 Comparison case of periventricular nodular heterotopia (PVNH). In a 2 year old with seizures, a 3 T MRI demonstrated left PVNH (*arrows*) that appears similar to normal ependymitis granularis on the opposite side (*dashed arrows*) as shown on coronal T1WI (*left*), sagittal T1WI (*middle*), and coronal FLAIR (*right*)

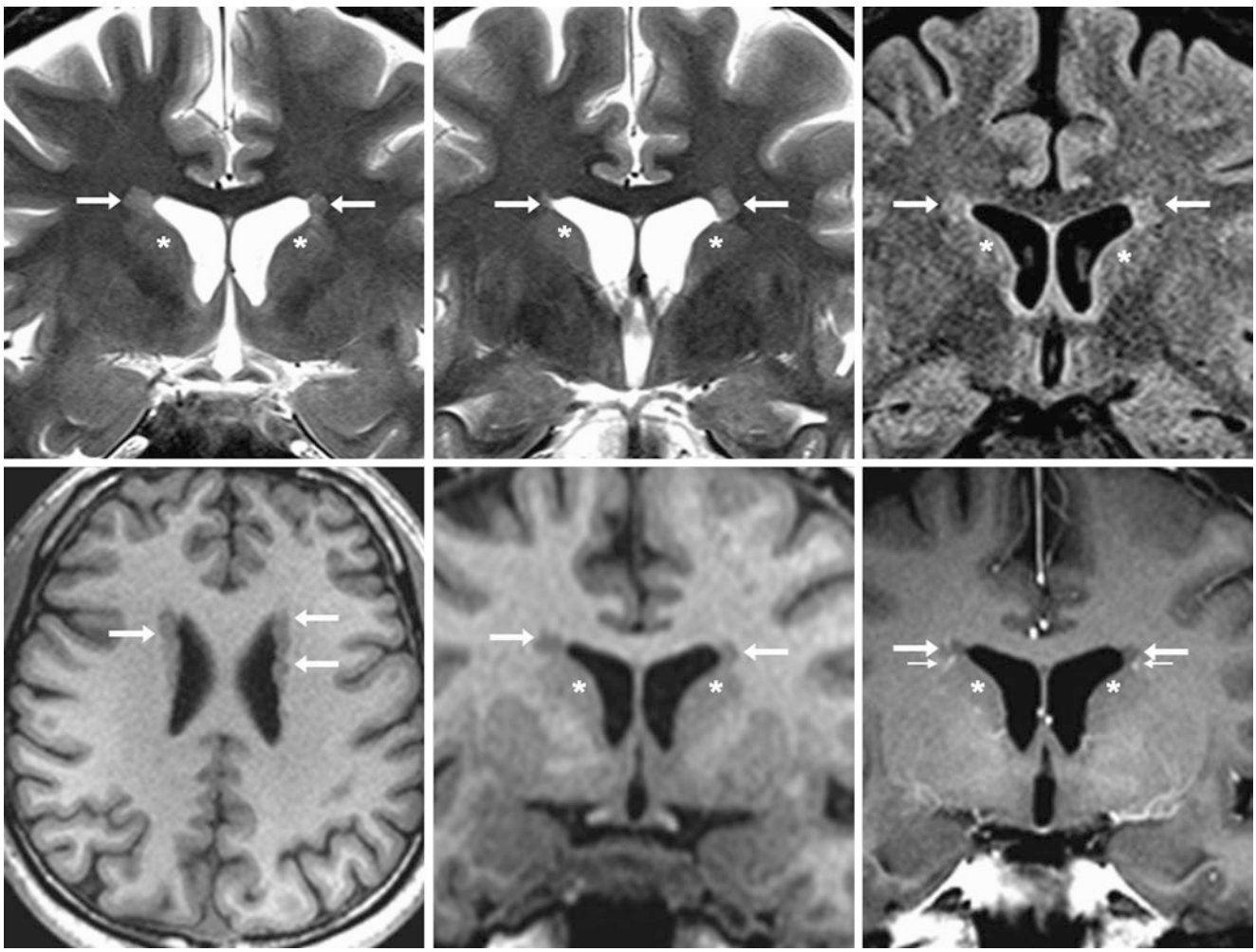

Fig. 12.60 Comparison case of bilateral PVNH. In a 19 year old with seizures, a 3 T MRI with coronal T2WIs (*top left and middle*) showed bilateral gray matter-like nodular foci (*arrows*) just above the caudate nuclei (*) but difficult to visualize on FLAIR (*top right*). Axial T1WI (*bottom left*) confirmed the nodularity of these foci, although the nodular appearance was more difficult to discern on coronal T1WI (*bottom middle*). The faint enhancement noted just outside of these lesions (*tiny arrows*), rather than within them, is typical of PEP/ependymitis granularis

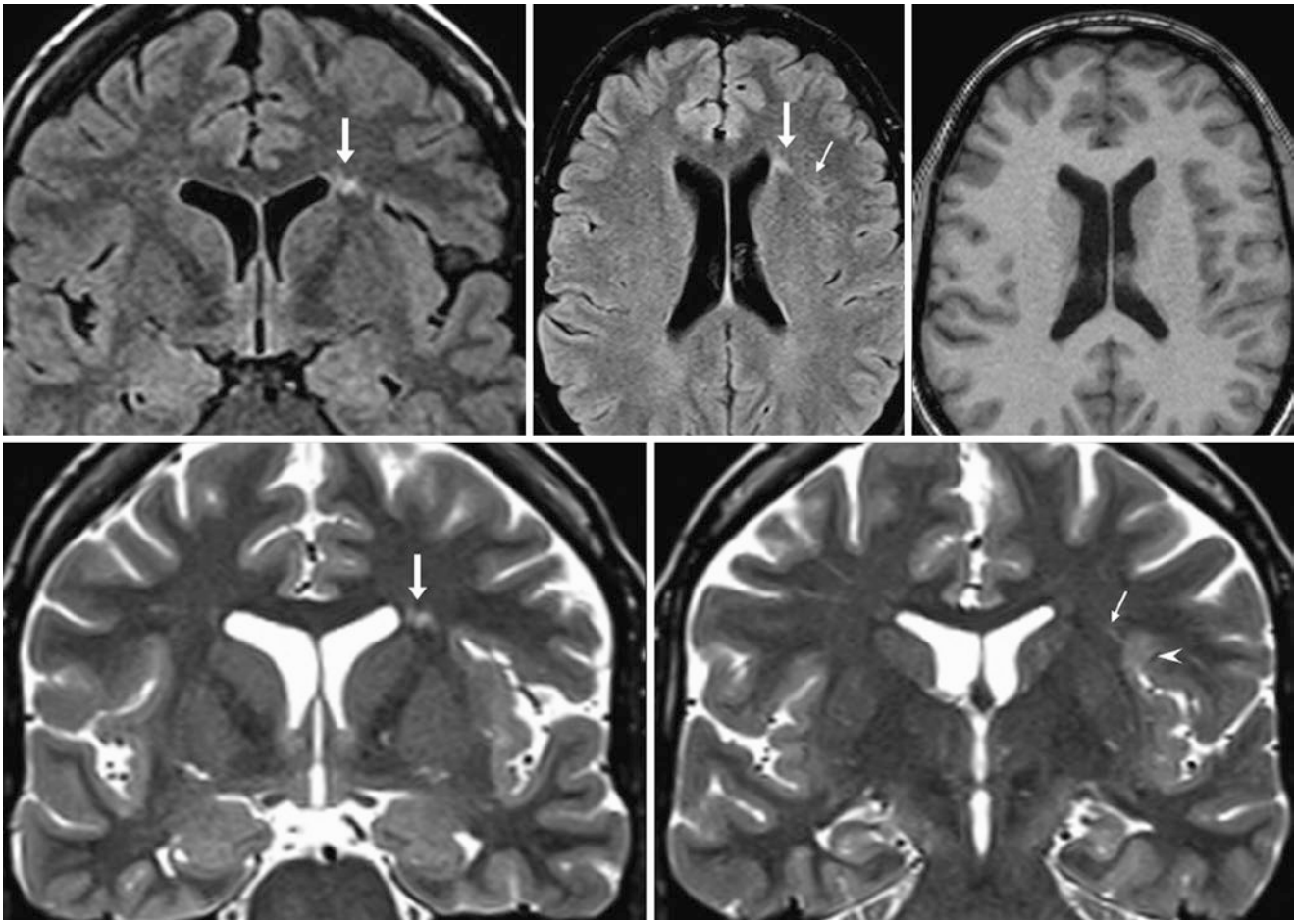

Fig. 12.61 Comparison case of focal cortical dysplasia. In a 34 year old with seizures, a 1.5 T MRI demonstrated focal periependymal signal (*arrows*) on coronal FLAIR (*top left*), with a radiating, tangential band on axial FLAIR (*top middle*). An axial T1WI (*top right*) appeared normal. Thin-section coronal T2WIs (*bottom row*) further demonstrated that peripherally there is faint cortical hyperintensity with blurring of the gray-white matter junction (*arrowhead*)

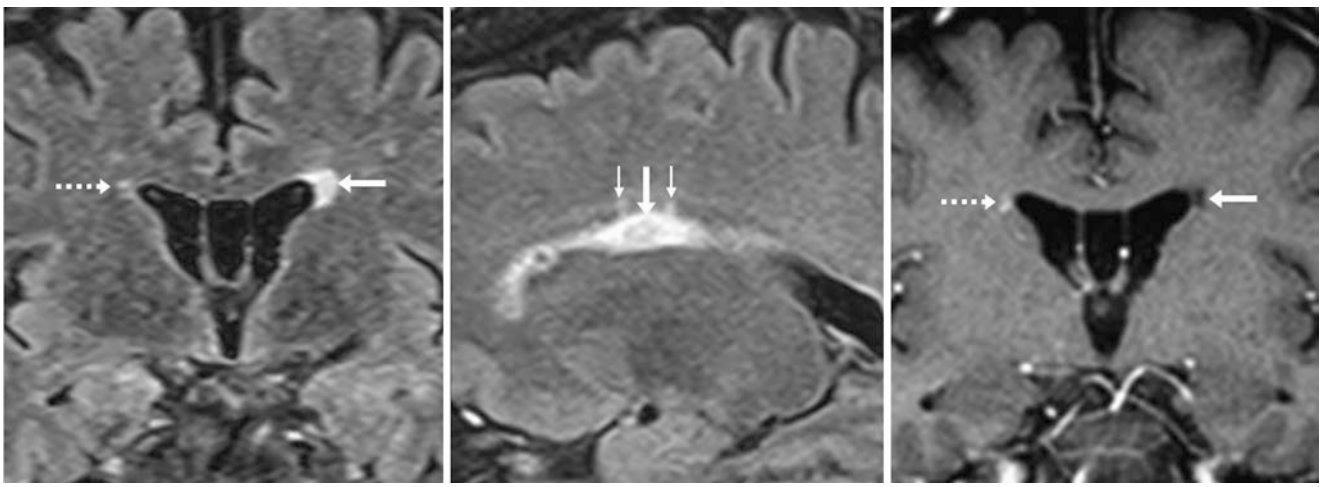

Fig. 12.62 Comparison case of multiple sclerosis. A 49 year old had a demyelinating lesion (*arrows*) noted on the left on coronal FLAIR MRI (*left*), with typical striations (*tiny arrows*) oriented perpendicular to the lateral ventricles on sagittal 2-mm thin FLAIR images (*middle*). The lesion has the appearance of a black hole that does not enhance on post-contrast T1WI (*right*). Note the faint enhancement of a normal PEP (*dashed arrows*) on the right side

References

1. Sze G, De Armond SJ, Brant-Zawadzki M, Davis RL, Norman D, Newton TH. Foci of MRI signal (pseudo lesions) anterior to the frontal horns: histologic correlations of a normal finding. Am J Roentgenol. 1986;147:331–7.

Suggested Reading

Barboriak DP, Doraiswamy PM, Krishnan KR, Vidyarthi S, Sylvester J, Charles HC. Hippocampal sulcal cavities on MRI: relationship to age and apolipoprotein E genotype. Neurology. 2000;54:2150–3.

Bronen RA, Cheung G. MRI of the temporal lobe: normal variations, with special reference toward epilepsy. Magn Reson Imaging. 1991;9:501–7.

Chen W, Song X, Zhang Y. Alzheimer's disease neuroimaging initiative. Assessment of the Virchow-Robin spaces in Alzheimer disease, mild cognitive impairment, and normal aging using high-field MR imaging. Am J Neuroradiol. 2011;32:1490–5.

De Vita E, Thomas DL, Roberts S, Parkes HG, Turner R, Kinchesh P, et al. High resolution MRI of the brain at 4.7 Tesla using fast spin echo imaging. Br J Radiol. 2003;76:631–7.

Epelman M, Daneman A, Blaser SI, Ortiz-Neira C, Konen O, Jarrín J, et al. Differential diagnosis of intracranial cystic lesions at head US: correlation with ct and mr imaging. Radiographics. 2006;26:173–96.

Gutierrez J, Rundek T, Ekind MS, Sacco RL, Wright CB. Perivascular spaces are associated with atherosclerosis: an insig ht from the northern Manhattan study. Am J Neuroradiol. 2013;34:1711–6.

Kier EL, Kim JH, Fulbright RK, Bronen RA. Embryology of the human fetal hippocampus: MR imaging, anatomy, and histology. Am J Neuroradiol. 1997;18:525–32.

Larcos G, Gruenewald SM, Lui K. Neonatal subependymal cysts detected by sonography: prevalence, sonographic findings, and clinical significance. Am J Roentgenol. 1994;162:953–6.

Neema M, Guss ZD, Stankiewicz JM, Neema M, Guss ZD, Stankiewicz JM. Normal findings on brain fluid-attenuated inversion recovery MR images at 3 T. Am J Neuroradiol. 2009;30:911–6.

Pal BR, Preston PR, Morgan ME, Rushton DI, Durbin GMI. Frontal horn thin walled cysts in preterm neonates are benign. Arch Dis Child Fetal Neonatal Ed. 2001;85:F187–93.

Sasaki M, Sone M, Ehara S, Tamakawa Y. Hippocampal sulcus remnant: potential cause of change in signal intensity in the hippocampus. Radiology. 1993;188:743–6.

Thun-Hohenstein L, Forster I, Kunzle C, Martin E, Boltshauser E. Transient bifrontal solitary periventricular cysts in term neonates. Neuroradiology. 1994;36:241–4.

Tan ZYJ, Naidoo P, Kenning N. Ultrasound and MRI features of connatal cysts: clinicoradiological differentiation from other supratentorial periventricular cystic lesions. Br J Radiol. 2010;83:180–3.

Midline Variants of the Septum Pellucidum, Corpus Callosum, and Massa Intermedia

13

13.1 Cavum Septum Pellucidum, Cavum Et Vergae, and Cavum Velum Interpositum

The cavum septum pellucidum (CSP) is a normal variant fluid potential space of CSF density (on CT) and signal intensity (on MRI). A CSP may simulate a cystic lesion and can occasionally even appear to cause mass effect or can be confused with hydrocephalus. Three general variations of the septum pellucidum exist: the standard *cavum septum pellucidum* (CSP), the *cavum septum pellucidum et vergae* (CEV), and the *cavum velum interpositum* (CVI). To understand the difference between these three variations, a brief description of the anatomy and embryology is necessary. The normal septum pellucidum consists of two leaflets/septations of white matter that are separated in nearly all fetuses in utero. Typically, these septations (i.e., septi pellucidi) fuse in the posterior to anterior direction soon before or after the neonatal period, especially by adulthood. Thus, the CSP exists when the two leaves fail to fuse; it is situated somewhere posterior to the genu of the corpus callosum but anterior to the columns of the fornix.

It is estimated that some form of CSP is present in 100 % of fetuses, fusing by 3–6 months of age in 85 % of the population and persisting to some degree in 59–85 % of normal healthy adults as less than 5 mm in size; it is present as a cystic dilation of greater than 5 mm in size in 1–6 % of adults. Regarding the CEV variant, a CEV is when this CSF-intensity space is filled with fluid but lies posterior to the columns of the fornix. A CEV has been noted in about 20–30 % of children and in about 2–10 % of adults and the elderly. These varying incidences relate to whether a true cyst is seen versus a tiny potential space at necropsy. The CSP and CEV are usually interconnected, and accordingly both fuse posterior to anterior. Hence, a CEV is typically nearly (but not always) associated with a CSP.

The CVI is a cystic-appearing anatomic variation that occurs anywhere within the cistern of the velum interpositum, a potential space located at the top of the third ventricle and below the forniceal columns, possibly extending as far forward as the foramen of Monro anteriorly to as far as the pineal region posteriorly. A CVI may even extend below the splenium of the corpus callosum. CVIs may mimic a simple pineal cyst but on closer inspection they usually reveal that the small, enhancing pineal gland is separate from a CVI. Typically, the internal cerebral veins course along the floor of a CVI.

A CVI usually develops independent of the septum pellucidum, where it is believed to result from abnormal separation of the crura (posterior limbs) of the fornices. However, the CSP, CEV, and CVI may all occur simultaneously. In such a case, the CEV is separated from the CVI by the forniceal crura. Notably, a CVI has been estimated to occur in as many as 20–35 % of infants and children. The literature in adults is not as well described but it may occur in up to 10 %.

It should be mentioned that a CSP has often been referred to as the fifth ventricle and a CEV as the sixth ventricle, Verga ventricle, the ventricle of Strambio, the ventriculus fornicis, or the ventriculus triangulus (due to its oft-triangular appearance). However, these cystic-appearing prominences should not be considered as part of the true ventricular system, since the CSF is not truly formed within them, they often do not communicate with the ventricular system (except occasionally), and they are potential spaces that regress to varying degrees and are not required for normal CSF flow. Thus, terms such as fifth ventricle or sixth ventricle are now considered misnomers in the current literature.

A number of studies have been published over the years that have suggested associations between the presence of a CSP with numerous other disorders, including congenital

A.M. McKinney, *Atlas of Normal Imaging Variations of the Brain, Skull, and Craniocervical Vasculature*,
DOI 10.1007/978-3-319-39790-0_13

CNS malformations, mental retardation, schizophrenia, obsessive compulsive disorder, dementia pugulistica ("punch drunk syndrome" in boxers now considered a form of chronic traumatic encephalopathy [CTE]), craniofacial disorders (such as craniosynostoses), teratogen exposures, and other abnormalities. However, the significance of these associations is often controversial, and many are still being debated.

It should be noted that an enlarged or cystic CSP should not cause *hydrocephalus*. If hydrocephalus is present, concern should be directed at the presence of an intraventricular *arachnoid cyst (*neuroepithelial cyst*)*, a *colloid cyst*, or a *tumor* (such as an subependymoma or central neurocytoma). Inversion recovery (IR) images such as FLAIR may help discern a cyst wall, while postcontrast images can help distinguish tumors, since certain tumors enhance to some degree (Figs. 13.1, 13.2, 13.3, 13.4, 13.5, 13.6, 13.7, 13.8, 13.9, 13.10, 13.11, 13.12, 13.13, 13.14, 13.15, 13.16, 13.17, 13.18, 13.19, 13.20, 13.21, 13.22, and 13.23).

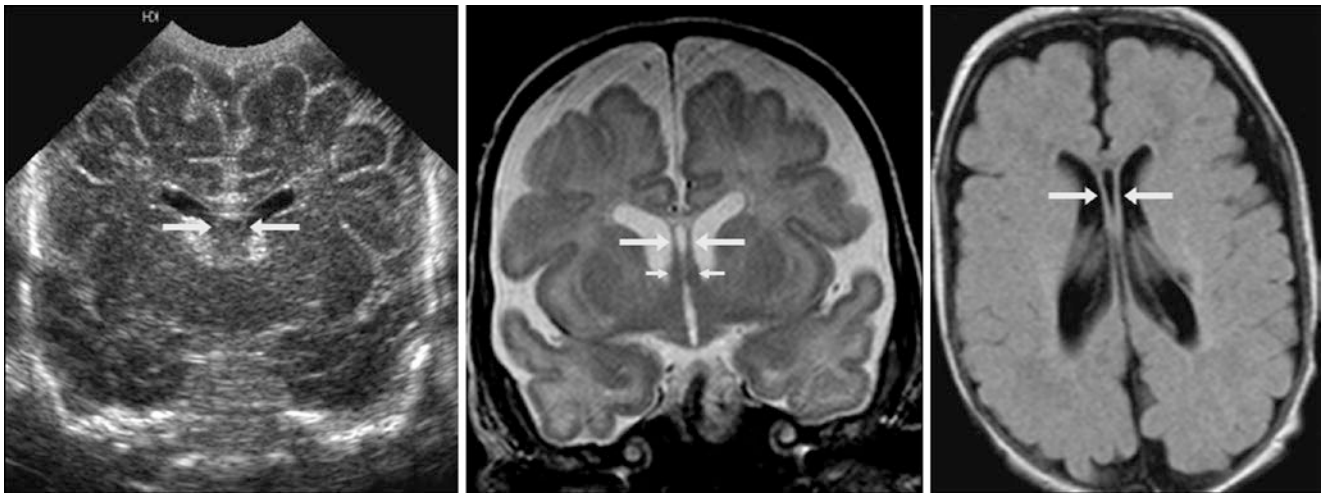

Fig. 13.1 A 3 month old with a CSP (*arrows*) on coronal ultrasound (*left*), T2WI (*middle*), and axial FLAIR (*right*) images. Note the columns of the fornix (*tiny arrows*) on the T2WI. There is also benign prominence of the subarachnoid spaces of infancy, which is typically self-limiting and usually resolves within the first 18–24 months of life

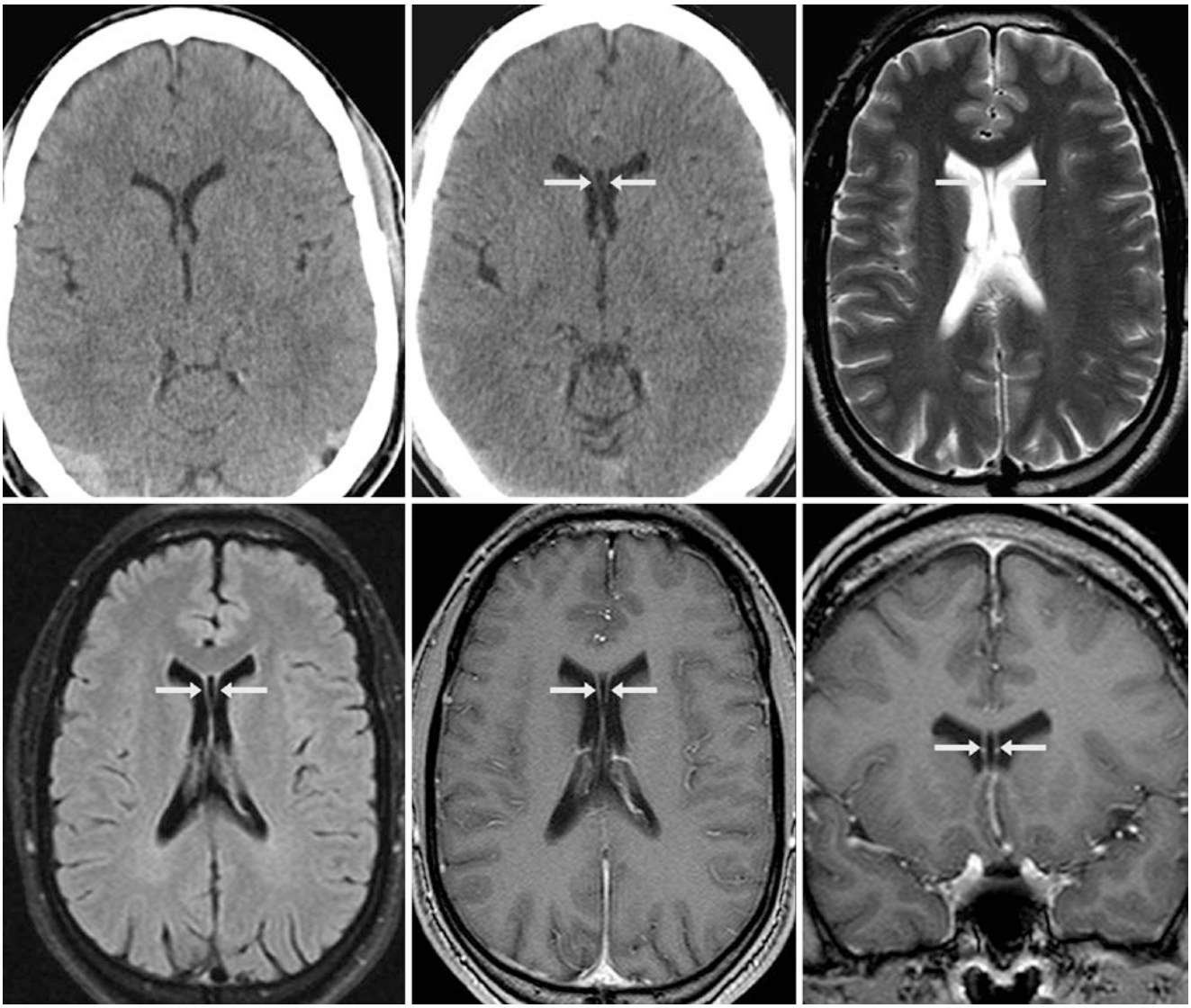

Fig. 13.2 A 35 year old with a CSP that is present but poorly seen on a 7-mm thickness NECT (*left*). A 2-mm thickness NECT 8 years earlier (*middle*) better demonstrates the CSP. This is only present anteriorly, as seen on axial T2WI (*top right*), FLAIR (*bottom left*), and axial (*bottom middle*) and coronal (*bottom right*) postcontrast T1WIs

Fig. 13.3 A 19 year old with a NECT showing a cystic CSP (*arrows*). There is no hydrocephalus

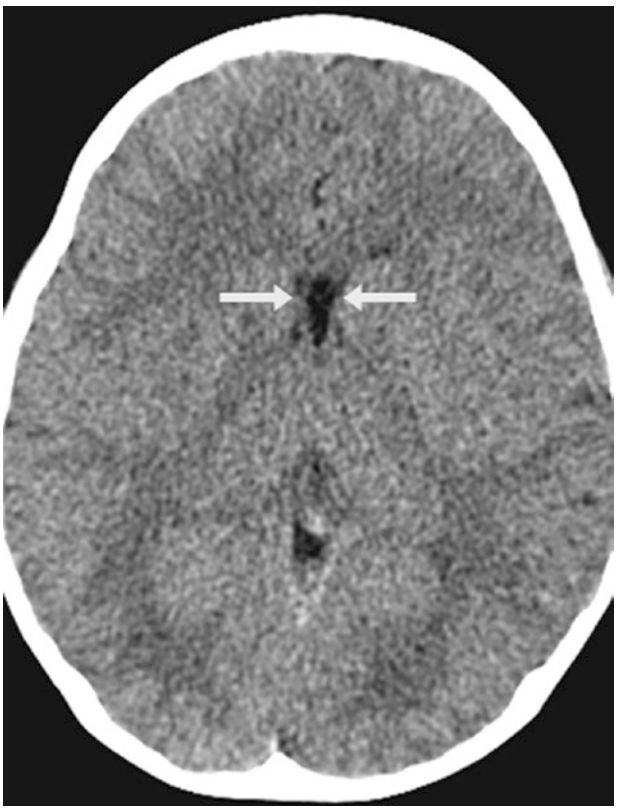

Fig. 13.4 A 6 year old with a tiny CSP on NECT that does not extend posteriorly (*arrows*). The ventricles are normal

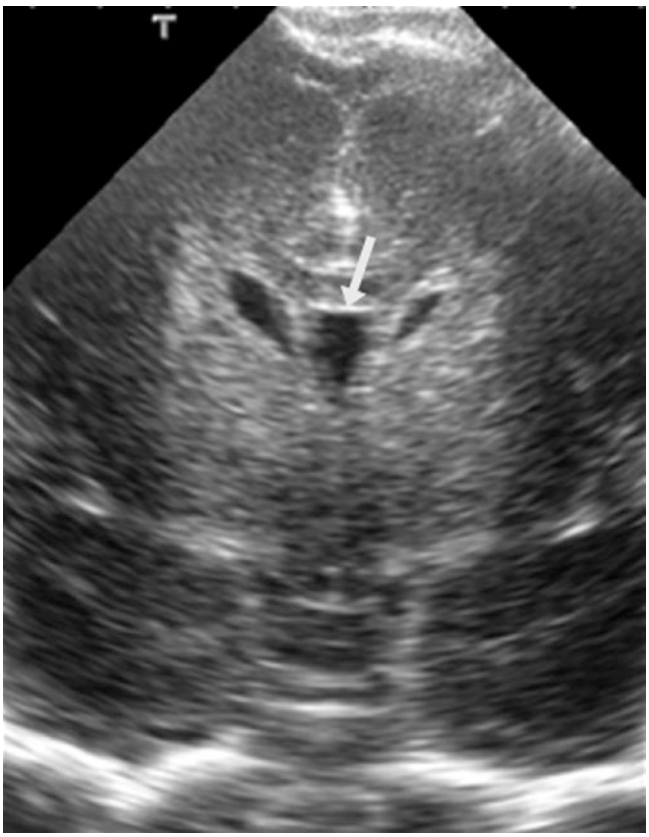

Fig. 13.5 A 7-day-old infant with a small normal CSP (*arrow*) on a coronal US image. The ventricles are normal in size

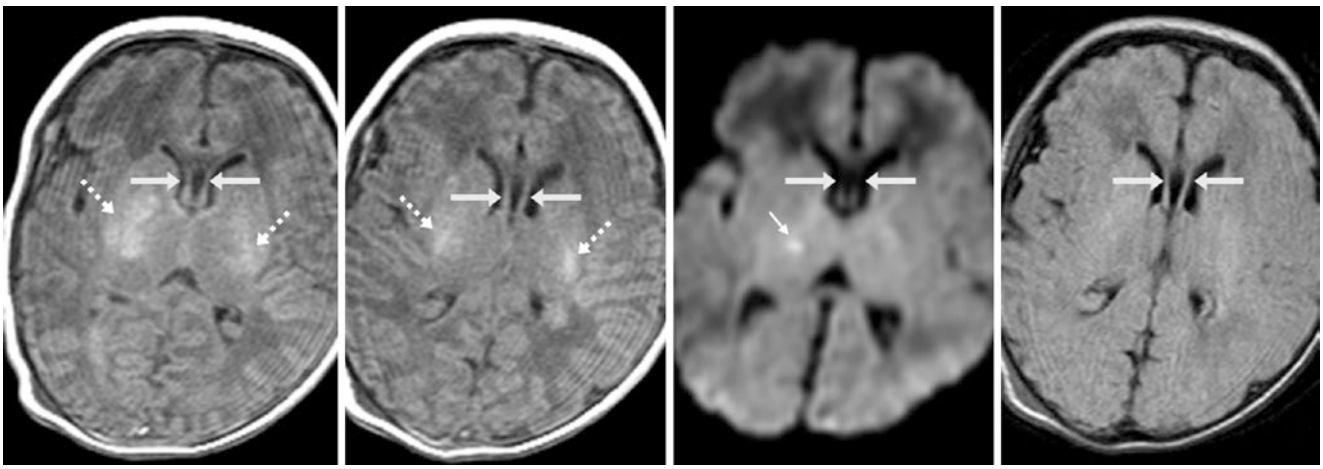

Fig. 13.6 A 2-day-old term infant with severe hypoxic-ischemic injury (HII, *dashed arrows*) on MRI and an incidental, tiny CSP (*arrows*) anteriorly. The HII is represented by bright T1 signal within the posterior putamina on axial T1WI (*dashed arrows*, *left two images*) and by punctate thalamic reduced diffusion on DWI (*tiny arrow*, *right middle*). Note the lack of abnormalities on FLAIR (*right*), which may appear normal in neonates even with severe HII

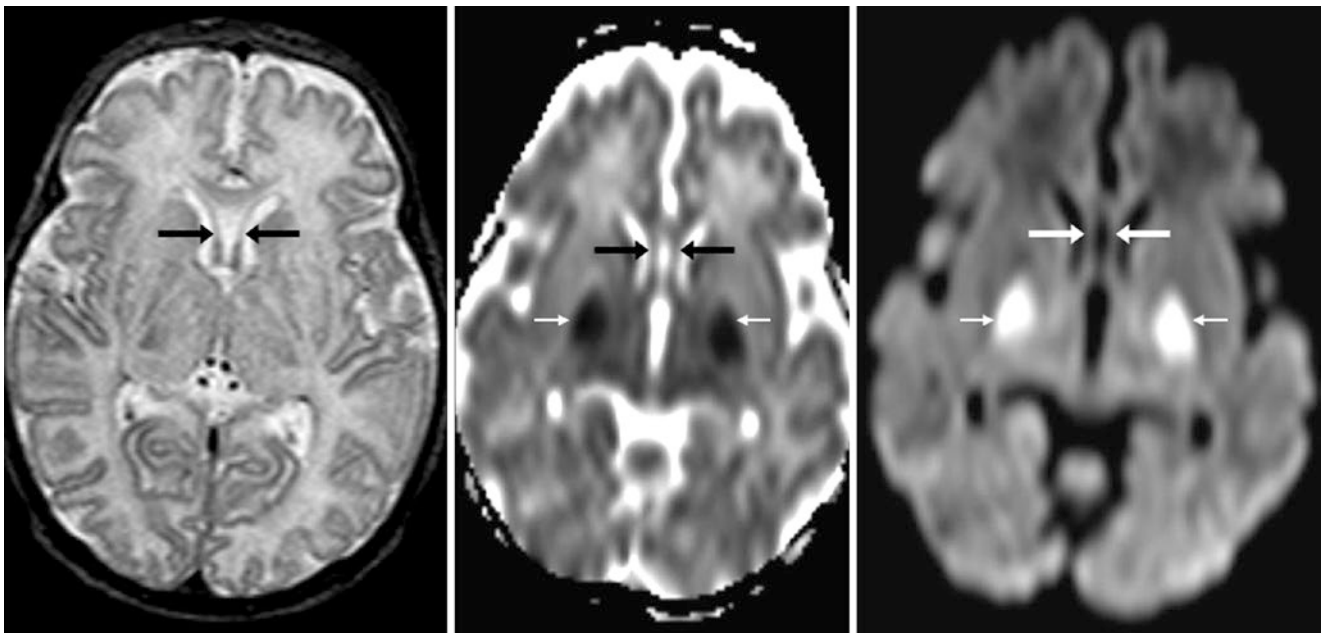

Fig. 13.7 A 1-week-old term infant with severe HII who had an incidental tiny CSP (*arrows*). MRI demonstrates abnormal signal (*tiny arrows*) in the putamina and globi pallidi on axial T2WI (*left*), ADC map (*middle*), and DWI (*right*)

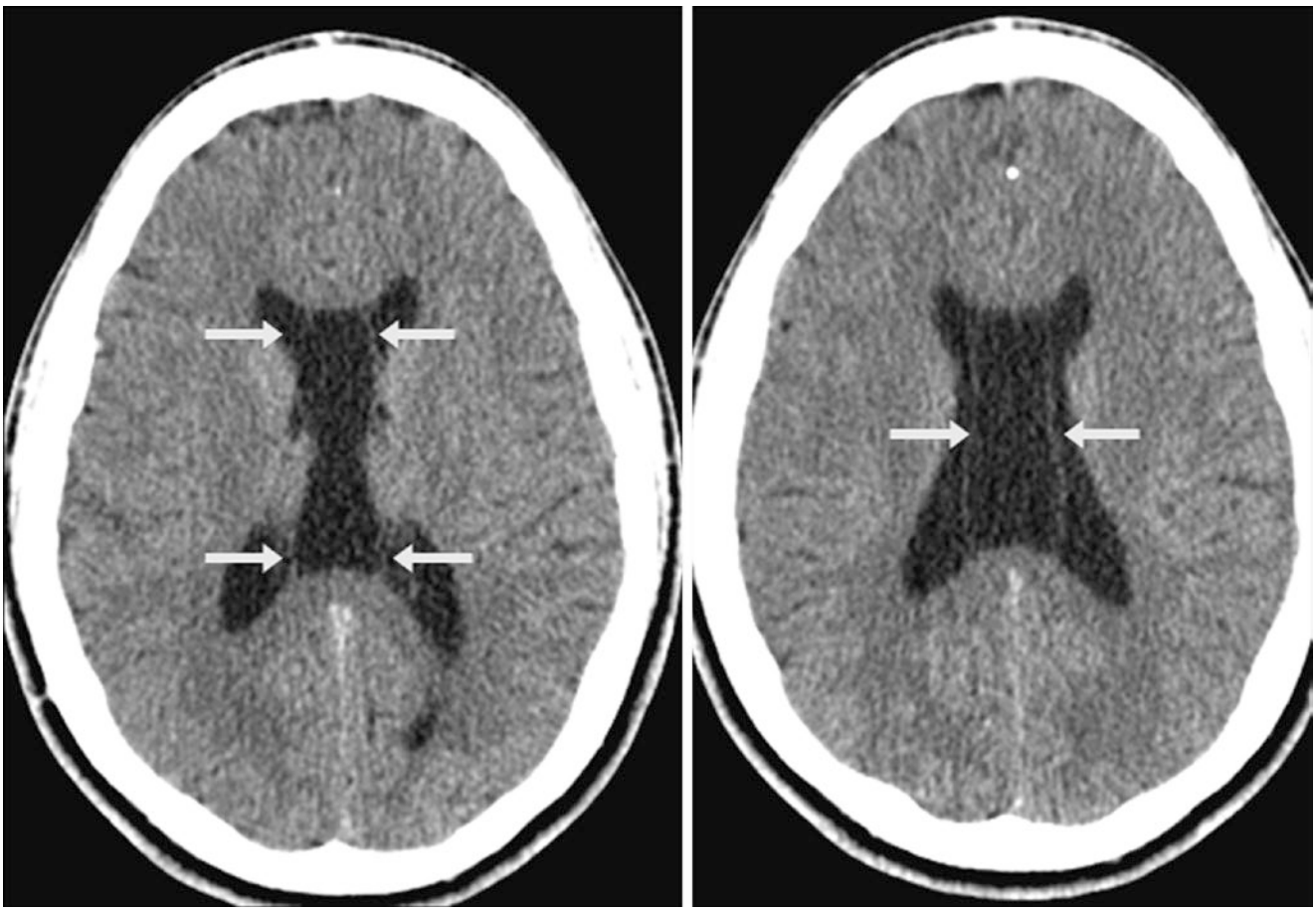

Fig. 13.8 A 20 year old with a CEV (*arrows*) on NECT. This extends posterior to the column of the fornices, just up to the callosal splenium

Fig. 13.9 A 67 year old; a CEV (*arrows*) did not change by 1 year on NECT (*not shown*)

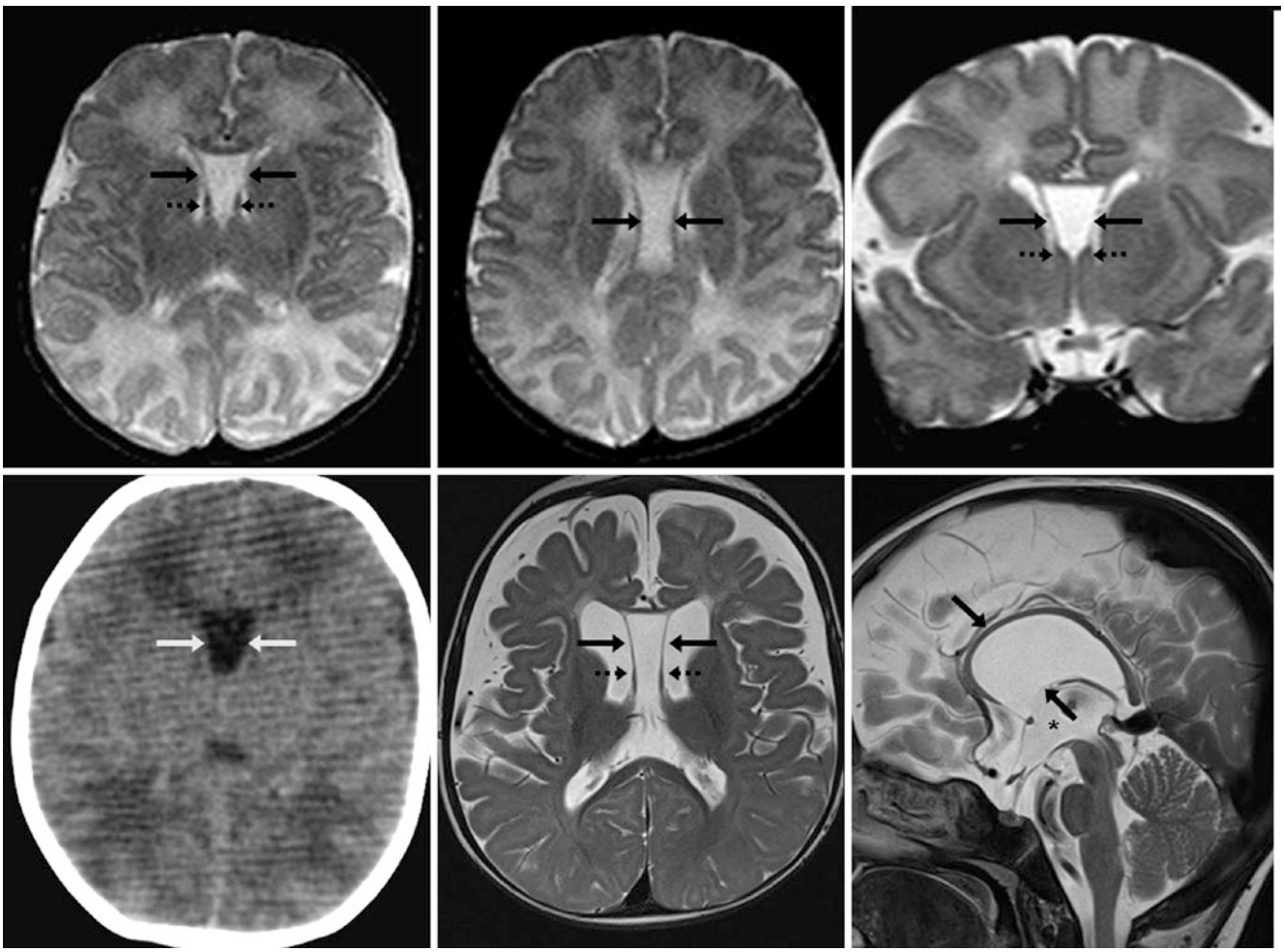

Fig. 13.10 A 2-week-old infant with a CEV (*arrows*) on axial (*top left and top middle*) and coronal T2WI (*top right*). Note the normal forniceal columns (*dashed arrows*). A NECT 1 month later is shown (*bottom left*). At 8 months of age, an axial T2WI (*bottom middle*) showed normal myelination but diffuse cerebral atrophy owing to congenital heart disease, making the CEV appear slightly larger. Inferiorly, note the third ventricle (*) on a midline sagittal T2WI (*bottom right*)

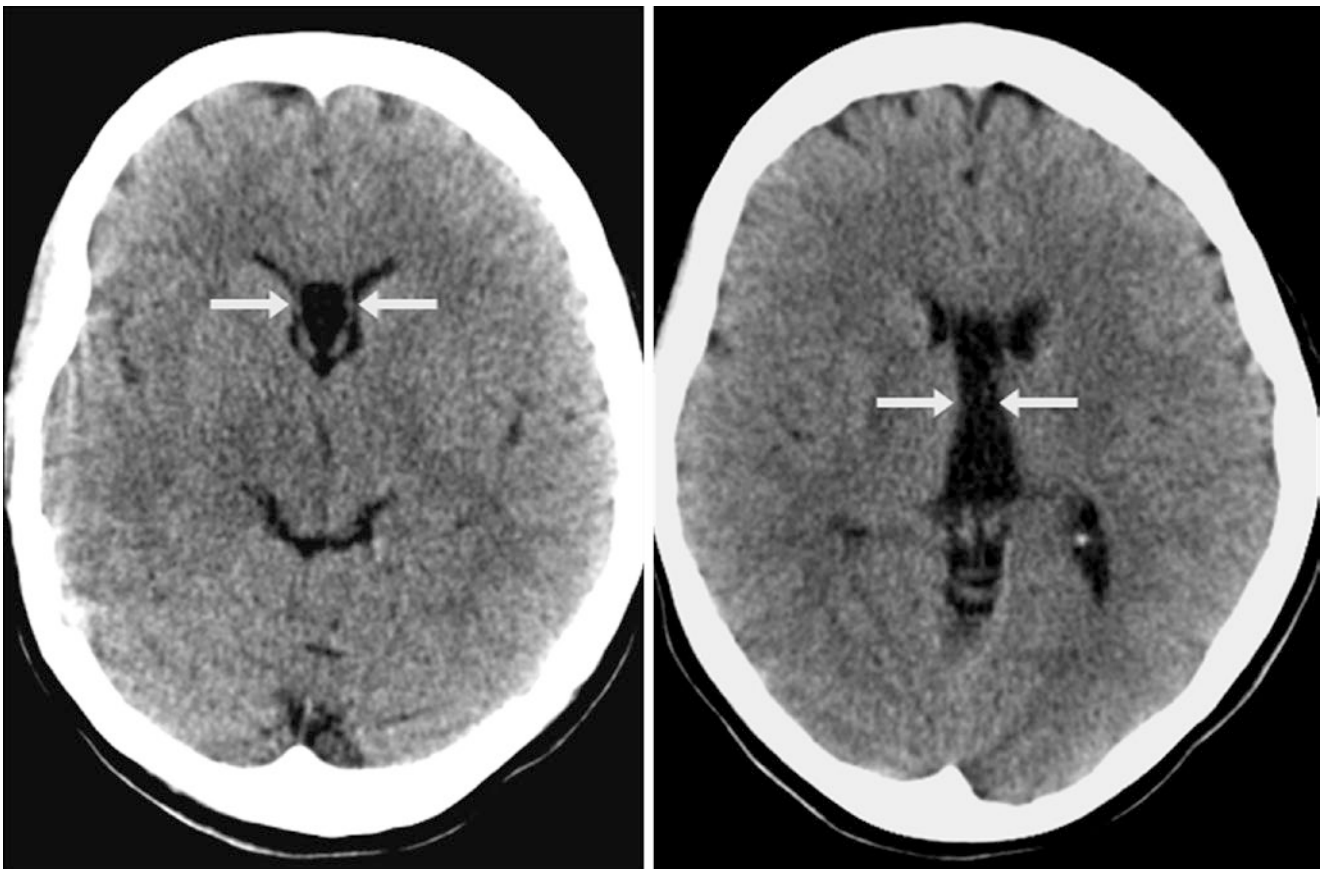

Fig. 13.11 A 44-year-old patient with a CEV (*arrows*) on NECT. The cyst-like CEV should not be confused with the third ventricle, although the two may communicate

Fig. 13.12 A 23-year-old patient who was given a NECT that depicts an incidental CEV (*arrows*)

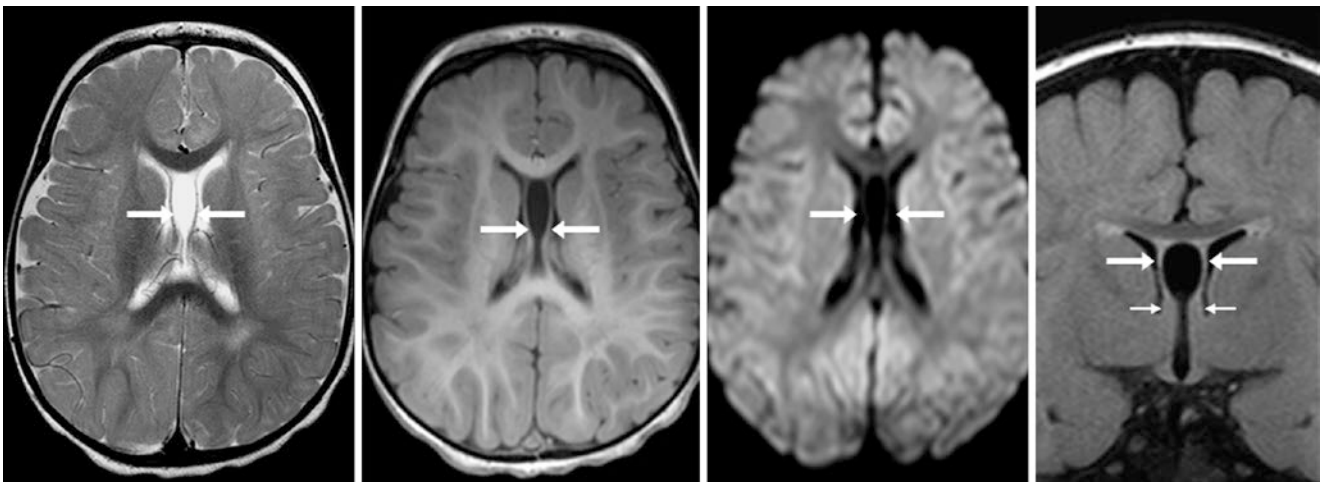

Fig. 13.13 A 1 year old who underwent a 3T MRI that shows the extent of a CEV (*arrows*) on axial T2WI (*left*), T1WI (*left middle*), and DWI (*right middle*). Coronal FLAIR images (*right*) depict how the septae connect to the forniceal columns (*tiny arrows*)

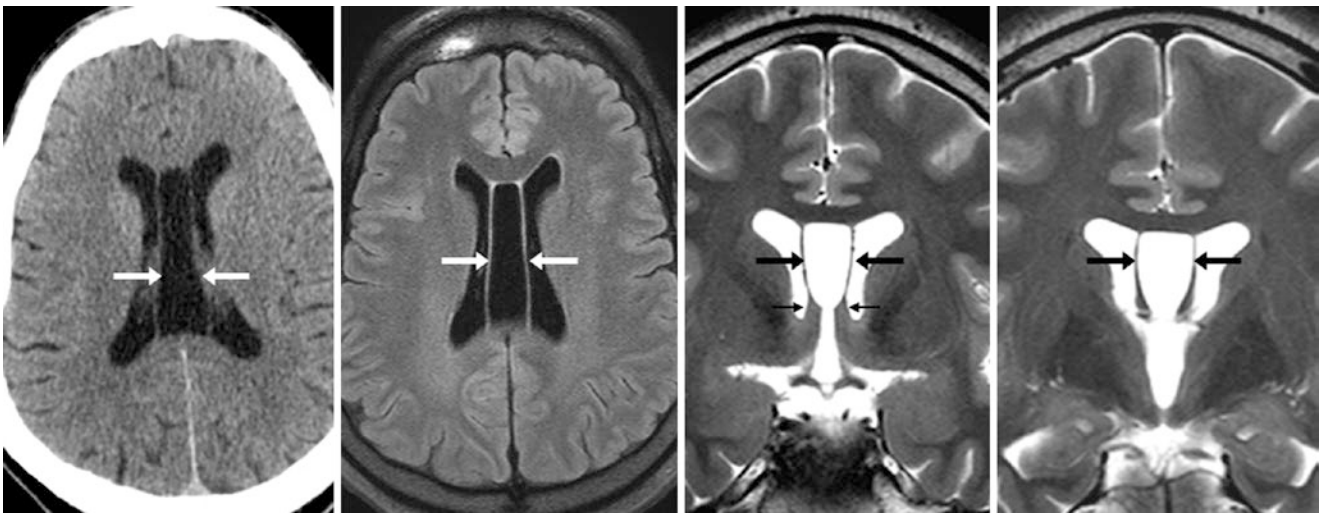

Fig. 13.14 A 38 year old with a CEV on a NECT (*left*). On a 3T MRI, the extent of the CEV is demonstrated on axial FLAIR (*left middle*) and on coronal T2WIs (*right middle and right*). Note the forniceal columns (*tiny arrows*)

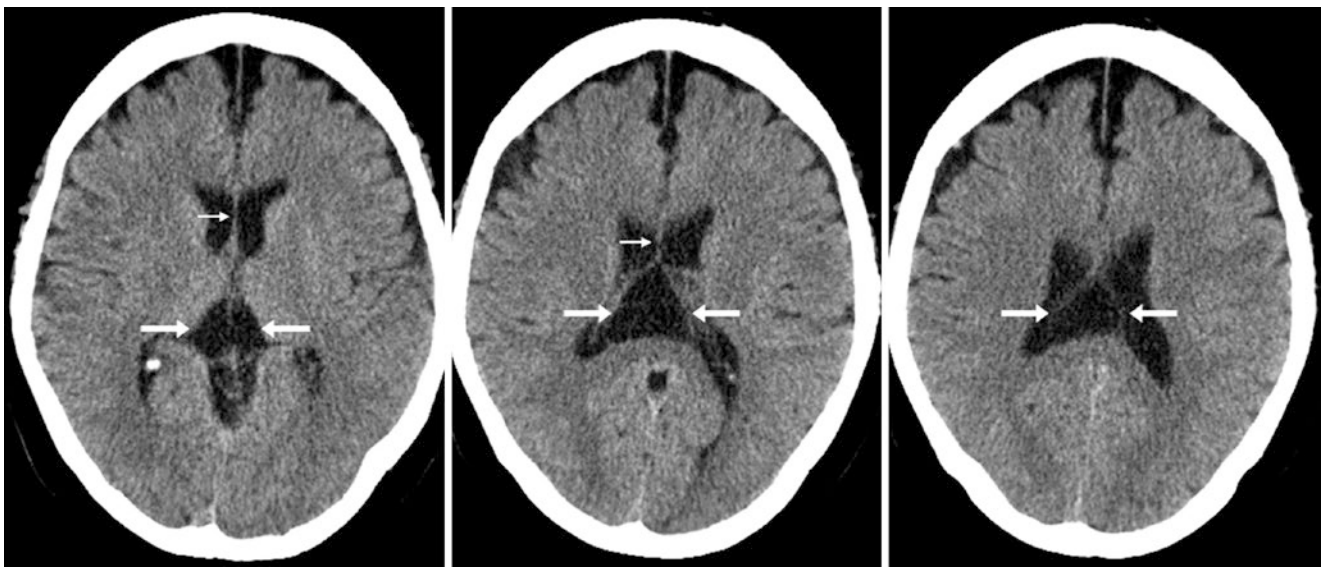

Fig. 13.15 A 62 year old with a CVI on NECT. Note the single midline septum of the septum pellucidum anteriorly (*tiny arrows*)

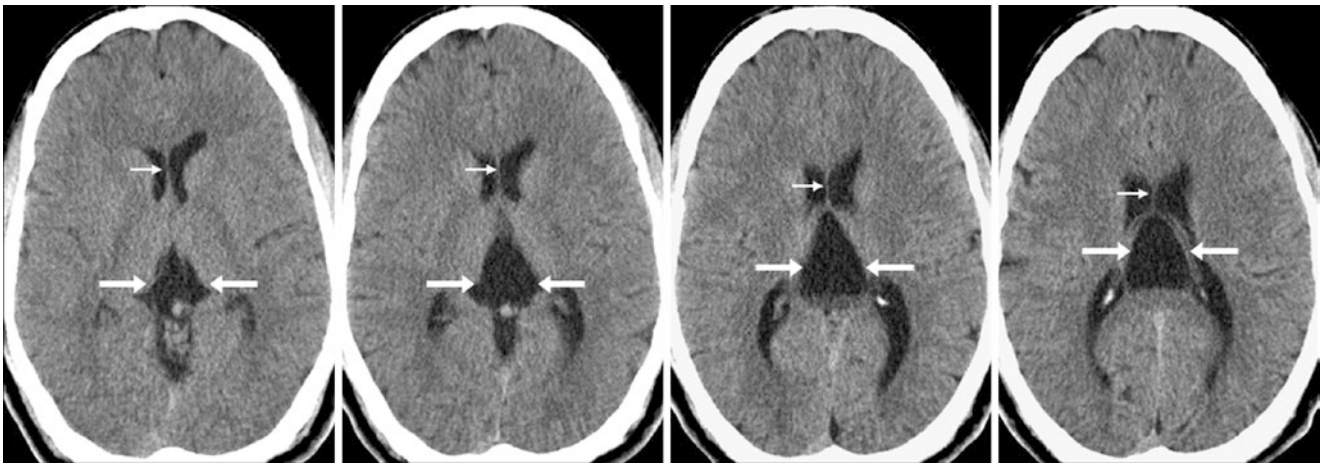

Fig. 13.16 A 25 year old with a CVI on NECT. Note the single midline septum of the septum pellucidum anteriorly (*tiny arrows*)

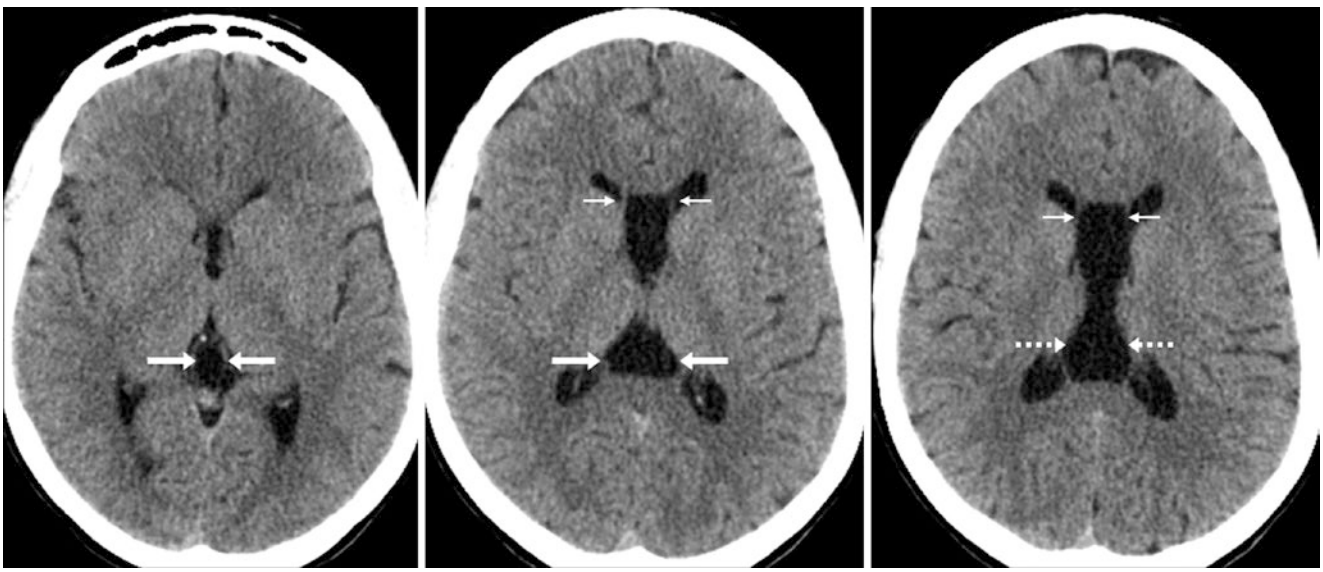

Fig. 13.17 A 22-year-old patient; a presumed CVI (*arrows*) exists along with a CEV (*dashed arrows*) on NECT. While the septae of the CSP-CEV are split anteriorly (*tiny arrows*), the extension of the cyst into the suprapineal region (beneath the callosal splenium) implies the existence of a CVI. Alternatively, this could be a CEV with an incidental pineal cyst

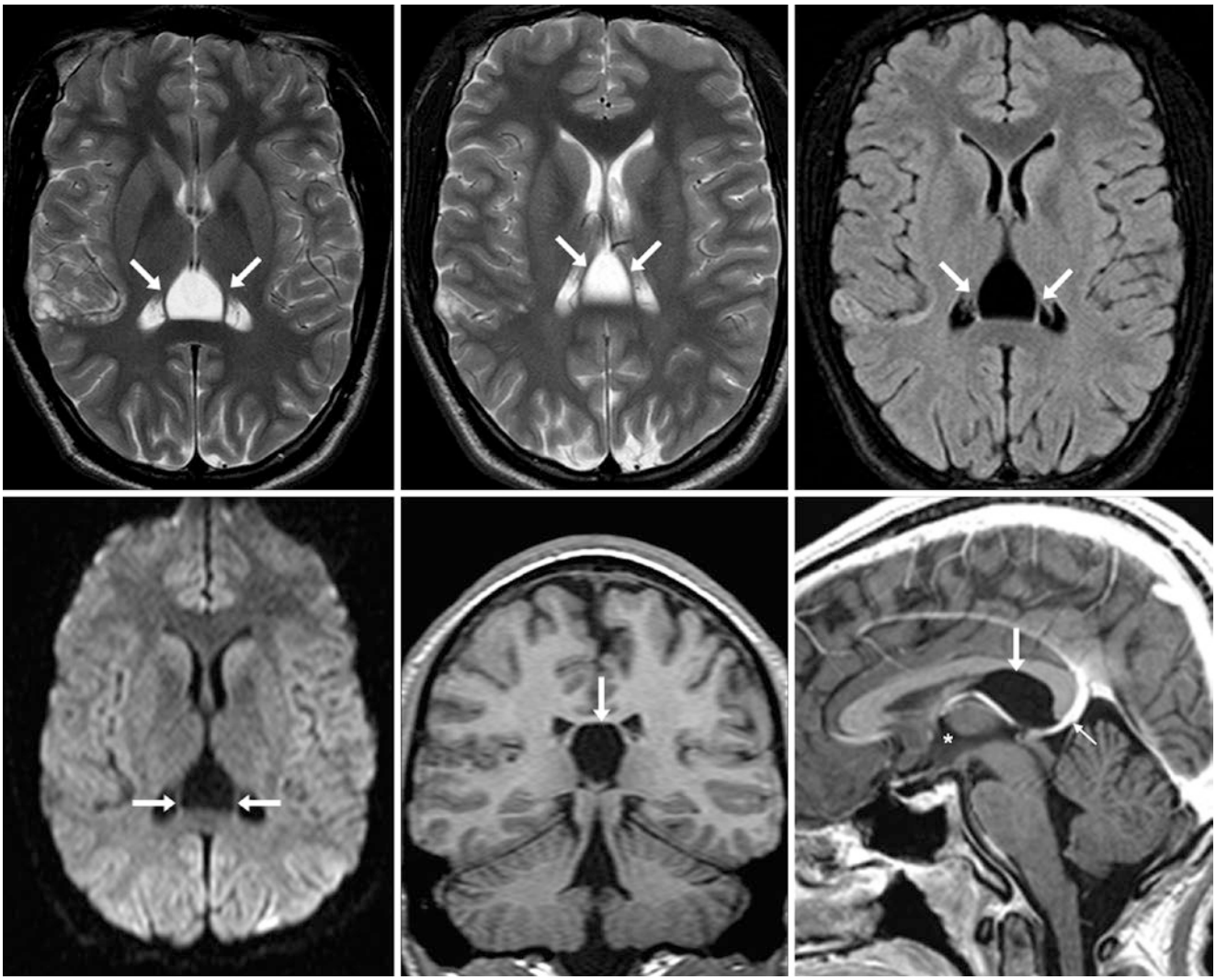

Fig. 13.18 A 20 year old with a CVI (*arrows*) shown on MRI T2WI (*top left and top middle*), FLAIR (*top right*), DWI (*bottom left*), coronal T1WI (*bottom middle*), and postcontrast sagittal T1WI (*bottom right*). Note an internal cerebral vein (*tiny arrow*) coursing along the floor of the CVI and that the pineal region is not involved. Also, note the third ventricle (*)

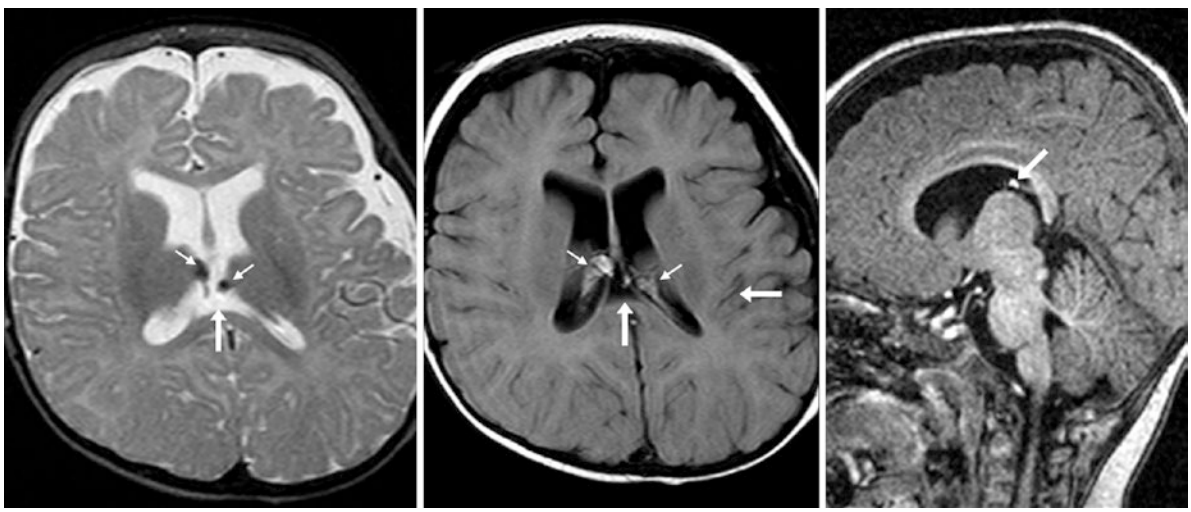

Fig. 13.19 A 5 month old with a CVI (*arrows*) as well as choroid plexus lipomas (*tiny arrows*) on MRI. Choroid plexus lipomas are often associated with callosal/pericallosal (interhemispheric) lipomas, which may be associated with callosal dysgenesis (not seen here). They also have T1-bright, T2-dark, and DWI-dark signal, distinguishing them from normal xanthogranulomas. Xanthogranulomas are more common in the elderly and are less frequent in children

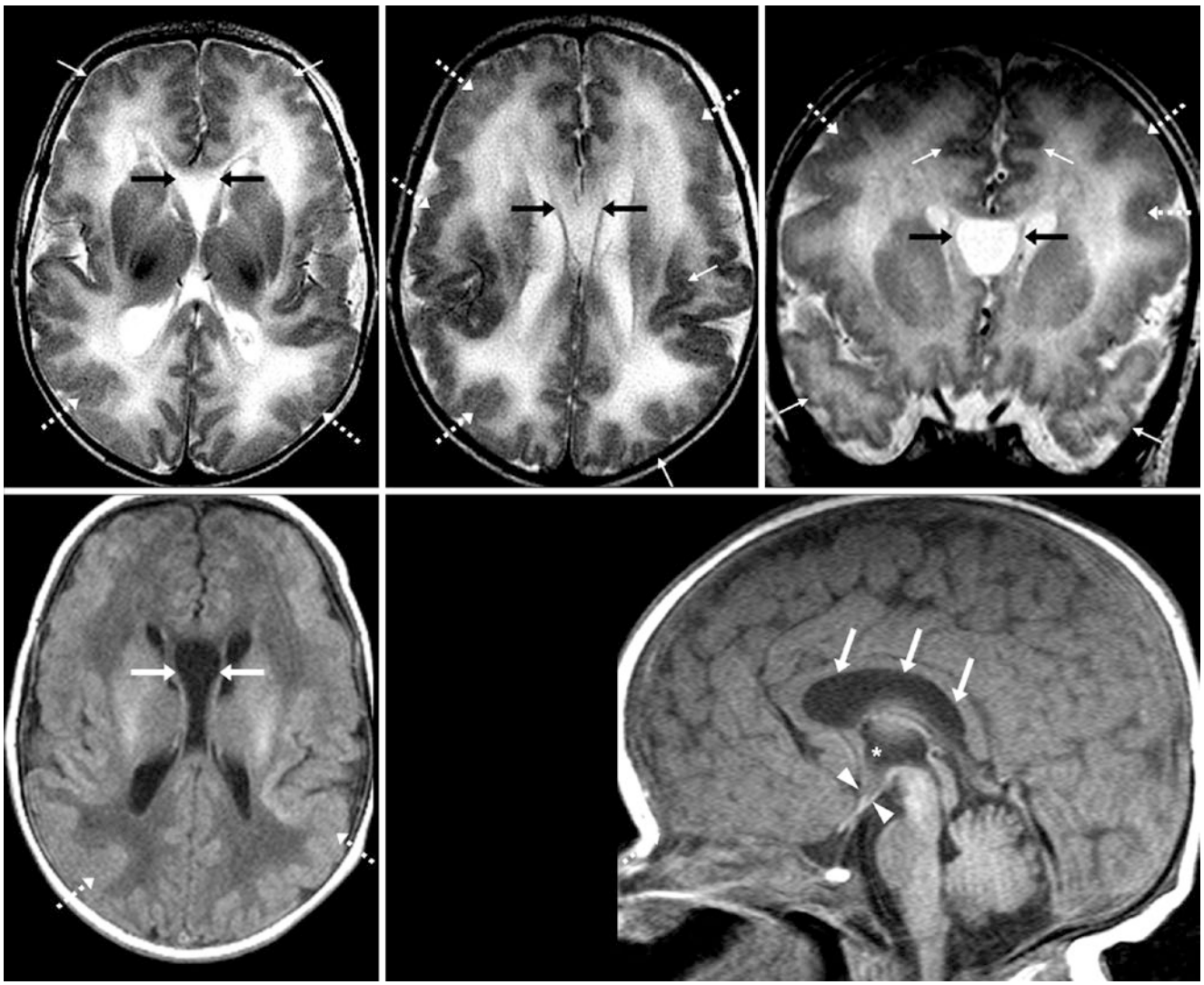

Fig. 13.20 Comparison case of CSP in macrocephaly-polydactyly-polymicrogyria-hydrocephalus (MPPH) syndrome**.** A 1-day-old infant with macrocephaly (head circumference >3 standard deviations above normal), polymicrogyria (*dashed arrows*), and polydactyly (of digits), but without hydrocephalus (not present here and not always present in MPPH). *Tiny arrows* denote a normal cortex as opposed to the blurred gray-white matter junction of areas of polymicrogyria. A CSP-CEV (*arrows*) is usually present in this syndrome, as shown on axial (*top left and top middle*) and coronal (*top right*) T2WIs and on an axial T1WI (*bottom left*). On a sagittal T1WI (*bottom right*), note that the anterior recesses (*arrowheads*) of the third ventricle (*) are thin, confirming a lack of hydrocephalus

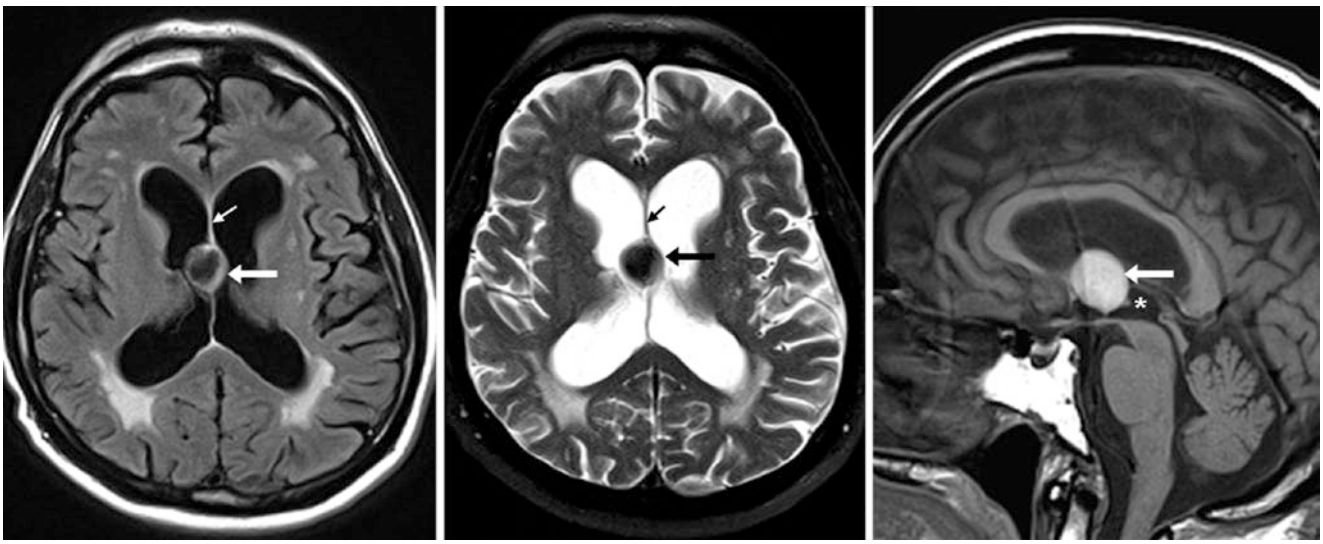

Fig. 13.21 Comparison case of a third ventricular colloid cyst. A 74 year old had a cystic mass (*arrows*) within the roof of the third ventricle (*), with dark signal on FLAIR (*left*) and T2WI (*middle*) and was bright on noncontrast sagittal T1WI (*right*). The septum pellucidum is normal and fused (*tiny arrows*). There are age-related findings of cerebral volume loss. Hydrocephalus is unlikely because the anterior recesses of the third ventricle are not enlarged

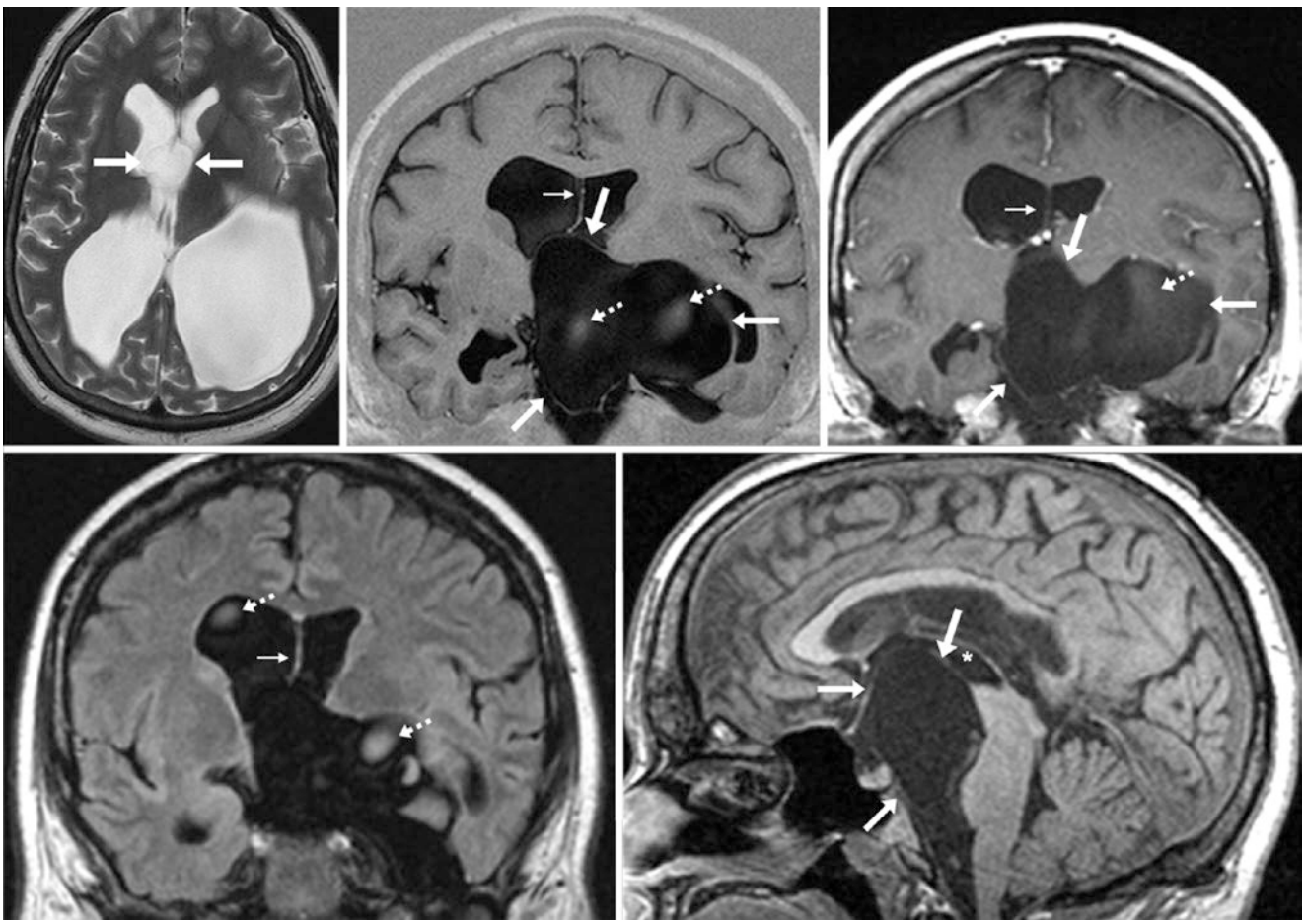

Fig. 13.22 Comparison case of an intraventricular arachnoid cyst. A 22 year old with an extensive cyst (outlined by the *arrows*) that had bright signal on T2WI (*top left*), dark signal on coronal T1WI-IR (*top middle*), and nonenhancment on postcontrast T1WI (*top right*). The cyst extends into and displaces the third ventricle (*) and left lateral ventricle, as shown on coronal FLAIR (*bottom left*) and sagittal T1WI (*bottom right*). The septum pellucidum is fused (*tiny arrows*). There is age-related cerebral volume loss. Flow voids within the cyst (*dashed arrows*) suggest communication with the ventricles

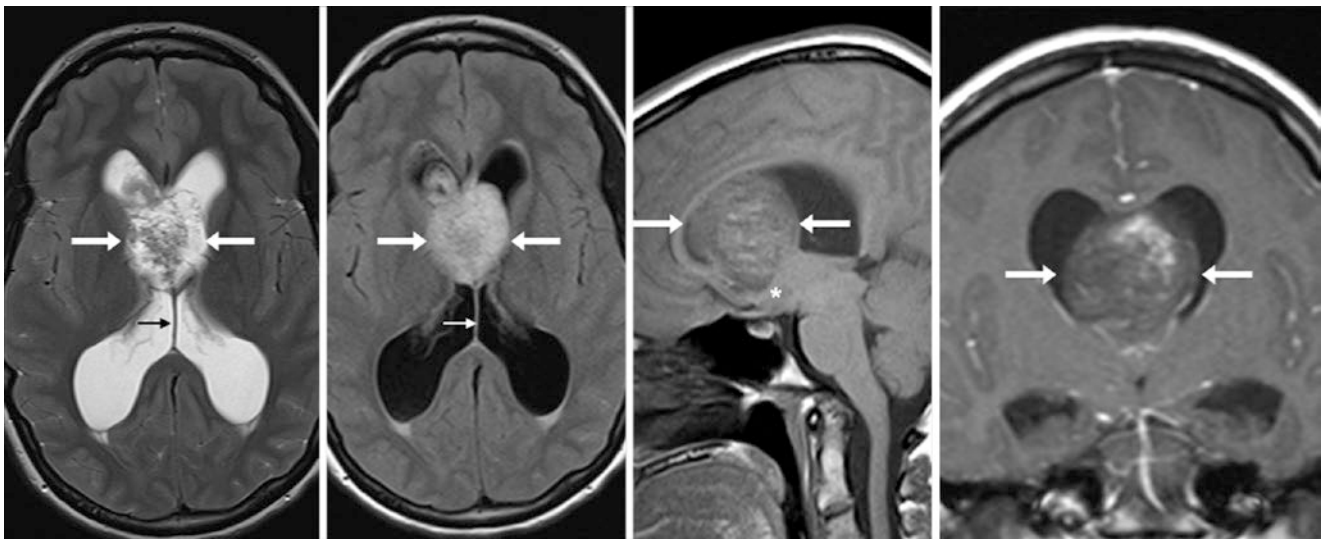

Fig. 13.23 Comparison case of a central neurocytoma of the septum pellucidum compressing the third ventricle. A 20 year old had a mass (*arrows*) with bright signal on T2WI (*left*) and FLAIR (*left middle*), with slightly bright signal internally on sagittal noncontrast T1WI (*right middle*). The mass is located above the third ventricle (*), and the septum pellucidum is replaced by tumor anteriorly while being normal posteriorly (*tiny arrows*). Postcontrast coronal T1WI (*right*) depicts slight internal enhancement and enlarged temporal horns, indicating hydrocephalus

13.2 Subcallosal/Paraterminal Pseudomass on Midline Sagittal Images

On midline or near midline sagittal images, a pseudomass is occasionally visualized immediately below the rostrum of the corpus callosum and anterior to the third ventricle. The *paraterminal gyrus* (i.e., the *subcallosal gyrus*) is medial and is located along the frontal lobe, just anterior to the lamina terminalis (which constitutes the anterior wall of the third ventricle by extending vertically between the anterior commissure and the optic chiasm), behind the parolfactory area, and superior to the optic chiasm. Review of axial and coronal images with localization software will confirm that no mass is present and that this pseudomass often arises from volume averaging of the paraterminal/subcallosal gyri near the midline. A *subcallosal pseudomass* can be exacerbated by and appear even larger on FLAIR images because of volume averaging combined with CSF-flow related artifact. Also, a very thin cistern of the lamina terminalis (located anterior to the lamina terminalis) may leave room for the subcallosal gyri to appose each other. This pseudomass may mimic a *meningioma*, a craniopharyngioma, an *optic glioma,* a *hypothalamic glioma*, or even an *aneurysm* (Figs. 13.24, 13.25, 13.26, 13.27, 13.28, and 13.29).

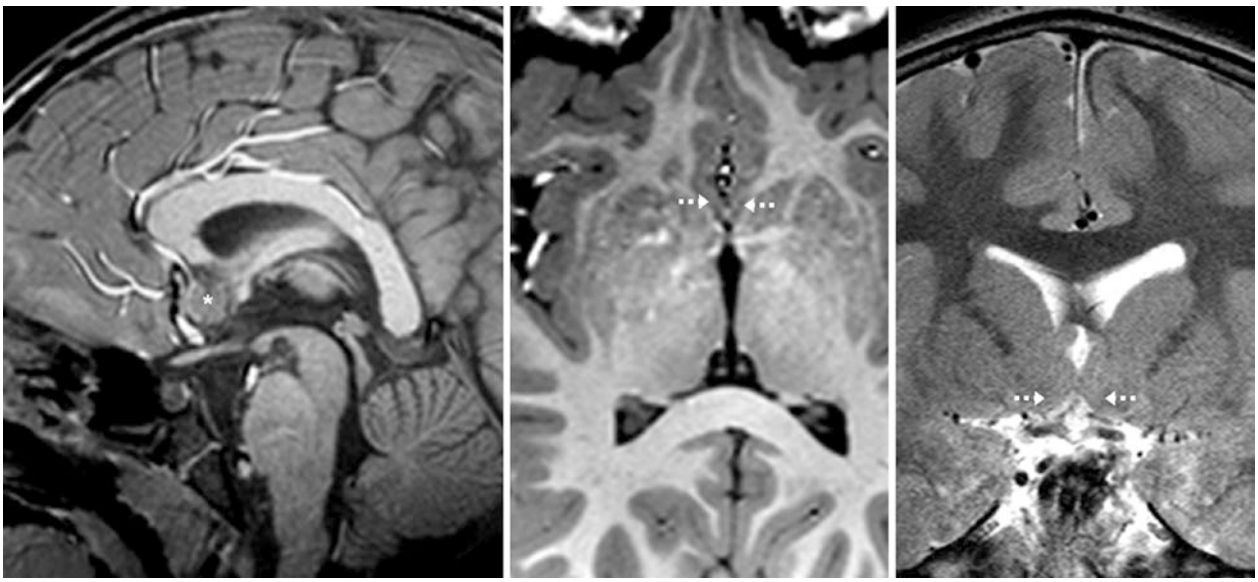

Fig. 13.24 A 7 year old with a 3T MRI that was performed for developmental delay. There is a subcallosal pseudomass (*) on a midline sagittal T1WI (*left*). Axial T1WI (*middle*) and coronal T2WI (*right*) do not demonstrate any mass in the region of the paraterminal gyri (*dashed arrows*) on either side

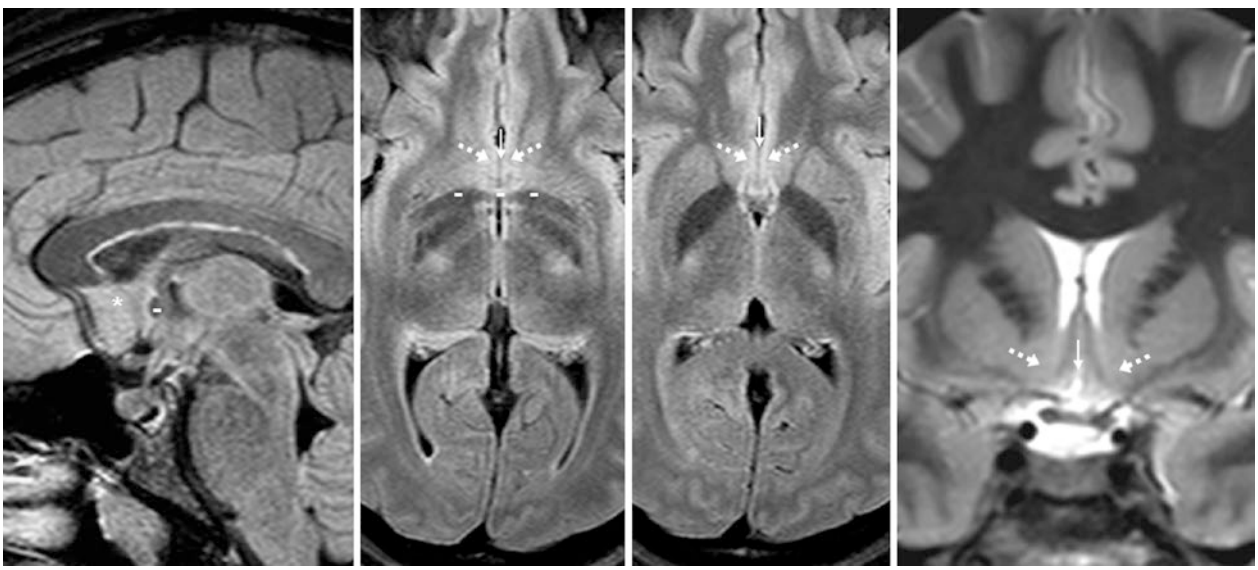

Fig. 13.25 A 30-year-old patient; a 3T MRI performed for headaches demonstrated a subcallosal pseudomass (*) on a midline sagittal FLAIR image (*left*) caused by a combination of volume averaging of the paraterminal gyri (*dotted arrows*) as well as a thin, diminutive cistern of the lamina terminalis (*thin arrows*). Axial FLAIR (*left middle and right middle*) and coronal T2WI (*right*) do not depict any mass in that region on either side. Note the anterior commissure posteriorly (–)

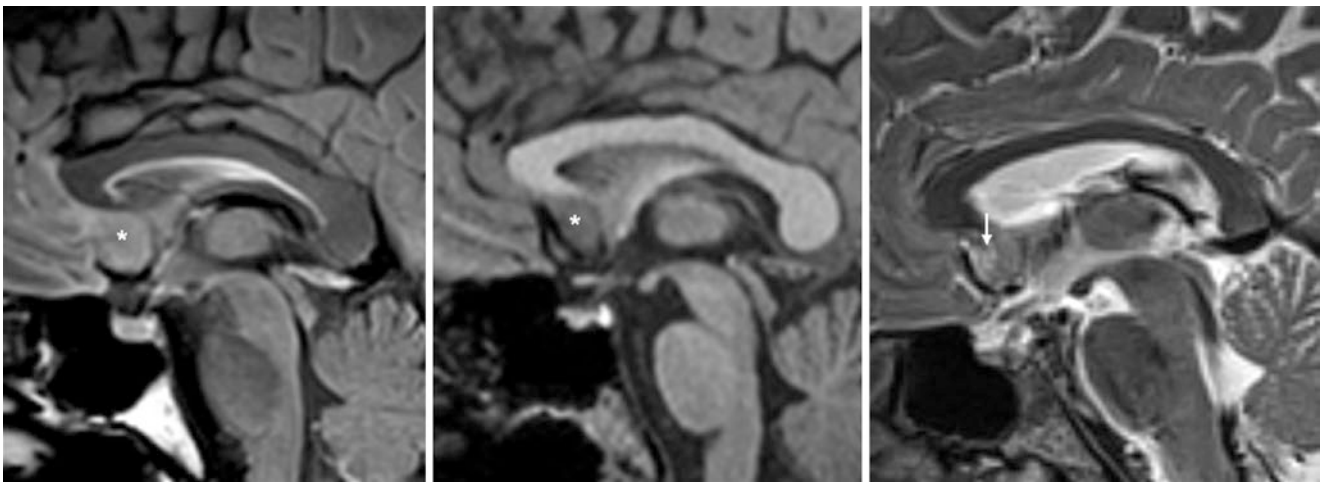

Fig. 13.26 A 48 year old who had a 3T MRI performed for a research study; this demonstrates a pseudomass in the subcallosal region (*) on a midline sagittal FLAIR image (*left*). Sagittal T1WI (*middle*) and T2WI (*right*) do not confirm a mass in that region. CSF is noted (*thin arrow*) within the cistern of the lamina terminalis on T2WI, proving that the pseudomass arises from a combination of volume averaging of the paraterminal gyri with CSF flow artifact

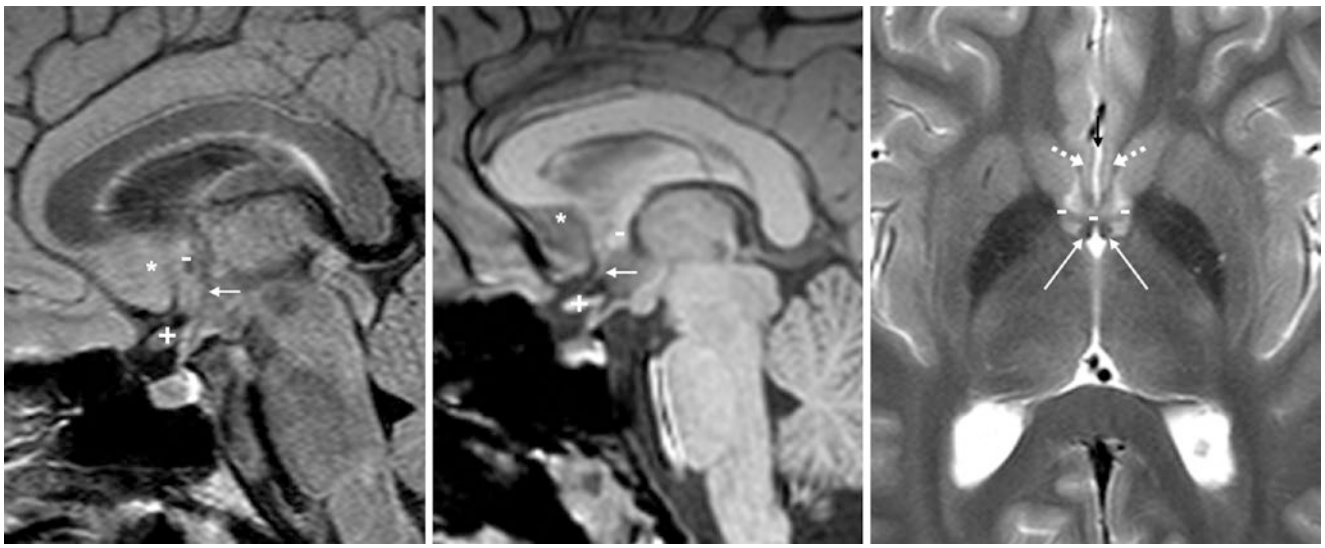

Fig. 13.27 An 18 year old in whom a 3T MRI showed a subcallosal pseudomass (*) on a midline sagittal FLAIR image (*left*), but sagittal T1WI (*middle*) and axial T2WI (*right*) did not confirm a mass. CSF is noted (*thin black arrow*) within a thin cistern of the lamina terminalis, indicating that the pseudomass is the result of volume averaging of the paraterminal gyri with CSF flow artifact. Note the lamina terminalis (*thin white arrow*) on sagittal T1WI at the midline; it extends between the anterior commissure (–) and the optic chiasm (+). Note the columns of the fornix (*long arrows*) just posteriorly

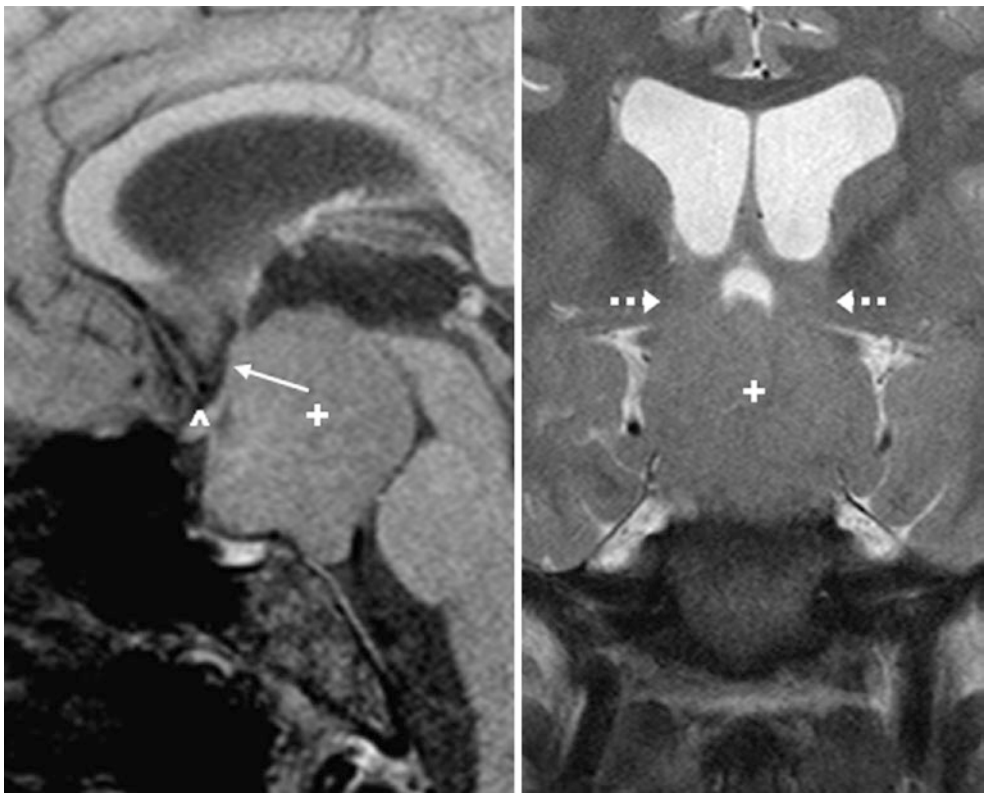

Fig. 13.28 Comparison case of hypothalamic glioma. A 15 year old with gelastic seizures. Sagittal T1WI (*left*) and coronal T2WI (*right*) depicted a mass (+). Note the optic chiasm (^), the lamina terminalis (*arrows*), the subcallosal gyrus, and the paraterminal gyri (*dashed arrows*)

Fig. 13.29 Comparison case of optic glioma. A 23 month old with neurofibromatosis type 1 had a chiasmatic mass (+) on sagittal T1WI (*left*) and coronal T2WI (*right*). Note a normal subcallosal pseudolesion superiorly (*), with the lamina terminalis located posteroinferiorly (*thin arrow*)

13.3 Massa Intermedia Pseudomass on Sagittal T1WI

At the midline on sagittal T1WI, the *massa intermedia* (i.e., the interthalamic adhesion or middle commissure) can appear as a pseudomass. This appearance can be exacerbated by flow-related artifacts within the third ventricle on multiple echo images such as spin-echo T1WI, T2WI, or FLAIR. The massa intermedia is a relatively large structure that connects the thalami on both sides directly but is composed of gray matter, and for that reason many deem it inappropriate to refer to it as a commissure. No known neurologic deficit has been attributed to its absence. This pseudolesion is common on sagittal T1WIs and can be readily confirmed to be normal on corresponding axial images. The massa intermedia may be enlarged in some congenital abnormalities of the posterior fossa such as a Chiari II malformation or in primary brain neoplasms such as astrocytomas. This pseudo-lesion can mimic nonenhancing *low-grade gliomas* but can be distinguished from them by their bright signal on FLAIR and by the asymmetric mass effect caused by such neoplasms (Figs. 13.30, 13.31, 13.32, 13.33, and 13.34).

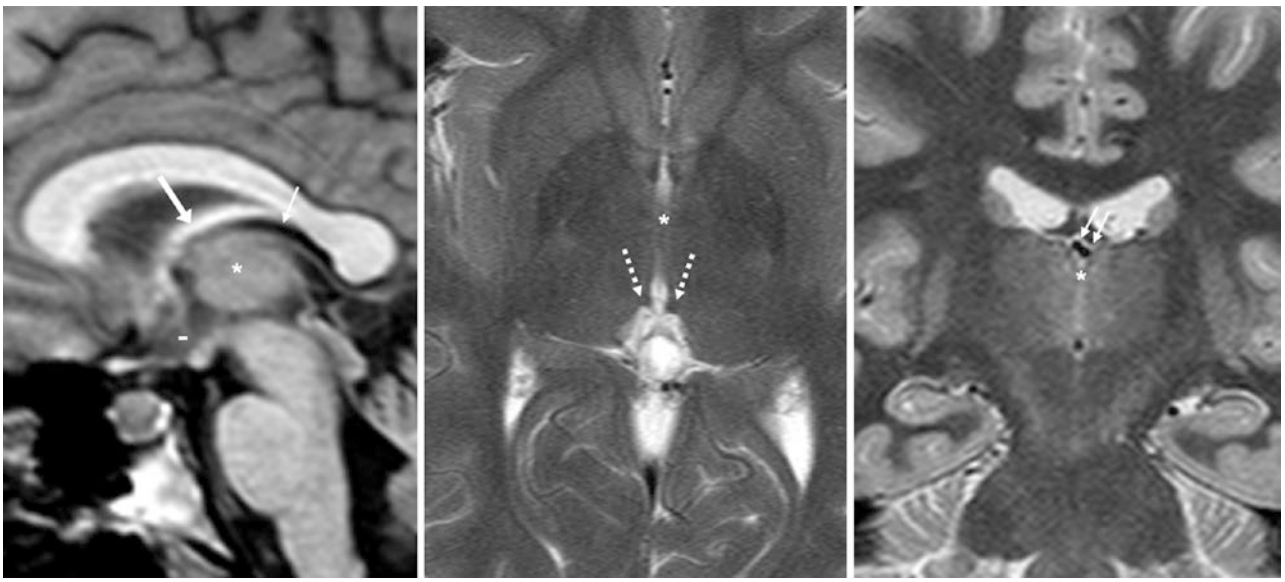

Fig. 13.30 A 28 year old with a 3T MRI performed for seizures (negative study), which demonstrated a pseudomass of the massa intermedia (*) on midline sagittal T1WI (*left*). This was confirmed to be normal on axial (*middle*) and coronal (*right*) T2WI. On sagittal T1WI, note the internal cerebral veins (*thin arrows*) and the body of the fornix (*arrow*) just superiorly, the third ventricle anteroinferiorly (–), and the habenula (*dashed arrows*) posteriorly

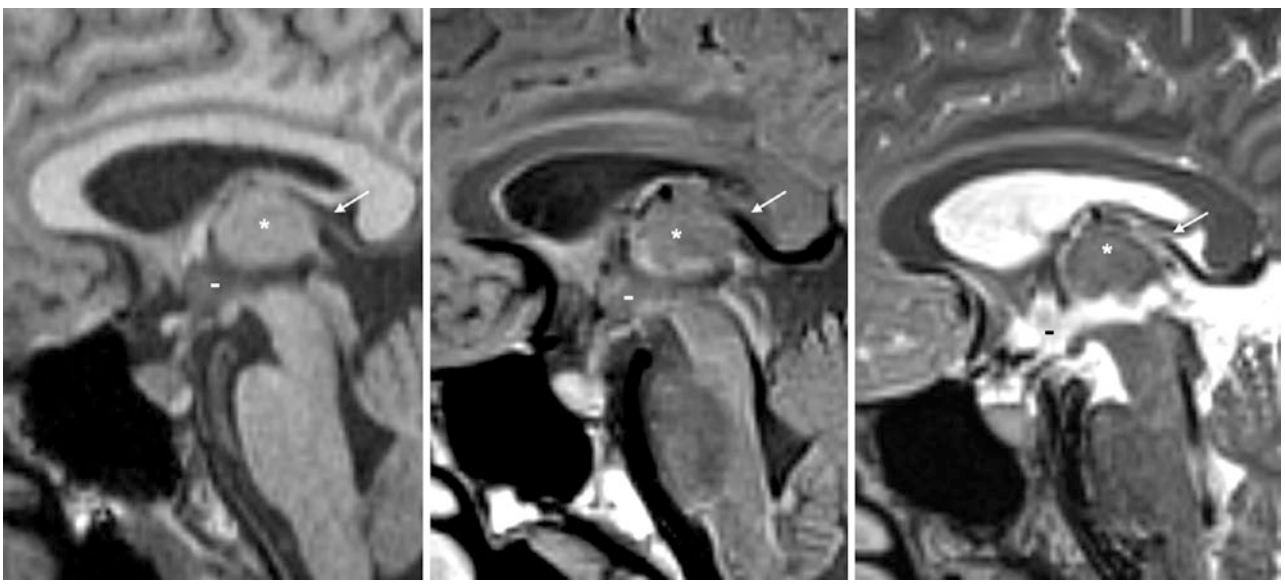

Fig. 13.31 A 47 year old with a 3T MRI performed as part of a research study, which demonstrated a pseudomass of the massa intermedia (+) on a midline sagittal T1WI (*left*), T2WI (*middle*), and FLAIR (*right*). Note the internal cerebral veins (*thin arrows*) just posterior to the massa intermedia and the third ventricle anteroinferiorly (–)

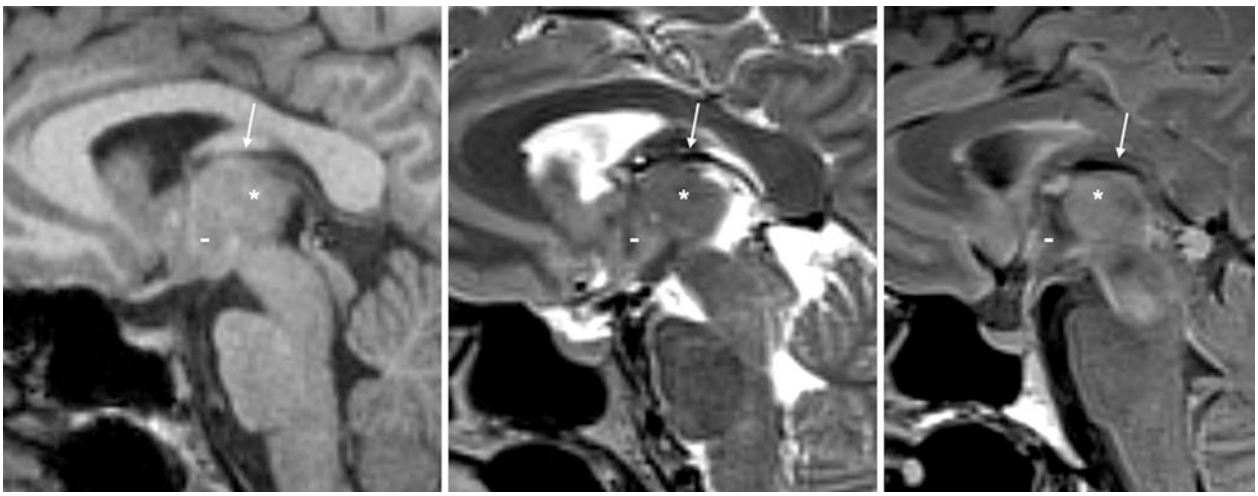

Fig. 13.32 A 25 year old who underwent a 3T MRI performed as part of a research study; it demonstrated a mass intermedia pseudomass (*) on a midline sagittal T1WI (*left*), T2WI (*middle*), and FLAIR (*right*). This appears mass-like as a result of CSF flow artifacts in the third ventricle (–) on T1WI and T2WI, which disappear on FLAIR. Note the internal cerebral veins (*arrows*)

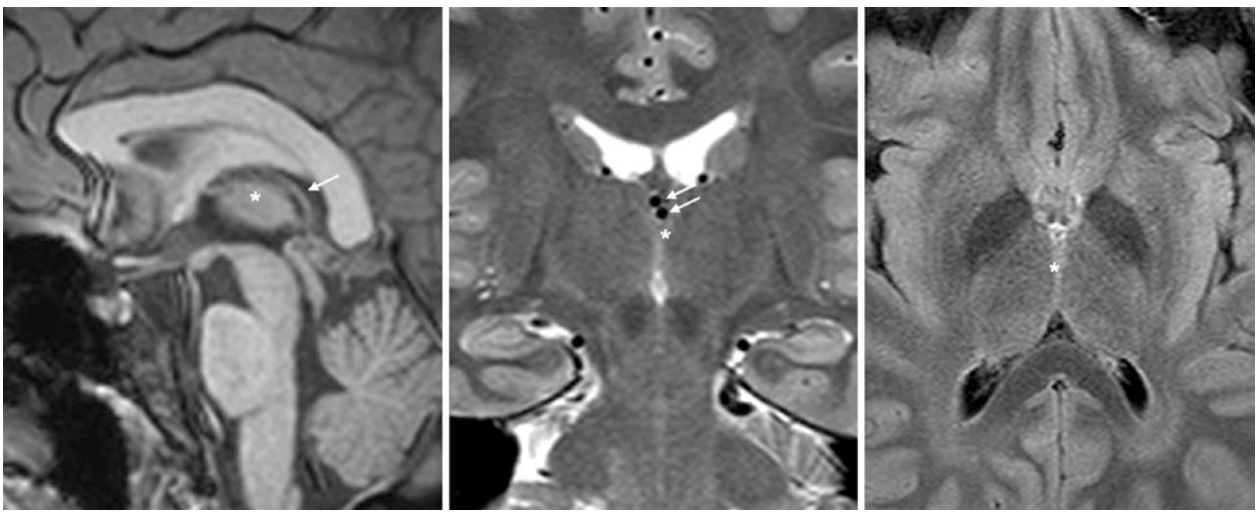

Fig. 13.33 A 27 year old who had a 3T MRI performed for headaches, which showed a pseudomass of the massa intermedia (*) on a midline sagittal T1WI (*left*). Coronal T2WI (*middle*) and axial FLAIR (*right*) did not confirm a mass and depicted the thin connection between the thalami. Note the internal cerebral veins (*arrows*) behind the massa intermedia

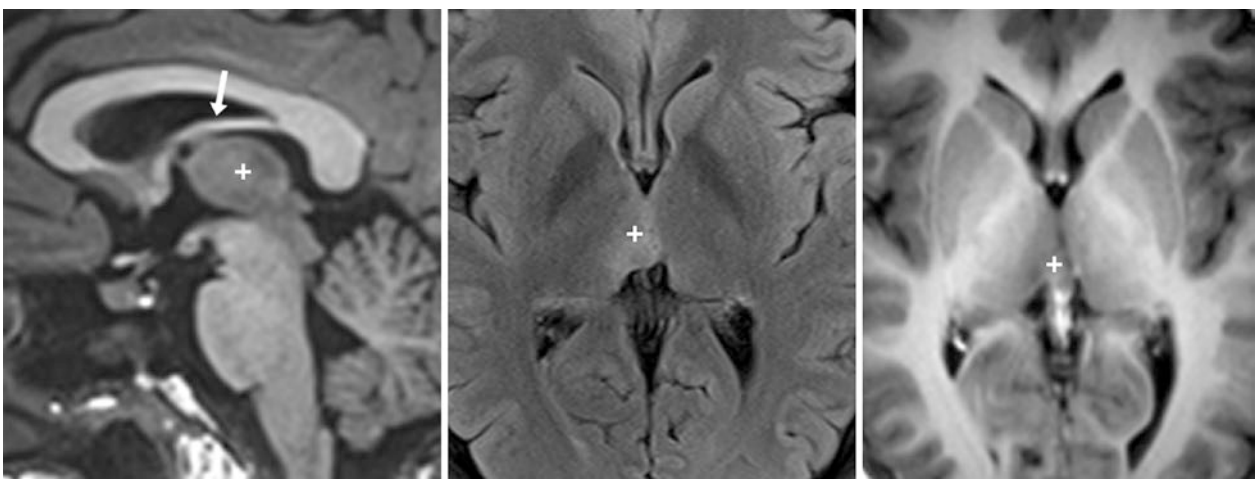

Fig. 13.34 Comparison case of low-grade glioma. An 18 year old with a 3T MRI that depicts a mass involving the massa intermedia (+) on a midline sagittal T1WI (*left*). Axial FLAIR (*middle*) and a postcontrast T1WI (*right*) confirm a mass in that region. Note the body of the fornix superiorly (*thick arrow*). A biopsy found a low-grade astrocytoma

13.4 Callosal-Septal and Pericallosal Pseudolesions on Sagittal FLAIR MRI

At the midline, there can be normal linear hyperintense signal at the *callosal-septal interface* on thin (1–3 mm) sagittal FLAIR images. This signal may be related to an artifact at the junction of these two structures with the CSF or could relate to a form of *ependymitis granularis*. Such signal is typically parallel to the orientation of the lateral ventricles. This is important because periventricular hyperintense notches have been found to be relatively sensitive for detecting early demyelinating lesions of *multiple sclerosis* on sagittal FLAIR images along the inner surface or undersurface of the corpus callosum; such notches are oriented perpendicular to the curve of the corpus callosum and lateral ventricles.

Thus, midline lesions may occur within the corpus callosum or at the callosal-septal interface that have an irregular margin with the lateral ventricle, are perpendicular to the ventricle, and appear nonlinear. When these occur in a parasagittal or more lateral location off midline, they have been termed *subcallosal striations*. Thus, a normal subependymal hyperintense signal on sagittal FLAIR images is located at the interface between the ependyma and the CSF or at the interface between the corpus callosum and the septum pellucidum at the midline, whereas laterally this normal signal occurs along the undersurface of the corpus callosum. These normal variations can be distinguished from lesions caused by *multiple sclerosis* (MS), which typically have a perpendicular orientation to the lateral ventricles; early lesions appear as striations, whereas larger, more evolved lesions have the classic appearance of Dawson fingers (Figs. 13.35, 13.36, 13.37, 13.38, 13.39, 13.40, 13.41, 13.42, and 13.43).

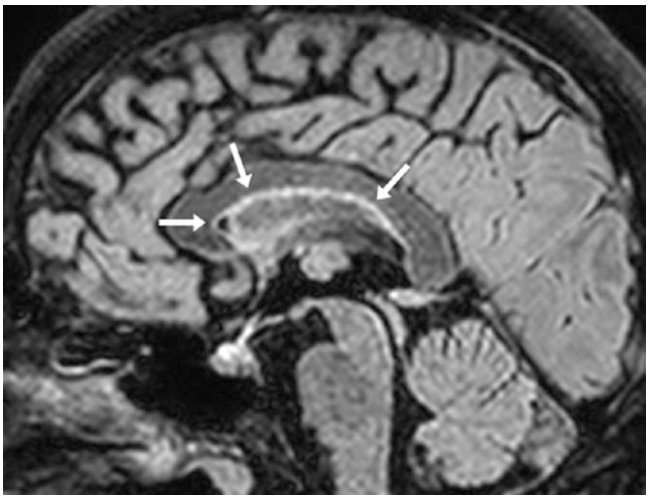

Fig. 13.35 A 41 year old with normal hyperintensity (*arrows*) of the callosal-septal interface, which runs parallel to the corpus callosum on a midline three-dimensional acquired sagittal FLAIR image

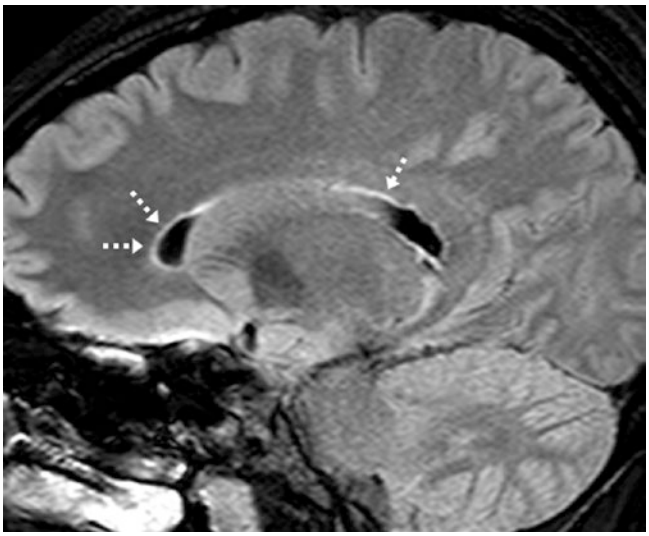

Fig. 13.36 A 30 year old with normal subcallosal hyperintensity (*dashed arrows*) oriented parallel to the ventricles on a sagittal FLAIR image lateral to the corpus callosum

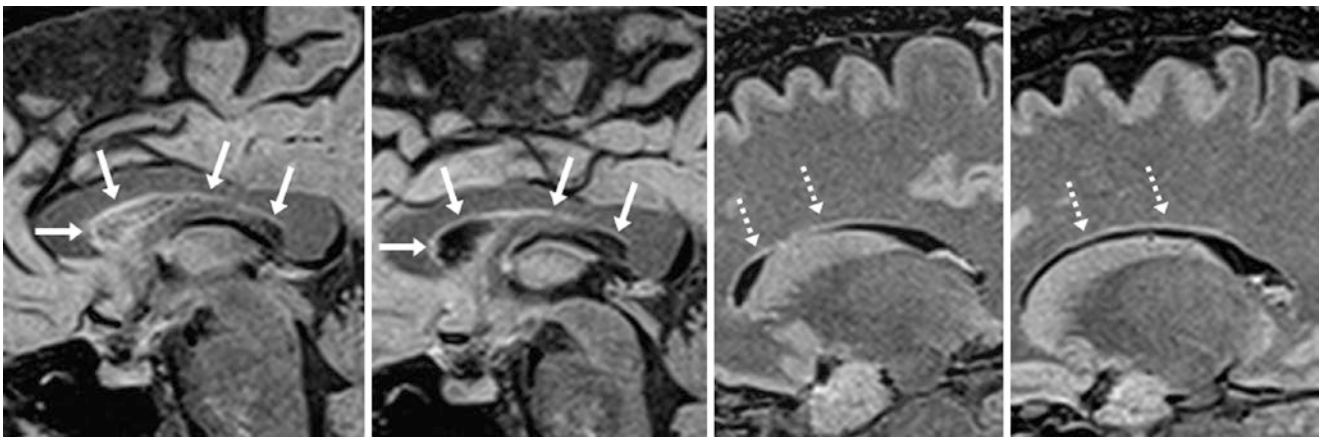

Fig. 13.37 A 33 year old with normal, mild, linear hyperintense signal (*arrows*) in a parallel, nonirregular orientation relative to the lateral ventricles on midline 3T sagittal FLAIR images (*left two images*) at the callosal-septal interface. More laterally, at the subcallosal interfaces on the right (*right middle*) and left (*right*) sides, similar hyperintensities are visualized (*dashed arrows*). Multiple sclerosis lesions are typically oriented perpendicular to the lateral ventricles

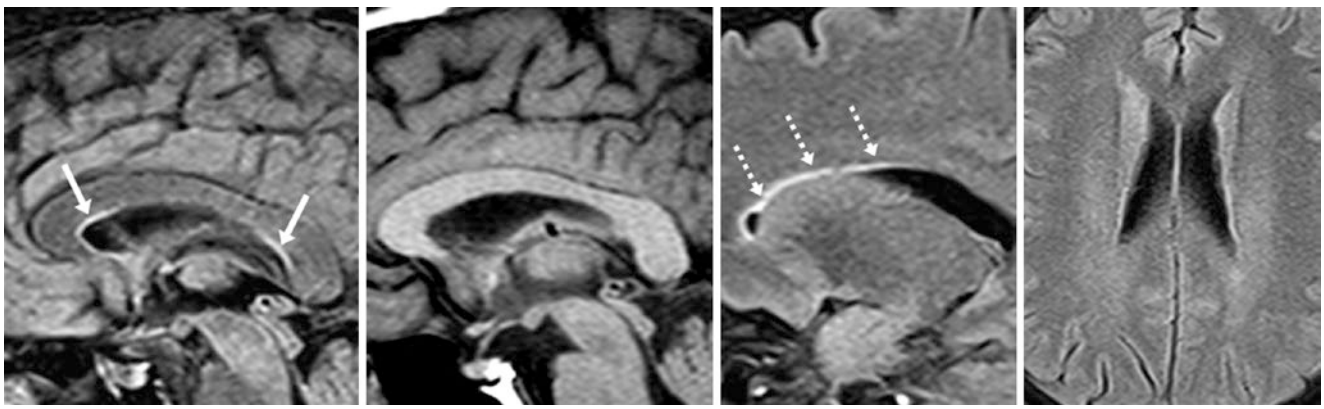

Fig. 13.38 A 53 year old who had normal bright signal (*arrows*) parallel to the lateral ventricles on a midline sagittal FLAIR image (*left*) at the callosal-septal interface, not seen on a sagittal T1WI (*left of middle*). More laterally, at the subcallosal interface, similar normal hyperintensity is noted on the right (*dashed arrows*). Axial FLAIR images (*right*) do not depict any periventricular white matter abnormalities. This patient was not found to have demyelinating disease clinically

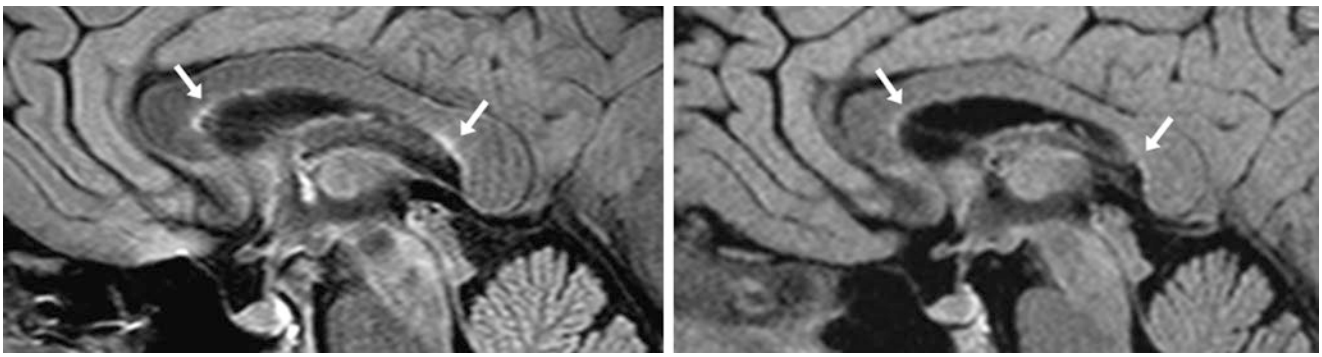

Fig. 13.39 A 37 year old with a 3T MRI that was performed for headaches (interpreted as negative) demonstrating mild, normal hyperintensity anteriorly and posteriorly (*arrows*) on a midline sagittal FLAIR image (*left*). A midline sagittal FLAIR image repeated 1 year later at 3T (*right*) showed that the hyperintensity was less apparent

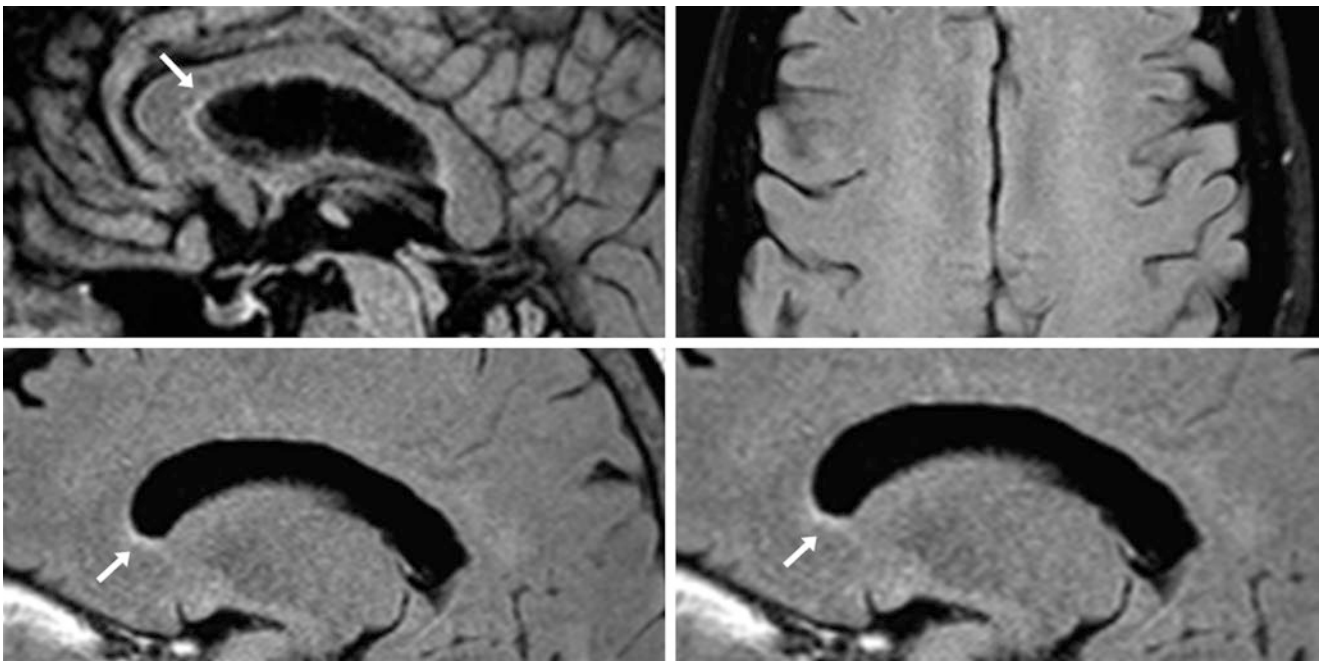

Fig. 13.40 A 63 year old who underwent a 3T MRI (interpreted as negative) that demonstrated minimal, normal hyperintensity anteriorly (*arrows*) on a midline sagittal FLAIR image (*top left*) with normal axial FLAIR images (*top right*). FLAIR images of the left (*bottom left*) and right (*bottom right*) sides also depict minimal focal hyperintensity anteriorly

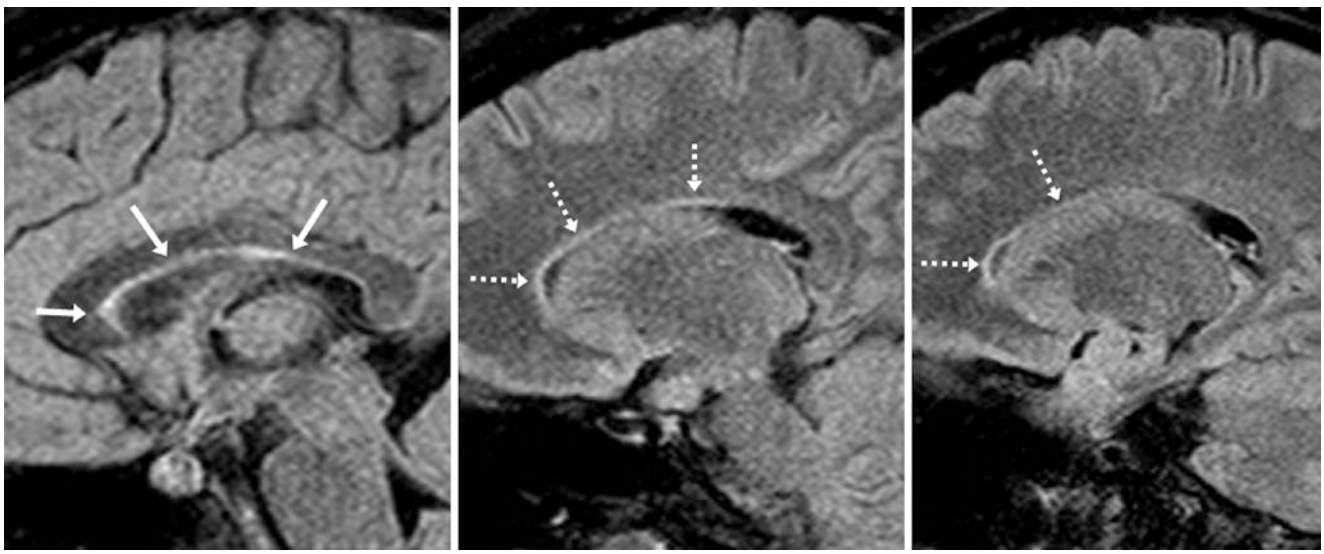

Fig. 13.41 A 24 year old with normal, mild hyperintense signal (*arrows*) parallel to the lateral ventricles on a midline sagittal FLAIR image (*left*) at the callosal-septal interface. More laterally, sagittal FLAIR images of the right (*middle*), and left (*right*) sides demonstrate a normal, regular contour of the subcallosal interface bilaterally (*dashed arrows*), which is probably related to ependymitis granularis. This patient did not have a history of demyelinating disease

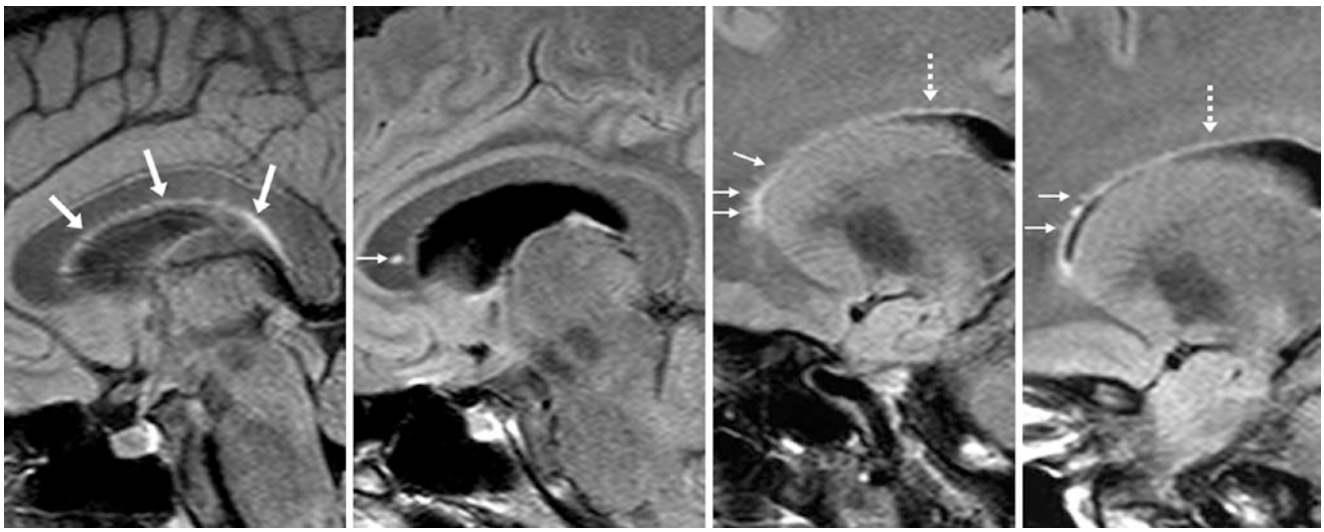

Fig. 13.42 Comparison case of a patient with early multiple sclerosis (MS). An 18 year old had normal bright signal at the callosal-septal interface (*arrows*) oriented parallel to the lateral ventricles on a sagittal FLAIR midline image (*left*). Just left of the midline (*left middle*), there was an MS lesion (*tiny arrow*) within the callosal genu. More laterally on the left (*right middle*) and right sides (*far right*), thin subcallosal striations (*tiny arrows*) were seen at the subcallosal interface, oriented perpendicular to the ventricles. Two to three other white matter lesions were also noted. Combined with the clinical findings, these findings together were indicative of early MS

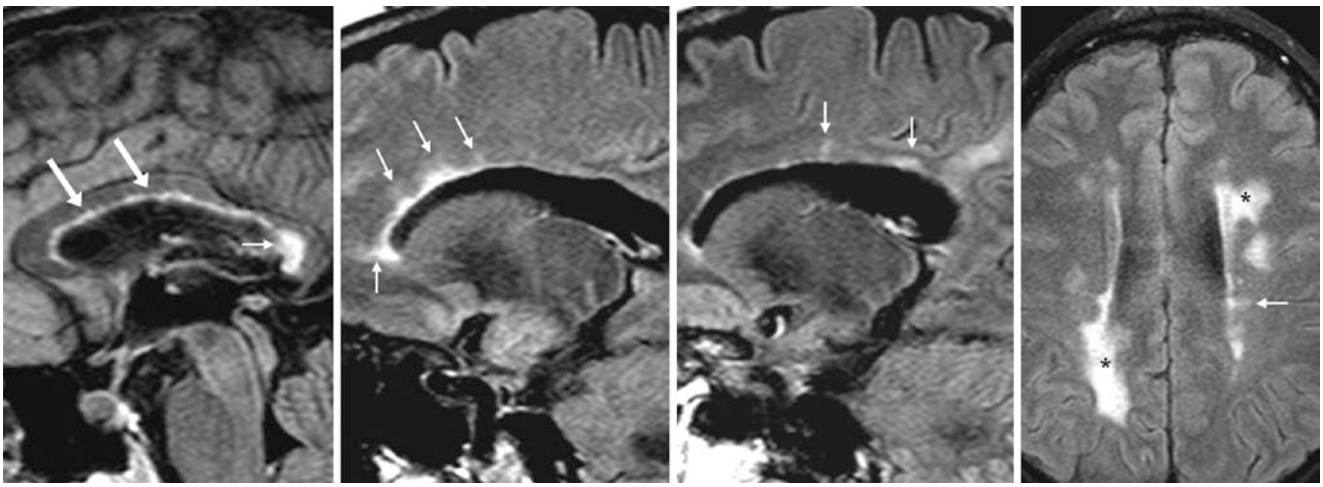

Fig. 13.43 Comparison case of a patient with multiple sclerosis (MS). A 37 year old with worsening disease had normal hyperintense signal anteriorly at the callosal-septal interface (*arrows*) on a midline sagittal FLAIR image (*left*), but there was an irregular margin posteriorly; a focal lesion was noted within the splenium (*tiny arrow*). More laterally on the left (*left middle*) and right sides (*right middle*), perpendicularly oriented lesions (*tiny arrows*) were noted at the subcallosal interfaces that were larger than striations. Axial images (*right*) show larger, more confluent MS lesions (*)

13.5 Callosal Isthmus

At the midline on sagittal T1WI, the *callosal isthmus* (i.e., isthmus of the corpus callosum), which is located at the junction of the posterior body and splenium, can normally appear thinned relative to the remainder of the corpus callosum. The isthmus is the site of interconnecting axons between the two hemispheres, particularly the superior temporal and parietal lobes. A normal, thin isthmus may simulate lesions, most notably focal atrophy of the corpus callosum, which can be seen in a variety of disorders, such as patients with *cerebral palsy* (typically long term following perinatal hypoxia), *demyelinating disorders* (e.g., multiple sclerosis), following *trauma,* or even *leukodystrophies*. Notably, in a pediatric patient with a chronic history of ventriculostomy *shunt catheterization*, the corpus callosum may be thinned either diffusely or focally and should be distinguished from a normally thin isthmus. Correlation with the clinical history and detecting corresponding abnormalities on FLAIR images within the adjacent periventricular white matter (PVWM) can identify true abnormalities of the posterior body and the splenium of the corpus callosum (Figs. 13.44, 13.45, 13.46, 13.47, 13.48, 13.49, 13.50, 13.51, 13.52, and 13.53).

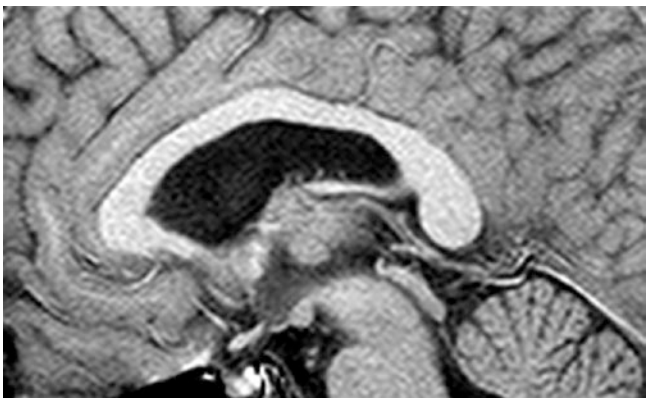

Fig. 13.44 A 49 year old with a typical normal-appearing corpus callosum that lacks thinning of the isthmus

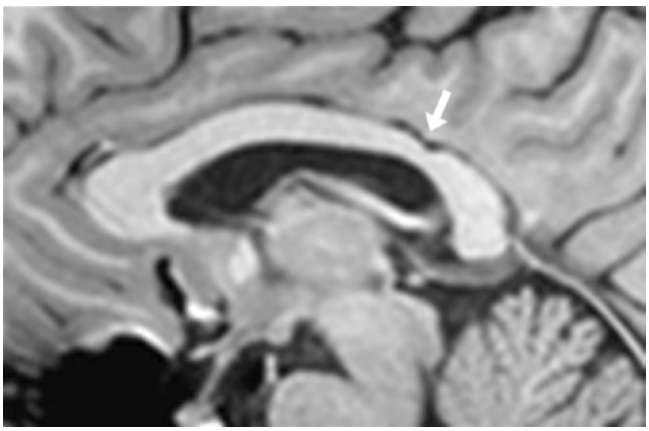

Fig. 13.45 A 29 year old with a normal region of slight thinning located at the callosal isthmus (*arrow*)

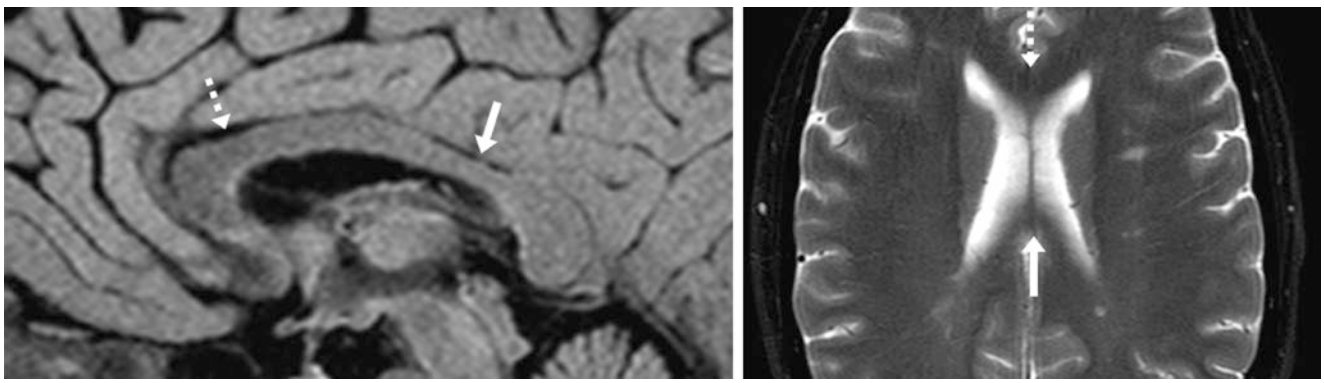

Fig. 13.46 A 36 year old who underwent an MRI obtained for headaches (MRI was negative). There was a normal, slightly thinned callosal isthmus on a midline sagittal FLAIR image (*arrows, left*). An axial T2WI (*right*) adequately demonstrated the disparate thickness of the isthmus of the corpus callosum (*arrows*) relative to the anterior body (*dashed arrows*)

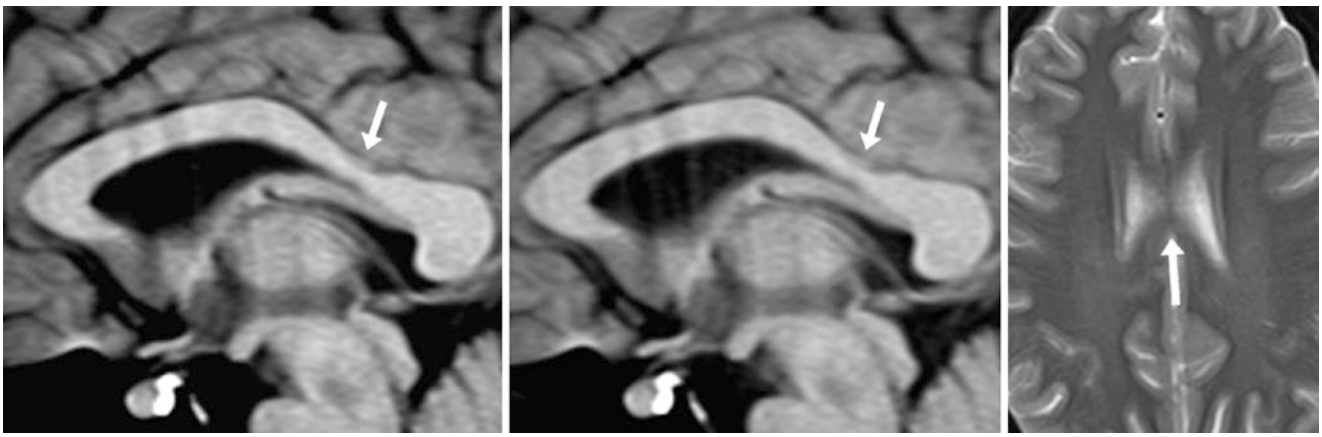

Fig. 13.47 A 27-year-old patient; an otherwise negative MRI obtained for headaches showed a normal, moderately thinned callosal isthmus (*arrows*) on midline sagittal T1WIs (*left and middle*). An axial T2WI (*right*) did not show the thinning clearly

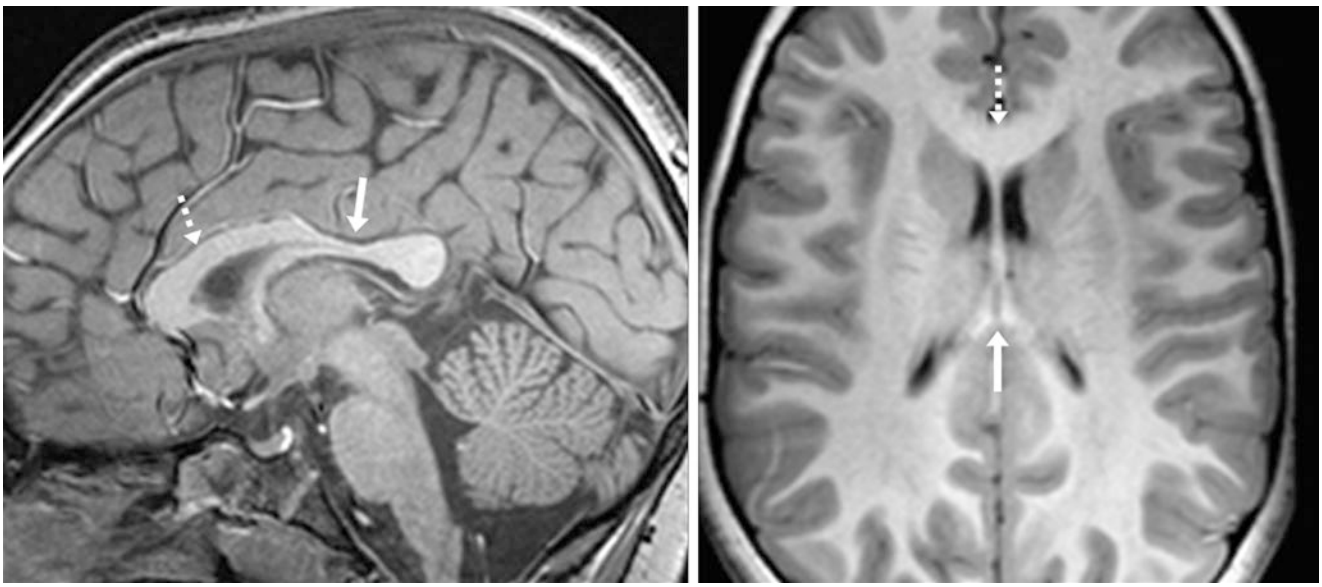

Fig. 13.48 A 4 year old with an otherwise negative 3T MRI obtained for a behavioral disorder. It depicted a normal, moderately thin callosal isthmus on a midline sagittal T1WI (*arrows, left*). An axial T1WI (*right*) through the isthmus demonstrated the disparate thickness of the isthmus relative to the anterior body (*dashed arrows*)

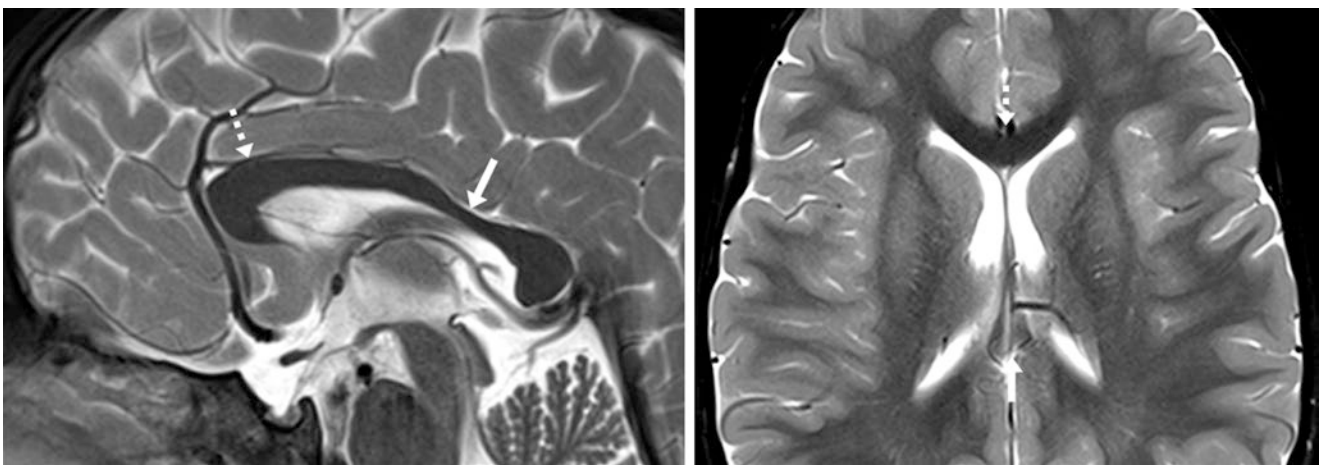

Fig. 13.49 A 3 year old with an otherwise negative 3T MRI obtained for seizures that demonstrated a normal, moderately thin callosal isthmus (*arrows*) on a midline sagittal T2WI (*left*). An axial T2WI through the level of the isthmus (*right*) confirmed the disparate thickness of the callosal isthmus relative to the anterior body (*dashed arrows*)

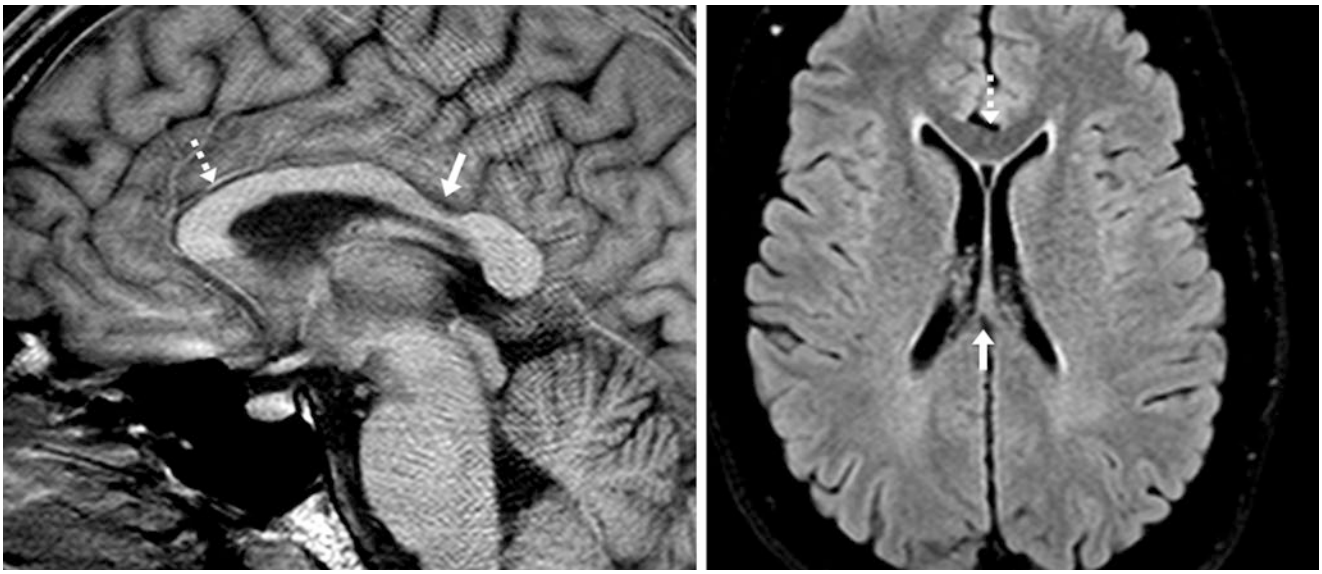

Fig. 13.50 A 46 year old with an MRI obtained to rule out an aneurysm (the MR angiogram was negative). There was a normal, thin callosal isthmus on a midline sagittal T1WI (*arrows, left*). An axial FLAIR image (*right*) confirmed the disparate thickness of the isthmus (*arrows*) relative to the anterior body (*dashed arrows*)

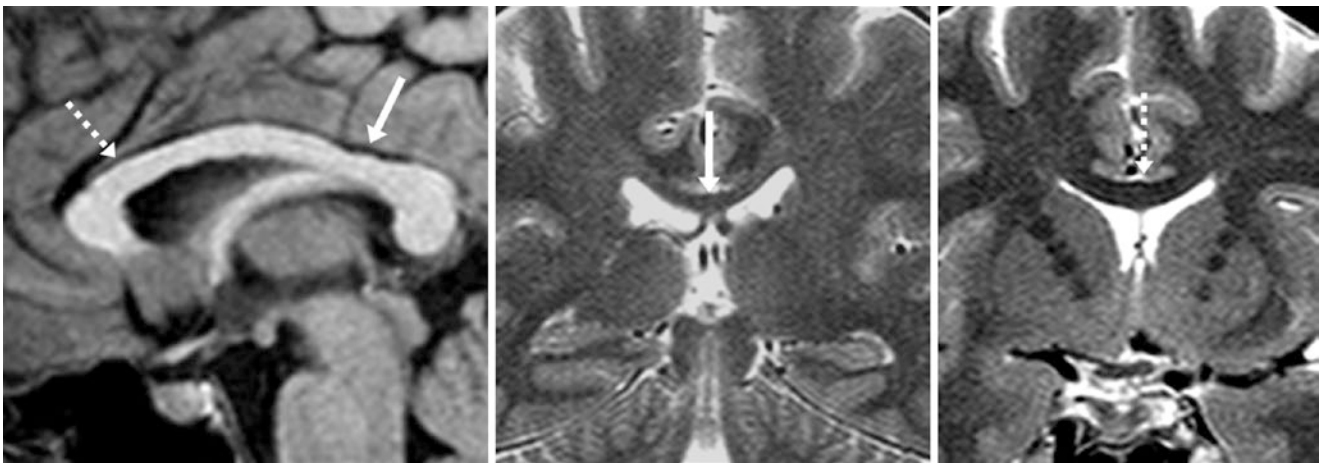

Fig. 13.51 A 31 year old with an otherwise negative MRI obtained for headaches, which showed a normal callosal isthmus on a midline sagittal T1WI (*arrow, left*). Coronal T2WIs through the callosal isthmus (*middle*) and anterior body (*right*) demonstrated the disparate thickness of the isthmus (*arrows*) relative to the anterior body (*dashed arrows*)

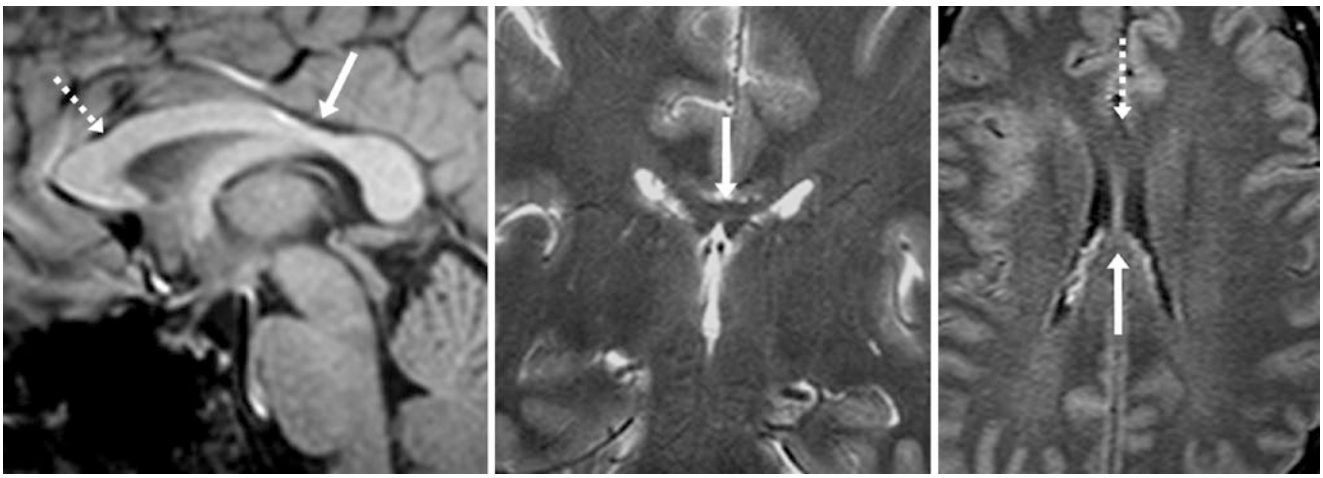

Fig. 13.52 A 44 year old with an otherwise negative MRI obtained for nonspecific symptoms that demonstrated a normal isthmus on a midline sagittal T1WI (*arrow, left*). Coronal T2WI through the isthmus (*middle*) and an axial FLAIR image (*right*) show the disparate thickness of the isthmus (*arrows*) relative to the anterior body (*dashed arrows*)

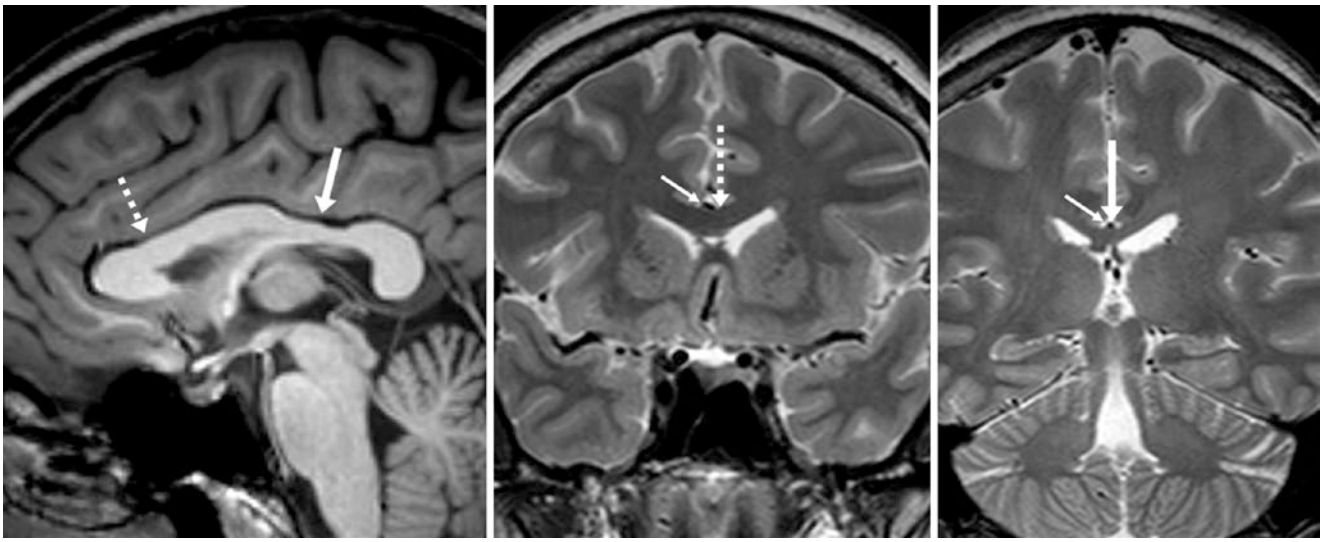

Fig. 13.53 A 28 year old with a normal isthmus (*arrows*) shown on a 3T MRI sagittal T1WI (*left*). Coronal T2WIs through the anterior body (*middle*) and isthmus (*right*) show the disparate thickness between the isthmus (*arrows*) and the anterior body (*dashed arrows*). Indentation by the pericallosal arteries (*thin arrows*) may contribute to the apparent thinning

13.6 Callosal Vascular Indentation by the Anterior Cerebral Artery or Its Branches

On midline sagittal images, a false impression/indentation of the corpus callosum can occur at any site but is particularly common at the posterior genu or anterior body. This is not a congenitally thin region, such as occurs at the callosal isthmus. Rather, such indentation is usually related to a *pericallosal artery*, which usually arises from an A3 segment of the anterior cerebral artery (ACA) that supplies most of the corpus callosum while traveling within the pericallosal sulcus. Thus, such an indentation can mimic a congenital anomaly (e.g., *callosal hypogenesis*) or *atrophy*. This normal variant can be seen in any age group (Figs. 13.54, 13.55, 13.56, 13.57, 13.58, 13.59, 13.60, 13.61, 13.62, 13.63, 13.64, 13.65, 13.66, 13.67, 13.68, and 13.69).

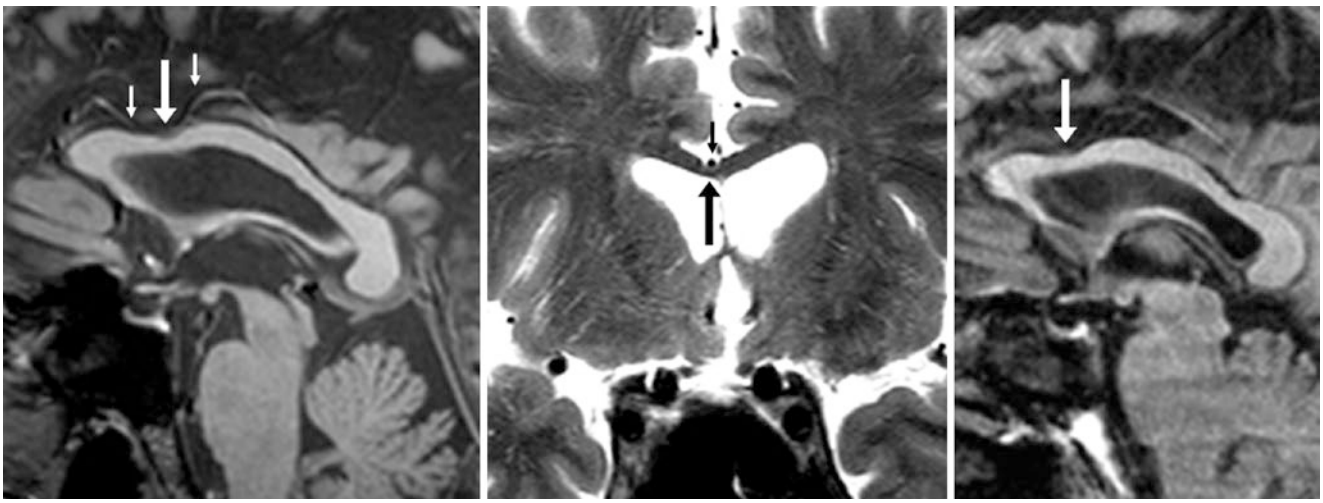

Fig. 13.54 A 62 year old who underwent a 3T MRI (negative) demonstrating normal compression of the posterior genu–anterior body of the corpus callosum (*arrows*) on a sagittal midline T1WI (*left*). A coronal T2WI (*middle*) showed that this compression was from the right pericallosal artery (*thin arrows*). A sagittal T1WI 2 years later (*right*) showed that this was unchanged

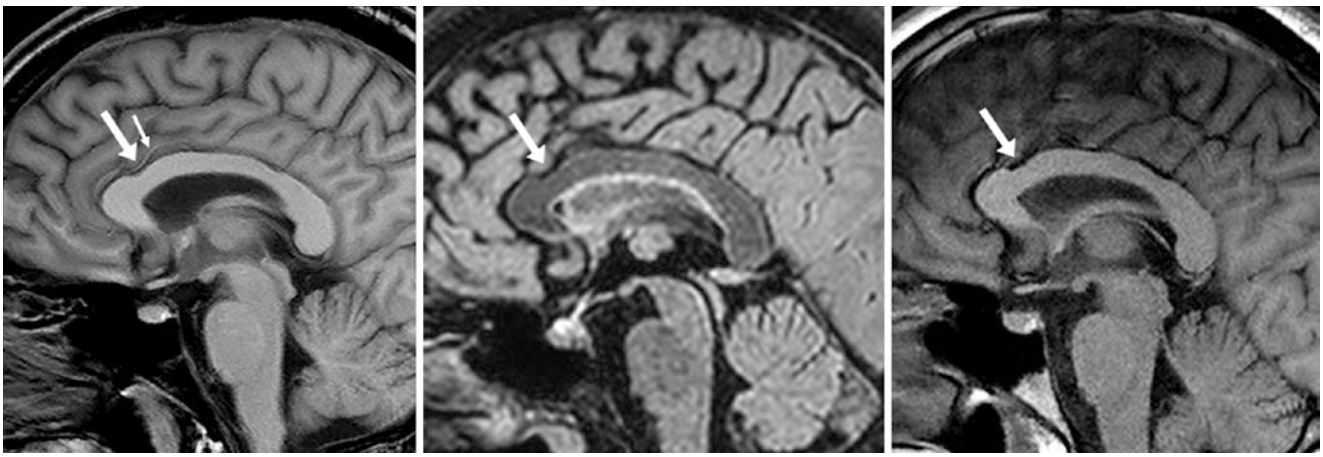

Fig. 13.55 A 33 year old with a negative 3T MRI demonstrating normal compression of the posterior genu–anterior body of the corpus callosum (*arrows*) on a sagittal midline T1WI (*left*) and FLAIR image (*middle*). This compression is from a pericallosal artery (*thin arrow*). A sagittal T1WI 6 months later (*right*) showed that this was unchanged

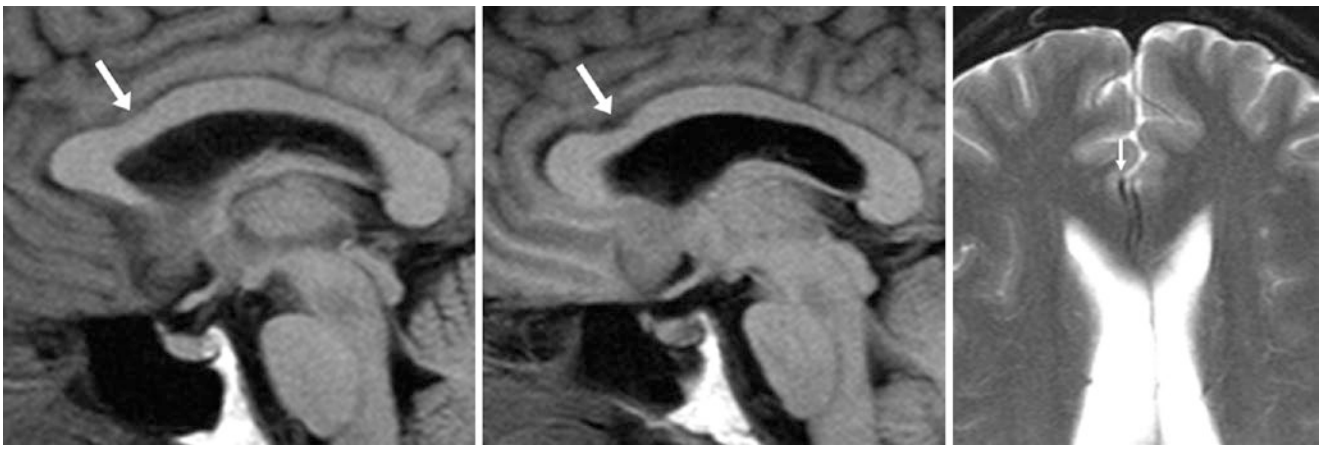

Fig. 13.56 A 49 year old underwent an MRI (negative result) showing apparent compression of the anterior body of the corpus callosum (*arrows*) on T1WIs at the midline (*left*) and just to the right of the midline (*middle*), simulating a congenital defect. An axial T2WI at that level (*right*) showed that this relates to compression from the right pericallosal artery (*thin arrow*)

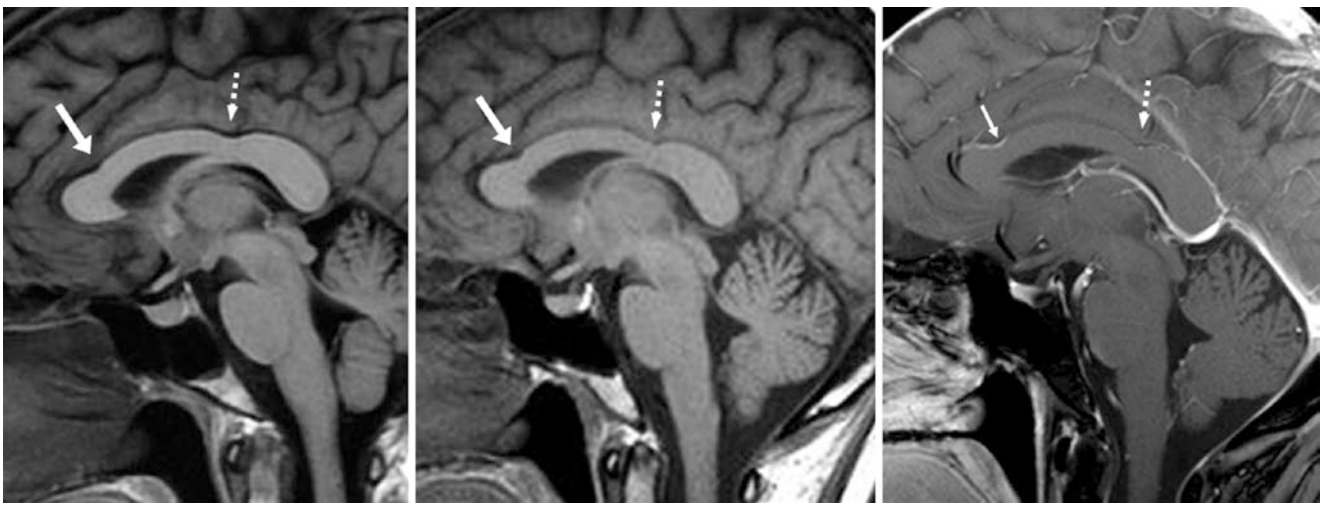

Fig. 13.57 A 45 year old who underwent a 1.5T MRI demonstrating normal, mild compression of the callosal posterior genu–anterior body (*arrows*) from a pericallosal artery (*thin arrow*) on a sagittal midline T1WI (*left*). This was unchanged 8 years later on pre- (*middle*) and postcontrast (*right*) T1WIs. Note a normal callosal isthmus posteriorly (*dotted arrows*)

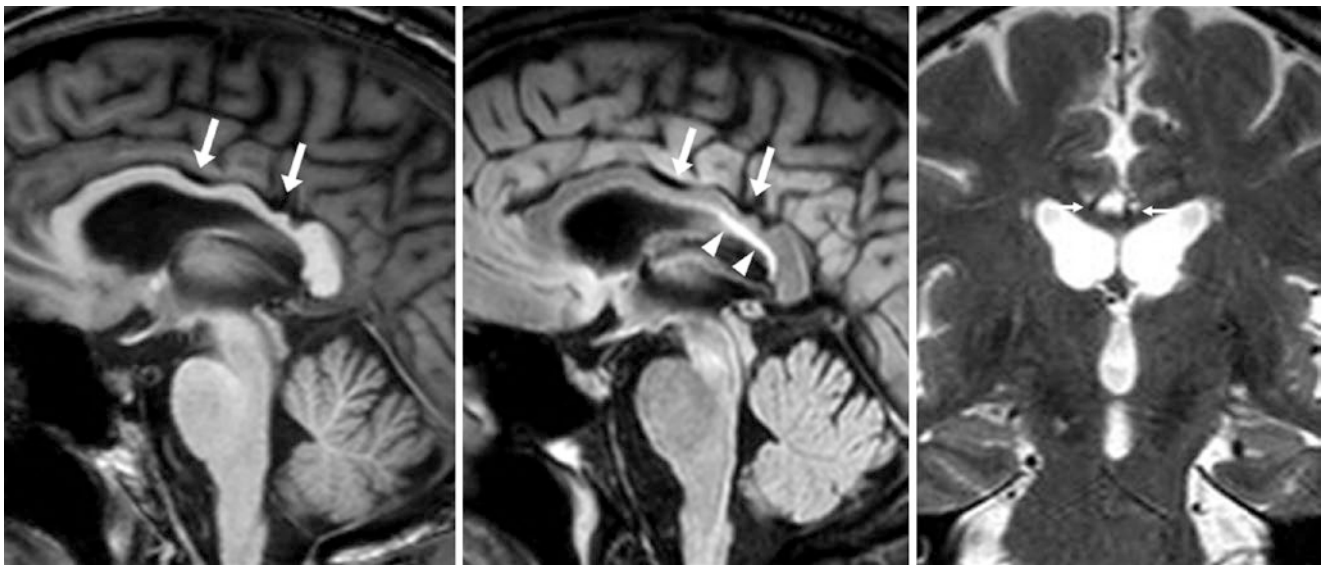

Fig. 13.58 A 35 year old who underwent with a 3T MRI (negative) demonstrating mild compression (*arrows*) of the midposterior callosal body from pericallosal arteries (*thin arrows*) on a midline sagittal T1WI (*left*), FLAIR (*middle*), and coronal T2WI (*right*). Note the normal callosal-septal interface signal (*arrowheads*) on FLAIR, which is oriented parallel to the ventricular margin

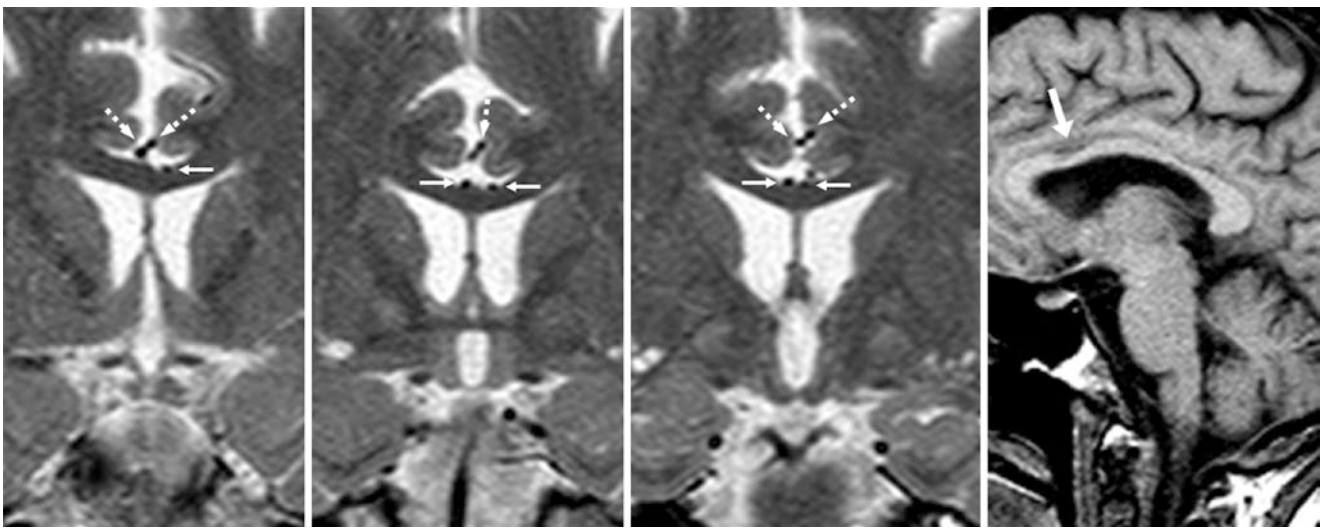

Fig. 13.59 A 69 year old with seizures. There was normal, mild compression of the corpus callosum (*arrow*) on serial coronal T2WIs (*left three images*) by pericallosal anterior cerebral artery (ACA) branches (*thin arrows*). On a sagittal T1WI (*right*), this indentation may mimic focal callosal atrophy or gliosis. Note the normal callosal marginal arteries (*dashed arrows*)

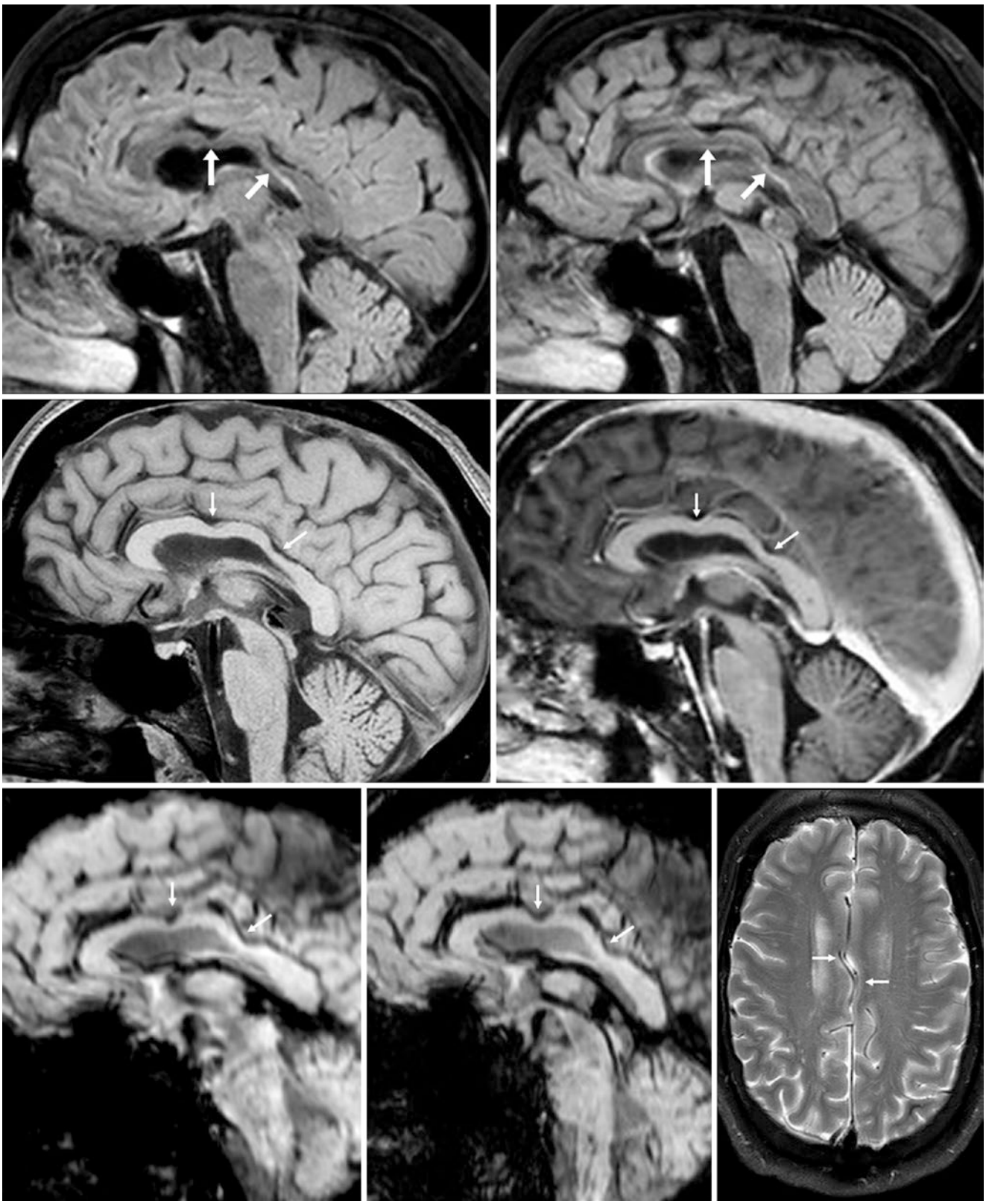

Fig. 13.60 A 54 year old with a 3T MRI performed to evaluate for traumatic lesions. *Top row:* there is normal, moderate indentation of the posterior genu–anterior body of the corpus callosum (*arrows*) on sagittal FLAIR images. *Middle row:* sagittal precontrast (*left*) and postcontrast (*right*) GE T1WI confirm that this impression is related to pericallosal or other distal ACA branches (*thin arrows*). *Bottom row:* sagittal SWIs at 2-mm (*left*) and 7-mm (*right*) thickness depict flow voids of the distal ACA branches (*thin arrows*), which cause the callosal indentations. A T2WI (*right*) shows tortuosity of the distal ACA branches

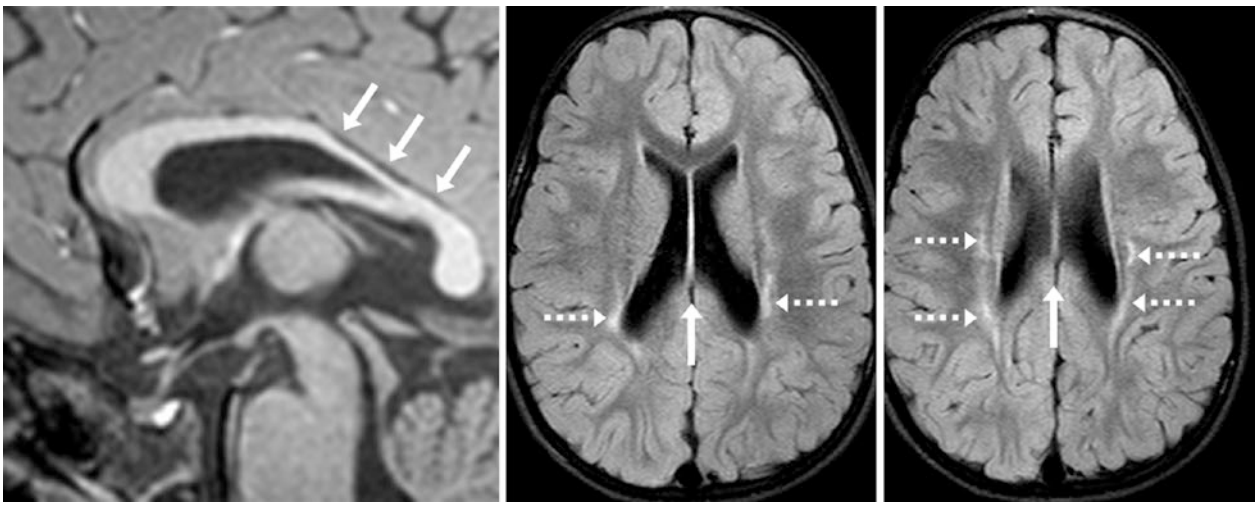

Fig. 13.61 Comparison case of atrophy from perinatal ischemia. A 3 year old born prematurely at 29 weeks' gestational age subsequently developed a spastic gait disorder. A 3T MRI depicted severe, focal atrophy of the posterior callosal body and isthmus (*arrows*) on sagittal T1WI (*left*). FLAIR images (*middle and right*) demonstrated multifocal periventricular white matter abnormalities (*dotted arrows*), presumed to be sequelae of a perinatal insult

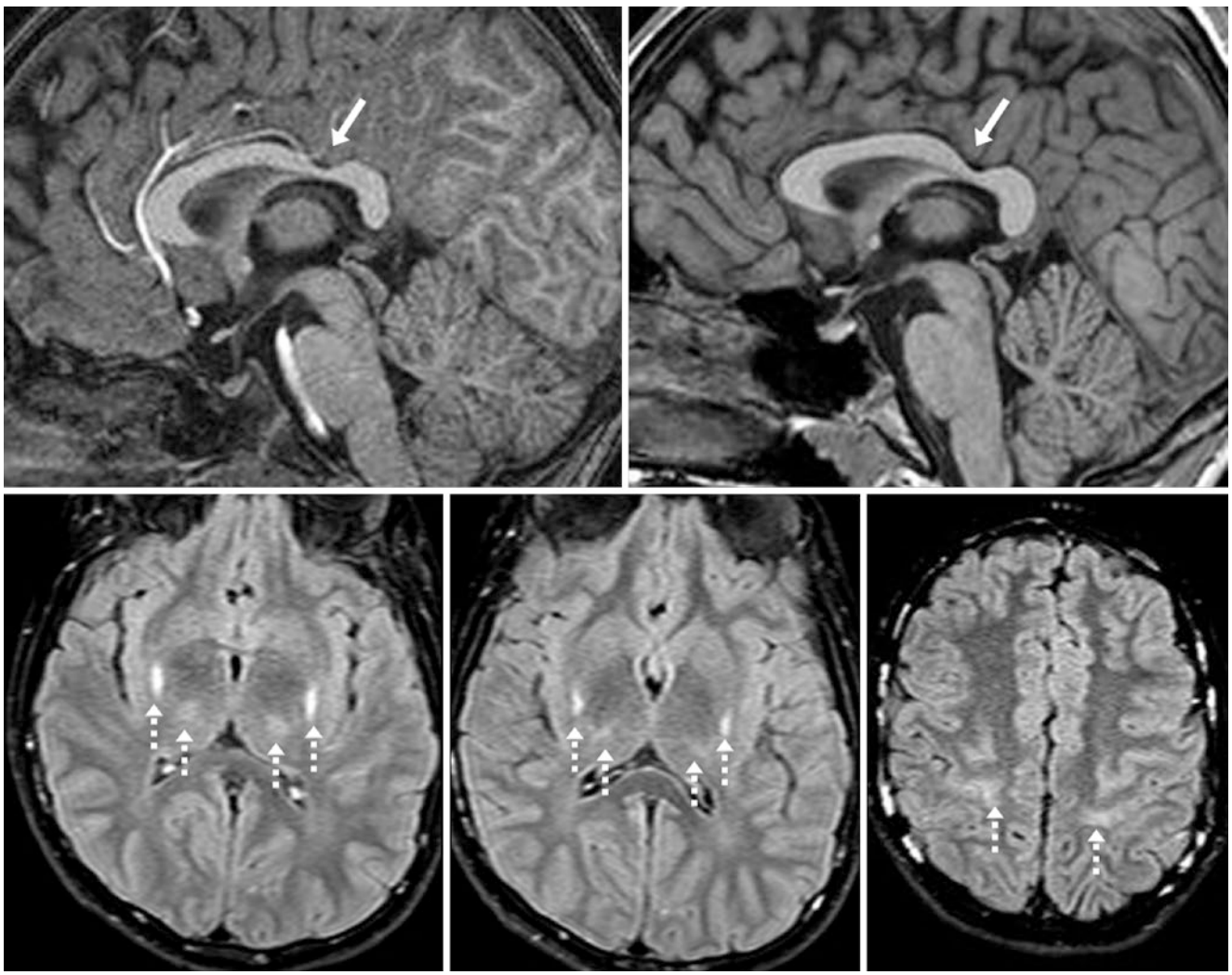

Fig. 13.62 Comparison case of atrophy from remote perinatal ischemia**.** In a 6 year old born with a history of a perinatal insult, a 1.5T MRI depicted severe atrophy of the posterior callosal body and isthmus (*arrows*) on a sagittal T1WI (*top left*), unchanged 10 years later on a T1WI (*top right*). Axial FLAIR (*bottom row*) showed corresponding abnormalities (*dotted arrows*) of the ventrolateral thalami, the internal capsules, and the precentral subcortical white matter

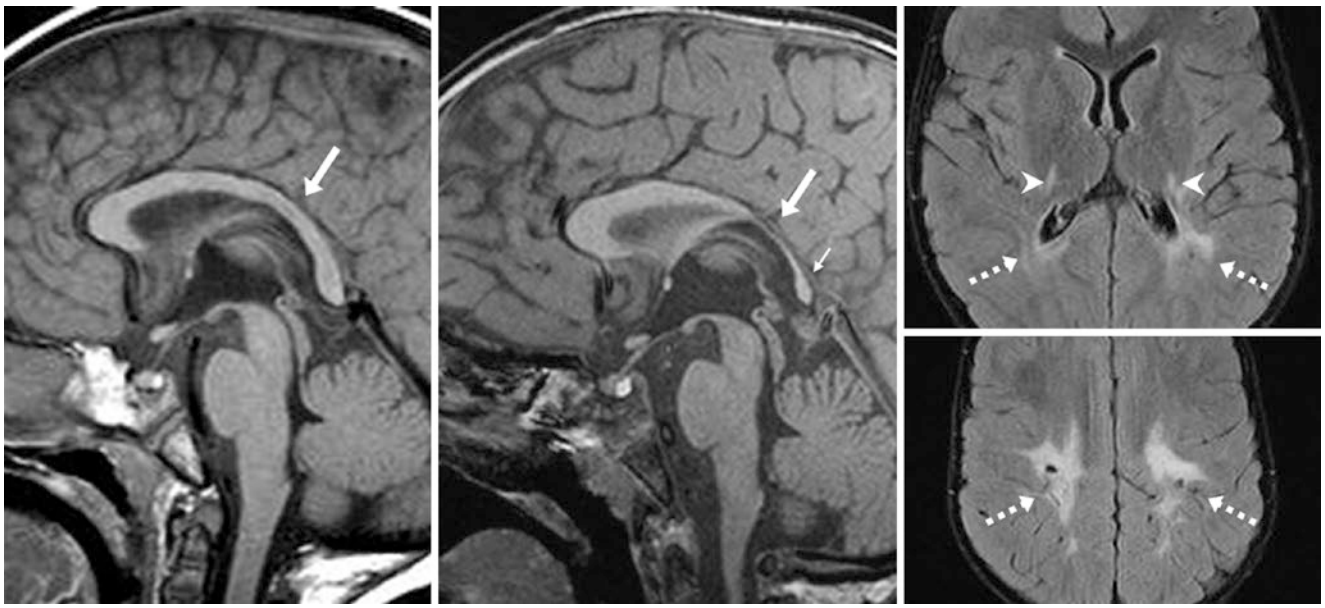

Fig. 13.63 Comparison case of Krabbe/globoid cell leukodystrophy (GLD). A 1 year old female had no callosal atrophy at birth on sagittal T1WI (*left*), but by 3 years of age (*middle*) there was severe atrophy of the posterior body (*arrows*) and to a lesser degree of the splenium (*thin arrow*). There were typical abnormalities along the path of the corticospinal tracts (*arrowheads*) and within the deep white matter (*dotted arrows*) on FLAIR (*right*)

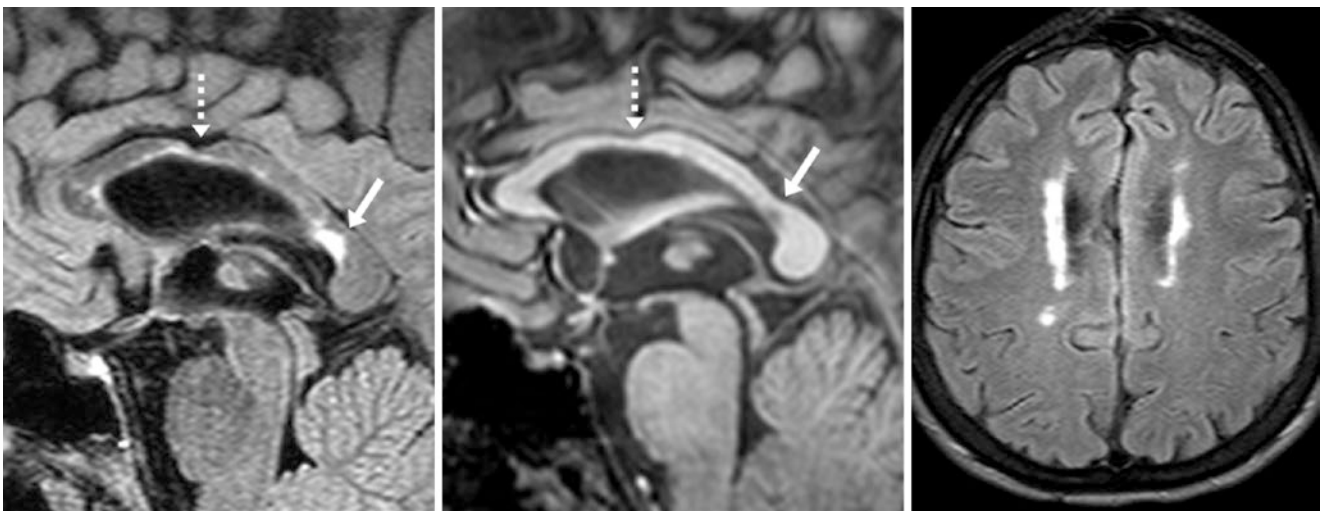

Fig. 13.64 Comparison case of multiple sclerosis (MS). A 44 year old with chronic MS had focal atrophy (*dashed arrows*) of the callosal body on sagittal FLAIR (*left*) and T1WI (*middle*). Note lesions of the callosal-septal interface at the midline, one being in the isthmus (*arrows*). An axial FLAIR image (*right*) further depicts the white matter lesions

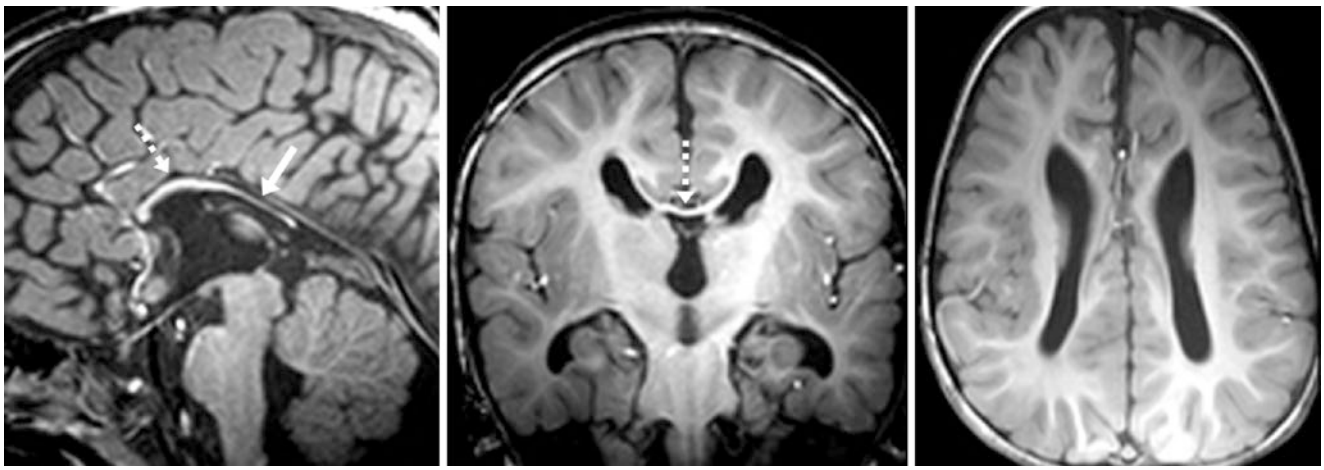

Fig. 13.65 Comparison case of callosal hypogenesis. A 2 year old had a diffusely severe hypogenetic corpus callosum, while the anterior body of the corpus callosum (*dashed arrows*) was thicker and more developed than the posterior body (*arrows*) and splenium, as depicted on sagittal (*left*), coronal (*middle*), and axial (*right*) T1WIs

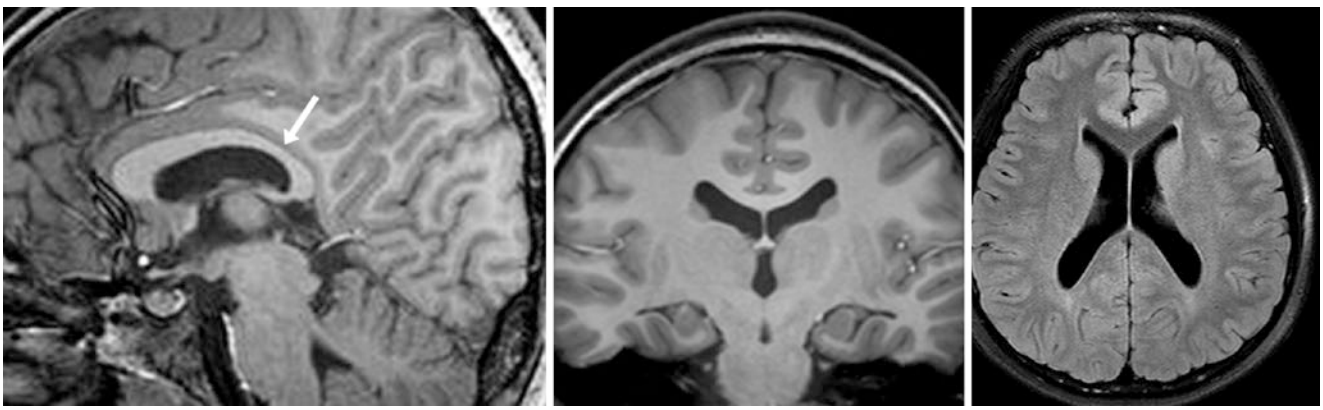

Fig. 13.66 Comparison case of callosal hypogenesis**.** A 12 year old had hypogenesis of the posterior body and callosal splenium (*arrow*), where the anterior body (*dashed arrows*) was thicker and more normal, as shown on sagittal T1WI (*left*), coronal T1WI (*middle*), and axial FLAIR (*right*). Note the slightly enlarged lateral ventricles posteriorly

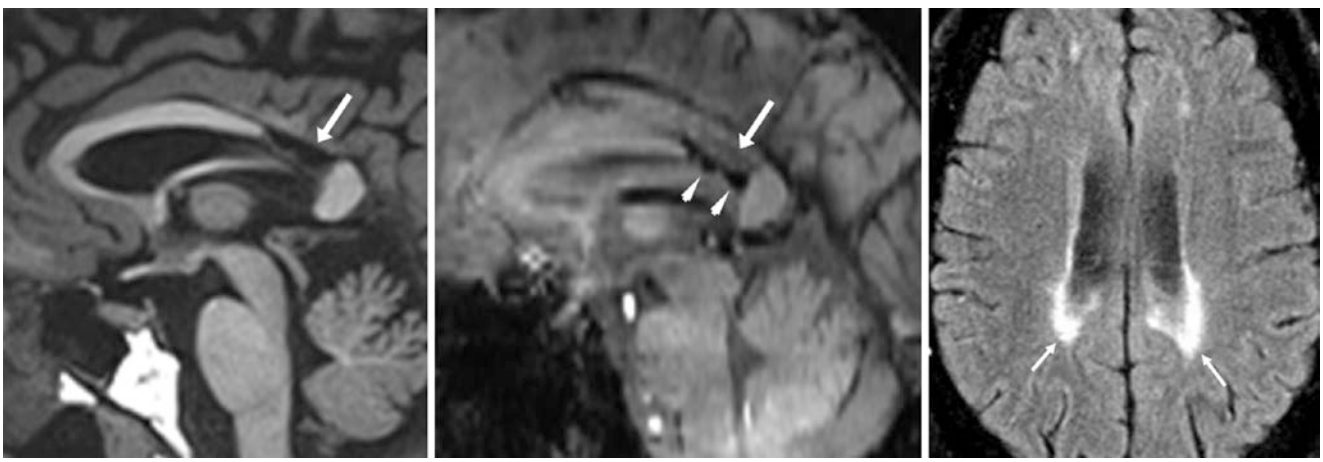

Fig. 13.67 Comparison case of remote injury. A 55 year old with severe isthmic atrophy (*arrows*) on 3T sagittal T1-FLAIR (*left*) and SWI (*middle*). On SWI, there were frontotemporal hemorrhages and isthmic hemorrhage (*arrowheads*), with periventricular abnormalities on FLAIR (*right*). The insults were thought to be related to an old traumatic or perinatal injury

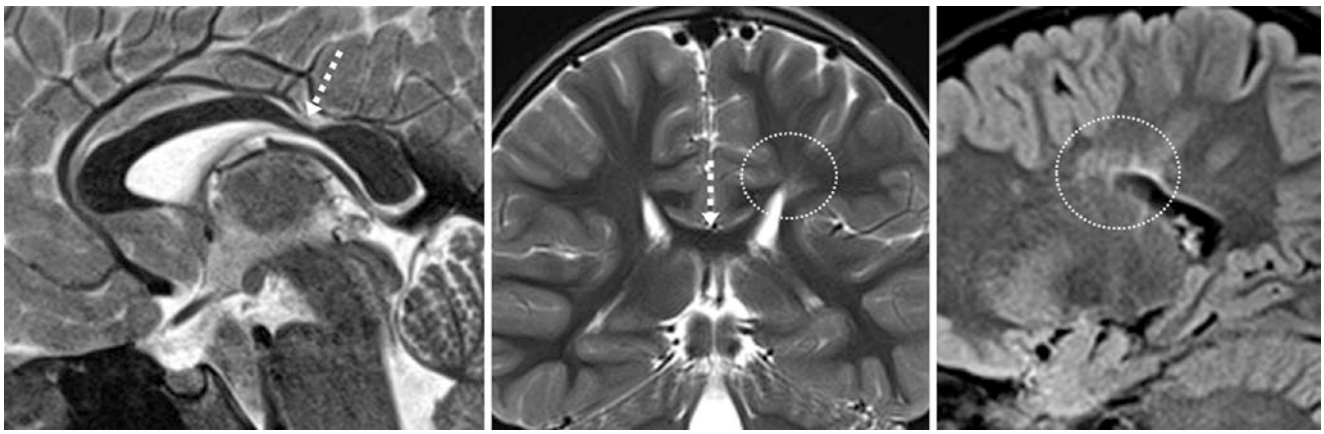

Fig. 13.68 Comparison case of atrophy**.** An 8 year old with cerebral palsy had a 3T MRI that showed focal atrophy of the callosal isthmus (*dashed arrows*) on sagittal T2WI (*left*), with periventricular hyperintensity (*dotted circles*) on the left side on coronal T2WI (*middle*) and on sagittal FLAIR (*right*); ex vacuo dilatation of the left lateral ventricle was also observed

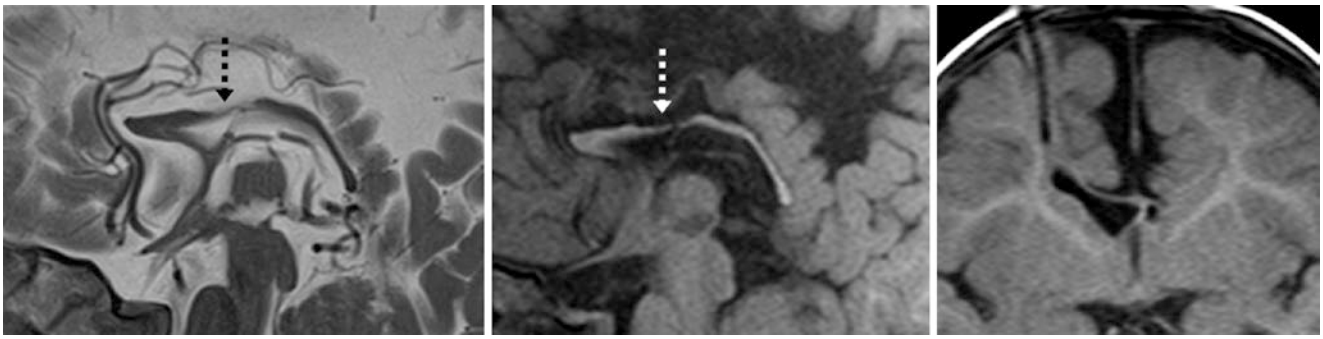

Fig. 13.69 Comparison case of iatrogenic atrophy from shunting. An 11 month old had had a shunt catheter since birth. 3T MRI demonstrated severe thinning and focal atrophy of the callosal body (*arrows*) on sagittal T2WI (*left*) and T1WI (*middle*). On a coronal T1WI (*right*), note the catheter with enlarged frontal horn caused by instrument-related atrophy

Suggested Reading

Born CM, Meisenzahl EM, Frodl T, Pfluger T, Reiser M, Möller HJ, Leinsinger GL. The septum pellucidum and its variants. An MRI study. Eur Arch Psychiatry Clin Neurosci. 2004;254:295–302.

Chen CY, Chen FH, Lee CC, Lee KW, Hsiao HS. Sonographic characteristics of the cavum velum interpositum. AJNR Am J Neuroradiol. 1998;19:1631–5.

Farruggia S, Babcock DS. The cavum septi pellucidi: its appearance and incidence with cranial ultrasonography in infancy. Radiology. 1981;139:147–50.

Gean-Marton AD, Vezina LG, Marton KI, Davis KR. Abnormal corpus callosum: a sensitive and specific indicator of multiple sclerosis. Radiology. 1991;180:215–21.

Hagino H, Suzuki M, Kurokawa K, Mori K, Nohara S, Takahashi T, et al. Magnetic resonance imaging study of the cavum septi pellucidi in patients with schizophrenia. Am J Psychiatry. 2001;158:1717–9.

Kier EL, Truwit CL. The normal and abnormal genu of the corpus callosum: an evolutionary, embryologic, anatomic, and MR analysis. AJNR Am J Neuroradiol. 1996;17:1631–41.

Kwon JS, Shenton ME, Hirayasu Y, Salisbury DF, Fischer IA, Dickey CC, et al. MRI study of cavum septi pellucidi in schizophrenia, affective disorder, and schizotypal personality disorder. Am J Psychiatry. 1998;155:509–15.

Macpherson P, Teasdale E. CT demonstration of a 5th ventricle – a finding to KO boxers? Neuroradiology. 1988;30:506–10.

Nakashima I, Fujihara K, Miyazawa H, Misu T, Fujimori J, Sato S, Itoyama Y. Relevance of callosal and periventricular MRI lesions to oligoclonal bands in multiple sclerosis. Acta Neurol Scand. 2006;113:125–31.

Neema M, Guss ZD, Stankiewicz JM, Arora A, Healy BC, Bakshi R. Normal findings on brain fluid-attenuated inversion recovery MR images at 3T. AJNR Am J Neuroradiol. 2009;30:911–6.

Nopoulos P, Swayze V, Flaum M, Ehrhardt JC, Yuh WT, Andreasen NC. Cavum septi pellucidi in normals and patients with schizophrenia as detected by magnetic resonance imaging. Biol Psychiatry. 1997;41:1102–8.

Okamoto K, Ito J, Tokiguchi S. The MR findings on the corpus callosum of normal young volunteers [Japanese]. Nippon Igaku Hoshasen Gakkai Zasshi. 1990;50:954–63.

Picard L, Leymarie F, Roland J, Sigiel M, Masson JP, André JM, Renard M. Cavum veli interpositi. Roentgen anatomy – pathology and physiology. Neuroradiology. 1976;10:215–20.

Sarwar M. The septum pellucidum: normal and abnormal. AJNR Am J Neuroradiol. 1989;10:989–1005.

Schwidde JT. Incidence of cavum septi pellucidi and cavum vergae in 1032 human brains. AMA Arch Neurol Psychiatry. 1952;67:625–32.

Simon JH, Holtas SL, Schiffer RR, Rudick RA, Herndon RM, Kido DK, Utz R. Corpus callosum and subcallosal-periventricular lesions in multiple sclerosis: detection with MR. Radiology. 1986;160:363–7.

Dilated Perivascular Spaces

14

A *perivascular space* (PVS) or a *Virchow-Robin space* is a typically narrow tract that is the drainage pathway for the cerebral parenchyma. As there is no lymphatic system within the cerebrum, the PVSs drain interstitial/extracellular fluid peripherally outward to the *subarachnoid space* (SAS) but are thought not to communicate directly with the SAS. PVSs are also termed Virchow-Robin spaces, which surround small perforating arteries in multiple locations. They have also been described as potential spaces created by leptomeninges that penetrate the cerebral parenchyma and surround blood vessels. The literature suggests that tiny, normal PVSs may be seen in up to 80 % of the pediatric population, while irregular or ectatic PVSs (status cribrosum) may be noted in 1–2 %. However, on standard imaging, slightly prominent PVSs are visible in 33 % of patients greater than or equal to 65 years of age [1–6].

The most common location of these normal variant mildly dilated PVSs is surrounding the lenticulostriate arteries within the *anterior perforated substance*, posterior to the anterior commissure and inferior to the inferior aspect of the putamen (*type I*). They are also fairly common along perforating medullary vessels within the *subcortical white matter* (SCWM) and *periventricular white matter* (PVWM) as they enter the cortex (*type II*) and *midbrain/cerebral peduncle* (*type III*). Less commonly, dilated PVSs can be seen within the corpus callosum, thalami, dentate nuclei, subinsular region, and within the anterior temporal white matter or optic radiations. Those within the PVWM or SCWM often radiate peripherally. Usually, the tiny perforating vessel is not seen, but if it is present the uncommon finding of a perforating vessel confirms the diagnosis.

Innumerable tiny PVSs seen throughout the basal ganglia in the elderly population has been termed *état criblé* (translated as cribriform state or status cribrosum); this is sometimes difficult to distinguish from multifocal lacunar infarcts. As this cribriform imaging appearance has been associated with the elderly and/or vasculopaths (i.e., those patients with atherosclerotic disease such as hypertension, diabetes, or chronic smoking), it has long been questioned whether even a noncribriform appearance of PVSs is found with an increasing frequency in such vasculopathic patients or in the elderly. Indeed, although many consider *état criblé* to represent tiny but dilated PVSs, a high correlation has been shown between the presence of *état criblé* with the presence of lacunar infarcts and leukoariosis (i.e., chronic small vessel ischemic disease within the white matter on CT and MRI); this suggests an underlying vasculopathy/arteriopathy of small perforating vessels. Such patients have been shown to have an association with the presence of vascular dementias.

More recent literature has also demonstrated that perivascular spaces are found more frequently within patients who are vasculopaths, particularly those with a history of hypertension or carotid plaques. It has also been shown that PVSs in most previously described locations have an increased number and frequency with increasing age. Such evidence has suggested that the pathophysiologic processes that lead to atherosclerosis and vasculopathic findings (such as within the white matter or basal ganglia) are related to the development of PVSs. In particular, it seems that dilated PVSs are especially associated with the degree of lacunar ischemic infarcts and white matter abnormalities on T2WI or FLAIR MRI.

Also notable is the fact that the cystic-appearing foci traditionally called *hippocampal cysts* probably represent PVSs, which are also normal variants and are noted with increased frequency with age; they are visible in up to 40–50 % of the elderly [1–6]. This point is controversial because it has been traditionally thought that hippocampal cavities or cysts are related to the persistence of the hippocampal sulcus and perhaps to even incomplete hippocampal infolding. Interestingly, they have been noted to histologically resemble PVSs, and they do seem to occur at the site of the residual hippocampal sulcus remnant at the deepest portion of the expected sulcus' location, between the dentate gyrus and the cornus ammonis of the hippocampus. This

A.M. McKinney, *Atlas of Normal Imaging Variations of the Brain, Skull, and Craniocervical Vasculature*,
DOI 10.1007/978-3-319-39790-0_14

topic is covered elsewhere in this book (Sects. 12.1 and 12.2) along with hippocampal variants and *choroidal fissure cysts*. Thus, only a small number of corresponding images are provided in this section.

On MRI, the vast majority of dilated PVSs follow CSF signal intensity on all sequences. As stated previously, the PVSs represent potential spaces containing interstitial fluid similar to CSF, and the imaging findings reflect that. Thus, PVSs are expected to completely saturate (become dark) on FLAIR and DWI MRI and to appear bright on T2WI and on ADC maps. This is in contradistinction to *lacunar infarcts*, which by definition are smaller than 1.5 cm in size and are commonly confused with or difficult to distinguish from normally dilated PVSs. Such lacunar infarcts typically have a lack of complete saturation in the manner of CSF on FLAIR (often with a hyperintense rim or central region) and are often not linear or radiating in appearance. Occasionally they may have a central linear vessel represented by a thin T2-dark flow void or a contrast-enhancing vascular structure that is best seen on MRI at higher field strengths (i.e., at 3T and above). Recent evidence has raised the possibility that PVSs may slowly dilate in various inflammatory disorders that follow them, such as multiple sclerosis (MS), since they are thought to transport leukocytes/lymphocytes as an inflammatory response. Of interest is the fact that the perivascular spaces in the basal ganglia usually have two separate layers of surrounding leptomeninges, while those in the SCWM extending into the cortex only have one such layer. However, the imaging significance of this histolopathologic finding is not yet known.

In this author's experience an exception to this rule of saturation of PVSs akin to the CSF are the quite common thin and tiny PVSs (<1–2 mm thickness) that may be easily seen on higher resolution T2WI, while at times they appear nearly completely invisible on T1WI and FLAIR MRI (i.e., representing the up to "80 %" of patients in whom tiny PVSs can be seen). Another exception is the rare *giant or tumefactive PVS* (>1.5–2 cm). On MRI, giant PVSs are typically bright on T2WI, dark on T1WI, FLAIR, and DWI, do not have dark calcium or hemorrhage on SWI or nonenhanced CT (NECT), and do not enhance after intravenous contrast agent administration. Such a giant PVS may simulate a *low-grade brain tumor* such as a *juvenile pilocytic astrocytoma* that can even appear multiloculated or clustered. One reason that a giant PVS may simulate a low-grade tumor is that it may have surrounding T2WI or a FLAIR hyperintense signal (thought to represent gliosis). Additionally, although quite rare, giant PVSs can enlarge slowly over time and may even cause mass effect and hydrocephalus. Rarely, they may cause symptoms as they enlarge, such as cranial nerve symptoms (if they are located within the brainstem), seizures (if they are near the medial temporal lobe or subcortical), and ataxia, headaches, vertigo, syncope, or visual changes.

In summary, the differential diagnosis for dilated PVSs varies slightly, depending on their location. When in the basal ganglia and anterior perforated substance (type I), the differential diagnosis includes *lacunar infarcts* (described previously), *MS* (usually hyperintense on FLAIR and enhance in active lesions, with callosal lesions that are perpendicular to the lateral ventricles), *vasculitis* (e.g., Neuro-Behçet syndrome, in which the lesions enhance and may be bright on DWI), and *cryptococcal infection* (usually hyperintense on FLAIR in immunocompromised patients). When they occur within the PVWM and SCWM (type II), the differential diagnosis includes *lacunar infarcts, MS, cystic periventricular leukomalacia* (multiple cysts within the PVWM near the trigones of lateral ventricles but showing gliosis on T2WI and FLAIR), and rarely *mucopolysaccharidoses* (dilated PVSs diffusely isointense to CSF with a proper clinical history but possibly with associated gliosis on T2WI/FLAIR). Dilated PVSs occurring within the midbrain and cerebral peduncles (type III) have the differential diagnosis of *lacunar infarcts, multiple sclerosis,* and the sequela of *vasculitis* (e.g., neuro-Behçet). When larger they may simulate a cystic *low-grade glioma* such as a juvenile pilocytic astrocytoma (which usually has mass effect, surrounding hyperintensity, and does not suppress on FLAIR). Giant PVSs may simulate a *neuroepithelial cyst* (it usually occurs along ventricles but in some locations can be indistinguishable from a PVS), an *arachnoid cyst* (usually occurs along convexities or in the cerebellopontine angle but has a signal similar to that of a PVS), or, as described above, *low-grade tumors*, particularly cystic primary brain neoplasms.

14.1 Dilated Perivascular Spaces: Type I

Again, the most common location of normal variant mildly dilated PVSs is in the general location of the lenticulostriate arteries within the anterior perforated substance, located posterior to the anterior commissure and inferior to the inferior aspect of the putamen. These can be single or multiple. They can be confused with vascular etiologies (e.g., lacunar infarcts, which do not suppress and become dark like CSF on FLAIR MRI) or various inflammatory (e.g., vasculitis, multiple sclerosis) or infectious (e.g., cryptococcal meningitis) etiologies (Figs. 14.1, 14.2, 14.3, 14.4, 14.5, 14.6, 14.7, 14.8, 14.9, and 14.10).

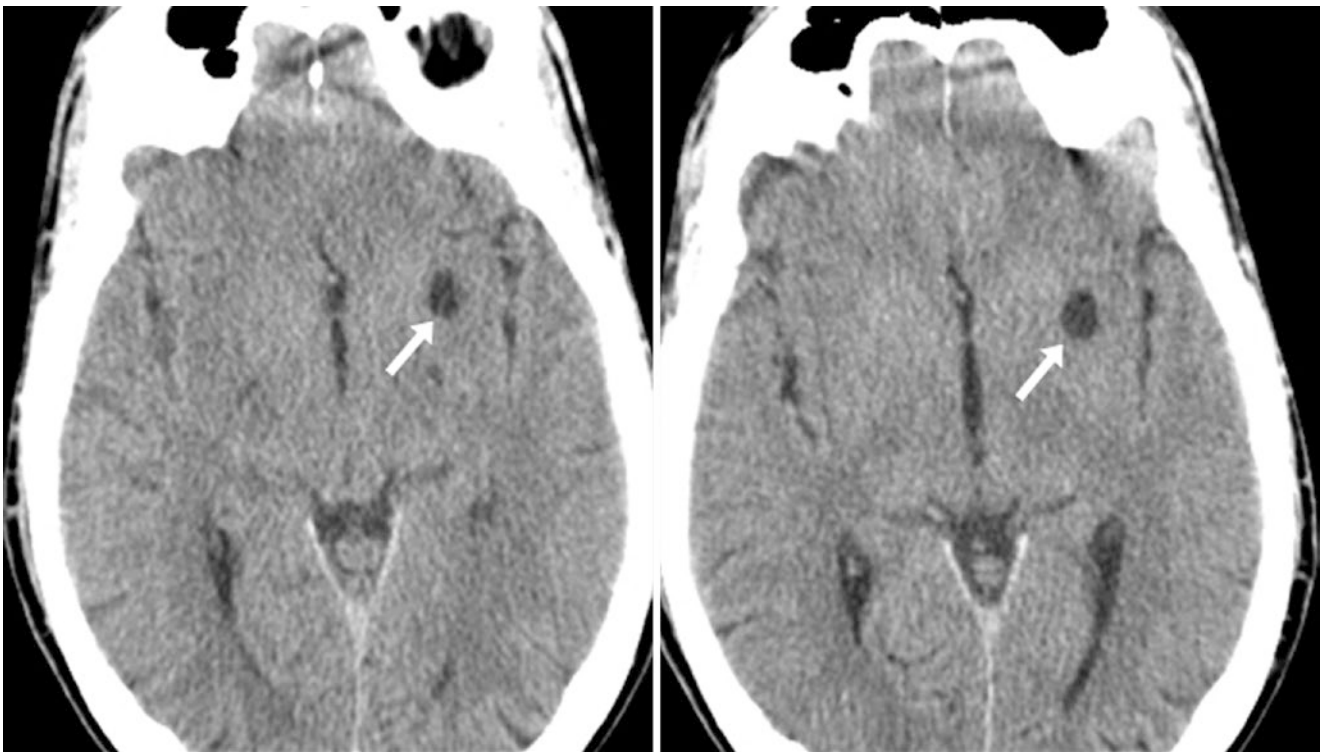

Fig. 14.1 A 38 year old had a moderately dilated PVS (*arrows*) within the inferior left putamen on NECT. As expected, the PVS had a density nearly identical to that of the CSF. Note the lack of surrounding edema and mass effect

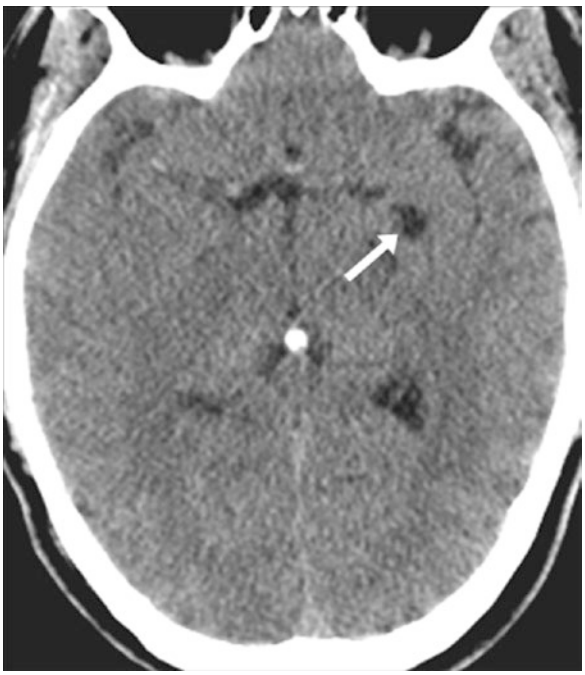

Fig. 14.2 A 48 year old with a dilated PVS (*arrow*) within the anterior perforated substance inferior to the putamen

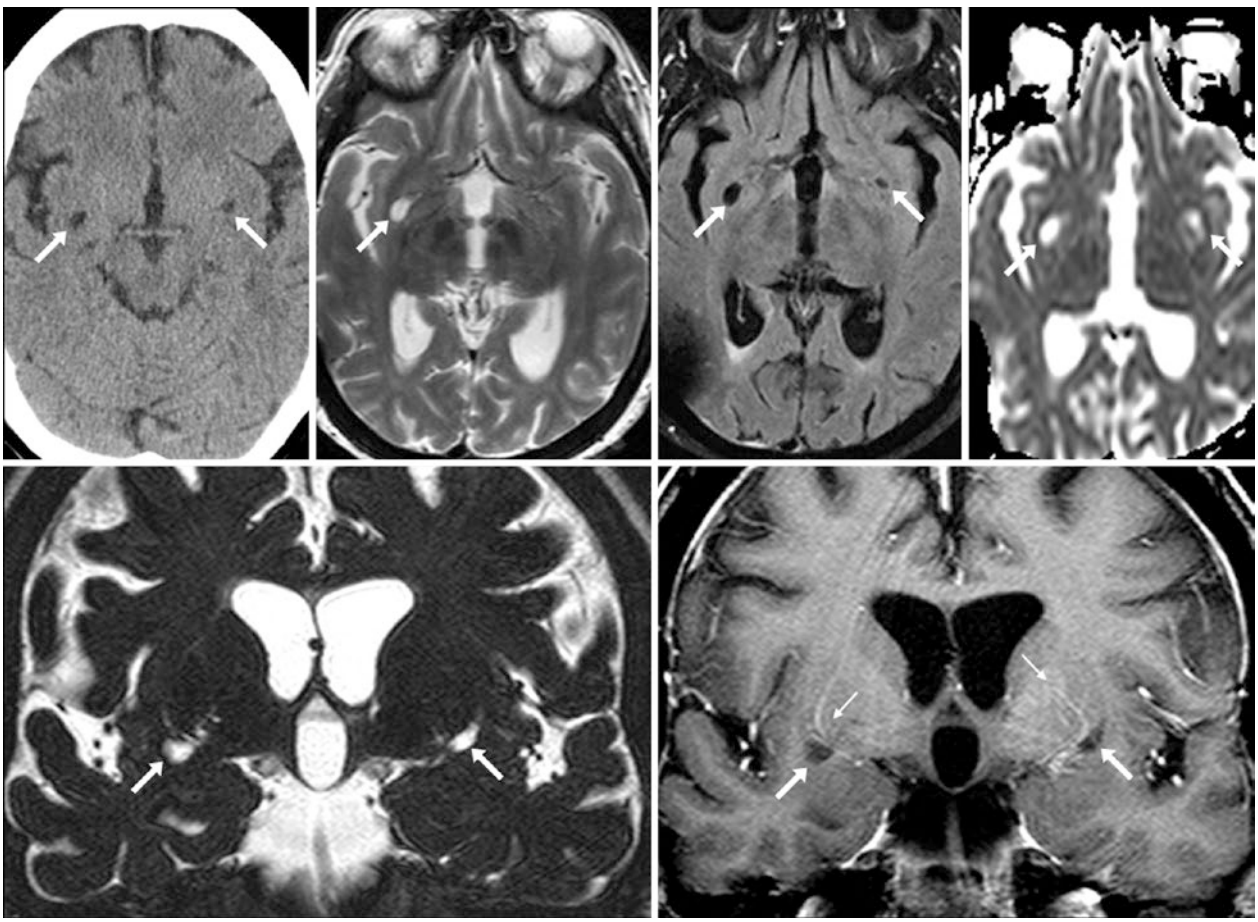

Fig. 14.3 A 46 year old had dilated PVSs bilaterally (*arrows*) within the inferior putamina on axial NECT (*top left*), T2WI (*top, left middle*), FLAIR (*top, right middle*), and an ADC map (*top right*). The PVSs suppress with CSF on FLAIR and are bright on ADC maps. Thin-section (0.8 mm) balanced echo three-dimensional T2WI (*bottom left*) optimizes CSF versus a parenchymal signal. The PVSs do not enhance on postcontrast T1WI (*bottom right*), although small enhancing lenticulostriate vessels (*tiny arrows*) are seen to perforate the PVSs; they were unchanged 3 years later (*not shown*)

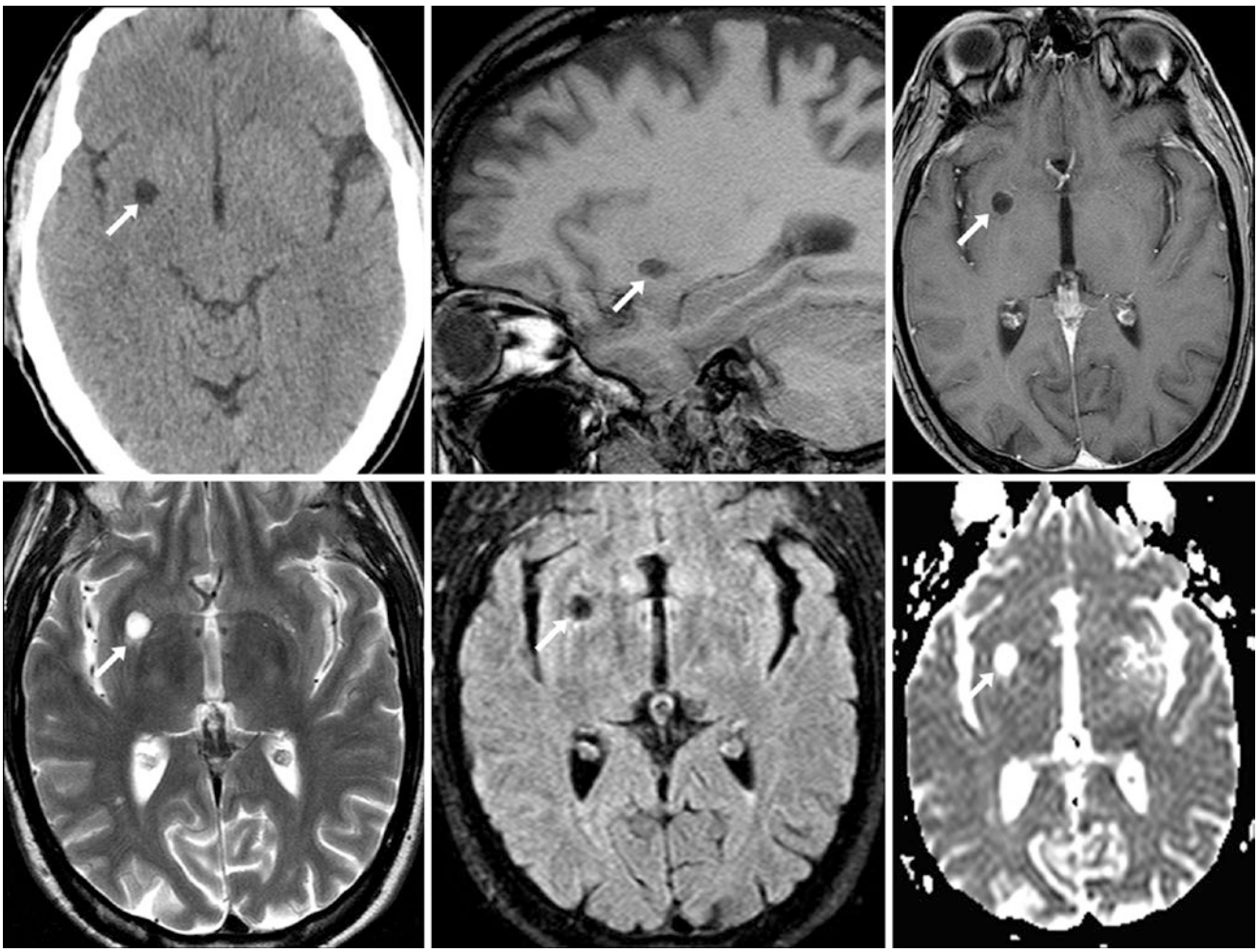

Fig. 14.4 A 52 year old had a dilated PVS (*arrows*) within the inferior right putamen on a NECT (*top left*), sagittal T1WI MRI (*top middle*), postcontrast axial T1WI MRI (*top right*), axial T2WI (*bottom left*), FLAIR (*bottom middle*), and an ADC map (*bottom right*). As expected, the PVS suppresses with CSF on FLAIR and is bright on the ADC map

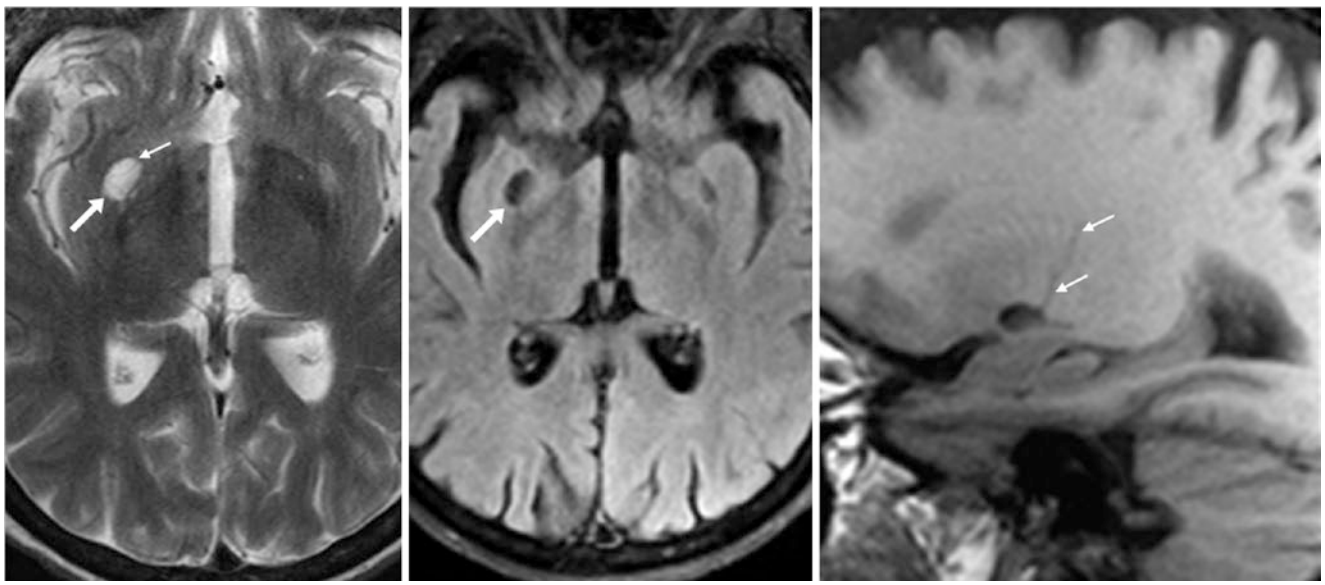

Fig. 14.5 A 55 year old with a dilated PVS (*arrows*) within the anterior perforated substance/inferior putamen on a 3T axial T2WI MRI (*left*) in which a faint, tiny, perforating lenticulostriate vessel may be seen (*tiny arrows, left*). The PVS suppresses on FLAIR (*middle*). A sagittal T1WI MRI of the right side (*right*) also depicts the perforating vessel as it penetrates and passes through the dilated PVS. Note a smaller, dilated PVS on the left side in a similar location

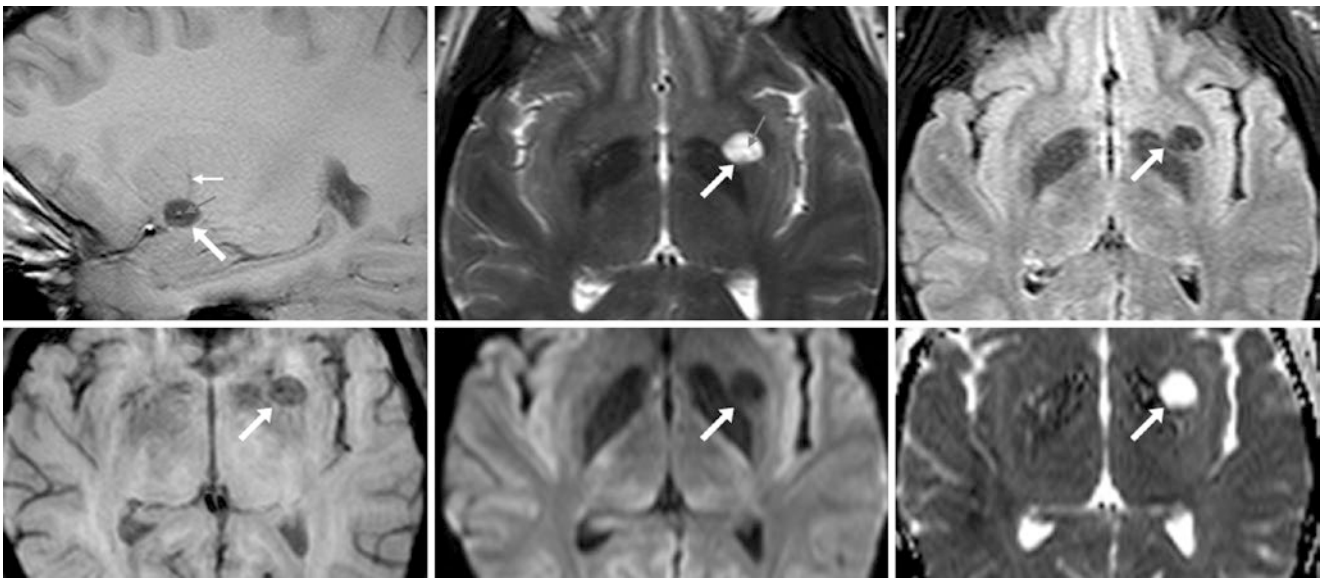

Fig. 14.6 A 35 year old with a dilated PVS (*arrows*) on a sagittal T1WI (*top left*), axial T2WI (*top middle*), FLAIR (*top right*), SWI (*bottom left*), DWI (*bottom middle*), and an ADC map (*bottom right*). The PVS surrounds a tiny lenticulostriate vessel (*tiny arrows*) that travels up into the basal ganglia. On an MRI 1 year later (*not shown*), the PVS was unchanged

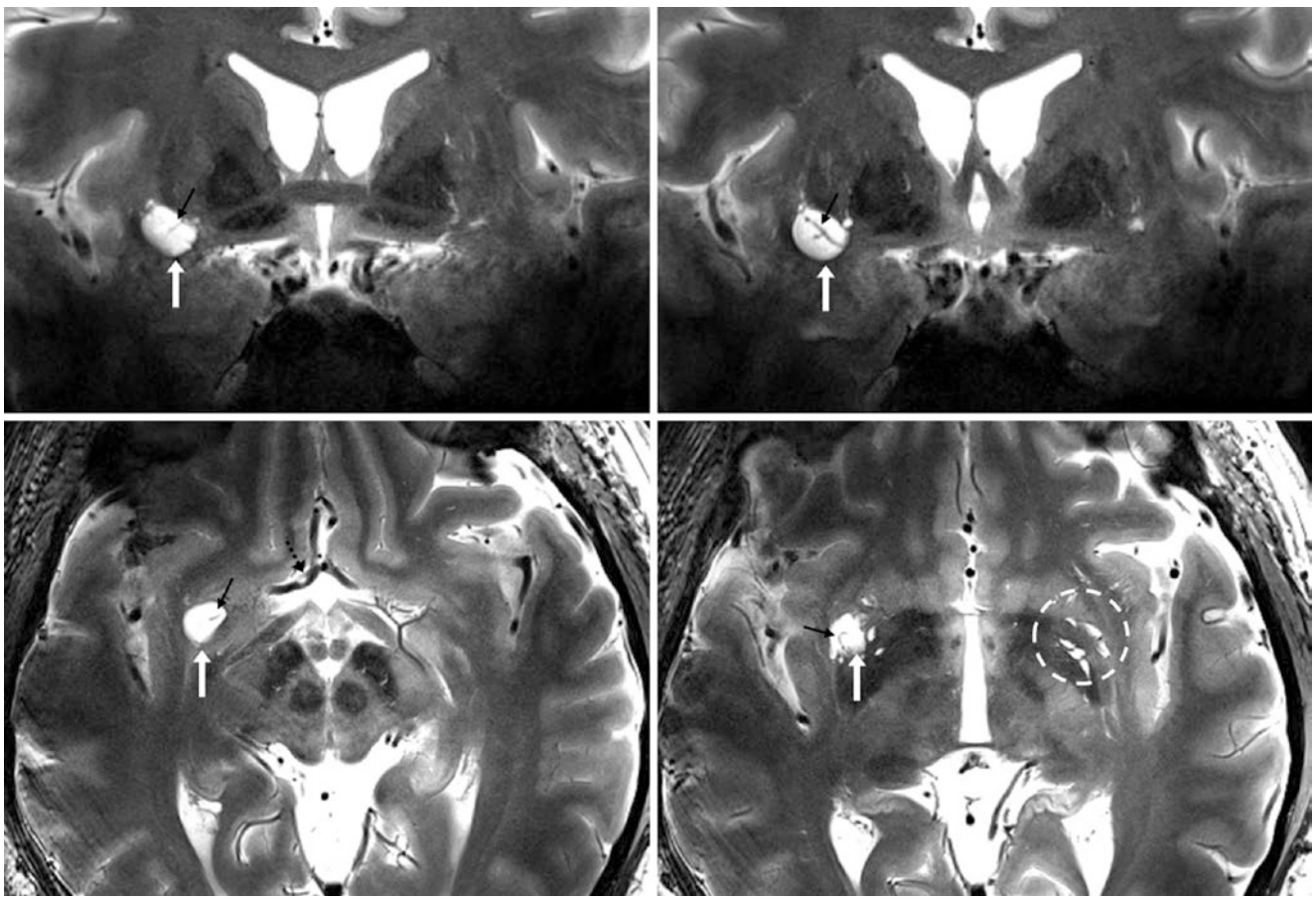

Fig. 14.7 In a 35-year-old volunteer a dilated PVS (*white arrows*) is noted on a 7T scanner within the inferior right putamen on coronal (*top row*) and on axial (*bottom row*) T2WIs. There is a tiny vessel (*tiny black arrows*) traversing the PVS centrally, probably a lenticulostriate vessel. Smaller PVSs are noted in a similar contralateral location (*dashed circle, bottom right*). Also note an incidental right ACA A1 segment fenestration (*dotted black arrow*, *bottom left*)

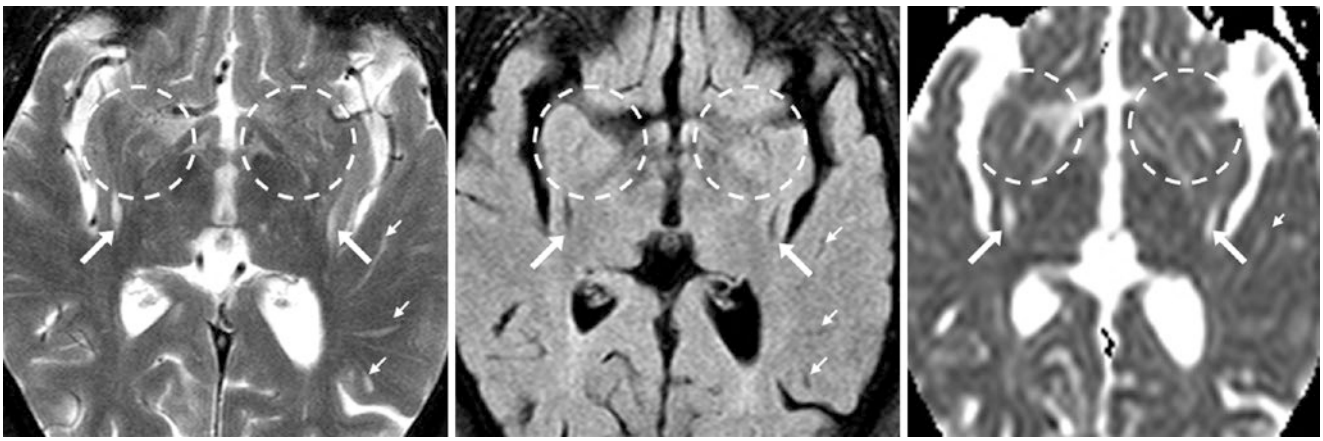

Fig. 14.8 A 52 year old had bilateral dilated PVSs of the posterior putamina/insula (*arrows*), also with poorly defined PVSs more anteriorly of the anterior perforated substance on axial T2WI (*left*). All PVSs suppress on FLAIR (*middle*) and are hyperintense on ADC maps (*right*). The ill-defined PVSs border on being *état criblé* (*dashed circles*)

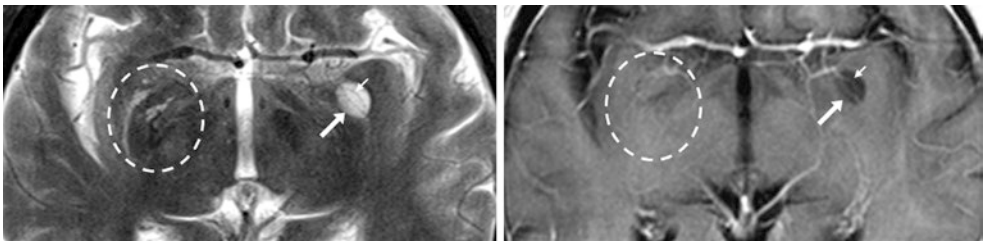

Fig. 14.9 A 65 year old had a dilated PVS (*arrows*) of the left anterior perforated substance on T2WI at 3T (*left*) and on postcontrast T1WI (*right*); it suppresses on FLAIR (*not shown*). There are tiny perforating vessels (*tiny arrows*) that traverse the PVS. Additionally, there is an appearance bordering on *état criblé* on the right (*dashed circles*)

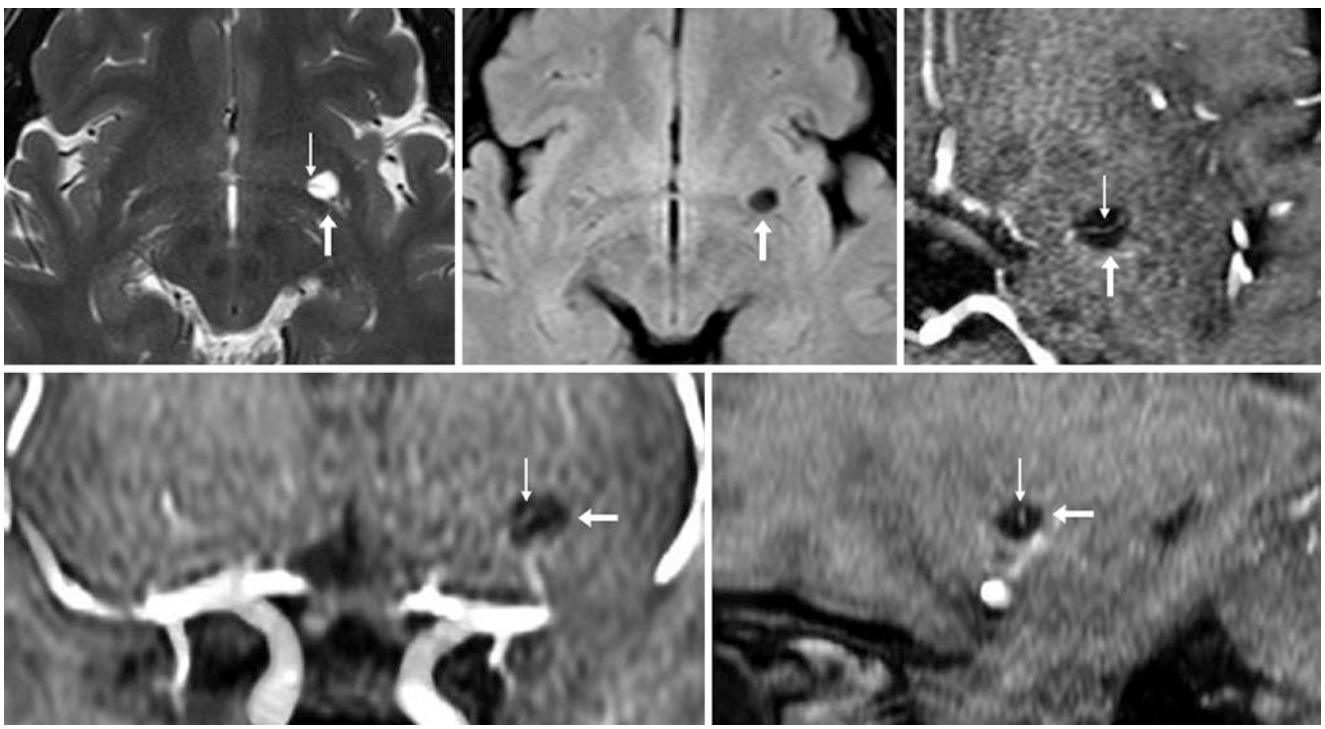

Fig. 14.10 A 30 year old with an otherwise normal MRI had a dilated PVS (*arrows*) of the left inferior putamen on T2WI (*top left*), FLAIR (*top middle*), and magnified 3D time-of-flight (TOF) MRA reconstructions in axial (*top right*), coronal (*bottom left*), and sagittal (*bottom right*) planes. A small vessel (*tiny arrows*) traverses the PVS, arising from a lenticulostriate artery

14.2 Extensive Type 1 Dilated Perivascular Spaces: *État Criblé*

The cribriform appearance (i.e., status cribrosum) of *état criblé* is characteristic on T2WI but may hardly be visible on FLAIR. It is typically associated with the elderly. The diffuse PVSs should suppress on FLAIR in the normal elderly, whereas the persistence of numerous hyperintensities on FLAIR suggests underlying multiple *lacunar infarcts* and severe *vasculopathy* (i.e., chronic small vessel ischemic disease) (Figs. 14.11, 14.12, 14.13, 14.14, 14.15, 14.16, 14.17, 14.18, 14.19, 14.20, and 14.21).

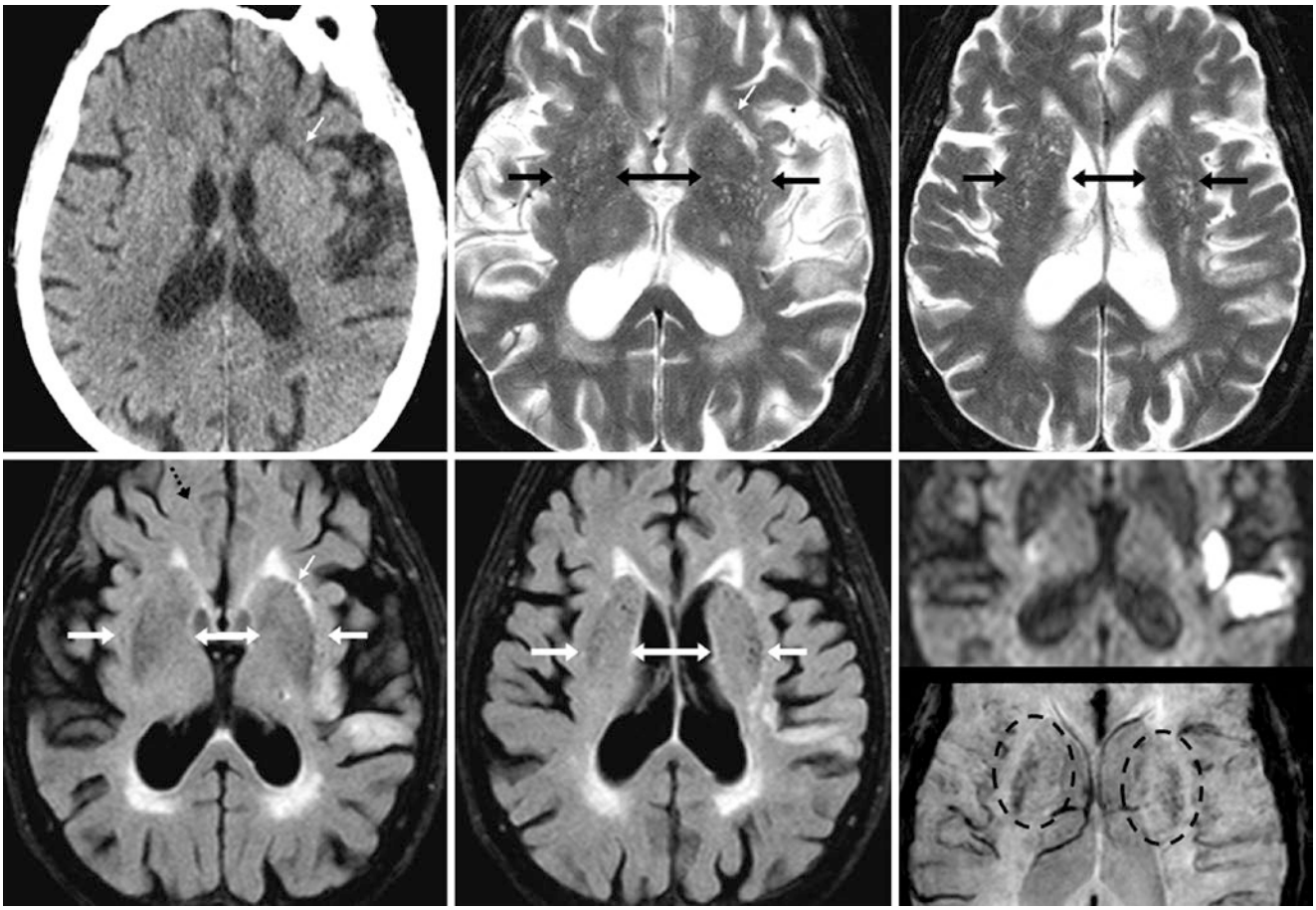

Fig. 14.11 A 92 year old had cribriform tiny PVSs (*between arrows*) throughout the basal ganglia (*état criblé),* on NECT (*top left*) and T2WI MRI (*top, middle, and right*). The PVSs mostly suppress on FLAIR (*bottom, left, and middle*); note encephalomalacia anteriorly (*tiny arrows*). DWI shows a new acute infarct (*bottom right, top image*). SWI (*bottom right, bottom image*) depicts mild putaminal iron (*dashed circles*) without hemorrhage, which is normal in the elderly. This case illustrates how *état criblé* may coexist in the setting of vasculopathy and lacunar infarcts

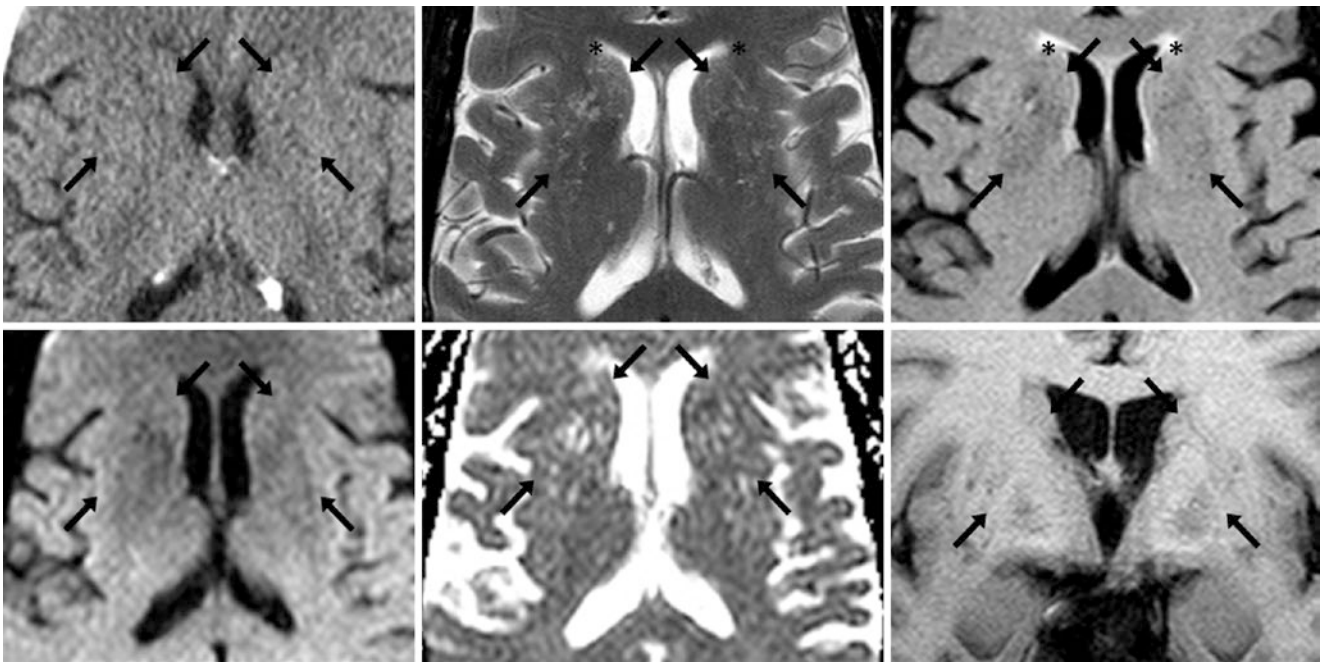

Fig. 14.12 A 76 year old had bilateral cribriform-appearing basal ganglial PVSs (i.e., *état criblé between arrows)* on NECT (*top left*), T2WI (*top middle*), FLAIR (*top right*), DWI (*bottom left*), ADC map (*bottom middle*), and coronal T1WI (*bottom right*). There are mild chronic small vessel ischemic findings/leukoariosis (*) without lacunar infarcts

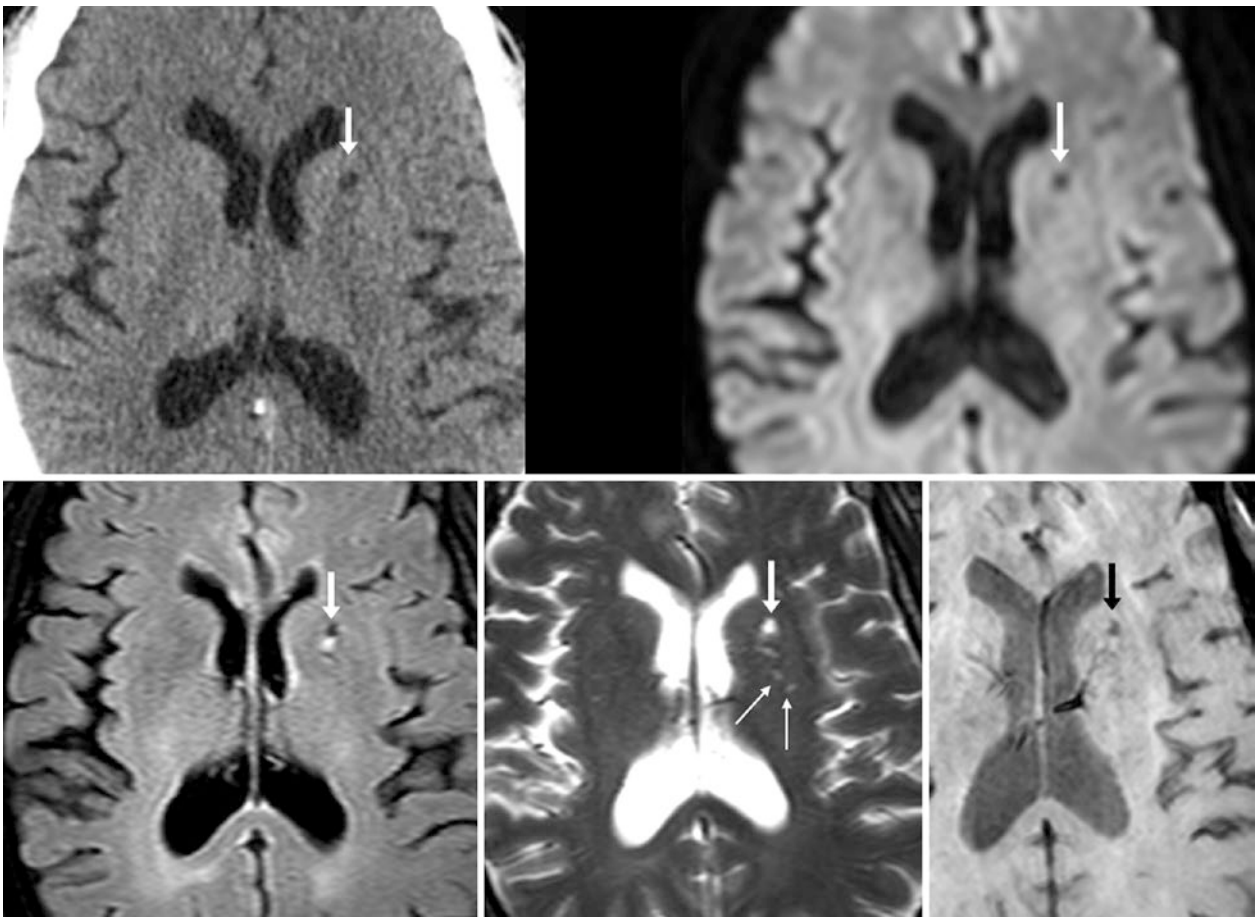

Fig. 14.13 Comparison case of lacunar infarct. A 54 year old had a lacune (*dashed arrows*) identified on NECT (*top left*), as its density was greater than that of the CSF. On MRI it was dark on DWI MRI (*top right*), bright on FLAIR (*bottom left*), and had CSF-like signal on T2WI (*bottom middle*) with tiny PVSs posteriorly (*thin arrows*). There was no definite hemorrhage associated on SWI, where the signal appeared to be that of CSF (*bottom right*)

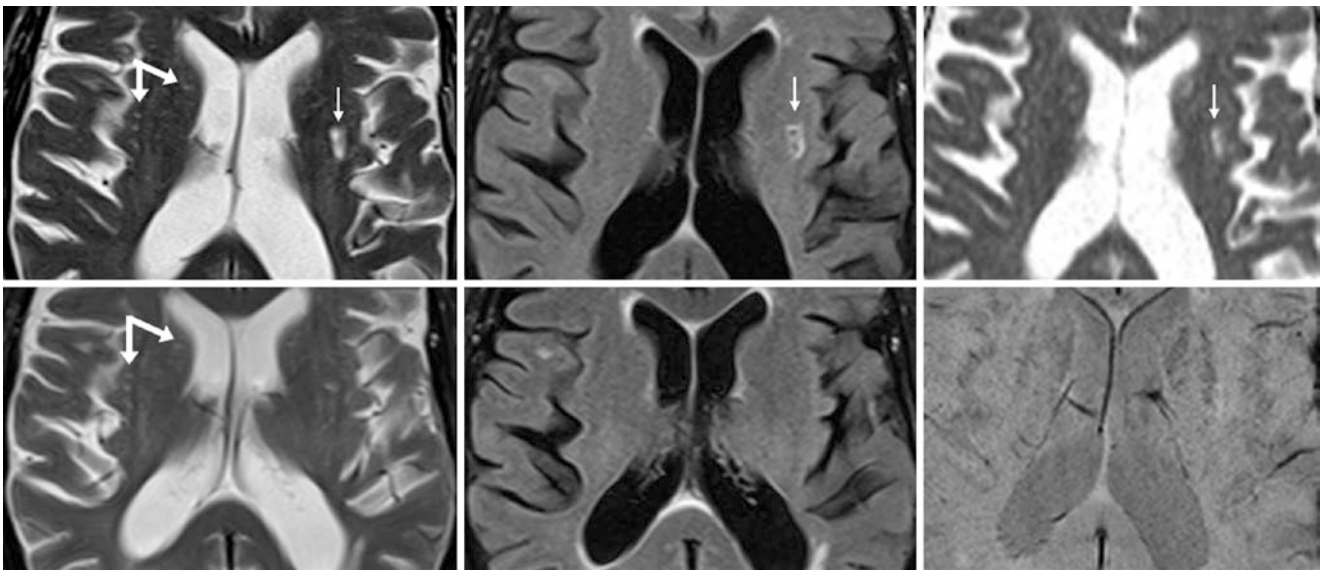

Fig. 14.14 Comparison case of lacunar infarct. A 51 year old had a small left putaminal lesion (*thin arrows*) on 1.5T MRI T2WI (*top left*) that was bright on FLAIR (*top middle*) and ADC map (*top right*). It was new from images that were done 9 months prior on T2WI (*bottom left*), FLAIR (*bottom middle*) and SWI (*bottom right*). Note tiny PVSs in the right putamen (*arrows*)

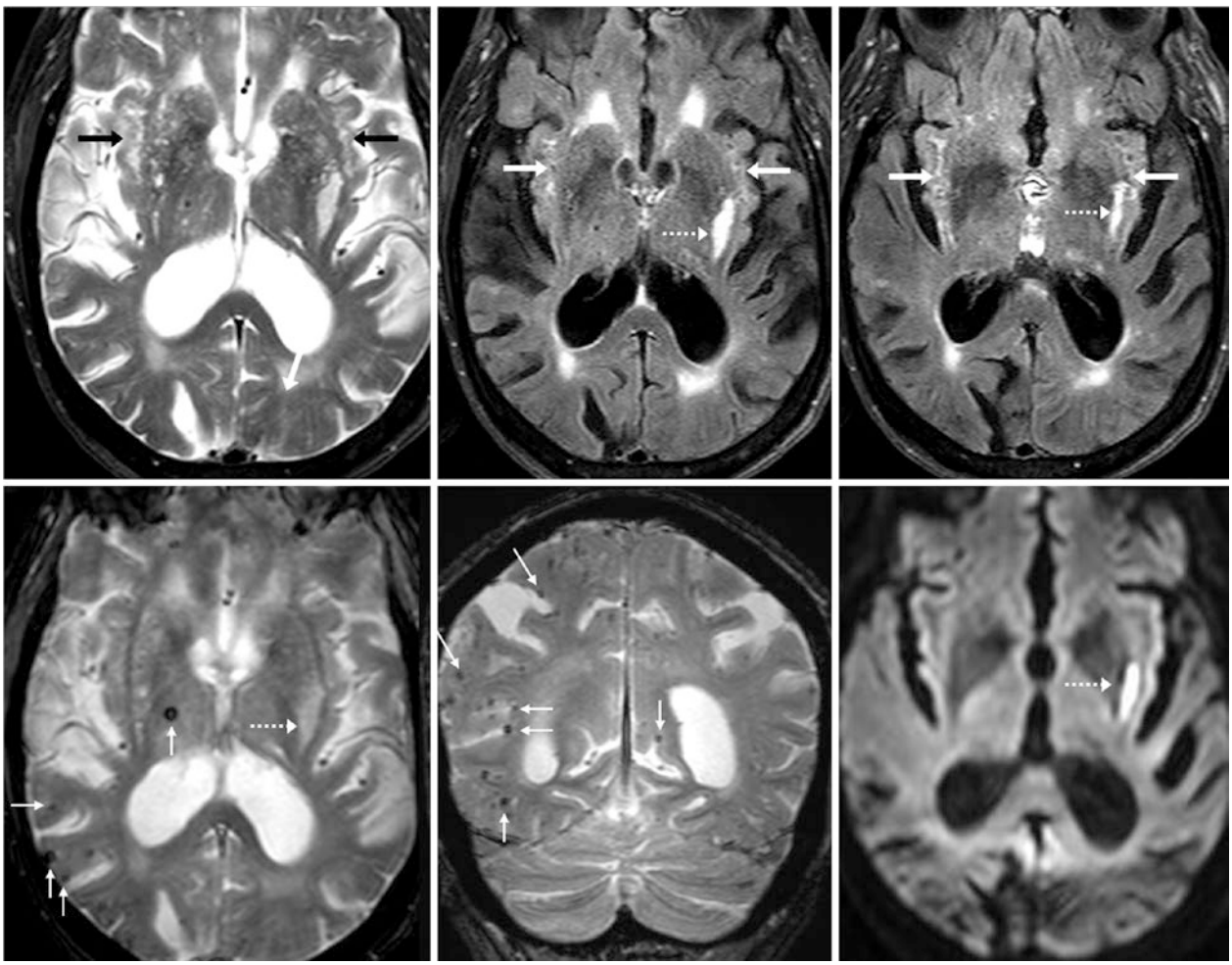

Fig. 14.15 Comparison case of vascular dementia, stroke, and *état criblé*. An 82 year old with dementia had a diffuse, cribriform appearance of PVSs (*arrows*) throughout the basal ganglia, as shown on axial T2WI (*top left*), which mostly suppress on FLAIR (*top middle, and right*). Note numerous microhemorrhages (*tiny arrows*) on axial and coronal T2*WIs (*bottom left and middle*), with a superimposed acute infarct (*dotted arrows*) on DWI (*bottom right*)

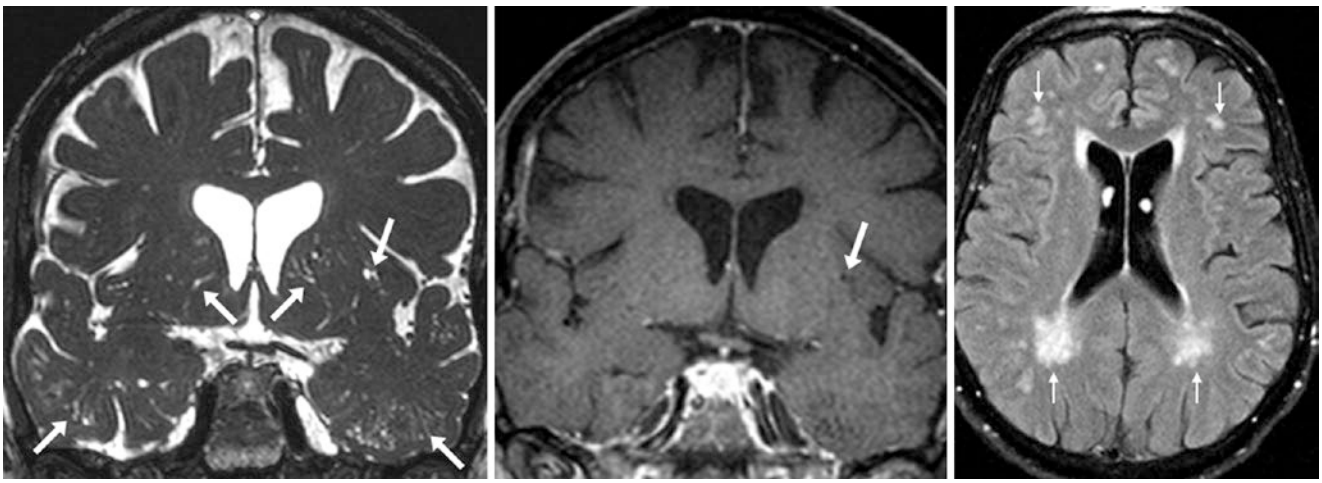

Fig. 14.16 Comparison case of leukoariosis superimposed on diffuse PVSs (*état criblé*). A 73 year old had a diffuse, cribriform appearance of PVSs throughout the basal ganglia (*état criblé*) and the subcortical white matter on a 0.8-mm thickness coronal T2WI (*left*). The PVSs are nearly invisible on T1WI (*middle*) and FLAIR (*right*), although extensive findings of chronic small vessel ischemic disease (leukoariosis) are noted on FLAIR (*tiny arrows*)

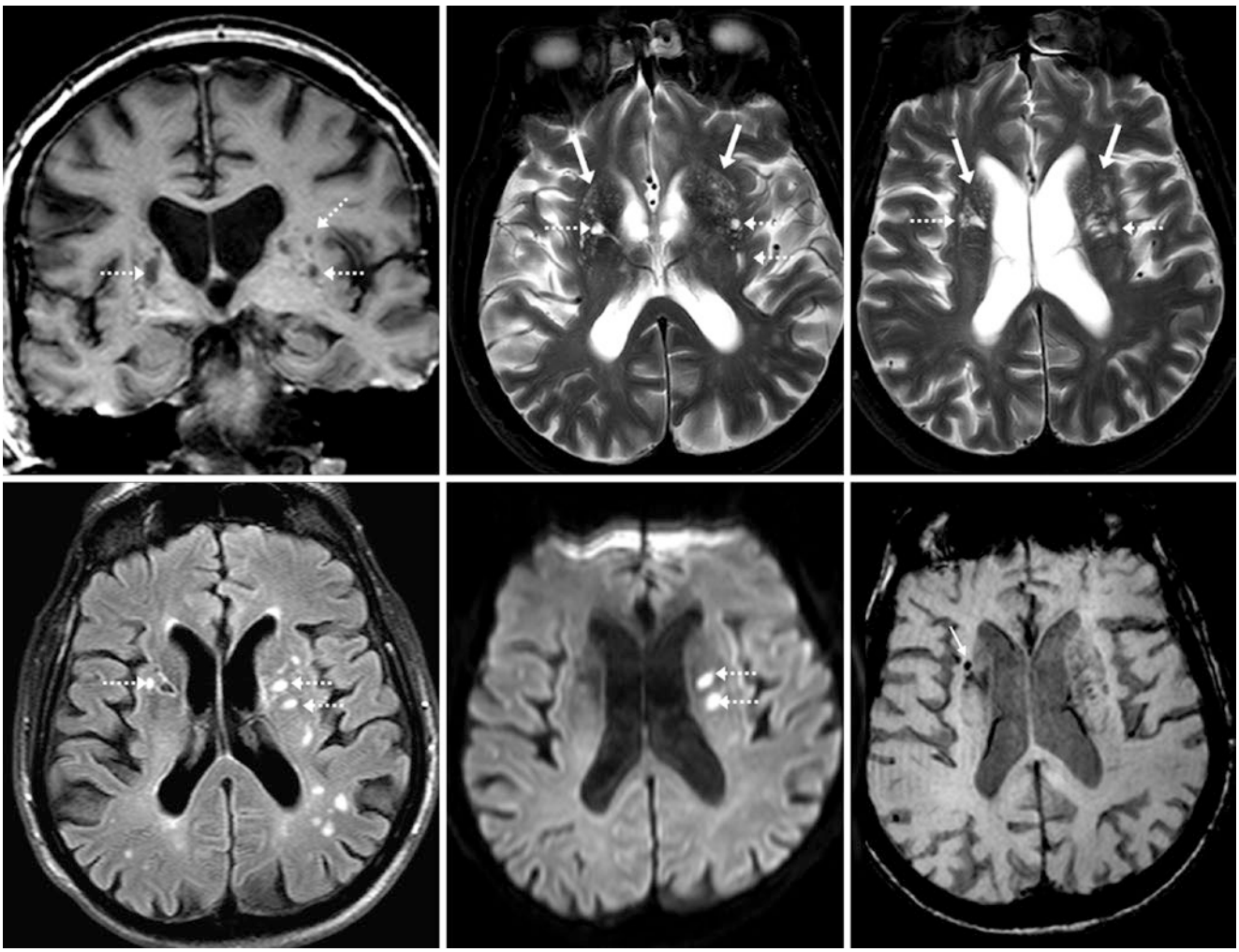

Fig. 14.17 Comparison case of acute lacunar infarcts superimposed on PVSs (*état criblé*). A 69 year old had diffuse, PVSs (*solid arrows*) of the basal ganglia on T1WI (*dashed arrows, top left*) and T2WI (*top middle and top right*), but within the left putamen some did not suppress on FLAIR (*bottom left*), while two had reduced diffusion, indicating acute infarcts (*bottom middle*). A right putaminal lesion had remote gliosis on FLAIR, with remote microhemorrhage on SWI (*tiny arrow, bottom right*). This case illustrates how *état criblé* may coexist with acute lacunar infarcts

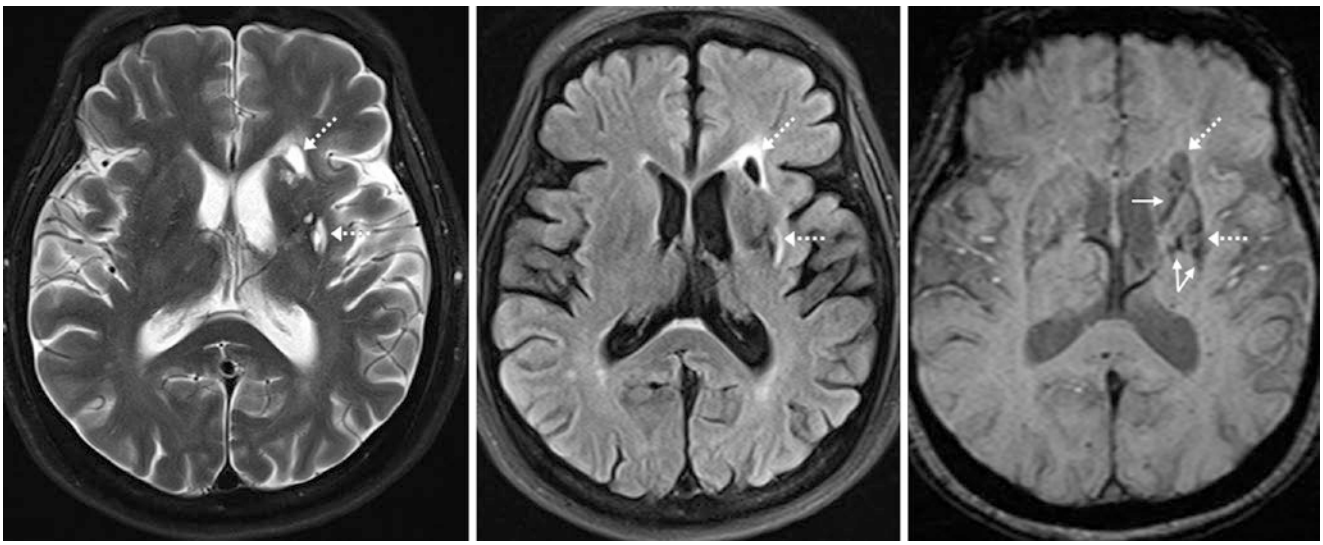

Fig. 14.18 Comparison case of chronic lacunar infarcts. A 59 year old with dementia had chronic lacunar infarcts (*dotted arrows*) on T2WI (*left*), with mild surrounding hyperintense signal on FLAIR (*middle*) caused by resultant gliosis. Note that on SWI (*right*), these lacunar infarcts also contain internal remote punctate microhemorrhages (*thin arrows*)

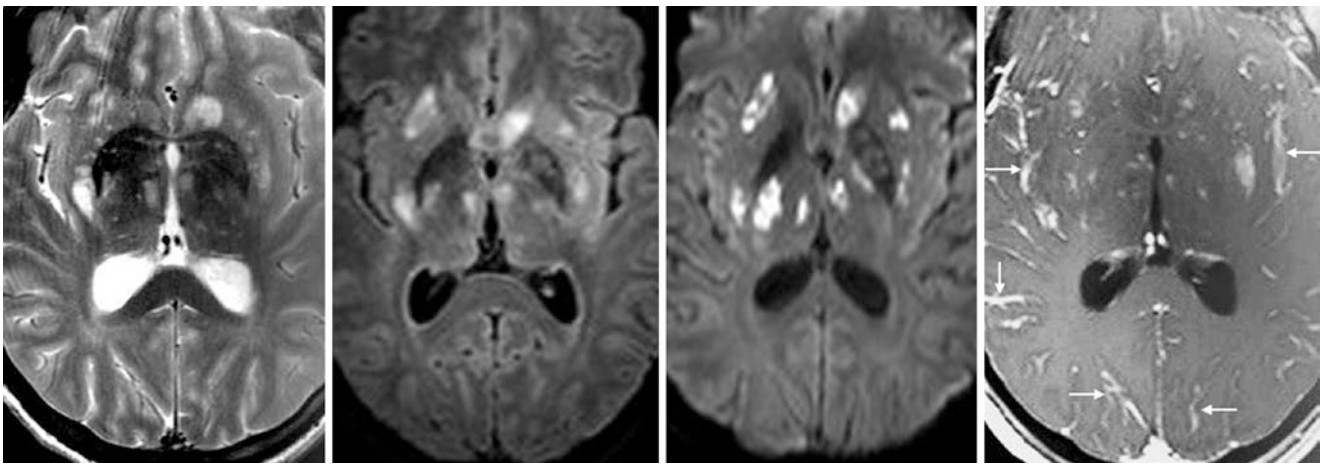

Fig. 14.19 Comparison case of cryptococcal meningitis. On a 3T MRI, an HIV+ 33 year old had numerous bright basal ganglia lesions on T2WI (*left*), which were also bright on FLAIR (*left middle*) and DWI (*right middle*). On postcontrast T1WI (*right*), most lesions enhanced. There was also abnormal enhancement of the leptomeninges (*thin arrows*)

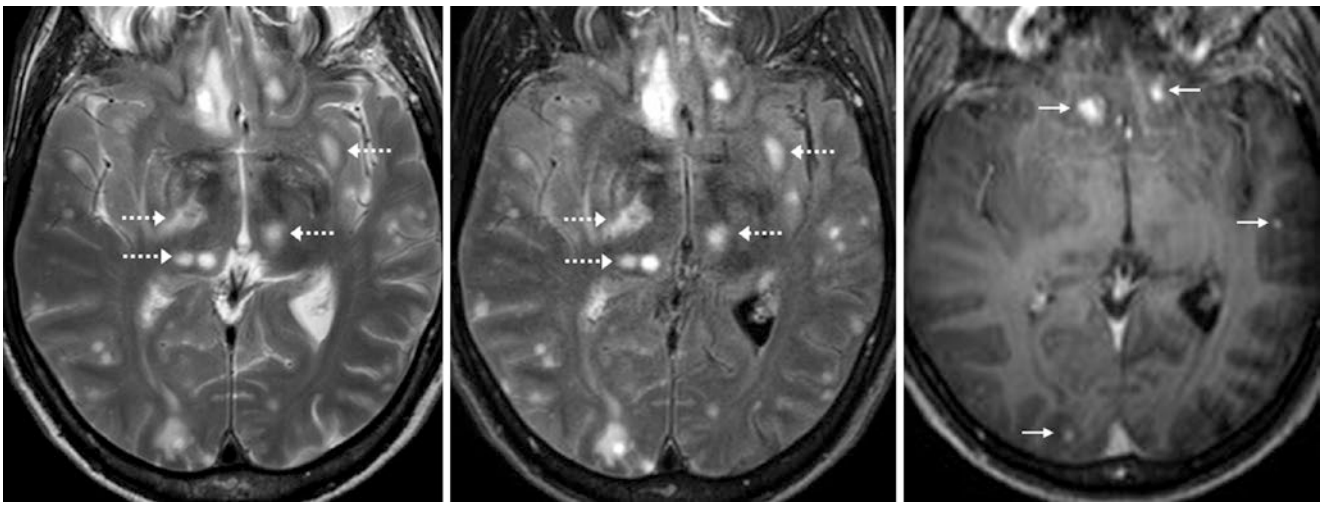

Fig. 14.20 Comparison case of central nervous system toxoplasmosis. An immunocompromised 42 year old had numerous hyperintense lesions throughout the basal ganglia (*dotted arrows*) as well as throughout the subcortical white matter on a 3T MRI with axial T2WI (*left*) and FLAIR (*middle*). On postcontrast T1WI (*right*), some lesions enhanced (*thin arrows*)

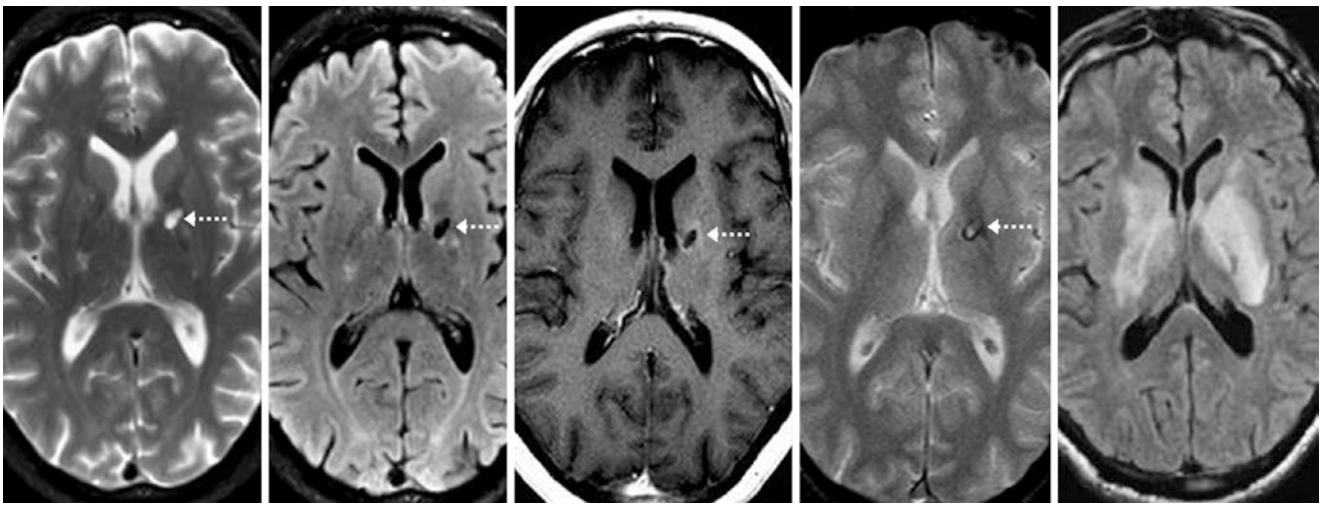

Fig. 14.21 Comparison case of neuro-Behçet syndrome sequela. In a 40-year-old male with prior neuro-Behçet a focal hyperintensity was seen within the left basal ganglia (*dotted arrows*) on a 1.5T MRI with axial T2WI (*left*) and FLAIR (*left middle*), with faint surrounding enhancement on postcontrast T1WI (*middle*) and hemorrhage on GE T2*WI (*right middle*). An MRI 2 years prior at the time of onset of disease showed edema of the basal ganglia on FLAIR (*right*)

14.3 Dilated Perivascular Spaces: Type II

PVSs within the s*ubcortical white matter* (SCWM*)* and deep *periventricular white matter* (PVWM) are considered type II. These are quite common and can be seen with increasing frequency the higher the field strength, resolution, and age. Although as yet there may not be substantial literature on this in children, they are not uncommon in adolescents, particularly at higher field strengths. Such type II PVSs are easily distinguished from *demyelinating lesions* such as MS, even though their distribution may be similar by their complete suppression/darkening along with CSF on FLAIR with lack of residual hyperintensity, which is always present in MS lesions (Figs. 14.22, 14.23, 14.24, 14.25, 14.26, 14.27, 14.28, 14.29, 14.30, 14.31, 14.32, 14.33, 14.34, 14.35, 14.36, 14.37, 14.38, 14.39, 14.40, 14.41, 14.42, 14.43, and 14.44).

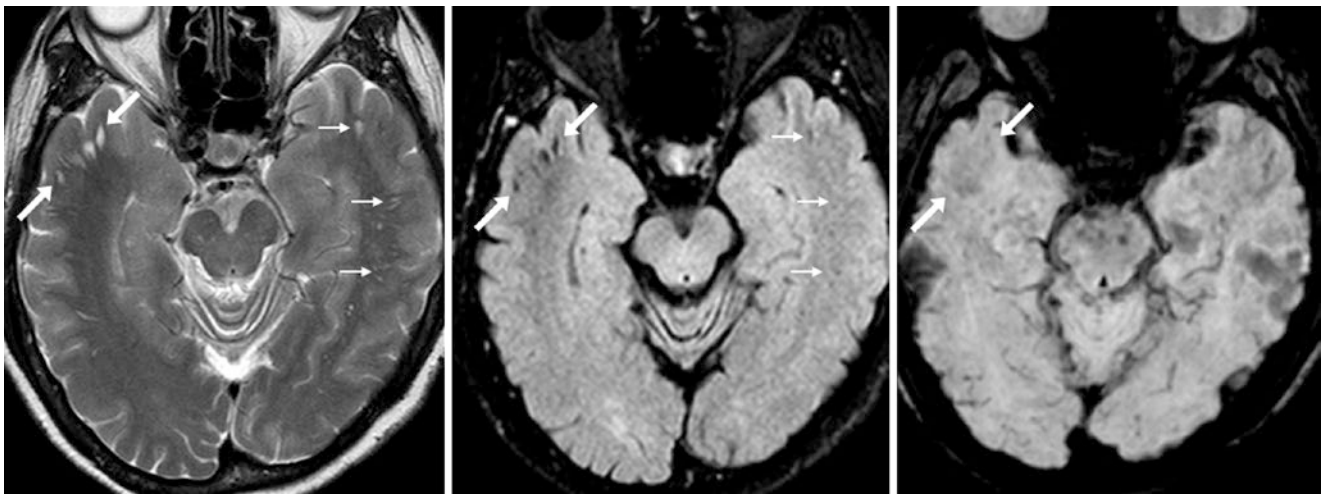

Fig. 14.22 A 57 year old had dilated PVSs of the temporal subcortical white matter bilaterally (between *arrows* on the right side and *thin arrows* on the left), seen as radiating foci that are hyperintense on T2WI (*left*), suppress on FLAIR (*middle*), and are invisible on SWI (*right*) and DWI. These were unchanged on an MRI 1 year later (*not shown*)

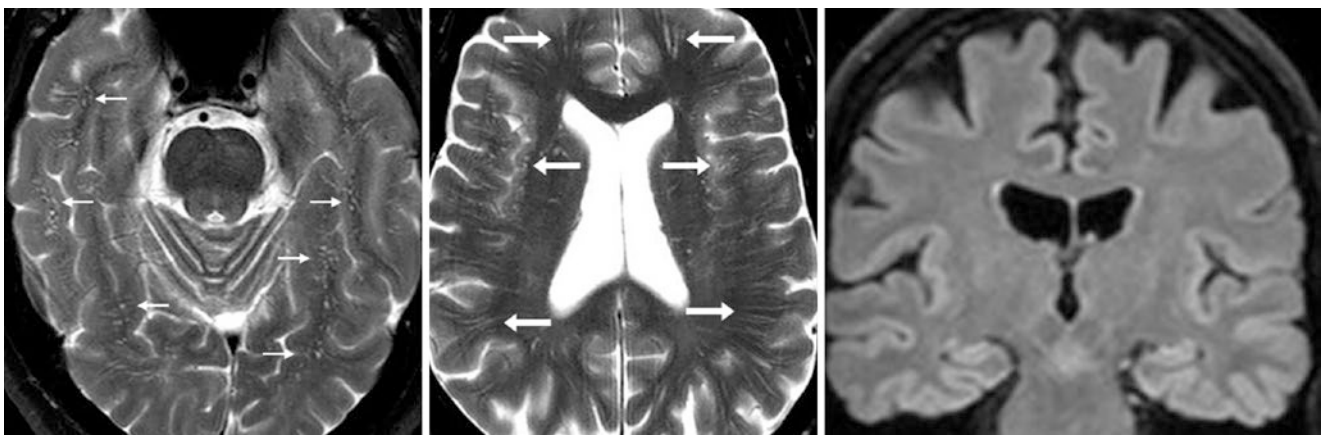

Fig. 14.23 A 62 year old had innumerable slightly dilated PVSs on a 3T MRI with T2WIs (*left and middle*). The PVSs were located throughout the temporal white matter (*thin arrows, left*) and frontoparietal white matter (*arrows, middle*). These appear as radiating ovoid foci that are hyperintense on T2WI and nearly disappear on coronal FLAIR (*right*)

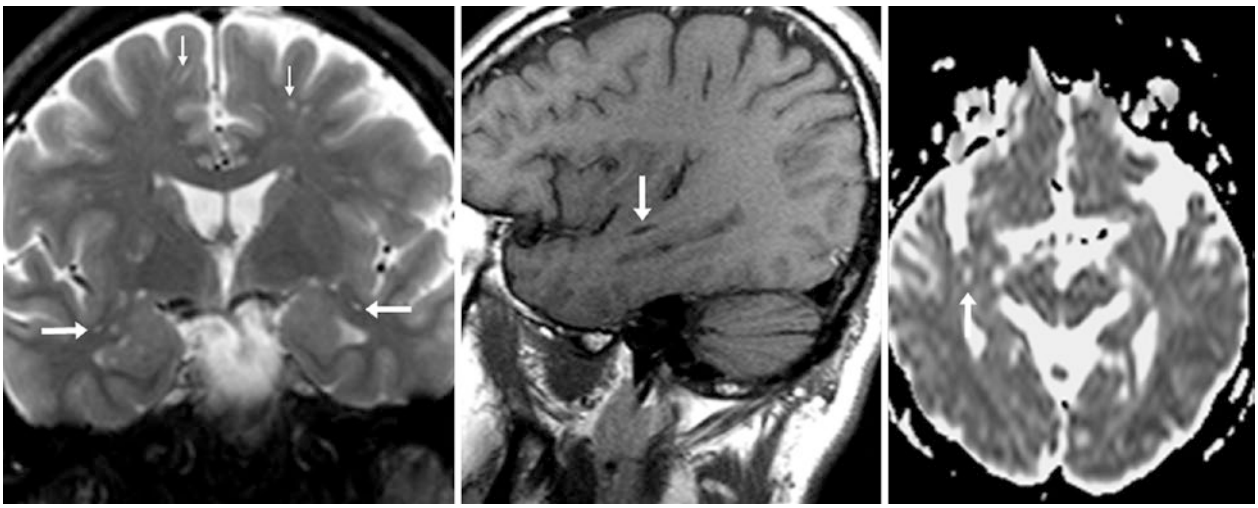

Fig. 14.24 A 48 year old had bilateral dilated PVSs within the deep white matter of the temporal stems (*arrows*) bilaterally on coronal T2WI (*left*) and sagittal T1WI (*middle*), with increased diffusion on an ADC map (*right*). On the T2WI, smaller PVSs with a radiating appearance (*tiny arrows*) are visualized within the subcortical frontal white matter

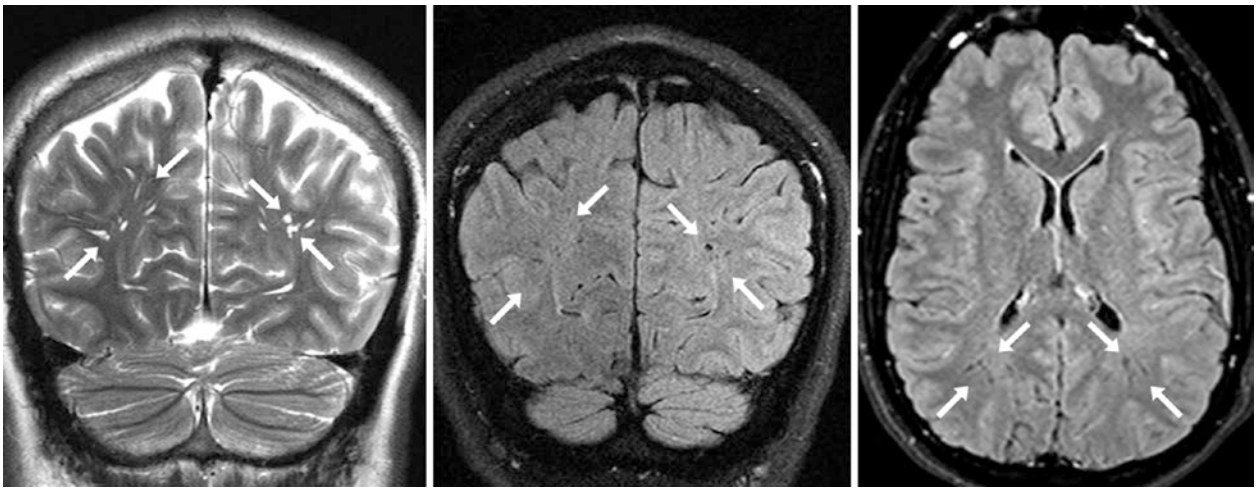

Fig. 14.25 A 24 year old had PVSs of the parieto-occipital white matter bilaterally (*between arrows*) on a 3T MRI. The PVSs are radiating ovoid foci on coronal T2WI (*left*) that suppress on coronal (*middle*) and axial (*right*) FLAIR images

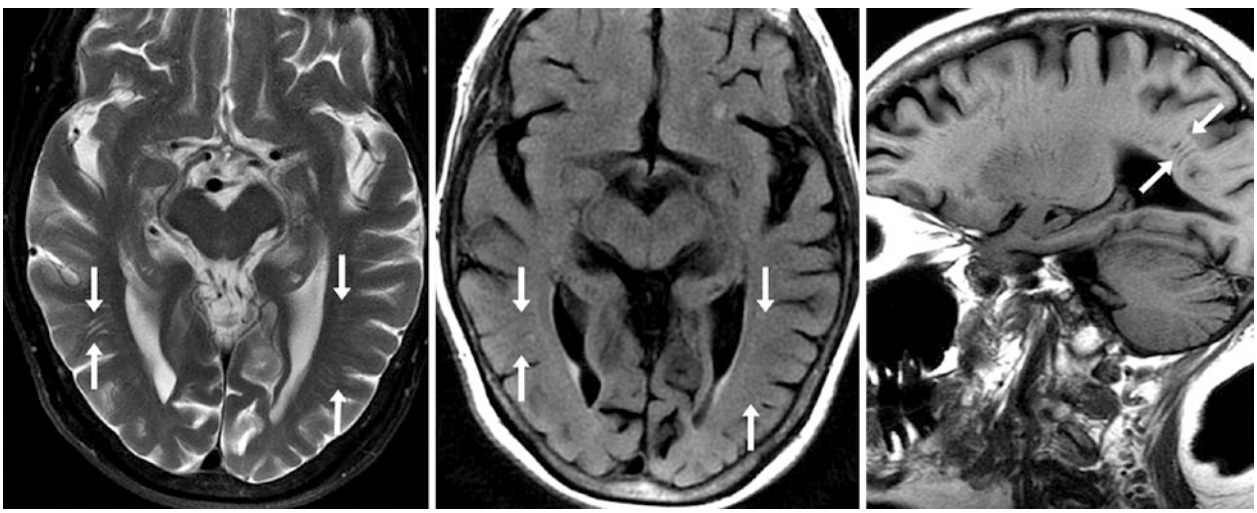

Fig. 14.26 A 73 year old had bilateral PVSs located within the deep temporal white matter (*between arrows*). The PVSs are ovoid, radiating foci on T2WI (*left*) that suppress on FLAIR (*middle*). They appear linear on sagittal T1WI (*right*)

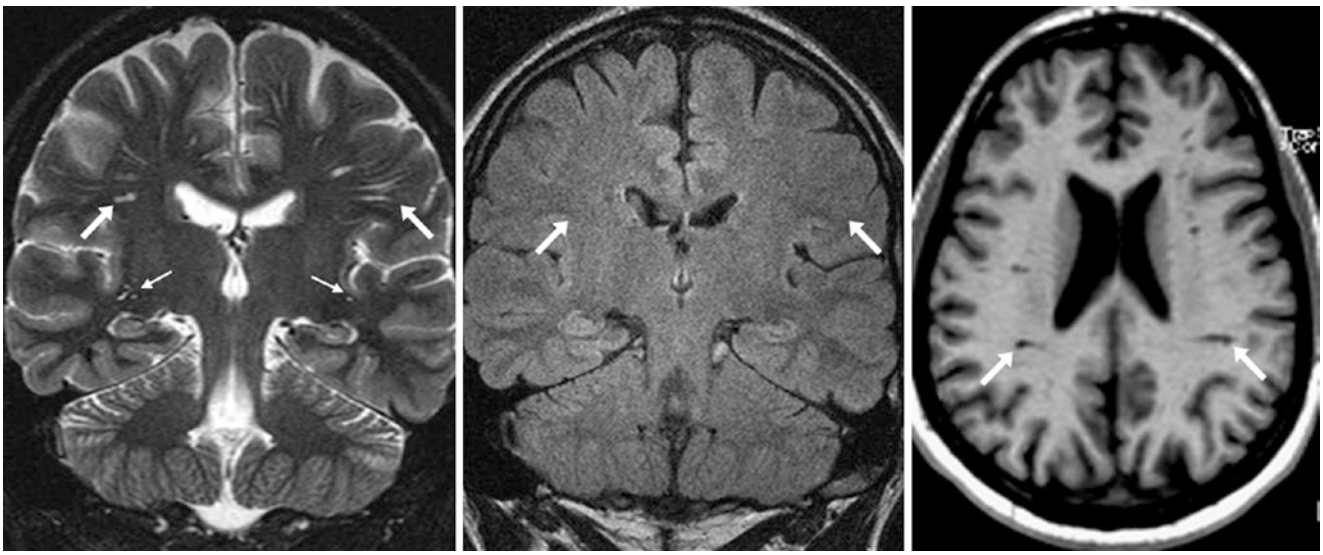

Fig. 14.27 A 35 year old had dilated PVSs within the posterior frontal and anterior parietal white matter bilaterally (*arrows*). They appear radiating and ovoid and are hyperintense on coronal T2WI (*left*), suppress on FLAIR (*middle*), and are nearly as dark as CSF on T1WI (*right*). Tiny PVSs are also noted within the temporal stems (*tiny arrows*)

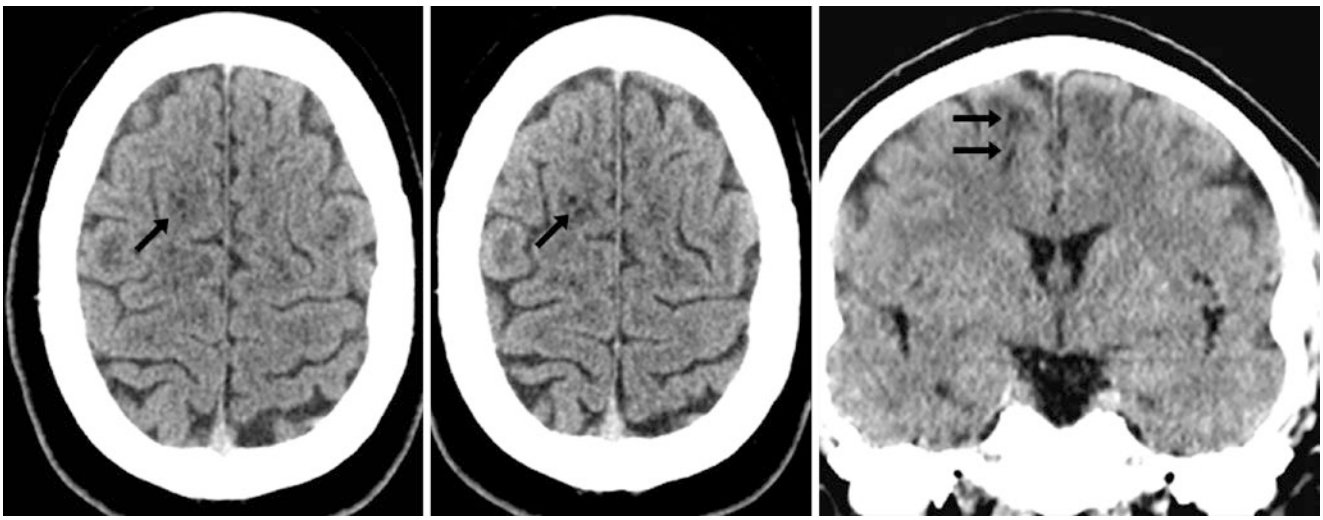

Fig. 14.28 A 41 year old with dilated PVSs within the right frontal subcortical white matter (*arrows*) on axial (*left and middle*) and coronal (*right*) NECT images. The coronal reformat illustrates their linear and radiating appearance. There are no definite findings of chronic small vessel disease (i.e., leukoariosis) or lacunar infarcts, which PVSs can mimic

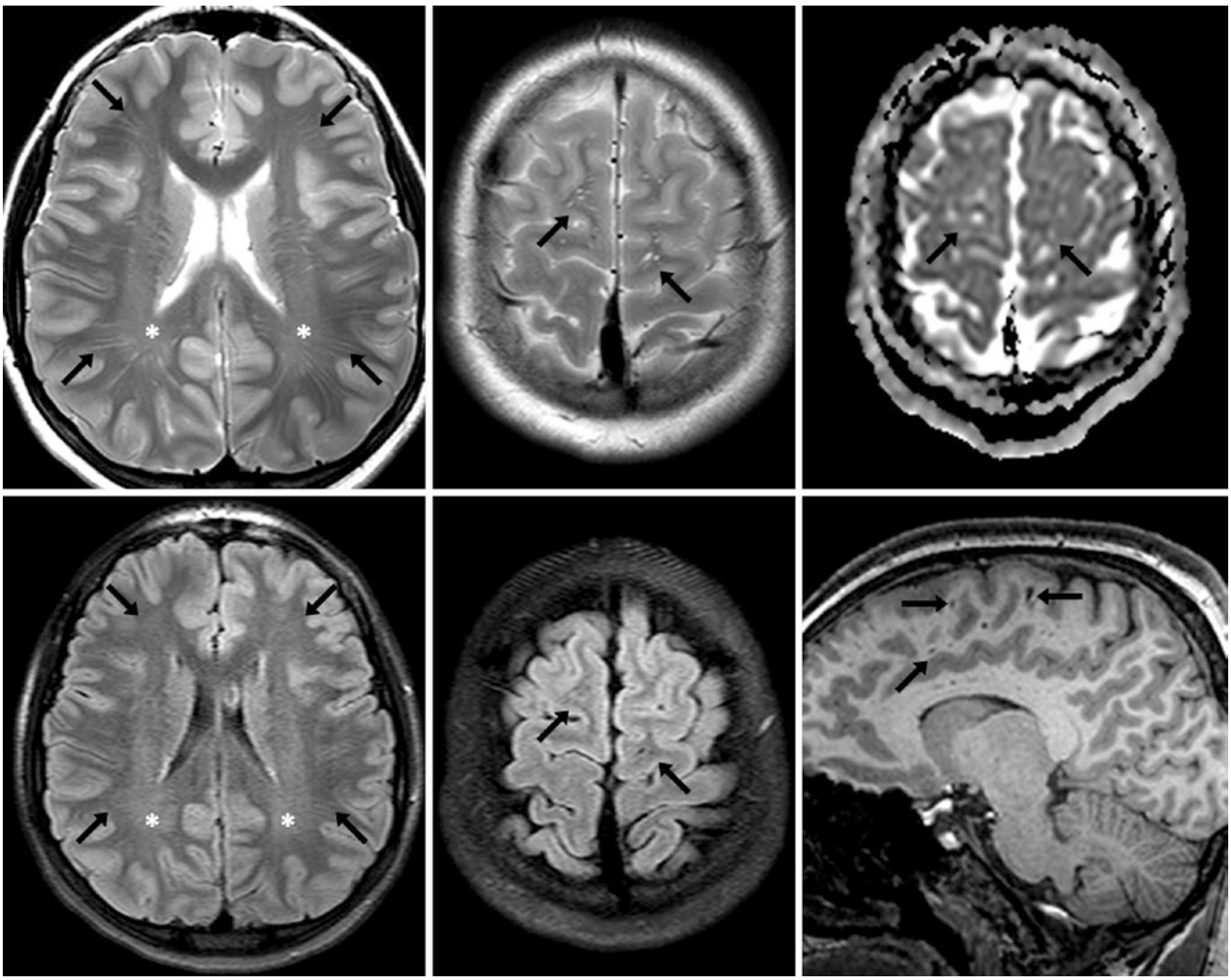

Fig. 14.29 A 13 year old had mildly dilated PVSs throughout the subcortical white matter (*arrows*) on 3T MRI axial T2WIs (*top, left two images*), being nearly invisible on FLAIR (*bottom, left two images*). These appear to radiate from the lateral ventricles and corpus callosum. Axial ADC maps (*top right*), FLAIR, and sagittal T1WIs (*bottom right*) confirmed their CSF-like signal. This boy had new seizures; note mildly hyperintense periventricular terminal zones (*), a normal variant. Notably, subcortical PVSs can mimic the radial bands seen in tuberous sclerosis

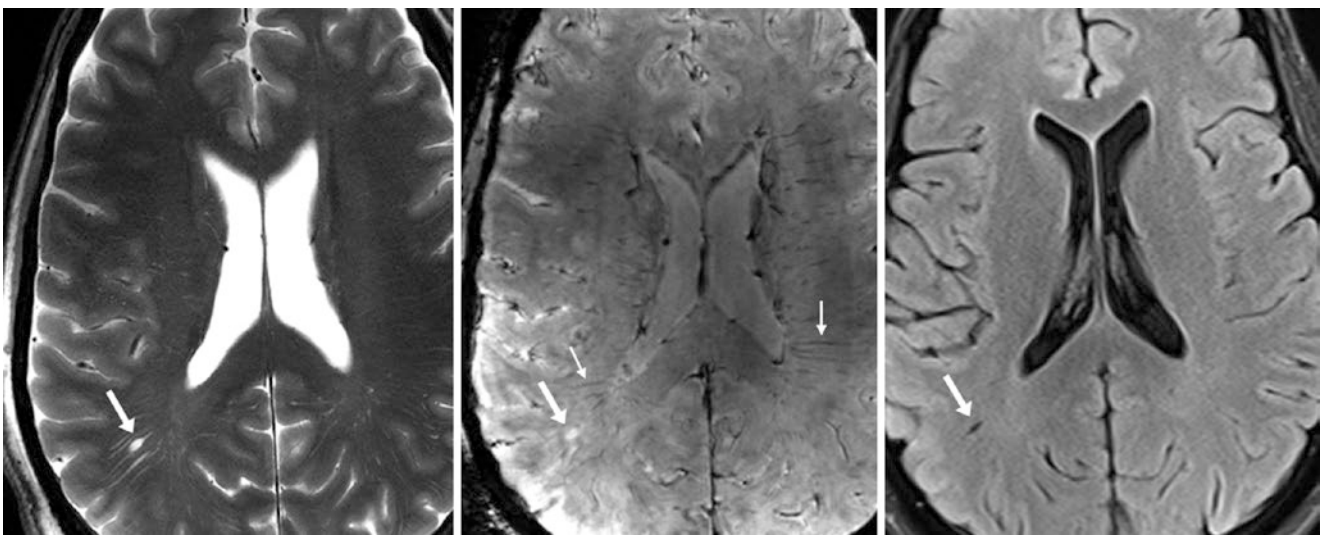

Fig. 14.30 A 59 year old had dilated PVSs within the right parietal deep white matter bilaterally (*arrows*) on a 7T T2WI MRI (*left*), seen as radiating, ovoid, and linear foci similar in orientation to radiating perimedullary veins (*thin arrows*) on SWI (*middle*). These PVSs suppress on 3T FLAIR images from a different magnet (*right*) in the same patient

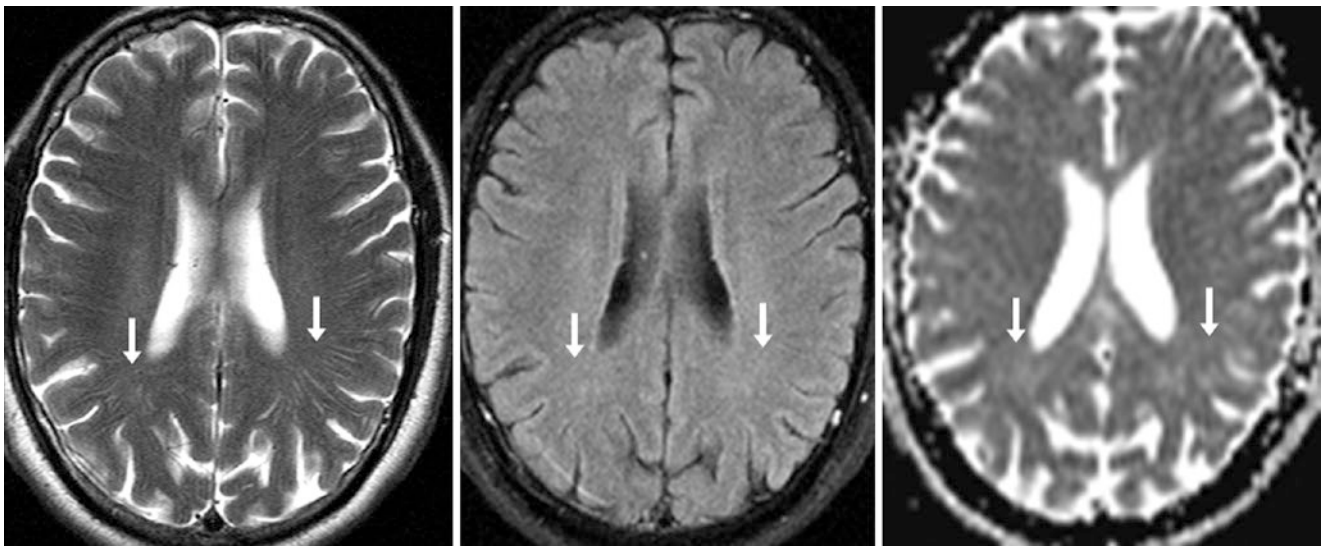

Fig. 14.31 A 62 year old had dilated PVSs within the parietal-occipital subcortical white matter bilaterally (*arrows*) on T2WI (*left*), seen as radiating, ovoid, and linear foci that suppress and are nearly invisible on FLAIR (*middle*), along with increased diffusion on ADC maps (*right*). Such discrete, type II PVSs can be seen in patients of nearly any age

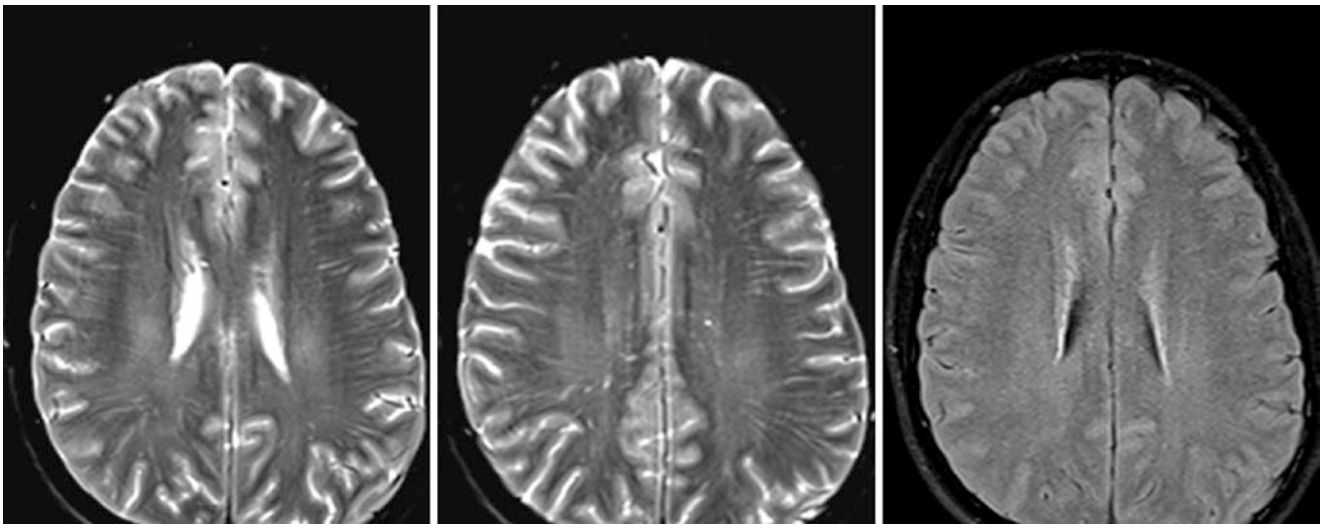

Fig. 14.32 A 23 year old had extensive radiating hyperintensities throughout the deep white matter of the supraventricular white matter on 3T MRI T2WI (*left and middle*), which suppress on FLAIR (*right*). If one is solely viewing the T2WIs, the findings could resemble the radiating bands (abnormal migration tracts) of tuberous sclerosis. However, note the lack of cortical abnormalities (tubers) on FLAIR

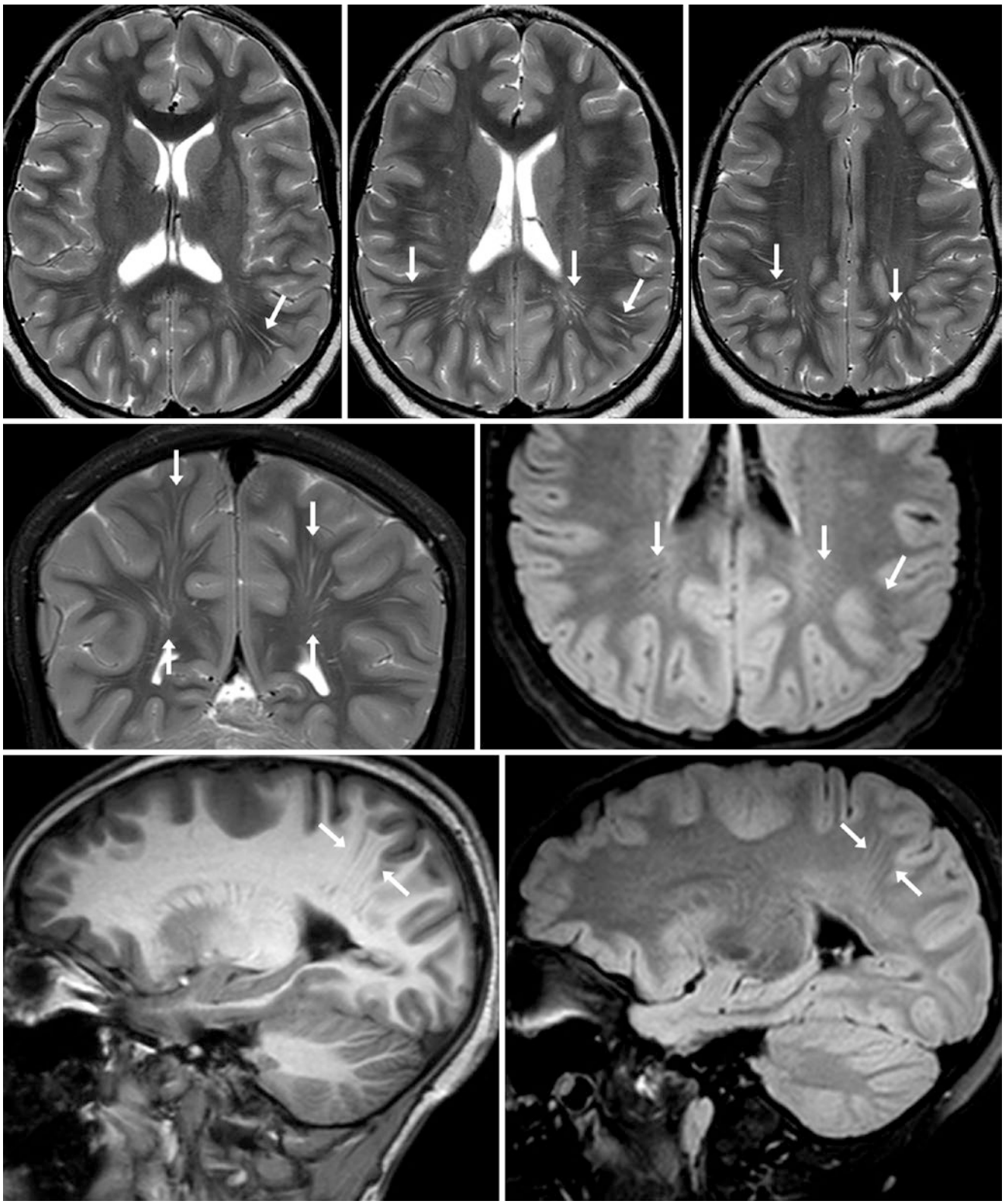

Fig. 14.33 The patient is an 8-year-old normal boy with a history of seizures. *Top row:* on a 3T MRI, there are bilateral dilated PVSs within the deep parietal white matter (*arrows*) on T2WI. Note their linear appearance that radiates from the lateral ventricles and the lack of overlying cortical atrophy or gliosis. The MRI was otherwise interpreted as normal. *Middle row:* on coronal T2WI (*left*), the dilated PVSs within the deep parietal white matter (*between arrows*) are rather diffuse but suppress on a reconstructed axial 3D FLAIR image (*right*). *Bottom row:* on sagittal 3D T1WI (*left*) and 3D FLAIR (*right*), the dilated PVSs are delineated but are still not as well visualized as on the T2WIs

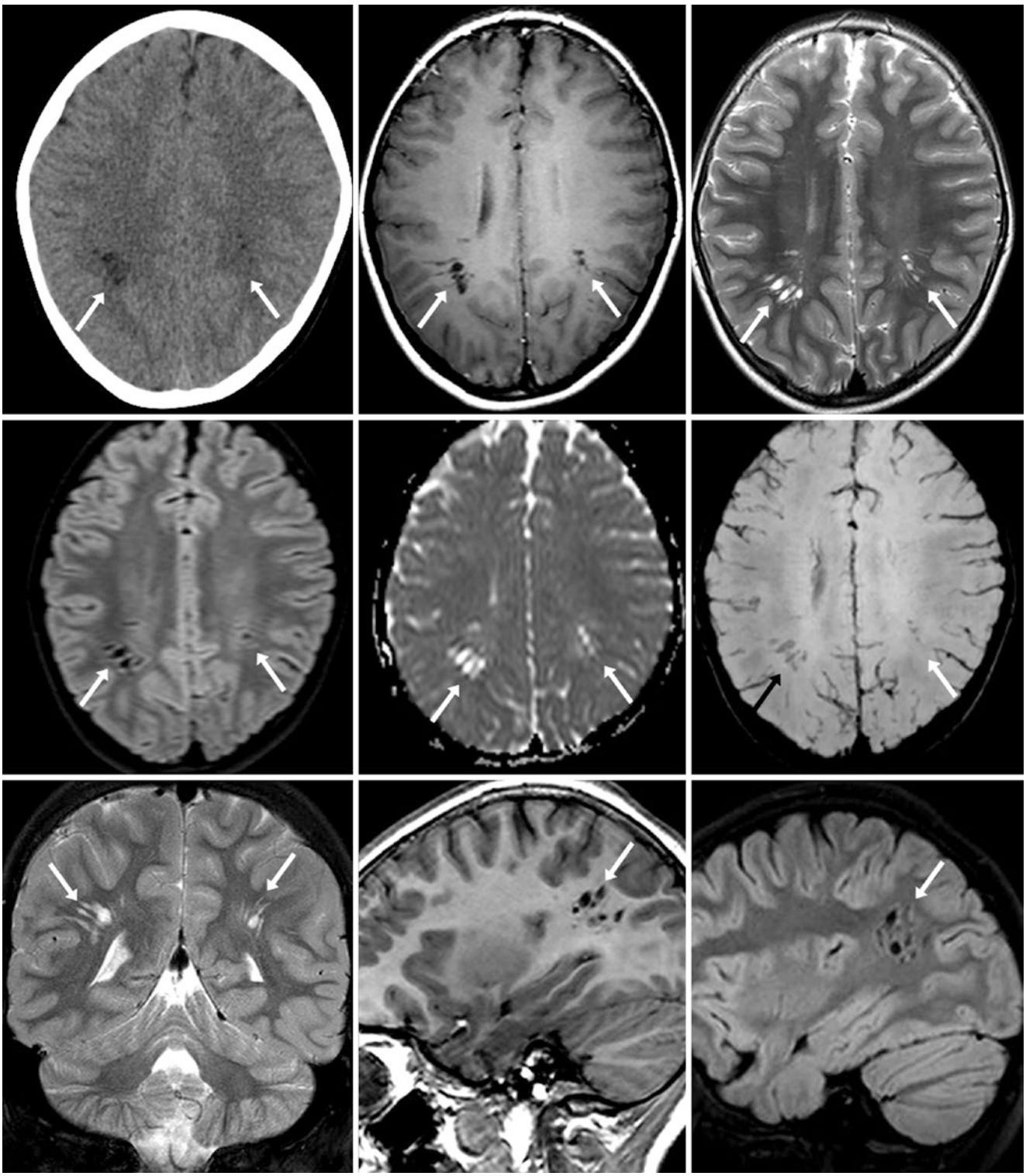

Fig. 14.34 The patient is an 8-year-old otherwise normal boy with headaches. *Top row:* there are bilateral dilated PVSs within the deep parietal white matter (*arrows*) on NECT (*left*), and on 3T MRI with T1WI (*middle*) and T2WI (*right*). *Middle row:* the PVSs are radiating, ovoid, and orient perpendicular to the ventricles on DWI (*left*), an ADC map (*middle*), and SWI (*right*). *Bottom row:* on coronal T2WI (*left*), sagittal three-dimensional T1WI MRI (*middle*) and FLAIR (*right*), the signal intensity is akin to that of CSF, as the PVSs suppress on FLAIR. The coronal T2WI also illustrates their orientation perpendicular to the ventricles. This patient's symptoms were deemed to be from migraines, with the PVSs being a normal variation

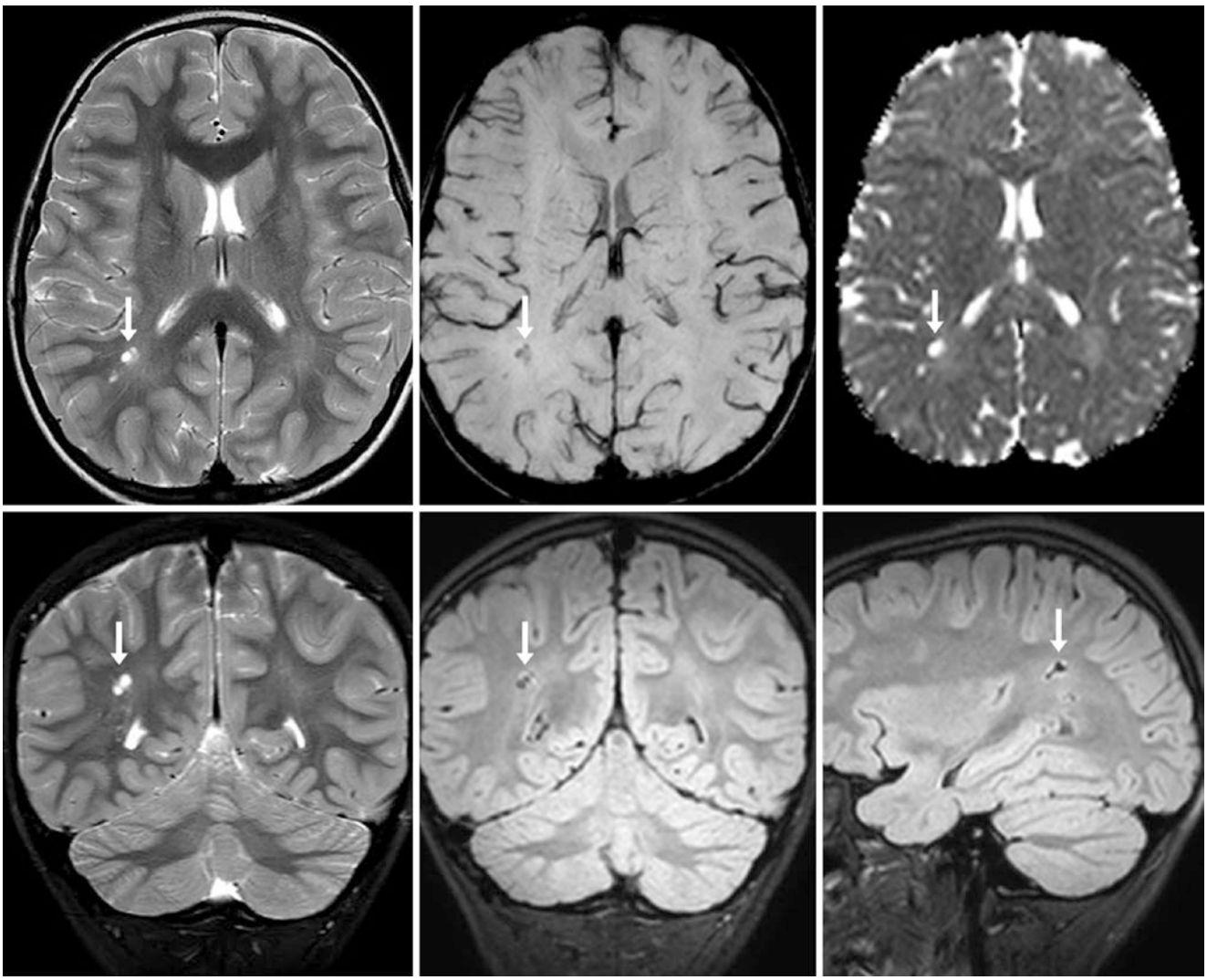

Fig. 14.35 A 6 year old with nonspecific headaches had focally dilated PVSs within the right periatrial white matter (*arrows*) on a 3T MRI with axial T2WI (*top left*), SWI (*top middle*), an ADC map (*top right*), coronal T2WI (*bottom left*), coronal three-dimensional FLAIR (*bottom middle*), and sagittal three-dimensional FLAIR (*bottom right*). Because the foci suppress with CSF and do not have a surrounding bright signal on FLAIR, they are consistent with dilated PVSs. Note the lack of hemorrhage on SWI

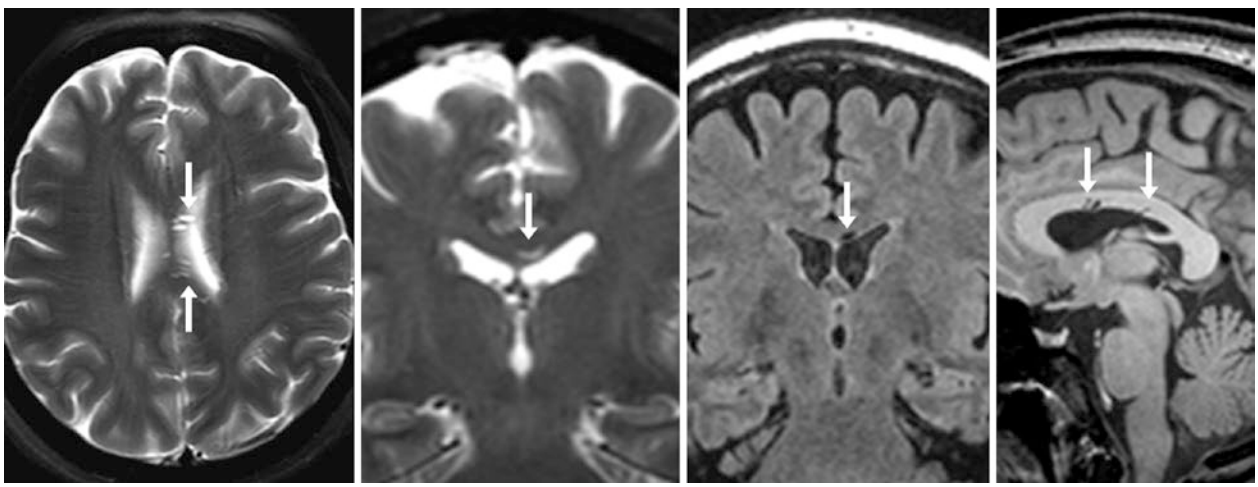

Fig. 14.36 A 43 year old had an uncommon appearance of dilated PVSs within the corpus callosum body (*arrows*) on axial (*left*) and coronal (*left middle*) T2WIs. These appear ovoid, linear, and suppress on coronal FLAIR images (*right middle*), being isointense to CSF on sagittal T1WI (*right*). These can simulate the pericallosal lesions of MS; however, no lesions were noted elsewhere in this patient. Typically, MS lesions will not suppress on FLAIR unless they are black holes; but even black holes typically exhibit bright signal along their periphery

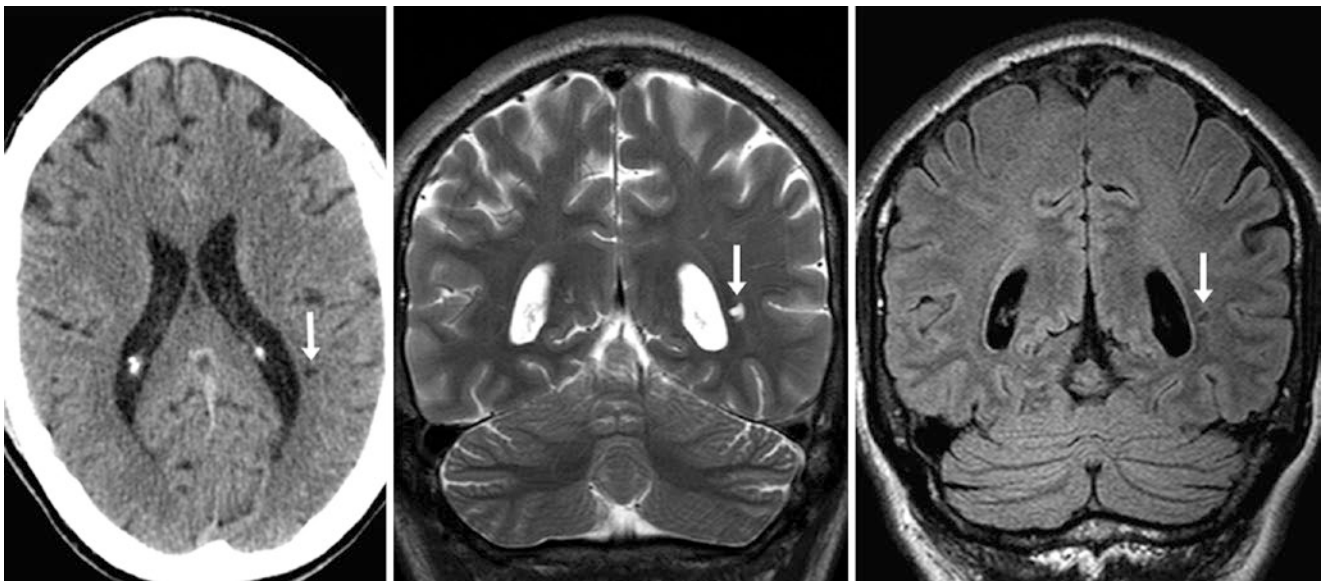

Fig. 14.37 A 52 year old had a single dilated PVS (*arrows*) with the left parietal PVWM, adjacent to the lateral ventricle on NECT (*left*). A 3T MRI confirmed this to be a focal PVS, as it was hyperintense on T2WI (*middle*) and suppressed on FLAIR (*right*). Thus PVSs located within the PVWM may be solitary and may simulate a small lacunar infarct

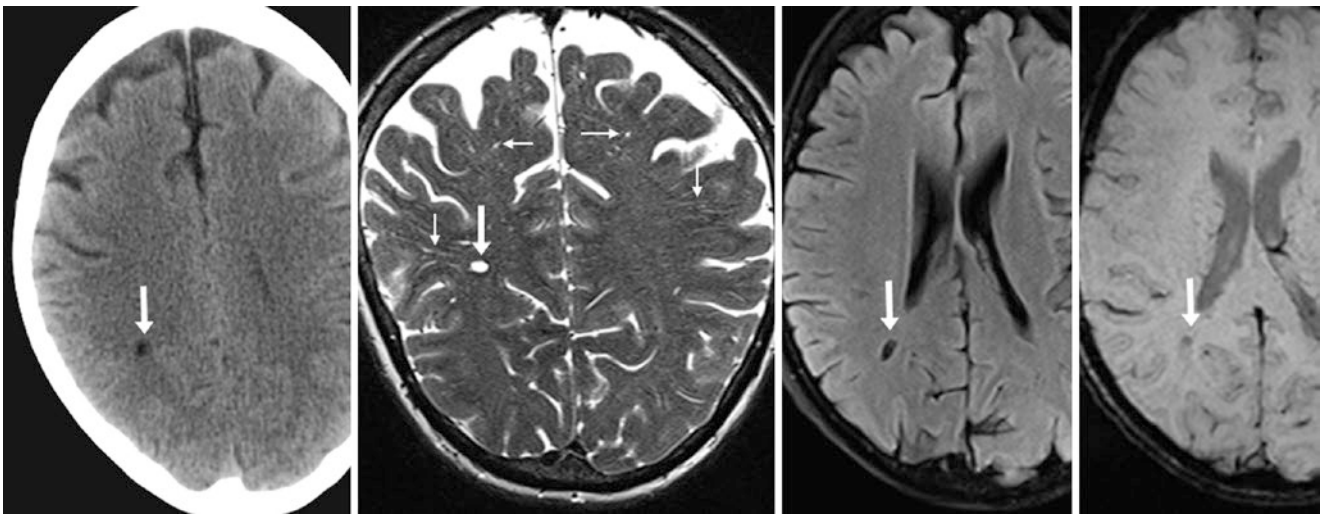

Fig. 14.38 A 57 year old had a single dilated PVS (*arrows*) within the right parietal PVWM adjacent to the lateral ventricle on NECT (*left*). On a 3T MRI, it was hyperintense on a coronal T2WI (*left middle*), suppressed on axial FLAIR (*right middle*), and was barely visible on SWI (*right*). This is an example of how PVSs may be solitary and can mimic lacunar infarcts. Thin PVSs are also present on T2WI within the subcortical white matter bilaterally (*tiny arrows*)

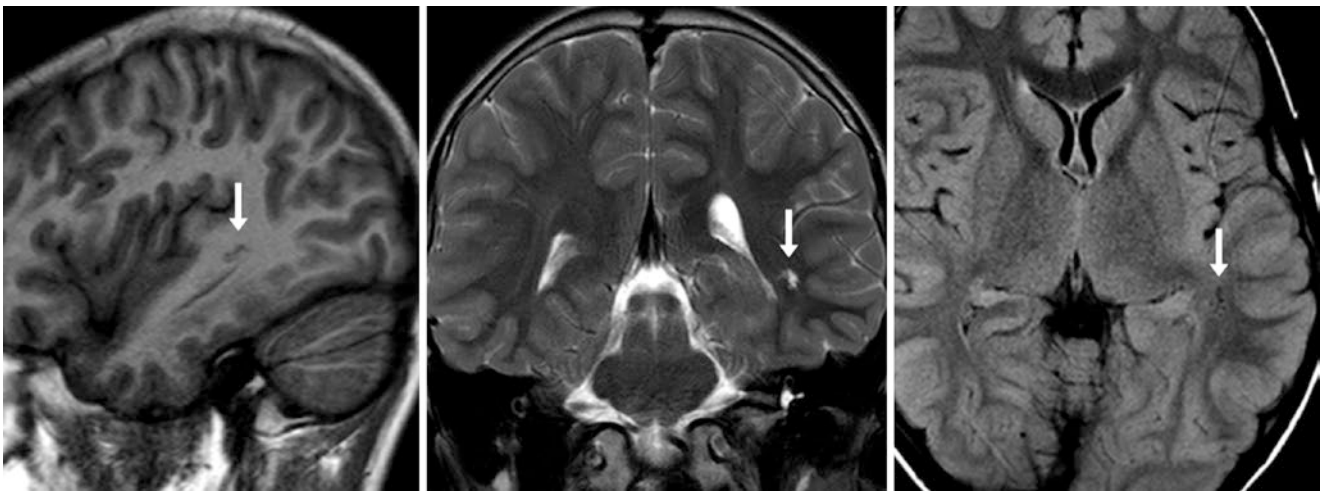

Fig. 14.39 A 10 year old with headaches had a dilated PVS (*arrows*) of the left temporal lobe near the left lateral ventricle on sagittal T1WI (*left*) and coronal T2WI (*middle*). There was no white matter atrophy next to the ventricle, given the lack of hyperintensity around the PVS on FLAIR (*right*). Thus, this did not represent gliosis or leukomalacia

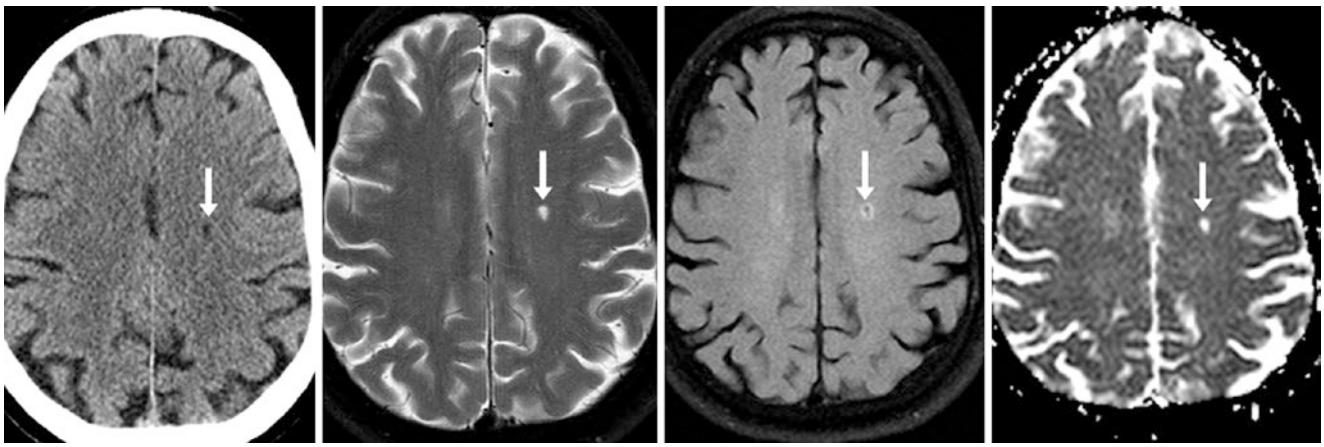

Fig. 14.40 Comparison case of lacunar infarct. A 76 year old had a focal hypodensity (*arrows*) of the centrum semiovale on NECT (*left*) that was hyperintense on T2WI MRI (*left middle*) and only partially suppressed on FLAIR (*right middle*), with high diffusivity on an ADC map (*right*). A dilated PVS of that size should entirely suppress on FLAIR

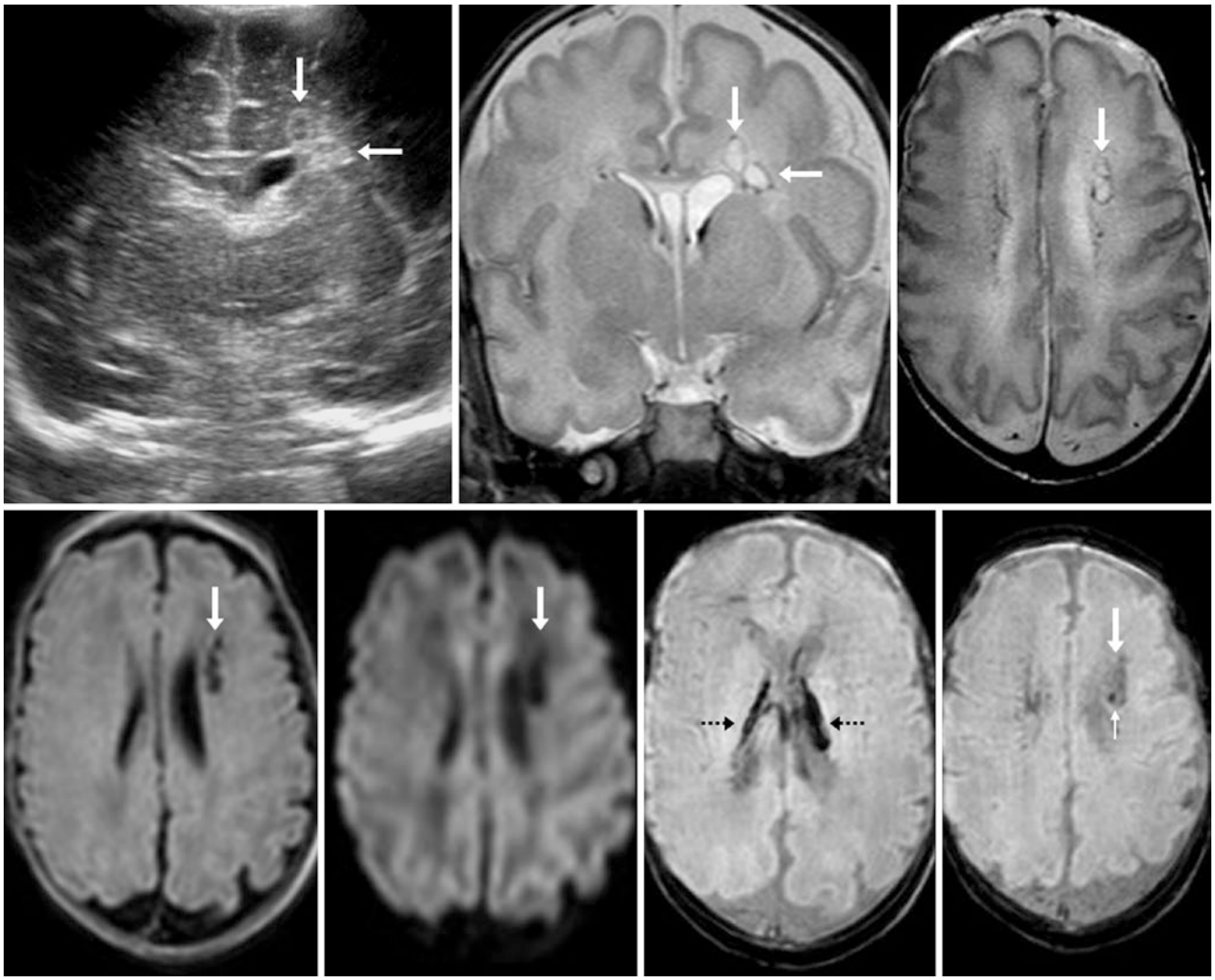

Fig. 14.41 Comparison case of periventricular leukomalacia (PVL). A premature infant born at 34 weeks had left frontal PVWM abnormalities (*arrows*) on a coronal ultrasound (*top left*) and a grade 1 germinal matrix hemorrhage (GMH) within the left caudothalamic groove. On an MRI at term equivalent age 6 weeks later, coronal T2WI (*top middle*) and axial T2WI (*top right*) showed cystic PVL, which is dark on FLAIR (*bottom, left*) and DWI (*bottom, left middle*). SWIs (*bottom right images*) depict bilateral GMH (*dotted arrows*) as well as hemosiderin at the site of PVL (*thin arrow*)

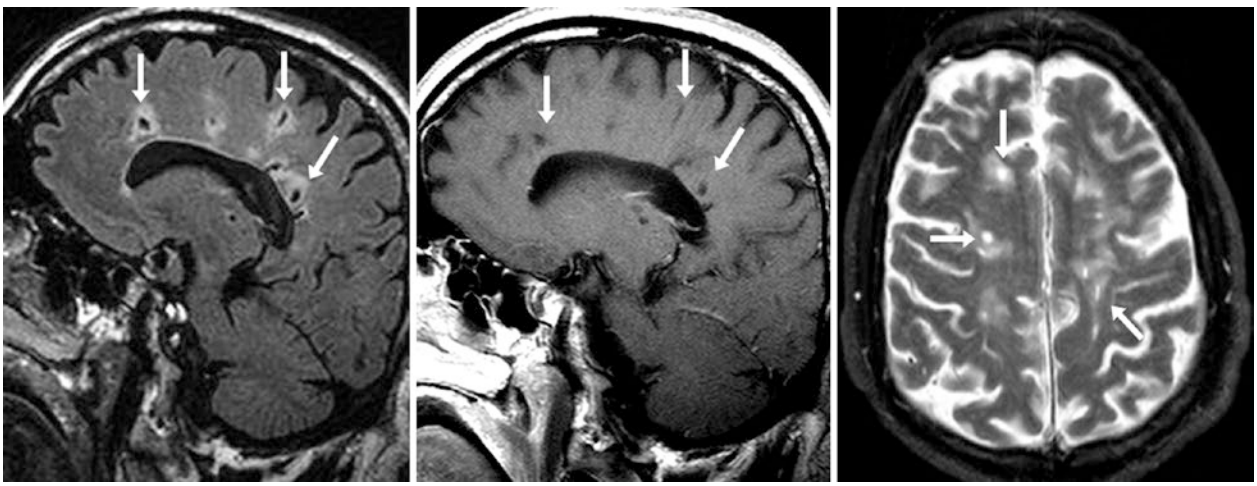

Fig. 14.42 Comparison case of black holes in MS. A 48 year old had multifocal hyperintensities surrounding a black hole (*arrows*) on sagittal FLAIR MRI (*left*) that were severely dark on sagittal T1WI (*middle*) and bright on T2WI (*right*). These lesions are oriented perpendicular to the corpus callosum, which is characteristic of MS

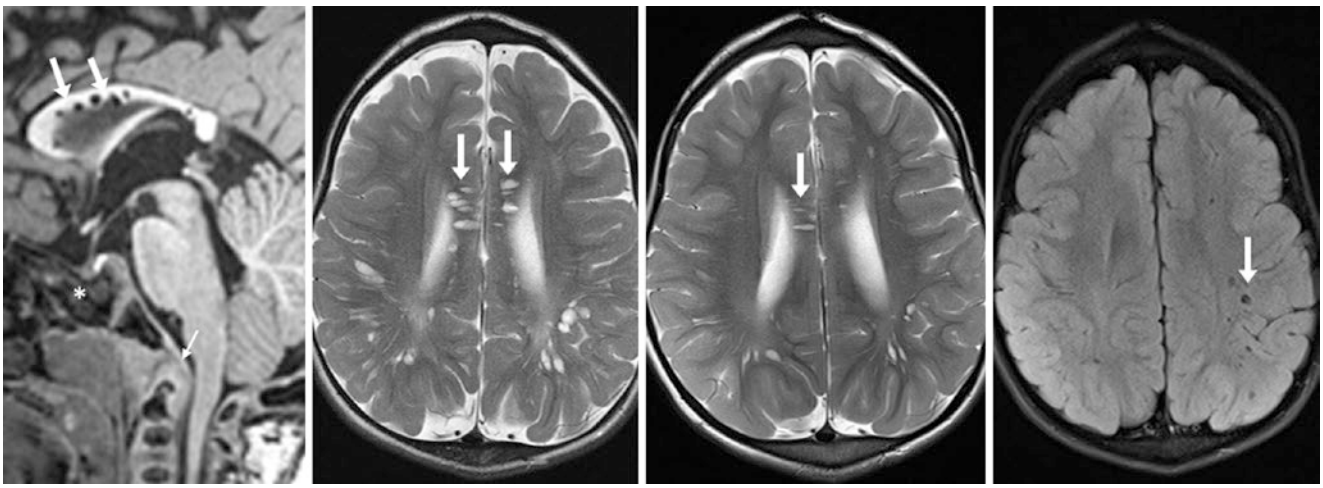

Fig. 14.43 Comparison case of Hurler syndrome. A 2 year old had dilated PVSs of the corpus callosum (*arrows*) and PVWM on sagittal T1WI (*left*) and on axial T2WI (*left middle*). The patient underwent a marrow transplant; the PVSs then decreased 3 years later on T2WI (*right middle*); the PVSs followed the CSF on FLAIR (*right*). Note the J-shaped sella (*) and odontoid capping (*tiny arrow*), which are typical of Hurler syndrome. The PVSs are too extensive to be normal; in patients with mucopolysaccharidoses, they represent deposition of mucopolysaccharide material

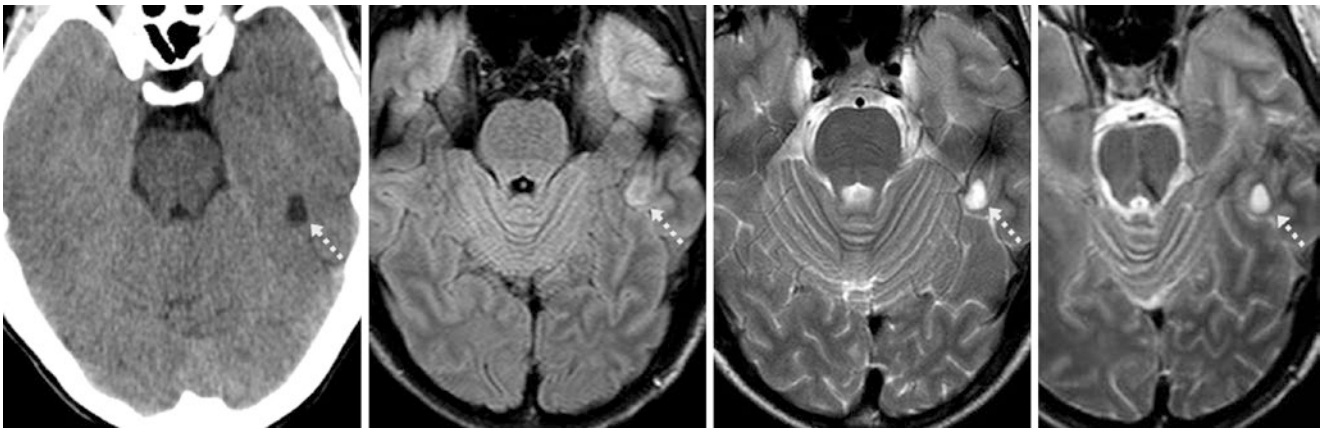

Fig. 14.44 Comparison case of dysembryoplastic neuroepithelial tumor (DNET). A 21 year old with seizures had a left temporal hypodensity (*dotted arrows*) on NECT (*left*) thought to be a PVS versus a low-grade cystic neoplasm. Axial FLAIR (*left middle*) and T2WI (*right middle*) did not confirm the cyst signal. On postcontrast T1WI (*not shown*), the lesion did not enhance. It was unchanged 2 years later on T2WI (*right*). It was later proven to be a DNET

14.4 Dilated Perivascular Spaces: Type III

Dilated PVSs of the *midbrain* or *cerebral peduncles* have been termed type III. As with the other types, they are increasingly identified in normal patients with increasing age, MR scanner field strength, and resolution, particularly on T2WI sequences. Again, a lack of suppression of punctate foci on FLAIR is suggestive of either *vascular etiology* (e.g., lacunar infarcts), *demyelinating disease* (e.g., MS), or as a chronic *sequela of trauma* (e.g., diffuse axonal injury) (Figs. 14.45, 14.46, 14.47, 14.48, 14.49, 14.50, 14.51, 14.52, 14.53, and 14.54).

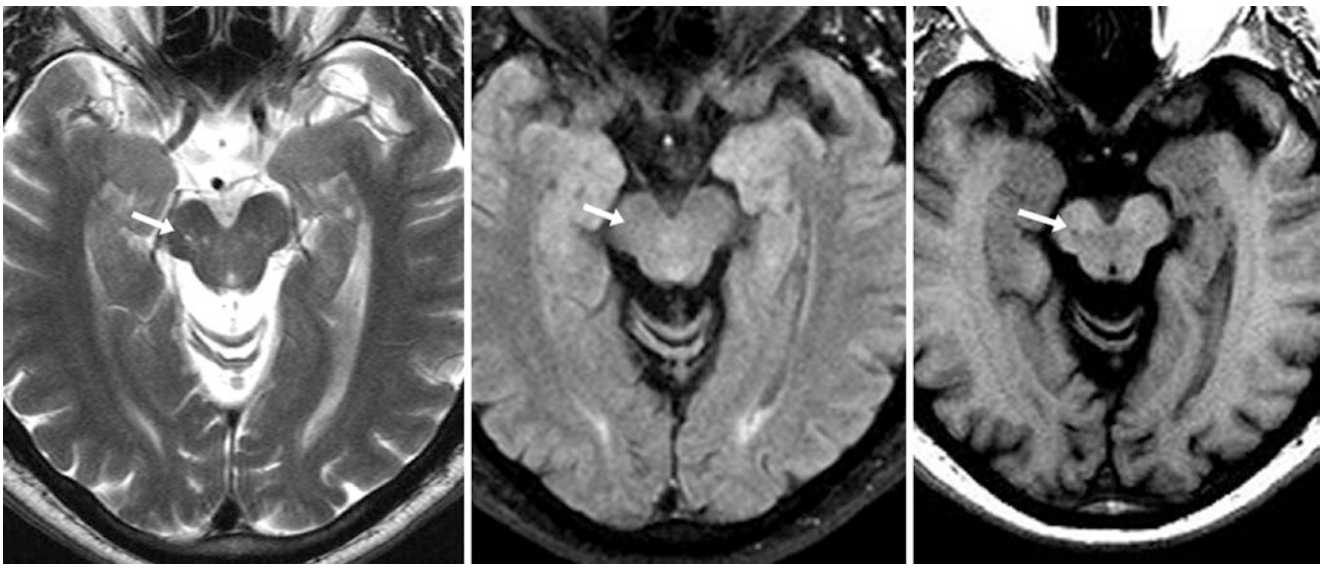

Fig. 14.45 A 60 year old had tiny PVSs (*arrows*) of the right midbrain and cerebral peduncle on axial T2WI (*left*), which suppress with CSF and are nearly invisible on FLAIR (*middle*). These PVSs are also barely visualized on T1WI (*right*)

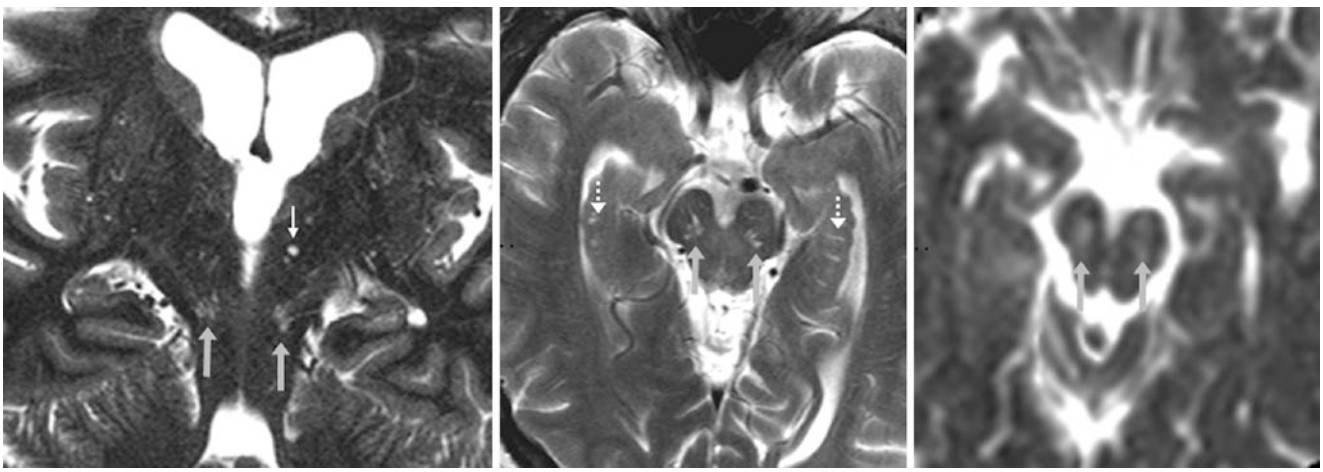

Fig. 14.46 A 60 year old had bilateral dilated PVSs of the midbrain/cerebral peduncles (*arrows*) on coronal T2 IR (*left*), on axial T2WI (*middle*), and on an ADC map (*right*). There is also a tiny PVS of the left cerebral peduncle (*tiny arrow, left*). Tiny hippocampal cysts are noted bilaterally (*dashed arrows*), which are also a normal variant

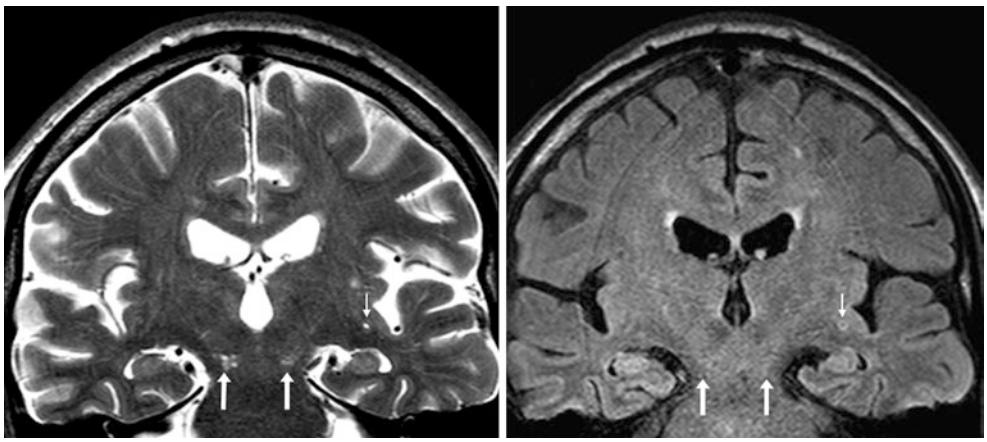

Fig. 14.47 A 78 year old had bilateral dilated PVSs within the midbrain/cerebral peduncles (*arrows*) on coronal T2WI (*left*), which suppress on FLAIR (*right*). There is also a tiny PVS of the left external capsule/temporal stem (*tiny arrows*)

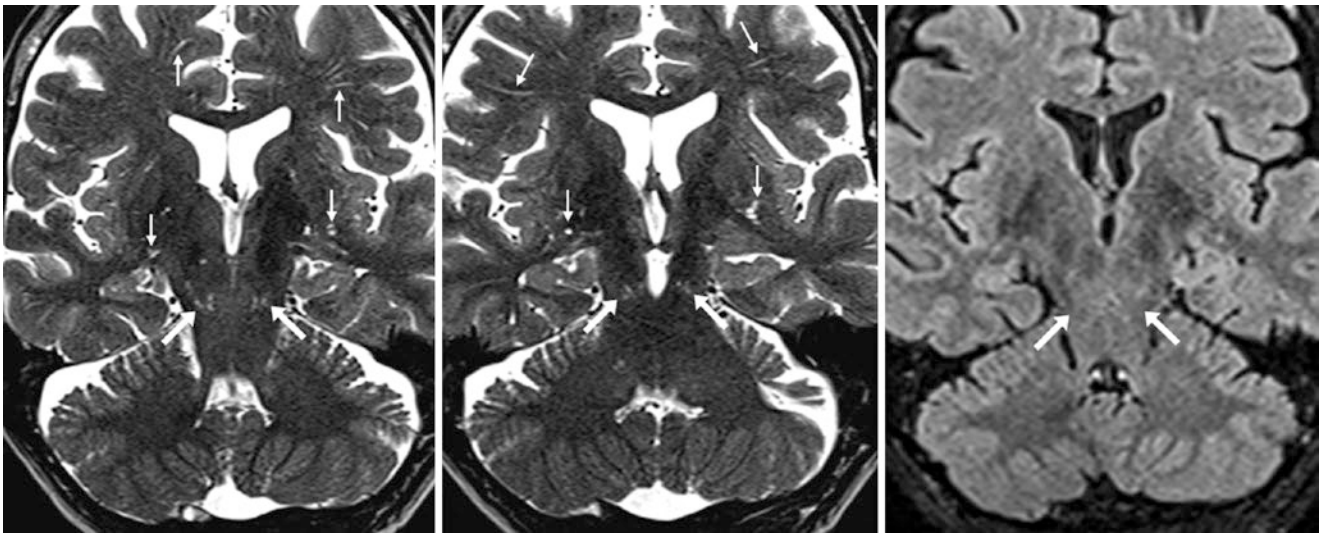

Fig. 14.48 A 67 year old had dilated PVSs within the midbrain (*arrows*) on 3T MRI coronal T2WI (*left two images*), which suppress similar to CSF on FLAIR (*right*). Dilated PVSs are also noted on T2WI throughout the subcortical white matter and inferior putamina bilaterally (*tiny arrows*). This MRI was interpreted as normal for the patient's age

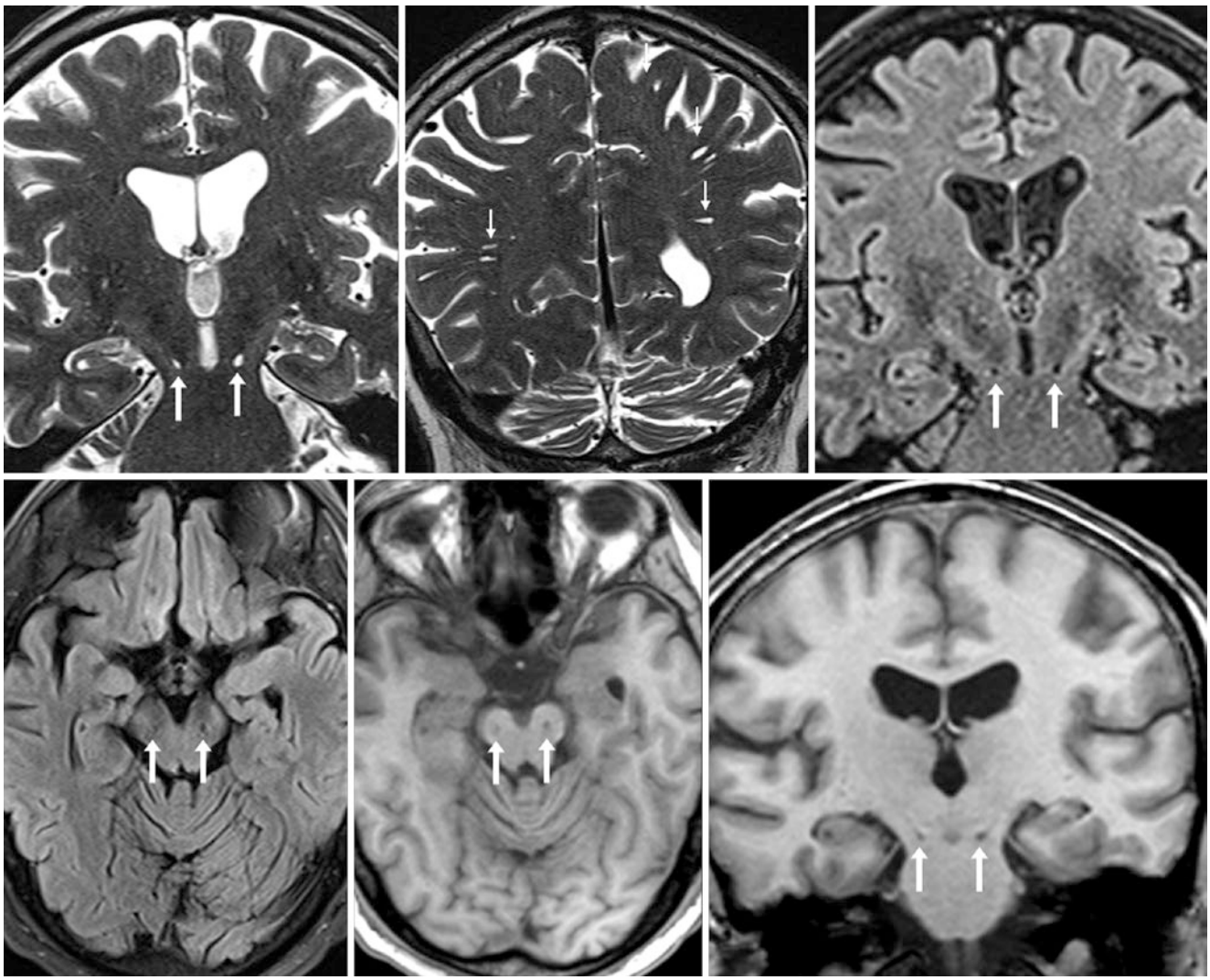

Fig. 14.49 A 62 year old had dilated PVSs within the midbrain/cerebral peduncles (*arrows*) on coronal T2WI (*top left and top middle*) and within the subcortical white matter posteriorly (*tiny arrows*), which suppress on FLAIR (*top right*). The PVSs are also noted on axial FLAIR (*bottom left*), axial T1WI (*bottom middle*), and coronal T1WI (*bottom right*)

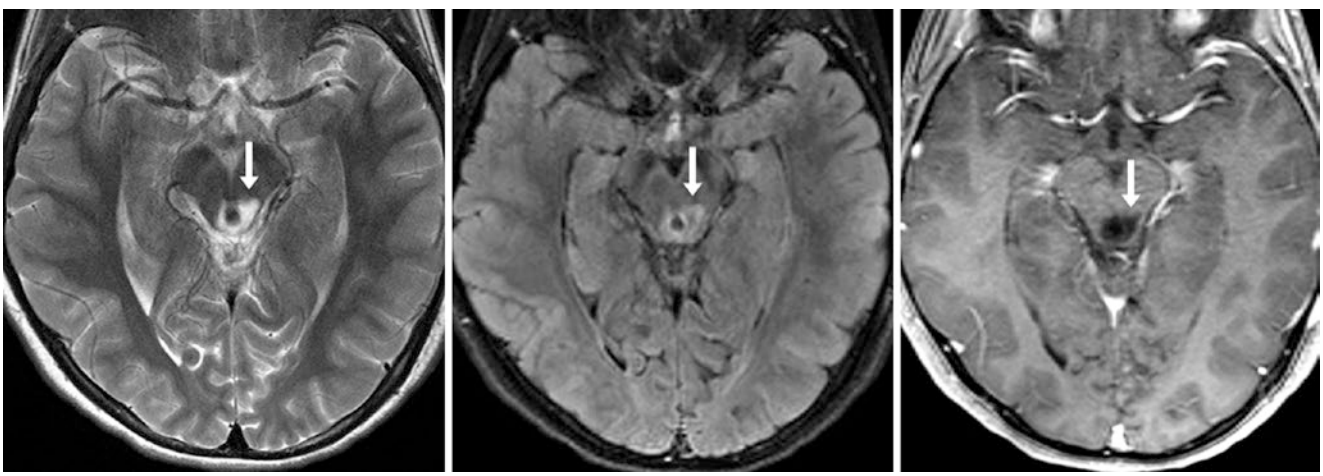

Fig. 14.50 Comparison case of low-grade glioma. A 15 year old had a hyperintense abnormality (*arrows*) on a 3T MRI with T2WI (*left*) and FLAIR (*middle*); the lesion surrounded the aqueduct, involving the left midbrain tegmentum and tectum. It did not enhance on postcontrast axial T1WI (*right*). This lesion did not change over several years

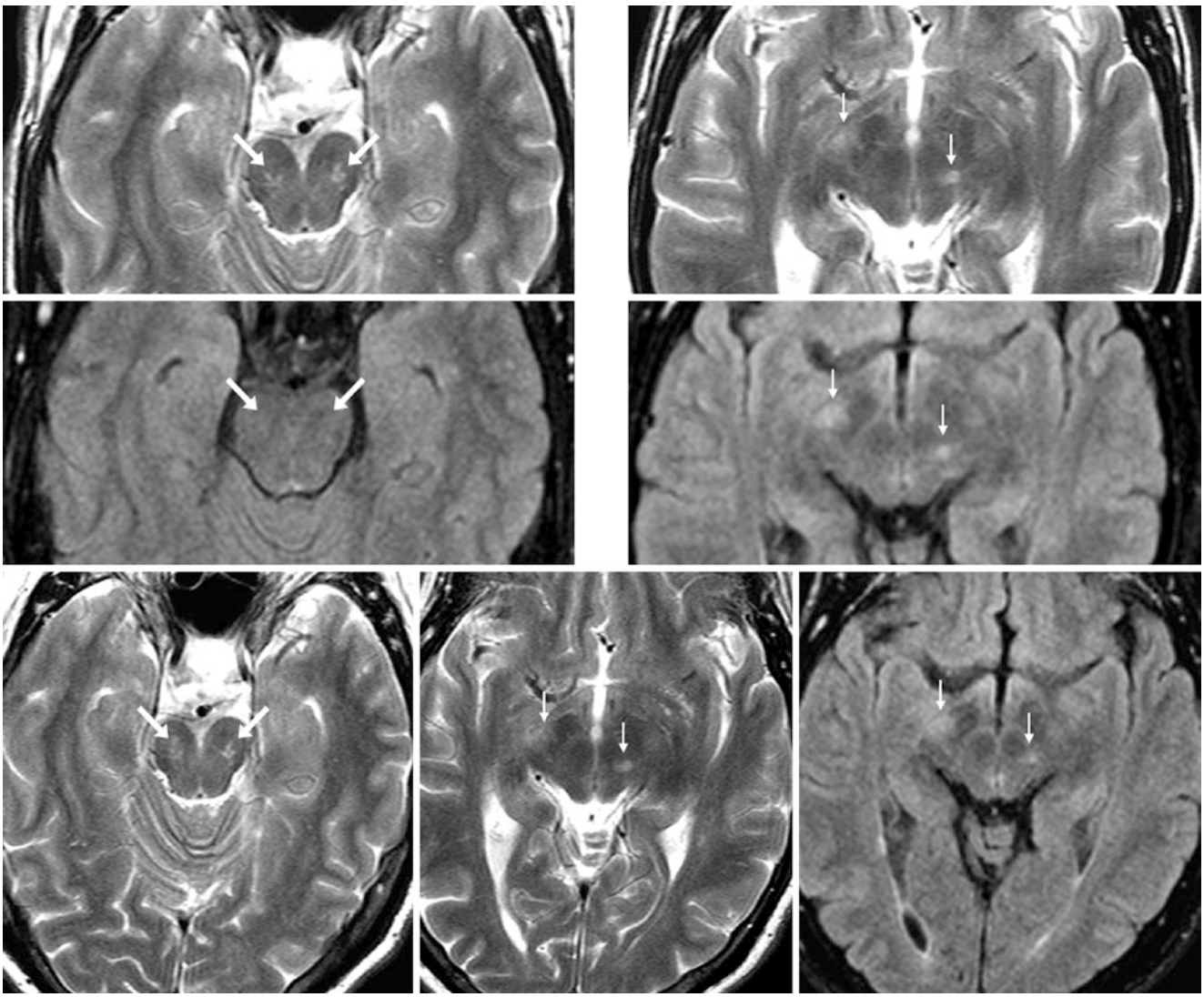

Fig. 14.51 Comparison case of MS plaques within the midbrain and dilated PVSs. A 42 year old with MS. *Top row:* there were dilated PVSs bilaterally within the midbrain and cerebral peduncles (*arrows*) on T2WI (*left*); the patient also had MS plaques (*tiny arrows)* on T2WI at another level (*right*). *Middle row:* The corresponding FLAIR images are provided at the same levels as the T2WIs, showing that the PVSs within the midbrain suppressed on FLAIR, while the MS plaques persisted. *Bottom row:* a follow-up MRI obtained 2.5 years later was unchanged, using axial T2WIs (*bottom left and middle*) and axial FLAIR (*bottom right*)

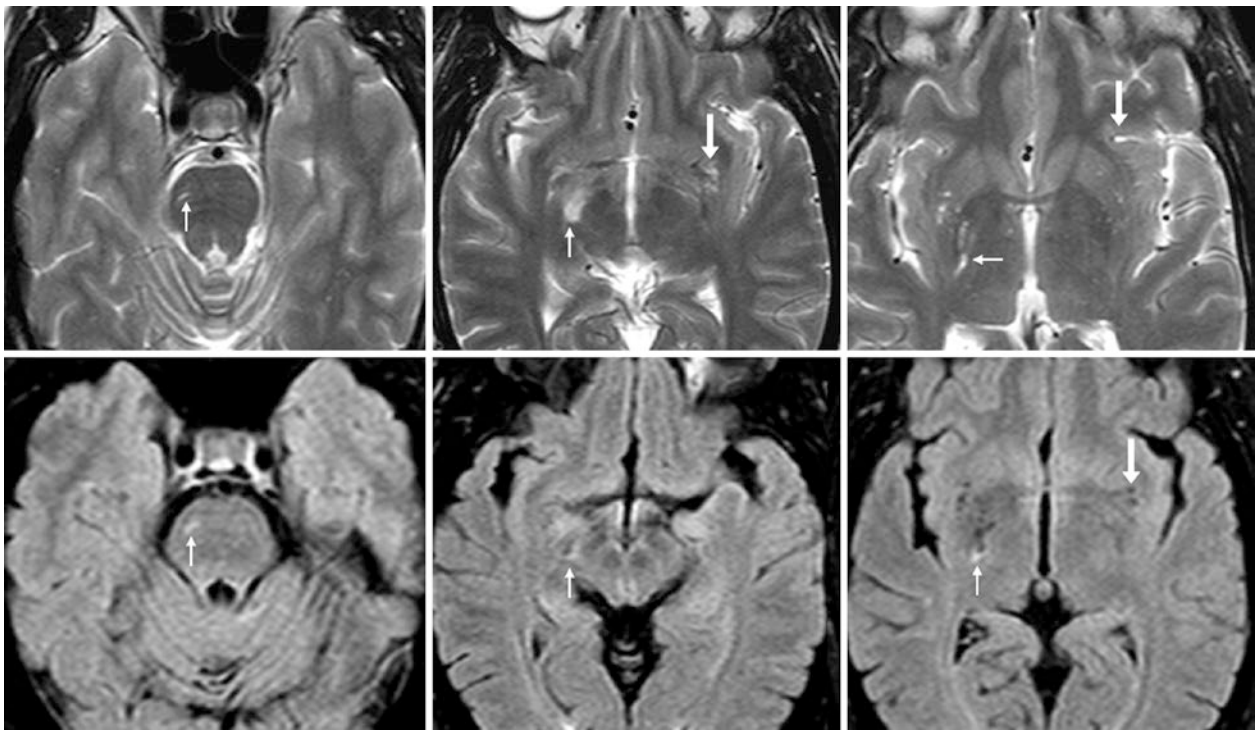

Fig. 14.52 Comparison case of chronic insult and gliosis amid dilated PVSs. A 35 year old boxer with upper motor neuron signs underwent an MRI, which showed normal dilated PVSs within the left anterior perforated substance (*arrows*) on T2WI (*top row*) that suppressed on FLAIR (*bottom row*). However, there was abnormal hyperintense signal along the corticospinal tracts (*tiny arrows*) that did not suppress on FLAIR, suggesting a chronic traumatic injury

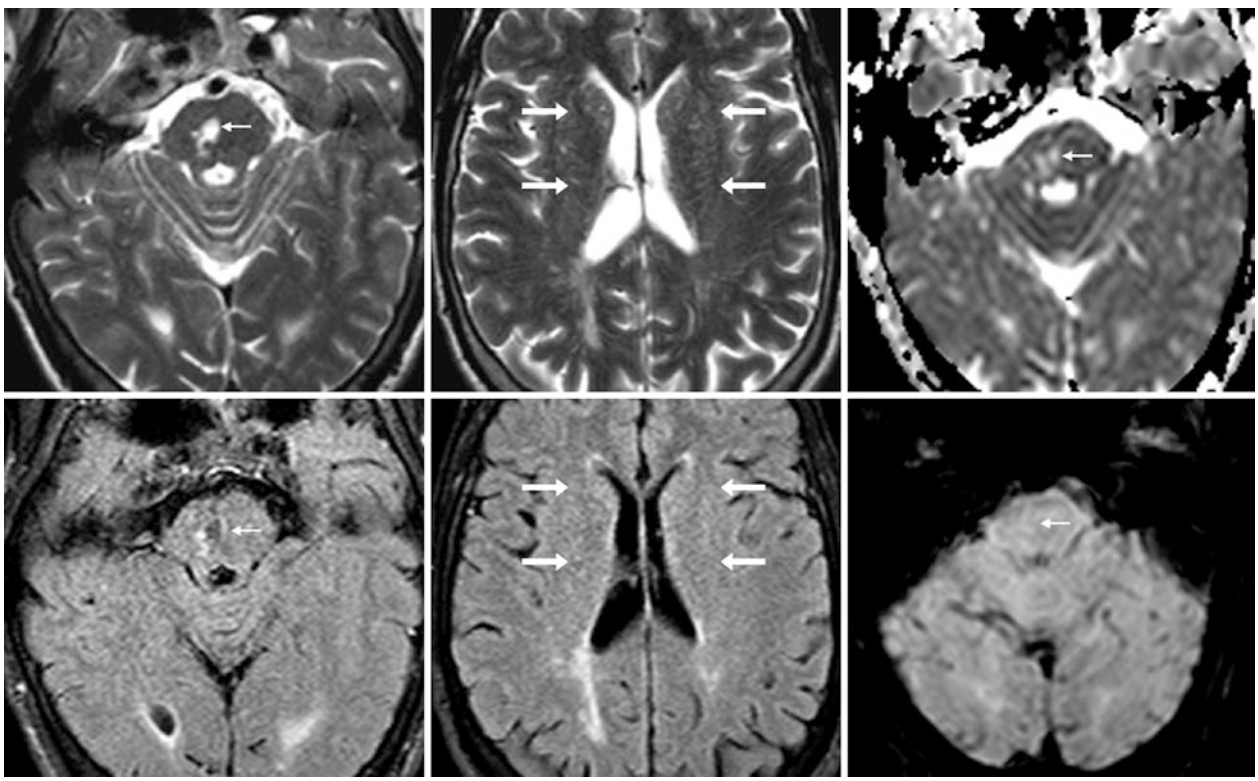

Fig. 14.53 Comparison indeterminate case of an old lacunar infarct versus a dilated PVS. A 57 year old with a cystic lesion (*tiny arrows*) within the right hemipons on T2WI MRI (*top left*) had an *état criblé* appearance (*arrows*) of PVSs within the basal ganglia on T2WI at a higher level (*top middle*). The brainstem lesion was hyperintense on ADC maps (*top right*) and partially suppressed on FLAIR (*bottom left and middle*). There was also hyperintensity within the PVWM on FLAIR, indicative of chronic small vessel ischemic disease. SWI (*bottom right*) did not depict any pontine hemorrhage. The right hemipons appeared to have mild atrophy; therefore a remote lacunar infarct was the favored diagnosis

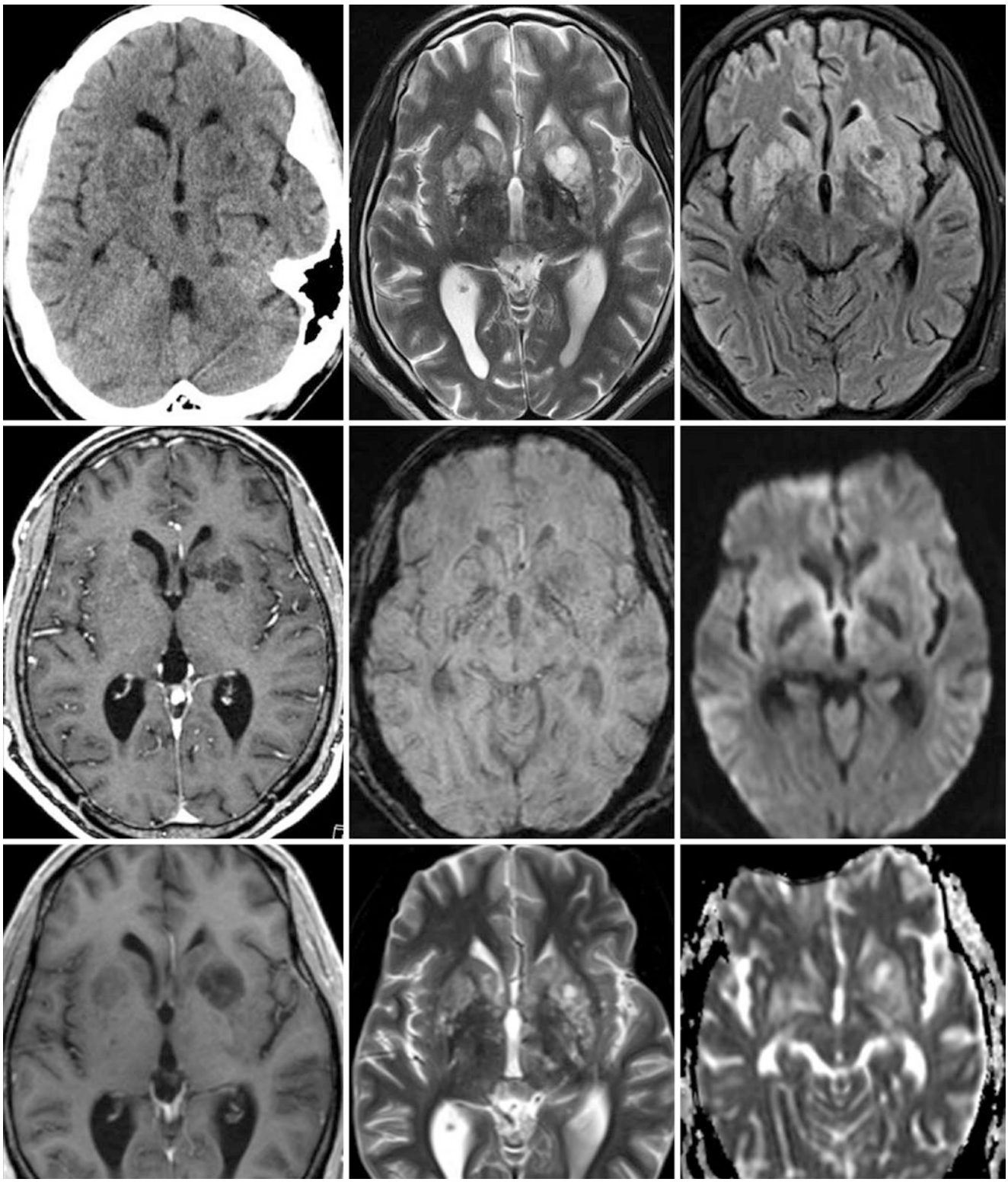

Fig. 14.54 Comparison case of cryptococcal meningitis with dilated PVSs. *Top row:* a 31 year old with HIV and AIDS had diffuse low attenuation throughout the basal ganglia on NECT (*left*). On T2WI (*middle*), there were diffusely markedly dilated PVSs bilaterally throughout the basal ganglia, which only partially suppressed on FLAIR (*right*). *Middle row:* Postcontrast T1WI (*left*) did not reveal any enhancement of the PVSs, which is not atypical in AIDS patients with cryptococcal infections. SWI (*middle*) and DWI (*right*) results are unremarkable. *Bottom row:* a follow-up MRI several days later was unchanged, with postcontrast T1WI (*left*), T2WI (*middle*), and a matching ADC map (*right*)

14.5 Tumefactive Perivascular Spaces

Tumefactive PVSs (>1.5–2 cm) are rare. They can be difficult to distinguish from *low-grade gliomas* containing cystic components, since huge PVSs can be surrounded by a mild signal on FLAIR, possibly due to gliosis. Distinguishing factors may be the lack of enhancement, reduced diffusion, and the fact that the size of the PVSs is disproportionate to the degree of FLAIR hyperintensity. (Usually cystic gliomas have a greater degree of vasogenic edema) (Figs. 14.55 and 14.56).

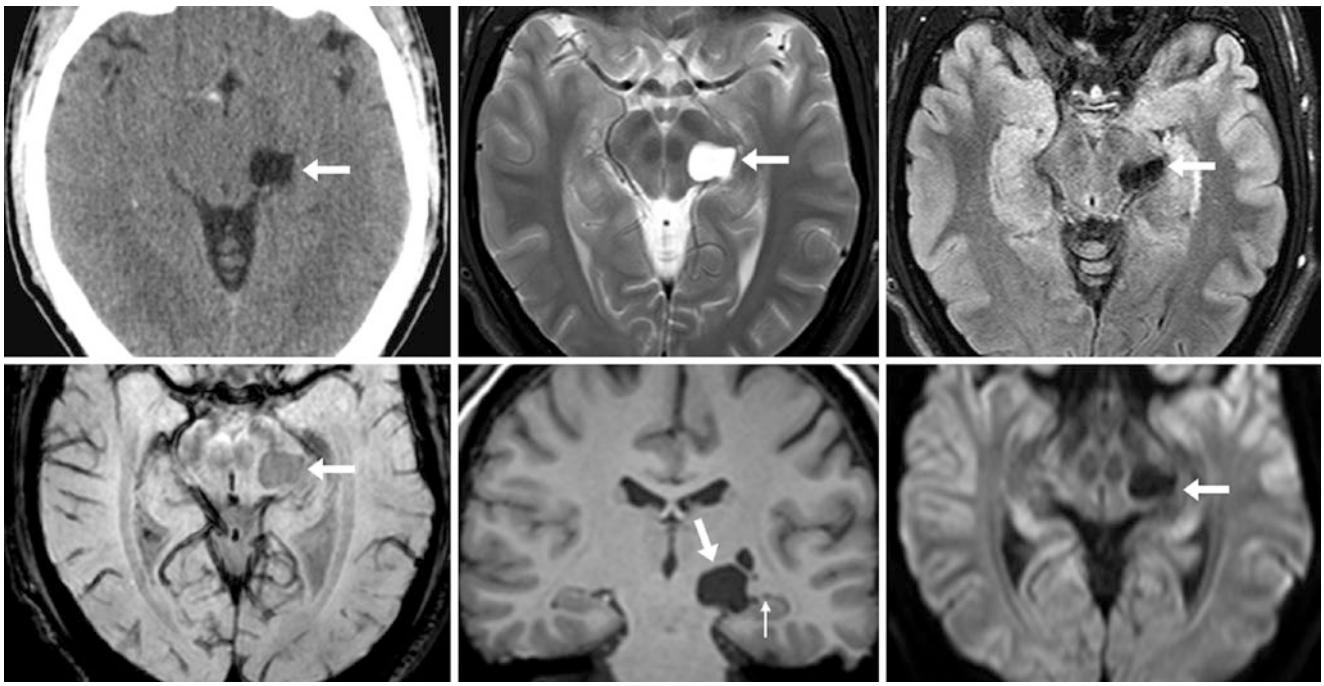

Fig. 14.55 A 27 year old had a NECT (*top left*) after a fall, in which there was a cyst greater than 2 cm (*arrows*) with CSF density located in the lateral left midbrain. A 3T MRI two days later showed that the cystic lesion had CSF signal intensity on T2WI (*top middle*), FLAIR (*top right*), SWI (*bottom left*), T1WI (*bottom middle*), and DWI (*bottom right*). Note that this is not a neuroepithelial cyst, since it is not within the choroidal fissure (*thin arrows*)

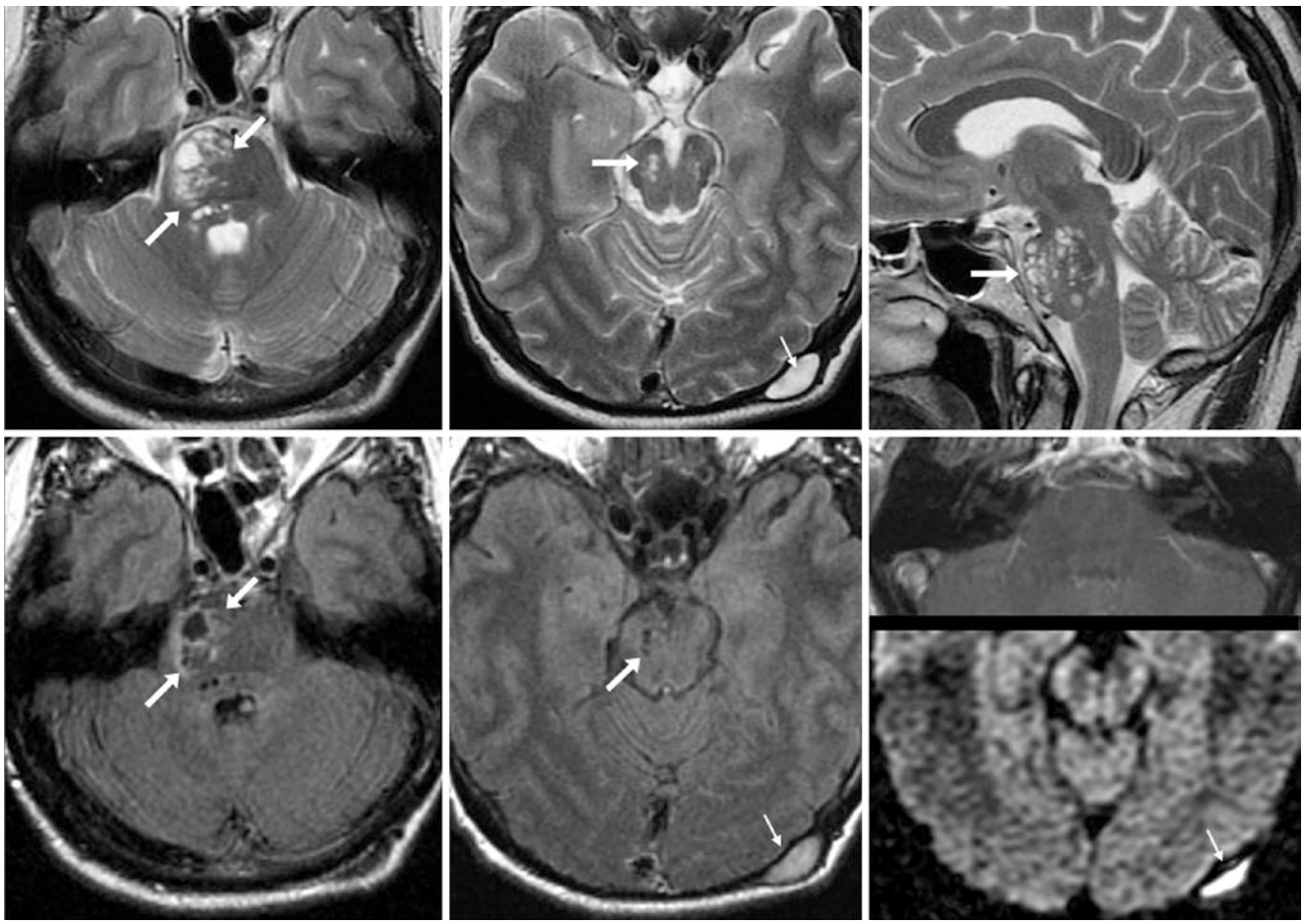

Fig. 14.56 Tumefactive (giant) dilated PVSs. A 38 year old had mild, chronic headaches and a reportedly stable brainstem lesion (*arrows*) for 11 years (*old images were not available*). The PVSs are multiloculated, with CSF intensity on axial (*top left*) and coronal (*top right*) T2WIs and suppression of the majority of the spaces on FLAIR images (*bottom left, bottom middle*) but with surrounding hyperintensity that is thought to be related to gliosis. No enhancement was noted on T1WI (*bottom right, top*) and there was no reduced diffusion on DWI (*bottom right, bottom*). Five years later, the patient remained without related symptoms. Also, note an incidental scalp epidermoid cyst (*tiny arrows*)

References

1. Heier A, Bauer CJ, Schwartz L, Zimmerman RD, Morgello S, Deck MD. Large Virchow-Robin spaces: MR-clinical correlation. AJNR Am J Neuroradiol. 1989;10:929–36.
2. Gutierrez J, Rundek T, Ekind MS, Sacco RL, Wright CB. Perivascular spaces are associated with atherosclerosis: an insight from the Northern Manhattan Study. AJNR Am J Neuroradiol. 2013;34:1711–6.
3. Kwee RM, Kwee TC. Virchow-Robin spaces at MR imaging. Radiographics. 2007;27:1071–86.
4. Groeschel S, Chong WK, Surtees R, Hanefeld F. Virchow-Robin spaces on magnetic resonance images: normative data, their dilatation, and a review of the literature. Neuroradiology. 2006;48:745–54.
5. Zhu YC, Dufouil C, Mazoyer B, Soumaré A, Ricolfi F, Tzourio C, Chabriat H. Frequency and location of dilated Virchow-Robin spaces in elderly people: a population-based 3D MR imaging study. AJNR Am J Neuroradiol. 2011;32:709–13.
6. Chen W, Song X, Zhang Y. Alzheimer's disease neuroimaging initiative. Assessment of the Virchow-Robin spaces in Alzheimer disease, mild cognitive impairment, and normal aging using high-field MR imaging. AJNR Am J Neuroradiol. 2011;32:1490–5.

Suggested Reading

Bastos AC, Andermann F, Melancon D, Cendes F, Guberman A, Dubeau F, Olivier A. Late-onset temporal lobe epilepsy and dilatation of the hippocampal sulcus by an enlarged Virchow-Robin space. Neurology. 1998;50:784–7.

Bronen RA, Cheung G. MRI of the temporal lobe: normal variations, with special reference toward epilepsy. Magn Reson Imaging. 1991;9:501–7.

De Vita E, Thomas DL, Roberts S, Parkes HG, Turner R, Kinchesh P, et al. High resolution MRI of the brain at 4.7 Tesla using fast spin echo imaging. Br J Radiol. 2003;76:631–7.

Doubal FN, MacLullich AM, Ferguson KJ, Dennis MS, Wardlaw JM. Enlarged perivascular spaces on MRI are a feature of cerebral small vessel disease. Stroke. 2010;41:450–4.

Hervé D, Gautier-Bertrand M, Labreuche J, Amarenco P; GENIC Investigators. Predictive values of lacunar transient ischemic attacks. Stroke. 2004;35:1430–5.

Jungreis CA, Kanal E, Hirsch WL, Martinez AJ, Moossy J. Normal perivascular spaces mimicking lacunar infarction: MR imaging. Radiology. 1988;169:101–4.

Patankar TF, Mitra D, Varma A, Snowden J, Neary D, Jackson A. Dilatation of the Virchow-Robin space is a sensitive indicator of cerebral microvascular disease: study in elderly patients with dementia. AJNR Am J Neuroradiol. 2005;26:1512–20.

Pollock H, Hutchings M, Weller RO, Zhang ET. Perivascular spaces in the basal ganglia of the human brain: their relationship to lacunes. J Anat. 1997;191(Pt 3):337–46.

Salzman KL, Osborn AG, House P, Jinkins JR, Ditchfield A, Cooper JA, Weller RO. Giant tumefactive perivascular spaces. AJNR Am J Neuroradiol. 2005;26:298–305.

Sasaki M, Sone M, Ehara S, Tamakawa Y. Hippocampal sulcus remnant: potential cause of change in signal intensity in the hippocampus. Radiology. 1993;188:743–6.

Wuerfel J, Haertle M, Waiczies H, Tysiak E, Bechmann I, Wernecke KD, et al. Perivascular spaces—MRI marker of inflammatory activity in the brain? Brain. 2008;131(Pt 9):2332–40.

Enlargement or Asymmetry of the Lateral Ventricles Simulating Hydrocephalus

15

The *lateral ventricles* have a wide range of appearances that can be considered normal. There may be variations in size between sides or between different regions (e.g., the bodies may be larger than the temporal horns, or vice versa). Such asymmetry occurs in about 5–20 % of the population, depending on what is considered asymmetry and which portions of the ventricle are compared to the opposite side. More commonly, for unknown reasons the right lateral ventricle is larger than the left by about a 3:1 ratio. This may be seen at any age, from the fetus to the elderly population. Such asymmetry should be considered normal as long as the ventricular size and configuration do not fit the criteria for hydrocephalus. Additionally, varying degrees of cerebral atrophy (and particularly adjacent white matter atrophy surrounding the lateral ventricles) can accentuate this appearance and mistakenly lead to the diagnosis of communicating hydrocephalus, leading to unnecessary shunting.

At this point, we would like to clarify that this chapter is focused on those appearances of the lateral ventricles that should not be mistaken for *hydrocephalus* or *cysts*. In this chapter, atrophy is considered a "don't touch lesion," that is, is not to be treated by ventriculostomy. This is not to say that all atrophy is normal. Indeed, a common problem occurs when atrophy (diffuse cerebral volume loss) that is disproportionate to age is called hydrocephalus. However, that distinction has been addressed by a significant amount of literature over the years as to what is appropriate for age, which is not the primary focus of this chapter. Rather, we will focus on how to distinguish *volume loss* from *hydrocephalus*. In this regard, it helps to pay attention to adjacent *periventricular white matter* (PVWM).

Several criteria have been proposed to distinguish normal ventricular asymmetry from volume loss (i.e., atrophy) and from hydrocephalus. The most common and traditional method is to evaluate the size and the presence of an acute angle of the *temporal horns*; in hydrocephalus, the temporal horns become rounded and enlarged. Additionally, the *anteroinferior recesses of the third ventricle*, best evaluated on sagittal images, become widened in hydrocephalus, since these recesses normally have very acute angles. In particular, in this author's experience, the optic recess (anterior) may be more sensitive than the infundibular recess (posterior) to becoming widened in the earlier stages of hydrocephalus. The size of the *cerebral aqueduct* should also be evaluated, since aqueductal stenosis is one of the more common causes of obstructive (noncommunicating) hydrocephalus. The radiologist should also evaluate for several other secondary findings of hydrocephalus, such as PVWM abnormality (hypodensity on CT, hyperintensity on FLAIR or T2WI), sulcal effacement, or the presence of an obstructive lesion (e.g., a mass, web, or hemorrhage). Notably, periventricular hypodensity (on CT) or hyperintensity (on MRI) may be present in *chronic small vessel ischemic disease* (i.e., leukoariosis), *demyelinating disorders*, or *toxic/metabolic leukoencephalopathies*; therefore such hypodensity/hyperintensity is a nonspecific finding. Also of note is that atrophy/volume loss usually leads to concomitant enlargement of the cerebral sulci along with and proportionate to the ventricular system; however, disproportionate atrophy of the PVWM relative to gray matter/cortex can occur in those same aforementioned disorders. Therefore atrophy can simulate hydrocephalus if such insults are focused in the posterior periventricular regions leading to an appearance of *culpocephaly* (enlargement of the posterior bodies or occipital horns of the lateral ventricles relative to the remainder of the ventricles).

One notable example that causes the appearance of culpocephaly is *periventricular leukomalacia* (PVL), in which neonatal premature infants (or fetuses) are at a high risk of developing hypoxic-ischemic injury to the developing brain when they are born at less than 33 weeks' gestational age as a result of their centrifugal blood supply at that age. (In the late third trimester this converts to the typical centripetal outside-in vascular supply.) Such infants develop and may continue into adulthood with white matter volume loss/thin-

A.M. McKinney, *Atlas of Normal Imaging Variations of the Brain, Skull, and Craniocervical Vasculature*,
DOI 10.1007/978-3-319-39790-0_15

ning manifested focally in the posterior periventricular regions and by culpocephaly; more severe cases suffer hemorrhages and cystic degeneration. Culpocephaly can also arise from a number of congenital or developmental abnormalities, the most notable being *corpus callosum agenesis*.

The *choroidal fissure* is the site of attachment of the choroid plexus in the lateral ventricle. The fissure communicates between the temporal horn and the peri-mesencephalic cistern and is retro-thalamic (retro-pulvinar) as well. It can be asymmetrical in size and can simulate disease processes such as *mesial temporal sclerosis* or sequelae of *previous trauma or infection*. Normal asymmetry can be discerned from disease, as diseases usually have an abnormal signal on T2WI or FLAIR with volume loss/atrophy (Figs. 15.1, 15.2, 15.3, 15.4, 15.5, 15.6, 15.7, 15.8, 15.9, 15.10, 15.11, 15.12, 15.13, 15.14, 15.15, 15.16, 15.17, 15.18, 15.19, 15.20, 15.21, 15.22, 15.23, 15.24, 15.25, 15.26, 15.27, 15.28, 15.29, 15.30, 15.31, and 15.32).

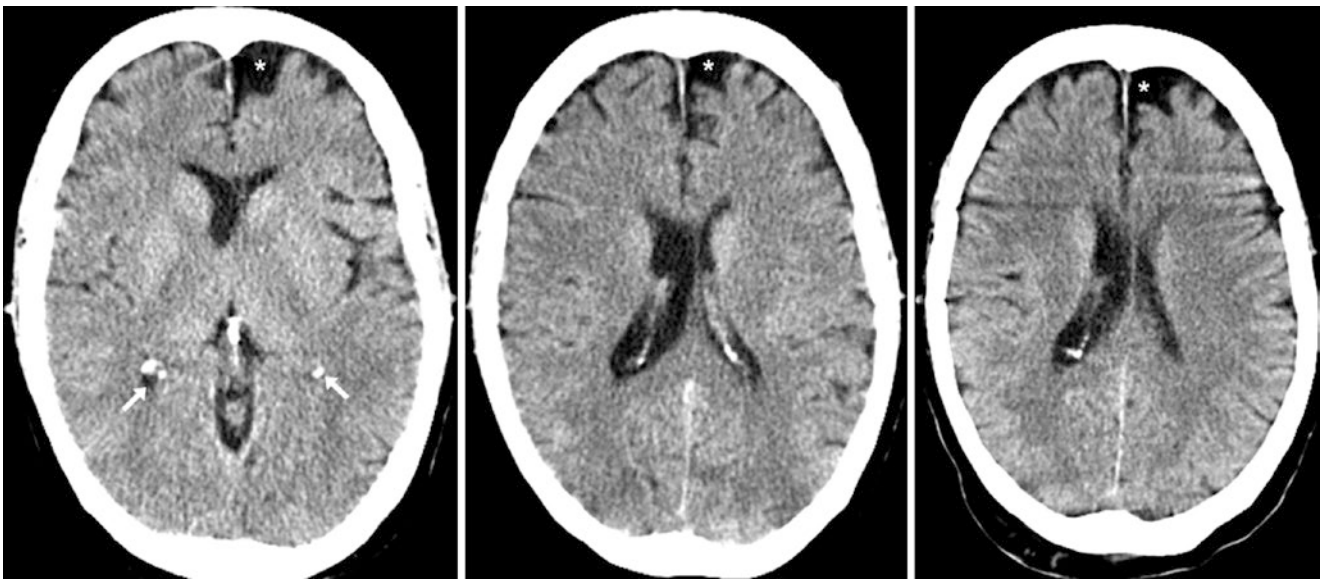

Fig. 15.1 A 67 year old underwent a NECT (*left and middle*) that showed an asymmetrically prominent right lateral ventricle without enlargement of the trigones (*arrows*) or temporal horns (*not shown*). The prominence of the subarachnoid space (*) along the left frontal convexity was also noted, confirming that atrophy is present. The ventricular asymmetry was unchanged 2 years later on a NECT (*right*), while the atrophy had mildly progressed

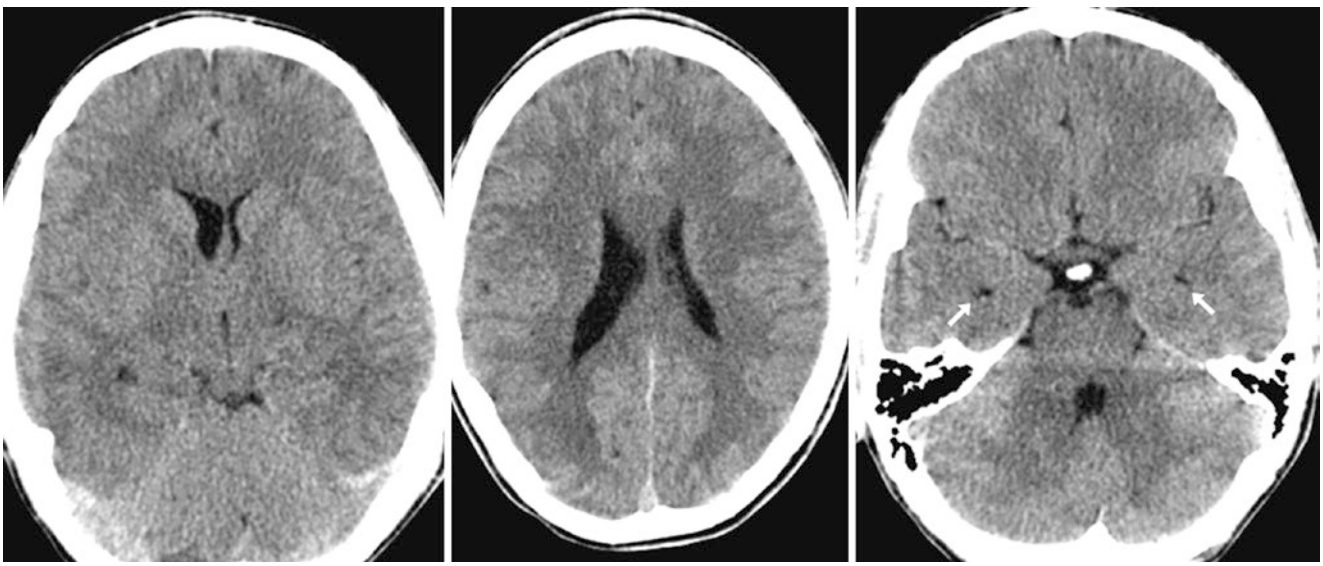

Fig. 15.2 A 15 year old whose NECT images demonstrated asymmetric enlargement of the body of the right lateral ventricle without enlargement of the temporal horns (*arrows*). A follow-up NECT was not obtained. This should not be mistaken for PVL because there is no significant PVWM thinning or evidence of focal gliosis

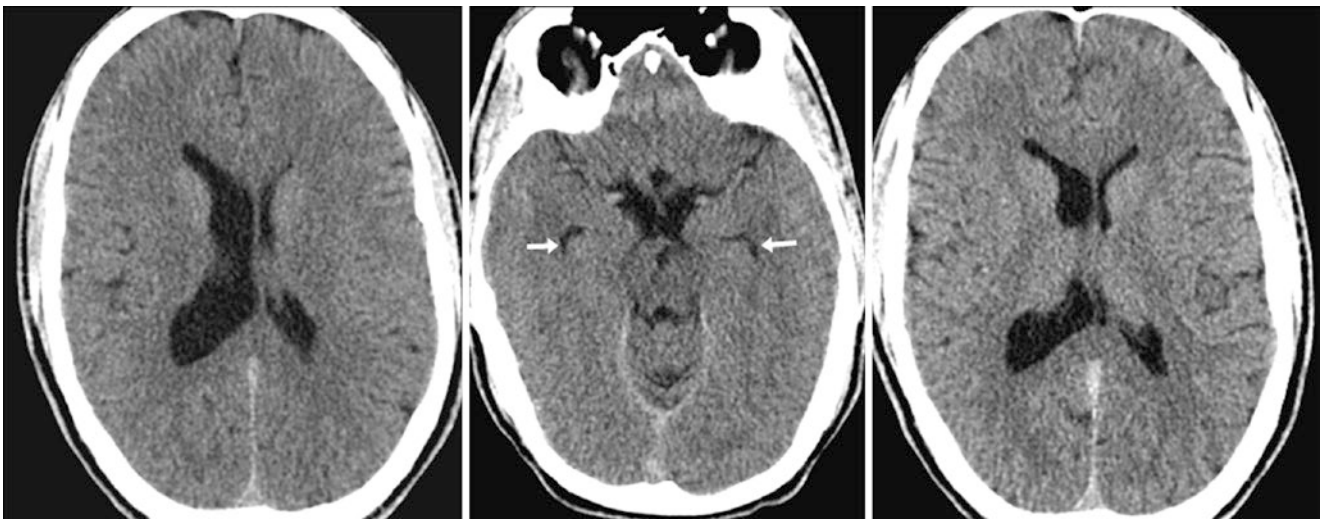

Fig. 15.3 A 25 year old's NECT images (*left and middle*) demonstrated an asymmetrically enlarged body of the right lateral ventricle without enlargement of the temporal horns (*arrows*). This was unchanged 1 month later on another NECT (*right*). Again this should not be mistaken for PVL because there is no significant PVWM thinning or focal atrophy

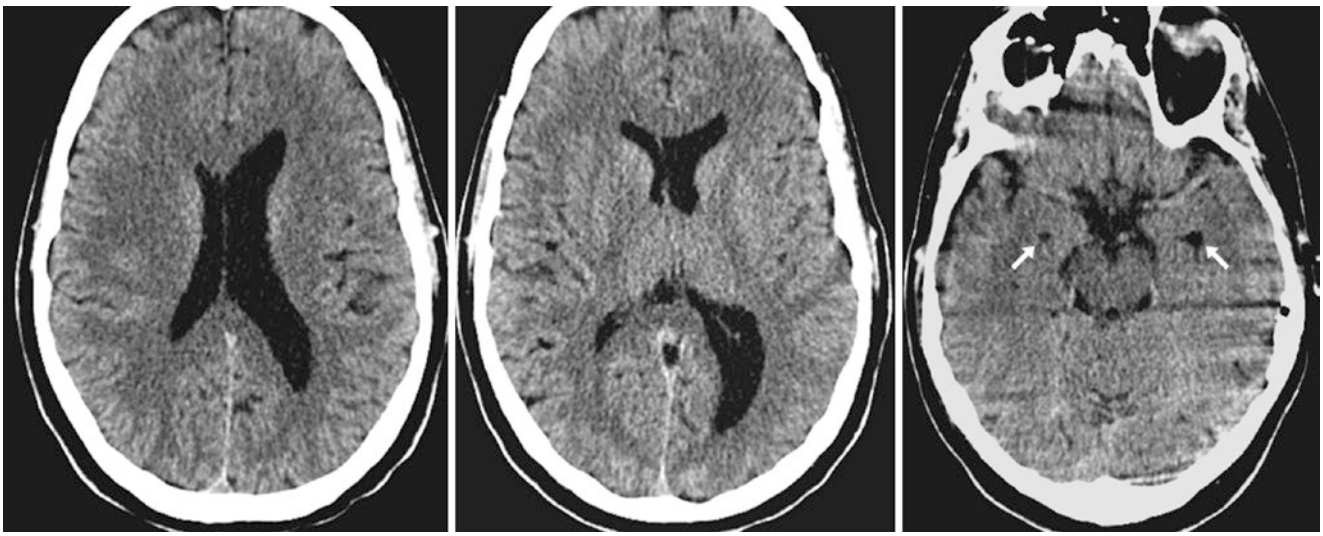

Fig. 15.4 A 45 year old's NECT images demonstrated asymmetric enlargement of the body of the left lateral ventricle without enlarged temporal horns (*arrows*). Again, this should not be mistaken for PVL because there is no significant PVWM thinning/atrophy. The asymmetry is exacerbated by the tilting of the patient's head within the gantry

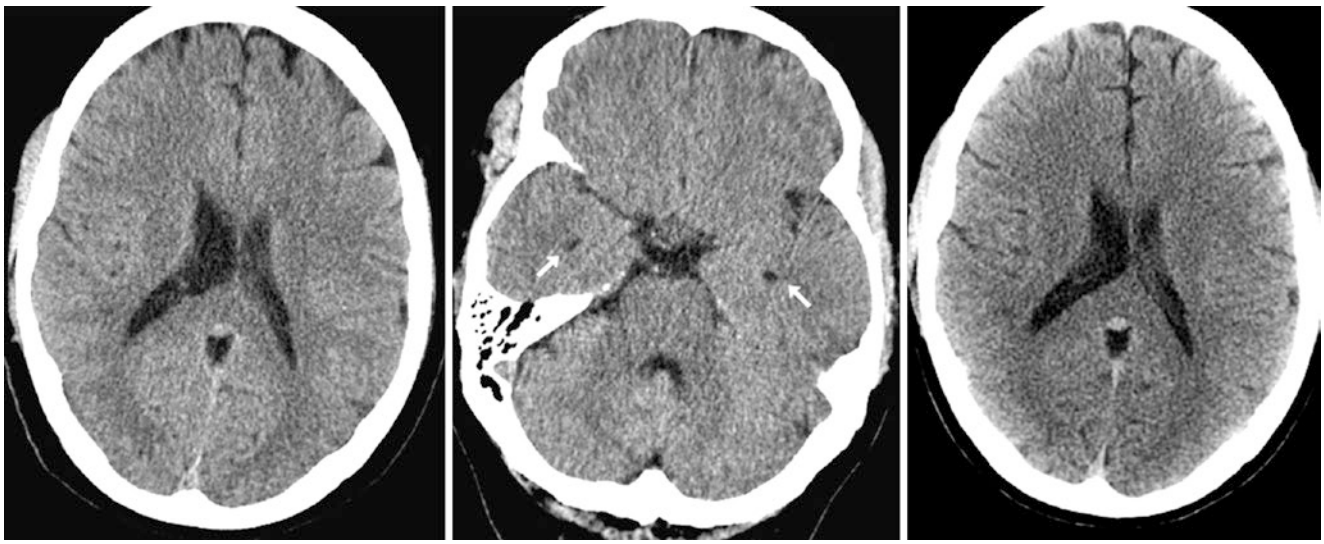

Fig. 15.5 A 49 year old's initial NECT images (*left and middle*) demonstrated asymmetric enlargement of the body of the right lateral ventricle without enlarged temporal horns (*arrows*). This also should not be mistaken for PVL because there is no significant PVWM thinning. This was unchanged on a NECT performed 4 years later (*right*)

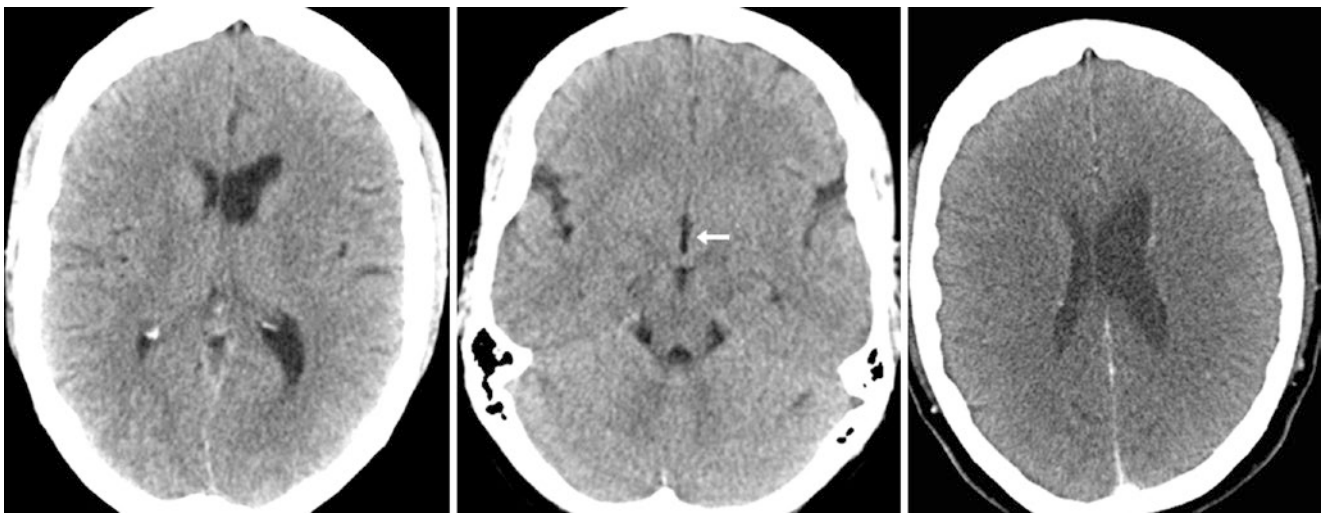

Fig. 15.6 A 59 year old whose NECT images (*left and middle*) demonstrated asymmetric enlargement of the body and trigone of the left lateral ventricle without enlarged anterior recess of the third ventricle (*arrow*). This should not be mistaken for PVL because there is no significant PVWM thinning. A CECT (*right*) weeks later appears similar

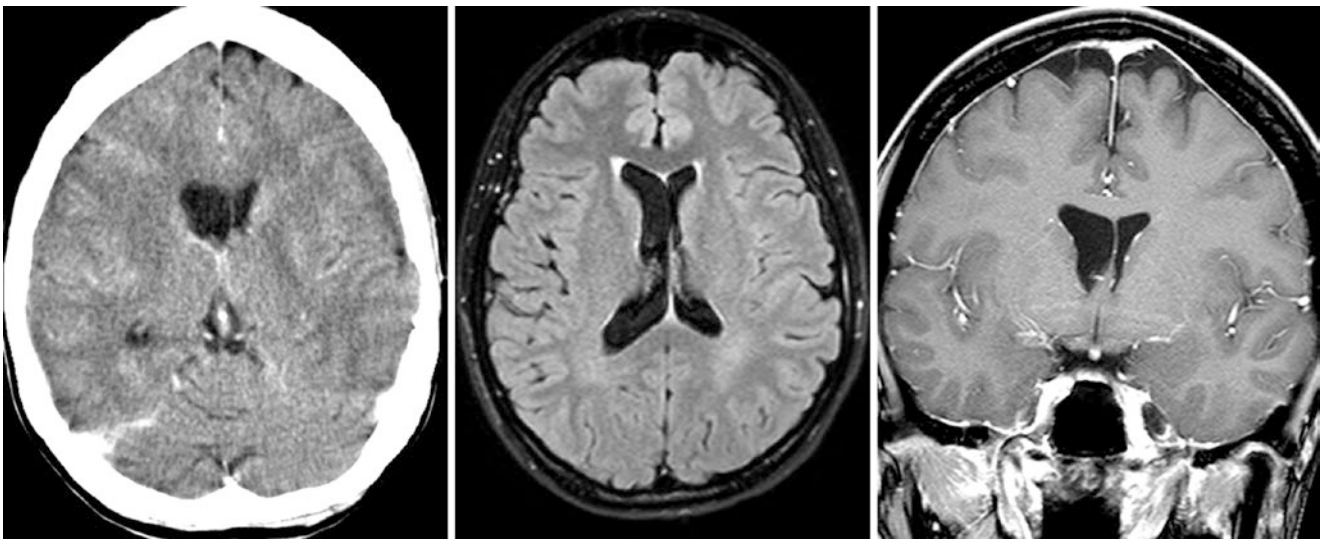

Fig. 15.7 A 38 year old had axial NECT (*left*), axial FLAIR (*middle*), and coronal postcontrast T1WI (*right*) that demonstrated normal, asymmetric enlargement of the body of the right lateral ventricle. The PVWM does not appear to be thinned

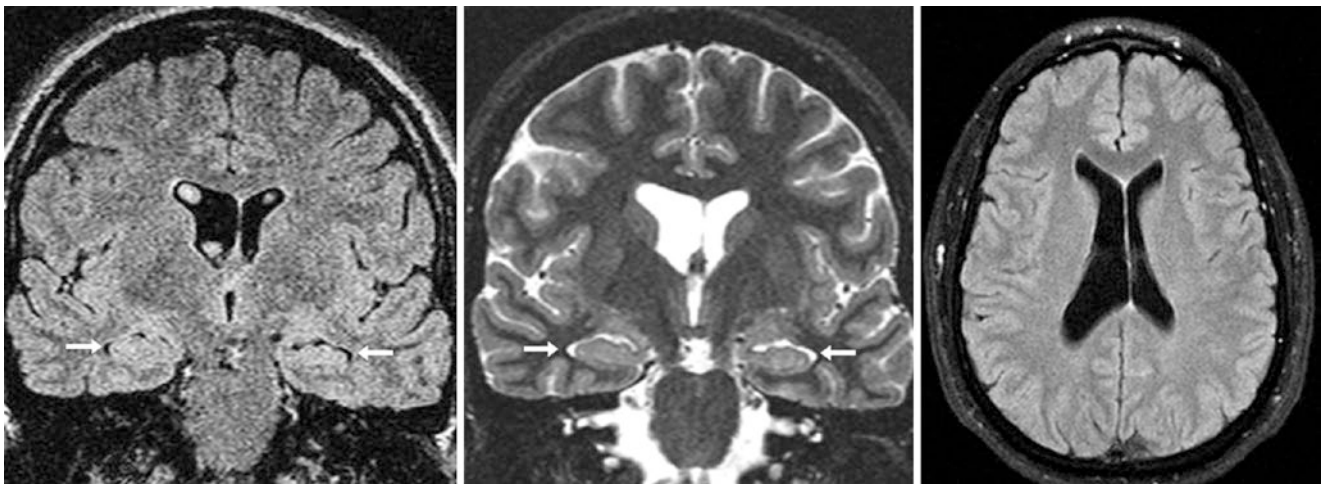

Fig. 15.8 A 37 year old underwent coronal FLAIR (*left*) and T2WI (*middle*) that demonstrated asymmetric enlargement of the body of the right lateral ventricle without enlarged temporal horns (*arrows*). Axial FLAIR images (*right*) are also shown. This should not be mistaken for PVL because there is no significant PVWM thinning

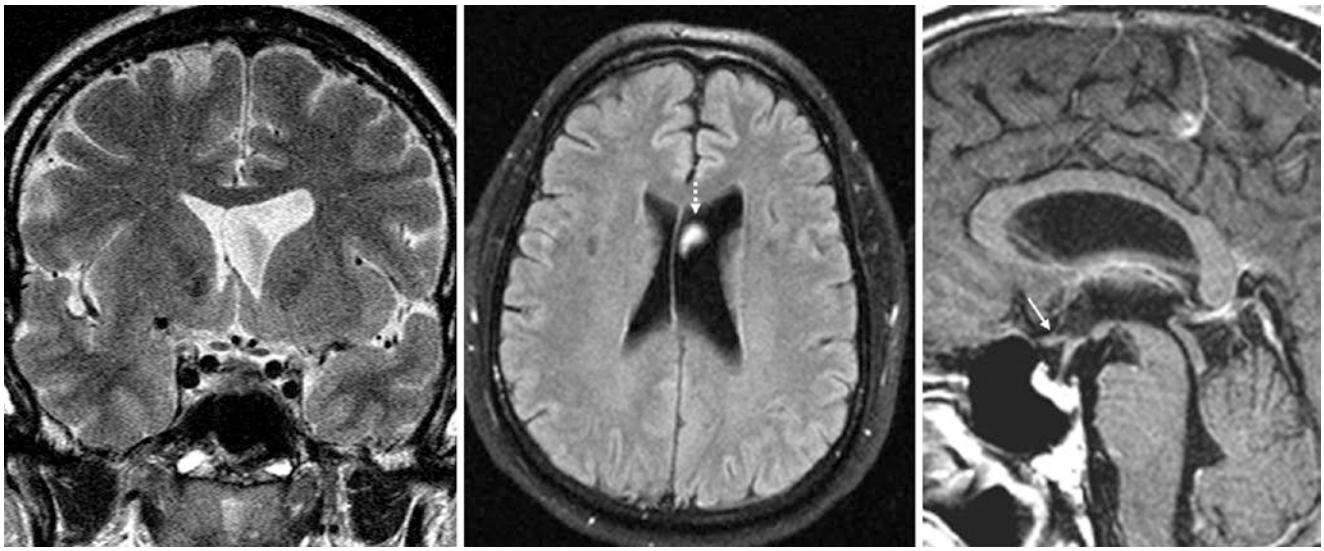

Fig. 15.9 A 55-year-old patient in whom coronal T2WI (*left*) and axial FLAIR (*middle*) images showed asymmetric enlargement of the left lateral ventricular body. On sagittal T1WI (*right*), the third ventricle's optic recess (*thin arrow*) is not enlarged, confirming that there is no hydrocephalus. Note a normal artifactual CSF flow-related hyperintensity (*dotted arrow*) on FLAIR

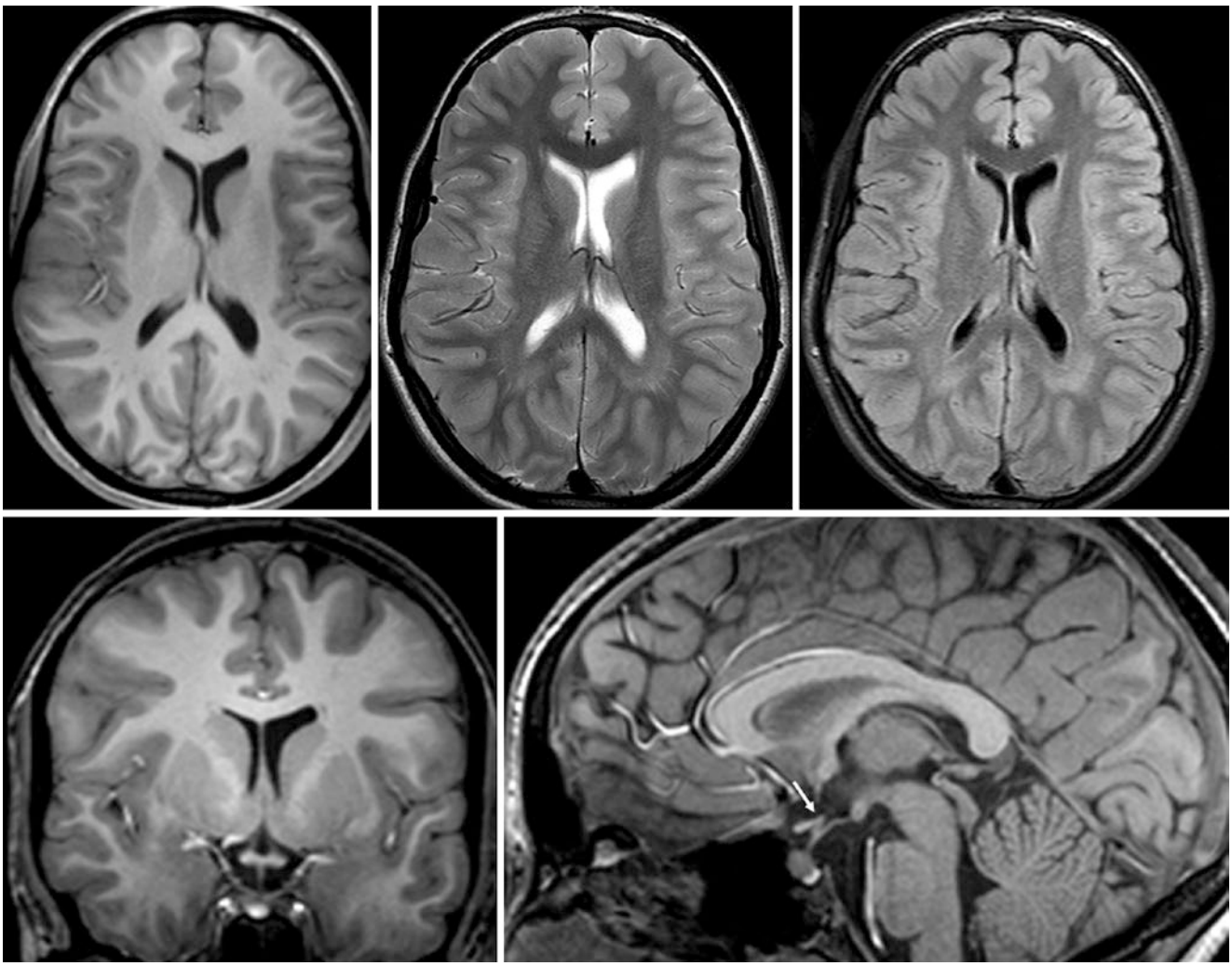

Fig. 15.10 A 12-year-old patient whose 3T MRI included axial T1WI (*top left*), T2WI (*top middle*), FLAIR (*top right*), coronal T1WI (*bottom left*), and sagittal T1WI (*bottom right*). The MRI depicts a slightly asymmetric and enlarged body of the left lateral ventricle. Sagittal T1WI confirms that the optic recess of the third ventricle (*thin arrow*) is not enlarged

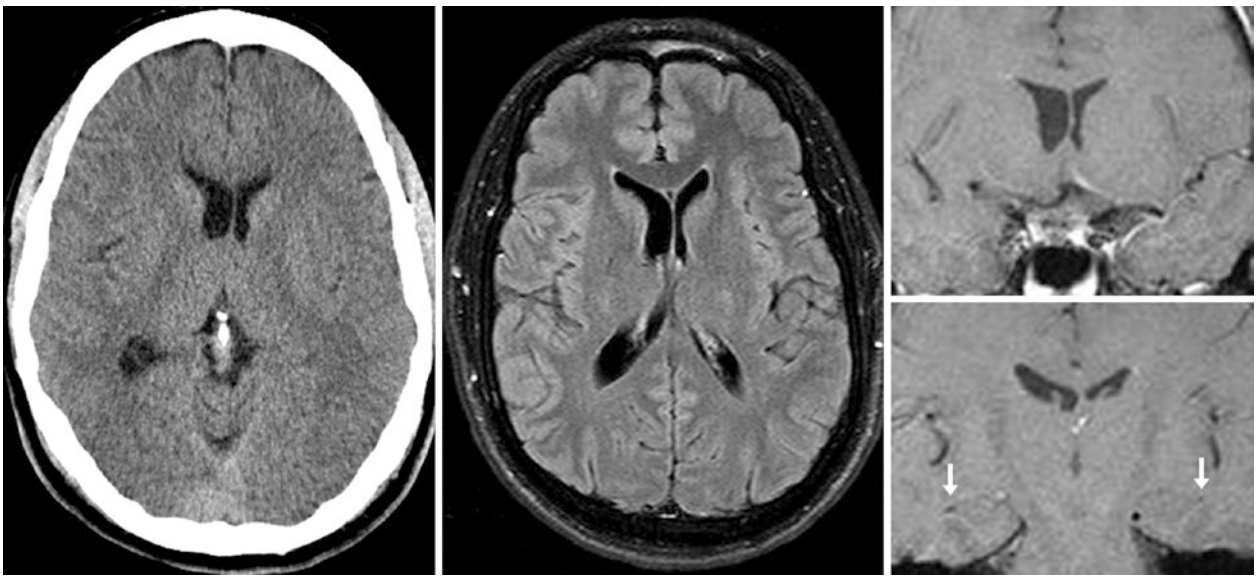

Fig. 15.11 A 32 year old with normal, mild, and asymmetric enlargement of the body and trigone of the right lateral ventricle on NECT (*left*). On an MRI with FLAIR (*middle*) and coronal T1WIs (*right, top, and bottom*), the asymmetry is slightly less pronounced, and the temporal horns (*arrows*) and the remainder of the ventricles are within normal limits

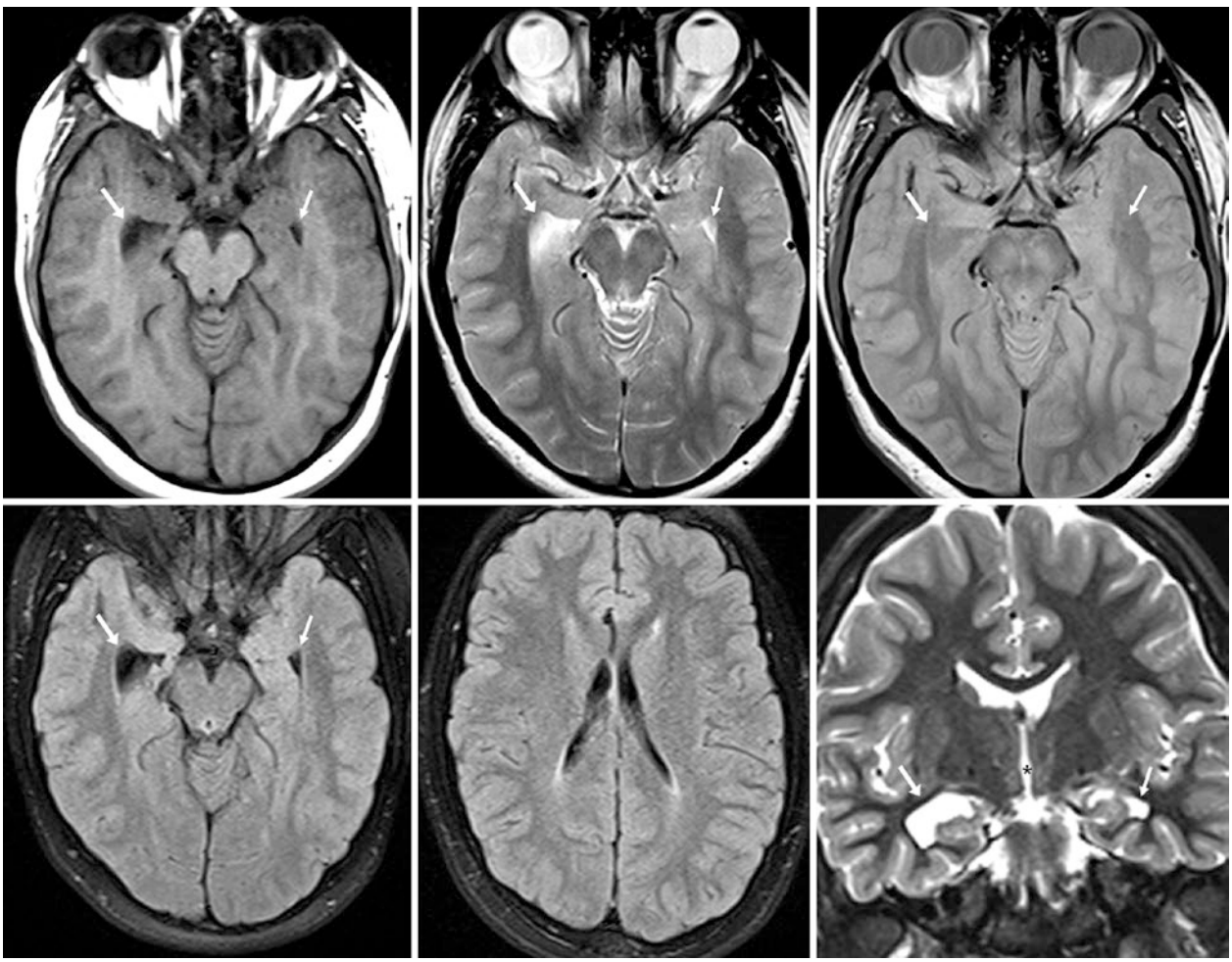

Fig. 15.12 A 14 year old underwent axial T1WI (*top left*), T2WI (*top middle*), proton-density-weighted (*top right*), FLAIR (*bottom left, and middle*), and coronal T2WI (*bottom right*) that depicted an enlarged right temporal horn (*arrows*) that was focal and asymmetric. Note that the contralateral temporal horn (*thin arrows*) and lateral ventricular bodies are not enlarged. This should not be called a choroidal fissure (neuroepithelial cyst) since it is not within that fissure and is not round

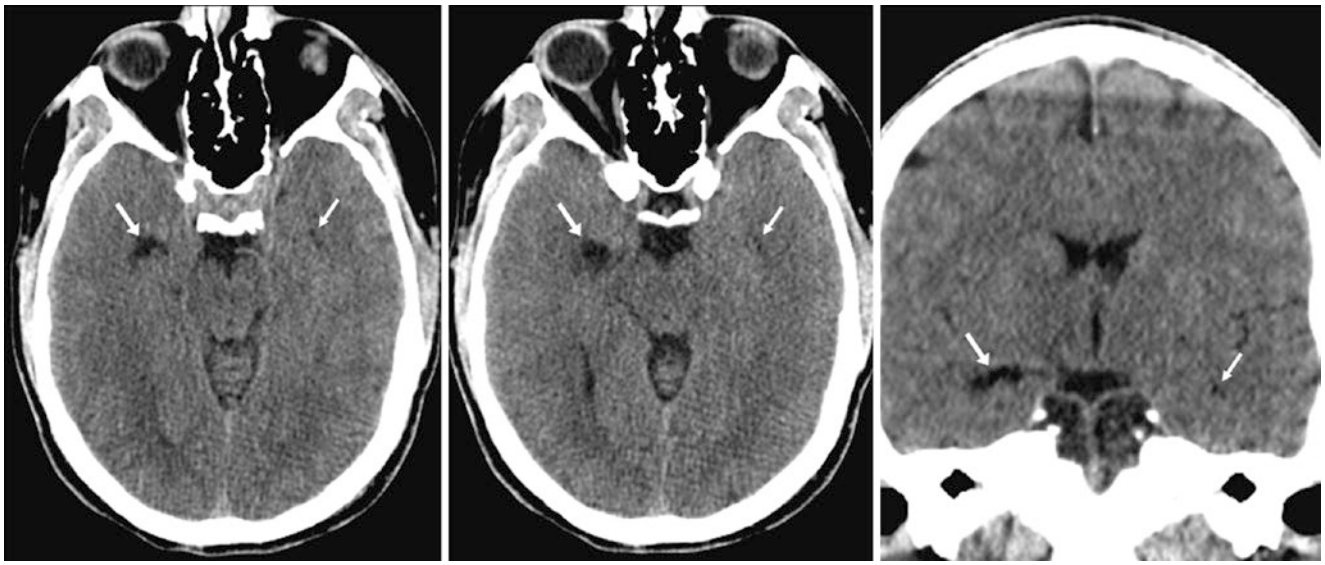

Fig. 15.13 A 33-year-old patient had mild asymmetric enlargement of the temporal horn (*arrows*) of the right lateral ventricle as compared with the left side (*thin arrows*) on axial NECT (*left two images*). On a coronal reformat (*right*), the finding is shown to be within the temporal horn and should not be mistaken for a choroidal fissure cyst because it is not within that fissure

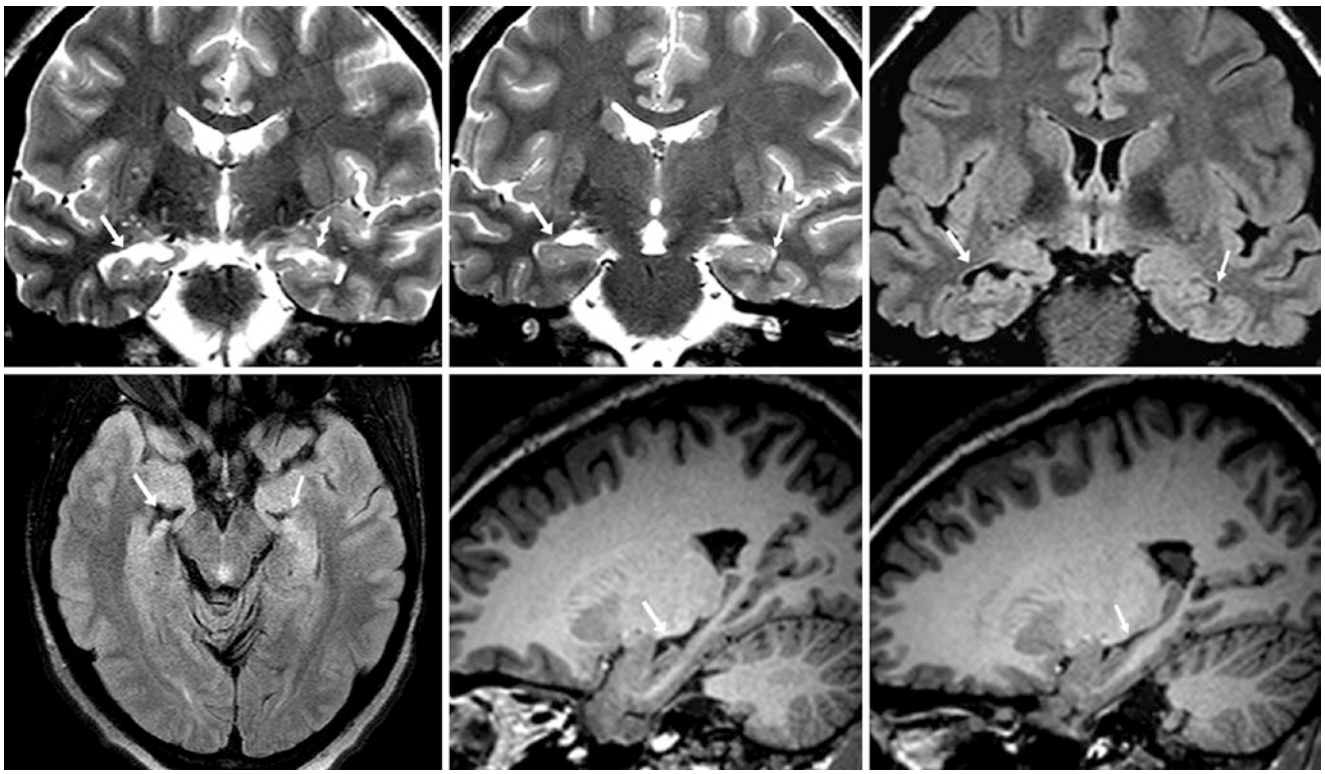

Fig. 15.14 A 21 year old was given a coronal T2WI MRI (*top left, top middle*) that demonstrated prominence of the right temporal horn anteriorly (*arrows*) as compared to the left (*thin arrows*). This is clearly indicated to be within the ventricular system on coronal (*top right*) and axial (*bottom left*) FLAIR images and is therefore shown not to be a cyst. Sagittal T1WIs of the right (*bottom middle*) and left (*bottom right*) sides further depict the temporal horns

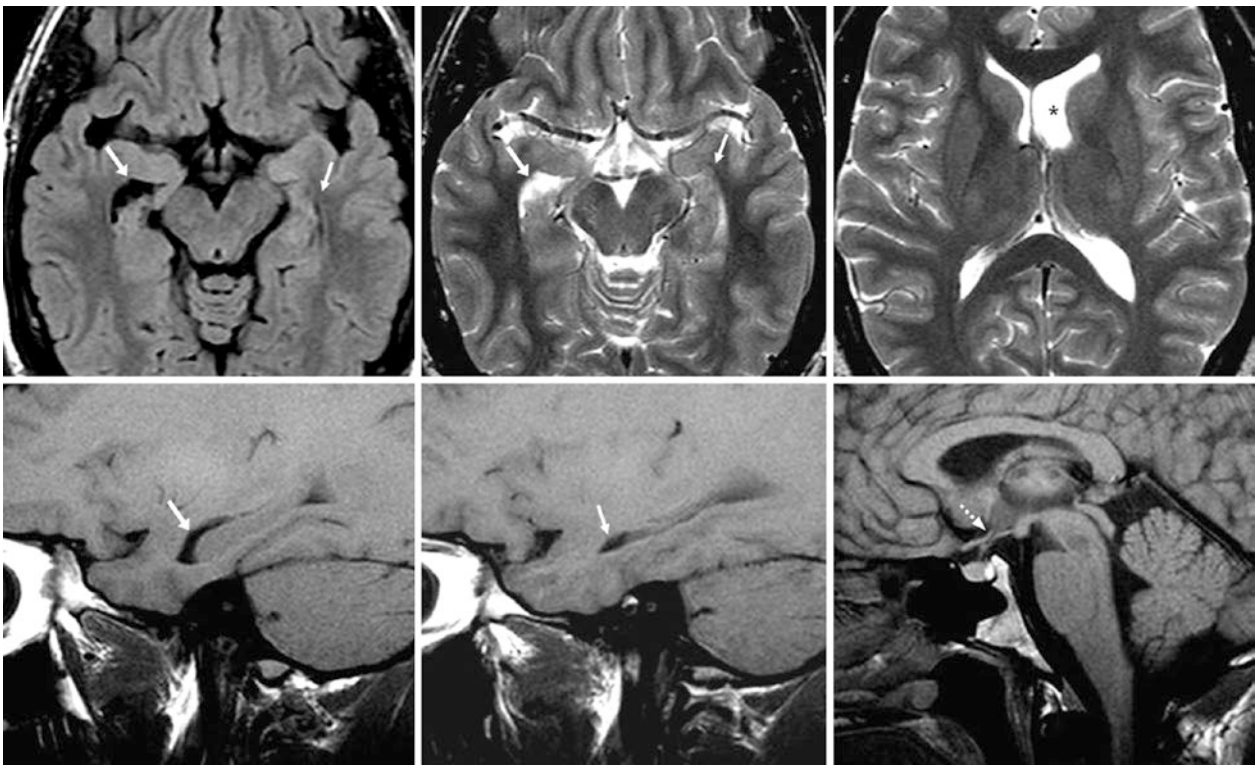

Fig. 15.15 An 18 year old with asymmetric prominence of the right temporal horn (*arrows*) on FLAIR (*top left*) and T2WI (*top middle*) when compared with the left one (*thin arrows*). The left lateral ventricle's frontal horn (*) and body appear larger on higher images (*top right*); this is also a normal variation. The cyst-like right temporal horn is confirmed to be intraventricular on sagittal T1WI (*bottom left*) as compared to T1WIs of the right side (*bottom middle*). A midline T1WI (*bottom right*) shows no hydrocephalus, since the optic recess (*dotted arrow*) is normal in size

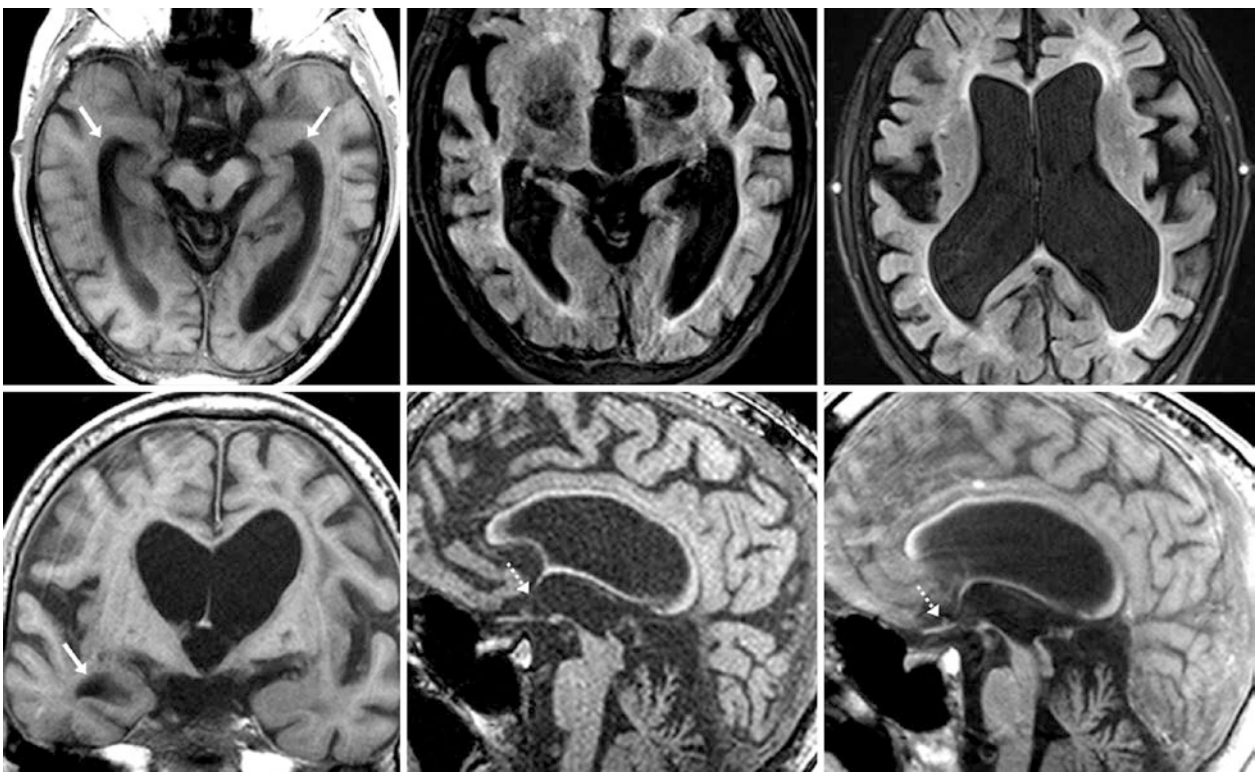

Fig. 15.16 A 54-year-old patient was considered to have atrophy simulating hydrocephalus. On a 3T MRI with axial T1WI (*top left*), FLAIR (*top middle and right*), and coronal T1WI (*bottom left*), there are enlarged temporal horns (*arrows*) and lateral ventricular bodies (*top right*). However, on midline sagittal T1WIs (*bottom middle and right*), the optic recess of the third ventricle (*dotted arrows*) is not enlarged. The PVWM is severely atrophied; such atrophy can simulate hydrocephalus

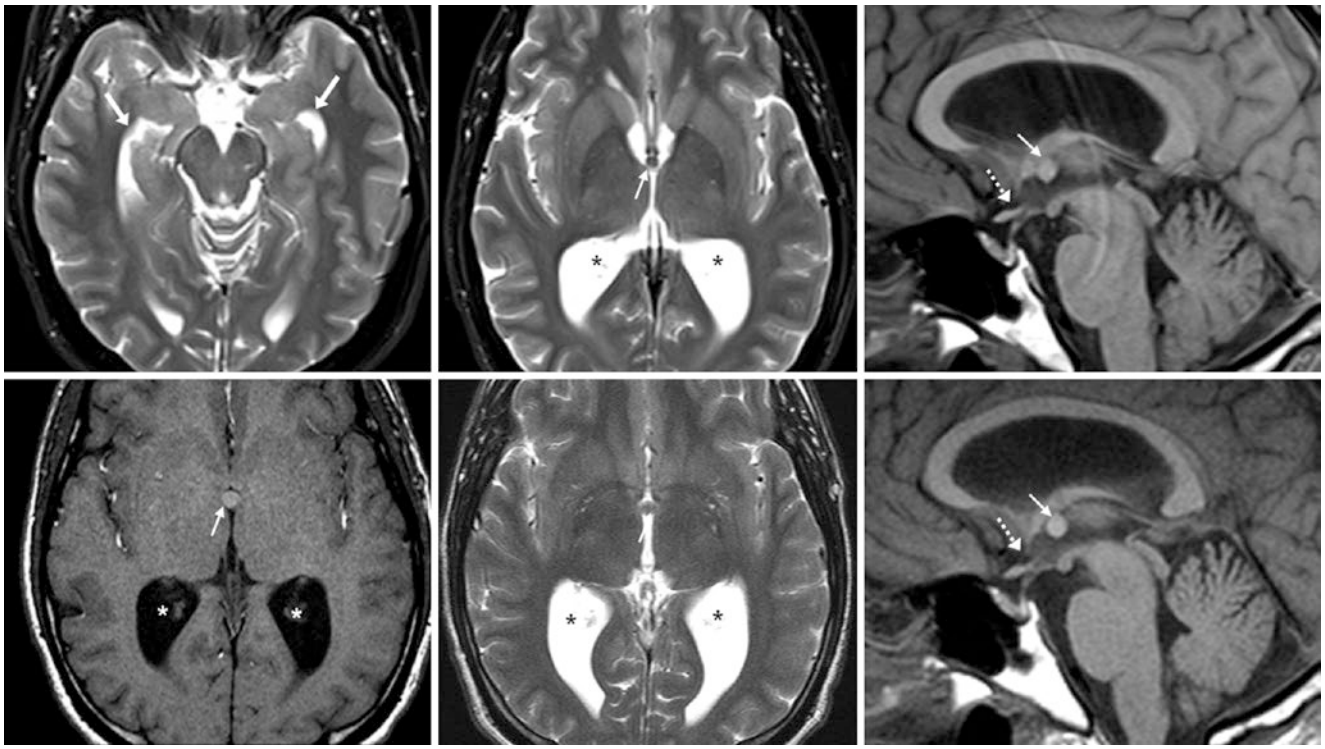

Fig. 15.17 A 37 year old was seen with culpocephaly simulating hydrocephalus. Axial T2WIs (*top left* and *middle)* showed a small colloid cyst at midline where the foramina of Monro meet (*thin arrows*), and there are prominent temporal horns and mildly enlarged lateral ventricular bodies (*). However, on sagittal T1WI (*top right*), the optic recess (*dotted arrows*) was normal. Six months later, the axial T1WI (*bottom left*), T2WI (*bottom middle*), and sagittal T1WI (*bottom right*) were unchanged

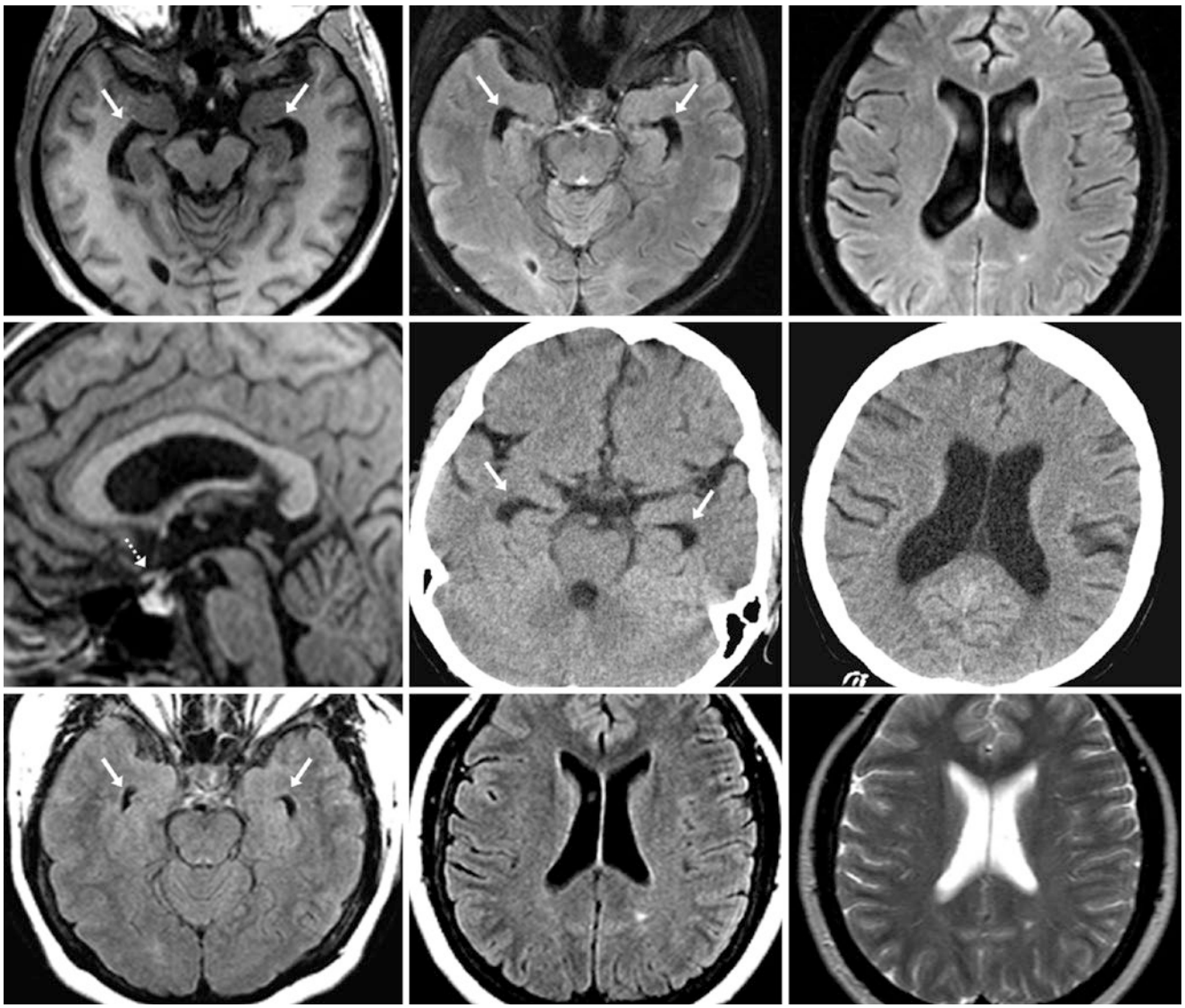

Fig. 15.18 An 18-year-old patient was seen with cerebral volume loss that simulated hydrocephalus. *Top row:* axial T1WI (*left*) and FLAIR (*middle and right*) show enlarged temporal horns of the lateral ventricles (*arrows*) mimicking hydrocephalus. Mild white matter abnormalities were also noted on FLAIR. *Middle row:* However, on sagittal T1WI (*left*), the optic recess of the third ventricle (*dotted arrow*) is not enlarged. A NECT 1 year later showed no change in size (*middle and right*), with prominent sulci. *Bottom row:* FLAIR (*left and middle*) and T2WI (*right*) were then found from 9 years earlier that showed normal lateral ventricles. Thus, the patient had developed atrophy disproportionate to age (unknown etiology) but not hydrocephalus

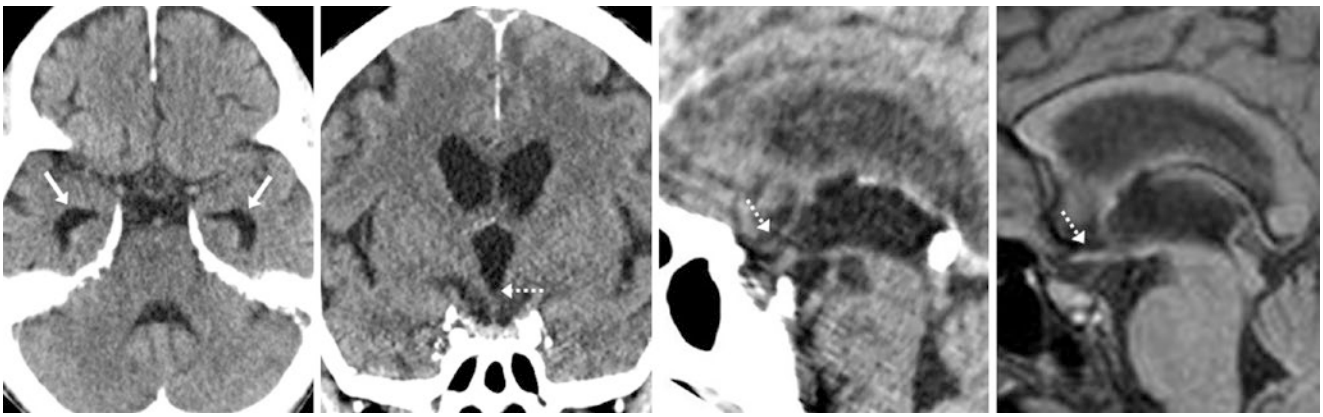

Fig. 15.19 A 65 year old with diagnosed atrophy. Axial (*left*) and coronal (*left middle*) NECT show enlarged temporal horns (*arrows*) and bodies of the lateral ventricles, mimicking hydrocephalus. However, note the sulcal prominence and that on sagittal NECT (*right middle*) and T1WI MRI (*right*), the third ventricle's optic recess (*dotted arrows*) is not enlarged

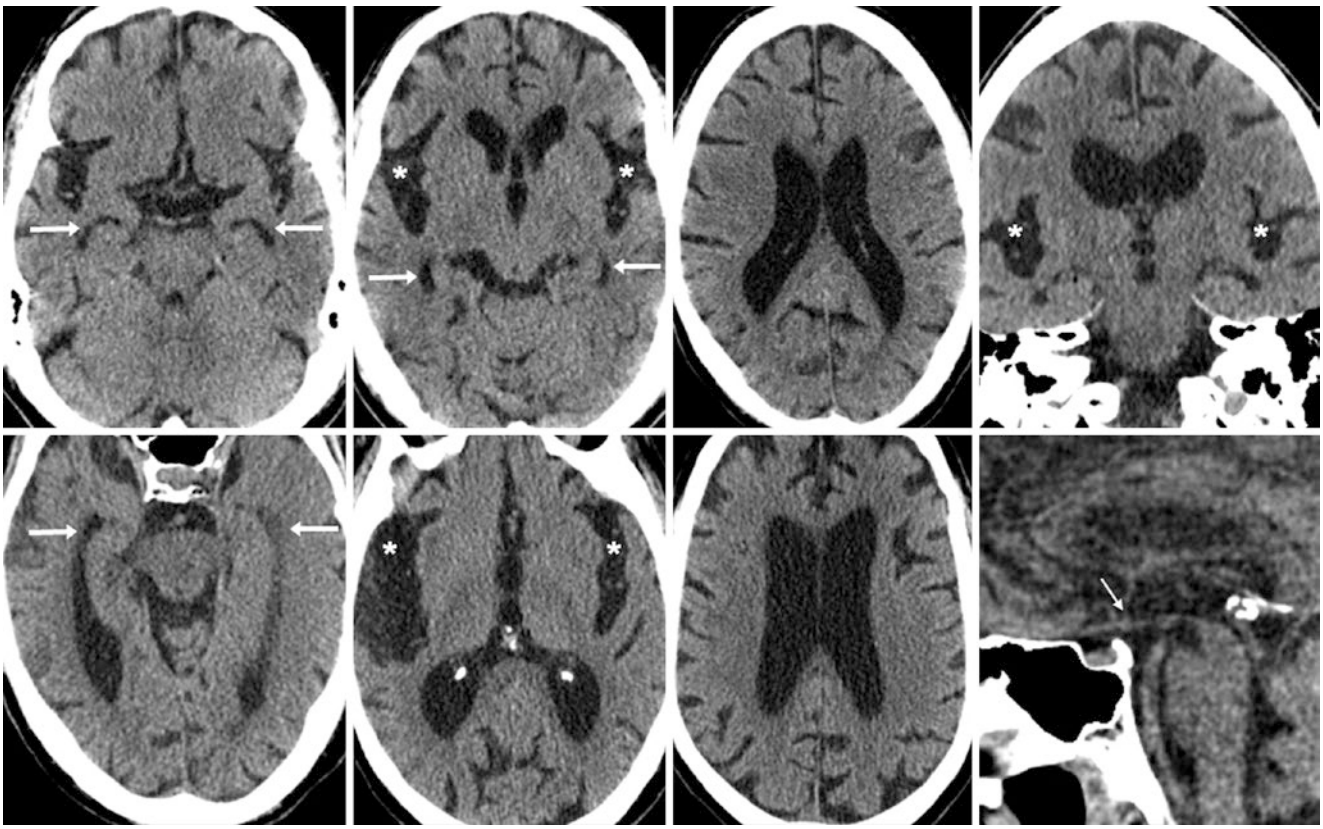

Fig. 15.20 A 63-year-old patient whose axial (*top row*) and coronal (*top right*) NECT images show mildly enlarged temporal horns (*arrows*), sylvian fissures (*), and sulci, suggesting volume loss. On a NECT 4 years later (*bottom row*), the temporal horns have mildly enlarged, simulating hydrocephalus, along with the bodies of the lateral ventricles. However, sagittal reformats (*bottom right*) depicted a normal optic recess (*thin arrows*), confirming that there is no hydrocephalus

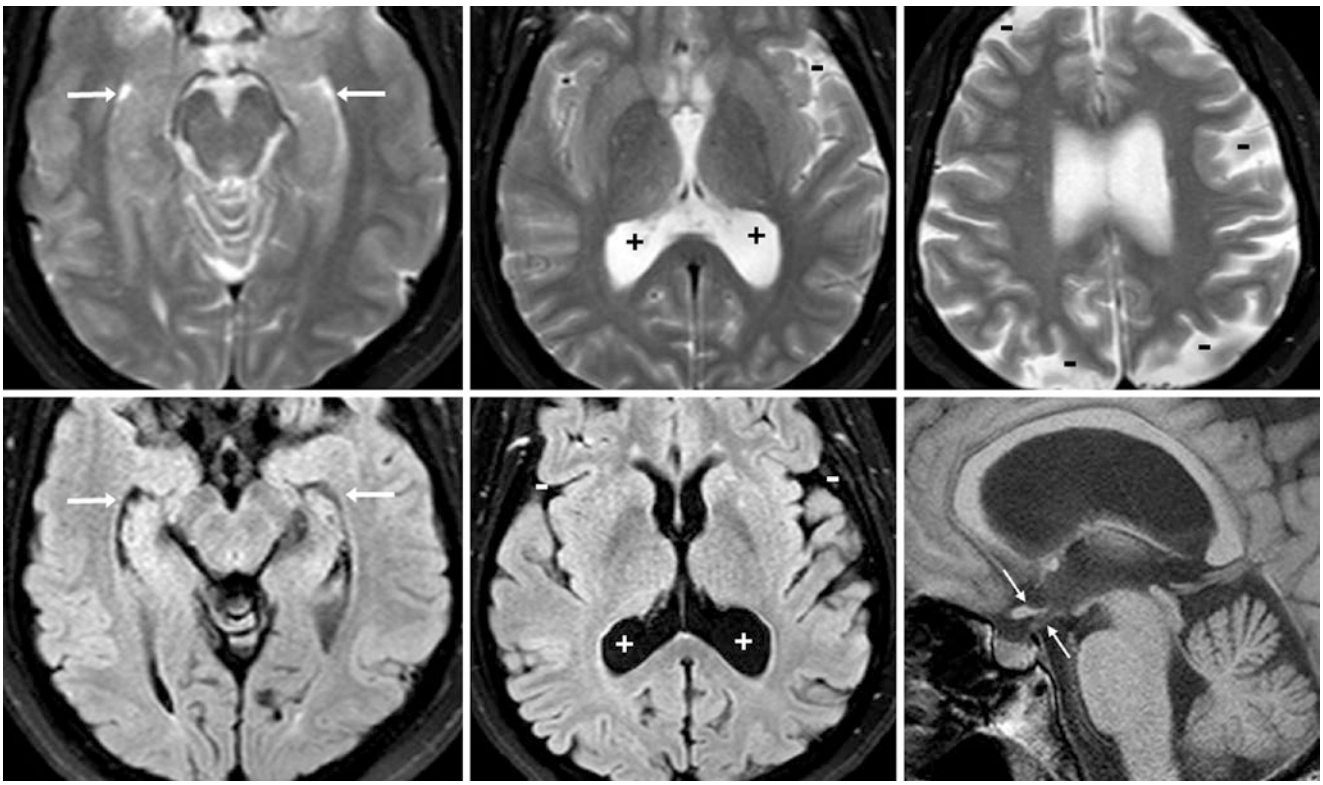

Fig. 15.21 A 51 year old patient whose 1.5T MRI with T2WIs (*top row*) and FLAIR (*bottom left and middle*) depicted normal-sized temporal horns (*arrows*) but mildly enlarged atria of the lateral ventricles (+) and scattered prominent sulci (−); these were indications of atrophy, not hydrocephalus. On sagittal T1WI (*bottom right*), the third ventricular recesses are normal (*thin arrows*)

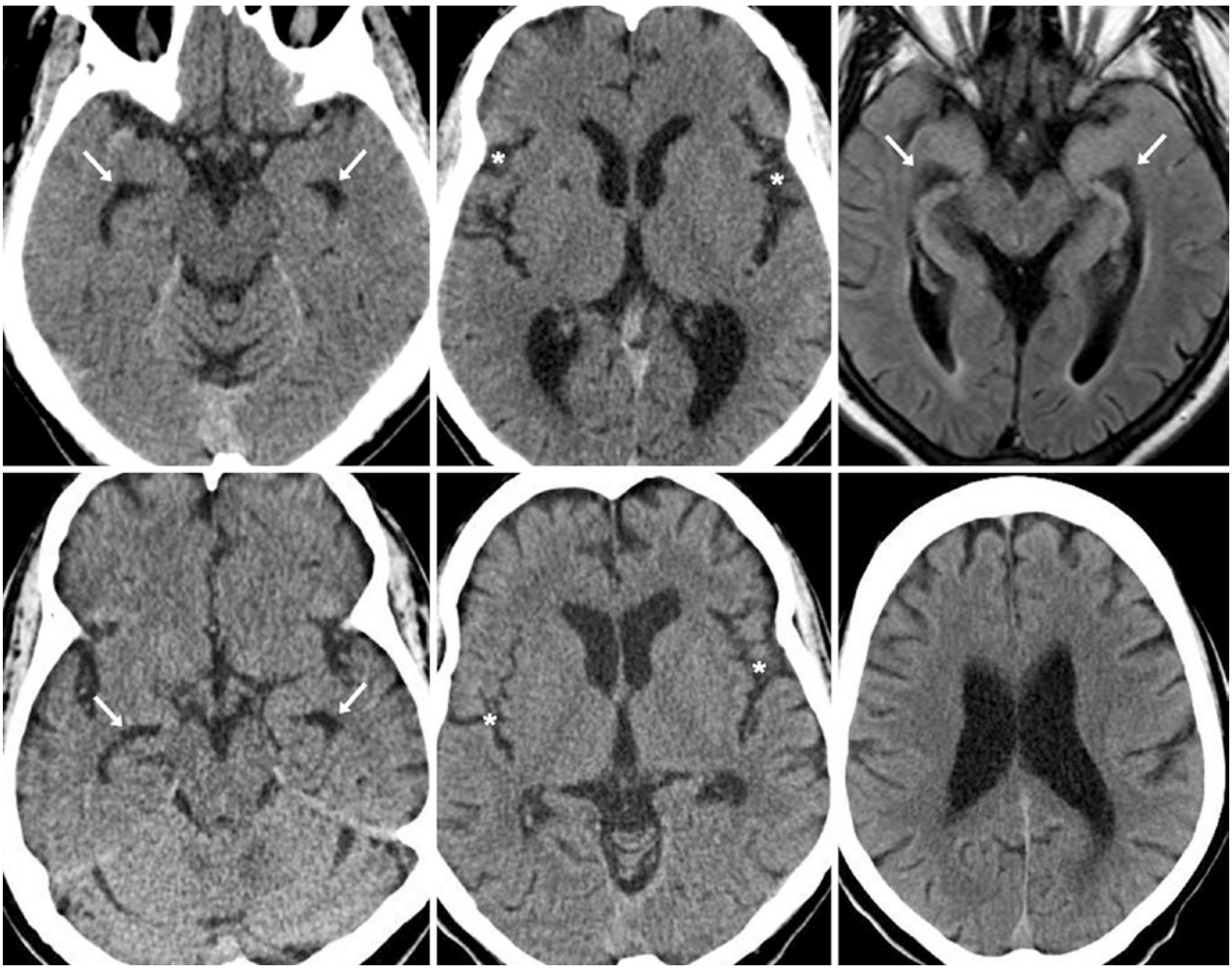

Fig. 15.22 A 58 year old who showed mild prominence of the temporal horns (*arrows*) on NECT (*top left and middle*), and on 1.5T FLAIR MRI (*top right*). The temporal horns were noted to be larger than on a NECT 7 years prior (*bottom row*), but this did not represent hydrocephalus because the sulci, including the sylvian fissures (*), are similarly enlarged

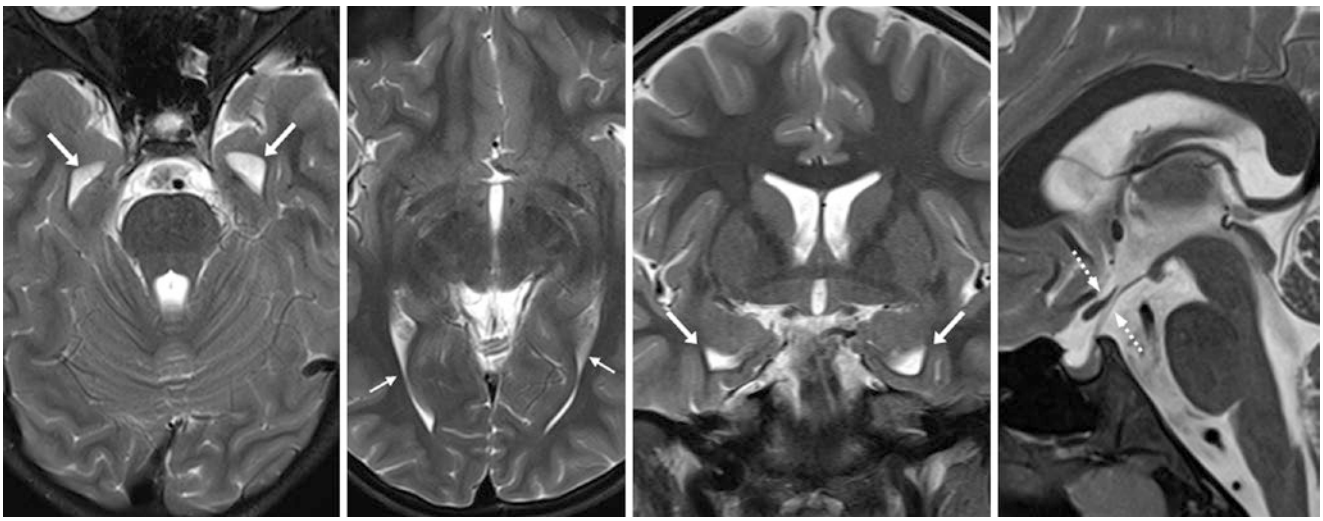

Fig. 15.23 A 7 year old with mild prominence of only the anterior temporal horns bilaterally (*arrows*) compared with the posterior/occipital horns (*thin arrows*) on axial (*left and left middle*) and coronal (*right middle*) 3T MRI T2WIs. On sagittal T2WI (*right*), note that the anterior recesses of the third ventricle (*dotted arrows*) have normal acute angles

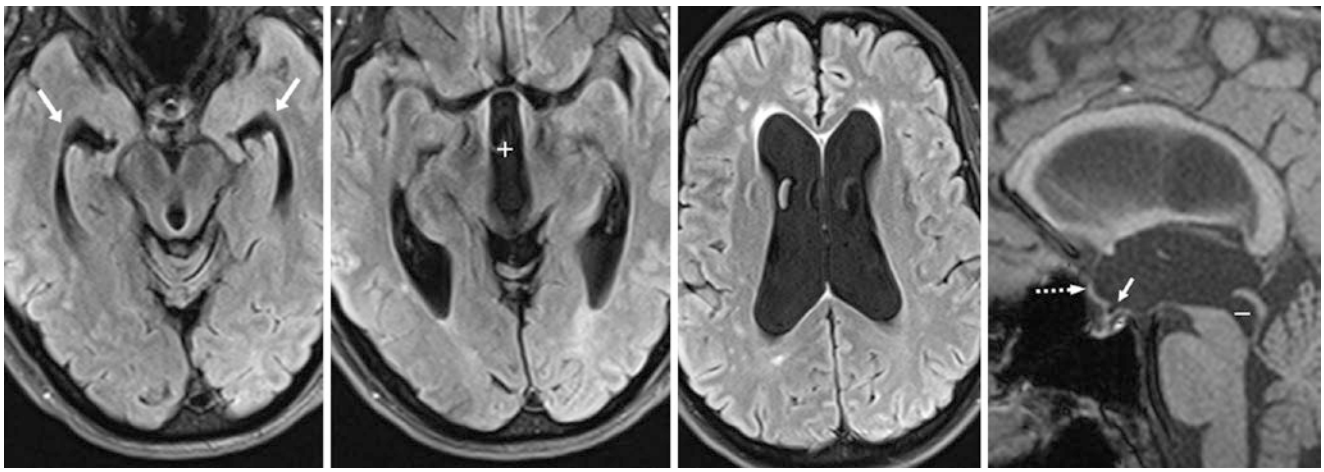

Fig. 15.24 Comparison case of hydrocephalus from aqueductal stenosis. A 48 year old had mild enlargement of the temporal horns anteriorly (*arrows*) and the third ventricle (+) on serial FLAIR images (*left three images*), while on sagittal T1WI (*right*) the optic recess of the anterior third ventricle (*dotted arrow*) was also enlarged. Note the normal-sized infundibular recess (*thin arrow*) just posterior to the optic recess, while there is an enlarged cerebral aqueduct (–)

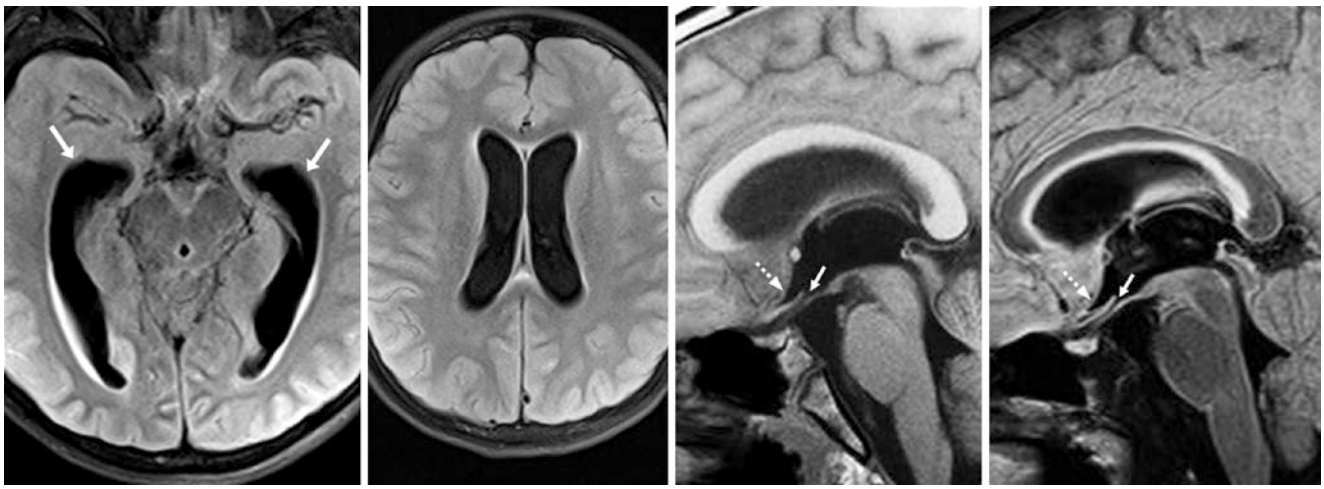

Fig. 15.25 Comparison case of hydrocephalus from bacterial meningitis. An 11 year old had mild to moderately enlarged temporal horns (*arrows*) and bodies of the lateral ventricles on axial FLAIR images (*left two images*). On sagittal T1WI (*right middle*) and FLAIR (*right*), the optic recess of the anterior third ventricle (*dotted arrows*) is mildly prominent, confirming hydrocephalus. Also, note the nonenlarged infundibular recess (*thin arrows*) of the third ventricle, while transependymal signal on FLAIR suggests a more recent development of hydrocephalus

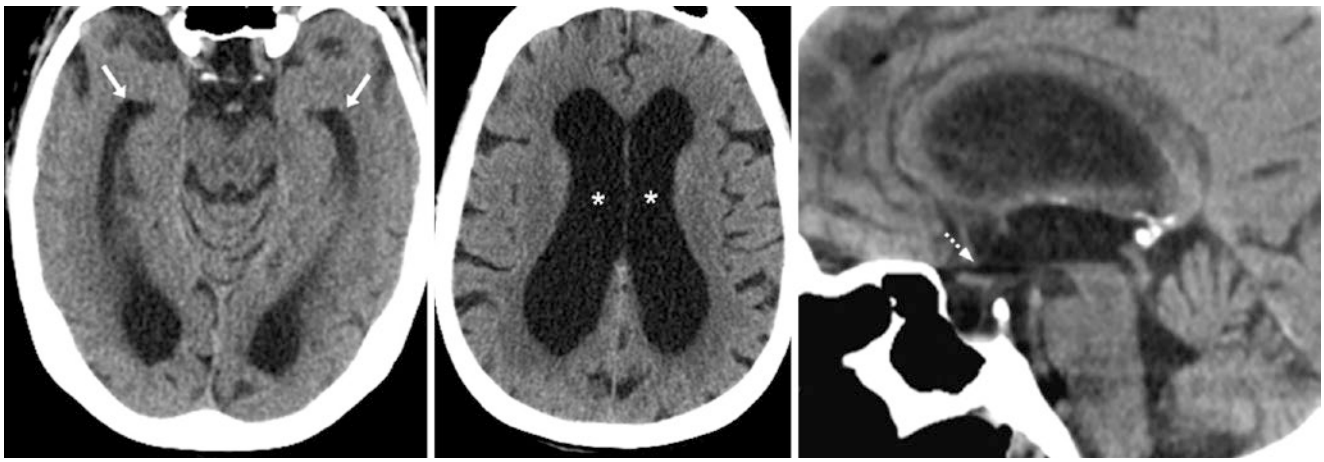

Fig. 15.26 Comparison case of mild hydrocephalus**.** A 75 year old had mildly enlarged temporal horns (*arrows*) and bodies (*) of the lateral ventricles on axial NECT (*left two images*), while on sagittal reformats (*right*), the optic recess of the anterior third ventricle (*dotted arrow*) is also moderately enlarged. Although there is atrophy present, the enlargement of the third ventricle anteriorly would suggest an underlying component of hydrocephalus as well

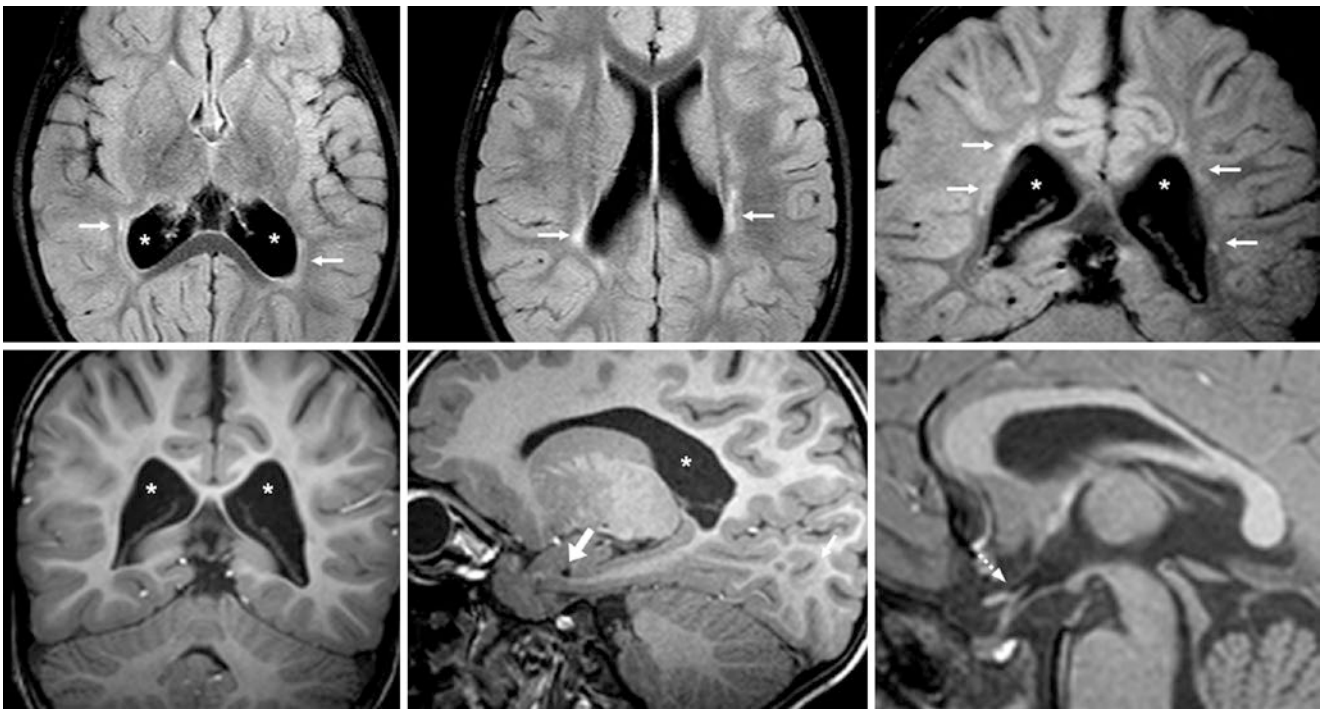

Fig. 15.27 Comparison case of PVL. In a 3 year old, a 3T MRI showed mildly enlarged posterior bodies (*) of the lateral ventricles on axial FLAIR (*top left and middle*), coronal FLAIR (*top right*), coronal T1WI (*bottom left*), and sagittal T1WI (*bottom middle and right*). Note the hyperintense and thinned PVWM (*thin arrows*). Both the temporal horns (*arrow*) and optic recess (*dotted arrows*) appear normal, excluding hydrocephalus

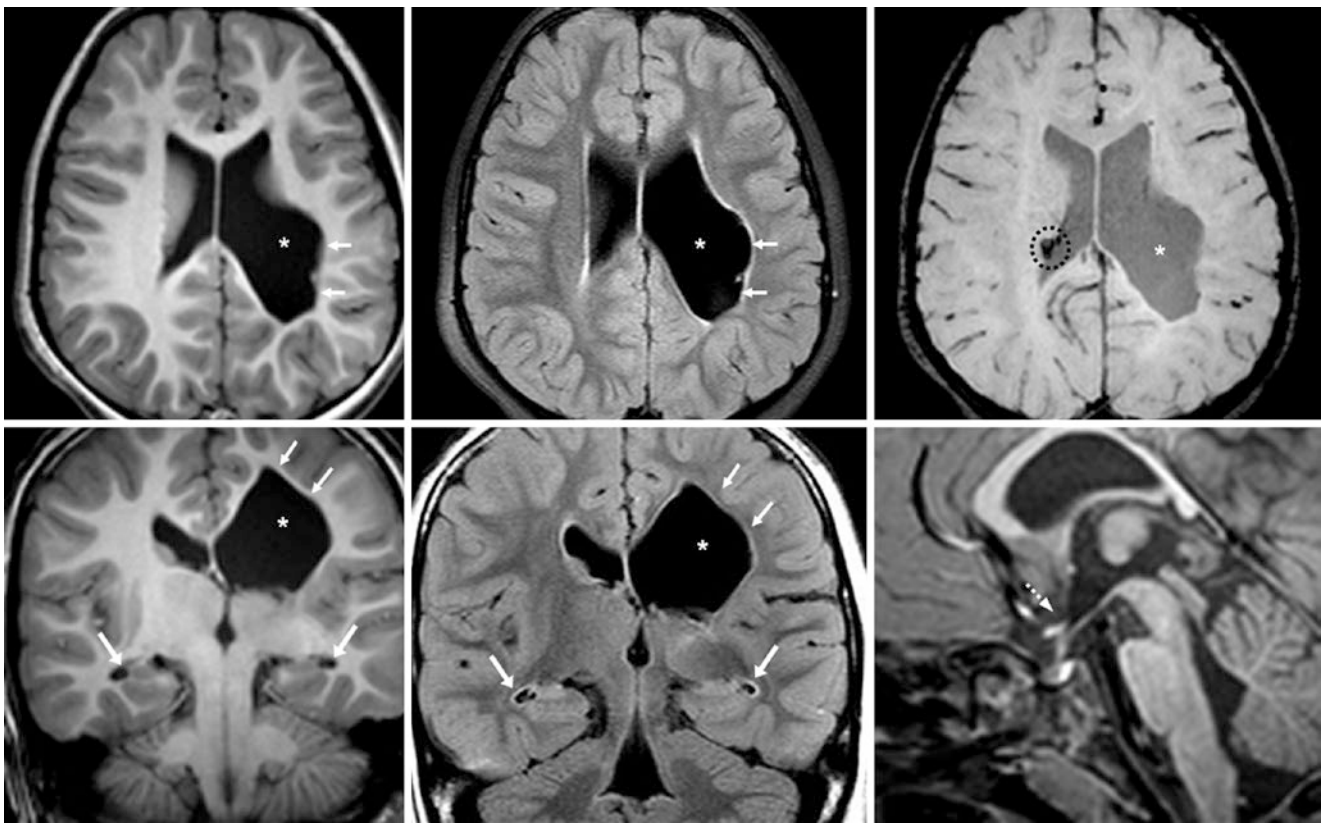

Fig. 15.28 Comparison case of PVL. A 5 year old who underwent a 3T MRI had an enlarged left lateral ventricular posterior body (*) on axial T1WI (*top left*), FLAIR (*top middle*), and SWI (*top right*), with thinned PVWM (*thin arrows*). The findings are also shown on coronal T1WI (*bottom left*), FLAIR (*bottom middle*), and sagittal T1WI (*bottom right*). SWI depicts a tiny germinal matrix hemorrhage (*dotted circle*). The normal optic recess (*dotted arrows*) excludes hydrocephalus

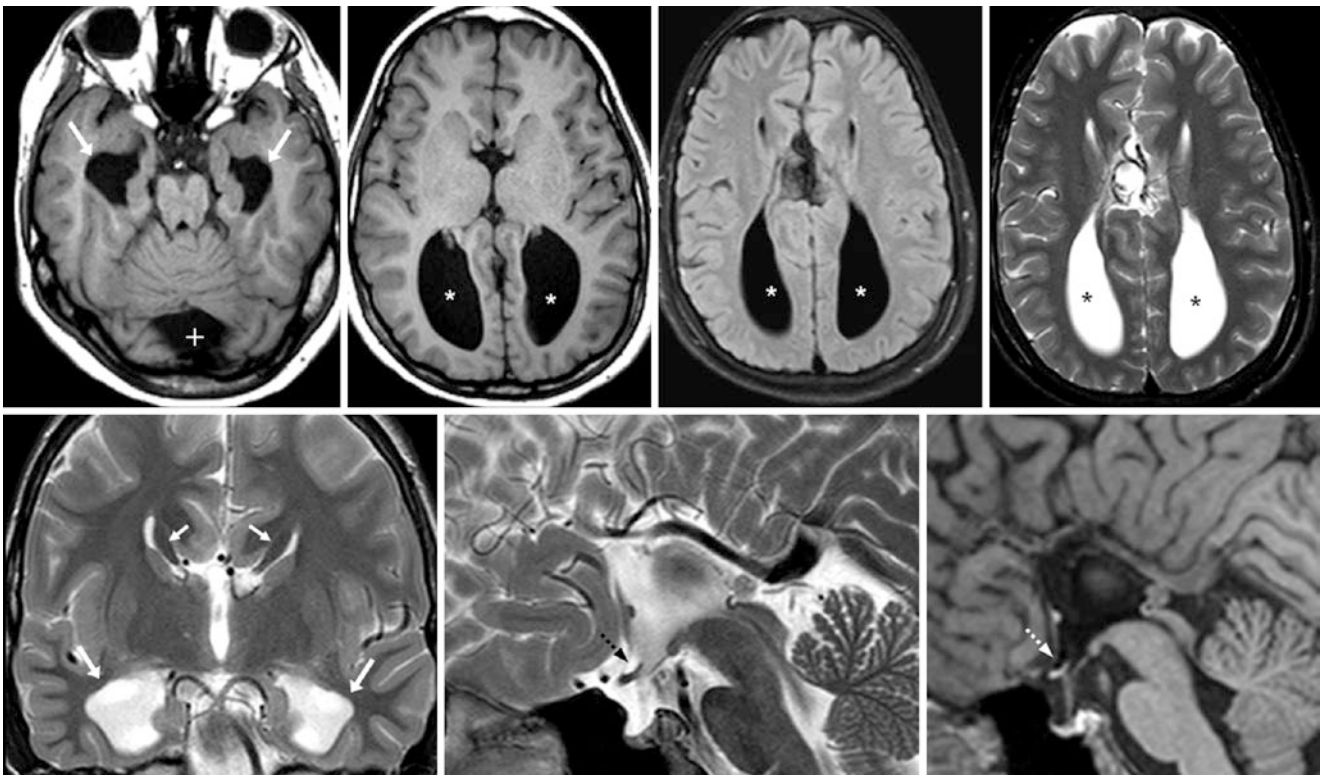

Fig. 15.29 Comparison case of culpocephaly from callosal agenesis. A 12 year old had enlarged posterior bodies (*) and temporal horns (*arrows*) of the lateral ventricles that mimic hydrocephalus on T1WI (*top left* and *left middle*), FLAIR (*top, right middle*), and T2WI (*top right*). Callosal agenesis is suggested by straightened lateral ventricles on axial images, and a steer horn appearance on coronal T2WI (*bottom left*) with Probst bundles (*thin arrows*). Midline sagittal T2WI (*bottom middle*) and T1WI (*bottom right*) both depict a normal optic recess (*dotted arrows*)

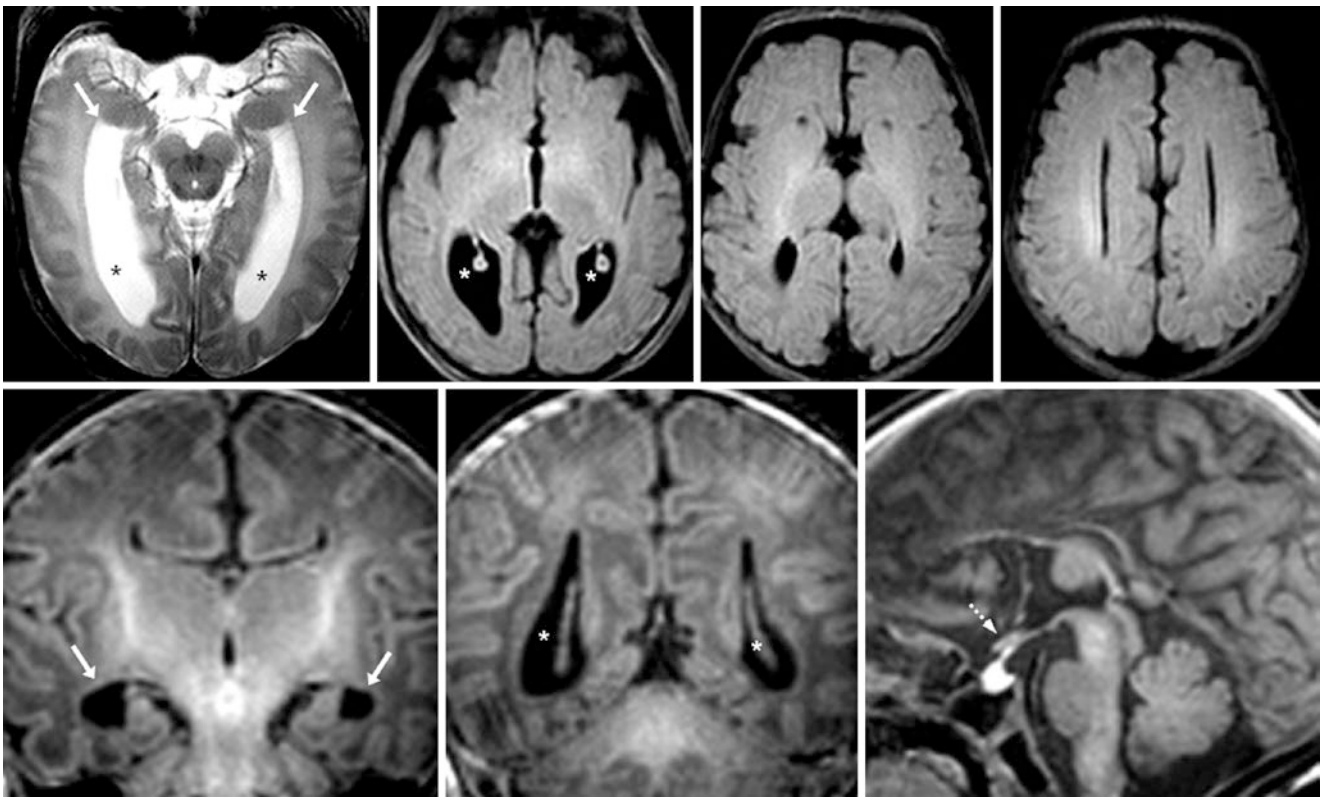

Fig. 15.30 Comparison case of culpocephaly caused by callosal agenesis. A 2 day old infant had enlarged temporal horns (*arrows*) and culpocephaly (*), which simulate hydrocephalus on T2WI (*top left*), and FLAIR (*top right three images*). Note the straightened lateral ventricles with a steer horn appearance on coronal T1WI (*bottom left and middle*). On a sagittal T1WI (*bottom right*), the optic recess (*dotted arrow*) appears normal, which excludes hydrocephalus

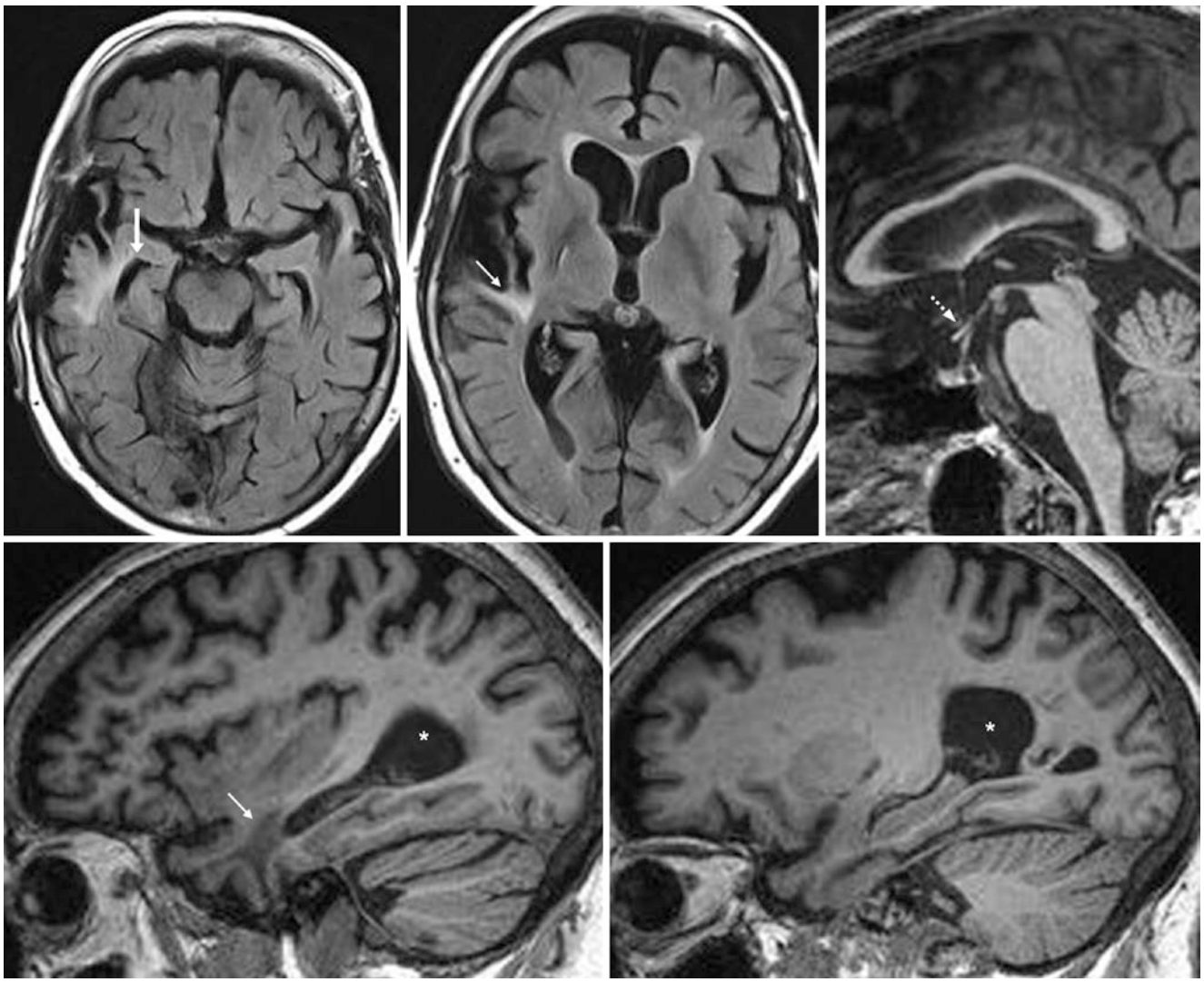

Fig. 15.31 Comparison case of enlargement from focal atrophy. A 75 year old had right temporal horn enlargement (*arrows*) caused by focal right temporal atrophy (*thin arrows*) on axial FLAIR (*top left and middle*). Note a normal optic recess (*dotted arrow*) on midline sagittal T1WI (*top right*). On sagittal T1WI of the right (*bottom left*) and left (*bottom right*) sides, the trigones of the lateral ventricles (*) are also prominent, probably the result of age-related mild global cerebral atrophy

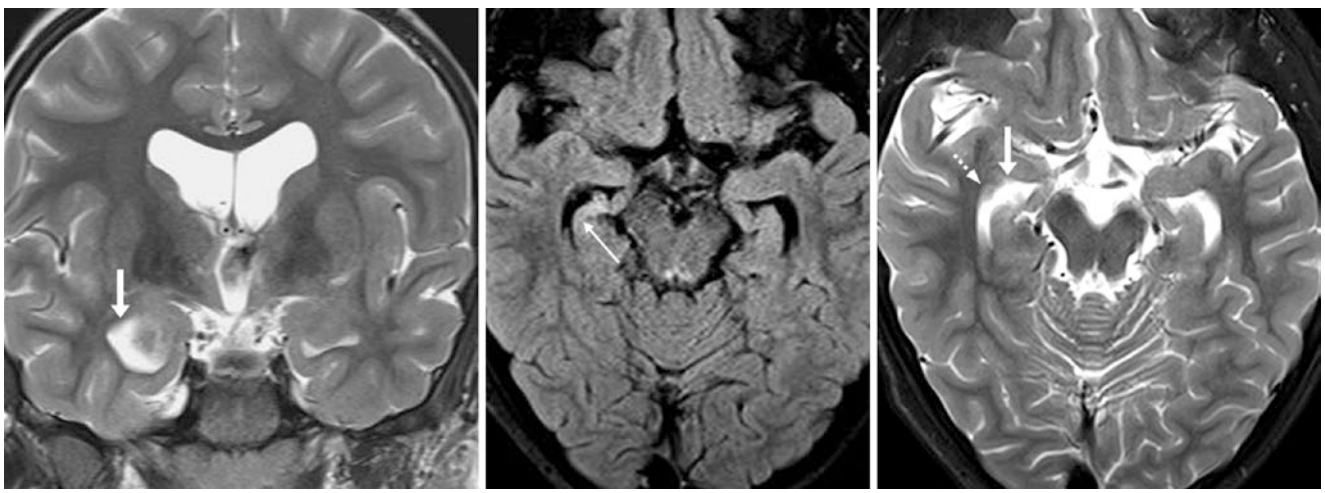

Fig. 15.32 Comparison case of enlargement from focal atrophy. A 9 year old with seizures had subtle anterior temporal horn enlargement (*arrows*) on coronal T2WI 3T MRI (*left*) caused by focal right hippocampal sclerosis (*thin arrow*), as shown on axial FLAIR (*middle*). On axial T2WI (*right*), a tiny nodular heterotopia (*dotted arrow*) portrays the seizure's etiology

Suggested Reading

Achiron R, Yagel S, Rotstein Z, Inbar O, Mashiach S, Lipitz S. Cerebral lateral ventricular asymmetry: is this a normal ultrasonographic finding in the fetal brain? Obstet Gynecol. 1997;89:233–7.

Barkovich AJ. Hydrocephalus. In: Barkovich AJ, editor. Pediatric neuroimaging. 4th ed. Philadelphia: Lippincott Williams & Wilkins; 2005. p. 686–9.

Grosman H, Stein M, Perrin RC, Gray R, St Louis EL. Computed tomography and lateral ventricular asymmetry: clinical and brain structural correlates. Can Assoc Radiol J. 1990;41:342–6.

Kiroğlu Y, Karabulut N, Oncel C, Yagci B, Sabir N, Ozdemir B. Cerebral lateral ventricular asymmetry on CT: how much asymmetry is representing pathology? Surg Radiol Anat. 2008;30:249–55.

Voigt K, Bockenheimer S. Neuroradiologic and clinical correlations in asymmetric lateral ventricles and posterior cornua in pneumoencephalograms. Fortschr Neurol Psychiatr Grenzgeb. 1978;46:440–51.

Cerebral or Cerebellar Volume Loss Simulating Subdural Hematomas, Hygromas, and Arachnoid Cysts

16

Cerebral volume loss and *cerebellar volume loss* (i.e., atrophy) are usually apparent on imaging because of the prominence of the *subarachnoid spaces* (SASs) with associated widening of the sulci, along with mild, progressive enlargement of the ventricles, particularly the lateral ventricles. Typically, white matter volume loss, particularly of the *periventricular white matter* (PVWM) also accompanies such findings, all of which typically progress with age. However, bilateral, *chronic hypodense subdural hematomas or hygromas* (SDHs) are not uncommon in the elderly; in particular, patients who have been receiving long-term anticoagulation therapy are at risk for developing SDHs. Such chronic or acute SDHs are usually distinguishable from global volume loss (i.e., atrophy), which can even appear asymmetric between sides. One quite practical method to distinguish SDH from atrophy is to note the location and path of the *cortical veins*. With atrophy, the cortical veins traverse the CSF-density, hypoattenuating fluid, while with SDHs the vessels are pushed inward and compressed against the cortical surface. SDHs may also cause a mass effect if they are large enough. Also, any internal density or layering of isodense or hyperdense material indicates hemorrhage, typically the more recent acute or subacute component.

Additionally, it can be quite difficult to distinguish focal areas of cortical volume loss along the convexities from *small arachnoid cysts* (ACs) or small *focal SDHs* or *epidural hematomas* (EDHs). Mild, asymmetric volume loss may be present normally, while *focal encephalomalacia* from a remote injury may be superimposed on diffuse global cerebral volume loss, which can be a source of confusion. ACs are typically asymptomatic if they are not extremely large, and therefore this distinction is usually academic. However, it is important to be aware that ACs occasionally enlarge, particularly after trauma or with anticoagulation, which can at times lead to bleeding within them.

Thus, although cerebral and cerebellar volume loss with prominent SASs is not normal in younger patients, this is a "don't touch" appearance whenever it occurs no matter what the cause, since volume loss or atrophy can be confused with SDHs, ACs, or even hydrocephalus. (Methods to distinguish hydrocephalus are noted in prior chapters, such as Chapter 15). Additionally, diffuse atrophy can be considered normal in the elderly if it is not disproportionate to the patient's age. Notably, volume loss or atrophy affecting certain lobes more than others can be hallmarks in some chronic *neurodegenerative disorders* that cause dementia. The principle behind this section is distinguishing volume loss/atrophy from pathologic conditions that may acutely worsen or cause mass effects, such as SDHs, ACs, and hydrocephalus.

16.1 Cerebellar (Without Cerebral) Volume Loss Simulating Chronic Subdural Hematomas or Hygromas

Cerebellar volume loss or atrophy is usually less prominent than the degree of cerebral volume loss in a given patient and is only rarely asymmetric from side-to-side. Rarely, cerebellar volume loss is disproportionate to that of the cerebrum. It can be difficult to discern severe cerebellar atrophy from bilateral subdural fluid collections such as *hygromas* or *hematomas*. However, bilateral, extra-axial fluid collections in the posterior fossa are quite uncommon (Figs. 16.1 and 16.2).

A.M. McKinney, *Atlas of Normal Imaging Variations of the Brain, Skull, and Craniocervical Vasculature*,
DOI 10.1007/978-3-319-39790-0_16

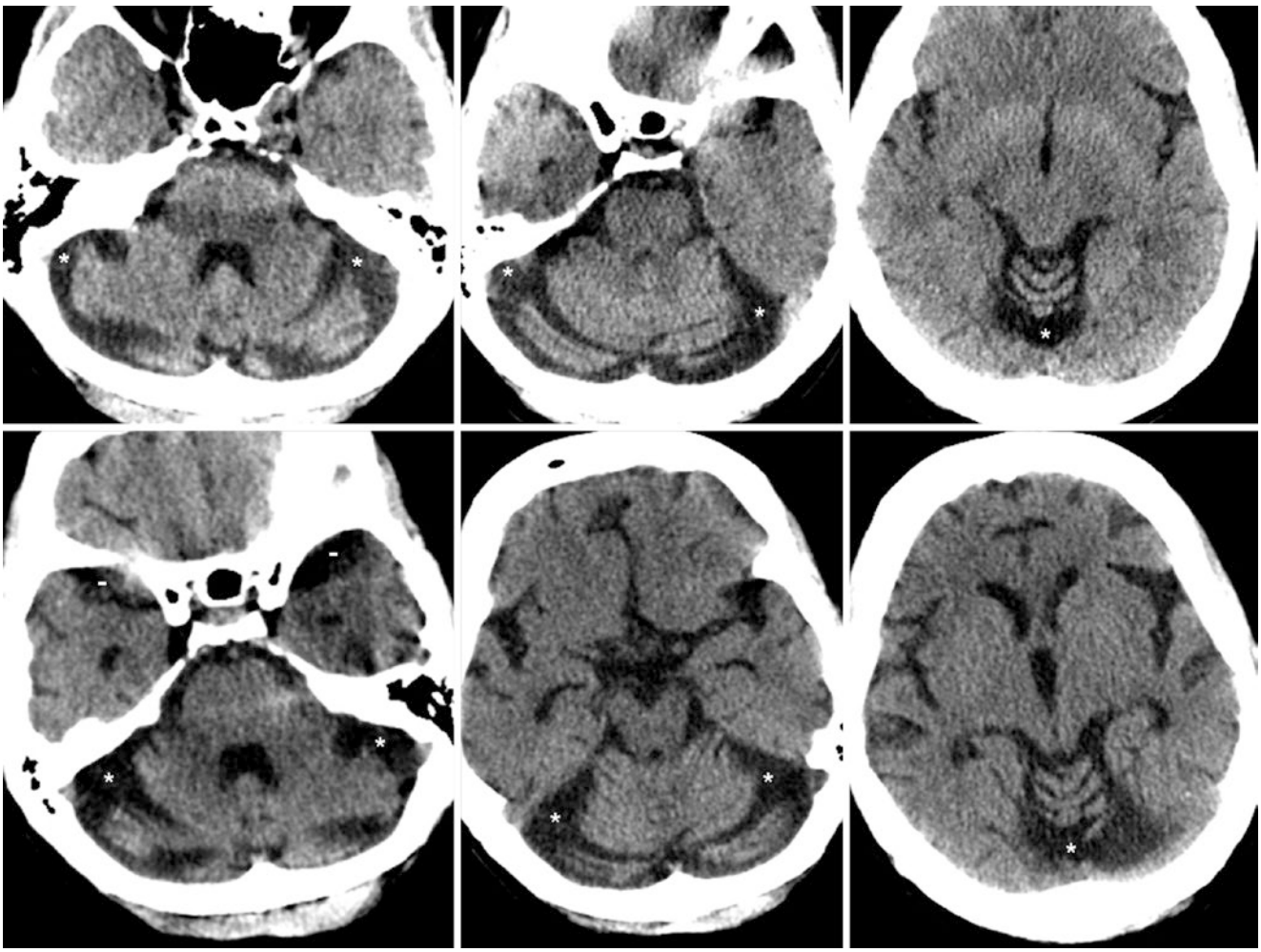

Fig. 16.1 The NECT (*top row*) of a 62 year old shows bilateral, prominent SASs (*) along the cerebellar convexities that simulate chronic SDHs and are disproportionate to the SASs around the cerebrum; note the mildly prominent sylvian fissures. On a NECT 2 years later, the SASs along the cerebellar convexities and sylvian fissures progressed, confirming atrophy. The bilateral, prominent SASs in the middle cranial fossa (–) also increased, thus simulating ACs

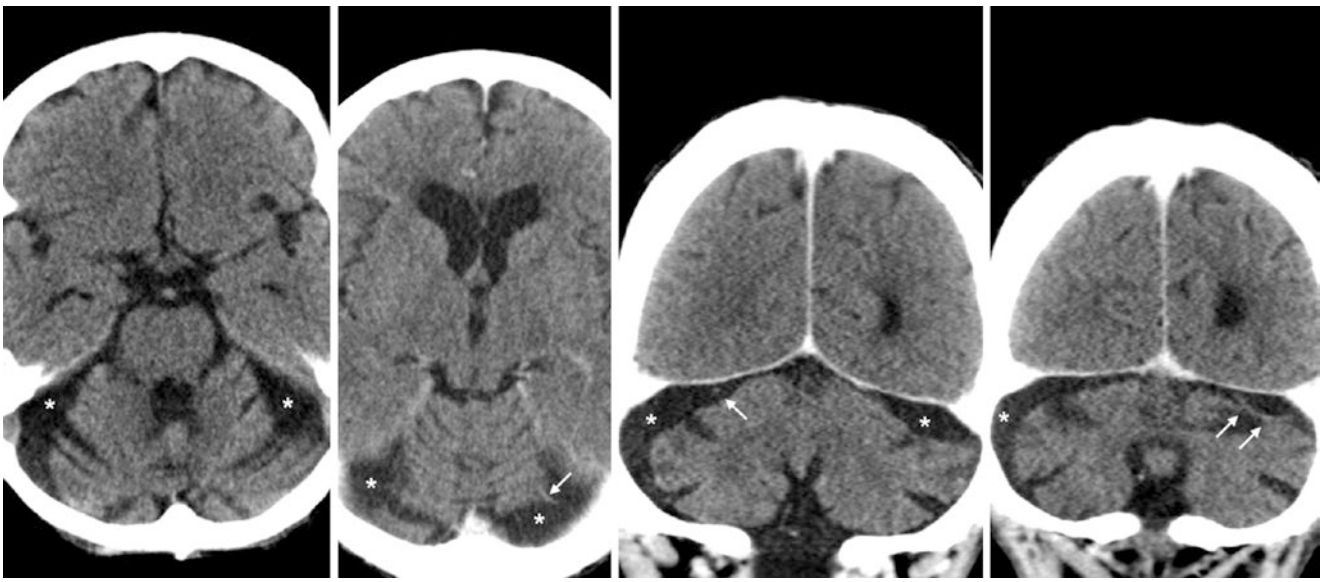

Fig. 16.2 A 63 year old underwent an axial NECT (*left*) that depicted fluid collections (*) along the cerebellar convexities, simulating chronic SDHs. However, CECT axial (*left middle*) and coronal (*right middle*) images show that these do not have a mass effect and that they have the density of CSF. The cerebellar sulci are also quite prominent relative to the cerebral sulci. These represent prominent SASs, as evidenced by the small veins (*arrows*) traversing them. The patient was found to be on chronic antiepileptic medication, which can cause disproportionate cerebellar atrophy

16.2 Cerebellar and Cerebral Atrophy Simulating Chronic Subdural Hematomas or Hygromas

A much more common occurrence is when *cerebellar* and *cerebral atrophy* are present together, typically with more prominent involvement of the cerebrum. Note that cerebral atrophy can more focally involve certain lobes or distributions in certain *neurodegenerative disorders*, some of which can even be asymmetric from side-to-side (e.g., the semantic variant of frontal-temporal dementia). Again, the cortical vein sign is typically visible on multiplanar CT with reconstructions; if necessary, CTA/CTV or MRI can be helpful (particularly with FLAIR, which suppresses CSF) in confirming the presence or absence of veins crossing the fluid collections (Figs. 16.2, 16.3, 16.4, 16.5, 16.6, 16.7, 16.8, and 16.9).

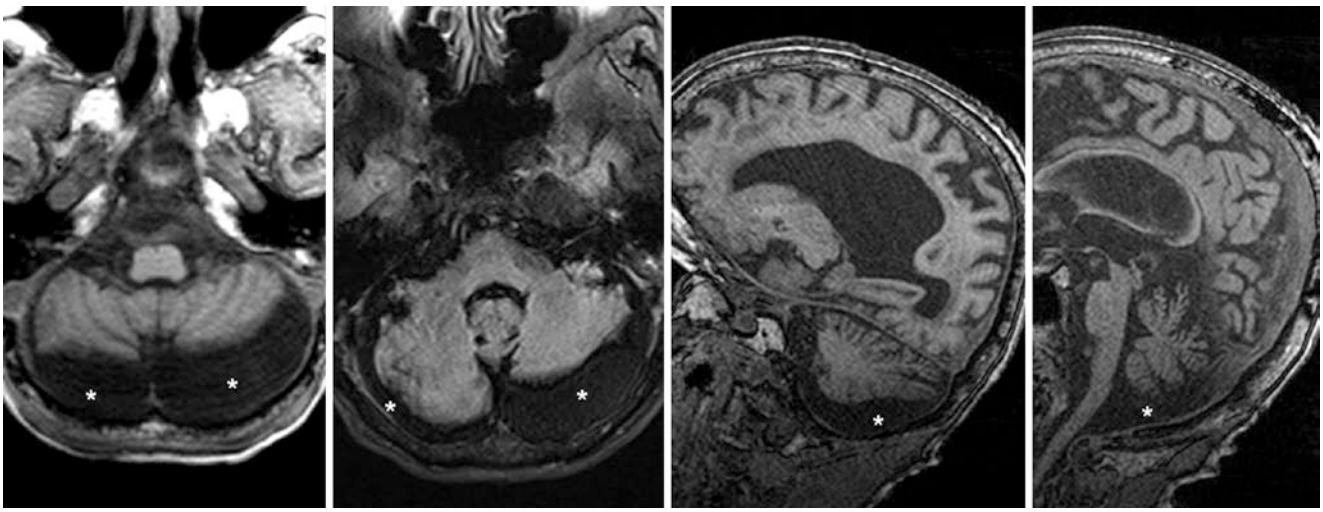

Fig. 16.3 A 3T MRI of a 54 year old showed bilateral fluid collections (*) along the cerebellar convexities on axial T1WI (*left*) and FLAIR (*left middle*), which mimic chronic SDHs. Notice the lack of mass effect and that the signal intensity is the same as that of CSF. These represent prominent SASs that are also numerous along the left cerebral convexity on sagittal T1WI (*right middle and right*). This is not a prominent cisterna magna, since there is no posterior fossa enlargement

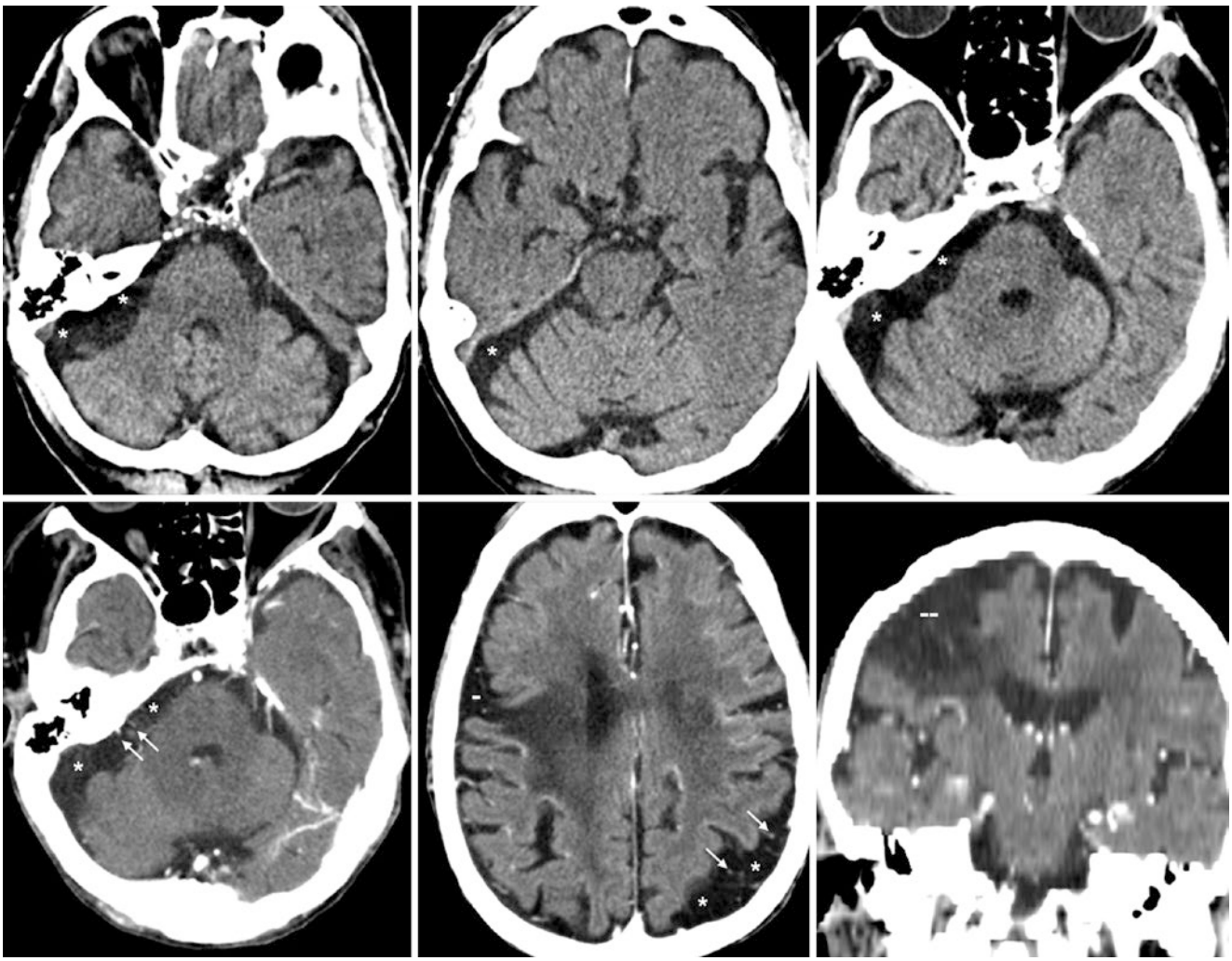

Fig. 16.4 A NECT (*top row*) of a 72 year old showed prominence of the SAS (*) along the right cerebellar convexity (*top left and middle*), simulating a chronic SDH. A repeat NECT 5 years later (*top right*) showed that the volume loss remained prominent along the right cerebellar convexity. Contrast-enhanced computed tomogaphy (CECT) on the same day (*bottom left*) confirmed prominent veins within the SAS fluid in several areas (*thin arrows*), consistent with atrophy. Additionally, there was focal atrophy along the left cerebral convexity that simulated an AC (*bottom middle*), which is also traversed by cortical veins. A focus of encephalomalacia/gliosis (non-CSF density) is noted (−−), as shown on a coronal reformat (*bottom right*)

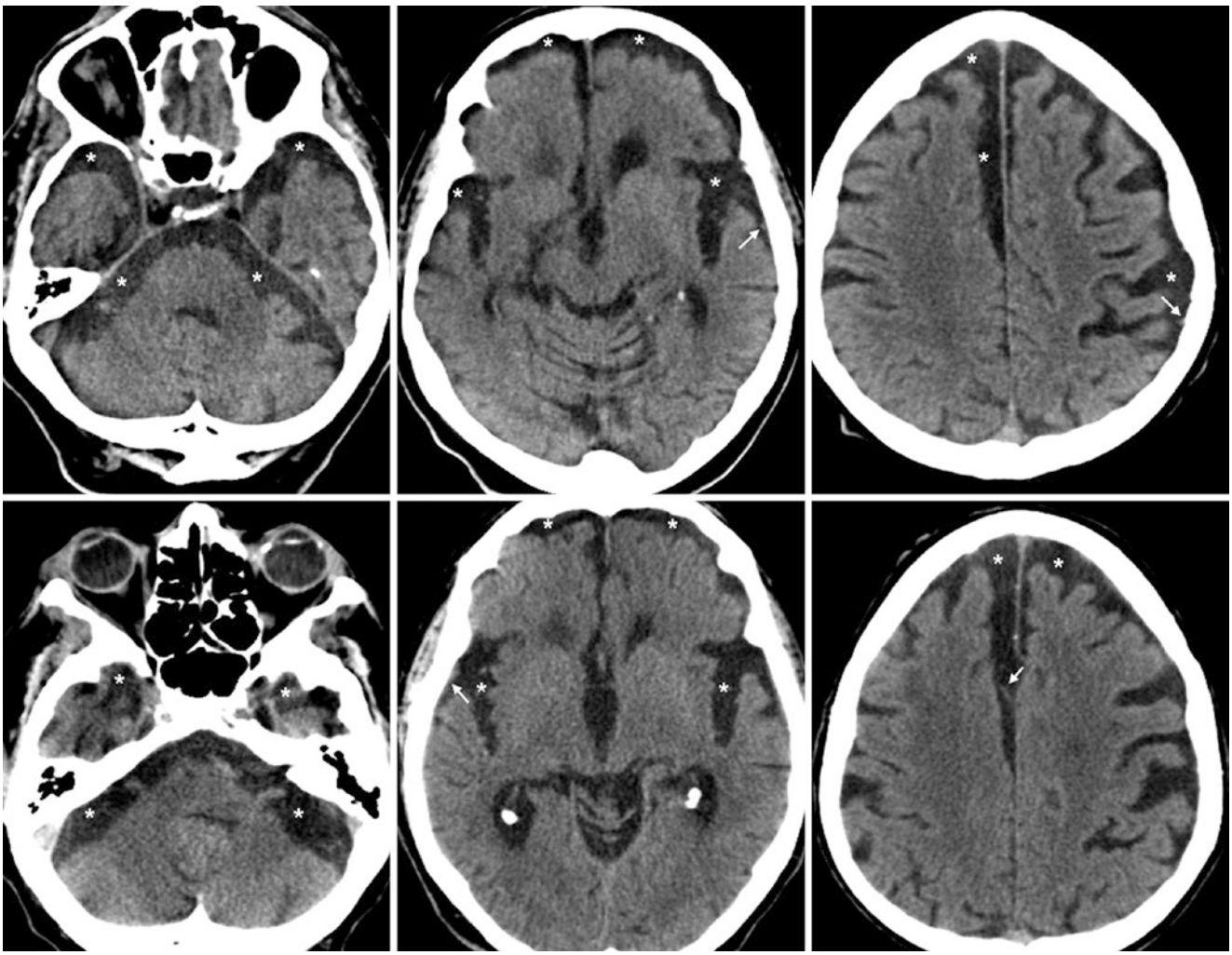

Fig. 16.5 A NECT (*top row*) from a 92 year old showed bilateral prominence of the SAS (*) along the cerebellar convexities and orbitofrontal convexities (*top middle*), with asymmetry of the interhemispheric fissure (*top right*); together, such findings simulate bilateral chronic SDHs. However, note the severe volume loss of the sylvian fissures and the cortical veins superficial to the fluid in several areas (*thin arrows*), indicating atrophy. Chronic SDHs would displace the cortical veins inward. These findings were not changed on a NECT 1 year later (*bottom row*)

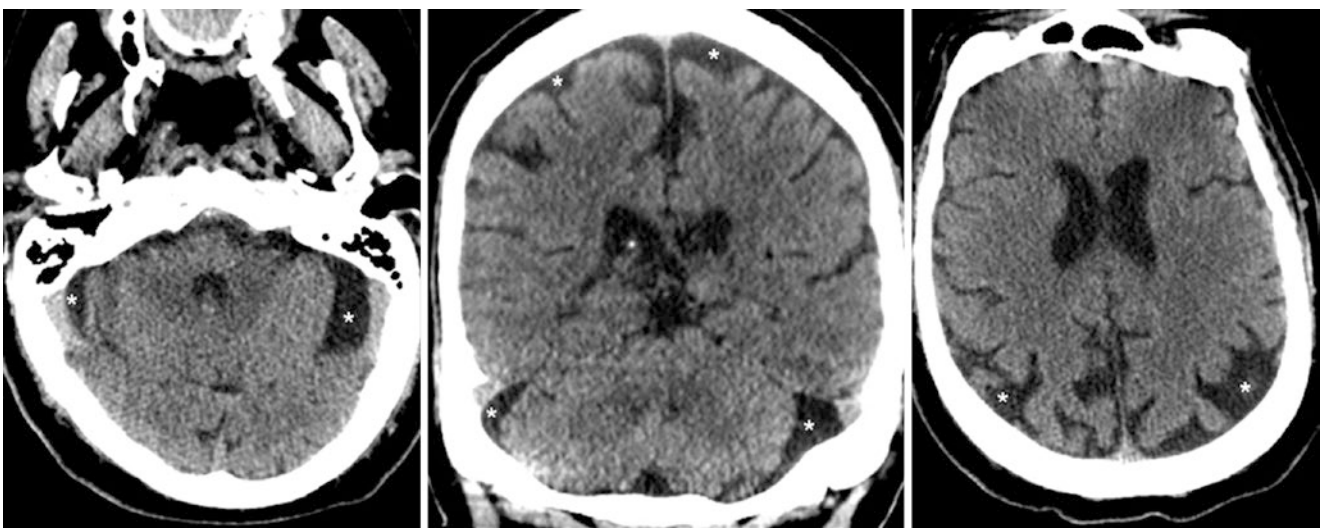

Fig. 16.6 A NECT from a 71 year old with axial (*left*) and coronal (*middle*) reformats showed CSF-density collections (*) along the cerebellar convexities, simulating chronic SDHs, hygromas, or ACs. However, the cerebral sulci are prominent relative to the cerebellar sulci, which is due to prominent SASs (*), as noted on a higher axial image (*right*)

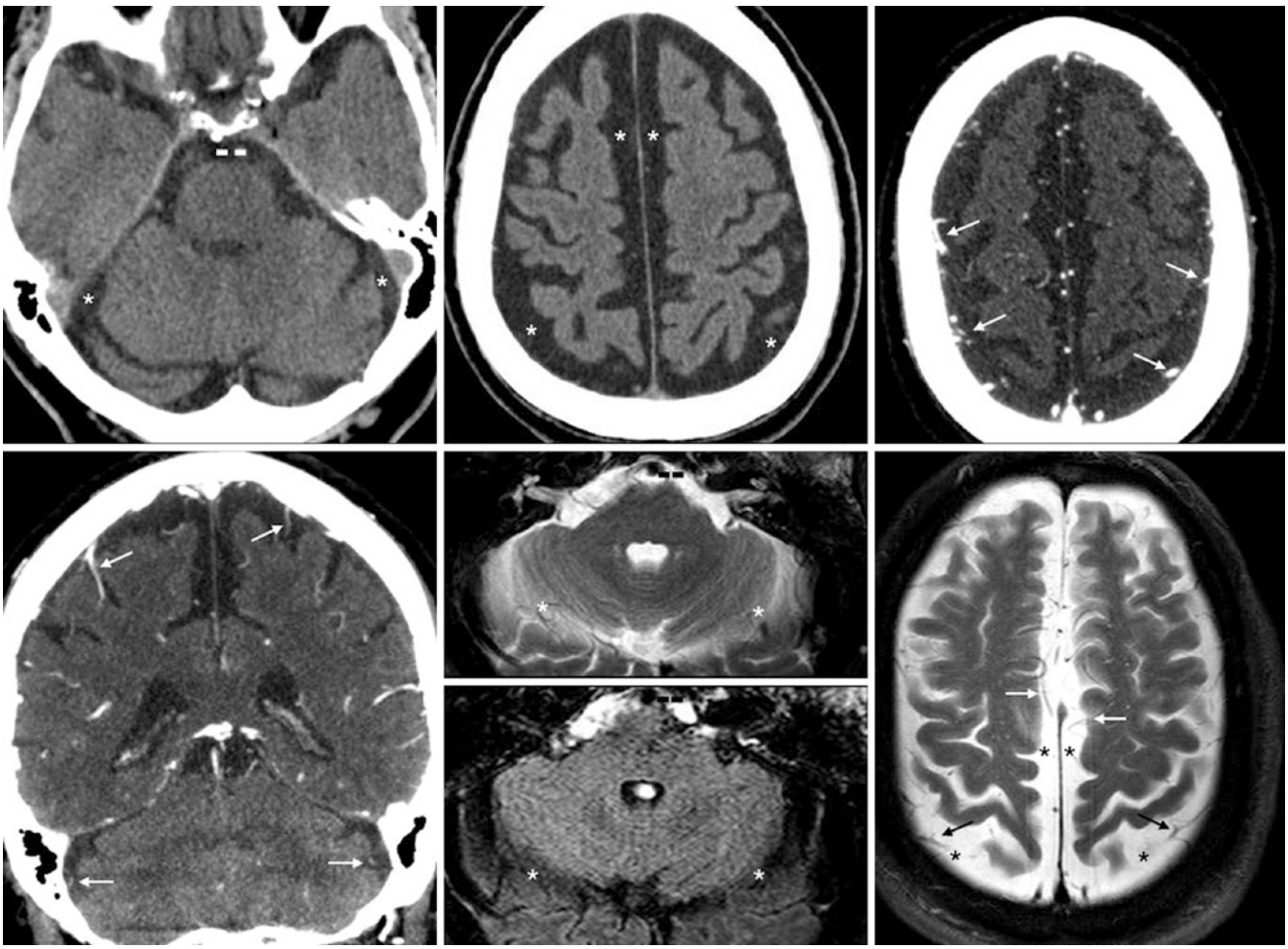

Fig. 16.7 A 69 year old underwent a NECT (*top left and middle*) that demonstrated prominent SASs (*) along the cerebellar and cerebral convexities and within the prepontine cistern (−−), which simulated chronic SDHs. CECT axial (*top right*) and coronal (*bottom left*) reformats depicted cortical veins (*thin arrows*) superficial to and crossing these spaces, confirming atrophy. An MRI also defined the cortical veins on axial T2WI and FLAIR (*bottom middle and bottom right)*

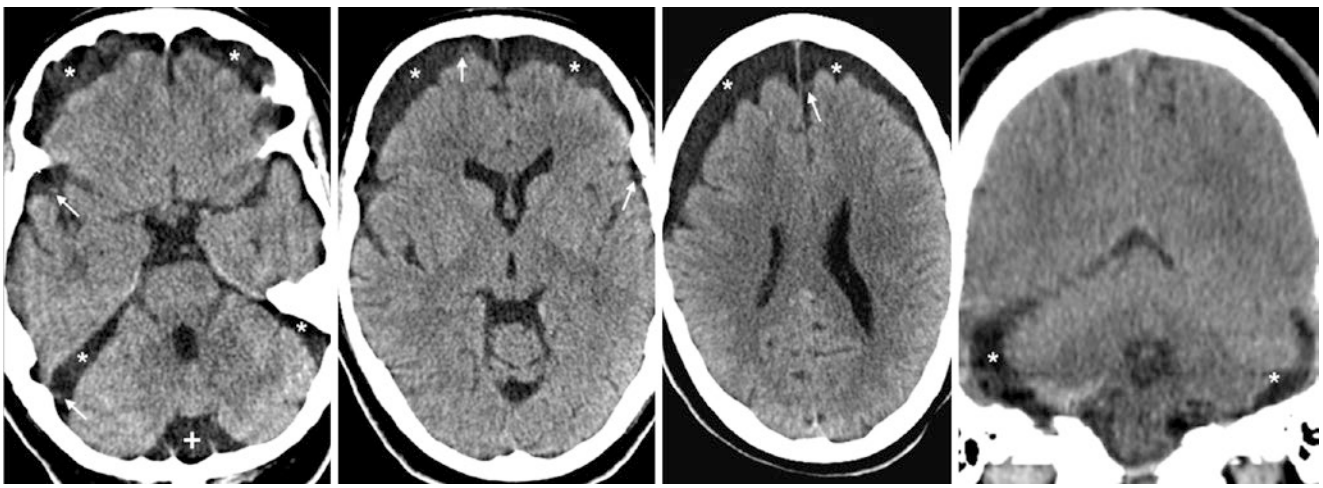

Fig. 16.8 A 58 year old had a NECT that showed prominent SASs (*) along the cerebral convexities simulating bilateral chronic SDHs. However, the SASs were also prominent along the cerebellar convexities, and there were visible cortical veins (*thin arrows*) passing through the SASs in some areas, along with a prominent cisterna magna (+); this is consistent with atrophy. Note the coronal reformats of the cerebellum (*right*)

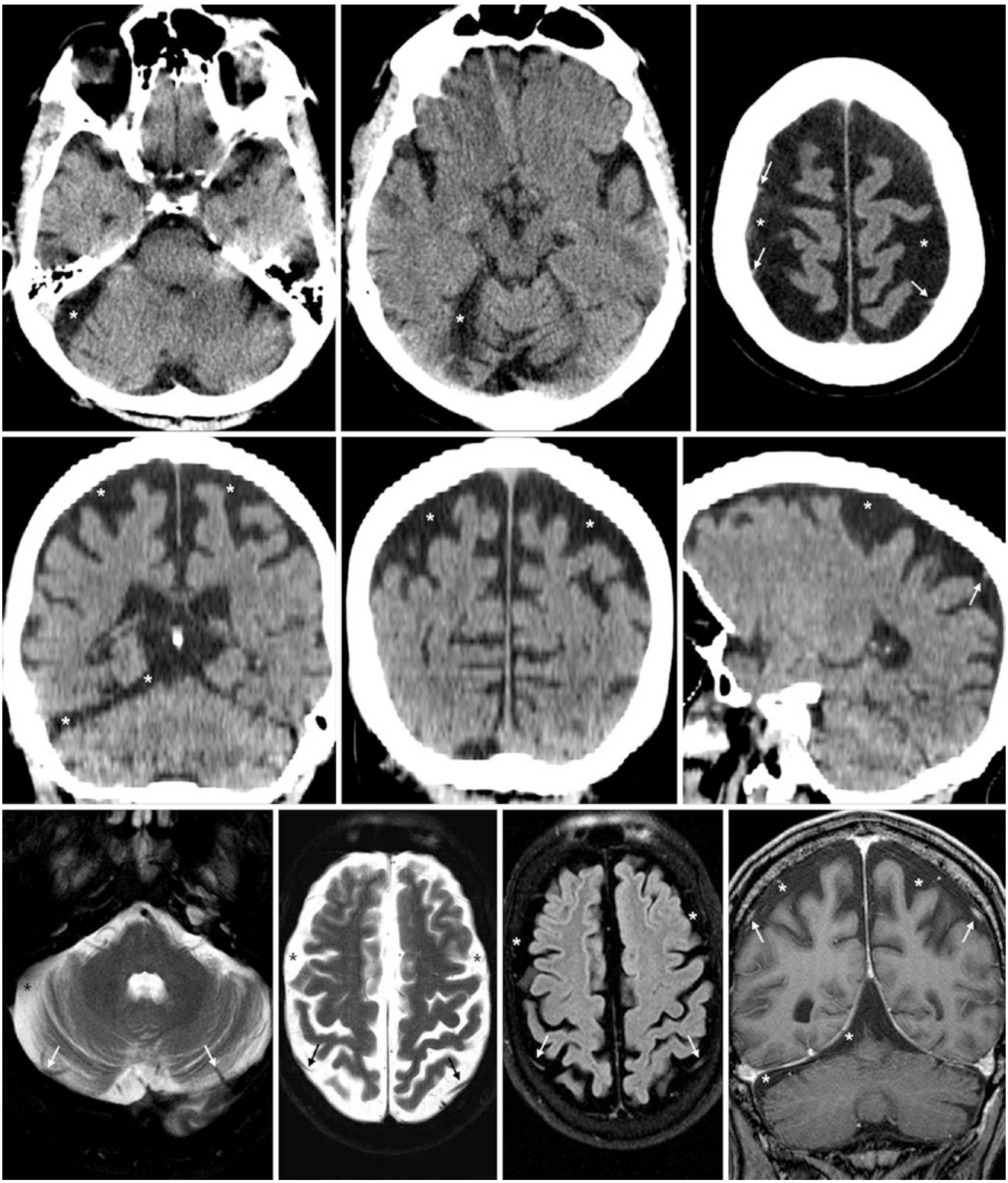

Fig. 16.9 Atrophy simulating subdural hygromas. The patient was a 55 year old with headaches. *Top row:* the patient underwent a NECT, which demonstrated prominent SASs (*) along the cerebral convexities and along the right cerebellar convexity, which could simulate chronic SDHs. At this time these were called SDHs, although tiny cortical veins (*thin arrows*) were visualized superficial to the fluid collections on both sides. *Middle row:* on a NECT 2 years later, the atrophy was unchanged on coronal (*left and middle*) and sagittal (*right*) reformats, and cortical veins were visualized, confirming atrophy. *Bottom row:* an MRI 3 days later also depicted crossing cortical veins on axial T2WI (*left images*), FLAIR (*right middle*), and coronal postcontrast T1WI (*right*)

16.3 Cerebral (Without Cerebellar) Atrophy Simulating Chronic Subdural Hematomas or Hygromas

Again, *cerebral volume loss* or atrophy can be present to a much greater degree than or even in the absence of cerebellar volume loss. Cerebral atrophy may not always be diffuse and can be more focal or regional in certain *neurodegenerative disorders,* some of which can even be asymmetric from side-to-side (e.g., the semantic variant of frontal-temporal dementia). Again, the cortical vein sign is typically visible on multiplanar CT with reconstructions, while MRI can help in difficult cases (Figs. 16.10 and 16.11).

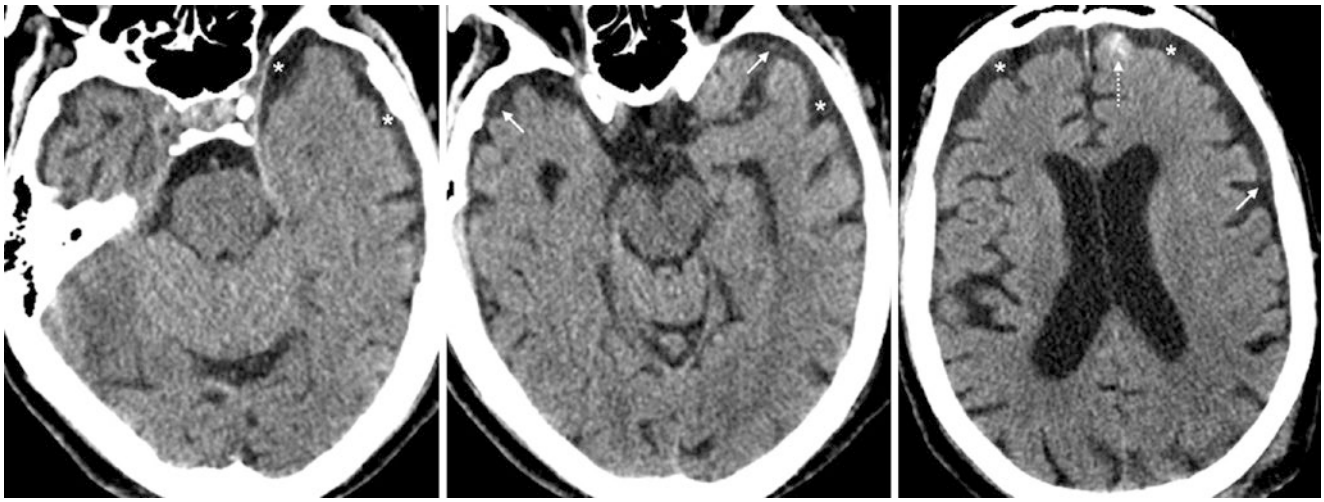

Fig. 16.10 A NECT (*left*) of an 80-year-old patient showed asymmetric prominence of the SAS (*) along the left temporal convexity. Higher images (*middle and right*) showed a milder prominence of the right SAS as well. Such prominence of the SASs may simulate bilateral, chronic SDHs. Note that there are prominent cortical veins superficial to the fluid (*thin arrows*), also consistent with atrophy. Also note a focal beam hardening artifact that simulates SAH (*dotted arrow, right*)

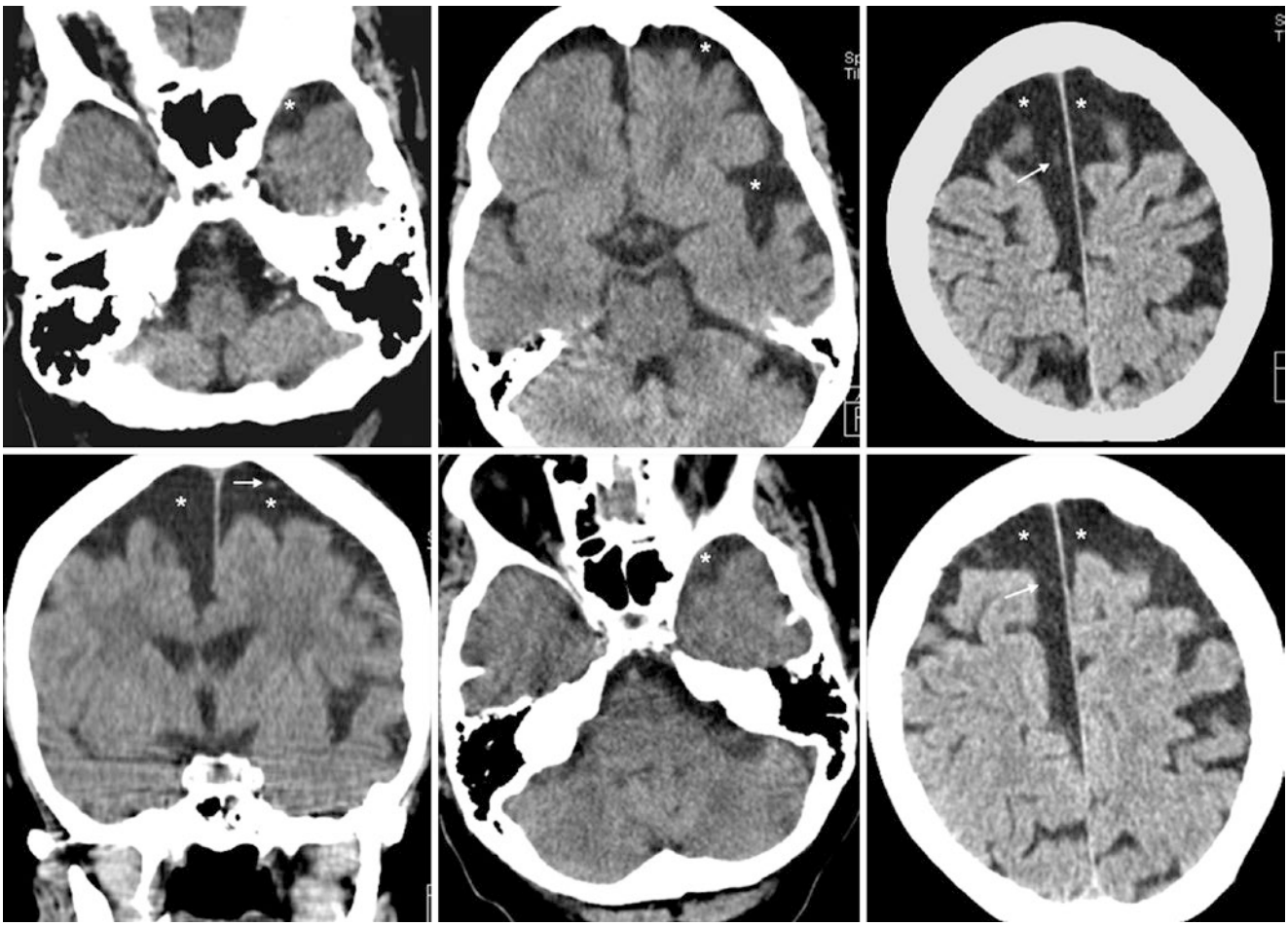

Fig. 16.11 Axial NECT images of a 71 year old showed prominence of the SASs (*) along the left cerebral convexity that was asymmetric and simulated a chronic SDH or AC anterior to the left temporal pole (*top left*). Note that the SAS is prominent within the left sylvian fissure and along the left cerebellar convexity as well. A higher axial image (*top right*) and a coronal reformat (*bottom left*) depicted a lesser degree of right-sided cerebral atrophy and indicated that cortical veins (*thin arrows*) traverse the SASs. A repeat NECT 5 years later (*bottom middle and right*) showed no change

16.4 Enlarged Subarachnoid Spaces Simulating Cyst, Subdural, or Encephalomalacia

Focal enlargement of the subarachnoid spaces may simulate a small subdural or epidural hematoma, an AC, or encephalomalacia. More commonly, this occurs on CT but occasionally can be problematic on MRI if the acquisition is not multiplanar. Fortunately, T2WI often depicts small, crossing cortical veins (Figs. 16.12, 16.13, 16.14, 16.15, 16.16, 16.17, 16.18, 16.19, 16.20, 16.21, 16.22, 16.23, 16.24, 16.25, 16.26, 16.27, 16.28, and 16.29).

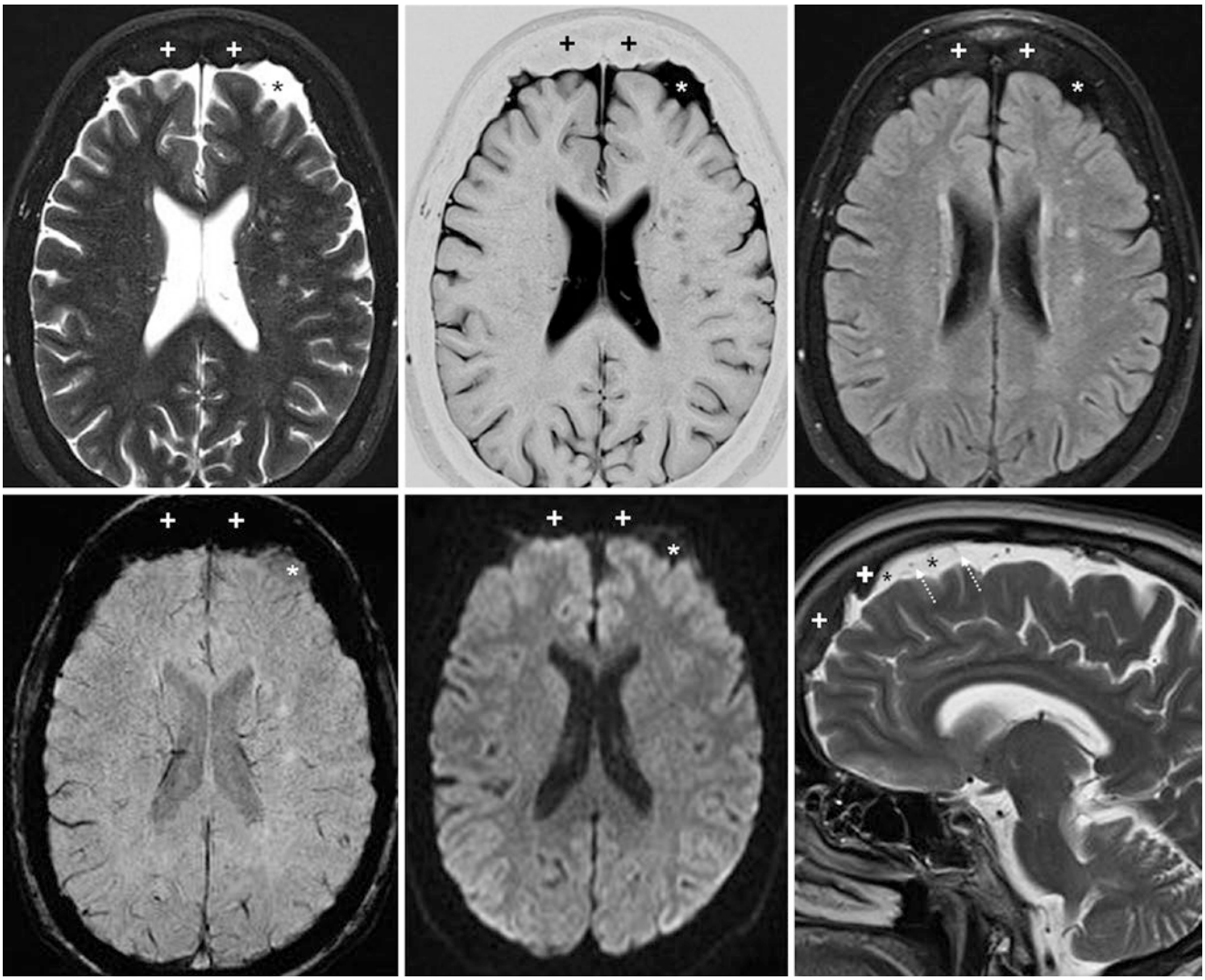

Fig. 16.12 The patient was a 67-year-old female with dizziness and focal SAS prominence (*) on 1.5T MRI axial T2WI (*top left*), T1 inversion recovery (*top middle*), FLAIR (*top right*), SWI (*bottom left*), DWI (*bottom middle*), and sagittal T2WI (*bottom right*). This could simulate an AC or focal encephalomalacia. However, note the vascular structures (*dotted arrows*) passing through the SAS and the incidental benign hyperostosis frontalis (+)

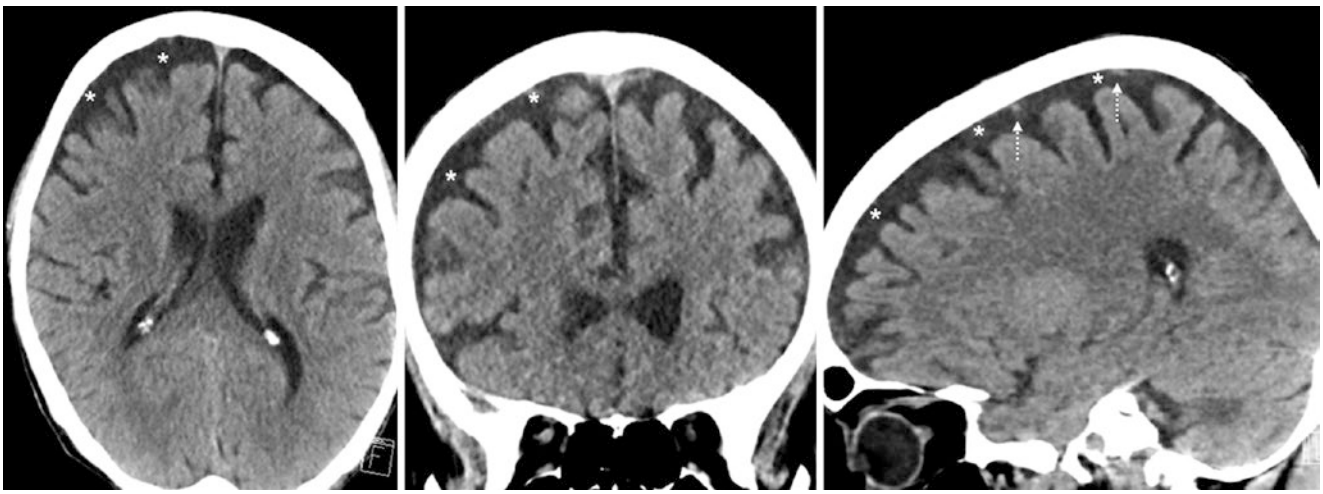

Fig. 16.13 Axial (*left*), coronal (*middle*), and sagittal (*right*) reformats of a NECT of a 73 year old depicted asymmetric extra-axial SAS prominence along the right cerebral convexity (*) that mimicked a SDH, hygroma, or AC. However, the sagittal reformat (*right*) clearly showed that the cortical veins (*dotted arrows*) were not displaced inward

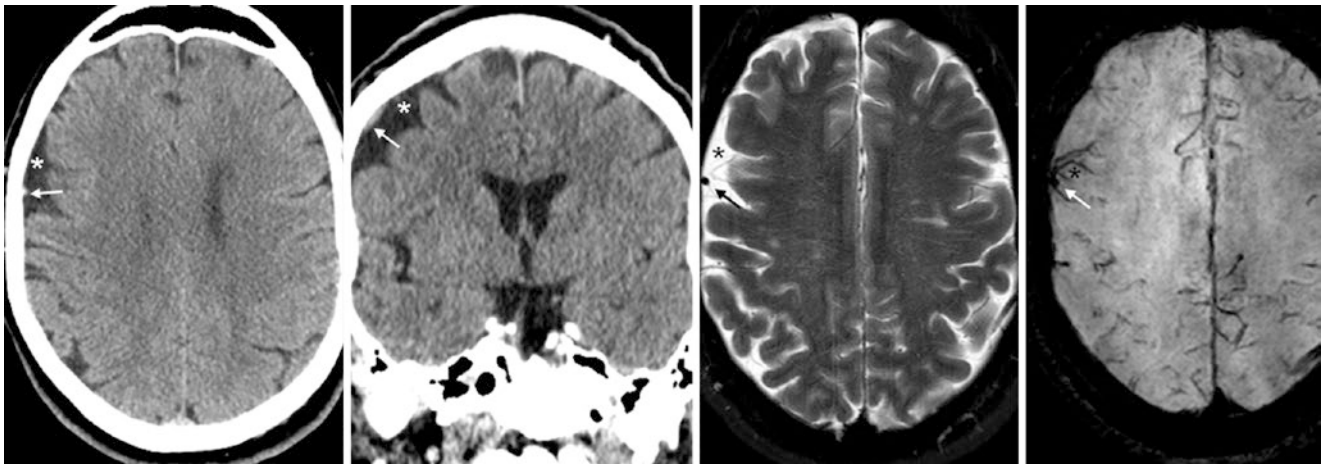

Fig. 16.14 Axial (*left*) and coronal (*left middle*) NECT images of a 65 year old depicted asymmetric SAS prominence (*) of the right frontal convexity, simulating an AC, while a small vessel (*arrows*) simulated a small SDH on the coronal image. A 1.5T MRI with axial T2WI (*right middle*) and SWI (*right*) confirmed that vessels traversed the SAS

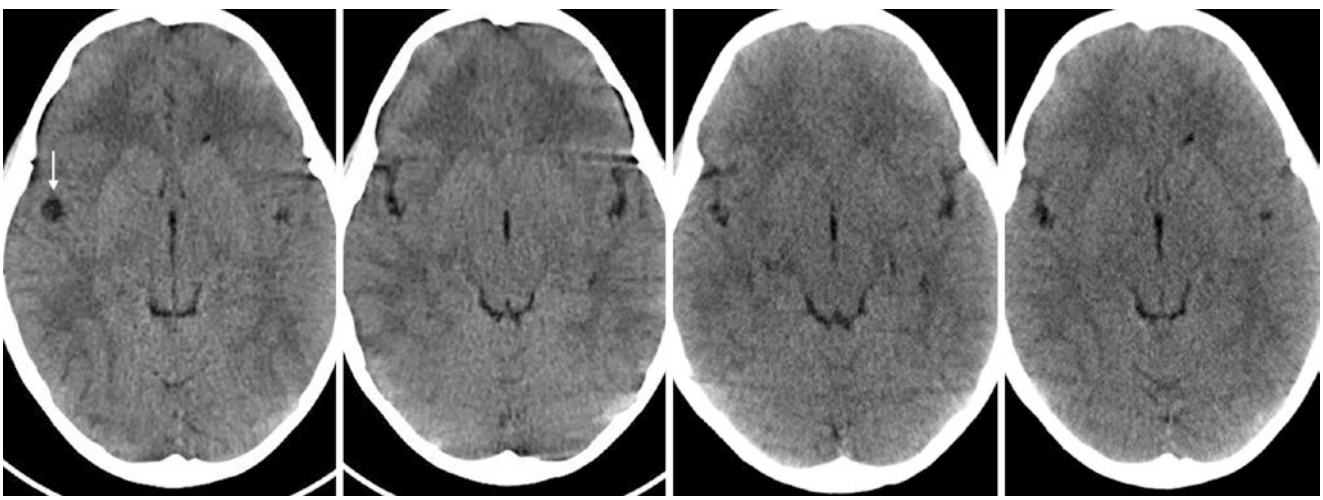

Fig. 16.15 A 7 year old underwent axial (*left and left middle*) reformats of a NECT that depicted a cyst-like focus (*arrow*) within the right sylvian fissure, simulating an AC, neurocysticercosis, or other type of extra-axial cyst. On repeat CT images 6 months later (*right middle and right*), this was confirmed to be simply a prominent fissure relative to the remainder of the cerebral sulci

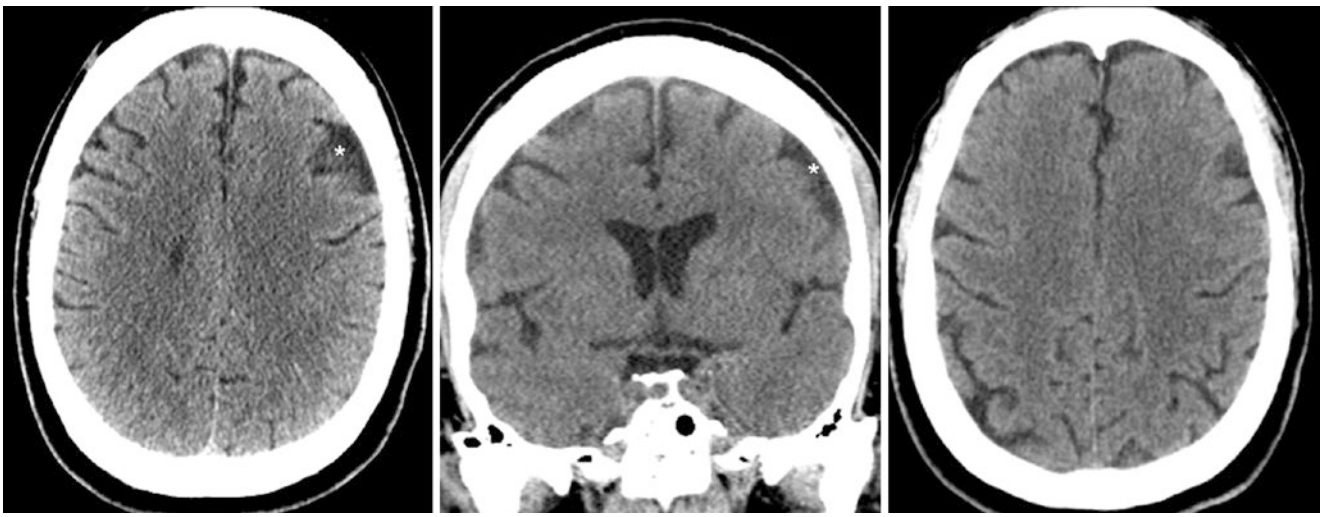

Fig. 16.16 The patient was a 50 year old with headaches. Focal SAS prominence (*) on axial (*left*) and coronal (*middle*) reformats simulated an AC, an extra-axial collection, or focal encephalomalacia. However, a NECT 5 years later with slightly different angulation (*right*) confirmed this to be a prominent sulcus that was volume-averaged with the cerebrum

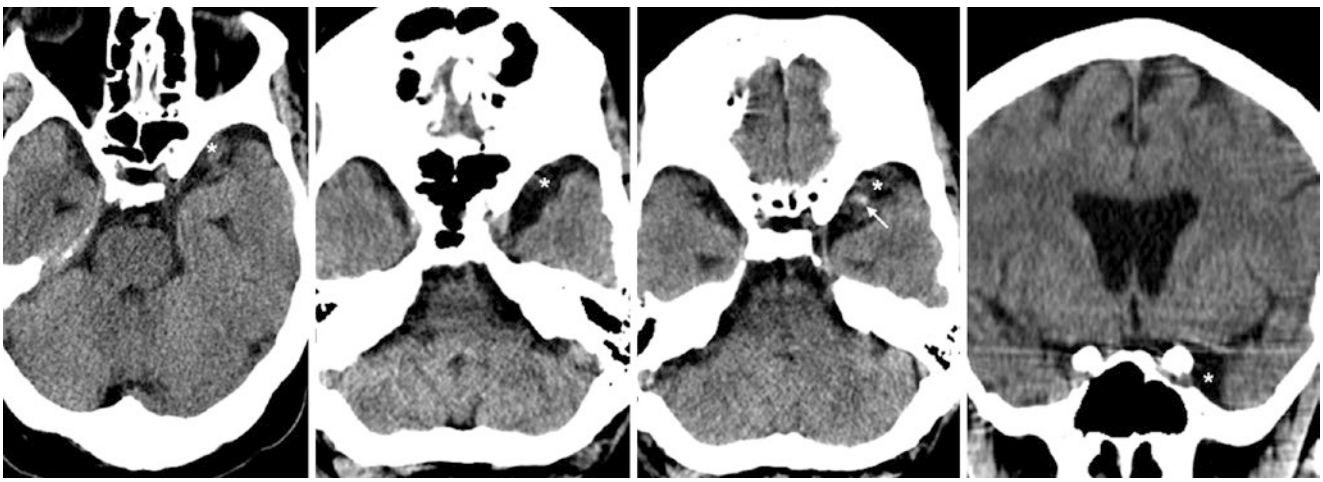

Fig. 16.17 A NECT of a 37-year-old patient shows cyst-like fluid (*) within the left middle cranial fossa anterior to the temporal pole (*left*), which mimics an AC. An axial NECT was unchanged 2 years later (*left middle*), with a coronal reconstruction (*right*). The SASs are prominent along the convexities, while a vein was noted to traverse the cyst (*thin arrows*)

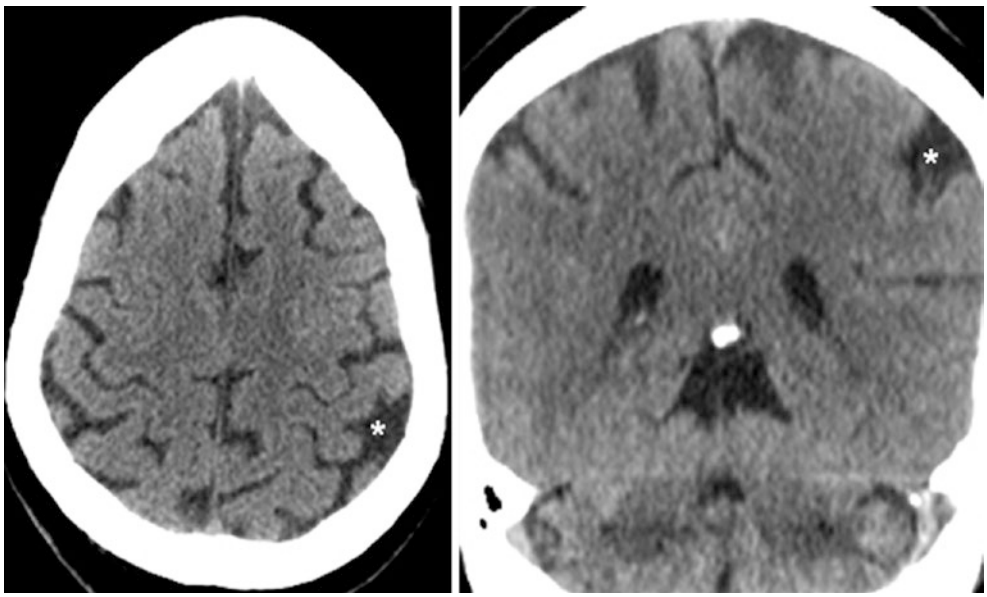

Fig. 16.18 An axial NECT (*left*) of a 68-year-old patient depicted a cyst-like focus along the left convexity (*), simulating an AC. However, a coronal reformat (*right*) showed this to be focal atrophy or a sulcus

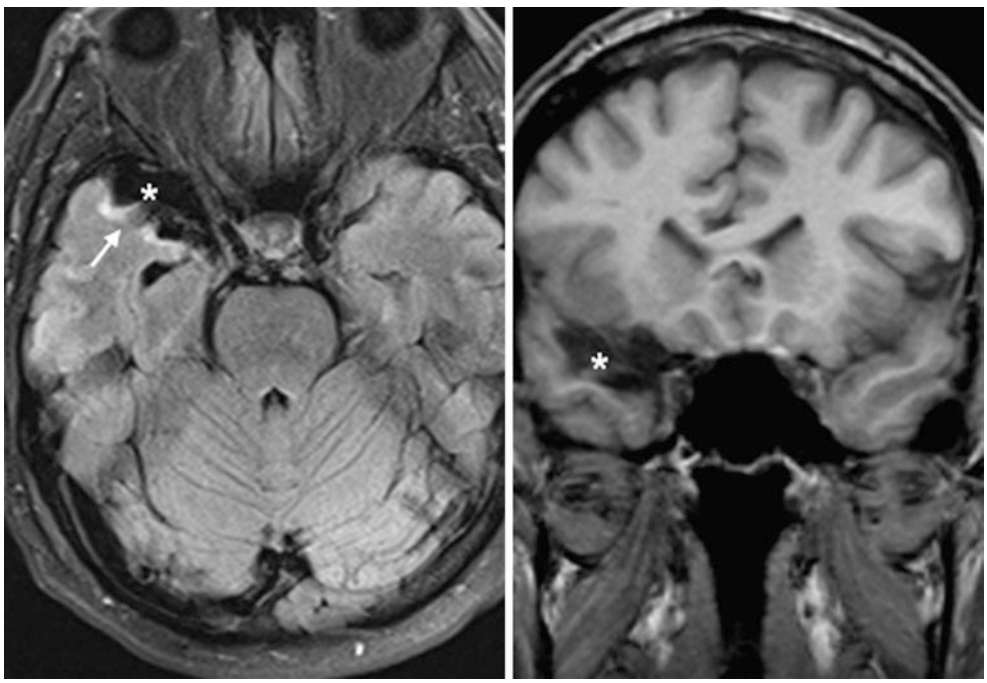

Fig. 16.19 A 3T MR axial FLAIR (*left*) and coronal T1WI (*right*) of a 50 year old showed an AC-like focus (*), but the presence of gliosis on FLAIR (*thin arrows*) and enlargement of the adjacent temporal horn confirmed that this is atrophy

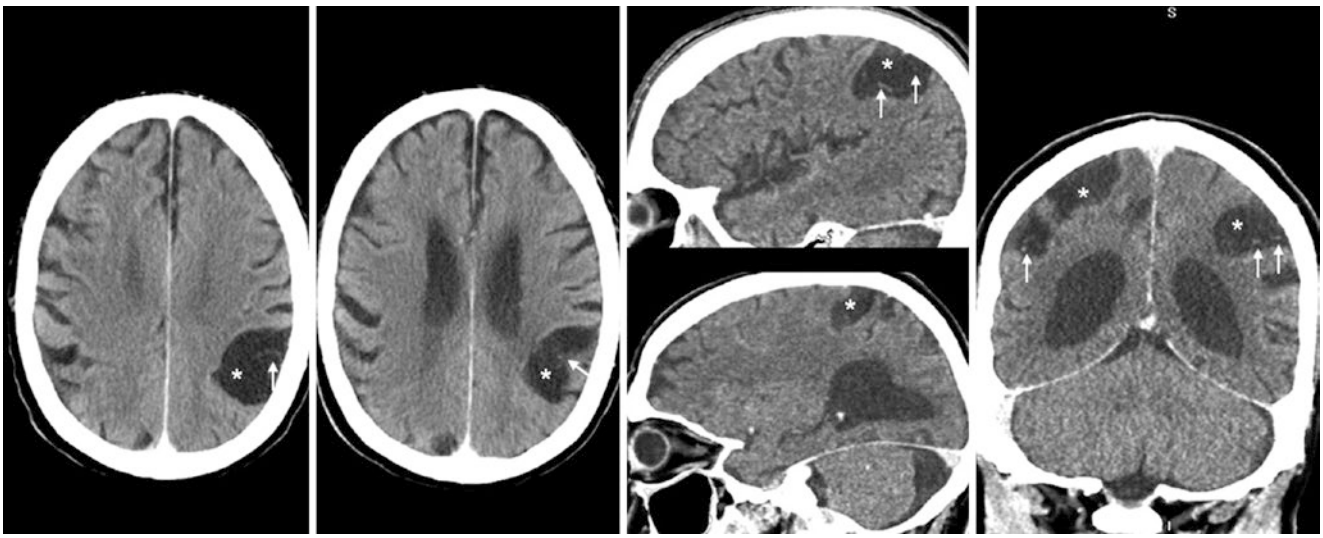

Fig. 16.20 An 88 year old with memory loss had an axial NECT (*left two images*) that showed a prominent cyst-like collection (*) within the left postcentral sulcus that simulated an AC. However, sagittal reformats of the left (*right middle, top*) and right (*right middle, bottom*) sides and coronal reformats (*right*) illustrated that the SASs are prominent bilaterally in similar locations (*) and that veins (*thin arrows*) traverse these cysts, confirming atrophy

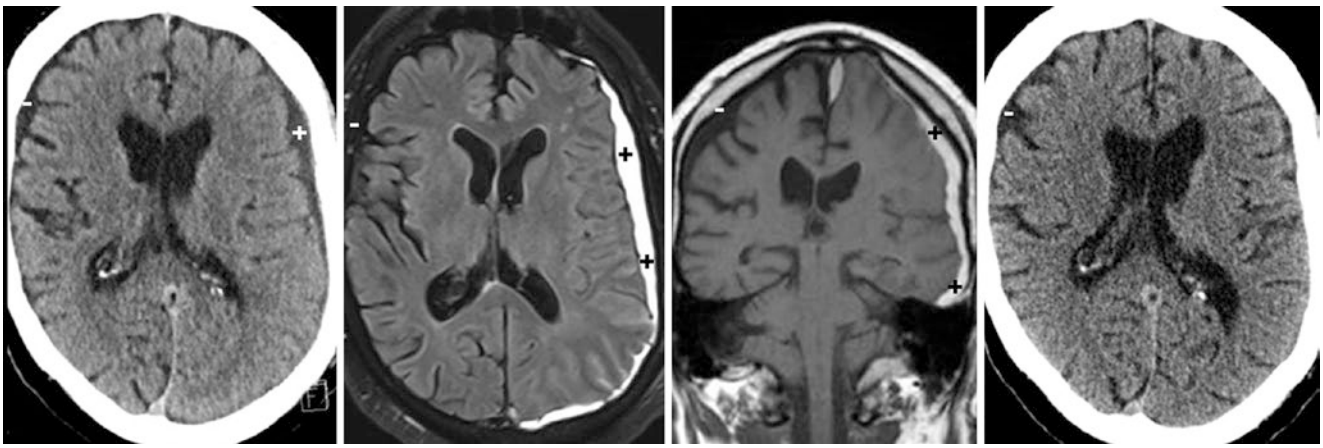

Fig. 16.21 Comparison case: chronic SDH. In a 72 year old without known trauma, a NECT (*left*) depicted an isodense SDH (+) along the left cerebral convexity. On a 1.5T MRI with FLAIR (*left middle*) and a coronal T1WI (*right middle*), the SDH was confirmed to be subacute in age (bright on T2WI, FLAIR, and T1WI). Compare this to the right-sided volume loss with SAS prominence (−). The left-sided SDH had resolved 30 days later on a repeat NECT (*right*)

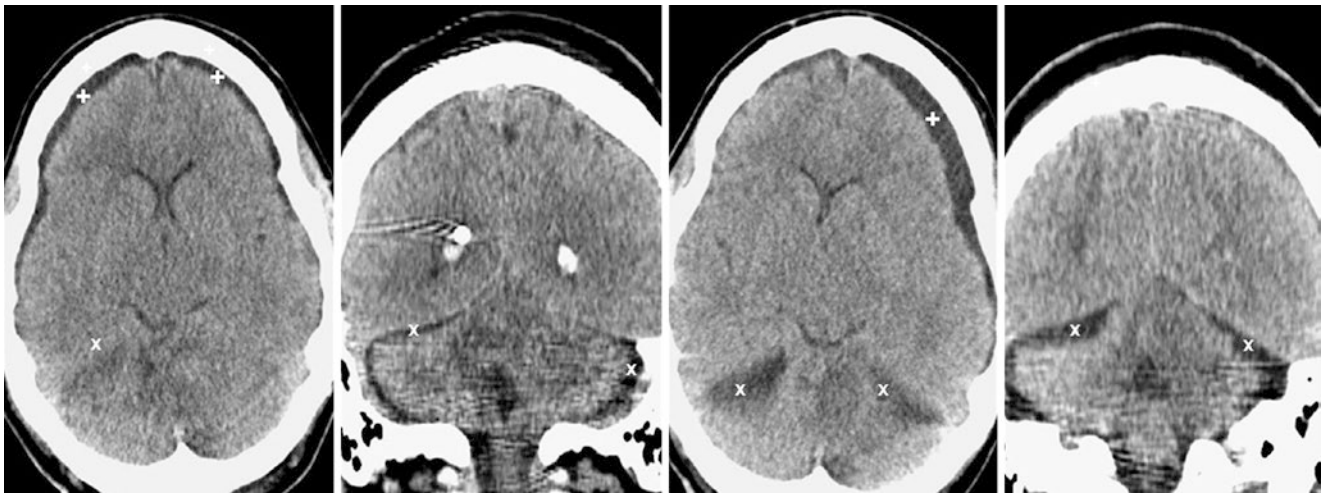

Fig. 16.22 Comparison case of posterior fossa postsurgical subdural collections. NECT axial (*left*) and coronal (*left middle*) reformats in a 47 year old showed small bilateral subdural collections along the cerebral (+) and cerebellar (×) convexities after evacuation of a cerebellar hemorrhage (*not shown*). Repeat NECT axial (*right middle*) and coronal (*right*) reformats 1 week later showed that each collection had enlarged with worsening midline shift

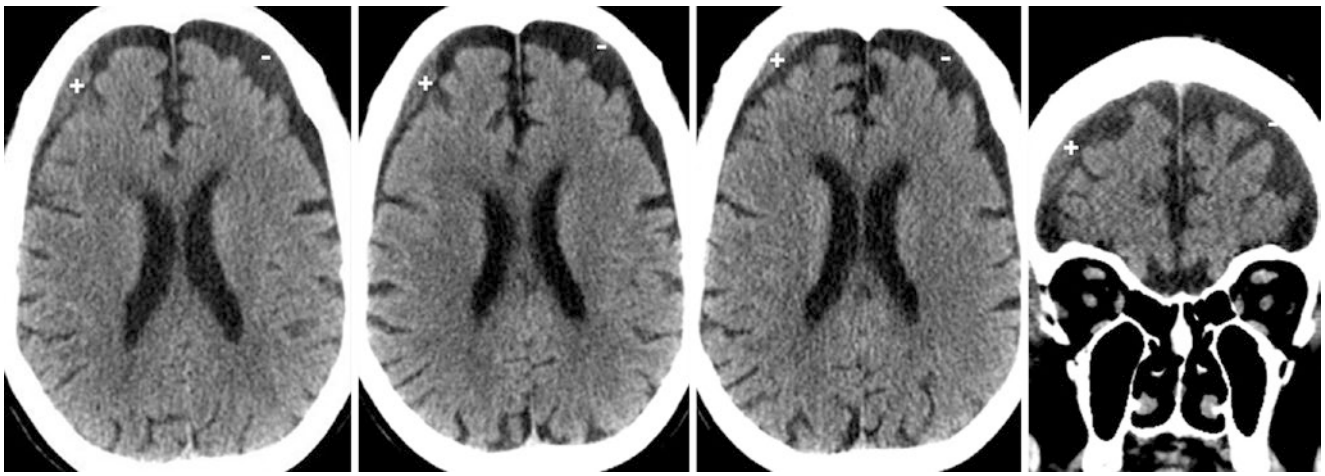

Fig. 16.23 Comparison case of chronic SDH. In a 67 year old non-trauma patient a NECT (*left*) depicted an isodense SDH (+) that was unchanged at 3 months (*left middle*) and 5 months later (*right middle*). Compare this to the left-sided volume loss with SAS prominence (–) on a coronal reformat (*right*), which is from the 5-month follow-up NECT

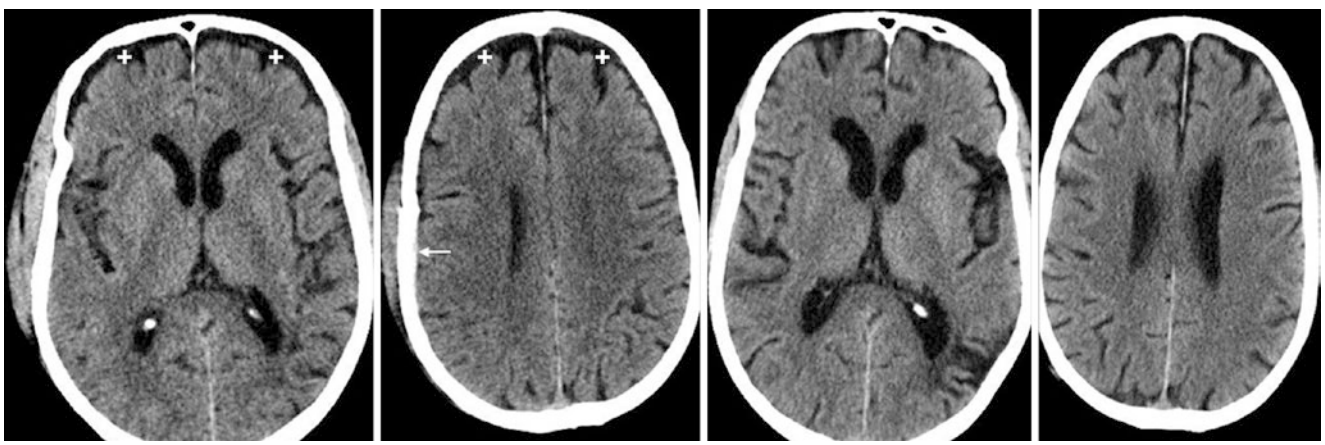

Fig. 16.24 Comparison case of SDHs. NECT (*left, left middle*) in a 76 year old who suffered head trauma. There are small, bilateral SDHs (+) along the frontal convexities; their low density indicates that they are chronic. A tiny EDH is noted along the right convexity (*thin arrow*). On a 7-month follow-up NECT (*right middle and right*), the fluid collections have resolved, with residual moderate diffuse cerebral volume loss

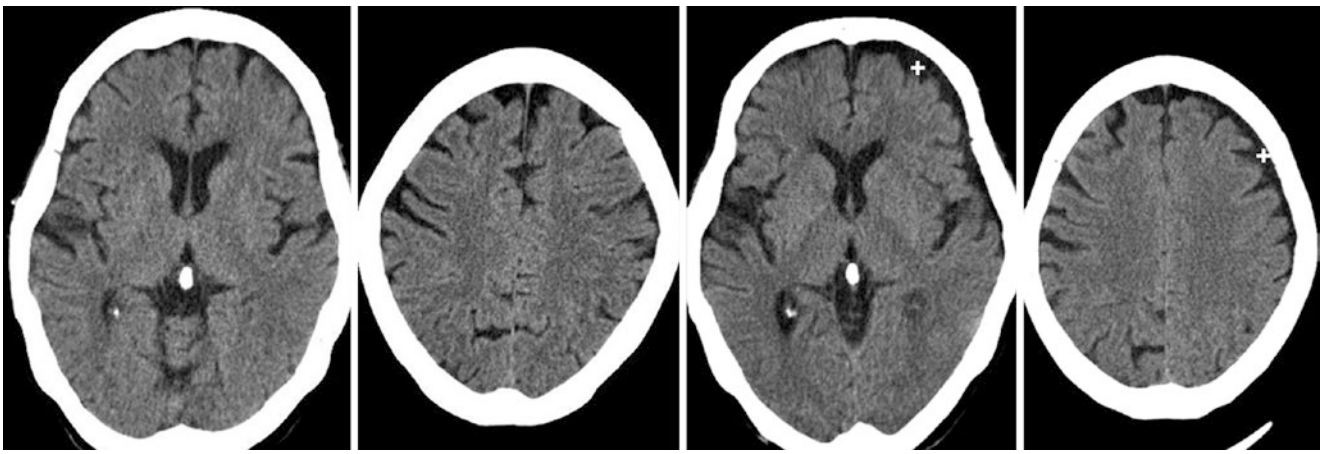

Fig. 16.25 Comparison case of unilateral chronic subdural hematoma or hygroma (SDH). A NECT (*left, left middle*) in an 80 year old was normal for age. One month later, performed just after a fall, a NECT (*right middle and right*) demonstrated a small unilateral hypodense SDH or hygroma along the left frontal convexity (+)

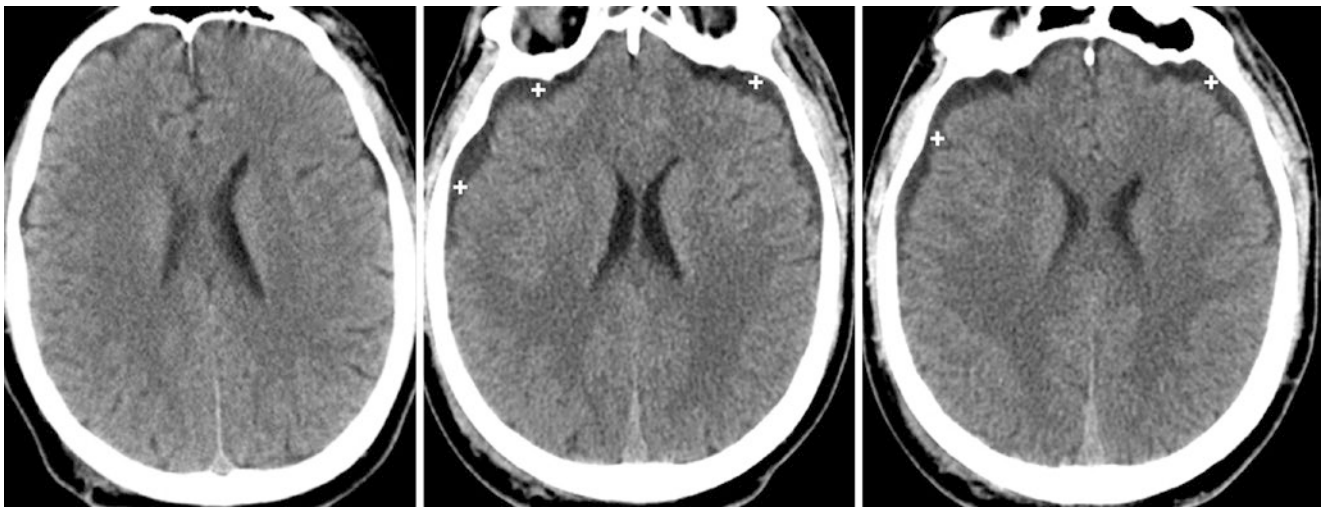

Fig. 16.26 Comparison case: acute subdural hygromas from trauma. An initial NECT (*left*) was interpreted as negative in an 18 year old the day of the traumatic incident. However, a NECT one day later (*middle and right*) noted new, bilateral subdural hygromas (+). In this case, the hygromas may have arisen from a tear in the dura, through which CSF leaked

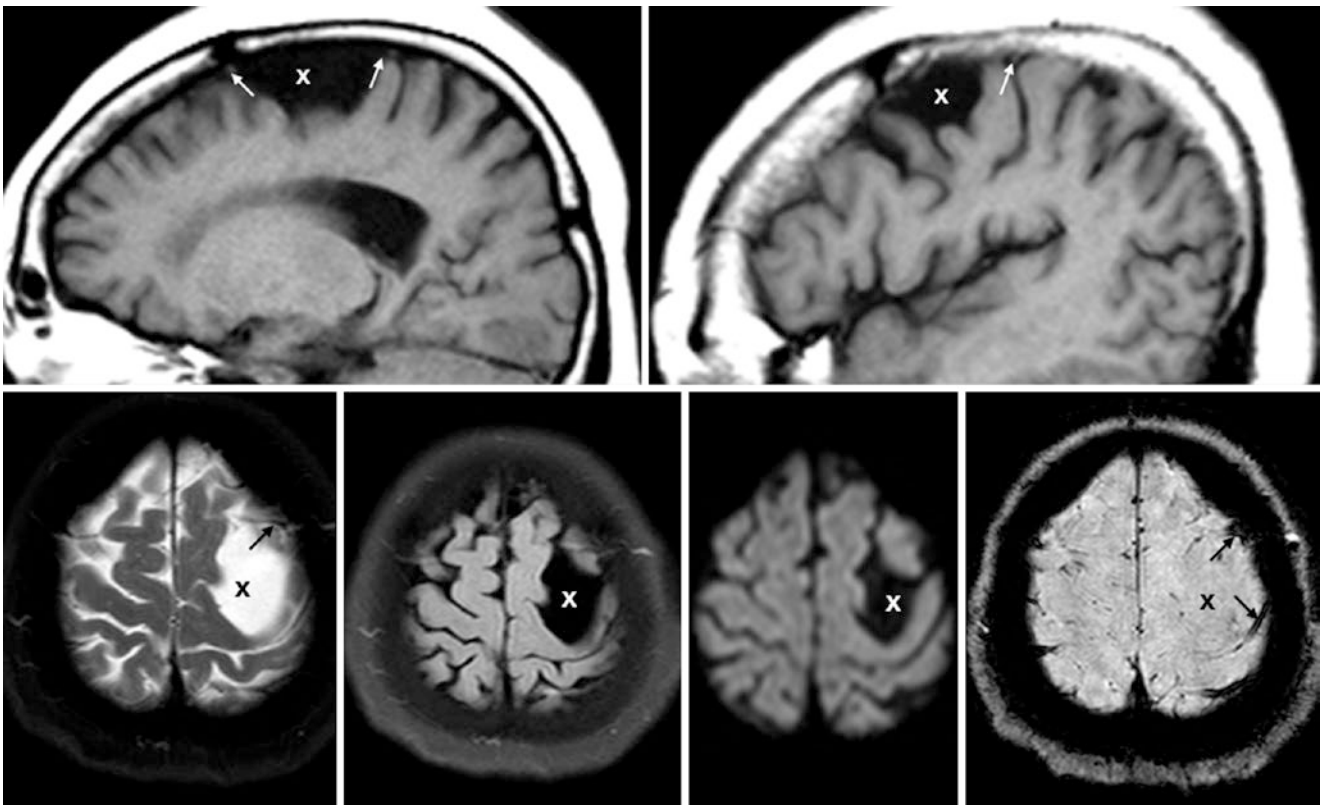

Fig. 16.27 Comparison case of bilateral cerebral convexity ACs. In a 76 year old with headaches, sagittal T1WIs showed left- (*top left*) and right-sided (*top right*) ACs (×) displacing cortex and adjacent vascular structures (*thin arrows*). Axial T2WI (*bottom left*), FLAIR (*bottom left middle*), and DWI (*bottom right middle*) demonstrate that the signal intensity is akin to CSF, but SWI (*bottom right*) and T2WI depict the displaced vasculature

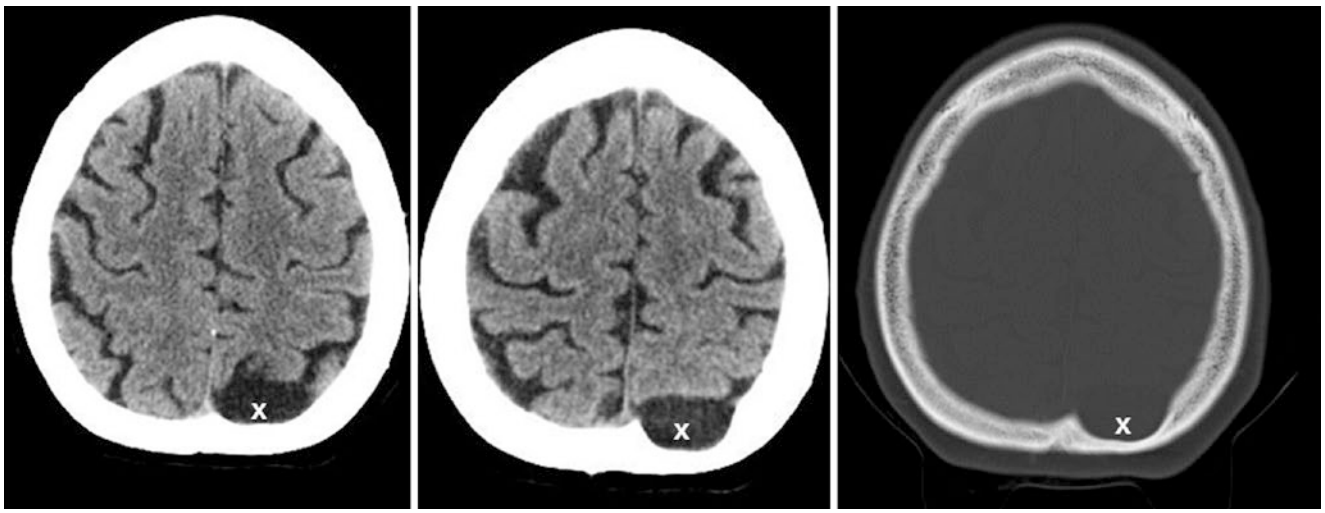

Fig. 16.28 Comparison case of a convexity AC. A 46 year old asymptomatic patient underwent a routine post-trauma NECT otherwise (negative). Axial images in the brain window (*left two images*) demonstrated a small left frontal convexity AC (×) only slightly displacing the adjacent cortex. Bone windows (*bottom right*) demonstrated mild scalloping of the inner table of the calvarium, an infrequent but confimatory finding of an AC

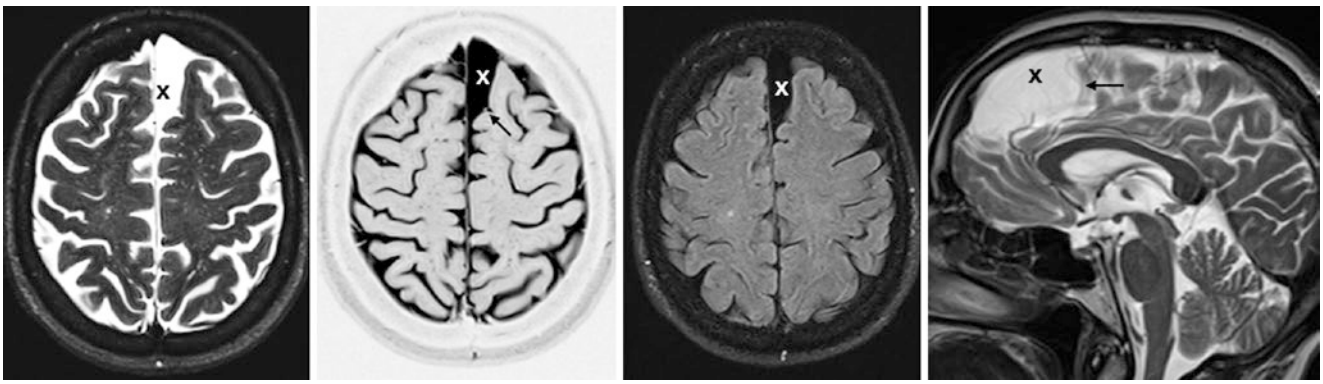

Fig. 16.29 Comparison case of a parafalcine AC. A 69 year old asymptomatic patient underwent an MRI for routine follow-up of a cyst from an outside institution. Axial T2WI (left), inverted T1IR (*left middle*), FLAIR (*right middle*), and sagittal T2WI (*right*) demonstrated the AC (×), which displaced adjacent arteries (*thin arrows*)

Suggested Reading

Aoki N. Extracerebral fluid collections in infancy: role of magnetic resonance imaging in differentiation between subdural effusion and subarachnoid space enlargement. J Neurosurg. 1994;81:20–3.

Brant-Zawadzki M, Kelly W, Kjos B, Newton TH, Norman D, Dillon W, Sobel D. Magnetic resonance imaging and characterization of normal and abnormal intracranial cerebrospinal fluid (CSF) spaces. Neuroradiology. 1985;27:3–8.

Fobben ES, Grossman R, Atlas SW, Hackney DB, Goldberg H, Zimmerman RA, Bilaniuk LT. MR characteristics of subdural hematomas and hygromas at 1.5T. AJNR Am J Neuroradiol. 1989;10:687–93.

Deltour P, Lemmerling M, Bauters W, Siau B, Kunnen M. Posttraumatic subdural hygroma: CT findings and differential diagnosis. JBR-BTR. 1999;82:155–6.

Lee KS. The pathogenesis and clinical significance of traumatic subdural hygroma. Brain Inj. 1998;12:595–603.

McCluney KW, Yeakley JW, Fenstermacher MJ, Baird SH, Bonmati CM. Subdural hygroma versus atrophy on MR brain scans: “the cortical vein sign.”. AJNR Am J Neuroradiol. 1992;13:1335–9.

Zanini MA, Resende LA, Freitas CC, Yamashita S. Traumatic subdural hygroma: five cases with changed density and spontaneous resolution. Arquivos de neuro-psiquiatria. 2007;65:68–72.

Dural Calcifications: Normal Locations and Appearances

17

Normal physiologic *calcifications of the dura* increase in frequency with increasing age and are typically not of any clinical significance. They are particularly common among the elderly and are rare in children. However, in children they can be related to an underlying etiology or metabolic disorder, while in adults they are considered abnormal only if they are marked and progressive. Etiologies that may lead to the abnormally progressing dural calcifications include underlying inflammation or fibrosis such as arises from *chronic subdural hematoma* (SDH), *dural osteoma*, *intracranial hypotension*, *sarcoidosis*, *tuberculosis*, *hyperparathyroidism*, *basal cell nevus syndrome* (in children), chronic involvement by *lymphoma* or *plasmacytoma* (or any other tumor that invades the dura mater), *chronic renal failure*, or rarely, *nephrogenic systemic fibrosis*. It should be noted that since extra-axial lesions can cause hyperostosis or dural calcification as a reactive phenomenon, the presence of dural calcifications should alert the radiologist to exclude an adjacent mass. However, the overwhelming majority of dural calcifications are physiologic, particularly in the elderly. Such calcifications may enlarge very slowly. Dural calcifications may also occur in conjunction with *hyperostosis* of the calvarial bones, most commonly along the vertex of the skull (especially *hyperostosis frontalis*) or even along the inner aspect of the sphenoid or temporal bones.

The order of most common to least common normal locations of dural calcifications includes the falx (anteriorly or posteriorly), along the *petroclinoid ligament*, at the *tentorium*, the *retroclival region*, and occasionally along the *convexities*. Typically these are not a source of confusion on CT. However, on an MRI with the absence of a CT scan, these calcifications occasionally cause a confusing appearance of either an extra-axial tumor or hemorrhage, since their appearance may vary on T1WI with or without fat saturation, particularly in the sagittal plane near the midline (such as falcine calcifications). One clue that a T1-bright abnormality on T1WI is a dural calcification is the presence of dark signal on SWI or GE T2*WI that does not follow hemorrhage on other MR sequences. Typically, such calcifications are dark on T2WI as well and may be invisible or dark on FLAIR and both DWI and its corresponding ADC map. They may extend laterally along the convexities and may even surround the dural sinuses (which are enveloped by the leaves of the dura).

Another important point to note is that since meningiomas, SDHs, and surgery may cause reactive dural calcification or hyperostosis, it can be particularly difficult to differentiate a focal, completely *calcified meningioma* (i.e., a "burnt-out" meningioma) that has been stable for many years from a focal, rounded dural calcification. The presence of enhancement would suggest a meningioma. Indeed, completely calcified meningiomas may be indistinguishable from focal dural calcifications, although dural calcifications should not cause mass effect or focal (asymmetric) hyperostosis and should not enhance (Figs. 17.1, 17.2, 17.3, 17.4, 17.5, 17.6, 17.7, 17.8, 17.9, 17.10, 17.11, 17.12, 17.13, 17.14, 17.15, 17.16, 17.17, 17.18, 17.19, 17.20, 17.21, 17.22, 17.23, 17.24, 17.25, 17.26, 17.27, 17.28, 17.29, 17.30, 17.31, 17.32, 17.33, 17.34, 17.35, 17.36, and 17.37).

A.M. McKinney, *Atlas of Normal Imaging Variations of the Brain, Skull, and Craniocervical Vasculature*,
DOI 10.1007/978-3-319-39790-0_17

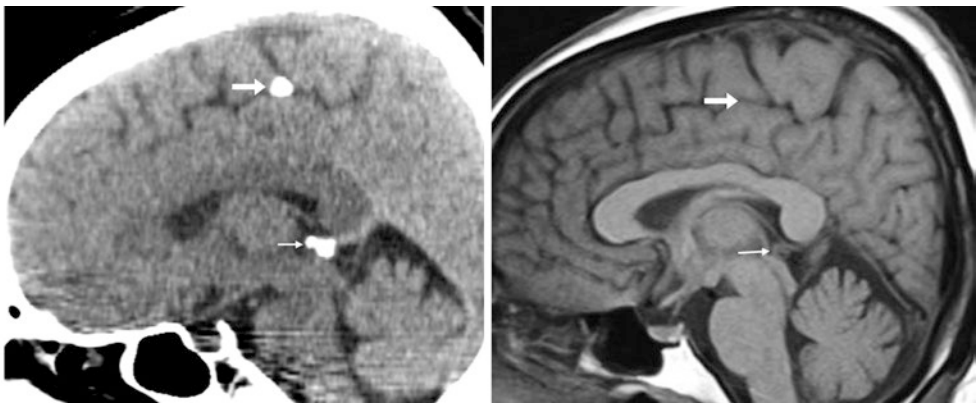

Fig. 17.1 A 52 year old with a dural/falx calcification (*arrows*) that is shown at the midline on sagittal NECT (*left*). Also note a normal, pineal calcification (*thin arrows*). These are relatively invisible on sagittal SE T1WI MRI (*right*) in this case

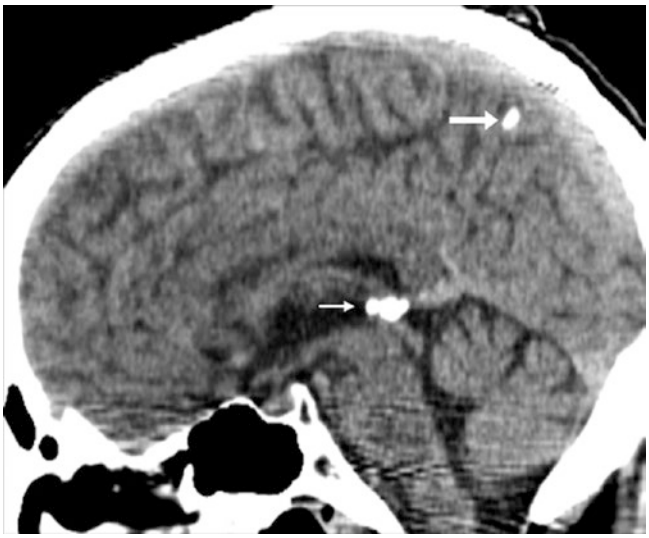

Fig. 17.2 A 43 year old who has a small falcine calcification (*arrow*) and an incidental pineal calcification (*thin arrow*)

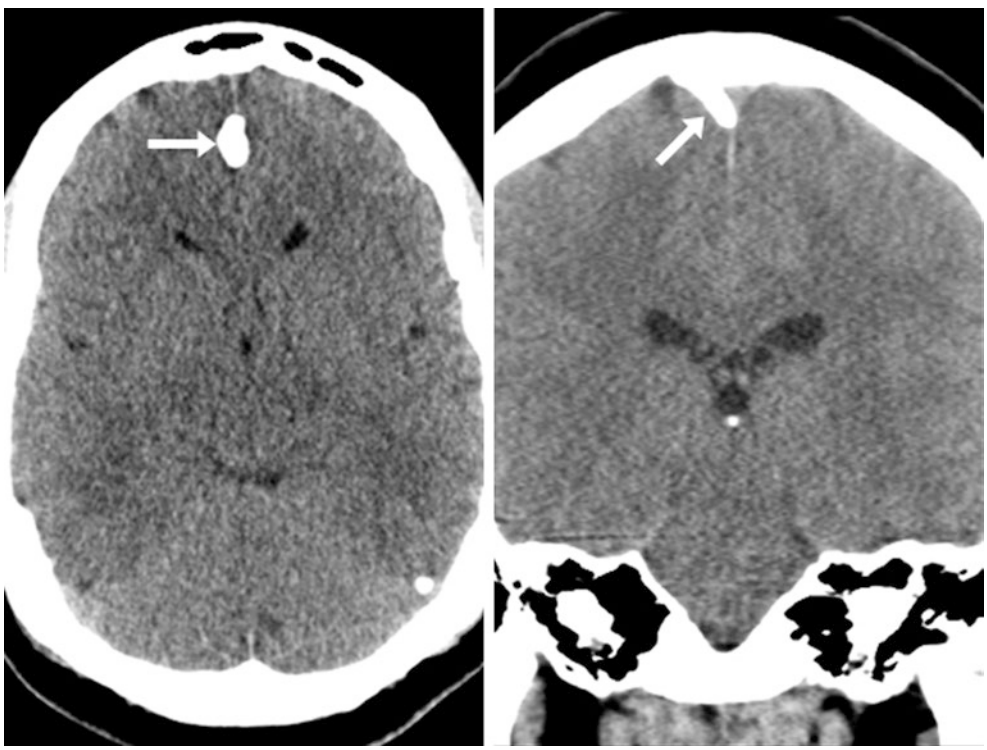

Fig. 17.3 A 22 year old with falcine calcifications (*arrow*) seen on NECT (*left*) extending along the superior sagittal sinus (*right*)

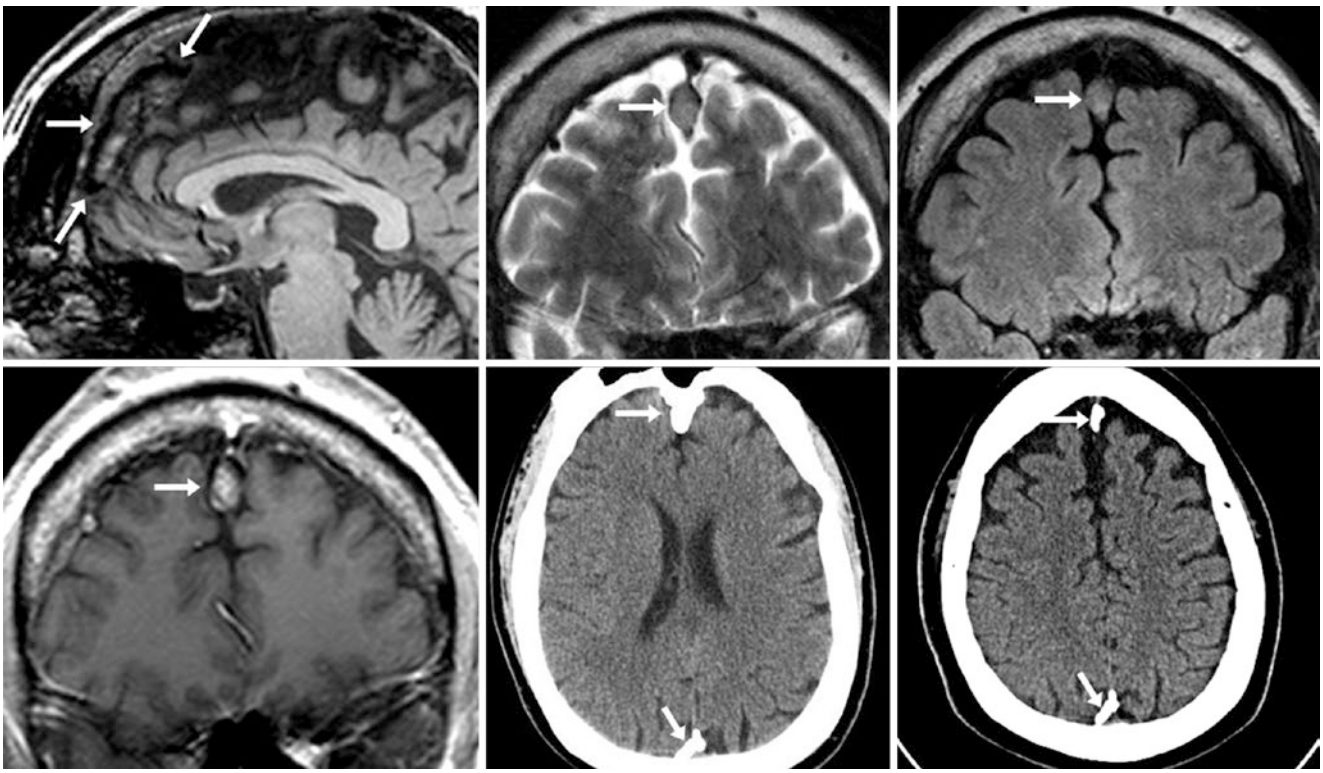

Fig. 17.4 A 30 year old with a large, extra-axial lesion that is isointense (*arrows*) to gray matter as shown on a noncontrast 3T MRI with sagittal SE T1WI (*top left*), coronal T2WI (*top middle*), and FLAIR (*top right*). There is pseudo-enhancement on postcontrast SE T1WI (*bottom left*), mistakenly thought to be a meningioma. A NECT (*bottom middle*) confirmed a falcine calcification with dural calcifications posteriorly partially surrounding the superior sagittal sinus (*bottom right*)

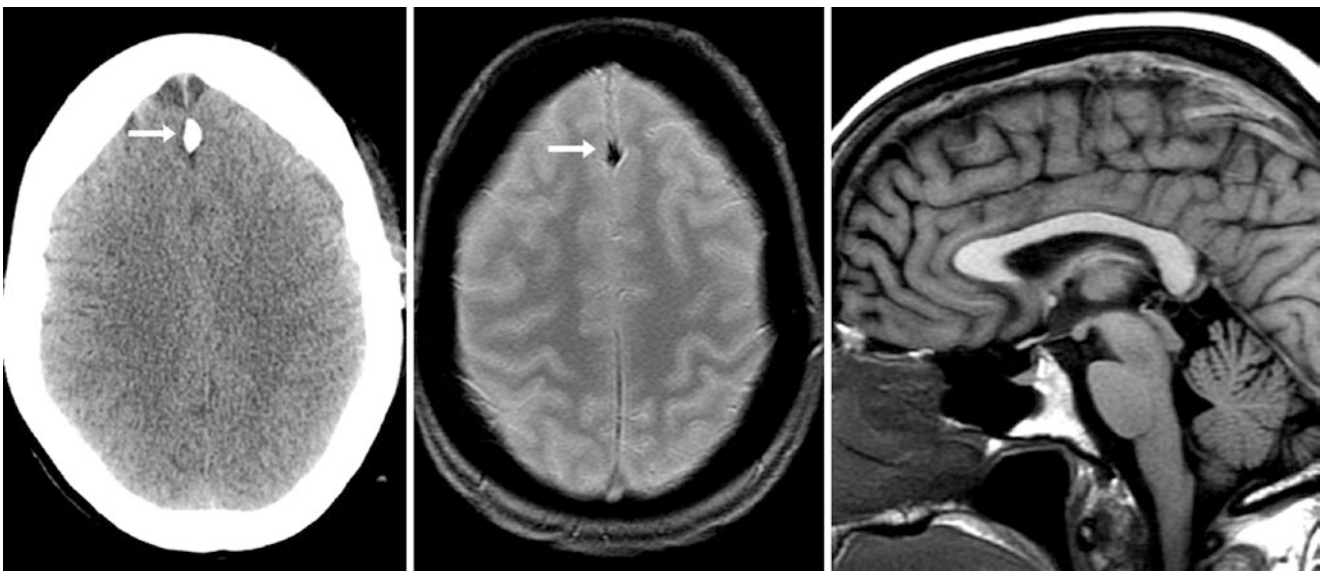

Fig. 17.5 A 51-year-old patient with head trauma who underwent a negative NECT (*left*) that demonstrated an incidental dural calcification of the falx (*arrows*). This is dark on GE T2*WI (*middle*) but is invisible on SE T1WI (*right*)

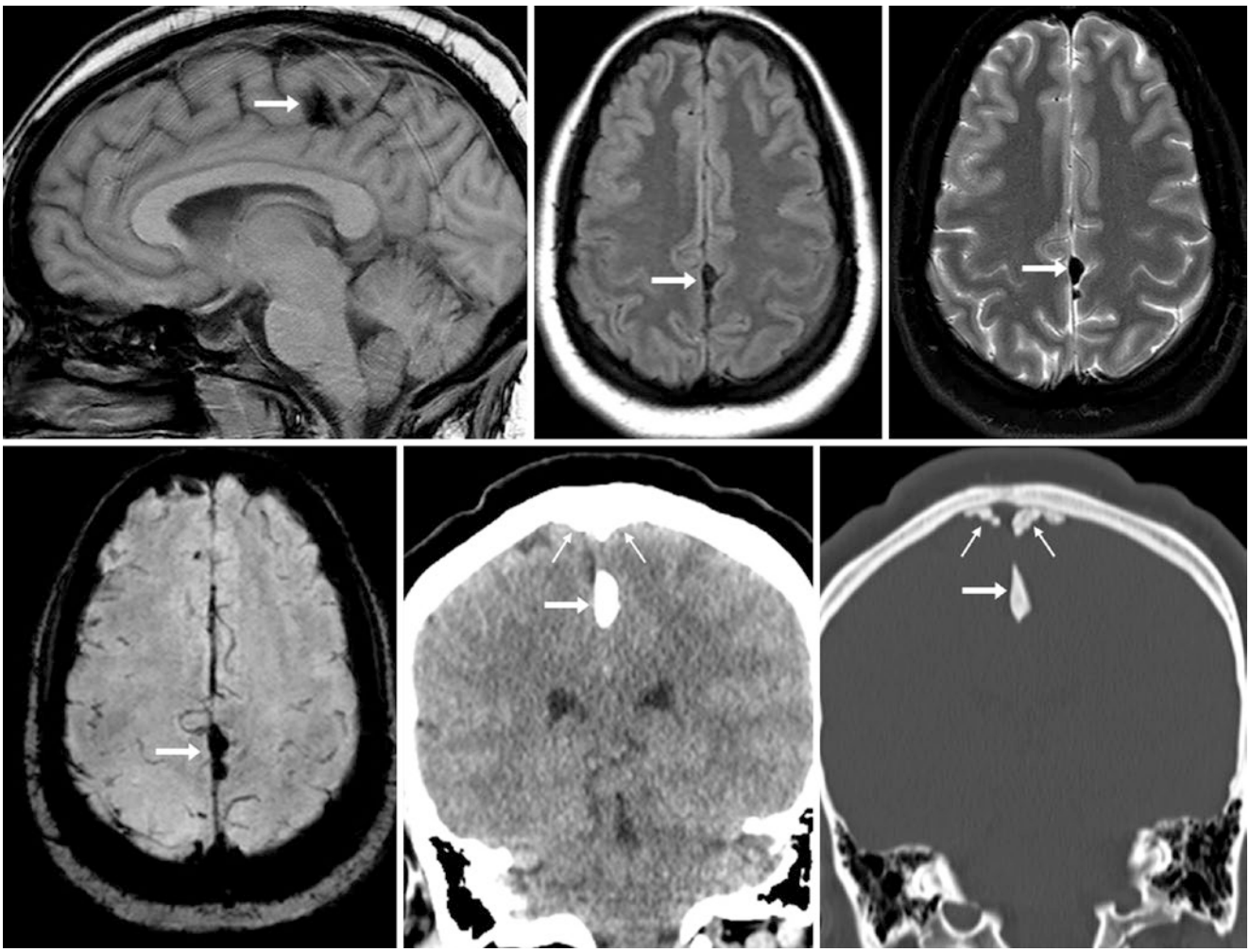

Fig. 17.6 A 35 year old who had dark dural calcifications (*arrows*) on sagittal SE T1WI (*top left*), axial FLAIR (*top middle*), T2WI (*top right*), and SWI (*bottom left*). On NECT, coronal soft tissue (*bottom middle*) and bone windows (*bottom right*) demonstrated the calcification along the falx as well as its lateral extension along the convexities (*thin arrows*)

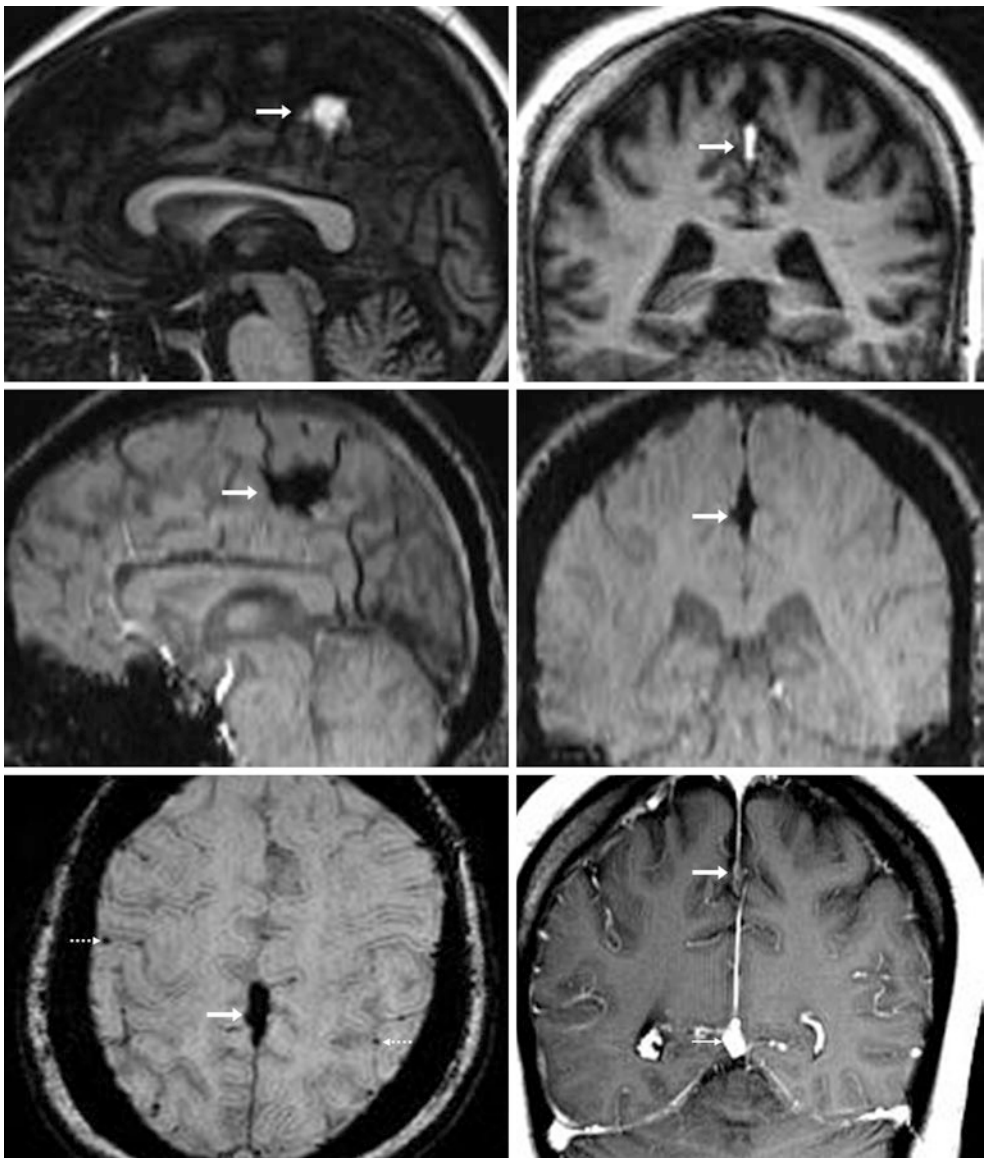

Fig. 17.7 A 52 year old with headaches. *Top row:* there is a T1-bright focus (*arrow*) on midline sagittal (*top left*) and coronal (*top right*) GE T1WIs attributable to falx calcification. *Middle row:* this is also defined on sagittal (*middle left*) and coronal (*middle right*) SWIs. Note that on SWI alone this calcification cannot be discerned from prominent vasculature. *Bottom row:* on axial SWI (*bottom left*) the falx calcification appears darker than the cortical vessels (*dotted arrows*). On coronal postcontrast T1WI (*bottom right*), note that the falx calcification does not enhance nearly as much as the normal dural venous sinuses (*thin arrows*). Thus, an extra-axial calcified meningioma can be excluded

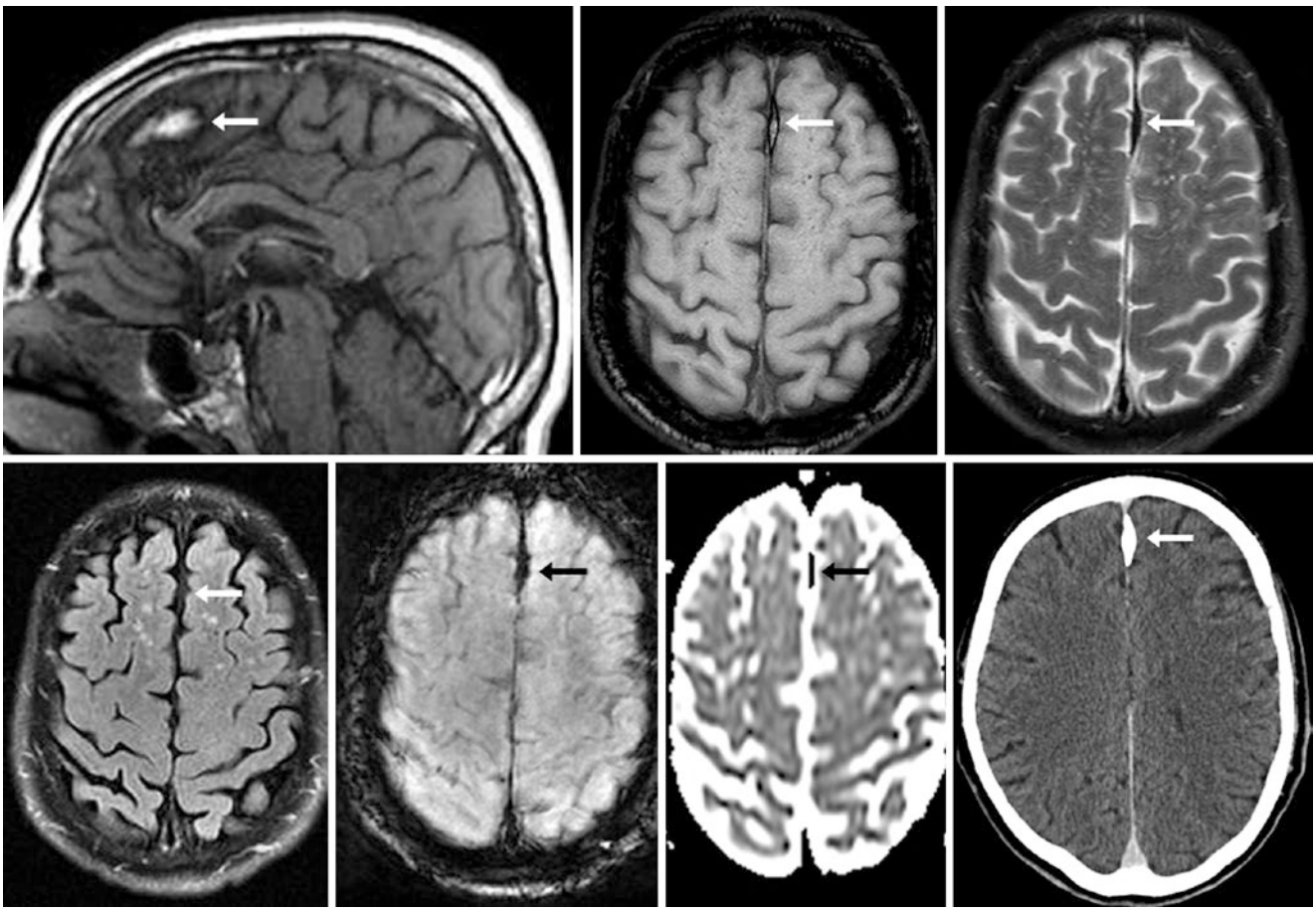

Fig. 17.8 A 68 year old had a bright anterior falx (*arrows*) on noncontrast sagittal SE T1WI (*top left*), which is less bright than on axial GE T1WI (*top middle*) and is dark on T2WI (*top right*). It is nearly invisible on FLAIR (*bottom left*) and was dark on SWI (*bottom, left middle*), with T2 blackout dark signal on an ADC map (*bottom, right middle*). It was initially thought to be a meningioma, but a subsequent postcontrast CT (*bottom right*) confirmed calcification

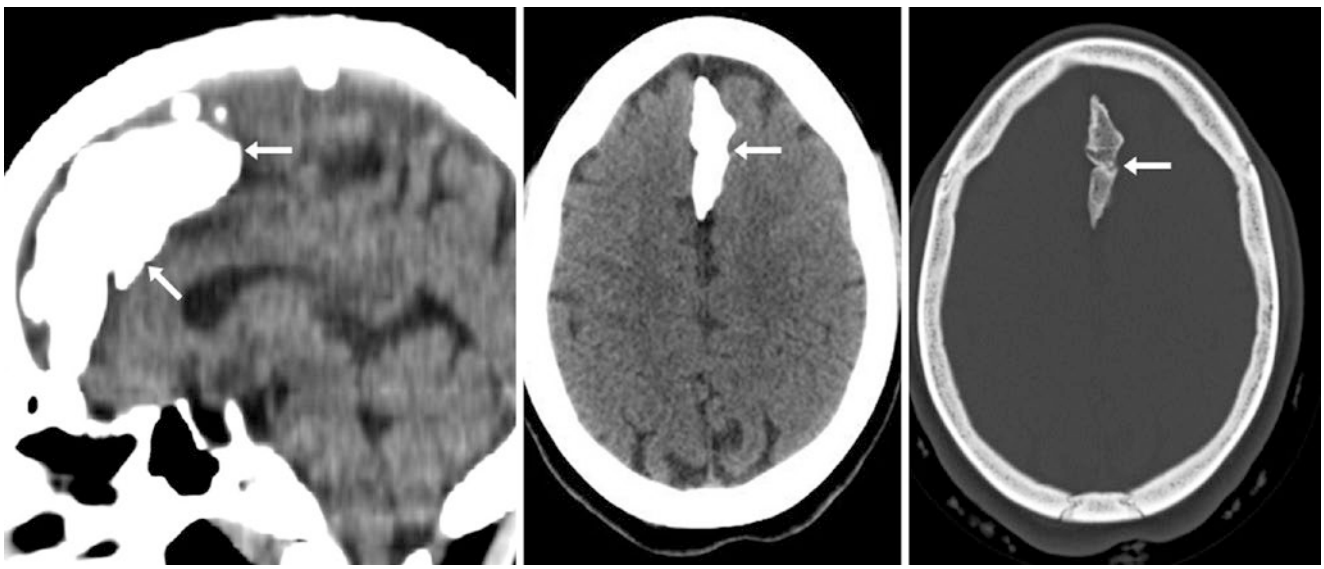

Fig. 17.9 A 38 year old had a large midline dural calcification (*arrows*) of the falx within the anterior interhemispheric fissure, as demonstrated on sagittal NECT (*left*), axial brain windows (*middle*), and bone windows (*right*). This falcine calcification is so large that it mildly displaces the adjacent superior frontal lobe on both sides

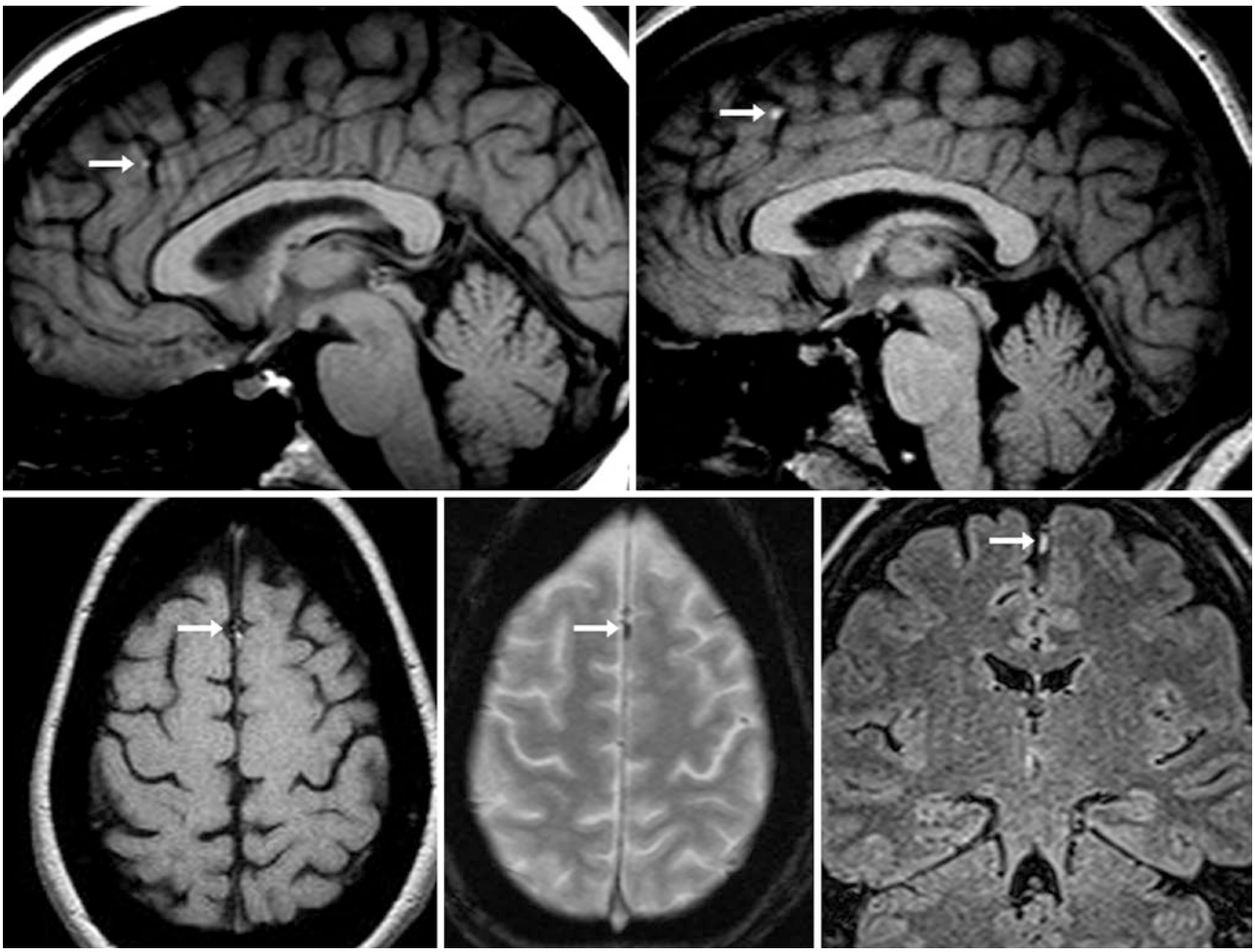

Fig. 17.10 A 29 year old was shown to have a tiny T1-bright focus (*arrows*) on a midline sagittal SE T1WI (*top left*) that probably represented a tiny falcine calcification. This was slightly larger 8 years later on repeat sagittal (*top right*) and axial (*bottom left*) SE T1WIs. It was dark on GE T2*WI (*bottom middle*) and slightly bright on coronal FLAIR (*bottom right*)

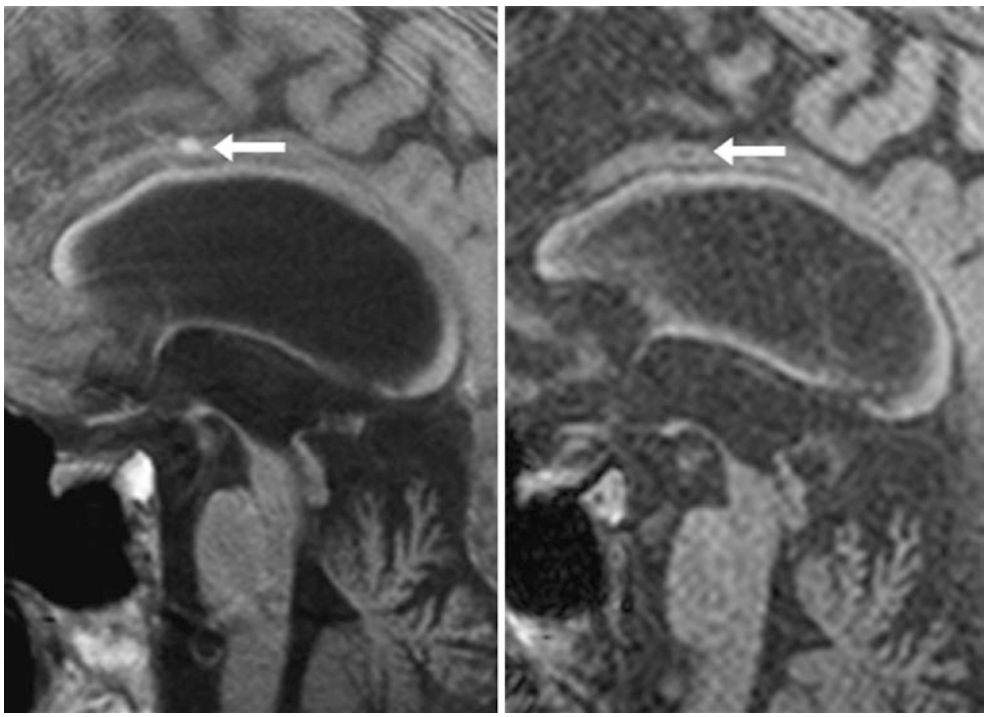

Fig. 17.11 A 54 year old was shown to have small falx calcification anteriorly (*arrows*) on a 3T MRI sagittal SE T1WI (*left*), which was invisible on a GE T1WI (*right*) at the midline

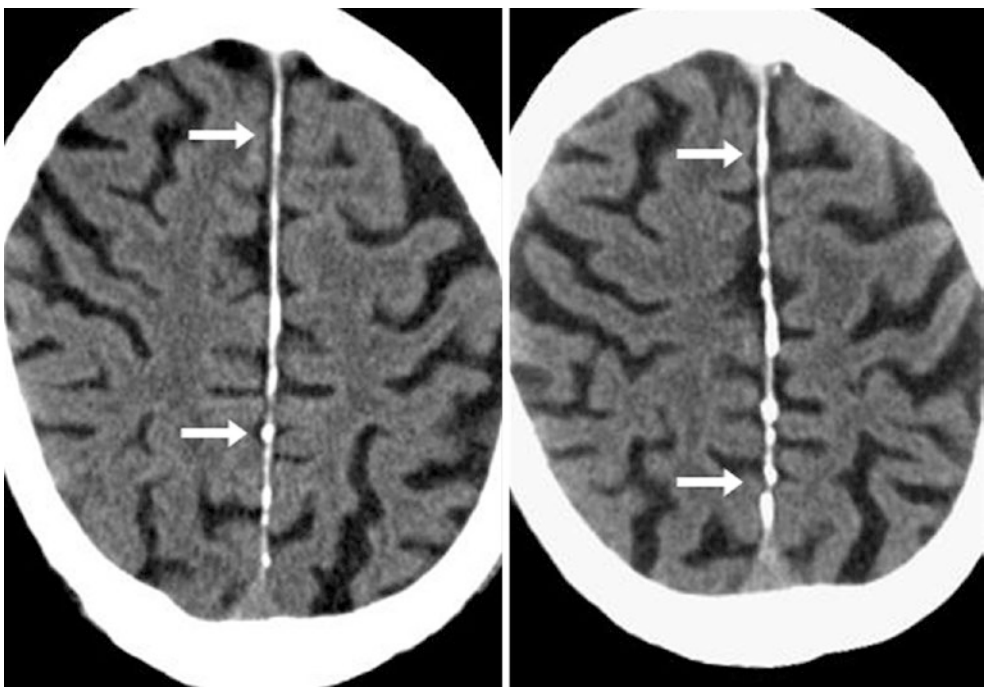

Fig. 17.12 A 77 year old with scattered falx calcifications (*arrows*) on two sequential axial NECT images from the same examination

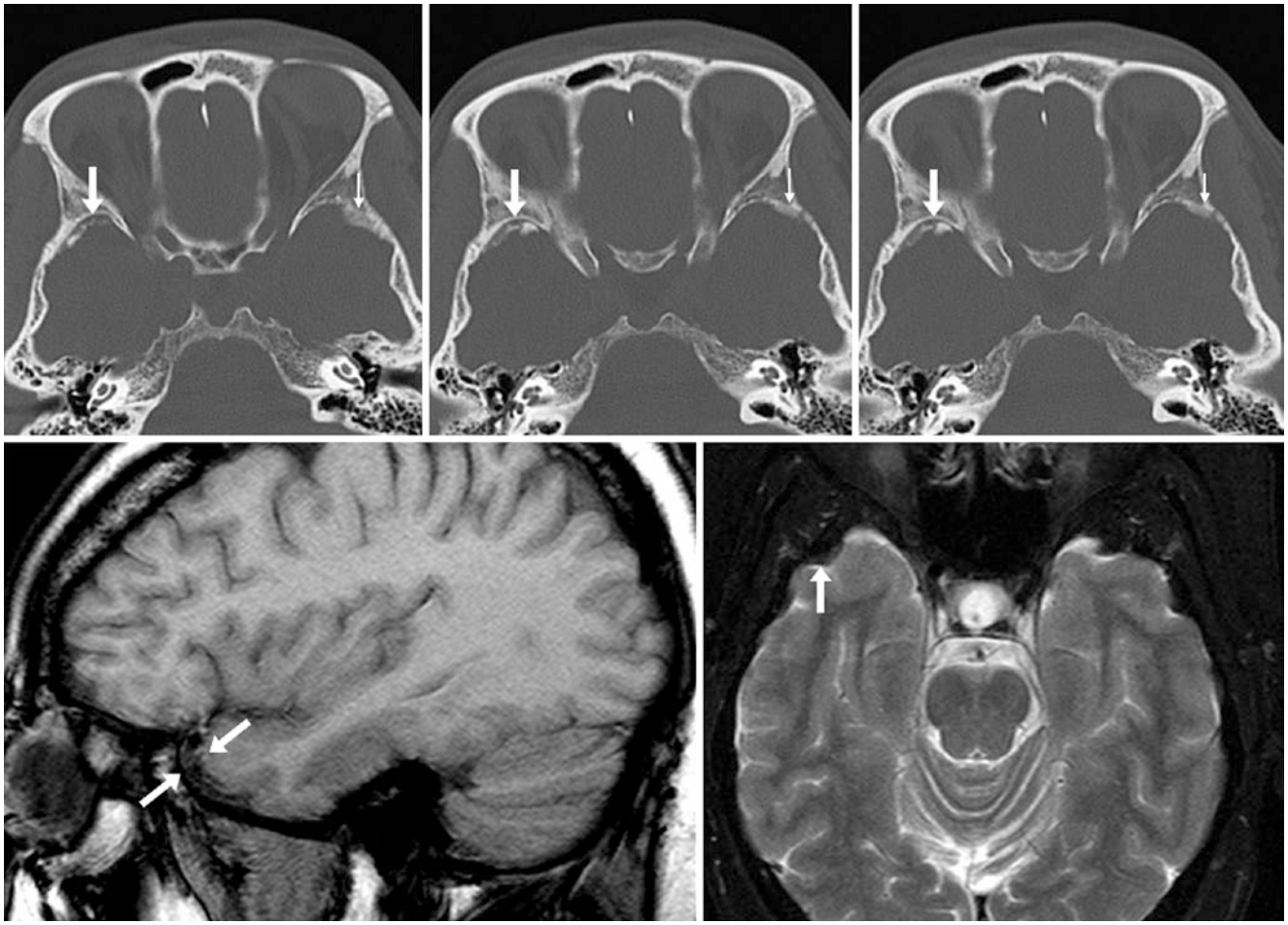

Fig. 17.13 A 54 year old with dural calcifications along the right temporal pole (*arrows*) in the middle cranial fossa on NECT (*top row*). Also note mild benign hyperostosis (*thin arrows*) along the inner aspect of the sphenoid's greater wing contralaterally. On sagittal T1WI (*bottom left*) and axial T2WI (*bottom right*), dural calcifications in this location are quite dark and nearly invisible. This illustrates how dural calcifications may occur in conjunction with hyperostosis

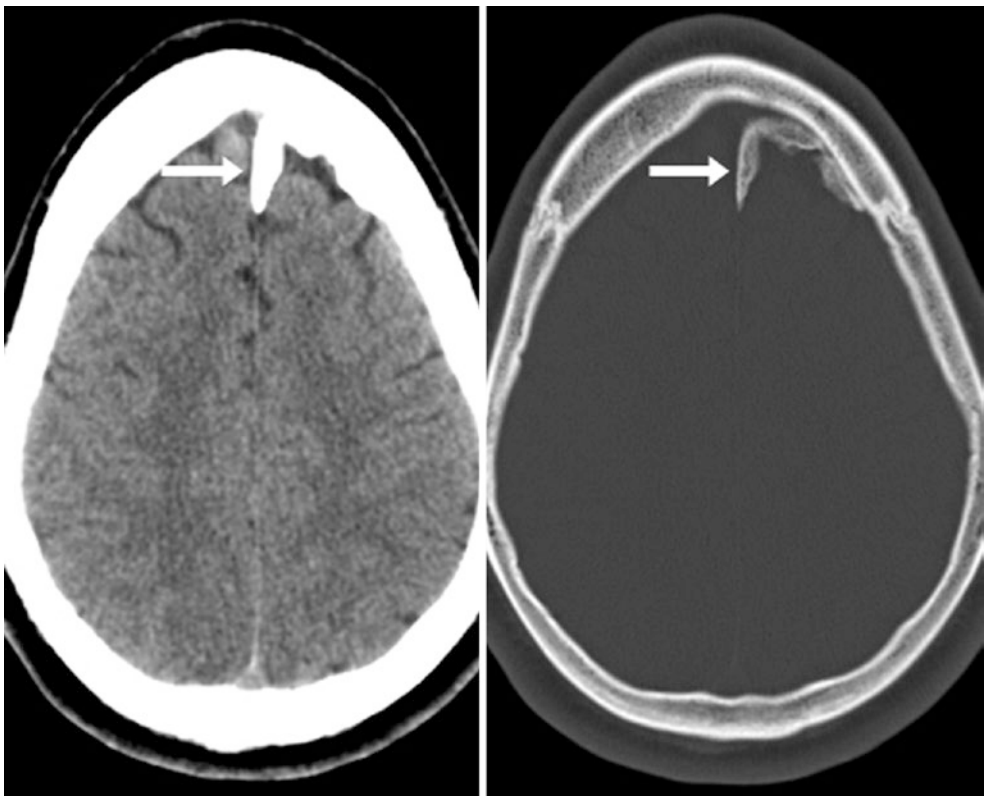

Fig. 17.14 A 25 year old with a dural calcification along the falx and left convexity (*arrows*) on NECT brain (*left*) and bone (*right*) windows. The configuration and patient age raise the question if this is from a prior SDH

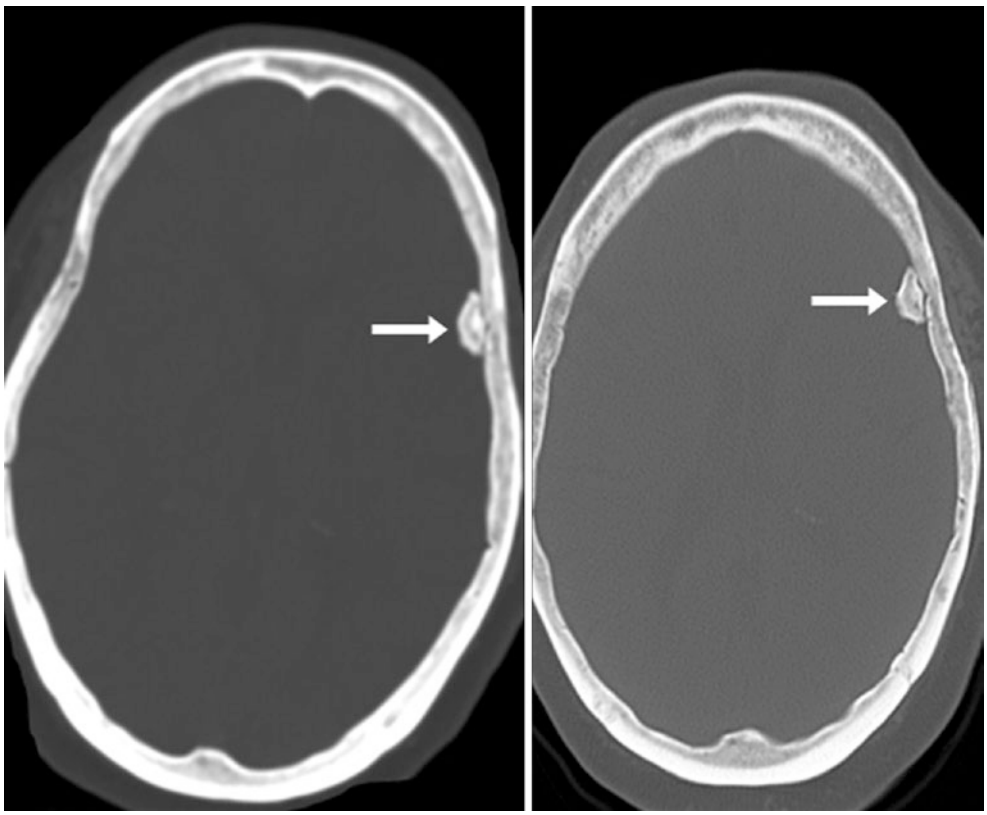

Fig. 17.15 A 64 year old was shown to have a left convexity calcification (*arrows*) on a NECT with bone windows (*left*), which was unchanged 2 years later (*right*). No underlying lesion was found. This was thought to be a chronic, reactive phenomenon

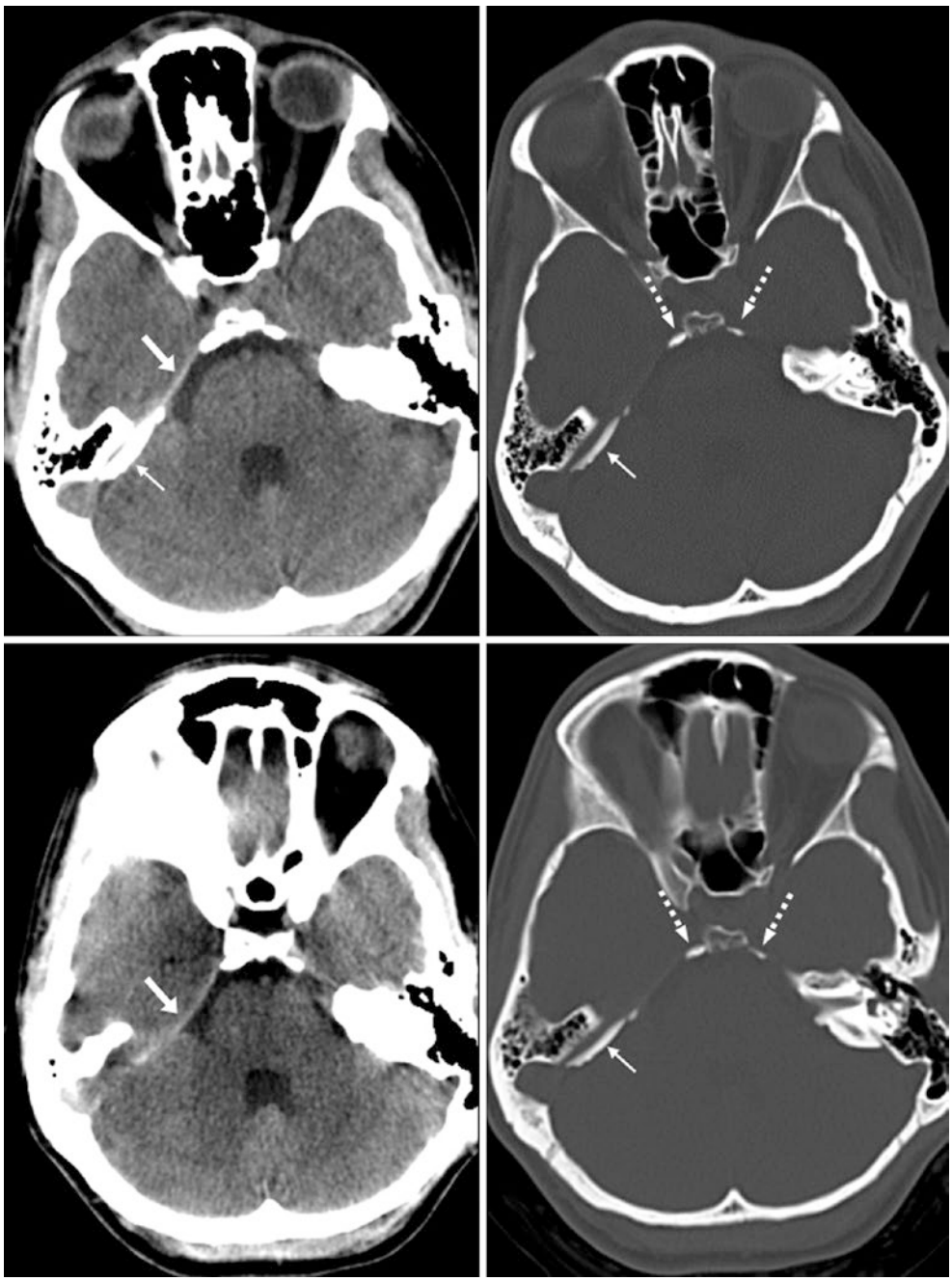

Fig. 17.16 A 22 year old with trauma who had an asymmetric, mildly hyperdense right PCL on NECT (*top left*), initially questioned to be an SDH. However, on bone window (*top right*), there was calcification both near the posterior clinoid (*dashed arrows*) as well as near the petrous apex (*thin arrows*), consistent with PCL calcification. This was unchanged 2 months later (*bottom row*)

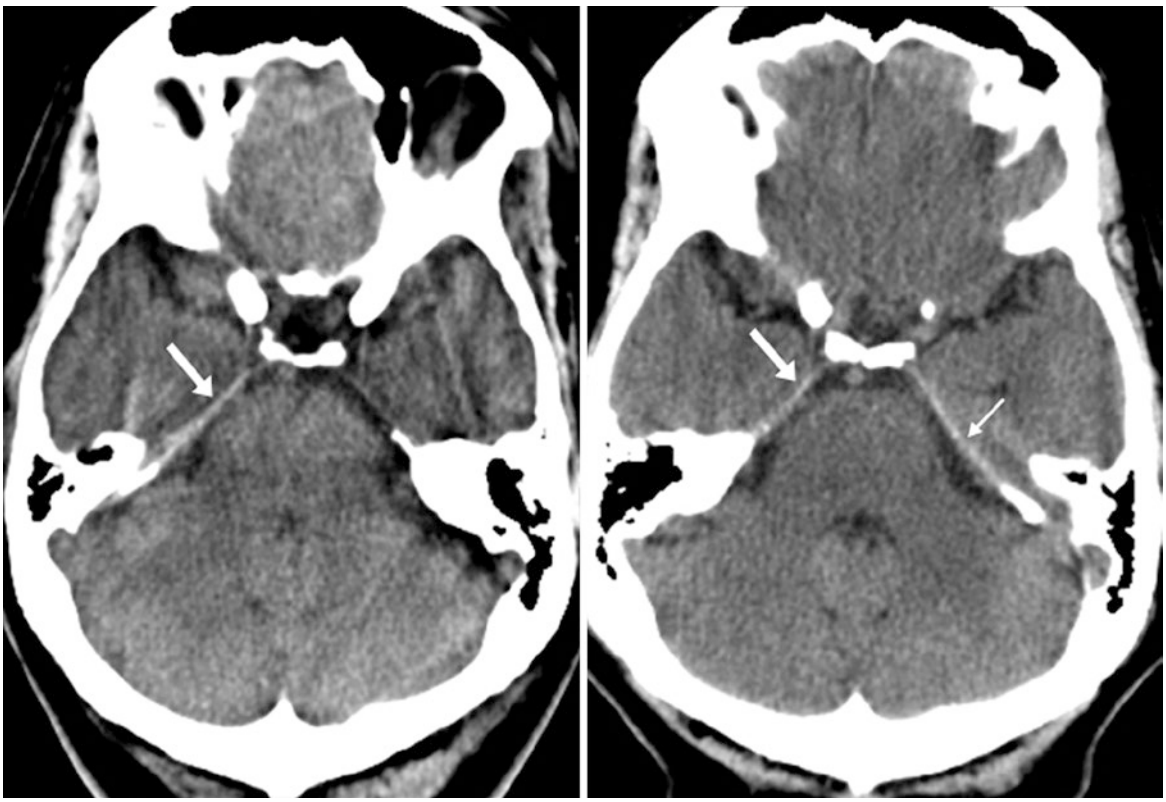

Fig. 17.17 On an initial NECT, a 50 year old had a dense right petroclinoid ligament calcification (PCL) (*arrows*, *top*) that was thought to be a SDH. This was present 4 years later (*bottom*); by then, the left PCL (*thin arrow*) began to calcify

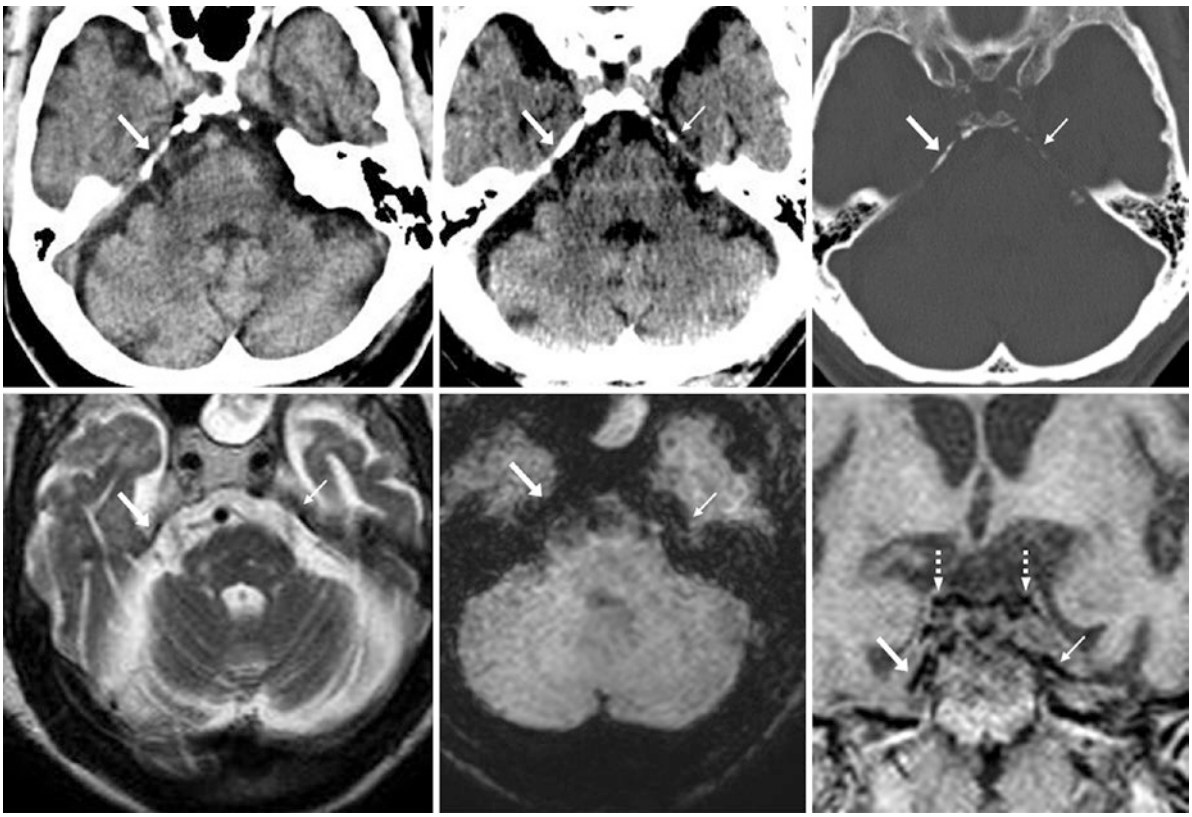

Fig. 17.18 An 81 year old with a calcified right PCL on NECT (*top left*), which had further calcified on a NECT 7 years later (*top middle*, with bone windows at *top right*); the left PCL had also further calcified (*thin arrows*). The calcifications are not visualized on T2WI MRI (*bottom left*), while on SWI (*bottom middle*), artifact from gas within the mastoids obscured the PCLs. On coronal GE T1WI (*bottom right*), the posterior clinoids (*dashed arrows*) are also depicted

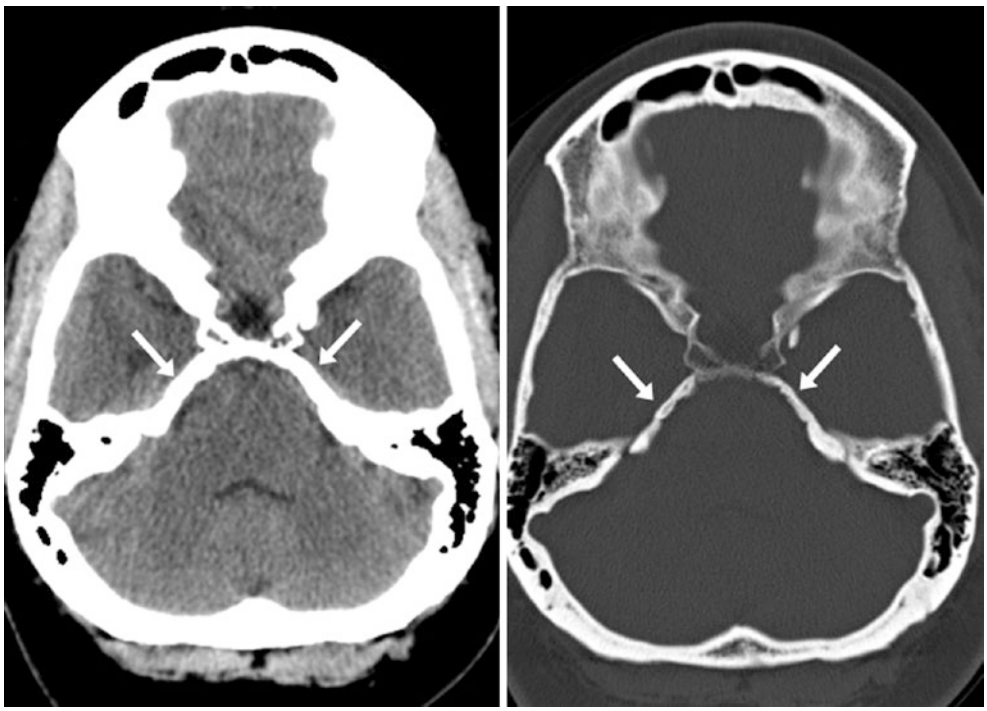

Fig. 17.19 A 40 year old with ossified PCLs bilaterally (*arrows*) on brain windows (*left*) and on bone windows (*right*). This case demonstrates the nearly ossified end of the spectrum of PCL ligament calcification

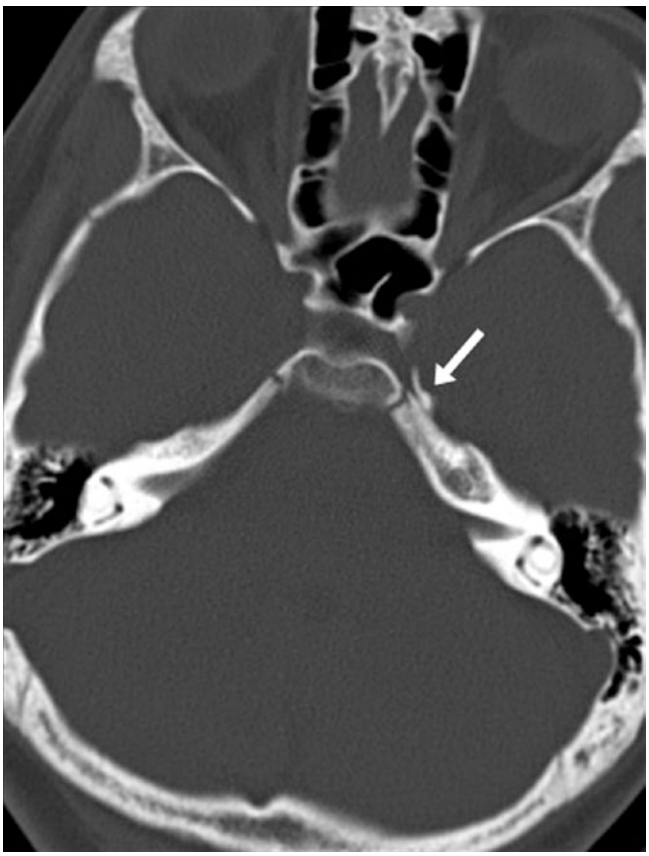

Fig. 17.20 A 13 year old with early calcifications of the left PCL (*arrow*). This may mimic a fracture in a patient with trauma

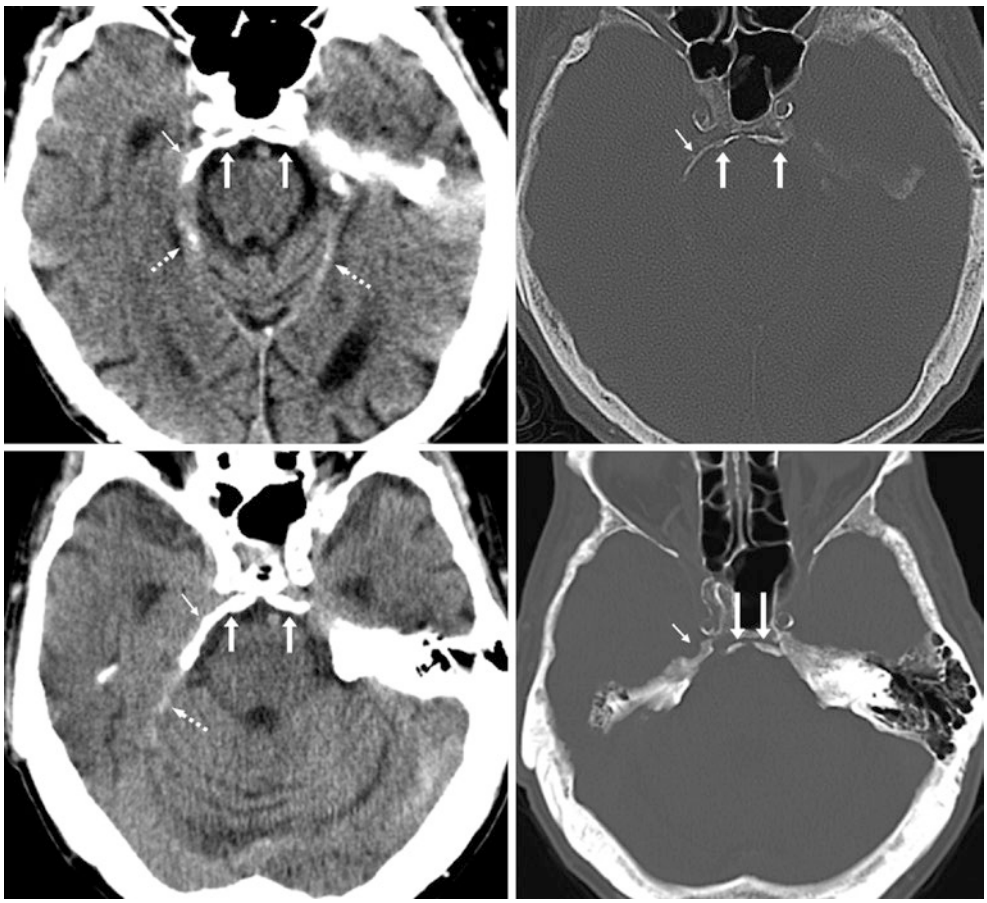

Fig. 17.21 A 73 year old had retroclival dural calcifications (*arrows*) on NECT, as shown on brain (*top left*) and bone (*top right*) windows. These had mildly increased 4 years later (*bottom*). Note that these are contiguous with right PCL calcifications (*thin arrows*). Mild tentorial calcifications are also present (*dashed arrows*)

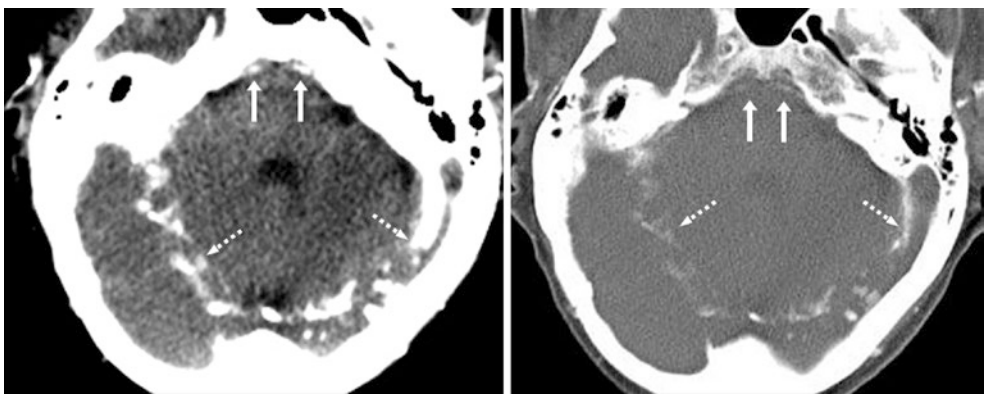

Fig. 17.22 A 45 year old had retroclival dural calcifications (*arrows*) on brain windows (*left*) and bone windows (*right*), with extensive tentorial dural calcifications as well (*dashed arrows*)

Fig. 17.23 A 77 year old was shown to have right tentorial dural calcifications (*arrows*) on NECT, with falcine calcifications (*dashed arrow*)

Fig. 17.25 A 97 year old had scattered, bilateral tentorial calcifications on NECT

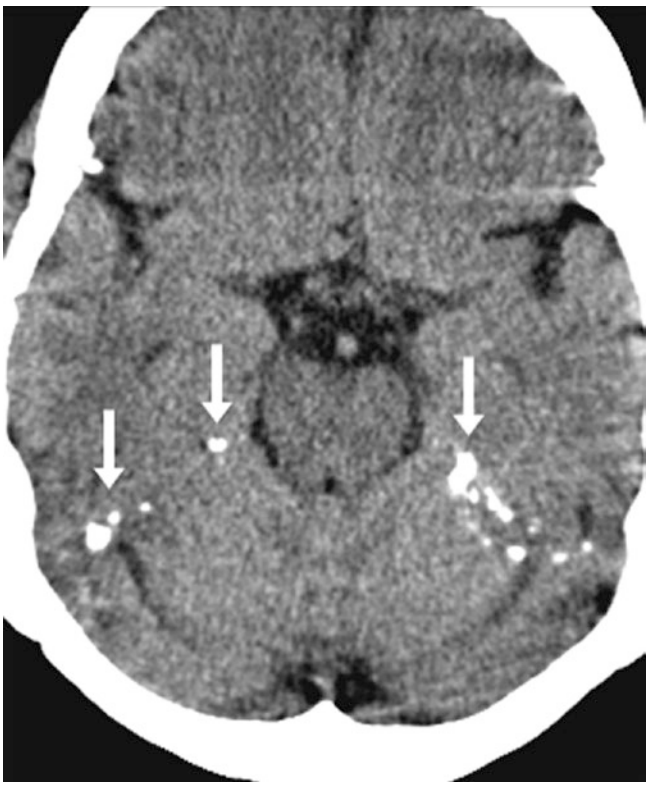

Fig. 17.24 A 75-year-old patient had bilateral, multifocal tentorial calcifications (*arrows*) on NECT

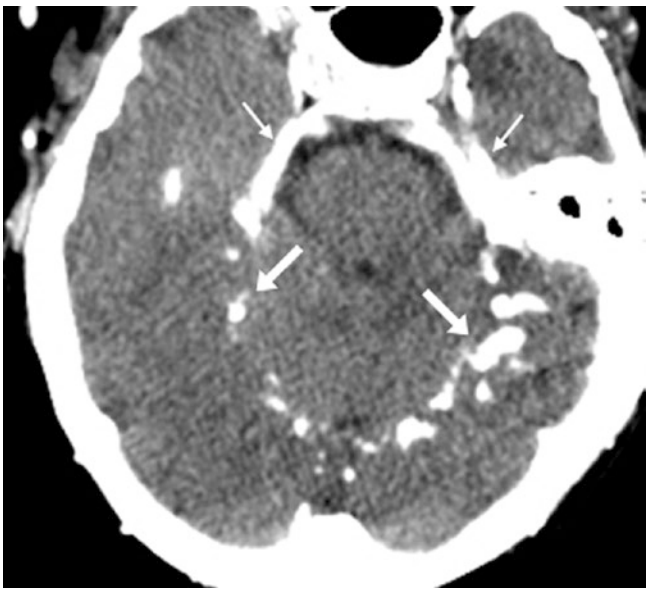

Fig. 17.26 A 43 year old with extensive and lobular tentorial calcifications (*arrows*) on NECT. Note the PCL calcifications (*thin arrows*) anteriorly as well

Fig. 17.27 A 22 year old was found to have tentorial calcifications (*arrows*) surrounding a transverse sinus. Note a falcine calcification (*dashed arrow*)

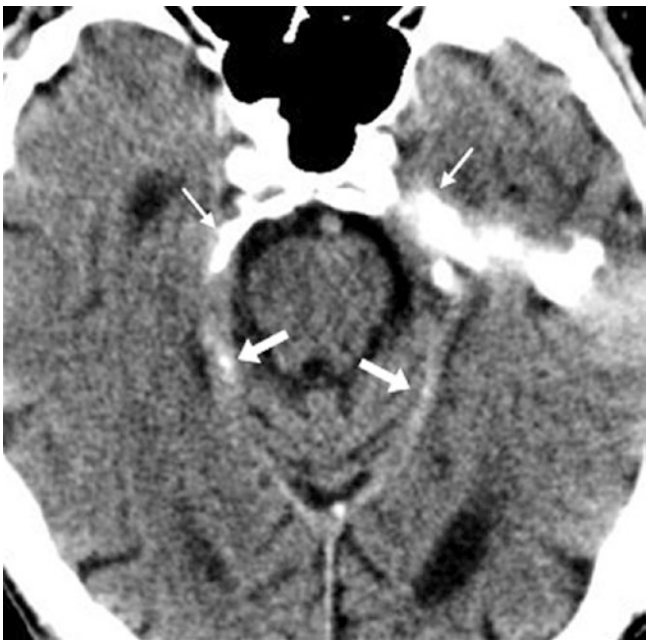

Fig. 17.28 A 77 year old with only mild tentorial calcifications (*arrows*). Also, note profound calcification of the PCL bilaterally (*thin arrows*)

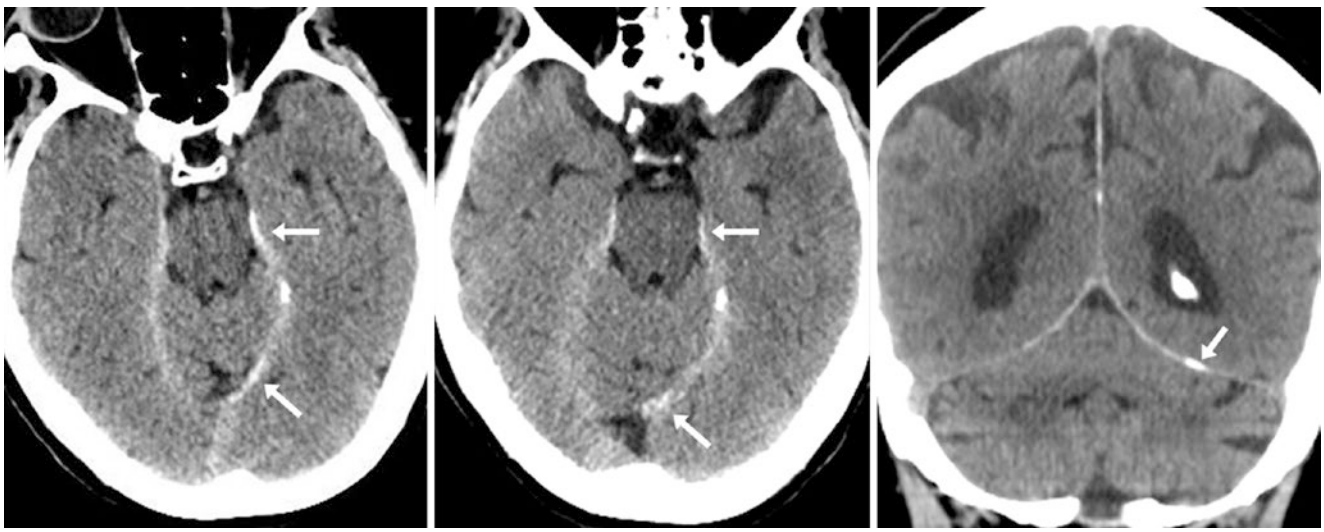

Fig. 17.29 A 95 year old who had left-sided tentorial dural calcifications (*arrows*) on axial NECT (*left*), which were unchanged on axial (*middle*) and coronal (*right*) NECT images 1 year later. Additional lower dose images of the skull base from 7 years earlier (*not shown*) confirmed that these had not changed

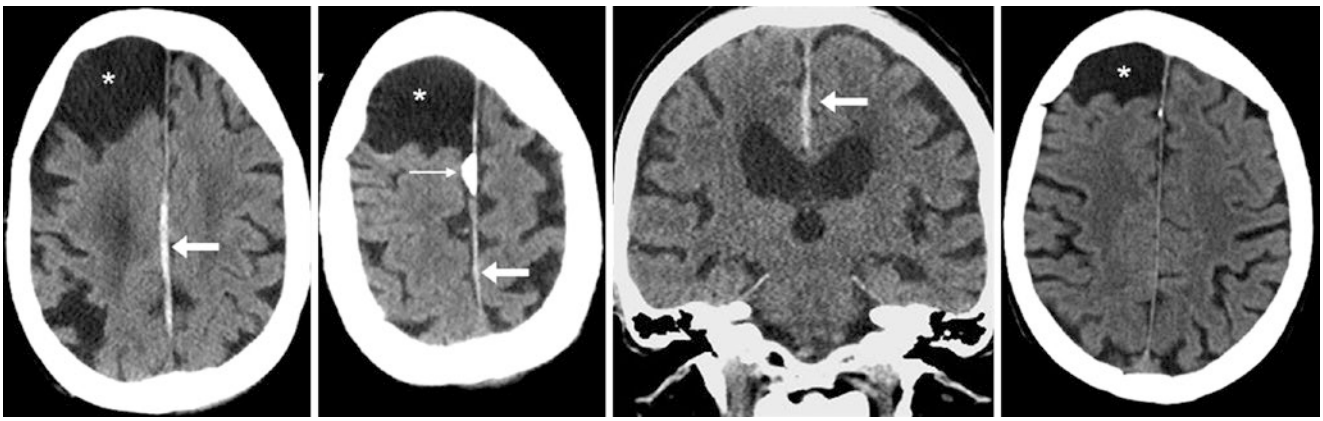

Fig. 17.30 Comparison case of interhemispheric SDH. An 84 year old with SDH along the falx (*arrows*) on axial (*left and left middle*) and coronal (*right middle*) NECT images also had a normal dural calcification (*thin arrows*). The SDH had not been present on a NECT 10 years prior (*right*). Note an incidental arachnoid cyst (*)

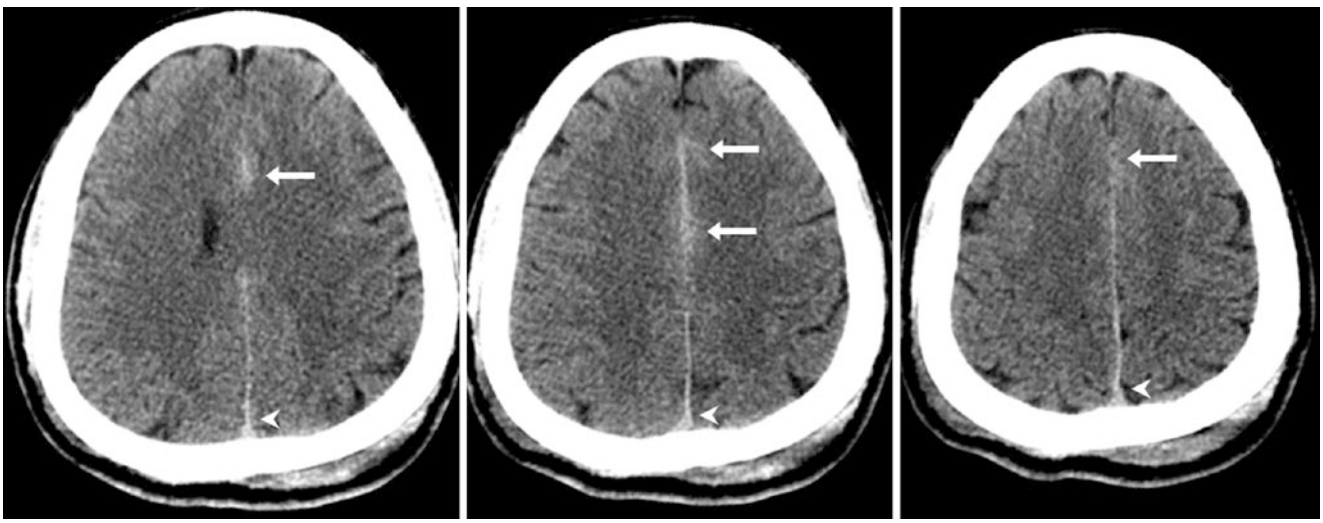

Fig. 17.31 Comparison case of interhemispheric subarachnoid hemorrhage (SAH). A 42 year old had SAH along the falx (*arrows*) on serial NECT images. Interhemispheric SAH may be mistaken for early calcification and vice versa. Also, dense venous vasculature, as in this patient (*arrowheads*), may be mistaken for hemorrhage

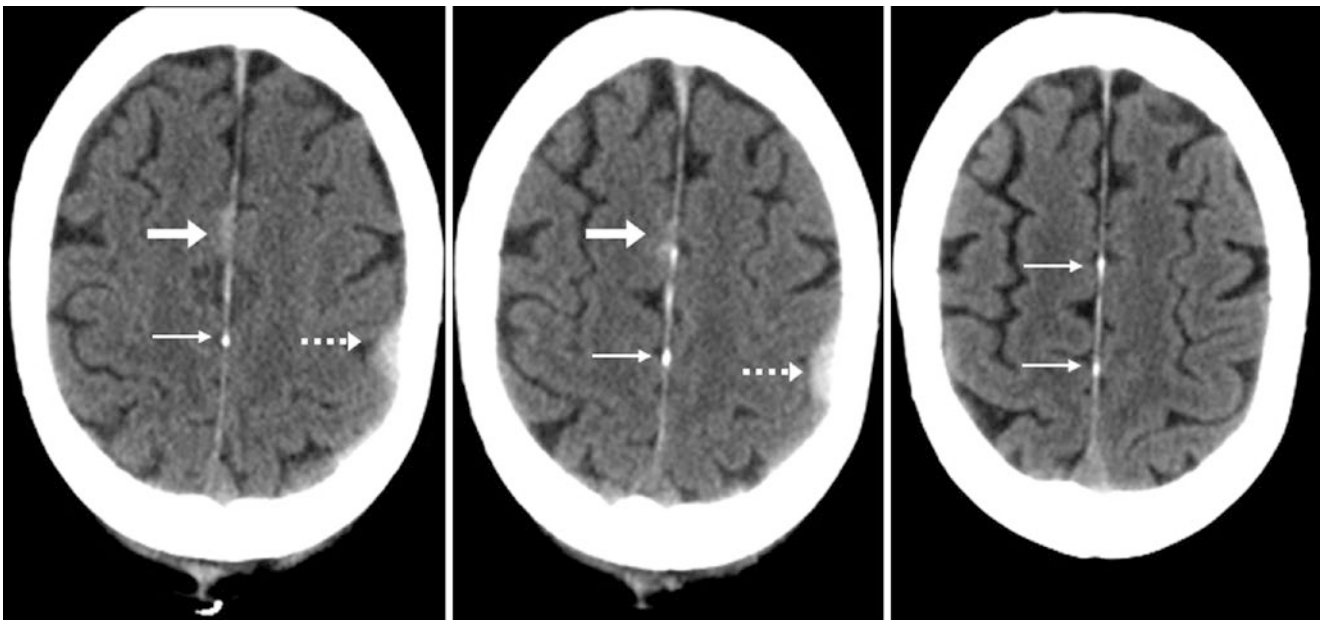

Fig. 17.32 Comparison case of interhemispheric SAH. A 77 year old had SAH along the falx (*arrows*) on an initial NECT (*left and middle*), along with a small epidural hemorrhage (*dashed arrows*). Note the greater density of tiny falcine dural calcifications (*thin arrows*). A follow-up NECT 1 month later (*right*) was normal

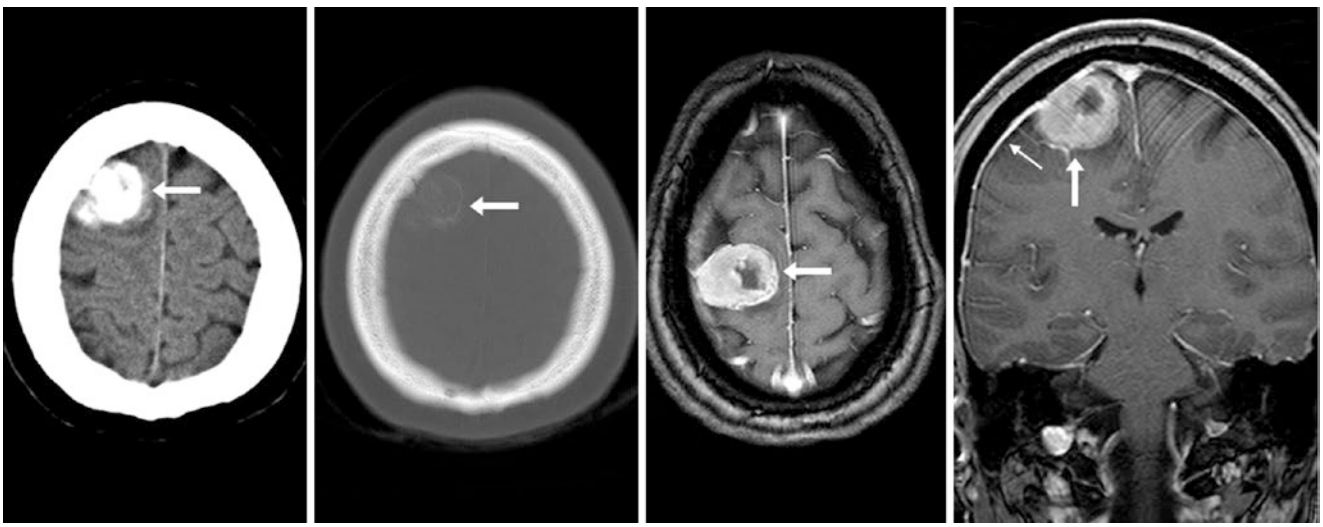

Fig. 17.33 Comparison case of calcified meningioma. A 49 year old had a focal extra-axial mass (*arrows*) along the right frontal convexity on NECT brain (*left*) and bone (*left middle*) windowed images. The lesion enhances avidly on postcontrast axial (*right middle*) and coronal (*right*) T1WIs. Note a dural tail (*thin arrow*) extending from the mass

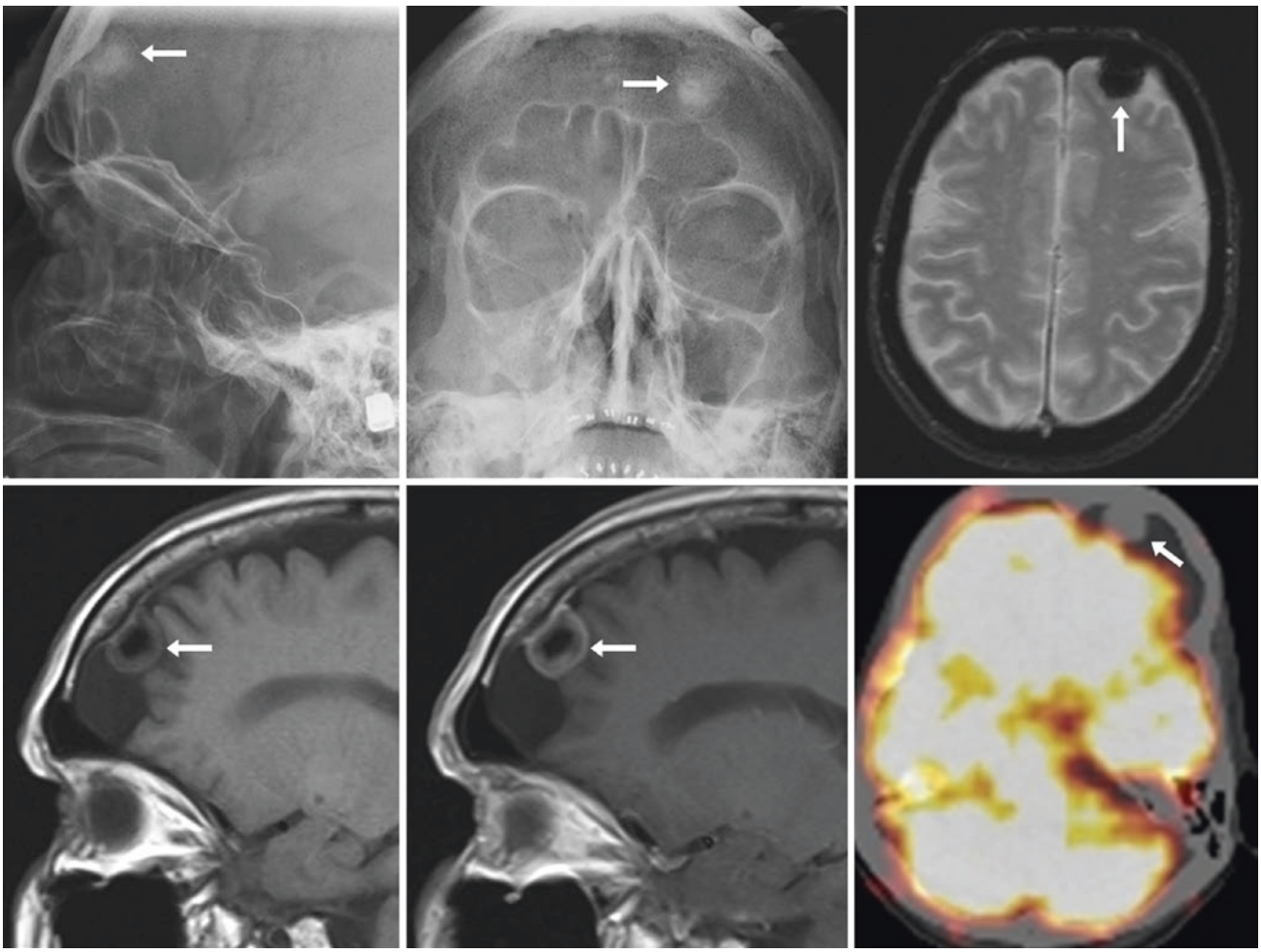

Fig. 17.34 Comparison case of calcified meningioma. An 82 year old with a history of lung cancer had an extra-axial calcification (*arrows*) on lateral (*top left*) and anteroposterior (*top middle*) plain films. On MRI, there was dark signal on GE T2*WI (*top right*) and noncontrast sagittal T1WI (*bottom left*), with mild enhancement on postcontrast T1WI (*bottom middle*). A PET-CT (*bottom right*) did not show elevated metabolic activity, confirming a benign mass

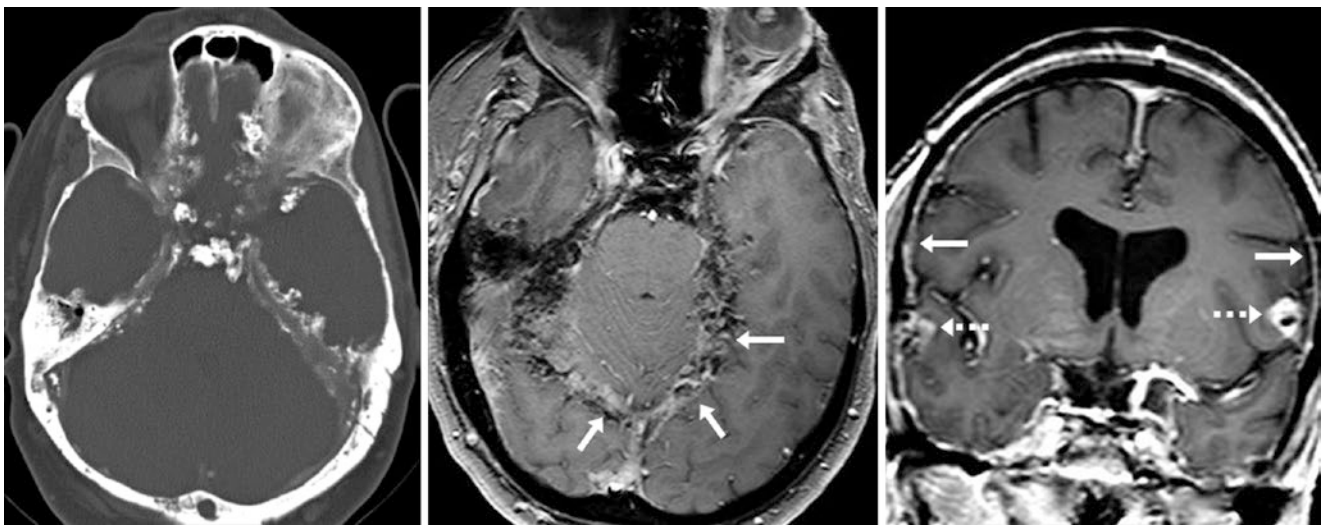

Fig. 17.35 Comparison case of basal cell nevus syndrome (Gorlin syndrome). A 52 year old had marked dural calcifications on NECT (*left*). Postcontrast axial (*middle*) and coronal (*right*) T1WIs showed dark calcium mixed with diffuse dural enhancement (*arrows*), meningiomas (*dashed arrows*), mandibular keratocysts (*not shown*), and scalp lesions (*not shown*), all features of this syndrome that occur in addition to profound dural calcifications

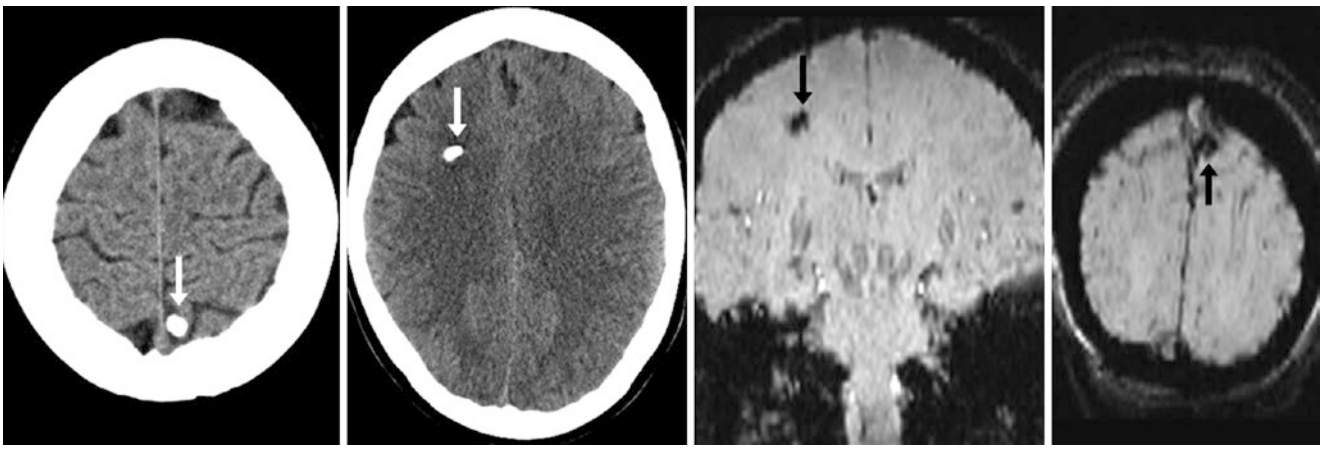

Fig. 17.36 Comparison case of neurocysticercosis. A 38 year old with seizures had a focal parietal calcification (*arrows*) that could either be intra- or extra-axial on axial NECT (*left and left middle*). A second right-sided parenchymal calcification was noted (*thin arrows*). A 3T MRI with SWI in coronal reformats (*right middle and right*) confirmed their parenchymal locations, and it was later found that the patient had been previously treated for neurocysticercosis

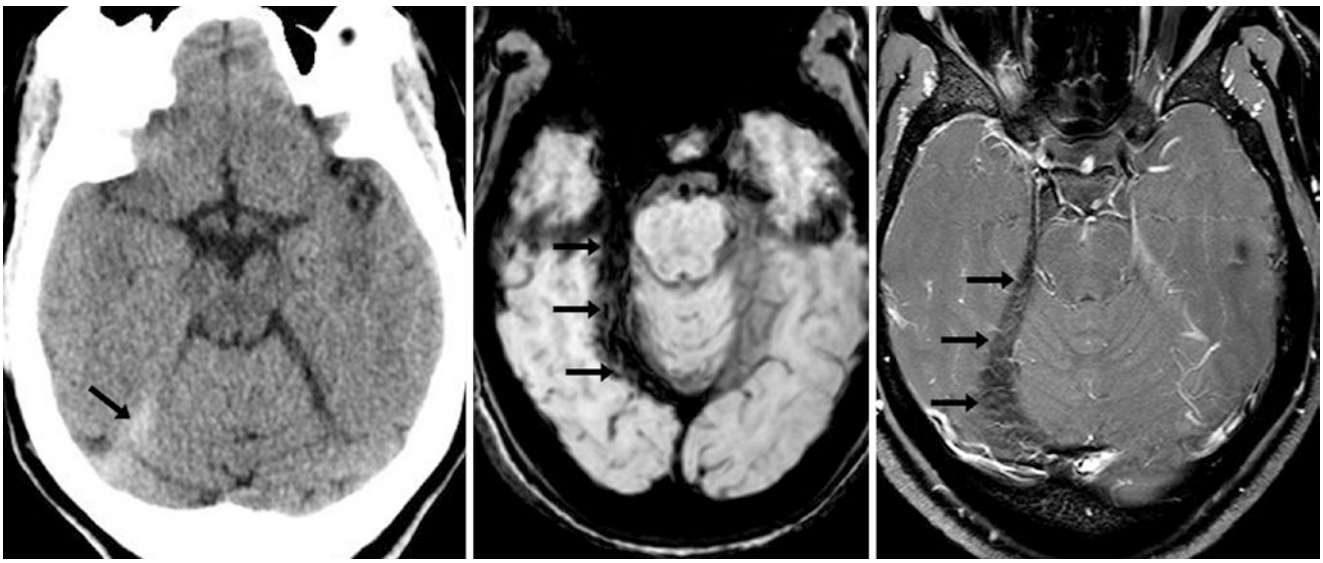

Fig. 17.37 Comparison case of idiopathic hypertrophic pachymeningitis (inflammatory pseudotumor). A 22 year old had hyperdensity of the right tentorium (*arrows*) on a NECT (*left*), but the lack of a history of trauma as well as the degree of hyperdensity made a diagnosis of SDH unlikely. A 3T MRI showed dark signal on SWI (*middle*) and T2WI (*not shown*); the region lacked enhancement on postcontrast T1WI (*right*). The patient improved with steroid therapy

Suggested Reading

Al-Motabagani M, Haroun H, Meguid EA. Calcification and ossification of the convexity of the falx cerebri and related subdural space in human cadavers. Neurosciences (Riyadh). 2004;9:261–4.

Dorenbeck U, Leingärtner T, Bretschneider T, Krämer BK, Feuerbach S. Tentorial and dural calcification with tertiary hyperparathyroidism: a rare entity in chronic renal failure. Eur Radiol. 2002;12 Suppl 3:S11–3.

Kıroğlu Y, Callı C, Karabulut N, Oncel C. Intracranial calcifications on CT. Diagn Interv Radiol. 2010;16:263–9.

Makariou E, Patsalides AD. Intracranial calcifications. Applied Radiol. 2009;38:48–60.

Rao SR, Rao TR, Ovchinnikov N, McRAE A, Rao AVC. Unusual isolated ossification of falx cerebri: a case report. Neuroanatomy. 2007;6:54–5.

Shiraishi T, Ikegami T, Okubo Y, Yato Y, Honda M. Cervical peridural calcification in patients undergoing long-term hemodialysis. Report of two cases. J Neurosurg. 2004;100:284–6.

Skrzat J, Walocha J, Jaworek JK, Mroz I. The clinical significance of the petroclinoid ligament. Folia Morphol. 2007;66:39–43.

Whitehead MT, Oh C, Raju A, Choudhri AF. Physiologic pineal region, choroid plexus, and dural calcifications in the first decade of life. AJNR Am J Neuroradiol. 2015;36:575–80.

Zelasko S, Hollingshead M, Castillo M, Bouldin TW. CT and MR imaging of progressive dural involvement by nephrogenic systemic fibrosis. AJNR Am J Neuroradiol. 2008;29:1880–2.

Pseudo-leptomeningeal Contrast Enhancement

18

The meninges covering the cerebrum and cerebellum consist of two types: the *leptomeninges* (thin covering, also known as pia mater) and the *pachymeninges* (tough covering, also known as dura mater). The vessels of the pachymeninges are outside of the blood-brain barrier and therefore certain compounds may leak through it (particularly in reactive or postoperative states), while the leptomeninges typically only exhibit enhancement with breakdown of the blood-brain barrier (e.g., infectious, inflammatory, or neoplastic conditions). Leptomeningeal contrast enhancement is usually irregular and often gyriform (i.e., not smooth along the convexity of the brain but rather following the gyri) and extends into the sulci, subarachnoid space, cerebellar folia, and around the pons, while pachymeningeal enhancement typically appears smooth and occurs along the inner surface of the bony calvarium, along the falx, and along the tentorium.

It has been described that the leptomeninges or pachymeninges may have prominent or even exuberant enhancement on contrast-enhanced CT (CECT) that will usually be less prominent on contrast-enhanced MRI following intravenous gadolinium administration. This section focuses on exuberant vascular enhancement, which may simulate *leptomeningeal contrast enhancement* (LMCE*)*. This phenomenon is particularly common in sedated pediatric patients on CECT and on contrast-enhanced MRI (CEMRI). However, on MRI this phenomenon is much more variable and depends on factors such as field strength, sequence, two-dimensional versus three-dimensional acquisition, slice thickness, contrast bolus timing, and perhaps the type of intravenous gadolinium-based contrast agent and the concentration of that agent. Generally, higher field strengths such as 3T with spin-echo sequences and thinner slices are more likely to exhibit this appearance, particularly in pediatric patients undergoing intravenous (IV) sedation.

In general, this author's experience is that it can be at times difficult to distinguish normal, robust LMCE from abnormal, mild LMCE based on CECT alone, especially in sedated pediatric patients. Thus, CEMRI is preferred to CECT in patients in whom meningitis, carcinomatosis, or other disorders of the leptomeninges are clinically suspected. There is debate as to whether FLAIR is more sensitive than CET1WI in detecting meningeal disease. Similar factors enter into this debate, as described above, but the literature suggests that overall, postcontrast two-dimensional FLAIR sequences may be a bit more sensitive than standard spin-echo T1WI; however, such sequences may be less specific, since multiple nonpathologic factors can cause a bright sulcal signal on FLAIR. However, if fat suppression is added to T1WI, there may be increased performance of CET1WI relative to FLAIR. Furthermore, if three-dimensional and/or fat suppression is added to FLAIR, there may be better performance of three-dimensional FLAIR relative to three-dimensional gradient echo T1WI (GET1WI). To this author's knowledge this has not yet been directly compared to spin echo T1WI (SET1WI) in evaluating for LMCE.

Some general guidelines (other than experience) may help discern actual from *pseudo-LMCE* on MRI. First, it is recommended to perform both CET1WI and CEFLAIR in at least the *axial plane* if leptomeningeal disease is suspected. This enables a direct comparison between the two sequences and can increase the certainty of diagnosis. A subtle finding on CET1WI can become more apparent on CEFLAIR, but on the other hand subtle, apparent enhancement on FLAIR (such as from motion) may not be real. Again, CEFLAIR is likely more sensitive but less specific than CE SET1WI. Second, *fat suppression* for FLAIR or T1WI can be quite helpful, as it removes bright fatty signal from the scalp, calvarium, or falx from the image. Also, a comparison with another plane is recommended, since apparent LMCE may wane or become less apparent in another plane, particularly on coronal sections. Occasionally, *subtraction imaging* can be useful to detect or confirm LMCE as long as the patient is not moved out of the scanner in the interval between pre- and postcontrast imaging.

This author's experience is that pseudo-LMCE usually represents prominent venous vasculature of the subarachnoid space and is particularly common in younger, sedated pediat-

A.M. McKinney, *Atlas of Normal Imaging Variations of the Brain, Skull, and Craniocervical Vasculature*,
DOI 10.1007/978-3-319-39790-0_18

ric patients (usually <7 years old). This is relatively uncommon in adults but still is anecdotal because adults less commonly undergo intravenous sedation. This phenomenon may relate to several factors that have only recently been discussed: (1) Those receiving higher concentrations or fractions of *inspired oxygen* have been shown to have pseudo-LMCE (however, this phenomenon has primarily been described with noncontrast FLAIR, not with CE T1WI). (2) In particular, IV *propofol* has been shown to increase the partial pressure of arterial CO_2 from respiratory depression, leading to compensatory vascular dilatation caused by vascular smooth muscle dilation (vascular autoregulation is preserved even under sedation). (3) Perhaps the leptomeninges are particularly *more reactive or sensitive in children* compared with adults and that effect may be amplified by sedation. Unfortunately, exuberant pseudo-LMCE in young children may simulate *meningitis* and lead to a lumbar puncture. Therefore the radiologist should exhaust available imaging sequences to exclude pseudo-LMCE prior to the patient's leaving the MR scanner. The most common scenario seems to be that a child with an unrelated diagnosis (e.g., developmental delay, autism, chronic seizures) is imaged under propofol sedation, making the finding of pseudo-LMCE spurious, and resultant lumbar punctures are negative. Our preliminary data suggest that the phenomenon of asymptomatic pseudo-LMCE is more common and occurs to a greater degree on SE T1WI compared with GE T1WI; preliminarily, the degree of prominence of the pseudo-LMCE appears inversely proportional to age and weight in children who are sedated intravenously with propofol (Figs. 18.1, 18.2, 18.3, 18.4, 18.5, 18.6, 18.7, 18.8, 18.9, 18.10, 18.11, 18.12, 18.13, 18.14, 18.15, 18.16, 18.17, 18.18, 18.19, and 18.20).

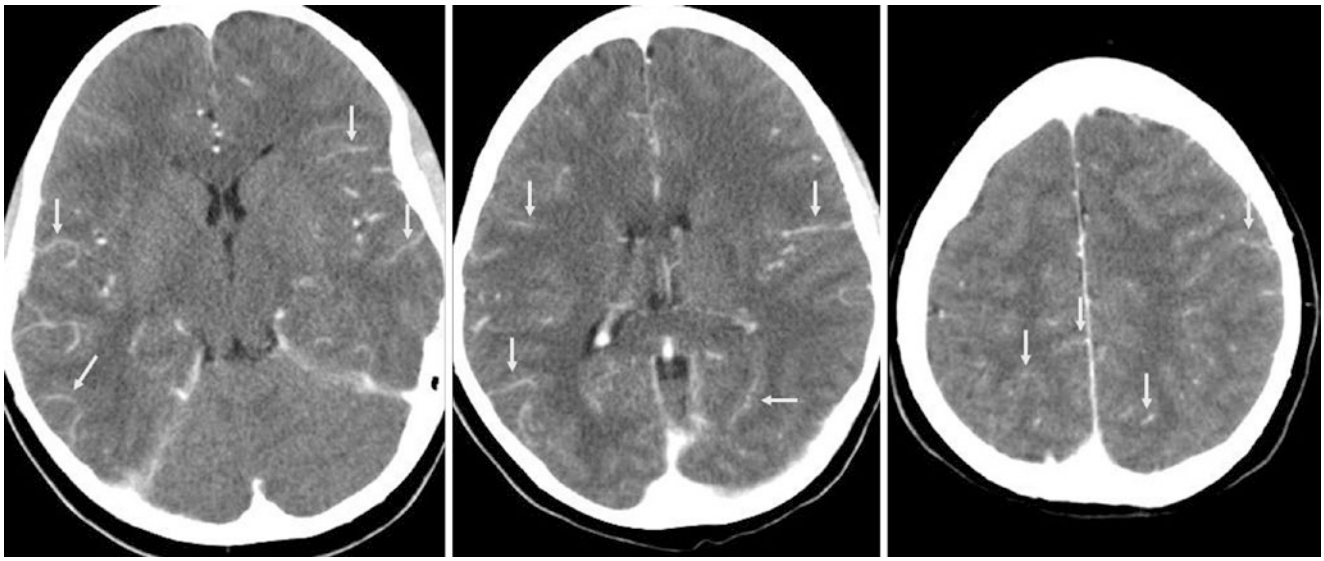

Fig. 18.1 A 15 year old male with fever and headache who had pseudo-LMCE (*arrows*) on CECT, most likely caused by prominent vasculature. A lumbar puncture was negative. Note the lack of such pseudo-LMCE along the cerebellum

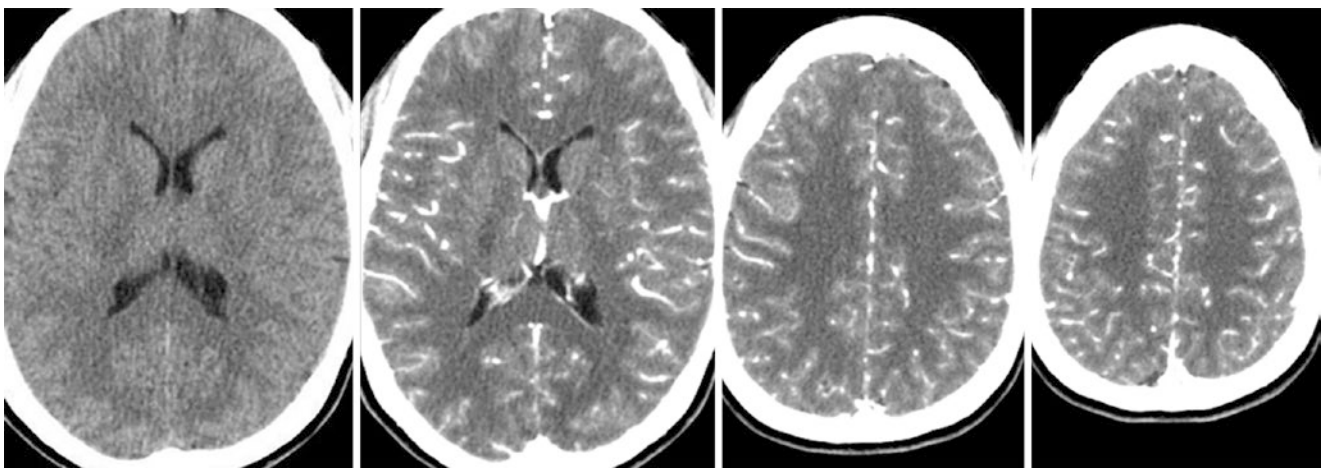

Fig. 18.2 A 25 year old male with new headaches. The patient had a normal NECT (*left*) but had exuberant pseudo-LMCE on CECT (*right three images*), most likely due to prominent vasculature. A lumbar puncture was negative

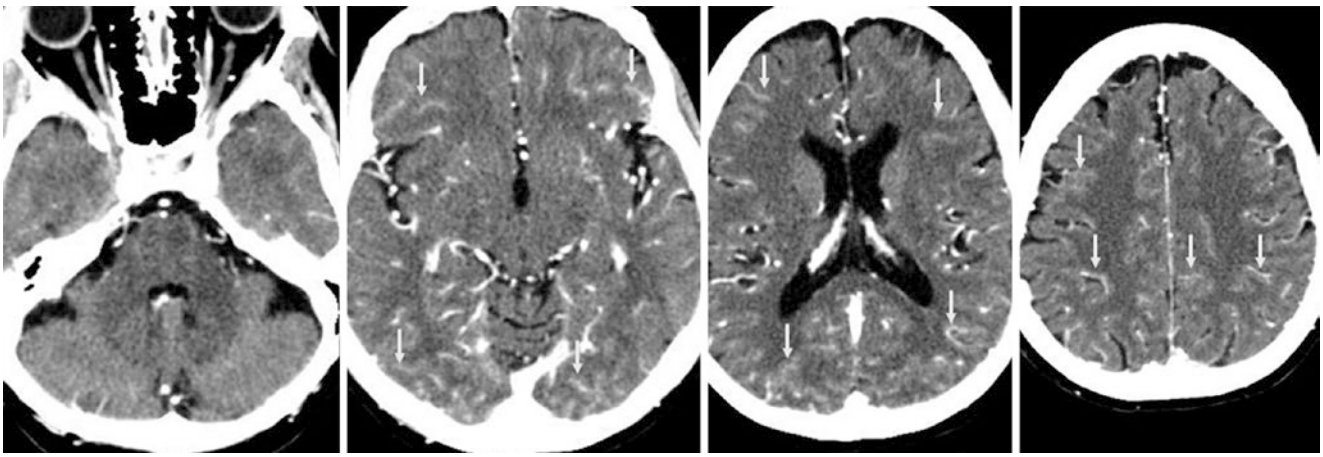

Fig. 18.3 A 51-year-old HIV-positive female who had headaches after trauma (normal NECT). CECT demonstrated avid pseudo-LMCE (*arrows*). Note the lack of pseudo-LMCE in the posterior fossa. A lumbar puncture was negative

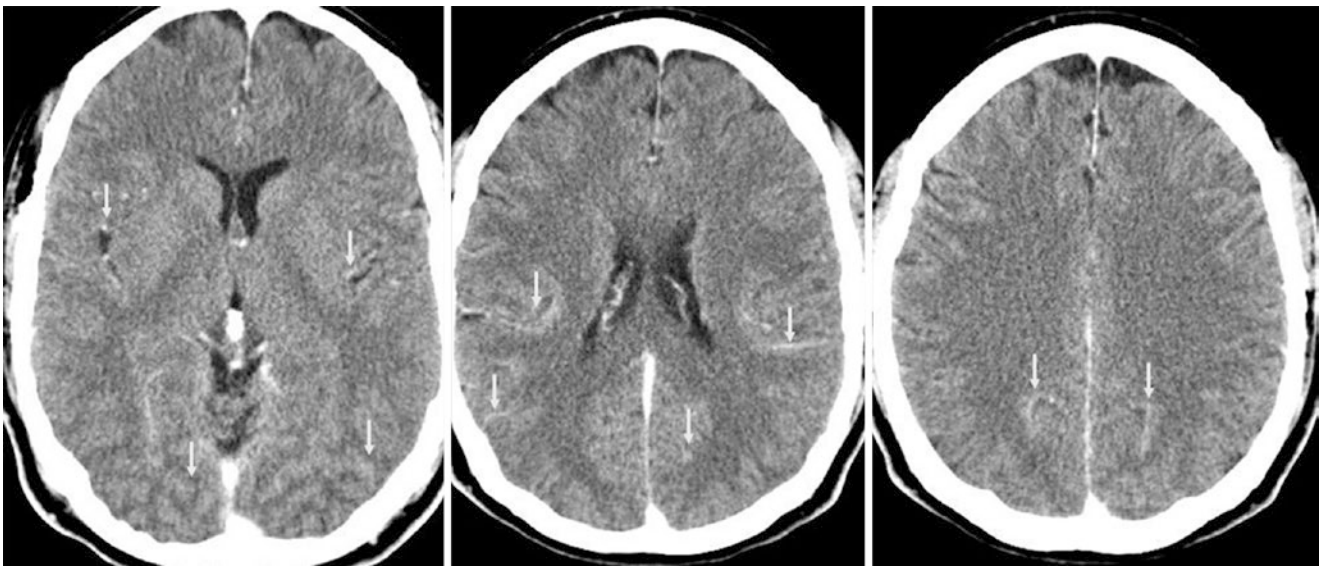

Fig. 18.4 A 31 year old male with a germ cell tumor (non-intracranial) with mild pseudo-LMCE (*arrows*) indicated on CECT. A lumbar puncture was negative for subarachnoid tumor. This is most prominent in the parieto-occipital region

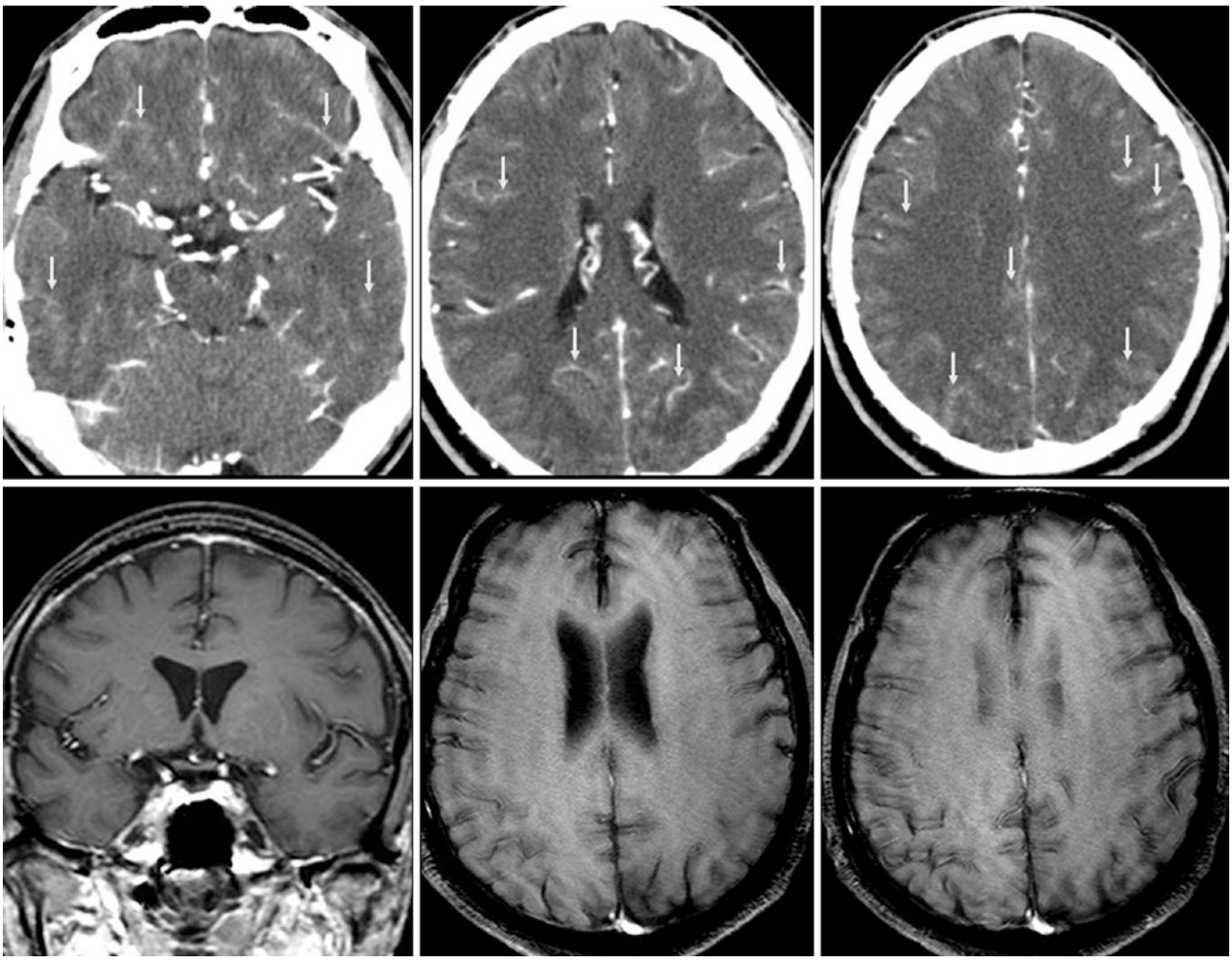

Fig. 18.5 A 57 year old male with a history of lung cancer underwent CECT (*top row*) to evaluate for metastatic disease. There was an appearance of pseudo-LMCE (*arrows*) on CECT. However, a lumbar puncture was negative. A 3T MRI did not depict LMCE on postcontrast coronal (*bottom left*) or axial (*bottom middle and bottom right*) SE T1WIs

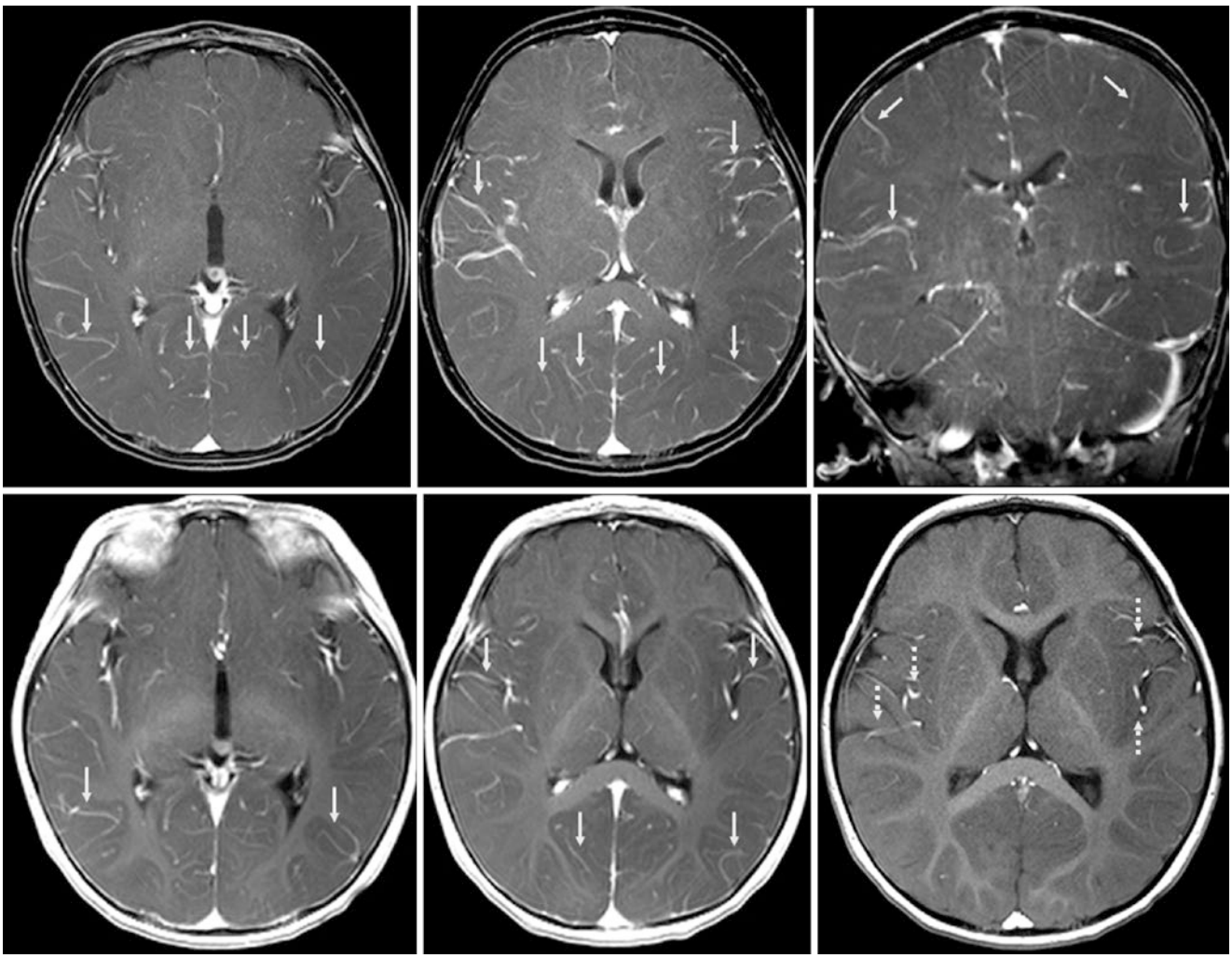

Fig. 18.6 A 9 month old male with nystagmus underwent an otherwise normal 3T MRI with sedation. CEMRI axial (*top left and top middle*) and coronal (*top right*) SE T1WIs showed pseudo-LMCE (*arrows*) simulating meningeal inflammation. However, the symptoms were not acute. The pseudo-LMCE was less pronounced on CEMRI GET1WIs (*bottom left and middle*). Note that on noncontrast GET1WI (*bottom right*) some vessels were already bright (*dotted arrows*)

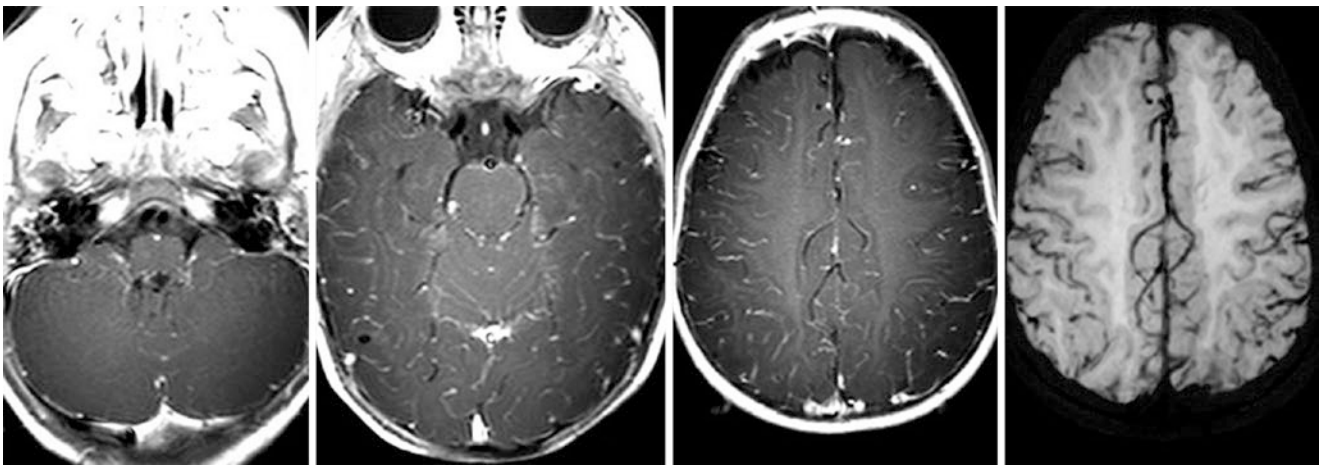

Fig. 18.7 A 10 month old with developmental delay underwent a 3T MRI with IV sedation. Diffuse pseudo-LMCE was present on postcontrast axial SET1WIs (*leftmost three images*) simulating meningeal inflammation. Note that the pseudo-LMCE spares the posterior fossa (*left*). A 10-mm sliding MIP SWI (*right*) at the same level of a SET1WI (*right middle*) demonstrated that the pseudo-LMCE was present in regions of prominent venous vascularity

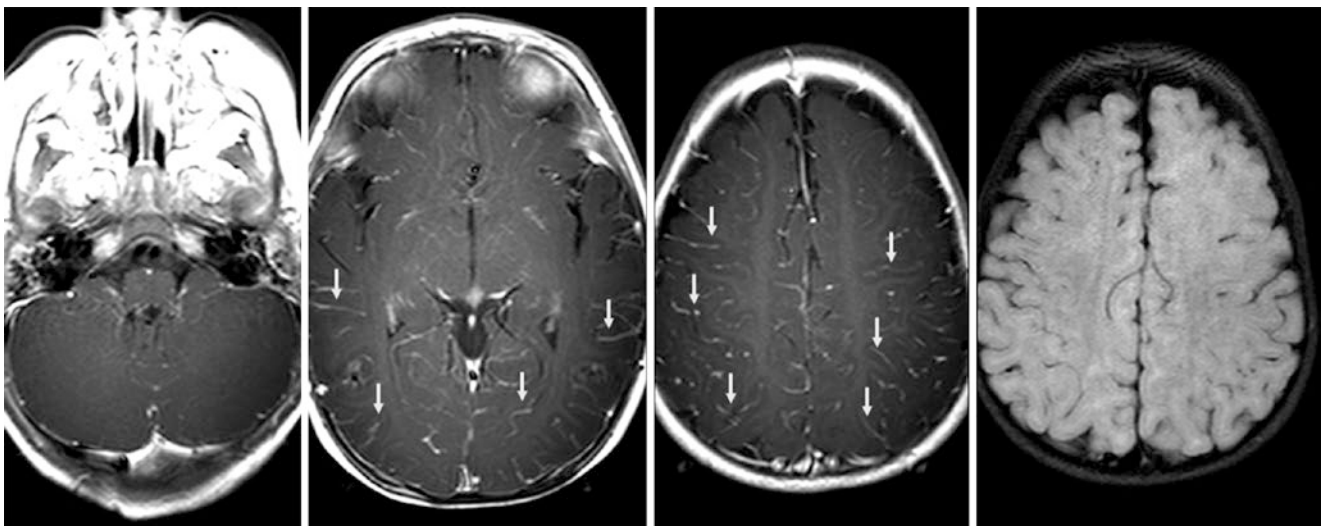

Fig. 18.8 A 10 month old male with developmental delay who underwent a 3T MRI with sedation. CEMRI SET1WI depicted mild to moderate pseudo-LMCE (*arrows*) simulating meningeal inflammation, but there were no acute symptoms. Note that this was not present along the cerebellum. Also, on noncontrast FLAIR (*right*), there was no hyperintense sulcal signal

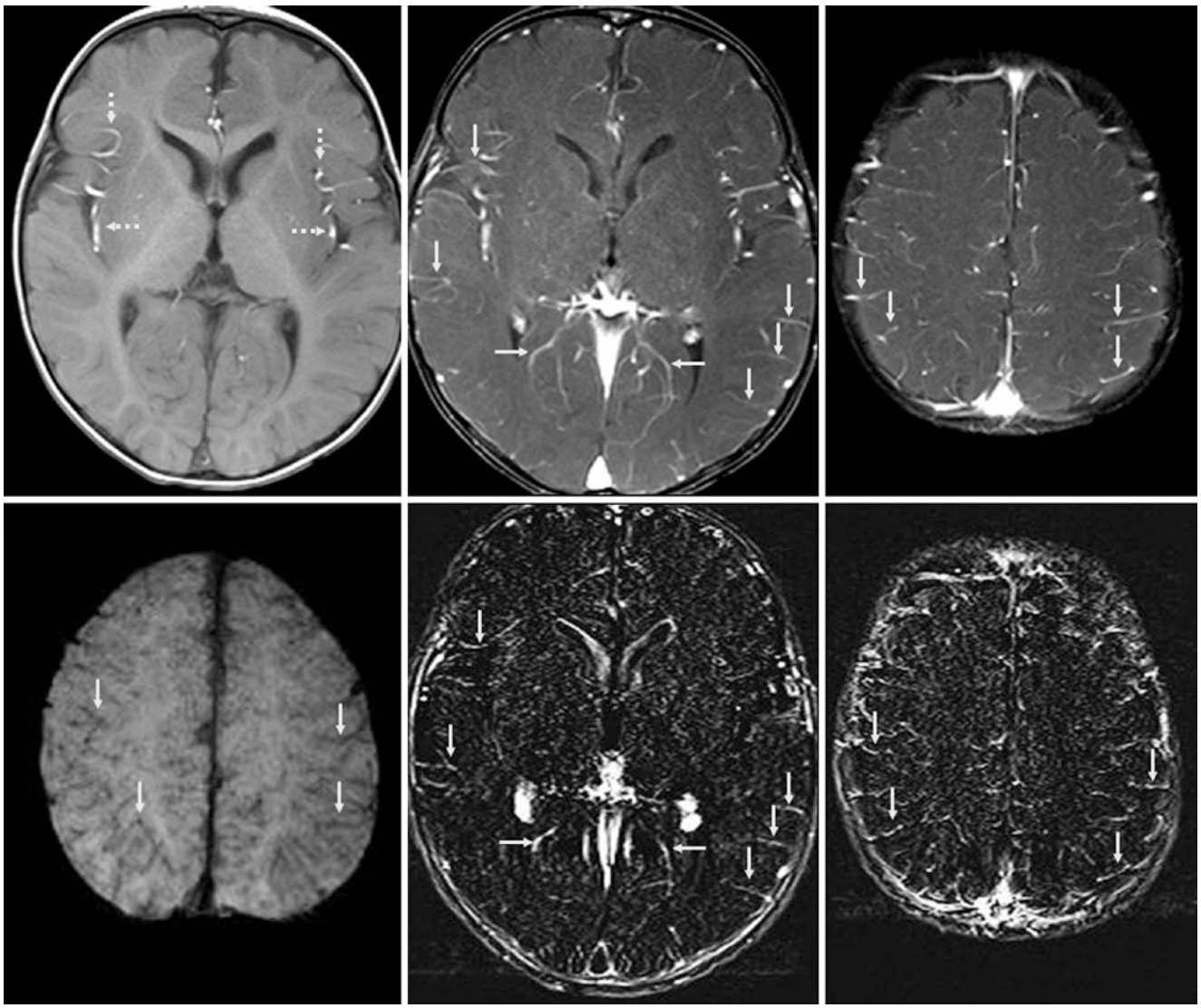

Fig. 18.9 A 1 year old had a questionable history of a remote neonatal infection and lacked acute symptoms. A negative 3T MRI with IV sedation showed normal vascularity (*dotted arrows*) on noncontrast GET1WI (*top left*) with mild pseudo-LMCE (*arrows*) on CEMRI GET1WIs obtained with fat suppression (*top middle and right*). SWI (*bottom left*) and subtraction images (precontrast subtracted from postcontrast GET1WIs, *bottom middle and right*) also depict such vasculature

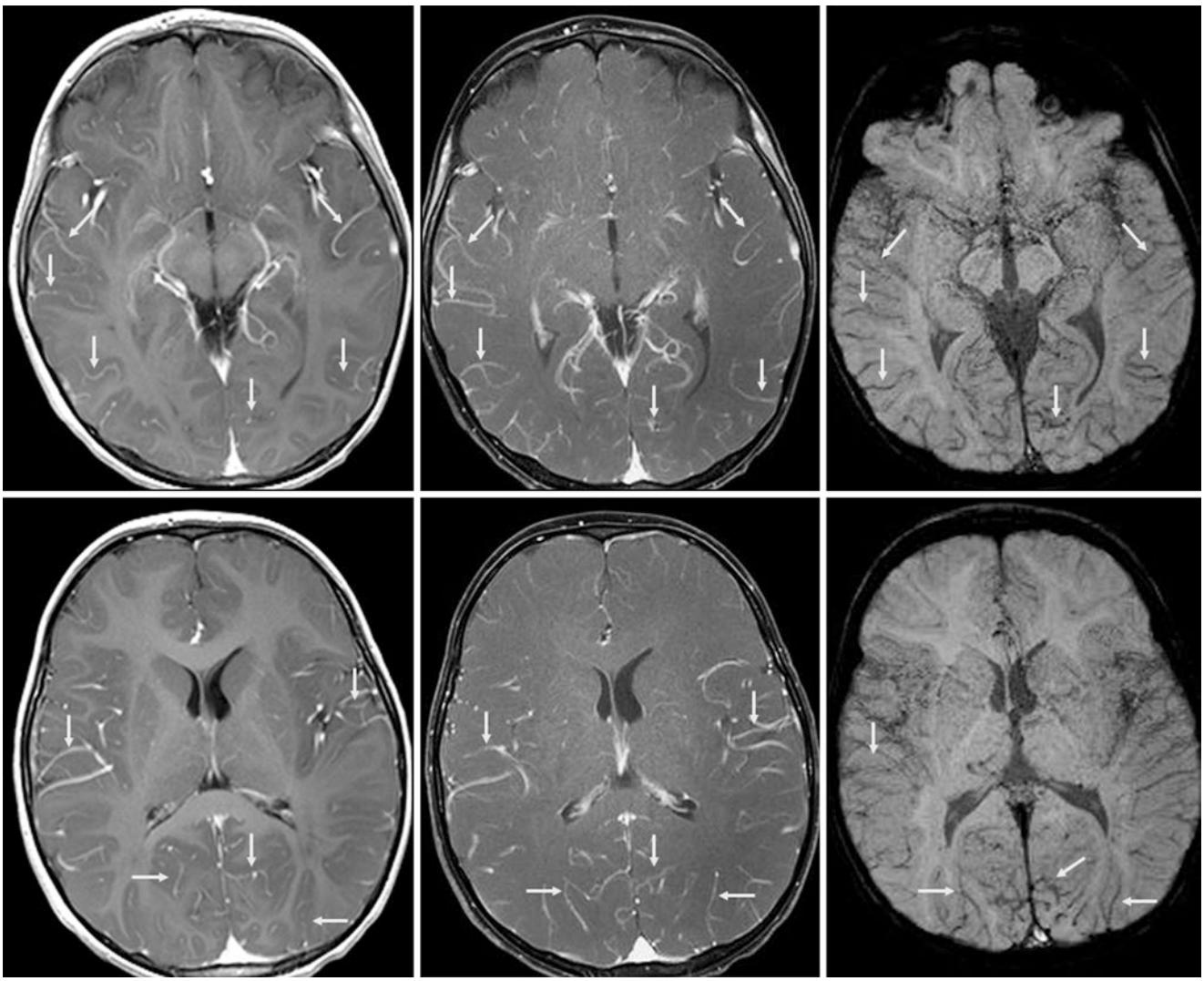

Fig. 18.10 A 2 year old with esotropia (nonacute) had a negative 3T MRI with IV sedation that showed mild pseudo-LMCE (*arrows*) on postcontrast GET1WIs (*left column*), which was a bit more pronounced on fat-suppressed SE T1WIs (*middle column*). On SWI (*right column*), the visibility of the venous vasculature is probably attributable to deoxyhemoglobin

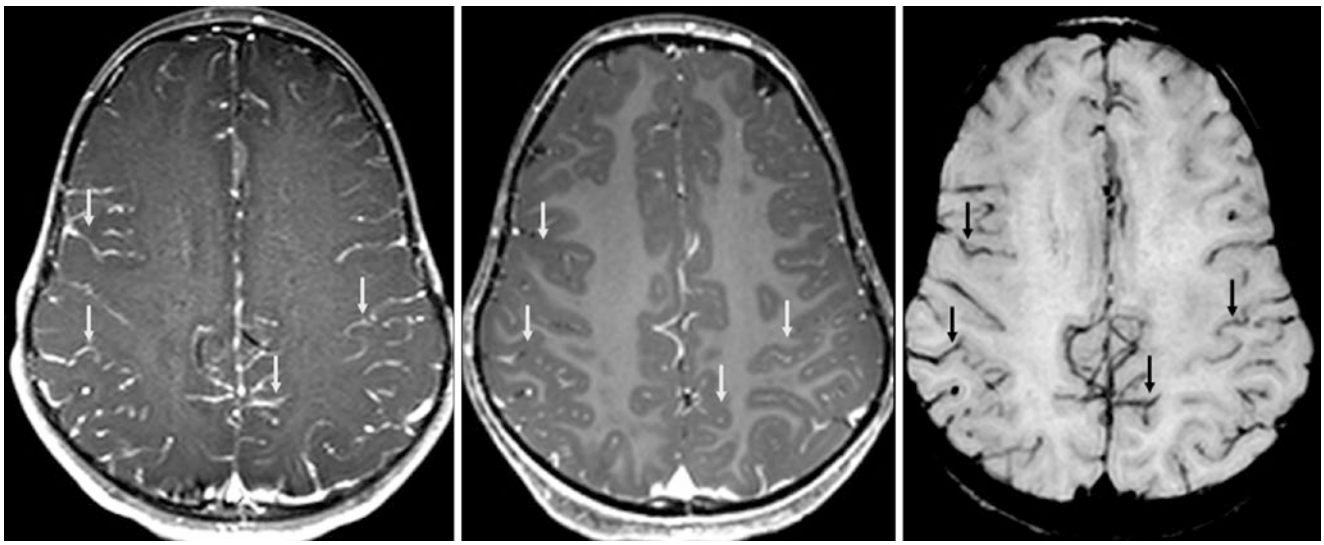

Fig. 18.11 A 4 year old with developmental delay: a negative 3T MRI with IV sedation showed moderate, diffuse pseudo-LMCE (*arrows*) on CEMRI SE T1WI (*left*) simulating meningeal inflammation, but there were no acute symptoms. This was less prominent on GE T1WI (*middle*). SWI (*right*) demonstrates venous structures in these locations

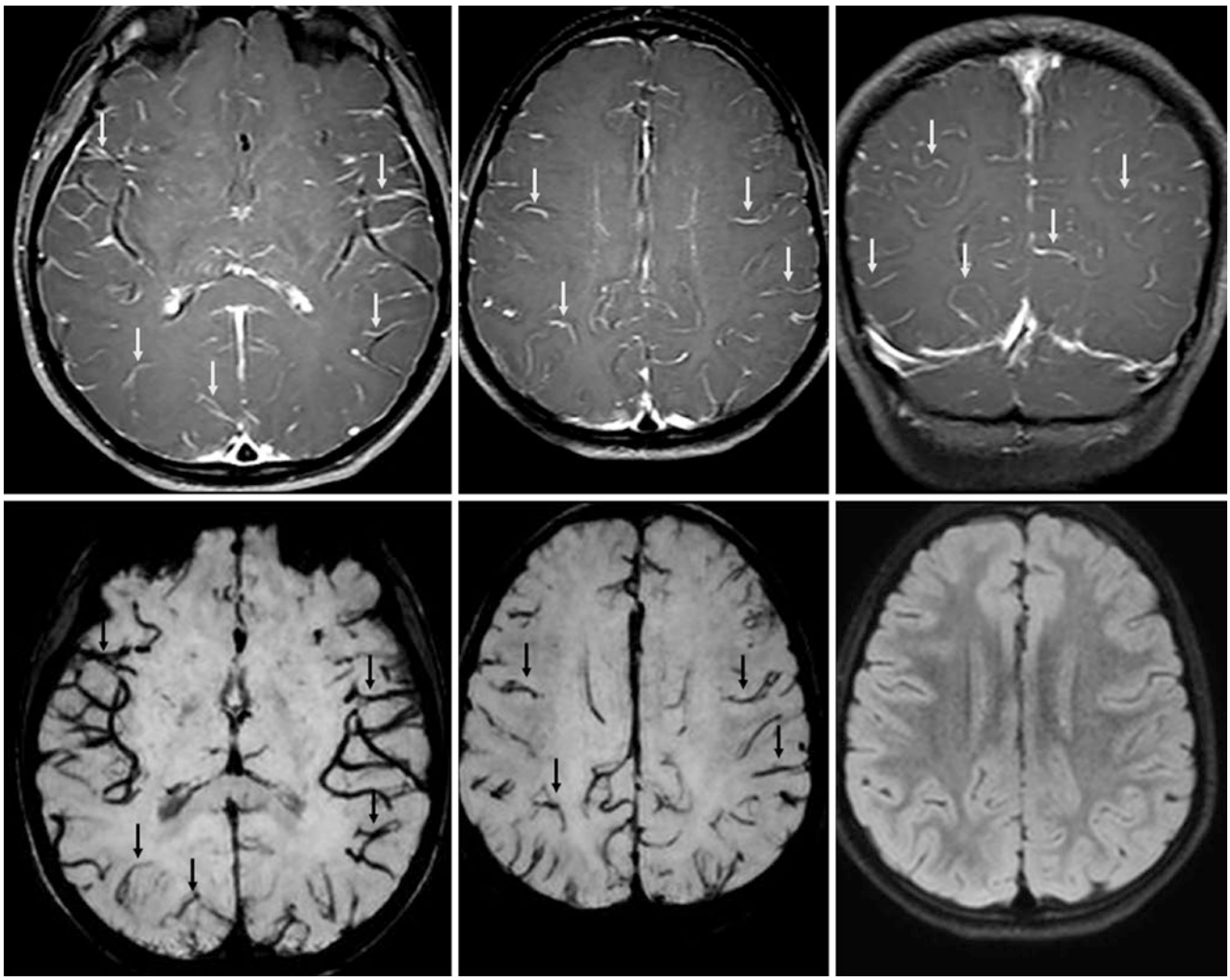

Fig. 18.12 A 5 year old with chronic visual symptoms had a negative 3T MRI under IV sedation that showed moderate pseudo-LMCE (*arrows*) on axial (*top left and middle*) and coronal (*top right*) SET1WIs. On 10 mm-thick sliding MIP SWIs (*bottom left and middle*), these sites indicate vasculature. Note the lack of hyperintensity within the sulci on noncontrast FLAIR (*bottom right*), which, given the lack of a clinical history, confirms that the findings are not caused by meningitis

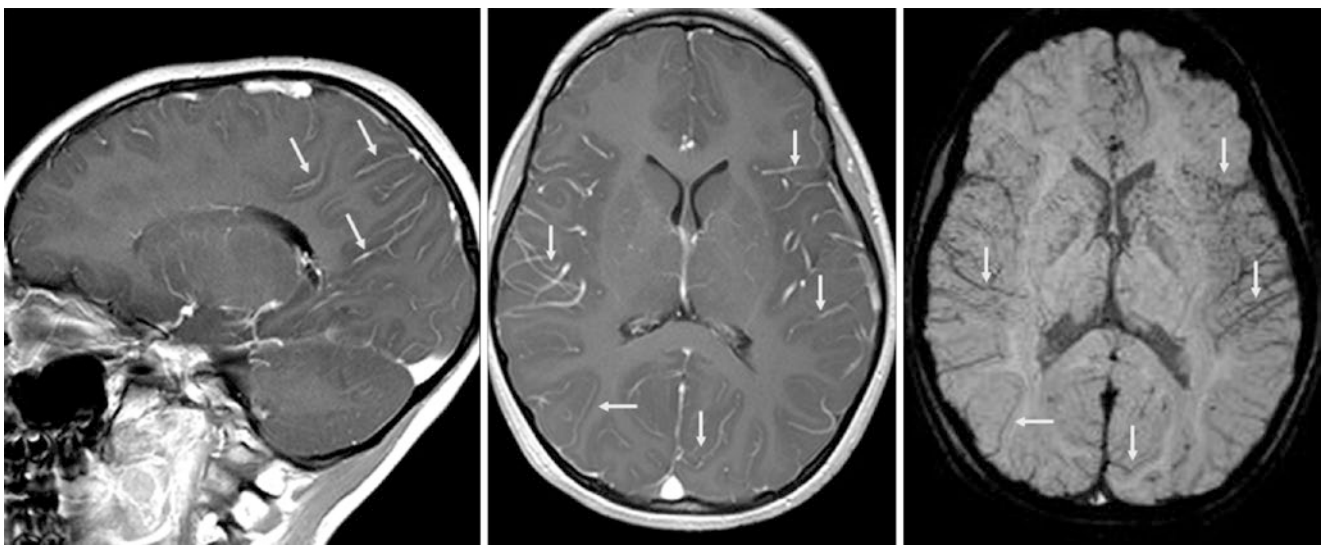

Fig. 18.13 A 6 year old with nausea and vomiting underwent a 3T MRI with IV sedation. A CEMRI with sagittal (*left*) and axial (*middle*) GET1WIs showed mild sulcal enhancement (*arrows*), initially worrisome for meningeal inflammation. However, on 20-mm thick SWI (*right*), these foci corresponded to vasculature. A lumbar puncture was negative

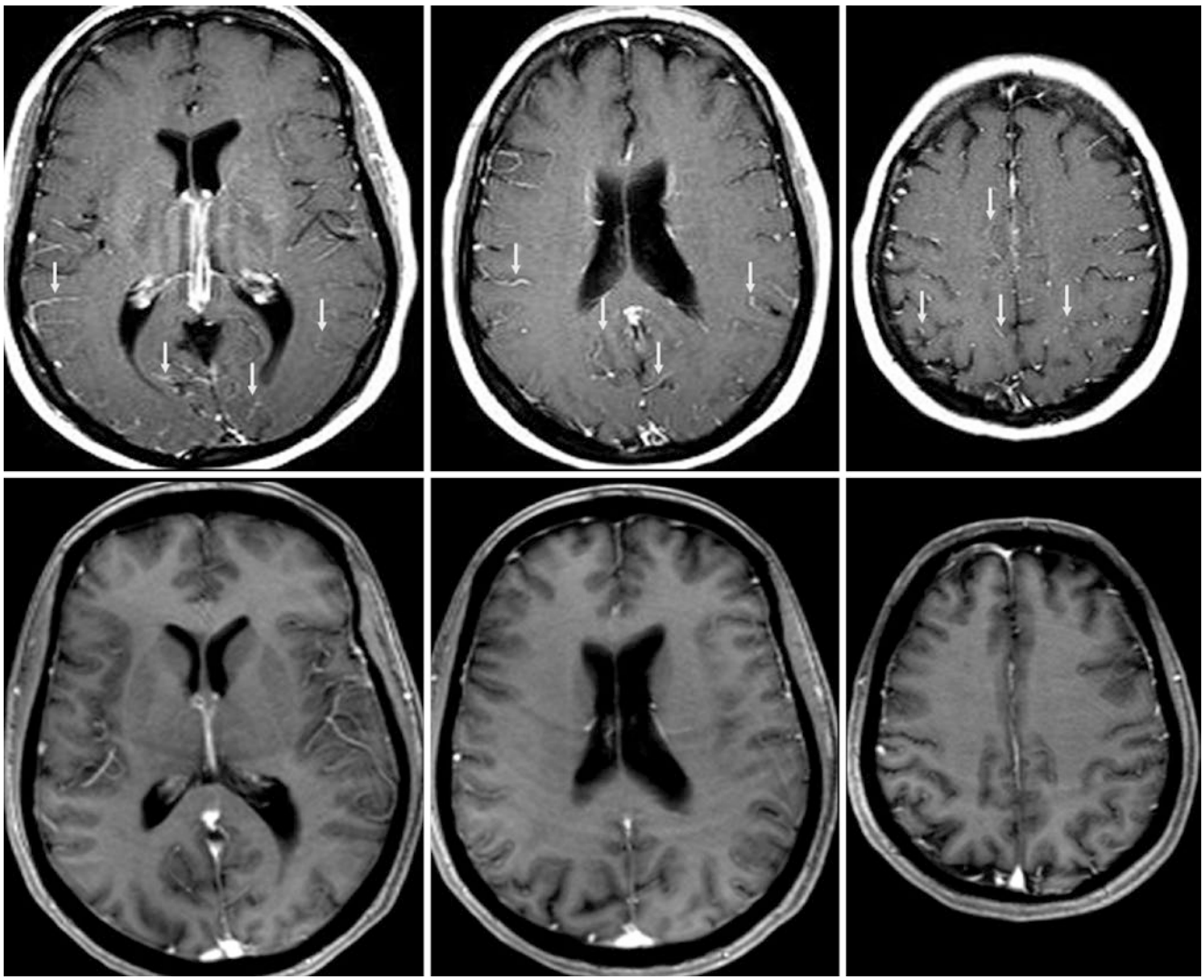

Fig. 18.14 A 40 year old with cranial nerve XII symptoms had a negative 3T MRI (without sedation) that showed slight pseudo-LMCE (*arrows*) on CE SET1WIs (*top row*), which disappeared on CE GET1WIs (*bottom row*). This demonstrates how there can be subtle differences in the degree of vascular or leptomeningeal enhancement between sequences

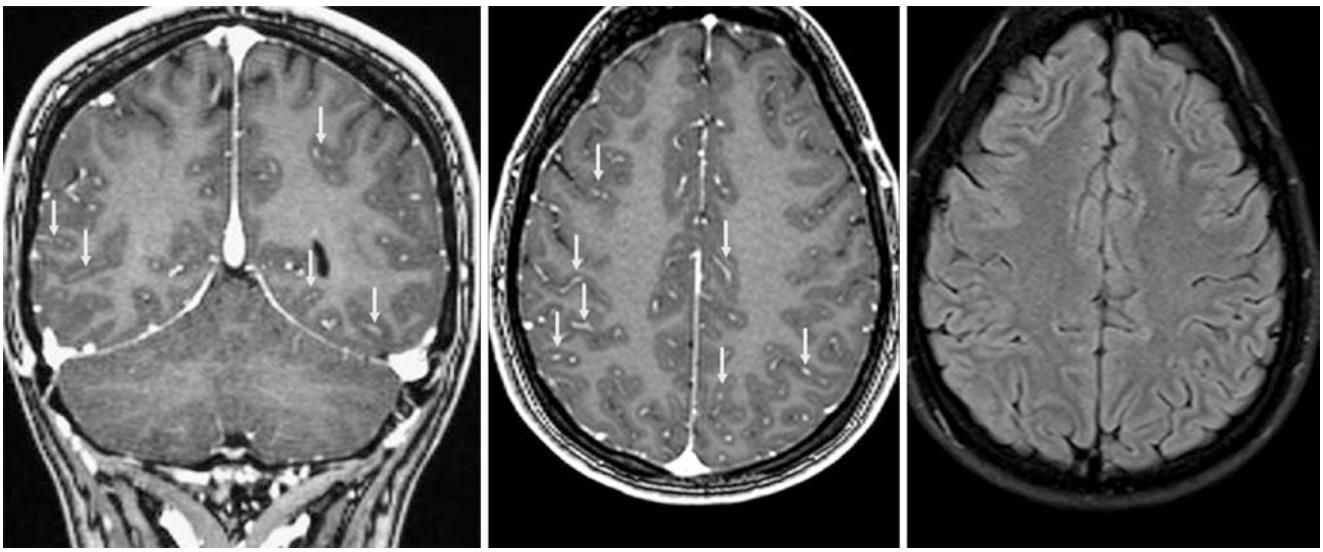

Fig. 18.15 A 24 year old with chronic headaches and memory loss had a 1.5T MRI (without sedation) with CEMRI coronal (*left*) and axial (*middle*) GET1WIs that showed mild pseudo-LMCE (*arrows*), initially worrisome for meningeal inflammation. However, there was no sulcal hyperintensity on noncontrast FLAIR (*right*). A lumbar puncture was also negative

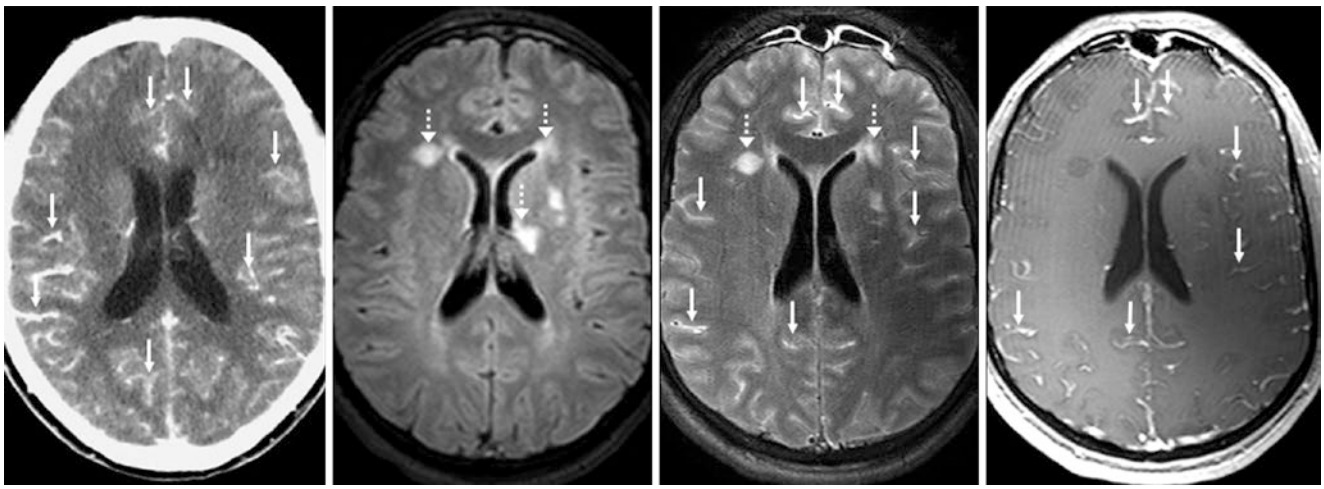

Fig. 18.16 Comparison case of cryptoccal meningitis. A 33-year-old HIV+ man had diffuse LMCE on CECT (*left*). A 3T MRI with FLAIR (*left middle*) and DWI (*not shown*) showed bilateral acute periventricular and basal ganglia infarcts (*dotted arrows*) probably due to vascular inflammation. True LMCE (*arrows*) was noted on both postcontrast FLAIR (*right middle*) and SET1WI (*right*). Note the thickened appearance of the enhancing leptomeninges

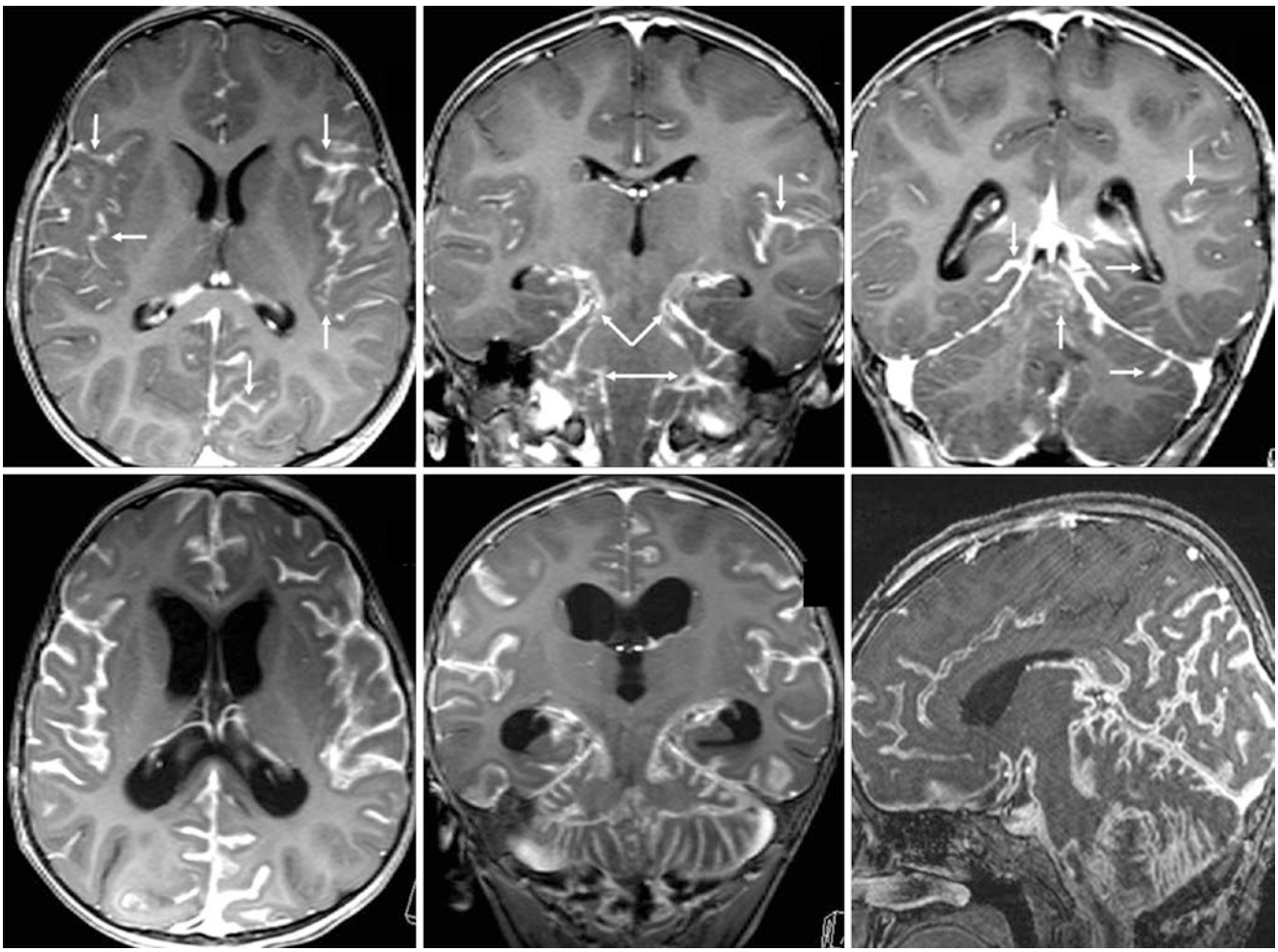

Fig. 18.17 Comparison case of medulloblastoma. A 22-month-old female had a history of a treated medulloblastoma. A 3T CEMRI that implemented GET1WIs (*top row*) showed true LMCE and subarachnoid spread (*arrows*). Only 13 days later, a repeat 3T CEMRI (*bottom row*) depicted worsening spread, along with the development of hydrocephalus

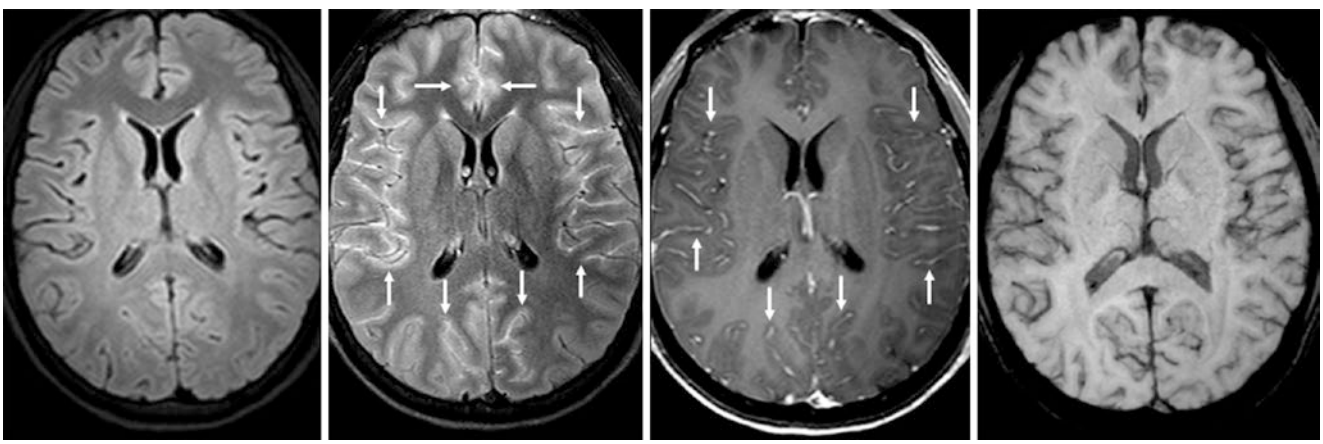

Fig. 18.18 Comparison case of viral (unspecified) meningitis**.** A 16-year-old immunocompetent female with a severe headache had a normal noncontrast FLAIR at 3T (*left*), but postcontrast FLAIR (*left middle*) and GET1WI (*right middle*) confirmed true LMCE. Note the mildly thickened enhancing sulci (*arrows*). In comparison to SWI results (*right*), the sulcal enhancement on postcontrast T1WI and FLAIR images is out of proportion to the dark sulcal vasculature on SWI

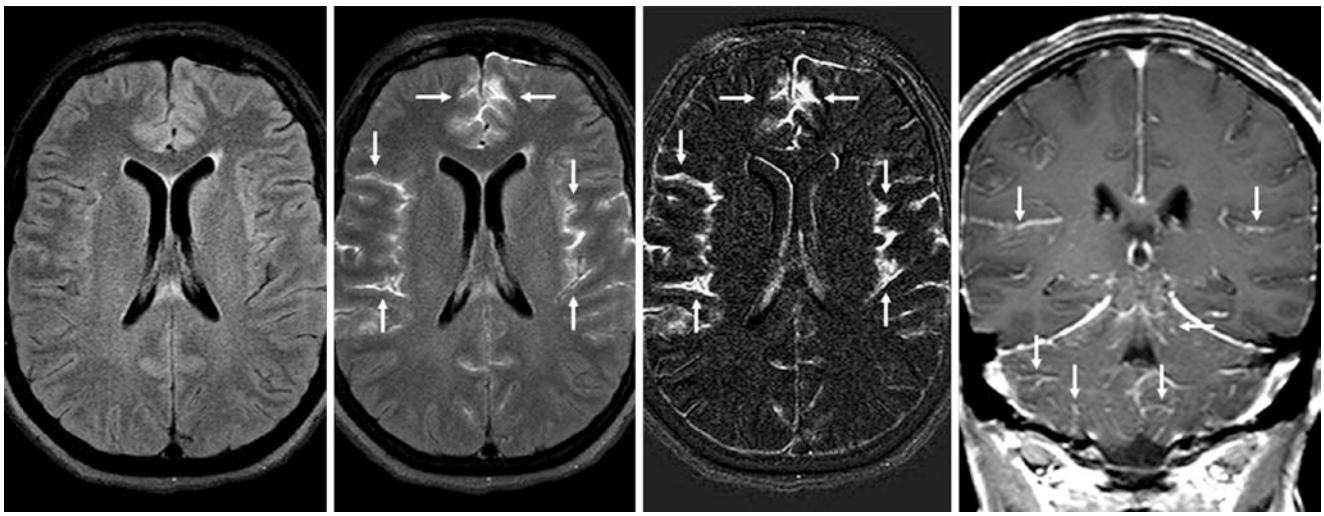

Fig. 18.19 Comparison case of herpes simplex virus (HSV) meningitis**.** A 39-year-old HIV+ female with a fever and altered mental status had normal noncontrast FLAIR at 3T (*left*). However, postcontrast FLAIR (*left middle*) depicted true LMCE (*arrows*), confirmed by subtraction images (*right middle*). The temporal lobes appeared normal. Cerebellar LMCE on coronal CE GET1WI (*right*) is not common with pseudo-LMCE. A lumbar puncture revealed HSV A lumbar puncture revealed HSV via polymerase chain reaction (PCR) testing

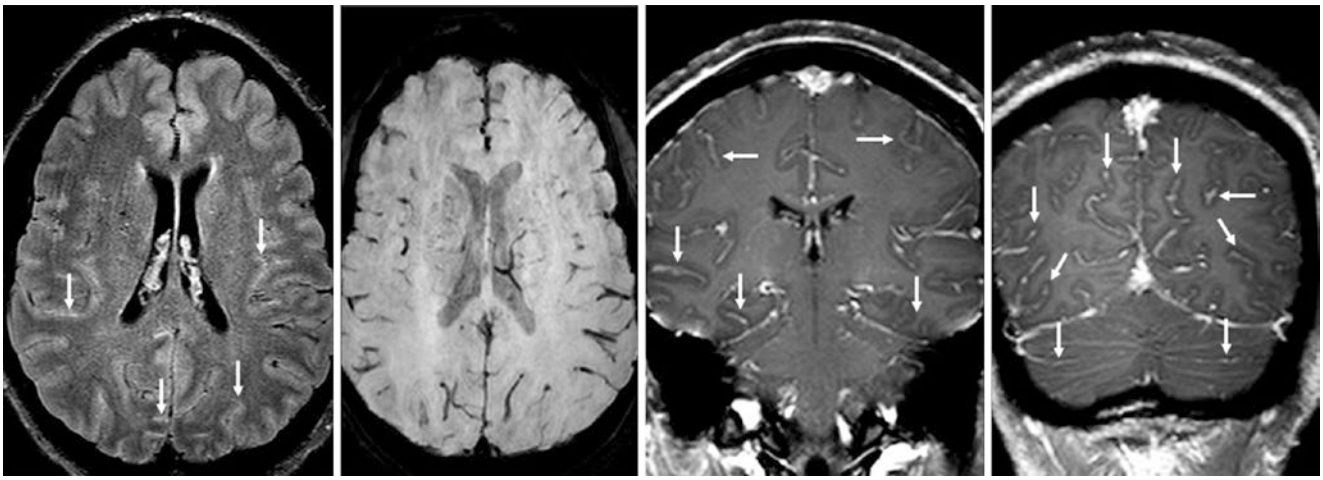

Fig. 18.20 Comparison case of cryptococcal meningitis**.** A 20-year-old HIV+ female with altered mental status had subtle LMCE (*arrows*) on 3T CE FLAIR (*left*). SWI (*left middle*) also showed that the LMCE was out of proportion to the vasculature within the sulci on SWI. The LMCE is slightly more pronounced on coronal CE GET1WI (*right middle and right*)

Suggested Reading

Ashkanian M, Borghammer P, Gjedde A, Ostergaard L, Vafaee M. Improvement of brain tissue oxygenation by inhalation of carbogen. Neuroscience. 2008;156:932–8.

Bloomfield EL, Masaryk TJ, Caplin A, Obuchowski NA, Schubert A, Hayden J, et al. Intravenous sedation for MR imaging of the brain and spine in children: pentobarbital versus propofol. Radiology. 1993;186:93–7.

Brian Jr JE. Carbon dioxide and the cerebral circulation. Anesthesiology. 1998;88:1365–86.

Chappell PM, Pelc NJ, Foo TK, Glover GH, Haros SP, Enzmann D. Comparison of lesion enhancement on spin-echo and gradient-echo images. AJNR Am J Neuroradiol. 1994;15:37–44.

Ercan N, Gultekin S, Celik H, Tali TE, Oner YA, Erbas G. Diagnostic value of contrast-enhanced fluid-attenuated inversion recovery MR imaging of intracranial metastases. AJNR Am J Neuroradiol. 2004;25:761–5.

Filippi CG, Ulug AM, Lin D, Heier LA, Zimmerman R. Hyperintense signal abnormality in subarachnoid spaces and basal cisterns on MR images of children anesthetized with propofol: new fluid-attenuated inversion recovery finding. AJNR Am J Neuroradiol. 2001;22:394–9.

Frigon C, Shaw DW, Heckbert SR, Weinberger E, Jardine DS. Supplemental oxygen causes increased signal intensity in subarachnoid cerebrospinal fluid on brain FLAIR MR images obtained in children during general anesthesia. Radiology. 2004;233:51–5.

Fukuoka H, Hirai T, Okuda T, Shigematsu Y, Sasao A, Kimura E, Yamashita Y. Comparison of the added value of contrast-enhanced 3D fluid-attenuated inversion recovery and magnetization-prepared rapid acquisition of gradient echo sequences in relation to conventional postcontrast T1-weighted images for the evaluation of leptomeningeal diseases at 3 T. AJNR Am J Neuroradiol. 2010;31:868–73.

Galassi W, Phuttharak W, Hesselink JR, Healy JF, Dietrich RB, Imbesi SG. Intracranial meningeal disease: comparison of contrast-enhanced MR imaging with fluid-attenuated inversion recovery and fat-suppressed T1-weighted sequences. AJNR Am J Neuroradiol. 2005;26:553–9.

Gawande R, Kiragu A, Knoll B, Truwit CL, McKinney AM. Pseudo-Leptomeningeal Contrast Enhancement at 3.0T in Pediatric Patients Sedated by Propofol. Oral Presentation. ASNR National Meeting. 2014.

Griffiths PD, Coley SC, Romanowski CAJ, Hodgson T, Wilkinson ID. Contrast-enhanced fluid-attenuated inversion recovery imaging for leptomeningeal disease in children. AJNR Am J Neuroradiol. 2003;24:719–23.

Klein KU, Fukui K, Schramm P, Stadie A, Fischer G, Werner C, et al. Human cerebral microcirculation and oxygen saturation during propofol-induced reduction of bispectral index. Br J Anaesth. 2011;107:735–41.

Komada T, Naganawa S, Ogawa H, Matsushima M, Kubota S, Kawai H, et al. Contrast-enhanced MR imaging of metastatic brain tumor at 3 tesla: utility of T(1)-weighted SPACE compared with 2D spin echo and 3D gradient echo sequence. Magn Reson Med Sci. 2008;7:13–21.

Mathews VP, Caldemeyer KS, Lowe MJ, Greenspan SL, Weber DM, Ulmer JL. Brain: gadolinium-enhanced fast fluid-attenuated inversion-recovery MR imaging. Radiology. 1999;211:257–63.

McKinney A, Palmer C, Short J, Lucato L, Truwit C. Utility of fat-suppressed FLAIR and subtraction imaging in detecting meningeal abnormalities. Neuroradiology. 2006;48:881–5.

Meltzer CC, Fukui MB, Kanal E, Smirniotopoulos JG. MR imaging of the meninges. Part I. Normal anatomic features and nonneoplastic disease. Radiology. 1996;201:297–308.

Sedlacik J, Lobel U, Kocak M, Loeffler RB, Reichenbach JR, Broniscer A, et al. Attenuation of cerebral venous contrast in susceptibility-weighted imaging of spontaneously breathing pediatric patients sedated with propofol. AJNR Am J Neuroradiol. 2010;31:901–6.

Singh SK, Leeds NE, Ginsberg LE. MR imaging of leptomeningeal metastases: comparison of three sequences. AJNR Am J Neuroradiol. 2002;23:817–21.

Smirniotopoulos JG, Murphy FM, Rushing EJ, Rees JH, Schroeder JW. Patterns of contrast enhancement in the brain and meninges. Radiographics. 2007;27:525–51.

Basal Ganglia: Physiologic Calcifications

19

Basal ganglia (BG) *calcifications* are a common cause of either confusion or misinterpretation, particularly when the degree of calcification is only mild or unilateral. In general, although there is no landmark recent literature regarding the incidence of idiopathic, asymptomatic BG calcifications on CT, the incidence is thought to be less than 2 % in the overall population and has been shown to increase with age. Such calcifications should not be present in pediatric patients in children under 13–15 years of age (based on scant literature, anecdotal reports, and this author's experience). Notably, for the purposes of this section, the term BG refers to the traditional definition of those nuclei involved in voluntary motor initiation consisting of the *globi pallidi* (GP), *caudate nuclei* (CN), as well as the *substantia nigra* (SN) and the *subthalamic nuclei* (STN). Also, it is important to point out that physiologic calcifications in the SN and the STN are much less common than in the other nuclei. Additionally, the dentate nuclei (DN) are one of the three sets of paired deep nuclei of the cerebellum, and physiologic calcifications are also not uncommon in this location in the elderly.

One particular difficulty arises when a radiologist (often a trainee) measures mildly hyperdense BG calcifications and the result is within the density range (measured in HUs) of acute hemorrhage, i.e., between 50 and 100 HU, although calcium would be expected to have a density of greater than 120 HU. This probably occurs as a result of the speckled or punctate calcifications within the GP or putamen intermixed with normal cerebral parenchyma. Thus, the appearance, location, and symmetric distribution of such cases of mild calcification, in addition to lack of surrounding hypodense edema, can differentiate such calcifications from true parenchymal hemorrhage.

Also important is that BG calcification may be difficult to discern from normal *BG iron* (especially present within the globi pallidi and putaminal nuclei) when MRI is the initial imaging modality. Iron is nearly always T2-dark, becoming increasingly so with higher field strengths and dark on SWI, FLAIR, and DWI, while the signal of calcium is variable on T1WI depending on the sequence. Larger amounts of calcium may have combinations or heterogeneous mixtures of bright and dark signals on T1WI, which may also vary with magnet field strength to some degree.

Metabolic (i.e., endocrine) *disorders* of calcium or parathyroid hormone metabolism are the most common nonidiopathic causes of profound BG calcifications. These include hypoparathyroidism, pseudohypoparathyroidism, pseudopseudohypoparathyroidism, hyperparathyroidism, and occasionally hypothyroidism. These typically exhibit calcifications on CTs outside of the BG as well in later stages, including the cerebellar folia and the gray-white matter junction of the cerebrum. Several *congenital disorders* may manifest with pronounced BG calcifications, but these typically show profound calcifications, even at a young age. Such disorders include Fahr disease *(*familial idiopathic basal ganglia calcification*)* and other, much rarer disorders, including ataxia-telangiectasia, Cockayne syndrome, neurofibromatosis, tuberous sclerosis, methemoglobinopathy, Leigh disease (as well as other mitochondrial disorders), and lipoid proteinosis. Also, *intrauterine exposure of congenital infectious or inflammatory disorders* can have such an appearance, which may also occasionally appear symmetric, such as toxoplasmosis, rubella, cytomegalovirus, measles, and HIV. However, such congenital infectious causes typically are accompanied by other cerebral anomalies. Rarely, a *neoplastic disorder* such as diffuse, infiltrating astrocytoma, lymphoma, or teratoma (infantile) may have bilateral calcifications involving the BG, but typically the degree of mass effect facilitates the diagnosis of a neoplastic disorder. Additionally, prominent calcifications can occur in the BG bilaterally and symmetrically in the form of a long-term sequela of a *hypoxic-ischemic insult* or a *metabolic insult* such as an ingestion of extraneous or environmental toxins. Examples of ingested or enviromental toxic

A.M. McKinney, *Atlas of Normal Imaging Variations of the Brain, Skull, and Craniocervical Vasculature*,
DOI 10.1007/978-3-319-39790-0_19

insults that selectively injure the BG (particularly the globi pallidi) can be denoted by the acronym COMA(H), which is an acronym based on the oft-occurring clinical presentation of the patient being comatose. This denotes Carbon monoxide poisoning (CO), Cyanide, Overdose of illicit drugs (e.g., Opiates), Osmotic, Manganese (selectively injures the globi pallidi), Methanol, Anoxia, Antifreeze (Ethylene glycol), Hypoxia, Hyperammonemia, and Hydrogen sulfide (Figs. 19.1, 19.2, 19.3, 19.4, 19.5, 19.6, 19.7, 19.8, 19.9, 19.10, 19.11, and 19.12).

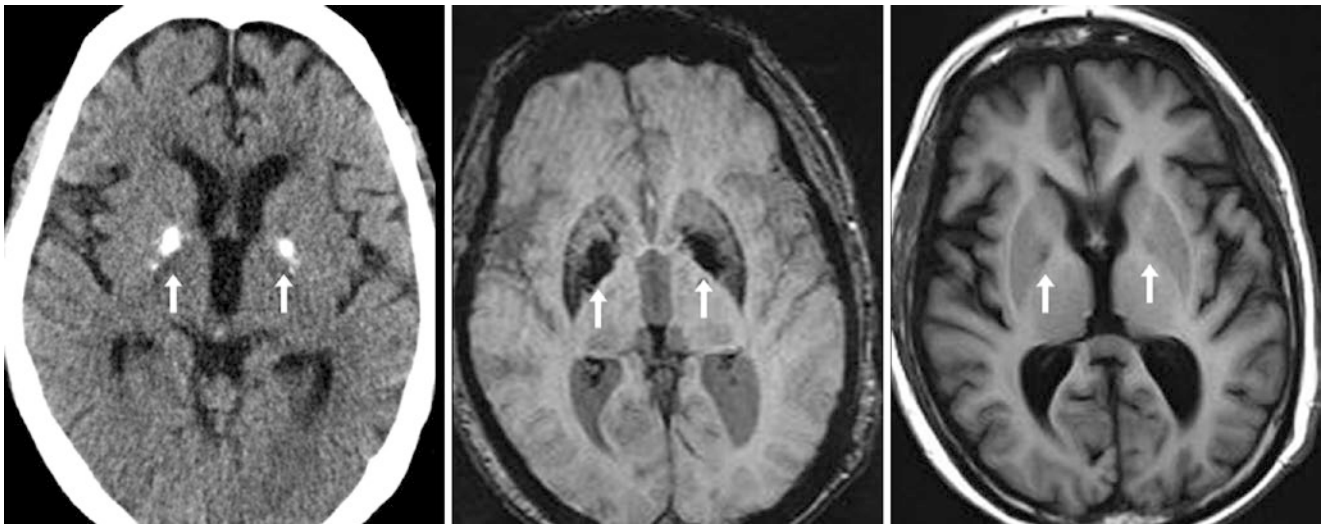

Fig. 19.1 A 63 year old was found to have bilateral prominent BG calcifications (*arrows*) that could simulate intraparenchymal hemorrhages (IPHs) on NECT (*left*), but there is a lack of surrounding hypodense edema. Axial SWI (*middle*) and T1WI (*right*) also depict the areas of calcification

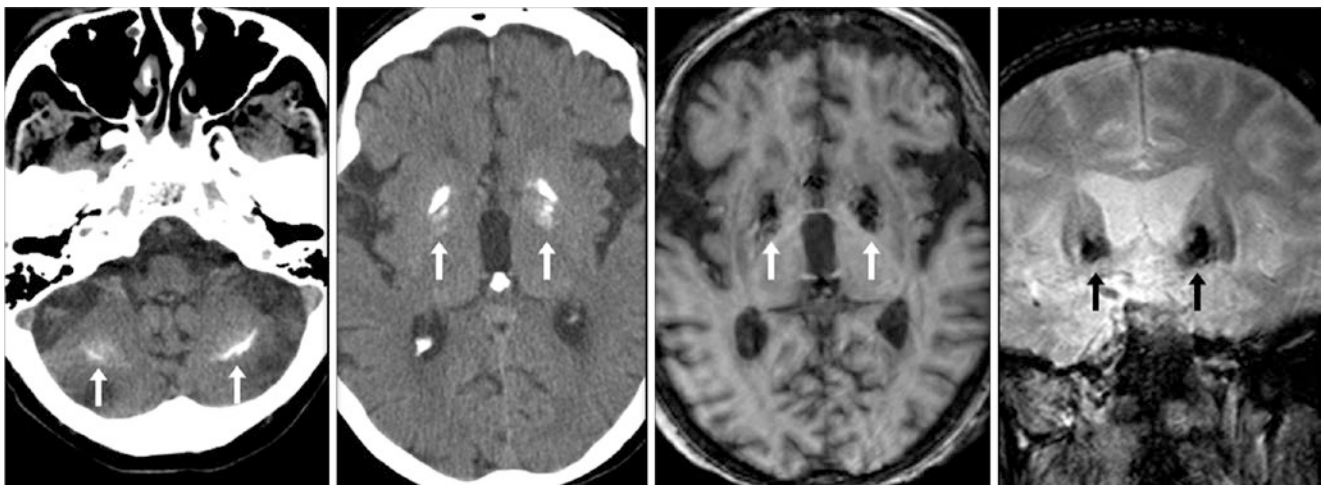

Fig. 19.2 A 65 year old who had bilateral prominent BG calcifications (*arrows*) within the cerebellum near the dentate nuclei on NECT (*left*) as well as within the globi pallidi (*left middle*). An MRI with axial T1WI (*right middle*) and coronal T2*WI (*right*) also demonstrated the calcifications. Calcifications within the dentate nuclei are less common but normal in the elderly. Also, note that both pallidal calcium and iron are dark on T2*WI but only calcium is hyperdense on CT

Fig. 19.3 An 85 year old with very dense GP calcifications (*arrows*) on NECT

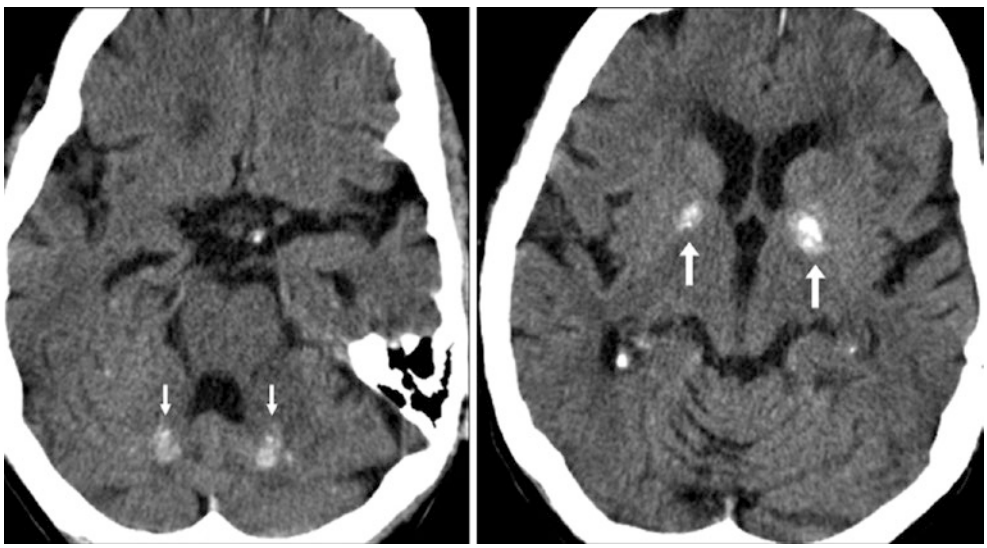

Fig. 19.4 An 89 year old with physiologic calcifications of the dentate nuclei (*thin arrows*) and GP (*arrows*) on NECT

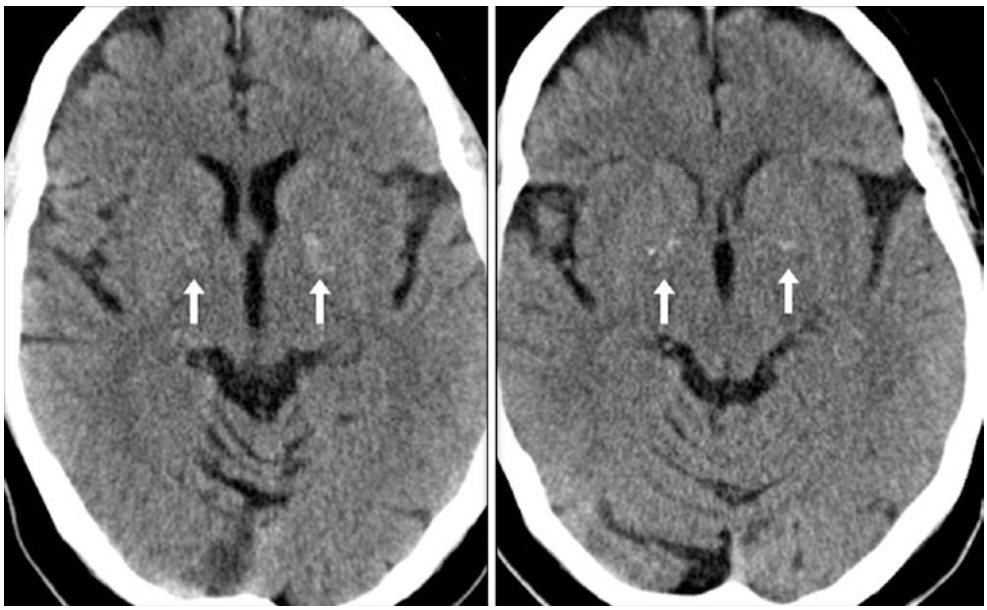

Fig. 19.5 A 65 year old who was post trauma had mild, speckled calcifications on NECT. This was initially questioned to be hemorrhage by the radiology resident. However, there was a lack of surrounding edema

Fig. 19.6 A 47 year old with patchy BG calcifications (*arrows*) on NECT, initially thought to represent hemorrhage

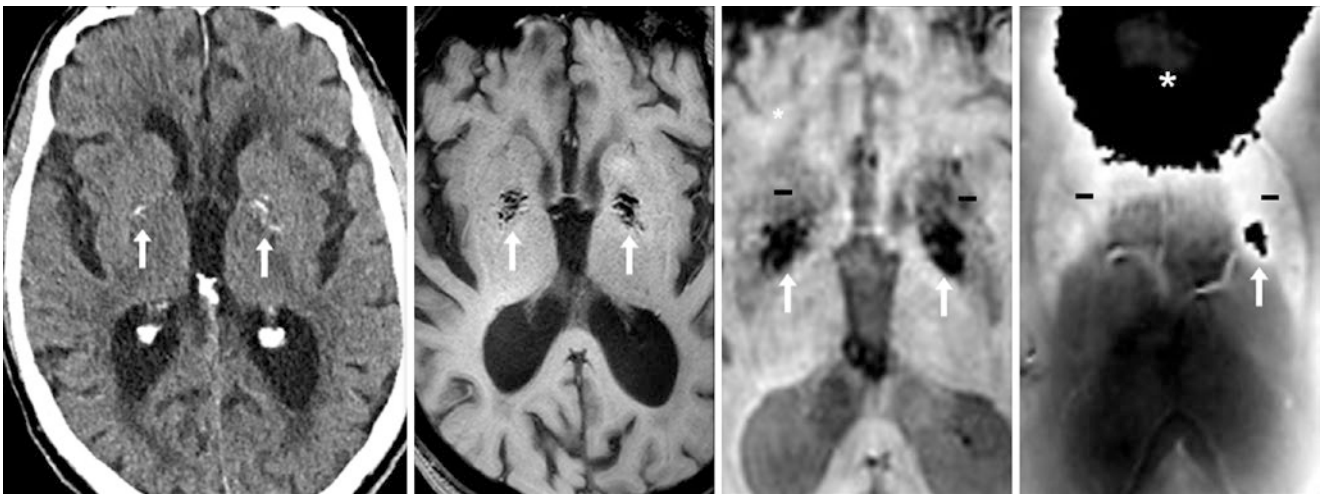

Fig. 19.7 An 85-year-old patient underwent NECT (*left*) which showed left side dominant BG calcifications (*arrows*) that were dark on T1WI (*left middle*) and dark on a magnified SWI image (*right middle*). Surrounding mildly dark signal on SWI is bright on an unfiltered phase map (*right*) owing to larger areas of paramagnetic iron deposition (–). On the left side, the calcium is large enough to appear dark (i.e., diamagnetic). Note the susceptibility artifact at air-bone interfaces on the phase map (*). On some scanners, calcium is dark and iron bright on the SWI phase maps, while others show the opposite effect because of polarity differences

Fig. 19.8 A 31 year old whose tests showed mild BG calcifications on NECT. Such subtle calcifications can be noted in adults as early as in their twenties

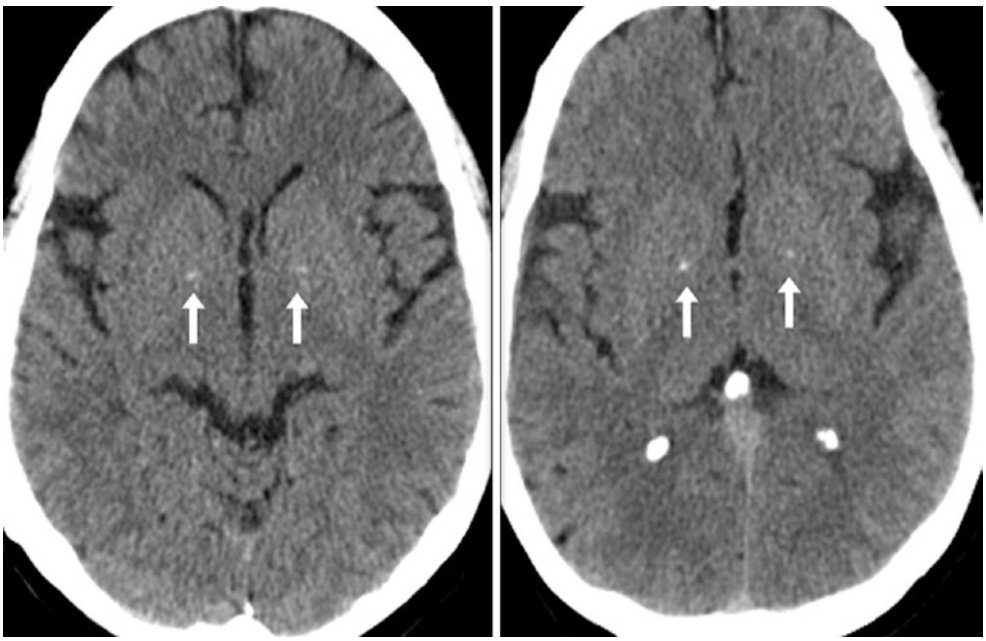

Fig. 19.9 A 48 year old had tiny, bilateral BG calcifications (*arrows*) on a NECT (*left*), which were unchanged on a repeat NECT performed over 10 years later (*right*)

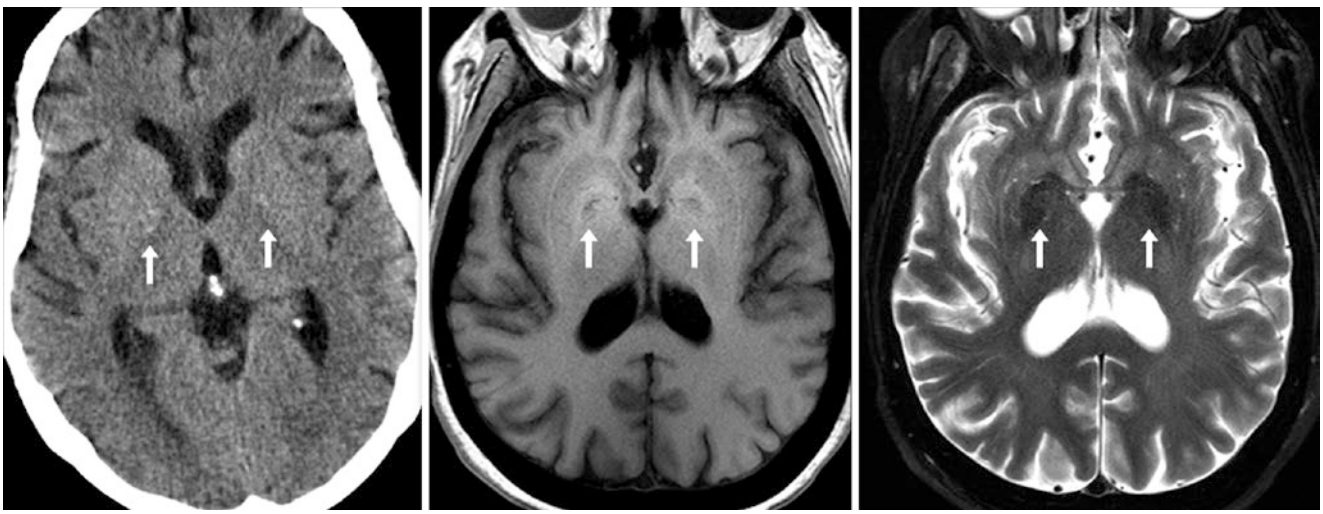

Fig. 19.10 A 59 year old with early, mild BG calcifications (*arrows*) on a NECT (*left*). Axial T1WI (*middle*) and T2WI (*right*) from a 3T MRI demonstrated a combination of a mildly bright but speckled signal of the globi pallidi, which was dark on T2WI. There is probably iron deposition as well, since the area of the T2-dark signal is larger than that of calcium on NECT

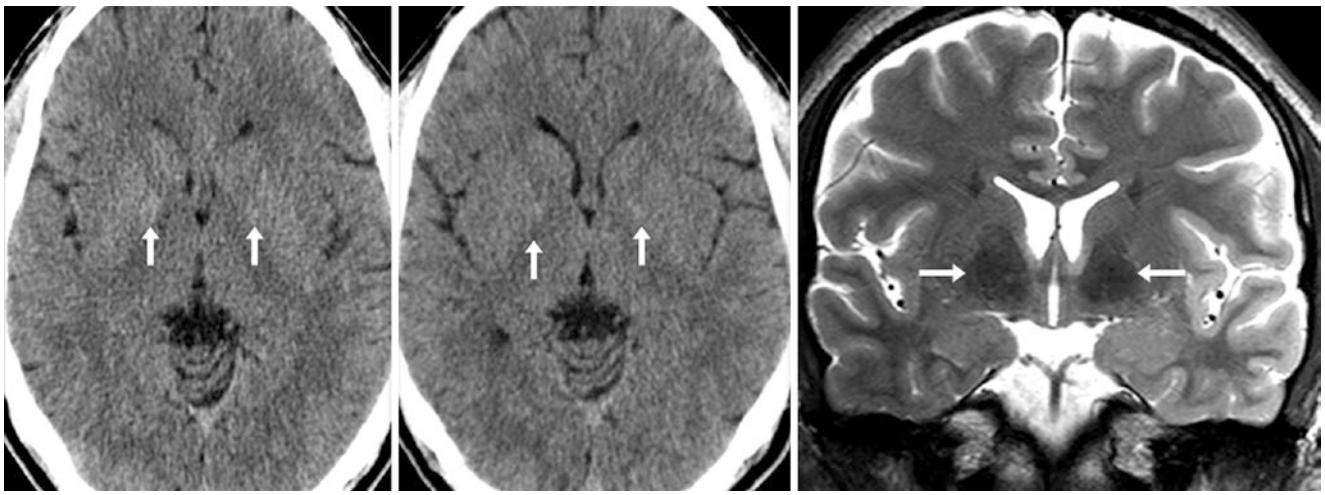

Fig. 19.11 A 27 year old with faint, early, BG calcifications (*arrows*) on NECT (*left*) that were unchanged 1 year later (*middle*). A coronal T2WI MRI at 3T (*right*) showed dark signal of the globi pallidi (and to a lesser degree the putamina) probably also related to iron deposition, since the region of dark signal on T2WI is larger than that of calcium on NECT

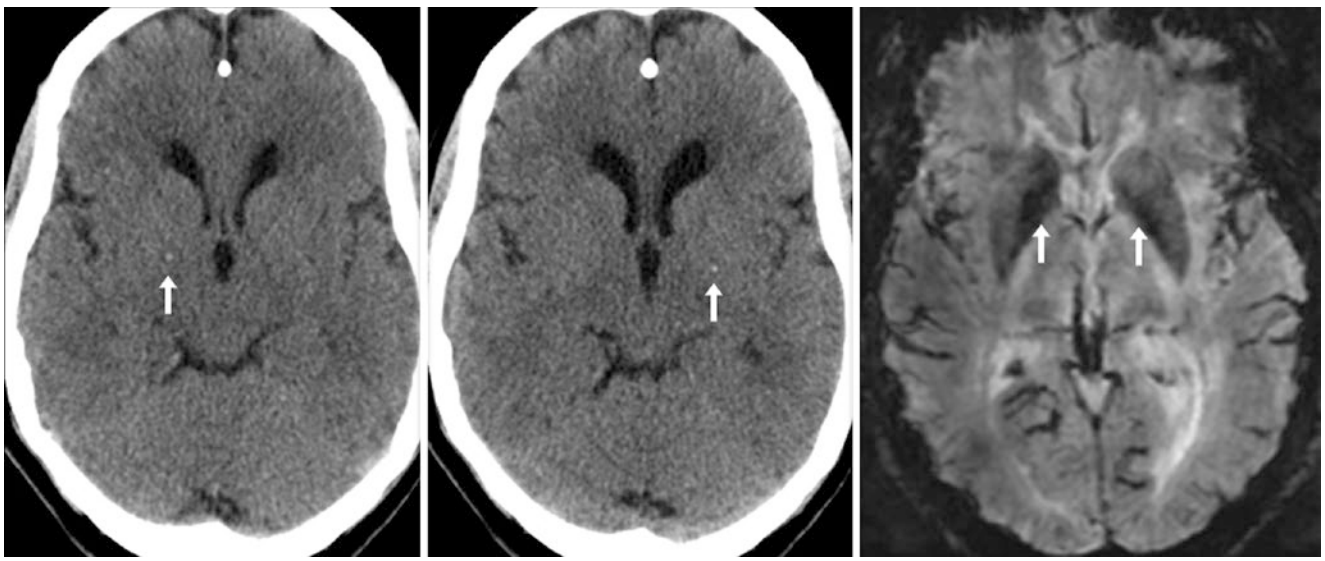

Fig. 19.12 A 49 year old with bilateral very tiny BG calcifications (*arrows*) on NECT images (*left and middle*). On SWI MRI at 1.5T (*right*), there was a larger region of iron deposition as well, since the extent of the T2-dark signal on SWI is disproportionate to the degree of calcium on the NECT examination

19.1 Basal Ganglia Calcifications: Unilateral or Asymmetric

Although they are less common than bilateral calcifications, unilateral or *asymmetric calcifications of the basal ganglia* (BG) may occur. These can be problematic in the early phase when there is only faint calcification that occasionally simulates *parenchymal hemorrhage* (particularly if the HU density is measured and is less than 100HU). The characteristic location of these calcifications in the globi pallidi and their progressively increased density on NECT over time can identify them as calcium (Figs. 19.13, 19.14, 19.15, 19.16, 19.17, 19.18, 19.19, 19.20, 19.21, 19.22, 19.23, 19.24, and 19.25).

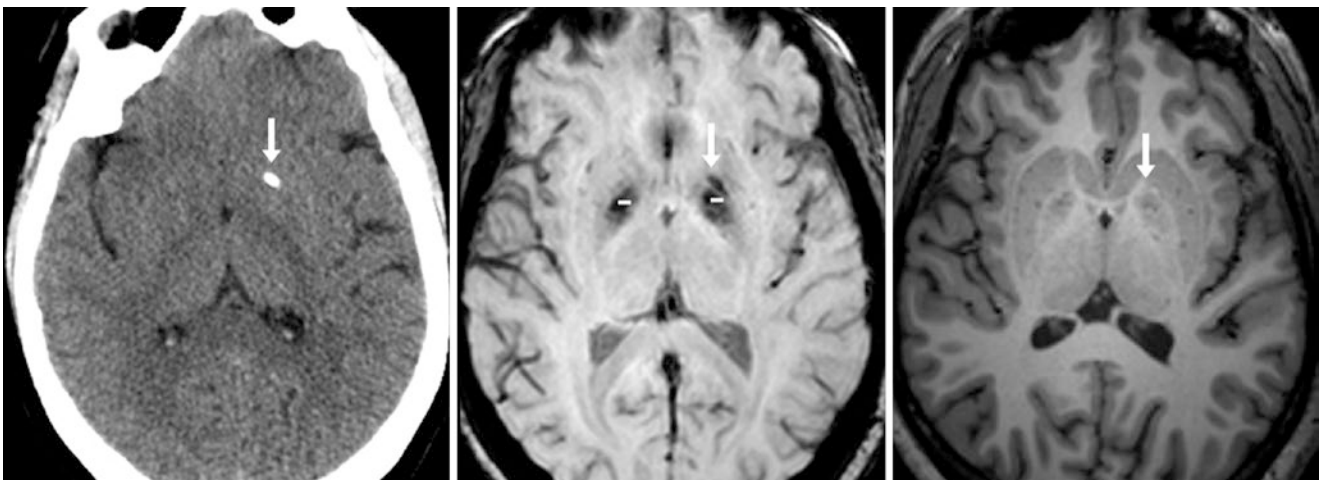

Fig. 19.13 A 28 year old with a prominent left BG calcification (*arrows*) on NECT (*left*) and on 3T SWI MRI (*middle*). Note that on SWI, the regions of the bilateral iron deposits (–) are much larger than those of the left BG calcium. Also, both the calcium and iron are nearly invisible on a three-dimensional magnetization prepared rapid GE T1WI sequence (*right*)

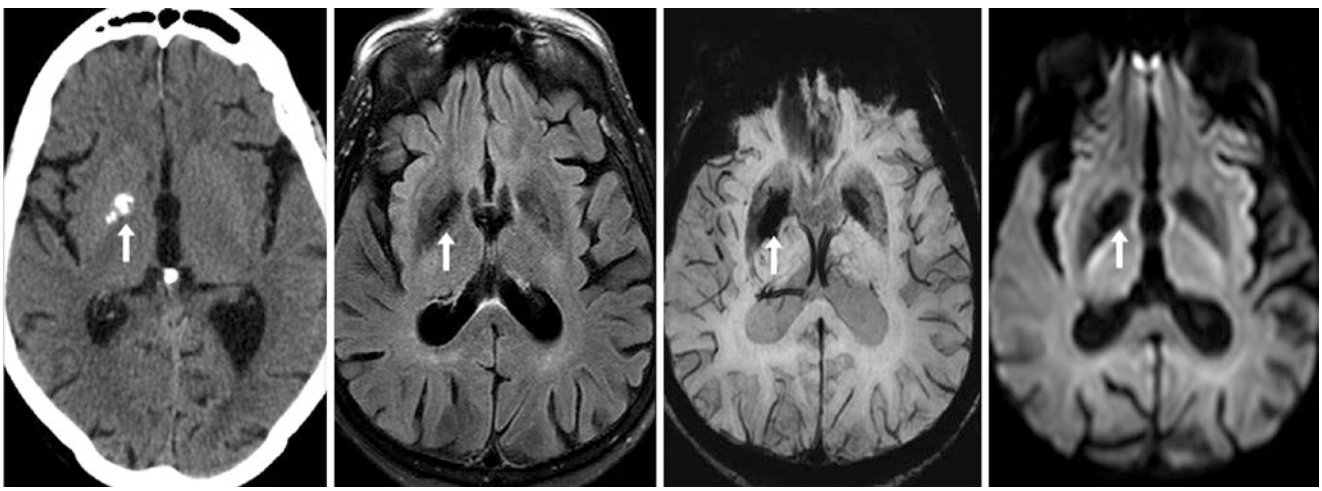

Fig. 19.14 An 80 year old had a right BG calcification (*arrows*) on NECT (*left*) and on a 3T MRI with FLAIR (*left middle*), SWI (*right middle*), and DWI (*right*). Note that the area of T2-dark signal on each sequence is larger than the calcification on CT, and observe the lack of calcium within the T2-dark left GP, which confirms the presence of bilateral pallidal iron

Fig. 19.15 A 56 year old had a faint, unilateral left BG calcification (*arrow*) on NECT

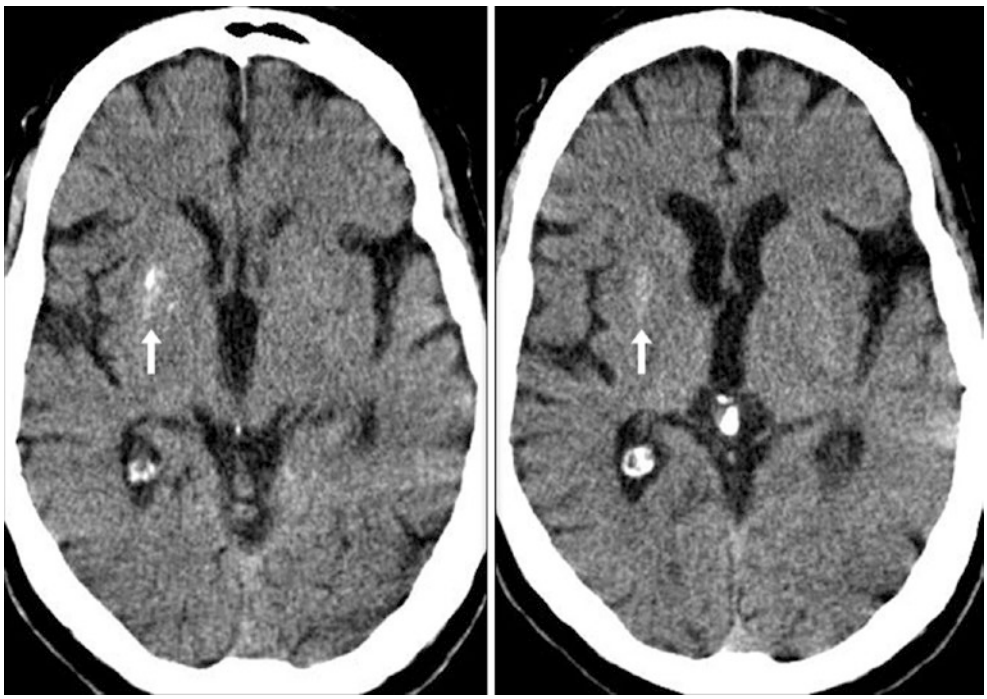

Fig. 19.16 A 62 year old had moderate, unilateral right BG calcifications (*arrows*) on NECT without a visible area of calcification on the contralateral side

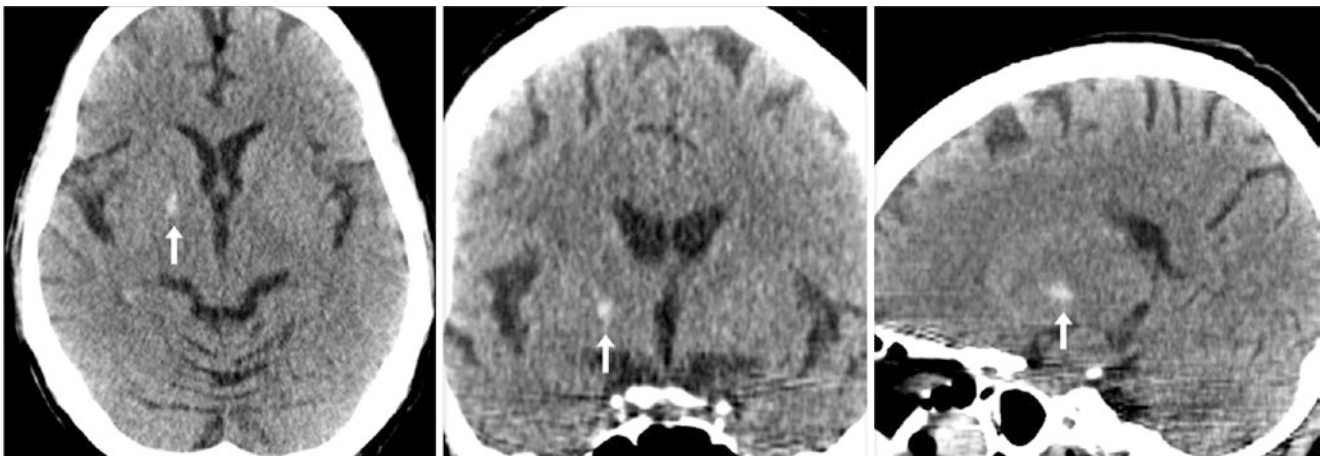

Fig. 19.17 A 62 year old had a unilateral, moderate-sized right BG calcification (*arrows*) on NECT with axial (*left*), coronal (*middle*), and sagittal (*right*) reformats. No calcification was noted on the opposite side

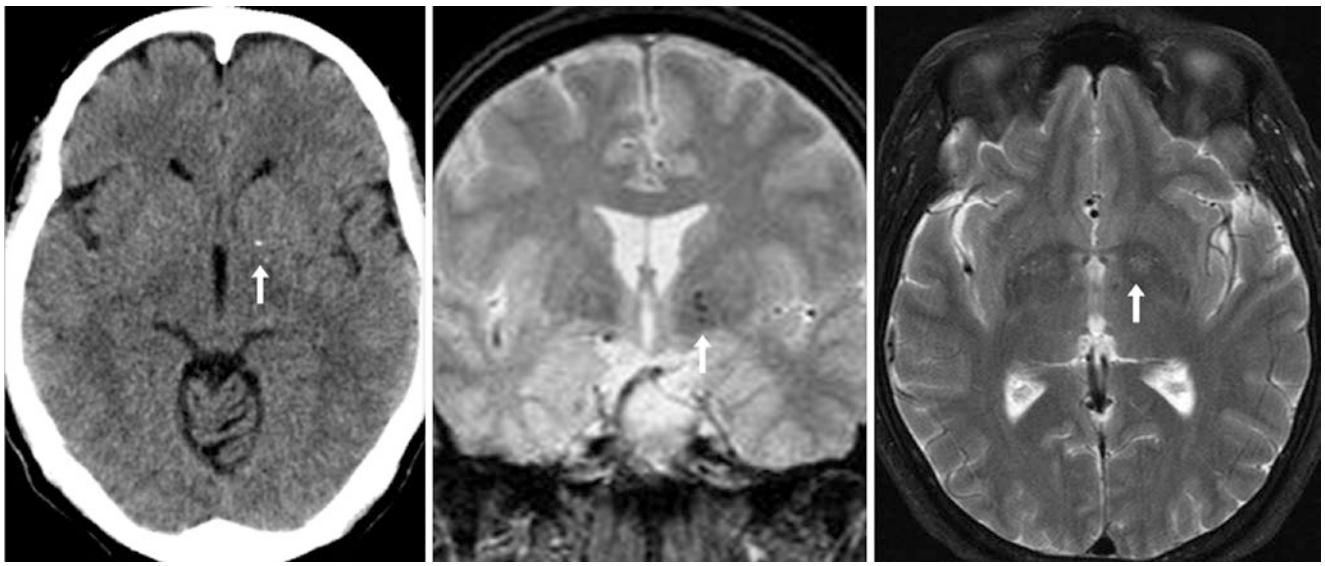

Fig. 19.18 A 71 year old who had a tiny left BG calcification (*arrows*) on NECT (*left*) and on a 1.5T MRI with GE T2*WI (*middle*). On routine T2WI (*right*), the calcification is not noted, as turbo spin echo images remove much of the susceptibility effects of calcium by multiple 180° refocusing pulses (turbo factor)

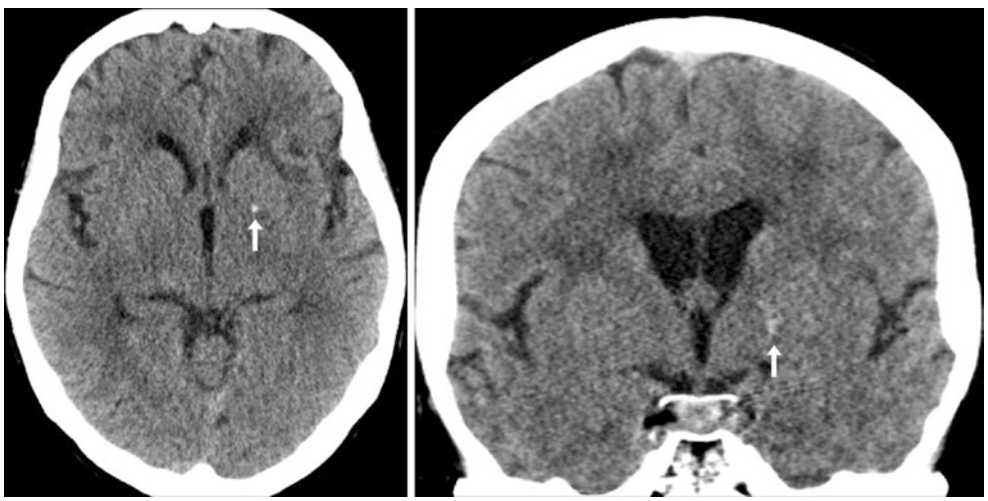

Fig. 19.19 A 73 year old with a tiny left BG calcification (*arrows*) on a NECT with axial (*left*) and coronal (*right*) reformats. On the coronal reformat, the calcification appears a bit larger but less dense than on the axial image

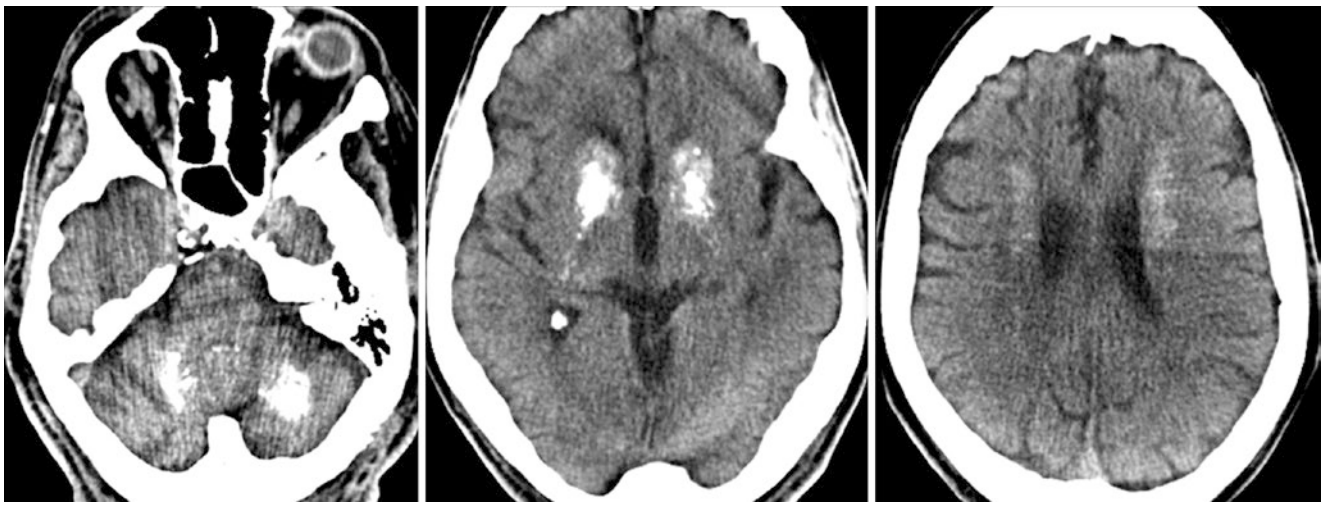

Fig. 19.20 Comparison case of pseudohypoparathyroidism**.** A 56 year old male had profound, diffuse BG calcifications on a NECT. The degree of calcification is disproportionate to the patient's age. Additionally, the calcifications are also abnormal in that they involve the cerebellar (*left*) and cerebral (*right*) deep white matter

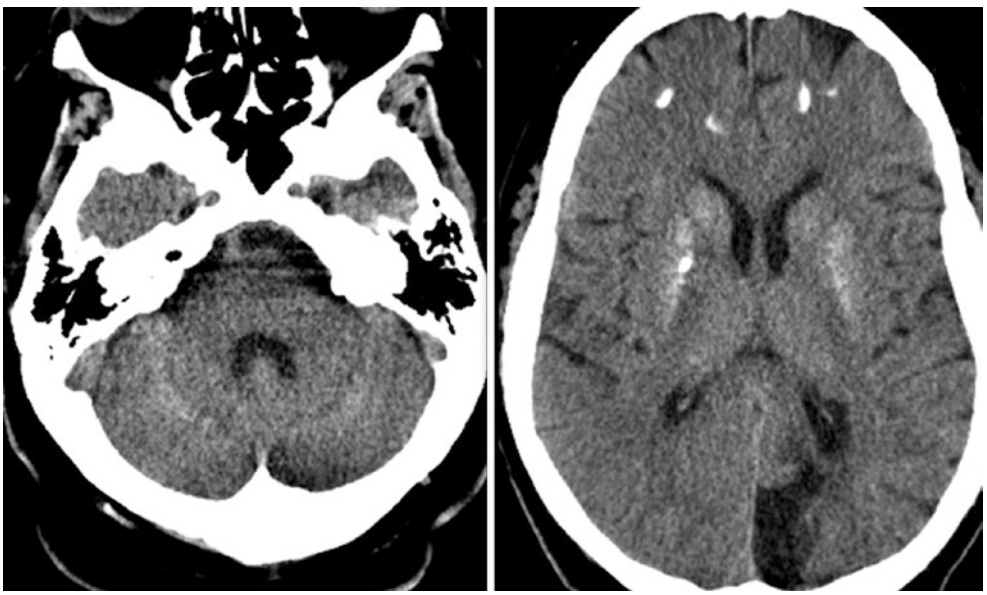

Fig. 19.21 Comparison case of hypoparathyroidism. A 56 year old male had diffuse BG calcifications on NECT, which also involved the cerebral and to a lesser degree the cerebellar, subcortical, and deep white matter

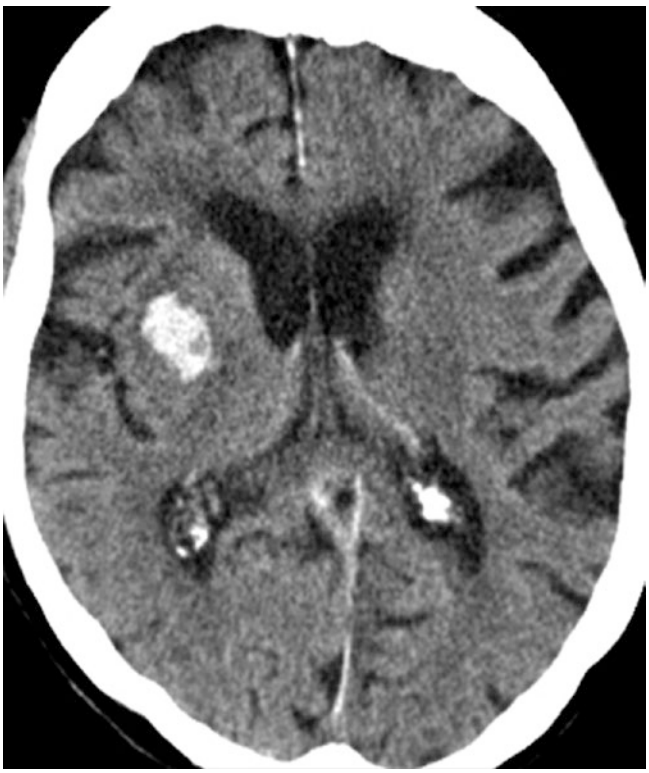

Fig. 19.22 Comparison case of hemorrhage. An 82 year old had a right BG hemorrhage that lacked surrounding edema on NECT

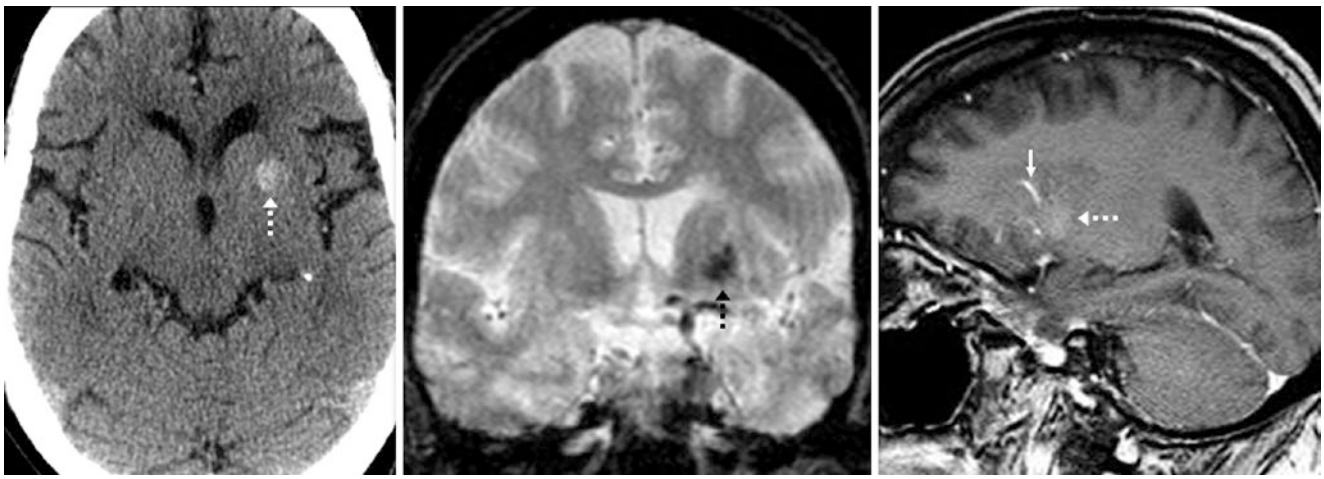

Fig. 19.23 Comparison case of cavernoma and developmental venous anomaly (DVA). A 75 year old had hyperdensity of the lateral left putamen (*dashed arrows*) on NECT (*left*). This hyperdensity is not physiologic, as it is not located within the globus pallidus and contains hemosiderin on GE T2*WI (*middle*). There is an associated DVA with a small vein (*tiny arrow*) draining the cavernoma, best visualized on sagittal postcontrast T1WI (*right*). The cavernoma faintly enhances

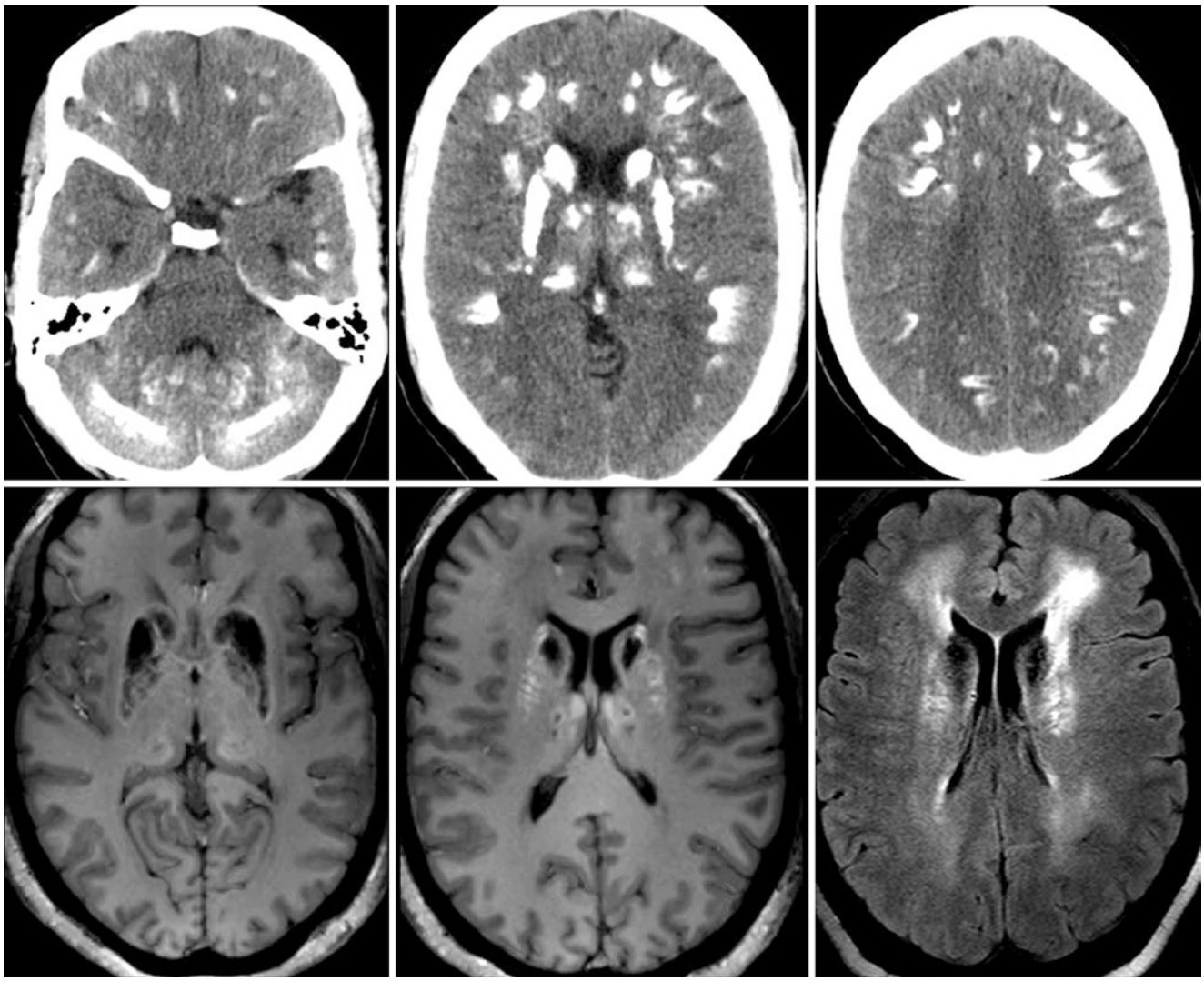

Fig. 19.24 Comparison case of Fahr disease. A 52-year-old female had diffuse, severe BG calcifications on a NECT (*top row*), which also involved the cerebral and cerebellar subcortical and deep white matter. On a 3T MRI with GE T1WI (*bottom left and middle*), the heavily calcified basal ganglia are variably bright and dark in signal. On FLAIR images (*bottom right*), there is diffuse deep white matter hyperintensity, presumably caused by concomitant vasculopathy

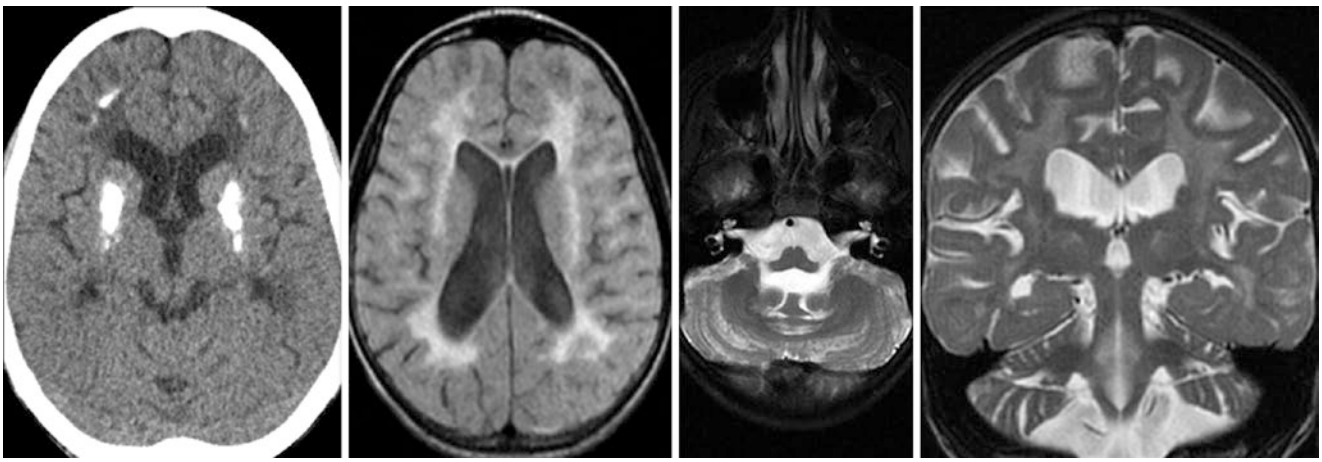

Fig. 19.25 Comparison case of Cockayne syndrome. A 13-year-old male had severe BG calcifications and subcortical calcifications that were quite disproportionate to his age on a NECT (*left*). A 1.5T MRI showed moderate to severe cerebral and cerebellar atrophy on axial FLAIR (*left middle*), on T2WI (*right middle*), and on a coronal T2WI (*right*)

Suggested Reading

Adams AE. Basal ganglia calcification. Characteristics of CT scans and clinical findings. Neurosurg Rev. 1980;3:201–3.

Bennett JC, Maffly RH, Steinbach HL. The significance of bilateral basal ganglia calcification. Radiology. 1959;72:368–78.

Cohen CR, Duchesneau PM, Weinstein MA. Calcification of the basal ganglia as visualized by computed tomography. Radiology. 1980;134:97–9.

Harrington MG, Macpherson P, McIntosh WB, Allam BF, Bone I. The significance of the incidental finding of basal ganglia calcification on computed tomography. J Neurol Neurosurg Psych. 1981;44:1168–70.

Ho VB, Fitz CR, Chuang SH, Geyer CA. Bilateral basal ganglia lesions: pediatric differential considerations. Radiographics. 1993;13:269–92.

Kıroğlu Y, Callı C, Karabulut N, Oncel C. Intracranial calcifications on CT. Diagn Interv Radiol. 2010;16:263–9.

Koller WC, Klawans HL. Cerebellar calcification on computerized tomography. Ann Neurol. 1980;7:193–4.

Legido A, Zimmerman RA, Packer RJ, Bilaniuk LT, Siegel KR, D'Angio G. Significance of basal ganglia calcification on computed tomography in children. Pediatr Neurosci. 1988;14:64–70.

Makariou E, Patsalides AD. Intracranial calcifications. Applied Radiol. 2009;38:48–60.

Susceptibility-Weighted Imaging: Concepts, Basal Ganglia Variation in Age-Related Iron Deposition, and Artifacts

20

Susceptibility-weighted imaging (SWI) is a novel technique that has been increasingly utilized over the past several years to visualize vasculature, hemorrhage, and deposits of calcium or metals as well as other causes of susceptiblity artifact. SWI combines both magnitude and phase data in order to optimize, visualize (and sometimes quantify) magnetic susceptibility effects. The foundations for this technique were developed in the late 1990s, initially intended as an MR venographic technique (by Reichenbach and coworkers in 1997), as it was designed to take advantage of the paramagnetic properties of *deoxygenated hemoglobin*, which is higher concentrations within venous blood, and thus it was considered to be a form of blood oxygen level–dependent (BOLD) imaging at that time. While BOLD imaging went on to become the mainstay for functional MRI (fMRI) imaging, several later iterations and contributions were involved in the eventual evolution to the technique of SWI that is currently available today for routine implementation from the major MRI scanner manufacturers.

In brief, the final form of SWI, although varying slightly among manufacturers, essentially involves multiplying a T2*-based gradient echo "magnitude" image a variable number of times by a phase mask (which is obtained from high-pass filtering of the original phase image). Notably, the original magnitude image is sensitive to T2* effects, as it typically implements a low flip angle and intermediate time to echo (TE), although the degree to which arterial or venous components are visualized depends on the selected TE; higher flip angles can better demonstrate regions of edema while still enabling visualization of the T2* effects of hemorrhage. Notably, one can actually set the standard gradient echo T2*-weighted images (GE T2*WI) available on the MR scanner to an identical time to repeat (TR), TE, flip angle, and thickness as that of an SWI sequence, but the resultant images are not identical to those of SWI since SWI implements both magnitude and phase data. In contrast, GE T2*WI only implements magnitude data, as illustrated in the following pages. As compared to routine GE T2*WI, SWI typically removes more unwanted background susceptibility effects, has a higher resolution, and can better demonstrate *venous vasculature* and *microhemorrhages* (MHs) than GE T2*WI (at least two to three times as many MHs can be visualized on SWI as compared to GE T2*WI). These factors all improve with increasing MRI field strength, while advanced postprocessing methods continue to be updated to improve the visualized final SWI images. Additionally, as SWI is typically obtained as a three-dimensional acquisition, the data have the potential to be reconstructed quite thin and in nearly any plane, depending on the resolution and quality of the acquisition. One of the most common ways to visualize the SWI data involves reviewing both thinner axial plane data (at 1–4 mm thickness), which best depicts the MHs, along with a "sliding" minimum intensity projection (MinIP) of 10–20-mm thickness (with variable overlap), which may improve visualization of deoxygenated blood such as venous vasculature in order to visualize venous anatomy.

The "filtered" phase map that is utilized to optimize the SWI can be useful in distinguishing hypointense signals from *hemorrhage* or *iron* from *calcium, manganese,* and *copper*, based on the presence of a positive (bright) or negative (dark) phase, which also depends on whether the magnet is left-handed or right-handed. Positive phase substances on a left-handed system include paramagnetic substances such as deoxyhemoglobin, higher concentrations of deposits of iron nanoparticles (such as in the basal ganglia), and manganese, while the negative phase is caused by diamagnetic substances such as calcium. The reverse appearances are present on right-handed systems. Note that the unfiltered phase map may be useful but can be misleading because of extensive artifacts from susceptibility caused by gas, air, and metal; unfortunately, not all vendors have filtered phase maps routinely available.

Given the excellent depiction of veins on SWI, one should be aware of normal venous vasculature, particularly trans-

A.M. McKinney, *Atlas of Normal Imaging Variations of the Brain, Skull, and Craniocervical Vasculature*,
DOI 10.1007/978-3-319-39790-0_20

medullary/perimedullary veins oriented perpendicular to the bodies of the lateral ventricles in the supratentorial white matter as well as normal deep veins. When these veins are traveling perpendicular to the slice (particularly to the axial plane), they may simulate MH, so one must carefully review the thin images to follow the course of the smaller vessels that are invisible on routine MR imaging if a MH is suspected. Interestingly, in *acute stroke, perimedullary veins* are often actually increased in prominence. In this regard, the normal anatomy and examples of such trans-/perimedullary veins are covered separately within this text within the vascular section under the topic of Susceptibility-Weighted Images: Deep Veins, Transmedullary Veins, and Subventricular Veins (Sect. 40.6). The focus of this section is rather on the concepts behind SWI, variations in basal ganglial appearance on SWI, and artifacts on SWI that simulate disease, with relevant examples.

20.1 Susceptibility-Weighted Imaging: Phase Maps

In addition to detecting MHs or occult, low-flow vascular lesions, SWI-generated phase maps can be useful in distinguishing SWI-dark signal from *diamagnetic* versus *paramagnetic* substances. These maps (in combination with other MR sequences) may help to distinguish hemorrhage, iron, manganese, or calcium deposits based on the presence of a negative (dark) or positive (bright) phase and also depending on whether the magnet is left-handed or right-handed (polarity). Positive phase substances that are bright on a left-handed system include paramagnetic deoxyhemoglobin (present in high concentrations in deoxygenated blood) and depositions of iron nanoparticles and manganese, whereas diamagnetic substances appear dark (e.g., calcium). The reverse appearances are visualized on a right-handed system (Figs. 20.1, 20.2, and 20.3).

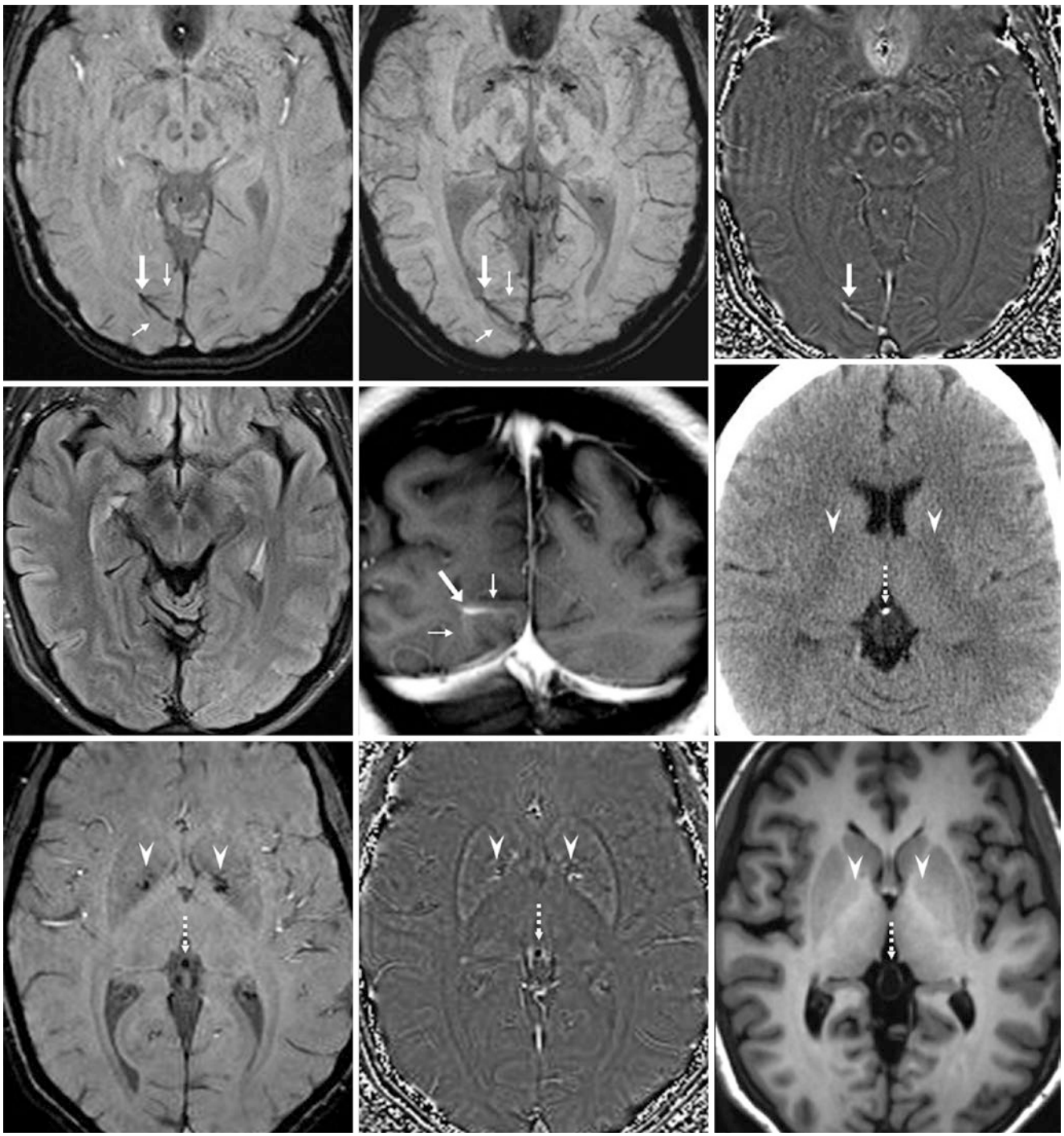

Fig. 20.1 A 55 year old with breast cancer in whom a left-handed 3T MRI was negative for metastases. *Top row:* 2-mm-thick SWI (*left*) depicted a draining vein (*arrows*) from a DVA, with as faint caput" (*thin arrows*), also shown on a 10-mm MIP (*middle*). The phase map (*right*) demonstrates bright signal from paramagnetic deoxygenated blood. *Middle row:* an axial postcontrast FLAIR image (*left*) does not demonstrate the DVA as well as coronal postcontrast SE T1WI (*middle*). On axial NECT (*right*), there is a pineal calcification (*dotted arrows*) within a pineal cyst. On NECT, note the lack of calcifications within the globi pallidi (*arrowheads*). *Bottom row:* the pineal calcification is dark on both SWI (*left*) and phase map (*middle*) from diamagnetic calcium. There is a mostly dark signal at the periphery of the globi pallidi (*arrowheads*) on SWI, which is bright on phase maps, which excludes calcium (also excluded by NECT). Paramagnetic manganese is also excluded because of the lack of bright signal on T1WI (*right*). The bright portion of the pallidal signal is likely related to paramagnetic iron deposits

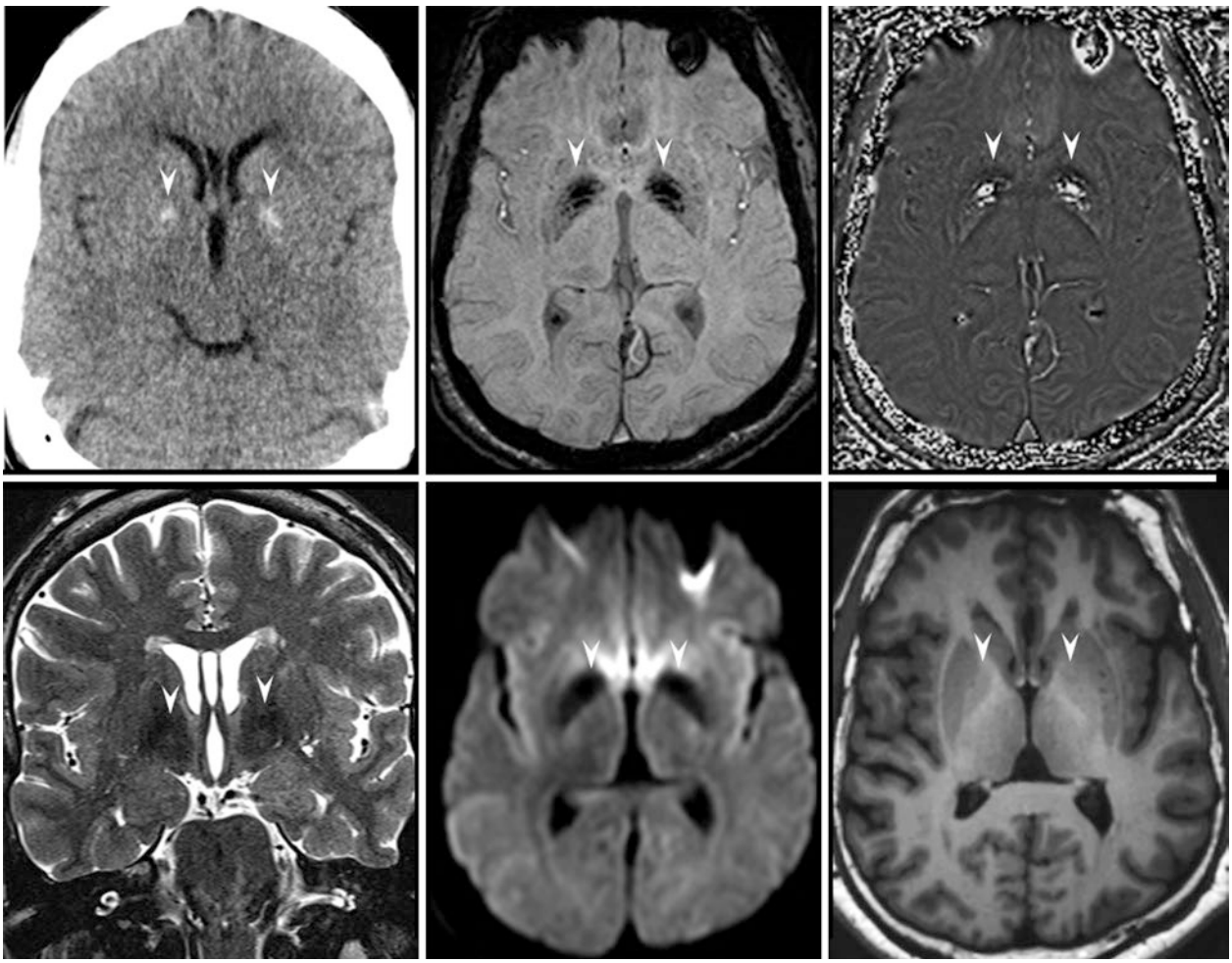

Fig. 20.2 In a 51 year old pallidal calcium (*arrowheads*) on a NECT (*top left*) are, on a left-handed 3T MRI, located within larger areas of dark signal on SWI (*top middle*) that are bright on phase maps (*top right*) and dark on T2WI (*bottom left*) and DWI (*bottom middle*). The dark signal on SWI is from paramagnetic iron; smaller amounts of diamagnetic calcium are dark on phase maps. T1WI (*bottom right*) does not show bright pallidal signal, excluding manganese

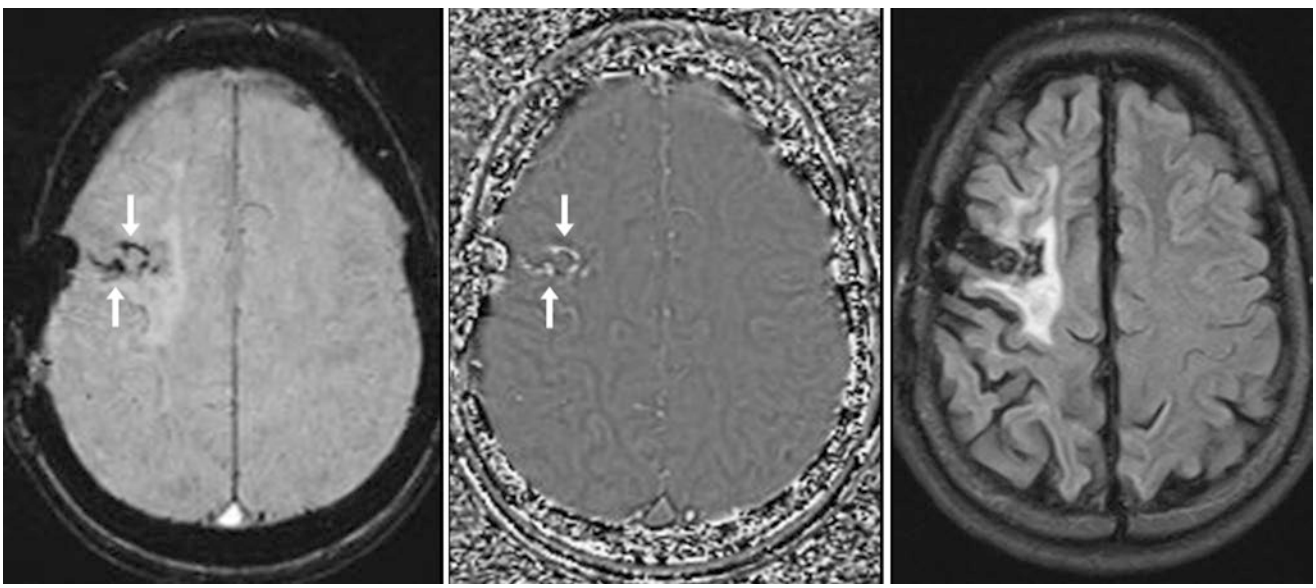

Fig. 20.3 Example of hemosiderin (ferritin) outside of the basal ganglia: On a 1.5T left-handed MRI, a 28 year old had hemosiderin deposition (*arrows*) within a region of encephalomalacia (post-trauma) on SWI (*left*), phase map (*middle*), and FLAIR (*right*). The paramagnetic property of hemosiderin causes it to appear bright on phase maps

20.2 Susceptibility-Weighted Images: Normal Basal Ganglial Iron Deposition

On susceptibility-weighted imaging (SWI), one can visualize normal stored iron deposits (nanoparticles) within the basal ganglia, as stated previously. Iron normally accumulates with increasing age within the *corpus striatum* (caudate, putamen, and globus pallidus, collectively) in asymptomatic patients, although the exact mechanism for this deposition is unknown. Pallidal iron begins to accumulate as early as the first year of life and begins accumulating exponentially by the second to third decade, reaching its plateau or "saturation" by about 35–40 years of age. Putaminal iron accumulates more slowly and less exponentially, typically reaching its plateau around 50–60 years. In adolescence and early adult years, normal iron deposition also occurs within the substantia nigra, dentate nuclei, and red nuclei. Normal, age-related accumulation may continue to the point where the signal intensity of the caudate and putamen becomes equivalent to that of the globus pallidus by the eighth decade. However, accelerated iron deposition in various structures may be present in certain disorders (discussed below). Thus, "dark" iron on SWI is normal and expected to be present within the globi pallidi, dentate nuclei, red nucleus, and substantia nigra, even in late adolescents and teenagers. In general, it is considered normal if a lesser degree of iron is visualized within these structures than expected for age.

Accelerated or *abnormal iron concentrations* can be found in certain disorders. For example, patients with *Alzheimer disease* and its presumed precursor, mild cognitive impairment, have higher concentrations of iron than controls within the globi pallidi and substantia nigra and perhaps also within the hippocampi, putamina, caudate nuclei, and dentate nuclei. In addition, both conditions have an increased frequency of cerebral MHs, which are easily detected on SWI (thought to be associated with β-amyloid deposition). Thus, while dark signal throughout the basal ganglia in an elderly patient can be normal, the presence of profoundly dark signal on SWI throughout the basal ganglia along with characteristic geographic locations of cerebral atrophy and microhemorrhages is highly suggestive of either Alzheimer disease or mild cognitive impairment.

Additionally, syndromes of *neurodegeneration with brain iron accumulation* (NBIA) have abnormal amounts of iron deposition within the basal ganglia, which appear profoundly dark on SWI to the point of having very dark signal even on spin-echo T2WI (SE T2WI. Note that spin-echo T2WI is relatively insensitive to susceptibility effects compared to other MR sequences; therefore the presence of dark signal on T2WI indicates that the iron concentration is quite high). Notably, NBIA consists of at least nine as yet identified disorders, all but two of which are recessively inherited. In this regard, pantothenate kinase-associated neurodegeneration is the most common form of NBIA, constituting nearly half of all NBIA patients, and it usually presents in childhood. The other, less common NBIA disorders include aceruloplasminemia, neuroferritinopathy (the only genetically dominant form of NBIA identified as of yet), neuroaxonal dystrophy (in both infantile and adult forms), mitochondrial-membrane protein-associated neurodegeneration, fatty acid hydroxylase-associated neurodegeneration, Kufor-Rakeb disease, Woodhouse-Sakati syndrome, and an idiopathic form of NBIA.

Finally, when correcting for age, SWI may distinguish *Parkinson disease* (PD) from atypical forms of Parkinsonism such as progressive supranuclear palsy (PSP) and multisystem atrophy (MSA), and SWI may also help distinguish PSP from MSA. Based on a visual perspective, both PSP and MSA may have greater degrees of hypointense iron within the putamina, red nuclei, and dentate nuclei as compared to both typical PD and controls, while PSP may have a greater concentration of iron within the red nuclei than both PD and MSA. There are conflicting results as to whether the substantia nigra has greater visibly detectable hypointensity on SWI regarding PD as compared to both atypical PD (MSP and PSP) and controls, although preliminary data suggest that PD has measurably different SWI signal in that structure. After correction for age, some studies suggest that typical PD may actually have less iron in the abovementioned structures, which may relate to the theory that the pathophysiology of PD involves impaired iron handling with a concomitant decrease in ferritin (the storage protein for iron). More recently, detecting the lack of high signal (i.e. within Nigrosome 1 subregions of the posterior third of the substantia nigra (SN) have been described by Schwarz et al. to have a high accuracy of detecting idiopathic Parkinson disease. It has been theorized that this decreased signal (so-called "swallow-tail sign") may relate to either increased iron deposition or decreased neuromelanin (leading to increased free iron) within these structures, but this phenomenon needs to be studied further.

Iron deposition may also be visualized on sequences such as SE T2WI, GE T2*WI, DWI, or BOLD (blood oxygenation level dependent) imaging, while being visible on FLAIR to a lesser degree. As stated earlier in this chapter, SWI utilizes both magnitude and phase data via postprocessing in order to optimize the visualization of parenchymal susceptibility effects while minimizing artifacts. Thus, while nano-deposits of iron may be visualized on various sequences, it is best to confirm iron deposition on SWI with filtered phase maps in order to exclude other substances. As stated previously, the accumulation of other substances may occur in the basal ganglia of normal patients, such as with *calcium* (most commonly in the globus pallidus, which is diamagnetic). Other substances may also accumulate in

pathologic conditions, such as with *manganese* (selectively of the globus pallidus in hepatic failure, being paramagnetic) or *copper* (in Wilson disease, often paramagnetic). Such deposits are easily visualized on SWI, and the type of mineral is identified by a combination of SWI with phase maps, the site of deposits, and clinical findings.

Note: unless otherwise stated, the SWI images displayed in this section are of 2-mm thicknes and were obtained on a 3.0 Tesla (3 T) magnet.

20.3 Susceptibility-Weighted Images: Normal Iron Deposition at 0 to 10 Years of Age

At the age of 0–10 years on SWI, there is very little physiologic iron deposition within basal ganglial structures, although later in that decade small amounts can be visualized within the *globi pallidi* and *substantia nigra* (the earliest structures to accumulate physiologic iron) and perhaps within the *red nuclei* (Figs. 20.4, 20.5, and 20.6).

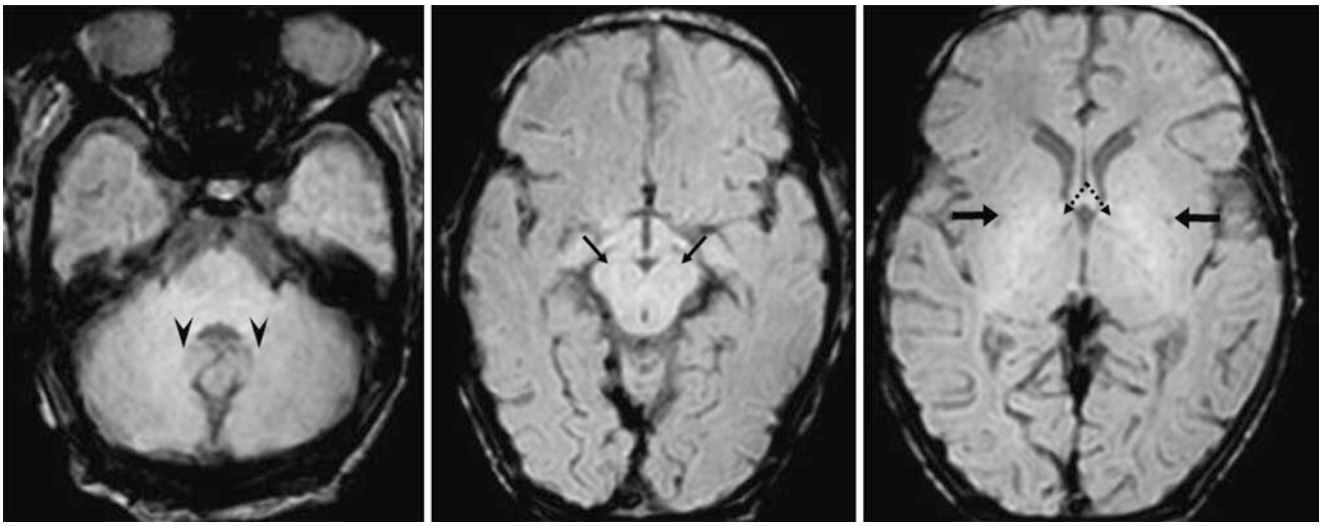

Fig. 20.4 A 5-day-old patient who underwent a negative 3T MRI to evaluate for hypoxic-ischemic injury. The patient's milestones were normal on clinical examinations at 1 and 2 years of age. Axial SWI images show no visible iron deposition. *Arrowheads* indicate dentate nuclei; *dotted arrows* indicate globi pallidi (GP); *arrows* indicate putamina; *thin arrows* indicate substantia nigra (SN)

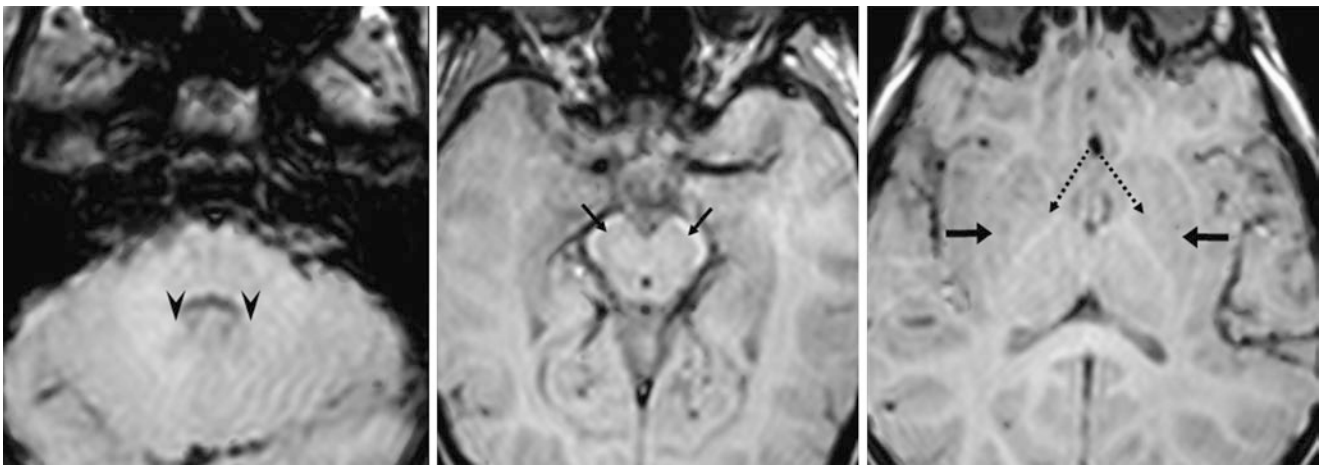

Fig. 20.5 A developmentally normal 3 year old underwent a negative 3T MRI to evaluate for a seizure. Axial SWIs illustrate that there has not yet been visible deposition of iron within the dentate nuclei (*arrowheads*), SN (*thin arrows*), or GP (*dotted arrows*). *Arrows* indicate putamina

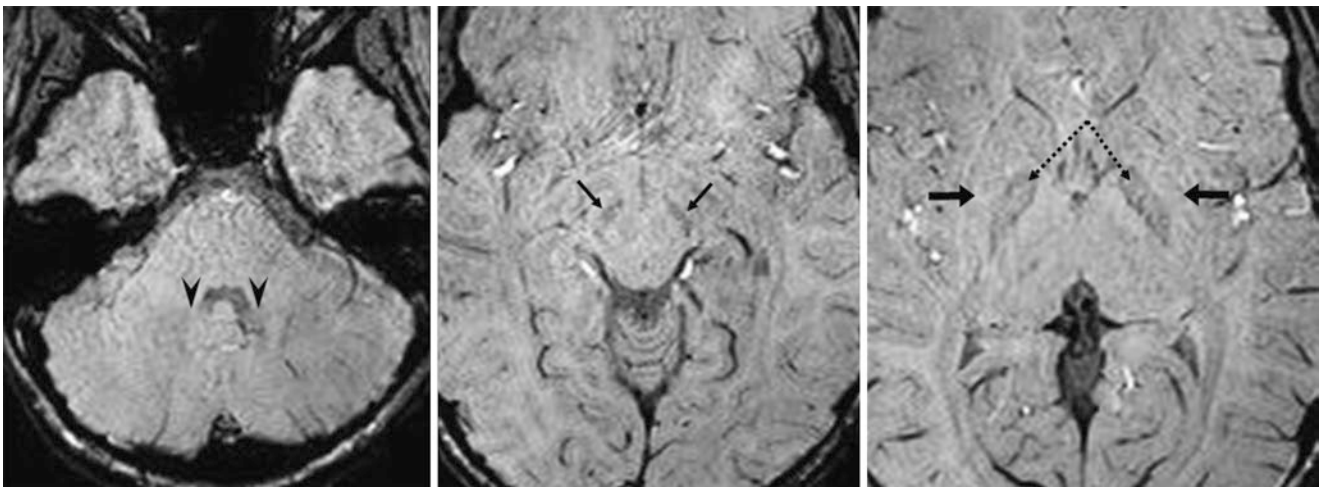

Fig. 20.6 A 7 year old with growth deficits underwent a negative 3T MRI to evaluate the pituitary. Axial SWIs show no visible deposition of iron within the dentate nuclei (*arrowheads*), while there is early iron deposition within the SN (*thin arrows*) and GP (*dotted arrows*). *Arrows* indicate putamina

20.4 Susceptibility-Weighted Images: Normal Iron Deposition at 10 to 20 Years of Age

At the age of 10–20 years on SWI, there should be a clearly visibly dark signal from iron within the *globi pallidi* and *substantia nigra* (typically the earliest structures to accumulate physiologic iron); however, it should not be exceedingly dark and not within the putamina. The red nuclei and perhaps even the dentate nuclei may have a very faintly dark signal in in this age group (Figs. 20.7, 20.8, 20.9, 20.10, and 20.11).

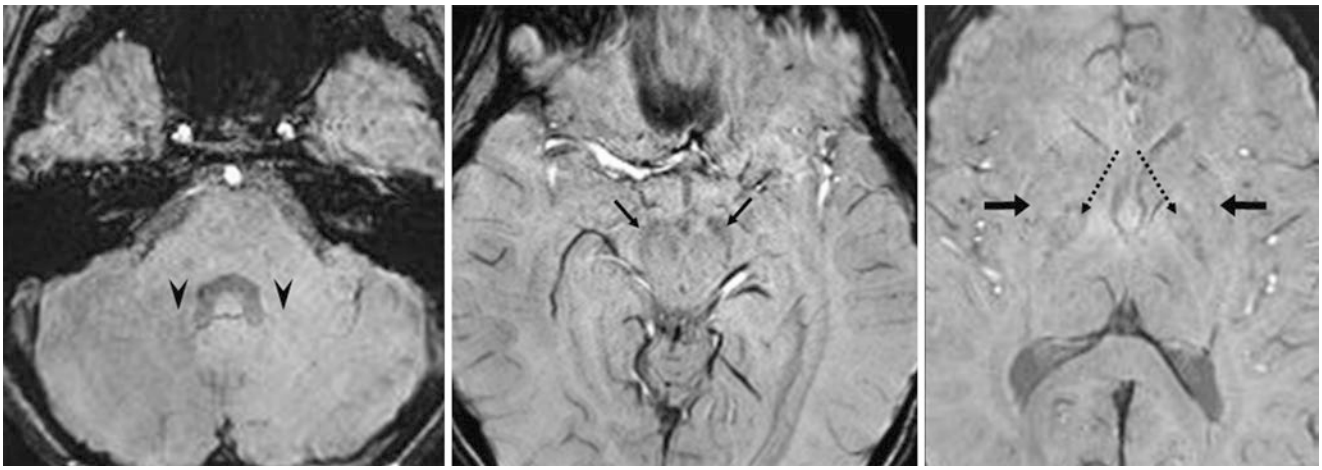

Fig. 20.7 A 10 year old who underwent an otherwise negative 3T MRI for a middle ear mass. Axial SWIs show no visible iron deposition in the dentate nuclei (*arrowheads*), while there is very early deposition within the SN (*thin arrows*) and GP (*dotted arrows*) but not the putamen (*arrows*)

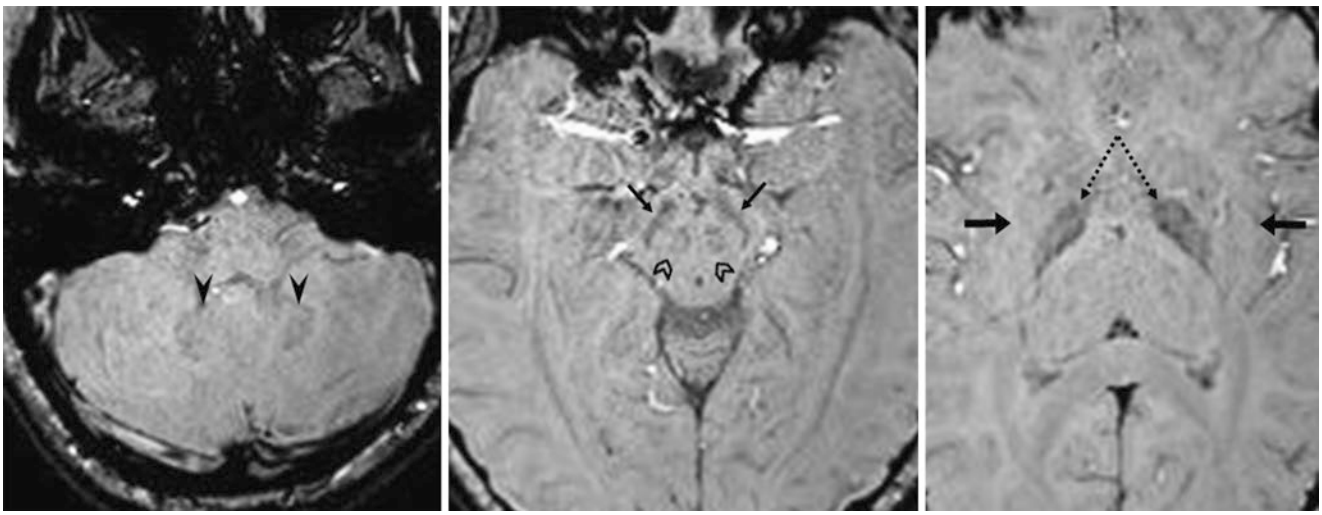

Fig. 20.8 A 12 year old with a negative 3T MRI for headaches: axial SWIs illustrate early iron deposition within the dentate nuclei (*arrowheads*) as well as within the SN (*thin arrows*) and GP (*dotted arrows*) but not the putamen (*arrows*). Also, note faint iron within the red nuclei (*chevrons*)

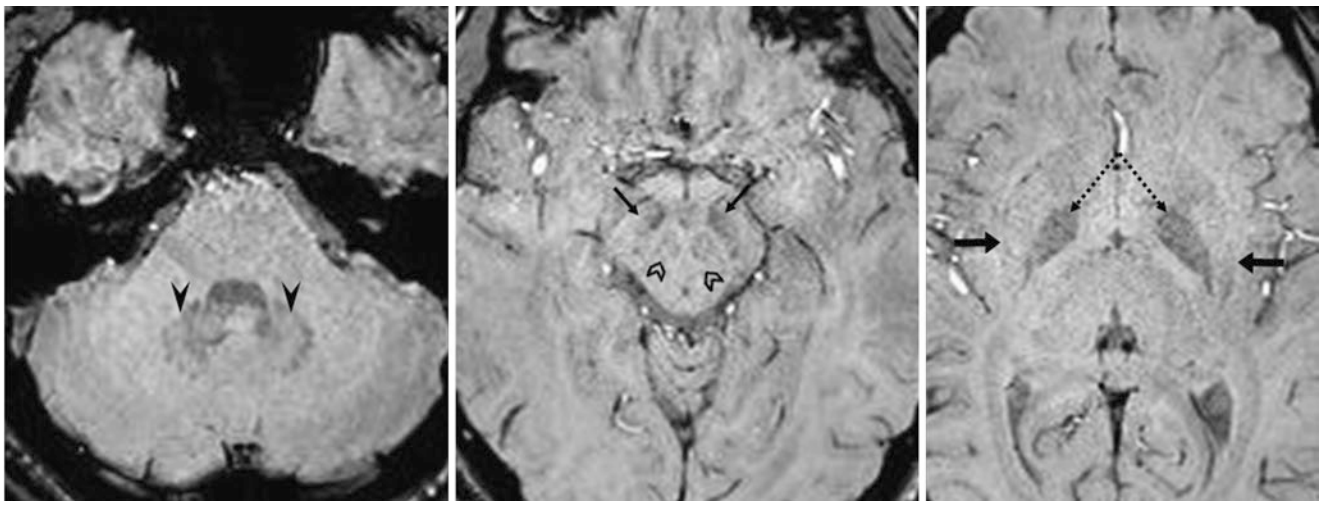

Fig. 20.9 A 15 year old with a negative 3T MRI for headaches. Axial SWIs show early iron deposition within the dentate nuclei (*arrowheads*) as well as within the SN (*thin arrows*) and GP (*dotted arrows*). Also, note faint iron deposition within the red nuclei (*chevrons*). *Arrows* indicate putamina

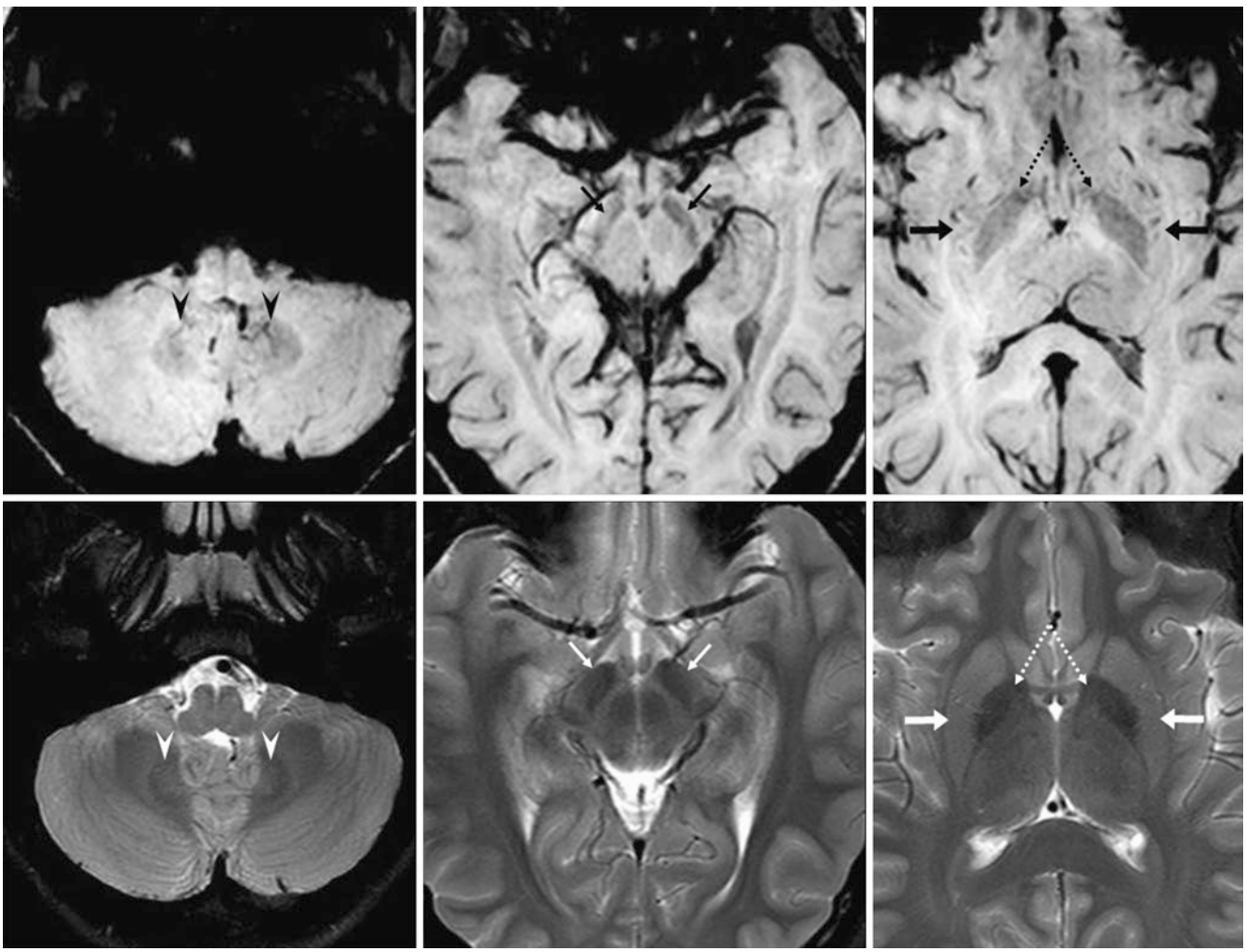

Fig. 20.10 A 15 year old with a normal 3T MRI for headaches. There is mild, early iron deposition within the dentate nuclei (*arrowheads*), SN (*thin arrows*), and GP (*dotted arrows*) on axial SWIs (*top row*). The putamen (*arrows*) has not yet accumulated much iron. T2WIs are also provided (*bottom row*). The amount of visible iron within these structures varies mildly in this age group

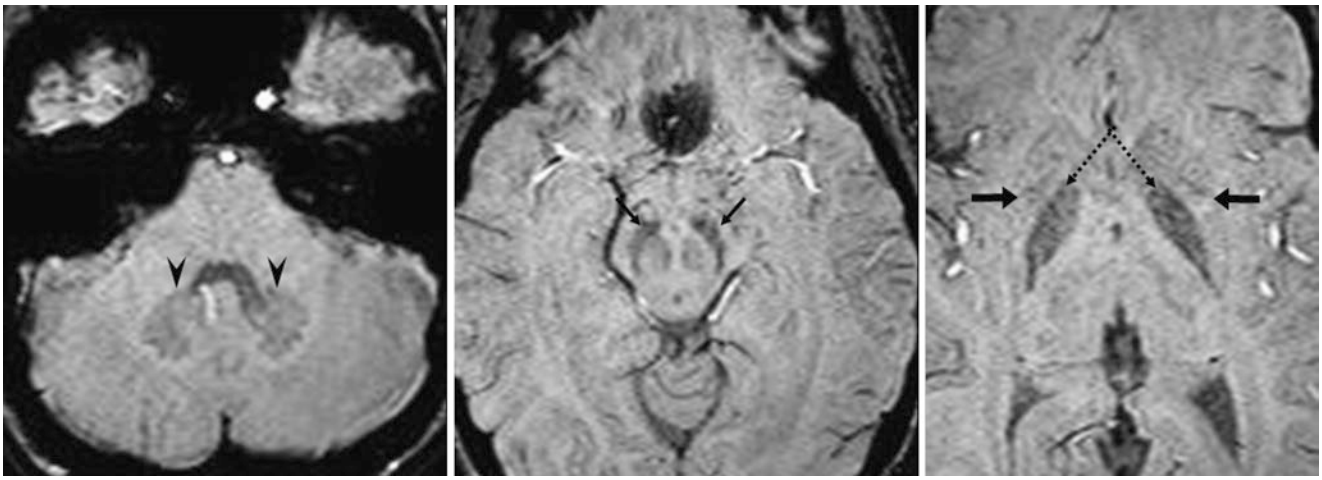

Fig. 20.11 A 20 year old with a negative 3T MRI for headaches. Axial SWIs illustrate that there has been increasing iron deposition within the dentate nuclei (*arrowheads*), SN (*thin arrows*), and GP (*dotted arrows*). However, there is still a paucity of putaminal iron

20.5 Susceptibility-Weighted Images: Normal Iron Deposition at 20 to 40 Years of Age

At the age of 20–40 years on SWI a normal dark signal from iron is already quite evident within the *globi pallidi, substantia nigra,* and *red nuclei*, while a faintly dark signal may become evident within the *putamina* and *dentate nuclei*. However, the putaminal signal should not be nearly as dark as one within the globi pallidi (Figs. 20.12, 20.13, 20.14, 20.15, and 20.16).

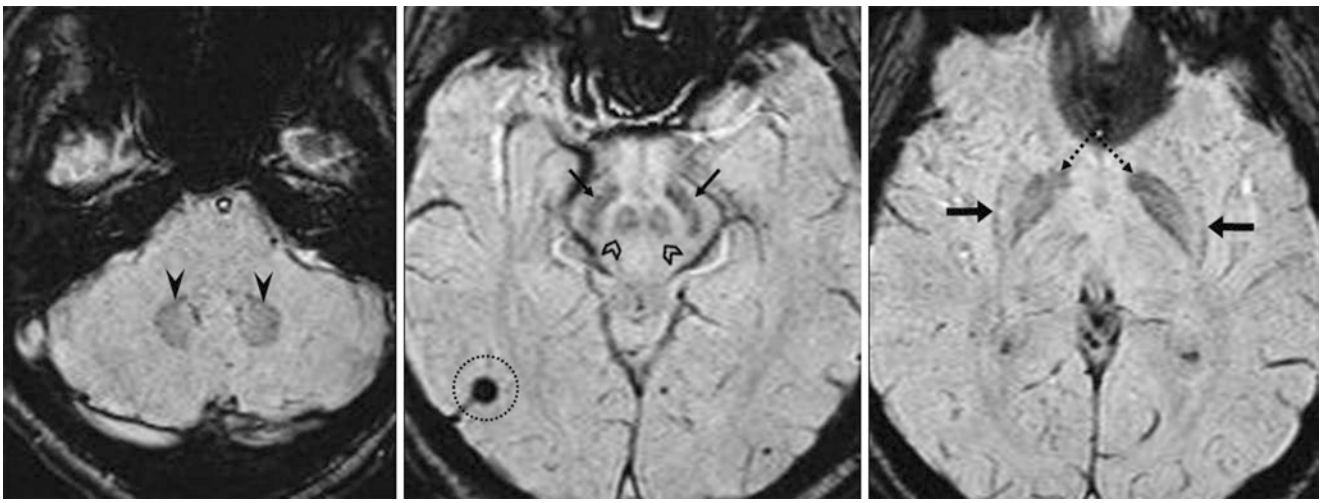

Fig. 20.12 A 25 year old who had a 3T MRI performed for headaches. The MRI showed an incidental cavernoma (*dotted circle*). On SWI, there was mild iron deposition within the dentate nuclei (*arrowheads*), SN (*thin arrows*), and GP (*dotted arrows*). Also, note the increasing deposition of iron within the red nuclei (*chevrons*) and further deposition within the posterolateral portions of the putamina (*arrows, right*)

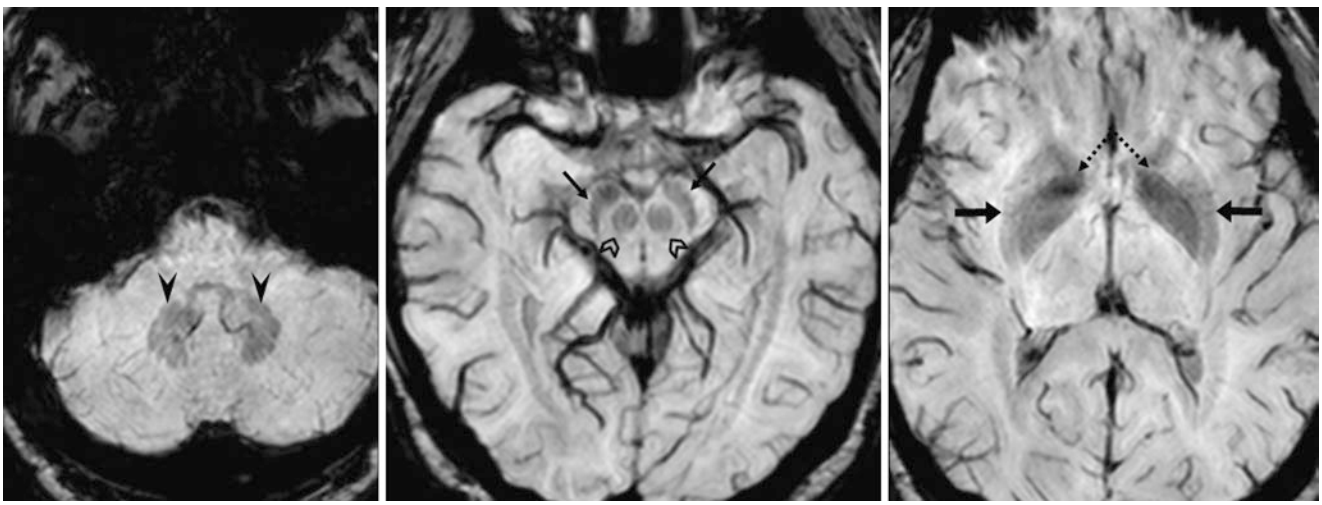

Fig. 20.13 A 33 year old with a negative 3T MRI performed for headaches. A 5-mm-thickness SWI depicts increasing iron deposition within the dentate nuclei (*arrowheads*), SN (*thin arrows*), GP (*dotted arrows*), putamina (*arrows*), and red nuclei (*chevrons*). In particular, the putamina are becoming more homogeneously dark in signal as iron begins to accumulate more rapidly (*arrows, right*)

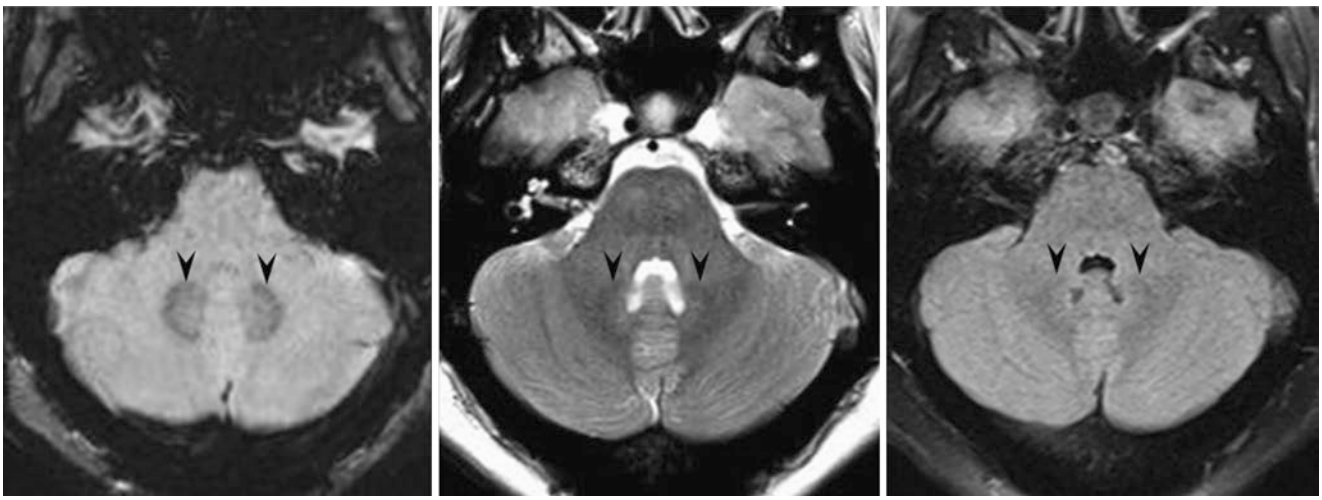

Fig. 20.14 A 35 year old with a negative 3T MRI performed to evaluate for multiple sclerosis. SWI (*left*) depicts iron within the dentate nuclei (*arrowheads*). The dentate nuclei can often be visualized on T2WI (*middle*) in the middle aged and elderly as a result of the T2* effects of iron. This dark signal from iron is usually less visible on FLAIR (*right*)

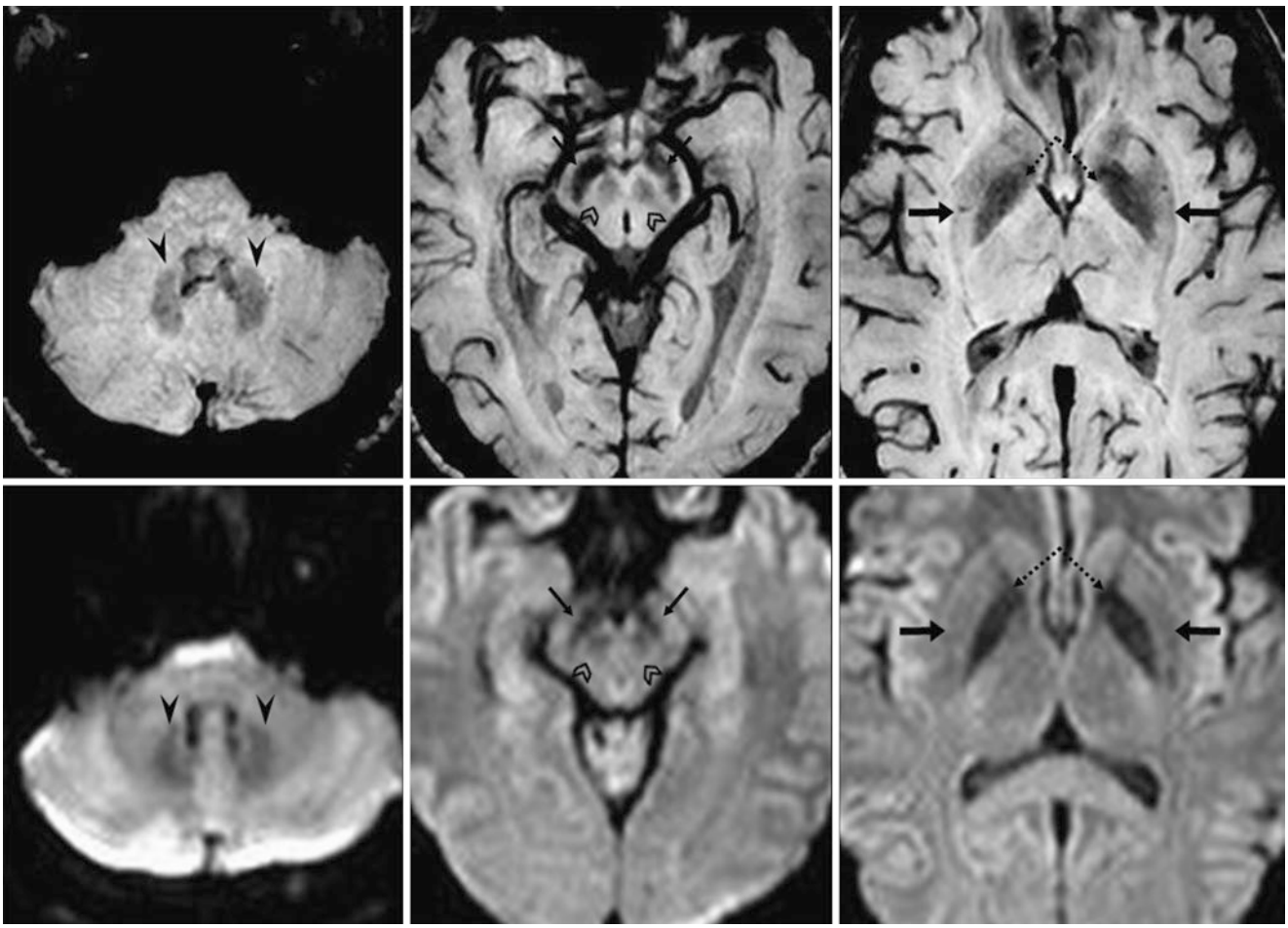

Fig. 20.15 A 39 year old with a negative 3T MRI for headaches. SWIs (*top row*) show iron deposition within the dentate nuclei (*arrowheads*), SN (*thin arrows*), GP (*dotted arrows*), putamina (*arrows*), and red nuclei (*chevrons*). The putamina have become darker in signal as iron continues to accumulate (*arrows, right*). These nuclei are also dark on DWIs (*bottom row*) because of the iron's susceptibility effects

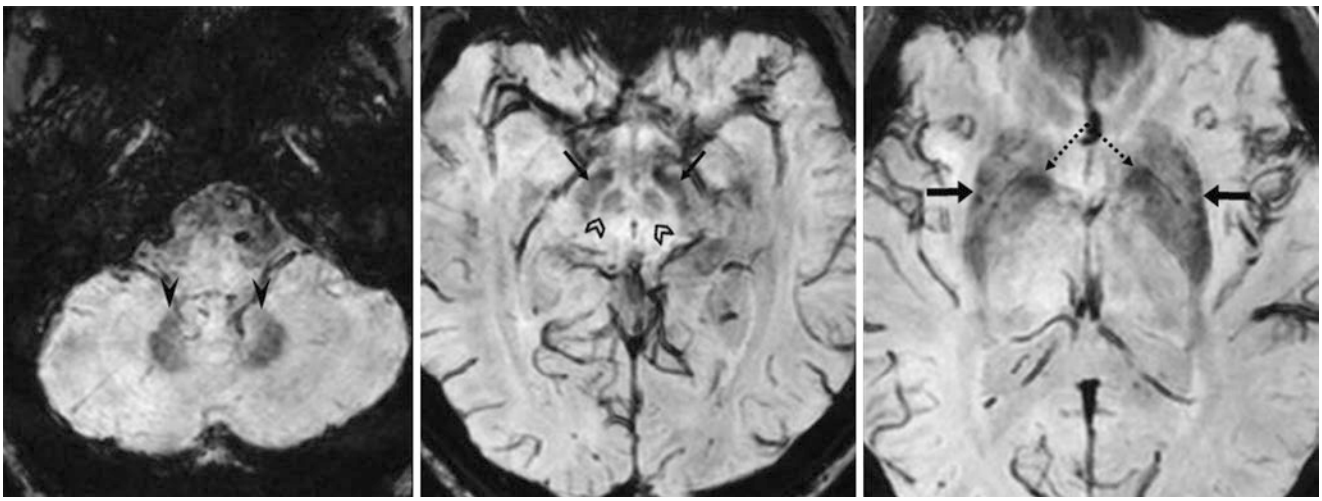

Fig. 20.16 A 40 year old with a negative 3T MRI performed for seizures. SWIs depict iron deposition within the dentate nuclei (*arrowheads*), SN (*thin arrows*), GP (*dotted arrows*), red nuclei (*chevrons*), and putamina (*arrows*). The putamina have darkened in signal, particularly more laterally

20.6 Susceptibility-Weighted Images: Normal Iron Deposition at 40 to 60 Years of Age

At the age of 40–60 years on SWI, a normal dark signal from iron is increasingly prominent within the *putamina* and *dentate nuclei*. However, the putaminal signal should still not be quite as dark as the one from the globi pallidi, although the lateral edges of the putamen may appear quite dark. The dentate nuclei may be almost as dark as the globi pallidi (Figs. 20.17, 20.18, 20.19, 20.20, and 20.21).

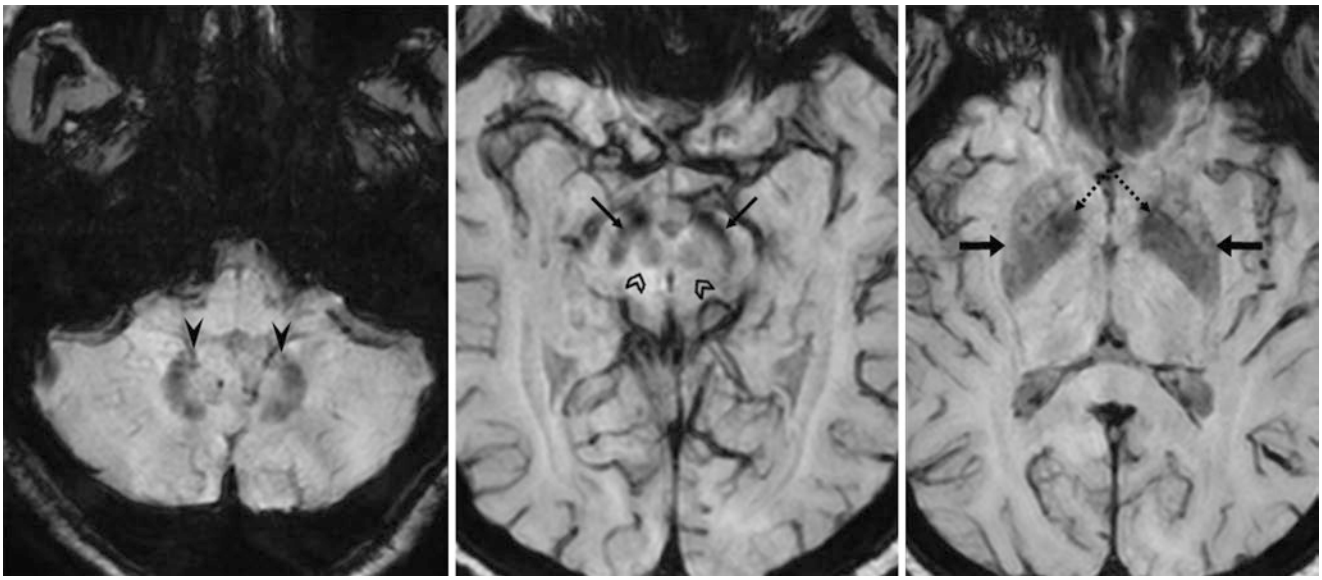

Fig. 20.17 A 41 year old with a negative 3T MRI performed for altered mental status. SWIs demonstrate iron deposition within the dentate nuclei (*arrowheads*), SN (*thin arrows*), GP (*dotted arrows*), putamina (*arrows*), and red nuclei (*chevrons*). The putamina are becoming more hypointense

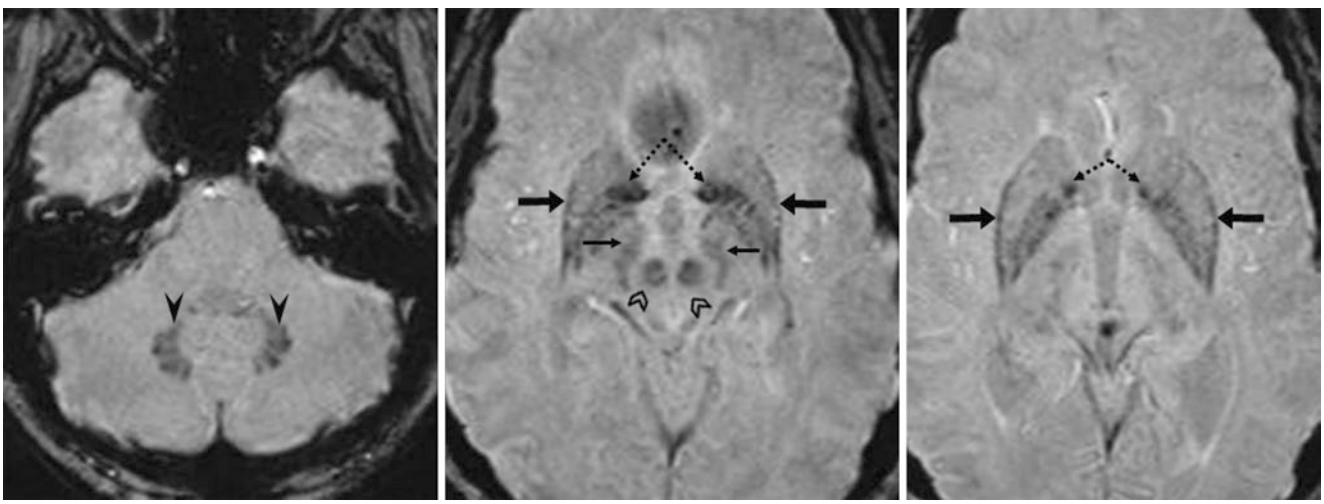

Fig. 20.18 A 45 year old with a negative 3T MRI performed for altered mental status. SWIs illustrate iron deposition within the dentate nuclei (*arrowheads*), SN (*thin arrows*), GP (*dotted arrows*), putamina (*arrows*), and red nuclei (*chevrons*). The putamina are more hypointense laterally

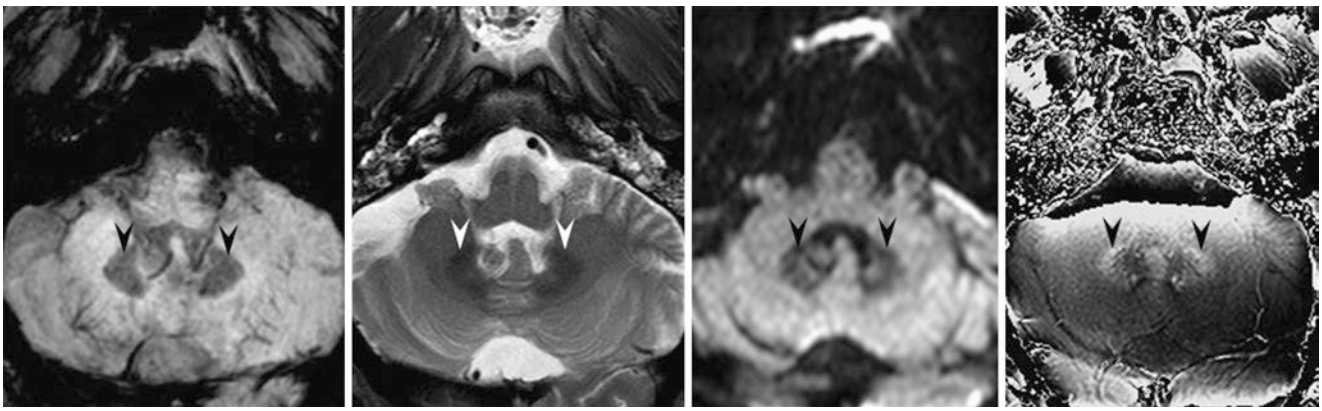

Fig. 20.19 A 54 year old; a 3T MRI demonstrates dark signal of the dentate nuclei on SWI (*left*), T2WI (*left middle*), and DWI (*right middle*). Corresponding bright signal on an unfiltered SWI phase map (*right*) confirms paramagnetic iron

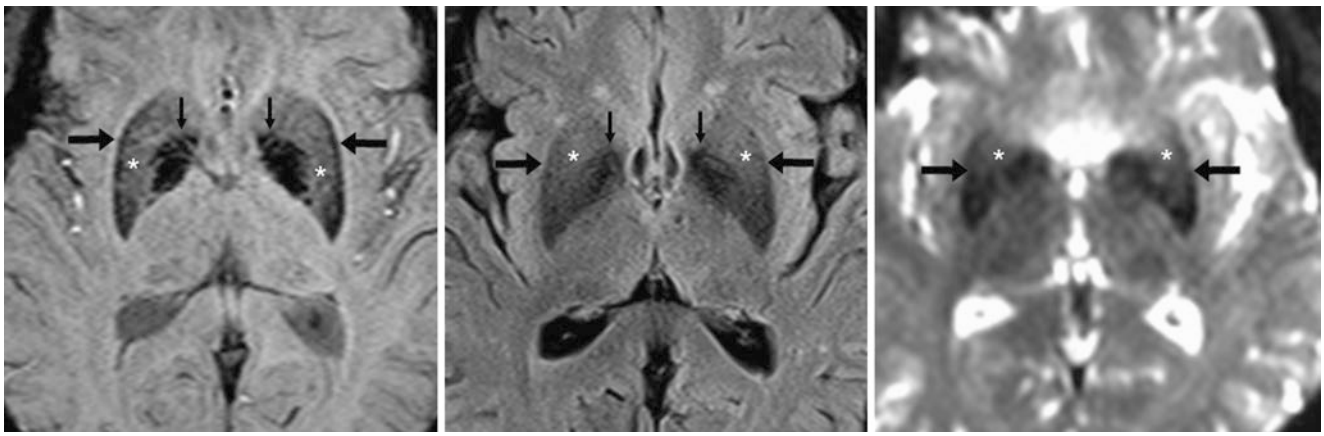

Fig. 20.20 A 63 year old in whom 3T MRI SWI (*left*) and FLAIR (*middle*) depict iron throughout the lentiform nuclei, being most prominent within the GP but even darker within the medially located GP interna (*thin arrows*). Iron is less prominent within the medial putamina (*) but is more prominent along the lateral edge of the putamina (*arrows*). Note corresponding findings on b = 0 map from DWI (*right*), which is a single echo echoplanar sequence that has T2-weighting but also T2* effects, as DWI is usually obtained by a single echo, gradient echo sequence

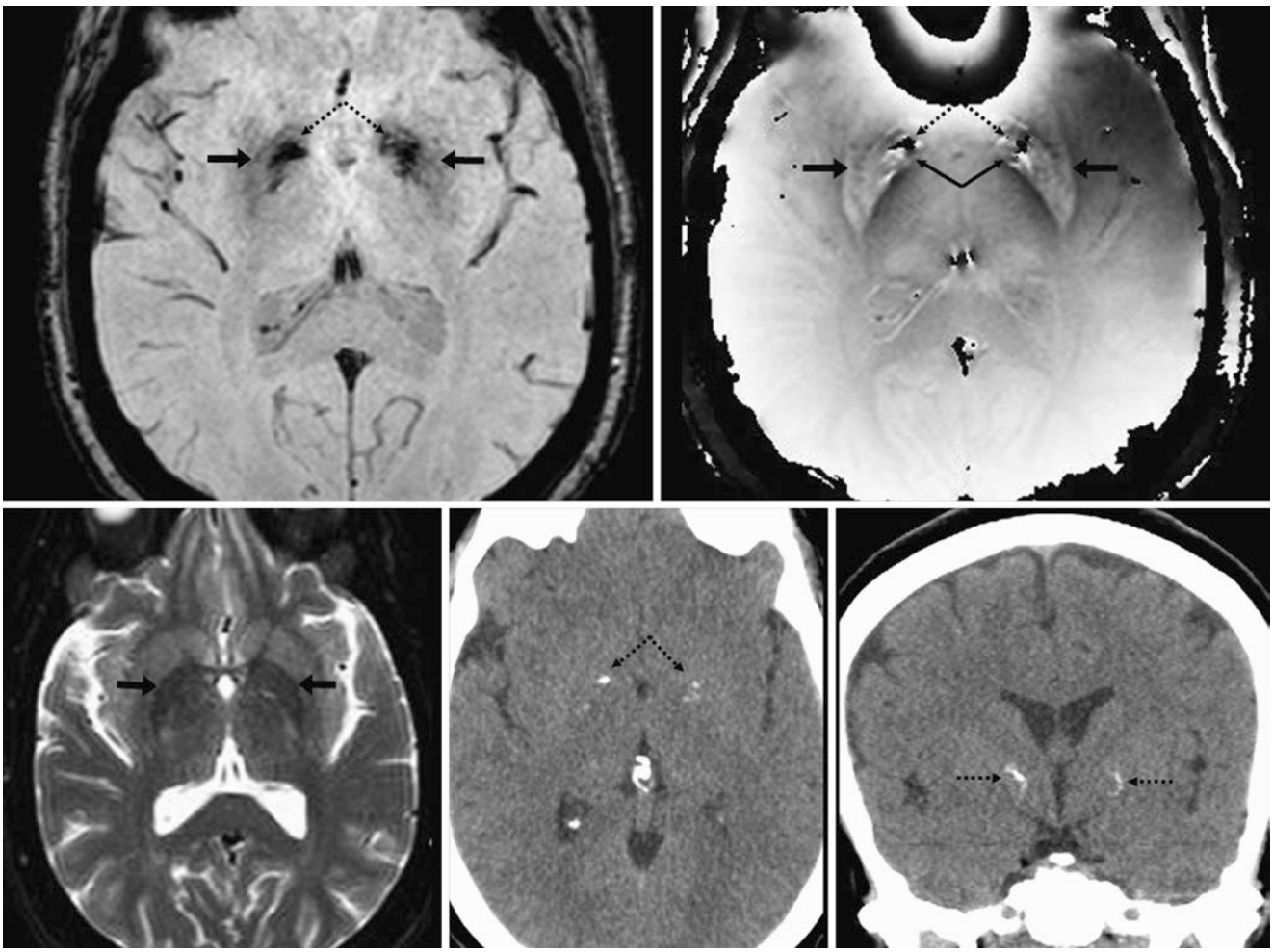

Fig. 20.21 A 64 year old; on a 3T MRI (negative study), SWI (*top left*) shows dark signal from iron within the putamina (*arrows*), with smaller areas of dark signal within the GP (*dotted arrows*). An unfiltered phase map (*top right*) shows that the smaller foci of the dark signal centrally within the GP are diamagnetic calcium, while the larger areas of bright signal within the GP (*thin arrows*) and putamina (*arrows*) are from paramagnetic iron. T2WI (*bottom left*) shows dark iron within the lentiform nuclei. Axial (*bottom middle*) and coronal (*bottom right*) NECT images confirm GP calcium

20.7 Susceptibility-Weighted Images: Normal Iron Deposition at 60+ Years of Age

At the age of 60 years and older on SWI, the normal dark signal from iron can be quite prominent within the *putamina* and *dentate nuclei* and can appear as dark as in the globi pallidi. This can make it difficult to discern excess iron deposition, such as is present in NBIA without the use of additional sequences (Figs. 20.22, 20.23, 20.24, 20.25, 20.26, 20.27, 20.28, and 20.29).

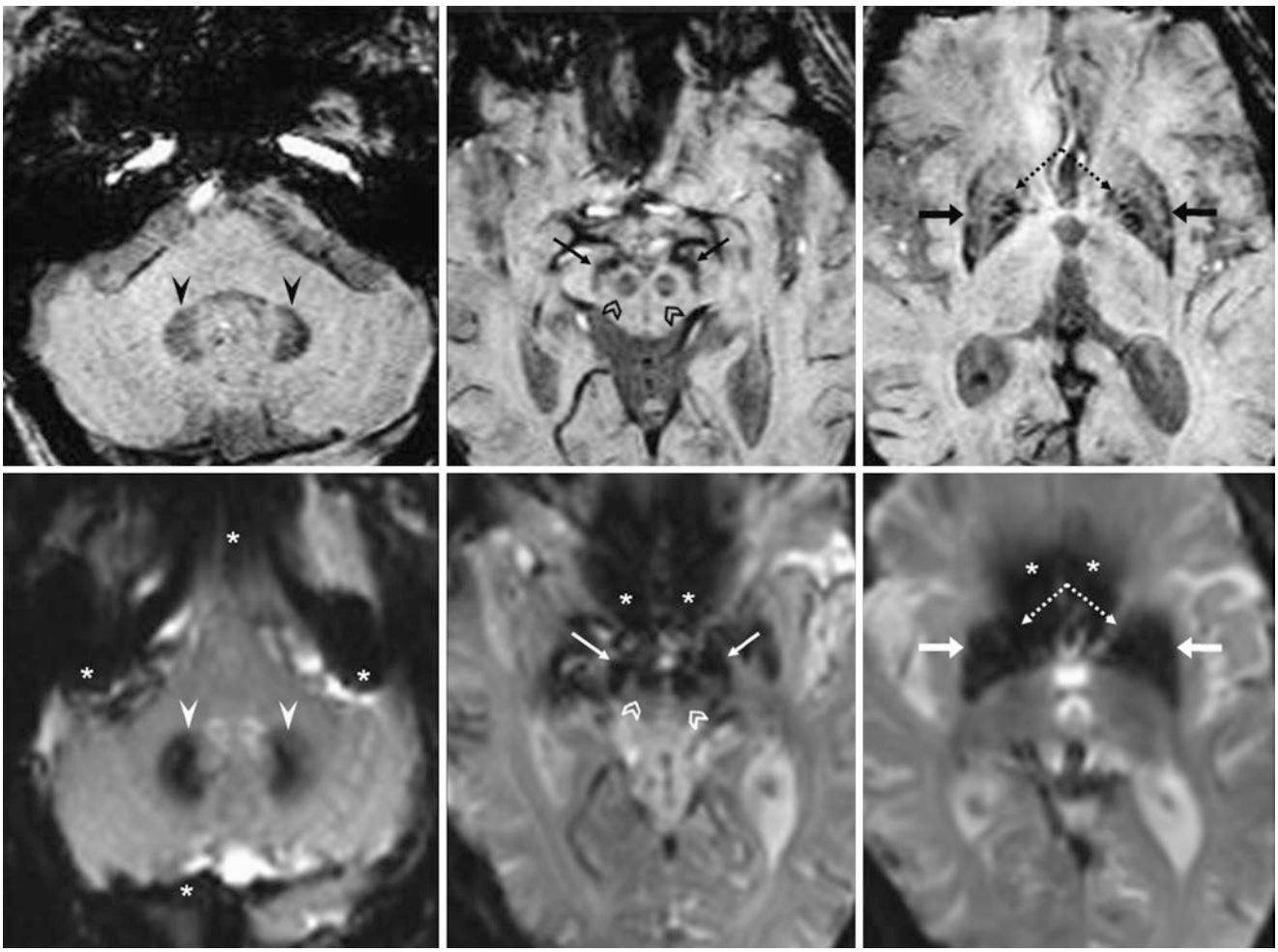

Fig. 20.22 A 76 year old; on a 3T MRI (negative study), SWIs (*top row*) showed a dark signal from iron within the dentate nuclei (*arrowheads*), GP (*dotted arrows*), putamina (*arrows*), and red nuclei (*chevrons*). On matched noncontrast BOLD images (*bottom row*) utilized to acquire an MR perfusion study, such nuclei appear even more hypointense but suffer extensive gas-related artifacts (*) from the paranasal sinuses, mastoid air cells, and externally, all of which obscure the margins with the cerebrum

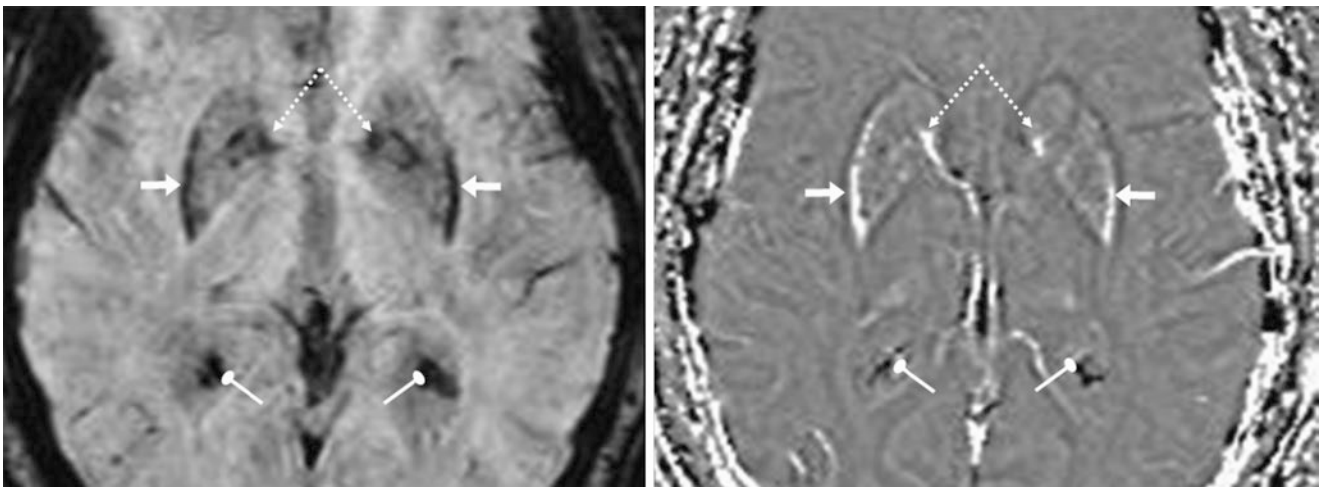

Fig. 20.23 A 79 year old with a negative 1.5T MRI performed for seizures. On SWI (*left*), there is dark signal from iron deposits medially within the GP (*dotted arrows*), along with a crescent of dark signal along the lateral margin of the putamina. On a filtered phase map (*right*), the bright signal represents paramagnetic iron deposition. In contrast, note the dark signal that results from calcifications of the choroid plexi (*circle tip arrows*), as calcium is a diamagnetic substance

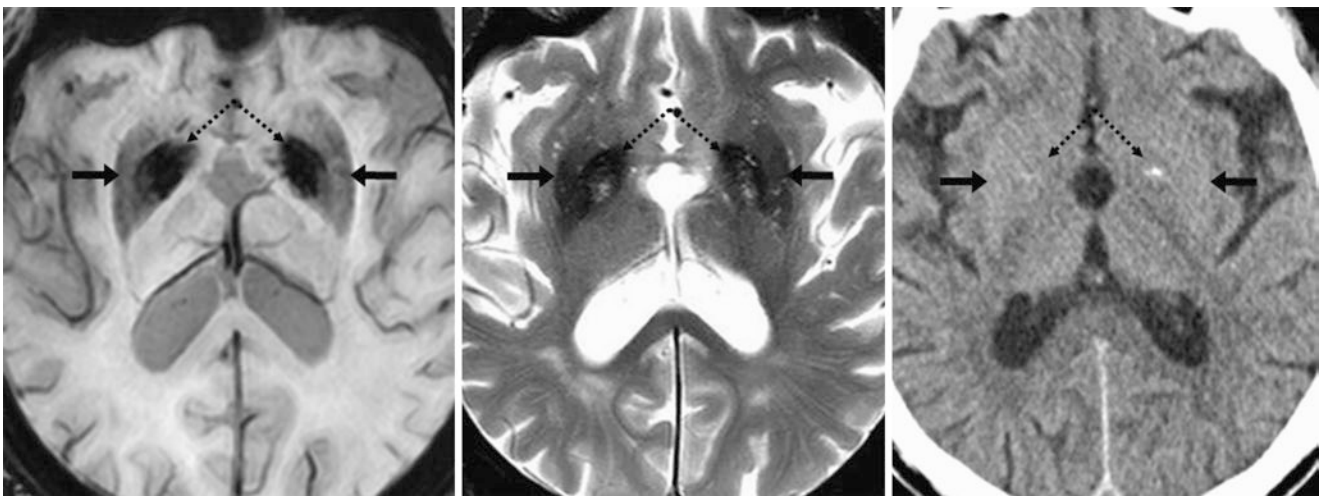

Fig. 20.24 An 81 year old had a negative 3T MRI performed for altered mental status. An SWI (*left*) demonstrates iron deposition within the lentiform nuclei (i.e., GP [*dotted arrows*] and putamina [*arrows*]). T2WI (*middle*) shows similarly dark signal. A NECT (*right*) confirms that the dark signal is largely due to iron, as there is only a small amount of GP calcium bilaterally

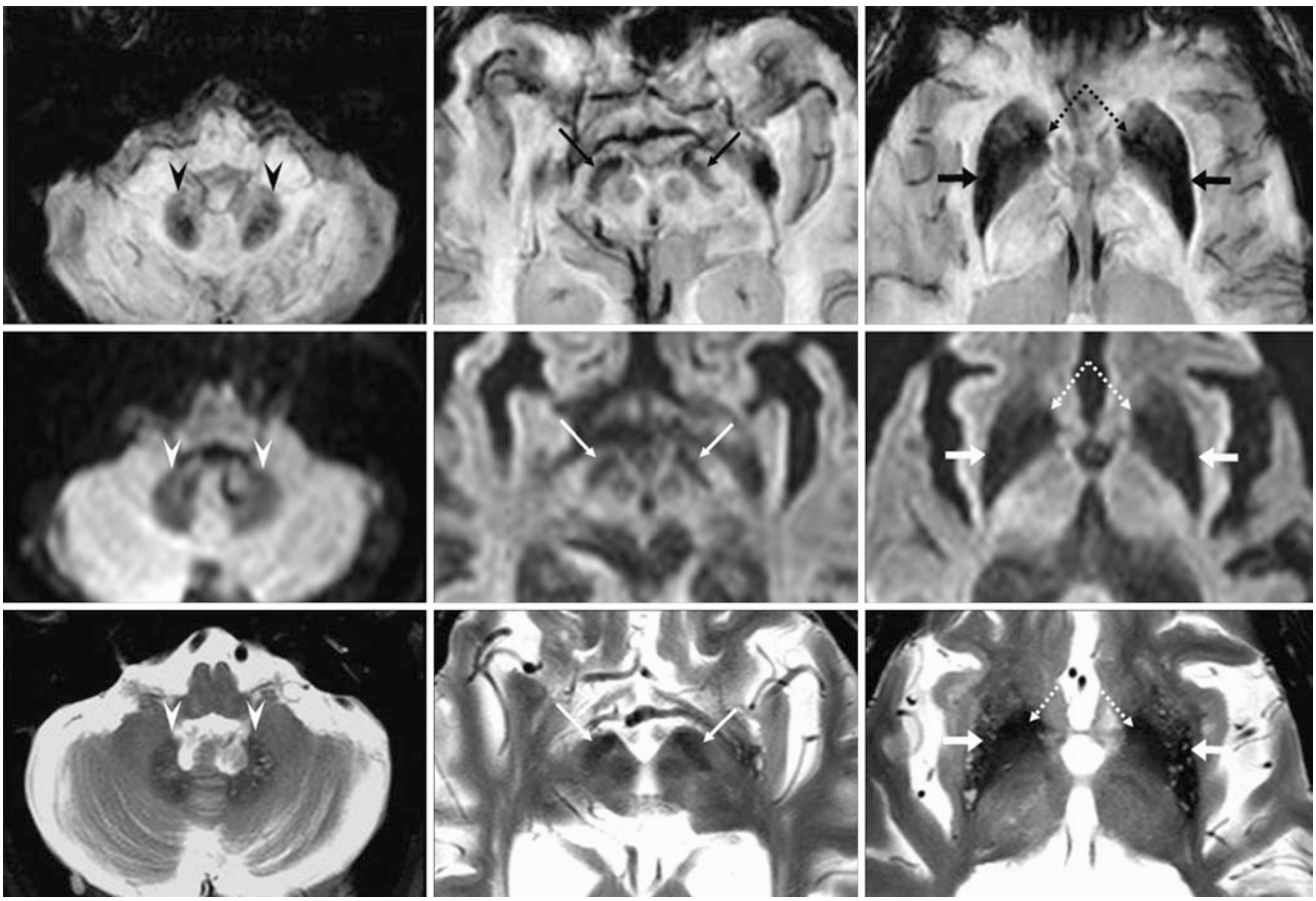

Fig. 20.25 A 91 year old with a negative 3T MRI performed for altered mental status. *Top row:* SWIs show iron deposition of the dentate nuclei (*arrowheads*), SN (*thin arrows*), and GP (*dotted arrows*). Both the GP and lentiform nuclei have become homogeneously dark bilaterally. *Middle row:* on DWI, there is dark signal throughout these nuclei owing to iron. *Bottom row:* T2WIs also depict prominent iron deposition within these nuclei. This case demonstrates how iron may appear on all three sequences

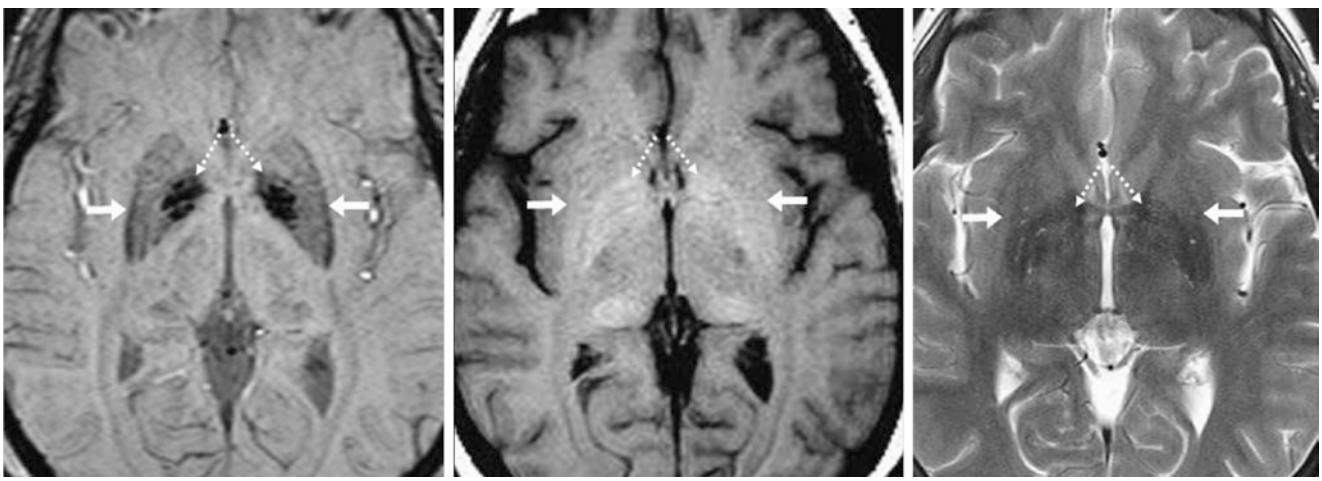

Fig. 20.26 Comparison case: Manganese (Mn) deposition within the GP. A 49 year old with chronic liver disease: On a 3T MRI, the GP (*dotted arrows*) appear dark on SWI (*left*), bright on T1WI (*middle*), and dark on T2WI (*right*). On a NECT (*not shown*), no calcium was noted within the GP, thus indicating paramagnetic manganese within the GP. As compared to the GP, the putamina (*arrows*) are less dark on SWI and less bright on T1WI, suggesting iron deposition within the GP rather than manganese. In liver disease, manganese selectively collects within the GP

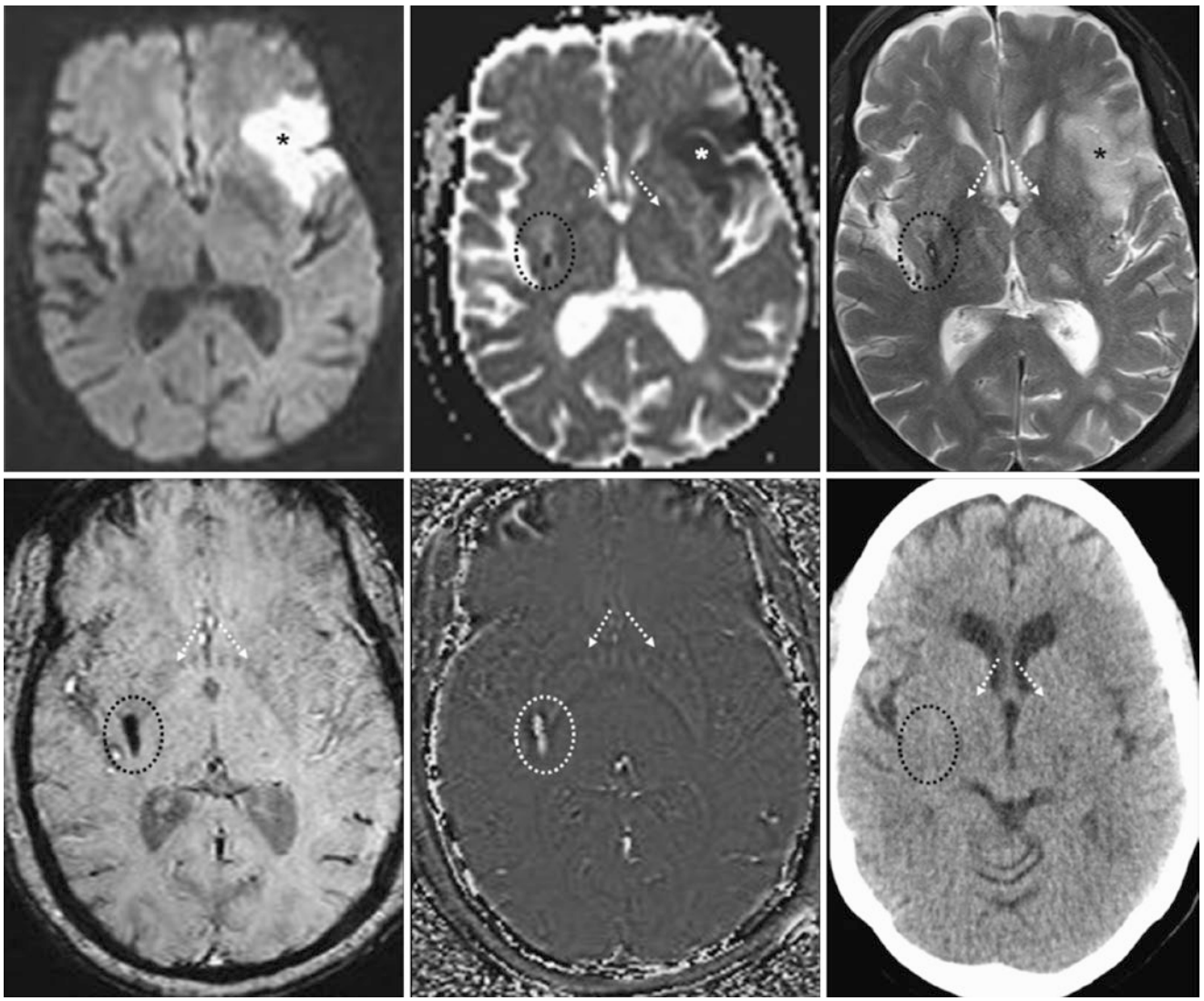

Fig. 20.27 Comparison case: acute stroke and hemosiderin**.** A 73 year old had an acute left MCA infarct (*) on 1.5T DWI MRI (*top left*), ADC map (*top middle*), and T2WI (*top right*). SWI (*bottom left*) also showed focal dark signal within the contralateral right putamen (*dotted circles*), with only scant iron deposition of the GP (*dotted arrows*). There was no infarct there on DWI. On a filtered phase map (*bottom middle*), the right putaminal abnormality exhibited bright signal because of paramagnetic iron from hemosiderin. On NECT (*bottom right*), no calcium was noted there

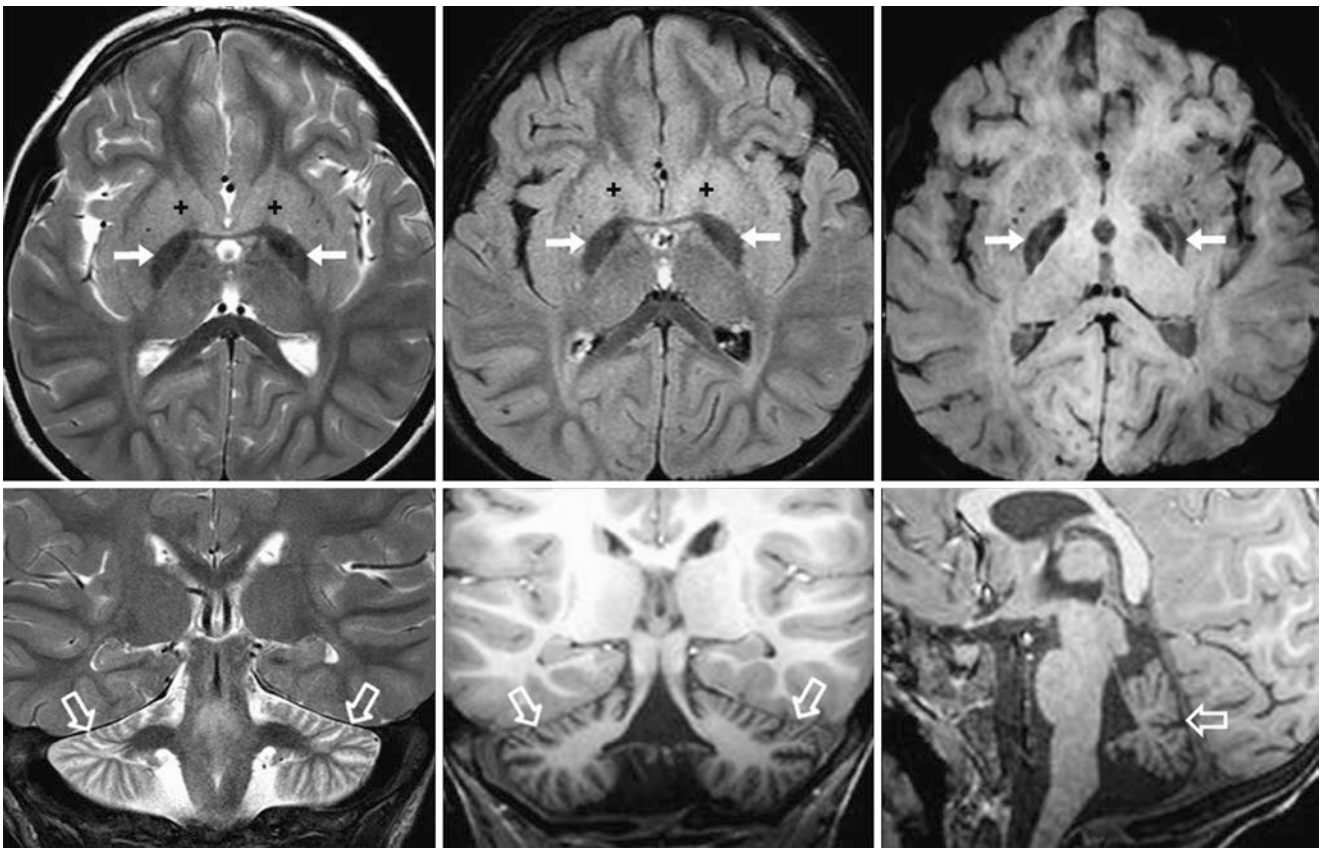

Fig. 20.28 Comparison case of NBIA: infantile neuraxonal dystrophy (INAD)**.** After being diagnosed with INAD as an infant, a 3 year old underwent a 3T MRI that showed abnormally dark GP (*arrows*) on T2WI (*top left*), FLAIR (*top middle*), and SWI (*top right*). There was severe cerebellar atrophy (*open arrows*), as noted on coronal T2WI (*bottom left*), T1WI (*bottom middle*), and sagittal T1WI (*bottom right*), consistent with the diagnosis of INAD. There was also probably mild edema within the caudate and putaminal nuclei (+), as shown on T2WI and FLAIR

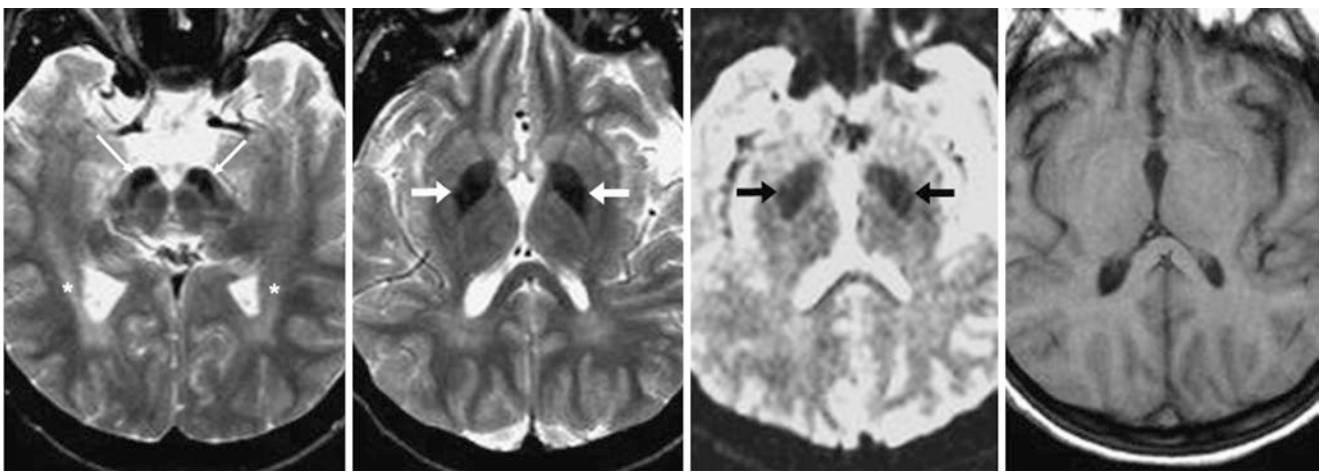

Fig. 20.29 Comparison case of NBIA: pantothenate kinase associated neurodegeneration (PKAN). A 14 year old female underwent a 1.5T MRI that showed abnormally dark GP (*arrows*) and SN (*thin arrows*) on T2WI (*left and left middle*) and on the gradient echo b = 0 map used to form a DWI (*right middle*), which is sensitive to susceptibility effects. T1WI (*right*) appeared normal. The findings were consistent with abnormally accelerated deposition of iron within those structures for the patient's age. Also, note subtle abnormalities within the optic radiations (*)

20.8 Susceptibility-Weighted Images: Artifacts Simulating Hemorrhages

Artifacts on SWI are many, and most are similar to the causes of susceptibility artifact on GE T2*WI. These include *phase wrapping* (i.e., aliasing because the field of view is too small), *poor filtering* of the phase map, *air-bone interface* (such as the calvarium, mastoid air cells, or where paranasal sinuses meet the skull base), *metal*, and *motion-related* artifacts. These can particularly simulate hemorrhage or microhemorrhage (MH) in post-trauma cases where the region of interest is in close proximity to such an air-bone interface or if there is a large amount of gas, such as near the floor of the anterior cranial fossa (just above the cribriform plate), mastoid air cells, the temporal lobe, or at the skull base. Additionally, motion-related artifacts not only degrade the image but may also generate pseudo-abnormalities. Such motion artifacts vary depending on the severity of patient motion; they generally appear as hazy or patchy regions of hypointensity and may simulate *hemorrhage*. Motion artifacts presumably simulate hemorrhage because of volume averaging of normal darker structures such as vasculature, cerebrospinal fluid, or gas with normal brighter parenchyma, resulting in regions of "hazy" intermediate signal (Fig. 20.30).

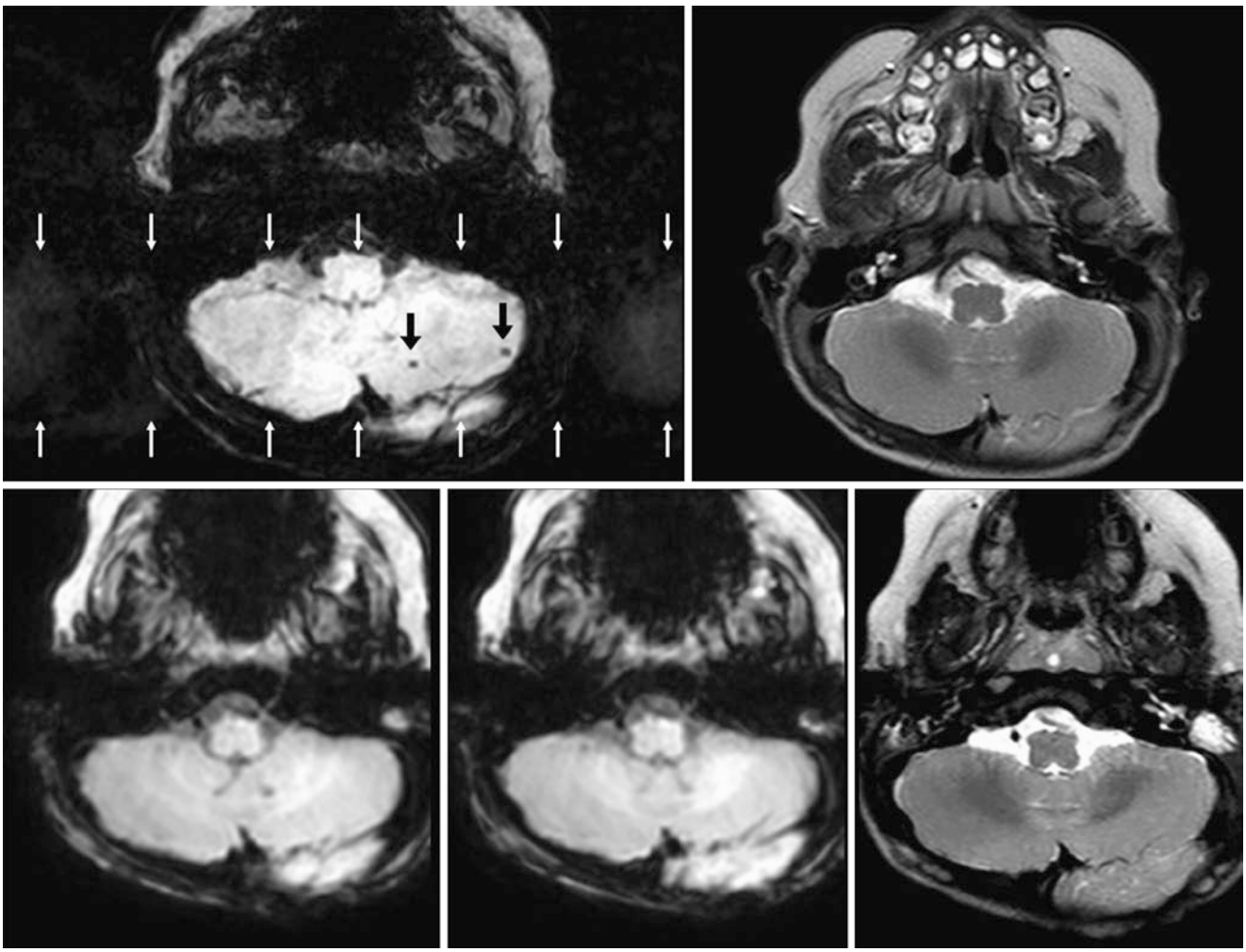

Fig. 20.30 Phase wrapping artifact. A 7 month old with hypotonia underwent a 1.5T MRI. On a 2-mm-thick SWI (*top left*) there were two punctate, dark foci (*arrows*) that simulated MHs. However, the SWI suffered moderate phase-related artifact (delineated by *thin arrows*), while T2WI (*top right*) appeared normal. On a repeat MRI at 3T performed at 12 months of age, both the SWIs (*bottom left and middle*) and T2WI (*bottom right*) appeared normal. The repeat MRI and the lack of a relevant clinical history for MH indicated that these were artifactual

20.9 Susceptibility-Weighted Images: Artifact from Air-Bone Interfaces and Gas

Artifacts from *air-bone interfaces* and *gas* can be quite prominent on SWI and are relatively proportional to the degree of aeration of the aerated bone (such as mastoid air cells or paranasal sinus). This can extend inward to obscure the adjacent cerebrum or cerebellum. It can particularly obscure the posterior fossa, the anterior fossa just above the ethmoids, or the temporal lobe just above the mastoids. Fast (turbo) spin-echo (FSE) T2WI is the most resistant to this artifact and can confirm suspected abnormalities. Turbo FLAIR is also relatively resistant to such artifacts as a result of the multiple 180° pulses that follow the initial 180° radio-frequency pulse and the second 90° pulse (Figs. 20.31, 20.32, 20.33, 20.34, 20.35, 20.36, 20.37, 20.38, 20.39, 20.40, 20.41, 20.42, 20.43, 20.44, and 20.45).

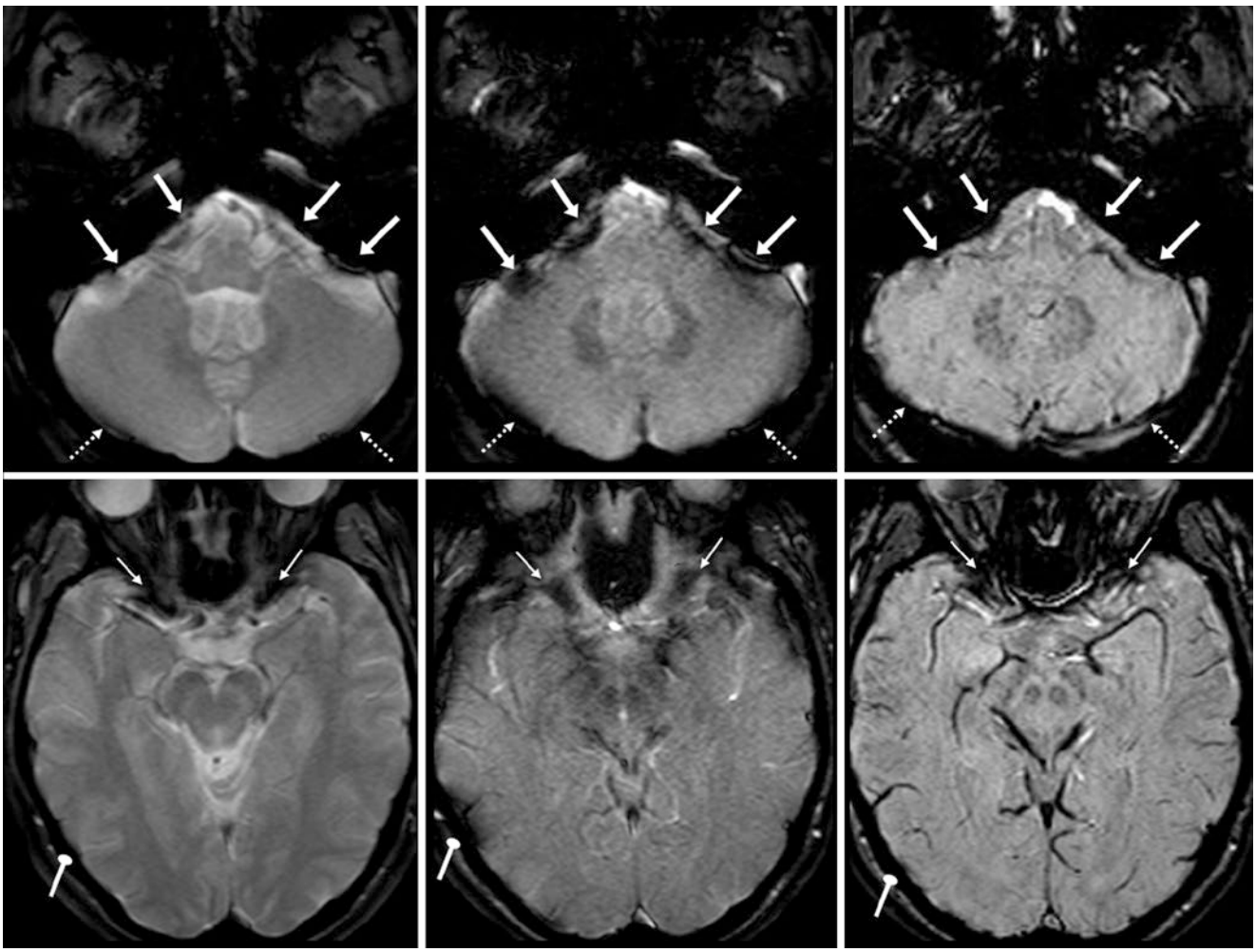

Fig. 20.31 Air-bone interface artifact from several locations**.** A 37 year old with headaches underwent 1.5T MRI with three separate 2-mm-thickness sequences: routine GE T2*WI (*left column*), modified GE T2*WI (*middle column*, with flip angle, TR, and TE identical to the SWI sequence) and the true three-dimensional SWI acquisition (*right column*). The modified T2*WIs suffer the presence of greater artifacts from phase loss (T2* affect) but are more sensitive in detecting hemorrhage than standard GE T2*WIs. *Top row:* as expected, T2* effects are most noticeable on the modified GE T2*WI, being most prominent at air-bone interfaces such as along the petrosal surfaces of the cerebellopontine angles (*arrows*) and the cerebellar convexities (*dotted arrows*) to a lesser degree. *Middle row:* note artifacts from the anterior clinoids (*thin arrows*). *Bottom row:* the T2* effects are also noticeable on the modified T2*WI along the cerebral convexities bilaterally (*circle tip arrows*). Note an incidental developmental venous anomaly (DVA, *arrowheads*), which is most visible on SWI, as SWI best depicts deoxygenated blood within the DVA due to paramagnetic deoxyhemoglobin

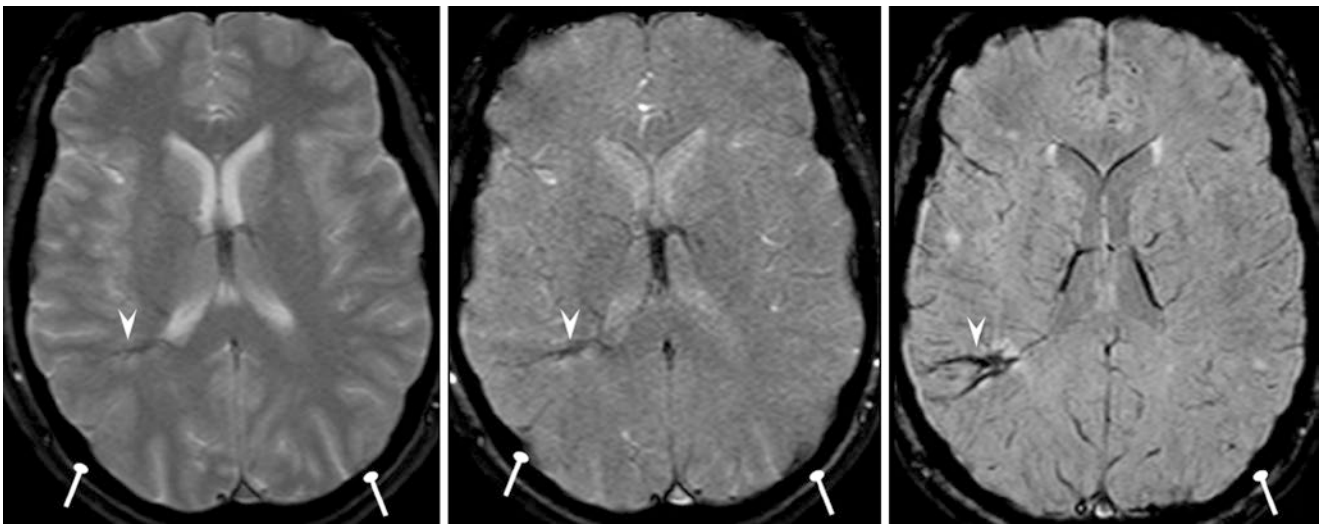

Fig. 20.31 (continued)

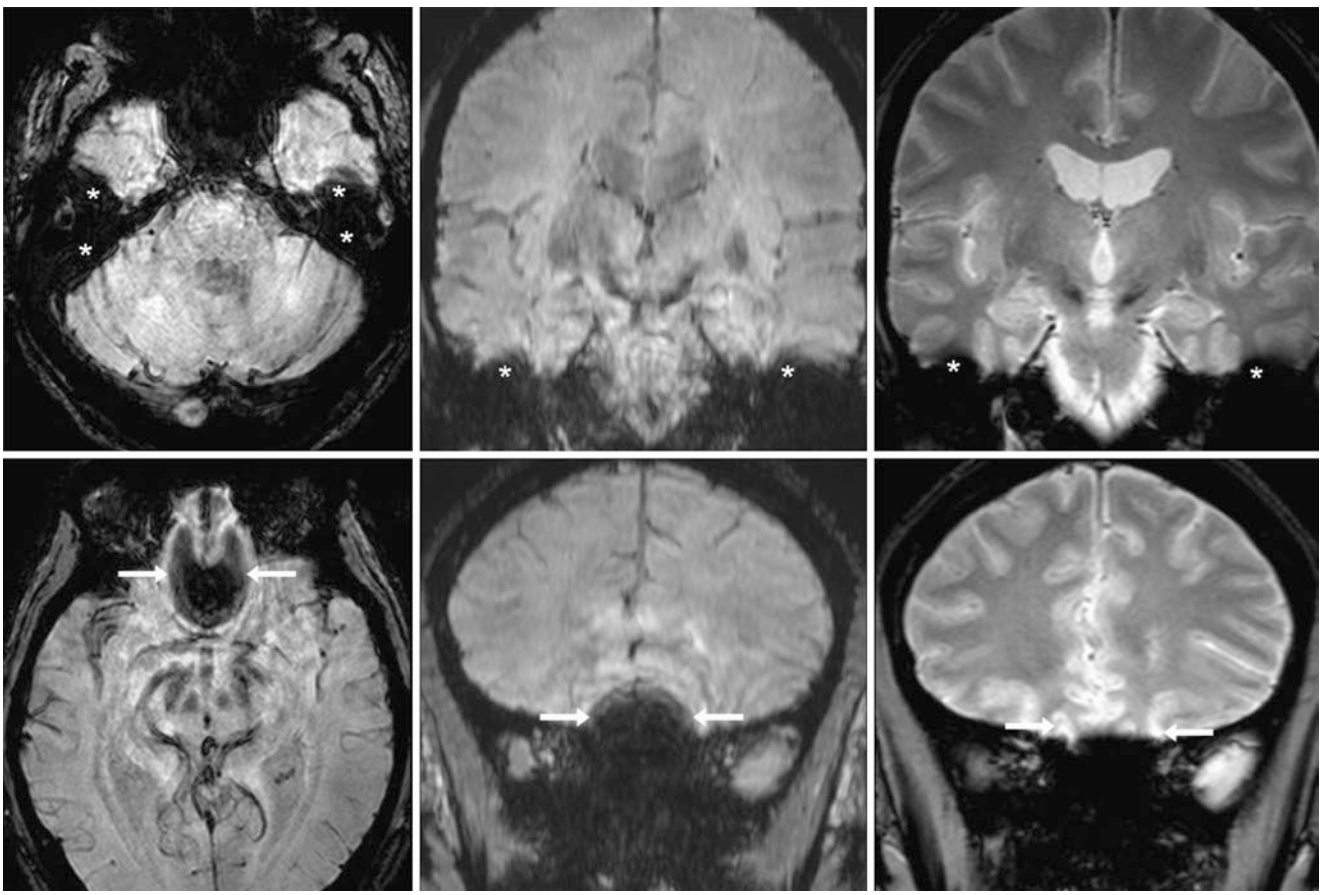

Fig. 20.32 Air-bone interface artifact from the mastoid air cells**.** A 47 year old was found to have prominent T2* effects just above the mastoid air cells (*) on 1.5T MRI 3-mm-thick axial (*top left*) and coronal (*top middle*) SWI and on coronal T2*WI (*top right*), obscuring the inferior temporal gyri. Also, artifact from air within the ethmoid air cells (*arrows*) obscures the orbitofrontal gyri and anterior cranial fossa on 3-mm thick axial (*bottom left*) and coronal (*bottom middle*) SWIs; the artifact is less severe on coronal T2*WI (*bottom right*)

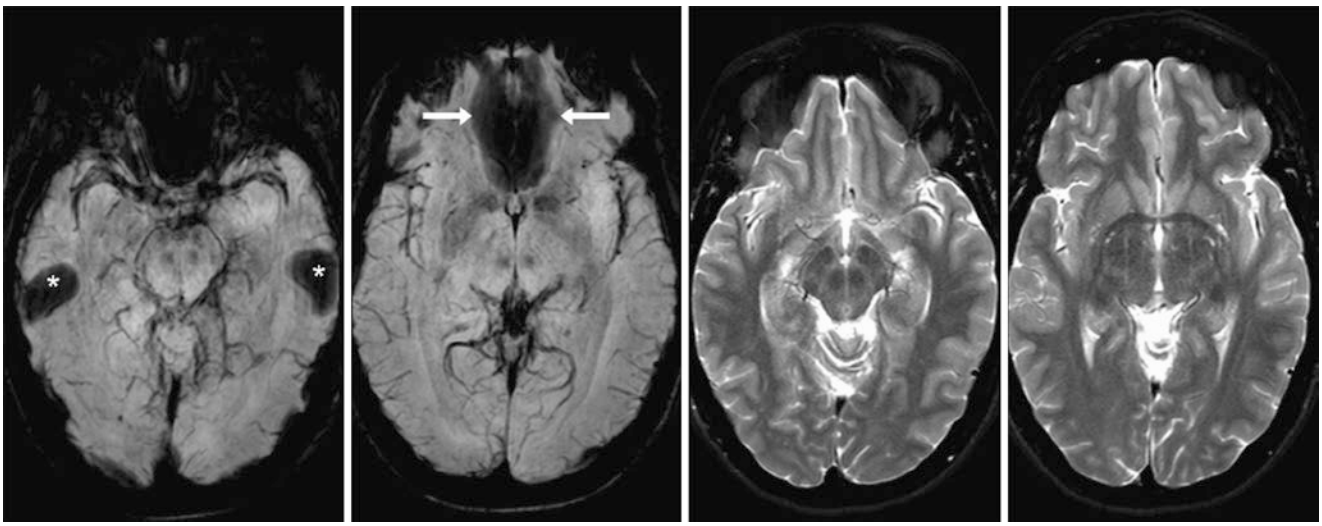

Fig. 20.33 Air-bone interface artifact from the mastoid air cells and ethmoid sinuses**.** A 39 year old underwent a 3T MRI with 10-mm-thick SWI minIPs (*left two images*) that showed that T2* effects are most prominent at air-bone interfaces such as just above the mastoids (*) and ethmoid air cells (*arrows*). On SE T2WI at the same levels (*right two images*), such artifacts are not present. On SWI, such artifacts appear worse with greater slice thickness

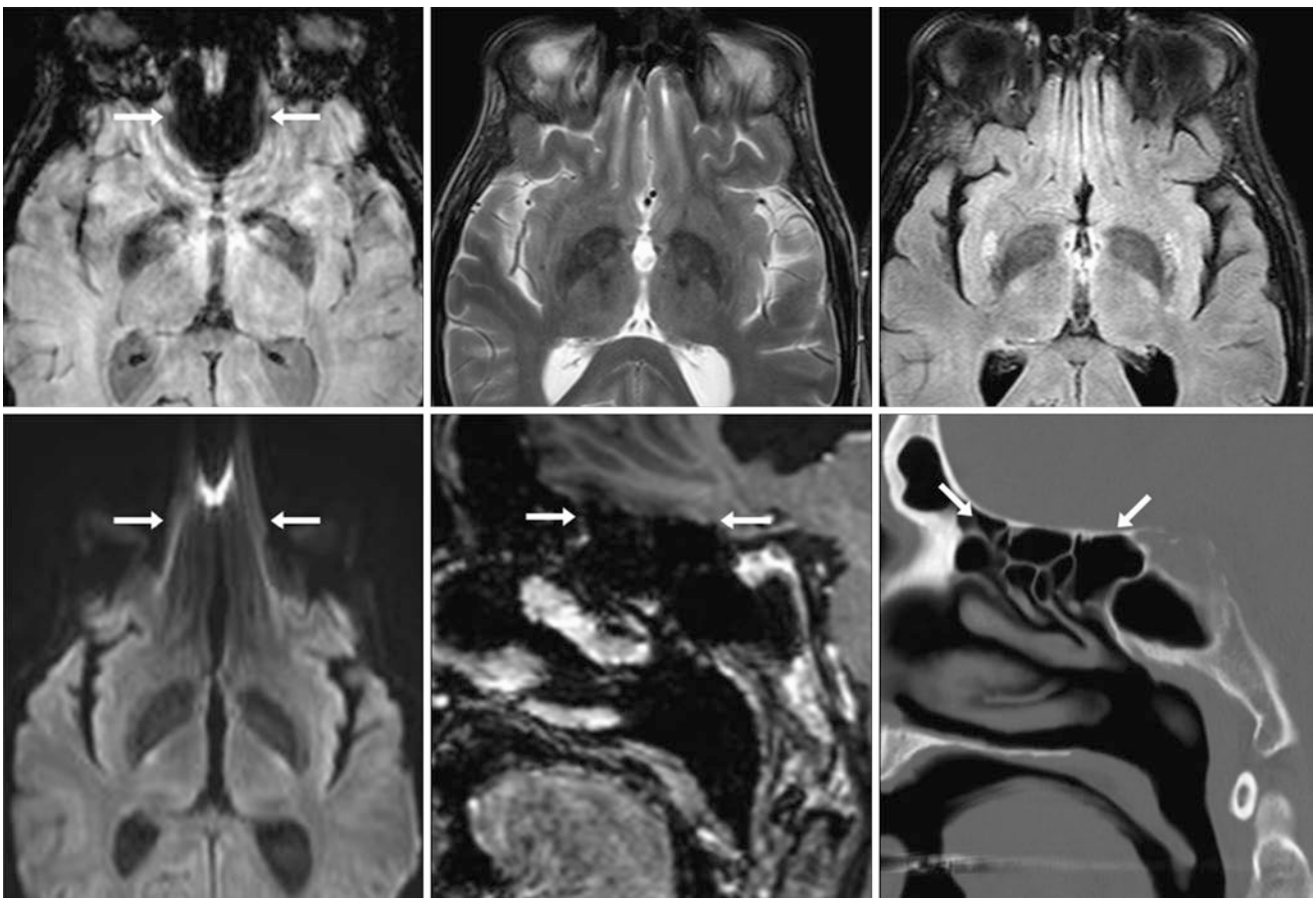

Fig. 20.34 Air-bone interface artifact from the ethmoid air cells**.** A 57 year old with prominent T2* effects just above the ethmoid air cells (*arrows*) on 3-mm-thick SWI at 3T (*top left*) but not present on SE T2WI (*top middle*) or FLAIR (*top right*), owing to the suppression of artifact from multiple echoes (turbo factor). Such artifact also affects DWI (*bottom left*). The source of artifact from the ethmoid air cells is illustrated on postcontrast sagittal GE T1WI (*bottom middle*) and on sagittal NECT reformats (*bottom right*)

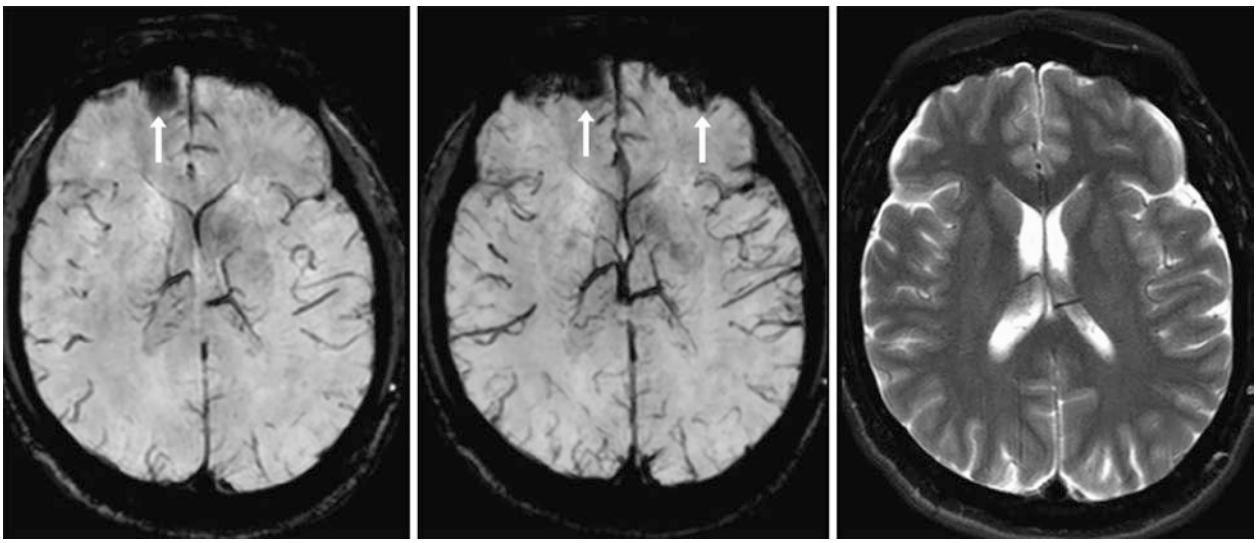

Fig. 20.35 Air-bone interface artifact from the frontal sinuses**.** A 49 year old with trauma having asymmetric T2* effect from right ethmoid and frontal sinus gas (*arrows*) on 2-mm-thick SWI at 1.5T (*left*), which could simulate hemorrhage from an orbitofrontal contusion. However, on 12-mm-thick sliding minIP (*middle*), the artifact appears bilateral. On a SE T2WI (*right*), the artifact disappears owing to the relative suppression of susceptibility effect by the multiple echoes (turbo factor)

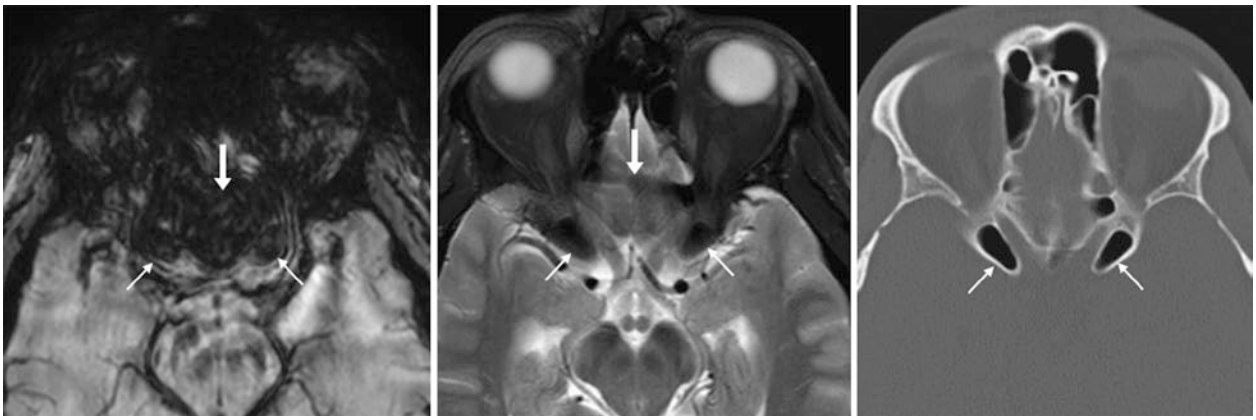

Fig. 20.36 Air-bone interface artifact from anterior clinoid processes**.** A 54 year old with T2* effects bilaterally due to aerated anterior clinoids (*thin arrows*), as shown on 2-mm-thick SWI at 3T (*left*), which are present to a lesser degree on T2WI (*middle*). NECT (*right*) confirms the aerated clinoid processes. Also note the orbitofrontal artifact (*arrows*) caused by aeration of the ethmoid air cells

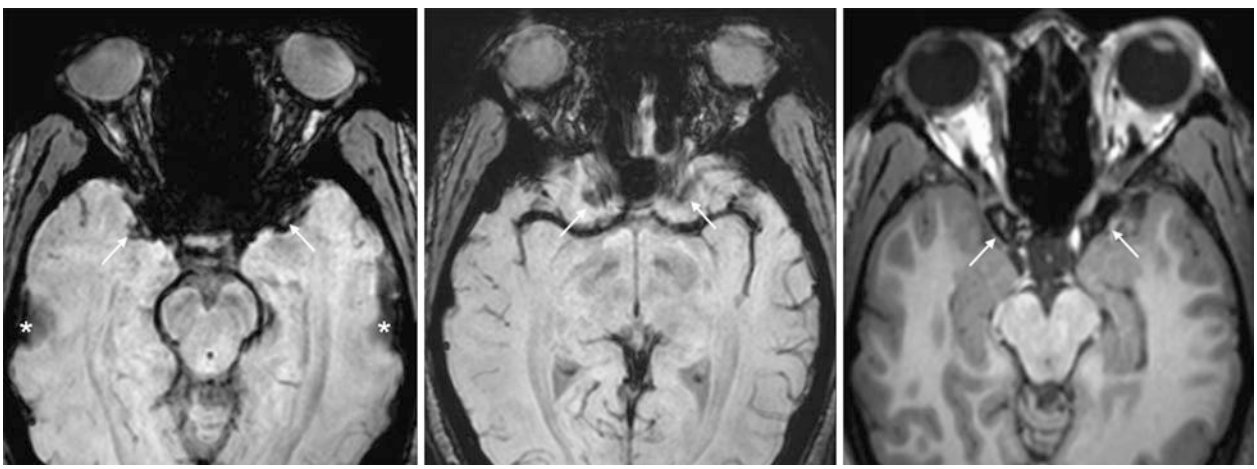

Fig. 20.37 Air-bone interface artifact from anterior clinoid processes**.** A 24 year old with T2* effects bilaterally caused by aerated anterior clinoids (*thin arrows*) as demonstrated on 2-mm-thick SWI at 3T (*left and middle*), and present to a lesser degree on GE T1WI (*right*). Also, note artifact along the temporal convexities (*), arising from aeration of the top of the mastoid air cells

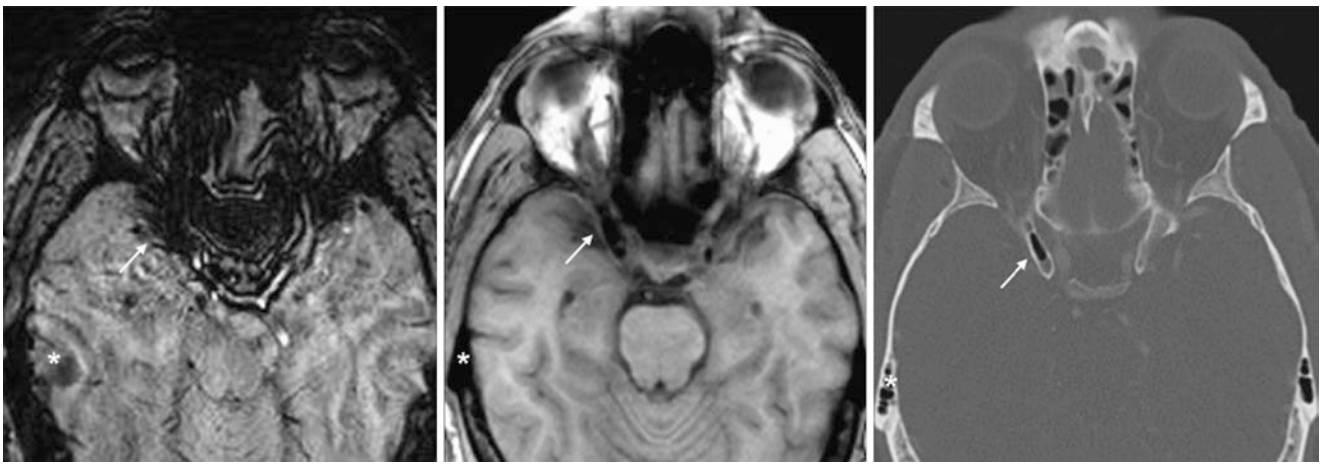

Fig. 20.38 Air-bone interface artifact from an anterior clinoid process. A 56 year old with asymmetric T2* effects from a unilaterally aerated right anterior clinoid process (*thin arrows*) on 2-mm-thick SWI at 3T (*left*) and present to a lesser degree on GE T1WI (*middle*). NECT (*right*) confirms the aerated right anterior clinoid process. Also, note artifact caused by aeration of the top of the right mastoid air cells (*)

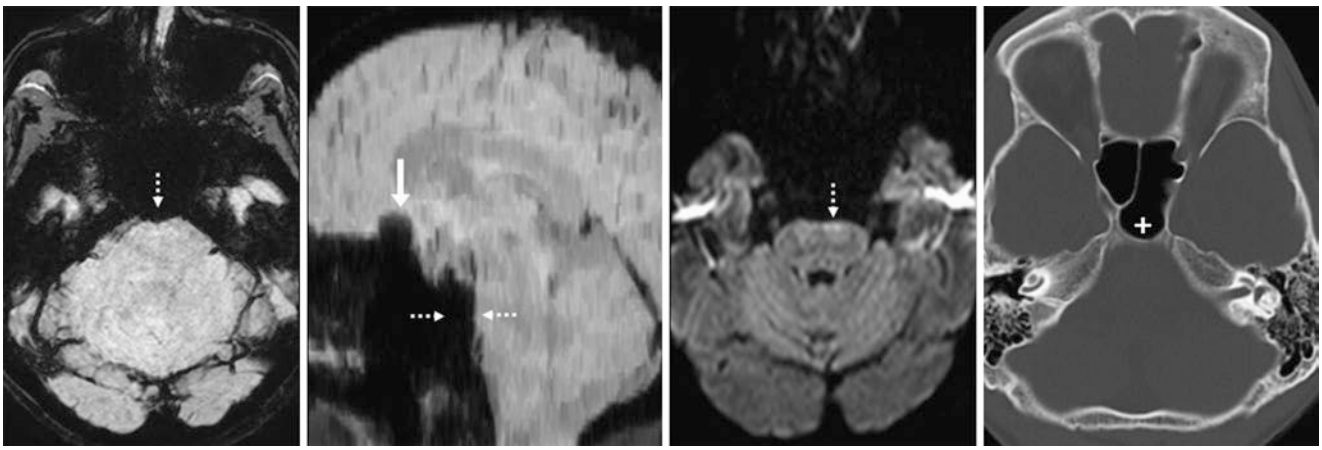

Fig. 20.39 Air-bone interface artifact from the sphenoid sinus. A 34 year old with T2* effects that protrude into the prepontine cistern and brainstem (*dotted arrows*) from sphenoid sinus air, as demonstrated on 2-mm-thick SWIs at 1.5T in axial (*left*) and 5-mm-thick sagittal (*left middle*) planes. DWI (*right middle*) suffers from a similar artifact along the ventral brainstem. NECT (*right*) confirms sinus air (+), with a thin posterior sinus wall. Also, note the artifact arising from aeration of the top of the ethmoid air cells (*arrow*)

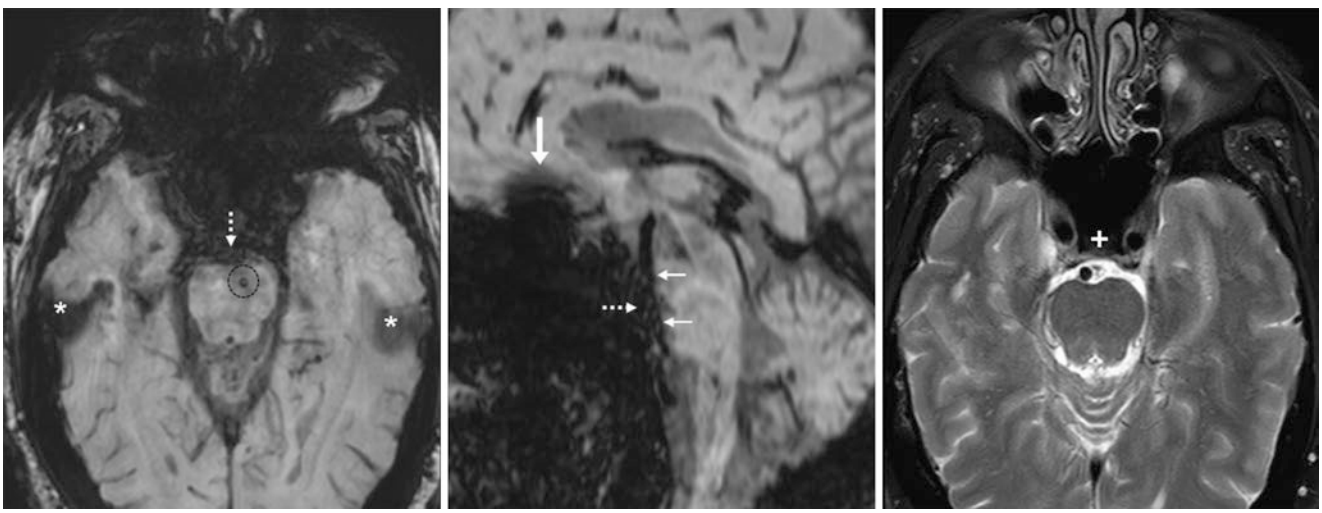

Fig. 20.40 Air-bone interface artifact from the sphenoid sinus**.** A 54 year old with T2* effects that protrude into the prepontine cistern (*dotted arrows*) from sphenoid sinus air, as shown on 2-mm-thick SWIs at 3T in axial (*left*) and sagittal (*middle*) planes and not present on T2WI (*right*), which shows the sinus air (+). On SWI, the air obscures the basilar artery (*thin arrows*). Also, note artifact from aeration at the top of the mastoids (*) and ethmoid air cells (*arrows*) as well as a true pontine MH (*circle*)

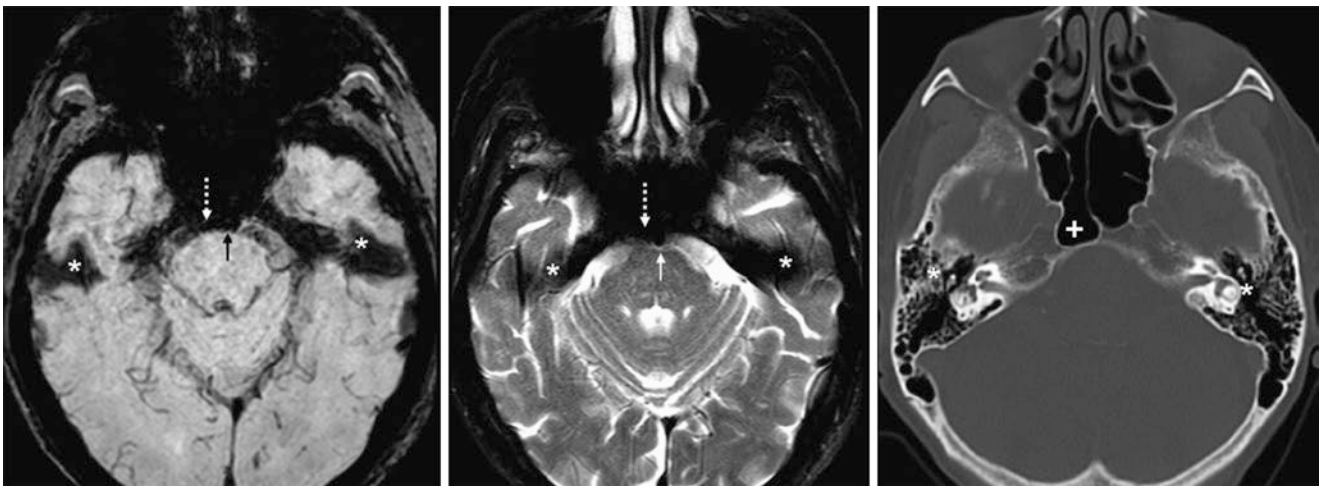

Fig. 20.41 Air-bone interface artifact from the sphenoid sinus**.** An 84 year old with T2* effects that extend into the prepontine cistern (*dotted arrows*), which arise from air within the sphenoid sinus, as demonstrated on 2-mm-thick SWI at 1.5T (*left*). This artifact is present to a lesser degree on SE T2WI (*middle*) but still obscures the basilar artery flow void (*thin arrows*). NECT (*right*) confirms an aerated sphenoid sinus (+) with a thin posterior wall. Also note artifact arising from aeration of the top of the mastoids (*)

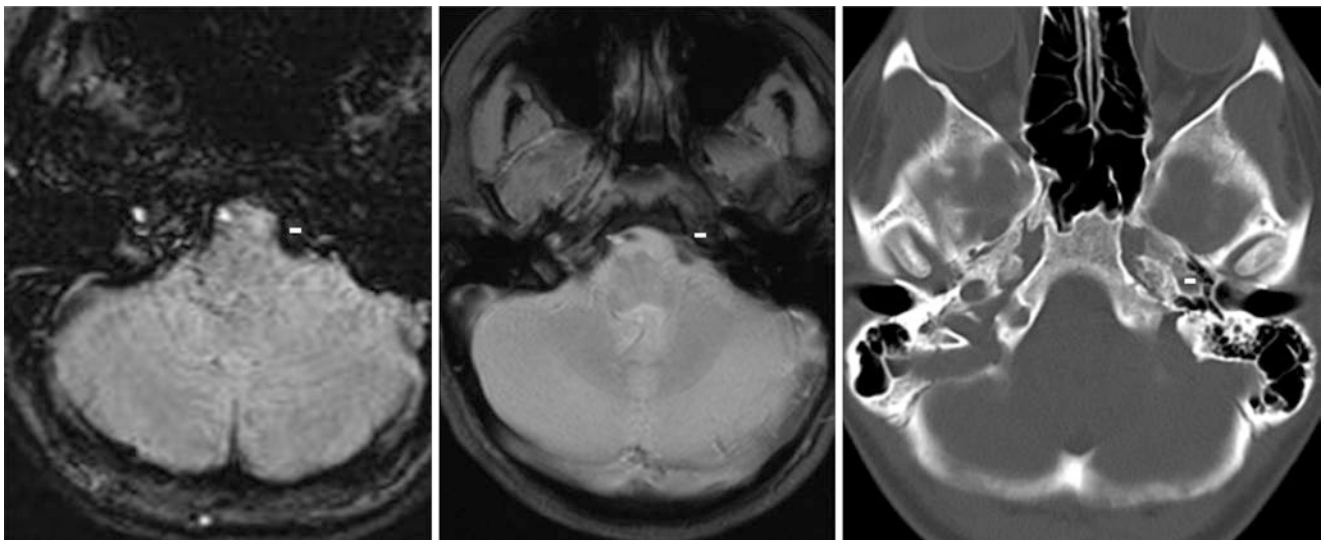

Fig. 20.42 Air-bone interface artifact from a petrous apex**.** A 25 year old with T2* effects at the skull base protruding into the left side of the cerebellopontine angle and medulla (–) from normal left petrous apex aeration on 2-mm-thick SWI at 1.5T (*left*) and on GE T2* WI (*middle*). NECT (*right*) confirms the petrous apex air (–). Note that the artifact is greater on SWI than GE T2*WI in this case. On SWI, this could simulate an enlarged flow void from an aneurysm or calcifications within a meningioma

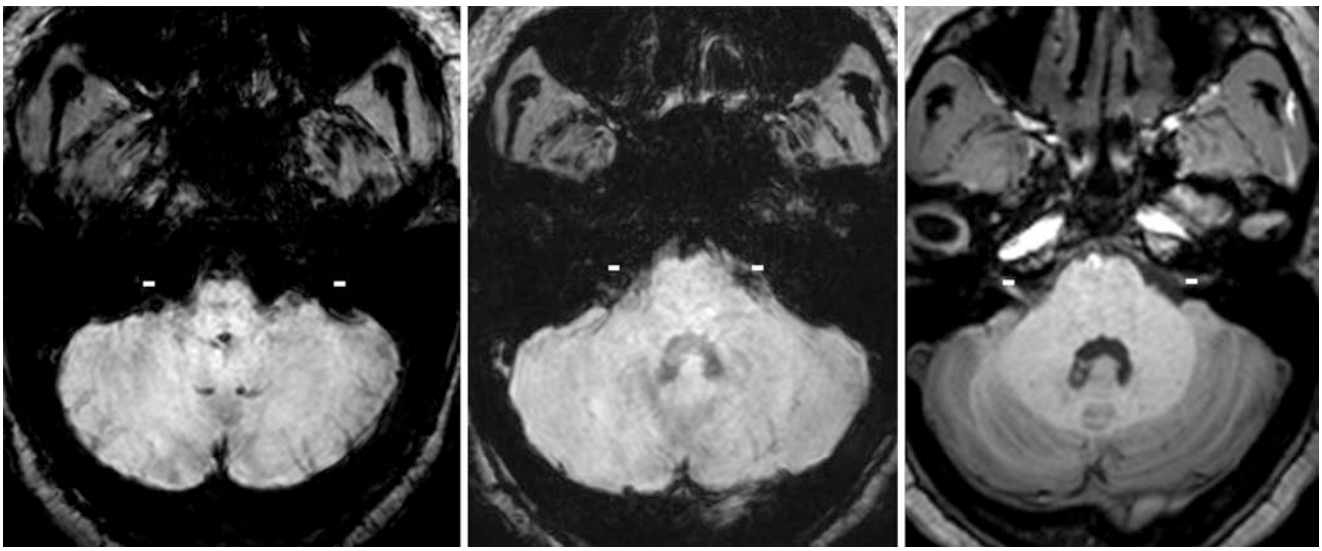

Fig. 20.43 Air-bone interface artifact from the petrous apices and mastoids**.** A 24 year old with T2* effects at the skull base (–) that obscure the internal auditory canals bilaterally, arising from normal air cell aeration of the petrous apices on 2-mm-thick SWIs at 3T (*left and middle*). This artifact is much more attenuated on GE T1WI (*right*). On SWI, such an artifact can either simulate subarachnoid hemorrhage or can mimic flow voids from aneurysms. Such susceptibility artifacts also obscure adjacent normal anatomy

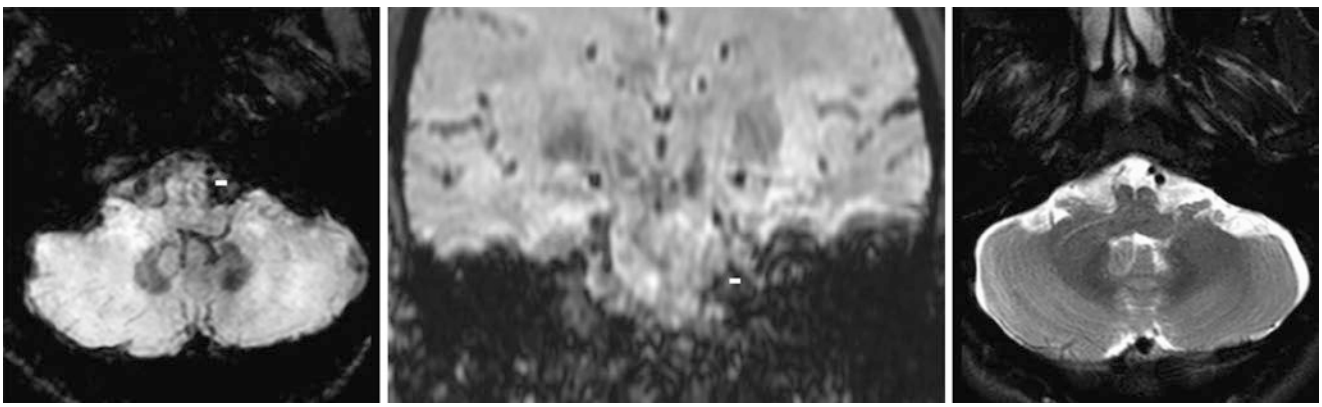

Fig. 20.44 Air-bone interface artifact from a petrous apex. A 49 year old with T2* effects at the skull base (–) that mimic a mass compressing the left side of the medulla, as demonstrated on 2-mm-thick SWI at 1.5T with axial (*left*) and coronal (*middle*) reformats; however it is not present on SE T2WI (*right*). Such artifact can simulate hemorrhage, flow voids from an aneurysm, or a calcified extra-axial mass

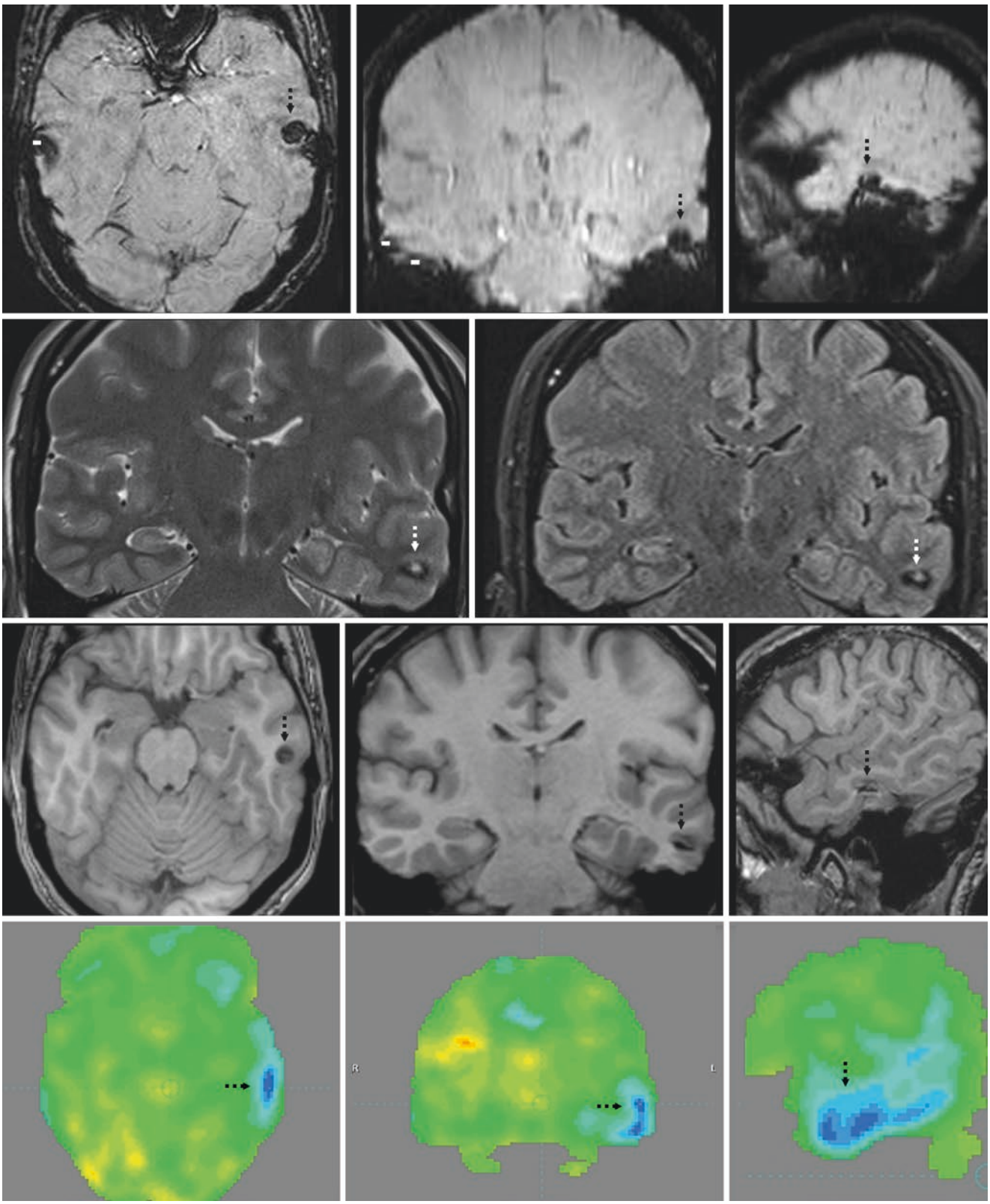

Fig. 20.45 Comparison case of focal temporal hemorrhage simulating air-bone interface artifact**.** *Top row:* a 44 year old with seizures underwent a 3T MRI to determine the cause. On SWI, focal left temporal T2* effect (*dotted arrows*) was noted just above the mastoids, initially thought to be air-bone interface artifact from mastoid aeration. On the right, note normal T2* effect from air-bone interface artifact just above the mastoids (–). *Second row:* However, on coronal T2WI (*left*) and FLAIR (*right*), which are relatively resistant to susceptibility artifact due to the multiple fast spin echo technique (i.e., turbo spin echo), the hemosiderin stain is evident, with centrally mildly hyperintense signal. *Third row*: On multiplanar spoiled GE T1WI, the hemosiderin stain is confirmed. *Bottom row:* On ^{18}F-FDG PET, there is hypometabolism with the left temporal focus, likely further confirming that the left temporal focus was the site of seizure origin. The findings likely represented a cavernoma versus being related to the patient's remote history of closed head injury

20.10 Susceptibility-Weighted Images: Artifacts from Metal Extensively Obscuring the Cranium

Susceptibility artifacts from metal are typically much more extensive and overt on SWI as compared to those from air-bone interfaces and gas. Such artifacts can extend so far inward so as to not only obscure adjacent cerebrum or cerebellum but also can render certain regions that are nondiagnostic for interpretation such as the posterior fossa and the anterior fossa just above the ethmoids (such as with braces or other oral or odontogenic implants). The degree of artifact becomes greater with increasing field strength. Again, FSE T2WI and turbo FLAIR are the more resistant sequences to this artifact but can still be nondiagnostic in cases with large amounts of adjacent metal (Figs. 20.46, 20.47, 20.48, 20.49, and 20.50).

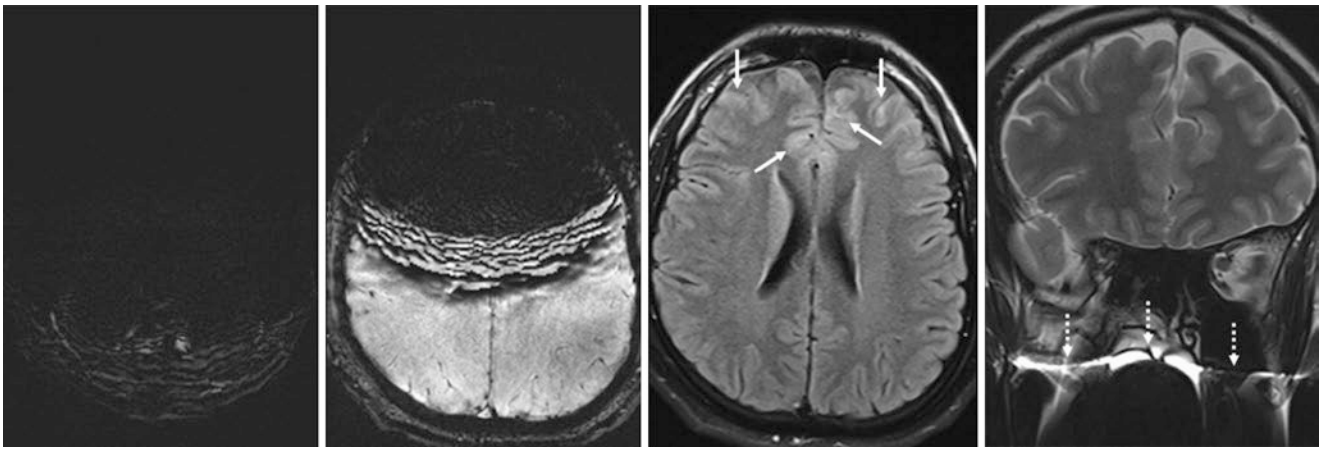

Fig. 20.46 Metal-related artifact**.** A 22 year old with dental amalgam that caused artifact that completely obscured the skull base at the level of the medulla (*left*) and most of the cranium at the level of the bodies of the lateral ventricles (*left middle*) on axial SWI. At that same level, the artifact is not visualized on FLAIR (*right middle*), although it causes "pseudo-hyperintensity" of the frontal cortices (*arrows*). Coronal SE T2WI (*right*) shows the artifact's source (*dotted arrows*)

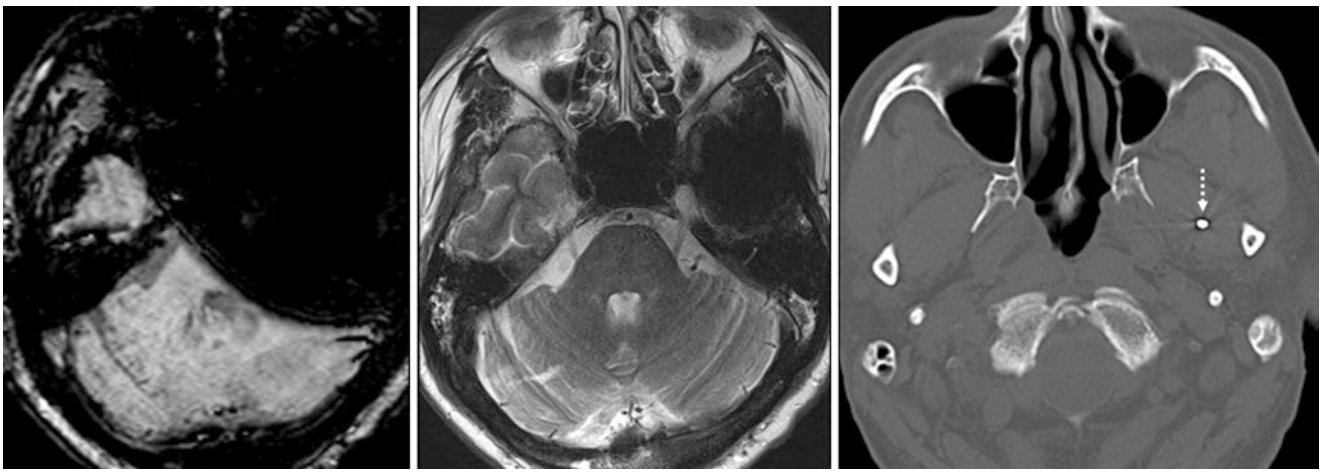

Fig. 20.47 Metal-related artifact**.** A 62 year old with susceptibility artifact that obscures most of the left middle cranial fossa and brainstem on SWI (*left*), which is much less extensive on SE T2WI (*middle*). A NECT (*right*) revealed the source of artifact to be a metallic foreign body (i.e., a "BB" pellet) that is embedded within the left pterygoid musculature (*dotted arrow*)

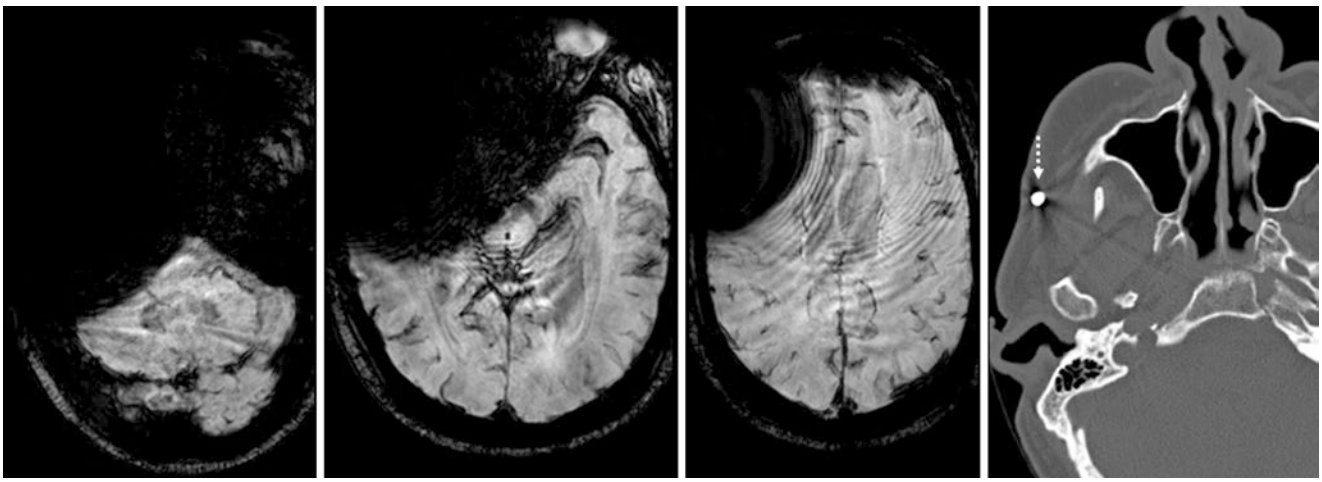

Fig. 20.48 Metal-related artifact**.** A 27 year old in whom an artifact entirely obscures the right skull base and most of the frontal lobe on SWI (*left three images*). A NECT (*right*) confirms that the source of artifact is a "BB" pellet overlying the right zygoma (*dotted arrows*)

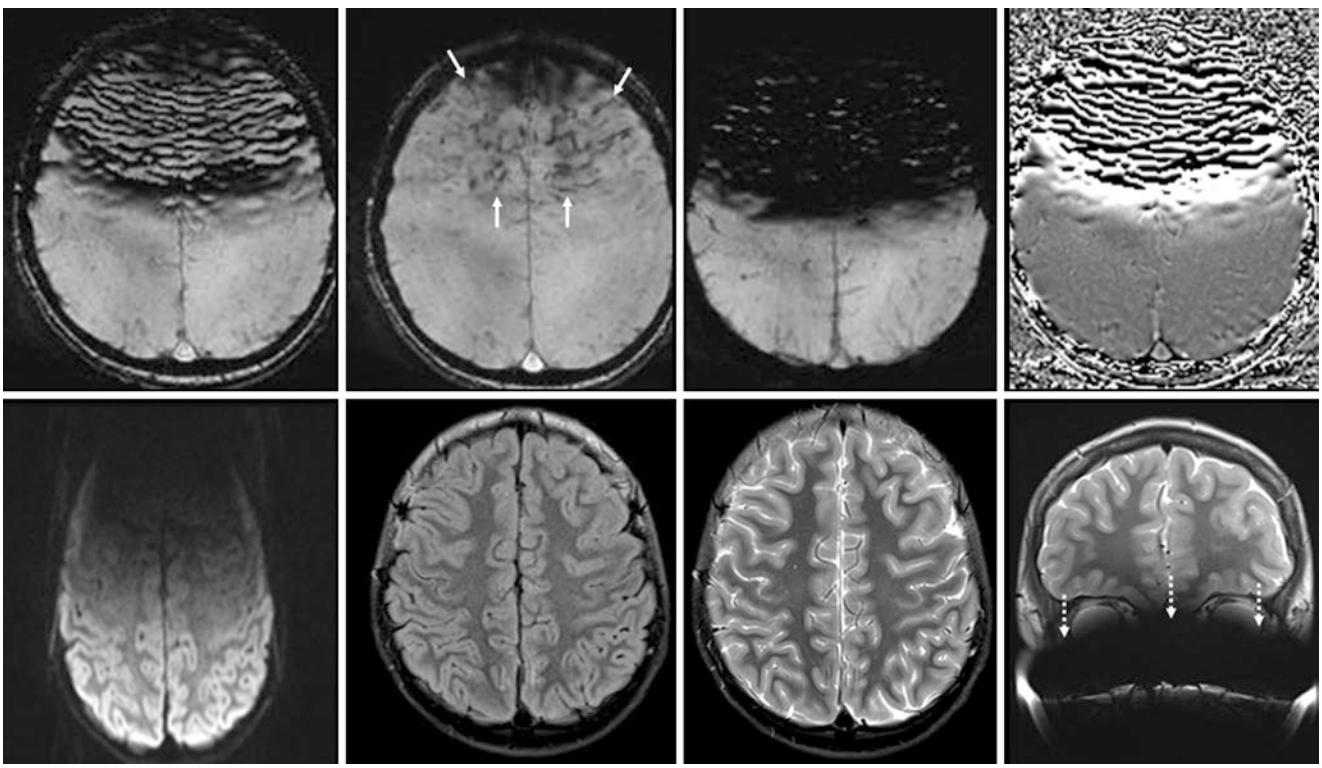

Fig. 20.49 Metal-related artifact**.** A 13 year old with artifact from dental amalgam that obscured the frontal lobes on 2-mm-thick (*top left*), magnitude (*top, left middle*), and 10-mm-thick (*top, right middle*) SWIs, with a corresponding phase map (*top right*). This mimics subarachnoid hemorrhage (*thin arrows*) on the magnitude image, which does not incorporate phase data. Note the "stretching" of brain in the anteroposterior direction on DWI (*bottom left*), while FLAIR (*bottom, left middle*) and T2WI (*bottom, right middle*) are normal. A coronal SE T2WI (*bottom right*) depicts the artifact's source (*dotted arrows*)

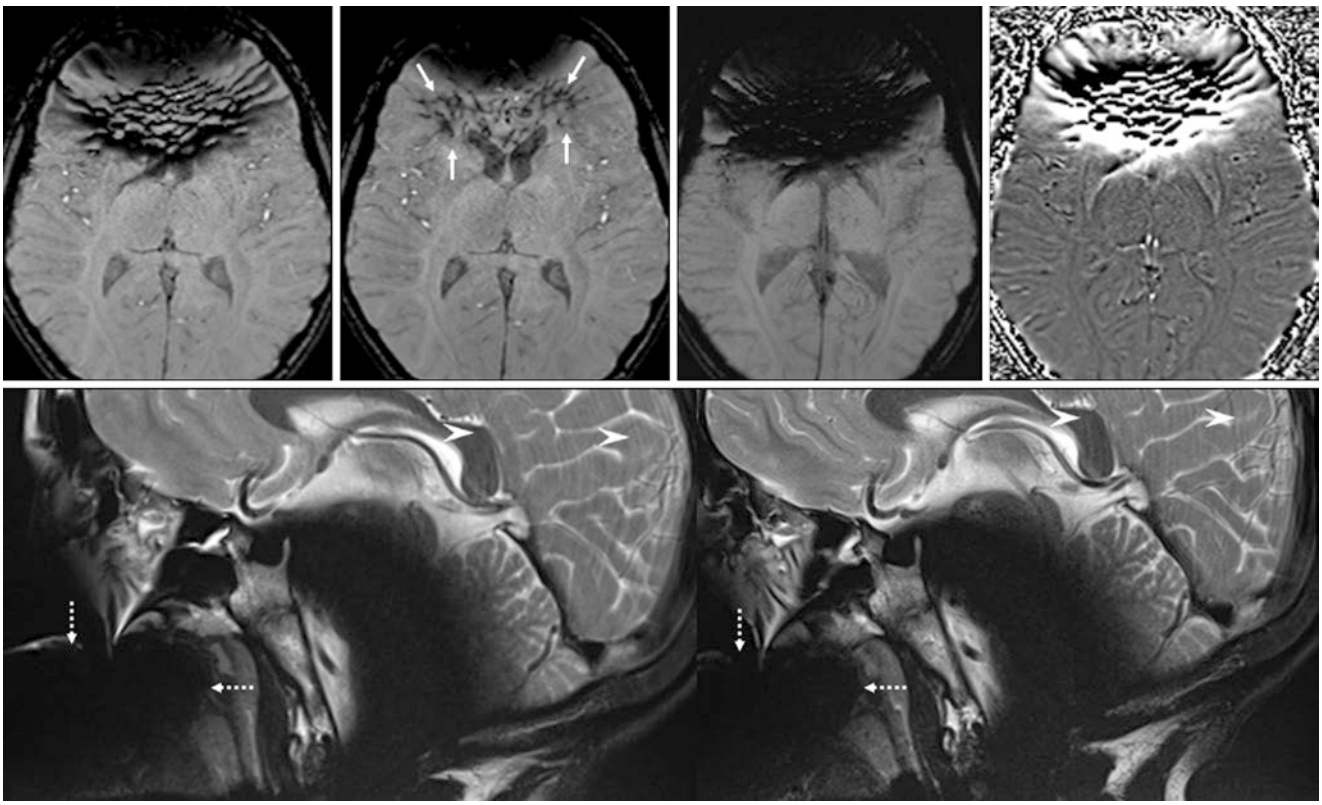

Fig. 20.50 Metal-related artifact**.** An 8 year old with artifact from dental amalgam that obscured the frontal lobes on 2-mm-thick (*top left*), magnitude (*top, left middle*), and 10-mm-thick (*top, right middle*) SWIs, with a phase map (*top right*). This mimics hemorrhage (*thin arrows*) on the magnitude image. Sagittal SE T2WIs (*bottom row*) show the source of the artifact (*dotted arrows*) with mild motion artifact as well (*arrowheads*). Even on SE T2WI, the posterior fossa is completely obscured

20.11 Susceptibility-Weighted Images: Motion-Related Artifact

Motion-related artifact is usually evident on SWI, since it is most often present on other sequences. However, mild motion may not be as evident on SWI as other sequences (such as T2WI), since the finding of darker deoxygenated blood within venous structures can be blunted (i.e., not as dark as expected), which can be overlooked on SWI. Other findings that indicate motion, such as poor visualization of sulci and curved artifacts following the contour of the cranium, can also suggest compromise of images caused by motion. It is important to note the presence of such artifacts because they can compromise the detection of hemorrhage, particularly MHs (Figs. 20.51, 20.52, 20.53, 20.54, 20.55, and 20.56).

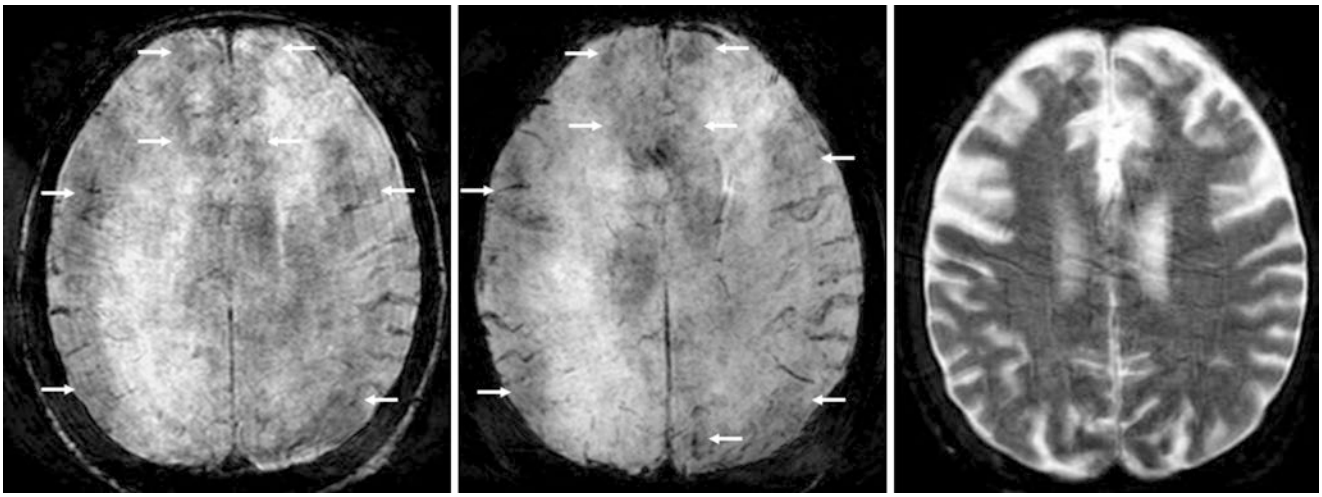

Fig. 20.51 Motion-related artifact**.** A 65 year old with diffuse, moderate artifact from motion on 2-mm- (*left*) and 10-mm-thick (*middle*) SWIs at 1.5T as well as on SE T2WI (*right*). This patchy artifact presumably relates to volume averaging of parenchyma with darker veins, CSF, or gas and obscures normal dark veins (deoxygenated blood). FLAIR (*not shown*) was not affected

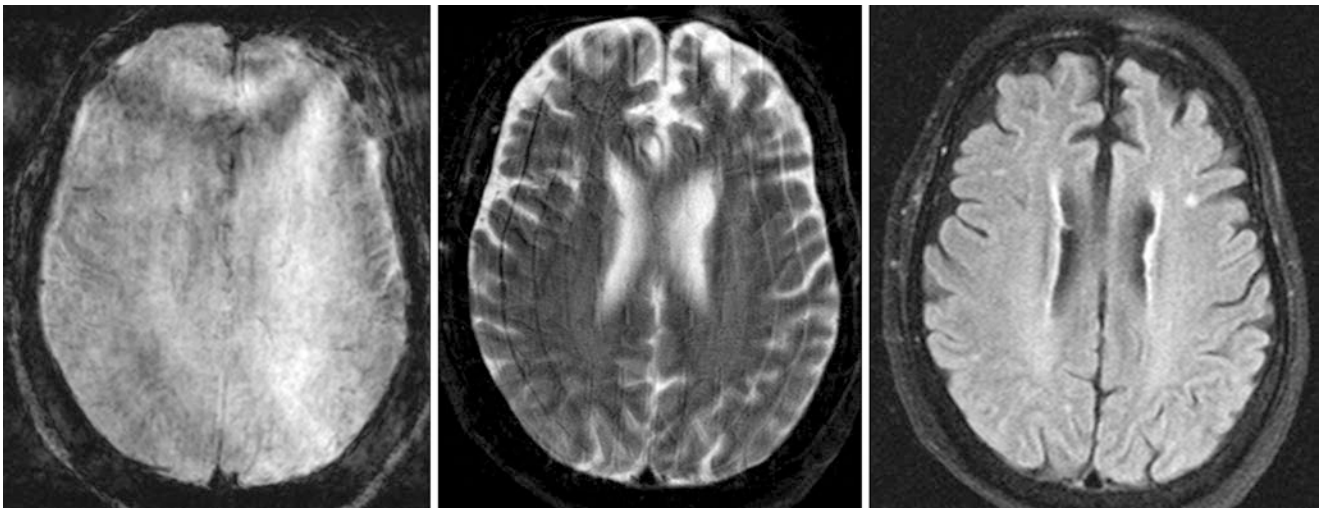

Fig. 20.52 Motion-related artifact**.** A 64 year old with moderate-severe artifact from motion on 2-mm-thick (*left*) and on SE T2WI (*middle*) SWI at 1.5T. The artifact is hazy and obscures the normally dark veins (deoxygenated blood). FLAIR (*right*) was not affected

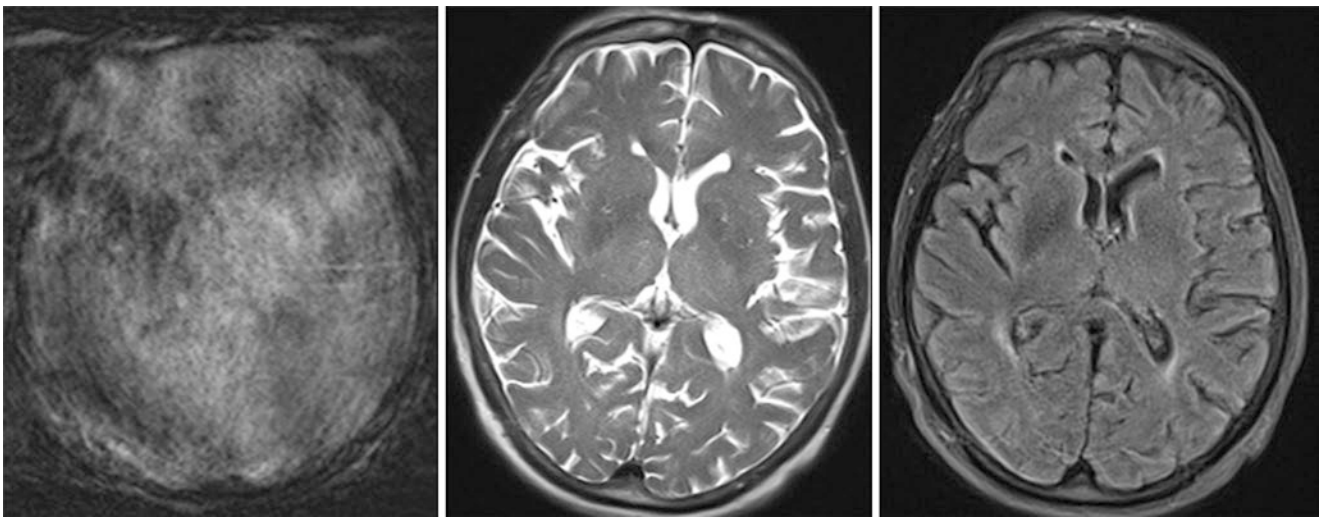

Fig. 20.53 Motion-related artifact**.** A 67 year old with a severely degraded image on 2-mm-thick SWI (*left*) caused by a severe degree of motion-related artifact. This is mitigated to some degree on ultrafast HASTE-T2WI (*middle*) and on motion-corrected (BLADE) FLAIR (*right*) images at 3T. The trade-off is that these latter two sequences have a lower signal-to-noise ratio

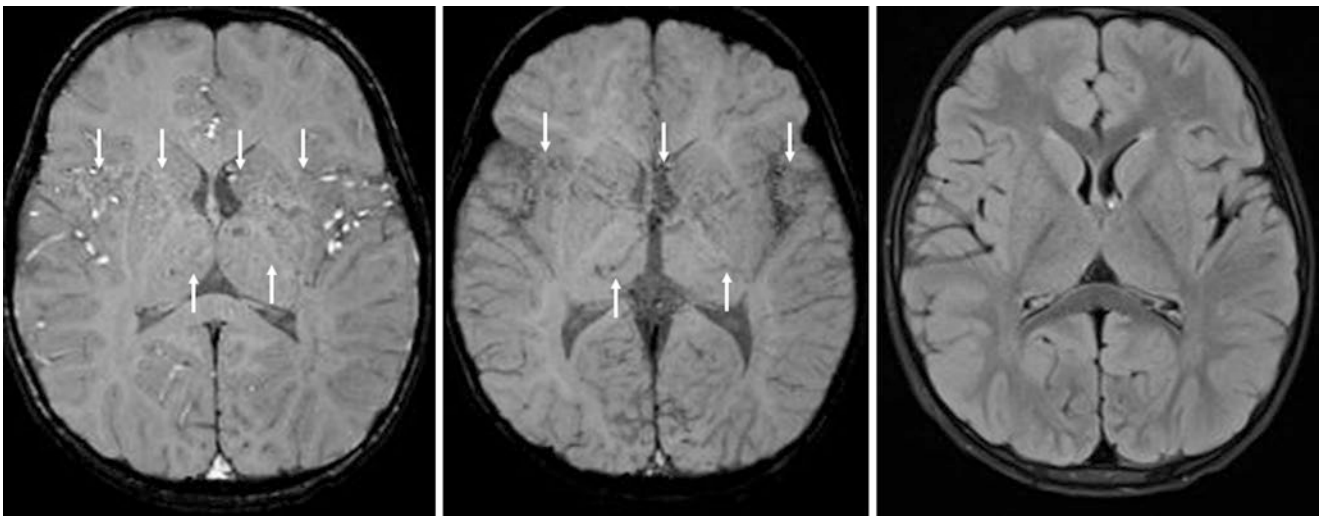

Fig. 20.54 Motion-related artifact**.** A 2 year old with subtle motion-related artifact on 2-mm-thick (*left*) and 10-mm-thick (*middle*) SWI at 3T. The artifact appears hazy or "blotchy" (*arrows*), while FLAIR (*right*) appears normal. This artifact also may be exacerbated by phase direction-artifact from vascular pulsation. Such an artifact can simulate multifocal MHs such as may occur with shear injury, or it can simulate prominent vasculature such as occurs with vascular malformations

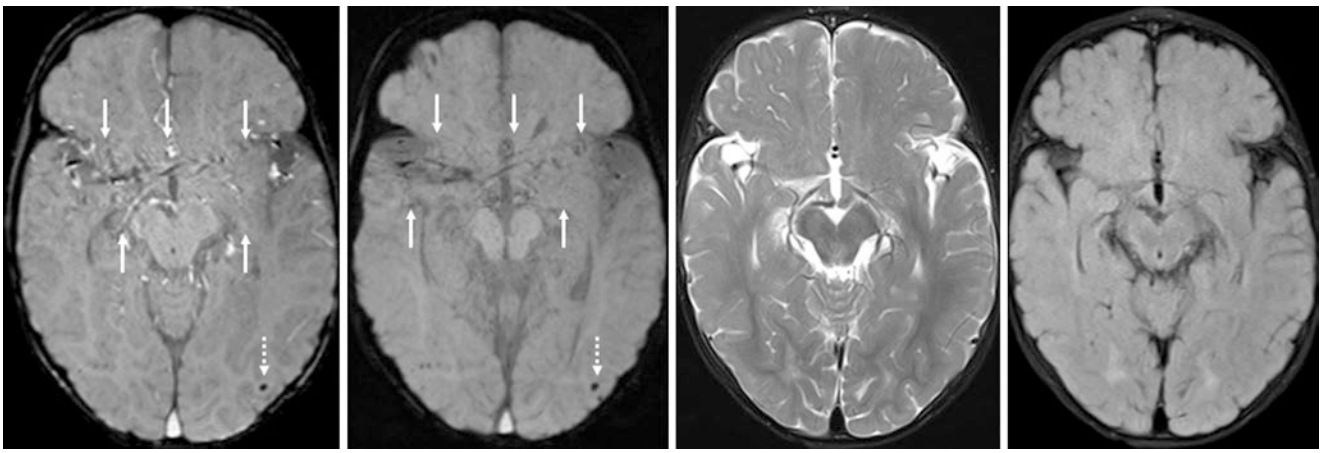

Fig. 20.55 Motion-related artifact**.** The patient was 12 months old with congenital cytalomegalovirus infection. There is subtle motion-related or pulsation-related artifact on 2-mm-thick (*left*) and 10-mm-thick (left middle) SWIs at 3T. The artifact appears blotchy (*arrows*), while T2WI (*right middle*) and FLAIR (*right*) are not affected. Such an artifact can simulate MHs or vasculature of an AVM. Note a true MH (*dotted arrows*)

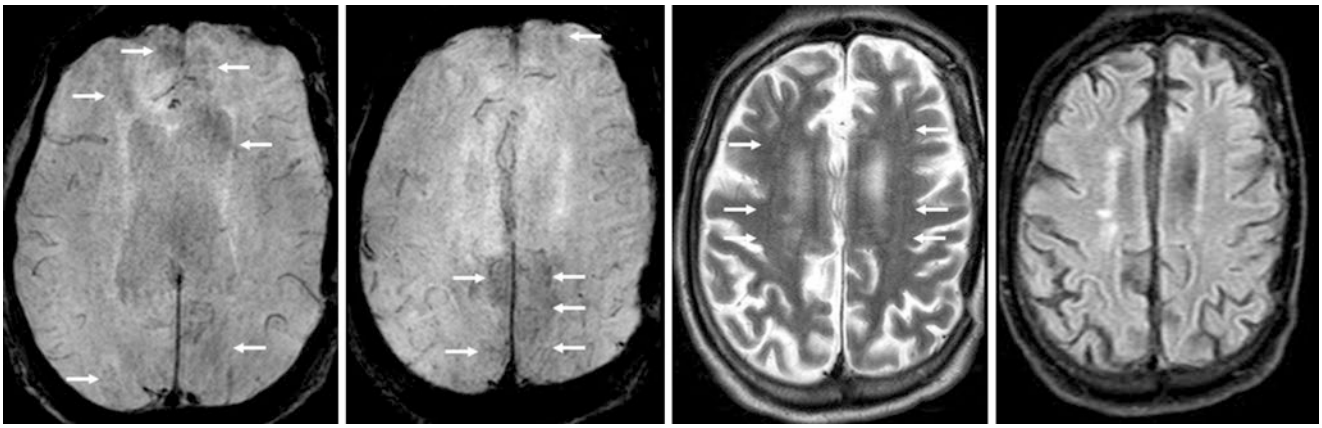

Fig. 20.56 Motion-related artifact**.** A 70 year old with mild to moderate motion artifact on 2-mm-thick (*left and left middle*) SWIs at 1.5T. The artifact appears hazy or blotchy (*arrows*), perhaps due to volume averaging of parenchyma with darker CSF, vasculature, or regions of gas. Motion artifact is noted to a lesser degree on T2WI (*right middle*) but disappears on FLAIR (*right*)

20.12 Susceptibility-Weighted Images: Vasculature Simulating Microhemorrhages

On SWI, various normal (or normal variant) *vasculature structures* can simulate MHs. These include vasculature that travels perpendicular to the imaging plane (which can be confirmed by visualization in other planes or by scrolling), calcifications (whether choroid plexus, dural, or of the basal ganglia), or artifacts (as discussed previously). Correlation with other planes of imaging should be performed, since SWI is typically obtained by a three-dimensional acquisition. One should also correlate with other routine MR imaging sequences or CT (e.g., to identify calcifications) in order to identify the etiology of such SWI-dark foci (Figs. 20.57 and 20.58).

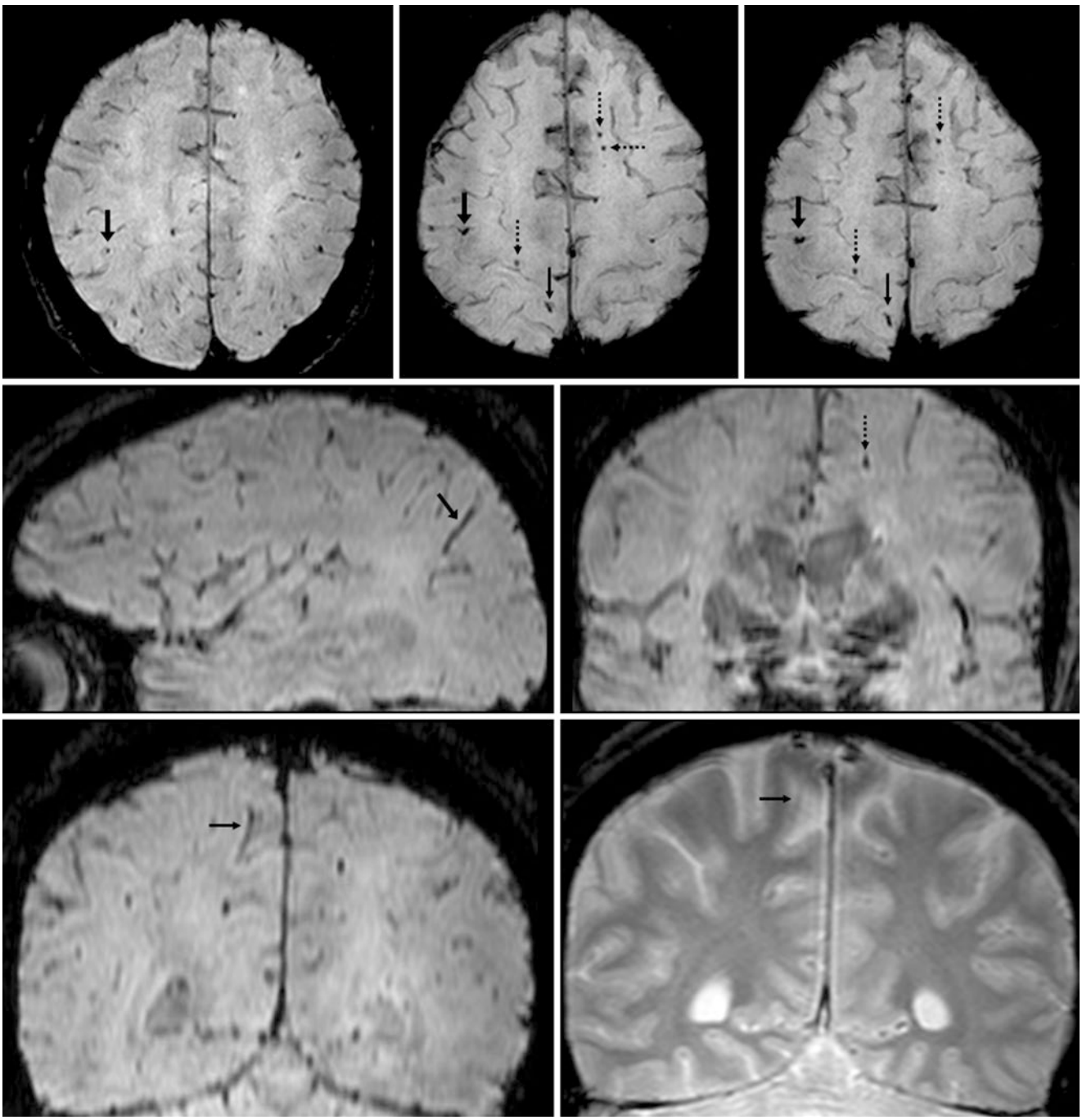

Fig. 20.57 A 47 year old with seizures. *Top row*: a punctate hypointense focus (*arrows*) within the lateral right parietal lobe simulates MH on a 2-mm-thick axial SWI obtained at 3T. Medially, another focus also simulates a MH (*thin arrows*). There are several other foci that were later confirmed to be true MHs (*dotted arrows*). *Middle row:* the lateral focus (*arrows*) appears linear like a vessel on sagittal SWI (*left*). Compare these to actual MHs (*dotted arrows*) confirmed on both axial (*top row*) and coronal (*right*) 2-mm-thick SWI's. *Bottom row*: the more medial focus is confirmed to be vasculature on coronal SWI (*left*) and is not visualized on GE T2*WI (*right*)

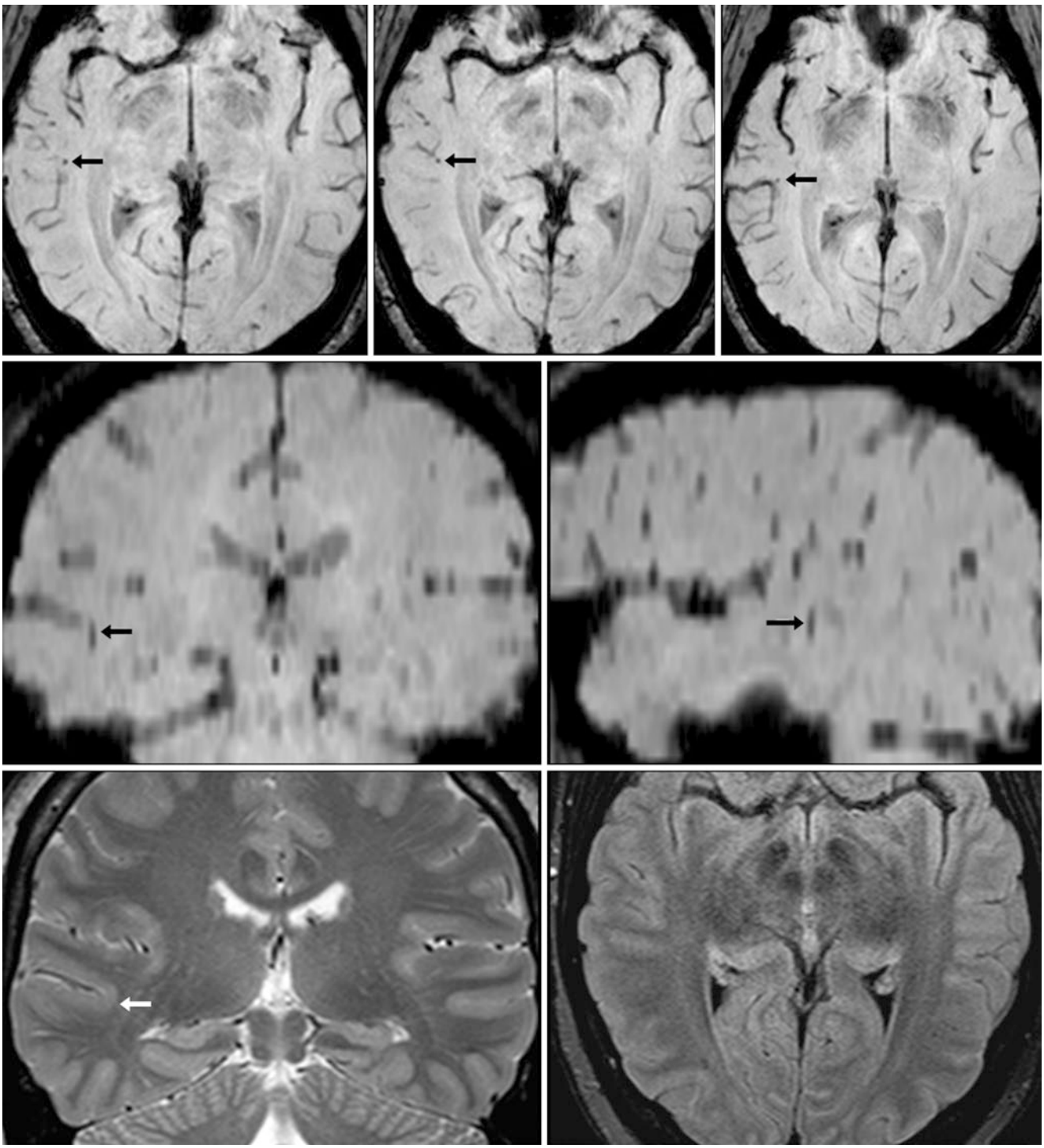

Fig. 20.58 A 24 year old with seizures. *Top row*: a punctate hypointense focus (*arrows*) is noted within the right temporal lobe, which simulates a MH on 2-mm-thick SWIs obtained at 3T. This does not appear to connect to a vessel. *Middle row*: using localization, the punctate focus is shown to be a small cortical vessel on coronal (*left*) and sagittal (*right*) SWIs. *Bottom row*: that region also appears normal on coronal T2WI (*left*) and axial FLAIR (*right*)

20.13 Susceptibility-Weighted Images: Choroid Plexus Simulating Microhemorrhages

On SWI, normal (or normal variant) *choroid plexus* can simulate MHs. These foci can be identified as choroid plexus based on their typical location, particularly within the trigones of the lateral ventricles, choroidal fissures, or foramina of Luschka. Occasionally, they can be problematic when they are densely calcified and cause confusion if a CT is not available. Postcontrast MRI can help identify a typical configuration of choroid plexus, and NECT can confirm calcification, if present, in a typical location for choroid plexus (Figs. 20.59 and 20.60).

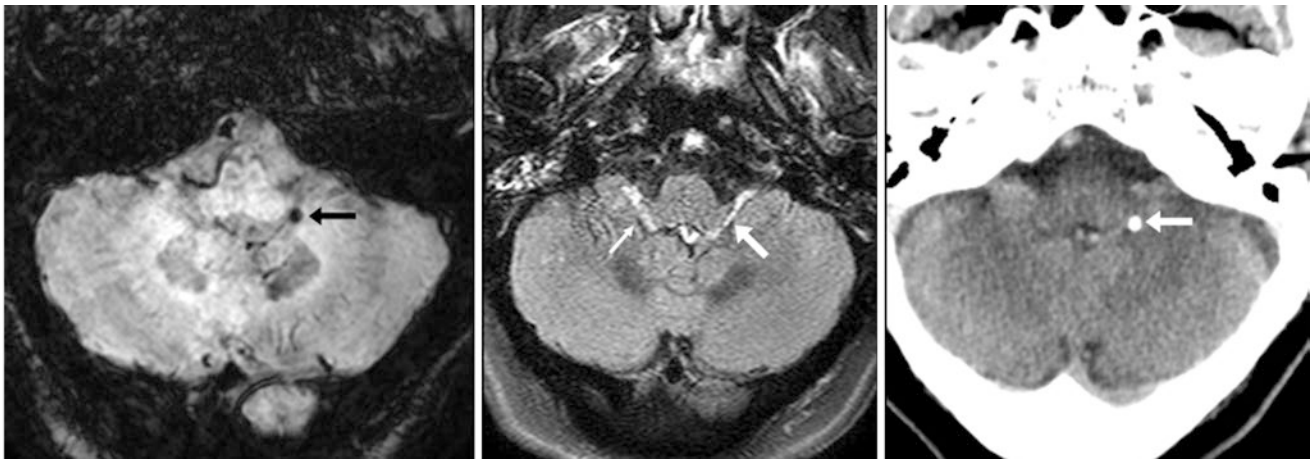

Fig. 20.59 A 70 year old with acute weakness. A punctate hypointense focus (*arrows*) was noted near the lateral brainstem on a 2-mm-thick SWI obtained at 3T (*left*), simulating a MH. However, axial postcontrast FLAIR (*middle*) depicted enhancement within the left foramen of Luschka owing to choroid plexus in that location; the *thin arrow* also depicts normal contralateral choroid plexus enhancement. Later, a NECT (*right*) confirmed that this was calcified choroid

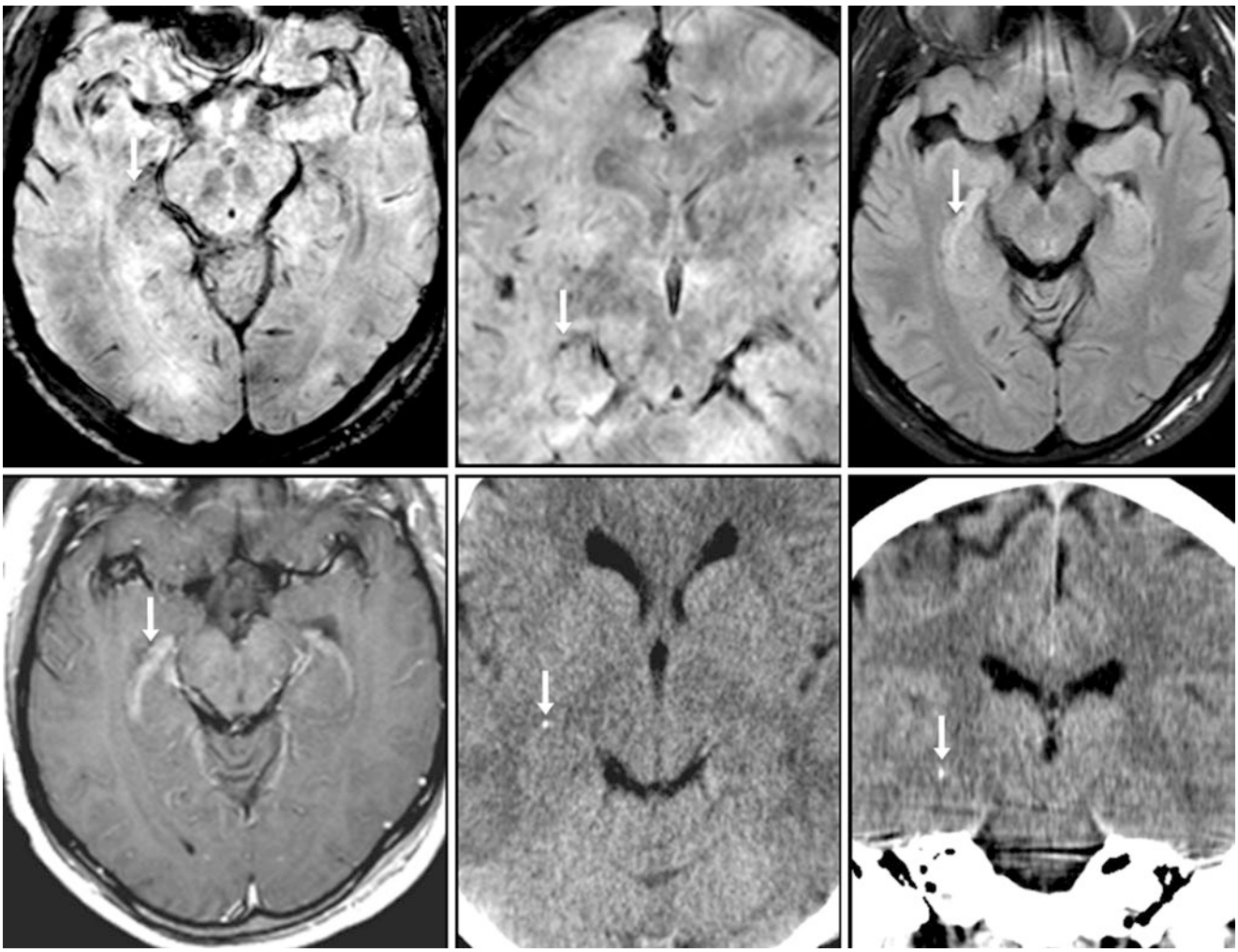

Fig. 20.60 A 40 year old with headaches had a punctate hypointense focus (*arrows*) along the medial right temporal lobe on 2-mm-thick axial (*top left*) and coronal (*top middle*) SWIs obtained at 1.5T. This simulated a remote MH. However, postcontrast axial FLAIR (*top right*) and T1WI (*bottom left*) showed enhancing choroid plexus within the choroidal fissure. Axial (*bottom middle*) and coronal (*bottom right*) NECT images confirmed slightly calcified choroid plexus within the choroidal fissure

20.14 Susceptibility-Weighted Images: Postcontrast Appearance and the Use of Subtraction Imaging

One should be aware of the appearance of *postcontrast susceptibility-weighted imaging* (SWI). Gadolinium-based contrast agents (GBCAs) cause variable enhancement of the vasculature (depending on a number of factors such as the TE), while injury to the blood-brain barrier (BBB) leads to parenchymal enhancement on SWI. Briefly, on SWI, GBCAs can actually be visualized as a bright signal in a fashion similar to that seen on T1WI (T1 shine-through). This is typically due to BBB injury, breakdown, or increased permeability, whether from *neoplasm*, infarction (typically subacute phase), endothelial injury (e.g., endothelial injury in posterior reversible encephalopathy syndrome), *vascular inflammation*, or *meningeal inflammation*. This appearance on postcontrast SWI may be important to be aware of because future research may incorporate the utilization of pre- and postcontrast SWI in characterizing vascular anomalies such as *arteriovenous malformations* or *fistulas* (AVMs or AVFs), neoplasms such as recurrent high-grade primary brain tumors (e.g., glioblastomas), or in assessing perfusion/permeability (e.g., stroke or neoplasm). Additionally, the precontrast SWI may be subtracted from the postcontrast SWI in situations where underlying dark hemorrhage is present in order to detect enhancing lesions within hemorrhagic regions; for example, SWI subtraction may reveal recurrent tumor in *glioblastoma multiforme* (Figs. 20.61, 20.62, 20.63, 20.64, 20.65, 20.66, 20.67, and 20.68).

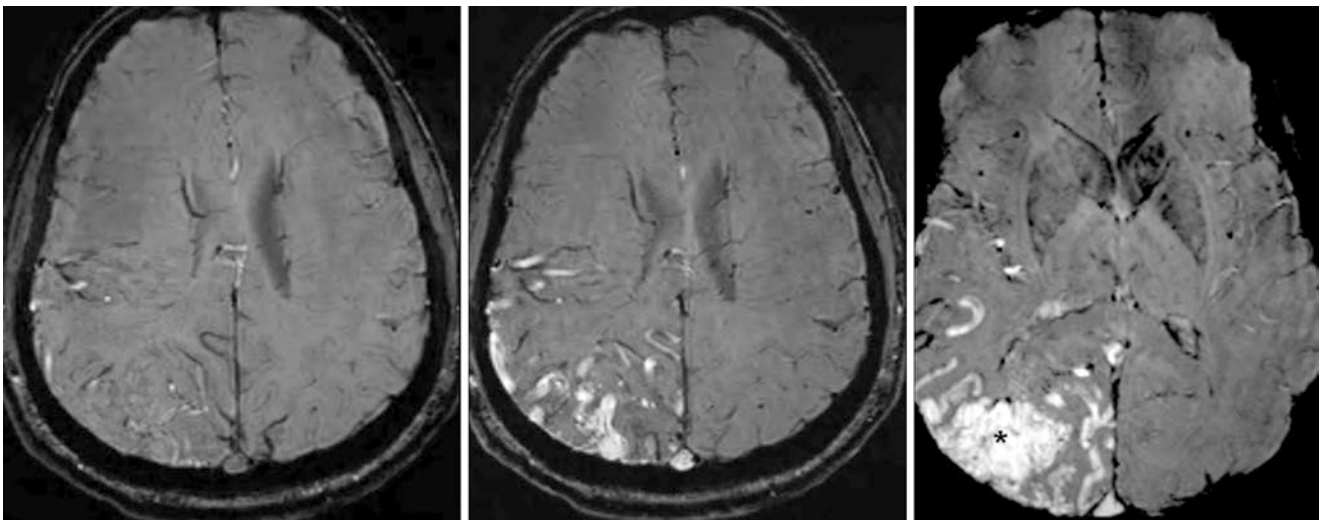

Fig. 20.61 A 56 year old with an AVM. On a noncontrast 3T SWI MRI (*left*), there is subtle bright arterial signal. On a postcontrast SWI at that level (*middle*), there is signal within both the supplying arteries and draining veins. On another postcontrast SWI at a lower level (*right*), the large AVM nidus is shown (*)

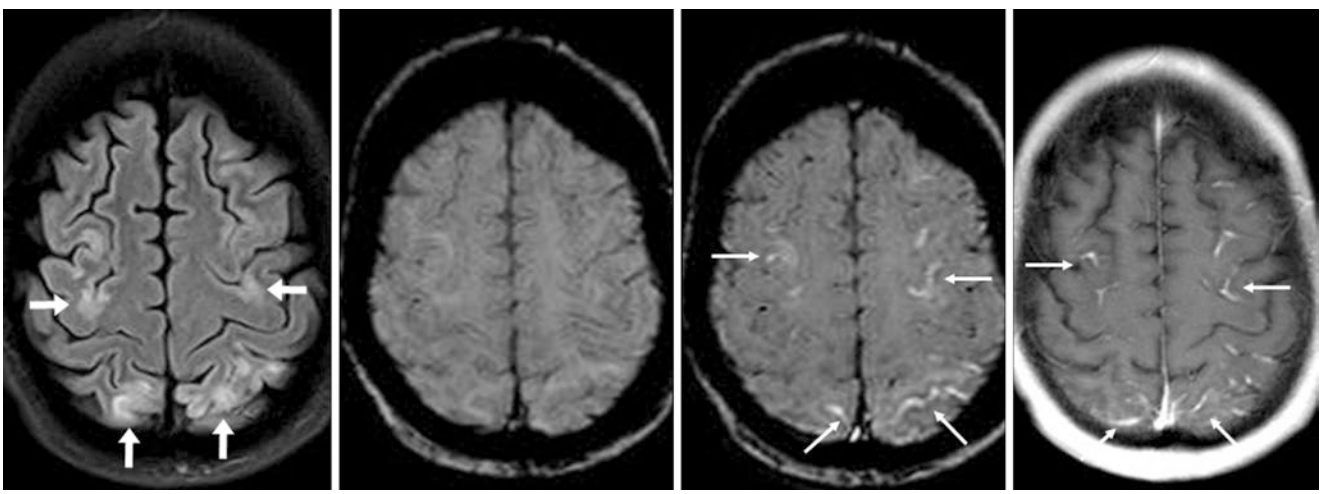

Fig. 20.62 A 24 year old on cyclosporine, with seizures from posterior reversible encephalopathy syndrome (PRES**).** A noncontrast 3T FLAIR MRI (*left*) showed cortical/subcortical edema (*arrows*) of the posterior frontal and anterior parietal lobes near the vertex, typical of PRES. On noncontrast SWI (*left middle*), there was no MH (note: MH occurs in over half of PRES patients). On postcontrast SWI, (*right middle*), pial enhancement was present (*thin arrows*), which was confirmed on postcontrast T1WI (*right*). Pial (leptomeningeal) enhancement occurs in up to 30–40 % of PRES cases

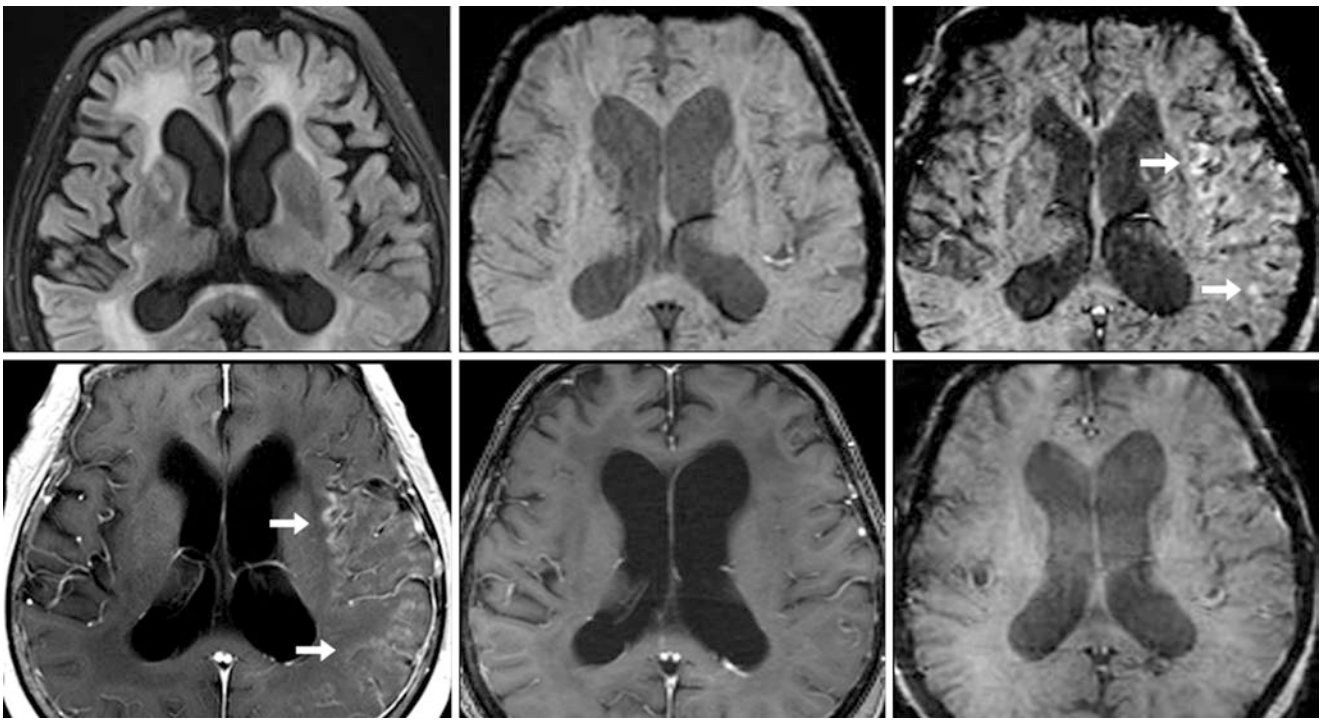

Fig. 20.63 A 68 year old with SMART syndrome (stroke-like migraine attacks after radiation therapy). Fifteen years after cranial radiation for a grade 2 astrocytoma, the patient presented with severe headaches who had since had yearly MRIs that were negative for recurrence. A noncontrast 3T FLAIR MRI (*top left*) showed postradiation findings, while SWI (*top middle*) did not show MHs (often noted after radiation). On postcontrast SWI (*right*), there was gyral enhancement (*arrows*), also present on postcontrast T1WI (*bottom left*), which resolved 11 days later on postcontrast T1WI (*bottom middle*) and SWI (*bottom right*). This entity can simulate recurrent tumor or meningeal inflammation

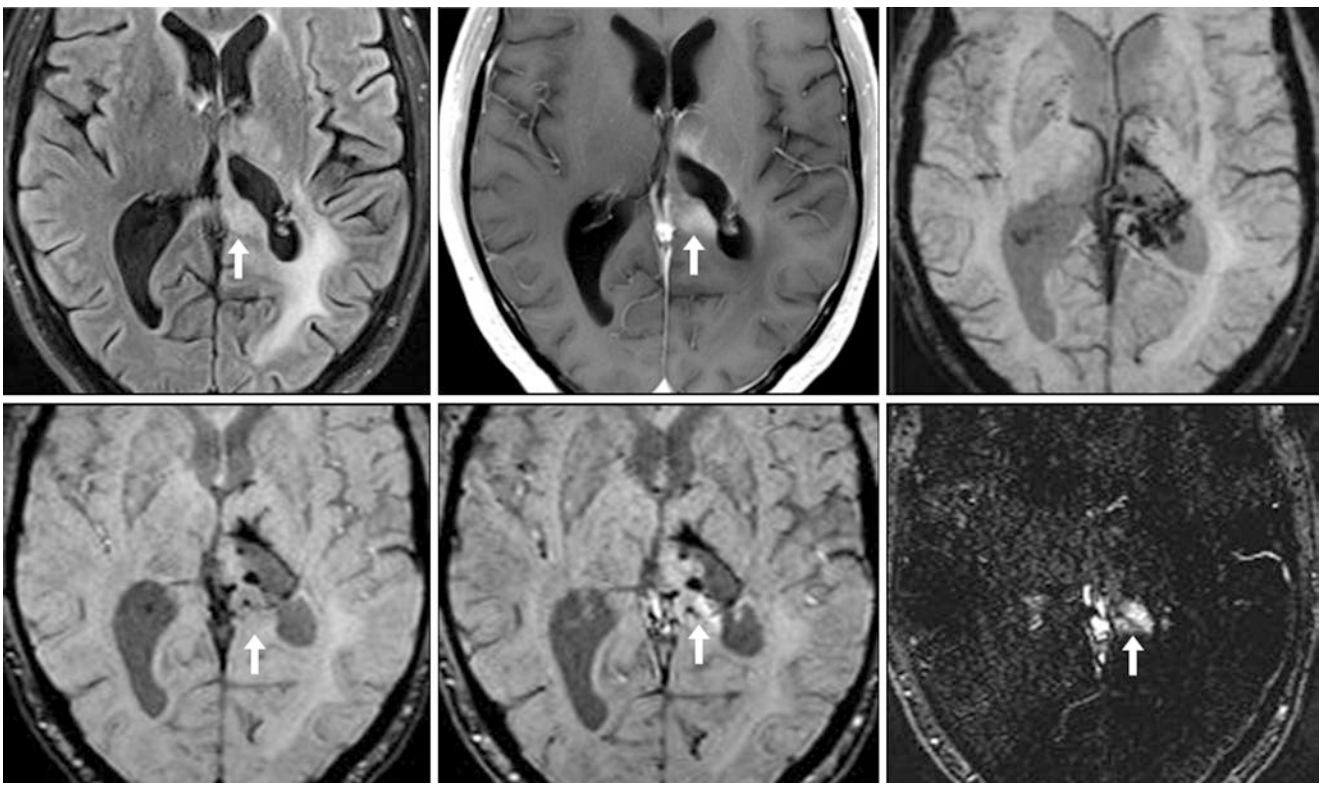

Fig. 20.64 SWI subtraction to detect recurrent tumor**.** A 48 year old with a previous astrocytoma had enlarging nodularity at the margin of a prior resection (*arrows*) on FLAIR (*top left*), with new enhancement on postcontrast T1WI (*top middle*). On 16-mm-thick precontrast SWI (*top right*), hemosiderin was seen around the resection site, also shown on 2-mm-thick SWI (*bottom left*). On a postcontrast SWI (*bottom middle*), nodular enhancement (*arrows*) is shown by subtraction (*bottom right*) of the pre- from the postcontrast SWI. This was proven to be a recurrent high-grade tumor

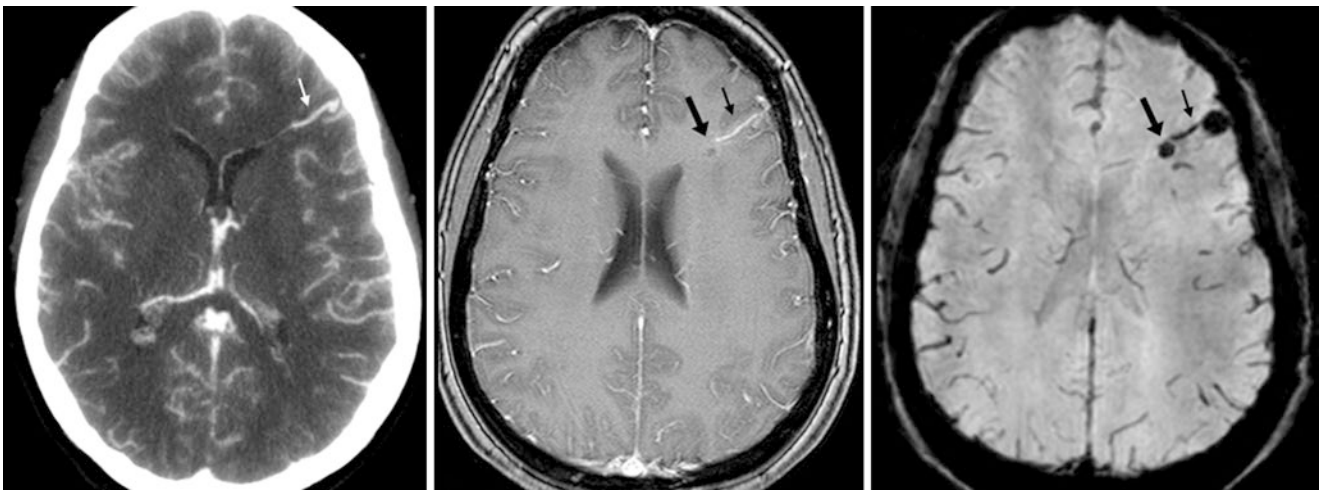

Fig. 20.65 Comparison case of cavernoma**.** A 40 year old had focal left frontal subarachnoid hemorrhage that was initially noted on NECT (*not shown*). A CT venogram (*left*) demonstrated an enlarged draining vein (*thin arrow*s). A subsequent catheter angiogram was negative. On a 1.5T MRI, postcontrast SE T1WI (*middle*) also depicted the enlarged draining vein, deep to which a cavernoma (*arrows*) was found on a 2-mm-thick SWI (*right*)

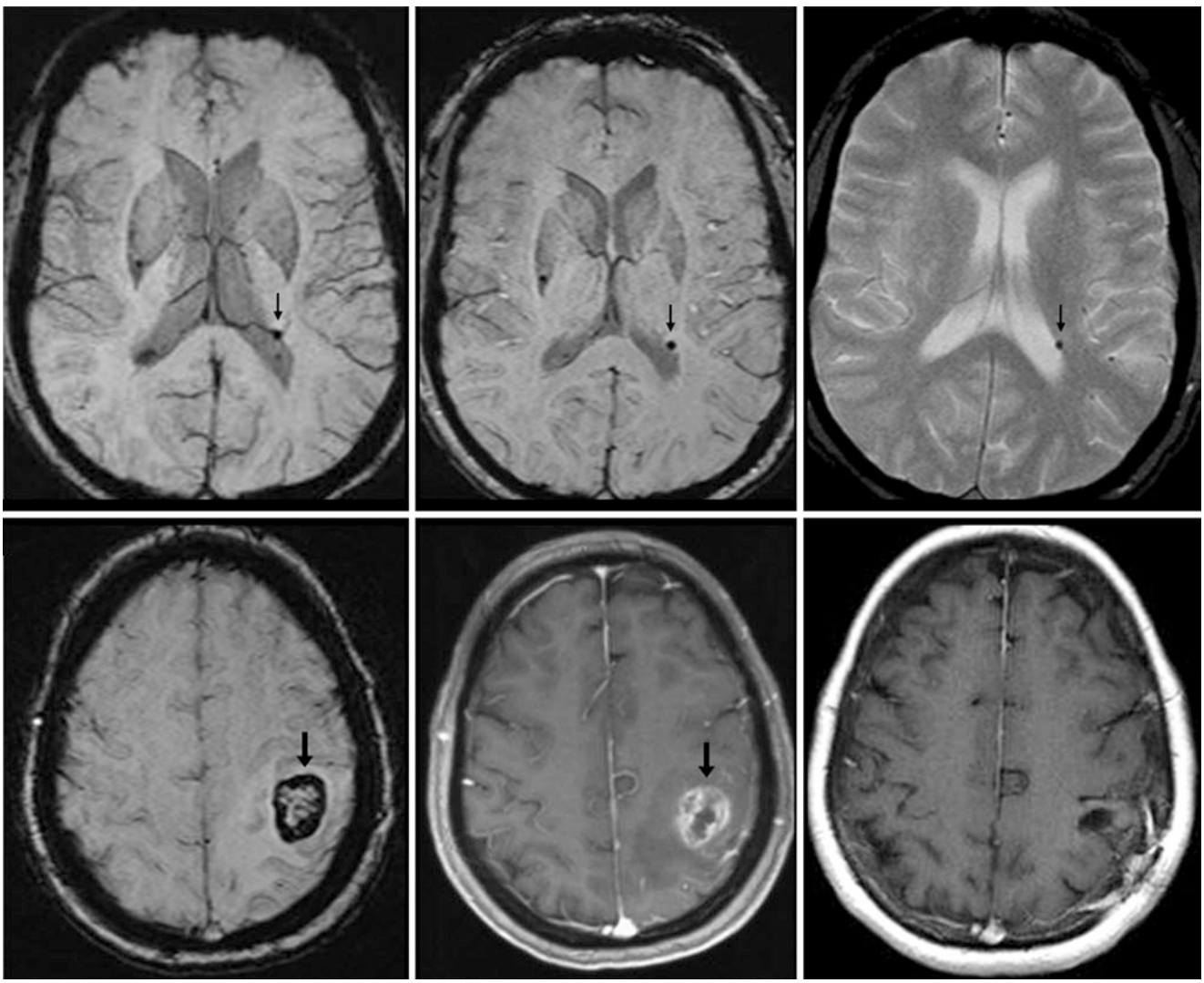

Fig. 20.66 Comparison case of cavernomas**.** A 58 year old with weakness had a MH (*thin arrow*s) that was obscured on a 10-mm-thick SWI (*top left*) but was shown to be separate from medullary veins on a 2-mm-thick SWI (*top middle*) and on GE T2*WI (*top right*). A larger, symptomatic cavernoma (*arrows*) appeared necrotic on 2-mm SWI (*bottom left*) with an enhancing rim on postcontrast SE T1WI (*bottom middle*), thus simulating a high-grade glioma. After resection, this was proven to be a cavernoma. It did not recur at 5 years on postcontrast SE T1WI (*bottom right*)

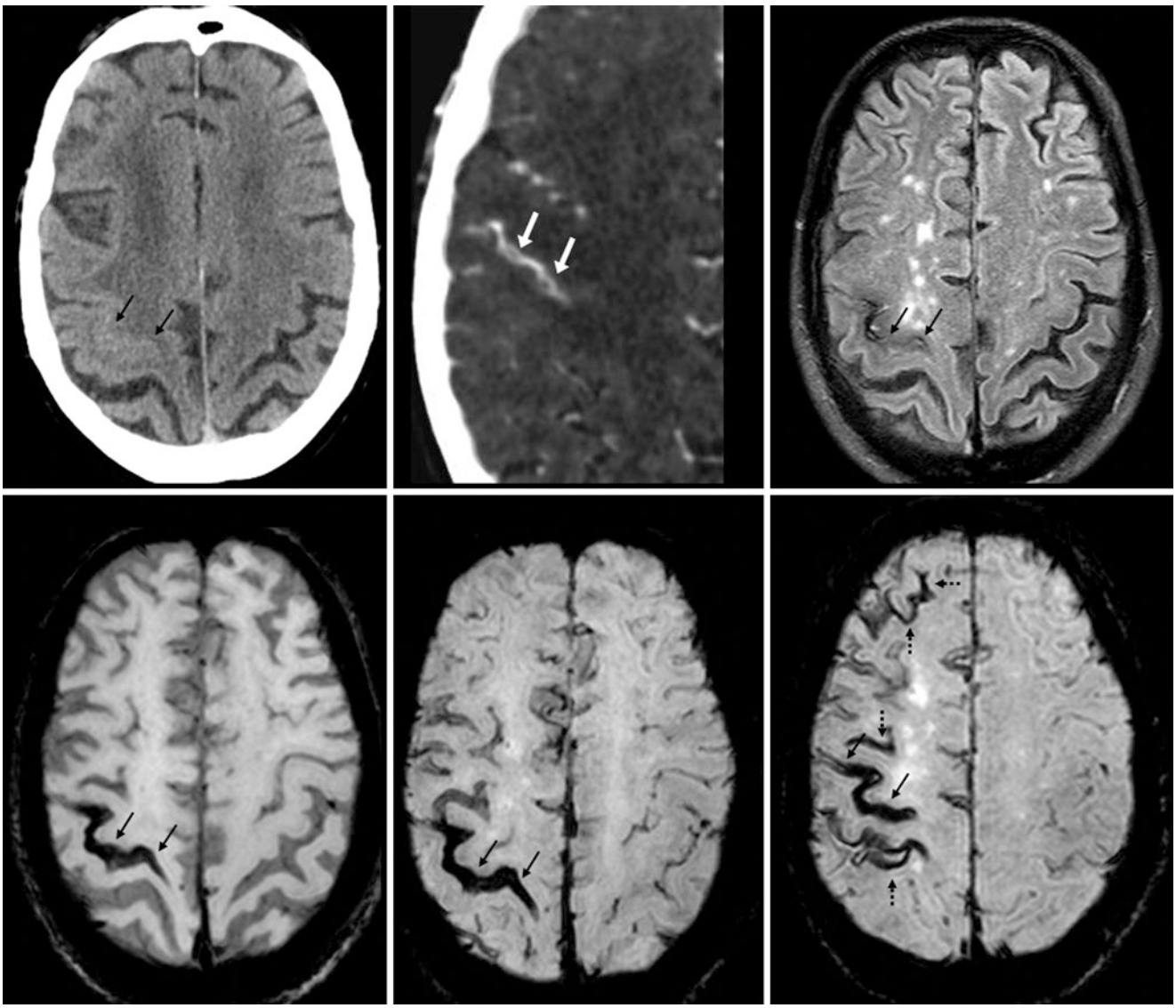

Fig. 20.67 Comparison case of cortical vein thrombosis**.** A 65 year old with an acute headache and left-sided weakness had loss of the right central sulcus (*thin arrows*) on NECT (*top left*), with an enlarged cortical vein (*arrows*) on a CT venogram (*top middle*). On a 1.5T FLAIR MRI (*top right*), there was T2-dark acute subarachnoid hemorrhage (SAH) or venous clot, which was also dark on 1-mm- (*bottom left*) and 5-mm-thick (*bottom middle*) SWIs. Four months later, SWI (*bottom right*) confirmed hemosiderin from SAH in that location and elsewhere (*dotted arrows*)

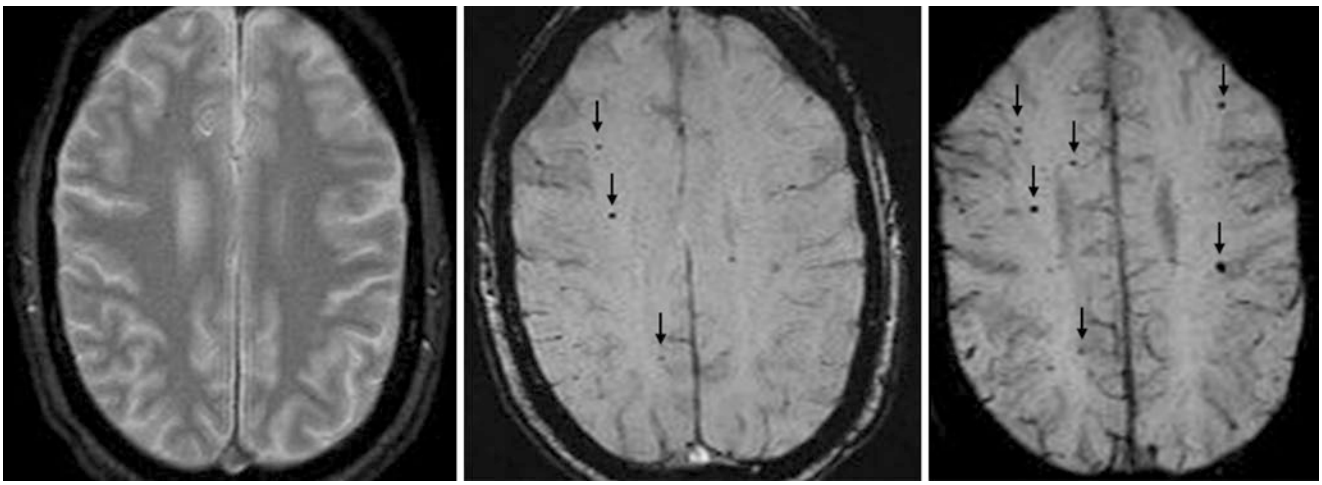

Fig. 20.68 Comparison case of cavernomas (i.e., vascular dysplasias). A 42 year old with cranial irradiation more than 20 years prior for medulloblastoma had no tumor recurrence and had no lesions on GE T2*WI (*left*). However, 2-mm-thick SWI (*middle*) depicted multiple punctate, dark foci (*thin arrow*s), with even more foci visualized on 10-mm-thick minIPs (*right*)

Suggested Reading

Abduljalil AM, Schmalbrock P, Novak V, Chakeres DW. Enhanced gray and white matter contrast of phase susceptibility-weighted images in ultra-high-field magnetic resonance imaging. J Magn Reson Imaging. 2003;18:284–90.

Aquino D, Bizzi A, Grisoli M, Garavaglia B, Bruzzone MG, Nardocci N, et al. Age-related iron deposition in the basal ganglia: quantitative analysis in healthy subjects. Radiology. 2009;252:165–72.

Baudendistel KT, Reichenbach JR, Metzner R, Schroeder J, Schad LR. Comparison of functional MR-venography and EPI-BOLD fMRI at 1.5T. Magn Reson Imaging. 1998;16:989–91.

Cumings JN. The copper and "organic" iron content of human tissues. Biochem J. 1935;29:480–6.

Dexter DT, Jenner P, Schapira AHV, Marsden CD. Alterations in levels of iron, ferritin, and other trace metals in neurodegenerative diseases affecting the basal ganglia. Ann Neurol. 1992;32:S94–100.

Drayer B, Burger P, Darwin R, Riederer S, Herfkens R, Johnson GA. Magnetic resonance imaging of brain iron. AJNR Am J Neuroradiol. 1998;7:373–80.

El-Koussy M, Schroth G, Gralla J, Brekenfeld C, Andres RH, Jung S, et al. Susceptibility-weighted MR imaging for diagnosis of capillary telangiectasia of the brain. AJNR Am J Neuroradiol. 2012;33:715–20.

Gupta D, Saini J, Kesavadas C, Sarma PS, Kishore A. Utility of susceptibility-weighted MRI in differentiating Parkinson's disease and atypical parkinsonism. Neuroradiology. 2010;52:1087–94.

Haacke EM, Reichenbach JR, editors. Susceptibility Weighted Imaging in MRI. Hoboken: John Wiley & Sons; 2011.

Haacke EM, Xu Y, Cheng YC, Reichenbach JR. Susceptibility weighted imaging (SWI). Magn Reson Med. 2004;52:612–8.

Haacke EM, Mittal S, Wu Z, Neelavalli J, Cheng YC. Susceptibility-weighted imaging: technical aspects and clinical applications, part 1. AJNR Am J Neuroradiol. 2009;30:19–30.

Haller S, Bartsch A, Nguyen D, Rodriguez C, Emch J, Gold G. Cerebral microhemorrhage and iron deposition in mild cognitive impairment: susceptibility-weighted MR imaging assessment. Radiology. 2010;257:764–73.

Haller S, Badoud S, Nguyen D, Barnaure I, Montandon ML, Lovblad KO, Burkhard PR. Differentiation between Parkinson disease and other forms of parkinsonism using support vector machine analysis of susceptibility-weighted imaging (SWI): initial results. Eur Radiol. 2013;23:12–9.

Hallgren B, Sourander P. The effect of age on the non-haemin iron in the human brain. J Neurochem. 1958;3:41–51.

Hermier M, Nighoghossian N. Contribution of susceptibility-weighted imaging to acute stroke assessment. Stroke. 2004;35:1989–94.

Jagadeesan BD, Delgado Almandoz JE, Benzinger TL, Moran CJ. Postcontrast susceptibility-weighted imaging: a novel technique for the detection of arteriovenous shunting in vascular malformations of the brain. Stroke. 2011;42:3127–31.

Li N, Wang WT, Pham DL, Butman JA. Artifactual microhemorrhage generated by susceptibility weighted image processing. J Magn Reson Imaging. 2015;41:1695–700.

Lotfipour AK, Wharton S, Schwarz ST, Gontu V, Schäfer A, Peters AM, et al. High resolution magnetic susceptibility mapping of the substantia nigra in Parkinson's disease. J Magn Reson Imaging. 2012;35:48–55.

Martin WR, Ye FQ, Allen PS. Increasing striatal iron content associated with normal aging. Mov Disord. 1998;13:281–6.

McKinney AM, Sarikaya B, Gustafson C, Truwit CL. Detection of microhemorrhage in posterior reversible encephalopathy syndrome using susceptibility-weighted imaging. AJNR Am J Neuroradiol. 2012;33:896–903.

Nair JR, Van Hecke W, De Belder F, Gontu V, Rodesch G, Mercier P, Söderman M. High-resolution susceptibility-weighted imaging at 3T with a 32-channel head coil: technique and clinical applications. Am J Roentgenol. 2010;195:1007–14.

Noh Y, Sung YH, Lee J, Kim EY. Nigrosome 1 detection at 3T MRI for the diagnosis of early-stage idiopathic Parkinson disease: assessment of diagnostic accuracy and agreement on imaging asymmetry and clinical laterality. AJNR Am J Neuroradiol. 2015;36:2010–16.

Reichenbach JR, Venkatesan R, Schillinger DJ, Kido DK, Haacke EM. Small vessels in the human brain: MR venography with deoxyhemoglobin as an intrinsic contrast agent. Radiology. 1997;204:272–7.

Reichenbach JR, Jonetz-Mentzel L, Fitzek C, Haacke EM, Kido DK, Lee BC, Kaiser WA. High-resolution blood oxygen-level dependent MR venography (HRBV): a new technique. Neuroradiology. 2001;43:364–9.

Schenker C, Meier D, Wichman W, Boesiger P, Valavanis A. Age distribution and iron dependency of the T2 relaxation time in the globus pallidus and putamen. Neuroradiology. 1993;35:119–24.

Schwarz ST, Afzal M, Morgan PS, et al. The 'swallow tail' appearance of the healthy nigrosome - a new accurate test of Parkinson's disease: a case-control and retrospective cross-sectional MRI study at 3T. PLoS ONE. 2014;9:e93814.

Yates PA, Sirisriro R, Villemagne VL, et al.; AIBL Research Group. Cerebral microhemorrhage and brain β-amyloid in aging and Alzheimer disease. Neurology. 2011;77:48–54.

Zhu WZ, Zhong WD, Wang W, Zhan CJ, Wang CY, Qi JP, et al. Quantitative MR phase-corrected imaging to investigate increased brain iron deposition of patients with Alzheimer disease. Radiology. 2009;253:497–504.

Slow-Flow, Asymptomatic Vascular Malformations: Brain Capillary Telangiectasias and Developmental Venous Anomalies

21

This chapter focuses on two slow-flow vascular malformations of the brain: *brain capillary telangiectasias* (BCTs) and *developmental venous anomalies* (DVAs). Both occur as incidental findings in the general population, are typically asymptomatic when existing as solitary lesions, and can occur along a spectrum of being barely visible (usually only on postcontrast imaging) to being quite large to the point of simulating symptomatic lesions such as a *neoplasm* (owing to avid enhancement and size in a BCT) or frank *arteriovenous malformation* (AVM, due to large venous flow voids in a DVA). Besides size, they can both occur concomitantly in symptomatic cases when associated with symptomatic slow-flow vascular lesions, typically *cavernomas* (e.g., cavernous hemangiomas, cavernous malformations). Both lesions have dedicated, longer discussions in this chapter about the spectrum of their appearance on various sequences and when they can simulate symptomatic lesions as well as their appearance on more recently available MR sequences, most notably susceptibility-weighted imaging (SWI). Comparison cases are provided at the end of the chapter for both lesions, with a focus on cavernomas and AVMs.

21.1 Brain Capillary Telangiectasias

BCTs are nearly always an incidental finding on a brain MRI, being considered by many as a normal variation or at the very least as a "don't touch" lesion. This is because they are benign vascular entities that angiographically demonstrate low flow. They are the second most frequent vascular malformations next to DVAs (also known as venous angiomas), accounting for about 5–15 % of brain vascular malformations. They are estimated to occur in 0.4–0.7 % of the population, based on both autopsies and susceptibility-weighted imaging (SWI) MRI. However, this frequency may increase in the future, as BCTs can be tiny, but continually improving MR imaging has proceeded to identify increasingly smaller BCTs. Histologically, they are composed of thin-walled vascular spaces/capillaries that are larger in caliber than normal brain capillaries. Thus, their incidence may be increasing with the increasing utilization of MR imaging, particularly with the development of SWI in the last several years and higher field strengths.

The appearance of BCTs on MRI varies with sequence and field strength, and as such BCTs are usually invisible on nonenhanced CT (NECT), while larger BCTs may be only barely visible if a contrast-enhanced CT (CECT) is performed. On MRI, the characteristic patterns described typically include no hyperintensity (or only faint hyperintensity in larger lesions) on T2WI or FLAIR, near-invisibility on T1WI, mild hypointensity on T2* gradient-echo (T2*WI), faint hypointensity on DWI, and a mild or faint puff of enhancement on T1WI obtained postcontrast. Notably, the degree of enhancement within these lesions may vary with field strength (the greatest enhancement occurs at higher field strengths such as 3 T), sequence (enhancement is typically visualized better on postcontrast spin echo [SE] T1WI than on GE T1WI), and time delay (a longer time in the range of 5–10 min may improve their visibility). However, perhaps the best way to visualize capillary telangiectasias is their characteristic hazy signal loss (hypointensity) on SWI, particularly at higher field strengths such as 3T, thought to be related to the relatively high concentration of deoxyhemoglobin in these lesions. On SWI, these lesions typically exhibit a homogeneous "fluffy" dark signal with poorly defined borders in a pattern akin to their manner of contrast enhancement. In some cases, linear hypointensities may be noted radiating from BCTs on SWI, thought related to the presence of draining vascular channels. A newer contrast and iron-based agent, ferumoxytol, may augment the signal loss (hypointensity) within BCTs on SWI MRI, thus increasing their visualization. It should also be noted that other than SWI, older (or more traditional) T2*-weighted gradient echo (GE T2*WI) or echoplanar sequences may also depict the faint signal of deoxygenated hemoglobin to a lesser degree, such as blood oxygen level–dependent images (BOLD, used

A.M. McKinney, *Atlas of Normal Imaging Variations of the Brain, Skull, and Craniocervical Vasculature*,
DOI 10.1007/978-3-319-39790-0_21

for functional MRI or MR perfusion source data), "b = 0" maps (used to create DWI images), or phase contrast MR images. Telangiectasias can also be visualized on CECT in the late arterial/early venous phase, or even on postcontrast time-of-flight (TOF) MRA.

The location of BCTs can be nearly anywhere within the brainstem or cerebral or cerebellar parenchyma, although the *pons* is by far the most common location (about 75–80 %). Other locations include the medulla or midbrain, the *cerebellum*, the *basal ganglia,* the *cerebral parenchyma* (i.e., lobar), or the *basal forebrain* (e.g., substantia innominata). Notably, they can be missed when located in the posterior fossa because of adjacent gas from the sphenoid sinus, or the tentorial vasculature, or if they are located near the fourth ventricle (due to a calcified choroid plexus or vascular flow voids). Visualization of SWI in multiple planes helps confirm the presence and location of these lesions.

BCTs almost always have an unremarkable clinical course and do not change over time, unless they are associated with other vascular malformations such as *cavernomas* or *arteriovenous malformations/fistulae* (AVMs/AVFs). BCTs typically do not exhibit mass effect or cause symptoms (<5 % have been stated to cause symptoms, but even this number is controversial), unless in the quite rare case that they are larger than 1 cm in size. Even in such a scenario of a giant BCT, they are still unlikely to be symptomatic. However, a prominent draining vein may be identified in up to 30–40 % of BCTs, and 10–15 % have an associated DVA, whereas DVAs (also considered don't touch lesions) may be associated with cavernomas (see following topic). Such findings have led to speculation that these three entities may be on a spectrum from typically a normal variation (e.g., BCTs) to don't touch lesions (e.g., DVAs) to lesions that are more likely to be symptomatic (e.g., cavernomas). Thus, the presence of a BCT in concert with a DVA or a prominent draining vein should prompt a search for a cavernoma, which often exhibits a "popcorn-like" appearance of a T2-dark hemosiderin ring (typically a large blotch on SWI) that has a variegated signal on T1WI but lacks contrast enhancement. DVAs are discussed separately in a following section (21.3).

21.1.1 Brain Capillary Telangiectasias: Pontine

Pontine BCTs are the most common location. As such, their true incidence may actually be unknown, since they are increasingly recognized with improving resolution and higher field strengths both on postcontrast T1WI as well as on noncontrast SWI. Occasionally, small BCTs may be relatively invisible on a prior postcontrast T1WI MRI but become visible on a follow-up MRI simply because of timing of contrast. Often, these fill in over time 5–10 min after contrast administration on T1WI, but they may be difficult to visualize on early postcontrast imaging. Larger pontine BCTs may simulate enhancing lesions, such as occurs with *metastatic disease* (Figs. 21.1, 21.2, 21.3, 21.4, 21.5, 21.6, 21.7, 21.8, 21.9, 21.10, 21.11, 21.12, and 21.13).

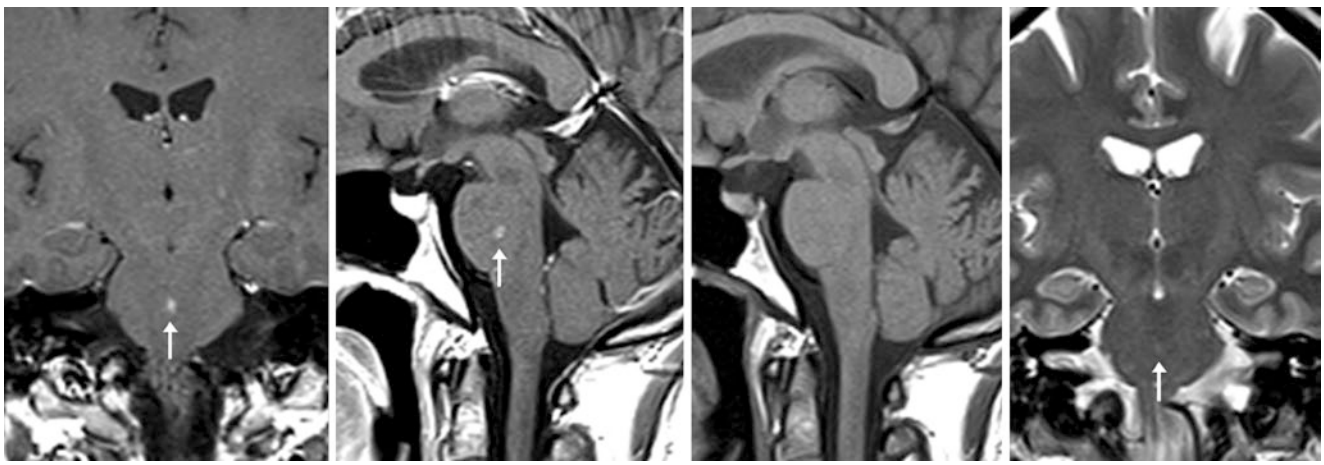

Fig. 21.1 In a 33 year old with hyperprolactinemia, incidental faint enhancement within a pontine BCT (*arrows*) was found on 1.5T MRI postcontrast coronal (*left*) and sagittal (*left middle*) T1WI, being invisible on noncontrast T1WI (*right middle*). T2WI depicts only faint hyperintense signal (*right*)

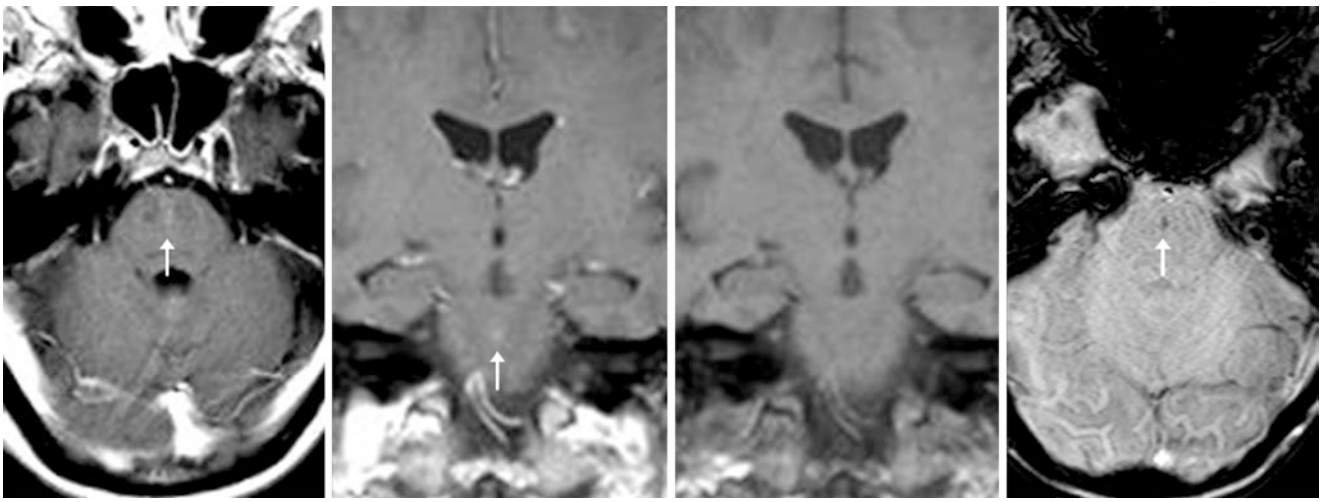

Fig. 21.2 A 51 year old with a seizure was found to have faint enhancement within a small pontine BCT (*arrows*) on 1.5T MRI postcontrast axial (*left*) and coronal (*left middle*) T1WIs, which was invisible on noncontrast T1WI (*right middle*). SWI depicts an associated faint puff of dark signal on SWI (*right*)

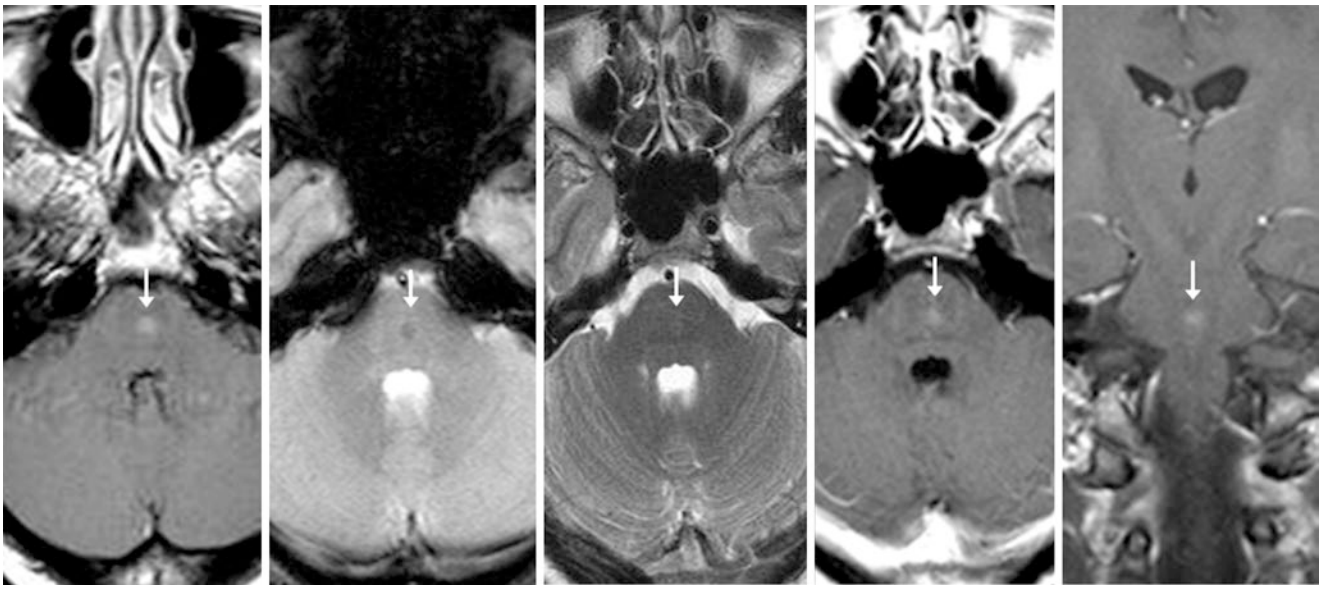

Fig. 21.3 A 26 year old who had a frontal tumor (*not shown*). Mild enhancement is demonstrated within a pontine BCT (*arrows*) on a 1.5T MRI with postcontrast T1WI (*left*). There is a puff of dark signal on GE T2*WI (*left middle*), with a normal T2WI (*middle*). Postcontrast axial (*right middle*) and coronal (*right*) T1WIs 3 years later show no change

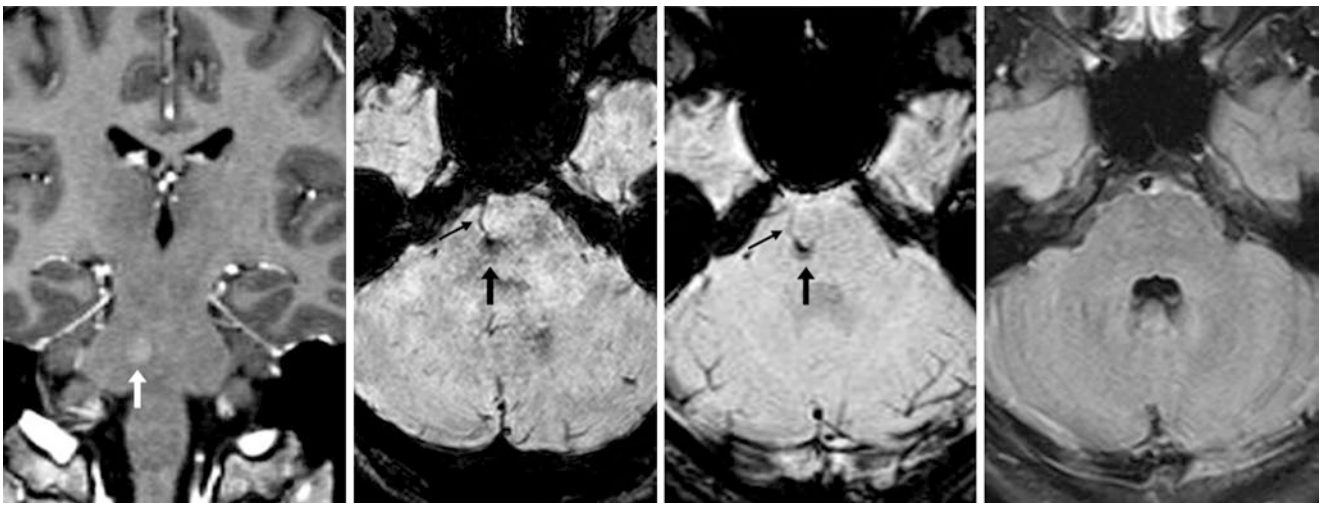

Fig. 21.4 A 17 year old experiencing nausea had faint enhancement of a pontine BCT (*arrows*) on a 1.5T MRI with a postcontrast coronal GRE T1WI (*left*), a faint dark signal on a 2-mm-thick SWI (*left middle*), and a dilated draining vein (*thin arrow*). This was unchanged on SWI 3 months later (*right middle*), while FLAIR remained normal (*right*)

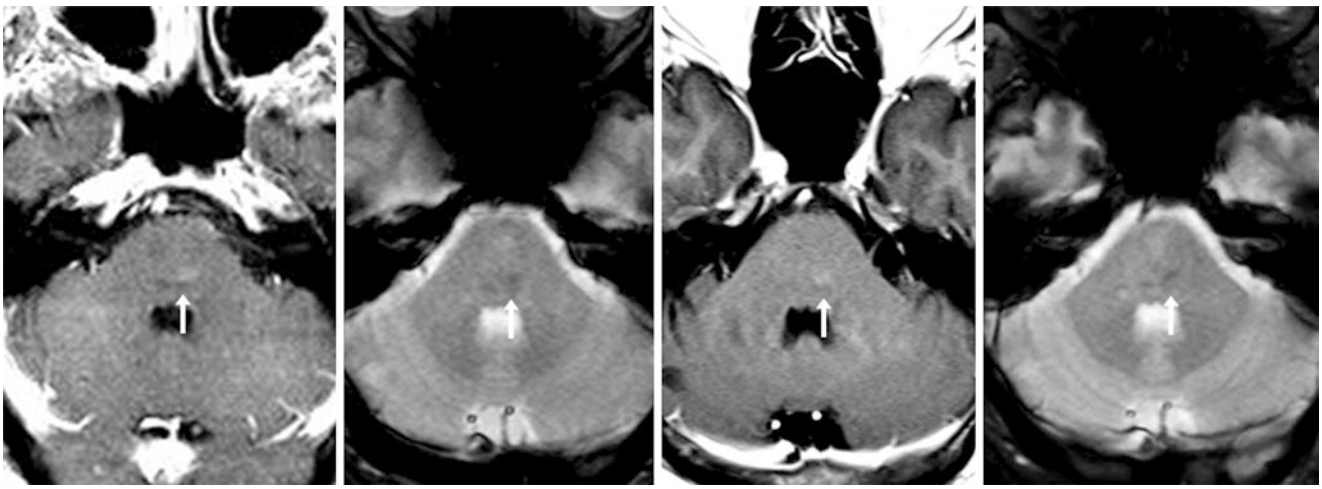

Fig. 21.5 A 43 year old was examined for altered mentation. There was faint enhancement of a pontine BCT (*arrows*) on a 1.5T MRI with postcontrast SE T1WI (*left*), and a faint dark signal on GE T2*WI (*left middle*). Seven years later, the BCT was unchanged on a postcontrast SE T1WI (*right middle*) and on a GE T2*WI (*right*)

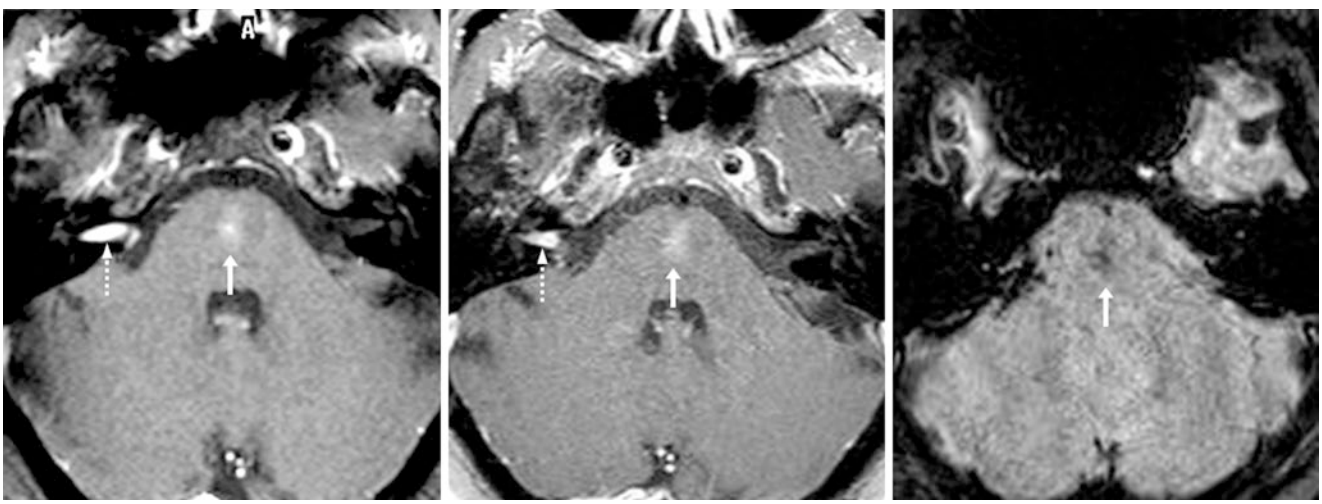

Fig. 21.6 A 41 year old was found to have a schwannoma (*dashed arrows*) within the right internal auditory canal. Additionally, there was a blush of enhancement from a pontine BCT (*arrows*) on a postcontrast T1WI (*left*), which was unchanged on an MRI obtained 7 years later (*middle*). SWI at that time (*right*) depicted "spidery" dark signal of deoxyhemoglobin

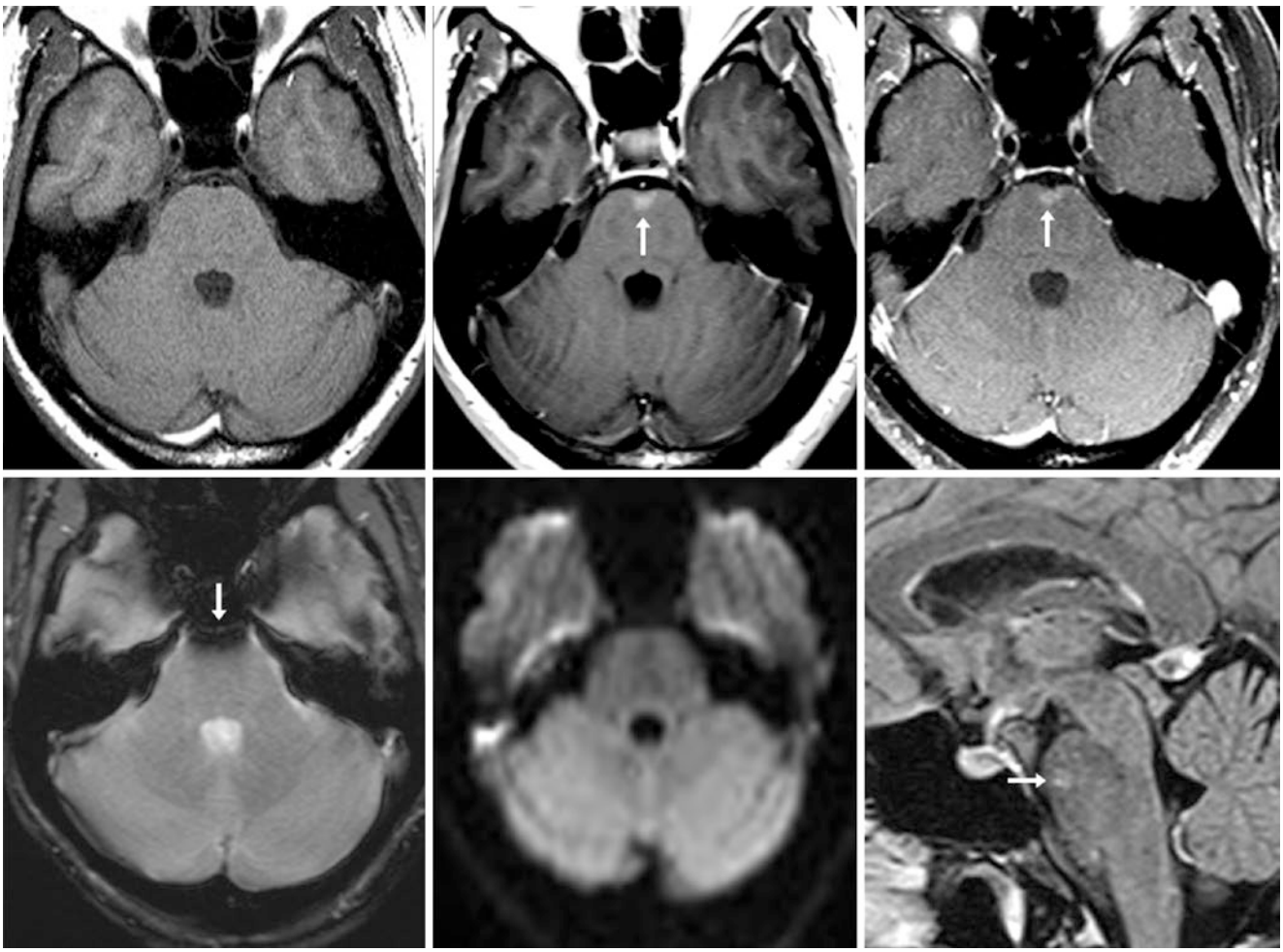

Fig. 21.7 A 39 year old with hearing loss underwent a 1.5T MRI that included a normal-appearing precontrast T1WI (*top left*). There was faint enhancement of a ventral pontine BCT (*arrows*) on postcontrast GE T1WI (*top middle*) and on SE T1WI (*top right*). This is obscured on GE T2*WI (*bottom left*) due to gas artifact from the sphenoid sinus. DWI is normal (*bottom middle*). Postcontrast sagittal FLAIR (*bottom right*) also depicts the enhancing telangiectasia

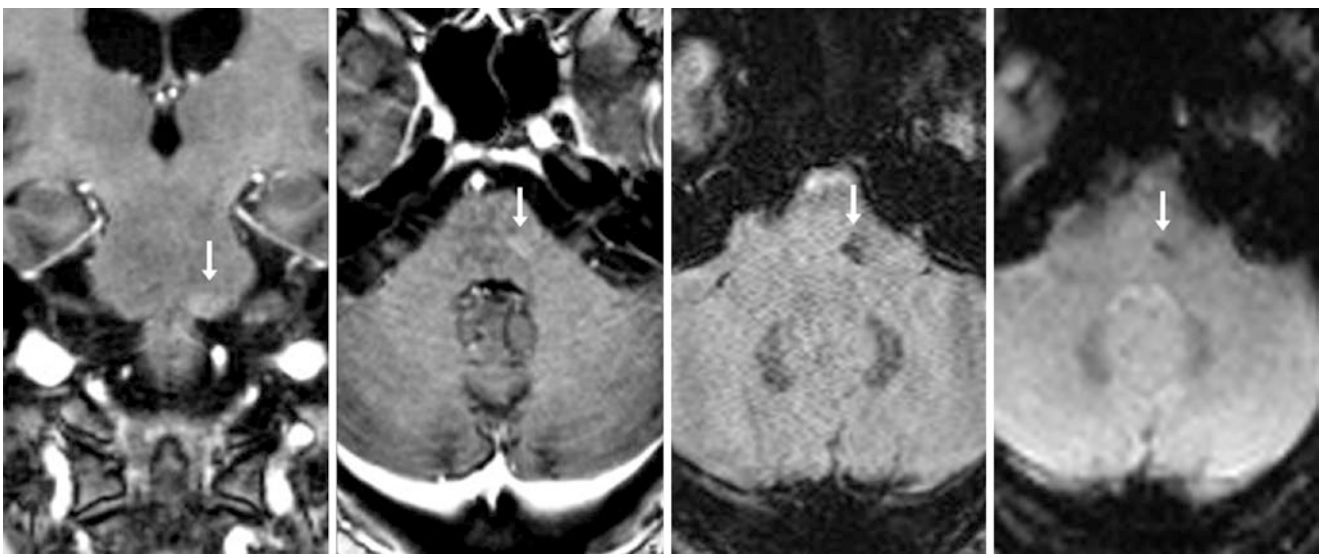

Fig. 21.8 A 64 year old with altered mentation who had only faint enhancement within a BCT located at the pontomedullary junction (*arrows*) on a 1.5T MRI with postcontrast coronal (*left*) and axial (*left middle*) GE T1WIs. On SWI (*right middle*), the telangiectasia's hypointensity was more evident. BOLD imaging (*right*) from MR perfusion data demonstrated the BCT to a lesser degree, since BOLD does not optimize phase data to the degree that SWI does

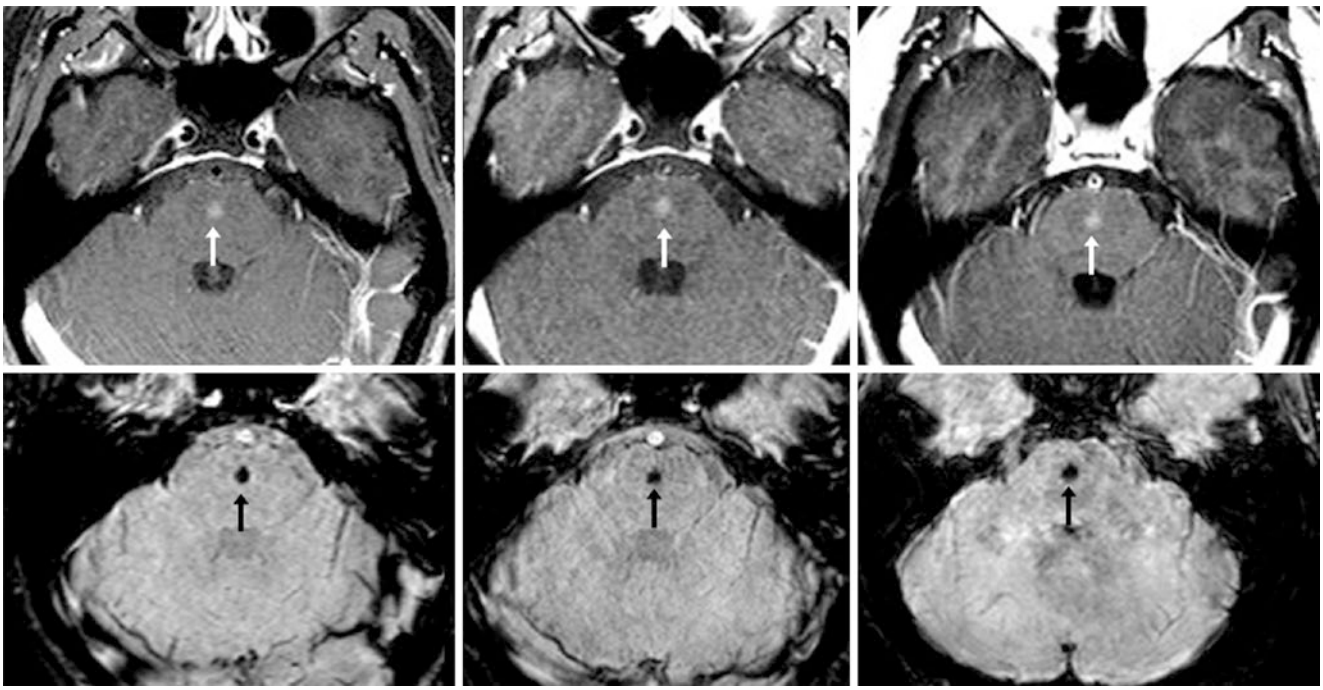

Fig. 21.9 A 26 year old with hearing deficits had a pontine BCT (*arrows*) on otherwise negative serial 1.5T MRIs that were obtained annually over 3 years; this included postcontrast axial T1WIs (*top row*) and SWIs (*bottom row*). The BCT mildly enhanced and was quite hypointense on SWI but appeared normal on T2WI/FLAIR (*not shown*)

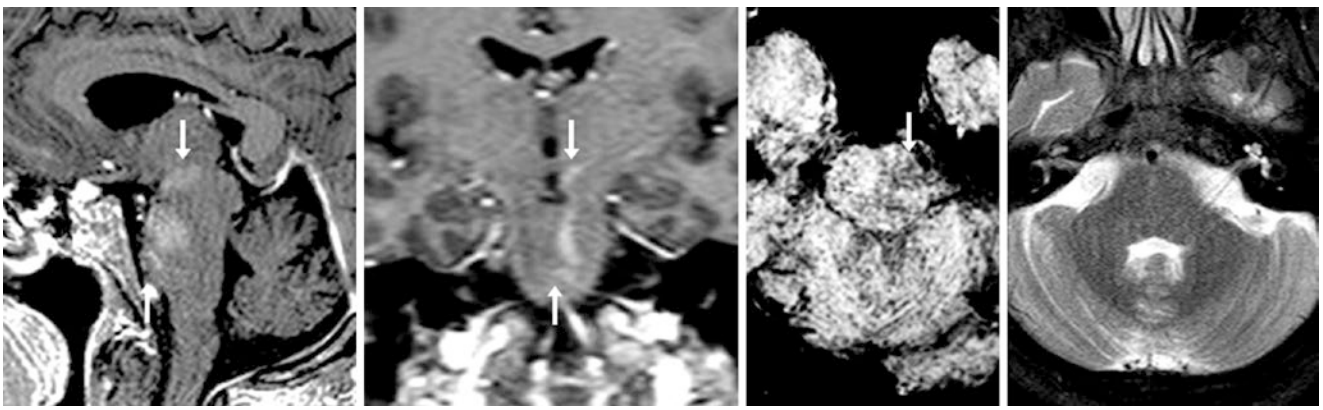

Fig. 21.10 A 37 year old with altered mentation who had had either a diffuse, multilevel BCT or three separate BCTs at the level of the midbrain, mid-pons, and lower pons (*arrows*) on a 1.5T MRI with postcontrast sagittal (*left*) and coronal (*left middle*) GE T1WIs. On an SWI that was mildly compromised because of motion (*right middle*), the BCT had mild hypointensity. The T2WI (*right*) appeared normal

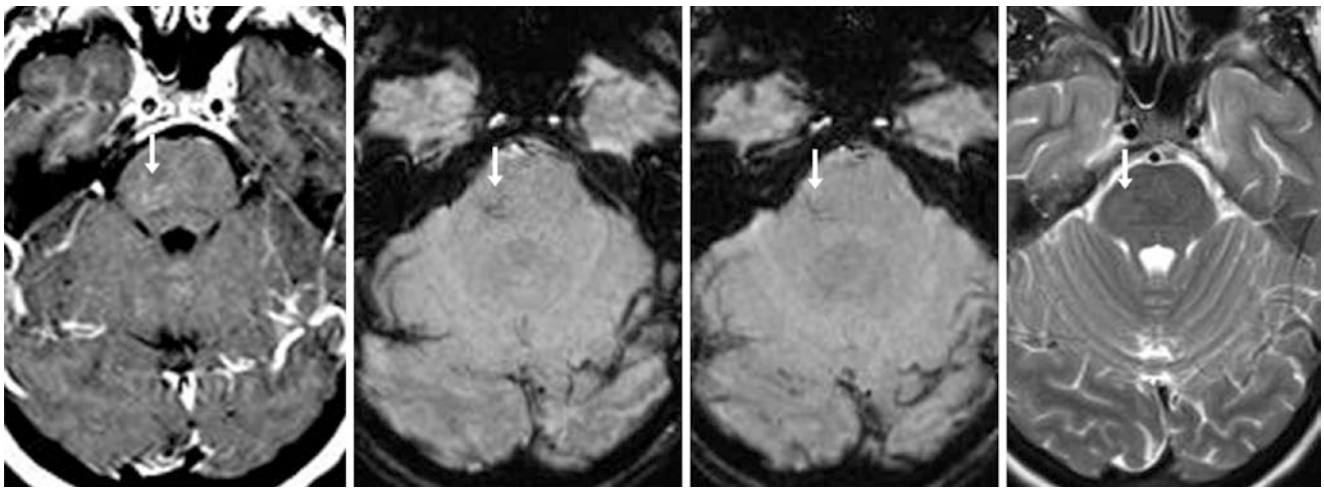

Fig. 21.11 In a 48 year old with gait difficulty an otherwise normal 1.5T MRI demonstrated only faint enhancement of a right pontine BCT (*arrows*) on postcontrast T1WI (*left*), with a small vascular tuft on SWIs (*left middle and right middle*). T2WI (*right*) and FLAIR (*not shown*) were normal. This subtle case of BCT could have been missed if SWI had not been obtained

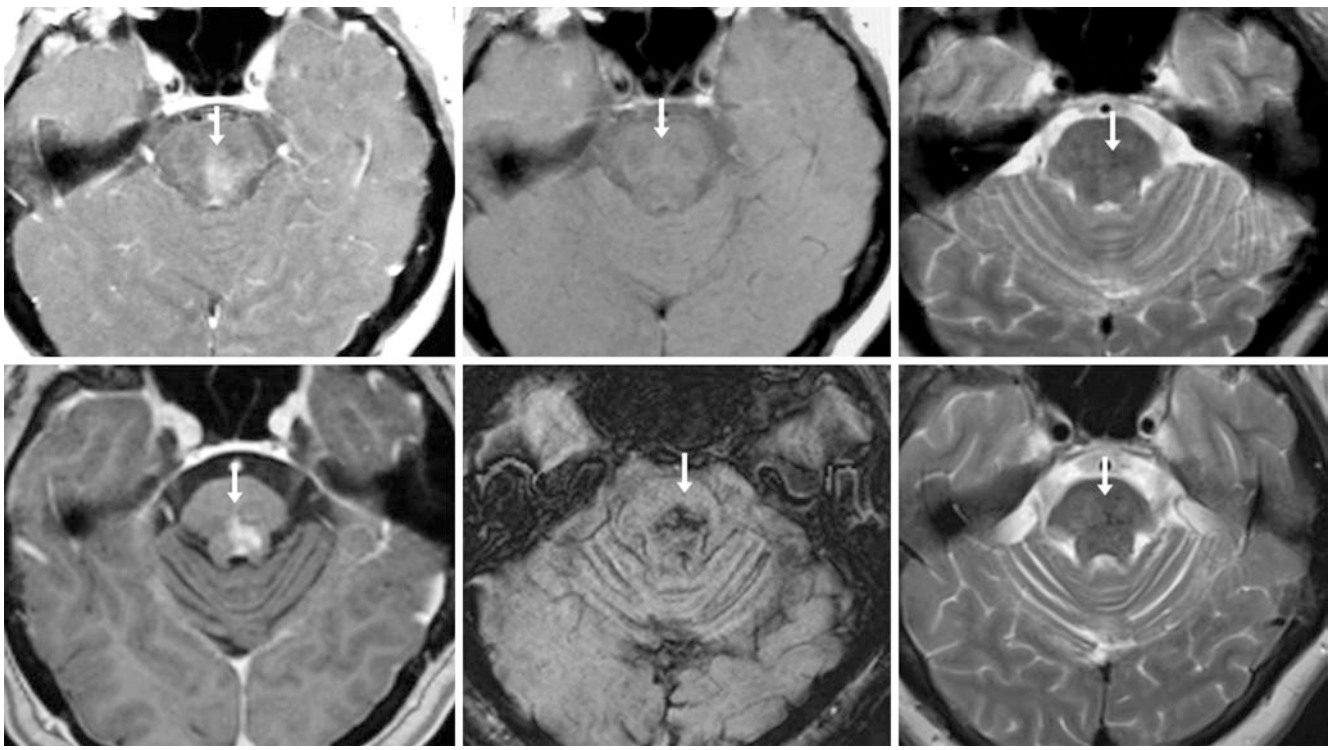

Fig. 21.12 Large pontine BCT in a 58 year old with ataxia. On a 1.5T brain MRI, postcontrast SE T1WI (*top left*) depicted rather avid enhancement, whereas precontrast T1WI (*top middle*) and T2WI (*top right*) were unremarkable. On a 1.5T MRI obtained 15 years later, postcontrast GE T1WI (*bottom left*) shows that the BCT is more discrete, while SWI (*right middle*) shows a darker signal than is typically seen within a BCT. The T2WI (*bottom right*) is unchanged

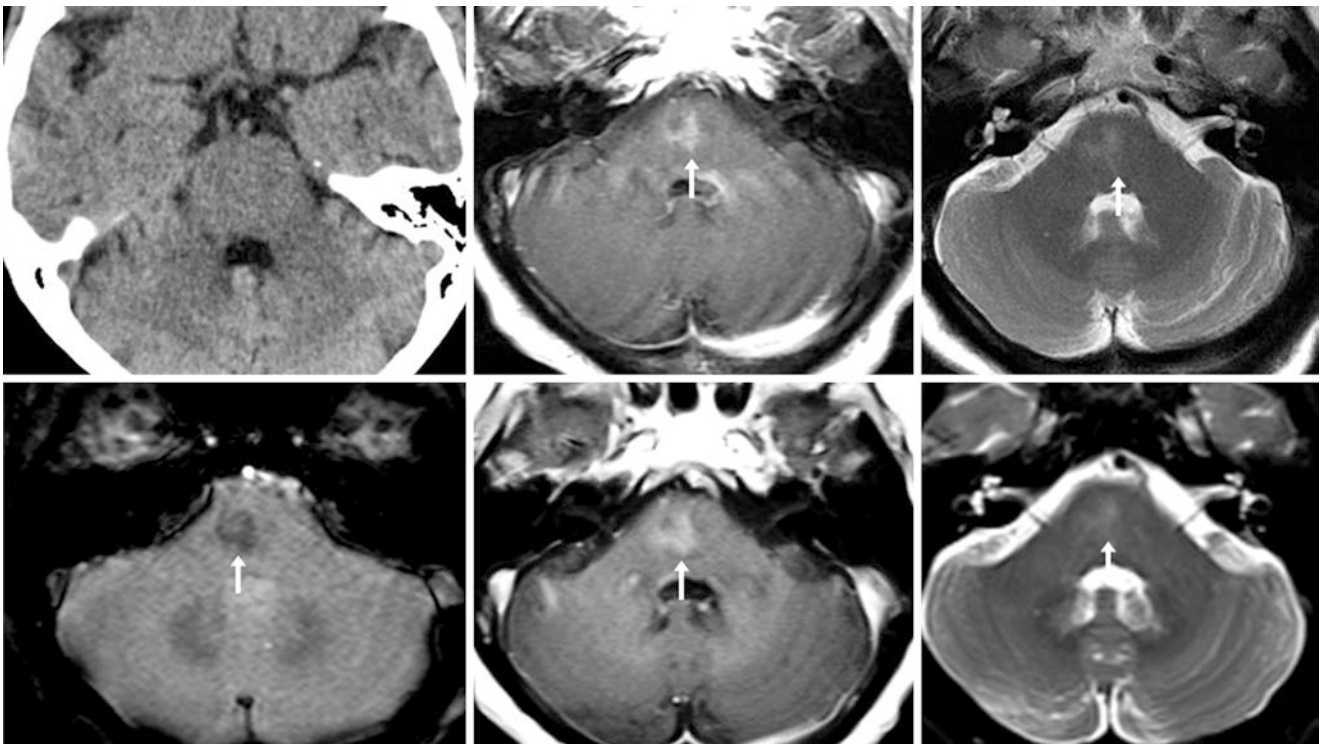

Fig. 21.13 A 62 year old had lung cancer without metastasis. A NECT (*top left*) was negative but a 1.5T MRI showed a 1.7 cm enhancing lesion (*arrows*) on postcontrast T1WI (*top middle*), with mild hyperintensity on T2WI (*top right*). This was not thought to be a metastasis because of the faint hyperintensity, but a follow-up MRI was recommended. On an MRI 1.5 years later, SWI (*bottom left*) showed "hazy" hypointensity of the BCT, and the BCT was unchanged on postcontrast T1WI (*bottom middle*), with persistent hyperintensity on T2WI (*bottom right*)

21.2 Capillary Telangiectasias: Cerebellar and Medullary

Cerebellar and *medullary* locations of *BCTs* are much less common than pontine types. Their appearance on SWI and enhancement pattern on postcontrast T1WI are similar to the pontine BCTs, but they are often much smaller and at times hardly visible. Some BCTs in these locations may be large and focal enough to resemble an enhancing focus of *metastatic disease* or *infectious etiology* (e.g., tuberculoma) (Figs. 21.14 and 21.15).

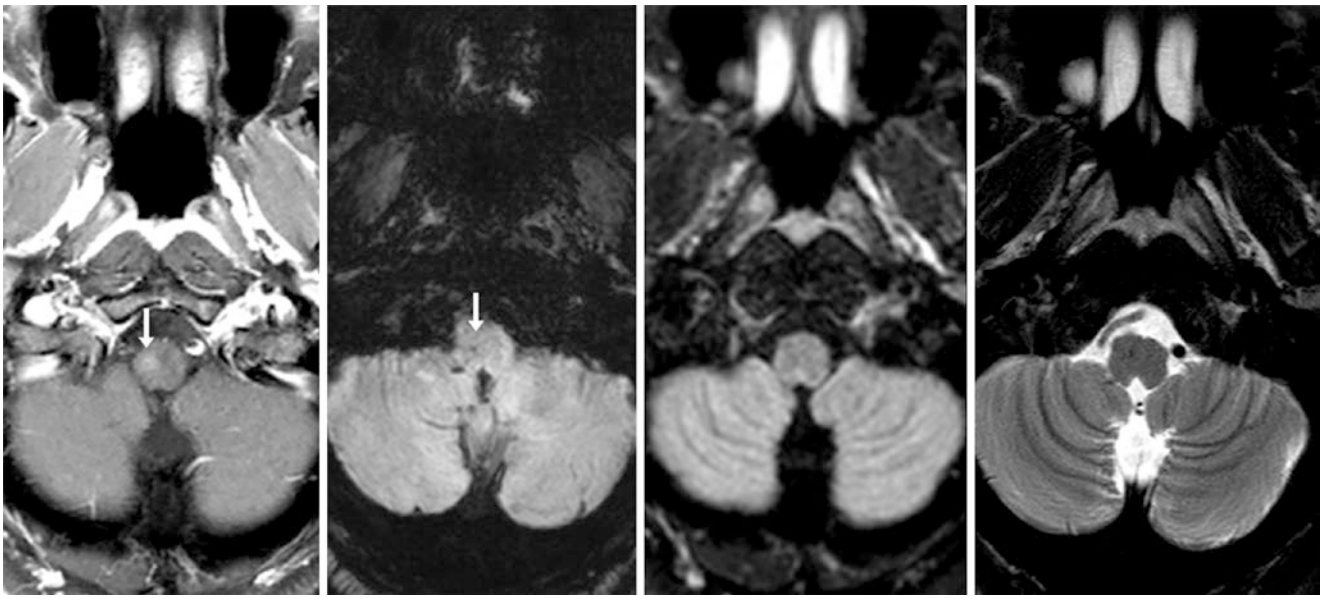

Fig. 21.14 A 55 year old with hyperesthesias had faint enhancement of a medullary BCT (*arrows*) on 1.5T MRI postcontrast axial SE T1WI (*left*), with faint low signal on SWI (*left middle*). The BCT is invisible on FLAIR (*right middle*) and T2WI (*right*) but does not simply represent flow void artifact from the vertebral artery since it is not present on T2WI

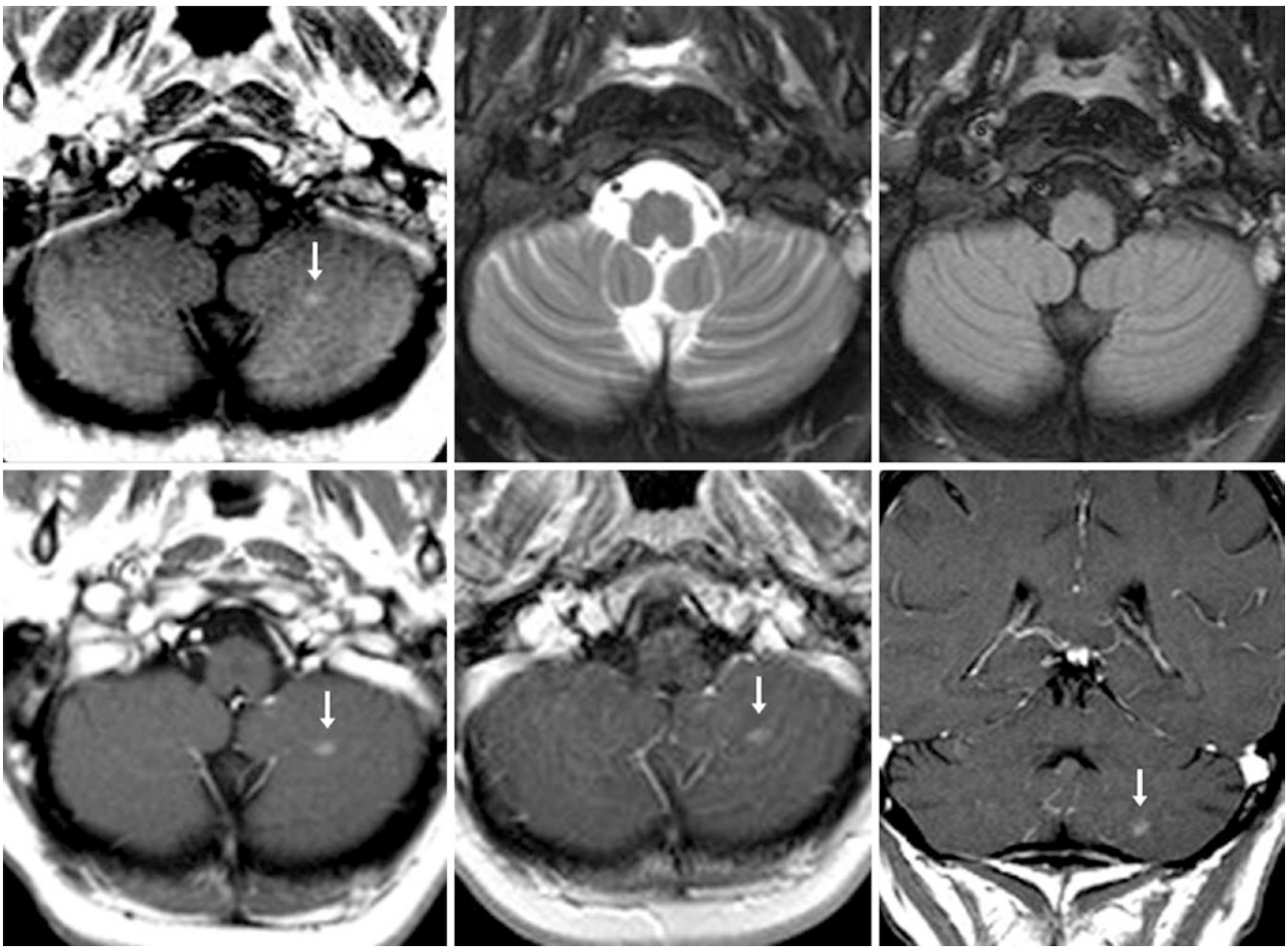

Fig. 21.15 A 42 year old had newly diagnosed lung cancer, with a 1.5T screening MRI that showed faint enhancement within the cerebellum (*arrows*) on a postcontrast SE T1WI (*top left*), which was questioned to be a metastasis. T2WI (*top middle*) and FLAIR (*top right*) were normal, and there were no enhancing lesions elsewhere. Repeat postcontrast T1WI at 3 months (*bottom left*) and 6 months (*bottom middle*) with coronal images (*bottom right*) showed no change in the presumed BCT. An untreated metastasis typically would have enlarged during that time

21.2.1 Capillary Telangiectasias: Basal Ganglial, Capsular, Frontal Basal, Insular, and Thalamic

Basal ganglial, frontobasal, and *thalamic BCTs* are also quite uncommon but can be troublesome when they mimic pathology, depending on location, sequence, and appearance. For example, as in other locations, they can simulate a solitary *neoplasm* or *metastatic disease* when focal and avidly enhancing. Another example is in the basal ganglia and thalami, where they may simulate a *subacute infarct with microhemorrhage* if avidly enhancing with dark signal on SWI (Figs. 21.16, 21.17, 21.18, 21.19, 21.20, and 21.21).

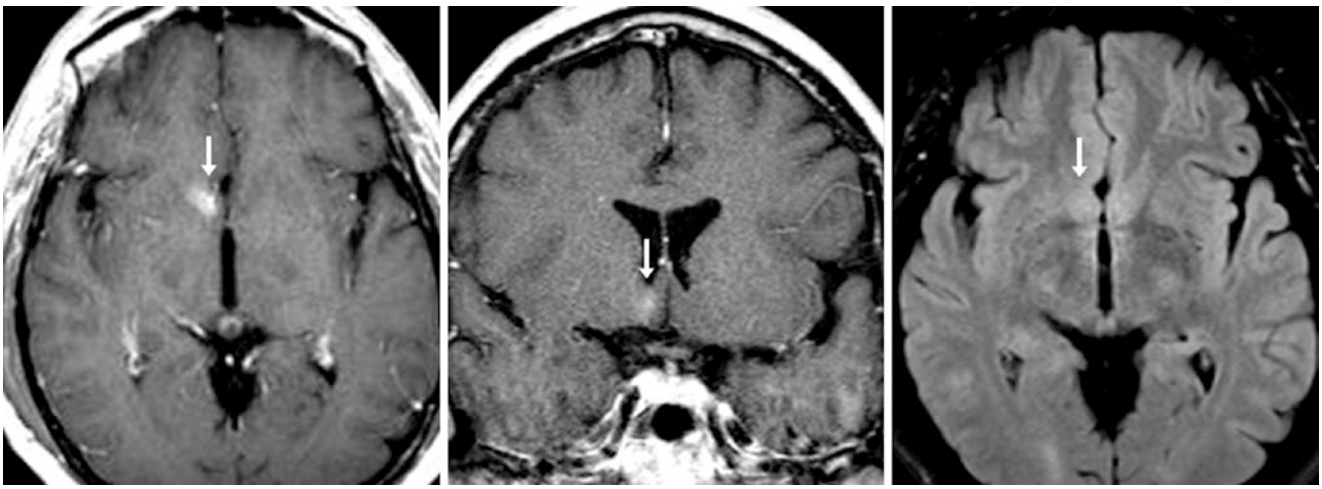

Fig. 21.16 A 45 year old with transient unconsciousness. Found on a 1.5T brain MRI, axial (*left*) and coronal (*middle*) postcontrast T1WIs was right frontal basal enhancement, while FLAIR (*right*) and T2WI (*not shown*) were normal. The patient requested a biopsy, since an outside physician told the patient that a low-grade neoplasm was probable, although it had been stable for 2 years. The biopsy confirmed a BCT, but the patient had a poor outcome because of an infarction

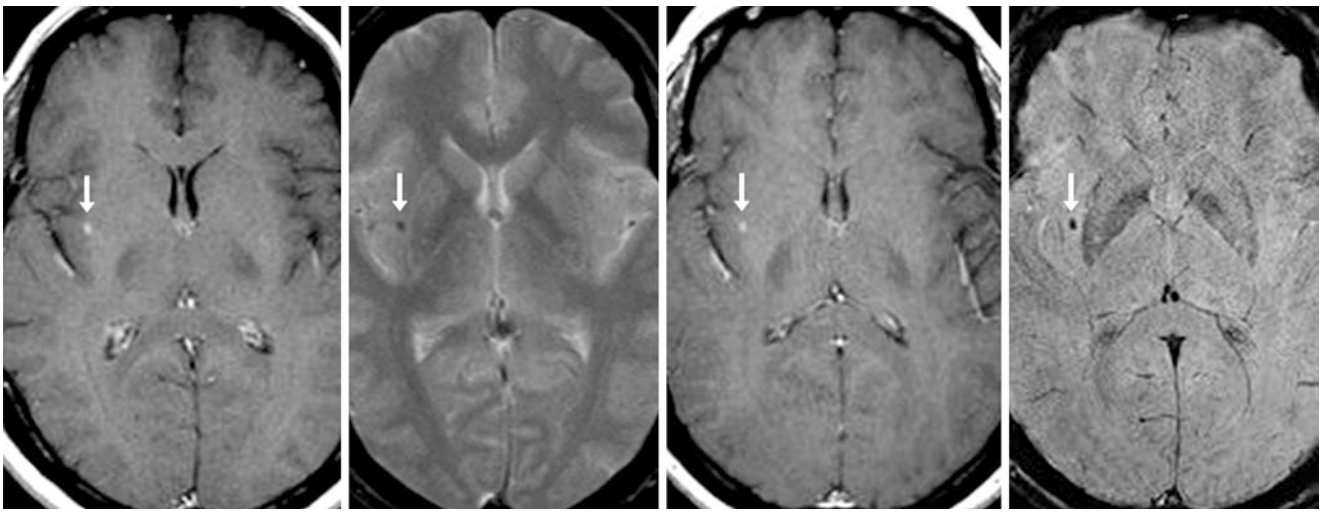

Fig. 21.17 A 53 year old with spinal myelitis underwent an otherwise negative 1.5T brain MRI that depicted a small focus of right external capsular enhancement (*arrows*) on postcontrast SE T1WI (*left*) and faint hypointensity on GE T2*WI (*left middle*). On MRI 2 years later, postcontrast SE T1WI (*right middle*) was stable, with hypointensity on SWI (*right*) indicative of a BCT that simulates microhemorrhage. FLAIR images remained normal

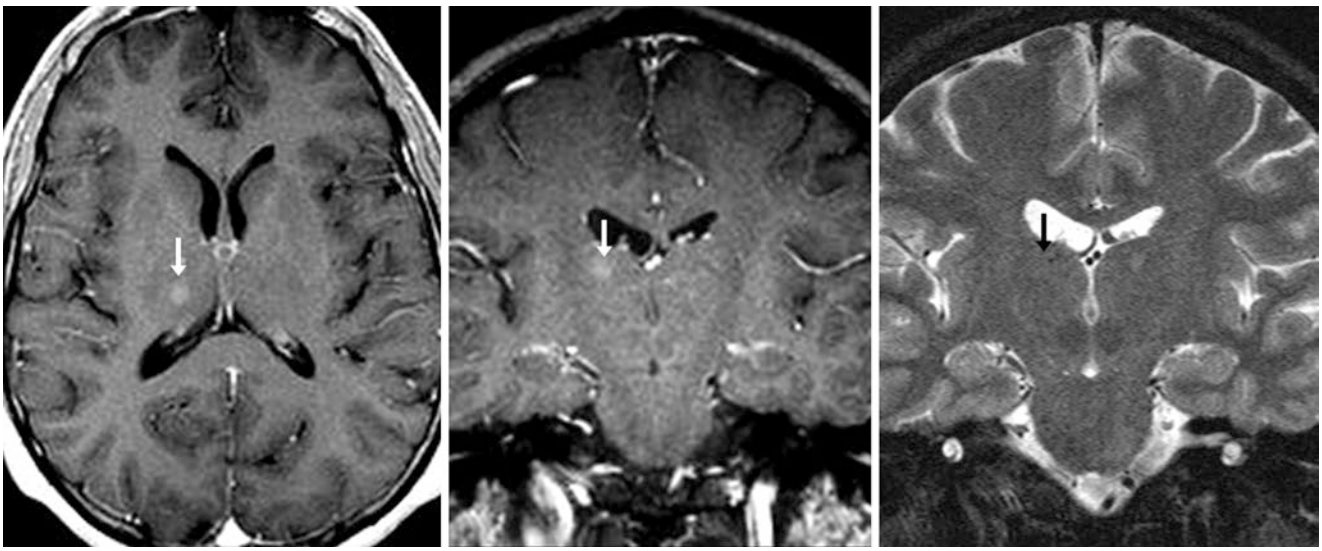

Fig. 21.18 A 32 year old with headaches underwent a 1.5T brain MRI, which showed a small, faint focus of enhancement within the right thalamus that simulated a solitary neoplasm on postcontrast axial (*left*) and coronal (*middle*) T1WIs, without corresponding edema on coronal T2WI (*right*). SWI was not available at that time, but the findings were considered consistent with a BCT

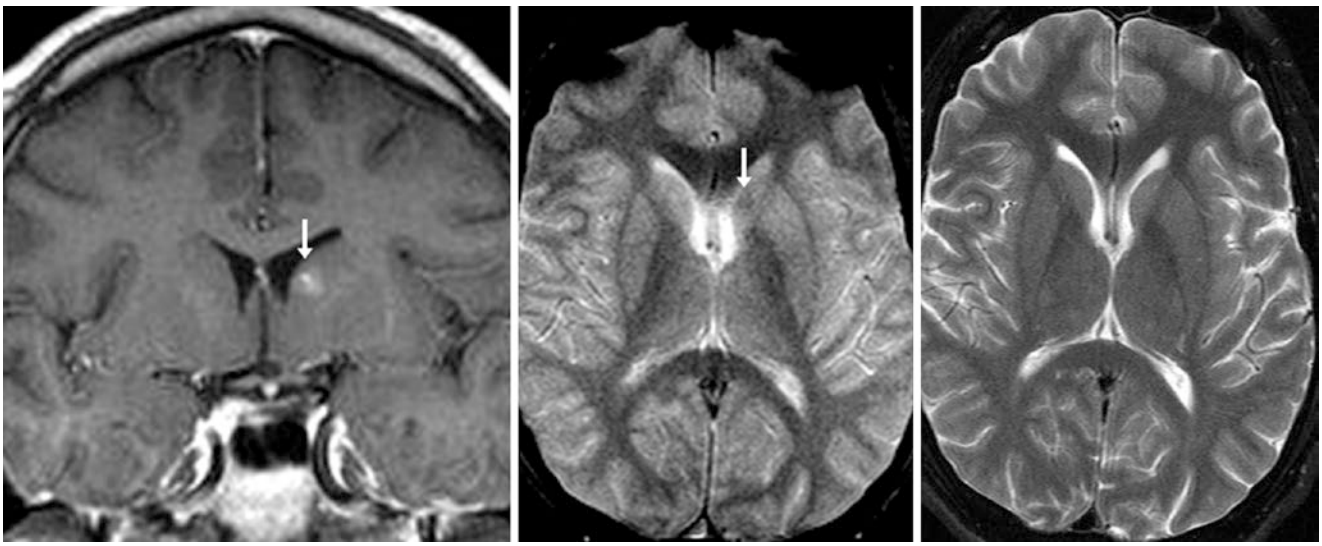

Fig. 21.19 A 27 year old with dizziness; on a 1.5T MRI, there was a region of poorly circumscribed but a moderate degree of enhancement (*arrows*) within the left caudate head on postcontrast coronal SE T1WI (*left*) with only faint internal dark signal on GRE T2*WI (*middle*), while T2WI (*right*) appeared normal. No other enhancing lesions were noted

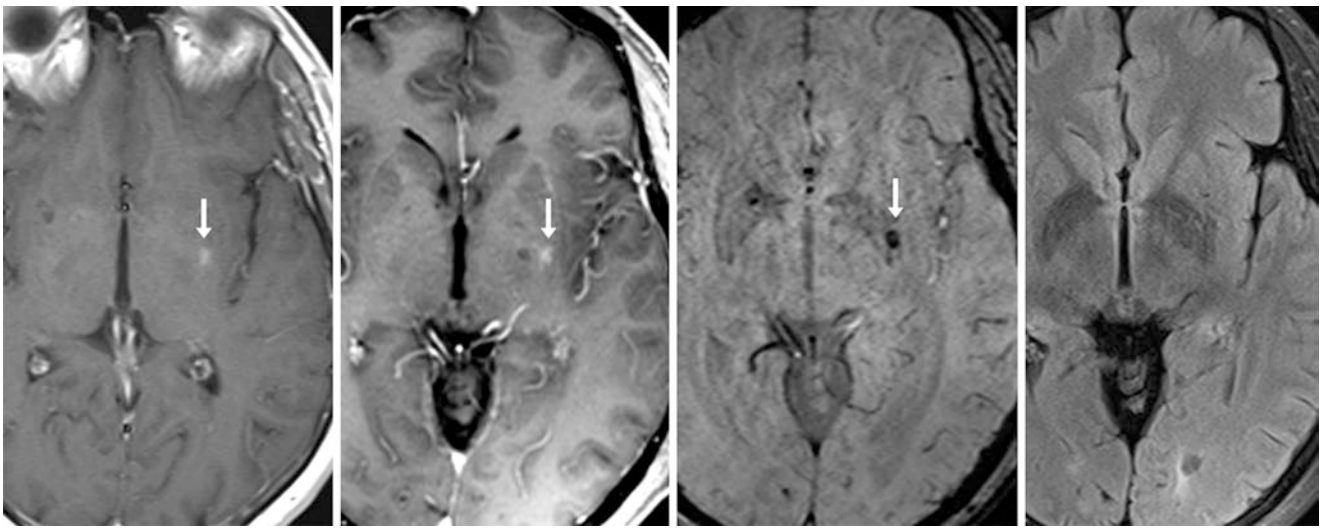

Fig. 21.20 A 44 year old with a tiny sphenoidal meningioma whose Initial 1.5T MRI showed a small focus of left putaminal enhancement (*arrows*) on postcontrast SE T1WI (*left*). This was unchanged 6 years later on GE T1WI (*left middle*). The hypointensity on SWI (*right middle*) and normal FLAIR (*right*) signal were indicative of a BCT. On SWI, this basal ganglial BCT could simulate a subacute infarct with microhemorrhage if no follow-up MRI was available

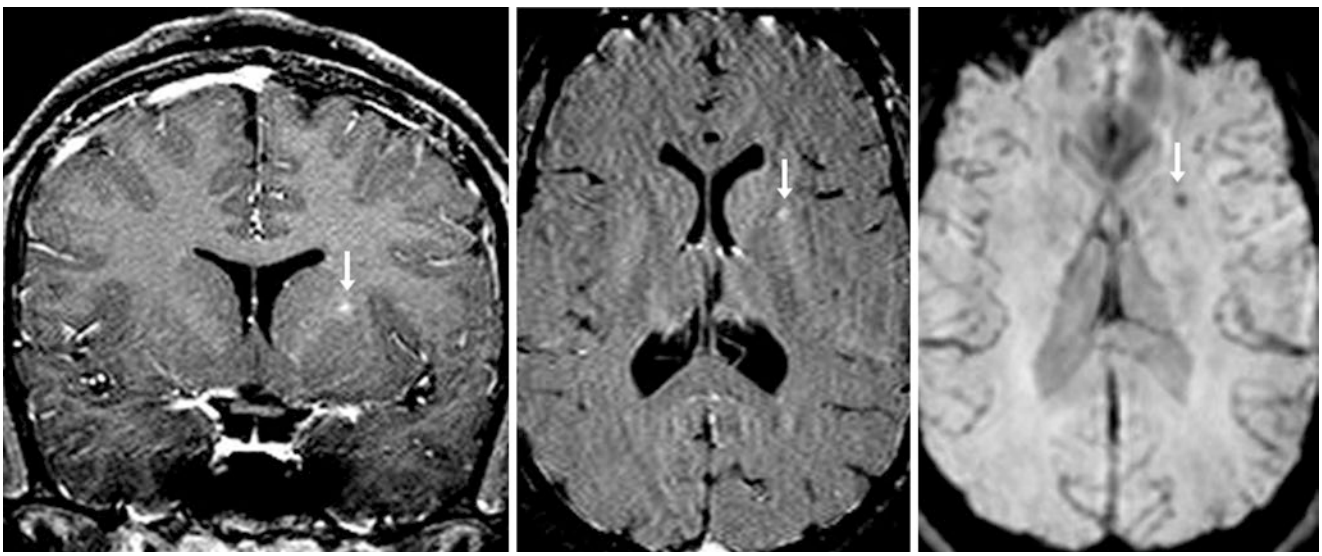

Fig. 21.21 An 11 year old with an unrelated cranial nerve VI palsy underwent an otherwise negative 1.5T MRI on which faint enhancement was demonstrated (*arrows*) within the left internal capsule on postcontrast coronal SE T1WI (*left*) and on GE phase contrast images (*middle*). SWI (*right*) demonstrated a faint focus of signal loss consistent with a BCT

21.2.2 Capillary Telangiectasias: Callosal and Cingulate

Callosal and *cingulate BCTs* are rare. BCTs in these locations may mimic pathology such as *demyelinating disease* (when focally avidly enhancing), focal *traumatic brain injury* (due to a dark signal on SWI), or a *neoplasm* (e.g., a solitary enhancing lesion of metastatic disease or primary brain tumor) (Figs. 21.22, 21.23, and 21.24).

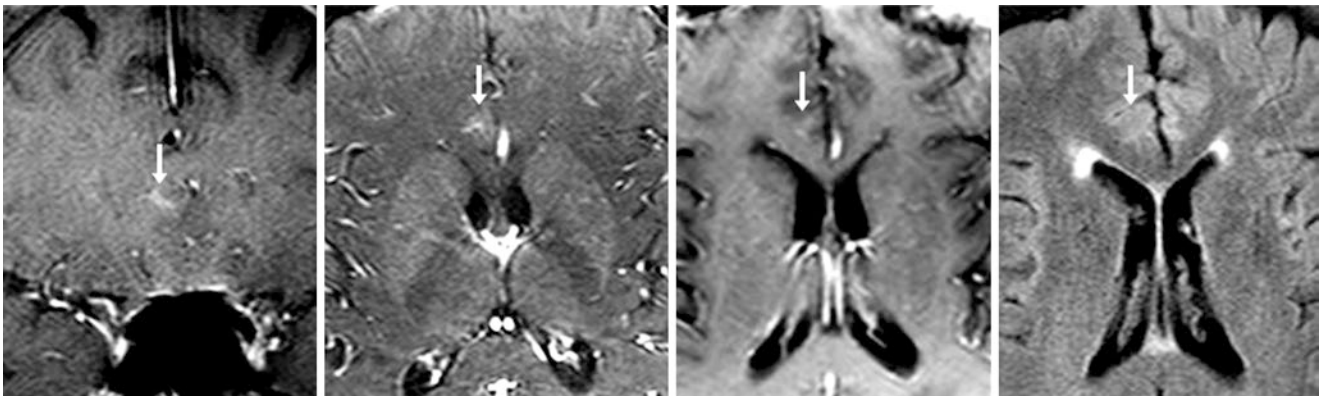

Fig. 21.22 A 69 year old who had visual deficits underwent an otherwise negative 3T MRI that demonstrated a small, faint focus of enhancement (*arrows*) within the right cingulate gyrus on postcontrast coronal (*left*) and axial (*left middle*) SE T1WIs. This BCT was not as well visualized on postcontrast axial GE T1WIs (*right middle*) and was not visible on FLAIR (*right*)

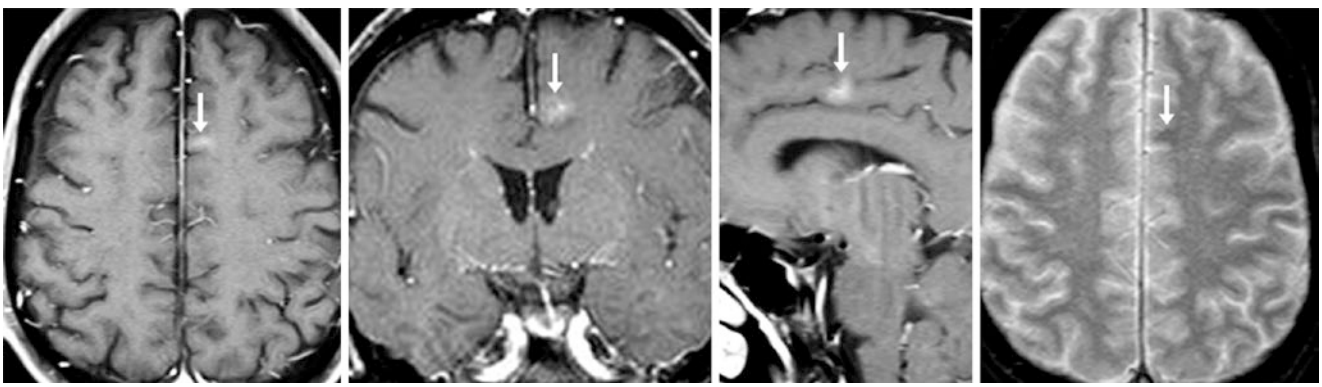

Fig. 21.23 A 65 year old with dizziness underwent an otherwise negative 1.5T MRI that depicted a small enhancing focus (*arrows*) within the left cingulate gyrus on postcontrast axial (*left*), coronal (*left middle*), and sagittal (*right middle*) SE T1WIs. There was only very faint hypointensity on axial GE T2*WI (*right*). This BCT was not visible on T2WI/FLAIR (*not shown*)

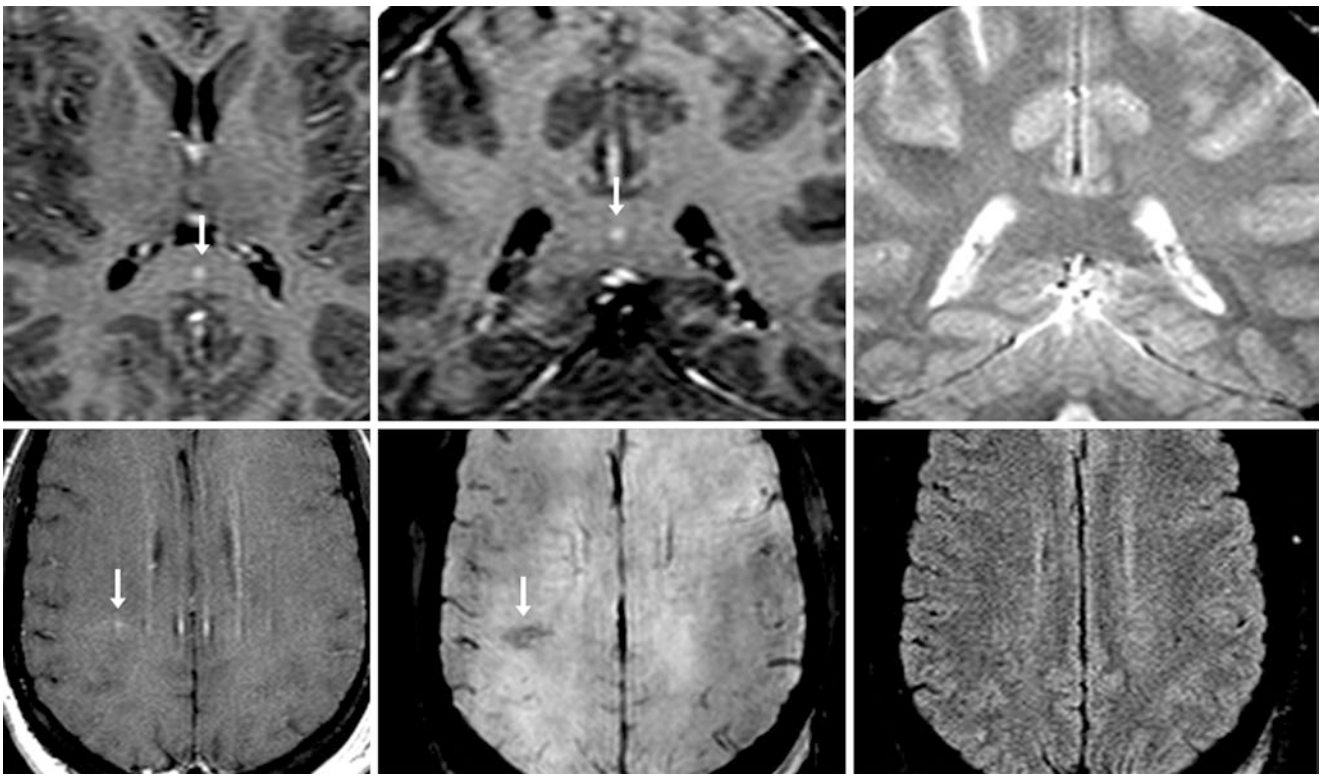

Fig. 21.24 A 42-year-old post-trauma patient with two BCTs. On a 1.5T brain MRI, postcontrast axial (*top left*) and coronal (*top middle*) GE T1WIs showed focal enhancement of a BCT within the callosal splenium, while GE T2*WI (*top right*) was normal, indicating this was not a shear injury. Also, a second small lobar BCT was found within the right parietal lobe, as shown on postcontrast SE T1WI (*bottom left*) and SWI (*bottom middle*) but normal on FLAIR (*bottom right*). These were not trauma-related hemorrhages, as they enhanced and were not punctate on SWI

21.2.3 Capillary Telangiectasias: Lobar

Lobar BCTs occurring within the parenchyma of the frontal, occipital, parietal, or temporal lobes are also quite rare, typically located within the subcortical or deep white matter. BCTs in these locations may also mimic pathology such as *demyelinating disease* (when focally avidly enhancing), focal *traumatic brain injury* (due to a dark signal on SWI), or *neoplasm* (e.g., a solitary enhancing lesion of metastatic disease or a primary brain tumor) (Figs. 21.25 and 21.26).

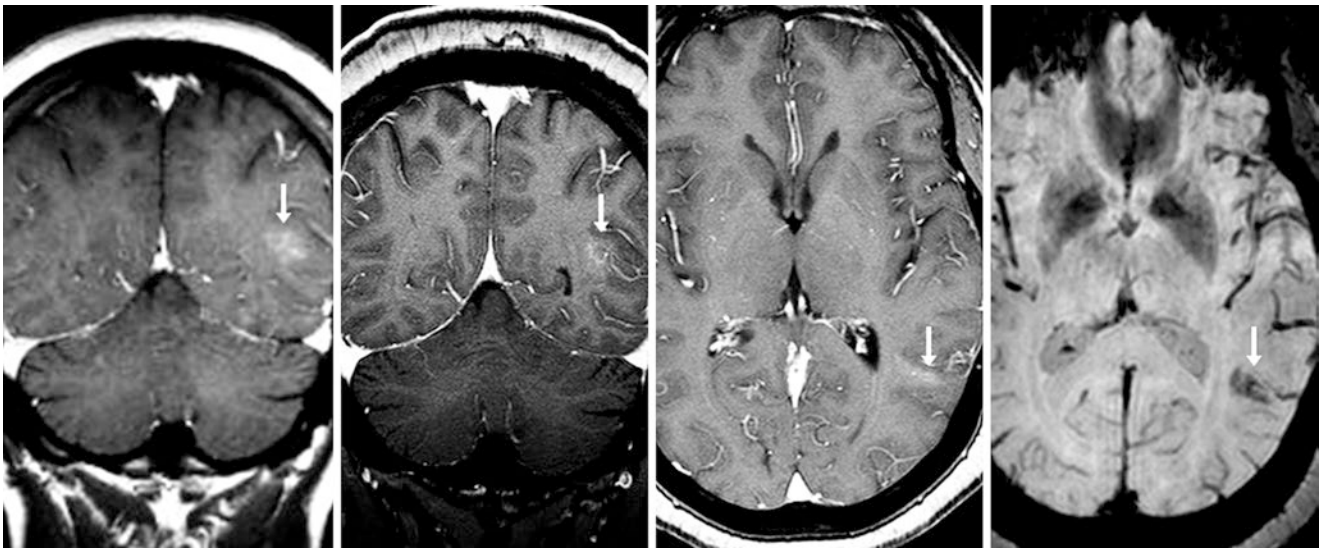

Fig. 21.25 A 50 year old with chronic headaches underwent an otherwise negative 1.5T brain MRI that depicted mild enhancement within the posterior left temporal white matter (*arrows*) on postcontrast SE T1WI (*left*). Over 10 years later, this was unchanged on coronal (*left middle*) and axial (*right middle*) postcontrast GE T1WI, while T2WI (*not shown*) was normal. On SWI (*right*) the blush of hypointensity indicated a BCT

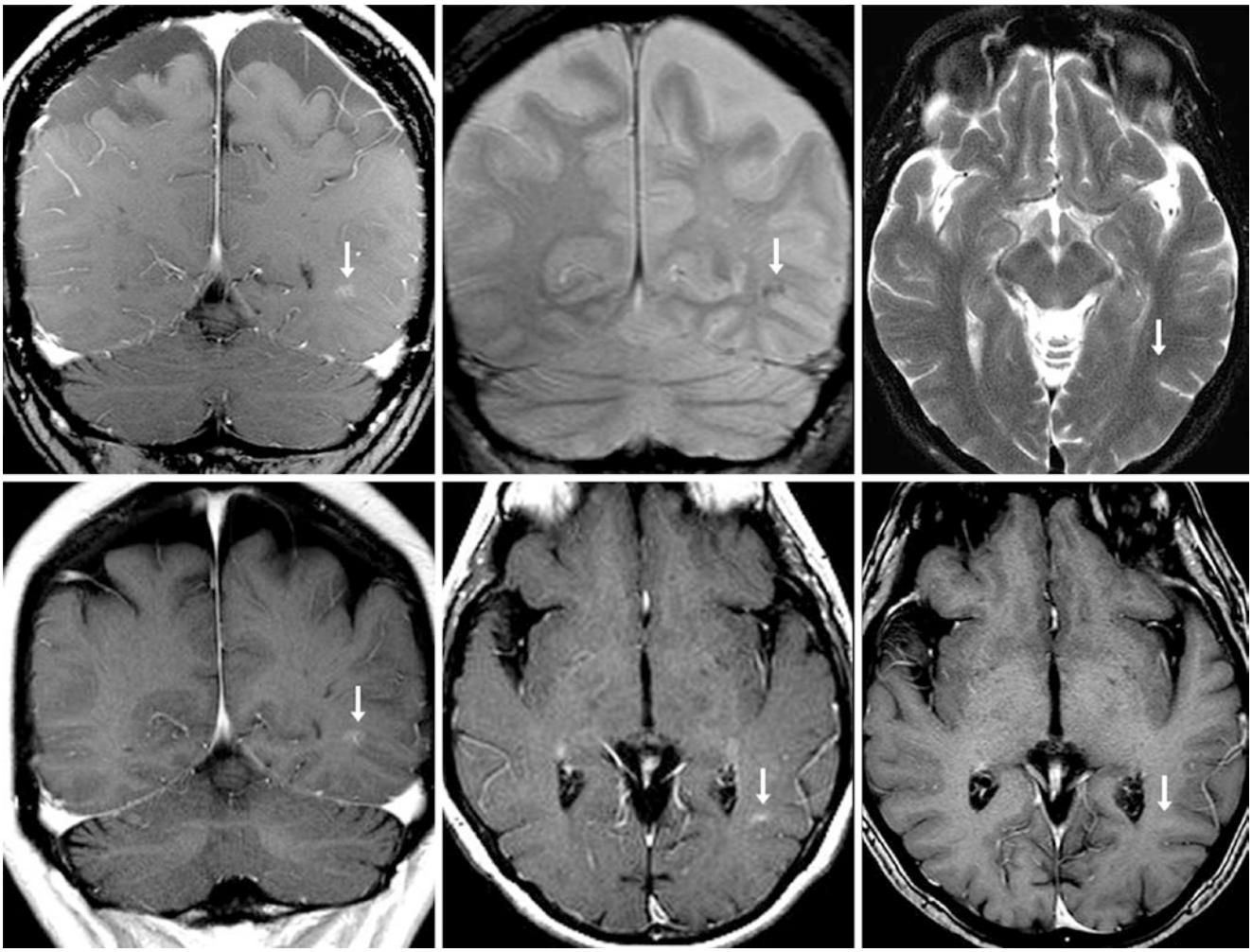

Fig. 21.26 A 64 year old with renal cancer whose 1.5T MRI, postcontrast axial GE T1WI (*top left*) showed a faint parietal focus of enhancement with faint dark signal on coronal T2*WI (*top middle*), and lacking edema on T2WI (*top right*). This was called a BCT; no metastases were noted. Two years later, coronal postcontrast GE (*bottom left*) and axial SE (*bottom middle*) T1WIs were unchanged, consistent with a BCT. Note that spoiled postcontrast GE T1WI (*bottom right*) hardly shows the enhancing BCT, as the contrast-to-noise ratio of GE T1WI is not as high as SE T1WI

21.3 Developmental Venous Anomalies

As stated earlier, *developmental venous anomalies* (DVAs, also known as venous angiomas) are the most common cerebral vascular malformations, representing about 50–60 % of such lesions. They appear as a spoke-wheel or *caput medusa* of enlarged veins that drain into a larger vein; the larger vein eventually drains into a dural venous sinus, cortical vein, or another major intracranial vein. They are not to be confused with AVMs, since DVAs lack an arterial component (although some reports have claimed to identify one). Their most common location (approximately 40–60 %) is the frontal or parietal lobes, but up to 30 % can be seen within the cerebellar hemispheres.

DVAs are estimated to occur in 0.5–2.5 % of the population based on both autopsies and recent studies that have implemented SWI MRI. This number may increase as improved susceptibility imaging and higher field strengths are utilized. SWI is able to demonstrate DVAs because of the high concentration of paramagnetic deoxyhemoglobin in the deoxygenated (i.e., venous) blood within them. DVAs are considered to be low-flow lesions that are purely venous, histologically consisting of thickened, hyalinized abnormally enlarged veins. The pathophysiology of their development is still debated, but it has been proposed that collateral dilated veins develop as a result of impaired or occluded normal cortical venous drainage or deep medullary venous drainage in early life. As such, the enlarged draining veins are considered abnormal.

Initially, DVAs were thought to have a high rate of hemorrhage or to portend the development of an AVM; however, more recent data suggest that DVAs are basically "don't touch" lesions because their annual risk of hemorrhage has been reported to be quite low at 0.15–0.70 % based on the lack of symptom development at long-term follow-up in the vast majority. Also, these are typically "don't touch" lesions since they drain normal cerebral parenchyma, and treatment or resection of these lesions may lead to horrible complications, such as venous ischemia or thrombosis. Some even consider DVAs to be at the extreme end of normal variation. However, more recent evidence based on SWI MRI suggests that these are actually not normal variants, since hypointense foci that are presumed to represent remote microhemorrhages or tiny *cavernomas* have been found in up to 62 % of DVAs! This percentage had previously been reported to be much lower (at 7 to 18 %); conversely, DVAs have been found in 8–33 % of patients with cavernomas. Therefore, the evidence linking DVAs to the higher risk cavernomas is increasing and argues against DVAs being true normal variations. DVAs can occasionally be confused with AVMs when they are larger, particularly if only noncontrast images are available.

The appearance of the "caput medusae", or spoke-wheel of radiating vessels associated with a DVA is quite consistent and typically cements the diagnosis of DVA on postcontrast imaging; the type of T1WI sequence usually does not matter for diagnosis (but may make a difference to visualize the extent) unless the lesion is quite tiny. Postcontrast FLAIR imaging can also help to visualize DVAs. However, an intravenous contrast agent is not always administered for MRIs, and thus on noncontrast routine MR images DVAs are only variably visualized as dark flow voids on T2WI, related to the size, extent, and flow rate of these lesions. However, the use of SWI on all routine noncontrast examinations may obviate the use of intravenous contrast material in discriminating DVAs from AVMs, since SWI is quite accurate in detecting DVAs. It is also important to note that white matter hyperintensity may be visualized in DVAs based on FLAIR or T2WI, and such hyperintensity is more common when there is also hypointensity (thought to be old hemorrhages or cavernomas) immediately surrounding the DVA. There is no gold standard to detect DVAs; however, both noncontrast SWI and postcontrast SWI can easily depict DVAs and discriminate them from AVMs. Catheter angiography was initially utilized to diagnose larger DVAs, but because DVAs are low flow, invasive methods are unnecessary in the majority of patients unless they are extensive or in the rare instance where their appearance overlaps that of an AVM.

Hence, DVAs should only be treated if there are clearly related symptoms such as *thrombosis,* or if they are quite large and strategically placed to cause symptoms (e.g., seizures), which occurs only rarely. Also, extremely rare cases have been described of a holohemispheric type of DVA that involves the entire cerebral or cerebellar hemisphere, which may have associated cerebral atrophy and cause symptoms such as seizures. Interestingly, to the best of this author's knowledge there have not been any clear descriptions of enlargement of a DVA progressively over time, which is in direct contrast to AVMs.

The most clinically important (and interesting) point regarding DVAs is their debatable association with the presence of *cavernomas* (also known as cavernous angiomas). The rate of their occurring together varies widely, probably related to whether the study quoting the number is subselected from a cohort selected from solely DVAs, from patients with cavernomas, from a group with vascular lesions in general, or from autopsy data at large. As stated above, more recent literature has suggested that faint microhemorrhages or cavernomas occur on SWI in over 60 % of DVAs, a frequency much higher than the traditional 7–18 %, while 8–33 % of cavernomas have been found to have an underlying DVA. This frequency of cavernomas associated with DVAs appears to be increasing, probably as a result of improved detection related to utilization of SWI, which can depict both the hemosiderin stain of a cavernoma as well as

the caput drainage appearance of a DVA. It is currently thought (based on imaging and histology) that the presence of hemorrhage surrounding a DVA is overwhelmingly likely to represent a cavernoma, but the radiologist should exclude the uncommon possibility of thrombosis of the DVA.

As discussed in the previous topic, 10–15 % of incidental brain capillary telangiectasias (BCTs) have an associated DVA, and they may occasionally have a tiny draining vein but lack the caput of a DVA. This has led to speculation that BCTs, DVAs, and cavernomas exist on a spectrum of vascular malformations; indeed, there are reports of all three phenomena occurring together in a patient. Notably, cavernomas are much less common (about 0.5 % of the population) than either DVAs or BCTs. Even if an asymptomatic cavernoma presents in association with a DVA, the risk of hemorrhage per year remains quite low (just under 1.0 % annually).

21.3.1 Developmental Venous Anomalies: Cerebellar

DVAs can occur just about anywhere within the brainstem, cerebrum, or cerebellar hemispheres, but they are quite common and have a characteristic appearance within the cerebellum. The cerebellum is a site of DVAs in about one third of cases but is typically asymptomatic. The appearance of a caput with an enlarged draining vein is characteristic, typically best seen on either postcontrast T1WI or as a blush of deoxygenated venous structure with a single draining vein on higher resolution SWI. Larger cerebellar DVAs may simulate an *arteriovenous malformation*. Also, note the presence of a concomitant *brain capillary telangiectasia* (BCT, asymptomatic) or hemosiderin from a *cavernoma* (seen in up to one third of DVAs) on SWI, as *cavernomas* can be symptomatic and are common in the posterior fossa (Figs. 21.27, 21.28, 21.29, 21.30, and 21.31).

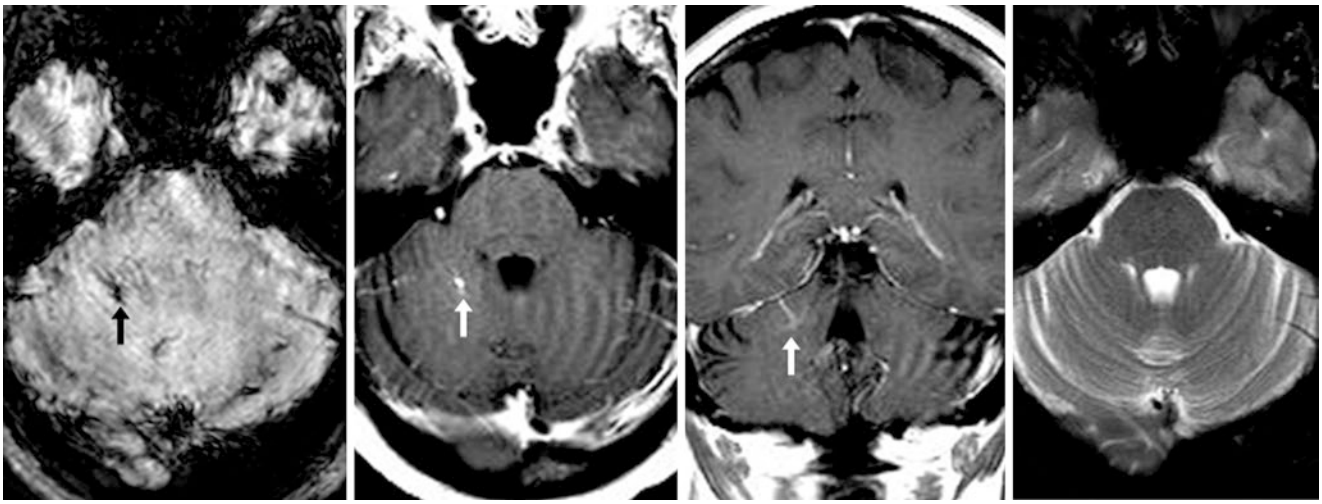

Fig. 21.27 A 49 year old with headaches and syncope underwent an otherwise negative 1.5T brain MRI that depicted a small draining vein (*arrows*) arising from a tuft of enhancement within the superior right hemicerebellum on SWI (*left*) and on postcontrast axial (*left middle*) and coronal (*right middle*) SE T1WIs. T2WI (*right*) appeared normal

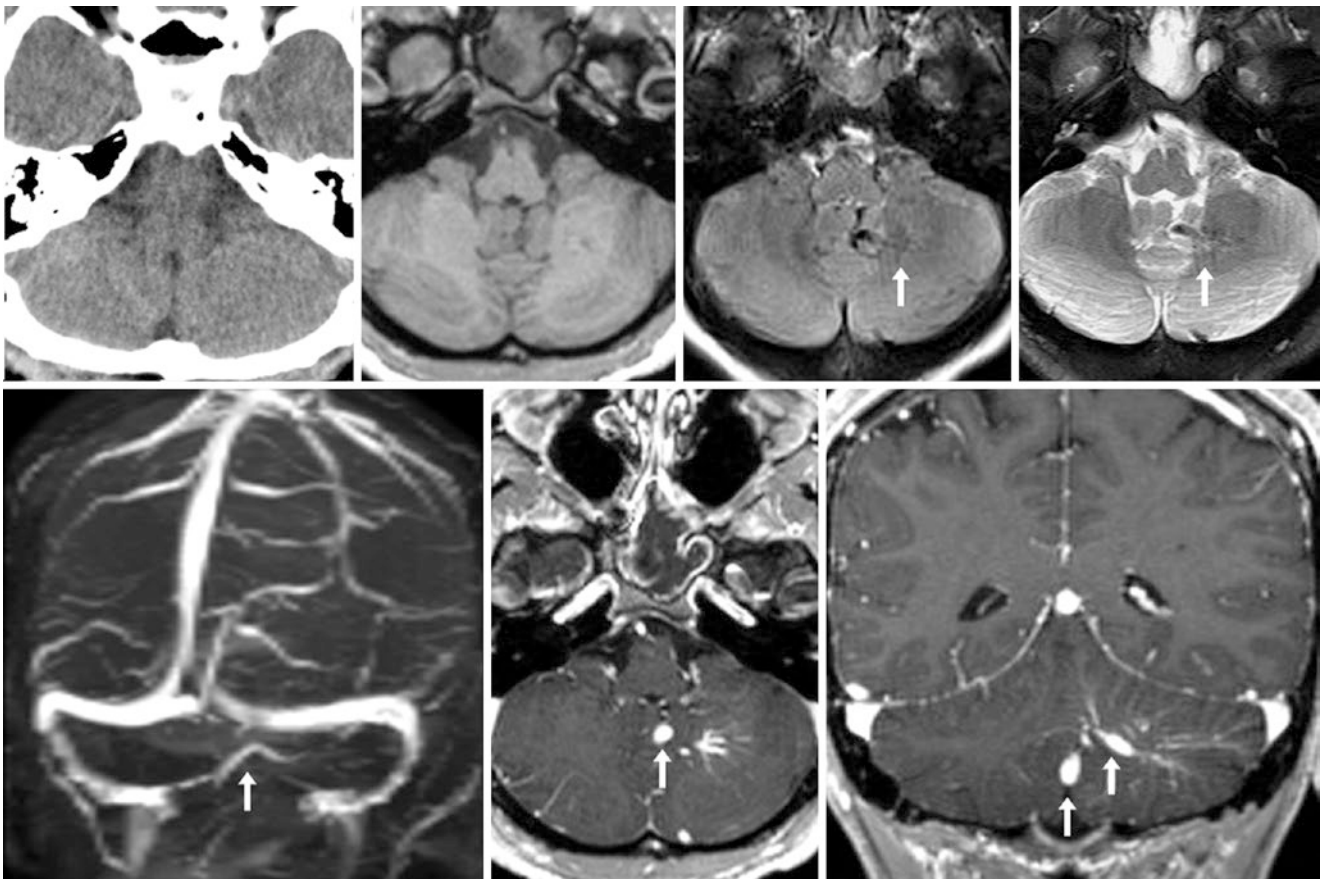

Fig. 21.28 A 25 year old with chronic headaches: axial NECT, GE T1WI, FLAIR, and T2WI (*top row, respectively*) did not depict a DVA. However, noncontrast TOF MRV (*PA view, bottom left*) and axial (*bottom middle*) and coronal (*bottom right*) GE T1WIs showed a caput of left cerebellar enhancement with an enlarged vein draining medially (*arrows*)

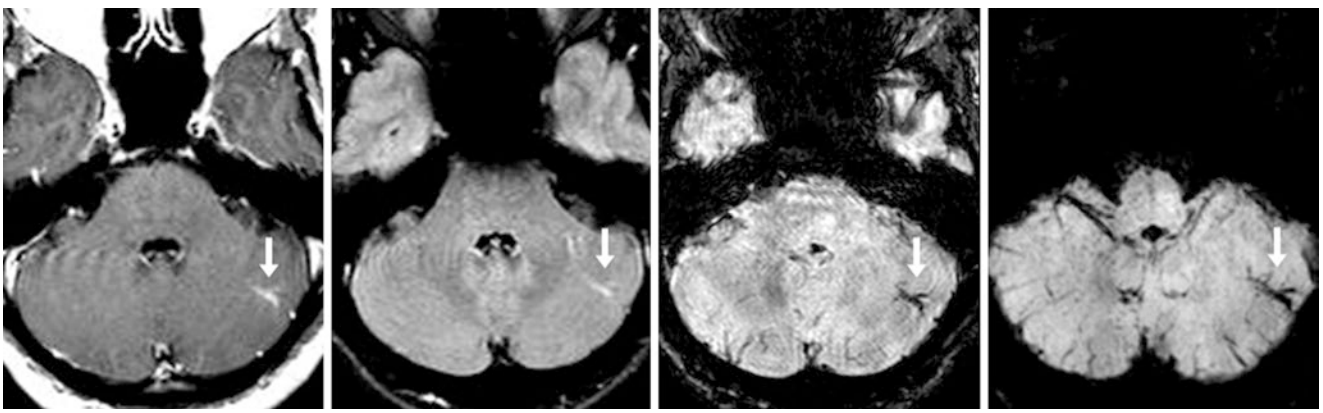

Fig. 21.29 A 48 year old with memory loss in whom an otherwise negative 1.5T brain MRI noted a small draining vein (*arrows*) within the left hemicerebellum on postcontrast SE T1WI (*left*), postcontrast FLAIR (*left middle*), 2 mm SWI (*right middle*), and thick 15 mm SWI (*right*). Note how thicker SWI images better illustrate the course of the draining vein

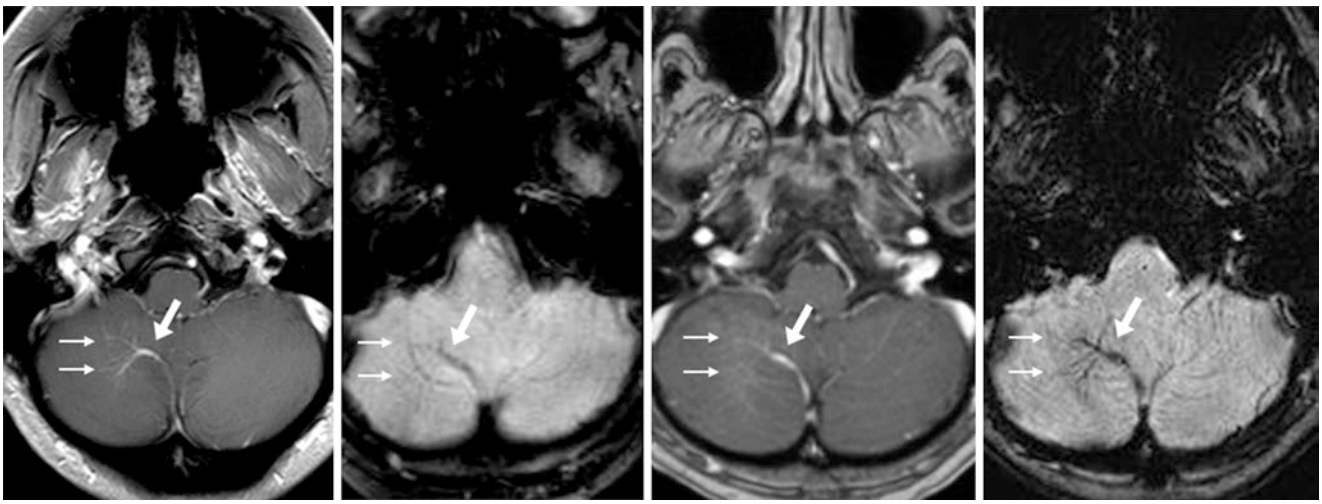

Fig. 21.30 A 49 year old followed for a frontal oligodendroglioma in whom a 1.5T brain MRI noted a small vein (*arrows*) that drained medially from a caput of vessels (*thin arrows*) within the right hemicerebellum on postcontrast SE T1WI (*left*) and on GE T2*WI (*left middle*). A repeat MRI 8 years later was performed with postcontrast GE T1WI (*right middle*), and on 2-mm SWI (*right*). Note that SWI delineates DVA better than GE T2*WI, probably because SWI better displays deoxygenated blood. Also, postcontrast SE T1WI may better portray a DVA than GE T1WI

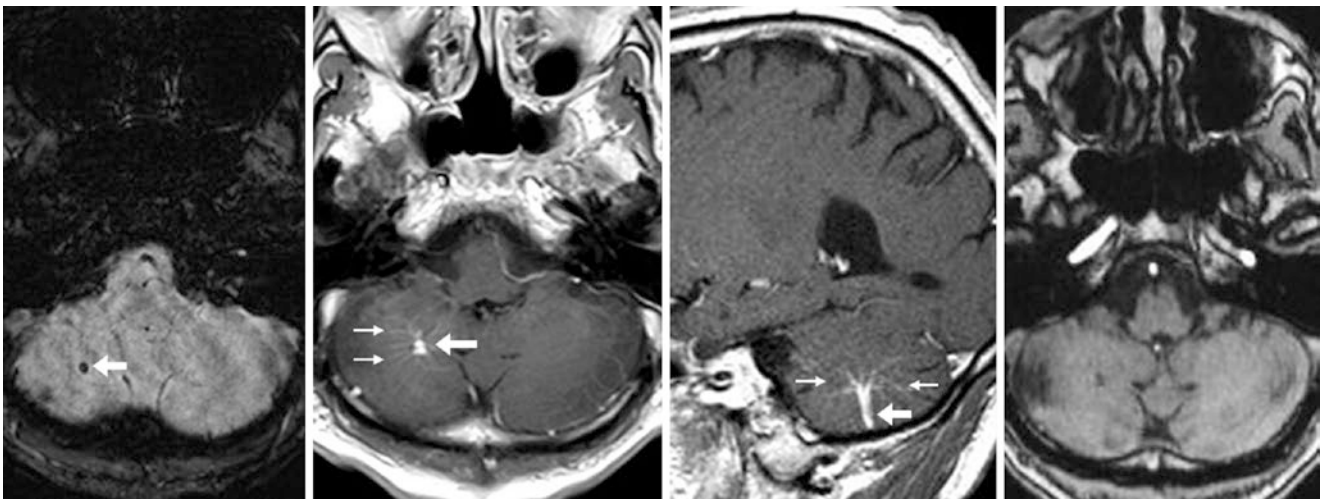

Fig. 21.31 A 64 year old followed for a pituitary lesion in whom a 1.5T brain MRI noted a moderate-sized vein (*arrows*) draining inferiorly from a caput of vessels (*thin arrows*) within the right hemicerebellum on SWI (*left*) and on postcontrast axial (*left middle*) and sagittal (*right middle*) SE T1WIs. The caput is better visualized on postcontrast T1WIs in this patient, which is atypical. The DVA is not visualized on a 3DTOF MRA, which portrays only arterial flow (*right*)

21.3.2 Developmental Venous Anomalies: Lobar

Lobar cerebral DVAs are quite common, and the overwhelming majority are incidental and asymptomatic. Most commonly these are in the frontal lobe, but they can occur virtually anywhere within the cerebrum and typically are best visualized on either postcontrast T1WI or as a blush of a deoxygenated venous structure with a single draining vein on SWI. Faintly hyperintense signal on FLAIR is associated with some lobar DVAs. Again, larger lobar DVAs may mimic an *arteriovenous malformation* if the DVA is large. A concomitant brain capillary telangiectasia (BCT, asymptomatic) or incidental (but abnormal) cavernoma may also be noted along with a lobar DVA (present simultaneously in up to one third of DVAs on SWI) (Figs. 21.32, 21.33, 21.34, 21.35, 21.36, and 21.37).

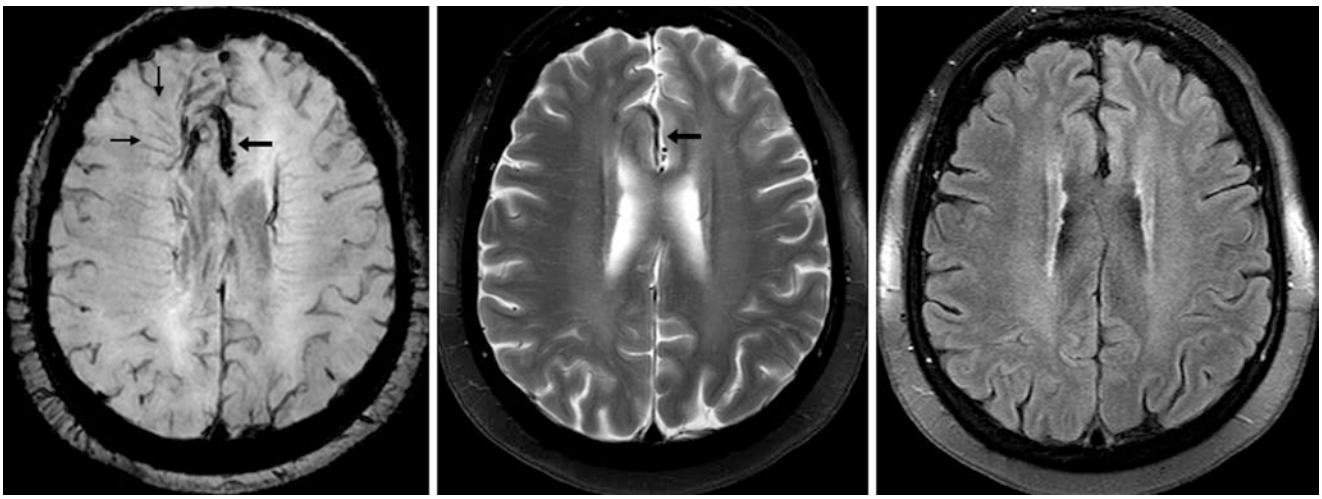

Fig. 21.32 A 77 year old with headaches in whom a 3T MRI with SWI (*left*) demonstrated a very large DVA that had quite a prominent draining vein (*arrows*) that drained a caput of smaller vessels (*thin arrows*). This enlarged vein is only partially visible on T2WI (*middle*) and is nearly invisible on FLAIR (*right*), which illustrates the utility of SWI. This sizable DVA could simulate an AVM, but no enlarged arterial structures were noted

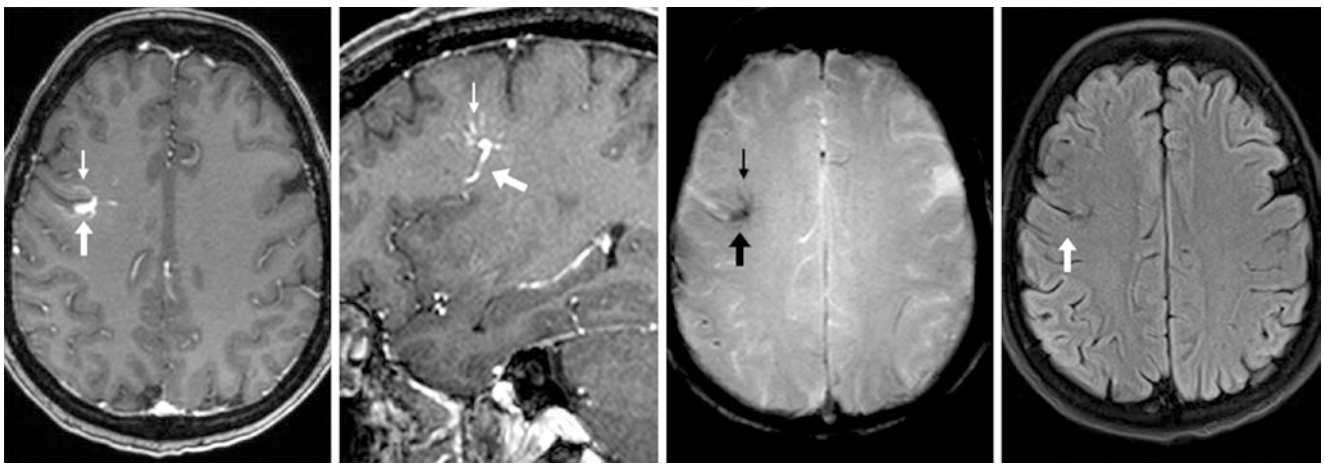

Fig. 21.33 A 59 year old with an acute speech deficit underwent a 3T MRI with postcontrast axial (*left*) and sagittal (*left middle*) GE T1WIs that delineated a moderate-sized draining vein (*arrows*) from a DVA with a spoke-wheel appearance of surrounding vessels (*thin arrows*), also shown on GE T2*WI (*right middle*). FLAIR (*right*) and DWI (*not shown*) were normal

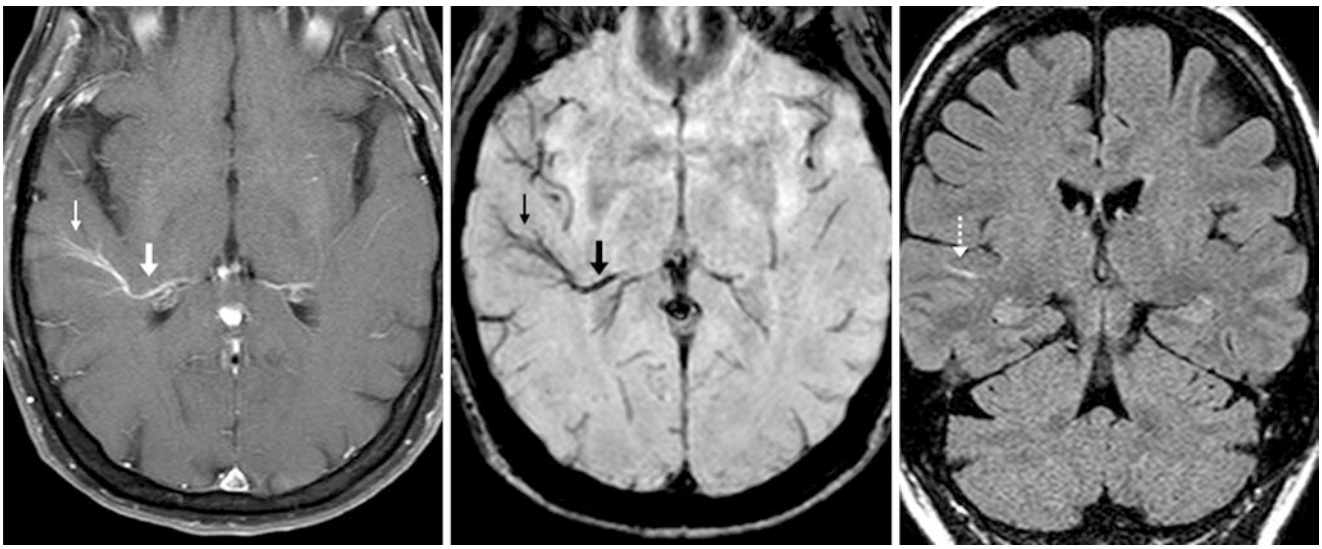

Fig. 21.34 A 37 year old with headaches had a 1.5T MRI with axial postcontrast T1WI (*left*) and SWI (*middle*) that depicted a mildly prominent right temporal draining vein (*arrows*) from a DVA, fed by caput vessels (*thin arrows*). On FLAIR (*right*), there was faint hyperintense signal, which can be seen in some DVAs. DWI was normal (*not shown*)

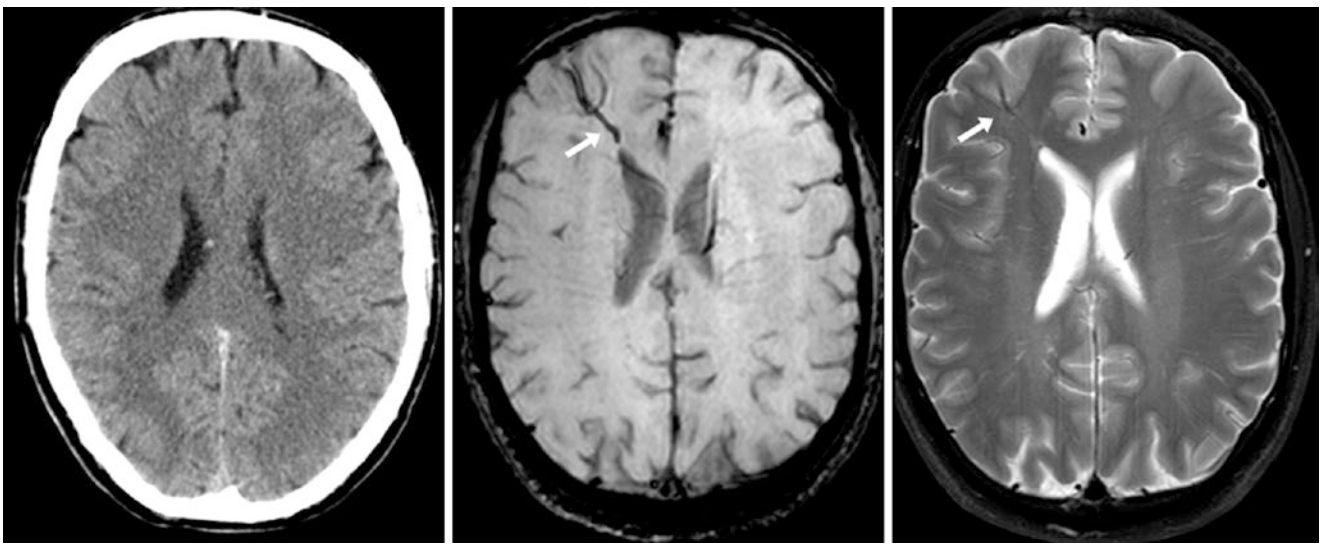

Fig. 21.35 A 50 year old with psychosis in whom a NECT (*left*) was called negative, while a 3T MRI demonstrated a relatively large DVA (*arrows*) on SWI (*middle*). On T2WI (*right*), the vessels contributing to the DVA are barely visualized

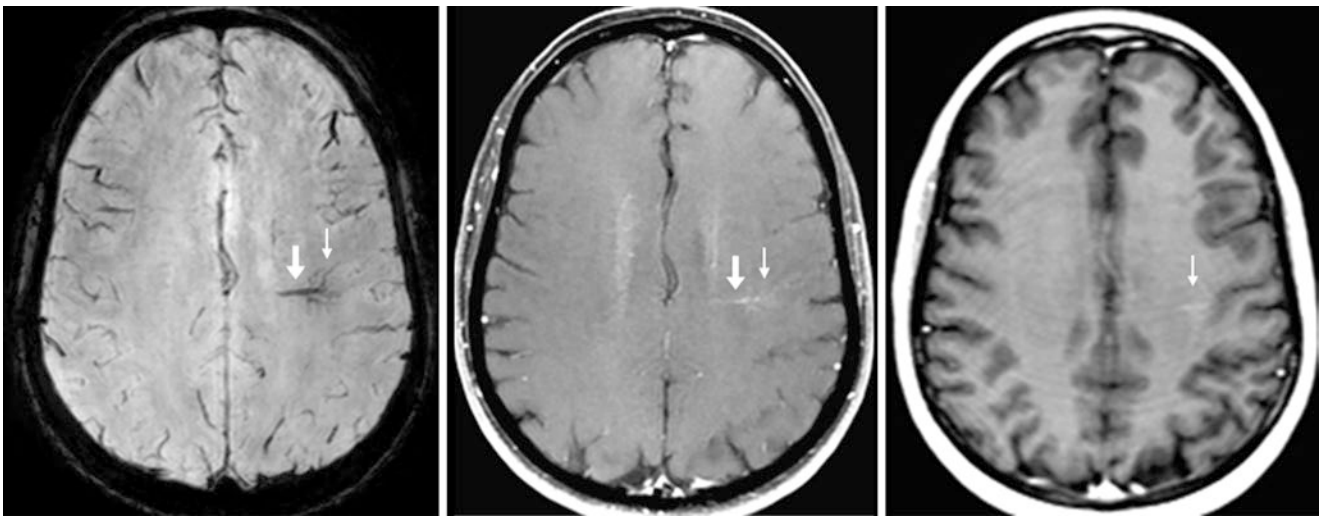

Fig. 21.36 A 44 year old with headaches, in whom a 1.5T MRI with SWI (*left*) demonstrated both the DVAs draining vein (*arrows*) and its associated caput (*thin arrows*). On postcontrast SE T1WI (*middle*), the draining vein is difficult to visualize, while on postcontrast GE T1WI (*right*) the draining vein is invisible with the caput barely visualized

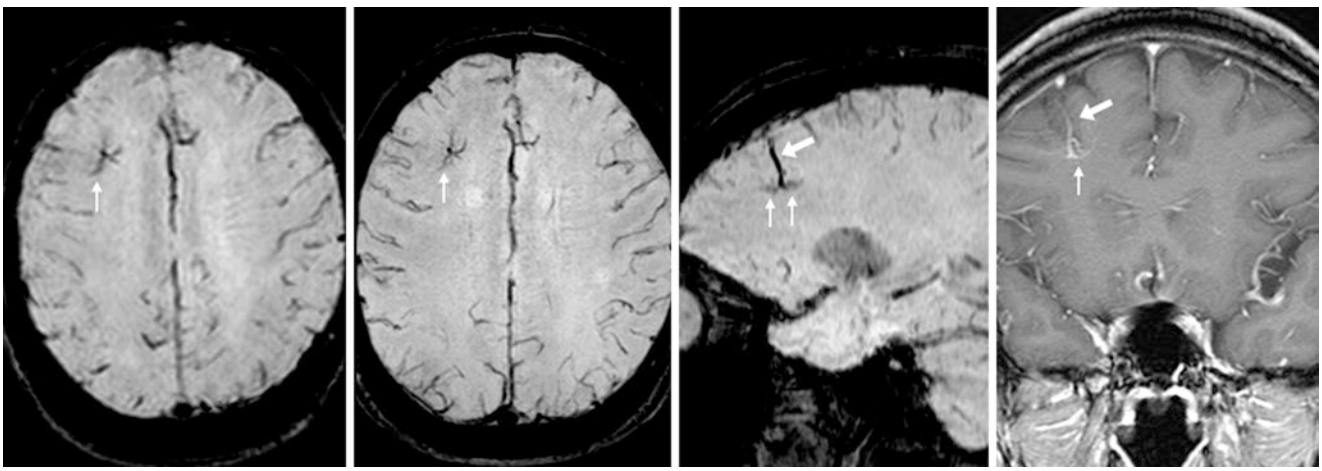

Fig. 21.37 A 48 year old with vertigo, in whom a 1.5T MRI with SWI (*left*) demonstrated a DVA's caput of hazy vessels (*thin arrows*), which was unchanged on a 1.5T MRI with SWI 1 year later (*left middle*). Sagittal reformats best depicted the draining vein (*arrows*), while a postcontrast SE T1WI (*right*) depicted the caput better than the draining vein

21.3.3 Developmental Venous Anomalies: Giant and Holohemispheric Types

Giant or *holohemispheric DVAs* are quite rare and can occur within the cerebrum or cerebellum. They are so large that the typical caput appearance may not be immediately apparent, since the enlarged draining vein and network of veins leading into that vein can be quite complex, that is, not appear to have the simple drainage of a typical DVA. Thus, such giant cerebral or cerebellar DVAs often simulate an AVM. When present, these are quite evident on either postcontrast CT or T1WI with a single draining vein, while on SWI, a simple pattern of numerous veins leading centrally toward a solitary draining vein is apparent. This can also be noted on MR venography (MRV). The lack of enlarged supplying arterial structures as well as the lack of multidirectional draining veins (complex pattern) distinguishes these large DVAs from true AVMs (Figs. 21.38, 21.39, and 21.40).

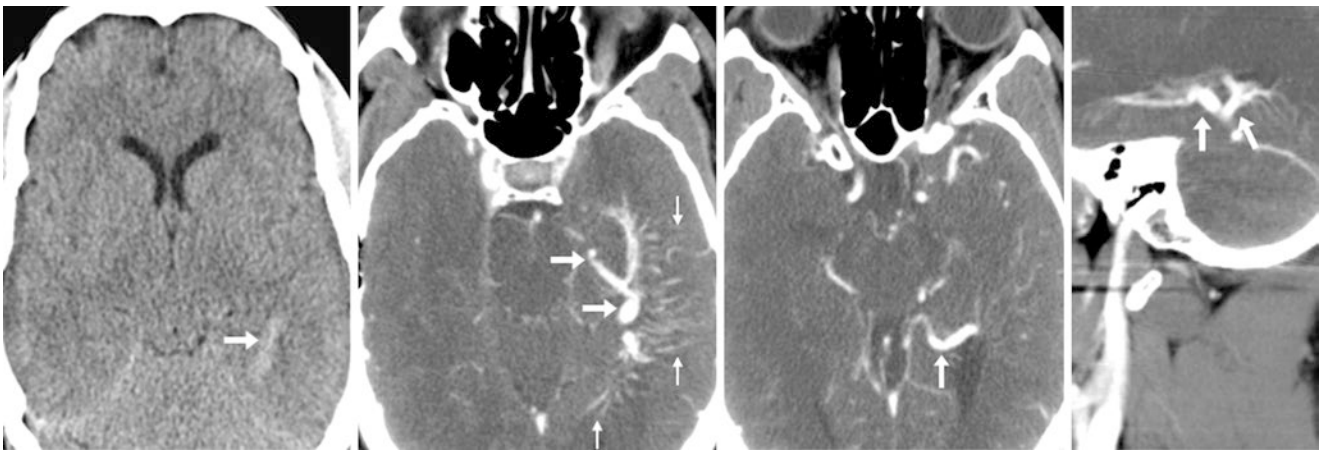

Fig. 21.38 DVA: holohemispheric variant. A 47 year old had a noncontrast neck CT (*left*) that showed a large vascular-appearing structure within the left temporal lobe that was mildly hyperdense (*arrows*). On postcontrast axial (*left middle and right middle*) and sagittal (*right*) images, the hyperdensity was found to be a giant DVA that involved nearly the entire temporal lobe, which drained innumerable tiny caput-type vessels (*thin arrows*)

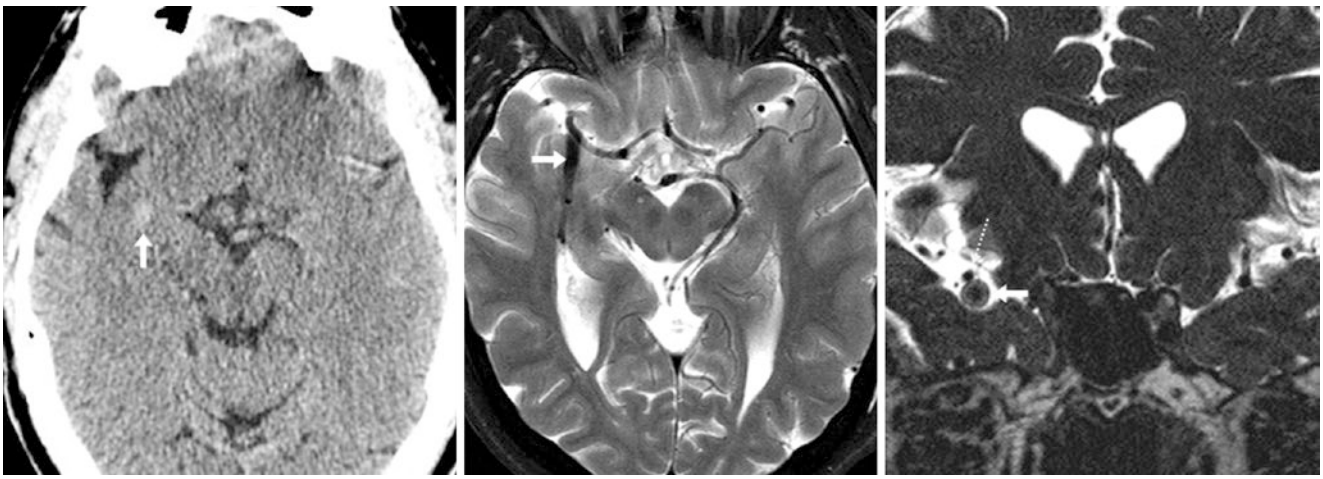

Fig. 21.39 DVA: Giant draining vein simulating hemorrhage. In a 56 year old with chronic headaches, a NECT (*left*) showed a focal hyperdensity (*arrows*) within the right temporal lobe, which was initially called a hemorrhage (note the lack of surrounding edema) and was unchanged 1 day later (*not shown*). On a 3T MRI, there was a giant flow void from a DVA draining vein (*arrows*) that appeared in close proximity to the middle cerebral artery (MCA) on an axial T2WI (*middle*). Coronal 3D T2WIs (*right*) confirmed the vein to be separate from the MCA (*dotted arrow*). Neither postcontrast imaging nor SWI were obtained, and therefore the caput was not visualized

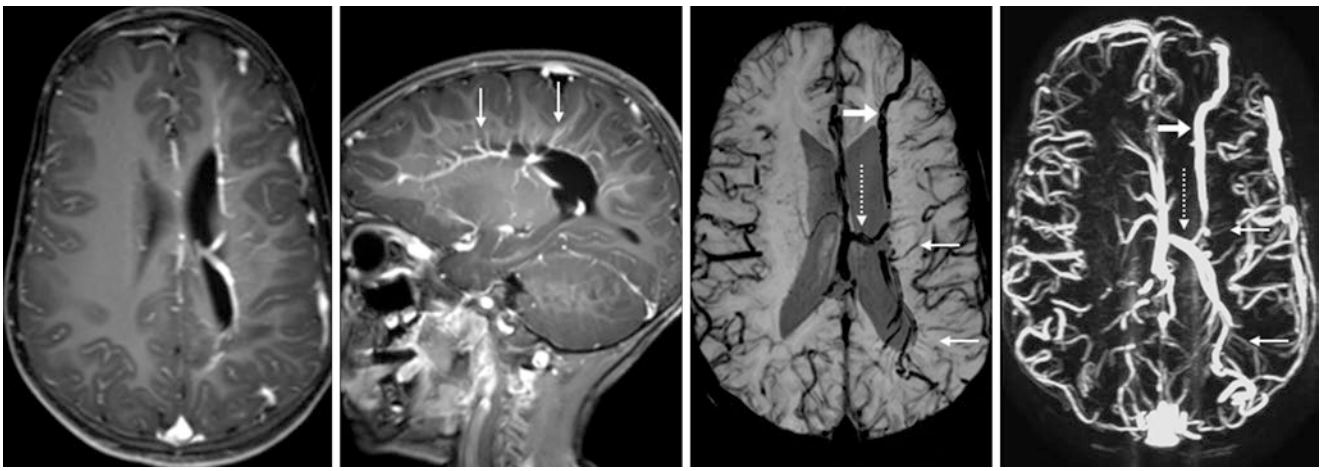

Fig. 21.40 DVA: holohemispheric variant. A 4 year old with cerebral palsy had multiple caput veins (*thin arrows*) that drained into a giant thalamostriate vein centrally (*dotted arrows*) while peripherally draining into a vein (*arrows*) that eventually led into large cortical veins, as shown on postcontrast axial (*left*) and sagittal (*left middle*) T1WIs and on 20-mm-thick SWI (*right middle*) and phase contrast MRV (*right*). There were no enlarged arteries on MRA (*not shown*), and no nidus of an AVM. On FLAIR (*not shown*), there was left periventricular white matter gliosis

21.3.4 Overlap Between Developmental Venous Anomaly and Capillary Telangiectasia

As DVAs and BCTs are both quite common within the cerebrum, cerebellum, and brainstem, these two entities can occur together. However, there is no agreed upon rate of how frequently they occur together in the asymptomatic population, since both entities are increasingly detected with higher resolution imaging, particularly on noncontrast SWI. Preliminarily, it appears that it can also be difficult at times to distinguish one entity from the other with smaller lesions, since their appearances can overlap; the caput of a small DVA may appear similar to the blush of a BCT. This overlap in appearance as well as their relatively frequent rate of occurring together lends credence to the theory that both slow-flow malformations originate on the same spectrum of anomalies in normal venous development (Figs. 21.41, 21.42, and 21.43).

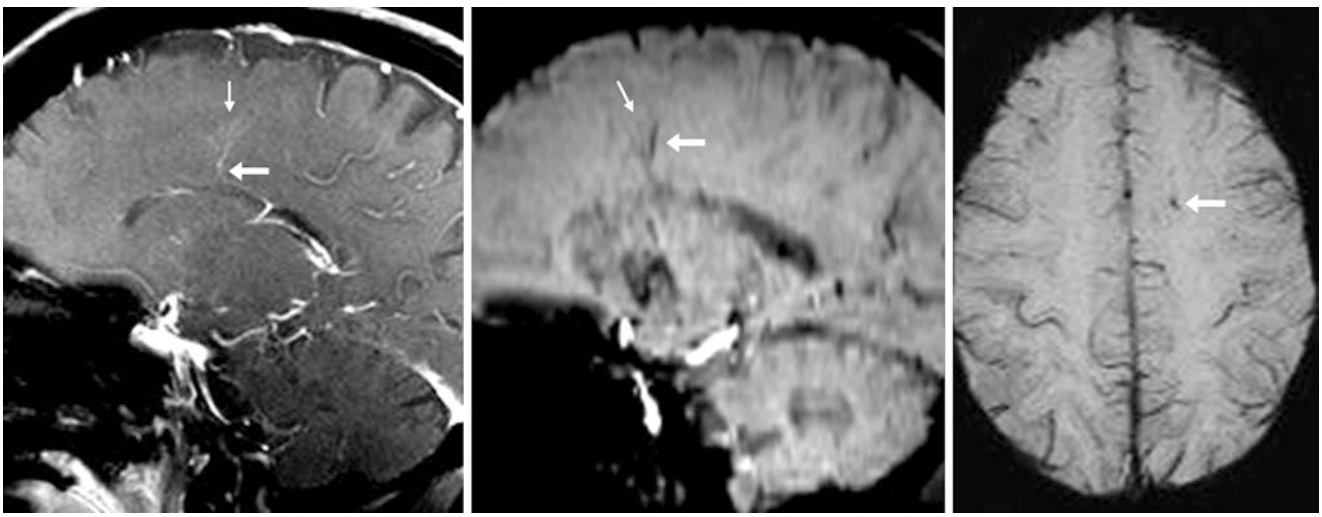

Fig. 21.41 A 61 year old with headaches in whom a postcontrast sagittal SE T1WI at 1.5T (*left*) had faint enhancement (*thin arrows*), perhaps the blush of a BCT versus the caput of a DVA. On sagittal (*middle*) and axial (*right*) SWIs, there was a small draining vein (*arrows*). Thus, components of both a small DVA and BCT might be present

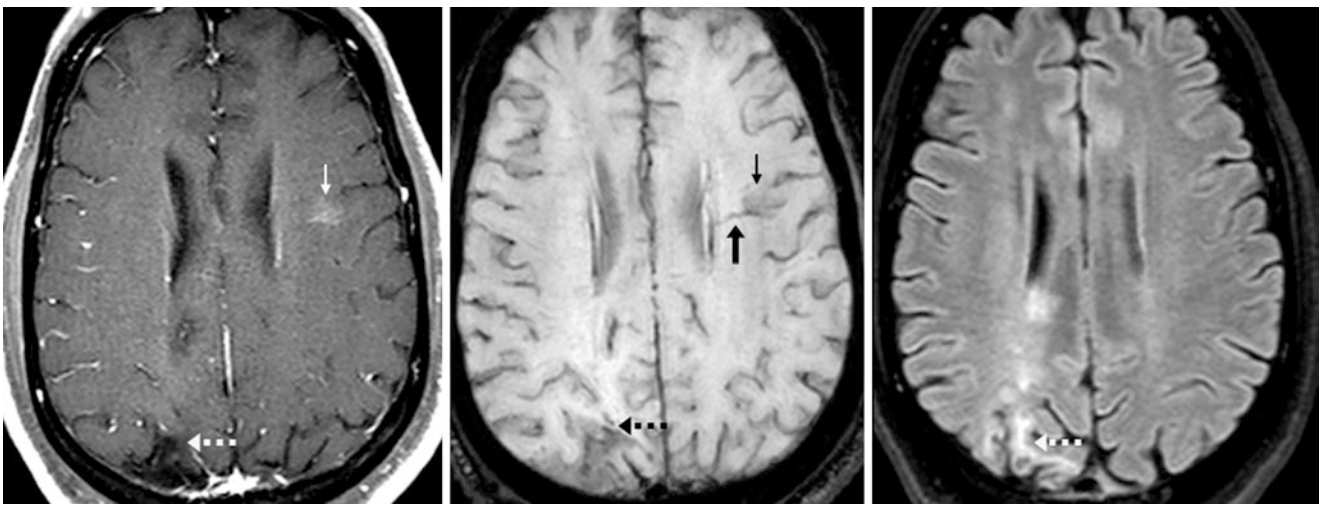

Fig. 21.42 A 59 year old with weakness; a postcontrast axial SE T1WI at 1.5T (*left*) showed a faint tuft of enhancement (*thin arrows*), perhaps the blush of a BCT versus the caput of a DVA. On SWI (*middle*), there was a small draining vein (*arrows*), not visualized on FLAIR (*right*). Note focal right parieto-occipital encephalomalacia (*dotted arrows*)

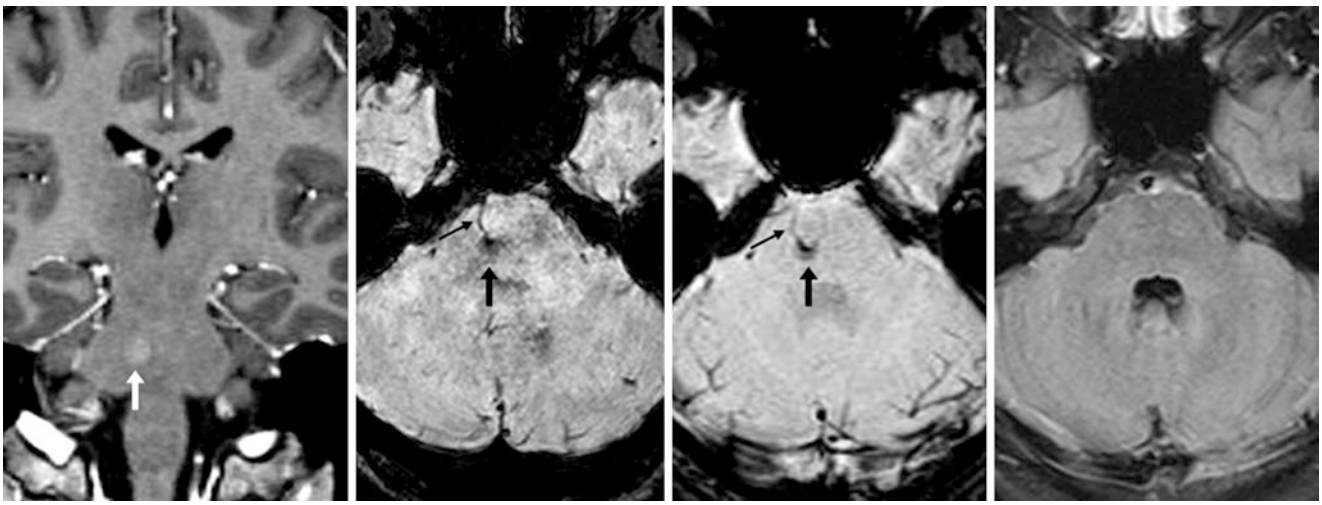

Fig. 21.43 A 17 year old with nausea in whom a 1.5T MRI demonstrated faint enhancement of a pontine BCT (*arrows*) on postcontrast coronal GE T1WI (*left*) having faint dark signal on 2-mm-thick SWI (*left middle*), with a small draining vein (*thin arrows*), perhaps a DVA. This was unchanged on SWI 3 months later (*right middle*). FLAIR was normal (*right*)

21.3.5 Comparison Cases of Symptomatic Developmental Venous Anomalies

Rarely, DVAs can become symptomatic, perhaps because of *venous ischemia.* Venous ischemia can be reversible but occasionally leads to frank focal venous infarction with resultant encephalomalacia. In the rare case in which a DVA is symptomatic and results in an infarction, a focal, small area of encephalomalacia may be difficult to distinguish from a focal cortical infarction of arterial origin other than that the draining vein of a DVA from that region may still be evident on postcontrast T1WI or SWI (Figs. 21.44 and 21.45).

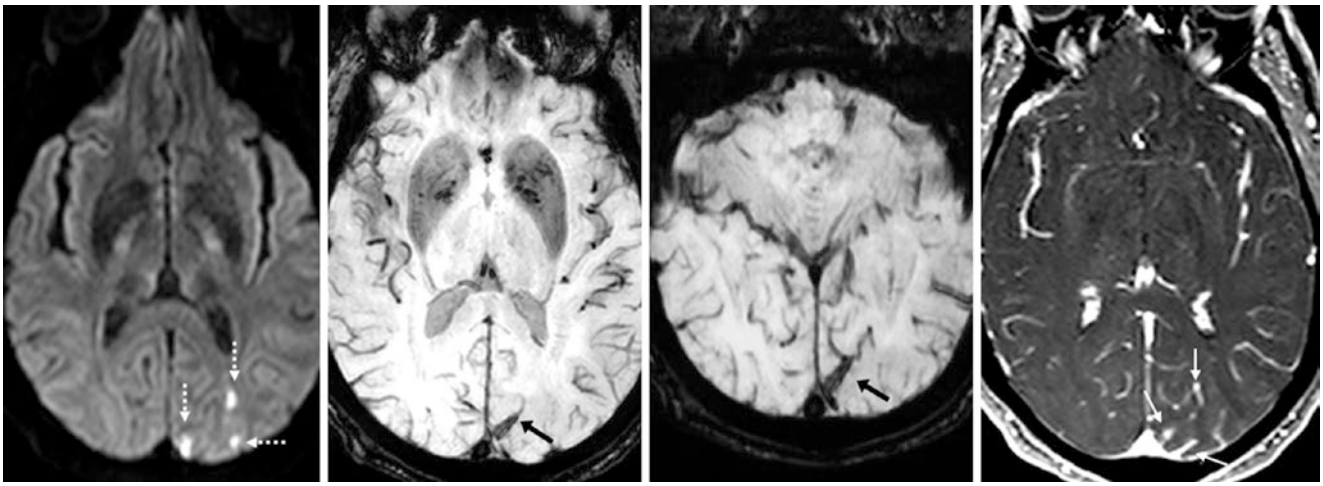

Fig. 21.44 Comparison case of DVA associated with stroke. A 53 year old with acute visual symptoms underwent a 3T MRI, which demonstrated small occipital infarcts (*dotted arrows*) on DWI (*left*); within this region was an enlarged draining vein (*arrows*) from a DVA on 2-mm-thick axial SWI (*left middle*), which was better defined on 3-mm oblique axial SWI (*right middle*). Postcontrast GE T1WI (*right*) showed ill-defined cortical/leptomeningeal enhancement, likely related to venous infarcts. The infarcts were presumed to be related to spontaneous thrombosis of the DVA

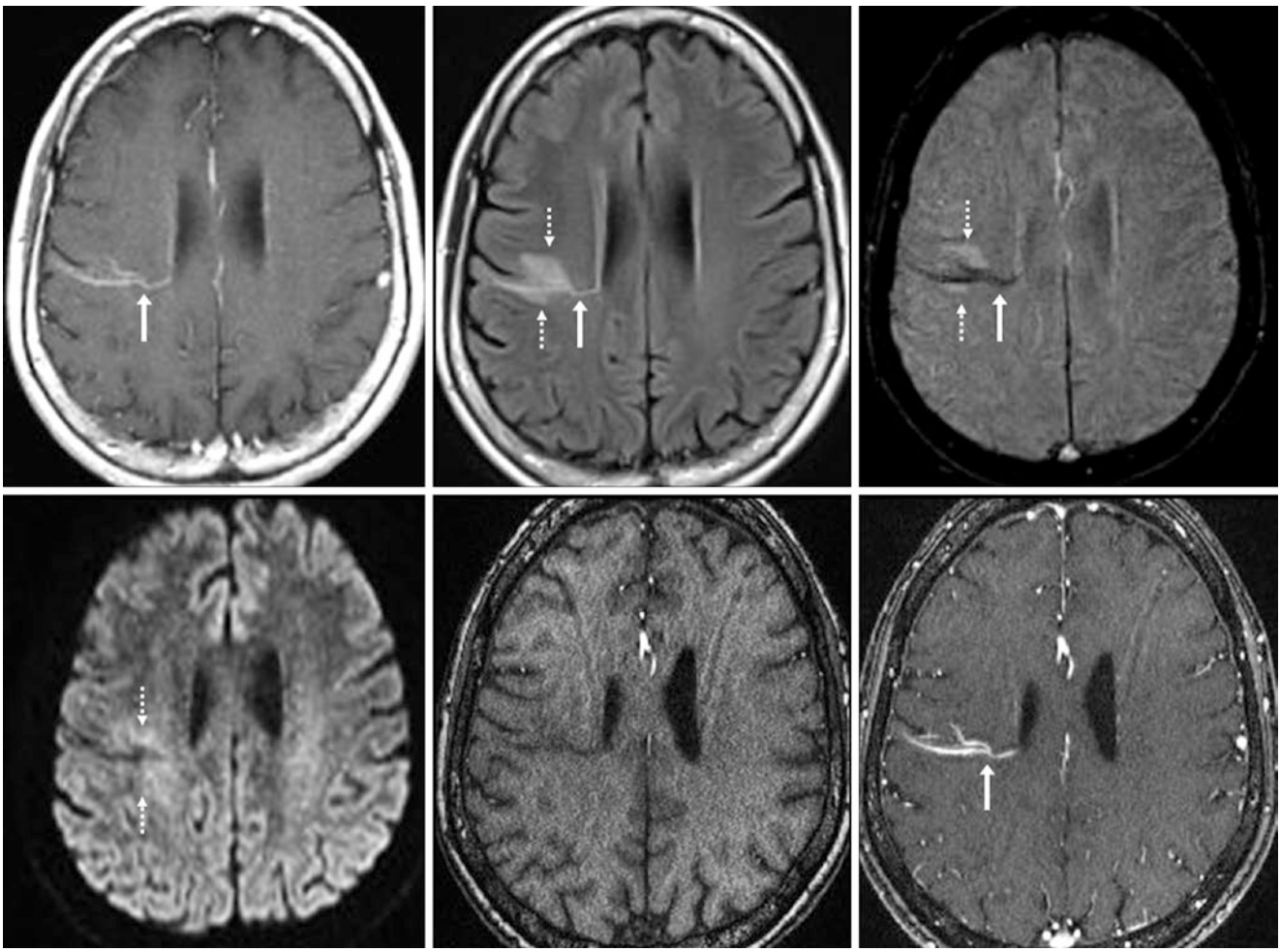

Fig. 21.45 Comparison case of DVA with venous ischemia. A 65 year old had had a known DVA, with the draining vein (*arrows*) shown on a postcontrast SET1WI (*top left*) from a 1.5T MRI. Six months later, the patient presented with acute left facial numbness. There was edema surrounding the DVA (*dotted arrows*) on postcontrast FLAIR (*top middle*) and SWI (*top right*), with mildly reduced diffusivity on DWI (*bottom left*); this was thought to be related to reversible venous ischemia. Noncontrast 3DTOF MRA (*bottom middle*) and postcontrast MRA (*bottom right*) confirmed the lack of an arterial component. Overall, the findings were thought to be related to spontaneous thrombosis of the DVA

21.3.5.1 Comparison Cases: Cavernomas with Developmental Venous Anomalies and Arteriovenous Malformation

Finally, a few cases of concomitant *DVA with cavernoma* are demonstrated here, given their propensity to occasionally occur together (perhaps again making the theory plausible that slow-flow malformations originate on the same spectrum). An example of *AVM* is also provided for comparison with the large draining vein of a DVA. AVMs (unless quite small) typically have enlargement of both arterial and venous supplying/draining structures as well as a nidus of enhancement that is visible as flow-voids on noncontrast imaging (such as SWI) and on postcontrast T1WI. Catheter angiography distinguishes such high-flow AVMs from the aforementioned slow-flow venous malformations in difficult cases (Figs. 21.46, 21.47, 21.48, and 21.49).

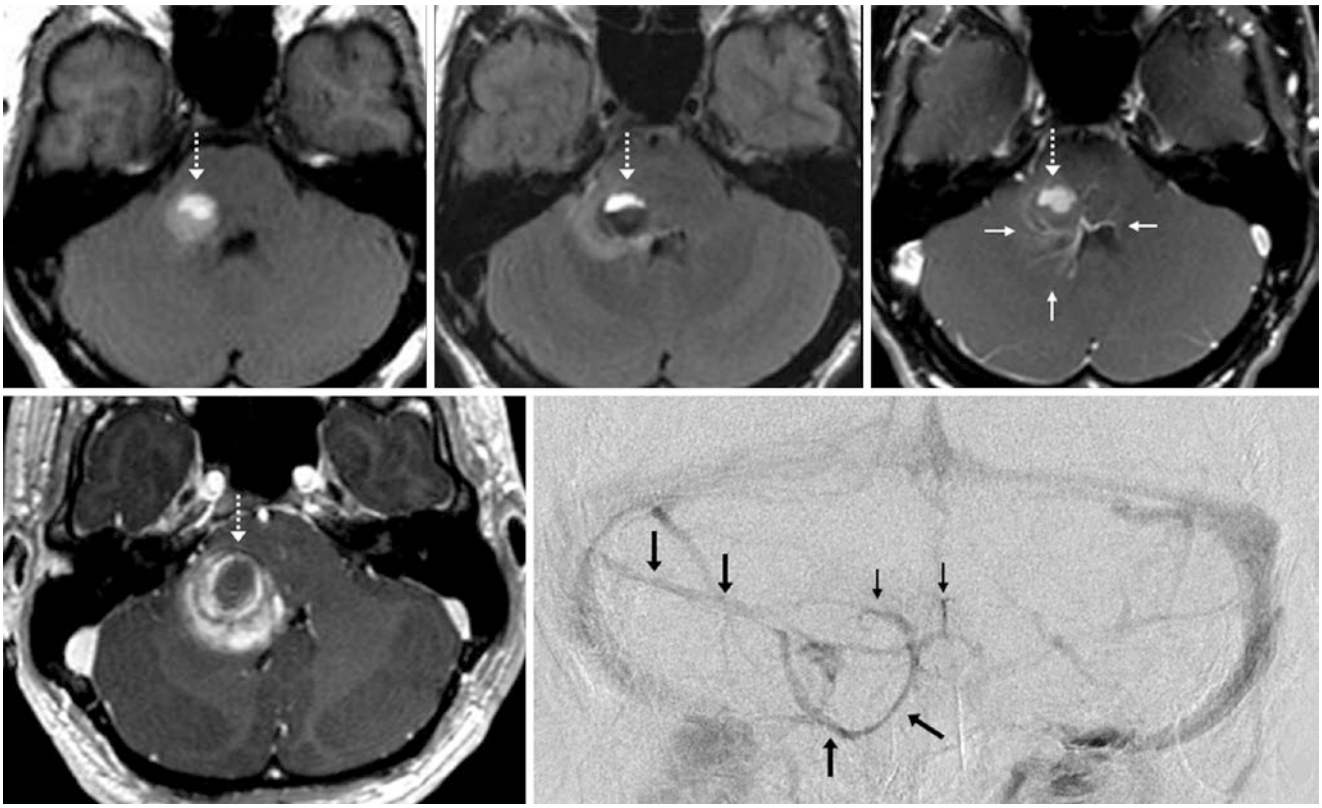

Fig. 21.46 Comparison case of a cavernoma with a DVA. A 30 year old with an acute headache: On a 1.5T MRI, there was hemorrhage within the right middle cerebellar peduncle (*dotted arrows*) on SE T1WI (*top left*), FLAIR (*top middle*), and on postcontrast SE T1WI (*top right*), with enhancing caput vessels from an underlying DVA (*thin arrows*). On an MRI only 3 weeks later, the cavernoma had enlarged on postcontrast GE T1WI (*bottom left*). A catheter DSA at that time (AP view, *bottom right*) showed no arterial component but did note the DVAs draining vein (*arrows*)

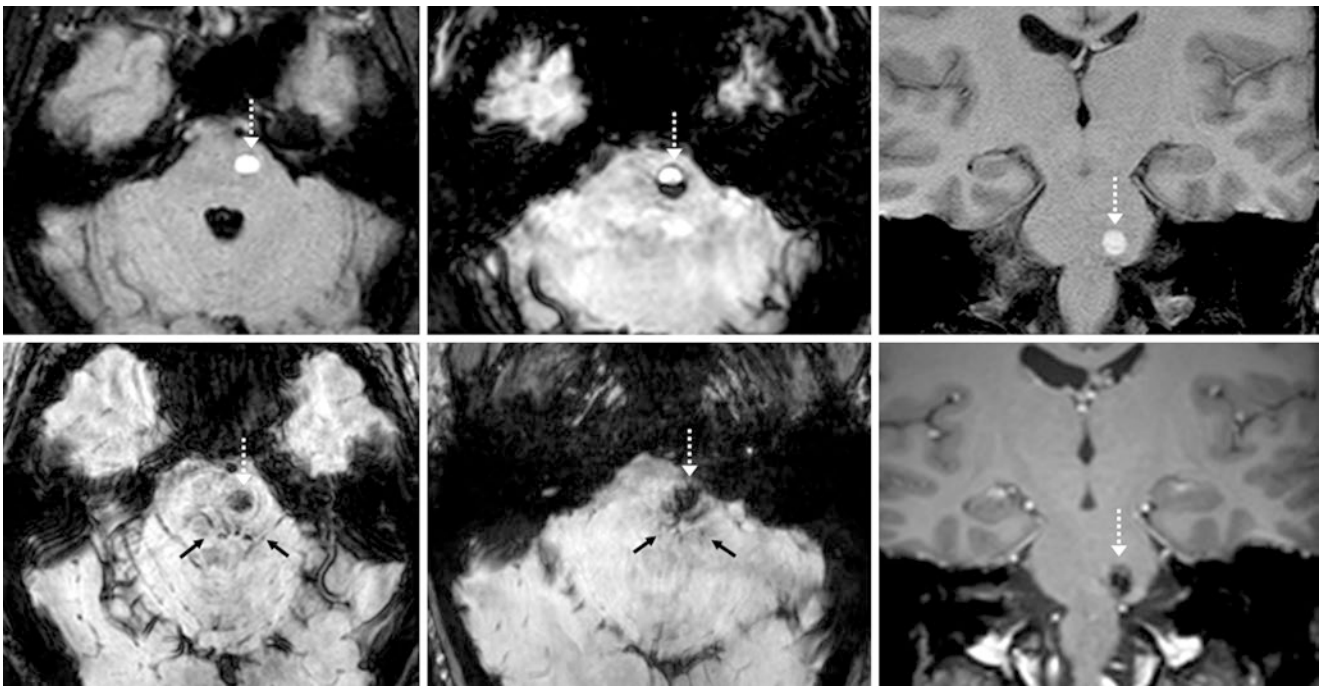

Fig. 21.47 Comparison case of a cavernoma with DVA. A 30 year old had focal hemorrhage of the left hemipons on a 1.5T MRI (*dotted arrows*) with FLAIR (*top left*), SWI (*top middle*), and coronal T1WI (*top right*). At 6 months, SWI 2-mm and 4-mm reformats (*bottom left and middle*) and postcontrast T1WI (*bottom right*) showed that the cavernoma became entirely dark, while caput flow voids (*thin arrows*) became better visualized from the underlying DVA

Fig. 21.48 Comparison case of a cavernoma with DVA. A 28 year old with an abrupt-onset headache and vertigo had a left cerebellar hemorrhage *(dotted arrows)* on NECT (*left*), also shown on a 3T MRI with noncontrast T1WI (*left middle*). Postcontrast T1WI (*right middle*) and SWI (*right*) depicted caput vessels (*thin arrows*) from an underlying DVA

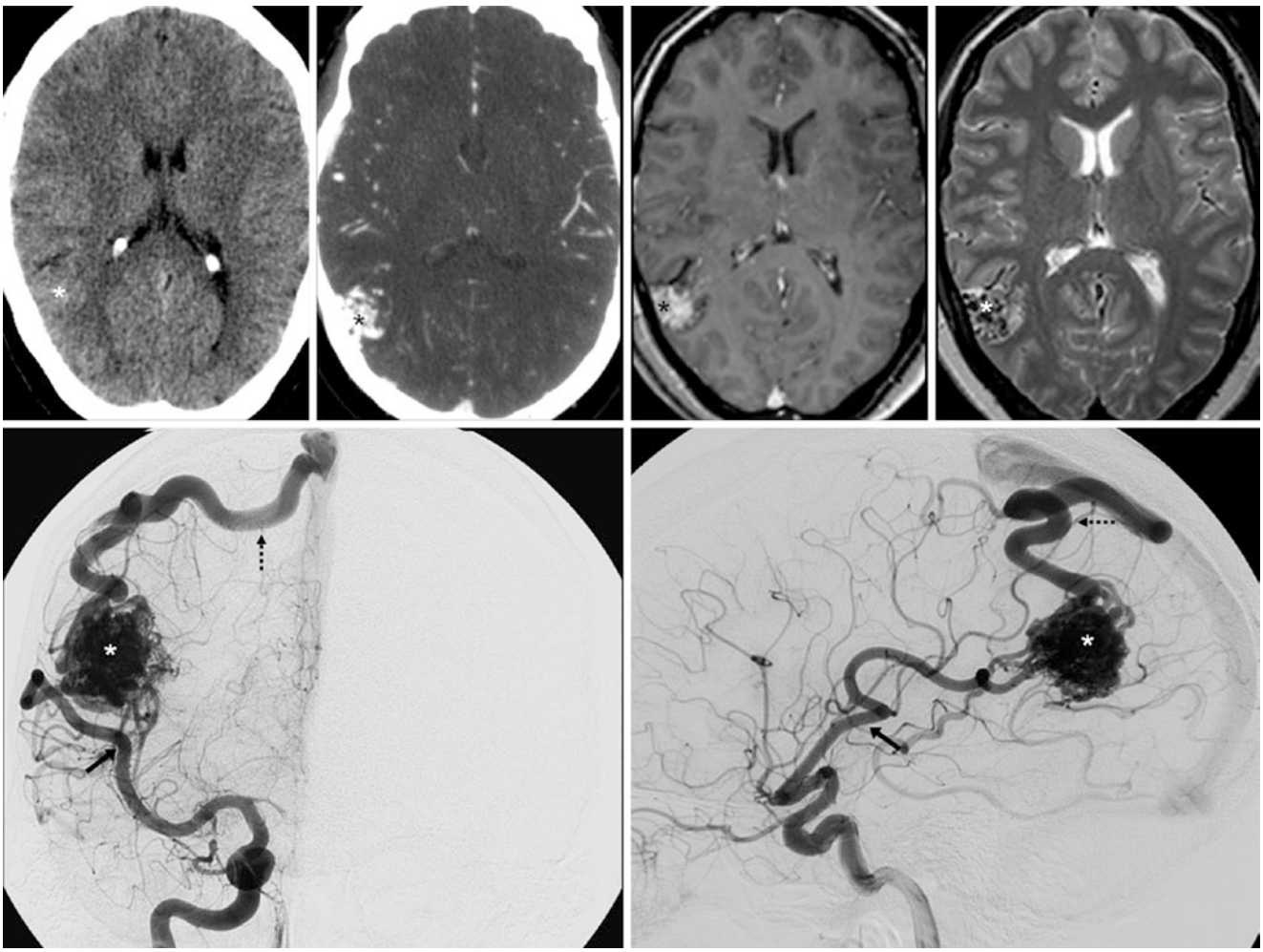

Fig. 21.49 Comparison case of an AVM. A 28 year old had a dense parietal focus (*) on NECT (*top, left*), later confirmed to be an AVM nidus on CTA (*top, left middle*) and on a 1.5T MRI with postcontrast T1WI (*top, right middle*) and T2WI (*top, right*). On a right internal carotid catheter DSA, the middle cerebral artery was enlarged (*arrows*), with a draining vein (*dotted arrows*), as shown on anteroposterior (*bottom left*) and lateral (*bottom right*) views

Suggested Reading

Abdulrauf SI, Kaynar MY, Awad IA. A comparison of the clinical profile of cavernous malformations with and without associated venous malformations. Neurosurgery. 1999;44:41–6.

Abla AA, Lekovic GP, Turner J, de Oliveira JG, Porter R, Spetzler RF, et al. Advances in the treatment and outcome of brain stem cavernous malformation surgery: a case series of 300 surgically treated patients. Neurosurgery. 2011;68:403–14.

Augustyn GT, Scott JA, Olson E, Gilmor RL, Edwards MK. Cerebral venous angiomas: MR imaging. Radiology. 1985;156:391–5.

Barr RM, Dillon WP, Wilson CB. Slow-flow vascular malformations of the pons: capillary telangiectasias? AJNR Am J NeuroradiolAm J Neuroradiol. 1996;17:71–8.

Buhl R, Hempelmann RG, Stark AM, Mehdorn HM. Therapeutical considerations in patients with intracranial venous angiomas. Eur J Neurol. 2002;9:165–69.

Cakirer S. De novo formation of a cavernous malformation of the brain in the presence of a developmental venous anomaly. Clin Radiol. 2003;58:251–6.

Campeau NG, Lane JI. De novo development of a lesion with the appearance of a cavernous malformation adjacent to an existing developmental venous anomaly. AJNR Am J Neuroradiol. 2005;26:156–9.

Casey MA, Lahoti S, Gordhan A. Pediatric holohemispheric developmental venous anomaly: definitive characterization by 3D susceptibility weighted magnetic resonance angiography. J Radiol Case Rep. 2011;5:10–8.

Castillo M, Morrison T, Shaw JA, Bouldin TW. MR imaging and histologic features of capillary telangiectasia of the basal ganglia. AJNR Am J Neuroradiol. 2001;22:1553–5.

Chaloupka JC, Huddle DC. Classification of vascular malformations of the central nervous system. Neuroimaging Clin N Am. 1998;8:295–321.

Chaudhry US, De Bruin DE, Policeni BA. Susceptibility-weighted MR imaging: a better technique in the detection of capillary telangiectasia compared with T2* gradient-echo. AJNR Am J Neuroradiol. 2014;35:2302–5.

Cheong WY, Tan KP. Cerebral venous angioma-a misnomer? Ann Acad Med Singapore. 1993;22:736–41.

Dósa E, Tuladhar S, Muldoon LL, Hamilton BE, Rooney WD, Neuwelt EA. MRI using ferumoxytol improves the visualization of central nervous system vascular malformations. Stroke. 2011;42:1581–8.

El-Koussy M, Schroth G, Gralla J, Brekenfeld C, Andres RH, Jung S, et al. Susceptibility-weighted MR imaging for diagnosis of capillary telangiectasia of the brain. AJNR Am J Neuroradiol. 2012;33:715–20.

Fontaine S, de la Sayette V, Gianfelice D, Melanson D, Ethier R. CT, MRI, and angiography of venous angiomas: a comparative study. Can Assoc Radiol J. 1987;38:259–63.

Garner TB, Del Curling Jr O, Kelly Jr DL, Laster DW. The natural history of intracranial venous angiomas. J Neurosurg. 1991;75:715–22.

Gross BA, Puri AS, Popp AJ, Du R. Cerebral capillary telangiectasias: a meta-analysis and review of the literature. Neurosurg Rev. 2013;36:187–93.

Hodel J, Blanc R, Rodallec M, Guillonnet A, Gerber S, Pistocchi S, et al. Susceptibility-weighted angiography for the detection of high-flow intracranial vascular lesions: preliminary study. Eur Radiol. 2013;23:1122–30.

Jagadeesan BD, Delgado Almandoz JE, Moran CJ. Postcontrast susceptibility-weighted imaging: a novel technique for the detection of arteriovenous shunting in vascular malformations of the brain. Stroke. 2011;42:3127–31.

Jellinger K. Vascular malformations of the central nervous system: a morphological overview. Neurosurg Rev. 1986;9:177–216.

Lai PH, Chen PC, Pan HB, Yang CF. Venous infarction from a venous angioma occurring after thrombosis of a drainage vein. Am J Roentgenol. 1999;172:1698–9.

Lasjaunias P, Burrows P, Planet C. Developmental venous anomalies (DVA): the so-called venous angioma. Neurosurg Rev. 1986;9:233–42.

Lee C, Pennington MA, Kenney CM. MR evaluation of developmental venous anomalies: medullary venous anatomy of venous angiomas. AJNR Am J Neuroradiol. 1996;17:61–70.

Lee RR, Becher MW, Benson ML, Rigamonti D. Brain capillary telangiectasia: MR imaging appearance and clinicohistopathologic findings. Radiology. 1997;205:797–805.

Lee BC, Vo KD, Kido DK, Mukherjee P, Reichenbach J, Lin W, et al. MR high-resolution blood oxygenation level-dependent venography of occult (low-flow) vascular lesions. AJNR Am J Neuroradiol. 1999;20:1239–42.

McLaughlin MR, Kondziolka D, Flickinger JC, Lunsford S, Lunsford LD. The prospective natural history of cerebral venous malformations. Neurosurgery. 1998;43:195–200.

Merten CL, Knitelius HO, Hedde JP, Assheuer J, Bewermeyer H. Intracerebral haemorrhage from a venous angioma following thrombosis of a draining vein. Neuroradiology. 1998;40:15–8.

Mullan S, Mojtahedi S, Johnson DL, Macdonald RL. Cerebral venous malformation-arteriovenous malformation transition forms. J Neurosurg. 1996a;85:9–13.

Mullan S, Mojtahedi S, Johnson DL, Macdonald RL. Embryological basis of some aspects of cerebral vascular fistulas and malformations. J Neurosurg. 1996b;85:1–84.

Naff NJ, Wemmer J, Hoenig-Rigamonti K, Rigamonti DR. A longitudinal study of patients with venous malformations: documentation of a negligible hemorrhage risk and benign natural history. Neurology. 1998;50:1709–14.

Okudera T, Huang YP, Fukusumi A, Nakamura Y, Hatazawa J, Uemura K. Micro-angiographical studies of the medullary venous system of the cerebral hemisphere. Neuropathology. 1999;19:93–111.

Oran I, Kiroglu Y, Yurt A, Ozer FD, Acar F, Dalbasti T, et al. Developmental venous anomaly (DVA) with arterial component: a rare cause of intracranial haemorrhage. Neuroradiology. 2009;51:25–32.

Pinker K, Stavrou I, Knosp E, Trattnig S. Are cerebral cavernomas truly nonenhancing lesions and thereby distinguishable from arteriovenous malformations? MRI findings and histopathological correlation. Magn Reson Imaging. 2006;24:631–7.

Pozzati E, Marliani AF, Zucchelli M, Foschini MP, Dall'Olio M, Lanzino G. The neurovascular triad: mixed cavernous, capillary, and venous malformations of the brainstem. J Neurosurg. 2007;107:1113–9.

Rabinov JD. Diagnostic imaging of angiographically occult vascular malformations. Neurosurg Clin N Am. 1999;10:419–32.

Ruíz DS, Yilmaz H, Gailloud P. Cerebral developmental venous anomalies: current concepts. Ann Neurol. 2009;66:271–83.

Saba PR. The caput medusae sign. Radiology. 1998;207:599–600.

San Millán Ruíz D, Delavelle J, Yilmaz H, Gailloud P, Piovan E, Bertramello A, et al. Parenchymal abnormalities associated with developmental venous anomalies. Neuroradiology. 2007;49(San Millán Ruíz D):987–95.

Santucci GM, Leach JL, Ying J, Leach SD, Tomsick TA. Brain parenchymal signal abnormalities associated with developmental venous anomalies: detailed MR imaging assessment. AJNR Am J Neuroradiol. 2008;29:1317–23.

Sarwar M, McCormick WF. Intracerebral venous angioma: case report and review. Arch Neurol. 1978;35:323–25.

Sayama CM, Osborn AG, Chin SS, Couldwell WT. Capillary telangiectasias: clinical, radiographic, and histopathological features—clinical article. J Neurosurg. 2010;113:709–14.

Somasundaram S, Kesavadas C, Thomas B. Susceptibility weighted imaging in holohemispheric venous angioma with cerebral hemiatrophy. Neurol India. 2008;56:103–4.

Töpper R, Jürgens E, Reul J, Thron A. Clinical significance of intracranial developmental venous anomalies. J Neurol Neurosurg Psychiatry. 1999;67:234–8.

Truwit CL. Venous angioma of the brain: history, significance, and imaging findings. Am J Roentgenol. 1992;159:1299–307.

Uchino A, Imada H, Ohno M. Magnetic resonance imaging of intracranial venous angiomas. Clin Imaging. 1990;14:309–14.

Vieira Santos A, Saraiva P. Spontaneous isolated non-haemorrhagic thrombosis in a child with development venous anomaly: case report and review of the literature. Childs Nerv Syst. 2006;22:1631–3.

Wilms G, Bleus E, Demaerel P, Marchal G, Plets C, Goffin J, et al. Simultaneous occurrence of developmental venous anomalies and cavernous angiomas. AJNR Am J Neuroradiol. 1994;15:1247–54.

Wilms G, Demaerel P, Robberecht W, Plets C, Goffin J, Carton H, Baert AL. Coincidence of developmental venous anomalies and other brain lesions: a clinical study. Eur Radiol. 1995;5:495–500.

Yamasaki F, Kurisu K, Arita K, Yamanaka M, Ohba S, Hanaya R, et al. Contrast enhanced fast fluid-attenuated inversion-recovery MR imaging for diagnosing cerebral venous angioma: report of two cases. No To Shinkei. 2003;55:537–41.

Yoshida Y, Terae S, Kudo K, Tha KK, Imamura M, Miyasaka K. Capillary telangiectasia of the brain stem diagnosed by susceptibility-weighted imaging. J Comput Assist Tomogr. 2006;30:980–82.

Brain MRI Pseudolesions: 3.0 T Imaging, FLAIR, and Diffusion-Weighted Imaging

22

Fluid attenuated inversion recovery (FLAIR) imaging is considered a vital sequence for routine brain evaluation by MR imaging. Again, FLAIR implements an inversion time, or time to inversion (TI), to null the signal from cerebrospinal fluid (CSF), thereby enabling improved discrimination of structures immediately adjacent to CSF, such as the cerebral cortex, brainstem, periventricular white matter, or hippocampi. A number of artifacts can occur on FLAIR imaging and can simulate disease. Many of these require increasing awareness at higher field strengths or with the implementation of volumetric 3D acquisition.

One of the most problematic "pseudoabnormalities" is cerebral parenchymal hyperintensity on FLAIR, T2-weighted imaging (T2WI), or diffusion-weighted imaging (DWI); this hyperintensity occurs in certain regions more frequently than in other regions and is exacerbated at higher field strengths such as 3.0 T (3 T), though it can occur even at 1.5 T. At 3 T, perhaps up to three quarters of patients exhibit such "pseudolesions" somewhere within the brain on FLAIR. The locations most frequently affected (in order of greatest to least frequency) are the *periventricular white matter* (PVWM) diffusely, especially within the centrum semiovale just above the level of the lateral ventricles; the *corticospinal tracts* (CSTs), whether within the brainstem, the *posterior limb of the internal capsule* (PLIC), or within the corona radiata; the *decussation of the superior cerebellar peduncle* (DSCP); and the *superior cerebellar peduncle* (SCP). Such regions can be similarly hyperintense on T2WI or DWI (as discussed in the following section) but are usually most prominent on FLAIR. Also, the cerebral cortex may show hyperintensity that is diffuse or is localized to certain regions; this is a normal (or artifactual) appearance on FLAIR/T2WI/DWI, and is most prevalent (in this author's experience) in the *hippocampi, insula, cingulate, orbitofrontal region,* and *parieto-occipital cortices*. These areas can also appear hyperintense on inversion recovery (IR) sequences, particularly IR T2WI in the coronal plane. Such cortical hyperintensity also may be diffuse throughout the cerebrum or cerebellum and may simulate early findings of hypoxic-ischemic encephalopathy/injury (HIE/HII); the apparent diffusion coefficient (ADC) maps accompanying the DWI will lack cortical or subcortical white matter abnormalities in such normal cases. (Acute HIE will have a dark cortex on ADC maps, and subacute HIE more than 5–7 days old will have deep white matter dark signal on ADC maps.) Cortical hyperintensity may appear asymmetric and greater in the frontal region (particularly at 3 T) than in posterior regions, a difference that may be exaggerated by the fact that the perirolandic cortices (precentral and postcentral gyri) have normally darker signal at 3 T than the frontal cortices.

The reasons for parenchymal FLAIR, T2WI, and DWI pseudolesions are unknown. However, such pseudolesions seem to be noted most commonly in regions that undergo myelination later (*e.g.*, the PVWM posteriorly), at the edge of or within regions of active myelination in children (*e.g.*, PVWM or CST in infants), or in regions of high diffusion *anisotropy* (*e.g.*, CST or DSCP). The concept of structures with normal, relatively higher anisotropy causing normal hyperintensity focally on DWI is covered in more detail later in the subsection focused on DWI, along with DWI-specific artifact. The concept that non-free fluid (CSF is free fluid) or *interstitial edema* is bright on FLAIR or DWI would suggest that there may be subtly increased underlying amounts of fluid in these locations relative to other regions that are darker on FLAIR, or the bright signal in these regions could be related to a slightly lesser degree of myelination (*i.e.*, less tightly packed axons). Alternatively, this phenomenon could be entirely artifactual because of a "*dielectric resonance effect*" (*i.e.*, hyperintensity of deep structures relative to superficial structures) that occurs at higher field strengths. The problem with the theory of the dielectric effect is that cases of cortical hyperintensity are quite common, which is contrary to the concept that deeper structures tend to be more hyperintense. Thus, the cause of hyperintensities in such locations is unknown but may vary depending on the location.

Additionally, with the increasing utilization of *3D volumetric imaging*, particularly for FLAIR imaging, it should be pointed out that bright signal in the same regions mentioned

A.M. McKinney, *Atlas of Normal Imaging Variations of the Brain, Skull, and Craniocervical Vasculature*,
DOI 10.1007/978-3-319-39790-0_22

above, particularly along the white matter tracts of the CST, DSCP, SCP, and the middle cerebellar peduncle (MCP), can become more prominent with 3D acquisitions, particularly at the 3 T MR field strength. The reason for such increased hyperintensity with 3D acquisitions of FLAIR versus 2D acquisitions is unclear, but has been proposed to be related to a longer echo time (TE), higher turbo factors, less partial volume effects, or even a "diffusion sensitivity" effect that may occur at the lower refocusing flip angles utilized. Overall, such effects are thought to increase the visibility of white matter structures at 3 T when FLAIR is obtained by a 3D volumetric acquisition.

The various common MRI artifacts that can limit interpretation are not covered here, as those well-known artifacts can be found in separate texts and their appearance on imaging is well established. Common or misleading artifacts on FLAIR and DWI are covered to some degree because they are more likely to be mistaken for disease and the available literature on these artifacts is less established.

22.1 FLAIR and DWI Pseudolesions at 3 T

22.1.1 Cingulate, Insula, and Orbitofrontal Cortices

On 3 T FLAIR and DWI, perhaps the most common sites by far for normal, mild hyperintensity relative to other areas are the *cingulate, insula*, and *orbitofrontal cortices.* On FLAIR, this is distinguished from true pathology by the lack of swelling or mass effect. On DWI, there is a lack of dark signal on ADC maps, and no bright signal on "exponential" diffusion images (*i.e.*, the T2 component is removed), indicating the absence of cytotoxic edema. Differential considerations include causes of cortical edema, such as *HIE, acute hepatic or hyperammonemic encephalopathy* (AHE, which most commonly involves the insula), or *inflammatory or infectious* involvement of cortices, such as meningoencephalitis (Figs. 22.1, 22.2, 22.3, 22.4, 22.5, 22.6, 22.7, 22.8, 22.9, 22.10, 22.11 and 22.12).

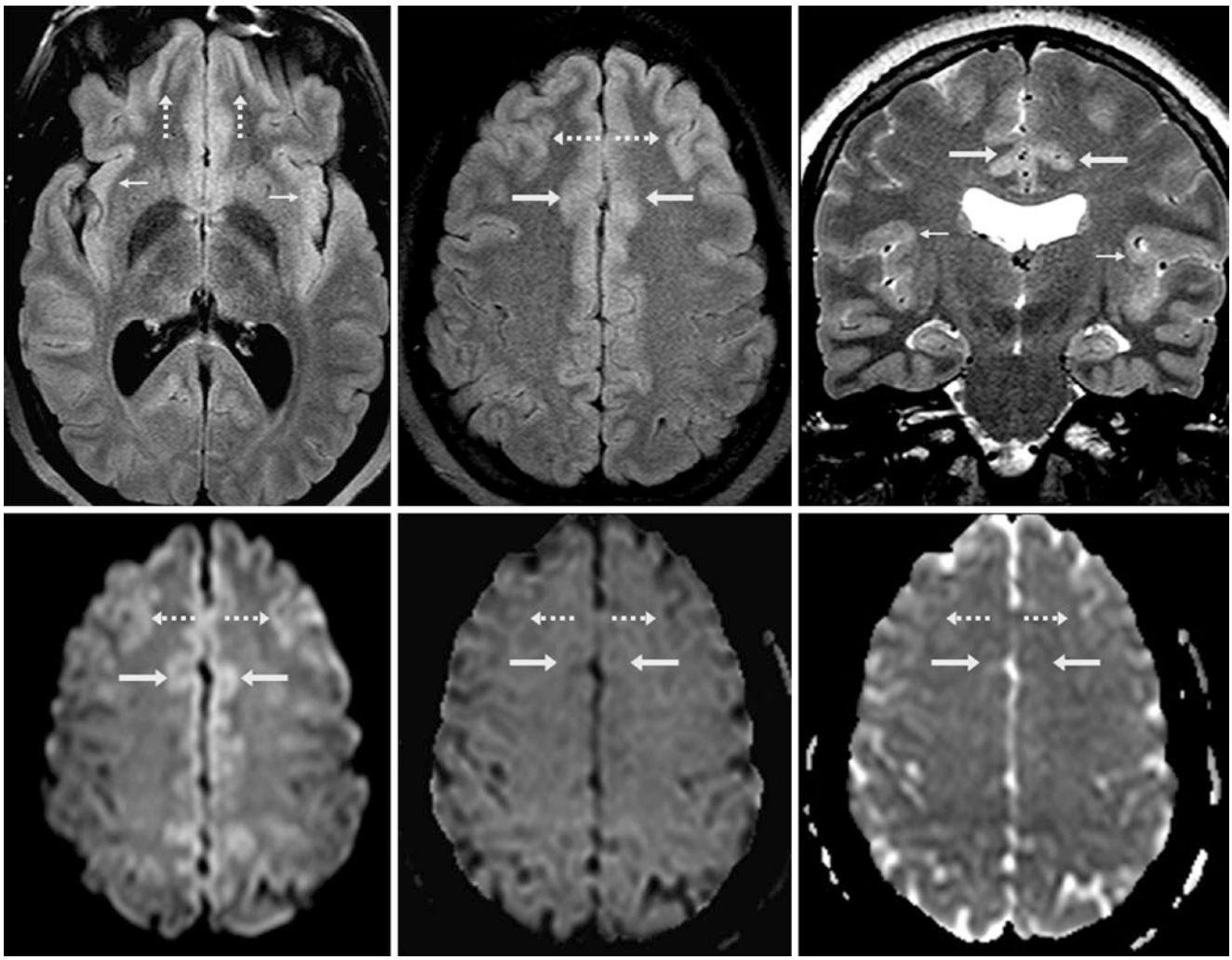

Fig. 22.1 A 22-year-old patient underwent a 3 T MRI that illustrates hyperintense cortices of the cingulate (*arrows*), insular (*thin arrows*), and orbitofrontal gyri (*dashed arrows*) on fluid-attenuated inversion recovery (FLAIR) imaging (*top left and middle*), coronal T2-weighted imaging (T2WI) (*top right*), and diffusion-weighted imaging (DWI) (*bottom left*). The appearance resembles cytotoxic edema, such as hypoxic-ischemic encephalopathy (HIE), but this is not HIE, as the gyri are not bright on "exponential" DWI (*bottom middle*), which removes the T2 component of DWI, and they are not dark on apparent diffusion coefficient (ADC) maps (*bottom right*)

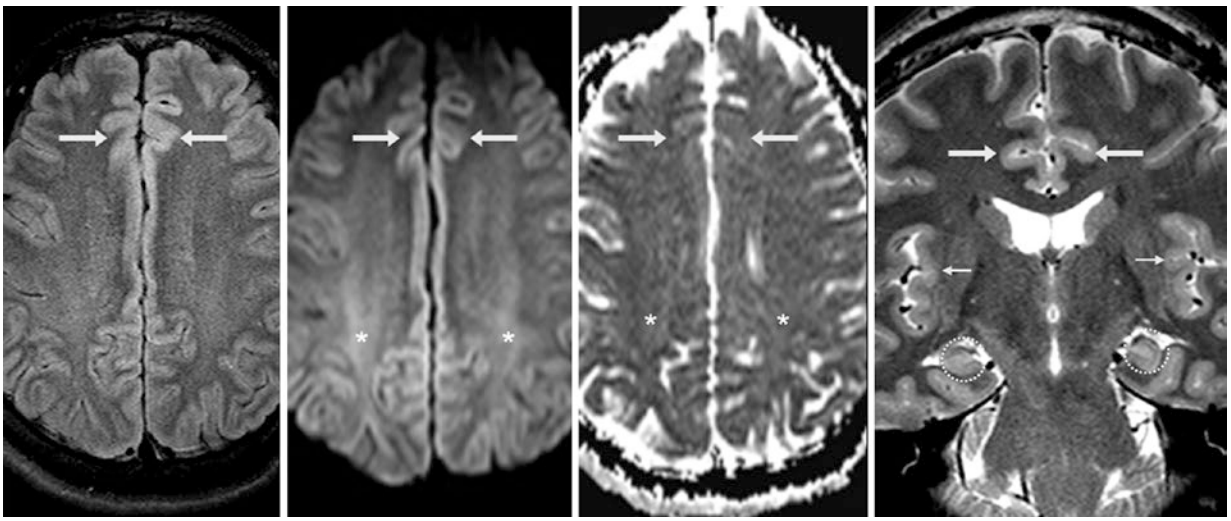

Fig. 22.2 A 27-year-old underwent a 3 T MRI that shows hyperintense cortices of the cingulate (*arrows*) and insular (*thin arrows*) gyri, relative to the parieto-occipital gyri, on axial FLAIR (*left*), DWI (*left middle*), and coronal T2WI (*right*). These gyri exhibit normal signal intensity on ADC maps (*right middle*). Also note normal hyperintensity within the periventricular white matter (PVWM) on DWI (*asterisk*) and within the hippocampi on coronal T2WI (*dotted circles*), which may also simulate HIE

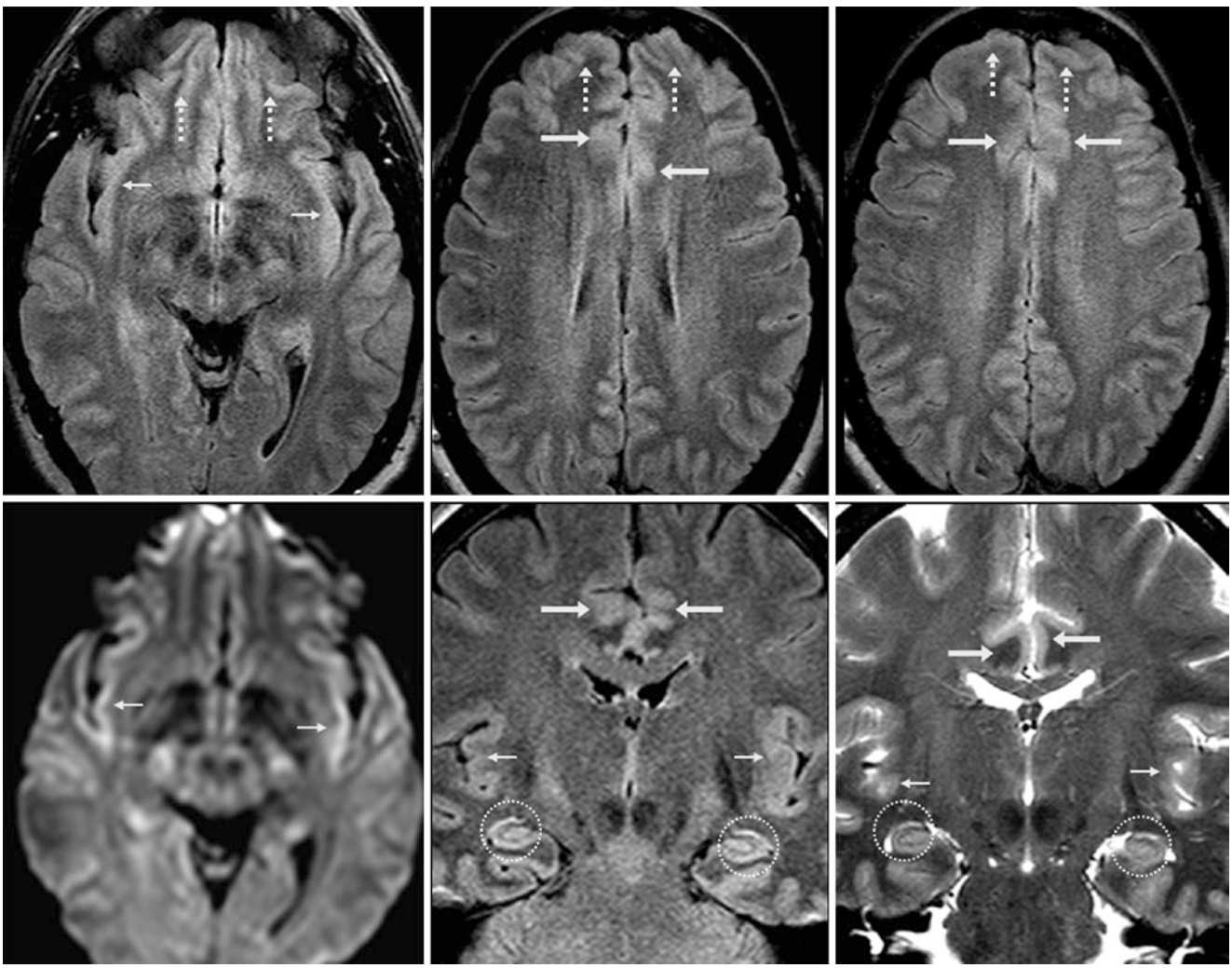

Fig. 22.3 A 37-year-old underwent a 3 T MRI that illustrates hyperintense cortices of the cingulate (*arrows*), insular (*thin arrows*), and orbitofrontal (*dashed arrows*) gyri on axial FLAIR images (*top row*). Only the insular gyri are hyperintense on DWI (*bottom left*). The cortices of these gyri are also bright on coronal FLAIR (*bottom middle*) and T2WI (*bottom right*). The hippocampi (*dotted circles*) are also relatively hyperintense (but normal) on the coronal images

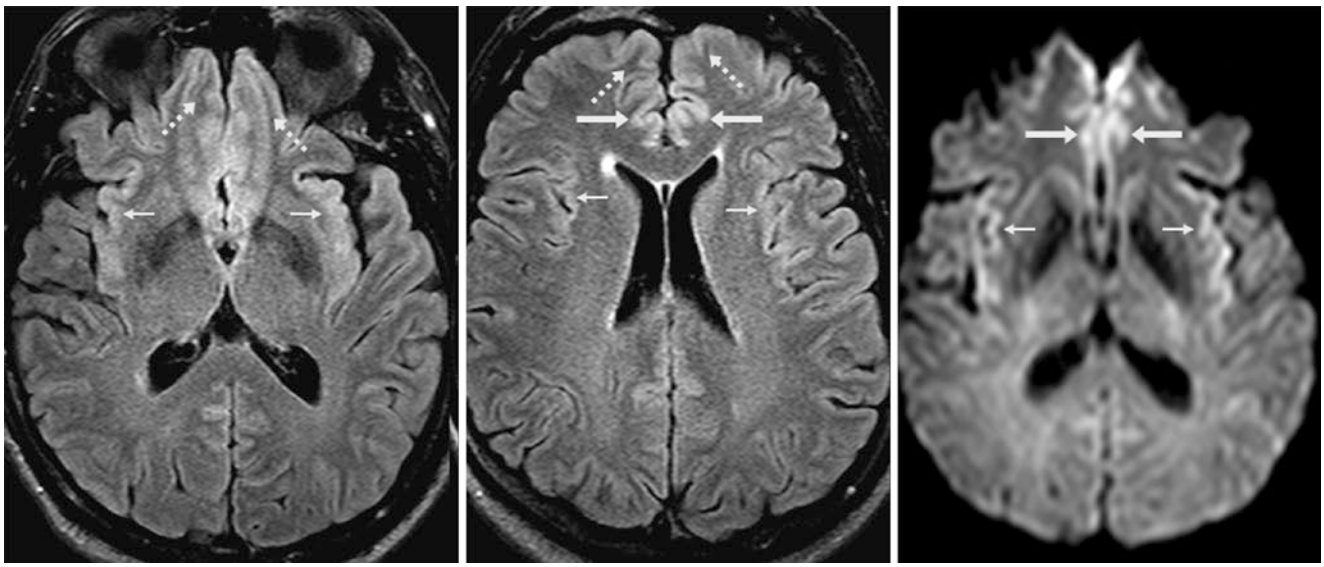

Fig. 22.4 A 64-year-old underwent a 3 T MRI that demonstrates hyperintense cortices of the cingulate (*arrows*), insular (*thin arrows*), and orbitofrontal (*dashed arrows*) gyri on axial FLAIR images (*left and middle*). These gyri are also hyperintense on DWI (*right*). Note the normal signal intensity of the temporal and parieto-occipital gyri

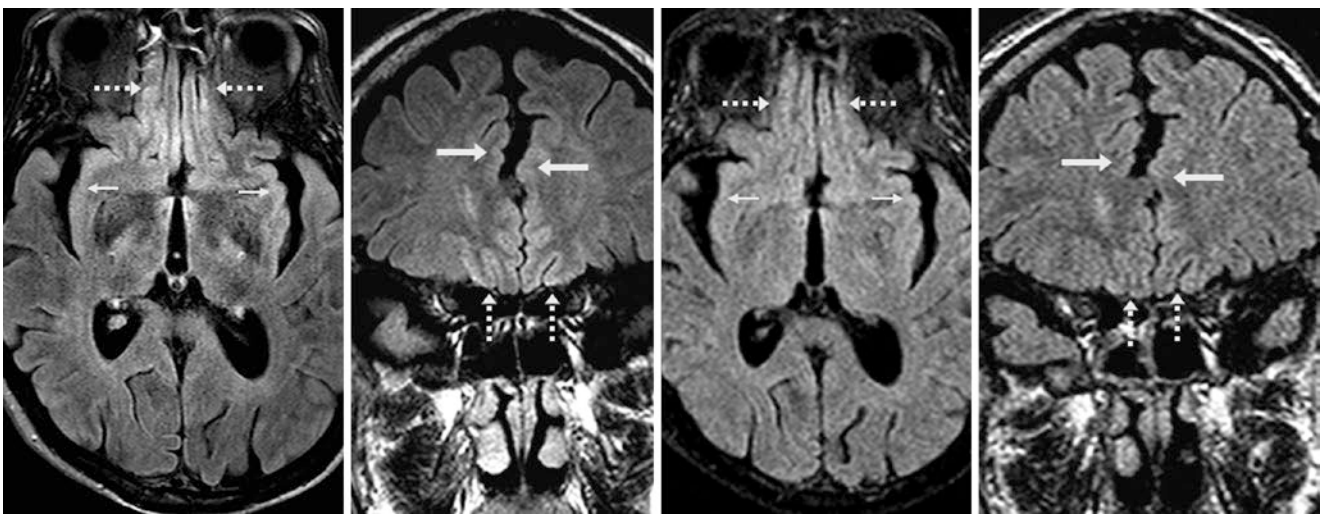

Fig. 22.5 A 62-year-old underwent a 3 T MRI that illustrates hyperintense cortices of the cingulate (*arrows*), insular (*thin arrows*), and orbitofrontal (*dashed arrows*) gyri on axial (*left*) and coronal (*left middle*) FLAIR images. On a 2-year follow-up 1.5 T MRI with axial (*right middle*) and coronal (*right*) FLAIR images, these gyri appear to have normal signal intensity

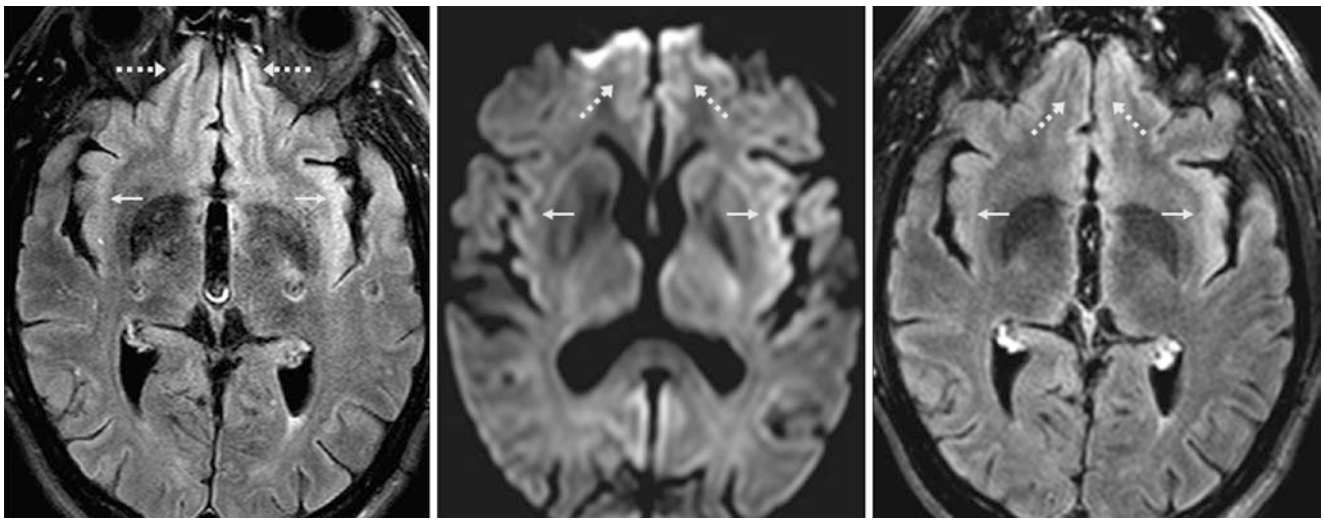

Fig. 22.6 A 64-year-old underwent a 3 T MRI that shows asymmetrically hyperintense left insular cortex (*thin arrows*) and left orbitofrontal gyri (*dashed arrows*) on FLAIR (*left*) and DWI (*middle*). Repeat motion-corrected PROPELLER FLAIR images (*right*) have inherently decreased signal and thus cause the hyperintensity to appear less prominent

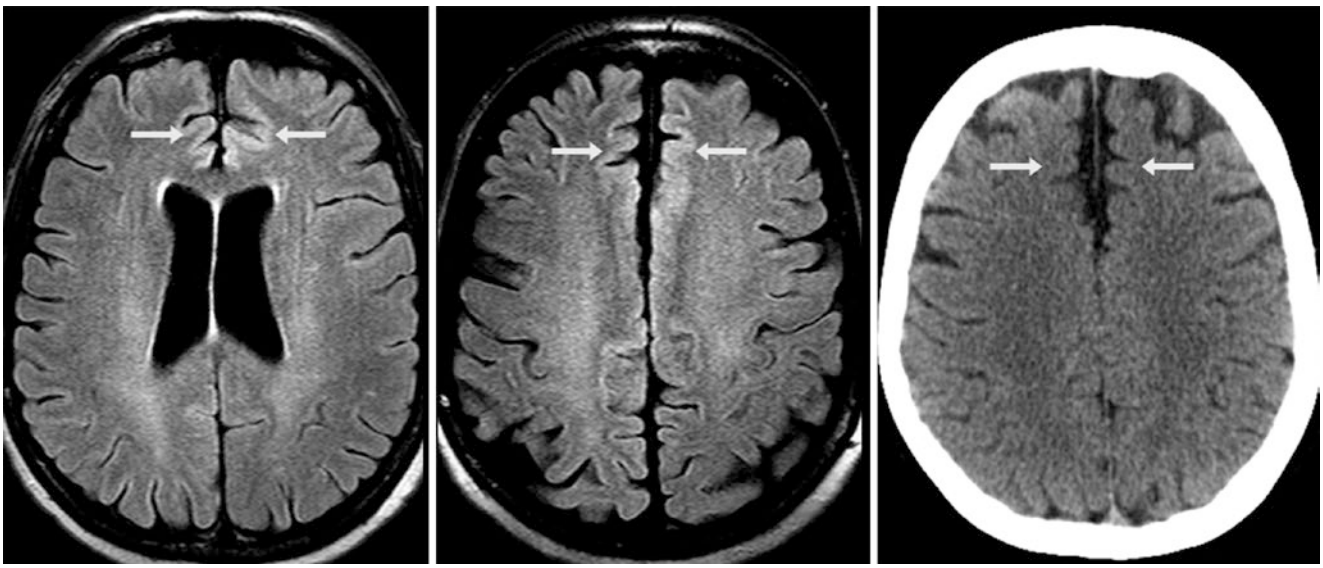

Fig. 22.7 A 60-year-old with headaches underwent an otherwise normal 3 T MRI that demonstrates mildly hyperintense cortices of the orbitofrontal gyri (*arrows*) on FLAIR (*left and middle*). A nonenhanced CT (NECT) scan (*right*) depicts a normal appearance

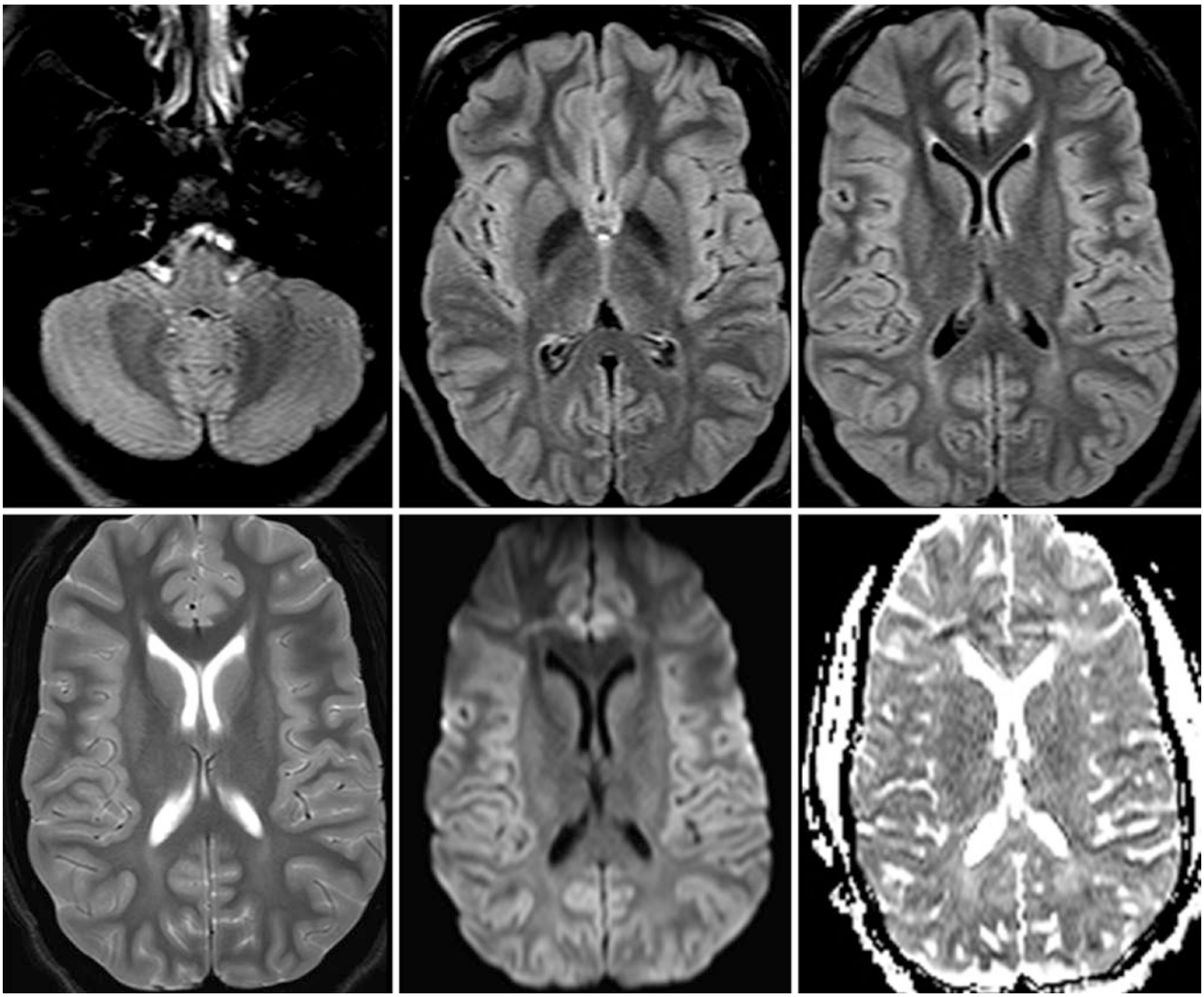

Fig. 22.8 A 19-year-old with weakness (which resolved soon after) had a normal 3 T MRI that illustrates diffusely hyperintense cerebellar and cerebral cortices on FLAIR images (*top row*), T2WI (*bottom left*), and DWI (*bottom middle*). This hyperintensity simulates diffuse cortical injury of HIE, but the ADC maps appear normal (*bottom right*), indicating that HIE is not present

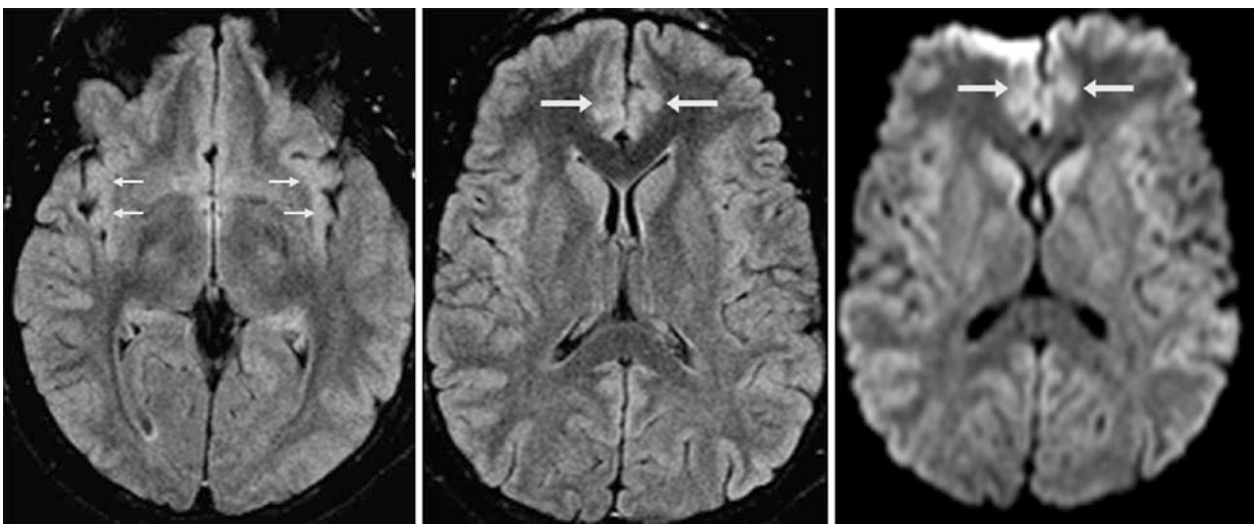

Fig. 22.9 A 24-year-old with headaches had a 1.5 T MRI that depicts mild, diffusely hyperintense cingulate (*arrows*) and insular (*thin arrows*) cortices on FLAIR (*left and middle*) and DWI (*right*). This case demonstrates how normal hyperintensity can occur even at 1.5 T, although to a lesser degree (and less commonly) than at 3 T

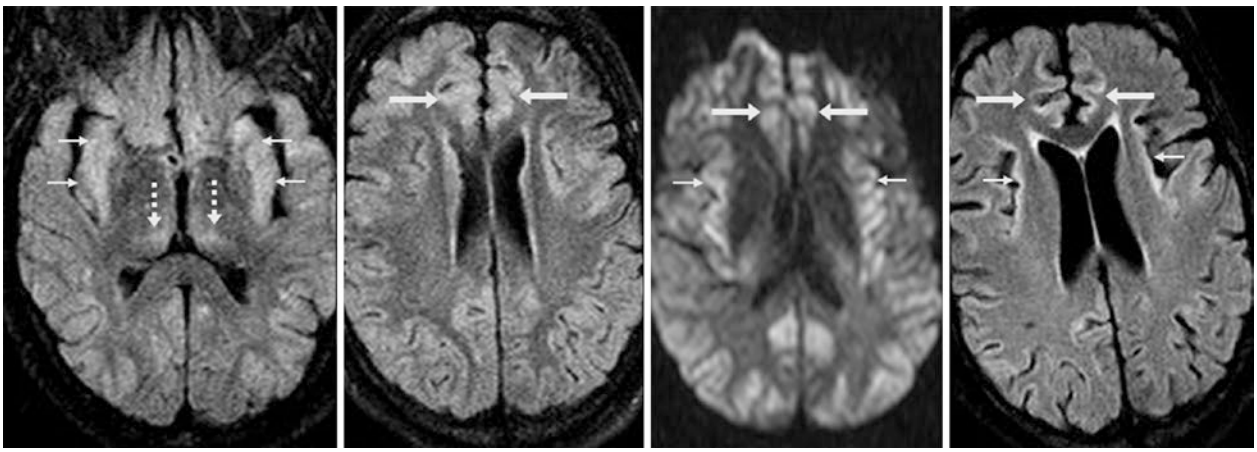

Fig. 22.10 Comparison case of acute hepatic encephalopathy (AHE) with diffuse cortical involvement: This 57-year-old with hyperammonemia from hepatic failure had a 1.5 T MRI that showed diffuse cortical edema on FLAIR (*left images*) and DWI (*right middle*), particularly involving the cingulate gyri (*arrows*) and insula (*thin arrows*), with characteristic involvement of the thalami (*dashed arrows*). On FLAIR images 13 days later (*right*), there was mild residual cortical edema (*arrows*). Diffuse cortical involvement shows a relatively severe form of AHE, which can be fatal

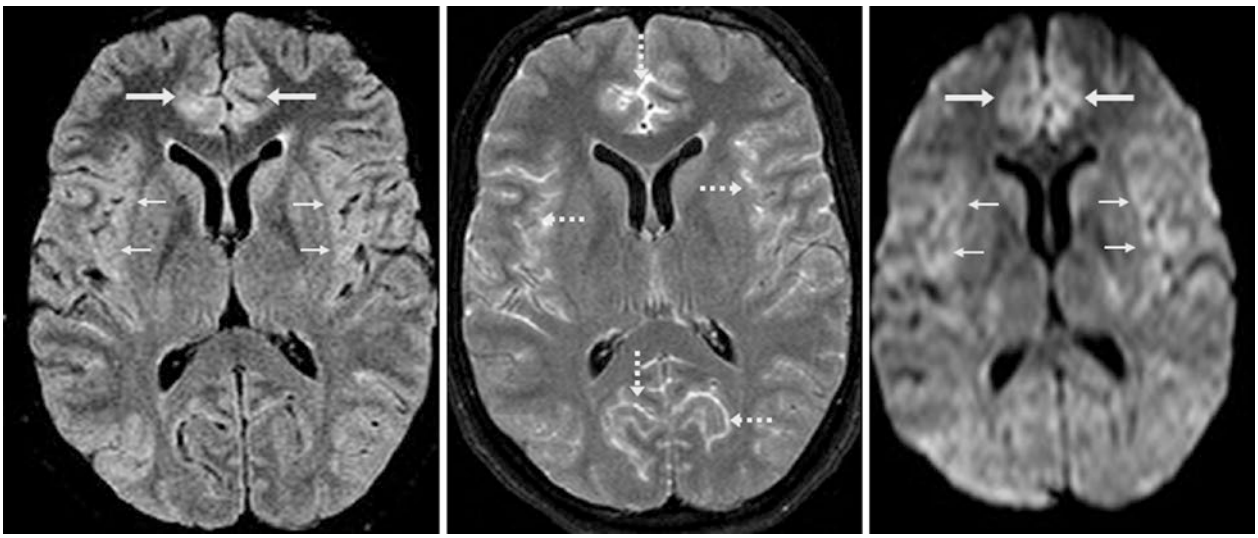

Fig. 22.11 Comparison case of herpes simplex viral (HSV) encephalitis: This 37-year-old underwent a 3 T MRI, which demonstrated subtle, multifocal cortical edema on FLAIR (*left*) and DWI (*right*), particularly involving the cingulate gyri (*arrows*) and insula (*thin arrows*). Postcontrast FLAIR images (*middle*) demonstrated diffuse leptomeningeal enhancement (*dotted arrows*). Serology found evidence of HSV infection

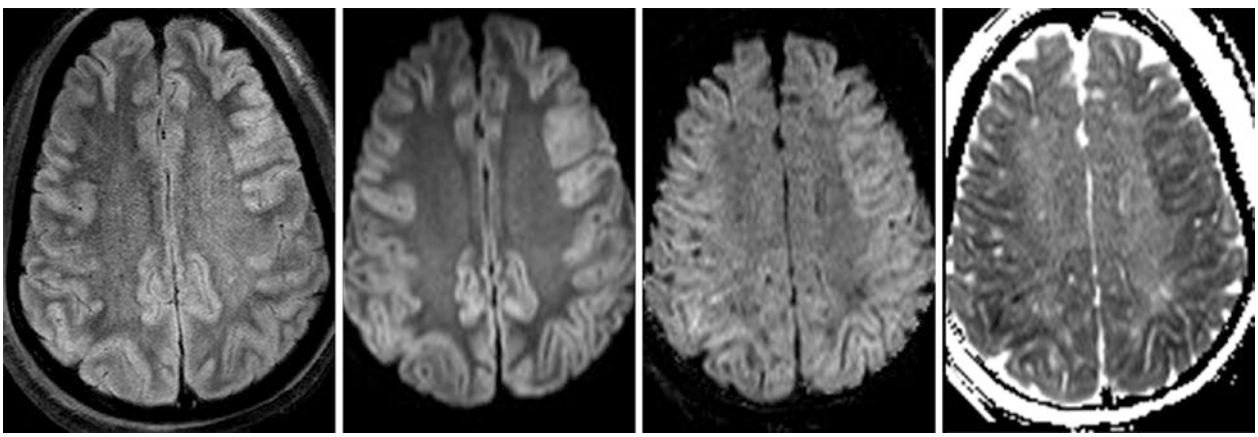

Fig. 22.12 Comparison case of hypoxic ischemic encephalopathy (HIE) in a 58-year-old after an overdose of sedatives. A 3 T MRI showed mild, diffuse cortical edema on FLAIR (*left*) and DWI (*left middle*). An exponential DWI (*right middle*) removes the T2 component of edema and shows diffuse cortical injury from HIE, as confirmed by dark cortical signal diffusely on an ADC map (*right*)

22.1.2 Periventricular White Matter

On 3 T FLAIR and DWI, other common sites for normal, mild hyperintensity are located within the *periventricular white matter* (PVWM), particularly within the corona radiata, the supraventricular centrum semiovale, and forceps major or minor. Differential considerations are vast, and include causes of deep white matter or subcortical edema, in addition to the most common cause which is chronic vasculopathic disease, such as the delayed (subacute) phase of *HIE; acute toxic leukoencephalopathy* (ATL), which can be due to many causes; *postinfectious or inflammatory* acute disseminated encephalomyelitis (ADEM); or *inflammatory disorders of demyelination* such as multiple sclerosis (MS), *amyotrophic lateral sclerosis* (ALS), or rarely demyelinating *leukodystrophies* (Figs. 22.13, 22.14, 22.15, 22.16, 22.17, 22.18, 22.19 and 22.20).

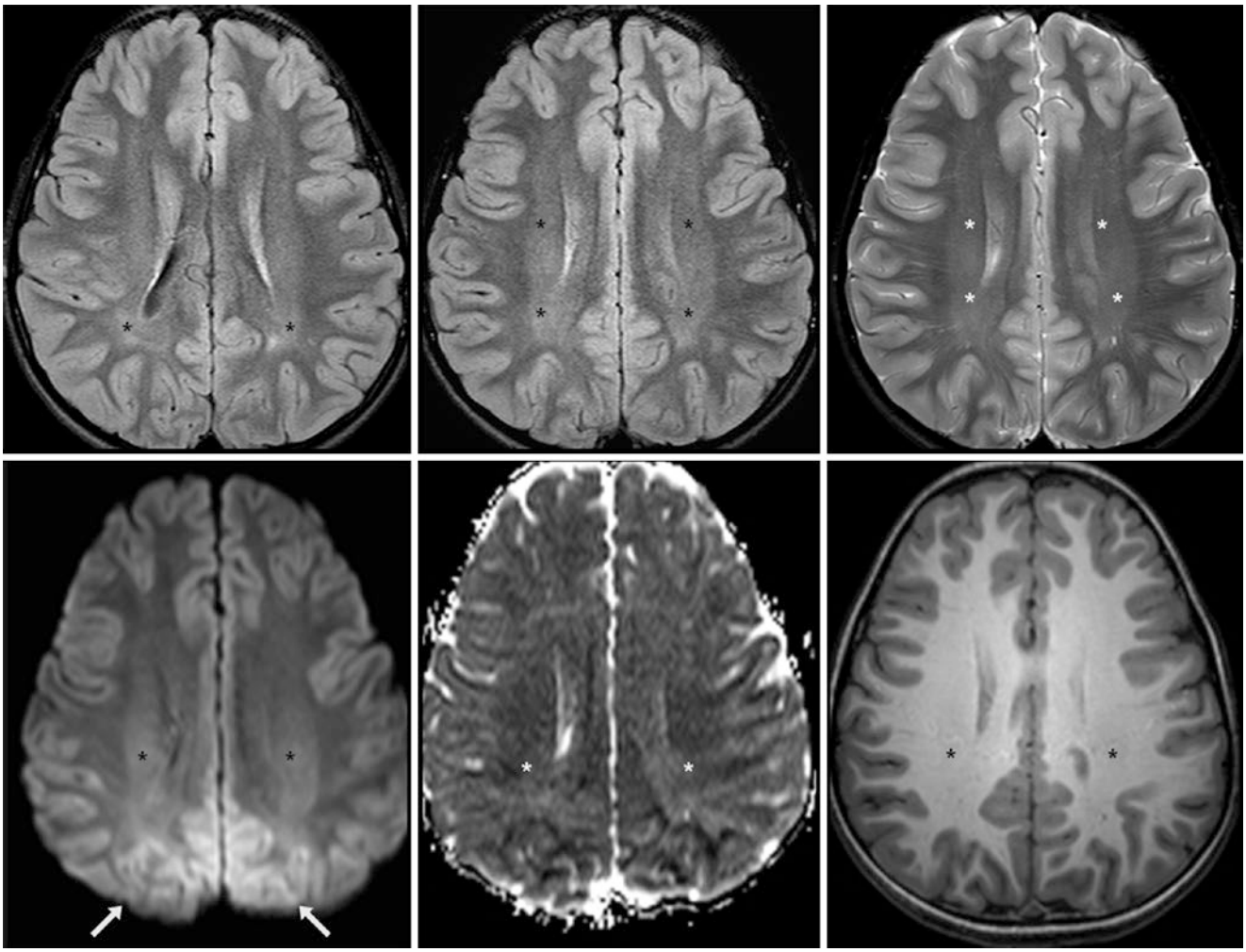

Fig. 22.13 A 9-year-old with migraines had a negative 3 T MRI that demonstrated mild PVWM hyperintensity (*asterisk*) on FLAIR (*top left and top middle*), which is slightly less prominent on T2WI (*top right*), and DWI (*bottom left*). Although there is mild PVWM hyperintensity on DWI, the corresponding ADC map (*bottom middle*) and gradient echo (GE) T1WI (*bottom right*) are unremarkable. Note the artifactual hyperintensity of the parieto-occipital cortices on DWI (*arrows*), likely due to air-bone and bone-tissue interfaces with subsequent field inhomogeneities

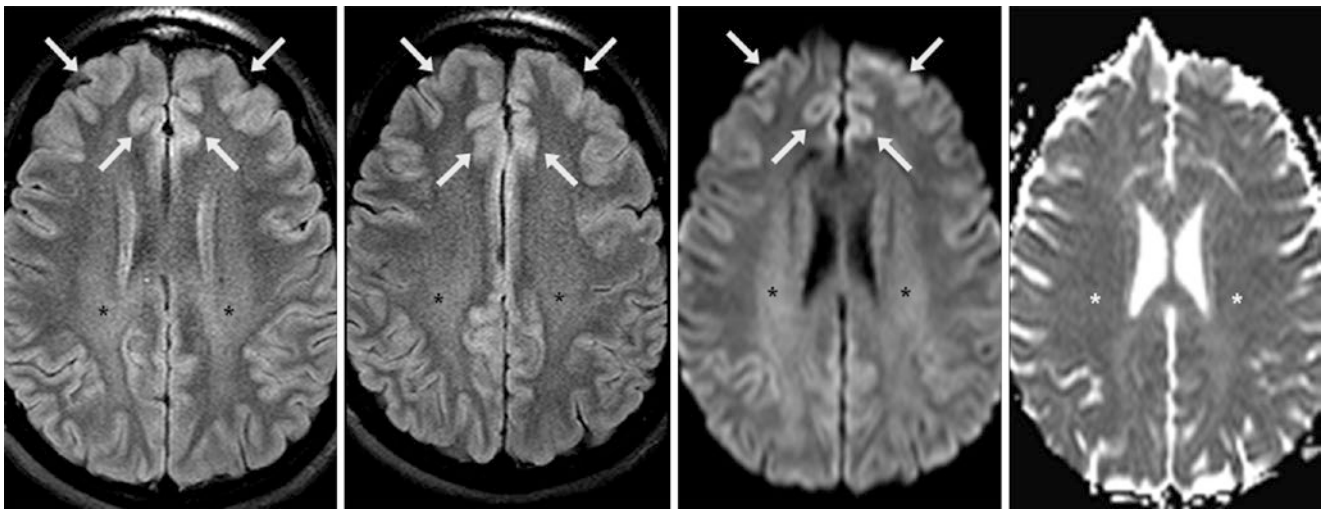

Fig. 22.14 A 38-year-old with altered mental status had a negative 3 T MRI. FLAIR (*left and left middle*), DWI (*right middle*), and the ADC map (*right*) demonstrate mild, normal hyperintensity diffusely and bilaterally within the PVWM of the centrum semiovale (*asterisk*), without corresponding abnormally dark signal on the ADC map (*right*). Note also the normal-variant bright frontal and cingulate cortices on FLAIR (*arrows*), which are brighter than the parieto-occipital cortices posteriorly

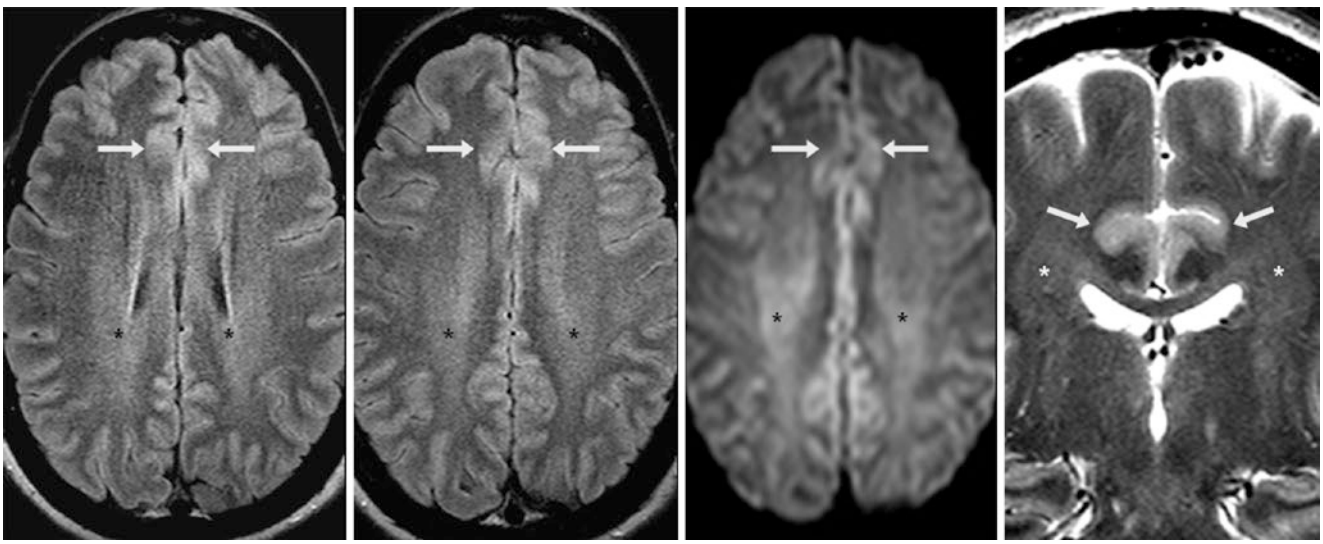

Fig. 22.15 A 37-year-old had transient weakness that resolved hours later. A negative 3 T MRI with FLAIR (*left and left middle*), DWI (*right middle*), and coronal T2WI (*right*) showed normal, mild hyperintensity within the PVWM diffusely and bilaterally, centered within the centrum semiovale (*asterisk*), without dark signal on an ADC map (not shown). Also, note mildly hyperintense cingulate (*arrows*) and frontal cortices on T2WI (*right*), which are also normal variants at 3 T

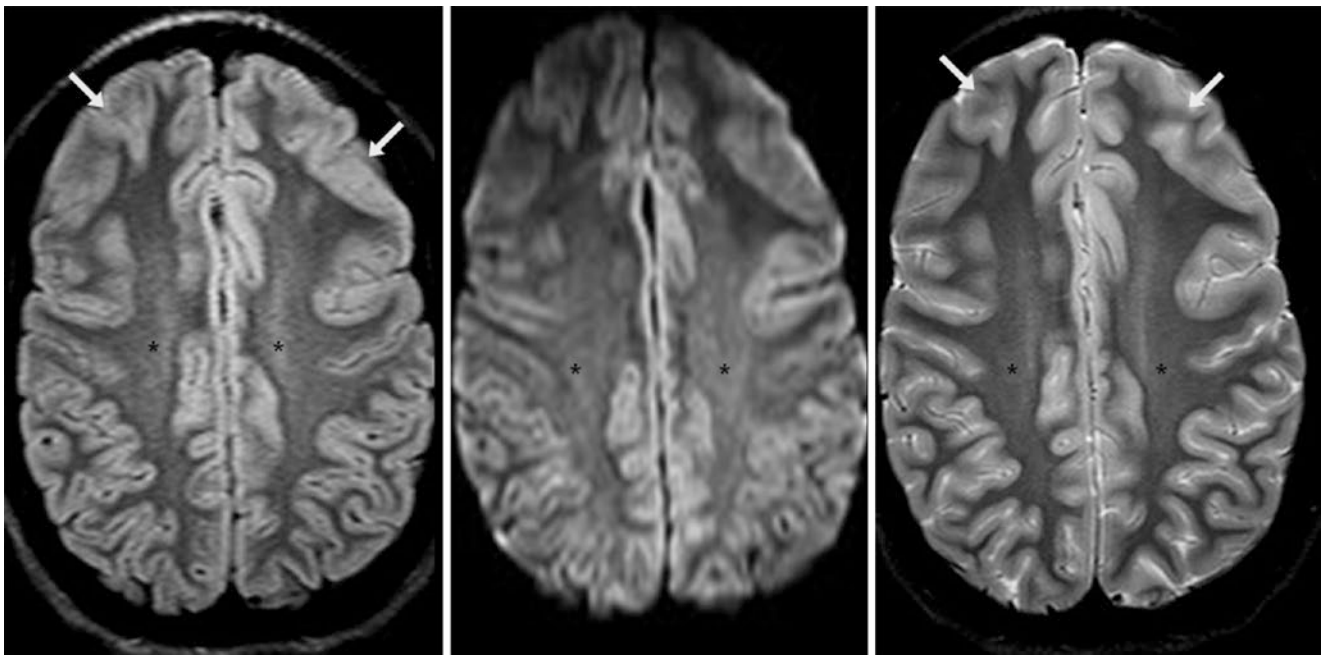

Fig. 22.16 A 19-year-old had concussive symptoms that resolved soon after. A negative 3 T MRI with FLAIR (*left*), DWI (*middle*), and T2WI (*right*) showed normal, subtle hyperintensity of the PVWM bilaterally on each sequence, centered in the centrum semiovale (*asterisk*). Also, note the normal, mildly hyperintense frontal cortices (*arrows*) on FLAIR

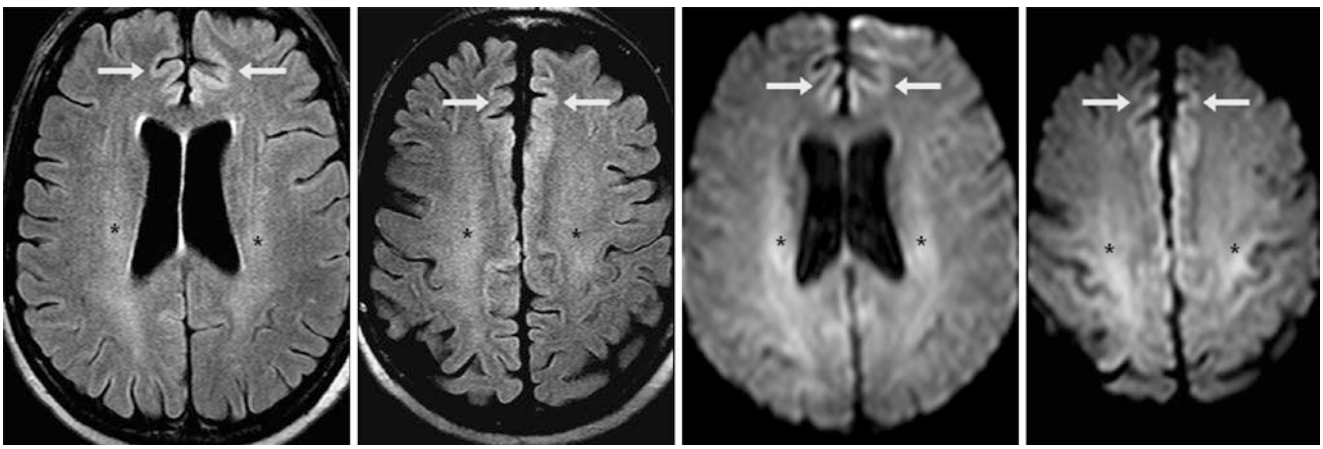

Fig. 22.17 A 60-year-old with altered mental status had symptoms that resolved within 1 day. A 3 T MRI with FLAIR (*left and left middle*) and DWI (*right and right middle*) showed normal, mild hyperintensity throughout the PVWM and within the corona radiata, extending up to the centrum semiovale (*asterisk*). Also, note the normally bright cingulate cortices (*arrows*)

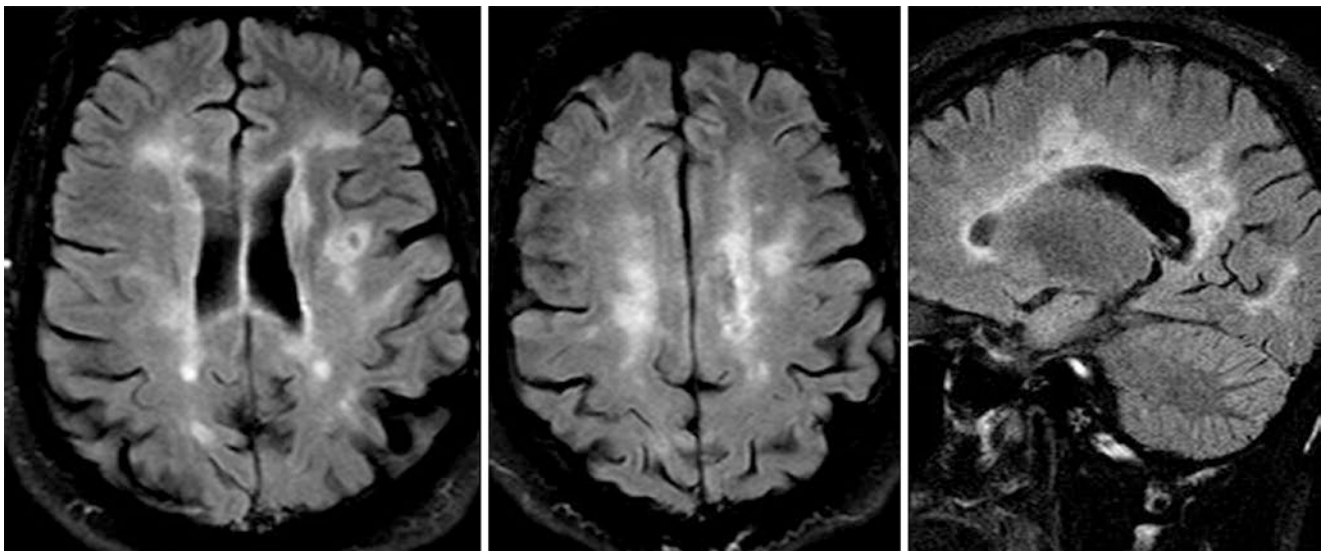

Fig. 22.18 Comparison case of confluent lesions in multiple sclerosis (MS) in a 44-year-old with worsening symptoms. A 1.5 T MRI demonstrated confluent abnormalities throughout the PVWM on axial (*left and middle*) and sagittal (*right*) FLAIR images. Note the irregular PVWM lesions that are oriented perpendicular to the ventricles, typical of MS

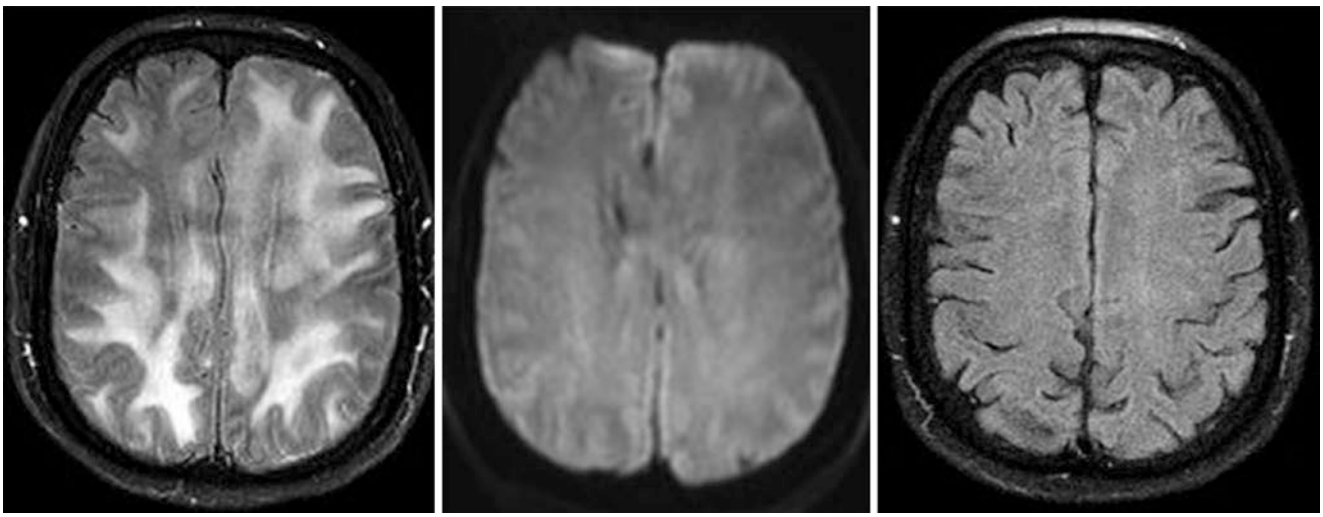

Fig. 22.19 Comparison case of acute disseminated encephalomyelitis (ADEM). A 58-year-old underwent a 1.5 T MRI, which demonstrated confluent abnormalities throughout the deep PVWM on axial FLAIR (*left*), but did not show reduced diffusivity on DWI (*middle*). Six months later, the abnormalities had entirely resolved on FLAIR (*right*)

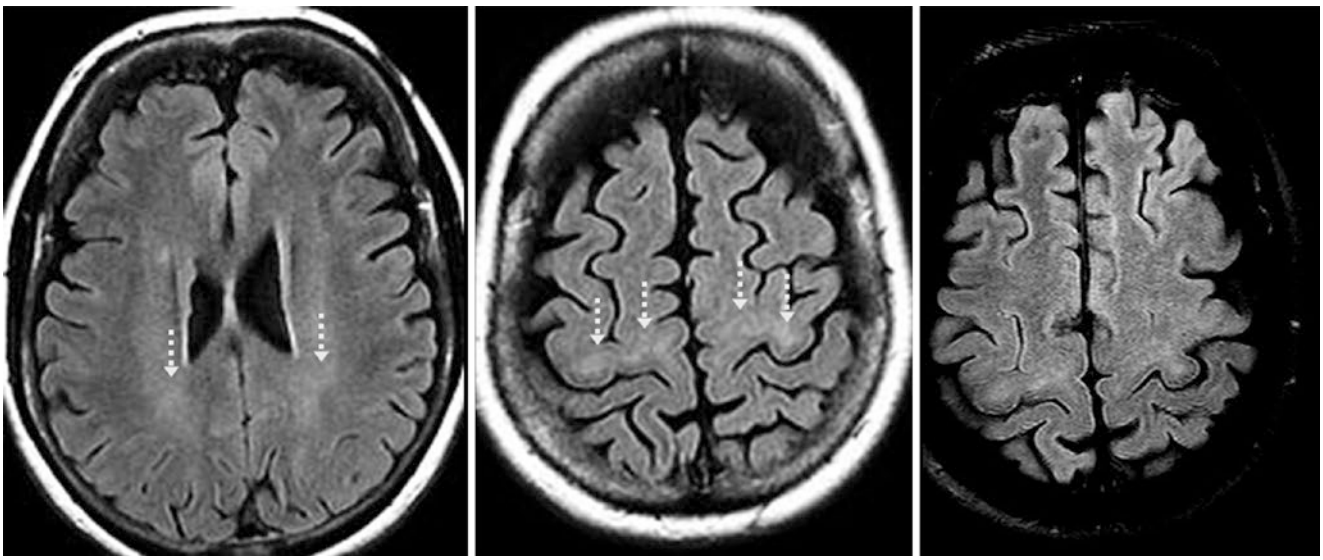

Fig. 22.20 Comparison case of amyotrophic lateral sclerosis (ALS). A 54-year-old with progressive motor weakness underwent a 3 T MRI. FLAIR images (*left and middle*) demonstrated subtle abnormal signal within the posterior PVWM (*dotted arrows*), which extended into the subcortical white matter of the precentral gyri (primary motor region). Such findings can be seen in ALS. FLAIR images obtained 5 years later remained unchanged (*right*)

22.1.3 Corticospinal Tracts

On 3 T FLAIR and DWI, another quite common site for normal, mild hyperintensity is within the *corticospinal tracts* (CSTs), most commonly at the level of the *posterior limb of the internal capsule* (PLIC) but possibly at any level from the brainstem up to the subcortical white matter and centrum semiovale just below the primary motor cortex of the of the frontal lobe. The cause is unknown, but could relate to increased interstitial water or a lesser degree of myelination (T2WI brightness) versus a greater degree of anisotropy (DWI brightness). The appearance is most commonly bilateral, but it may seem asymmetric or unilateral. Differential considerations include vascular or *ischemic conditions* (lacunar infarction), *demyelinating disorders* such as multiple sclerosis (MS) or *amyotrophic lateral sclerosis* (ALS), *acute hepatic encephalopathy* (AHE), or rare demyelinating leukodystrophies (Figs. 22.21, 22.22, 22.23, 22.24, 22.25, 22.26, 22.27 and 22.28).

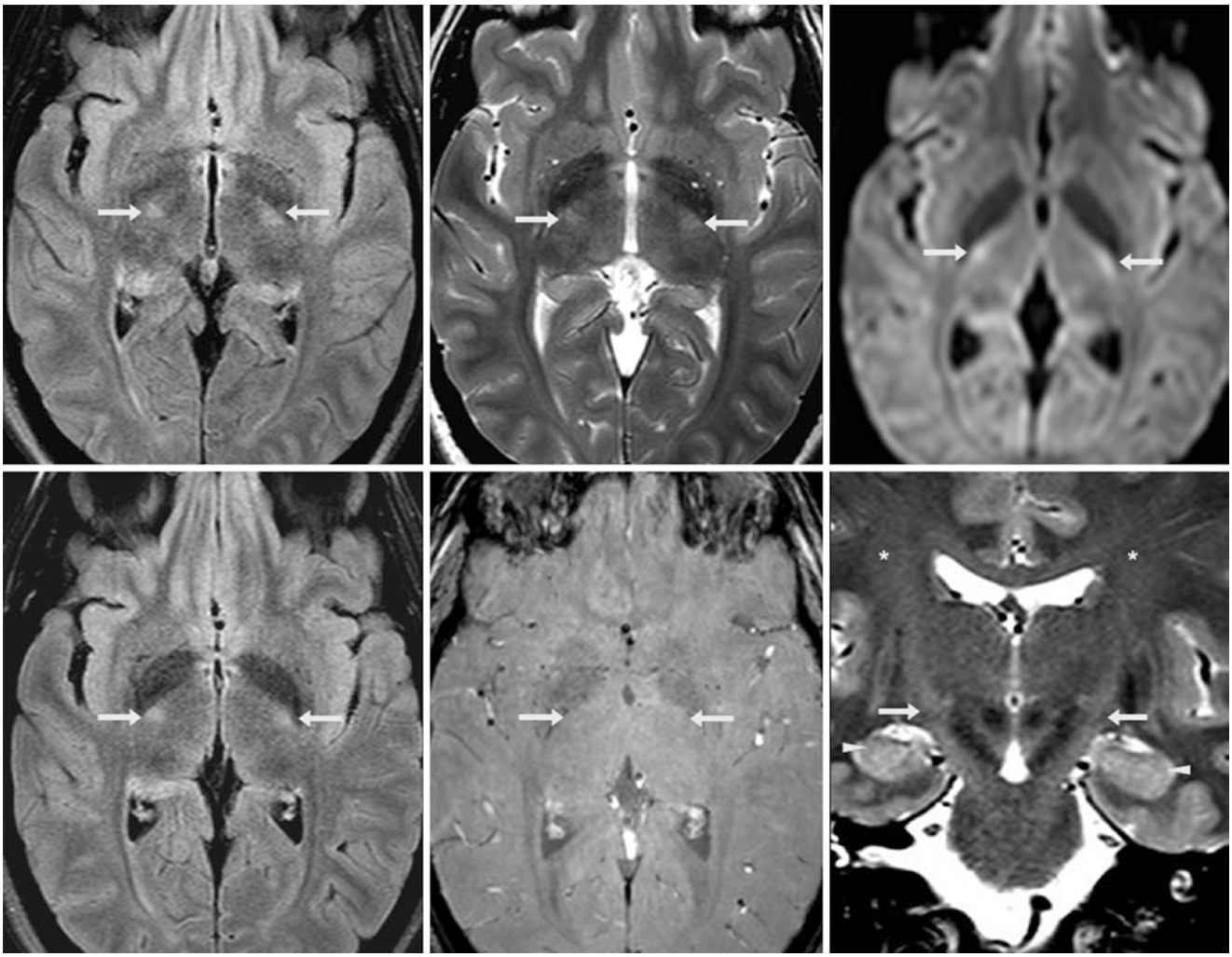

Fig. 22.21 A 29-year-old underwent a 3 T MRI with FLAIR (*left*), T2WI (*middle*), and DWI (*right*), which illustrate normal, mild hyperintensity within the CSTs (*arrows*). These findings were not changed 3 years later on FLAIR (*bottom left*); susceptibility weighted imaging (SWI) was also normal (*bottom middle*). Note the bright signal of the CSTs within the PLICs, extending down to the cerebral peduncles at the level of the brainstem, as shown on coronal T2WI (*bottom right*). Also note normal, mildly bright signal at 3 T within the PVWM at the level of the corona radiata (*asterisk*), as well as within the hippocampi (*arrowheads*)

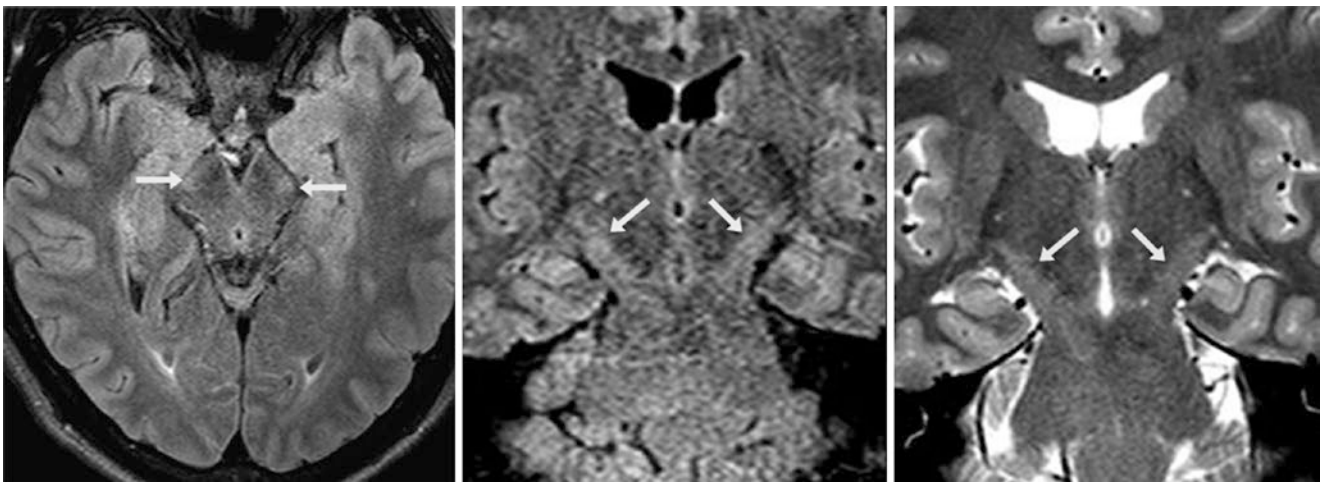

Fig. 22.22 A 27-year-old underwent a 3 T MRI. Axial FLAIR (*left*) demonstrates that the CSTs (*arrows*) are hardly bright, but the bright signal of the CSTs is much more prominent on a coronal FLAIR image (*middle*) and on a T2WI (*right*), which illustrate normal hyperintensity of the CSTs within the cerebral peduncles at the level of the midbrain. This case demonstrates how CST hyperintensity may appear more prominent in the coronal plane on FLAIR or T2WI

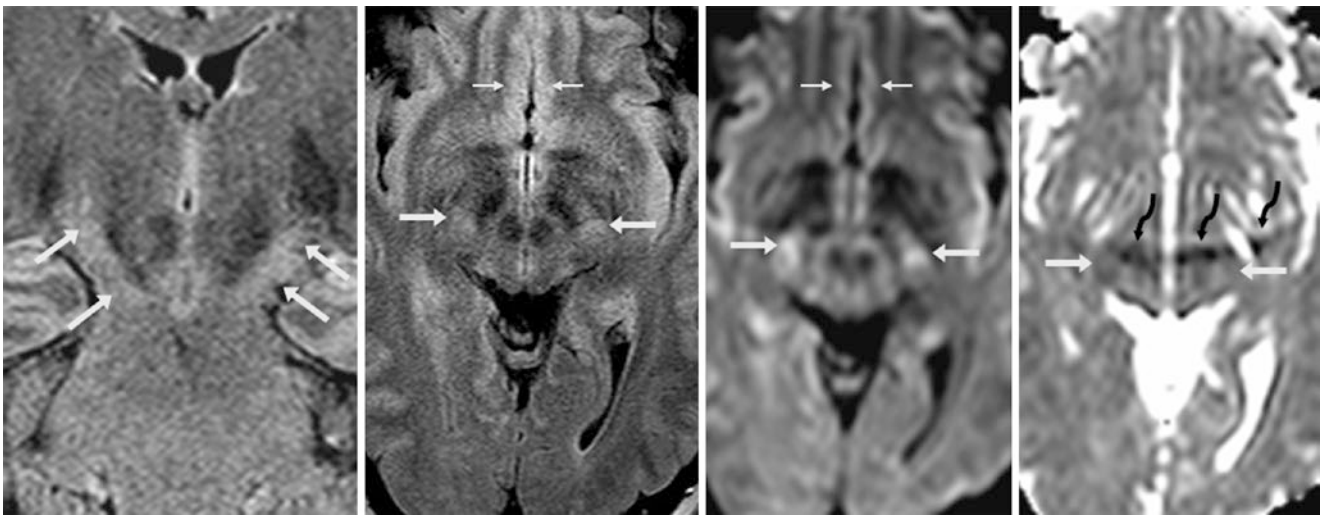

Fig. 22.23 A coronal FLAIR image (*left*) from a 3 T MRI in a 37-year-old shows normal, but quite hyperintense, CSTs (*arrows*) within the cerebral peduncles and subthalamic regions; these are less intense on axial FLAIR (*left middle*) and DWI (*right middle*). Also note the bright orbitofrontal cortices (*thin arrows*), a normal finding at 3 T. ADC maps (*right*) do not show dark signal within the CSTs (*arrows*), although there is a curvilinear inhomogeneity artifact, likely representing "unfolding" artifact from parallel acquisition (*curved arrows*)

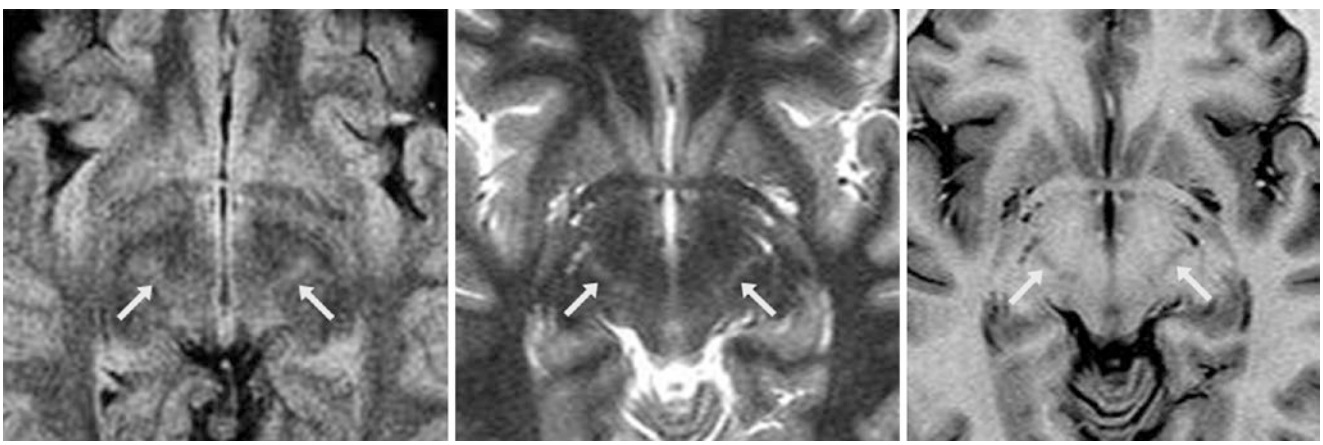

Fig. 22.24 A 23-year-old underwent a 1.5 T MRI. Axial FLAIR (*left*) and inversion recovery (IR) T2WI (*middle*) images show that the CSTs (*arrows*) are mildly bright and have a linear appearance within the cerebral peduncles. The CSTs also appear mildly hypointense on IR T1WI (*right*). Thus, this case demonstrates how such normal CST hyperintensity may also appear linear

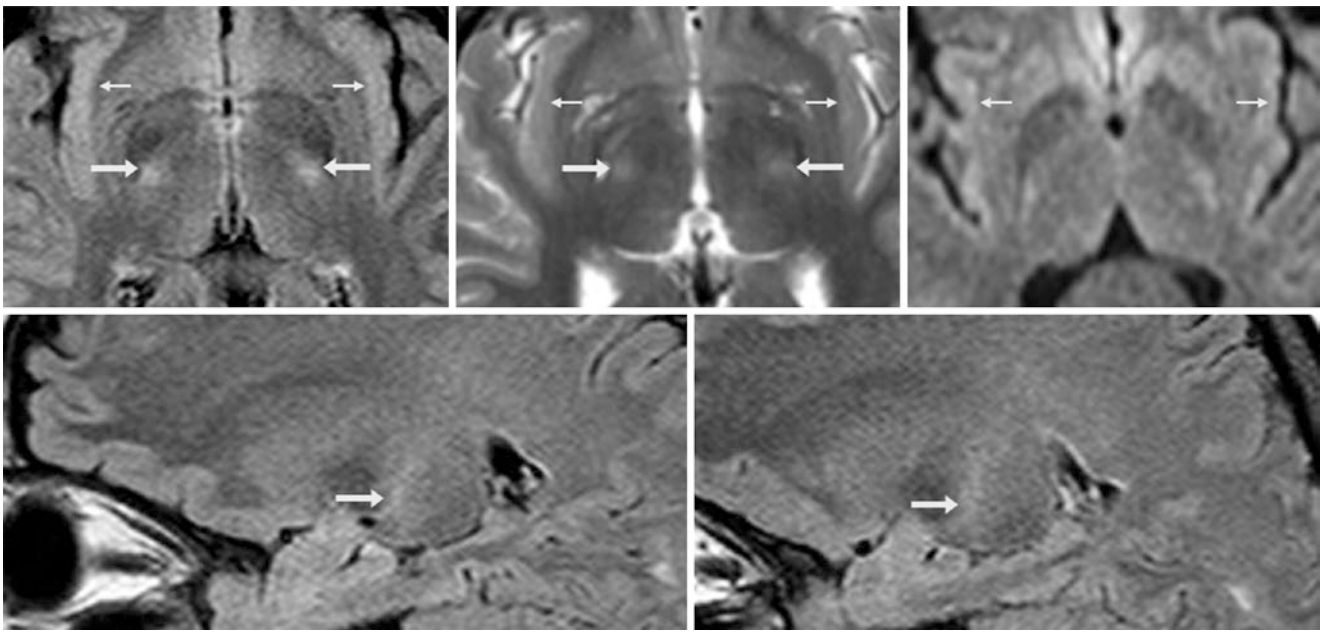

Fig. 22.25 A 19-year-old with headaches had a normal 1.5 T MRI with FLAIR (*top left*) and T2WI (*top middle*). There is mildly bright signal within the CSTs (*arrows*) and insula (*thin arrows*) bilaterally, somewhat prominent for a 1.5 T MRI, but such signal in these sites is normal. DWI (*right*) did not show such hyperintensities, and the ADC maps were normal (*not shown*). Note the mildly bright signal of the CSTs on sagittal FLAIR images of the right and left sides (*bottom row*). These images show how such areas of normal hyperintensity may seem prominent even at 1.5 T

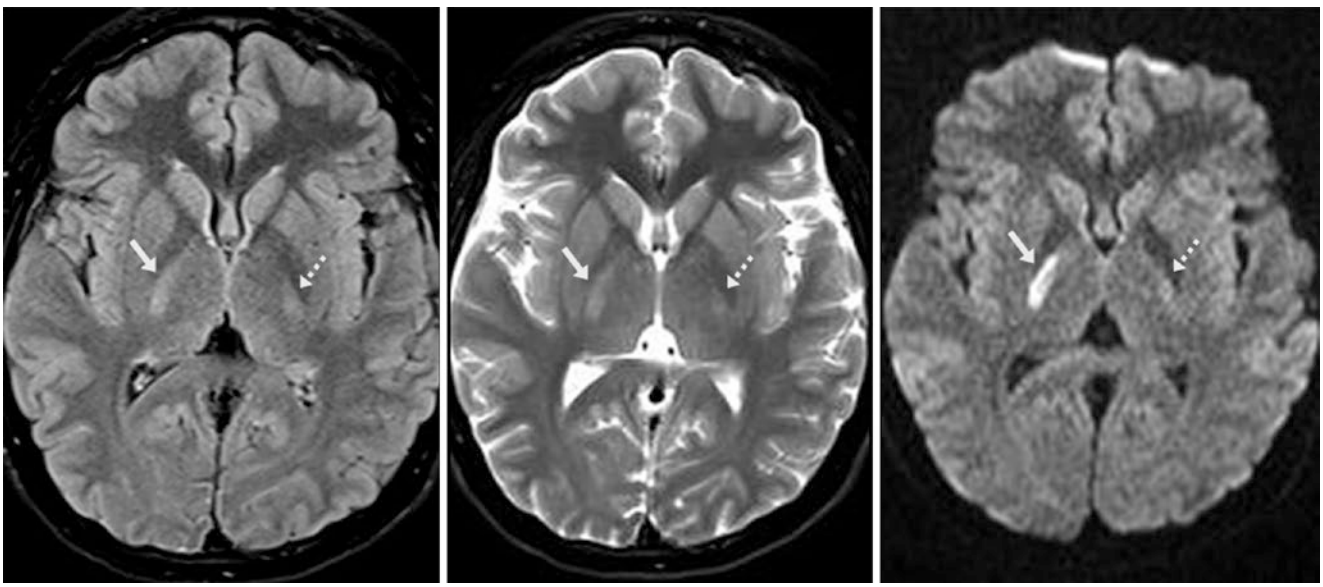

Fig. 22.26 Comparison case of lacunar infarct. A 17-year-old had a 1.5 T MRI that showed a subtle CST lesion within the right PLIC (*arrows*) on FLAIR (*left*) and T2WI (*middle*). The lesion was brighter on DWI (*right*), consistent with an acute/early subacute lacunar infarct. Note mild, normal hyperintensity within the left CST/PLIC (*dashed arrows*)

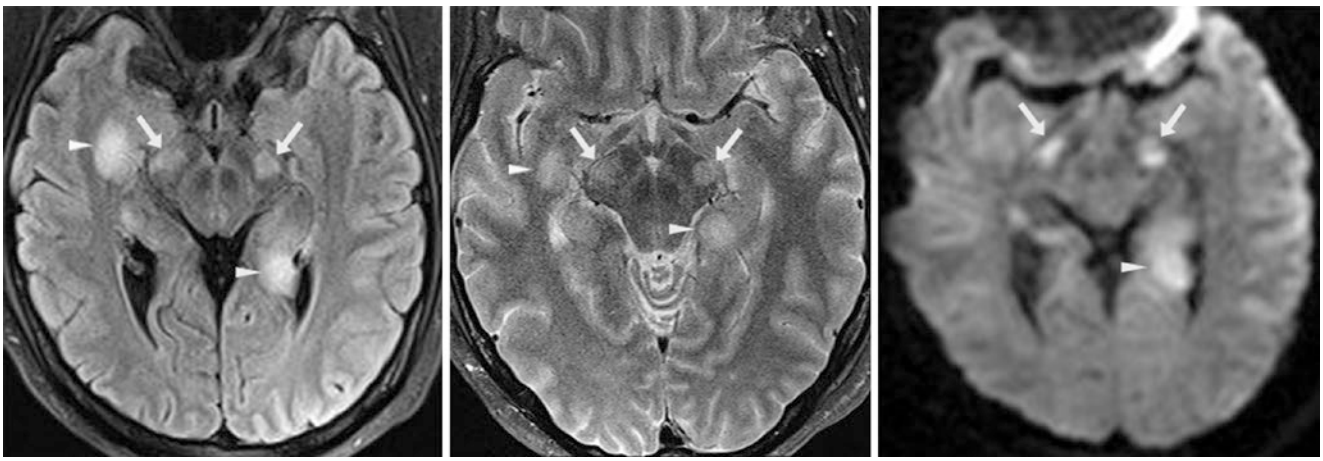

Fig. 22.27 Comparison case of multiple sclerosis (MS). A 36-year-old had a 3 T MRI that showed bilateral CST lesions (*arrows*) on FLAIR (*left*), T2WI (*middle*), and DWI (*right*). Other periventricular lesions were noted within the medial temporal lobes (*arrowheads*). This patient was known to have MS, a demyelinating disease

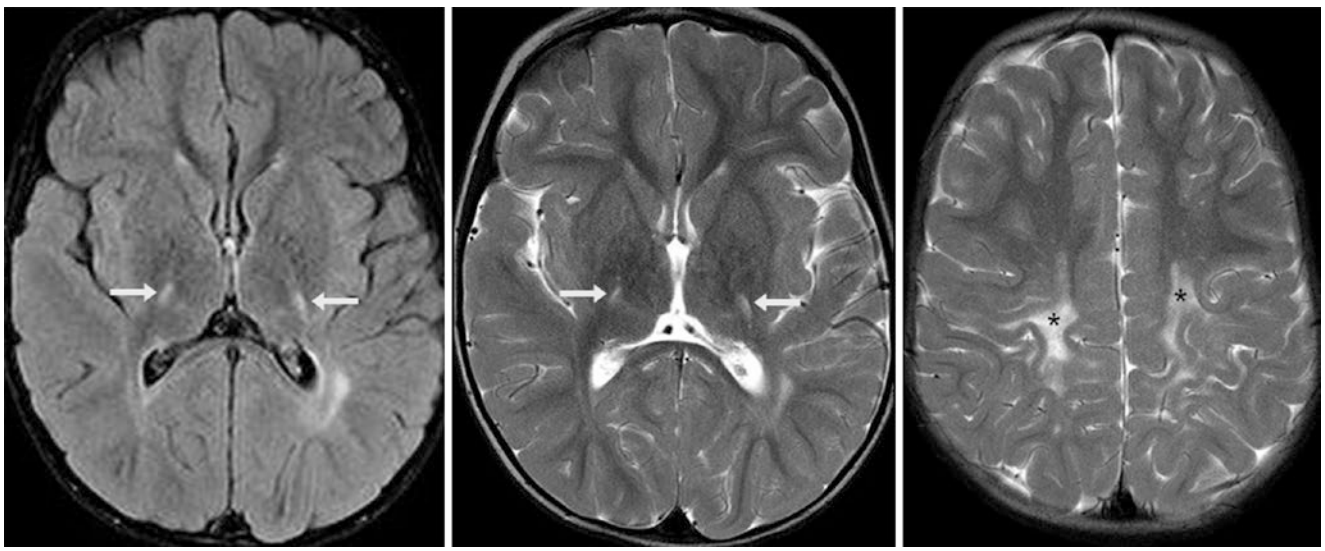

Fig. 22.28 Comparison case of globoid cell leukodystrophy (Krabbe disease). In a 3-year-old with Krabbe disease, a 3 T MRI depicted characteristic bilateral CST abnormalities (*arrows*) within the PLICs on FLAIR (*left*) and T2WI (*middle*), being contiguous with subcortical white matter hyperintensity (*asterisk*). There was moderate precentral gyral atrophy

22.1.4 Decussation of the Superior Cerebellar Peduncle

On 3 T FLAIR and DWI, the *decussation of the superior cerebellar peduncles* (DSCP) is another fairly common site for mild hyperintensity, likely owing to normal high anisotropy, which may be the cause of the bright signal on DWI, with a mildly bright signal on T2WI ("T2 shine-through," perhaps due to focally prominent interstitial fluid). Occasionally, this signal occurs in the SCPs themselves. Whatever the cause of this normal signal, differential considerations include *vascular/ischemic conditions* (lacunar infarction), *demyelinating disorders* such as MS, *metabolic disorders* such as Wernicke's encephalopathy, or *infectious disorders* like rhombencephalitis (Figs. 22.29, 22.30, 22.31, 22.32, 22.33, 22.34, 22.35 and 22.36).

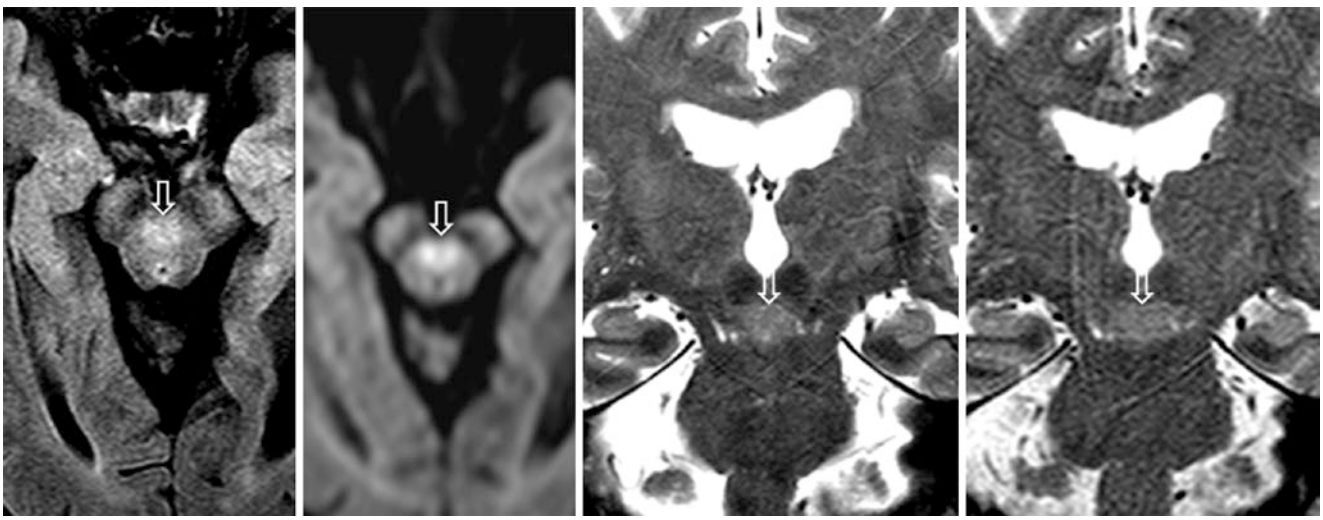

Fig. 22.29 A 62-year-old had a 3 T MRI with axial FLAIR (*left*), DWI (*left middle*), and coronal T2WI (*right middle*), on which the decussation of the superior cerebellar peduncles (DSCP) (*open arrows*) appeared hyperintense. This finding was unchanged 2 years later on a coronal T2WI obtained at 3 T (*right*). The DSCP is a quite common site of normal bright signal on T2WI and FLAIR, and anisotropy on DWI

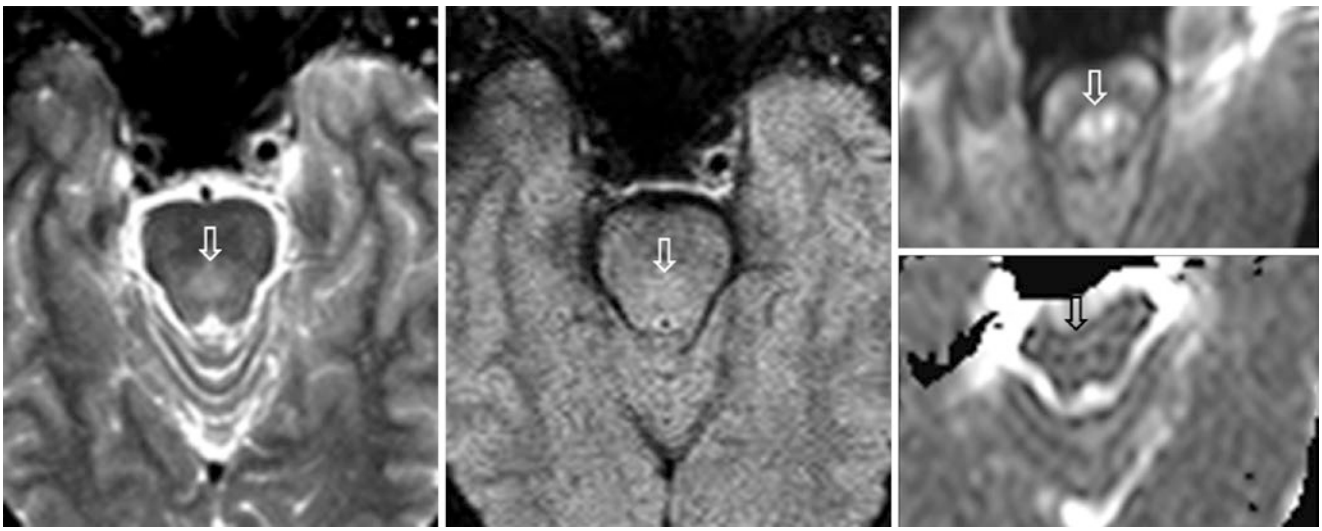

Fig. 22.30 In a 54-year-old with a 1.5 T MRI, the DSCP (*open arrows*) was hyperintense on axial T2WI (*left*) but had near normal signal intensity on FLAIR (*middle*). On DWI, however, the DSCP also appeared quite hyperintense (*right*, *top image*), with normal signal intensity on the corresponding ADC map (*right*, *bottom image*). Note how the DSCP may appear mildly hyperintense on T2WI, FLAIR, or DWI, even at the lower 1.5 T field strength

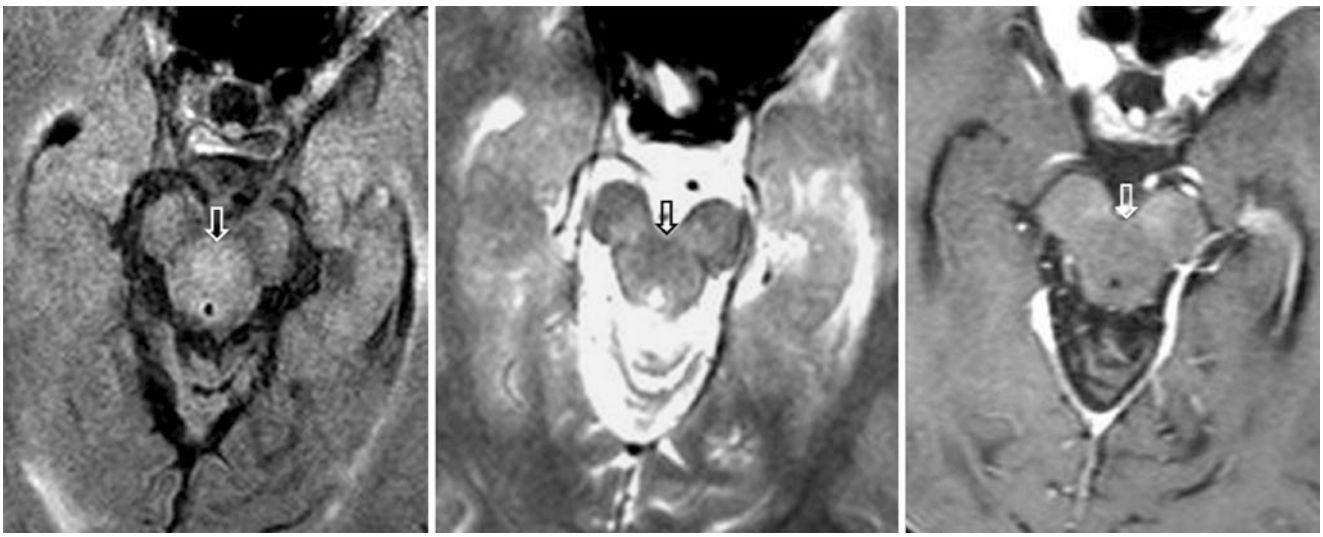

Fig. 22.31 In a 77-year-old with a 1.5 T MRI, axial FLAIR (*left*) shows that the DSCP (*open arrows*) appeared mildly bright, but was slightly dark on T2WI (*middle*), and unremarkable on postcontrast T1WI (*right*). These images are an example of how the DSCP may appear mildly hyperintense on one sequence and have normal or even low signal intensity on another. Again, note how the DSCP may appear mildly bright on an MRI, even at the lower 1.5 T field strength

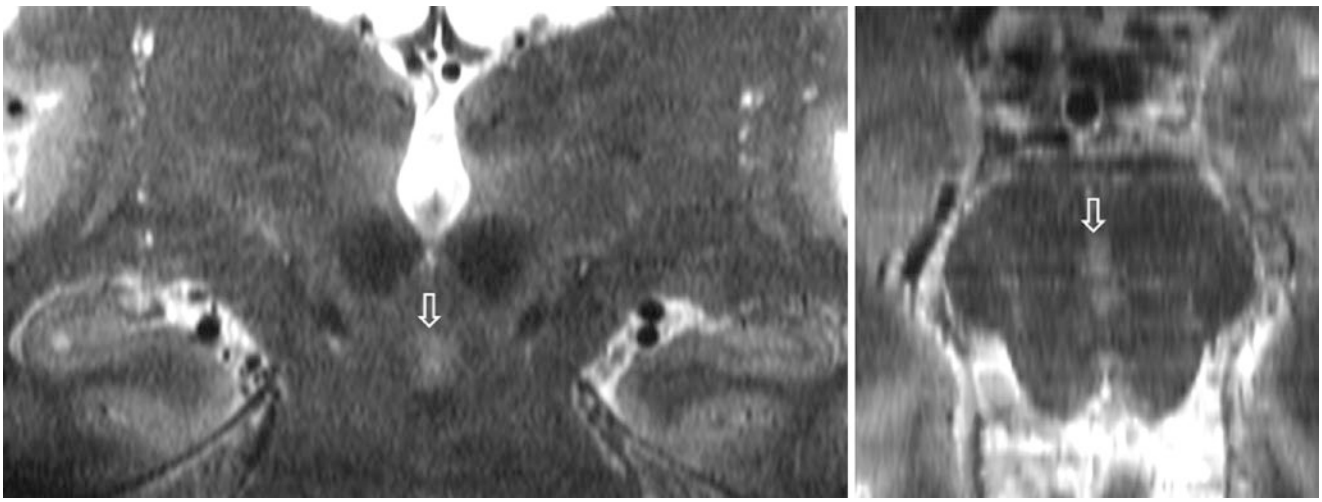

Fig. 22.32 A 52-year-old volunteer with a 7 T MRI. Coronal (*left*) and axial (*right*) T2WIs illustrate a mildly hyperintense DSCP (*open arrows*)

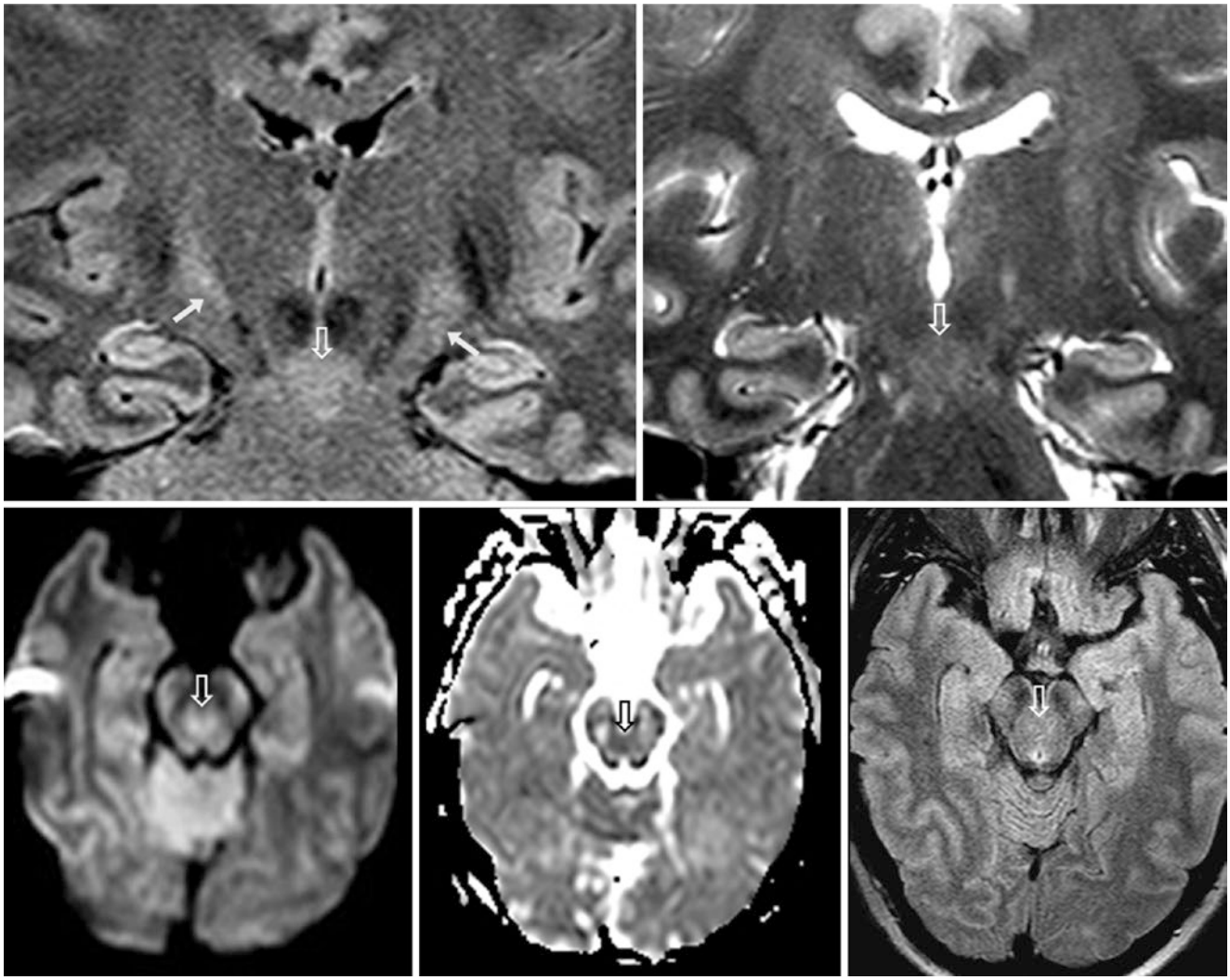

Fig. 22.33 A 37-year-old with a 3 T MRI. Coronal FLAIR (*top left*) and T2WI (*top right*) show mildly bright signal of the DSCP (*open arrows*), which is also mildly hyperintense on DWI (*bottom left*), without corresponding hypointensity on the ADC map (*bottom middle*), or bright signal on FLAIR (*bottom right*). Additionally, there is normal hyperintensity within the CSTs (*arrows*). This case demonstrates how mild hyperintensity within the DSCP on FLAIR, T2WI, or DWI may not be apparent on all three sequences or may be present in only one plane or only on one sequence

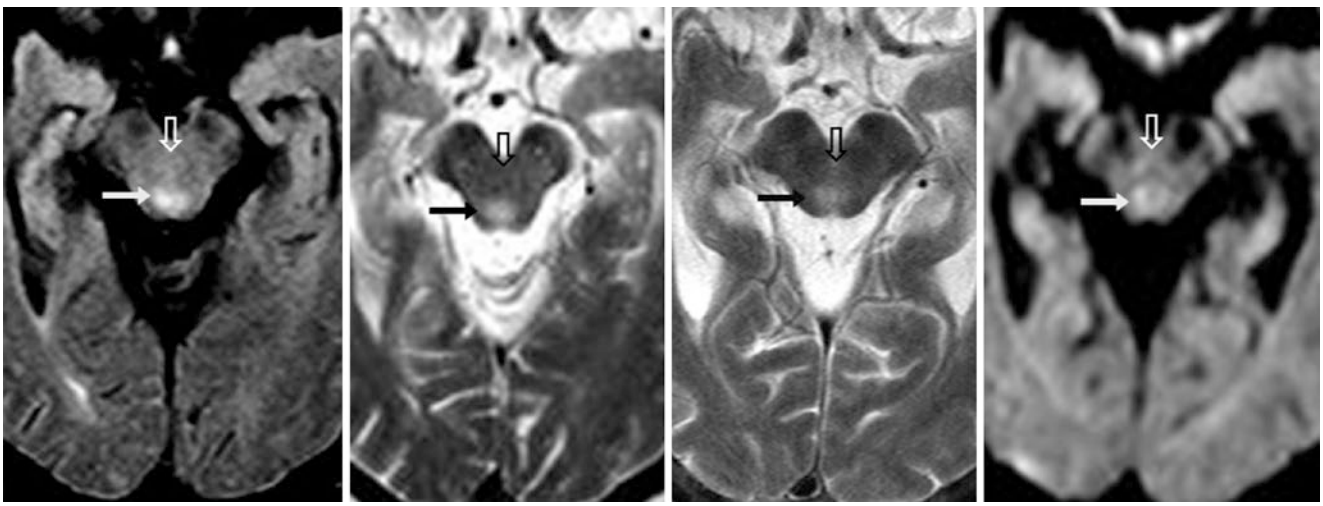

Fig. 22.34 Comparison case of Wernicke encephalopathy in a 65-year-old with confusion. On a 1.5 T MRI, periaqueductal edema (*arrows*) was noted on FLAIR (*left*) and T2WI (*left middle*), just dorsal to the DSCP (*open arrows*), which was unchanged 3 weeks later on T2WI (*right middle*). The periaqueductal gray was mildly bright on DWI (*right*), owing to "T2 shine-through"

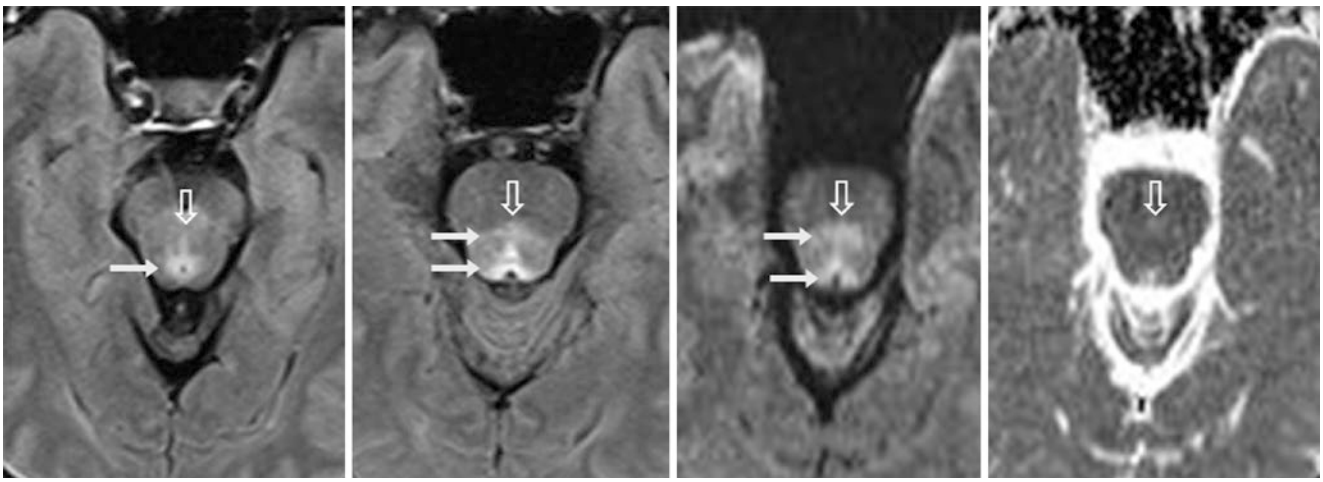

Fig. 22.35 Comparison case of rhombencephalitis in a 54-year-old with cranial nerve III-IV palsy. Periaqueductal edema (*arrows*) was present on a 1.5 T MRI with FLAIR (*left and left middle*). At its anterior extent, it involved the DSCP (*open arrows*) and was bright on DWI (*right middle*), perhaps owing to "T2 shine-through" (see ADC map, *right*)

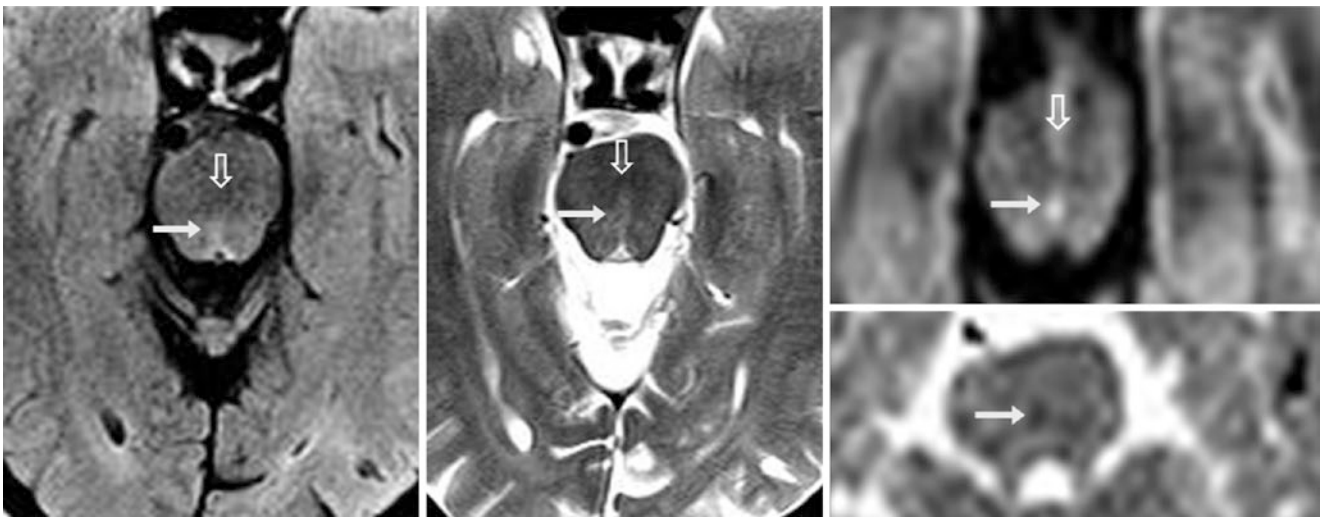

Fig. 22.36 Comparison case of lacunar infarct in a 58-year-old with internuclear ophthalmoplegia. A 1.5 T MRI with FLAIR (*left*) and T2WI (*middle*) depicted a tiny lesion just right of midline, located within the medial longitudinal fasciculus (*arrows*) and just posterior to the DSCP (*open arrows*). The lesion represents an acute or early subacute infarct, as it was bright on DWI (*right*, *top*) and was mildly dark on the ADC map (*right*, *bottom*)

22.1.5 Hippocampi and Amygdalae

On 3 T FLAIR and DWI, the *hippocampi* and *amygdalae* may have normal, mild hyperintensity that is symmetric. Normal signal here can be problematic, particularly when an MRI is ordered for epilepsy. Differential considerations are *infection* (herpes encephalitis), *postictus* (*i.e.*, hippocampal hyperintensity secondarily after seizures), *mesial temporal sclerosis* (MTS, *i.e.*, the primary site of seizure), *low-grade glioma,* or *toxic-metabolic conditions* such as carbon monoxide inhalation (Figs. 22.37, 22.38, 22.39, 22.40, 22.41, 22.42, 22.43, 22.44 and 22.45).

Fig. 22.37 A 63-year-old had a 3 T MRI with bright hippocampi (*arrowheads*) on axial (*top left*) and coronal (*top right*) FLAIR. Such hyperintensity mimics herpetic encephalitis, limbic encephalitis, or seizure sequelae. The DSCPs (*open arrows*) are also bright. Two years later, a 1.5 T MRI showed resolution of these bright regions on axial (*bottom left*) and coronal (*bottom right*) FLAIR, likely due to the lower field strength

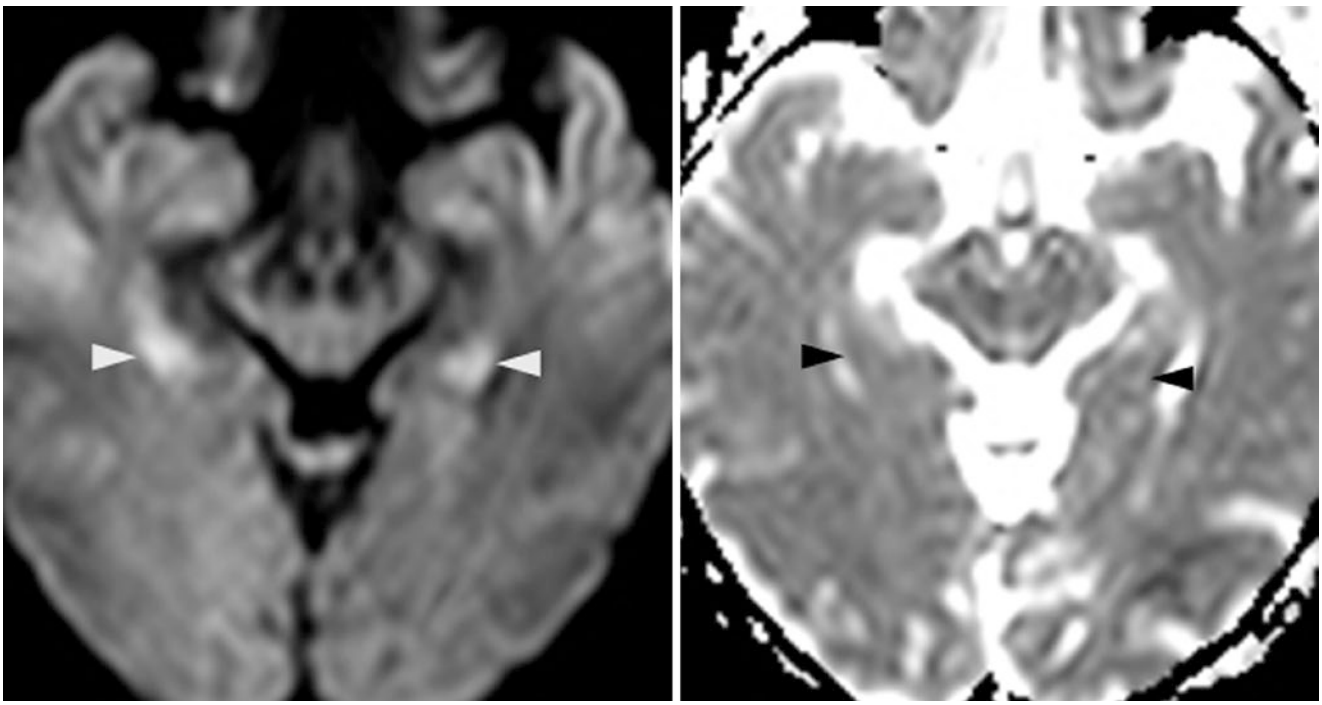

Fig. 22.38 A 53-year-old had a 3 T DWI MRI (*left*) with bright hippocampi posteriorly (*arrowheads*), but corresponding low signal was lacking on the ADC map (*right*)

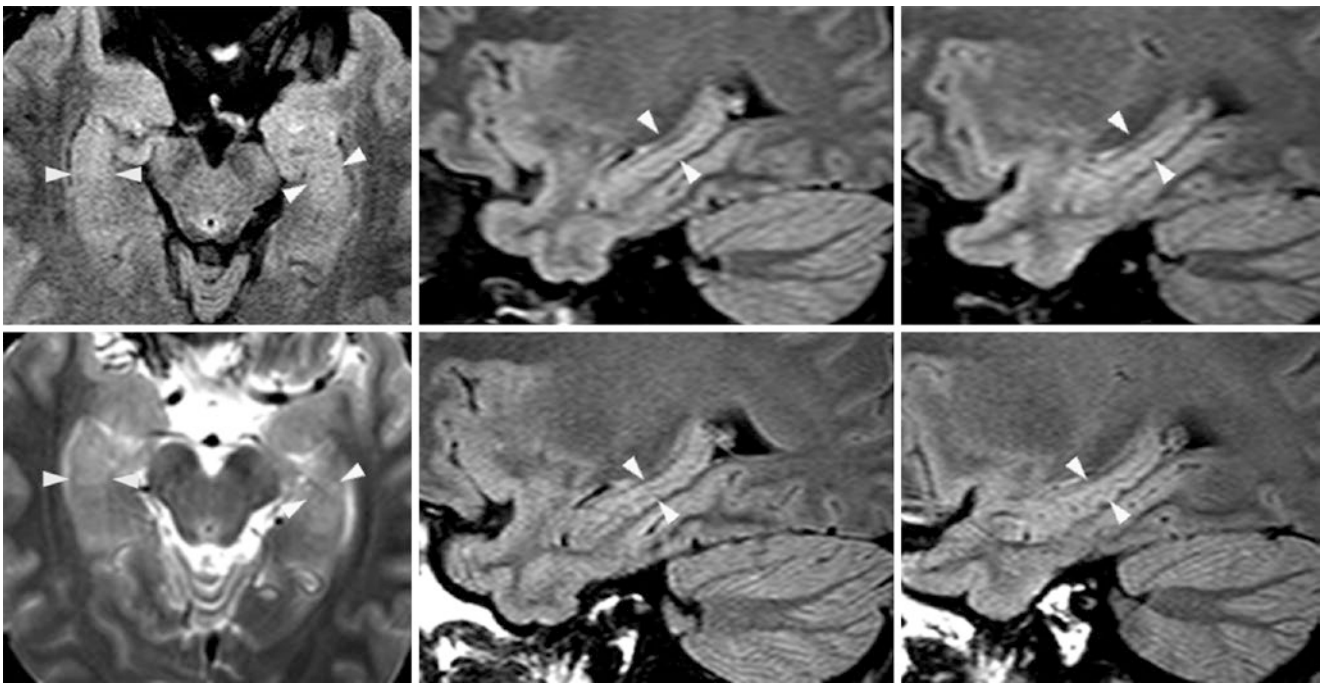

Fig. 22.39 A 28-year-old had a 3 T MR with axial (*top left*) and sagittal FLAIR images of the right (*top middle*) and left (*top right*) sides, which depict bilaterally hyperintense hippocampi, amygdala, and superior temporal gyri (*all between arrowheads*). These temporal lobe areas remained hyperintense at 1 year on a repeat 3 T MRI, as shown on axial T2WI (*bottom left*) and on paired sagittal FLAIR images of the right (*bottom middle*) and left (*bottom right*) sides

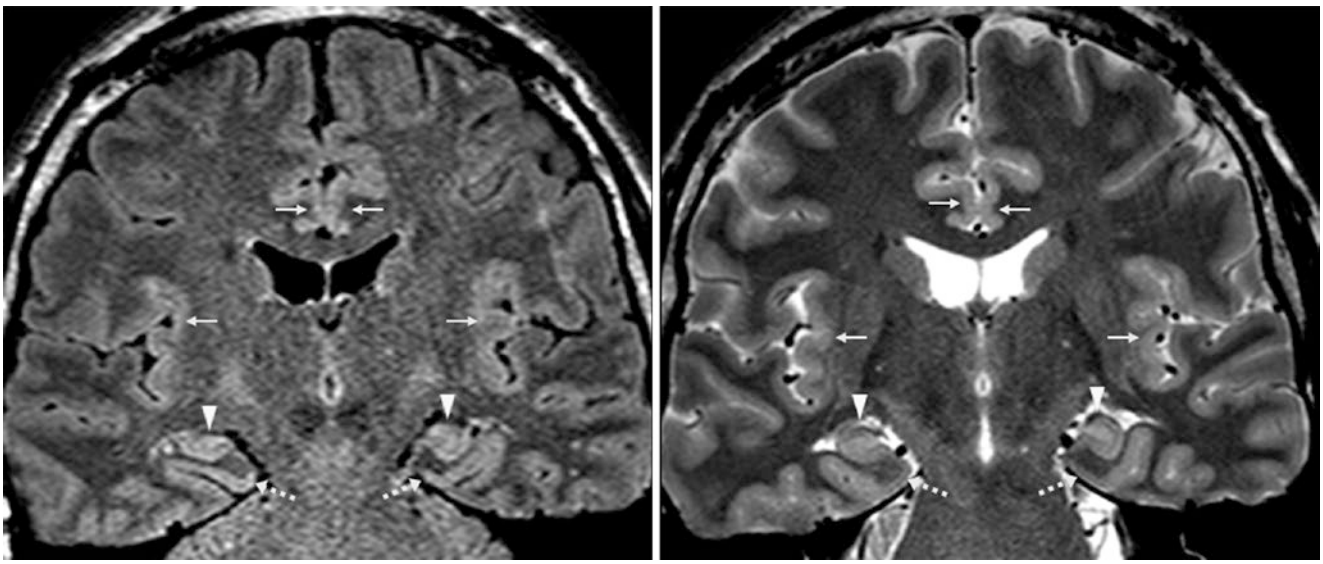

Fig. 22.40 A 27-year-old with a first-time seizure had a 3 T MRI with coronal FLAIR (*left*) and T2WI (*right*), which showed mildly bright hippocampi (*arrowheads*) and cortices of the parahippocampal gyri (*dotted arrows*), without atrophy. The MRI was deemed negative. The cingulate and insular cortices (*thin arrows*) were also slightly hyperintense

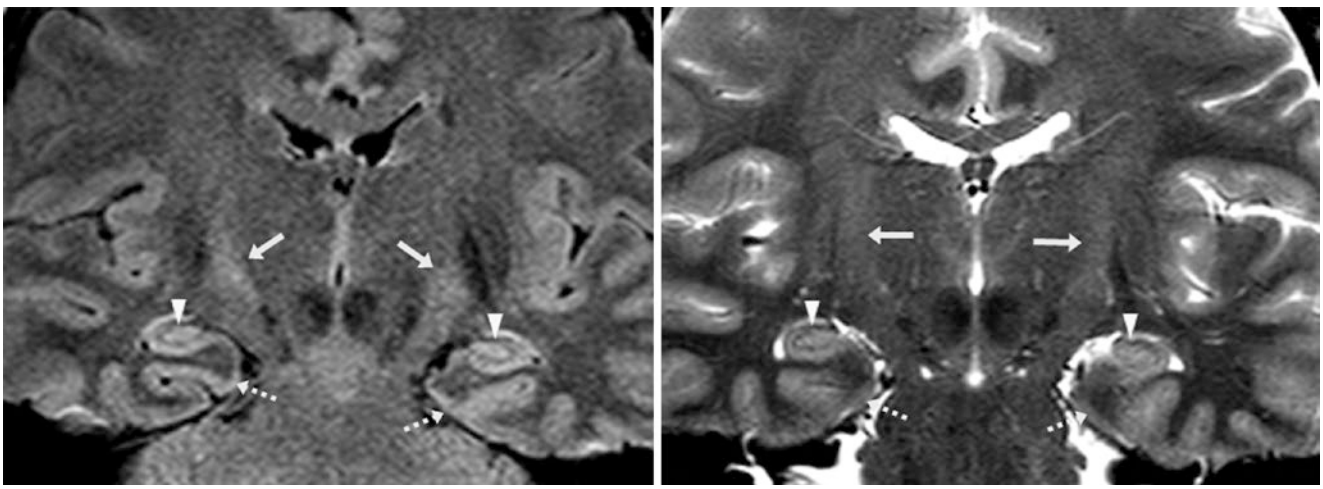

Fig. 22.41 A 37-year-old with transient ischemic symptoms underwent a 3 T MRI that was interpreted as negative. The MRI demonstrated normal hyperintensity of the cortices of the hippocampi (*arrowheads*) and the parahippocampal gyri (*dotted arrows*) on coronal FLAIR (*left*) and T2WI (*right*). Normal CST hyperintensity (*arrows*) is also seen

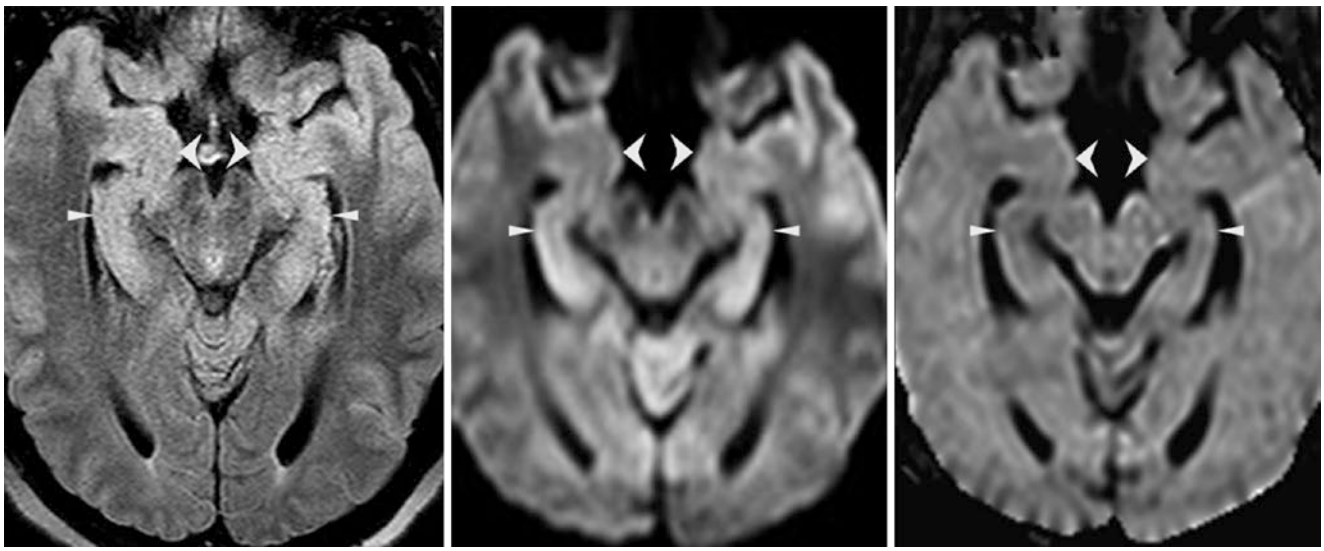

Fig. 22.42 A 22-year-old with headaches months after trauma. An otherwise normal 3 T MRI illustrates mildly hyperintense hippocampi (*small arrowheads*) and amygdalae (*large arrowheads*) bilaterally on FLAIR (*left*) and DWI (*middle*). An exponential DWI (*right*) removes the T2 component of the hyperintensity, thereby ruling out cytotoxic edema. This normal "pseudo-signal" within the medial temporal lobes is quite common at 3 T

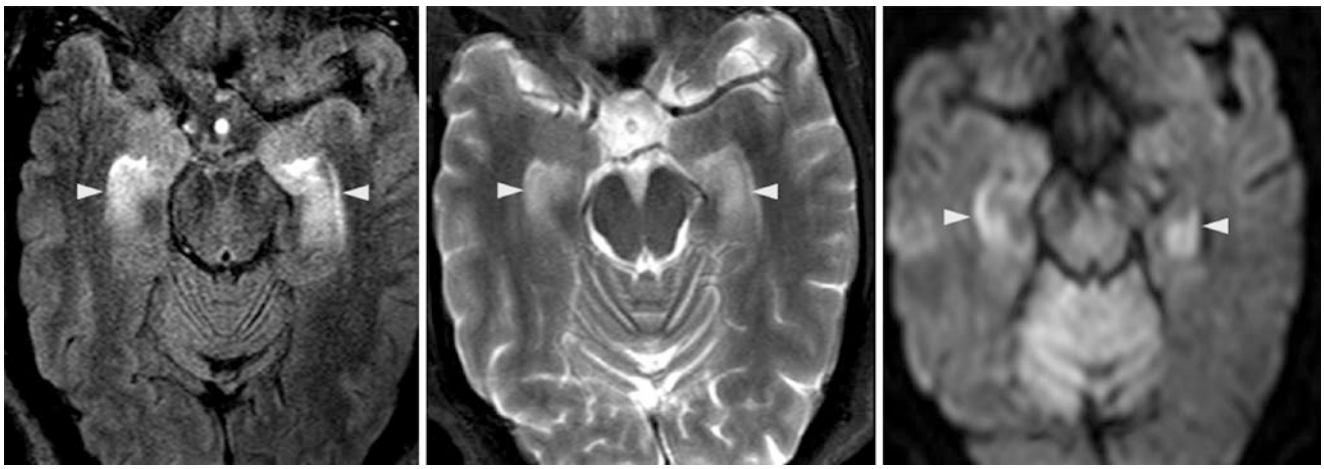

Fig. 22.43 Comparison case of herpetic encephalitis. A 50-year-old with altered mental status underwent a 3 T MRI, which demonstrated edema of the hippocampi bilaterally (*arrowheads*) on axial FLAIR (*left*) and T2WI (*middle*), with mildly reduced diffusion on DWI (*right*). Later, serology tests confirmed the presence of herpetic encephalitis

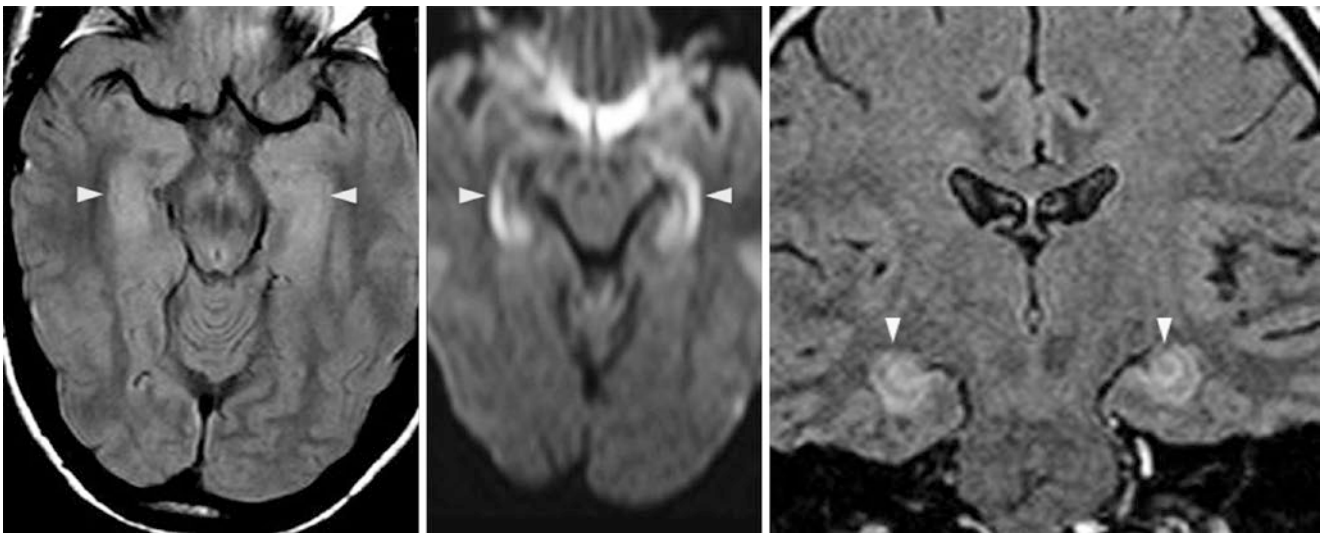

Fig. 22.44 Comparison case of carbon monoxide toxicity. An unresponsive 27-year-old patient underwent a 1.5 T MRI, which demonstrated edema of the hippocampi bilaterally (*arrowheads*) on axial FLAIR (*left*), with moderately reduced diffusion on DWI (*middle*) and edema on coronal FLAIR (*right*). On FLAIR and DWI, carbon monoxide toxicity usually presents with involvement of either the hippocampi, periventricular white matter, or (in severe cases) the basal ganglia

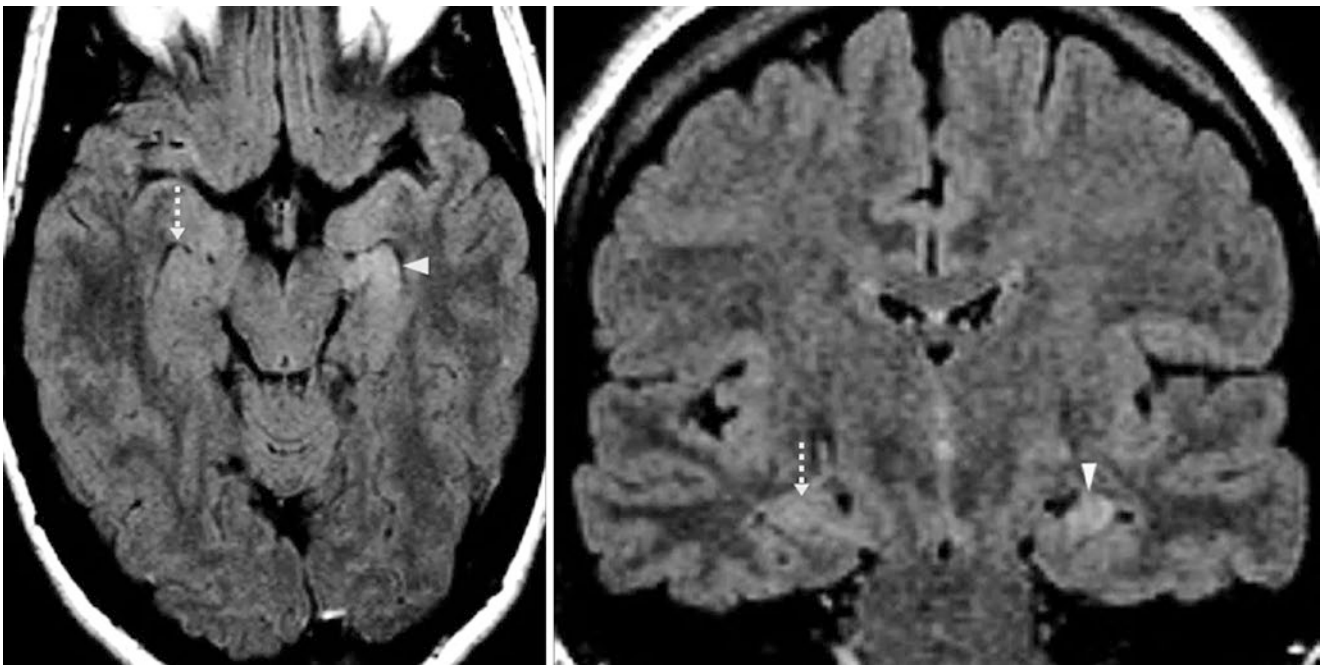

Fig. 22.45 Comparison case of mesial temporal sclerosis. A 35-year-old with seizures underwent a 1.5 T MRI that showed subtle hyperintensity and mild atrophy of the left hippocampus (*arrowheads*) on axial (*left*) and coronal (*right*) FLAIR images, which correlated with the EEG findings. Note the normal right hippocampus (*dotted arrows*)

22.2 FLAIR Pseudolesions at 3 T Due to 3D Acquisition

On 3 T FLAIR, *pseudolesions* from normal, mild hyperintensity may be noted in areas identical to the aforementioned locations, such as the DSCPs, SCPs, CSTs, cingulate cortices, medial lemnisci, and insulae. These pseudolesions are more prominent at 3 T, but they can also be noted from 3D acquisition with 1.5 T magnets. Again, the cause is not well understood. Differential considerations are as mentioned previously for the individual regions. Comparison to 2D FLAIR proves that these pseudolesions are nonpathologic (Figs. 22.46, 22.47, 22.48, 22.49, 22.50 and 22.51).

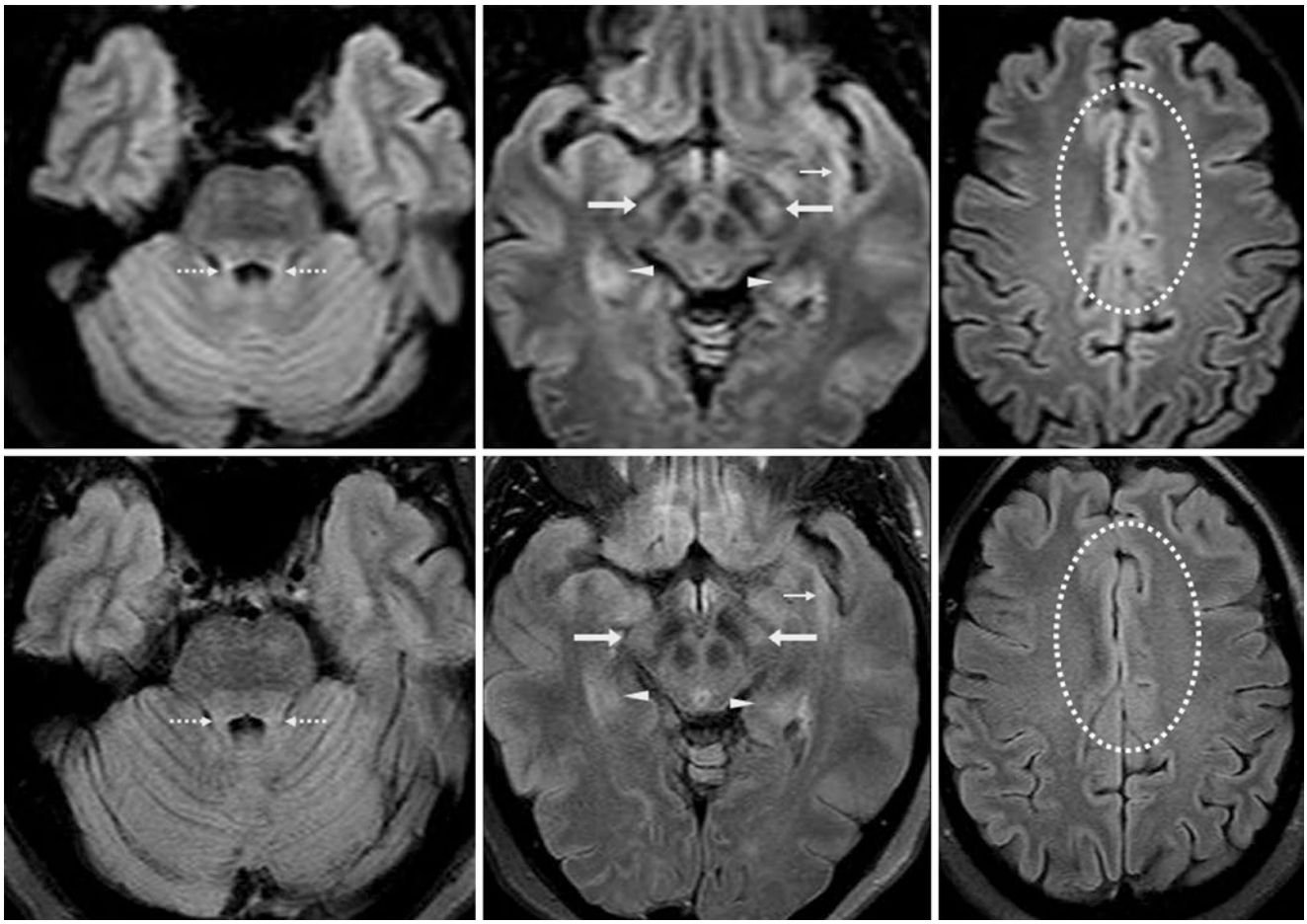

Fig. 22.46 In a 53-year-old, axial reformats from a 3D FLAIR acquisition at 3 T (*top row*) show normal hyperintensity in various sites, being brighter than 2D FLAIR images from 2 years prior (*bottom row*). Bright signal is seen within the CSTs (*arrows*), SCPs (*thin dotted arrows*), hippocampi (*arrowheads*), insula (*thin arrows*), and cingulate gyri (*dotted circles*)

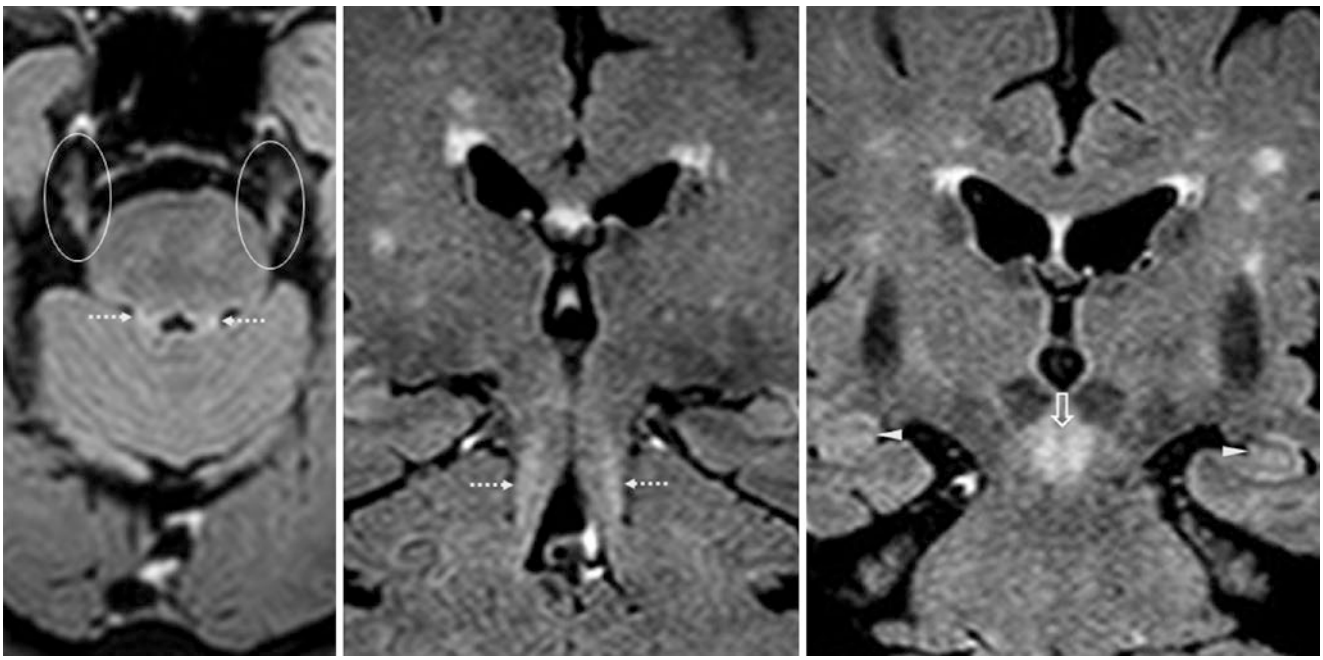

Fig. 22.47 An 84-year-old underwent a 3 T MRI with a 3D FLAIR acquisition. Axial (*left*) and coronal (*middle and right*) reformats show hyperintensities of the SCPs (*thin dotted arrows*), DSCP (*open arrow*), hippocampi (*arrowheads*), and cranial V cisternal segments (*thin circles*). Also note scattered leukoaraiosis of the periventricular white matter

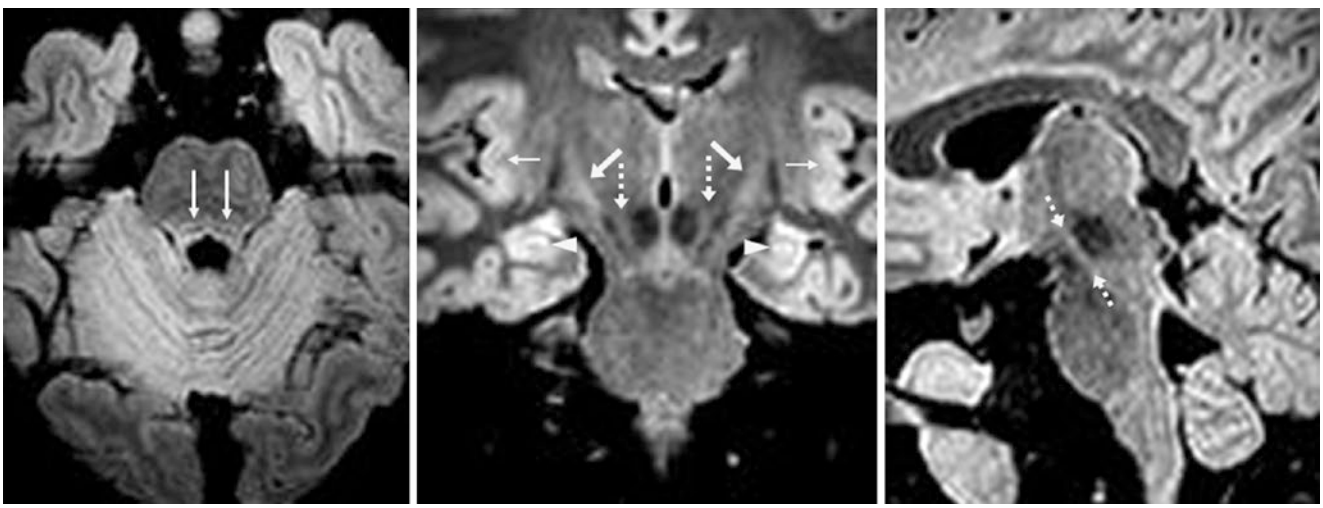

Fig. 22.48 In a normal 16-year-old, axial reformats (*left*) from a 3D FLAIR at 3 T show normal, slightly bright medial lemnisci (*long arrows*). On coronal reformats (*middle*), the CSTs (*arrows*), insulae (*thin arrows*), substantia nigra (*dotted arrows*), and hippocampi (*arrowheads*) are also bright. Sagittal reformats (*right*) also define the substantia nigra

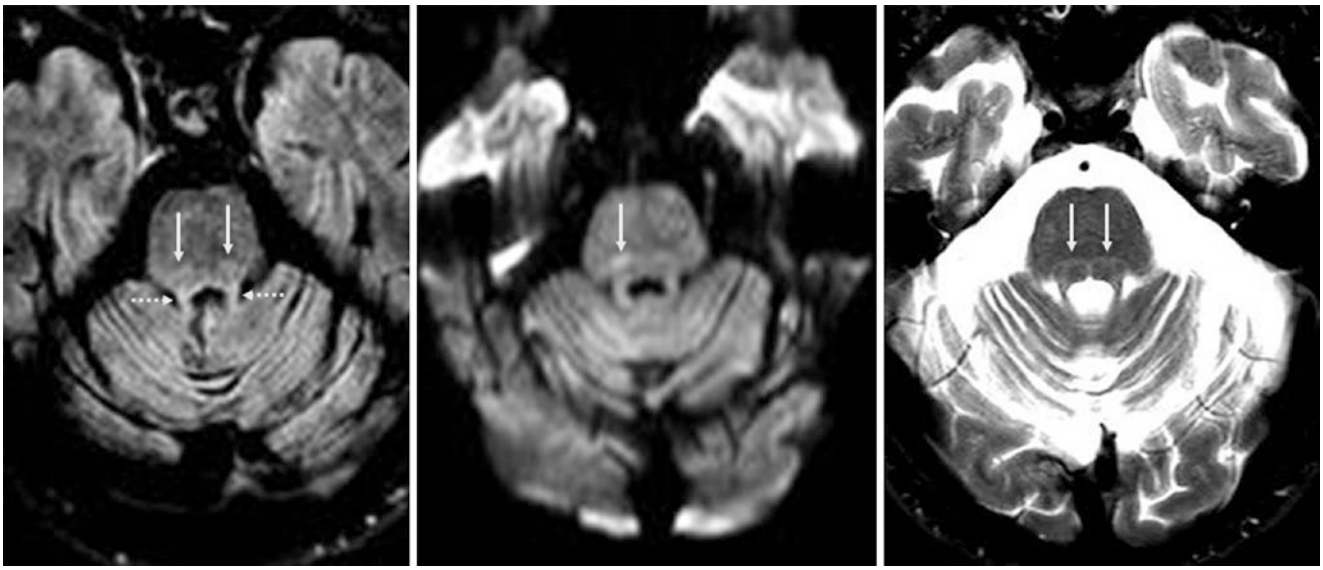

Fig. 22.49 A 59-year-old with headaches had a 3 T MRI with an axial 3D FLAIR reformat (*left*) that depicts normal, mild hyperintensity of the SCPs (*thin dotted arrows*) and medial lemnisci (*long arrows*) within the dorsal brainstem. Only the right medial lemniscus is prominent on DWI (*middle*), but they are clearly visible bilaterally on T2WI (*right*)

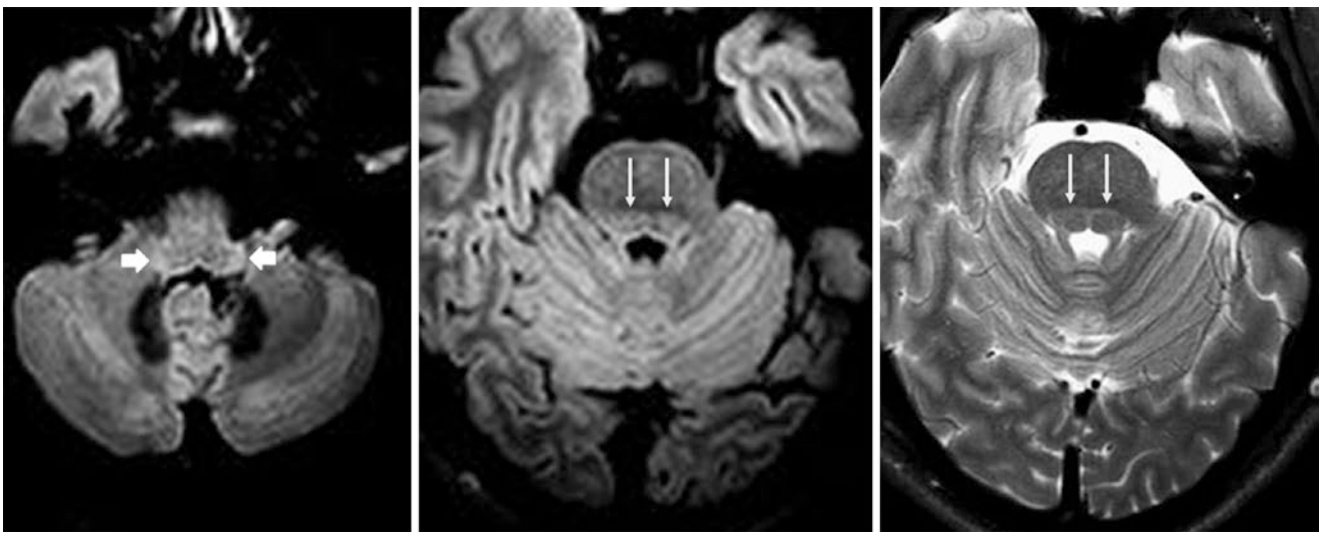

Fig. 22.50 A 51-year-old with a 3D FLAIR acquisition at 3 T. Axial reformats of the FLAIR images (*left and middle*) demonstrate hyperintensities of the inferior cerebellar peduncles (*wide arrows*) and of the medial lemnisci (*long arrows*) within the dorsal brainstem. The medial lemnisci also appear mildly hyperintense on T2WI (*right*)

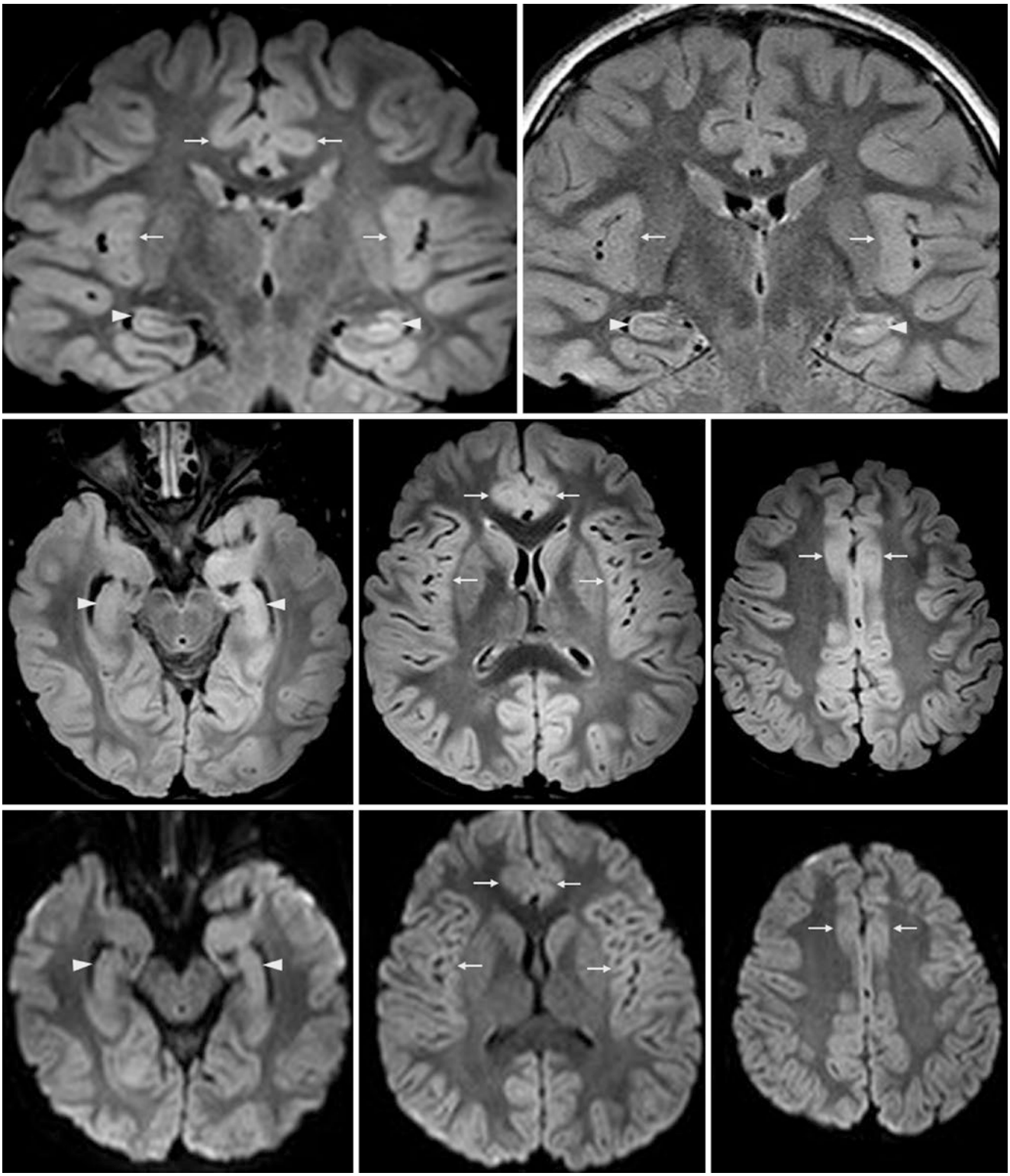

Fig. 22.51 Comparison between 3D and 2D FLAIR in causing cortical pseudolesions in images from a 6-year-old with an otherwise negative 3 T MR for altered mentation. *Top row*: A 3D-reformatted coronal FLAIR image (*left*) shows bilaterally hyperintense hippocampi (*arrowheads*), and insulae and cingulate gyri (*thin arrows* for both). The artifacts are more prominent centrally and are not nearly as hyperintense on coronal FLAIR images from a 2D acquisition (*right*). *Middle row*: Axial reconstructions of the 3D FLAIR images further demonstrate the relatively bright hippocampi, amygdalae, cingulate gyri, and insulae. The distribution of such hyperintensities suggests that they may be related to the dielectric effect, as they are more prominent centrally. *Bottom row*: DWI appears essentially normal

22.3 DWI Artifacts and Causes of Hyperintensity

Diffusion-weighted imaging (DWI) is considered vital for routine brain MRI evaluation. It is deemed necessary to evaluate the DWIs in tandem with the corresponding ADC maps. DWI may be the single MRI sequence that has had the largest impact on *acute stroke* evaluation in the past decade, because of its ability to discriminate "reduced" or "restricted" diffusion (bright on DWI, dark on the ADC map), which typically represents cytotoxic edema. In the setting of acute stroke, this finding represents acute, irreversible cerebral infarction, although recently there has been recognition that some portion of the cytotoxic edema on DWI may be reversible in infarcts, and that other reversible causes of reduced diffusion exist. The cause of reduced diffusion is likely to be related to the underlying pathophysiology. In acute infarcts, it is due to cellular swelling with failure of the Na+/K+ pump to exchange water between the intracellular and extracellular spaces. In *high-grade tumors,* high cellularity leads to diminished extracellular space, with resultant reduced diffusion and movement of free water within the interstitium. In reversible insults such as *toxic leukoencephalopathies*, intramyelinic edema (*i.e.*, within the myelin sheath) causes reduced diffusion within the white matter.

Hence, all that is bright on DWI does not represent cytotoxic edema; there are other causes of bright signal. Bright signal intensity on DWI arises from several factors, in decreasing order of contribution: ADC value (of the tissue), T2 value (of tissue), *b* value (selected by the technologist), and spin density (slight contribution). Some causes of bright signal on DWI are artifactual, whereas others relate to the T2-bright signal overwhelming the ADC values to cause bright signal on DWI (*e.g.*, "*T2 shine-through*").

To understand these causes, a brief explanation is in order of how routine DWI and ADC maps are compiled, and the artifacts that affect them. First, the "trace" DWI that is most commonly used for routine image interpretation is a composite of a single-shot, echoplanar gradient sensitization in three orthogonal directions. This approach attenuates the inherent *anisotropy* (unequal movement of water that favors certain directions) of cerebral structures, particularly within white matter, where *anisotropy* results from the integrity of myelin sheaths and the direction of fibers. A certain degree of anisotropy can be normal and is expected in certain myelinated structures; it is more pronounced in young children because of *progressing myelination*. The images displayed on the ADC map are a calculation of the magnitude obtained via the matrix from these three gradients. For more detailed descriptions, see the articles by Schaefer et al. and Beauchamp et al. in the Suggested Reading.

To generate a "trace" DWI for standard image review, at least two acquisitions with differing *b* values must be obtained. The "*b* value" is the strength of the diffusion gradient, where the higher the selected *b* value, the greater the diffusion weighting; the lower the *b* value, the greater the "T2 weighting" of the DWI image. Thus, DWI has a component of T2 weighting, and the degree of diffusion weighting is determined by the maximum *b* value, where the minimum is often set to zero (*i.e.*, $b = 0$ s/mm^2) and the maximum in routine brain imaging is typically 1000 (*i.e.*, $b = 1000$ s/mm^2). Notably, one can visualize an abnormality that is hyperintense on DWI without being dark on ADC maps, because of the logarithmic nature of the equation, which involves a combination of the ADC values and a component of T2-bright contrast. Thus, the "trace" DWI is quite sensitive for identifying *cytotoxic edema,* but it cannot be interpreted completely without inspecting the matching ADC map to exclude brightness (on both DWI and ADC maps) from T2 shine-through (*i.e.*, bright signal on DWI from vasogenic edema). Examples of T2 shine-through from extremely T2-bright lesions are seen in *MS, chronic infarcts,* and *posterior reversible encephalopathy syndrome* (PRES). One way to ameliorate the appearance of T2 shine-through is to generate an exponential DWI, which removes the T2-bright component of the image, but doing so can decrease the sensitivity of the DWI. An opposite concept is "*T2 washout*," in which there may be little or no hyperintensity on DWI, with dark signal on the ADC map. This occasionally occurs in cases of severe vasogenic edema. A third phenomenon on DWI is "*T2 blackout*," which is dark signal on DWI due to extremely dark foci on ADC maps from susceptibility effects, such as hematoma, or high concentrations of iron or calcium.

Normal, focal hyperintensity may occur on DWI from several factors. One is the relative anisotropy of certain myelinated structures, which can appear bright on images in one of the three orthogonal planes, thus overwhelming the signal intensity of the other two planes. This most commonly occurs within the posterior limb of the internal capsule (PLIC) or corticospinal tract (CST), the decussation of the superior cerebellar peduncle (DSCP), superior cerebellar peduncle (SCP), or less commonly, in the medial lemnisci, pyramidal decussation, inferior cerebellar peduncle (ICP), or the callosal splenium. To demonstrate this concept, some structures, such as the DSCP or PLIC, are quite bright on the two planes that are oriented orthogonal (90°) to the plane of that structure on DWI, and are dark on the gradient-sensitized images in the direction parallel to that structure. This phenomenon was demonstrated in some general examples in the prior section along with FLAIR imaging (22.2), but further cases are provided here with a focus on DWI and sensitization to its directional gradients.

There can be other causes of artifactual bright or dark signal on DWI, including susceptibility effects (from air, gas, or metal) and T2 blackout. Other potential causes of artifacts include *phase ghosting*, *motion*, and *unfolding artifacts. Eddy*

current artifacts can be induced by rapid on/off gradient switching during DWI acquisition; rarely, such gradients may even displace tissue by mechanical vibration. Most such artifacts are more likely to occur at higher magnetic field strengths (*e.g.*, at 3 T rather than 1.5 T). Another situation that may mimic disease on DWI is the *lack of a head coil*, or one that is improperly calibrated.

In the following sections, examples of varying *b* values on DWI, T2 shine-through, T2 washout, T2 blackout, and various DWI-based artifacts are illustrated. As other texts have dealt in detail with MRI artifacts, their appearance on routine MR images such as T1WI, T2WI, and FLAIR are not covered here. This section focuses on the common or misleading DWI artifacts, in particular those that may simulate disease.

22.3.1 DWI: Effect of Varying *b* Values on CSF Contrast and Normal White Matter Anisotropy

As stated previously, the *b* values that refer to gradient strength affect the appearance of CSF on DWI. Lower *b* values have greater degrees of CSF hyperintensity, where the lowest "b = 0" map essentially is a "poor man's" T2-weighted image. Standard *b* values for brain imaging are typically 0, 500, and 1000 s/mm^2. Higher *b* values above 1000 may have a greater sensitivity for detecting cytotoxic edema, but they become less specific, as greater degrees of anisotropy are accentuated, simulating abnormalities (Figs. 22.52, 22.53, 22.54, 22.55, 22.56, 22.57, 22.58 and 22.59).

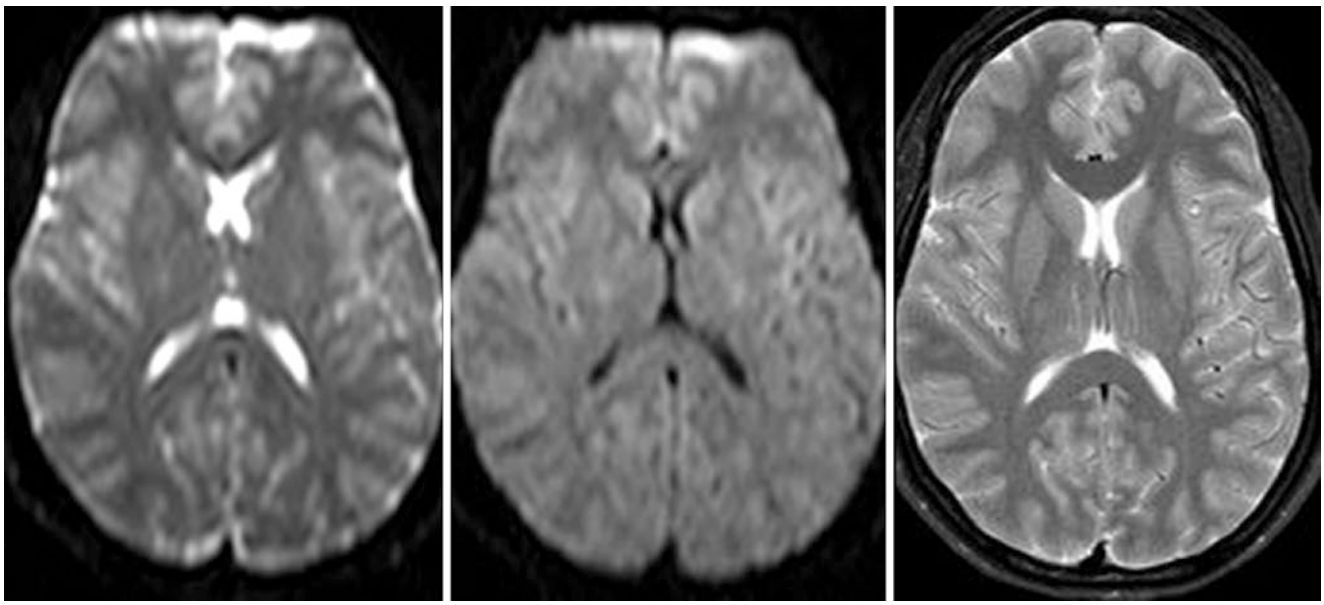

Fig. 22.52 A 24-year-old with a normal 1.5 T MRI. DWIs with values of $b = 0$ s/mm^2 (*left*), and $b = 1000$ s/mm^2 (*middle*) are shown. Note that the closer the *b* value is to zero, the more T2 weighting is present, although DWI utilizes a single-shot, gradient-echo technique. A spin echo T2WI in the same patient is provided for comparison (*right*)

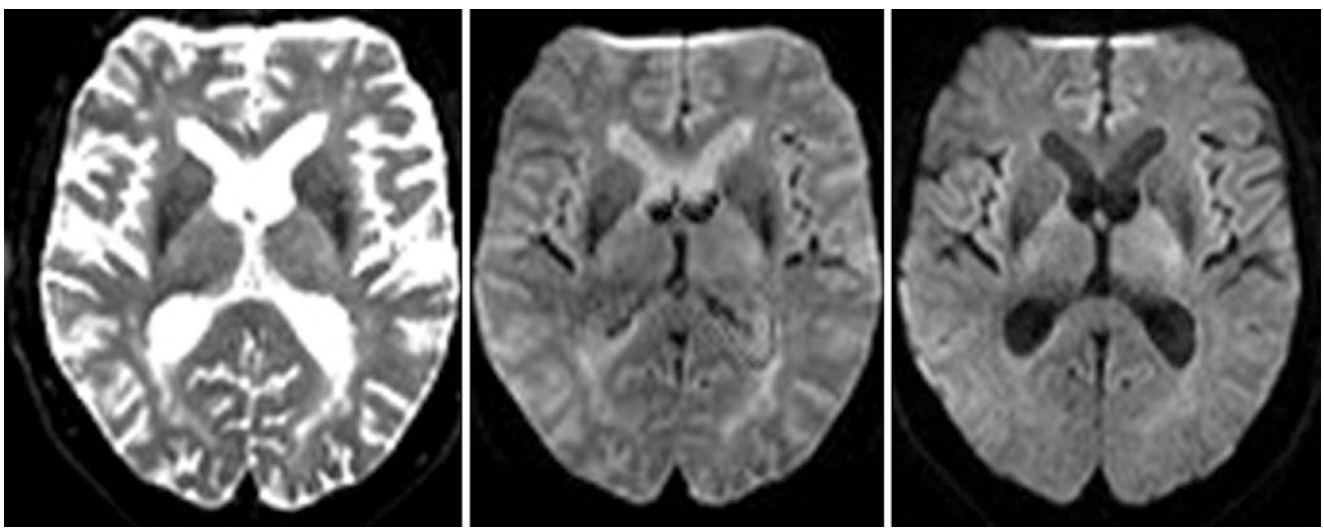

Fig. 22.53 A 71-year-old with a normal 3 T MRI. DWI was obtained with *b* values of 0 (*left*), 500 (*middle*), and 1000 (*right*) s/mm^2. Note that the closer the *b* value is to zero, the more the image appears to be a rudimentary T2WI, whereas at higher *b* values, the CSF becomes quite dark

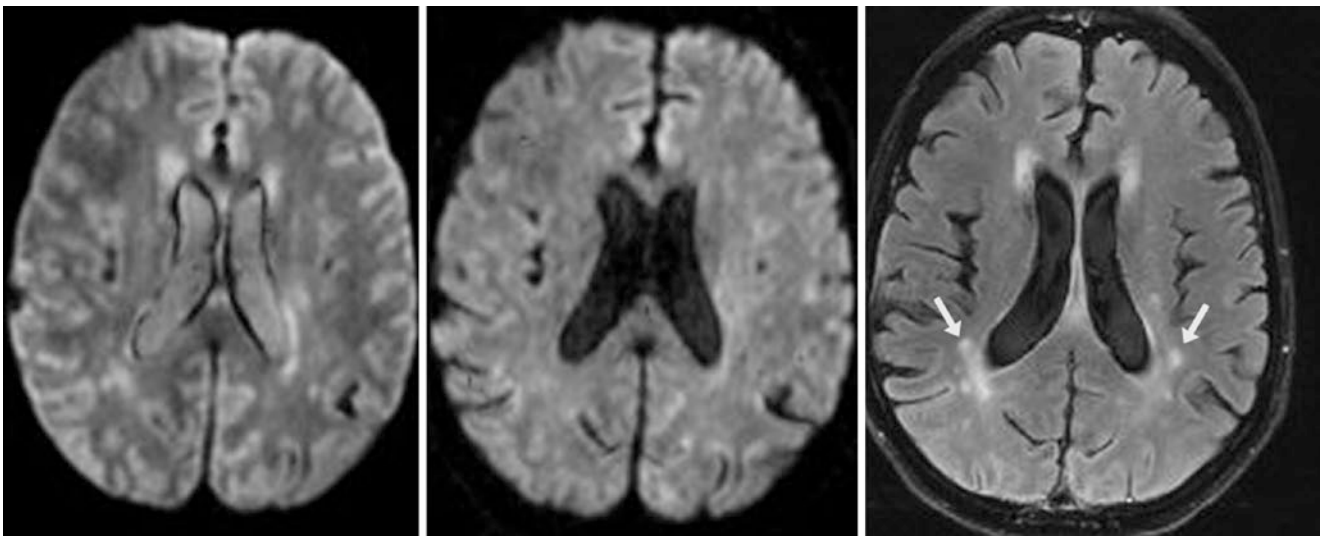

Fig. 22.54 A 59-year-old with a 1.5 T MRI had DWI that utilized *b* values of 500 (*left*) and 1000 (*middle*) s/mm^2. FLAIR images (*right*) show the classic T2 hyperintensities of chronic small vessel ischemic disease (leukoaraiosis) within the periventricular white matter (*arrows*), without an acute infarct. Note the darkening of CSF with increasing *b* value

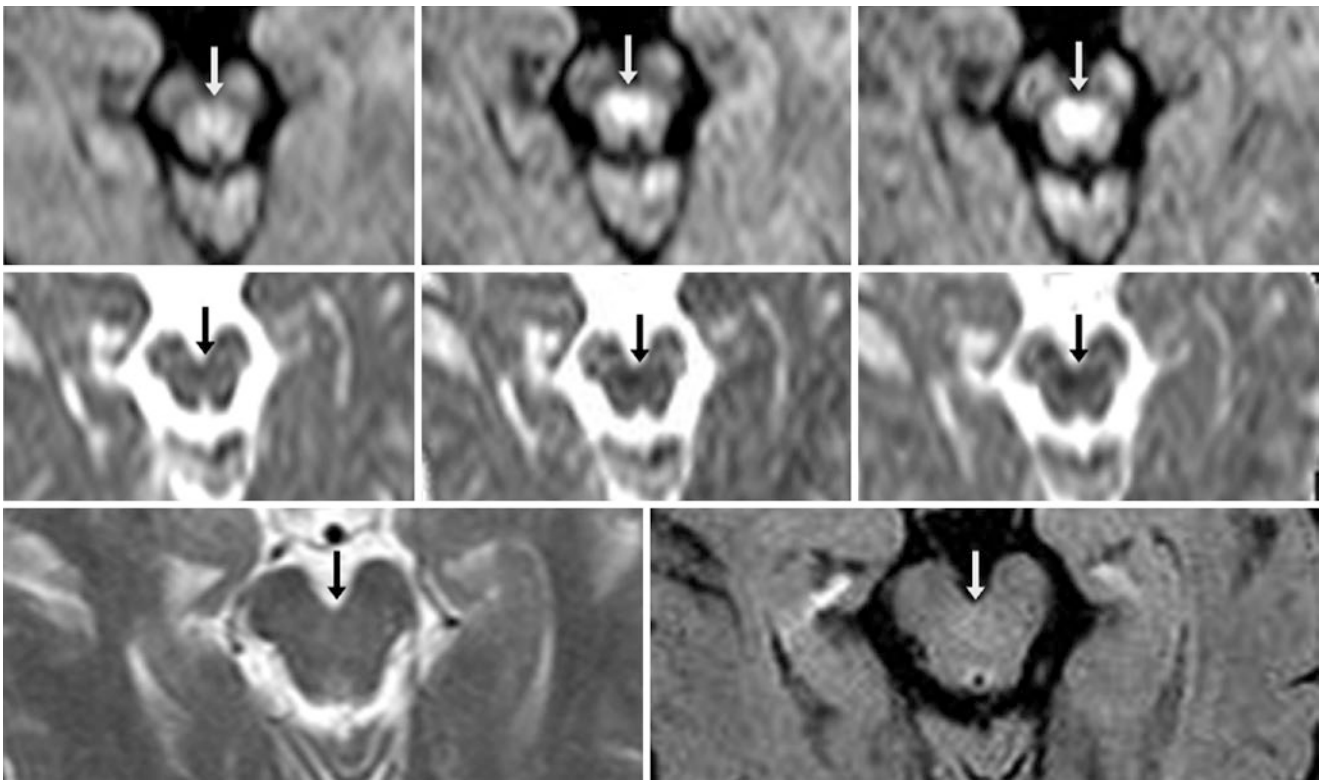

Fig. 22.55 An 81-year-old with a 1.5 T MRI. *Top row*: A $b=1000$ DWI (*left*) shows normal mild hyperintensity of the DSCP (*arrows*), which is increasingly visible at *b* values of 1500 (*middle*), and 2000 (*right*) s/mm^2. The brightness is due to intense white matter anisotropy at that site. *Middle row*: Matched ADC maps are shown for $b=1000$ (*left*), $b=1500$ (*middle*), and $b=2000$ (*right*) s/mm^2. *Bottom row*: T2WI (*left*) and FLAIR (*right*) are normal, and lack the DSCP hyperintensity

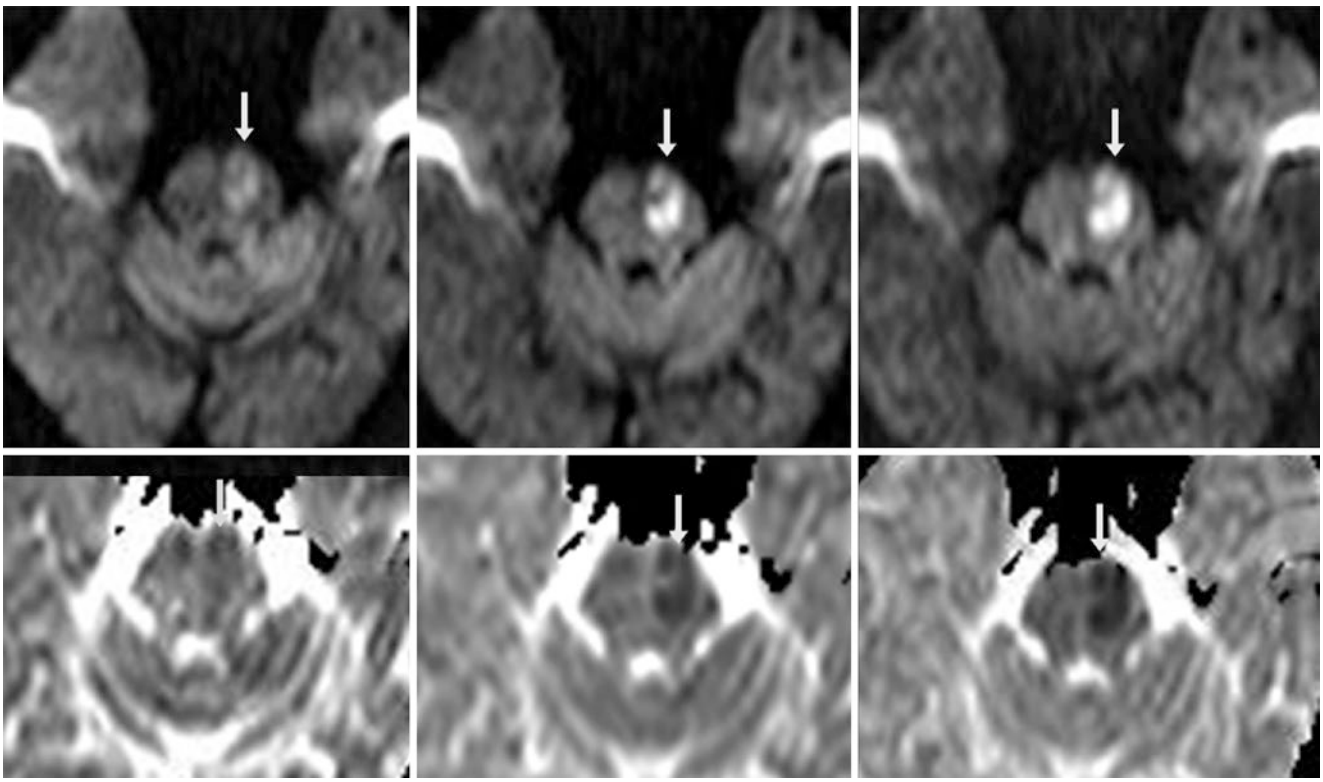

Fig. 22.56 Comparison case of brainstem infarct. A 66-year-old had a left-sided brainstem infarct (*arrows*) on a 1.5 T MRI, which is not well visualized on $b = 1000$ DWI (*top left*) or ADC map (*bottom left*), but is better visualized on DWI at $b = 1500$ (*top middle*) with its ADC map (*bottom middle*). On the $b = 2000$ DWI (*top right*) and its corresponding ADC map (*bottom right*), the infarct is more clearly visualized. This example illustrates the utility of DWI with higher *b* values

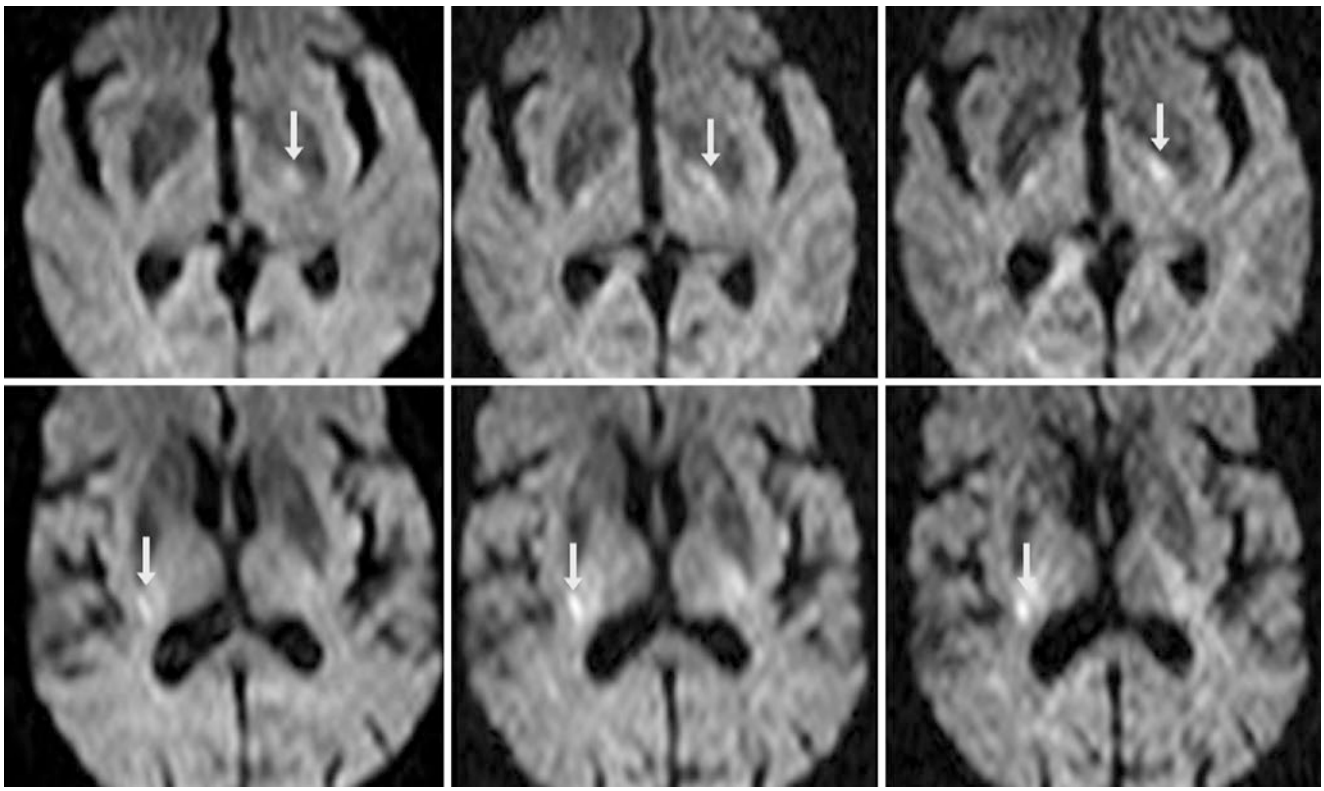

Fig. 22.57 An 80-year-old with a 1.5 T MRI. There is increasing normal hyperintensity (from anisotropy in the craniocaudal direction) of the left PLIC/CST (*arrows*) on DWIs with *b* values of 1000 (*top left*), 1500 (*top middle*) and 2000 (*top right*) s/mm^2. More superiorly, this occurs within the right CST/PLIC on DWI at *b* values of 1000 (*bottom left*), 1500 (*bottom middle*) and 2000 (*bottom right*) s/mm^2. The unilateral appearance is from the patient's head being tilted; brighter signal occurs when the CST is oriented more orthogonal relative to the "z axis" of the magnet

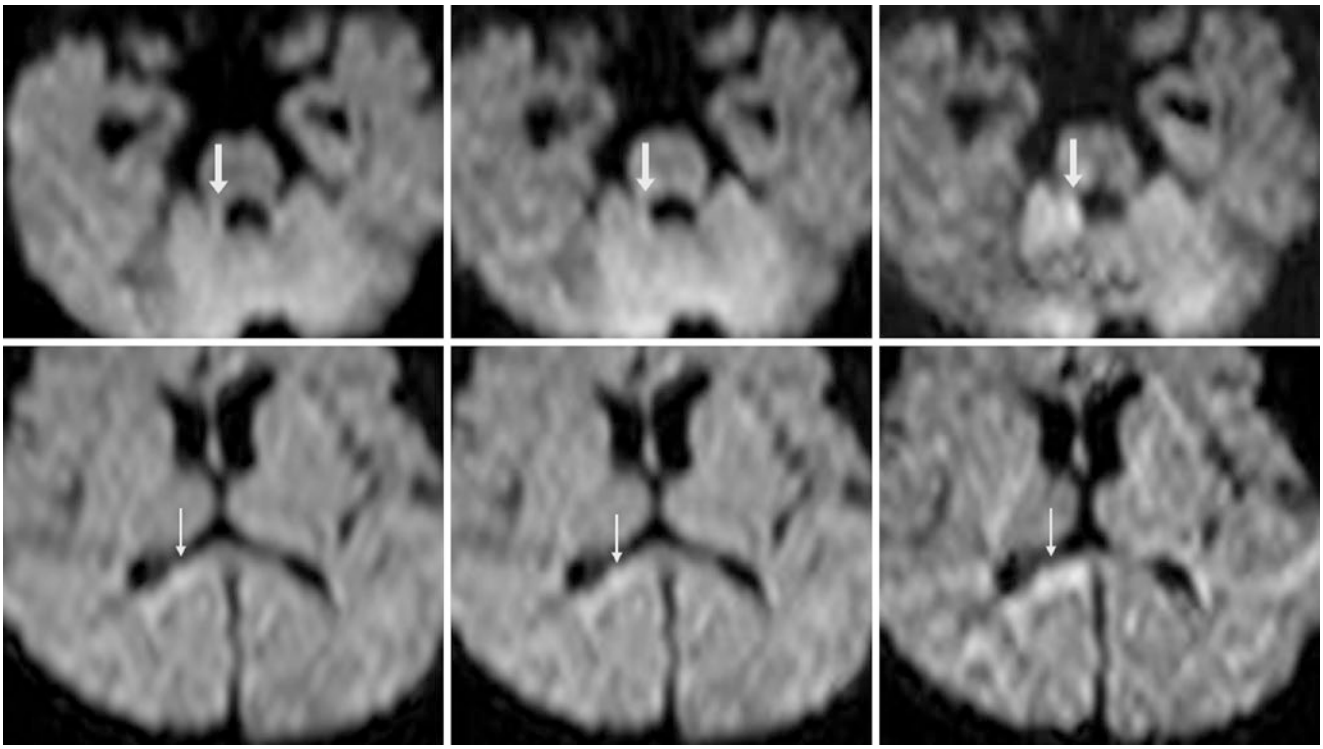

Fig. 22.58 *Top row*: A 1-year-old with an otherwise normal 1.5 T MRI for developmental delay, which illustrates increasingly bright signal (from normal anistropy in the AP direction) of the right superior cerebellar peduncle (SCP) (*arrows*) on DWI at *b* values of 1000 (*left*), 1500 (*middle*) and 2000 (*right*) s/mm^2. *Bottom row*: This signal also occurs along the callosal splenium's right side (transverse fiber direction) at *b* values of 1000 (*left*), 1500 (*middle*), and 2000 (*right*) s/mm^2. The unilaterality may be due to head tilt relative to the scanner's z axis and mimics a focal splenial lesion on the $b = 2000$ images

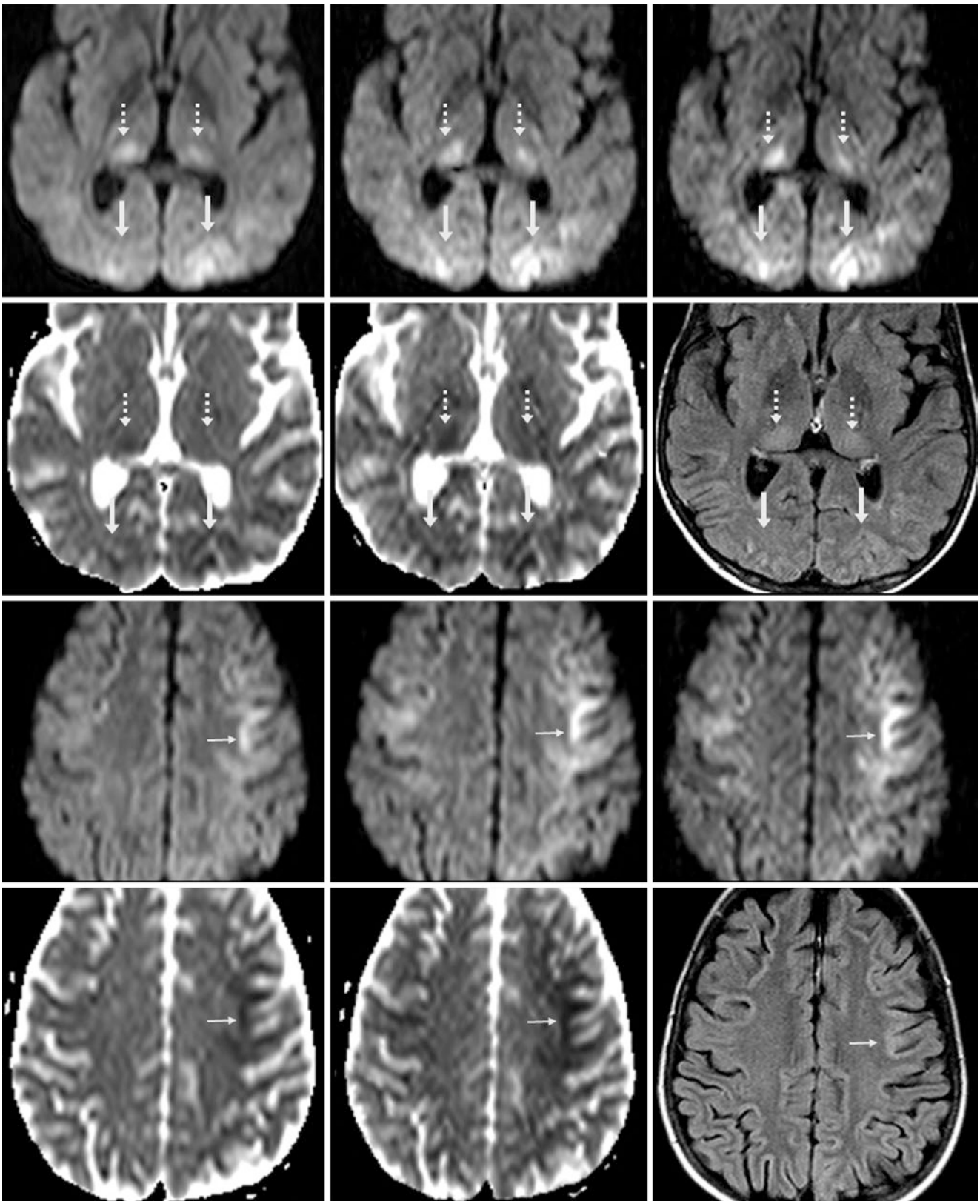

Fig. 22.59 Comparison case of hypoxic ischemic encephalopathy (HIE) in a 4-year-old who suffered cardiac arrest after trauma. *Top row*: A 1.5 T MRI with DWI shows increasingly visible cortical (*arrows*) and thalamic (*dashed arrows*) findings of HIE at $b = 1000$ (*left*), 1500 (*middle*), and 2000 (*right*) s/mm^2. *Second row*: The ADC maps appear almost normal at $b = 1000$ s/mm^2 (*left*) but seem more abnormal at $b = 2000$ s/mm^2 (*middle*). FLAIR (*right*) also appears nearly normal. *Third row*: At a more superior level, DWI depicts increasingly visible cortical HIE (*thin arrows*) at $b = 1000$ (*left*), 1500 (*middle*), and 2000 (*right*) s/mm^2. *Bottom row*: The corresponding ADC maps (*left and middle*) are provided for the third row's DWIs, and confirm that the DWI findings are real. On FLAIR (*right*), the cortical/subcortical abnormalities are barely visible. These images illustrate how increasing the *b* value improves the visualization of cortical insults (particularly HIE) on DWI

22.3.2 DWI: Directional Anisotropy Demonstrated in Three Orthogonal Planes

As the *"trace" DWI* (the most commonly used for routine DWI interpretation) is a composite of a single-shot, echoplanar gradient sensitization in three orthogonal directions, the appearance of certain tracts can be bright or dark depending on the plane of gradient sensitization. In particular, the strongest *anisotropy* is noted on the DWI gradient map sensitized orthogonal to (*i.e.*, 90° to) the plane of acquisition. For example, on the craniocaudal-sensitized DWI image, the callosal splenium (a transverse structure) is bright, and the posterior limbs of the internal capsules (a craniocaudal structure) appear dark. Thus, structures in the plane of the applied gradient appear dark. Neuroradiologists do not routinely review all three maps, but rather only the composite "trace" image. (Its signal intensity is a cube root of the three planes' signal intensities multiplied together.) This composite trace image essentially averages the three planes so that structures do not appear bright in the absence of pathology. Occasionally, however, strong but normal anisotropy in certain structures "shines through" onto the trace image and appears mildly bright on "trace" DWI. The following pages show examples of such anisotropy within several structures (Figs. 22.60, 22.61, 22.62, 22.63, 22.64, 22.65, 22.66, 22.67 and 22.68).

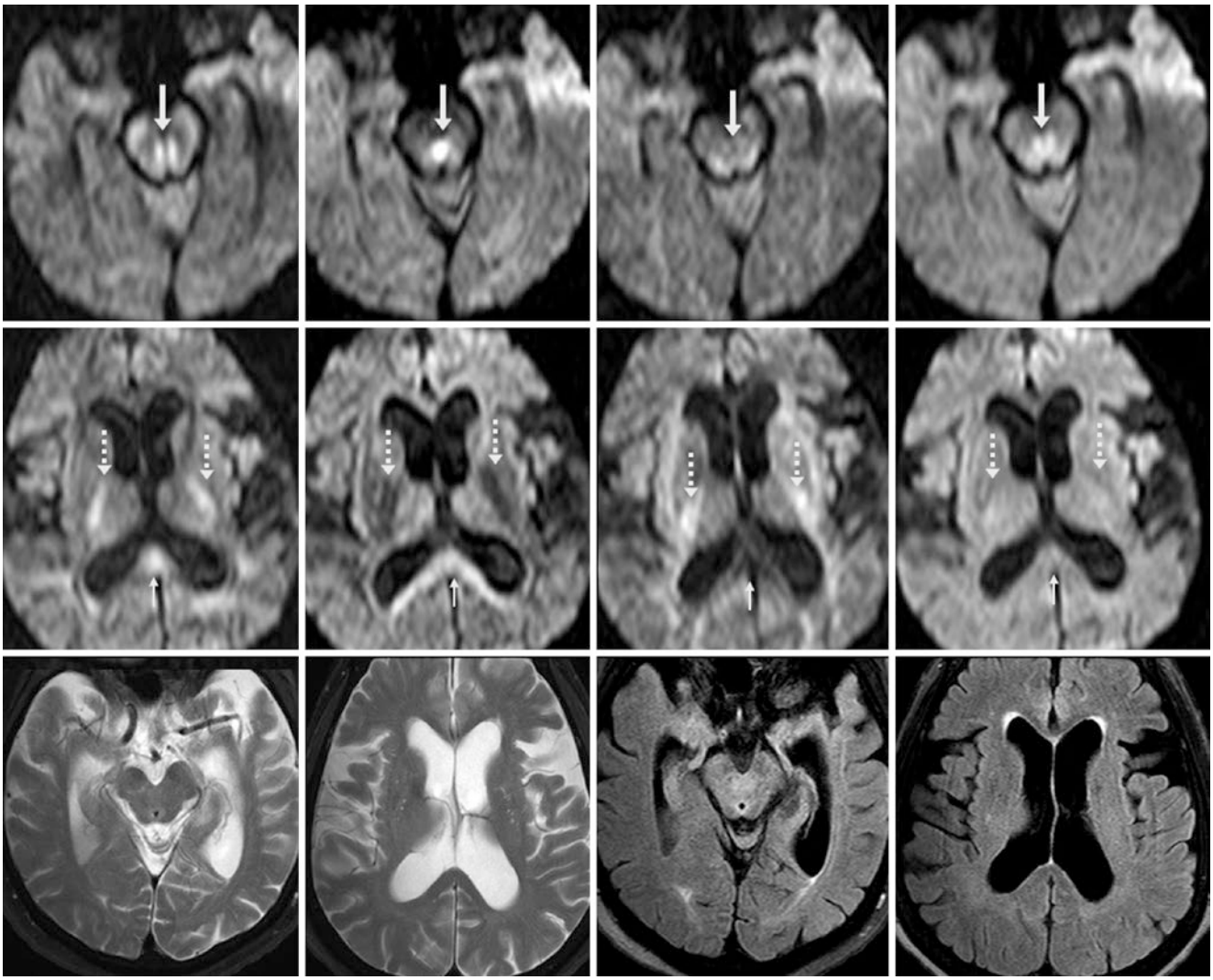

Fig. 22.60 A 76-year-old with a 1.5 T MRI. *Top and middle rows*: DWIs in three orthogonal directions illustrate normal anisotropy at $b = 1000$ s/mm^2. DWIs sensitized to AP (*left*), craniocaudal (*left middle*), and transverse (*right middle*) directions depict bright signal of the DSCP (*arrows*), the PLIC (*dashed arrows*), and the callosal splenium (*thin arrows*). The "trace" maps (*right*) are a compilation of all three planes. The DSCP still appears bright on the trace map, a normal variation. Note that the DSCP is not bright on the transverse image, as the fibers travel in that direction; this similarly is true for the callosal splenium. The PLIC is dark on the craniocaudal image, as that is the direction that those fibers travel. *Bottom row*: Corresponding axial T2WIs (*left*) and FLAIR images (*right*) are provided

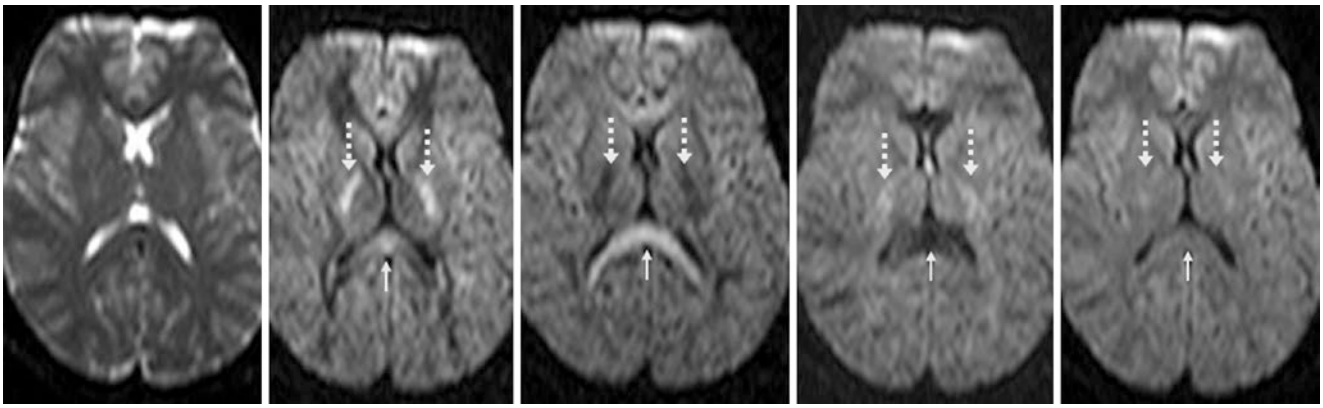

Fig. 22.61 3T MRI DWI in three orthogonal directions, to illustrate normal anisotropy in a 24-year-old normal volunteer. A "*b*0" (*i.e.*, $b=0$ s/mm^2) map appears similar to a rudimentary T2WI (*left*). The DWIs are provided for $b=1000$ s/mm^2, as shown in AP (*left middle*), craniocaudal (*middle*), and transverse (*right middle*) planes, with trace map (*right*). The PLIC (*dashed arrows*) is dark on craniocaudal images; the splenium (*thin arrows*) is dark on transverse images. These images illustrate how a structure appears dark on DWI sensitized to the same plane in which the white matter tract travels

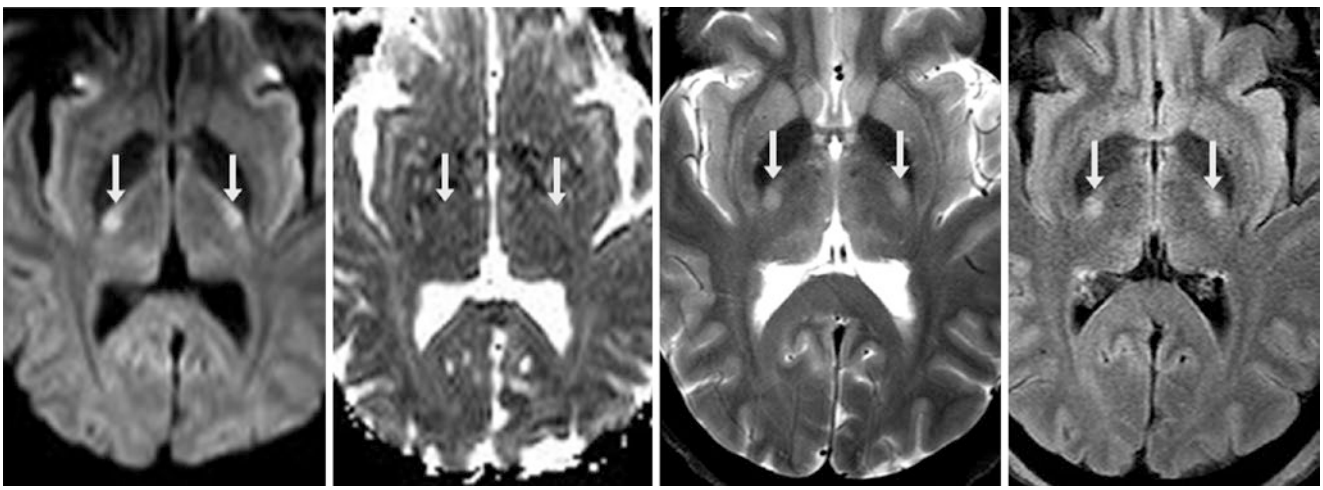

Fig. 22.62 A 49-year-old with a 3 T MRI that demonstrates hyperintensity within the PLICs bilaterally (*arrows*) on the regular "trace" DWI map (*left*) but without corresponding bright signal (*i.e.*, edema) on the ADC map (*left middle*). There is also normal, bright signal within that location on T2WI (*right middle*) and FLAIR (*right*). This hyperintensity likely results from the normal, relatively high anisotropy present within the tightly-packed white matter tracts of the PLIC and CSTs

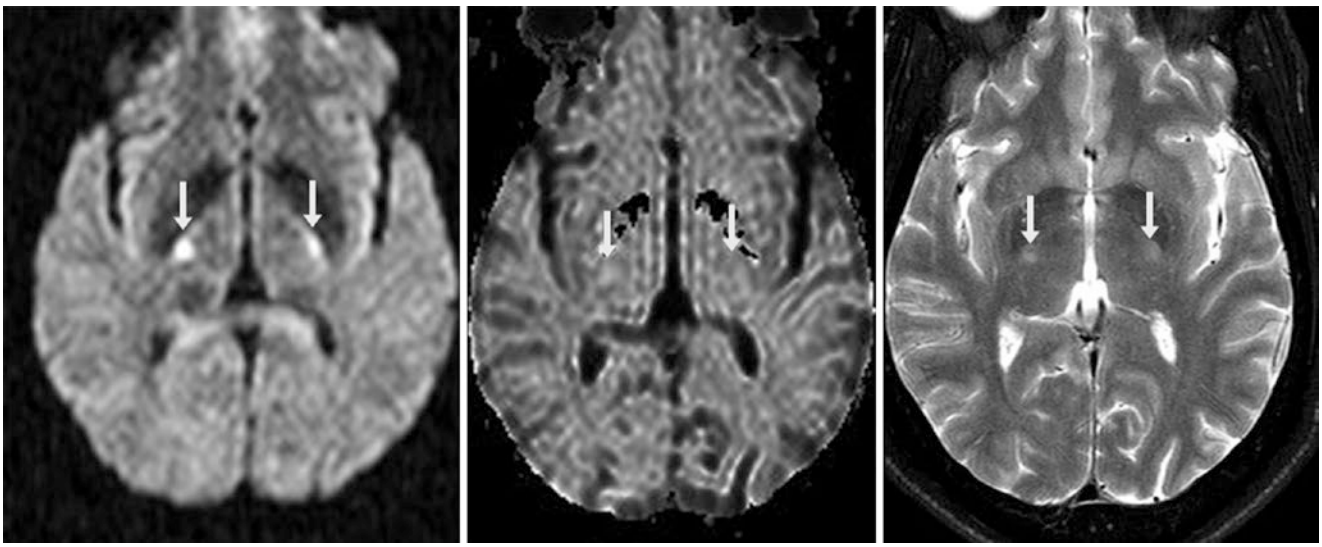

Fig. 22.63 A 3 T MRI in a 50-year-old illustrates hyperintensity within the PLICs and CSTs bilaterally (*arrows*) on DWI (*left*), but without corresponding bright signal on exponential DWI (*middle*), which removes the T2-bright component of the image. There is also normal, bright signal within that location on T2WI (*right*) and FLAIR (*not shown*). This signal results from perhaps either a relatively higher degree of anisotropy within the CST as compared to surrounding structures, or from increased interstitial fluid

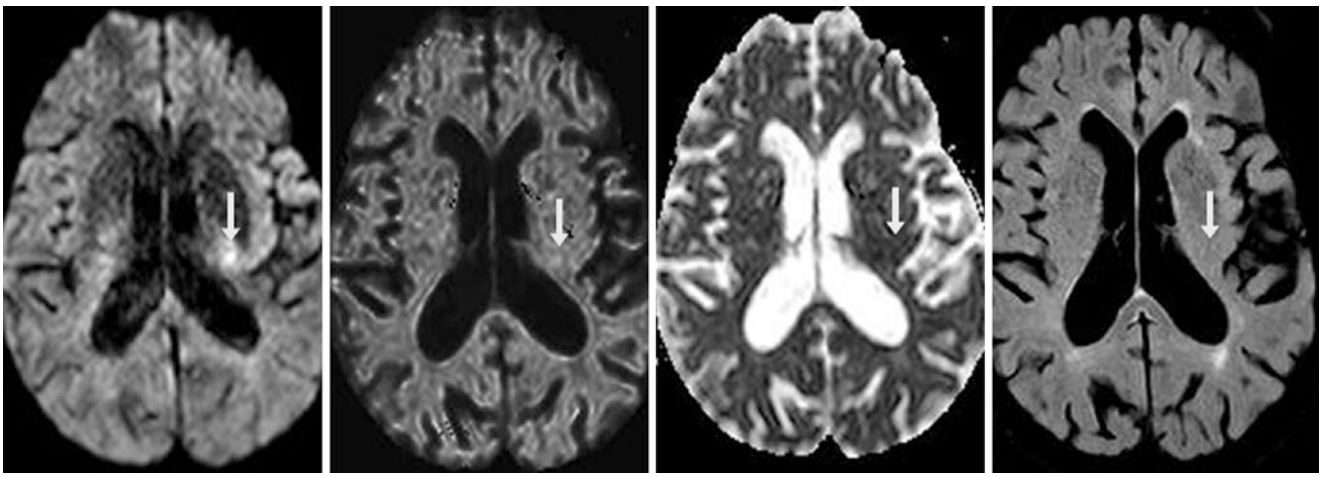

Fig. 22.64 A 1.5 T MRI in a 78-year-old shows unilateral hyperintensity within the left PLIC/CST (*arrows*) on DWI (*left*). On initial review, this appeared to be a small lacunar infarct, but there was no corresponding bright signal on exponential DWI (*left middle*), which removes T2-bright signal (*i.e.*, vasogenic edema) from the image, and no edema on the ADC map (*right middle*) or FLAIR (*right*). This finding results from normal anisotropy of the CST

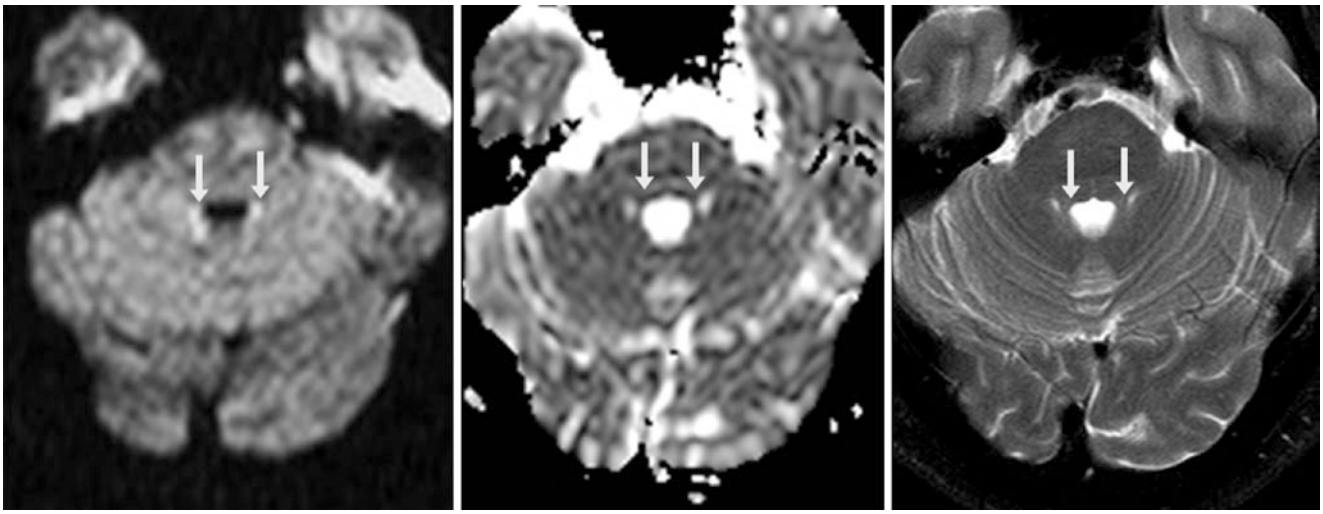

Fig. 22.65 A 1.5 T MRI in a 49-year-old contains hyperintensity (*arrows*) within the superior cerebellar peduncle (SCP) bilaterally on DWI (*left*), but without corresponding bright signal (*i.e.*, edema) on the ADC map (*middle*). There is normal bright signal within that location on T2WI (*right*) and FLAIR (not shown). This finding is most likely a result of the normal, relatively high degree of anisotropy present from tightly-packed fibers in that location

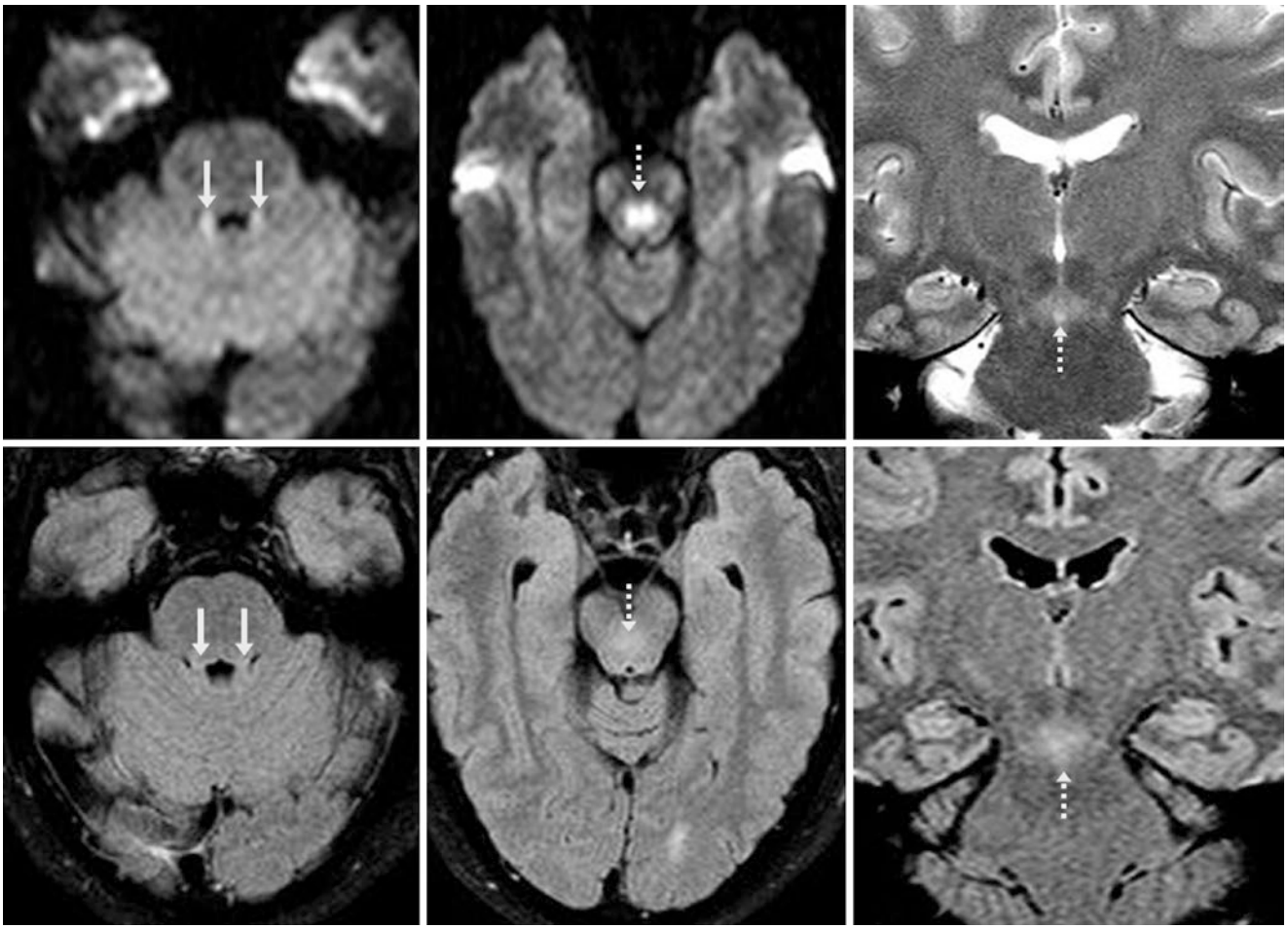

Fig. 22.66 A 1.5 T MRI in a 35-year-old shows hyperintensity of the SCPs (*arrows*) and their decussation (DSCP) (*dotted arrows*) on DWI (*top left* and *top middle*), but without corresponding dark signal on the ADC map (*not shown*). The hyperintensity within the DSCP could simulate an infarct or an inflammatory lesion (*e.g.*, from MS). There is also normal, hyperintense signal within that location on coronal T2WI (*top right*), which is less bright on axial (*bottom left* and *bottom middle*) and coronal (*bottom right*) FLAIR images

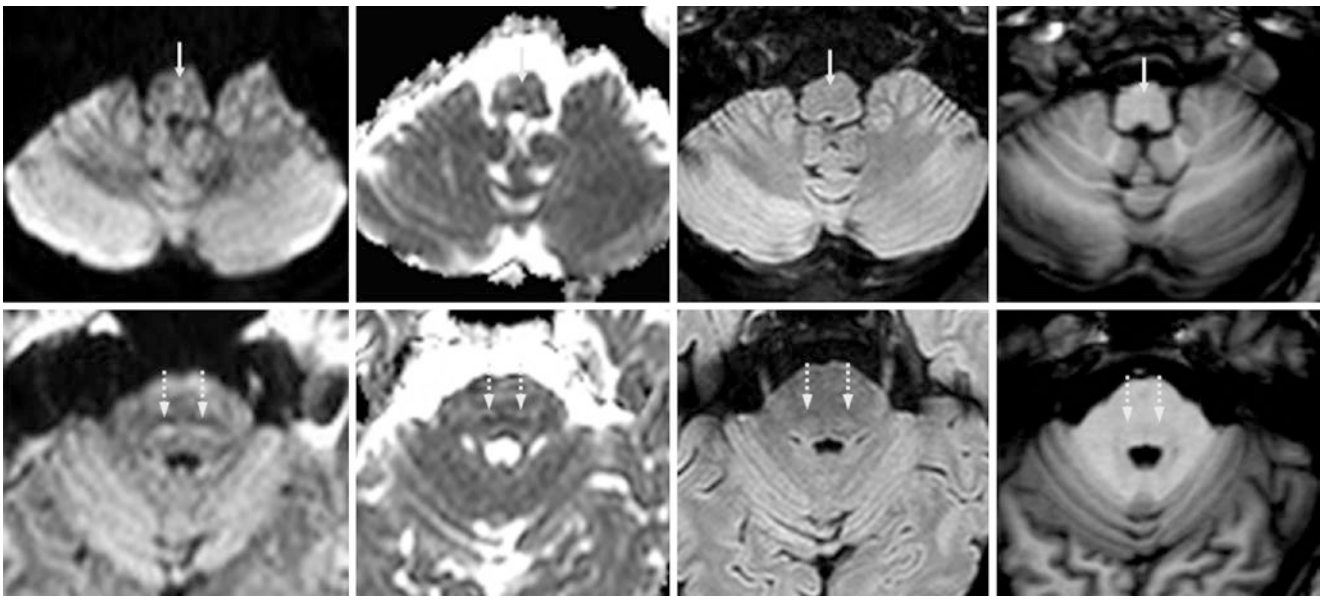

Fig. 22.67 A 38-year-old with a normal 3 T MRI. *Top row*: There is hyperintensity within the pyramidal decussation (*thin arrows*) on DWI (*left*), but no corresponding dark signal on the ADC map (*left middle*); 3D-reformatted FLAIR (*right middle*) and T1WI (*right*) are normal. *Bottom row*: There are bright medial lemnisci (*dotted arrows*) on DWI (*left*), with dark signal on the ADC map (*left middle*). 3D FLAIR (*right middle*) and T1WI (*right*) appear normal

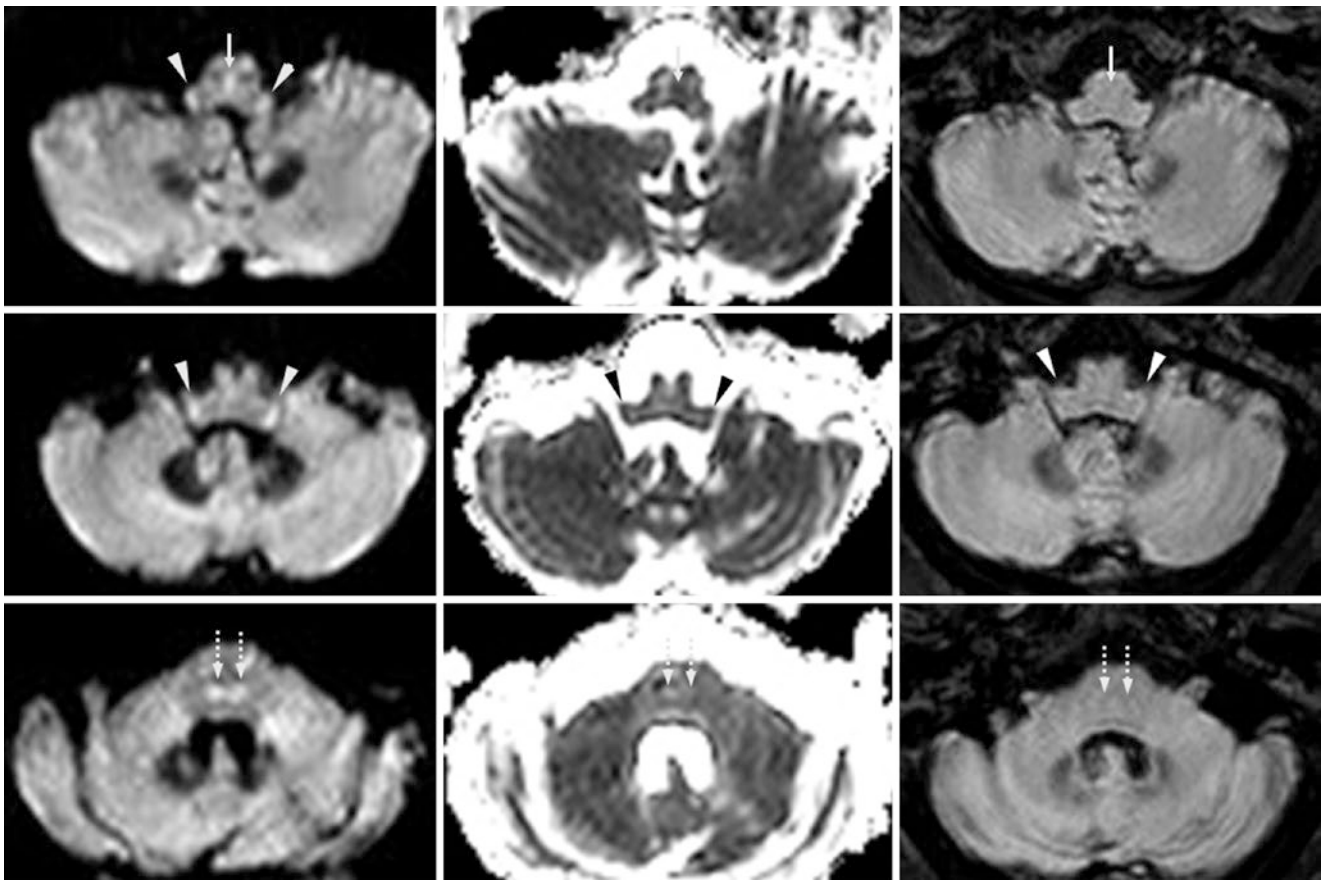

Fig. 22.68 A 54-year-old with a normal 3 T MRI. *Top row*: There is hyperintensity within the pyramidal decussation (*thin arrows*) on DWI (*left*), without dark signal on the ADC map (*middle*) or on 3D-reformatted FLAIR (*right*). There is also bright signal on DWI within the inferior cerebellar peduncles (ICPs) bilaterally (*arrowheads*). *Middle row*: There is hyperintensity within the ICPs (*arrows*) on DWI (*left*), without dark signal on the ADC map (*middle*) or on 3D FLAIR (*right*). *Bottom row*: There is bright signal on DWI within the medial lemnisci (*dotted arrows*) without abnormal signal on the ADC map (*middle*) or on 3D FLAIR (*right*)

22.3.3 DWI Pseudolesions: Cortical Hyperintensity at 3 T Mimics Hypoxic-Ischemic Encephalopathy

As stated previously, DWI is excellent at detecting *hypoxic-ischemic encephalopathy/injury* (HIE/HII), which appears as diffuse cortical bright signal on DWI and is dark on ADC maps. However, DWI occasionally (particularly at 3 T) has mild, diffusely bright *cortical* signal, likely related to either the effects mentioned in the section on FLAIR artifacts at 3 T (mildly T2-bright cortical signal) or to some degree of subcortical white matter normal anisotropy. This normal, mildly bright cortical signal can occasionally simulate HIE or other uncommon insults to the cortex, such as *acute hepatic encephalopathy* (AHE) or *encephalitis*. There are some ways to avoid this pitfall: 1) Note the relative lack of dark cortical signal on ADC maps; 2) Be aware of regions where such bright signals typically occur (in similar locations as on FLAIR, including the orbitofrontal, cingulate, insular, and hippocampal cortices); 3) Note the lack of cortical swelling or sulcal effacement (Figs. 22.69, 22.70, 22.71 and 22.72).

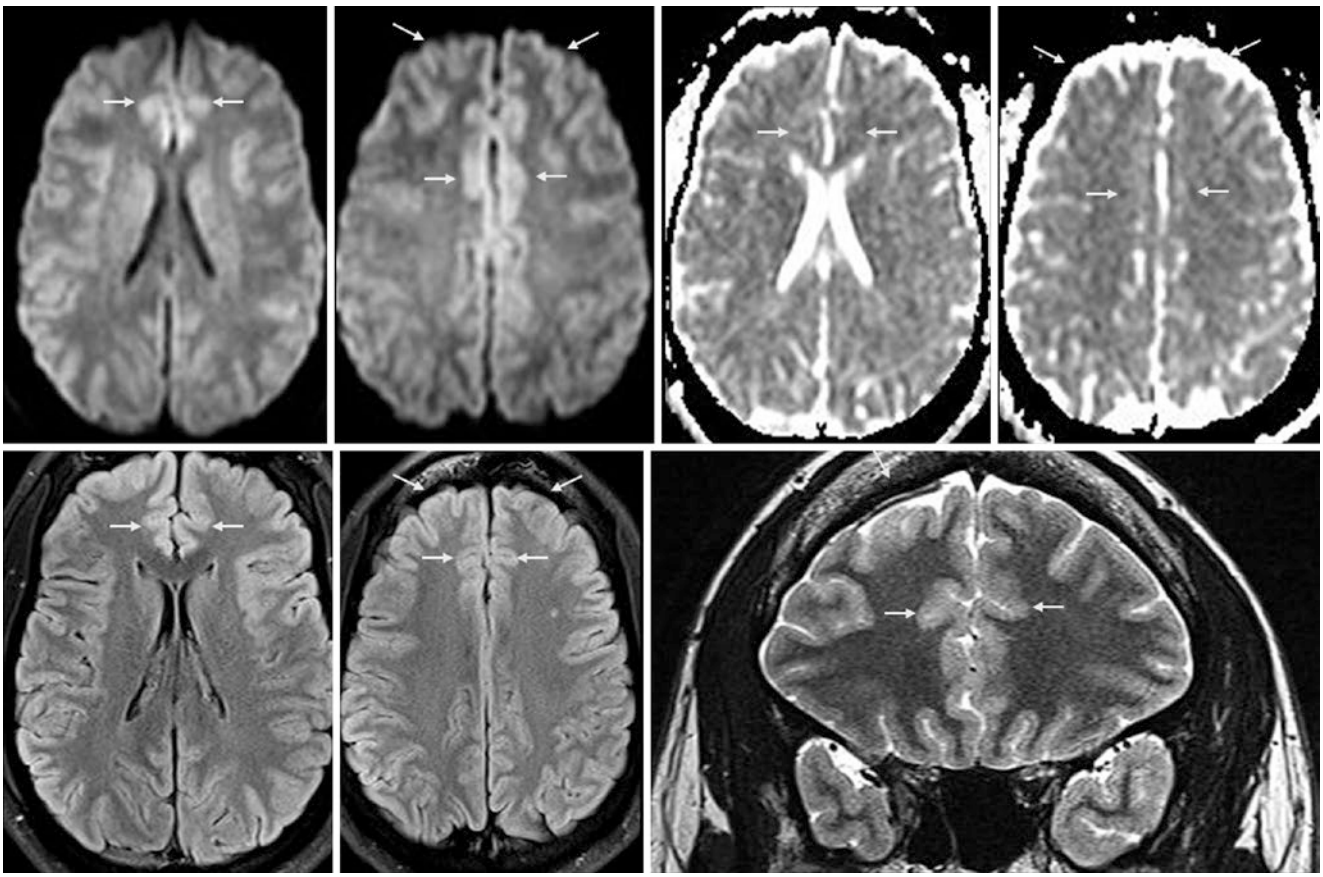

Fig. 22.69 A 3 T MRI from a 27-year-old illustrates mild, normal cortical hyperintensity in multiple locations on DWI (*top left*), most notably in the cingulate gyri and frontal poles (*thin arrows*) without corresponding dark signal on ADC maps (*top right*). There is also mild hyperintensity on FLAIR (*bottom left* and *bottom middle*), relative to the parieto-occipital gyri posteriorly. These findings could simulate multifocal HIE, but note the lack of cortical swelling or sulcal effacement. On a coronal T2WI (*bottom right*), the cingulate gyri are slightly hyperintense

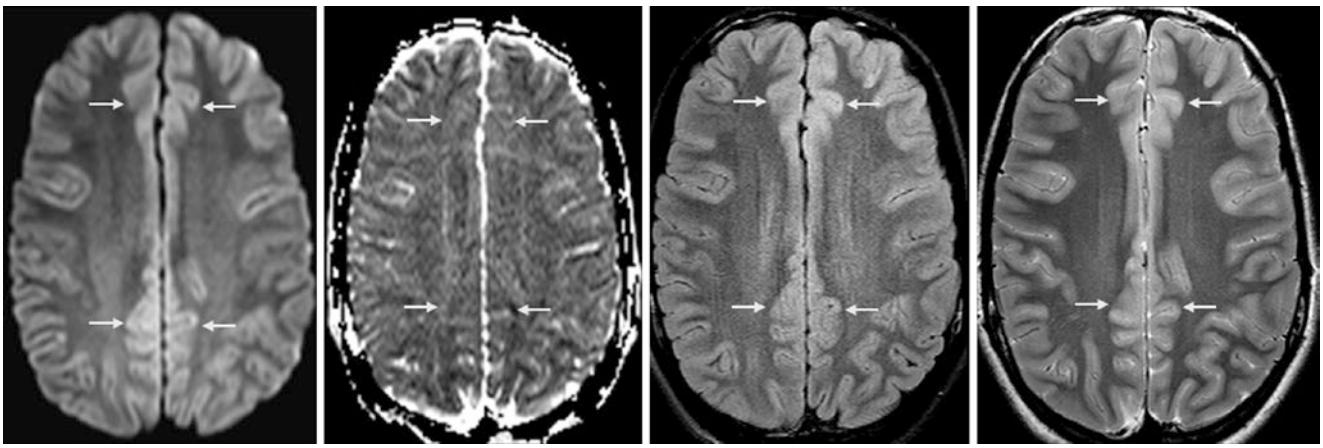

Fig. 22.70 A 16-year-old with headaches had a 3 T MRI that shows normal, multifocal cortical hyperintensity on DWI (*left*), FLAIR (*right middle*), and T2WI (*right*), particularly in the cingulate gyri and frontal poles (*thin arrows*), mimicking HIE. These areas do not appear dark on the ADC map (*left middle*), and note the lack of cortical swelling or sulcal effacement

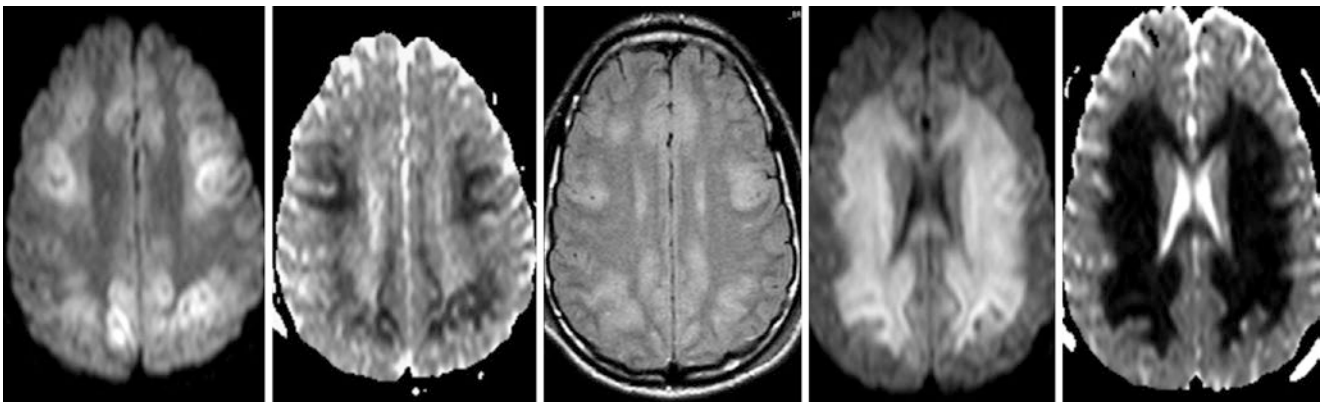

Fig. 22.71 Comparison case of HIE. In a 13-year-old, a 3 T MRI obtained 5 days after cardiac arrest from drowning showed multifocal hyperintense cortices on DWI (*left*), with corresponding dark signal on ADC maps (*left middle*), and with hyperintensity on FLAIR (*middle*). At 9 days after the arrest, the abnormalities involved the deep periventricular white matter on DWI (*right middle*) and the ADC map (*right*), a phenomenon that often occurs in the subacute phase of HIE

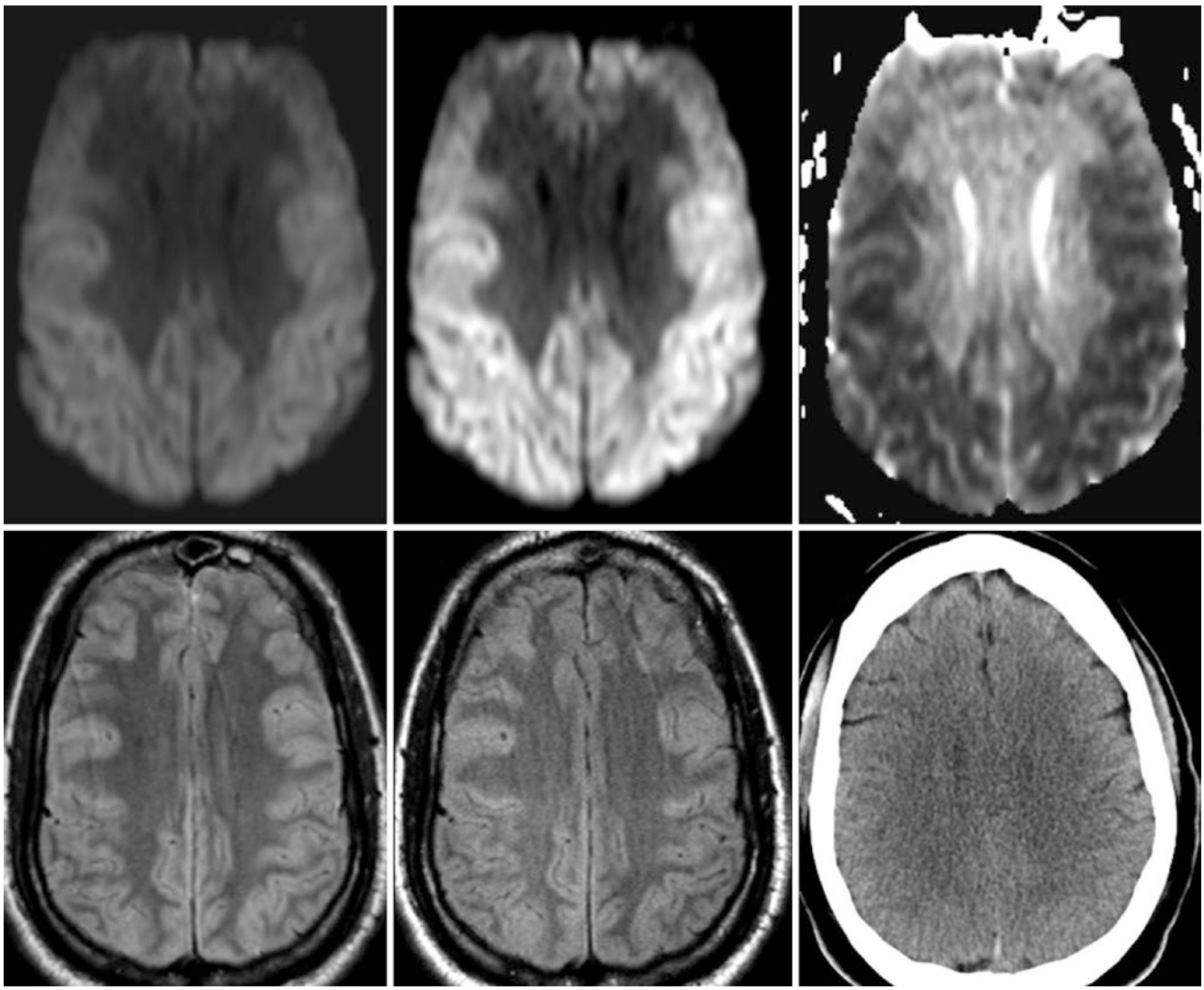

Fig. 22.72 Comparison case of "superscan" on DWI in HIE. A 3 T MRI in a 19-year-old 3 days after he hung himself showed homogeneously hyperintense cerebral cortices on improperly windowed DWI (*top left*), representing a so-called DWI superscan (mistakenly called normal by the on-call resident). Optimized windowing (*top middle*) showed profound cortical insults, confirmed by an ADC map (*top right*), with cortical edema and effacement of the sulci on T2WI (*bottom left*) and FLAIR (*bottom middle*). A CT scan 1 day earlier appeared normal (*bottom right*)

22.3.4 DWI Pseudolesions: Periventricular White Matter

Pseudoabnormalities can also be noted on DWI within the *periventricular white matter* (PVWM), particularly in the parieto-occipital regions and forceps major, and particularly at 3 T. These are presumably due to normal anisotropy, as noted previously. They may also be synonymous with normal "*terminal zones*" of myelination in the posterior PVWM, which are common in adolescence and may persist into adulthood. Such pseudoabnormalities can mimic pathologies such as *acute toxic leukoencephalopathy* (ATL); *acute disseminated encephalomyelitis* (ADEM), the *subacute phase of HIE*, following the acute, cortical phase; or *progressive multifocal leukoencephalopathy* (PML) (Figs. 22.73, 22.74, 22.75, 22.76, 22.77 and 22.78).

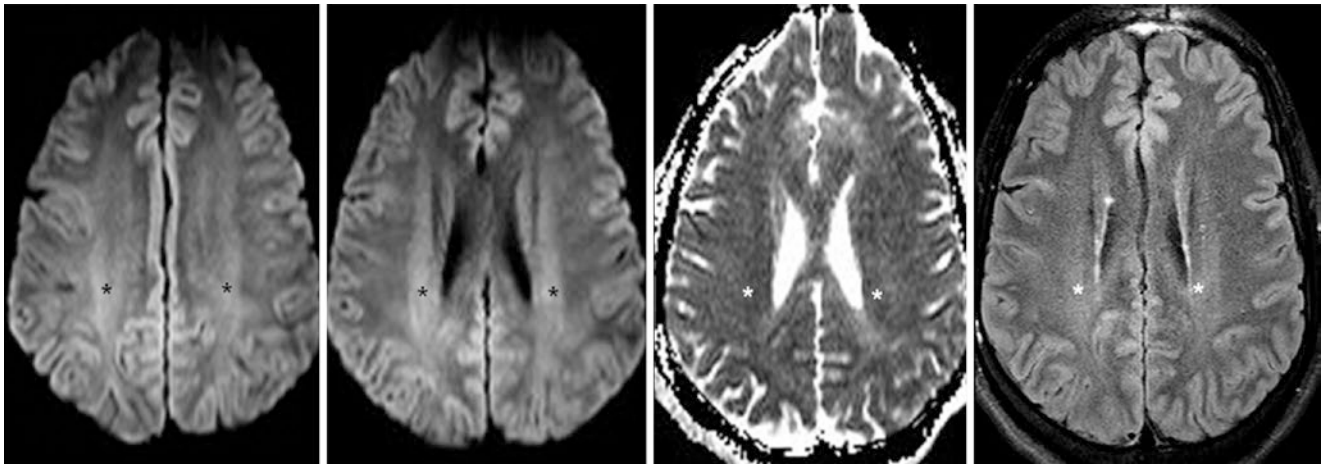

Fig. 22.73 A 3 T MRI in a 27-year-old shows normal hyperintensity within the periventricular white matter (PVWM) (*asterisk*) bilaterally on DWI (*left*), with normal appearance on the ADC map (*right middle*). There is also mild hyperintensity on FLAIR (*right*)

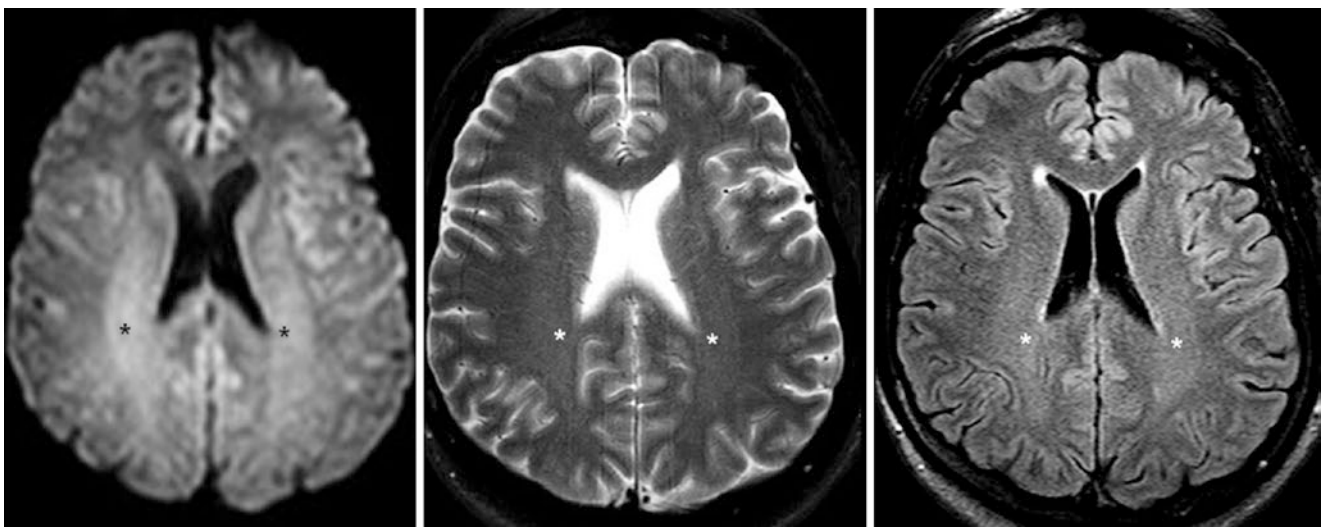

Fig. 22.74 A 3 T MRI in a 65-year-old illustrates normal hyperintensity within the PVWM (*asterisk*) bilaterally on DWI (*left*), also having faint hyperintensity on T2WI (*middle*) and on FLAIR (*right*). An ADC map (not shown) was normal

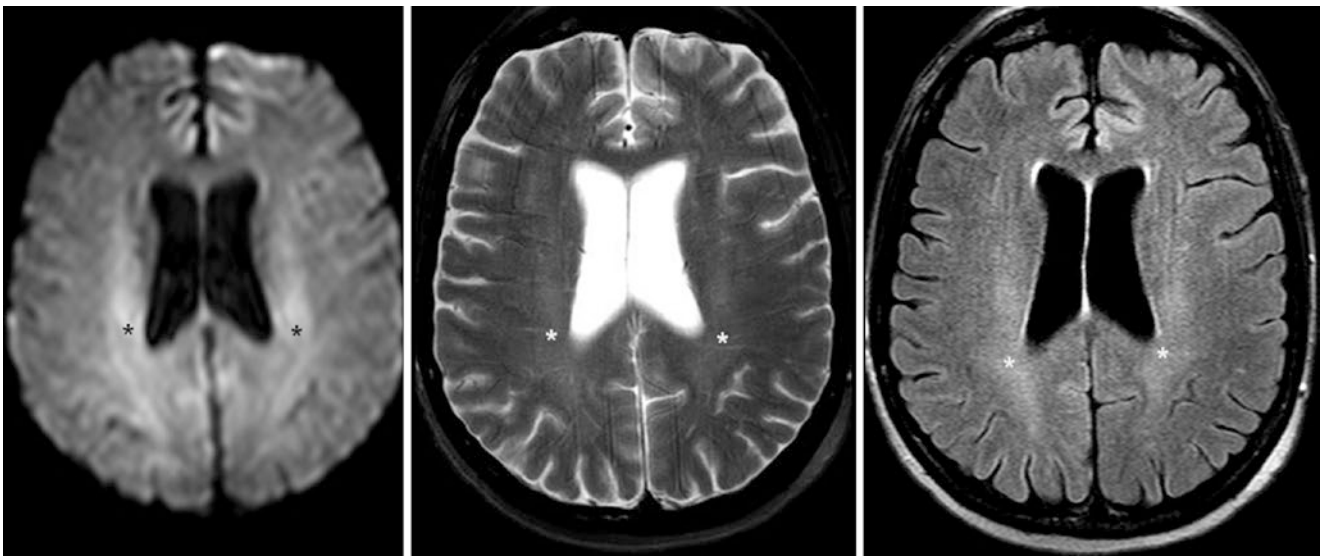

Fig. 22.75 A 3 T MRI in a 60-year-old shows normal hyperintensity within the PVWM (*asterisk*) bilaterally on DWI (*left*), with mild corresponding hyperintensity on T2WI (*middle*) and on FLAIR (*right*). An ADC map (*not shown*) was normal

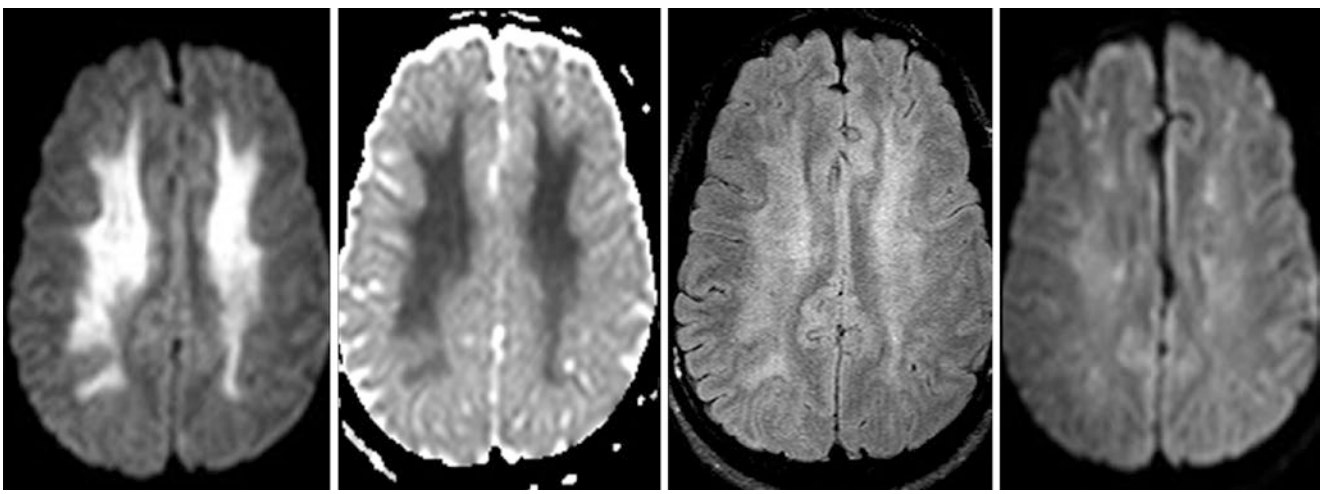

Fig. 22.76 Comparison case of acute toxic leukoencephalopathy (reversible) from carbon monoxide toxicity. An unresponsive 20-year-old underwent a 3 T MRI, which demonstrated diffuse abnormalities throughout the PVWM on DWI (*left*), ADC map (*left middle*), and FLAIR (*right middle*). Two weeks later, the abnormalities on DWI (*right*) had markedly improved, and had also nearly resolved on FLAIR (*not shown*)

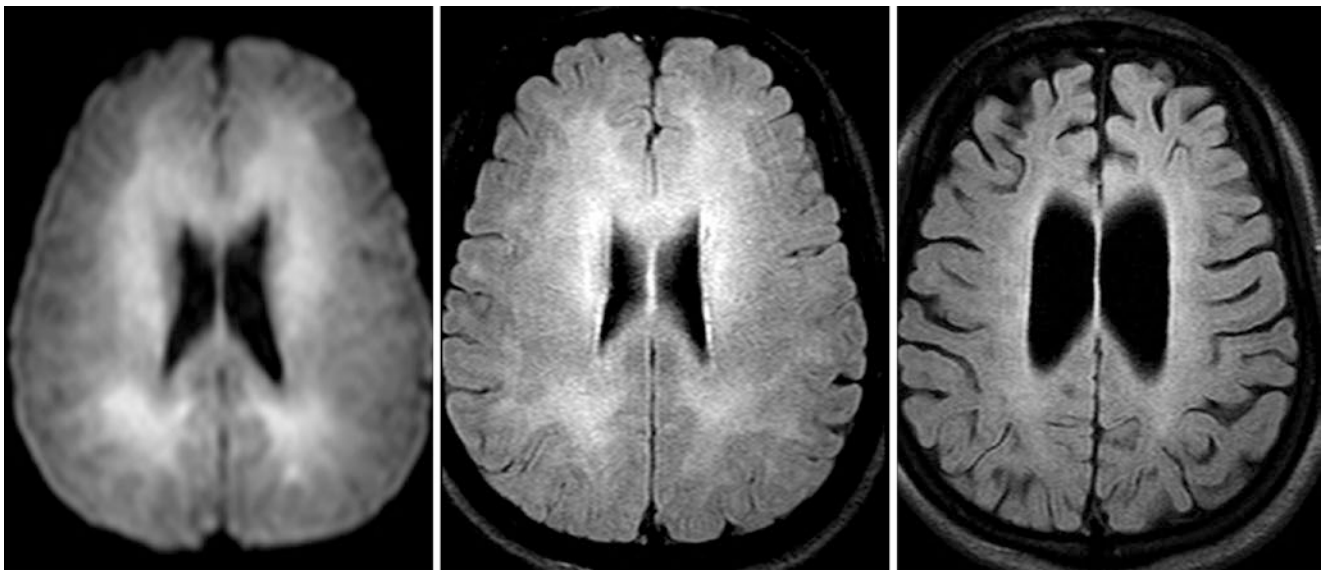

Fig. 22.77 Comparison case of acute toxic leukoencephalopathy from heroin inhalation ("chasing the dragon"). An unresponsive 24-year-old underwent 3 T MRI, which demonstrated diffuse abnormalities throughout the PVWM on DWI (*left*) and FLAIR (*middle*), along with mild sulcal effacement. FLAIR images 1 year later (*right*) showed resultant severe global cerebral atrophy, predominantly involving the white matter

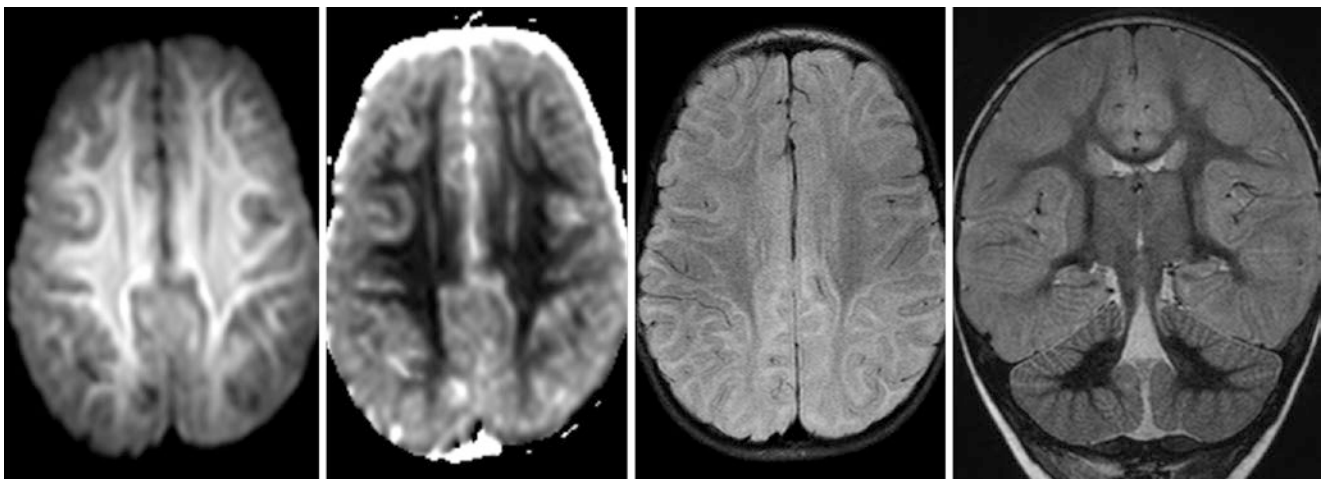

Fig. 22.78 Comparison case of subacute HIE. A 3 T MRI in a 9-month-old infant with status epilepticus at 7 days postinsult showed confluent periventricular white matter abnormalities on DWI (*left*), ADC map (*left middle*), and FLAIR (*right middle*), along with diffuse cortical swelling on coronal T2WI (*right*). The presence of cortical edema on FLAIR differentiates HIE from acute toxic leukoencephalopathy (ATL), which lacks cortical edema

22.3.5 DWI: T2 Shine-Through Effect

"*T2 shine-through*" is abnormal and usually occurs when bright signal on DWI is extremely bright on T2WI or FLAIR. The ADC contribution varies somewhat and is debatable. Typically, there is elevated ADC in such regions, although occasionally the ADC values are normal or slightly decreased. In the latter case, the bright signal on DWI arises from the overwhelming effect of T2-bright edema. T2 shine-through appears dark on exponential DWI, which removes the T2-bright component of the edema. Common causes of this appearance include *posterior reversible encephalopathy syndrome* (PRES), *MS*, or *peritumoral edema* (Figs. 22.79, 22.80, 22.81, 22.82 and 22.83).

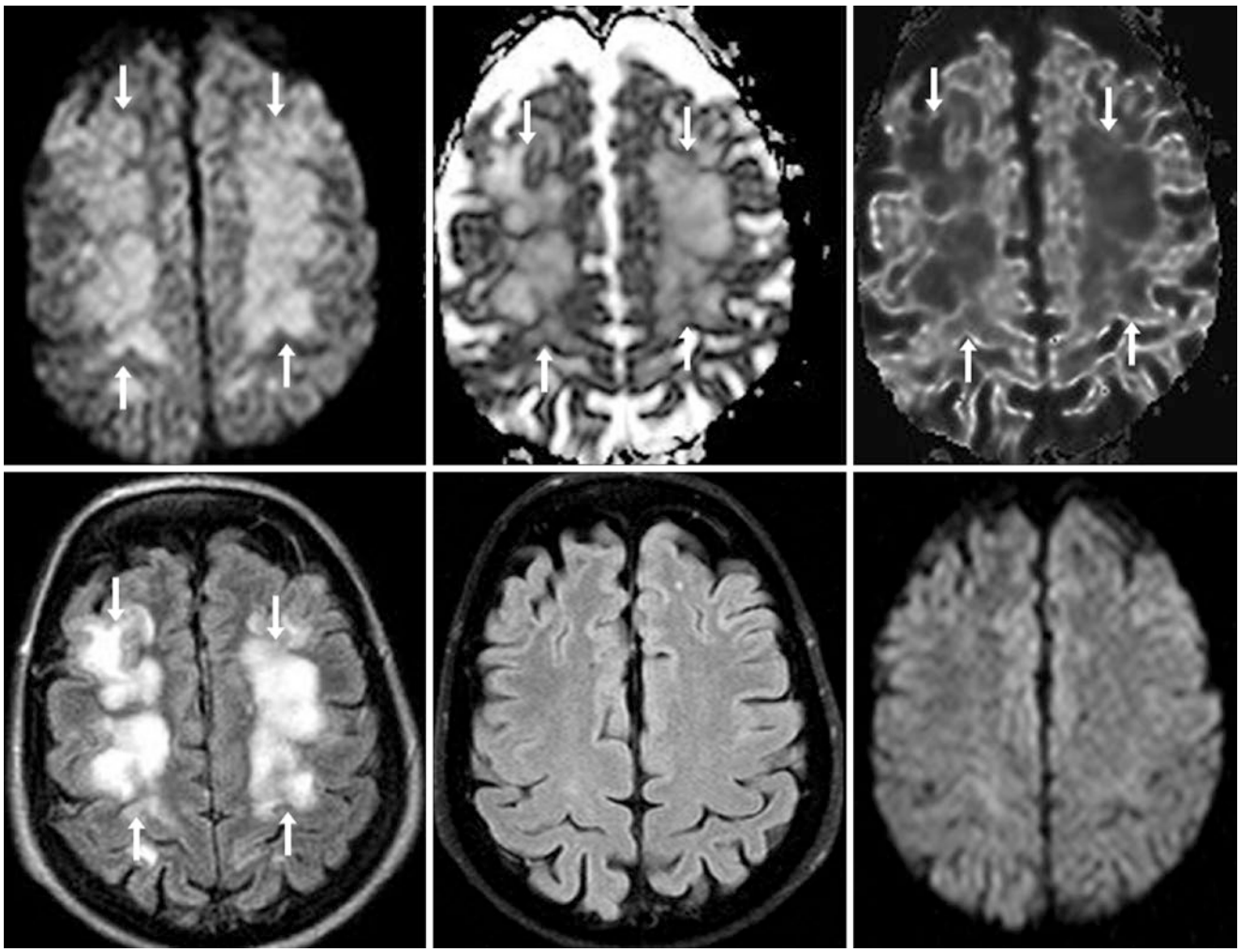

Fig. 22.79 A 1.5 T MRI in a 52-year-old illustrates confluent, bright T2 shine-through signal (*arrows*) from hypertensive posterior reversible encephalopathy syndrome (PRES) on DWI (*top left*). This signal arises from extremely bright vasogenic (as opposed to cytotoxic) edema and is confirmed by bright signal on the ADC map (*top middle*), which darkens on "exponential" DWI (*top right*). The "severe" extent of edema on FLAIR (*bottom left*) resolved 3 weeks later on FLAIR (*bottom middle*) and DWI (*bottom right*)

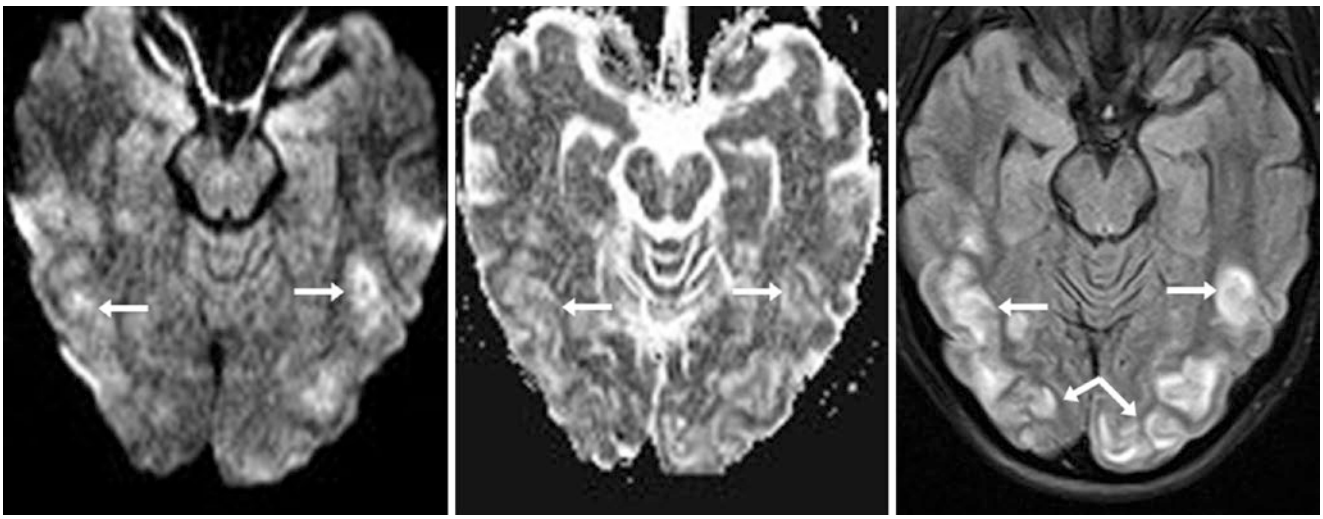

Fig. 22.80 A 21-year-old with systemic lupus had a 1.5 T MRI that shows T2 shine-through bright signal (*arrows*) from PRES-related vasogenic edema within the temporo-occipital regions on DWI (*left*). These regions are depicted as bright on an ADC map (*middle*). A FLAIR image (*right*) demonstrates the typical cortical-subcortical edema from PRES

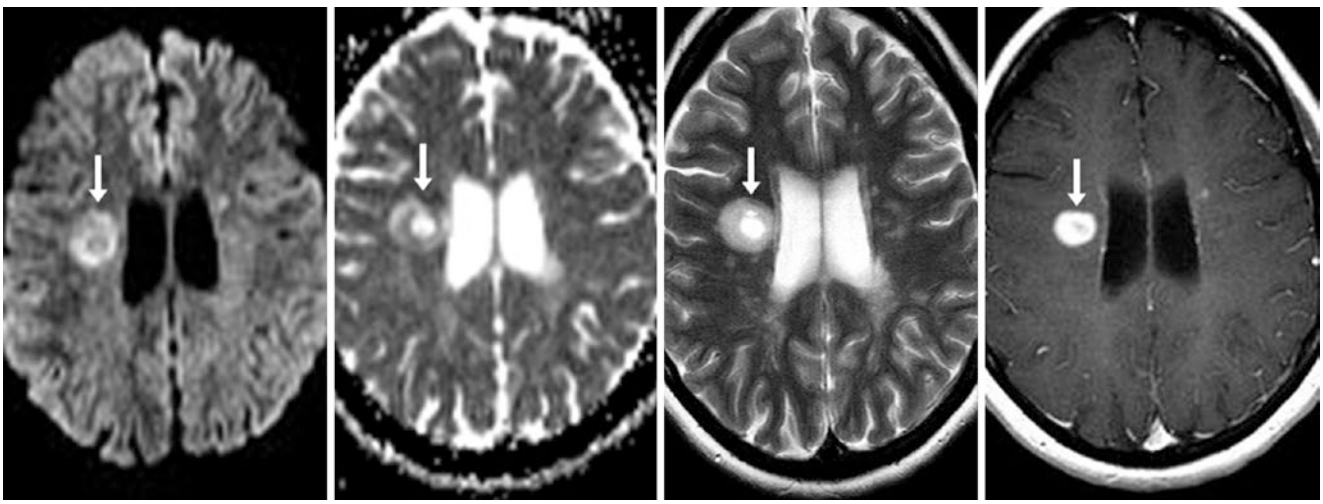

Fig. 22.81 A 1.5 T MRI in a 26-year-old with MS depicts a masslike lesion (*arrows*) of T2 shine-through hyperintense signal on DWI (*left*) within the periventricular white matter. The lesion is bright on an ADC map (*left middle*) and T2WI (*right middle*), and enhances on postcontrast T1WI (*right*), representing active demyelination

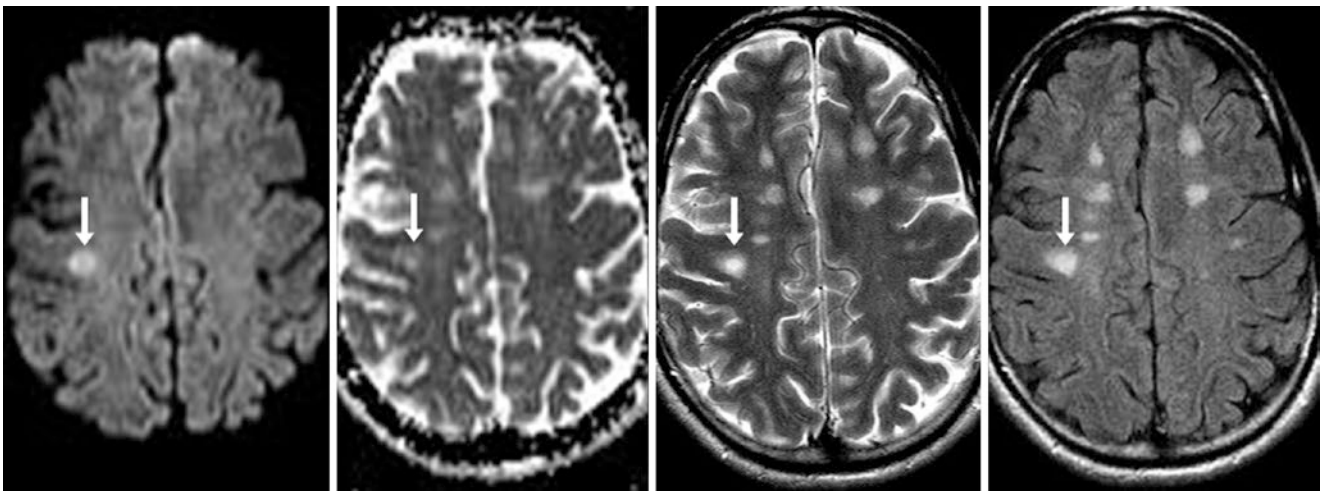

Fig. 22.82 In a 34-year-old with MS, a 1.5 T MRI demonstrates a right frontal focus of hyperintense signal (*arrows*) on DWI (*left*) from MS, representing T2 shine-through, based on corresponding bright signal on the ADC map (*left middle*). T2WI (*right middle*) and FLAIR (*right*) demonstrate the T2-hyperintense focus along with other lesions

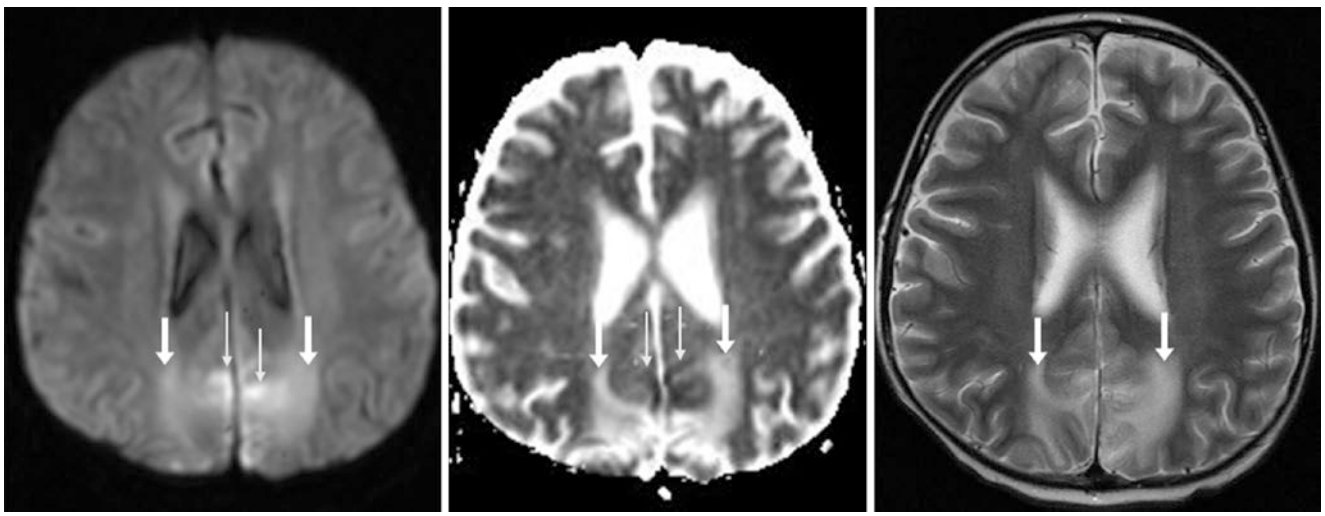

Fig. 22.83 In a 10-year-old with PRES from methotrexate, a 3 T MRI shows parieto-occipital vasogenic edema with T2 shine-through signal (*arrows*) on DWI (*left*), ADC map (*middle*), and T2WI (*right*). There are also bilateral, smaller areas of cytotoxic edema medially in parasagittal locations, which have mildly reduced diffusion (*thin arrows*) and are darker on the ADC map. About 15–20 % of PRES cases show focal regions of cytotoxic edema on DWI

22.3.6 DWI: T2 Washout Effect

"*T2 washout*" occurs when profoundly T2-bright and FLAIR-bright signal is present (*i.e.*, comes close to CSF) on ADC maps and causes resultant dark signal on DWI. It is abnormal and is not a normal variant, but its appearance is important to recognize. T2 washout appears dark on "exponential" DWI, which removes the T2 component of vasogenic edema; typically, the ADC values are extremely high in such regions. Though uncommon, T2 washout occurs in scenarios in which edema is focally quite severe, such as *PRES*, *MS*, or *peritumoral edema* of malignancy (Figs. 22.84, 22.85, 22.86, 22.87, 22.88 and 22.89).

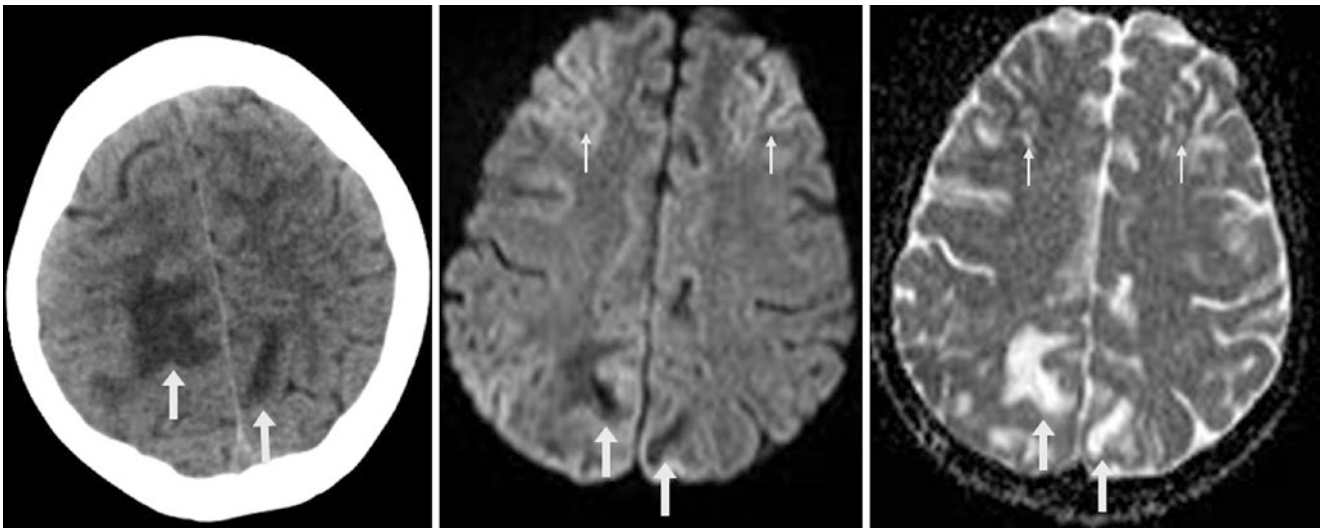

Fig. 22.84 An 11-year-old with bilateral parieto-occipital edema (*arrows*) of PRES (due to cyclosporine toxicity) on nonenhanced CT (*left*). On a 3 T MRI, there is dark signal on DWI (*middle*) and bright signal on the corresponding ADC map (*right*). Such "T2 washout" relates to extremely T2-bright vasogenic edema. Areas of milder vasogenic edema, which cause mild T2 shine-through (*thin arrows*), are noted in the frontal lobes anteriorly and bilaterally

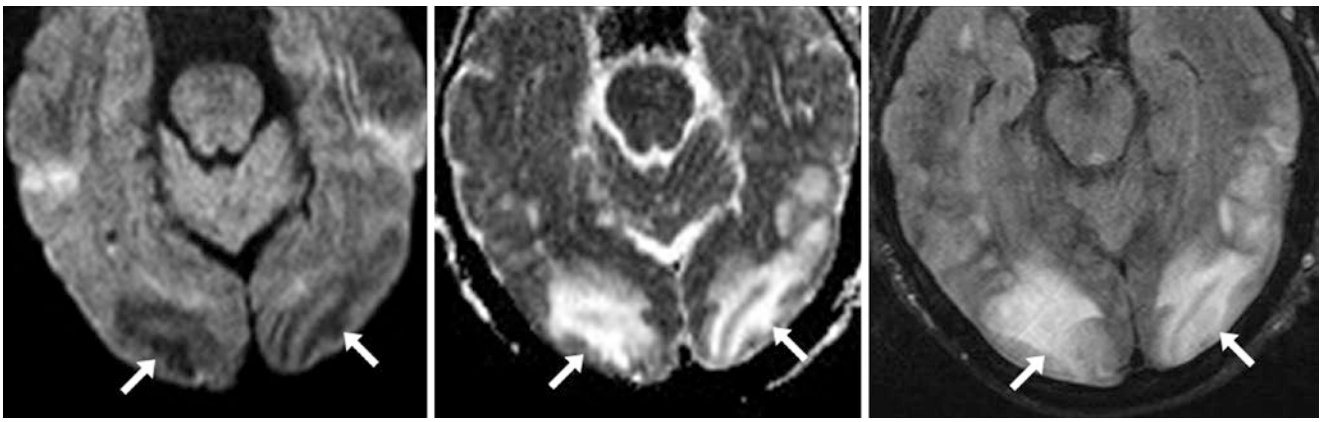

Fig. 22.85 A 1.5 T MRI in a 63-year-old with PRES from cyclosporine. Vasogenic edema (*arrows*) from PRES causes left parieto-occipital T2-washout on DWI (*left*), being bright on the ADC map (*middle*). There is moderate cortical-subcortical edema on FLAIR (*right*). Severe edema from PRES extends inwards to the ventricular margins

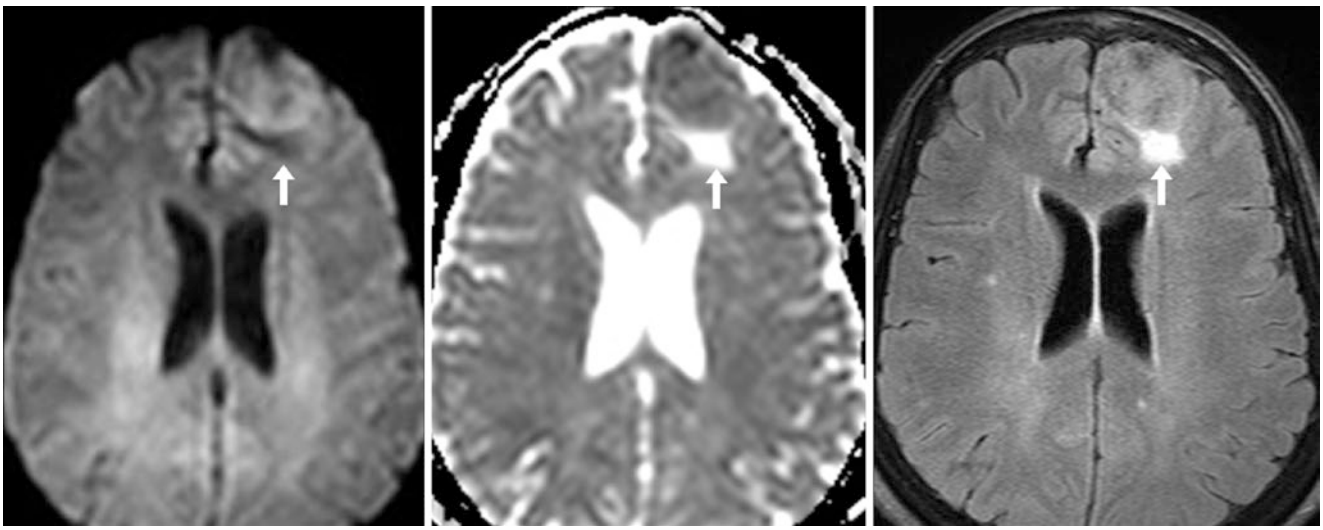

Fig. 22.86 A 64-year-old with a high-grade oligodendroglioma. A 3 T MRI showed avid contrast enhancement on T1WI (not shown), with dark signal from T2 washout on DWI (*left*), caused by peritumoral edema along the tumor's posterior border. There is corresponding extremely bright signal in that location on an ADC map (*middle*) and on FLAIR (*right*)

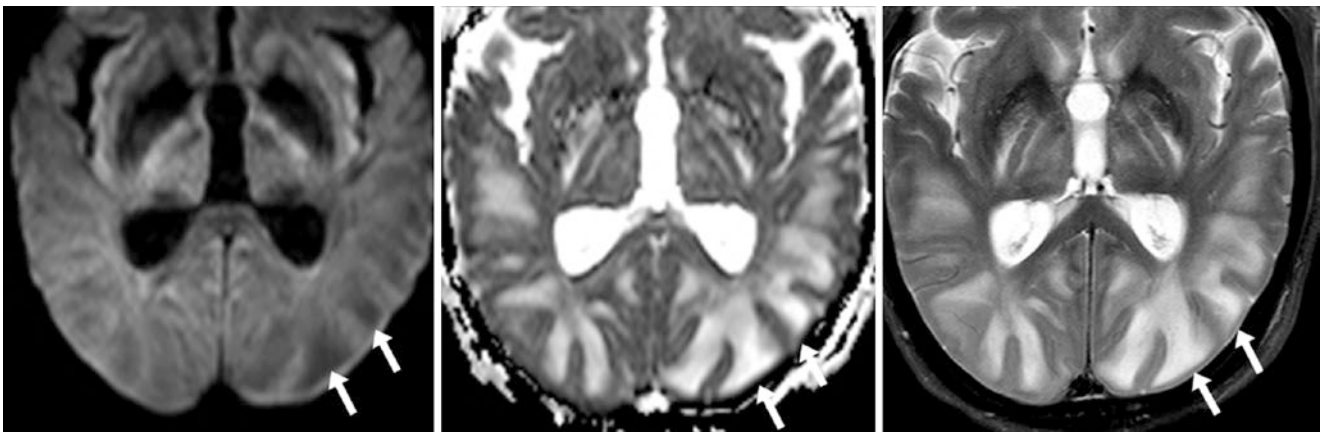

Fig. 22.87 A 3 T MRI in a 60-year-old with PRES from rituximab therapy. The bright vasogenic edema (*arrows*) from PRES caused T2 washout unilaterally within the left temporal and occipital lobes on DWI (*left*) and was bright on the ADC map (*middle*). There was severe subcortical edema on FLAIR (*right*), as the edema extended to the ventricular margins

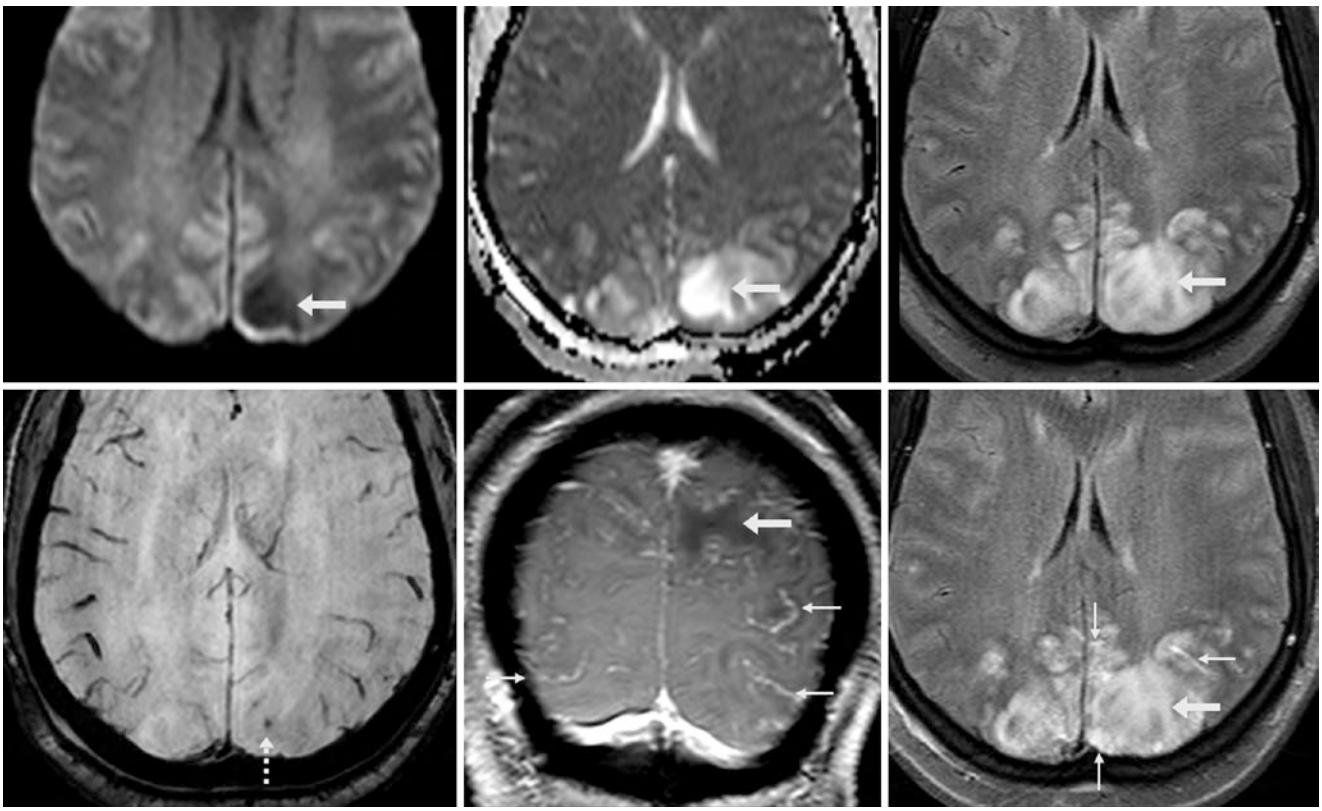

Fig. 22.88 In a 30-year-old with PRES from eclampsia, profound vasogenic edema (*arrows*) caused left occipital T2 washout on DWI (*top left*) and the ADC map (*top middle*), with a moderate degree of cortical-subcortical edema on FLAIR (*top right*). Susceptibility-weighted imaging (SWI) (*bottom left*) shows a microhemorrhage (*dotted arrow*), which is present in 50–70 % of PRES cases. Leptomeningeal enhancement (*thin arrows*) on postcontrast T1WI (*bottom middle*) or FLAIR (*bottom right*) is present in 30–40 %

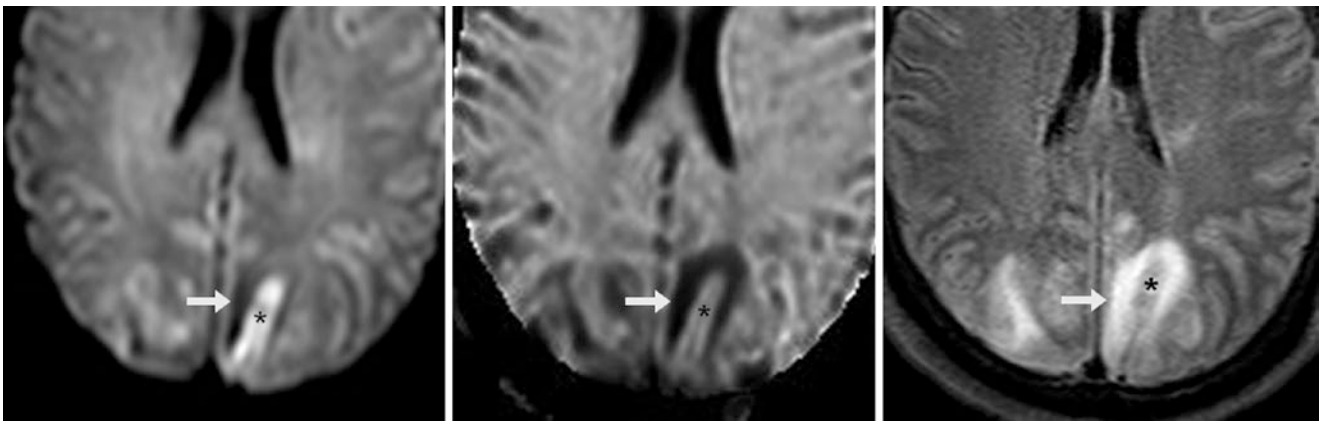

Fig. 22.89 A 55-year-old with PRES from gemcitabine. On DWI at 1.5 T (*left*), there is T2 washout from vasogenic edema (*arrows*) within the left occipital region, with gyriform bright signal centrally (*asterisk*) within the larger area of edema. An exponential DWI (*middle*) removes T2-bright edema, but isointense signal on DWI remains, suggesting that there is mild cytotoxic edema centrally within the larger region of vasogenic edema, which is demonstrated on FLAIR (*right*)

22.3.7 DWI: T2 Blackout Effect

"*T2 blackout*" occurs when dark T2 signal causes resultant dark signal on the DWI, which is dark on ADC maps and on T2WI and FLAIR. T2 blackout will typically appear dark on all other MRI sequences. It can be either abnormal (*e.g.*, hemorrhage) or a normal variant (*e.g.*, age-related basal ganglia calcification or iron). T2 blackout can occur from common, normal, highly concentrated deposits of *calcium* or metals such as *iron*, but it can also occur from deposits of uncommon materials (such as manganese in hepatic failure), albeit to a lesser degree (Figs. 22.90, 22.91, 22.92, 22.93, 22.94, 22.95, 22.96, and 22.97).

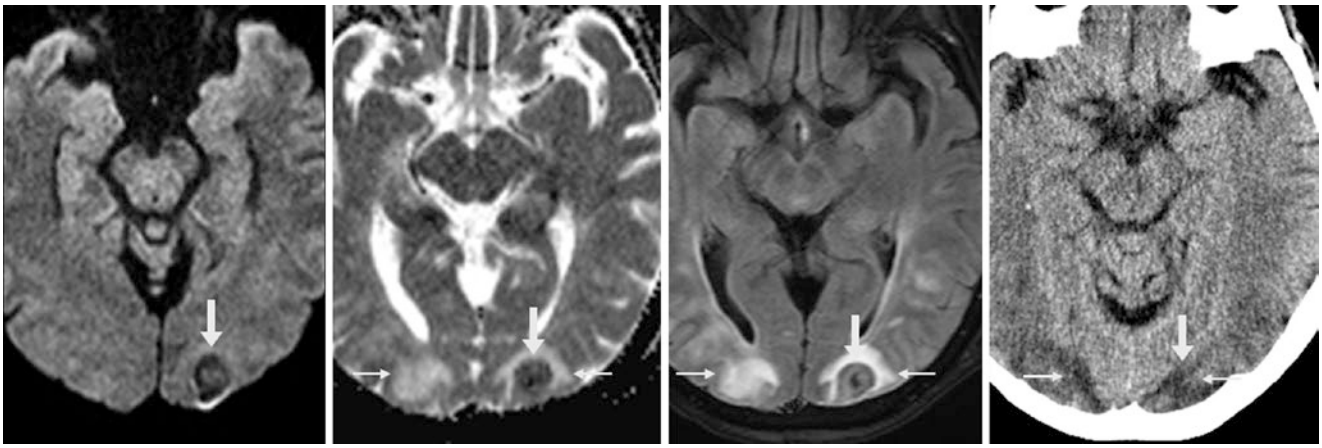

Fig. 22.90 A 1.5 T MRI in a 53-year-old that illustrates "T2 blackout" (*arrows*) from focal, acute parenchymal hemorrhage that resulted from PRES due to cyclosporine toxicity. The hemorrhage is dark on DWI (*left*). There was also T2-bright vasogenic edema (*thin arrows*) from PRES within the occipital regions on the ADC map (*left middle*) and on FLAIR (*right middle*). A CT scan from 2 days earlier (*right*) showed edema, without overt hemorrhage at that time

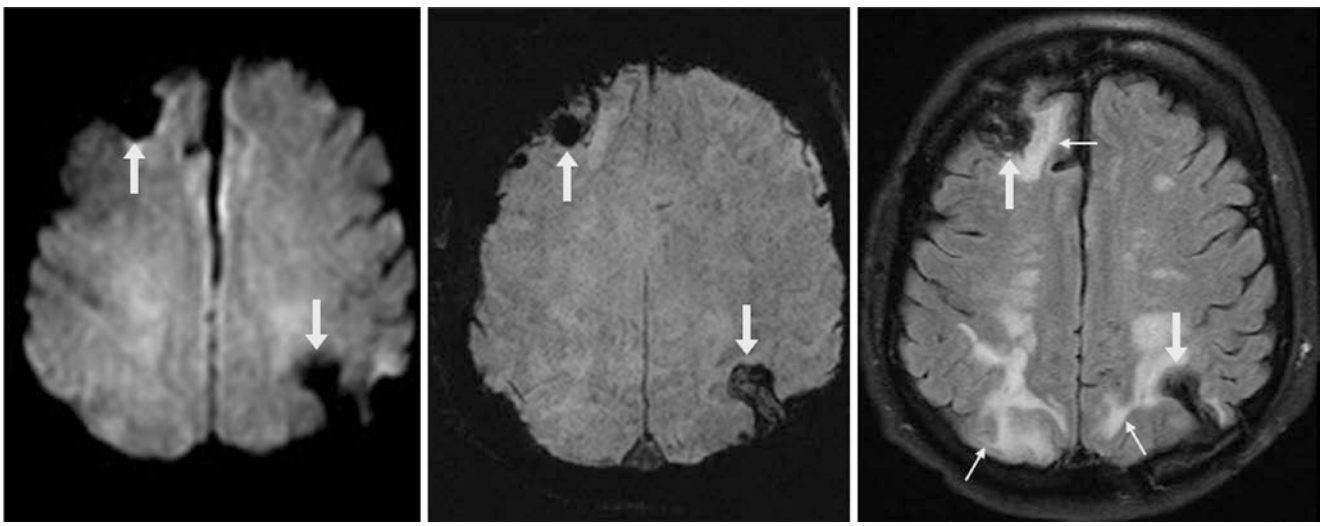

Fig. 22.91 A 3 T MRI in a 58-year-old shows two foci of T2 blackout (*arrows*) in acute parenchymal hemorrhages that arose from PRES. (The patient had received chemotherapy.) These foci are dark on DWI (*left*), SWI (*middle*), and FLAIR (*right*). There is "mild-moderate" cortical-subcortical vasogenic edema from PRES (*thin arrows*) on FLAIR

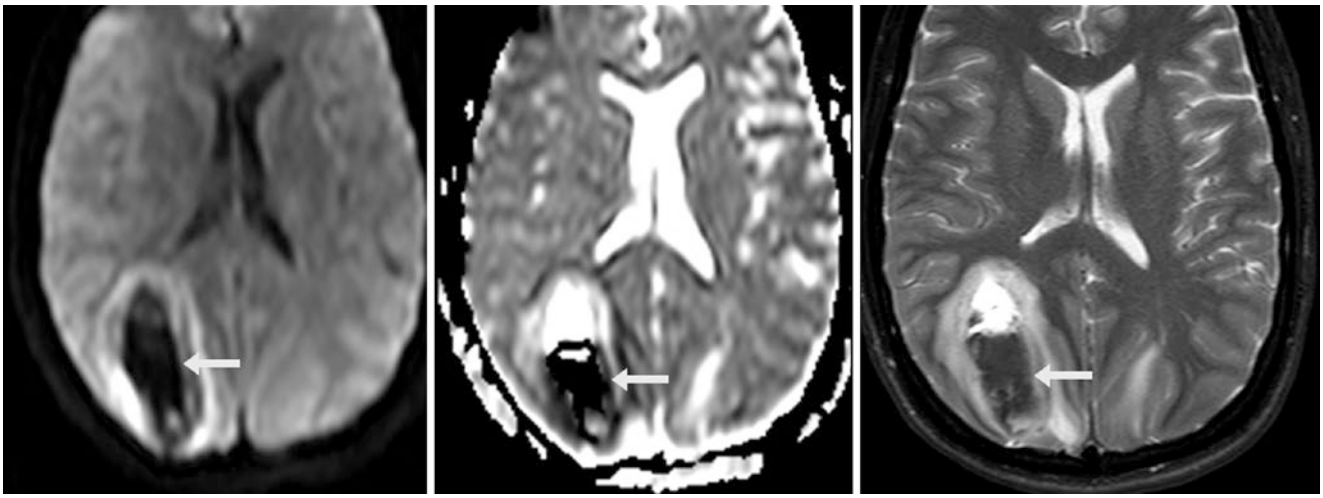

Fig. 22.92 A 1.5 T MRI in a 39-year-old shows a large occipital acute parenchymal hematoma, the result of PRES in a chemotherapy patient. T2 blackout (*arrows*) results from the blood being acute age, dark on DWI (*left*), ADC map (*middle*), and T2WI (*right*). There is "mild-moderate" bilateral cortical-subcortical edema on T2WI

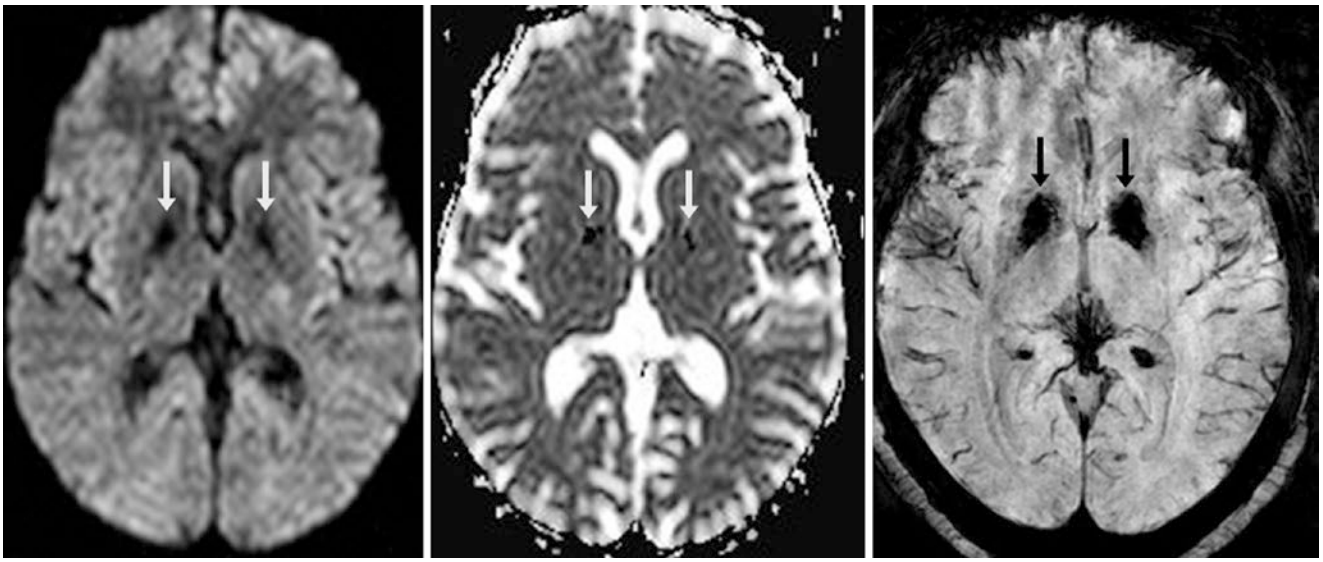

Fig. 22.93 A 3 T MRI DWI (*left*) in a 48-year-old has dark signal within the globi pallidi owing to T2 blackout, which also appears dark on an ADC map (*middle*) and SWI (*right*). SWI suggests that this susceptibility artifact is probably due to iron, or less likely, calcium. In this patient, the blackout most likely results from prominent iron deposition for age

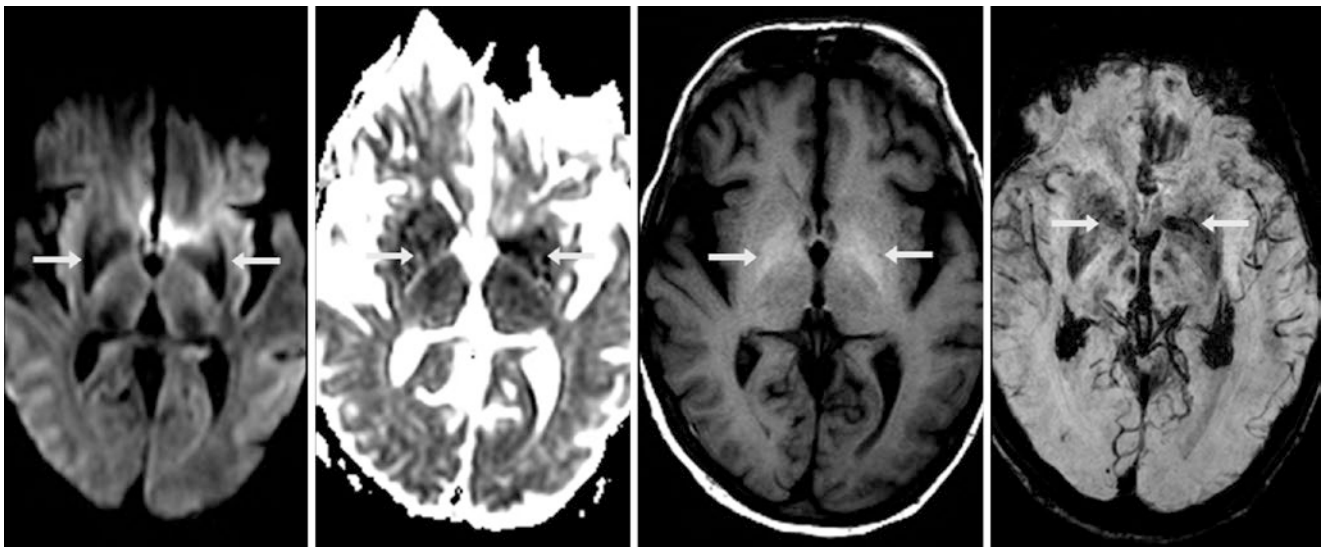

Fig. 22.94 A 56-year-old with chronic hepatic failure had moderately T2-dark signal (*arrows*) that caused a milder degree of T2 blackout within the lentiform nuclei (especially the globi pallidi) on a 1.5 T MRI with DWI (*left*) and ADC map (*left middle*). The blackout in this patient is likely due to pallidal manganese deposition, based on bright signal on T1WI (*right middle*), along with mildly dark signal on SWI (*right*), and a lack of hyperdensity on CT (not shown)

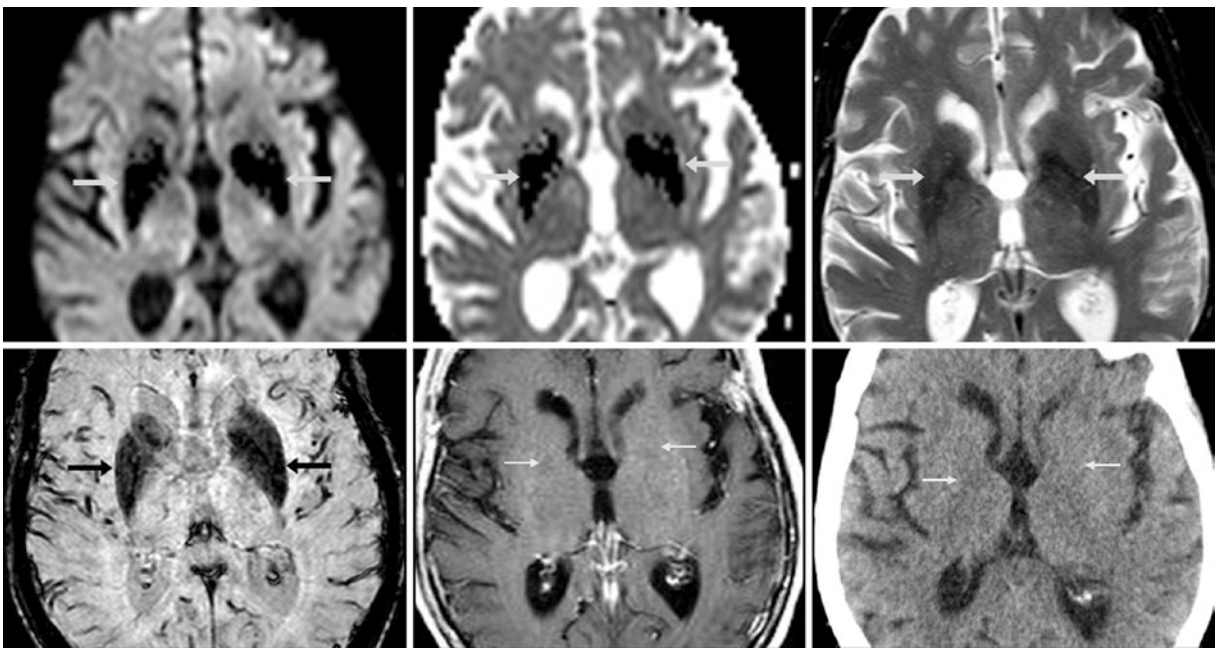

Fig. 22.95 A 79-year-old with a 1.5 T MRI that shows T2 blackout (*arrows*) within the lentiform nuclei on DWI (*top left*), ADC map (*top middle*), T2WI (*top right*), and SWI (*bottom left*). T1WI (*bottom middle*) was normal. This finding represents age-related iron deposition rather than calcium, given the lack of pallidal calcium (*thin arrows*) on NECT (*bottom right*)

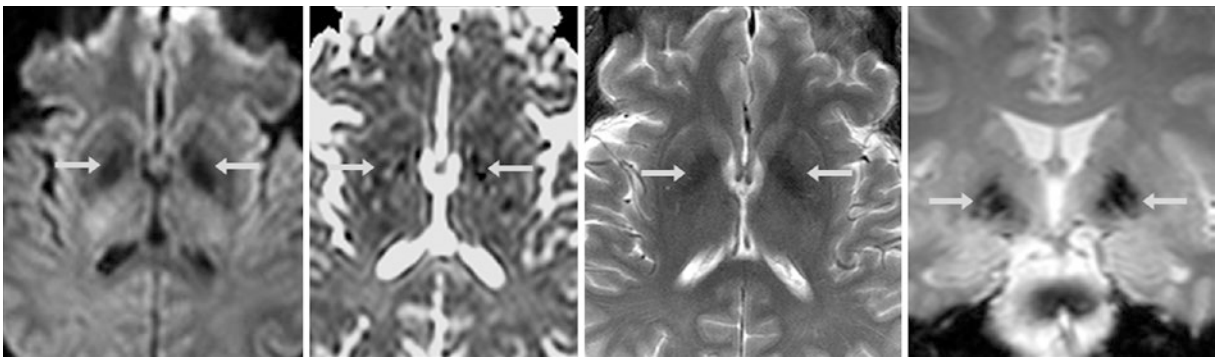

Fig. 22.96 A 3 T MRI from a 62-year-old demonstrates a mild degree of T2 blackout (*arrows*) on DWI (*left*), ADC map (*left middle*), T2WI (*right middle*), and coronal gradient-echo T2*WI (*right*). The blackout is due to iron deposition focally within the globi pallidi, which is normal for age. In this case, the putamen laterally is not dark on the MRI sequences

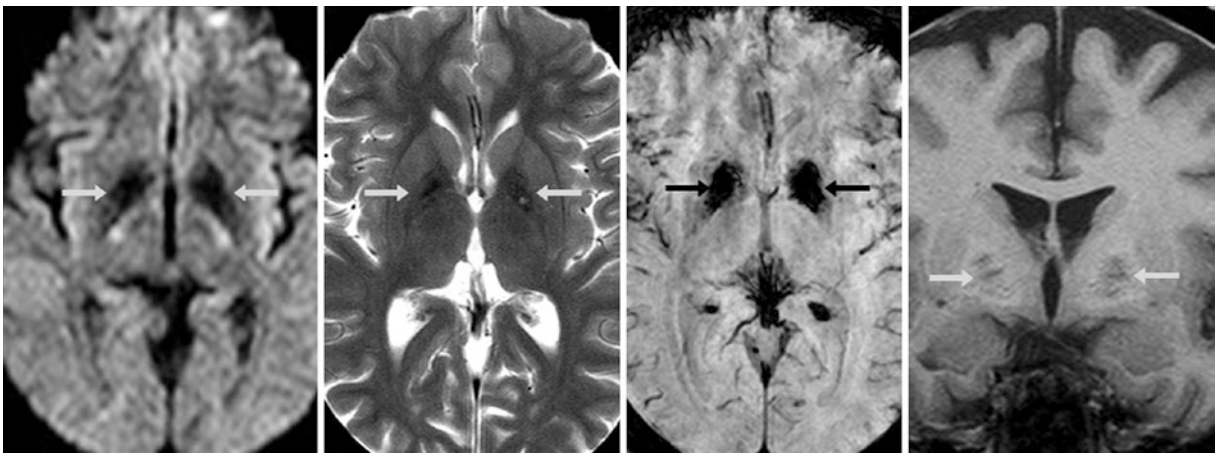

Fig. 22.97 A 1.5 T MRI in a 48-year-old shows T2 blackout (*arrows*). It is dark on DWI (*left*), T2WI (*left middle*), and SWI (*right middle*), from accelerated deposition of pallidal iron, which is disproportionate for age. The presence of iron rather than calcium is clear from its location, its dark signal on T1WI (*right*), and its profoundly dark appearance on SWI

22.3.8 DWI: Susceptibility Artifacts

Susceptibility artifacts ("blooming"), perhaps the most common artifacts on DWI, can occur from several sources: *metallic hardware* (such as from craniotomy, clips, or coils), *air-bone* or *gas-tissue interfaces* (such as above the ethmoid air cells or at the junction of calvarium with air), heavily concentrated *calcified lesions*, or *hemorrhage*. Such artifacts are related to the local paramagnetic effect of the substance, causing frequency and phase sampling errors. These errors are most pronounced in the phase-encoding direction and at the skull base, where there is more bone than brain (as well as adjacent gas within the paranasal sinuses) on axial images through that region. When it arises from the paranasal sinuses, the artifact can be alleviated to some degree by focusing on the anatomy. For example, regarding the brainstem and posterior fossa, such artifact can usually be minimized by acquisition in the AP direction, with a mildly oblique plane of axial acquisition, so the sphenoid sinus and brainstem are not on the same axial image. The artifact can also be alleviated by techniques such as multishot (rather than routine single-shot) echoplanar acquisition of DWI, line-scan DWI, or periodically rotated overlapping parallel lines with enhanced reconstruction (PROPELLER) imaging (Figs. 22.98, 22.99, 22.100, 22.101, 22.102, 22.103, 22.104, 22.105, 22.106 and 22.107).

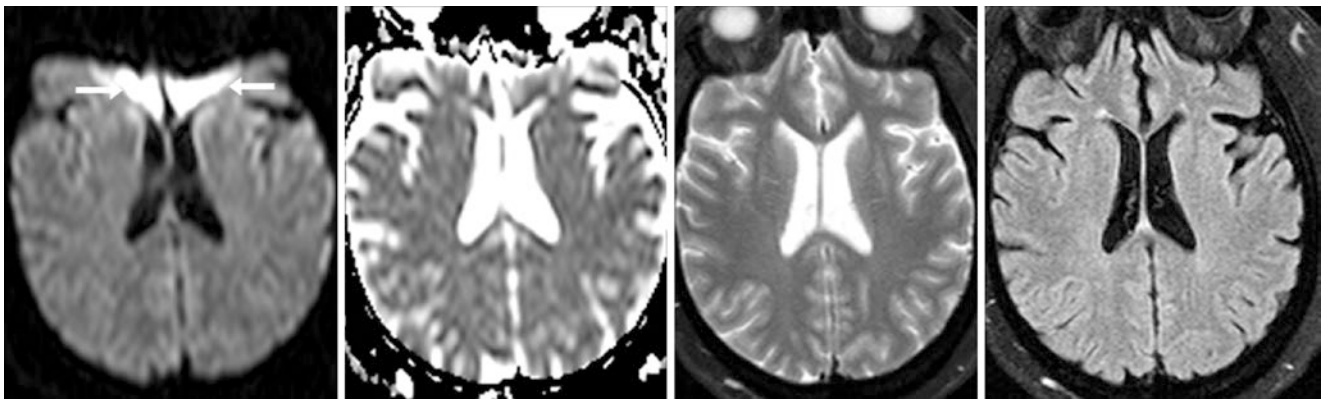

Fig. 22.98 A 1.5 T MRI in a 41-year-old is affected by dental amalgam, which causes "blooming" susceptibility artifact (*arrows*) on DWI (*left*). The orbitofrontal region is obscured and does not register signal on the ADC map (*left middle*). Axial T2WI and FLAIR (*right middle* and *right*) do not suffer such artifact because of their "multishot" acquisition

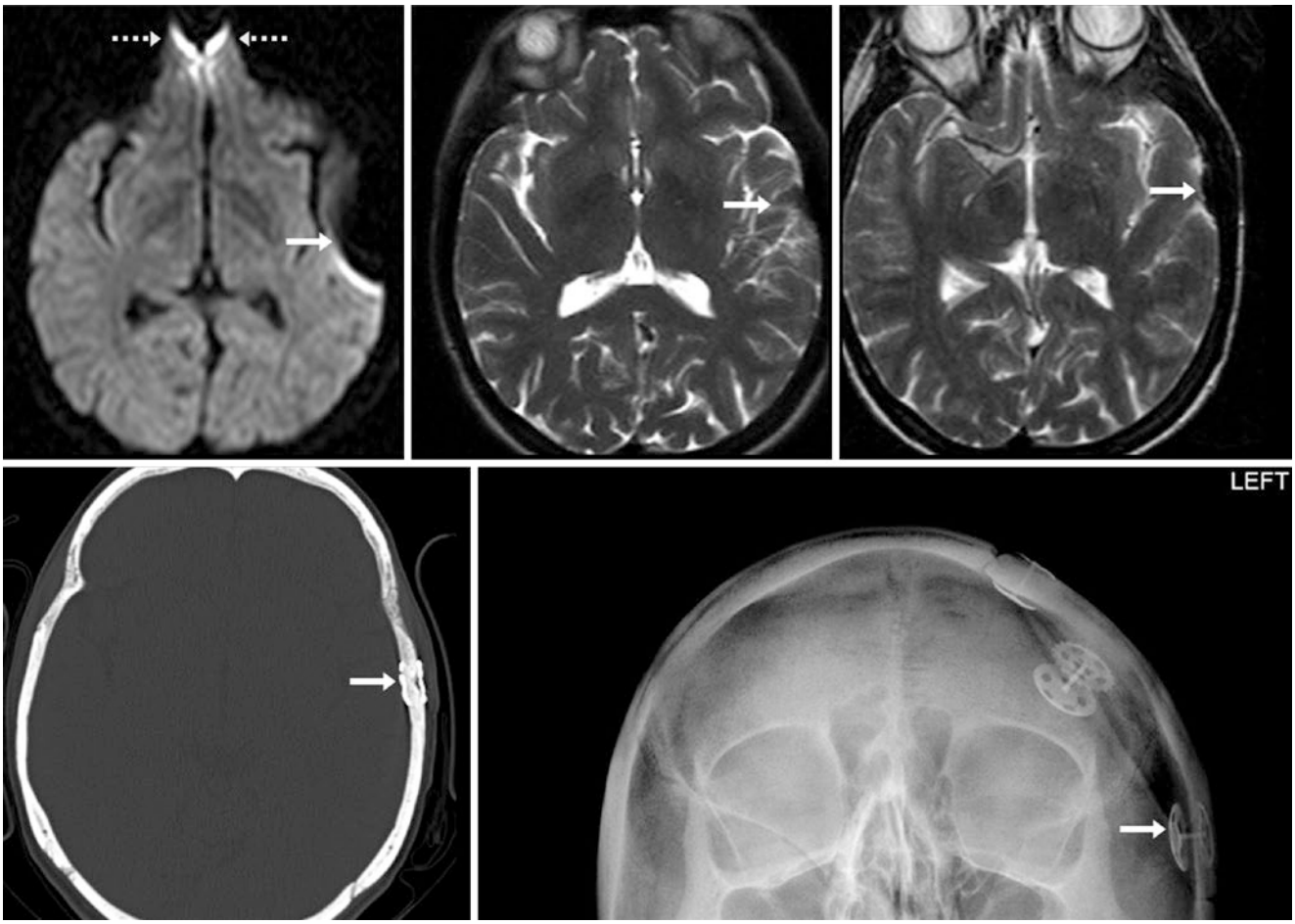

Fig. 22.99 A 35-year-old had craniotomy hardware that caused "blooming" susceptibility artifact (*arrows*) on a 1.5 T DWI MRI (*top left*). The artifact is present to a lesser degree on single-shot T2WI (*top middle*) and is barely notable on turbo spin-echo (TSE, turbo factor of 20) T2WI (*top right*); the artifact is far less on TSE T2WI because the multiple lines used to fill k-space inherently correct for such artifacts to some degree. Metallic hardware from the craniotomy is noted within the temporal bone on CT (*bottom left*) and plain film (*bottom right*). Another common source of susceptibility artifact is noted at the floor of the anterior cranial fossa (*dotted arrows*) owing to gas within the ethmoid air cells

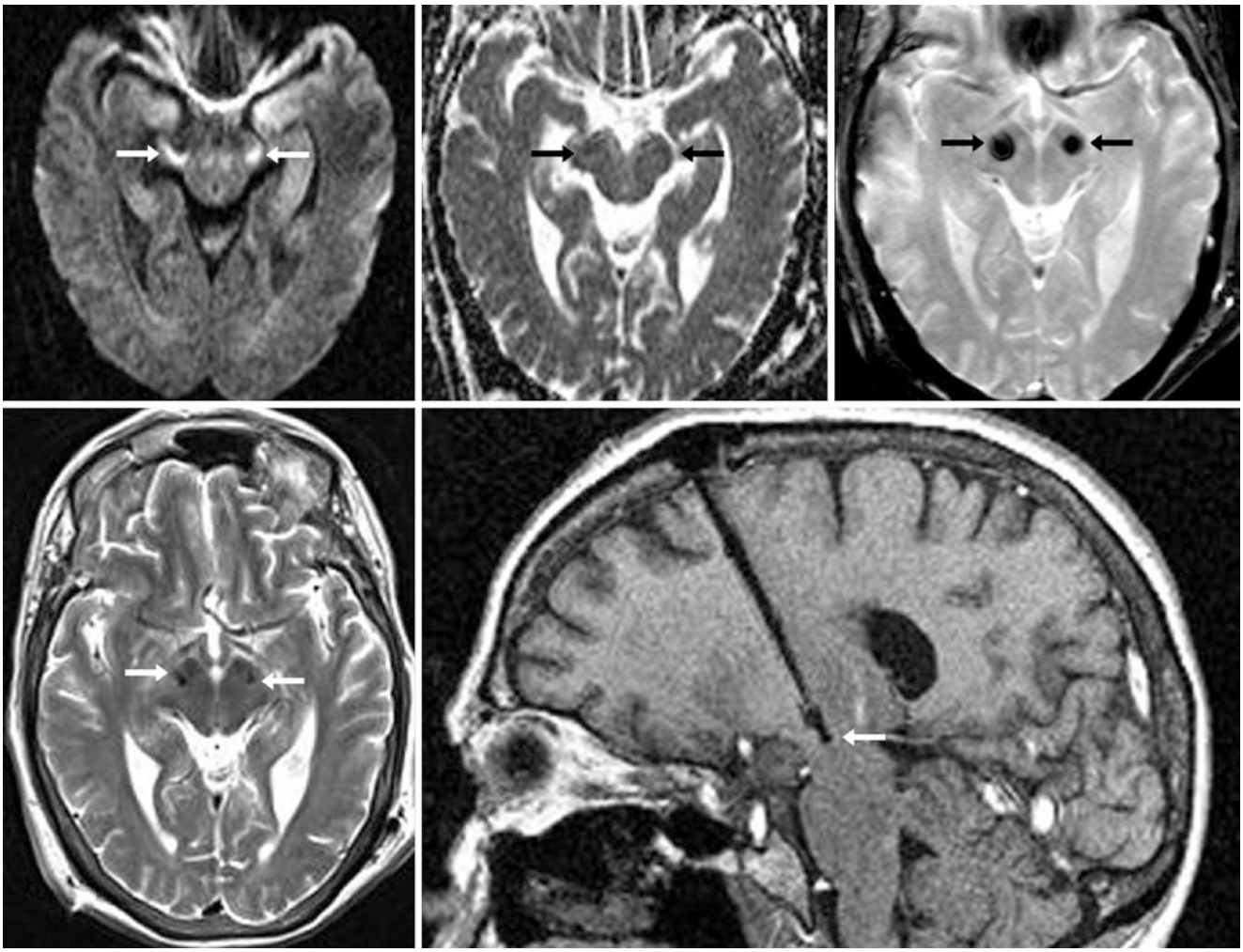

Fig. 22.100 A 65-year-old with "blooming" susceptibility artifacts (*arrows*) on 1.5 T DWI MRI (*top left*) from bilateral deep brain stimulators (for parkinsonism) with their tips in the tops of the cerebral peduncles or subthalamic regions. Though not easily visualized on the ADC map (*top middle*), these images are clearly demonstrated to represent susceptibility artifact on GE T2*WI (*top right*). The artifact is far less noticeable on TSE T2WI (*bottom left*). A sagittal T1WI (*bottom right*) depicts the left lead tip in the subthalamic region

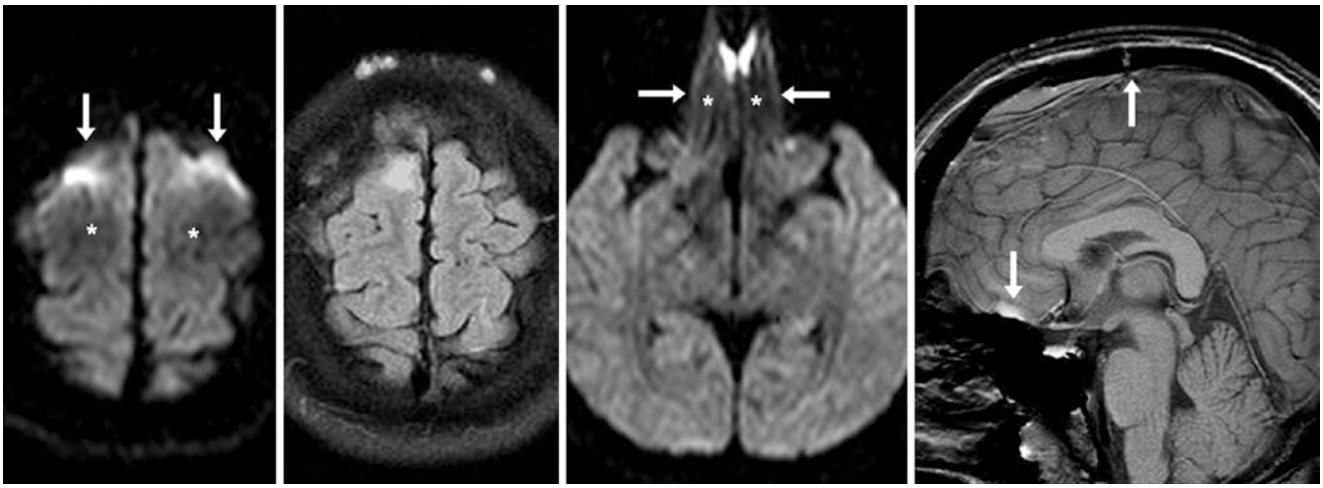

Fig. 22.101 A 24-year-old was postoperative for a meningioma resection near the vertex. A 1.5 T DWI MRI (*left*) showed alternating bright susceptibility artifact (*arrows*) with darker regions of signal dropout (*asterisk*), not present on FLAIR (*left middle*). There is also susceptibility artifact from the ethmoid air cells on axial DWI at the floor of the anterior cranial fossa (*right middle*), obscuring the orbitofrontal gyri. Sagittal T1WI (*right*) shows the sites of these artifacts

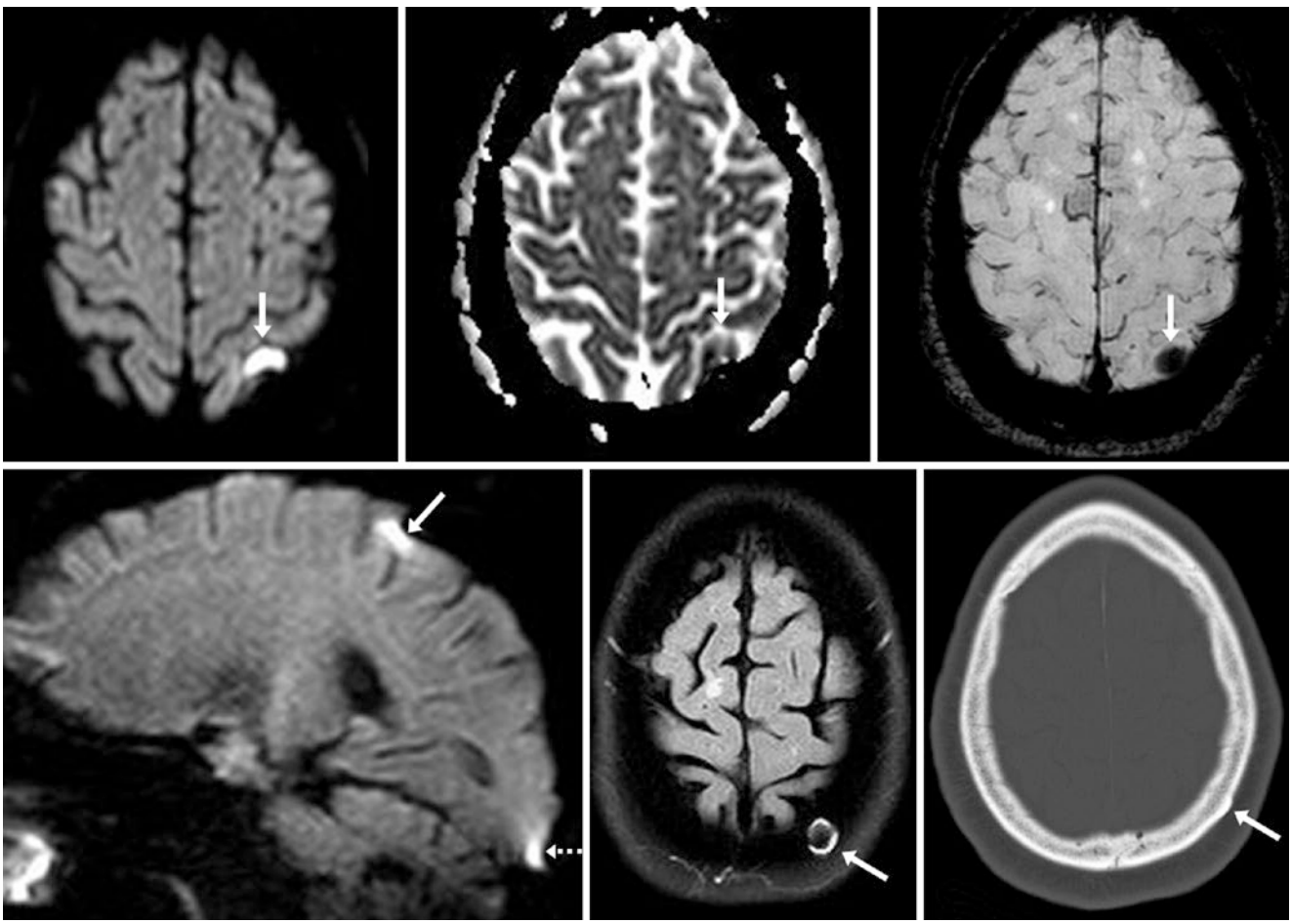

Fig. 22.102 A 62-year-old had focal bright signal (*arrows*) overlying the left postcentral gyrus on a 1.5 T DWI (*top left*), being dark on an ADC map (*top middle*). This image simulated a small cortical infarct, but on SWI (*top right*), it clearly represents susceptibility artifact. This was also noted on sagittal DWI (*bottom left*), with a second focus of similar artifact in the left occipital lobe (*dashed arrow*). FLAIR (*bottom middle*) depicts the origin of the artifact. On NECT (*bottom right*), it can be related to focal calvarial thickening or simply to the air-bone interface

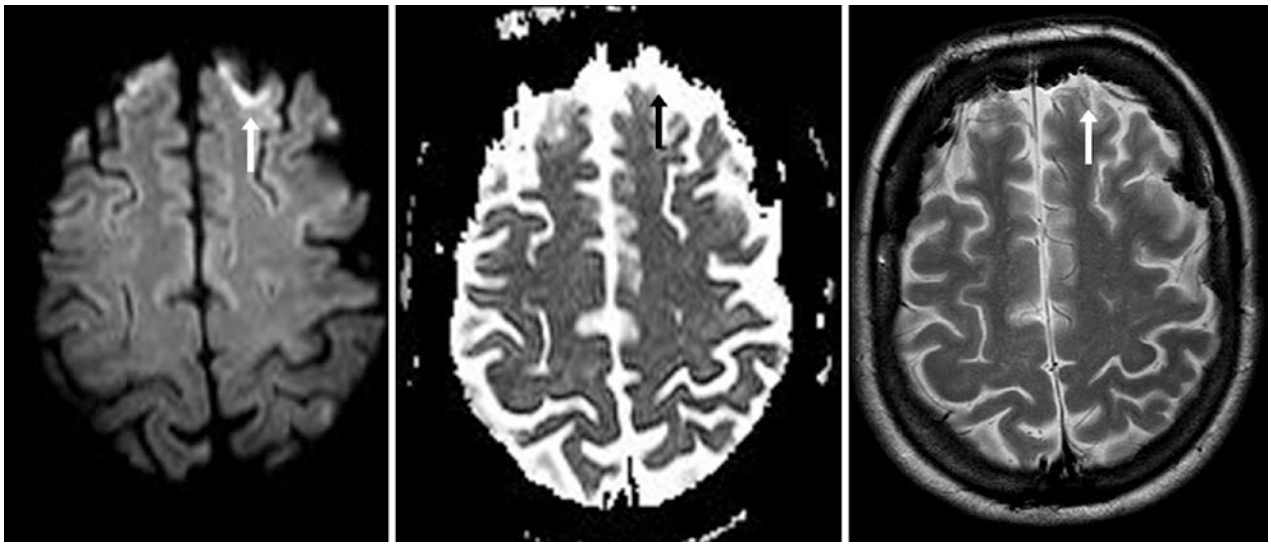

Fig. 22.103 A 3 T DWI MRI (*left*) in a 53-year-old has focal bright susceptibility artifact (*arrows*), which is only minimally visible on an ADC map (*middle*). On T2WI (*right*), the air-bone interface artifact is not noted, as TSE T2WI is one of the sequences most resistant to susceptibility artifacts because of the multiple echoes used to form the image

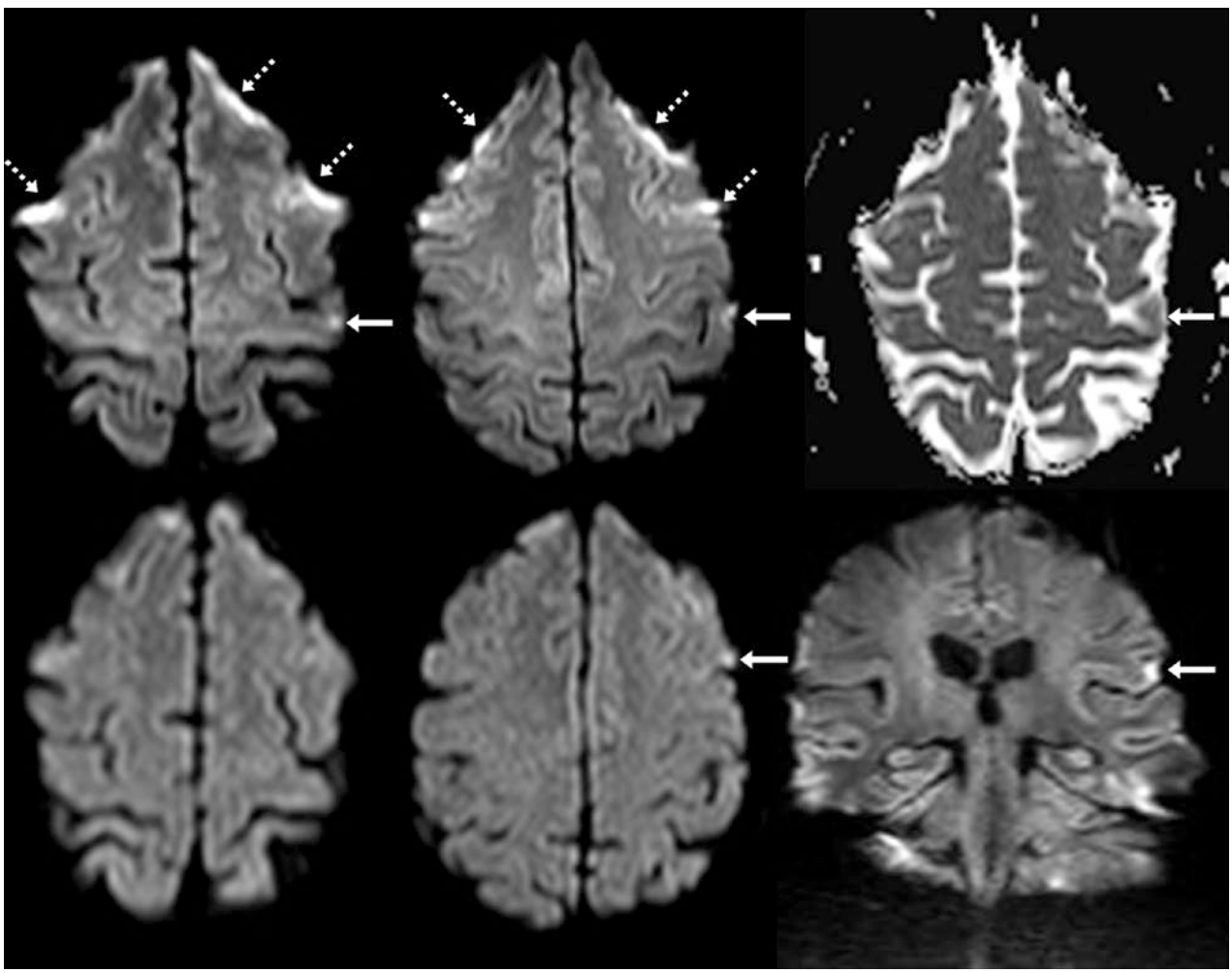

Fig. 22.104 A 53-year-old with alcohol intoxication had two suspected punctate abnormalities (*arrows*) on 4 mm–thickness DWI at 1.5 T, located within the left precentral gyrus (*top left*) and postcentral gyrus (*top middle*), simulating cortical infarcts. The ADC maps appeared normal (*top right*). The DWIs were repeated at 5 mm thickness with slight reangling (*bottom left* and *middle*), and were called negative. Note other foci of susceptibility artifacts along the frontal convexities (*dashed arrows*). Coronal DWI (*bottom right*) confirmed that the suspected foci were due to susceptibility artifacts

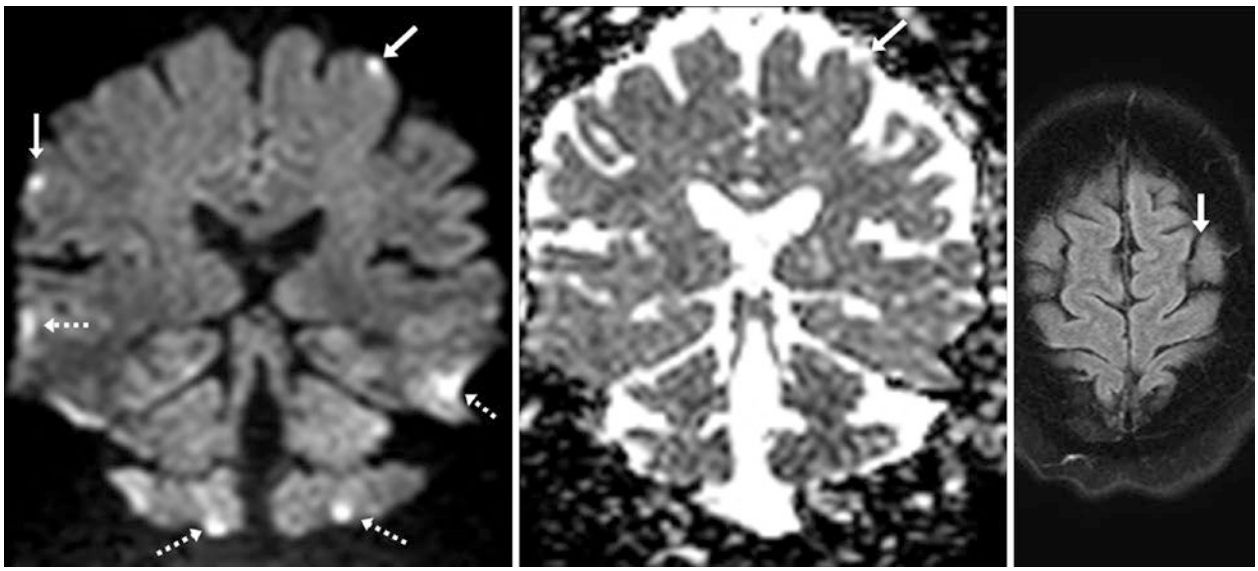

Fig. 22.105 In a 60-year-old with tinnitus, two punctate abnormalities (*arrows*) on coronal DWI at 1.5 T (*left*) simulated cortical infarcts. These were deemed to be due to susceptibility effects, as the ADC maps appeared normal (*middle*). Note other foci of susceptibility artifacts along the temporal and cerebellar convexities (*dashed arrows*). A normal axial FLAIR image through the left frontal focus (*right*) confirmed that the foci were susceptibility artifacts

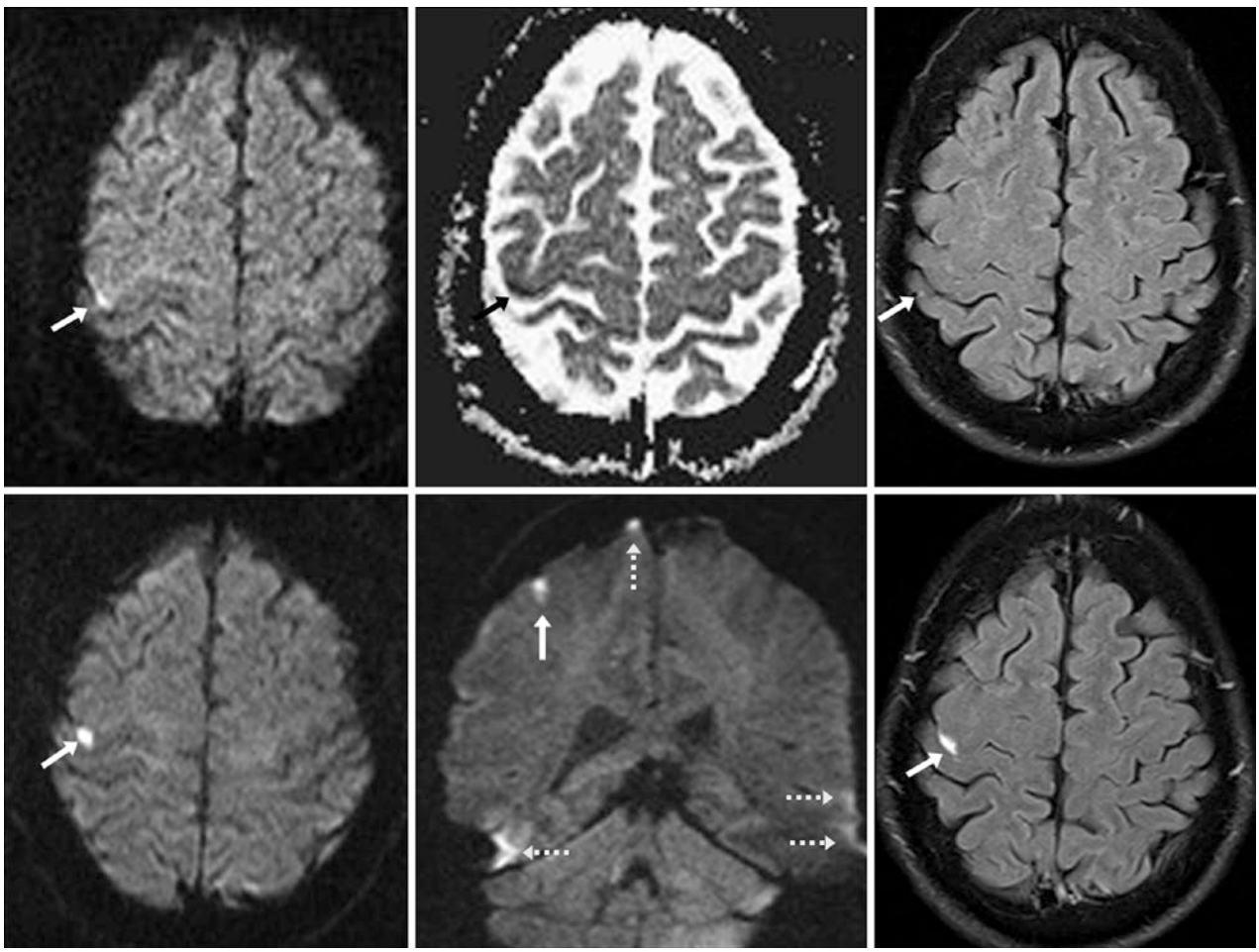

Fig. 22.106 Comparison case of focal cortical infarct. A 44-year-old with acute speech difficulties underwent a 3 T MRI, which showed focal bright signal in the right precentral gyrus (*arrows*) on DWI MRI (*top left*), but it was not noticed on an ADC map (*top middle*) or on FLAIR (*top right*). It was mistakenly thought to represent susceptibility artifact. A repeat MRI the next day with slightly different positioning clearly depicted the cortical infarct on axial DWI (*bottom left*) and coronal DWI (*bottom middle*), with areas of true susceptibility effect denoted (*dotted arrows*). Repeat FLAIR images showed the infarct (*bottom right*), as edema on FLAIR becomes visible more than 8 h after symptom onset

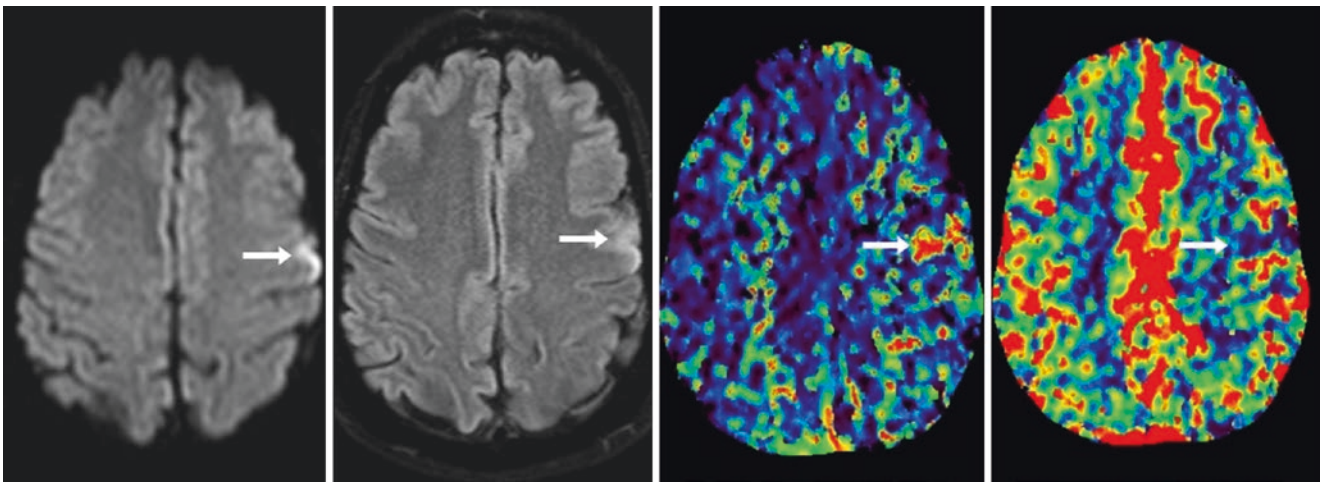

Fig. 22.107 Comparison case of focal cortical infarct. In a 54-year-old with acute aphasia, a 1.5 T MRI DWI (*left*) showed focal bright cortical signal (*arrows*) that was not visualized on an ADC map (not shown) but was visible on FLAIR (*left middle*), and so was interpreted as positive. A CT perfusion exam performed earlier the same day depicted focal increased mean transit time abnormality in that location (*right middle*), with low cerebral blood flow (*right*). There was a normal cerebral blood volume map (*not shown*), which may occur with early infarcts less than 1.5 cm in size

22.3.9 DWI: Phase Ghosting Artifact

DWI phase ghosting artifact (also called "N/2 artifact" or "N/2 ghost") occurs in echoplanar diffusion imaging owing to the acquisition technique, which is based on the reversal of echoes by a gradient pulse; the reversal process may introduce phase errors into the alternating lines of k-space. N/2 artifact arises from differences (phase errors) between the alternating even and odd lines in k-space, and usually relates to hardware deficiencies (such as field inhomogeneity, imperfect shimming, or eddy currents). Such artifact is exacerbated by gradient on-and-off switching and causes the DWI and the ADC map to have a shift of half of the field of view in the phase-encoding direction, usually manifest as an anterior-posterior or transverse shift of a portion of the image, depending on acquisition. This artifact often requires a service visit to fix it, but it is also relieved by greater field homogeneity, reduction of eddy currents, and potentially the use of higher *b* values (Figs. 22.108 and 22.109).

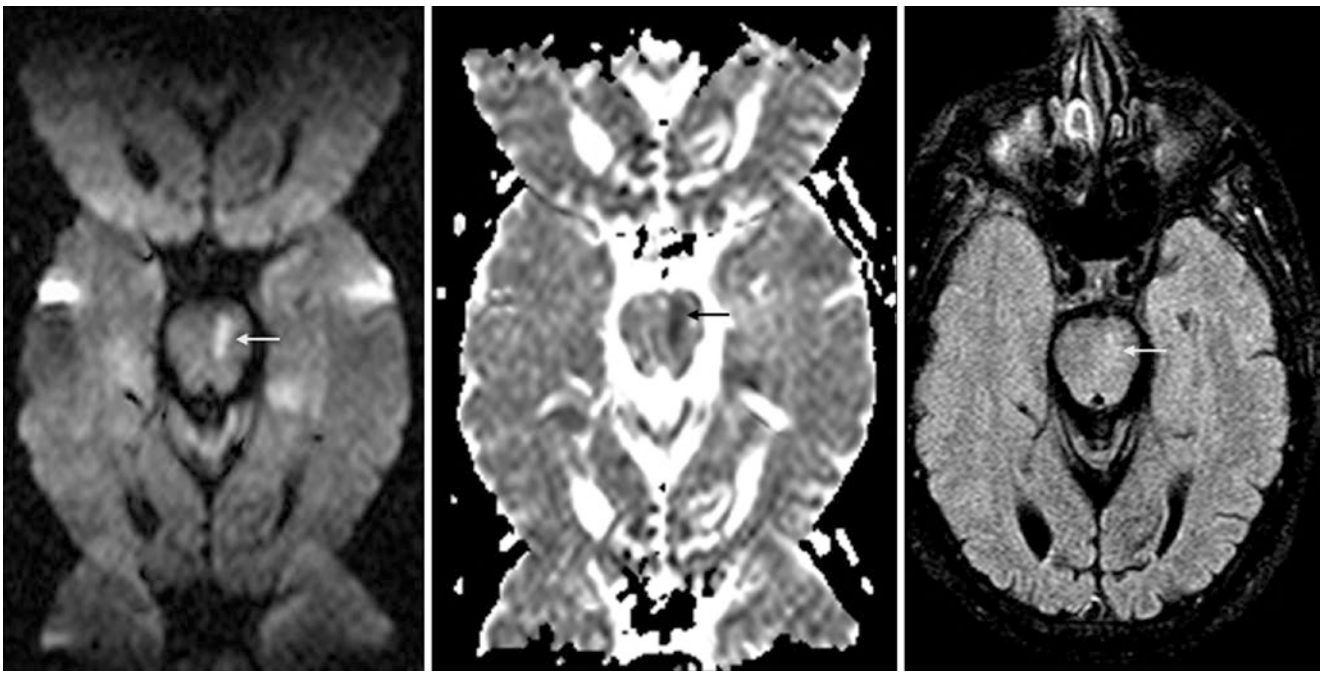

Fig. 22.108 In a 3 T MRI of a 71-year-old, the axial DWI (*left*) and ADC map (*middle*) are affected by N/2 ghost artifact. This is represented as a shift of one half of the field of view in the anterior-posterior (AP) direction. This shift is not present on FLAIR (*right*), which does not undergo the same degree of gradient switching, as it is not an echoplanar sequence. There is a small lacunar infarct (*thin arrows*) within the brainstem, which is acute, as there is only faint hyperintensity on FLAIR

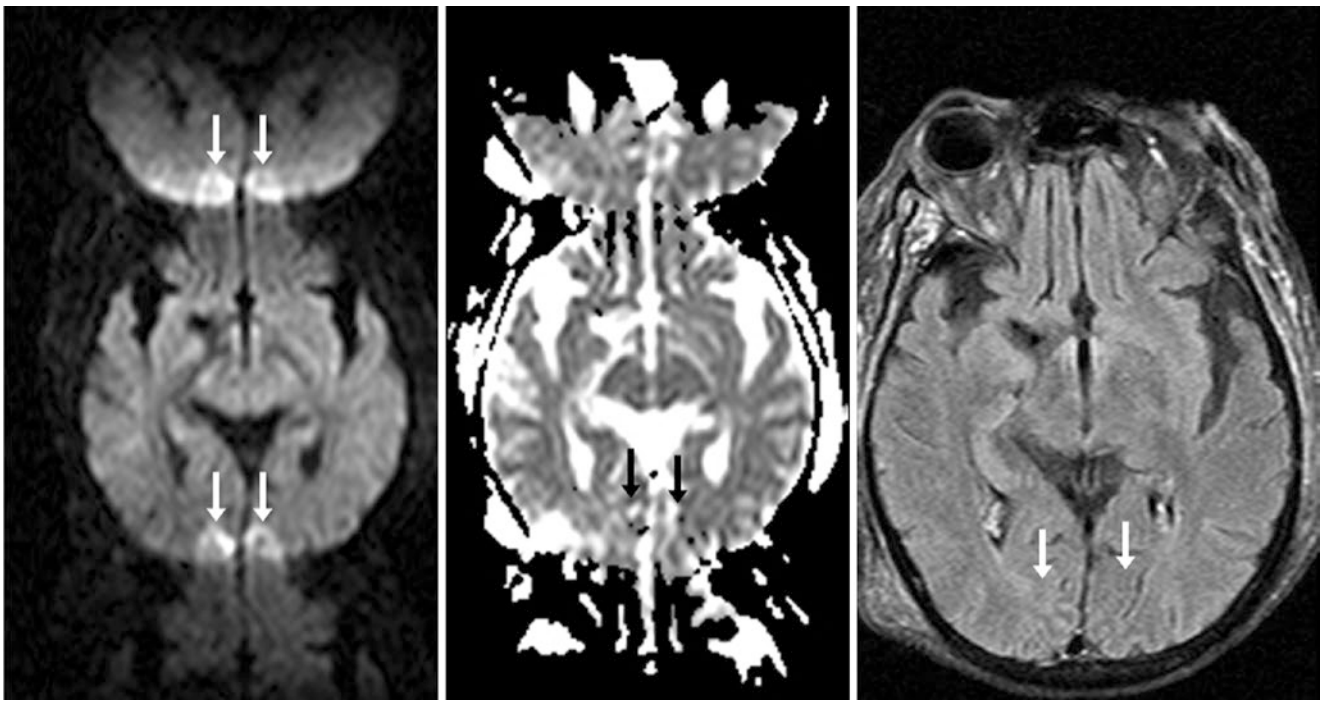

Fig. 22.109 In a 69-year-old with a 1.5 T MRI, the axial DWI (*left*) and ADC map (*middle*) are affected by phase ghosting artifact (N/2 artifact). This artifact is represented as a shift of one half of the field of view in the AP direction, which simulates bilateral occipital infarcts or cytotoxic edema on DWI (*arrows*). This artifact is not present on FLAIR (*right*)

22.3.10 DWI: Motion Artifact

On DWI, *motion-related artifacts* are the most common cause of serious image degradation. the motion can be head rotating ("shaking"), which can be alleviated somewhat by available motion correction techniques such as parallel lines with enhanced reconstruction (PROPELLER) imaging, but this increases the acquisition time. Craniocaudal ("z-axis") motion is more difficult to correct and necessitates advance techniques. Severe motion is most often recognizable, but milder degrees of motion may be overlooked and may simulate any of numerous types of pathology. To identify whether motion is the cause of a suspected pseudoabnormality, it helps to have stalwart performing technologists who remark and note in the record the degree of patient motion (Figs. 22.110, 22.111 and 22.112).

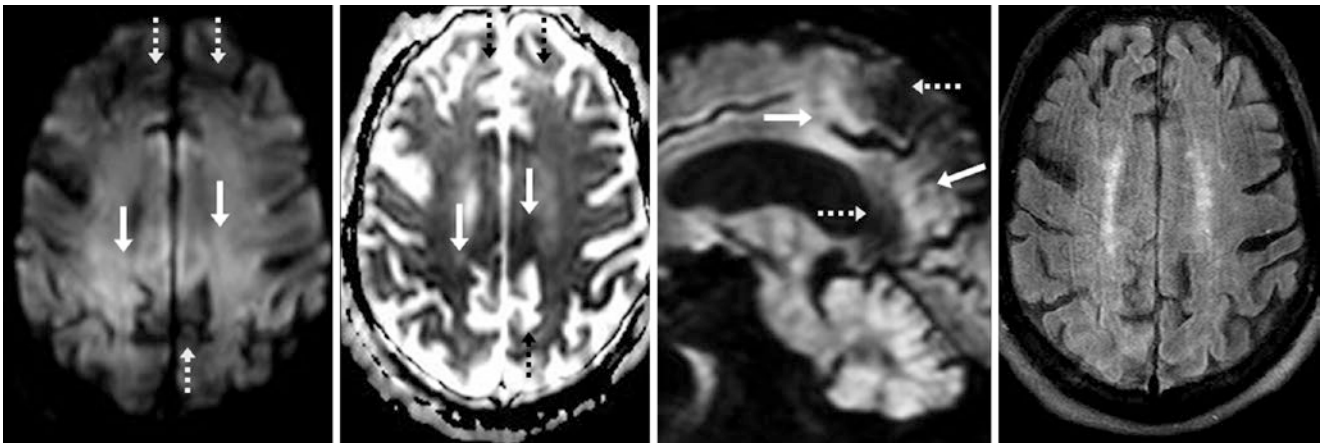

Fig. 22.110 A 3 T MRI from an 80-year-old shows motion artifact causing patchy regions of both bright signal (*arrows*) and dark signal (*dashed arrows*) on DWI (*left*), with the reverse appearance on an ADC map (*left middle*). A sagittal DWI (*right middle*) was obtained, which has a similar appearance. On FLAIR (*right*), typical curvilinear blurring artifacts from motion are more noticeable. In such situations with motion on DWI, it can be difficult to detect a small infarct

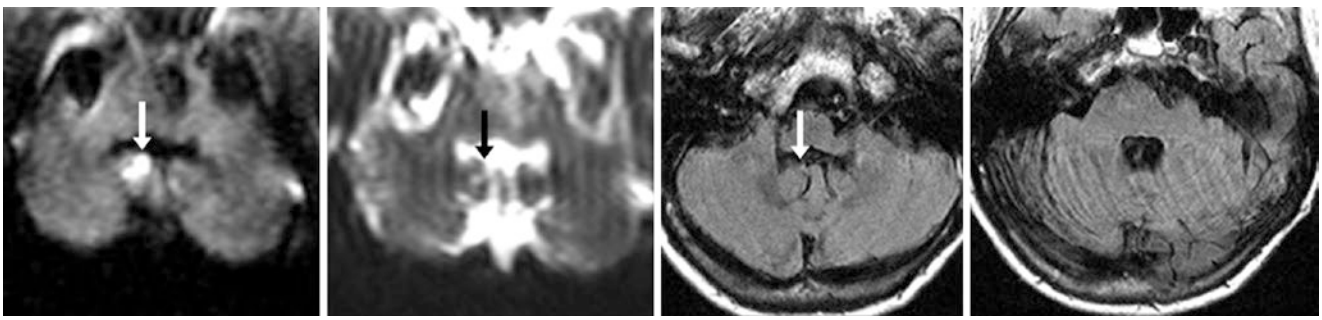

Fig. 22.111 In an 81-year-old with 1.5 T MRI, motion causes focal hyperintensity (*arrows*) in the right hemicerebellum on DWI (*left*). DWI ($b=0$) shows blurred curvilinear artifacts from motion (*left middle*), with varying degrees of motion on FLAIR (*right middle*, *right*), but no abnormality, confirming artifact from CSF flow, venous pulsation, or head motion

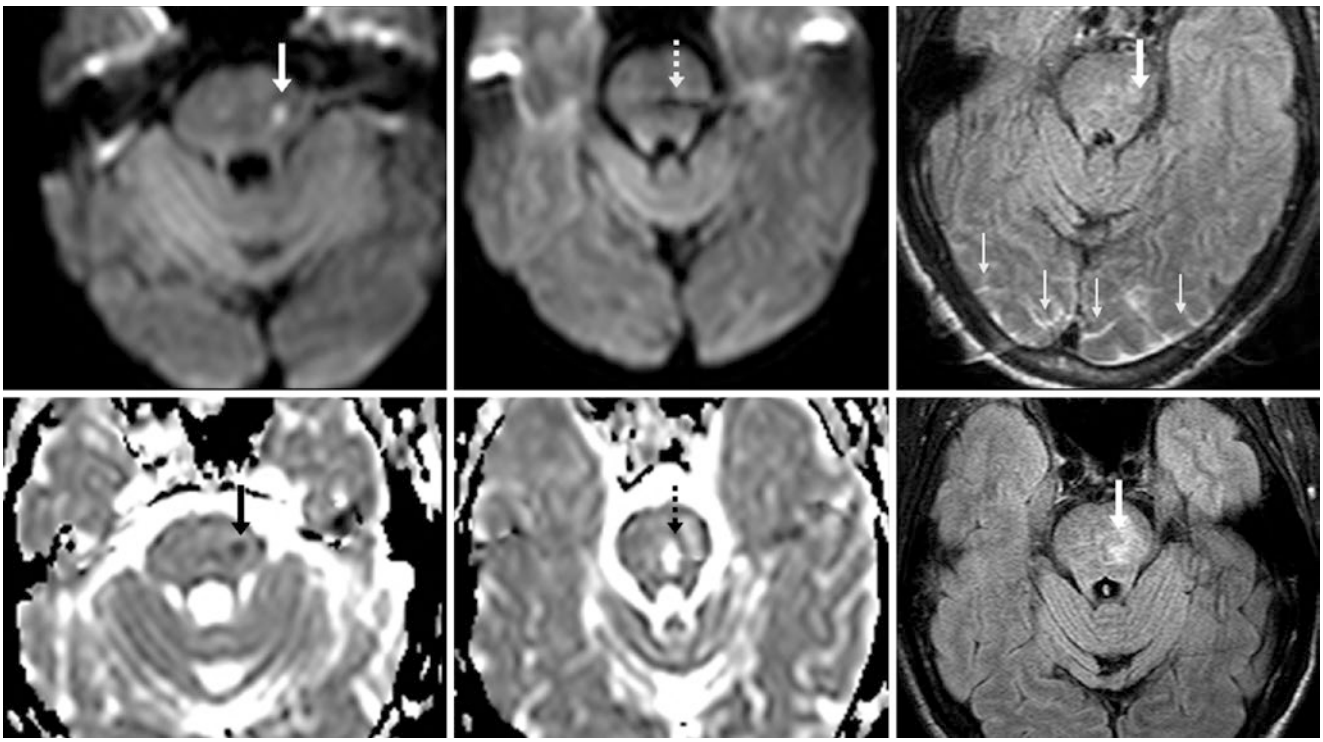

Fig. 22.112 Comparison case of lacunar infarct combined with motion artifact. A 71-year-old with a 3 T MRI had focal bright signal within the left hemipons (*arrows*) on DWI (*top left*); the image was dark on DWI at a level just above that (*top middle*). Motion artifact with resultant sulcal hyperintensity (*thin arrows*) was seen on FLAIR (*top right*), simulating meningeal disease. ADC maps (*bottom left* and *middle*) also showed perplexing signal. FLAIR images 2 weeks later confirmed a pontine abnormality (*bottom right*), whereas the prior occipital sulcal signal was artifactual

22.3.11 DWI: Unfolding Artifacts from Parallel Acquisition

DWI is routinely performed using a single-shot, echoplanar technique, which involves a relatively short amount of time and a good signal-to-noise ratio. Adequate images of the entire brain are often obtained in less than 1 min. Additionally, parallel imaging techniques can be utilized to minimize geometrical distortions from susceptibility artifacts, particularly at higher field strengths. However, "*unfolding artifacts*" may result from parallel imaging if care is not taken to optimize the sensitivity profiles for the radiofrequency coils. Such artifacts can be removed by applying a saturation band across the causative region of susceptibility artifact, but doing so may lead to stray signal elsewhere in the brain (most commonly the globes, aerated sinuses or mastoid air cells at the skull base, hardware, etc.). The use of a higher *b* value also can alleviate the artifact (Figs. 22.113 and 22.114).

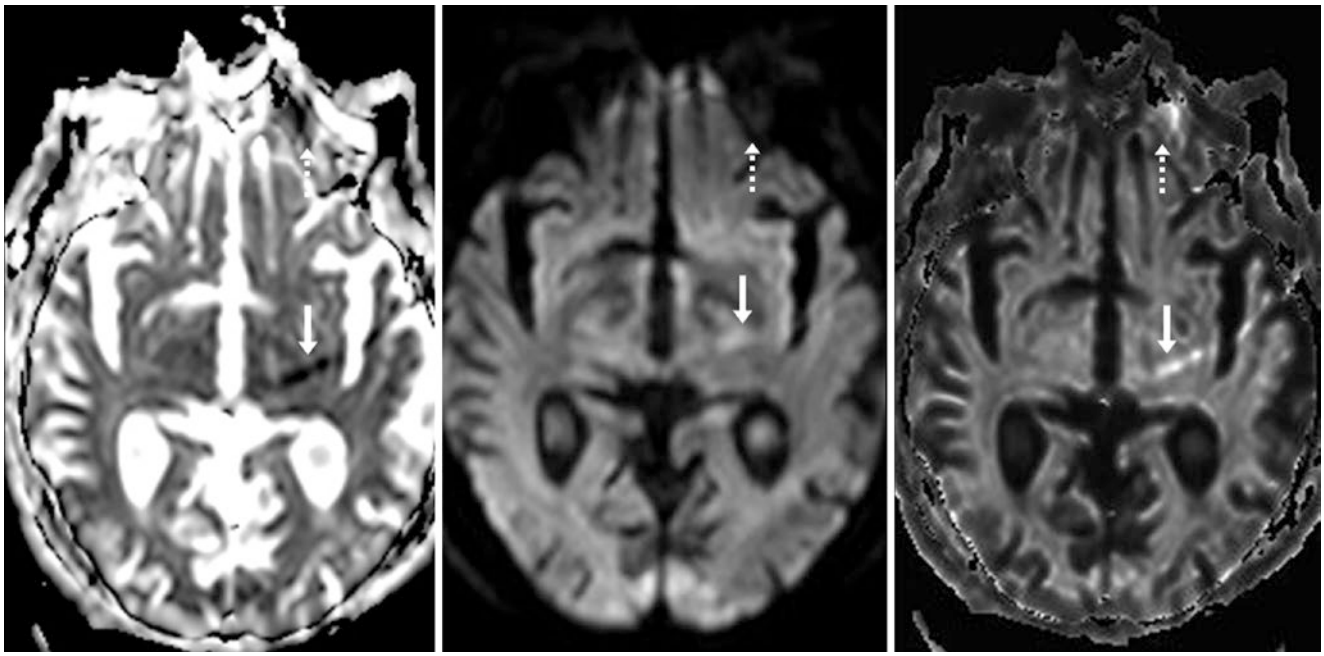

Fig. 22.113 80-year-old with a negative 3 T MRI demonstrating a left thalamic unfolding artifact (*arrows*) on an ADC map (*left*) and DWI (*middle*), worsened on "exponential" DWI (*right*), likely from frontal sinus or scalp-related susceptibility artifact (*dotted arrows*). The left thalamus appears normal on FLAIR and T2WI (*not shown*)

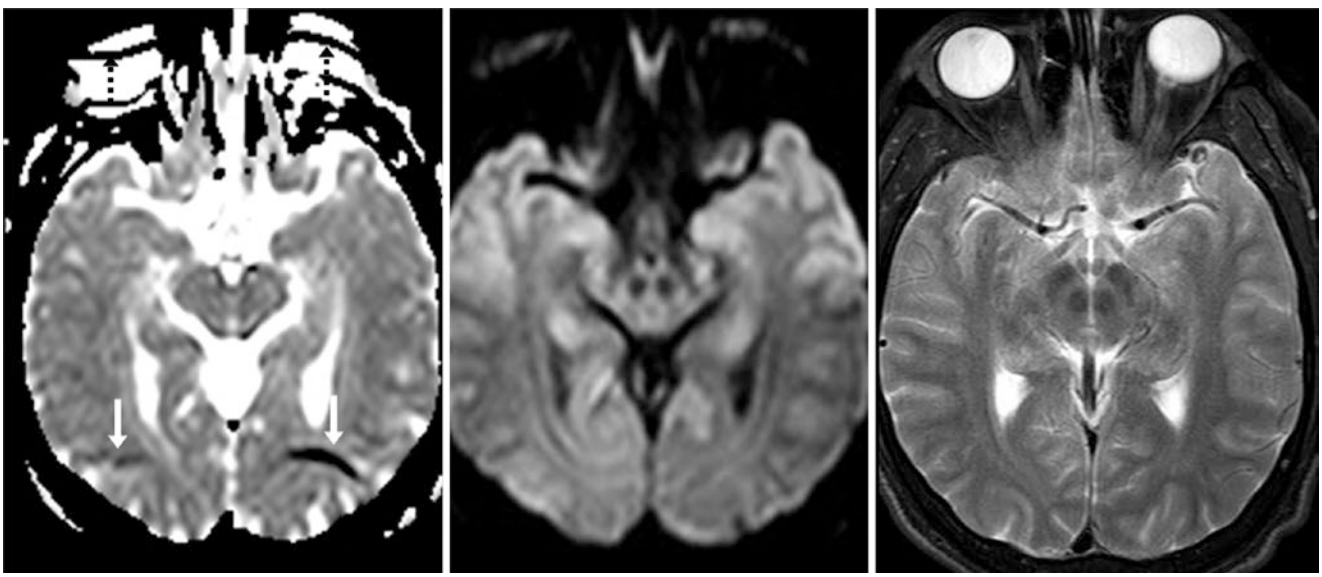

Fig. 22.114 In a 30-year-old normal patient, 3 T MRI shows parieto-occipital unfolding artifacts (*white arrows*) on the ADC map (*left*), likely from the globes (*black dotted arrows*), as the phase direction is anterior to posterior on most routine DWI acquisitions. However, that region appears normal on DWI (*middle*) and on T2WI (*right*)

22.3.12 DWI: Mechanical Vibration and Eddy Current Artifacts

Eddy currents are electrical currents that are induced in a conductor (such as tissue, wires, coils, etc.) by a changing magnetic field. With regards to MRI, they represent magnetic fields that are residua of fast gradient switching. In echoplanar DWI MRI, this occurs following gradients being rapidly switched on and off and is often most profound during routine echoplanar single-shot DWI, or on single-shot diffusion tensor imaging (DTI). Eddy currents cause image distortion by interfering with both the echoplanar imaging gradients and the motion-probing gradients. Stronger eddy currents can cause displacement of neural tissue (Lorentz forces), leading to focal intravoxel dephasing. Stronger gradients with faster switching can even lead to mechanical vibration, which can further exacerbate image distortion and has been shown to worsen with increasing *b* value and possibly with patient weight. Such mechanical distortion artifact can theoretically occur in any intracranial location, but a characteristic location seems to be the superior cerebellar vermis, for some reason.

These artifacts often appear as foci of image distortion and blurring, although occasionally they may appear larger, multifocal, or diffuse. They may also appear as either bright or dark signal on DWI, with the reverse signal on an ADC map. Correction or prevention of such artifacts may improve with specialized postprocessing, precompensation, or future advances in gradient design and shielding (Figs. 22.115, 22.116, 22.117, 22.118 and 22.119).

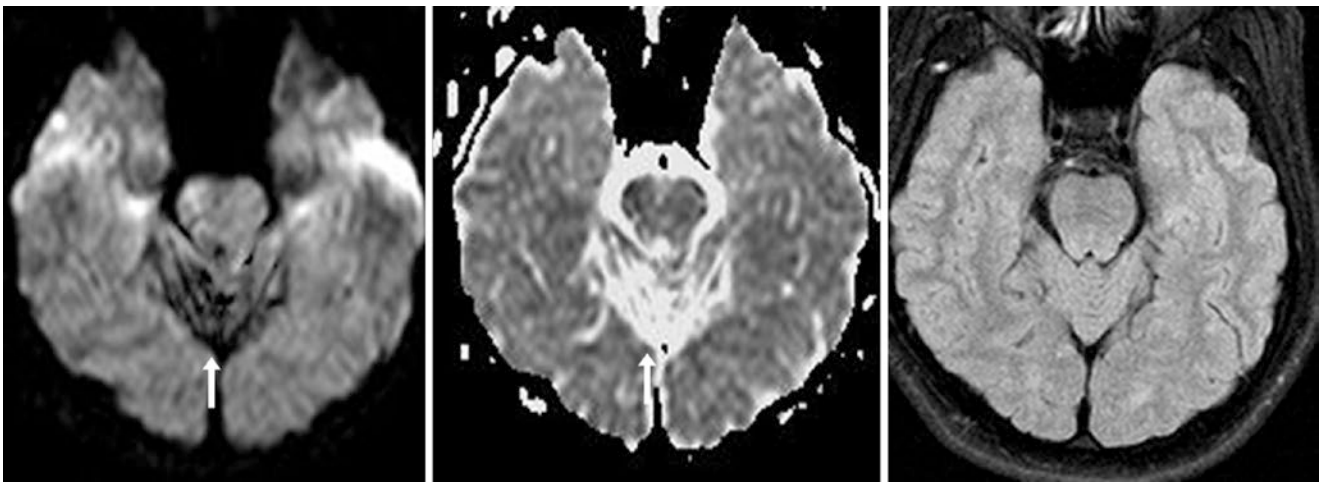

Fig. 22.115 An 80-year-old had a large area of dark artifact overlying the midline superior cerebellum (*arrows*) on DWI MRI at 3 T (*left*). This can be a characteristic location of mechanical vibration artifact, or the artifact could be related to residual eddy currents with Lorentz forces. Note bright signal on ADC maps (*middle*) and a normal FLAIR image (*right*)

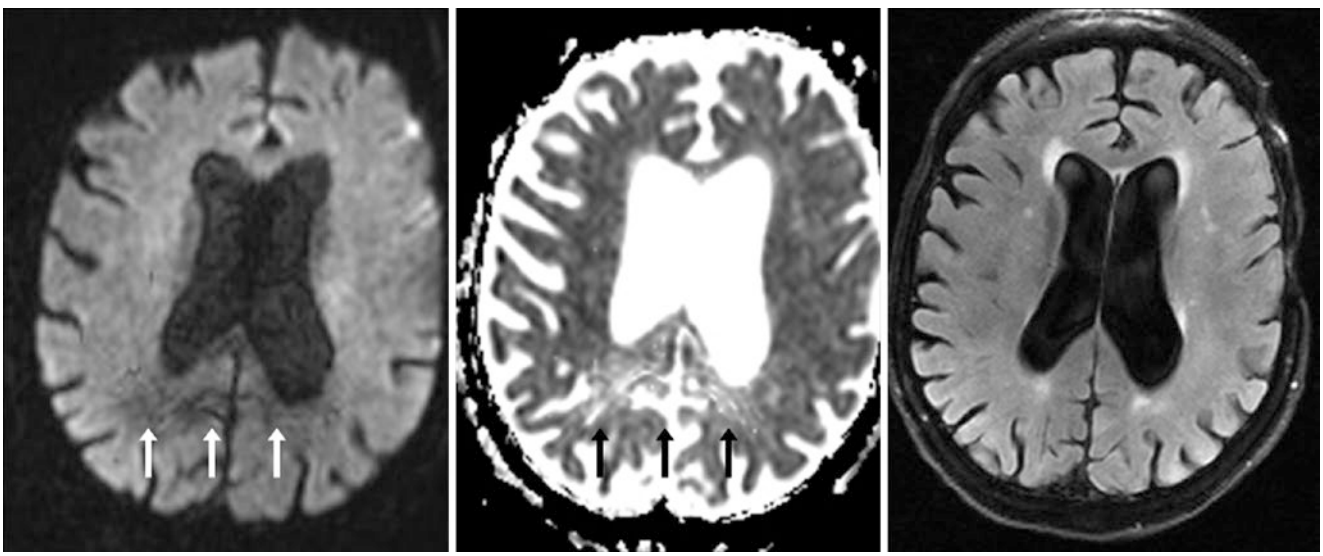

Fig. 22.116 An 85-year-old had a small, focal region of dark artifact within the parieto-occipital region on DWI MRI (*left*) at 3 T, thought related to eddy currents and Lorentz forces (*arrows*); it also could be due to mechanical vibration. There is corresponding bright signal on the ADC map (*middle*), while FLAIR appears normal in that location (*right*)

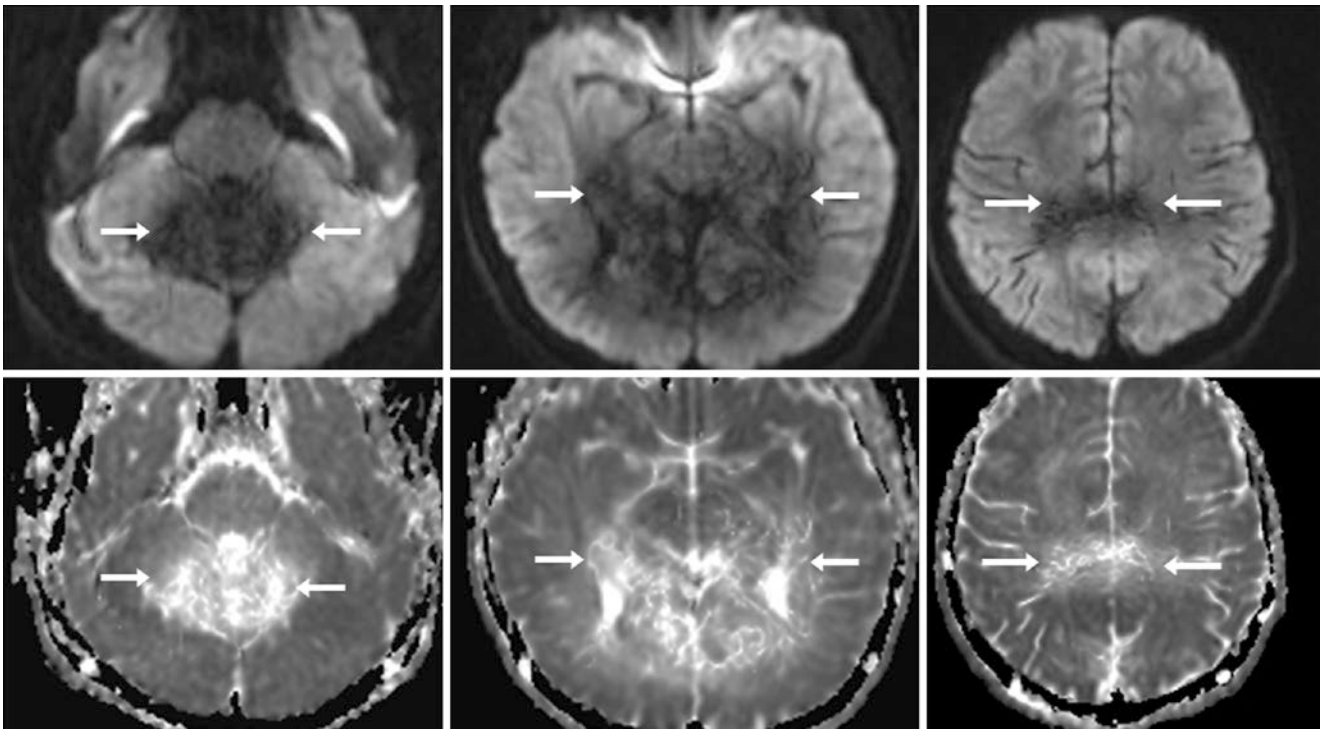

Fig. 22.117 An 11-year-old with a large region of dark artifact from eddy currents or mechanical vibration (*arrows*), as shown on DWI at 3 T (*top row*), with bright signal on ADC maps (*bottom row*). FLAIR and T2WI were normal (*not shown*)

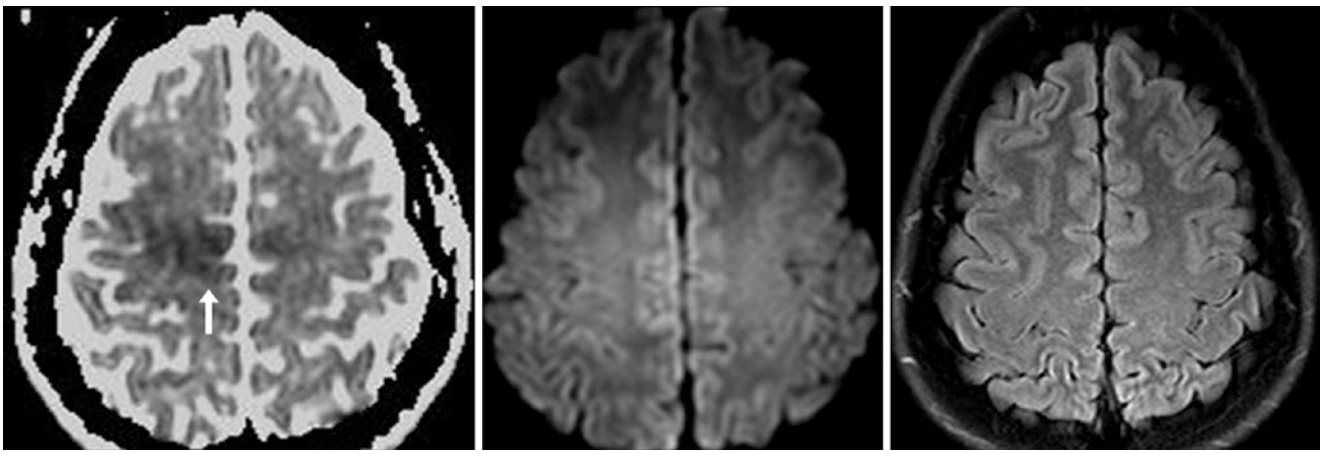

Fig. 22.118 In a 33-year-old, a focal region of dark artifact was likely due to eddy currents with Lorentz forces (*arrows*), as shown on an ADC map at 3 T (*left*). The region appears normal on DWI (*middle*) and FLAIR images (*right*)

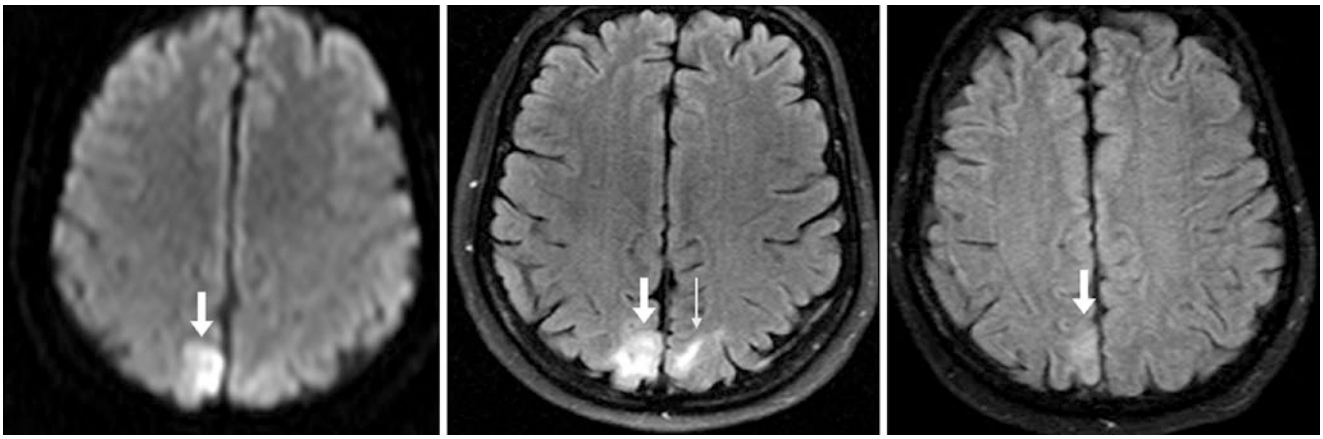

Fig. 22.119 Comparison case of infarct in PRES. A 57-year-old had a 1.5 T DWI MRI (*left*) that demonstrated focal reduced diffusion (*arrows*) within a larger region of "mild" cortical edema on FLAIR (*middle*). Contralateral edema (*thin arrows*) is also seen. On a repeat FLAIR image 1 month later, the edema had improved bilaterally (*right*)

22.3.13 DWI: Susceptibility and Field Inhomogeneity Artifacts in Head Coil Absence

A head coil or "bird cage" coil is typically utilized to bring the coil in proximity to the tissue of interest (brain), with the intent of achieving greater magnetic field homogeneity and uniform excitation of the tissue. This results in optimum signal and the least amount of noise. Occasionally, however, a patient's head cannot fit into a coil, but can fit into the standard magnet bore. The exception to this is "open" magnets, which vary in configuration and utility, and often use lower field strengths with lower signal-to-noise ratio.

The situation of cranial imaging without a dedicated head coil usually occurs due to the patient's head size, a severe kyphosis, or worsening claustrophobia with the coil in place. The *lack of a head coil* typically necessitates the use of either the surrounding "whole body" coil, or some other compromise that will inherently lead to far less signal-noise in comparison to an acquisition with the appropriate head coil. Such "non-head coil" MR image acquisitions often suffer large regions of field inhomogeneity and a greater degree of susceptibility artifacts. These artifacts may simulate large *infarcts*, regions of *cytotoxic* or *vasogenic edema*, or other pathology on DWI.

Often, patient sedation must be used to obtain images with a head coil, but newer MR systems may utilize solely the coil base just posterior to the skull, which can obtain images that are much better than images using only the body coil and lead to a reasonable compromise in patient comfort and signal-to-noise (Figs. 22.120 and 22.121).

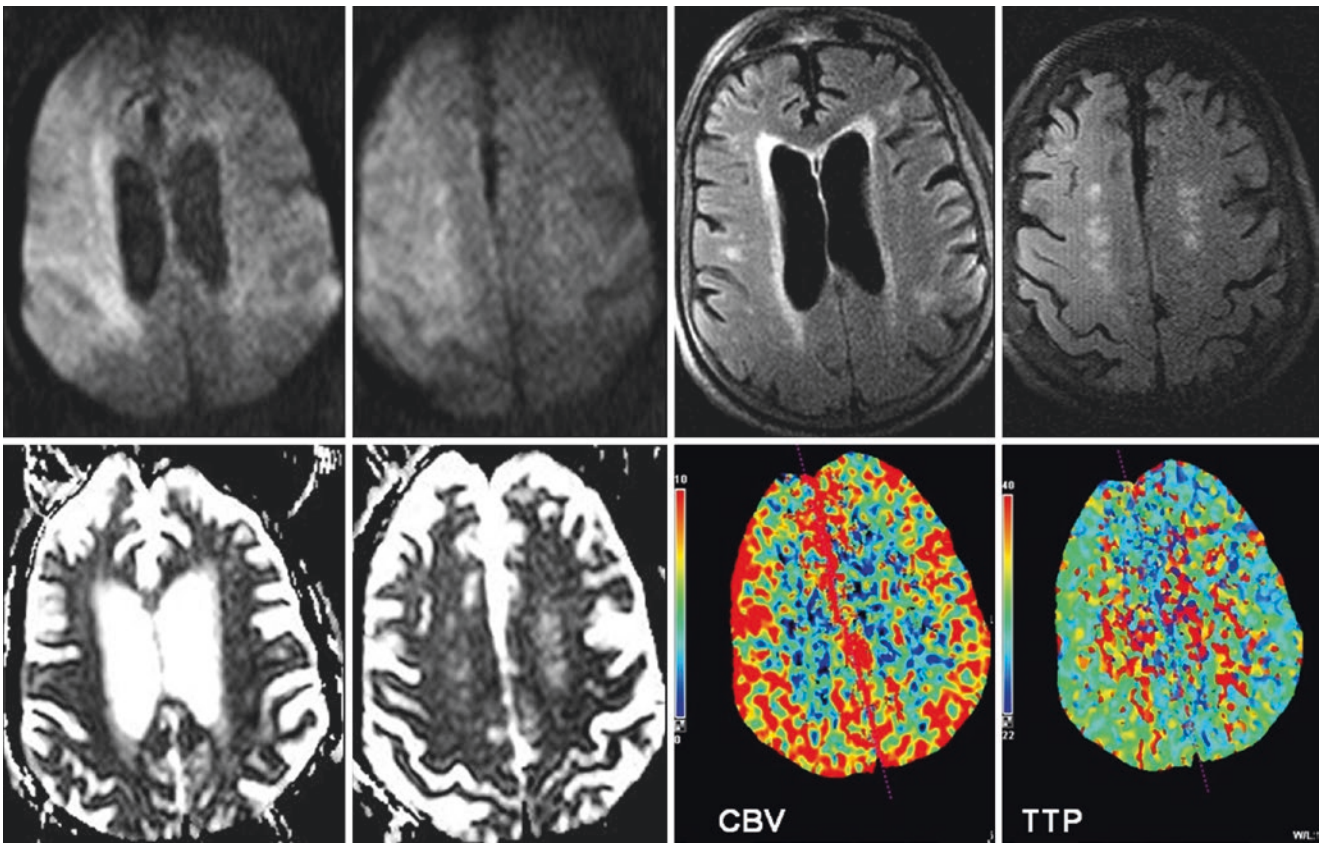

Fig. 22.120 A 79-year-old with severe kyphosis could not be fit into the head coil for a 1.5 T MRI. Hence, the MRI was obtained without a head coil. DWI (*top left*) showed bright signal throughout the right cerebrum, with darker signal on the left, which could simulate an acute middle cerebral artery infarct on DWI. On FLAIR, however (*top right*), there is also bright signal throughout the right hemisphere. ADC maps (*bottom left*) showed no corresponding dark signal of the right hemisphere, thus confirming that the signal was artifactual. A CT perfusion examination showed normal cerebral blood volume (CBV) and time-to-peak (TTP) images (*bottom right*), confirming that there were no perfusion abnormalities or infarcts. (An infarct would appear low/blue on a CBV map, and high/red on a TTP map.)

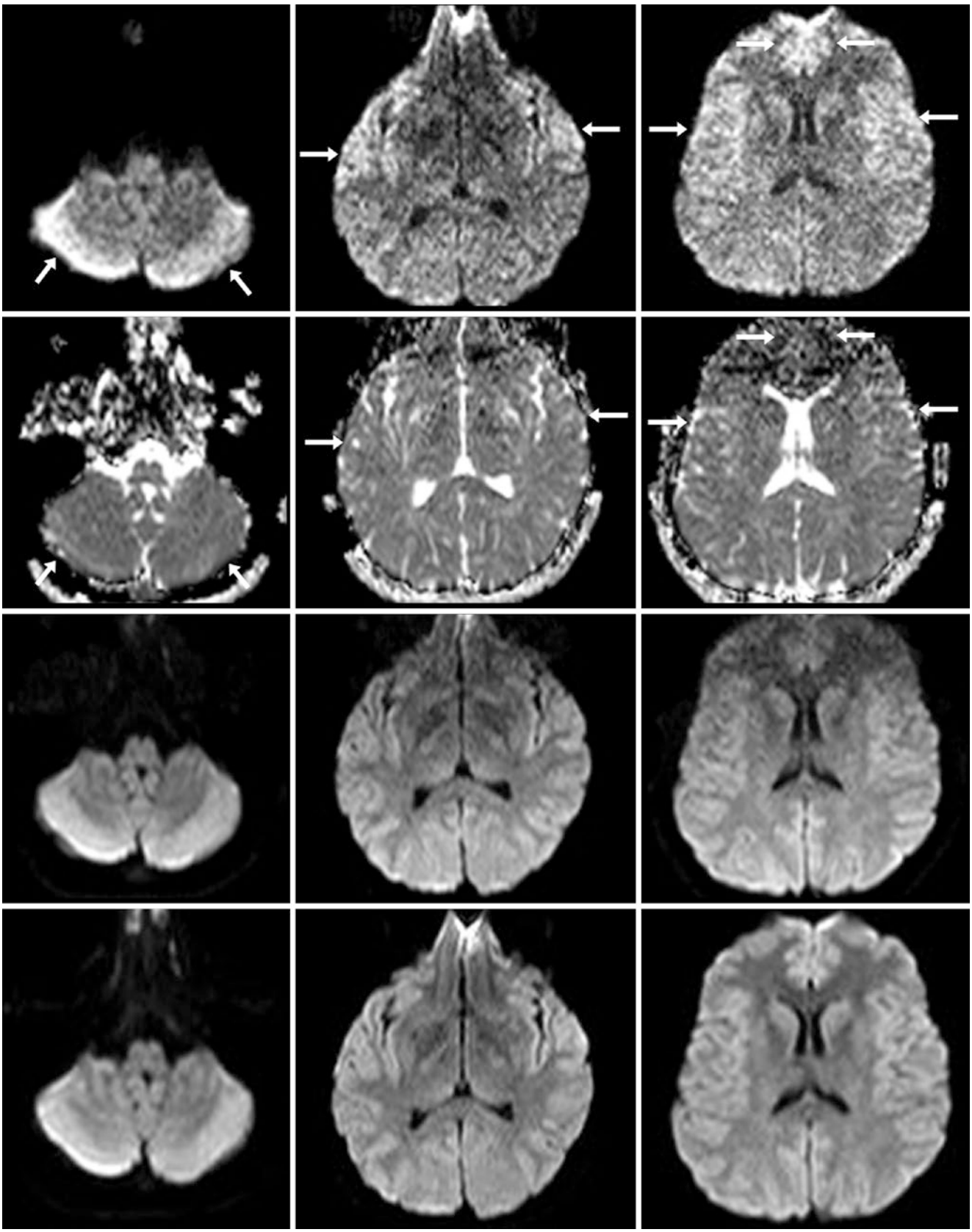

Fig. 22.121 A 27-year-old normal volunteer underwent DWI with no head coil (*i.e.*, using a body coil) (*top row*), with matched ADC maps (*second row*); using only a posterior base coil (*third row*); and using a typical "bird cage" head coil (*bottom row*). *Top row*: Note that the lack of a dedicated head coil causes bright "pseudoinfarcts" (*arrows*). *Second row*: The ADC maps are normal in such regions, and the artifact is most prominent in anterior-most locations. *Third row*: The use of a posterior-only base coil, which the head rests on directly, removes most of the pseudoinfarcts but there is still loss of signal in anterior-most locations such as the orbitofrontal regions. *Bottom row*: The use of a dedicated "bird cage" head coil markedly improves signal at all three levels shown. Even the orbitofrontal regions, a common site of susceptibility artifact and signal loss, are markedly improved

Suggested Reading

Beauchamp Jr NJ, Ulug AM, Passe TJ, van Zijl PC. MR diffusion imaging in stroke: review and controversies. Radiographics. 1998;18:1269–83.

Chou MC, Wang CY, Liu HS, Chung HW, Chen CY. Pseudolesions arising from unfolding artifacts in diffusion imaging with use of parallel acquisition: origin and remedies. AJNR Am J Neuroradiol. 2007;28:1099–101.

Hiwatashi A, Zhong J. Pitfalls and artifacts of DW imaging. In: Moritani T, Ekholm S, Westeson P-L, editors. Diffusion-weighted MR imaging of the brain. New York: Springer; 2005. p. 23–35.

Kakeda S, Korogi Y, Hiai Y, Ohnari N, Sato T, Hirai T. Pitfalls of 3D FLAIR brain imaging: a prospective comparison with 2D FLAIR. Acad Radiol. 2012;19:1225–32.

Kamada K, Kakeda S, Ohnari N, Moriya J, Sato T, Korogi Y. Signal intensity of motor and sensory cortices on T2-weighted and FLAIR images: intraindividual comparison of 1.5T and 3T MRI. Eur Radiol. 2008;18:2949–55.

Kitajima M, Hirai T, Shigematsu Y, Uetani H, Iwashita K, Morita K, et al. Comparison of 3D FLAIR, 2D FLAIR, and 2D T2-weighted MR imaging of brain stem anatomy. AJNR Am J Neuroradiol. 2012;33:922–7.

Le Bihan D, Poupon C, Amadon A, Lethimonnier F. Artifacts and pitfalls in diffusion MRI. J Magn Reson Imaging. 2006;24:478–88.

Lettau M, Laible M. 3 T high-*b*-value diffusion-weighted MR imaging in hyperacute ischemic stroke. J Neuroradiol. 2013;40:149–57.

McKinney AM, Kieffer SA, Paylor RT, SantaCruz KS, Kendi A, Lucato L. Acute toxic leukoencephalopathy: potential for reversibility clinically and on MRI with diffusion-weighted and FLAIR imaging. AJR Am J Roentgenol. 2009;193:192–206.

Meyer JR, Gutierrez A, Mock B, Hebron D, Prager JM, Gorey MT, Homer D. High-*b*-value diffusion-weighted MR imaging of suspected brain infarction. AJNR Am J Neuroradiol. 2000;21:1821–9.

Mukherjee P, Chung SW, Berman JI, Hess CP, Henry RG. Diffusion tensor MR imaging and fiber tractography: technical considerations. AJNR Am J Neuroradiol. 2008;29:843–52.

Neema M, Guss ZD, Stankiewicz JM, Arora A, Healy BC, Bakshi R. Normal findings on brain fluid-attenuated inversion recovery MR images at 3 T. AJNR Am J Neuroradiol. 2009;30:911–6.

Provenzale JM, Engelter ST, Petrella JR, Smith JS, MacFall JR. Use of MR exponential diffusion-weighted images to eradicate T2 "shine-through" effect. AJR Am J Roentgenol. 1999;172:537–9.

Provenzale JM, Petrella JR, Cruz Jr LC, Wong JC, Engelter S, Barboriak DP. Quantitative assessment of diffusion abnormalities in posterior reversible encephalopathy syndrome. AJNR Am J Neuroradiol. 2001;22:1455–61.

Schaefer PW, Grant PE, Gonzalez RG. Diffusion-weighted MR imaging of the brain. Radiology. 2000;217:331–45.

Sohn CH, Sevick RJ, Frayne R, Chang HW, Kim SP, Kim DK. Fluid attenuated inversion recovery (FLAIR) imaging of the normal brain: comparisons between under the conditions of 3.0 Tesla and 1.5 Tesla. Korean J Radiol. 2010;11:19–24.

Weigel M, Henning J. On the diffusion sensitivity of 2D- and 3D-turbo spin sequences. In: Proceeding of the 19th annual meeting of the International Society for Magnetic Resonance in Medicine, Montreal, Quebec, Canada. 6–13 May 2011.

Yoshiura T, Wu O, Zaheer A, Reese TG, Sorensen AG. Highly diffusion-sensitized MRI of brain: dissociation of gray and white matter. Magn Reson Med. 2001;45:734–40.

Zhuo J, Gullapalli RP. AAPM/RSNA physics tutorial for residents: MR artifacts, safety, and quality control. Radiographics. 2006;26:275–97.

Pediatric Brain: Normal Variations in Development, Maturation, and Myelination

23

This chapter focuses on neonates, infants, adolescents, and to a lesser degree, teenagers. With the advent of 3T MRI, norms for development and maturation of white matter structures have changed and evolved somewhat. Though it is critical to note the appropriate signal intensities within myelinating and maturing structures in the neonate and within the first 2 years of life, the focus is largely on T2-weight imaging (T2WI) in infants and young children when assessing normal development; fluid-attenuated inversion recovery (FLAIR) is less useful. For example, in neonates, T1-bright signal within the basal ganglia can be a source of consternation and may or may not be abnormal, depending on location, degree, and signal intensity relative to adjacent structures. Additionally, in young children, juveniles, and adolescents, knowledge of normal terminal zones of myelination is necessary to distinguish normal maturation from true pathology. It is also important to mention that CT has been used with decreasing frequency in children (particularly neonates and infants) over the past 10 years, as the lifetime risk of developing malignancy due to the radiation dose increases with decreasing age. Although newer, lower-dose protocols that implement iterative reconstruction have improved the dose profile, it is important to be aware of the cumulative risk of CT over time to children, particularly those with neoplasm or malignancies, who are expected to undergo multiple future CT-based studies. Thus, MRI is increasingly becoming the method of initially diagnosing and following most chronic disorders or neoplasms in children, until positron emission tomography (PET)-MRI becomes routinely available.

This chapter attempts to bring together current knowledge of normal maturation in neonates and young children, and to focus on those normal variations in development that can persist into adolescence and adulthood, with a greater focus on MRI and CT. Certain variants, most notably benign enlargement of the subarachnoid spaces of infancy (BESSI), are mentioned here as normal variations or as "don't touch lesions" that typically disappear by a certain age, though correlation with disease later in life has not been disproven.

In this author's opinion, it is important to use follow-up imaging, particularly MRI, when necessary to assess myelination and maturation. In particular, questionable cases of normal myelination and maturation can be difficult to assess on an initial MR examination, particularly when the history or reason for the examination is questionable or the patient is unsedated, or even with a technically adequate study at certain ages (*e.g.*, assessing myelination at 7–11 months of age). Though cost to the patient is important, noncontrast MRI using standard MR protocols for children offers little risk, and 3T versus 1.5T field strengths can be useful in detecting subtle abnormalities. It is important to note, however, that in neonates, preterm infants, and young children, 3T imaging is likely to be more sensitive than 1.5T in detecting abnormalities in myelination and maturation.

A.M. McKinney, *Atlas of Normal Imaging Variations of the Brain, Skull, and Craniocervical Vasculature*,
DOI 10.1007/978-3-319-39790-0_23

23.1 Neonatal "Patchy" White Matter Hypoattenuation on CT

CT scans can be quite sensitive for detecting intracranial hemorrhage, even in a neonate, but it can demonstrate normal "*patchy*" *hypoattenuation* that may simulate abnormalities in neonates. Such patchy low attenuation is scattered throughout the deep white matter, particularly the *periventricular white matter* (PVWM), and may involve the *subcortical white matter* (SCWM) to a lesser degree. The cause of this pseudoabnormality is likely related to several factors, the most prominent probably being that the concentration of water is higher in the neonatal brain, as the water concentration progressively decreases at later ages. Such hypoattenuation may be problematic in that it can simulate edema from *hypoxic-ischemic encephalopathy/injury* (HIE/HII), an infectious etiology such as *meningitis*, or a developmental or congenital anomaly such as *hypomyelination*.

Thus, there is potential for overdiagnosis of white matter abnormalities in neonates by nonenhanced CT (NECT), and the presence of such pseudoabnormalities on CT in term neonates has a low correlation with the presence of disease on MRI sequences such as diffusion-weighted imaging (DWI), FLAIR, and T2WI. Additionally, the specificity and sensitivity of CT is rather low overall for detecting white matter abnormalities. Low attenuation on CT is abnormal within the basal ganglia, however, and simultaneous findings such as cortical edema, mass effect, effacement of the basal cisterns, and loss of gray-white matter differentiation are all suggestive of underlying edema if white matter hypoattenuation is present. Thus, the presence of patchy hypoattenuation in the PVWM is typically normal by itself, but if there are such other associated abnormalities, an MRI should be performed.

This variant is becoming less commonly seen, as MRI has largely been accepted as the preferred modality in the initial workup of term neonates, given the awareness of the need to minimize radiation exposure because of its potential stochastic effects later in life (such as cancer). Additionally, the progressively decreasing doses and size/weight-variable doses from newer CT scanners may also decrease the likelihood of seeing this variant, as lower doses often lead to decreased discrimination between gray and white matter (Figs. 23.1, 23.2, 23.3, 23.4, 23.5, 23.6, 23.7, 23.8, 23.9 and 23.10).

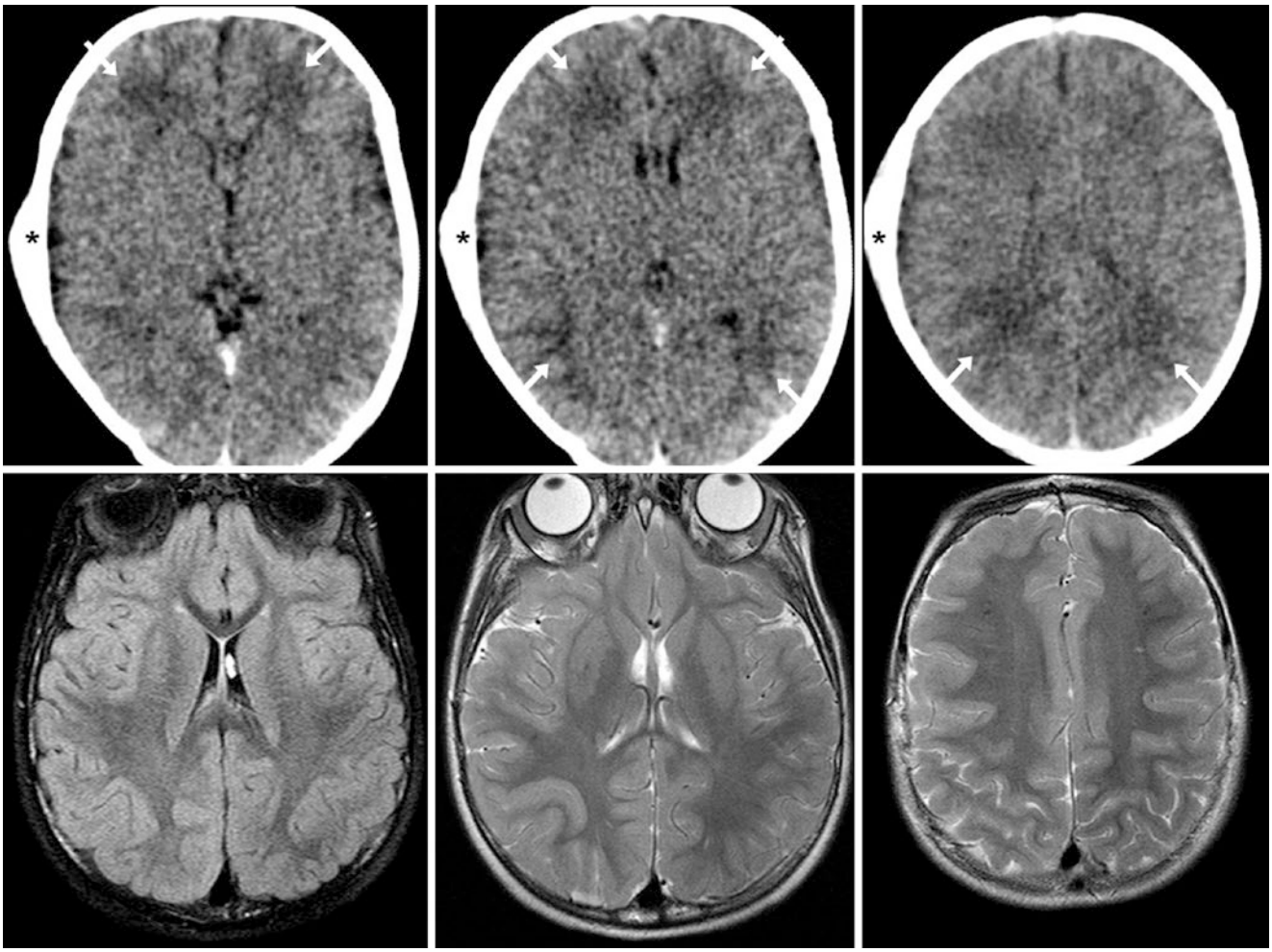

Fig. 23.1 An 8-day-old term neonate had a nondisplaced right temporal skull fracture and an overlying cephalohematoma (*asterisk*) after being dropped, without intracranial hemorrhage on a nonenhanced CT (NECT) (*top row*). There were patchy, hypodense areas throughout the periventricular white matter (PVWM) (*arrows*). Two years later, a 3T MRI was normal, without hemorrhage or atrophy, as shown on fluid-attenuated inversion recover (FLAIR) (*bottom left*) and T2-weighted imaging (T2WI) (*bottom middle* and *right*). The patient's clinical developmental was normal

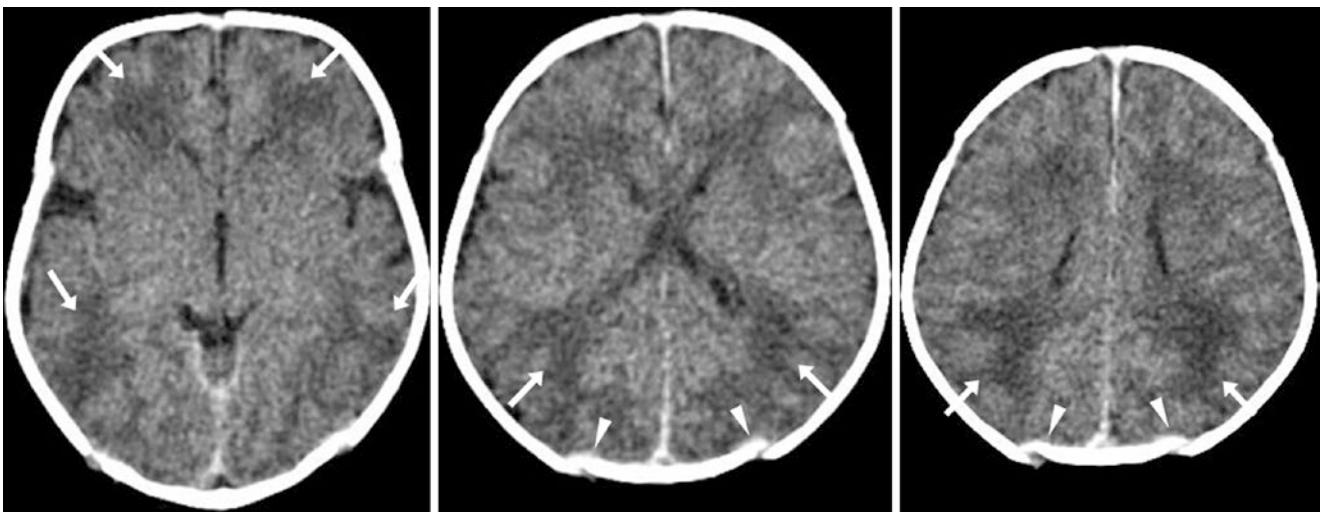

Fig. 23.2 A 7-day-old term neonate underwent a NECT for perinatal respiratory depression. There were patchy areas of low attenuation scattered throughout the PVWM (*arrows*) that were more prominent posteriorly in the parieto-occipital regions. A repeat NECT was not performed, but the infant's development was normal. Note the normal sutural overlap posteriorly (*arrowheads*), due to compression from delivery, which typically resolves by 3–4 weeks of age

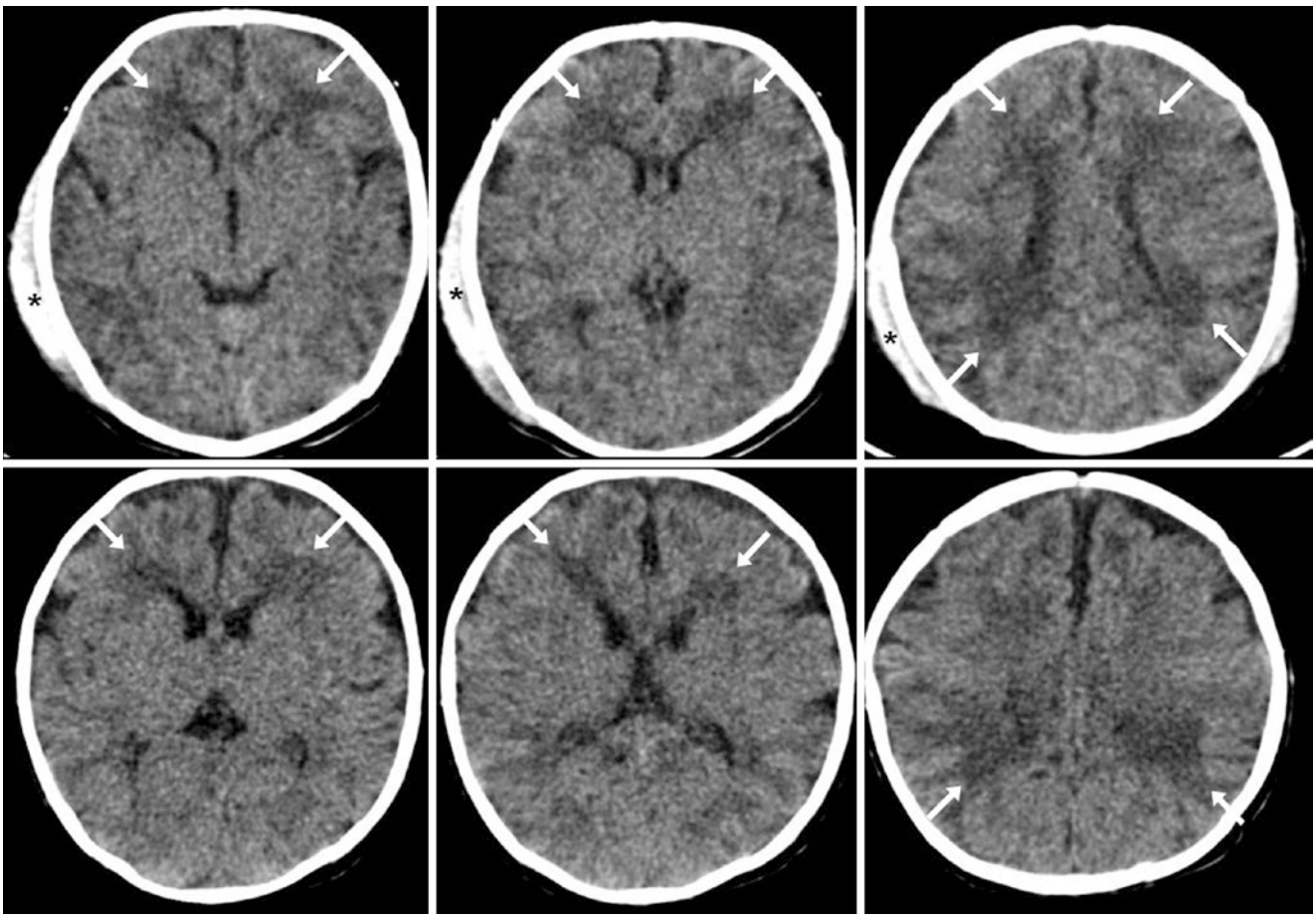

Fig. 23.3 A 13-day-old term neonate had a nondisplaced right temporal skull fracture, with a cephalohematoma (*asterisk*), after being dropped from a height, without intracranial hemorrhage on NECT (*top row*). There were patchy, hypodense regions throughout the PVWM (*arrows*). A repeat NECT several days later was normal (*bottom row*), and the infant was neurologically intact. Note that the intact overlying cortical gray matter, indicating that although the white matter appears hypoattenuated, the gray-white matter differentiation is not blunted

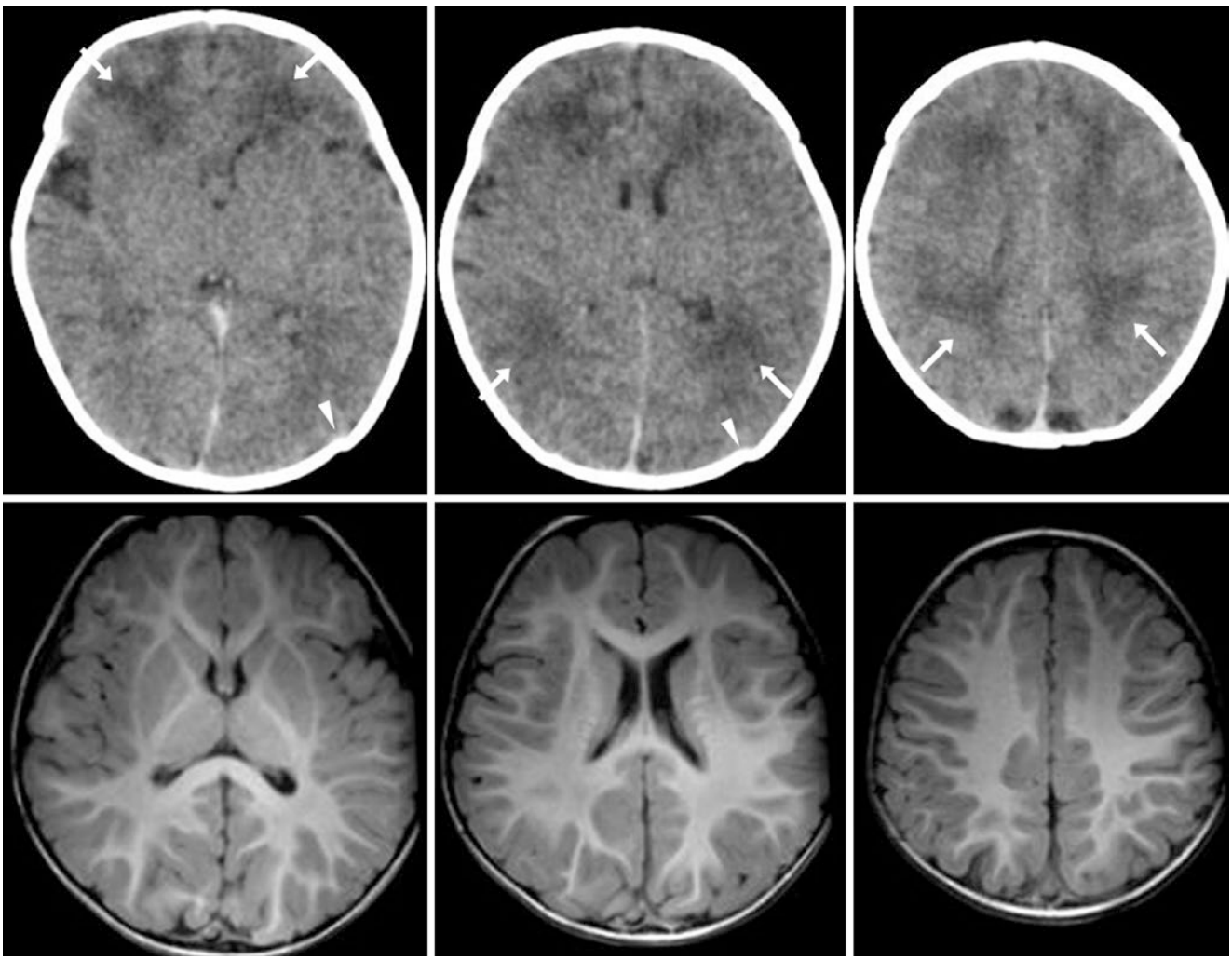

Fig. 23.4 A 3-day-old term neonate with bradycardia had an otherwise negative NECT (*top row*) that showed patchy areas of hypoattenuation throughout the PVWM (*arrows*). Note the normal, slight sutural overlap (*arrowheads*). One year later, a 3T MRI with T1-weighted imaging (T1WI) was normal (*bottom row*). The infant's neurologic development was normal

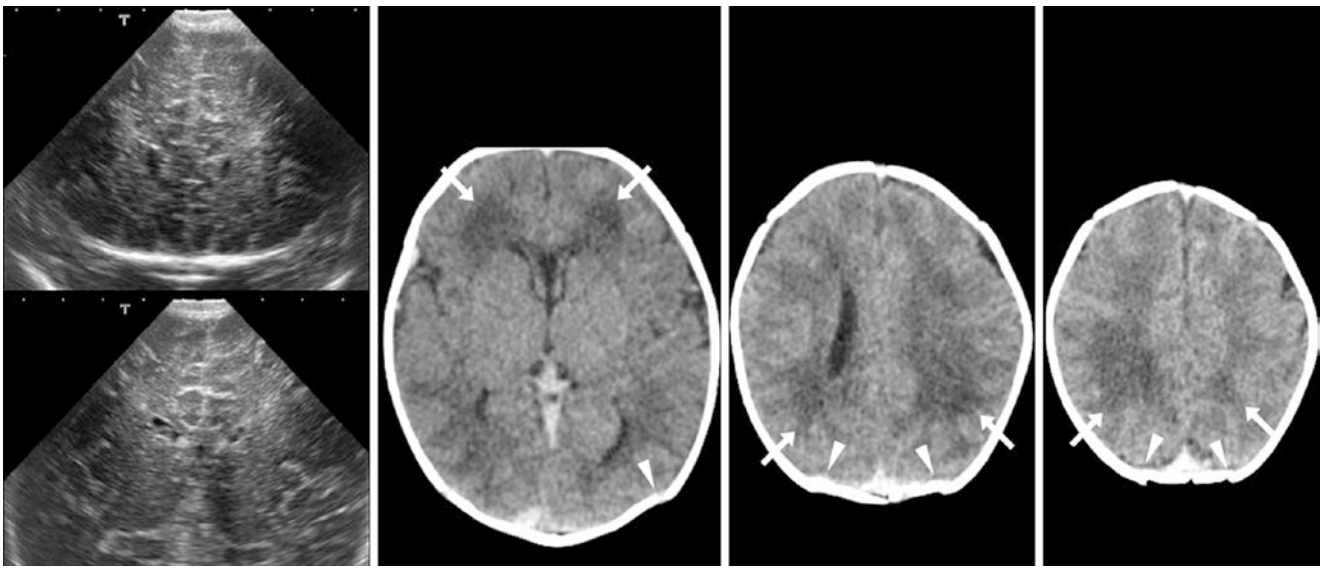

Fig. 23.5 A 3-day-old term neonate with decreased responsiveness had a coronal ultrasound (*left*), which was questioned to have a tiny amount of intraventricular hemorrhage. An otherwise negative NECT the next day (*middle and right*) showed only patchy regions of hypoattenuation throughout the PVWM (*arrows*), with normal, slight sutural overlap (*arrowheads*). The infant's clinical neurologic development was subsequently normal

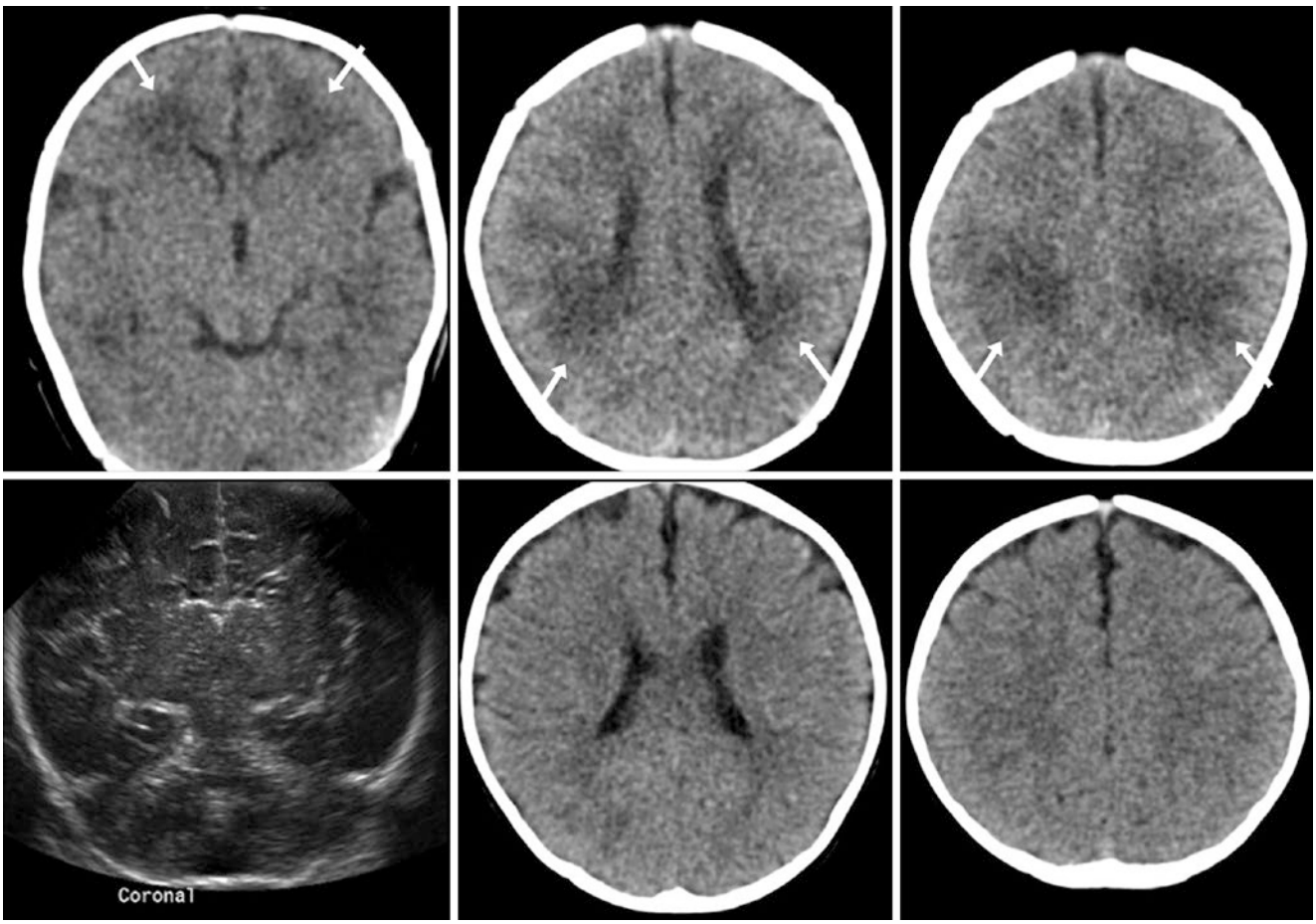

Fig. 23.6 A 4-day-old term neonate with a possible hypoxic event had an otherwise negative NECT (*top row*), which showed scattered, patchy regions of hypoattenuation throughout the PVWM (*arrows*). A coronal ultrasound (*bottom left*) was also called negative. Note the intact overlying cortical gray matter. A repeat NECT at 6 months of age (*bottom middle* and *bottom right*) showed resolution of the patchy white matter, and the patient's neurologic development at that time was considered normal

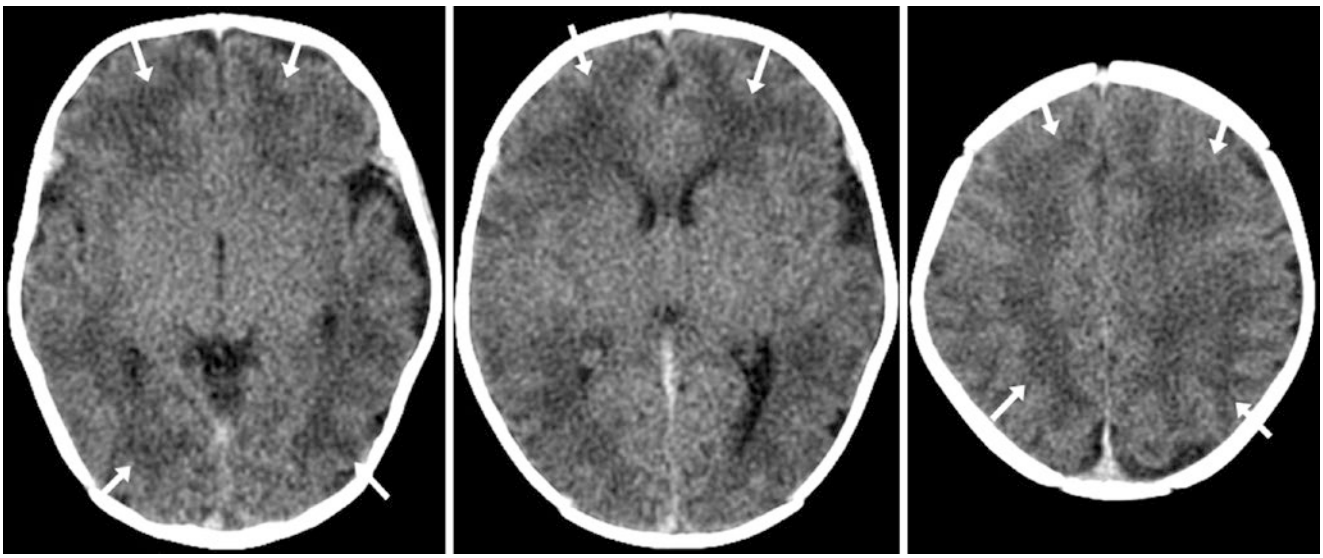

Fig. 23.7 A 2-day-old neonate with apnea had an otherwise negative NECT that showed only patchy hypoattenuation scattered throughout the PVWM (*arrows*). The infant's neurologic development was subsequently normal, so no further imaging was obtained

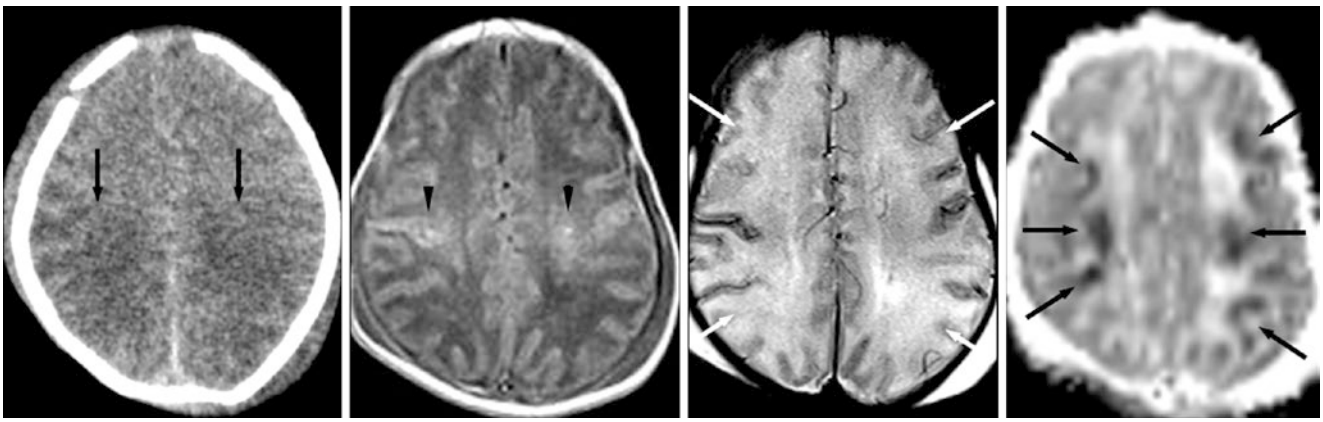

Fig. 23.8 Comparison case of hypoxic-ischemic injury (HII). A 3-day-old term neonate had a CT scan (*left*) that showed subcortical low attenuation with loss of cerebral sulci posteriorly, and loss of gray-white matter differentiation called cerebral edema. A 3T MRI depicted patchy perirolandic hyperintensity (*arrowheads*) on gradient echo (GE) T1WI (*left middle*), with multifocal areas lacking a normal dark cortical ribbon (*arrows*) on spin echo (SE) T2WI (*right middle*). Diffusion-weighted imaging (DWI) (not shown) showed abnormalities in such regions, as confirmed by apparent diffusion coefficient (ADC) maps (*right*)

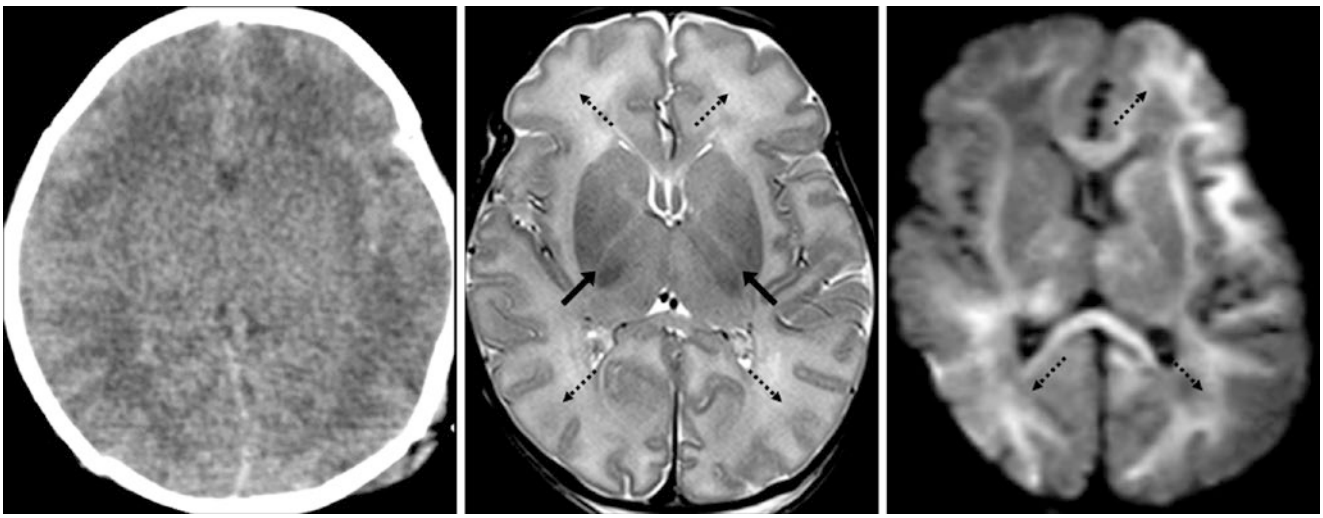

Fig. 23.9 Comparison case of HII. A 2-day-old term neonate had a CT scan (*left*) that showed diffuse subcortical low attenuation thought to be cerebral edema, with loss of sulci. A 3T MRI the next day depicted mild diffuse cortical edema on SE T2WI (*middle*), poor visualization of the normal posterior limb of the internal capsule (PLIC) (*arrows*), and some focal regions that lacked the normal T2-dark cortical ribbon (*dotted arrows*). DWI was diffusely abnormal (*right*)

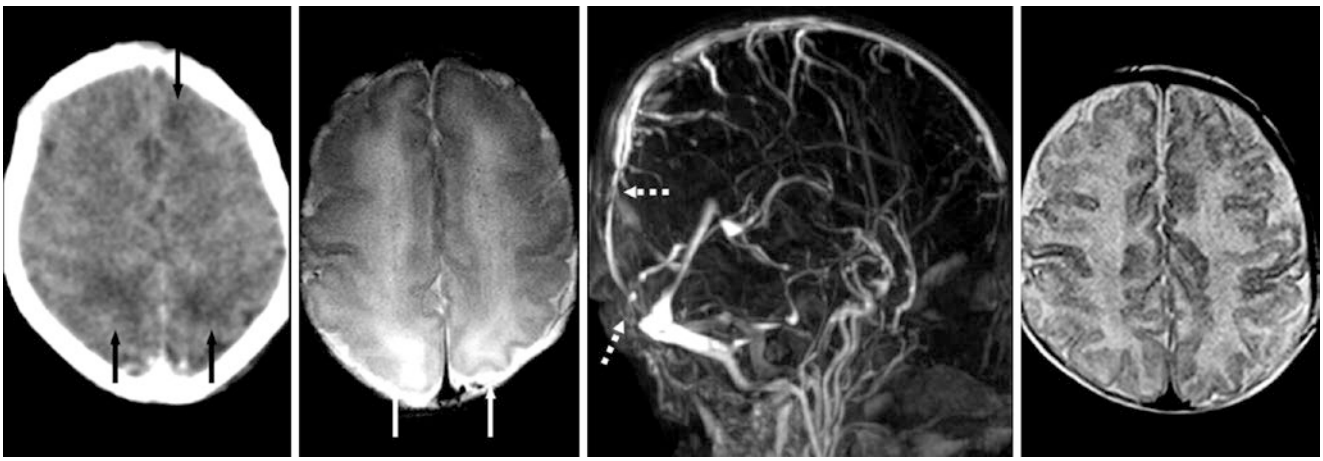

Fig. 23.10 Comparison case of reversible edema from venous stenosis. A 4-day-old term neonate with congenital heart disease (presurgery) had bilateral, subcortical low attenuation on CT (*left*), called cerebral edema (*arrows*). A 3T MRI with T2WI (*left middle*) demonstrated focal loss of the normal T2-dark cortical "ribbon" in those locations. Postcontrast MR venography (MRV) from a sagittal view (*right middle*) depicted multifocal severe stenoses (*dotted arrows*) of the superior sagittal sinus, with venous collaterals. Two months later, the edema had resolved following cardiac surgery (*right*)

23.2 Normal T1-Bright Basal Ganglia in Term Neonates on 3T MRI

T1-bright signal in the *posterior limb of the internal capsule* (PLIC) is entirely normal in a term neonate (*i.e.*, >38 weeks gestational age), and it also may be present in the *ventrolateral thalami* (VLT), *globi pallidi* (GP), *posterior putamina* (PP), and *subthalamic nuclei* (STN), to a lesser degree. Diffusion-weighted imaging (DWI) can be quite helpful, as it can confirm suspected findings of *hypoxic-ischemic encephalopathy* (HIE) or injury (HII), particularly within the basal ganglia or cortices. DWI is useful only within the acute or early subacute phase of HII, however (within 7 days post-insult), when infants suspected to have HII may immediately undergo either head-only or whole-body cooling for the first 72 h to induce hypothermia, which has been shown to improve outcome. Thus, there is a window of only a few days in which to implement DWI. Also, as DWI may underestimate the final extent of insult, T1-weighted imaging (T1WI) and T2WI can also be helpful. FLAIR images are of little use in the neonate, except to evaluate subdural collections or tumors.

Several criteria based on MRI have been proposed to evaluate for the presence of HII and its extent. A detailed discussion is beyond the scope of this text, but one of the scoring systems that showed a strong association with outcome was shown by Barkovich et al. in 1998 to be based largely on an abnormal appearance of the basal ganglia, thalami, or cortices [1, 2]. In short, cortical abnormal signal is relatively easily visualized on T1WI, particularly within the perirolandic cortex (PRC), which will appear much brighter in HII than the faintly bright signal that may or may not be present in normal term infants. Such bright signal may also appear to extend from the PRC down through the corticospinal tracts (CST) within the corona radiata to the PLIC. A helpful finding that can confirm cortical involvement by HII is that the cerebral cortex normally has a uniformly dark "ribbon" on T2WI relative to the underlying T2-bright subcortical white matter (SCWM), which has not yet myelinated. Thus, in HII, edema effaces the involved regions, and the dark layer is lost.

In the absence of abnormal cortical signal on T1WI, T2WI, or DWI, however, the appearance of bright signal on T1WI within the basal ganglia can be difficult to assess. There can be normal bright signal within certain basal ganglial and thalamic structures on T1WI, which may simultaneously appear slightly hypointense on T2WI. A number of studies have described this appearance, and have even attempted to quantify the degree to which such hyperintensity is abnormal in these structures [3–12]. In general, although there may be mild, normal T1 hyperintensity within the VLT, the lentiform nuclei (the GP together with the putamen), and the PLIC/CST, the signal should be greater in the PLIC and CST than in the other structures on T1WI in normal, term infants. In HII, T1 hyperintensity is greater within the PP than in the adjacent PLIC, and is greater within the PRC than in the immediately subjacent corona radiata [3–5]. T1 hyperintensity within the VLT and the PLIC/CST also may be much greater than normal. It should be pointed out that T1 hyperintensity within these structures, particularly the STN and GP, is typically a transient phenomenon that usually subsides by the end of the first month of life. Such structures may also appear bright on susceptibility-weighted imaging (SWI), possibly owing to "T1 shine-through" effects (which can occur on gradient echo-based images), in combination with the fact that there is not yet iron deposition within these structures in a neonate.

This assessment may be even more complex with T1WI at 3T [11, 12]. As discussed in other sections of this text, there is greater T1 signal at 3T, but the T1 times between gray and white matter decrease, which can lead to less intracerebral tissue contrast on standard spin echo T1WI (SE T1WI). Therefore, various other methods of obtaining T1WI have arisen to better visualize the contrast between gray and white matter at 3T. These include spoiled gradient echo T1WI (GE T1WI), inversion recovery T1WI (IR T1WI), video inversion of T2WI (from whichever type of acquisition), and 3D SE T1WI. Preliminary data have shown that, at 3T, GE T1WI appears to show a greater number of "myelinated" (*i.e.*, T1-bright) structures, and an apparently greater degree of brightness, than SE T1WI, although it has not yet been proven whether such structures are truly myelinated or are simply precursors to myelination [11, 12]. Additionally, the T1-brightness of the lentiform nuclei (especially the GP) may be more pronounced at 3T, and may appear similar in signal to the PLIC and CST. Although this assessment may be complex, it is fortunate that DWI can be more specific at 3T in detecting HII. In particular, although SE T1WI was traditionally the best sequence for assessing myelination at 1.5T, recent evidence suggests that GE T1WI is better at 3T, and SE T2WI may be just as sensitive [11, 12]. This concept is also discussed in the following section on normal myelination.

It is necessary to be careful in deeming that a term neonate has HII based solely on T1-bright signal within the basal ganglia, unless such hyperintensity is profound within the lentiform nuclei and PRC, is disproportionate to the signal of the PLIC and CST, or is quite pronounced within the VLT and CST. In questionable cases, it is important to search for other clues, such as abnormalities on DWI; lack of the normal, dark cortical ribbon on T2WI; lack of the normally small PLIC on T2WI; or abnormalities on SWI (such as hemorrhages). It is important to note that, while specific, the sensitivity of DWI may be lower within the first 1–2 days of life in term neonates, particularly within deep gray matter structures. This author's experience is that the ADC maps must be carefully compared with the corresponding DWI images and T1WI and T2WI images in questionable cases of HII involving the basal ganglia, PLIC, and thalami (Figs. 23.11, 23.12, 23.13, 23.14, 23.15, 23.16, 23.17, 23.18, 23.19, 23.20 and 23.21) [13, 14].

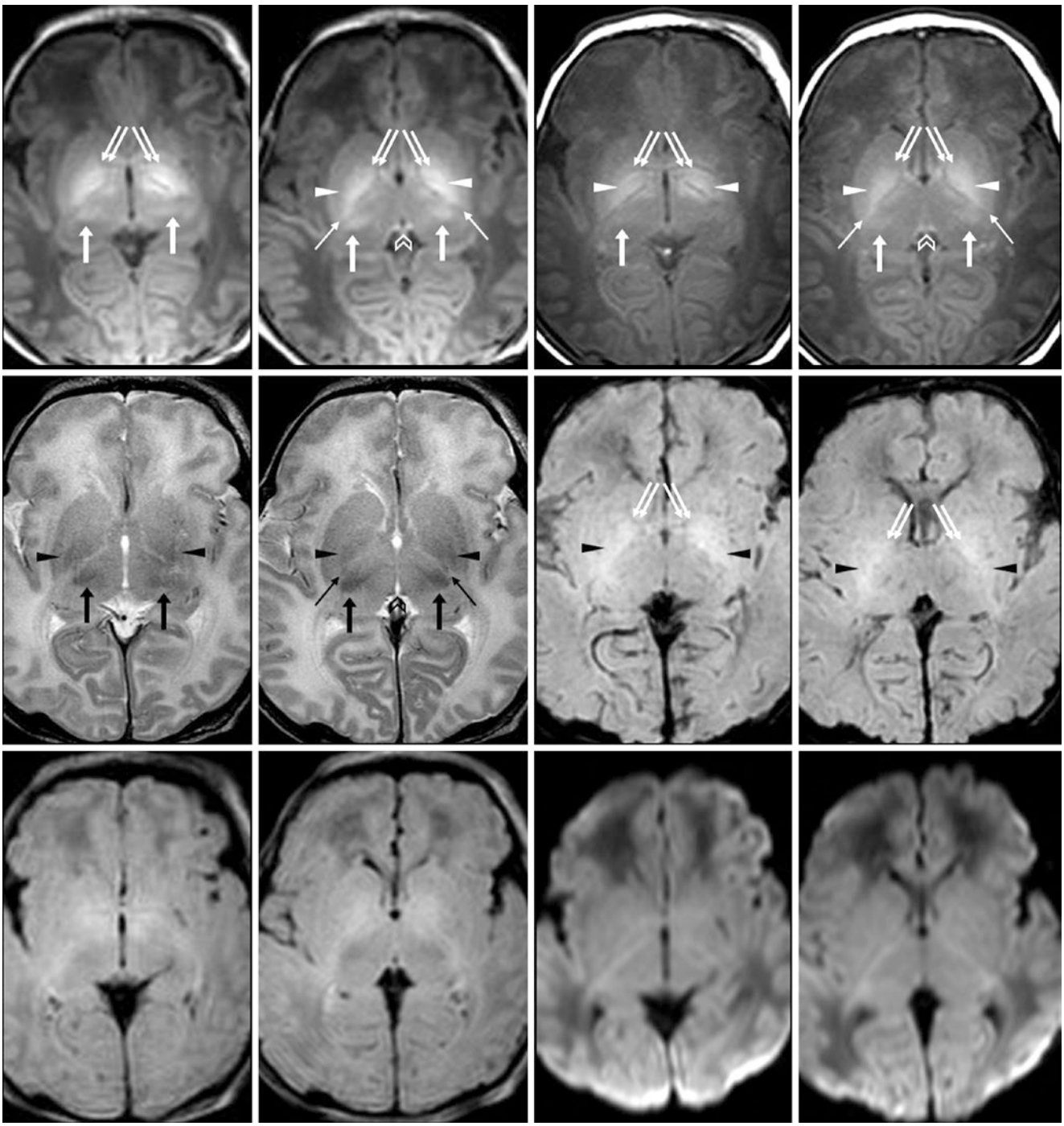

Fig. 23.11 A 1-day-old term neonate with a solitary seizure and a normal 3T MRI. *Top row*: Spoiled GE T1WI (*left*) and SE T1WI (*right*) both show bright signal of the globi pallidi (GP) (*double arrows*) and posterior putamina (PP) (*arrowheads*)—that is, of the lentiform nuclei (LN)—and the ventrolateral thalami (VLT) (*arrows*), being brighter on GE T1WI. The PLIC (*thin arrows*) is also bright, although its proximity to the PP makes it difficult to discern. Note the bright habenular commissure (*chevrons*). Such normal structures usually appear brighter on GE T1WI, particularly at 3T. *Middle row*: On SE T2WI (*left*), the GP/PP and VLT are mildly hypointense, but the PLIC can be discerned as a tiny tract. Again, the habenular commissure is visible (*chevrons*). Susceptibility-weighted imaging (SWI) shows no hemorrhage, but there is mild "T1 shine-through" of the GP/PP (*right*). *Bottom row*: FLAIR (*left*) is typically not useful in evaluating neonates. DWI (*right*) was normal. A 1-year follow-up neurologic exam was normal

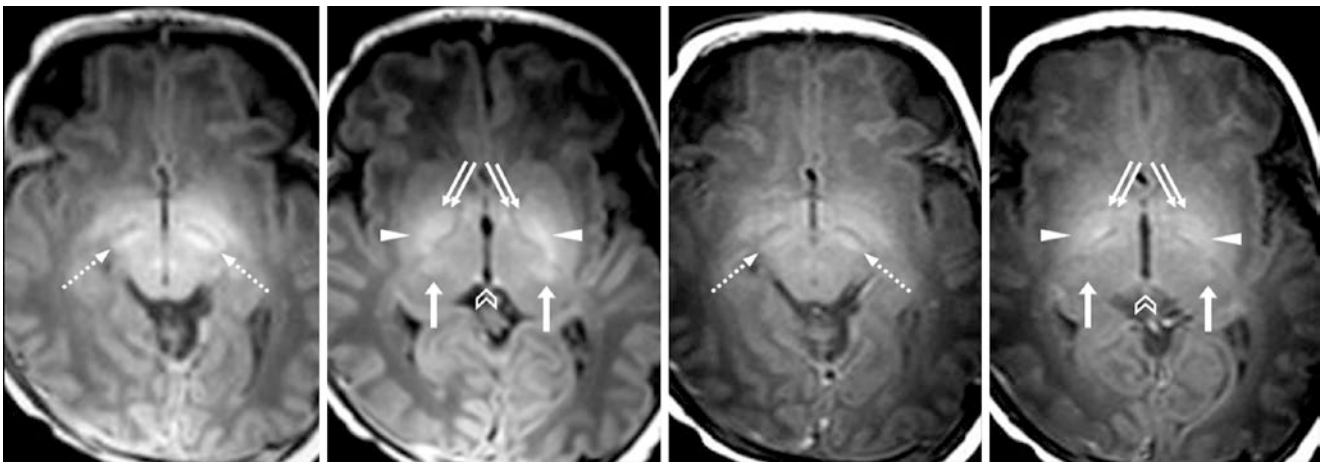

Fig. 23.12 A 3-day-old term neonate with a seizure had a normal 3T MRI, which included spoiled GE T1WIs (*left two images*) and SE T1WIs (*right two images*). Note the bright signal of the GP (*double arrows*), PP (*arrowheads*), VLT (*arrows*), and subthalamic nuclei (STN) (*dotted arrows*), being brighter on GE T1WI. The habenular commissure (*chevrons*) is also bright, being normal. The infant's 1-year clinical exam was normal

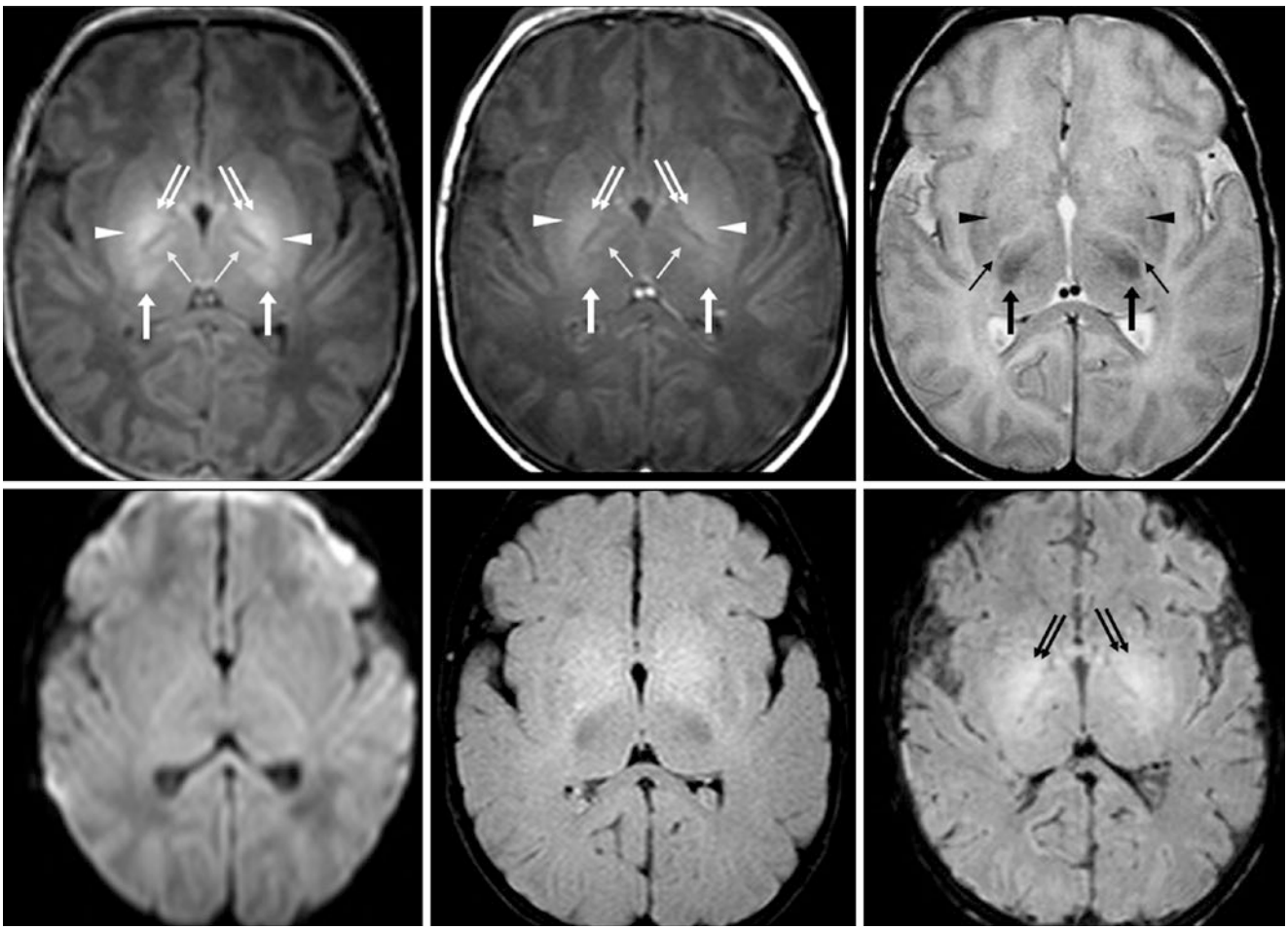

Fig. 23.13 A 4-day-old term neonate with a hypoxic event had a normal 3T MRI, which included spoiled GE T1WI (*top left*), SE T1WI (*top middle*), SE T2WI (*top right*), DWI (*bottom left*), FLAIR (*bottom middle*), and SWI (*bottom right*). Note that the LN are brighter on GE T1WI. On T2WI, the PLIC (*thin arrows*) is tiny but is visible, as is the normal, dark cortical ribbon. On SWI, the LN are bright, perhaps due to "T1 shine-through." The 1-year clinical exam was normal

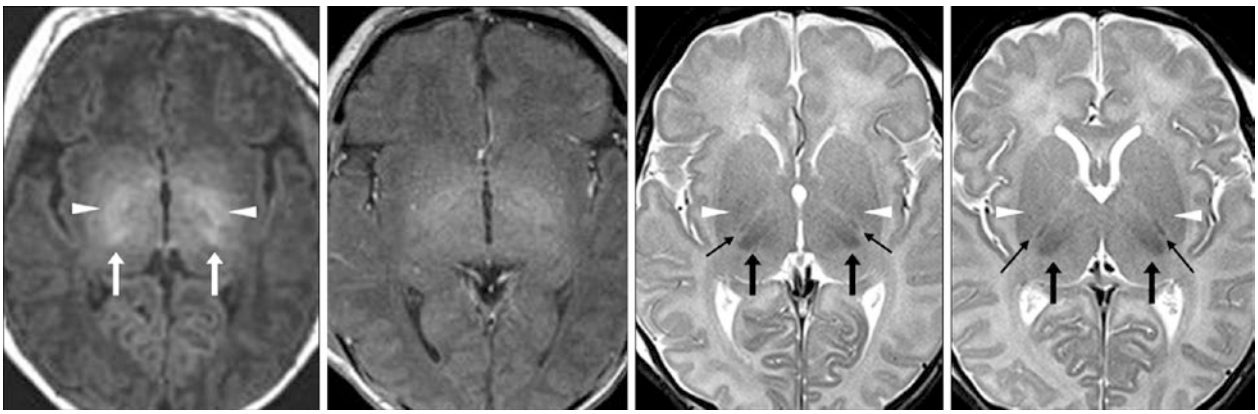

Fig. 23.14 A 5-day-old term neonate with a possible hypoxic event at birth had a normal 3T MRI that included two types of spoiled GE T1WIs: multiplanar 3D magnetization-prepared rapid acquisition gradient echo (MPRAGE) (*left*) and 2D fast low-angle shot (FLASH) (*left middle*), as well as SE T2WIs (*right*). The LN are brighter on the MPRAGE T1WI than on the FLASH GE T1WI, but the PLIC is difficult to distinguish from the PP (*arrowheads*). On the T2WIs, the PLIC (*thin arrows*) is tiny but is clearly visible as being separate from the LN/PP. The 1-year clinical follow-up exam was normal

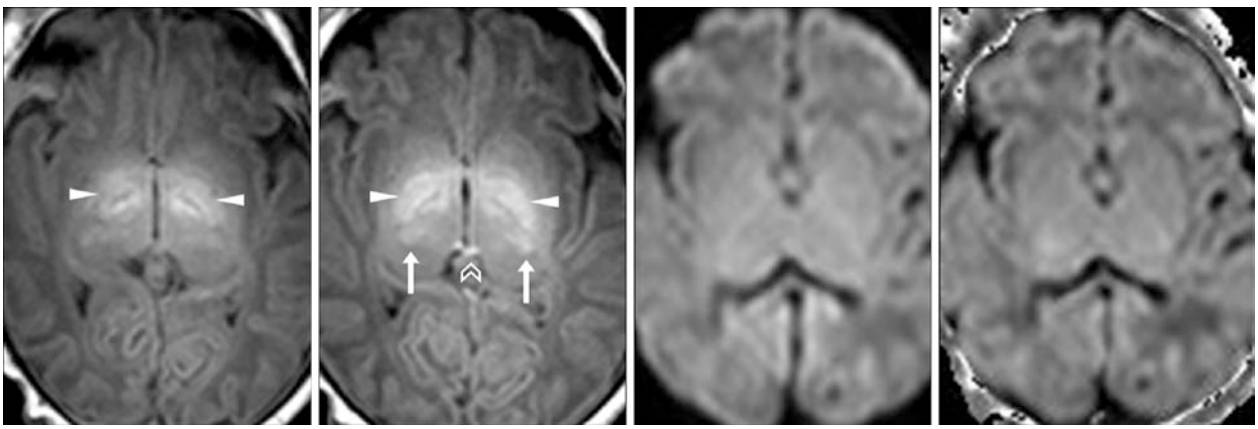

Fig. 23.15 A 7-day-old term neonate with a seizure at birth and respiratory depression had a normal 3T MRI that included GE T1WI (*left* and *left middle*). DWI (*right middle*) and an exponential DWI that removes vasogenic edema (*right*) both showed no basal ganglial cytotoxic edema. Note brightness of the posterior putamina (*arrowheads*), ventrolateral thalami (*arrows*), and habenular commissure (*chevron*); the PLIC is bright, but difficult to visualize. The infant's follow-up neurologic examination at 1 year was normal

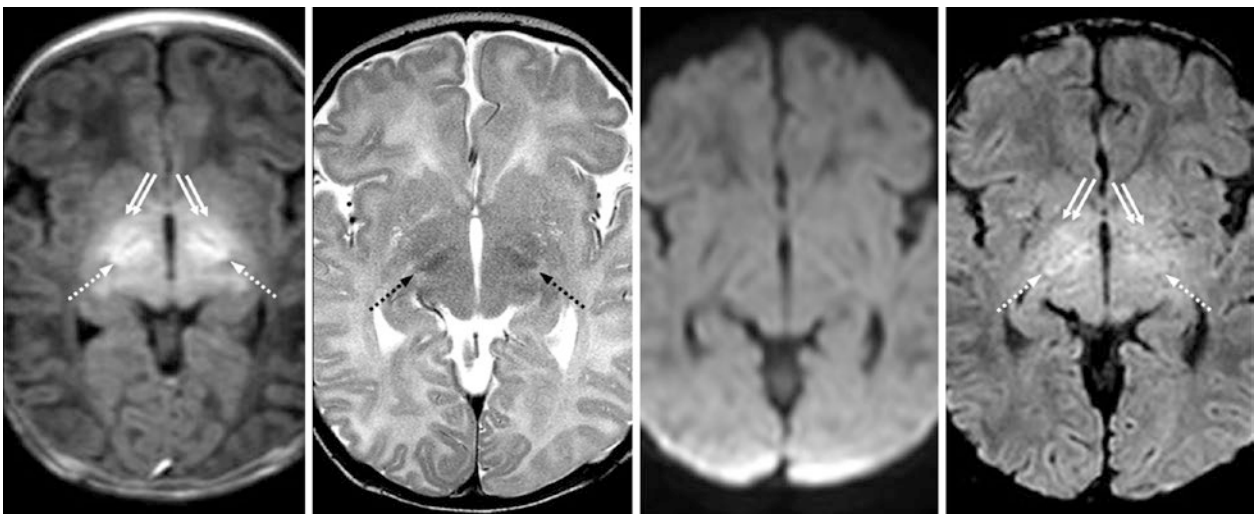

Fig. 23.16 A 15-day-old term neonate with respiratory depression at birth had a normal 3T MRI, which included spoiled GE T1WI (*left*), SE T2WI (*left middle*), DWI (*right middle*), and SWI (*right*). Both the subthalamic nuclei (STN) (*dotted arrows*) and GP (*double arrows*) are bright on GE T1WI; only the STN is dark on T2WI. On SWI, there is bright signal within the STN and GP, likely owing to "T1 shine-through" effect, as SWI is a gradient echo-based image. The follow-up clinical examination at 1 year was normal

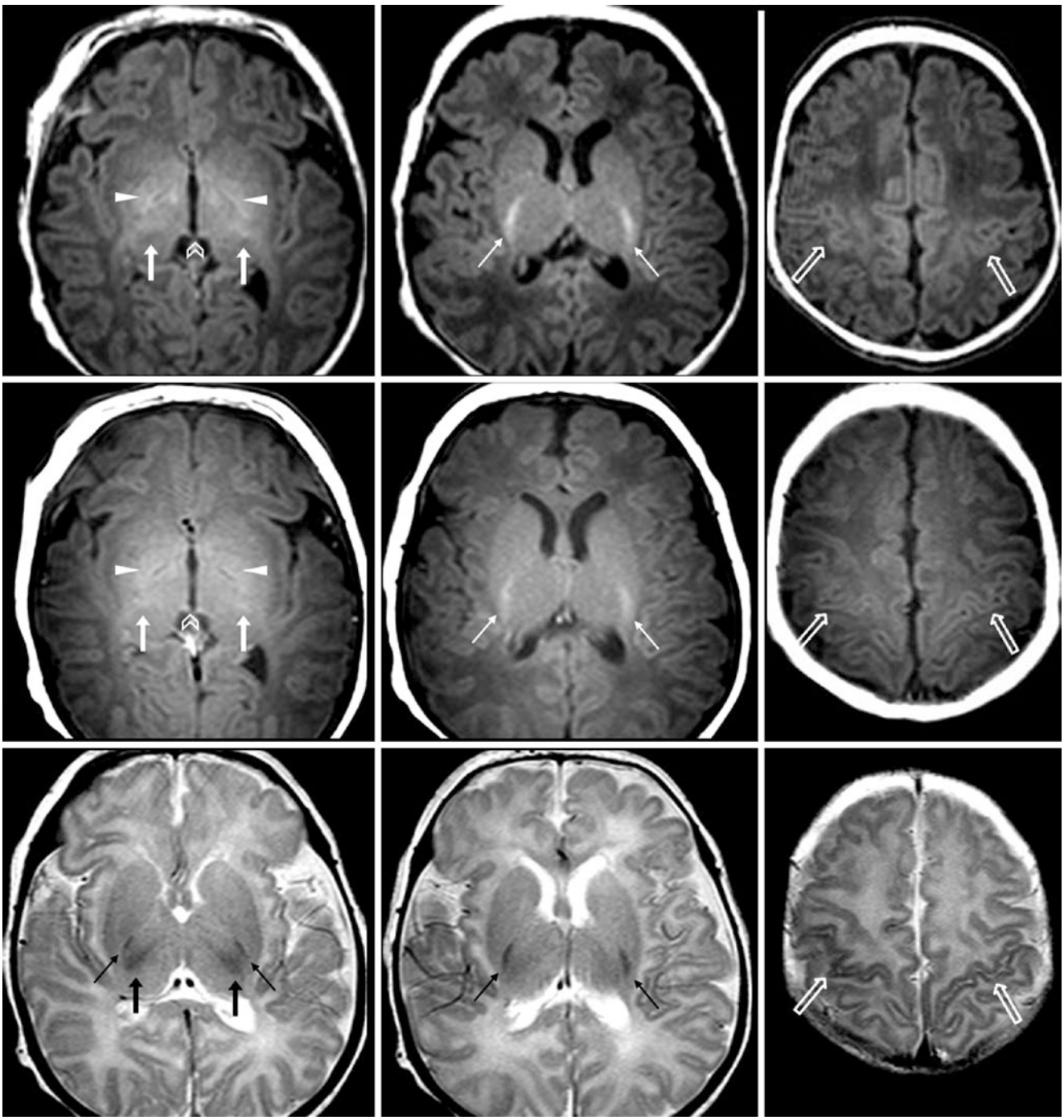

Fig. 23.17 A 21-day-old term neonate with poor feeding and a normal 3T MRI. *Top row*: Spoiled GE T1WI shows only mildly bright signal within the posterior putamina (*arrowheads*) and VLT (*arrows*). *Middle row*: SE T1WI shows even less bright GP and VLT, compared with GE T1WI. Note a mildly bright habenular commissure (*chevrons*). *Bottom row*: SE T2WI shows continued dark signal within the GP and VLT. The PLIC (*thin arrows*) continues to stay bright on GET1WI and SE T1WI. Note the normal, dark perirolandic cortex (PRC) (*open arrows*) bilaterally, which is darker than the normally dark "ribbon" of cortices elsewhere

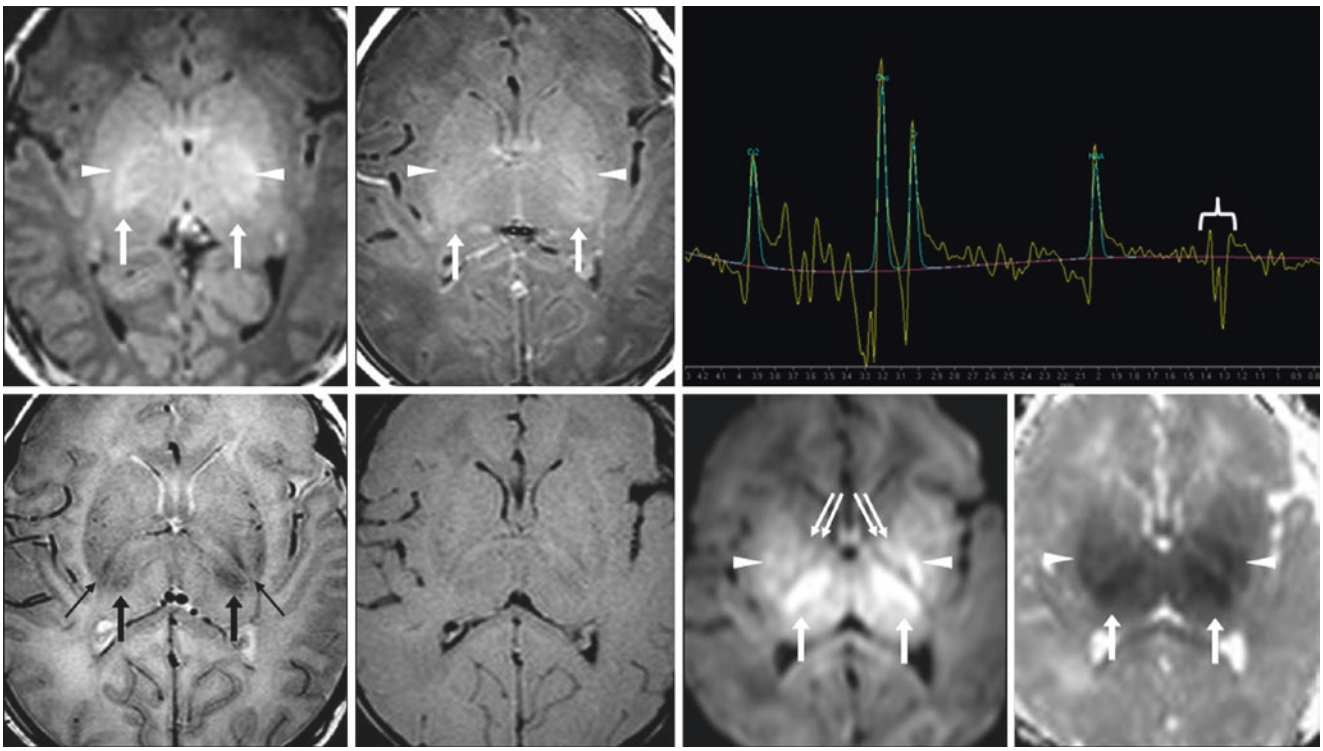

Fig. 23.18 Comparison case of hypoxic-ischemic injury (HII). A 4-day-old term neonate with a hypoxic event, seizure, and an abnormal EEG had a abnormal 3T MRI, which included "blotchy" basal ganglia and globi pallidi (*double arrows*) that appeared too bright and bunched together on GE T1WI (*top left*) and SE T1WI (*top middle*). MR spectroscopy (*top right*) showed a lactate peak (*bracket*); it is inverted due to the echo time (TE) of 144 ms. SE T2WI (*bottom left*) suggested LN edema, but FLAIR (*bottom*, *left middle*) did not. DWI (*bottom*, *right middle*) and the ADC map (*bottom right*) showed insults of the VLT (*arrows*) and LN, especially the PP (*arrowheads*)

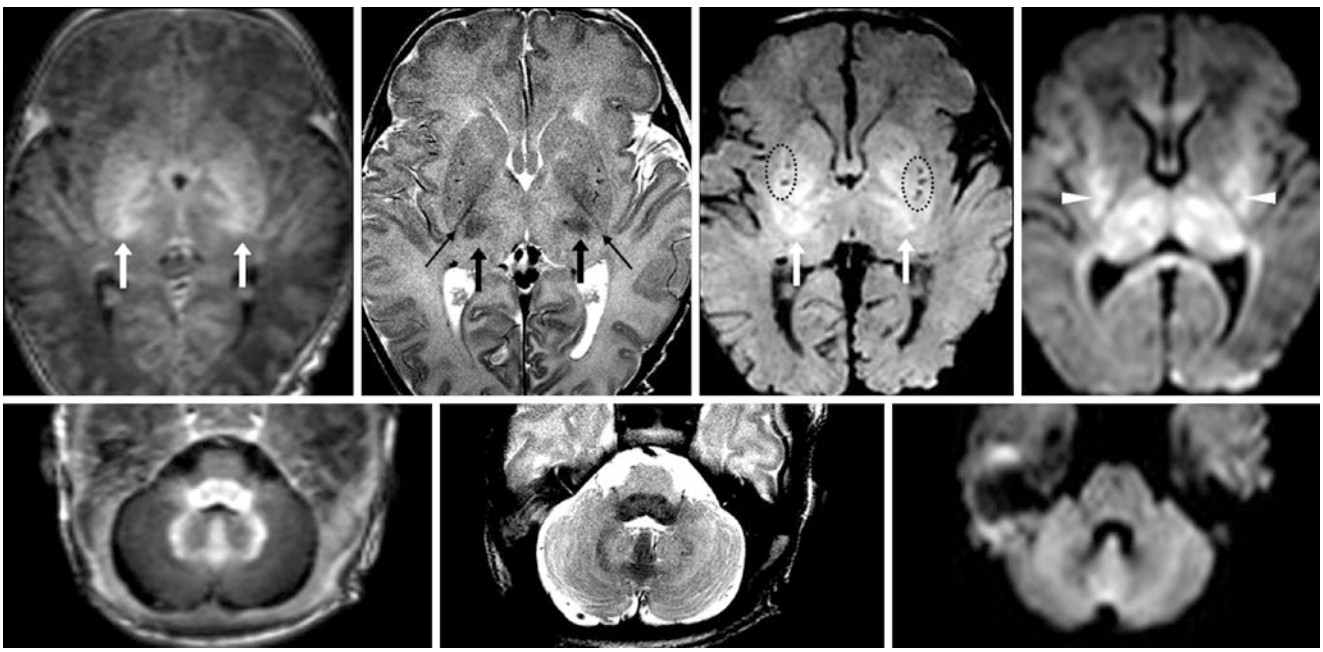

Fig. 23.19 Comparison case of HII. A 4-day-old term neonate with hypoxia and a seizure underwent a 3T MRI. The LN and VLT (*arrows*) were uniformly bright on GE T1WI (*top left*), with mild edema on SE T2WI (*top*, *left middle*). On SWI (*top*, *right middle*) the LN and VLT were bright due to "T1 shine-through," with punctate hemorrhages laterally (*dotted circles*). DWI (*top right*) confirmed PP (*arrowheads*), thalamic, and callosal insults. GE T1WI (*bottom left*) and T2WI (*bottom middle*) also showed T1-bright, T2-dark insults of the cerebellum and dorsal brainstem, not being bright on DWI (*bottom right*)

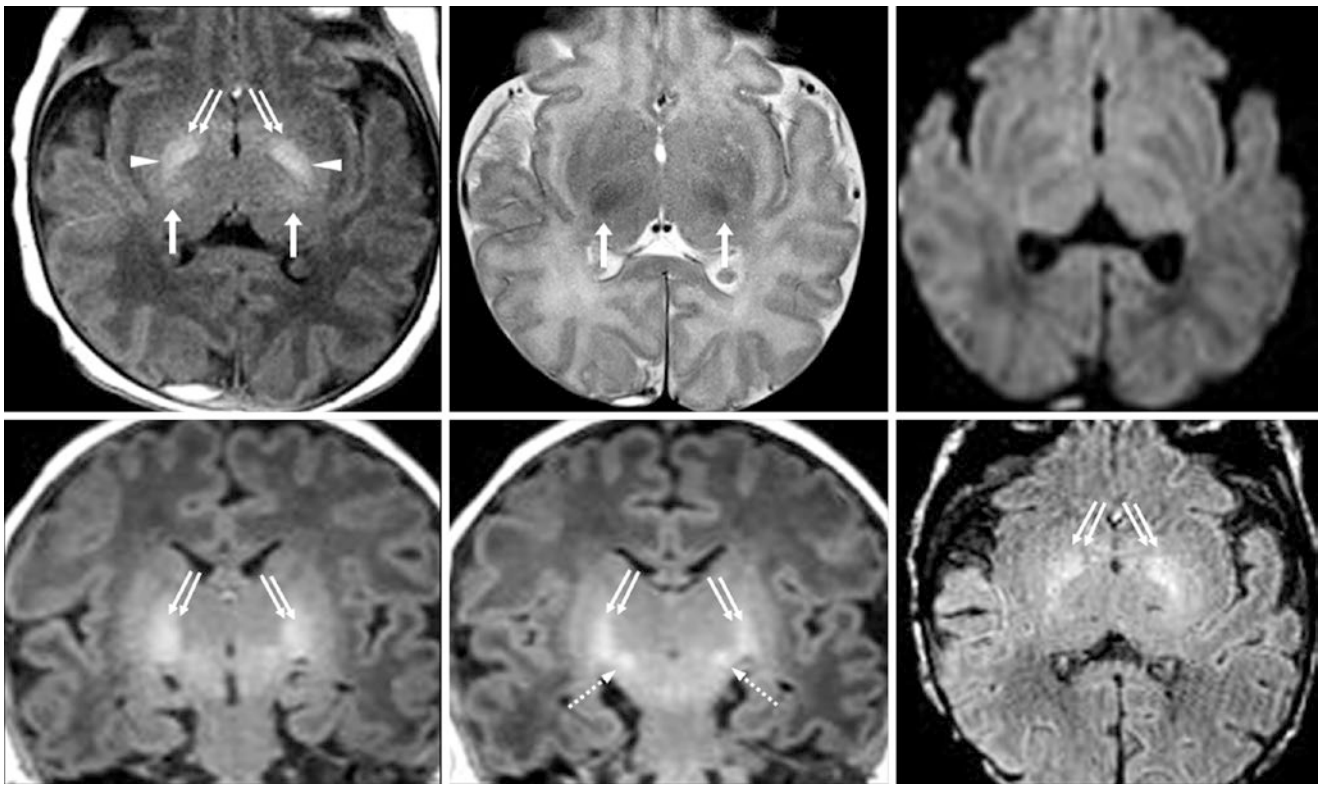

Fig. 23.20 Comparison case of kernicterus. A 15-day-old term neonate with hyperbilirubinemia and hypertonia had a 1.5T MRI that showed profoundly bright signal of the GP (*double arrows*) on GE T1WI (*top left*), with minimal findings on SE T2WI (*top middle*), perhaps representing a milder degree of insult. The lack of findings on DWI (*top right*) likely relates to the subacute age of the insults. Coronal GE T1WIs (*bottom left* and *middle*) also showed the T1-bright insults within the GP (*double arrows*) and STN (*dotted arrows*), which are usually affected. The bright GP on SWI (*bottom right*) is thought to be due to T1 shine-through

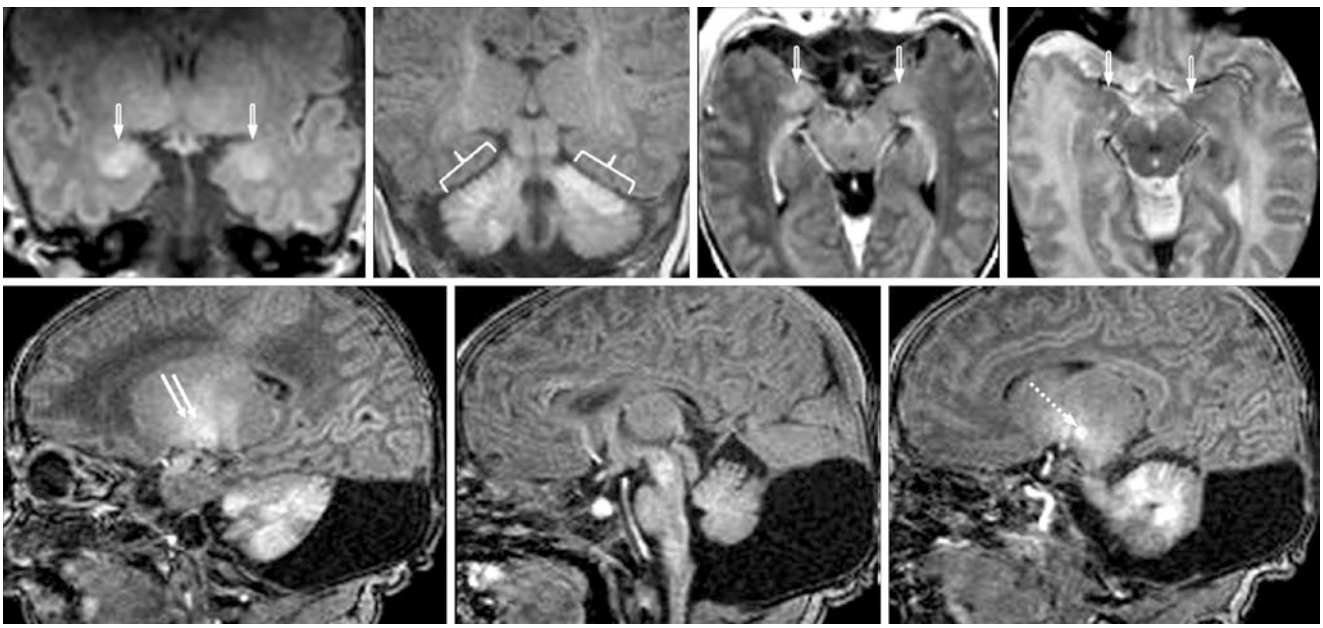

Fig. 23.21 Comparison case of neurocutaneous melanosis. A 3-day-old term neonate with seizures (without hypoxia) had a 1.5T MRI that showed bright signal within the amygdalae (*beveled arrows*) on coronal GE T1WI (*top left* and *left middle*) and postcontrast T1WI (*top*, *right middle*), being dark on SE T2WI (*top right*). There was also T1-bright signal of the cerebellar cortices (*brackets*), being even brighter than the GP (*double arrows*) and STN (*dotted arrows*), as shown on sagittal T1WIs (*bottom row*). DWI (*not shown*) was negative. Also, note cerebellar hypoplasia and an enlarged posterior fossa

23.3 Normal Myelination and Variation in Term Neonates at 3T

The following sections display *normal myelination in term infants* with normal neurologic and developmental outcomes at clinical follow-up. As previously discussed, *T1-bright signal* may be present in term infants at birth within the posterior limb of the internal capsule (PLIC), *ventrolateral thalami* (VLT), *globus pallidi* (GP), *posterior putamina* (PP), and the *subthalamic nuclei* (STN) [6–12]. White matter tracts that have been described to be myelinated in nearly all term infants or term-equivalent infants (*i.e.*, premature infants imaged at a corrected postnatal gestational age of 38–42 weeks) at 3T include the *brachium of the inferior colliculus* (BIC), *decussation of the superior cerebellar peduncle* (DSCP), and *medial leminisci* (ML), whether on spoiled GE T1WI or on SE T2WI; the *PLIC* should be seen in all infants on both sequences, but may appear rather tiny on T2WI [11, 12]. With regards to GE T1WI, additional structures that are visualized as bright—that is, presumed to be "myelinated"—in more than 90% of infants at term or term-equivalent age include the *habenular commissure* (HC), *lateral leminisci* (LL), *pyramidal decussation* (PD), and the *superior cerebellar peduncles* (SCP). On SE T2WI, an additional structure that is visualized as dark (presumed to be myelinated) in nearly all infants at term or term-equivalent age is the *inferior cerebellar peduncle* (ICP). These findings are based on infants who were subsequently developmentally normal [11, 12]. Although not always present, other white matter tracts that appear myelinated in the majority of infants at term or term-equivalent age include the optic tracts (OT) on both GE T1WI and SE T2WI. On GE T1WI, this is present in a majority along the fascicle of cranial nerve V (CNV) within the brainstem, as well as the corticospinal tracts (CST) at the level of the corona radiata. Most are also myelinated within the HC, medial longitudinal fasciculus (MLF), PD, PLIC, SCP, and spinal tracts of V (STV) on SE T2WI. Table 23.1 provides a quick reference to help in remembering these structures.

Therefore, the assessment of myelination in a term or term-equivalent infant may appear complex, but may be facilitated by the identification of certain structures as "myelinated" on GE T1WI and SE T2WI at 3T. It is recommended that both sequences are assessed, at a minimum [11, 12]. Of course, such findings should be correlated with the presence or absence of findings such as cytotoxic edema on DWI, which can show most (but not all) findings of *hypoxic-ischemic injury* (HII), particularly within the basal ganglia, white matter tracts, or cortices. DWI is typically useful only within the acute or early subacute phase of HII (0–7 days post-insult), and it may actually underestimate the final extent of insult [13, 14]. FLAIR images are of quite limited use in the neonate evaluation, with the exception of extraaxial *hemorrhage* or neonatal *meningitis*, as FLAIR is better than noncontrast T2WI or T1WI at detecting exudate or hemorrhage within the subarachnoid or subdural space.

The prior topic briefly discussed several criteria to evaluate for the presence of HII, including an abnormal appearance of the basal ganglia, thalami, or cortices on T1WI, DWI, and SWI, along with the oft-helpful findings of

Table 23.1 Normal Myelination in Term Neonates at 3T

Myelination (presumed)	GE T1WI	SE T2WI
Present in 90–100% of term or term-equivalent infants	BIC	BIC
	DSCP	DSCP
	HC	ICP
	LL	ML
	ML	PLIC (but tiny)
	PD	
	PLIC	
	SCP	
Present in >50% of term or term-equivalent infants	CNV	HC
	CST	MLF
	ICP	OT
	OT	PD
		PLIC
		PRC
		SCP
		STV

BIC brachium of the inferior colliculus, *CNV* fascicle of cranial nerve V, *CST* corticospinal tracts, *DSCP* decussation of the superior cerebellar peduncle, *GE T1WI* gradient echo T1-weighted imaging, *HC* habenular commissure, *ICP* inferior cerebellar peduncle, *LL* lateral leminisci, *ML* medial leminisci, *MLF* medial longitudinal fasciculus, *OT* optic tracts, *PD* pyramidal decussation, *PLIC* posterior limb of the internal capsule, *PRC* perirolandic cortex, *SCP* superior cerebellar peduncles, *SE T2WI* spin echo T2-weight imaging, *STV* spinal tracts of V

multifocal loss of the normal, uniformly dark "ribbon" on T2WI relative to the underlying T2-bright subcortical white matter (SCWM). Again, in HII, cortical abnormal signal is usually relatively easily visualized on T1WI if present, particularly within the perirolandic cortex (PRC), which will appear much brighter in HII than the faintly bright signal that may or may not be present in normal term infants. Such bright signal can extend from the PRC down through the CST within the corona radiata to the PLIC [9–17]. Therefore, this section focuses on the appearance of what is presumed (although not entirely proven) to be either myelination or a precursor of normal myelination, based on the presence of bright signal on GE T1WI or dark signal on T2WI. As infants are now commonly evaluated by 3T MR imaging, this section focuses on appearances at the higher 3T field strength rather than at 1.5T; it is safe to say that structures that appear bright at 1.5T are even brighter at 3T on GE T1WI, although they may appear less bright on SE T1WI (owing to the closer T1 times of gray and white matter at 3T).

23.3.1 Normal Myelination in Term Neonates at 3T: Craniocervical Junction to the Mid Medulla

On 3T axial GE T1WI and SE T2WI at levels from the craniocervical junction and medulla, the *inferior cerebellar peduncle* (ICP), *pyramidal decussation* (PD), and *spinal tract of V* (STV) are commonly seen and can be routine markers to indicate normal, healthy myelination. Notably, the PD and the decussation of the ML are either one axial image away from each other, or volume-averaged together on one axial image, so for the purposes of this text, the term "PD" is utilized. Other cranial nerve nuclei, such as the vestibular nuclei and inferior olivary nuclei, may also be visualized in most patients at these axial levels, if the slice thickness and sequence are optimal, but these nuclei are not focused on here, as they can be difficult to identify at times with certainty. 3D FLAIR acquisitions, though exquisite, are often of little help in assessing myelination (Figs. 23.22, 23.3, 23.4, 23.5, 23.6 and 23.27).

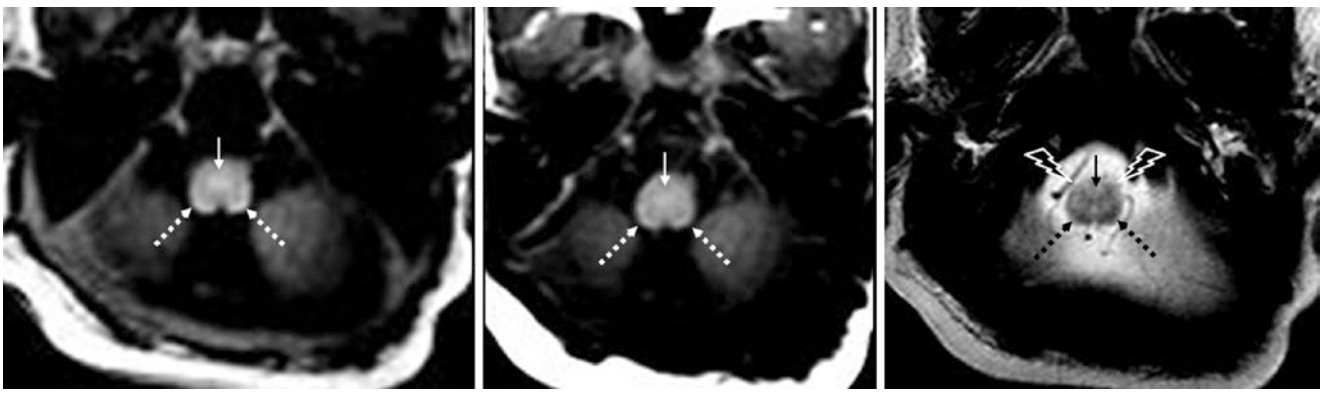

Fig. 23.22 A 3-day-old term neonate had a normal 3T MRI, including spoiled GE T1WI (*left*), SE T1WI (*middle*) and SE T2WI (*right*). Note the mildly T1-bright and T2-dark pyramidal decussation (PD) (*tiny arrows*) and spinal tracts of V (STV) (*dotted arrows*). Note tiny, inferior olivary nuclei (*lightning bolts*)

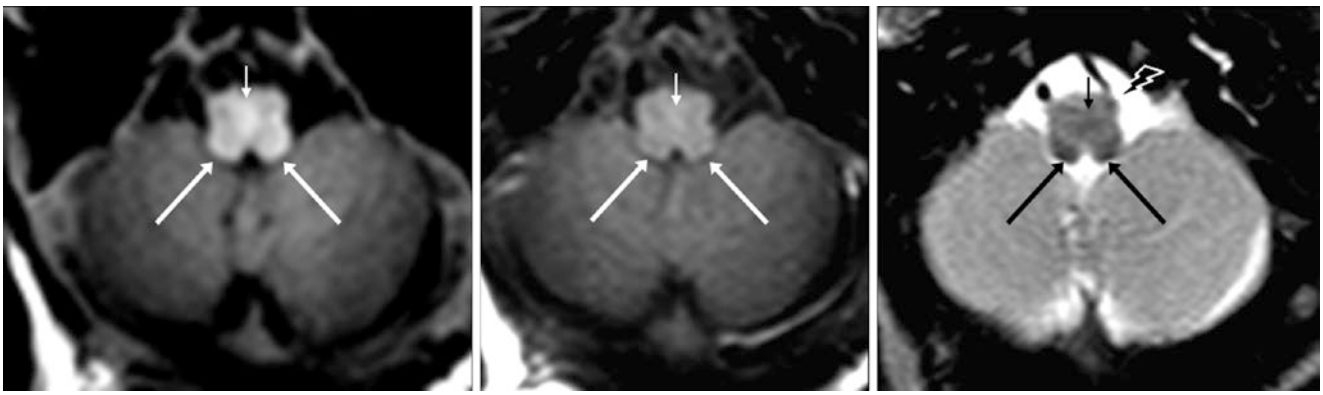

Fig. 23.23 A 7-day-old term neonate had a normal 3T MRI, including spoiled GE T1WI (*left*), SE T1WI (*middle*) and SE T2WI (*right*). Note the mildly T1-bright and T2-dark PD (*tiny arrows*) and inferior cerebellar peduncles (ICP) (*long arrows*). Note a tiny, left inferior olivary nucleus (*lightning bolt*)

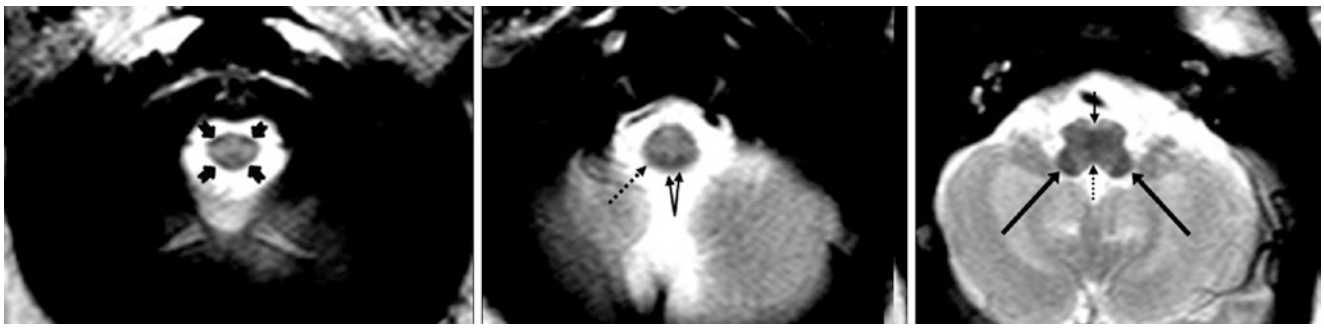

Fig. 23.24 A 21-day-old term neonate had a normal 3T MRI with SE T2WI. There were mildly dark ICP (*long arrows*), PD (*tiny arrow*), and right STV (*dotted arrows*), along with gracile fasciculi (*split arrows*). Both the anterior and posterior spinocerebellar tracts are visible (*notched arrows*), as well as the medial longitudinal fasciculus (*tiny dotted arrow*), located dorsal to the PD/ML decussation

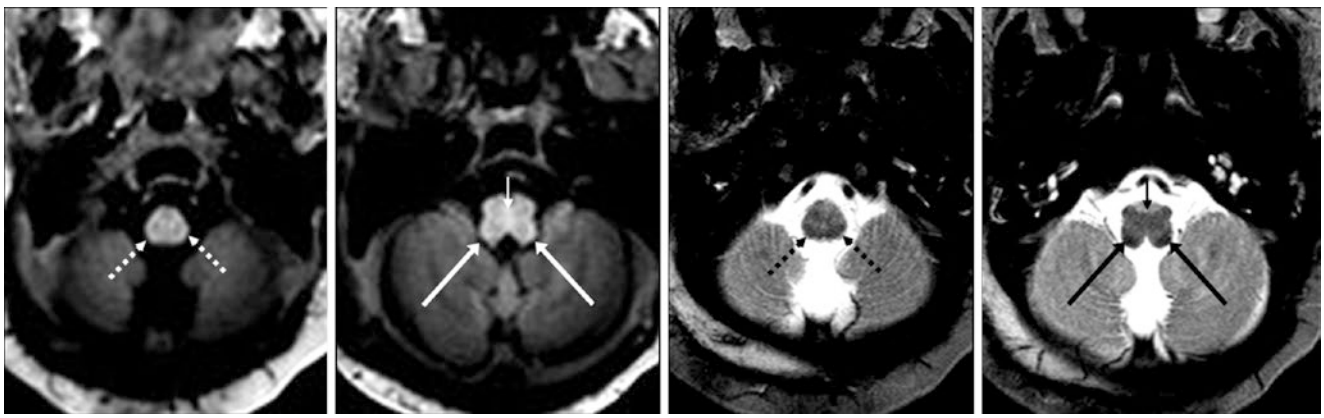

Fig. 23.25 A 4-day-old term neonate had a normal 3T MRI with GE T1WI (*left images*) and SE T2WI (*right images*). Note the ICP (*long arrows*) and STV (*dotted arrows*), which are better visualized on SE T2WI. The PD (*tiny arrow*) is not well seen on SE T1WI (*not shown*) or on SE T2WI

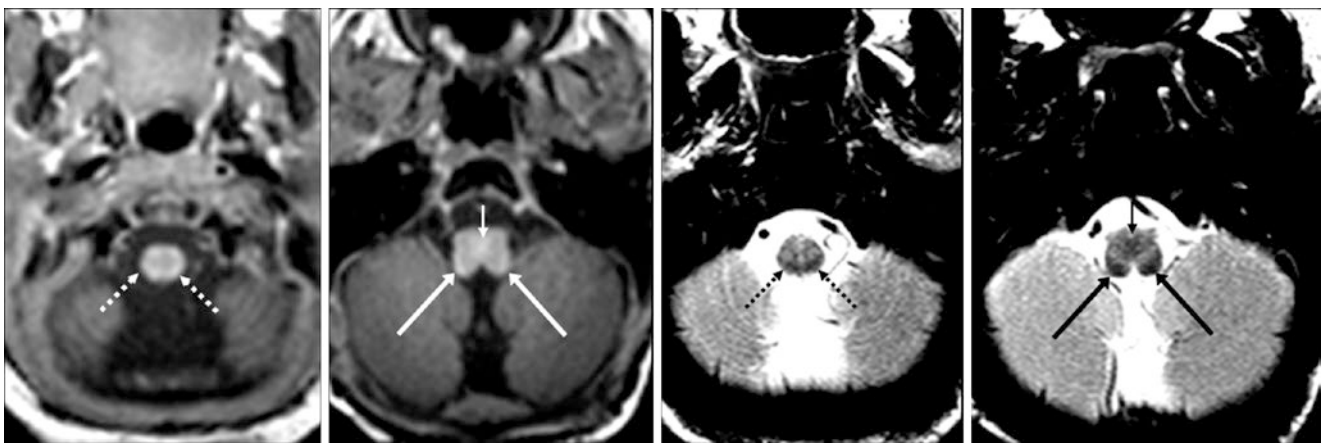

Fig. 23.26 A 6-day-old term neonate had a normal 3T MRI with GE T1WI (*left images*) and SE T2WI (*right images*). Note the ICP (*long arrows*), PD (*tiny arrows*), and STV (*dotted arrows*). This case illustrates how lower medullary structures are often better visualized on SE T2WI

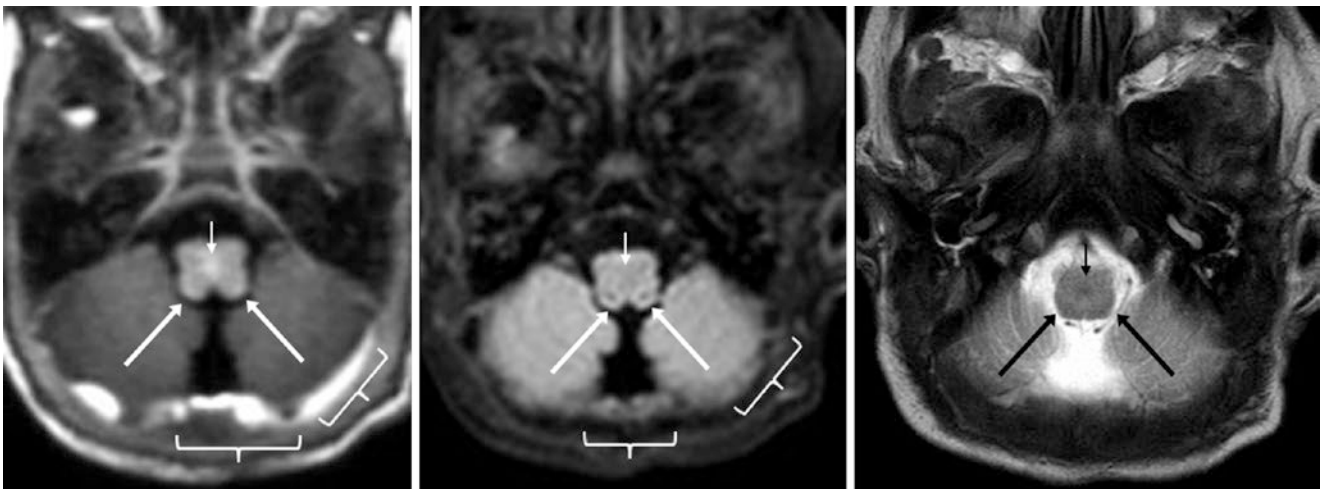

Fig. 23.27 A 17-day-old term neonate had a normal 3T MRI with GE T1WI (*left*), 3D FLAIR axial reconstruction (*middle*), and SE T2WI (*right*). Note that the ICP (*long arrows*) and PD (*tiny arrows*) are faintly visible on both GE T1WI and SE T2WI. On axial 3D FLAIR at the same thickness, the PD is not visible, but the ICPs have mild, low signal along their inner aspects. Note a typical subdural hematoma posteriorly (*brackets*), being present in many asymptomatic neonates

23.3.2 Normal Myelination in Term Neonates at 3T: Upper Medulla to Mid Pons

On 3T axial GE T1WI and SE T2WI at levels from the upper medulla up to the mid pons, structures such as the *ICP*, *LL*, *ML*, and the *SCP* should be routinely visualized in nearly all term neonates (along with the dorsal pons); the *CNV* can be recognized in at least half on GE T1WI. Additionally, dark signal should be present within the *cerebellar nodulus*, *vermis*, and *corpus medullare* (central white matter of the cerebellum) in all term neonates who are subsequently developmentally normal. Again, SE T1WI is usually not as helpful at 3T in assessing myelination, particularly with regards to the subtle anatomy of the brainstem. 3D FLAIR acquisitions can yield high-resolution images but are usually of little help in assessing myelination (Figs. 23.28, 23.29, 23.30, 23.31, 23.32, 23.33, 23.34 and 23.35).

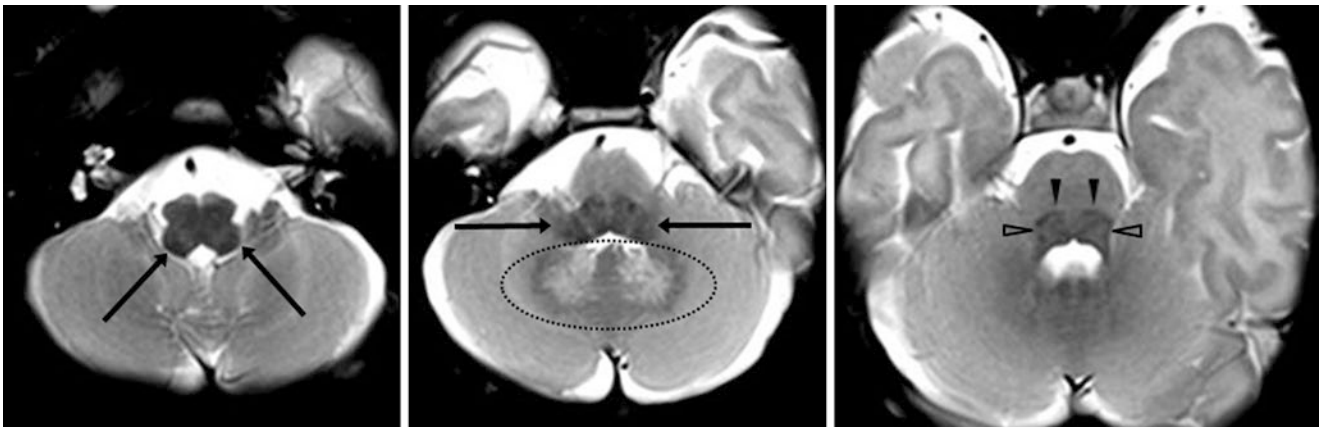

Fig. 23.28 A 1-day-old term neonate had a normal 3T MRI with SE T2WIs, which demonstrate the ICP (*long arrows*) at two levels. Also, note the lateral leminisci (LL) (*open arrowheads*) and medial leminisci (ML) (*arrowheads*). The cerebellar nodulus and corpus medullare are darkening on T2WI (*dotted oval*)

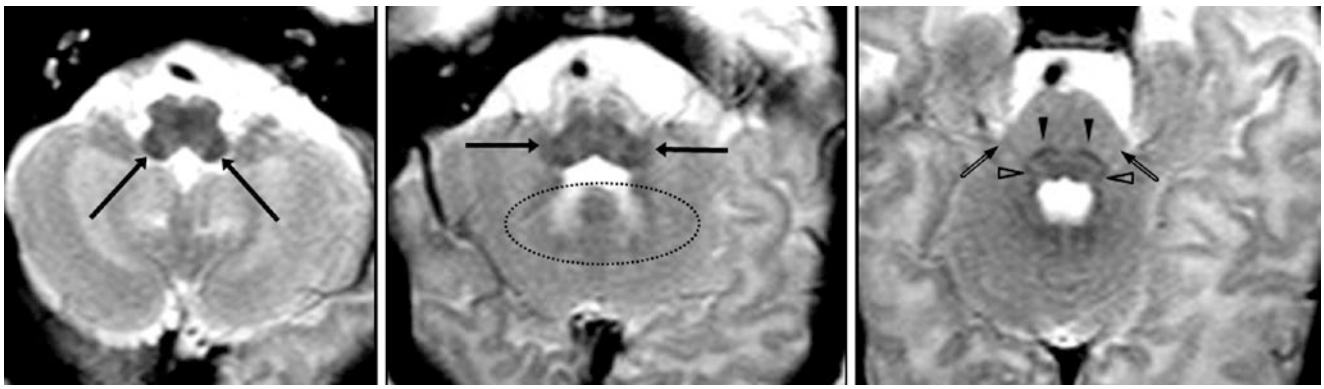

Fig. 23.29 A 21-day-old term neonate had a normal 3T MRI with SE T2WIs, which demonstrate the ICP (*long arrows*) at two levels. Also, note the LL (*open arrowheads*), ML (*arrowheads*), and cranial nerve V fascicles (CNV) (*beveled arrows*). Again, note the darkening cerebellar nodulus and corpus medullare (*dotted oval*)

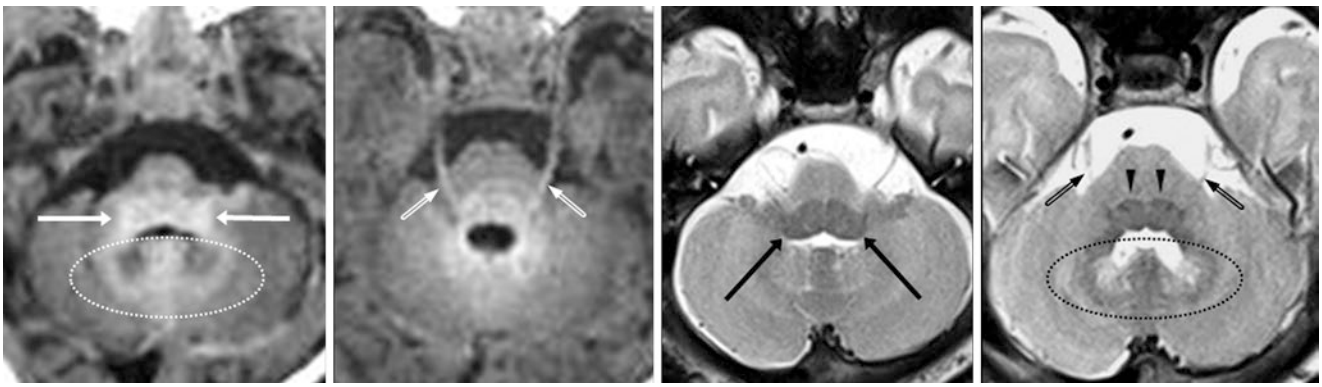

Fig. 23.30 A 4-day-old term neonate had a normal 3T MRI with GE T1WI (*left images*) and SE T2WI (*right images*). Note the ICP (*long arrows*), ML (*arrowheads*), and CNV (*beveled arrows*). Note that the cerebellar nodulus and corpus medullare are "myelinating" (*dotted ovals*)

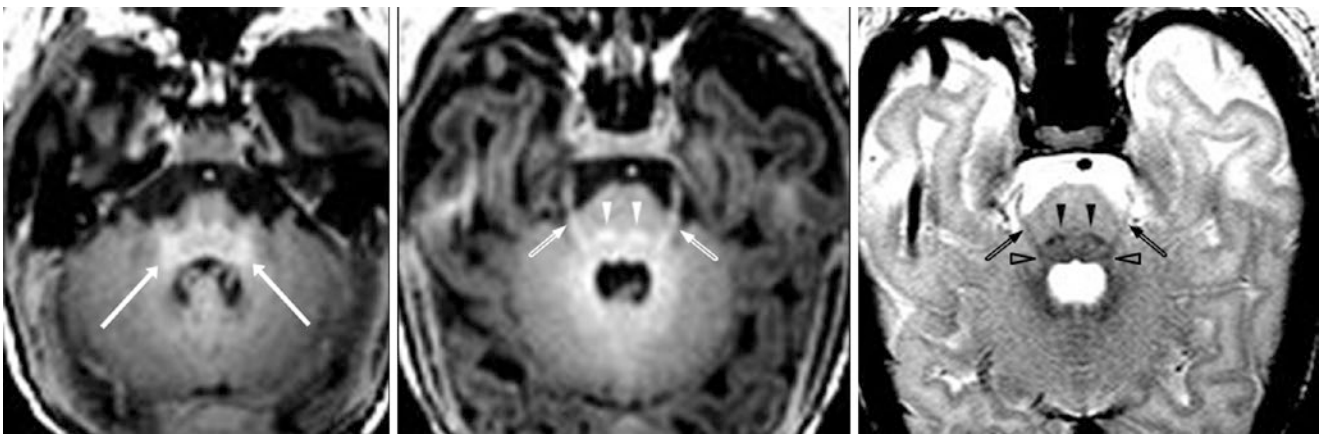

Fig. 23.31 A 6-day-old term neonate had a normal 3T MRI with GE T1WI (*left* and *middle*) and SE T2WI (*right*). Note the ICP (*long arrows*), LL (*open arrowheads*), ML (*arrowheads*), and CNV (*beveled arrows*). The fascicles of CNV can be followed anteriorly as the nerves into the cistern on both sides

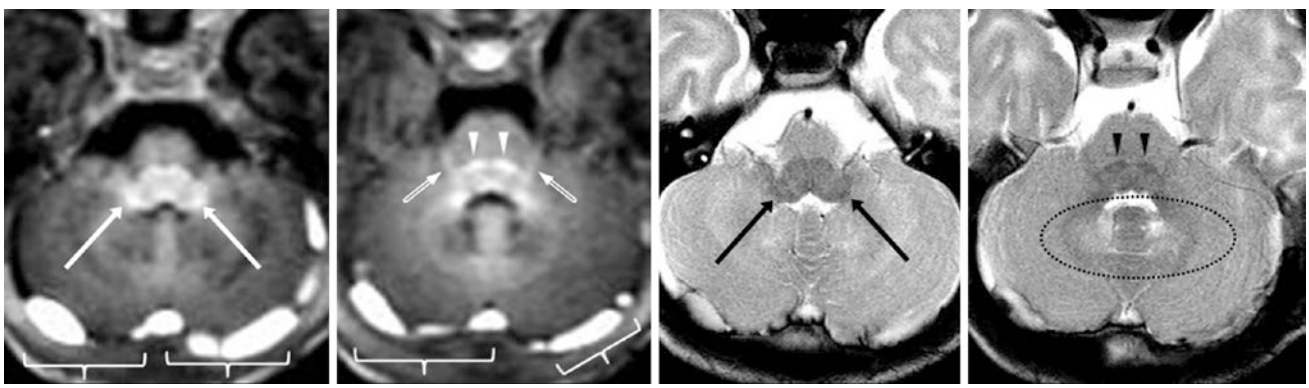

Fig. 23.32 A 17-day-old term neonate had a normal 3T MRI with GE T1WI (*left images*) and SE T2WI (*right images*). Note the CNV (*beveled arrows*), ICP (*long arrows*), and ML (*arrowheads*). Note the darkening cerebellar nodulus and corpus medullare on SE T2WI (*dotted oval*). Also, note the asymptomatic posterior fossa subdural hematoma (*brackets*), which is present in many newborns

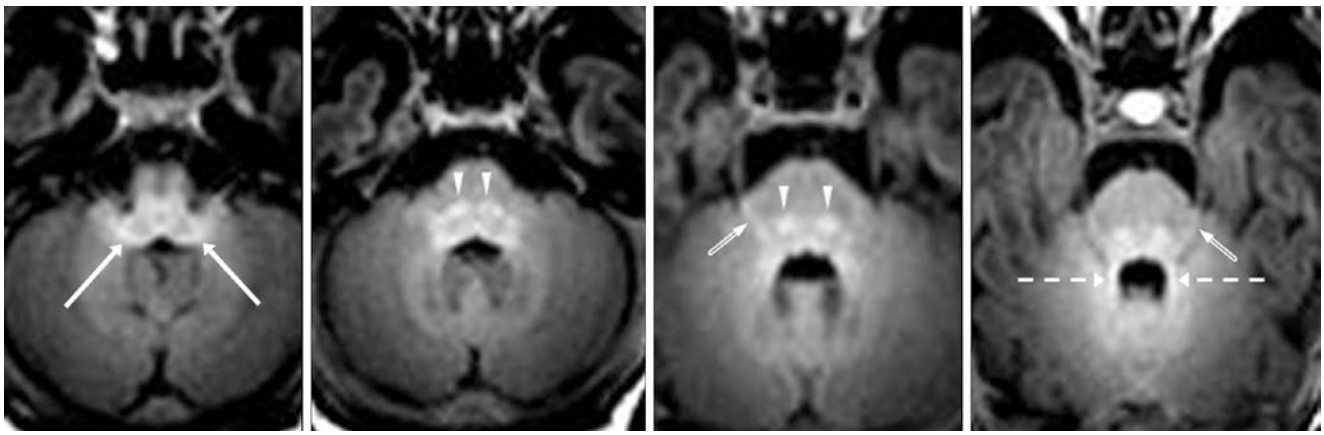

Fig. 23.33 A 5-day-old term neonate had a normal 3T MRI with GE T1WIs. Note the ICP (*long arrows*), ML (*arrowheads*), and CNV (*beveled arrows*). The fascicles of CNV can be followed anteriorly as the nerves into the cistern on both sides. Also, note the bottom of the superior cerebellar peduncles (SCP) (*dashed arrows*)

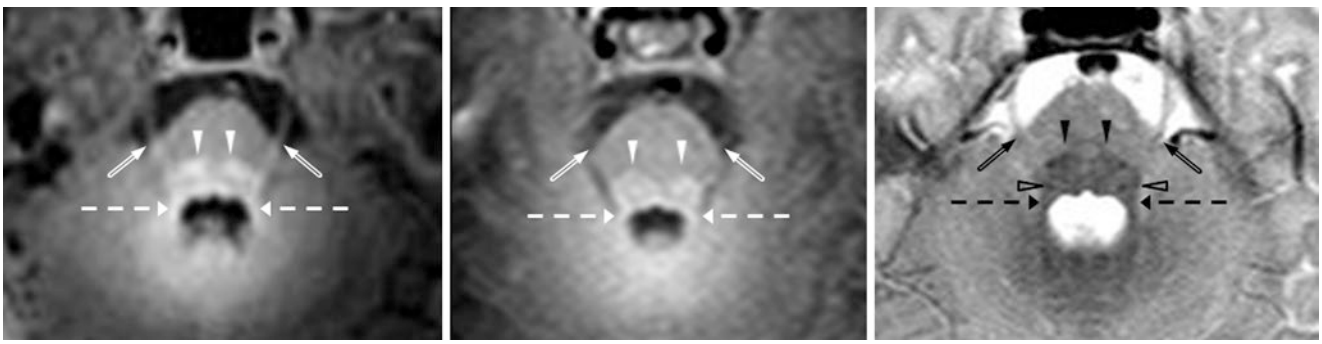

Fig. 23.34 A 4-day-old term neonate had a normal 3T MRI with GE T1WI (*left*), SE T1WI (*middle*), and SE T2WI (*right*). Note the CNV (*beveled arrows*), LL (*open arrowheads*), ML (*arrowheads*), and SCP (*dashed arrows*). The fascicles of CNV can be followed to the nerves into the cistern on both sides

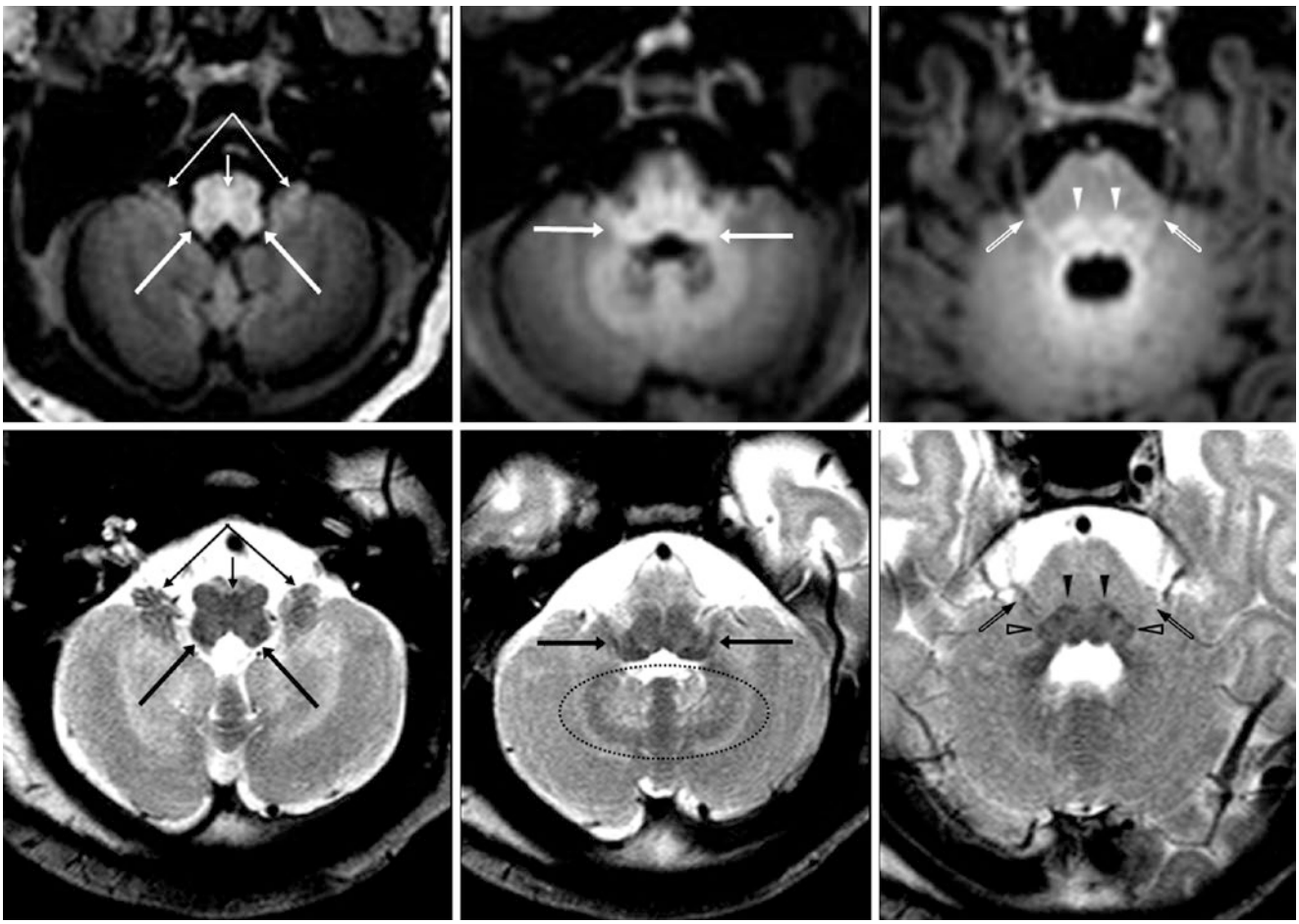

Fig. 23.35 A 3-day-old term neonate had a normal 3T MRI with GE T1WI (*top row*) and SE T2WI (*bottom row*). Note the CNV (*beveled arrows*), ICP (*long arrows*), LL (*open arrowheads*), ML (*arrowheads*), and PD (*tiny arrows*). On SE T2WI, myelination of the cerebellar floculi (*split arrows*) as well as of the nodulus and corpus medullare (*dotted oval*) are better visualized, while CNV and PD are better visualized on GE T1WI

23.3.3 Normal Myelination in Term Neonates at 3T: Mid Pons to Mid Mesencephalon

On 3T axial GE T1WI and SE T2WI at levels from the upper pons through the midbrain, the *BIC* and *DSCP* are routinely seen as myelinated in all term neonates and term-equivalent infants who are subsequently normal; these can be considered routine markers to indicate normal, healthy myelination. Additionally, the *SCP* should be visible on in all term neonates on GE T1WI, and in the large majority on SE T2WI. Also, the *optic tracts* usually appear myelinated on both sequences, but the optic nerve anteriorly usually does not. Additionally, at these axial levels, other structures that may exhibit T1-bright and/or T2-dark myelination include the cerebellar vermis, medial geniculate nuclei (MGN), and amygdalae (Figs. 23.36, 23.37, 23.38, 23.39, 23.40, 23.41, 23.42 and 23.43).

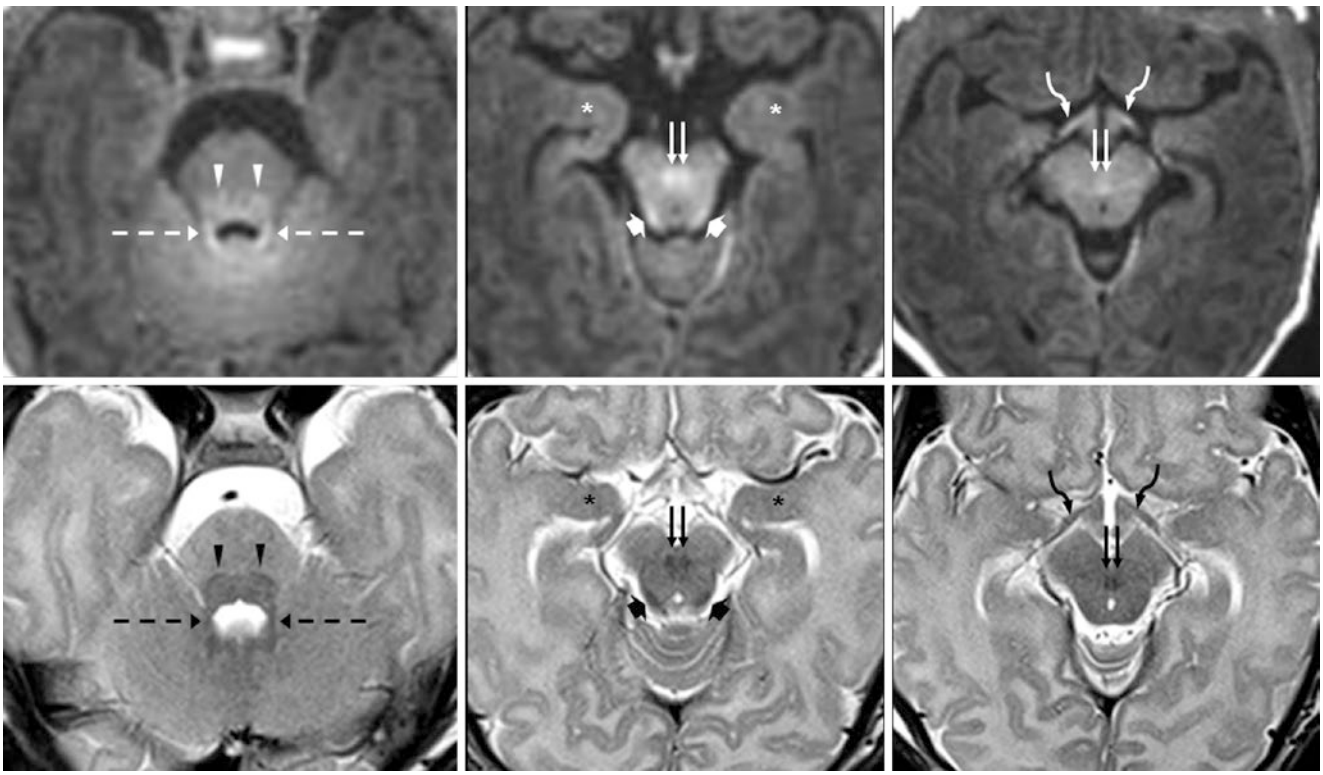

Fig. 23.36 A 4-day-old term neonate had a normal 3T MRI with GE T1WIs (*top row*) and SE T2WIs (*bottom row*). Note the brachia of the inferior colliculi (BIC) (*wide arrows*), the decussation of the SCP (DSCP) (*double arrows*), the ML (*arrowheads*), and the SCP (*dashed arrows*). The optic tracts (*curved arrows*) are myelinated in this patient, and are visualized as such in most term neonates. There may also be early myelination of the amygdalae (*asterisks*), better visualized on T2WI

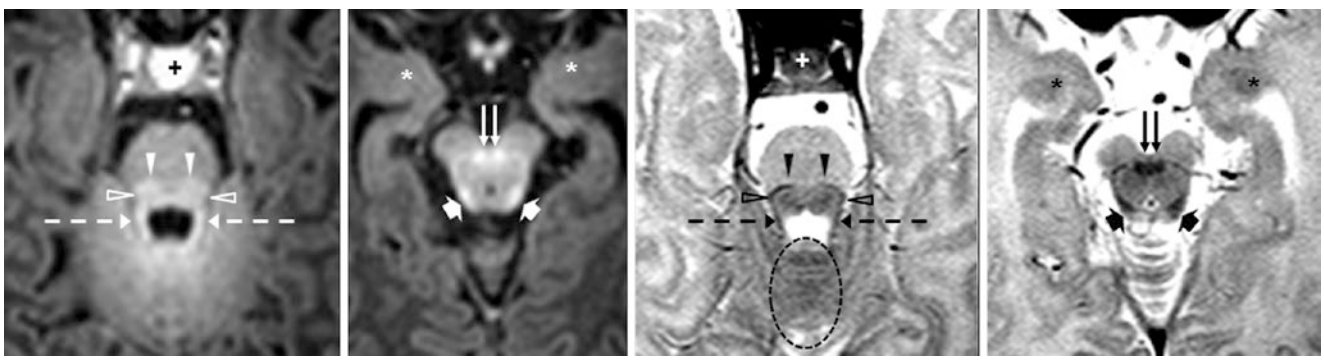

Fig. 23.37 A 6-day-old term neonate had a normal 3T MRI with GE T1WIs (*left images*) and SE T2WIs (*right images*). The BIC/inferior colliculi (*wide arrows*), DSCP (*double arrows*), LL (*open arrowheads*), ML (*arrowheads*), and SCP (*dashed arrows*) all appear myelinated. Note "myelination" of the superior cerebellar vermis (*dotted oval*), and perhaps the amygdalae (*asterisks*), along with a normal, homogenously T1-bright pituitary (*plus sign*)

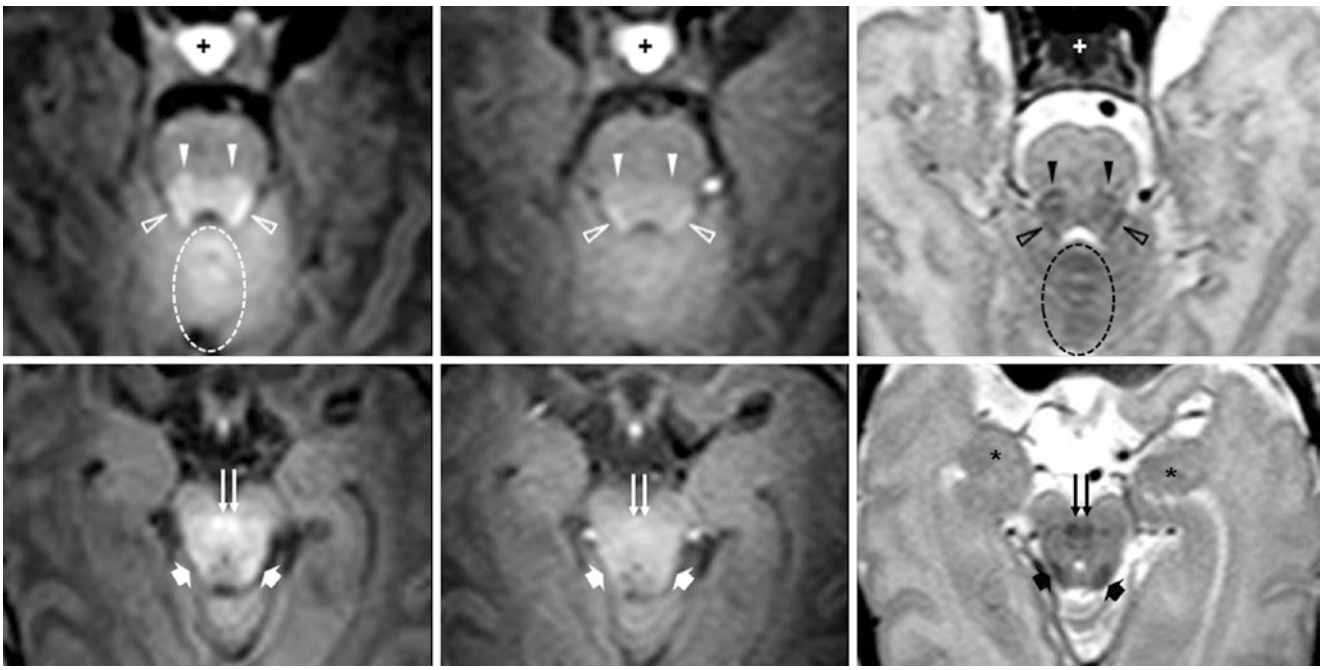

Fig. 23.38 A 7-day-old term neonate had a 3T MRI with GE T1WI (*left column*) and SE T2WI (*right column*), on which both the BIC (*wide arrows*) and the DSCP (*double arrows*) should be visible in all term neonates, but are not well seen on SE T1WI (*middle column*). Also, note myelination of the LL (*open arrowheads*), ML (*arrowheads*), cerebellar vermis (*dotted ovals*) and amygdalae (*asterisks*). A T1-bright and T2-dark pituitary (*plus sign*) is normal at this age; it usually evolves into the typical adult appearance by about 6 weeks of age

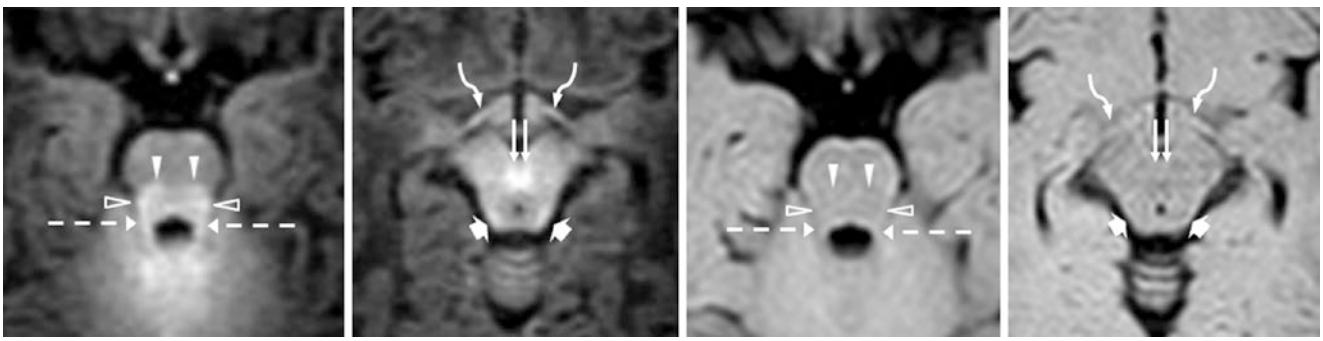

Fig. 23.39 A 17-day-old term neonate had a normal 3T MRI with axial GE T1WIs (*left images*) and 3D FLAIR (*right images*). There is T1-bright myelination of the BIC (*wide arrows*), DSCP (*double arrows*), LL (*open arrowheads*), ML (*arrowheads*), optic tracts (*curved arrows*), and SCP (*dashed arrows*). FLAIR does not depict myelination well

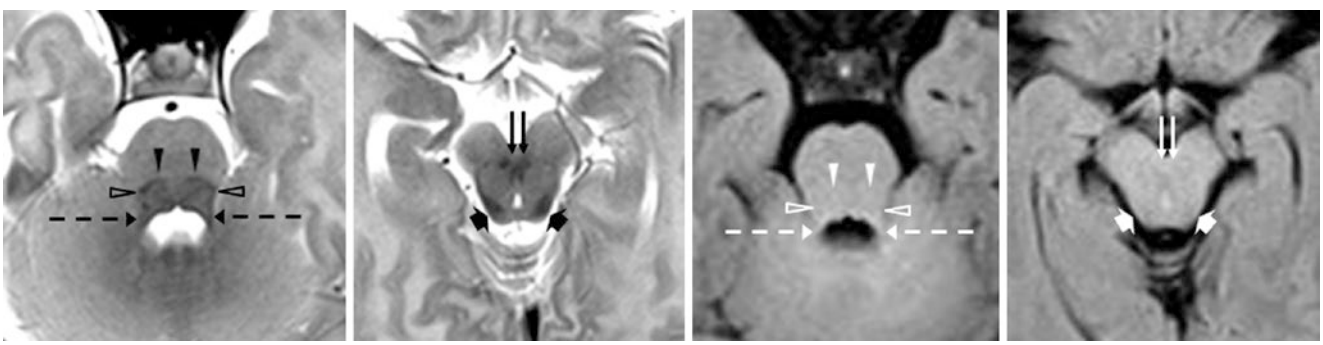

Fig. 23.40 A 1-day-old term neonate had a normal 3T MRI with axial SE T2WIs (*left images*) and 2D FLAIR (*right images*). There is T2-dark myelination of the BIC (*wide arrows*), DSCP (*double arrows*), LL (*open arrowheads*), ML (*arrowheads*), and SCP (*dashed arrows*) Again, FLAIR does not depict myelination well

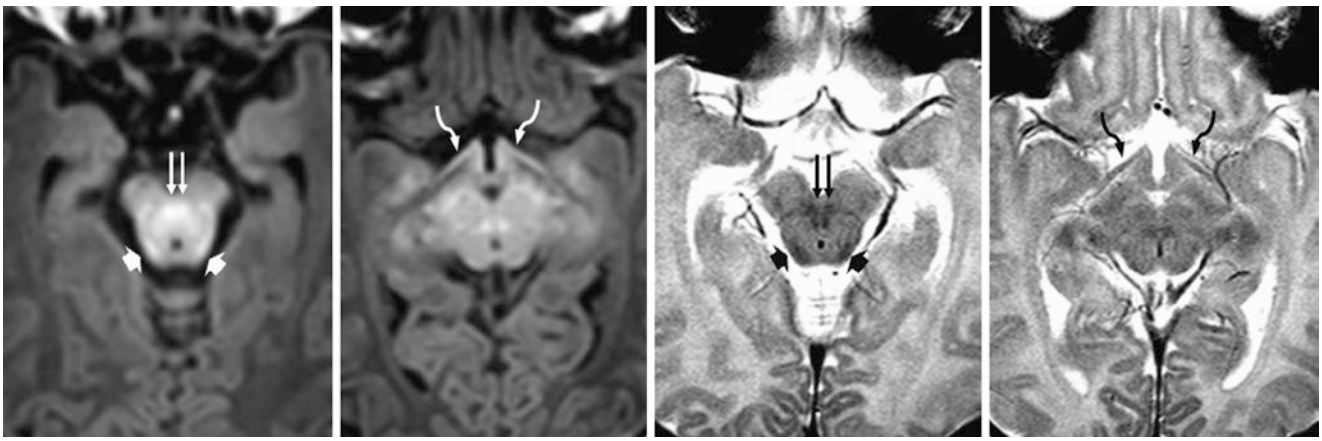

Fig. 23.41 A 4-day-old term neonate had a normal 3T MRI with GE T1WIs (*left images*) and SE T2WIs (*right images*). The BIC/inferior colliculi (*wide arrows*), DSCP (*double arrows*), and optic tracts (*curved arrows*) appear myelinated, being bright on T1WI and dark on T2WI

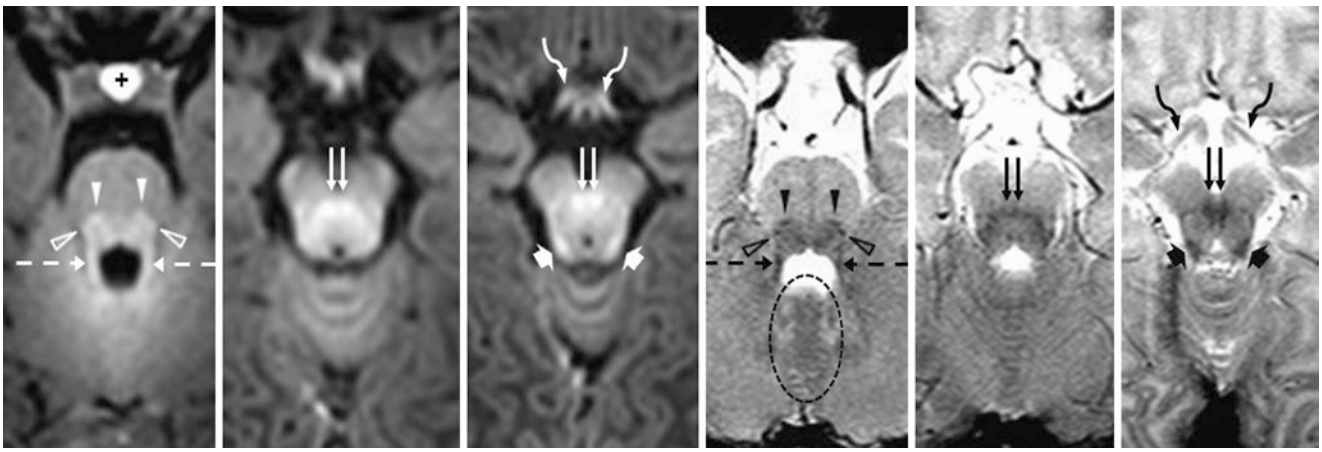

Fig. 23.42 A 5-day-old term neonate had a normal 3T MRI with GE T1WIs (*left 3 images*) and SE T2WIs (*right 3 images*). The BIC/inferior colliculi (*wide arrows*), DSCP (*double arrows*), LL (*open arrowheads*), ML (*arrowheads*), optic tracts (*curved arrows*), and SCP (*dashed arrows*) all appear myelinated, along with normal "myelination" of the superior cerebellar vermis (*dotted oval*). Also, note the normal, homogenously T1-bright pituitary gland (*plus sign*)

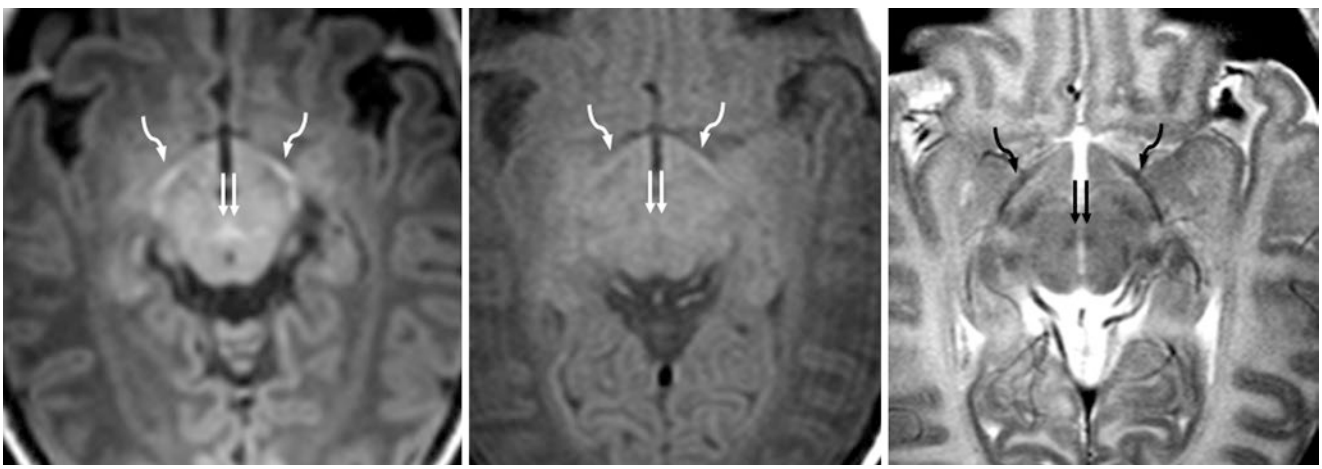

Fig. 23.43 An 11-day-old term neonate had a normal 3T MRI with GE T1WI (*left*), SE T1WI (*middle*), and SE T2WI (*right*). The DSCP (*double arrows*) and optic tracts (*curved arrows*) appear myelinated. The myelination of these structures is not well visualized on SE T1WI

23.3.4 Normal Myelination in Term Neonates at 3T: Basal Ganglia and Thalami

This section focuses on the presumed "*myelination*" of structures within or around the *basal ganglia* rather than on the T1-bright basal ganglia themselves, which can be visualized in normal *term neonates* at 3T. As stated previously, *T1-bright signal* in the *posterior limb of the internal capsule* (PLIC) is entirely normal in a term neonate (*i.e.*, >38 weeks gestational age), but also may be present in the *ventrolateral thalami* (VLT), *globi pallidi* (GP), *posterior putamina* (PP), and *subthalamic nuclei* (STN). At the level of the basal ganglia, other structures that are myelinated in nearly all term infants are the hippocampal commissure (HC) and PLIC on GE T1WI; on SE T2WI, T2-dark myelination of both of these structures is usually seen, but it may not be present in all infants. Notably, the PLIC appears quite small and thin relative to the PLIC and CST on GE T1WI. Occasionally, on GE T1WI only at 3T, subtle hyperintensity may also be noted within the *anterior commissure*, presumably representing early myelination. Similarly, T2-dark signal is sometimes noted within the *callosal splenium* on SE T2WI, presumably representing early myelination; if present, this is generally a marker of healthy myelination (Figs. 23.44, 23.45, 23.46, 23.47, 23.48, 23.49 and 23.50).

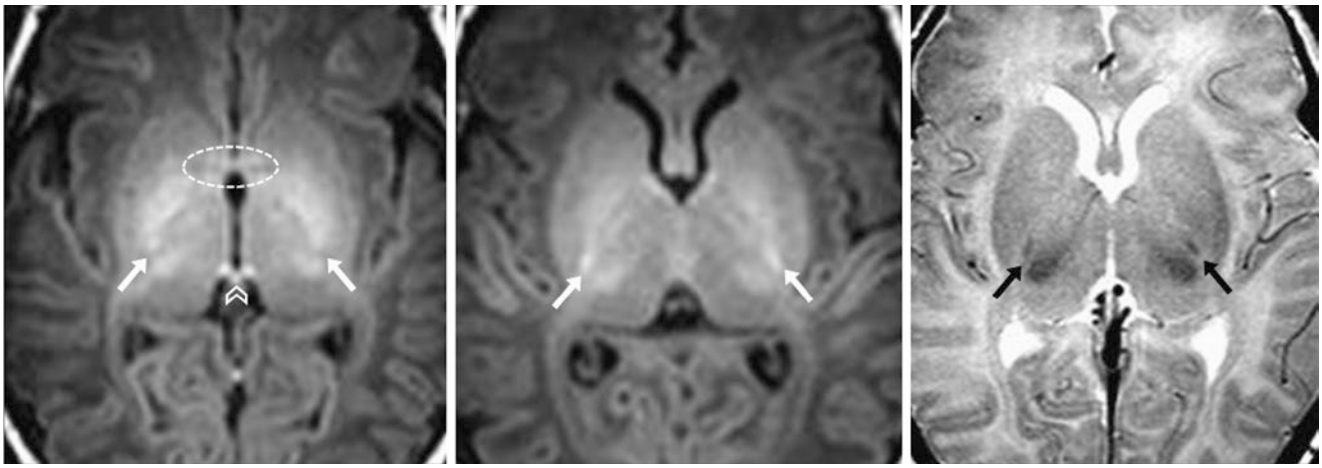

Fig. 23.44 A 5-day-old term neonate had a normal 3T MRI with GE T1WIs (*left* and *middle*) and SE T2WI (*right*). The habenular commissure (HC) (*chevron*) and posterior limbs of the internal capsules (PLIC) (*arrows*) are better visualized on GE T1WI; they seem clearly myelinated but appear smaller on SE T2WI. Note possible early myelination within the anterior commissure on GE T1WI (*dotted oval*)

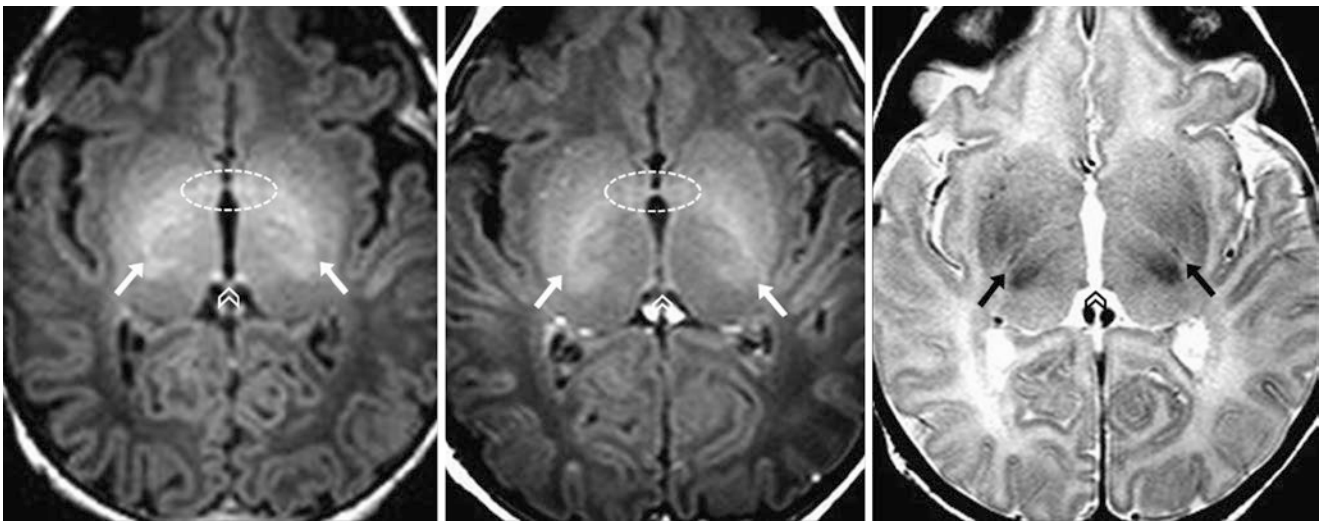

Fig. 23.45 A 6-day-old term neonate had a normal 3T MRI with GE T1WI (*left*), SE T1WI (*middle*), and SE T2WI (*right*). The HC (*chevrons*) and PLIC (*arrows*) are better visualized on GE T1WI, but they appear myelinated on both sequences. On T1WI, the PLIC is a bit difficult to separate from the normal, bright PP anteriorly and VLT posteriorly, but it is clearly myelinated. Note possible early myelination within the anterior commissure on GE T1WI and on SE T1WI (*dotted ovals*)

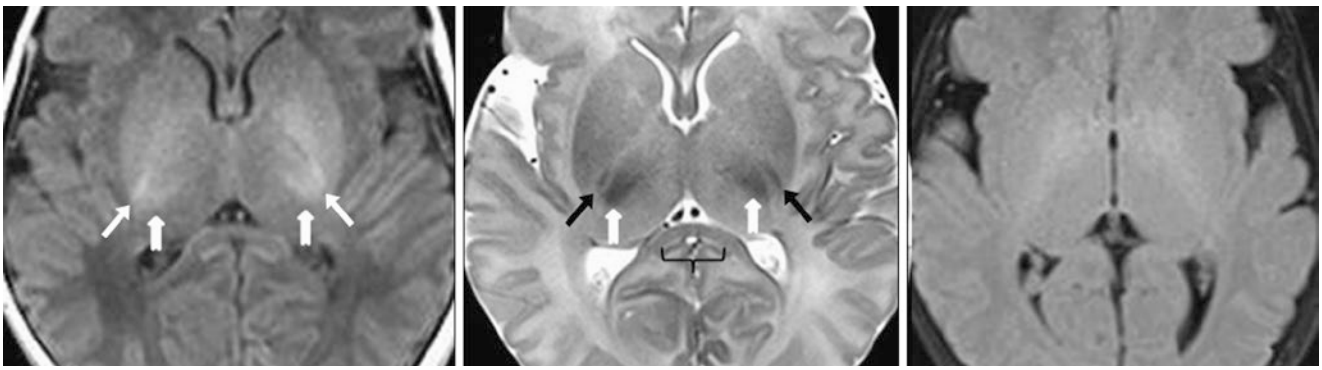

Fig. 23.46 A 1-day-old term neonate had a normal 3T MRI with GE T1WI (*left*), SE T2WI (*middle*), and 2D FLAIR (*right*). The PLIC (*arrows*) is well visualized on both GE T1WI and T2WI, but not on FLAIR. Note the T1-bright, T2-dark VLT (*notched arrows*), situated posterior and medial to the PLIC. There may be very early myelination of the callosal splenium on T2WI (*bracket*)

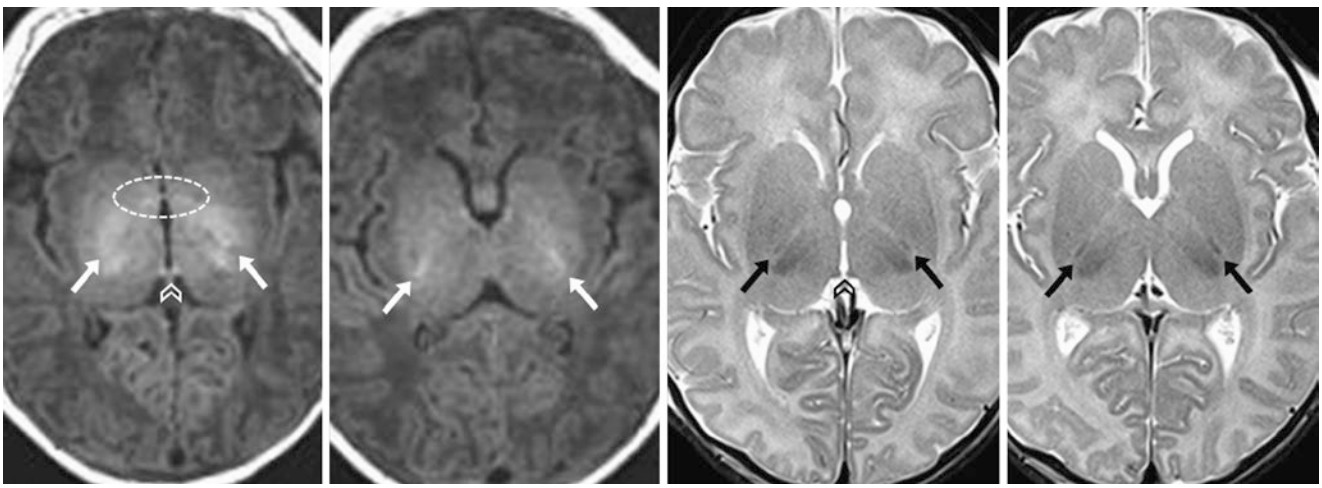

Fig. 23.47 A 4-day-old term neonate had a normal 3T MRI with GE T1WI (*left images*) and SE T2WI (*right images*). The HC (*chevrons*) and PLIC (*arrows*) are better visualized on GE T1WI, but they appear myelinated on both sequences. Note questionable early myelination within the anterior commissure (*dotted oval*) on GE T1WI

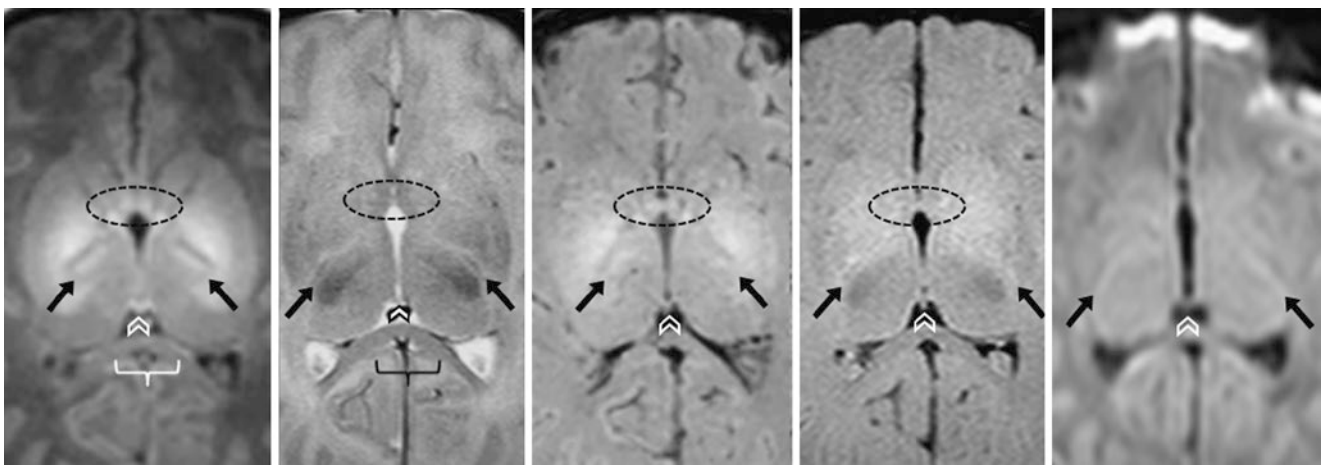

Fig. 23.48 A different 4-day-old term neonate had a normal 3T MRI with GE T1WI (*left*), SE T2WI (*left middle*), SWI (*middle*), FLAIR (*right middle*), and DWI (*right*). The HC (*chevrons*) and PLIC (*arrows*) appear myelinated and are better visualized on GE T1WI. Note the lack of myelination within the callosal splenium (*brackets*) and anterior commissure (*dotted ovals*)

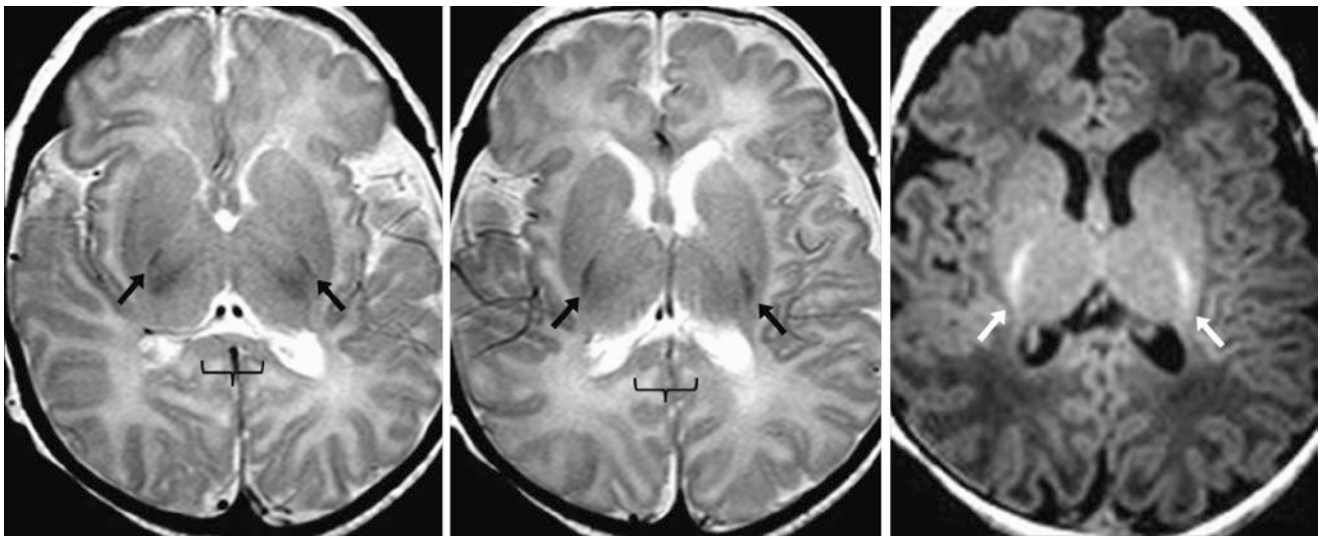

Fig. 23.49 A 21-day-old term neonate had a normal 3T MRI with SE T2WIs (*left and middle*) and GE T1WI (*right*). The PLIC (*arrows*) is visualized on both sequences and appears clearly myelinated. The HC is not included on these images because of angling. Note possible early myelination within the callosal splenium on SE T2WI (*brackets*)

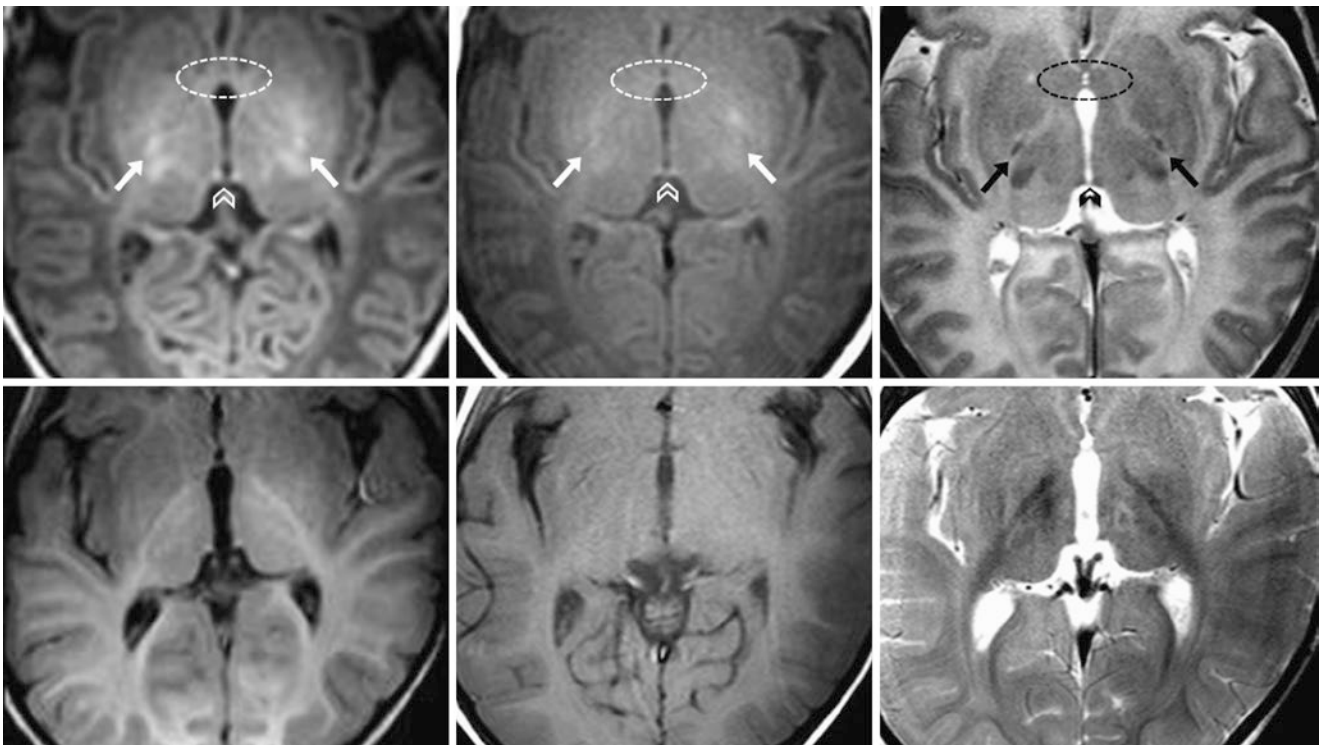

Fig. 23.50 An 11-day-old term neonate had a normal 3T MRI with GE T1WI (*top left*), SE T1WI (*top middle*), and SE T2WI (*top right*). The PLIC (*arrows*) and HC (*chevrons*) both appear myelinated on each sequence. Note that the anterior commissure does not (*dotted ovals*). A follow-up MRI at 1 year demonstrated normal myelination on corresponding GE T1WI (*bottom left*), SE T1WI (*bottom middle*), and SE T2WI (*bottom right*), although there was some motion on the examination

23.3.5 Normal Myelination in Term Neonates at 3T: Perirolandic Cortex and Corona Radiata

As stated earlier, the *CST* within the *corona radiata* are visualized as being myelinated (T1-bright) on GE T1WI in most subsequently normal term neonates at 3T, and the *PRC* is visible as being T2-dark in most. The PRC generally consists of the precentral gyrus (the primary motor cortex within the frontal lobe) anteriorly and the postcentral gyrus (the primary sensory cortex within the parietal lobe) posteriorly; the PRC surrounds the central sulcus. Again, the T2-dark cortical "ribbon" of the cerebral cortex should appear continuous throughout in the normal term neonate; regions of discontinuity should be viewed with suspicion in the setting of potential *hypoxic-ischemic encephalopathy or injury* (HIE/HII) and should be correlated with DWI and with findings within the basal ganglia (Figs. 23.51, 23.52, 23.53, 23.54, 23.55 and 23.56).

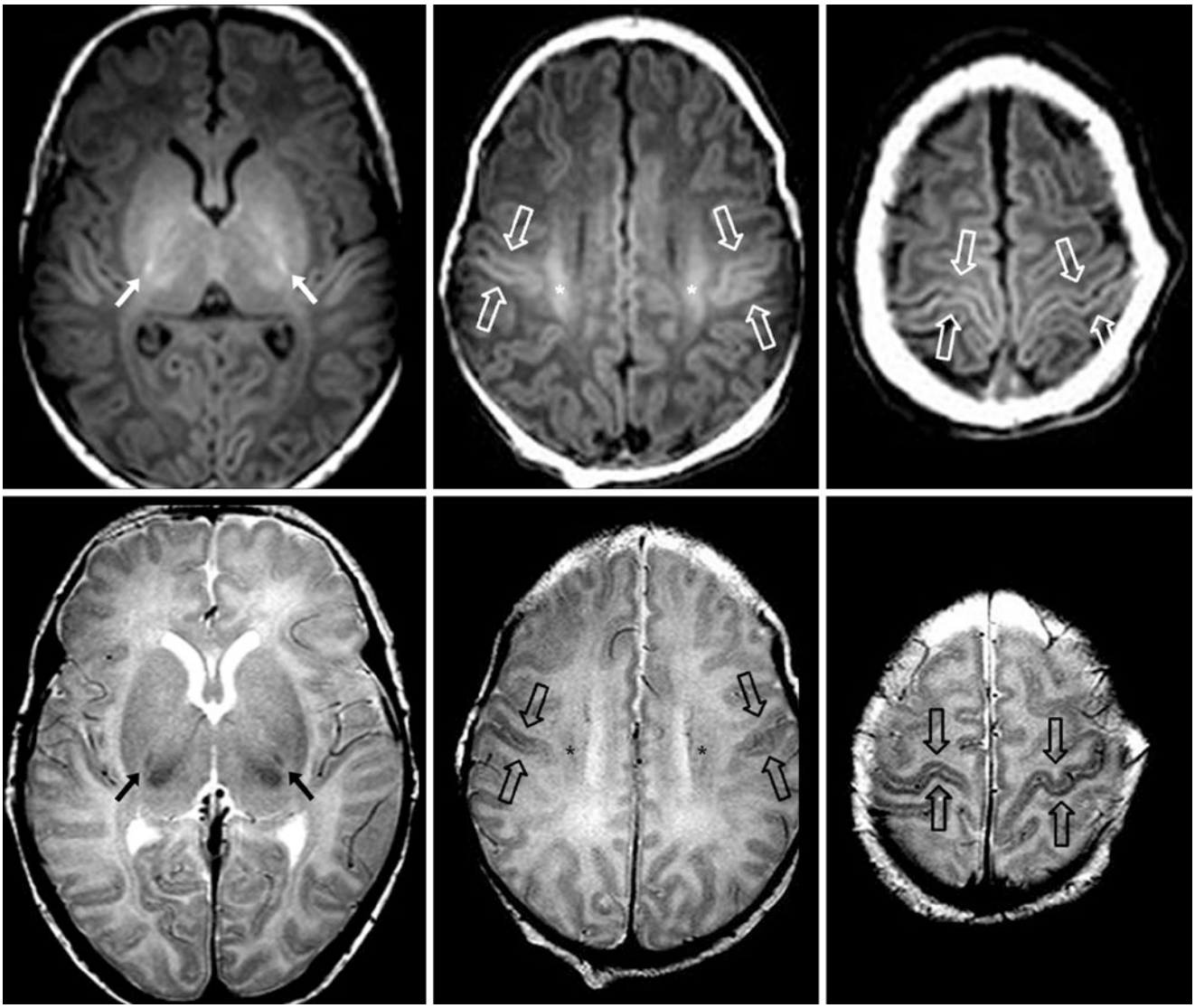

Fig. 23.51 A 5-day-old term neonate had a normal 3T MRI with GE T1WIs (*top row*) and SE T2WIs (*bottom row*). The PLIC/corticospinal tracts (CSTs) (*arrows*) are quite bright on GE T1WI; they are less visible, but present, on SE T2WI. This finding is contiguous with T1-bright signal within the corona radiata (*asterisk*). The perirolandic cortex (PRC) (*open arrows*) is slightly bright on GE T1WI, but clearly appears myelinated on SE T2WI, appearing darker and thicker than the remainder of the cortex. Note the T2-dark cortical "ribbon" diffusely

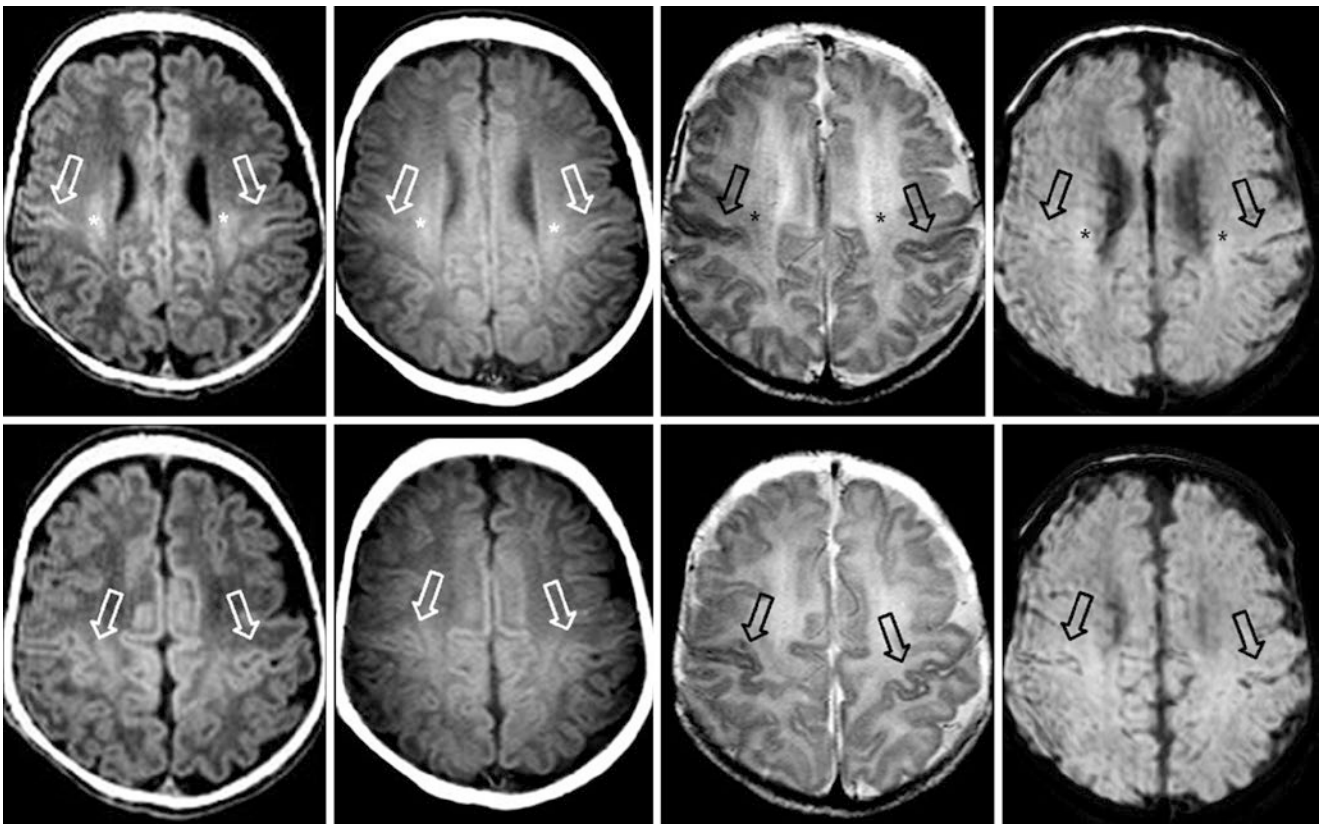

Fig. 23.52 A 21-day-old term neonate had a normal 3T MRI with GE T1WI (*left column*), SE T1WI (*left middle column*), SE T2WI (*right middle column*), and SWI (*right column*). The CSTs within the corona radiata (*asterisks*) are bright on GE T1WI but less so on SE T1WI; the dark signal is less visible on SE T2WI. There is slight "T1 shine-through" on SWI. The CSTs are contiguous with the white matter subjacent to the PRC (*open arrows*). The PRC is mildly bright on GE T1WI; it clearly appears myelinated on SE T2WI, appearing darker and thicker than the remainder of the cortex

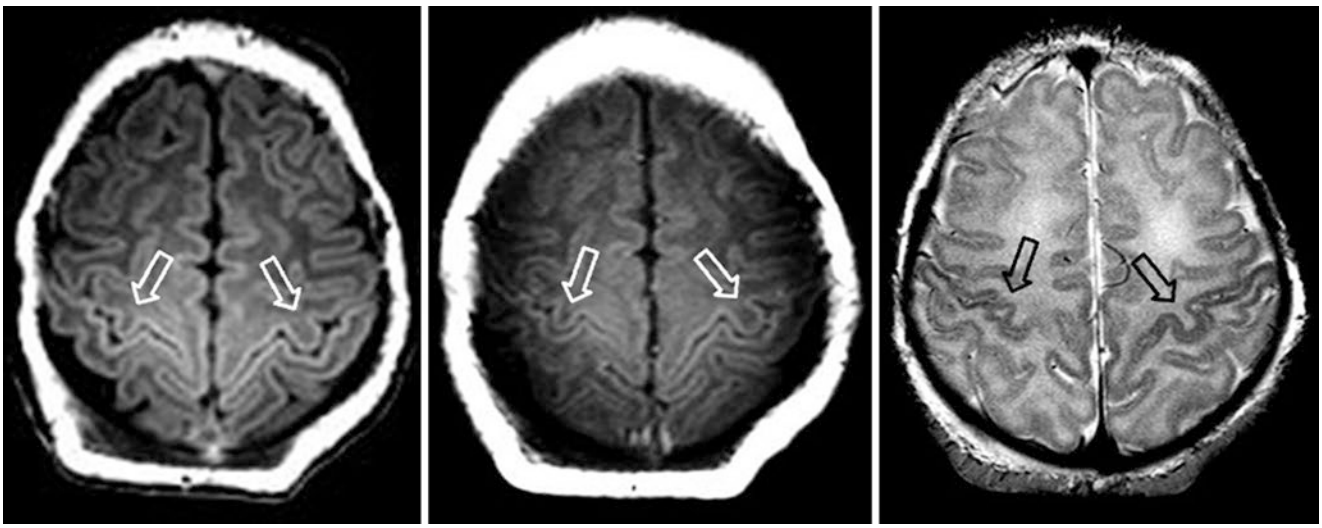

Fig. 23.53 A 3-day-old term neonate had a normal 3T MRI with GE T1WI (*left*), SE T1WI (*middle*), and SE T2WI (*right*). The PRC (*open arrows*) appears slightly bright on GE T1WI, and slightly darker than the remainder of the cortices on SE T2WI

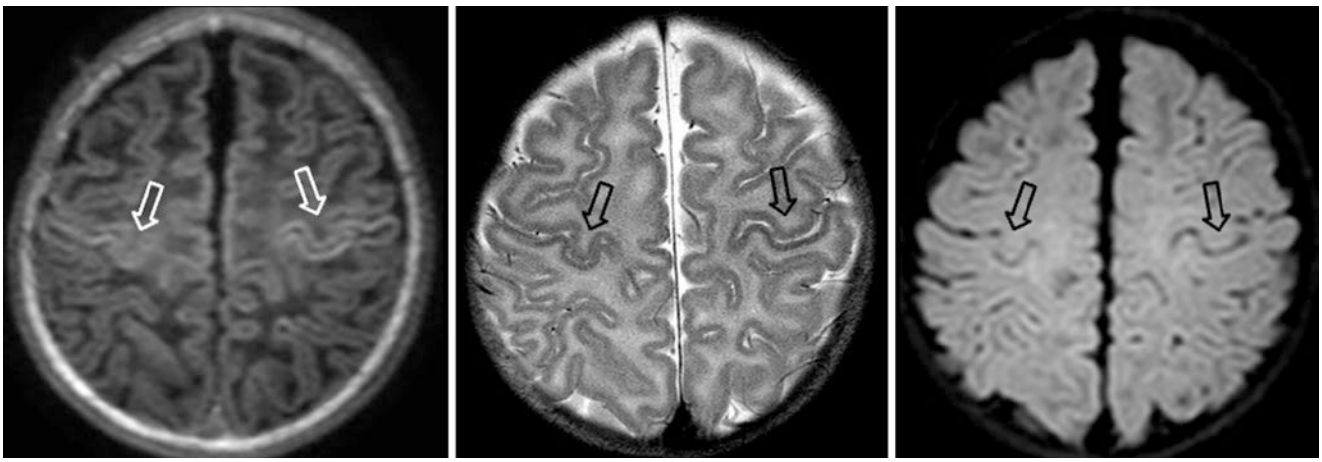

Fig. 23.54 A 17-day-old term neonate had a normal 3T MRI with GE T1WI (*left*), SE T2WI (*left middle*), and axial reformats from a 3D FLAIR acquisition (*right*). The PRC (*open arrows*) is visualized as slightly brighter than the remainder of the cortex on GE T1WI, but clearly appears T2-dark (myelinated) and thicker than the remainder of the cortex on SE T2WI

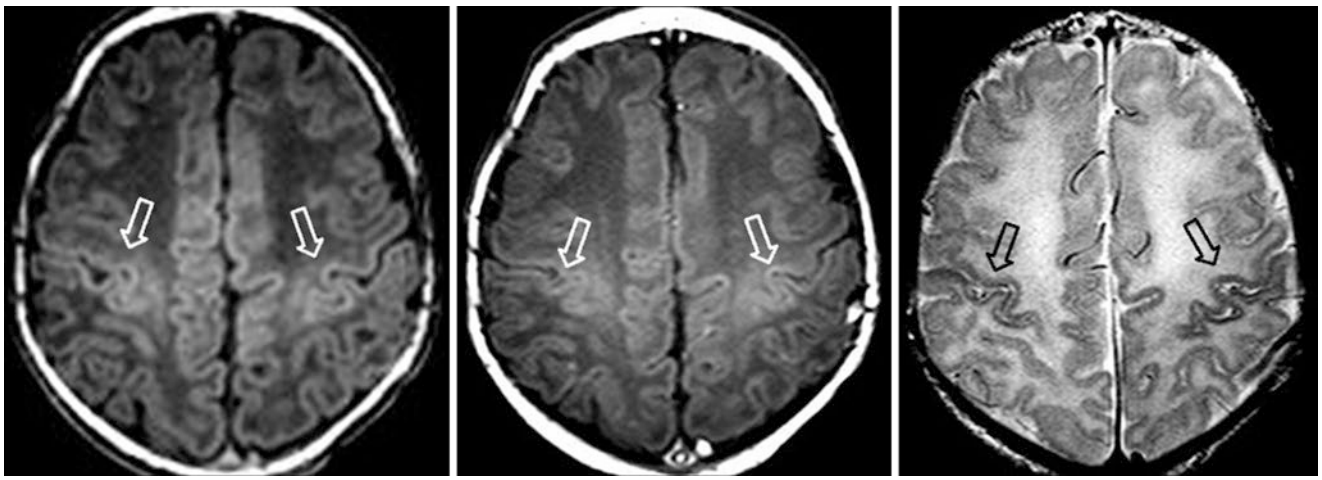

Fig. 23.55 A 6-day-old term neonate had a normal 3T MRI with GE T1WI (*left*), SE T1WI (*left middle*), and SE T2WI (*right*). The PRC (*open arrows*) is visualized as slightly bright on GE T1WI, but clearly appears myelinated on SE T2WI, appearing darker and thicker than the remainder of the cerebral cortex. Note the T2-dark cortical "ribbon" diffusely

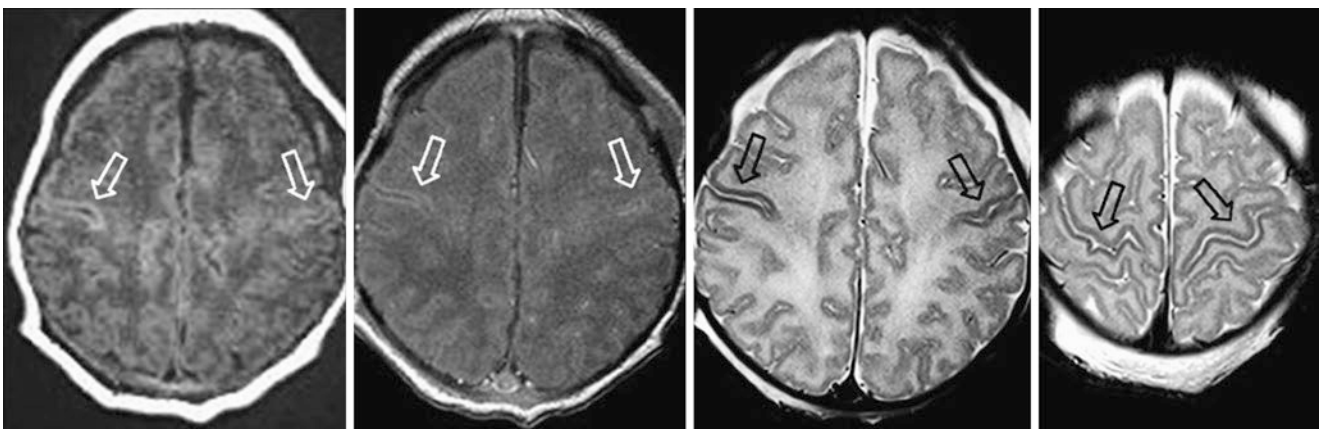

Fig. 23.56 A 4-day-old term neonate had a normal 3T MRI with GE T1WI (*left*), SE T1WI (*left middle*), and SE T2WIs (*right middle* and *right*). The PRC (*open arrows*) is visualized as slightly bright on GE T1WI, but it clearly appears myelinated on SE T2WI, appearing darker and thicker than the remainder of the cerebral cortex. Note the T2-dark cortical "ribbon" diffusely

23.4 Comparison Cases of Hypoxic-Ischemic Injury and Other Insults in Term Neonates

The abnormal cases shown in Figs. 23.57, 23.58, 23.59, 23.60, 23.61, 23.62 23.63 and 23.64 should be compared with the appearance of T1 hyperintensity and corresponding T2 hypointensity within normally developing structures in the term neonate, as well as T1-bright basal ganglia, VLT, PLIC, CST, and so forth. In particular, *hypoxic-ischemic encephalopathy* or *injury* (HIE/HII) should be suspected in the following situations: loss of the normally T2-dark cortical "ribbon" on SE T2WI; loss of the myelinated appearance of the PLIC on SE T2WI or GE T1WI; or a "blotchy" T1-bright appearance of the basal ganglia, VLT, PLIC, CST, or PRC on T1WI. Again, DWI is helpful to confirm findings, but it has been described as normal in some scenarios of confirmed insults, particularly when severely ill infants in the intensive care unit eventually undergo MRI at more than 1 week of age. The "blotchy" or "patchy" hyperintensity of the basal ganglia can be one of the hardest signs to discern. It has been suggested that bright signal within the PP greater than the PLIC on T1WI should raise suspicion for HII because the PLIC should be brighter, but this finding has yet to be confirmed prospectively at 3T.

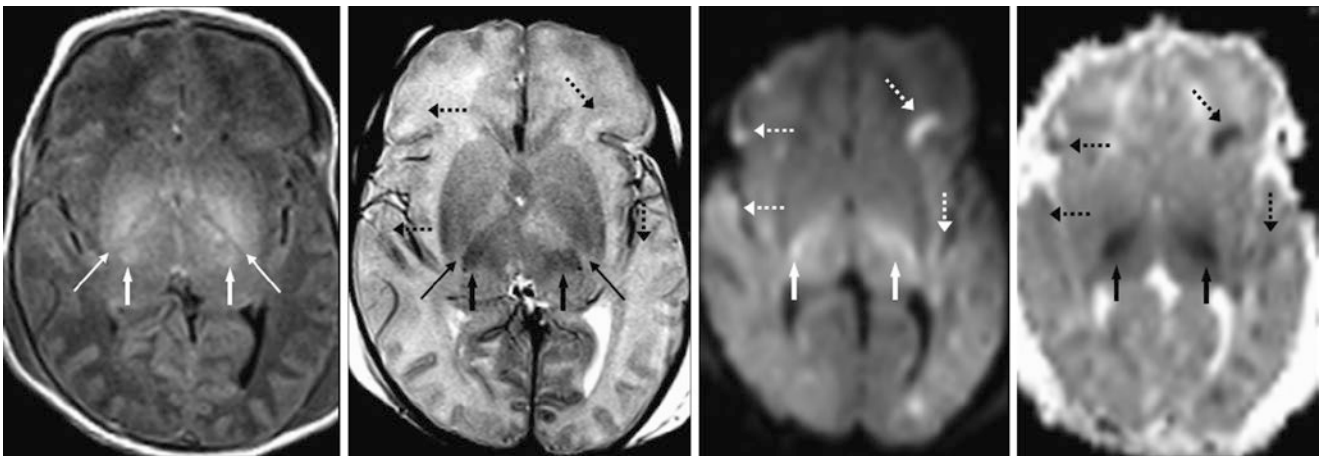

Fig. 23.57 Comparison case of severe HII. A 2-day-old term neonate with respiratory distress had a 3T MRI. GE T1WI (*left*) showed loss of the normally T1-bright PLIC (*thin arrows*). The normally thin PLIC was also not visualized on SE T2WI (*left middle*), and a normal, T2-dark cortical "ribbon" was missing in several locations (*dotted arrows*). DWI (*right middle*) and an ADC map (*right*) confirmed HII in multifocal cortical regions, as well as in the VLT (*arrows*)

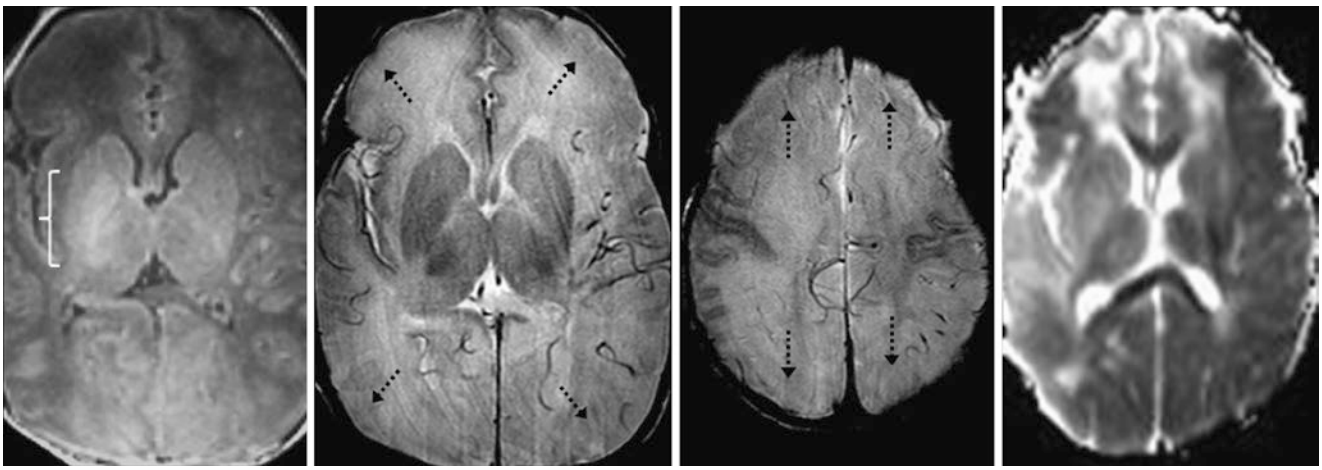

Fig. 23.58 Comparison case of severe HII. A 4-day-old term neonate with hypotonia following a respiratory event had a 3T MRI. GE T1WI (*left*) showed loss of the normal T1-bright central structures on the left, such as the basal ganglia, VLT, and PLIC, while on the right (*bracket*), these were too hyperintense, "blotchy," and could not be discerned separately from each other. Note loss of the sulci (*dotted arrows*) and of the normal, T2-dark cortical "ribbon" on SE T2WIs (*middle two images*). DWI (*not shown*) and ADC maps (*right*) confirmed diffuse HII, worse on the left side

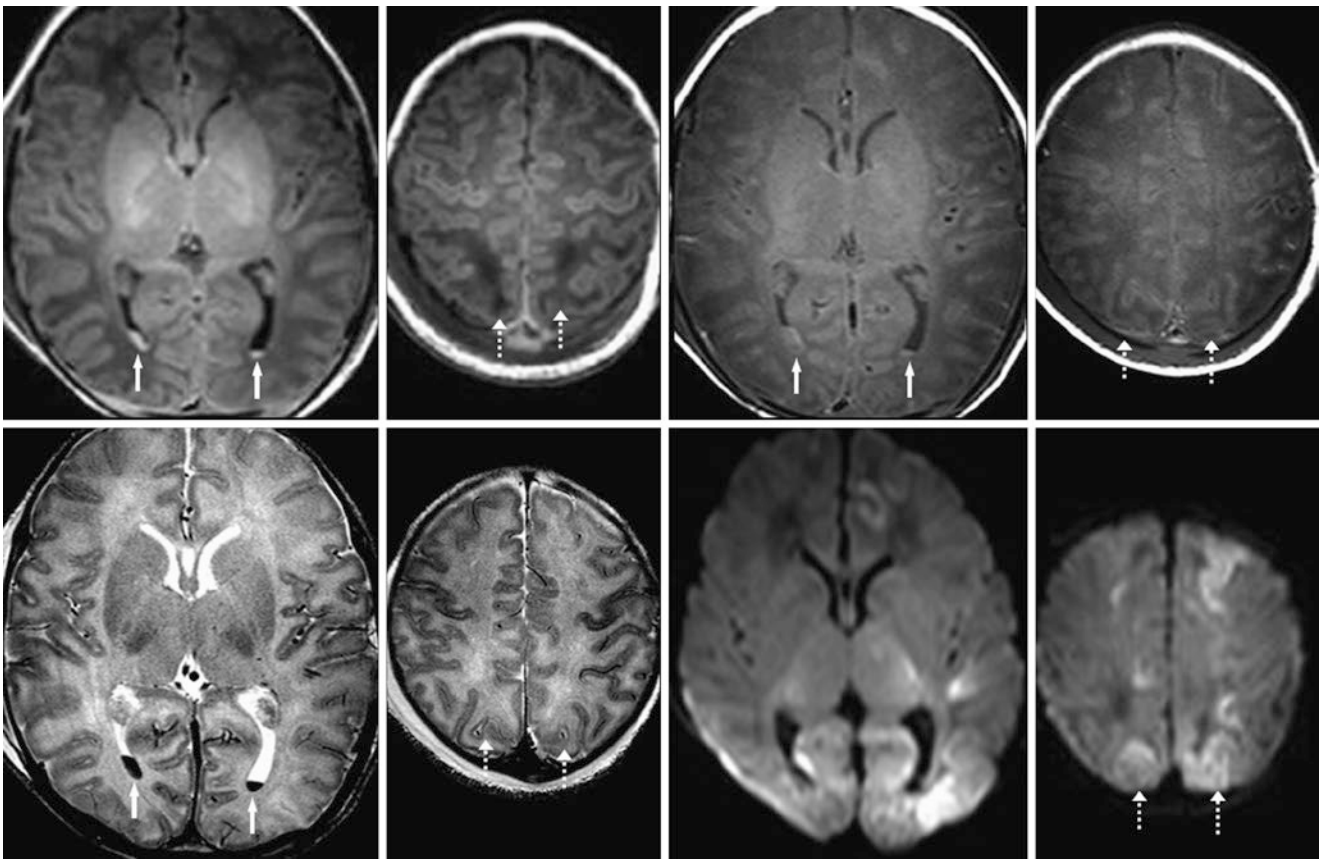

Fig. 23.59 Comparison case of mild HII. A 1-day-old term neonate with prolonged seizures. *Top row*: 3T MRI with GE T1WI (*left* and *left middle*) showed intraventricular hemorrhage in the lateral ventricles (*arrows*), parietal edema (*dotted arrows*), and normal-appearing basal ganglia; SE T1WI was not useful (*right middle* and *right*). *Bottom row*: SE T2WI showed similar findings (*left* and *left middle*); DWI confirmed HII (*right middle* and *right*)

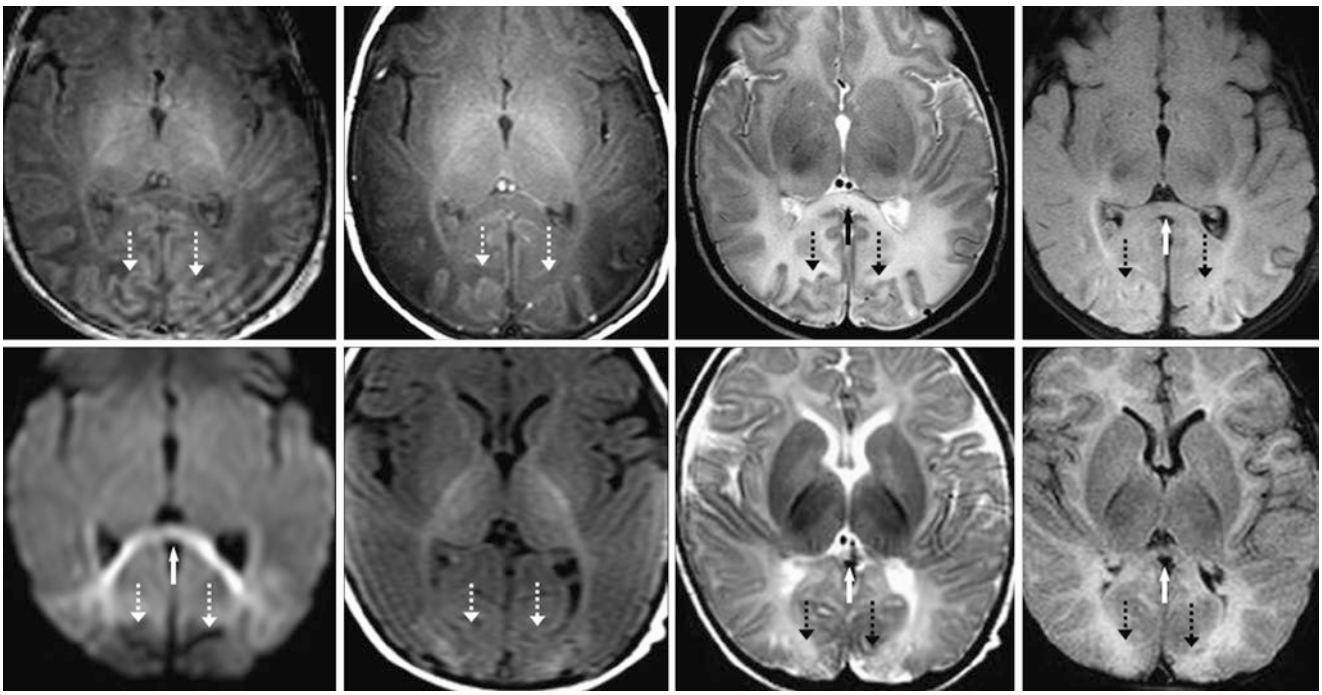

Fig. 23.60 Comparison case of mild HII. An 8-day-old term neonate with birth asphyxia. *Top row*: On 3T MRI, the basal ganglia, PLIC, and VLT were normal on GE T1WI (*left*) and SE T1WI (*left middle*); SE T2WI (*right middle*) and FLAIR (*right*) both showed subtle edema within the callosal splenium (*arrows*) and occipital cortices (*dotted arrows*). *Bottom row*: DWI (*left*) confirmed only the splenial findings. At 4 months of age, a repeat 3T MRI with GE T1WI (*left middle*), SE T2WI (*right middle*), and FLAIR (*right*) showed both splenial and occipital atrophy. This illustrates how DWI occasionally may not show abnormalities (such as those in the occipital lobe in this case)

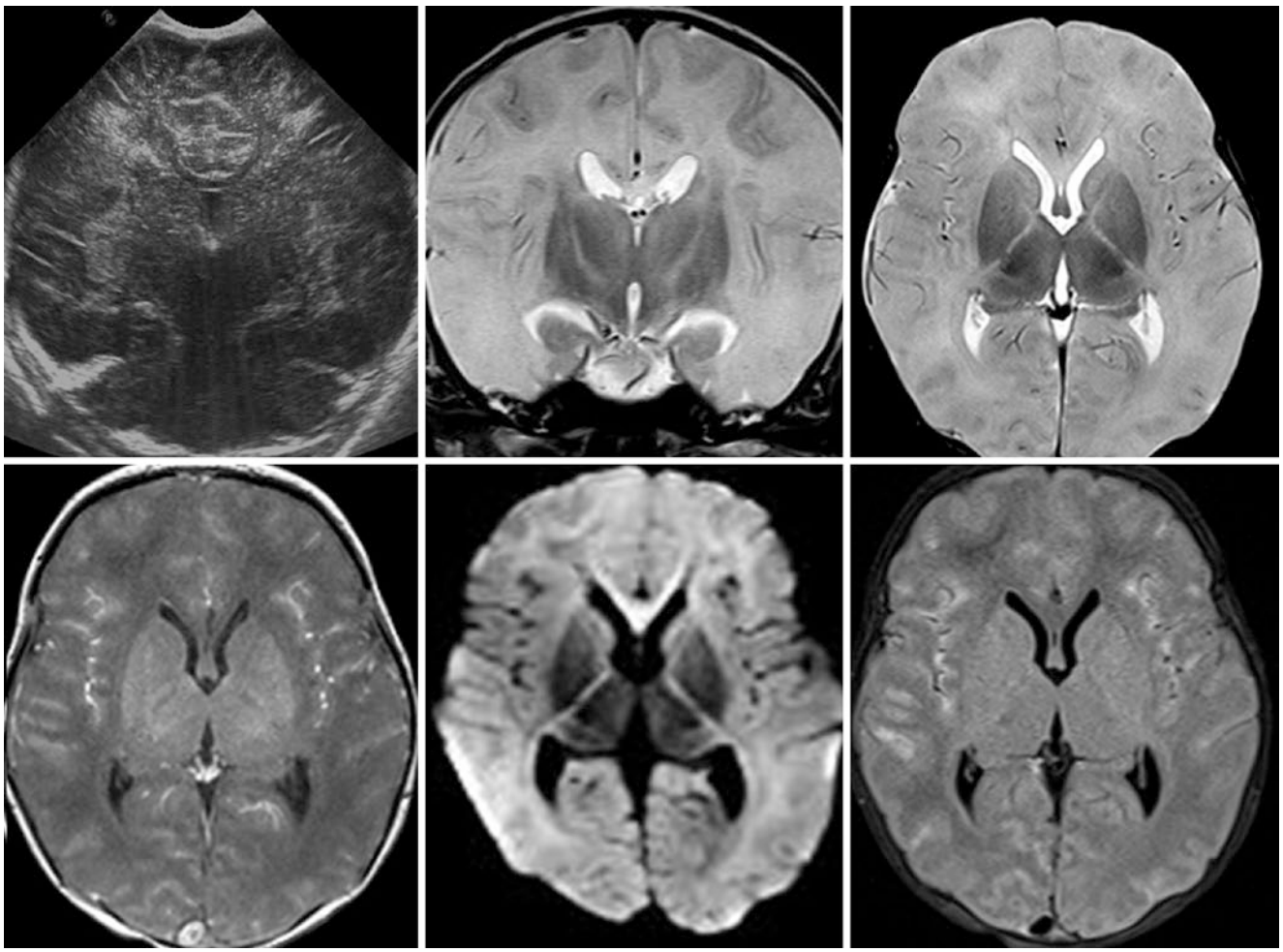

Fig. 23.61 Comparison case of severe HII. *Top row*: A 3-day-old term neonate with respiratory failure had a coronal ultrasound (*left*) that noted cerebral edema. 3T MRI demonstrated diffuse, severe edema with loss of the sulci and of the normal, T2-dark cortical "ribbon," as shown on coronal (*middle*) and axial (*right*) SE T2WIs. *Bottom row*: The normally T1-bright basal ganglia, VLT, and PLIC were not present on an axial GE T1WI (*left*), and the basal ganglia were also too dark on SE T2WI. On DWI (*middle*), nearly the entire cortex and subjacent white matter were abnormal. Note how FLAIR (*right*) is underwhelming, even in the setting of severe HII

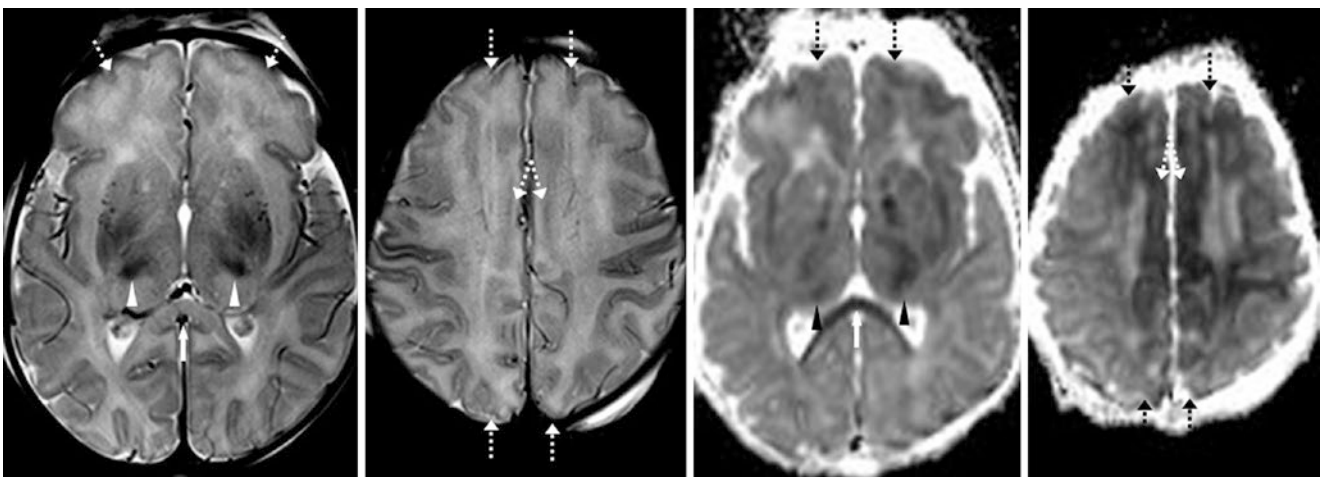

Fig. 23.62 Comparison case of moderate HII. A 2-day-old term neonate delivered after fetal distress had a 3T MRI. SE T2WIs (*left and left middle*) demonstrated a normal, thin PLIC and basal ganglia, but the normal, T2-dark cortical "ribbon" was missing in several locations (*dotted arrows*), while the VLT (*arrowheads*) was too dark. DWI (not shown) and the ADC map (*right middle* and *right*) confirmed multifocal cortical HII, as well as injury of the VLT and callosal splenium (*white arrows*)

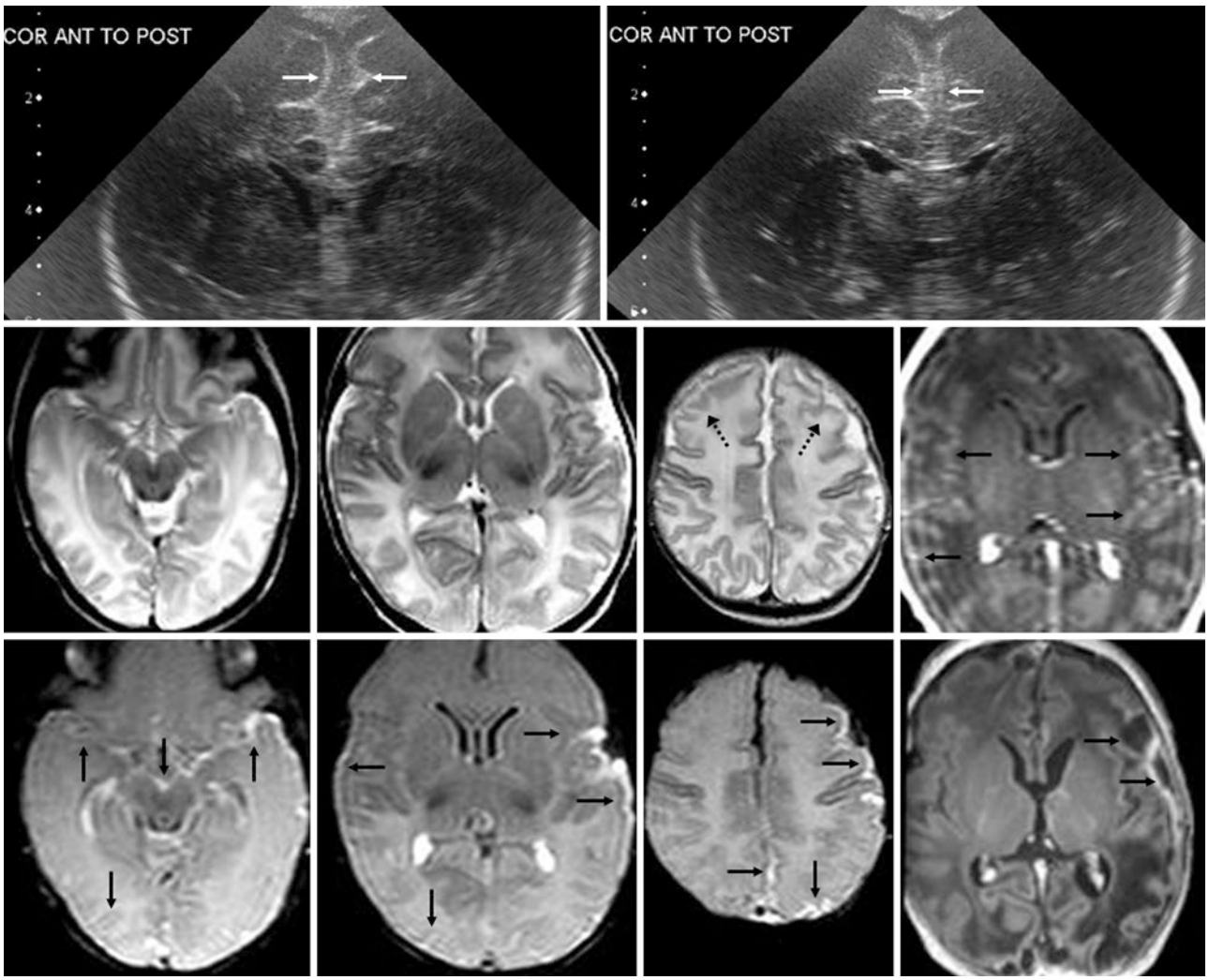

Fig. 23.63 Comparison case of group B streptococcal meningitis. *Top row*: A 21-day-old term neonate with prolonged fevers and altered mental status had coronal ultrasound images that demonstrated echogenic material within the subarachnoid space (*arrows*), which was considered suspicious for exudate. A 3T MRI was ordered the next day (with contrast, given the clinical history). *Middle row*: On MRI, SE T2WI (*left three images*) showed subtle blurring of the normal cortical ribbon (*dotted arrows*). Postcontrast GE T1WI (*right*) showed leptomeningeal enhancement (*thin arrows*), but suffered from motion. *Bottom row*: Postcontrast FLAIR (*left images*) better depicts the enhancement (*thin arrows*). One month later, a repeat contrast-enhanced GE T1WI (*right*) shows a new subdural empyema along the left convexity, with subjacent brain atrophy

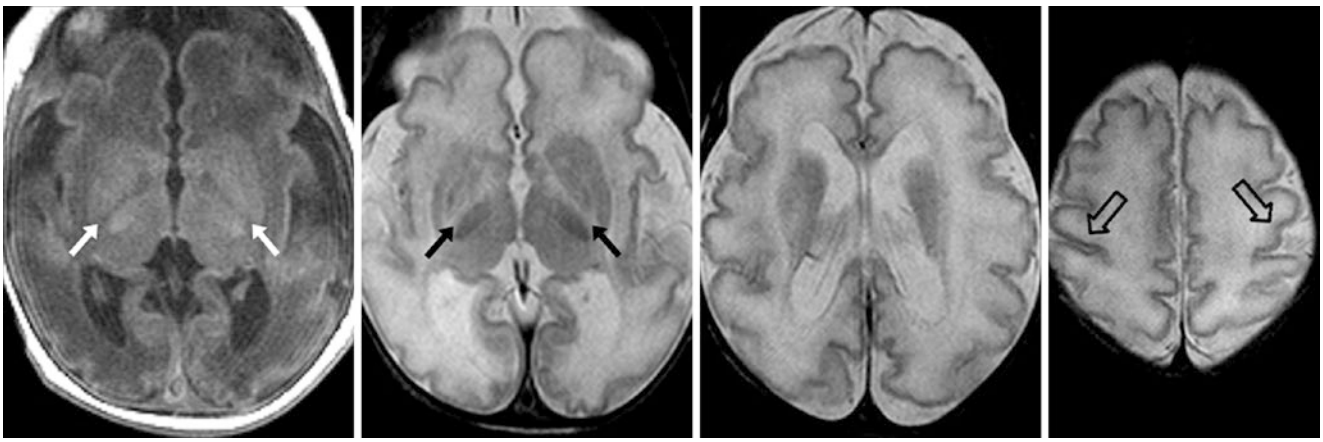

Fig. 23.64 Comparison case of hypomyelination and delayed sulcation. A 4-day-old term neonate with severe hypotonia had a 1.5T MRI that showed a lack of the normal, bright PLICs (*arrows*) on GE T1WI (*left*) and SE T2WI (*left middle*). At higher levels, SE T2WIs demonstrate a lack of the normally dark CSTs within the corona radiata (*right middle*), and lack of the normally dark PRC (*open arrows*). The sulci were shallow, and the gyri undersulcated, akin to those of an infant born at 32–33 weeks gestational age. Various tests did not identify the presumed genetic etiology

23.5 Subcortical Low Signal on Diffusion-Weighted Imaging in Neonates and Very Young Infants

On diffusion-weighted imaging (DWI) in the neonate, a transient appearance of certain regions of white matter can be seen in normal neonates, and can persist until about 1–2 months of age. This characteristically *dark appearance on DWI of the subcortical white matter* (SCWM) and deep, periventricular white matter (PVWM) is usually noted within the frontal and parietal deep white matter. This appearance is likely related to the low signal on T1WI and high signal on T2WI, which are postulated to be due to the relatively high water content within such regions at this age, as demonstrated on apparent diffusion coefficient (ADC) maps and on prior diffusion tensor imaging (DTI) studies. This temporary appearance on DWI is also likely akin to the patchy, dark white matter appearance on CT at this age, which has been presumed related to the high water content. As the various white matter tracts myelinate and mature, the degree of anisotropy increases, reflecting tighter packing of fibers and a progressively decreasing concentration of free water (Figs. 23.65, 23.66, 23.67 and 23.68).

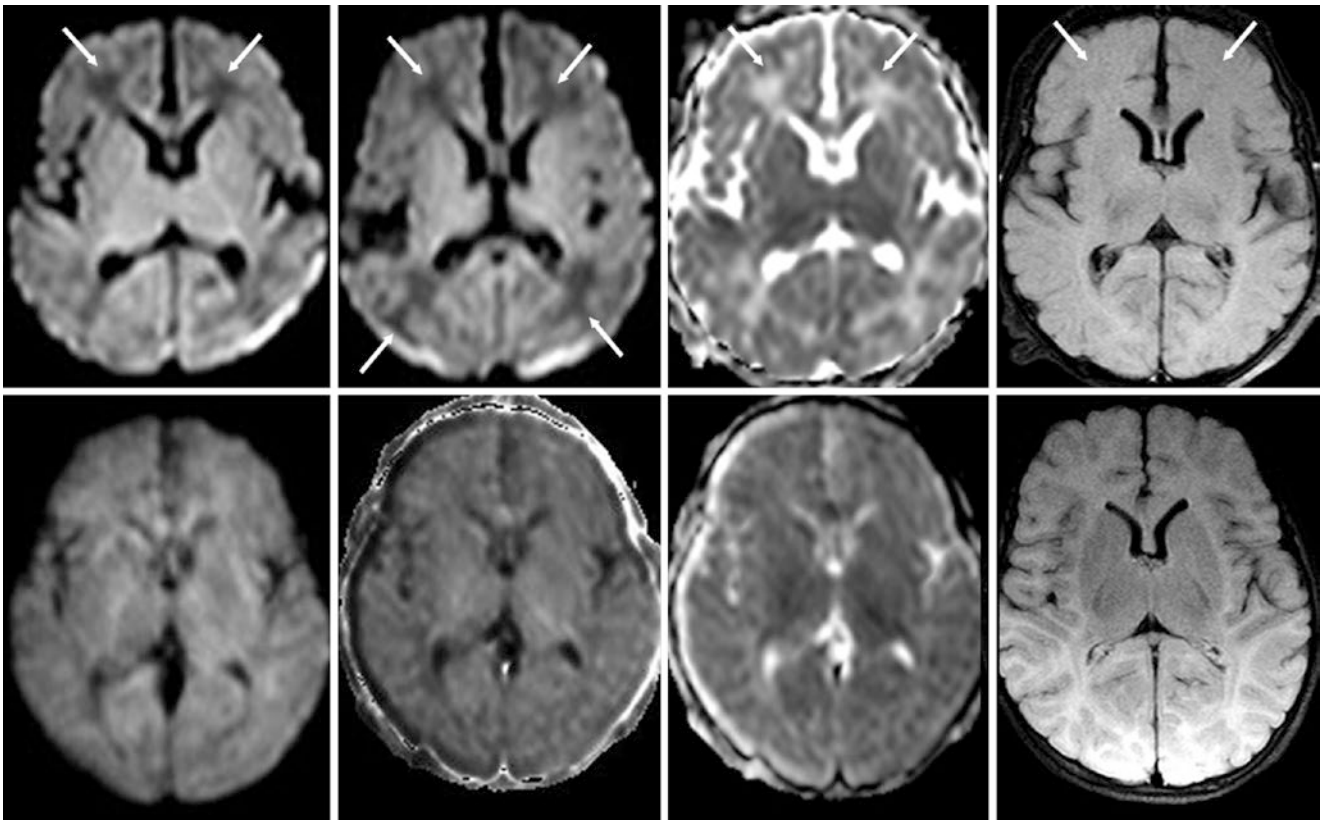

Fig. 23.65 An 8-day-old term neonate with hypotonia had a normal 3T MRI and subsequent development. *Top row*: On DWI (*left* and *left middle*) there are patchy regions of hypointensity (*arrows*) that are bright on an ADC map (*right middle*) and dark on FLAIR (*right*), indicating a higher concentration of free water. *Bottom row*: another MRI at 2.5 months of age shows that the white matter and gray matter are isointense on DWI (*left*), "exponential" DWI (*left middle*), and on an ADC map (*right middle*). Note that on FLAIR (*right*), the white matter is now hyperintense relative to gray matter, which is a normal transition on FLAIR in infants

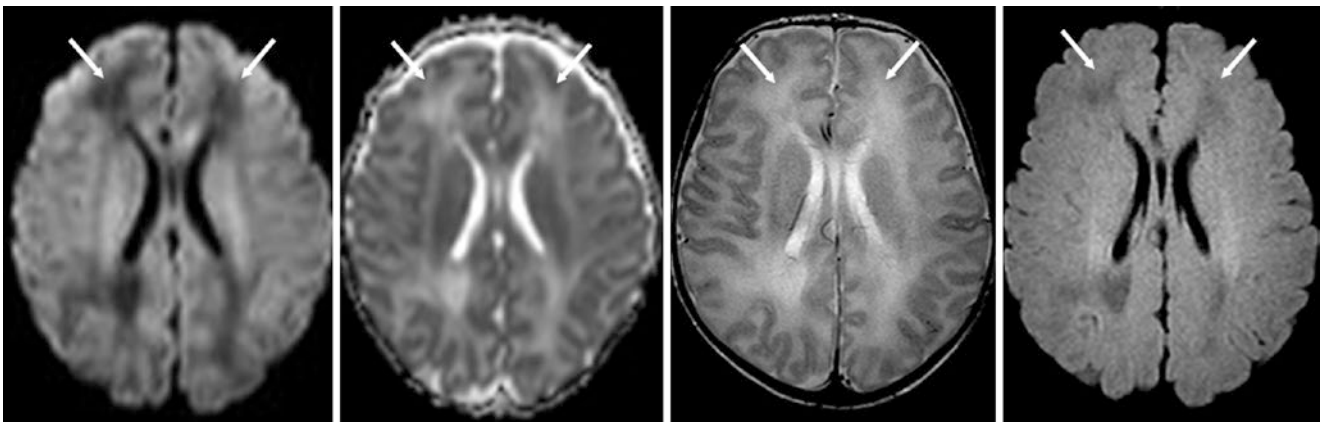

Fig. 23.66 A 1-month-old term infant with difficulty breathing at birth (no imaging at that time) had a normal 3T MRI. On DWI (*left*), there was patchy low signal (*arrows*) in white matter areas that are bright on the ADC map (*left middle*) and SE T2WI (*right middle*), with dark signal on FLAIR (*right*), suggesting high water content. The patient developed normally

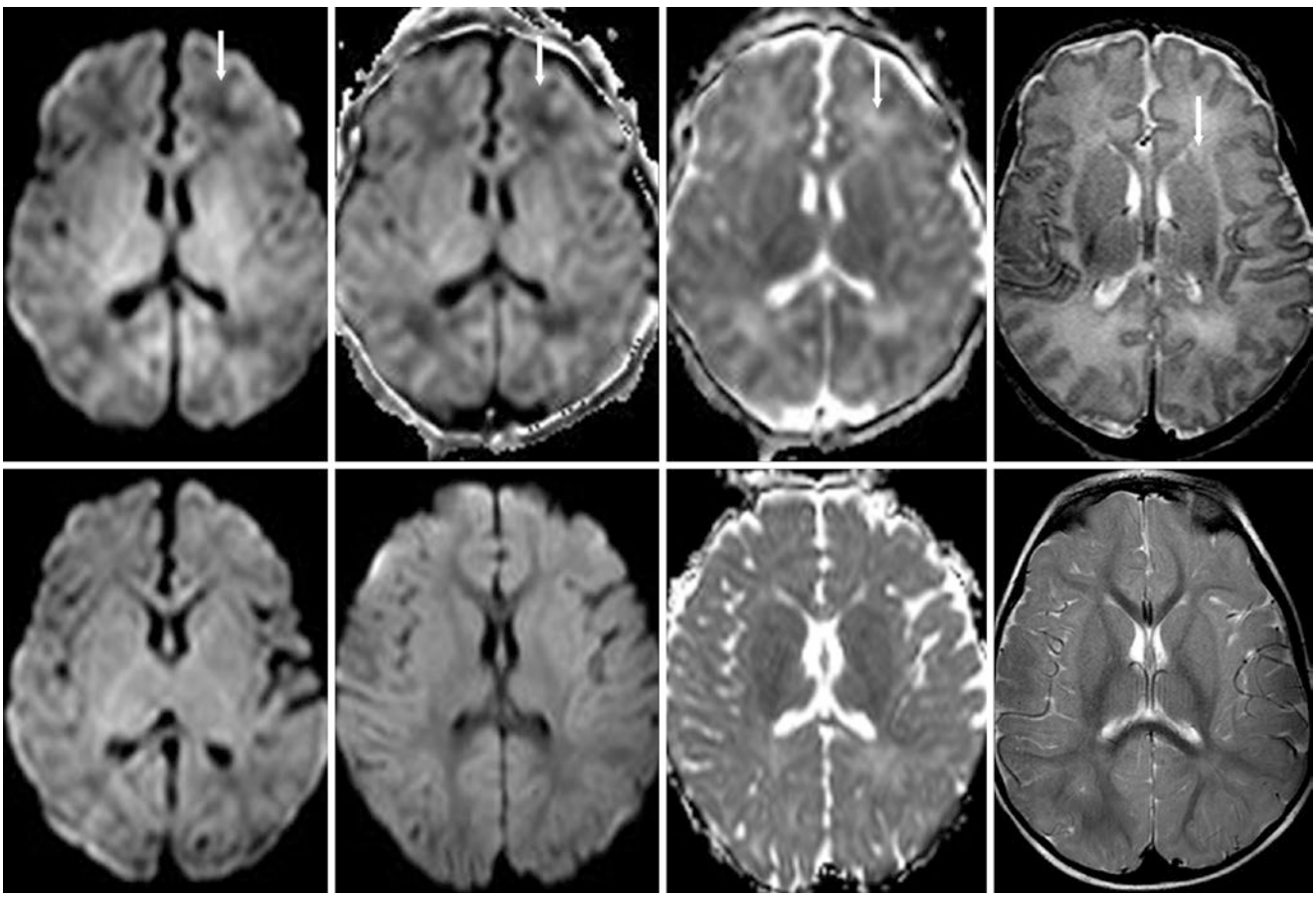

Fig. 23.67 A 7-day-old term infant with weakness had a normal 3T MRI. *Top row*: On DWI (*left*) and exponential DWI (*left middle*), which removes the T2 component of the DWI, there was asymmetric low signal (*arrows*) of left frontal PVWM, which was mildly bright on the ADC map (*right middle*) and SE T2WI (*right*). *Bottom row*: At 2.5 months of age, the gray matter and white matter are isointense on DWI (*left*). At 10 months, the white matter is again slightly darkened relative to gray matter on DWI (*left middle*), but there is no white matter edema on an ADC map (*right middle*) or on T2WI (*right*). This higher signal of the cortex at birth may be due to its greater cell density on DWI (relative to white matter), while the SCWM and deep WM are still undergoing myelination and may have a higher water concentration

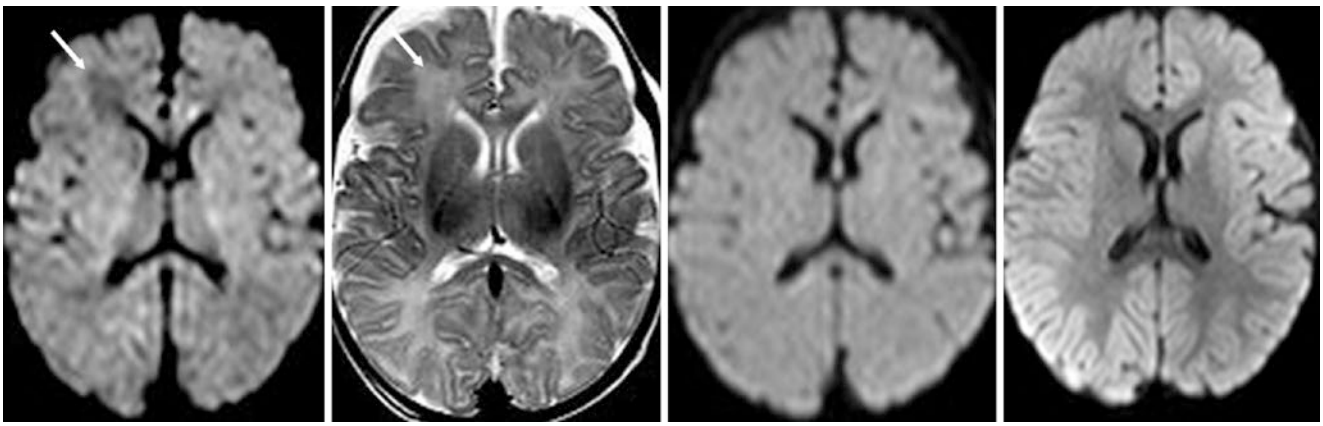

Fig. 23.68 A 1-month-old term infant with poor feeding and normal 3T MRI. (No neonatal imaging was performed.) On DWI (*left*), there was unilateral, patchy low signal (*arrow*) in the right frontal PVWM, in a location that was normal on SE T2WI (*left middle*). At 3 months of age, DWI (*right middle*) showed gray and white matter that were isointense to each other. At 1 year of age (*right*), the white matter is diffusely mildly dark again relative to gray matter on DWI a normal appearance

23.6 Normal Myelination in Infants and Young Children

The figures in this section illustrate the appearance of *normal myelination* and development at several age points ranging from 1 month to 2 years. It is quite important to be aware of the major milestones at these intervals, as many congenital or genetic inborn errors of metabolism that may be asymptomatic at birth or relatively invisible on neonatal MRI can become more apparent as the white matter matures. Additionally, other anomalies such as *malformations of cortical development* (including cortical dysplasias), *white matter lesions*, and sequelae of *hypoxic-ischemic encephalopathy* or *injury* can become more evident with normal brain maturation. Another reason to be aware of such milestones is that development at certain stages can even obscure lesions. For example, at approximately 8–10 months of age, the cortex and subjacent white matter can appear isointense to each other on T2WI. It is important to note that these milestones may be visualized a bit earlier at 3T field strength than at 1.5T.

It is helpful to be aware of a general overall pattern of myelination [6, 7, 15–24]. The most common rule of thumb has been that myelination generally progresses from *posterior to anterior* and *caudal to cephalad*, based on structures the infant needs first:

1. **Caudal to Cephalad** and **Dorsal to Ventral**
   Examples: Brainstem → cerebellum; basal ganglia → cerebral cortex
2. In a particular region, **Posterior to Anterior**
   Examples: Dorsal brainstem → ventral brainstem; Occipital white matter → frontal white matter
3. **Myelination progresses more rapidly in systems used earlier in life**
   Examples: Brainstem: MLF, ML, ICP, SCP myelinated at birth → MCP later (transmits motor to cerebellum)
   Examples: Cerebral white matter: calcarine (visual) and pre/postcentral gyri → posterior parietal, temporal, frontal white matter later
4. Most myelination is **completed by 2 years of age** (except some PVWM and other terminal zones)
5. Best times and sequences to assess myelination: **T1WI**: **0–8 months**; **T2WI**: **8–24 months**

Other rules that may be helpful are described below. The subject of *terminal zones* (regions that are mildly hyperintense on T2WI and myelinate later) on T2WI and FLAIR is discussed later, with more detailed descriptions of the PVWM, SCWM, and other locations. The images used in this chapter are from patients who were subsequently developmentally normal on clinical follow-up.

Table 23.2 is a brief compilation of particular milestones can be visualized with T1WI and T2WI at specific ages after the neonatal stage in term infants. It is not a comprehensive list; many more specifically named structures have been identified in detailed literature and texts [6, 7, 15–24]. Many of these structures are smaller and are not always visualized owing to technique (such as brainstem nuclei or tiny supratentorial nuclei).

Table 23.2 Myelination by age

Age	T1WI (high signal)	T2WI (low signal)	Other
4–5 weeks	**Perirolandic gyri**, deep cerebellar WM, optic tracts & optic chiasm	**Perirolandic gyri**, deep cerebellar WM, posterior limb of the internal capsule more apparent; optic tracts & optic chiasm	**DWI**: SCWM still dark *vs* cortex
2 months	Patchy ↑T1 in centrum semiovale	Patchy ↓T2 in centrum semiovale	**DWI**: SCWM nears gray matter signal
3 months	**ALIC**, occipital/calcarine WM; cerebellum being "adult-like"; SCWM brightening	**Middle cerebellar peduncle**, occipital/calcarine WM, optic radiations, **callosal splenium** (at 3T), SCWM patchy (esp. at 3T), darkening of frontal and parietal gyri	**FLAIR**: **bright PVWM** (*vs* gray matter), dark PLIC
4 months	**Callosal splenium**	**Perirolandic gyri similar to others**; cerebral peduncles	**DWI**: SCWM no longer dark
6 months	Ventral pons (3–6 mo); **callosal genu**	**Callosal splenium** (1.5T); ventral brainstem now dark on T2; cerebral (6–12 mo) & cerebellar WM arborization (5–8 mo)	
8 months	**Adult appearance** (except anterior commissure & external capsule)	**Callosal genu**, most of ALIC, PVWM but "patchy" subcortical WM regions not yet myelinated begin to appear diffusely	
10 months	**Anterior commissure**	**WM & gray matter isointense** to each other (8–10 mo)	
12 months	Anterior temporal lobe and orbitofrontal SCWM appear myelinated	**ALIC completed** (about 9–11 mo); cerebral WM arborization (occurs from 6 to 12 mo)	**FLAIR**: isointense WM and gray matter
18 months		**Most WM completed** except deep & anterior temporal	**FLAIR**: WM darkens
2 years		**Adult appearance** except for terminal zones	**FLAIR**: WM darker

ALIC anterior limb of the internal capsule, *DWI* diffusion-weighted imaging, *FLAIR* fluid-attenuated inversion recovery, *PLIC* posterior limb of the internal capsule, *PVWM* periventricular white matter, *SCWM* subcortical white matter, *WM* white matter

23.6.1 Normal Myelination in Infants: Appearance at the Age of 1–2 Months

At the age of 1–2 months, the extent of myelination is similar to that of the term infant. For example, the *ventral brainstem* remains hyperintense relative to the dorsal brainstem (pons and midbrain). However, those structures that are questionably myelinated (that is, T1-bright or T2-dark) are more discernibly myelinated at 4–8 weeks age, such as the *cranial nerve V fascicle* (CNV) and *optic tract* (OT), particularly on GE T1WI at 3T. On SE T2WI, the *perirolandic cortex* (PRC) may appear darker than adjacent frontal or parietal gyri; within the cerebellum, myelination of the *nodulus* and *corpus medullare* should be clearly present. The optic chiasm (OC) and habenular commissure (HC) are myelinated but variably seen, usually owing to slice thickness. The posterior limb of the internal capsule (PLIC) should be more apparent on SE T2WI. Finally, the callosal splenium (CS) may begin to darken at this age on SE T2WI, but this is an advanced finding. Later, around 6–8 weeks of age, the white matter begins to appear patchy on T1WI and T2WI within the deep, periventricular white matter (PVWM) of the centrum semiovale. On FLAIR, just after 2 months age, the white matter becomes transiently hyperintense relative to gray matter; this finding typically is no longer present by 10–12 months of age, but this phenomenon is not well described (Figs. 23.69, 23.70, 23.71, 23.72, 23.73, 23.74 and 23.75).

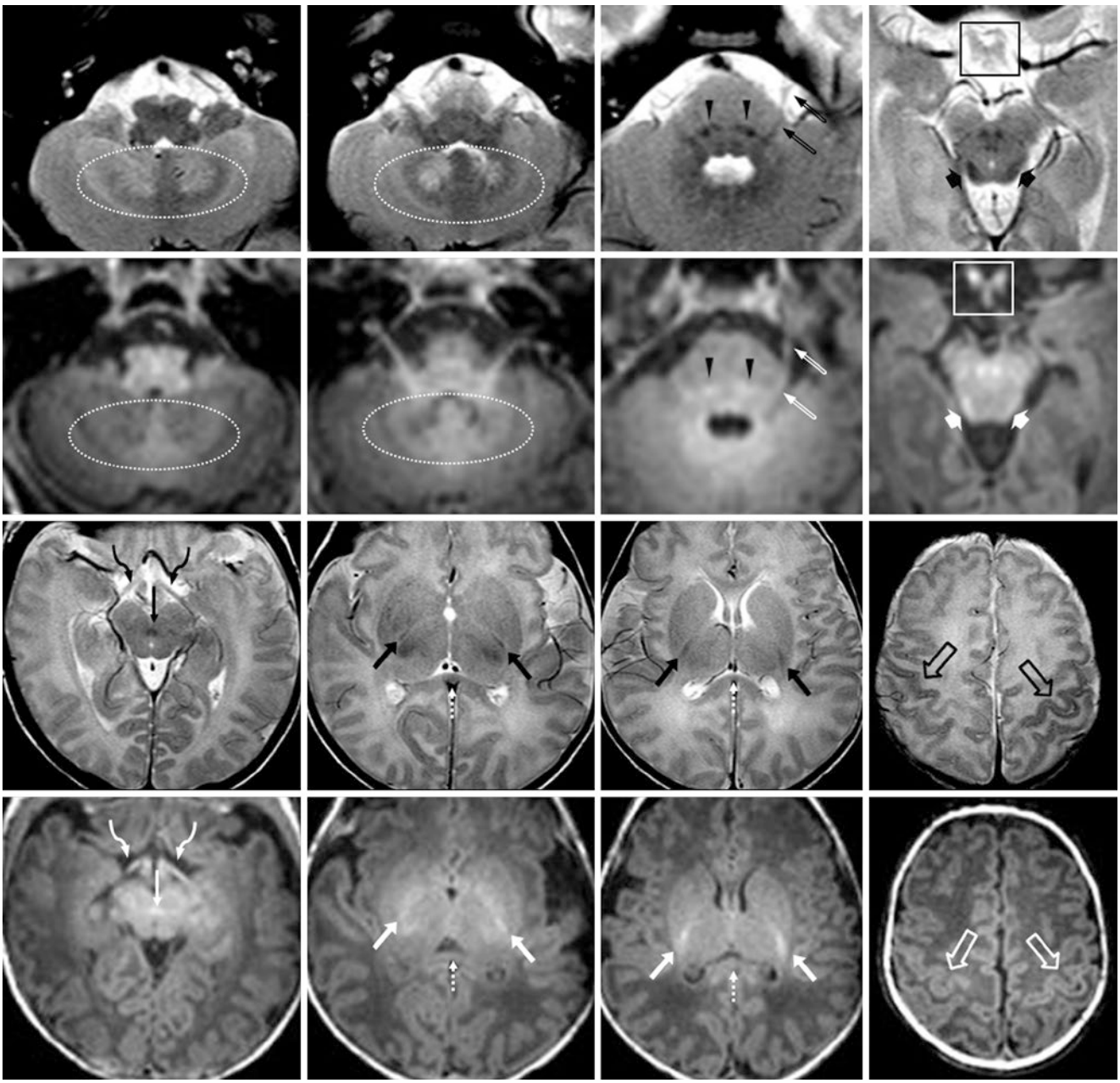

Fig. 23.69 A 4-week-old with fevers but a negative 3T MRI. The patient was subsequently developmentally normal. *Top row*: SE T2WIs show darkening cerebellar white matter and nodulus (*dotted ovals*), medial leminisci (*arrowheads*), left CNV (*beveled arrows*), and inferior colliculi (*wide arrows*). The ventral brainstem overall remains hyperintense. *Second row*: GE T1WIs do not depict the myelination of the cerebellar deep white matter and nodulus as well, but the optic chiasm (OC) is better visualized as myelinated than on SE T2WI (*box*). The dorsal brainstem is slightly hyperintense. *Third row*: SE T2WIs depict myelinating optic tracts (*curved arrows*), PLICs (*arrows*), and DSCP (*thin arrows*). There may be early myelination of the CS (*dotted arrows*), better visualized on SE T2WI. *Bottom row*: GE T1WIs depict the myelinating optic tracts and PLICs better than SE T2WI, although the DSCP is not as well seen. The dark PRC (*open arrows*) is better visualized on T2WI

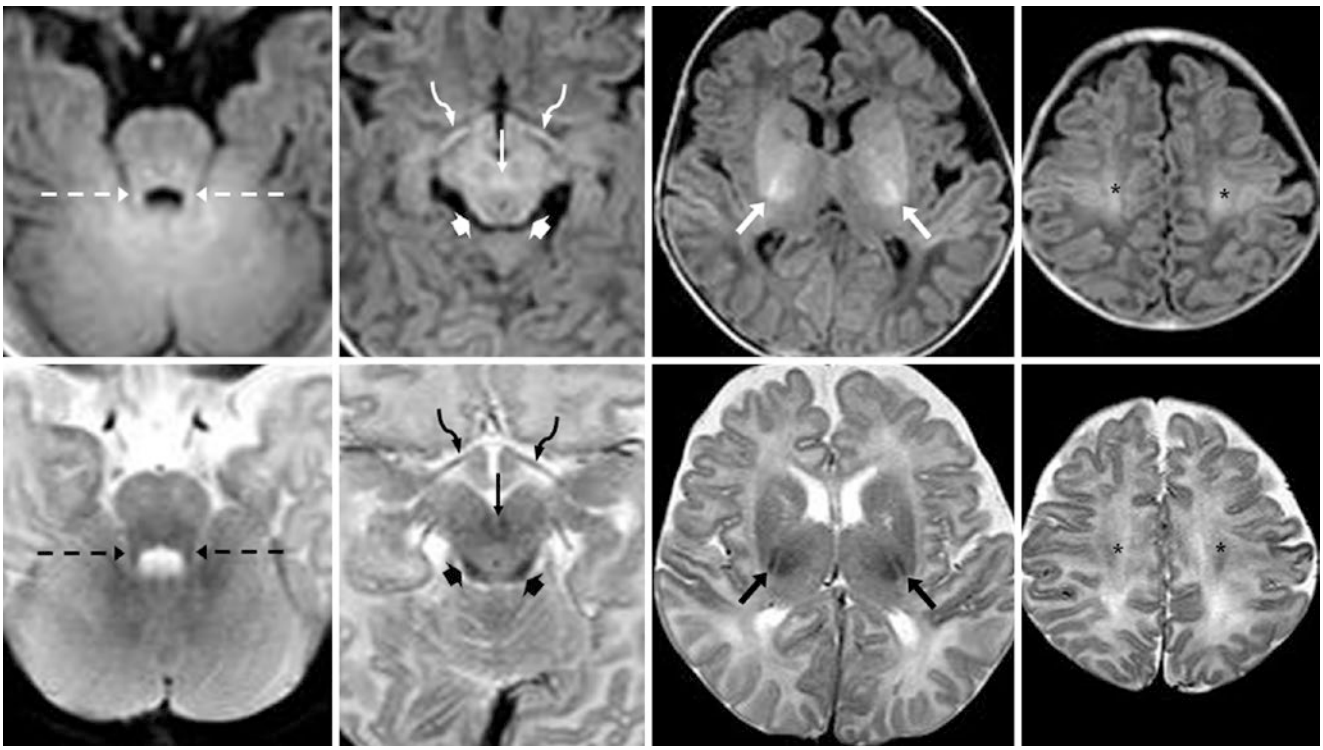

Fig. 23.70 A 5-week-old with fevers and a negative 1.5T MRI. GE T1WIs (*top row*) show myelinated superior cerebellar peduncles (*dashed arrows*), optic tracts (*curved arrows*), PLICs (*arrows*), and centrum semiovale (*asterisks*), which are present but less visible on SE T2WIs (*bottom row*). SE T2WIs better depict the inferior colliculi (*wide arrows*) and DSCP (*thin arrows*), but these are not as dark as expected because the image was obtained at 1.5T

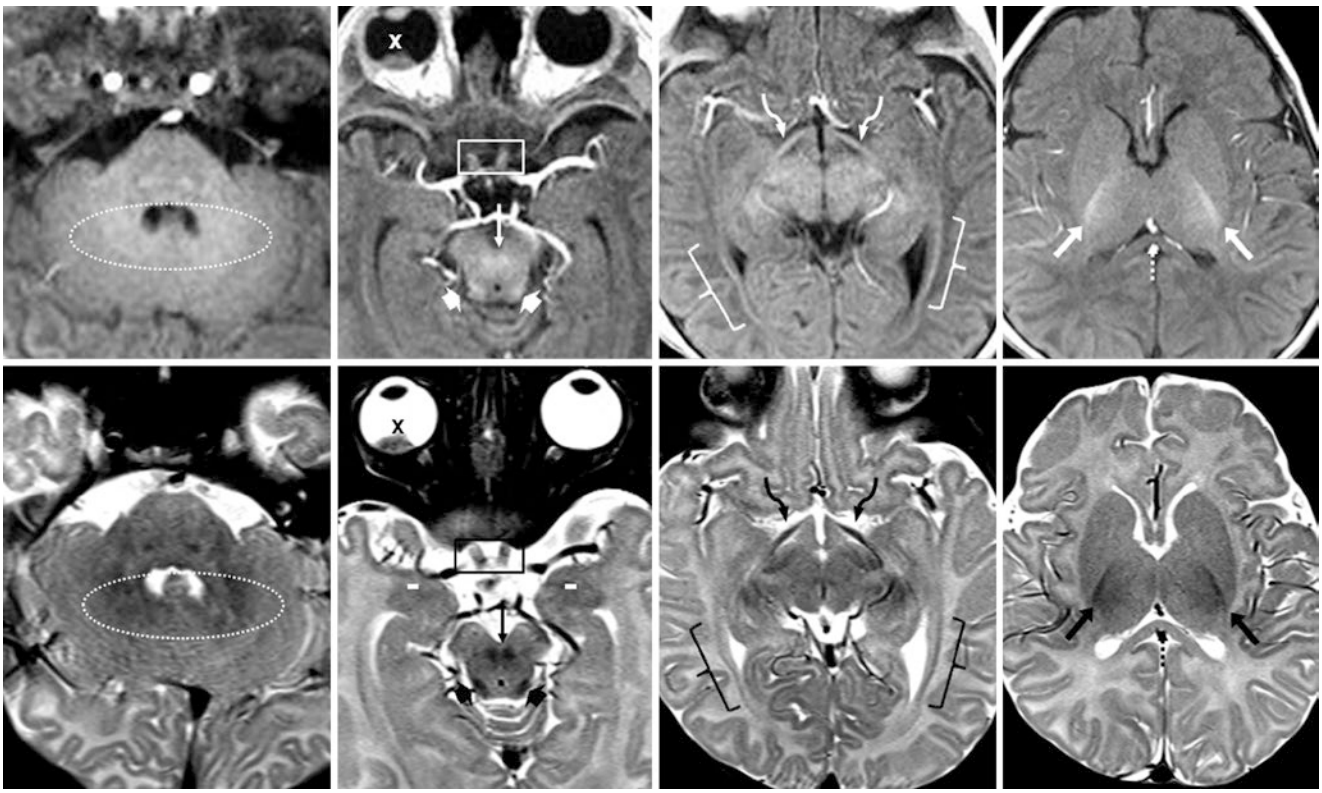

Fig. 23.71 A 6-week-old with a normal 1.5T MRI obtained for suspected retinoblastoma (X). Both spoiled GE T1WIs (*top row*) and SE T2WIs (*bottom row*) depict myelinated cerebellar white matter and nodulus (*dotted ovals*), inferior colliculi (*wide arrows*), DSCP (*thin arrows*), optic tracts (*curved arrows*), optic nerves (*boxes*), and PLICs (*arrows*). SE T2WIs show early darkening of the callosal splenium (*dotted arrows*). At this age, there is advanced myelination of the optic radiations (*brackets*). Note T2-dark amygdalae (*white dashes on left middle image*), not visible on T1WI

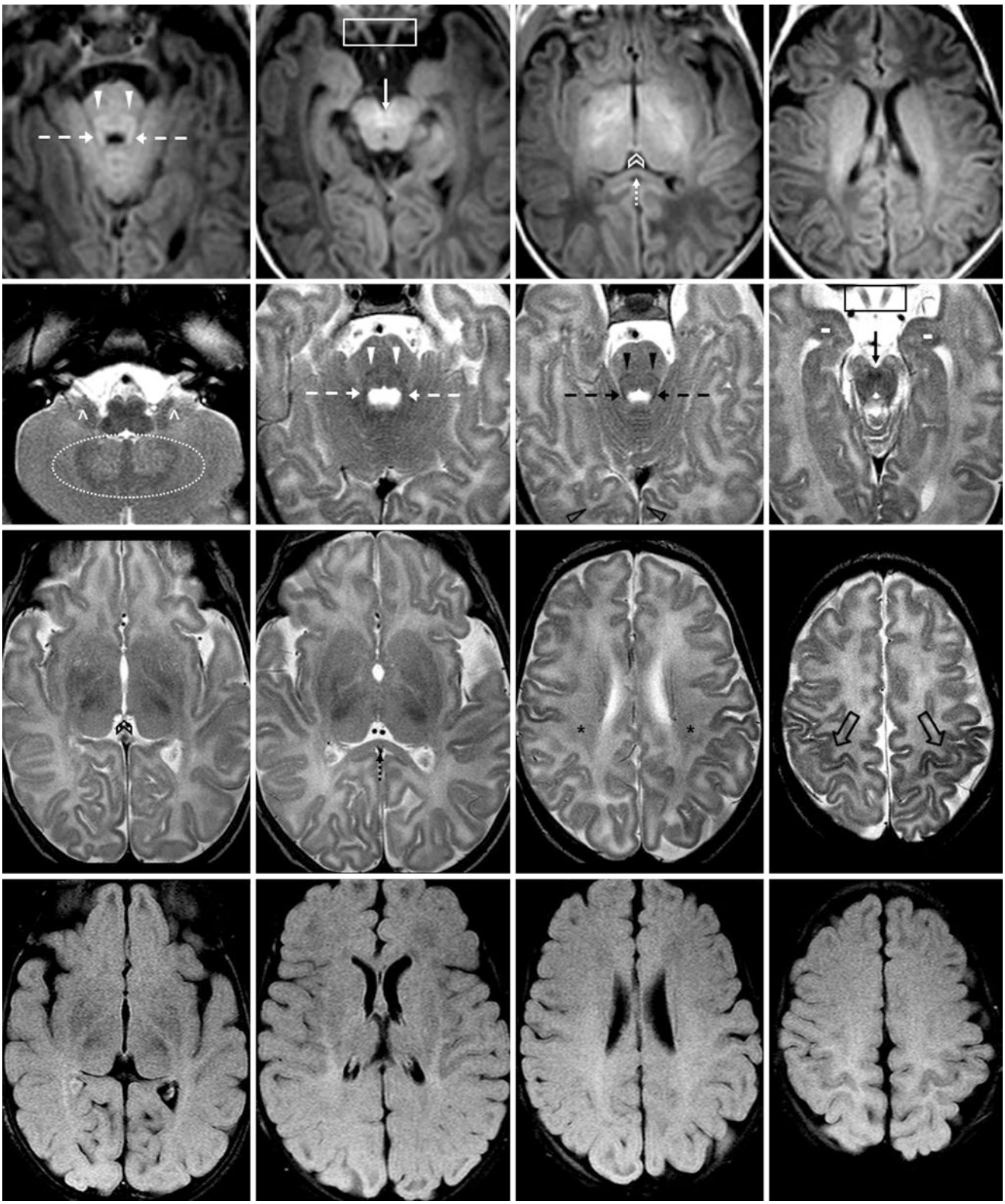

Fig. 23.72 A 7-week-old with leg weakness and a negative 3T MRI of the brain and spine. *Top row*: GE T1WIs show myelinating superior cerebellar peduncles (*dashed arrows*), their decussation (*thin arrows*), medial leminisci (*arrowheads*), optic nerves (*box*), and HC (*chevron*). The PLIC is still quite bright. *Second row*: On SE T2WIs, note T2-dark signal of the same structures, as well as a darkening ventral brainstem, deep cerebellar white matter and nodulus (*dotted oval*), flocculi (^), and optic nerves. Also, note the T2-dark amygdalae (*white dashes*). *Third row*: SE T2WIs at a higher level show the darkening HC and callosal splenium (*dotted arrows*). Also, note darkening white matter within the centrum semiovale (*asterisks*). The PRC (*open arrows*) remains darker than the adjacent gyri. *Bottom row*: on FLAIR images, the optic radiations and PVWM are beginning to appear hyperintense relative to the overlying cortices and to the basal ganglia. This phenomenon is transient, lasting until about 1 year of age

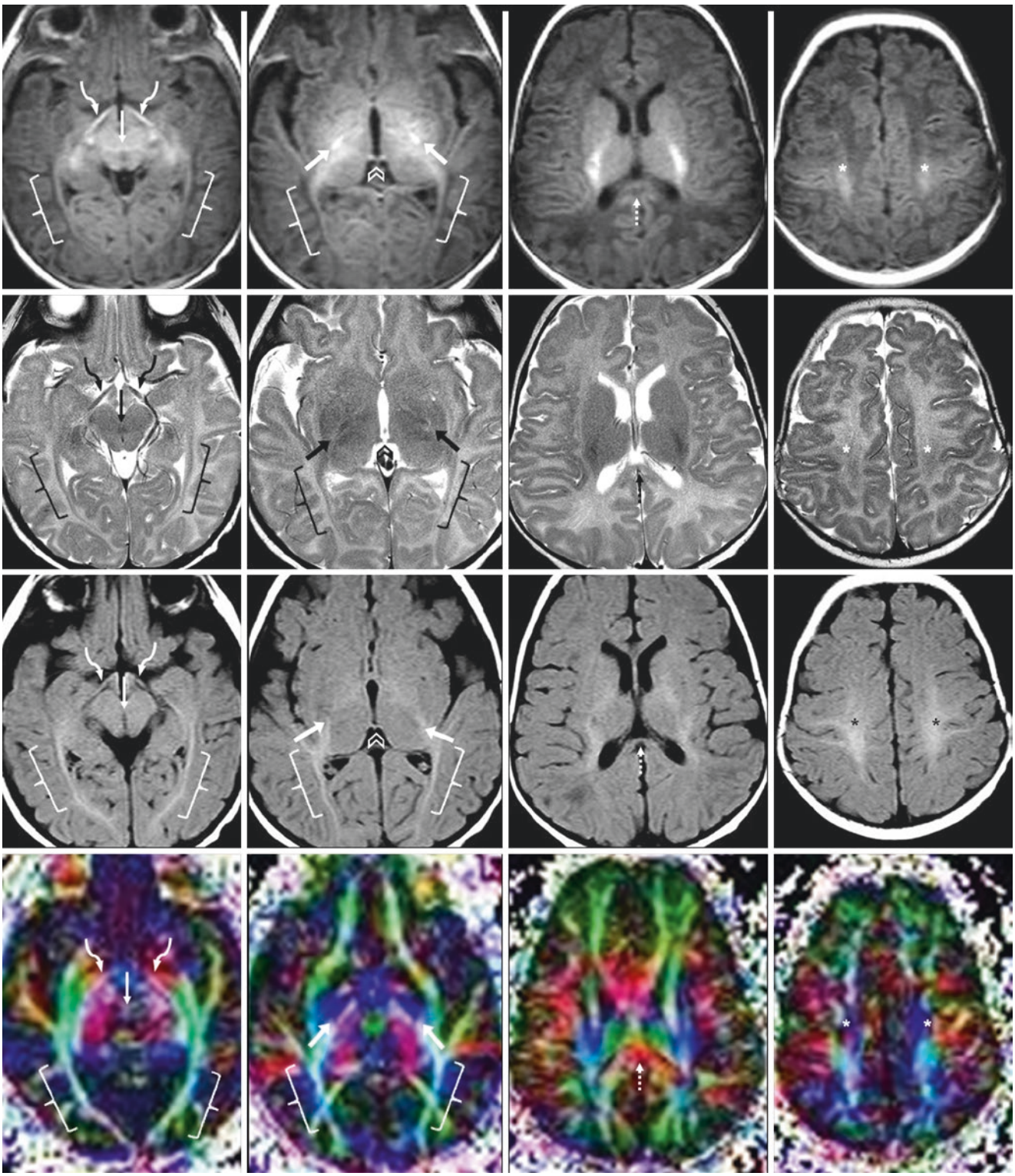

Fig. 23.73 An 8-week-old with questioned trauma but a negative 3T MRI, who thereafter developed normally. *Top row*: GE T1WIs depict clear myelination of the optic tracts (*curved arrows*), DSCP (*thin arrow*), HC (*chevron*), and PLICs (*arrows*). The centrum semiovale continues to brighten (*asterisks*). *Second row*: SE T2WIs show evident myelination in the same structures; the HC and optic tracts are now clearly myelinated. Also, note darkening optic radiations (*brackets*) and CS (*dotted arrow*), better seen on SE T2WI. *Third row*: FLAIR images illustrate how the deep WM and PVWM have become hyperintense as compared with gray matter. This phenomenon is transient and typically fades later in the first year of life as the white matter matures. *Bottom row*: Six-directional diffusion tensor images were obtained to evaluate the fiber tracts, which were normal. *Blue* = craniocaudally oriented fibers; *Green* = anterior-posteriorly oriented fibers; *Red* = transversely oriented fibers

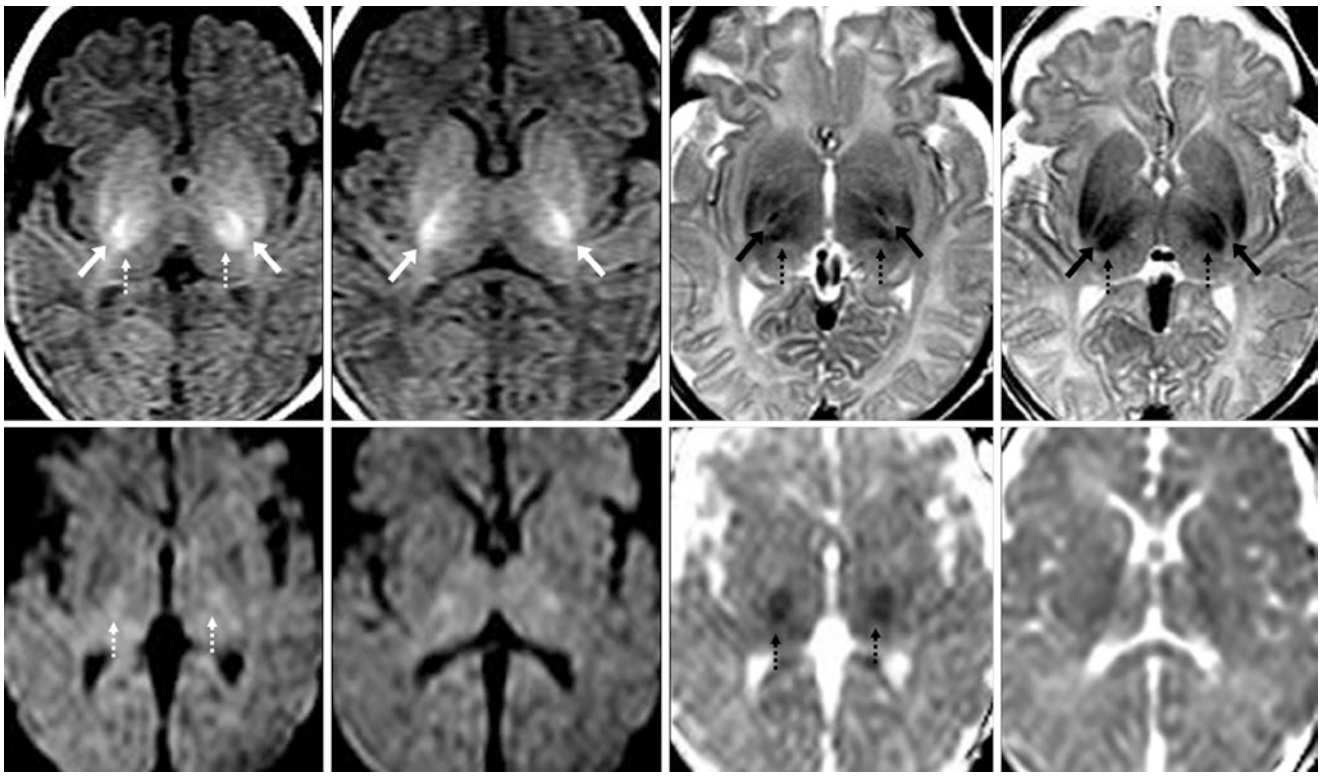

Fig. 23.74 Comparison case of mild HII in a 5-week-old with recurring apnea. *Top row*: GE T1WI (*left images*) and SE T2WI (*right images*) show "blotchy" bright signal on T1WI and dark signal on T2WI of the ventrolateral thalami (*dotted arrows*), posterior putamina, and PLICs (*arrows*), which appear somewhat blended together. *Bottom row*: DWI (*left images*) is negative at this stage, probably because it is several weeks postnatal, but abnormal signal remains on ADC maps (*right images*) within the thalami (*dotted arrows*)

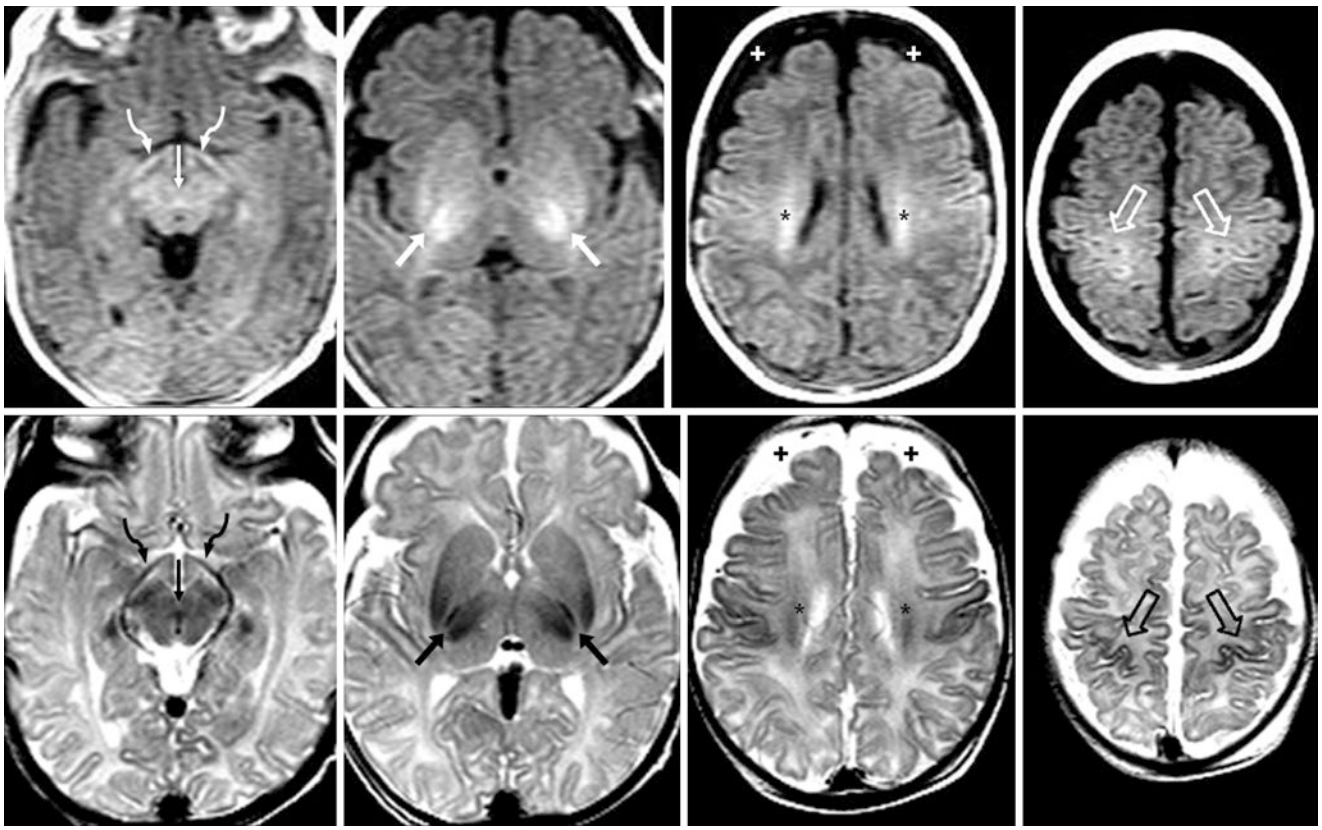

Fig. 23.75 Comparison case of subtle HII: A 4-week-old had benign enlargement of subarachnoid spaces (*plus signs*). GE T1WIs (*top row*) and SE T2WIs (*bottom row*) show normal myelination of the optic tracts (*curved arrows*), DSCP (*thin arrow*), and PRC (*open arrows*), but the bright signal on T1WI and dark signal on T2WI of the ventrolateral thalami, posterior putamina, PLICs (*arrows*), and corona radiata (*asterisks*) is too profound

23.6.2 Normal Myelination in Infants: Appearance at the Age of 3–4 Months

By the age of 3–4 months, the extent of myelination is demonstrably quite different from the extent at 1–2 months in several key locations. For example, the *ventral brainstem* (pons and midbrain) typically becomes darker and nearer in signal intensity to the dorsal brainstem by this age on both GE T1WI and SE T2WI at 3T. Thus, structures such as the *medial and lateral leminisci*, *cranial nerve V fascicle*, and the *superior cerebellar peduncle and its decussation* become nearly isointense to the remainder of the brainstem on both sequences, and are much less discernible. On GE T1WI at 3T, the *anterior limb of the internal capsule* (ALIC) and the *callosal splenium* (CS) are key structures that should appear "myelinated" at 3T on both sequences by age 4 months, particularly at 3T. As the white matter continues to "myelinate" it progresses generally posteriorly to anteriorly, which includes not only the corpus callosum, but also the frontal and parietal regions. Generally, the PVWM and SCWM tend to progress outwards from the PRC as well. By age 3 months, the adjacent frontal and parietal cortices are darkening on T2WI; they become the same or nearly the same signal intensity as the PRC by 4 months. At 1.5T, the PVWM and SCWM begin to appear "patchy" by age 3 months on SE T1WI, and they may start appear isointense to, or difficult to discern from, the cortices by 3–4 months of age, although this appearance may occur slightly later (at 5–6 months) on GE T1WI or SE T1WI at 3T.

On FLAIR images at this age, the white matter typically appears homogeneously hyperintense within PVWM of the corona radiata, centrum semiovale, and optic radiations, relative to gray mattter. Again, this phenomenon is not well described, but it seems to abate to near the signal of cortex by age 10–12 months. Because of T2 hypointensity, the PLIC appears dark. On DWI, the PVWM-SCWM, darker than cortex neonatally and at 1–2 months of age, now becomes isointense (Figs. 23.76, 23.77, 23.78, 23.79, 23.80, 23.81 and 23.82).

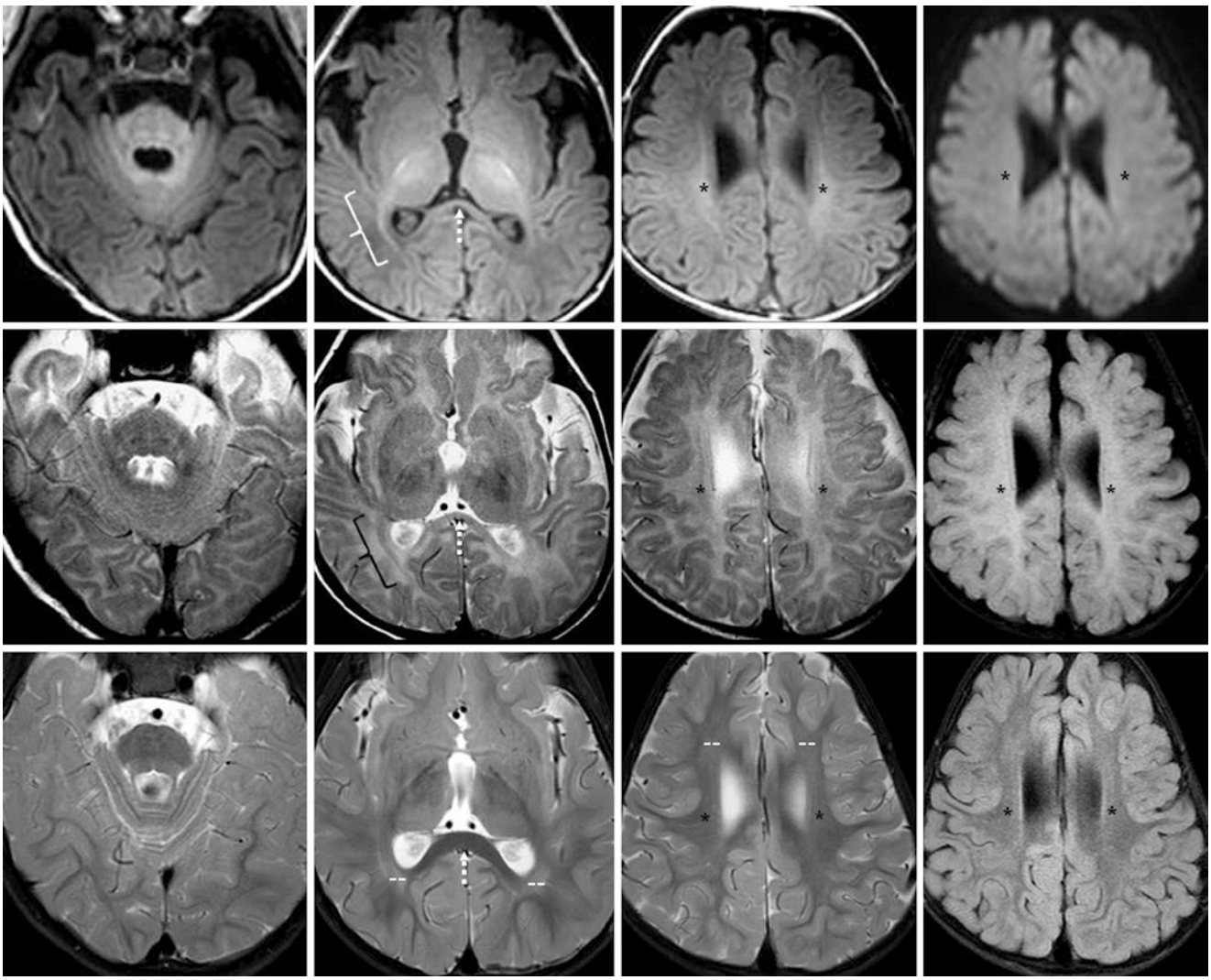

Fig. 23.76 A 10-week-old with motor delays had a negative 3T MRI. *Top row*: GE T1WIs (*left images*) illustrate how the ventral pons is almost isointense to the dorsal pons. The optic radiations (*brackets*) are myelinating. Bright white matter of the corona radiata (*asterisks*) is extending further anteriorly and posteriorly. DWI (*right*) shows isointense PVWM-SCWM. *Middle row*: SE T2WIs (*left images*) also show that the ventral brainstem is becoming more isointense relative to the dorsal brainstem. The CS is darkening (*dotted arrows*), along with the corona radiata and optic radiations. The frontal and parietal cortices are darkening. Note hyperintense white matter on FLAIR (*right*). *Bottom row*: at 2.5 years of age, repeat SE T2WIs (*left images*) show clearly normal myelination in the structures noted above. The CS and optic radiations have myelinated normally. Note normal terminal zones of incomplete myelination (*white double dashes*). On FLAIR (*right*), the PVWM-SCWM have now become hypointense relative to gray matter

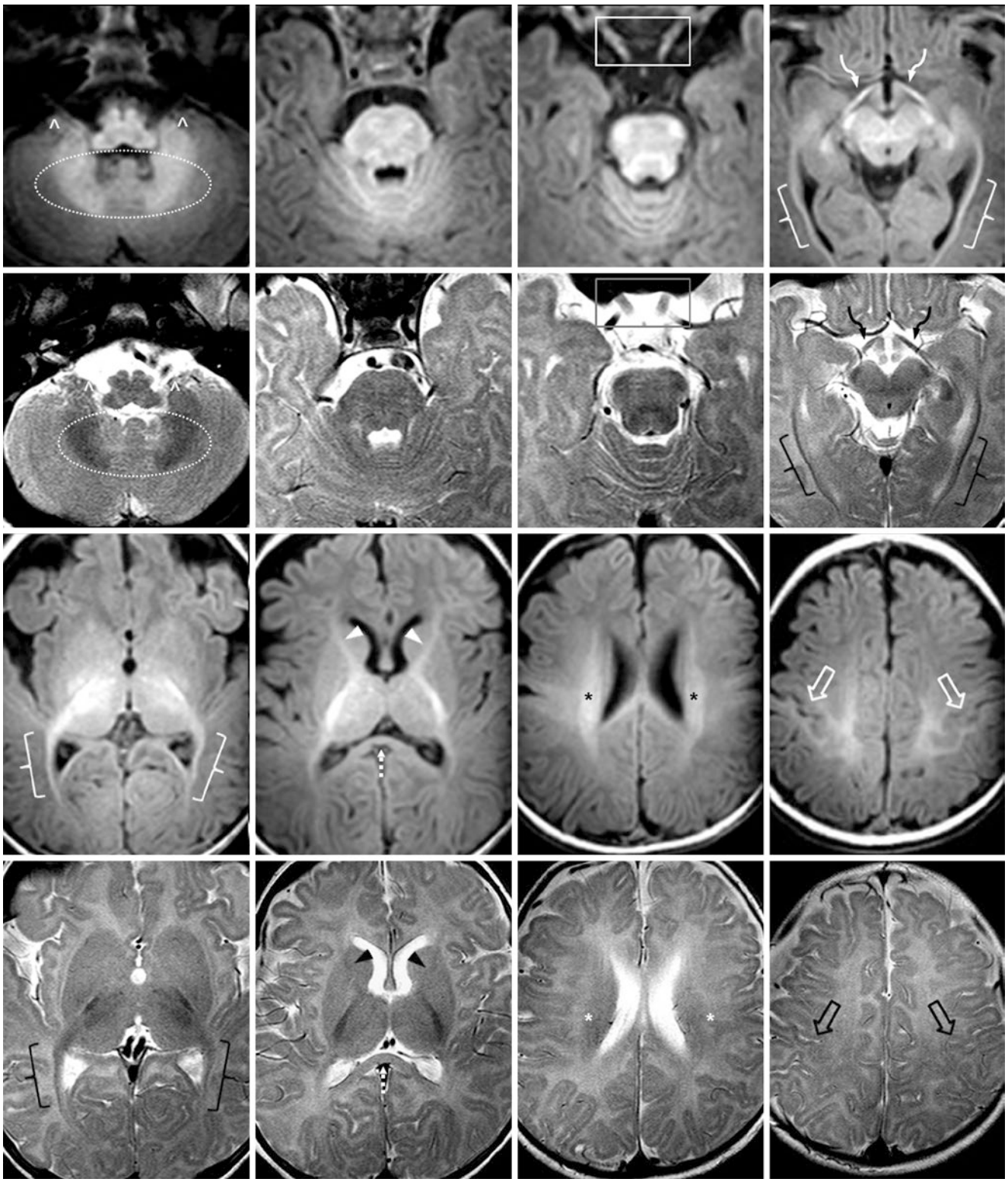

Fig. 23.77 An 11-week-old with questioned trauma, who had a negative 3T MRI, and thereafter developed normally. *Top row*: GE T1WIs depict clear myelination of the cerebellar deep white matter and nodulus (*dotted oval*), and flocculi (^). Note myelination of the optic radiations (*brackets*), optic tracts (*curved arrows*), and optic nerves (*box*). *Second row*: SE T2WIs show evident myelination in the same structures noted on GE T1WI. In addition, note that the ventral brainstem is nearly isointense with the dorsal brainstem, and the optic radiations are quite T2-dark. *Third row*: GE T1Ws at higher levels demonstrate early myelination of the ALIC (*arrowheads*) and CS (*dotted arrow*). The deep PVWM of the corona radiata (*asterisks*) and centrum semiovale are becoming more diffuse and patchy. *Bottom row*: SE T2WIs do not show early myelination of the ALIC (*arrowheads*) as well as GE T1WIs. As myelination of the deep white matter spreads, the frontal and parietal gyri darken to the degree of the PRC (*open arrows*)

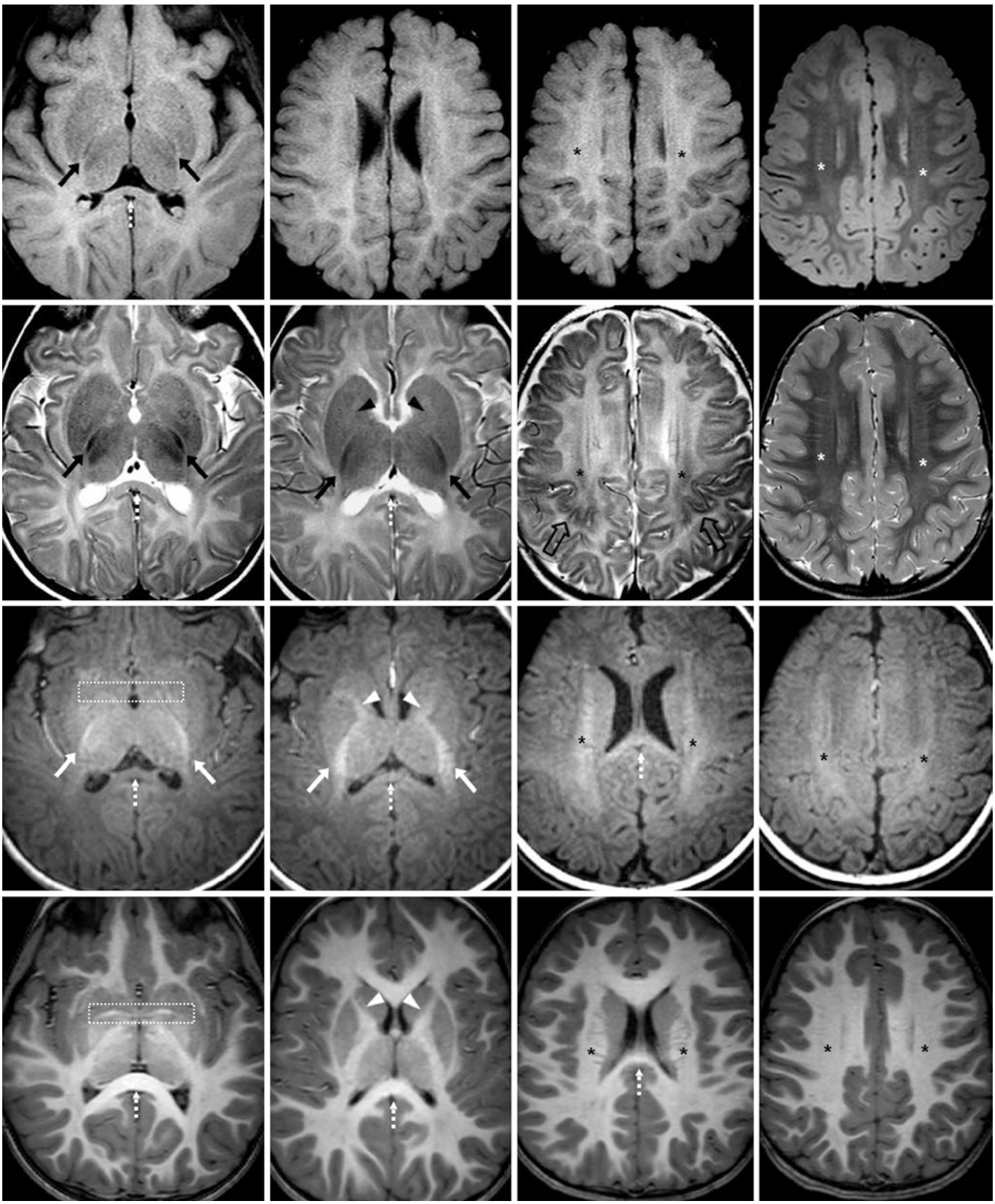

Fig. 23.78 A 13-week-old with possible abusive trauma, who had a negative 3T MRI, and developed normally. *Top row*: FLAIR images show the hyperintense PVWM and SCWM, which regresses by 1 year of age. Note the dark PLIC (*arrows*). At 3 years of age (*right*), note that the gray matter-white matter pattern has reversed to the adult appearance. *Second row*: SE T2WIs show PLIC myelination. The centrum semiovale is darkening (*asterisks*). The frontoparietal gyri have darkened nearly to the PRC (*open arrows*). At 3 years of age, there is white matter reversal akin to an adult (*right*). *Third row*: GE T1WIs show myelinating PLIC-corticospinal tracts. The ALIC (*arrowheads*) has early myelination, as does the CS (*dotted arrows*), which are not as well seen on SE T2WI. The centrum semiovale (*asterisks*) is myelinating. *Bottom row*: Repeat GE T1WIs at 3 years of age illustrate completed myelination, with normal appearances of the ALIC, CS, and the centrum semiovale (*asterisks*). Note that myelination of the anterior commissure (*dotted box*) is also completed

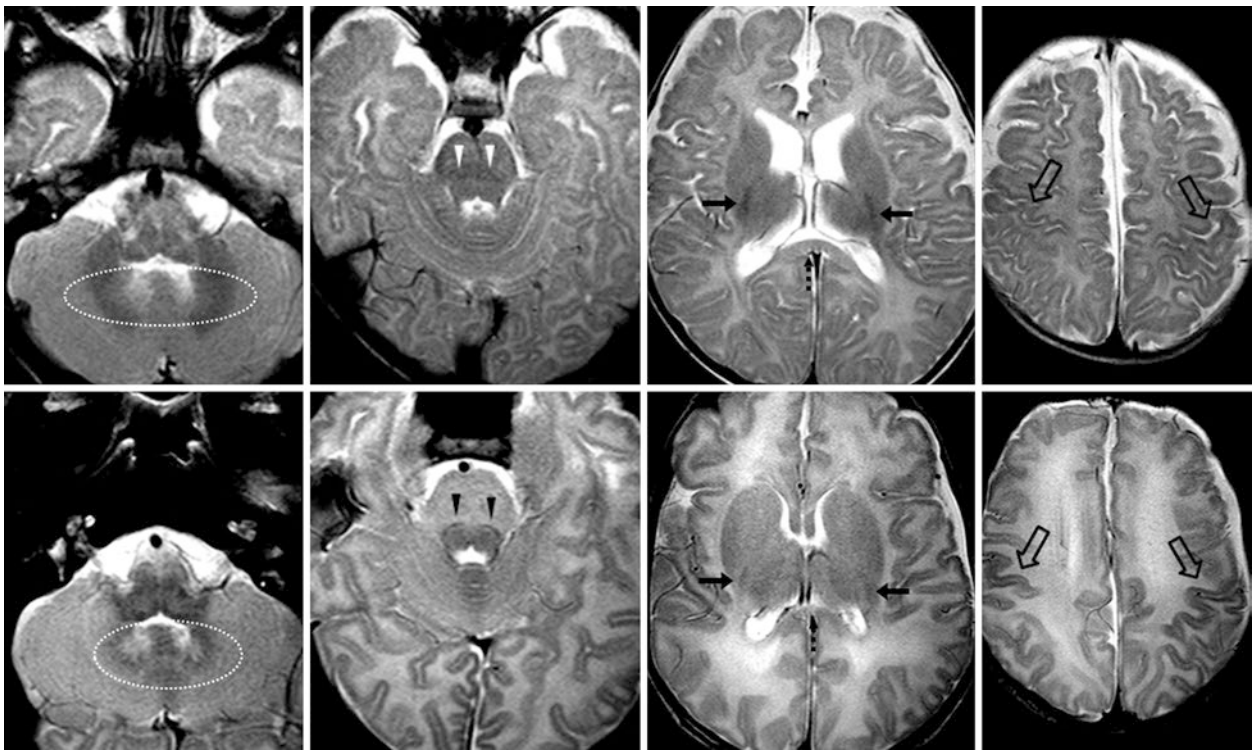

Fig. 23.79 A 14-week-old with possible seizures had a negative 3T MRI with SE T2WIs (*top row*). Compared with a 3T MRI at 5 days of age (*bottom row*), the pons is now homogeneous in signal, the medial leminisci (*arrowheads*) are no longer discernible within the pons, and the PLIC (*arrows*) has become more discernible and entirely dark. The frontal and parietal gyri are nearly isointense to the PRC (*open arrows*). The cerebellar white matter is myelinated (*dotted ovals*)

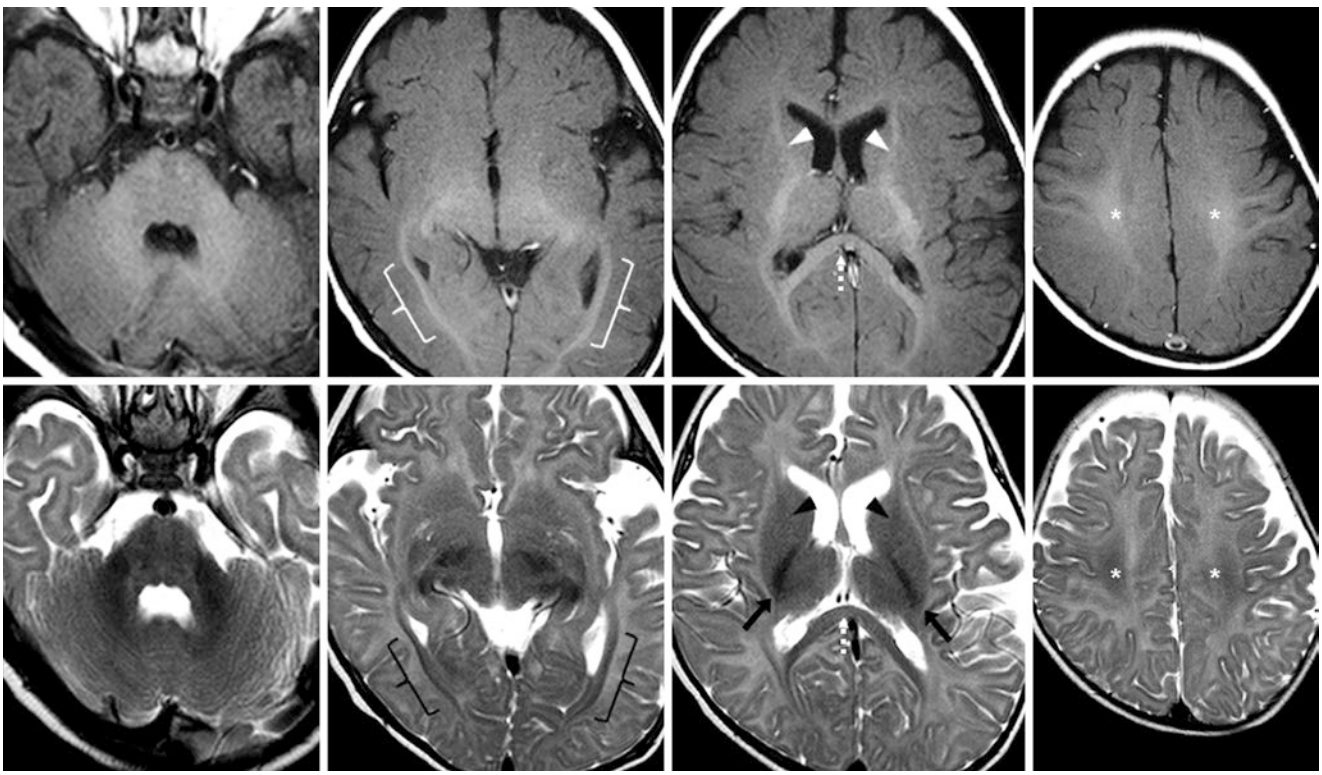

Fig. 23.80 A 16-week-old with head enlargement (benign enlargement of subarachnoid spaces) had a negative 3T MRI with GE T1WIs (*top row*) and SE T2WIs (*bottom row*). The pons is homogeneous in signal. Myelination of cerebellar white matter appears complete. The ALICs (*arrowheads*) appear to be myelinating on T1WI, but are not well visualized on T2WI. There has been progression in myelination of the optic radiations (*brackets*), CS (*dotted arrows*), and centrum semiovale (*asterisks*) on both sequences

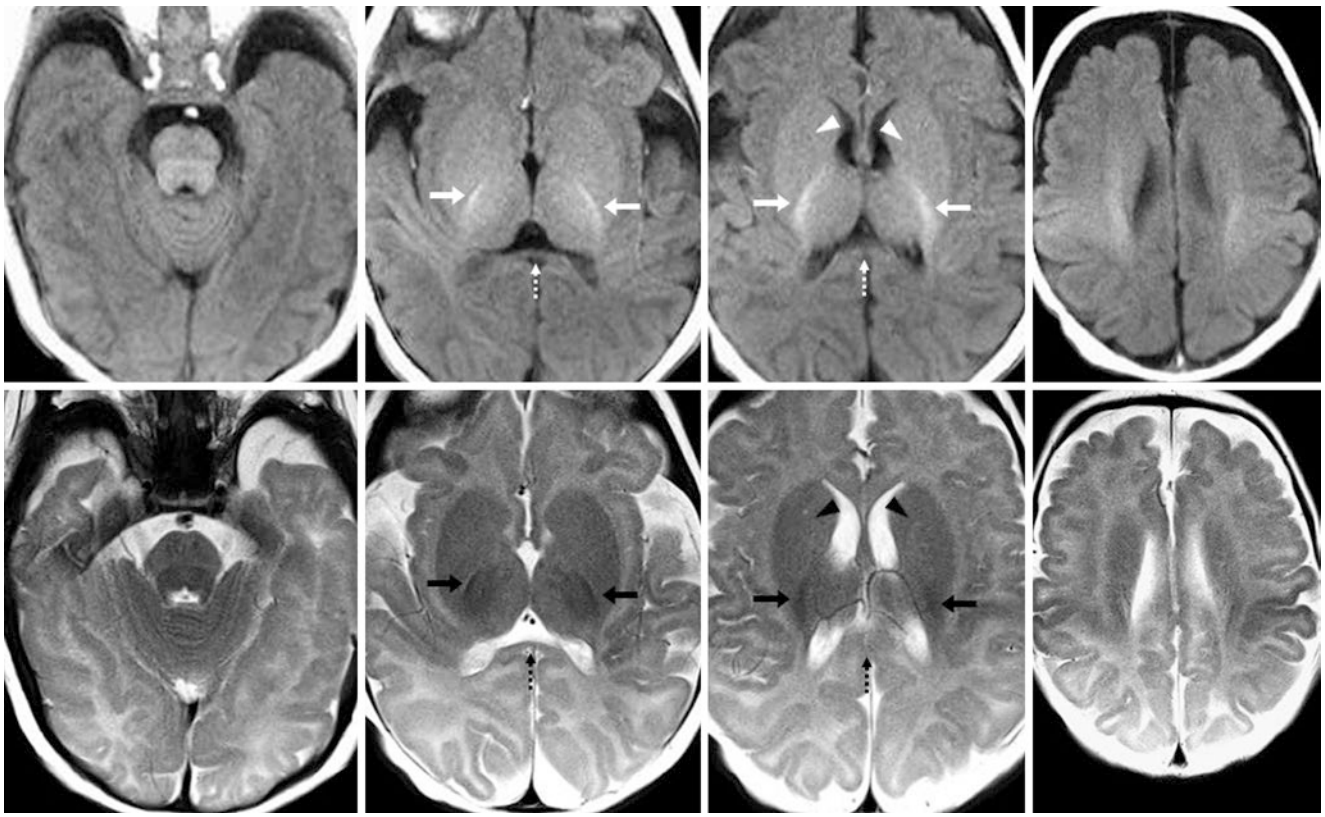

Fig. 23.81 Comparison case of mild hypomyelination in cobalamin C defect. A 14-week-old with developmental delay had a 3T MRI with GE T1WIs (*top row*) and SE T2WIs (*bottom row*). Although there appears to be maturation (*i.e.*, myelination) of the PLICs-corticospinal tracts (*arrows*) on both sequences, the ALIC (*arrowheads*) and CS (*dotted arrows*) should be myelinated by this age, and myelination has not spread far enough within the corona radiata

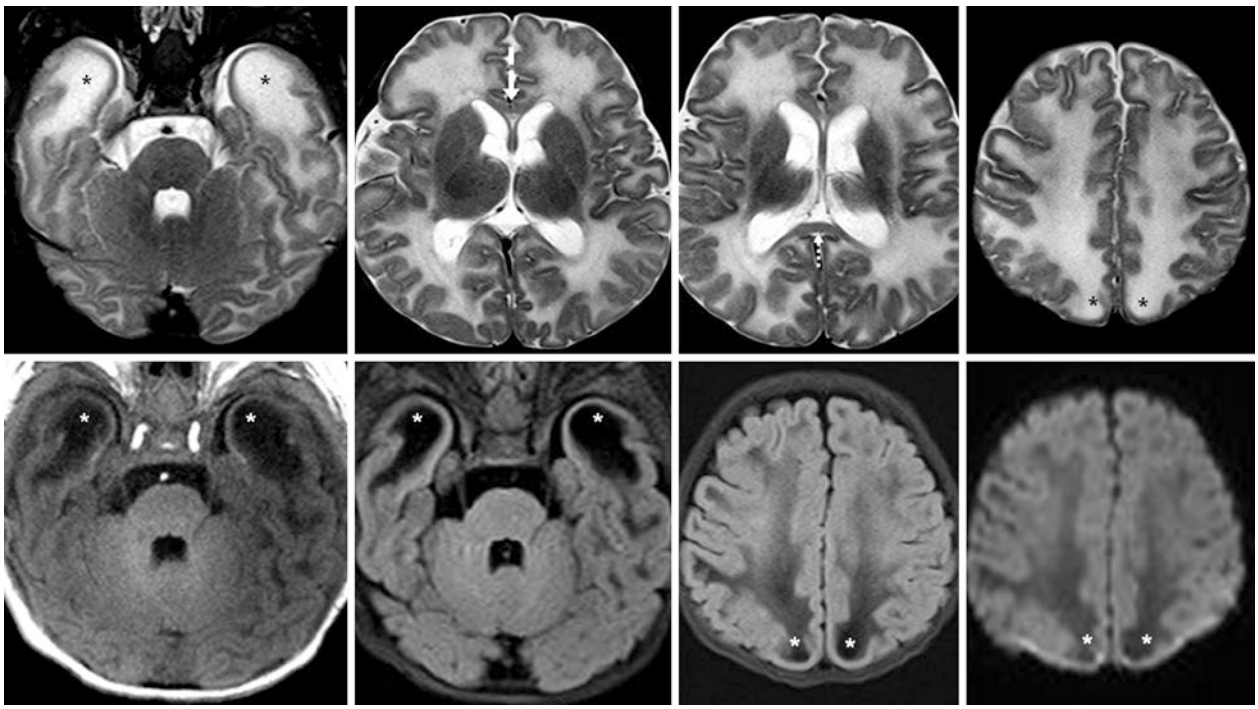

Fig. 23.82 Comparison case of megancephalic leukoencephalopathy with subcortical cysts (van der Knaap disease). A 14-week-old with motor delay had a 3T MRI with SE T2WIs (*top row*). Note the quite T2-bright edema that has been called "cysts" within the anterior temporal and high parietal lobes (*asterisks*), which are dark on both T1WI (*bottom left*) and FLAIR (*bottom*, *left and right of middle*). On DWI (*bottom right*), these are nearly as dark as CSF. Also, on T2WI, note that the callosal genu (CG) (*dashed arrow*) and the callosal splenium (CS) (*dotted arrow*) are relatively spared

23.6.3 Normal Myelination in Infants: Appearance at the Age of 5–6 Months

By the age of 6 months, several keys structures should be clearly myelinated. Most notably, the *ventral brainstem* (pons and midbrain) has darkened to the point that the brainstem should appear homogeneously hypointense on SE T2WI. Thus, the various pontine nuclei and tracts should be far less discernible and nearly isointense to the remainder of the pons on both sequences. The *callosal genu* (CG) should be visibly myelinated on GE T1WI at 3T, and typically on SE T2WI as well, if performed at 3T; the CG may appear myelinated a bit later (at 8 months) at 1.5T. By 5–6 months, the *callosal splenium* (CS) should appear clearly myelinated on both sequences, particularly at 3T, as should the *cerebral peduncles* (CP). At about 5 months of age, the CS may appear quite bright relative to the CG on T1WI in the sagittal plane; this appearance is normal and at times is striking. Both the *anterior limb of the internal capsule* (ALIC) and *external* and *extreme capsules* (EC) should have definite bright signal on T1WI at both 1.5T and 3T, but they may not be visible on SE T2WI, whether at 1.5T or 3T. In general, at 3T, white matter maturation on SE T2WI may be nearly equivalent to GE T1WI or may lead GE T1WI in some structures, whereas at 1.5T, the visualization of white matter maturation on SE T2WI definitely trails both GE T1WI and SE T1WI.

As the myelination of the white matter continues, it progresses further anteriorly, and also peripherally into the SCWM from the PVWM. By 6 months, the adjacent frontal and parietal cortices have darkened on T2WI so that they are of the same signal intensity as the PRC. Notably, myelination of the SCWM commences at about 3 months of age (exception for motor and visual regions, which are earlier), and the white matter continues to myelinate in a general posterior-to-anterior direction, so that the *anterior temporal white matter* (ATWM) myelinates last (except for normal PVWM "*terminal zones*") [1, 6–8]. At this age, there is usually visible myelination of the deep white matter (WM) and SCWM underlying the PRC and occipital regions, whereas the anterior frontal and parietal gyri are less mature. Barkovich also describes myelination extending peripherally in the SCWM until about 7 months of age in the occipital region and by 8–11 months in the frontotemporal regions. Thus, by this author's experience, the PVWM and SCWM can appear inhomogeneous at this age, and can obscure subtle abnormalities such as *malformations of cortical development*, white matter insults such as *focal gliosis*, or mild *hypomyelination*. In such instances, it may be prudent to recommend follow-up imaging at about 1 year of age, when the white matter is more mature. On FLAIR, deep WM and PVWM of the corona radiata, centrum semiovale, and optic radiations remain hyperintense relative to gray matter (Figs. 23.83, 23.84, 23.85, 23.86, 23.87, 23.88, 23.89 and 23.90).

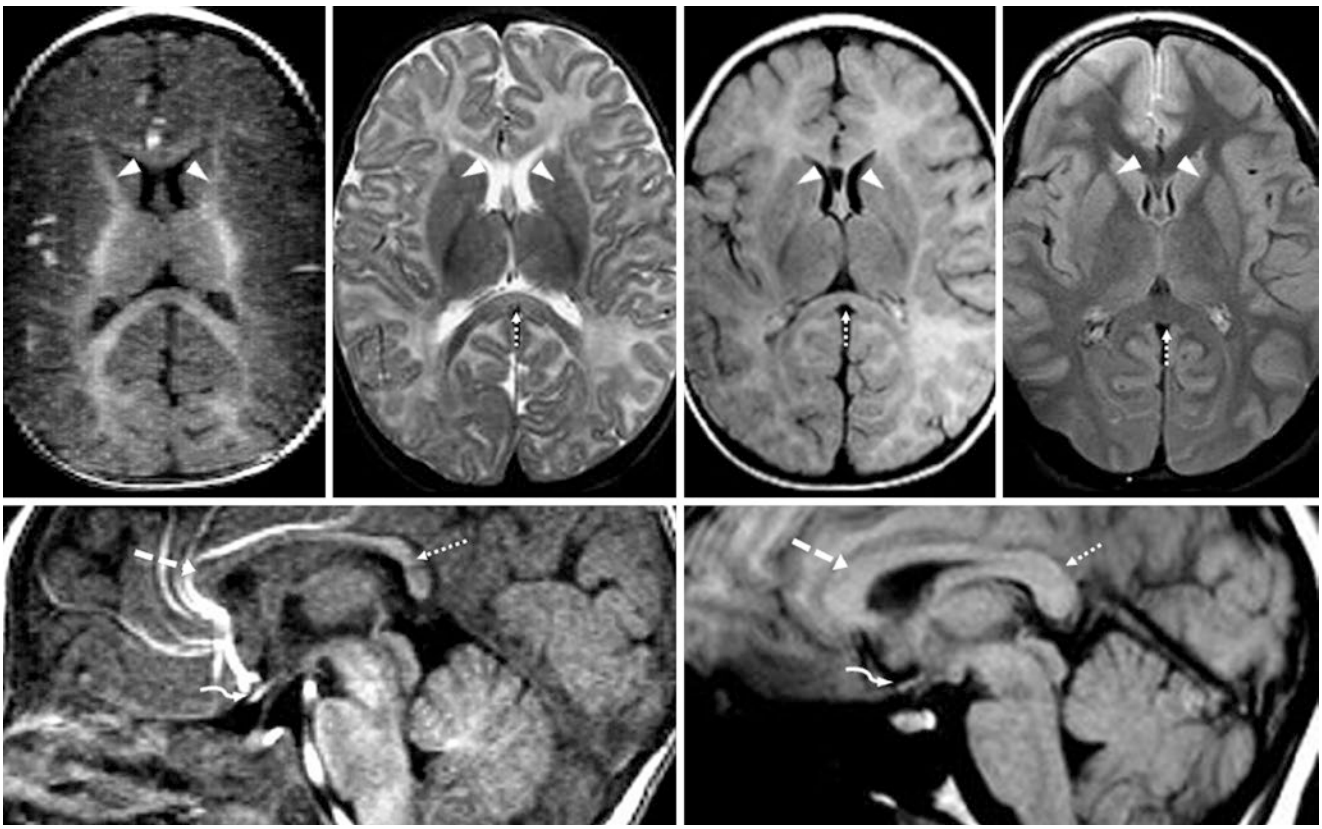

Fig. 23.83 A 5.5-month-old with a possible visual deficit had a negative 1.5T MRI with GE T1WI (*top left*), SE T2WI (*top*, *left middle*), and FLAIR (*top*, *right middle*). The ALICs (*arrowheads*) are maturing on T1WI and are only slightly dark on T2WI. The PVWM is bright on FLAIR; a FLAIR image 13 years later in the same patient (*top*, *right*) shows the PVWM reversal. On a sagittal GE T1WI at 5.5 months of age (*bottom left*), note the bright CS (*dotted arrow*) and dark CG (*dashed arrow*), as compared with a SE T1WI at age 13 years (*bottom right*). Also note the myelinated optic chiasm (*curved arrows*)

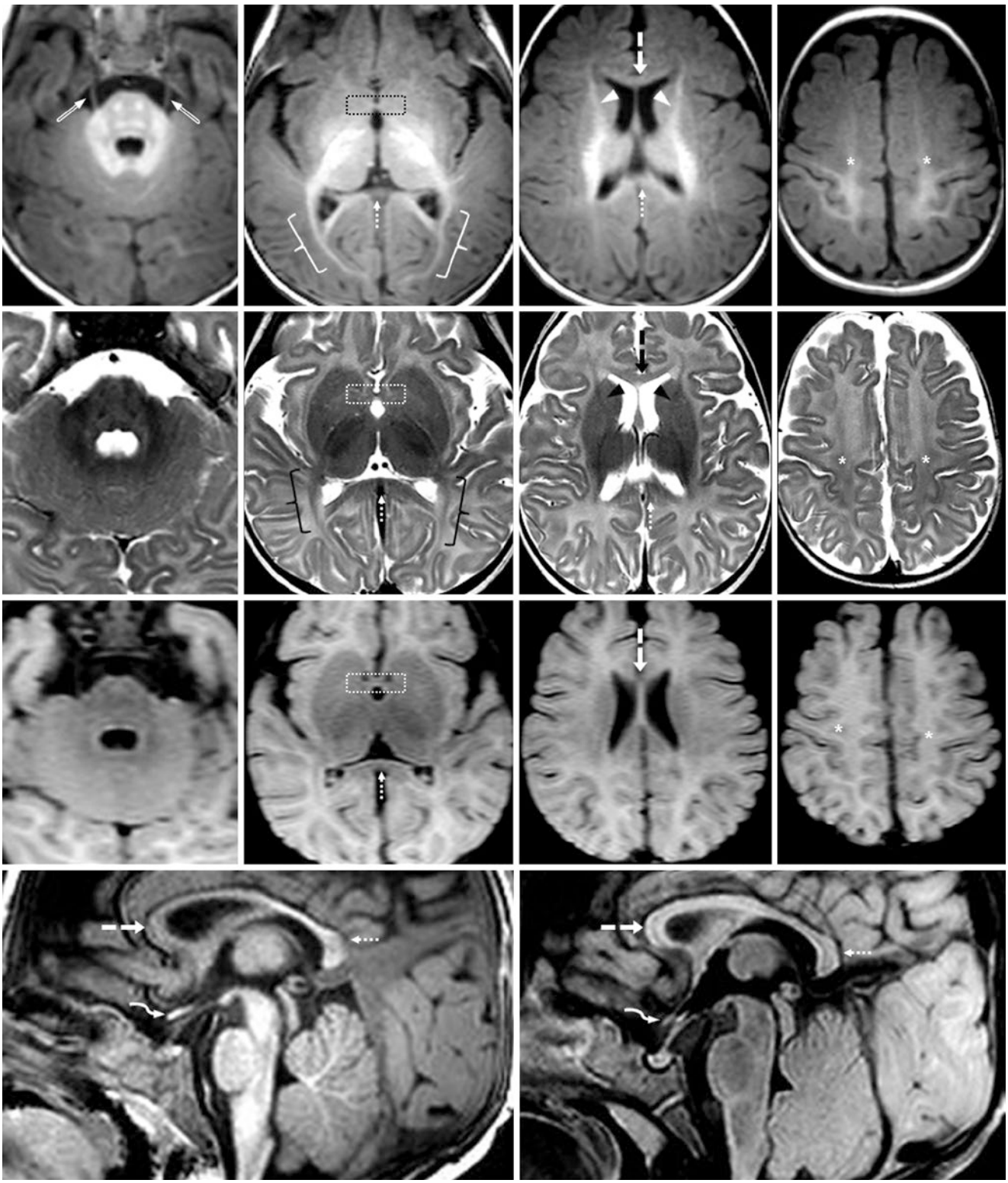

Fig. 23.84 A 5.5-month-old with a possible seizure, who had a negative 3T MRI and thereafter developed normally. *Top row*: GE T1WIs show clear myelination of the cerebellar deep WM. Note cranial nerve V fascicles (*beveled arrows*) and myelination of the optic radiations (*brackets*), ALIC (*arrowheads*), and CS (*dotted arrow*). *Second row*: SE T2WIs illustrate the brainstem's homogeneously dark appearance. The CS has undergone myelination, but the CG (*dashed arrows*) has not. The frontoparietal gyri are nearly isointense to the PRC. *Third row*: 3D acquisition axial FLAIR images illustrate how the PVWM and SCWM remain hyperintense. The anterior commissure can be discerned (*dotted box*, and is not yet myelinated on T1WI or T2WI. *Bottom row*: 3D sagittal GE T1WI (*left*) and FLAIR (*right*) show T1-bright myelination of the CS but not the CG, causing the CG to appear bright on FLAIR but dark on T1WI. Note the myelinated optic chiasm (*curved arrows*)

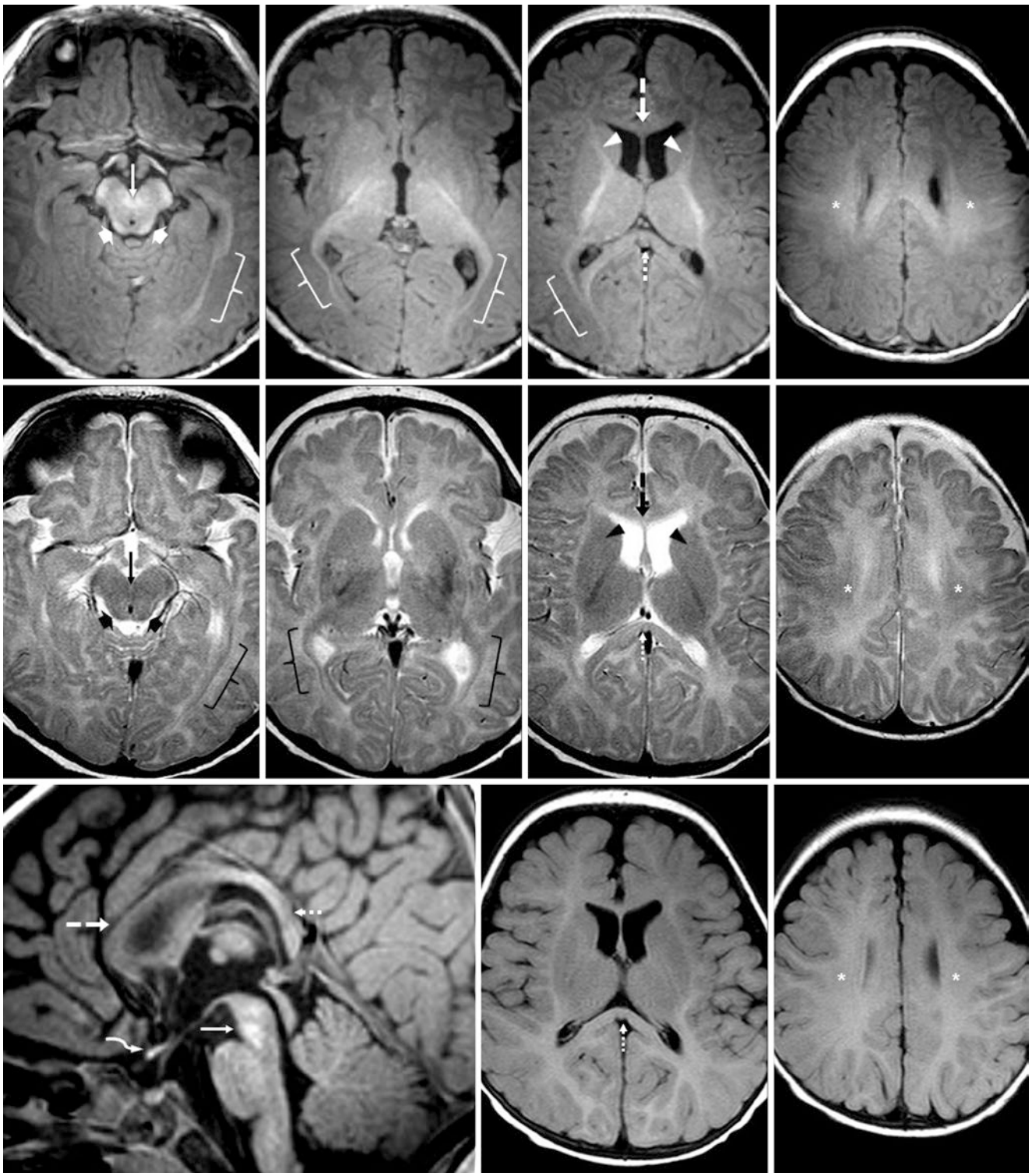

Fig. 23.85 A 5.75-month-old with a questioned developmental delay, who had a negative 1.5T MRI and subsequently normal development. In general, note progressing myelination within the centrum semiovale (*asterisks*), as the PRC and occipital deep WM and SCWM are mostly myelinated; the frontal and parietal WM are less mature. *Top row*: GE T1WIs illustrate that the decussation of the cerebellar peduncles (*thin arrows*) and brachia of the inferior colliculi (*wide arrows*) still appear hyperintense relative to the remainder of the midbrain on T1WI. The optic radiations (*brackets*), CS (*dotted arrow*), and ALIC (*arrowheads*) all appear to be myelinating. *Second row*: On SE T2WIs, the decussation of the superior cerebellar peduncles and brachia of the inferior colliculi do not stand out relative to the rest of the brainstem, as they do on T1WI. Note that the optic radiations and CS show slight maturation/myelination, but to a lesser degree than on T1WI, perhaps because this is at 1.5T. *Bottom row*: On a sagittal T1WI at midline (*left*), note bright signal within the CS and posterior callosal body, whereas the CG still appears unmyelinated. Note the myelinated optic chiasm (*curved arrow*). Even at 1.5T field strength on FLAIR (*middle and right*), the PVWM and SCWM appear hyperintense relative to cortical gray matter

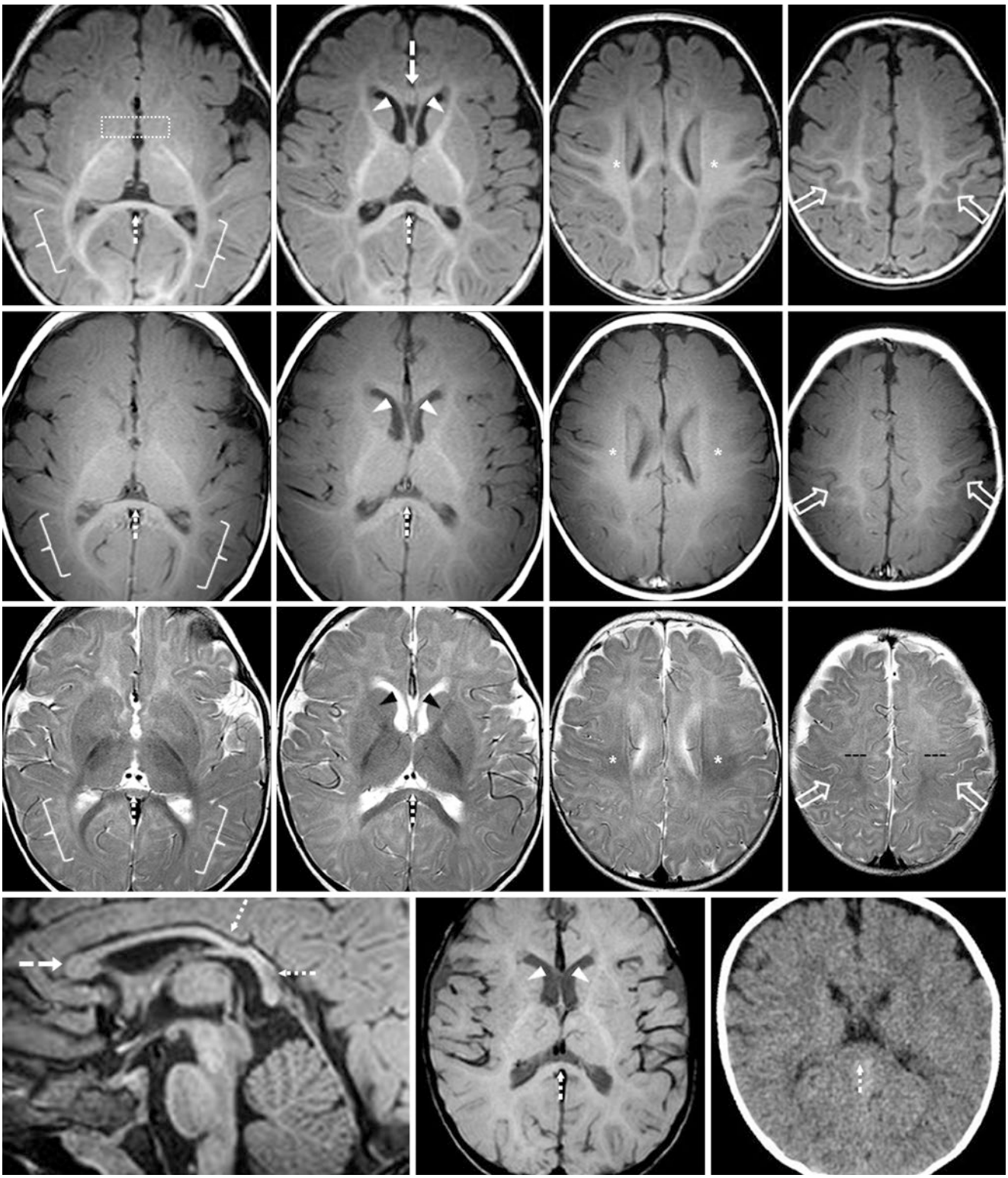

Fig. 23.86 A 6-month-old with altered mental status underwent a negative 3T MRI, and thereafter developed normally. Note progressing myelination within the centrum semiovale (*asterisks*), as the PRC (*open arrows*) and occipital white matter are quite mature. *Top row*: GE T1WIs illustrate myelination of the optic radiations (*brackets*), CS (*dotted arrows*) and ALIC (*arrowheads*). The CG (*dashed arrow*) is mildly hyperintense. The anterior commissure (*dotted box*) is unmyelinated. *Second row*: SE T1WIs also demonstrate myelination of the abovementioned structures, but they are much less visible on SE T1WI at 3T than on GE T1WI. Note clearly myelinated white matter underlying the PRC (*open arrows*). *Third row*: SE T2WIs also depict myelination of the abovementioned structures, which is slightly less visible than on GE T1WI, especially the optic radiations and ALIC. However, the "edge" of myelination is more visible on T2WI (*black dashes*). *Bottom row*: On a midline sagittal T1WI (*left*), note bright signal within the CS and posterior callosal body (*dotted arrows*); the CG (*dashed arrow*) is unmyelinated. On SWI (*middle*), the ALIC and CS are slightly bright. A NECT (*right*) is normal

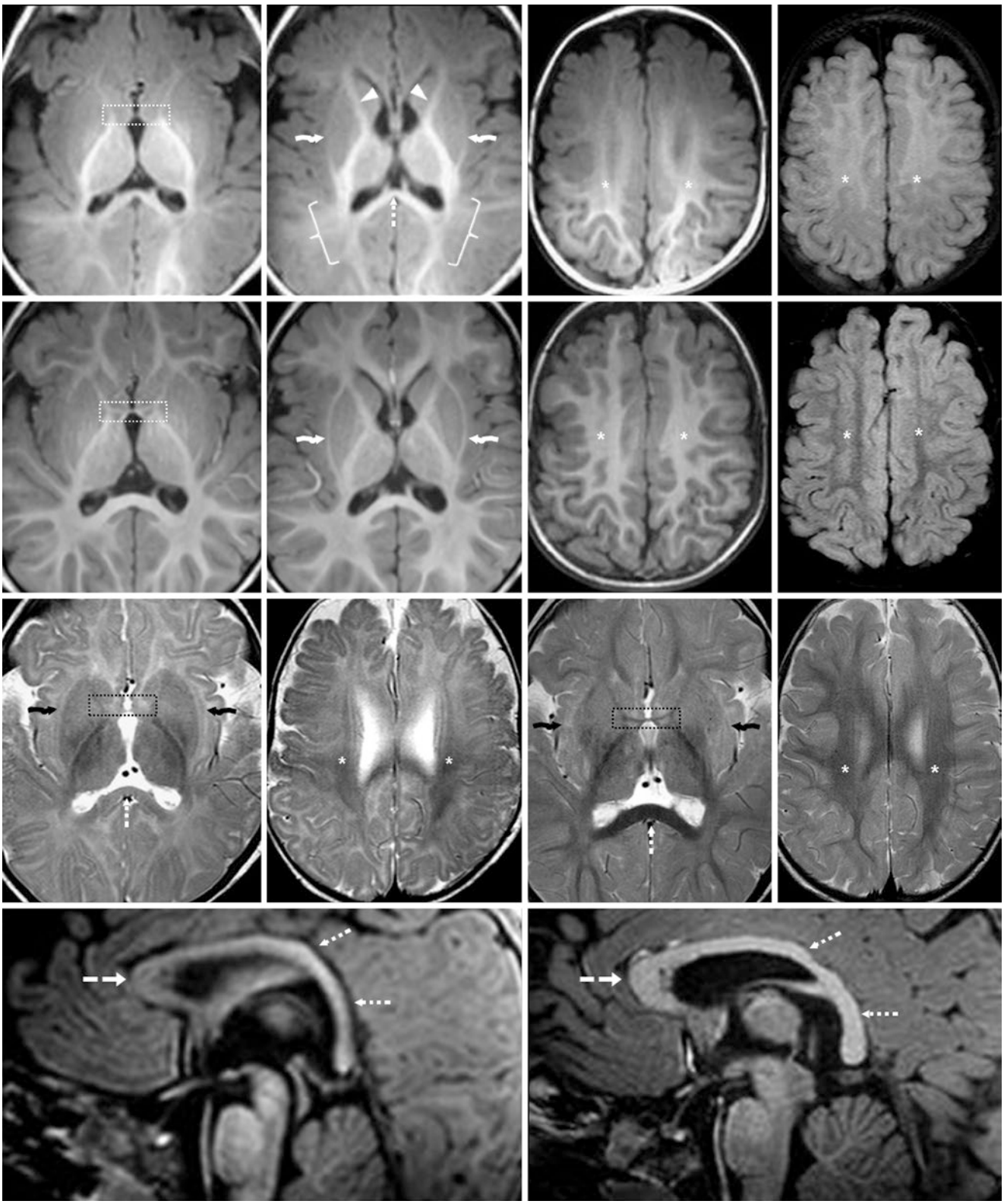

Fig. 23.87 A 6-month-old with "spells" who underwent a negative 3T MRI and thereafter developed normally, with another normal MRI at 15 months of age. Note progressing myelination of the centrum semiovale (*asterisks*). *Top row*: GE T1WIs (*leftmost images*) illustrate myelination of the optic radiations (*brackets*), CS (*dotted arrow*) and ALIC (*arrowheads*). The external capsules (*crooked arrows*) are maturing. Note bright white matter on FLAIR (*right*). *Second row*: GE T1WIs (*leftmost images*) at 15 months of age show further myelination of the structures noted above. The centrum semiovale has darkened on FLAIR (*right*). The anterior commissure (*dotted box*) has myelinated. *Third row*: SE T2WIs at ages 6 months (*left two images*) and 15 months (*right two images*) illustrate progressive myelination of the anterior commissure, CS, and coronal radiata, though the external capsule is not completed. *Bottom row*: On a midline sagittal T1WI at age 6 months (*left*), note bright signal of the CS and posterior callosal body (*dotted arrows*); the CG (*dashed arrow*) is unmyelinated. At age 15 months (*right*), the CG has myelinated and is thicker

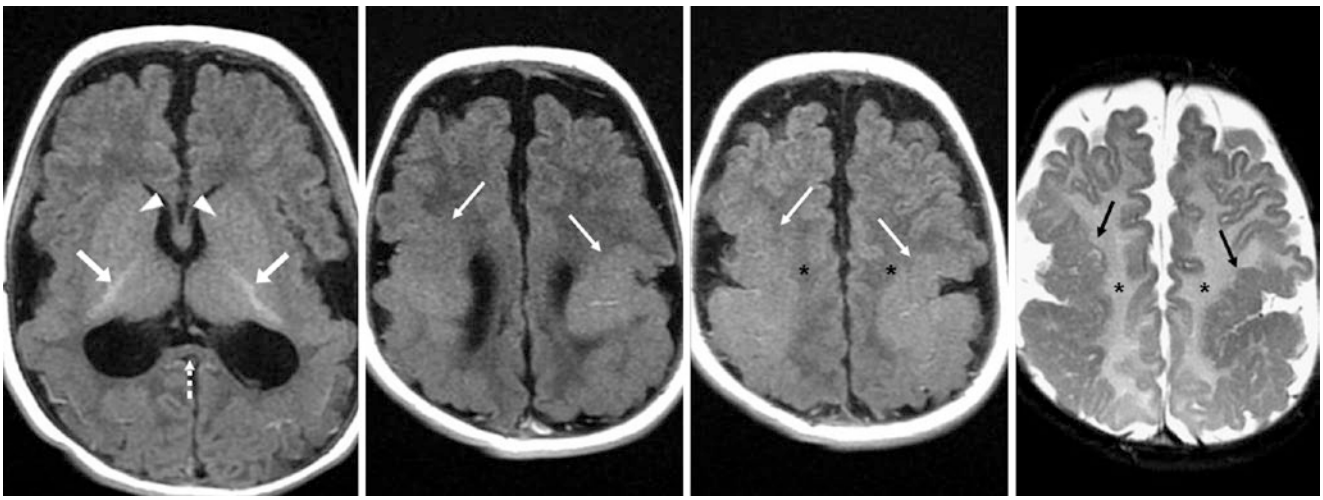

Fig. 23.88 Comparison case of hypomyelination in congenital perisylvian polymicrogyria. A 5-month-old with motor delays had a 1.5T MRI with T1 FLAIR (*leftmost images*) and SE T2WI (*right*). The ALICs (*arrowheads*), CS (*dotted arrow*) and CG (*dashed arrow*) were poorly myelinated, whereas the PLICs (*arrows*) were myelinated. The centrum semiovale (*asterisks*) is poorly myelinated. The polymicrogyria (*thin arrows*) is better visualized on SE T2WI in this patient

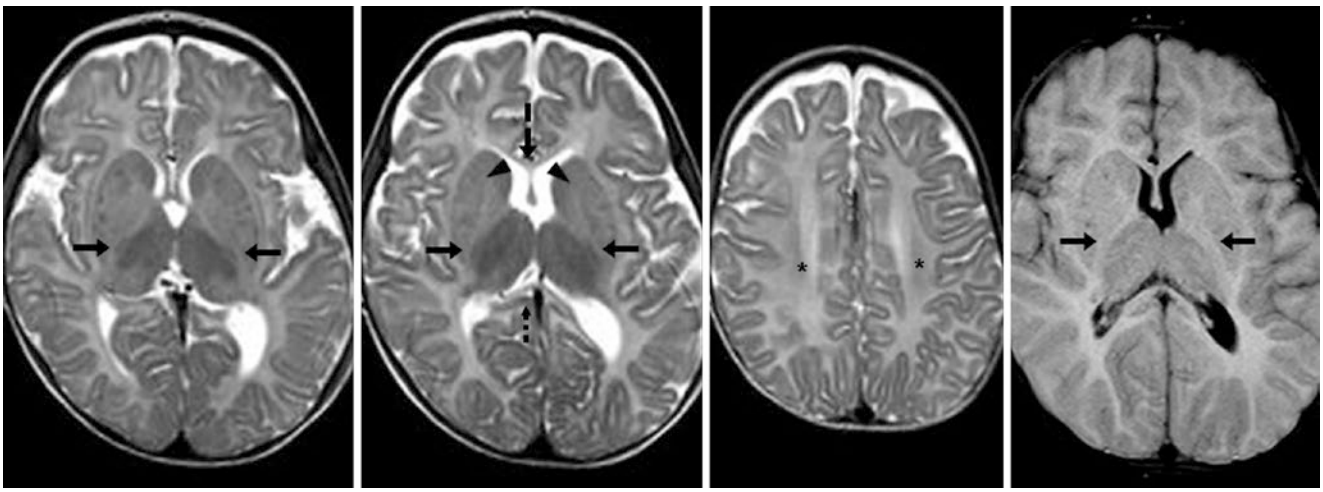

Fig. 23.89 Comparison case of hypomyelination in GM1 gangliosidosis. A 5.5-month-old with weakness had a 1.5T MRI with SE T2WIs (*leftmost images*) and FLAIR (*right*). The ALICs (*arrowheads*), CS (*dotted arrow*), and CG (*dashed arrow*) were unmyelinated. The PLICs (*arrows*) were small and unmyelinated. The centrum semiovale (*asterisks*) is poorly myelinated. On FLAIR, note the lack of the normal, dark PLIC. The thalami are darkened relative to the basal ganglia

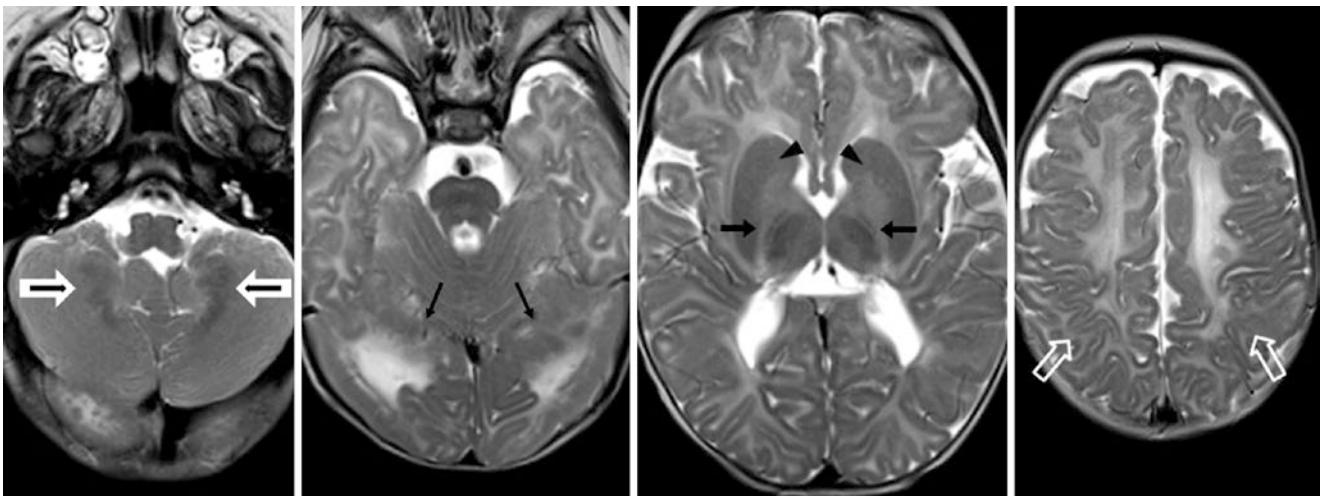

Fig. 23.90 Comparison case of hypomyelination in congenital muscular dystrophy (unknown type). A 6-month-old with seizures had a 1.5T MRI with SE T2WIs. The ALICs (*arrowheads*) and the CG (*not shown*) were not myelinated. The PLIC (*arrows*) was too small and largely unmyelinated. Note bilateral occipital polymicrogyria (*thin arrows*), abnormal central cerebellar WM (*bolded arrows*), and a lack of SCWM maturation deep to the PRC (*open arrows*)

23.6.4 Normal Myelination in Infants: Appearance at the Age of 7–8 Months

An important concept is that by the age of 7–8 months, the white matter appearance on T1WI in general should appear nearly the same as for an adult, with the exception of small patches within the *PVWM* or *SCWM* in the most anterior temporal or frontal lobes, or in normal *terminal zones* (discussed later 23.6.7). In particular, on T1WI at 3T, by this time the SCWM should appear myelinated out to the cortex in the posterior occipital regions (especially the visual cortex), whereas the SCWM within the most anterior portions of the frontal and temporal lobes may lag until 11 months, perhaps creating an appearance of "*patchy SCWM*," which is discussed in more detail in the next section 23.6.5. Such tiny regions of incomplete myelination (as well as normal terminal zones) may be better visualized on T1WI if obtained at 3T with thinner sections, particularly by a GE T1WI 3D acquisition that is isotropic (*i.e.*, equal diameter of the acquired voxel in all three dimensions). In general, however, SE T2WI usually better depicts incomplete white matter maturation after 7 months of age, whether such regions are normal or not.

On GE T1WI at 3T, each of the structures mentioned in prior sections should again be clearly myelinated by this time, including the *anterior limb of the internal capsule* (ALIC), the *callosal genu*, and the *optic radiations*, though small regions of incompletely myelinated white matter may be seen in certain locations only on higher resolution or thinner-section (<4 mm) images. The *external capsule* and *extreme capsule* are difficult to discern from each other, but should appear myelinated on GE T1WI at 3T. Notably, one such structure that is often not visibly myelinated or mature by this point is the *anterior commissure*; it usually appears myelinated by 9–10 months on T1WI. These rules generally apply whether the acquisition is at 1.5T or 3T, although at 3T, GE T1WI is preferred to assess the degree of myelination.

On SE T2WI, however, the appearance and degree of myelination may appear quite different and overall much less mature than that seen on T1WI, both globally and for particular structures, especially if it is compared with GE T1WI at 3T. This difference likely relates to the dynamic component of PVWM and SCWM within the frontal WM anterior to the perirolandic regions, supraventricular WM, and deep temporal WM at this point, where there can be a fair amount of variability between patients. Therefore, this is an important age to be aware of critical milestones for maturation. For example, by the age of 7–8 months, the ALIC may not appear entirely myelinated on SE T2WI, although it should be clearly apparent on T1WI; on T2WI, this maturation may not occur until about 9–10 months. This structure often appears slightly darkened on SE T2WI at 3T, but it is usually not nearly as dark as the PLIC. The callosal genu should appear to be maturing and is darkening on T2WI, although it may not appear as dark as the callosal splenium. The external or extreme capsules may now be visible as they start to darken as well. Regarding the PVWM of the centrum semiovale (just above the lateral ventricles on axial images) and corona radiata (on axial images near the top of the lateral ventricles just above the PLIC as the fibers "radiate" into the PVWM), such regions of PVWM may appear quite patchy on T2WI because of incomplete myelination, and this "*patchy white matter*" *appearance is much more visible on T2WI than on T1WI*. Typically, the PVWM and SCWM appear to myelinate in a generally bidirectional fashion that extends both anteriorly and posteriorly from the *perirolandic cortices* (PRC) and the subjacent SCWM. This appearance also occurs at earlier ages, but it can vary between being rather pronounced versus a slow gradient of myelination bidirectionally from the PRC. Similarly, by this point, the frontal and parietal cortices at the same level as the PRC on axial images should appear isointense to the PRC, even if their subjacent SCWM is slightly less mature. The occipital SCWM surrounding the visual cortex and the optic radiations also should appear quite mature, with the exception of periatrial terminal zones immediately surrounding the lateral ventricles. Further anteriorly on axial images, the *anterior temporal lobes* may exhibit sparse deep WM or SCWM myelination and maturation.

On FLAIR, white matter within the deep WM and PVWM of the corona radiata, centrum semiovale, and optic radiations remains hyperintense relative to gray matter, but the deep WM is starting to darken. White matter typically becomes isointense to gray matter on FLAIR at about 11–12 months of age, after which it further darkens relative to cortex (Figs. 23.91, 23.92, 23.93, 23.94 and 23.95).

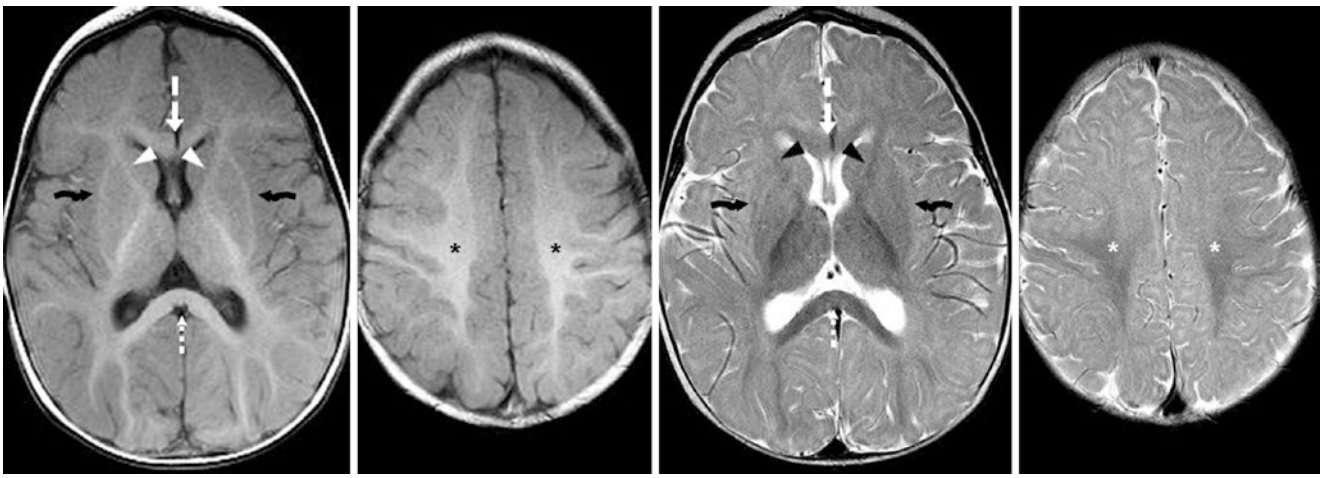

Fig. 23.91 A 7-month-old with focal, palpable hyperostosis anteriorly had a normal 3T MRI with GE T1WIs (*left images*) and SE T2WIs (*right images*). Note maturation of the CS (*dotted arrows*) on both sequences. The external capsules (*curved arrows*), CG (*dashed arrows*), and ALIC (*arrowheads*) have started to darken on T2WI, but are not complete. Note bright PVWM anteriorly on T2WI; the WM subjacent to the PRC (*asterisks*) appears mature (*right*)

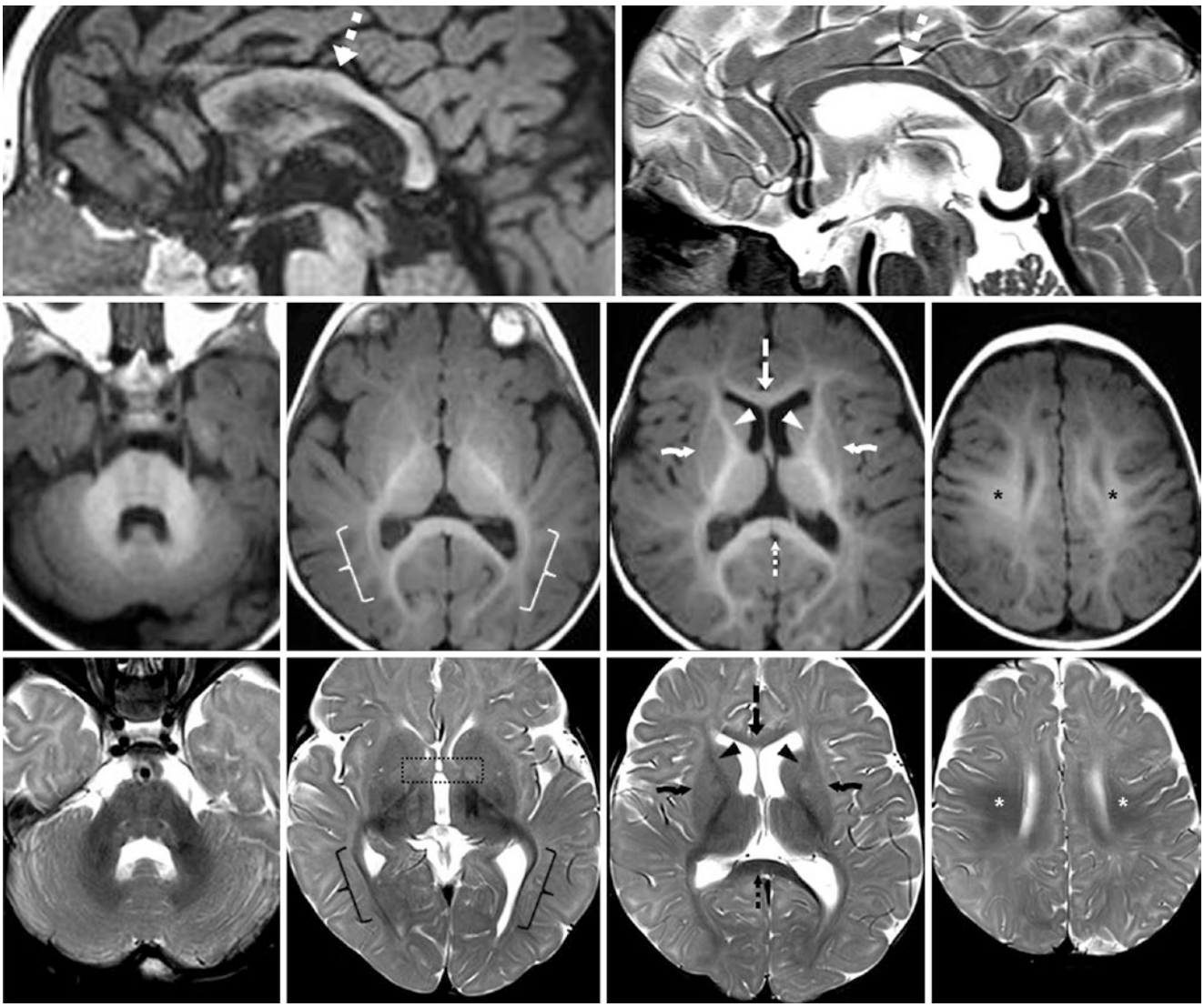

Fig. 23.92 A 7.5-month-old with a scalp lesion underwent a negative 3T MRI, and thereafter developed normally. On these images, note the steep, bidirectional gradient of myelination from the white matter subjacent to the PRC. *Top row*: A midline sagittal GE T1WI (*left*) and sagittal SE T2WI (*right*) illustrate that the brightest area of myelination on T1WI is the callosal midbody (*large dotted arrow*). The CG is not as bright as the CS, and the CS is thickening. *Second row*: Axial GE T1WIs illustrate maturation of the optic radiations (*brackets*), CS (*dotted arrow*) and ALIC (*arrowheads*); the CG (*dashed arrow*) is also bright, but less so. The external capsules (ECs) (*crooked arrows*) are relatively mature. *Bottom row*: SE T2WIs also illustrate early myelination of the ALIC and CG. The ECs are not as mature as on GE T1WI, and the anterior commissure has not matured (*dotted box*). Note that the deep white matter of the optic radiations and PRC (*asterisks*) are myelinated but the orbitofrontal regions are not

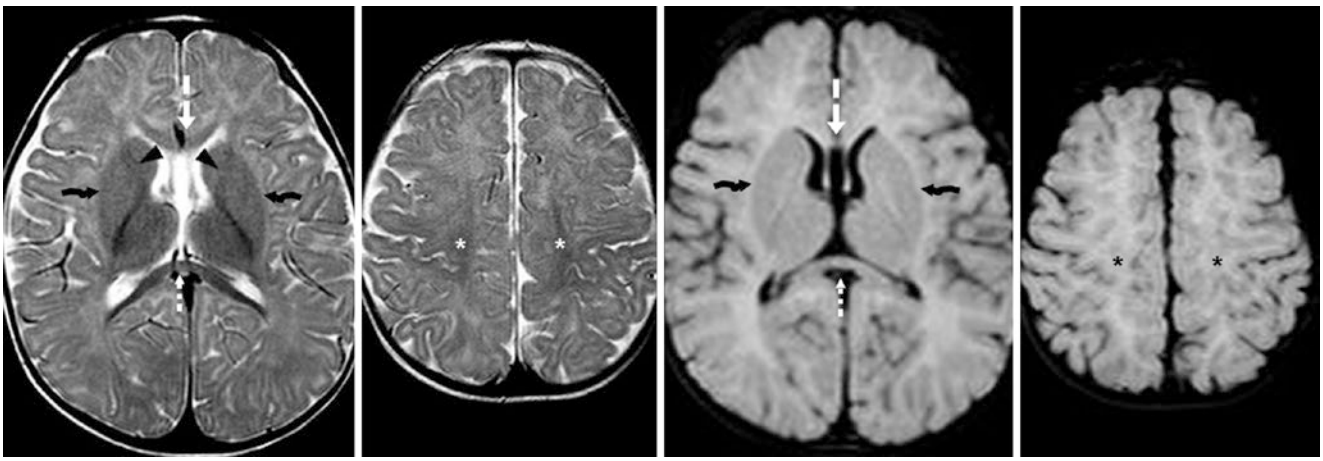

Fig. 23.93 A 7.5-month-old with developmental delay with a negative 3T MRI. SE T2WIs (*left images*) and FLAIR (*right images*) show early maturation of the ALIC (*arrowheads*), CG (*dashed arrows*), and ECs (*crooked arrows*), which are all mildly dark, but not as much as the CS (*dotted arrows*). The white matter deep to the PRC is rather mature, and is much darker than the anterior frontal or posterior parietal deep white matter. The orbitofrontal white matter is quite immature

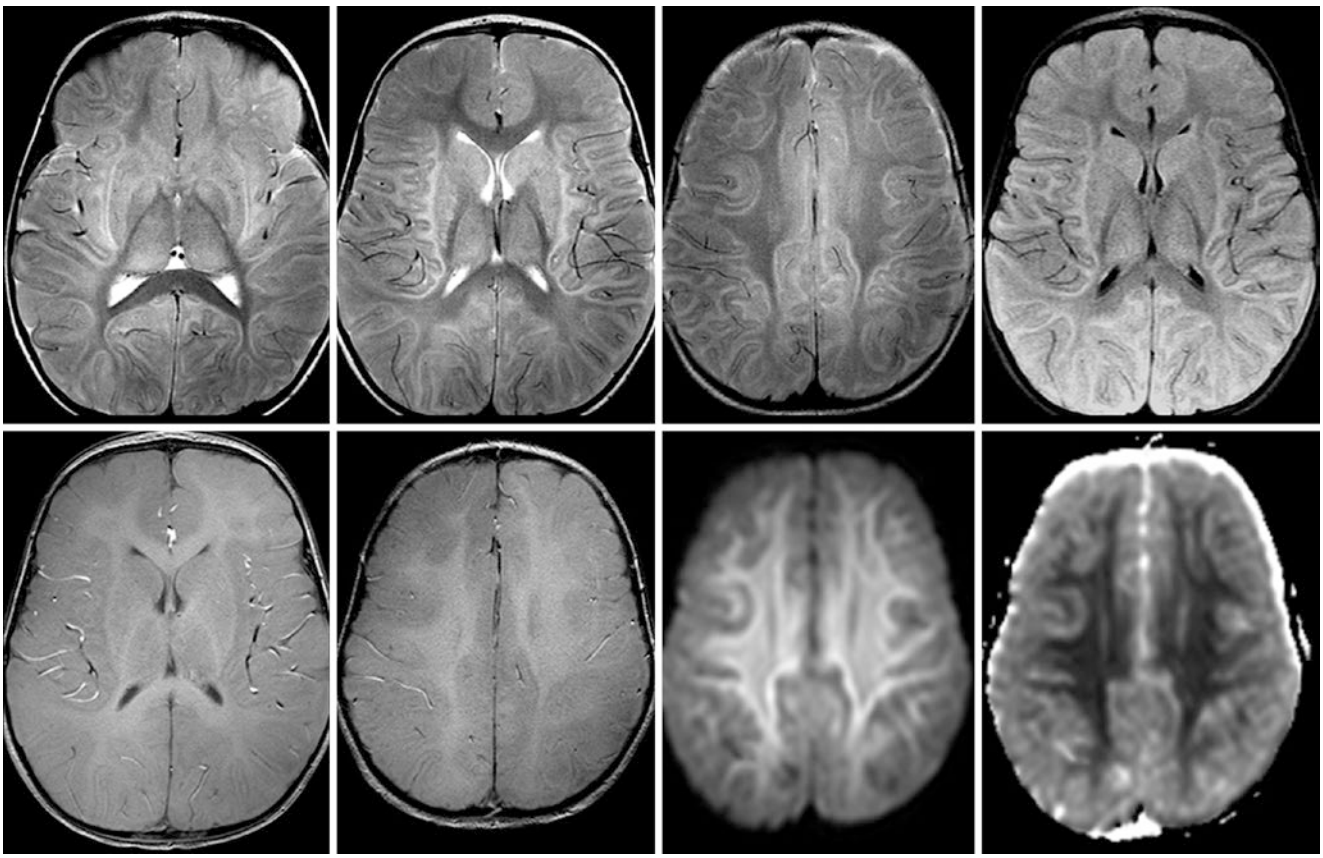

Fig. 23.94 Comparison case of subacute hypoxic-ischemic injury (HII). A 7-month-old remained unresponsive 8 days after a prolonged seizure from a febrile illness. A 3T MRI demonstrated diffuse hyperintensity of the cortex and basal ganglia on SE T2WIs (*top*, *left three images*) and on FLAIR (*top*, *right*). GE T1WIs (*bottom*, *left two images*) show diffuse edema and blunting of gray-white matter differentiation. DWI (*bottom*, *right middle*) and ADC map (*bottom*, *right*) depict a diffuse deep WM and SCWM insult that is typical of the subacute phase of severe HII

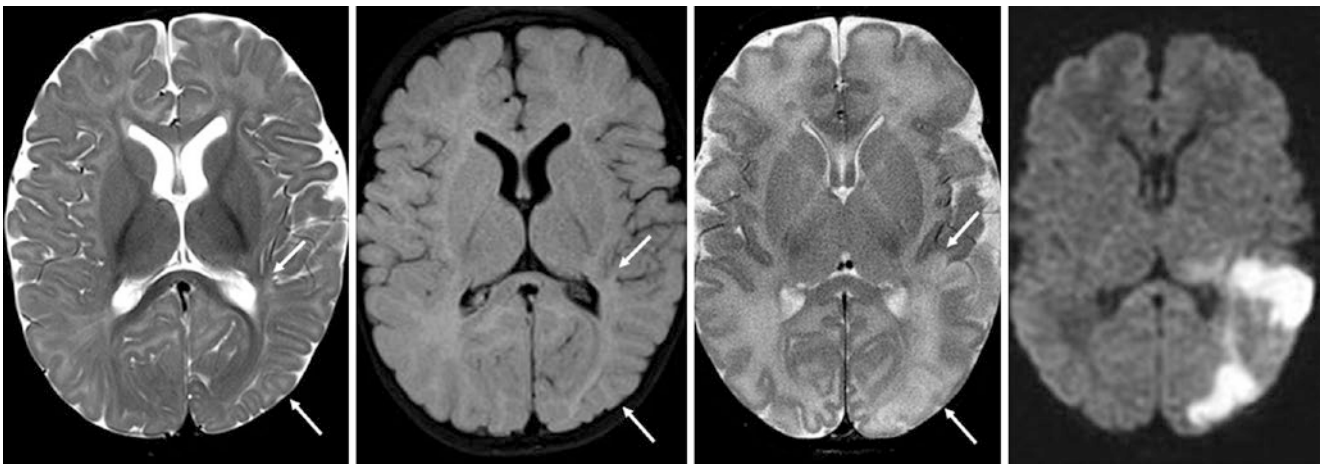

Fig. 23.95 Comparison case of sequela of infarction. A 7-month-old with right-sided weakness had a 3T MRI that showed thinning of the left optic radiations white matter, with overlying small, shrunken gyri (*thin arrows*) on T2WI (*left*) and FLAIR (*left middle*), as well as prominence of the lateral ventricular trigone. The prior MRI from age 7 days confirmed findings of left middle cerebral artery distribution infarcts on T2WI (*right middle*) and DWI (*right*)

23.6.5 Normal Myelination in Infants: Appearance at the Age of 9–10 Months

By the age of 9–10 months, the white matter appearance on T1WI generally is nearly that of an adult; it appears to have matured even within the PVWM and SCWM, although there is often sparing of myelination within the most anterior temporal or frontal lobes, or in normal terminal zones (discussed later 23.6.7). In particular, by this time, the SCWM on GE T1WI at 3T appears myelinated out to the cortex in all but the most anterior portions of the frontal and temporal lobes, which may lag until 11–12 months. On SE T2WI, such lagging may create the appearance of *patchy SCWM*, which can be seen even overlying normally myelinating and maturing deep WM in regions that are immediately anterior and posterior to the SCWM of the perirolandic cortices, while appearing entirely myelinated on T1WI. This appearance of patchy SCWM likely lasts until about 12 months of age. Again, in general, SE T2WI is usually superior for assessing white matter maturation after the age of 7–8 months, and for detecting subtle regions of *hypomyelination*, because the white matter appears mature on T1WI by that age.

On GE T1WI at 3T, each of the structures mentioned in prior sections should again be clearly myelinated by this time, including the *anterior limb of the internal capsule* (ALIC), *callosal genu* (CG), *external and extreme capsules* (difficult to separate from each other on sections thicker than 1 mm), and the *optic radiations*. The SCWM and deep WM should appear mature in all but the most anterior temporal and anterior and inferior frontal lobes (such as the orbitofrontal region). The *anterior commissure* should be myelinated/mature by this point; it usually appears myelinated by 9–10 months on T1WI. These rules generally apply whether the acquisition is at 1.5T or 3T, although at 3T, GE T1WI is preferred to assess the degree of myelination.

Again, the appearance and degree of myelination is quite different and seems less mature on SE T2WI than on T1WI, especially using GE T1WI at 3T. The difference is likely related to the dynamic myelination of PVWM and SCWM at this time. At 9–10 months of age, within the frontal WM anterior to the perirolandic regions, supraventricular WM, and deep temporal WM, there can be a fair amount of variability between patients, particularly with regards to the appearance of the "patchy SCWM". Critical milestones to be aware of at this age are that the ALIC should be almost completely myelinated on SE T2WI, and should appear nearly as dark as the posterior limb of the internal capsule (PLIC). The *callosal genu* (CG) also should appear nearly as dark as the *callosal splenium* (CS). The *external or extreme capsules* (EC) are usually becoming apparent, but typically are not nearly as dark as the internal capsule (whether ALIC or PLIC) on SE T2WI at 3T, although the EC appears quite mature on GE T1WI at 3T. Regarding the PVWM of the centrum semiovale (just above the lateral ventricles on axial images) and the corona radiata (on axial images near the top of the lateral ventricles just above the PLIC as the fibers "radiate" into the PVWM), such regions of PVWM continue to also appear quite "patchy" on T2WI. This "patchy WM" appearance is becoming less so as the WM myelination is extending in a generally bidirectional fashion both anteriorly and posteriorly from the PRC and at the same time is becoming more homogeneous. By this point, the frontal and parietal cortices at the same level as the PRC on axial images should appear isointense with the PRC, even if their subjacent SCWM is slightly less mature. Finally, the far *anterior temporal lobes* and the anteriormost *orbitofrontal gyri* (*i.e.*, the gyrus rectus and the medial, middle, and lateral orbital gyri) may have little deep WM or SCWM myelination at this time. Another interesting finding at the level of the brainstem is that the *dorsal brainstem* may start to appear mildly hyperintense at this age, particularly the pons and pontomesencephalic junction, though it appears homogeneous in signal on T1WI.

On FLAIR, white matter within the deep WM and PVWM of the corona radiata, centrum semiovale, and optic radiations remains hyperintense relative to gray matter. However, the deep WM is starting to darken. The isointense appearance of white matter and gray matter on FLAIR typically occurs at about 11–12 months of age, after which the white matter further darkens relative to cortex. However, normal *terminal zones* within the PVWM (such as within the peritrigonal regions) start to become apparent as mildly bright signal on FLAIR at this time. They can be mistaken for disease such as *periventricular leukomalacia*, sequela of term neonatal *hypoxic-ischemic encephalopathy or injury, white matter disease*, or *hypomyelination* (Figs. 23.96, 23.97, 23.98, 23.99, 23.100, 23.101 and 23.102).

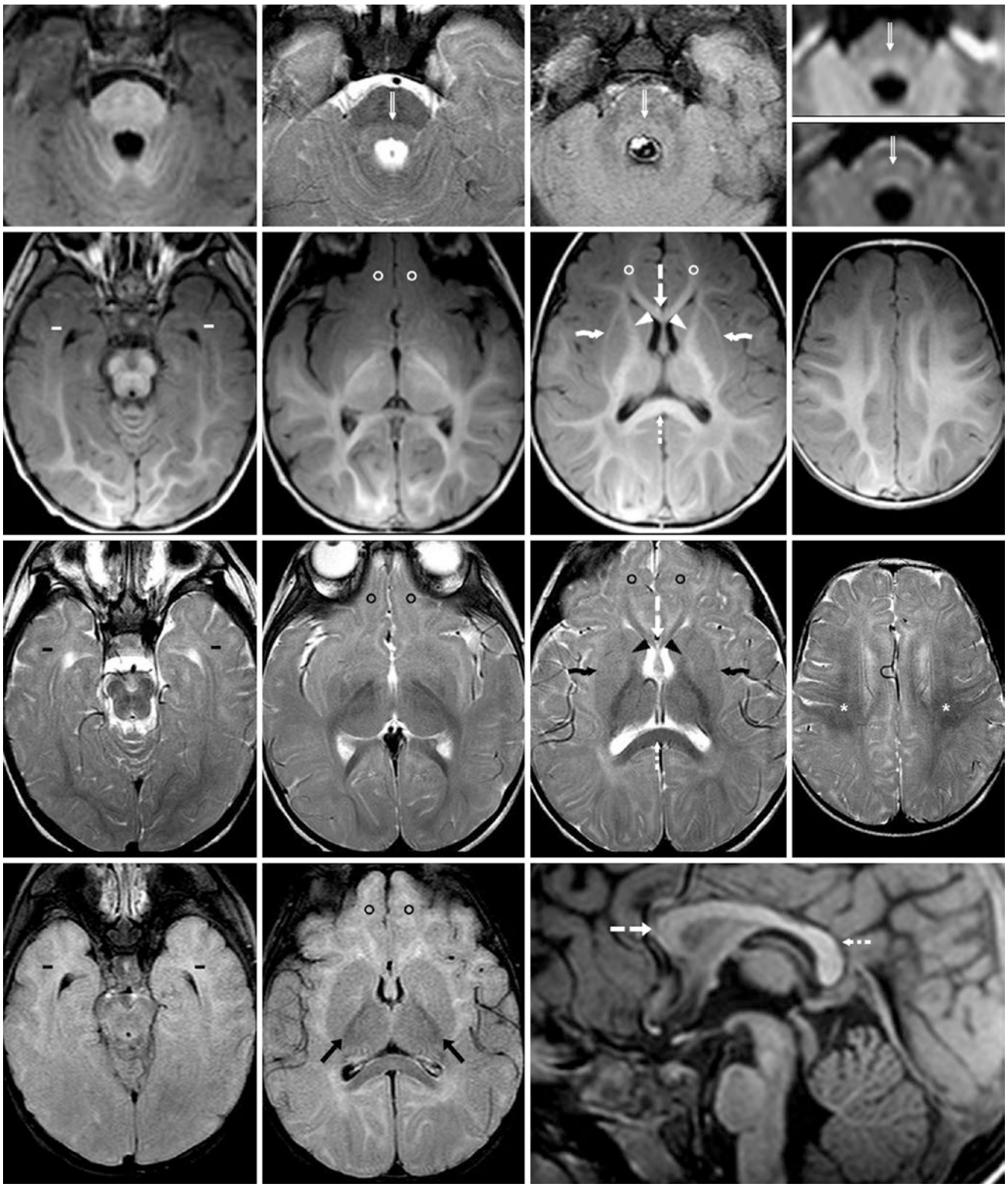

Fig. 23.96 A 8.75-month-old with mild motor delays underwent a negative 3T MRI, and thereafter developed normally. In general, the SCWM on these images appears much more mature on GE T1WI than on SE T2WI. *Top row*: The pons is homogeneous in signal on GE T1WI (*left*), but is mildly bright dorsally (*beveled arrows*) on T2WI (*left middle*) and FLAIR (*right middle*). DWI (*right*, *top*) and exponential DWI (*right*, *bottom*) show no edema. *Second row*: Axial GE T1WIs illustrate myelination of the ALIC (*arrowheads*), CG (*dashed arrow*), CS (*dotted arrow*) and EC (*crooked arrows*). Note incomplete maturation of the anterior temporal white matter (ATWM) (*dashes*) and orbitofrontal WM (OFWM) (*circles*). *Third row*: SE T2WIs also depict progressive myelination of the ALIC and CG. The ECs are hardly dark, and not as mature as on GE T1WI. Note that white matter subjacent to the PRC (*asterisks*) is myelinated, but the orbitofrontal regions are not. *Bottom row*: FLAIR images (*left two images*) show that the white matter remains bright relative to gray matter, and the PLIC (*arrows*) remains dark. A midline sagittal T1WI (*right*) shows that the CG is still less hyperintense than the CS

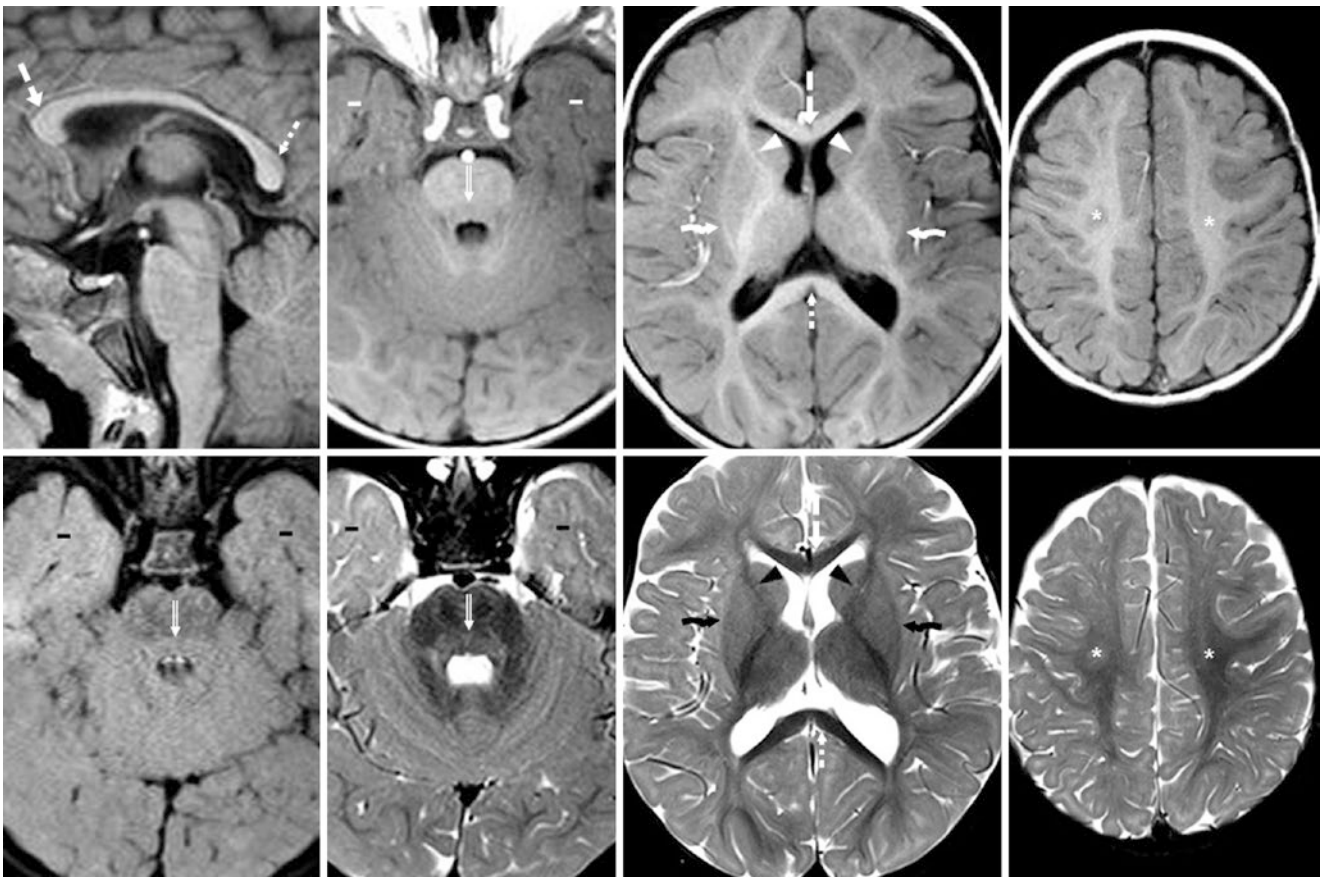

Fig. 23.97 A 9.5-month-old with abnormal movements had a negative 3T MRI, and normal development. Sagittal GE T1WI (*top*, *left*) shows a mature CS (*dotted arrow*) and CG (*dashed arrow*). Axial T1WIs (*top*, *right three images*) show mature ALICs (*arrowheads*) and ECs (*crooked arrows*), which are mildly dark on SE T2WIs (*bottom*, *right three images*), but not as much as the CS. The WM deep to the PRC (*asterisks*) is mature and is much darker than the anterior temporal deep WM and SCWM (*dashes*). Note a mildly bright dorsal pons (*beveled arrows*) on T2WI and on FLAIR (*bottom left*)

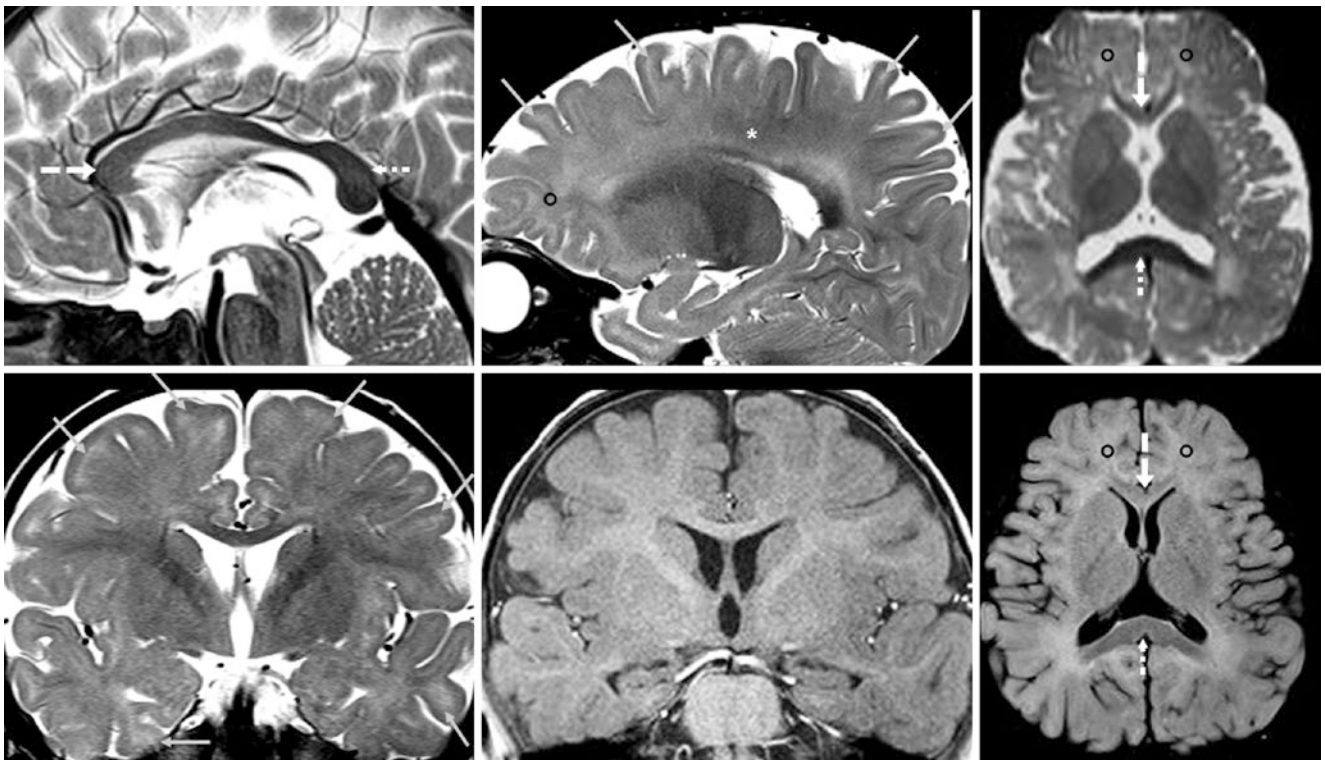

Fig. 23.98 A 9.75-month-old with growth hormone deficit had a normal pituitary MRI at 3T. A sagittal SE T2WI (*top left*) shows a mature CS (*dotted arrow*); the CG (*dashed arrow*) is slightly less T2-dark. Further laterally, T2WI (*top middle*) depicts mature WM deep to the PRC (*asterisk*), but the OFWM (*circle*) is far less mature. This finding is also shown on a T2-like $b=0$ DWI (*top right*). Note the normal, "patchy" frontal SCWM (*thin arrows*) on sagittal and coronal T2WIs (*bottom left*). A coronal T1WI (*bottom middle*) is normal. There is still mildly bright WM on FLAIR (*bottom right*)

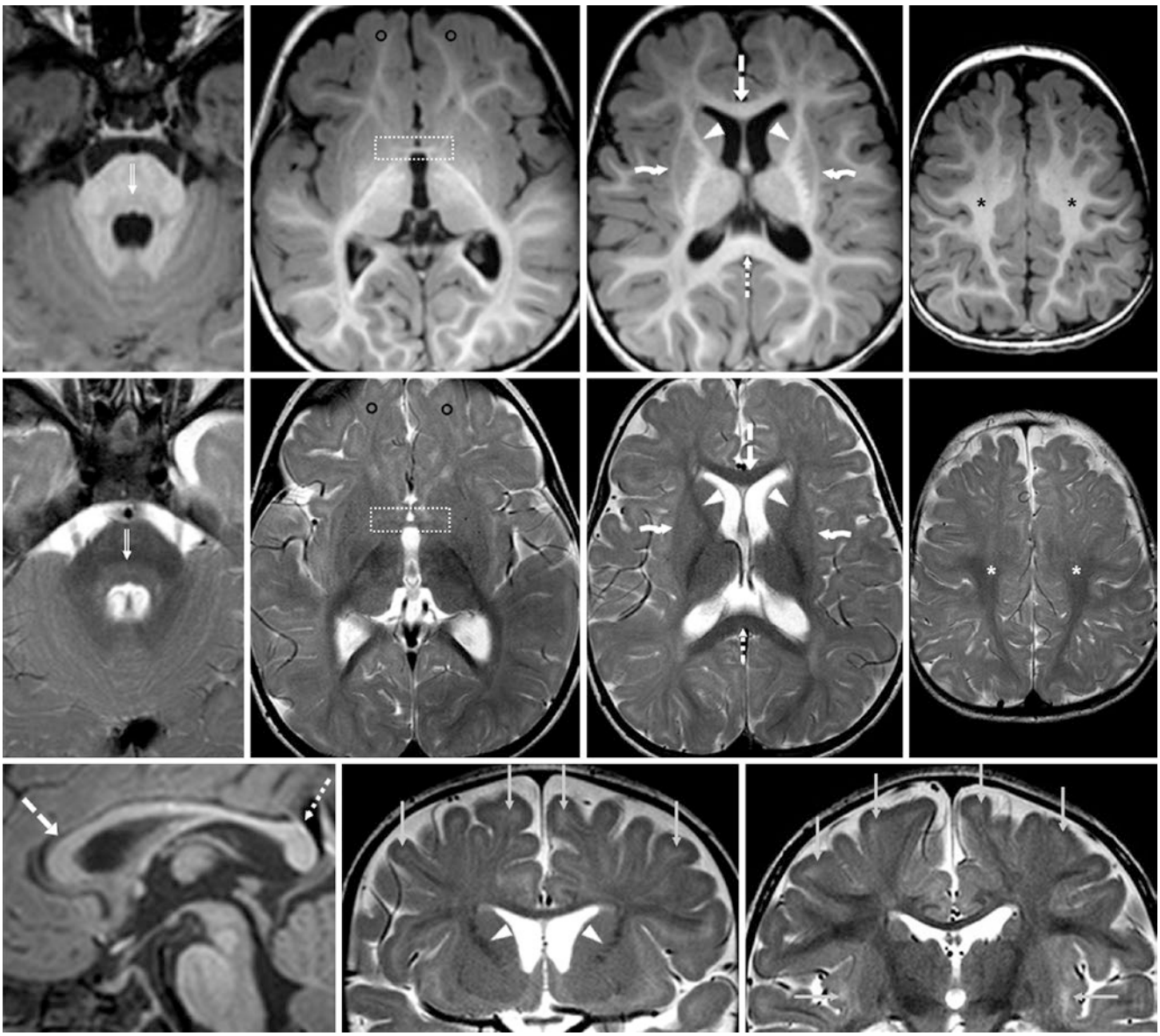

Fig. 23.99 A 10-month-old with failure to thrive underwent a negative 3T MRI. In these images, the SCWM appears generally much more mature on GE T1WI than on SE T2WI, particularly within the OFWM (*circles*). *Top row*: On GE T1WI, the pontine signal is relatively homogeneous (*beveled arrows*). The anterior commissure is now mature (*dotted box*). The CS (*dotted arrow*), CG (*dashed arrow*), and EC (*crooked arrows*) are mature. *Second row*: SE T2WIs illustrate a mildly hyperintense dorsal brainstem. The ALIC is myelinated (*arrowheads*); the EC and anterior commissure are less mature. Note myelination deep to the PRC (*asterisks*), which tapers anteriorly. *Bottom row*: A sagittal GE T1WI (*left*) shows that the CG is still less bright than the CS. Note "patchy" SCWM (*thin arrows*) on coronal SE T2WIs (*middle and right*), being more prominent anteriorly, where the SCWM is less mature

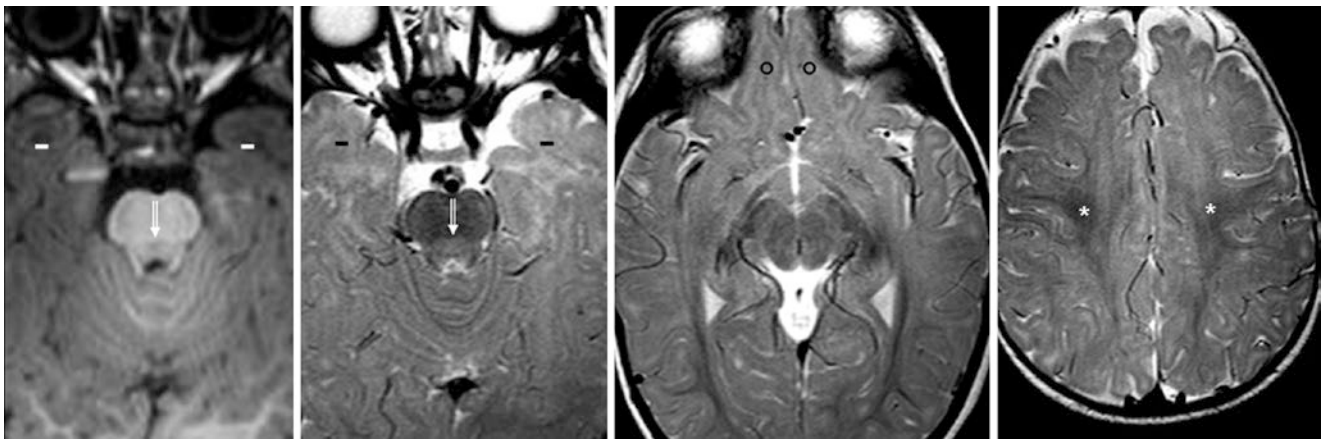

Fig. 23.100 A 10-month-old with a seizure had a negative 3T MRI, and developed normally. A GE T1WI (*left*) shows the dorsal pons (*beveled arrows*) to be slightly dark, but better visualized as bright on SE T2WIs (*right three images*). The WM deep to the PRC (*asterisks*) is mature and is much darker than the anterior temporal SCWM (*dashes*) and orbitofrontal SCWM (*circles*)

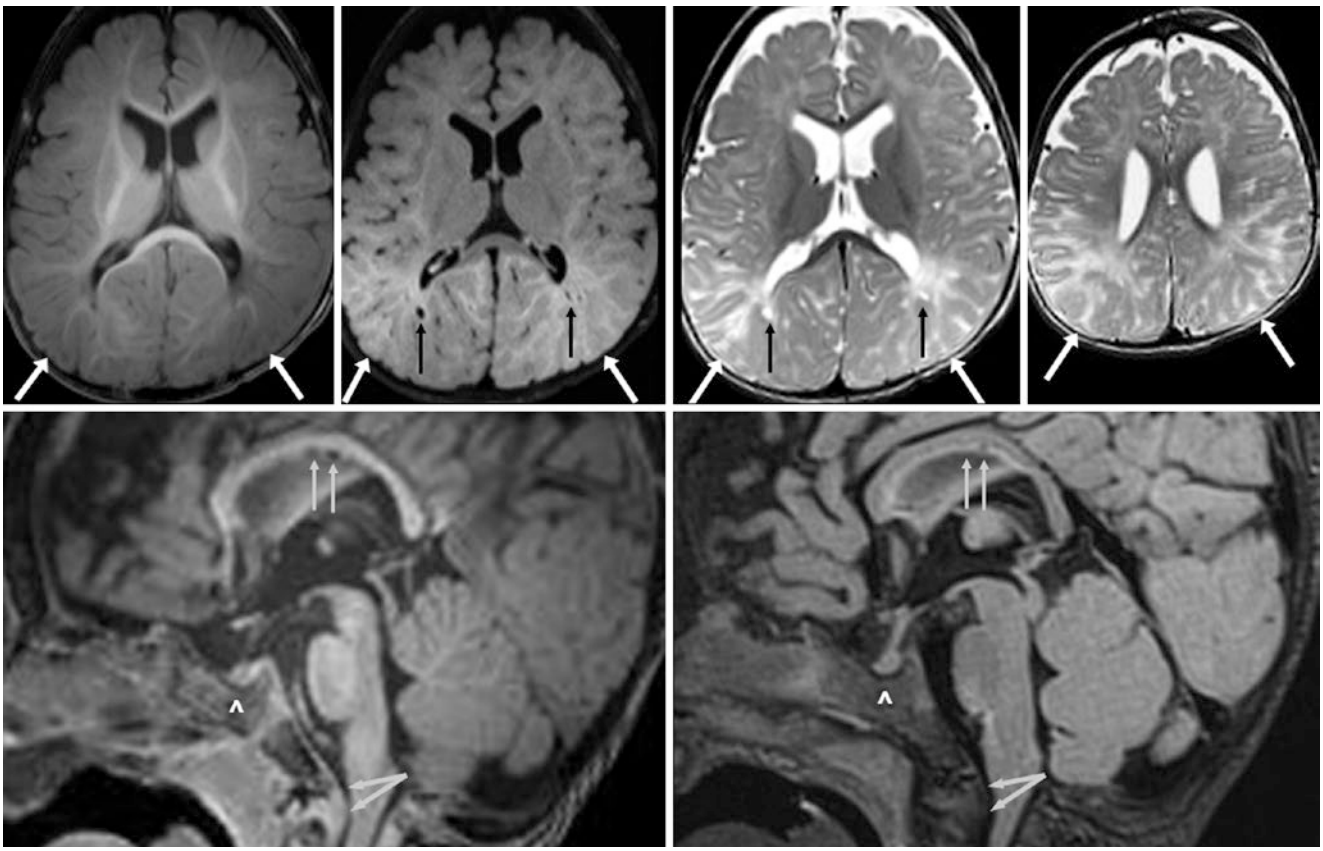

Fig. 23.101 Comparison case of Hurler's mucopolysaccharidosis. A 9.5-month-old had abnormal deep WM and SCWM on a 3T MRI, with blurring of the gray-white junction (*arrows*) on GE T1WI (*top*, *left*), FLAIR (*top*, *left middle*), and SE T2WI (*top*, *right two images*). Typically, the posterior white matter is more mature, but the reverse is true in this case. Note dilated perivascular spaces (*thin arrows*). Also, on sagittal GE T1WI (*bottom left*) and sagittal 3D FLAIR (*bottom right*), there is a "J-shaped" contour of the bony sella (^) and odontoid capping (*split arrows*), which is typical of Hurler's

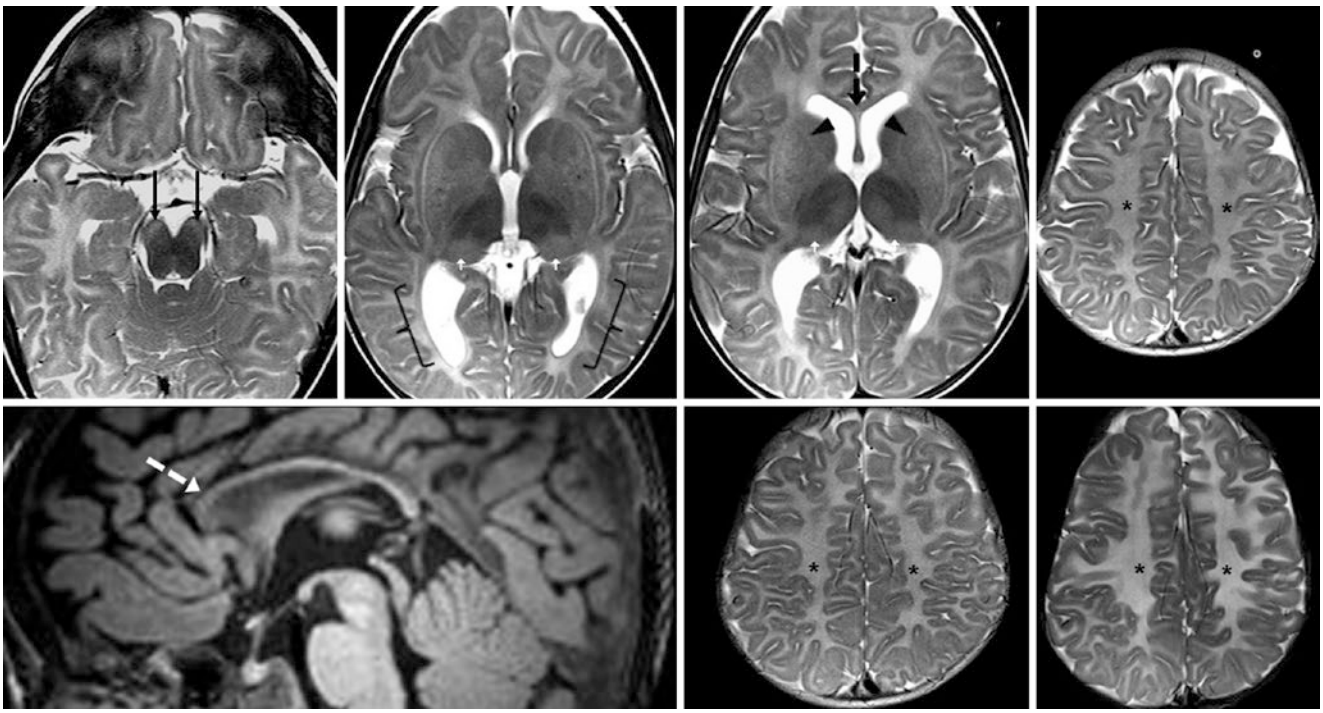

Fig. 23.102 Comparison case of GM2 gangliosidosis (Sandhoff's disease). In a 10-month-old, a 3T MRI showed diffusely poor myelination on SE T2WIs (*top row*), with a severely thin corpus callosum on sagittal T1WI (*bottom left*). Note failed myelination of the ALIC (*arrowheads*), CG (*dashed arrows*), optic radiations (*brackets*), and corona radiata (*asterisks*). There are abnormalities within the cerebral peduncles (*thin arrows*) and pulvinar nuclei (*small white upward arrows*). At ages 13 months (*bottom middle*) and 16 months (*bottom right*), repeat SE T2WIs at 3T show little progression in myelination

23.6.6 Normal Myelination in Infants: Appearance at the Age of 11–13 Months

By the age of 11–12 months, the white matter appearance on T1WI appears the same as in an adult. It has further matured within the PVWM and extends further peripherally into the SCWM. The myelination may still be immature within the *anterior temporal WM* (ATWM), *orbitofrontal WM* (OFWM), and in *normal terminal zones* (discussed later 23.6.7). By this time on GE T1WI at 3T, the SCWM appears myelinated out to the cortex in all but the most anterior portions of the frontal and temporal lobes, which should appear myelinated by 12–13 months (*i.e.*, by the end of the first year of life). SE T2WI often still show the lagging of maturation within subcortical WM, and this "*patchy SCWM*" appearance can be seen even overlying mature deep WM in the anteriormost frontal and temporal lobes. Such patchy SCWM should not be present subjacent to or immediately anterior or posterior to the *perirolandic cortices* (PRC). This appearance of patchy SCWM likely lasts until about 12–13 months of age, but it has not been well described. In general, SE T2WI is usually superior in the assessment of WM maturation after age 7–8 months, and it is also superior to T1WI in detecting WM lesions after that time.

On GE T1WI at 3T, each of the structures mentioned in prior sections, such as the *anterior commissure*, *ALIC*, *CG*, *EC*, and *optic radiations*, should be clearly myelinated by this time. There may be areas of isointense white matter (relative to gray matter) on T1WI that are analogous to the "patchy SCWM" on T2WI, lasting on T1WI until about 12–13 months of age. Note that normal terminal zones posterolateral to the lateral ventricular trigones may also appear isointense to gray matter.

On SE T2WI, the appearance and degree of myelination appears quite different and less mature than on T1WI, but the WM anterior and posterior to the perirolandic regions has been rapidly extending, particularly posteriorly, where even the SCWM of the occipital and parietal regions should be almost completely mature (again, with the exception of normal terminal zones). A gradient of myelination/maturity of the WM on axial images often remains just above the lateral ventricles, where the anteriormost deep WM may still appear slightly immature. The far *anterior temporal lobes*, the anteriormost *orbitofrontal gyri* (the gyrus rectus and the medial, middle, and lateral orbital gyri), and the *subinsular WM* may still have relatively immature deep WM or SCWM at this time, but it should be progressing. Finally, the dorsal brainstem may remain mildly bright.

On FLAIR, white matter within the deep WM and PVWM of the corona radiata, centrum semiovale, and optic radiations starts to appear isointense to gray matter, as the white matter continues to darken relative to the cortex. However, normal terminal zones within the PVWM (*e.g.*, within the peritrigonal regions) start to become even more apparent as mildly bright signal on FLAIR at this time, and can be mistaken for disease; they can simulate *periventricular leukomalacia*, sequela of *hypoxic-ischemic encephalopathy or injury*, or *hypomyelination* (Figs. 23.103, 23.104, 23.105, 23.106, 23.107, 23.108, 23.109, 23.110, 23.111 and 23.112).

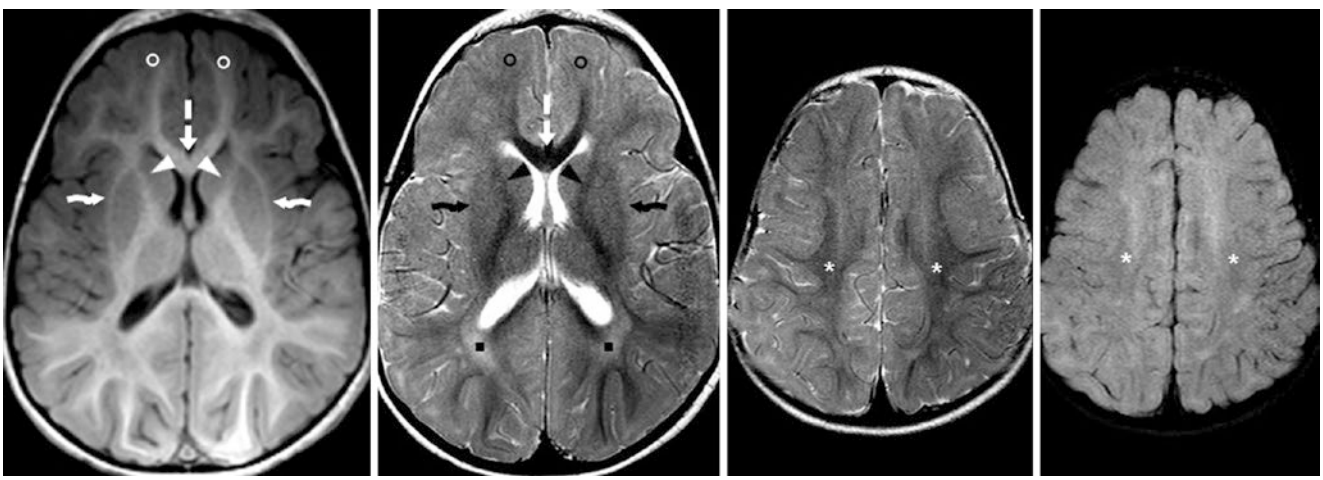

Fig. 23.103 A 12-month-old with a mildly enlarged head circumference had a negative 3T MRI, and developed normally. A GE T1WI (*left*) and SE T2WIs (*middle images*) illustrate that the ALICs (*arrowheads*), CG (*dashed arrows*), EC (*crooked arrows*), and centrum semiovale white matter deep to the PRC (*asterisks*) are mature. Myelination of the supraventricular white matter has progressed anteriorly. The white matter within the centrum semiovale remains darker than the orbitofrontal SCWM (*circles*). Note that normal terminal zones are becoming visible, appearing mildly hyperintense within the periatrial WM (*squares*)

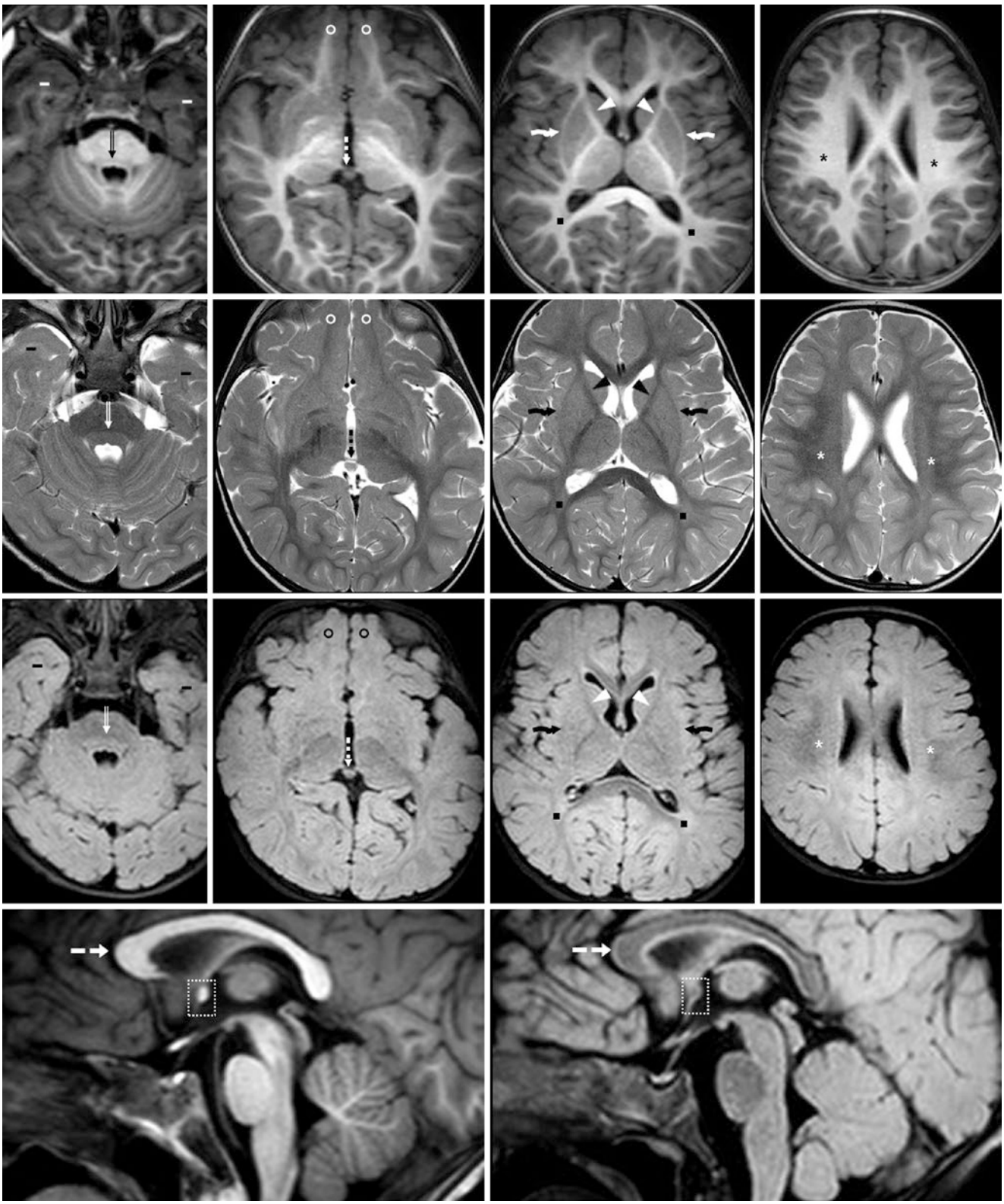

Fig. 23.104 A 12-month-old with seizures had a negative 3T MRI, and developed normally. On these images, the SCWM generally appears nearly as mature on SE T2WI as on GE T1WI, except for the anterior temporal lobes. *Top row*: Axial GE T1WIs illustrate a mature ALIC (*arrowheads*), CG (*dashed arrows*), and EC (*crooked arrows*). On T1WIs and T2WIs, the ATWM (*dashes*) and the OFWM (*circles*) appear more mature than at earlier ages. *Second row*: The pons (*beveled arrow*) is still mildly bright dorsally. The ALIC, CG, and EC are mature. Note the posterior commissure (*dotted arrow*). The anterior temporal and frontal SCWM has been maturing. *Third row*: 3D FLAIR images with axial reformats shows progressive myelination of the corona radiata (*asterisks*) deep to the PRC; with slightly less in the orbitofrontal regions. Note subtle, normal periatrial terminal zones (*squares*). *Bottom row*: A midline sagittal GE T1WI (*left*) and sagittal 3D FLAIR image (*right*) show that the corpus callosum is homogeneous in signal at this point, indicating maturity. Note a mature anterior commissure (*dotted boxes*)

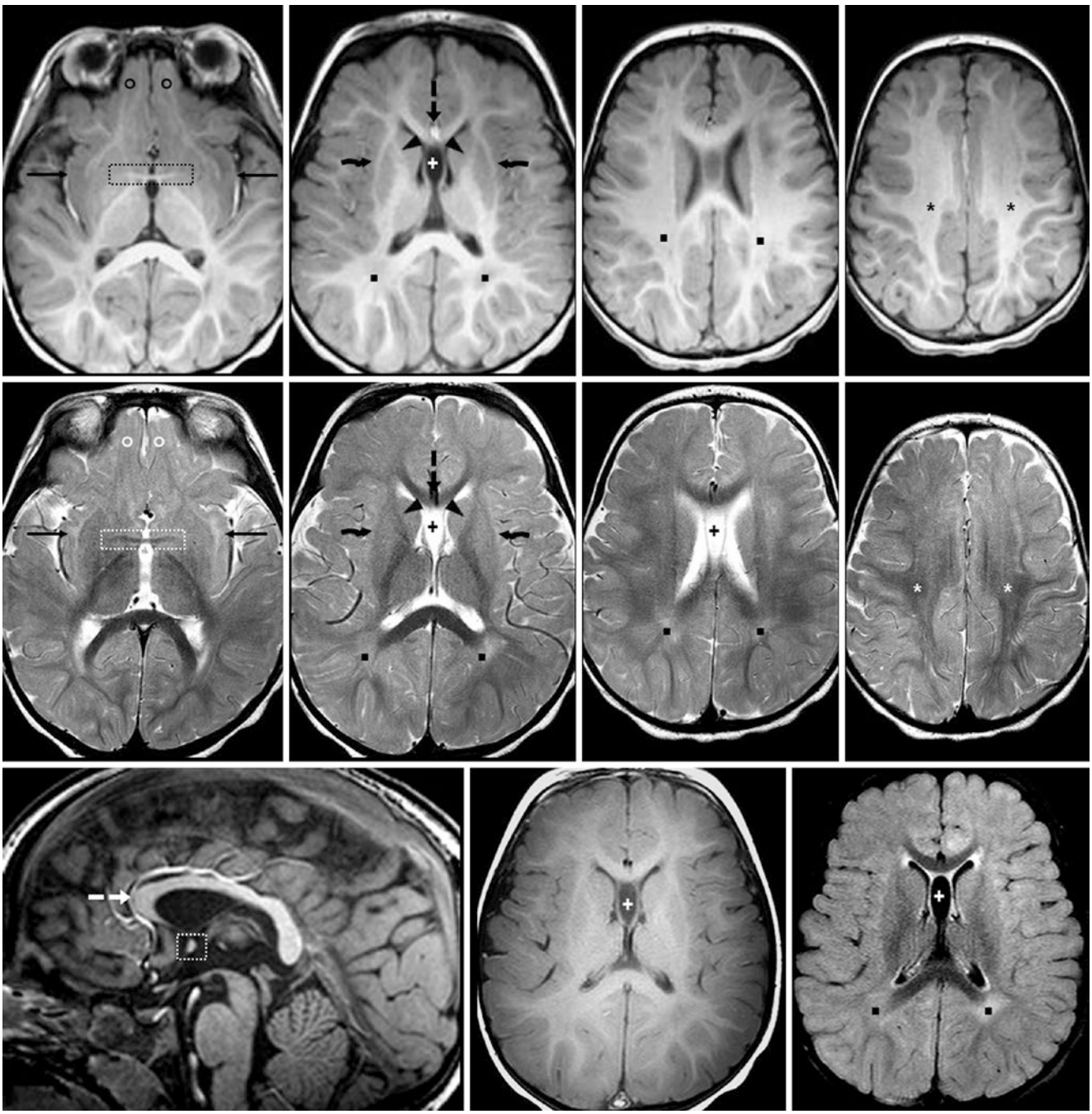

Fig. 23.105 A 12.25-month-old with seizures had a negative 3T MRI, and developed normally. In these images, the SCWM appears nearly as mature on SE T2WIs as on GE T1WIs. Note a normal cavum septum pellucidum (*plus sign*). *Top row*: GE T1WIs show maturity of the ALIC (*arrowheads*), anterior commissure (*dotted box*), CG (*dashed arrow*), and EC (*crooked arrows*). White matter of the orbitofrontal regions (*circles*) and centrum semiovale (*asterisks*) appears mature. *Second row*: On SE T2WIs, the aforementioned structures appear mature, as does the deep WM, except for OFWM and terminal zones in the peritrigonal regions (*squares*) and subinsular regions (*thin arrows*). *Bottom row*: A sagittal T1WI (*left*) shows normal myelination of the CG and anterior commissure. Myelination is less visible on SE T1WI (*middle*). FLAIR (*right*) depicts mild hyperintensity of normal periatrial terminal zones (*squares*)

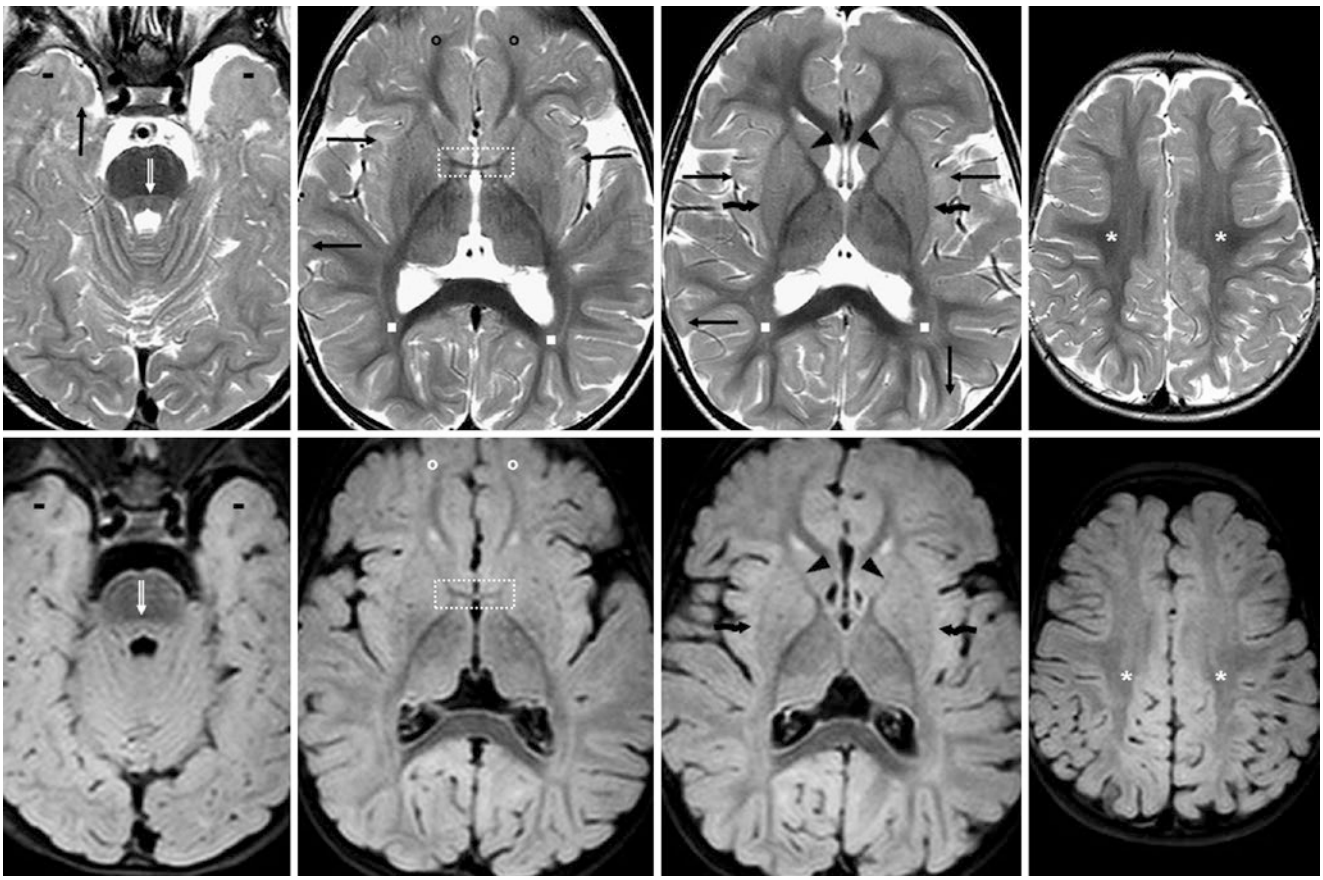

Fig. 23.106 A 12.5-month-old with a skin lesion had a negative 3T MRI, and developed normally. SE T2WIs (*top row*) and axial 3D FLAIR (*bottom row*) illustrate that the ALICs (*arrowheads*), EC (*crooked arrows*), and centrum semiovale WM (*asterisks*) are mature. Myelination of the supraventricular WM, orbitofrontal SCWM (*circles*), and ATWM (*dashes*) is also nearly completed, but there are small focal "islands" of "patchy" SCWM that remain hyperintense in such regions, some being terminal zones, such as within the subinsular WM (*thin arrows*). Peritrigonal terminal zones are also becoming increasingly visible (*squares*). The dorsal brainstem (*beveled arrows*) is bright on both sequences

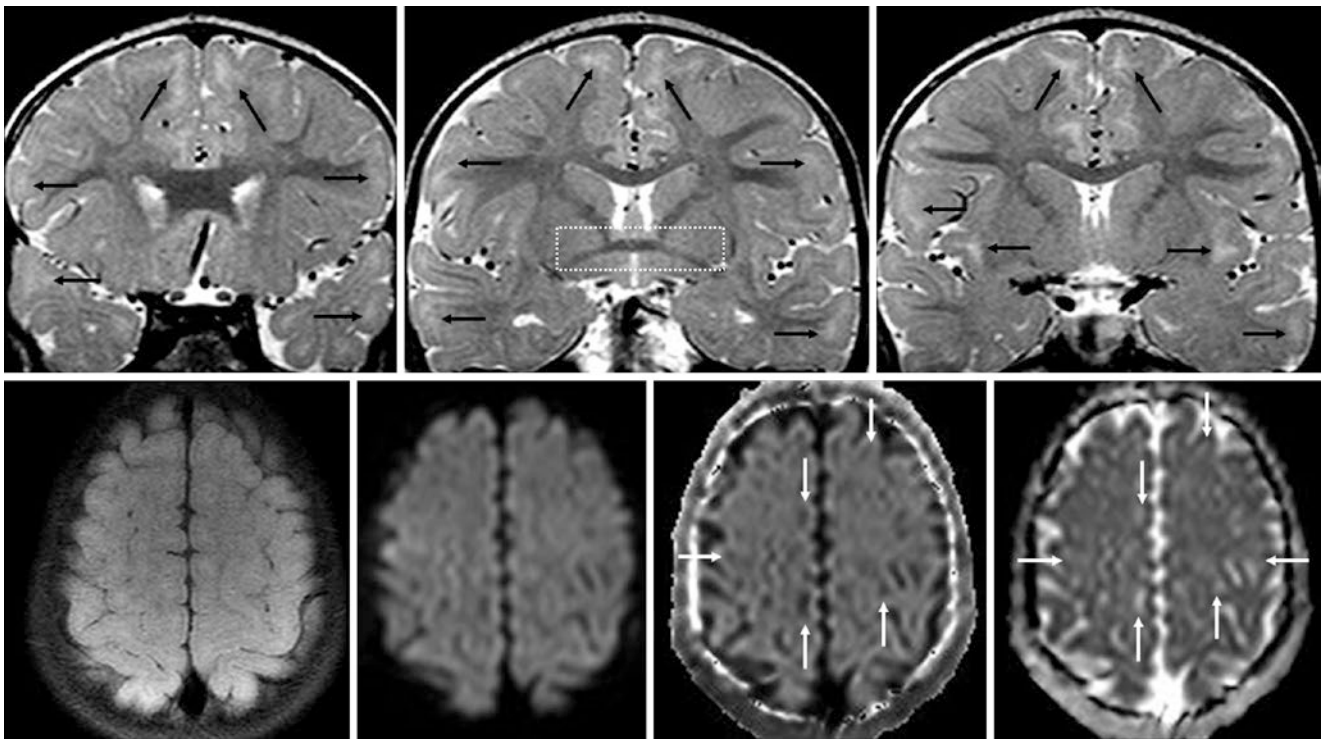

Fig. 23.107 Example of normal "patchy" islands of SCWM. A 12.5-month-old with a normal 3T pituitary MRI. Thin coronal SE T2WIs (*top row*) best demonstrate such islands of residual, nonmyelinated SCWM (*thin arrows*). Note that these are more prominent anteriorly in the frontal and temporal lobes (*top left*). Also, note the mature anterior commissure (*dotted box*). Axial FLAIR (*bottom*, *left*) and DWI (*bottom*, *left middle*) do not depict such "islands" very well, but they can be seen on an exponential DWI (*bottom*, *right middle*) with its ADC map (*bottom*, *right*)

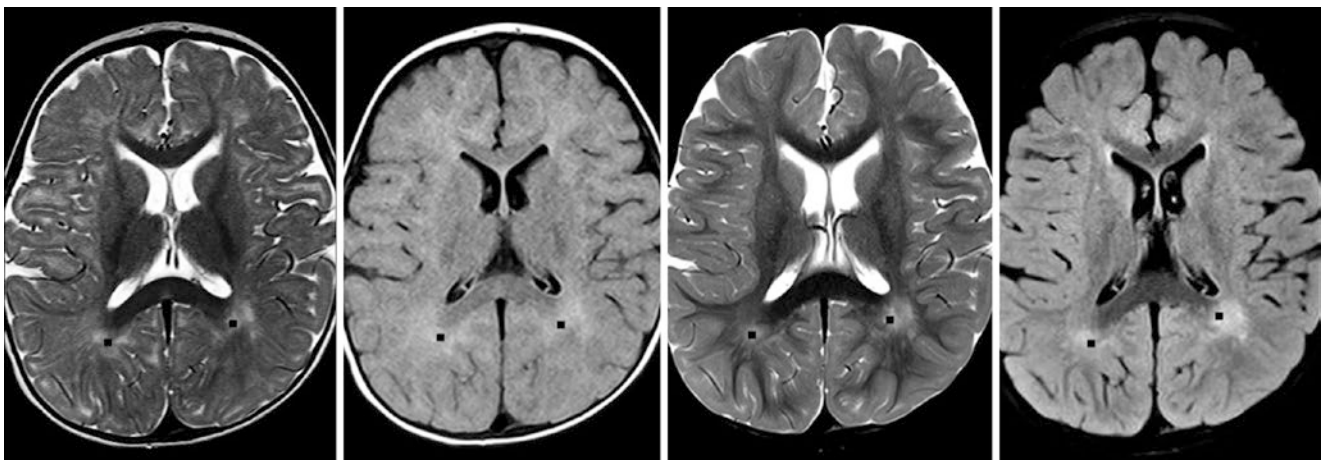

Fig. 23.108 Comparison case of 3-methylglutaconic aciduria (type I). An 11-month-old with microcephaly (by history) had multifocal, abnormal deep WM and PVWM (*squares*) on a 3T MRI with SE T2WI (*left*) and FLAIR (*left middle*), while the CG, CS, ALIC, and SCWM regions appeared normal. A repeat MRI at 2 years of age with T2WI (*right middle*) and FLAIR (*right*) shows normal maturation of the aforementioned structures, but the periatrial PVWM abnormalities persisted

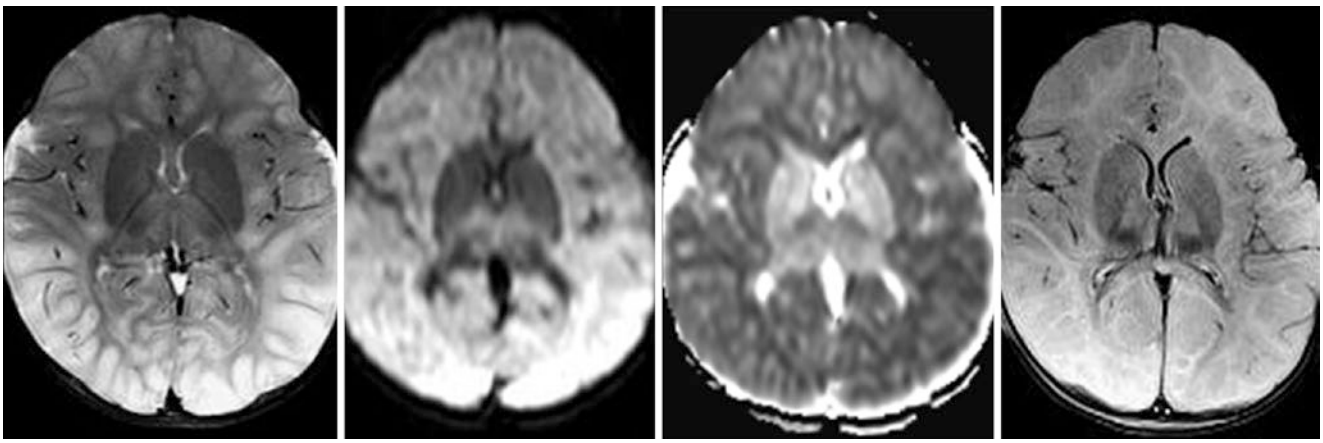

Fig. 23.109 Comparison case of urea cycle disorder (UCD, ornithine transcarbamylase deficiency). An 11-month-old with acute encephalopathic symptoms had diffuse cerebral edema on a 3T MRI with SE T2WI (*left*). On DWI (*left middle*) and the corresponding ADC map (*right middle*), the edema was confirmed to be cytotoxic in nature. On a follow-up MRI 6 days later, FLAIR (*right*) showed persistent diffuse edema, with the deep WM and PVWM much brighter than should be seen on FLAIR. It is not uncommon for UCDs to present with diffuse cortically cytotoxic edema on DWI, which can simulate hypoxic-ischemic encephalopathy, but the injury in UCDs can be partly reversible

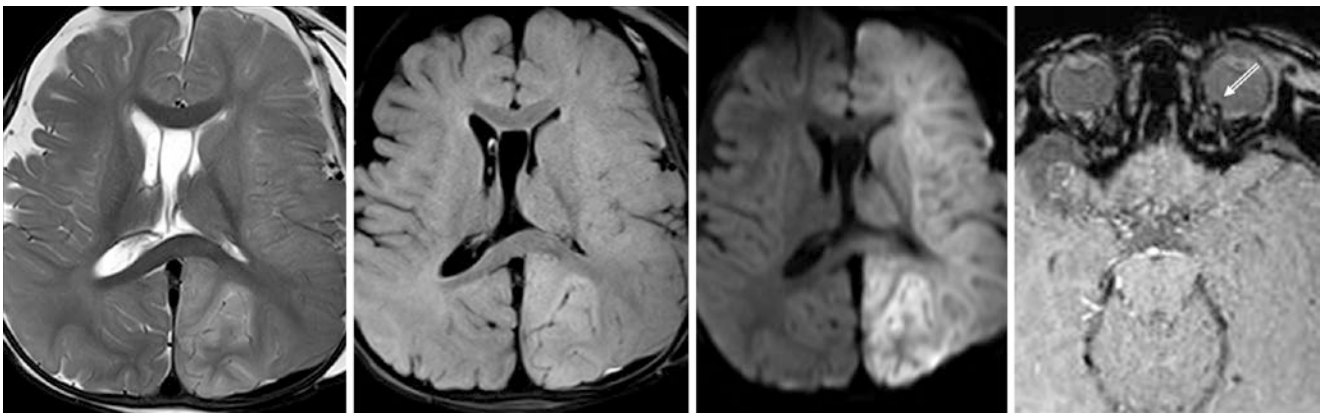

Fig. 23.110 Comparison case of hypoxic-ischemic injury (HII) from abusive head trauma, i.e. non-accidental trauma (AHT, i.e. NAT). An 11-month-old had diffuse, but largely unilateral, cytotoxic edema on a 3T MRI with SE T2WI (*left*), FLAIR (*left middle*), and DWI (*right middle*); the presence of unilateral HIE in an infant should raise the question of AHT. SWI (*right*) depicts unilateral retinal hemorrhage on the left side (*beveled arrow*), which was confirmed clinically

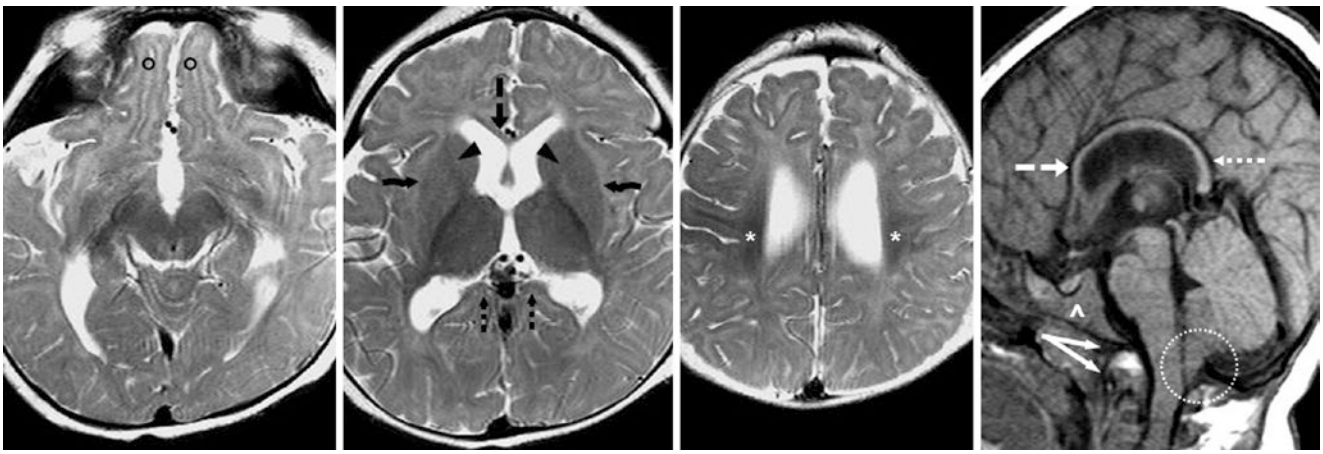

Fig. 23.111 Comparison case of mucolipidosis II (I-cell disease). A 12-month-old had delayed maturation of deep WM and SCWM on a 3T MRI with SE T2WIs (*left three images*). The ALIC (*arrowheads*), CG (*dashed arrow*), CS (*dotted arrows*), optic radiations, OFWM (*circles*), and deep WM anterior to the PRC (*asterisks*) are poorly myelinated. There is atrophy of the CG and CS, as shown on a sagittal GE T1WI (*right*). I-cell disease resembles Hurler's; thus, note a "J-shaped" contour of the bony sella (^), odontoid capping (*split arrows*), and tonsillar herniation (*dotted circle*)

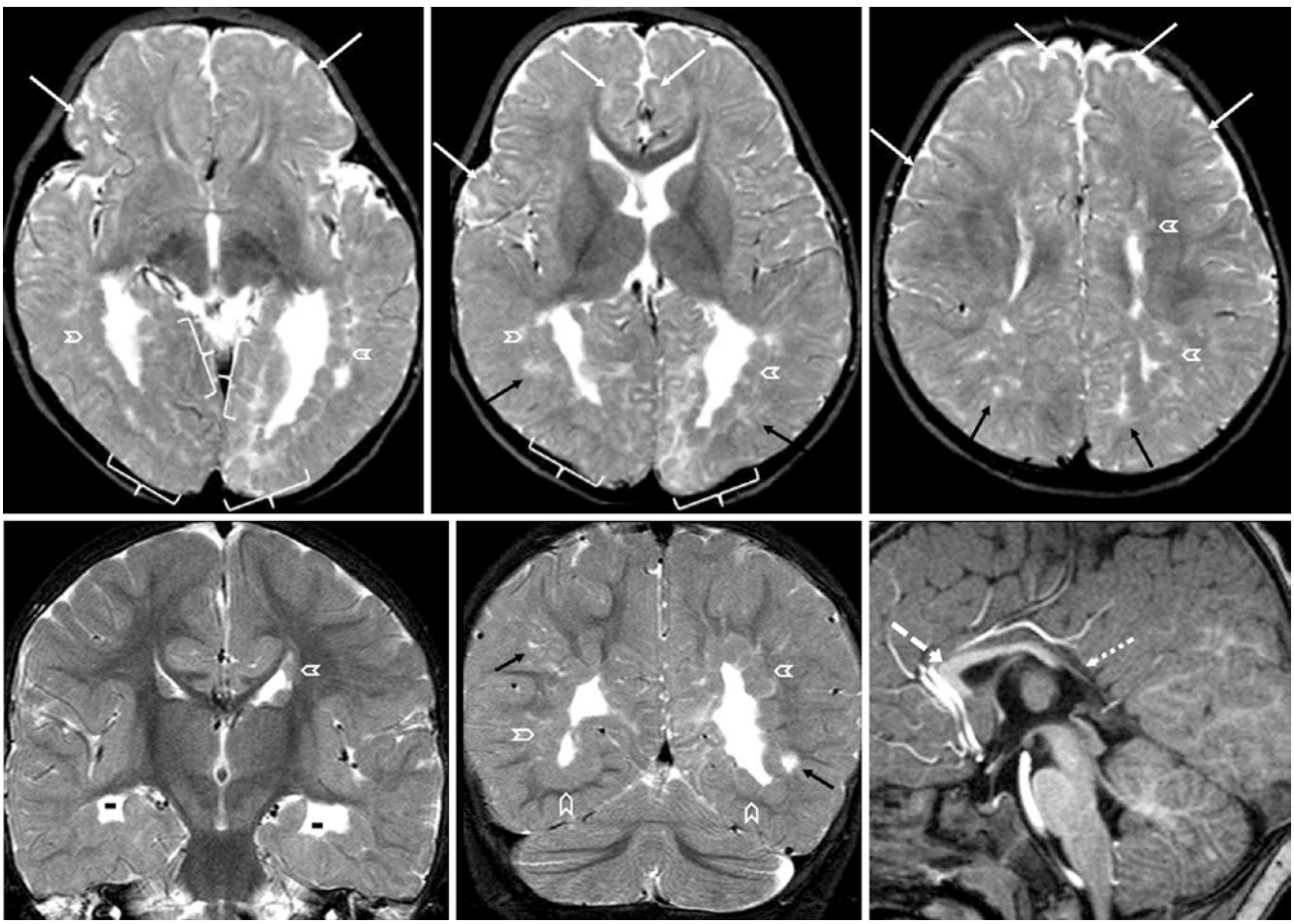

Fig. 23.112 Comparison case of diffuse periventricular nodular heterotopia (PVNH) and polymicrogyria (PMG). A 12-month-old had diffuse PVNH (examples shown by *chevrons*), on a 3T MRI with axial (*top row*) and coronal (*bottom left and middle*) SE T2WIs. The PVNH is more prominent posteriorly, likely with bilateral medial occipital PMG as well (*brackets*). Note the abnormal, scarred subjacent white matter from gliosis (*black arrows*), in contrast to normal, "patchy" SCWM islands of incomplete myelination (*white arrows*). A sagittal GE T1WI (*bottom right*) shows CS agenesis (*dotted arrow*), with a normal and myelinated CG (*dashed arrow*)

23.6.6.1 Normal Myelination: Appearance at the Age of 14–18 Months

By the age of 13–14 months, the white matter appearance on T1WI appears as that of an adult, and the PVWM and SCWM should appear mature, even in the ATWM and OFWM. Residual, incompletely myelinated, normal *terminal zones* may still be seen in periatrial regions or the optic radiations, but are better visualized on T2WI, and are hardly visible on T1WI (discussed later 23.6.7). Again, SE T2WI is usually superior in the assessment of WM maturation after 7–8 months age and is also superior to T1WI in detecting WM lesions after that time. GE T1WI at 3T is superior to routine SE T1WI in the assessment of myelination, but this is not an important distinction at 13–14 months of age, as SE T2WI is preferred over T1WI in general.

On SE T2WI, the SCWM again appears almost entirely myelinated out to the cortex in all but the most anterior portions of the frontal and temporal lobes. Even at the age of 14–18 months, SE T2WI may still show subtle "patchy" *islands of SCWM* far anteriorly and inferiorly. The structures such as the *anterior commissure*, *ALIC*, *CG*, *EC*, and *optic radiations* should have been myelinated previously, so they will not be discussed further. The far anterior ATWM, OFWM, and subinsular WM (SIWM) may still have subtle foci of patchy" SCWM at this time, but these foci should be just subjacent to the cortex; they usually disappear by age 20–24 months. In some patients, they persist as normal terminal zones of hyperintensity on SE T2WI.

On FLAIR, white matter within the deep WM and PVWM of the corona radiata, centrum semiovale, and optic radiations should have darkened relative to the more isointense cortex and basal ganglia. However, normal terminal zones within the PVWM (such as within the periatrial or peritrigonal regions) may become even more apparent as mildly bright signal on FLAIR at this time. As discussed in the previous section, such SCWM hyperintensity can be mistaken for disease, most commonly *periventricular leukomalacia* but also uncommon disorders such as *tuberous sclerosis* (Figs. 23.113, 23.114, 23.115, 23.116, 23.117, 23.118, 23.119, 23.120, 23.121, 23.122, 23.123, 23.124, 23.125 and 23.126).

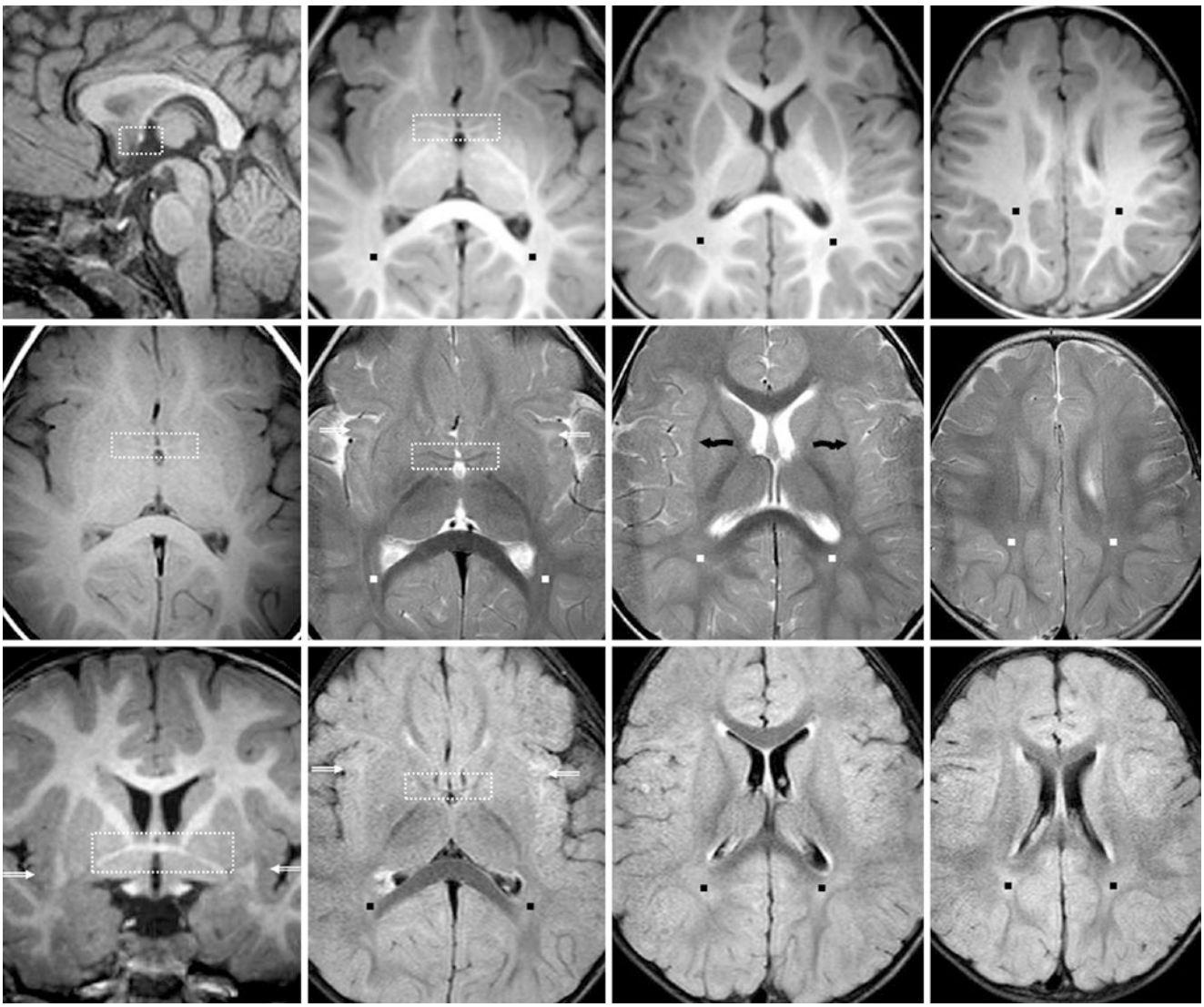

Fig. 23.113 A 14-month-old with possible hypotonia and a negative 3T MRI. *Top row*: Sagittal (*left*) and axial (*right three images*) GE T1WIs show that the anterior commissure (*dotted boxes*) is mature. *Middle row*: An axial SE T1WI (*left*) does not show myelination as well. On SE T2WIs (*right three images*), note that the PVWM and the ECs (*crooked arrows*) are mature, with the exception of terminal zones in peritrigonal (*squares*) and subinsular (*beveled arrows*) regions. *Bottom row*: A coronal GE T1WI (*left*) shows slightly darker signal of the subinsular terminal zones, relative to overlying insular cortex. On FLAIR (*right three images*), note mild hyperintensity within the terminal zones

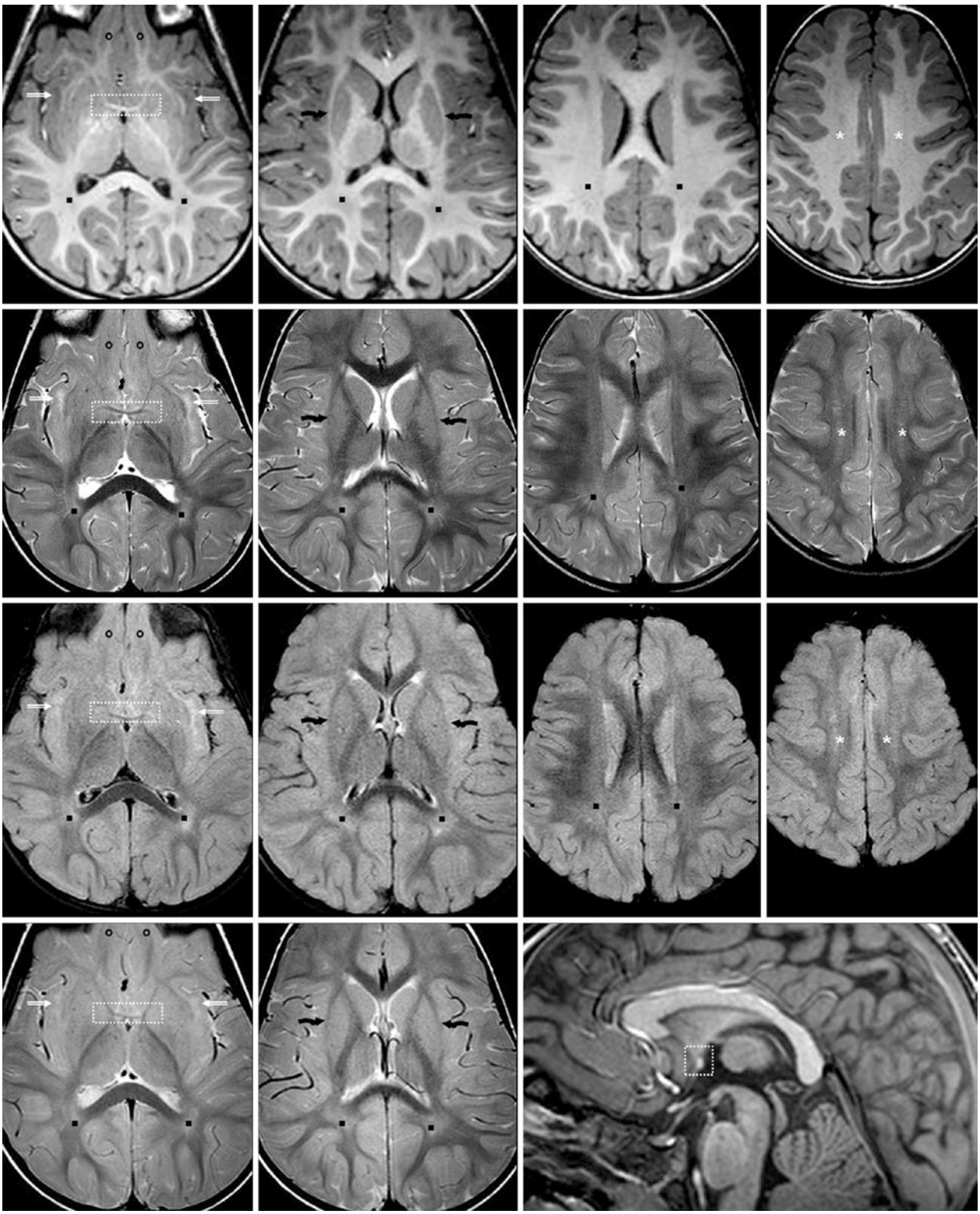

Fig. 23.114 A 14-month-old with abnormal gait had a normal 3T MRI. On GE T1WIs, the anterior commissure (*dotted boxes*) and EC (*crooked arrows*) appear mature. Note subtle low signal in the subinsular WM (SIWM) (*beveled arrows*). *Top row*: GE T1WIs show maturity of the ALIC, anterior commissure (*dotted box*), CG, and EC (*crooked arrows*). The deep WM and SCWM of the orbitofrontal regions (*circles*) and centrum semiovale (*asterisks*) appears mature. *Second row*: On axial SE T2WIs, note that the PVWM is relatively mature, with the exception of terminal zones in the periatrial (*squares*) and SIWM. On more superior images (*right*), the SCWM appears quite mature. *Third row*: Axial FLAIR images demonstrate mild hyperintensity of subinsular terminal zones, relative to the insular cortex. There is also hyperintensity within the periatrial PVWM, which can simulate periventricular leukomalacia. *Bottom row*: Axial proton density-weighted images (*left and middle*) illustrate hyperintensity in the same regions as described above. On a sagittal GE T1WI (*right*), note the maturation/myelination of the anterior commissure

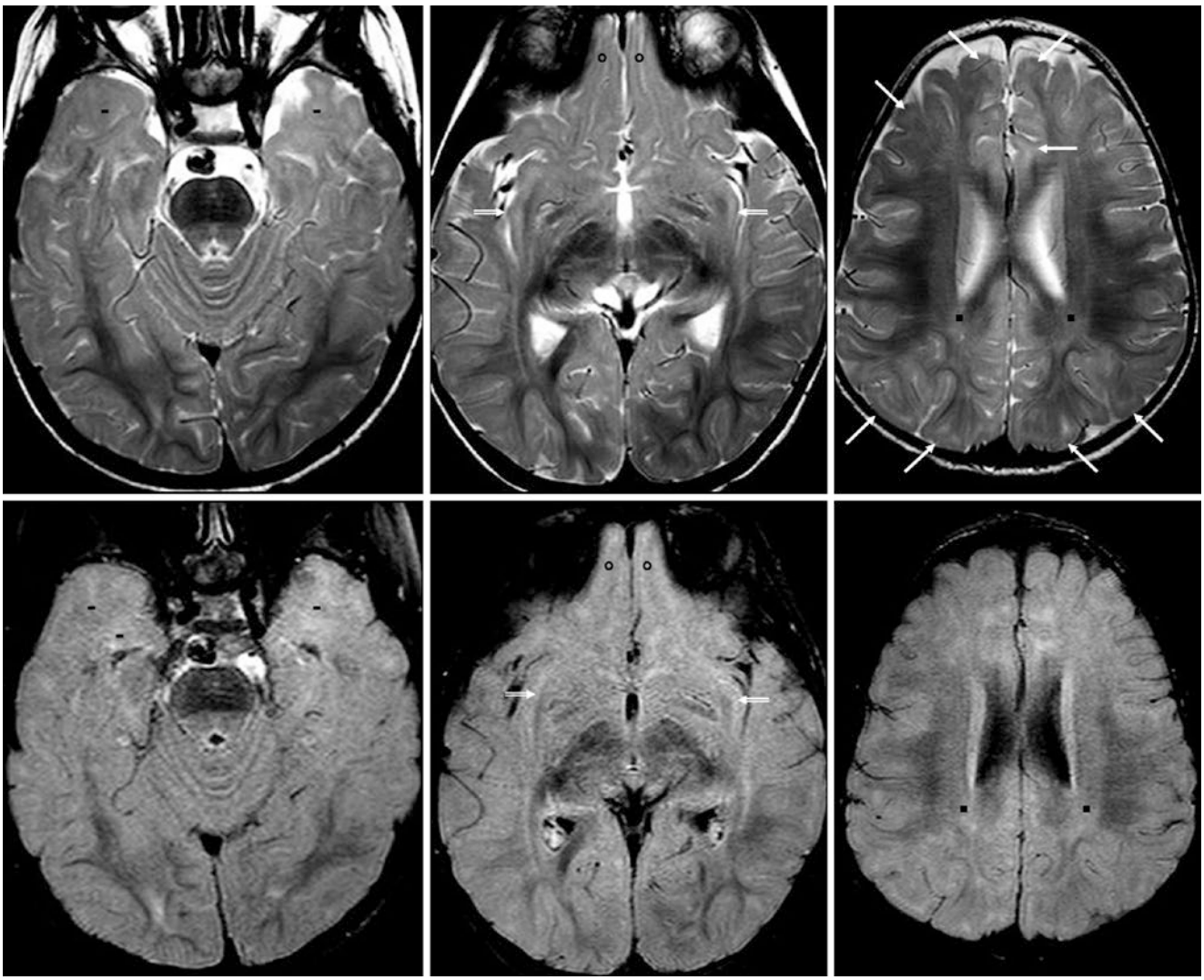

Fig. 23.115 A 14-month-old with a febrile seizure had a normal 3T MRI. On SE T2WIs (*top row*), note hyperintensity of the deep WM and SCWM of the ATWM (*dashes*), OFWM (*circles*), and SIWM (*beveled arrows*). There are also hyperintense SCWM foci within the high anterior frontal and parietal lobes (*thin arrows*). Such SCWM "islands" of hyperintensity are more prominent farther from the perirolandic gyri, and are not well visualized on FLAIR (*bottom row*)

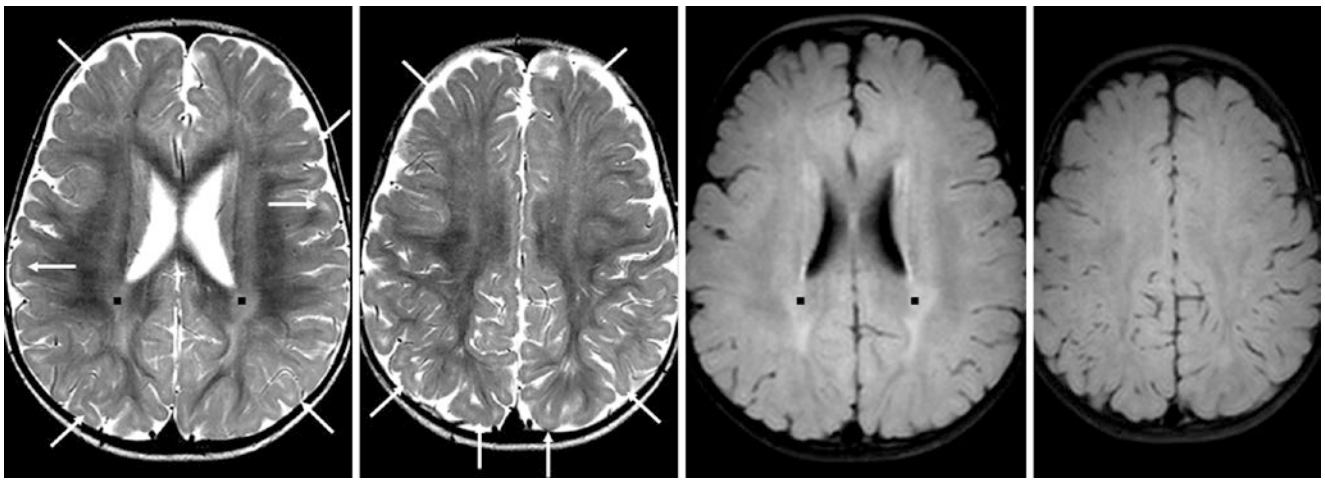

Fig. 23.116 A 14-month-old with mild head enlargement (from slight enlargement of the subarachnoid spaces) had a 3T MRI with SE T2WIs (*left images*) that showed multiple SCWM hyperintense foci (*thin arrows*) within frontal and parietal SCWM, which are not visible on 3D FLAIR (*right images*). The PVWM (*squares*) is also hyperintense on T2WI and FLAIR

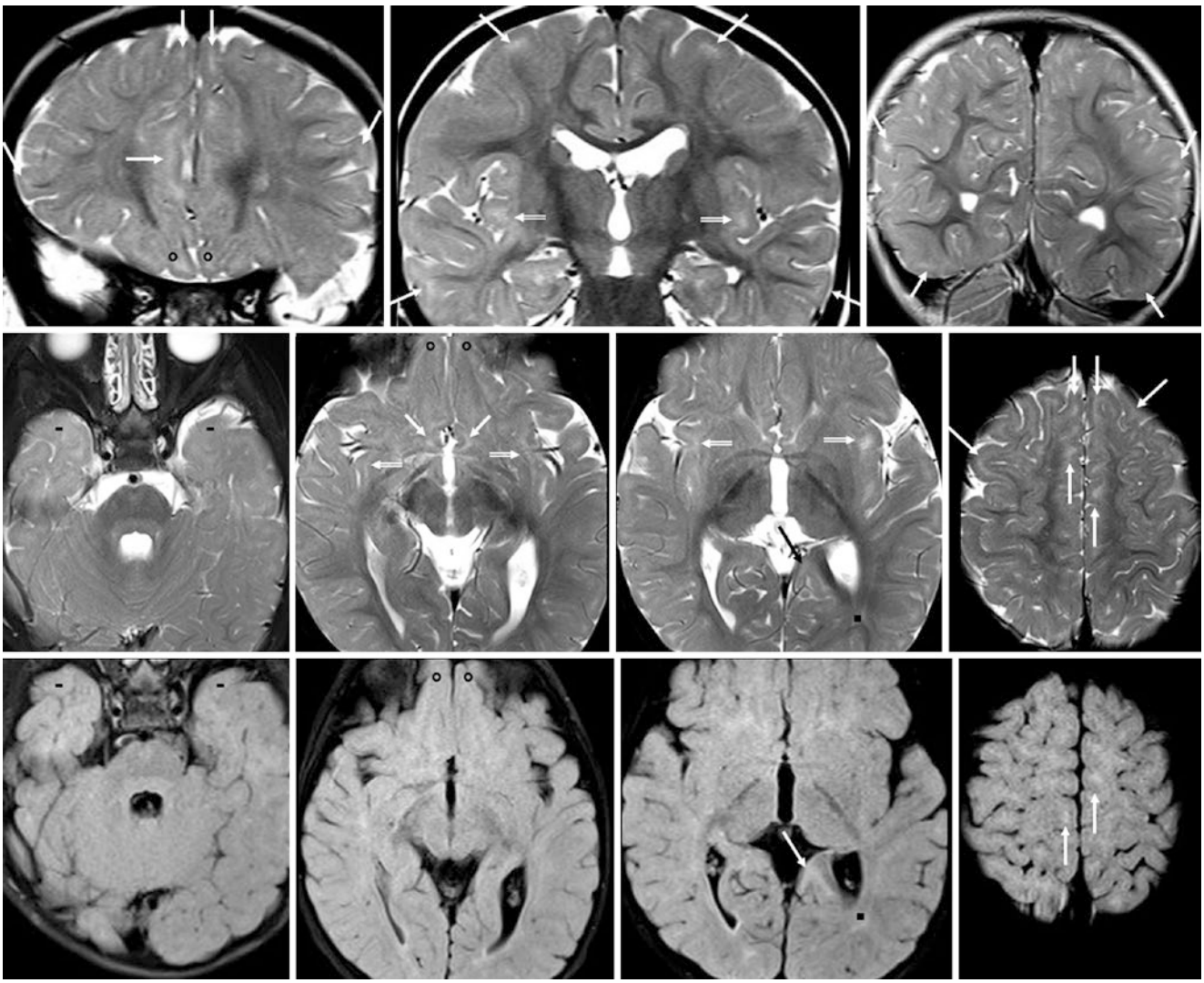

Fig. 23.117 *Top row*: a 14.5-month-old with motor delays had a normal 3T MRI with coronal SE T2WIs. Note hyperintense, patchy SCWM foci (*thin arrows*), which are most prominent anteriorly and inferiorly in the frontal and temporal lobes. *Second row*: On axial SE T2WIs, note that the PVWM is relatively mature, with the exception of terminal zones in the periatrial WM (*squares*) and SIWM (*beveled arrows*). Note patchy ATWM (*dashes*) and OFWM (*circles*). *Bottom row*: On axial FLAIR images, note that the deep WM and SCWM are nearly isointense to cerebral cortex, with the exception of terminal zones in the periatrial WM (*square*), and peripherally immature SCWM foci (*thin arrows*)

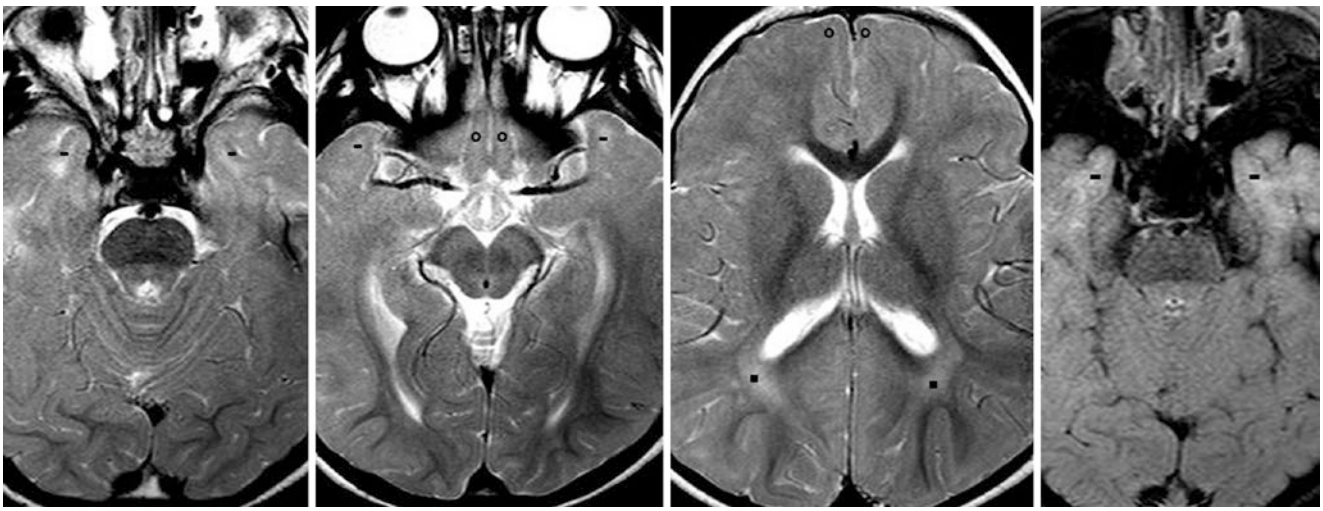

Fig. 23.118 A developmentally normal 14.5-month-old with a head circumference that was not enlarging fast enough underwent a normal 3T MRI with SE T2WIs (*left three images*) and FLAIR (*right*). Note residual SCWM hyperintensity in ATWM (*dashes*) and the OFWM (*circles*). Periatrial terminal zones (*squares*) are normal

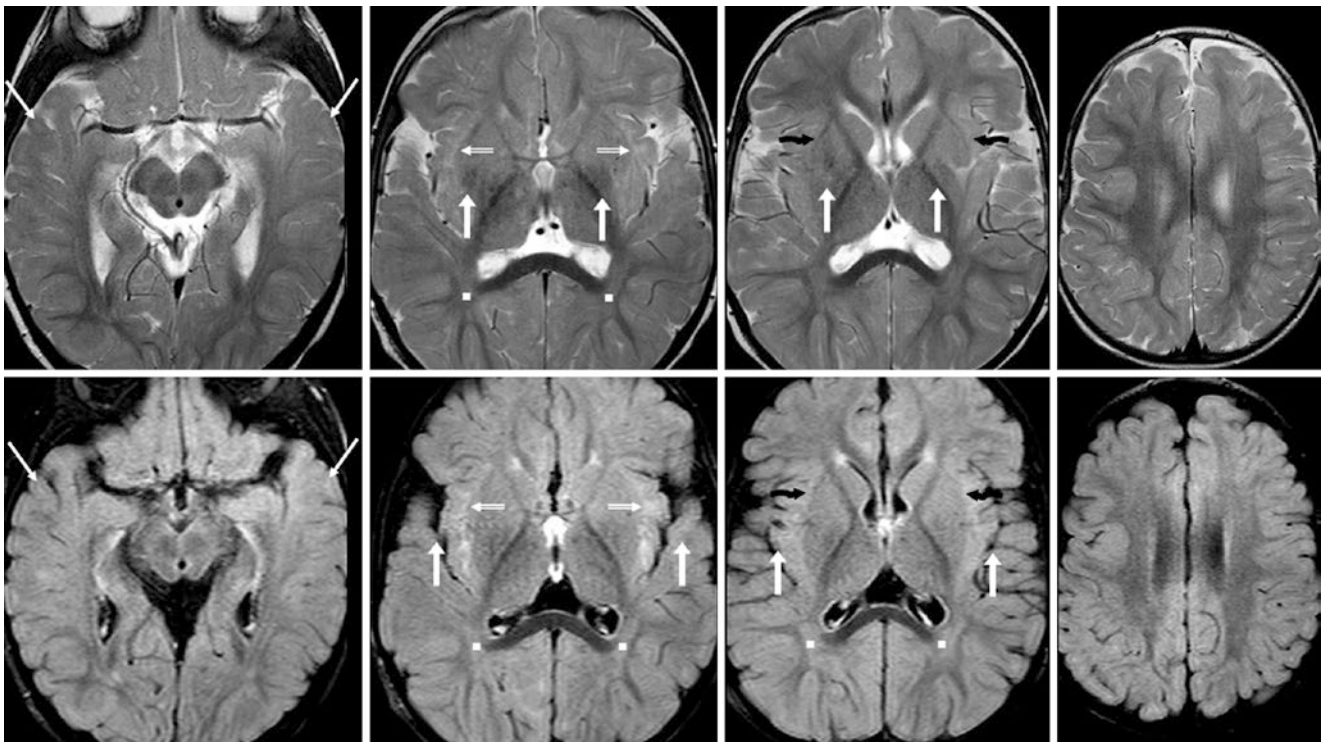

Fig. 23.119 A developmentally normal 15.5-month-old with "spells" had a normal 3T MRI. The anterior commissure and EC (*crooked arrows*) are myelinated on axial SE T2WIs (*top row*) and FLAIR images (*bottom row*). There is mild hyperintensity of the SIWM terminal zones (*beveled arrows*) and subtle patchy SCWM foci elsewhere (*thin arrows*). Note tiny periatrial terminal zones (*squares*) bilaterally on both sequences. There is also motion artifact (*arrows*)

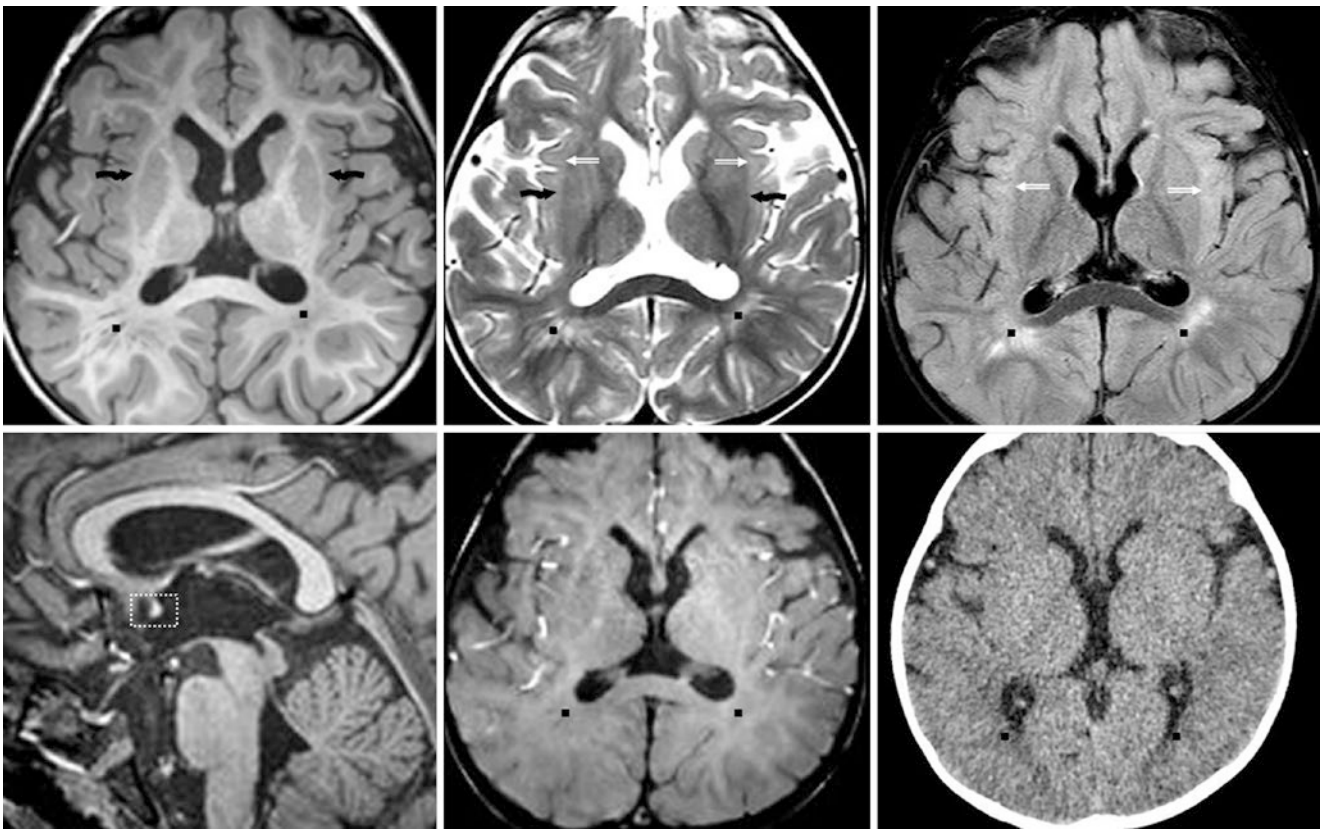

Fig. 23.120 A developmentally normal 16-month-old with nausea had a normal 3T MRI. The EC (*crooked arrows*) appears mature on axial GE T1WI (*top left*) and SE T2WI (*top middle*). FLAIR (*top right*) shows mildly hyperintense subinsular terminal zones (*beveled arrows*). Note myelination of the anterior commissure (*dotted box*) on sagittal GE T1WI (*bottom left*). SWI (*bottom middle*) and NECT (*bottom right*) show periatrial terminal zones (*squares*)

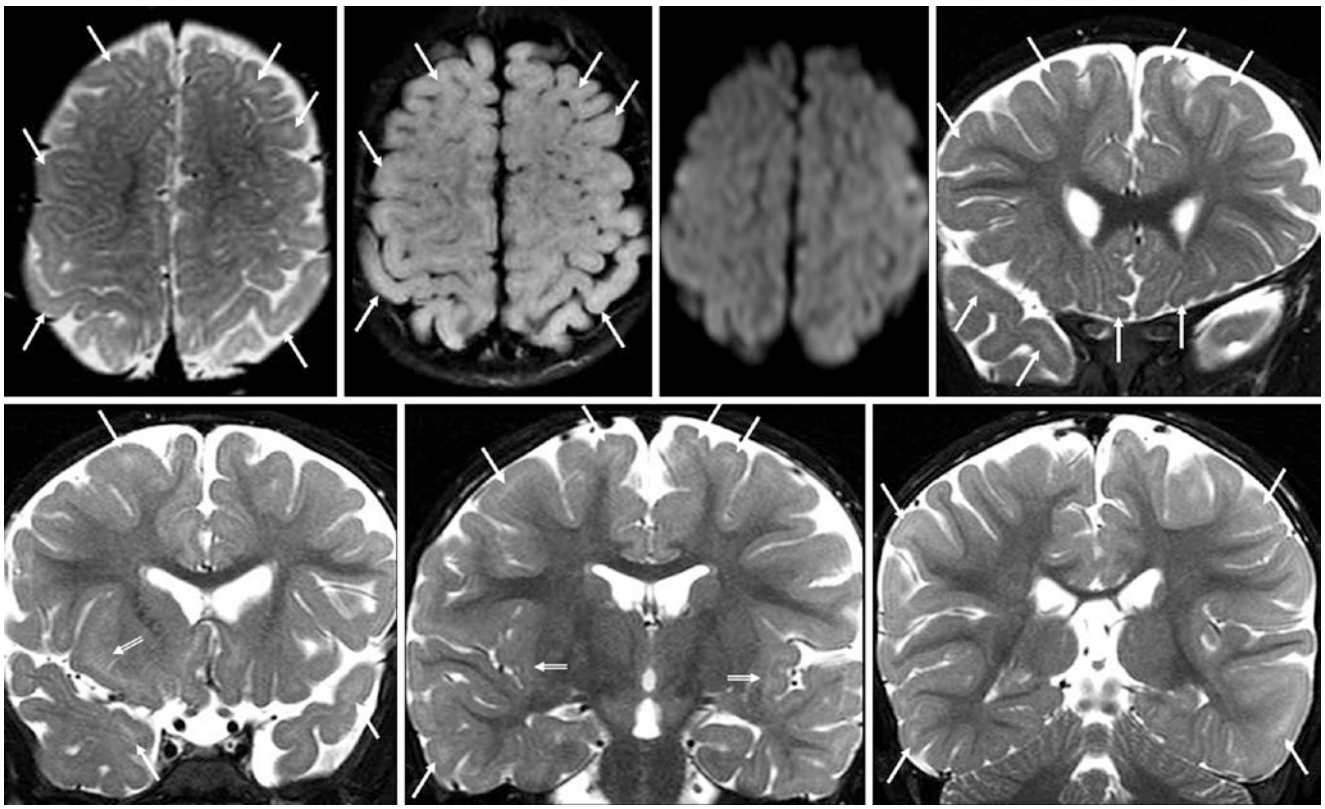

Fig. 23.121 "Patchy" SCWM in a 16.5-month-old with seizures on a 1.5T MRI. The myelination pattern was normal, but with patchy SCWM (*thin arrows*) that is most visible within the anterior and inferior frontal and temporal lobes, as well as within the SIWM (*beveled arrows*), on axial SE T2WI (*top left*). The SCWM foci are not well visualized on FLAIR (*top*, *left middle*) or DWI (*top*, *right middle*) in this patient. Coronal SE T2WIs (*top right* and *bottom row*) from anterior to posterior illustrate that the posterior SCWM seems more mature, and has less patchy hyperintensity

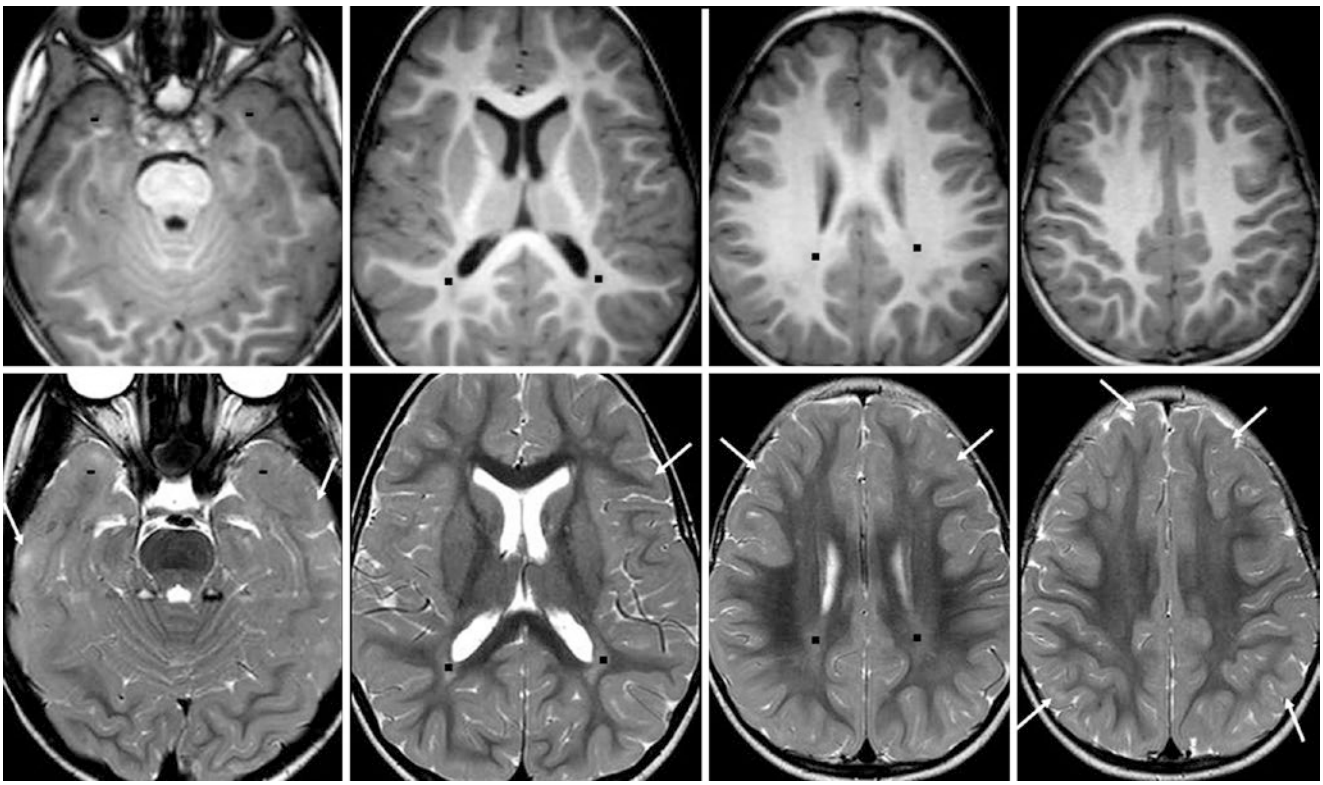

Fig. 23.122 Minimal "patchy" SCWM. A 17.5-month-old with seizures had a 3T MRI, with a normal myelination pattern on GE T1WIs (*top row*) and SE T2WIs (*bottom row*). There is only minimal SCWM hyperintensity (*thin arrows*), which is most visible within the anterior and inferior frontal and temporal poles (*dashes*). Note periatrial terminal zones (*squares*). Also, note that after the age of 8 months, the ventral brainstem can be mildly hyperinense relative to the dorsal brainstem

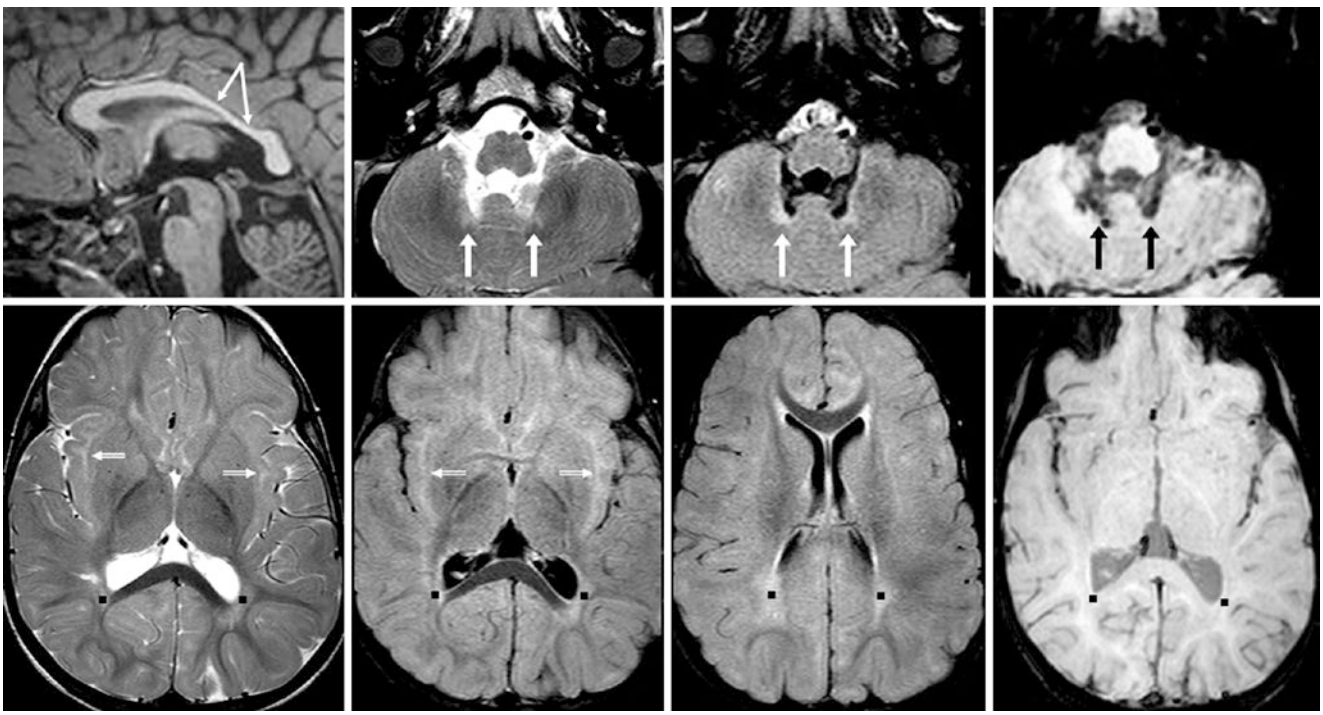

Fig. 23.123 Comparison case of periventricular leukomalacia (PVL) sequelae. A 14-month-old with motor delays had a 3T MRI. The callosal isthmus (*split arrow*) is thinned on a sagittal T1WI (*top*, *left*). On axial T2WI (*top*, *left middle*) and FLAIR (*top*, *right middle*), there is cerebellar WM atrophy (*arrows*), with hemorrhage on SWI (*top*, *right*). T2WI (*bottom*, *left*), FLAIR (*bottom*, *left and right middle*), and SWI (*bottom*, *right*) images at a higher level show diffuse thinning of periatrial WM (*squares*) and SIWM (*beveled arrows*), with bright gliotic signal. Note that normal terminal zones should not be associated with atrophy

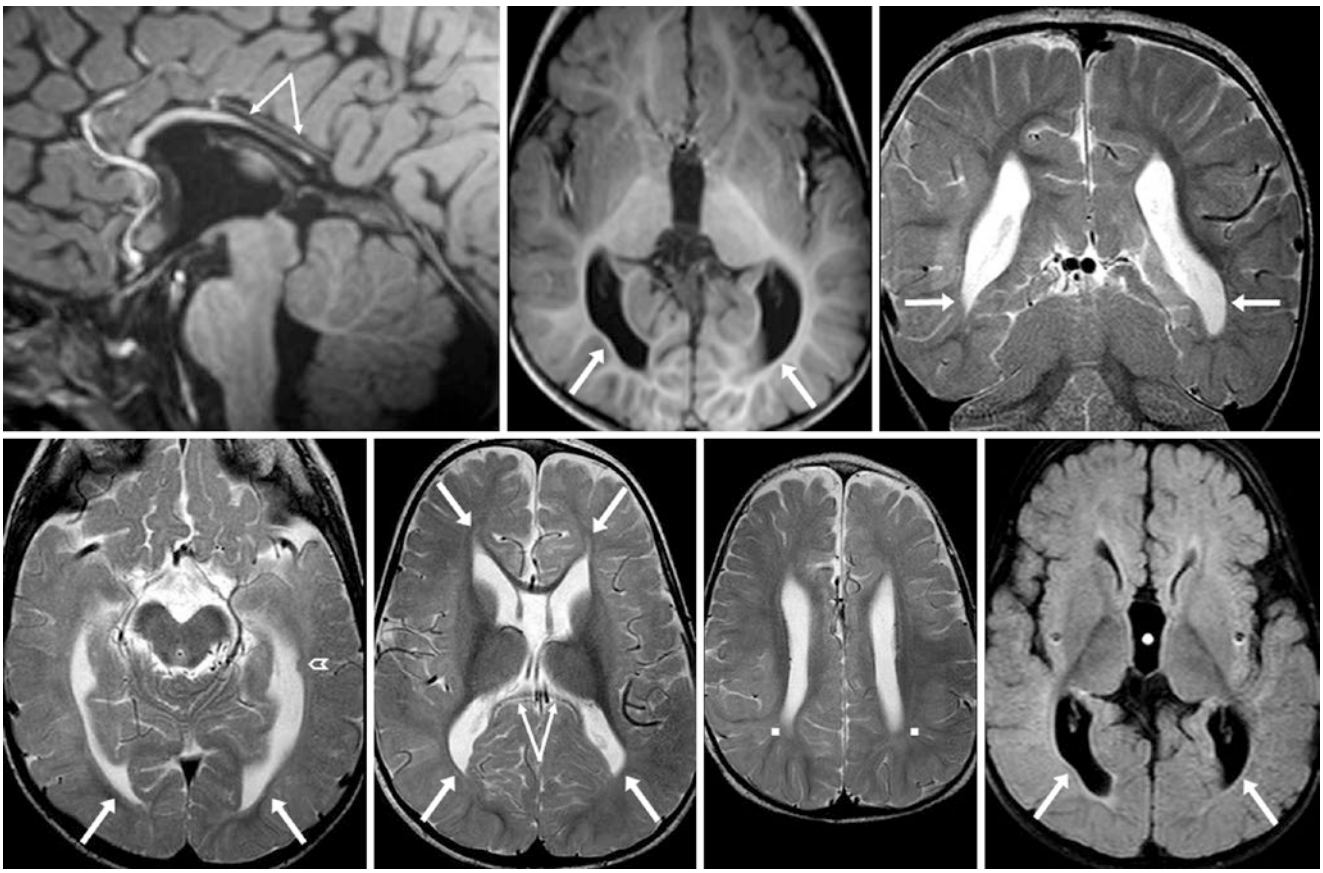

Fig. 23.124 Comparison case of callosal dysgenesis and leukomalacia. A 15-month-old had a 3T MRI that showed severe thinning of the posterior body and splenium of the corpus callosum (*split arrows*) on sagittal T1WI (*top left*), axial T1WI (*top middle*), and coronal T2WI (*top right*). There is periatrial gliosis (*squares*), with WM atrophy/thinning, to a lesser degree near the frontal horns (*arrows*), also depicted on axial T2WIs (*bottom*, *left three images*) and FLAIR (*bottom right*). Note a focus of nodular heterotopia (*chevron*, *bottom left*). The findings suggest intrauterine hypoxic injury

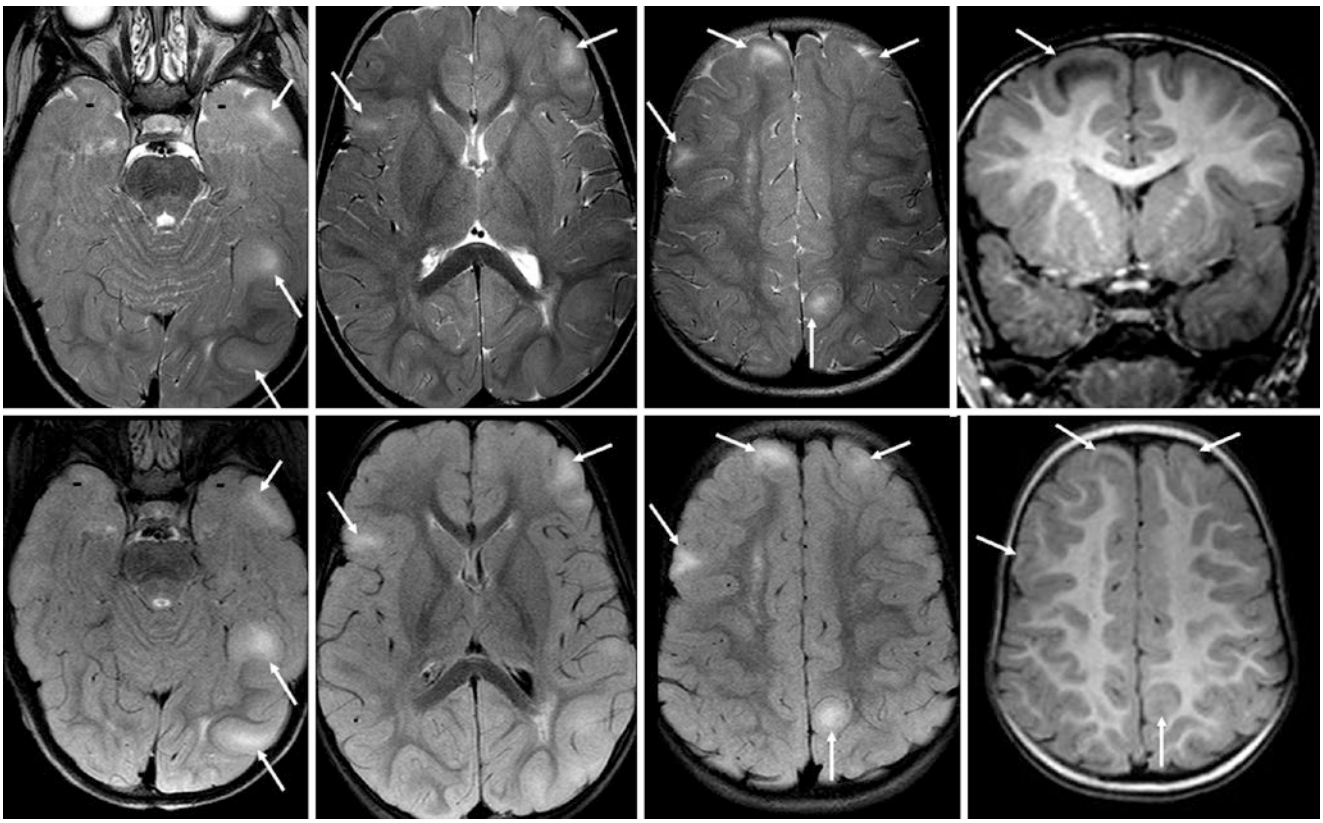

Fig. 23.125 Comparison case of tuberous sclerosis. A 15.5-month-old with seizures underwent a 3T MRI, which depicted multiple cortical tubers (*thin arrows*) on axial SE T2WIs (*top*, *left three images*), coronal GE T1WI (*top*, *right*), FLAIR (*bottom*, *left three images*), and axial GE T1WI (*bottom*, *right*). Contrast these multiple cortical tubers (which appear as "swollen" gyri, representing harmatomas or dysplasias) to normal anterior temporal "patchy" SCWM (*dashes*) (*left*, *top and bottom*)

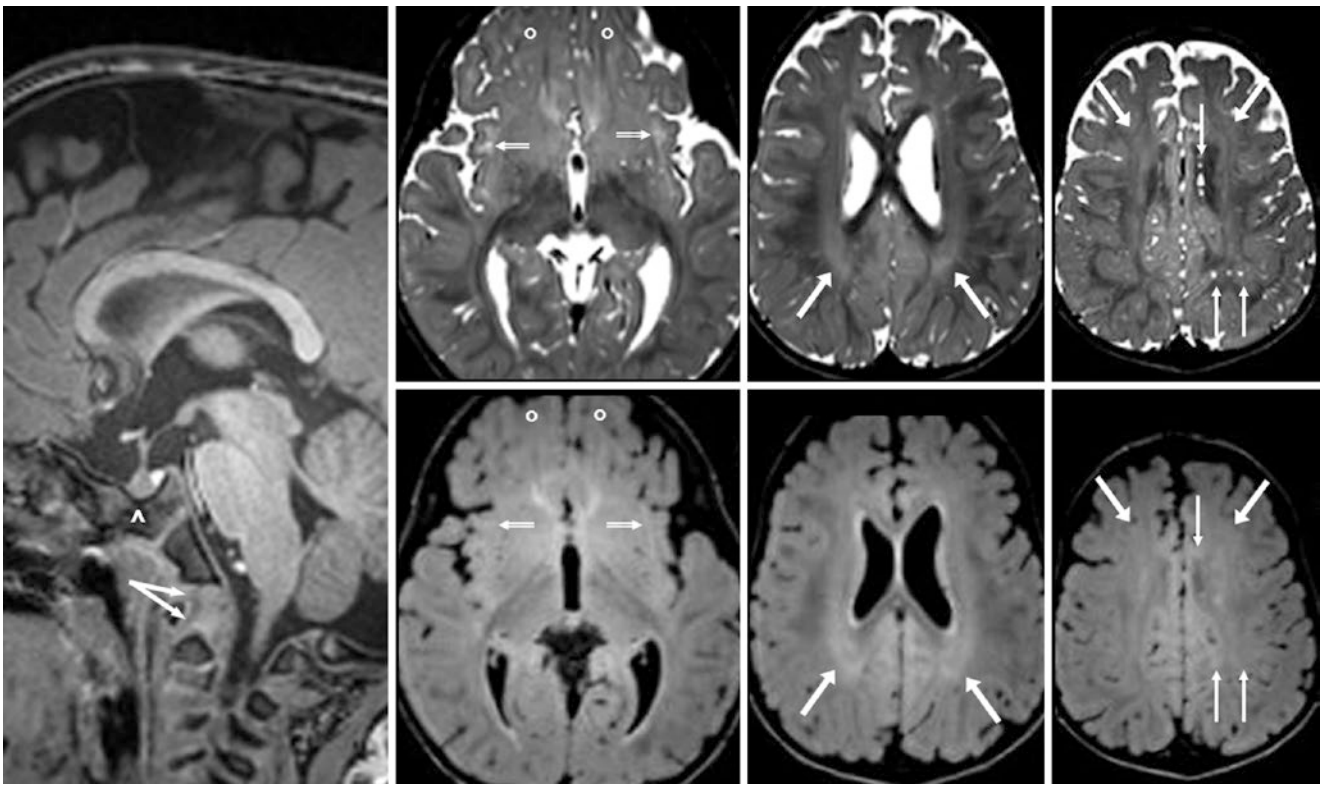

Fig. 23.126 Comparison case of Hurler's mucopolysaccharidosis. A 17-month-old had a 3T MRI that showed a "J-shaped" bony sella (^) with odontoid capping (*split arrows*) on a sagittal GE T1WI (*left*). On axial 3D SE T2WIs (*top row*) and 3D FLAIR (*bottom row*), the OFWM (*circles*), SIWM (*beveled arrows*), and periatrial WM (*arrows*) are not quite as myelinated as would be expected for the patient's age. Note dilated perivascular spaces (*thin arrows*)

23.6.6.2 Normal Myelination: Appearance at the Age of 18–24 Months

By the age of 18 months, the white matter appearance on T1WI has long since appeared as adult (usually by 7–8 months), and the PVWM and SCWM should appear mature, even the ATWM and OFWM. On SE T2WI, the SCWM should appear nearly completely myelinated out to the cortex, even in the most anterior portions of the frontal and temporal lobes; thus, the "patchy" regions of SCWM on SE T2WI may still be barely visible at this age in the most anterior and inferior regions of the frontal lobes, basal forebrain, and temporal lobes, but they usually disappear by 21–24 months. Thus, *an adult appearance should also be present on SE T2WI around 21–24 months* of age, except for residual incompletely myelinated, normal *terminal zones*. Such zones are often still visible within the optic radiations, periatrial WM, and sometimes the SIWM; they are better visualized on T2WI and hardly visible on T1WI.

FLAIR becomes increasing helpful to distinguish edema or gliosis within the WM, as well as to evaluate WM maturity, after the age of 16–18 months. Because FLAIR images are essentially T2-weighted, the maturity of WM on FLAIR images parallels that seen on T2WI. White matter within the deep WM and PVWM of the corona radiata, centrum semiovale, and optic radiations should have continued to darken relative to the more isointense cortex and basal ganglia. Again, normal terminal zones within the PVWM may become apparent as mildly bright signal on FLAIR. As discussed in the next section, such normal terminal zones may persist for many years, albeit to a decreasing degree with increasing age (Figs. 23.127, 23.128, 23.129, 23.130, 23.131, 23.132, 23.133, 23.134, 23.135 and 23.136).

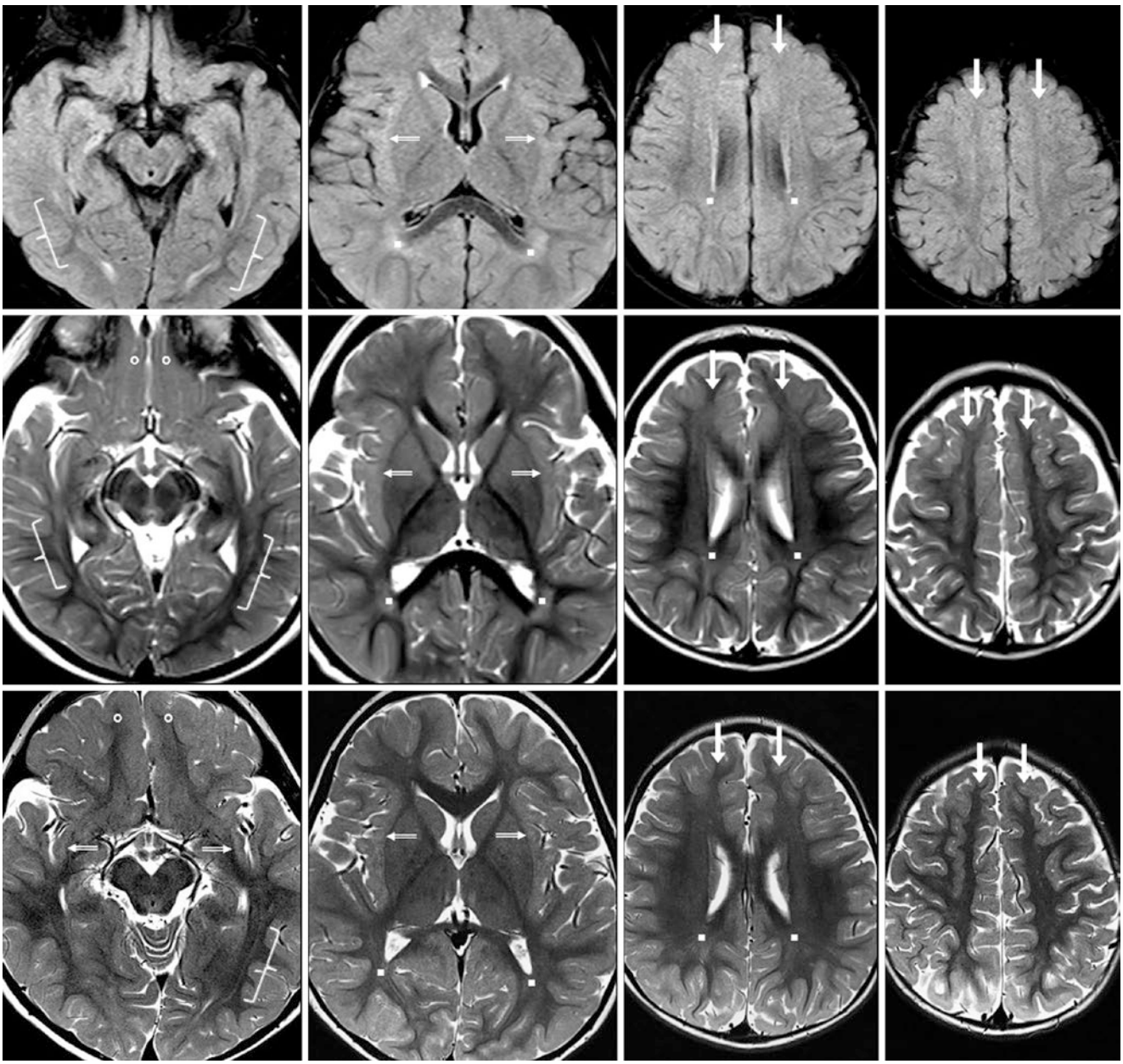

Fig. 23.127 An 18-month-old with suspected developmental delays had a normal 3T MRI. On these images, note the periatrial terminal zones (*squares*), OFWM (*circles*), optic radiations (*brackets*), and SIWM (*beveled arrows*). *Top row*: On FLAIR images, there is mild hyperintensity within the optic radiations, periatrial-supraventricular WM, and SIWM. Incompletely myelinated regions of the frontal SCWM (*arrows*) are not bright on FLAIR. *Second row*: On SE T2WIs, note that the PVWM is quite mature, with the exception of periatrial and SIWM terminal zones, which were also mildly bright on FLAIR. Note incomplete superior frontal myelination (*arrows*). *Bottom row*: On SE T2WIs at 24 months of age, subinsular and periatrial WM are less bright, indicating progressing WM maturity. The maturity of the optic radiations and superior frontal WM has also progressed (*arrows*)

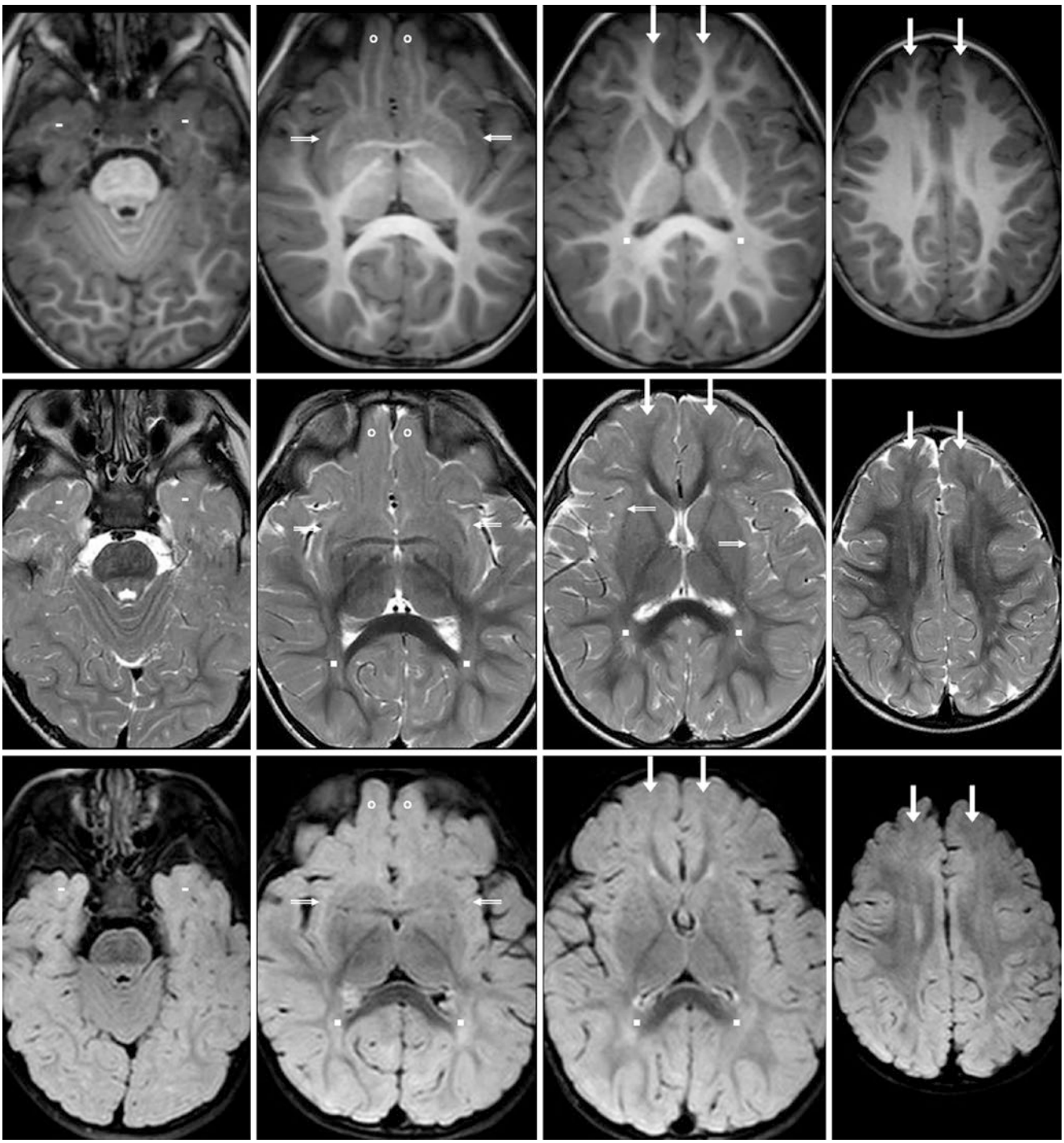

Fig. 23.128 An 18-month-old with "spells" had a normal 3T MRI. On these images, note the periatrial terminal zones (*squares*), OFWM (*circles*), ATWM (*dashes*), and the SIWM (*beveled arrows*). The appearance is nearly that of an adult. *Top row*: On GE T1WIs, the myelination appearance is that of an adult, with the exception of subtle hypointensity within the SIWM and ATWM. The dorsal brainstem is slightly hypointense on this sequence. *Second row*: On SE T2WIs, the PVWM seems mature, except for the terminal zones and the OFWM (*circles*). Note immature anterior frontal SCWM (*arrows*). The dorsal brainstem is mildly hyperintense. *Bottom row*: Axial reformats of a 3D FLAIR acquisition show the subinsular and periatrial WM to be mildly bright. The persistent bright signal in these two regions simulates periventricular leukomalacia, but there is no atrophy

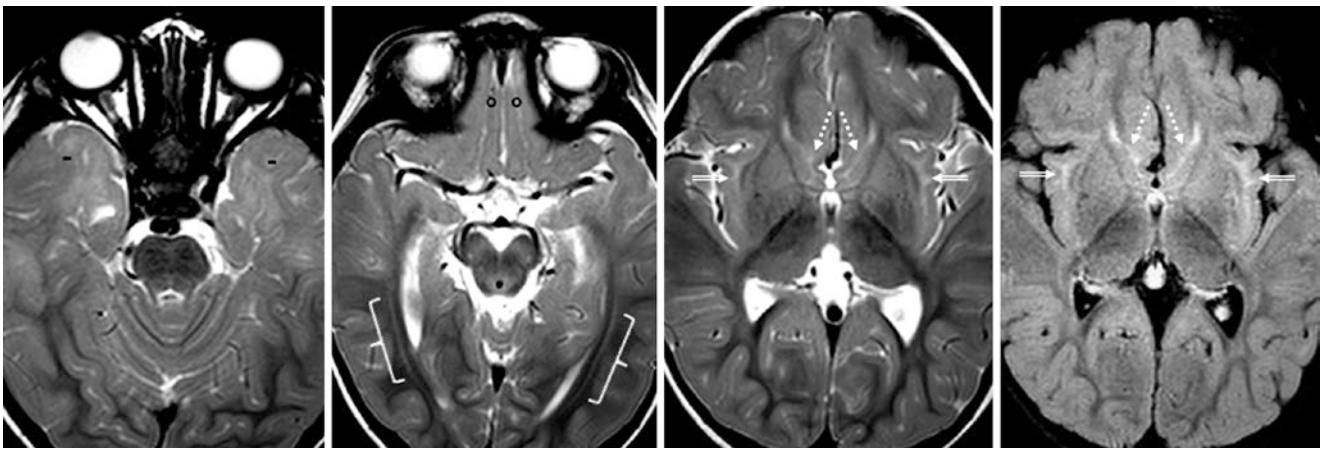

Fig. 23.129 A 19-month-old with "altered mentation" was developmentally normal and had a normal 3T MRI. On SE T2WIs (*left three images*) and FLAIR (*right*), note immaturity of the WM of the orbitofrontal gyri (*circles*) and basal forebrain (*dotted arrows*), along with normal terminal zones within the ATWM (*dashes*), optic radiations (*brackets*), and SIWM (*beveled arrows*)

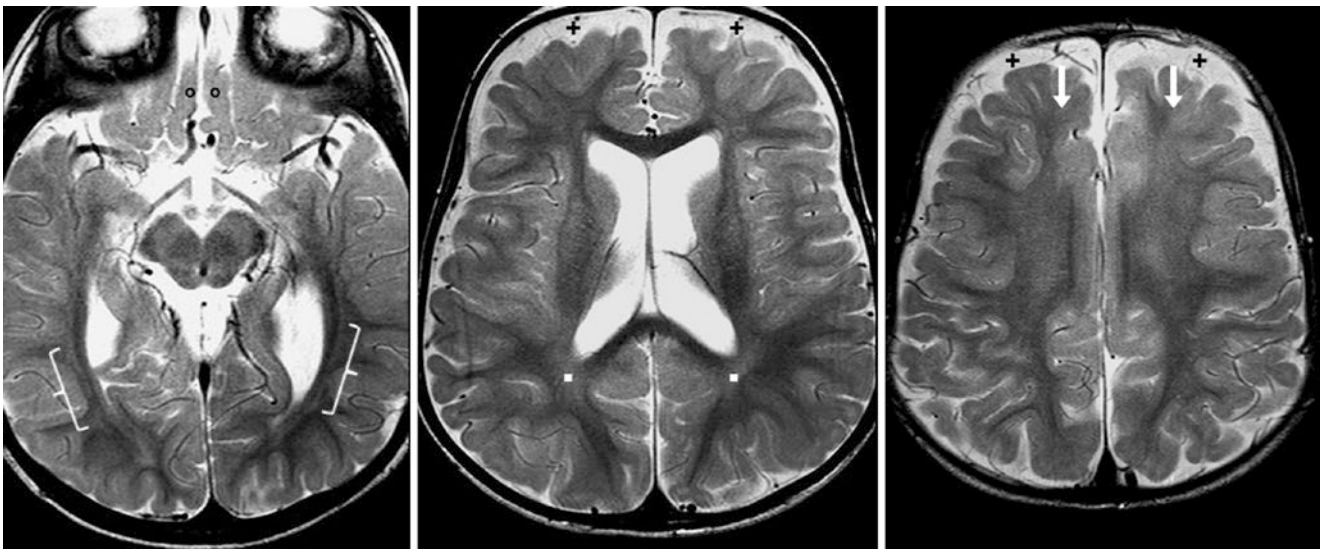

Fig. 23.130 A 20-month-old who was neurologically normal had macrocephaly and benign enlargement of subarachnoid spaces (*plus signs*), with an otherwise normal 3T MRI. On SE T2WIs, note incomplete SCWM maturity of the orbitofrontal (*circles*) and superior frontal gyri (*arrows*). The periatrial (*squares*) and optic radiations (*brackets*) terminal zones are normal

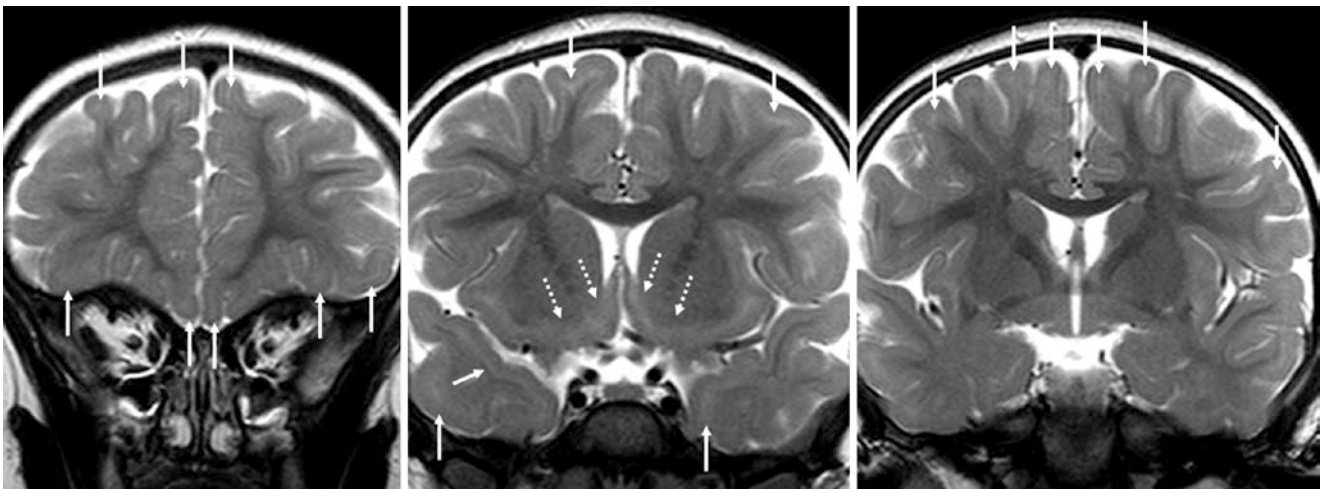

Fig. 23.131 A 21-month-old with obesity had a normal 3T MRI. On coronal SE T2WIs, note residual, hyperintense "patchy" SCWM (*thin arrows*) within the anterior-inferior frontal WM, superior frontal gyrus anteriorly, and ATWM. Additionally, note residual bright signal representing immaturity within basal forebrain areas, including the diagonal gyrus, paraterminal gyrus, nucleus accumbens, and substantia innominata (*dotted arrows*)

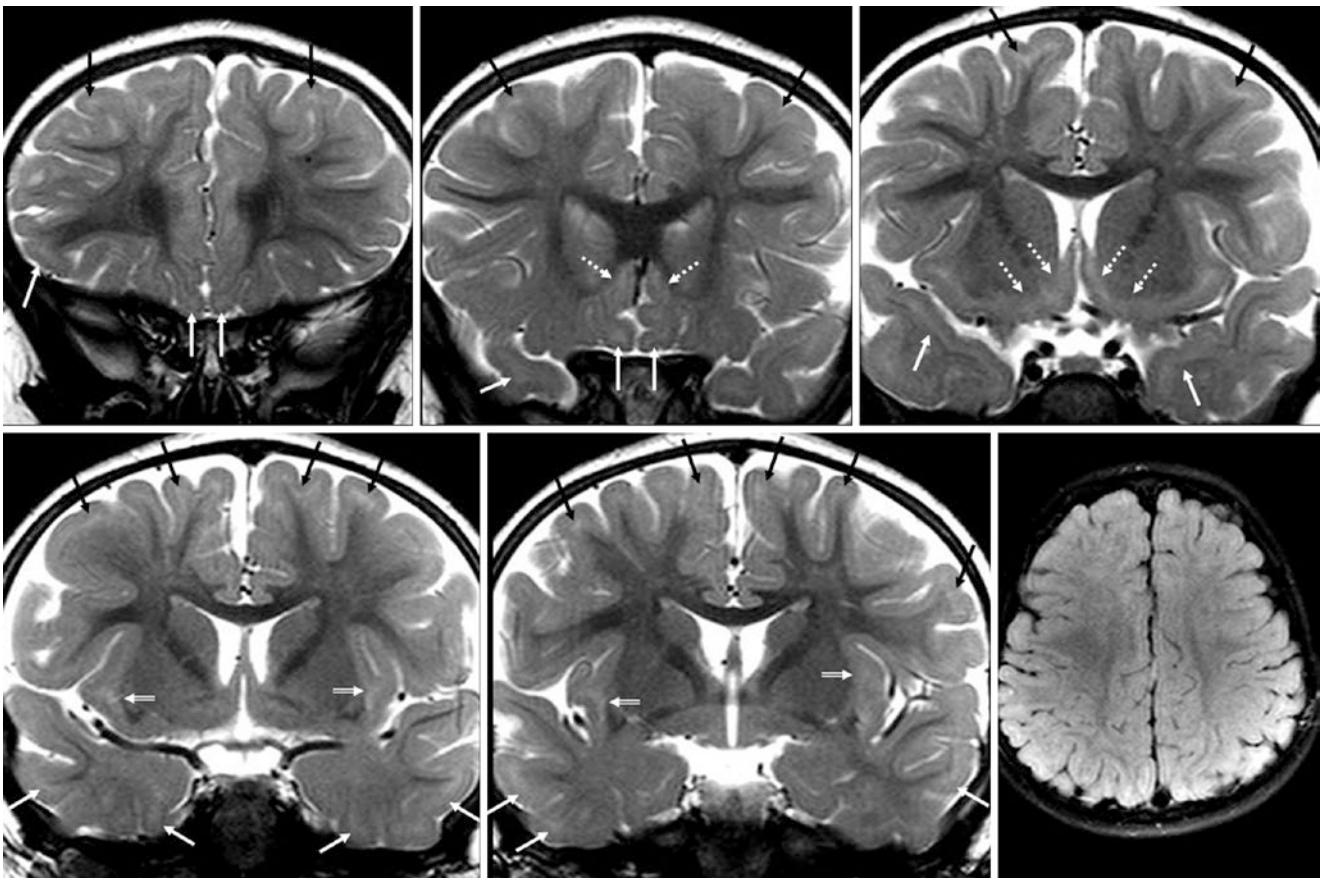

Fig. 23.132 A 21.5-month-old with symptoms of rage and obesity had a normal 3T MRI. On coronal SE T2WI (*top row and bottom left and middle*), note tiny residual patchy SCWM hyperintensity (*thin arrows*) within the anterior-inferior frontal WM, anterior superior frontal gyri, and ATWM. Also, note bright signal from immaturity within the SIWM (*beveled arrows*) and basal forebrain, which includes the nuclei accumbens, diagonal gyri, paraterminal gyri, and substantia innominata (*dotted arrows*). On FLAIR (*bottom right*), the SCWM hyperintensities are not visible

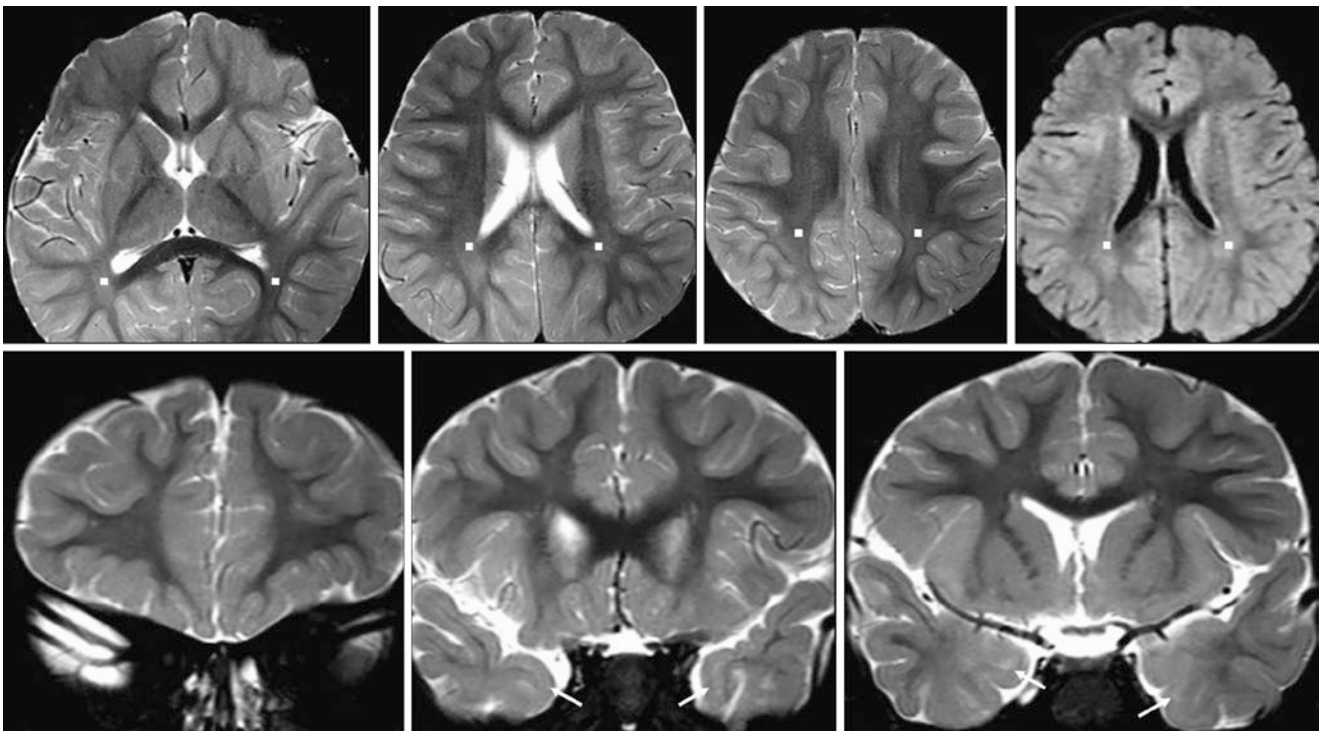

Fig. 23.133 A 23.9-month-old with possible ataxia had a normal 3T MRI. On axial SE T2WIs (*top*, *left three images*), there were only mild residual periatrial terminal zones (*squares*), which are barely visible on FLAIR (*top*, *right*). Coronal SE T2WIs show that the patchy SCWM hyperintensity has nearly disappeared in the orbitofrontal regions (*bottom left*) and anterior-superior frontal regions (*bottom middle and right*), but persists in the anteriormost temporal SCWM (*thin arrows*)

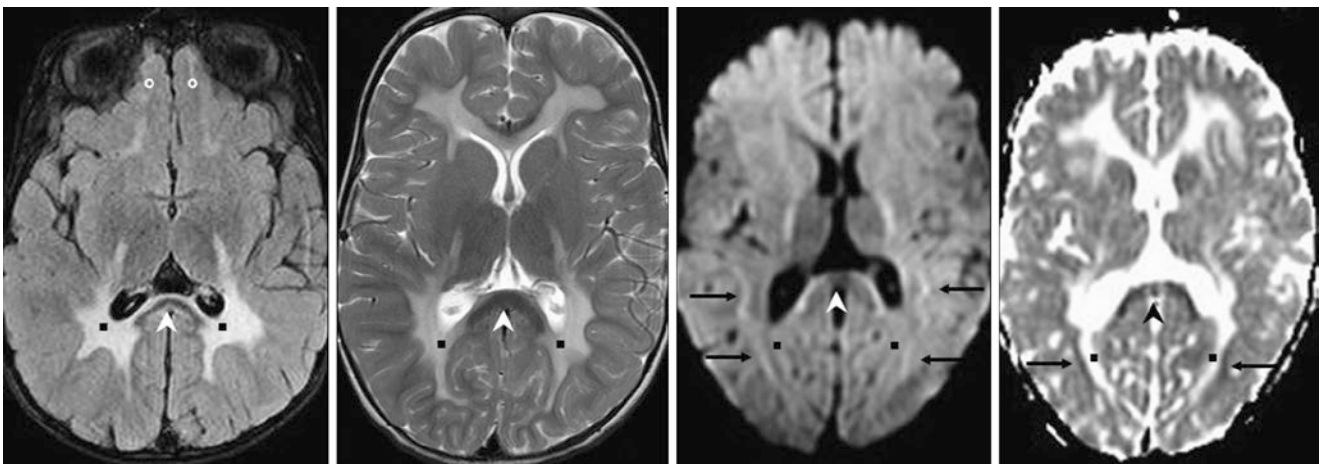

Fig. 23.134 Comparison case of metachromatic leukodystrophy (MLD). A 22-month-old had a 1.5T MRI that showed signal abnormalities of periatrial WM (*squares*), OFWM (*circles*), and frontal PVWM on FLAIR (*left*) and T2WI (*left middle*), with sparing of the callosal splenium (*arrowhead*). Reduced diffusion (*thin arrows*) is present on DWI (*right middle*) and the ADC map (*right*). Splenial sparing suggests MLD rather than adrenoleukodystrophy (ALD)

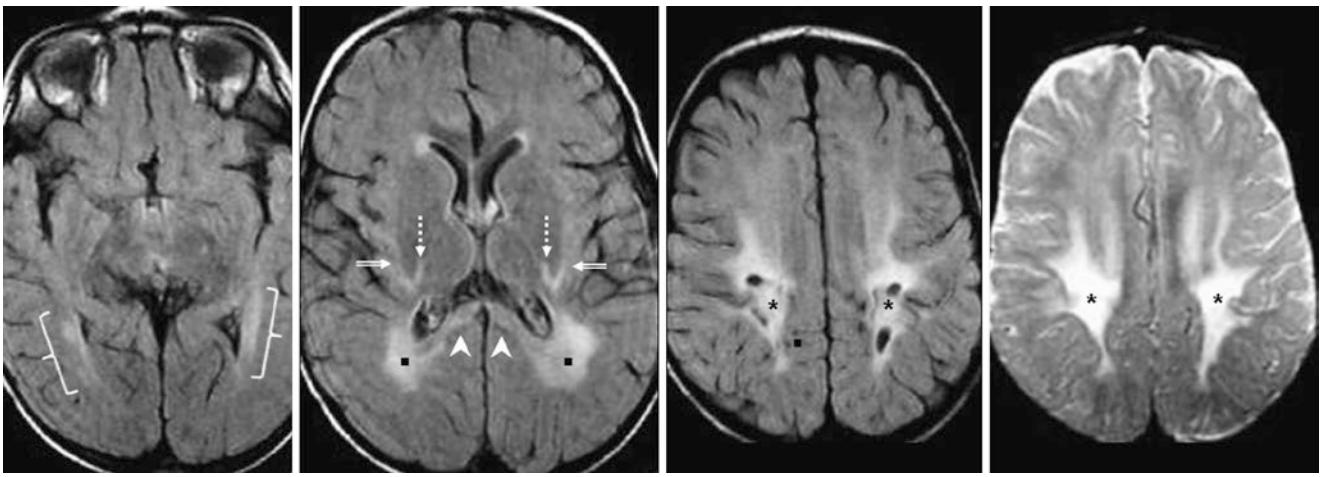

Fig. 23.135 Comparison case of globoid leukodystrophy (GLD, Krabbe disease). A 23-month-old had a 1.5T MRI that showed abnormal signal and cystic leukomalacia of periatrial WM (*squares*), optic radiations (*brackets*), supraventricular WM (*asterisks*), SIWM (*beveled arrows*), and the internal capsules' posterior limbs (*dotted arrows*) on FLAIR (*left three images*) and T2WI (*right*). The involvement of the posterior limbs is typical of GLD

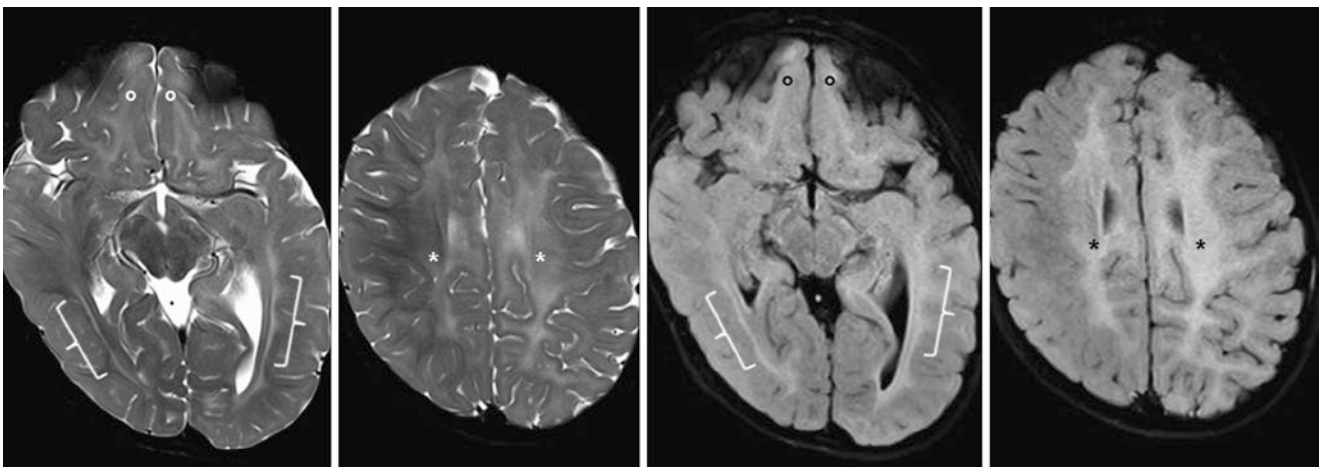

Fig. 23.136 Comparison case of velocardiofacial syndrome (VCFS, 22q11.2 deletion syndrome). A 23-month-old had a 3T MRI that showed hyperintense signal within the optic radiations (*brackets*), OFWM (*circles*), and supraventricular WM (*asterisks*) on FLAIR (*left images*) and T2WI (*right images*), being affected more on the left. Studies have demonstrated parieto-occipital and temporal atrophy, as well as congenital anomalies, in VCFS

23.6.7 Terminal Zones After 2 Years of Age

Myelination typically progresses in a predictable fashion, generally from posterior to anterior while at the same time "radiating" towards the anterior and posterior poles from a central point, the *perirolandic* (pericentral) *gyri*. Typically, this *myelination is nearly complete by the age of 18–24 months on T2WI and FLAIR*. The exception is normal, residual *terminal zones*, which can be visualized within the white matter for years after birth. The exact age at which these terminal zones disappear is not known: Several sources have given this age as about 20–24 months; others have said 3–4 years, and yet others have described the persistence of such normal terminal zones in patients as old as 20–30 years! Perhaps such discrepancies within the literature may relate to both technique and the patient cohort studied. Regarding technique, it is well known that subtle T2-bright phenomena, whether mild abnormalities or even normal anisotropy (as in the sections on diffusion imaging and FLAIR), can be visualized at 3T but appear unremarkable at 1.5T, and periventricular findings, such as terminal zones, may be better visualized on certain sequences such as FLAIR or double inversion recovery images. Regarding patient cohort, it is possible that studies based on a patient cohort with clinical histories such as "developmental delay" or other clear neurodevelopmental symptoms may have a higher incidence of such terminal zones, or they could last longer in such patients. Many of the patients shown in this text have such a clinical history. However, preliminary data taking into account terminal zones and SCWM has found that the extent of myelination in such regions is no less in patients with congenital-metabolic or congenital-structural developmental delay than in controls. These findings suggest that the persistence of such terminal zone regions in children should not raise alarm.

Terminal zones presumably represent regions of unmyelinated, or incompletely mature, WM. One hypothesis states that this appearance relates to the increasing concentration of myelin (itself consisting of T1-bright cholesterol and glycolipids) and decreasing concentration of water (decreasing the T2-bright signal) in maturing WM with increasing age. By this hypothesis, terminal zones persist in regions such as the *peritrigonal regions*, which are the last to myelinate. Another hypothesis describes that terminal zones may have a higher concentration of perivascular spaces than other regions of the cerebrum. The problem with that hypothesis is that, although peritrigonal regions have a higher number of perivascular spaces, there is as yet no evidence that these constitute the entirety of the T2-bright signal. Additionally, T2-bright perivascular spaces nearly always darken (suppress) on FLAIR, whereas terminal zones may have mildly bright signal on FLAIR. A third hypothesis is that there is a lower concentration of myelinated fibers in such terminal zones, particularly the peritrigonal regions, and potentially a higher amount of interstitial water, which may explain both why mildly bright signal may persist on FLAIR, as well as why terminal zones may normally persist into adulthood.

The most common location of terminal zones is generally within the PVWM that is immediately adjacent and lateral to or superior to the lateral ventricles, particularly within the *periatrial* or *peritrigonal regions*, the last regions of the cerebrum to "mature." (Note: the word "myelination" may not be the best choice here, given that the reason for their appearance is not entirely known.) Other locations are also commonly noted, however, including the *SIWM*, *ATWM*, *optic radiations*, and to a lesser degree, the *SCWM*. Another region that "matures" or "myelinates" much later, in this author's experience (although not as late as the peritrigonal WM) is the *basal forebrain*, which includes structures such as the diagonal gyrus, paraterminal gyrus, nucleus accumbens, substantia innominata, and nucleus basalis of Meynert. Notably, after age 24 months, the OFWM should appear mature, and this is not typically considered a terminal zone. The ages at which such regions of normal terminal zones entirely disappear is controversial, but they generally become less and less common at older ages, being fairly uncommon in 18- to 20-year-olds and rather rare after that. A general rule is that the SIWM and SCWM terminal zones should disappear by 36–48 months (3–4 years) of age, but periatrial and peritrigonal terminal zones can persist much longer, even into early adulthood.

Nevertheless, one should exercise caution when calling T2-bright and FLAIR-bright foci immediately adjacent to the lateral ventricles "normal terminal zones," as several disorders favor those locations. The most common one, and potentially the most difficult to distinguish from normal terminal zones, is *periventricular leukomalacia* (PVL). In PVL, there is loss of PVWM; in the mildest form, it may involve WM thinning that can be subtle and difficult to visualize, but at the more severe end of the spectrum there can be cystic leukomalacia, hemorrhage (best visualized on SWI, particularly if punctate), and even overlying cortical atrophy. Other abnormalities that have a predilection for PVWM or peritrigonal WM include *congenital-genetic inborn errors of metabolism* (CIEM); *tuberous sclerosis* (with T2-bright radial lines or "streaks" of migration); trauma-induced gliosis from *diffuse axonal injury*, usually visible on DWI, FLAIR, or SWI within the PVWM and gray-white matter interface; *hypoxic-ischemic encephalopathy/injury*, usually visible on DWI in the cortex in the acute phase and within the PVWM in the subacute phase; *acute toxic leukoencephalopathy*, typically having bright PVWM on DWI in the acute phase and potentially chronically on FLAIR; *multiple sclerosis* (rare in young children); *Lyme disease* (uncommon); and other rare hematologic disorders, such as *Langerhans cell histiocytosis* (*i.e.*, eosinophilic granulomatosis) (Figs. 23.137, 23.138, 23.139, 23.140, 23.141, 23.142,

23.143, 23.144, 23.145, 23.146, 23.147, 23.148, 23.149, 23.150, 23.151, 23.152, 23.153, 23.154, 23.155, 23.156, 23.157, 23.158, 23.159, 23.160, 23.161, 23.162, 23.163, 23.164, 23.165, 23.166, 23.167, 23.168, 23.169, 23.170, 23.171, 23.172, 23.173 and 23.174.

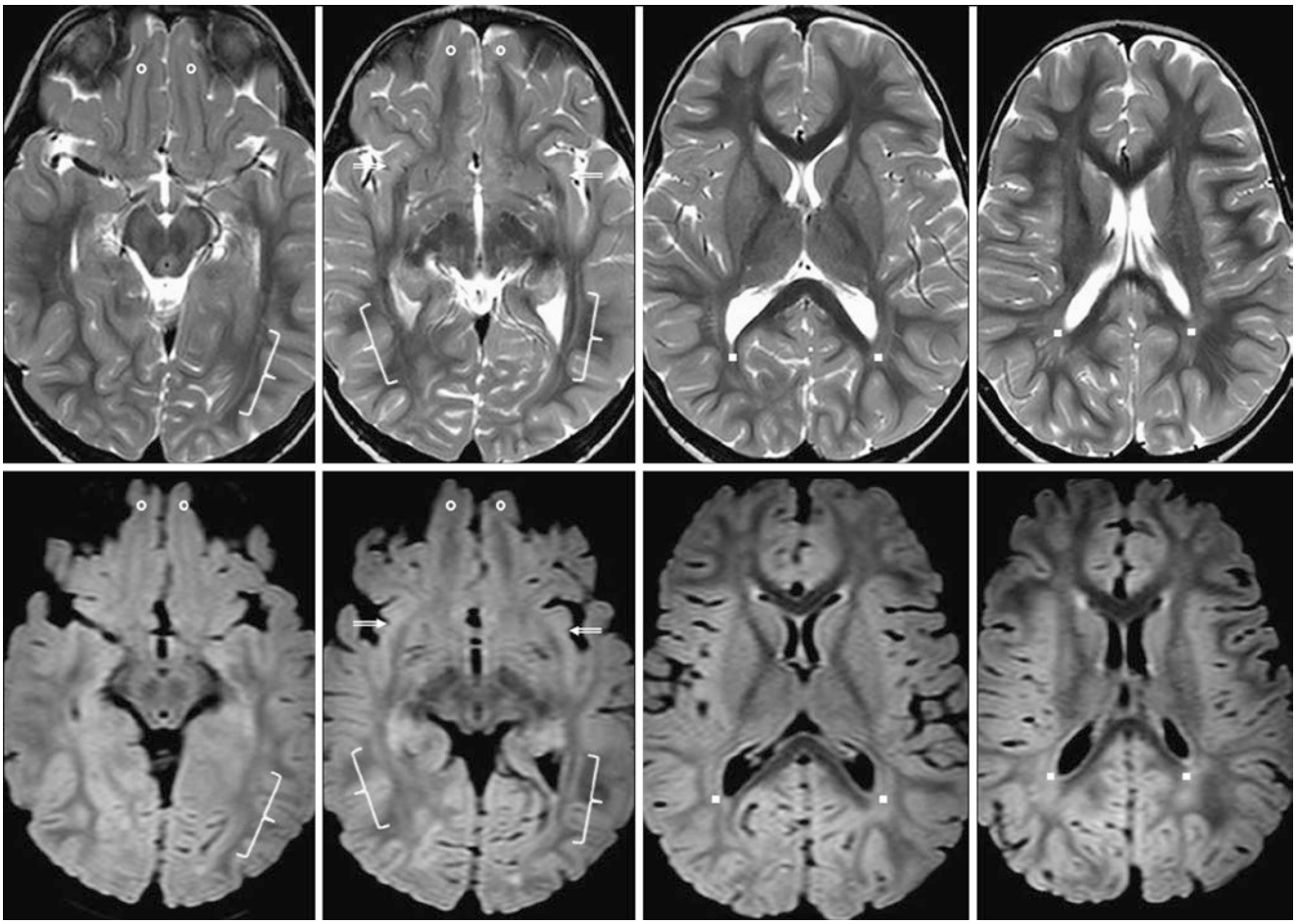

Fig. 23.137 A 2.1-year-old with a seizure had a normal 3T MRI. On SE T2WIs (*top row*), note hyperintense, residual SIWM (*beveled arrows*), whereas the ATWM and OFWM (*circles*) appear mature. Also, note bright signal from incomplete maturity of the optic radiations (*brackets*). On 3D axial FLAIR (*bottom row*), these regions do not appear quite as hyperintense. There is bright signal on both sequences in the most commonly noted and typical terminal zone location, the peritrigonal WM (PTWM) (*squares*)

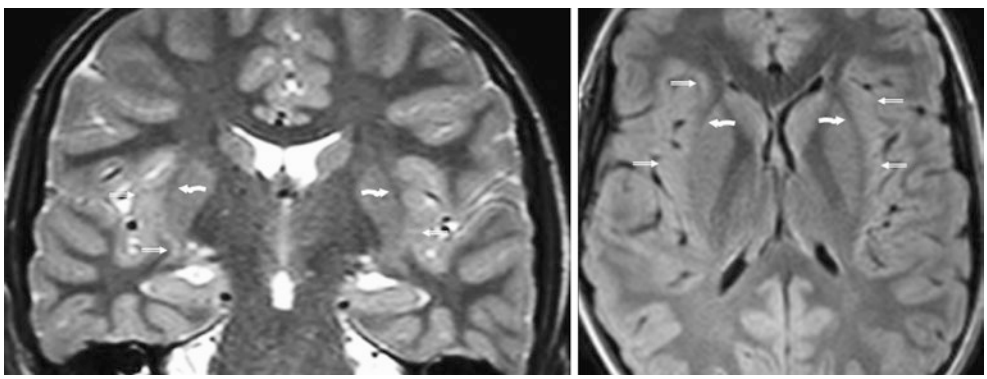

Fig. 23.138 A 2.5-year-old with a seizure had a normal 3T MRI. On a coronal SE T2WI (*left*), note the subtle, residual SIWM terminal zone (*beveled arrows*), where the external capsule (*curved arrows*) does not appear entirely continuous through the SIWM. On axial FLAIR (*right*), these terminal zones within the SIWM do not appear as hyperintense

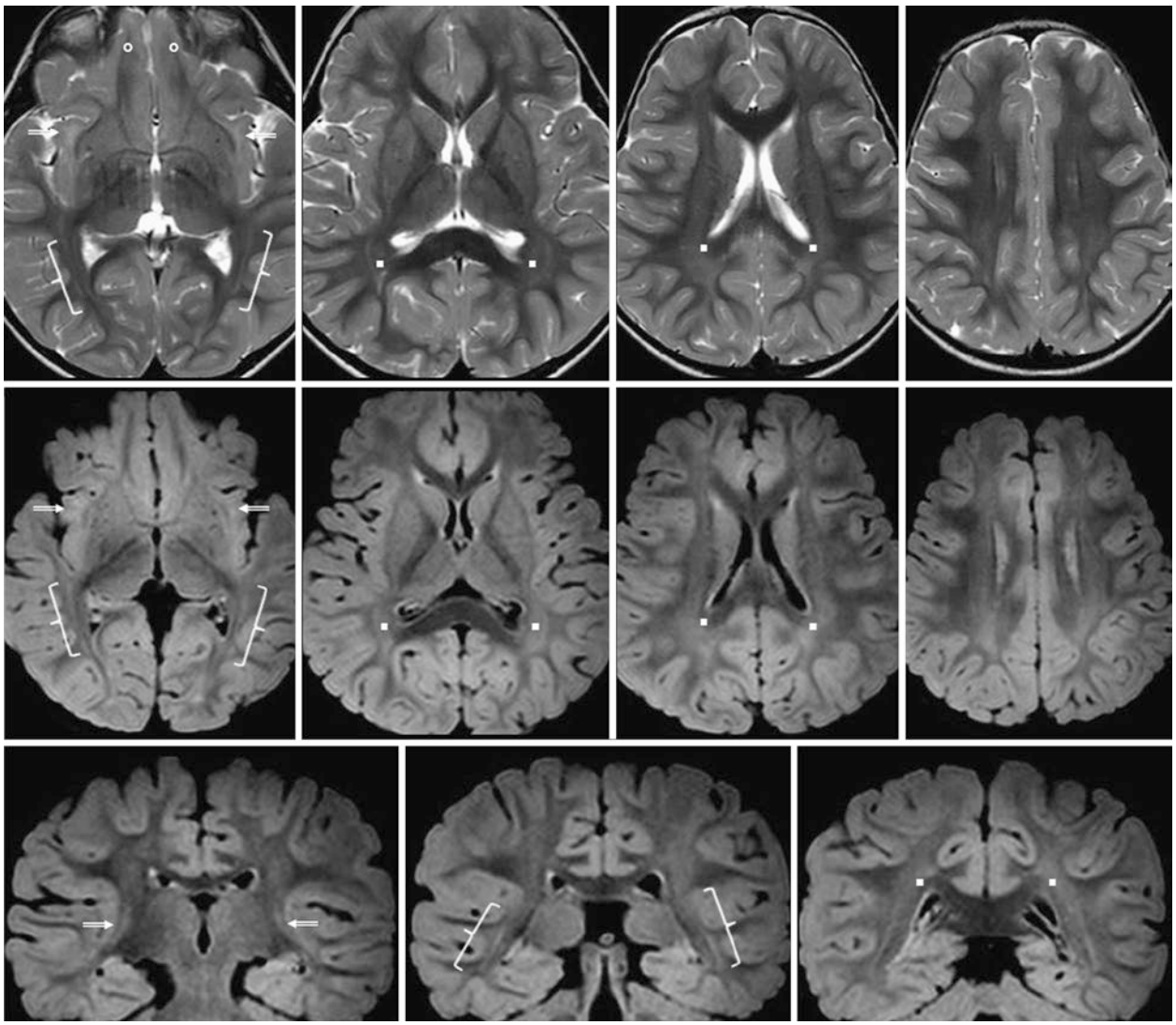

Fig. 23.139 A 2.25-year-old with seizures after trauma had a normal 3T MRI. *Top row*: On SE T2WIs, note residual terminal zones within the SIWM (*beveled arrows*) and optic radiations (*brackets*). The ATWM and OFWM (*circles*) appear mature. Note normal PTWM terminal zones (*squares*) as well. *Middle row*: On 3D axial FLAIR images, the terminal zones mentioned above are slightly bright, but do not appear as bright as on SE T2WIs. Hyperintense signal in the typical PTWM terminal zones extends up into the centrum semiovale (*right*). *Bottom row*: On 3D coronal FLAIR images, these terminal zone regions also appear slightly bright. The coronal images better demonstrate the continuity between terminal zones within the SIWM, optic radiations, and PTWM

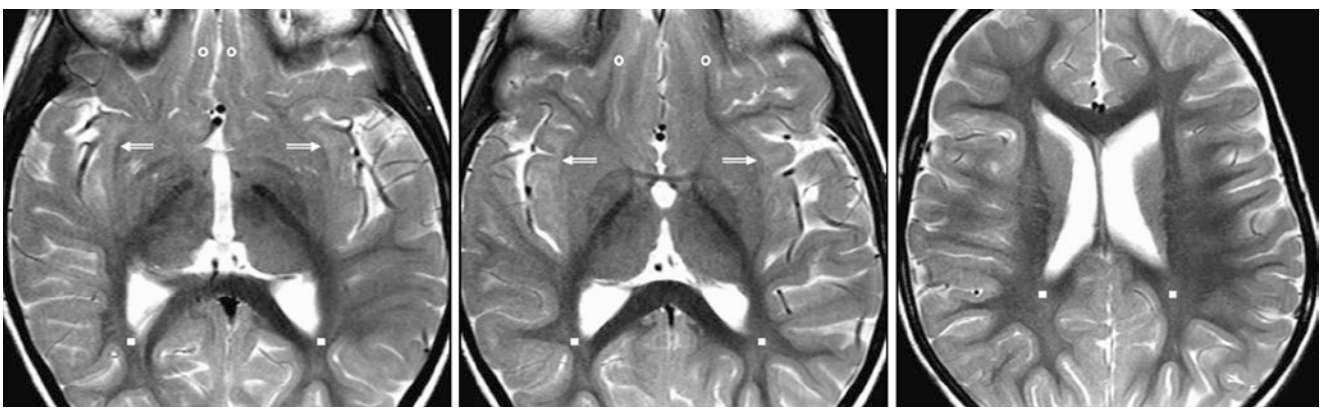

Fig. 23.140 A 2.75-year-old with cerebellar symptoms had a normal 3T MRI. On SE T2WIs, note hyperintense, residual terminal zones within the SIWM (*beveled arrows*), whereas the OFWM (*circles*) appears almost completely mature. Also, note typical bright signal from immaturity of the PTWM (*squares*). This child subsequently developed normally

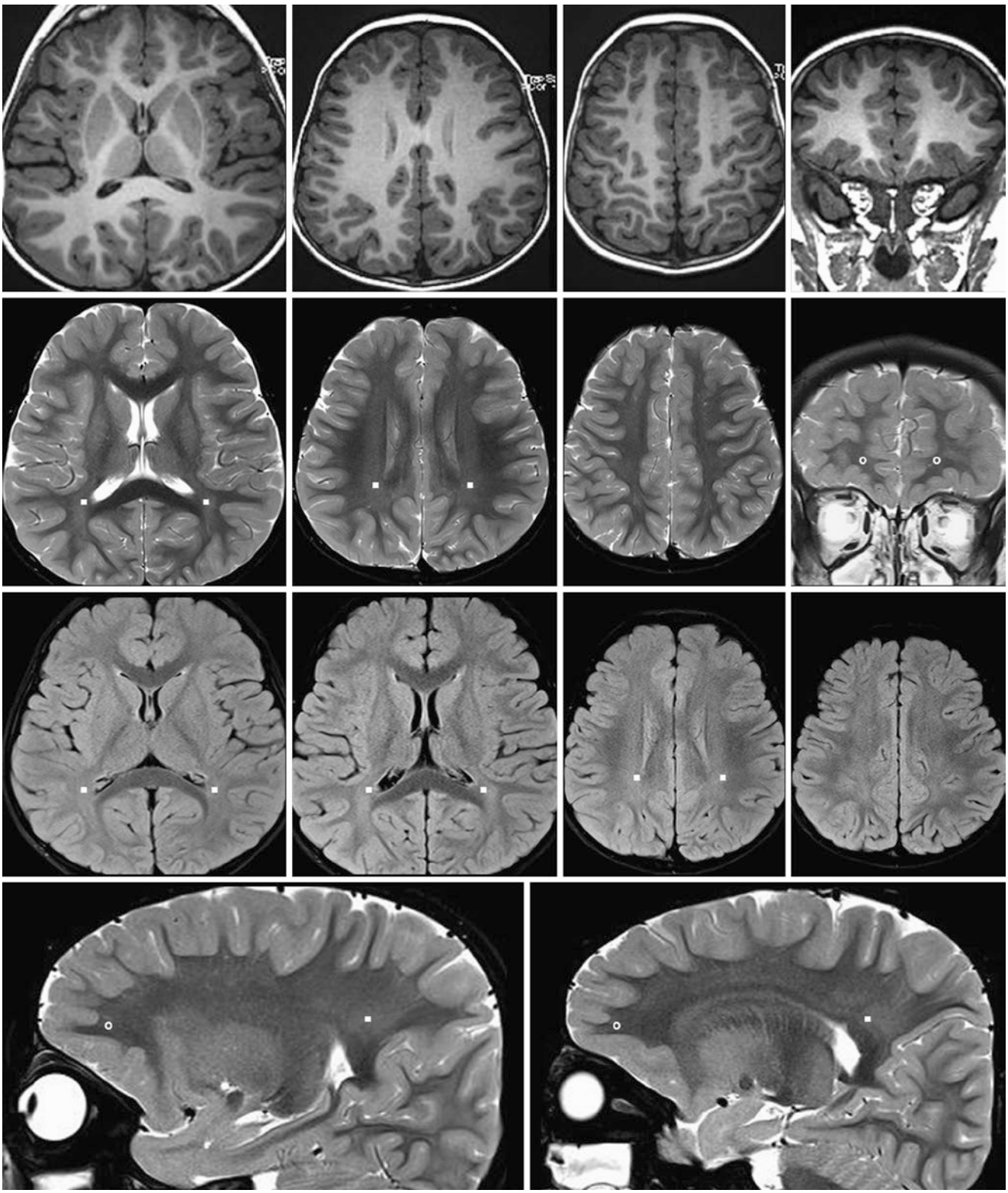

Fig. 23.141 A 2.75-year-old with "skin spots" had a normal 3T MRI. The child's neurodevelopment was normal. *Top row*: On axial GE T1WIs (*left three images*), the myelination pattern appears normal, as in an adult. The residual terminal zones are hardly visible. A coronal GE T1WI anteriorly (*right*) shows normal OFWM. *Second row*: On axial SE T2WIs (*left three images*), the myelination pattern appears normal, as in an adult, with the exception of mild, residual PTWM terminal zones (*squares*). A coronal SE T2WI anteriorly (*right*) shows normal OFWM (*circles*). *Third row*: On axial FLAIR images, note the mild, residual PTWM terminal zones. In this patient, the extent of these terminal zones into the corona radiata and centrum semiovale is better visualized on FLAIR images than in T2WIs. *Bottom row*: On sagittal SE T2WIs of the left (*left*) and right (*right*) sides, note the mild, residual PTWM terminal zones. Also, note the mature OFWM anteriorly; it typically matures before the ATWM, SIWM, and PTWM terminal zones

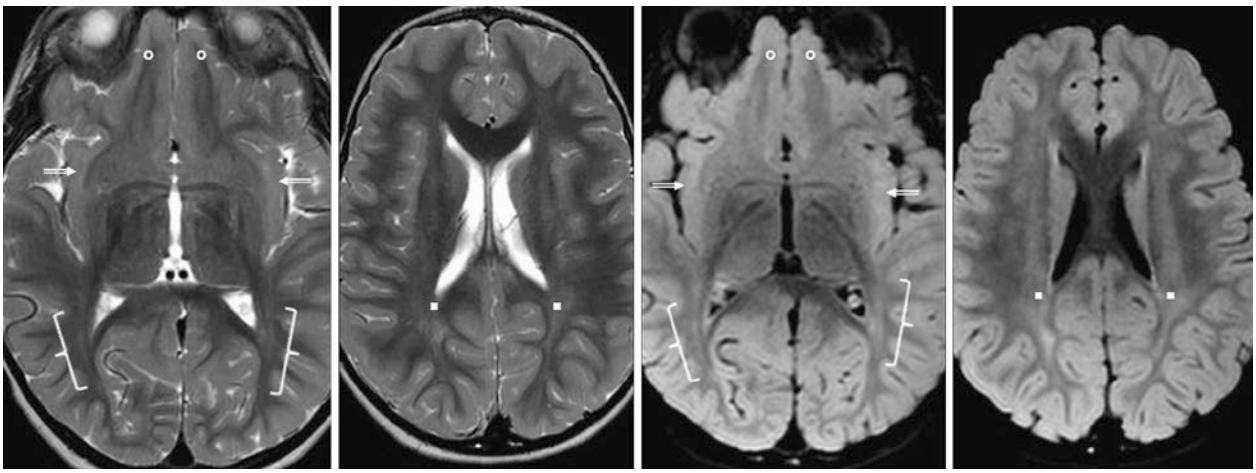

Fig. 23.142 A 3.0-year-old with a fever of unknown origin had a 3T MRI with SE T2WIs (*left images*) and 3D FLAIR (*right images*). Note the mild, residual PTWM terminal zones (*squares*), as well as the optic radiations (*brackets*) and SIWM (*beveled arrows*). The OFWM (*circles*) appears mature

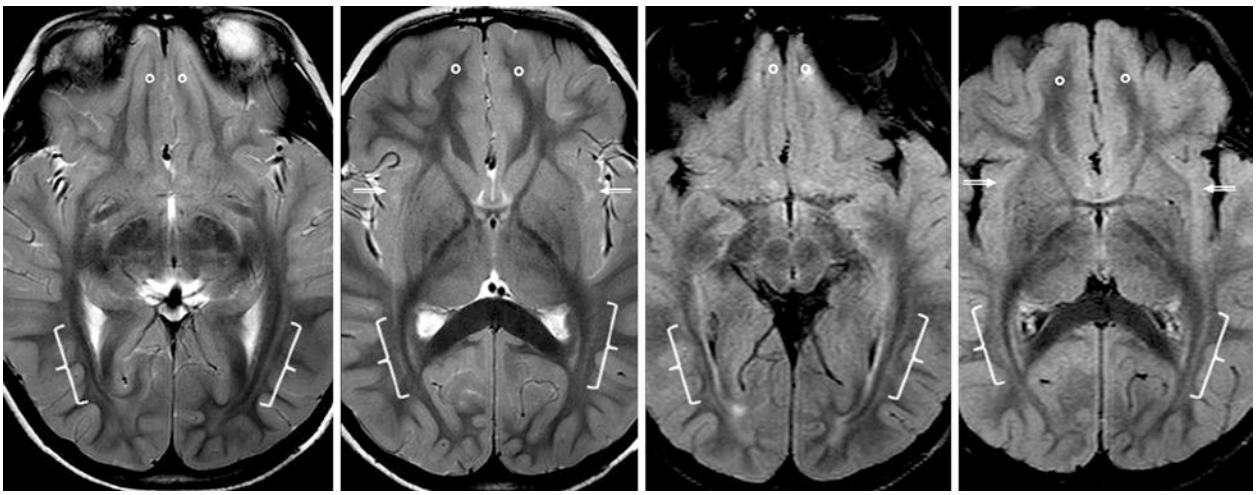

Fig. 23.143 A 3.0-year-old with seizures had a 3T MRI with SE T2WIs (*left images*) and 2D FLAIR images (*right images*). There are mild, residual terminal zones within the PTWM, optic radiations (*brackets*), and SIWM (*beveled arrows*). The OFWM (*circles*) and the rest of the PVWM are mature

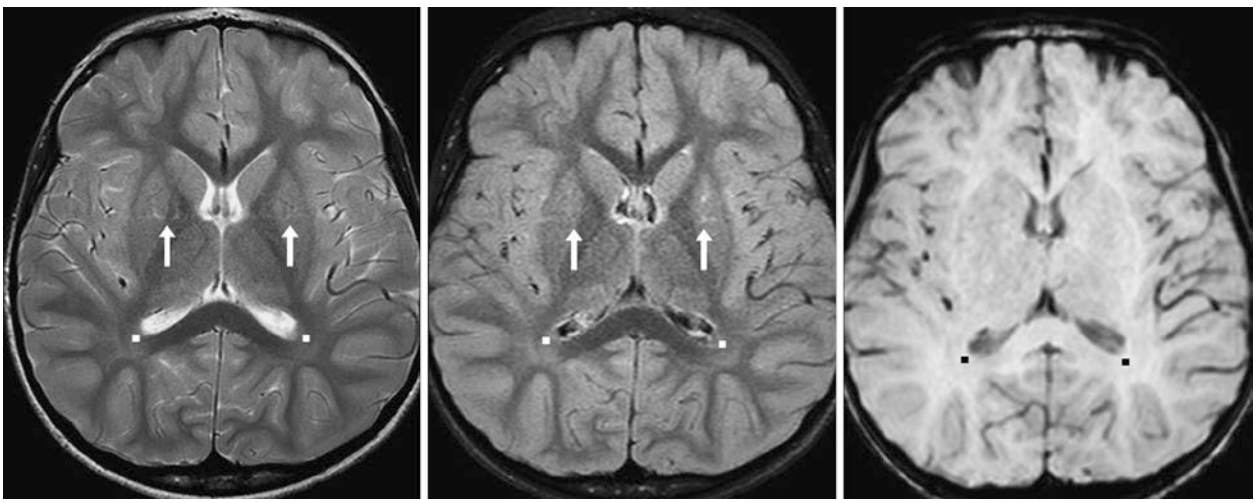

Fig. 23.144 A 3.0-year-old with weakness had a 3T MRI with SE T2WI (*left*), FLAIR (*middle*), and SWI (*right*). There are mild, residual PTWM terminal zones (*squares*), but the rest of the deep WM and PVWM are mature. Note CSF pulsation artifact (*arrows*)

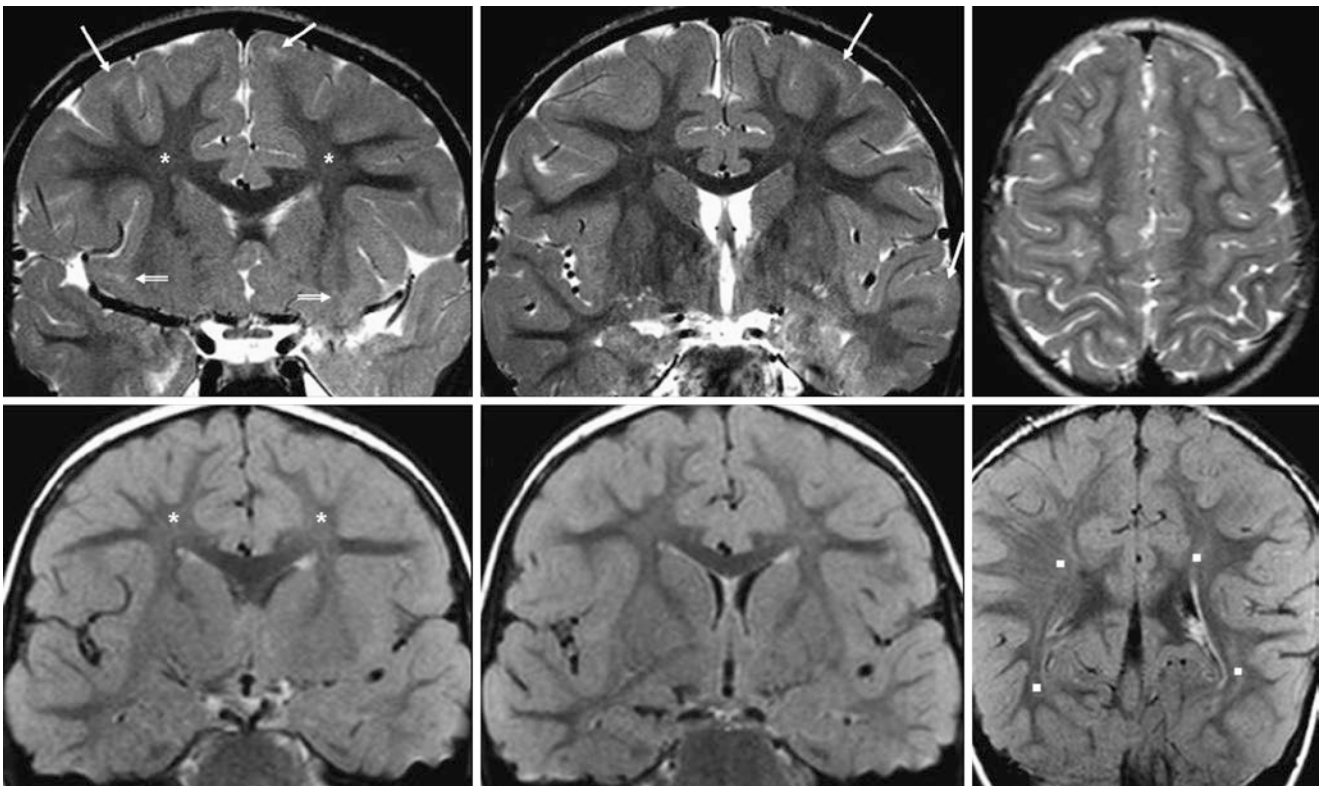

Fig. 23.145 A 3.5-year-old with seizures. *Top row*: 3T MRI coronal SE T2WI (*left* and *middle*) depicts subtle, patchy regions of incomplete maturation of SCWM (*thin arrows*), not visible on axial SE T2WI (*right*). *Bottom row*: Such SCWM terminal zones are also not visible on 2D coronal FLAIR; note subtle, terminal zones of the PTWM (*squares*), SIWM (*beveled arrows*), and frontal PVWM (*asterisks*)

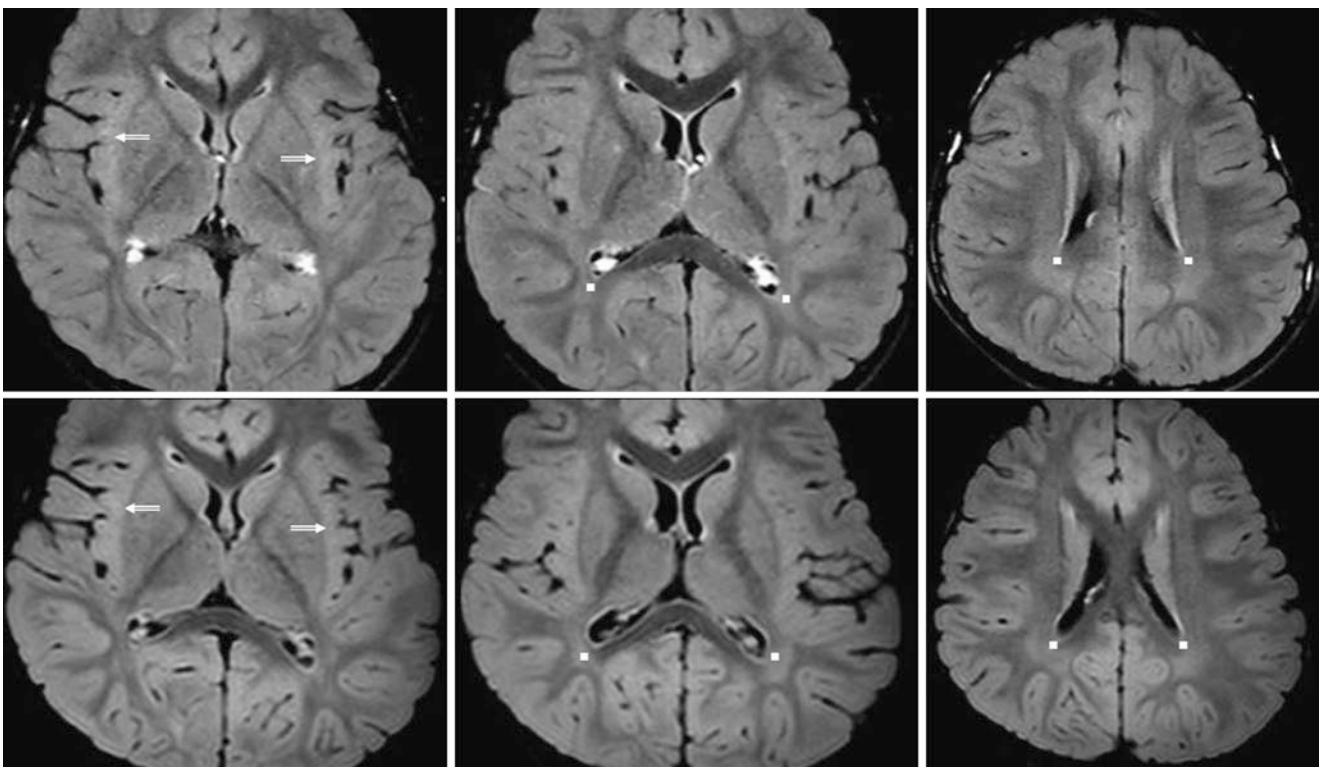

Fig. 23.146 A 3.5-year-old with seizures, illustrating terminal zones both on 2D FLAIR and 3D FLAIR at 3T. *Top row*: Axial 2D FLAIR images (*top row*) show residual terminal zones within the PTWM (*squares*) and SIWM (*beveled arrows*). *Bottom row*: CSF suppression is better on axial reformats of 3D FLAIR images, and lacks pulsation artifacts, but the SIWM terminal zones are less visible

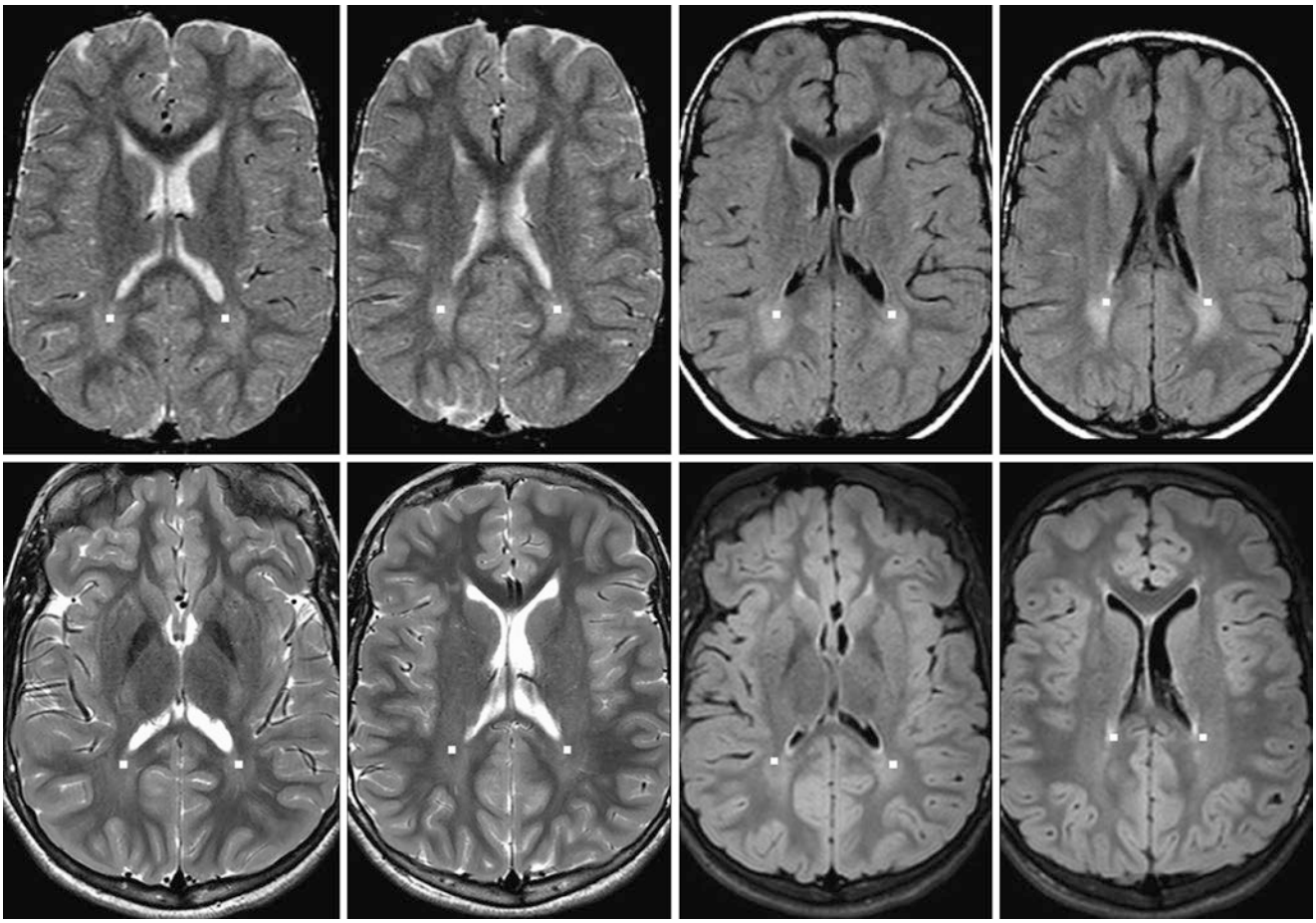

Fig. 23.147 A 4.0-year-old with autism. *Top row*: 1.5T SE T2WI (*left images*) and FLAIR (*right images*) showed patchy terminal zone regions of incomplete PTWM maturation (*squares*). *Bottom row*: A 3T MRI was repeated 10 years later at 14 years of age. It showed improved PTWM terminal zones (*squares*) on SE T2WI (*left images*) and FLAIR (*right images*)

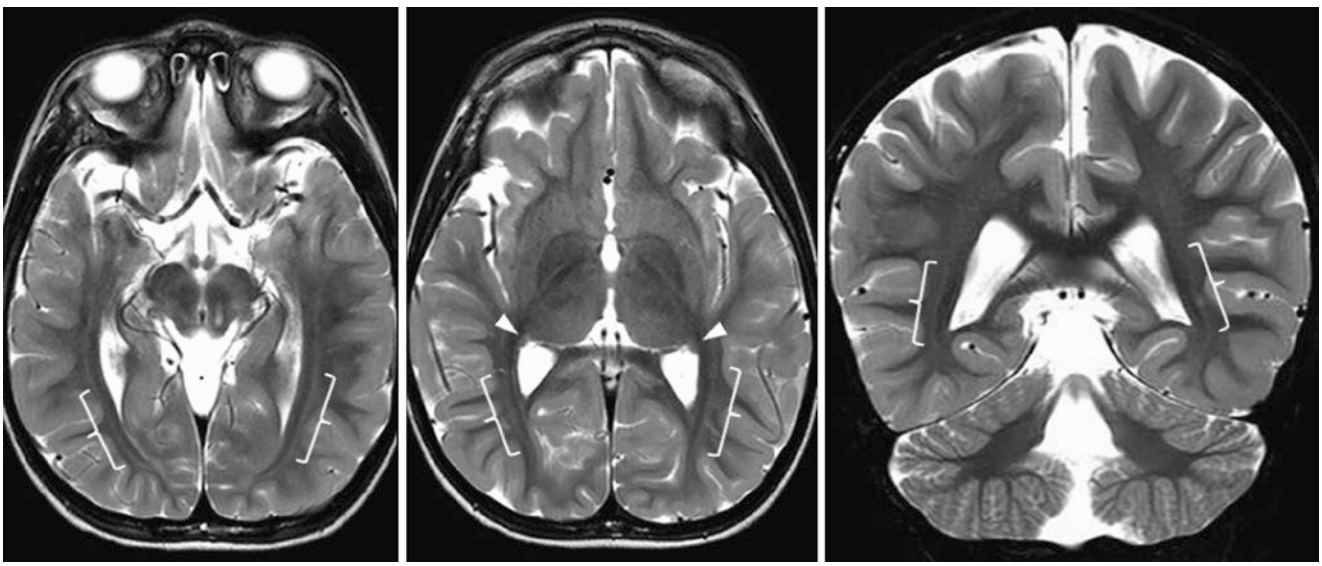

Fig. 23.148 A 4.0-year-old with altered mentation. A 3T MRI with SE T2WI in axial (*left* and *middle*) and coronal (*right*) planes demonstrated terminal zones in the optic radiations (*brackets*), being normal for age. Note normal caudate tails (*arrowheads*)

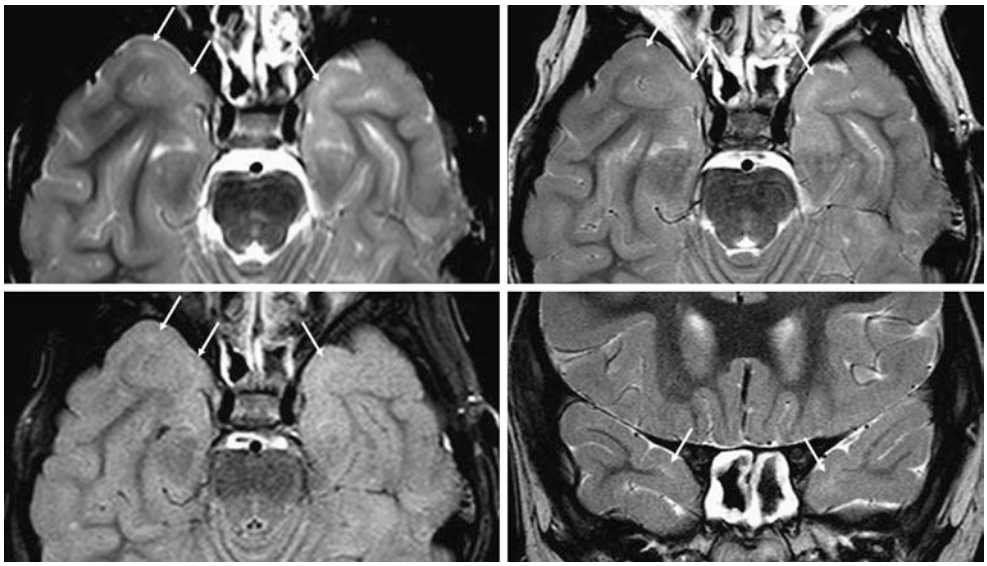

Fig. 23.149 A 4.0-year-old with visual symptoms, which soon resolved. A normal 3T MRI with axial SE T2WI with thickness of 5 mm (*top left*) and 3 mm (*top right*), axial 2D FLAIR (*bottom left*), and coronal SE T2WI (*bottom right*). Note subtle terminal zones that are manifested as patchy anterior temporal SCWM (*thin arrows*) on T2WI, being relatively invisible on FLAIR

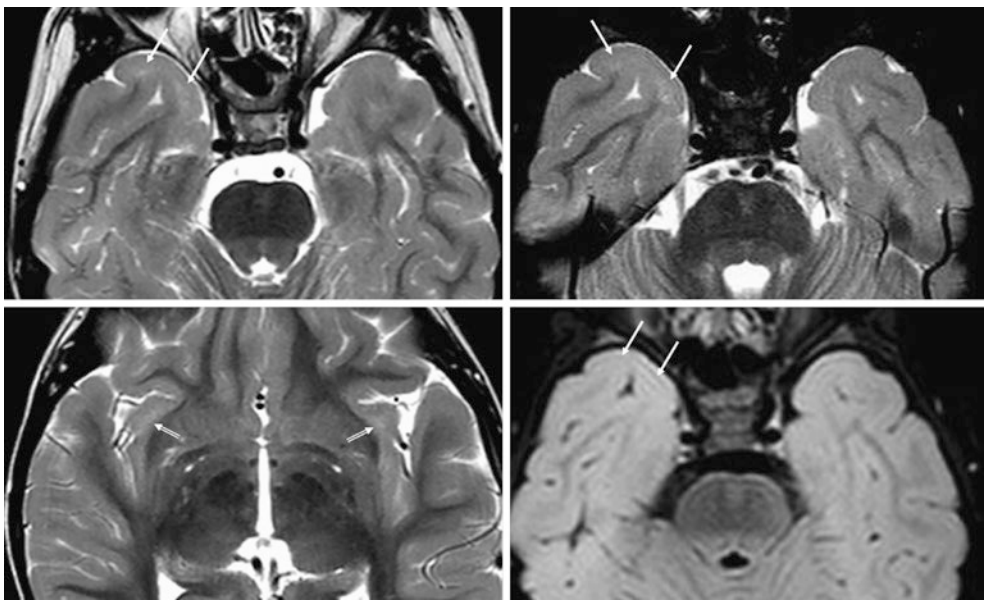

Fig. 23.150 A 4.25-year-old with a concussion. Normal 3T axial SE T2WI with 5 mm (*top left*) and 3 mm thickness (*top right* and *bottom left*), as well as 3D FLAIR (*bottom right*). Note subtle terminal zones manifested as patchy anterior right temporal SCWM (*thin arrows*) on T2WI, which are hardly visible on FLAIR. Also, note bilateral SIWM terminal zones (*beveled arrows*, *bottom left*)

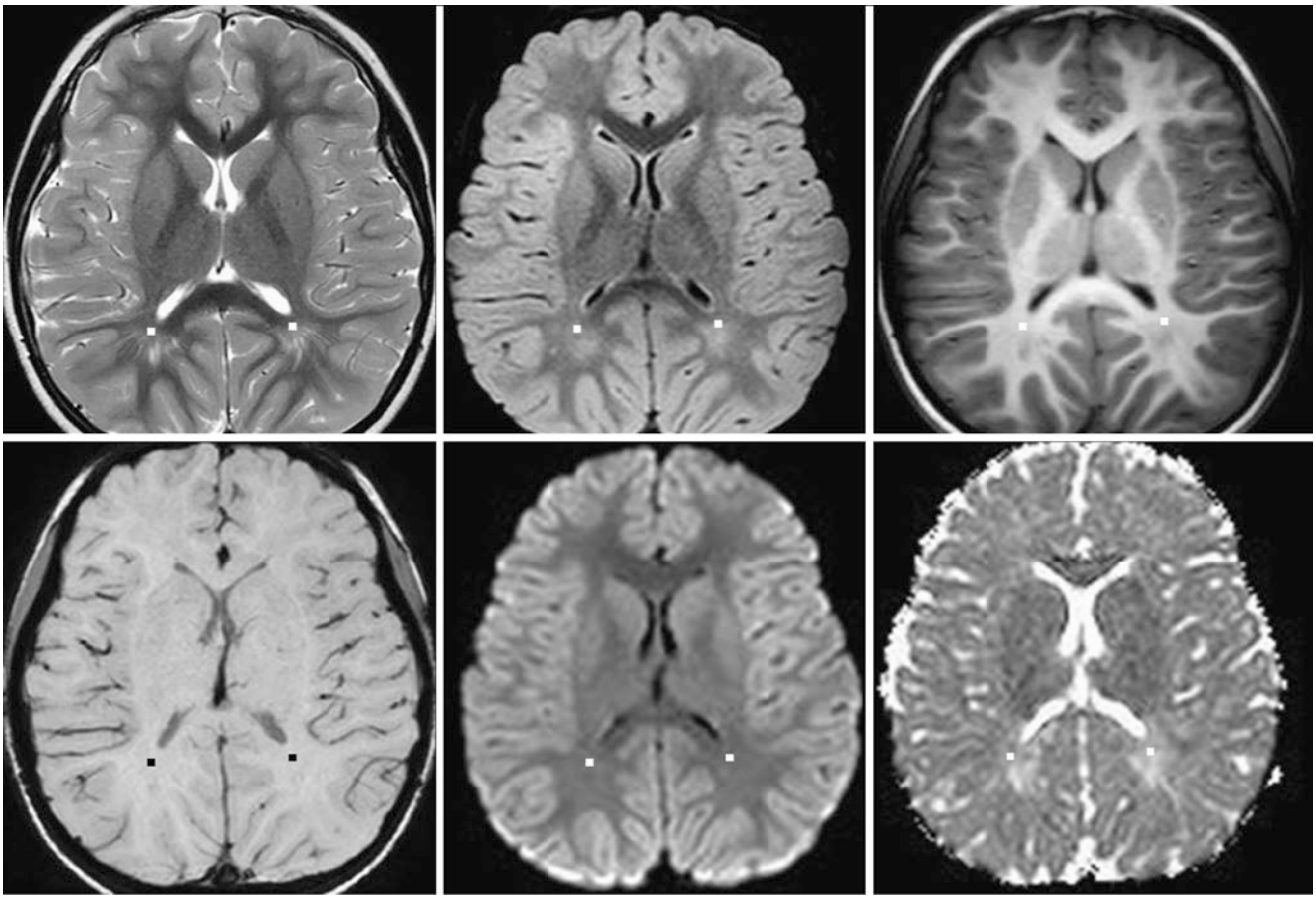

Fig. 23.151 A 4.25-year-old with gait symptoms, with normal 3T SE T2WI (*top left*), 3D FLAIR (*top middle*), GE T1WI (*top right*), SWI (*bottom left*), DWI (*bottom middle*), and ADC map (*bottom right*). Note terminal zones bilaterally within the PTWM (*squares*) on T2WI, FLAIR, T1WI, and the ADC map, without corresponding abnormality on SWI or DWI

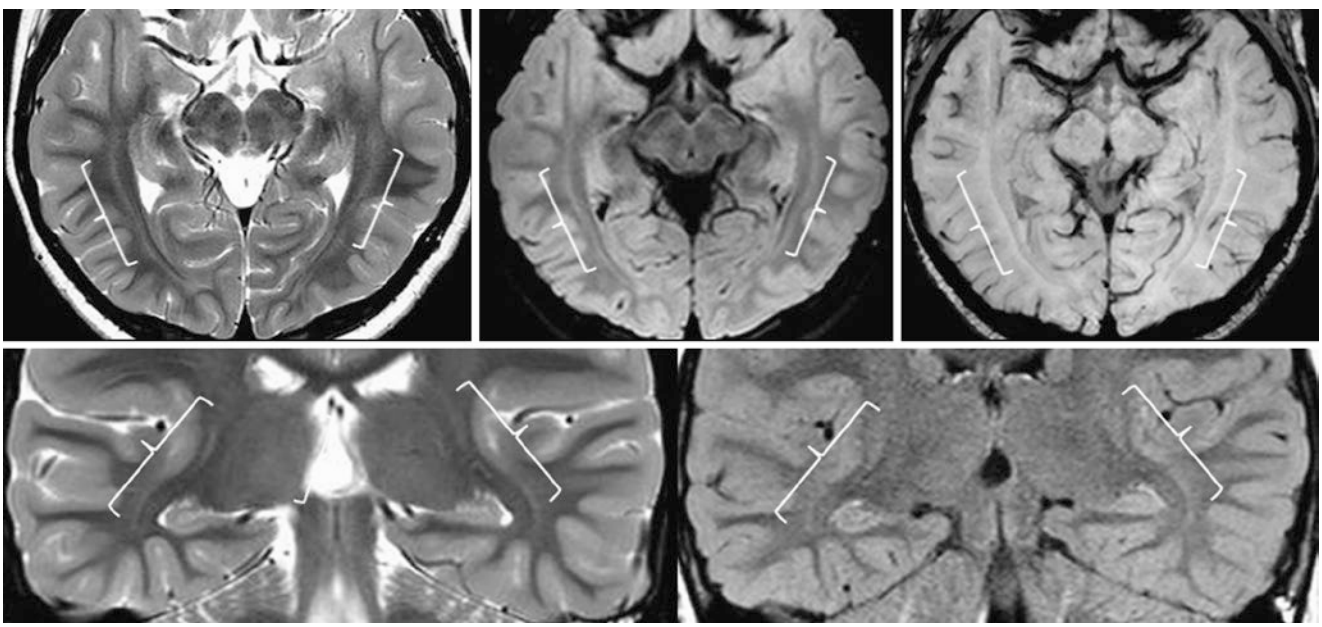

Fig. 23.152 A 4.5-year-old with a solitary seizure. 3T axial SE T2WI (*top left*), 3D FLAIR (*top middle*), and SWI (*top right*), coronal T2WI (*bottom left*), and FLAIR (*bottom right*) were all normal. Note the contiguity and continuity of the terminal zones bilaterally within the optic radiations (*brackets*) on T2WI and FLAIR, without a corresponding abnormality on SWI

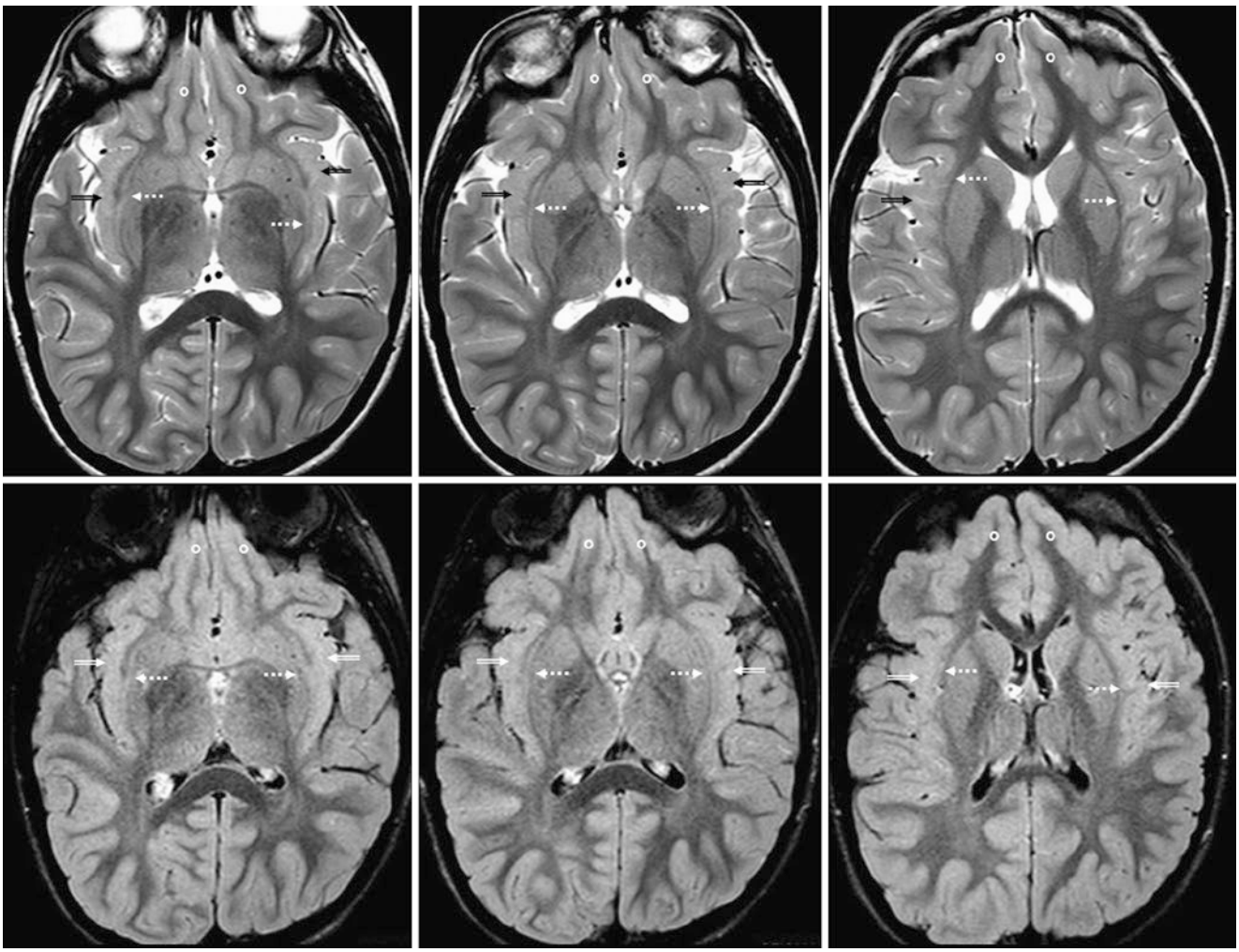

Fig. 23.153 A 5.25-year-old with headaches. 3T MRI axial SE T2WI (*top row*) and 3D FLAIR (*bottom row*) were normal. Note SIWM terminal zones (*beveled arrows*) bilaterally, being only mildly hyperintense on both sequences. Meanwhile, the subjacent claustrum is visible (*dotted arrows*). This shows that SIWM terminal zones can overlap with the normal claustrum and in some cases may be "volume averaged" with the developing claustrum. Also, note mature OFWM (*circles*) anteriorly

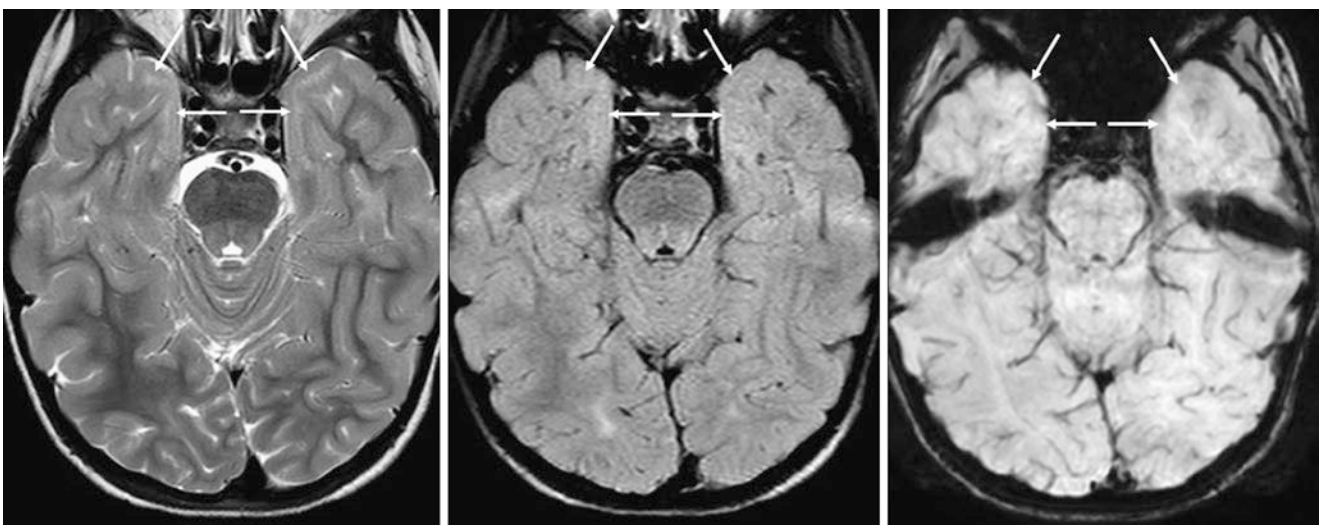

Fig. 23.154 A 5.75-year-old with migraines. 3T SE T2WI (*left*), 2D FLAIR (*middle*), and SWI (*right*) were normal. Note terminal zones within the anterior temporal SCWM bilaterally (*thin arrows*), being slightly hyperintense on T2WI and not visualized on FLAIR. On SWI (*right*), there is no hemorrhage, so the condition is likely not related to remote trauma or other insult

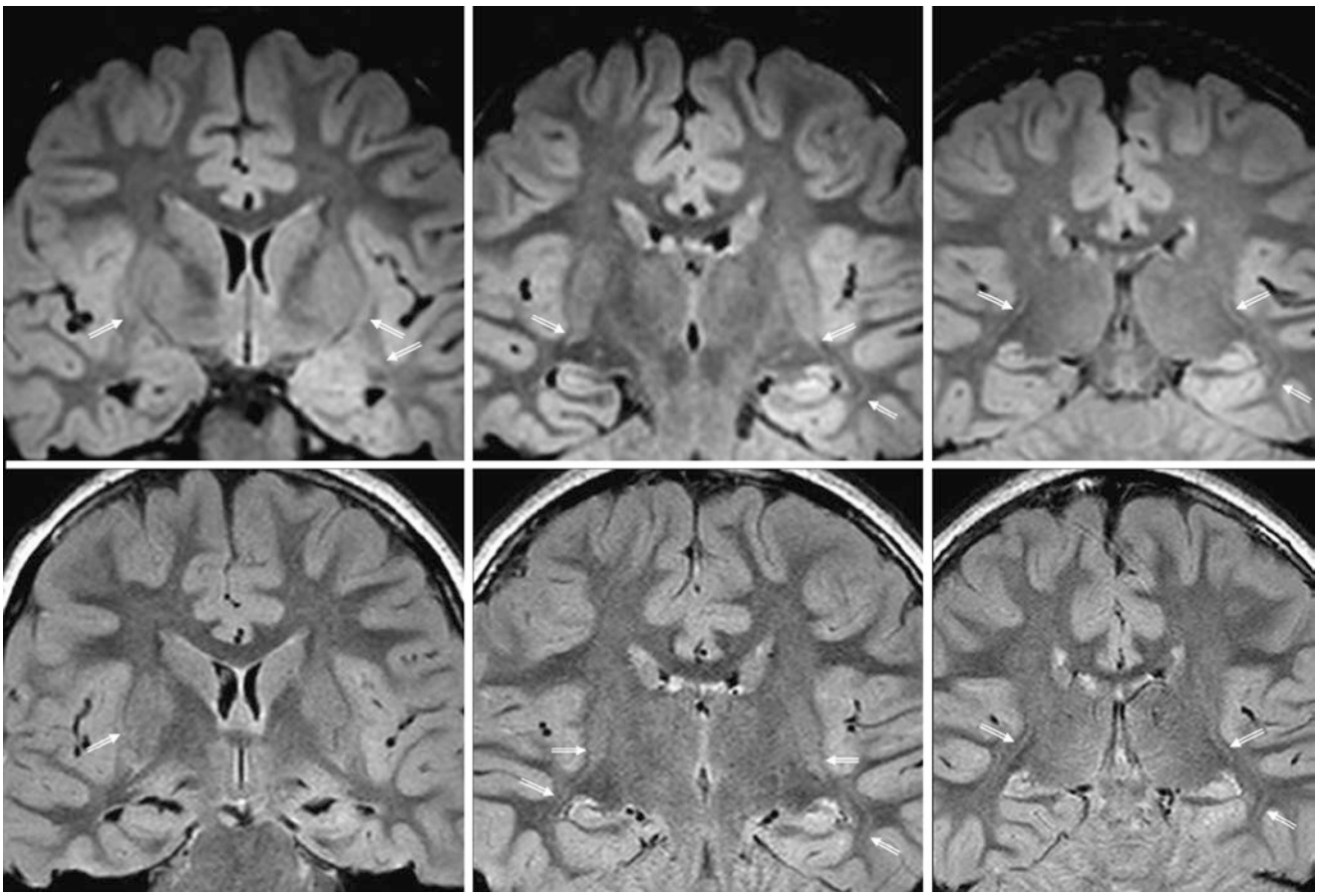

Fig. 23.155 A 6.0-year-old with nausea. Normal 3T MRI coronal FLAIR 3D (*top row*) and 2D (*bottom row*) acquisitions illustrate how the terminal zones may be contiguous bilaterally between the SIWM, optic radiations, and PTWM, although they are quite thin in this patient and are more prominent on the left. (The *beveled arrows* define the extent of the terminal zones.)

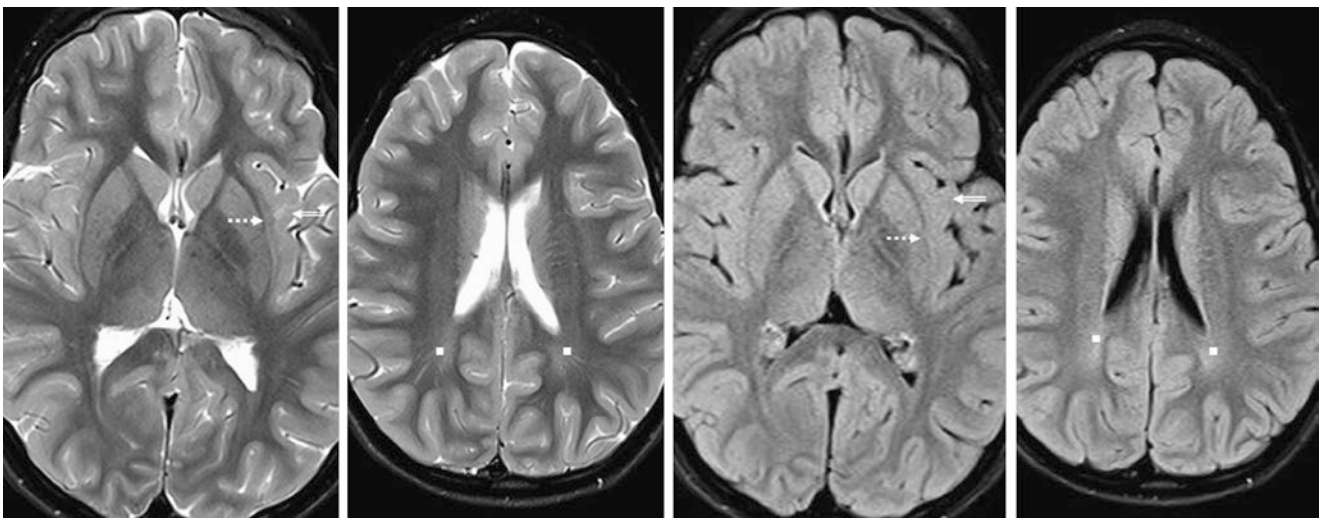

Fig. 23.156 A 6.0-year-old with altered mentation had a normal 3T MRI with SE T2WIs (*left images*) and 2D FLAIR (*right images*). On T2WI, note a focal terminal zone within the left SIWM (*beveled arrow*) that nearly overlaps with the claustrum (*dotted arrow*), although the claustrum is deep to the extreme capsule. Thus, SIWM signal can be "volume averaged" with claustrum to exaggerate normal, mildly bright terminal zones in that region. Also, note the PTWM terminal zones (*squares*)

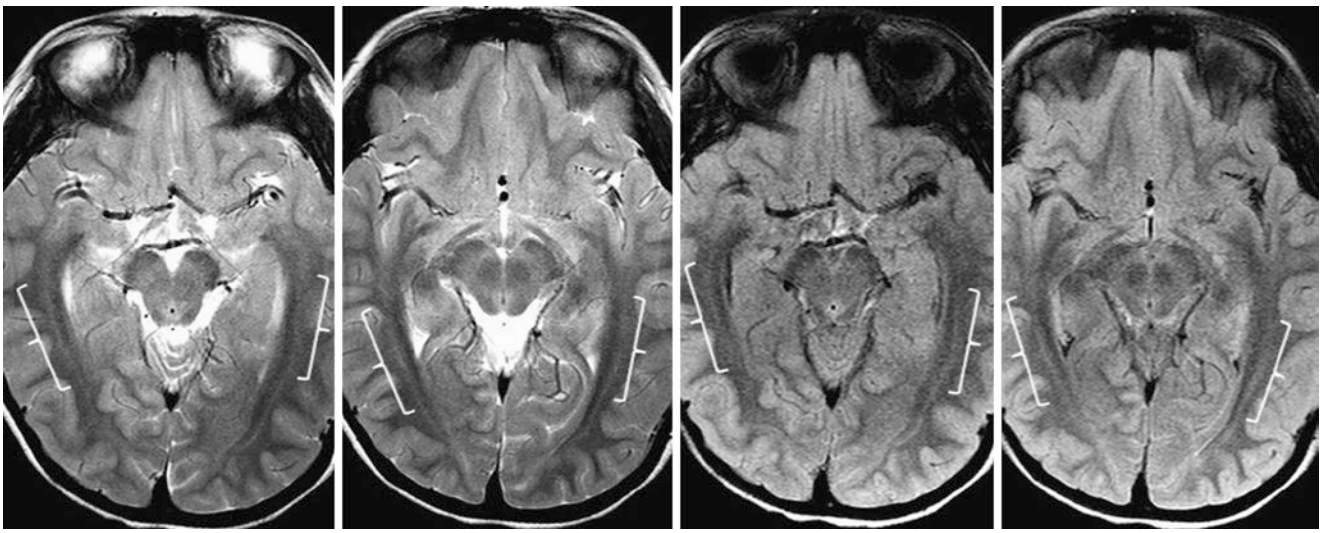

Fig. 23.157 A 6.5-year-old with developmental delay had a normal 3T MRI with SE T2WIs (*left images*) and 2D FLAIR (*right images*). Note terminal zones within the optic radiations (*brackets*), which are contiguous with quite subtle PTWM terminal zones (*not shown*). Terminal zones in this location can persist into late adolescence, the teenage years, and even into early adulthood

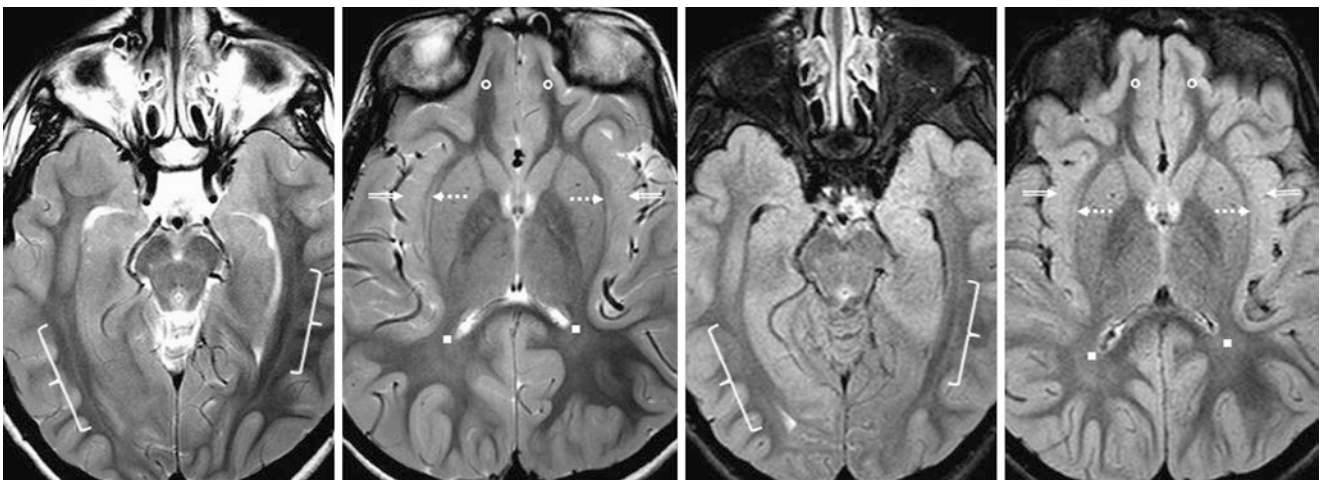

Fig. 23.158 A 6.75-year-old with seizures had a normal 3T MRI with SE T2WIs (*left images*) and 2D FLAIR (*right images*). Note terminal zones within the optic radiations (*brackets*), which are contiguous with subtle terminal zones within the PTWM (*squares*). Terminal zones in this location can persist even into early adult life. Also, note that the claustra (*dotted arrows*) are quite close to the SIWM (*beveled arrows*), although the SIWM appears only minimally bright in this patient

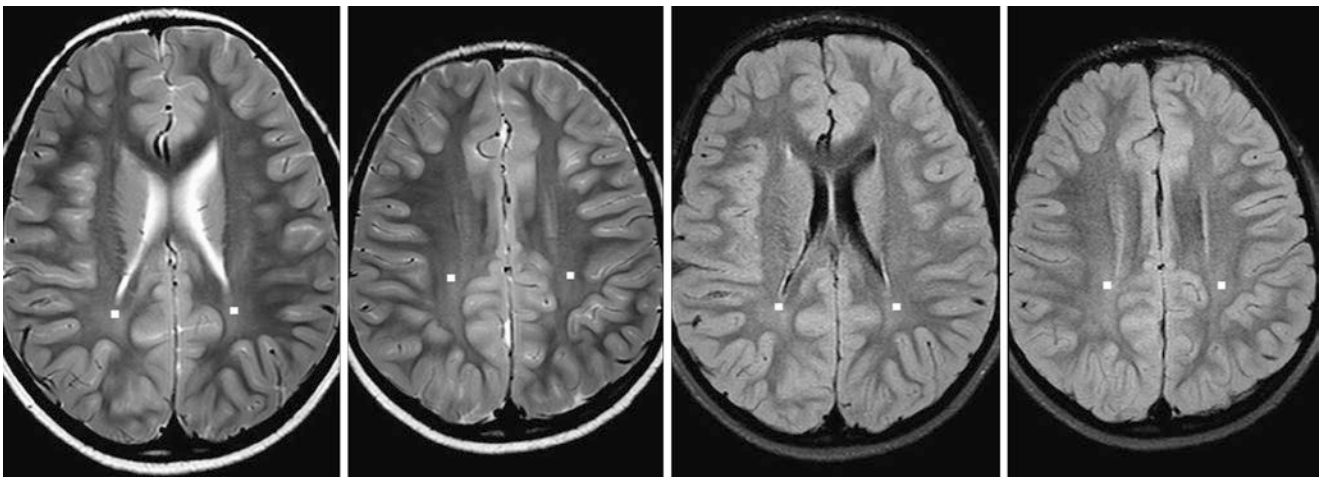

Fig. 23.159 A 7.0-year-old with gait abnormalities had a normal 3T MRI with SE T2WIs (*left images*) and 2D FLAIR (*right images*). Note residual terminal zones within the PTWM (*squares*) bilaterally; the remainder of the PVWM and deep WM are mature. Terminal zones in this location can persist into early adulthood

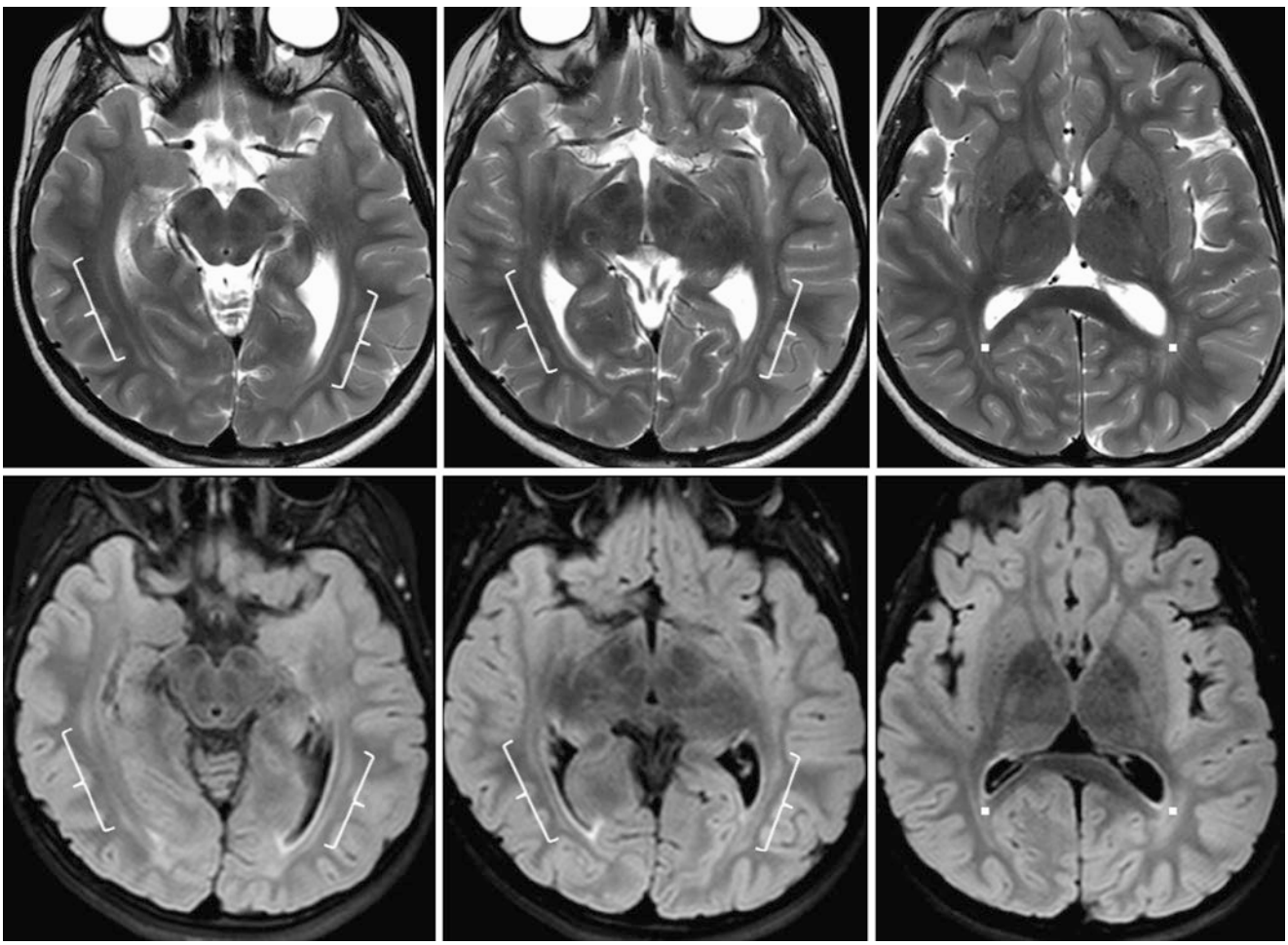

Fig. 23.160 A 9-year-old with hyperactivity disorder had a normal 3T MRI. Axial SE T2WIs (*top row*) and 3D FLAIR images (*bottom row*) illustrate terminal zones within the optic radiations (*brackets*) and PTWM (*squares*), which appear to be contiguous with each other

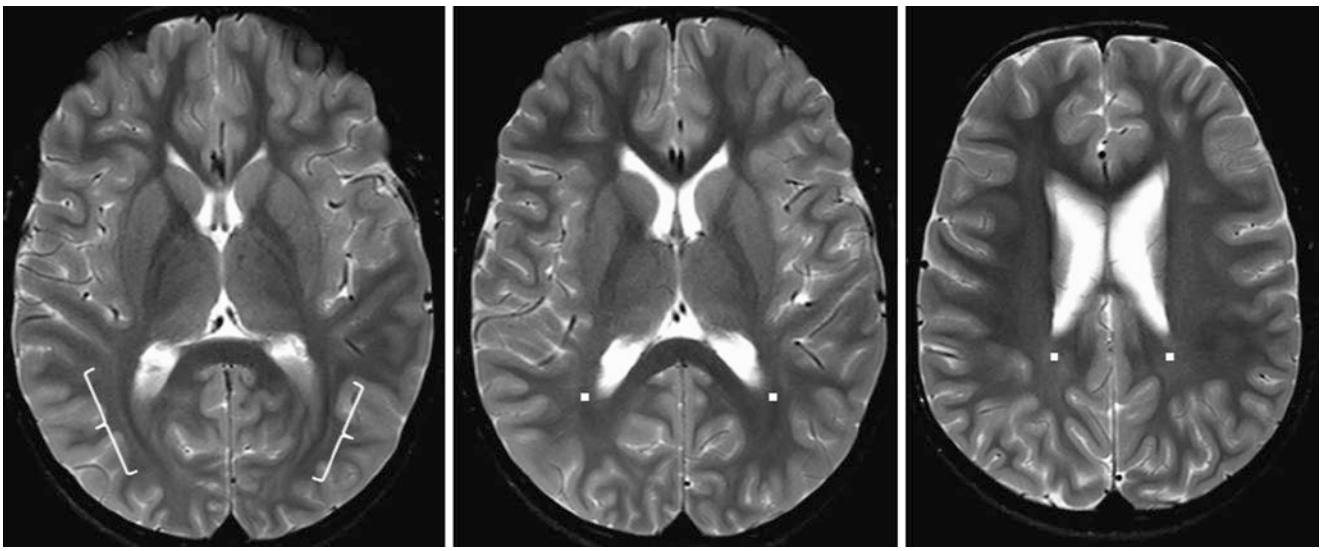

Fig. 23.161 A 9.5-year-old with a developmental delay had a normal 3T MRI. Axial SE T2WIs demonstrate faint, residual terminal zones within the optic radiations (*brackets*) and PTWM (*squares*), which appear to be contiguous with each other

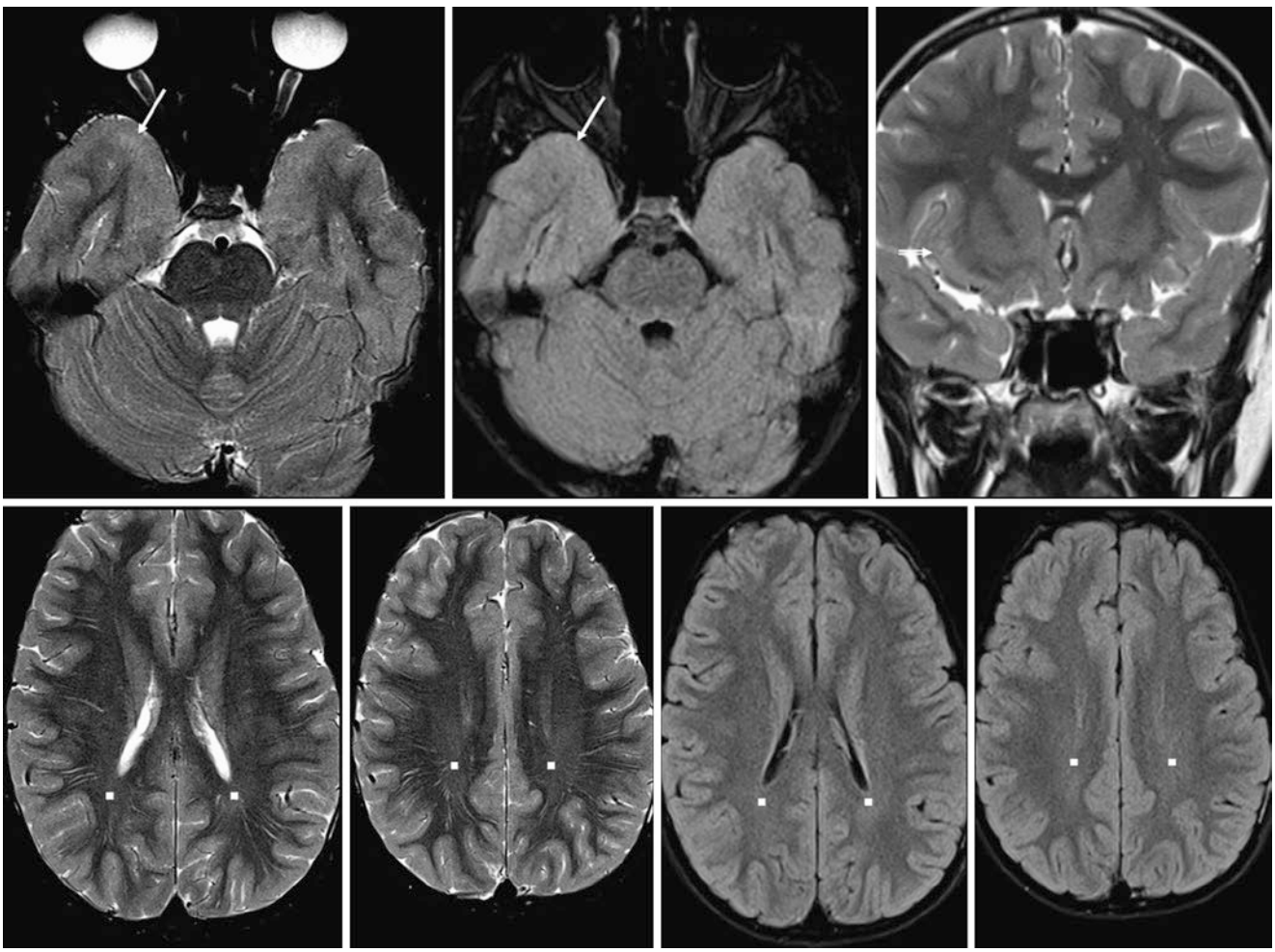

Fig. 23.162 A 10-year-old with chronic headaches had a normal 1.5T MRI. A focal terminal zone (*thin arrows*) is shown within the right ATWM on axial SE T2WIs (*top left*), but is not visible on 2D FLAIR (*top middle*); on coronal T2WI (*top right*), a tiny right SIWM terminal zone is also noted. Axial SE T2WIs (*bottom left*) and FLAIR images (*bottom right*) depict minimal residual PTWM terminal zones (*squares*), as well as many slightly enlarged perivascular spaces in the periatrial WM

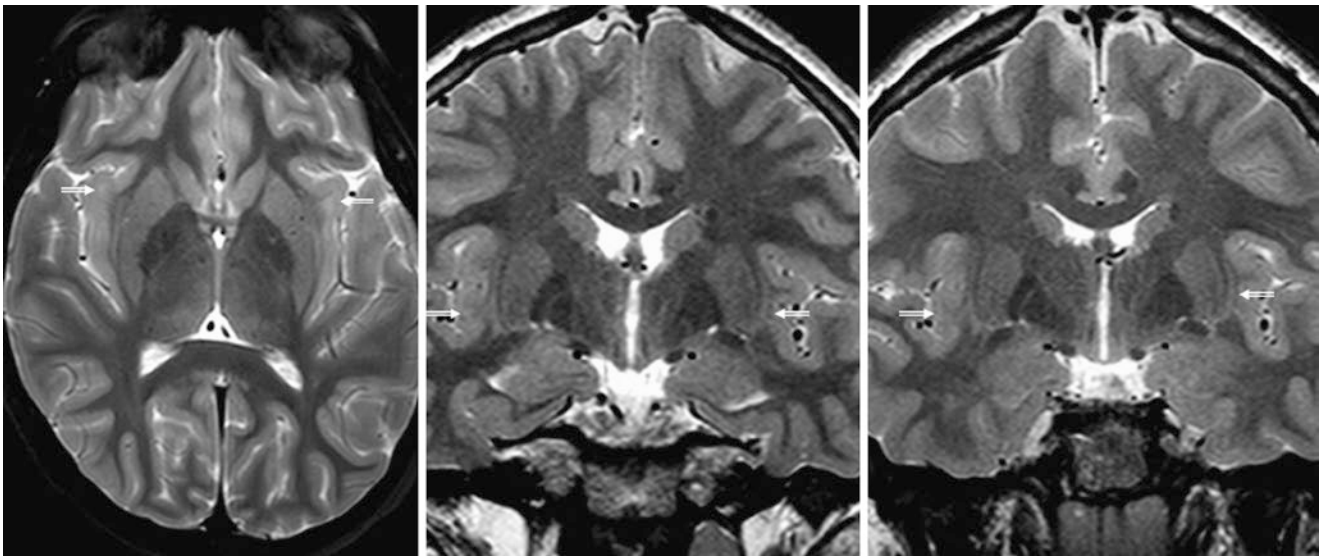

Fig. 23.163 An 11-year-old with headaches had a normal 3T MRI that showed bilateral subtle terminal zones within the SIWM (*beveled arrows*) on axial (*left*) and coronal (*middle*) SE T2WIs. On a follow-up coronal SE T2WI MRI 4 years later (*right*), there is decreasing SIWM hyperintensity

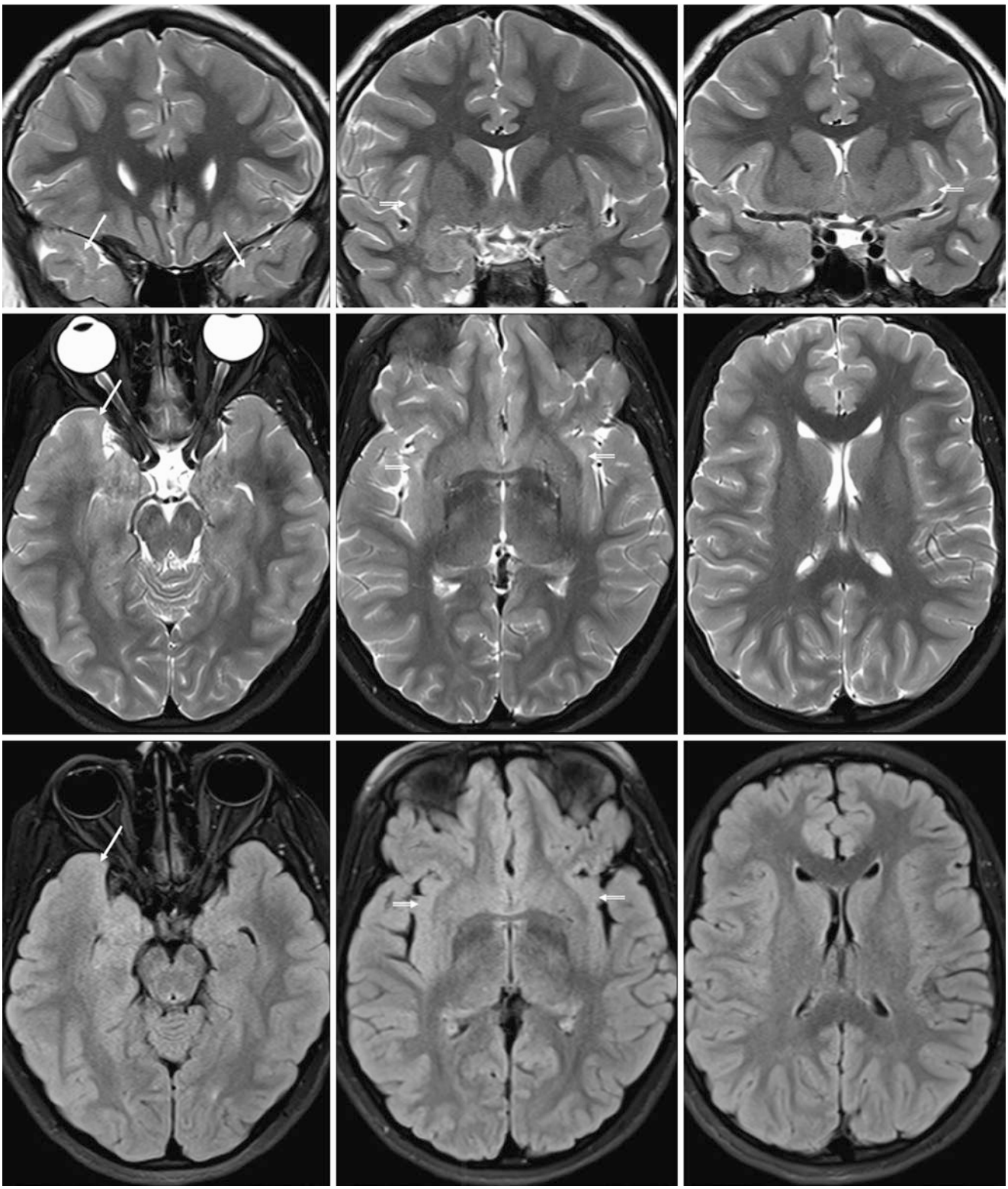

Fig. 23.164 An 11-year-old with a sleep disorder had a normal 3T MRI. *Top row*: Coronal SE T2WIs depict bilateral, subtle ATWM-SCWM terminal zones (*thin arrows*), which are quite focal. There are also bilateral small terminal zones within the SIWM. *Middle row*: Axial SE T2WIs further demonstrate the subtle terminal zones within the ATWM-SCWM terminal zones and SIWM (*beveled arrows*). The PTWM and optic radiations appear entirely normal, without terminal zones, although there are tiny dilated perivascular spaces (*right*). *Bottom row*: On axial FLAIR images, the ATWM-SCWM and SIWM terminal zones are not visualized. Additionally, there is little to no evidence of terminal zones within the PTWM posteriorly

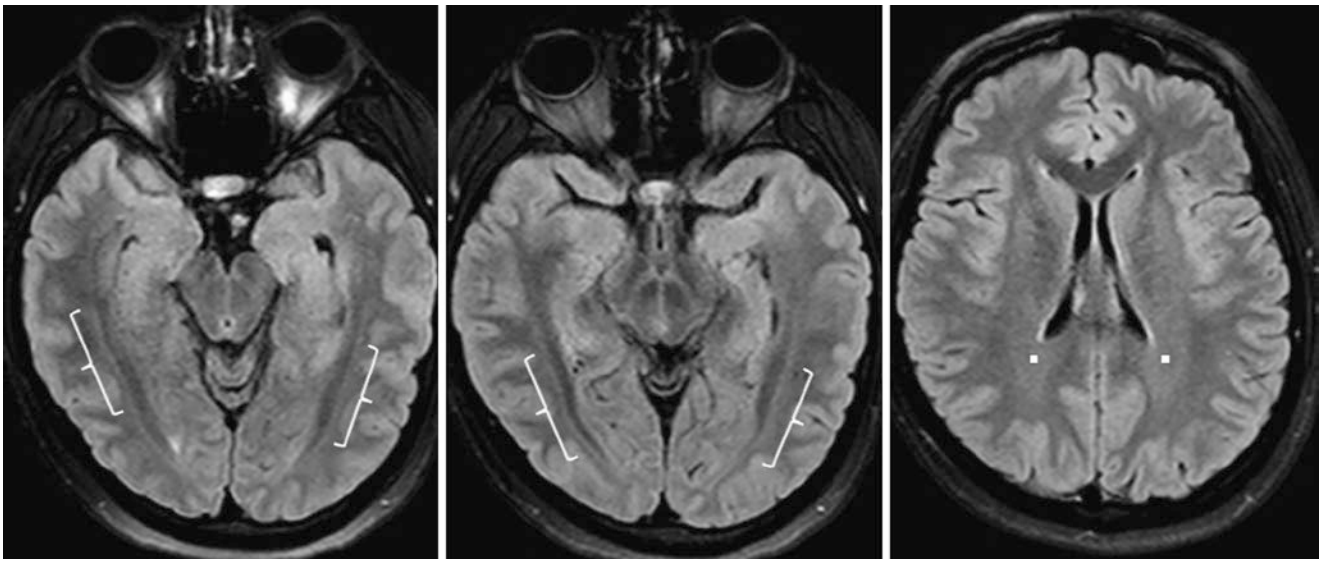

Fig. 23.165 A 15-year-old with headaches had a normal 3T MRI with axial FLAIR images that demonstrated bilateral, subtle terminal zones along the optic radiations (*brackets*). Also, note slight residual hyperintensity within the normal PTWM terminal zones (*squares*)

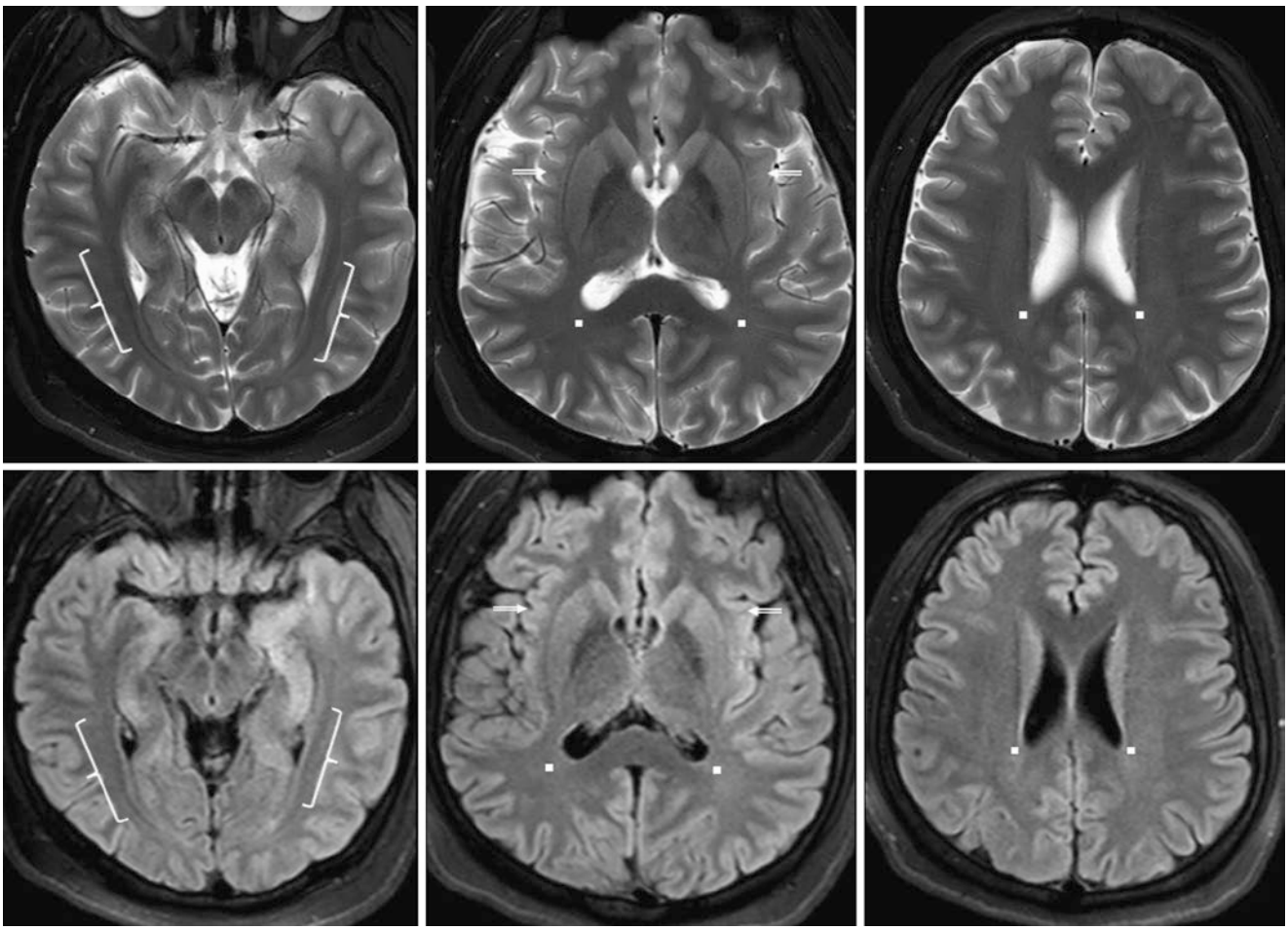

Fig. 23.166 An 18-year-old with headaches had a normal 3T MRI with SE T2WI (*top row*) and FLAIR images (*bottom row*), which demonstrated bilateral, subtle terminal zones along the optic radiations (*brackets*). There is minimal residual hyperintensity of the PTWM terminal zones (*squares*). The SIWM terminal zones (*beveled arrows*) are hardly visible, and residual bright signal there may be from normal claustra (*top middle*)

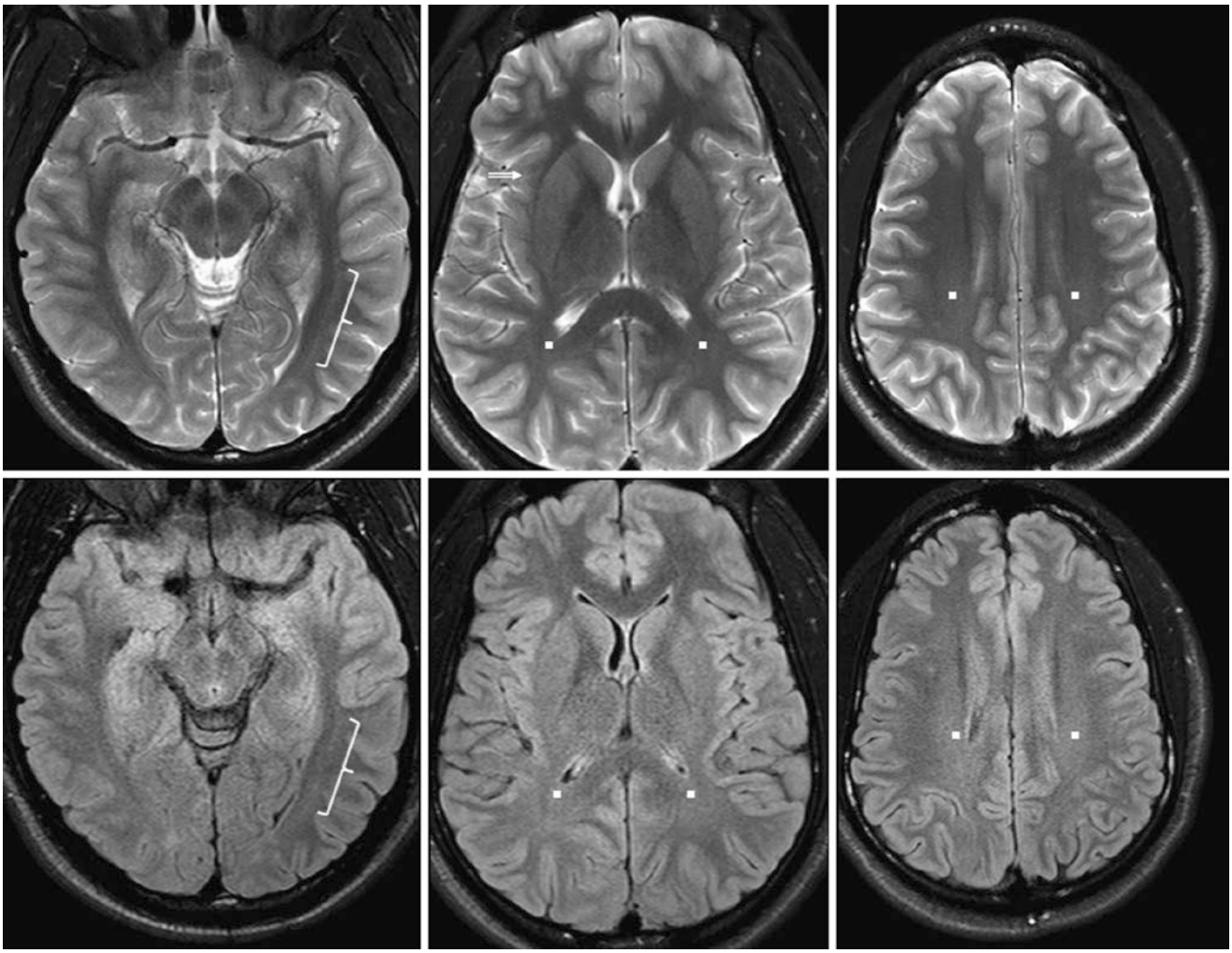

Fig. 23.167 A 19-year-old with chronic daily headaches had a normal 3T MRI with SE T2WI (*top row*) and FLAIR images (*bottom row*), which depict very subtle terminal zones within the optic radiations (*brackets*) only on the left side, and minimal hyperintensity within the PTWM (*squares*). A SIWM terminal zone may be visible only on the right side on T2WI, or this could simply be normal claustrum

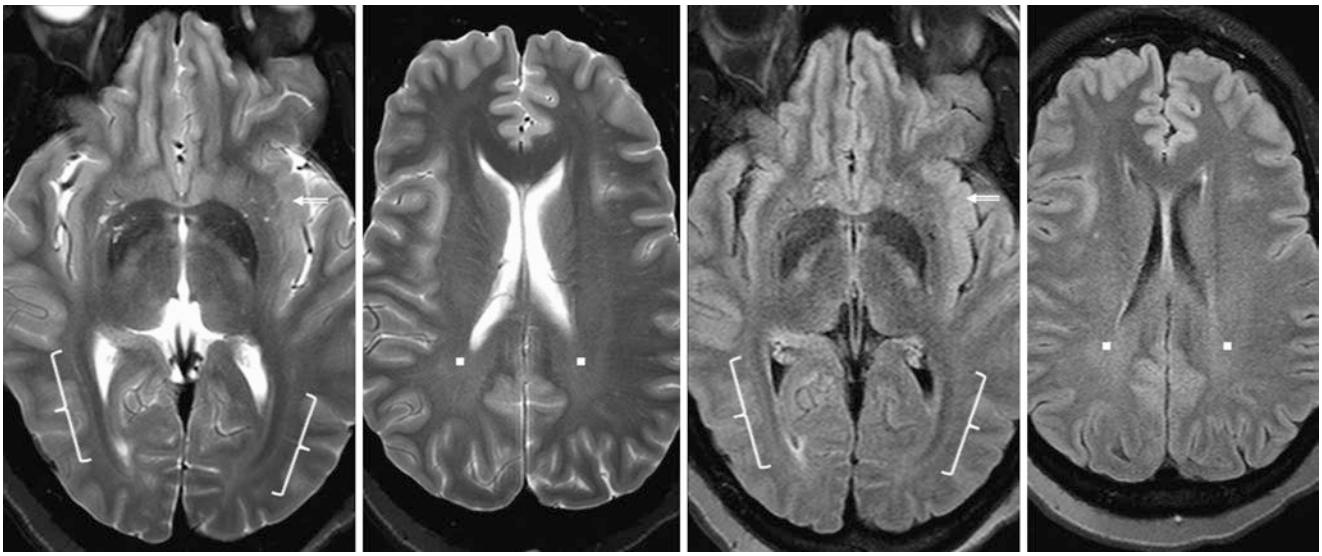

Fig. 23.168 A 29-year-old with nonmigraine headaches had a normal 3T MRI with SE T2WIs (*left images*) and FLAIR images (*right images*) that show subtle terminal zones within the optic radiations (*brackets*), which are barely visible on FLAIR, with mild PTWM hyperintensity (*squares*). A SIWM terminal zone (*beveled arrow*) may be visible only on the left side on T2WI, which could simply be normal claustrum

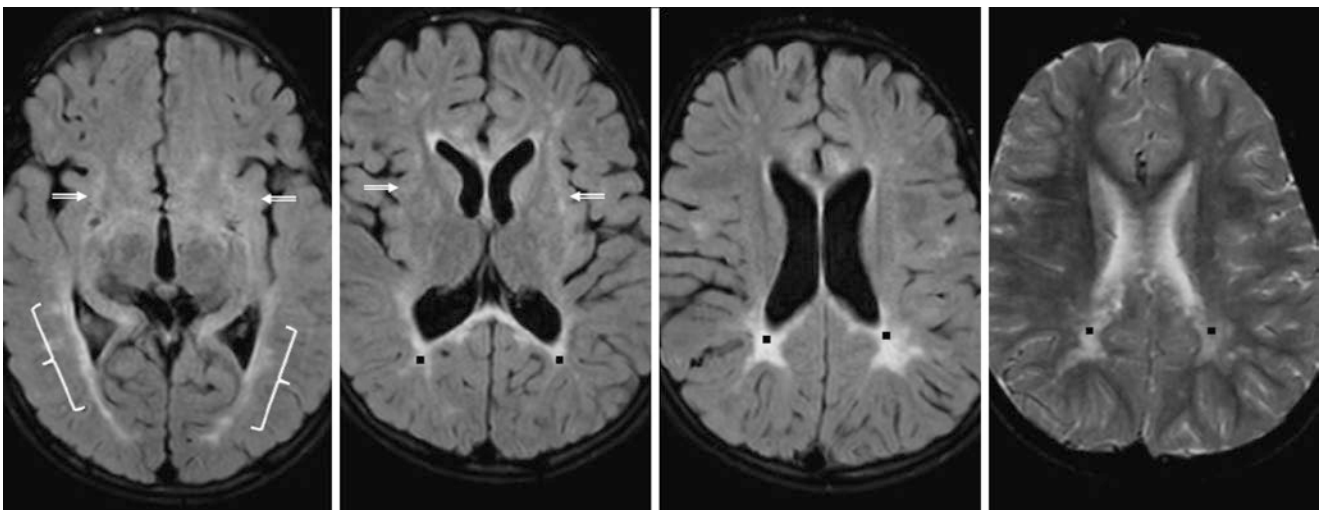

Fig. 23.169 Comparison case of Langerhan's cell histiocytosis (LCH, *i.e.*, eosinophilic granulomatosis). A 5-year-old with LCH underwent several rounds of chemotherapy over 2 years. A 3T MRI showed hyperintense optic radiations (*brackets*), SIWM (*beveled arrows*) and PTWM (*squares*), with resultant atrophy throughout the PVWM. In this patient, either the LCH itself, the rounds of chemotherapy, or both could be causing the white matter abnormalities

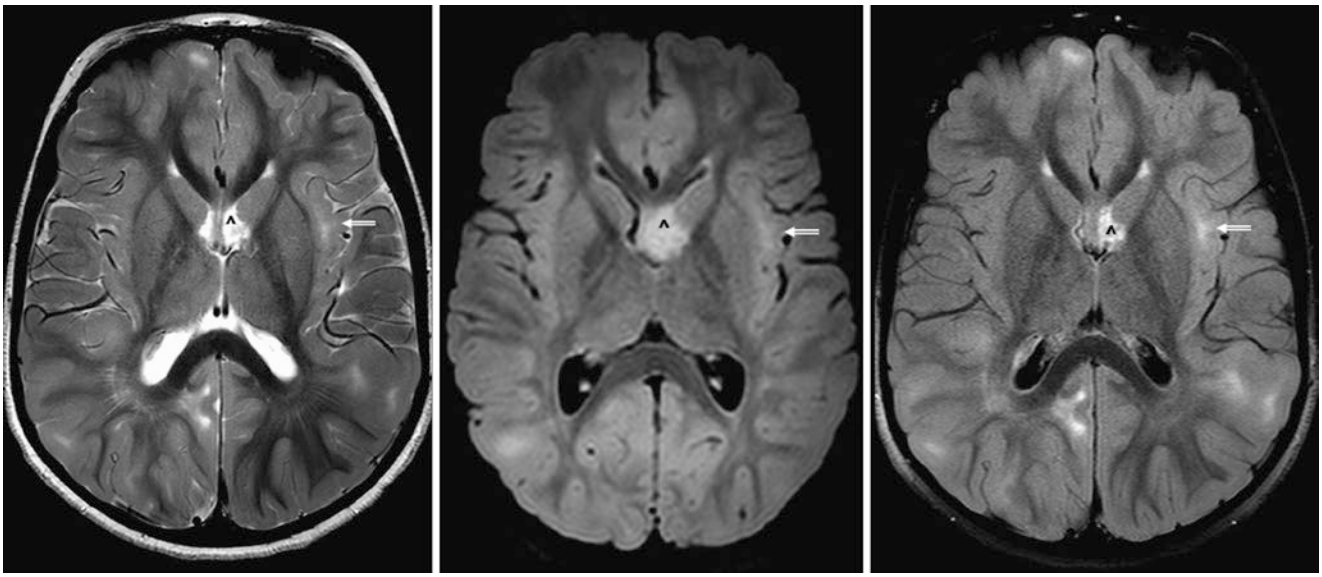

Fig. 23.170 Comparison case of tuberous sclerosis (TS). A 7-year-old had a 3T MRI that showed bright foci related to tubers/hamartomas throughout the SCWM on T2WI (*left*), 3D FLAIR (*middle*), and 2D FLAIR (*right*), from TS. One focus is denoted within the SIWM (*beveled arrows*); by itself, this focus could mistakenly seem to be a SIWM terminal zone. Note that the SIWM tuber is more visible on 2D FLAIR. Also, note a subependymal giant cell astrocytoma (^)

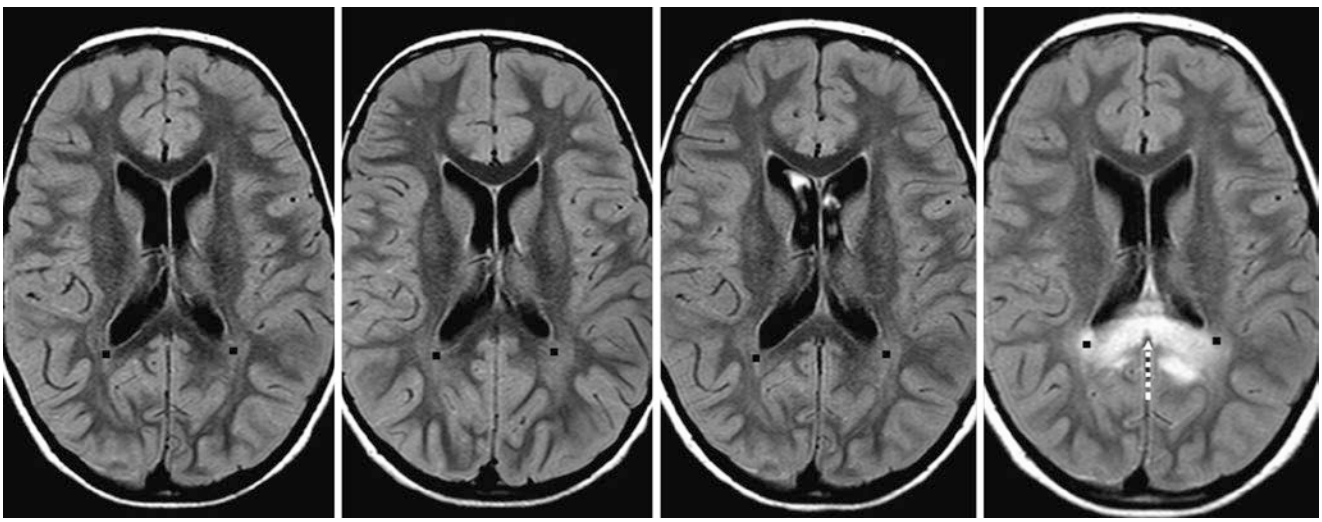

Fig. 23.171 Comparison case of adrenoleukodystrophy (ALD). A 5-year-old with worsening vision problems had what appear to be normal PTWM terminal zones (*squares*) on an initial 1.5T FLAIR image (*left*). However, subsequent yearly serial FLAIR MRIs show progressive involvement of not only the PTWM but also of the callosal splenium (*dotted arrow*) by 8 years of age (*right*). The teaching point is that terminal zones within the PTWM should lessen with time, not enlarge

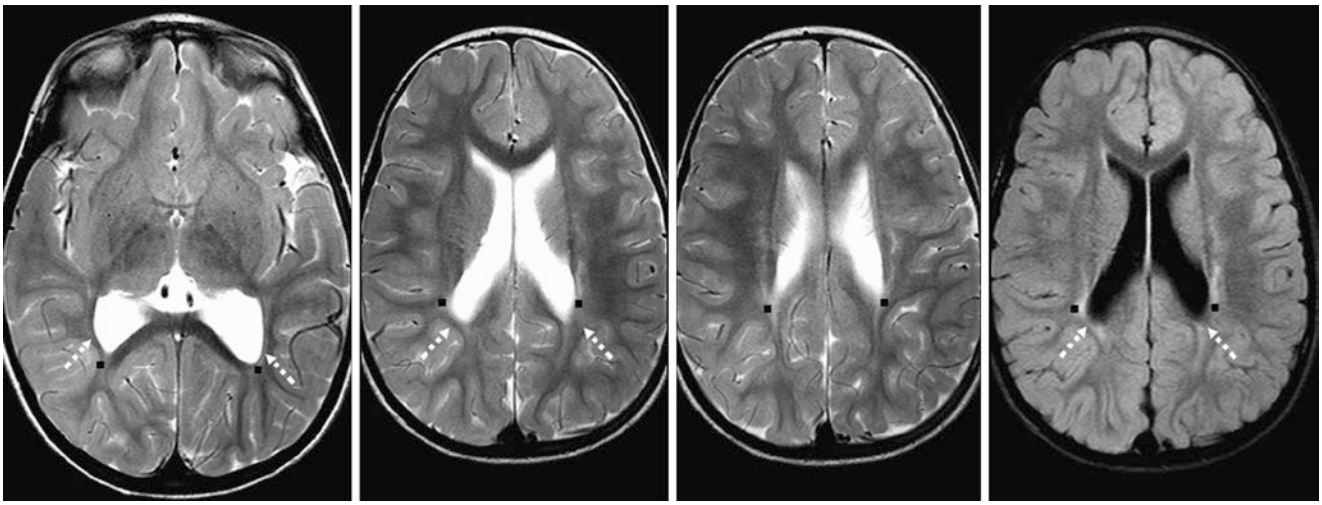

Fig. 23.172 Comparison case of periventricular leukomalacia (PVL). A 3-year-old with a history of prematurity and no prior MRI underwent a 3T MRI with SE T2WI (*left three images*) and FLAIR (*right*). The optic radiations and PTWM (*squares*) were hyperintense, with adjacent atrophy (*dotted arrows*). PVWM atrophy and hyperintensity characterize PVL

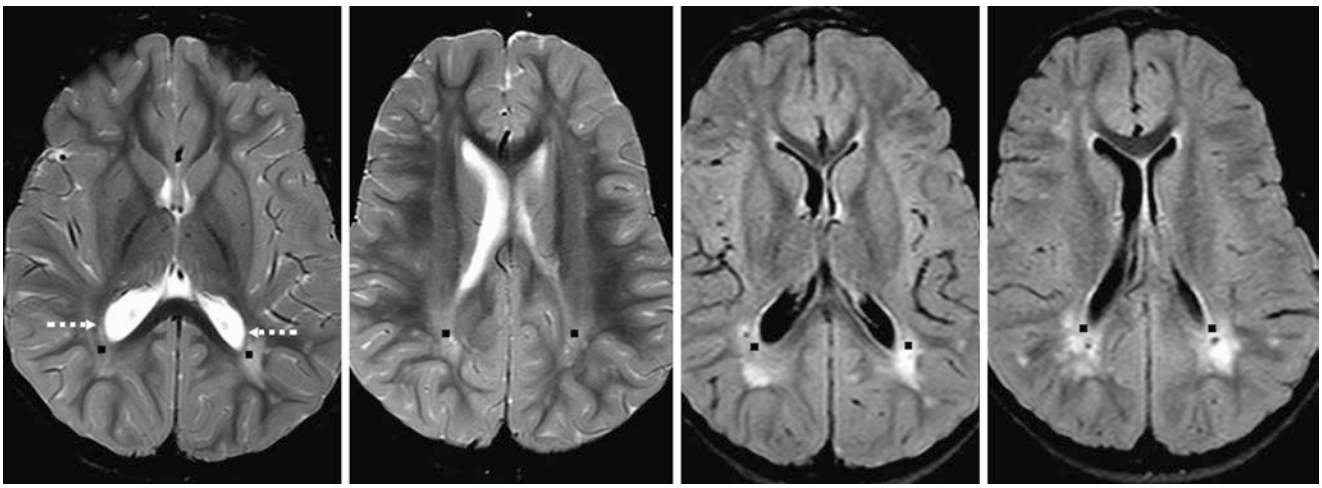

Fig. 23.173 Comparison case of an unknown white matter disease. A 2.5-year-old with motor delays underwent a 3T MRI. SE T2WI (*left images*) showed bright PTWM (*squares*), which was disproportionate to that normally seen at the patient's age. Also seen were tiny areas of cystic degeneration on FLAIR (*right images*), and mild PVWM atrophy (*dotted arrows*) on T2WI (*left*). As the birth history was normal, these findings were thought not related to PVL

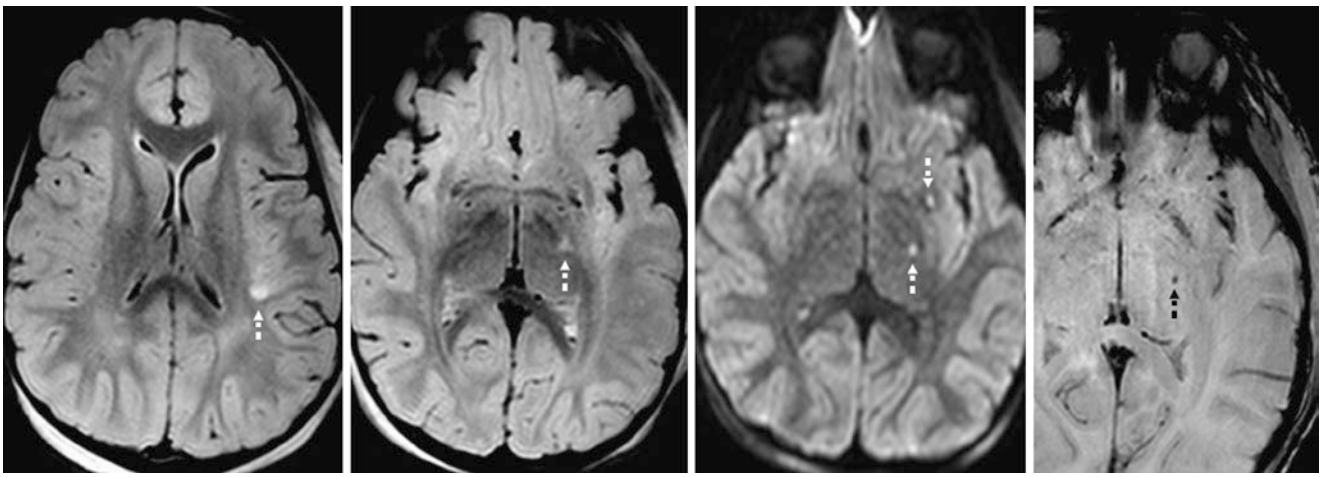

Fig. 23.174 Comparison case of diffuse axonal injury (DAI). A 3.5-year-old had altered mentation several days after blunt head trauma, with abnormal foci (*dotted arrows*) on 3T 3D FLAIR (*left two images*), and two punctate foci of cytotoxic edema on DWI (*right middle*), consistent with DAI. One focus was hemorrhagic, as shown on a magnified SWI (*right*)

23.6.8 Variants that Occur Solely in Young Infants

Many pediatric variants on brain MRI and CT that can persist into adulthood (such as cavum septum pellucidum, mega cisterna magna, and choroid plexus cysts) have been covered in previous sections. Because myelination (even of the normal terminal zones) should be completed in early adulthood, the preceding sections on white matter myelination and disease are focused in this pediatric section, but two variants occur only in young infants. These are the *residual germinal matrix* (RGM) and the *T1-bright anterior pituitary* in the young infant.

23.6.8.1 Residual Germinal Matrix in Preterm and Term Infants during the Neonatal Period

In both preterm and term infants, periventricular foci can be visualized that have increased echogenicity on ultrasound and are isointense to slightly bright on T1WI MRI, while being slightly hypointense on T2WI relative to white matter, and nearly isointense to cortical gray matter. These are thought to represent *residual germinal matrix* (RGM), a remnant. The vast majority occur immediately adjacent to the frontal horns of the lateral ventricles, but a few are seen more posteriorly. The RGM typically involutes and disappears by 1 month post-term age. It is important to exclude hemorrhage and gliosis, such as can occur with *periventricular leukomalacia*, and to exclude *periventricular nodular heterotopia* (PVNH) (Figs. 23.175, 23.176, 23.177, 23.178, 23.179, 23.180 and 23.181).

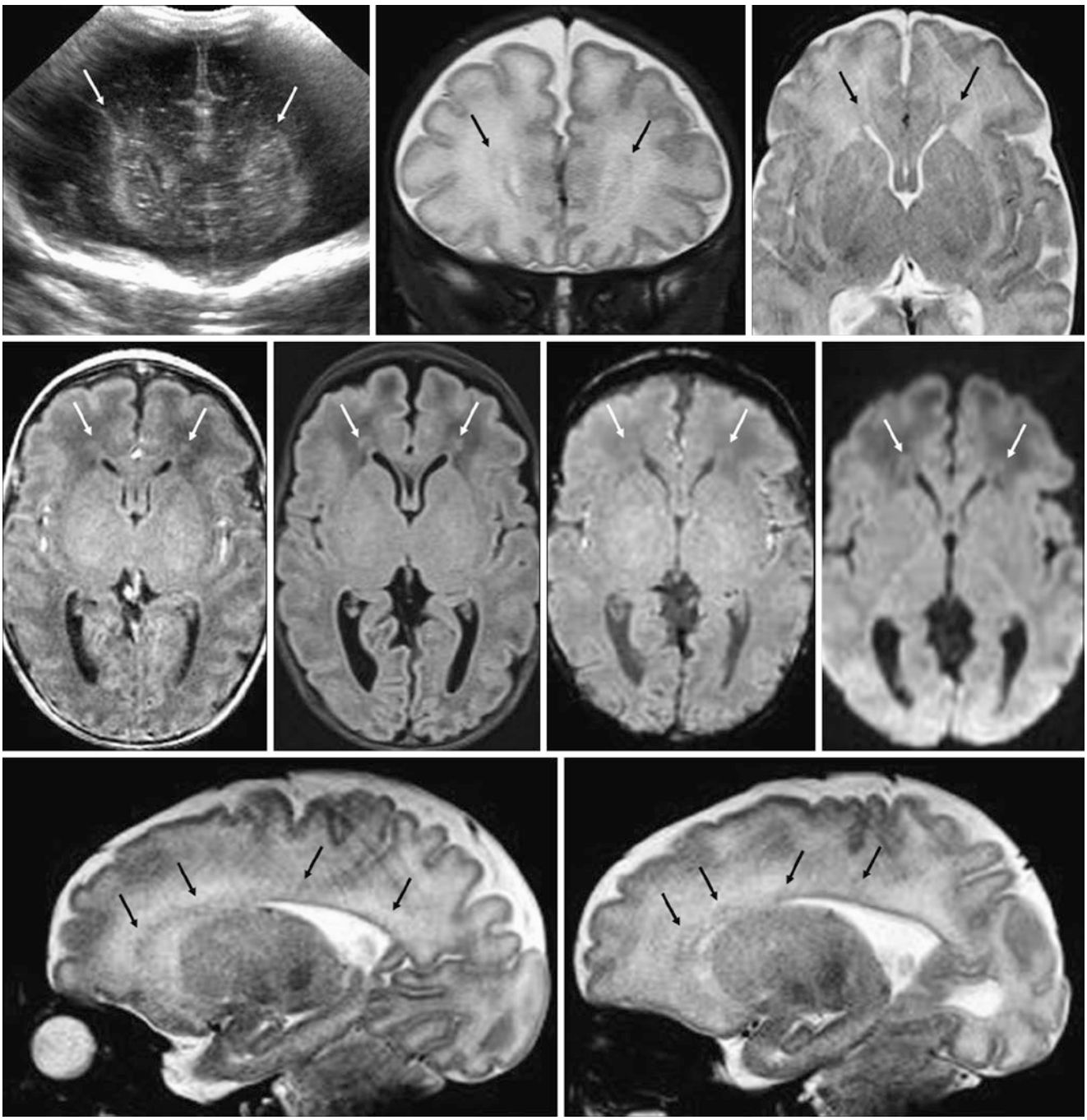

Fig. 23.175 *Top row*: A 36-week-old mildly premature infant had hyperechoic signal (*thin arrows*) along the frontal horns of the lateral ventricles on a coronal ultrasound (*left*); these areas were slightly dark on coronal (*middle*) and axial (*right*) SE T2WIs at 3T. This finding was presumed to represent residual germinal matrix (RGM), but motion on the axial T2WI made the RGM difficult to visualize. *Middle row*: On axial GE T1WI (*left*), the foci are shown to be in the typical location of presumed RGM, and they are nearly isointense to gray matter on FLAIR (*left middle*); no hemorrhage is noted in that location on SWI (*right middle*), while DWI appears normal (*right*), thus excluding sequelae of hypoxic-ischemic or perinatal injury. *Bottom row*: Sagittal SE T2WIs of the left side (*left*) and right side (*right*) confirm that the foci in question follow the contour of the lateral ventricles and are nearly isointense to the cortical gray matter, but minimally brighter in signal. Note that these presumed foci of RGM are much more visible anteriorly than posteriorly

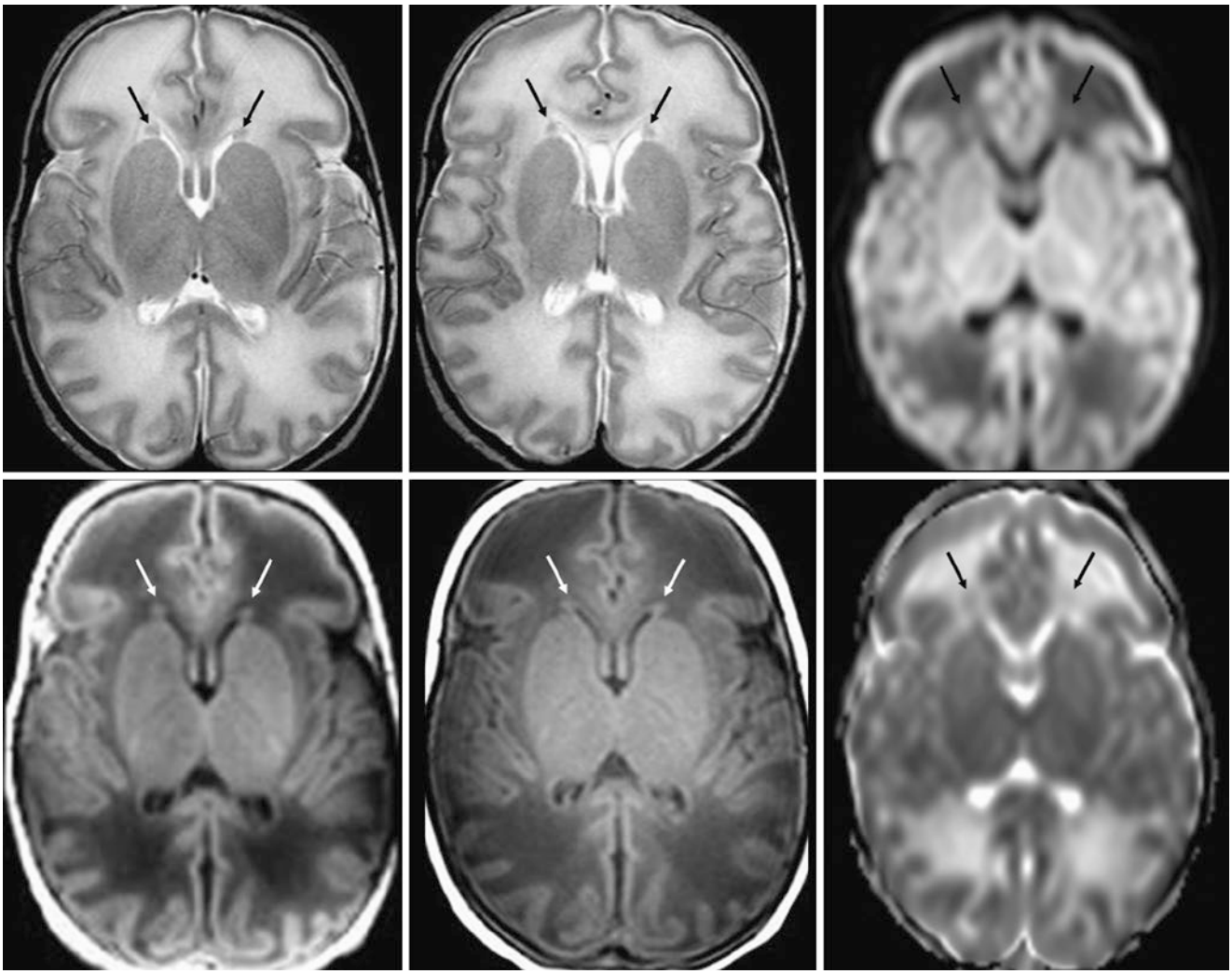

Fig. 23.176 A 36-week-old premature infant. *Top row*: Residual germinal matrix (RGM) (*thin arrows*) is adjacent to the lateral ventricles' frontal horns on 3T axial SE T2WI (*left* and *middle*) and DWI (*right*). *Bottom row*: RGM remnants are isointense to cortical gray matter on GE T1WI (*left*), but are more difficult to visualize on SE T1WI (*middle*) and the ADC map (*right*)

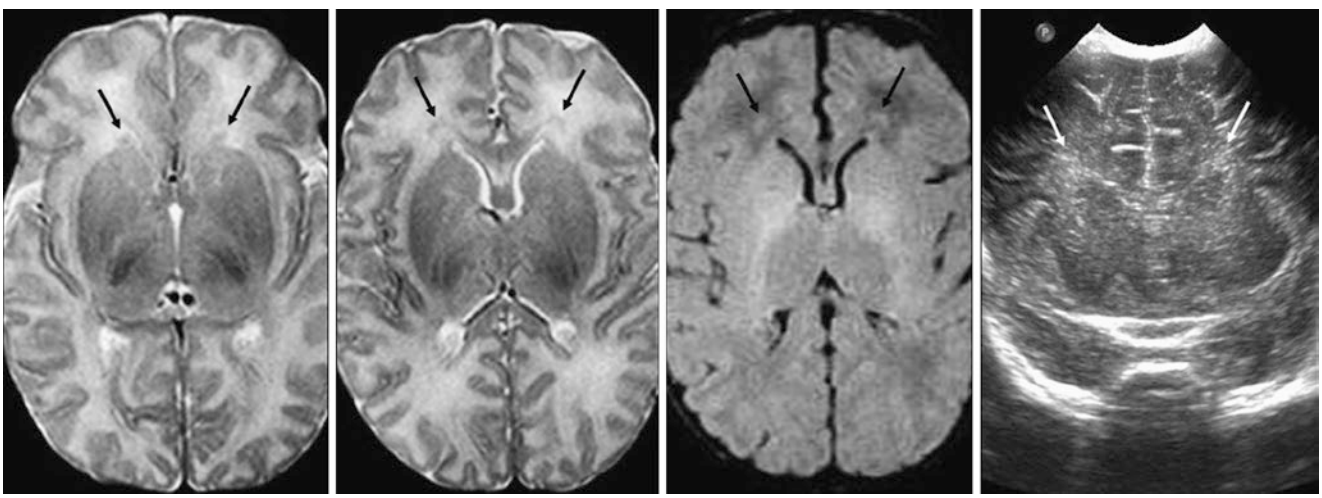

Fig. 23.177 A 40-week-old term infant had presumed RGM (*thin arrows*) on a 1.5T MRI with SE T2WIs (*left* and *left middle*), which were also visualized on FLAIR (*right middle*). DWI (*not shown*) and a corresponding ADC map (*not shown*) appeared normal. A coronal ultrasound image (*right*) showed mildly hyperechoic signal in that location

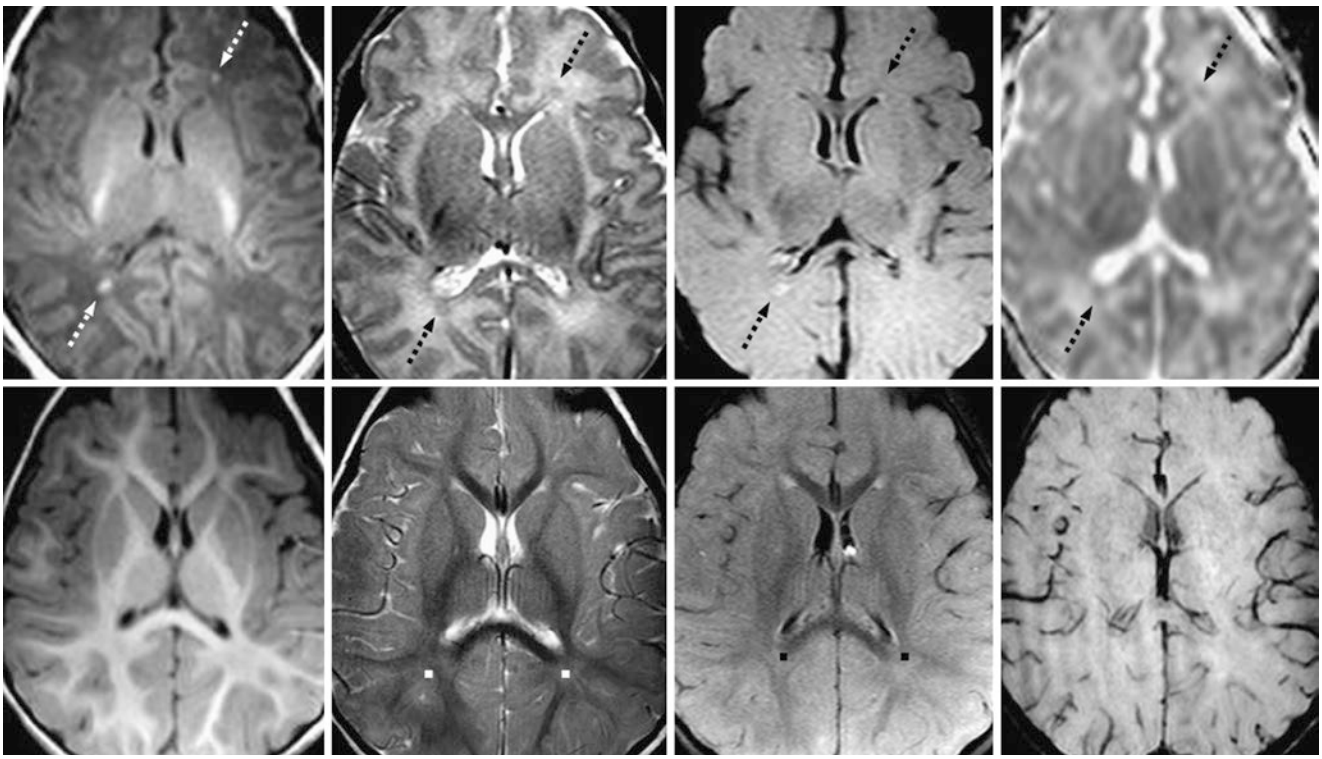

Fig. 23.178 Comparison case of noncavitary white matter injury. *Top row*: A 7-day-old term infant with respiratory difficulty had a 3T MRI that showed bright foci of WM injury (*dotted arrows*) on GE T1WI (*left*), which were isointense on T2WI (*left middle*) and FLAIR (*right middle*) and slightly dark on an ADC map (*right*, *normal DWI*). *Bottom row*: A repeat MRI 10 months later appeared normal on the same sequences; note the lack of hemorrhage on SWI (*right*), as well as normal PTWM terminal zones (*squares*). Such punctate, T1-bright foci of WM injury may resolve on follow-up MRI

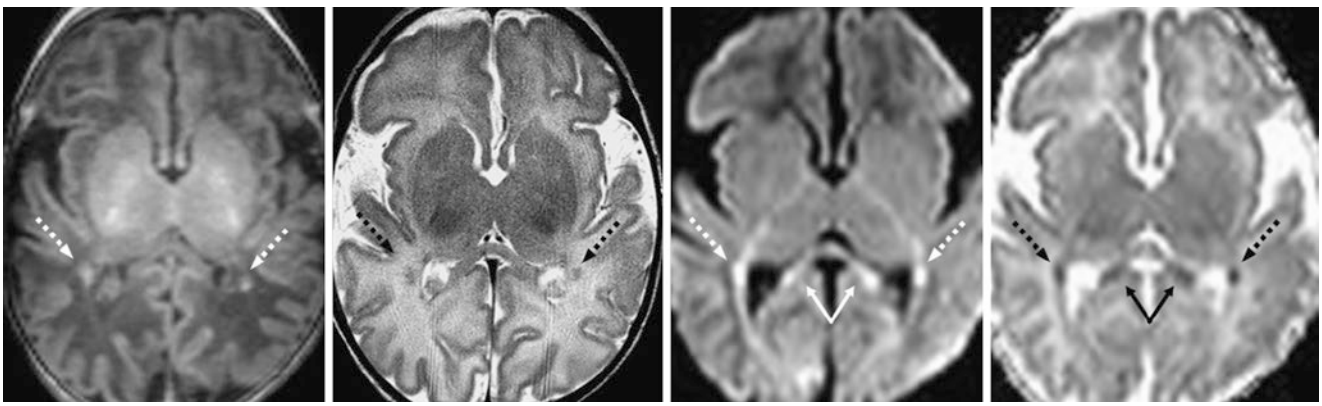

Fig. 23.179 Comparison case of hypoxic white matter injury. After cardiac arrest, a 9-day-old term infant had a 3T MRI that showed nonhemorrhagic periatrial foci (*dotted arrows*) on GE T1WI (*left*) and SE T2WI (*left middle*), found to be cytotoxic edema on DWI (*right middle*) and an ADC map (*right*). Note the callosal splenium injury (*split arrows*)

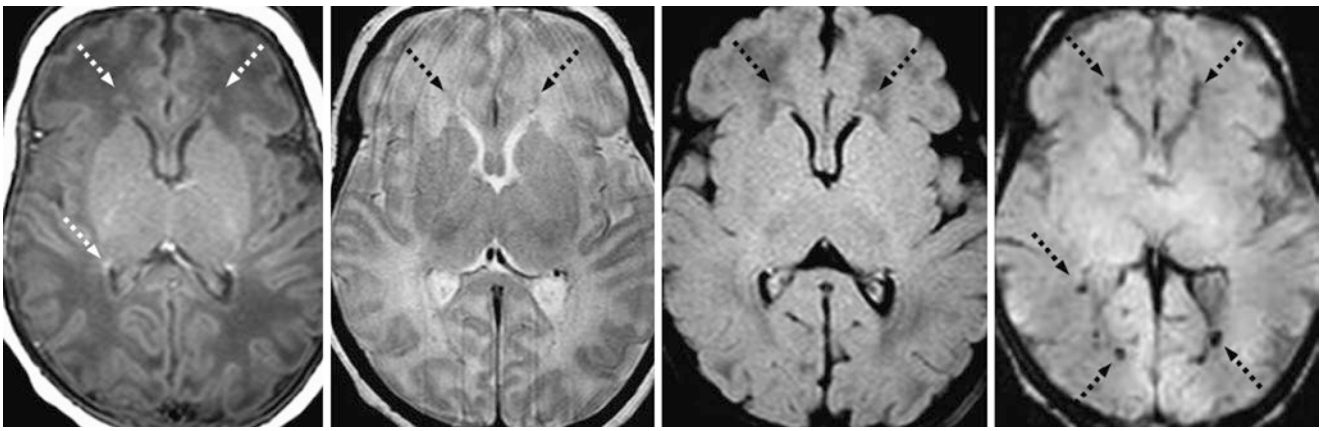

Fig. 23.180 Comparison case of early sequelae of PVL. A 4-week-old premature infant had a 3T MRI at term-equivalent age that showed PVWM foci (*dotted arrows*) along the periatrial and frontal horns on GE T1WI (*left*), SE T2WI (*left middle*), FLAIR (*right middle*) and SWI (*right*). Note PVWM hemorrhages, related to PVL, on SWI

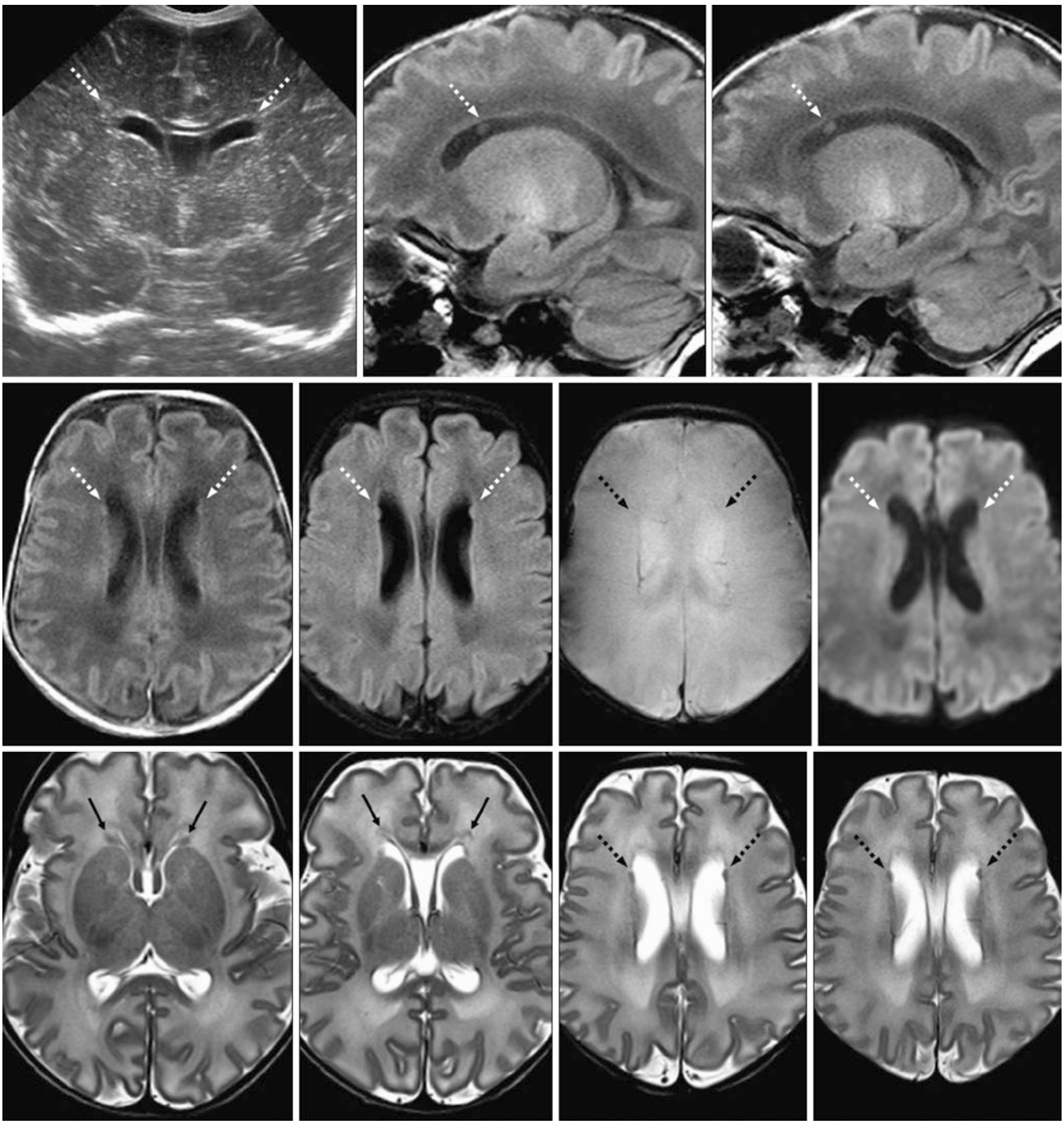

Fig. 23.181 Comparison case of tiny periventricular nodular heterotopia (PVNH). A 7-day-old infant born at 37 weeks gestational age had respiratory depression. An ultrasound and a 3T MRI were both requested. The ultrasound was interpreted as normal. *Top row*: Coronal ultrasound (*left*) appears relatively normal. On the 3T MRI, sagittal GE T1WIs of the right (*middle*) and left (*right*) sides demonstrated tiny nodular foci (*dotted arrows*) adjacent to the frontal horns of the lateral ventricles. The sulcal pattern is slightly less than expected at 37–38 weeks, appearing like a 35- to 36-week-old. *Middle row*: Axial GE T1WI (*left*), FLAIR (*left middle*), GE T2*WI (*right middle*), and DWI (*right*) images confirmed the tiny foci (*dotted arrows*) adjacent to the frontal horns. As these foci do not exhibit hemorrhage on T2*WI and do not have T1-bright signal, theye are not likely to represent WM injury, but are likely to represent tiny PVNH. *Bottom row*: Axial SE T2WIs confirmed the bilateral tiny foci (*dotted arrows*) adjacent to the frontal horns. These are not contiguous with, nor are they in a typical location for, residual germinal matrix, which can also be located near the frontal horns. Note normal residual germinal matrix slightly more anteriorly and inferiorly (*arrows*)

23.6.8.2 Normal Anterior Pituitary Hyperintensity in the Neonate and Early Infancy

The pituitary gland in the neonate may appear uniformly hyperintense on T1WI, owing to *bright signal in the anterior pituitary*, which lasts up to 6–7 weeks postnatal age. Although not entirely proven, it has been postulated that this appearance relates to histologic changes in the anterior lobe arising from the effect of high maternal estrogen levels; after the 25th week of gestation, prolactin-containing cells increase in the anterior pituitary and are numerous in the third-trimester fetus and neonate. These cells progressively decrease in number after birth and remain low in number during early childhood. Notably, such T1 hyperintensity of the anterior lobe will subside by 6–7 weeks after birth even in a premature infant, presumably owing to the lack of effects from maternal estrogen; differential considerations include *pituitary hemorrhage* or *adenoma*, which are very unlikely in a neonate or young infant (Figs. 23.182, 23.183, 23.184, 23.185, 23.186, 23.187 and 23.188).

Fig. 23.182 A 32-week-old premature infant had an entirely bright pituitary (*arrow*) on a sagittal GE T1WI

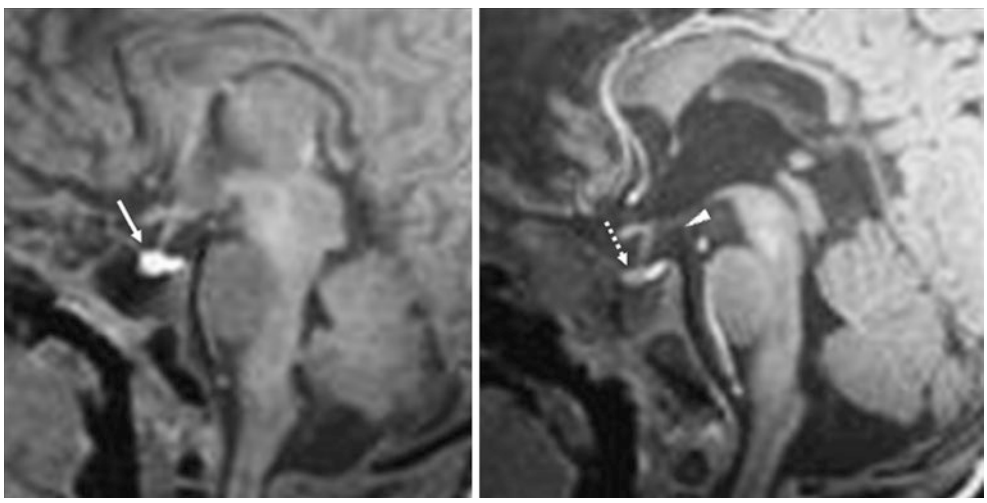

Fig. 23.183 A 5-day-old term infant had a uniformly bright pituitary gland (*arrows*) on a 3T sagittal GE T1WI (*left*). At 3.5 months of age (*right*), the anterior lobe (*dotted arrow*) is no longer bright, but the posterior lobe (*arrowhead*) remains so

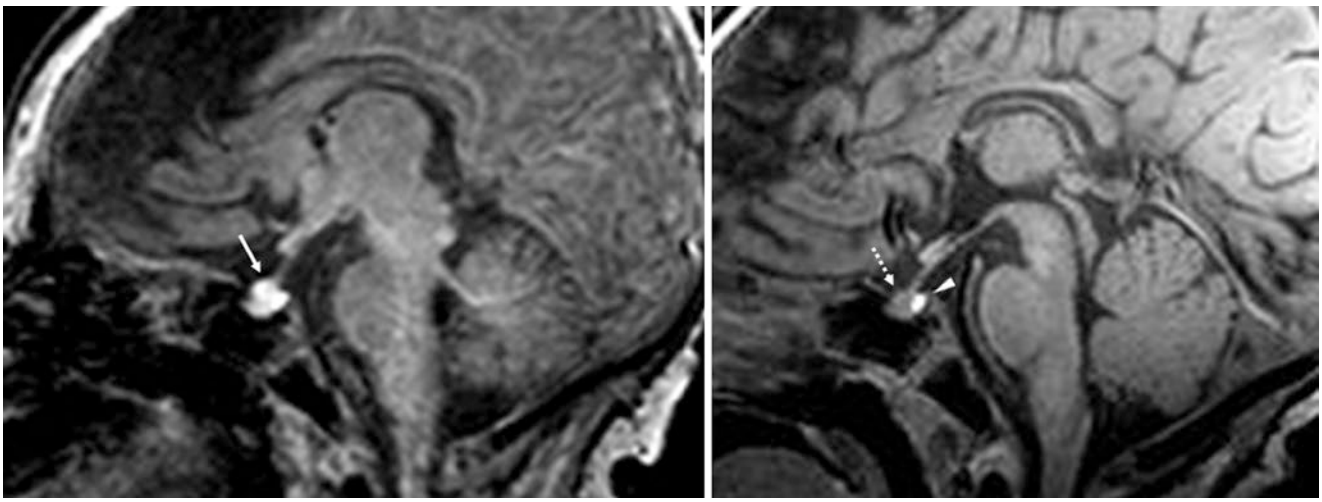

Fig. 23.184 An 8-day-old term infant with weakness had a uniformly bright pituitary gland (*arrow*) on a 3T MRI with sagittal GE T1WI (*left*). A follow-up 3T sagittal GE T1WI at age 2.5 months (*right*) shows that the anterior lobe of the gland (*dotted arrow*) is no longer hyperintense, but the posterior lobe (*arrowhead*) remains hyperintense

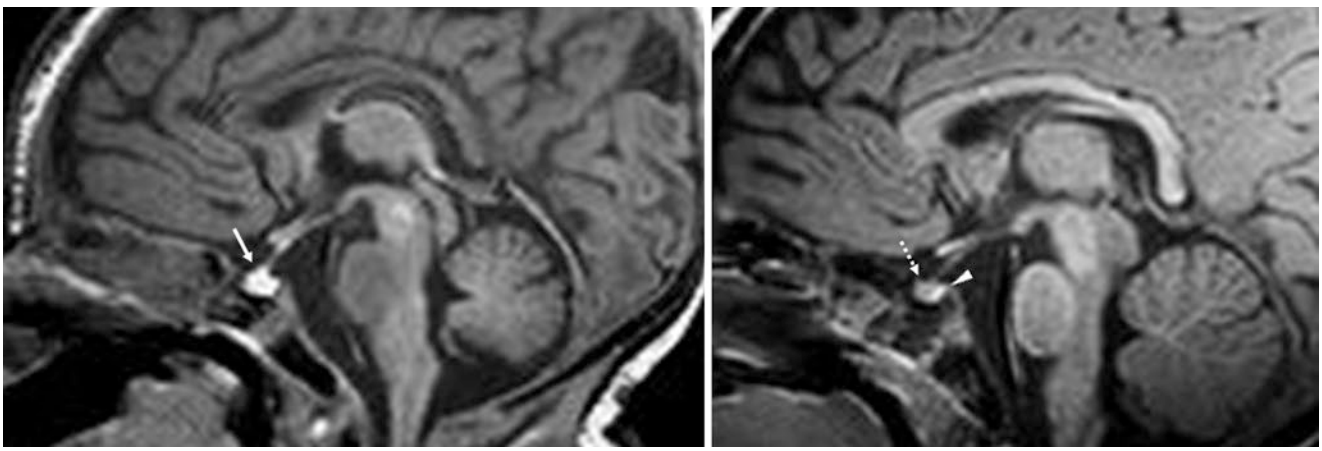

Fig. 23.185 A 9-day-old term infant with weakness had an entirely bright pituitary (*arrow*) on a 3T MRI with sagittal GE T1WI (*left*). A follow-up 3T sagittal GE T1WI at age 7 months (*right*) shows that the anterior pituitary (*dotted arrow*) is no longer hyperintense, but the posterior lobe (*arrowhead*) remains hyperintense

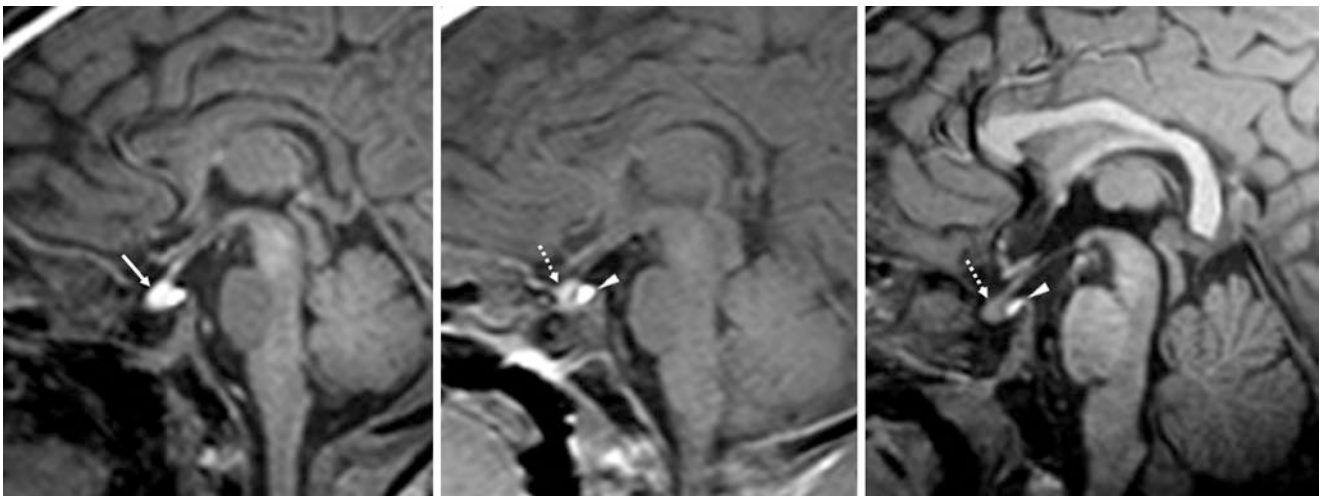

Fig. 23.186 A term 7-day-old had a uniformly bright pituitary (*arrow*) on a 3T sagittal GE T1WI (*left*). At 4 weeks (*middle*), the anterior lobe (*dotted arrow*) has mildly darkened, and can be discerned from the posterior lobe (*arrowhead*). By the age of 10 months (*right*), the anterior lobe appears isointense, and the posterior lobe remains bright

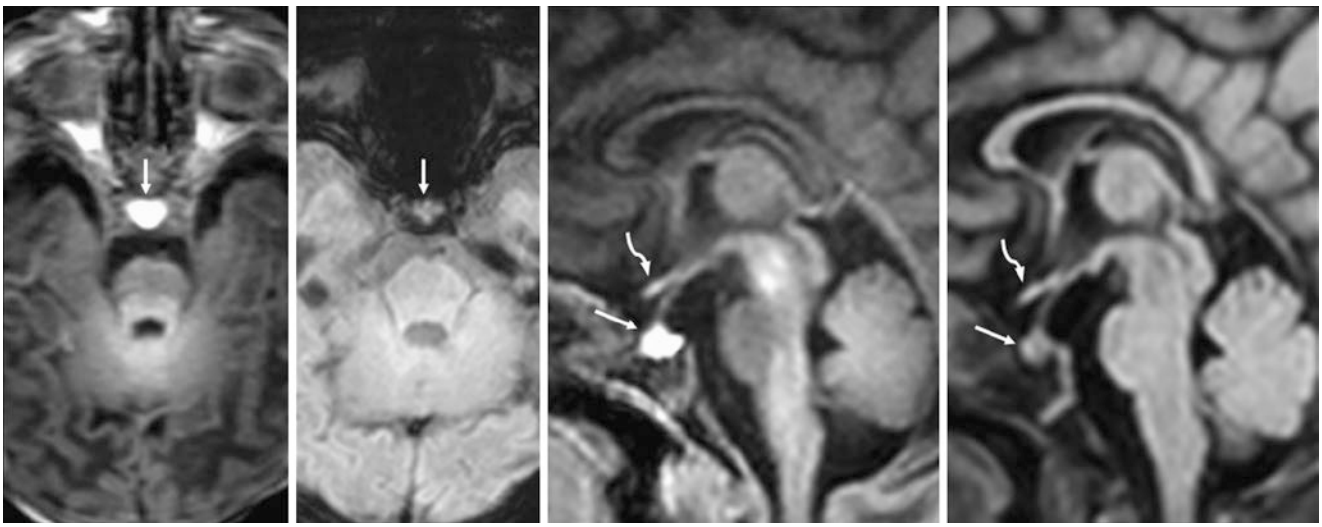

Fig. 23.187 A term 9-day-old had a uniformly hyperintense pituitary gland (*arrows*) on a 3T MRI with a 3D GE T1WI acquisition that was reconstructed in axial (*left*) and sagittal (*right middle*) planes. Note that the bright signal is not related to hemorrhage, as the gland is not dark on SWI (*left middle*). On a sagittal reformat from a 3D FLAIR image (*right*), the gland appears isointense. Note the optic chiasm superiorly (*curved arrows*)

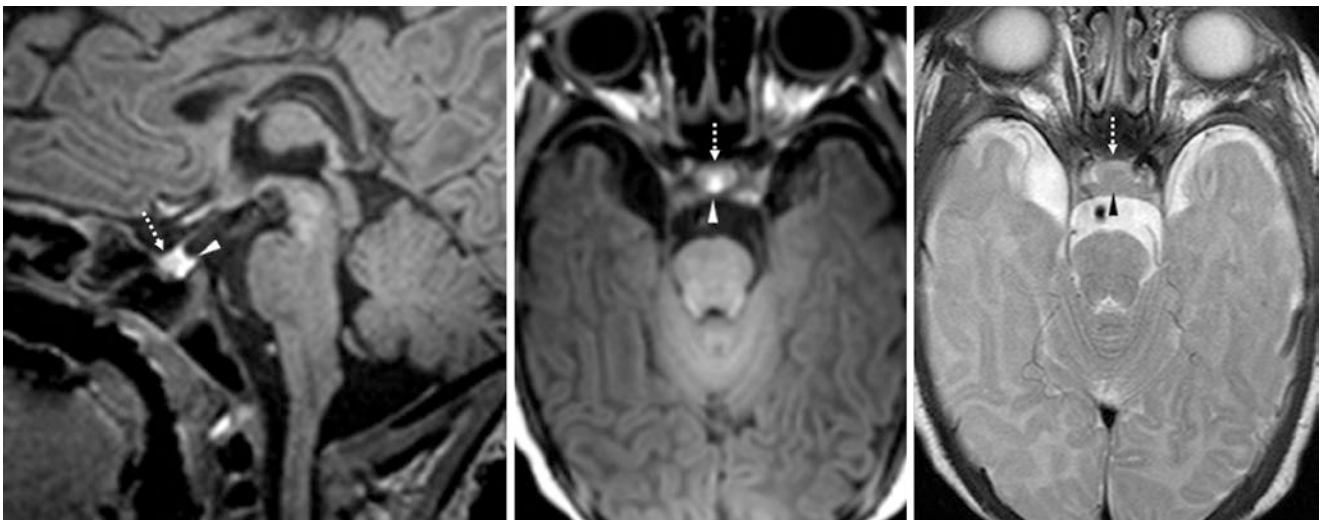

Fig. 23.188 A term 5.5-week-old had a mildly bright anterior lobe of the pituitary (*dotted arrows*) relative to the posterior lobe (*arrowheads*) on 3T GE T1WIs with sagittal (*left*) and axial (*middle*) reformats. On T2WI (*right*), the gland is uniformly isointense. This borderline bright signal is likely due to the fact that this age is around the time when the anterior lobe darkens

23.6.9 Benign Enlargement of the Subarachnoid Spaces of Infancy

The condition known as *benign enlargement of the subarachnoid spaces of infancy* (BESSI) has been called by many names, including benign prominence of the subarachnoid space of infancy, benign subarachnoid space enlargement, external hydrocephalus, extraventricular hydrocephalus, extra-axial collections of infancy, benign subdural effusions, benign extracerebral fluid collections, and pseudohydrocephalus megacephaly. All of these names refer to an entity of unknown etiology that is characterized by a rapidly enlarging head circumference in an otherwise normal infant with normal mental status and normal neurologic development. The rapid head enlargement typically normalizes between the ages of 13 and 24 months. The term "*external hydrocephalus*" may be particularly confusing, as it has not yet been clearly proven whether such a condition exists that leads to rapid enlargement of the extra-axial spaces and subsequent compression of the brain. This question was first raised by Dandy et al. in 1918. More recently, Barkovich has stressed that the term "benign enlargement of the subarachnoid spaces" should apply to such macrocephalic, but otherwise normal, infants.

The imaging appearance typically consists of enlarged *subarachnoid space* (SAS) along the frontal convexities, sometimes also affecting the parietal and temporal convexities, and often the sylvian fissures. These findings typically diminish, and eventually resolve, as the enlarging head circumference normalizes between the ages of 13 and 24 months. On CT and MRI, the prominent SAS follows CSF in density and signal intensity, being dark on CT, dark on T1WI, bright on T2WI, and suppressed with CSF on FLAIR. *Cortical veins* can often be discerned traversing the enlarged SAS, in a manner similarly described in the previous sections to discern volume loss (atrophy); such bridging veins confirm that these images show BESSI, and not *subdural hematomas* or *hygromas* (SDHs). These veins can be visualized and confirmed to be within the SAS on T2WI, SWI, postcontrast T1WI, MR angiography, or MR venography. Slight ventricular enlargement, may also be seen, but without frank *hydrocephalus*. The veins may also be peripheral to the cortices, and located just deep to the calvarium. In contrast, SDHs compress the cortical veins against the cortex or into the cerebral sulci.

Perhaps the confusing multitude of names for this rather benign condition inhibits its recognition among both radiologists and clinicians, and commonly leads to further unnecessary workups. This appearance should be distinguished from chronic SDHs (whether hematoma or hygroma), which may occur following trauma or in patients with disorders of coagulation, and it also should be distinguished from infectious subdural effusions. In patients with *nonaccidental trauma* (NAT), there are often other findings on whole body plain film examination, concomitant brain findings on MRI or CT (*e.g.*, brain or retinal hemorrhages on SWI, hypoxic-ischemic injury, or skull fractures), and the chronic SDHs often are complex with layering or membranes. It should also be noted that SDHs may occur in patients with BESSI, occurring either spontaneously or as a result of NAT or accidental trauma.

Some descriptions in the literature have suggested that uncommon or rare conditions may present with BESSI as the initial brain finding, where the brain parenchyma and ventricles otherwise appear normal. Such conditions include the *mucopolysaccharidoses*, *achondroplasia*, and a number of *congenital-genetic inborn errors of metabolism*. It is uncertain whether BESSI reflects the disease state in such disorders or is simply an incidental finding. The clinician should perform an adequate neurologic and neurodevelopmental examination and examine the family history to exclude the presence of such disorders. Overall, congenital-metabolic disorders are quite uncommon and are usually identified by other imaging features or by clinical or family history. Hence, the clinician should view any development of neurologic symptoms or failure to meet neurodevelopmental milestones with suspicion in a patient with BESSI.

In summary, the presence of BESSI in infants less than 1 year of age is benign and asymptomatic, although the clinician may note a dramatic increase in head size. As this condition typically resolves by 2 years of age, some state that it is not entirely normal, it is agreed upon that BESSI should be considered at least a "don't touch" appearance when it is detected. The presence or development of neurologic symptoms or neurodevelopmental delay regarding age-related milestones should be viewed with suspicion for an underlying condition, and BESSI should not be present after 2 years of age. If imaging abnormalities other than BESSI are present, then the condition may not be benign (Figs. 23.189, 23.190, 23.191, 23.192, 23.193, 23.194, 23.195, 23.196, 23.197, 23.198, 23.199, 23.200, 23.201, 23.202, 23.203 and 23.204).

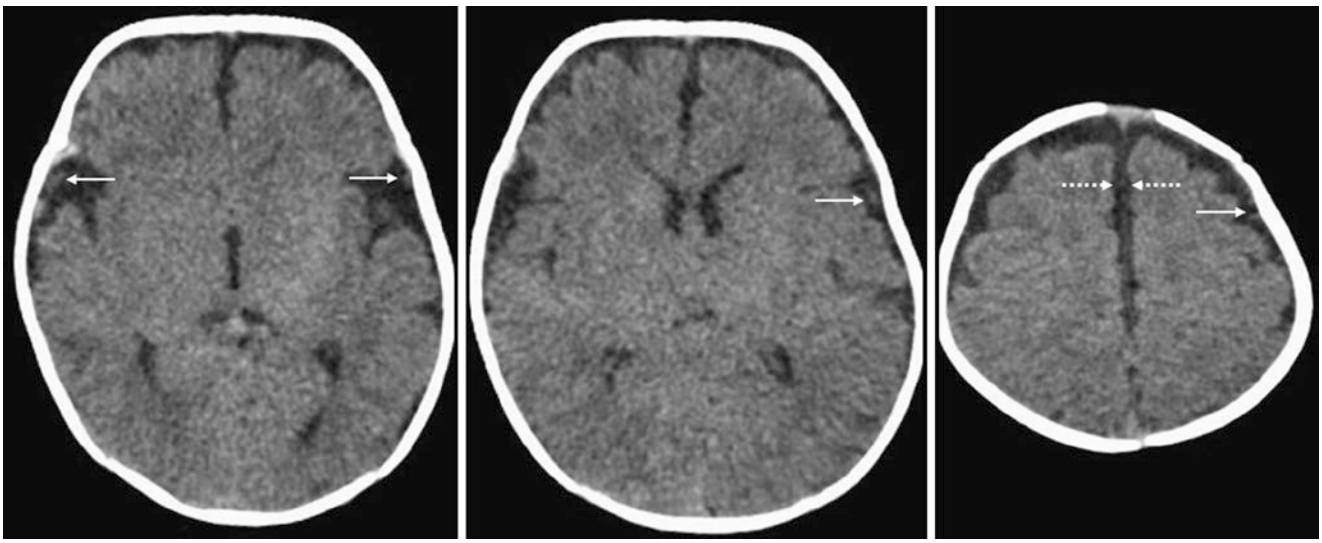

Fig. 23.189 A 6-week-old evaluated for trauma had benign enlargement of the subarachnoid spaces of infancy (BESSI) on an otherwise negative NECT, with bilaterally enlarged subarachnoid spaces (SASs) within the sylvian fissures and along the frontal convexities. The interhemispheric fissures (*dotted arrows*) are also prominent. Note small cortical veins (*thin arrows*) traversing the SASs. A follow-up CT scan was not obtained

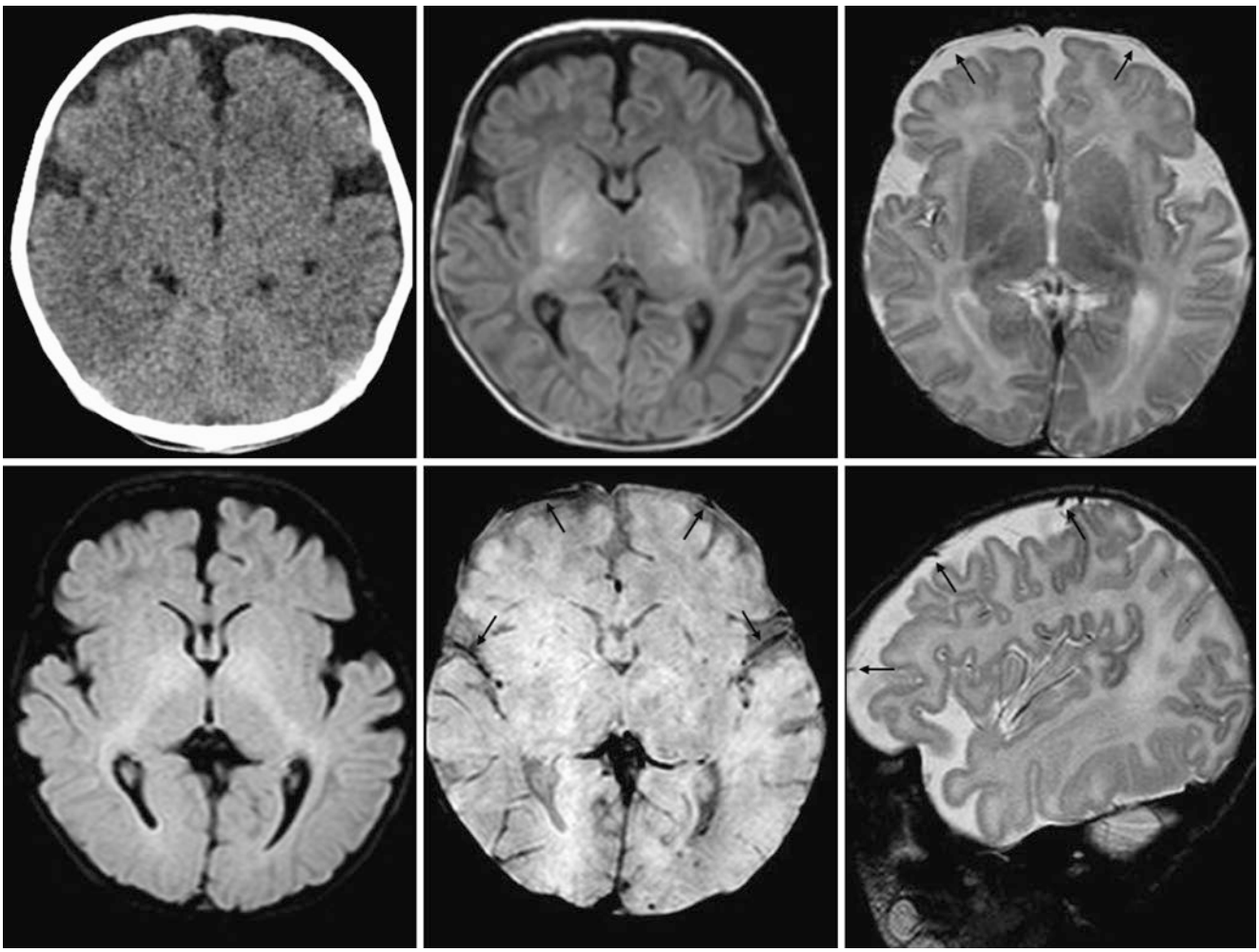

Fig. 23.190 An 8-week-old with "irritability" had BESSI on an NECT (*top left*), with enlarged SASs within the sylvian fissures and along the frontal convexities. An otherwise negative 1.5T MRI included axial T1WI (*top middle*), T2WI (*top right*), FLAIR (*bottom left*), SWI (*bottom middle*), and sagittal T2WI (*bottom right*). Note cortical veins (*thin arrows*) traversing the SASs. Follow-up imaging was not obtained. The patient's subsequent development was normal

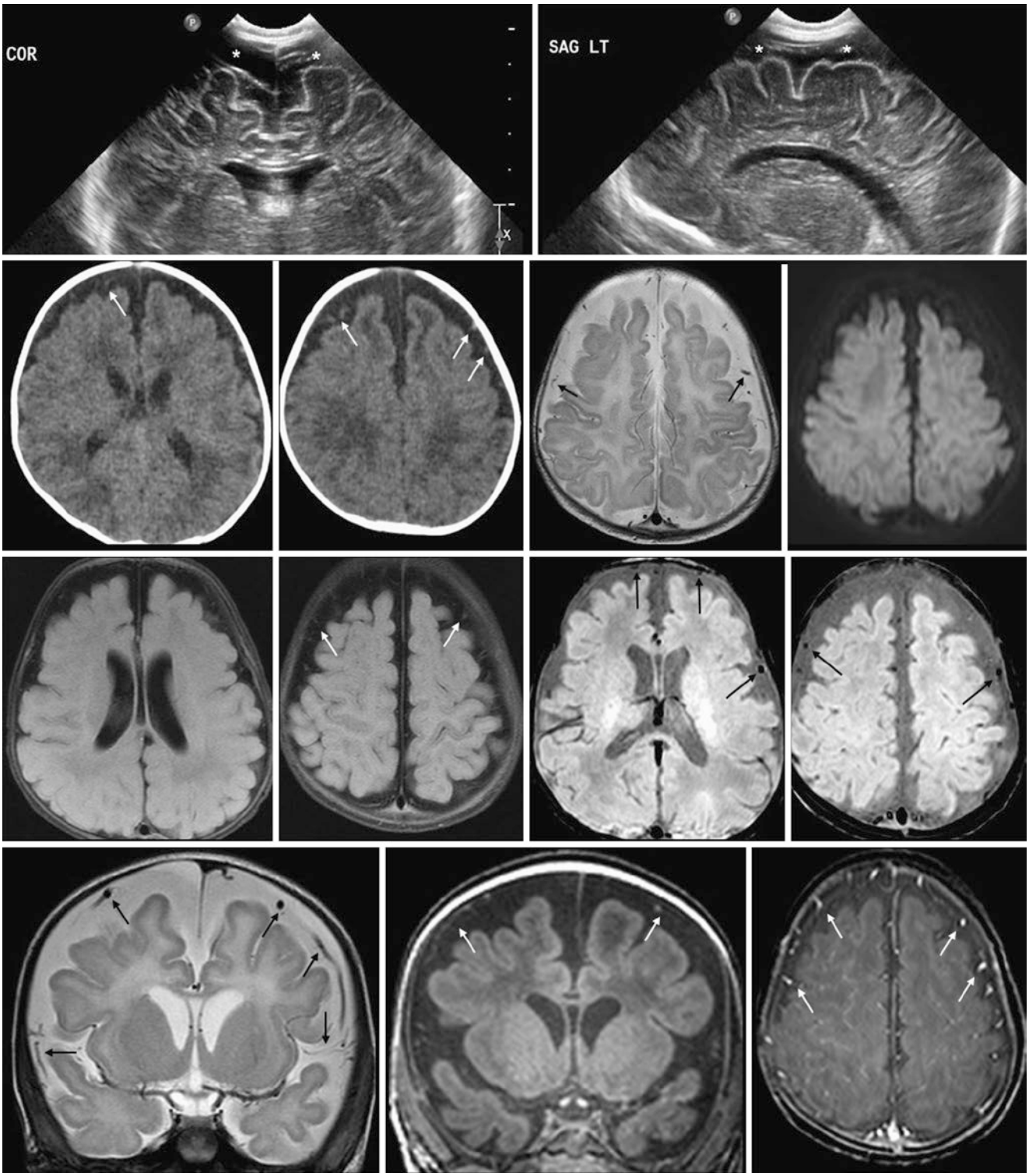

Fig. 23.191 An 11-week-old with BESSI. *Top row*: Ultrasound in a macrocephalic, developmentally normal infant showed what were thought to be enlarged SASs (*asterisks*), but further imaging was requested to exclude subdural hematomas or hygromas (SDHs) and hydrocephalus. *Second row*: Axial NECT images (*left* and *left middle*) and a 3T MRI with axial T2WI (*right middle*) and DWI (*right*) confirmed enlarged SASs. Note the small cortical veins (*thin arrows*) traversing the SASs. DWI was negative. *Third row*: axial FLAIR images (*left* and *left middle*) confirmed that the enlarged SASs suppressed with CSF. SWI (*right middle* and *right*) confirmed cortical veins (*thin arrows*) traversing the SASs. *Bottom row*: Coronal T2WI (*left*) and T1WI (*middle*) also depicted the small cortical veins, which are further illustrated on postcontrast T1WI (*right*)

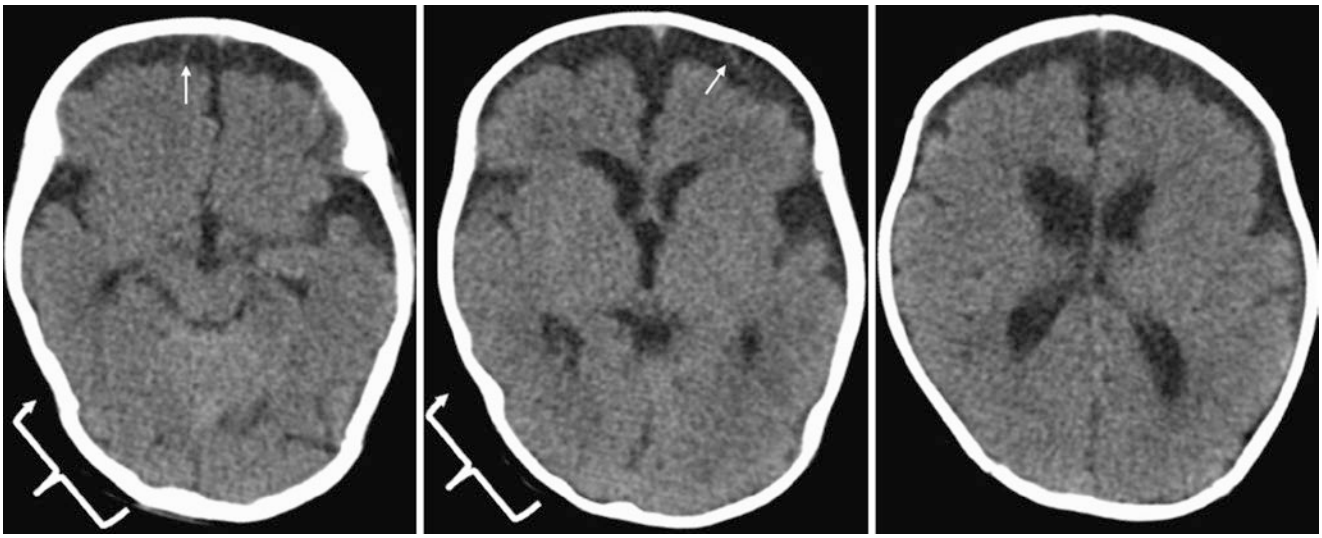

Fig. 23.192 On NECT, a 3-month-old with macrocephaly had enlarged SASs of the frontal convexities and sylvian fissures, which were traversed by small cortical veins (*thin arrows*). There was also mild right parieto-occipital calvarial flattening (*brackets*), representing mild benign positional plagiocephaly, as the sutures were patent

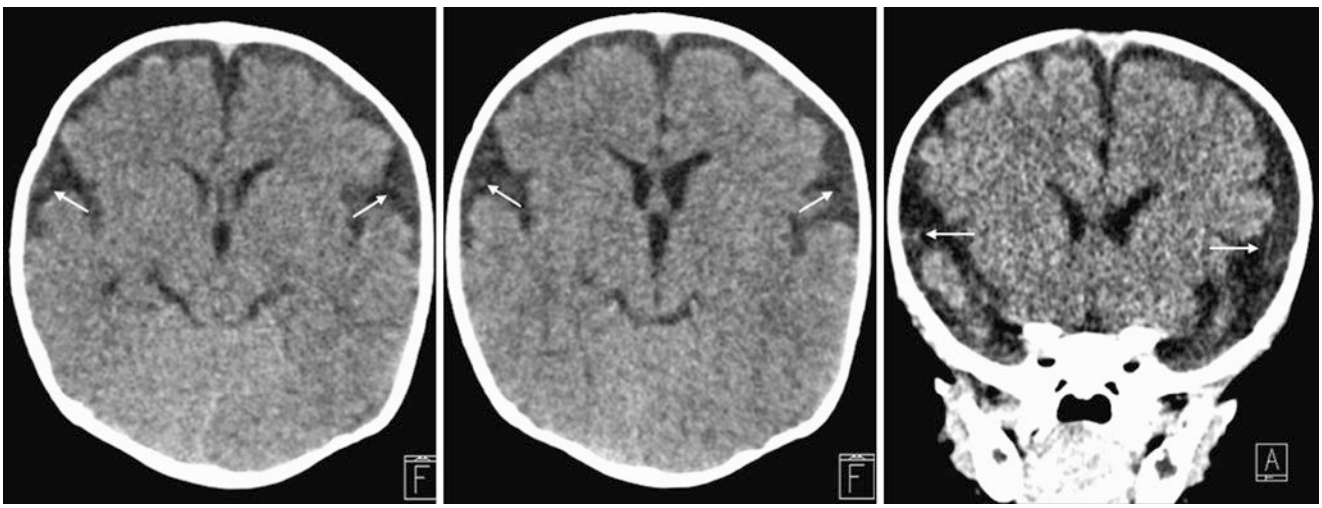

Fig. 23.193 A 3-month-old with macrocephaly had enlarged SASs of the frontal convexities and of the sylvian fissures on axial NECT (*left two images*). Both the axial images and coronal reformats (*right*) demonstrate that small cortical veins (*thin arrows*) traverse the enlarged SASs

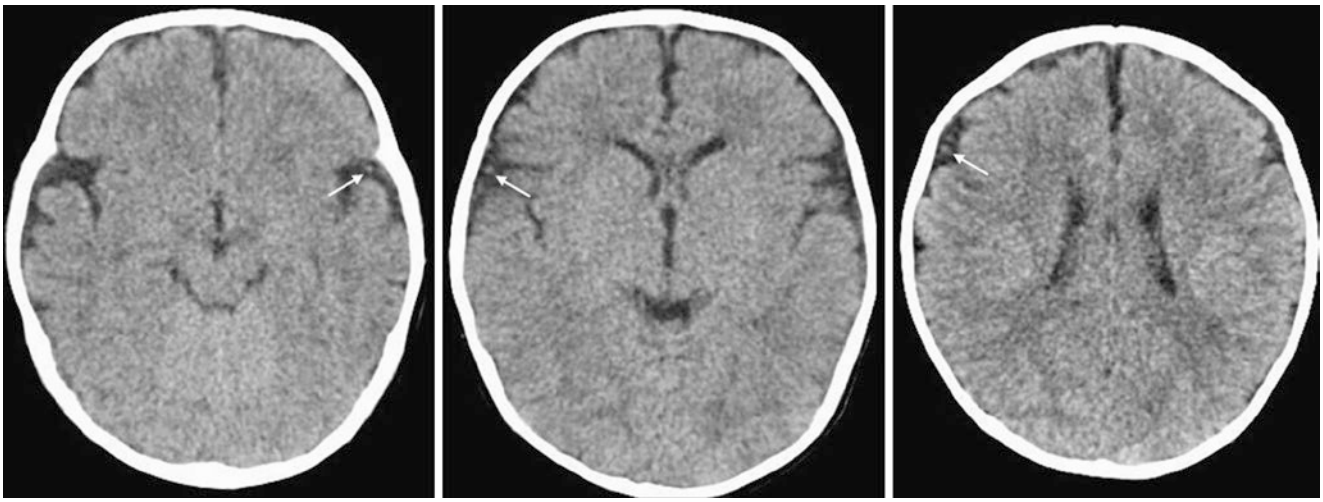

Fig. 23.194 A 3-month-old with macrocephaly had a milder degree of BESSI on NECT, having enlarged SASs predominantly within the sylvian fissures, whereas the SASs overlying the frontal convexities were only slightly prominent. Note cortical veins (*thin arrows*) traversing the SASs

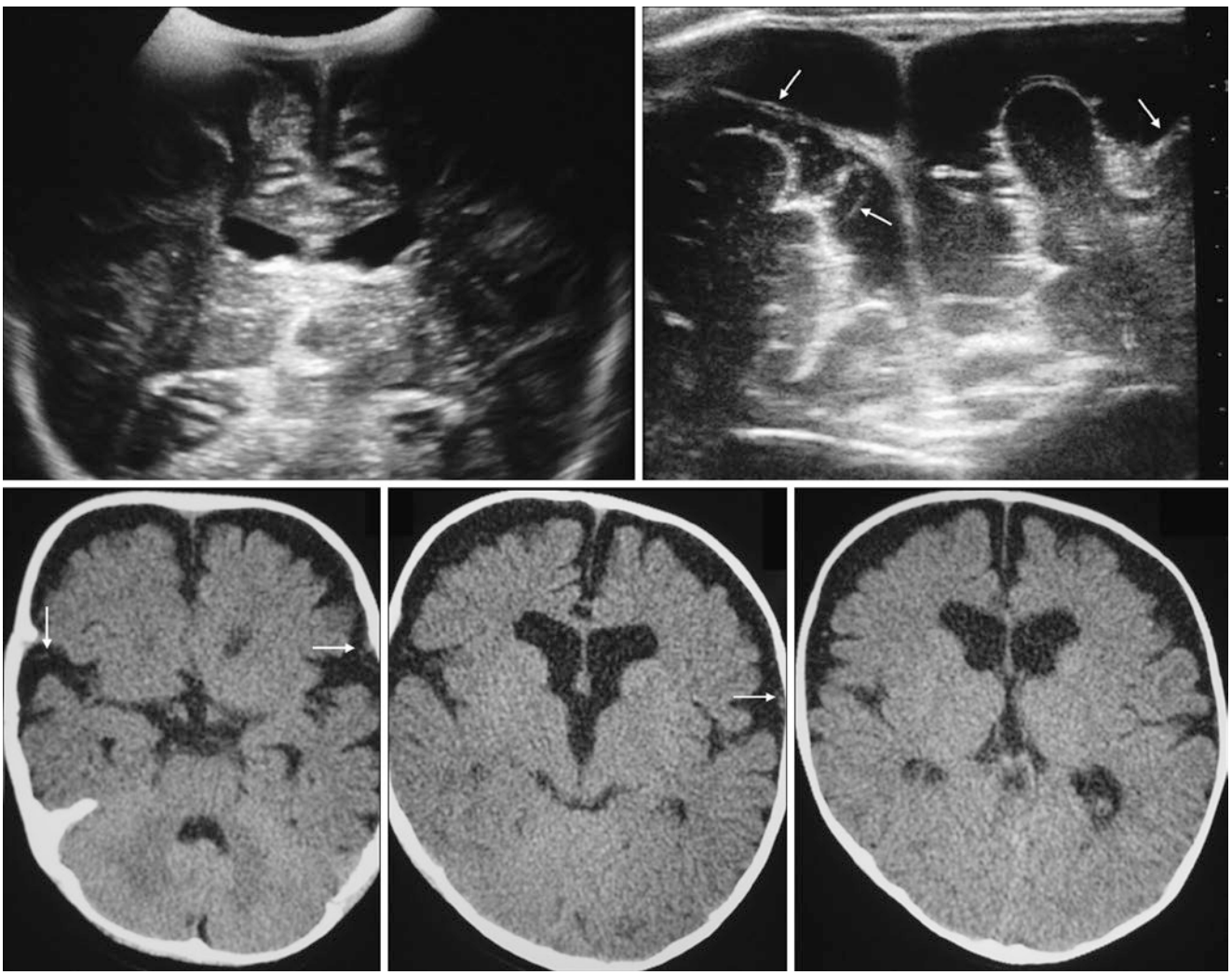

Fig. 23.195 A 4-month-old with macrocephaly had enlarged SASs of the frontal convexities and sylvian fissures bilaterally on coronal ultrasound images (*top row*). The SASs were traversed by small cortical veins (*thin arrows*). An NECT (*bottom row*) was ordered soon after to exclude the presence of SDHs, and the findings of BESSI were then confirmed

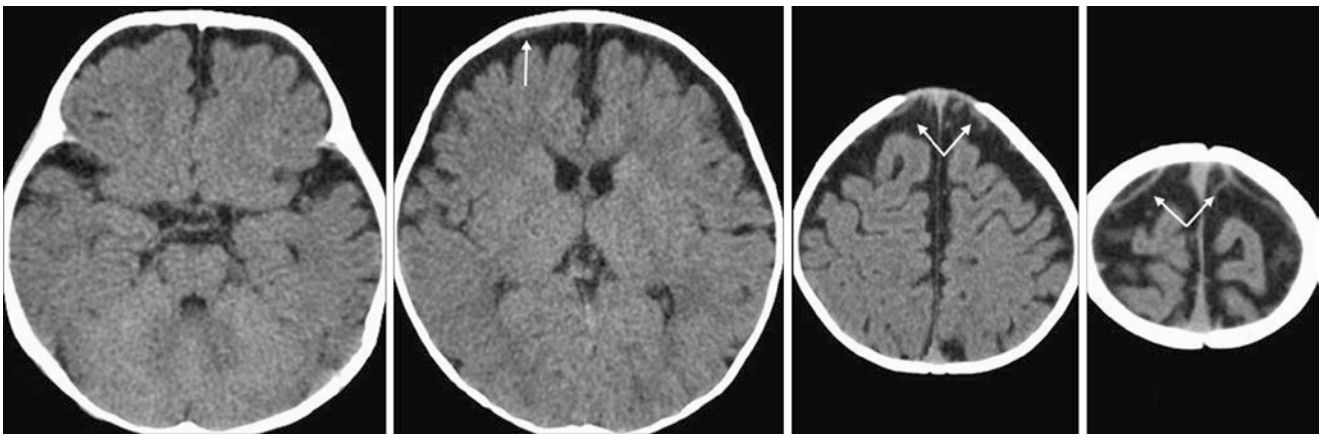

Fig. 23.196 A 6-month-old with macrocephaly had enlarged SASs of the frontal convexities and sylvian fissures bilaterally on NECT. The SASs were traversed by small, peripherally located cortical veins (*thin arrows*)

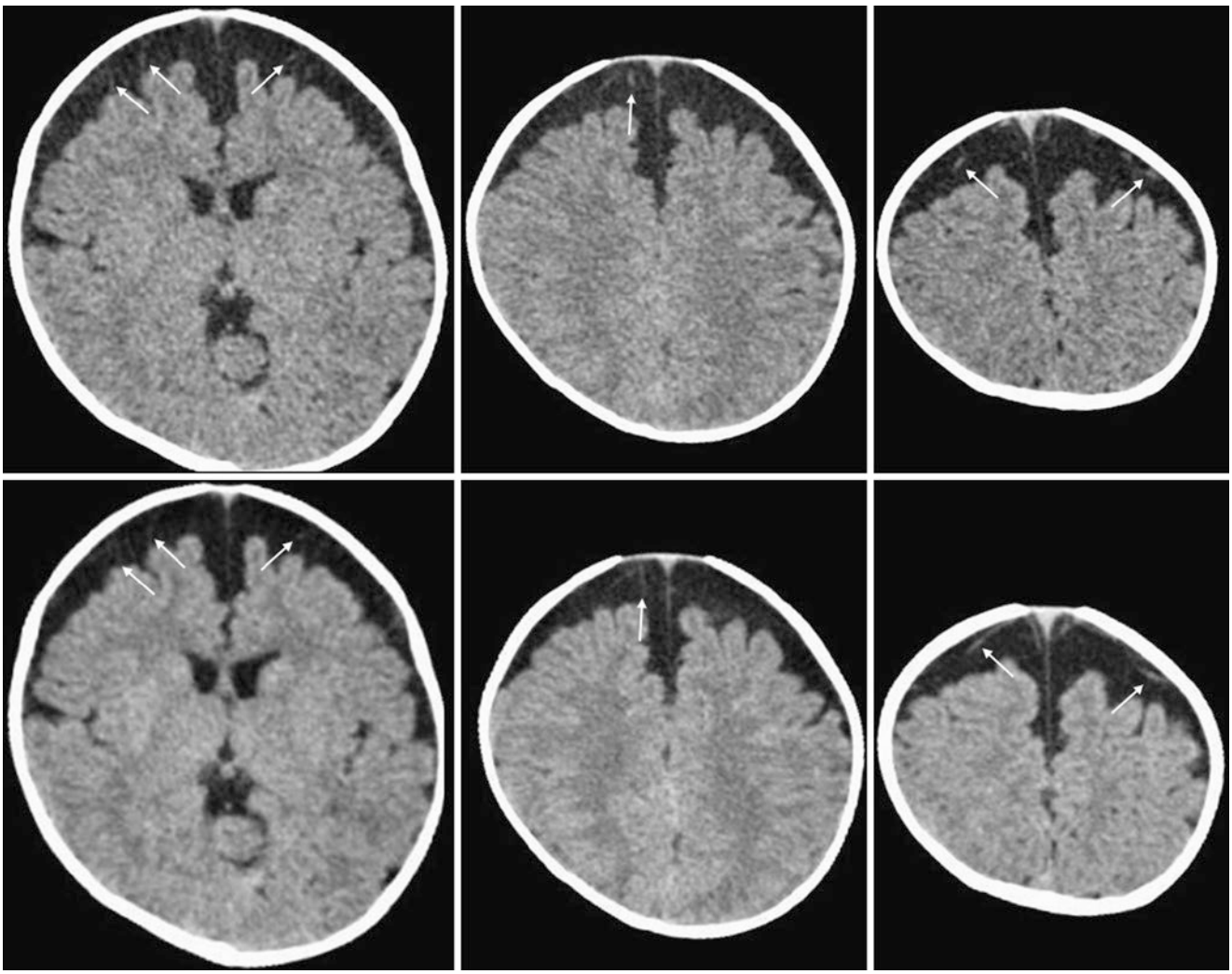

Fig. 23.197 A 7-month-old with trauma also was noted to have macrocephaly. NECT showed enlarged SASs of the frontal convexities, which were crossed by small cortical veins (*thin arrows*). The 0.8-mm thin-section images (*top row*) depict such tiny cortical veins better than the thicker 2.5-mm images (*bottom row*)

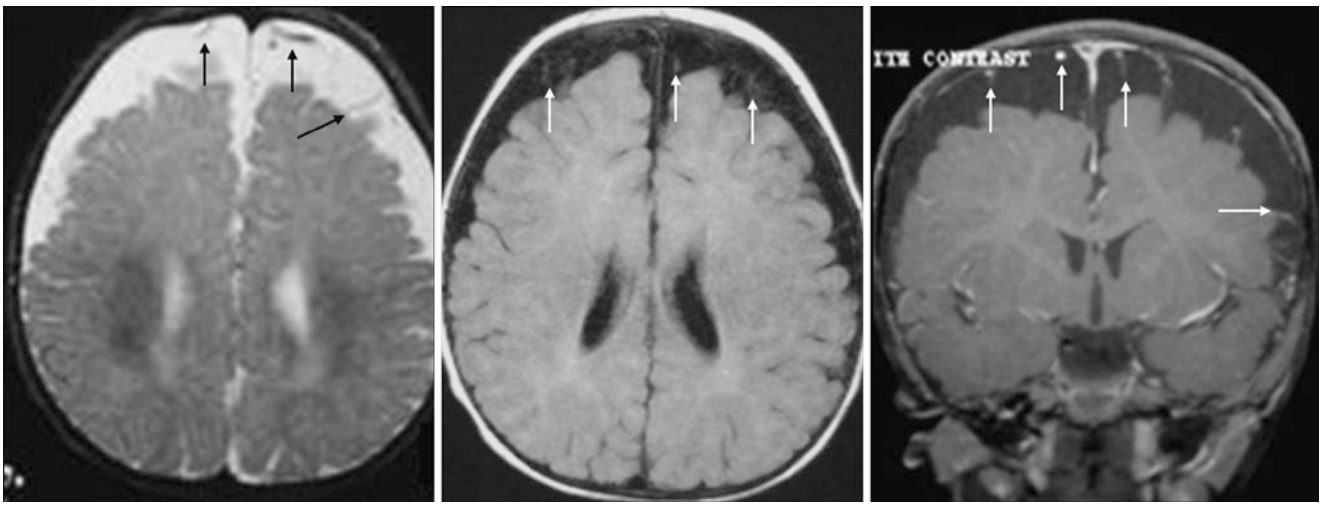

Fig. 23.198 A developmentally normal 10-month-old with macrocephaly underwent a 1.5T MRI. The SASs were moderately enlarged along the frontal convexities, and were crossed by multiple small cortical veins (*thin arrows*) on axial T2WI (*left*), FLAIR (*middle*), and coronal postcontrast T1WI (*right*). The SASs suppressed with CSF on FLAIR

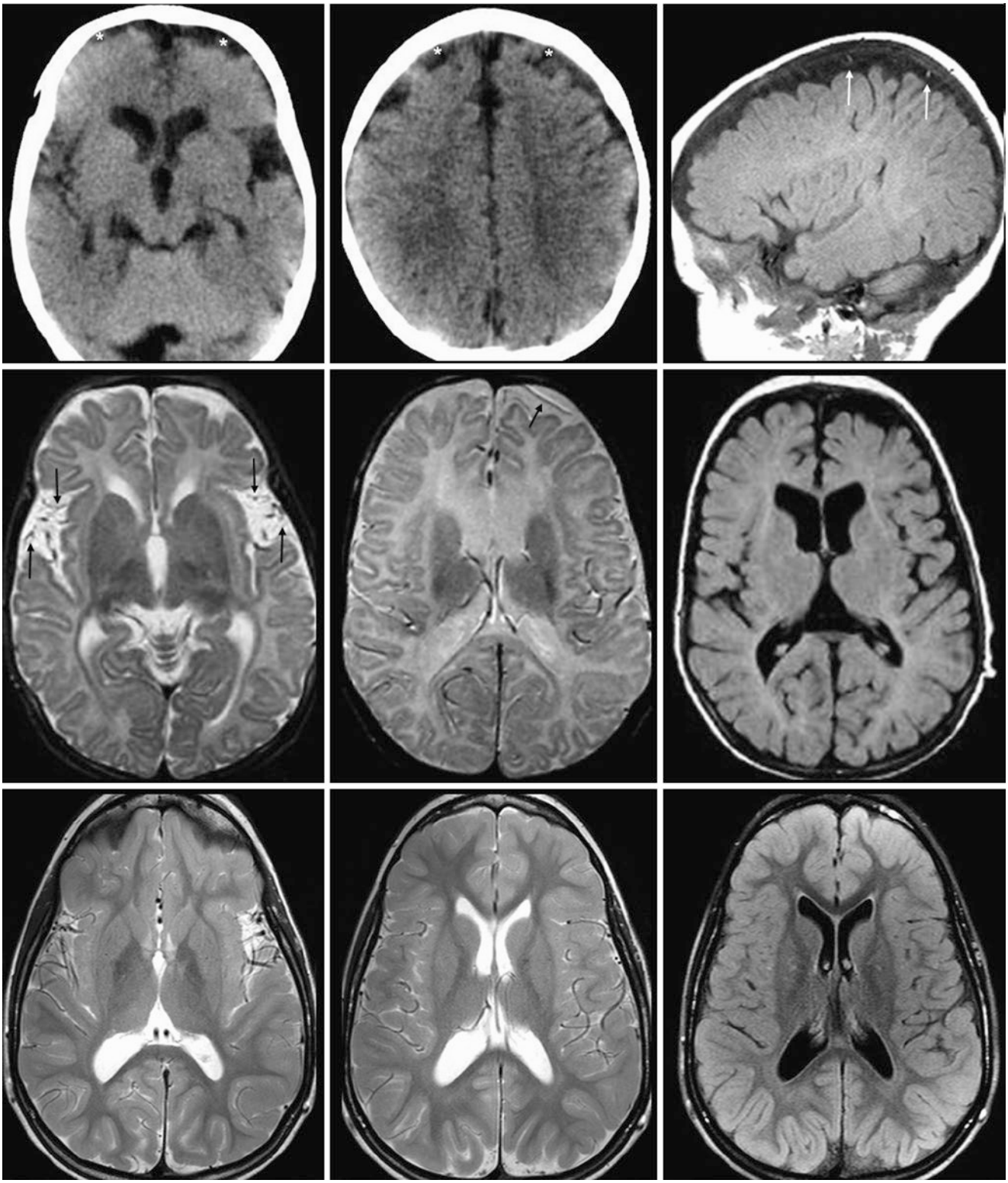

Fig. 23.199 A 10-year follow-up of BESSI. *Top row*: NECT (*left* and *middle*) in a developmentally normal, macrocephalic 7-month-old showed extra-axial space prominence (*asterisks*), but with density greater than that of CSF, perhaps artifactual, owing to combined motion and volume averaging. An MRI with sagittal T1WI (*right*) was obtained to exclude SDHs. *Middle row*: At 7 months of age, axial FLAIR T2WI (*left*), proton-density (*left middle*), and FLAIR (*right*) confirmed that the enlarged SASs suppressed with CSF, and depicted the cortical veins (*thin arrows*) crossing the SASs. *Bottom row*: On a 10-year repeat MRI, that was interpreted as normal T2WI (*left* and *middle*) and FLAIR (*right*) confirmed resolution of BESSI

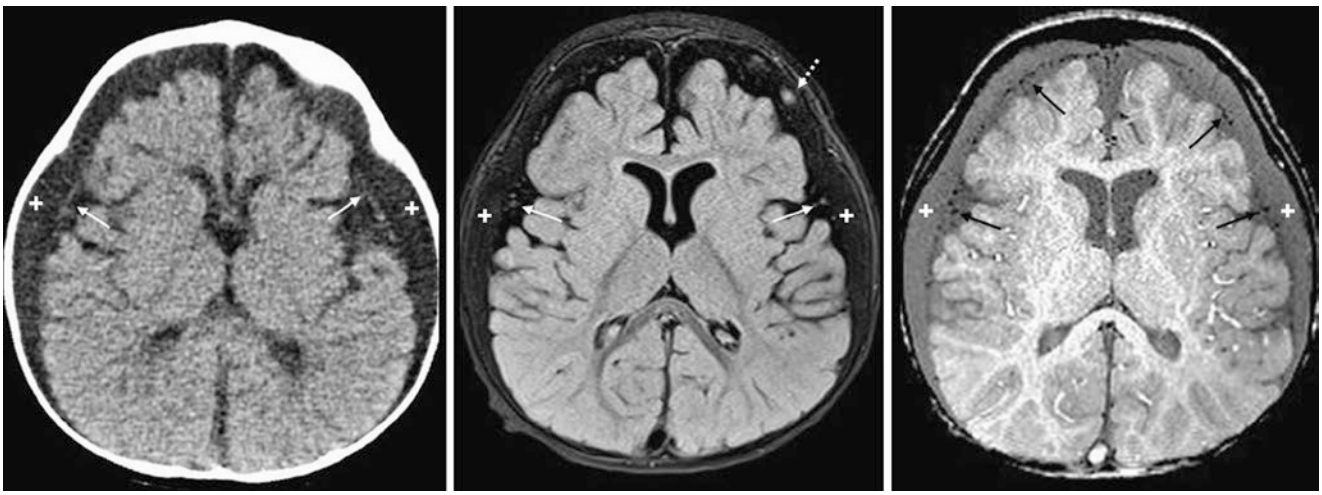

Fig. 23.200 Comparison case of subdural hygromas. NECT (*left*) in a macrocephalic 20-month-old with no history of trauma showed bilateral subdural collections (*plus signs*) along the convexities; cortical veins were displaced inwards (*thin arrows*). On a 3T MRI, these collections followed CSF on all sequences, including T2WI (not shown), FLAIR (*middle*), and SWI (*right*). One must exercise caution on FLAIR, as pulsation artifacts may mimic cortical veins (*dotted arrow*)

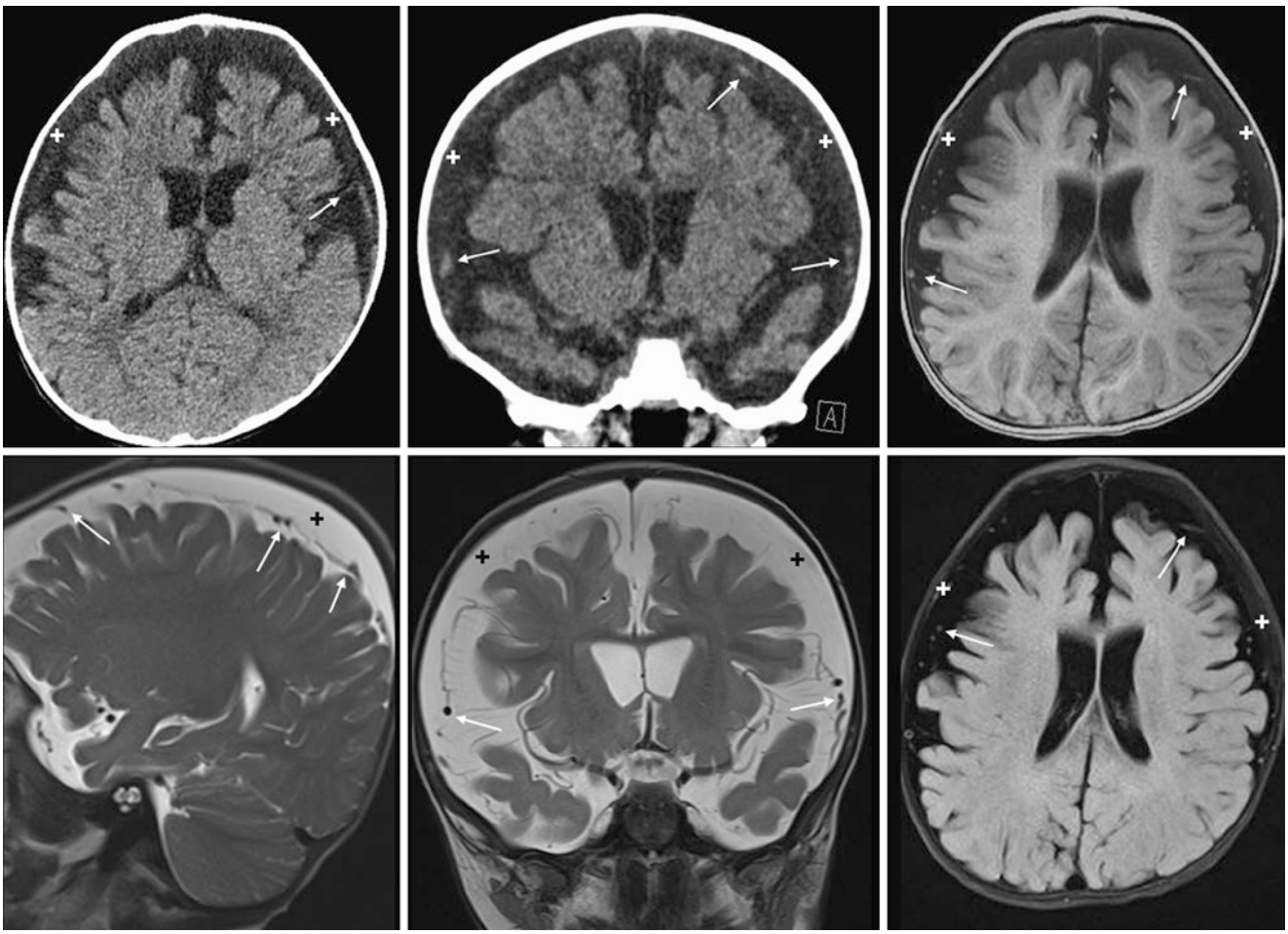

Fig. 23.201 Comparison case of subdural hygromas. NECT axial (*top left*) and coronal (*top middle*) reformats in a 14-month-old with no history of trauma show bilateral subdural collections (*plus signs*) along the convexities, which displace cortical veins inwards (*thin arrows*). On 3T MRI, these collections follow CSF on axial T1WI (*top right*), sagittal (*bottom left*) and coronal (*bottom middle*) T2WI, and suppress along with CSF on FLAIR (*bottom right*)

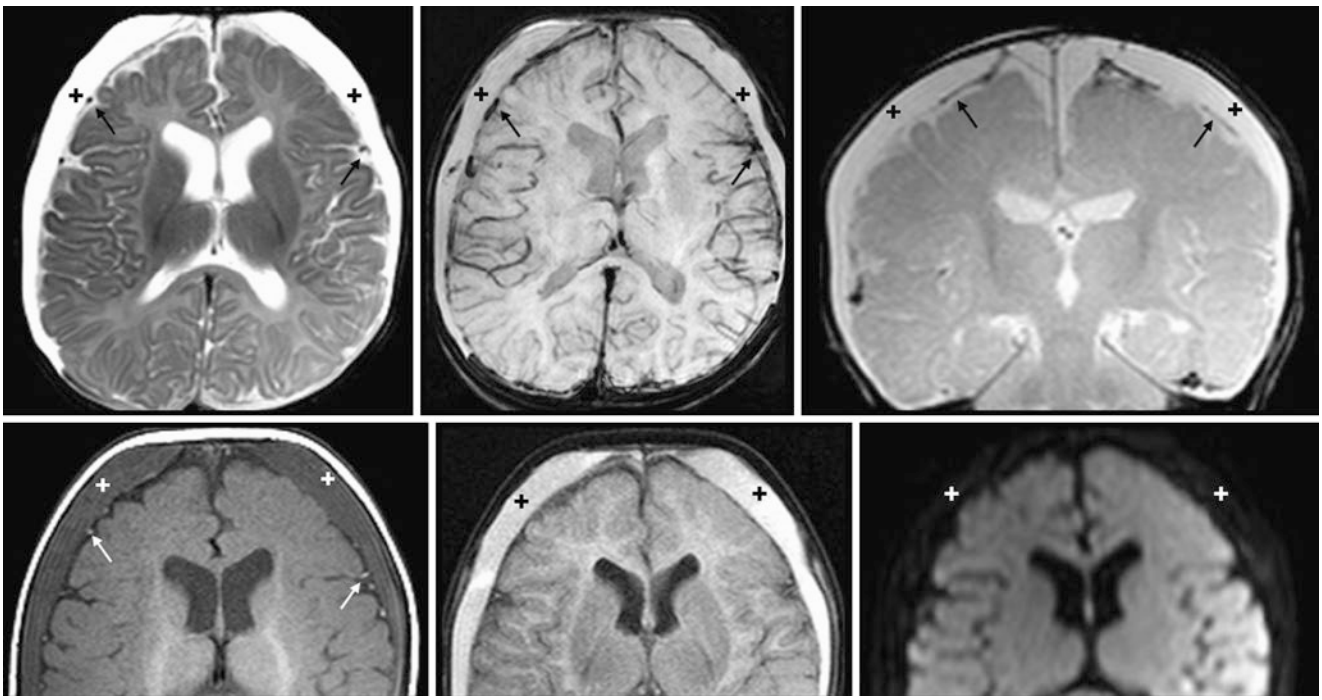

Fig. 23.202 Comparison case of subdural hematomas or hygromas in nonaccidental trauma (NAT). On 3T MRI, a 4-month-old with a history of NAT had bilateral collections (*plus signs*) on T2WI (*top left*), SWI (*top middle*), coronal GE T2*WI (*top right*), T1WI (*bottom left*), FLAIR (*bottom middle*), and DWI (*bottom right*), which did not suppress on FLAIR. Note the cortical veins displaced inwards (*thin arrows*)

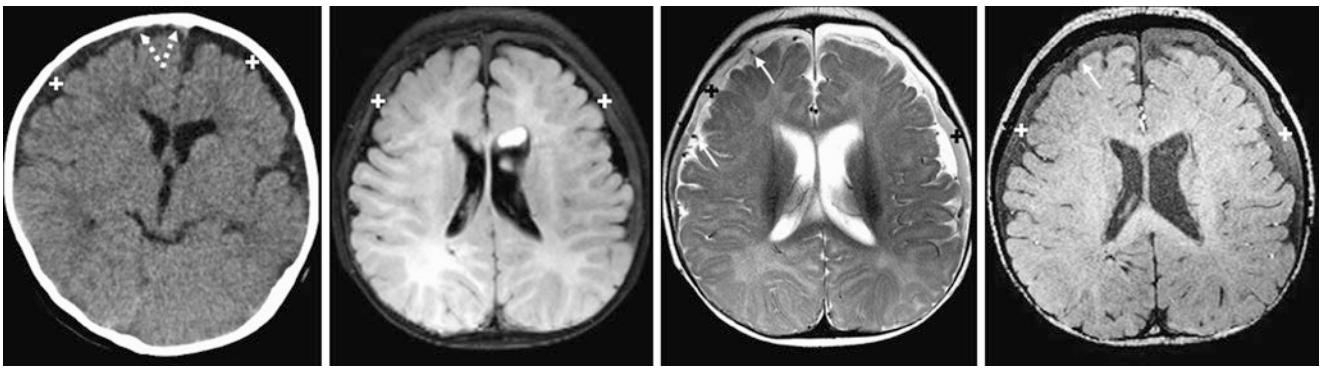

Fig. 23.203 Comparison case of chronic SDHs. In a 5-month-old, NECT (*left*) shows bilateral SDHs (*plus signs*) of the frontal convexities; hypodensity implies that these are chronic. The right SDH has acute hemorrhagic foci (*dotted arrows*). On a 3T MRI, the SDHs did not suppress with CSF on FLAIR (*left middle*). T2WI (*right middle*) and SWI (*right*) show cortical veins displaced inwards (*thin arrows*). A nonaccidental trauma workup was deemed negative

Fig. 23.204 Comparison case of enlarged SASs in mucopolysaccharidosis. In a 19-month-old, a T2WI MRI (*left*) showed mildly prominent SASs of the frontal convexities, with cortical veins (*thin arrows*) traversing them. On sagittal T1WI (*middle*), there was a nearly J-shaped sella (*dotted arrow*) and odontoid capping (between *arrows*), consistent with Hurler syndrome. On a T2WI MRI 5 years later (*right*), the SASs remained mildly prominent

References

1. Barkovich AJ. MR of the normal neonatal brain: assessment of deep structures. AJNR Am J Neuroradiol. 1998;19:1397–403.
2. Barkovich AJ, Hajnal BL, Vigneron D, Sola A, Partridge JC, Allen F, Ferriero DM. Prediction of neuromotor outcome in perinatal asphyxia: evaluation of MR scoring systems. AJNR Am J Neuroradiol. 1998;19:143–9.
3. Liauw L, Palm-Meinders IH, van der Grond J, Leijser LM, le Cessie S, Laan LA, et al. Differentiating normal myelination from hypoxic-ischemic encephalopathy on T1-weighted MR Images: a new approach. AJNR Am J Neuroradiol. 2007;28:660–5.
4. Liauw L, van der Grond J, van den Berg-Huysmans AA, Laan LA, van Buchem MA, van Wezel-Meijler G. Is there a way to predict outcome in (near) term neonates with hypoxic-ischemic encephalopathy based on MR imaging? AJNR Am J Neuroradiol. 2008;29:1789–94.
5. Liauw L, van Wezel-Meijler G, Veen S, van Buchem MA, van der Grond J. Do apparent diffusion coefficient measurements predict outcome in children with neonatal hypoxic-ischemic encephalopathy? AJNR Am J Neuroradiol. 2009;30:264–70.
6. Barkovich AJ, Kjos BO, Jackson Jr DE, Norman D. Normal maturation of the neonatal and infant brain: MR imaging at 1.5 T. Radiology. 1988;166:173–80.
7. Barkovich AJ, Mukherjee P. Normal development of the neonatal and infant brain, skull, and spine. In: Barkovich AJ, Raybaud C, editors. Pediatric neuroimaging. 5th ed. Philadelphia: Lippincott Williams & Wilkins; 2012. p. 20–80.
8. Counsell SJ, Maalouf EF, Fletcher AM, Duggan P, Battin M, Lewis HJ, et al. MR imaging assessment of myelination in the very preterm brain. AJNR Am J Neuroradiol. 2002;23:872–81.
9. Barkovich AJ, Hajnal BL, Vigneron D, Sola A, Partridge JC, Allen F, Ferriero DM. Prediction of neuromotor outcome in perinatal asphyxia: evaluation of MR scoring systems. AJNR Am J Neuroradiol. 1998;19:143–9.
10. Taoka T, Aida N, Ochi T, Takahashi Y, Akashi T, Miyasaka T, et al. Transient hyperintensity in the subthalamic nucleus and globus pallidus of newborns on T1-weighted images. AJNR Am J Neuroradiol. 2011;32:1130–7.
11. Sarikaya B, McKinney AM, Spilseth B, Truwit CL. Comparison of spin-echo T1- and T2-weighted and gradient-echo T1-weighted images at 3T in evaluating very preterm neonates at term-equivalent age. AJNR Am J Neuroradiol. 2013;34:1098–103.
12. Tyan AE, McKinney AM, Hanson TJ, Truwit CL. Comparison of spin-echo and gradient-echo T1-weighted and spin-echo T2-weighted images at 3T in evaluating term-neonatal myelination. AJNR Am J Neuroradiol. 2015;36:411–6.
13. Robertson RL, Ben-Sira L, Barnes PD, Mulkern RV, Robson CD, Maier SE, et al. MR line-scan diffusion-weighted imaging of term neonates with perinatal brain ischemia. AJNR Am J Neuroradiol. 1999;20:1658–70.
14. Forbes KP, Pipe JG, Bird R. Neonatal hypoxic-ischemic encephalopathy: detection with diffusion-weighted MR imaging. AJNR Am J Neuroradiol. 2000;21:1490–6.
15. Cowan MF. Magnetic resonance imaging of the normal infant brain: term to 2 years. In: Rutherford MA, editor. MRI of the neonatal brain. 4th ed. Philadelphia: WB Saunders; 2001.
16. Holland BA, Haas DK, Norman D, Brant-Zawadzki M, Newton TH. MRI of normal brain maturation. AJNR Am J Neuroradiol. 1986;7:201–8.
17. Brody BA, Kinney HC, Kloman AS, Gilles FH. Sequence of central nervous system myelination in human infancy. I. An autopsy study of myelination. J Neuropathol Exp Neurol. 1987;46:283–301.
18. Kinney HC, Brody BA, Kloman AS, Gilles FH. Sequence of central nervous system myelination in human infancy: patterns of myelination in autopsied infants. J Neuropathol Exp Neurol. 1988;47:217–34.
19. Dietrich RB, Bradley WG, Zaragoza 4th EJ, Otto RJ, Taira RK, Wilson GH, Kangarloo H. MR evaluation of early myelination patterns in normal and developmentally delayed infants. AJR Am J Roentgenol. 1988;150:889–96.
20. Bird CR, Hedberg M, Drayer BP, Keller PJ, Flom RA, Hodak JA. MR assessment of myelination in infants and children: usefulness of marker sites. AJNR Am J Neuroradiol. 1989;10:731–40.
21. Hayakawa K, Konishi Y, Kuriyama M, Konishi K, Matsuda T. Normal brain maturation in MRI. Eur J Radiol. 1991;12:208–15.
22. Staudt M, Schropp C, Staudt F, Obletter N, Bise K, Breit A, Weinmann HM. MRI assessment of myelination: an age standardization. Pediatr Radiol. 1994;24:122–7.
23. Parazzini C, Baldoli C, Scotti G, Triulzi F. Terminal zones of myelination: MR evaluation of children aged 20–40 months. AJNR Am J Neuroradiol. 2002;23:1669–73.
24. Maricich SM, Azizi P, Jones JY, Morriss MC, Hunter JV, Smith EO, Miller G. Myelination as assessed by conventional MR imaging is normal in young children with idiopathic developmental delay. AJNR Am J Neuroradiol. 2007;28:1602–5.

Suggested Reading

Asa SL, Kovacs K, Laszlo FA, Domokos I, Ezrin C. Human fetal adenohypophysis. Histologic and immunocytochemical analysis. Neuroendocrinology. 1986;43:308–16.

Ashikaga R, Araki Y, Ono Y, Nishimura Y, Ishida O. Appearance of normal brain maturation on fluid-attenuated inversion-recovery (FLAIR) MR images. AJNR Am J Neuroradiol. 1999;20:427–31.

Bartha AI, Yap KR, Miller SP, Jeremy RJ, Nishimoto M, Vigneron DB, et al. The normal neonatal brain: MR imaging, diffusion tensor imaging, and 3D MR spectroscopy in healthy term neonates. AJNR Am J Neuroradiol. 2007;28:1015–21.

Battin MR, Maalouf EF, Counsell SJ, Herlihy AH, Rutherford MA, Azzopardi D, Edwards AD. Magnetic resonance imaging of the brain in very preterm infants: visualization of the germinal matrix, early myelination, and cortical folding. Pediatrics. 1998;101:957–62.

Castillo M. Pituitary gland: development, normal appearances, and magnetic resonance imaging protocols. Top Magn Reson Imaging. 2005;16:259–68.

Chau V, Poskitt KJ, Sargent MA, Lupton BA, Hill A, Roland E, Miller SP. Comparison of computer tomography and magnetic resonance imaging scans on the third day of life in term newborns with neonatal encephalopathy. Pediatrics. 2009;123:319–26.

Cox TD, Elster AD. Normal pituitary gland: changes in shape, size, and signal intensity during the 1st year of life at MR imaging. Radiology. 1991;179:721–4.

Dietrich RB, Lis LE, Greensite FS, Pitt D. Normal MR appearance of the pituitary gland in the first 2 years of life. AJNR Am J Neuroradiol. 1995;16:1413–9.

Felderhoff-Mueser U, Rutherford MA, Squier WV, Cox P, Maalouf EF, Counsell SJ, et al. Relationship between MR imaging and histopathologic findings of the brain in extremely sick preterm infants. AJNR Am J Neuroradiol. 1999;20:1349–57.

Girard N, Raybaud C, Poncet M. In vivo MR study of brain maturation in normal fetuses. AJNR Am J Neuroradiol. 1995;16:407–13.

Heinz ER, Provenzale JM. Imaging findings in neonatal hypoxia: a practical review. AJR Am J Roentgenol. 2009;192:41–7.

Kitamura E, Miki Y, Kawai M, Itoh H, Yura S, Mori N, et al. T1 signal intensity and height of the anterior pituitary in neonates: correlation with postnatal time. AJNR Am J Neuroradiol. 2008;29:1257–60.

Liauw L, Palm-Meinders IH, van der Grond J, Leijser LM, le Cessie S, Laan LA, et al. Differentiating normal myelination from hypoxic-ischemic encephalopathy on T1-weighted MR Images: a new approach. AJNR Am J Neuroradiol. 2007;28:660–5.

Liauw L, van der Grond J, van den Berg-Huysmans AA, Laan LA, van Buchem MA, van Wezel-Meijler G. Is there a way to predict outcome in (near) term neonates with hypoxic-ischemic encephalopathy based on MR imaging? AJNR Am J Neuroradiol. 2008;29:1789–94.

Maalouf EF, Duggan PJ, Rutherford MA, Counsell SJ, Fletcher AM, Battin M, et al. Magnetic resonance imaging of the brain in a cohort of extremely preterm infants. J Pediatr. 1999;135:351–7.

Miller JH, McKinstry RC, Philip JV, Mukherjee P, Neil JJ. Diffusion-tensor MR imaging of normal brain maturation: a guide to structural development and myelination. AJR Am J Roentgenol. 2003;180:851–9.

Murakami JW, Weinberger E, Shaw DW. Normal myelination of the pediatric brain imaged with fluid-attenuated inversion-recovery (FLAIR) MR imaging. AJNR Am J Neuroradiol. 1999;20:1406–11.

Nelson MD, Jr. Session III: Neuroimaging of perinatal asphyxia in term infants. In: Acute perinatal asphyxia in term infants: report of the workshop. National Institutes of Health and National Institute of Child Health and Human Development. Philadelphia: Diane Publishing; 1997. p. 110–3.

Robertson RL, Robson CD, Zurakowski D, Antiles S, Strauss K, Mulkern RV. CT versus MR in neonatal brain imaging at term. Pediatr Radiol. 2003;33:442–9.

Rutherford MA. The asphyxiated term infant. In: Rutherford MA, editor. MRI of the neonatal brain. 4th ed. Philadelphia: WB Saunders; 2001.

Rutherford MA, Pennock JM, Schwieso JE, Cowan FM, Dubowitz LM. Hypoxic ischaemic encephalopathy: early magnetic resonance imaging findings and their evolution. Neuropediatrics. 1995;26:183–91.

van Wezel-Meijler G, van der Knaap MS, Sie LT, Oosting J, van Amerongen AH, Cranendonk A, Lafeber HN. Magnetic resonance imaging of the brain in premature infants during the neonatal period. Normal phenomena and reflection of mild ultrasound abnormalities. Neuropediatrics. 1998;29:89–96.

Wattjes MP, Lutterbey GG, Gieseke J, Träber F, Klotz L, Schmidt S, Schild HH. Double inversion recovery brain imaging at 3T: diagnostic value in the detection of multiple sclerosis lesions. AJNR Am J Neuroradiol. 2007;28:54–9.

Wolpert SM, Osborne M, Anderson M, Runge VM. The bright pituitary gland – a normal MR appearance in infancy. AJNR Am J Neuroradiol. 1988;9:1–3.

Part II

Skull

Skull: Introduction

24

The Skull section of this book is intended to address normal variations and do not touch lesions of the calvarium or structures that traverse the calvarium. Very little recent literature or texts have focused solely on the skull. Perhaps this is because the majority of variations are benign. As such, there are only a few recent works that address the normal sutures and their variants that occur as a neonate, infant, and young child, which may occasionally persist into adolescence and adulthood. Uncommonly, these sutures may not entirely fuse or may asymmetrically fuse in older children and adults and thus may mimic fractures.

Besides normal variants of the *cranial sutures*, there are many variations in the skull base and *cranial foramina* that may also simulate pathology, such as lytic neoplasms or erosions. Such *enlarged foramina* (such as parietal foramina) are most commonly not related to congenital or metabolic disorders, although in rare cases severely enlarged foramina may occur in certain disorders. Additionally, enlargement of such foramina can simulate erosions from an adjacent neoplasm.

Additionally, most *vascular channels* such as venous lakes, emissary veins, and uncommon arterial channels are readily recognizable. However, an uncommon or rare asymmetrically enlarged vascular channel can be problematic and simulate a neoplasm. Perhaps even more problematic are *low-flow vascular lesions* such as cavernous hemangiomas (cavernomas) of the calvarium, which can enhance and can have an ambiguous appearance when quite large.

There are also many *variations in the degree of aeration* (such as regarding the paranasal sinuses and mastoids), sclerosis (such as enostoses/exostoses), and *fatty deposition within the calvarium* (such as with calvarial arrested pneumatization of sinuses, lipomas, and hemangiomas) that can either be normal variations or "don't touch" lesions. To this author's knowledge, there are also scant existing references in this regard, and this section of the book is dedicated to also being a compilation of such uncommon variants. Some of these may be obvious to a radiologist as being benign, but it is still helpful to be able to correctly identify the variant to dissuade a referring physician who is inclined to send a patient to surgery.

Thus, the author acknowledges that this section has limitations, given the relatively new and sparingly addressed prior literature on such calvarial variants. Perhaps each of the following chapters of skull variations provides enough of a spectrum to generate future publications for some of the problematic variants described herein. Three-dimensional reconstructions of nonenhanced CT (NECT) are included for many of the variations when it would seem beneficial, such as when reviewing pediatric sutures in the setting of trauma to exclude fracture.

A.M. McKinney, *Atlas of Normal Imaging Variations of the Brain, Skull, and Craniocervical Vasculature*,
DOI 10.1007/978-3-319-39790-0_24

Pediatric Skull: Normal Pediatric Sutures on Computed Tomography

25

Knowledge of *normal suture lines* is necessary to recognize abnormalities and normal variants in pediatric patients and even later in adults. The typical, normally patent sutures that can be seen in children under 6 months of age are shown in Fig. 25.1. The following pages describe normal anatomy of the sutures of the skull base, basiocciput, and orbitofrontal region that can simulate *fractures* or other disease in children and less commonly in adults.

A.M. McKinney, *Atlas of Normal Imaging Variations of the Brain, Skull, and Craniocervical Vasculature*,
DOI 10.1007/978-3-319-39790-0_25

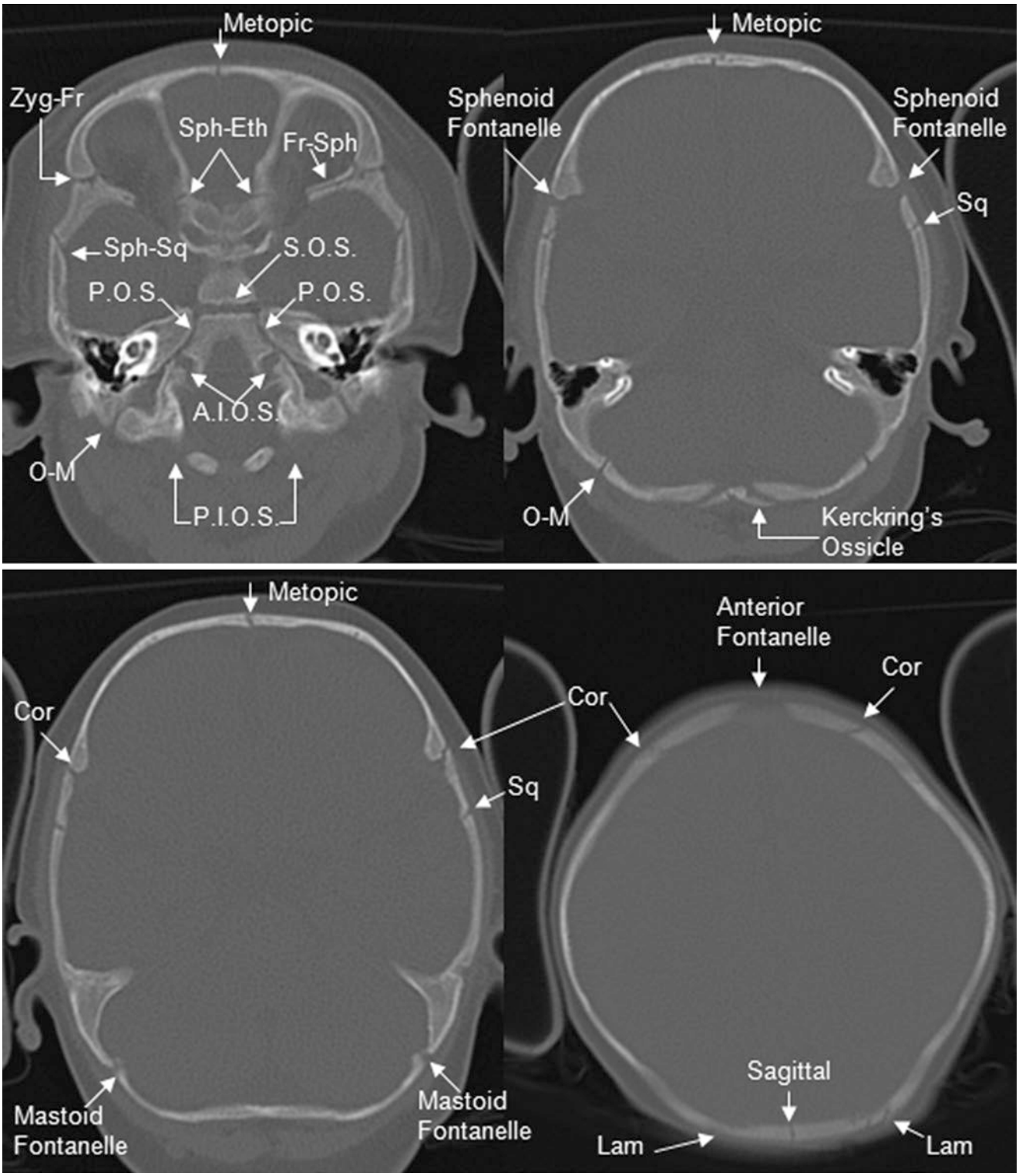

Fig. 25.1 A 4 month old with various sutures and foramina on axial NECT. *A.I.O.S* anterior intra-occipital synchondrosis; *Cor* coronal; *Fr-Sph* fronto-sphenoidal; *I.O.S.* intra-occipital synchondrosis; *Lam* lambdoidal; *O-M* occipito-mastoidal; *P.I.O.S.* posterior petro-occipital synchondrosis; *P.O.S.* petro-occipital synchondrosis; *S.O.S.* spheno-occipital synchondrosis; *Sph-Eth* spheno-ethmoidal; *Sph-Sq* spheno-squamosal; *Sq* Squamosal; *Zyg-Fr* zygomatico-frontal

25.1 Pediatric Skull Base: Intraoccipital Sutures and Kerckring Ossicle

The following data describe the fusion of the *anterior intraoccipital synchondrosis* (AIOS), *posterior petro-occipital synchondrosis* (PIOS), and *supraoccipital foramen/Kerckring ossicle*. Incomplete fusion (or scans obtained during fusion) can simulate *fracture defects*, pseudoforamina, or even appear as ossicles. The AIOS can have a normal "cruciate" appearance during its formation and persist as pseudoforamina or tiny clefts (Figs. 25.2, 25.3, 25.4, 25.5, 25.6, 25.7 and 25.8).

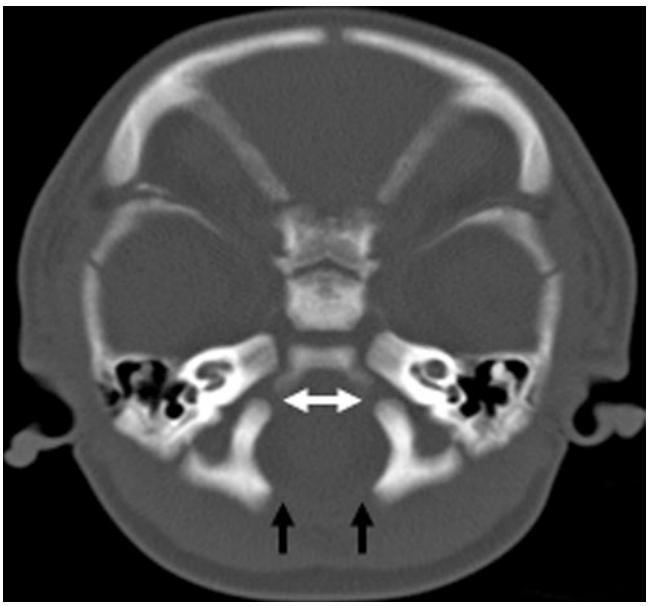

Fig. 25.2 A normal 2 week old. *White arrows* indicate AIOS; *black arrows* indicate PIOS

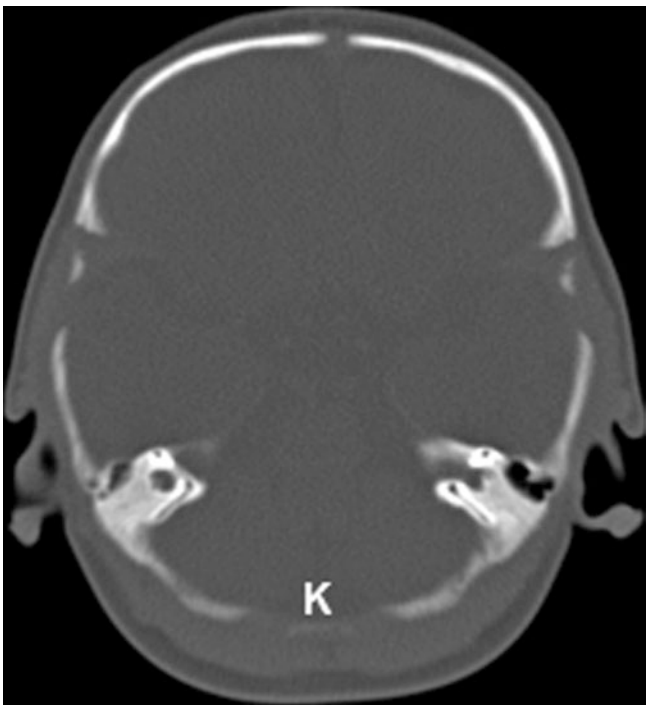

Fig. 25.4 A normal 2 month old. *K* indicates Kerckring ossicle in the supraoccipital foramen

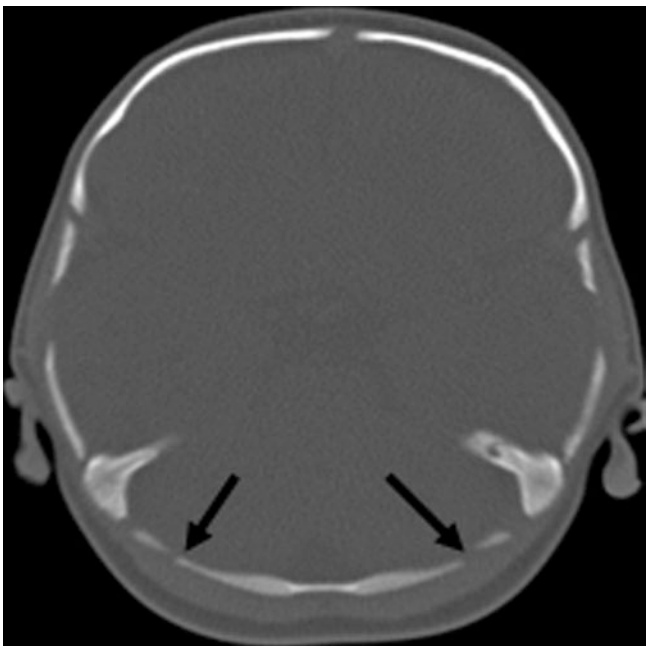

Fig. 25.3 A normal 2 month old. *Black arrows* indicate PIOS

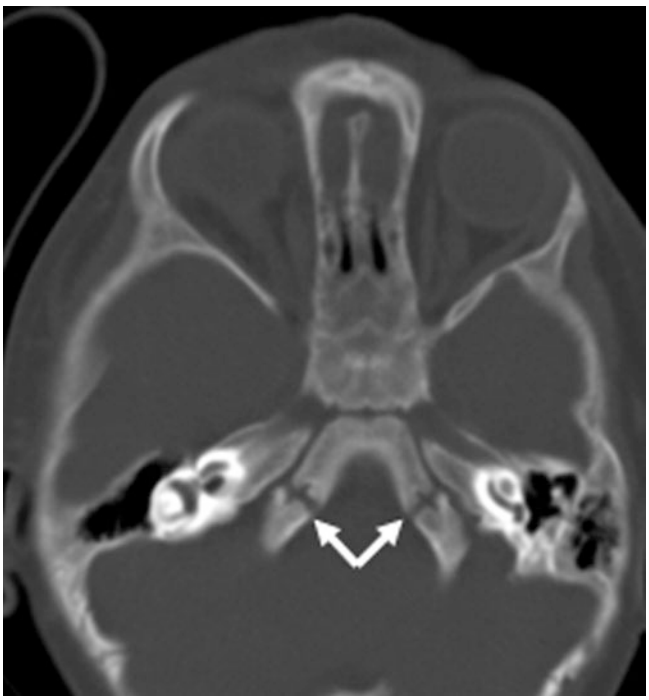

Fig. 25.5 A normal 1 year old with a cruciate AIOS (*white arrows*)

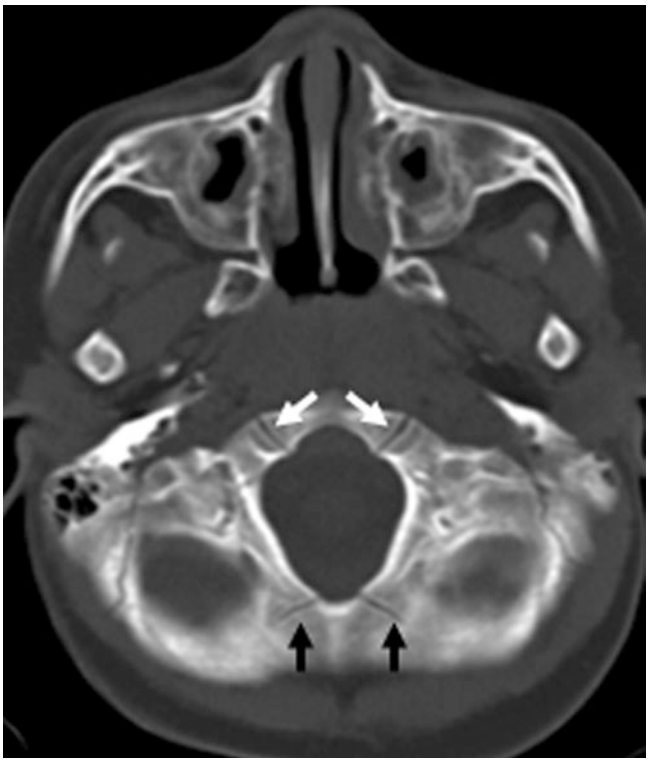

Fig. 25.6 A normal 2 year old with unfused AIOS (*white arrows*) and PIOS (*black arrows*)

Fig. 25.7 A normal 27 year old with bilateral AIOS pseudoforamina (*white arrows*)

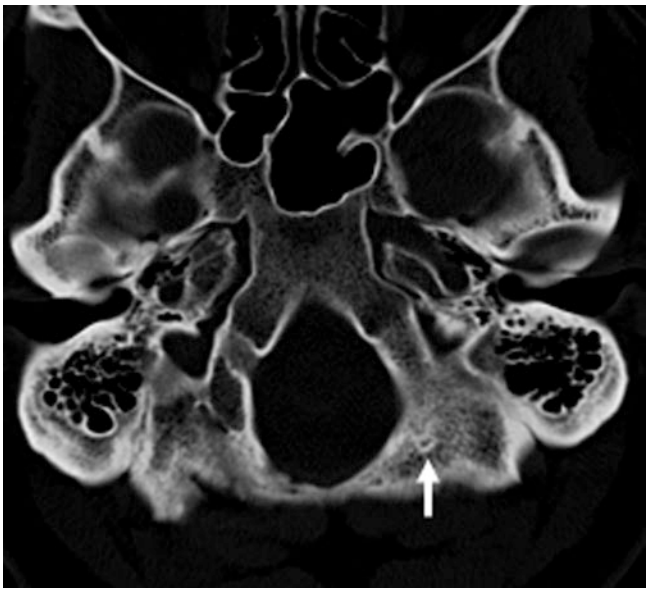

Fig. 25.8 A normal 50 year old with a posterior AIOS pseudoforamen (*white arrow*)

25.2 Pediatric Skull Base: Intraoccipital, Petrooccipital, and Occipitomastoid Sutures

Sutural development and fusion at the posterior skull base: The *anterior/posterior intra-occipital synchondroses* usually fuse in early childhood, starting at about 1–2 years, and they are usually completed by 7–10 years. The *spheno-occipital synchondrosis* usually fuses around the time of puberty or shortly thereafter. The *petro-occipital, sphenopetrosal, and occipitomastoid* (OM) sutures usually do not complete fusion until the late teens and may not fuse even in adults (Figs. 25.9, 25.10, 25.11 and 25.12).

Fig. 25.9 A normal 3 month old with an MPR slab (8-mm thickness) from a NECT. *White arrows* indicate AIOS; *black arrows* indicate PIOS; *arrowheads* indicate petro-occipital synchrondosis; *black dotted arrows* indicate the occipitomastoid suture

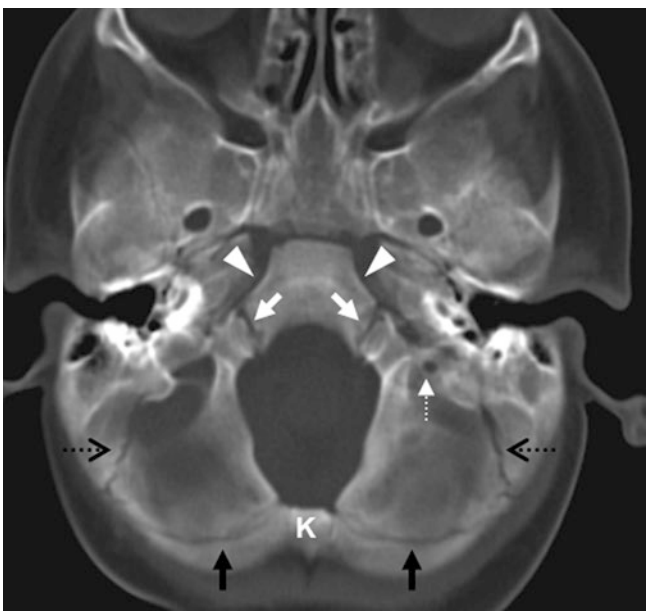

Fig. 25.10 A normal 1 year old with an MPR slab (11-mm thickness) from a NECT. *White arrows* indicate AIOS; *black arrows* indicate PIOS; *arrowheads* indicate petro-occipital synchrondosis; *dotted white arrow* indicates condylar canal; *dotted black arrows* indicate occipitomastoid sutures; *K* indicates Kerckring ossicle

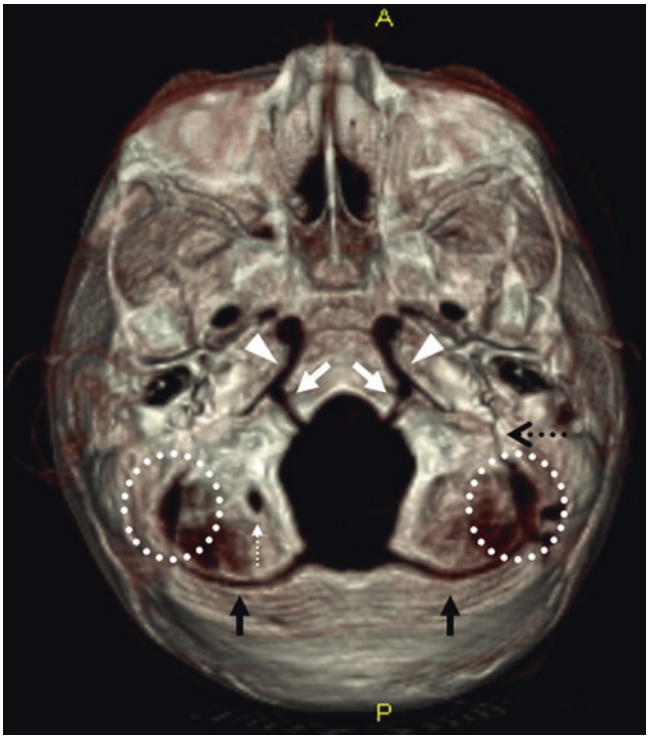

Fig. 25.11 A normal 3 month old with a three-dimensional reconstruction (*inferior view*) from a NECT. *White arrows* indicate AIOS; *black arrows* indicate PIOS; *arrowheads* indicate petro-occipital synchrondosis; *white dotted circles* indicate mastoid fontanelles; *White dotted arrow* indicates condylar canal

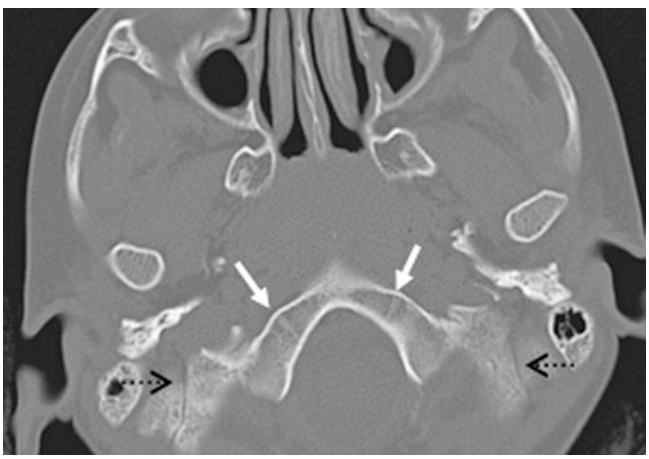

Fig. 25.12 A normal 9 year old. *White arrows* indicate AIOS; *dotted black arrows* indicate occipitomastoid sutures

25.3 Intraoccipital Suture Intrasutural Bone Normal Variant

Occasionally, the *AIOS* can persist for a while longer in infants or young children, even unilaterally, and may simulate a fracture. In this case, an "*AIOS bone*" persists, which should probably be considered a temporary intrasutural bone. This can cause confusion if the work-up is for trauma and when the child lays nonsymmetrically (or "cockeyed") in the scanner, as the unilaterality and asymmetry can simulate a *fracture* (Fig. 25.13).

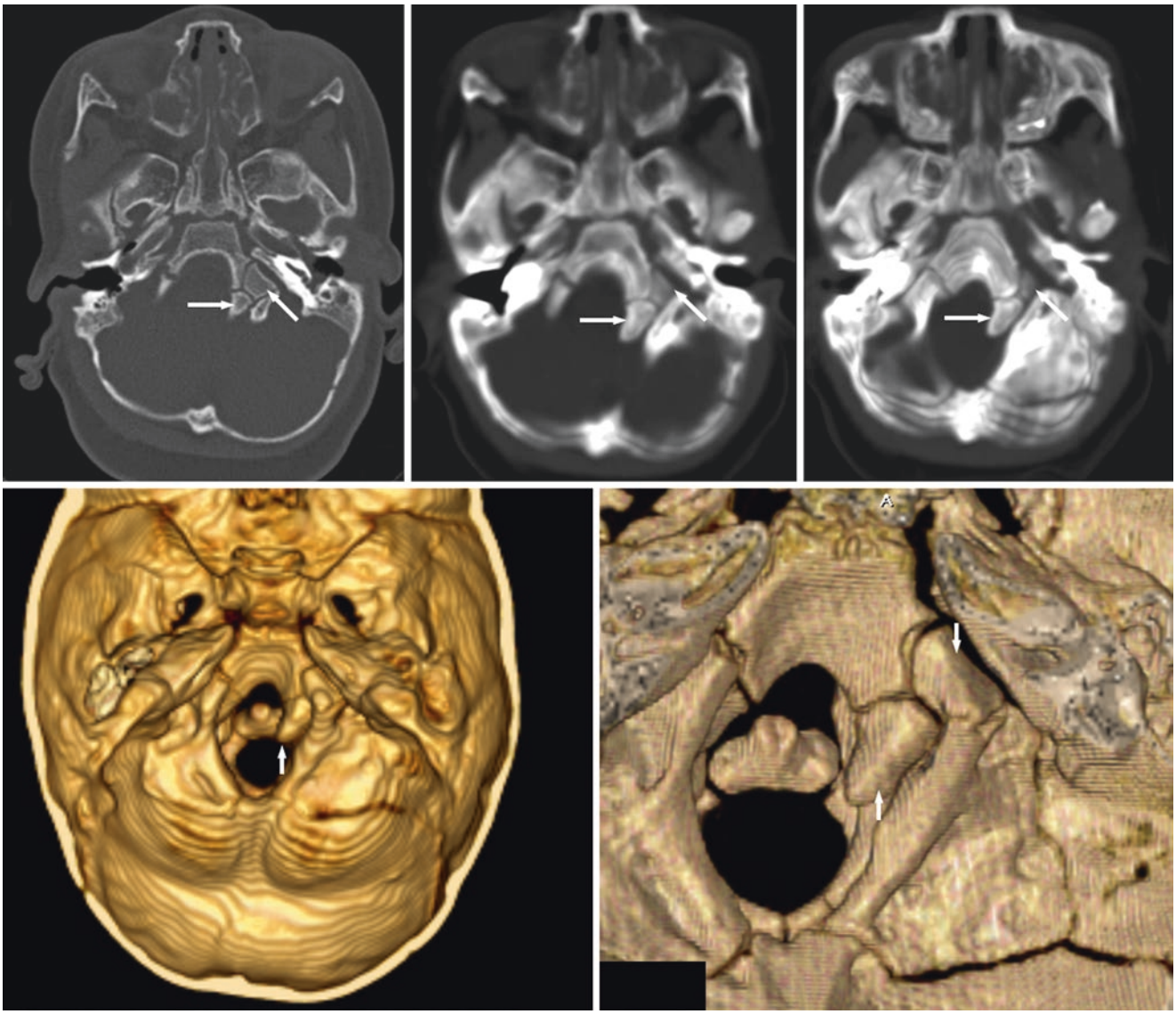

Fig. 25.13 A 13 month old with a work-up for nonaccidental trauma. Spiral CT (*top left*) demonstrated asymmetric lines in the region of the left occipital condyle (*white arrows*), with the patient lying obliquely in the scanner. However, on thicker MPR views that were corrected for the positioning (*top middle and top right*), the right AIOS was found to be fused, while intrasutural bones were noted on the left. This was best illustrated by three-dimensional images (*bottom row*, *views from superiorly*)

25.4 Kerckring Ossicle and Posterior Intraoccipital Suture Incomplete Fusion Persisting as "Pseudoforamina" or Clefts

Kerckring ossicle (at the top of the *PIOS/supraoccipital synchondrosis*) usually fuses within the first month of life, although persistence may lead to various ossicles or clefts even in teens and adults. Such an ossicle sometimes occurs within the Kerckring center of the supraoccipital region. Typically, a Kerckring ossicle consolidates with the remainder of the occipital bone just before birth or within the first 6–12 months of life. However, these can simulate a *fracture* when they persist later. Although the PIOS typically fuses within the first 2 years of age, it also may persist partially unilaterally or bilaterally and thus can be confused with fractures in the setting of trauma.

Also, a focal site of cartilaginous inclusion may persist at the site of Kerckring ossicle/supraoccipital synchondrosis, resulting in a defect of varying size and appear as a *pseudoforamen* (no arteries, veins, or nerves pass through). This pseudoforamen can occasionally simulate a fracture (Figs. 25.14, 25.15, 25.16, 25.17, 25.18, 25.19, 25.20, 25.21, 25.22, 25.23 and 25.24).

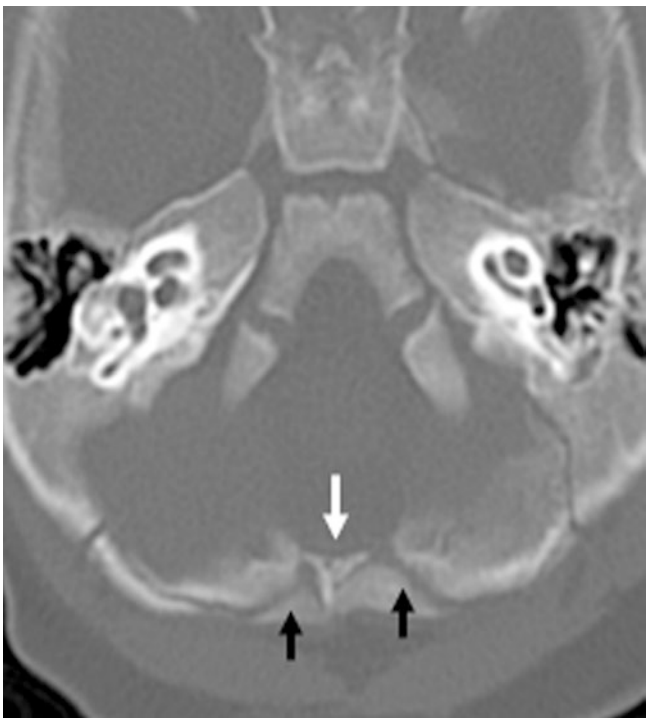

Fig. 25.14 A normal 4 month old with a Kerckring ossicle (*white arrow*). *Black arrows* indicate PIOS

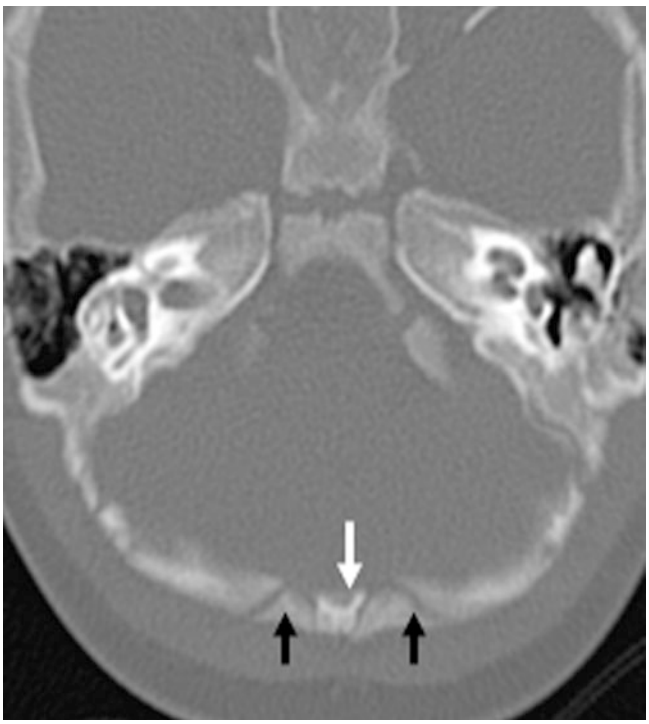

Fig. 25.15 A normal 5 month old with a Kerckring ossicle (*white arrow*). *Black arrows* indicate PIOS

Fig. 25.16 A normal 5 month old with normal Kerckring clefts (*white arrow*). *Black arrows* indicate PIOS

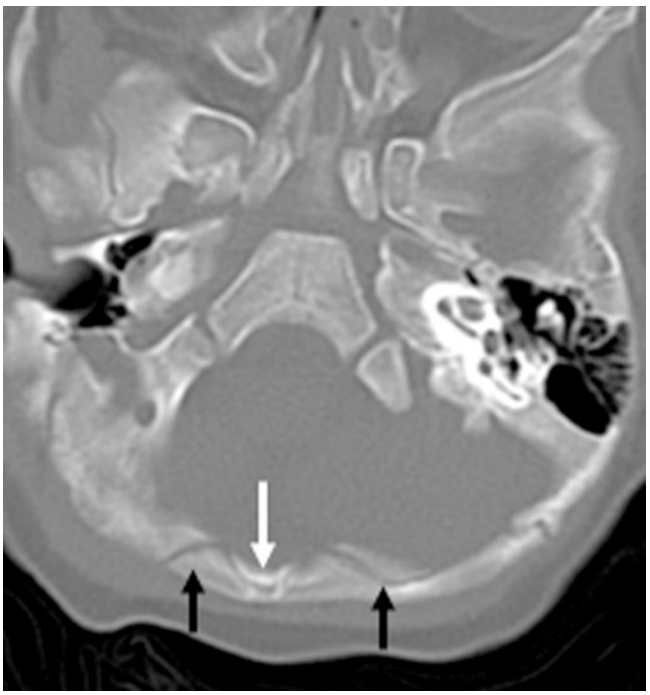

Fig. 25.18 A normal 5 month old with a partially fused Kerckring ossicle (*white arrows*). *Black arrows* indicate PIOS

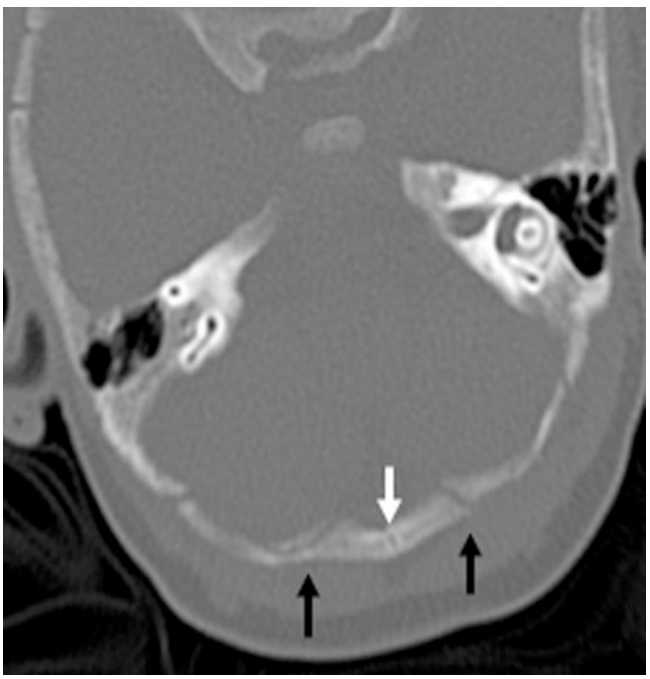

Fig. 25.17 A normal 5 month old with trauma and a cleft simulating a fracture. *White arrow* indicates the expected site of a prior Kerckring ossicle; *black arrows* indicate PIOS

Fig. 25.19 A 2.5 year old with bilateral nearly fused PIOSs (*black arrows*); the Kerckring ossicle has entirely fused

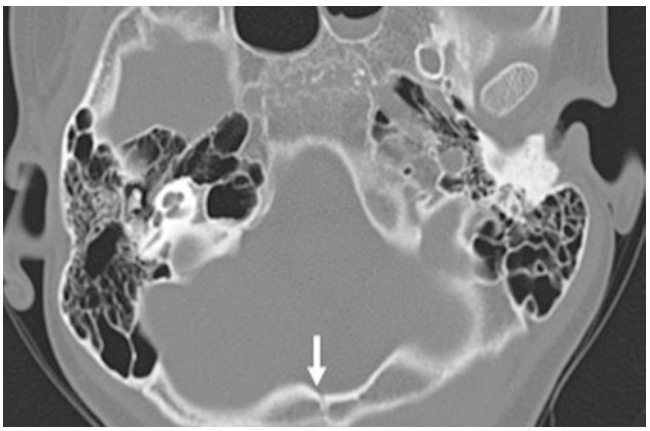

Fig. 25.20 A normal 11 year old with a posterior midline defect. *White arrow* indicates the expected site of a prior Kerckring ossicle

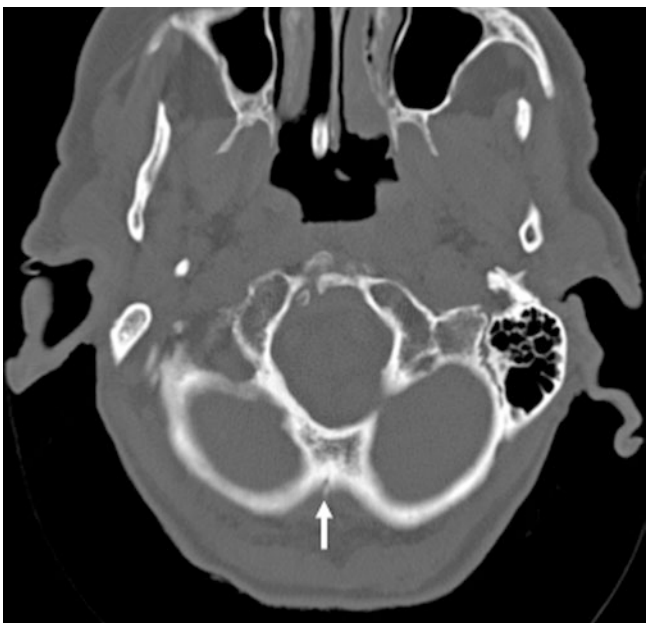

Fig. 25.21 A normal 80 year old with a posterior midline "pseudoforamen." *White arrow* indicates the expected site of a prior Kerckring ossicle

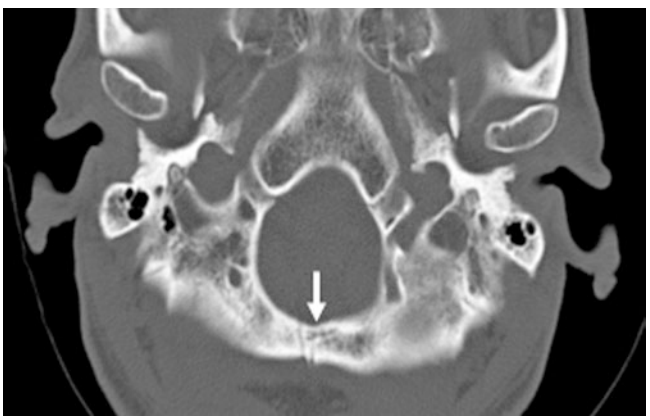

Fig. 25.22 A normal 63 year old with bilateral defects posteriorly. *White arrow* indicates the expected site of a prior Kerckring ossicle

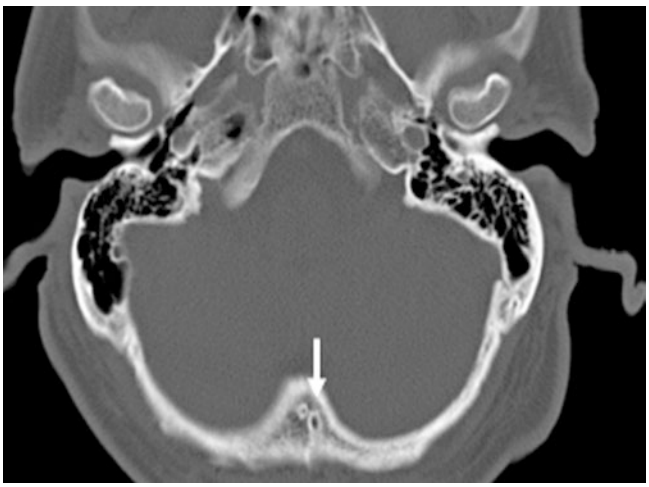

Fig. 25.23 A normal 64 year old with bilateral visual deficits and bilateral pseudoforamina. *White arrow* indicates site of prior Kerckring ossicle, the fusion of which likely led to these pseudoforamina

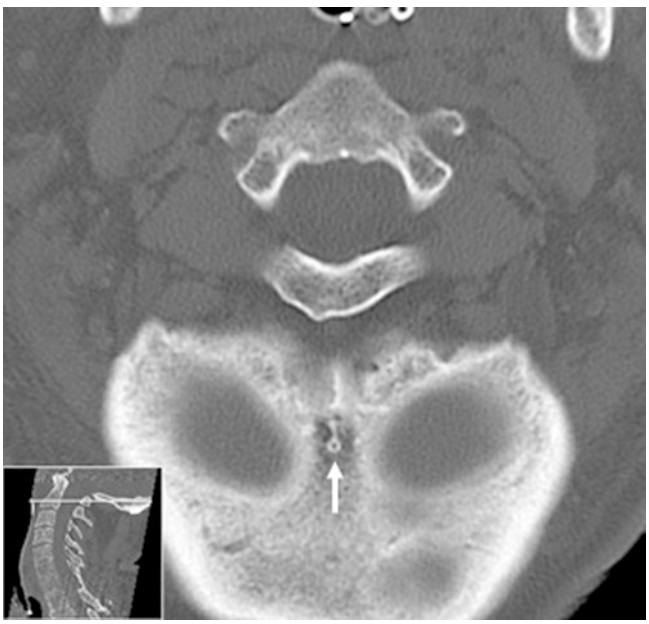

Fig. 25.24 A normal 63 year old with a single defect at the expected site of a prior Kerckring ossicle, the fusion of which likely led to this pseudoforamen (*white arrow*)

25.4.1 Occipito-Mastoid Suture: Variations in Fusion and Asymmetry

The OM suture is probably one of the most common sutures at the skull base, along with the *spheno-occipital synchondrosis* (SOS), to simulate a *fracture*. It can fuse symmetrically, asymmetrically, or persist to varying degrees even in the elderly. Additionally, this suture can commonly transmit an *emissary vein* between the dural sinuses and scalp, which can also simulate a fracture (Figs. 25.25, 25.26, 25.27, 25.28 and 25.29).

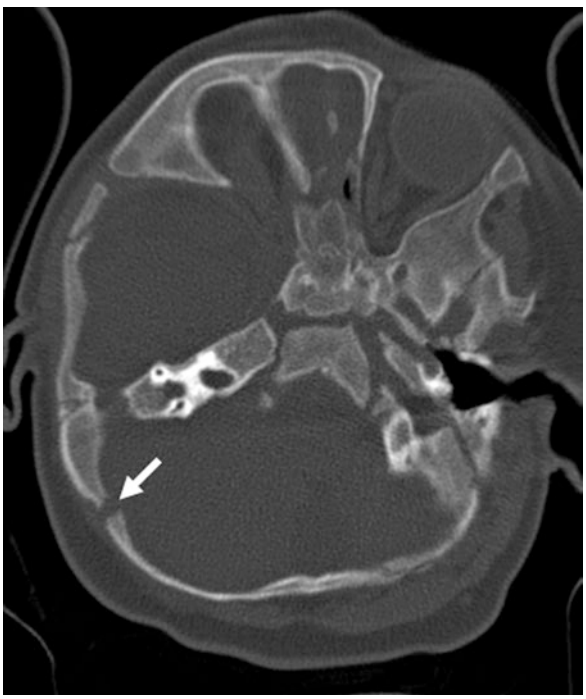

Fig. 25.25 A 3 month old with positional asymmetry that simulates a defect (*white arrow*)

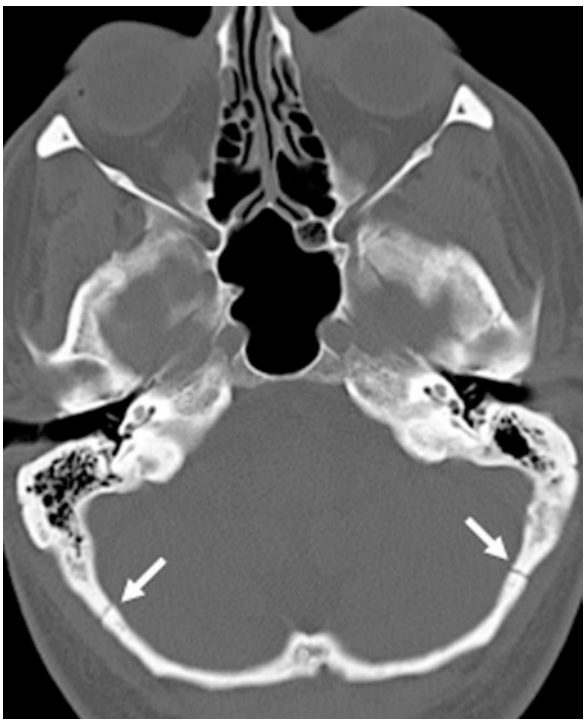

Fig. 25.26 A 44 year old with the typical, symmetric appearance of the occipitomastoidal sutures bilaterally (*white arrows*)

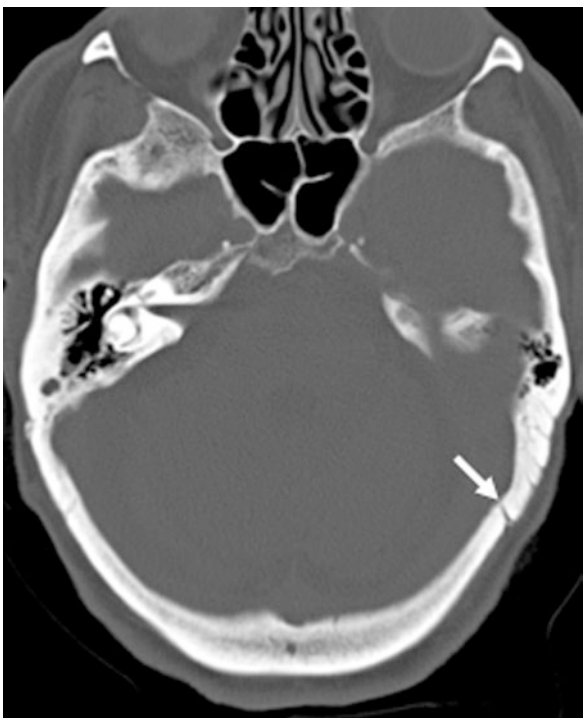

Fig. 25.27 An 80 year old with asymmetric occipitomastoidal sutures; the left suture (*arrow*) is unfused relative to the right suture (*white arrow*)

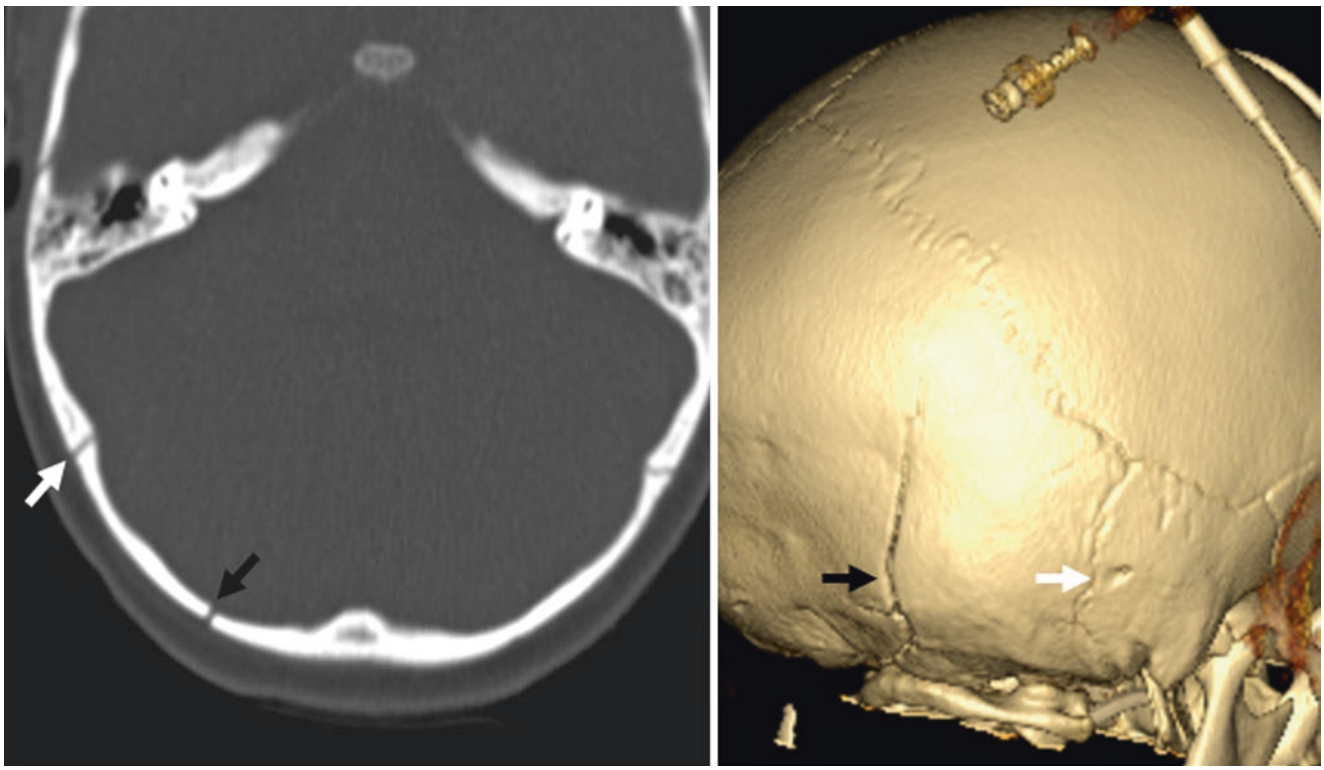

Fig. 25.28 Comparison case: a 3 year old with a fracture (*black arrows*) in contrast to a normal occipitomastoidal suture (*white arrows*). On a three-dimensional posterior view (*right*), note the fracture line's straighter configuration

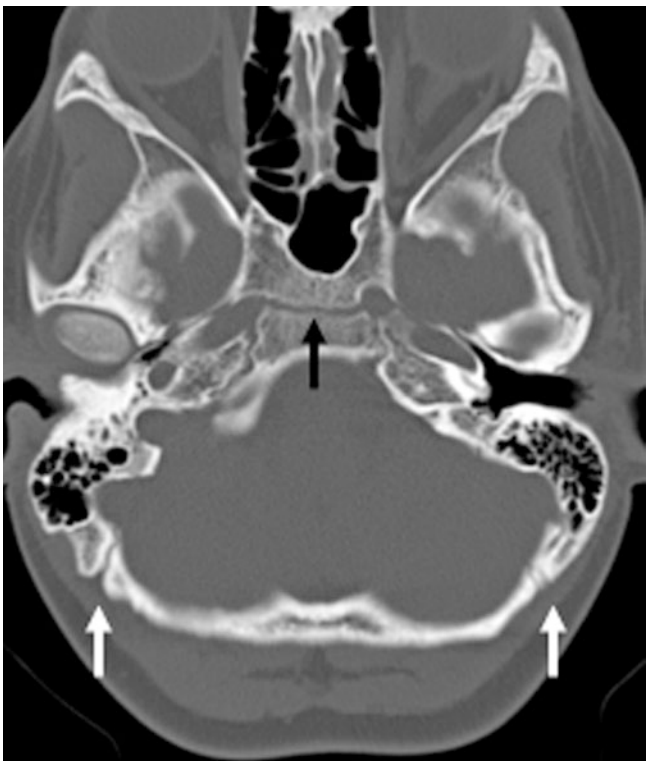

Fig. 25.29 An 11 year old with an asymmetric right occipitomastoidal suture (*white arrows*) and a patent SOS (*black arrow*)

25.4.2 Mendosal Sutures in Young Infants

Mendosal sutures are not typically seen unless the patient is imaged by a CT scan before 1–2 months age, at which point they also may have already fused. The suture runs from the *mastoid fontanelle* postero-supero-medially. The *lambdoid, squamosal, occipitomastoid,* and *posterior intraoccipital sutures* are also demonstrated here in two patients who were both less than 10 days old and were both evaluated for trauma because of being dropped (presumed accidental). Both NECTs were negative for fracture (Figs. 25.30 and 25.31).

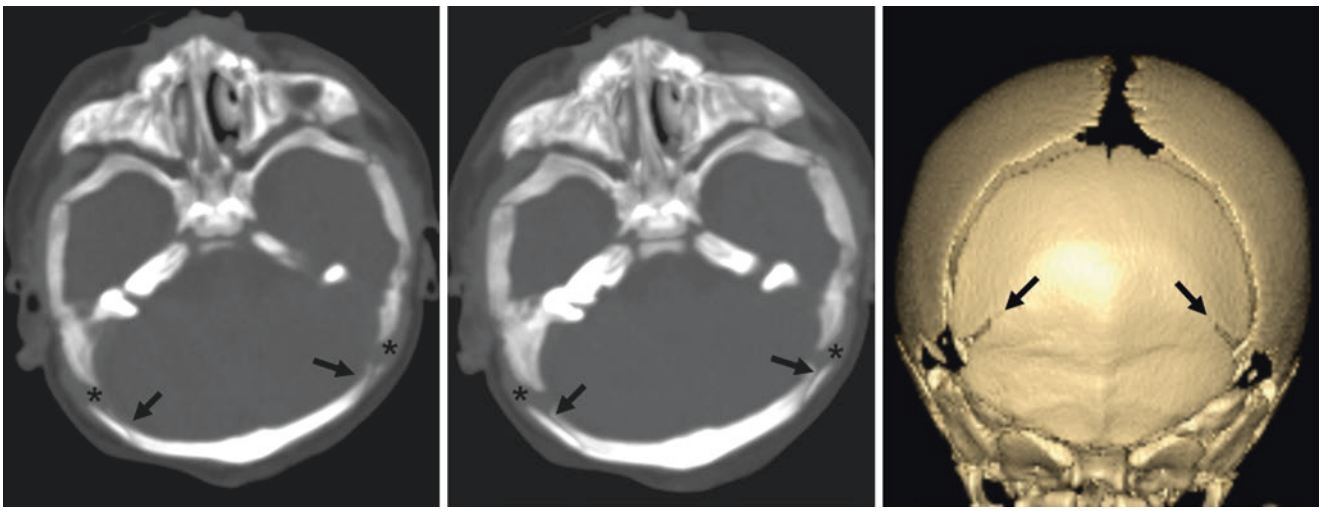

Fig. 25.30 A 10 day old infant. On axial NECT bone windows (*left*), the mendosal sutures (*black arrows*) appear faint and simulate a fracture, while thicker MPR slabs (*middle*) show that these are bilateral unfused sutures. Additionally, a three-dimensional reconstruction posterior view (*right*) confirms the normal bilateral appearance of the sutures. Also, note the normal mastoid fontanelles (*asterisk*)

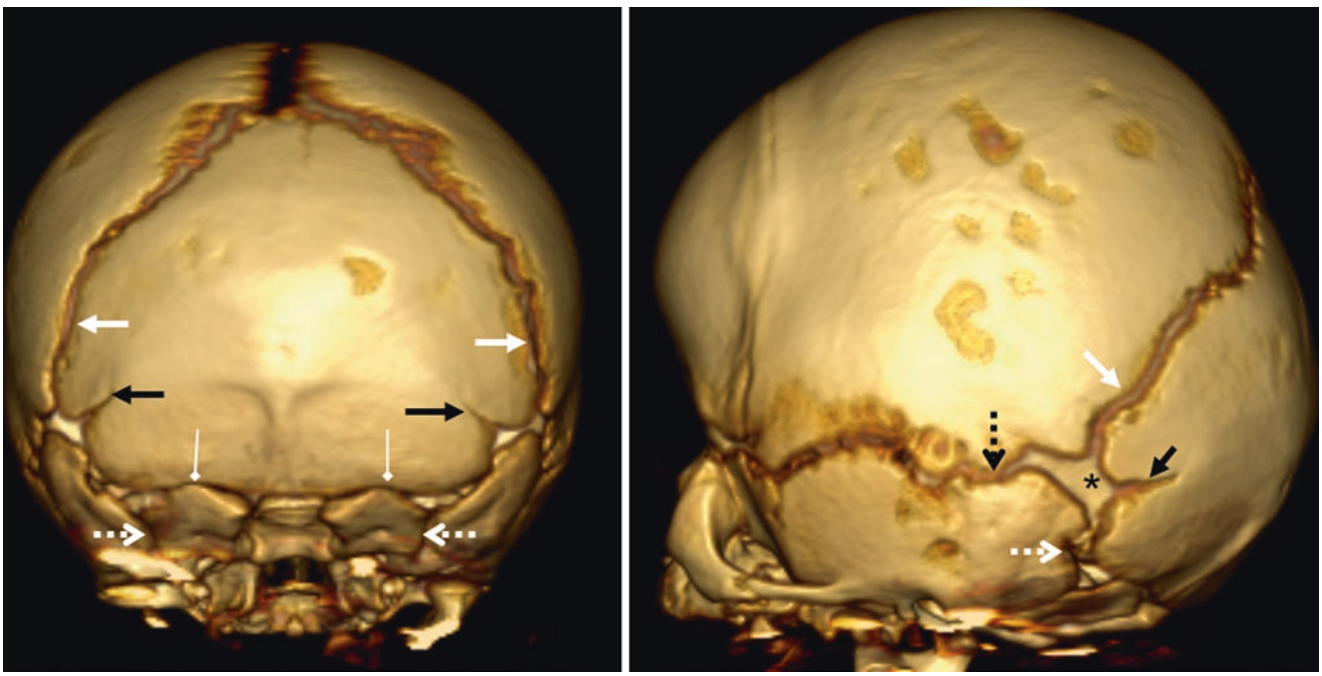

Fig. 25.31 A 3 day old neonate. There are bilateral mendosal sutures (*black arrows*), as depicted on three-dimensional reconstructions from a NECT, with posterior (*left*) and LPO (*right*) views. Also, note normal mastoid fontanelles (*asterisk*) as well as the lambdoid (*white arrows*), OM (*dashed white arrows*), squamosal (*dashed black arrows*), and posterior intraoccipital (*thin white arrows*) sutures

25.4.3 Sutures: Fronto-Ethmoidal, Spheno-Ethmoidal, Fronto-Sphenoidal, Zygomatico-Sphenoidal, and Zygomatico-Frontal Sutures

These sutures may cause confusion in infants with trauma, particularly when the patient is tilted and appears asymmetric, thus simulating a *fracture*. These sutures can be made to appear symmetric by constructing thicker MPR images. In particular, the *sphenoethmoidal suture* and the *frontosphenoidal suture* can appear jagged and asymmetric. The adjacent *zygomaticofrontal* and *zygomaticosphenoidal sutures* can also simulate orbital or frontal fractures. These sutures begin fusion at several months of age but may persist to some degree until about 10 years of age and occasionally can even be found in adults. The *sphenosquamosal* and *squamosal sutures* are also noted at similar time periods, along with the *sphenoid fontanelle* (Figs. 25.32, 25.33, 25.34, 25.35, 25.36, 25.37, 25.38, 25.39 and 25.40).

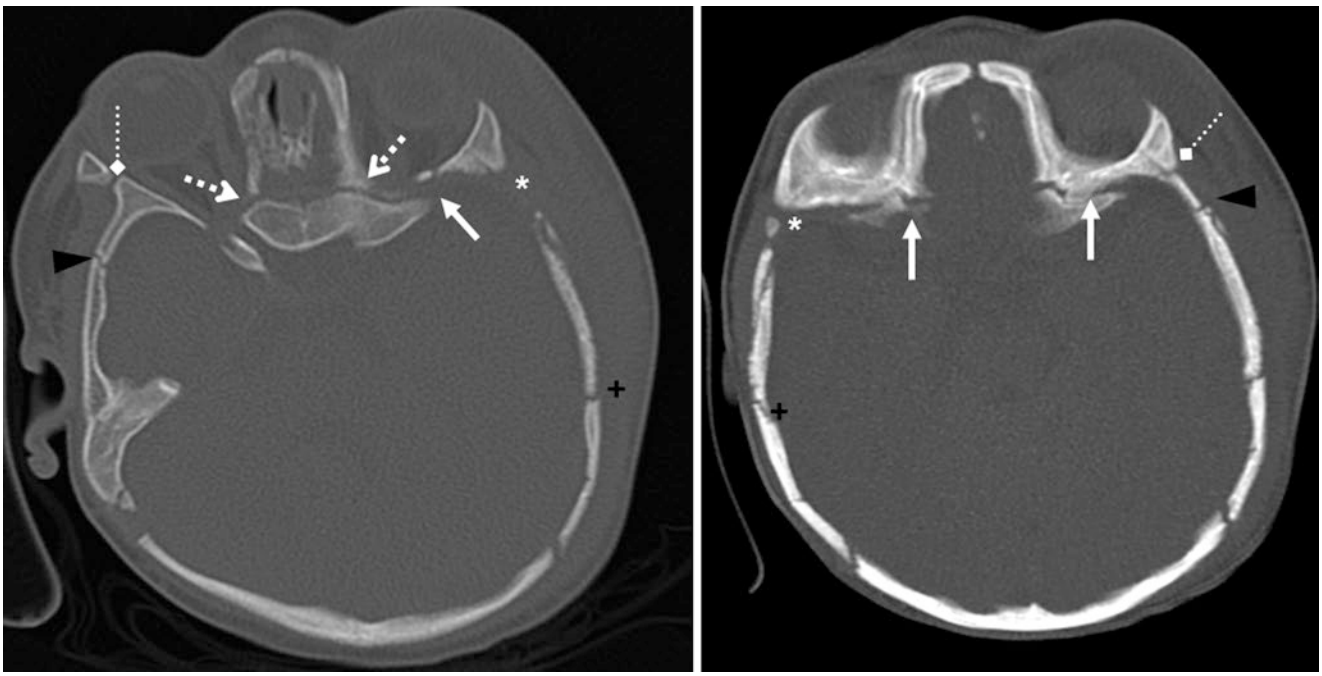

Fig. 25.32 A 3 month old with trauma (note left facial and scalp swelling) but lacking a fracture on NECT axial 2 mm (*left*) and 7 mm MPR (*right*) images. Note the sphenoethmoidal (*dashed white arrows*), frontosphenoidal (*solid white arrows*), zygomaticofrontal (*white arrowheads*), zygomaticosphenoidal (*dotted white arrows*), and sphenosquamosal (*black arrowheads*) sutures as well as the squamosal suture (*black plus sign*) and the sphenoid fontanelles (*asterisk*) (the right sphenoid fontanelle contains an intrasutural bone)

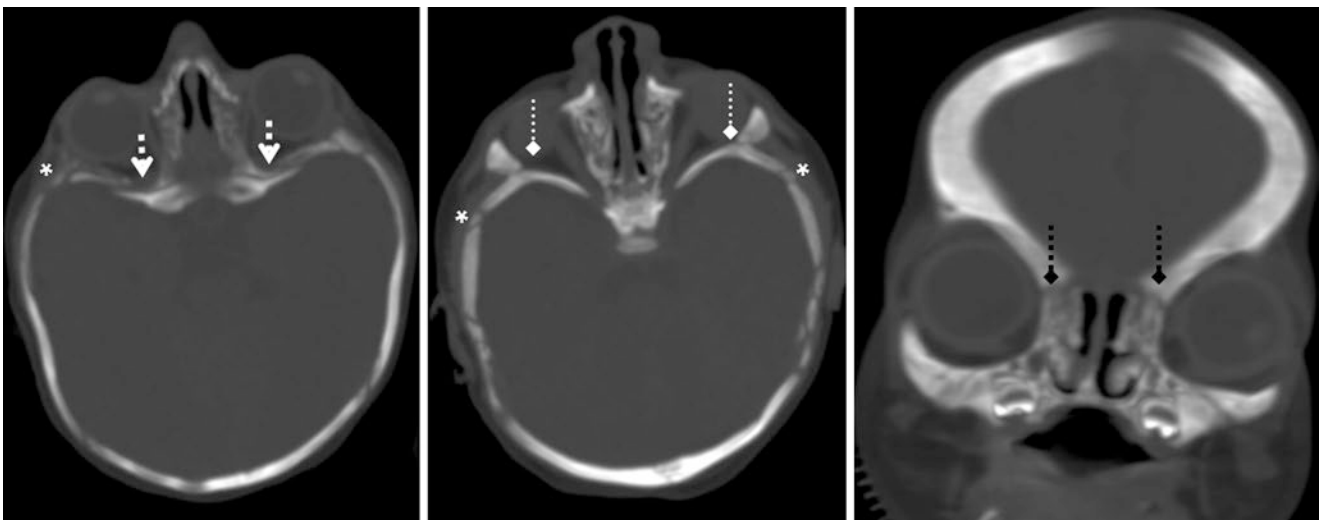

Fig. 25.33 A 10 day old with trauma and a negative CT with axial (*left two images*) and coronal (*right*) reformats. Note the sphenoethmoidal (*dashed white arrows*), frontoethmoidal (*dotted black arrows*), zygomaticosphenoidal (*dotted white arrows*), and sutures as well as the sphenoid fontanelles (*asterisk*)

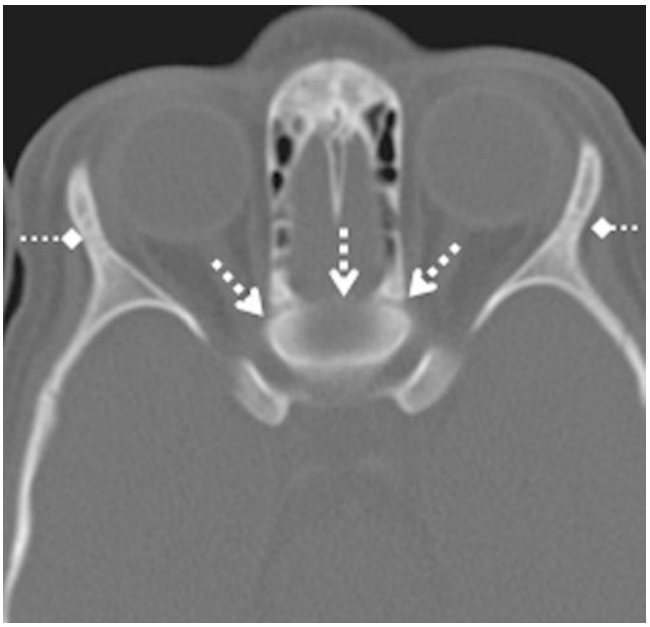

Fig. 25.34 An 18 month old with trauma having early fusion of the sphenoethmoidal suture (*dashed white arrows*). Note the zygomaticosphenoidal sutures (*dotted white arrows*)

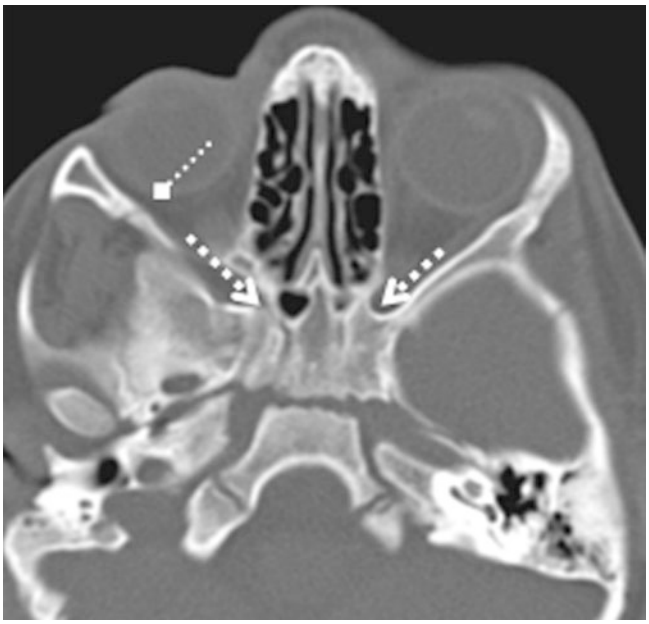

Fig. 25.36 A 9 year old with fused sphenoethmoidal (*dashed white arrows*) sutures and a rudimentary sphenoid sinus. Note the zygomaticosphenoidal sutures (*dotted white arrow*)

Fig. 25.35 A 3 year old with trauma having a partly fused zygomaticosphenoidal (*dotted white arrows*) suture

Fig. 25.37 A 22 year old with trauma having fused zygomaticosphenoidal (*dotted white arrows*) and frontosphenoidal (*solid white arrows*) sutures

Fig. 25.38 A 40 year old with trauma having a nonfused sphenoethmoidal (*dashed white arrows*) suture and a mostly fused zygomaticofrontal (*white arrowheads*) sutures. Both of these non-fused sutures could simulate fractures

Fig. 25.40 A 52 year old with trauma (no fracture) having nearly fused sphenoethmoidal (*dashed white arrows*) and frontosphenoidal (*solid white arrows*) sutures

Fig. 25.39 A 9 year old with trauma having fusion of the sphenoethmoidal (*dashed white arrows*), zygomaticofrontal (*white arrowheads*), and zygomaticosphenoidal (*dotted white arrows*) sutures (no fracture seen)

25.4.4 Zygomatico-Frontal and Spheno-Ethmoidal Sutures Versus Fractures

Following fusion, the sphenoid and ethmoid sinuses aerate, with minimal bone between them at the *sphenoethmoidal suture*. Again, the sphenoethmoidal suture may rarely remain partially patent in adults and occasionally may simulate a skull base *fracture* in the clinical setting of trauma. Note that the *zygomaticofrontal* and *zygomaticosphenoidal sutures* often are incompletely fused in adults, which can also simulate fractures but appear more typical of normal suture lines (Figs. 25.41 and 25.42).

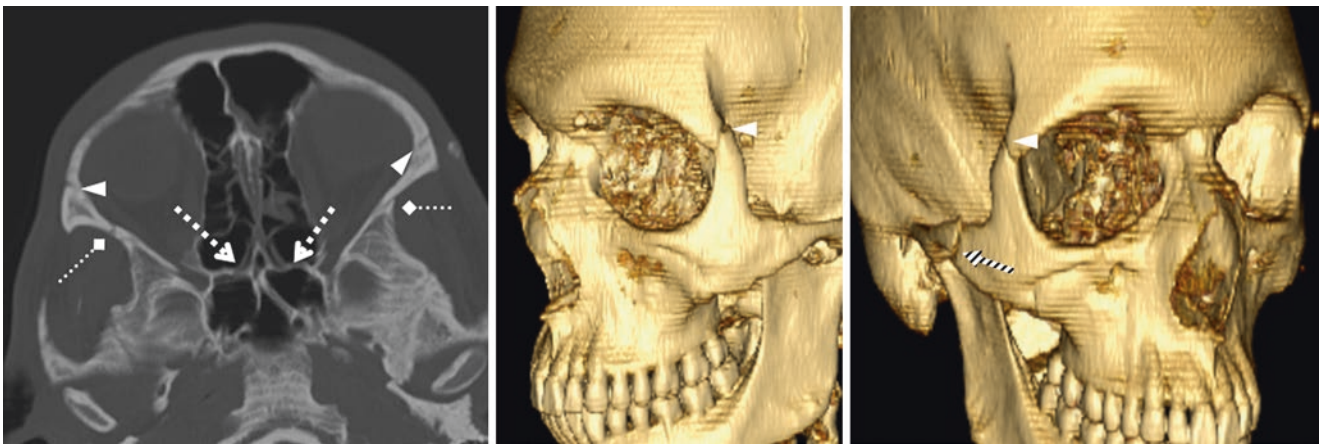

Fig. 25.41 A 22 year old with trauma. After axial NECT was performed (*left*), three-dimensional reconstructions with left lateral (*middle*) and RAO (*right*) views confirmed that the sphenoethmoidal (*dashed arrows*), zygomaticofrontal (*arrowheads*) and zygomaticosphenoidal (*dotted arrows*) sutures were normal and incompletely fused; however, there was also a true right zygomatic fracture (*zebra arrows*)

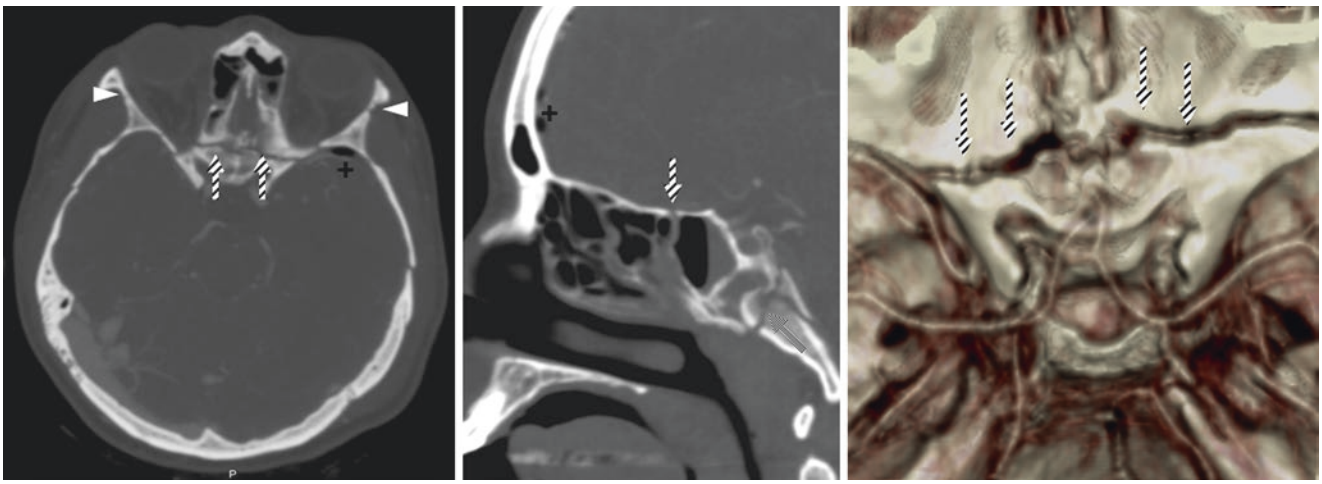

Fig. 25.42 Comparison case: A 23 year old with trauma, with axial (*left*) and sagittal (*middle*) reformats from a CTA. Note normal, incompletely fused zygomaticofrontal sutures bilaterally (*arrowheads*) but with a diastatic fracture line crossing the midline (*zebra arrows*) along the sphenoethmoidal suture. Note also how the fracture lines often follow a path of least resistance (i.e., suture lines). Pneumocephalus (*black plus sign*) is noted as well as a fracture along the spheno-occipital synchondrosis posteriorly (*shaded arrow, middle image*). Note an air-fluid level in the sphenoid sinus from that fracture, also depicted on a three-dimensional reconstruction (*right*, *superior view*)

25.4.5 Sphenoid Fontanelle, Frontosphenoidal Suture, and Sphenosquamosal Suture

The *frontosphenoidal* and *sphenosquamosal sutures* begin fusion at only a few months of age but may persist to a minor degree up to 5–10 years of age. The three-dimensional images in Figs. 25.43, 25.44 and 25.45 are each lateral views of the skull.

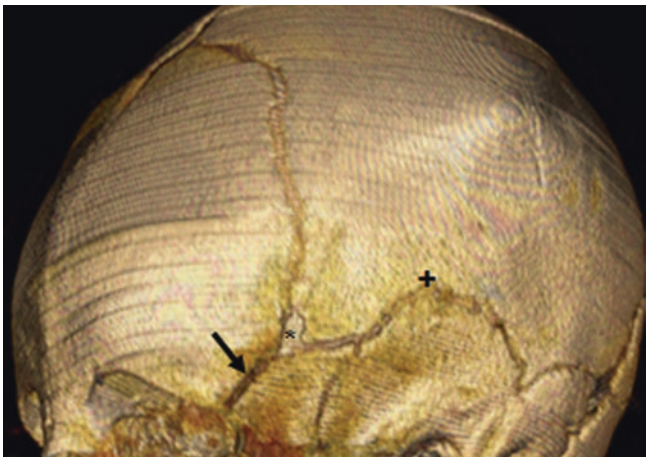

Fig. 25.43 A 3 month old with normal frontosphenoidal (*black arrow*) and sphenoid fontanelle (*asterisk*). *Plus sign* indicates squamosal suture

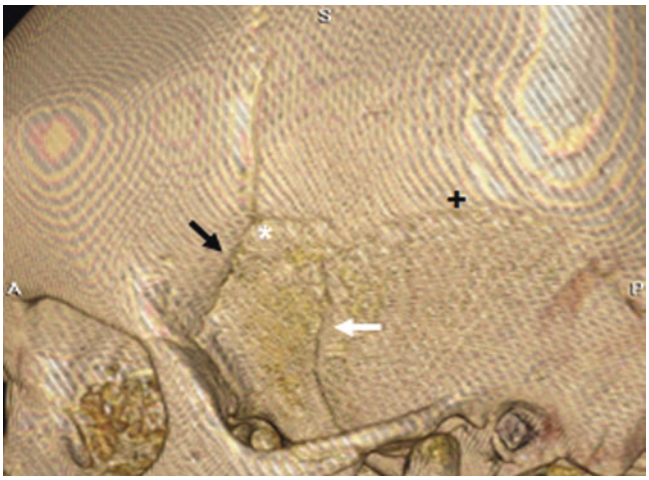

Fig. 25.44 A 1 year old with partially fused frontosphenoidal (*black arrow*) and sphenosquamosal sutures (*white arrow*). *Asterisk* indicates sphenoid fontanelle; *plus sign* indicates squamosal suture

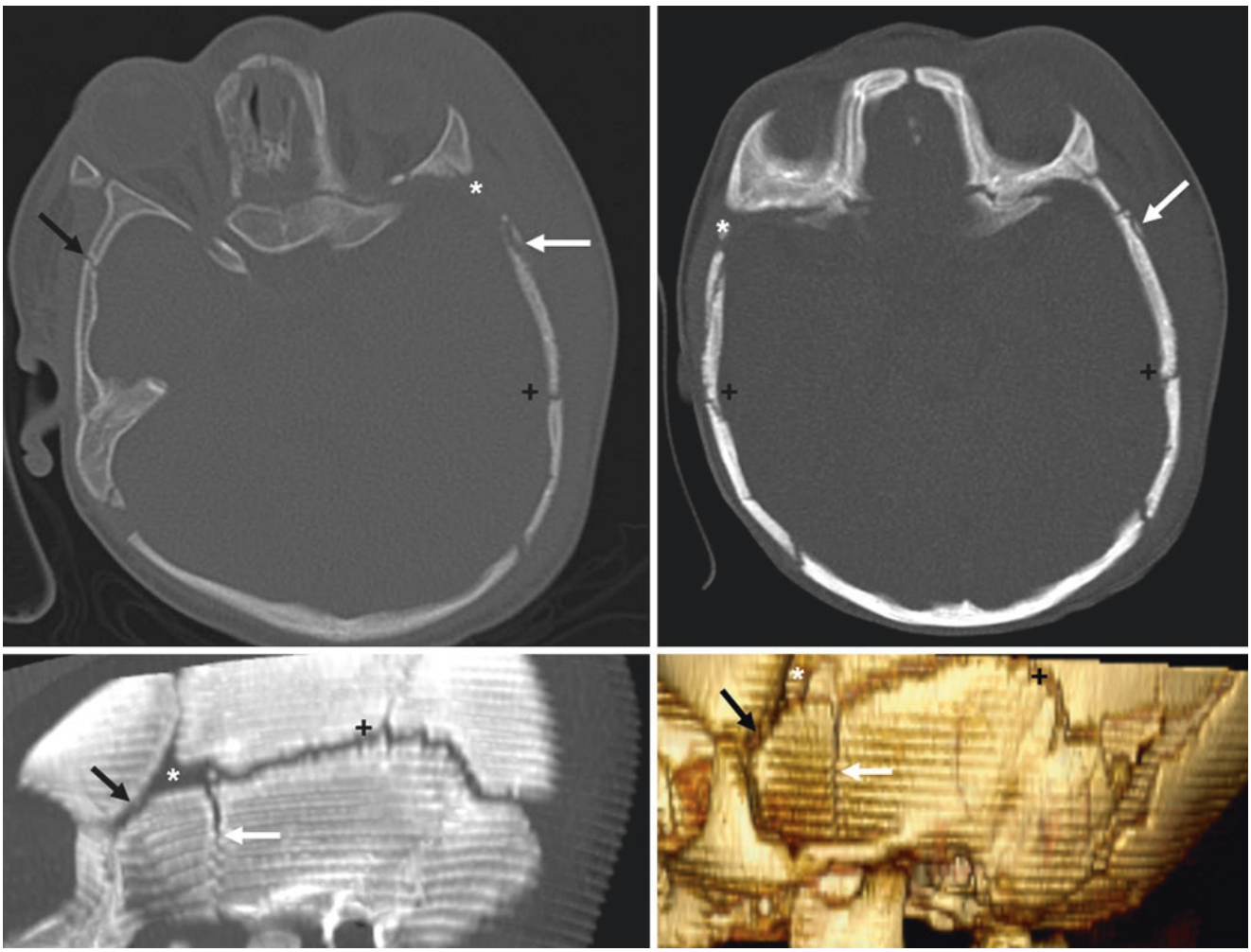

Fig. 25.45 A 3 month old with left orbital and scalp swelling. The CT (*top left*) raised the question of fractures (*white arrow*). The patient had been obliquely positioned; axial (*top right*), sagittal MPR (*bottom left*), and three-dimensional reconstruction (*bottom right*, *lateral view*) images showed that these were simply symmetric frontosphenoidal (*black arrows*), sphenosquamosal (*white arrows*), and squamosal sutures (*plus signs*). Note the normal sphenoid fontanelles (*asterisk*). On the three-dimensional images, note the "stair-step" artifacts from the incremental scan technique

25.4.6 Prominent Mastoid Fontanelle

The *mastoid fontanelle* can present some problems when evaluating infants, particularly when their heads are lying obliquely in the scanner. Furthermore, the obliquity may make it very difficult to evaluate a patient of this age because the adjacent *squamosal* and *occipitomastoid sutures* are not yet fused at less than 1 year of age, and the fontanelle can thus be confused with a *diastatic fracture* (Figs. 25.46 and 25.47).

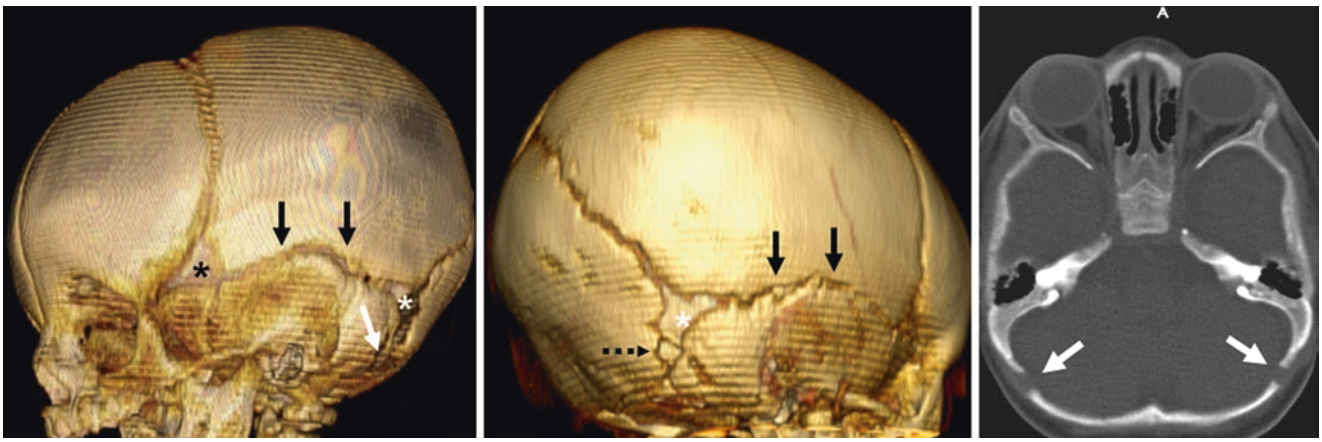

Fig. 25.46 A 3 month old with trauma. The NECT was negative for fracture. *White arrows indicate* OM suture; *black asterisks* indicate sphenoid fontanelle; *black arrows* indicate squamosal suture. Note a normal wormian bone (*black dashed arrow*) in a mastoid fontanelle (*white asterisks*) on the three-dimensional images. Shown are three-dimensional left lateral (*left*) and RPO (*middle*) reconstructions as well as axial (*right*) NECT images

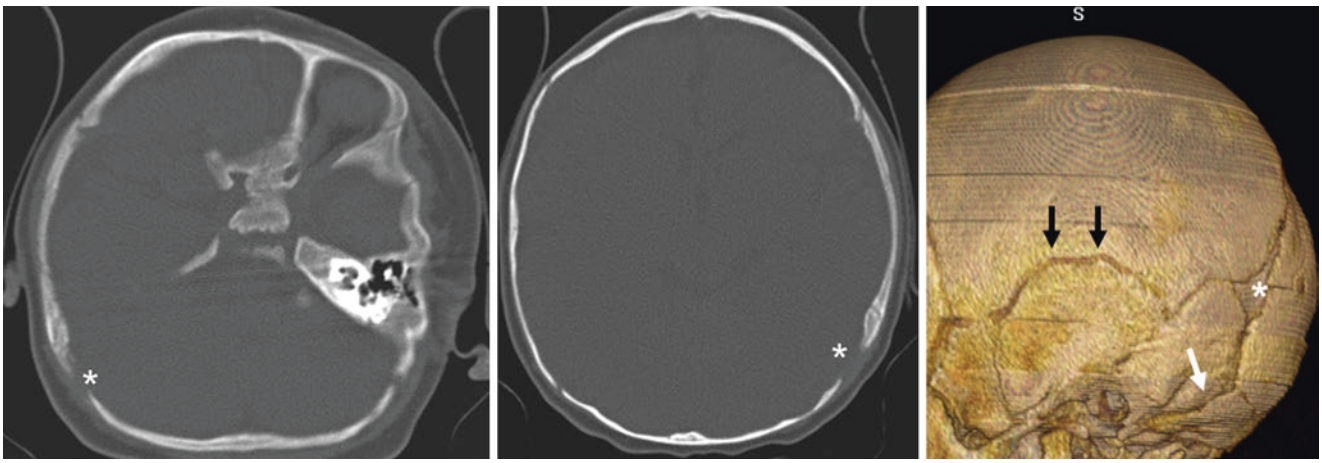

Fig. 25.47 A 3 month old with left scalp swelling from trauma. The patient was lying obliquely within the scanner. The left mastoid fontanelle (*white asterisks*) was problematic and was called a fracture by the resident radiologist, but the three-dimensional lateral views (*right*) excluded a fracture. *White arrow* indicates OM suture; *black arrows* indicate squamosal suture

Suggested Reading

Alcalá-Galiano A, Arribas-García IJ, Martín-Pérez MA, Romance A, Montalvo-Moreno JJ, Juncos JM. Pediatric facial fractures: children are not just small adults. Radiographics. 2008;28:441–61.

Belden CJ, Mancuso AA, Kotzur IM. The developing anterior skull base: CT appearance from birth to 2 years of age. AJNR Am J Neuroradiol. 1997;18:811–8.

Connor SE, Tan G, Fernando R, Chaudhury N. Computed tomography pseudofractures of the mid face and skull base. Clin Radiol. 2005;60:1268–79.

Dupuis O, Silveira R, Dupont C, Mottolese C, Kahn P, Dittmar A, Rudigoz RC. Comparison of "instrument-associated" and "spontaneous" obstetric depressed skull fractures in a cohort of 68 neonates. Am J Obstet Gynecol. 2005;192:165–70.

Furuya Y, Edwards MS, Alpers CE, Tress BM, Ousterhout DK, Norman D. Computerized tomography of cranial sutures. Part 1: comparison of suture anatomy in children and adults. J Neurosurg. 1984a;61:53–8.

Furuya Y, Edwards MS, Alpers CE, Tress BM, Norman D, Ousterhout DK. Computerized tomography of cranial sutures. Part 2: abnormalities of sutures and skull deformity in craniosynostosis. J Neurosurg. 1984b;61:59–70.

Freyschmidt J, Brossman J, Sternberg A, Wiens J. Skull. In: Freyschmidt's Koehler/Zimmer's borderlands of normal and early pathological findings in skeletal radiography. 5th ed. Tubingen: Thieme; 2003.

Glass RB, Fernbach SK, Norton KI, Choi PS, Naidich TP. The infant skull: a vault of information. Radiographics. 2004;24:507–22.

Gray H. The interior of the skull. In: Anatomy of the human body. 29th ed. Philadelphia: Lea & Feiger; 1918.

Hedlund G. Congenital frontal nasal masses: developmental anatomy, malformations, and MR imaging. Pediatr Radiol. 2006;36:647–62.

Keats TE, Anderson MW. Skull. In: Atlas of normal Roentgen variants that may simulate disease. 8th ed. Philadelphia: Mosby, Inc.; 2007.

Keskil S, Gözil R, Calgüner E. Common surgical pitfalls in the skull. Surg Neurol. 2003;59:228–31.

Madeline LA, Elster AD. Postnatal development of the central skull base: normal variants. Radiology. 1995a;196:757–63.

Madeline LA, Elster AD. Suture closure in the human chondrocranium: CT assessment. Radiology. 1995b;196:747–56.

Nemzek WR, Brodie HA, Hecht ST, Chong BW, Babcook CJ, Seibert JA. MR, CT, and plain film imaging of the developing skull base in fetal specimens. AJNR Am J Neuroradiol. 2000;21:1699–706.

Schratter M, Canigiani G, Karnel F, Imhof H, Kumpan W. Occult fractures of the skull. Radiologe. 1985;25:108–13.

Seeger JF. Normal variations of the skull and its contents. In: Zimmerman RA, editor. Neuroimaging: clinical and physical principles. New York: Springer; 1999. p. 415–53.

Skull Base Foramina: Normal Variations and Developmental Defects

26

This chapter is devoted to the normal variations in foramina at the skull base. Because these foramina can simulate *fractures, lytic lesions,* and *cephaloceles* based on their location, one can recognize the importance of being familiar with these variants. Although these foramina can be particularly prominent and problematic in younger children, their persistence in adults can cause confusion. Therefore the intent and methodology utilized here are to follow the normal anatomy and staying power of these variants from the pediatric to adult ages. A number of other skull base foramina are not covered in this text; those that are not mentioned either are not typically confused with other abnormalities or do not have significant asymmetry (e.g., optical canal, superior orbital fissure, carotid canal).

Our description is anatomic starting from the anterior (ethmoid) to the base of the sphenoid to the basiocciput foramina, followed by the cranial nerve foramina of the middle cranial fossa and posterior fossa. The variations above the skull base and of the cranial sutures above the skull base are presented later in the text. Please note that vascular variants (e.g., emissary veins) are covered separately, although some of these variants, such as the emissary vein of the foramen of Vesalius, overlap and may be mentioned separately elsewhere in the text.

26.1 Foramen Cecum

The *foramen cecum* is an embryonic remnant of a dural diverticulum and is a space where the dura briefly connects between the anterior cranial fossa and prenasally, even extending to the tip of the nose at one point. Thereafter the dura recedes, remaining intracranial. The prenasal space later disappears with fusion of the adjacent bones, although a tiny normal foramen cecum is present in many individuals between the *nasal process* of the frontal bone anteriorly and the *crista galli* posteriorly. This foramen is normal as long as no T1- or T2-bright (cephalocele or dermoid) mass is present. The foramen should be less than 3 mm at 5 years of age but may be larger in younger children.

Also, the foramen cecum may occasionally contain a tiny, imperceptible vein or dura, although usually only fibrous or mesenchymal tissue remains. The foramen's location and identity can be confirmed by multiplanar as well as three-dimensional (3D) reconstructions. When it is larger, this foramen can be confused with pathologic conditions such as *cephalocele* (skull base defect), *meningioma* (erosive mass), or *esthesioneuroblastoma* (erosive mass). (Figs. 26.1, 26.2, 26.3, 26.4 26.5, 26.6, and 26.7).

A.M. McKinney, *Atlas of Normal Imaging Variations of the Brain, Skull, and Craniocervical Vasculature*,
DOI 10.1007/978-3-319-39790-0_26

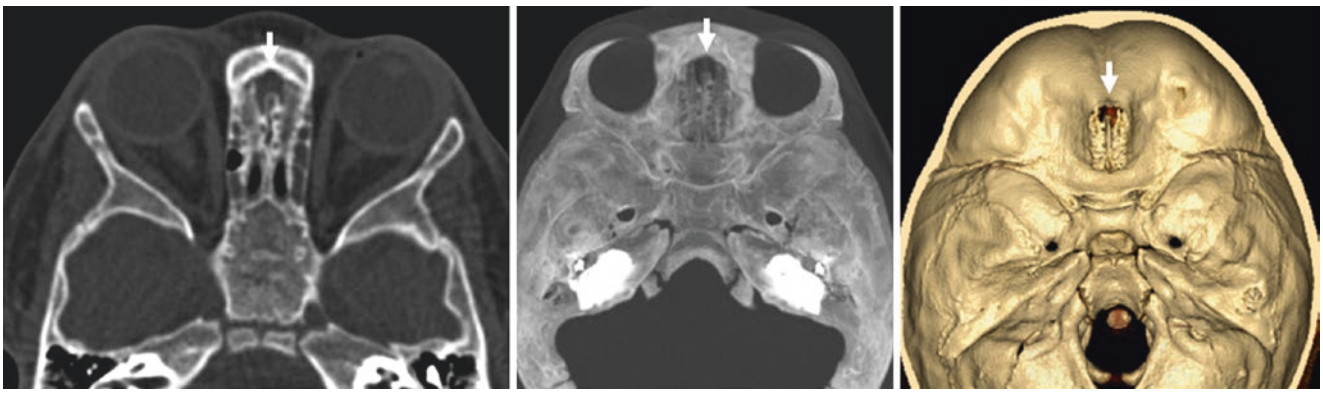

Fig. 26.1 An 11 month old with a sizeable but normal foramen cecum on axial CT (*left*), 24 mm MPR (*middle*) and 3D superior view (*right*)

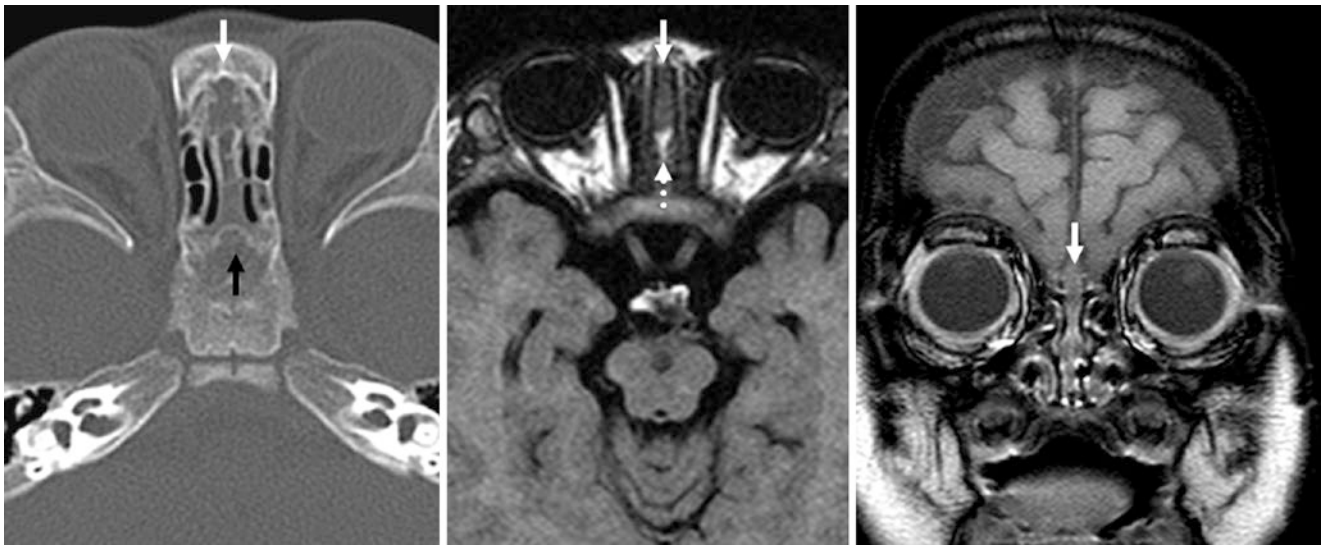

Fig. 26.2 A 1 year old with a foramen cecum (*arrows*) on CT (*left*), on axial FLAIR (*middle*), and on coronal T1WI (*right*) MRI. Also noted is an intraethmoidal defect posteriorly (*black arrows*). Note the T1-bright signal within the crista galli (*dashed arrow*)

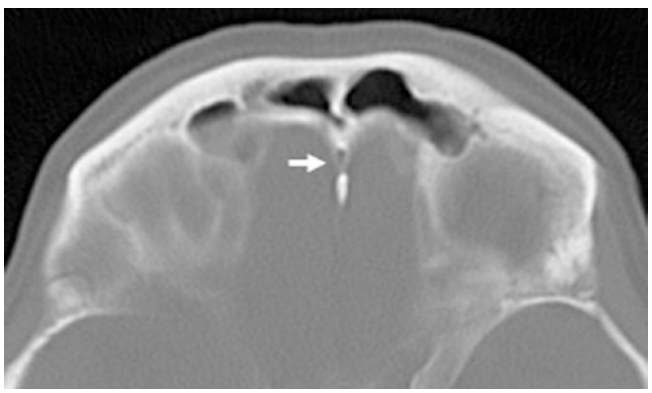

Fig. 26.3 A 73 year old with a tiny foramen

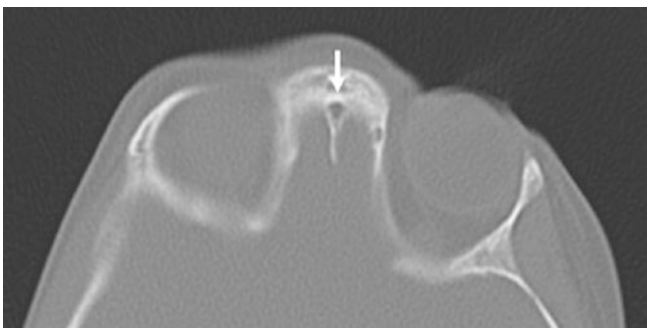

Fig. 26.4 A 4 year old with a sizeable foramen

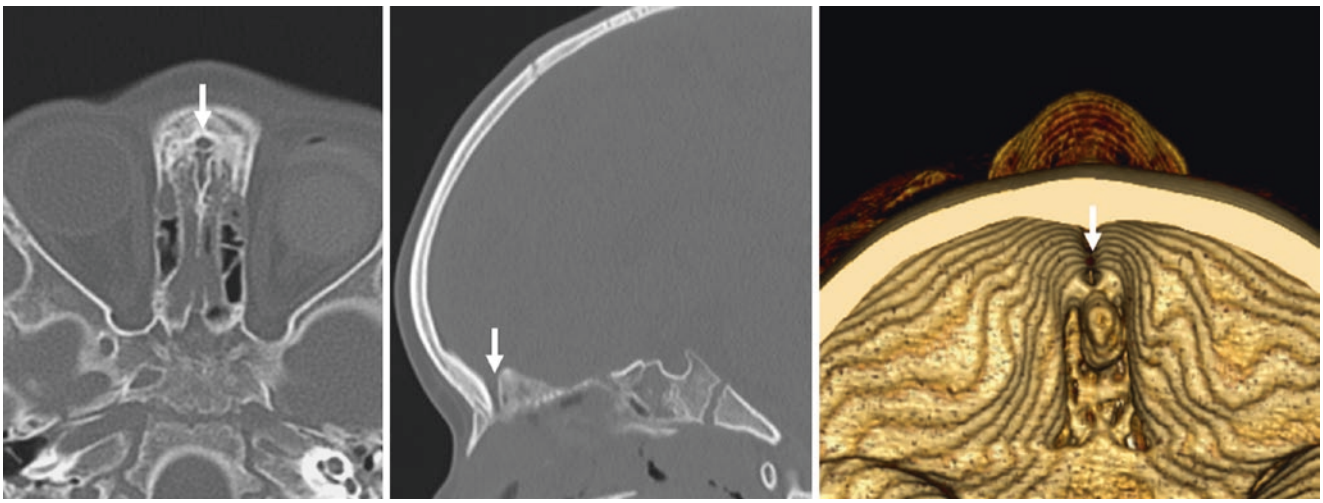

Fig. 26.5 A 4 year old with a patent foramen cecum on axial NECT (*left*), with sagittal MPR (*middle*) and 3D reconstruction (*right*, *superior view*) images

Fig. 26.6 A 17 year old with a tiny foramen cecum

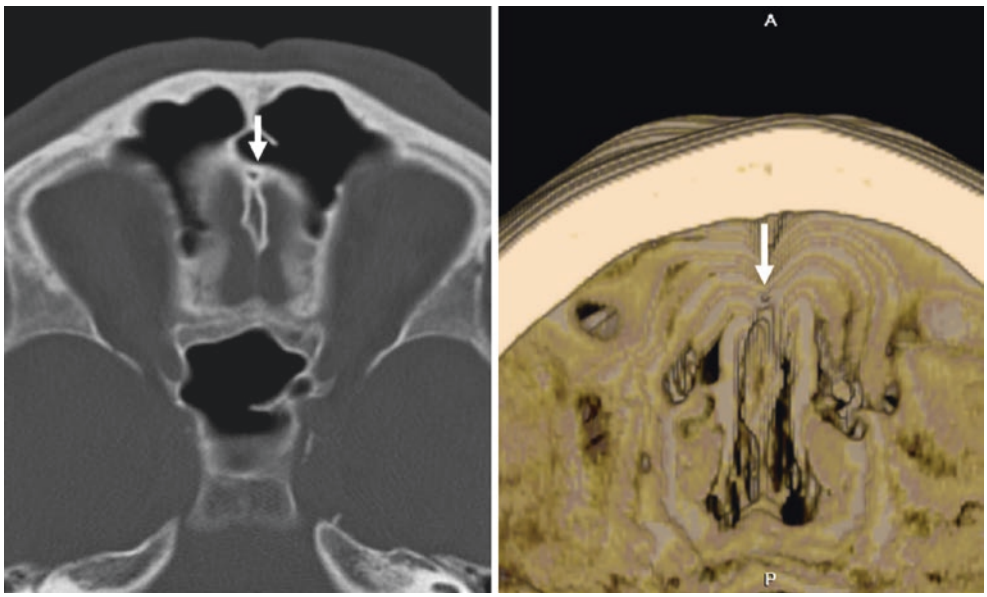

Fig. 26.7 A 52 year old with a tiny foramen cecum on axial (*left*) and 3D reconstruction (*right*, *superior view*) images

26.2 Interplanum Ethmoidal Defect

Interplanum ethmoidal defects (IED) are gaps that normally temporarily occur between the anterior aspect of the jugum (posteriorly), the orbito-/presphenoid on the sides and the ethmoid anteriorly. These usually disappear within the first few years of life: the presphenoid fuses at the midline and the ethmoids and sphenoids continue to aerate. No nerves or vascular structures or pathology is typically associated with this normal variant.

Unless otherwise noted, the images provided are axial nonenhanced CT (NECT) (Figs. 26.8, 26.9, 26.10, 26.11, and 26.12).

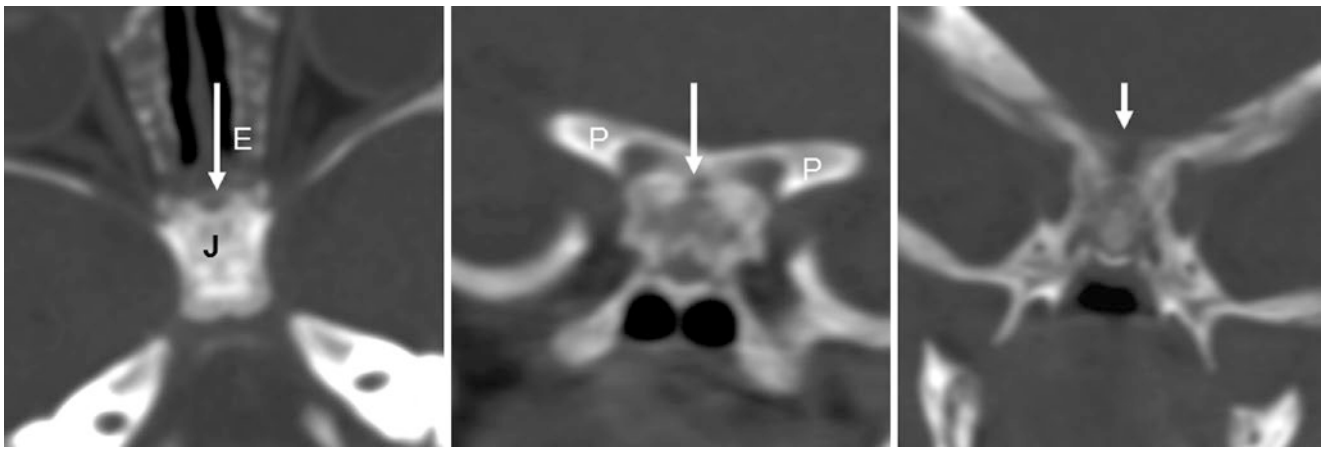

Fig. 26.8 A 3 month old with a small IED situated between the anterior aspect of the sphenoid jugum (*J*) and the ethmoid bones (*E*) on axial (*left*), coronal (*middle*), and oblique coronal (*right*) NECT reconstructions

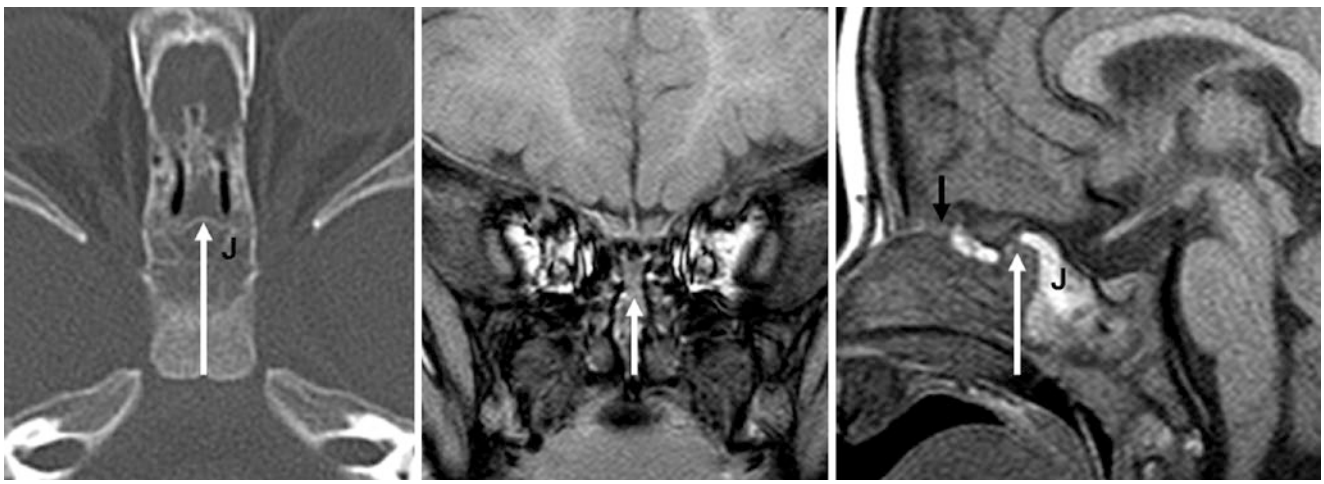

Fig. 26.9 A 1 year old with a larger IED (*white arrows*) on NECT (*left*) and a corresponding defect on MRI with coronal (*middle*) and sagittal (*right*) T1WI. The IED is located between the sphenoid jugum (***J***) and the ethmoid bones. An incidental foramen cecum is noted anteriorly (*black arrow*)

Fig. 26.10 A 5 month old with an IED on axial NECT

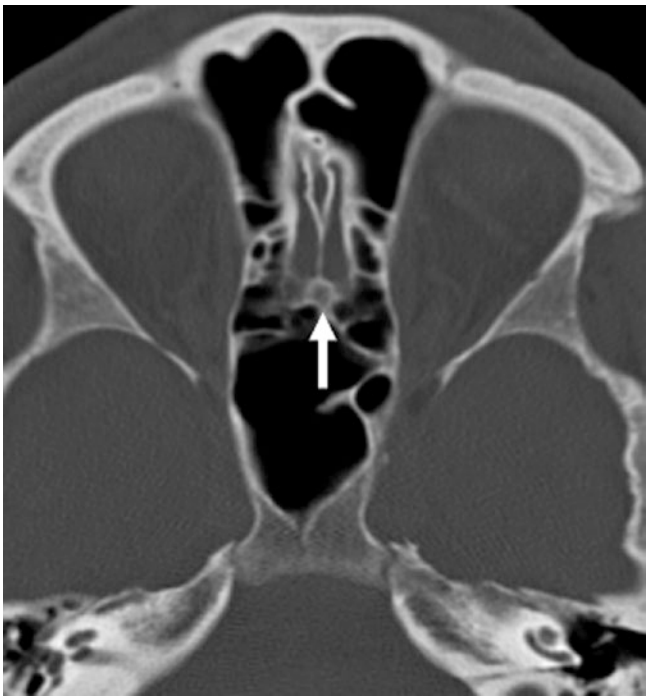

Fig. 26.12 A 52 year old with an IED between the ethmoid sphenoid sinuses on NECT

Fig. 26.11 A 4 year old with an IED between the orbitisphenoid and ethmoids on coronal reformats

26.3 Rostro-orbital Pseudoforamen

The *rostro-orbital pseudoforamen* (ROPF) is typically a bilateral defect along the lateral aspect of the presphenoid between the body of the anterior presphenoid and the orbitosphenoid. These often disappear within the first few years of life, although they may rarely persist in teens and early adults. No known nerves or vascular structures are transmitted.

Unless otherwise noted, the images provided are axial nonenhanced CT (NECT) (Figs. 26.13, 26.14, 26.15, 26.16, 26.17, 26.18, 26.19, 26.20, and 26.21).

Fig. 26.13 A 1 month old with bilateral ROPFs on axial NECT

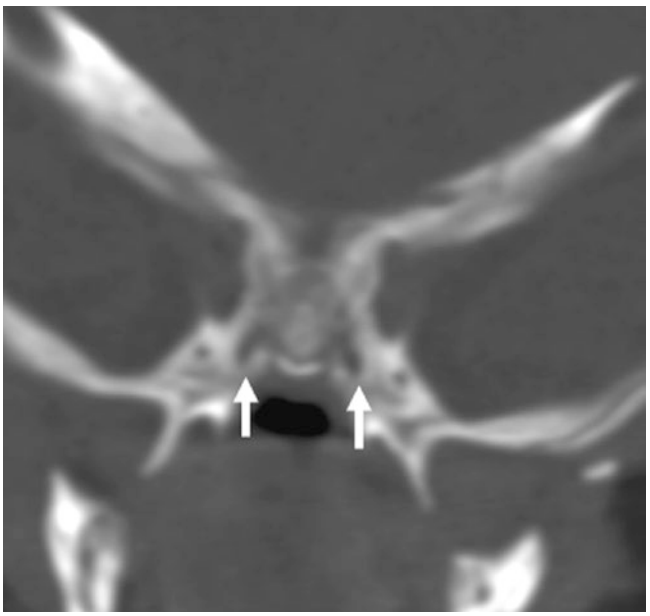

Fig. 26.14 A 3 month old with bilateral ROPF on coronal MPRs from NECT

Fig. 26.15 A 4 month old with tiny, bilateral ROPFs on axial NECT

Fig. 26.16 A 7 month old with bilateral asymmetric ROPFs on axial NECT

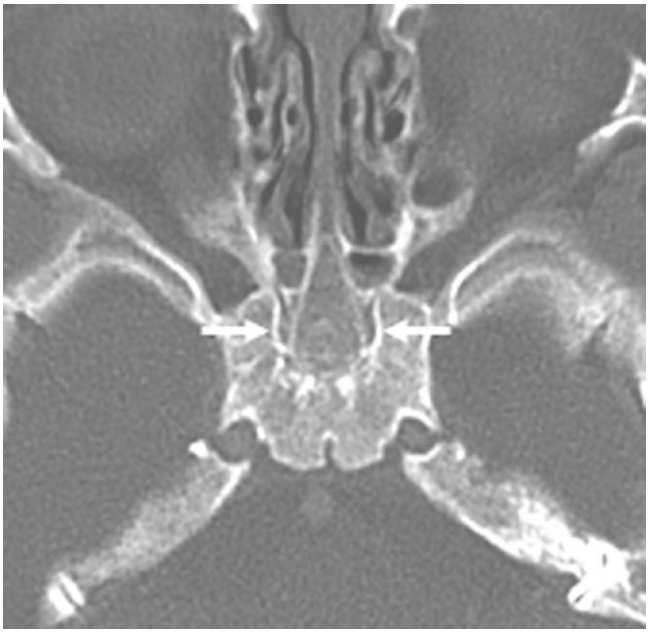

Fig. 26.17 A 9 month old with bilateral ROPFs on axial NECT

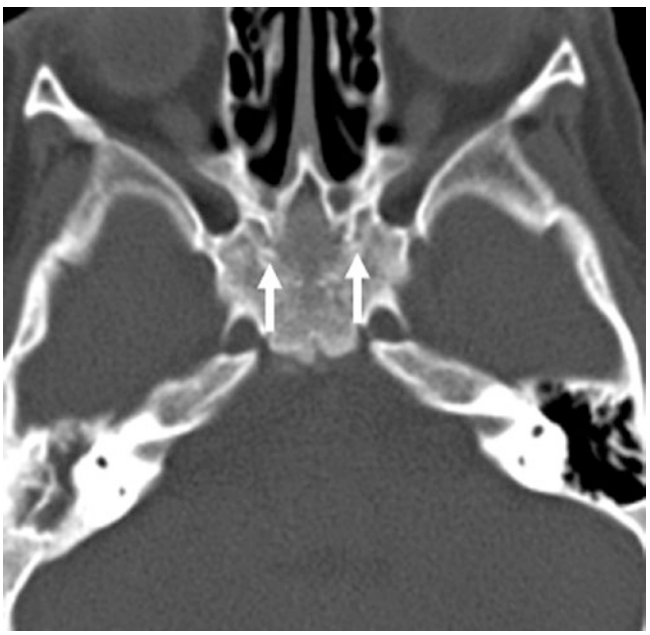

Fig. 26.18 An 18 month old with tiny bilateral ROPFs on axial NECT

Fig. 26.19 An 18 month old with tiny bilateral ROPFs on axial NECT

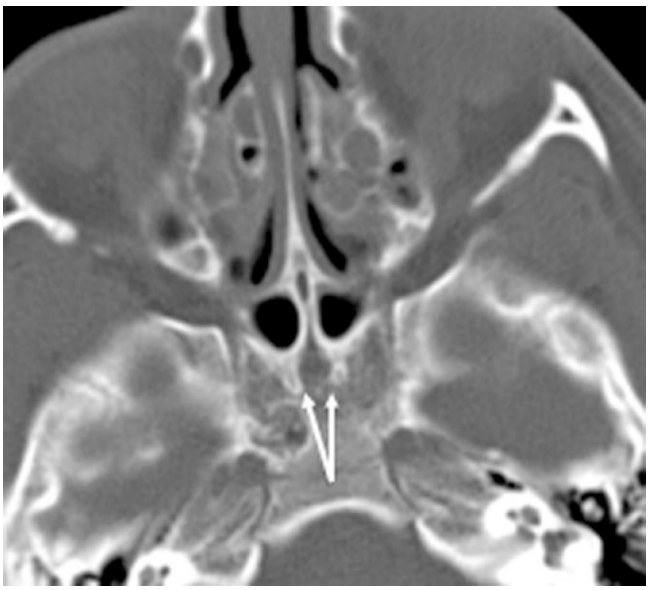

Fig. 26.20 An 8 year old with tiny bilateral ROPFs on axial NECT

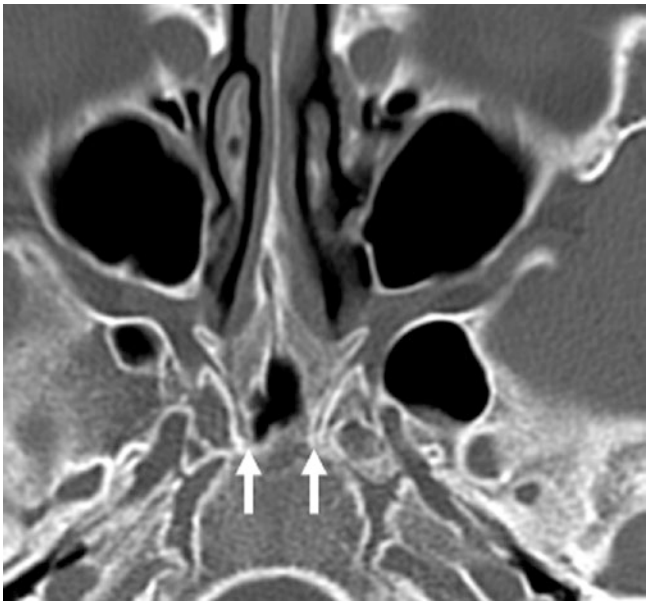

Fig. 26.21 An 18 year old with bilateral faint ROPFs on axial NECT

26.4 Anterior Foramen of Presphenoid

The *anterior foramen* (AF) is a defect of the presphenoid, usually noted in the first few months of life and containing cartilage. It is in the middle of the presphenoid. The term foramen may not be entirely appropriate because no nerves or vessels are known to pass through. Although initially a lucent and somewhat linear or triangular cartilaginous defect, it becomes rounded over the next 2–3 months and can persist in later infancy and early adolescence as linear or triangular sclerosis, particularly at its superior aspect. The *posterior foramen* (PF), also known as the *craniopharyngeal canal*, is just posterior between the middle and postsphenoid. Also noted in some cases are *intralateromedial lines/defects* (ILMDs) laterally. Some of the following cases are in patients who are older than the time of expected fusion of the AF. In each of the following cases, note that the AF is anterior to both the *spheno-occipital synchondrosis* and the PF. Included are examples of the AF from infancy onward, which only rarely persists in adults since it typically fuses in infancy.

Unless otherwise noted, the images provided are axial nonenhanced CT (NECT) (Figs 26.22, 26.23, 26.24, 26.25, 26.26, 26.27, 26.28, 26.29, and 26.30).

Fig. 26.22 A 1 month old with a large, unfused and triangular configuration of the AF (*white arrow*). Note the sphenooccipital synchondrosis (SOS) (*dashed lines*)

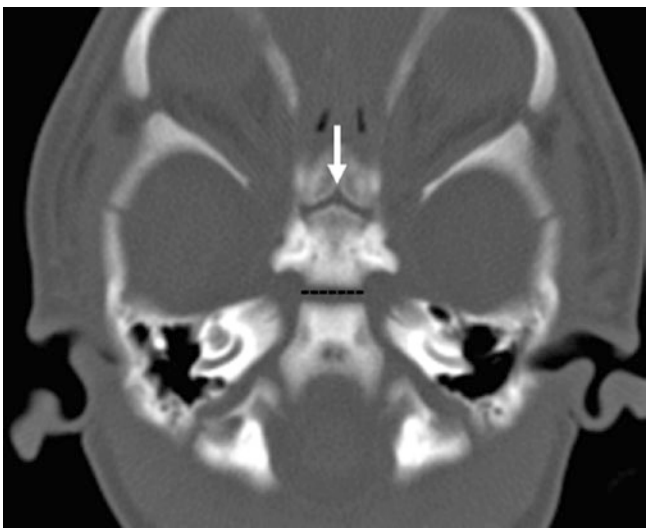

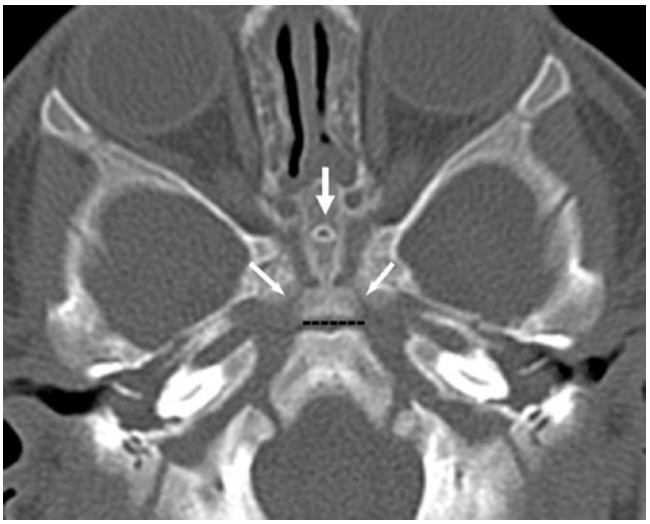

Fig. 26.23 A 1 month old with a small focal AF (*white arrow*) in the middle of the presphenoid. Note the sphenooccipital synchondrosis (*dashed lines*) and intralateromedial defects laterally (ILMD's), *(thin arrows*)

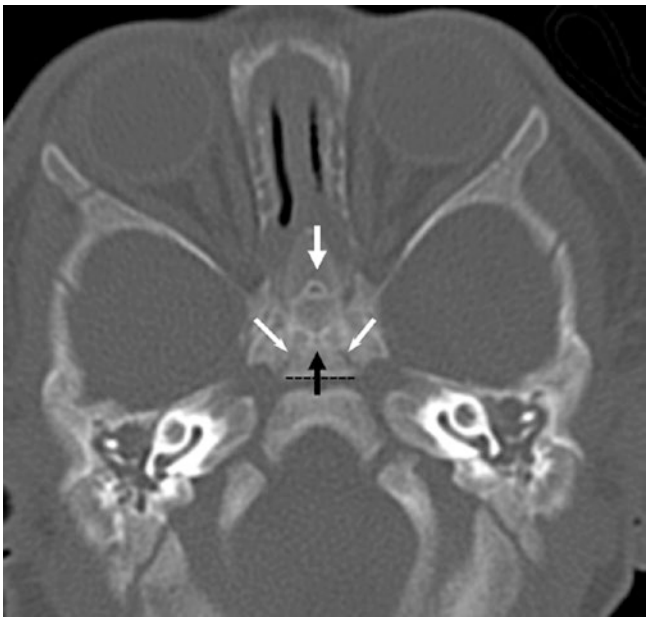

Fig. 26.24 A 7 week old with trauma but no fracture. Note a small AF (*white arrow*). *Black arrow* indicates posterior foramen (PF, craniopharyngeal canal). *Thin arrows* indicate intralateromedial defects (ILMDs)

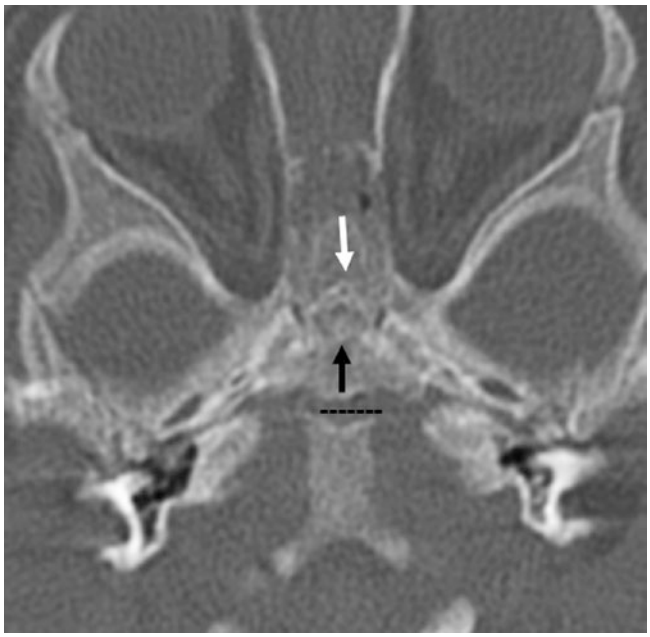

Fig. 26.25 A 3 month old with a triangular defect from an incompletely unfused AF (*white arrow*). *Black arrow* indicates PF, craniopharyngeal canal. *Dashed lines* indicate sphenooccipital synchondrosis (SOS)

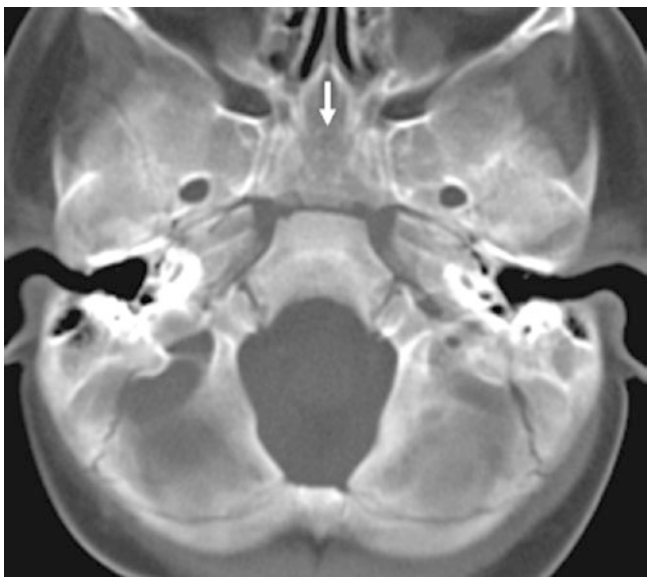

Fig. 26.26 A 1 year old with a residual, faint AF (*white arrow*) lucency on an axial 7-mm-thick MPR from NECT

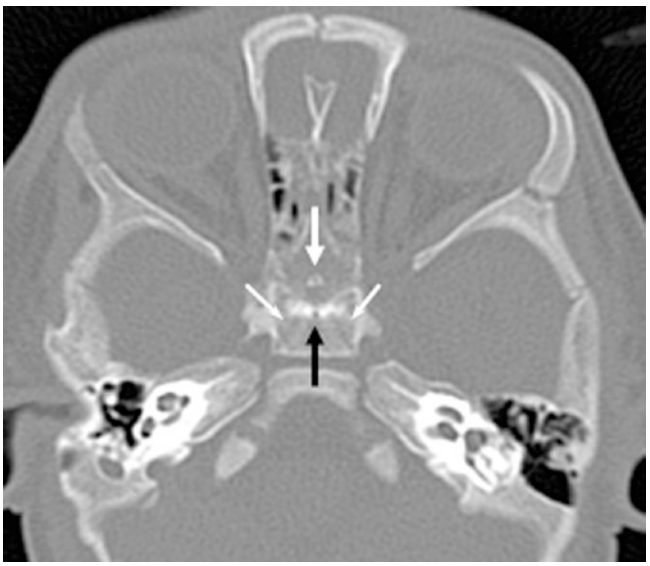

Fig. 26.27 A 5 month old with trauma but no fracture. A tiny AF (*white arrow*) can be seen anteriorly. *Black arrow* indicates PF, craniopharyngeal canal. *Thin arrows* indicate ILMDs

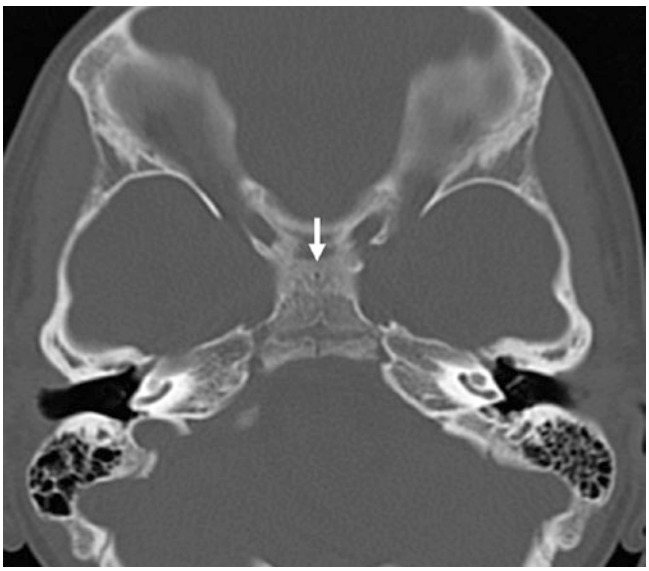

Fig. 26.29 A 6 year old with a tiny AF (*white arrow*) anterior to both the SOS and the sclerosis of the PF/CPC

Fig. 26.28 A 1 year old with a triangular, faintly sclerotic AF (*white arrow*) that is mostly fused. *Black arrow* indicates PF, craniopharyngeal canal

Fig. 26.30 A 30 year old with a residual tiny defect of the AF (*white arrow*) long after fusion

26.5 Posterior Foramen of the Sphenoid (also Known as the Craniopharyngeal Canal)

The *craniopharyngeal canal* (CPC) has many names, such as the *trans-sphenoidal canal, posterior sphenoidal foramen* (PF), *hypophyseal canal,* or the *basipharyngeal canal*. This bony canal transmits the Rathke pouch as it migrates rostrally to join with the infundibulum of the hypothalamus to form the pituitary (usually completed by 6–10 weeks' gestational age). Arrest of this migrational process can lead to the adenohypophysis' remaining below the bony sella, encephaloceles, and various other masses (craniopharyngiomas, hamartomas) or cysts (Rathke cleft cysts, dermoids, epidermoids). However, incidental, asymptomatic persistence of the canal (some sources state it is less than 2 mm in size) can be present in about 1 % of the population. The PF/CPC should be directly inferior to the sella, anterior to the *spheno-occipital synchondrosis*, and posterior to the *anterior foramen*.

The cases herein demonstrate that a normal PF, later known as a CPC, may persist and be seen in any age group. Both CT and MRI can demonstrate that a CPC is directly caudal to the bony sella and pituitary stalk and that the canal can theoretically communicate between the floor of the bony sella and the nasopharynx. Although the canal can be patent but asymptomatic, in a small segment of the population a *mass, cyst,* or *encephalocele* should be excluded when these are larger than 2–3 mm.

Unless otherwise noted, the images provided are axial nonenhanced CT (NECT) (Figs. 26.31, 26.32, 26.33, 26.34, 26.35, 26.36, and 26.37).

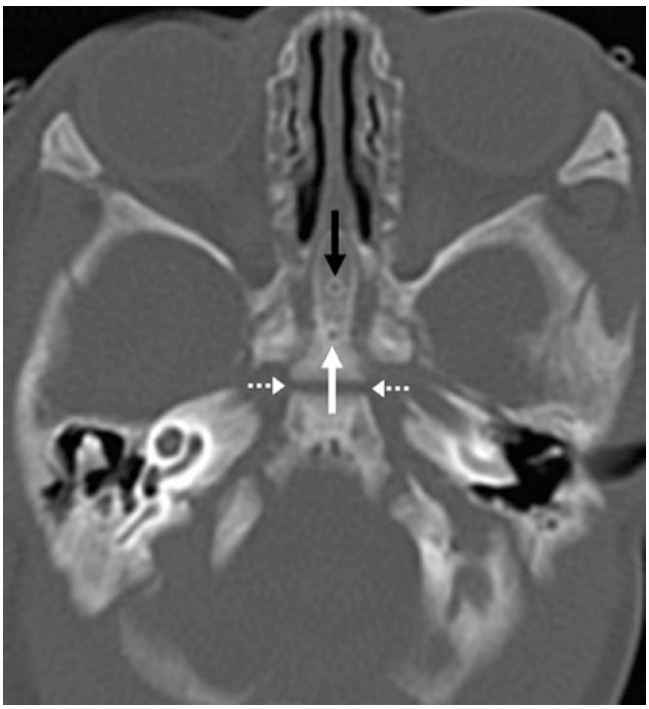

Fig. 26.31 A 10 day old with a tiny PF (*white arrow*) and a tiny AF (*black arrow*) on axial NECT. Note the patent SOS (*dashed arrows*) posteriorly

Fig. 26.32 A 1 month old with a tiny PF (*white arrow*) and a tiny AF (*black arrow*) on axial NECT. Note the patent SOS (*dashed arrows*) posteriorly

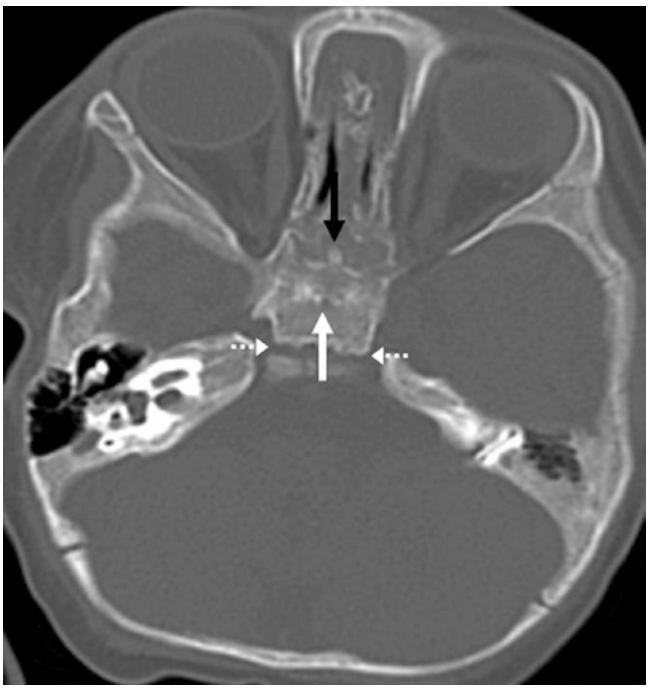

Fig. 26.33 A 5 month old with a tiny PF (*white arrow*) and a tiny AF (*black arrow*) on axial NECT. Note the patent SOS (*dashed arrows*) posteriorly.

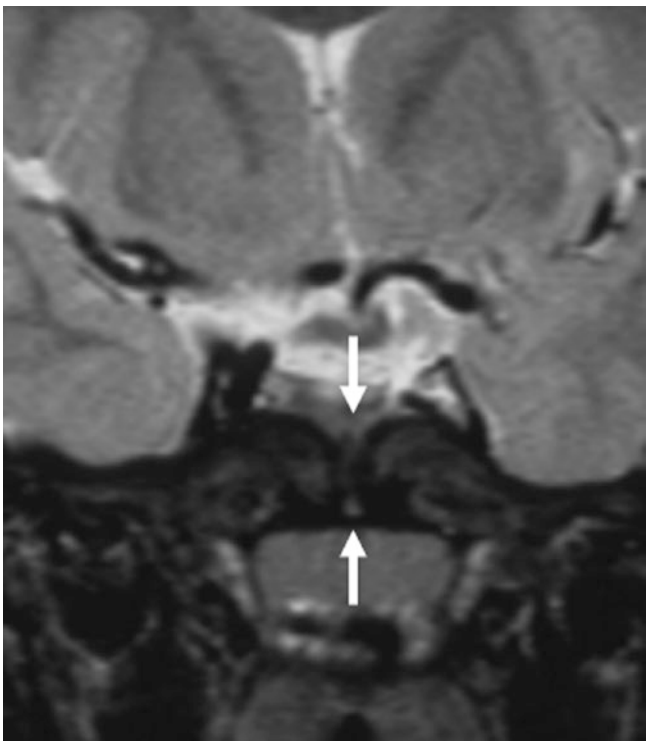

Fig. 26.35 A 6 year old with a coronal T2WI MRI that shows the patent extent of a PF/CPC (*arrows*)

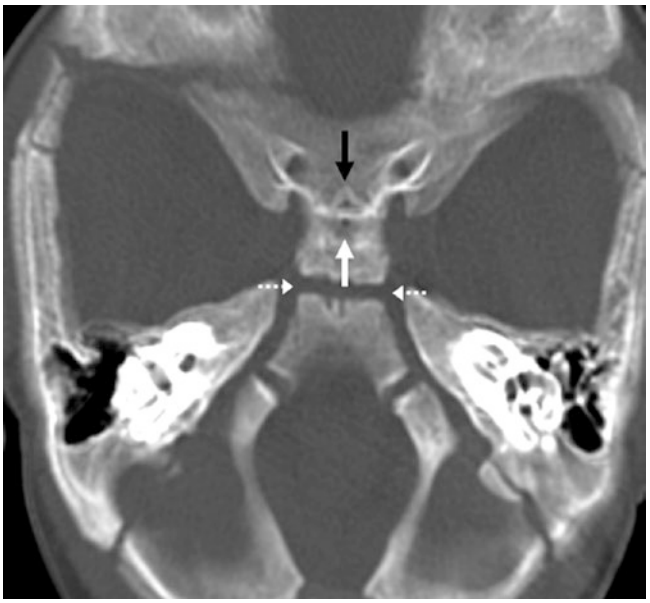

Fig. 26.34 A 5 month old with a mostly fused PF (*white arrow*) on MPR and a widely patent SOS (*dashed arrows*) posteriorly. The AF (*black arrows*) is patent

Fig. 26.36 A 20 year old with a residual patent PF (*arrow*) on axial NECT. The SOS has fused

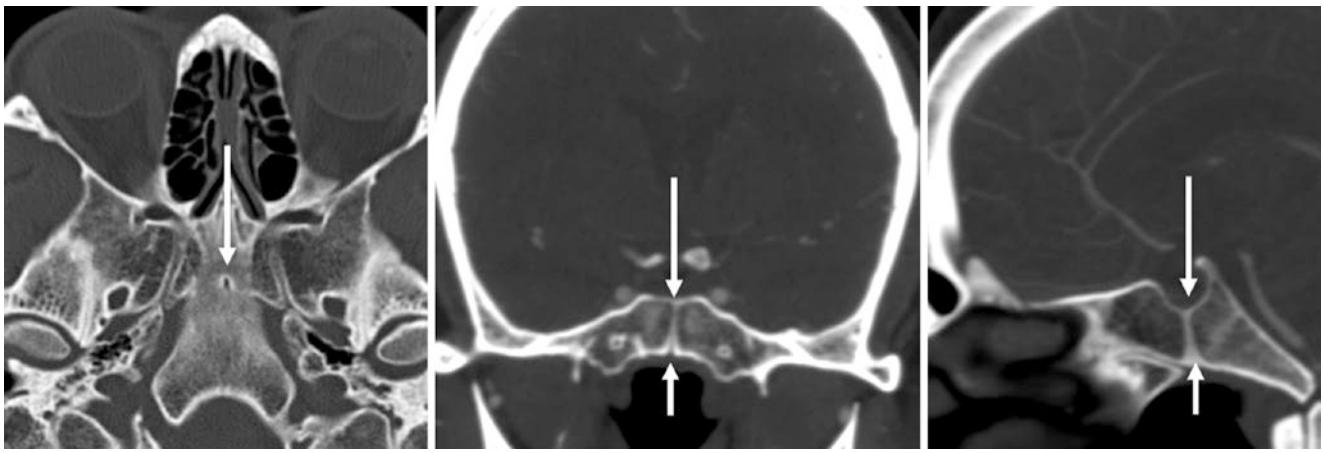

Fig. 26.37 A 50 year old with a patent PF (CPC) that is visible on axial (*left*), coronal (*middle*), and sagittal (*right*) images reconstructed from a CT angiogram. Note the fused SOS situated posteriorly

26.6 Intralateromedial Defects of the Postsphenoid

ILMDs are related to the lateral site of fusion of the postsphenoid. They are typically noticed on axial nonenhanced (NECT). In infants, small lines are seen at this site of fusion, usually disappearing in the first year of life. However, small, faint lines or even *pseudoforamina* may be present later in childhood, adolescence, or rarely in adults; they should not be mistaken for fractures and do not transmit nerves or vasculature. The *AF* (intrapresphenoidal) is also demonstrated in several examples because it is often present in the same time period as the ILMDs, typically within the first 6 months of life.

Unless otherwise noted, the images provided are axial NECT (Figs. 26.38, 26.39, 26.40, 26.41, 26.42, and 26.43).

Fig. 26.38 A 3 day old with tiny ILMDs (*arrows*) bilaterally. *Black arrow* indicates AF

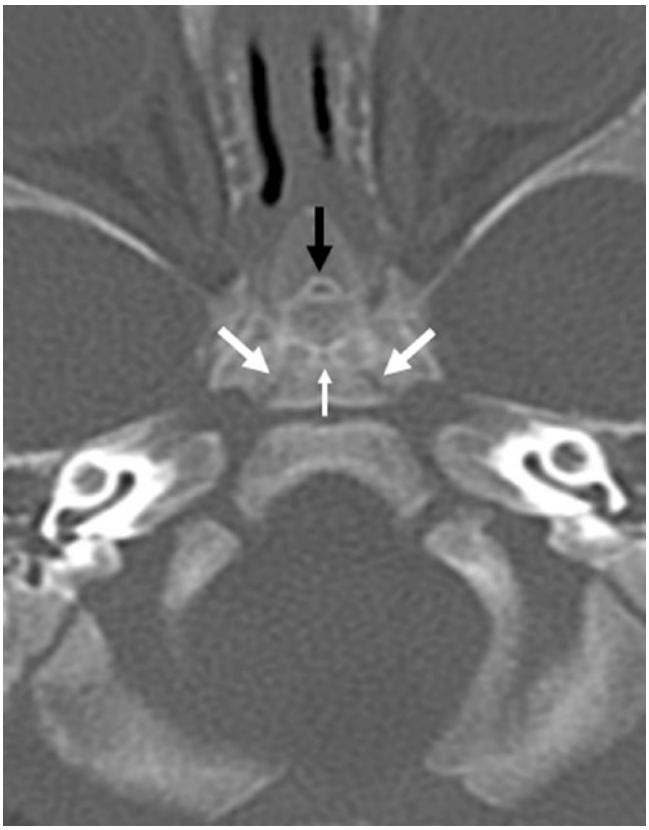

Fig. 26.39 A 1 month old with tiny ILMDs (*arrows*) bilaterally. *Black arrow* indicates AF. *Tiny arrow* indicates PF

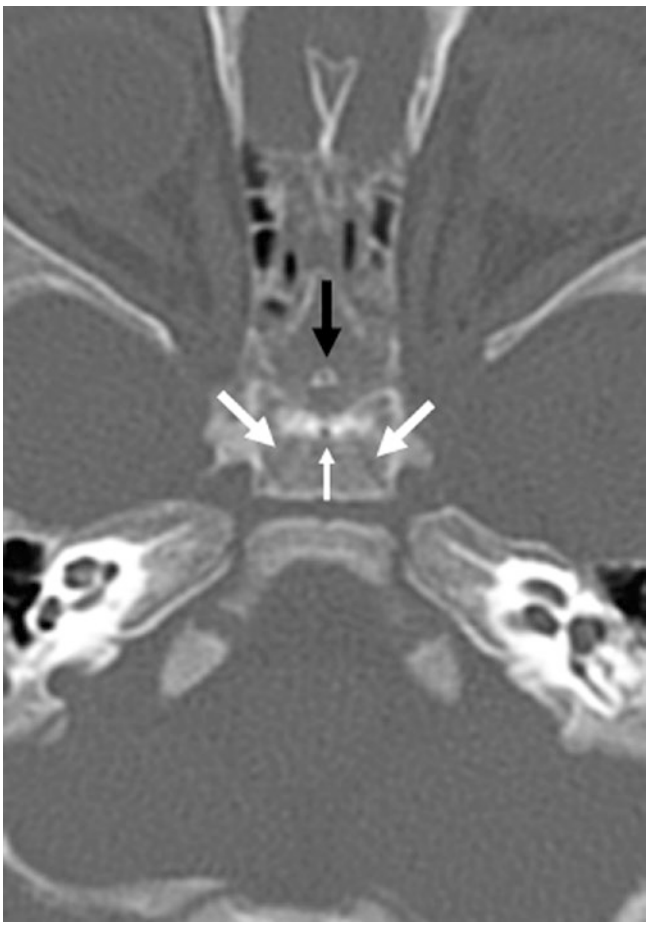

Fig. 26.40 A 5 month old with faint ILMDs (*arrows*) bilaterally. *Black arrow* indicates AF. *Tiny arrow* indicates PF

Fig. 26.42 A 49 year old with a unilateral left ILMD (*arrow*) persisting as small pseudoforamen

Fig. 26.41 A 45 year old with a unilateral left ILMD (*arrow*) persisting as a tiny pseudoforamen

Fig. 26.43 A 57 year old with a faint residual tiny left ILMD (*arrow*) pseudoforamen

26.7 Intrapostsphenoidal Pseudoforamen

The *intrapostphenoidal pseudoforamen* (IPSP, termed by Madeleine and coauthors) refers to a cartilaginous inclusion occurring at or near the *spheno-occipital synchondrosis* (SOS). This foramen is occasionally seen in adults upon or near fusion of the SOS and is typically noted on axial NECT images. This can be confused with a *craniopharyngeal canal* (i.e., posterior sphenoidal foramen); however, the IPSP does not communicate with the sella or pharynx. Seeing a foramen-like defect along or abutting the SOS (the CPC is anterior to the SOS) is the best way to discern this pseudoforamen. Unless otherwise noted, the images provided are axial nonenhanced CT (NECT) (Figs. 26.44, 26.45, 26.46, 26.47, 26.48, 26.49, and 26.50).

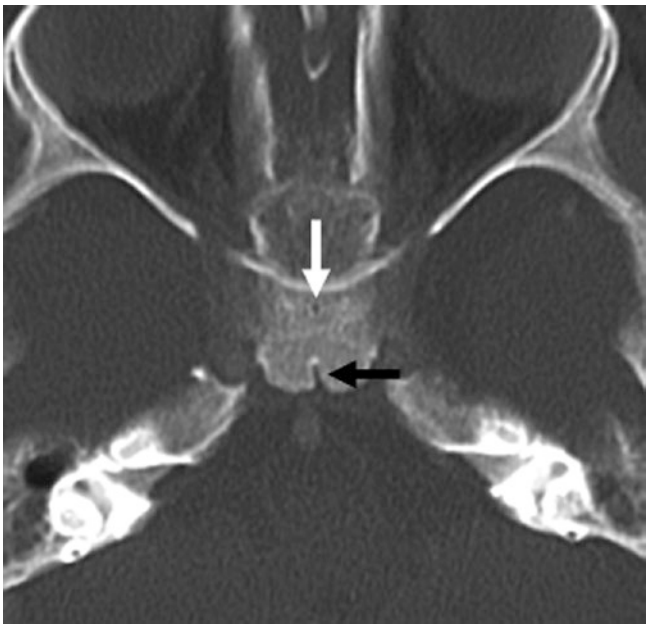

Fig. 26.44 A 9 month old with a postsphenoidal cleft (*black arrow*) and an IPSP (*white arrow*)

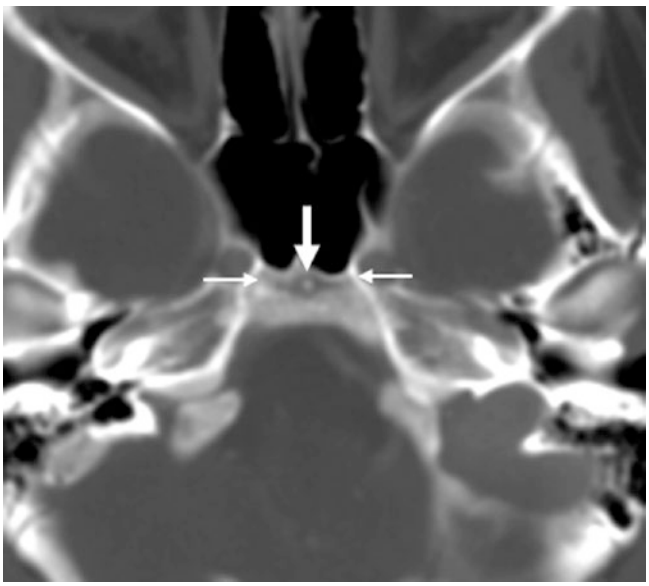

Fig. 26.45 A 12 year old with a tiny IPSP (*arrow*) and a marginally patent SOS (*thin arrows*)

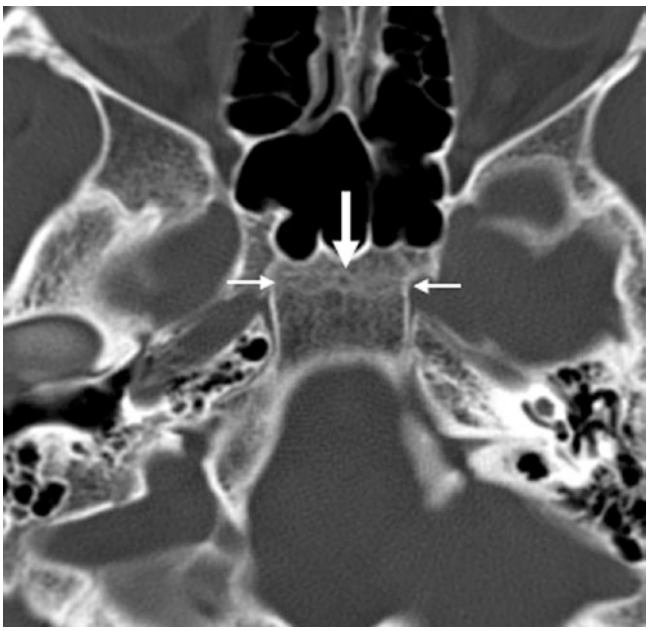

Fig. 26.46 In a 15 year old the SOS (*thin arrows*) is fusing and an early IPSP (*arrow*) has formed

Fig. 26.47 An 18 year old with a tiny IPSP (*arrow*)

Fig. 26.48 A 51 year old with a tiny midline defect that represents a residual IPSP (*arrow*)

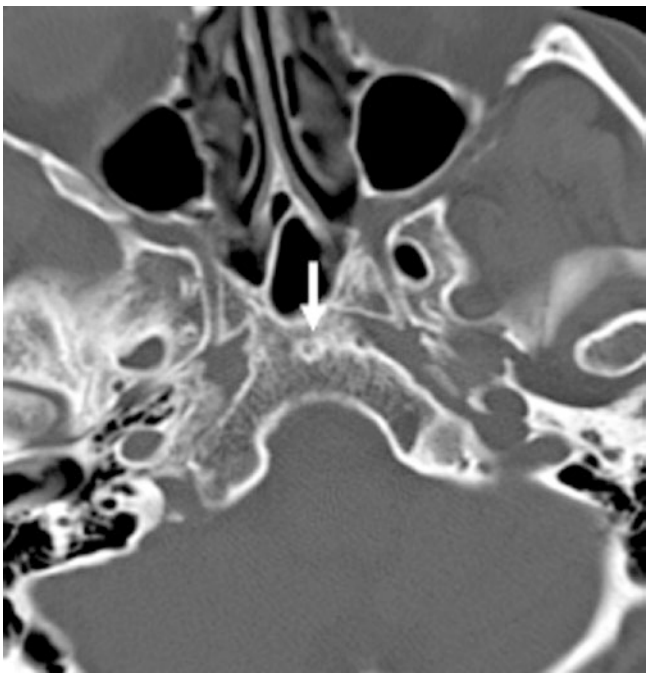

Fig. 26.49 A 48 year old with a tiny midline defect from a residual IPSP (*arrow*)

Fig. 26.50 A 37 year old with a pseudoforamen from an IPSP (*arrow*) noted along the SOS on the *middle image*; however it is not noted on axial CT images below (*left*) or above (*right*) that level. This demonstrates how the IPSP is a pseudoforamen that does not communicate above or below

26.8 Postsphenoidal Cleft

The *postsphenoidal clefts* (PSCs) and the *anterior basiocciptal clefts* (ABOCs) occur together in a majority of patients along the anterior and posterior aspects of the *SOS*. These clefts are common in childhood, when there is significant bone turnover, possibly lytic or blastic activity adjacent to the SOS, and are common between several months of age even into the late teens. Note that the PSCs are along the posterior aspect of the sphenoid, while the ABOCs are along the anterior aspect of the occipital bone. Both the PSCs and the ABOCs can have a cruciate appearance. Other variants seen in the cases below include the occipitomastoid suture (OMS) and a tiny CPC in one case.

Unless otherwise noted, the images provided are axial nonenhanced CT (NECT) (Figs. 26.51, 26.52, 26.53, 26.54, and 26.55).

Fig. 26.51 An 18 month old with trauma but no fracture and a small PSC (*arrow*)

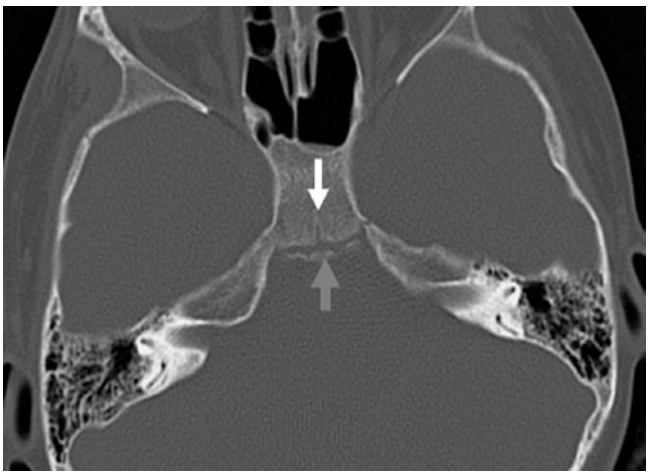

Fig. 26.52 A 9 year old with trauma but no fracture and a tiny PSC (*arrow*). *Gray arrow* indicates SOS

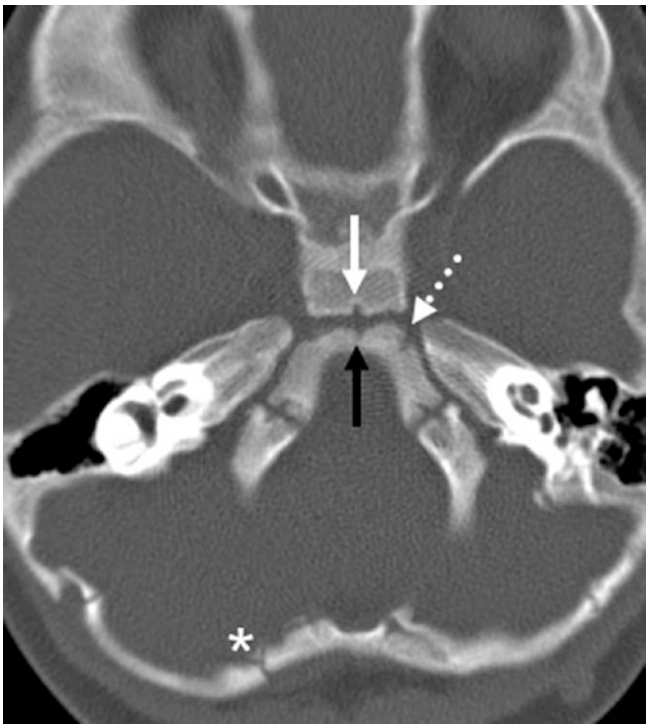

Fig. 26.53 A 1 year old with a PSC (*arrow*), anterior basioccipital cleft (ABOC) (*black arrow*), OMS (*dotted white arrows*), and a true occipital fracture (*asterisk*)

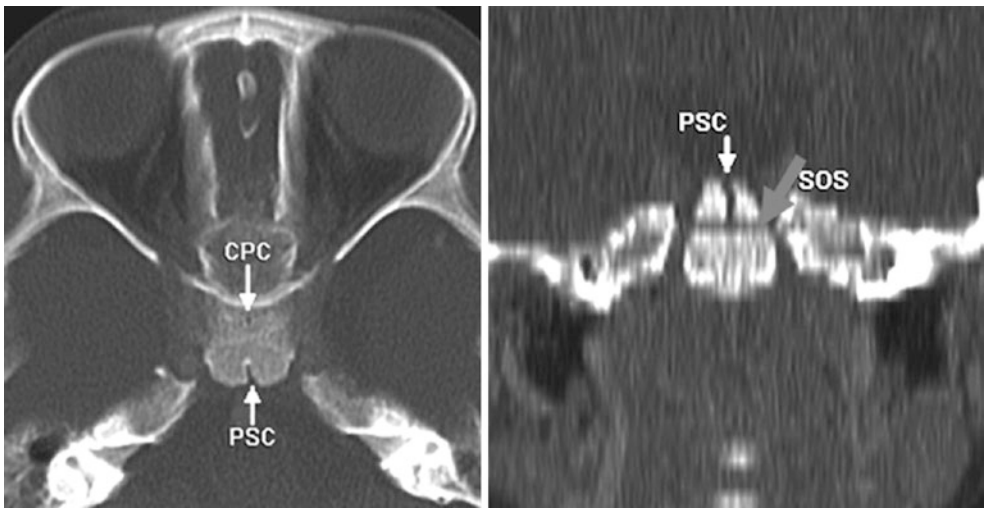

Fig. 26.54 A 9 month old with trauma but no fracture. Note the PSC, CPC, and SOS on axial (*left*) and coronal (*right*) NECT reformats; the PSC mimics a fracture on coronal MPR's

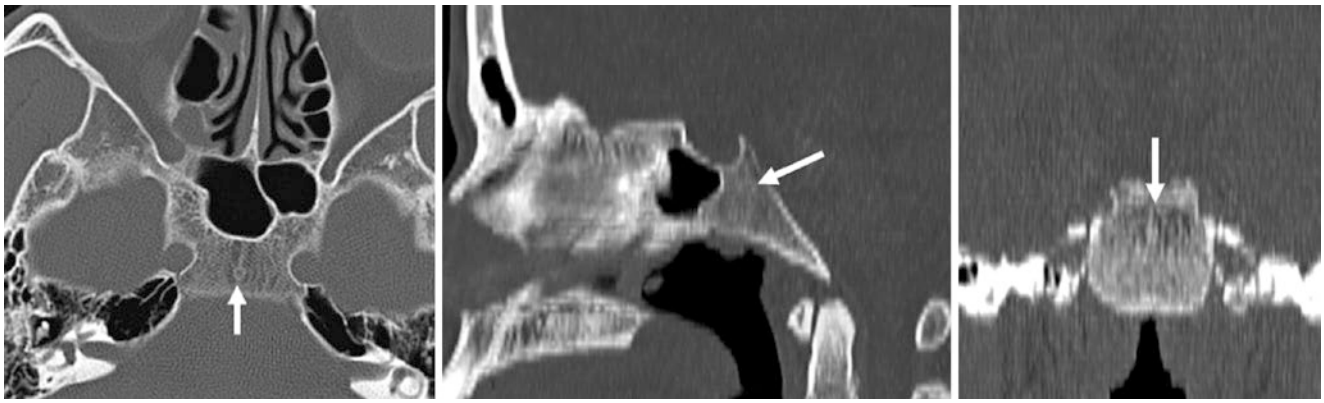

Fig. 26.55 A 37 year old with a tiny, tubular defect (*arrows*) at the top of the expected SOS but posterior to the expected location of the CPC on axial (*left*), sagittal (*middle*), and coronal (*right*) NECT reconstructions. This favors being a PSC remnant

26.9 Spheno-Occipital Synchondrosis

The *SOS* usually begins fusion about 6–8 years of age, and in the large majority of children (>95 %) completes fusion between 15 and 18 years of age. However, residual defects may be visualized in up to two thirds of patients and may be seen as faint areas of sclerosis or lucency in adults. These defects include small cleft-like defects, small ossified bodies within the cartilage-filled space yet to be ossified, or sclerotic lines, even in the later adult ages.

The figures in this section illustrate the SOS at various stages from birth to later in infancy, with examples also provided from later in life. The examples illustrate progressive sclerosis and fusion of the SOS from infancy to late childhood, early teens, adulthood, and even in the elderly. Note that the sclerosis denoting fusion of the SOS begins centrally, which can appear irregular as fusion commences. As the SOS progressively fuses, the surrounding and internal sclerosis ensues. Although fusion is typically completed or nearly completed by the ages of 18–21 years, varying degrees of residual sclerosis or faint defects can be noted and can persist even in the elderly. In *trauma*, this can simulate fractures or diastasis in any of these age groups, particularly during fusion. Thus, a true fracture can often be distinguished from a normal SOS by reformatting the axial sequences. However, one should be wary of true fractures that can extend along the SOS as a path of least resistance, particularly in older children or teens in whom the SOS is partially fused. It is recommended to look for fractures laterally with pneumocephalus extending along the carotid canal or for fluid in the adjacent sphenoid sinus or mastoid air cells.

Unless otherwise noted, the images provided are from axial nonenhanced CT (NECT) (Figs. 26.56, 26.57, 26.58, 26.59, 26.60, 26.61, 26.62, 26.63, 26.64, 26.65, 26.66, 26.67, 26.68, and 26.69).

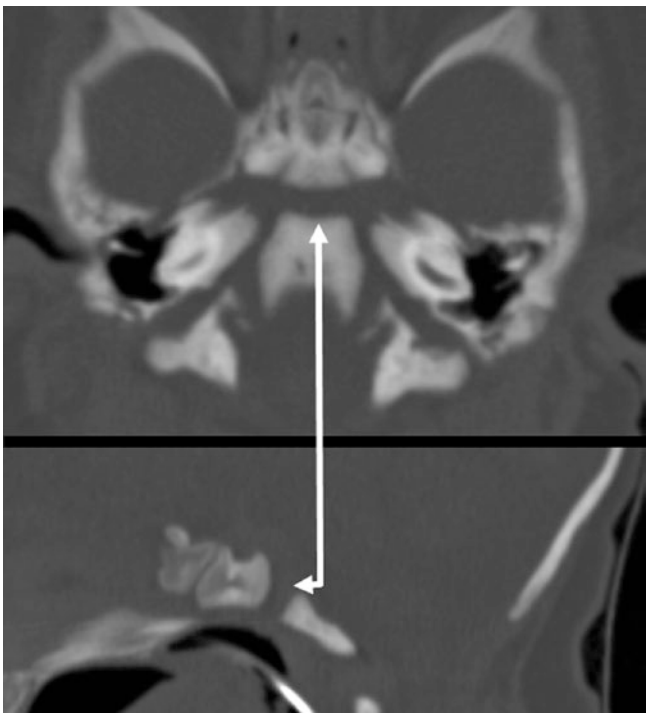

Fig. 26.56 A 1 day old with a widely patent SOS on axial (*top*) and sagittal (*bottom*) 5-mm-thickness reformats from NECT (*arrow*)

Fig. 26.57 A 1 month old with a typical SOS (*arrow*)

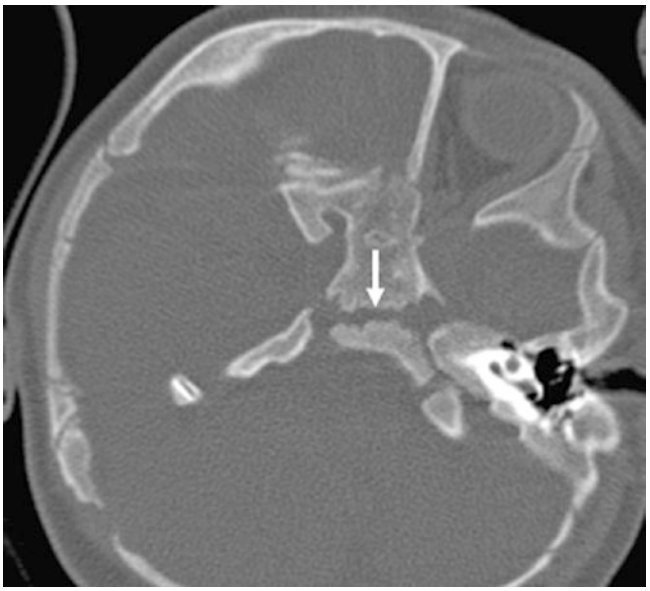

Fig. 26.58 A 3 month old whose body is tilted within the CT scanner. Note an irregular SOS (*arrow*)

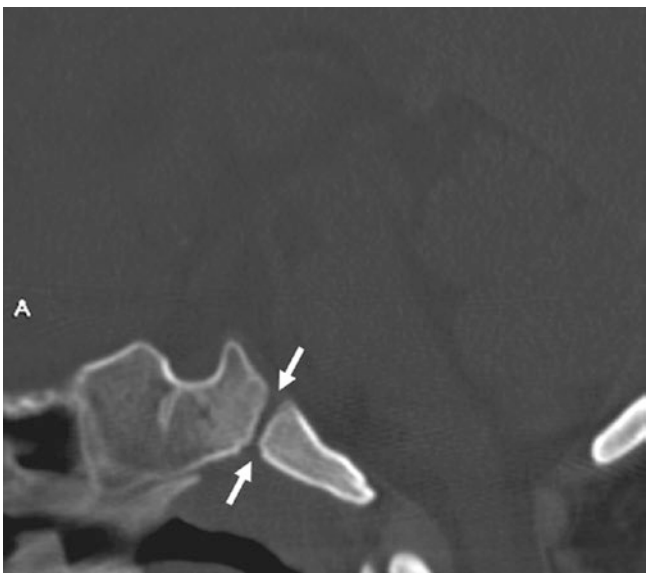

Fig. 26.59 A 1 year old with a normal patent SOS on a sagittal reformat from NECT

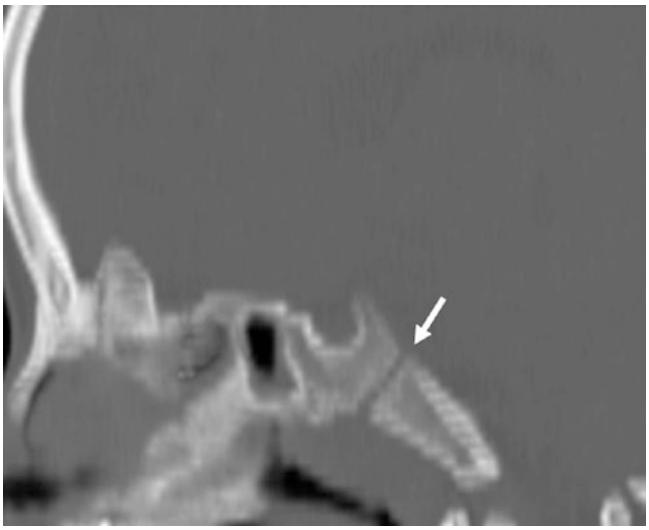

Fig. 26.60 A 4 year old with a patent SOS (*arrows*) noted on a sagittal MPR from NECT

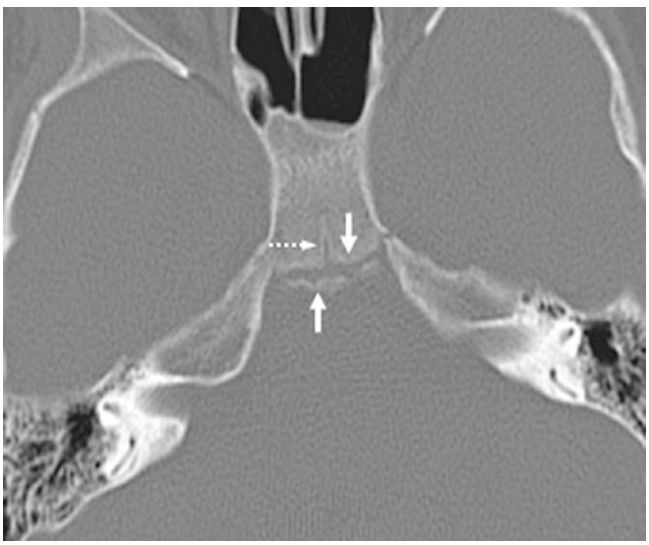

Fig. 26.61 A 9 year old with an irregular SOS (*arrows*) as well as a PSC (*dashed arrow*)

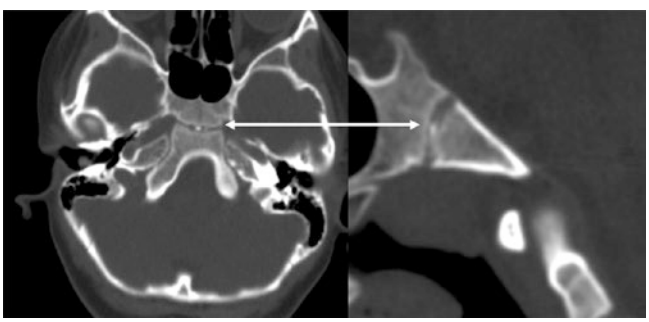

Fig. 26.62 An 8 year old with early ossification of the SOS (*arrow*) with internal ossicle-like sclerosis centrally on axial (*left*) and sagittal (*right*) MPRs from NECT

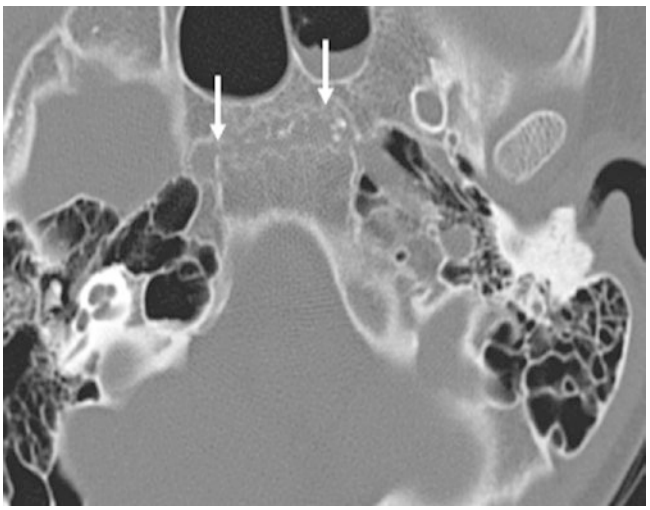

Fig. 26.63 An 11 year old with a sclerotic and irregular SOS (*arrows*) as the SOS is beginning to fuse

Fig. 26.64 An 11 year old with a sclerotic focus noted centrally near the midline of the SOS (*arrow*) while the SOS is partially fused

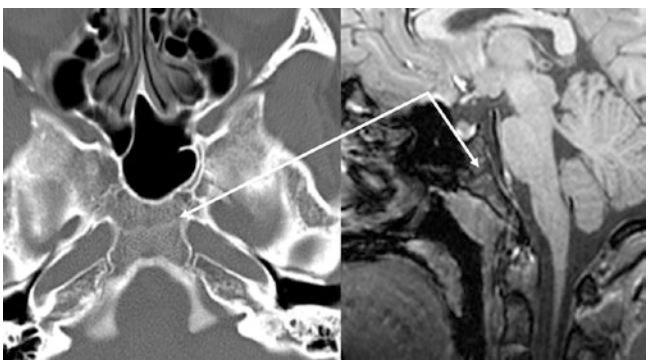

Fig. 26.65 An 18 year old with a sclerotic SOS (*arrow*) that is recently and nearly completely fused, as shown on axial NECT (*left*) and on a sagittal T1-weighted MRI (*right*) obtained at 3 T

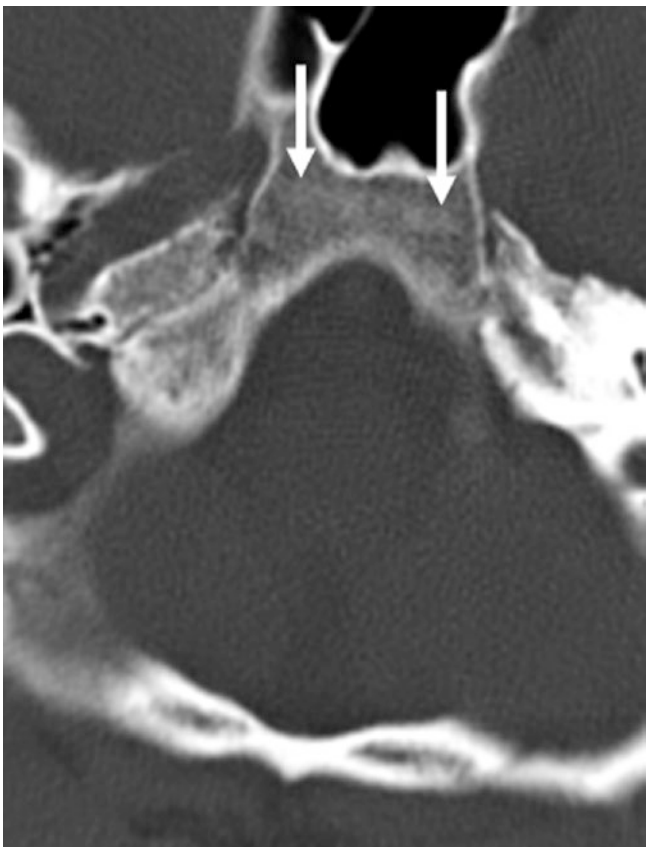

Fig. 26.66 A 45 year old with faint sclerosis of the SOS

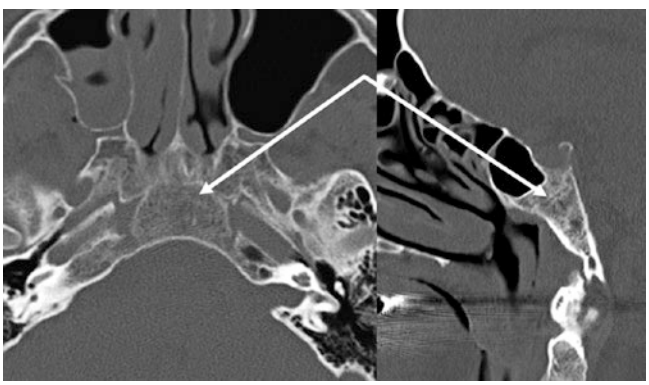

Fig. 26.67 A 71 year old with a tiny, hardly patent SOS (*arrows*) on axial NECT (*left*), which is best visualized on sagittal MPR (*right*)

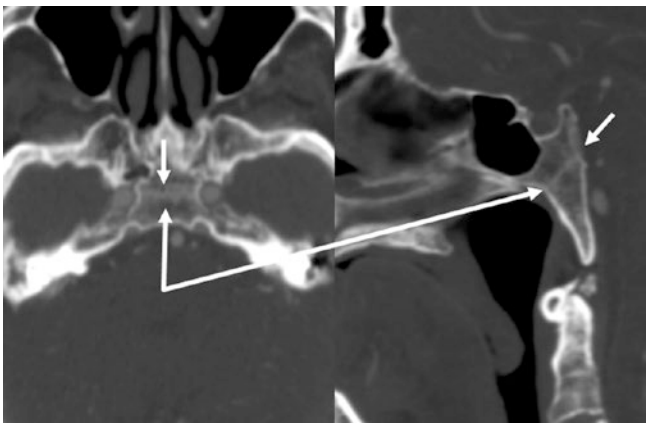

Fig. 26.68 A 74 year old with a residual sclerotic line from a fused SOS (*arrows*) shown on axial (*left*) and sagittal (*right*) MPRs

Fig. 26.69 A 79 year old with a line of faint sclerosis from SOS fusion (*arrow*)

26.10 Anterior Basioccipital Clefts

ABOC and *postsphenoidal clefts* occur together in a majority of patients. These clefts are common in childhood when there is significant bone turnover, possibly related to lytic/blastic activity adjacent to the *SOS*. There is no known synchondrosis along the anterior basiocciput's midline, supporting the theory that these clefts are related to absorption/resorption of bone and turnover adjacent to the active SOS. Therefore, particularly in ages between 3 months and 15 years (when there is active turnover in this region) jagged, irregular, or even a sclerotic and ossicular appearance in this location is within normal limits, although careful inspection should be performed in cases of trauma (all our cases were evaluated for trauma) to check if a *fracture* line crosses the SOS and other portions of the sphenoid and temporal bones. Also, correlation with the presence of pneumocephalus or debris in the mastoids or middle ear is helpful.

Unless otherwise noted, the images provided are from axial nonenhanced CT (NECT) (Figs. 26.70, 26.71, 26.72, and 26.73).

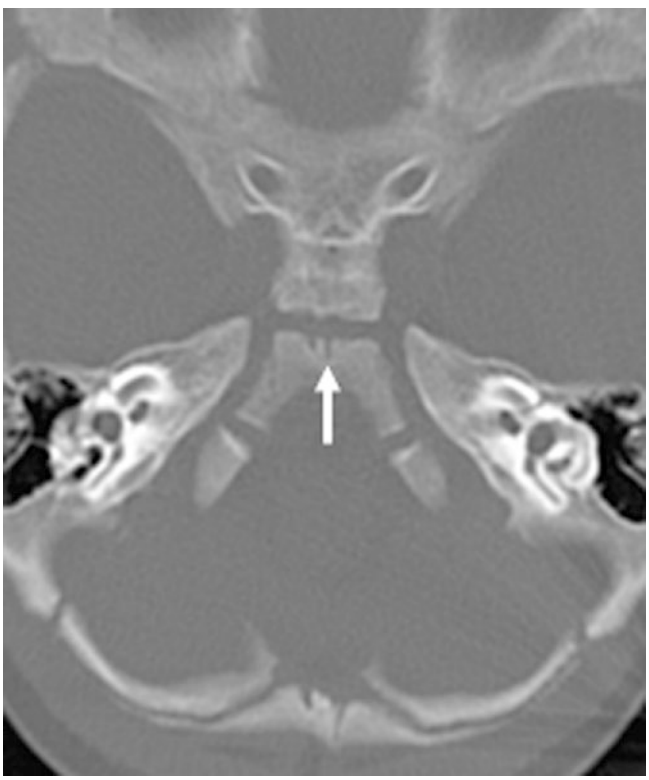

Fig. 26.70 A 5 month old with two tiny defects from ABOCs (*arrow*)

Fig. 26.71 A 3 year old with an ossicle-like ABOC (*arrow*)

Fig. 26.72 A 6 year old with a tiny ABOC defect (*arrow*)

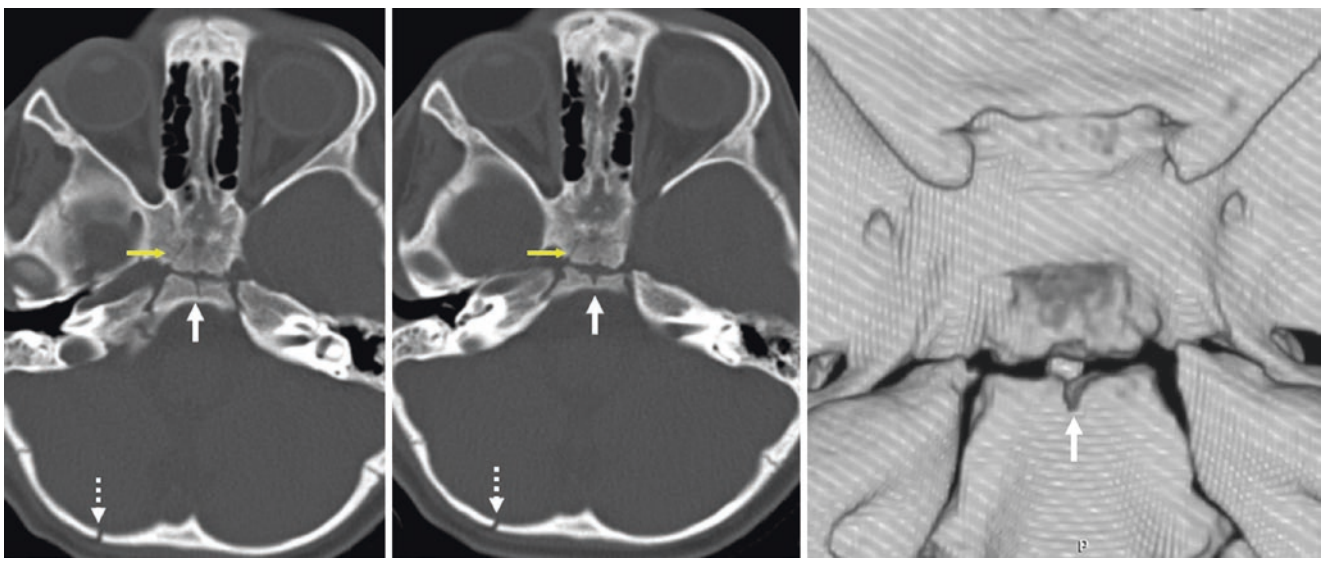

Fig. 26.73 A 6 month old who had trauma from a nondisplaced occipital fracture (*dotted arrows*). The ABOC (*white arrows*) is normal; a fracture line in that location would likely extend anteriorly into the ethmoids or laterally into the petrous apices. Another faint line (*yellow arrows*) was thought not to represent a fracture. Also, 3D images (*superior view*, *right*) did not depict a fracture

26.11 Parasagittal Defects of the Basiocciput (Basioticum Variant)

Parasagittal tubular defects (arrows) may be an uncommon form of incomplete fusion of the posterior parachordal centers and the adjacent occipital sclerotomes and are usually located just off of the midline. These may appear tubular or faint and can be bilateral. On sagittal or coronal reconstructions, they are usually linear and vertically oriented.

Unless otherwise noted, the images provided are from axial nonenhanced CT (NECT) (Figs. 26.74, 26.75, 26.76, 26.77, and 26.78).

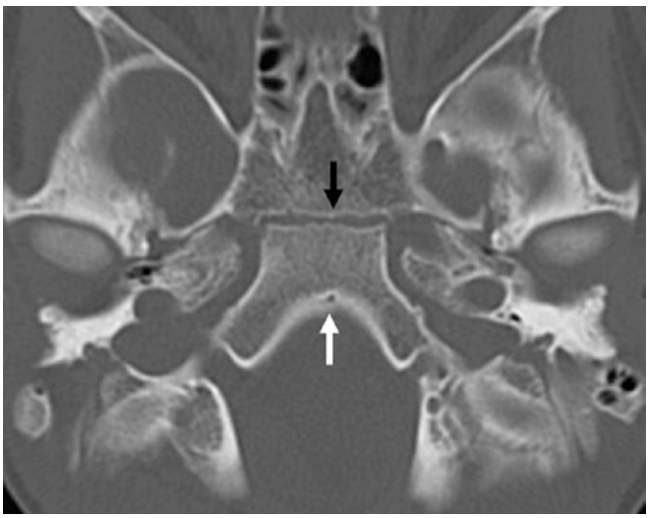

Fig. 26.74 An 11 year old with a tiny, tubular parasagittal defect (*white arrow*). Anteriorly, the spheno-occipital synchondrosis is patent (*black arrow*)

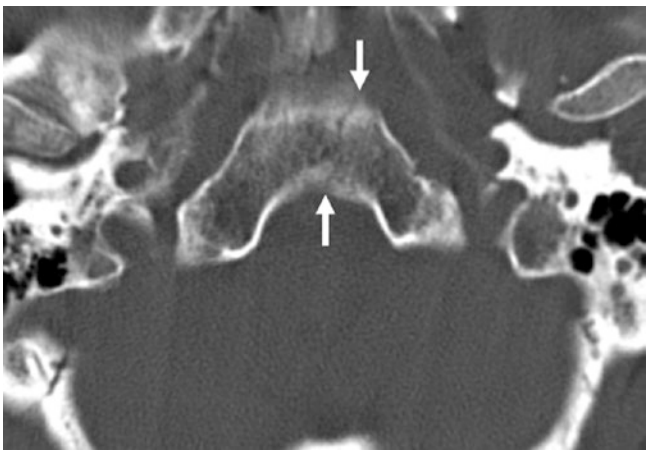

Fig. 26.76 A 76 year old in whom a tiny parasagittal defect (*arrows*) mimics a clival fracture

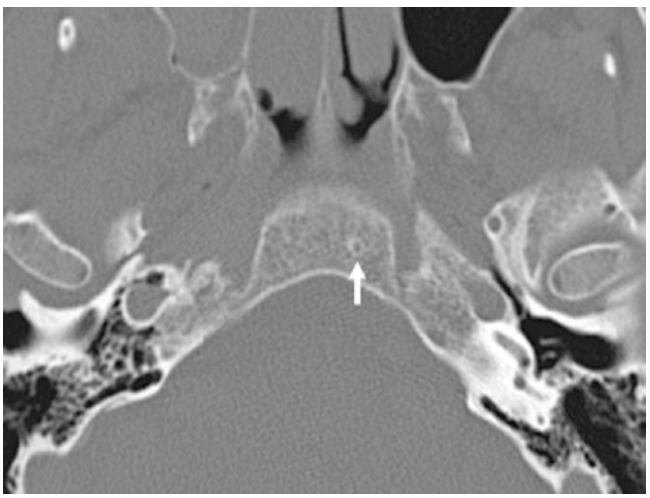

Fig. 26.75 An 11 year old with an off-midline tubular parasagittal defect (*arrow*)

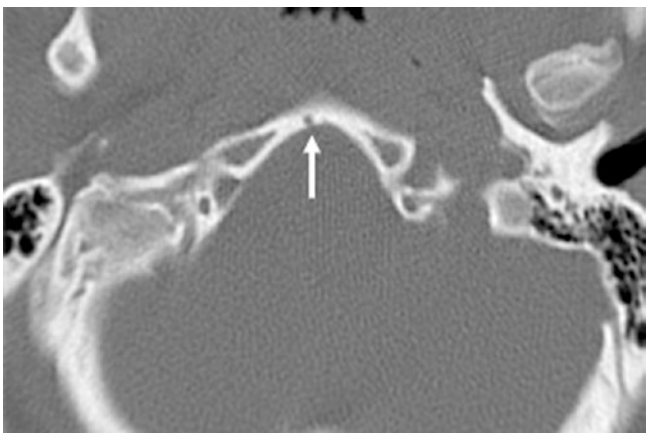

Fig. 26.77 A 25 year old with a small tubularparasagittal defect (*arrow*)

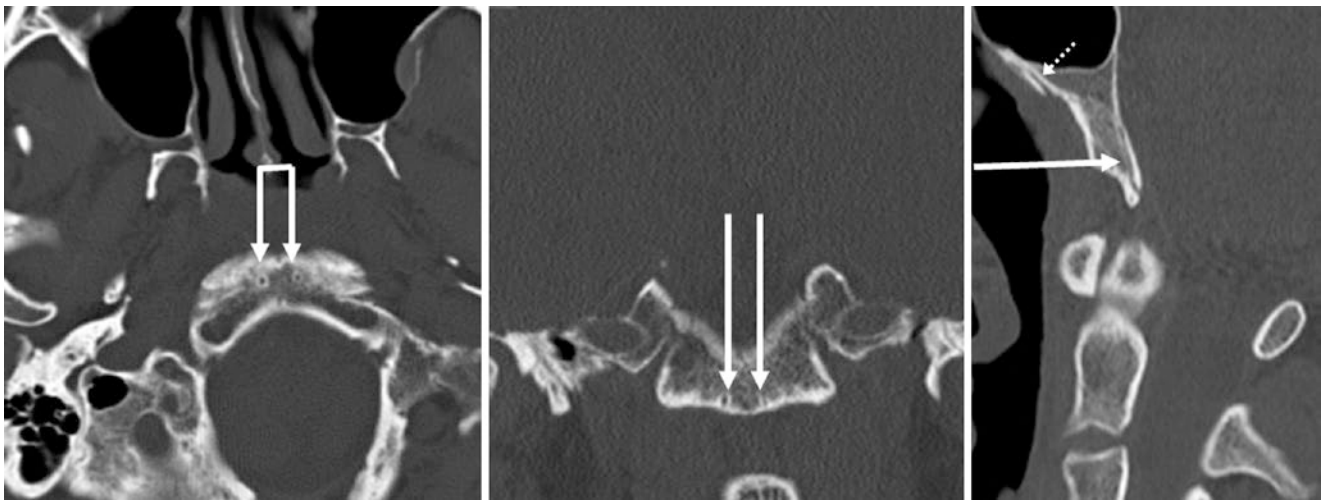

Fig. 26.78 A 36 year old with bilateral tubular parasagittal defects on axial (*left*), coronal (*middle*), and sagittal (*right*) NECT reconstructions. Note the sphenovomerine suture (*dotted arrows*)

26.12 Canalis Basilaris Medianus

The *canalis basilaris medianus* (CBM) is present in less than 2 % of the population and is a channel that is thought to be a notochordal remnant at its superior extent. The CBM is proposed to result from incomplete fusion of ossification centers around this remnant. It persists in varying degrees, being incomplete or complete, which can range among the basiocciput, the inferior aspect of the bony sella, and persist on the pharyngeal surface of the basiocciput as the *foveola pharyngica* (FP). As long as no meningocele or mass is contained within (a rare occurrence), the CBM is an asymptomatic normal variant. Note that it is located inferoposterior to the SOS.

Unless otherwise noted, the images provided are from axial nonenhanced CT (NECT) (Figs. 26.79, 26.80, 26.81, 26.82, 26.83, 26.84, 26.85, 26.86, and 26.87).

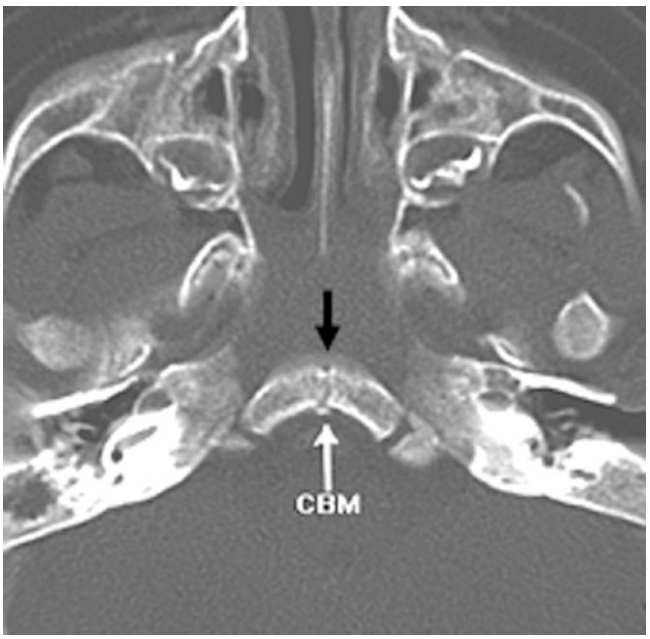

Fig. 26.79 A 9 month old with a CBM (*white arrow*) and an FP (*black arrow*)

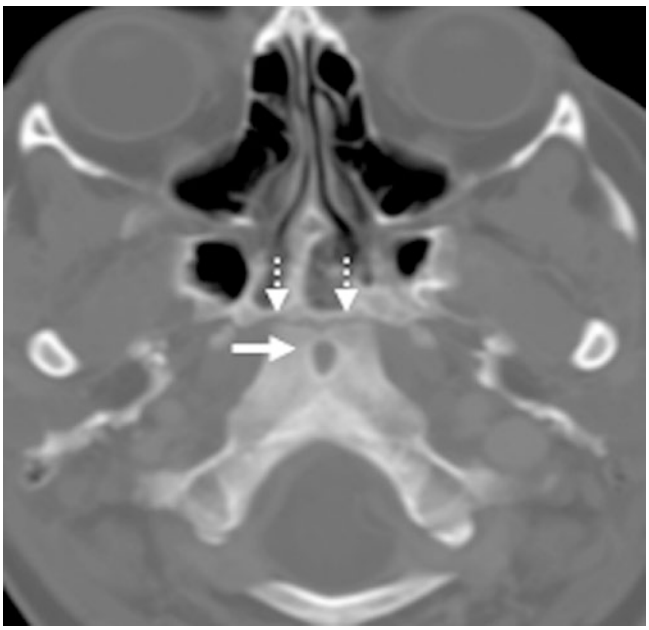

Fig. 26.81 A 12 year old with a CBM (*arrow*) and a patent SOS (*dashed arrows*)

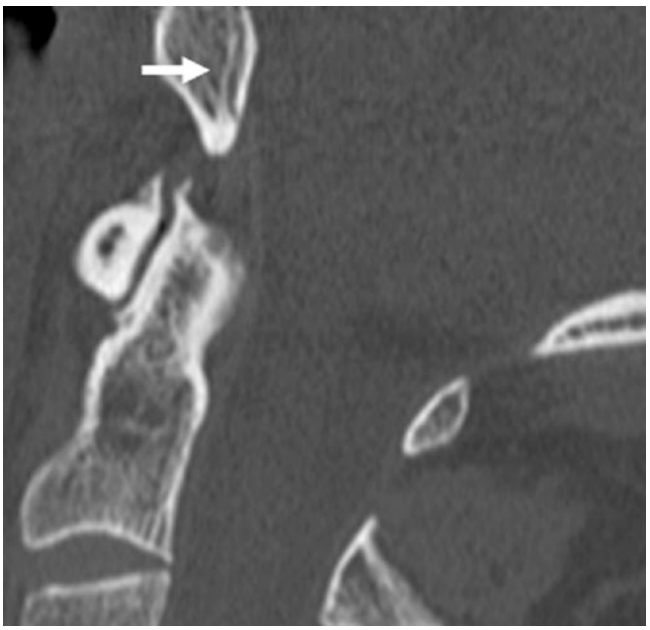

Fig. 26.80 A 46 year old with a CBM (*arrow*) at the top of a sagittal reformat from a cervical NECT

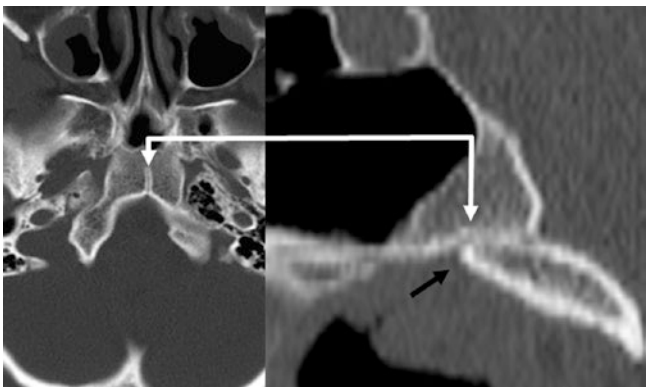

Fig. 26.82 A 15 year old in whom axial (*left*) and sagittal (*right*) reformatted NECT MPRs depict the superior aspect of incomplete notochordal fusion, with a FP anteriorly (*arrows*)

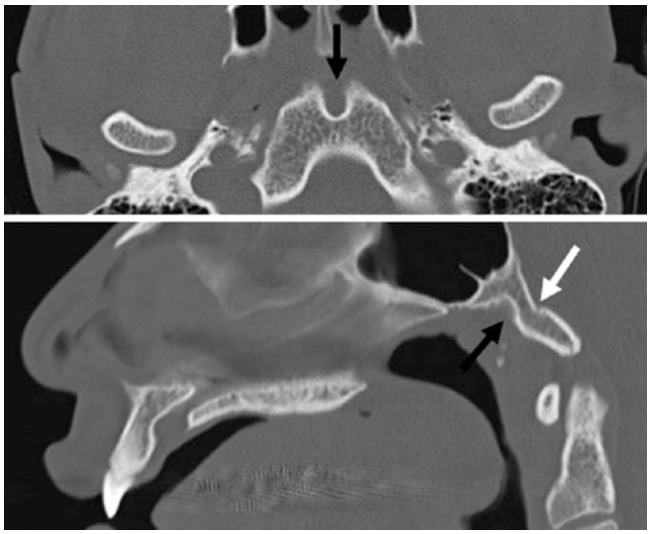

Fig. 26.83 A 23 year old with a tiny CBM and a big FP on axial (*top*) and sagittal (*bottom*) NECT reformats

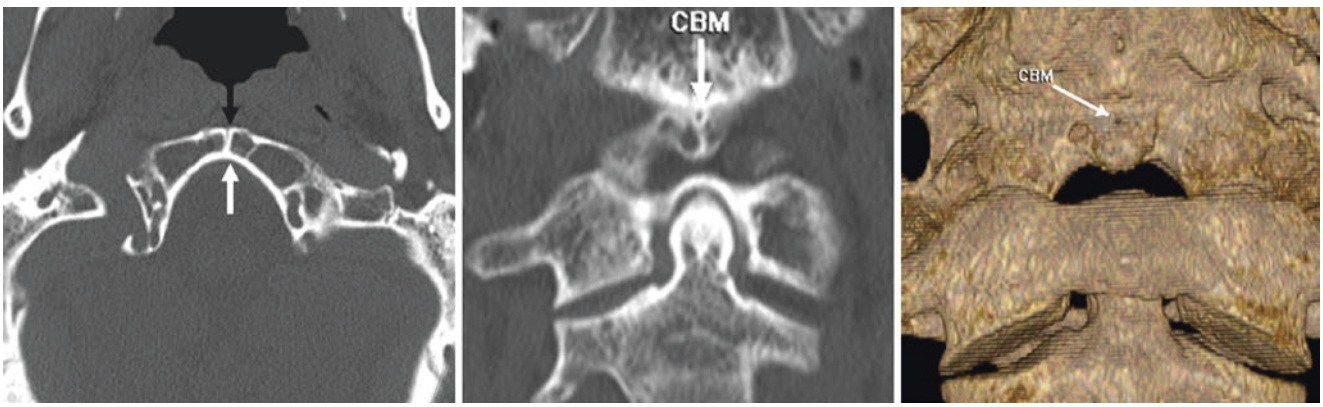

Fig. 26.84 A 50 year old with an incidental CBM (*arrows*) that was noted on coronal MPR (*middle*) and 3D reconstructions (*right*, *from anteriorly*) from axial NECT (*left*)

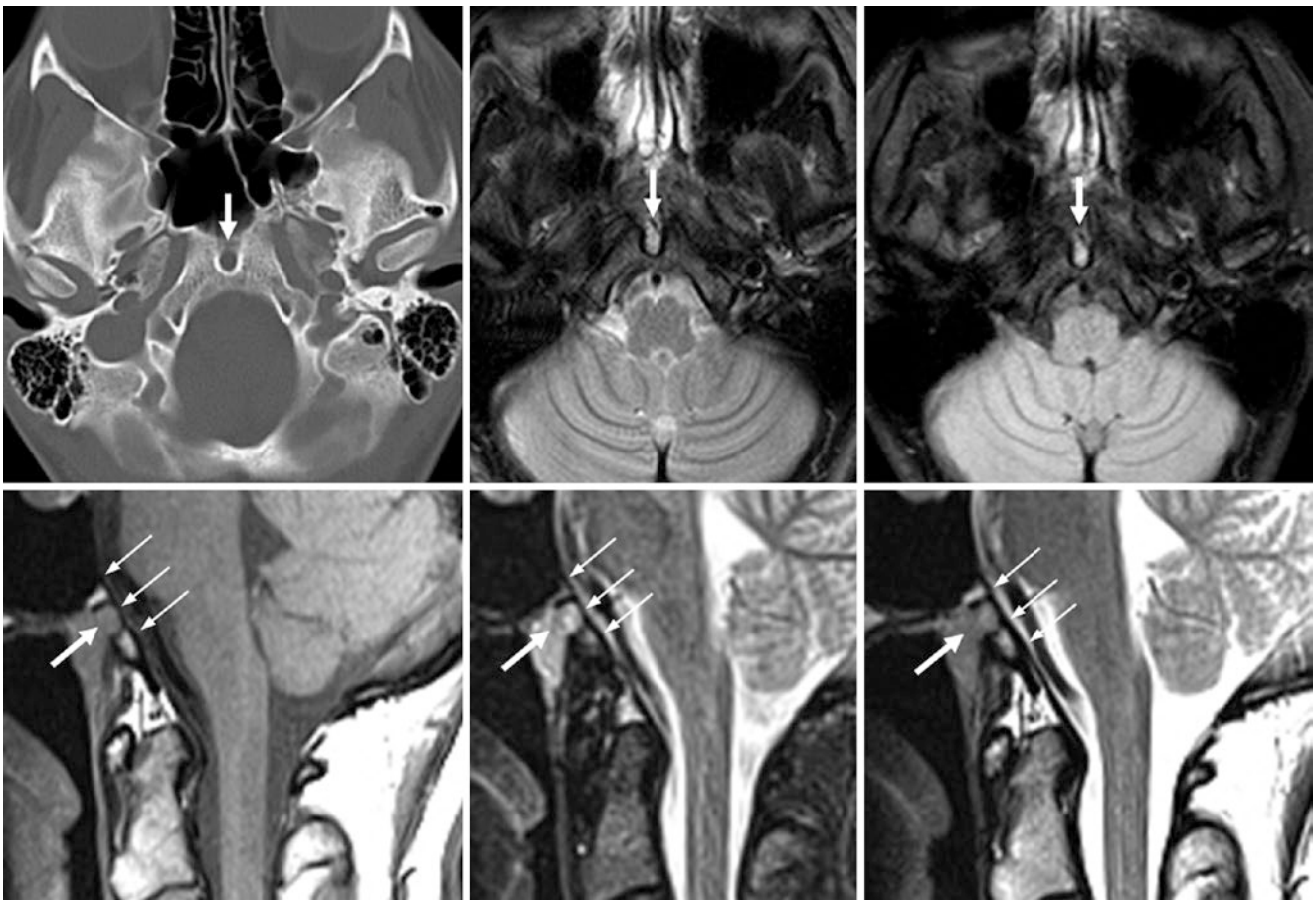

Fig. 26.85 *Top row*: A 23 year old with axial NECT (*left*) and T2WI (*middle*) and FLAIR MRI (*right*), which show bright signal within a FP from a CBM. *Bottom row*: on sagittal T1WI (*left*), STIR (*middle*), and T2WI (*right*), the FP/CBM extends through to the dura (*thin arrows*)

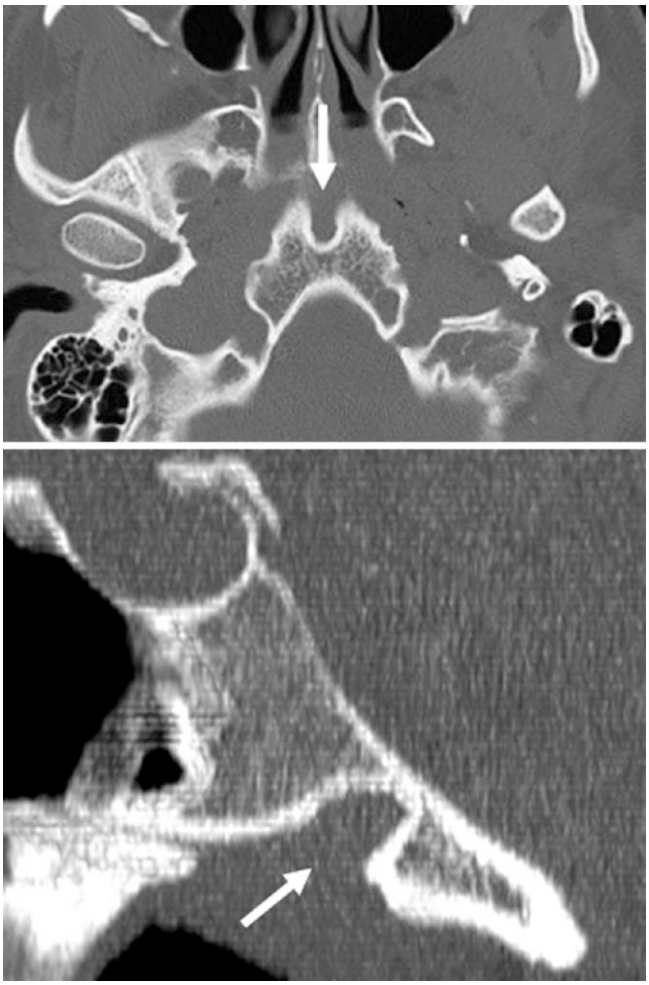

Fig. 26.86 A 25 year old with a large FP of a CBM on axial (*top*) and sagittal (*bottom*) MPRs

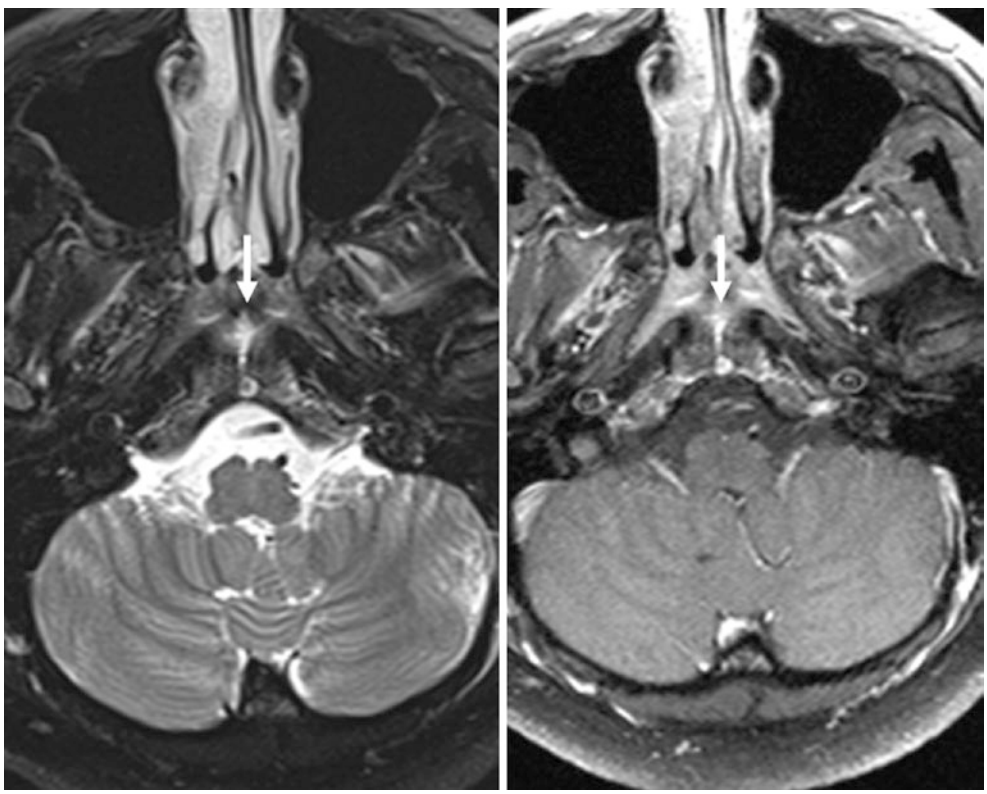

Fig. 26.87 A 57 year old with axial T2WI (*left*) and postcontrast T1WI (*right*) MR images that show a CBM and FP (*arrows*); there is bright signal and enhancing tissue within the CBM/FP, perhaps the result of mucosal tissue within the defect

26.13 Basioccipital Raphe

The *basioccipital raphe* has been described as a small, midline, medial faint defect (raphe) of the basiocciput, occurring in about 5–10 % of the population. Although it has primarily been described primarily in infants, faint defects in the same location in a number of adults have been seen. These may be difficult to differentiate from a persistent CBM, another midline normal variant. The cause of this appearance is not entirely known, but this variant has been postulated to relate to possible prenatal fusion of parachordal centers. In some patients this could simulate a *fracture*.

Unless otherwise noted, the images provided are from axial nonenhanced CT (NECT) (Figs. 26.88, 26.89, 26.90, 26.91, 26.92, and 26.93).

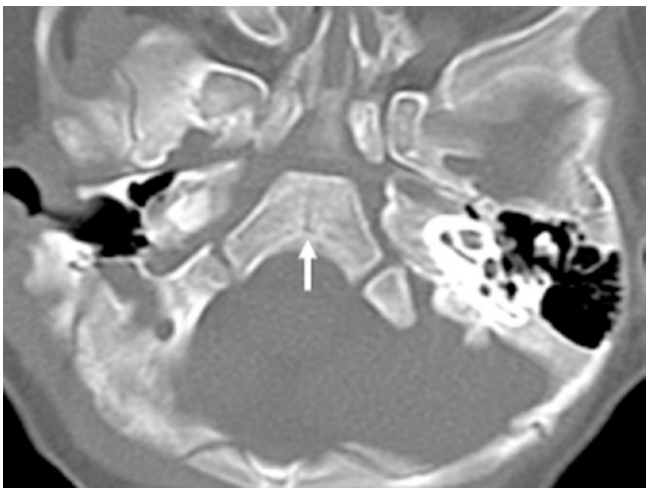

Fig. 26.88 A 5 month old with a thin BOR (*arrow*)

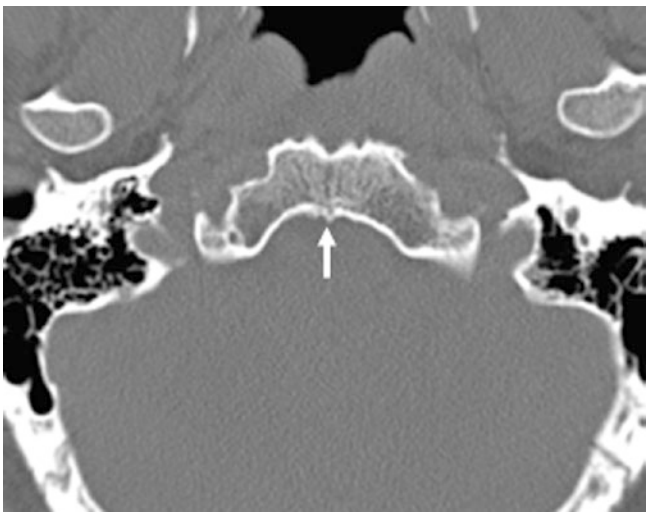

Fig. 26.90 A 46 year old with a thin BOR (*arrow*)

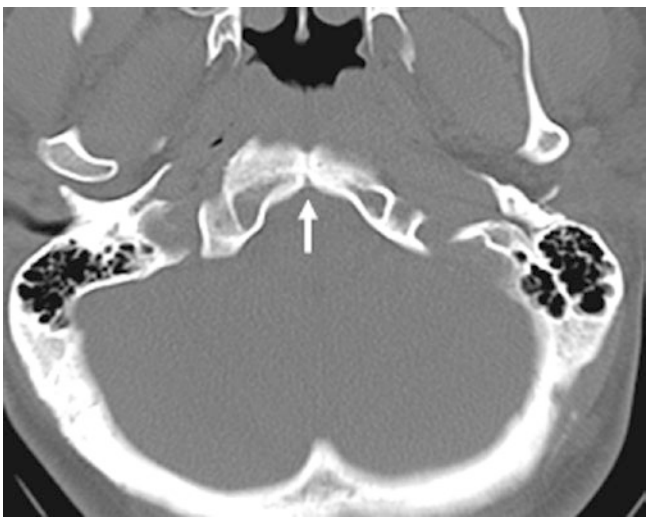

Fig. 26.89 A 24 year old with a thin BOR (*arrow*)

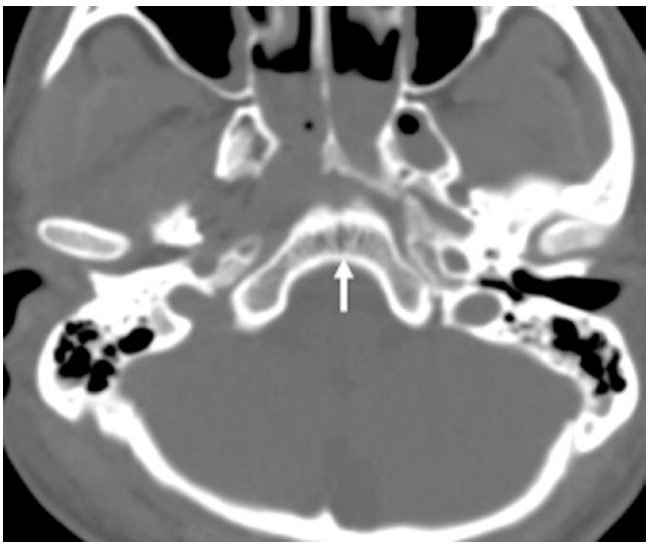

Fig. 26.91 A 26 year old with a tiny BOR (*arrow*)

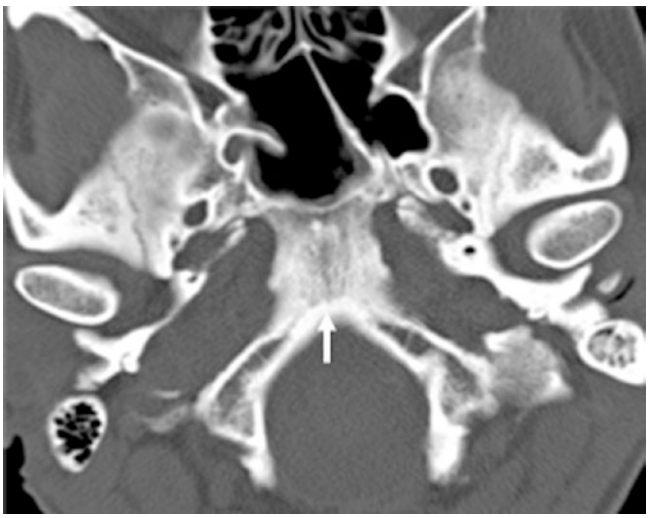

Fig. 26.92 A 51 year old with a faint BOR (*arrow*)

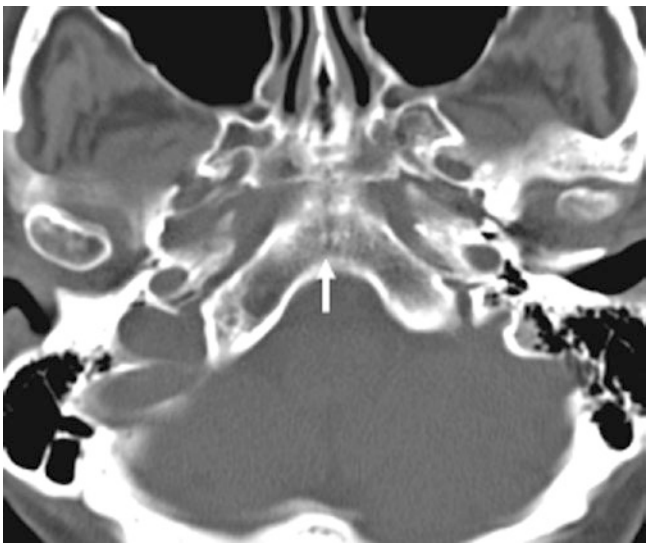

Fig. 26.93 A 59 year old with a faint BOR (*arrow*)

26.14 Normal Asymmetry or Prominence of Skull Base Foramina: Jugular and Hypoglossal

There can be normal mild asymmetry of skull base foramina without a mass being present as a result of several factors. These can simulate a mass that would correspond to traversing cranial nerves, such as with a schwannoma. One of the most common causes of normal foraminal enlargement (as mentioned within Chapters 40.1 and 40.2 within the Vascular section of this book that further discuss emissary veins and foraminal enlargement) is unilateral prominence of normal venous structures such as internal jugular veins (jugular foramen) or emissary veins (often the hypoglossal foramen); another simulated cause is asymmetric alignment of the patient in the axial plane. The most common foramina to demonstrate asymmetry are the *jugular foramen, condylar canal, hypoglossal, internal auditory canal,* and the *foramen ovale* (based on this author's experience). There may be asymmetry of other foramina that are usually not "in-plane" on axial head CT images; these are less common and often incidental findings. With asymmetric foramina, there is no scalloping or irregular cortical margin such as is typically seen with more aggressive masses (e.g., *chondrosarcomas* or *chordomas*); however, normal asymmetry of these foramina may be difficult to discern from slower growing masses such as in neurofibromatosis type 2, in which *schwannomas* or *meningiomas* can slowly enlarge (Figs. 26.94 and 26.95).

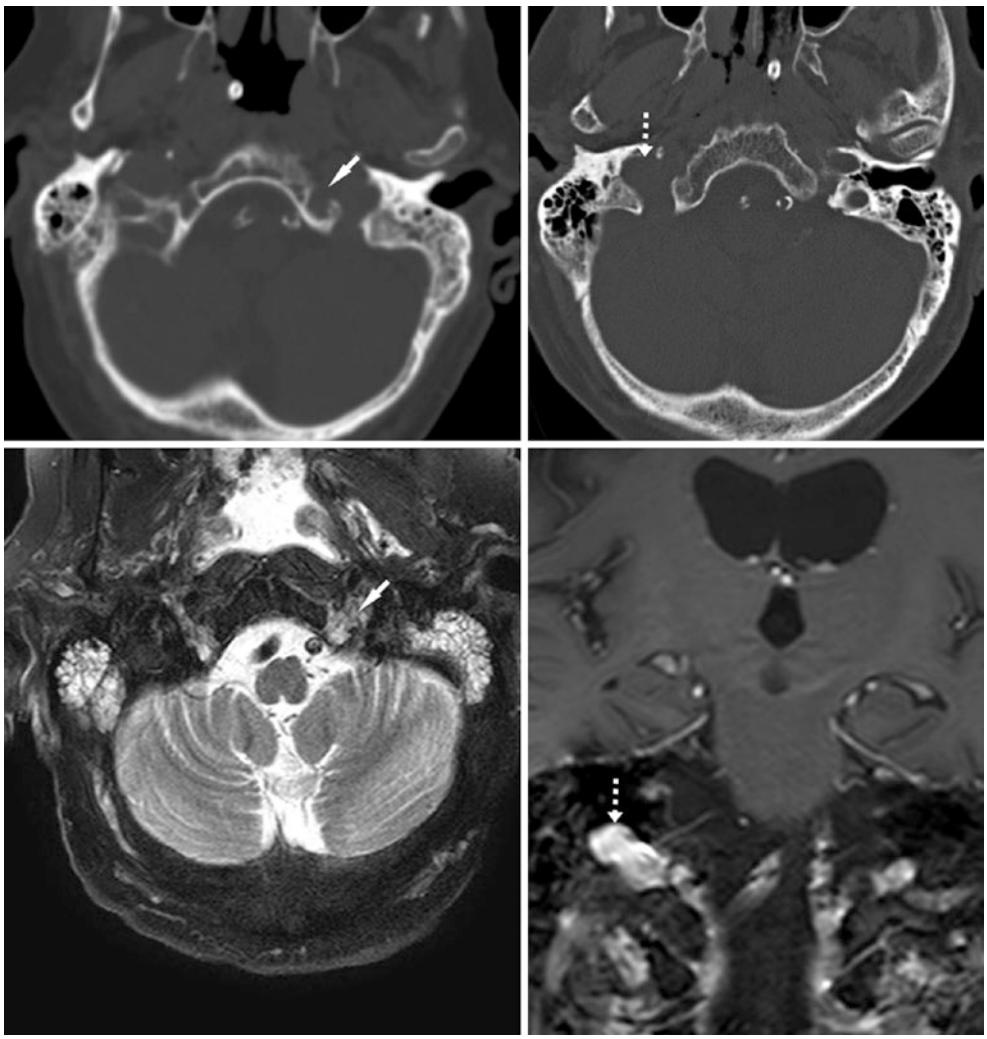

Fig. 26.94 *Top row*: on NECT, a 65 year old has an asymmetric prominence of the left hypoglossal canal (*arrows*) and right jugular foramen (*dashed arrows*). Axial T2WI MRI (*bottom left*) shows bright signal in both locations. Postcontrast coronal T1WI (*bottom right*) shows enhancement of the right IJV (*dashed arrows*). Thus, prominent venous structures are present in both locations

Fig. 26.95 A 36 year old with asymmetric hypoglossal canals (*arrows*). The right side connects to an emissary vein (*asterisk*) via the posterior condylar canal

26.15 Jugular Diverticulum (Also Known as "High-Riding Jugular Bulb" or Dehiscence)

A prominent *jugular diverticulum* (also called a *high-riding jugular bulb*) may simulate an erosive or expansile mass such as a *cholesteatoma, epidermoid cyst, glomus tumor,* or *schwannoma*. This appearance can be symmetric or asymmetric. Typically, this is called "high-riding" if it extends cephalad up above the bottom of the middle ear, sometimes even up to the level of the internal auditory canal. There is usually a thin rim of cortical bone present between the bulb and the middle ear, which distinguishes this entity from dehiscence of the jugular bulb. Although it is a normal variant, it may predispose to dehiscence of the bulb and hemorrhage from severe otomastoiditis or as a complication of surgery or trauma due to the proximity of the vein to the middle ear.

Although *jugular dehiscence* can arise from a middle ear mass, the most common form is a congenital extremely thin or absent plate of bone between the jugular foramen and the middle ear (a very thin bony plate is present in up to 10–15 % of the population). As with the high-riding jugular or jugular diverticulum, the knowledge of this anatomy is pertinent prior to surgery or after skull base trauma or infection. This normal variant is typically suspected on axial CT, although it is best confirmed on sagittal or coronal reconstructionss (Figs. 26.96 and 26.97).

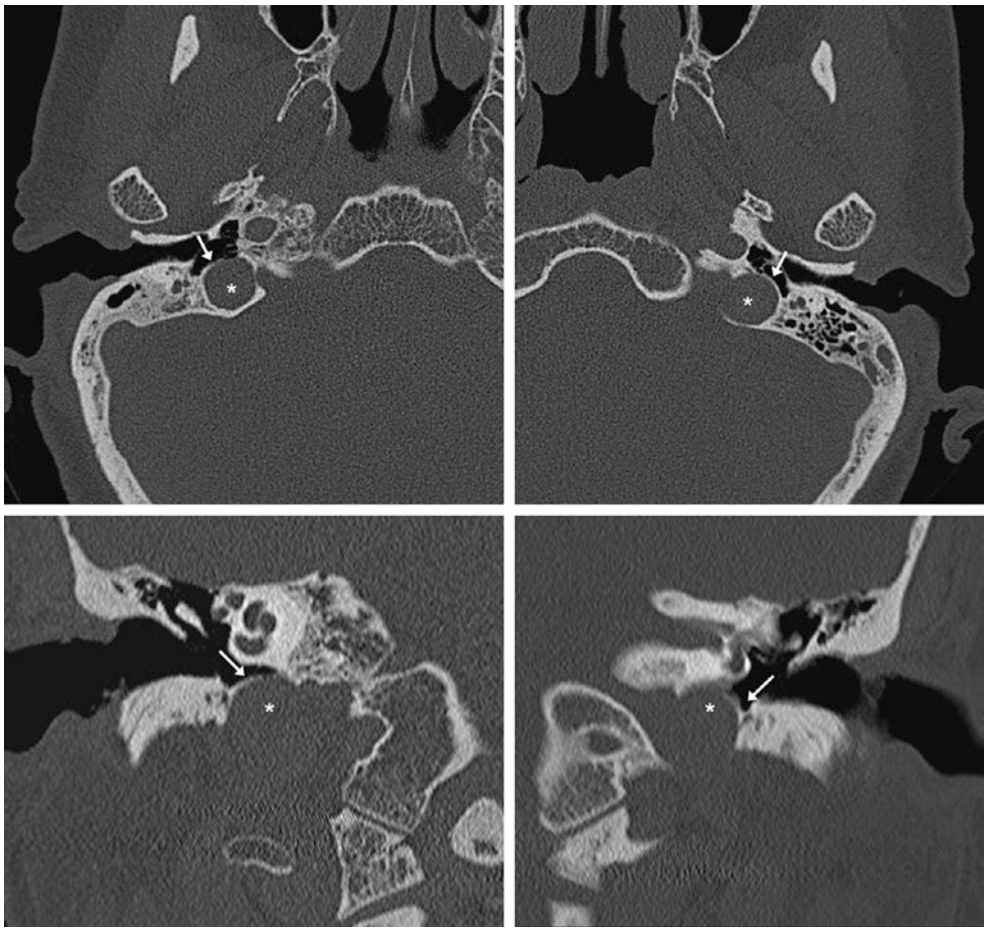

Fig. 26.96 A 66 year old with bilateral prominent jugular diverticula (*asterisks*) that are separated from the middle ears by a thin margin of cortical bone (*arrows*) but without frank dehiscence. Axial (*top row*) and coronal (*bottom row*) NECT images are provided

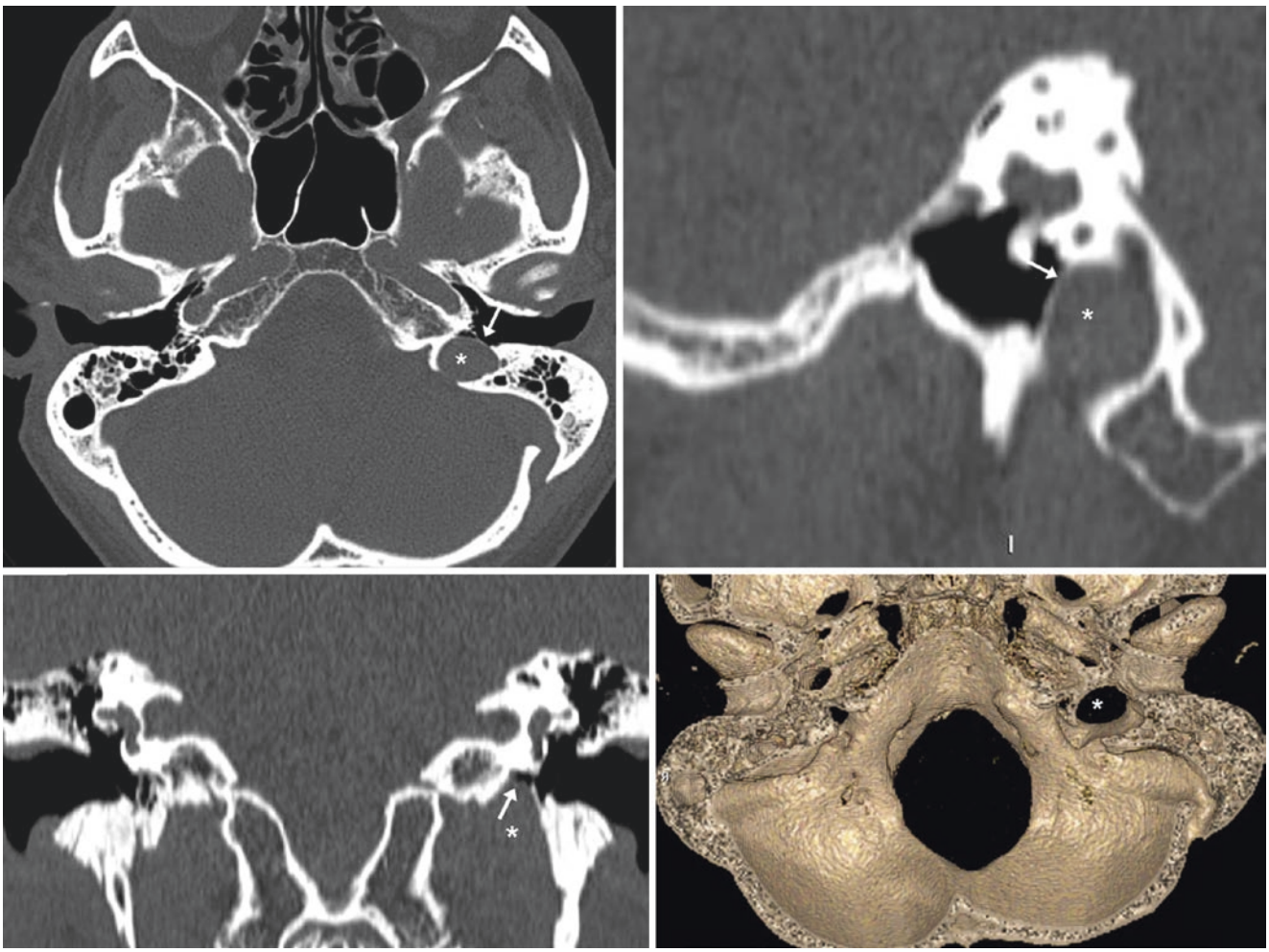

Fig. 26.97 A 71 year old with a unilateral left jugular diverticula (*asterisks*) that is separated from the middle ear by a thin margin of bone but has a focal area of dehiscence (*arrows*). This is demonstrated on sagittal (*top right*) and coronal (*bottom left*) MPRs from NECT. A 3D cut-away reformat (*superior view*, *bottom right*) illustrates the asymmetric jugular foramina

26.16 Comparison Cases: Masses of the Hypoglossal and Jugular Foramina

Below are examples of both aggressive and slow-growing *masses causing enlargement of the hypoglossal and jugular foramina*. The distinction between normal foraminal asymmetry and mass-related enlargement is less problematic with the hypoglossal and jugular foramina relative to the internal auditory canal (IAC), as these two foramina are not as commonly bilaterally and symmetrically involved by disease as the IAC (an example is with neurofibromatosis type 2) (Figs. 26.98, 26.99, and 26.100).

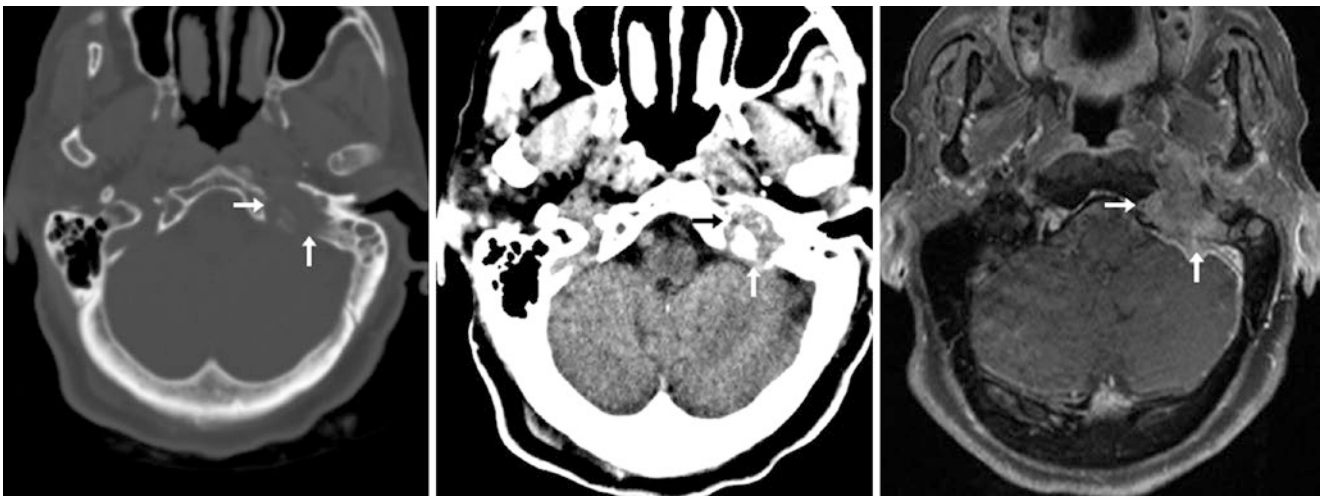

Fig. 26.98 Comparison case: a glomus jugulare enlarges the foramen with irregular edges and enhances with contrast (*arrows*)

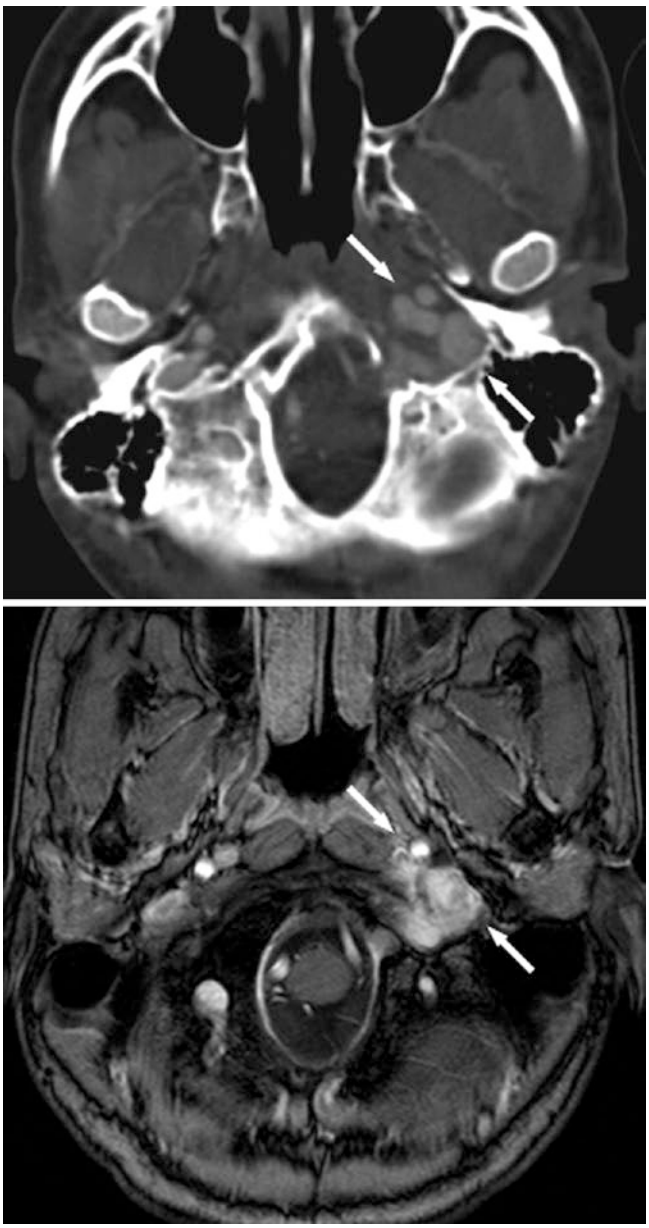

Fig. 26.99 Comparison case: a plexiform neurofibroma smoothly expands the left hypoglossal foramen in a patient with neurofibromatosis type 1

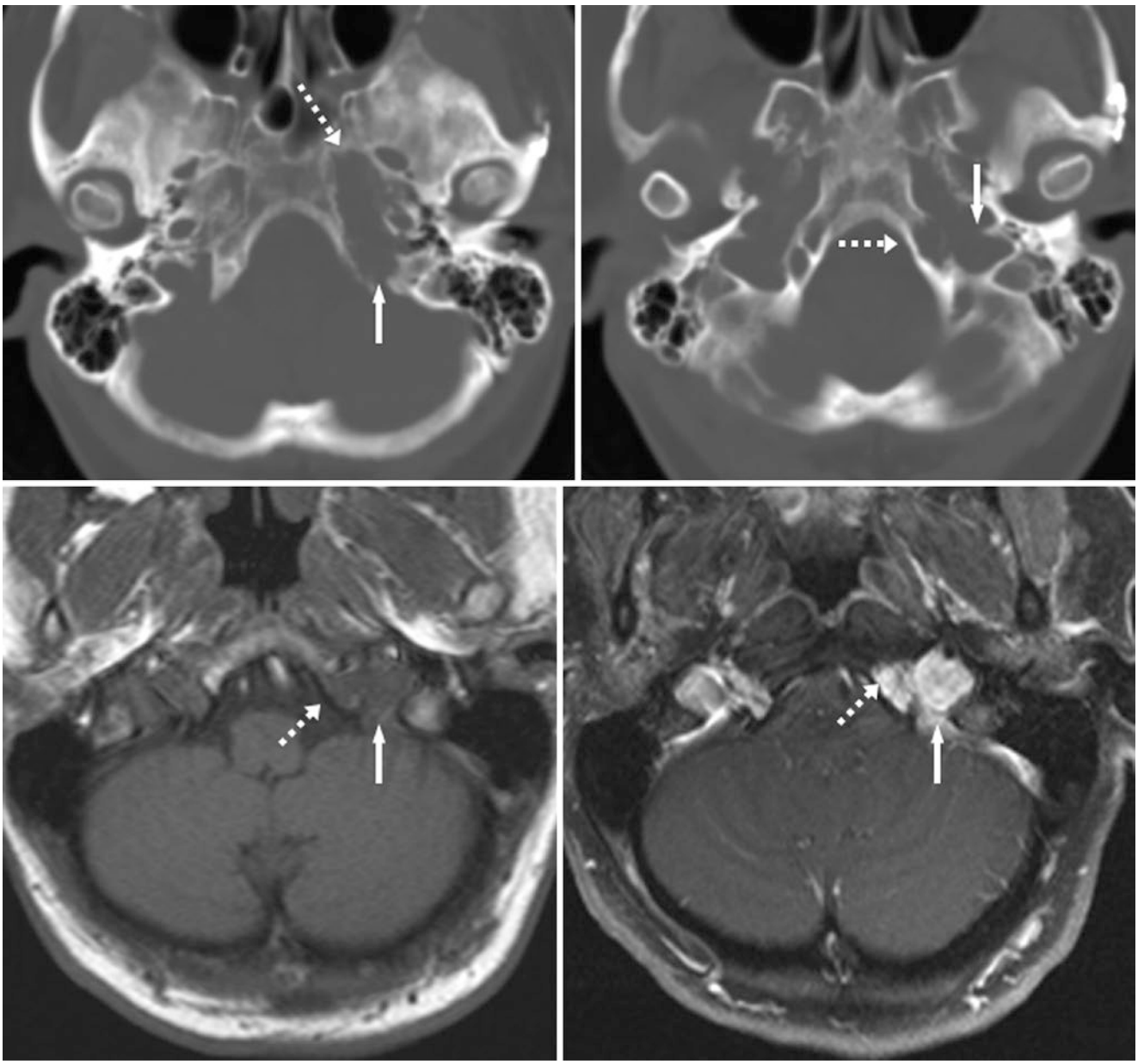

Fig. 26.100 Comparison case: a chondrosarcoma in the left jugular foramen (*arrows*) anteriorly involves the carotid canal and the lateral clivus (*dashed arrows*)

26.17 Normal Asymmetry or Prominence of Skull Base Foramina: Bulbous Internal Auditory Canals

The internal auditory canals (IACs) may also be slightly asymmetric or have a *bulbous appearance*, which could simulate *schwannomas*. Aggressive lesions (such as metastases) have irregular scalloping of the bone outlining the foramen, and it can be difficult to discern mild, normal bulbous ectasia of the IAC from slow growing, smaller, extra-axial lesions such as schwannomas. Hence, if the patient has symptoms of vertigo or deafness, these lesions cannot be excluded on the basis of CT alone, and an MRI of the skull base may be necessary (Figs. 26.101, 26.102, 26.103, 26.104, and 26.105).

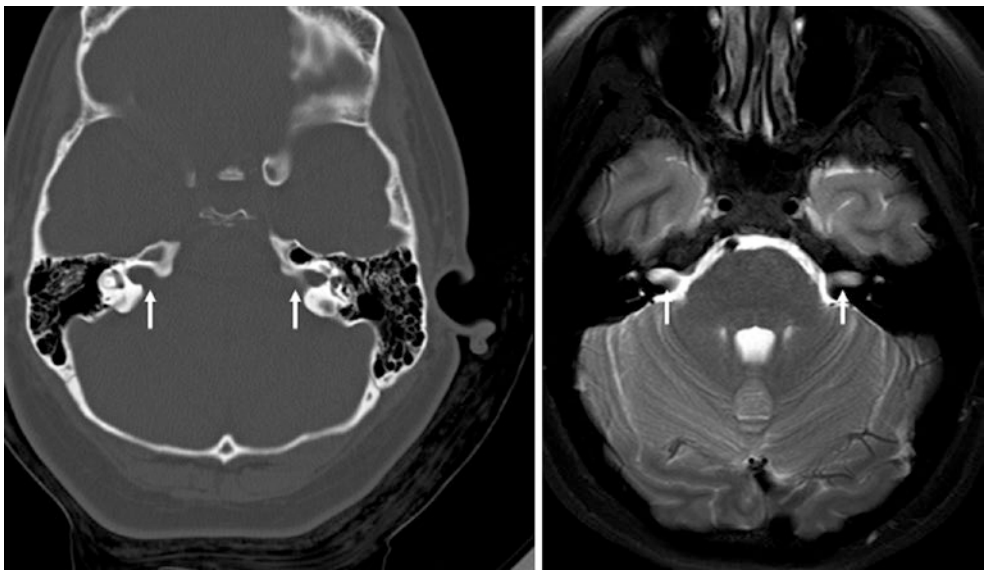

Fig. 26.101 A 24 year old with a normal bulbous appearance of the IACs on CT that is not as evident on T2WI MRI (*right*)

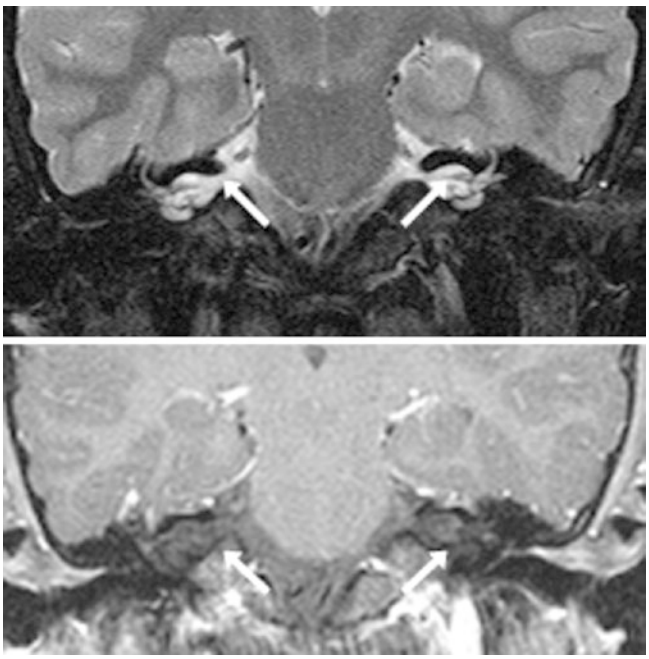

Fig. 26.102 A 12 year old with bulbous IACs on coronal T2WI (*above*) and postcontrast T1WI (*below*)

Fig. 26.103 A 68 year old with a bulbous-appearing left IAC. Note the fourth ventricular hemorrhage (*dashed circle*)

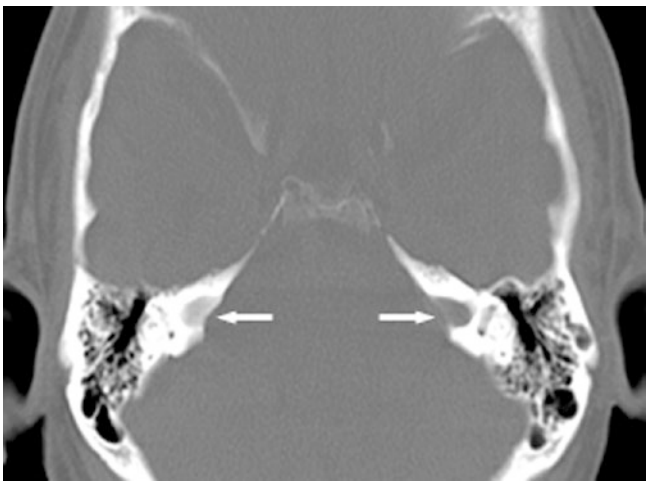

Fig. 26.104 A 79 year old with bulbous-appearing IACs on NECT (*arrows*)

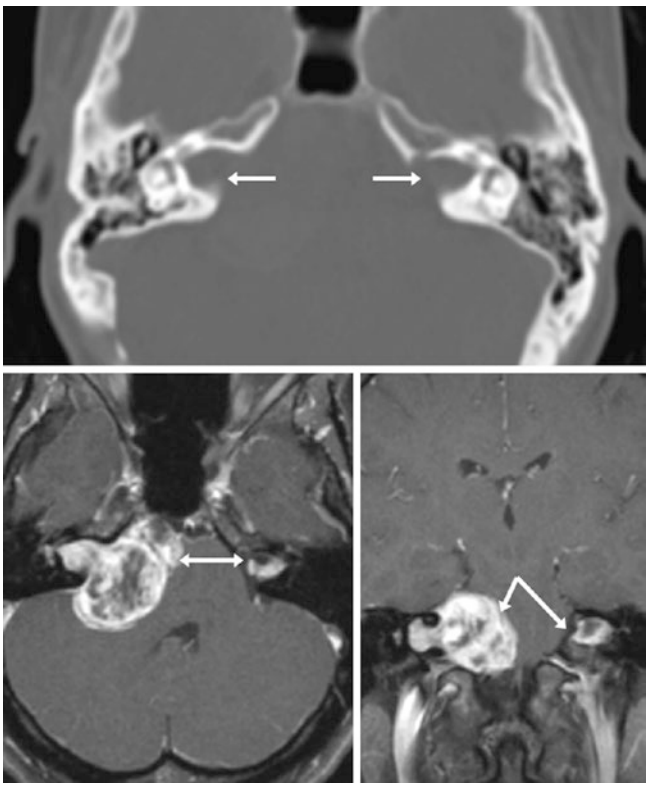

Fig. 26.105 Comparison case: There is a nearly symmetric IAC enlargement from schwannomas bilaterally in neurofibromatosis type 2 (*arrows*)

26.18 Normal Asymmetry or Prominence of Skull Base Foramina: Asymmetric Foramen Ovale

The *foramen ovale* may also have normal asymmetry, whether it is related to the plane of the slice (artifactual) or caused by actual asymmetry. Venous plexi can be transmitted through the foramen. The main consideration is to exclude a mass or erosions associated with enlargement of the bony margins of the foramen (Figs. 26.106 and 107).

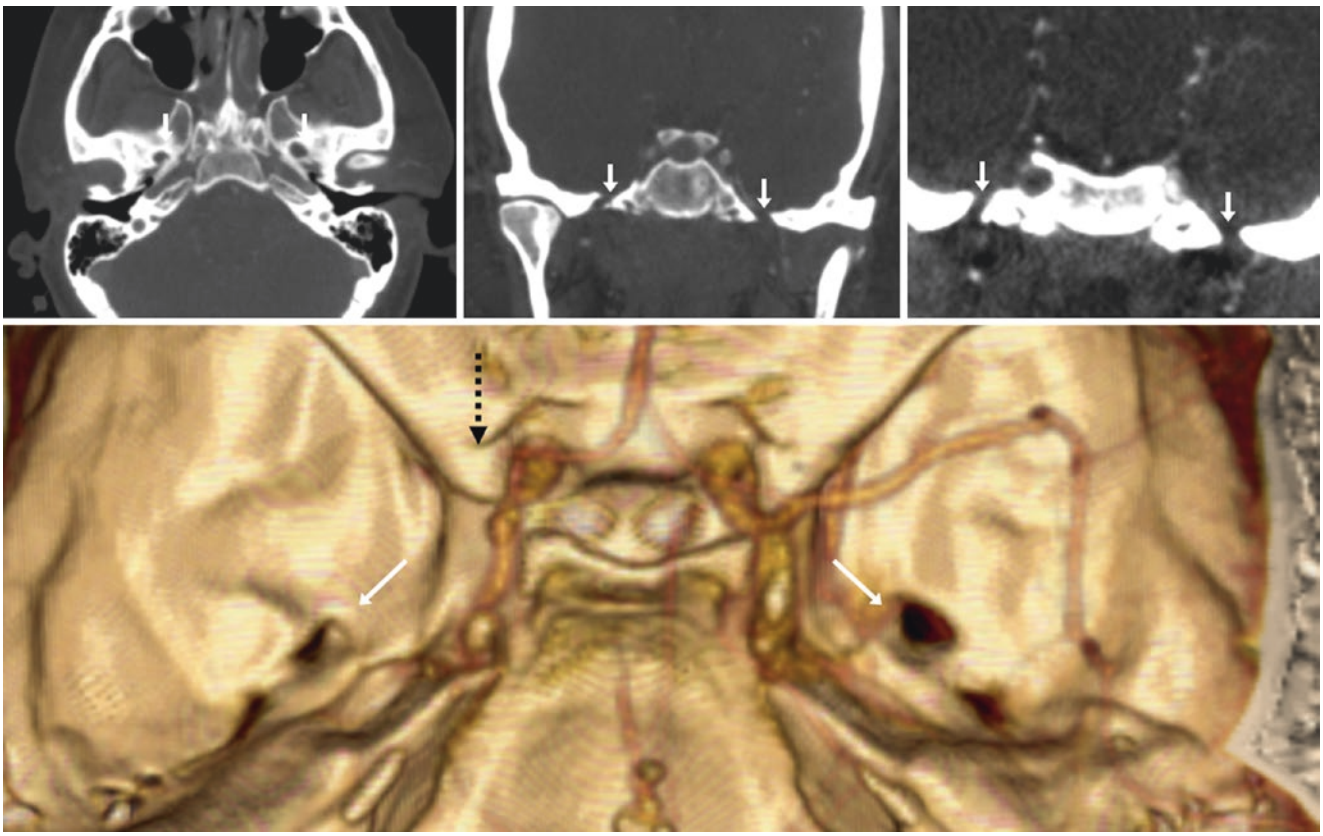

Fig. 26.106 A 43 year old with normal, asymmetric (left greater than right) foramen ovale (*arrows*) without a mass. This asymmetry was not likely related to the plane of slice selection, as confirmed by coronal (*top row*: *middle and right*) and by 3D VR images (*superior view*, *bottom*). The patient presented with stroke; note an occluded right middle cerebral artery (*dashed arrow*)

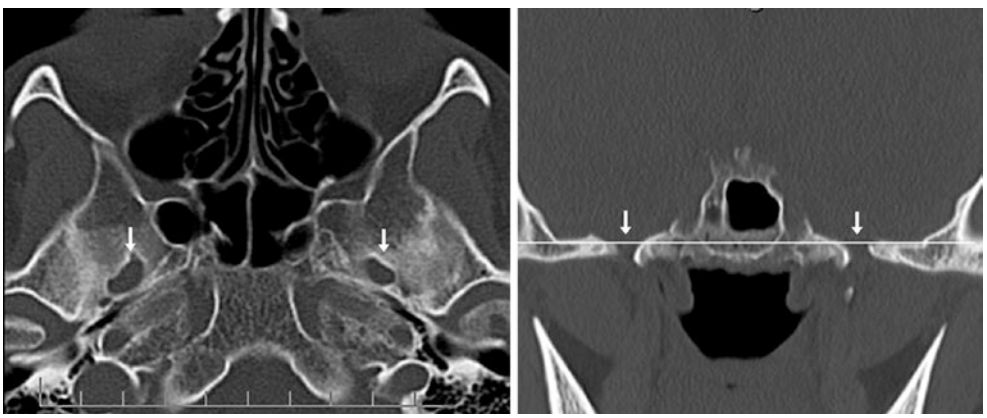

Fig. 26.107 A 32 year old with mild asymmetry of the foramen ovale (*left*). In this patient, the asymmetry was likely related to the selected axial plane of the slice. For example, on axial images, the right foramen ovale appears slightly larger, whereas on coronals (*right*) the left seems larger. Note the scout localizer's transverse plane on the coronal image

Suggested Reading

Alcalá-Galiano A, Arribas-García IJ, Martín-Pérez MA, Romance A, Montalvo-Moreno JJ, Juncos JM. Pediatric facial fractures: children are not just small adults. Radiographics. 2008;28:441–61.

Belden CJ, Mancuso AA, Kotzur IM. The developing anterior skull base: CT appearance from birth to 2 years of age. AJNR Am J Neuroradiol. 1997;18:811–8.

Berge JK, Bergman RA. Variations in size and in symmetry of foramina of the human skull. Clin Anat. 2001;14:406–13.

Connor SE, Tan G, Fernando R, Chaudhury N. Computed tomography pseudofractures of the mid face and skull base. Clin Radiol. 2005;60:1268–79.

Dupuis O, Silveira R, Dupont C, Mottolese C, Kahn P, Dittmar A, Rudigoz RC. Comparison of "instrument-associated" and "spontaneous" obstetric depressed skull fractures in a cohort of 68 neonates. Am J Obstet Gynecol. 2005;192:165–70.

Freyschmidt J, Brossman J, Sternberg A, Wiens J. Freyschmidt's Koehler/Zimmer's borderlands of normal and early pathological findings in skeletal radiography. 5th ed. Tubingen: Thieme; 2003. Chapter 4, Skull. p. 357–66.

Furuya Y, Edwards MS, Alpers CE, Tress BM, Ousterhout DK, Norman D. Computerized tomography of cranial sutures. Part 1: Comparison of suture anatomy in children and adults. J Neurosurg. 1984a;61:53–8.

Furuya Y, Edwards MS, Alpers CE, Tress BM, Norman D, Ousterhout DK. Computerized tomography of cranial sutures. Part 2: Abnormalities of sutures and skull deformity in craniosynostosis. J Neurosurg. 1984b;61:59–70.

Ginsberg LE. The posterior condylar canal. AJNR Am J Neuroradiol. 1994;15:969–72.

Glass RB, Fernbach SK, Norton KI, Choi PS, Naidich TP. The infant skull: a vault of information. Radiographics. 2004;24:507–22.

Gray H. Anatomy of the human body. 20th ed. Philadelphia: Lea & Febiger; 1918. Chapter 5D, the interior of the skull. Available at http://www.bartleby.com/107/47.html.

Hedlund G. Congenital frontal nasal masses: developmental anatomy, malformations, and MR imaging. Pediatr Radiol. 2006;36:647–62.

Keats TE, Anderson MW. Atlas of normal roentgen variants that may simulate disease. 8th ed. Philadelphia: Mosby, Inc.; 2007. Chapter 1: The skull. p. 3–117.

Keskil S, Gözil R, Calgüner E. Common surgical pitfalls in the skull. Surg Neurol. 2003;59:228–31.

Koesling S, Kunkel P, Schul T. Vascular anomalies, sutures and small canals of the temporal bone on axial CT. Eur J Radiol. 2005;54:335–43.

Lin SR, Lee KF, Stein GN, Lee I. Asymmetrical internal auditory canals. A normal variant. Arch Otolaryngol. 1973;98:164–9.

Madeline LA, Elster AD. Postnatal development of the central skull base: normal variants. Radiology. 1995a;196:757–63.

Madeline LA, Elster AD. Suture closure in the human chondrocranium: CT assessment. Radiology. 1995b;196:747–56.

Nemzek WR, Brodie HA, Hecht ST, Chong BW, Babcook CJ, Seibert JA. MR, CT, and plain film imaging of the developing skull base in fetal specimens. AJNR Am J Neuroradiol. 2000;21:1699–706.

Schmalfuss IM, Camp M. Skull base: pseudolesion or true lesion? Eur Radiol. 2008;18:1232–43.

Schratter M, Canigiani G, Karnel F, Imhof H, Kumpan W. Occult fractures of the skull. Radiologe. 1985;25:108–13.

Seeger JF Normal variations of the skull and its contents. In: Zimmerman RA, editor. Neuroimaging: clinical and physical principles. New York: Springer; 1999. p. 415–53.

Stuckey SL. Dilated venous plexus of the hypoglossal canal mimicking disease. AJNR Am J Neuroradiol. 1999;20:157–8.

Swartz JD, Harnsberg RH. Imaging of the temporal bone. 3rd ed. New York: Thieme; 1998.

Swischuk LE. Imaging of the newborn, infant, and young child. 5th ed. Philadelphia: Lippincott Williams & Wilkins; 2003.

Taccone A, Oddone M, Occhi M, Dell'Acqua AD, Ciccone MA. MRI "road-map" of normal age-related bone marrow. I. Cranial bone and spine. Pediatr Radiol. 1995;25:588–95.

Weissman JL, Hirsch BE. Imaging of tinnitus: a review. Radiology. 2000;216:342–9.

Normal Variations and Developmental Anatomy of the Calvarial Sutures and Fontanelles Above the Skull Base

27

This section focuses on the variations in sutural anatomy and development of the calvarium above the skull base that can mimic disease or cause confusion, particularly in the setting of blunt trauma. This includes the major cranial sutures, the *anterior and posterior fontanelles* in infants and young children, asymmetric or atypical configurations of the skull that may occur with suture closure, and *normal foramina* (such as emissary foramina) that can occur within the upper calvarium. The persistence of these sutures and fontanelles and their normal variations in adults can potentially cause difficulty in interpretation. Other variations can occasionally be problematic to identify on standard axial NECT images, such as normal *intrasutural bones, positional plagiocephaly*, and *bathrocephaly*. In such instances, three-dimensional (3D) volume-rendered (VR) reconstructions from thin axial NECT can readily identify such normal variations. For this reason, many pediatric neuroradiologists have advocated that thin (≤1-mm thickness) axial NECT images with bone windows should be standard for reviewing infants and young children with trauma, and that three-dimensional reconstructions should accompany them. As stated in prior chapters, the persistence of normal sutures can often be distinguished from fractures based on reviewing the 3D reconstructions of the cranium that are usually quite easy to produce on standard CT vendors' consoles. Also, if there is solely a question of fracture, extremely low-dose protocols can be obtained combined with iterative reconstruction to delineate such fractures, potentially using one third to one tenth of a standard axial NECT radiation dose to the head. Another point regarding NECT 3D reconstructions is that spiral (rather than sequential) acquisitions are optimal as source data, since sequential acquisitions can suffer from "stair-step" artifacts when reconstructed into 3D. Spiral scans also take less time to scan but often have a mildly higher dose for the same slice thickness, thereby decreasing motion effects to some degree.

The following sections are described anatomically from anteriorly to posteriorly. Again, vascular channels and emissary foramina in the skull base and upper calvarium are covered in detail in other sections. Unless otherwise noted, the images provided are axial nonenhanced CT (NECT).

A.M. McKinney, *Atlas of Normal Imaging Variations of the Brain, Skull, and Craniocervical Vasculature*,
DOI 10.1007/978-3-319-39790-0_27

27.1 Anterior Fontanelle and Metopic Suture

The *anterior fontanelle* (AF) is the largest fontanelle at birth and typically lasts the longest but has a wide range of normal age of closure: the extremes (highest and lowest fifth percentile) are at 4 and 26 months, with a median closure time of about 13–16 months of age but with a wide degree of variability [1–9]. This fontanelle is bordered by the *metopic suture* (MS, anteriorly), *coronal suture* (laterally on both sides), and the *sagittal suture* (posteriorly). Meanwhile, the sagittal and coronal sutures rapidly narrow within the first month and thereafter gradually but significantly narrow; these can persist to some degree in adults, but this subject is covered later in this chapter [1–9]. Hence, the MS lies at a four-way junction between the two frontal and two parietal bones, where premature closure of the fontanelle can arise from various disorders of *craniosynostosis* (it is important to check the plain films of the extremities), *trisomies* 13 or 18, or *skeletal dysplasias* (e.g., osteopetrosis) and other metabolic abnormalities. Delayed closure of the anterior fontanelle or an enlarged fontanelle may arise from *hydrocephalus*, trisomies 13 or 18, *metabolic disorders* (such as hypothyroidism) or *vitamin deficiencies* (such as rickets), to name a few.

In newborns, the AF is normally prominent with metopic suture patency in children less than 2 years of age but it may close anywhere from 3 months to 3 years. The MS may occasionally be seen in older children on NECT, although it is nearly always fused (based on plain films of the skull) in children 3 years or earlier, and a residual bone within the MS is rarely present. As the MS begins to fuse, it occasionally simulates a *fracture* with its sclerotic or faint linear appearance when it later persists to some degree. Hence, residual minimal patency or sclerosis of the MS can persist throughout life, based on CT. This should not be confused with a fracture, even in the setting of trauma. However, theoretically, *diastasis* of this suture could occur in trauma, via the path of least resistance phenomenon. Therefore, it is recommended to correlate the presence of this suture with the presence of soft-tissue swelling or other fractures and to make sure that the edges of the MS are closely apposed.

It is also important to note that the AF, coronal sutures, and MS can appear asymmetric, particular when the patient head is turning or in motion. The cases illustrated here are images of the above-named structures demonstrating fusion and asymmetry within the neonatal period, the first year of life in infancy, the second year of life, and rarely into adolescence and adulthood.

Finally, a residual bone within or along the posterior edge of the AF (i.e., the *bregmatic fontanelle*) has been termed an *os bregmaticum*, referring to the location. There is debate as to whether or not this is directly related to the AF. Regardless, a residual intrasutural (wormian) bone may be detected in the expected location of the AF in older children and adults, although the AF usually fuses within the first few years of life. This can be best depicted by a CT scan with 3D reconstructions. Notably, in contrast, there can abnormal intrasutural bone that occasionally occurs from sagittal craniosynostosis or chronic shunted hydrocephalus, but this occurs along the course of the sagittal suture and should be posterior to the expected location of the AF (Figs. 27.1, 27.2, 27.3, 27.4, 27.5, 27.6, 27.7, 27.8, 27.9, 27.10, 27.11, 27.12, 27.13, 27.14, 27.15, 27.16, 27.17, 27.18, 27.19, 27.20, 27.21, and 27.22).

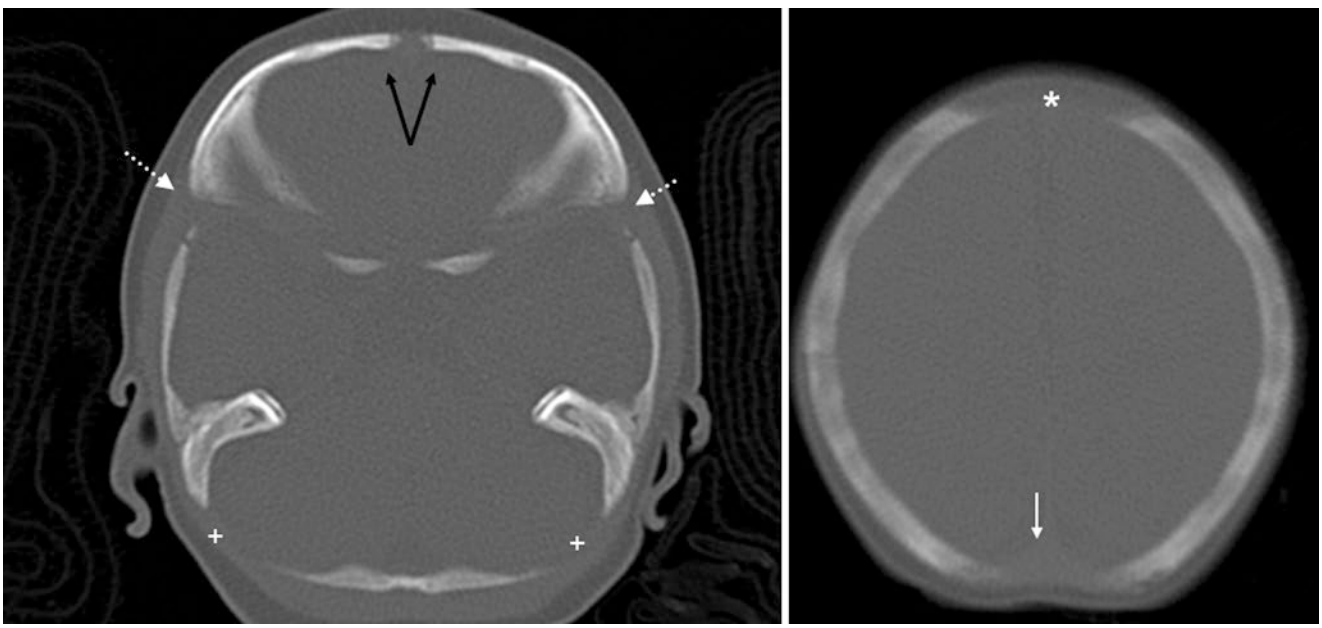

Fig. 27.1 A 20 day old whose images showed irregular edges of the MS (*double arrows*), while the AF (*) and PF (*thin arrow*) are both patent. Also note the sphenoid (*dotted arrows*) and mastoid (+) fontanelles

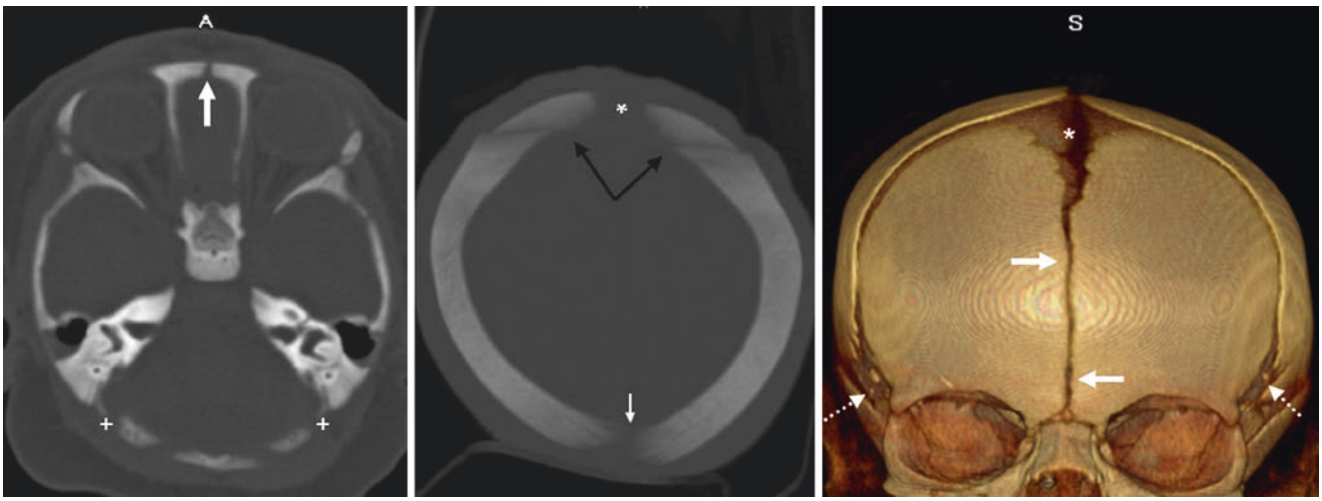

Fig. 27.2 A 3 day old with patency of the MS (*arrows*), AF (*), mastoid fontanelle (+), and posterior fontanelle (*thin arrow*) on axial 7-mm MPR (*left*), 20-mm MPR (*middle*), and 3D reconstruction in the anteroposterior view (*right*). Note the sphenoid fontanelles (*dotted arrows*). Also note a horizontal line (*double arrows*) across the axial MPR image from an streak artifact

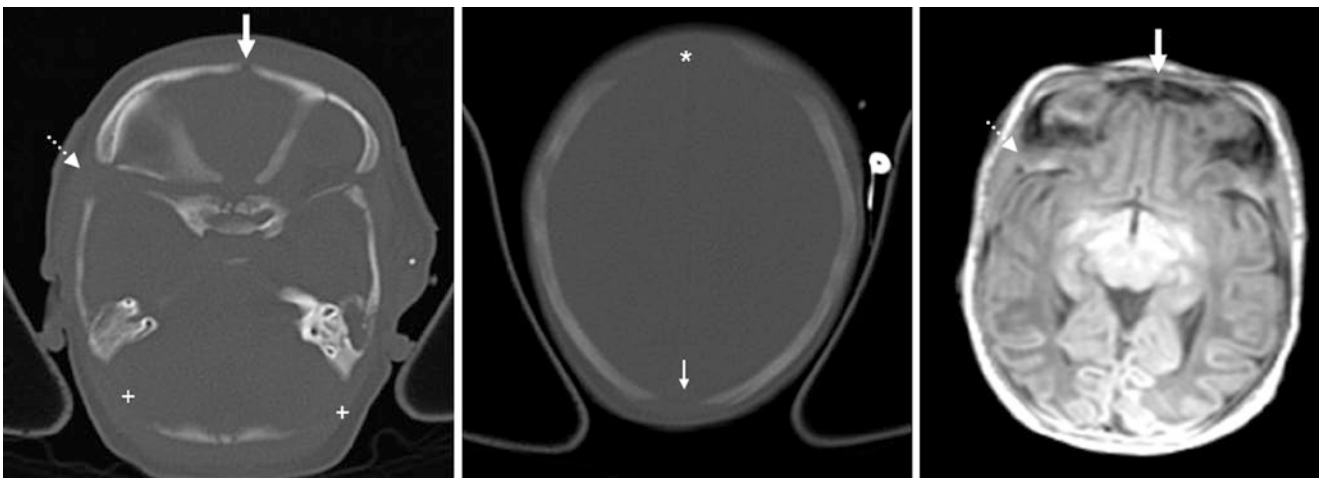

Fig. 27.3 A 6 day old with patency of the AF (*), posterior fontanelle (*thin arrow*), mastoid fontanelle (+), sphenoid fontanelle (*dotted arrows*), and MS (*arrows*) on axial CT (*left and middle*) and on gradient-echo T1WI MRI (*right*)

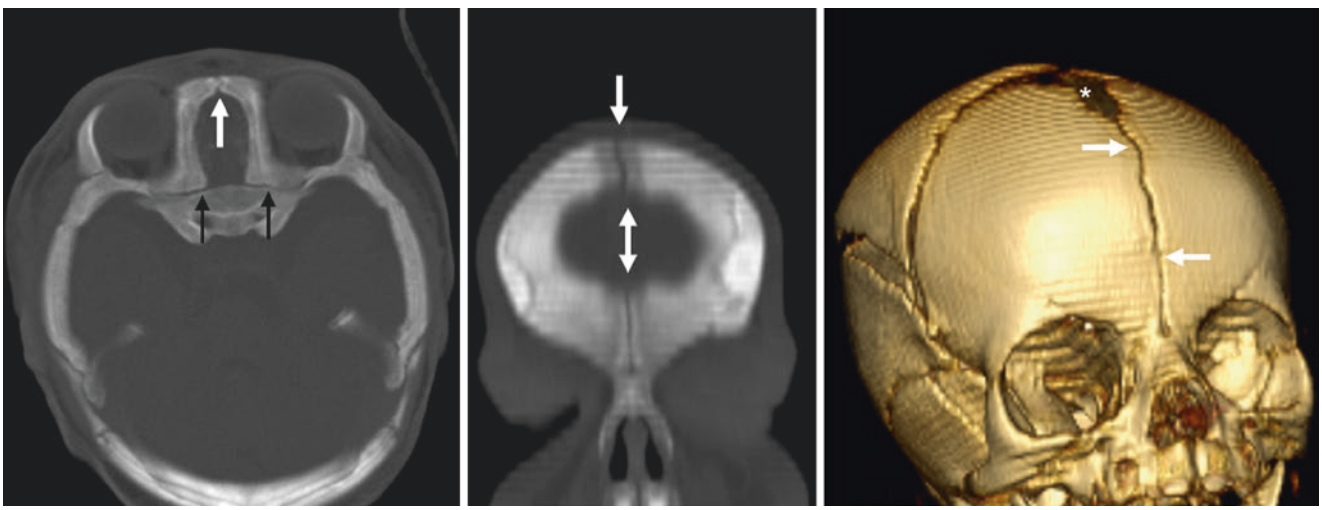

Fig. 27.4 A 1 month old with an unfused but narrowed MS (*arrows*) and patent AF (*), along with a patent sphenoethmoidal suture (*thin arrows*) on axial (*left*) and coronal 4-mm (*middle*) MPR, as well as on 3D VR reformats (*AP view*, *right*)

Fig. 27.5 A 1 month old with a half-fused MS on 3D VR CT (*AP-superior oblique view*) and a patent AF (*asterisk*)

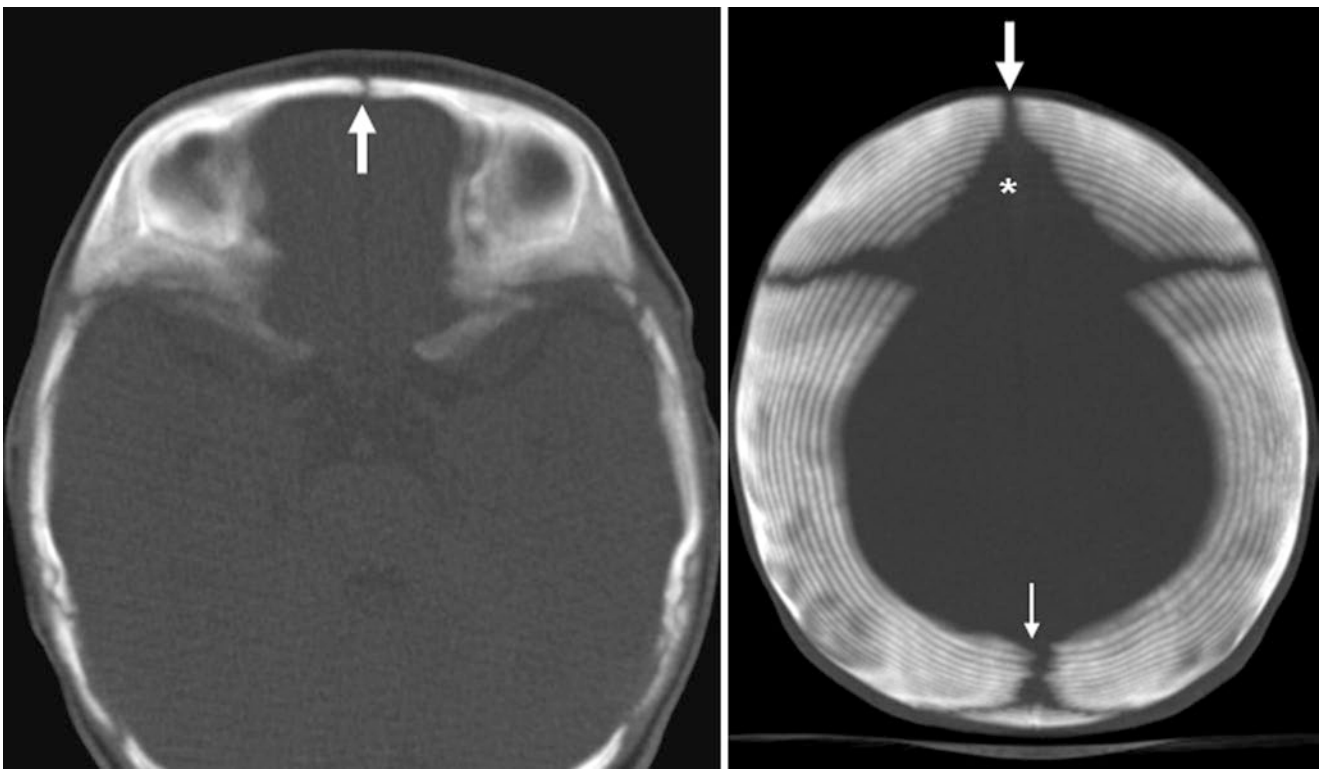

Fig. 27.6 A 3 month old with a small patent MS. There is also patency of both the AF (*asterisk*) and the PF (*thin arrow*)

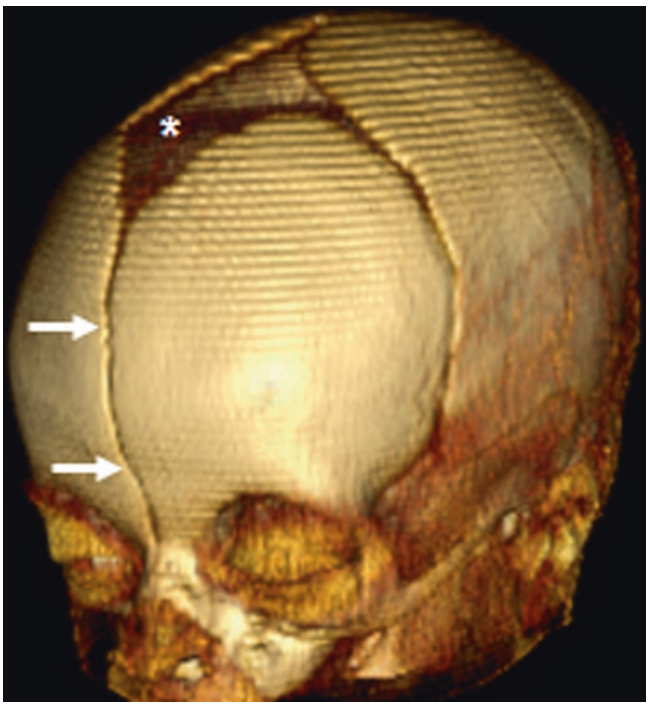

Fig. 27.7 A 3 month old; a 3D VR CT reconstruction demonstrates both the AF (*) and MS (*arrows*)

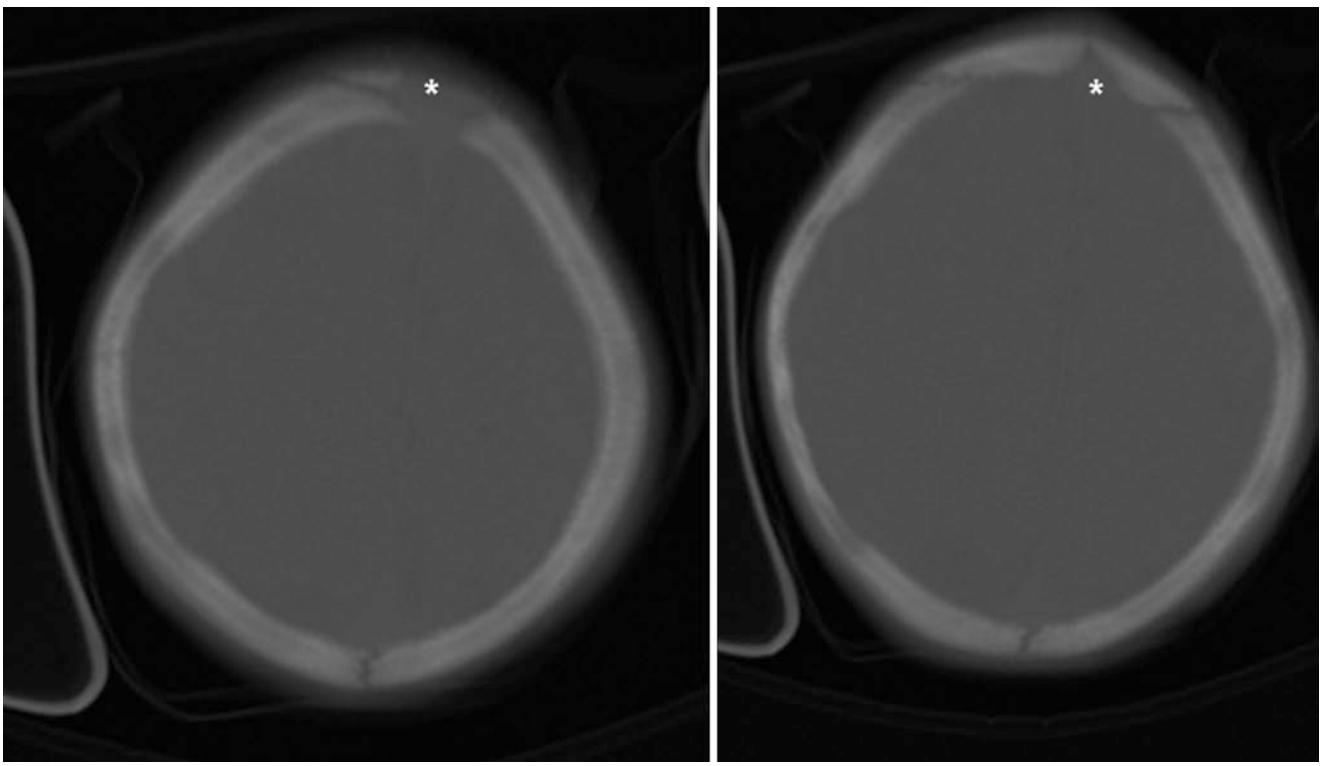

Fig. 27.8 A 5 month old with AF asymmetry (*) that is likely at least partially related to positioning. However, mild normal asymmetry of the AF can occasionally occur

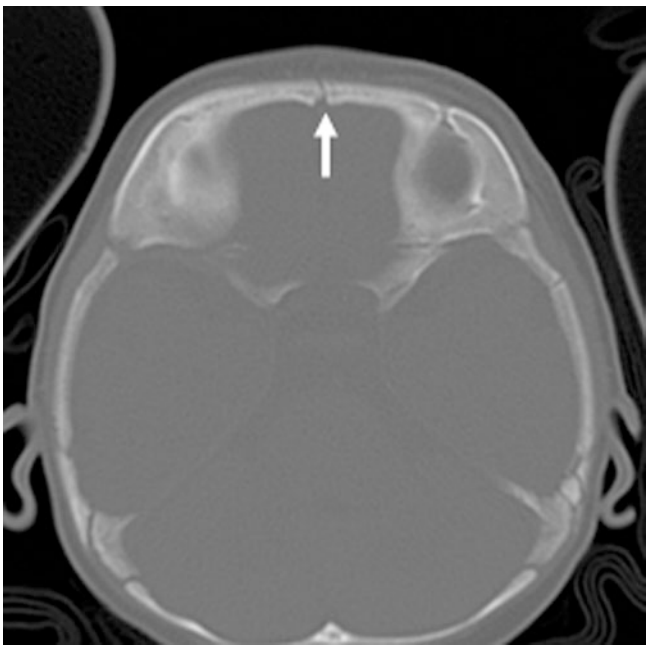

Fig. 27.9 A 5 month old with a small, patent MS (*arrow*) on axial NECT

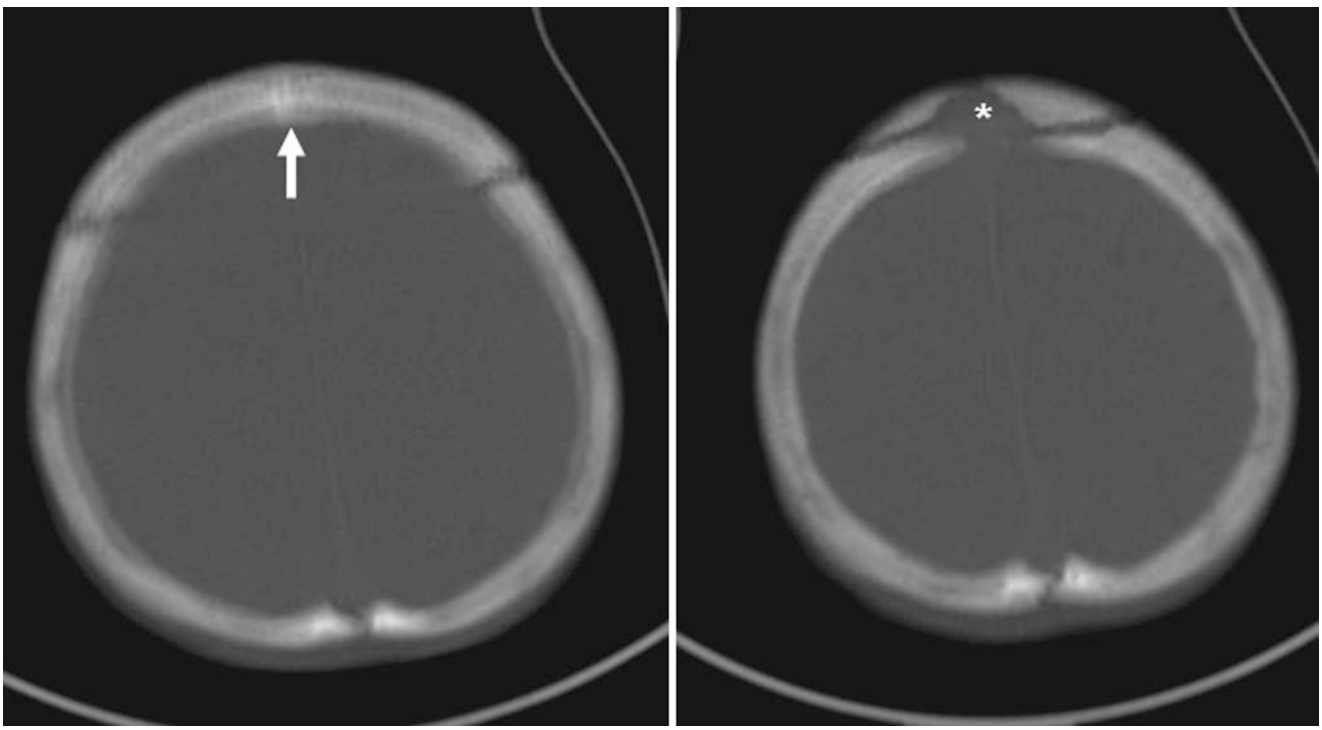

Fig. 27.10 An 8 month old with a mostly fused, sclerotic MS (*arrow*) and a small AF (*). Note that the coronal suture is entirely patent

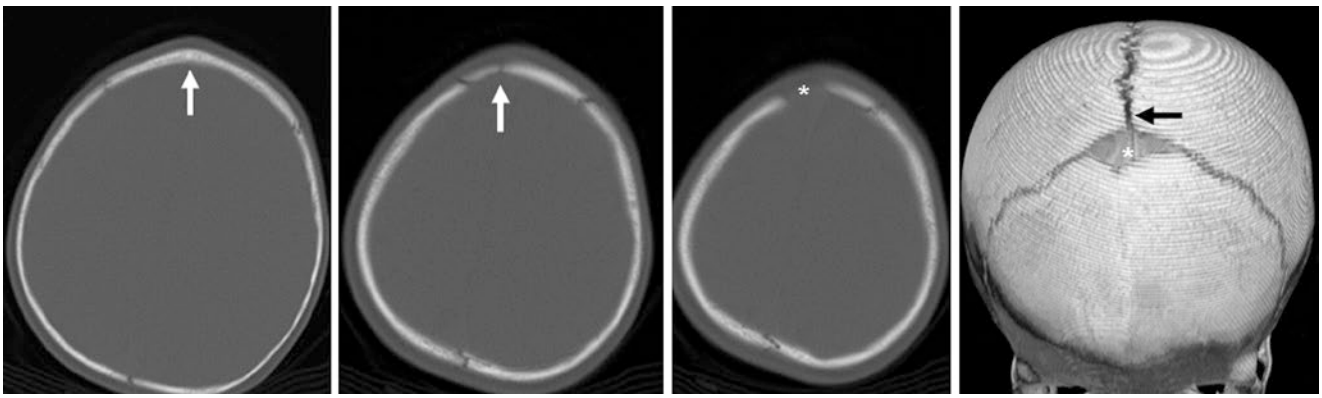

Fig. 27.11 A 9 month old with an asymmetric, small AF (*) and a short, residual portion of the MS (*arrows*). Note the sagittal suture (*black arrow*) on a 3D VR CT (*right*, *anterior view*)

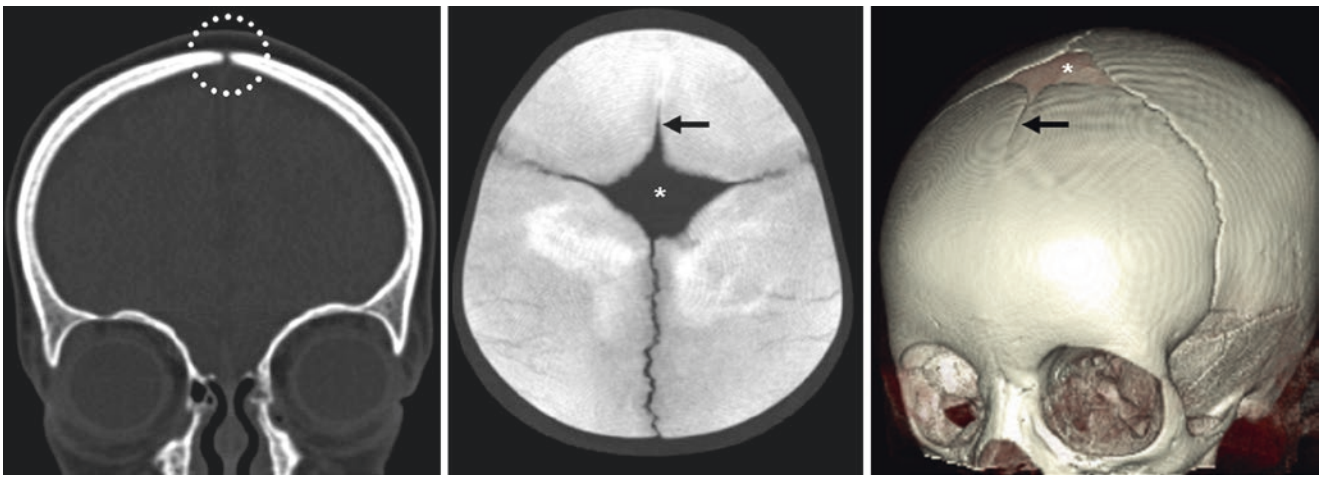

Fig. 27.12 An 11 month old with a partially fused MS (*black arrows and dashed circle*) on an 0.7-mm coronal MPR (*left*), axial 20-mm MPR (*middle*), and a 3D VR CT (*right*, *left anterior oblique* [*LAO*] *view*). There is an entirely patent AF (*asterisks*)

Fig. 27.13 A 1 year old with a normal fused MS that is slightly raised

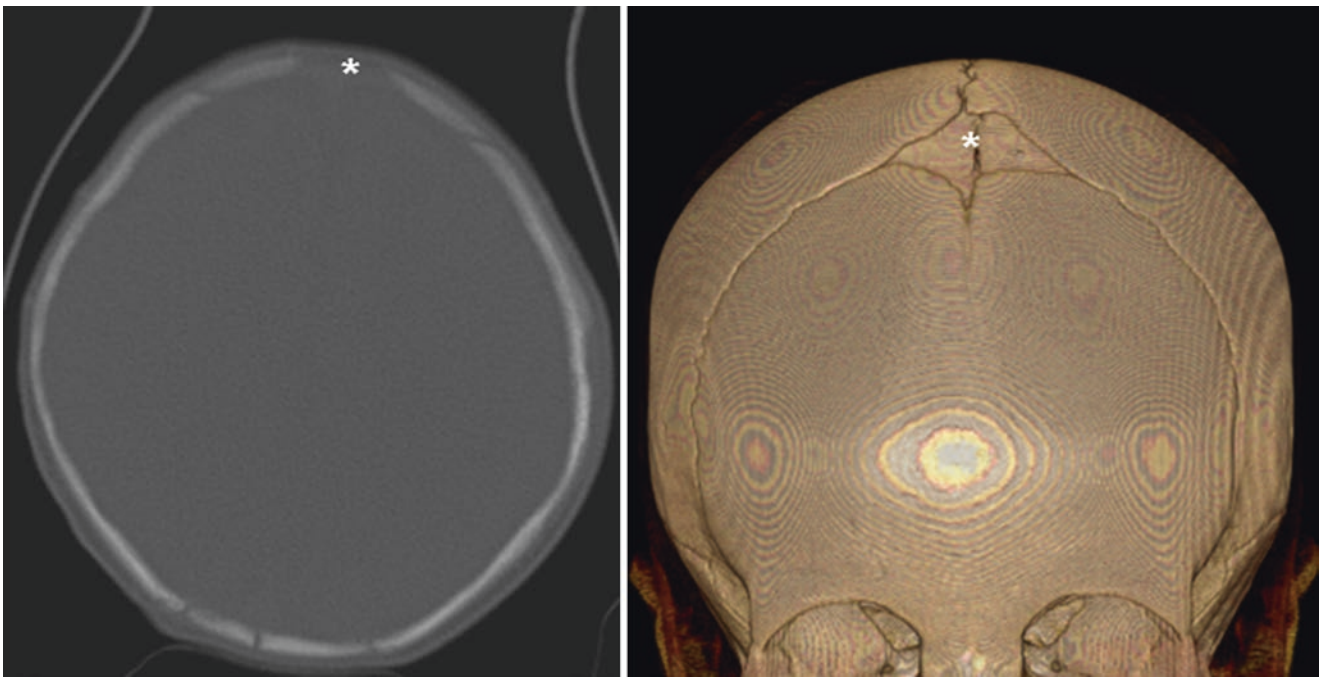

Fig. 27.14 A 1 year old with a fused MS and a patent AF on axial NECT (*left*) and 3D reformat (*right*, *anterior view*)

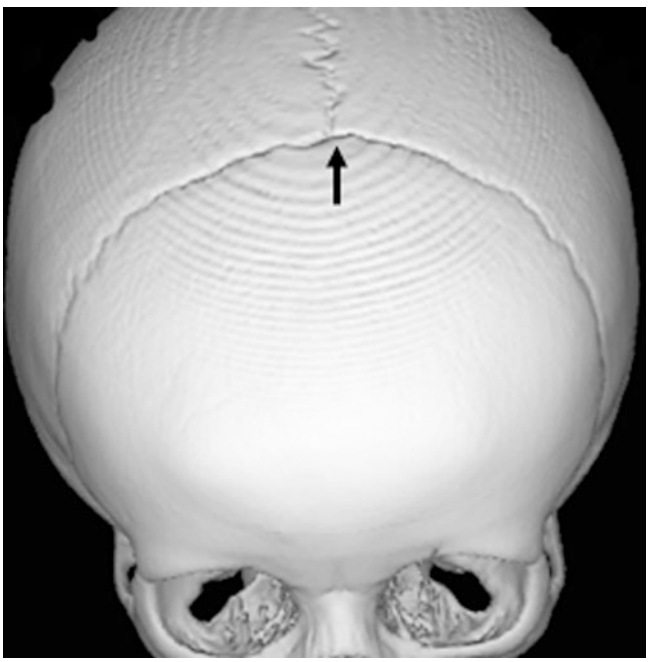

Fig. 27.15 An 18 month old in whom the MS fused and has a nearly closed AF

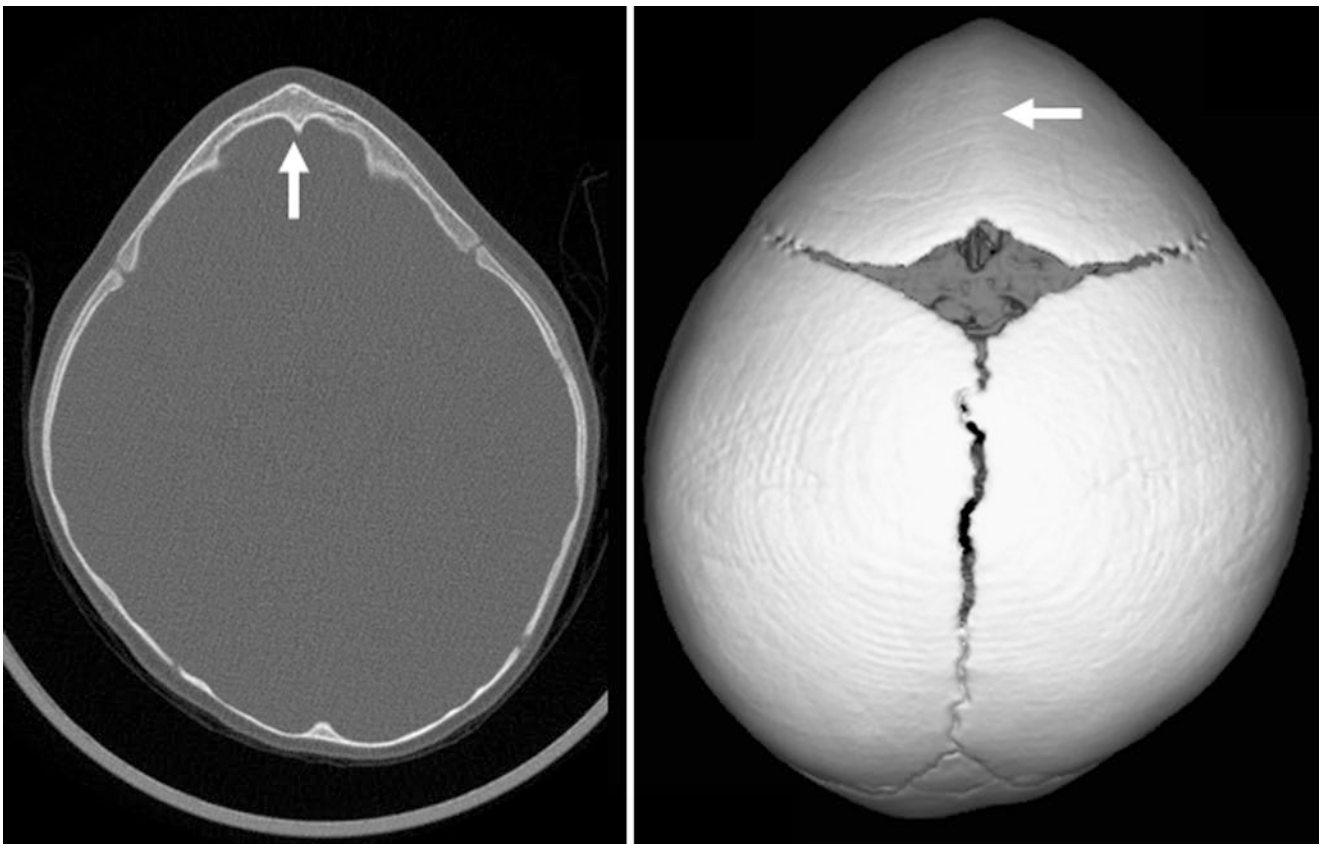

Fig. 27.16 Comparison case: A 7 month old with premature MS fusion causing trigonencephaly (*arrows*) with a patent AF

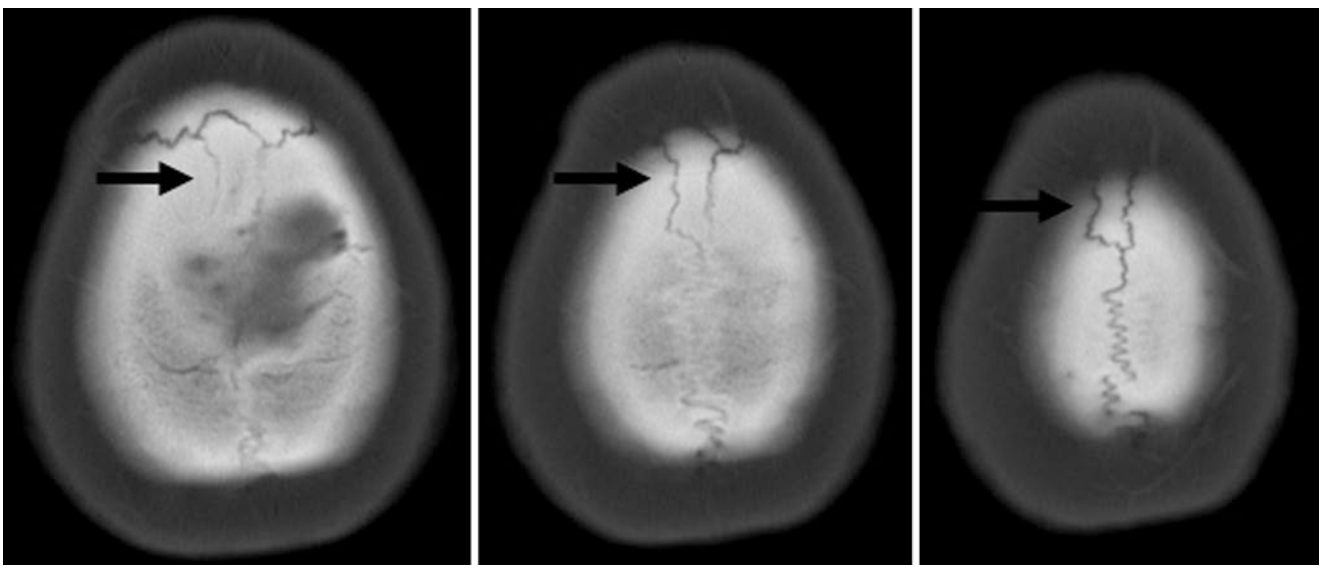

Fig. 27.17 A 58 year old: an os bregmaticum is located at the junction of the AF with the partly fused sagittal suture and thus represents a residual intrasutural bone in this asymptomatic adult

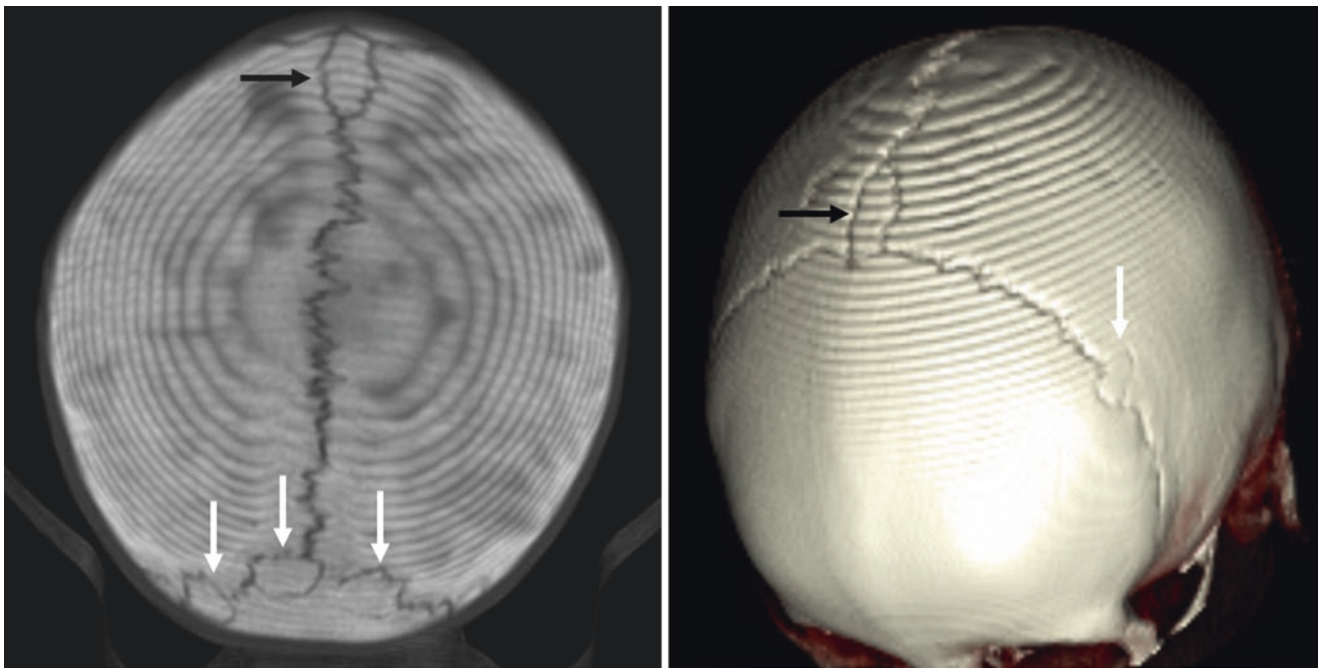

Fig. 27.18 A 7 year old: multiple intrasutural bones (*white arrows*) are depicted on a superior view of a 20-mm thickness MPR (*left*) and on a 3D VR CT (*right*, *oblique PA view*). One of the intrasutural bones is an os bregmaticum (*black arrows*), which lies along the sagittal suture's anterior margin

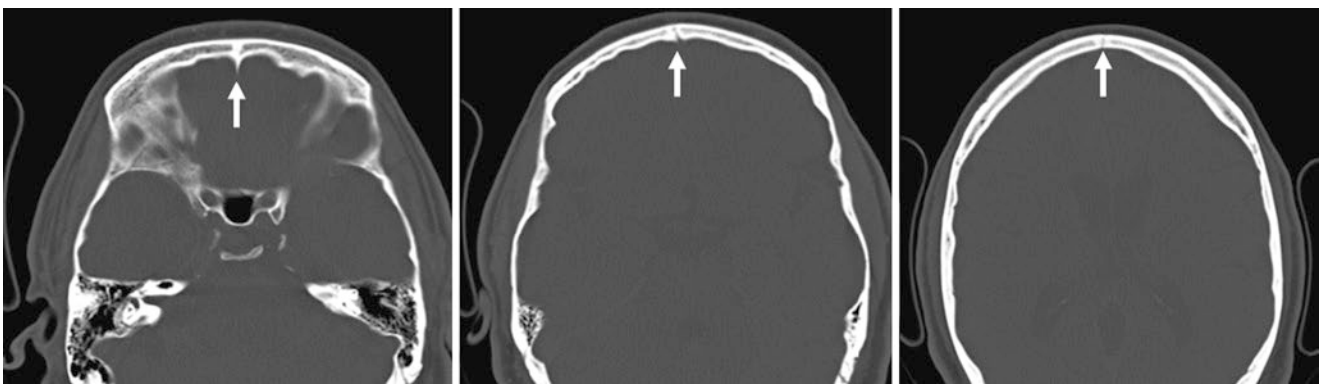

Fig. 27.19 A 49 year old with a nearly completely fused but very faint residual MS

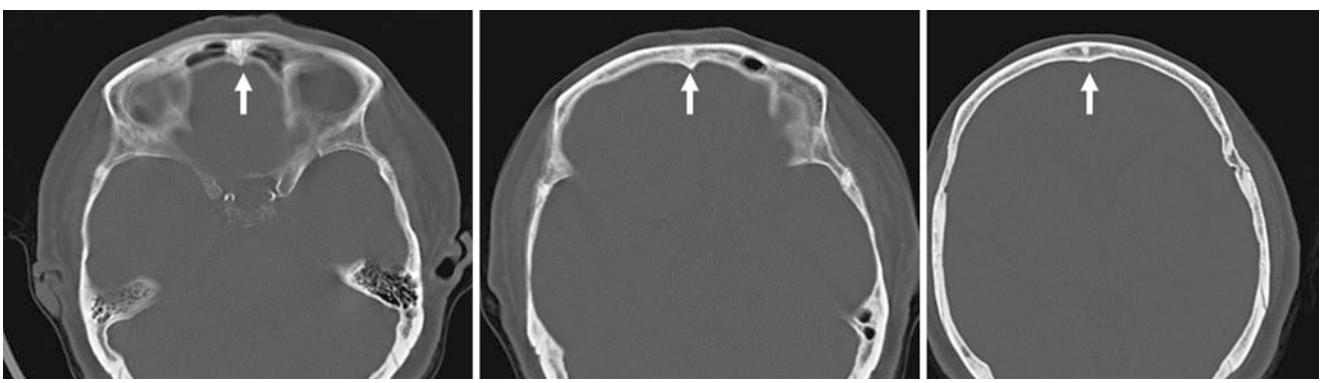

Fig. 27.20 A 67 year old with a largely fused and sclerotic-appearing MS

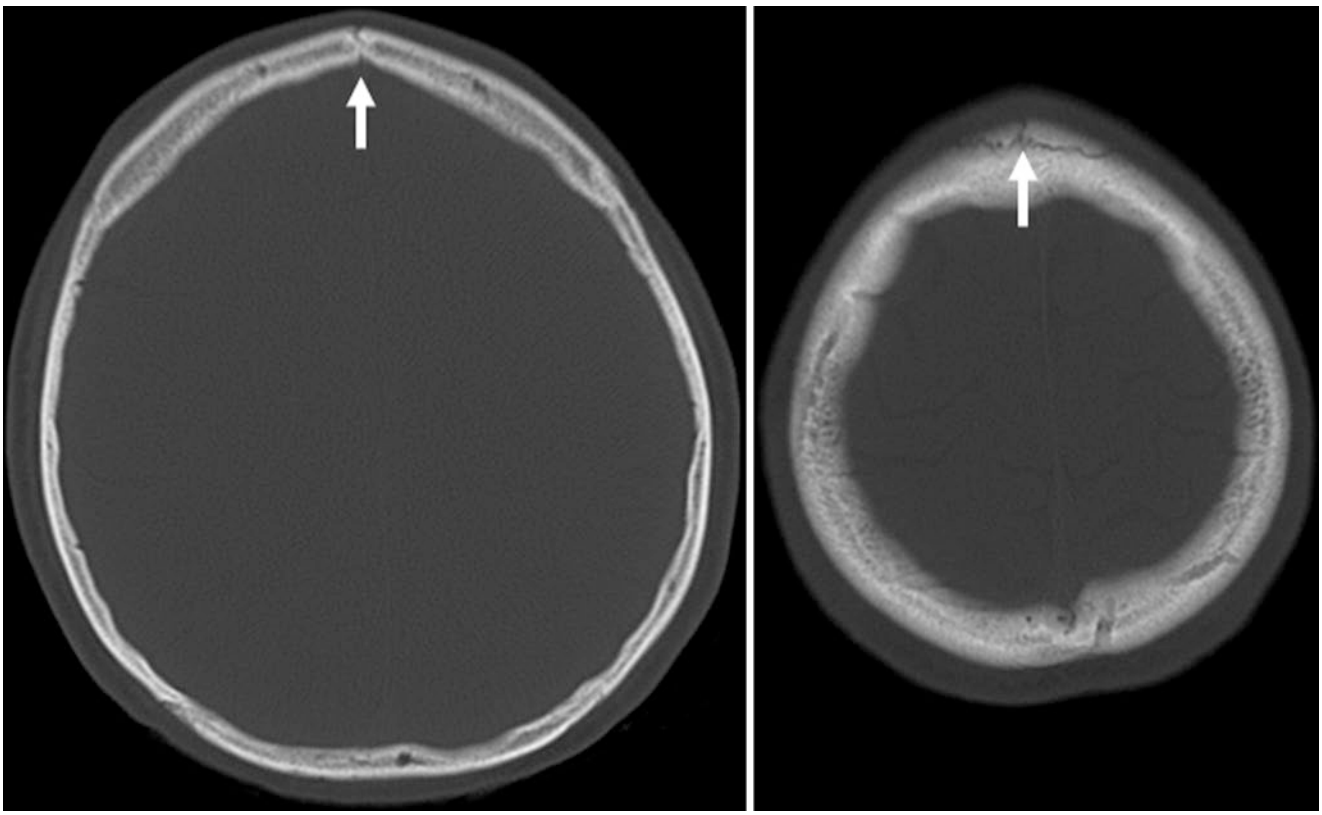

Fig. 27.21 A 23 year old with residual MS and a coronal suture

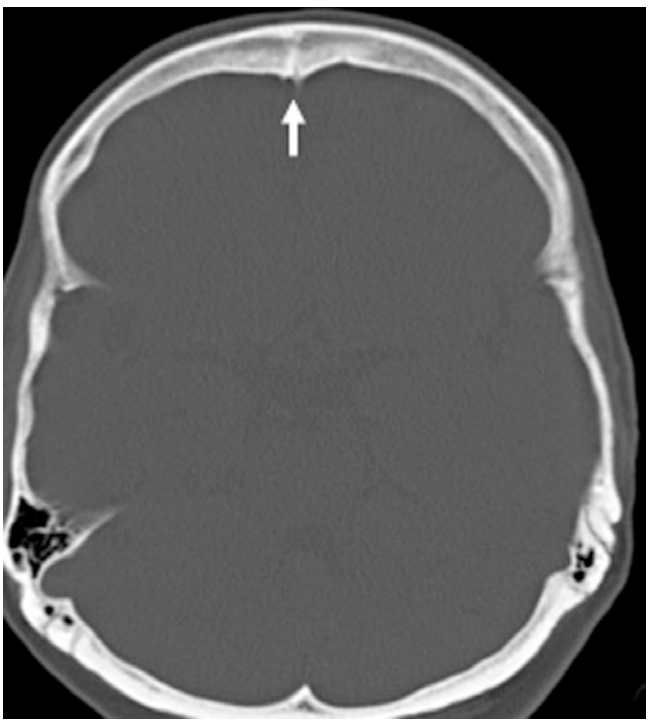

Fig. 27.22 A 60 year old with a MS that has almost entirely fused

27.2 Squamosal Suture and Petrosquamosal Fissure Persistence

The *squamosal suture* can occasionally persist in adults and simulate a *fracture*. This persistence may be unilateral or bilateral. An adjacent fissure that communicates with the squamosal suture is the *petrosquamosal fissure*, which can also mimic a fracture. This fissure is best noted in younger children along the superior aspect of the *squamosal portion of the temporal bone*, extending inferiorly from the posterior margin of the squamosal suture. This dilemma is usually solved by (1) evaluating for adjacent soft tissue swelling, (2) determining if this linear defect communicates with the coronal (anteriorly) and lambdoid (posteriorly) sutures if patent, and (3) the reconstruction of 3D images.

Additional cases are also demonstrated here of patent squamosal sutures and petrosquamosal fissures in adults. Their persistence may be unilateral or bilateral and may be difficult to connect with other sutures, since they may have already fused. Hence the importance of being familiar with their typical locations in children and their possible persistence in adults. These variants in suture and fissure closure can at times be problematic in adults when they simulate temporal fractures or sutural diastasis; in such cases, 3D volume-rendered (VR) reconstructions can be quite helpful (Figs. 27.23, 27.24, 27.25, 27.26, 27.27, 27.28, and 27.29).

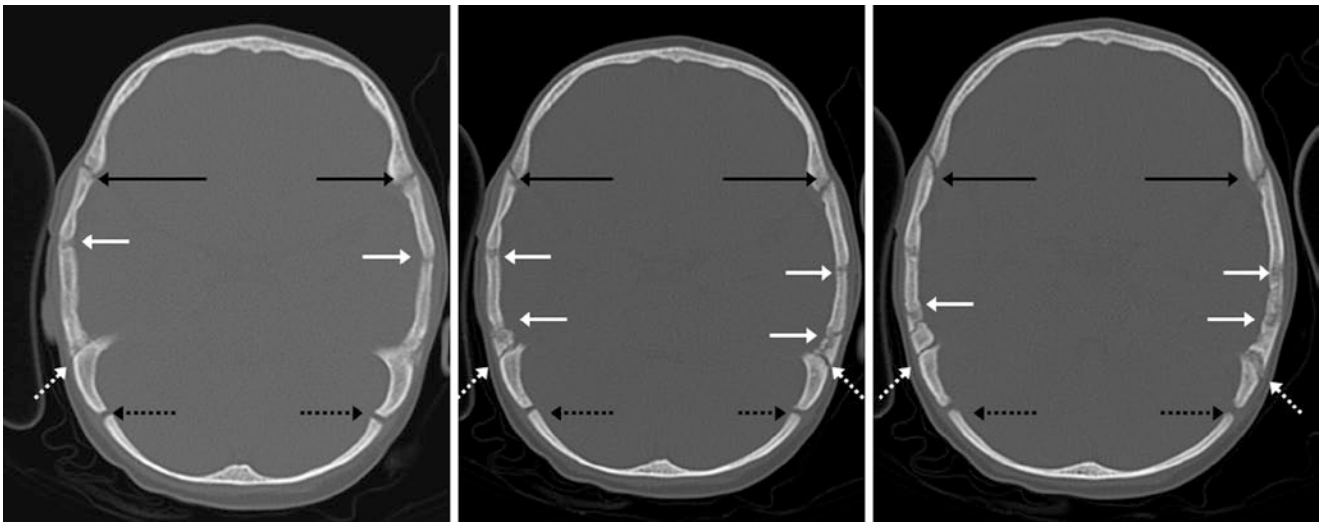

Fig. 27.23 A 5 month old: a normal infant's skull is provided to demonstrate the squamosal sutures (*solid white arrows*) in relation to the petrosquamosal fissure (*dotted white arrows*) for this age. Also note the coronal (*black arrows*) and lambdoid (*dotted black arrows*) sutures

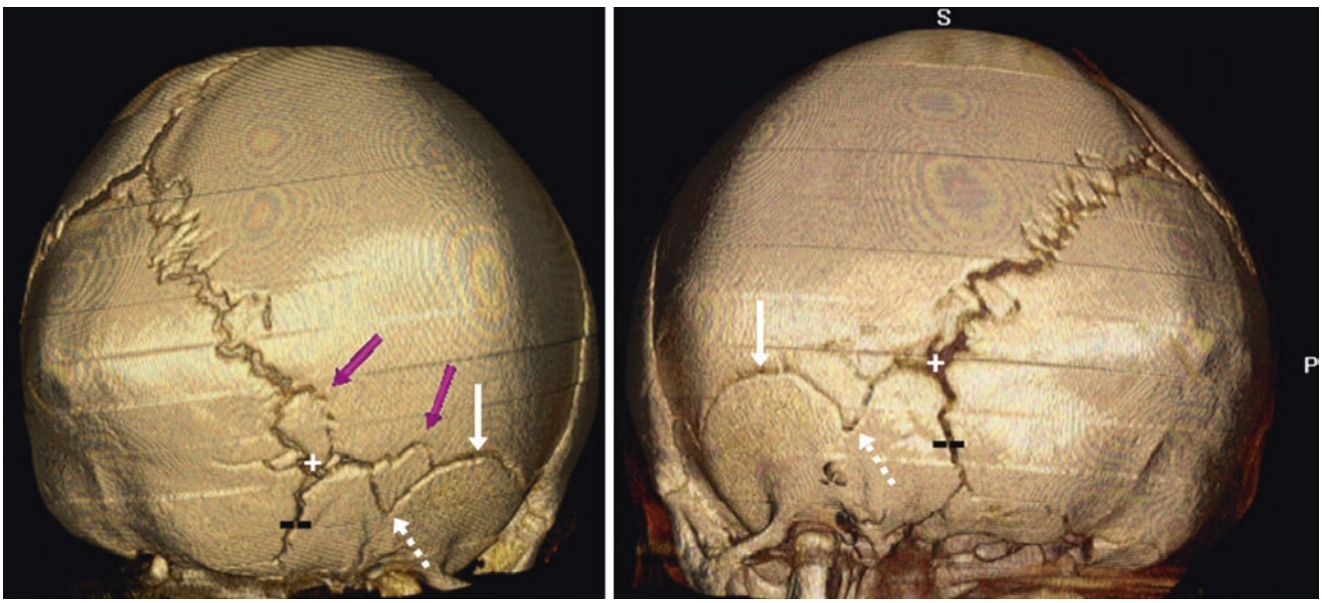

Fig. 27.24 In this 7 month old 3D VR reconstructions from a spiral CT demonstrated bilateral patent squamosal sutures (*solid white arrows*), petrosquamosal fissures (*dotted arrows*), and wormian bones (*pink arrows*) within the fissure on the right, on 3D VR CT right posterior oblique (RPO) (*left*), and on left posterior oblique (LPO) (*right*) projections. Note the mastoid fontanelles (+) and the occipitomastoid sutures (−)

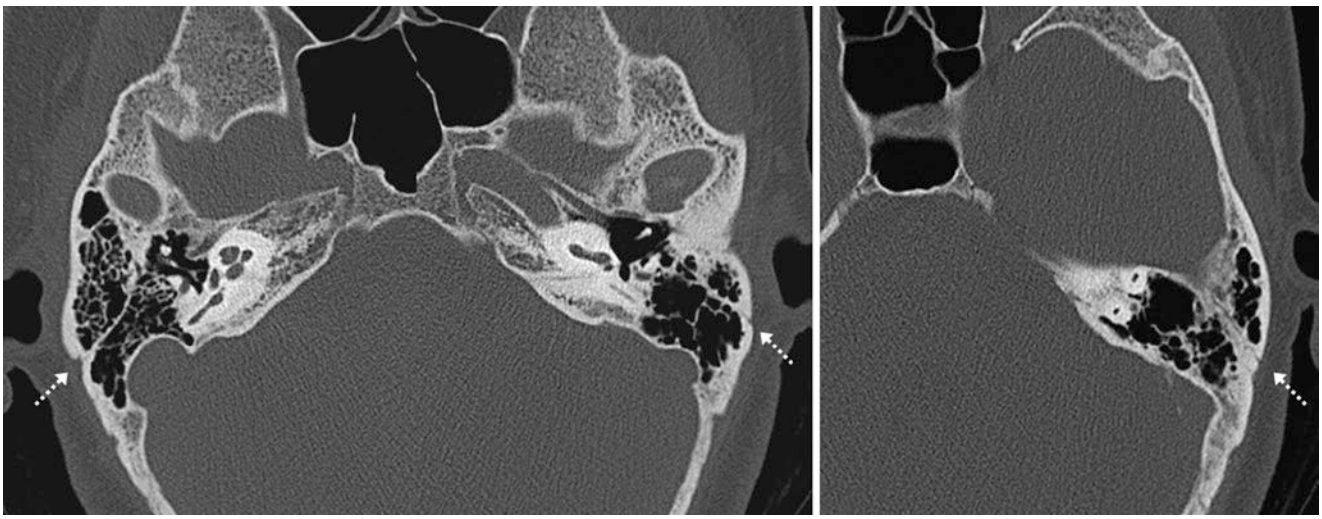

Fig. 27.25 In a 40 year old a persistent petrosquamosal fissure was noted (*dotted arrows*) on thin slices from a temporal bone CT, being more prominent on the left side but also present on the right to a lesser degree

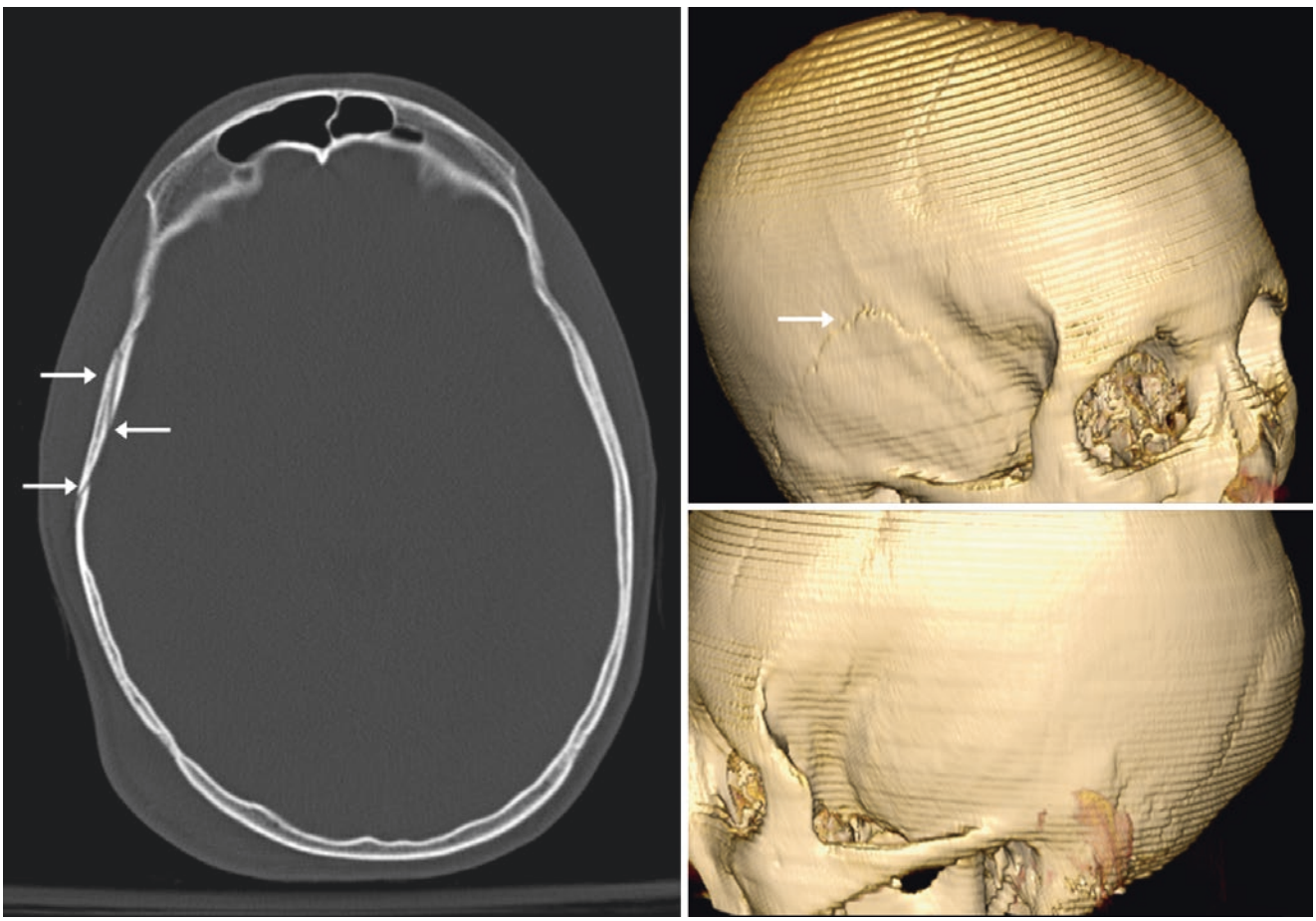

Fig. 27.26 In this 20 year old a fracture was initially suspected on NECT (*arrows*, *left*) but was later confirmed by 3D VR images to be the right squamosal suture on right lateral (*top right*) and left lateral (*bottom right*) views. The left squamosal suture had apparently previously fused

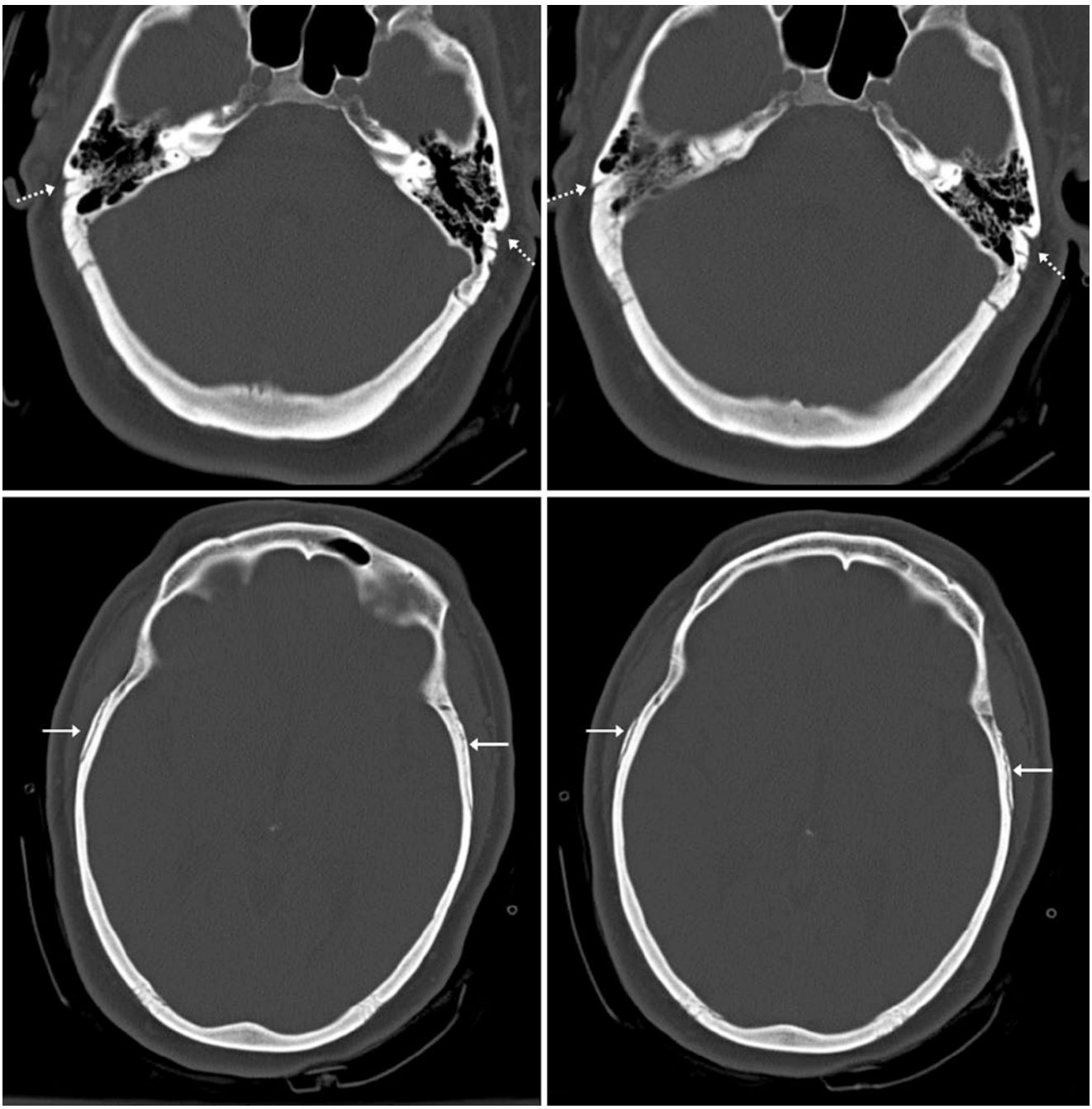

Fig. 27.27 In this 46 year old bilateral patent petrosquamosal fissures (*dashed arrows*, *top row*) were noted, along with patent squamosal sutures (*solid arrows*, *bottom row*) on a NECT that was negative for a fracture

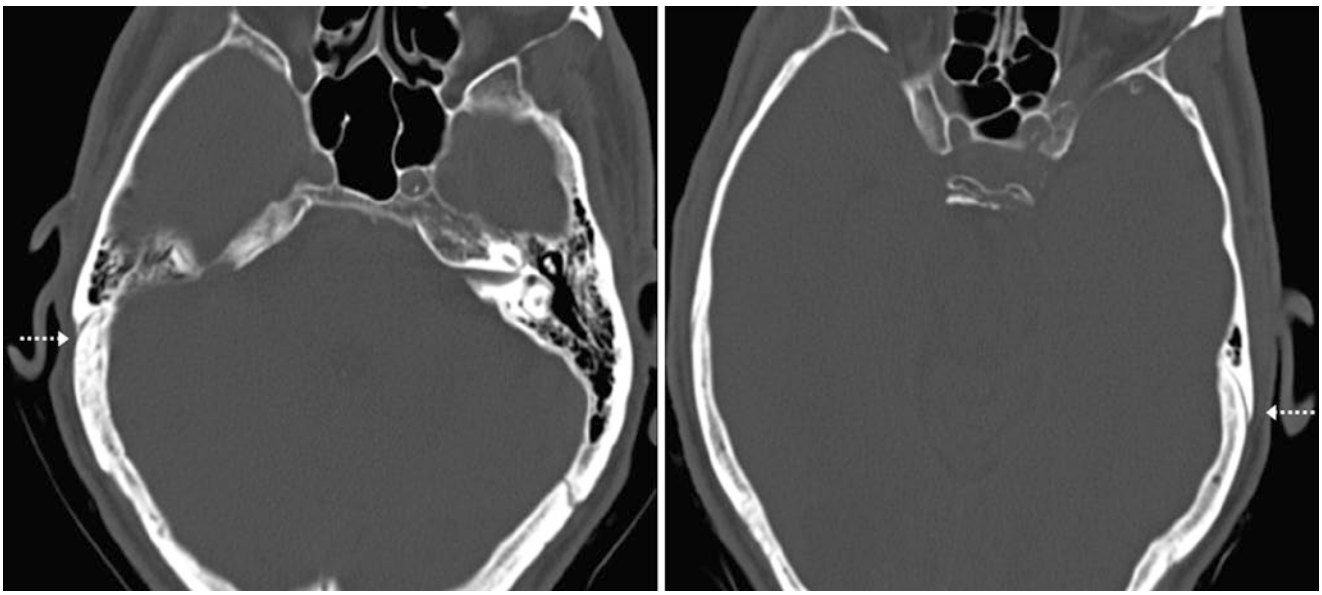

Fig. 27.28 A 55 year old had bilateral persistent petrosquamosal fissures (*dashed arrows*) on axial NECT images performed to evaluate blunt head trauma

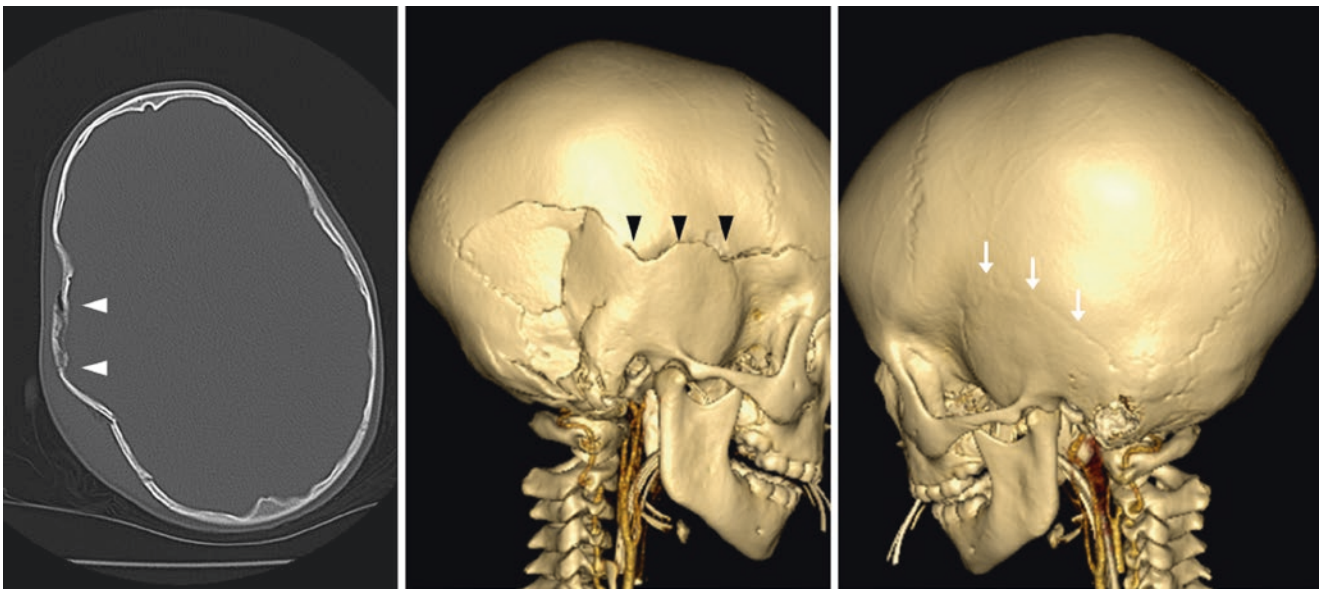

Fig. 27.29 Comparison case: A depressed fracture that contained gas and extended into the squamosal suture causing diastasis (*arrowheads*) on axial CT (*left*) was found in a 5 year old. This illustrates how fractures favor the path of least resistance. Note a normal, partly fused contralateral suture (*arrows*) on 3D VR CT right (*middle*) and left (*right*) lateral views

27.3 Posterior Fontanelle: Appearance in Newborns and Persistence Later in Life

The *posterior fontanelle* (PF) usually fuses before 6 months of age but varies in appearance. It can be entirely patent in the first few months or can develop a bone within it immediately; the bone may persist for several years before completely fusing with the adjacent *sagittal* and *lambdoid sutures*. The fontanelle and the bone within have many names, such as the *apical bone, os apicis,* preinterparietal bone, or the bone of the PF. This bone can have irregular, linear defects that can simulate fractures. The intrasutural bone within the posterior fontanelle could also be considered intrafonticular (i.e., within the fontanelle) rather than intrasutural, which is likely a purely academic distinction.

Thus, the following images provide examples of how the PF and the bone it variably contains within have continued irregularity, variability, and fusion within the first 6–7 months of age. Although a fusing bone is often present at 5–6 months of age, this may also be very irregular and simulate fractures on axial images, necessitating 3D reconstruction. Beyond the first year of life, the bone within the PF may persist, and adjacent intrasutural bones are also common in younger children. Also, irregularity of the edges of the fused PF may persist even in older children and adults and should not be misconstrued as fractures (Figs. 27.30, 27.31, 27.32, 27.33, 27.34, 27.35, 27.36, 27.37, 27.38, 27.39, 27.40, 27.41, 27.42, 27.43, 27.44, 27.45, 27.46, and 27.47).

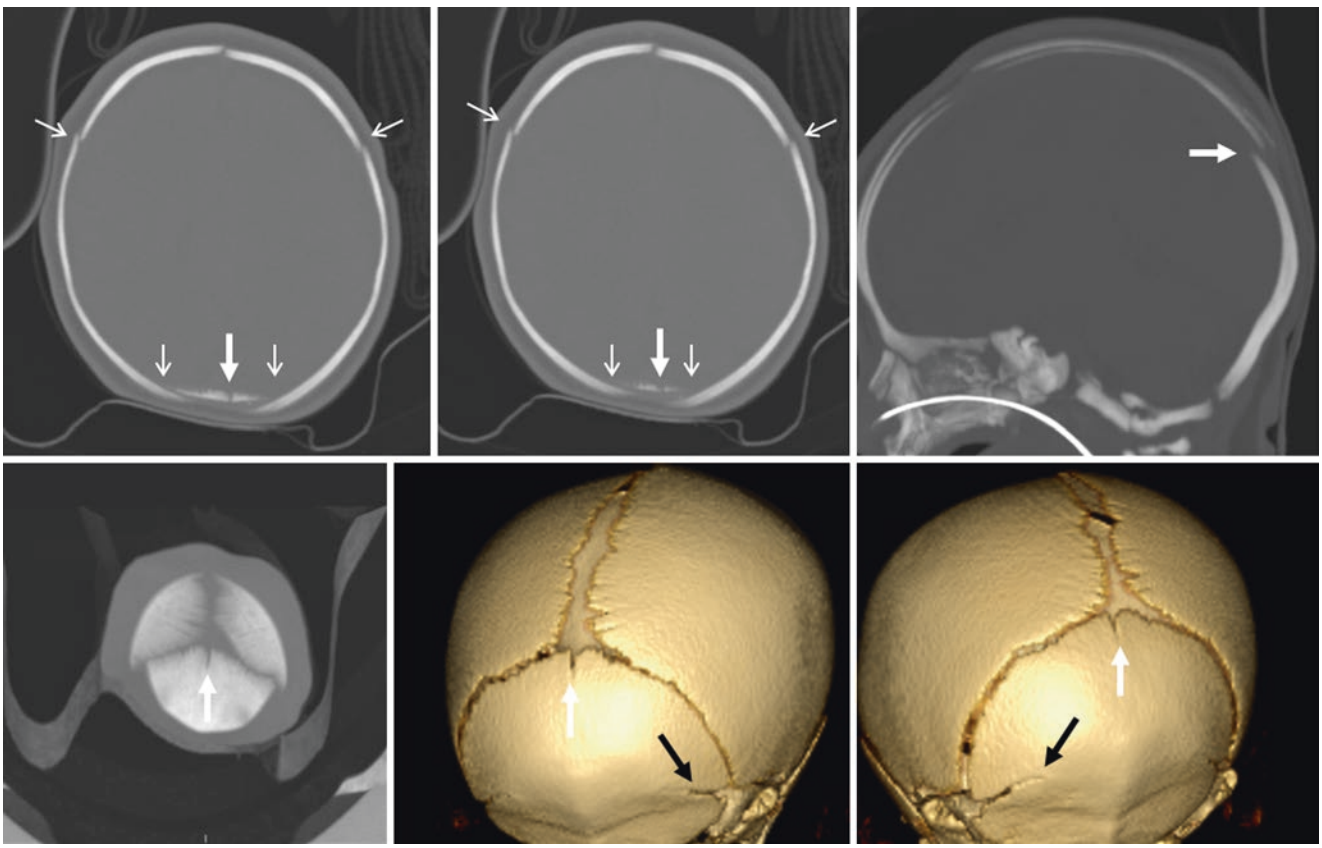

Fig. 27.30 A 3 day old with PF (*white arrows*) and an adjacent inferior defect on axial and sagittal (*top right*) MPRs. Note the normal neonatal overlap of the coronal and lambdoid sutures (*tiny arrows*). Also note the mendosal sutures (*black arrows*) on 3D VR CT posteroanterior views (*bottom middle and right*)

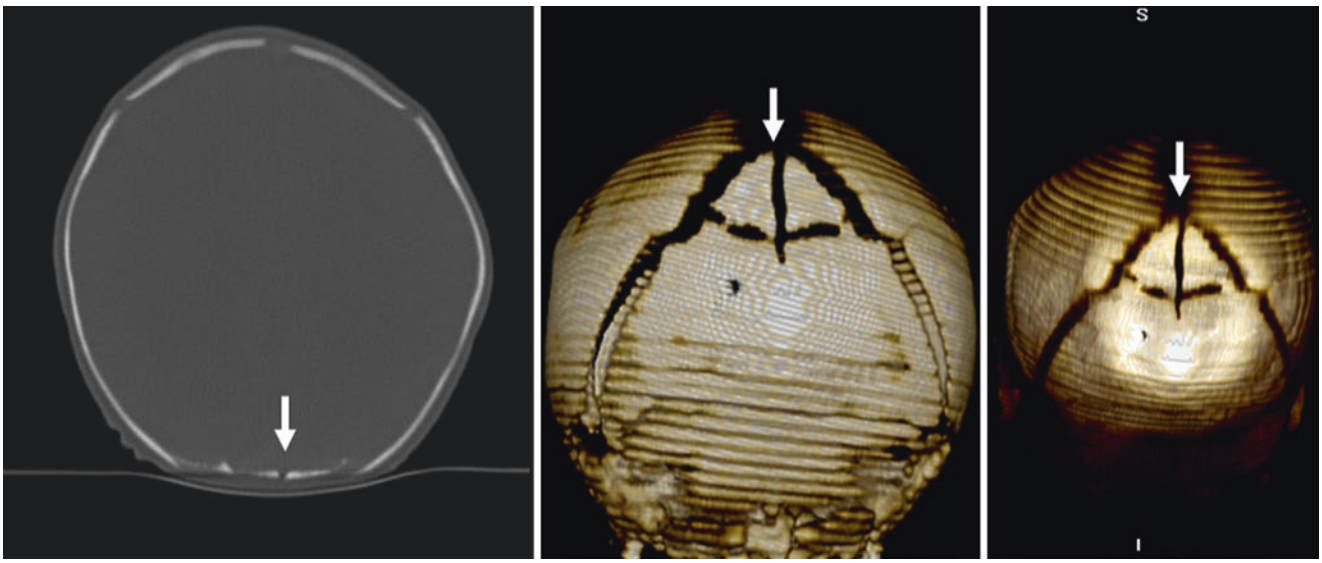

Fig. 27.31 A 4 day old with a normal linear defect of the PF bone that has a delta-like appearance on NECT (*left*). Note the normal overlapping sutures in a newborn on 3D VR posterior views (*middle and right*) obtained from a sequential acquisition. This type of acquisition accounts for the horizontal stair-step artifacts

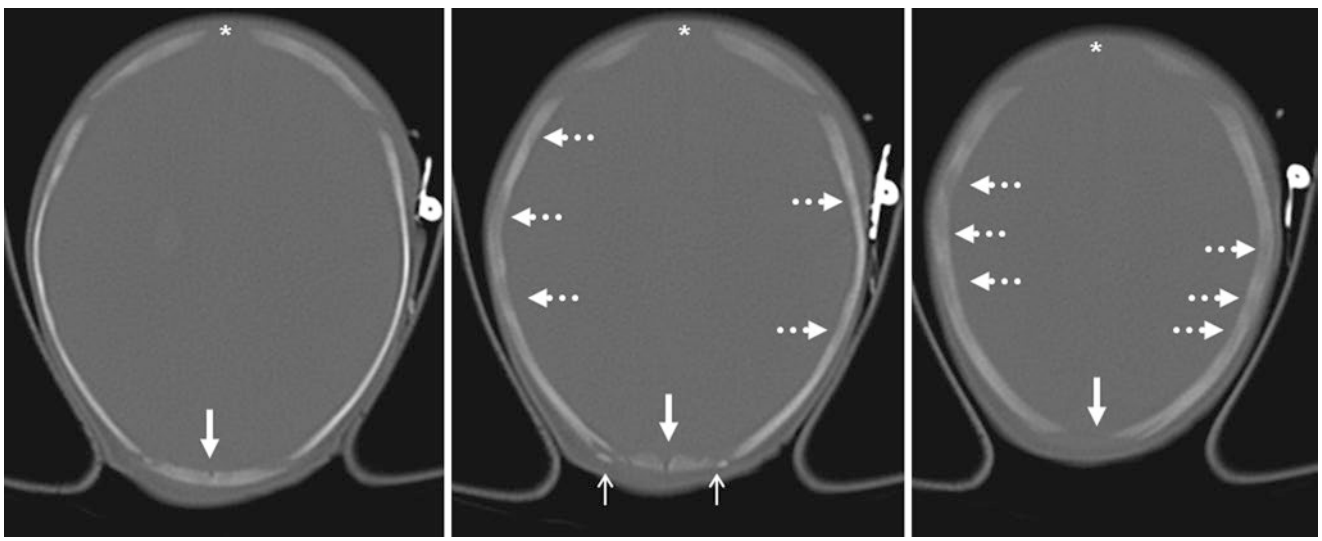

Fig. 27.32 A 6 day old (no trauma) with a PF bony defect (os apicis, *arrows*) having irregular edges (*thin arrows*) and normal marrow inhomogeneity (*dotted arrows*). Note the mild scaphocephalic contour with mild sutural overlap. Such overlap usually resolves over first 2 to 3 weeks of life

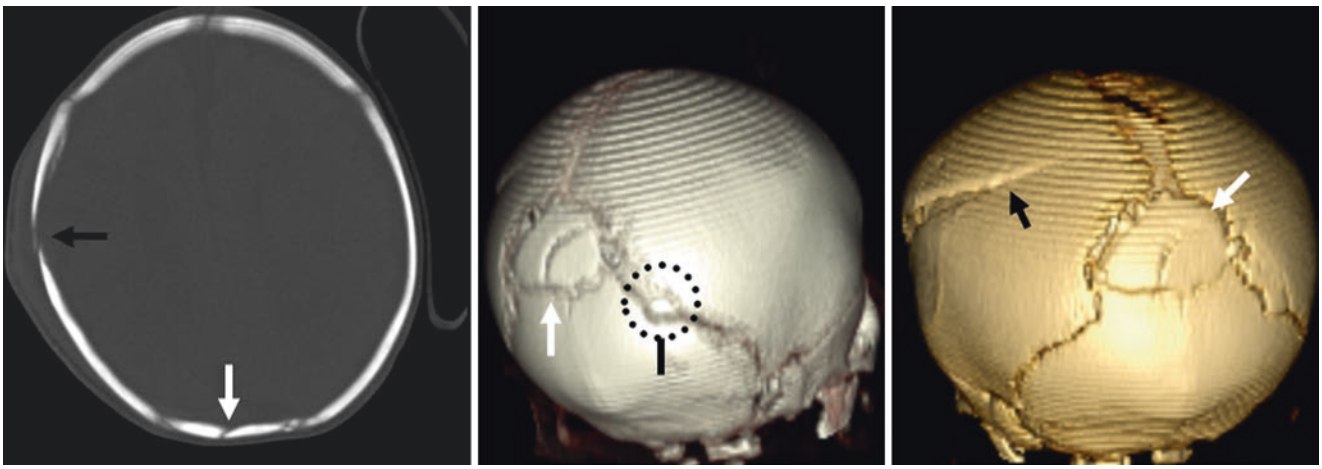

Fig. 27.33 A 1 month old post-trauma child showing an irregular margin of the PF (*thin arrows*) and an oblique defect (*arrows*) on NECT (*left*); this does not represent a fracture because fracture lines are absent in the adjacent bones. However, there is a true right parietal fracture (*black arrow*). Note a normal intrasutural bone (*dotted circle*) on 3D VR RAO (*middle*) and LAO (*right*) views

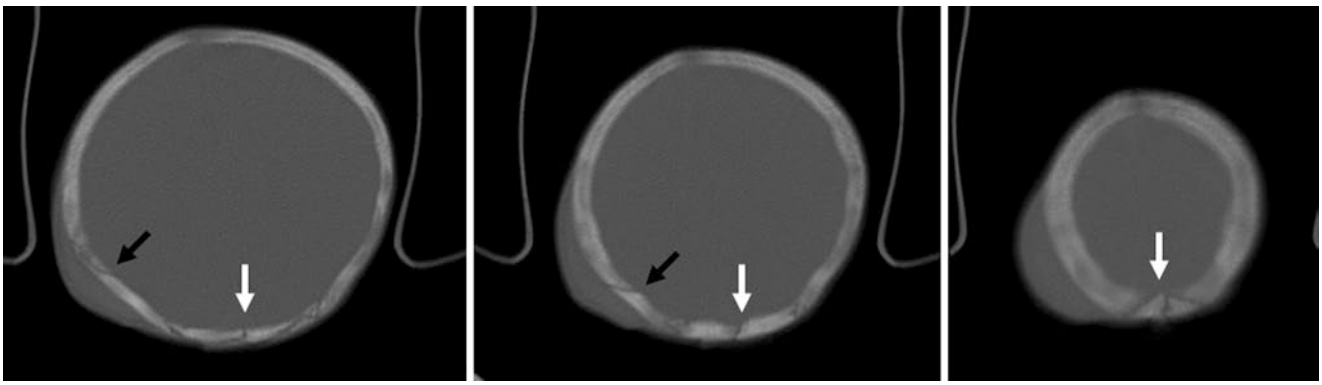

Fig. 27.34 A 3 month old with a normal defect in the PF bone (i.e., apical bone or os apices; *arrows*). However, note the true right parietal fracture and adjacent scalp swelling (*black arrows*)

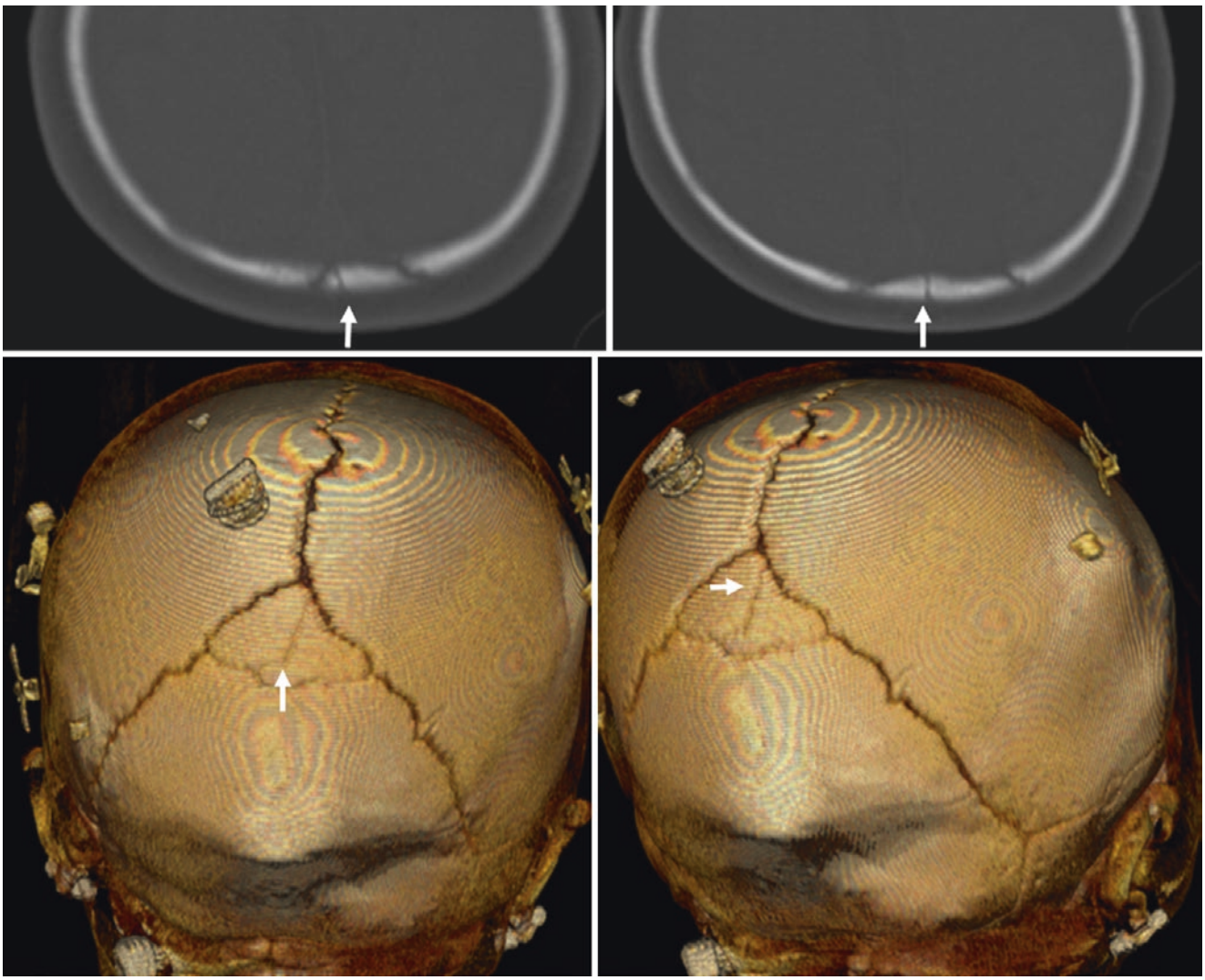

Fig. 27.35 *Top row*: NECT in a 6 month old evaluated for nonaccidental trauma with a jagged intrasutural defect, initially thought to be a fracture (which is usually straighter; note a lack of scalp swelling). *Bottom row*: 3D VR posteroanterior views (*bottom row*) confirm this to be an intrasutural bone

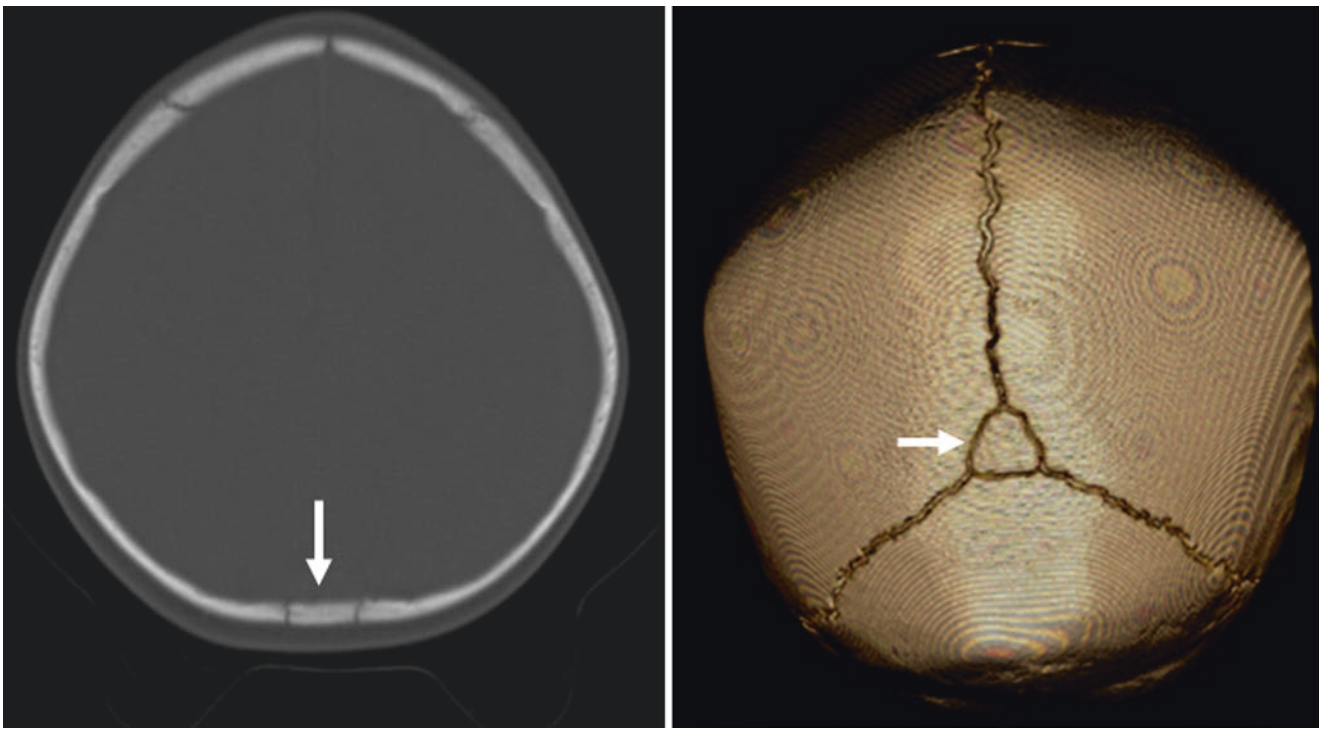

Fig. 27.36 An 11 month old with a normal intrasutural (intrafonticular) bone within the PF, also called a preinterparietal bone, apical bone, or an os apicis. A 3D VR posteroanterior view is provided (*right*)

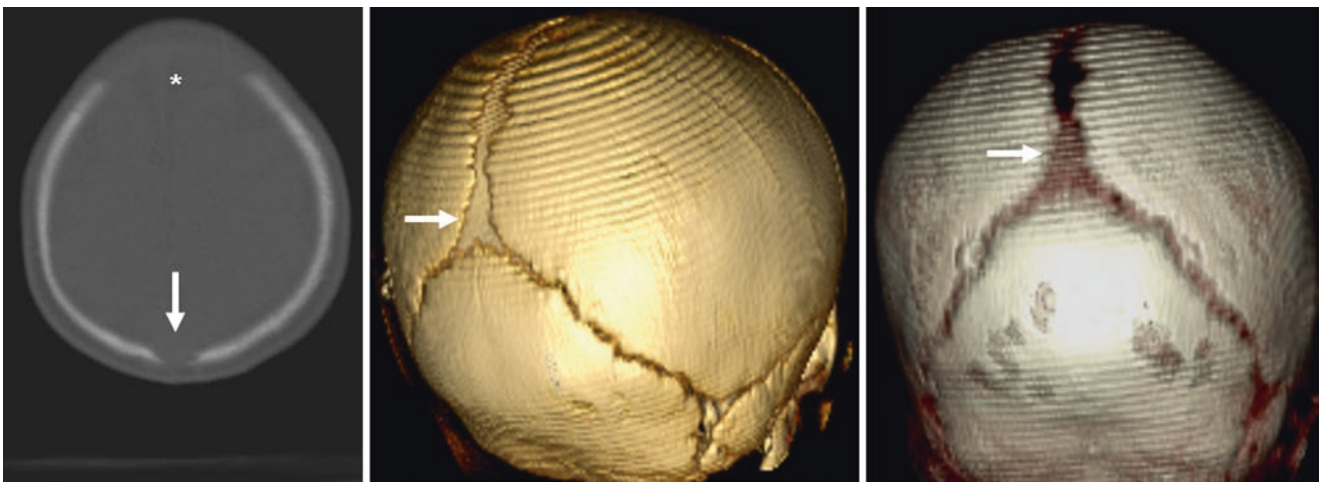

Fig. 27.37 A 3 month old with a small, patent PF (*arrow*) and AF (*asterisk*). 3D VR CT RPO (*middle*), and posterior/PA (*right*) views are also provided

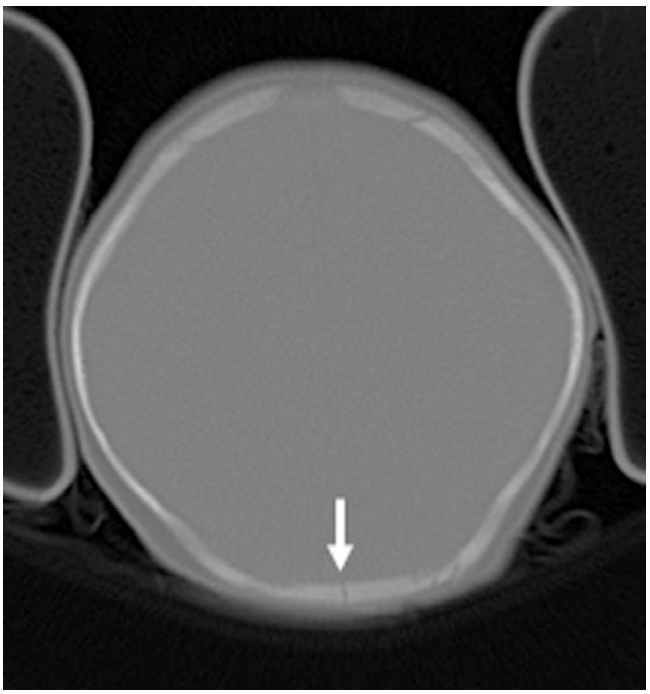

Fig. 27.38 A 3 month old with a tiny residual line from a fused PF

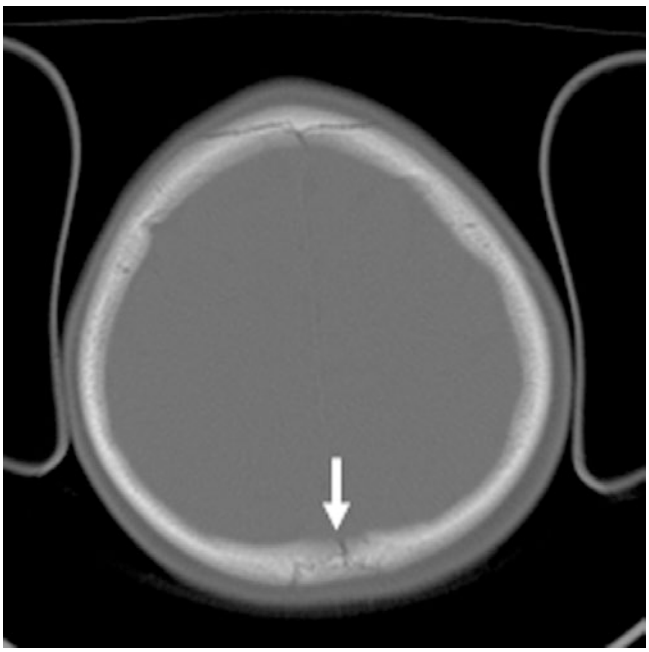

Fig. 27.40 A 5 month old with a fused PF

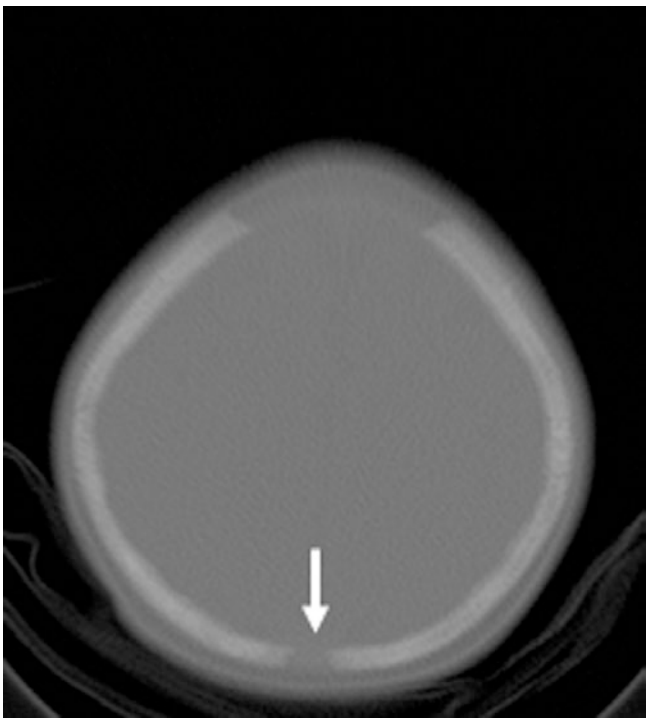

Fig. 27.39 A 4 month old with a patent PF

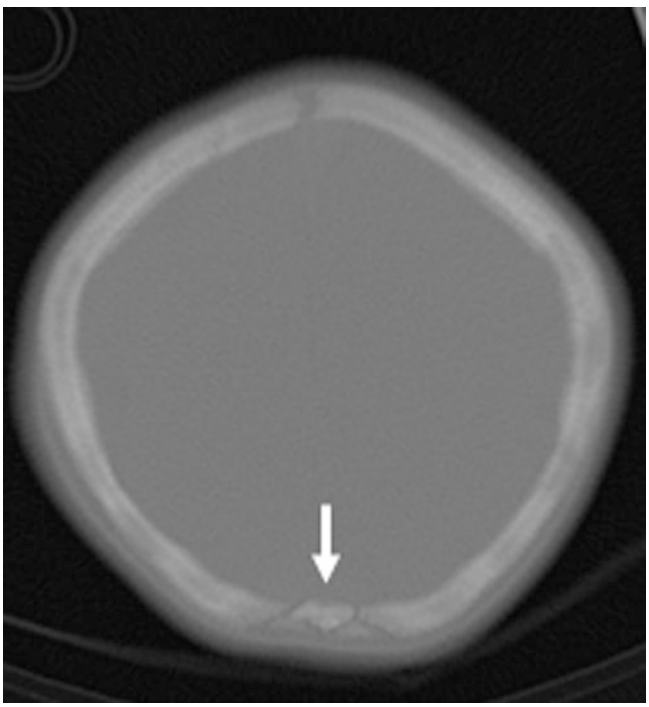

Fig. 27.41 A 5 month old with a small bone within the PF

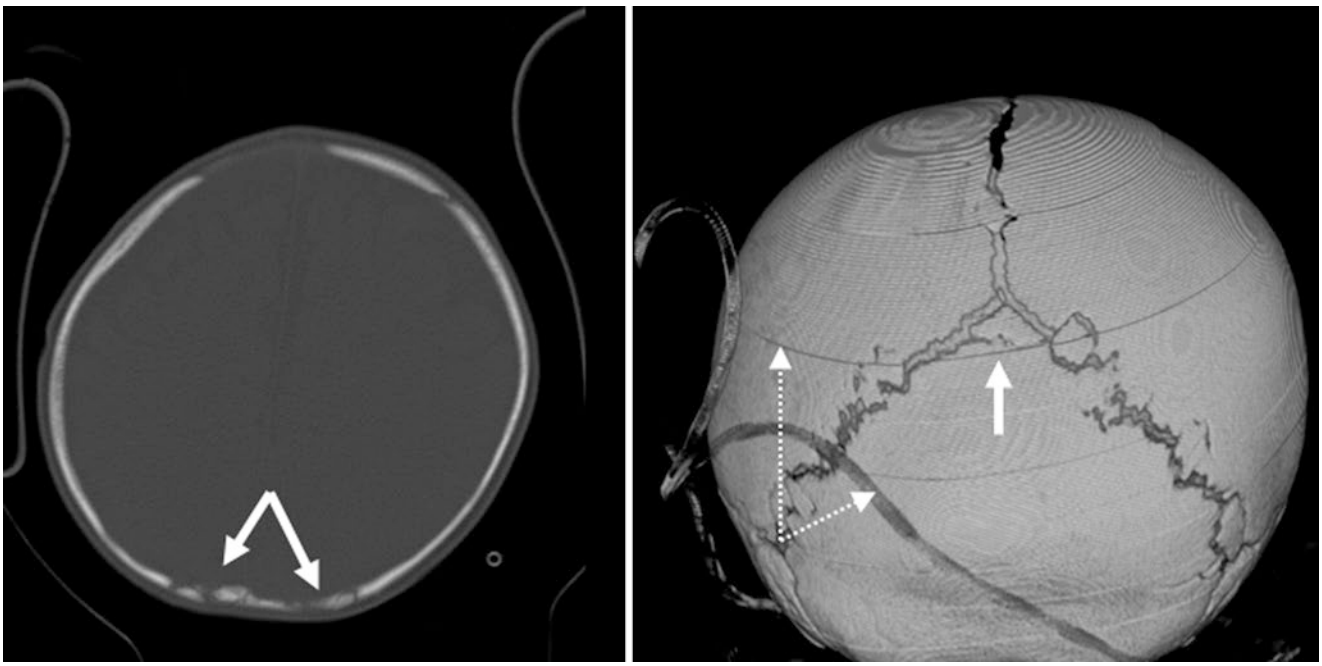

Fig. 27.42 A 7 month old with an irregular bone within the PF as well as other intrasutural bones on axial NECT (*left*) and 3D VR CT posteroanterior view (*right*). Note the motion artifact (*dotted arrows*)

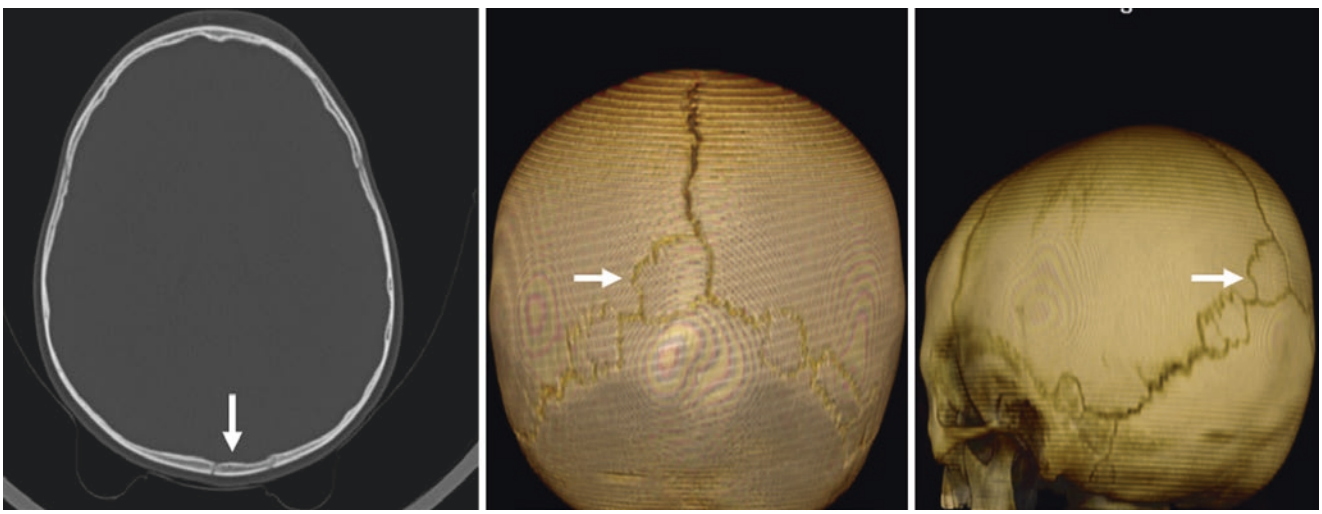

Fig. 27.43 A 2.5 year old with multiple intrasutural bones, including bones within the PF and lambdoid sutures on axial (*left*, and on 3D VR CT posteroanterior (*middle*) and LPO (*right*) views

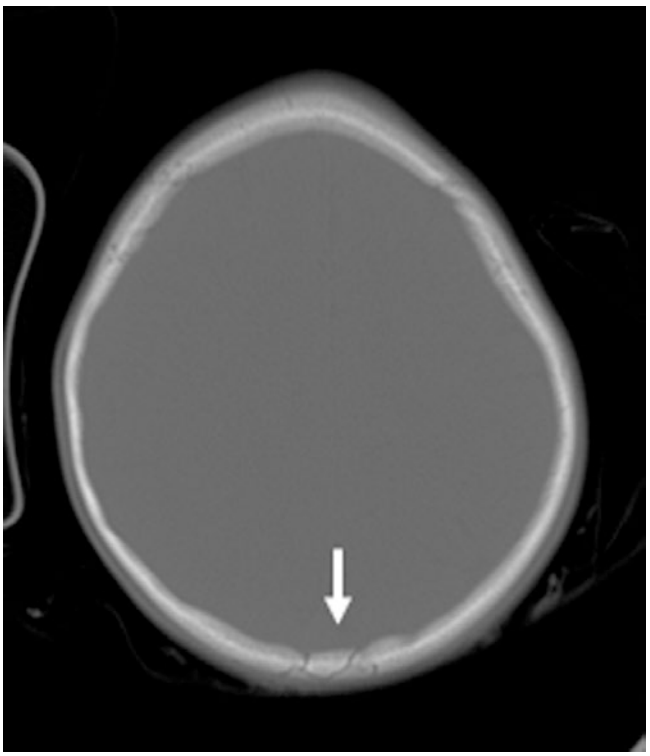

Fig. 27.44 A 3 year old with a fusing bone within the PF

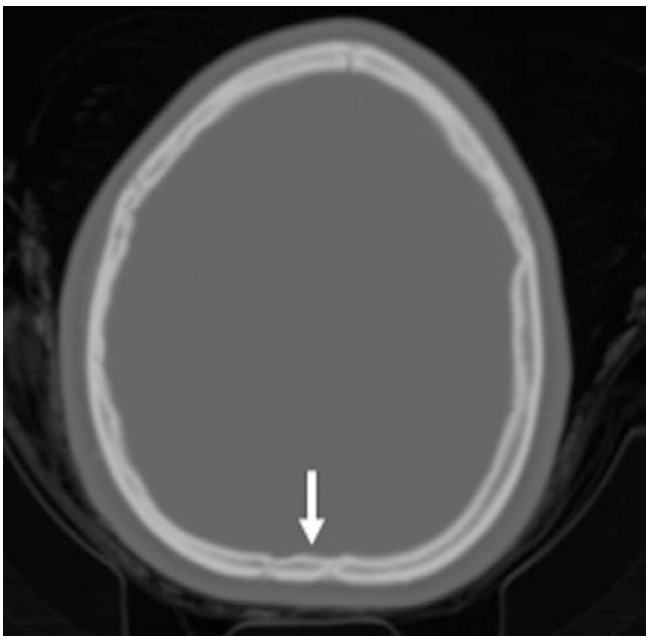

Fig. 27.45 A 14 year old with a tiny residual bone within the PF

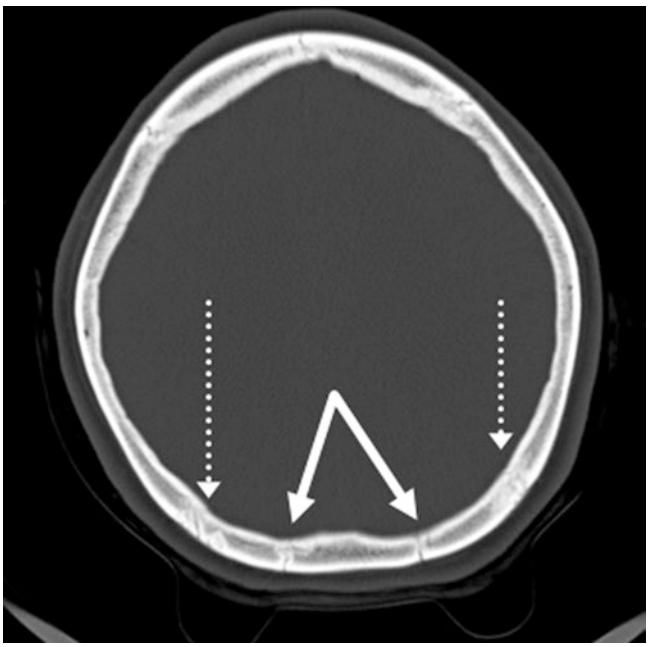

Fig. 27.46 A 26 year old in whom lines at sites of the PF and lambdoid sutures (*dotted arrows*) are thin

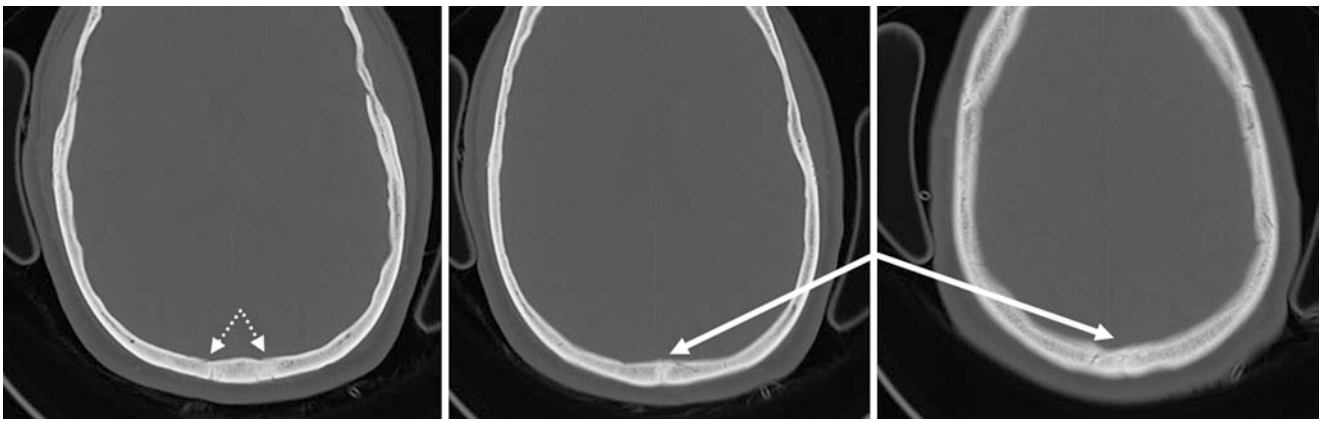

Fig. 27.47 A 46 year old with irregular, lucent lines in the expected locations of the PF or its bony remnant (*arrows*). Note the remnants of the top of the lambdoid sutures (*dotted arrows*)

27.4 Persistent Coronal, Lambdoid, and Sagittal Sutures in Adults

Although it may appear that the *cranial sutures (coronal, lambdoid, and sagittal)* are fused by early adulthood, a relative degree of minimal detectable patency of the suture lines (based on CT) is actually quite common regarding these sutures, even in the elderly. The cranial sutures may even remain more visible regionally in one portion of the suture or on one side compared to another location or side. Although complete ossification without detectable suture lines does occur in the majority by age 50 years, a mildly patent suture in a middle-aged or even elderly patient does not indicate a remote or acute *fracture*. These incompletely fused sutures may be potentially confused with diastatic fractures (Figs. 27.48, 27.49, and 27.50).

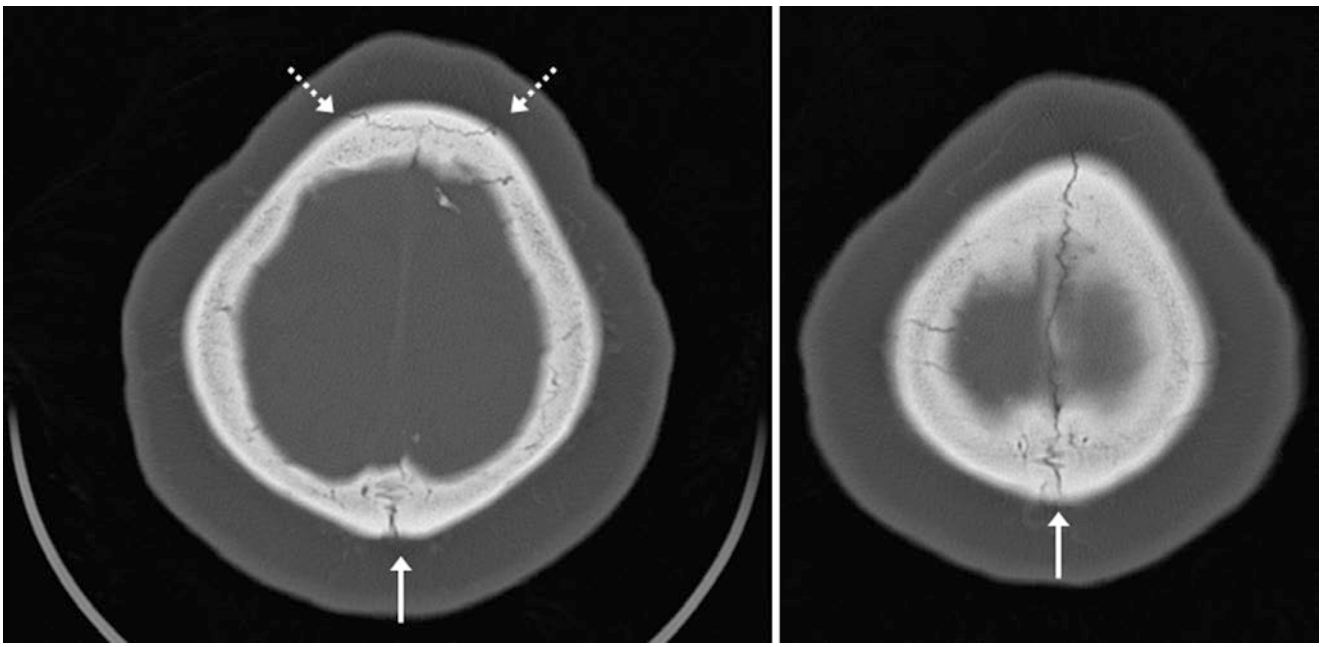

Fig. 27.48 A 45 year old in whom axial NECT images demonstrate a nearly fused coronal suture (*dashed arrows*) as well as a mildly patent sagittal suture (*solid arrows*). The lambdoid suture fusion is complete, and thus the suture is not visualized

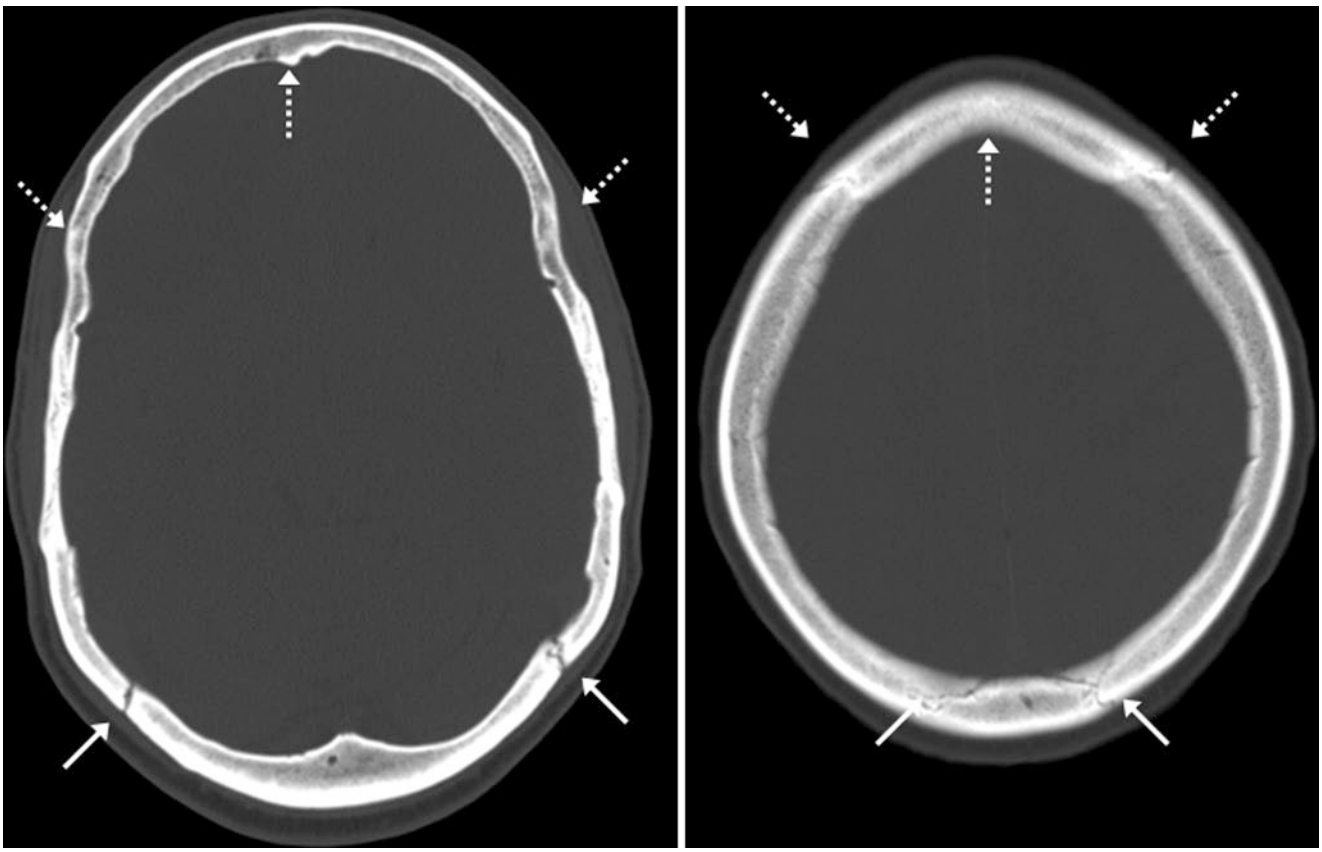

Fig. 27.49 A 38 year old in whom a NECT demonstrates almost entirely fused coronal and sagittal sutures (*dashed arrows*) with minimally detectable suture lines of the lambdoid sutures bilaterally (*solid arrows*)

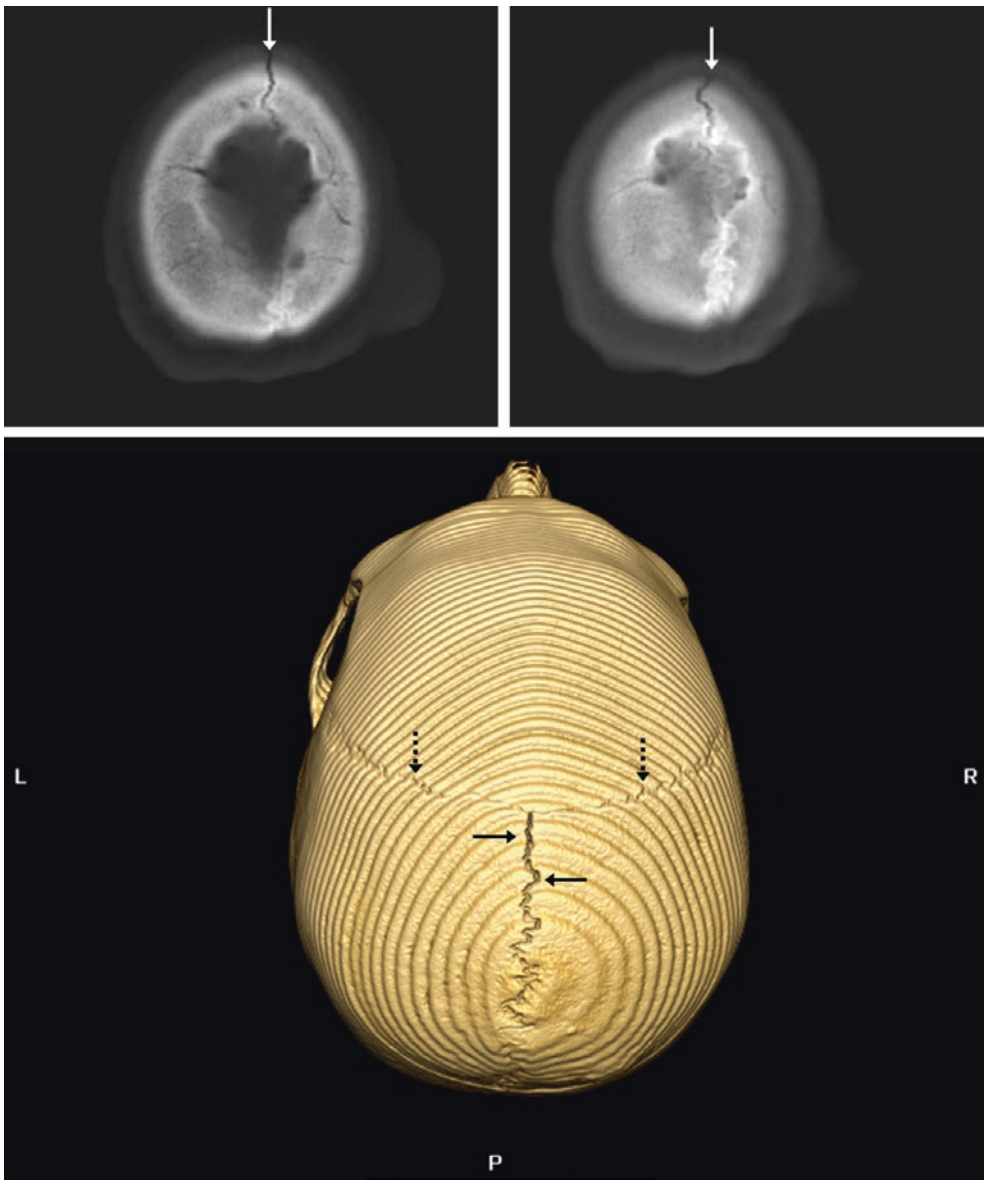

Fig. 27.50 *Top row*: in a 36 year old, axial 4-mm NECT images depict mild patency of the sagittal suture anteriorly (*arrows*). *Bottom row*: this is confirmed on a sequentially-acquired 3D VR CT (note the step artifact), which also shows that the coronal suture (*dotted arrows*) is minimally patent

27.5 Pediatric and Adult Skull: Intrasutural Bones

Intrasutural (wormian) bones are commonly seen on skull radiographs and CTs in infants and young children. These are normal variants in the large majority, particularly when isolated, but they are rarely associated with *skeletal dysplasias*. These are most common in the *lambdoid sutures* and less common in the coronal and sagittal sutures. It has been suggested that multiplicity (>10), larger size (>6 to 7 mm), and a mosaic arrangement suggest an underlying dysplasia. Technically, intrasutural bones within the fontanelles are termed intrafonticular. In addition to typical intrasutural bones, figures shown in this section will include other less common normal variants of intrasutural or intrafonticular bones, such as the *os bregmaticum, interparietal bone,* and *os inca*.

While such intrasutural (or sutural) bones are most commonly present in young children, they can be present at any age, even in the elderly. Since these intrasutural bones fuse later in adulthood, the presence of extra suture on CT may cause some questioning about the patient's normal calvarial anatomy. Hence, portions of these sutures may persist as odd or irregular lines on axial CT images. Three-dimensional VR images in multiple projections can help to resolve this problem when there is a question of "trauma" or "fracture" based on axial images. Spiral acquisitions are preferred because they can be reconstructed into 3D images with less stair-step artifact than the sequential scans, although with a mildly (approximately 10–30 %) increased dose. They are two to three times faster if a similar collimation and slice thickness are used; the faster spiral acquisition also mitigates motion (Figs. 27.51, 27.52, 27.53, 27.54, 27.55, 27.56, 27.57, 27.58, and 27.59).

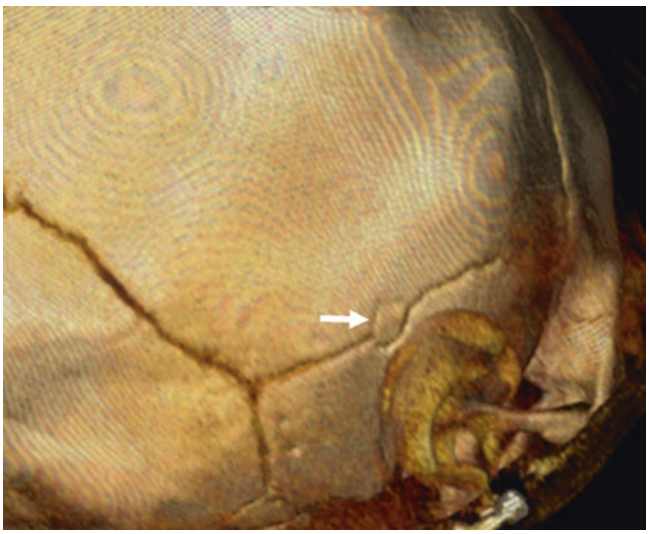

Fig. 27.51 A 6 month old with an intrasutural bone midway along the squamosal suture as shown on a 3D VR RPO view

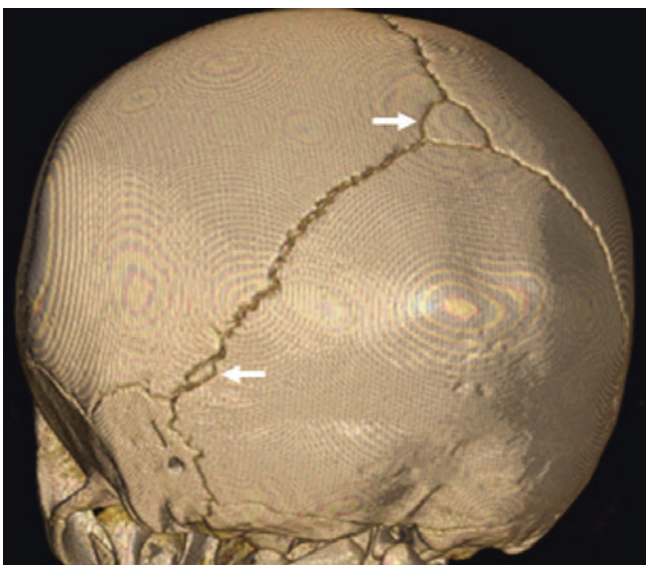

Fig. 27.52 A 1 year old with two denoted sutural bones, the upper being an os apicis, as shown on 3D VR posterior view

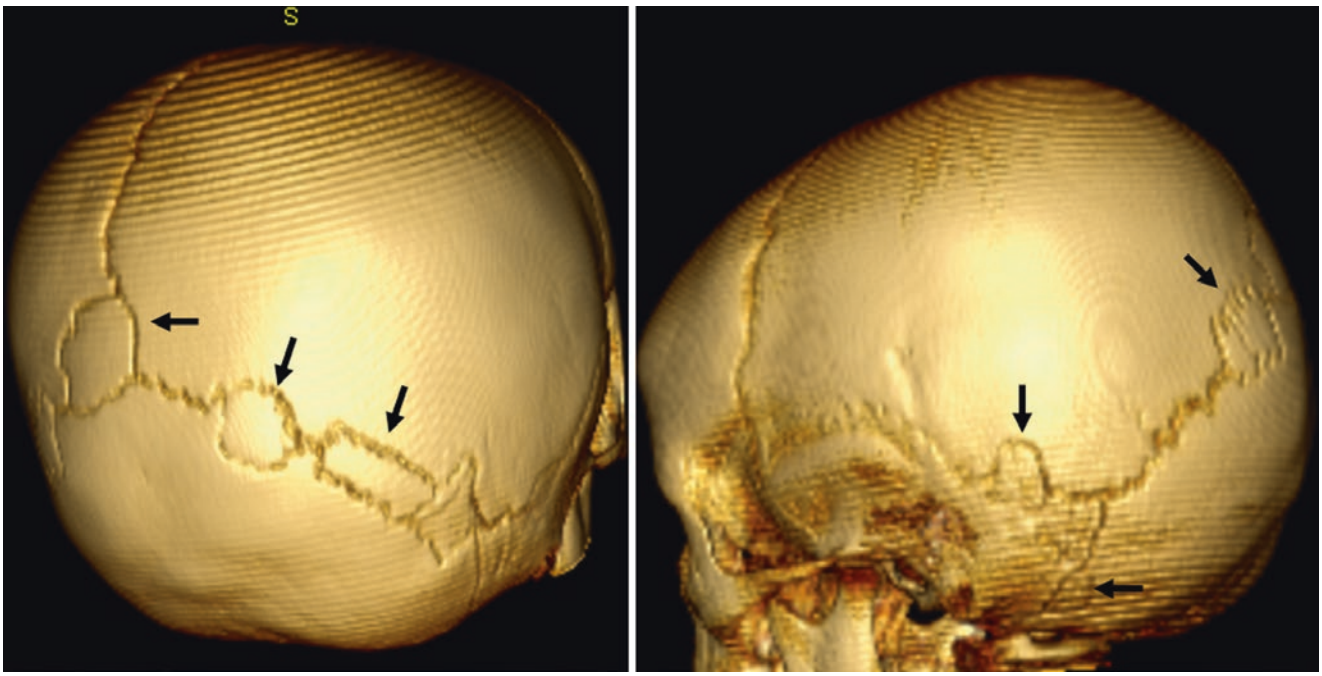

Fig. 27.53 A 2.5 year old with multiple intrasutural bones, including within the lambdoid, squamosal, and petro-occipital sutures. Note an intrafonticular bone (also known as an os apicis, apical bone, preinterparietal bone) within a fused PF. Shown are a 3D VR posterior view (*left*) and left lateral view (*right*)

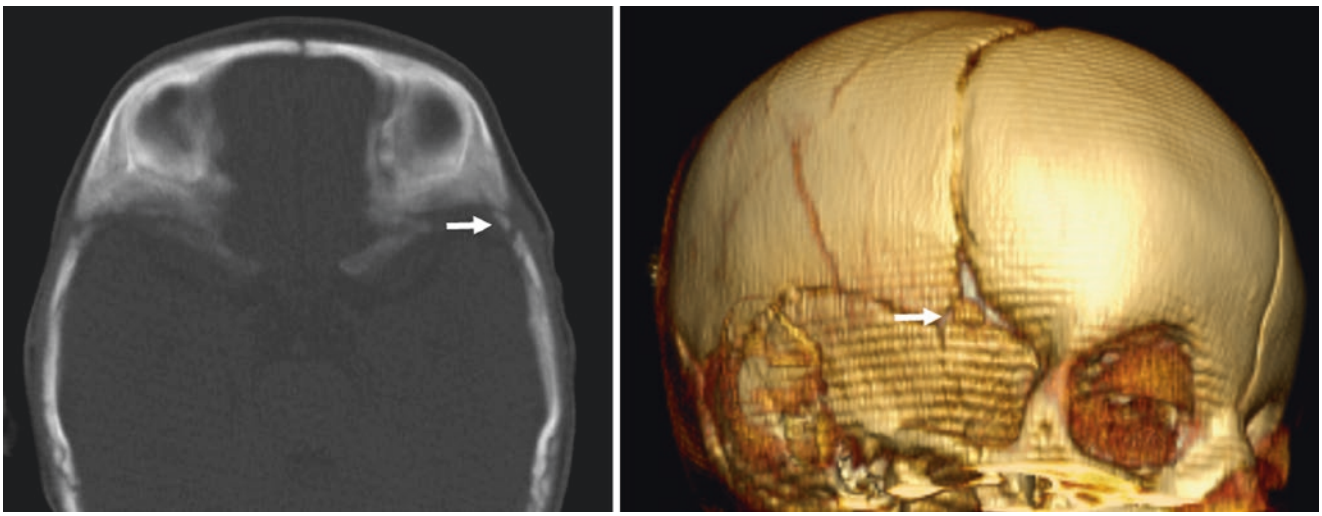

Fig. 27.54 In a 3 month old an intrafonticular sutural bone within the sphenoid fontanelle (*arrows*) is shown on axial 5-mm MPR (*left*) and on a 3D VR CT right lateral view (*right*)

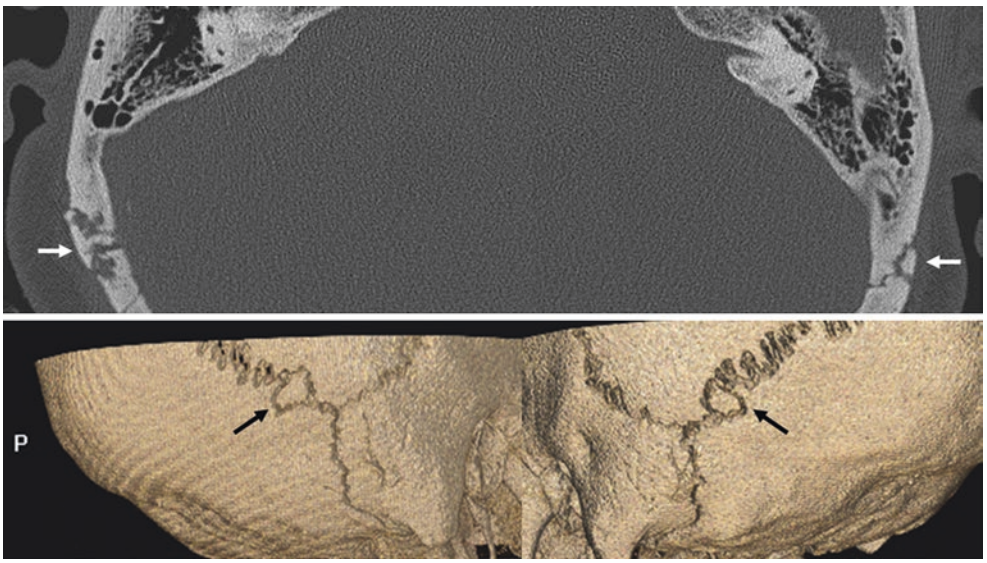

Fig. 27.55 In a 70 year old bilateral intrasutural bones are seen within the lambdoid sutures and on axial (*top row*) and right (*bottom left*) and left (*bottom right*) 3D VR lateral views, which can persist as normal variants in adults (*arrows*), since the irregularities can be bilateral. The lack of fusion may simulate fractures

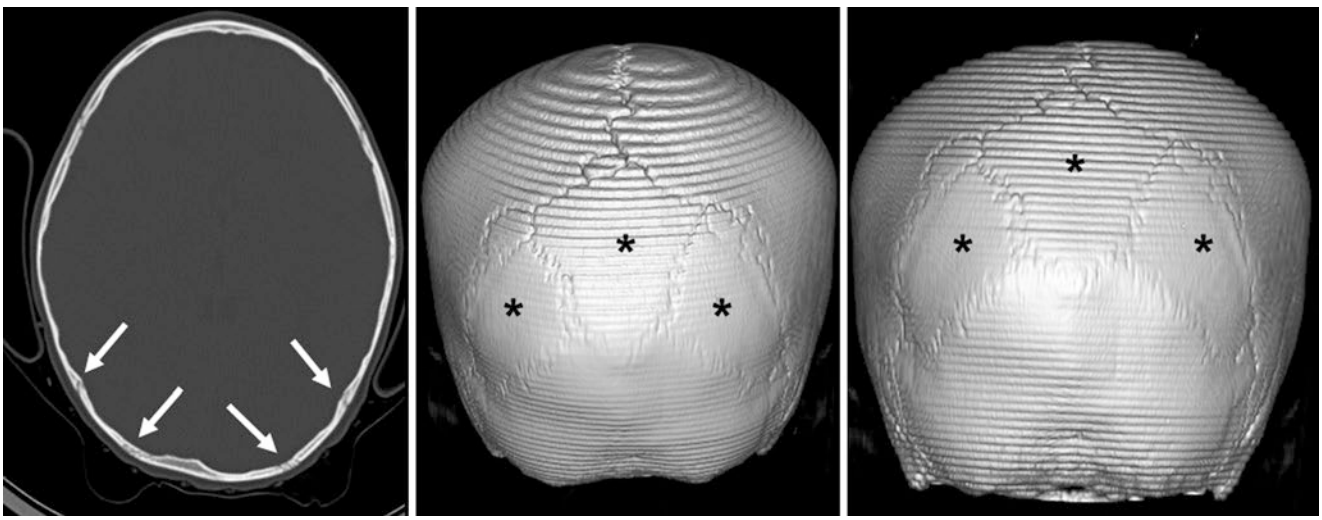

Fig. 27.56 A 3 year old with multiple wormian bones. A tripartite interparietal bone is present (*asterisks*) on axial CT (*left*) and on 3D VR posterior views (*middle and right*). This is an uncommon variant of what was classically (and perhaps incorrectly) termed the os incus. The arrows denote multiple intrasutural bones

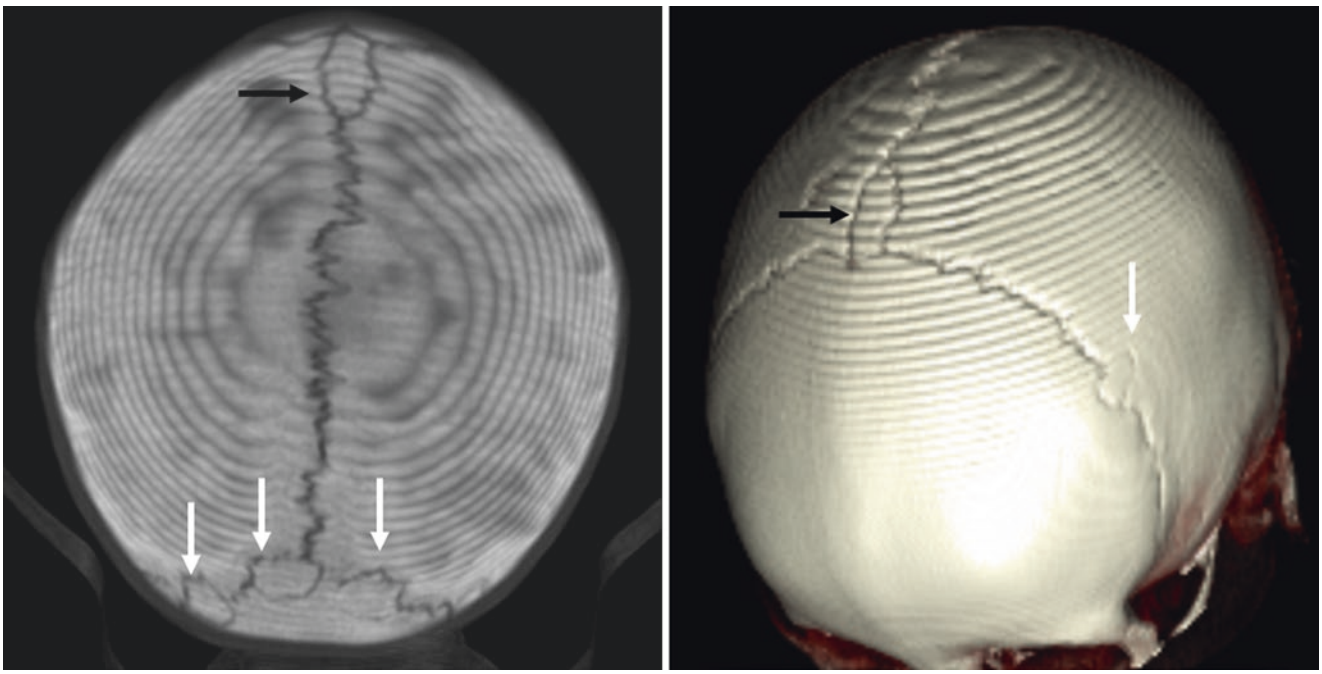

Fig. 27.57 A 7 year old with multiple intrasutural (wormian) bones (*arrows*). An intrasutural bone (also termed the os bregmaticum) lies in the sagittal suture's anterior margin (*black arrows*), as denoted on a 3D 20-mm thickness superior view (*left*) and on a left anterosuperior oblique view (*right*)

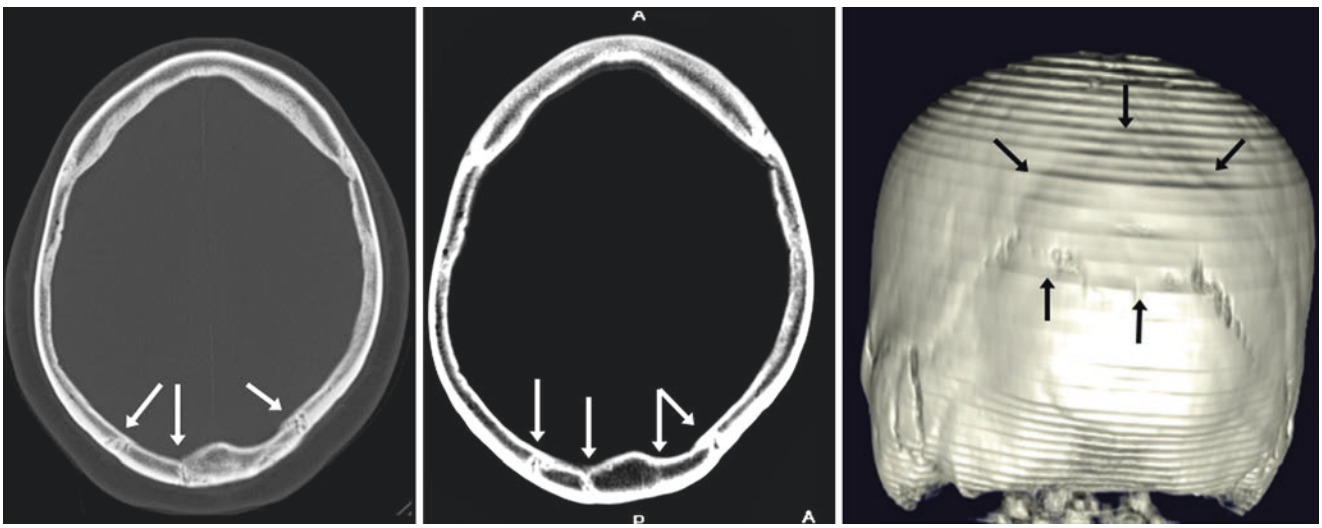

Fig. 27.58 A 57 year old with faint lines (*arrows*) noted on a 3-mm NECT (*left*) and on thicker 6-mm MPR images (*middle*); these were found to be residua of the fused interparietal bone (also termed an os incus), as outlined on a 3D reformat (*posterior view*, *right*)

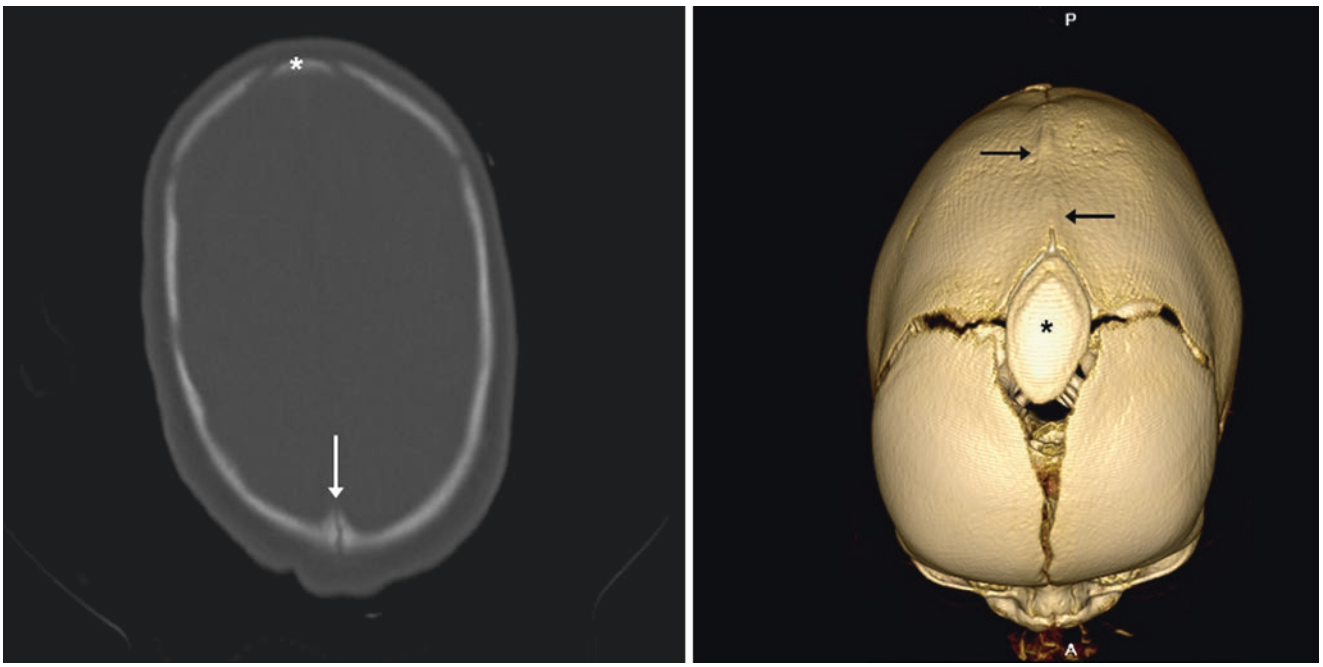

Fig. 27.59 Comparison case: a 2 month old with sagittal synostosis (*arrows*) on axial NECT (*left*) and a 3D VR superior view (*right*). There is an abnormal anterior fontanelle bone (*) extending into the sagittal suture, with scaphocephaly. Rarely, a normal anterior fontanelle may contain a wormian bone, but causes of hydrocephalus or synostosis should be excluded because these can also lead to an abnormal bone formation in this location

27.6 Overlapping Sutures and Scaphocephaly of Newborns, Children, and Adults

Overlapping sutures or ridging occurs in newborns from molding as the baby passes through the birth canal. These typically disappear within the first 2 weeks of life. However, they should be closely evaluated for the rare *fracture* that can occur (<1/10,000 births) from instrumental or even rarer from spontaneous delivery. A *temporary scaphocephalic configuration* of the skull is common with passage through the birth canal, normally resolving along with the overlap. The normal sutural overlap can be distinguished from true fractures via thin sections and by utilizing 3D reconstructions if necessary.

The lower sutures (such as the sphenosquamosal) can also exhibit normal overlap. True fractures are asymmetric, straight/linear, and usually have associated scalp swelling, while scalp swelling also commonly occurs without fracture as a cephalohematoma related to delivery.

A certain amount of scaphocephalic appearance can be constitutional, whereby the skull is somewhat elongated but without abnormally fused sutures (i.e., craniosynostosis). The included patients were otherwise asymptomatic but were found to have an incidentally scaphocephalic (oval-shaped and elongated) configuration of the skull. It is important to note the age of the patient; in early childhood the sagittal suture should not be fused, while in older patients an otherwise normally developed adult most likely does not suffer from craniosynostosis. Also, a *mosaic pattern of wormian bones* is characteristic of *craniosynostosis* (Figs.27.60, 27.61, 27.62, 27.63, 27.64, 27.65, 27.66, and 27.67).

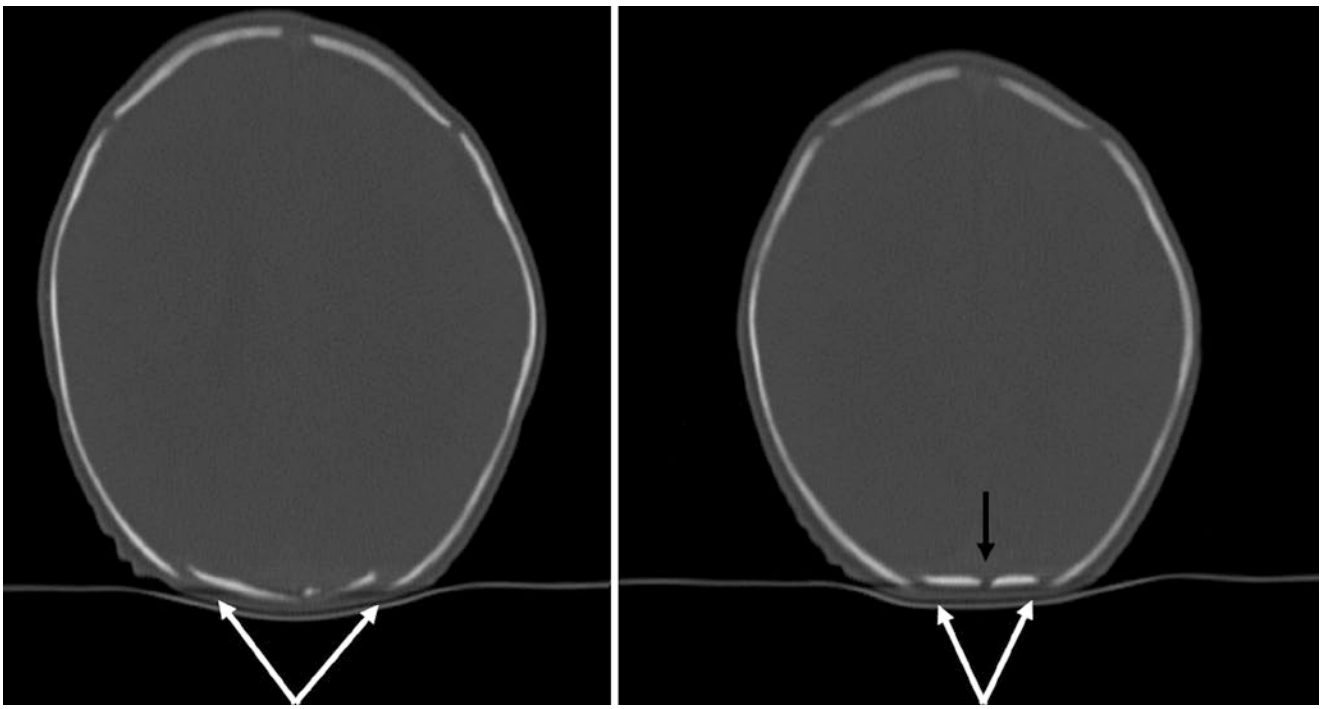

Fig. 27.60 A 4-day-old infant with overlapping lambdoid sutures without evidence of fracture or intracranial hemorrhage. Note a normal defect in a PF bone (*black arrow*)

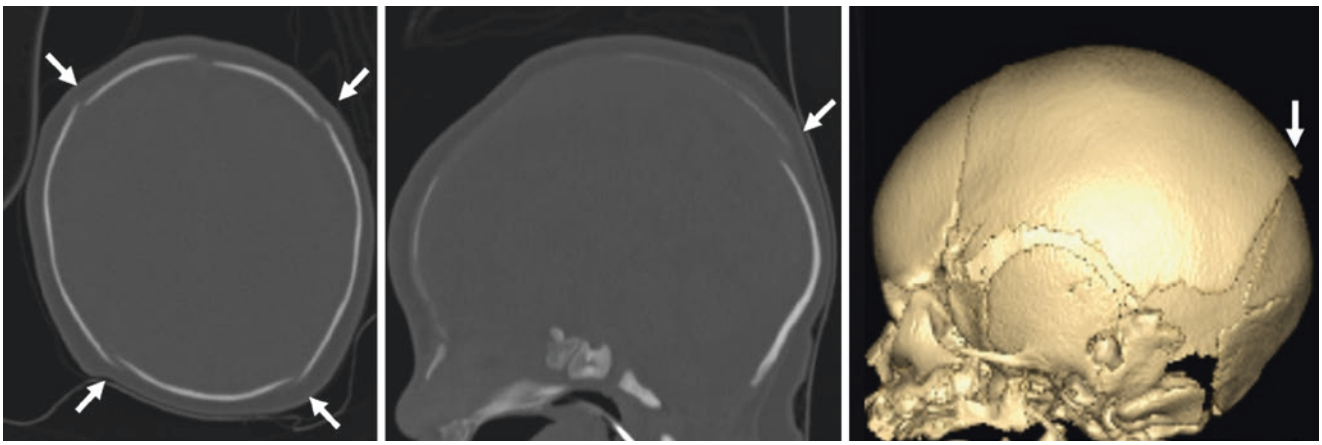

Fig. 27.61 A 3 day old with overlapping sutures on NECT without fracture or cerebral hemorrhage on axial (*left*) and sagittal (*middle*) views and on a 3D VR lateral view (*right*)

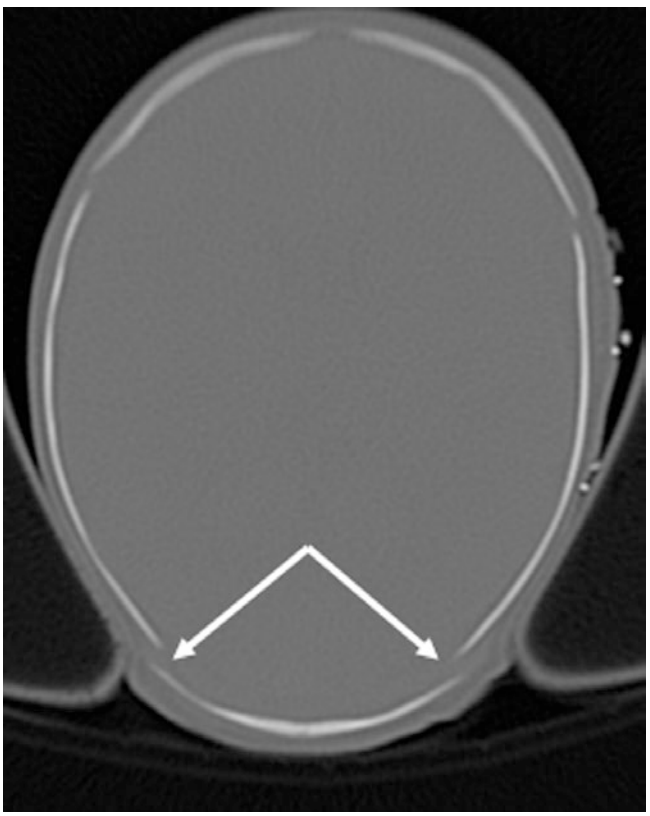

Fig. 27.62 A 6 day old with lambdoid suture overlap and a mildly scaphocephalic contour

Fig. 27.63 A 9 day old with only mild right sphenosquamosal suture overlap

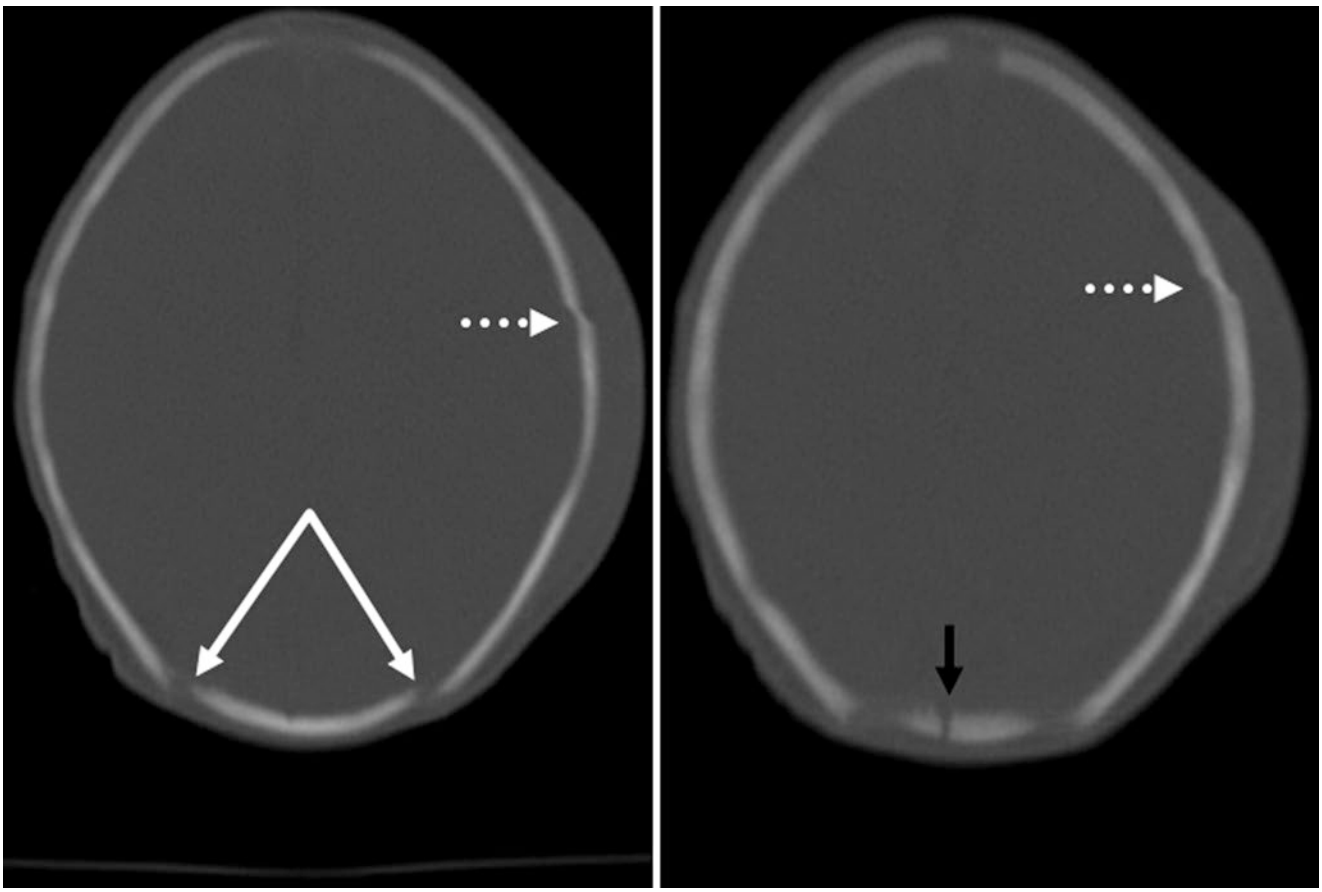

Fig. 27.64 Comparison case: An 11 day old with resolving sutural overlap (*arrows*) but also with a true fracture following delivery (*dashed arrows*). Note mild scaphocephaly and a normal defect within the PF (*black arrow*)

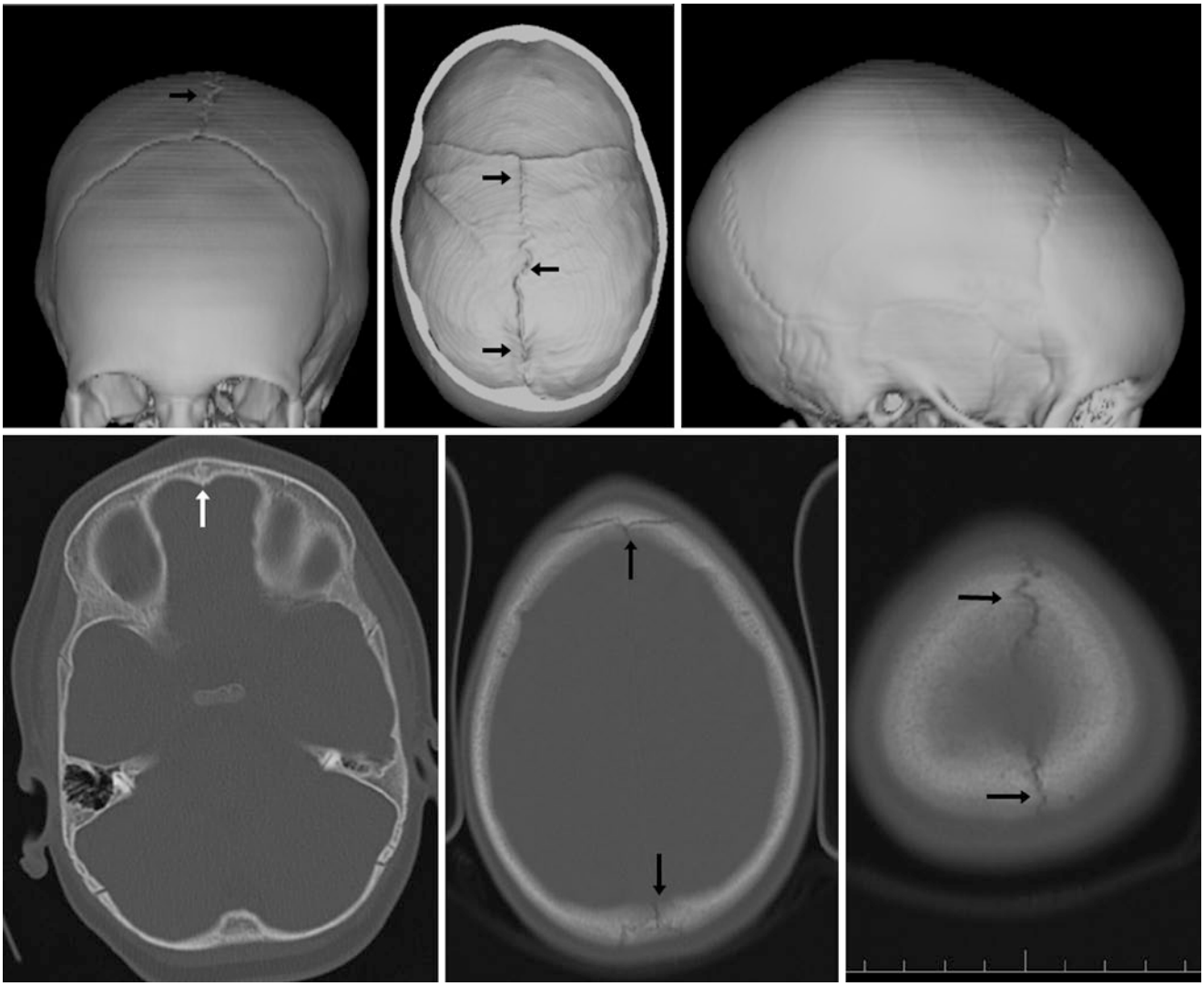

Fig. 27.65 In a 19 month old a NECT was ordered to evaluate for craniosynostosis (suspected sagittal suture fusion) due to a scaphocephalic shape. However, 3D reconstructions (*top row*) illustrated that the cranial sutures were patent as expected for age, with patent sagittal (*black arrows*), coronal, and lambdoid sutures. On axial images (*bottom row*), note normal metopic suture closure (*white arrow*), while the sagittal suture is patent (*black arrows*), as expected for age

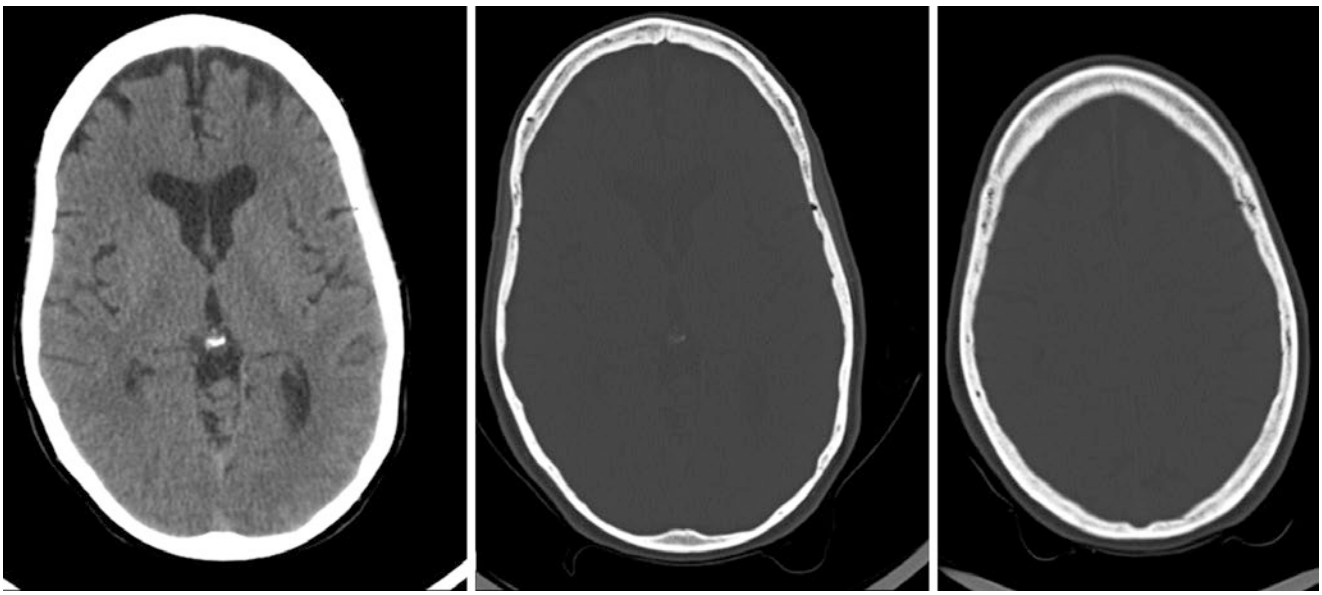

Fig. 27.66 In a 62 year old a CT scan was ordered to evaluate for hemorrhage after trauma in a previously asymptomatic patient. Note the scaphocephalic shape. There was no intracranial hemorrhage or fracture. No congenital-genetic history was present

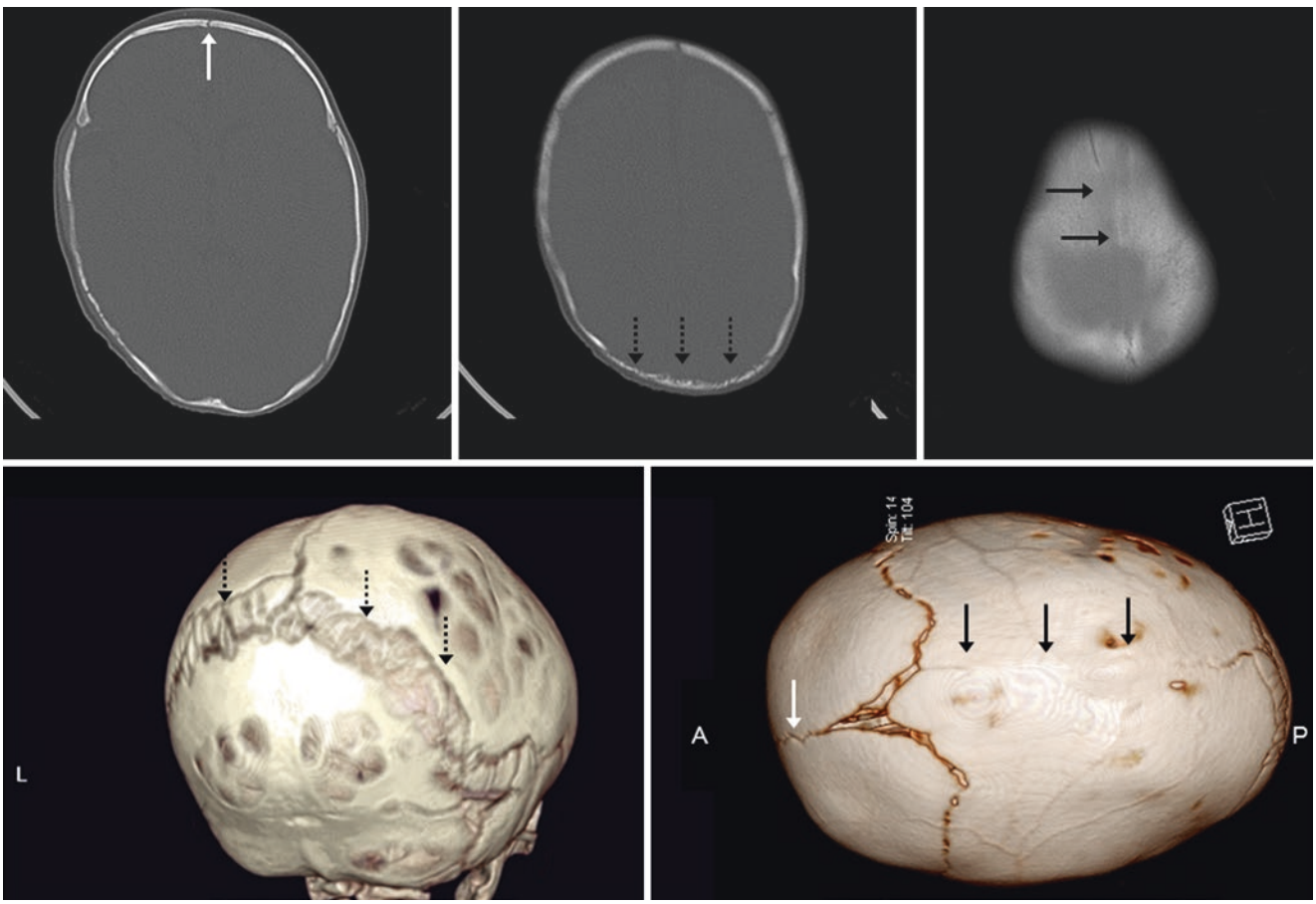

Fig. 27.67 Comparison case: A 5 month old with craniosynostosis on axial NECT (*top row*), along with 3D VR images in posterior (*bottom left*) and superior (*bottom right*) views. Note scaphocephaly, with fusion of the sagittal suture (*black arrows*), a patent MS (*white arrows*), and a diffuse mosaic pattern of intrasutural bones (*dashed arrows*); this pattern is characteristic of craniosynostosis

27.7 Positional Flattening (Plagiocephaly) of the Parieto-occipital Skull in Infants

Positional flattening can occur of the parieto-occipital skull in infants and is related to long-term oblique positioning (for days to weeks) of a supine infant. Most commonly, the infant lies in an oblique position for a prolonged period, causing a mild, posterior *positional plagiocephaly* that is only potentially problematic if chronic. This conditionally usually resolves by 1 year of age; most cases spontaneously resolve or can be treated by counter positioning, although controversy exists about the use of orthotic helmets or surgery in the most severe cases. The differential includes *lambdoid synostosis*, which is rather uncommon and accounts for a small minority (<5 %) of all cases with the clinical appearance of parieto-occipital plagiocephaly. The cases shown involve flattening in otherwise normal infants without clinical or radiographic evidence of craniosynostosis.

The parieto-occipital flattening can be bilateral or can appear somewhat unilateral. Since this flattening can appear prominent, the sutures should be carefully evaluated to exclude *craniosynostosis* if there is clinical concern. Usually these cases are not scanned by CT when the clinical history is correlated with the occipitofrontal circumference (OFC). However, if such a patient does undergo CT, one should exclude the presence of bony ridging or sutural fusion that is typically visualized with craniosynostosis. Again, 3D VR reconstructions can at times be helpful to depict the focal plagiocephaly and confirm that the overall calvarial configuration is otherwise normal elsewhere (Figs. 27.68, 27.69, 27.70, and 27.71).

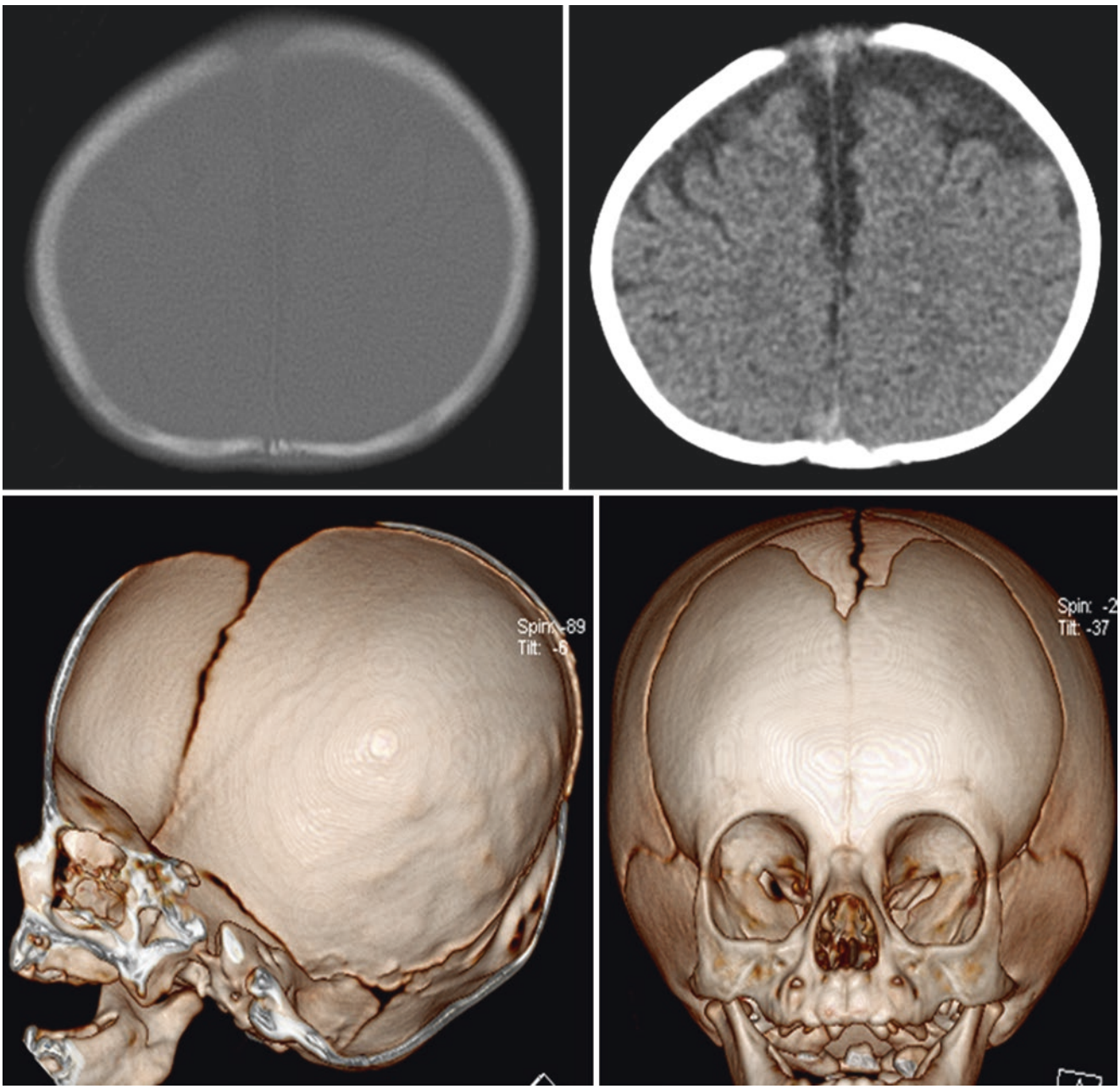

Fig. 27.68 A 5 month old with posterior flattening (positional plagiocephaly) on axial NECT (*top row*) and on 3D VR inside-out view (*bottom left*) and an anteroposterior view (*bottom right*)

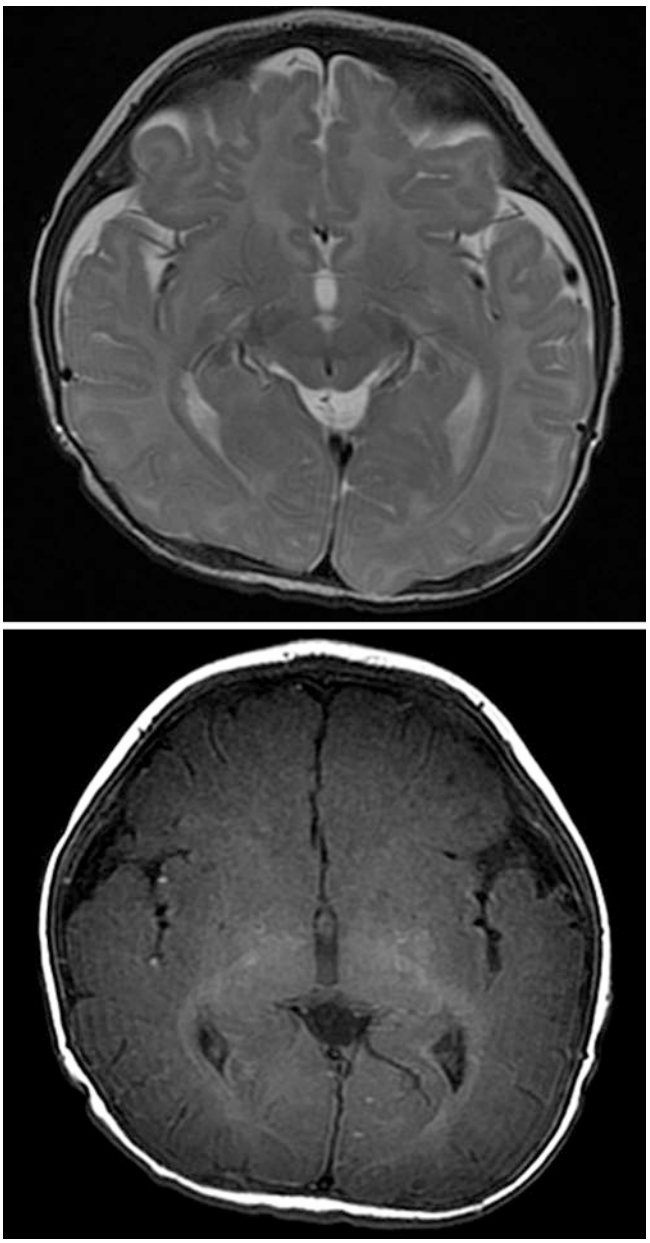

Fig. 27.69 A 2 month old showed flattening on axial T2WI (*top*) and T1WI (*bottom*) MRI

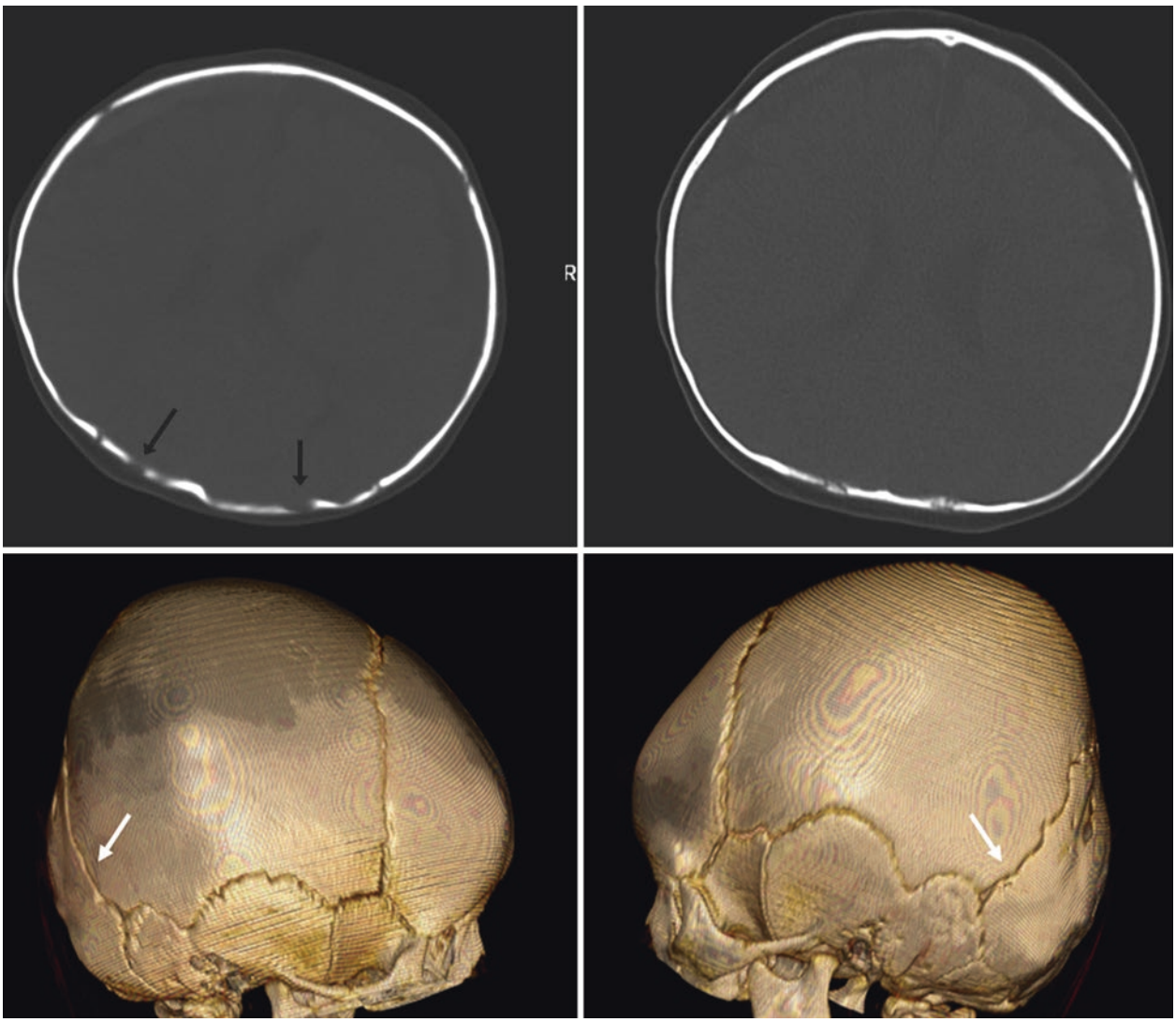

Fig. 27.70 A 6 month old: on axial NECT (*top row*) and on bilateral 3D reconstruction lateral views (*bottom row*) there is right parietal-occipital flattening but without synostosis, as lambdoid (*white arrows*), coronal, squamosal, and occipitomastoid sutures are patent. Note that normal variant occipital foramina are also present bilaterally (*black arrows*)

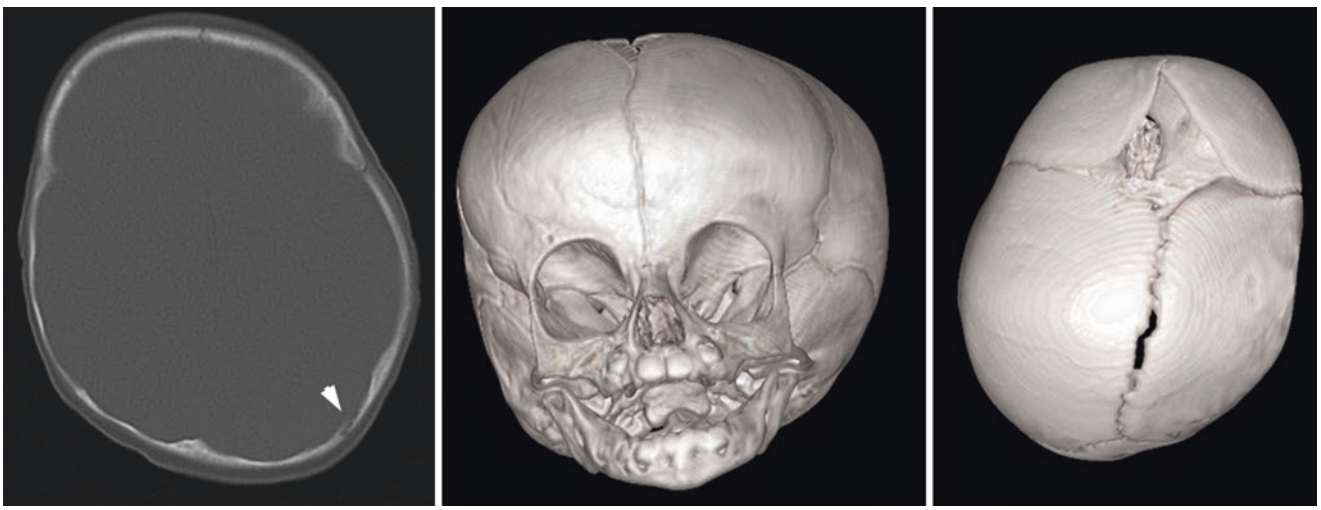

Fig. 27.71 Comparison case: a 5 month old had plagiocephaly on axial NECT (*left*) and on 3D reconstructions with anteroposterior (*middle*) and superior (*right*) views. This was related to isolated, unilateral right lambdoid suture synostosis; note a patent left lambdoid suture (*arrowheads*)

27.8 Bathrocephaly

A step-like bony protrusion of the posterior skull is termed *bathrocephaly*, which arises from the squamous portions of the occipital bone projecting past and between the two parietal bones. This may appear as an indentation of the suture and is most commonly an incidental finding in early infancy or neonates that soon resolves. While it is usually not very prominent in late infancy or early childhood, a mild degree of bathrocephaly may persist as a normal variant even into adulthood. This should be distinguished from the uncommon severe bathrocephaly, which typically occurs from early fusion of the posterior portion of the sagittal suture.

In adults, mild residual bathrocephaly may also occur as a normal variation of an outward, convex appearance of the occipital bone relative to the parietal bone. This occurs in the setting of an otherwise unremarkable skull. Examples of adults with this appearance where bathrocephaly occurs at the lambdoidal suture and the junction of the lambdoid with the sagittal suture are included. Occasionally in adults there may appear to be indentation of the lambdoidal suture (Figs. 27.72, 27.73, 27.74, and 27.75).

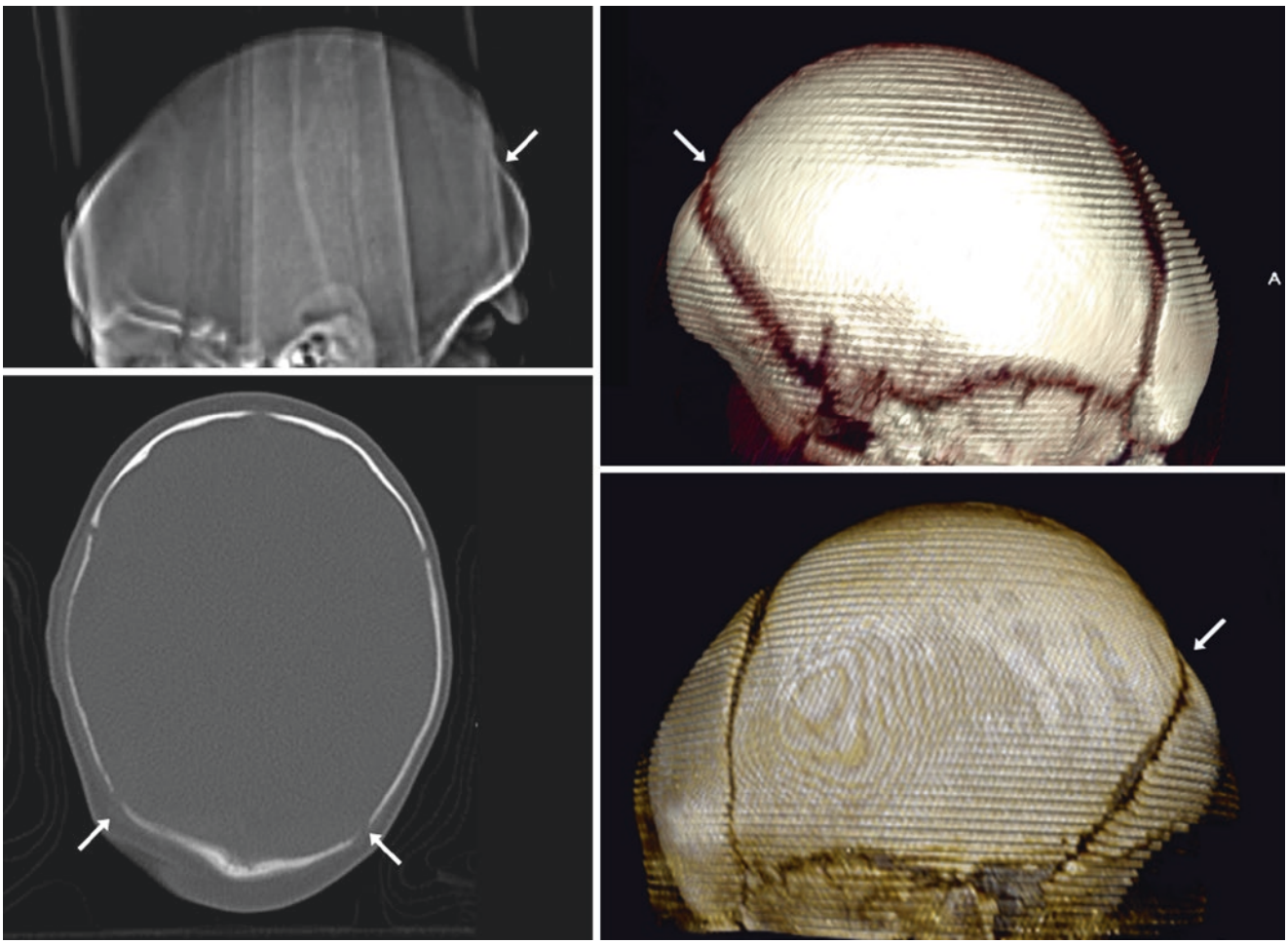

Fig. 27.72 In a 2 week old bathrocephaly was noted on scout films from the NECT (*top left*), with a step-off of the occipital bone protruding past the parietal bones, as shown on axial (*bottom left*) and on 3D VR images with right lateral (*top right*) and left lateral (*bottom right*) views

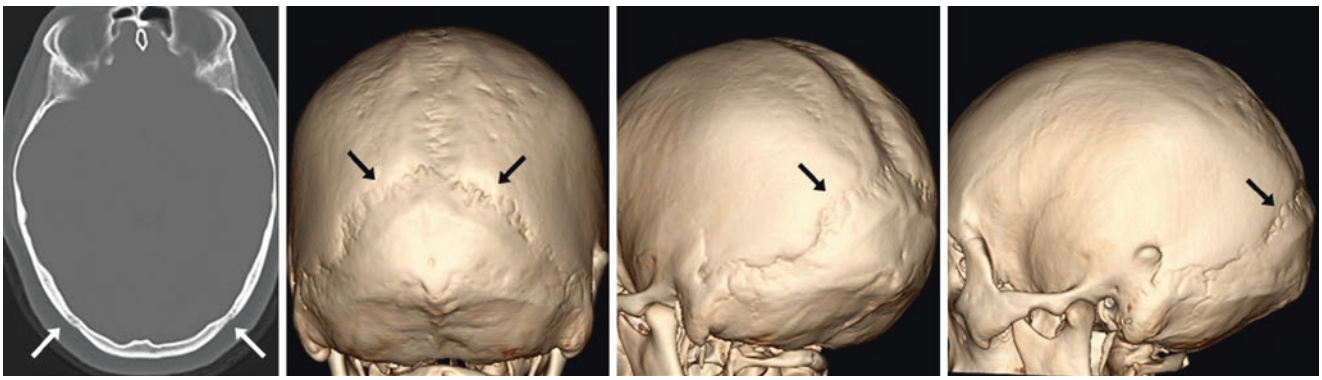

Fig. 27.73 A 16-year-old female patient was concerned about a dent she felt in her skull. While normal lambdoidal sutural fusion (*arrows*) was noted on axial CT (*left*), bathrocephaly was noted on multiple 3D reconstructions of the skull (*right three images*). Note the degree of indentation of the lambdoidal suture, which can be one feature of bathrocephaly

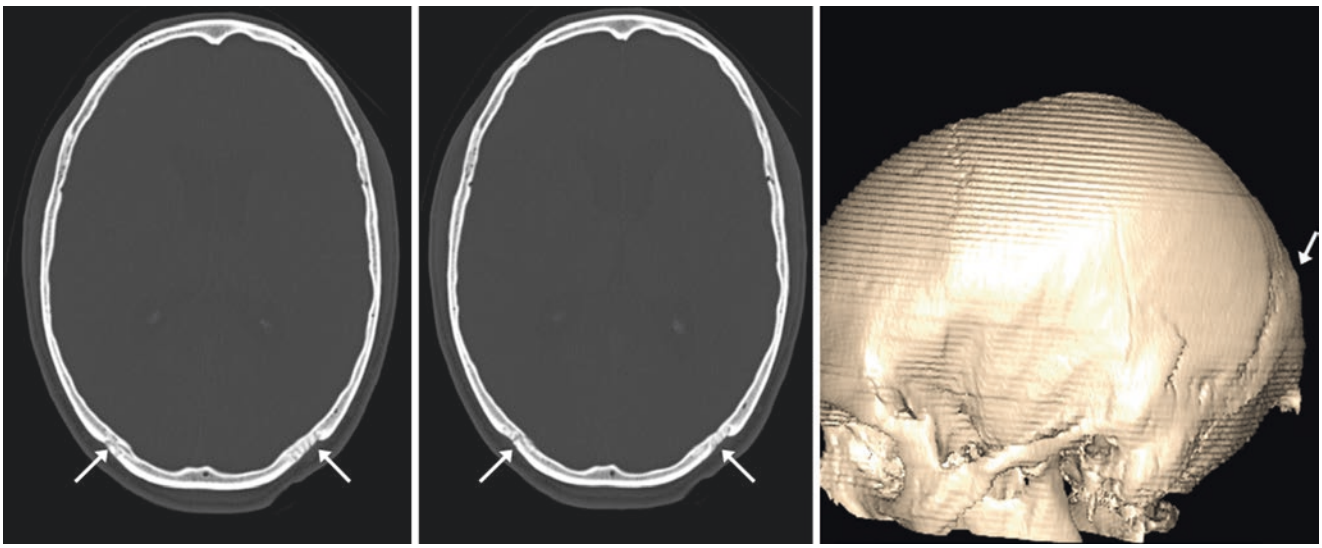

Fig. 27.74 A 29 year old with mild bathrocephaly and mild protrusion of the occipital bone past the adjacent parietal bones with step-off (*arrows*), as depicted on axial sequential NECT images (*left and middle*), and on a 3D VR lateral view (*right*). The step-like artifacts on the 3D reconstruction were obtained from reconstruction of a sequential CT acquisition

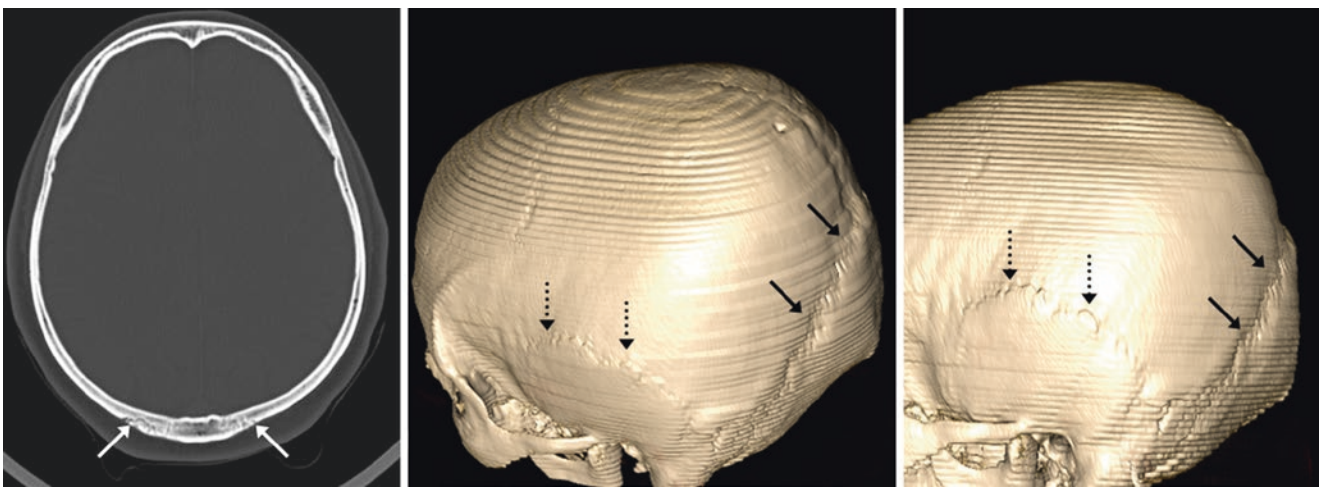

Fig. 27.75 In a 61 year old a mild, normal bathrocephaly was present with protrusion of the occipital bone between both parietal bones, resulting in a step-like appearance of the occiput (*arrows*). This is demonstrated on axial (*left*) and on 3D reconstructed (from sequential acquisition) oblique left lateral (*middle*) and direct lateral (*right*) views. Note the squamosal suture (*dotted arrows*)

References

1. Soboleski D, McCloskey D, Mussari B, Sauerbrei E, Clarke M, Fletcher A. Sonography of normal cranial sutures. Am J Roentgenol. 1997;168:819–21.
2. Furuya Y, Edwards MS, Alpers CE, Tress BM, Ousterhout DK, Norman D. Computerized tomography of cranial sutures. Part 1: comparison of suture anatomy in children and adults. J Neurosurg. 1984;61:53–8.
3. Furuya Y, Edwards MS, Alpers CE, Tress BM, Norman D, Ousterhout DK. Computerized tomography of cranial sutures. Part 2: abnormalities of sutures and skull deformity in craniosynostosis. J Neurosurg. 1984;61:59–70.
4. Kiesler J, Ricer R. The abnormal fontanel. Am Fam Physician. 2003;15:2547–52.
5. Aisenson MR. Closing of the anterior fontanelle. Pediatrics. 1950;6:223–6.
6. Pindrik J, Ye X, Ji BG, Pendleton C, Ahn ES. Anterior fontanelle closure and size in full-term children based on head computed tomography. Clin Pediatr. 2014;53:1149–57.
7. Mitchell LA, Kitley CA, Armitage TL, Krasnokutsky MV, Rooks VJ. Normal sagittal and coronal suture widths by using CT imaging. AJNR Am J Neuroradiol. 2011;32:1801–5.
8. Swischuk LE. Imaging of the newborn, infant, and young child. 5th ed. Philadelphia: Lippincott Williams & Wilkins; 2003.
9. Keats TE, Anderson MW. Atlas of normal roentgen variants that may simulate disease. 8th ed. Philadelphia: Mosby, Inc.; 2007. Chapter 1, The Skull. p. 3–117.

Suggested Reading

Berge JK, Bergman RA. Variations in size and in symmetry of foramina of the human skull. Clin Anat. 2001;14:406–13.

Dupuis O, Silveira R, Dupont C, Mottolese C, Kahn P, Dittmar A, Rudigoz RC. Comparison of "instrument-associated" and "spontaneous" obstetric depressed skull fractures in a cohort of 68 neonates. Am J Obstet Gynecol. 2005;192:165–70.

Freyschmidt J, Brossman J, Sternberg A, Wiens J. Chapter 4: Skull. In: Freyschmidt's Koehler/Zimmer's borderlands of normal and early pathological findings in skeletal radiography. 5th ed. Tubingen: Thieme; 2003. p. 357–66.

Glass RB, Fernbach SK, Norton KI, Choi PS, Naidich TP. The infant skull: a vault of information. Radiographics. 2004;24:507–22.

Gray H. Anatomy of the human body. 20th ed. Philadelphia: Lea & Febiger; 1918. Chapter 5D. The interior of the skull. Available at http://www.bartleby.com/107/47.html.

Hanihara T, Ishida H. Os incae: variation in frequency in major human population groups. J Anat. 2001;198:137–52.

Jinkins JR. Atlas of neuroradiologic embryology, anatomy, and variants. Philadelphia: Lippincott Williams & Wilkins; 2000. Chapter 2: Cranium.

Schratter M, Canigiani G, Karnel F, Imhof H, Kumpan W. Occult fractures of the skull. Radiologe. 1985;25:108–13.

Seeger JF. Normal variations of the skull and its contents. In: Zimmerman RA, editor. Neuroimaging: clinical and physical principles. New York: Springer; 1999. p. 415–53.

Sze RW, Hopper RA, Ghioni V, Gruss JS, Ellenbogen RG, King D, et al. MDCT diagnosis of the child with posterior plagiocephaly. Am J Roentgenol. 2005;185:1342–6.

Zimmerman RA. In: Zimmerman RA, Gibby W, Carmody R, editors. Neuroimaging: clinical and physical principles. New York: Springer; 1999. p. 415–65.

Emissary Veins, Vascular-Containing Foramina, and Vascular Depressions of the Skull

28

Emissary veins are channels of communication between the venous sinuses of the dura mater and the veins of the diploe and scalp. The skull base is the most common site of these veins, although they can be seen elsewhere as well. One of the more common sites is through or adjacent to the occipitomastoid suture (*mastoid emissary vein*). Other common locations include the condyle (*condylar emissary vein*), occiput (*occipital emissary vein*), foramen of Vesalius (*sphenoidal emissary vein*), and the parietal skull through the parietal foramina (*parietal emissary vein*). These can be unilateral, bilateral, or asymmetric.

Vascular-containing foramina include the relatively common *parietal foramina* and the uncommon *occipital foramina*, which may contain tiny communicating arteries or veins between the inner table of the skull or dura and the scalp. These also can be considered to transmit emissary veins, although there is debate as to whether these foramina always contain venous structures versus less commonly transmitting arteries. Parietal and occipital foramina have been described as containing emissary veins or occasionally arterial structures on histopathologic dissections, but these are not necessarily visualized on radiologic examinations. Therefore there is essentially probably no great difference between emissary venous foramina and various unnamed vascular-containing foramina, since both may be tiny and the vascular structure contained within may be too small to demonstrate radiologically.

Calvarial depressions (containing vasculature), *intradiploic venous plexi* (i.e., *venous lakes*), and *pacchionian (arachnoid) granulations* have similar appearances and may be interrelated but can be differentiated. Vascular calvarial depressions are related to cortical veins within the subarachnoid spaces or less commonly to arterial grooves on the inner surface of the skull. These may appear similar to pacchionian/arachnoid granulations (CSF-filled ingrowths of the arachnoid membranes into the dural venous sinuses or calvarium) on noncontrast CT, although on postcontrast CT these vascular depressions enhance with contrast media. MRI demonstrates CSF signal intensity within arachnoid granulations on T2WI. Intradiploic veins or venous lakes are prominent venous channels within the calvarium that may simulate a lytic lesion on CT, have a variable appearance on noncontrast MRI, and enhance with contrast. However, there may be some confusion among these entities because some texts have grouped venous lakes, pacchionian granulations, and calvarial depressions together; this grouping is not necessarily incorrect but it does not account for the slightly different imaging appearances among them as we have attempted to do here. Intradiploic veins are discussed in this section, while both vascular depressions and pacchionan granulations are not discussed at length; they are focused on in a later section titled "Don't Touch Lesions of the Skull (*Chapter 30*)."

Unless otherwise stated, the following images are axial nonenhanced CT (NECT). Notably, three-dimensional (3D) volume-rendered (VR) reconstructions can help discern many of these variants by depicting their relationship to the skull and skull base. Occasionally, CT angiography (CTA) or CT venography (CTV) may be necessary to confirm the presence of traversing vasculature.

28.1 Vascular Channels Through the Orbital Roof Simulating Fracture

Linear or curvilinear *vascular channels* are commonly present through the orbital roof. They are only of significance when they imitate *fractures*. The majority of cases can be discerned by evaluating for a sclerotic margin (vascular channel), connecting these with other vascular channels and evaluating for associated findings of true fractures such as soft-tissue swelling, other fractures, or orbital emphysema. These can be particularly problematic in pediatric patients under 7–10 years of age in whom the prominence of the forehead overhanging the face and the lack of pneumatization of the frontal sinus predispose to orbital roof fractures (considered skull fractures) as well as to intracranial injury.

A.M. McKinney, *Atlas of Normal Imaging Variations of the Brain, Skull, and Craniocervical Vasculature*,
DOI 10.1007/978-3-319-39790-0_28

By scrolling through axial images, one can usually discern vascular channels from true fractures. However, in the pediatric patient there can be significant difficulty in this delineation, since "ping-pong" fractures (akin to greenstick fractures of extremities) can occasionally occur that only partially travel through one table (either inner or outer) of the calvarium and are not through-and-through, as is typical of skull fractures in adults. Thin hairline fractures can also occur in children that may eventually travel across and only slightly widen cranial sutures. Usually there is associated soft-tissue swelling in such cases (Figs. 28.1, 28.2, 28.3, 28.4, 28.5, and 28.6).

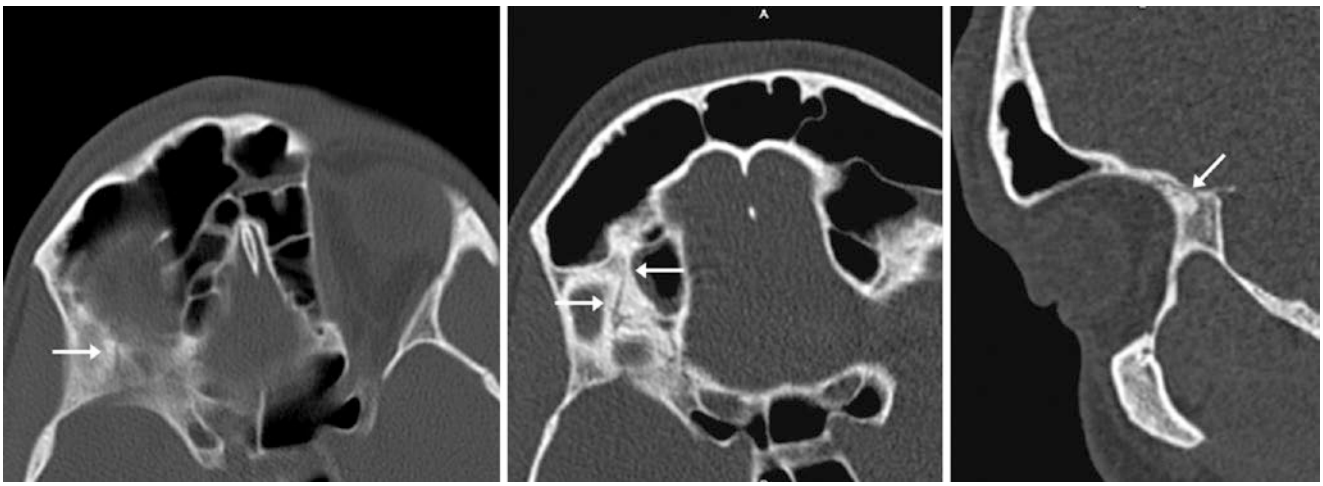

Fig. 28.1 A 20 year old with a vascular channel (*arrows*) through the right orbital roof as seen on routine axial NECT images. This was later confirmed as a vascular channel on multiplanar axial (*left*), oblique axial (*middle*), and sagittal (*right*) MPR images

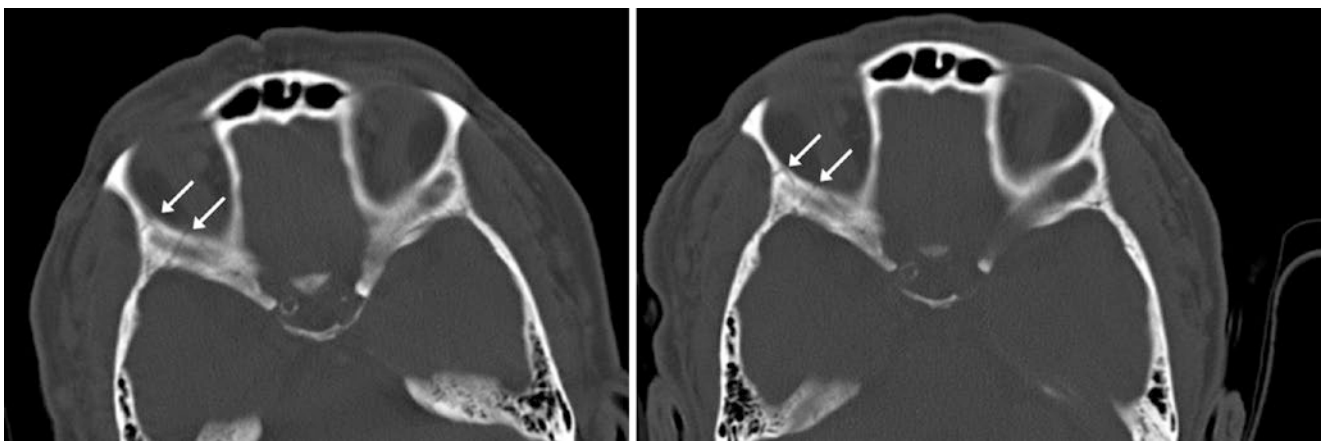

Fig. 28.2 A 74 year old who had vascular channels through the right orbital roof (*arrows, left*). These were unchanged from 2 years earlier (*arrows, right*) in a patient who had suffered only minimal trauma

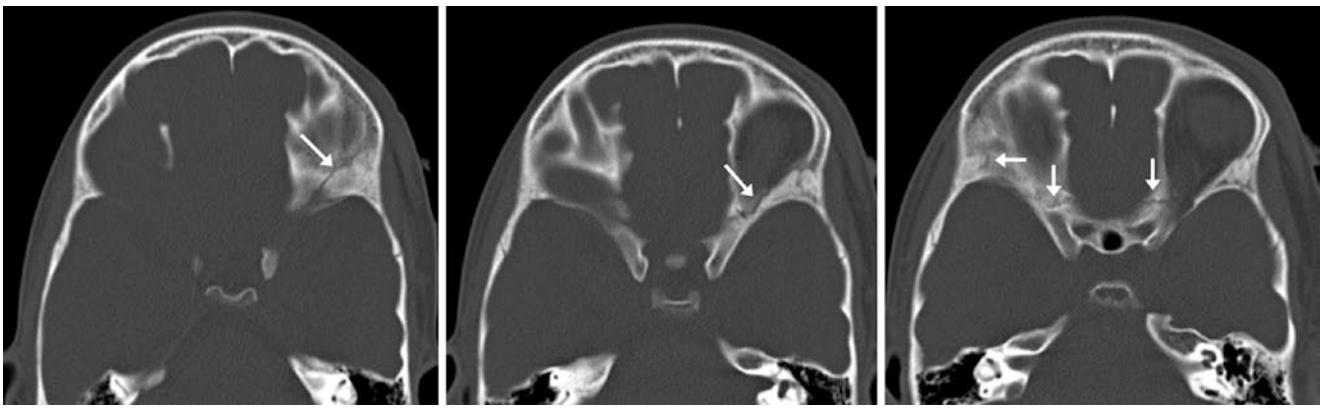

Fig. 28.3 A 12 year old in whom a vascular channel through the left orbital roof (*arrows*) was initially called a fracture, but it crossed midline (via the sphenoethmoidal suture) into the right orbital roof

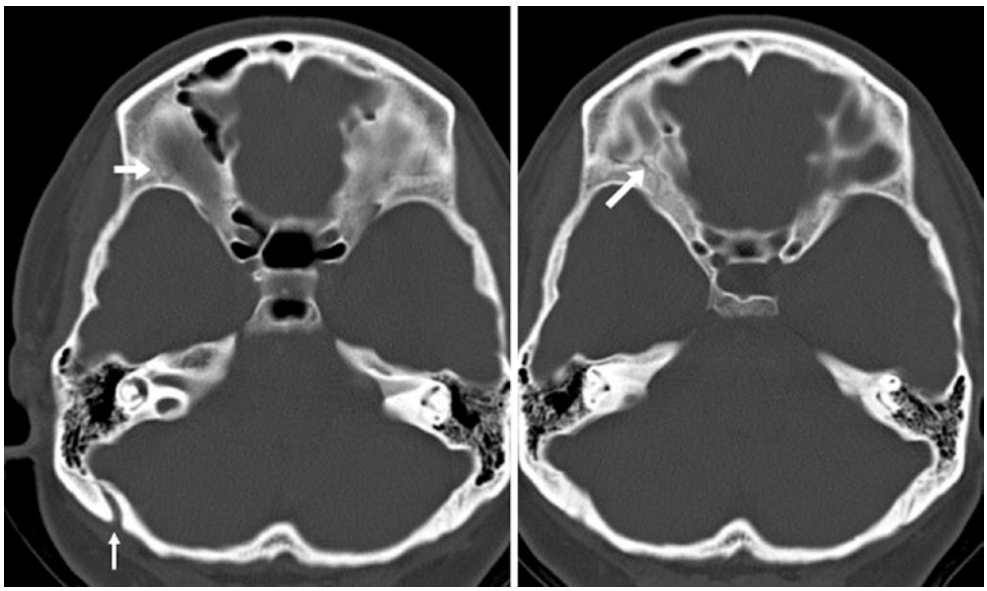

Fig. 28.4 A 43 year old with right orbital asymmetric connected channels (*arrows*) that do not continue through the cortex or superiorly. Note a mastoid emissary foramen (*thin arrow*)

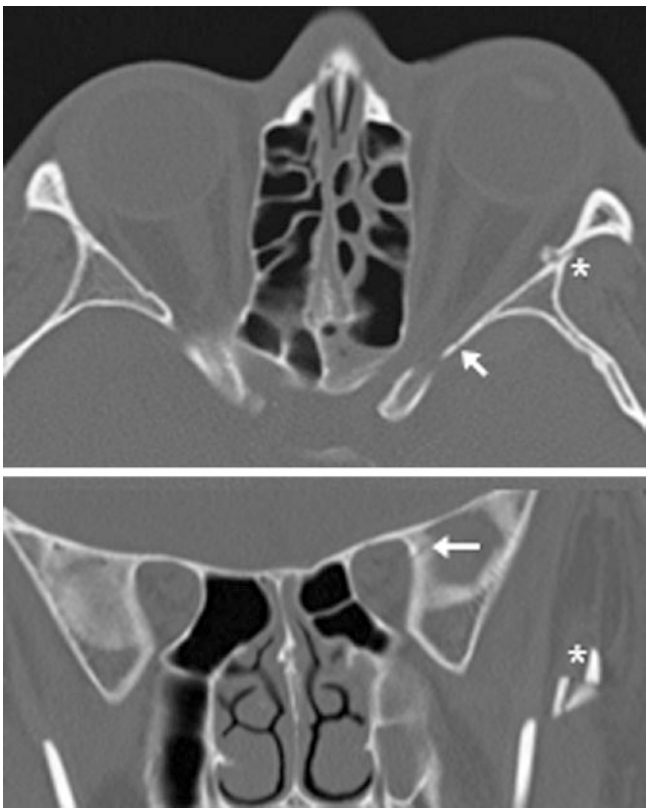

Fig. 28.5 Comparison case: A 24 year old with a fracture of the orbital roof (*arrows*). Also note lateral orbital and zygomatic fractures (*)

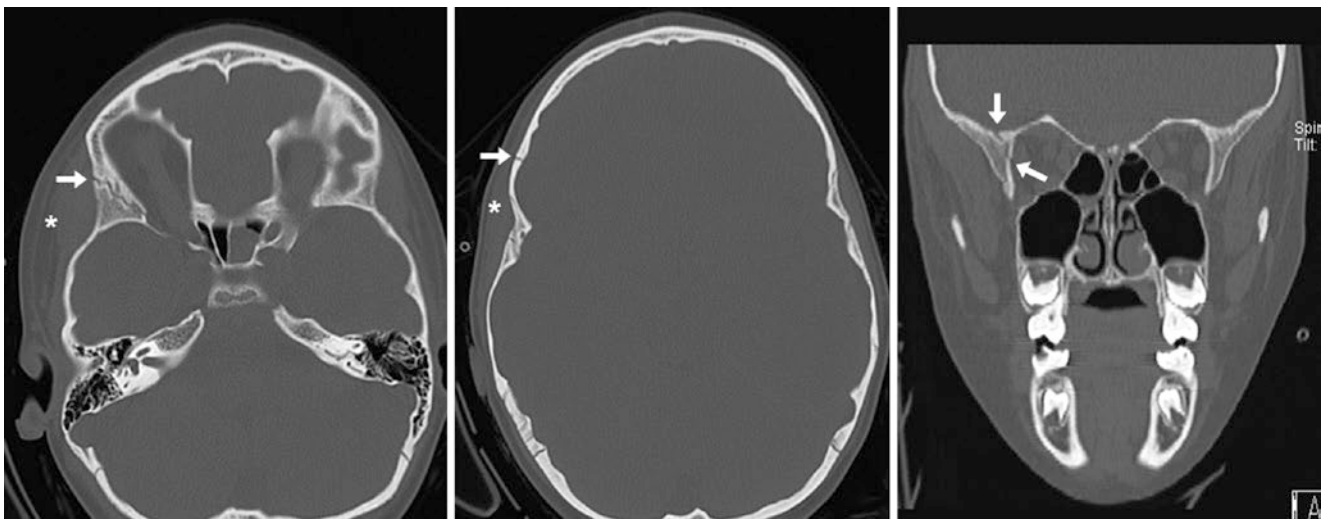

Fig. 28.6 Comparison case: A 9 year old with a fracture (*arrows*) of the orbital roof (involving the frontal bone and sphenoid greater wing) with moderate scalp swelling (*asterisks*). This was confirmed to be a fracture by scrolling through axial images and noting that the orbital roof defect continued superiorly as a right frontal bone fracture

28.2 Foramen of Vesalius and the Sphenoidal Emissary Vein

The *foramen of Vesalius* is located in the greater wing of the sphenoid bone, situated anteromedial to the *foramen ovale*. It varies in size but is usually tiny. The foramen (which transmits the sphenoidal emissary vein) is present in 30–50 % of people and is unilateral in 20–25 % of all skulls. It can simulate a *fracture* when viewed in the nonaxial plane on NECT, particularly in the reformatted coronal or sagittal planes.

In the following examples, note the thin sclerosis surrounding the foramen of Vesalius as well as the characteristic location anteromedial to the larger foramen ovale and *foramen spinosum*. This sclerotic rim is absent in fractures. Also, note the normal sutural articulation of the greater wing of the sphenoid with the bottom of the temporal bone at the level of the mandibular fossa (Figs. 28.7, 28.8, and 28.9).

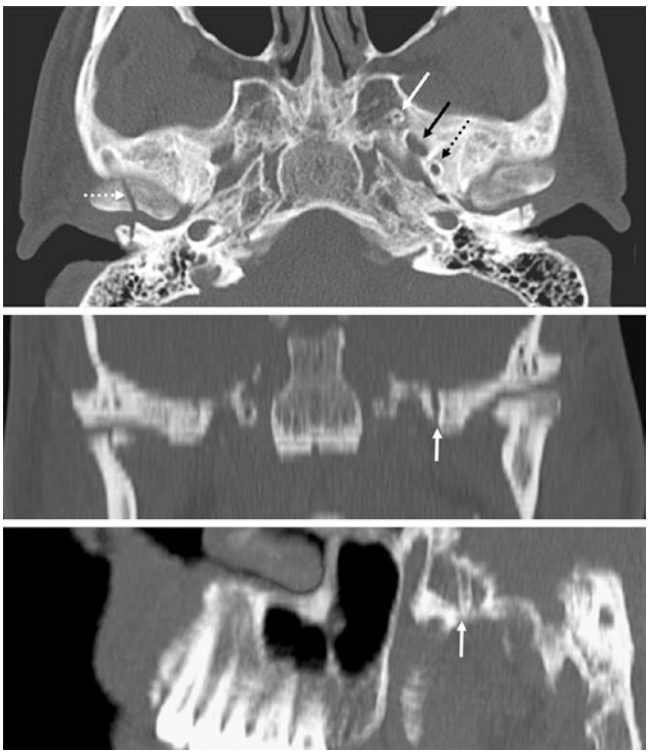

Fig. 28.7 A 34 year old with a tiny foramen of Vesalius (*white arrows*) on axial (*top*), coronal (*middle*), and sagittal (*bottom*) CT reformats. The foramen ovale (*black arrow*) and spinosum (*black dashed arrow*) are also shown, with a true fracture through the right temporomandibular joint/mandible (*dashed white arrow*). The foramen of Vesalius may simulate a fracture (*middle*), but note the subtle sclerosis around the foramen, which true fractures lack

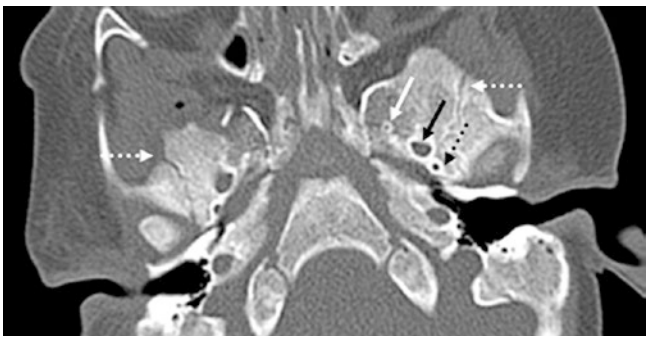

Fig. 28.8 A 3 month old with a unilateral left foramen of Vesalius (*arrows*). Note the foramen ovale (*black arrows*), foramen spinosum (*dashed black arrows*), and normal sutural articulation of the greater wing of the sphenoid with the temporal bone (*dashed white arrows*)

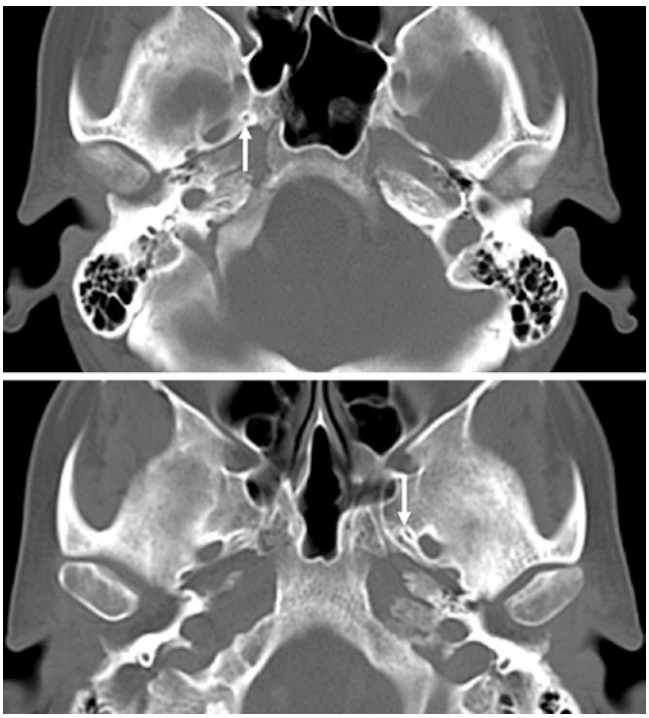

Fig. 28.9 *Above/below*: A 53 year old with bilateral foramina of Vesalius (*arrows*). Note the surrounding thin rim of sclerosis

28.3 Hypoglossal Canal Asymmetry and Emissary Veins

The *hypoglossal canal* transmits cranial nerve XII through the skull base. This canal may have significant asymmetry and may transmit *emissary veins* or *vascular channels* between the dural sinuses and the internal jugular veins. Also, there may be asymmetry in size as well as internal CSF intensity within these canals on MRI. Care must be taken to evaluate for soft-tissue signal prior to contrast, followed by enhancement; occasionally, a condylar *schwannoma* or *metastases* may present as a T2-hyperintense mass followed by enhancement. This may be problematic if either CT or MRI is the only study performed. Hence, correlation of these two modalities may be helpful in this scenario. While the hypoglossal canal can enhance within owing to the presence of an emissary vein, other variations include several linear, interconnected veins or a network of veins. The canal may also appear filled with CSF (Figs. 28.10, 28.11, 28.12, and 28.13).

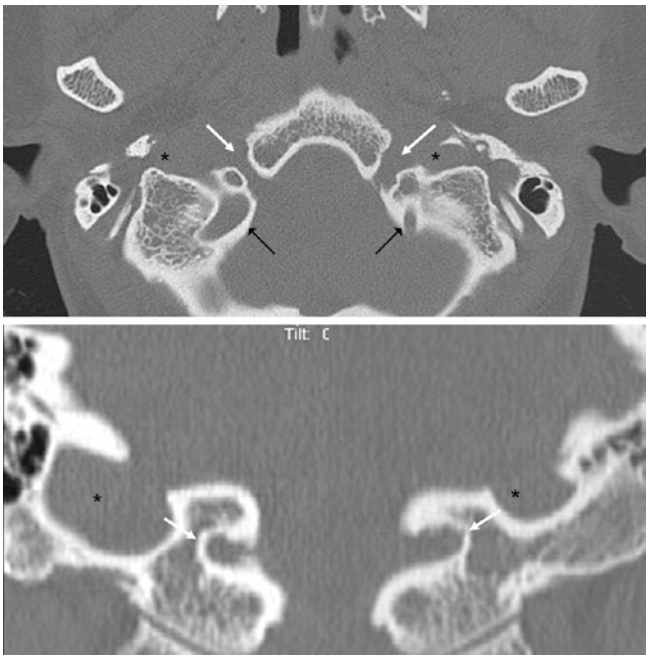

Fig. 28.10 A 47 year old with asymmetric hypoglossal canals (*arrows*) on axial (*top*) and coronal (*bottom*) reconstructions. Note normal adjacent condylar canals posteriorly (*black arrows*) as well as an asymmetric right, greater than left, caliber of the jugular foramina (*)

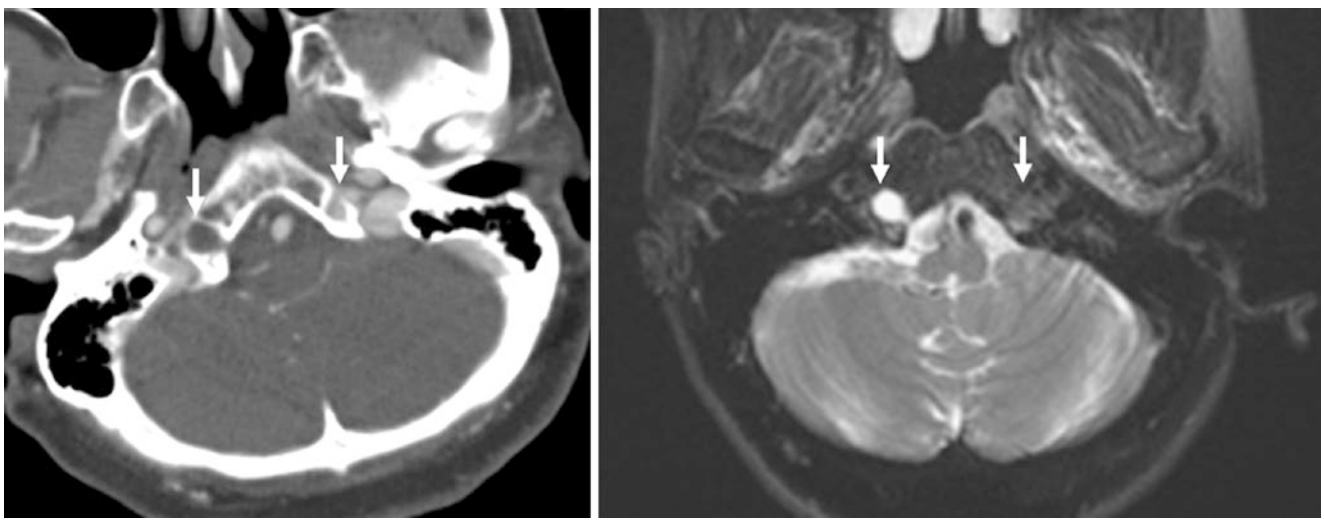

Fig. 28.11 A 71 year old: regarding the hypoglossal canals (*arrows*), a CSF-filled right canal is noted on postcontrast CT (*left*) with bright signal within from the CSF on axial T2WI MRI (*right*). Note an enhancing venous plexus within the left hypoglossal canal and jugular foramen (*)

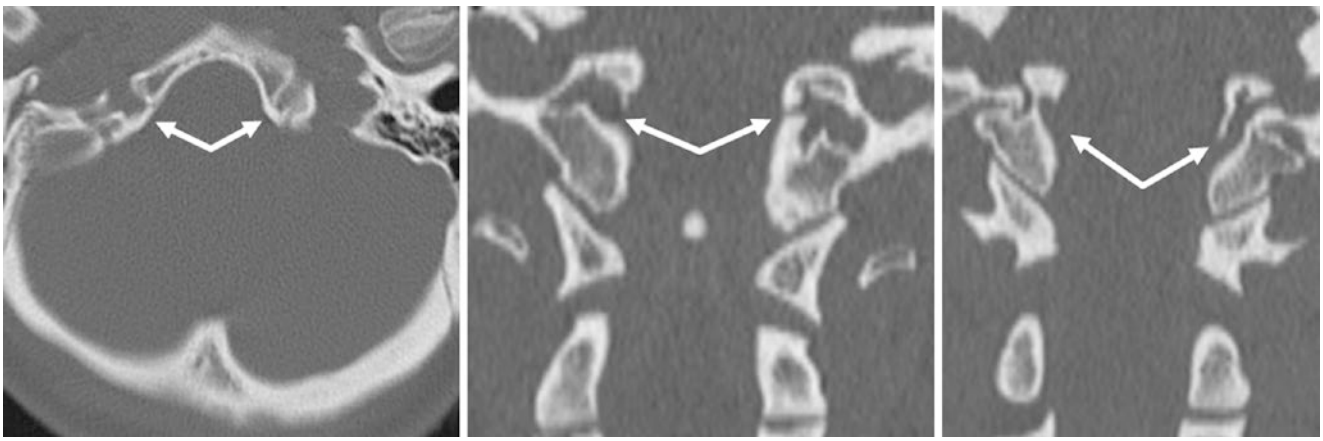

Fig. 28.12 A 24 year old with a venous plexus network extending throughout the hypoglossal canals bilaterally (*arrows*) seen on axial (*left*) and coronal (*middle and right*) NECT reconstructions

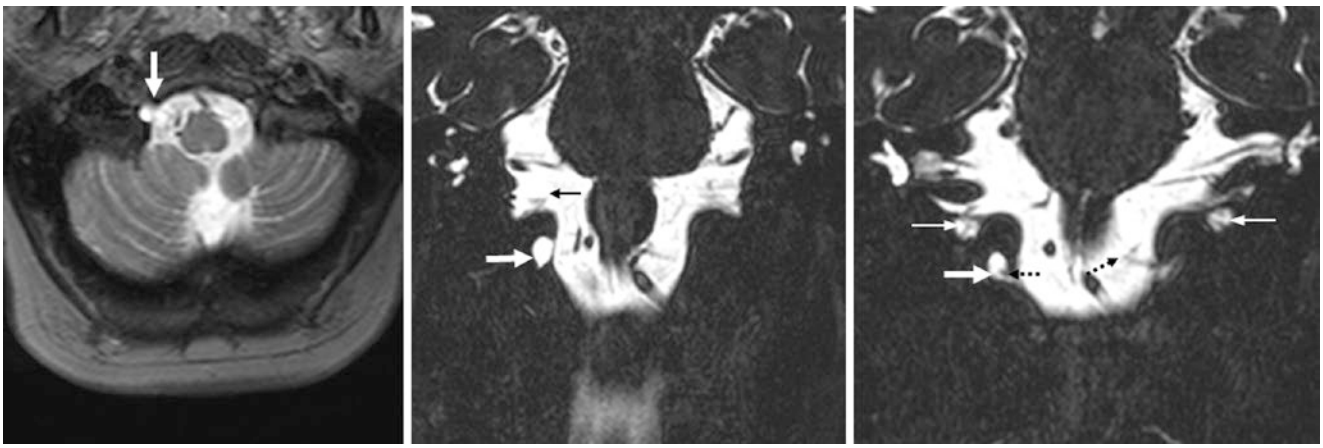

Fig. 28.13 A 45 year old with an asymmetric, CSF-filled right hypoglossal canal (*arrows*) on axial T2WI MRI (*left*) with coronal reformats from a 3D T2WI acquisition (*right two images*). Note cranial nerves X (*thin arrows*) and XII (*dotted arrows*)

28.4 Condylar Canal (Posterior) Emissary Veins

The *condylar emissary veins* pass through the *condylar canal* (also called the posterior condylar canal) usually just posterior to the occipital condyles. This vein can be unilateral or bilateral and variably travels between the transverse or sigmoid sinuses downward into the upper cervical region, usually toward the deep veins of the upper neck (often the suboccipital venous plexus). When it occurs, this vein is bilateral in about 50 % of the population, unilateral in about 33 %, and absent bilaterally in about 25 %. Note that many of the condylar canals presented here have a tubular appearance with sclerotic margins that is typical of larger emissary foramina (Figs. 28.14, 28.15, 28.16, and 28.17).

Fig. 28.14 A 3 month old in whom both condylar canals (*arrows*) appear tubular

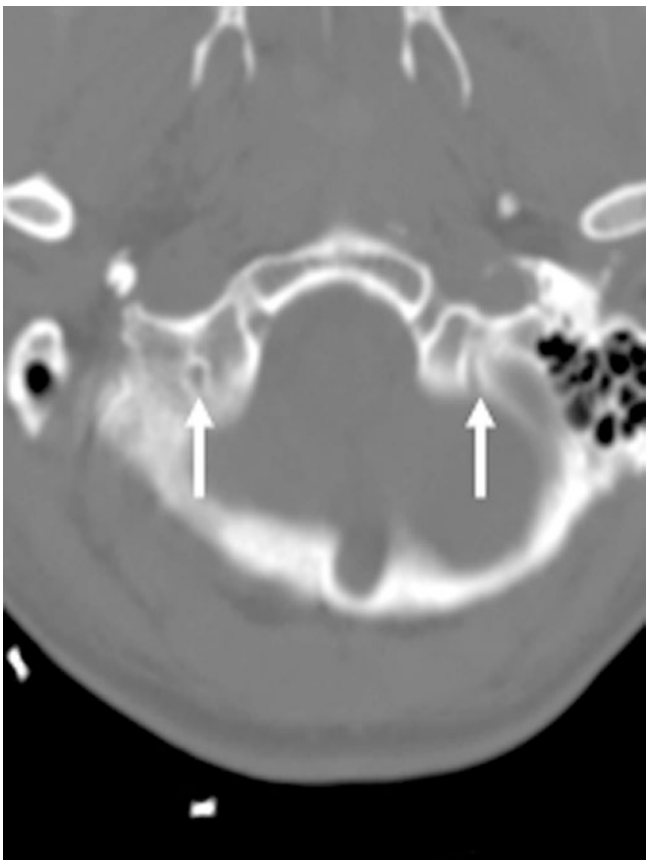

Fig. 28.15 A 26 year old with asymmetry of the condylar canals (*arrows*)

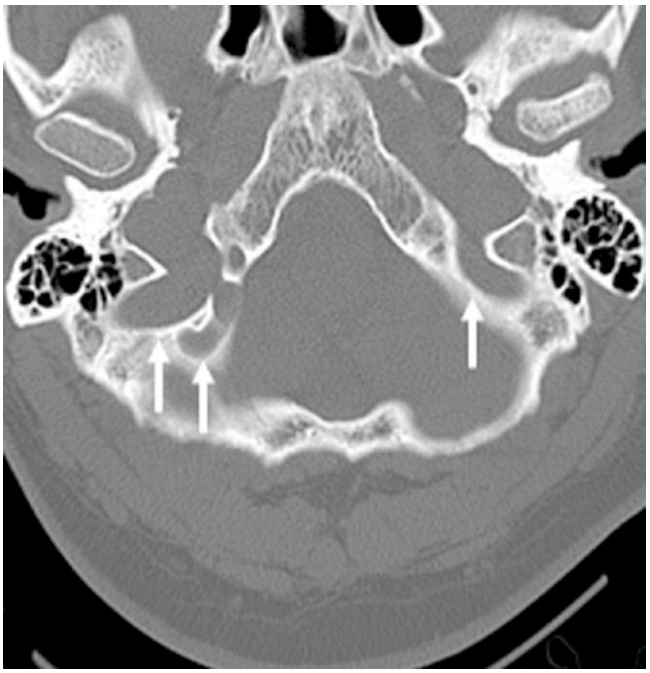

Fig. 28.16 A 36 year old with multiple large condylar canals (*arrows*) that appear tubular

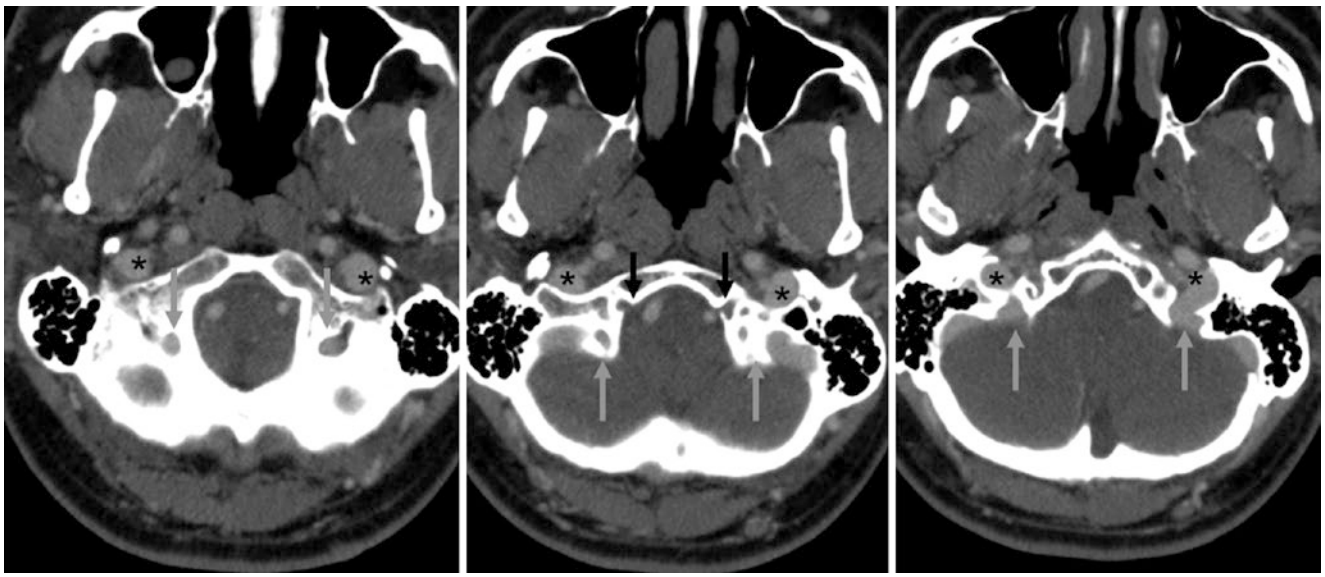

Fig. 28.17 A 45 year old: on postcontrast CT, the bilateral condylar veins (*grey arrows*) drain into the jugular foramina/veins (*asterisks*), which faintly opacify with contrast. Note the hypoglossal canals *(black arrows*)

28.5 Mastoid Emissary Veins Adjacent to or Through the Occipitomastoid Suture

The *mastoid emissary vein* is common and is usually visible in most adults. This vein runs through the *mastoid foramen*, connecting the transverse/sigmoid sinuses with the scalp's posterior auricular vein or occipital veins and ultimately with the vertebral venous plexus. Note that the mastoid canal/foramen is typically just lateral to the *occipitomastoid (OM) suture* or may appear to be partially situated within the suture. When present, this vein is bilateral in 50–90 % of the population (controversial), unilateral in 10–33 %, and is only occasionally bilaterally absent in 1–25 % (Figs. 28.18, 28.19, 28.20, and 28.21).

Fig. 28.18 A 36 year old with a unilateral right emissary vein (*arrow*) that passes through the right OM suture

Fig. 28.20 A 53 year old: bilateral emissary veins (*white arrows*) pass next to but not through the OM sutures (*black arrows*)

Fig. 28.19 A 30 year old with a unilateral left emissary vein (*arrow*) that travels through the OM suture

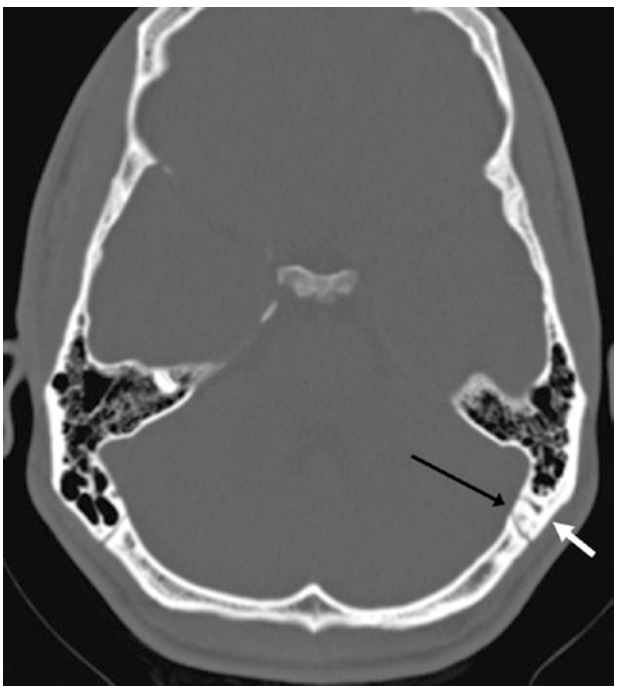

Fig. 28.21 A 20 year old: a unilateral left emissary vein (*white arrow*) passes lateral to the left OM suture (*black arrow*)

28.6 Occipital Foramina

Much less common than the parietal foramina, visible (on CT or cadavers) *occipital foramina* are normal variants that are present in less than 1 % of the population. These may variably connect the transverse sinus, torcular, or occipital sinus (if present) with venous plexi that travel within the occipital scalp. However, it is unclear how often these foramina transmit vessels, and in young children the surrounding occipital bone may be very thin and simulate vascular foramina. These may be unilateral or bilateral or can occasionally have the appearance of multiple foramina, which often regress or fuse closed with increasing age. As with many other normal variants, these can be troublesome in pediatric patients being evaluated by CT for trauma (Figs. 28.22 and 28.23).

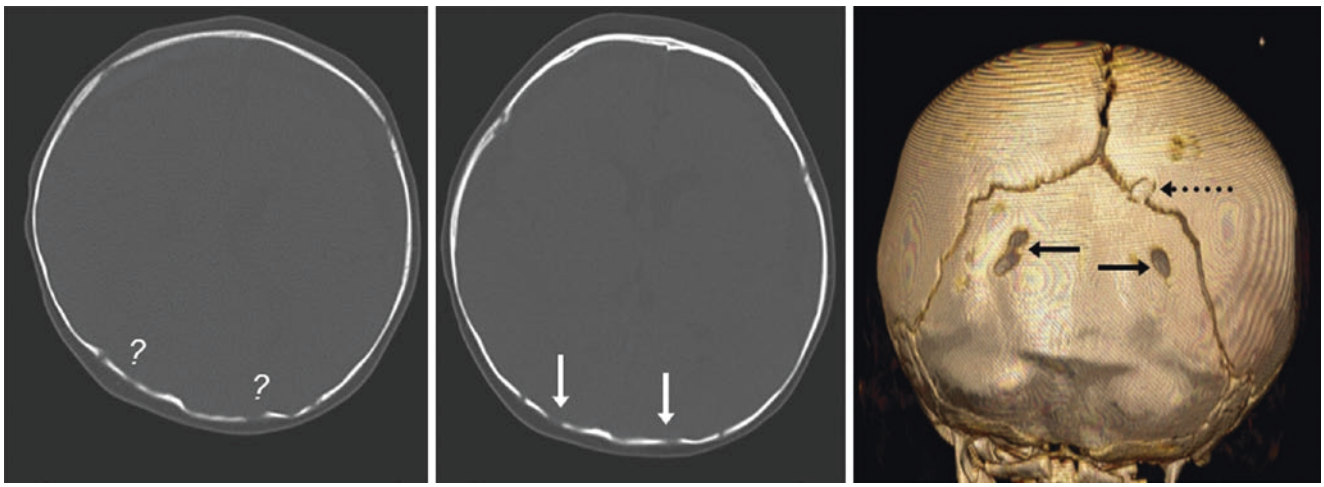

Fig. 28.22 A 6 month old lying obliquely in the CT scanner with curious occipital defects identified after head trauma (*?*). Axial images (3.5 mm) (*left and middle*) depict the occipital foramina (*arrows*), also shown on a 3D VR posterior view (*right*). Note a normal intrasutural bone (*dotted arrow*)

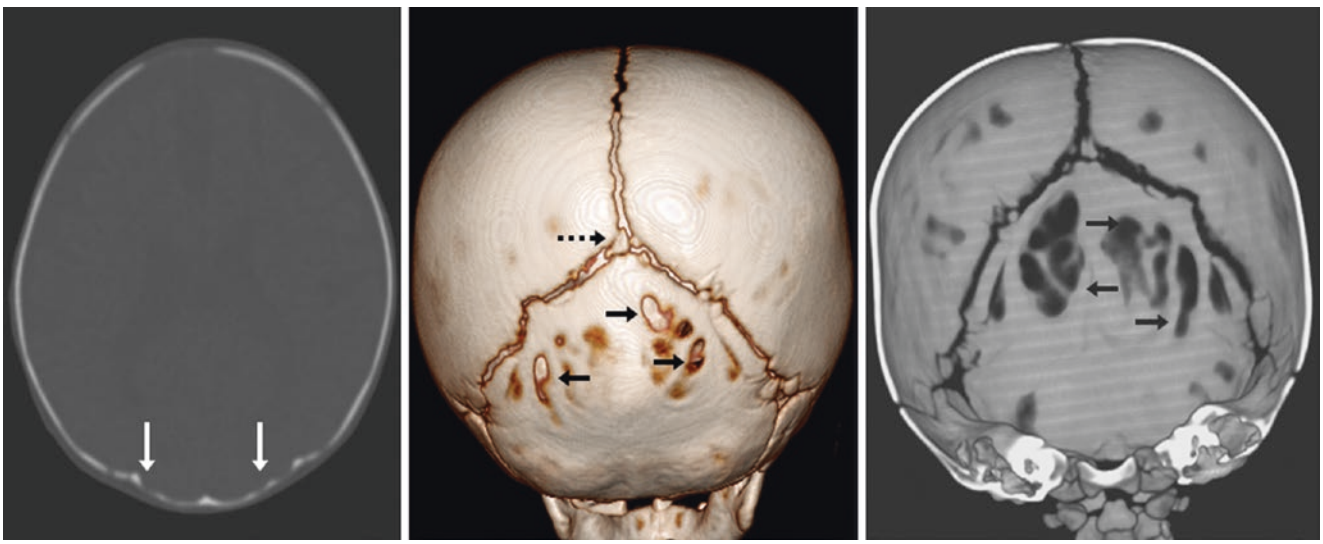

Fig. 28.23 A 5 month old with a thin occipital bone and multiple small foramina (*arrows*) noted on axial NECT post-trauma (*left*); the NECT was negative for fracture. Also, note a tiny posterior fontanelle bone (*dashed arrows*) on 3D posterior (*middle*) and inside (*right*) views

28.7 Parietal Foramina

The *parietal foramina* are located parasagittally, usually within 1–2 cm off the midline and about 2 cm superior to the lambdoid suture. Depending on whether or not these are considered visible on CT versus on histopathologic dissection (this gives rise to variable numbers in the literature), they are present in 10–60 % of people. Those that are entirely considered normal variations are typically less than 5 mm in size and are often present bilaterally; most commonly they appear as bilateral vascular channels. The larger than 5–7 mm foramina (large or *giant foramina*) are much less common (<1 %), and although they are usually asymptomatic, they are thought to have autosomal dominant inheritance and are sometimes associated with other intracranial abnormalities. The foramen either transmits an *emissary vein* to the scalp or, according to other sources, there is a tiny transcranial arterial communication between the meninges and the scalp. Another note regarding the parietal foramina is that they are probably present in a majority of patients as tiny defects or focal areas of sclerosis. They can be asymmetric from side-to-side. Occasionally, they are confused with lytic lesions of the skull or even mistakenly called burr holes when asymmetric. Again, the location and size usually confirm that they are normal variants (Figs. 28.24, 28.25, 28.26, 28.27, 28.28, 28.29, 28.30, 28.31, 28.32, 28.33, and 28.34).

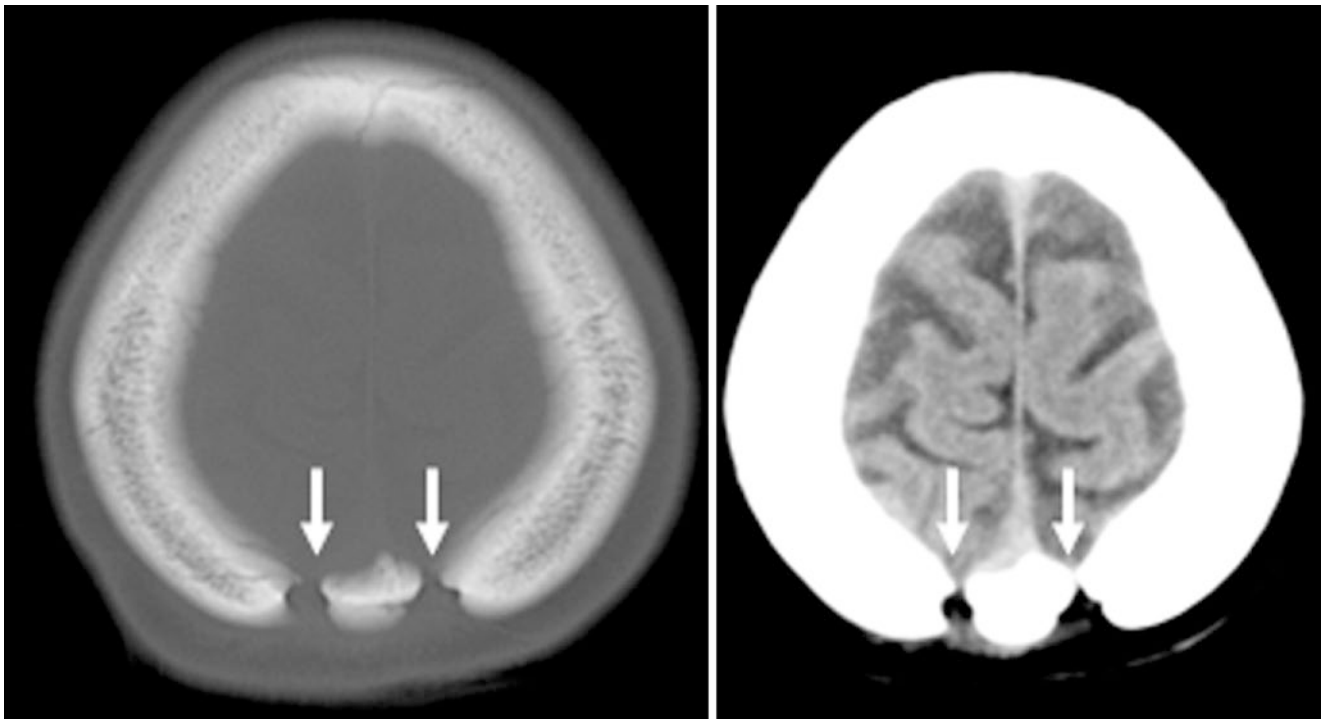

Fig. 28.24 A 56 year old with bilateral parietal foramina (*arrows*) on bone (*left*) and soft-tissue (*right*) windows

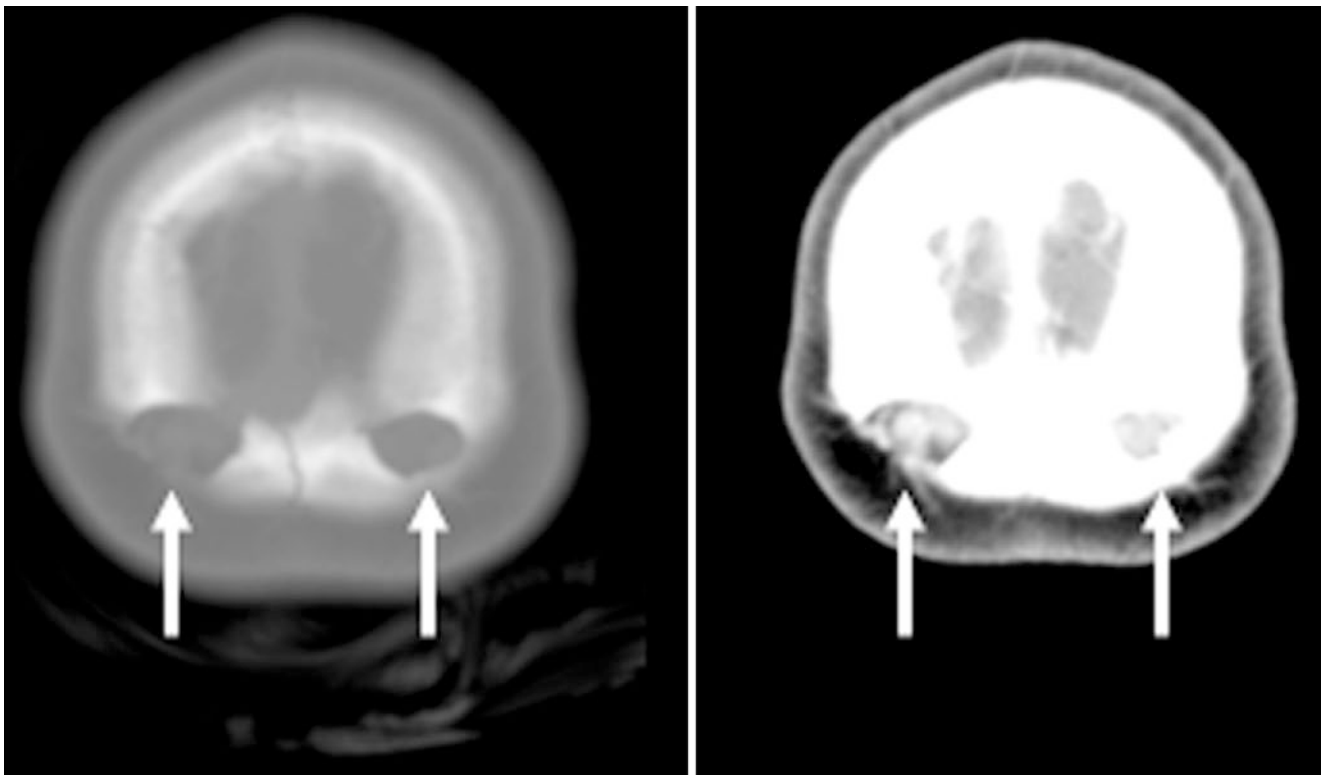

Fig. 28.25 An 8 year old in whom on bone (*left*) and soft tissue (*right*) windows parietal foramina (*arrows*) contain enhancing vessels

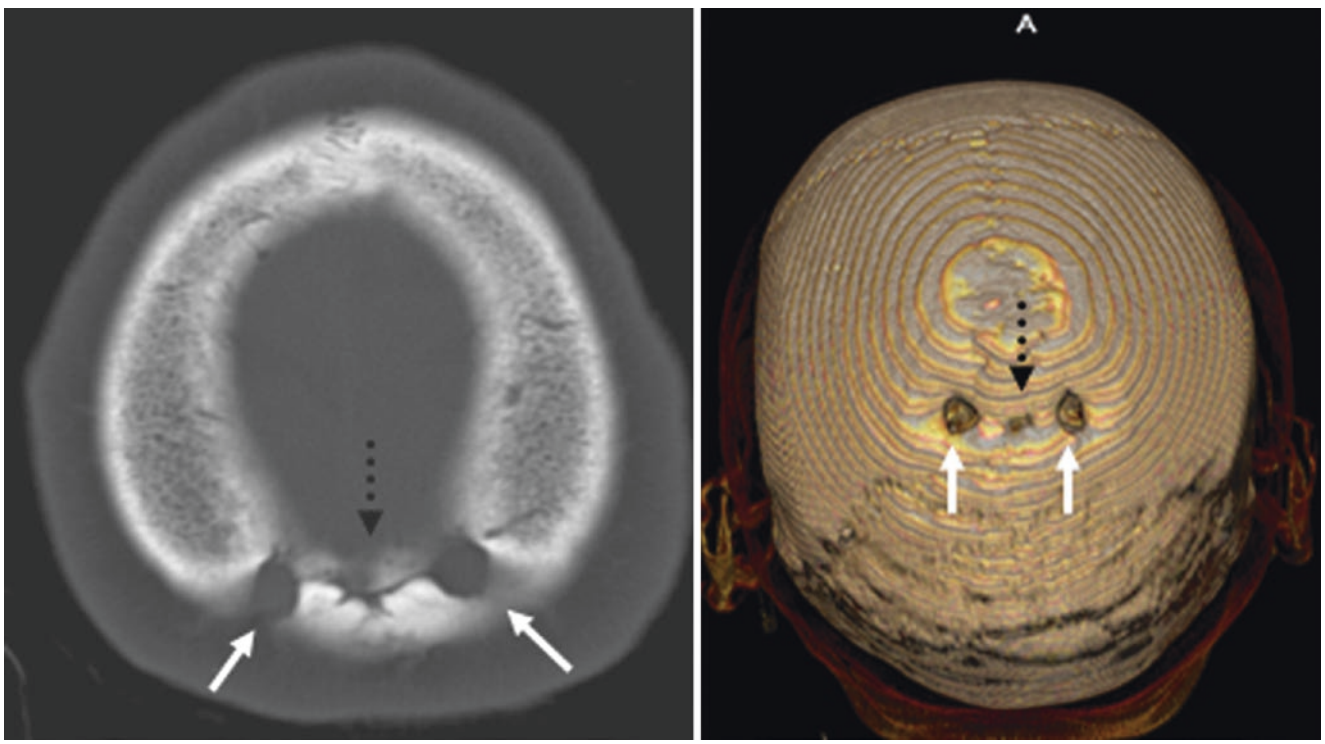

Fig. 28.26 A 57 year old: with parietal foramina, occasionally a midline defect (*black dashed arrows*) occurs with incomplete bony fusion. Note the foramina on a 3D VR superior view (*right*)

Fig. 28.27 A 30 year old with tiny bilateral parietal foramina that are similar to vascular channels

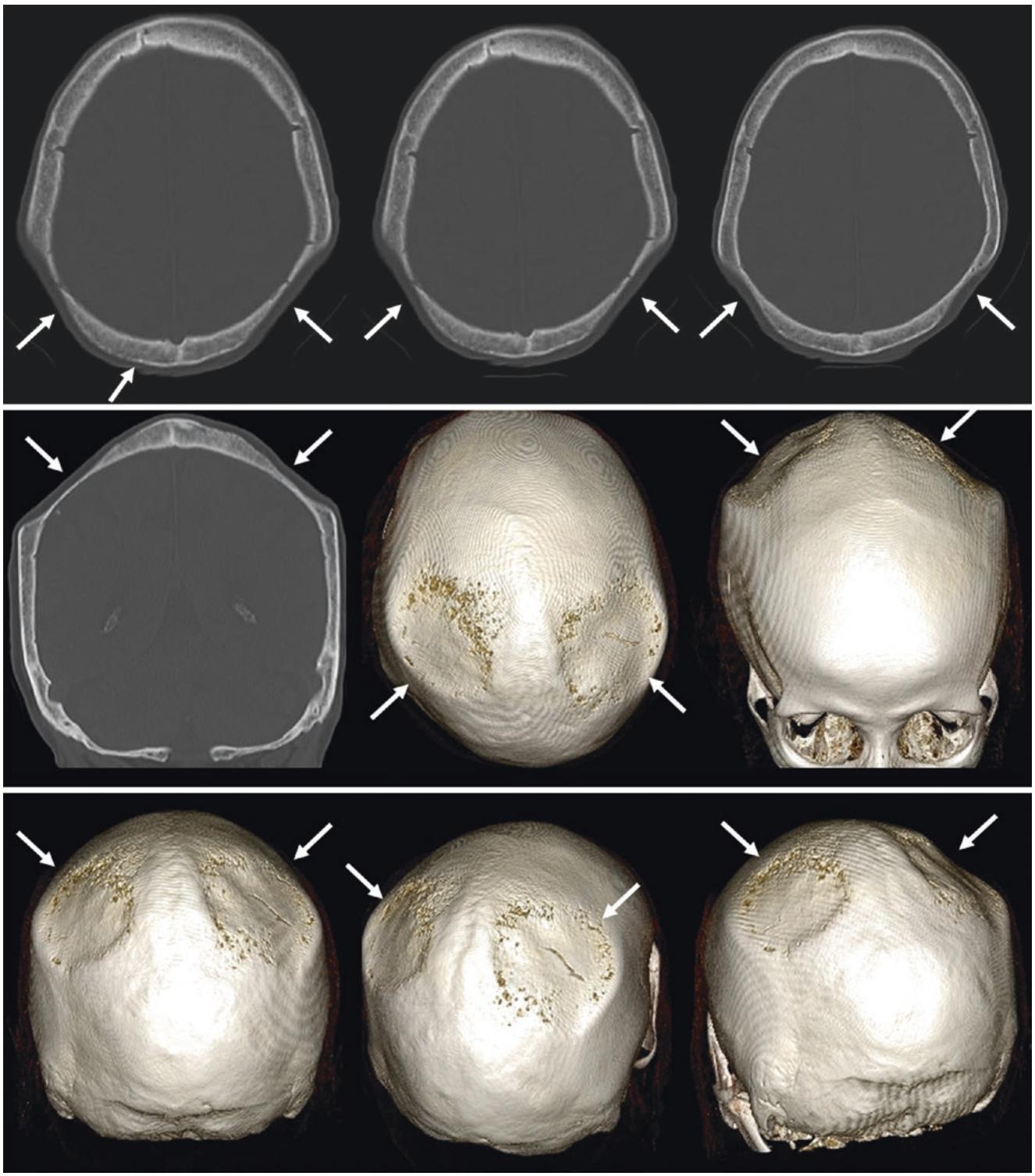

Fig. 28.28 An 80 year old with bilateral depressions of the parietal bones (*arrows*) but no history of trauma or surgery. NECT demonstrated a symmetric appearance, which would be unlikely with old fractures. Therefore these most likely represent bony fusions across what were once large parietal foramina. *Top row*: axial NECT images. *Middle row*: coronal reformats from NECT as well as 3D VR posterosuperior and anterior views. *Bottom row*: 3D VR posteroanterior and oblique views

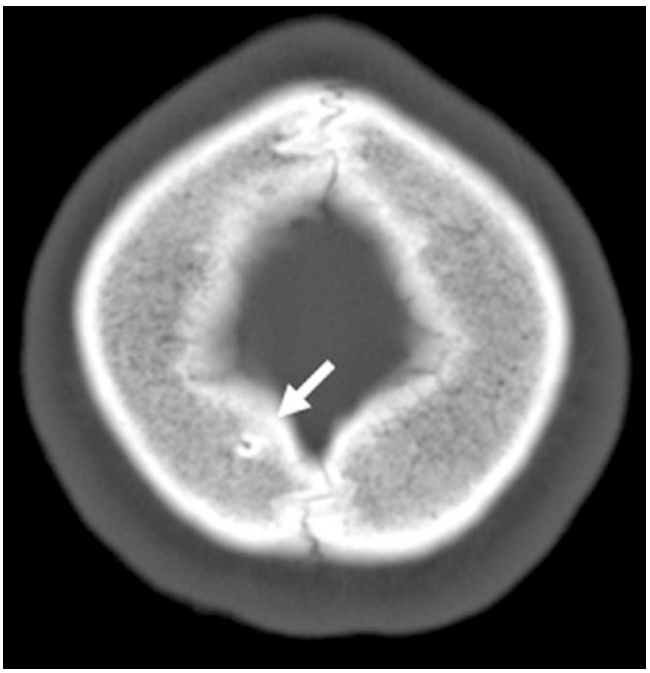

Fig. 28.29 A 20 year old with a tiny, unilateral parietal foramen present at the right vertex

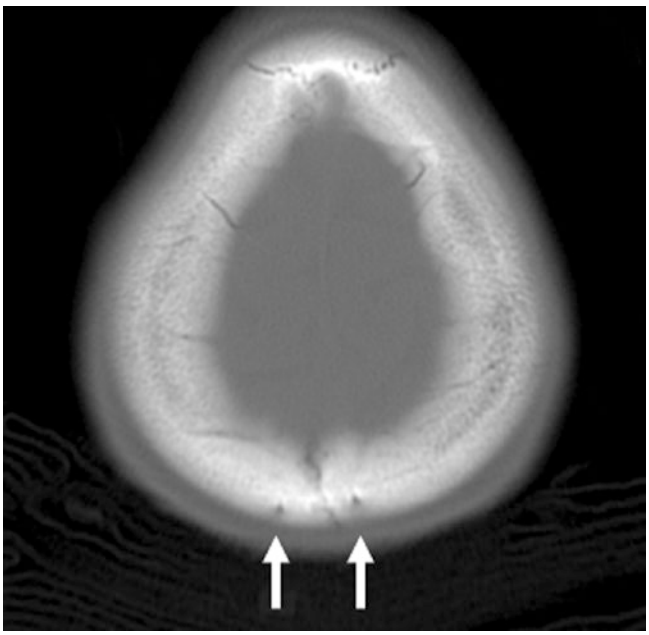

Fig. 28.31 A 30 year old with the most common appearance of tiny, bilateral foramina

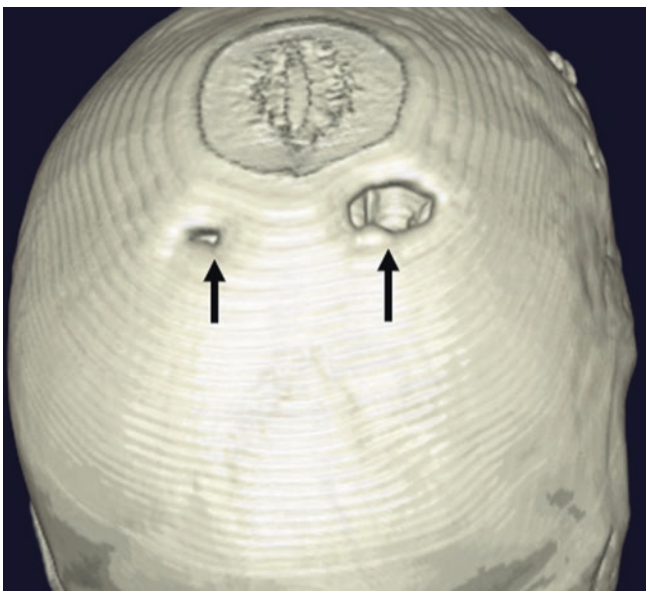

Fig. 28.30 An 18 year old with asymmetric parietal foramina on axial (*left*) and 3D VR posterior view (*right*) images (note: the top of the head was not covered). Note a stair-step artifact from sequential CT acquisition

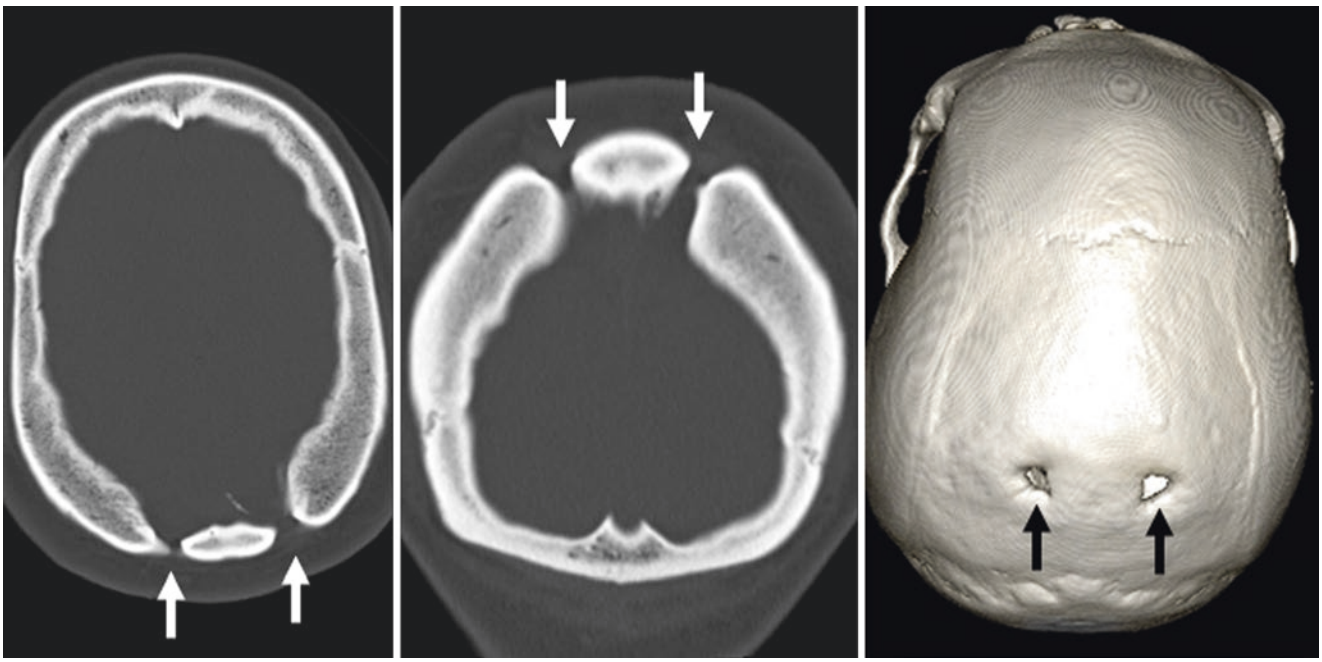

Fig. 28.32 A 32 year old: a NECT depicts symmetric, bilateral parietal foramina on axial (*left*), coronal (*middle*), and 3D VR (*right, superior view*) images

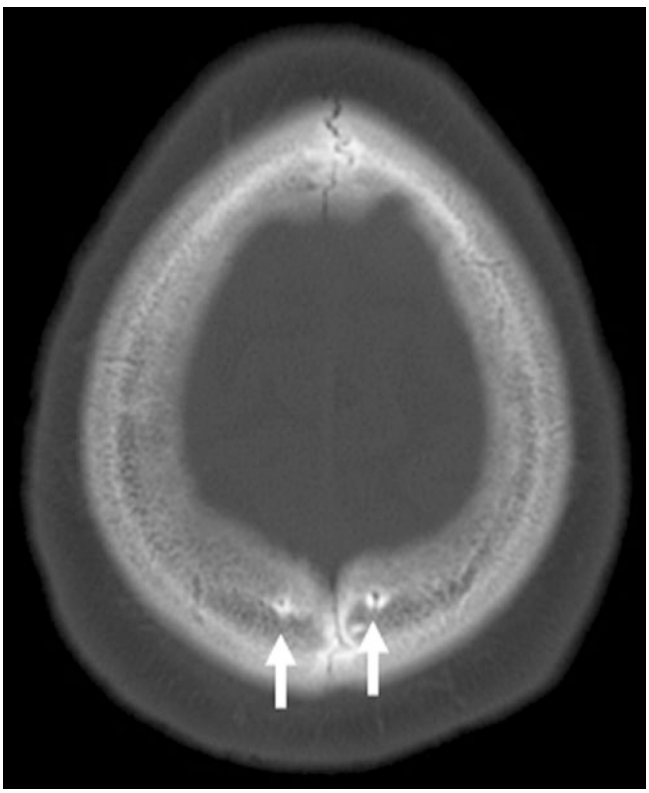

Fig. 28.33 A 52 year old with tiny parietal foramina or vascular channels

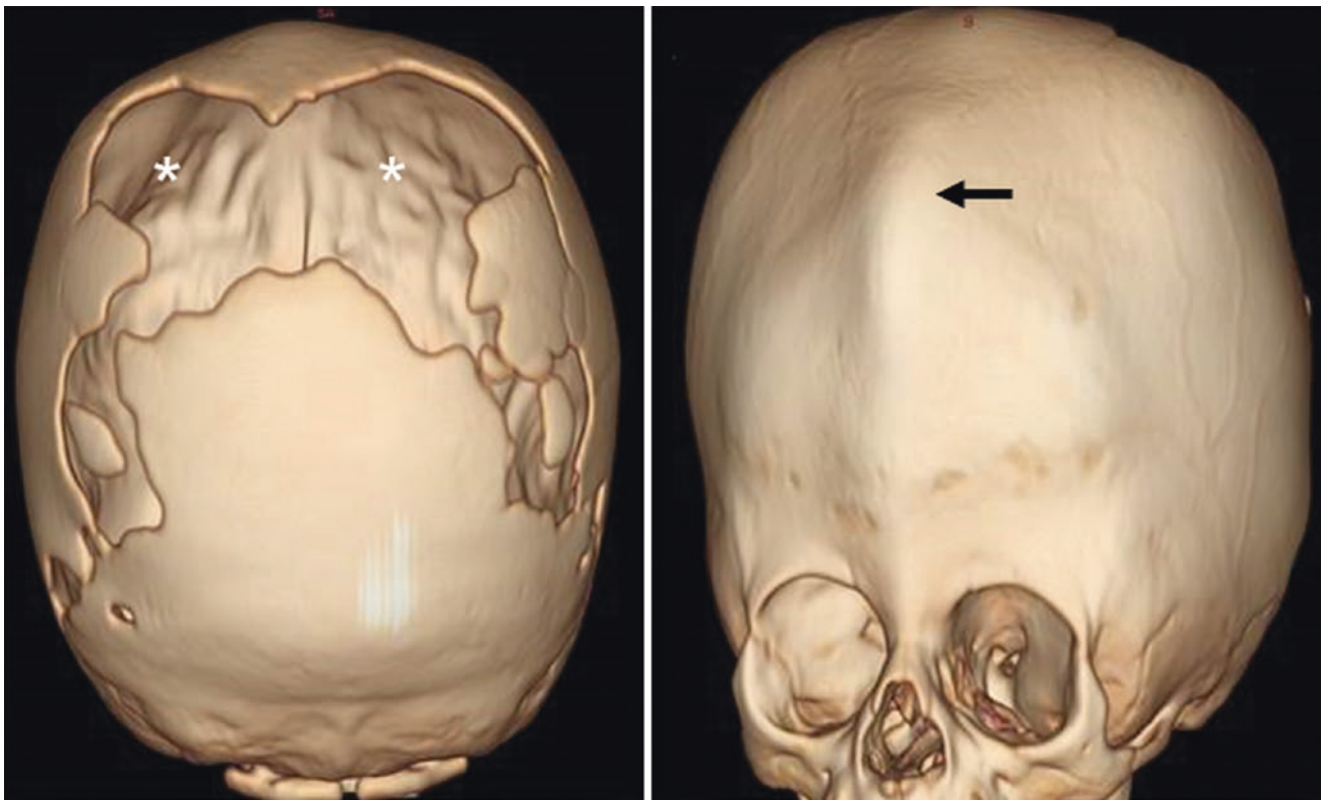

Fig. 28.34 Comparison case: In a 15 month old with trigonencephaly (*arrow*), 3D CT reformats with posteroanterior (*left*) and anteroposterior (*right*) views show severely enlarged parietal foramina that connect to enlarged lambdoid sutures inferolaterally (*)

28.8 Diploic Veins (Venous Lakes)

Diploic/intradiploic veins can be formidable to confirm because of their varied appearance as well as their propensity to simulate *lytic metastases*. They are probably most easily identified on skull radiography or CT as connecting vascular channels that may appear discontinuous at times. They can be problematic in distinguishing from pathology if they are enlarged, ovoid, and unilateral; they can also be problematic on a presenting MRI. Their appearance on CT typically is as described: vascular channels can be noted that may appear irregular and of varying caliber but can usually be demonstrated as connected and linear at some point if slice thicknesses are thin enough. On MRI, their appearance varies prior to contrast, probably because of the speed of flow within the channel; relatively fast flow may appear dark and not well visualized on spin-echo and FLAIR imaging, whereas slower flow may appear iso- or even slightly hyperintense. This can cause some confusion when a lack of hyperintensity is visualized on noncontrast MR images followed by enhancement after contrast administration; establishment of enhancing, connecting channels identifies these as normal variants.

MPR and 3D reconstructed images from NECT may also aid in distinguishing these normal variants from true lytic lesions by demonstrating the vascular channels after using cut-away views. Again, an appearance of linear, connecting, tubular, or serpiginous enhancement confirms this normal variation or don't touch lesion. Occasionally, abnormalities such as *arteriovenous malformations* (AVMs) may have enlarged arteries or veins crossing through the cranium, but these should supply or drain into and from enlarged vasculature within or outside the cranial vault (Figs. 28.35, 28.36, 28.37, 28.38, 28.39, and 28.40).

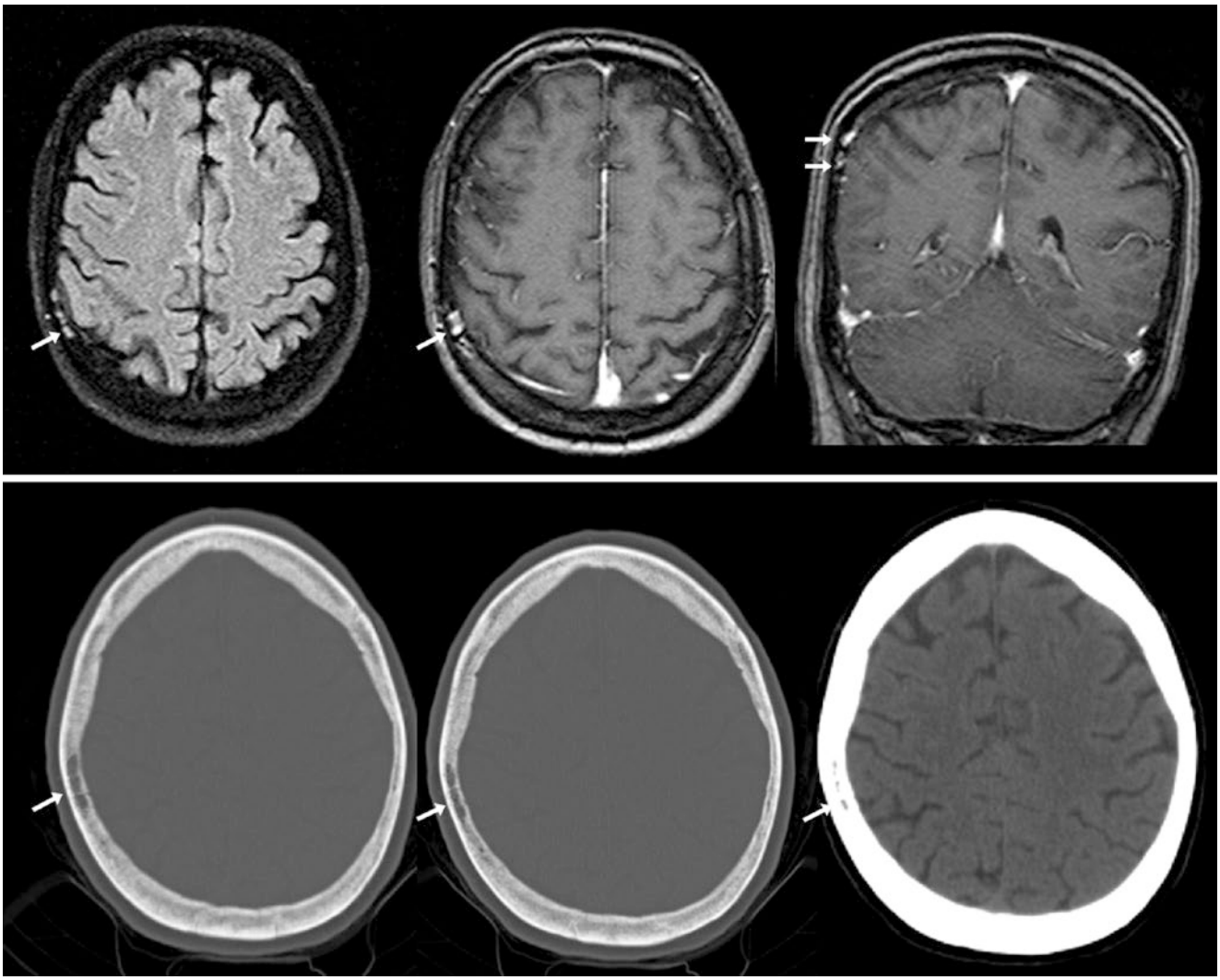

Fig. 28.35 A 57 year old: on noncontrast fat-suppressed FLAIR (*top left*), a focus enhances after IV contrast on both axial and coronal T1WI (*top middle and right*). This venous channel (*bottom*) is confirmed on CT by scrolling axial images (*bottom*) to verify a linear, connected appearance

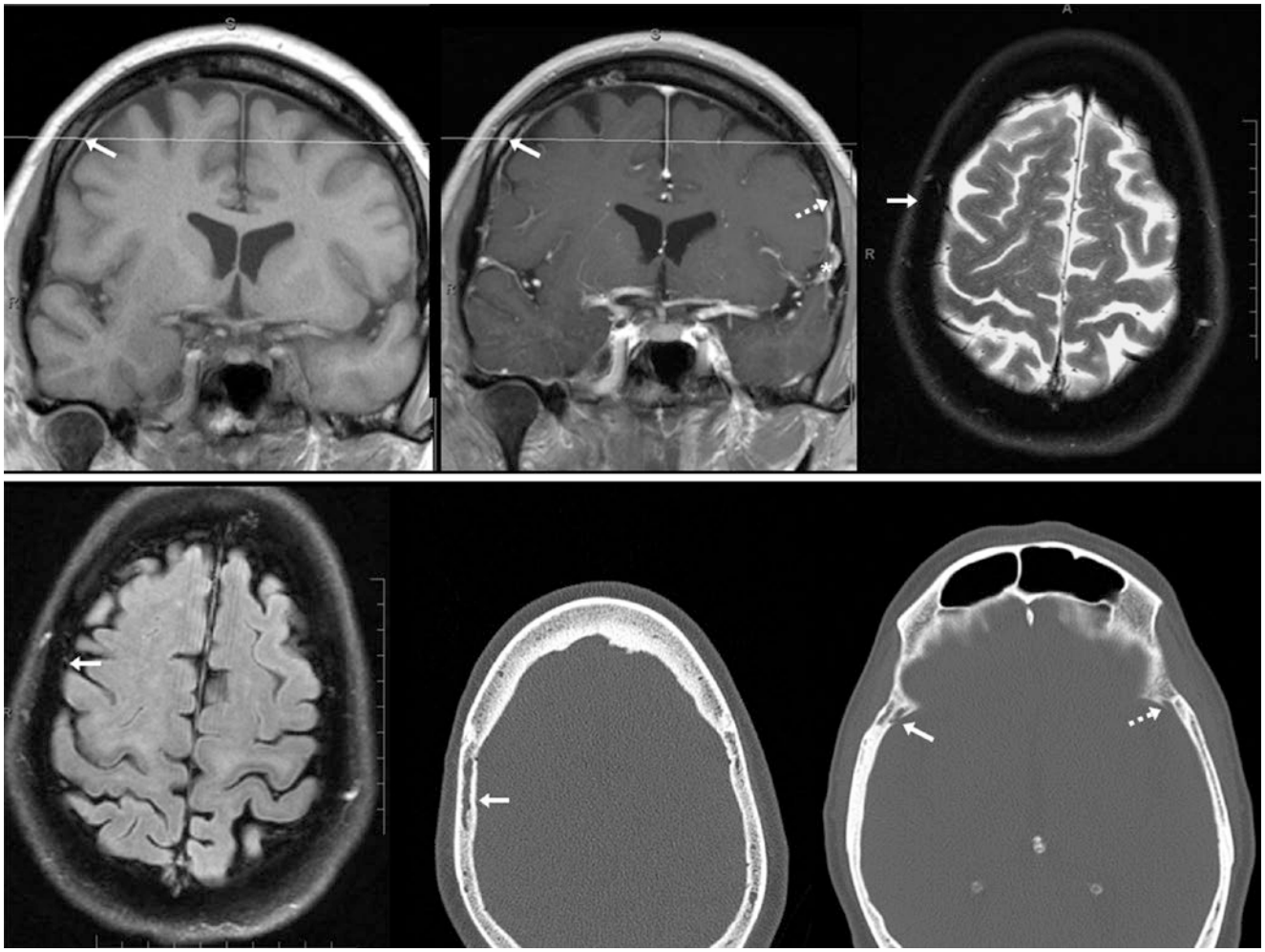

Fig. 28.36 A 52 year old: an ovoid-enhancing focus (*arrows*) on postcontrast T1WI (*top middle*) was not visualized on either fat-suppressed T2WI (*top right*) or FLAIR (*bottom left*). Scout lines (*top row*) confirmed the location. CT depicted a prominent vascular channel (*bottom right*) via scrolling through the images to demonstrate a linear, connected appearance. Note a diploic vein on the opposite side (*dashed arrows*), which connected to the left superficial middle cerebral vein (*)

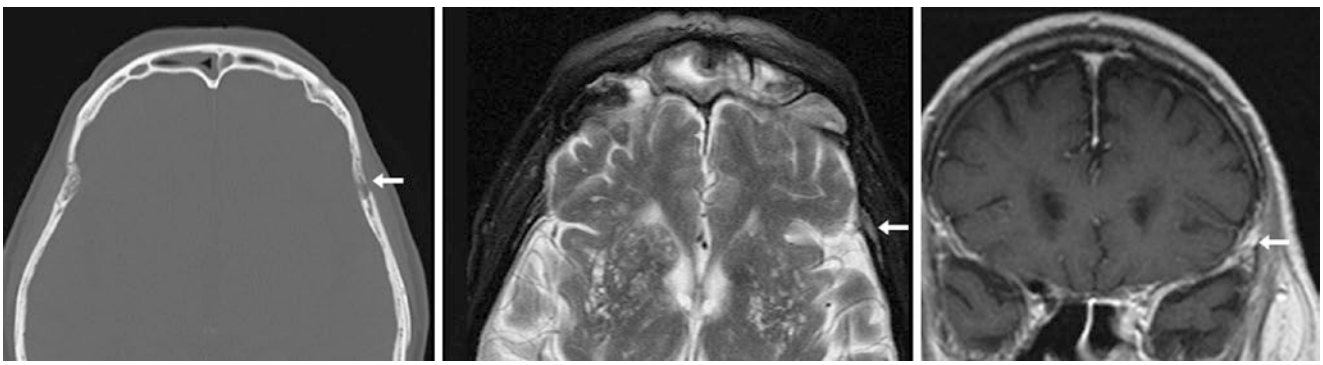

Fig. 28.37 An 85 year old: a diploic vein on CT (*left*) was mildly isointense to gray matter on T2WI (*middle*) and exhibited mild enhancement on postcontrast T1WI (*right*). Also on T2WI the patient has cribriform-appearing basal ganglia from dilated perivascular spaces (*état criblé*)

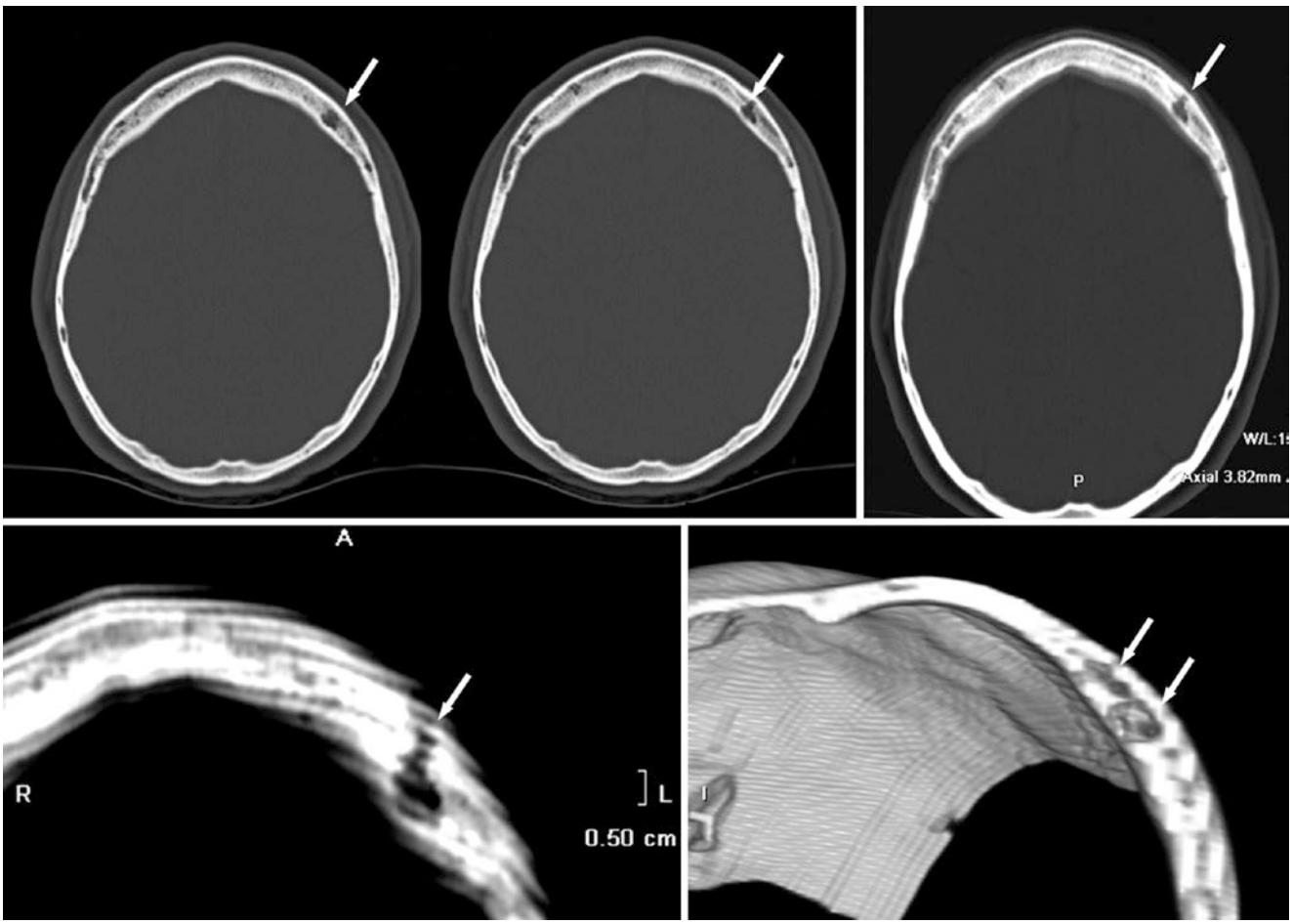

Fig. 28.38 A 38 year old with a questionable lytic lesion of the left frontal skull noted during a metastatic work-up. It was well circumscribed on axial NECT 2.5-mm (*top left and middle*) and 4- mm (*top right*) reconstructions. However, thicker 6.5-mm axial MPR images (*bottom left; note stair-step artifact from sequential acquisition*) and 3D cut-away sections in an axial oblique plain (*bottom right*) through midlesion confirmed it to be an (intra-) diploic vein

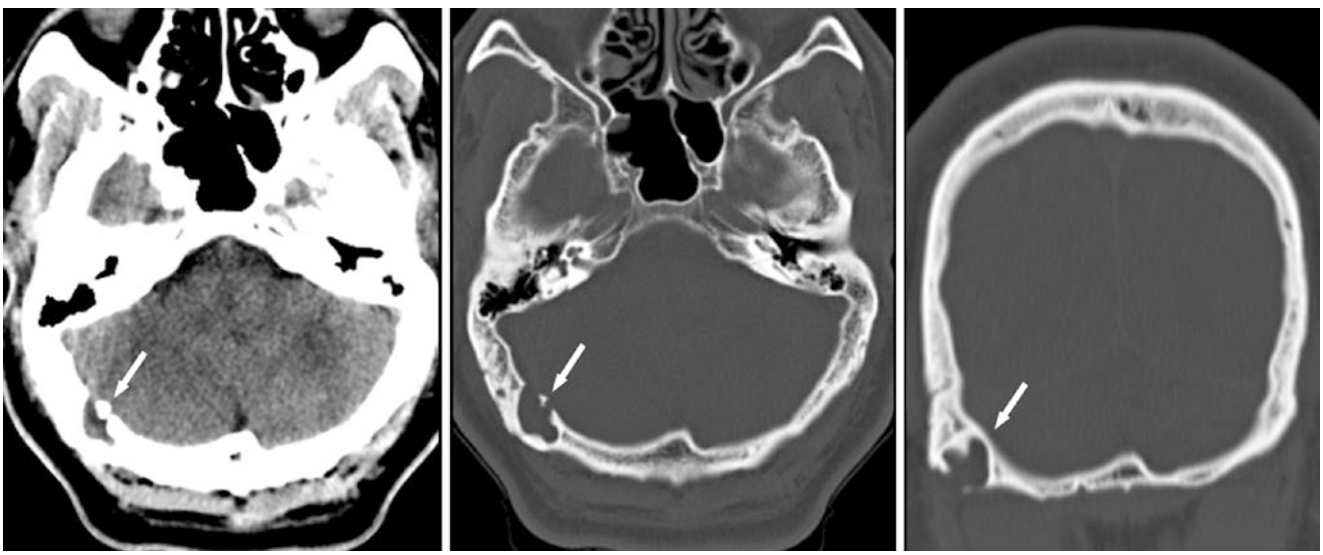

Fig. 28.39 A 37 year old with trauma: a large (intra-) diploic vein (*arrows*) was noted on a CT with soft tissue (*left*) and bone (*middle*) windows. This channel connected the cranial vault to the upper cervical veins. Coronal reformats (*right*) show a sclerotic rim, confirming its benignity

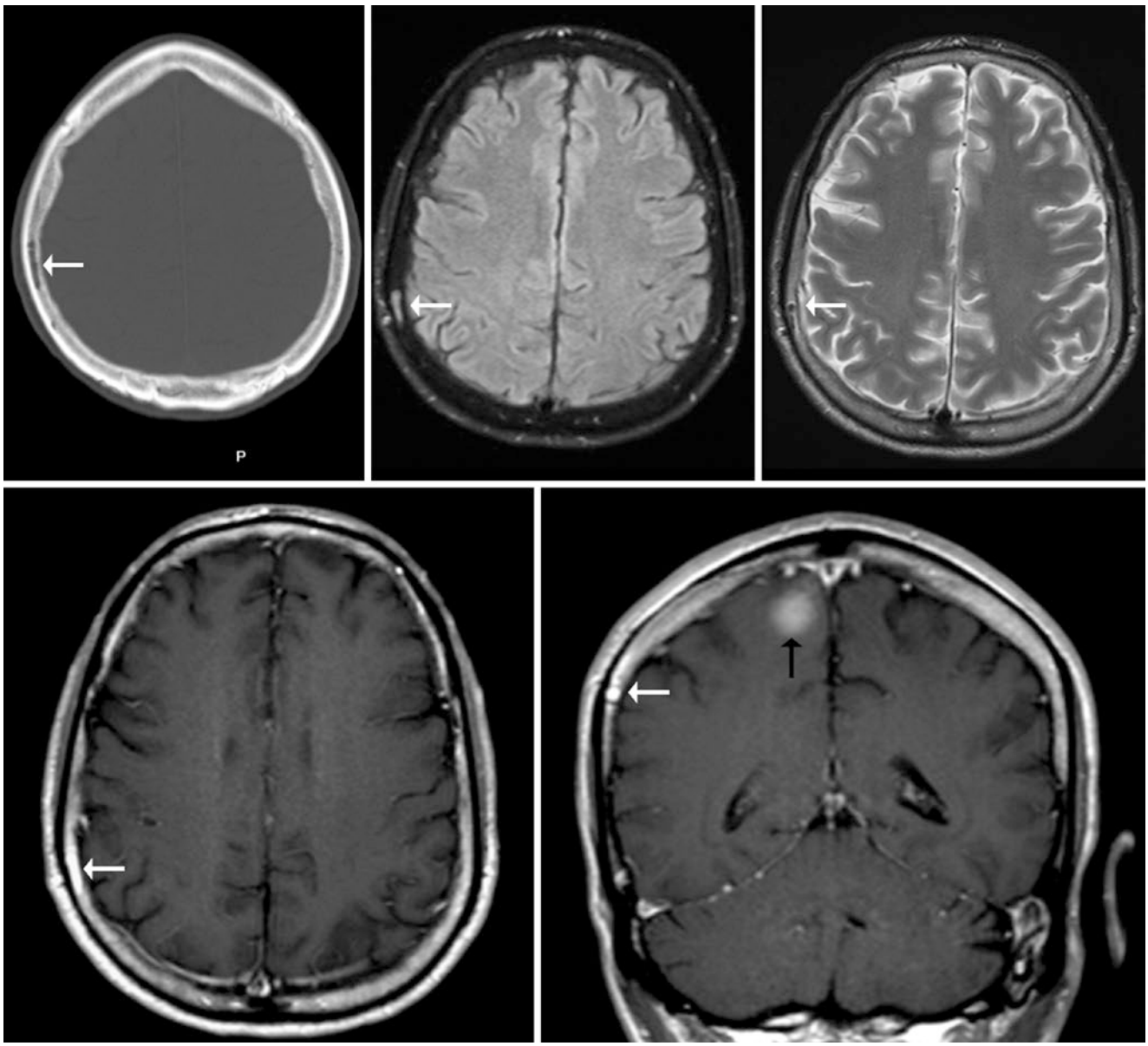

Fig. 28.40 A 75 year old with melanoma; NECT and MRI were performed to rule out metastases. *Top row*: a lytic-appearing focus within the right parietal bone on NECT (*left*) is bright on FLAIR (*middle*) but dark on T2WI (*right*). *Bottom row*: this enhances on postcontrast axial (*left*) and coronal (*right*) T1WI in a tubular fashion. Note a right parietal lobe metastasis (*black arrow*)

28.9 Other Emissary Veins or Linear Vascular Channels Simulating Fractures

It may be difficult to discern whether smaller vascular channels are *emissary veins* versus *diploic veins* (i.e., *venous lakes*), although this distinction is probably not of great significance. The more pertinent distinction is between such vascular channels and true fractures. Emissary veins and intradiploic veins may also be seen in several other less common locations. One of the most common of the uncommon locations of emissary veins is around the midline of the occiput; however, virtually any bone of the skull can transmit emissary or diploic veins. Emissary veins usually exhibit a smooth and tubular contour as opposed to the jagged appearance of fractures. Linear vascular channels also uncommonly traverse bony structures in other locations, even in areas not close to the scalp (e.g., the petrous apices) and sometimes communicate with vessels in the dura or with other channels within the calvarium. These thin channels are usually not as linear or as jagged as true *fractures*. The presence of a dense, sclerotic margin (not always seen) solidifies the recognition of these channels.

Again, 3D imaging can help in uncertain fractures when evaluating a linear defect above the skull base. However, this does not exclude the uncommon hairline fracture that does not completely traverse both the inner and outer tables of the skull (more common in pediatric patients). At the skull base, this can be difficult to diagnose, and knowledge of the normal sutures is vital. Fortunately, such spurious linear channels are not common at the bottom of the skull base.

Also shown are further examples of thin lucencies that could be confused with hairline fractures. An important means of differentiation is by scrolling through thin axial images to determine whether the faint lucency is tubular and not linear or jagged. Also, focal areas of dilatation or linear contrast enhancement can indicate a diploic vein. Again, a typical location or a tubular or sclerotic rim communication between the dura and scalp indicates an emissary vein (Figs. 28.41, 28.42, 28.43, 28.44, 28.45, 28.46, and 28.47).

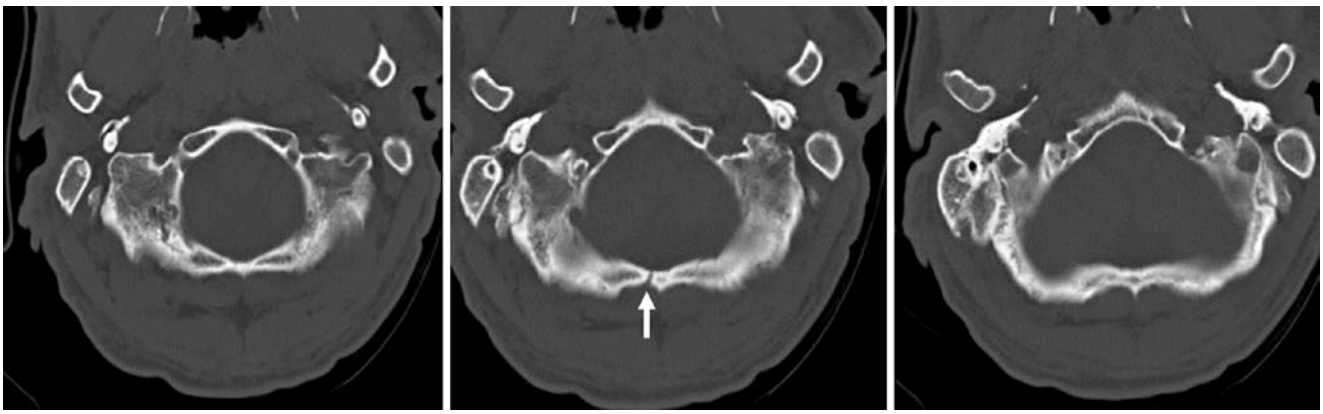

Fig. 28.41 A 45 year old with an off-midline emissary vein that was initially questioned to represent a fracture by a radiology resident. Note that the images below (*left*) and above (*right*) that level are negative. It is plausible that this small channel represents a sort of occipital emissary vein

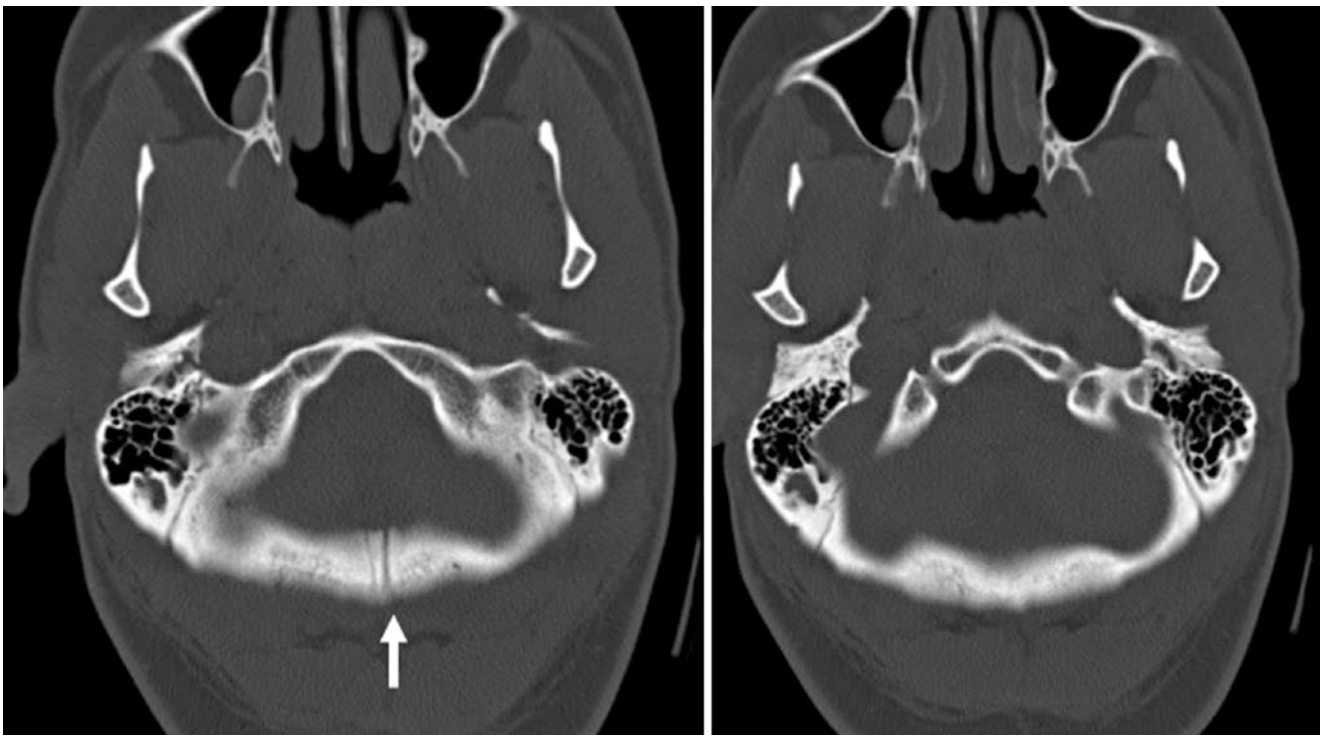

Fig. 28.42 A 36 year old: a midline vascular channel passes through the occipital bone and was not visualized on images above/below that level

Fig. 28.43 A 44 year old with a tiny channel that only partially traverses the occipital bone before returning to travel intracranially along dura mater

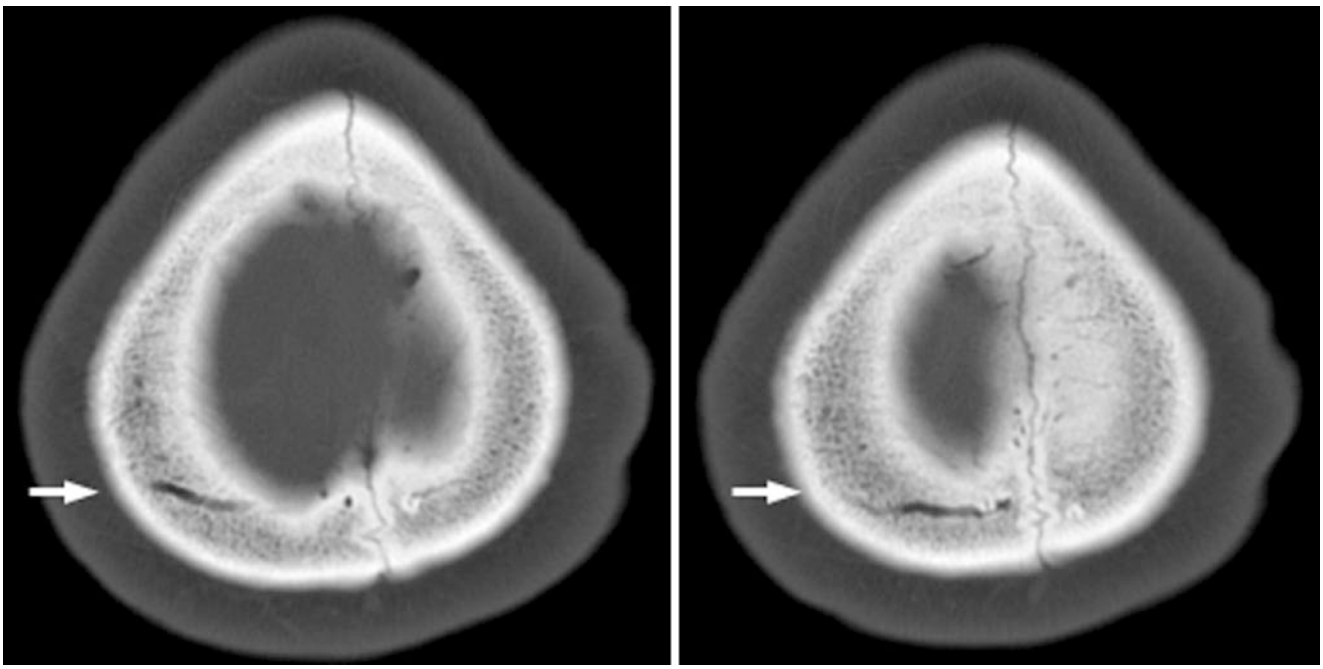

Fig. 28.44 A 38 year old: after trauma, a vascular channel initially thought by the resident to be a fracture does not continue through to the cortical surface

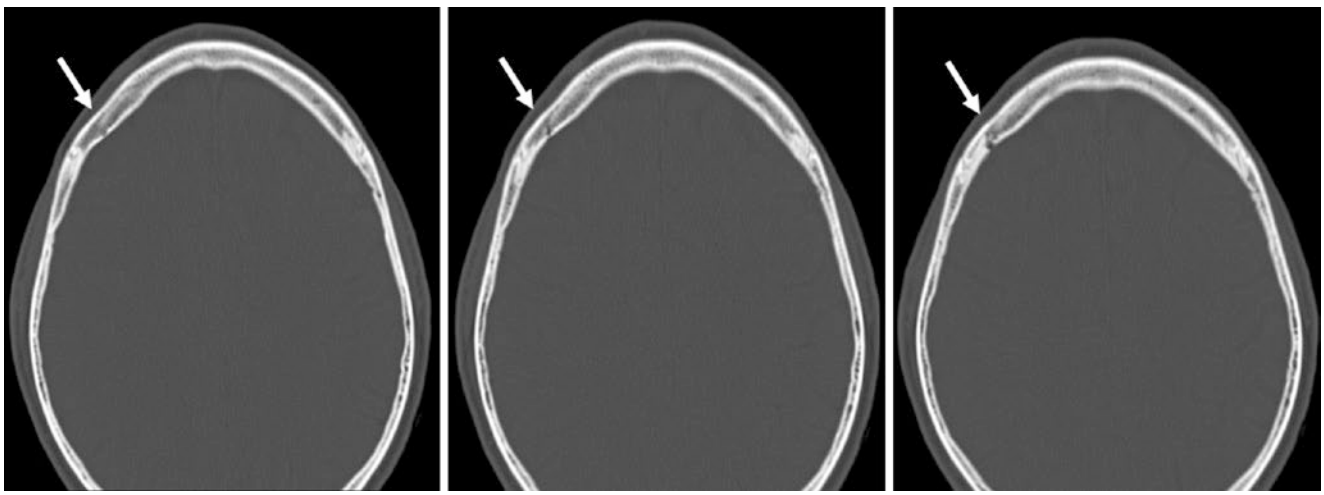

Fig. 28.45 A 32 year old with a vascular channel that does not pass through the outer cortical margin of the skull on NECT. On the topmost image (*right*), a focal dilatation suggests that this is a diploic vein

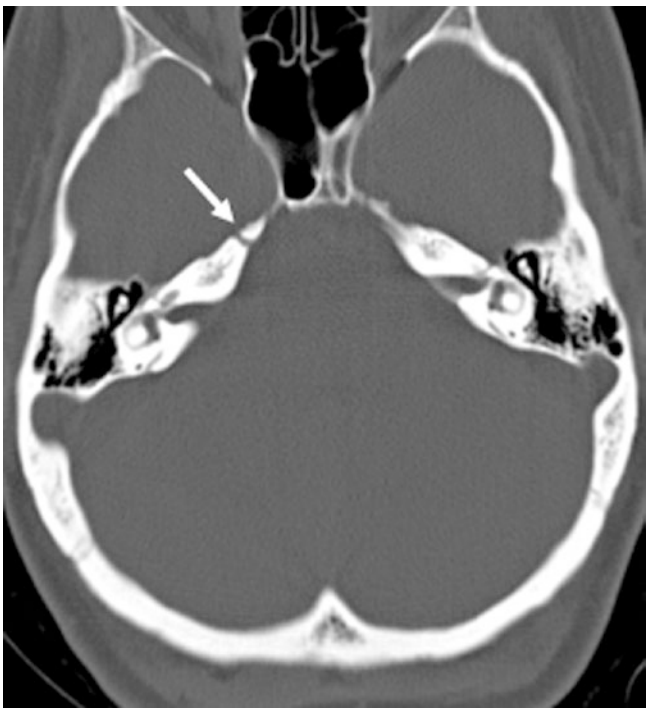

Fig. 28.46 A 31 year old: a vascular channel crosses the right petrous apex, and thus simulates a transverse temporal bone fracture

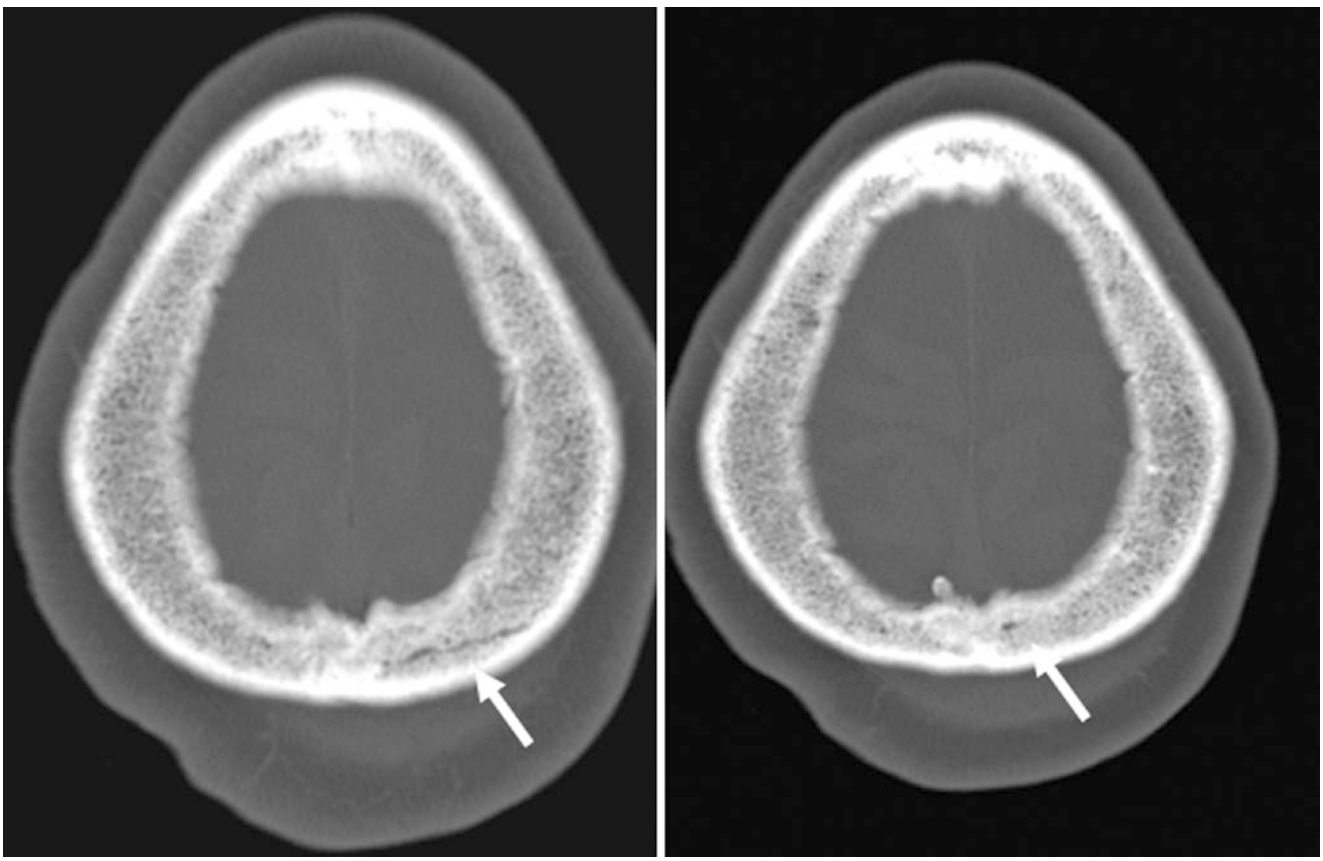

Fig. 28.47 An 81 year old: a thin, linear defect with adjacent scalp swelling, simulating a hairline fracture, did not pass through the outer cortex. A tubular contour on the top image (*right*) confirmed this to be a vascular channel

Suggested Reading

Berge JK, Bergman RA. Variations in size and in symmetry of foramina of the human skull. Clin Anat. 2001;14:406–13.

Freyschmidt J, Brossman J, Sternberg A, Wiens J. Freyschmidt's Koehler/Zimmer's borderlands of normal and early pathological findings in skeletal radiography. 5th ed. Tubingen: Thieme; 2003. Chapter 4, Skull. p. 357–66.

Gray H. Anatomy of the human body, 20th ed. Philadelphia: Lea & Febiger; 1918. Chapter 5D, The interior of the skull. Available at: http://www.bartleby.com/107/47.html.

Hershkovitz I, Greenwald C, Rothschild BM, Latimer B, Dutour O, Jellema LM, et al. The elusive diploic veins: anthropological and anatomical perspective. Am J Phys Anthropol. 1999;108:345–58.

Jinkins JR. Atlas of neuroradiologic embryology, anatomy, and variants. Philadelphia: Lippincott Williams & Wilkins; 2000. Chapter 2, Cranium. p. 62–85.

Keats TE, Anderson MW. Atlas of normal roentgen variants that may simulate disease. 8th ed. Philadelphia: Mosby, Inc.; 2007. Chapter 1: The Skull. pp. 3–117.

Koesling S, Kunkel P, Schul T. Vascular anomalies, sutures and small canals of the temporal bone on axial CT. Eur J Radiol. 2005;54:335–43.

Lanzieri CF, Duchesneau PM, Rosenbloom SA, Smith AS, Rosenbaum AE. The significance of asymmetry of the foramen of Vesalius. Am J Neuroradiol. 1988;9:1201–4.

Lo WW, Solti-Bohman LG. High-resolution CT of the jugular foramen: anatomy and vascular variants and anomalies. Radiology. 1984;150:743–7.

Premsagar IC, Lakhtakia PK, Bisaria KK. Occipital emissary foramen in Indian skulls. J Anat. 1990;173:187–8.

Schratter M, Canigiani G, Karnel F, Imhof H, Kumpan W. Occult fractures of the skull. Radiologe. 1985;25:108–13.

Seeger JF. Normal variations of the skull and its contents. In: Zimmerman RA, editor. Neuroimaging: clinical and physical principles. New York: Springer; 1999. p. 415–53.

Sharma PK, Malhotra VK, Tewari SP. Emissary occipital foramen. Anat Anz. 1986;162:297–8.

Swartz JD, Harnsberg RH. Imaging of the temporal bone. 3rd ed. New York: Thieme; 1998.

Tubbs RS, Smyth MD, Oakes WJ. Parietal foramina are not synonymous with giant parietal foramina. Pediatr Neurosurg. 2003a;39:216–7.

Tubbs RS, Smyth MD, Oakes WJ. Parietal foramina are not synonymous with giant parietal foramina. Pediatr Neurosurg. 2003b;39:216–7.

Weissman JL, Hirsch BE. Imaging of tinnitus: a review. Radiology. 2000;216:342–9.

West MS, Russell EJ, Breit R, Sze G, Kim KS. Calvarial and skull base metastases: comparison of nonenhanced and Gd-DTPA-enhanced MR images. Radiology. 1990;174:85–91.

Yoshioka N, Rhoton Jr AL, Abe H. Scalp to meningeal arterial anastomosis in the parietal foramen. Neurosurgery. 2006;58:ONS123–6.

Normal Variations in Calvarial Contour, Irregular Ossification/Aeration, and Inward/Outward Projections/ Protuberances

29

This subsection focuses on perceived abnormalities of osseous overgrowth or prominent protuberances that are within normal limits or are not atypical in certain age groups (e.g., benign hyperostosis frontalis in middle-aged females) [1–8]. This also includes perceived abnormalities of calvarial contour or multifocal irregularities in adults that may simulate disease. Many disease states that cause diffuse bony overgrowth are not covered here except as an occasional comparison case, since there can be a myriad causes/diseases for this appearance that range from malignant neoplastic (e.g., diffuse metastatic disease), benign (e.g., fibrous dysplasia), or metabolic (e.g., Paget disease or thalassemia).

This subsection also focuses on perceived abnormalities that result from bony projections when they are aerated or contain fat (e.g., the petrous apices) [1–8]. Many of these variants may be more of a source of confusion when seen on MRI compared to an initial presentation on CT (e.g., aerated clinoid processes and fatty petrous apices). Many skull abnormalities that are seen on MRI may be recognized more easily by sequences that incorporate fat suppression (FS) (e.g., fatty petrous apices). Hence, the intent is to address both CT and MRI appearances when appropriate. When in doubt, if the patient has had MR imaging and a normal variant versus pathology is in question, CT can easily exclude the presence of pathology in many scenarios, such as if calcification/ossification or aeration is suspected.

Focal areas of nonexpansile sclerosis can be present that may be normal or abnormal, but since small osteomas and sclerotic metastases (such as prostate metastases) can occasionally appear very similar to normal areas of sclerosis in the calvarium, this imaging differentiation is not attempted here, since it is this author's opinion that it may be difficult to discern. Hence, multifocal areas of sclerosis should be looked at in the clinical setting of suspected metastatic disease.

29.1 Convolutional Markings

As the normal brain grows with age, it can create normal indentations on the inner table of the skull termed *convolutional markings*. These are most prominent and commonly noticed in the period of fastest growth, usually over 3 years but under 9–10 years of age, although they can be seen even in adulthood. This normal variant should not be confused with *lacunar skull* (also known as luckenschadel or craniolacunae), which is a dysplasia of the membranous bones of the skull in various disorders such as *Chiari malformations* associated with cephaloceles or myelomeningoceles. These usually are present in patients less than 1–2 years of age and may disappear thereafter; however, convolutional markings should not be confused with a "silver-beaten" or "copper-beaten" skull, which are the chronic sequelae of increased intracranial pressure (i.e., *hydrocephalus*) (Figs. 29.1, 29.2, 29.3, 29.4, 29.5, and 29.6).

A.M. McKinney, *Atlas of Normal Imaging Variations of the Brain, Skull, and Craniocervical Vasculature*,
DOI 10.1007/978-3-319-39790-0_29

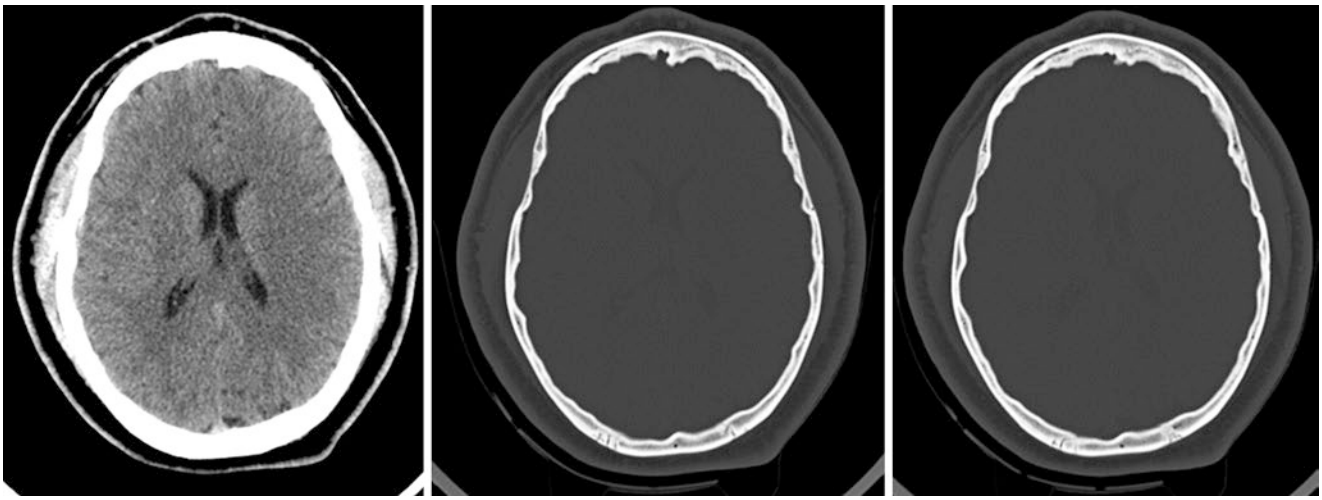

Fig. 29.1 A 32 year old with residual convolutional markings without evidence or history of hydrocephalus

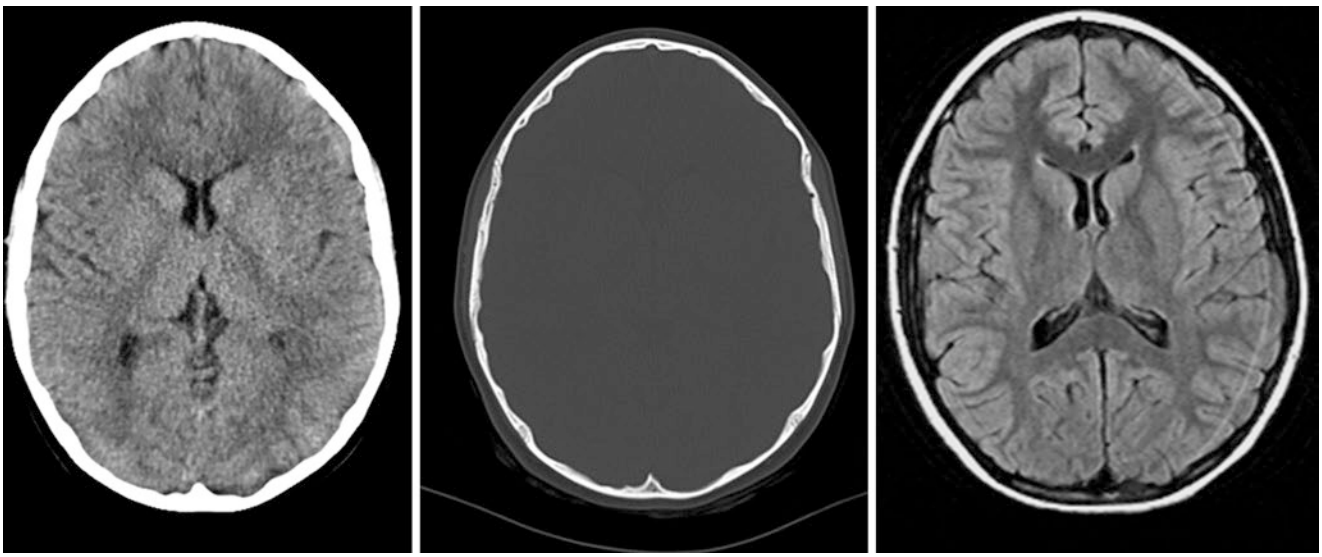

Fig. 29.2 A 12 year old with prominent convolutional markings and a normal-appearing underlying cerebrum on FLAIR MRI (*right*)

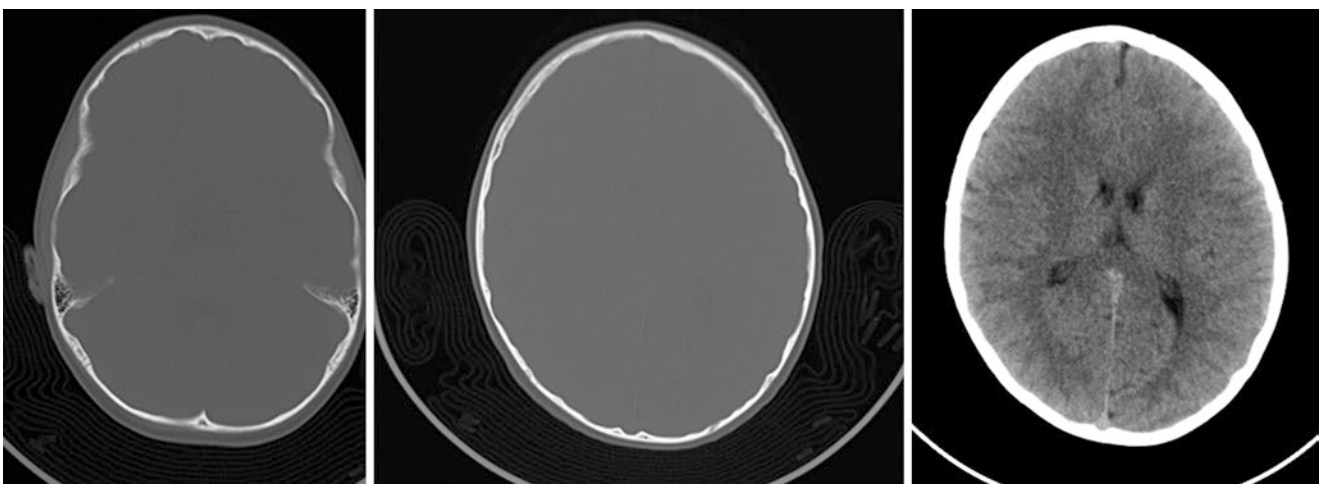

Fig. 29.3 A 6 year old with prominent convolutional markings who did not have hydrocephalus or a structural abnormality

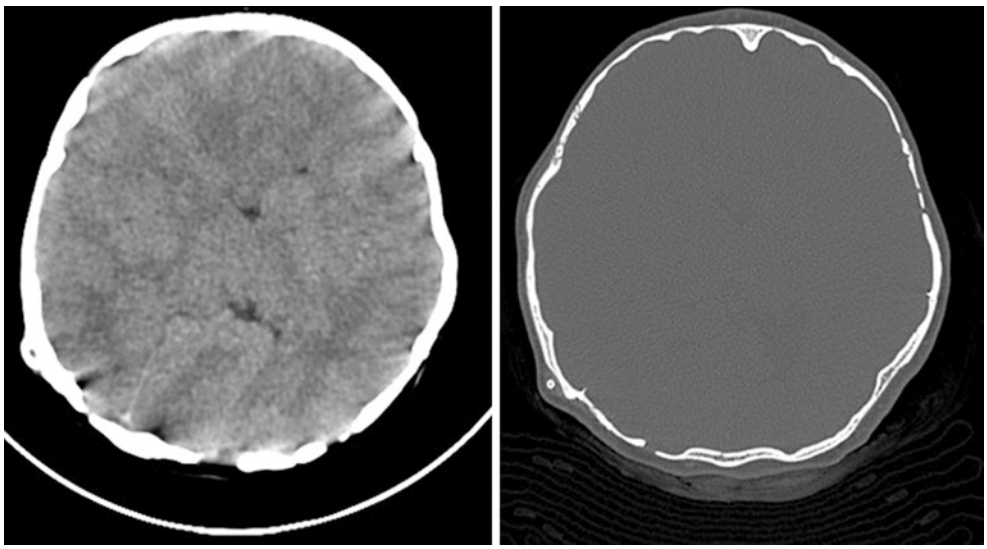

Fig. 29.4 Comparison case: an 8 month old with a Chiari II malformation and a ventricular shunt. There is a copper-beaten skull appearance at 6 years of age that is related to prior hydrocephalus

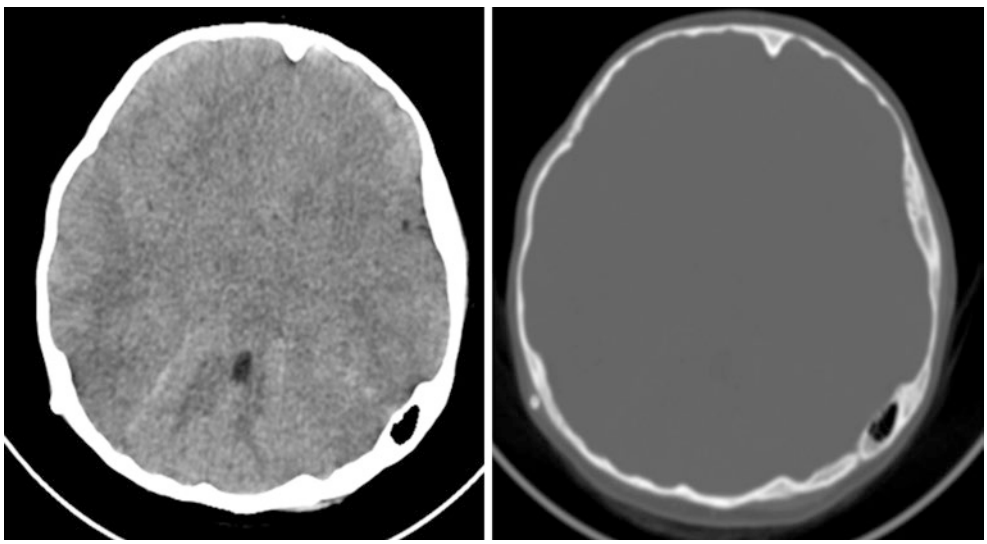

Fig. 29.5 Comparison case: a 5 year old has a beaten-metal appearance of the skull that is related to a shunted Chiari II malformation

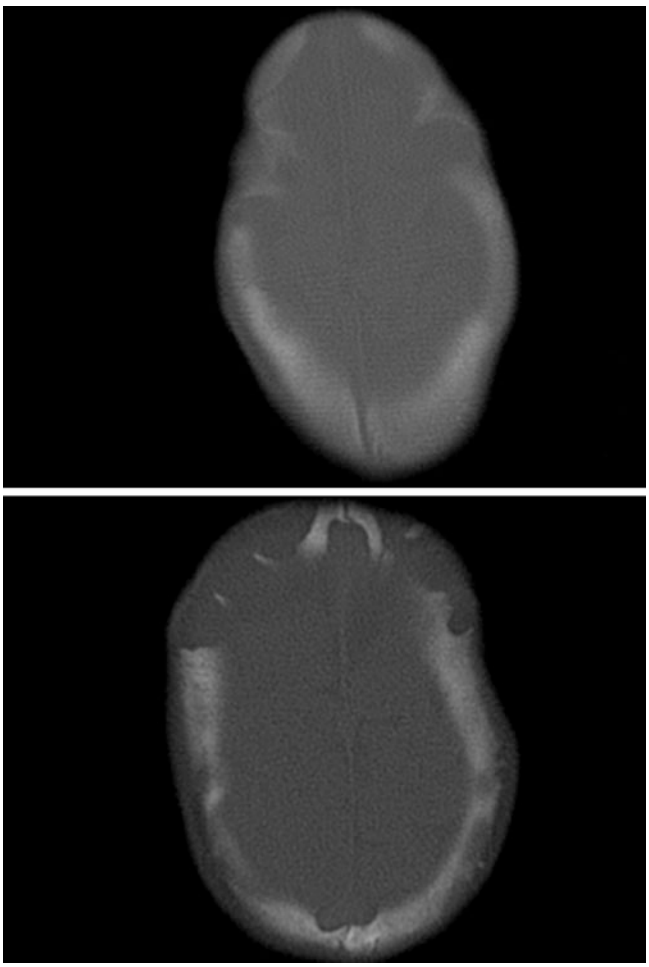

Fig. 29.6 Comparison case: craniosynostosis, scaphocephaly, and hydrocephalus are present on a CT in a 3 month old (*top*). The honeycomb-lacunar skull (craniolacunae) became more prominent at 9 months (*bottom*)

29.2 Cristal Galli on T1-Weighted MRI

The T1-bright signal of fatty marrow within a prominent *crista galli* (of the ethmoid bone) is an often noticed finding on MRI, specifically on sagittal or coronal T1WI. This is entirely normal and only causes a problem if it is considered for further work-up. If any doubts remain about the MRI appearance, a spiral nonenhanced CT scan (NECT) with multiplanar reconstruction can easily confirm the typical location. This can often suppress (become dark) on fat-saturated imaging owing to fatty marrow. Interestingly, even in the presence of fatty marrow, the crista galli may appear somewhat dense on NECT. However, extra-axial T1-brightness can also occur from *calcifications*, whether they are related to normal falx or prominent dural calcifications, or even from extra-axial lesions such as *meningiomas*. Hence, knowledge of normal anatomy and a characteristic appearance enable quick recognition of this normal structure.

The crista galli can be bright not only on T1WI but also on turbo spin-echo FLAIR or T2WI MRI, which can be confirmed with FS. Care should be taken not to interpret this finding on non-FS postcontrast T1WI as an extra-axial lesion such as a meningioma in questionable cases until fat-saturated images or NECT is available for confirmation (Figs. 29.7, 29.8, 29.9, 29.10, and 29.11).

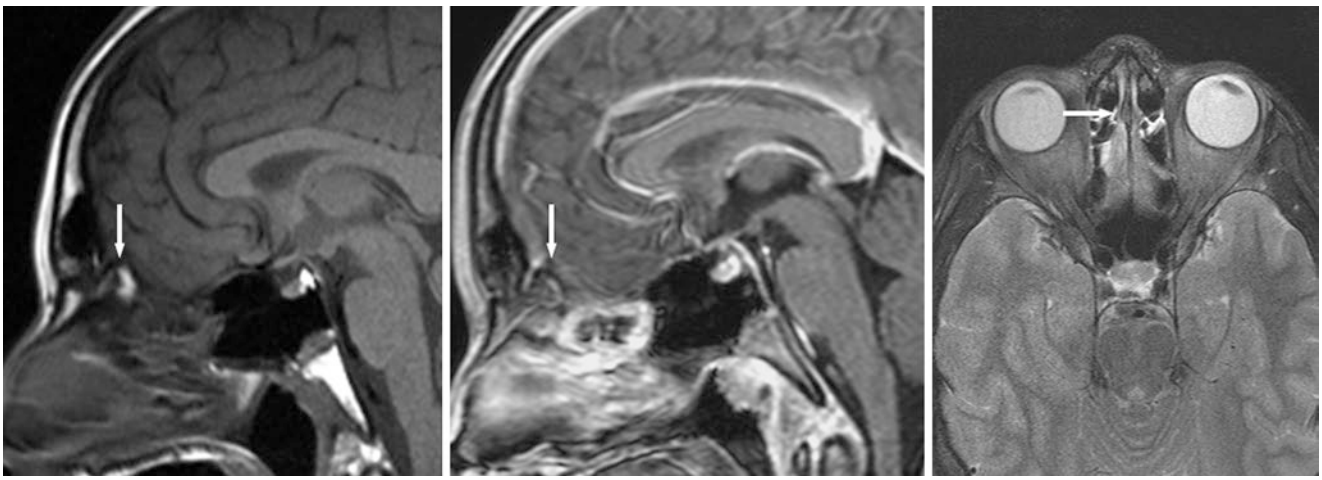

Fig. 29.7 A 14 year old with a bright crista galli on sagittal precontrast (*left*) and postcontrast T1WI (*middle*) that appears dark on axial FS T2WI (*right*)

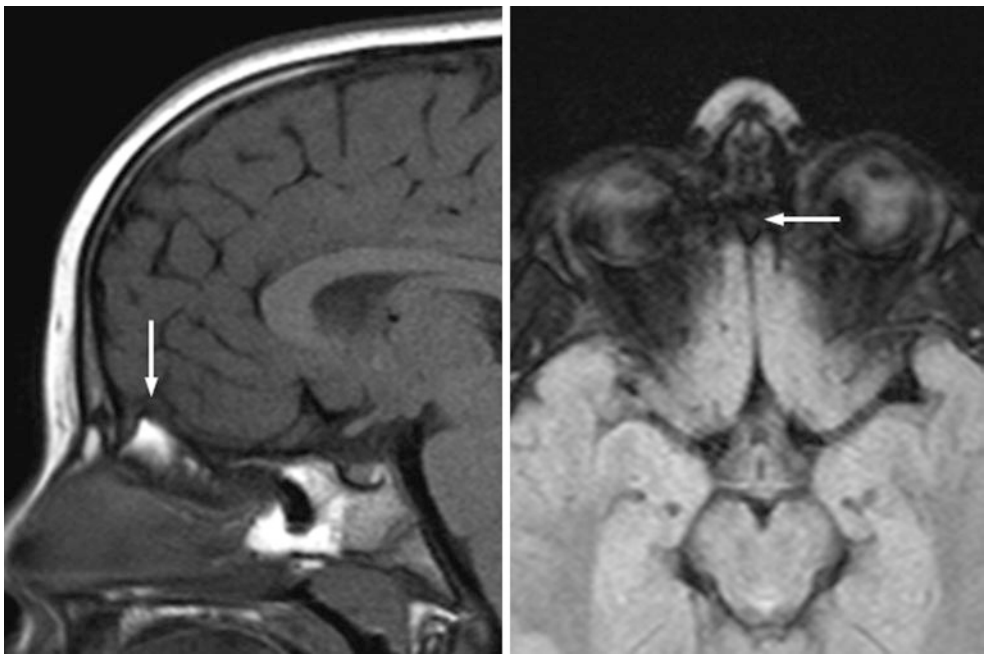

Fig. 29.8 A 5 year old with a T1-bright crista galli (*left*) that suppresses (darkens) on FS FLAIR (*right*) owing to the presence of internal fatty marrow

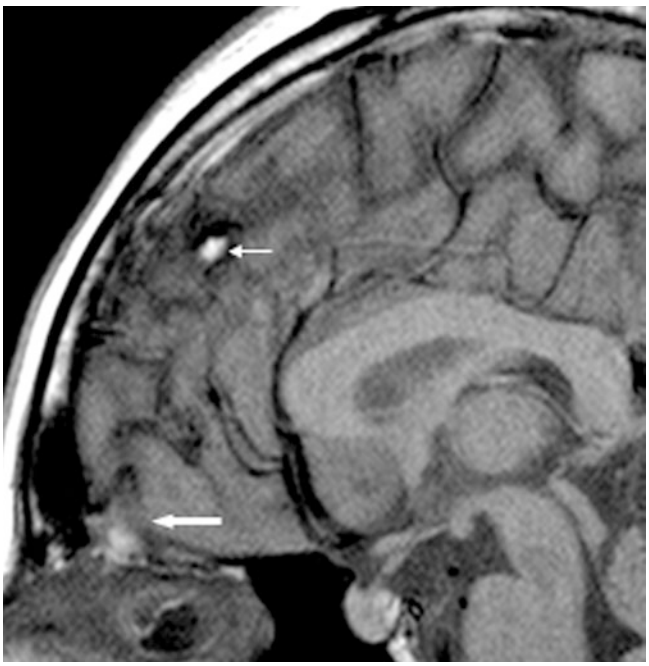

Fig. 29.9 A 34 year old with a T1-bright crista galli (*arrow*). Note an incidental falx calcification (*thin arrow*)

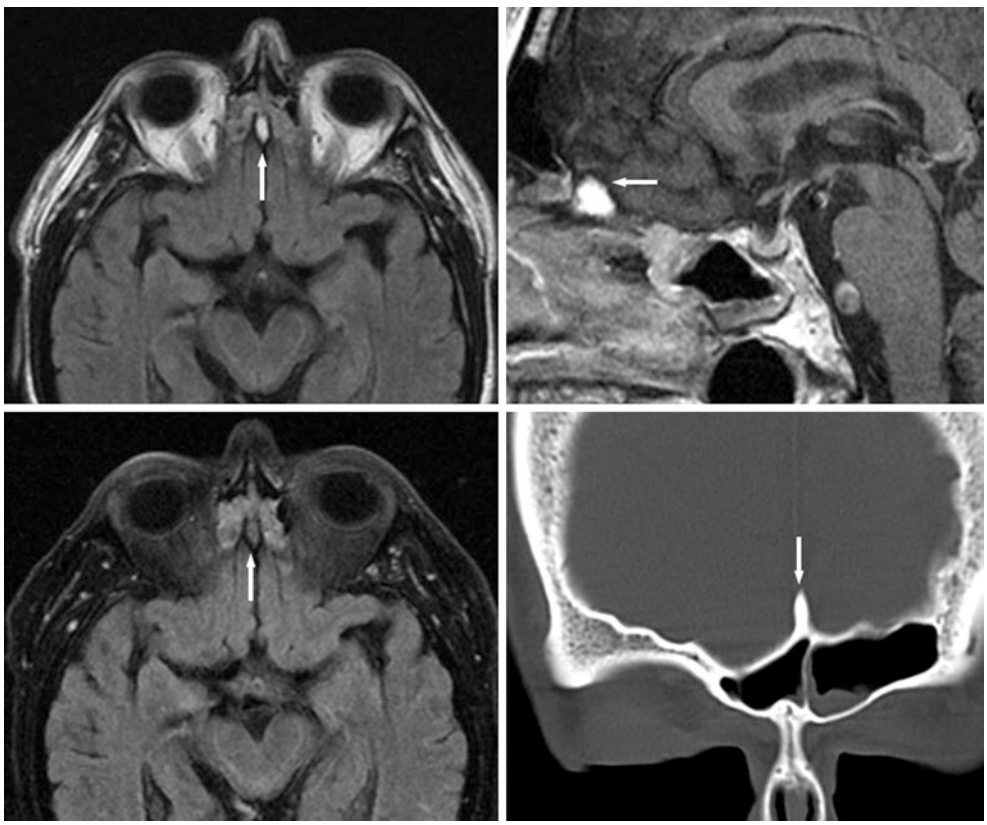

Fig. 29.10 A 65 year old with a T1-bright crista galli on axial non-FS FLAIR (*top left*) and on sagittal postcontrast T1WI (*top right*) that became dark on axial FS FLAIR (*bottom left*) due to fatty marrow. This was dense on coronal CT (*bottom right*)

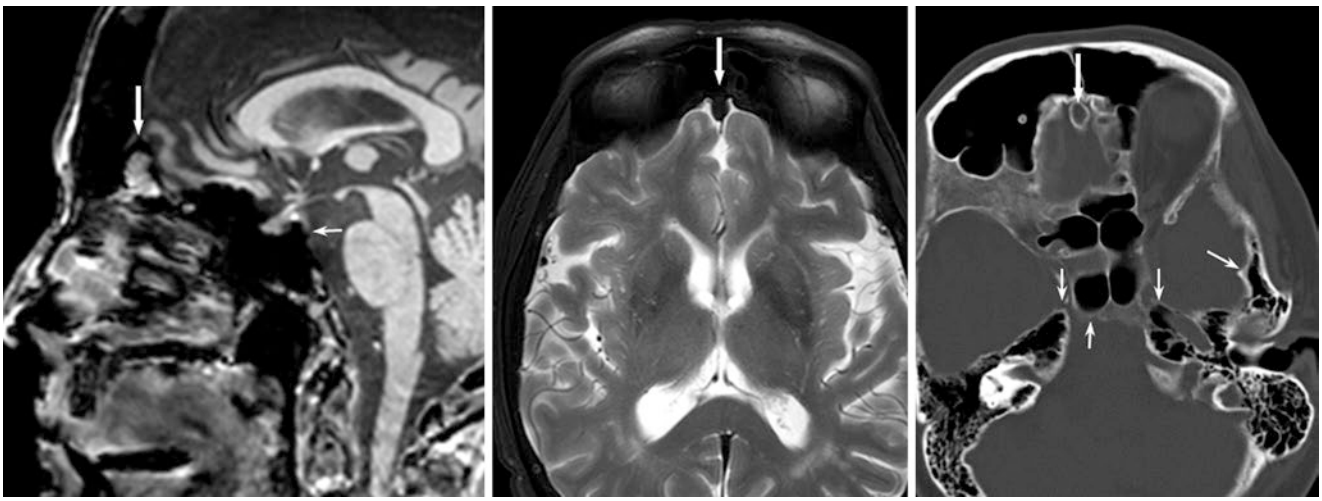

Fig. 29.11 A 71 year old with a bright crista galli on gradient echo T1WI (*left*) that was dark on FS T2WI (*middle*). On NECT (*right*) also note aeration of the petrous apices and dorsum sella (*thin arrows*)

29.3 Hyperostosis Frontalis Interna

Hyperostosis frontalis interna (HFI) is characterized by benign overgrowth of the inner table of the frontal bone. Although this had classically been described as part of various syndromes, it is idiopathic, usually asymptomatic (only very rarely causing symptoms via mass effect on the frontal lobes), and may be present in up to 10–20 % of females over 35–40 years age; 90–95 % of those affected are females from any culture or ethnicity, although males may also be affected [1–5, 9–17]. Hypotheses for this appearance are many and include increased leptin levels; also related are chronically increased estrogen stimulation and greater longevity (as HFI has become more prevalent in the past 100 years). A basis for an endocrine imbalance is that males with hormonal irregularities have been described to develop HFI [9–17].

The CT appearance can be irregular but is typically bilateral, symmetric, and following the expected signal of bone on MRI. This can slowly progress over time and at times appear rather pronounced to the point of partially "filling in" the volume loss of the cranial vault as the patient ages. Rarely, the cranium is involved diffusely; this is termed *hyperostosis calvaria diffusa* (HCD).

The hyperostosis can also be confluent with the falx cerebri. HCD is much less common and typically involves the bones in a contiguous fashion. After the frontal bone, the sphenoid, temporal, parietal, and occipital bones are involved. Typically, however, the frontal bones are the most affected part of the calvarium in HCD.

HFI should not be confused with metabolic abnormalities that thicken the calvarium diffusely such as *anemias, thalassemias, congenital disorders* of bone overgrowth, or multifocal disorders such as *Paget disease* or *fibrous dysplasia*. On MRI, HFI appears as a typical marrow signal, that is, it appears bright on T1WI and becomes dark with FS. HFI does not enhance after contrast administration, thus differentiating it from both fibrous dysplasia and Paget disease, both of which usually enhance avidly and diffusely due to vascularity. In particular, HCD can occasionally be confused with Paget disease, although the latter typically has bony overgrowth that enhances avidly on postcontrast imaging and involves most of the calvarium (Figs. 29.12, 29.13, 29.14, 29.15, 29.16, 29.17, 29.18, 29.19, 29.20, and 29.21).

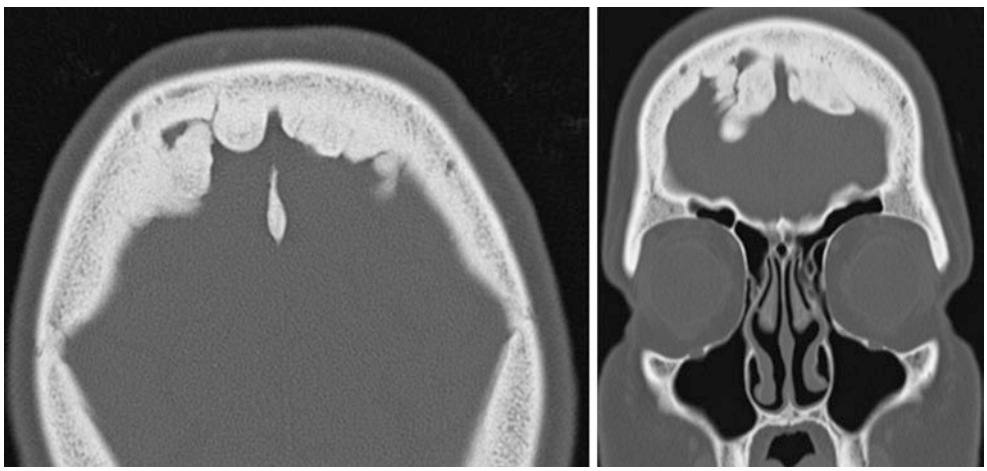

Fig. 29.12 A 52-year-old female with HFI on NECT with axial and coronal reconstructions

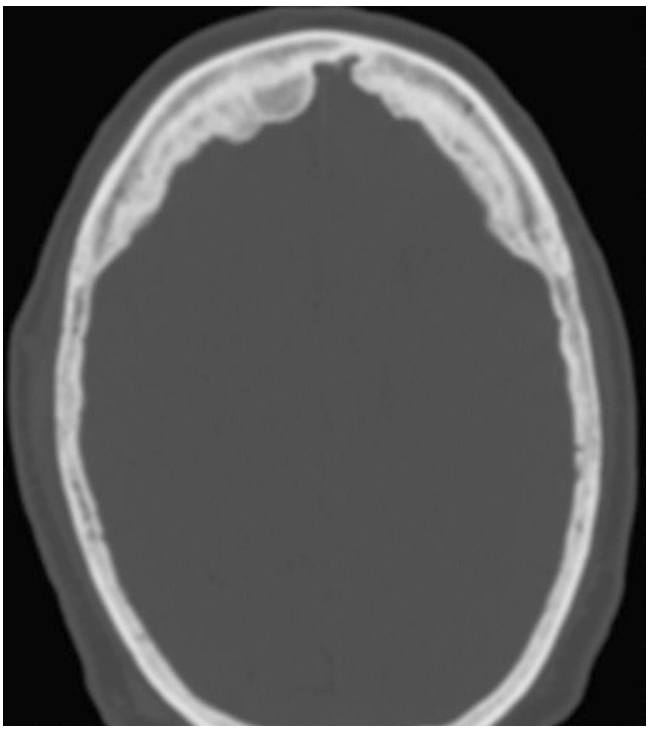

Fig. 29.13 A 64-year-old male with HFI

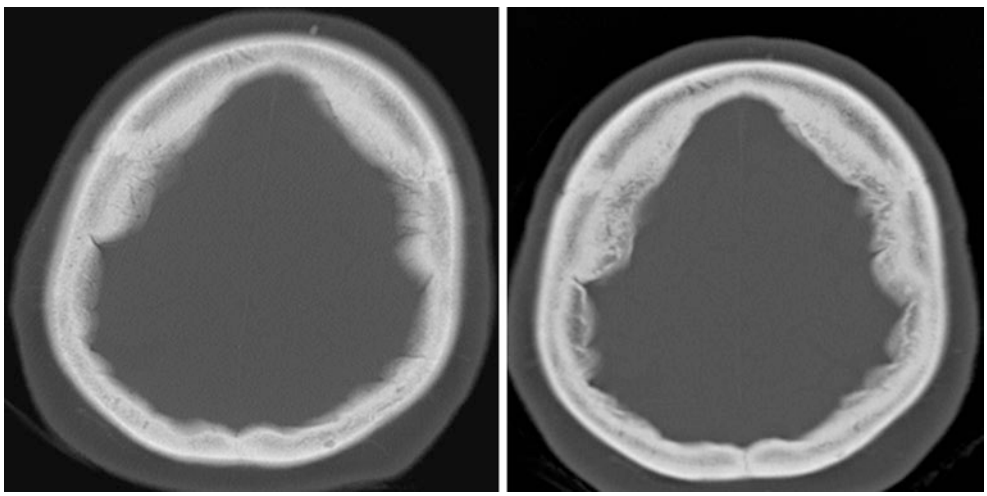

Fig. 29.14 A 59-year-old female with HFI that progressed over 5 years between initial (*left*) and follow-up (*right*) NECT examinations

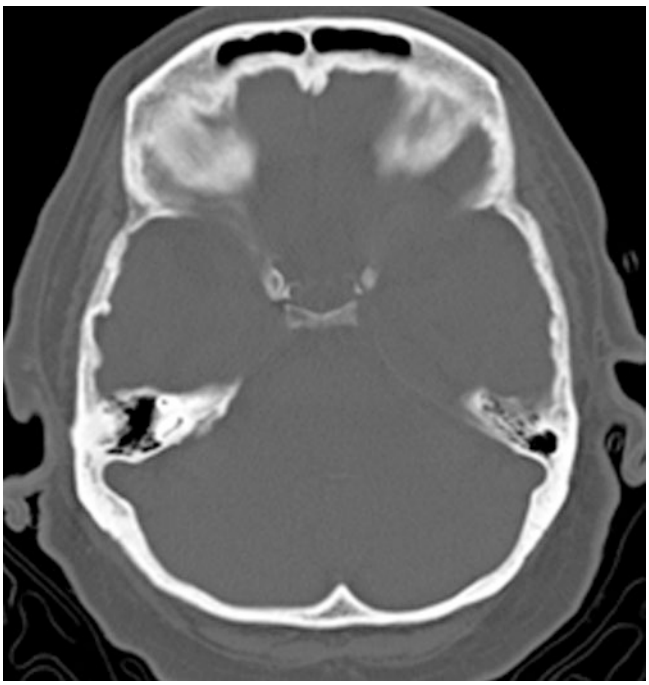

Fig. 29.15 An 81-year-old female with early/mild HCD

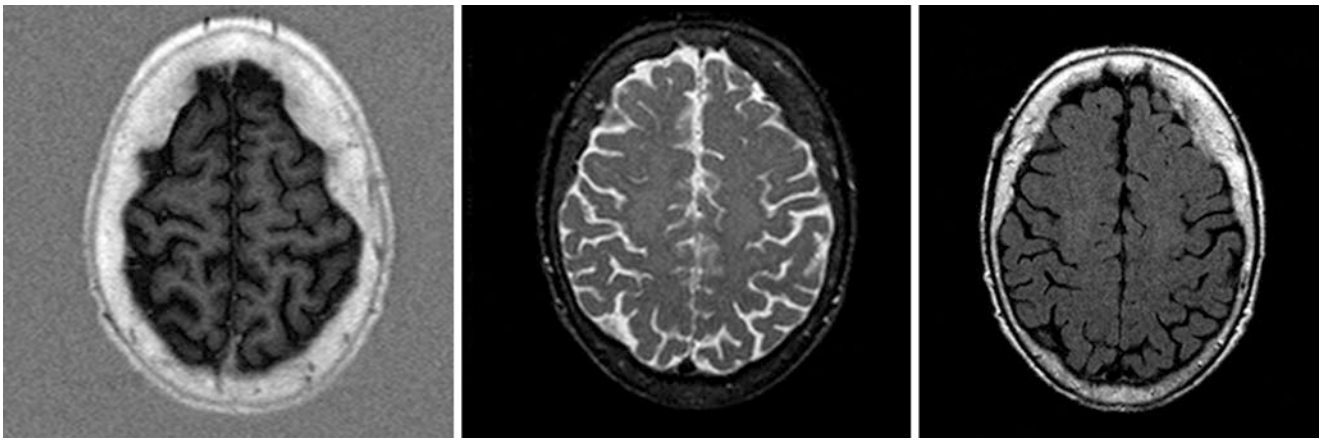

Fig. 29.16 A 79-year-old female with HFI on T1- (*left*) and T2-inversion recovery (*middle*) and non-FS FLAIR (*right*) MRI

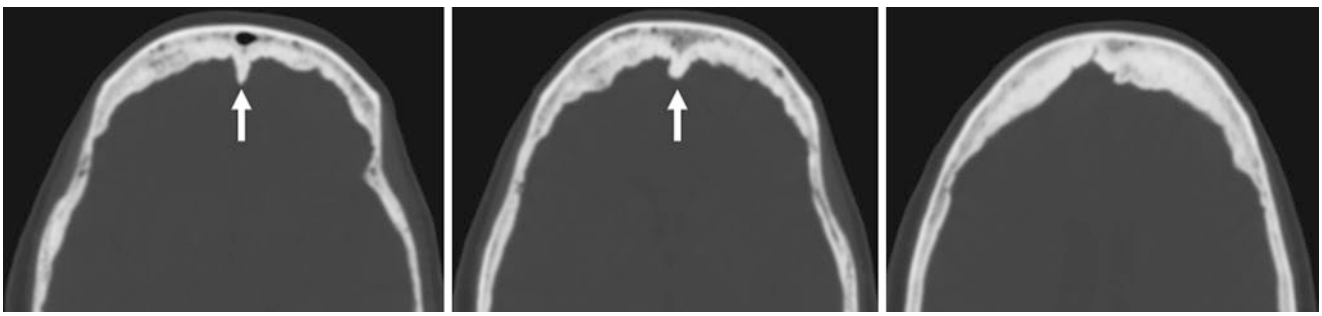

Fig. 29.17 An 80-year-old female with HFI that is contiguous with the falx cerebri (*arrows*)

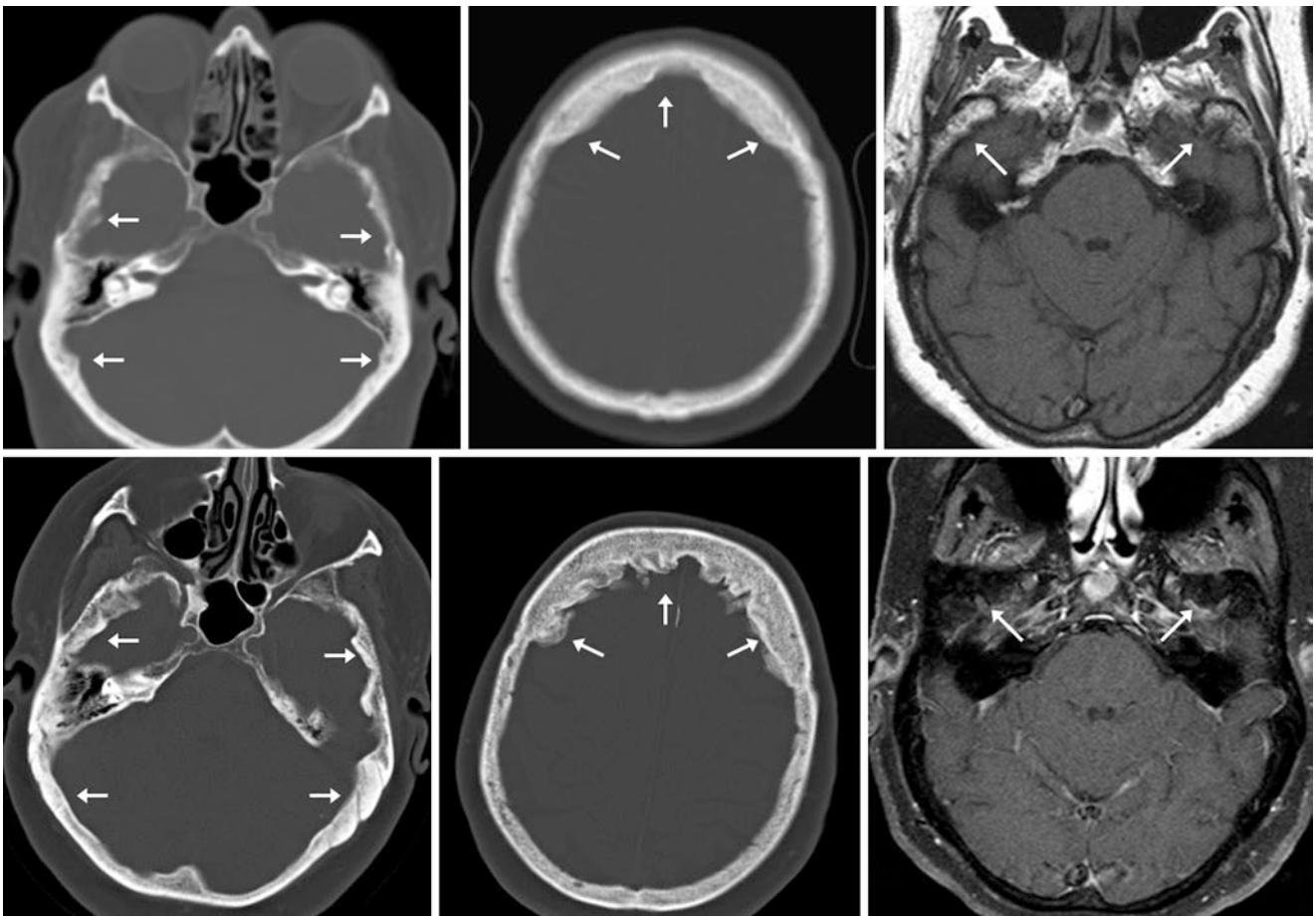

Fig. 29.18 An 80-year-old female with asymptomatic HCD noted on a NECT from 1997 (*top left and middle*). Note temporal bone hyperostosis on a 1.5T noncontrast T1WI MRI (*top right*). The hyperostosis had progressed on NECT 10 years later (*bottom left and middle*). Note suppression of bright fatty marrow on the later T1WI MRI, which utilized FS (*FS*, *bottom right*)

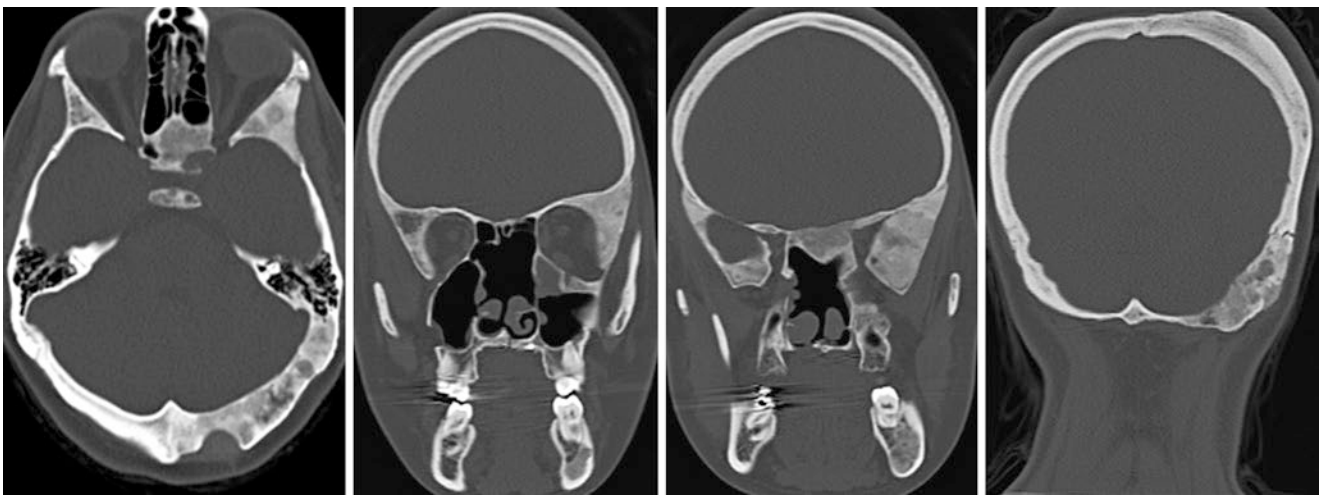

Fig. 29.19 Comparison case of fibrous dysplasia: In a 29-year-old female various areas of thickened, mixed lytic and ground-glass calvarium were noted on NECT in axial (*left*) and coronal (*right three images*) planes. While the sphenoid, occipital, temporal, and parietal bones are affected bilaterally, the sparing of some locations is typical of this disorder and not of Paget disease

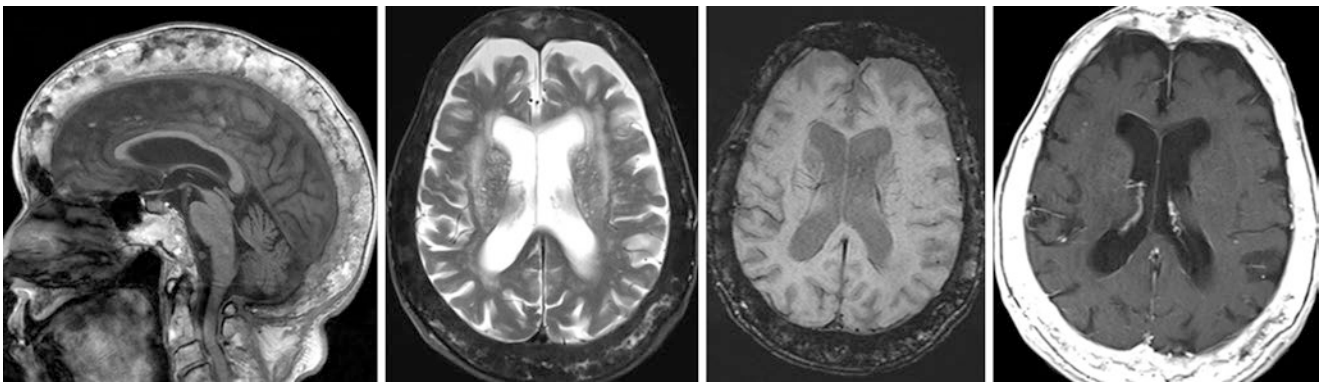

Fig. 29.20 Comparison case of Paget disease: In a 90-year-old female with a negative cancer work-up a diffusely enlarged and thickened skull with heterogeneous marrow was noted on 3T noncontrast sagittal T1WI (*left*), axial FS T2WI (*left middle*), and SWI (*right middle*). On axial postcontrast T1WI (*right*), the marrow diffusely enhances, typical of Paget disease

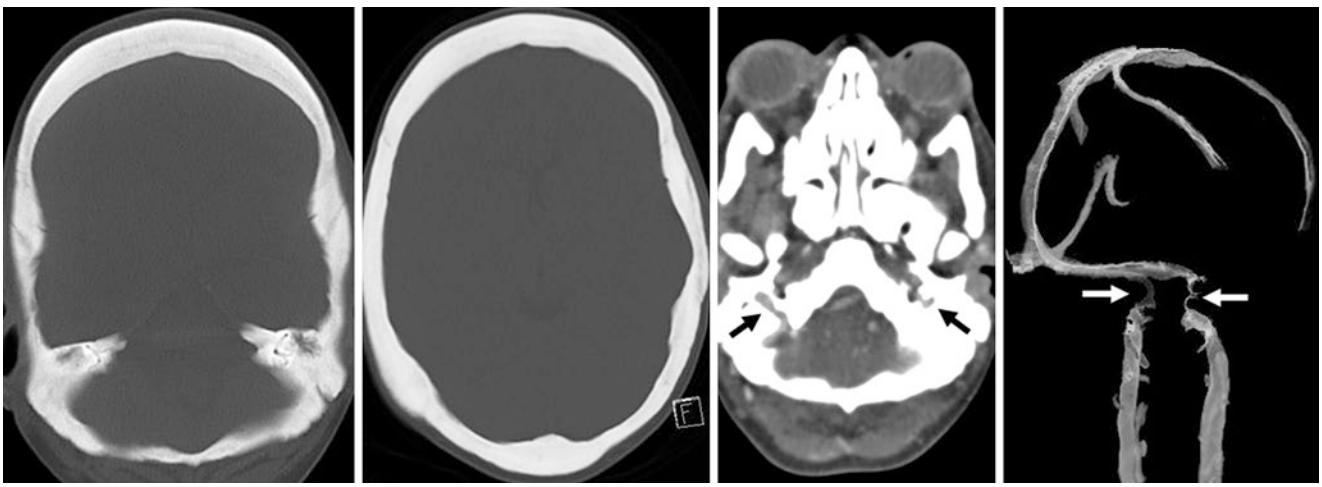

Fig. 29.21 Comparison case of osteopetrosis: In a 17-year-old female a diffusely thickened and hyperdense skull was noted on axial NECT (*left images*). A CT venogram (*right middle*) showed diminutive jugular foramina bilaterally (*arrows*), left greater than right, which was confirmed on three-dimensional VR venographic left posterior oblique images with bone segmented away (*right*)

29.4 Enostoses and Exostoses of the Calvarium

In musculoskeletal (MSK) radiology, the term *enostosis* has often been considered synonymous with bone island, while an *exostosis* has been considered to be synonymous with a bony or cartilaginous outgrowth such as an *osteoma* or *osteochondroma*. There can be confusion in reading divergent neuroradiologic literature in which some have perhaps mistakenly designated enostoses as protruding inward and exostoses as protruding outward. This terminology should be avoided because an enostosis (i.e., bone island) in pathology is considered a focus of concentrated, compact bone within cancellous bone (some consider this to be a form of *hamartoma*), while an exostosis is either an osteoma from a bony protrusion of membranous bone or rarely has cartilaginous elements such as osteochondroma. Thus, the variety within the literature as to actually what histopathology is present when a benign sclerotic lesion of the skull is encountered is cumbersome with fewer available larger case studies within the neuroradiologic literature [18–30]. To add to the confusion, some consider that sclerotic lesions cannot be true enostoses because they do not occur within the cancellous bones of the skull. Others believe that sclerotic-appearing foci of the skull that protrude should all be considered *osteomas* (i.e., lacking cartilaginous elements). Finally, further confusion occurs because some report an exostosis to refer solely to osteomas, while others consider extoses to refer only to osteochondromas. Such opinions are probably extreme and difficult to prove because most neuroimaging reports either do not indicate pathology or are anecdotal case reports [18–30].

In the author's experience, each of the above-mentioned observations has elements of truth to a degree but they are problematic if used by themselves. Some general guidelines may help describe and delineate the most likely histology of such lesions based on well-described appearances of such sclerotic lesions of the long bones [18–30]. First, true *enostoses* (bone islands) are rather uncommon in the calvarium but do occur rarely since they can be present anywhere within the skeleton, and there is cancellous bone present throughout the calvarium. They can occur along the skull's inner or outer table (usually frontal) or centrally within the calvarium and can be considered as focal areas of hyperostosis without bony expansion or surrounding hypoattenuation or protrusion outward or inward. Rarely, these have a characteristic thorny radiation, an appearance more typical elsewhere in the skeleton. Enostoses are usually solitary and asymptomatic but their appearance can be confirmed by their being cold on nuclear medicine scintigraphy. This is not necessary or cost effective in most cases unless the patient has a clinical history that necessitates to exclude metastatic disease. On MRI, enostoses are usually dark, nonprotruding structures; the susceptibility artifact on T2*WI and the lack of enhancement are clues that the structure is bone, while CT confirms an enostosis.

In contrast, *exostoses* are typically inward or outward protruding, may be pedunculated, and arise from membranous bone [18–30]. They are typically either osteomas (mature bony overgrowth) or osteochondromas (benign cartilagious elements). Again, rather than using the designation of some neuroradiology literature that has mistakenly termed solely protrusions outward from the outer table as exostoses via MSK radiologic criteria, protrusion either inward or outward can be termed an exostosis, which typically represents either an osteoma or a osteochondroma. Notably, other processes such as calcified ("burnt-out") *meningiomas*, remote *inflammatory or infectious insults*, postsurgical *calcifications*, or sequelae of *subdural hematomas* can appear to be extra-axial, densely calcified, and can seem to arise from the skull's inner table. By noting findings such as bony overgrowth (osteomas) or a cap of enhancement (osteochondromas), these lesions can be distinguished from each other. On post-contrast T1WI MRI, the rare *osteochondroma* has an enhancing cartilaginous cap, which is suspicious for malignant degeneration if it is greater than 1.5 cm in thickness; if it is less than 1.5 cm at detection, a follow-up in 1 year is probably prudent. Another rare appearance is that of a heterogeneously enhancing base with diffuse cartilaginous elements rather than a cap, similar to the appearance of a chondrosarcoma.

Whether it is an osteoma or osteochondroma, an exostosis can occasionally cause confusion on T2WI by appearing dark and simulating flow voids of *aneurysms* or calcified extra-axial lesions such as *meningiomas*. On nuclear medicine scintigraphy, osteochondromas have elevated uptake only in the active growth phase and then normalize relative to other bones over time, whereas osteomas have no increased uptake [18–30]. If the type of exostosis is unclear, following it over time such as at 1 year with either NECT or MRI is a prudent approach once a lesion is confirmed to be calvarial in nature.

Notably, there can be an overlap in appearance between enostoses and sessile exostoses, which has probably contributed to some of the confusion [18–30]. However, in either scenario such nonprotruding sclerotic foci should be "don't touch" lesions. Protruding exostoses, whether inward or outward, can be pedunculated and can rarely cause symptoms, particularly if they abut a cranial nerve. While osteochondromas are considered extremely rare in the calvarium, they may be present or multiple in the rare case of *Gardner syndrome* (polyposis with multiple hereditary exostoses). In this syndrome one should watch for the rare presence of an enhancing cartilaginous cap if an exostosis is present on a brain MRI. This author has also noted several cases in which *benign hyperostosis frontalis* occurs concomitantly with an

exostosis, which is interesting but likely of no clinical significance.

Also notable is that *osteoid osteomas* are also in the differential diagnosis; they typically have a centrally dense appearance surrounded by a hypoattenuating ring. These can be symptomatic and have an elevated uptake on nuclear medicine scintigraphy. They are not considered a "don't touch" lesion because of potential symptoms (Figs. 29.22, 29.23, 29.24, 29.25, 29.26, 29.27, 29.28, 29.29, 29.30, 29.31, 29.32, 29.33, 29.34, 29.35, 29.36, and 29.37).

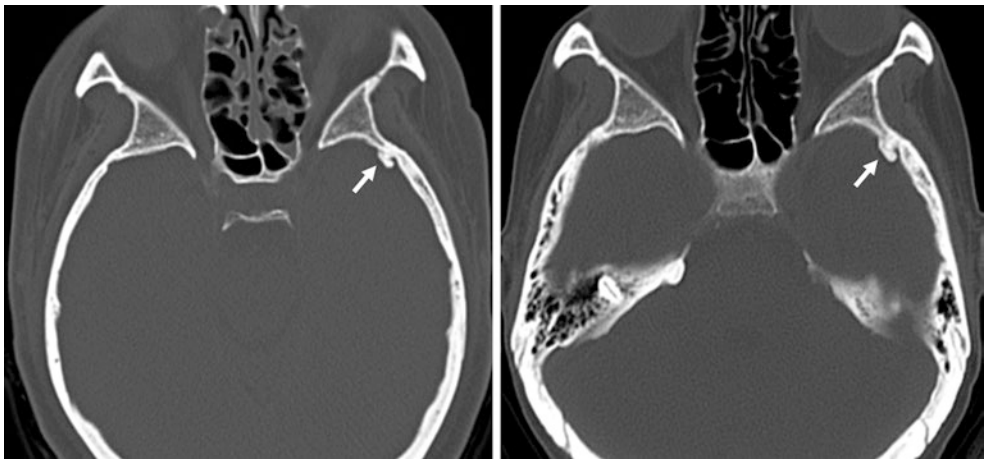

Fig. 29.22 A 36-year-old female with a small exostosis (*arrows*) present along the inner table of the greater wing of the left sphenoid on CT (*left*). It was unchanged 4 years later (*right*), probably representing an osteoma

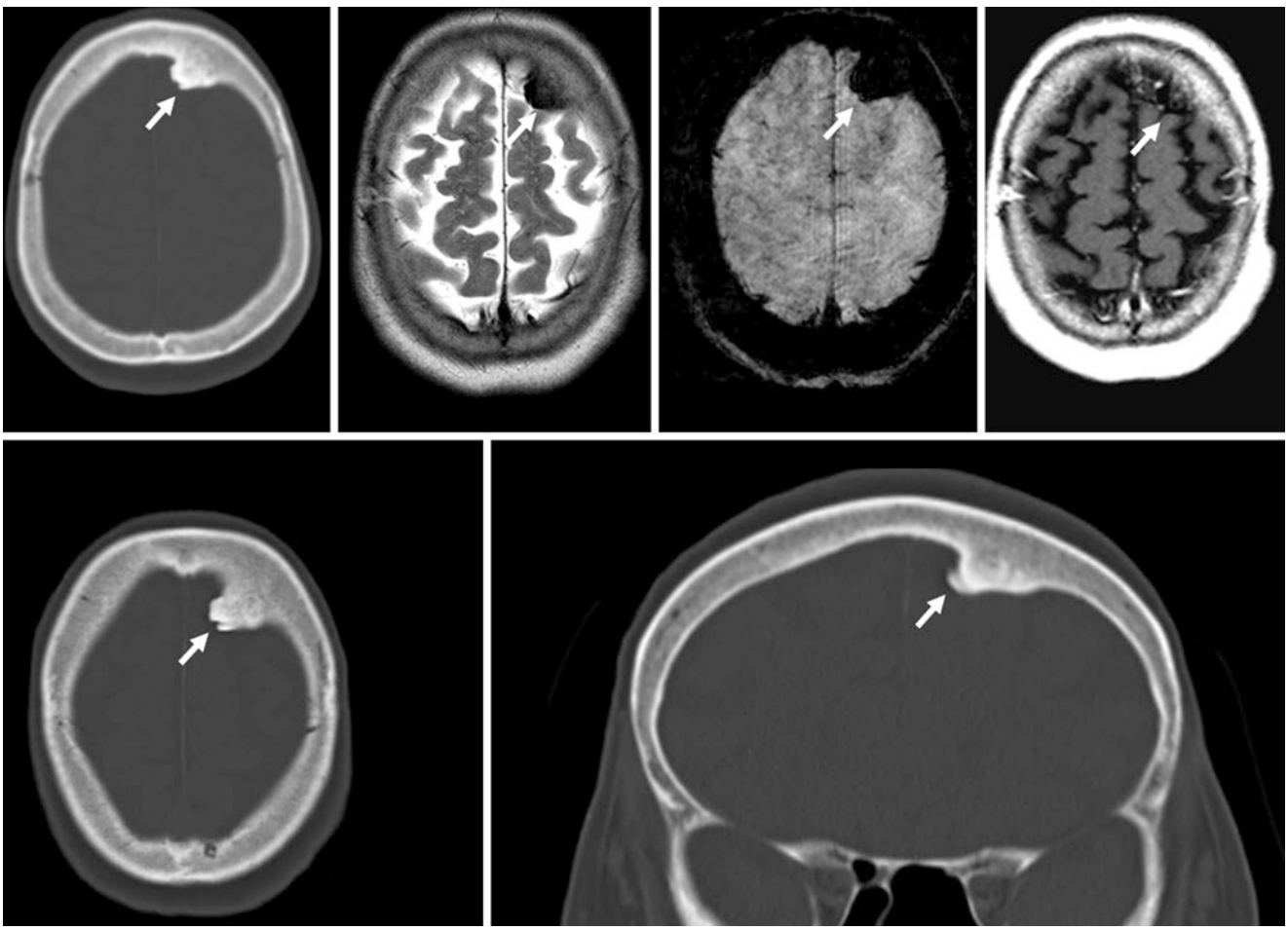

Fig. 29.23 An 89 year old: *Top row*: NECT (*left*) depicts a large exostosis (*arrows*) of the inner table of the frontal skull that is dark on T2WI (*left middle*), SWI (*right middle*), and T1WI after contrast (*right*). *Bottom row*: 5 years later it was unchanged on axial and coronal NECT, probably representing an osteoma

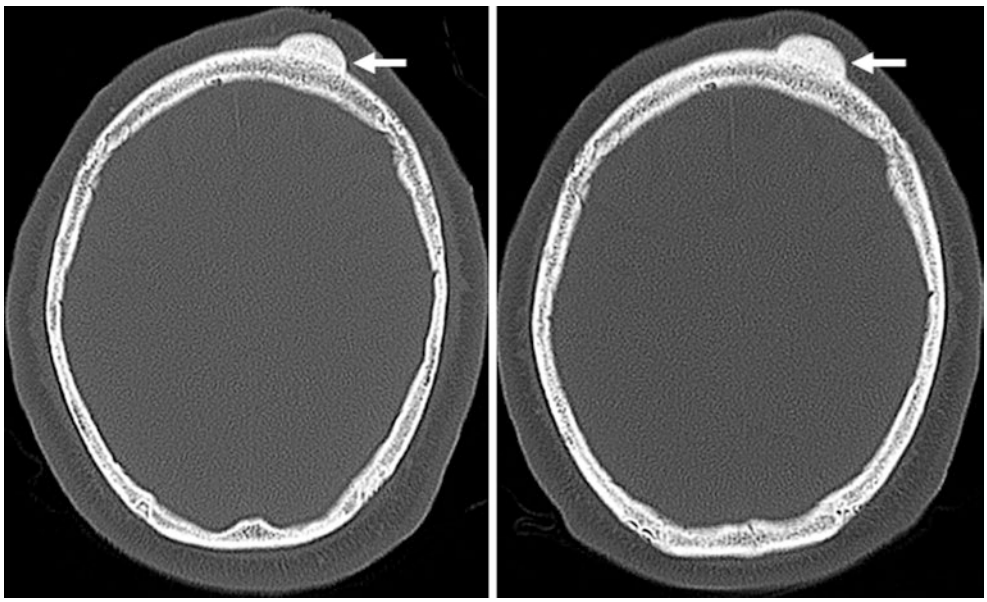

Fig. 29.24 A 62-year-old male who felt a frontal scalp "lump." NECT (*left*) showed a protruding exostosis (*arrows*) suggestive of an osteoma. The osteoma was unchanged 1 year later (*right*)

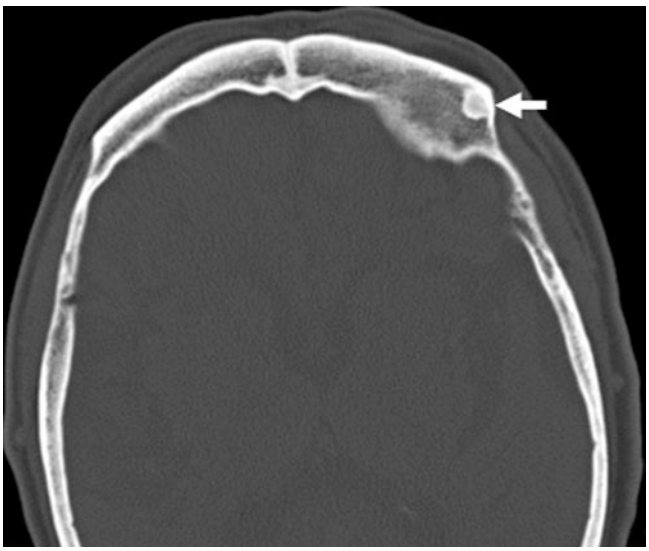

Fig. 29.25 A 63-year-old male with a skull enostosis or bone island (*arrow*)

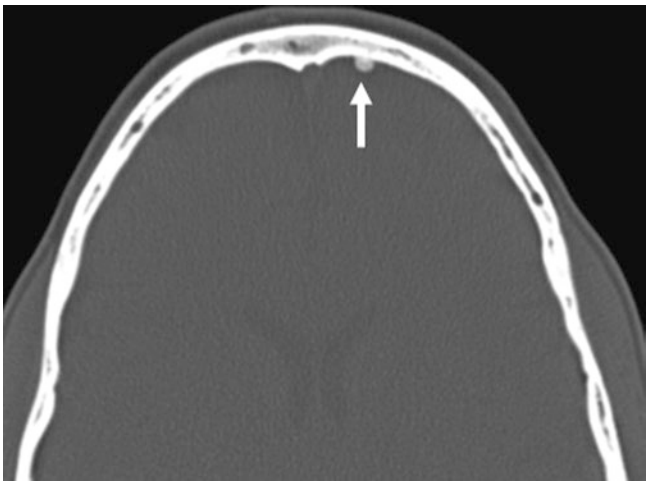

Fig. 29.26 A 40 year old with a very tiny exostosis, most likely an osteoma

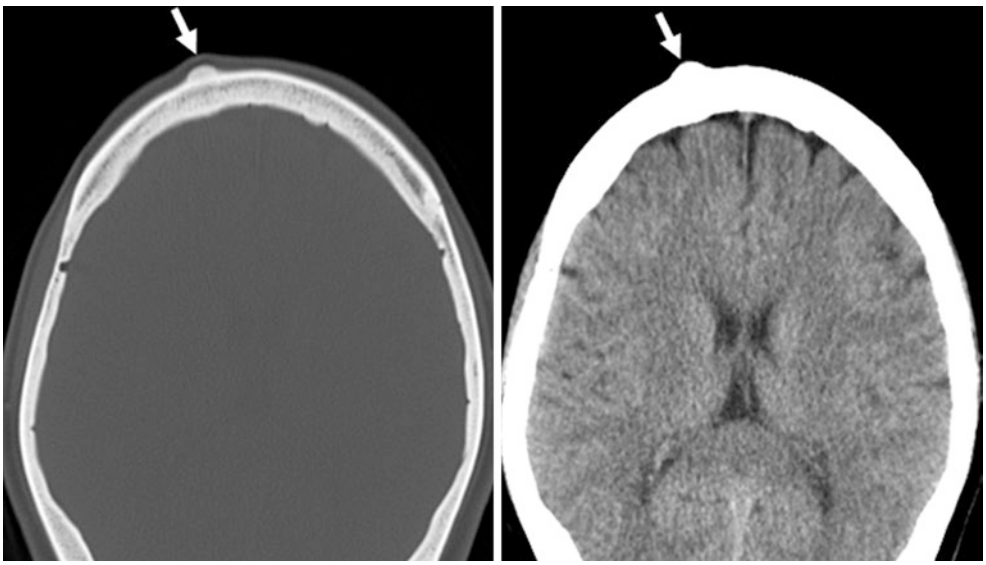

Fig. 29.27 A 48 year old with an outward-protruding exostosis (*arrows*) on NECT, probably an osteoma

Fig. 29.28 A 35-year-old male with a small pedunculated exostosis probably representing an osteoma

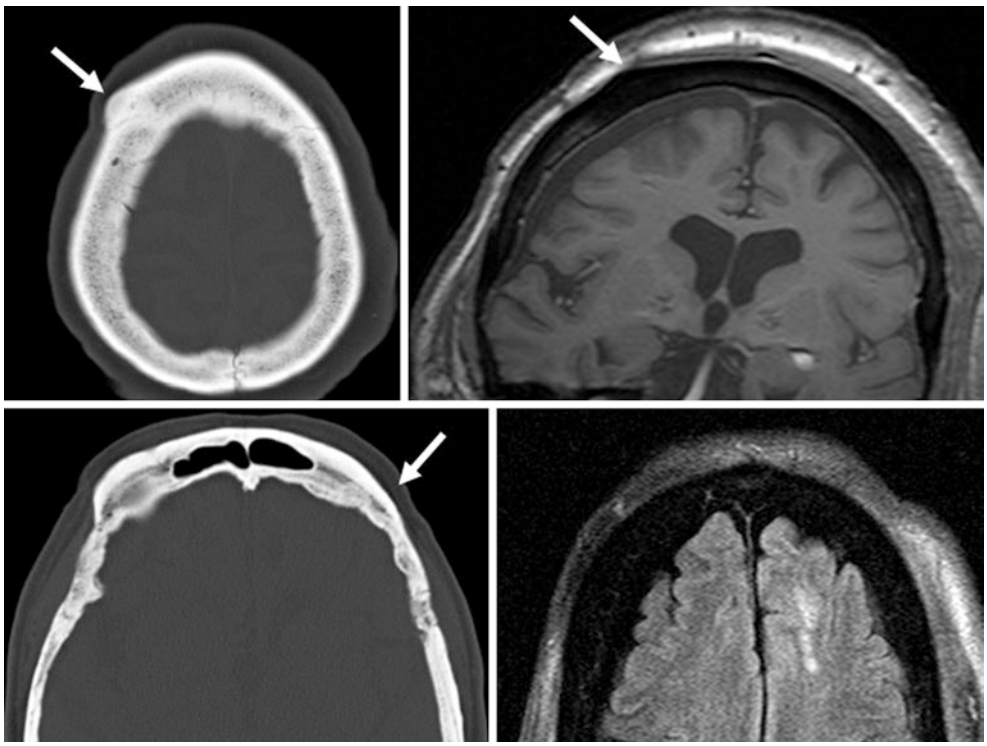

Fig. 29.29 A 67-year-old patient. *Top row*: an exostosis on NECT (*left*) that did not enhance on TWI MRI (*right*), suggesting an osteoma. *Bottom row*: Also note left-sided hyperostosis frontalis on NECT (*left*) and fat-suppressed FLAIR (*right*)

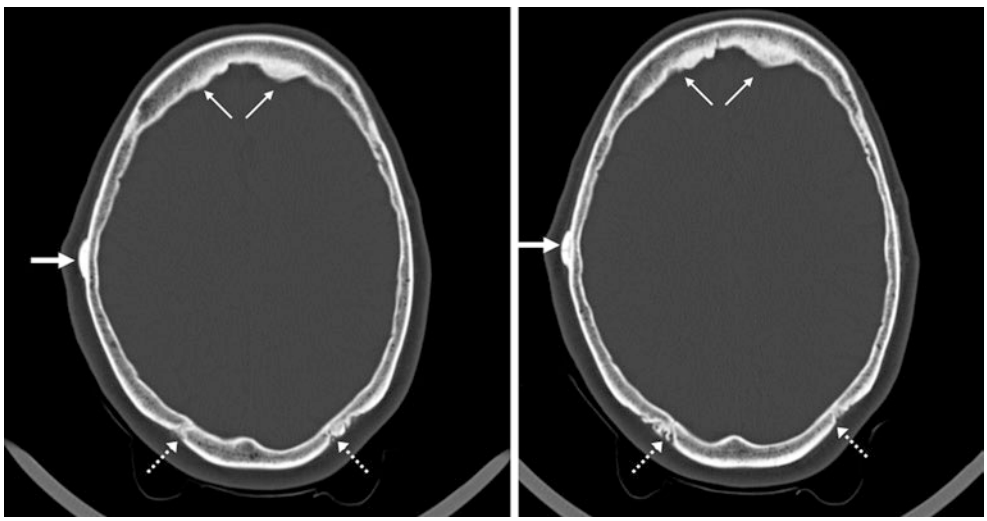

Fig. 29.30 A 66-year-old female with a right frontal exostosis (*arrows*) and hyperostosis frontalis bilaterally (*tiny arrows*) as well as incidental mild normal bathrocephaly (*dashed arrows*). This case again demonstrates that hyperostosis frontalis can simulate (or cause?) osteomas

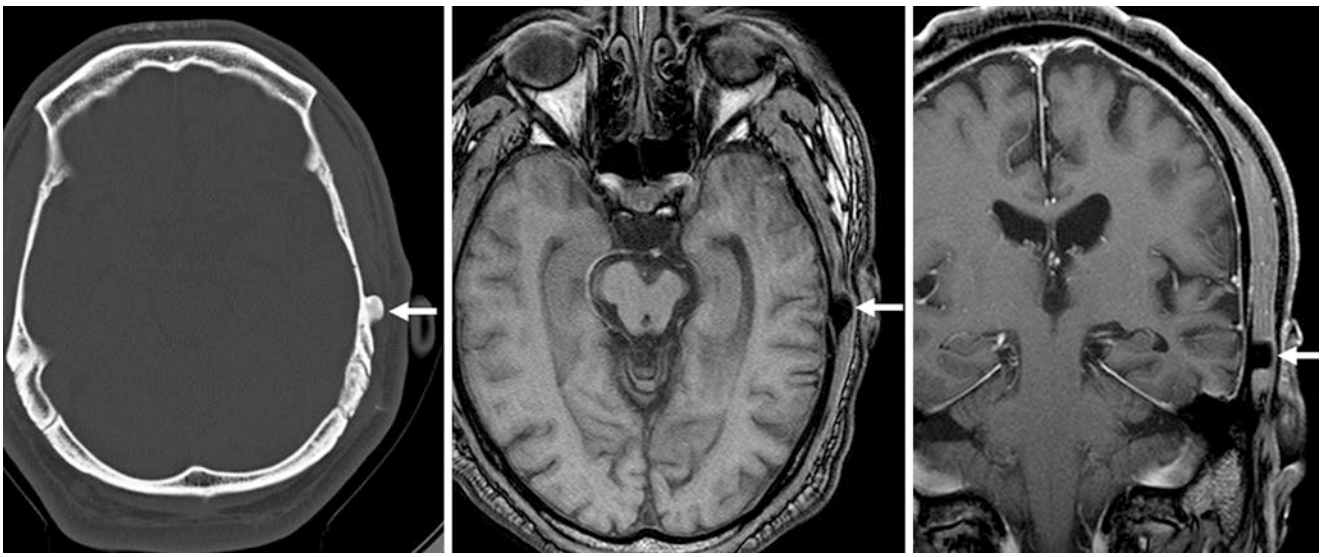

Fig. 29.31 A 49 year old with an exostosis (*arrows*) that protrudes from the calvarium on NECT (*left*), noncontrast axial T1WI (*middle*), and coronal postcontrast T1WI with FS (*right*). The lack of enhancement of a cartilaginous cap indicates an osteoma

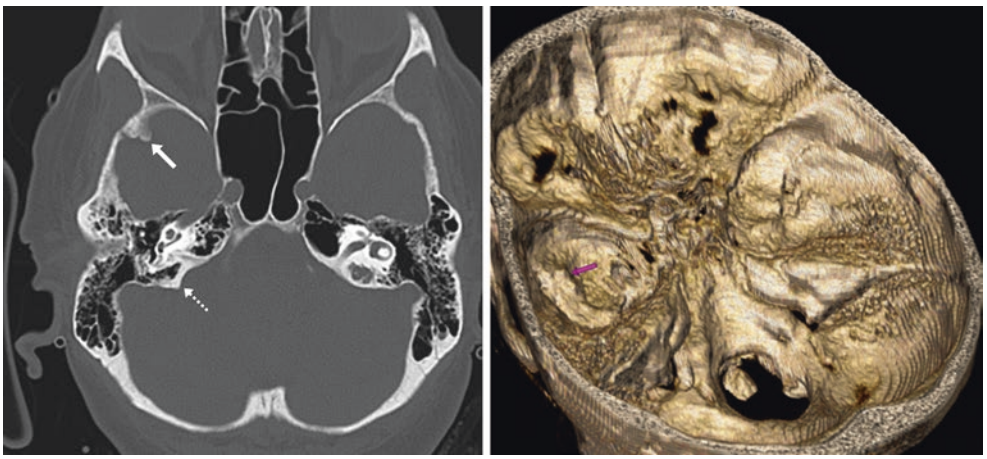

Fig. 29.32 A 60 year old with a focal exostosis that causes inward ridging over the right spheno-squamosal suture (*left, white arrow*); this likely represents an osteoma. A three-dimensional VR image (*right, inner superior view*) confirms the exostosis (*pink arrow*). Also present on the right side is a tiny area of hyperostosis along the petrous apex (*left, dashed arrow*)

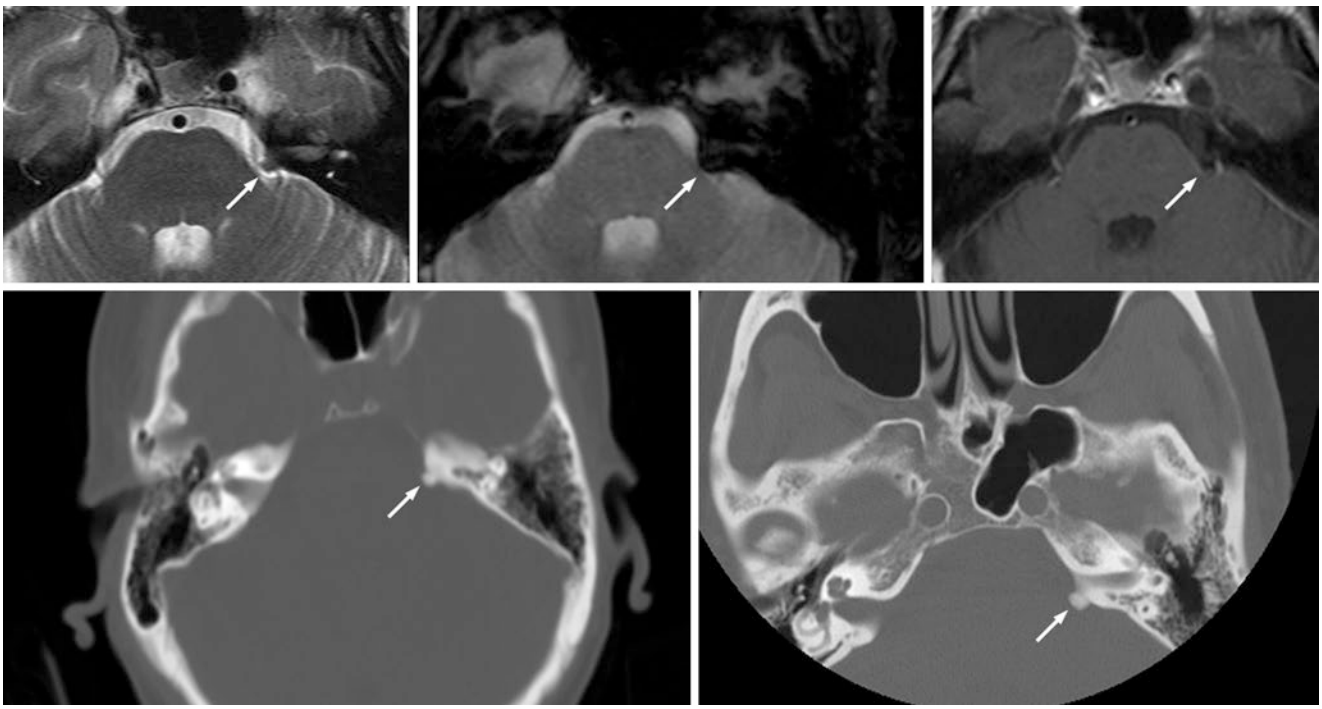

Fig. 29.33 A 52-year-old patient. *Top row*: a focus of dark signal within the left cerebellopontine angle mimicked an extra-axial lesion such as an aneurysm or a calcified meningioma on axial T2WI (*left*), T2*WI (*middle*), and postcontrast T1WI MRI (*right*). *Bottom row*: an exostosis (*arrows*) was present along the petrous apex on axial NECT, suggesting osteoma. This was the result of the presence of susceptibility artifact on T2*WI from ossification and the lack of enhancement on MRI

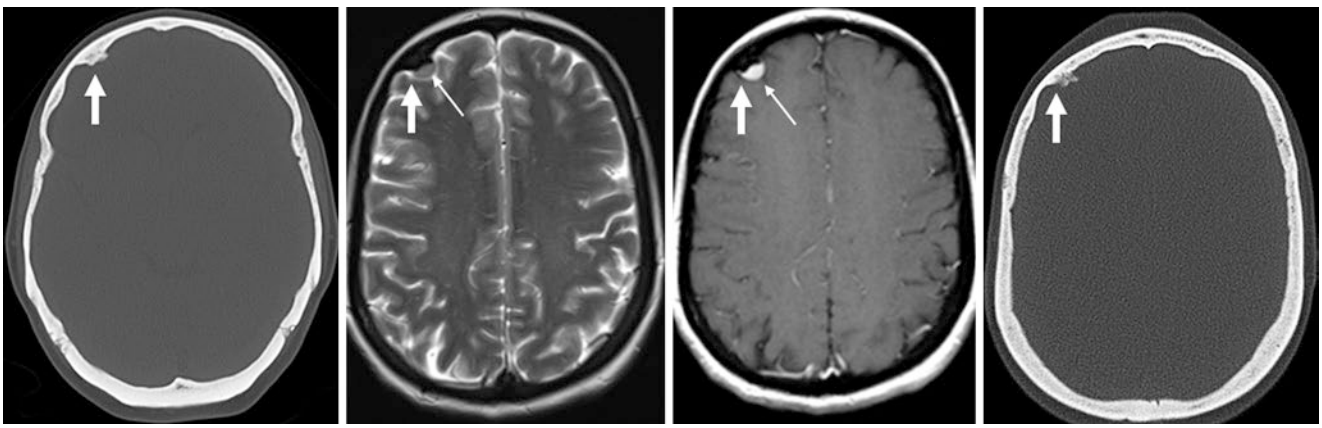

Fig. 29.34 A 59-year-old female with sinusitis had an incidental exostosis (*arrows*) oriented inward on axial NECT (*left*), initially questioned as secondary to meningioma. However, a 1.5T MRI showed a lack of a cleft between this lesion and the calvarium on T2WI (*left middle*), and there was an enhancing cap 5–6 mm thick (*thin arrows*) delineated on postcontrast FS T1WI (*right middle*) typical of a rare, benign osteochondroma. This was stable 2 years later on NECT (*right*)

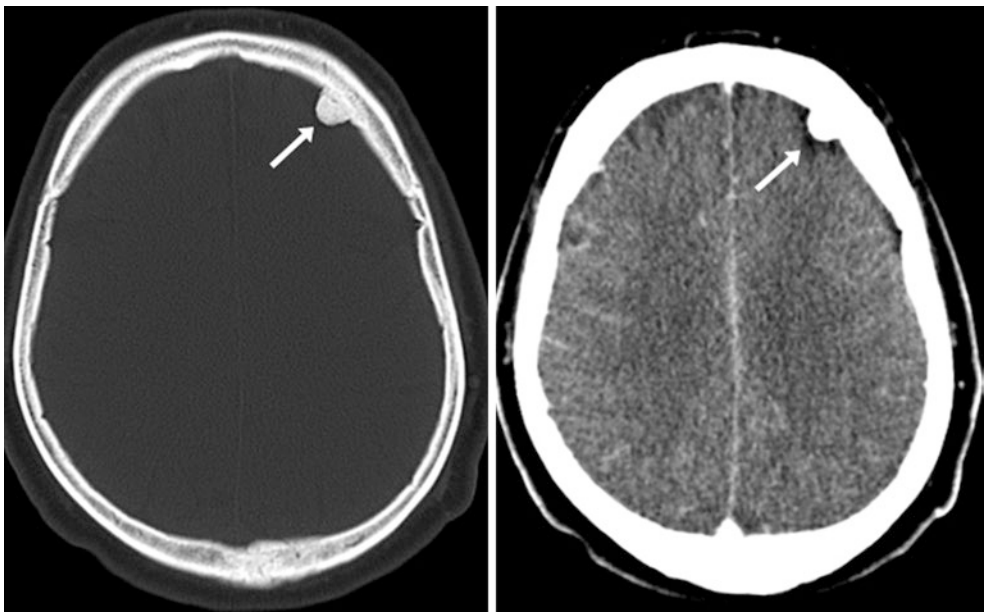

Fig. 29.35 A 52-year-old male with an otherwise negative noncontrast (*left*) and postcontrast (*right*) axial NECT. An exostosis (*arrows*) lacked an enhancing cap and lacked a cleft between it and the calvarium, identifying it as an osteoma

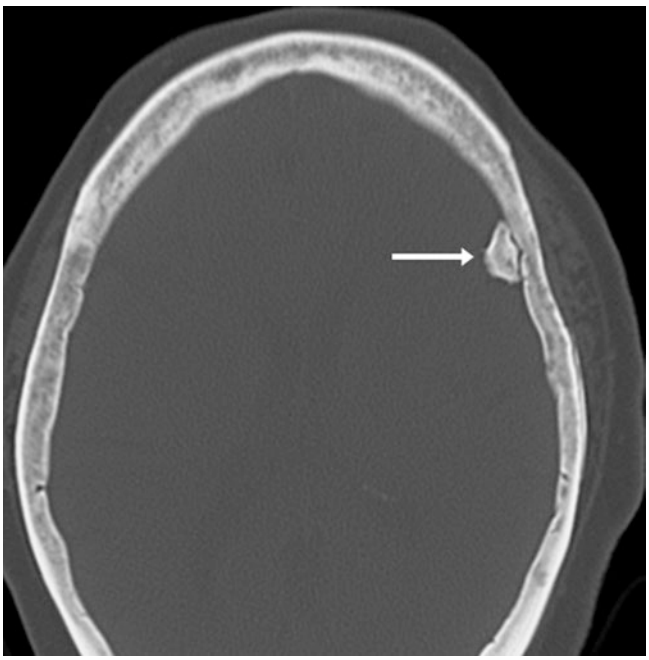

Fig. 29.36 Comparison case: dural calcification from a calcified meningioma, inflammation, or prior infection. Note a cleft between the lesion and the calvarium

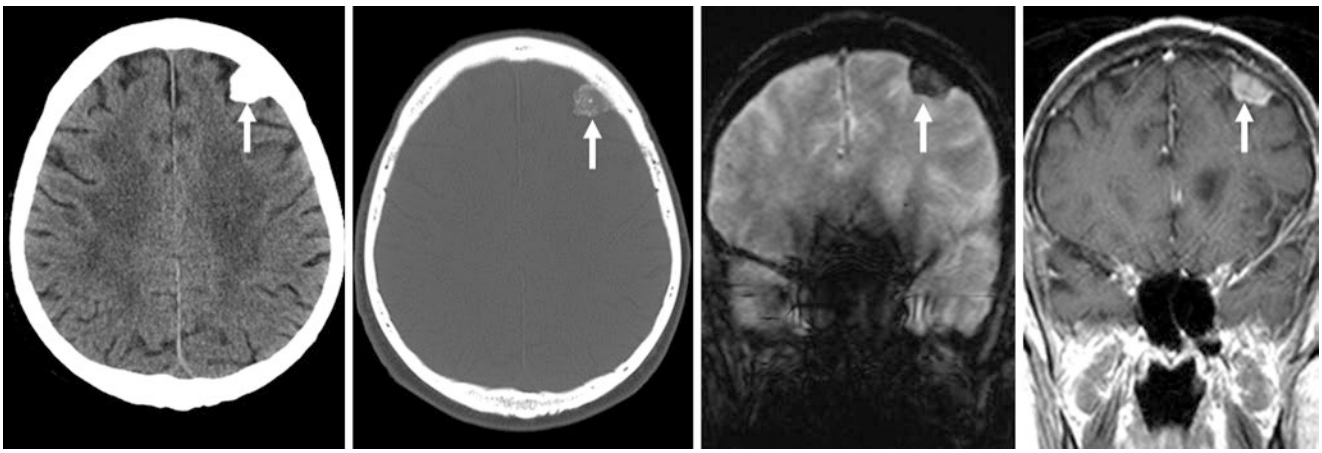

Fig. 29.37 Comparison case: a 62 year old with an extra-axial, dense lesion on CT (*left images*) that simulated an enostosis. This is dark on T2*WI (*right middle*) but enhances on T1WI MRI (*far right*), consistent with a calcified meningioma that is intimately associated with the calvarium

29.5 External and Internal Occipital Protuberances

The *EOP* and the *internal occipital protuberance* (IOP) are normal, midline, outward and inward projections of the occipital bone. They may occasionally appear quite prominent, have clefting, and have some asymmetry favoring one side or the other. These can sometimes mimic bony sclerotic lesions or reactive bone formation from extra-axial lesions such as *meningiomas*. They are only problematic when occasionally a patient (or their parent) will spontaneously notice an EOP and become concerned. On MRI, they usually follow cortical bone on most sequences; they are variably bright or dark on fast spin-echo T1WI and T2WI but usually appear dark on gradient-echo images. They typically darken following FS (Figs. 29.38, 29.39, 29.40, 29.41, 29.42, 29.43, and 29.44).

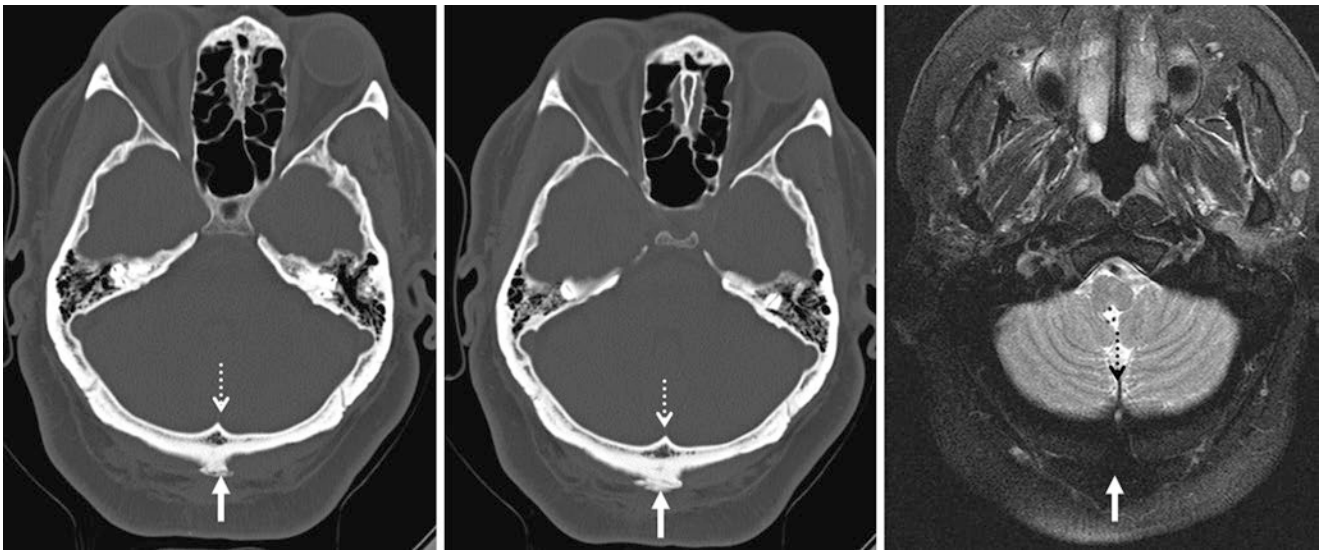

Fig. 29.38 A 63 year old with an EOP (*solid arrows*) and IOP (*dotted arrows*) on axial NECT (*left and middle*) and T2WI MRI (*right*)

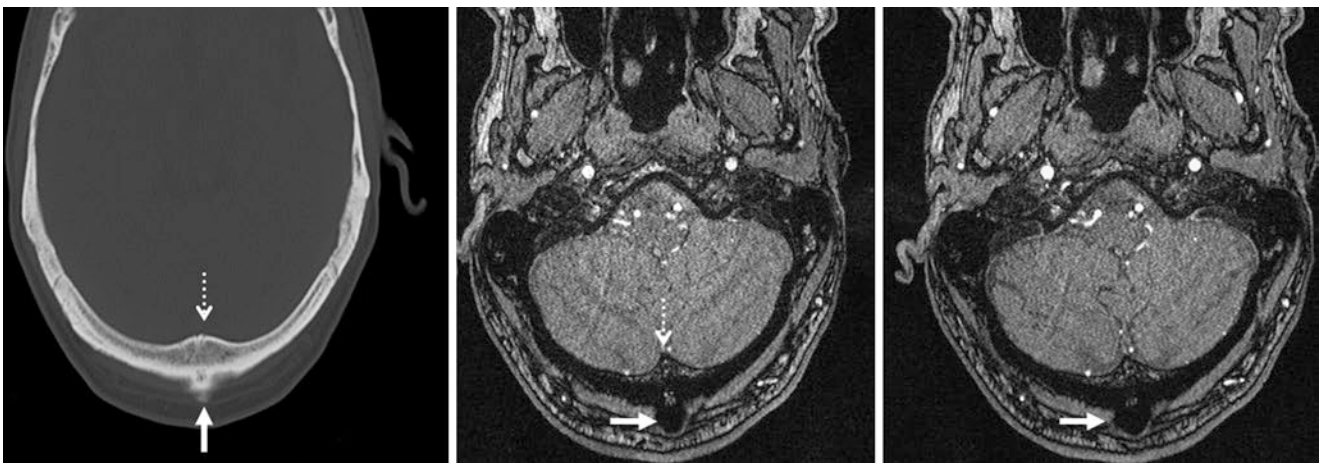

Fig. 29.39 A 56 year old with an EOP (*solid arrows*) and an IOP (*dotted arrows*) on axial NECT (*left*) and on three-dimensional TOF source MRA images (*middle and right*)

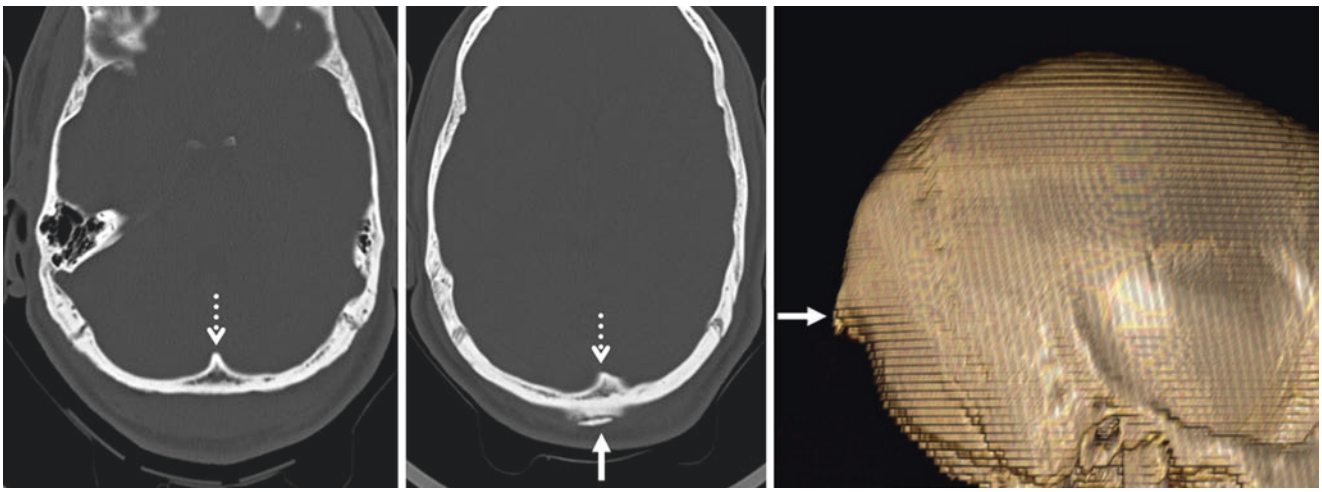

Fig. 29.40 A 19 year old with occipital trauma who had a cleft EOP (*solid arrows*) and IOP (*dotted arrows*) on axial NECT images (*left and middle*) and on a three-dimensional VR left lateral view (*right*)

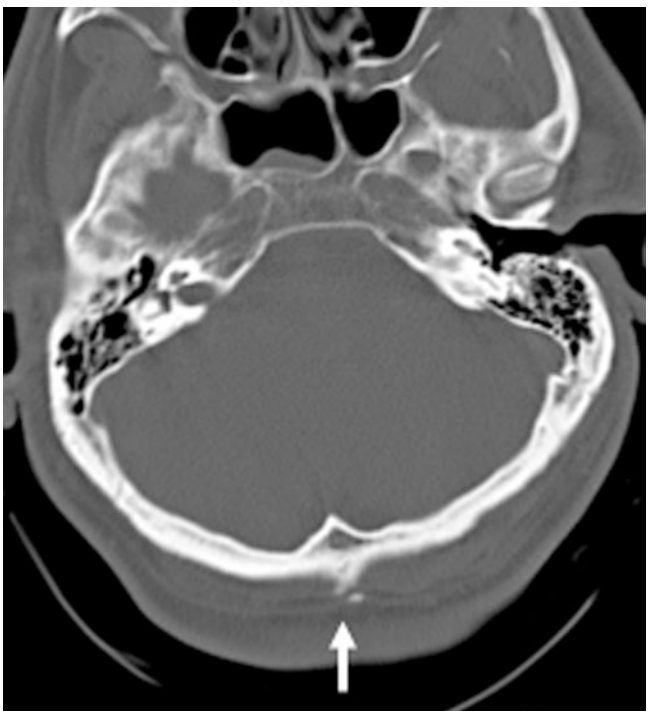

Fig. 29.41 A 41 year old with a cleft EOP on NECT that appears to mimic a fracture

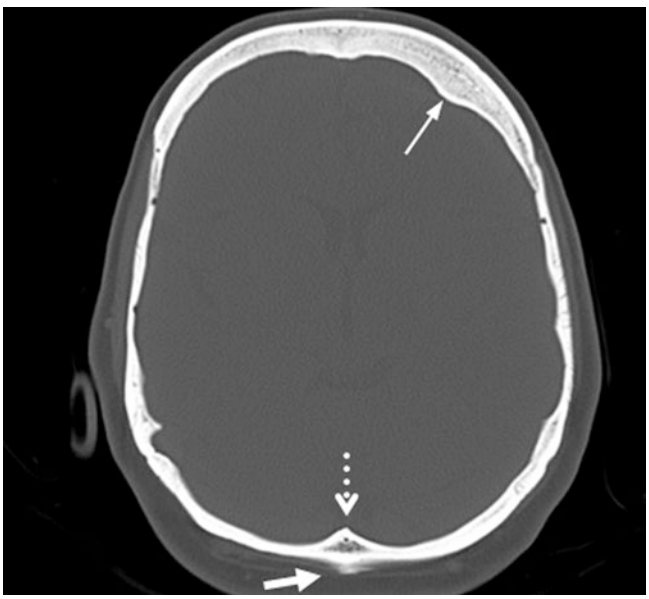

Fig. 29.42 A 50 year old with an EOP and IOP as well as unilateral benign left frontal hyperostosis (*thin arrow*)

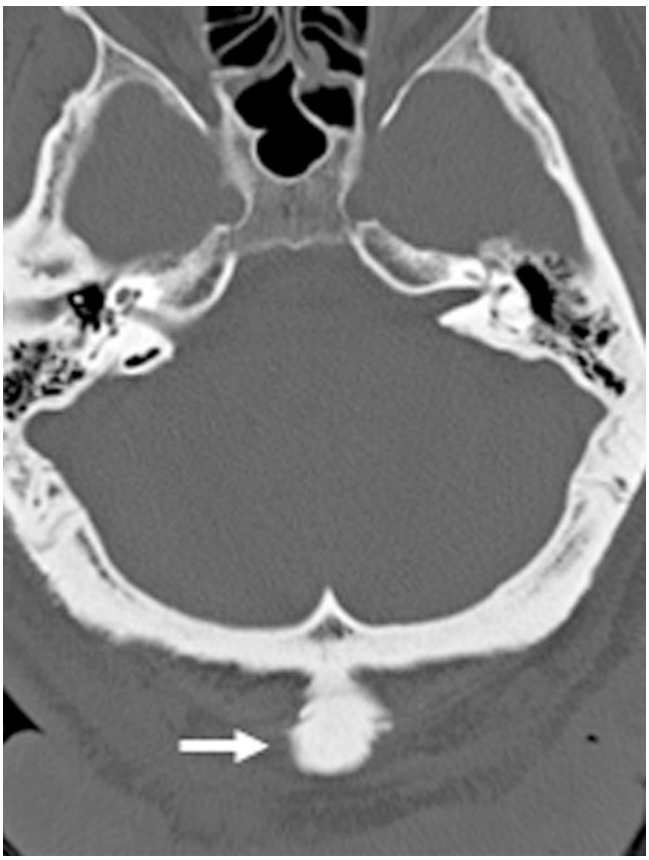

Fig. 29.43 A 49 year old in whom a large, partially cleft EOP mimics an osteoma

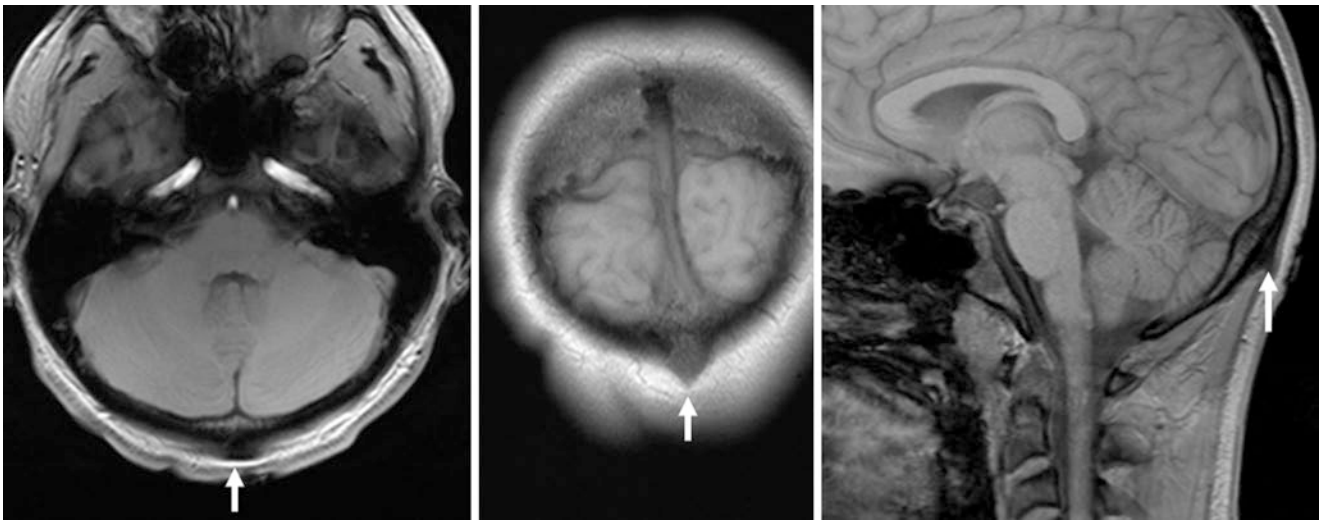

Fig. 29.44 A 16 year old: the patient's mother felt a skull mass that was found to be a prominent EOP (*arrows*) on 1.5T noncontrast gradient echo T1WI MRI in the axial (*left*), coronal (*middle*), and sagittal (*right*) planes

29.6 Petrous Apex Normal Variants that May Mimic Disease: Fatty Marrow, Aeration, Hyperostosis

Several variations in the appearance of the *petrous apex* can simulate disease [20, 21, 31–34]. One of the most common is normal *fatty marrow*, which can be bilateral, unilateral, or asymmetric. This appears as a bright signal on precontrast T1WI or with fast/turbo spin-echo acquisition used to obtain T2WI or FLAIR. It can mimic *cholesterol granulomas, dermoid/epidermoid cysts,* and even *meningiomas* or other tumors, depending on the sequence where the bright signal is noted. The fatty marrow can be discerned by implementing FS on these sequences. It is important to note that aerated petrous apices can trap fluid (i.e., effusions), perhaps originating from previous episodes of otitis.

Also, about 20–30% of people have normally *aerated petrous apices*, which are typically bilateral, but a minority may be asymmetric or unilateral. These are normal variants that are easily discerned on nonenhanced CT (NECT), but they can occasionally create difficulty in interpretation if an MRI is the presenting examination, as the gas may lead to field inhomogeneity or susceptibility artifacts. The dark, artifactual signal arising from air may simulate abnormalities at the petrous apex, the floor of the middle cranial fossa, or flow voids of the petrous internal carotid artery (ICA). Hence, *hemorrhage, aneurysm,* or other *vascular anomalies* may be incorrectly suspected based on the solitary interpretation of MR images. This effect is particularly pronounced on gradient echo-based acquisitions of T1WI, T2WI, or DWI.

Focal hyperostosis with bony overgrowth can also occur within the petrous apex, whether unilateral or symmetric and bilateral. As discussed previously, these may also be termed *osteomas* or *exostosis* if there are no enhancing components on postcontrast imaging. The term hyperostosis may also apply, as these are almost always not neoplasms and are very rarely symptomatic; rare cases of cranial nerve compression by such hyperostoses have been described. On NECT such foci may easily be discerned to be bony outgrowths, but hyperostoses can be problematic if the patient obtains an MRI with a large area of bright signal (simulating a *cholesterol granuloma*) or a dark signal (simulating an *aneurysm*) at the petrous apex. Focal areas of hyperostosis can also cause a confusing appearance on MRI, simulating cholesterol granulomas or even extra-axial lesions such as *schwannomas* or *meningiomas* if a previous NECT is not available, especially if FS is not utilized. Again, FS, MR angiography, or NECT can help if an MRI is suspicious (Figs. 29.45, 29.46, 29.47, 29.48, 29.49, 29.50, and 29.51).

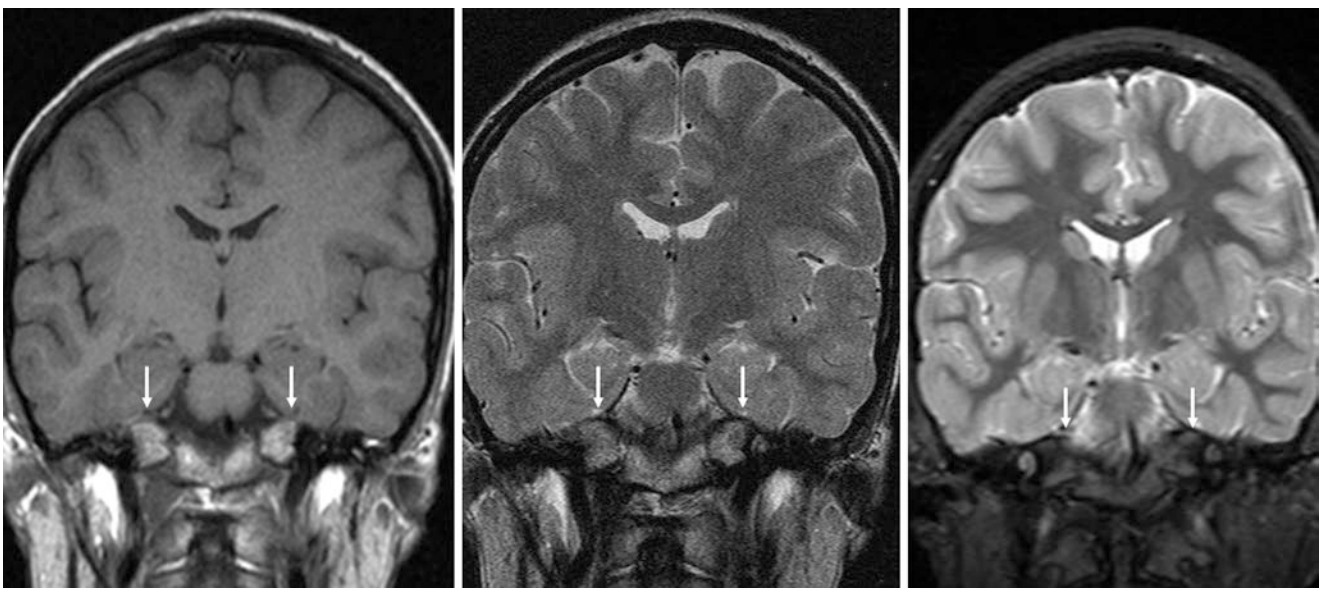

Fig. 29.45 A 21 year old with bilateral petrous apex fatty marrow (*arrows*), which is bright on coronal T1WI (*left*) and T2WI (*middle*) and disappears with FS on T2WI (*right*)

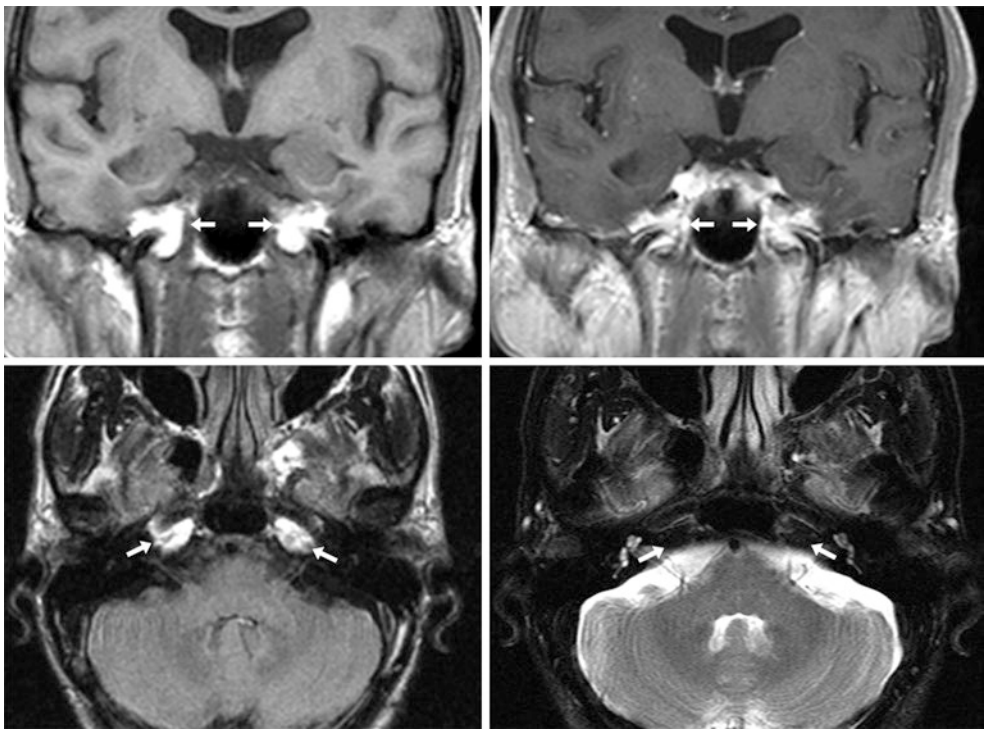

Fig. 29.46 A 50 year old with bilateral petrous apex T1-bright signal that is present on coronal T1WI (*top left*) and on postcontrast T1WI (*top right*). This fat was also bright on sequences using turbo FSE acquisition, such as on turbo FSE FLAIR (*bottom left*), but it suppresses with FS T2WI (*bottom right*), confirming the presence of normal fatty marrow

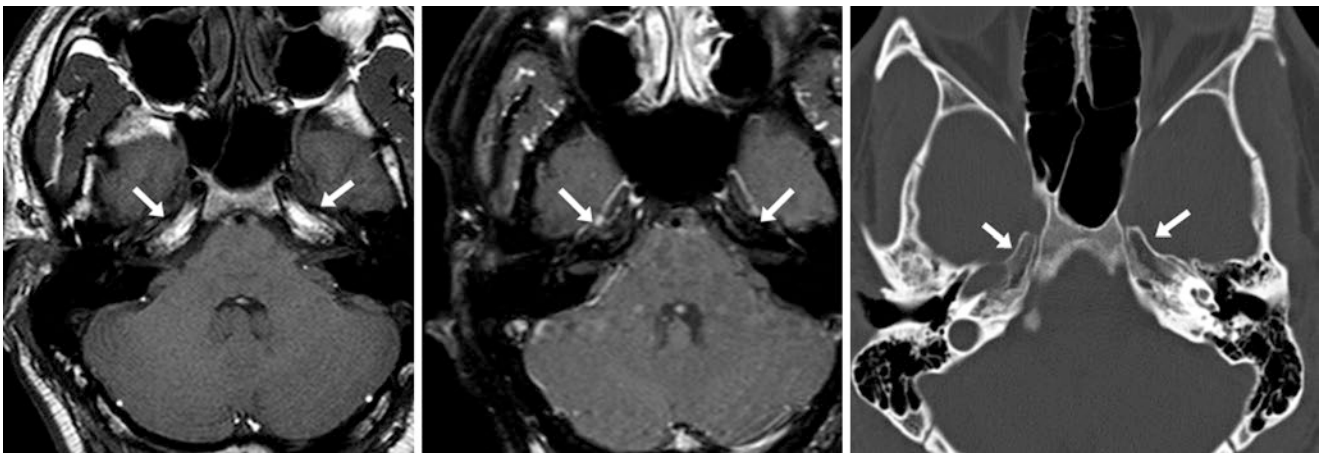

Fig. 29.47 A 19 year old with bilateral bright fatty signal within the petrous apices (*arrows*) on T1WI (*left*), which disappears after FS (*middle*). NECT (*right*) confirms fat density in that location

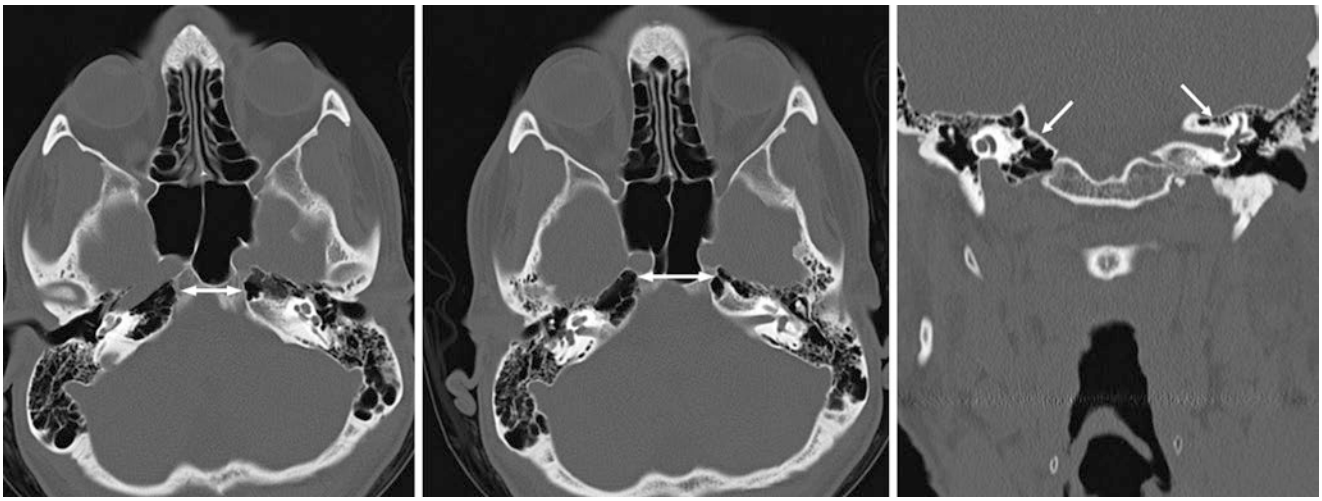

Fig. 29.48 A 32 year old with bilateral normally aerated petrous apices (*arrows*) on axial NECT (*left and middle*) and on coronal reconstructions (*right*)

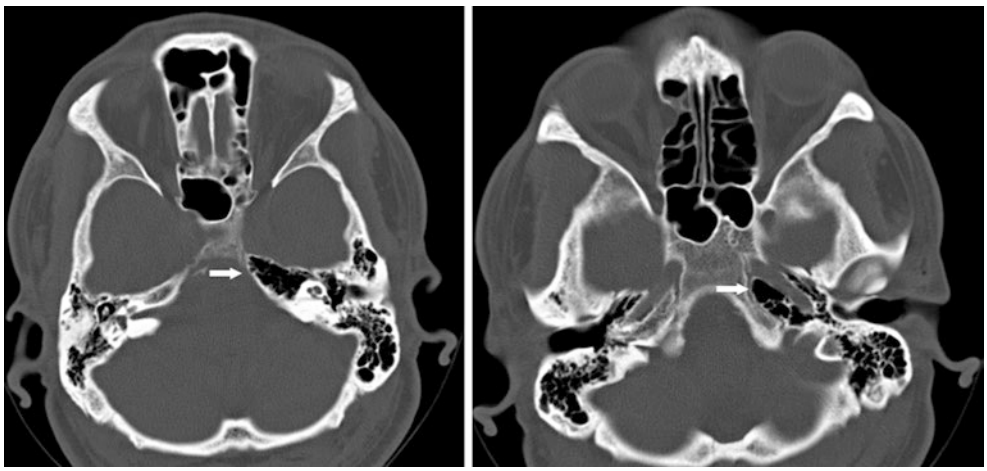

Fig. 29.49 A 32 year old with a unilateral aerated left petrous apex (*arrows*)

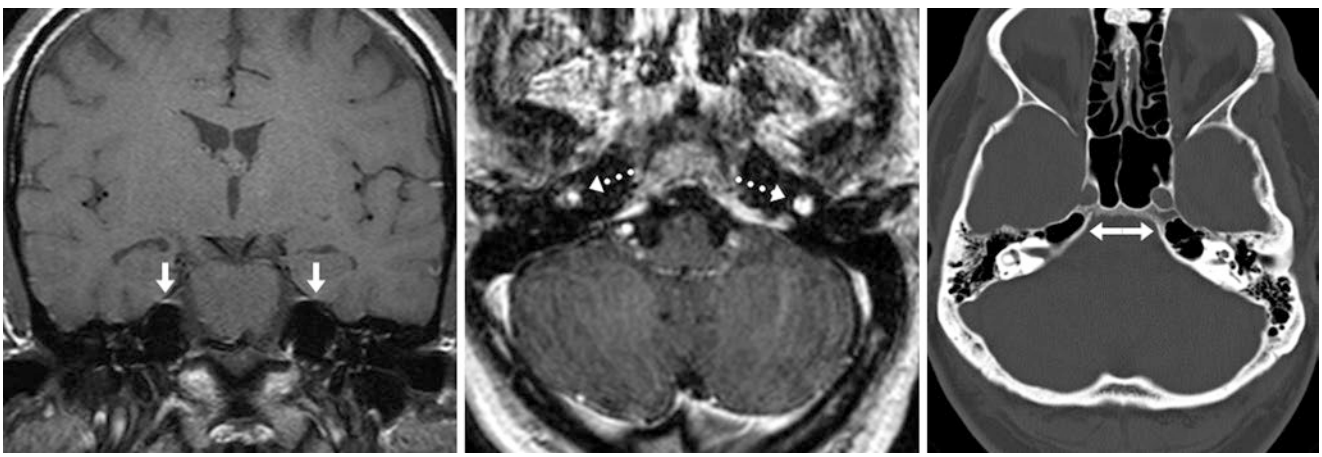

Fig. 29.50 A 46 year old male with artifacts at the petrous apices bilaterally (*arrows*) on coronal T1WI (*left*) that obscure and create artifact within the adjacent ICAs (*dashed arrows*) on axial postcontrast T1WI (*middle*); the artifact could be mistaken for a vascular abnormality such as thrombosis or dissection. Aerated petrous apices were later noted on a NECT (*arrows*)

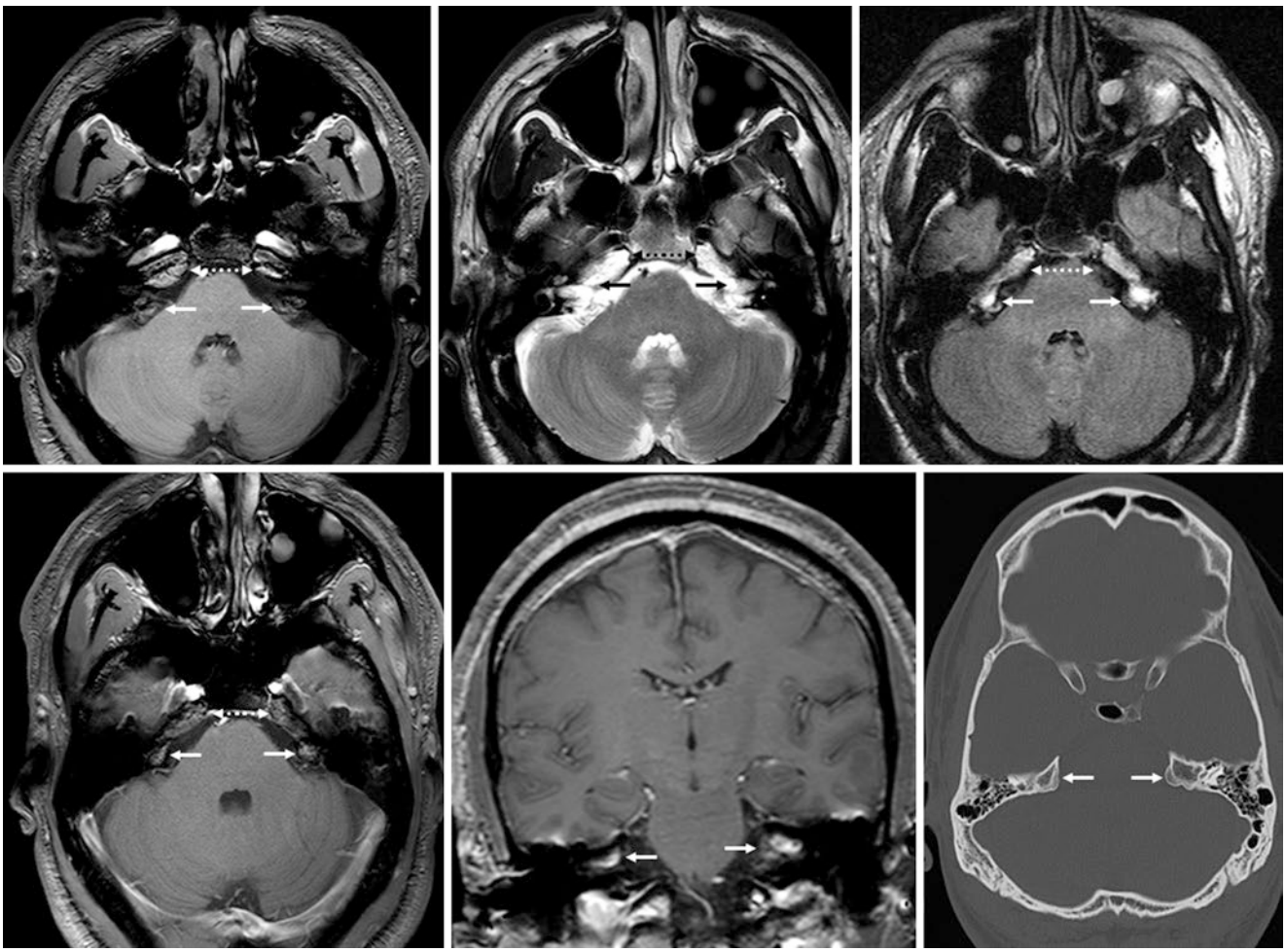

Fig. 29.51 A 31 year old was evaluated for recurrent metastatic disease after a frontal craniotomy (*note dural enhancement, bottom right*) hyperintense signal within the petrous apices bilaterally on all MR sequences (*arrows*), including T1WI (*top left*), T2WI (*top middle*), FLAIR (*top right*), and on postcontrast axial (*bottom left*) and coronal (*bottom middle*) T1WI. Enhancement was questioned because of a lack of FS. This was later confirmed to be focal hyperostosis on NECT (*bottom right*), with superimposed fatty marrow. Also note fatty marrow on the MRI (*dashed arrows*), located more anteriorly within the petrous apices

29.7 Anterior Clinoid, Posterior Clinoid, and Dorsum Sella Variants that Simulate Disease

Normal variations can occur in the bony *anterior* or *posterior clinoid processes* and within other areas of the sphenoid bone that are similar or identical to those of the petrous apices, although they are slightly less common [34–36]. These can simulate disease, particularly because of their relationship with the adjacent ICAs, cranial nerves, and parenchymal structures. Such variations include focal *fatty deposits* (confirmed by FS), bony *hyperostosis*, and *aeration* (which can occur unilaterally and communicate with the sphenoid sinus). These can simulate dural-based *tumors, metastases,* or even *aneurysms*.

Aerated clinoid processes can simulate *aneurysms* on MRI with the appearance of T2-dark or T1-dark flow voids. The anterior clinoids are aerated in about 10 % of patients; aerated anterior clinoid processes usually communicate with the sphenoid sinus (about 80 %) or less commonly with the ethmoid air cells (about 10 %). Posterior clinoid aeration is less common. NECT CT or multiplanar MRI can confirm the suspected flow void to be within the confines of normal bony marrow, which does not enhance after contrast administration, although it may be heterogeneous on various MRI sequences from a susceptibility artifact. MRA or CTA can also exclude the presence of a vascular lesion if the diagnosis is still in question.

The dorsum sella and posterior clinoid can also be prominent and aerated and can be in continuity with the sphenoid sinus, similar to the anterior clinoid (AC). Again, FS aids in diagnosing T1-bright marrow if an MRI is the presenting examination, although the marrow can still appear heterogeneous even after FS. NECT is typically the best study for confirmation (Figs. 29.52, 29.53, 29.54, 29.55, 29.56, and 29.57).

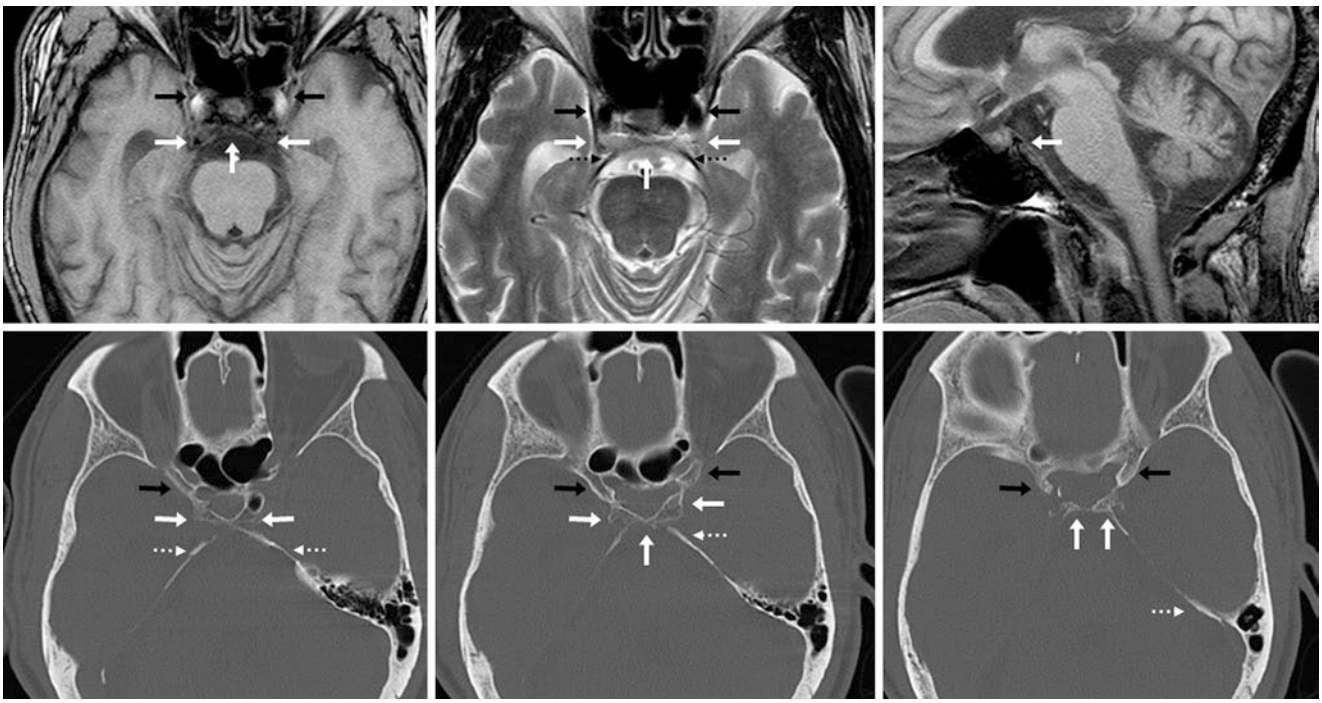

Fig. 29.52 A 70 year old with prominent anterior and posterior clinoid processes (*solid black and white arrows*) that were noted on T1WI MRI (*top left*), T2WI (*top middle*), sagittal T1WI (*top right*), and NECT (*bottom row*). These processes had heterogeneous signal on T1WI and T2WI, perhaps mimicking dural lymphoma or the tail of a meningioma if CT or contrast was not utilized. Note normal calcified petroclinoid ligaments, which are dark on T2WI but appear obvious on NECT (*dashed arrows*)

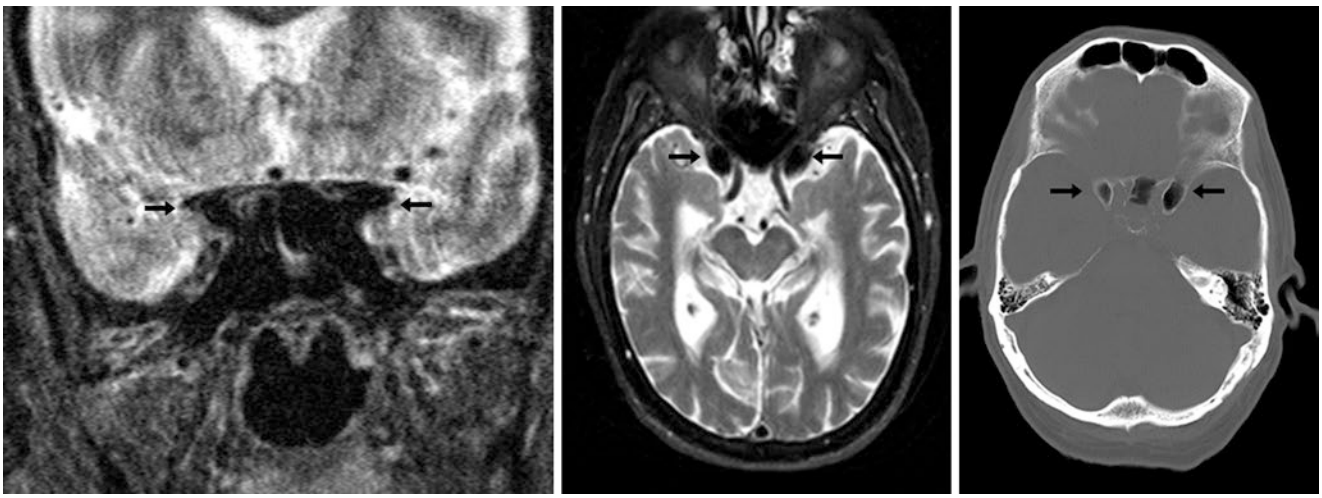

Fig. 29.53 A 75 year old with dark artifacts next to the ICAs on coronal (*left*), and axial (*middle*) T2WI, which resulted from aerated anterior clinoid processes and motion. These could mimic aneurysms on T2WI MRI (which can depict flow voids) but are clearly shown as being aerated on a NECT (*right*)

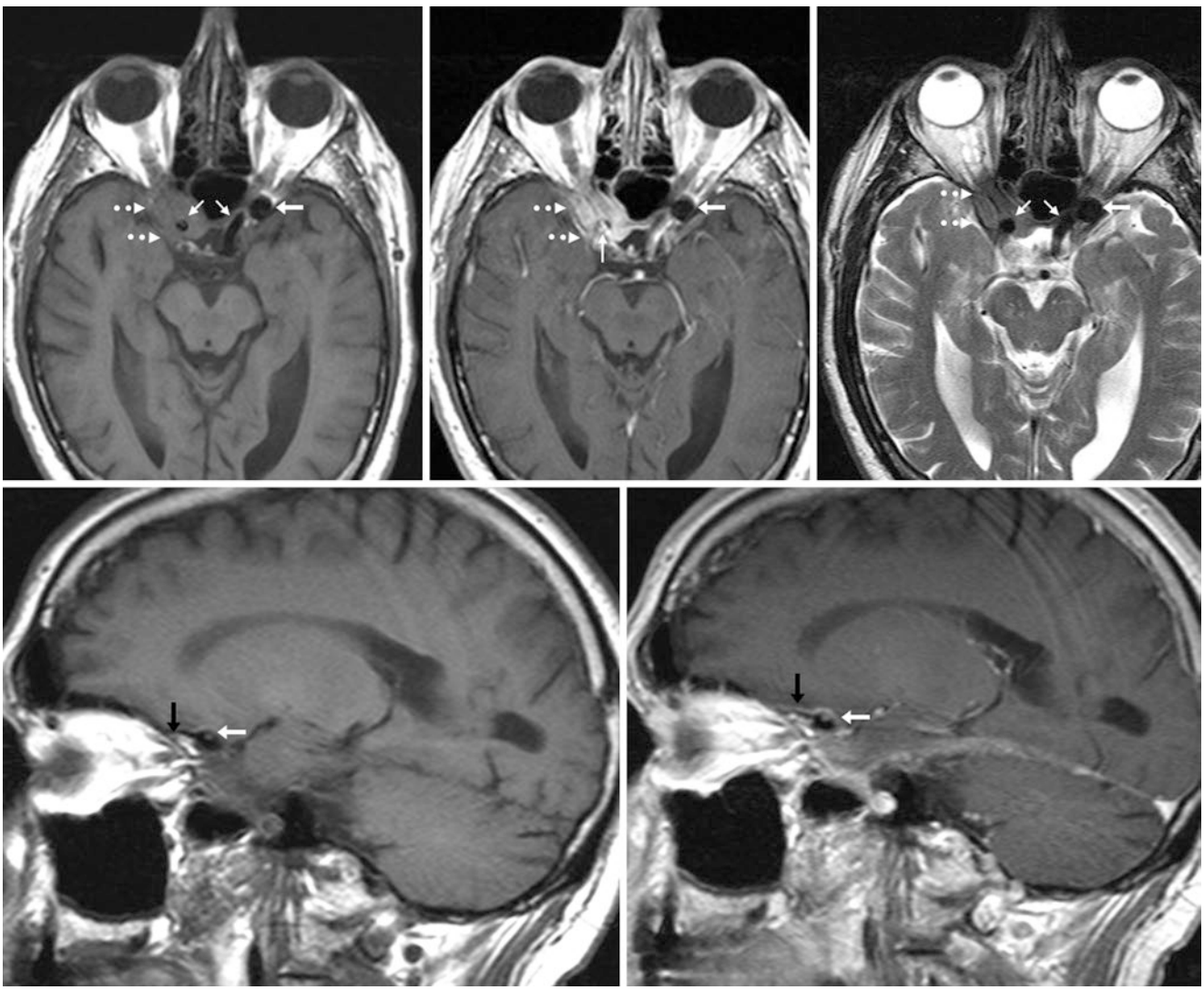

Fig. 29.54 *Top row*: An 84 year old with a focus of dark signal (*arrows*) that was initially called a flow void from an ICA aneurysm on axial T1WI MRI pre- (*left*) and postcontrast (*middle*) and T2WI (*right*). *Bottom row*: This was later found to be an aerated anterior clinoid on sagittal pre- (*left*) and postcontrast (*right*) T1WI, as it was contiguous with fatty marrow (*black arrows*) anteriorly. Note the ICA flow voids (*tiny arrows*); the right is surrounded by an enhancing meningioma (*dashed arrows*)

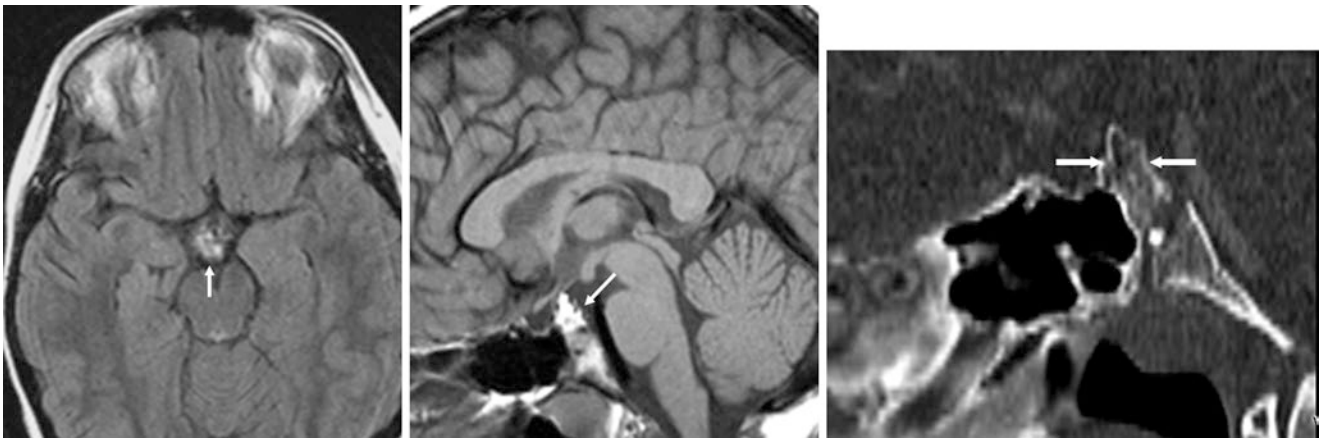

Fig. 29.55 A 12 year old with a bright focus on non–fat suppressed sagittal T1WI (*left*) and FLAIR (*middle*) MR images. This was thought to be a mass dorsal to the pituitary but was later found to be a prominent dorsum sella on sagittal NECT reconstructions (*right*) that contained fatty marrow

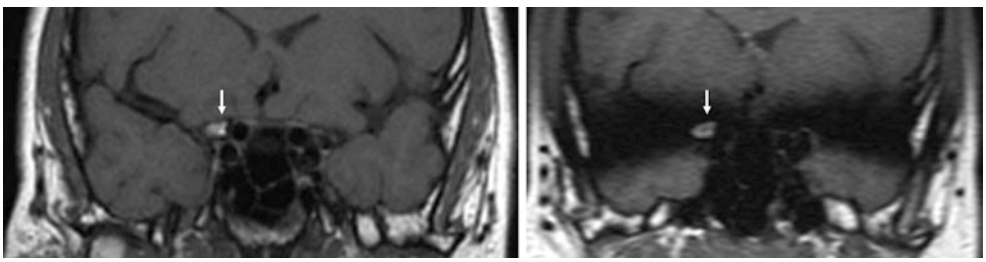

Fig. 29.56 A 35 year old with a unilateral focus of bright anterior clinoid marrow (*arrows*) on precontrast T1WI (*left*) that continued to be bright on the initial image of dynamic postcontrast T1WI (no contrast has entered the field of view yet), performed after failed FS (*right*)

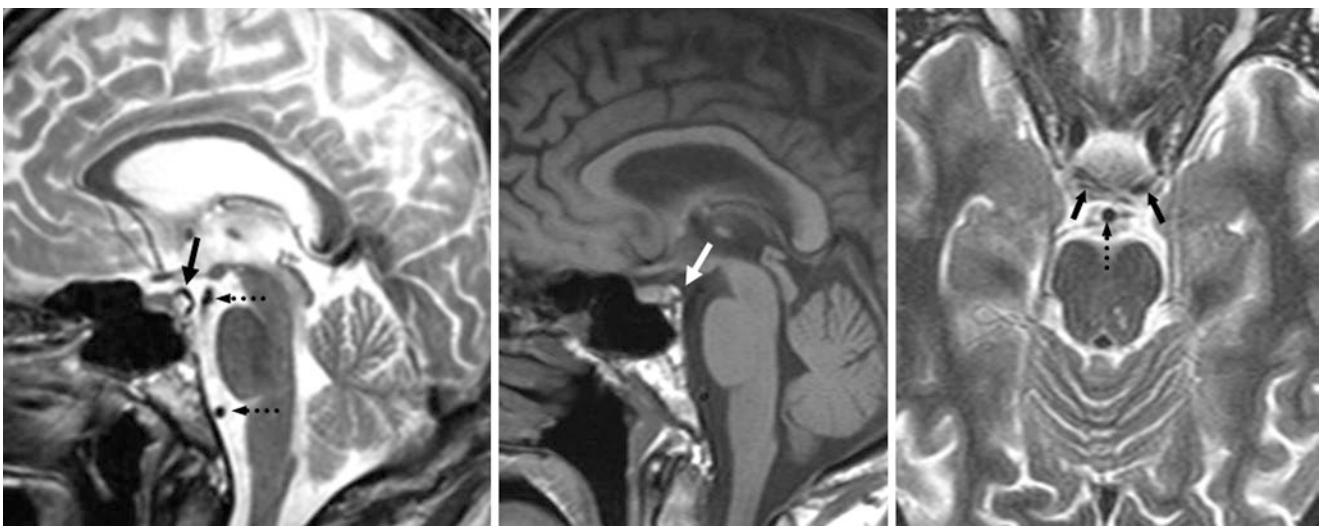

Fig. 29.57 A 46 year old with dark cortical bone of the dorsum sella (*arrows*), which simulates flow voids on sagittal T2WI (*left*); note a normal basilar artery flow void more posteriorly (*dashed arrow*). However, this was confirmed to be fatty marrow on sagittal non–fat suppressed T1WI (*middle*) and on fat-suppressed axial T2WI (*right*), as the focus exhibits a signal intensity similar to that of the clivus

29.8 Incomplete Aeration (Arrested Pneumatization) of the Skull Base

Incomplete pneumatization (i.e., *arrested pneumatization*) of the central skull base occurs at sites of expected aeration such as the sphenoid sinus as well as in previously described sites of normal variation in aeration (e.g., clinoid processes, pterygoid plates, basiocciput, petrous apices). Typically, these demonstrate well-defined margins of osseous or sclerotic density on CT and have interspersed foci of fat density internally on CT and MRI [37]. However, the internal density may appear to be that of soft tissue and may simulate focal masses such as *metastases, chordomas, osteomyelitis, ossifying fibromas,* or *giant cell tumors*; these may also simulate multifocal lesions such as *fibrous dysplasia*. They are located at a site of expected pneumatization, are nonexpansile with sclerotic and sharply circumscribed borders, and usually contain fatty-appearing internal material. Additionally, FS can be added to routine MRI sequences to distinguish these pseudolesions (Figs. 29.58, 29.59, 29.60, 29.61, 29.62, 29.63, 29.64, 29.65, 29.66, and 29.67).

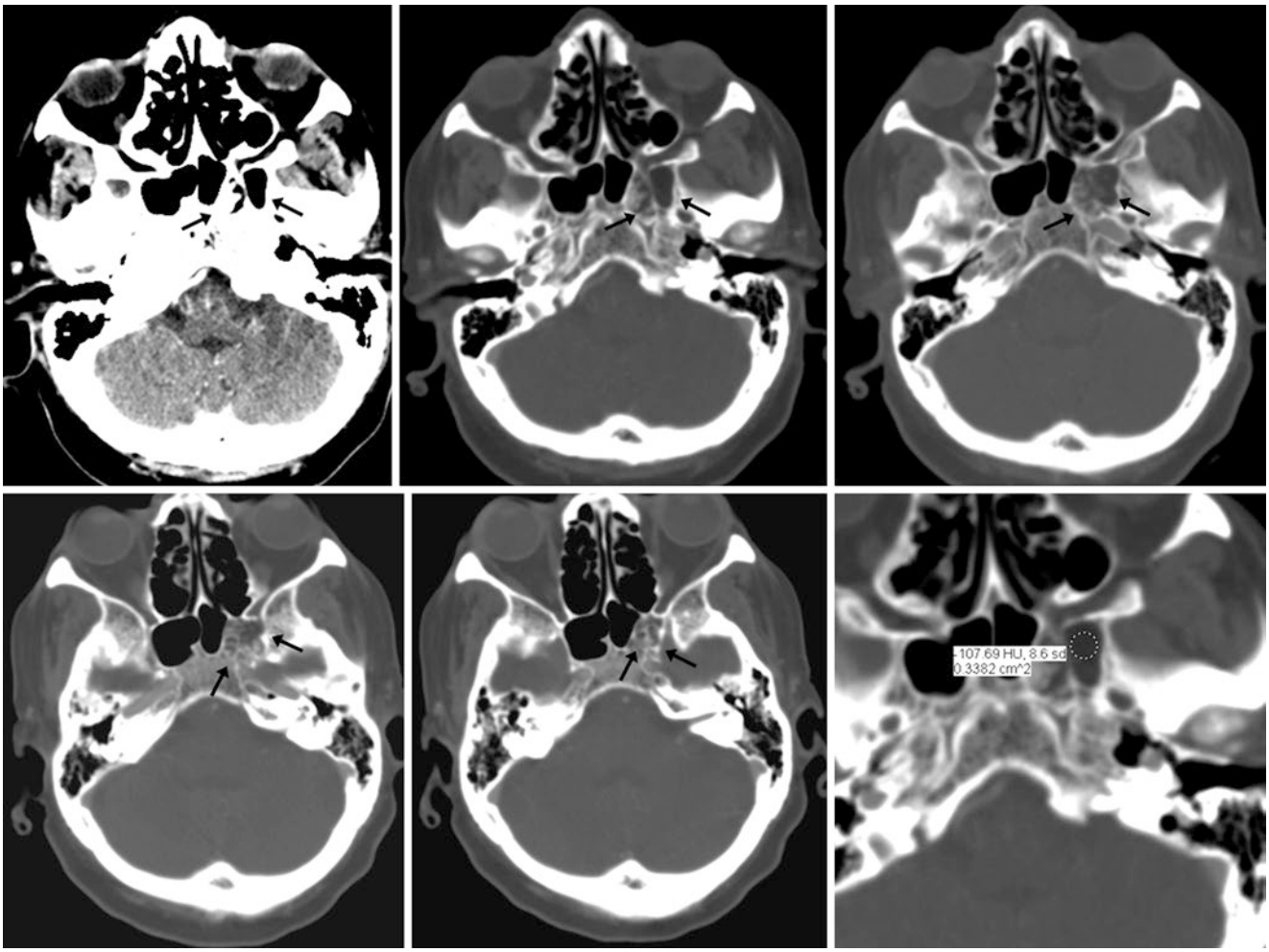

Fig. 29.58 A 75 year old with arrested pneumatization in the expected location of the left sphenoid locule, which appears similar to air on standard brain window width/level (80/40 HU, *top left*) and thus simulates gas. However, bone windows at several levels (2,500/500 HU) depict osseous density more cephalad (*bottom middle*), which is interspersed with fat density (−100 HU, *bottom right*) inferiorly

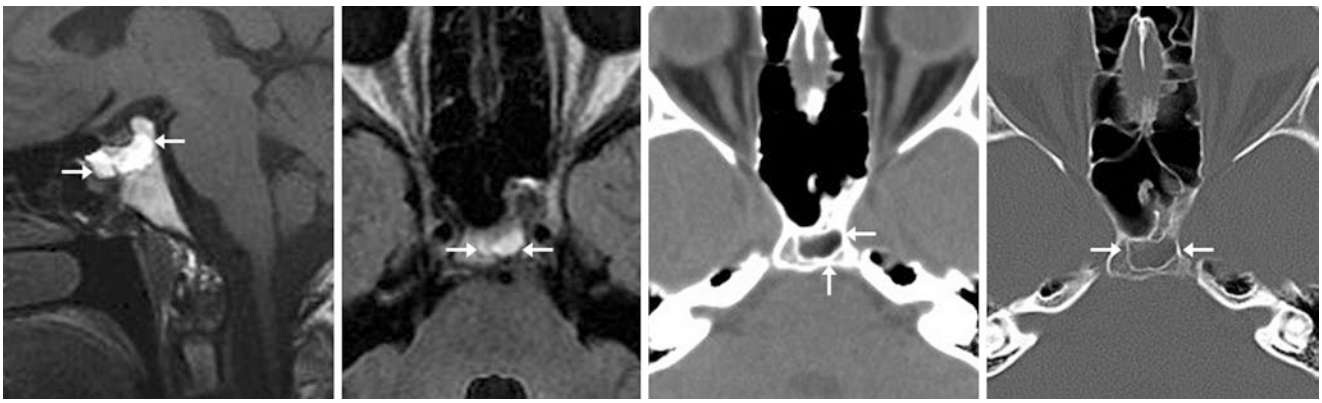

Fig. 29.59 A 19 year old in whom an incidental basisphenoid lesion was noted on a sagittal T1WI MRI (*left*). Axial FLAIR (*left middle*) depicted a well-circumscribed, bright clival lesion (*arrows*) with bright T1 signal exceeding that of adjacent bone marrow. A CT scan (*right images*) confirmed fat within the mass and a thin sclerotic rim, consistent with arrested pneumatization of the sphenoid sinus (*Courtesy of* Kirk M. Welker, MD, Mayo Foundation for Medical Education and Research, Rochester, MN, USA.)

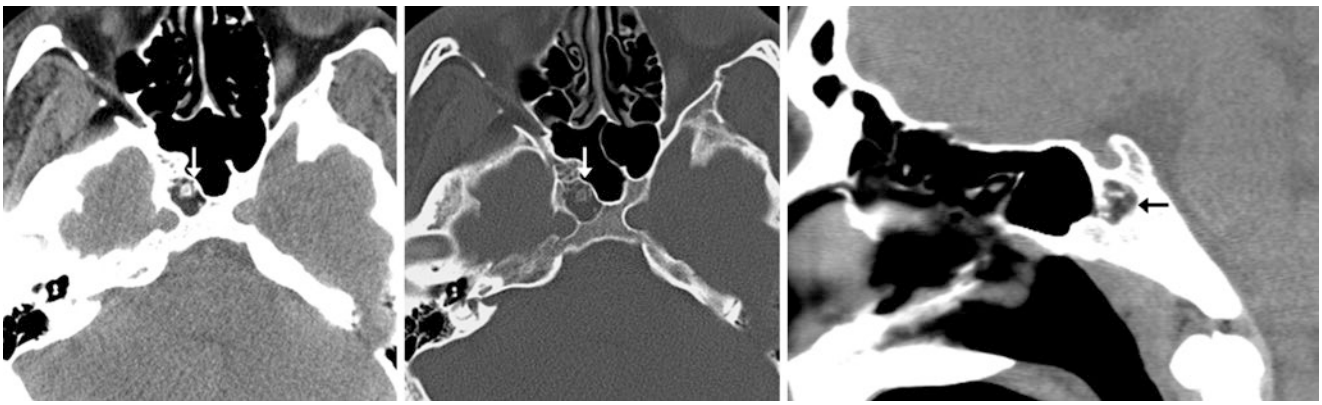

Fig. 29.60 A 27 year old in whom an incidental fat density (−31 HU) was noted within the clivus on soft-tissue windows (*left*). Bone windows (*middle*) showed central sclerosis. Sagittal reconstructions (*right*) depicted that this was just below the sella in the basisphenoid and had not changed over several years

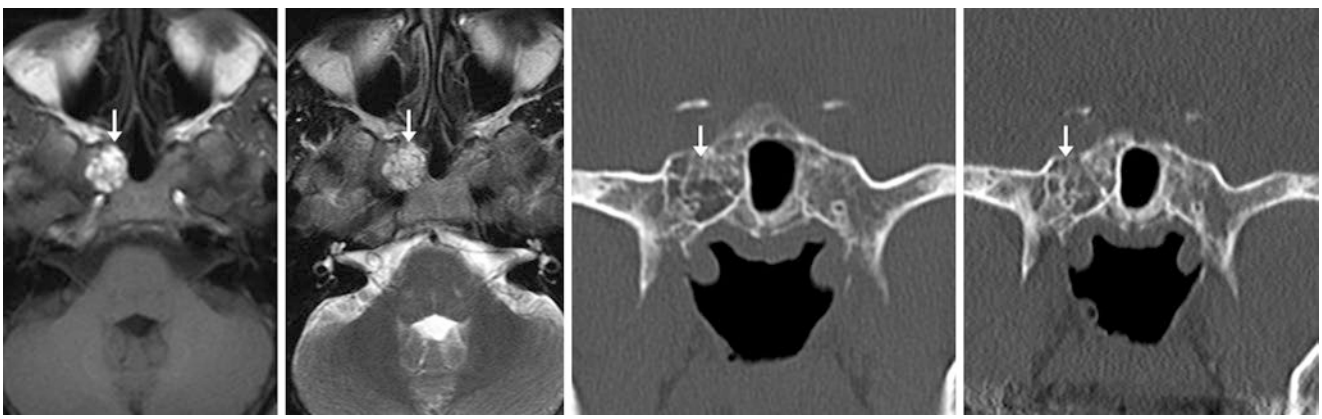

Fig. 29.61 A 43 year old in whom fat signal intensity (*arrows*) was noted within the right side of the sphenoid on non–fat-suppressed 1.5T MRI axial T1WI (*left*) and T2WI (*left middle*) in 2004. Coronal CT at that time (*right middle*) confirmed arrested pneumatization, which was unchanged in the year 2011 (*right*)

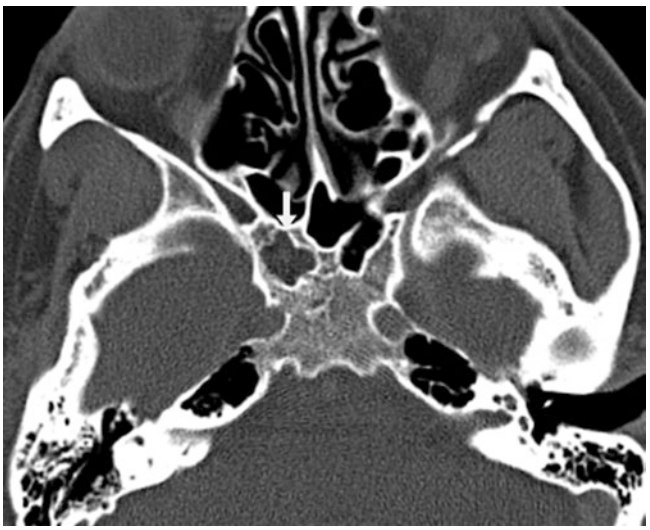

Fig. 29.62 A 31 year old in whom focal fat density (*arrow*) within the right basisphenoid on CT was consistent with arrested pneumatization

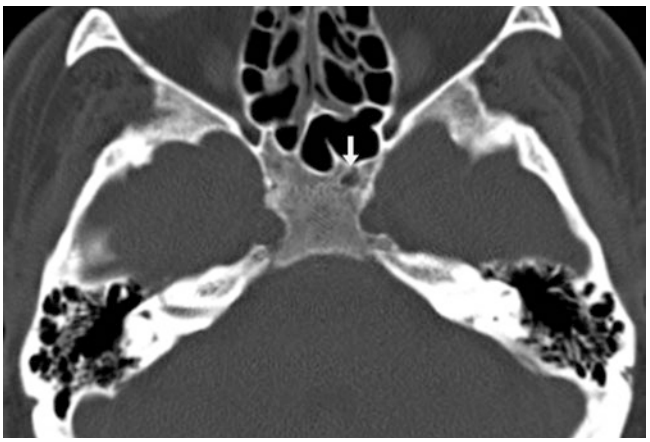

Fig. 29.63 A 58 year old in whom on CT, focal hypottenuation (too small to measure a density) was noted (*arrow*) within the basisphenoid, likely from arrested pneumatization

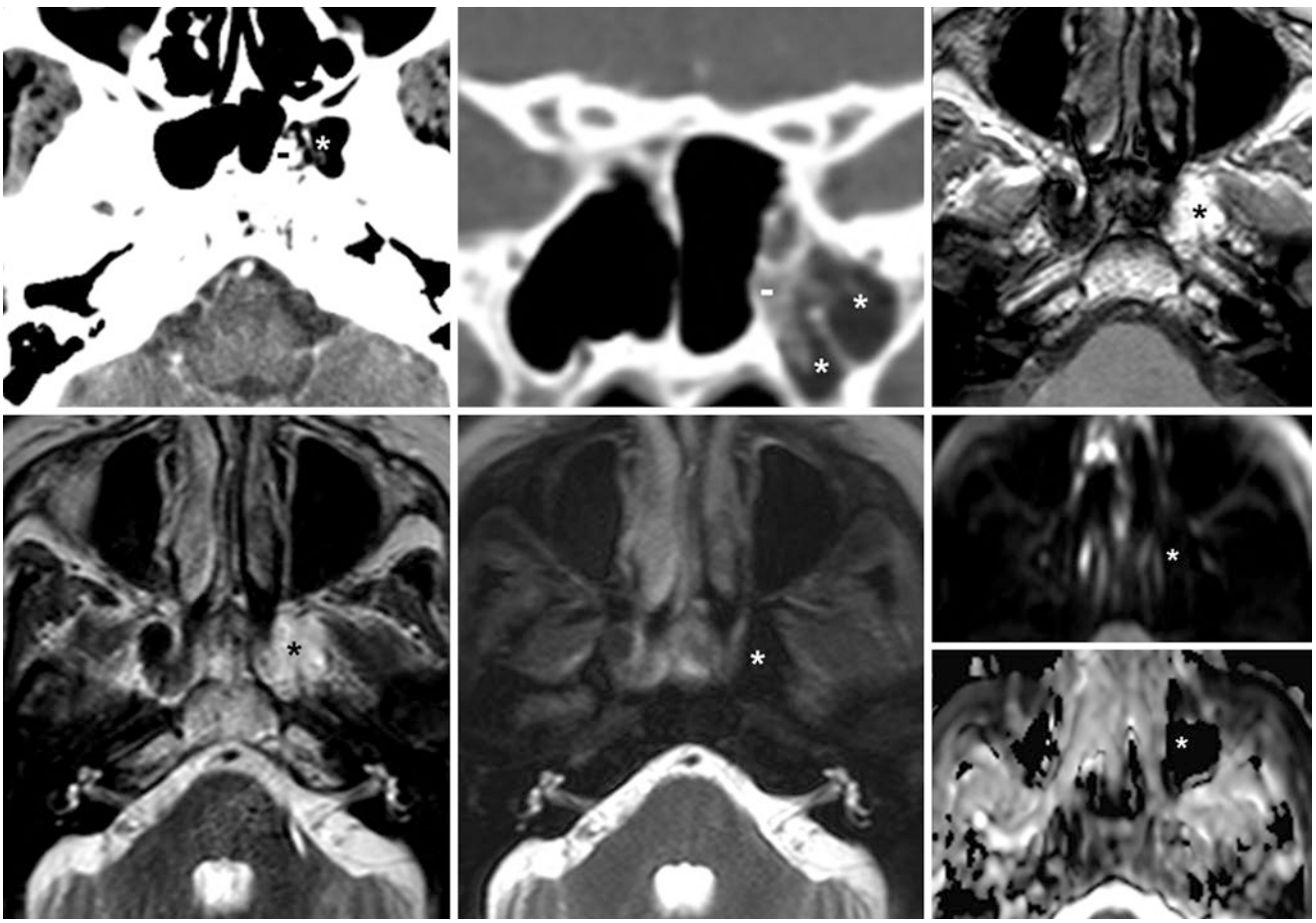

Fig. 29.64 A 75 year old in whom on axial (*top left*) and coronal (*top middle*) CECT fat density (−60 HU) was noted (*asterisk*) within the sphenoid, which was ossified medially (*dash*). On 3T MRI, this was bright on T1WI (*top right*) and T2WI (*bottom left*) and was dark on fat-suppressed T2WI (*bottom middle*). On DWI (*bottom right, top and bottom*), fat's dark signal confirmed arrested pneumatization

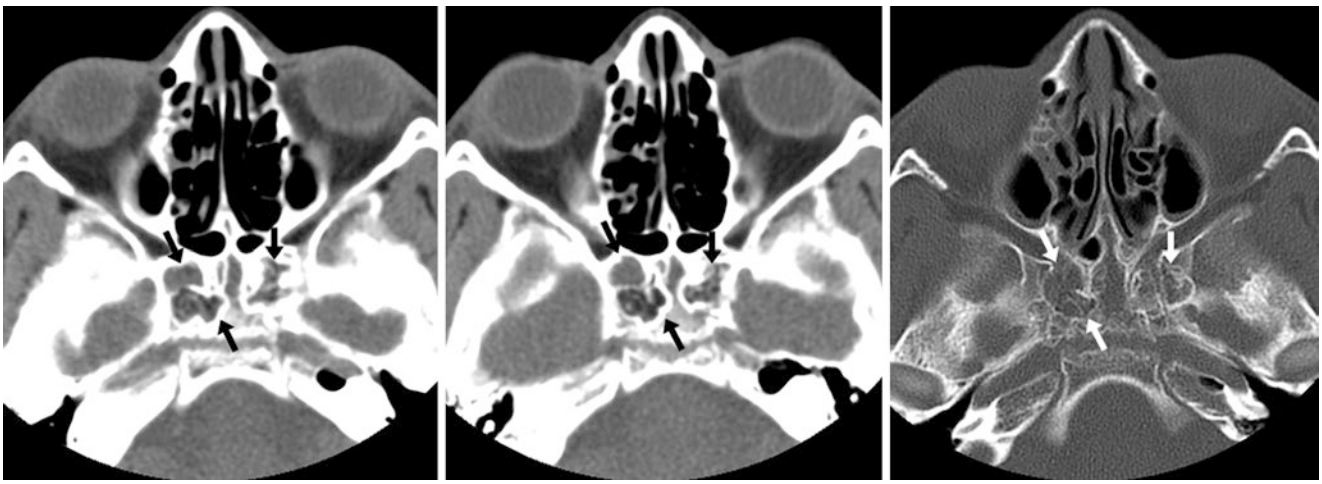

Fig. 29.65 A 9 year old in whom bilateral low-mixed density, although not clearly fat (3 HU) was noted (*arrows*) within the sphenoid bilaterally on soft tissue (*left and middle*) and bone (*right*) windows. The mixed ossification, fat and intermediate density are most consistent with arrested pneumatization

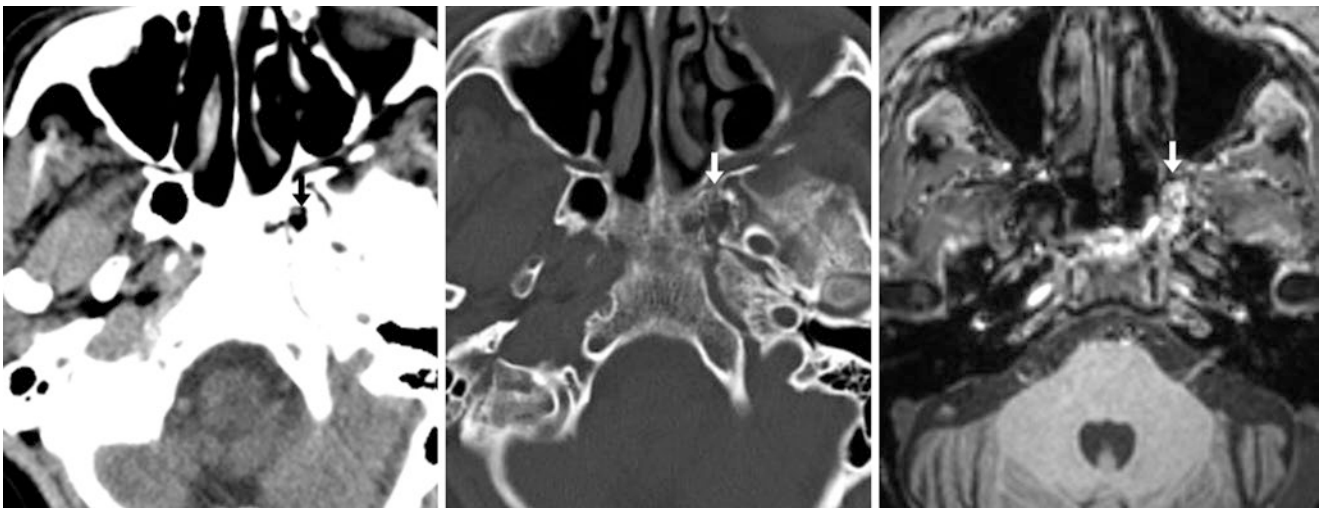

Fig. 29.66 A 58 year old in whom fat density (−60 HU) was noted (*arrows*) within the left pterygoid plate on CT with soft tissue (*left*) and bone (*middle*) windows, consistent with arrested pneumatization. On 3T MRI, a gradient-echo T1WI (*right*) confirmed the bright signal of fat

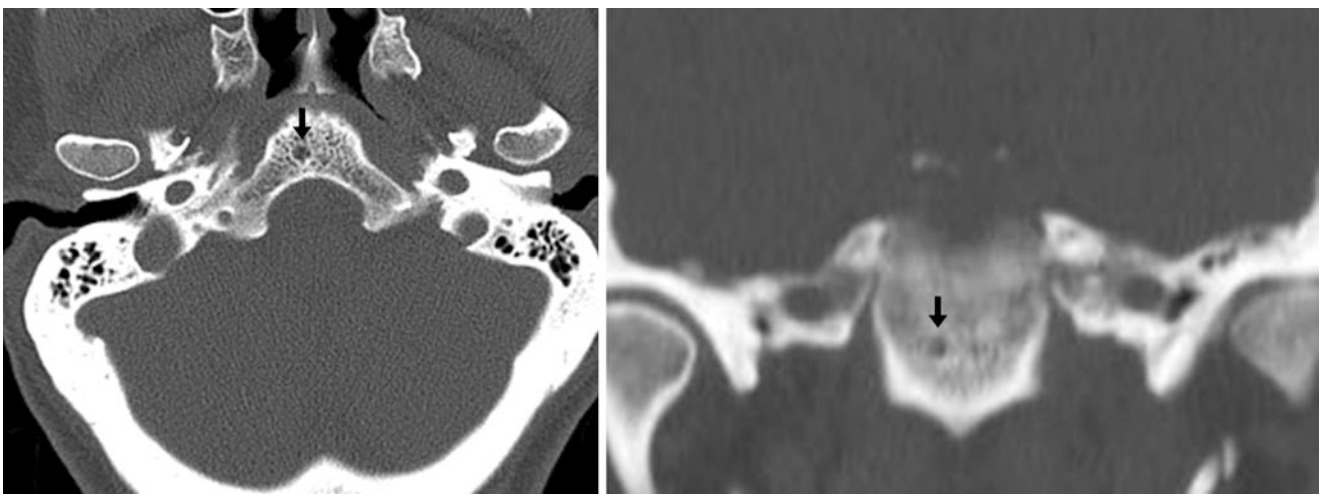

Fig. 29.67 A 58 year old in whom on CT a tiny focus of fat density (−40 HU) within the basiocciput (*arrows*) was noted on axial (*left*) and coronal (*right*) reconstructions, consistent with arrested pneumatization

References

1. Keats TE, Anderson MW. Atlas of normal roentgen variants that may simulate disease. 8th ed. Philadelphia: Mosby Inc.; 2007. Chapter 1, The skull. p. 3–117.
2. Freyschmidt J, Brossman J, Sternberg A, Wiens J. Freyschmidt's Koehler/Zimmer's borderlands of normal and early pathological findings in skeletal radiography. 5th ed. Tubingen: Thieme; 2003. Chapter 4, Skull. p. 358–463.
3. Seeger JF. Normal variations of the skull and its contents. In: Zimmerman RA, editor. Neuroimaging: clinical and physical principles. New York: Springer; 1999. p. 415–53.
4. Gray H. Anatomy of the human body. 20th ed. Philadelphia: Lea & Febiger; 1918. Chapter 5D, The interior of the skull. Available at http://www.bartleby.com/107/47.html.
5. Berge JK, Bergman RA. Variations in size and in symmetry of foramina of the human skull. Clin Anat. 2001;14:406–13.
6. Jinkins, JR. Atlas of neuroradiologic embryology, anatomy, and variants. Philadelphia: Lippincott Williams & Wilkins; 2000. Chapter 2, Cranium. pp. 62–85.
7. Weissman JL, Hirsch BE. Imaging of tinnitus: a review. Radiology. 2000;216:342–9.
8. Swartz JD, Harnsberg RH. Imaging of the temporal bone. 3rd ed. New York: Thieme; 1998.
9. Talarico Jr EF, Prather AD, Hardt KD. A case of extensive hyperostosis frontalis interna in an 87-year-old female human cadaver. Clin Anat. 2008;21:259–68.
10. Dihlmann W. Computerized tomography in typical hyperostosis cranii (THC). Eur J Radiol. 1981;1:2–8.
11. Querol MR, Aguirre JJ, Gahete C. Neuroimaging signs in a case of frontal internal hyperostosis. Neurologia. 2002;17:437.
12. Hershkovitz I, Greenwald C, Rothschild BM, Latimer B, Dutour O, Jellema LM, Wish-Baratz S. Hyperostosis frontalis interna: an anthropological perspective. Am J Phys Anthropol. 1999;109:303–25.
13. Smith S, Hemphill RE. Hyperostosis frontalis interna. J Neurol Neurosurg Psychiatry. 1956;19:42–5.
14. Raikos A, Paraskevas GK, Yusuf F, Kordali P, Meditskou S, Al-Haj A, Brand-Saberi B. Etiopathogenesis of hyperostosis frontalis interna: a mystery still. Ann Anat. 2011;193:453–8.
15. May H, Peled N, Dar G, Abbas J, Hershkovitz I. Hyperostosis frontalis interna: what does it tell us about our health? Am J Hum Biol. 2011;23:392–7.
16. May H, Mali Y, Dar G, Abbas J, Hershkovitz I, Peled N. Intracranial volume, cranial thickness, and hyperostosis frontalis interna in the elderly. Am J Hum Biol. 2012;24:812–9.
17. She R, Szakacs J. Hyperostois frontalis interna: case report and review of literature. Ann Clin Lab Sci. 2004;34:206–8.
18. Greenspan A. Bone island (enostosis): current concept – a review. Skeletal Radiol. 1995;24:111–5.
19. Ahmadi MS, Ahmadi M, Dehghan A. Osteoid osteoma presenting as a painful solitary skull lesion: a case report. Iran J Otorhinolaryngol. 2014;26:115–8.
20. Schutt CA, Guo JN, Bagwell KA, Bulsara KR, Malhotra A, Michaelides E. Bilateral osteomas and exostoses of the internal auditory canal. Am J Otolaryngol. 2015;36:583–6.
21. Mastromonaco P, Stöckli S. Hyperostosis of the internal auditory canal: an incidental finding? HNO. 2015;63:516–9.
22. Munakomi S, Bhattarai B. A rare case report on suboccipital region benign giant osteoma. Case Rep Neurol Med. 2016; Article ID: 2096701, 4 pages.
23. Abd Rabou A, Gaillard F. Osteoma. Radiopaedia.org. Accessed Apr 2016.
24. Knipe H, Jones J. Exostosis. Radiopaedia.org. Accessed Apr 2016.
25. Knipe H, Stanislavsky A. Enostosis. Radiopaedia.org. Accessed Apr 2016.
26. Brant WE, Helms CA. Fundamentals of diagnostic radiology. Philadelphia: Lippincott Williams & Wilkins; 2007.
27. Glassman SB, Delbeke D. Nuclear medicine case of the day. Hereditary multiple exostoses. Am J Roentgenol. 1992;158:1384.
28. Baik FM, Nguyen L, Doherty JK, Harris JP, Mafee MF, Nguyen QT. Comparative case series of exostoses and osteomas of the internal auditory canal. Ann Otol Rhinol Laryngol. 2011;120:255–60.
29. Beck DW, Dyste GN. Intracranial osteochondroma: MR and CT appearance. Am J Neuroradiol. 1989;10:7–8.
30. Hongo H, Oya S, Atsushi A, Matsui T. Solitary osteochondroma of the skull base: a case report and literature review. J Neurol Surg Rep. 2015;76:e13–7.
31. Moser T, Veillon F, Sick H, Riehm S. The hypodense focus in the petrous apex: a potential pitfall on multidetector CT imaging of the temporal bone. Am J Neuroradiol. 2008;29:35–9.
32. Taccone A, Oddone M, Occhi M, Dell'Acqua AD, Ciccone MA. MRI "road-map" of normal age-related bone marrow. I. Cranial bone and spine. Pediatr Radiol. 1995;25:588–95.
33. Jackler RK, Parker DA. Radiographic differential diagnosis of petrous apex lesions. Am J Otol. 1992;13:561–74.
34. Schmalfuss IM, Camp M. Skull base: pseudolesion or true lesion? Eur Radiol. 2008;18:1232–43.
35. Mikami T, Minamida Y, Koyanagi I, Baba T, Honkin K. Anatomical variations in pneumatization of the anterior clinoid process. J Neurosurg. 2007;106:170–4.
36. Bonneville F, Cattin F, Marsot-Dupuch K, Dormont D, Bonneville JF, Chiras J. T1 signal hyperintensity in the sellar region: spectrum of findings. Radiographics. 2006;26:93–113.
37. Welker KM, DeLone DR, Lane JI, Gilbertson JR. Arrested pneumatization of the skull base: imaging characteristics. Am J Roengenol. 2008;190:1691–6.

Other "Don't Touch" Skull Lesions: Arachnoid Granulations, Calvarial Depressions, Hemangiomas, and Intraosseous Lipomas

30

This subsection describes a few miscellaneous normal variants of the skull that can mimic lytic lesions [1–33]. These include the often encountered *pacchionian granulations*, *calvarial depressions*, and the quite uncommon *intraosseous lipomas* [1–33]. Pacchionian (arachnoid) granulations on CT could appear nearly identical to calvarial depressions from vascular channels; indeed, this distinction can be arbitrary and only based on the observation that calvarial depressions are filled with a clearly contrast-enhancing vascular channel, while arachnoid granulations are most commonly (but not always) filled with the T2-bright signal intensity of cerebrospinal fluid (CSF) on MRI, which suppresses/darken on FLAIR; uncommonly, these exhibit internal enhancement because of vasculature contained within. Intraosseous lipomas can be differentiated by their characteristic appearance and density on CT, although MRI can also help confirm that they are normal variants in questionable situations. Finally, *calvarial hemangiomas* can overlap with intraosseous lipomas if a hemangioma is small and T1-bright; however, larger hemangiomas have increasing enhancement, can be expansile, and can simulate lytic lesions such as metastases.

30.1 Arachnoid (Pacchionian) Granulations: CT and MRI Pitfalls

Arachnoid granulations can cause a good deal of confusion when they are multiple, irregular, and lytic-appearing on NECT and particularly when present in patients with a history of malignancy. These are meningiothelial-lined and CSF-filled invaginations of arachnoid villi in either the *cranium* or the *dural venous sinuses* or the dura near the venous sinuses. They favor being close to the midline, although they often occur off it. Please note that a detailed discussion of arachnoid granulations within the dural sinuses is included separately under the vascular variants section of this text, as this chapter focuses solely on calvarial variants. Also, for the purposes of this text, arachnoid granulations are distinguished from *calvarial depressions* (also known as *pacchionian depressions*), although other sources consider them the same entity [5–17]. Hence, a discussion of pacchionian depressions follows as the topic of the next chapter, since these entities may be related on a spectrum.

Arachnoid granulations can be troublesome in several ways, depending on their location and surrounding anatomy.

A.M. McKinney, *Atlas of Normal Imaging Variations of the Brain, Skull, and Craniocervical Vasculature*,
DOI 10.1007/978-3-319-39790-0_30

First, regarding location, pacchionian granulations or depressions extending into the calvarium are most commonly situated posteriorly within the occipital bone and adjacent to the dural sinuses or cortical veins, which makes sense as the transverse sinsuses are their most common location, although a large, adjacent vein may not be visualized on routine thickness (≥5 mm) NECT or MRI [5–17]. Such posterior granulations often occur just off the midline in the parieto-occipital region, can appear multilobulated or have an irregular appearance, and can thus simulate lytic metastases. Anteriorly, arachnoid granulations can also be bilateral and can simulate foramina, although no definite foramen occurs in this location. Therefore, such cases could be considered pseudoforamina, as no definite vascular or neural structures are transmitted.

Regarding their appearance on MRI, they typically but not always follow CSF on all MRI sequences [5–17]. Most granulations are typically hyperintense on T2WI and suppress on FLAIR with CSF, and they are usually discernible on thin (≤1 mm), heavily T2-weighted images. These T2-bright foci are usually well circumscribed without decreased diffusion on DWI and corresponding ADC maps; however, they may appear bright on DWI because of T2 shine-through effect. These can also seem septated or somewhat lobulated. Thus, granulations may simulate lytic, neoplastic bone lesions if they are large and irregular enough; however, on MRI, the lack of enhancement and the presence of increased diffusion on ADC maps enables differentiation. While the appearance of typical arachnoid granulations following CSF on all imaging modalities and sequences is pathognomonic, atypical appearances also exist that include internal signal intensity on MRI or density slightly different than CSF on NECT. Such atypical appearances with internal non-CSF signal intensity have been thought to be related to traversing veins, venous plexi, or volume averaging phenomenon.

On NECT, dedicated, bone-kernel reconstructions are recommended for their work-up in order to demonstrate their well-circumscribed appearance. Arachnoid granulations protruding into the dural venous sinuses can simulate nonocclusive *thrombus*, particularly when appearing low density on postcontrast CT, CT venography (CTV), or postcontrast MRI. Thin-section postcontrast CT, CTV, or postcontrast T1WI MRI can yield a confident diagnosis of an arachnoid granulation in most patients, since an arachnoid granulation follows CSF on postcontrast imaging (i.e., does not enhance).

Other points about arachnoid granulations that protrude into the skull are important to mention. One point is that they can be problematic to identify when they are small because of the volume averaging phenomenon, which may cause the appearance that a tiny arachnoid granulation does not follow CSF on standard MR sequences. Another point is that they typically do not enlarge over time; rarely they will enlarge over years but not over weeks to months in the fashion of *malignant neoplasms* or *thrombi*. Also, while these lesions more often appear well circumscribed and rounded, they can also appear lobulated or even slightly irregular on CT. When irregular-appearing they are still typically T2-hyperintense and lack contrast enhancement on MRI.

It is important to mention that a cortical vein or plexus may occasionally lie within a pacchionian "depression" that causes a non-CSF like signal, but such venous plexi should also be surrounded by CSF. These are most likely a separate entity from *venous lakes* (i.e., diploic veins), which are venous channels/plexi not surrounded by or communicating with CSF and lie entirely within the calvarium. Interestingly, recent evidence suggests that arachnoid granulations protruding into the calvarium may resorb CSF and drain into diploic veins situated within the granulation; this lends credence to the aforementioned theory that these entities may be interrelated [9, 13–16]. However, the debate continues as to whether arachnoid granulations, pacchyionian depressions, and diploic veins are all related, a discussion that is beyond this text. Thus, these are treated as separate entities in this chapter.

Additional atypical and potentially confusing appearances of arachnoid granulations with CT and MRI correlation are discussed at the end of this subsection. Occasionally, these present on MRI and are a diagnostic dilemma, particularly on DWI, which typically fills k-space with one pulse; this leads to skull artifacts near air interfaces such as at the periphery of the skull as causing internally non-CSF signal, thereby mimicking lytic lesions. These are distinguished by their true lack of reduced diffusion on ADC maps or their lack of enhancement internally on postcontrast MRI (Figs. 30.1, 30.2, 30.3, 30.4, 30.5, 30.6, 30.7, 30.8, 30.9, 30.10, 30.11, 30.12, 30.13, 30.14, 30.15, 30.16, and 30.17).

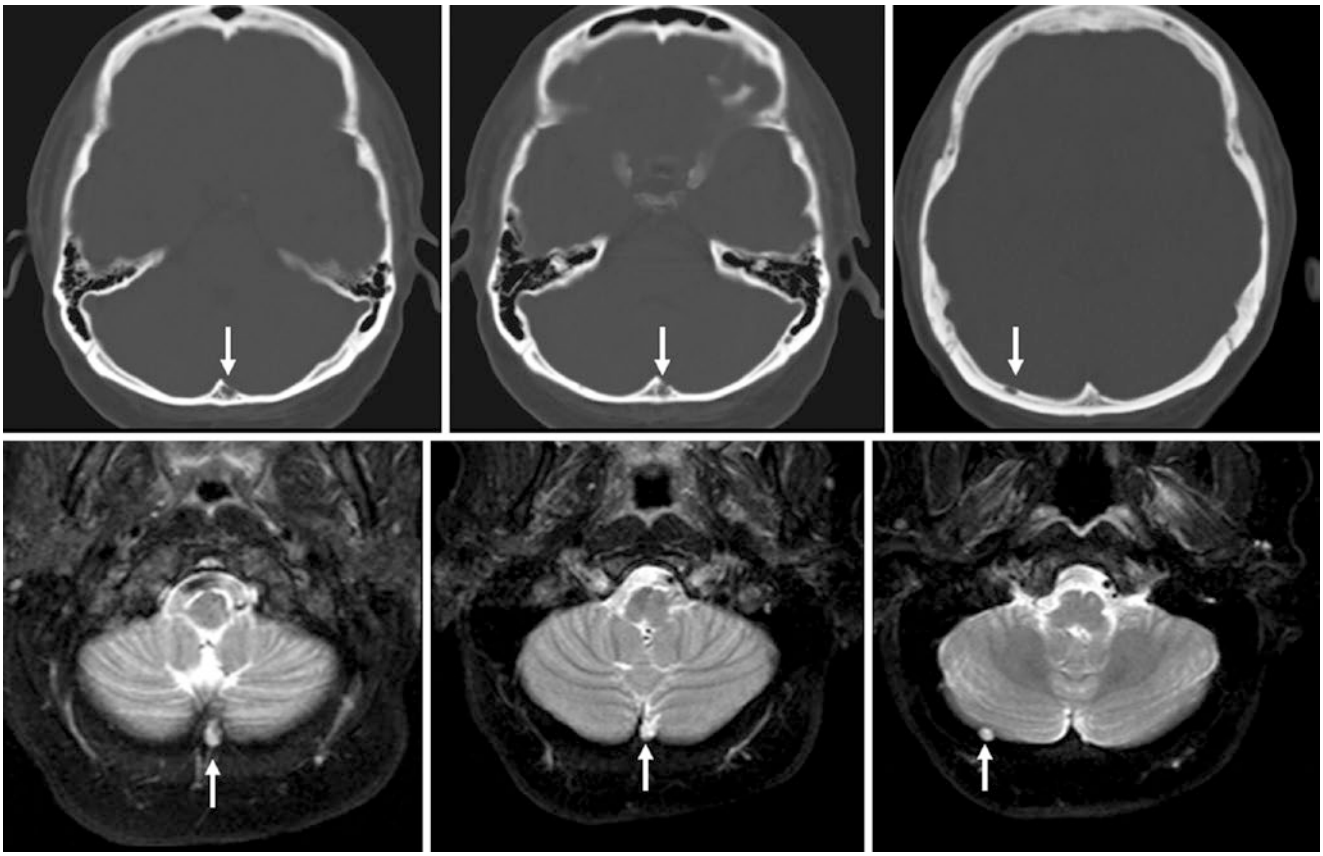

Fig. 30.1 A 51 year old with two occipital pacchionian granulations on both axial NECT (*top row*) and T2WI MRI (*bottom row*). Each pacchionian granulation is adjacent to the dural venous sinuses

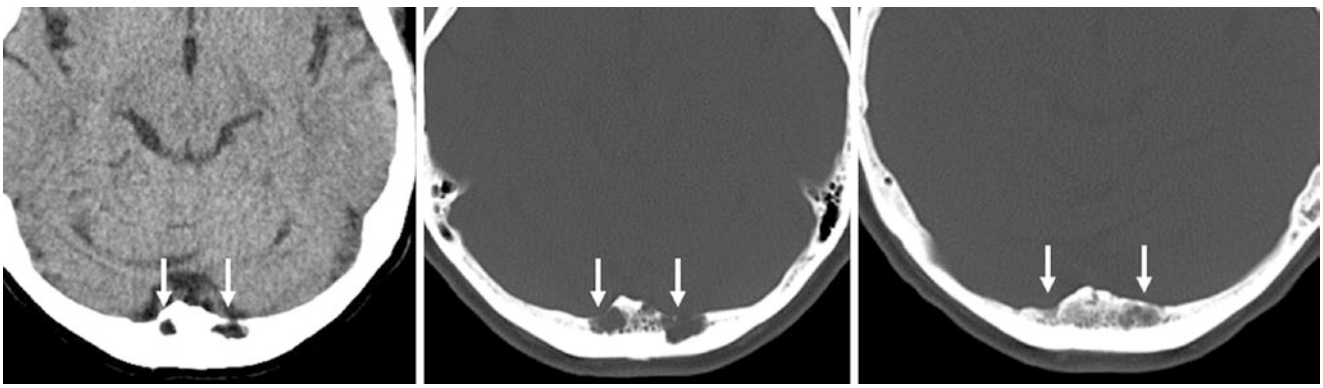

Fig. 30.2 A 72 year old male with lung cancer who had no metastases elsewhere. There were bilateral and somewhat irregular arachnoid granulations that appeared punched-out. Volume averaging through the top of the granulations mimics an ill-defined lytic metastasis

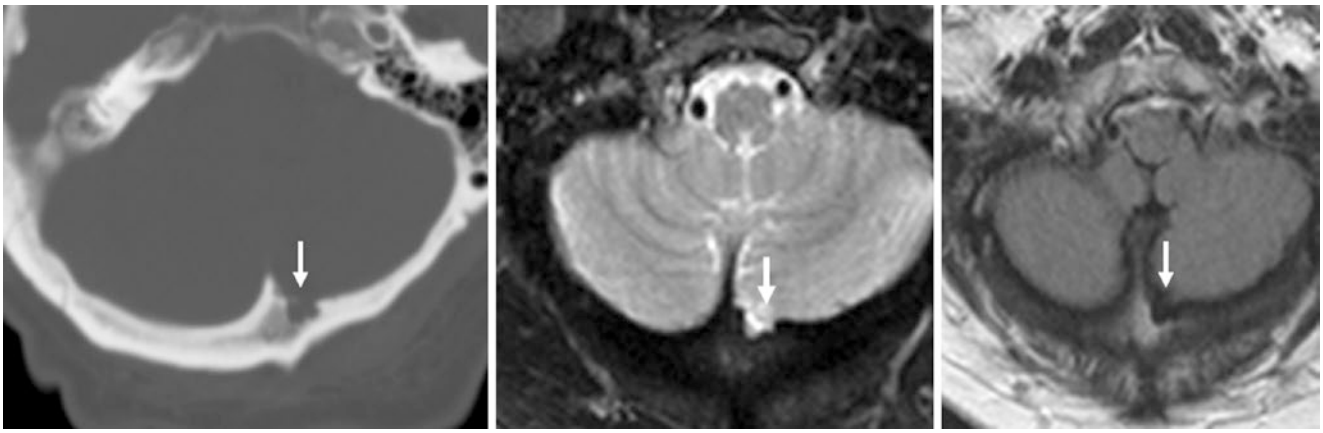

Fig. 30.3 A 60 year old with a small pacchionian granulation that appears lobulated on NECT (*left*), axial T2WI (*middle*), and postcontrast FLAIR MRI (*right*). Note the suppression of the CSF signal on FLAIR and the lack of any associated enhancement (*right*)

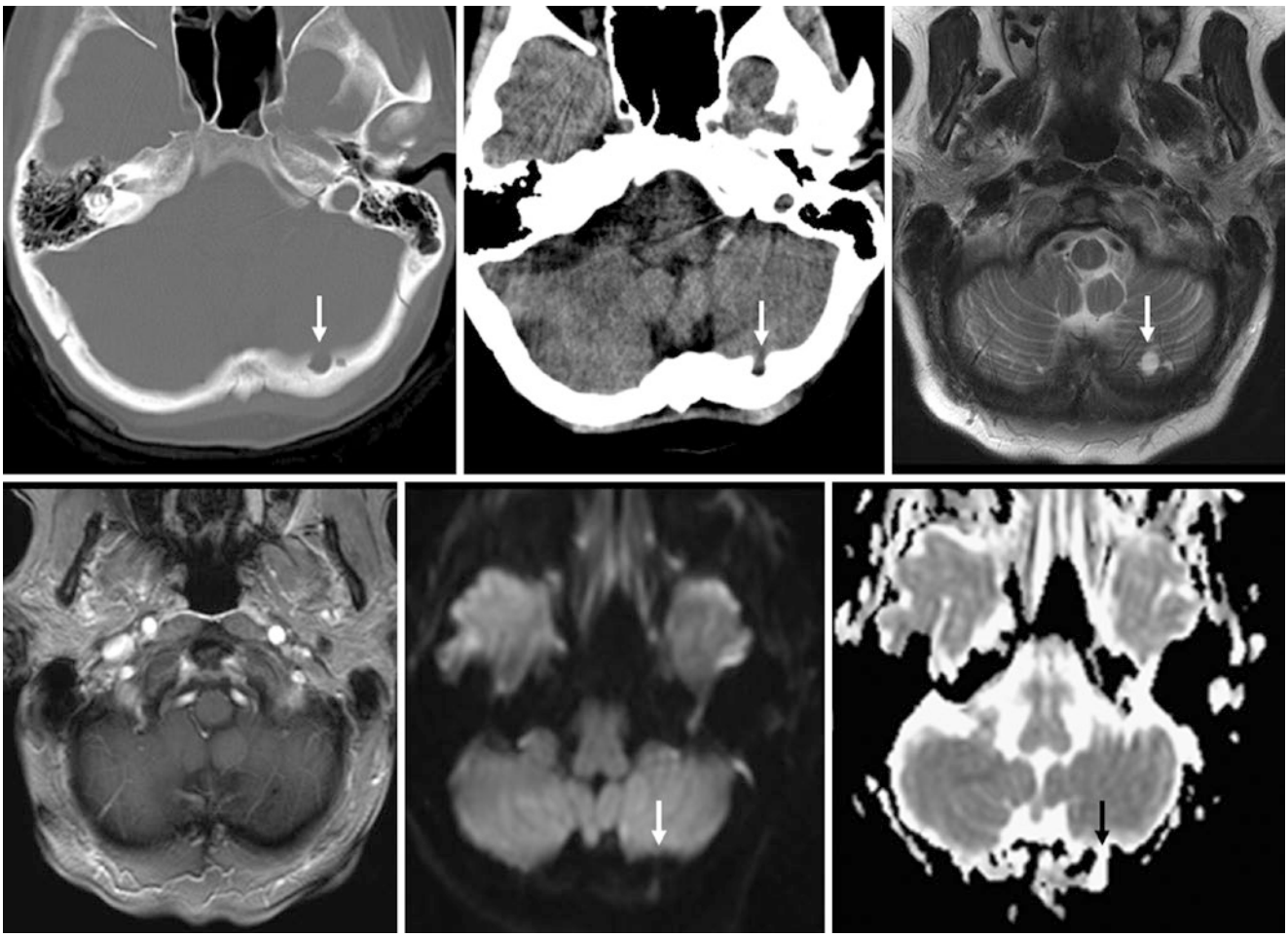

Fig. 30.4 A 65 year old with a small left occipital pacchionian granulation that is lobulated on NECT (*top left and middle*) and bright on T2WI MRI (*top right*). It lacks enhancement on T1WI (*bottom left*) and is without reduced diffusion on DWI (*bottom middle*) or ADC map (*bottom right*)

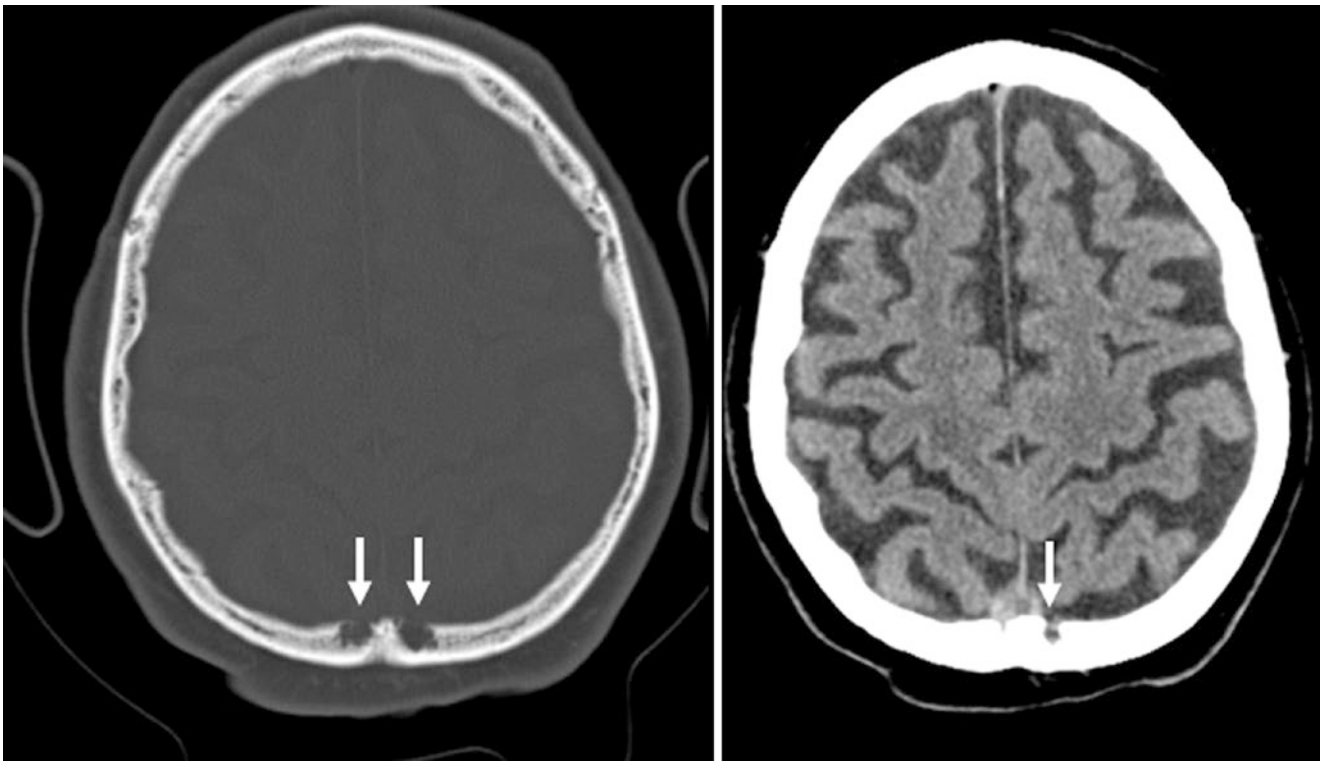

Fig. 30.5 An 83 year old with bilateral paramedian irregular parieto-occipital arachnoid (pacchionian) granulations

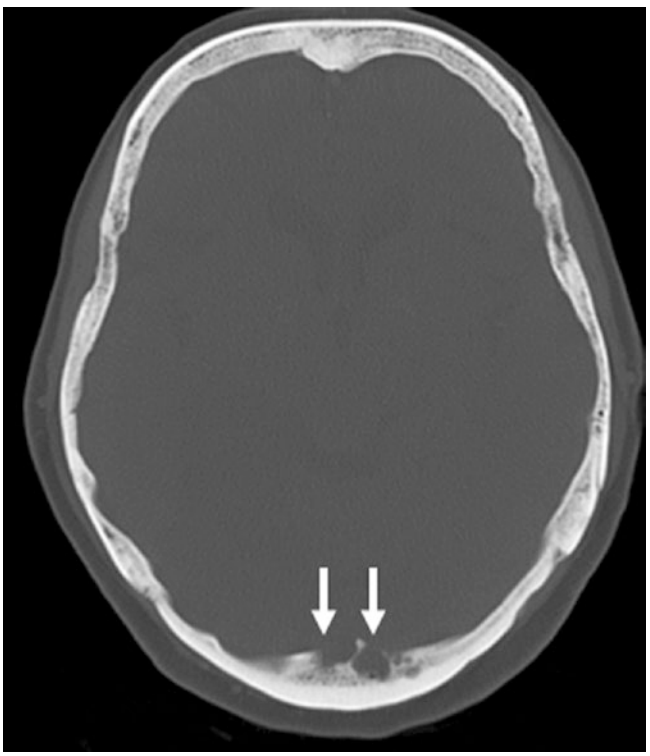

Fig. 30.6 A 74 year old with bilateral paramedian pacchionian granulations that appear irregular

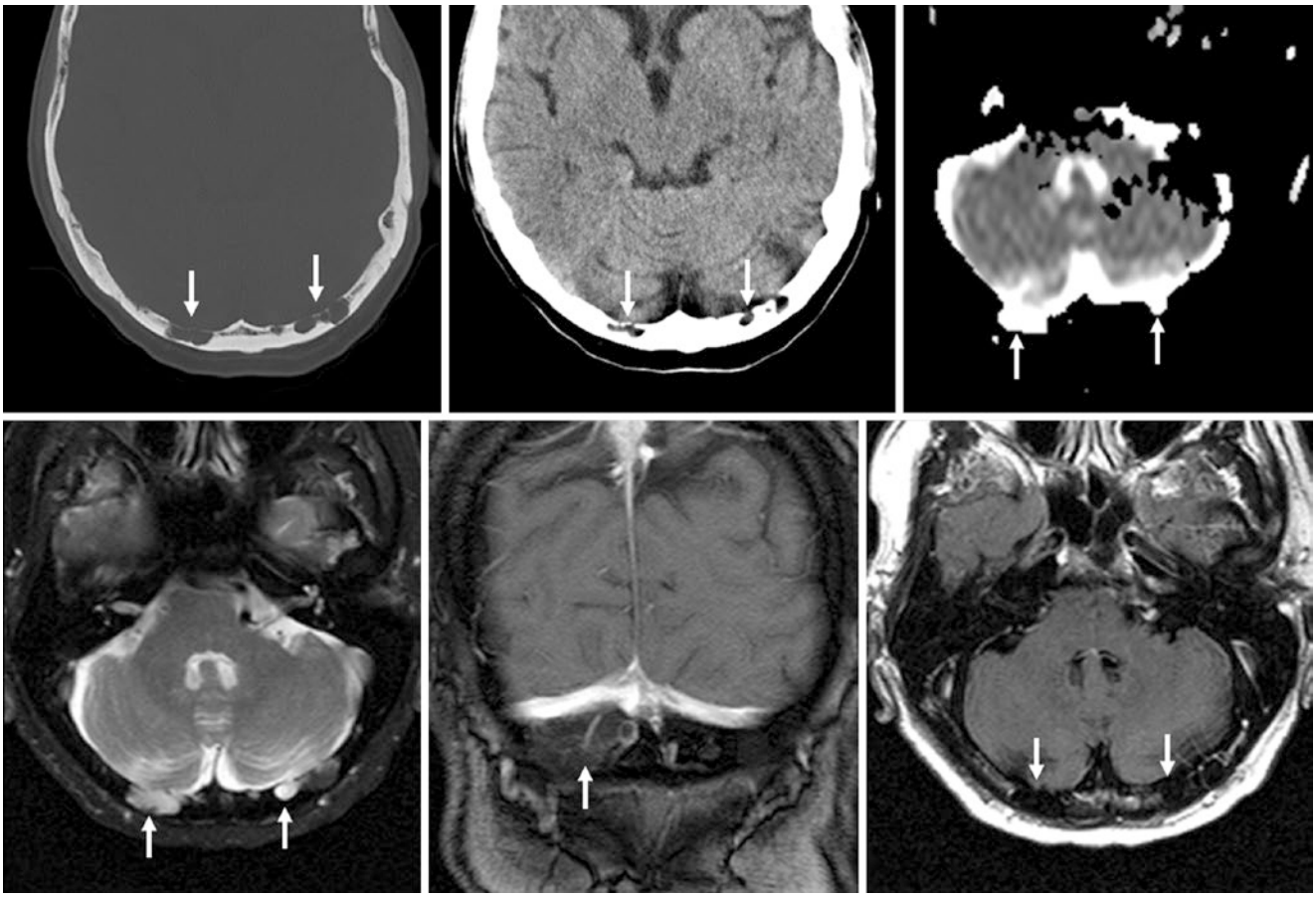

Fig. 30.7 A 75 year old with prostate cancer who had irregular pacchionian granulations of the occipital bone on NECT (*top left and middle*). These resembled CSF on ADC map (*top right*) and T2WI (*bottom left*) and did not enhance on T1WI (*bottom middle*) or FLAIR (*bottom right*)

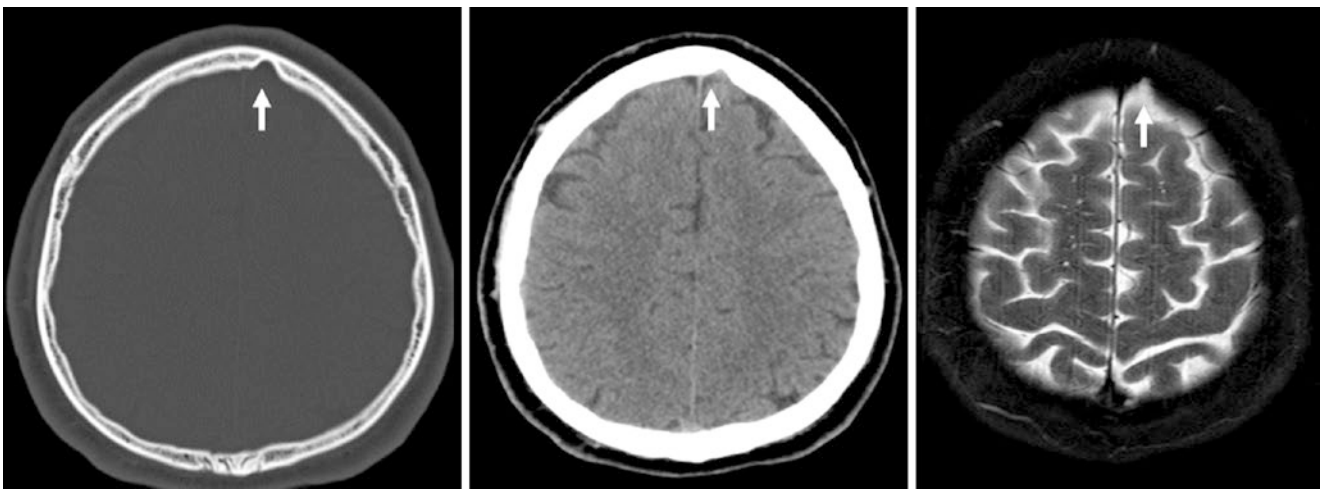

Fig. 30.8 A 52 year old with a small pacchionian granulation (*arrows*) that indents the skull on bone window (*left*) and on the brain window (*middle*) from NECT, being hyperintense on T2WI (*right*), thus following CSF in signal

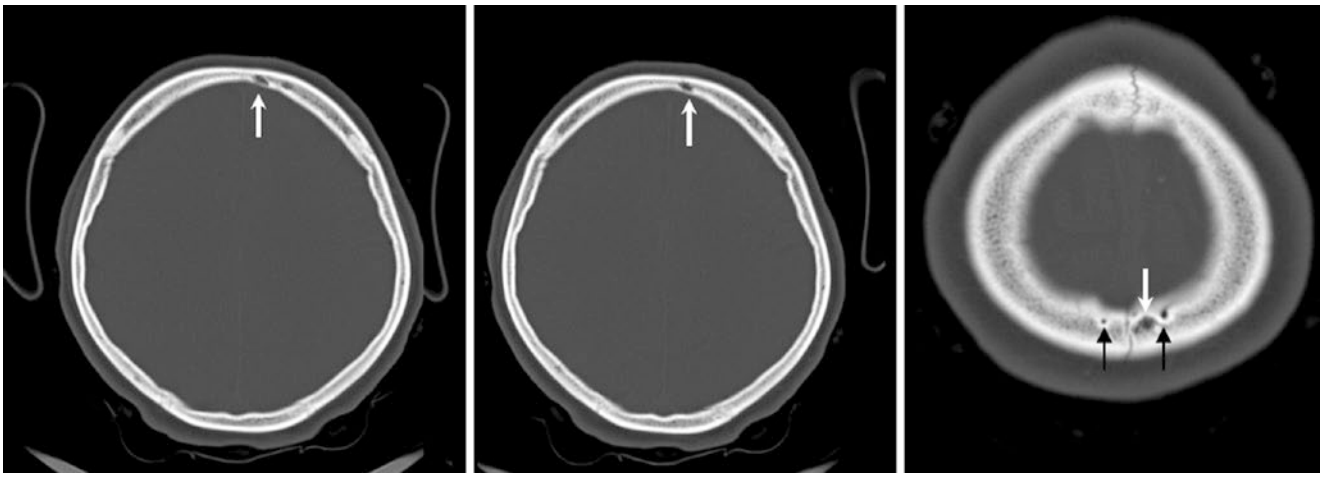

Fig. 30.9 A 5 year old with two incidental arachnoid granulations (*white arrows*) and two incidental parietal foramina (*black arrows*) on axial NECT images

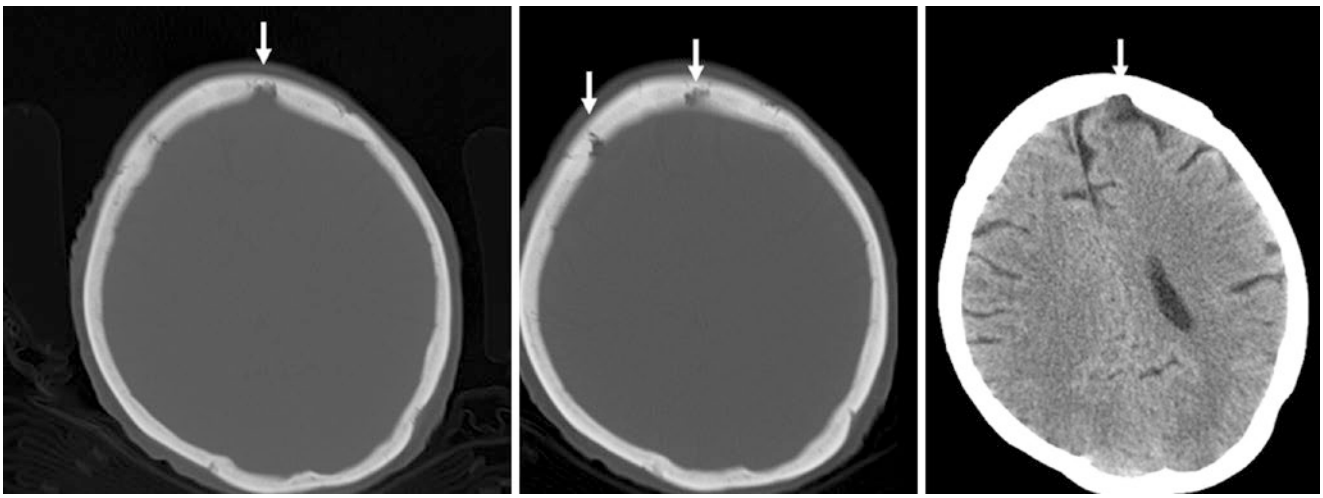

Fig. 30.10 A 59 year old who on NECT had two anterior frontal arachnoid granulations that are demonstrated on bone windows (*left and middle*) and are similar to CSF on brain windows (*right*)

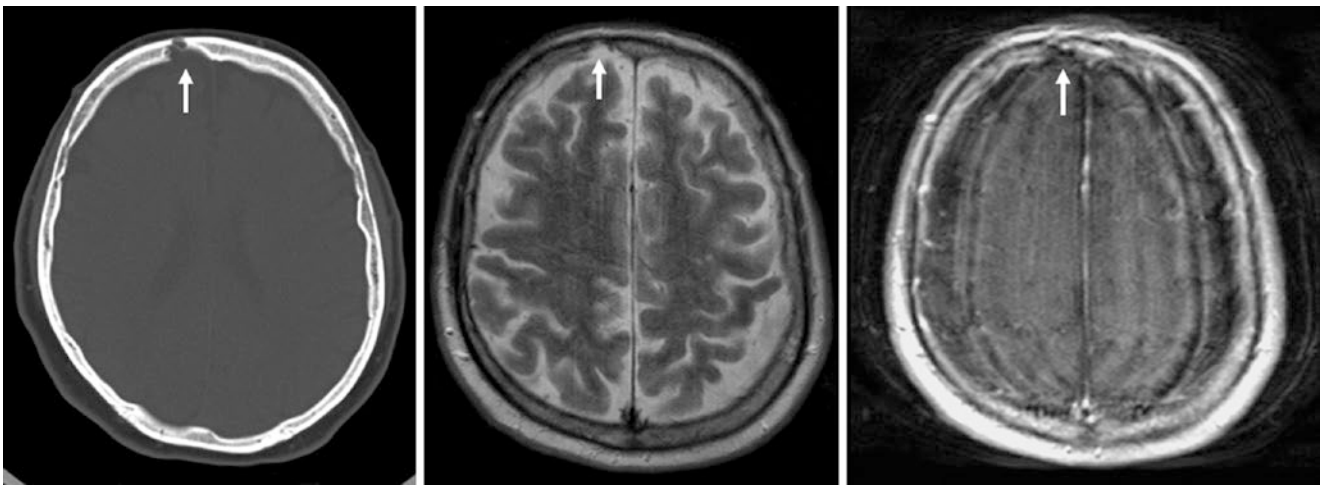

Fig. 30.11 A 61 year old: on an outside NECT (*left*), an arachnoid granulation was initially called a possible metastasis. On MRI, the potential lesion was found to follow the CSF signal on T2WI (*middle*) and FLAIR (*not shown*) and lacked enhancement on T1WI as well (*right*)

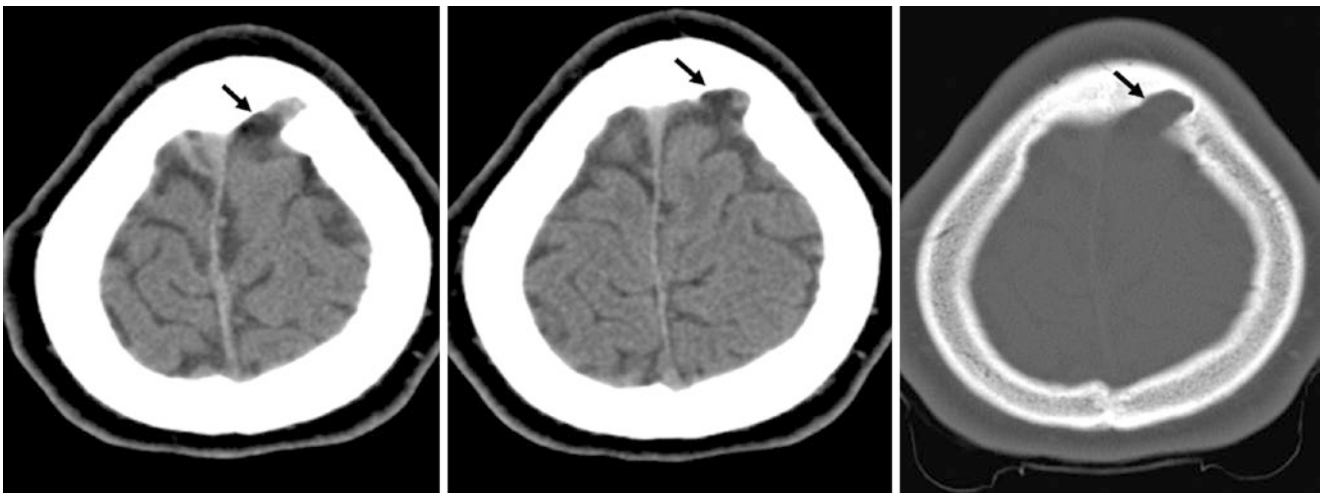

Fig. 30.12 A 20 year old who on NECT was found to have a unilateral, left frontal arachnoid granulation with mild internal density greater than CSF; however, it also contains CSF. Without contrast or an MRI, it is difficult to discern an arachnoid granulation from a diploic vein (i.e., a normal prominent vein or venous plexus within the skull). This also simulates a vascular foramen

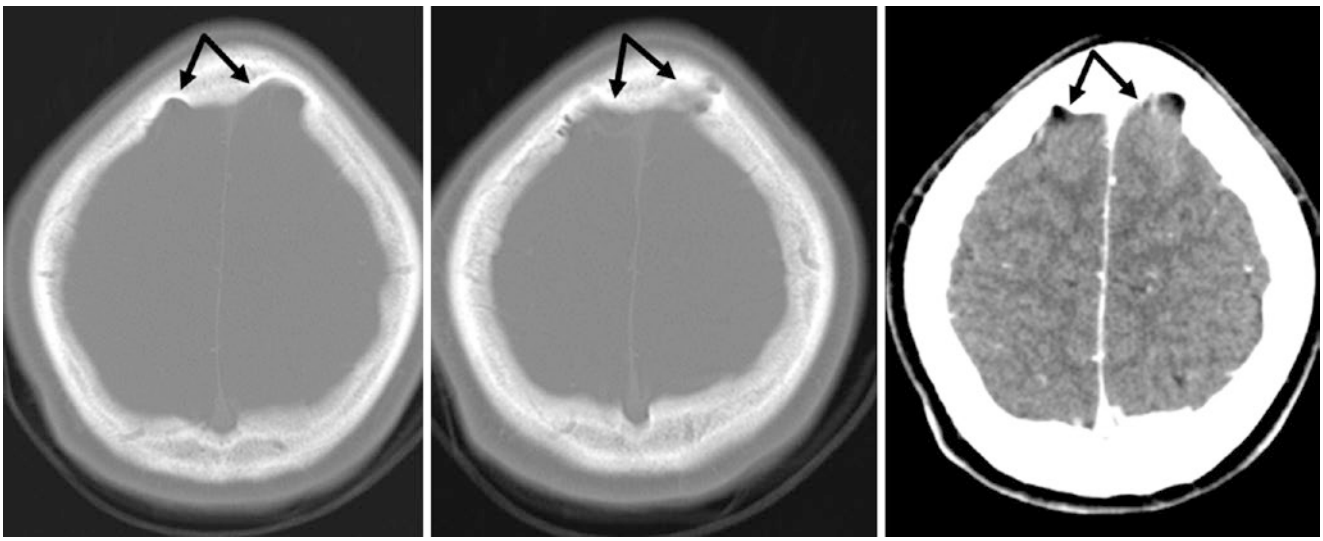

Fig. 30.13 A 17 year old with bilateral frontal arachnoid granulations on NECT (*left and middle*) that do not enhance on postcontrast CT (*right*). These simulate vascular foramina, but such foramina do not characteristically occur in this location. The left granulation contains a vessel

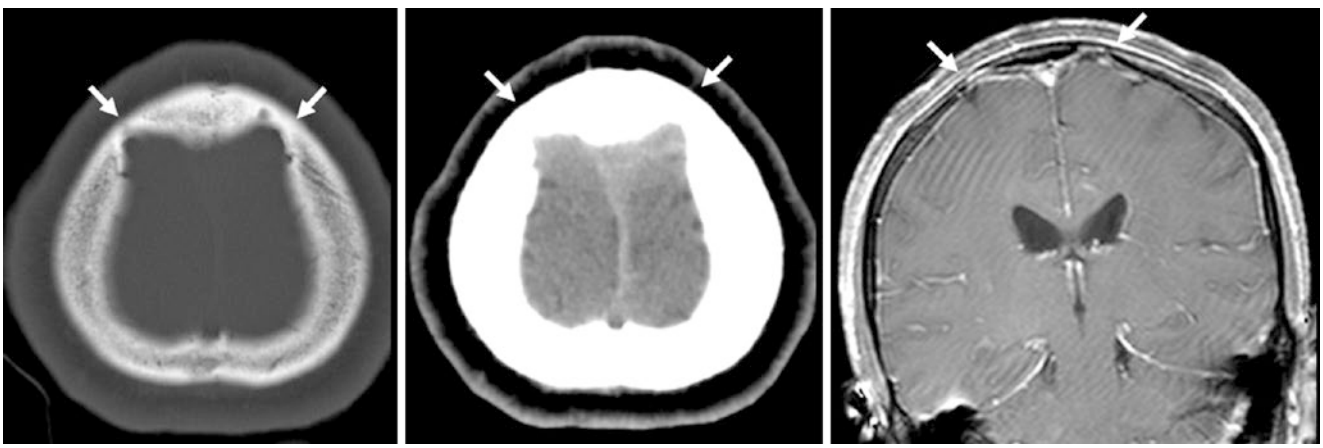

Fig. 30.14 A 48 year old with bilateral pacchionian granulations. Note that the cortical veins in the subarachnoid space pass through the granulations, which are surrounded by CSF. These can also be considered pacchionian depressions

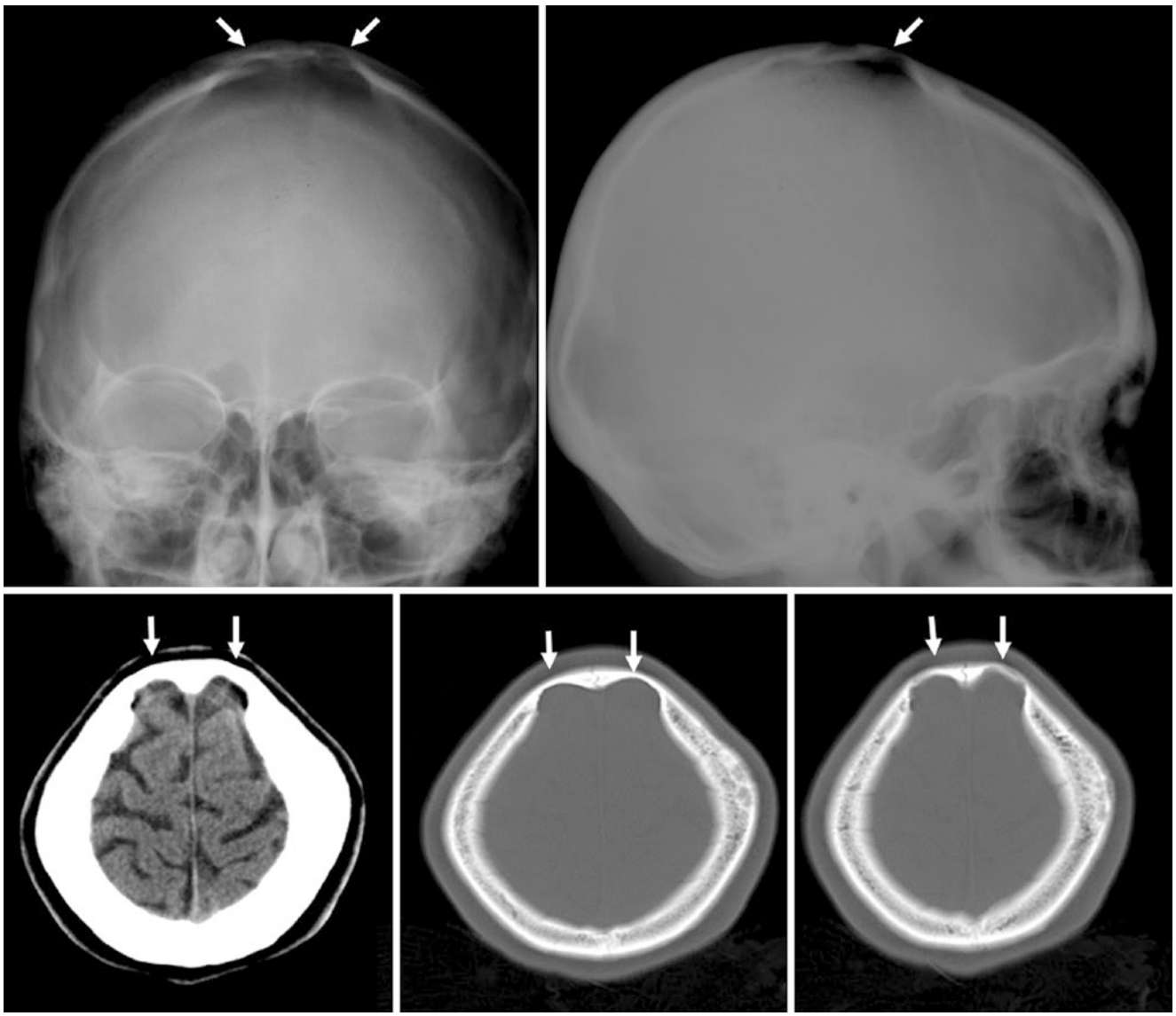

Fig. 30.15 *Top row:* A 12 year old with no fracture after trauma, but lytic lesions were questioned on plain films. *Bottom row:* NECT demonstrated bilateral pacchionian granulations, which also simulated foramina. No true foramina have been described in that location. These can also be considered pacchionian depressions

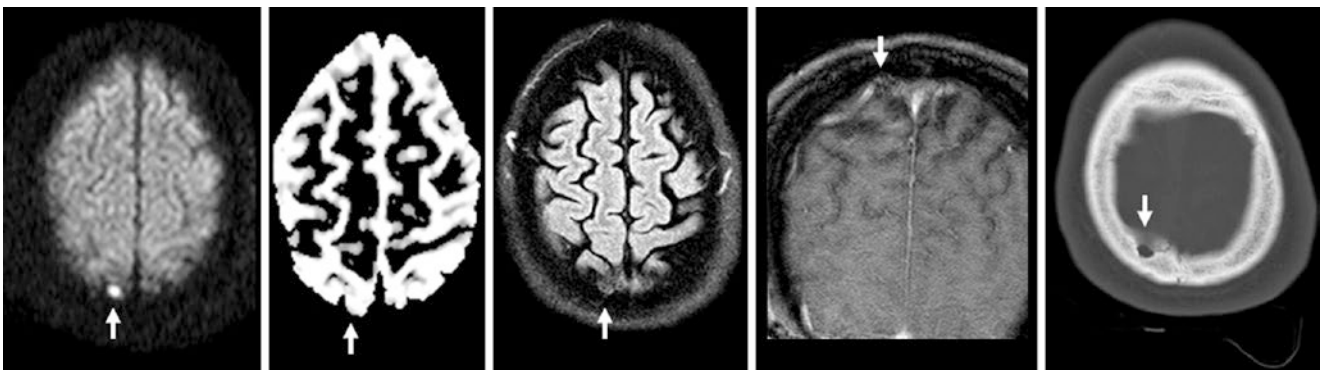

Fig. 30.16 A 54 year old: on MRI, a tiny infarct (*arrows*) was questioned on DWI (*left*), but it had a bright signal on ADC map (T2 shine-through, *left middle*), intermediate FLAIR signal (*middle*), and no enhancement on T1WI (*right middle*). NECT confirmed a small arachnoid granulation

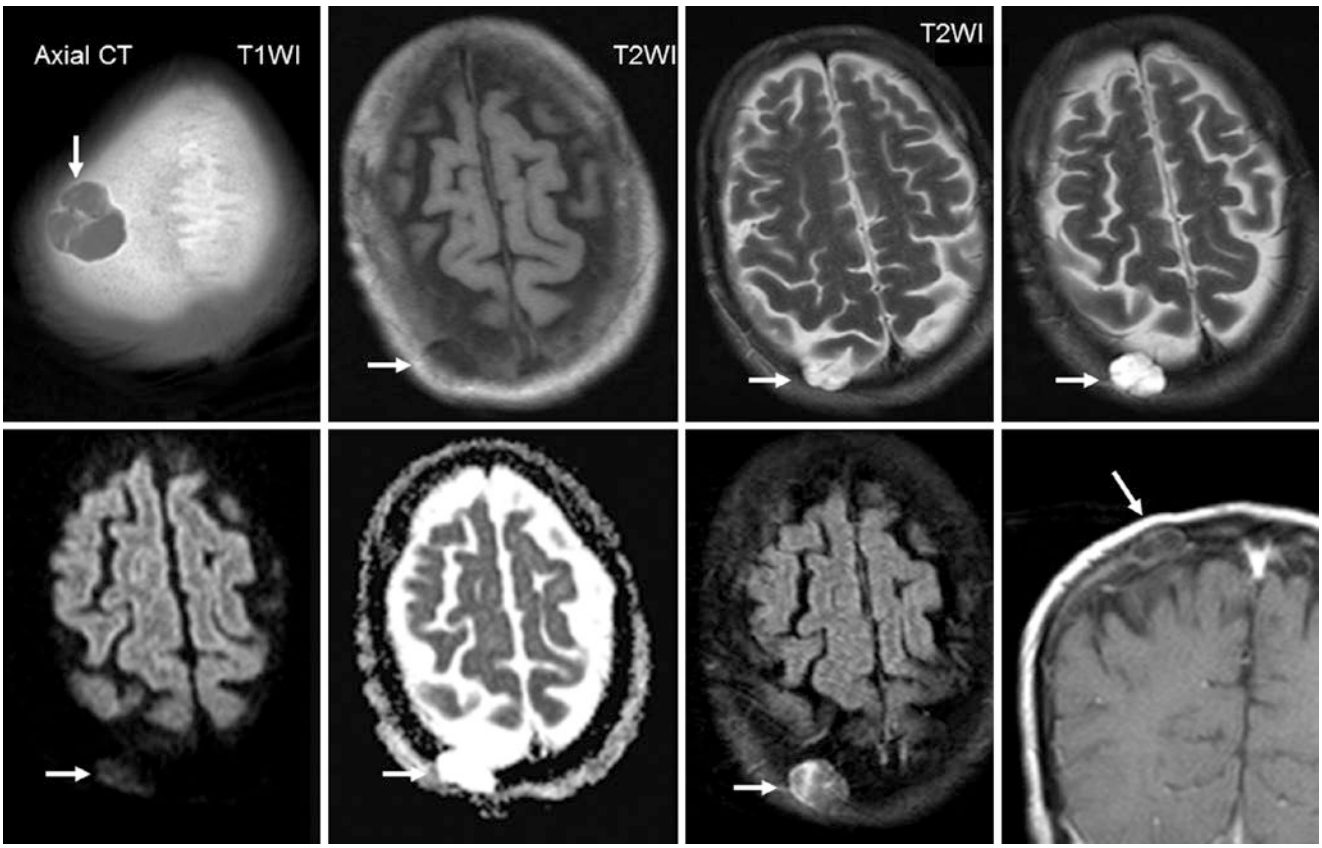

Fig. 30.17 A 48 year old: *Top row*: a septate and partly ossified arachnoid granulation on NECT (*left*) had signal akin to CSF on T1WI (*left middle*) and T2WI (*right images*). *Bottom row*: on DWI, there was decreased diffusion (*left*) with bright signal on ADC map (*left middle*) relative to gray matter but minimally brighter than CSF on DWI. There was no enhancement on postcontrast FLAIR (*right middle*) or on coronal T1WI (*right*)

30.2 Calvarial Depressions that Contain Vasculature, Mimicking Lytic Lesions

Calvarial depressions from vascular channels are quite common and are likely synonymous with the term *pacchionian depressions* [1–5, 13–16]. They differ from pacchionian granulations only in that these spaces are not entirely CSF-filled but rather are filled with an enhancing vessel. Thus, both entities may be the same or at least related on the same spectrum. The following cases are reconstructed from CT angiograms (CTAs) with overlapping 0.75-mm slices, partially in the venous phase. Inside-out three-dimensional reconstructions illustrate the internal venous channels well (Figs. 30.18, 30.19, and 30.20).

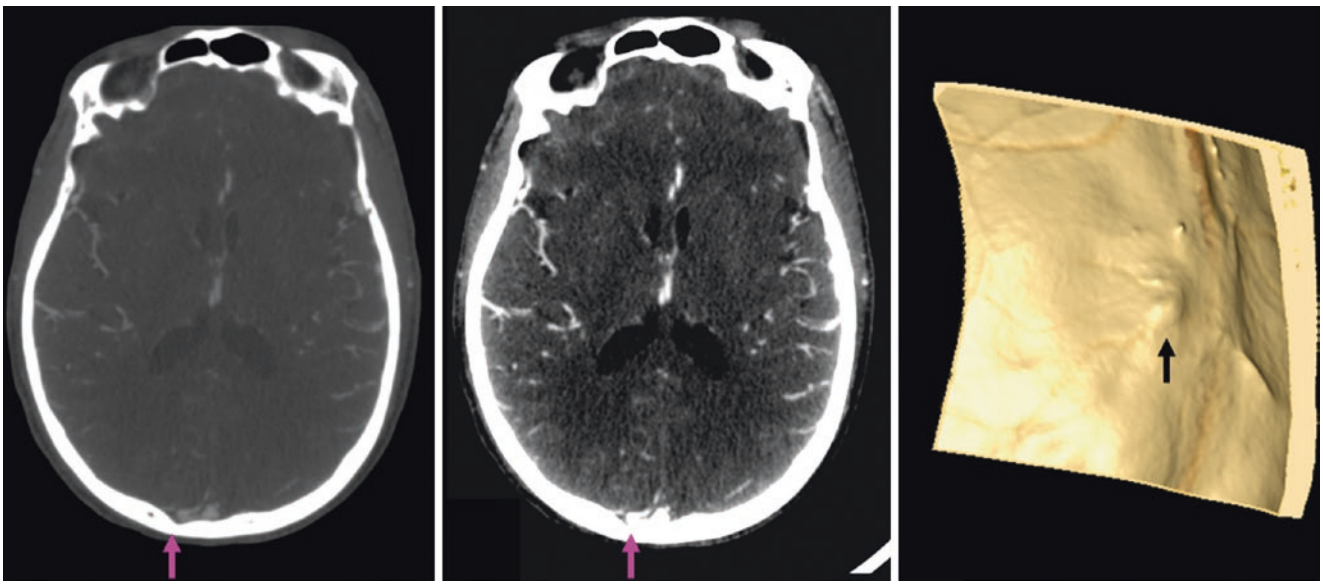

Fig. 30.18 A 58 year old in whom a cortical vein connecting to the superior sagittal sinus is contained within a calvarial depression on postcontrast source CTA images (*left and middle*). Three-dimensional VR reconstructions (inside-out view, *right*) can further depict a calvarial/pacchionian depression

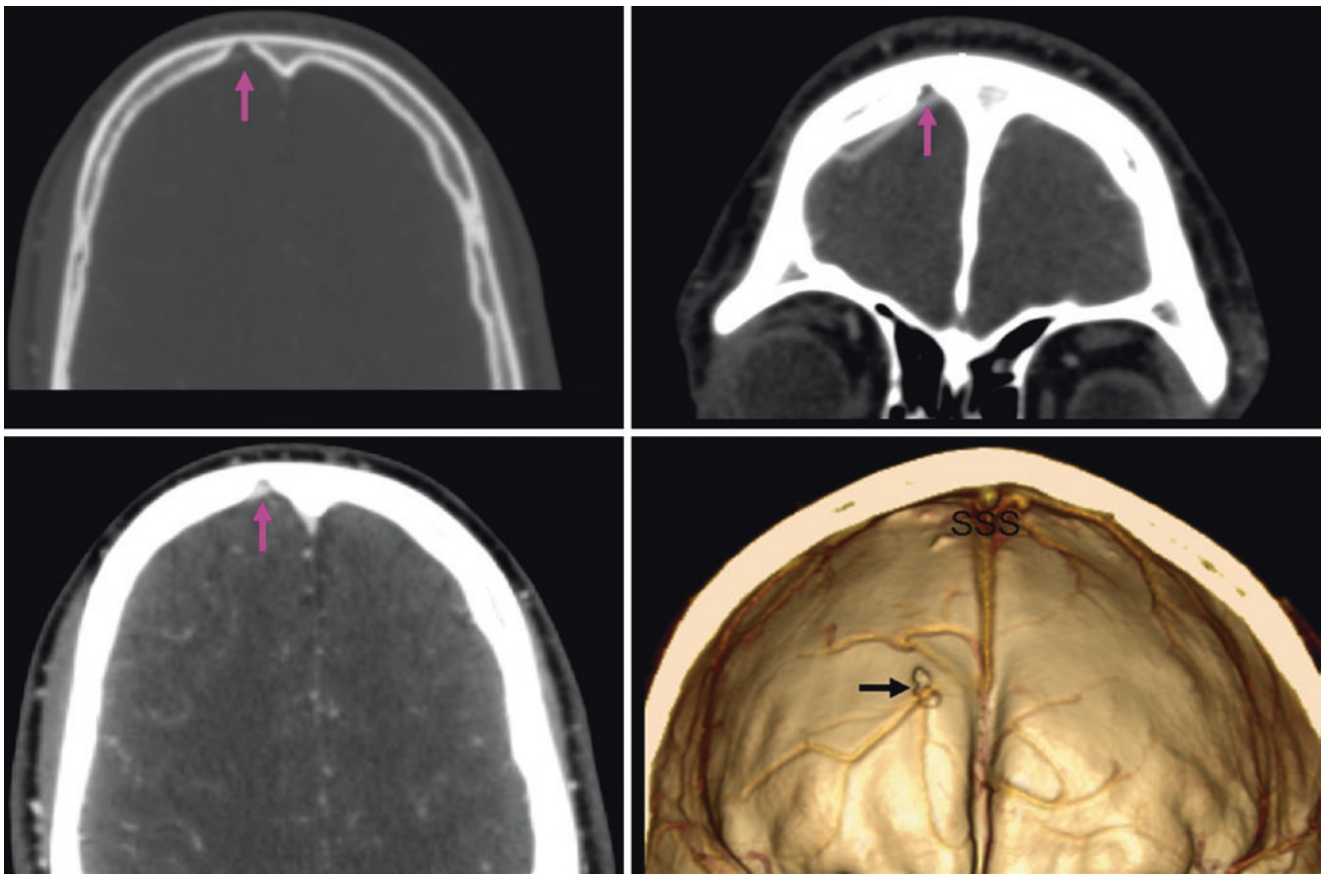

Fig. 30.19 Thin, less than 1-mm sections from a head CTA show small indentations of the skull's inner table, which are similar to arachnoid granulations on bone windows (*top left*). These contain venous channels on venous phase coronal (*top right*) and axial (*bottom left*) reformats. These depressions are well defined on three-dimensional inside-out view images (*bottom right*), which show scalloping of the inner calvarium. These vessels drain into the superior sagittal sinus (*SSS*)

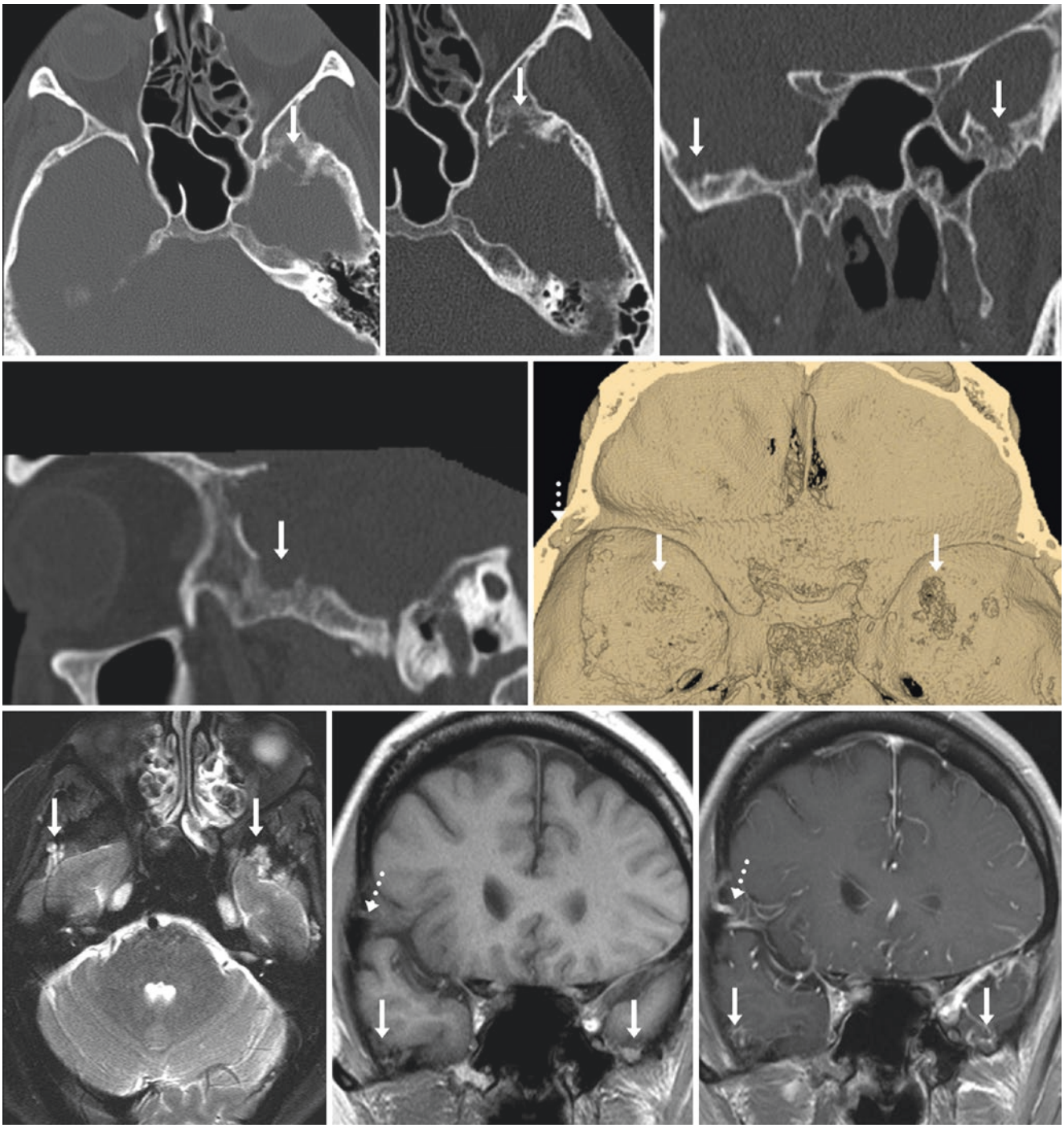

Fig. 30.20 A 61 year old with a lytic lesion questioned in the left middle cranial fossa floor on axial NECT (*top left*). Axial and coronal reformats (*top middle and right*) showed defects within the left sphenoid greater wing, also noted on sagittal (*middle row, left*) and three-dimensional VR superior view (*middle row, right*). MRI confirmed these to be calvarial depressions with venous plexi internally on T2WI (*bottom left*) and T1WI (*bottom middle*) but enhancing in a serpiginous fashion on T1WI (*bottom right*), potentially a confusing appearance. Note a right sphenoidal defect as well, from an intradiploic vein on the three-dimensional VR CT image and MRI (*dashed arrows*)

30.2.1 Calvarial (Intraosseous) Lipomas

Although *lipomas* are technically benign neoplasms, there is debate as to whether lipomas within the calvarium (*intraosseous lipomas*) are actually neoplasms at all, versus a response to various insults such as bone infarcts, trauma, and infections. Such lipomas of the calvarium are quite rare, with less than 20 cases described in the literature [18–22]. These should not be confused with *osteolipomas*, which may contain bony matrix and enlarge after a lipoma has undergone metaplasia. Included here is the uncommon, small, intraosseous lipoma as a don't touch lesion, since lipomas that are less than1.5 cm in size do not enlarge (per this author's unpublished data after following several over a number of years) and are asymptomatic. These have the density of fat on CT (−10 down to −150 HU), are of homogeneous dark density (not mixed with sclerotic density internally), and exhibit fat signal on MRI, that is, these are T1-bright and darken following *fat suppression* (FS). These may appear bright on T2WI when utilizing fast spin-echo sequences without FS and can be difficult to distinguish from smaller *hemangiomas* that are sometimes T1-bright on MRI (usually larger hemangiomas are expansile and have heterogeneous signal). On CT, hemangiomas usually demonstrate a "honeycomb" or mottled trabeculated appearance. Note that hemangiomas may also variably be bright on T1WI, whether on a gradient-echo or spin-echo acquisition. Hemangiomas are also most commonly dark on DWI and ADC maps, similar to cranial and scalp lipomas, but they have varying atypical appearances as well (Figs. 30.21, 30.22, 30.23, 30.24, 30.25, 30.26, and 30.27).

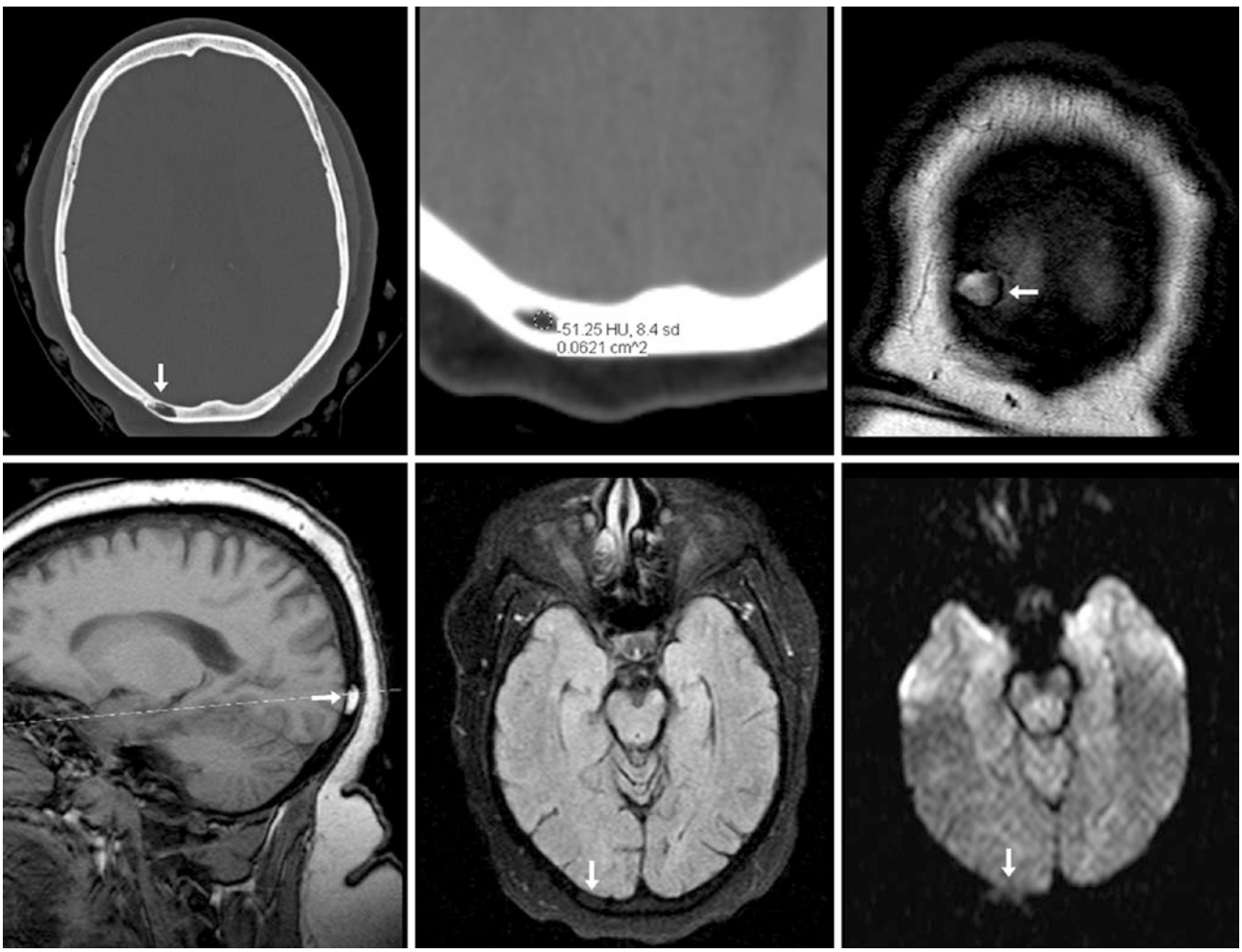

Fig. 30.21 A 51 year old with a focus having similar density to scalp fat (−51 HU) in the occipital bone on NECT (*top left and middle*). This was bright on noncontrast coronal (*top right*) and sagittal (*bottom left*) T1WI. It was dark on FS FLAIR (*bottom middle*) and DWI (*bottom right*); this uniform suppression of fat signal confirms a lipoma

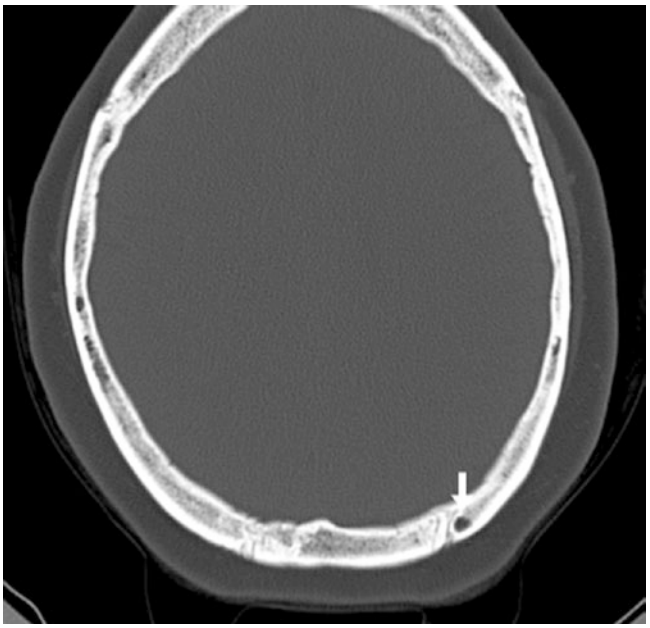

Fig. 30.22 A 29 year old with a tiny left parietal lipoma has internal fat density (−63 HU)

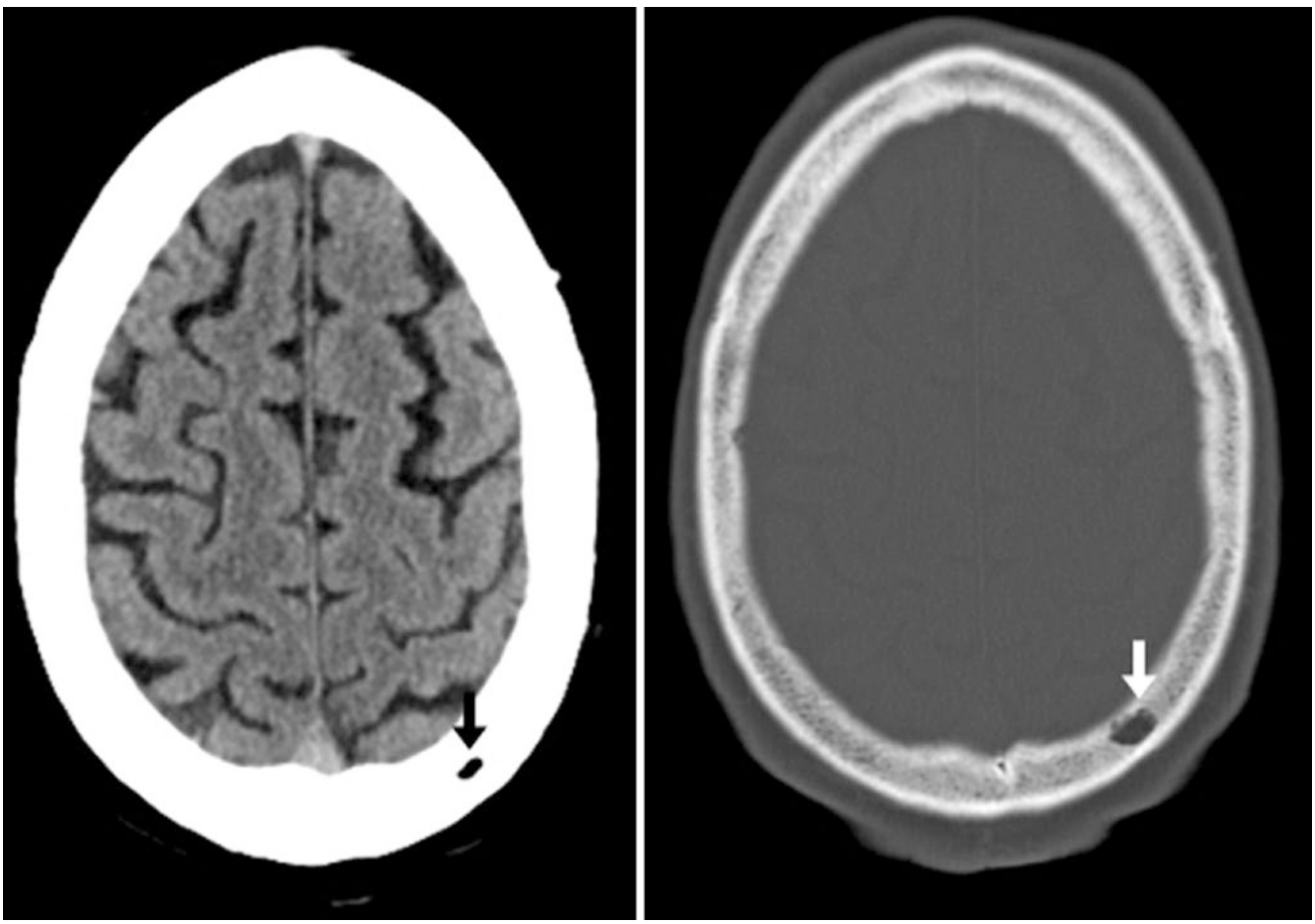

Fig. 30.23 A 71 year old with a small left parietal lipoma that has internal fat density (−55 HU)

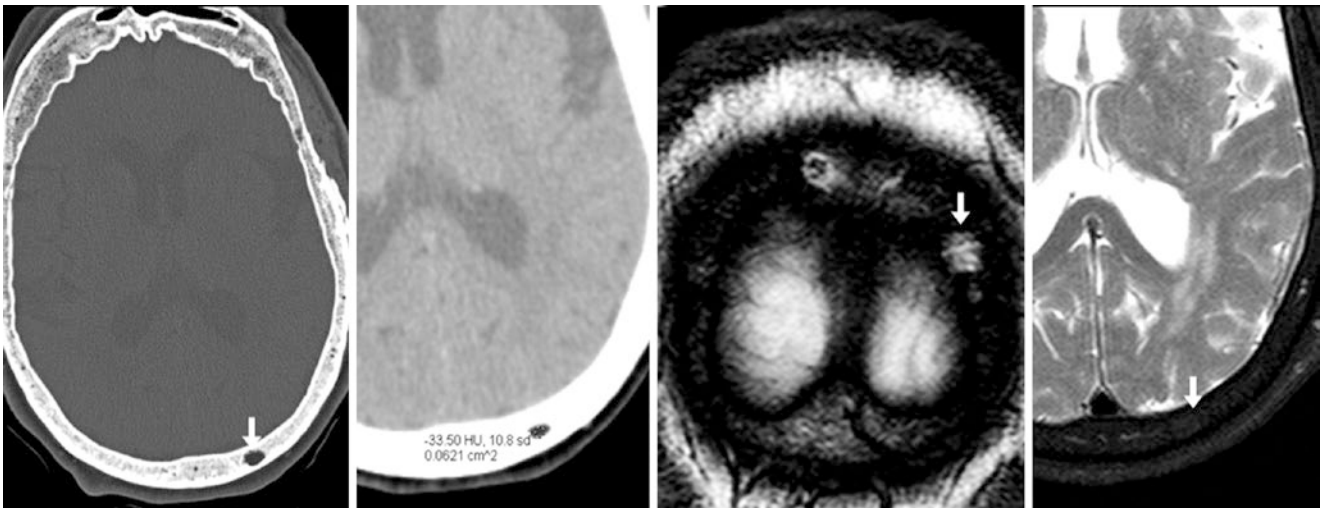

Fig. 30.24 A 73 year old with a focal calvarial hypodensity similar to that of scalp fat (−34 HU) within the left occipital calvarium on NECT bone (*left*) and soft tissue (*left middle*) windows that was mildly bright on coronal T1WI (*right middle*). This lipoma darkened on FS T2WI (*right*)

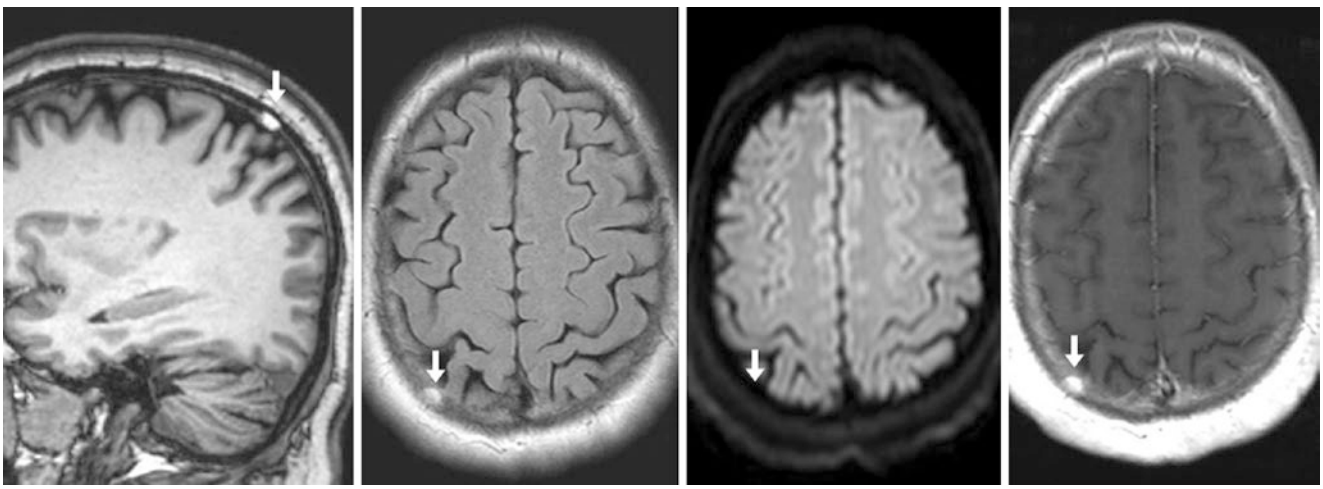

Fig. 30.25 A 76 year old in whom a focal T1-bright lesion within the right parietal calvarium was noted on sagittal T1WI (*left*) and FLAIR (*left middle*). This lipoma was dark on DWI (*right middle*) and retained its bright signal on postcontrast T1WI (*right*) since FS was not applied. Thus, this could simulate a skull metastasis if the noncontrast T1WIs are not reviewed closely

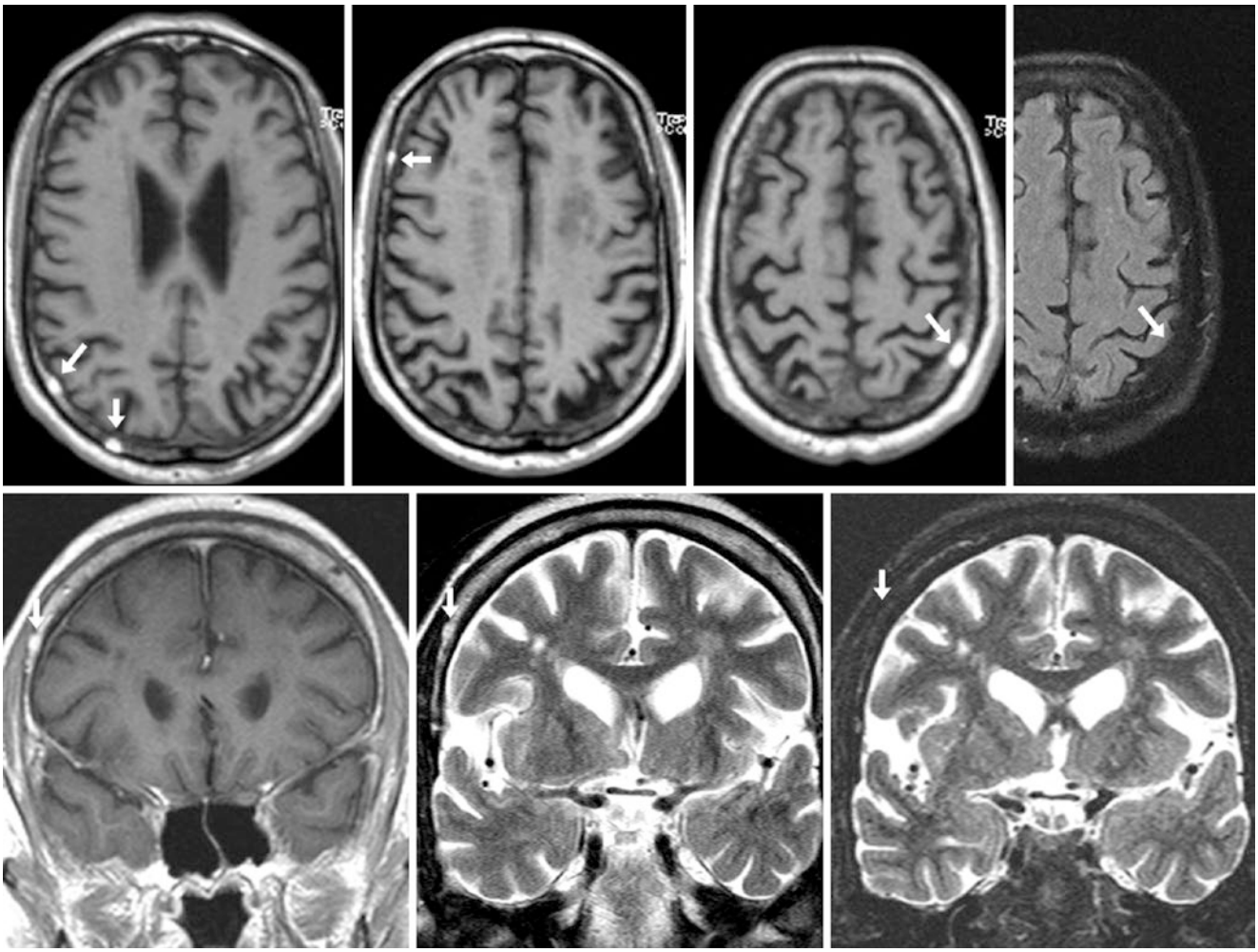

Fig. 30.26 A 59 year old: *Top row*: several small calvarial lipomas (*arrows*) on gradient-echo T1WI (*left three images*) have internal fat signal, which darkens on FS FLAIR (*right*). Focusing on the right frontal lipoma, spin-echo T1WI (*bottom left*) and T2WI (*bottom middle*) show that the fat of the T1- and T2-bright component darkens on fat-suppressed T2WI (*bottom right*)

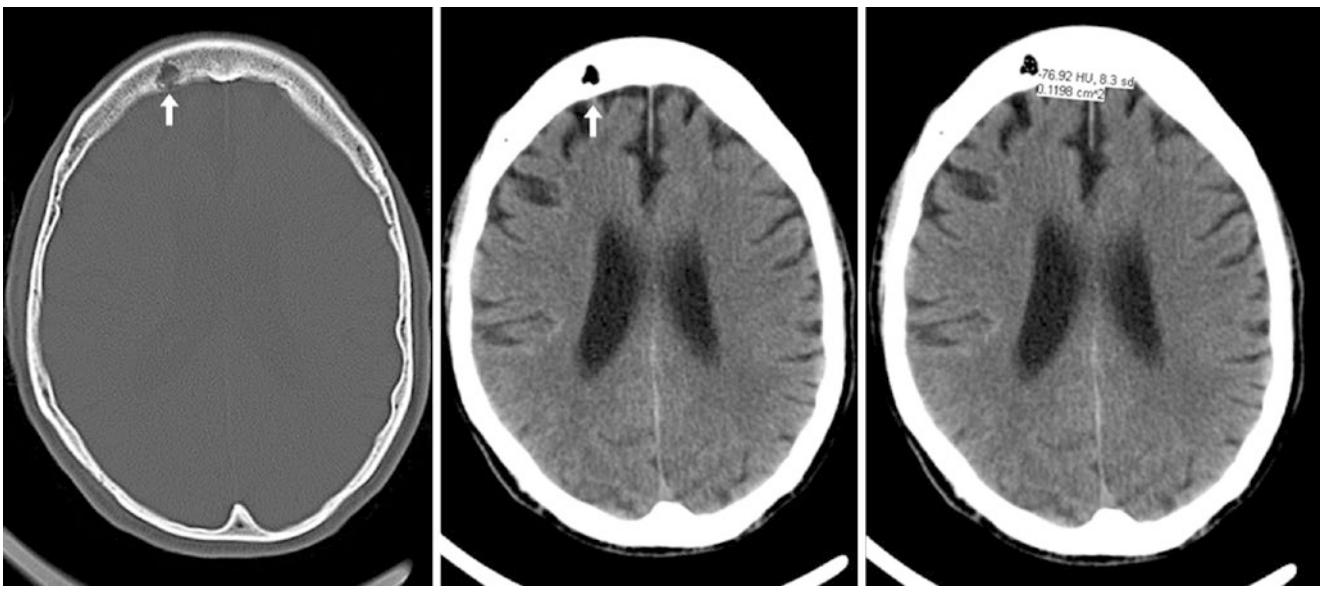

Fig. 30.27 A 76 year old with a small right frontal lipoma on axial NECT that has internal fat density (−76 HU)

30.2.2 Calvarial (Intraosseous) Hemangiomas

While the smaller *hemangiomas* may have T1-bright signal akin to that of intraosseous lipomas, *calvarial hemangiomas* typically have a different signal intensity than lipomas, given their underlying histopathologic makeup of clusters of dilated, thin-walled blood vessels lined often by only a single layer of endothelium [23–33]. Basically, the amount of T1-bright signal varies, most likely related to the degree of fat present within. These represent less than 0.5 % of all bone neoplasms, are more common in women than men (by a 3:1 ratio), and may be located anywhere within the skull [23–33]. Two different types have been described: "sessile" (the more common type that wends throughout the diploic space) and the rare "globular" (expansile and lytic) subtype. The sessile and smaller globular lesions are focused on here, since rarely globular lesions can become quite expansile and enlarge the calvarium. These most commonly occur in the frontal followed by the temporal bones.

Another increasingly more common, way to classify such intraosseous lesions is to view them as vascular *malformations* and thus classify them by the degree of flow. In such a classification, some have advocated dropping the term "hemangioma", as it invokes a wide spectrum of vascular-derived lesions and the reclassification of the subcategories as *low-flow* (i.e., slow flow, such as with traditional cavernous and capillary hemangiomas, cystic hygromas/venolymphatic malformations) versus *high-flow* (such as arteriovenous malformations). In this classification, an *intraosseous hemangioma* is a low-flow, intraosseous vascular malformation. This classification also applies in a similar fashion to soft-tissue vascular malformations of the head and neck.

The vast majority of smaller hemangiomas (<2.0 cm in size), whether sessile or globular, have some degree of enhancement on postcontrast T1WI MRI, while T2WI often demonstrates bright or mild hyperintensity with variable hyperintensity on noncontrast T1WI as well (again, most likely related to the amount of fat contained) [18–33]. Delayed contrast enhancement of a lesion with heterogeneous signal on T2WI is more commonly seen in larger lesions (>2–3 cm in size). Thus, there is some overlap of the smaller T1-bright hemangiomas and *intraosseous lipomas*, and their appearances differ on CT (lipomas have a homogeneous fat signal while hemangiomas can be heterogeneous but well circumscribed). Also, on postcontrast T1WI MRI, hemangiomas often enhance on fat-suppressed T1WI, whereas lipomas do not. On CT, hemangiomas often have a characteristic spoke-wheel or spiculated appearance centrally and are well circumscribed; occasionally, they have internal soft-tissue density. If so, they usually exhibit delayed enhancement after 1–5 min. The enhancement pattern of hemangiomas can at times simulate *metastases* or *plasmacytoma*, particularly if the calvarium expands with globular hemangioma enlargement; however, in the uncommon case where they enlarge, such hemangiomas develop internal flow voids, thereby revealing their benignity, while metastases usually do not. Another reason hemangiomas may simulate metastases is in the rare instance when they are multiple, such as in certain syndromes, which some have termed *"angiomatosis or hemangiomatosis"*. Rarely, these can become *giant calvarial hemangiomas (*cavernomas*).* Finally, regarding nuclear medicine studies, hemangiomas typically exhibit variable uptake on standard bone scans but usually demonstrate elevated uptake on delayed tagged red blood cell studies, further typifying their slow flow (Figs. 30.28, 30.29, 30.30, 30.31, and 30.32).

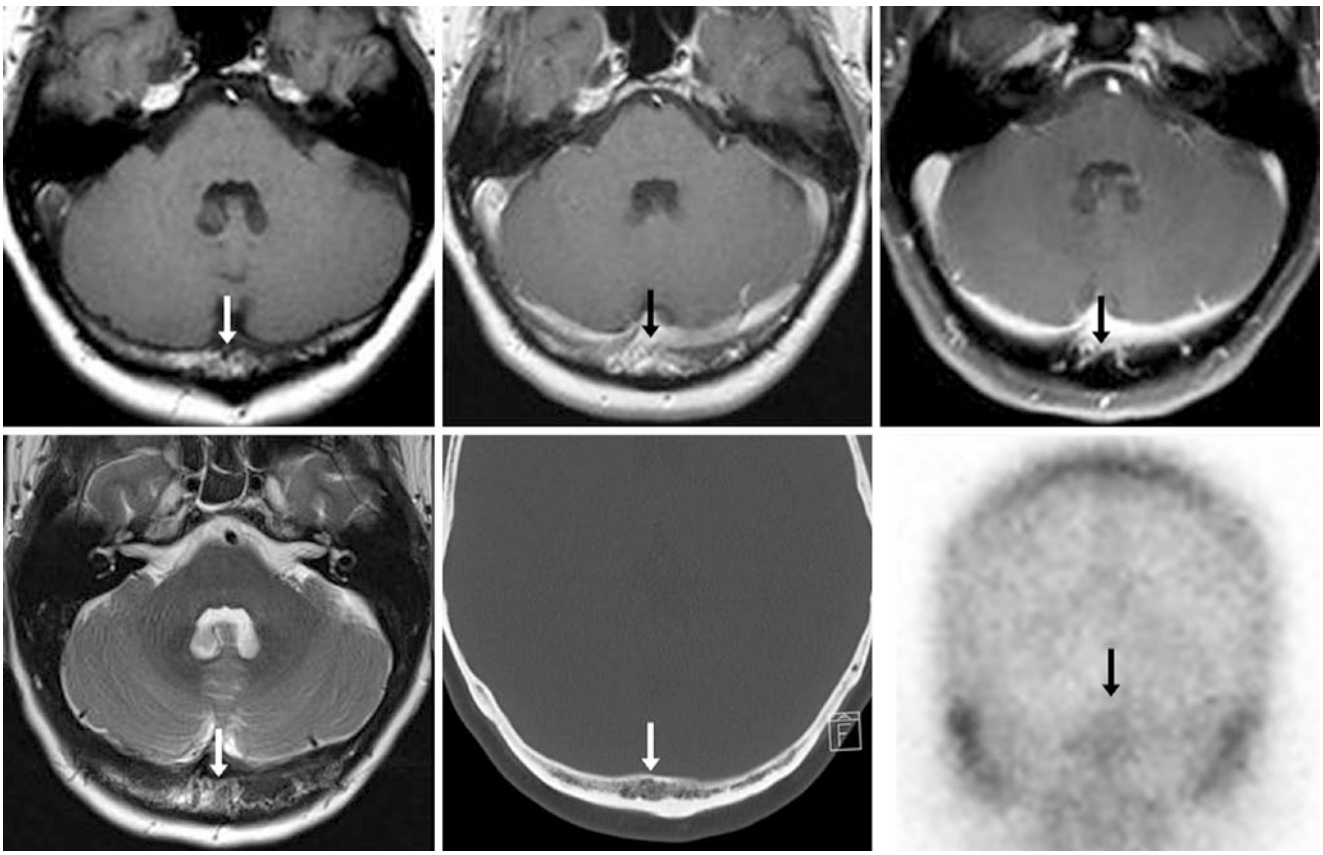

Fig. 30.28 A 42-year-old patient: *Top row*: on 1.5 T MRI, an occipital hemangioma (*arrows*) was bright on pre- (*left*) and postcontrast (*middle*) T1WI without FS; on FS T1WI (*right*), much of the brightness abated, but it retained mild enhancement. *Bottom row*: on T2WI (*left*), it was bright. On NECT (*middle*), it was sessile, not expanding the calvarium. On a posteroanterior view from a Tc99m bone scan (*right*), the lesion had uptake akin to the rest of the calvarium

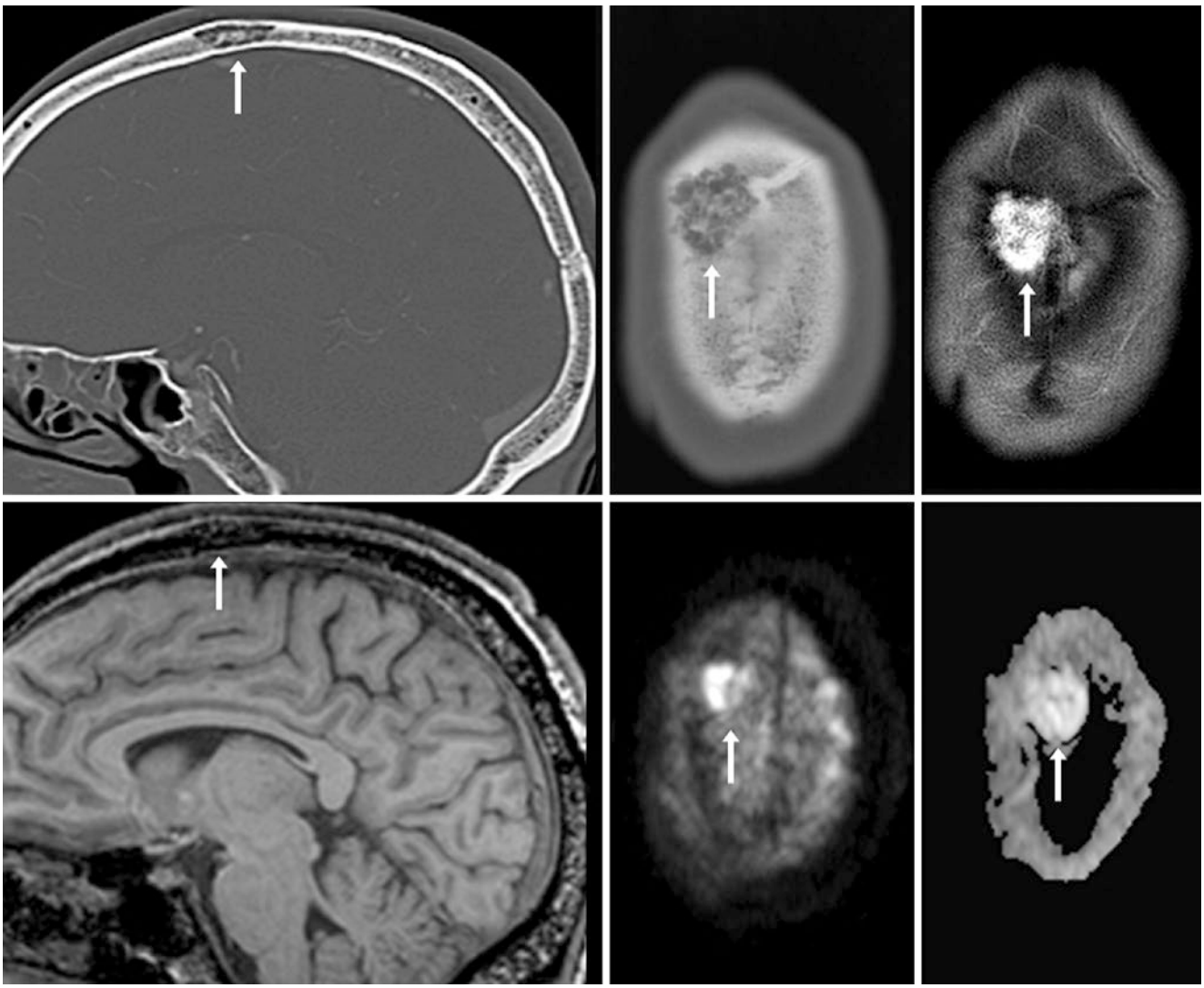

Fig. 30.29 A 42 year old with a frontal bone lesion (*arrows*) that was noted on sagittal (*top left*) and axial (*top middle*) NECT. On a 1.5 T MRI, fat-suppressed T2WI (*top right*) depicted that it was heterogeneous but mostly bright, being relatively dark on sagittal T1WI (*bottom left*). On DWI (*bottom middle*) and ADC map (*bottom right*), the lesion was bright, indicating T2-shine through. This hemangioma was unchanged 5 years later on NECT and on MRI (*not shown*)

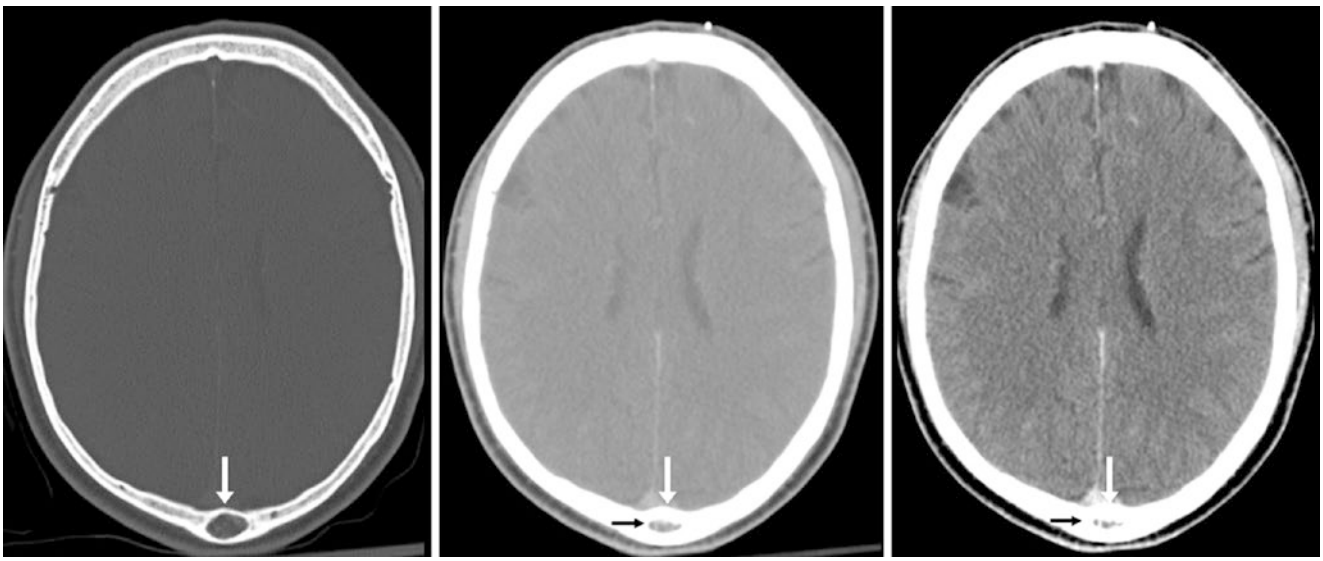

Fig. 30.30 A 56 year old with a midline parietal bone lesion (*arrows*) that was noted on axial postcontrast bone window (*left*), soft-tissue window (*middle*), and brain windows (*right*). This was presumed to be a hemangioma because of the well-circumscribed appearance and mild internal enhancement, which appeared to have internally enhancing vasculature (*thin arrows*)

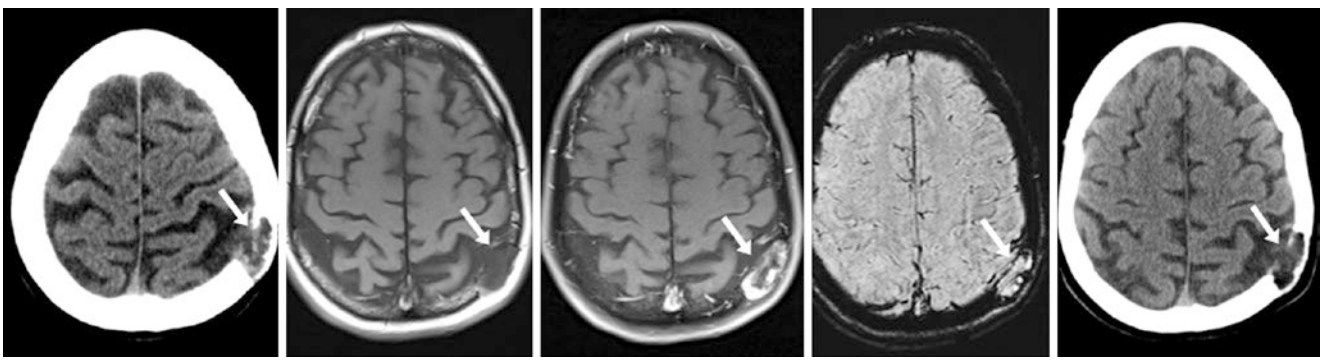

Fig. 30.31 A 47 year old with a parietal lesion (*arrows*) on NECT (*left*) that was shown to be hypointense on noncontrast T1WI (*left middle*), with peripheral enhancement after contrast (*middle*) on 1.5 T MRI; SWI (*right middle*) and DWI (*not shown*) depicted that it was mostly bright, likely due to T2-shine through effect. This was unchanged 3 years later on CT (*right*)

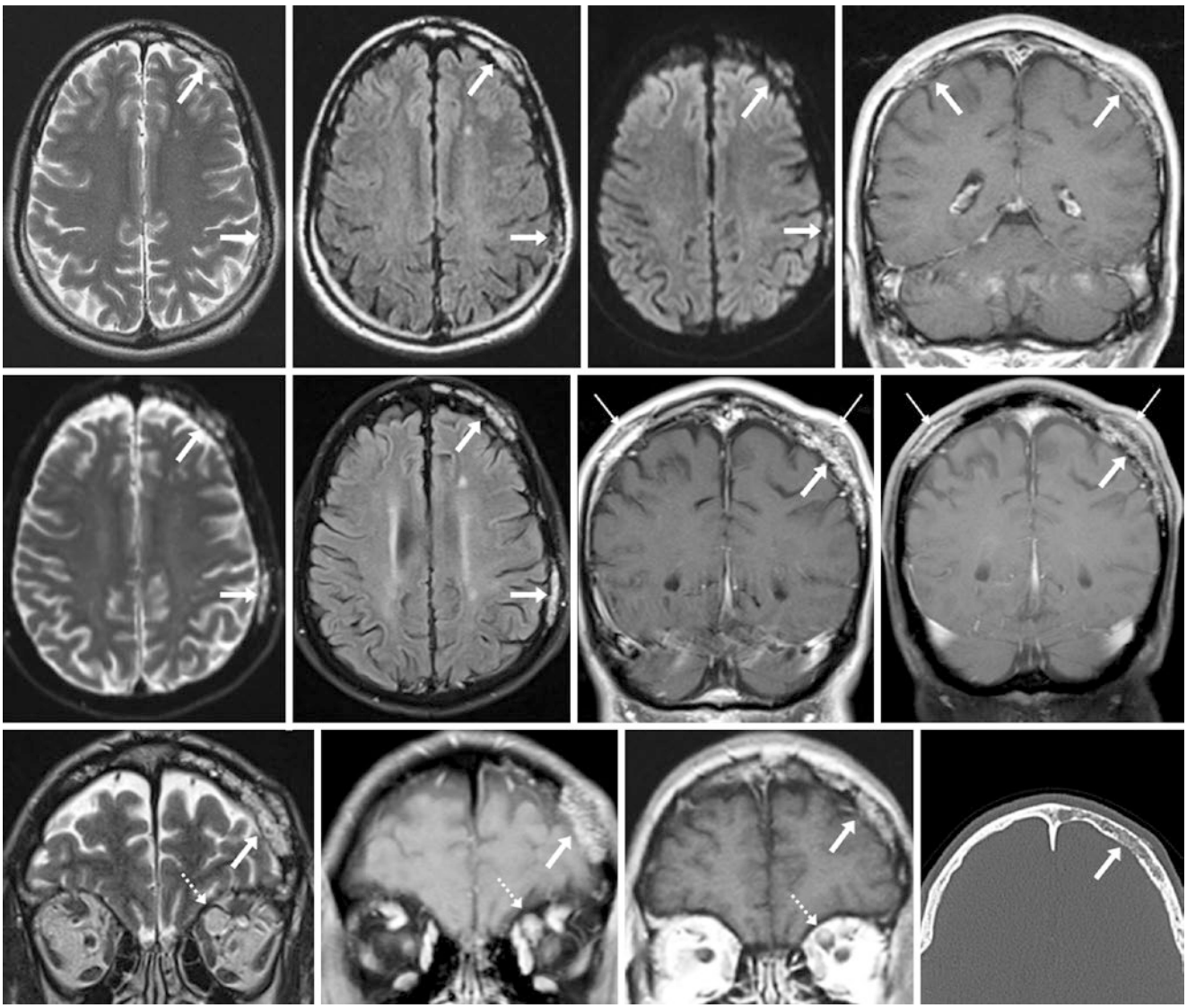

Fig. 30.32 A 48 year old with many hemangiomas (angiomatosis). *Top row*: multiple calvarial bright lesions (*arrows*) were noted on T2WI (*left*), FLAIR (l*eft middle*) DWI (*right middle*), and postcontrast T1WI (*right*). *Middle row*: 10 years later, these were unchanged on T2WI (*left*) and FLAIR (*left middle*), and enhanced on postcontrast coronal T1WI initially (*right middle*) and minutes later (*right*), typifying delayed enhancement of the superficial portion of the hemangioma (*thin arrows*). *Bottom row*: note an orbital hemangioma (*dotted arrows*) on T2WI (*left*) and postcontrast T1WI (*left middle*), which was unchanged from 10 years prior (*right middle*). Note a frontal hemangioma on NECT (*right*)

References

1. Keats TE, Anderson MW. Chapter 1: The skull. In: Atlas of normal roentgen variants that may simulate disease. 8th ed. Philadelphia: Mosby, Inc; 2007.
2. Seeger JF. Normal variations of the skull and its contents. In: Zimmerman RA, editor. Neuroimaging: clinical and physical principles. New York: Springer; 1999. p. 415–53.
3. Gray H. Chapter 5D: The interior of the skull. In: Anatomy of the human body. 20th ed. Philadelphia: Lea & Feiger; 1918.
4. Berge JK, Bergman RA. Variations in size and in symmetry of foramina of the human skull. Clin Anat. 2001;14:406–13.
5. Jinkins JR. Chapter 2: Cranium. In: Atlas of neuroradiologic embryology, anatomy, and variants. Philadelphia: Lippincott Williams & Wilkins; 2000.
6. Mamourian AC, Towfighi J. MR of giant arachnoid granulation, a normal variant presenting as a mass within the dural venous sinus. AJNR Am J Neuroradiol. 1995;16:901–4.
7. Roche J, Warner D. Arachnoid granulations in the transverse and sigmoid sinuses: CT, MR, and MR angiographic appearance of a normal anatomic variation. AJNR Am J Neuroradiol. 1996;17:677–83.
8. Leach JL, Jones BV, Tomsick TA, et al. Normal appearance of arachnoid granulations on contrast-enhanced CT and MR of the brain: differentiation from dural sinus disease. AJNR Am J Neuroradiol. 1996;17:1523–32.
9. Haroun AA, Mahafza WS, Al Najar MS. Arachnoid granulations in the cerebral dural sinuses as demonstrated by contrast-enhanced 3D magnetic resonance venography. Surg Radiol Anat. 2007;29:323–8.
10. Okamoto K, Ito J, Tokiguchi S, et al. Arachnoid granulations of the posterior fossa: CT and MR findings. Clin Imaging. 1997;21:1–5.
11. Koshikawa T, Naganawa S, Fukatsu H, et al. Arachnoid granulations on high-resolution MR images and diffusion-weighted MR images: normal appearance and frequency. Radiat Med. 2000;18: 187–91.
12. Ikushima I, Korogi Y, Makita O, et al. MRI of arachnoid granulations within the dural sinuses using a FLAIR pulse sequence. Br J Radiol. 1999;72:1046–51.
13. Celli P, Cervoni L, Quasho R. An asymptomatic hypertrophic pacchionian granulation simulating osteolytic lesion of the calvaria. Neurosurg Rev. 1999;22:149–51.
14. Kan P, Stevens EA, Couldwell WT. Incidental giant arachnoid granulation. AJNR Am J Neuroradiol. 2006;27:1491–2.
15. Tsutsumi S, Nakamura M, Tabuchi T, et al. Calvarial diploic venous channels: an anatomic study using high-resolution magnetic resonance imaging. Surg Radiol Anat. 2013;35:935–41.
16. Tsutsumi S, Ogino I, Miyajima M, et al. Cranial arachnoid protrusions and contiguous diploic veins in CSF drainage. AJNR Am J Neuroradiol. 2014;35:1735–9.
17. Trimble CR, Harnsberger HR, Castillo M, et al. "Giant" arachnoid granulations just like CSF?: NOT!! AJNR Am J Neuroradiol. 2010;31:1724–8.
18. Tomabechi M, Sako K, Daita G, et al. Lipoma involving the skull. Case report. J Neurosurg. 1992;76:312–4.
19. Arslan G, Karaali K, Cubuk M, et al. Intraosseous lipoma of the frontal bone. A case report. Acta Radiol. 2000;41:320–1.
20. MacFarlane MR, Soule SS, Hunt PJ. Intraosseous lipoma of the body of the sphenoid bone. J Clin Neurosci. 2005;12:105–8.
21. Milgram JW. Intraosseous lipomas. A clinicopathologic study of 66 cases. Clin Orthop Relat Res. 1988;277–302.
22. Milgram JW. Intraosseous lipomas: radiologic and pathologic manifestations. Radiology. 1988;167:155–60.
23. Naama O, Gazzaz M, Akhaddar A, et al. Cavernous hemangioma of the skull: 3 case reports. Surg Neurol. 2008;70:654–9.
24. Khanam H, Lipper MH, Wolff CL, Lopes MB. Calvarial hemangiomas: report of two cases and review of the literature. Surg Neurol. 2001;55:63–7.
25. Patel VH, Friedman L. Chapter 19: Normal anatomic variations. In: MRI of the brain: normal anatomy and normal variants. Philadelphia: W.B. Saunders Co; 1997.
26. Bastug D, Ortiz O, Schochet S. Hemangiomas in the calvaria: imaging findings. AJR Am J Roentgenol. 1995;164:683–7.
27. Gordhan A, Soliman J, Malpani A, Peg E. Symptomatic calvarial cavernous hemangioma: presurgical confirmation by scintigraphy. Radiol Case Rep. 2009;3:25–9.
28. Moore SL, Chun JK, Mitre SA, Som PM. Intraosseous hemangioma of the zygoma: CT and MR findings. AJNR Am J Neuroradiol. 2001;22:1383–5.
29. Heckl S, Aschoff A, Kunze S. Cavernomas of the skull: review of the literature 1975-2000. Neurosurg Rev. 2002;25(1–2):56–62.
30. Liu JK, Burger PC, Harnsberger HR, et al. Primary intraosseous skull base cavernous hemangioma: case report. Skull Base. 2003;13:219–28. 002;25:56–62.
31. Park BH, Hwang E, Kim CH. Primary intraosseous hemangioma in the frontal bone. Arch Plast Surg. 2013;40:283–5.
32. Politi M, Romeike BF, Papanagiotou P, et al. Intraosseous hemangioma of the skull with dural tail sign: radiologic features with pathologic correlation. AJNR Am J Neuroradiol. 2005;26: 2049–52.
33. Šarac H, Hajnšek S, Bašić S, et al. Giant cavernoma of the skull and skeletal-extraskeletal angiomatosis associated with paraproteinemia. Transl Neurosci. 2011;2:265–9.

Part III

Craniocervical Vasculature

Craniocervical Vasculature: Introduction

31

There are several important reasons to be familiar with normal variations and pitfalls of the *craniocervical vasculature*. First, prior knowledge of the variations in vascular origins of craniocervical vessels can prevent iatrogenic injury from a procedure or therapy. (A common example is an arch origin of the left vertebral artery during catheter angiography.) Second, a normal vessel in an unexpected location can simulate a mass, complicate biopsy of an adjacent structure, or lead to unnecessary or potentially dangerous treatment (such as with a retropharyngeal internal carotid artery). Third, some normal variations may simulate vascular abnormalities (such as normal infundibula of the intracranial vascular origins simulating aneurysms). Fourth, some of these normal variations, though not necessarily pathologic in and of themselves, carry a higher risk of associated pathology. (For instance, some fenestrations or duplications are associated with higher risks of aneurysm formation in certain locations.) Finally, the flow voids generated by vascular structures can become volume-averaged or generate artifacts that can lead to much consternation—a problem becoming more and more common as MRI usage increases.

In this chapter, the great vessel origins of the cervical vessels are covered first, followed by the skull base and intracranial portions, and then miscellaneous CT and MRI cross-sectional vascular variants or artifacts that can simulate intracranial disease. Thus, an attempt has been made to group the variations anatomically, although this can be somewhat difficult with cervical and cranial vasculature, as some variants span both cervical and cranial compartments and extend between the anterior and posterior circulation intracranially. Common variations in the craniocervical vessels and origins at the aortic arch are included in this chapter, as these are often encountered on cross-sectional imaging, but the extensive potential variations in the aortic arch and great vessel origins are not covered in great detail. That subject can constitute an entire text, and the reader is referred to a number of excellent vascular radiology and anatomy books on that subject. Rather, the focus of much of this chapter is on normal variants on *MRI* and *MR angiography* (MRA), *CT angiography* (CTA), and routine cross-sectional imaging, with catheter digital subtraction angiographic (DSA) correlation, when applicable or necessary. Table 31.1 lists the commonly used terms in this section.

It is important to pay close attention to the side of findings on PA, LPO, RPO, or superior views from 3D VR CTA, CTV, MRA, and MRV, as these 3D datasets are displayed corresponding to the angle of view. As a result, the finding may be on the opposite side of the image from an axial, coronal, or sagittal CT or MR image, based on the standard CT/MRI convention of looking up at the patient's feet. For example, on a "PA view" from a CTA/MRA, a *right* middle cerebral artery aneurysm will be on the *right* side of the 3D VR CTA/MRA image, but will be on the *left* side of the axial CT/MR image. However, as the AP plane is the convention for catheter DSA, the findings will be on the same side of the image as the axial CT/MRI.

A.M. McKinney, *Atlas of Normal Imaging Variations of the Brain, Skull, and Craniocervical Vasculature*,
DOI 10.1007/978-3-319-39790-0_31

Table 31.1 Terms commonly used in imaging craniocervical vasculature

2DTOF = Two-dimensional (2D) time-of-flight
3DTOF = Three-dimensional (3D) time-of-flight
3DDSA = 3D (rotational) digital subtraction angiography
AP = Anterior to posterior (view)
CCA = Common carotid artery
CECT = Contrast-enhanced CT
CEMRA = Contrast-enhanced MRA
CEMRV = Contrast-enhanced MRV
CTA = CT angiography
CTV = CT venography
DSA = catheter digital subtraction angiography
ICA = Internal carotid artery
LAO = Left anterior oblique (view, from anterior)
LCCA = Left common carotid artery
LICA = Left internal carotid artery
LPO = Left posterior oblique (view, from posterior)
LVA = Left vertebral artery
MIP = Maximum intensity projection
MPR = Multiplanar reformat
MRA = Magnetic resonance angiography
MRV = Magnetic resonance venography
NECT = Nonenhanced CT
PA = Posterior to anterior (view)
PCMRA/MRV = Phase contrast MRA/MRV
RAO = Right anterior oblique (view, from anterior)
RCCA = Right common carotid artery
RICA = Right internal carotid artery
RPO = Right posterior oblique (view, from posterior)
RVA = Right vertebral artery
SWI = Susceptibility-weighted imaging
T1WI = T1-weighted imaging
T2WI = T2-weighted imaging
VA = Vertebral artery
VR = Volume-rendered (3D reconstruction)

Aortic Arch and Great Vessel Origin Arterial Variants

32

Aortic arch variants are commonly encountered on neck CT or MR images and CTA/MRA, and this chapter illustrates a few of the more common or readily identifiable variants. Briefly, the normal configuration of the arch (in about 70 % of persons) gives rise to three vessels: the *innominate*, the *left common carotid*, and the *left subclavian* artery (Figs. 32.1, 32.2, and 32.3). The most common variations (which typically are asymptomatic) include a *common origin of the innominate and the left common carotid artery* (10–25 %, the so called "bovine arch" misnomer); *arch origin of the left vertebral artery* (about 5 %, between the origins of the left common carotid and left subclavian arteries); *left arch with retroesophageal right subclavian artery* (0.5–1 % of population, 10 % of which are associated with congenital cardiac anomalies); a *right-sided arch with a retroesophageal left subclavian artery* (about 0.1 %, a "true ring", of which 10 % are associated with cardiac anomalies); and a *right-sided arch without a retroesophageal left subclavian artery* (*i.e.*, "mirror image" right arch) [1–13]. The right and left arches with retroesophageal subclavian arteries are considered aberrant, but are usually asymptomatic variations unless there is esophageal compression from posteriorly by a "diverticulum of Kommerell."

The *"mirror image" right arch* is quite uncommon (<0.1 %) and is associated with congenital cardiac syndromes more than 90 % of cases. A *double arch* is even rarer (presumed to be <0.1 %), and may be symptomatic because both the trachea and esophagus are encircled. Other uncommon variants such as an interrupted arch, left arch atresia, or an isolated left subclavian artery are much rarer and are typically associated with symptoms. Because they are usually repaired quite early in life, they are not depicted in this book. It is important to note that the incidence of some of these variants may be increasing owing to greater numbers of observations from more frequent screening or incidental CT examinations. Readers are referred to a number of excellent radiologic and anatomic texts for further description and explanations of embryologic development [1–19].

A.M. McKinney, *Atlas of Normal Imaging Variations of the Brain, Skull, and Craniocervical Vasculature*,
DOI 10.1007/978-3-319-39790-0_32

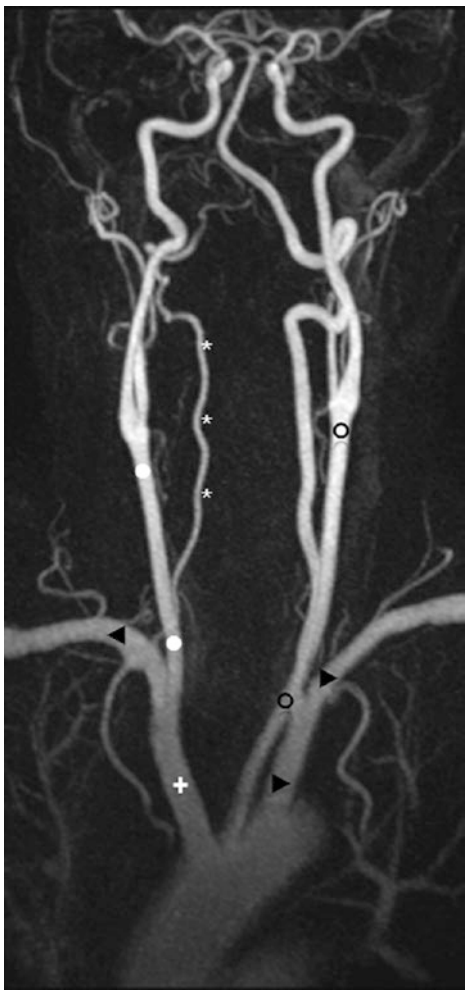

Fig. 32.1 18-year-old with a normal left-sided arch and a hypoplastic right vertebral artery (RVA) (*asterisks*), on a contrast-enhanced MRA AP view. *Aortic Arch* (*curved arrows*); *IA* Innominate Artery (+); *LCCA* Left Common Carotid Artery (○); *LSCLA* Left Subclavian Artery (▶); *RCCA* Right Common Carotid Artery (•); *RSCLA* Right Subclavian Artery (◀)

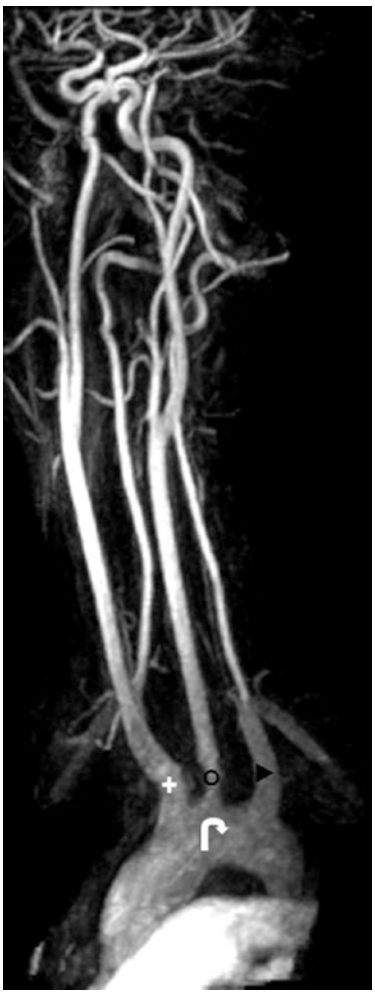

Fig. 32.3 25-year-old with a normal aortic arch (*curved arrow*), on a contrast-enhanced MRA left anterior oblique (LAO) view. *Aortic Arch* (*curved arrows*); *IA* Innominate Artery (+); *LCCA* Left Common Carotid Artery (○); *LSCLA* Left Subclavian Artery (▶); *RCCA* Right Common Carotid Artery (•); *RSCLA* Right Subclavian Artery (◀)

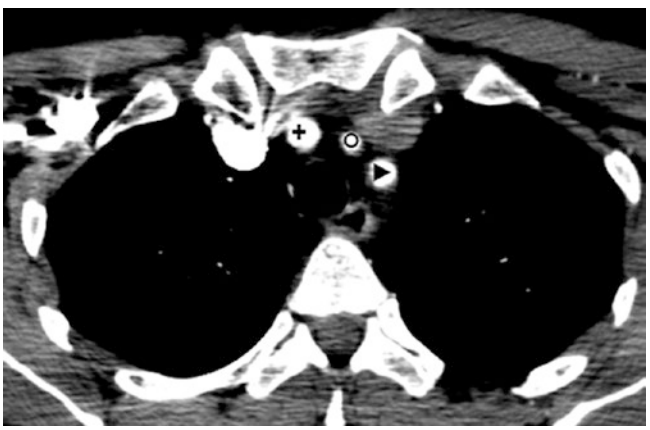

Fig. 32.2 51-year-old with typical origins of the great vessels off of the aortic arch on contrast-enhanced CT. *Aortic Arch* (*curved arrows*); *IA* Innominate Artery (+); *LCCA* Left Common Carotid Artery (○); *LSCLA* Left Subclavian Artery (▶); *RCCA* Right Common Carotid Artery (•); *RSCLA* Right Subclavian Artery (◀)

32.1 Common Origin ("Bovine Arch") and Truncus Bicaroticus

A *common origin of the innominate artery and the left common carotid artery* has been commonly but erroneously referred to as a "bovine arch"; cows do not actually have this configuration. In cows, usually only one great vessel arises directly from the aortic arch, so a "feline" or "canine" arch would be a better fit for this configuration, as both cats and dogs have two branches in the proximal aorta: a brachiocephalic artery followed by a left subclavian artery (LSCA) arising from the arch.

The reported incidence of this variation varies between 10 and 30 % of the population, perhaps depending on what one refers to as a "common origin"; the origins of these two great vessels can be in very close approximation. This variation is of significance particularly when attempting catheterization. Common origin can be very difficult to catheterize (particularly in older patients) with a routine catheter if the left common carotid artery (LCCA) makes an acute "right-angle turn" back to the left side after arising from or with the innominate artery (Figs. 32.4 and 32.5).

A *common origin of both common carotid arteries* is fairly uncommon, occurring in less than 0.5 % of the population. This anomaly is termed a "*truncus bicaroticus*" (Figs. 32.6, 32.7, 32.8, and 32.9). When seen, it usually is associated with an *aberrant right subclavian artery* (RSCA).

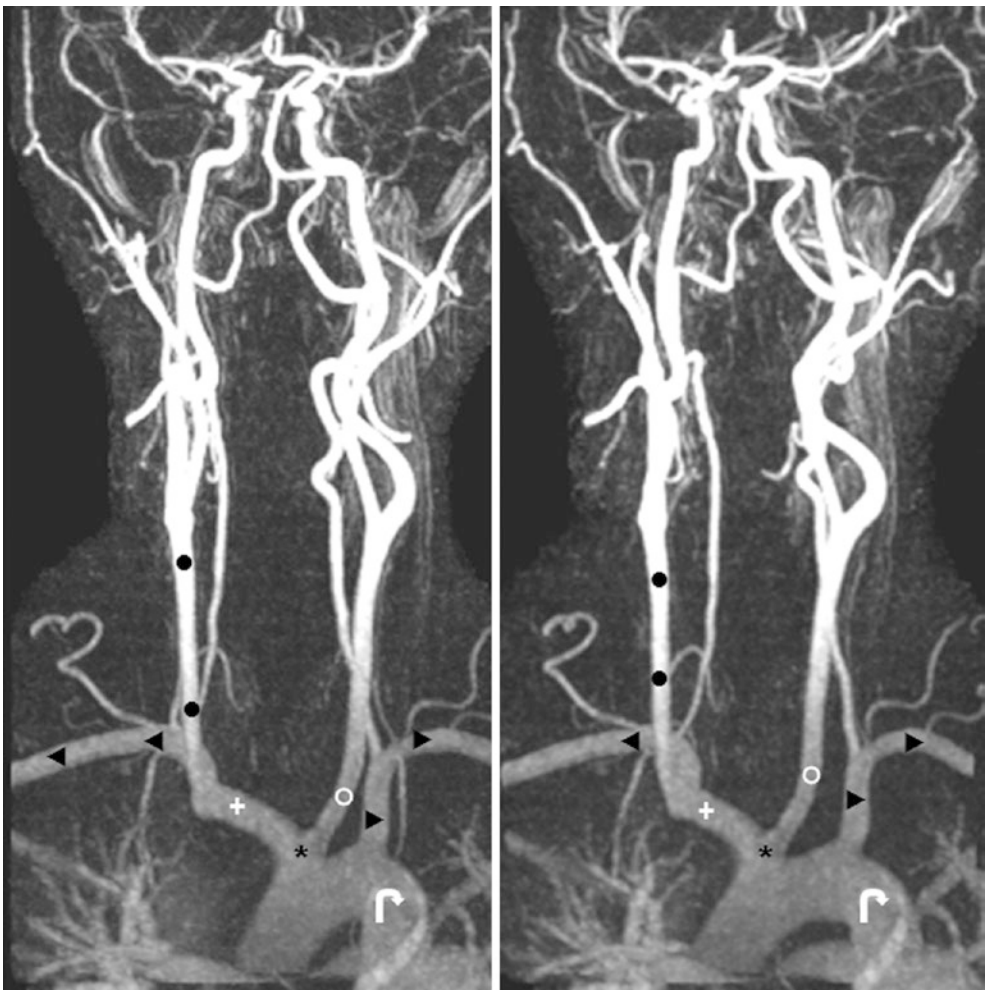

Fig. 32.4 42-year-old with the typical configuration of a "common origin" (*asterisks*) of the left common carotid artery (LCCA, *open circle*) and innominate artery (IA, *plus sign*) on contrast-enhanced MRA AP views. *Aortic Arch* (*curved arrows*); *IA* Innominate Artery (+); *LCCA* Left Common Carotid Artery (○); *LSCLA* Left Subclavian Artery (▶); *RCCA* Right Common Carotid Artery (•); *RSCLA* Right Subclavian Artery (◀)

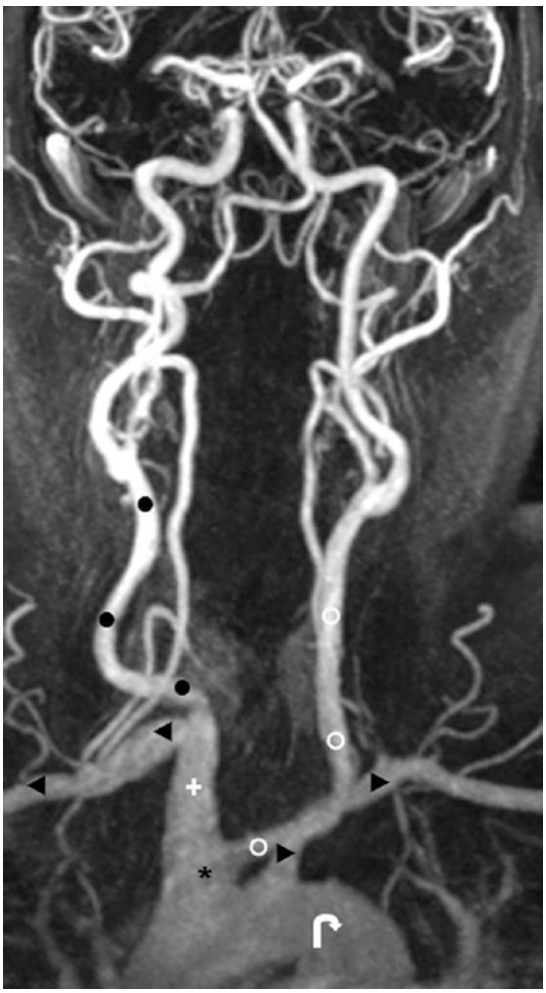

Fig. 32.5 55-year-old with a contrast-enhanced MRA AP view. From a common origin (*asterisk*) with the IA, the LCCA origin (*open circle*) is a "right angle," which can be difficult to catheterize. *Aortic Arch* (*curved arrows*); *IA* Innominate Artery (+); *LCCA* Left Common Carotid Artery (○); *LSCLA* Left Subclavian Artery (▶); *RCCA* Right Common Carotid Artery (•); *RSCLA* Right Subclavian Artery (◀)

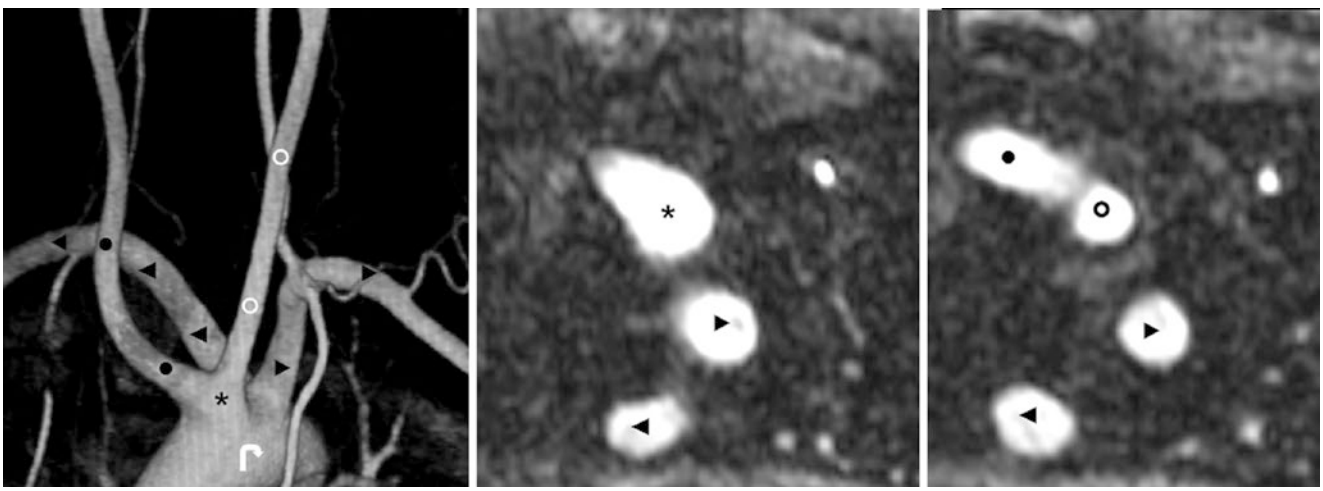

Fig. 32.6 53-year-old with a left-sided aortic arch (*curved arrow*), a "truncus bicaroticus" (*asterisk*), and a retroesophageal right subclavian artery (RSCA, *left-facing arrowhead*) on a 7 cm-thick maximum intensity projection (MIP) from a contrast-enhanced MRA (*left*), with axial source images (*middle, right*). *Aortic Arch* (*curved arrows*); *IA* Innominate Artery (+); *LCCA* Left Common Carotid Artery (○); *LSCLA* Left Subclavian Artery (▶); *RCCA* Right Common Carotid Artery (•); *RSCLA* Right Subclavian Artery (◀)

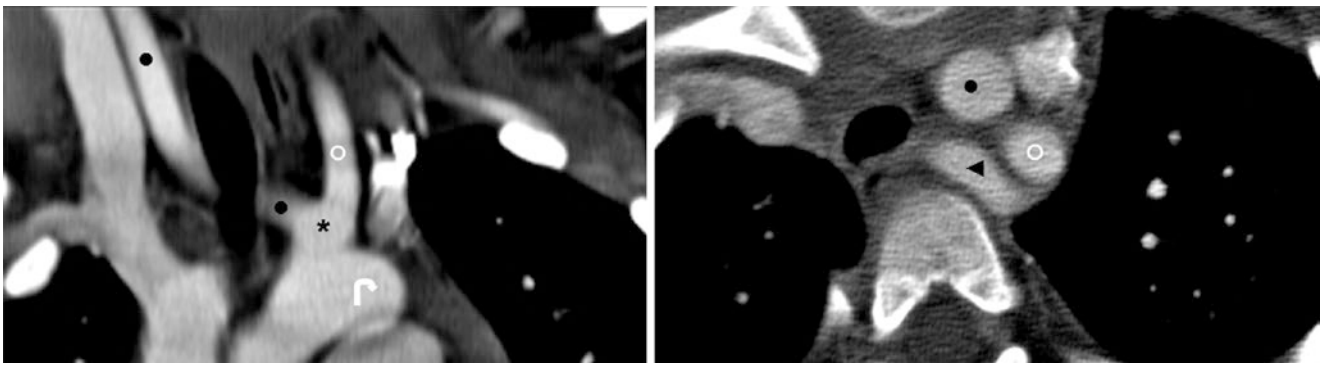

Fig. 32.7 4-year-old with a chest contrast-enhanced CT in the coronal (*left*), and axial (*right*) planes, which demonstrate a left-sided aortic arch and a common origin (*i.e.*, "truncus bicaroticus," *asterisk*), along with a retroesophageal RSCA. *Aortic Arch* (*curved arrows*); *IA* Innominate Artery (+); *LCCA* Left Common Carotid Artery (○); *LSCLA* Left Subclavian Artery (▶); *RCCA* Right Common Carotid Artery (•); *RSCLA* Right Subclavian Artery (◀)

Fig. 32.8 Catheter DSA left anterior oblique (LAO) view in a 60-year-old shows a left-sided arch (*curved arrows*), "truncus bicaroticus" (*asterisk*), and a retroesophageal RSCA. *Aortic Arch* (*curved arrows*); *IA* Innominate Artery (+); *LCCA* Left Common Carotid Artery (○); *LSCLA* Left Subclavian Artery (▶); *RCCA* Right Common Carotid Artery (•); *RSCLA* Right Subclavian Artery (◀)

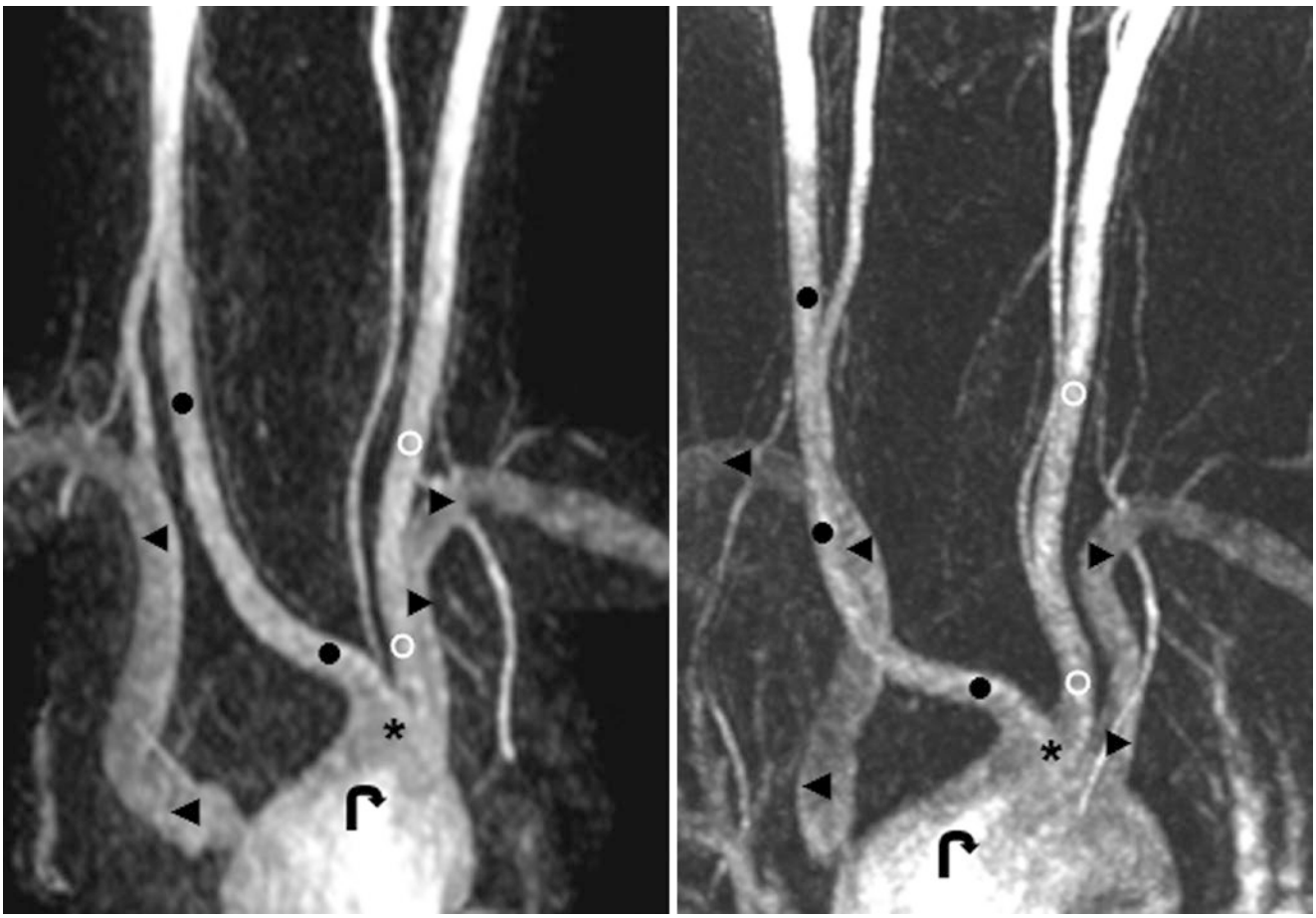

Fig. 32.9 51-year-old with contrast-enhanced MRA AP (*left*) and LAO (*right*) views of a left arch, a "truncus bicaroticus" (*asterisk*), and a RSCA (*left-facing arrowheads*) that is aberrant, as its diverticular origin is proximal to the right common carotid artery (RCCA, *black circles*) but is not retroesophageal (*Courtesy of* Dave Nascene, MD, University of Minnesota–M Health, Minneapolis, MN.). *Aortic Arch* (*curved arrows*); *IA* Innominate Artery (+); *LCCA* Left Common Carotid Artery (○); *LSCLA* Left Subclavian Artery (▶); *RCCA* Right Common Carotid Artery (•); *RSCLA* Right Subclavian Artery (◀)

32.2 Left Arch with Aberrant Right Subclavian Artery

Again, a *left-sided arch with an aberrant RSCA*, also known as "arteria lusoria," is an uncommon, but not rare, variation. It is present in approximately 0.5–1 % of the population, and about 10 % of cases are associated with congenital cardiac anomalies. Also, 10 % of patients with aberrant RSCA experience "dysphagia lusoria" owing to pressure from an enlarged *diverticulum of Kommerell* at the RSCA's origin. It is not uncommon to note a *truncus bicaroticus* (a common origin of both common carotid arteries) in combination with this variant. Most commonly, these are retroesophageal (80 %), but they can also occur between the trachea and esophagus (15 %) or anterior to the trachea (5 %) (Figs. 32.10, 32.11, and 32.12). It is also quite rare for the RSCA to arise separately from the right common carotid artery (RCCA). Figures 32.6, 32.7, 32.8, and 32.9 show examples of truncus bicaroticus and demonstrate a spectrum of such variants occurring in tandem with that anomaly.

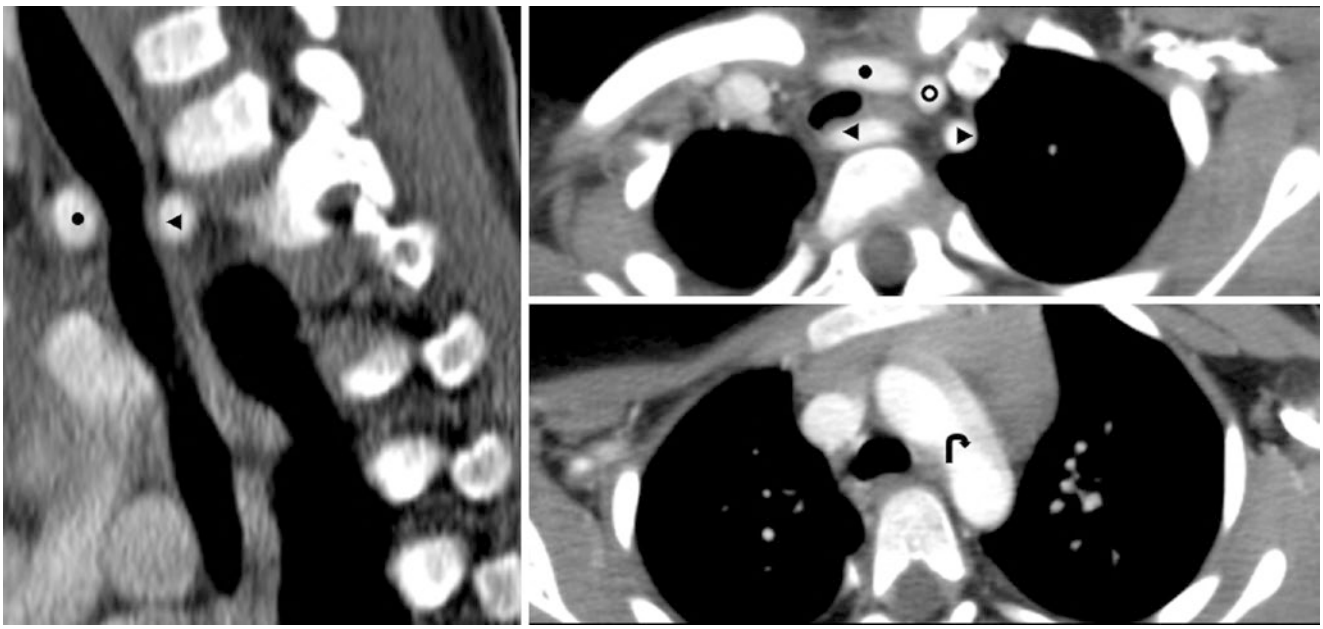

Fig. 32.10 In a 3-year-old, a sagittal postcontrast thoracic spine CT (*left*) demonstrates a left-sided aortic arch with a retroesophageal RSCA. Axial images from a chest CT (*right, top and bottom*) confirmed this finding. *Aortic Arch* (*curved arrows*); *IA* Innominate Artery (+); *LCCA* Left Common Carotid Artery (○); *LSCLA* Left Subclavian Artery (►); *RCCA* Right Common Carotid Artery (•); *RSCLA* Right Subclavian Artery (◄)

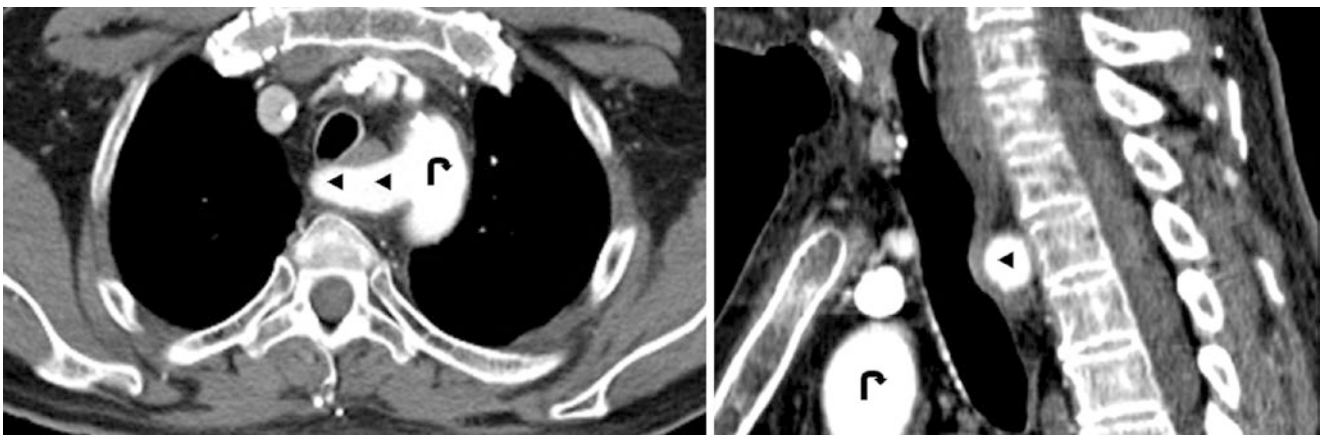

Fig. 32.11 51-year-old with a left-sided aortic arch (*curved arrow*) and a retroesophageal RSCA (*left-facing arrowheads*) noted on axial (*left*) and sagittal (*right*) reformats from a contrast-enhanced CT scan of the upper chest and lower neck. *Aortic Arch* (*curved arrows*); *IA* Innominate Artery (+); *LCCA* Left Common Carotid Artery (○); *LSCLA* Left Subclavian Artery (►); *RCCA* Right Common Carotid Artery (•); *RSCLA* Right Subclavian Artery (◄)

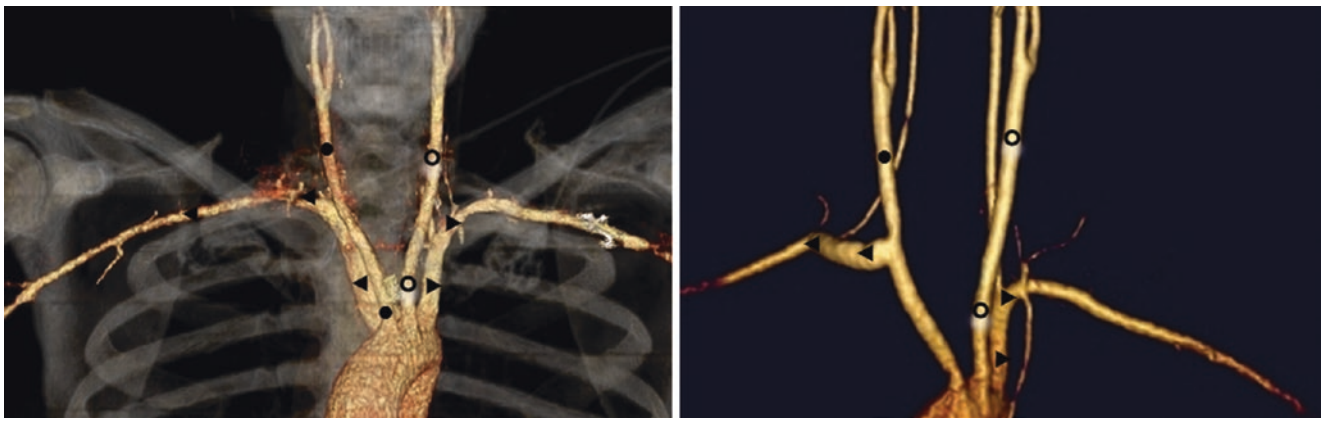

Fig. 32.12 43-year-old with a left arch and a retroesophageal RSCA (*left-facing arrowheads*) on an AP view from a CTA (*left*). Two weeks after the RSCA was detached and reimplanted to the right common carotid artery (RCCA, *black circle*), there was no stenosis at the vessel's origin on a contrast-enhanced MRA AP view (*right*). *Aortic Arch* (*curved arrows*); *IA* Innominate Artery (+); *LCCA* Left Common Carotid Artery (○); *LSCLA* Left Subclavian Artery (▶); *RCCA* Right Common Carotid Artery (•); *RSCLA* Right Subclavian Artery (◀)

32.3 Right-Sided Aortic Arch and Double Aortic Arch

A *right-sided aortic arch* is encountered in about 0.1 % of the population, and can be well demonstrated on CECT or CT angiography (CTA) (Figs. 32.13, 32.14, 32.15, 32.16, 32.17, and 32.18). These can be either a "*mirror image*" (Type I), being the reverse of normal great vessels' origins from a left-sided arch (80–85 % of right-sided arches), or a right-sided arch with an *aberrant left subclavian artery* but lacking an associated cardiac anomaly (Type II, 15–20 % of right-sided arches) [4–8]. "Mirror image" right-sided arches are typically associated with congenital cardiac anomalies, most commonly tetralogy of Fallot; about 25 % of tetralogy of Fallot patients are also reported to have a right-sided aortic arch [4–8]. Notably, the number of patients having a "mirror image" arch without cardiac anomalies is probably higher than previously thought; the association was said to be nearly 100 %, but current evidence from patients scanned by contrast-enhanced CT and CTA for noncardiac reasons suggests a range of 90–95 % instead [4–8].

A *double aortic arch* is less common, but is the most common vascular ring to cause symptoms [9–13]. Its incidence is poorly described, but is likely present in about 0.1 %, as the estimated incidence of aortic vascular rings is about 0.2–0.5 % [4–13]. It is typically not associated with congenital cardiac anomalies. The right-sided component of the arch is dominant in about 75 %, and the left in about 20 % [9–13].

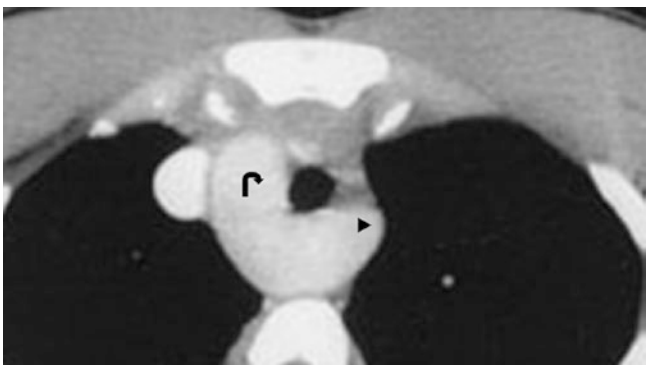

Fig. 32.13 Contrast-enhanced CT scan from a 10-year-old that depicts a right-sided aortic arch (*asterisk*), from which a retroesophageal LSCA (*right-facing arrowhead*) arises. This patient did not have an associated cardiac anomaly. *Aortic Arch* (*curved arrows*); *IA* Innominate Artery (+); *LCCA* Left Common Carotid Artery (○); *LSCLA* Left Subclavian Artery (▶); *RCCA* Right Common Carotid Artery (•); *RSCLA* Right Subclavian Artery (◀)

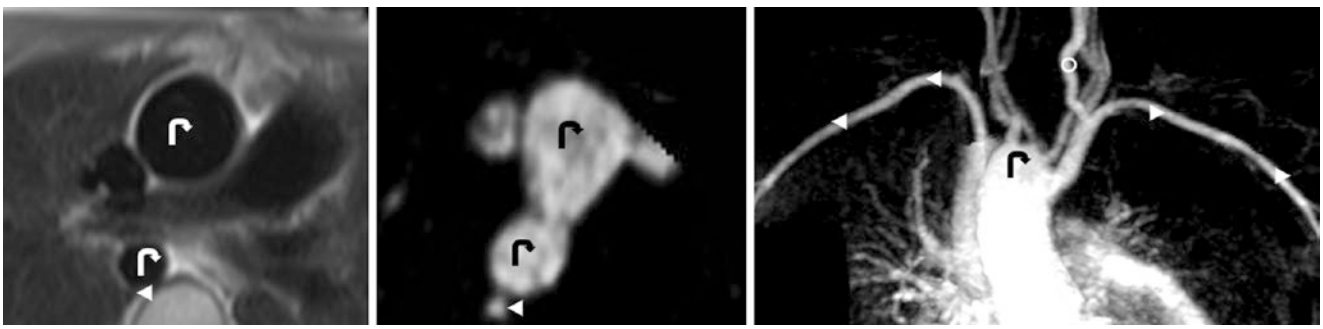

Fig. 32.14 11-year-old with Tetralogy of Fallot; the right arch (*curved arrows*) is not "mirror image" as both the RSCA and LSCA arise from it on axial T2WI (*lower left*), contrast-enhanced MRA 10 cm-thick AP view (*upper right*), and on axial contrast-enhanced MRA (*lower right*) (*Courtesy of* David Nascene, MD, University of Minnesota–M Health, Minneapolis, MN.). *Aortic Arch* (*curved arrows*); *IA* Innominate Artery (+); *LCCA* Left Common Carotid Artery (○); *LSCLA* Left Subclavian Artery (▶); *RCCA* Right Common Carotid Artery (•); *RSCLA* Right Subclavian Artery (◀)

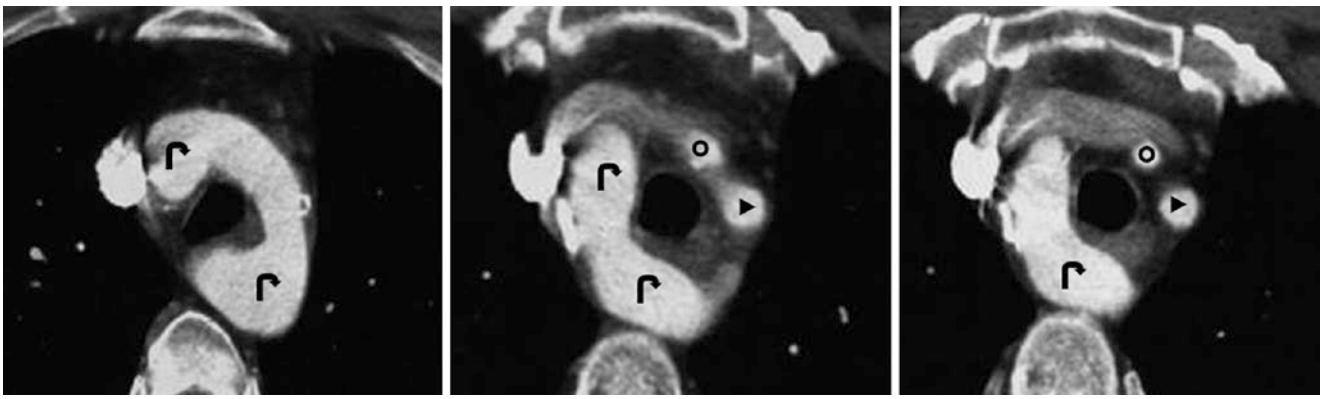

Fig. 32.15 In a 45-year-old patient, a contrast-enhanced CT (caudal to cranial images) demonstrates a double aortic arch (*curved arrows*) that surrounds both the trachea and esophagus. This patient suffered from recurrent aspiration pneumonia, necessitating surgical repair. *Aortic Arch* (*curved arrows*); *IA* Innominate Artery (+); *LCCA* Left Common Carotid Artery (○); *LSCLA* Left Subclavian Artery (►); *RCCA* Right Common Carotid Artery (•); *RSCLA* Right Subclavian Artery (◄)

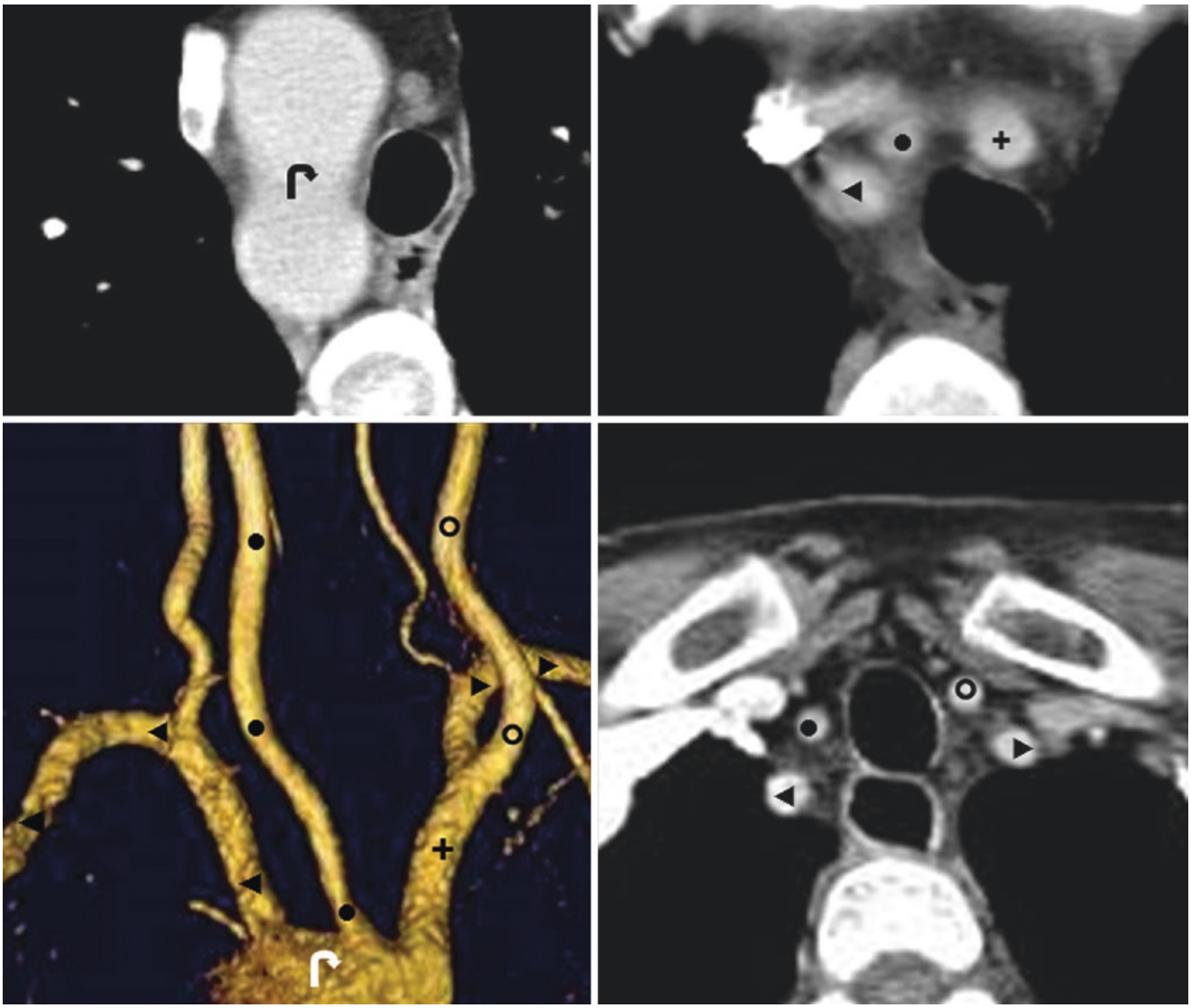

Fig. 32.16 A 23-year-old with an asymptomatic "mirror image" right-sided aortic arch on a contrast-enhanced CT (*top row* and *bottom right*) and on a 3D volume-rendered (VR) reconstruction from a contrast-enhanced MRA (*bottom left*). No other congenital defects were noted in this patient. *Aortic Arch* (*curved arrows*); *IA* Innominate Artery (+); *LCCA* Left Common Carotid Artery (○); *LSCLA* Left Subclavian Artery (►); *RCCA* Right Common Carotid Artery (•); *RSCLA* Right Subclavian Artery (◄)

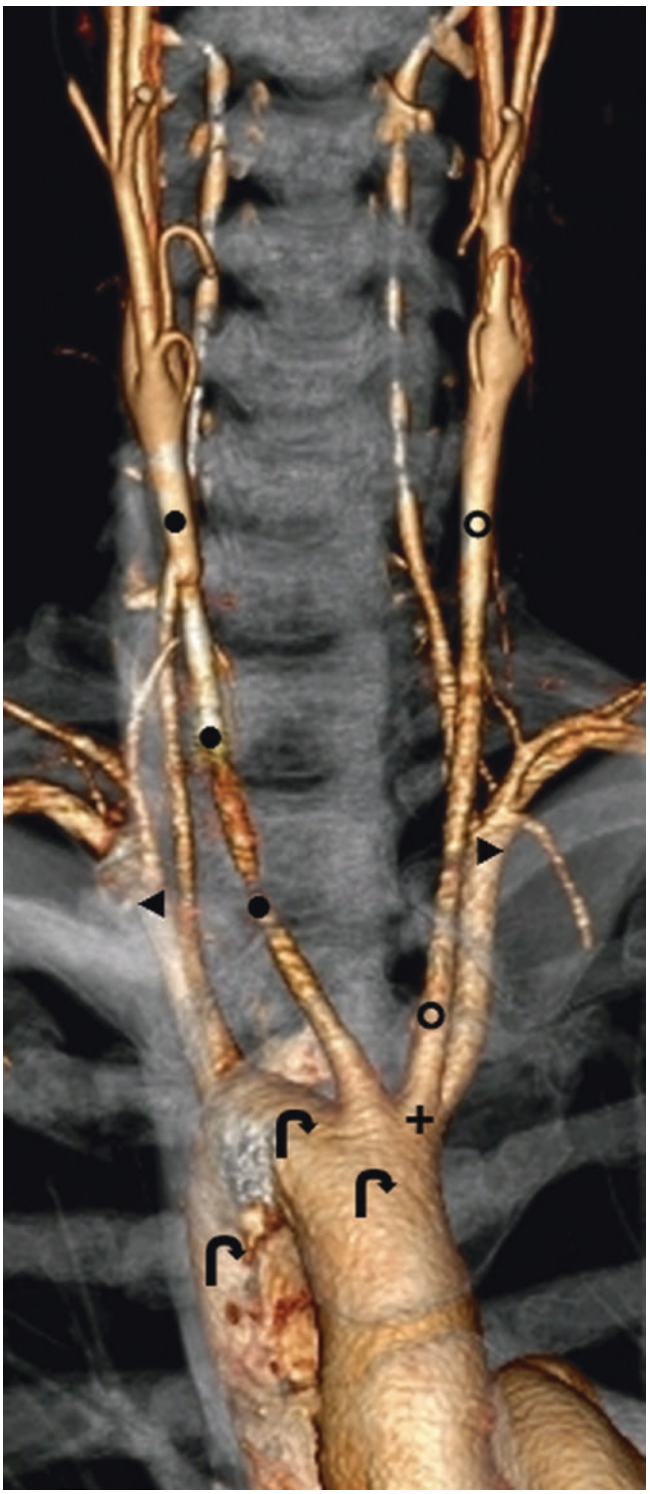

Fig. 32.17 36-year-old with a "mirror-image" right-sided arch on a 3D VR CTA (*AP view*). *Aortic Arch* (*curved arrows*); *IA* Innominate Artery (+); *LCCA* Left Common Carotid Artery (○); *LSCLA* Left Subclavian Artery (▶); *RCCA* Right Common Carotid Artery (•); *RSCLA* Right Subclavian Artery (◀)

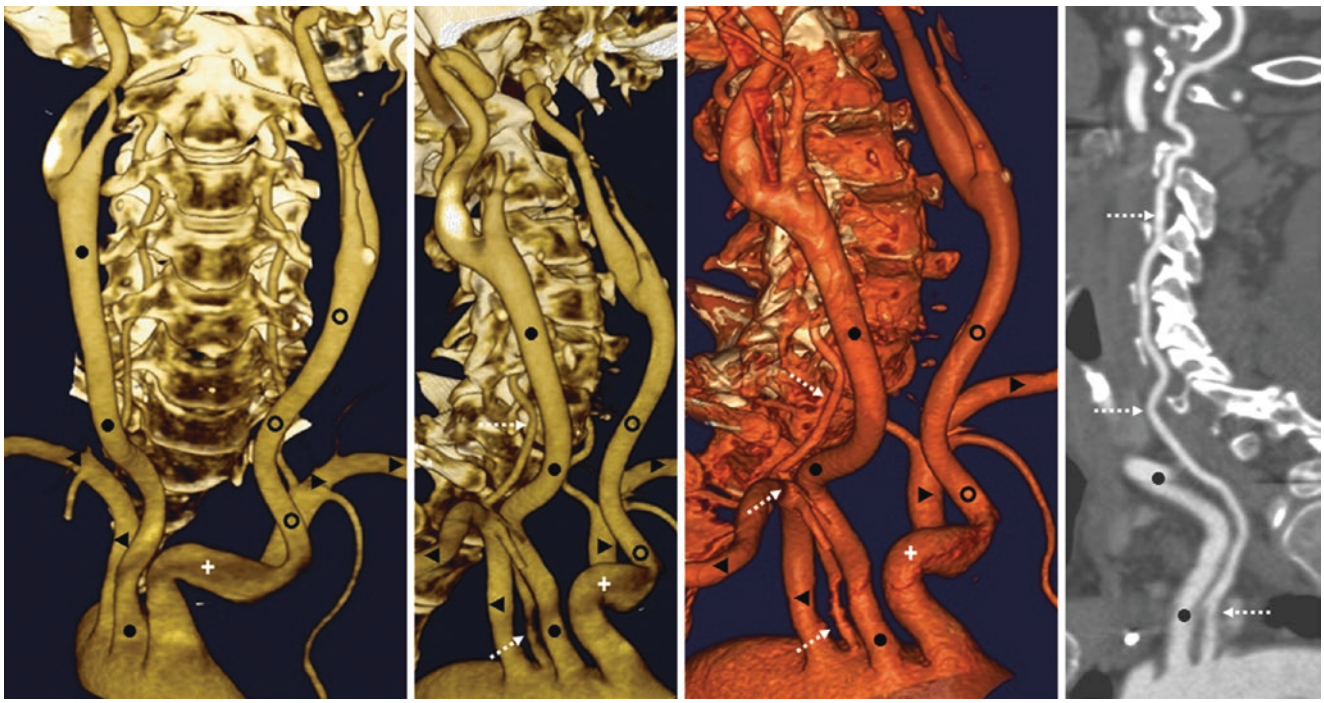

Fig. 32.18 62-year-old with an asymptomatic "mirror image" right-sided aortic arch (from Kartagener's syndrome with situs inversus) on a 3D VR CTA, with AP (*left*) and right anterior oblique (RAO) views (*left middle* and *right middle*). Also, a curved oblique sagittal MPR (*right*) demonstrates that the right vertebral artery (*dotted arrows*) arises directly from the aortic arch. *Aortic Arch* (*curved arrows*); *IA* Innominate Artery (+); *LCCA* Left Common Carotid Artery (○); *LSCLA* Left Subclavian Artery (▶); *RCCA* Right Common Carotid Artery (•); *RSCLA* Right Subclavian Artery (◀)

32.4 Arch Origin of Left Vertebral Artery and other Vertebral Artery Variant Arch Origins

An *arch origin of the left vertebral artery* (LVA) occurs in about 5 % of the population. The vast majority arise between the origins of the left common carotid artery (LCCA) and the left subclavian artery. Quite rare variations of vertebral artery origins from the aortic arch include distal arch origin of the LVA (*i.e.*, distal to the left subclavian origin), aberrant arch origin of the right vertebral artery (RVA), duplication of the vertebral artery, and origin from one of the carotid arteries (or carotid branches) (Figs. 32.19, 32.20, 32.21, 32.22, 32.23, 32.24, 32.25, 32.26, and 32.27). The latter variant is covered in Chapter 33, as this chapter focuses solely on aortic arch variations.

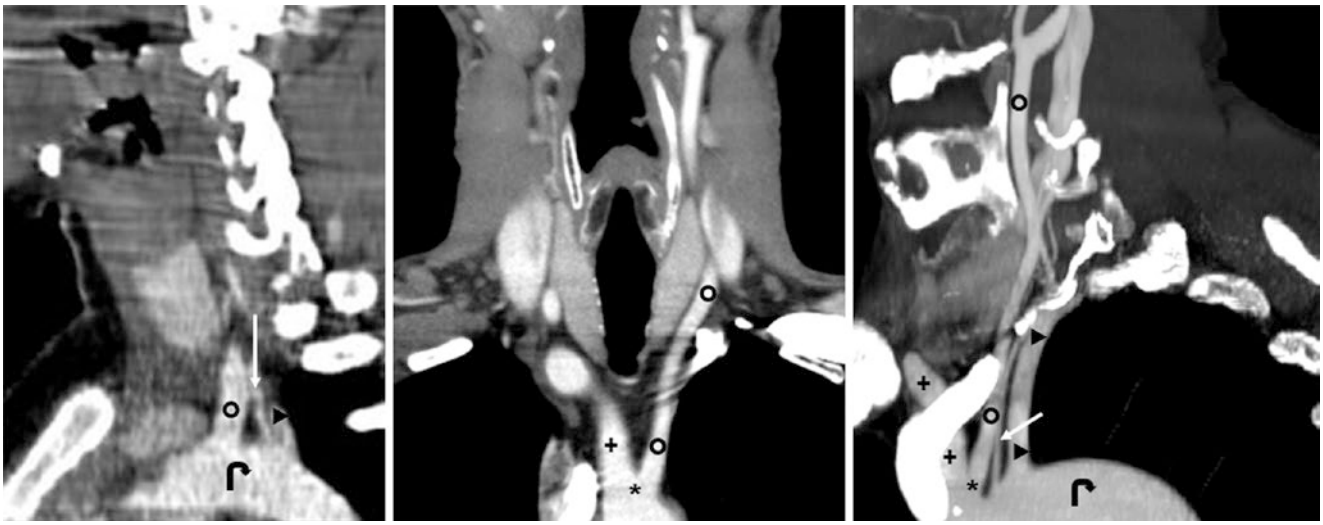

Fig. 32.19 45-year-old with an "arch origin" of the left vertebral artery (LVA) (*arrows*) on 3-mm sagittal (*left*), 6-mm coronal (*middle*), and 21-mm sagittal (*right*) MPRs from a CTA. There is also a common origin (*asterisk*) of the innominate artery (IA, *plus sign*) and the left common carotid artery (LCCA, *open circle*). *Aortic Arch* (*curved arrows*); *IA* Innominate Artery (+); *LCCA* Left Common Carotid Artery (○); *LSCLA* Left Subclavian Artery (▶); *RCCA* Right Common Carotid Artery (•); *RSCLA* Right Subclavian Artery (◀)

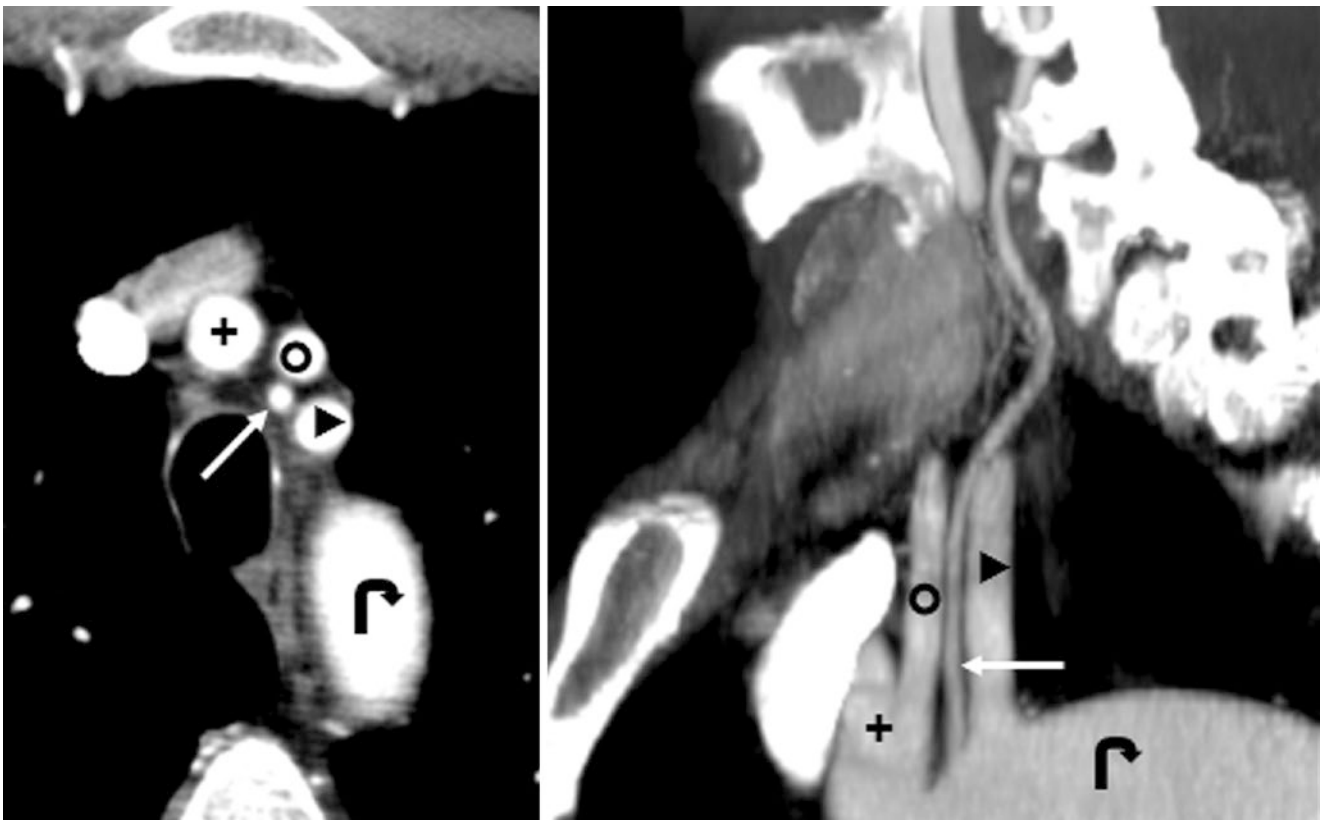

Fig. 32.20 42-year-old with a LVA "arch origin" (*arrows*) on a CTA axial view (*left*) and 15-mm MPR coronal LAO view (*right*). The LVA lies between the LCCA and the left subclavian artery (LSCA, *right-facing arrowhead*). *Aortic Arch* (*curved arrows*); *IA* Innominate Artery (+); *LCCA* Left Common Carotid Artery (○); *LSCLA* Left Subclavian Artery (▶); *RCCA* Right Common Carotid Artery (•); *RSCLA* Right Subclavian Artery (◀)

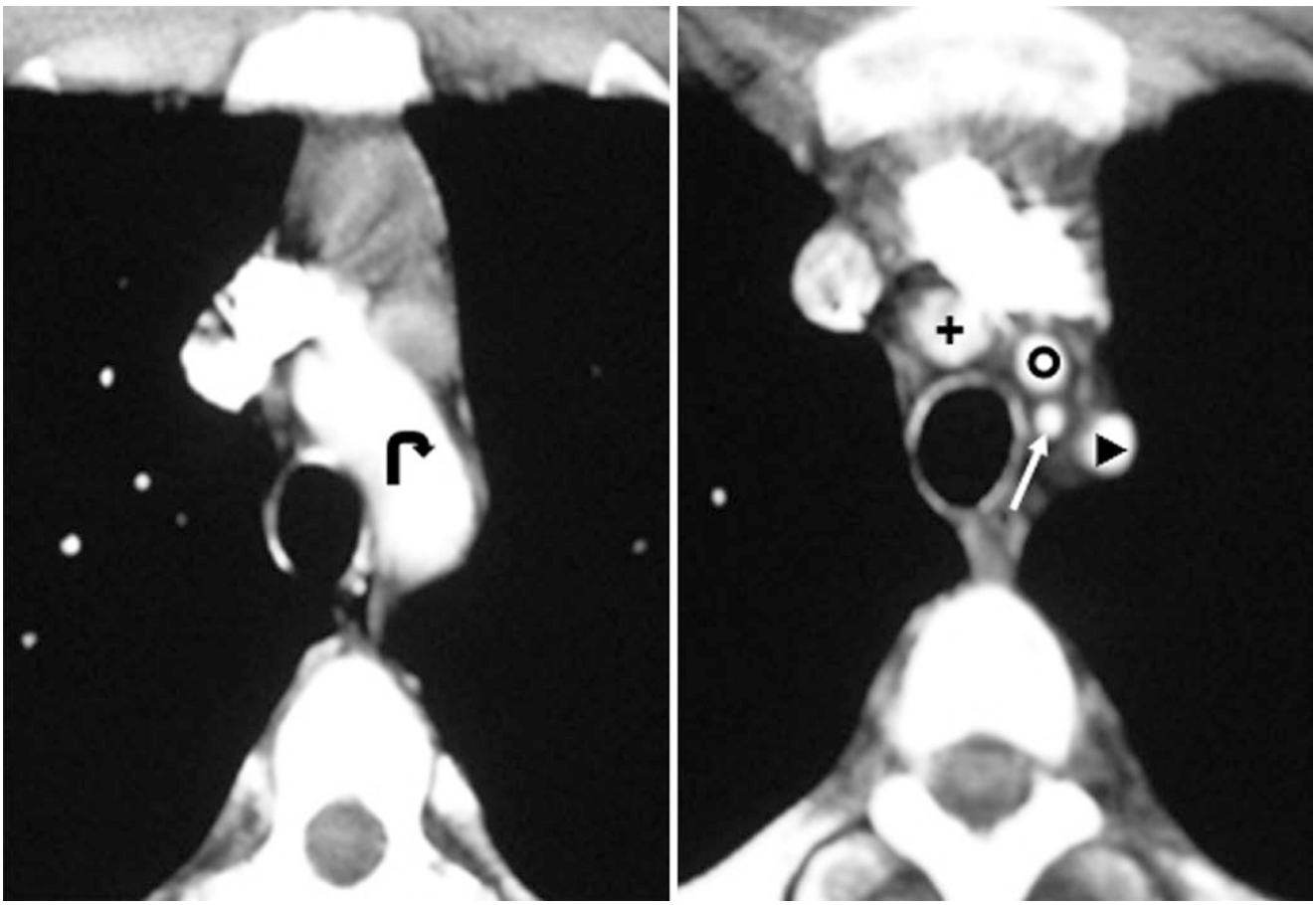

Fig. 32.21 33-year-old with the typical configuration of an "arch origin" of the LVA (*arrows*) on axial contrast-enhanced CT images at the level of the top of the arch. *Aortic Arch* (*curved arrows*); *IA* Innominate Artery (+); *LCCA* Left Common Carotid Artery (○); *LSCLA* Left Subclavian Artery (►); *RCCA* Right Common Carotid Artery (•); *RSCLA* Right Subclavian Artery (◄)

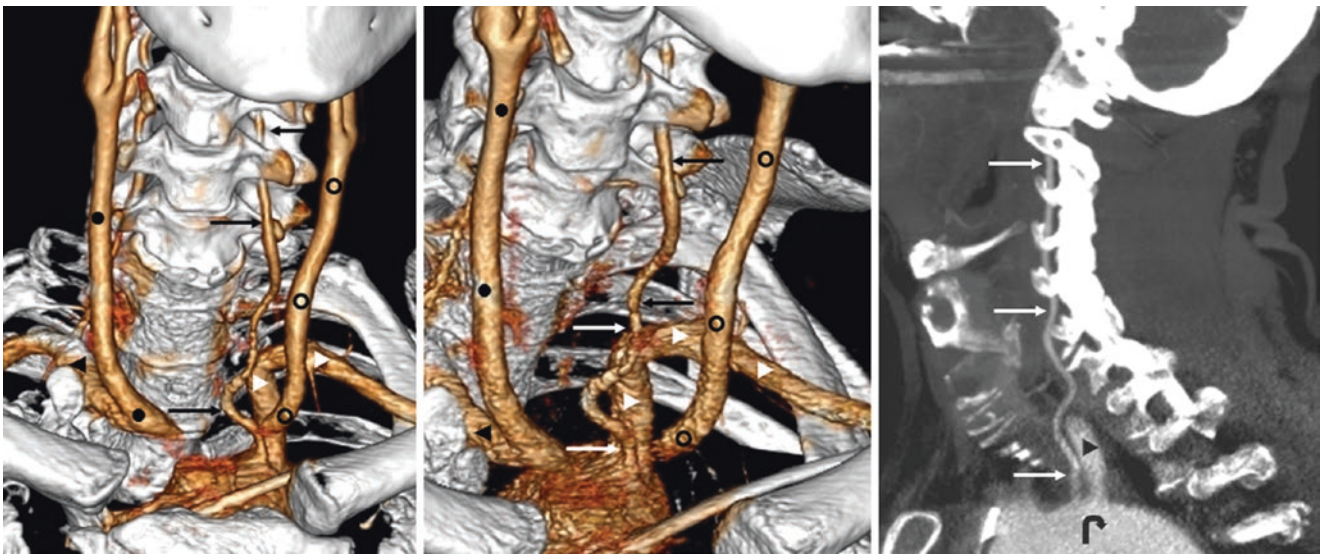

Fig. 32.22 50-year-old with an "arch origin" of the LVA (*arrows*) on a CTA with 3D VR AP (*left*) and RAO (*middle*) views, as well as on a 15-mm sagittal MPR (*right*). The MPR confirms that the LVA arises just proximal to the LSCA. *Aortic Arch* (*curved arrows*); *IA* Innominate Artery (+); *LCCA* Left Common Carotid Artery (○); *LSCLA* Left Subclavian Artery (▶); *RCCA* Right Common Carotid Artery (•); *RSCLA* Right Subclavian Artery (◀)

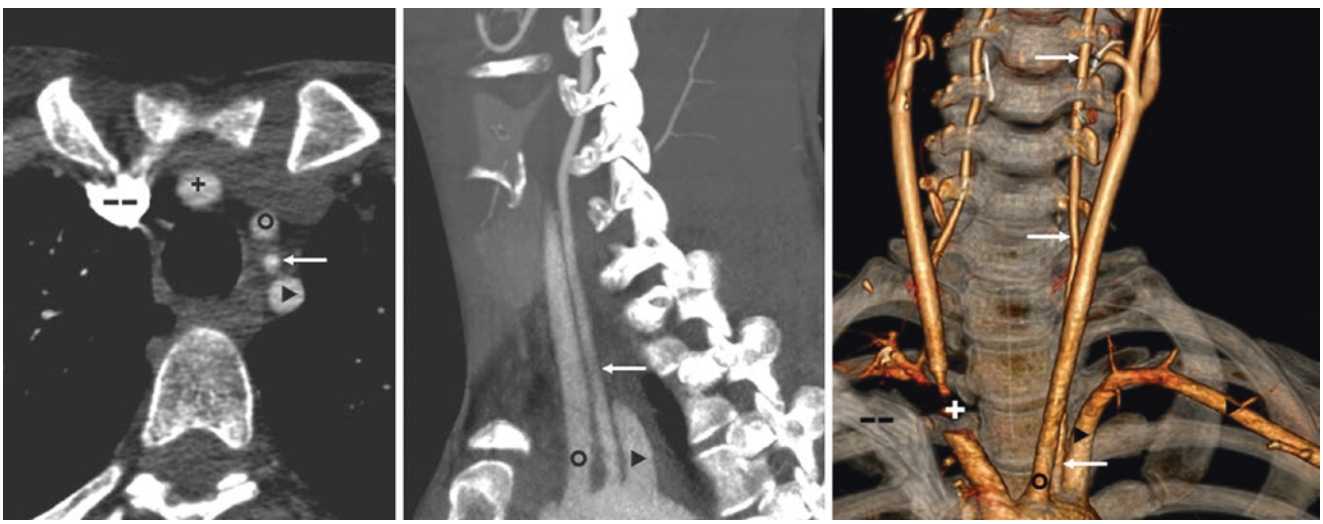

Fig. 32.23 In a 31-year-old, axial CTA source images (*left*) depict an "arch origin" of the LVA (*arrows*), situated between the LCCA and LSCA on an LAO 9-mm sagittal MPR (*middle*), as well as on a 3D VR CTA in an AP view (*right*). Note that the IA (*plus sign*) is focally obscured owing to streak artifact from contrast within the superior vena cava (*dashes*). *Aortic Arch* (*curved arrows*); *IA* Innominate Artery (+); *LCCA* Left Common Carotid Artery (○); *LSCLA* Left Subclavian Artery (▶); *RCCA* Right Common Carotid Artery (•); *RSCLA* Right Subclavian Artery (◀)

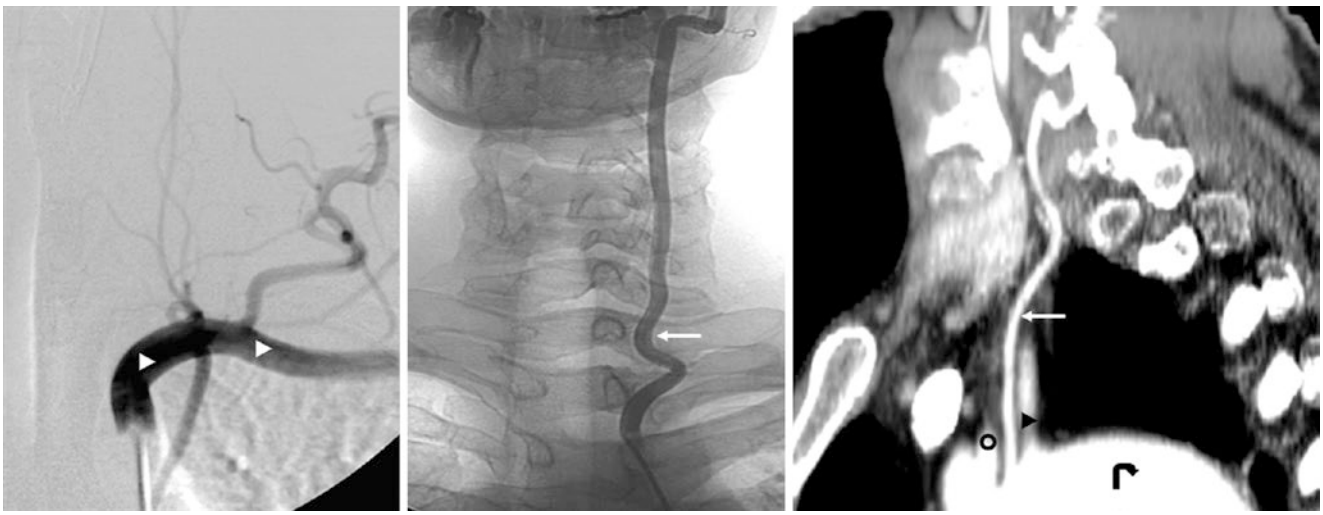

Fig. 32.24 In a 21-year-old, a catheter DSA injection of the LSCA origin in an AP view (*left*) did not depict the LVA origin, but its "arch origin" was found by selective catheterization (*middle*), and on an LAO MPR from a CTA (*right*). *Aortic Arch* (*curved arrows*); *IA* Innominate Artery (+); *LCCA* Left Common Carotid Artery (○); *LSCLA* Left Subclavian Artery (▶); *RCCA* Right Common Carotid Artery (•); *RSCLA* Right Subclavian Artery (◀)

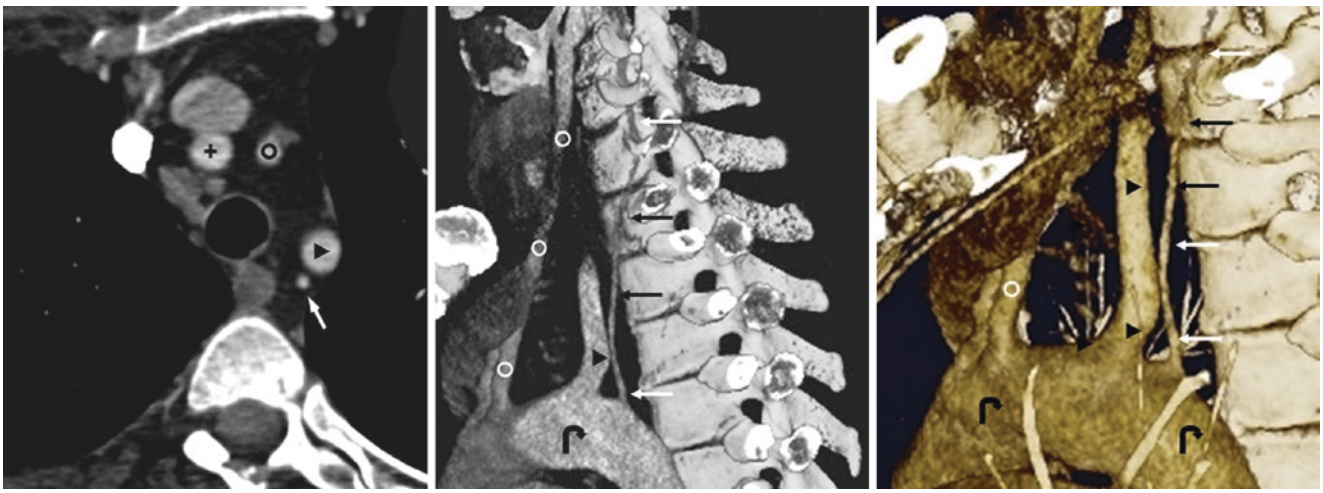

Fig. 32.25 54-year-old with a left-sided arch. An aberrant LVA (*arrows*) arises as a solitary vessel off of the aorta *distal* to the LSCA, rather than the typical variant, which arises proximal to the LSCA, as shown on various CTA reconstructions, including axial view (*left*), sagittal 15-mm view (*middle*), and a 3D VR left lateral view (*right*). *Aortic Arch* (*curved arrows*); *IA* Innominate Artery (+); *LCCA* Left Common Carotid Artery (○); *LSCLA* Left Subclavian Artery (▶); *RCCA* Right Common Carotid Artery (•); *RSCLA* Right Subclavian Artery (◀)

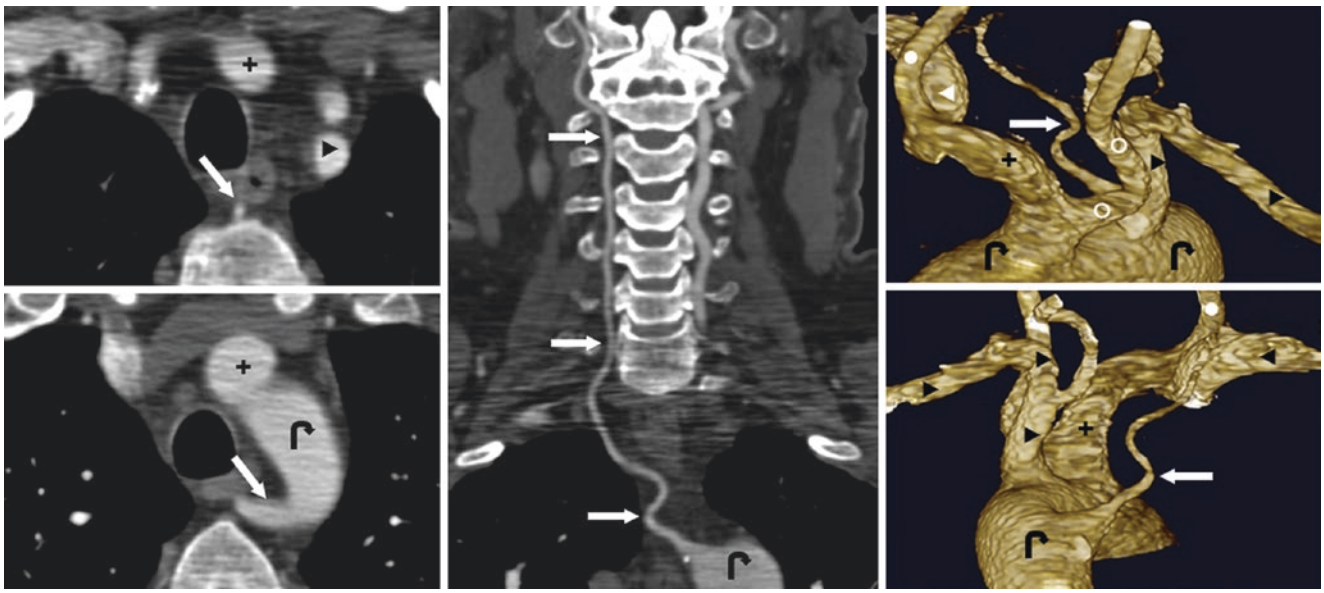

Fig. 32.26 54-year-old with a left arch, an IA/LCCA common origin, and a distal, aberrant, retroesophageal right vertebral artery (RVA) (*arrows*) on CTA axial views (*left*), coronal curved MPR view (*middle*), and on 3D VR AP (*right, top*) and posterior (*right, bottom*) views (*Courtesy of* Jeff Brace, MD, Suburban Radiologic Consultants, Edina, MN.). *Aortic Arch* (*curved arrows*); *IA* Innominate Artery (+); *LCCA* Left Common Carotid Artery (○); *LSCLA* Left Subclavian Artery (▶); *RCCA* Right Common Carotid Artery (•); *RSCLA* Right Subclavian Artery (◀)

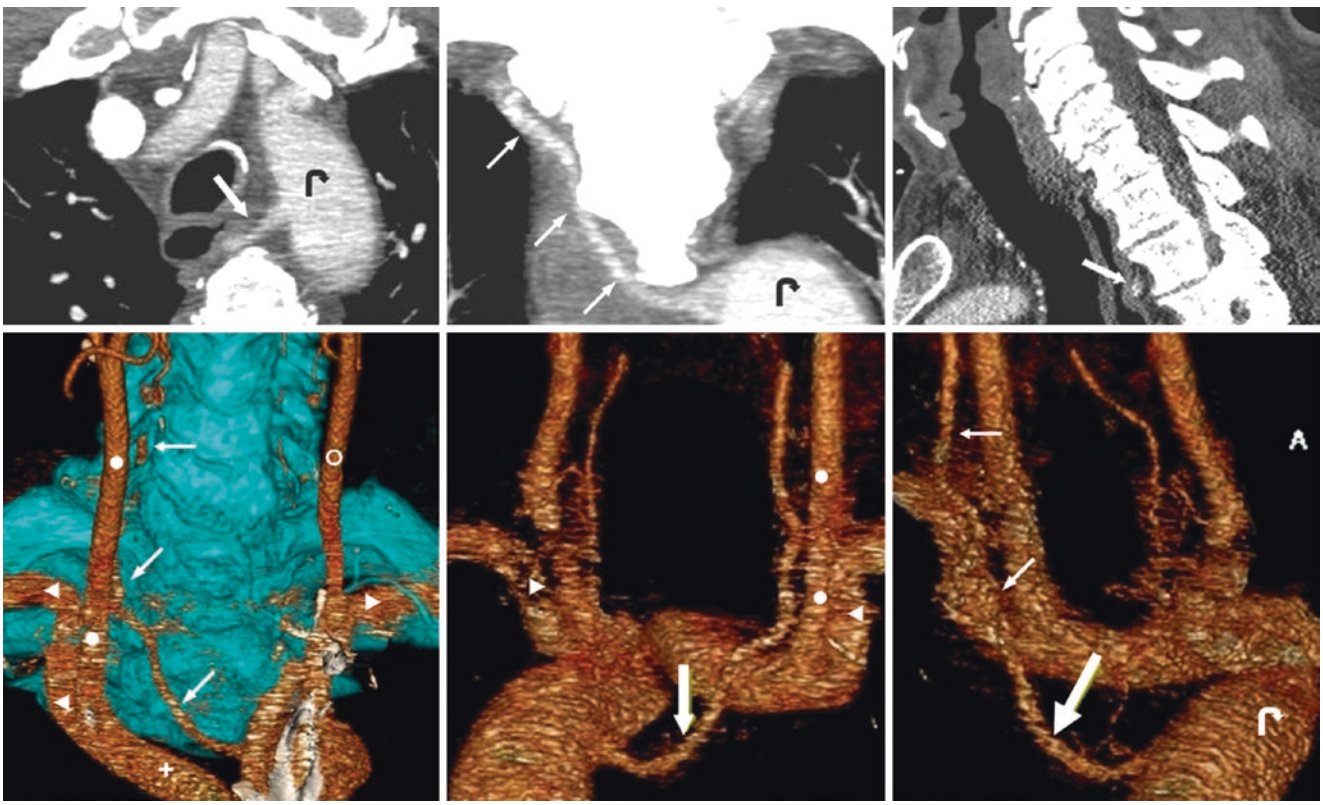

Fig. 32.27 A 78-year-old with a left-sided arch had an aberrant, retroesophageal RVA (*arrows*) arising off of the aorta, on various CTA MPRs, including axial (*top left*), coronal (*top middle*), and sagittal (*top right*) views. On 3D VR AP (*bottom left*), posterior (*bottom middle*), and right lateral (*bottom right*) views, the RVA's course is delineated. *Aortic Arch* (*curved arrows*); *IA* Innominate Artery (+); *LCCA* Left Common Carotid Artery (○); *LSCLA* Left Subclavian Artery (▶); *RCCA* Right Common Carotid Artery (•); *RSCLA* Right Subclavian Artery (◀)

32.5 Arch Origin of the External Carotid Artery

An *arch origin of the external carotid artery* (ECA) is another rare variant that can be entirely normal and asymptomatic, although one should exclude the concomitant presence of other rare, congenital vascular anomalies such as proatlantal arteries, double aortic arch, or persistent trigeminal arteries. These anomalies (and others) can be seen with right-sided or left-sided arches; when left-sided, the ECA is typically anterior to the internal carotid artery (ICA), and the right carotid bifurcation is a bit lower than normal. Although this variant is very rare and can be considered a form of "common carotid agenesis," it is typically asymptomatic unless an arterial stenosis exists simultaneously (Figs. 32.28 and 32.29).

Fig. 32.28 62-year-old woman with a left arch and an arch origin of the left external carotid artery (ECA) (*large arrows*) on axial images from a contrast-enhanced neck CT. Also note a separate left internal carotid artery (LICA) origin (*thin arrows*), and an anomalous vein arising from a vertebral vein (*dash*) (*Courtesy of* Chris Palmer, MD, Hennepin County Medical Center, Minneapolis, MN.). *Aortic Arch* (*curved arrows*); *IA* Innominate Artery (+); *LCCA* Left Common Carotid Artery (○); *LSCLA* Left Subclavian Artery (▶); *RCCA* Right Common Carotid Artery (•); *RSCLA* Right Subclavian Artery (◀)

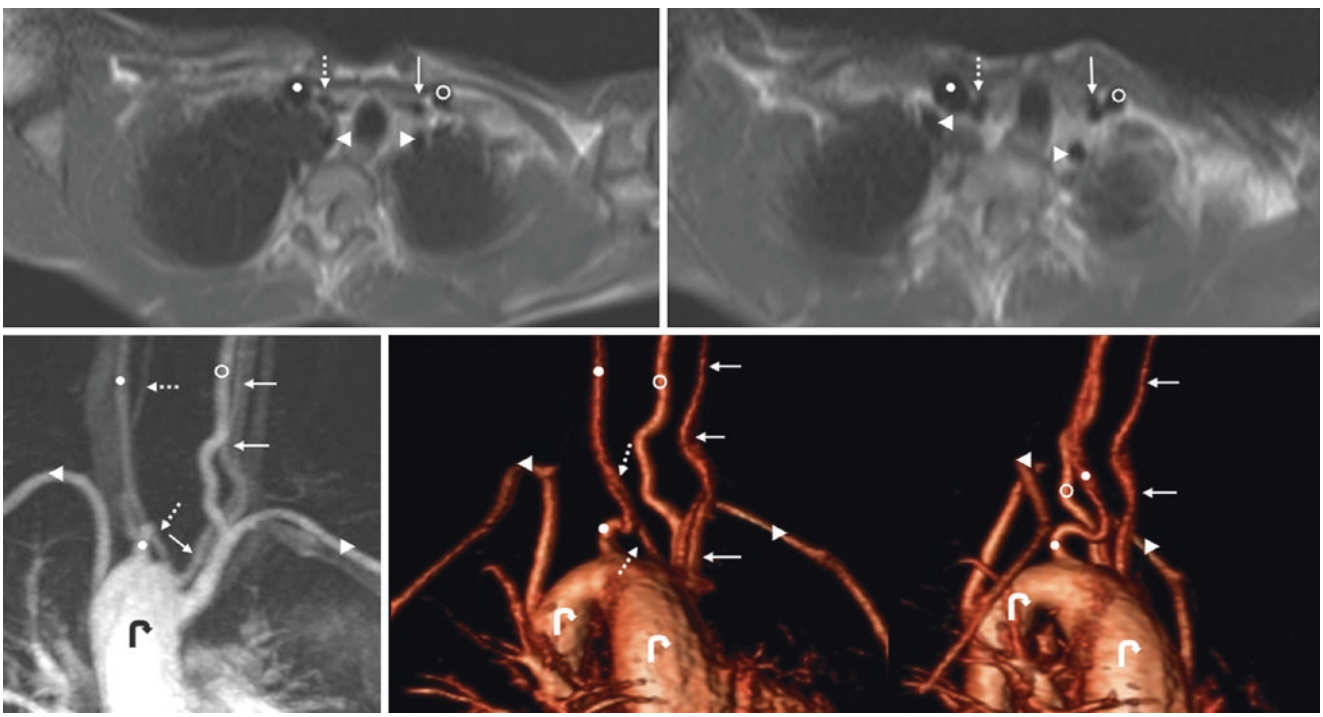

Fig. 32.29 11-year-old boy with tetralogy of Fallot, a right arch, and arch origins of both the right ECA (*dotted arrows*) and left ECA (*thin arrows*) on contrast-enhanced MRA AP view (*bottom left*), 3D VR mild LAO (*bottom middle*), and further oblique LAO (*bottom right*) views (*Courtesy of* David Nascene, MD, University of Minnesota–M Health, Minneapolis, MN.). *Aortic Arch* (*curved arrows*); *IA* Innominate Artery (+); *LCCA* Left Common Carotid Artery (○); *LSCLA* Left Subclavian Artery (▶); *RCCA* Right Common Carotid Artery (•); *RSCLA* Right Subclavian Artery (◀)

References

1. Osborn AG. Diagnostic cerebral angiography. Philadelphia: Lippincott Williams & Wilkins; 1999.
2. Sandhu JS, Wakhloo AK. Neuroangiographic anatomy and common cerebrovascular diseases. In: Bradley WG, editor. Neurology in clinical practice. 4th ed. Philadelphia: Elsevier; 2004.
3. Layton KF, Kallmes DF, Cloft HJ, Lindell EP, Cox VS. Bovine aortic arch variant in humans: clarification of a common misnomer. AJNR Am J Neuroradiol. 2006;27:1541–2.
4. Maldonado JA, Henry T, Gutierrez F. Congenital thoracic vascular anomalies. Radiol Clin North Am. 2010;48:11–4.
5. Knight L, Edwards JE. Right aortic arch. Types and associated cardiac anomalies. Circulation. 1974;50:1047–51.
6. Slisatkorn W, Laksanabunsong P, Thongcharoen P. Ruptured right aortic arch aneurysm. Asian Cardiovasc Thorac Ann. 2004; 12:360–2.
7. McElhinney DB, Hoydu AK, Gaynor JW, Spray TL, Goldmuntz E, Weinberg PM. Patterns of right aortic arch and mirror-image branching of the brachiocephalic vessels without associated anomalies. Pediatr Cardiol. 2001;22:285–91.
8. Hastreiter AR, D'Cruz IA, Cantez T, Namin EP, Licata R. Right-sided aorta. I. Occurrence of right aortic arch in various types of congenital heart disease. II. Right aortic arch, right descending aorta, and associated anomalies. Br Heart J. 1966;28:722–39.
9. Schlesinger AE, Krishnamurthy R, Sena LM, Guillerman RP, Chung T, DiBardino DJ, et al. Incomplete double aortic arch with atresia of the distal left arch: distinctive imaging appearance. AJR Am J Roentgenol. 2005;184:1634–9.
10. Kocis KC, Midgley FM, Ruckman RN. Aortic arch complex anomalies: 20-year experience with symptoms, diagnosis, associated cardiac defects, and surgical repair. Pediatr Cardiol. 1997;18:127–32.
11. Binet JP, Longlois J. Aortic arch anomalies in children and infants. J Thorac Cardiovasc Surg. 1977;73:248–52.
12. Nikaido H, Riker WL, Idriss FS. Surgical management of "vascular rings". Arch Surg. 1972;105:327–33.
13. Park JH, Kim JM, Roh JK. Hypoplastic vertebral artery: frequency and associations with ischaemic stroke territory. J Neurol Neurosurg Psychiatry. 2007;78:954–8.
14. Haramati LB, Glickstein JS, Issenberg HJ, Haramati N, Crooke GA. MR imaging and CT of vascular anomalies and connections in patients with congenital heart disease: significance in surgical planning. Radiographics. 2002;22:337–49.
15. VanDyke CW, White RD. Congenital abnormalities of the thoracic aorta presenting in the adult. J Thorac Imaging. 1994;9:230–45.
16. Das SK, Brow TD, Byrom R. Aortic root anomalies of the neck presenting in adults. Review of the literature with three case reports. Eur J Vasc Endovasc Surg. 2005;30:48–51.
17. Edwards JE. Anomalies of the derivatives of the aortic arch system. Med Clin North Am. 1948;32:925–49.
18. Satti SR, Cerniglia CA, Koenigsberg RA. Cervical vertebral artery variations: an anatomic study. AJNR Am J Neuroradiol. 2007;28:976–80.
19. Nogueira TE, Chambers AA, Brueggemeyer MT, Miller TJ. Dual origin of the vertebral artery mimicking dissection. AJNR Am J Neuroradiol. 1997;18:382–4.

Cervical Carotid and Vertebral Arterial Variants

33

This chapter covers congenital vascular variations in branching or anomalous entry points of *vertebral artery* (VA) and *internal carotid artery* (ICA) vasculature. These include *common carotid artery* (CCA) *origin of the VA, external carotid artery* (ECA) *origin of the VA, duplication of the VA, anomalous entry site of the VA into the vertebral transverse foramen, hypoplastic VA, hypoplastic ICA,* and *origin of ECA branches from the ICA*. *Tortuosity* that lacks abnormal branching or site of entry is covered in Chap. 34.

There are a multitude of potential congenital anomalous branches and courses of the various ECA branches, as well as branches from the thyrocervical and costocervical trunks that ascend into the cervical region. There are also potential anastamoses between these vessels, which can become more prominent or visible in the setting of pathology, particularly a proximal occlusion of a parent vessel, or in the uncommon arteriovenous malformation (AVM). Because of the normal, extreme variability in these branches, and because they are not usually encountered on routine neuroimaging and are unlikely to cause pathology or to be confused with abnormalities, they are not covered within this text.

Two of the most common settings in which knowledge of such variations is important are in the setting of *trauma* and in the setting of a dedicated vascular workup by catheter *digital subtraction angiography* (DSA). In the setting of trauma, a missing, small, or anomalous branching of a VA or ICA can lead to an erroneous diagnosis of occlusion from *blunt cerebrovascular injury* (BCVI) or to unnecessary catheter angiography, which, as an invasive procedure, does have some risk. In the setting of catheter angiography (most commonly to evaluate a suspected atherosclerotic stenosis), the lack of visualization of a CCA or VA can lead to the erroneous diagnosis that the vessel is occluded. In such cases, dedicated noninvasive imaging such as CT angiography (CTA) or MR angiography (MRA) prior to catheter DSA can be invaluable, which is one reason that neurointerventional and endovascular proceduralists have begun to favor noninvasive imaging in the initial workup of vascular abnormalities prior to endovascular therapy. Another reason is that a review of noninvasive imaging prior to the endovascular procedure has been shown to decrease the use of contrast and fluoroscopy time (hence, decreased radiation dose); such decreases are important, as an increase in each has been associated with greater risk of complications or morbidity.

A.M. McKinney, *Atlas of Normal Imaging Variations of the Brain, Skull, and Craniocervical Vasculature*,
DOI 10.1007/978-3-319-39790-0_33

33.1 Common Carotid Origin of the Vertebral Artery

Another very rare variant is a *VA origin from a CCA* instead of from a subclavian artery or even from the aortic arch. This type of origin occurs in far less than 1 % of the population; it can occur on either side. On the right side, it has been described to typically occur in conjunction with an *aberrant right subclavian artery* (RSCA), unless the patient has a right-sided aortic arch (Figs. 33.1, 33.2, and 33.3).

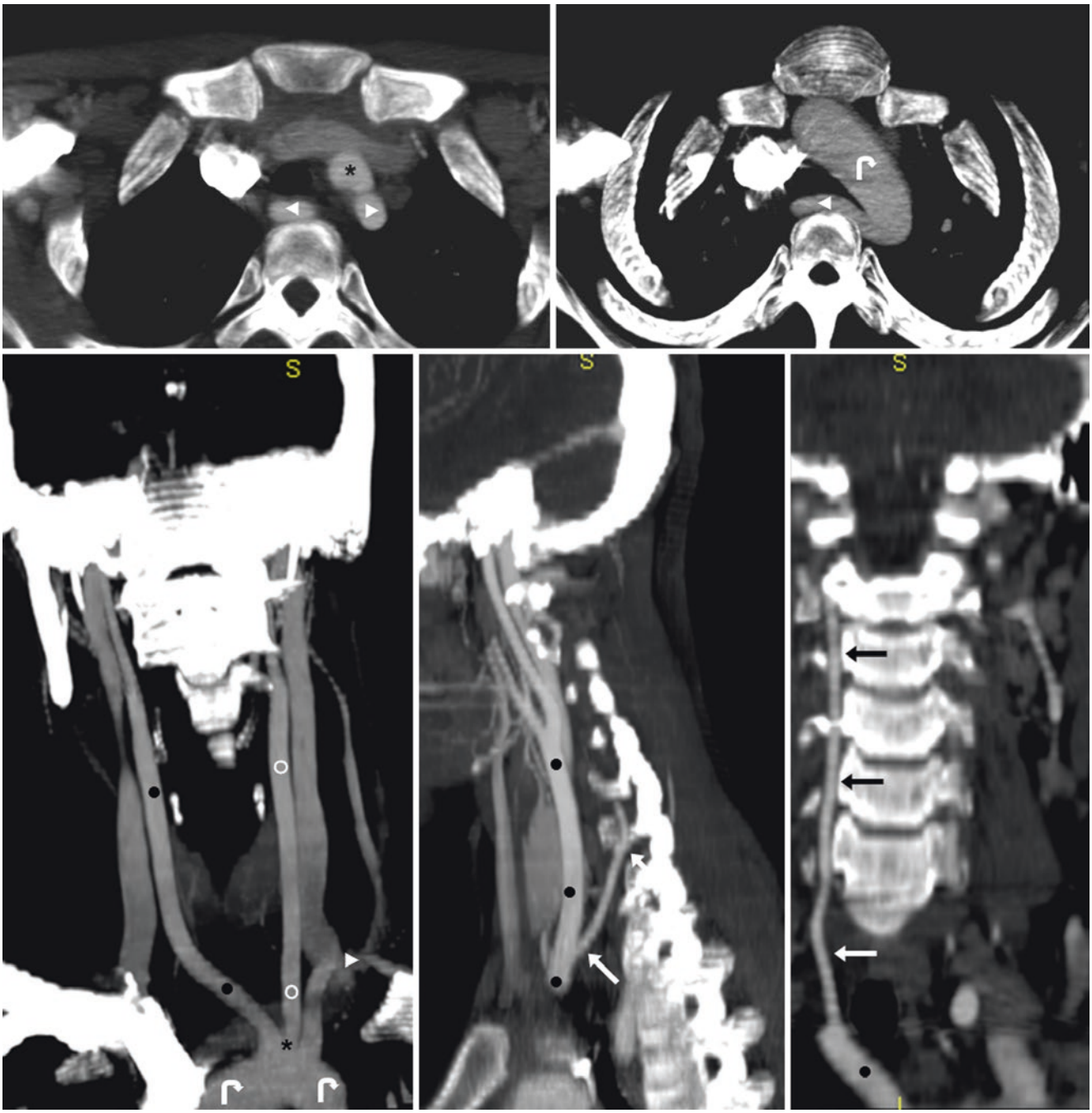

Fig. 33.1 *Top row:* 16-year-old with a left-sided aortic arch (*curved arrow*) and a retroesophageal right subclavian artery (RSCA, *left-facing arrowhead*) on CTA axial 3-mm (*left*) and 30-mm (*right*) images. *Bottom row:* Note the "truncus bicaroticus" (*asterisk*) on a coronal 30-mm MPR (*left*), which is usually accompanied by an aberrant RSCA. The right vertebral artery (RVA, *arrows*) arises from the right common carotid artery (RCCA, *black circles*) as shown on a sagittal 10-mm MPR (*middle*). A coronal 3-mm curved MPR (*right*) depicts the foraminal course of the RVA (*arrows*). *Aortic Arch* (*curved arrows*); *IA* Innominate Artery (+); *LCCA* Left Common Carotid Artery (○); *LSCLA* Left Subclavian Artery (▶); *RCCA* Right Common Carotid Artery (●); *RSCLA* Right Subclavian Artery (◀)

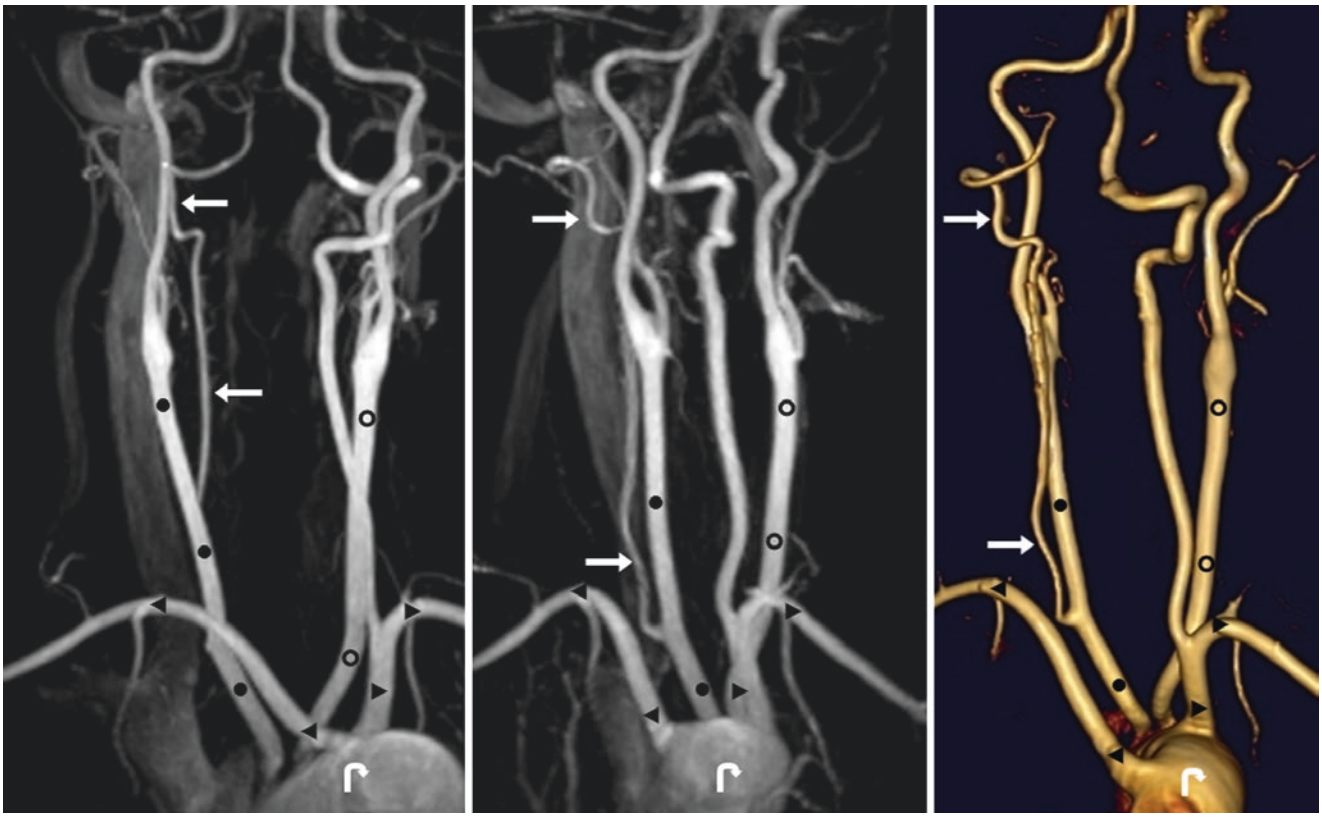

Fig. 33.2 46-year-old with a contrast-enhanced MRA that demonstrates a left-sided arch (*curved arrow*) with a retroesophageal RSCA (*left-facing arrowheads*) and the lack of an innominate artery (IA), on AP (*left*) and RAO (*middle*) views. On a further oblique RAO view (*right*, *veins removed*), the RVA (*arrows*) is demonstrated to arise from the RCCA (*black circles*). Also, the RVA appears hypoplastic intracranially. *Aortic Arch* (*curved arrows*); *IA* Innominate Artery (+); *LCCA* Left Common Carotid Artery (○); *LSCLA* Left Subclavian Artery (▶); *RCCA* Right Common Carotid Artery (●); *RSCLA* Right Subclavian Artery (◀)

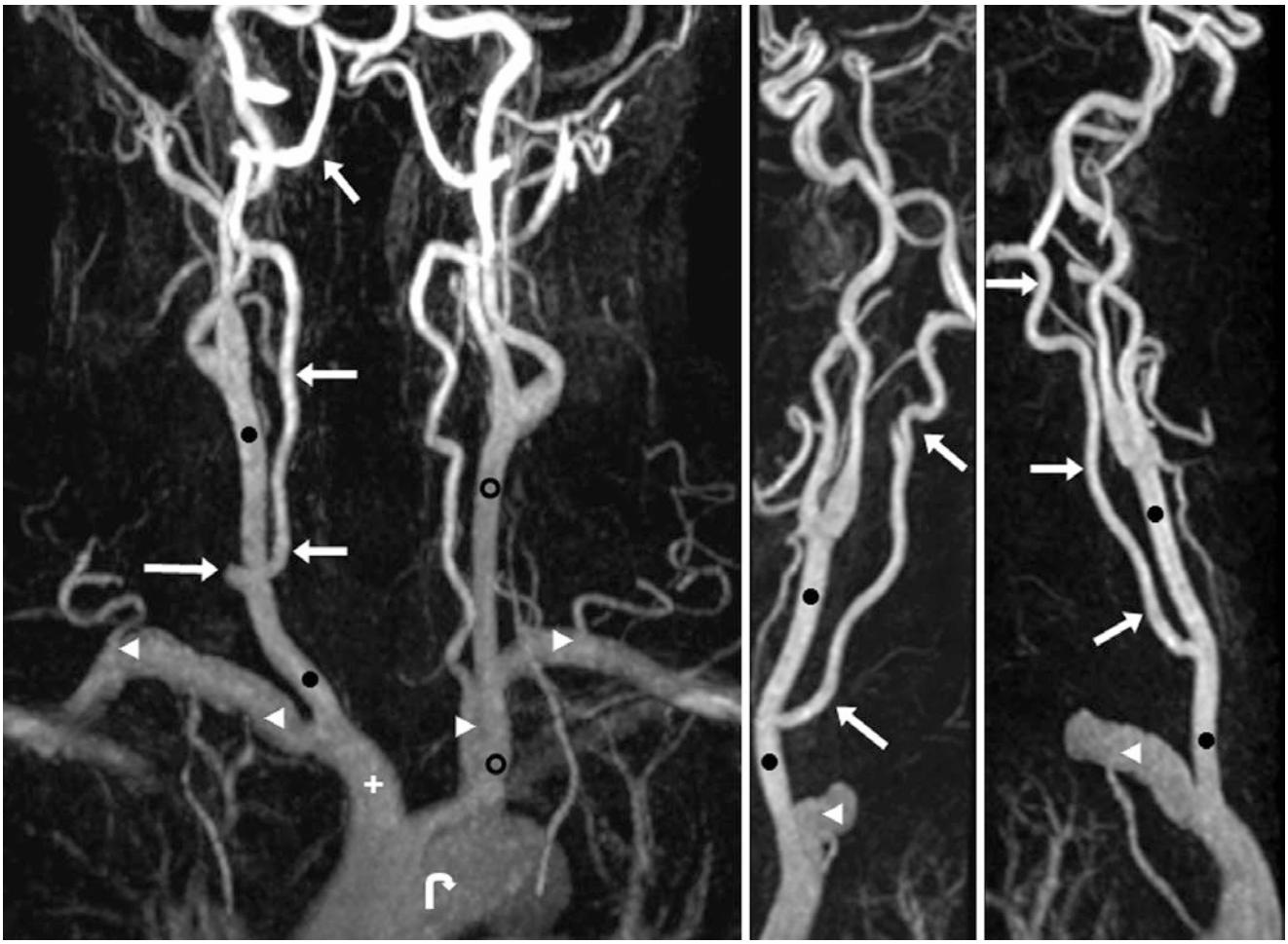

Fig. 33.3 49-year-old with a left-sided arch. The RVA (*arrows*) arises from the RCCA (*black circles*) on a contrast-enhanced MRA AP view (*left*), and on segmented LAO (*middle*) and RAO (*right*) views of only the right side. Neither an aberrant RSCA nor a right-sided arch is present, either of which is typical when the RVA arises from the RCCA. *Aortic Arch* (*curved arrows*); *IA* Innominate Artery (+); *LCCA* Left Common Carotid Artery (○); *LSCLA* Left Subclavian Artery (▶); *RCCA* Right Common Carotid Artery (●); *RSCLA* Right Subclavian Artery (◀)

33.2 Other Rare Vertebral Artery Origin Variants: External Carotid Origin and Duplication

Other quite rare variants of VA origins include *VA origin from the external carotid artery* (ECA), a *duplicated* or *triplicated origin*, or an *origin from the thyrocervical or costocervical trunks*. A duplication will usually fuse at some point in the upper cervical region, while the cranial portion of the VA appears normal. Also, if a duplication is focal, it may be termed a "fenestration," but *fenestrations* are much more common intracranially and have a single origin for both vessels. The term "duplication" is preferred if there are truly separate arterial origins that stay separate for long segments (Figs. 33.4 and 33.5).

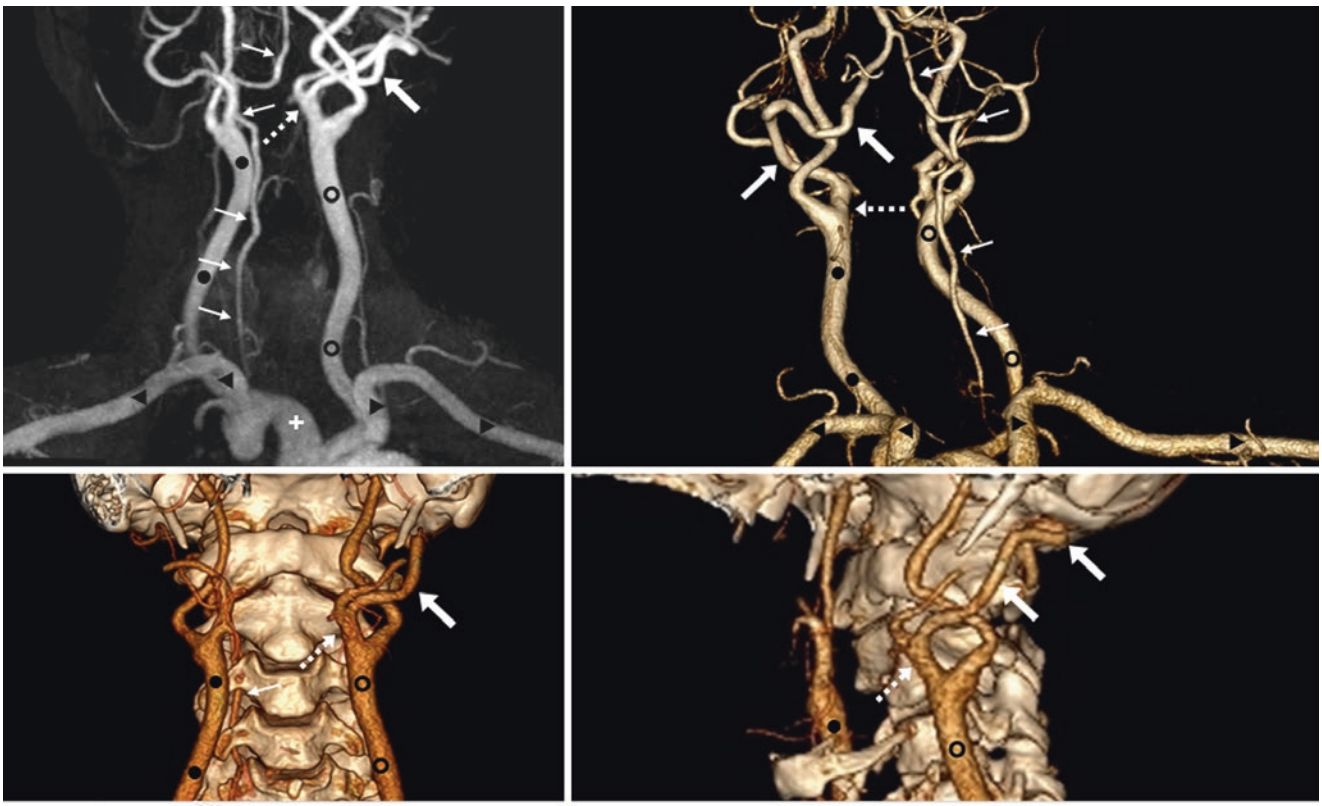

Fig. 33.4 *Top row*: 58-year-old with a contrast-enhanced MRA that demonstrates a left vertebral artery (LVA) origin (*large arrows*) that arises from the proximal external carotid artery (ECA, *dotted arrows*) on AP (*left*) and posterior/PA (*right*) views. *Bottom row*: Similar findings are noted on a CTA with AP (*left*) and left lateral (*right*) views. The RVA (*thin arrows*) is presented for comparison. *Aortic Arch* (*curved arrows*); *IA* Innominate Artery (+); *LCCA* Left Common Carotid Artery (○); *LSCLA* Left Subclavian Artery (▶); *RCCA* Right Common Carotid Artery (●); *RSCLA* Right Subclavian Artery (◀)

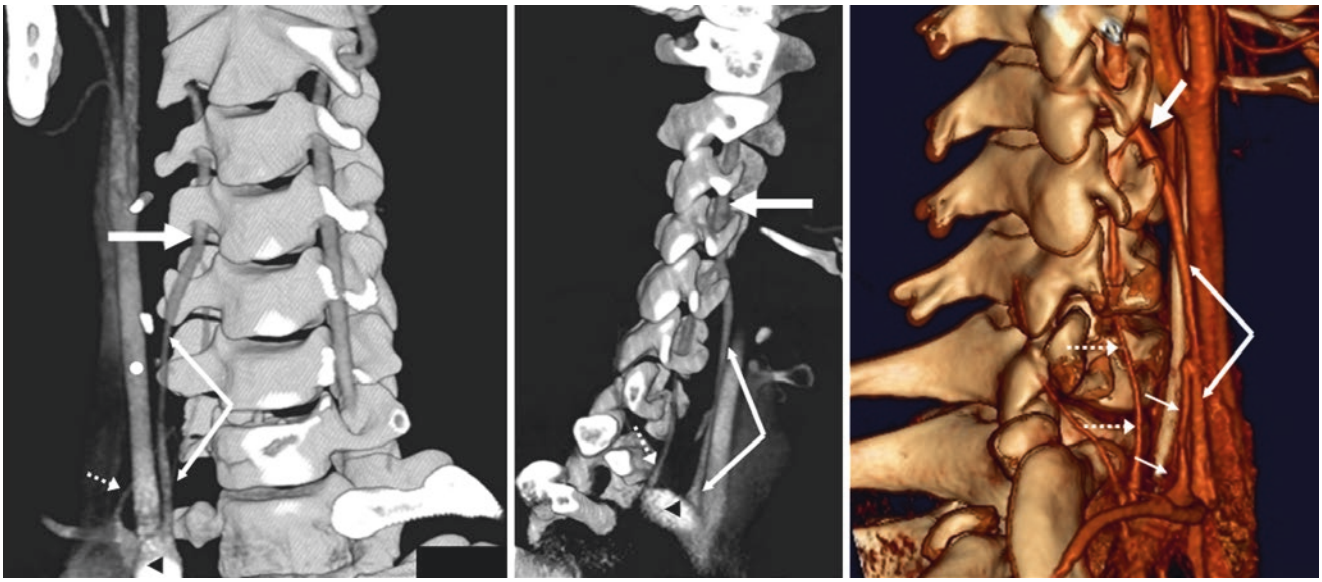

Fig. 33.5 17-year-old with a CTA that depicts RVA "triplication" on oblique AP (*left*) and lateral (*middle*) MPRs, and on a 3D VR lateral view (*right*). The three separate origins arise from the RSCA (*double arrows*), the thyrocervical trunk (*thin arrows*), and the costocervical trunk (*dotted arrows*). All combine superiorly (*large arrows*) at the level of the C4 vertebra to form a single RVA before it travels up through the foramen magnum. *Aortic Arch* (*curved arrows*); *IA* Innominate Artery (+); *LCCA* Left Common Carotid Artery (○); *LSCLA* Left Subclavian Artery (▶); *RCCA* Right Common Carotid Artery (●); *RSCLA* Right Subclavian Artery (◀)

33.3 Anomalous Level of Vertebral Artery Entry Into the Transverse Foramen or Dura

The *vertebral artery* (VA) in the V2 segment typically enters the *transverse foramen* (TF) at the level of C6 in approximately 90% of patients. In the other 10%, the entry point can be located anywhere between the levels of the C2 and C7 vertebrae. The bony contours of the transverse foramina that contain the VAs have also been described to be larger than those not containing a VA. These can be particularly problematic in a patient evaluated for *trauma* on noninvasive imaging; failure to visualize VA enhancement or its flow void within the foramen can mimic a dissection or occlusion from *blunt cerebrovascular injury* (BCVI). For example, this phenomenon can occur on a cervical spine MRI obtained to evaluate cervical trauma, on which the TF lacks normal, dark flow voids on T2WI, or on a postcontrast cervical CT, where the lack of the normal VA enhancement is apparent. However, noninvasive CTA, MRA, or catheter DSA can easily define the anomalous course of such VAs (Figs. 33.6, 33.7, 33.8, 33.9, 33.10, and 33.11).

Another rarer variant is *entry of the VA into the dura below the level of the foramen magnum*. The V1 segment of the VA runs from the origin to the V2 segment (where it enters the TF), whereas the V3 segment extends from the level of C2 to the dura, typically appearing as a "half square" appearance on catheter angiography AP views of each side. The V4 segment consists of the intradural portion, which is typically at the point where the VA becomes intracranial between the occiput and C1. Rarely, however, the VA may pierce the dura at a level lower than C1, and thus the V4 segment begins below the C1 vertebra. This variant is not likely to be symptomatic, but it may be of concern in situations of C1-2 fracture or subluxation, where it could present a higher risk for BCVI (Fig. 33.12).

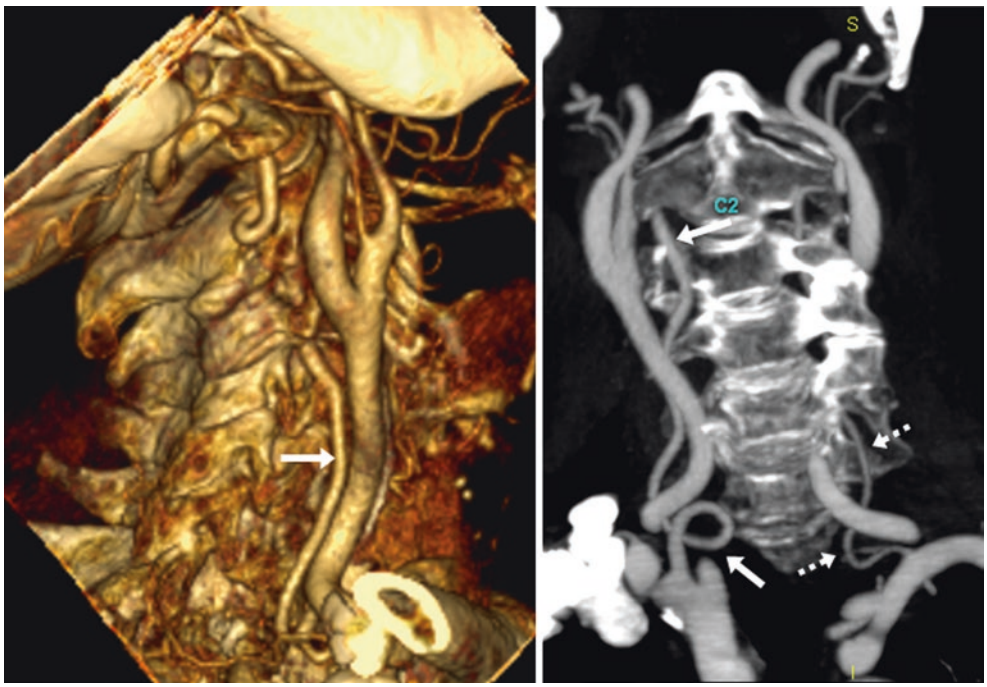

Fig. 33.6 In an 85-year-old, the RVA (*arrows*) enters the transverse foramen (TF) at the level of C2-3, whereas the LVA (*dotted arrows*) enters at the expected level, as demonstrated on a 3D VR lateral view (*left*) and on a 17 mm-thick coronal MPR AP view (*right*). The LVA is hypoplastic

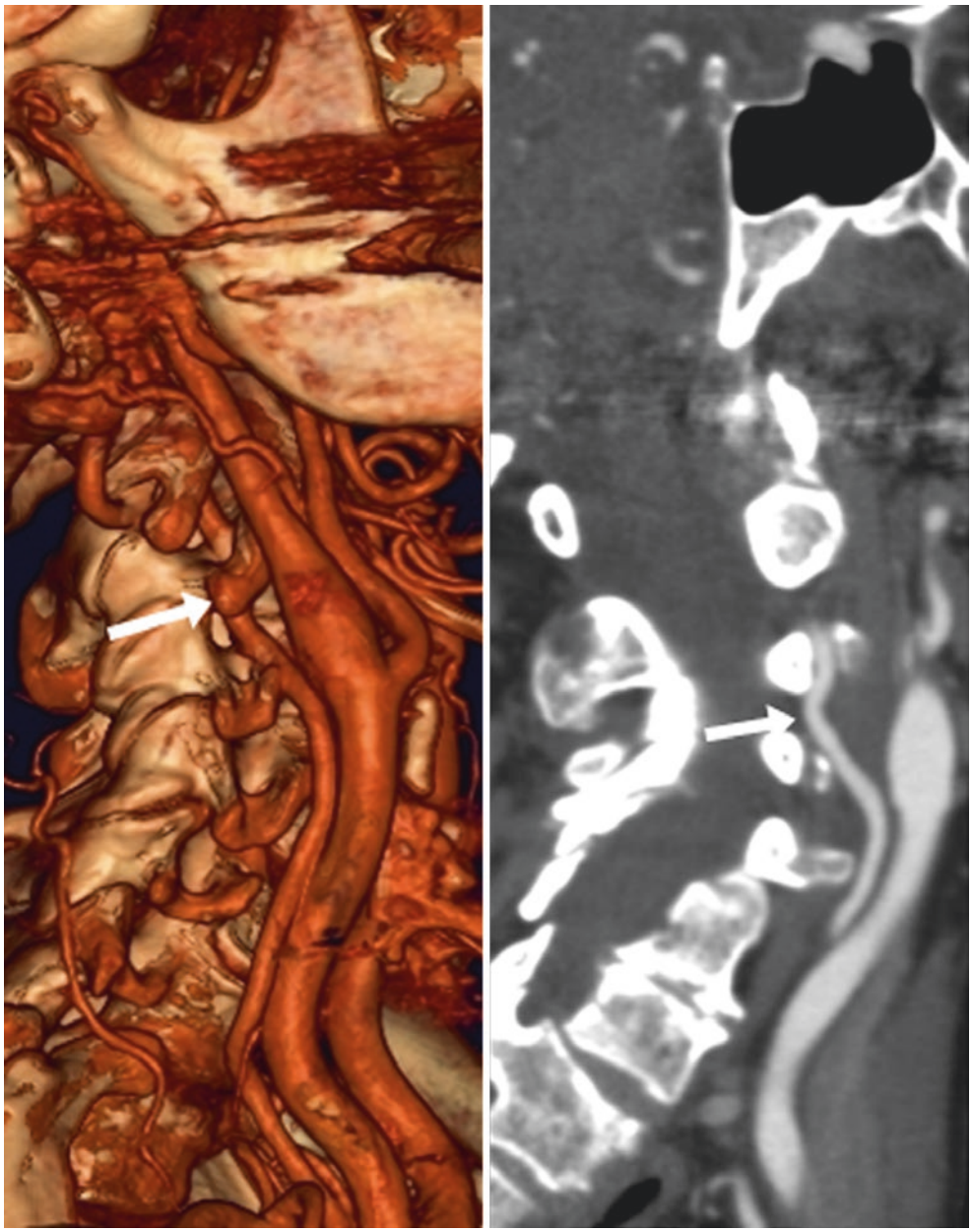

Fig. 33.7 In a 71-year-old, the RVA (*arrows*) enters the TF at C3-4, as shown on a 3D VR right lateral view (*left*) and a 5 mm-thick sagittal MPR view (*right*)

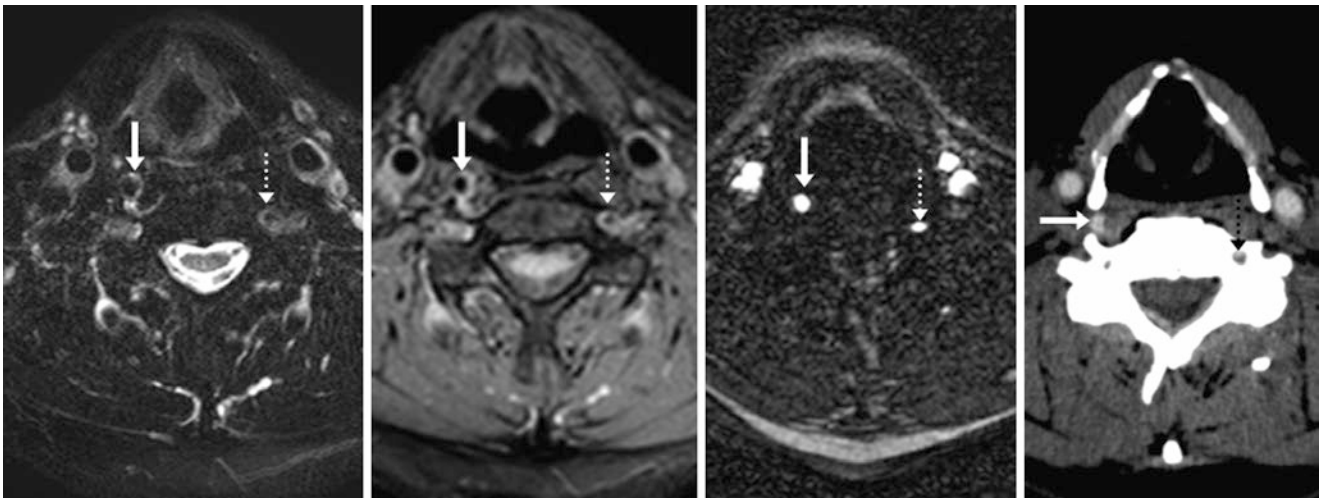

Fig. 33.8 In a 54-year-old trauma patient, the RVA (*large arrows*) was not visualized within the TF at the level of C5-6 (it enters higher, at the C4-5 level) on fat-suppressed T2WI (*left*) or on T1WI (*left middle*), but was certainly patent with cephalad flow on axial images from two-dimensional time-of-flight (2DTOF) MRA (*right middle*) and CTA (*right*). Note the LVA (*dotted arrows*)

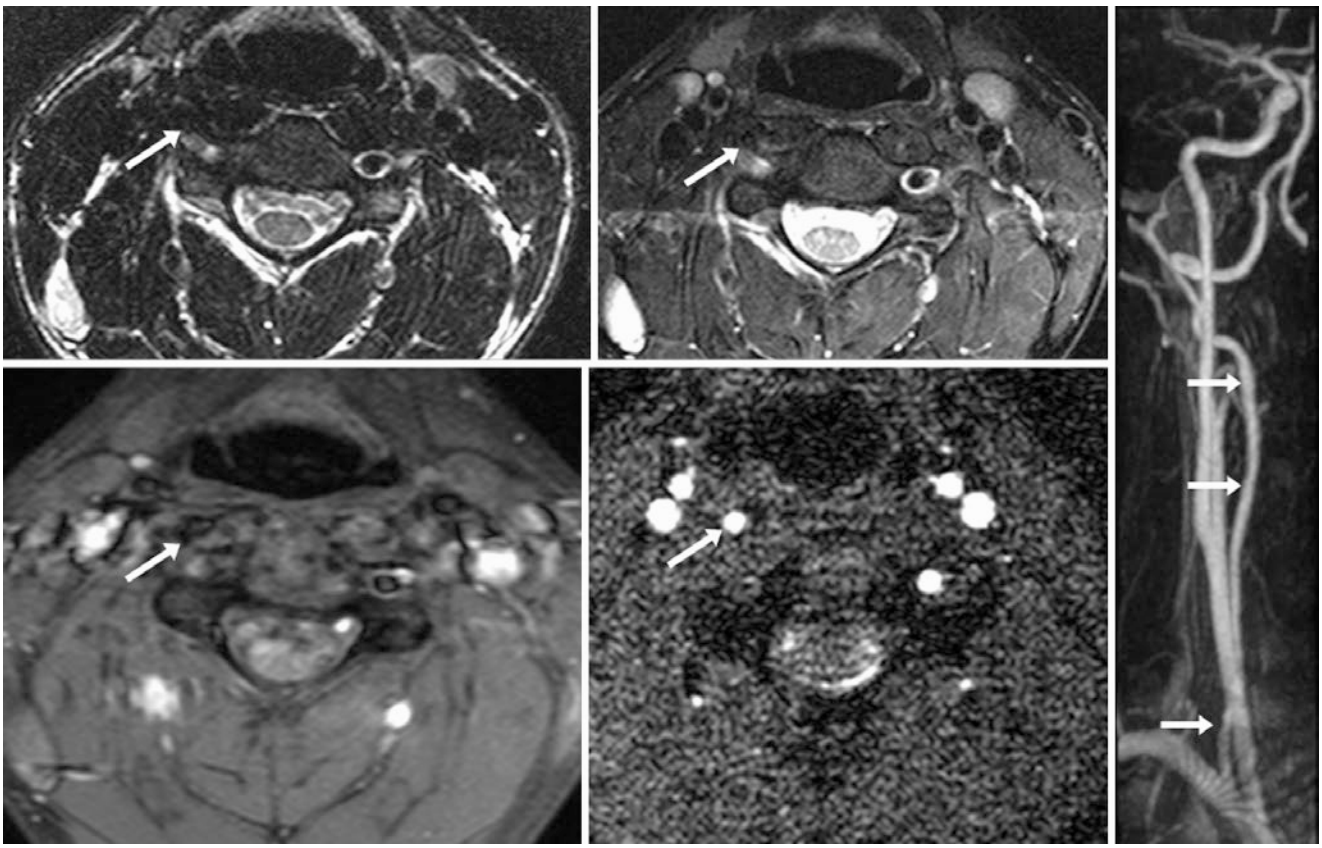

Fig. 33.9 A 17-year-old had a cervical spine fracture that involved the right TF at the C6 level; an MRI was ordered to rule out arterial injury. Initially, the RVA (*arrows*) was not identified prior to or after fat-suppression on T2WI *(top row*) or T1WI (*bottom left*), but it was noted to be outside of the C4-5 TF on 2DTOF MRA source images (*bottom right*); it entered the foramen at C3-4. Caudally flowing spins are saturated and thus not seen. Both a contrast-enhanced MRA AP view (*far right*) and a catheter DSA (*not shown*) were normal

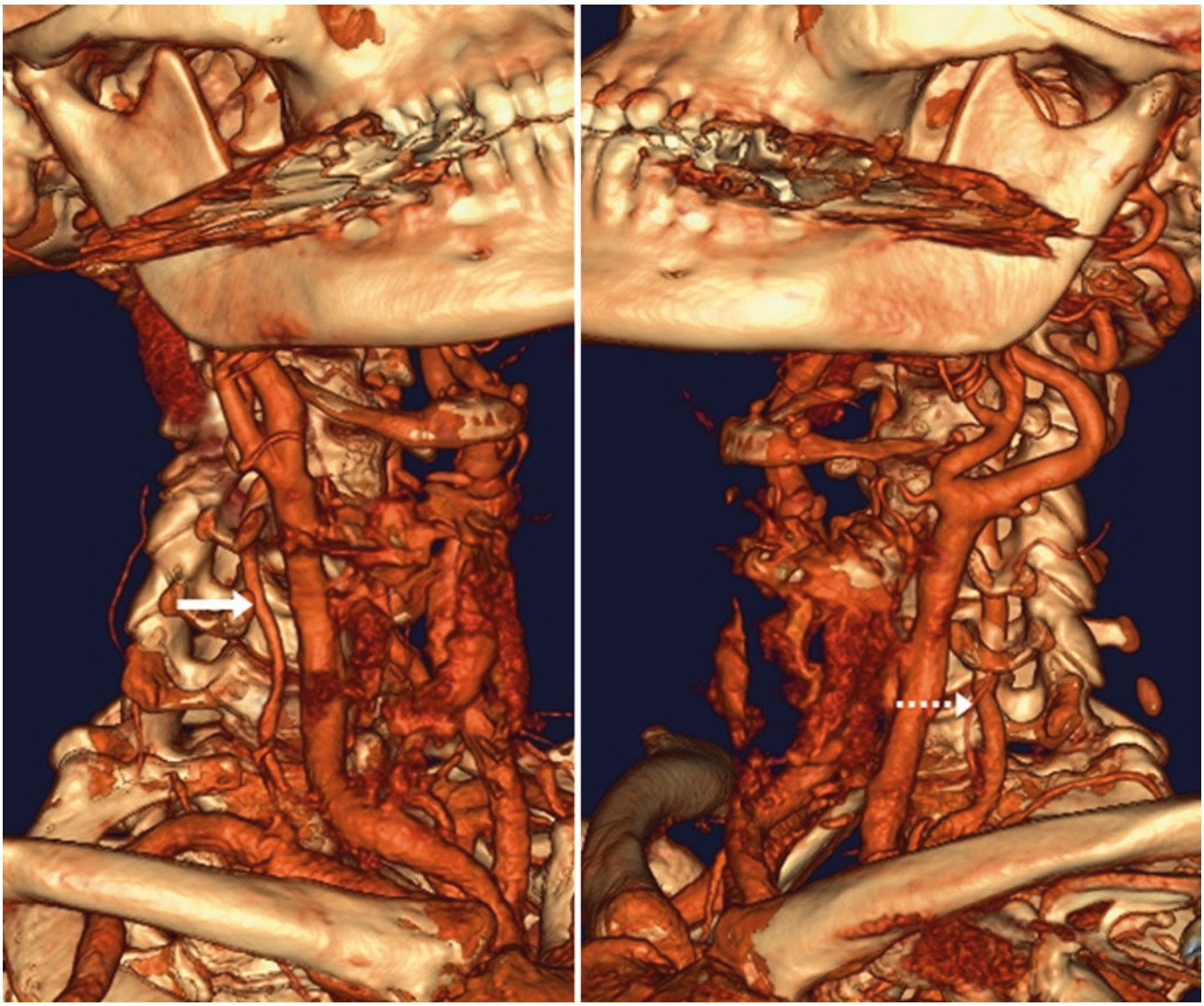

Fig. 33.10 In a 62-year-old, a CTA with 3D VR oblique views shows that the RVA (*arrow*) enters the TF at the C5-6 level (*left*), whereas the LVA (*dotted arrow*) enters the TF at the normal level of C6-7 (*right*)

Fig. 33.11 In a 29-year-old, a parasagittal MPR of a neck CTA (obtained for evaluation of the RVA following C6-7 dislocation and posterior fusion) showed entry of the RVA (*arrow*) into the TF at the C5-6 level, perhaps preventing vascular injury

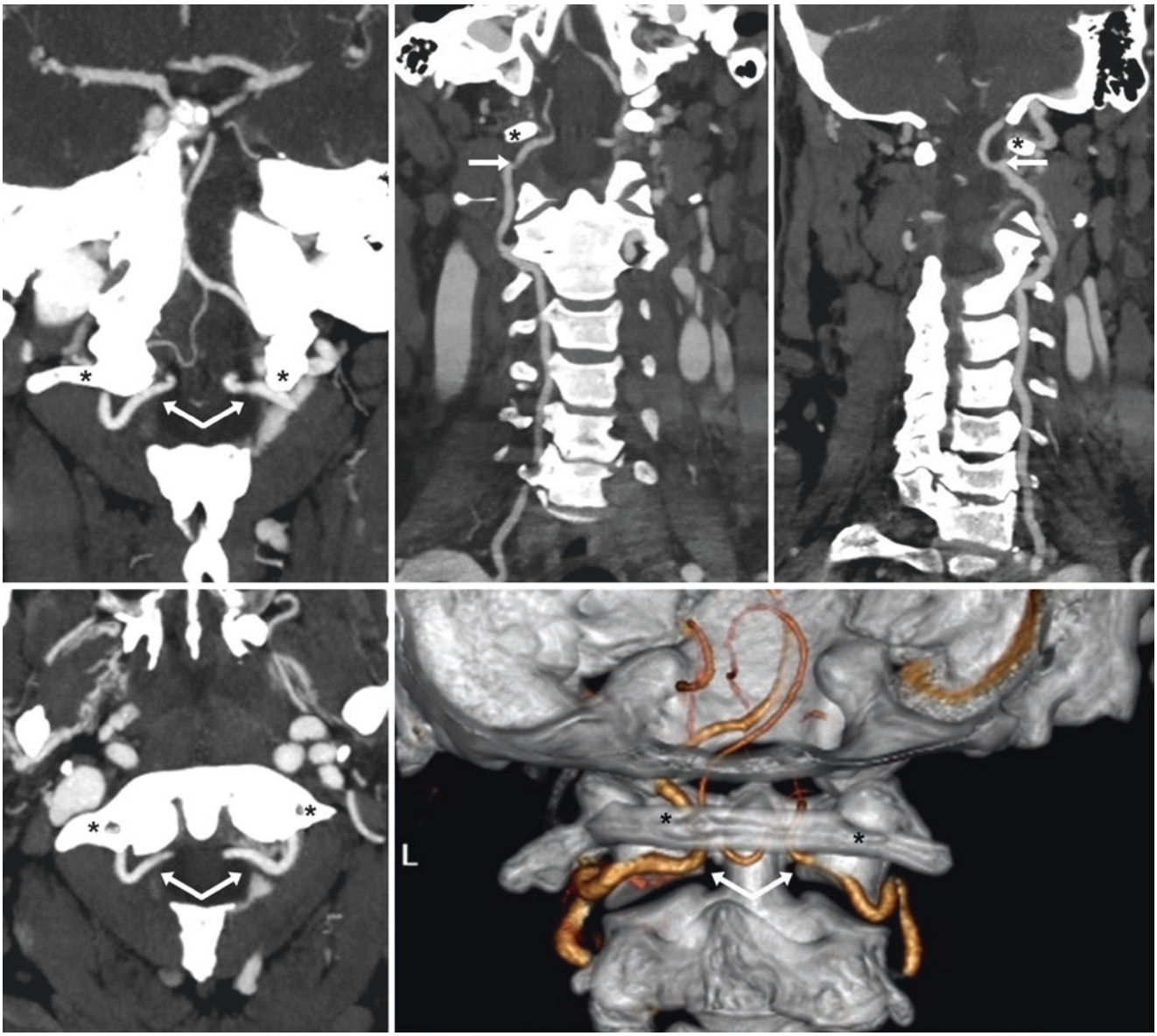

Fig. 33.12 In a 44-year-old with trauma and altered mentation (no cervical spine fracture), a CTA demonstrated anomalous entry of the V4 segments of both VAs into the dura (*arrows*) just below the level of C1 *(asterisks)*, on coronal MPR (*top left*), curved coronal MPR of the right (*top middle*) and left (*top right*) sides, and on axial MPR (*bottom left*). A PA view on 3D VR CTA (*bottom right*) best illustrates the VAs travelling medially just below the C1 arch

33.4 Hypoplastic Vertebral Artery

Hypoplastic VAs are common normal variants, which occur in about 10–30 % of the population. A typical example of how these can be problematic occurs in the scenario of "rule out dissection" or when the normal flow void in a hypoplastic artery is not visualized on a T2WI (perhaps because of slow or undetectable flow in a tiny artery). The result can be unnecessary tests and even potentially harmful iatrogenic injury if catheter angiography is performed within such a vessel. Thus, assessment by MRA (which also may fail to visualize an extremely hypoplastic artery well) or CTA should be performed first. The VA can also be so small as to terminate in the posterior inferior cerebellar artery (PICA), a variant estimated to occur in approximately 1 % of catheter angiograms.

There is debate as to whether the risk of stroke or injury is increased with a normal, hypoplastic VA in the setting of trauma. Such discussions are beyond the scope of this text. The literature on this subject is variable, perhaps because a patent but hypoplastic VA may erroneously appear occluded owing to slow flow on MRI, lower-quality CTA, or even suboptimal catheter DSA images (*e.g.*, if a small amount of contrast is injected) (Figs. 33.13, 33.14, 33.15, 33.16, 33.17, 33.18, 33.19, and 33.20).

Fig. 33.13 65-year-old with a hypoplastic RVA (*arrows*) on a coronal MPR from a CTA. The hypoplastic RVA has a smooth, regular contour, as opposed to a dissection, which has irregular margins with variegated luminal narrowing

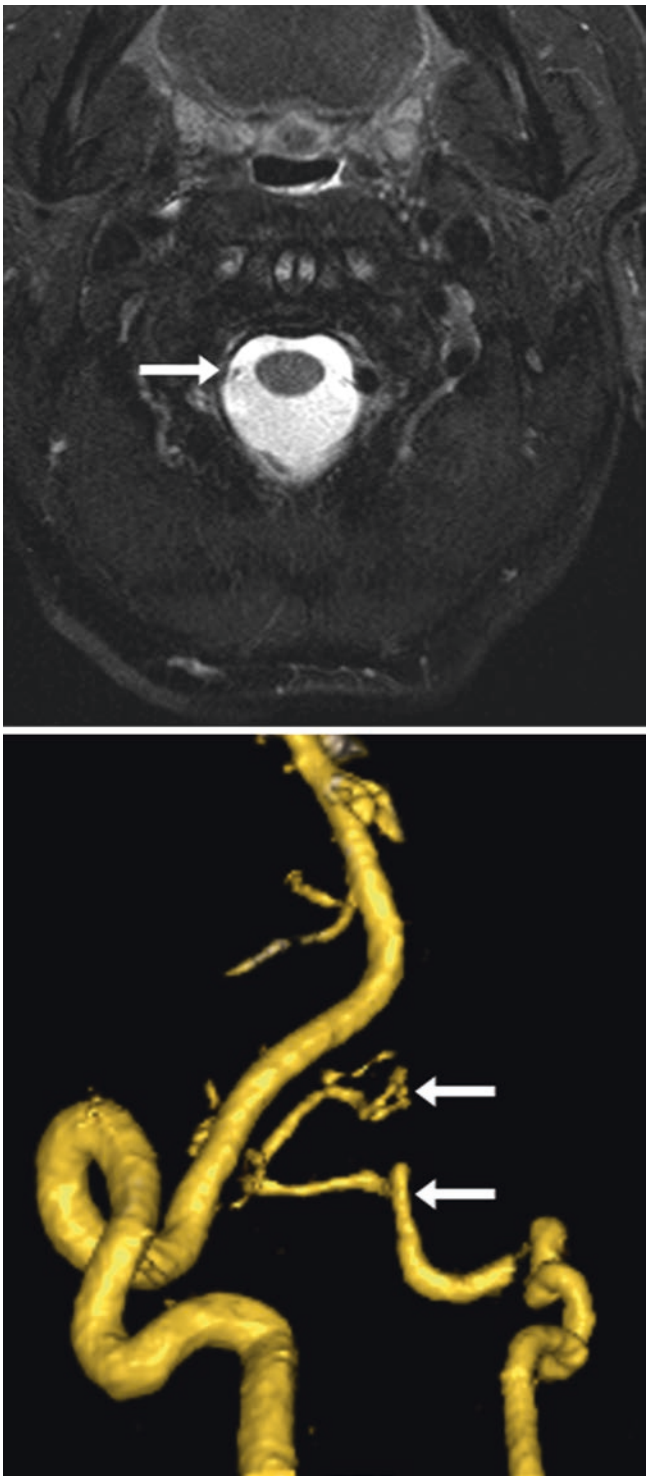

Fig. 33.14 In a 53-year-old, a tiny RVA on T2WI (*top*) lacked flow voids due to slow flow, but it had forward flow on a 3DTOF MRA VR PA view (*bottom*), confirming that the RVA terminated as the posterior inferior cerebellar artery (PICA)

Fig. 33.15 *Top row:* This 49-year-old has a hypoplastic RVA on post-contrast T1WI (*left*), gradient echo T1WI (*middle*), and on T2WI (*right*); the RVA's flow void is not visible because of slow flow. *Bottom row:* VA flow voids with antegrade flow are noted on coronal T2WI (*left*), and on TOF MRA with a 1-mm axial view (*middle*) and MIP AP view (*right*). Note a vertebrobasilar fenestration (*dotted arrows*) just cephalad

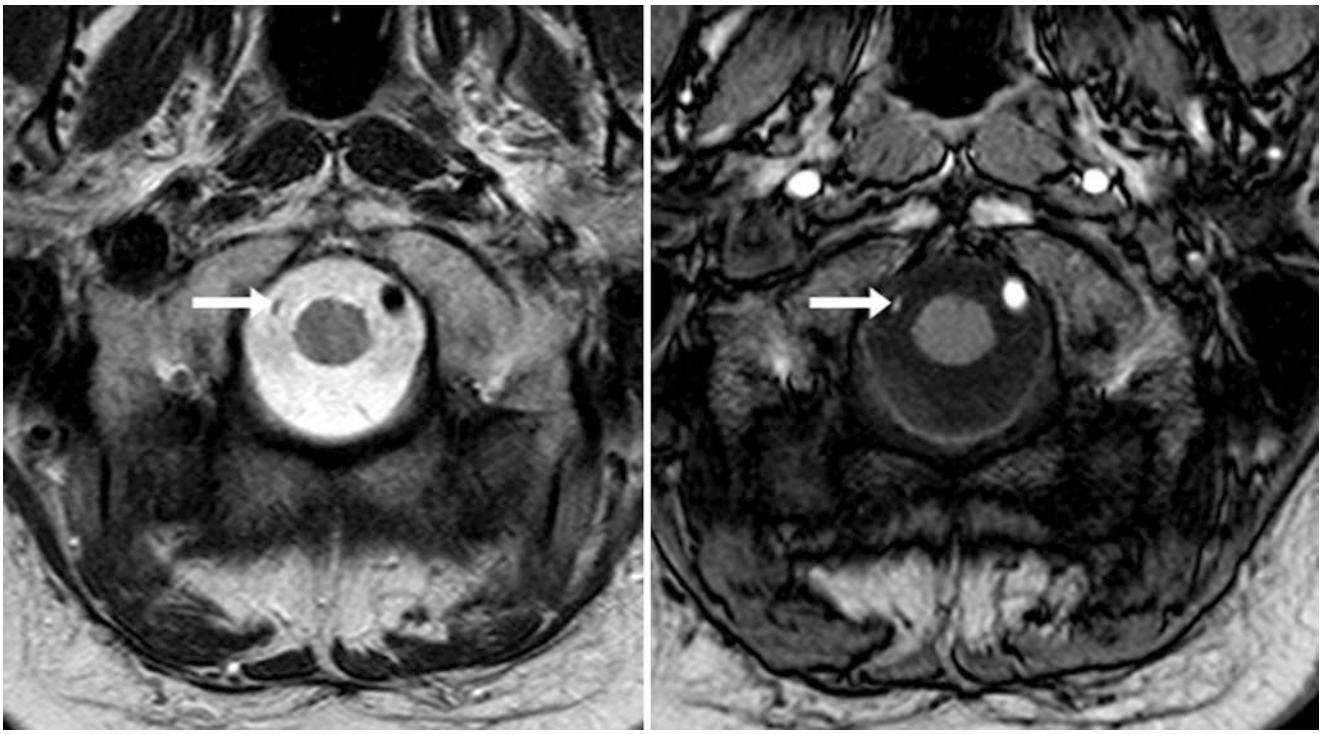

Fig. 33.16 60-year-old with a hypoplastic VA on axial T2WI (*left*) and on postcontrast T1WI (*right*). Note the lack of a flow void on T2WI, even though the tiny vessel is patent and enhances with contrast

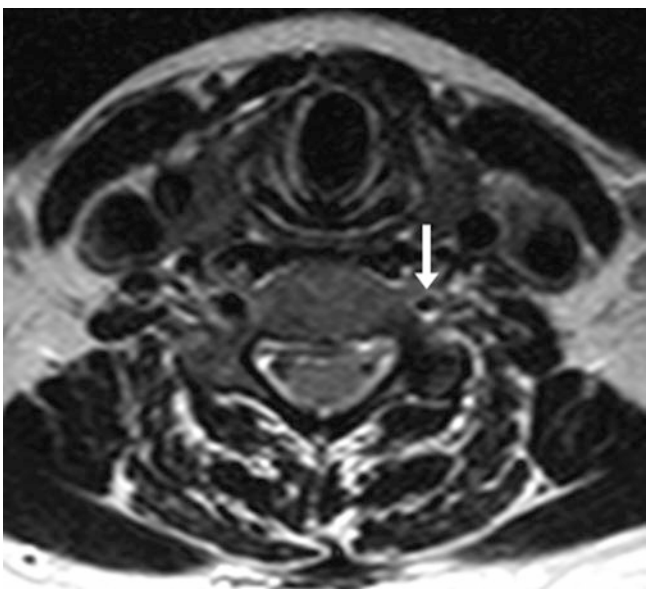

Fig. 33.17 35-year-old with a hypoplastic cervical LVA (*arrow*) at the C6 level on axial T2WI obtained for spinal evaluation

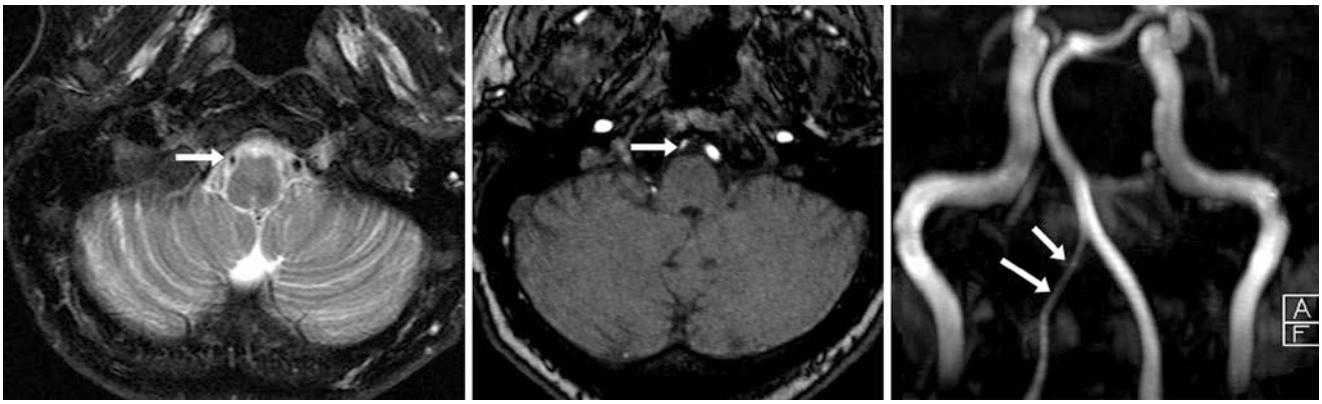

Fig. 33.18 52-year-old with a hypoplastic VA (*arrows*) on T2WI (*left*), axial source 3DTOF MRA images (*middle*), and on 3D MIP images in an AP view (*right*)

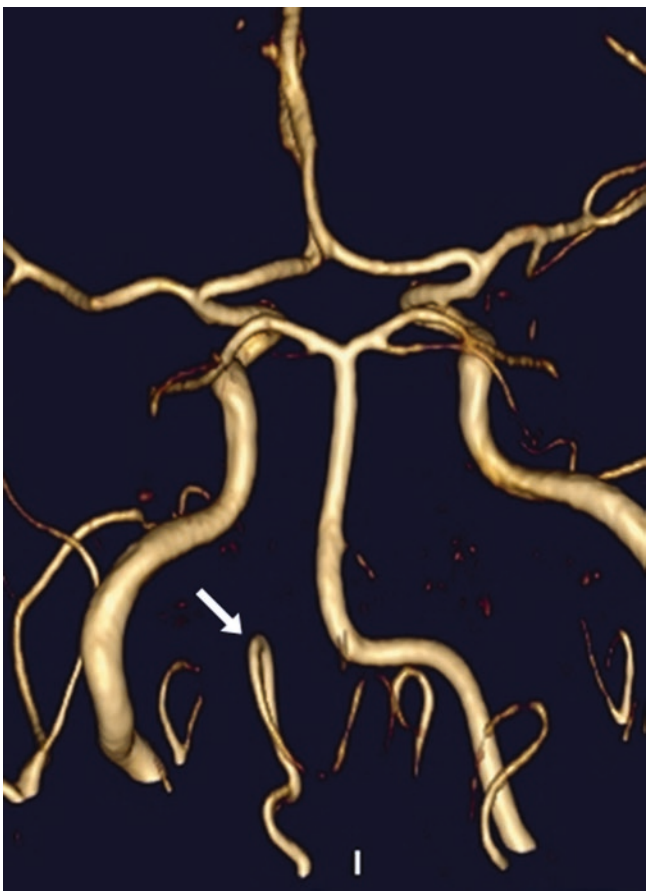

Fig. 33.19 21-year-old with a hypoplastic LVA (*arrow*) that ends in the PICA on a 3DTOF MRA VR PA view

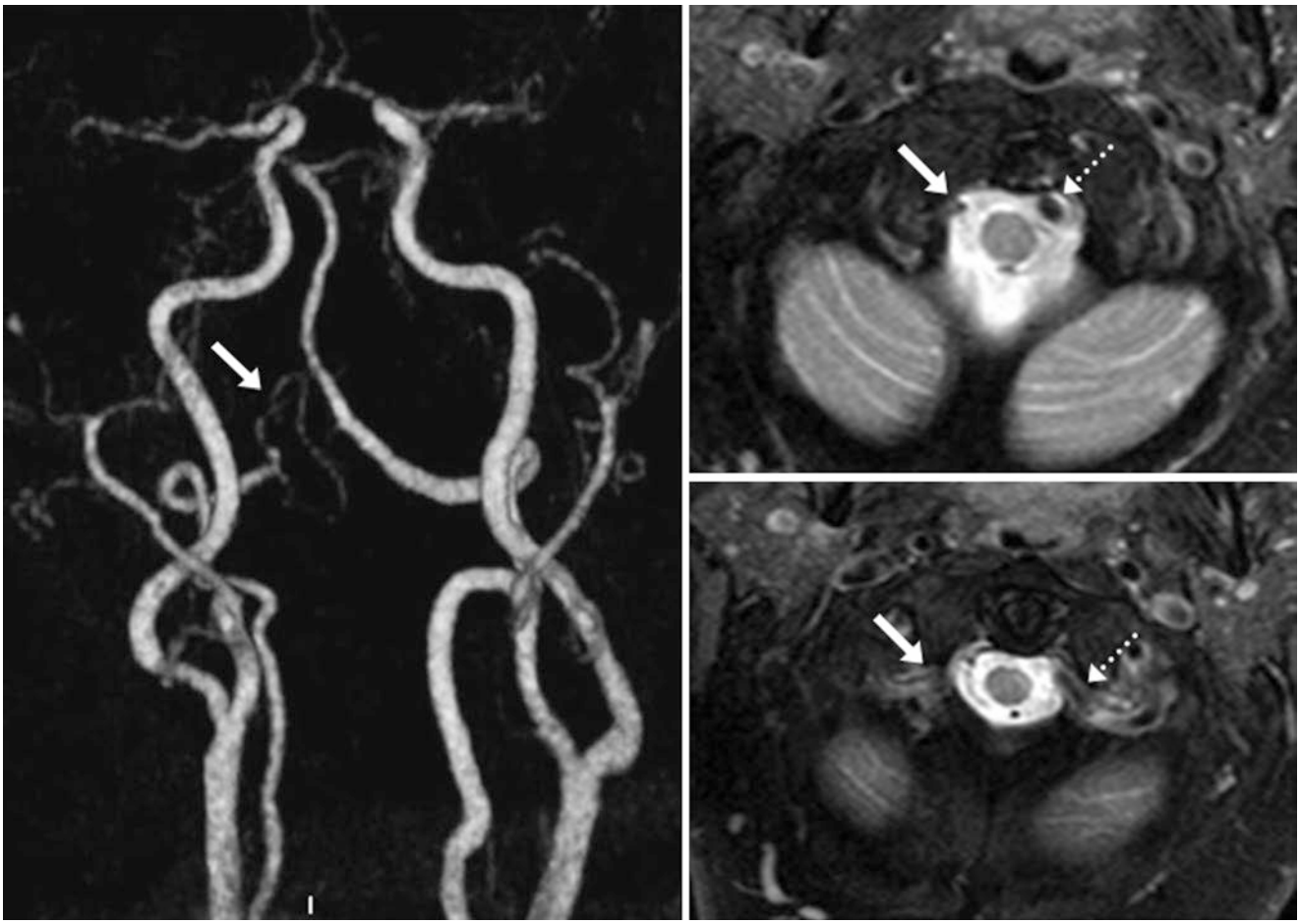

Fig. 33.20 78-year-old with a hypoplastic RVA terminating in the PICA on a contrast-enhanced MRA 3D VR AP view (*left*). On T2WI (*right*), note a diminished flow void due to slow flow, as opposed to a normal LVA flow void (*dotted arrows*)

33.5 Hypoplastic Internal Carotid Artery

Hypoplasia of the internal carotid artery (ICA) is a rare congenital anomaly occurring in less than 0.2 % of the population. It is usually (but not always) associated with other congenital vascular anomalies, and is commonly asymptomatic. The typical imaging pattern is of a small, bony petrous carotid canal on the hypoplastic side on a CT scan, with a mildly enlarged vertebrobasilar system and variable enlargement of the contralateral ICA. The ipsilateral common carotid artery (CCA) is also usually hypoplastic. It is extremely rare for this anomaly to be bilateral. Occasionally, ipsilateral facial hemiatrophy is noted. There is debate as to whether there the incidence of an *aneurysm* is increased on the contralateral side (perhaps due to increased flow); the literature is sparse on this subject. The ICA hypoplasia appears to be more common on the left. CTA, MRA, or catheter DSA can easily distinguish this variant (Figs. 33.21, 33.22, 33.23, 33.24, and 33.25).

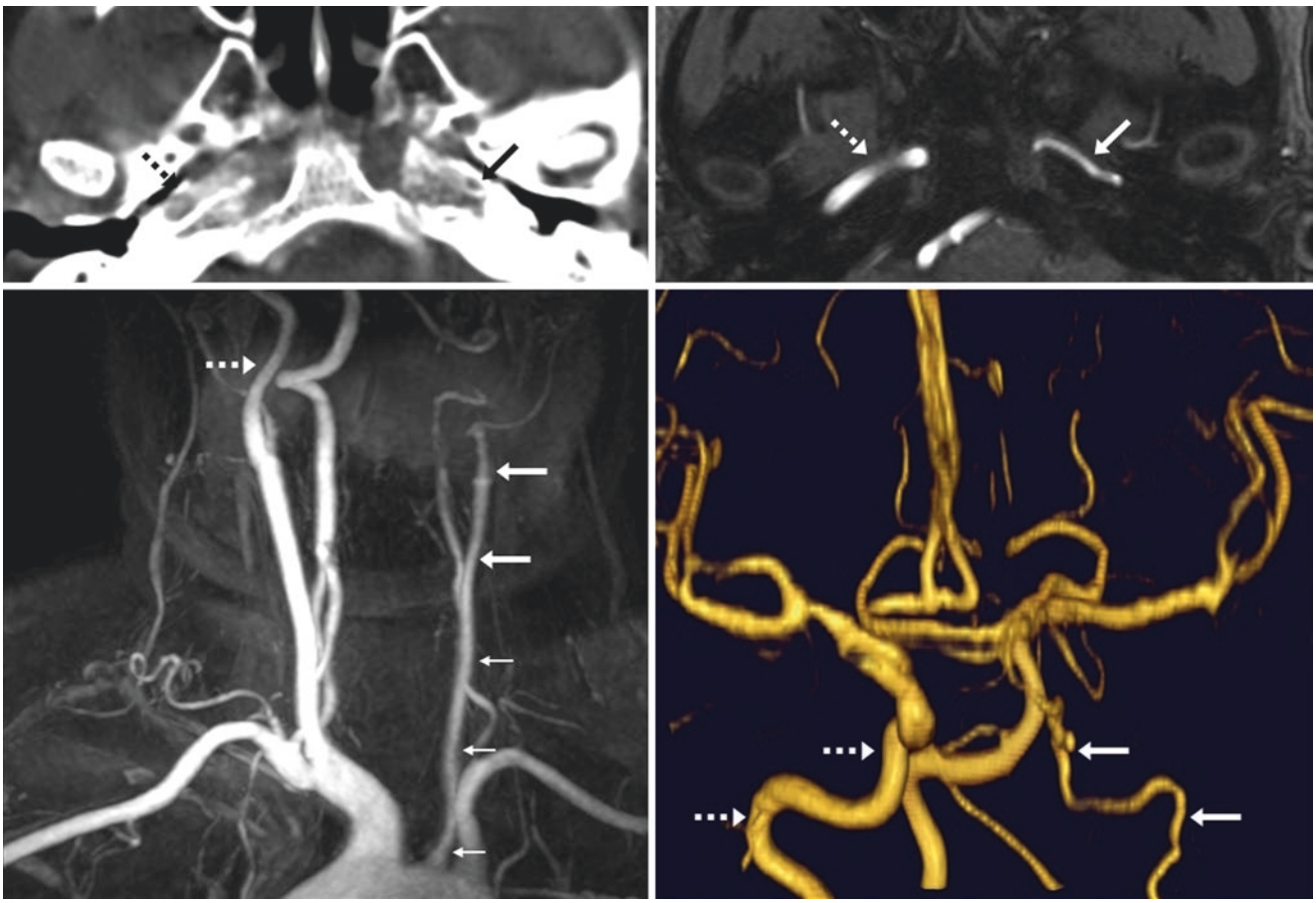

Fig. 33.21 29-year-old with a hypoplastic left internal carotid artery (ICA) (*large arrows*), as evidenced by a small, bony petrous ICA canal on nonenhanced CT (*top left*), 3DTOF MRA source (*top right*), and 3D VR AP view (*bottom right*) images. The left common carotid artery (CCA) was hypoplastic (*tiny arrows*) on a contrast-enhanced MRA MIP AP view (*bottom left*). Note the normal right ICA (*dotted arrows*)

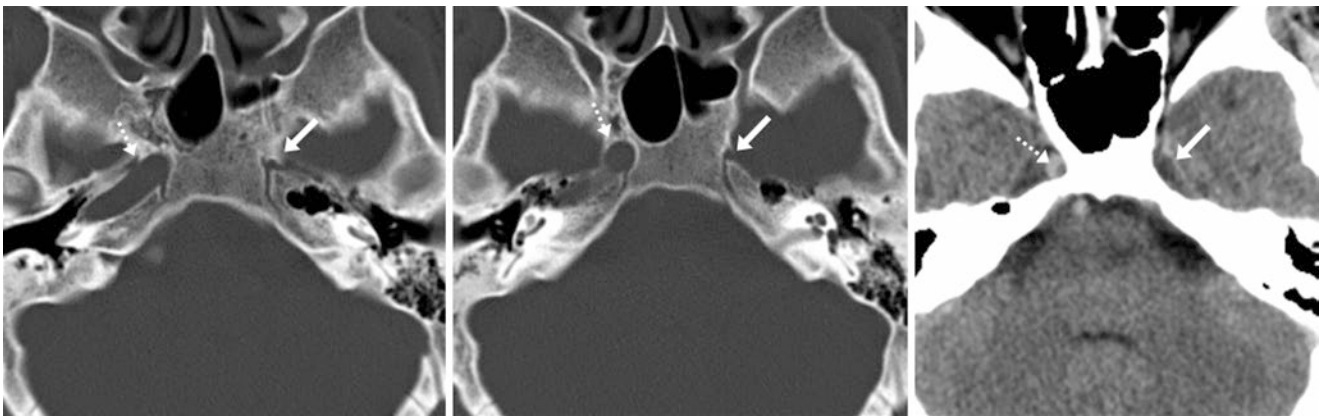

Fig. 33.22 25-year-old with a hypoplastic left ICA and bony canal (*arrows*) on bone windows (*left* and *middle*) and a soft tissue window (*right*) from nonenhanced CT, performed for screening after trauma. The patient was asymptomatic, and no skull fracture was identified. *Dotted arrows* denote the contralateral right ICA, which had a normal bony canal diameter

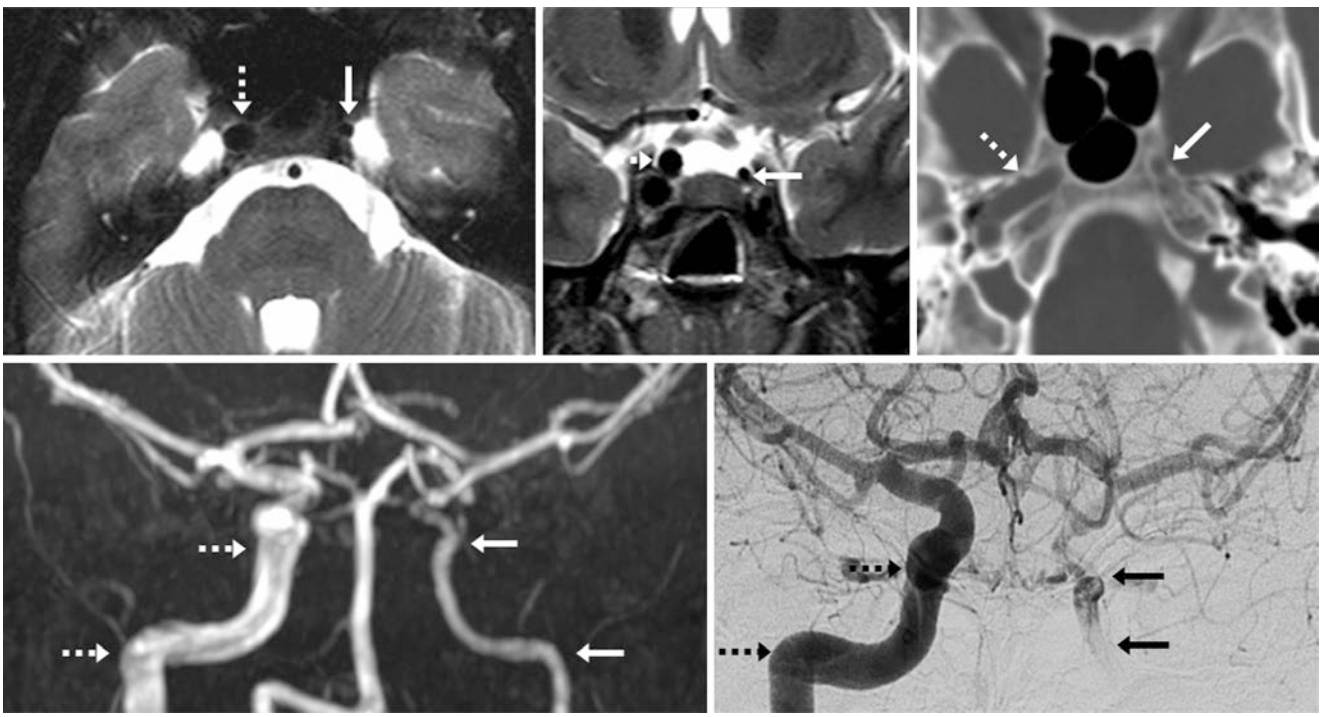

Fig. 33.23 *Top row:* In a 22-year-old, a hypoplastic left ICA (*arrows*) was suspected on a T2-weighted MRI in axial (*left*) and coronal (*middle*) views, and on nonenhanced CT (*right*), which demonstrated a small bony canal. *Bottom row:* A 3DTOF MRA AP view (*left*) confirmed left ICA hypoplasia, and a catheter DSA (*right*) showed that the left ICA was partially supplied via anterior communicating cross-filling from the right ICA (*dotted arrows*)

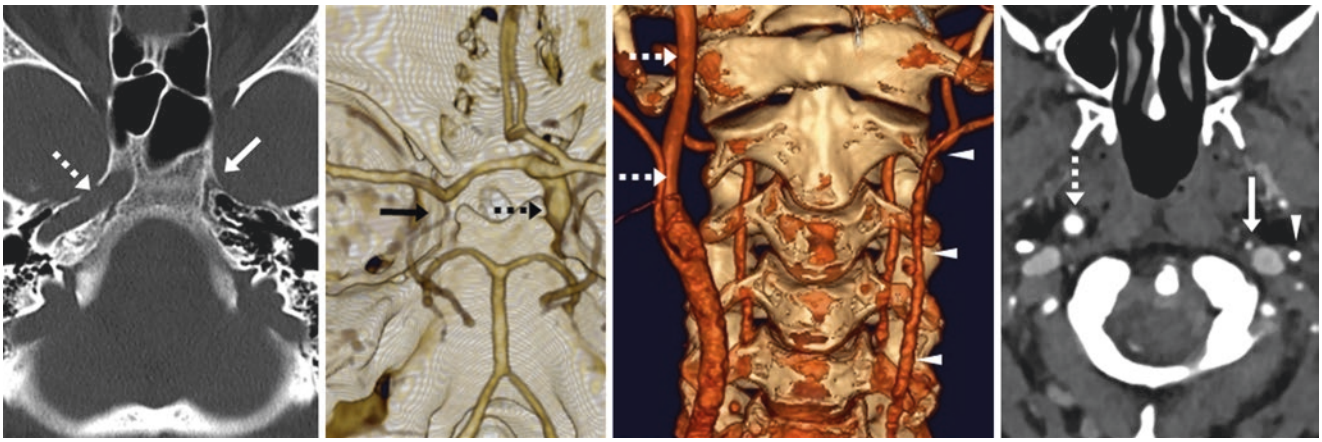

Fig. 33.24 A 39-year-old had a tiny, hypoplastic left ICA bony canal (*arrows*) on nonenhanced CT (*left*), with an absent left ICA on a CTA with a 3D VR superior head view (*left middle*), on a cervical AP view (*right middle*), and on source CTA images (*right*). The left ECA is patent (*arrowheads*), and the right ICA (*dotted arrows*) is normal

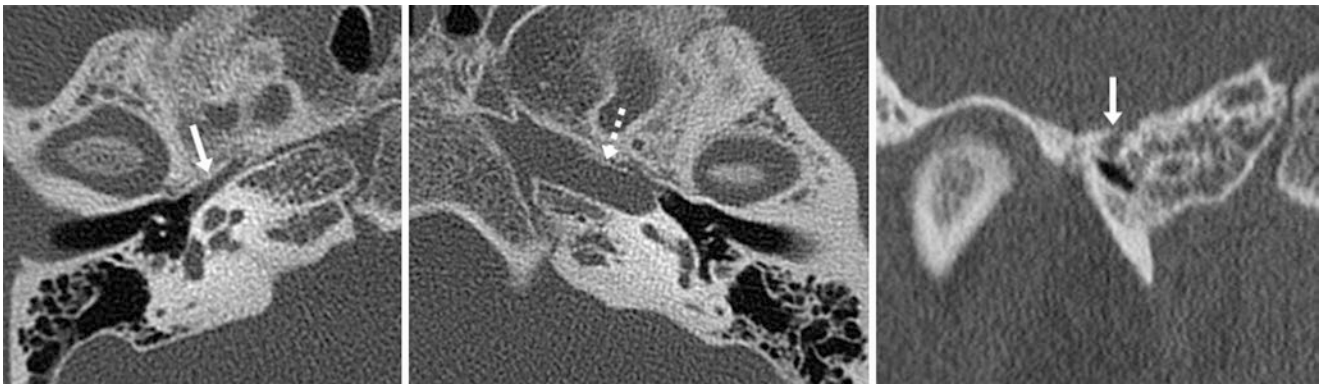

Fig. 33.25 14-year-old with a hypoplastic right ICA bony canal (*arrows*) on a temporal bone nonenhanced CT with axial (*left*) and coronal (*right*) images in bone windows, performed for bilateral hearing loss. (The etiology was unknown, as the examination was otherwise negative.) Note the normal, contralateral left ICA and bony canal (*dotted arrow*)

33.6 External Carotid Branches Arising from the Internal Carotid Artery

Branches of the *external carotid artery* (ECA) can rarely arise from the ICA. Although any branch could conceivably arise from the ICA, these rare variants more typically involve the *ascending pharyngeal artery*, *occipital artery*, *superior thyroidal artery*, or the *superficial temporal artery*. Also, some branches (particularly the ascending pharyngeal) can arise directly from the cervical carotid bifurcation. Knowledge of these variants, as well as of potential ECA-ICA collateral networks, is of particular import in the planning of endovascular embolization procedures (Figs. 33.26, 33.27, and 33.28).

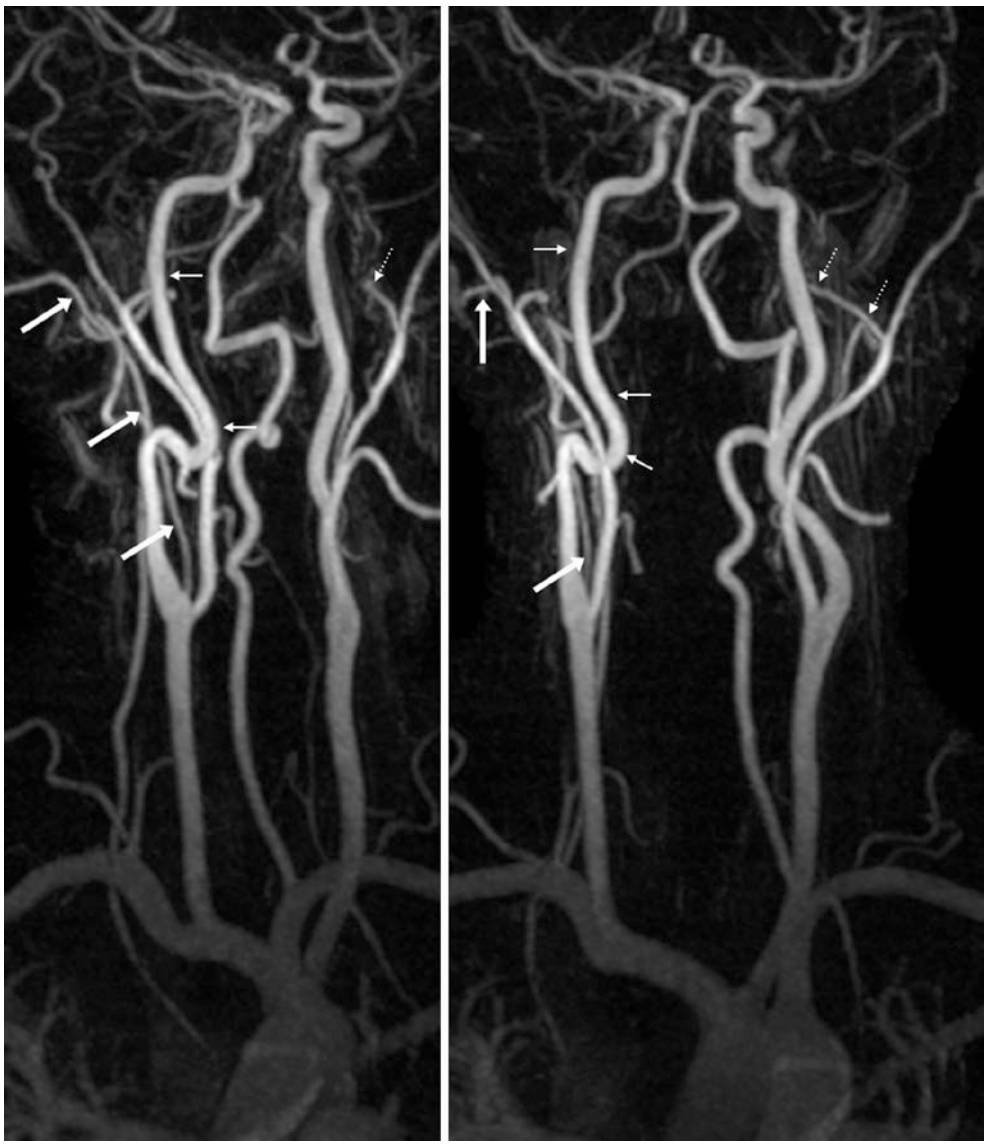

Fig. 33.26 53-year-old who underwent a contrast-enhanced MRA with RAO (*left*) and slightly LAO (*right*) views, which demonstrate that the right occipital artery (*large arrows*) arises from the right ICA (*thin arrows*), immediately distal to the carotid bifurcation. The left occipital artery (*dotted arrows*) arises as expected from the left external carotid artery (ECA)

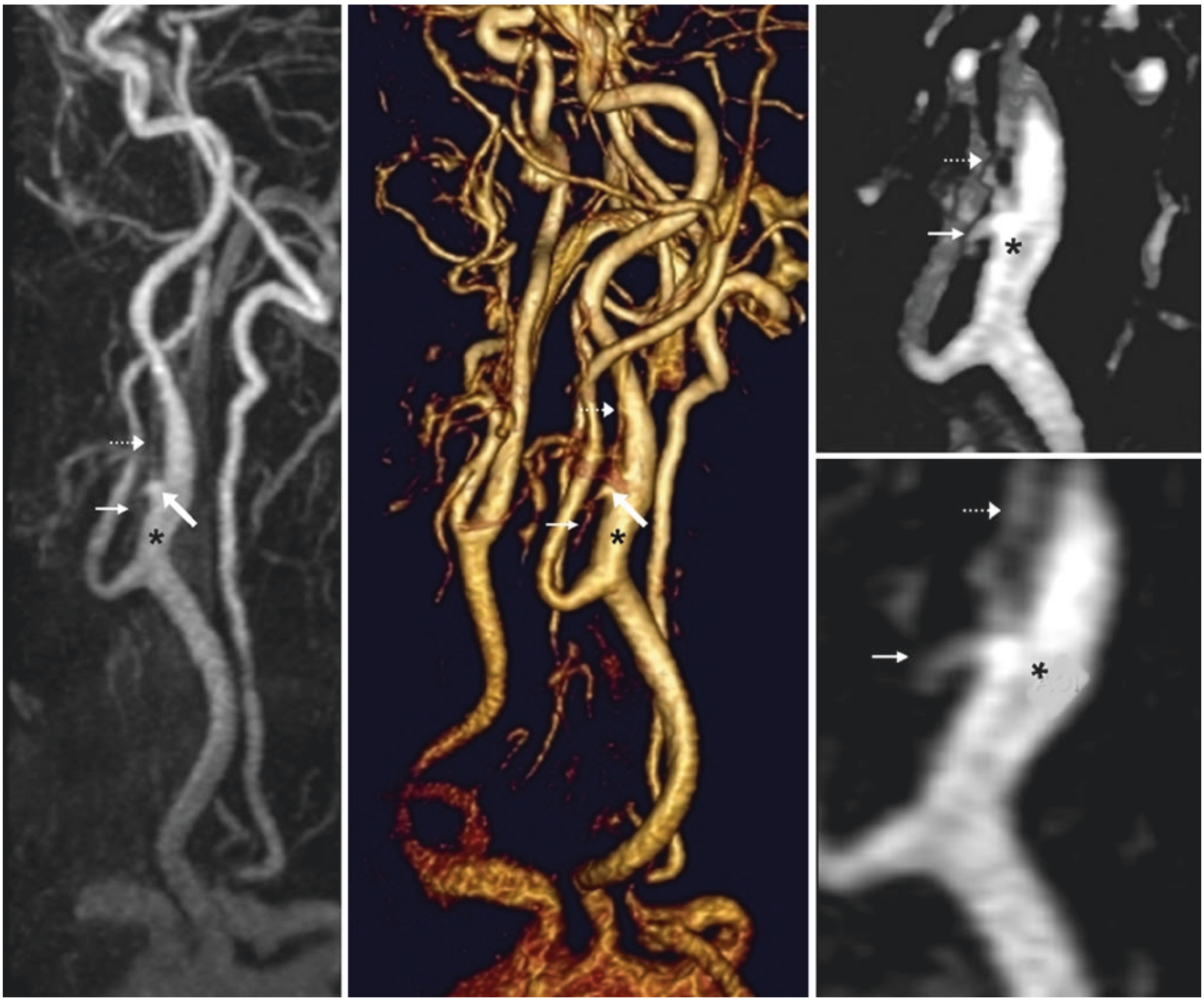

Fig. 33.27 In a 56-year-old, contrast-enhanced MRA (lateral MIP) (*left*), and 3D VR LAO (*middle*), lateral 3-mm MPR (*right, top*) and magnified lateral, 1-mm MPR (*right, bottom*) views depict a common trunk (*large arrows*) of the ascending pharyngeal artery (*dotted arrows*) and superior thyroidal artery (*thin arrows*), which arise from the proximal left ICA (*asterisk*)

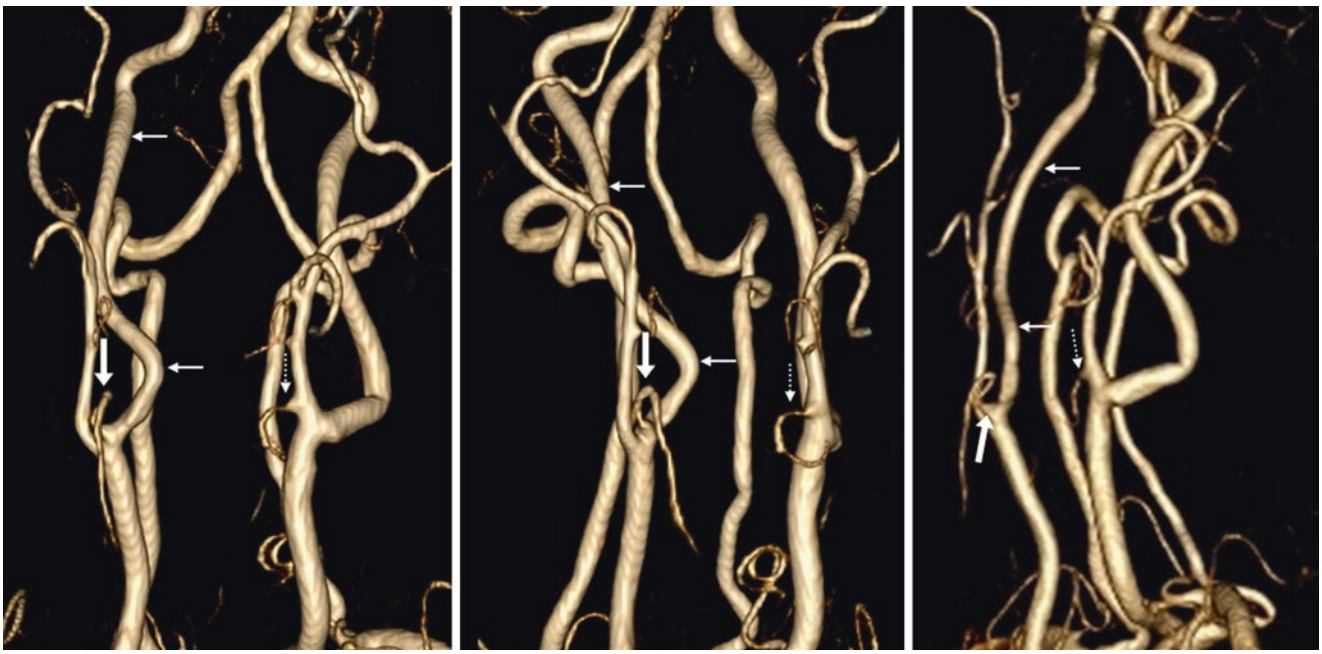

Fig. 33.28 In a 95-year-old, contrast-enhanced MRA and 3D VR AP (*left*), RAO (*middle*), and LAO MIP (*right*) views show that the right superior thyroidal artery (*large arrows*) arises from the proximal right ICA (*thin arrows*). As a comparison, note the normal origin of the left superior thyroidal artery (*dotted arrows*) from the left ECA

Suggested Reading

Afifi AK, Godersky JC, Menezes A, Smoker WR, Bell WE, Jacoby CG. Cerebral hemiatrophy, hypoplasia of internal carotid artery, and intracranial aneurysm. A rare association occurring in an infant. Arch Neurol. 1987;44:232–5.

Aggarwal NR, Krishnamoorthy T, Devasia B, Menon G, Chandrasekhar K. Variant origin of superior thyroid artery, occipital artery and ascending pharyngeal artery from a common trunk from the cervical segment of internal carotid artery. Surg Radiol Anat. 2006;28:650–3.

Benson MT, Hamer JD. Anomalous origin of the occipital artery from the cervical internal carotid artery. J Vasc Surg. 1988;8:6435.

Berge JK, Bergman RA. Variations in size and in symmetry of foramina of the human skull. Clin Anat. 2001;14:406–13.

Chen CJ, Wang LJ, Wong YC. Abnormal origin of the vertebral artery from the common carotid artery. AJNR Am J Neuroradiol. 1998;19:1414–6.

Goddard AJ, Annesley-Williams D, Guthrie JA, Weston M. Duplication of the vertebral artery: report of two cases and review of the literature. Neuroradiology. 2001;43:477–80.

Hong JT, Park DK, Lee MJ, Kim SW, An HS. Anatomical variations of the vertebral artery segment in the lower cervical spine: analysis by three-dimensional computed tomography angiography. Spine (Phila Pa 1976). 2008;33:2422–6.

Ionete C, Omojola MF. MR angiographic demonstration of bilateral duplication of the extracranial vertebral artery: unusual course and review of the literature. AJNR Am J Neuroradiol. 2006;27:304–6.

Jinkins JR. Atlas of neuroradiologic embryology, anatomy, and variants. Philadelphia: Lippincott Williams & Wilkins; 2000.

Katsanos AH, Kosmidou M, Kyritsis AP, Giannopoulos S. Is vertebral artery hypoplasia a predisposing factor for posterior circulation cerebral ischemic events? A comprehensive review. Eur Neurol. 2013;70:78–83.

Lasjaunias P, Braun JP, Hasso AN, Moret J, Manelfe C. True and false fenestration of the vertebral artery. J Neuroradiol. 1980;7:157–66.

Papon X, Pasco A, Fournier HD, Mercier P, Cronier P, Pillet J. Anastomosis between the internal carotid and vertebral artery in the neck. Surg Radiol Anat. 1995;17:335–7.

Park JH, Kim JM, Roh JK. Hypoplastic vertebral artery: frequency and associations with ischaemic stroke territory. J Neurol Neurosurg Psychiatry. 2007;78:954–8.

Quint DJ, Boulos RS, Spera TD. Congenital absence of the cervical and petrous internal carotid artery with intercavernous anastomosis. AJNR Am J Neuroradiol. 1989;10:435–42.

Seeger JF. Normal variations of the skull and its contents. In: Zimmerman RA, editor. Neuroimaging: clinical and physical principles. New York: Springer; 1999. p. 415–53.

Songur A, Gonul Y, Ozen OA, Kucuker H, Uzun I, Bas O, Toktas M. Variations in the intracranial vertebrobasilar system. Surg Radiol Anat. 2008;30:257–64.

Taşar M, Yetişer S, Taşar A, Uğurel S, Gönül E, Sağlam M. Congenital absence or hypoplasia of the carotid artery: radioclinical issues. Am J Otolaryngol. 2004;25:339–49.

Teal JS, Rumbaugh CL, Segall HD, Bergeron RT. Anomalous branches of the internal carotid artery. Radiology. 1973;106:567–73.

Tokuda K, Sugimoto S, Abe S, Takei H, Miyaskara K, Abe H, Tsuru M. Angiographic analysis of anomalous vertebral arteries. Neuroradiology. 1981;22:47.

Zümre O, Salbacak A, Ciçekcibaşi AE, Tuncer I, Seker M. Investigation of the bifurcation level of the common carotid artery and variations of the branches of the external carotid artery in human fetuses. Ann Anat. 2005;187:361–9.

Tortuous Cervical and Intracranial Arteries and Basilar-Carotid Dolichoectasia

34

Tortuosity most often occurs in the elderly or in the setting of *atherosclerosis*, but it also occurs in the uncommon patient with a *collagen vascular disorder*. The vertebral arteries can be tortuous at their origins or throughout the remainder of their course in the cervical and intracranial portions, and they can be particularly troublesome for interpretation or procedures in several scenarios.

First, attempting catheterization of *tortuous vertebral origins* for angiography can be extremely difficult and can lead to serious complications if extreme care is not exercised or if the angiographer is unaware of the vessel's course at the outset; one should always obtain images or angiographic runs of the vertebral arteries' origins prior to catheterization.

Second, tortuous vertebral artery origins can simulate *stenosis* on noninvasive imaging, whether MRA (due to artifacts such as in-plane saturation effects) or CTA (due to artifact and streaking from nearby bones). For example, routine T1WI and T2WI MRI sequences may be misleading, as small or hypoplastic vessels (with slow flow) or very tortuous vessels (causing in-plane saturation of spins) may lead to a misdiagnosis of occlusion or partial thrombosis.

Third, tortuosity in the cervical segments of the vertebral arteries may make it difficult to evaluate for a *dissection* on CTA or MRA, at times even having a "corkscrew" appearance on contrast-enhanced MRA similar to that seen in subclavian stenosis with retrograde vertebral arterial flow; 2D time-of-flight MRA with saturation bands above the cervical region can exclude the presence of downwards, retrograde flow.

Finally, the presence of tortuous vertebral arteries intracranially can lead one to question "*vascular contact*" against various structures such as the brainstem or cranial nerves if only axial images are obtained; the vast majority having this appearance intracranially are asymptomatic and of doubtful significance unless there is mass effect on the brainstem or if there is vascular enlargement indicative of an aneurysm.

The term "*dolichoectasia*" refers to a distended, elongated, and typically tortuous appearance of the vertebrobasilar arterial system greater than 4.5 mm in caliber. These are most commonly asymptomatic and are not uncommon on head CT scans from the emergency room as an unrelated finding in the elderly, akin to the concept of cerebral "age-related volume loss." A very small minority of these patients, however, may suffer symptoms related to progressive fusiform enlargement, as the pathogenesis of dolichoectasia can be related to systemic arterial hypertension and/or atherosclerosis with thinning of the internal elastic lamina. This fusiform enlargement can become *aneurysmal* and produce emboli, or (in the worst case scenario) basilar thrombosis. Because of mass effect, the symptoms may involve cranial neuropathies; rarely, a syndrome of thrombosis may occur with subsequent showering of emboli to the brainstem and posterior fossa that is difficult to treat and generally has a poor outcome. Recent studies suggest that these patients are at a higher risk for stroke and poor outcomes when observed 5–10 years after the initial CT or MRI [1–9].

In this author's opinion, dolichoectasia occurs along a spectrum and must be interpreted in a "gestalt" fashion: The vessel's appearance, including its size relative to the internal carotid arteries (ICAs), contour, and the presence of calcium or clot must be taken into consideration along with the patient's age. Irregular vessels with noncalcified plaque or thrombus are more likely to be symptomatic and unstable. The problem arises when dilated, tortuous vessels are visualized on axial images on a noncontrast head CT or MRI without a corresponding vascular study; the enlarged, tortuous arteries can appear to be an aneurysm or mass because of volume averaging in the axial plane. They may even mildly indent the brainstem, which is exceedingly likely to be asymptomatic. CTA or MRA can clarify questionable cases, and clinical correlation is often necessary.

Tortuosity and "kinking" of the upper cervical and intracranial internal carotid artery (ICA) is present in about 3–7 % of the population, and appears to be more common in the elderly, particularly those with atherosclerotic disease,

A.M. McKinney, *Atlas of Normal Imaging Variations of the Brain, Skull, and Craniocervical Vasculature*,
DOI 10.1007/978-3-319-39790-0_34

collagen vascular disease, or (less likely) polycystic kidney disease [10–16]. It is not rare to note this finding in middle-aged patients without atherosclerotic calcifications or a significant stenosis, however. Similarly, such tortuosity can lead to the presence of a *retropharyngeal ICA*, which can be problematic when a pharyngeal or nasopharyngeal mucosal lesion or abscess is present [16–22]. The presence of such tortuosity can occasionally cause difficulty in interpretation in various scenarios; for example, it may simulate a pseudoaneurysm after trauma, or it may cause stenosis measurements to be miscalculated. Tortuosity can also cause difficulty in catheterization. Notably, dolichoectasia of the ICAs can also occur, with an appearance similar appearance to that of the vertebrobasilar system, although it is perhaps less common. A tortuous appearance of the ICA at the skullbase can occur with an *aberrant internal carotid artery* [28, 29].

Therefore, mildly tortuous vertebral-basilar arteries or ICAs are most commonly asymptomatic and can be considered "don't touch" lesions. The exceptions are when they are symptomatic or problematic in only three scenarios: (1) Where severe dolichoectasia (stretching, dilatation, and tortuosity) occurs that may result in the uncommon severely enlarged, dissecting, fusiform aneurysm; (2) When the tortuous vertebrobasilar vasculature (or its branches) compresses a cranial nerve (such as VII)—a controversial but well-described phenomenon; (3) When an adjacent mass or abscess is present that needs to be excised (as with a retropharyngeal ICA).

CTA, MRA, and 3D T2WI can be helpful in the noninvasive workup to confirm patency of the ICAs. Notably, in large, dissecting vertebrobasilar aneurysms, CTA (with optimal timing and recirculation of contrast) may be the best modality for both initial and long-term followup, as even catheter angiography may have difficulty entirely visualizing a giant aneurysm, owing to a combination of in-flow from the opposite side and turbulence.

34.1 Tortuous Great Vessel Origins

The likelihood and degree of *tortuosity of the lower cervical and great vessel origins* increases with age. The origins of the great vessels and their cervical segments can be extremely tortuous, to the point where the aorta is also often elongated. This tortuosity most commonly occurs in elderly patients or vasculopaths with moderate or severe *atherosclerotic disease*. Its incidence is also increased in patients with *fibromuscular dysplasia* and *collagen vascular disorders*. One may occasionally note such tortuosity even in otherwise asymptomatic younger patients without a known history of collagen vascular disease or vasculopathy, although this scenario is rather uncommon (Figs. 34.1, 34.2, 34.3, 34.4, 34.5, 34.6, 34.7, and 34.8)

Although tortuous anatomy can be considered a normal variant in the absence of associated vascular disease, such variant anatomy can create significant problems when the angiographer or interventionalist attempts to catheterize or embolize through extremely tortuous vessels. The substantially increased fluoroscopy time, increased contrast dosage, and the use of multiple catheters can lead to a significantly increased procedural risk of thromboembolic infarcts or intimal injury in these patients. The subject of tortuosity and dolichoectasia of the upper cervical and intracranial arteries is discussed separately.

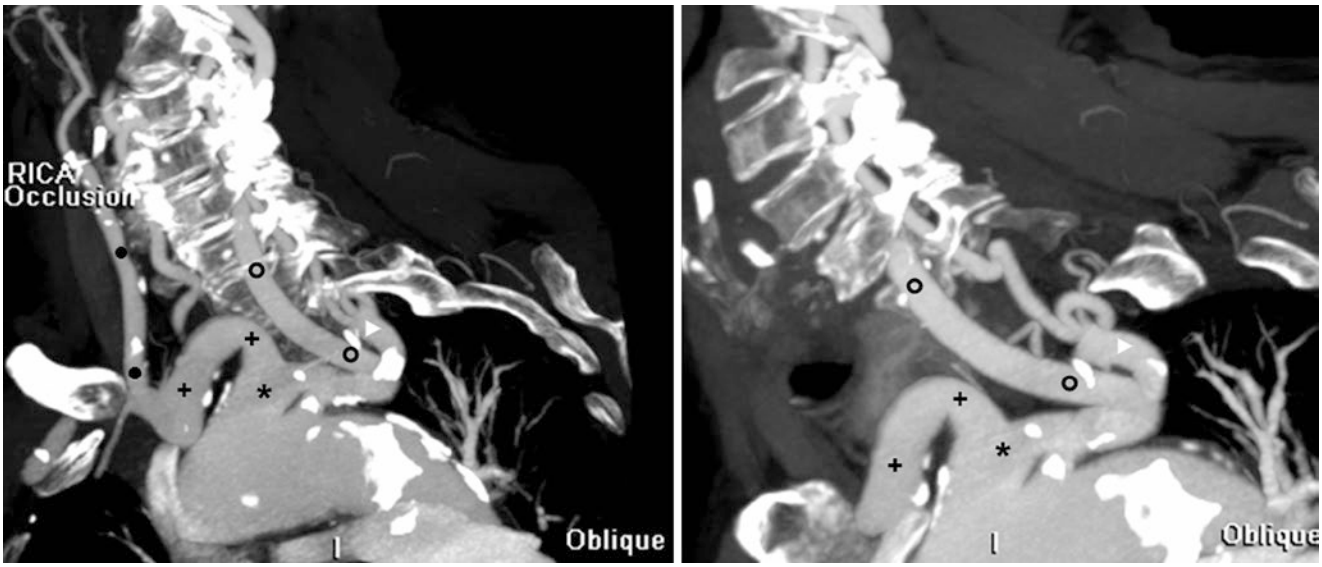

Fig. 34.1 84-year-old with extremely tortuous great vessel origins and extensive atherosclerotic calcifications on a CTA, as well as a common origin (*asterisk*) of the innominate artery (IA) (*plus sign*) and the left common carotid artery (LCCA) (*open circles*) on LAO MPR 32 mm-thick (*left*) and 16 mm-thick (*right*) views. Additionally, the right internal carotid artery (ICA) is occluded (*left*), while the right common carotid artery (RCCA) (*black circles*) is patent but has diffuse calcified plaque

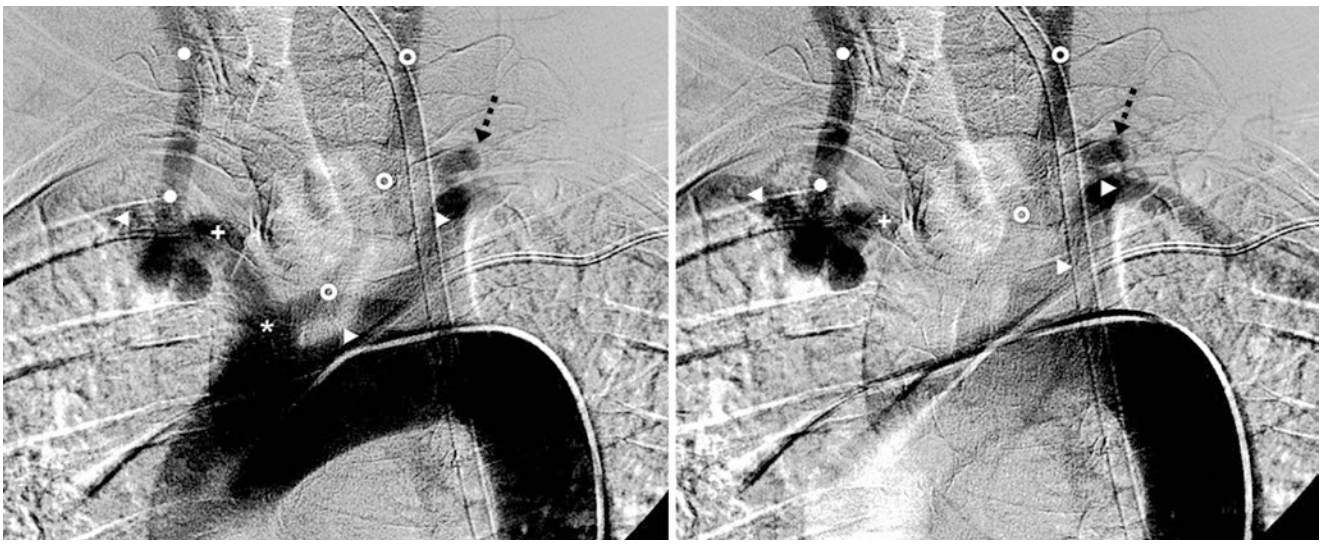

Fig. 34.2 76-year-old with an "elongated" aorta and mild to moderately tortuous great vessel origins on DSA LAO views in early (*left*) and late (*right*) arterial phases. A common origin (*asterisk*) of the IA and LCCA is present. Note tortuosity of the right subclavian artery (RSCA) (*left-facing arrowheads*), left subclavian artery (LSCA) (*right-facing arrowheads*), and RCCA origins, and also of the left vertebral artery (LVA) origin (*dotted arrows*)

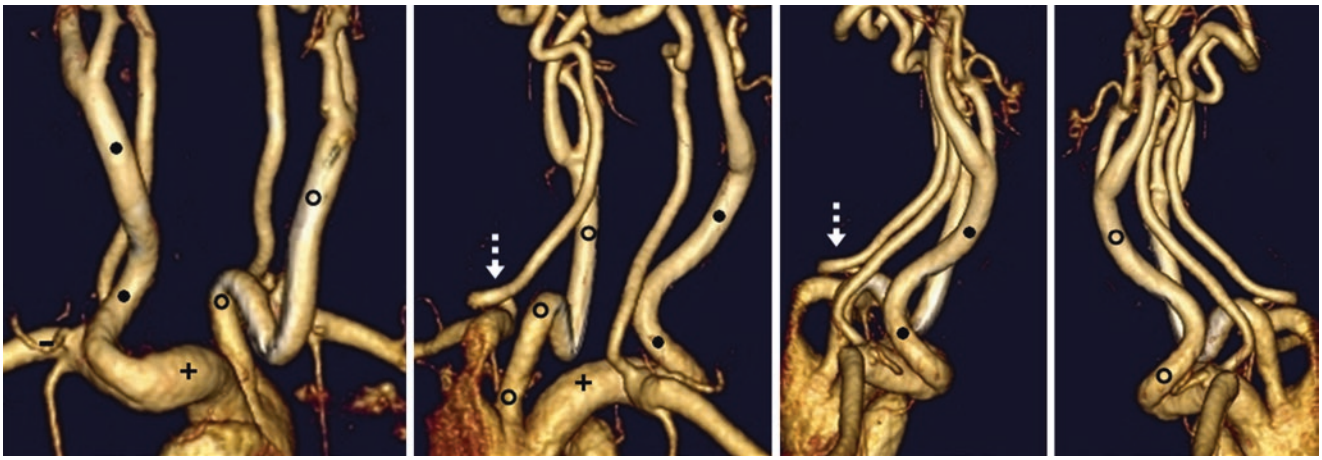

Fig. 34.3 81-year-old with a lower carotid bruit auscultated to the right of midline just above the sternum. On contrast-enhanced MRA, there was tortuosity of the origins of both the RCCA (*black circles*) and LCCA (*open circles*) on AP (*left*), PA (*left middle*), right lateral (*right middle*), and left lateral (*right*) views. Note tortuosity of the IA and RSCA origins, as well as of the LVA origin (*dotted arrows*) and the IA (*plus signs*)

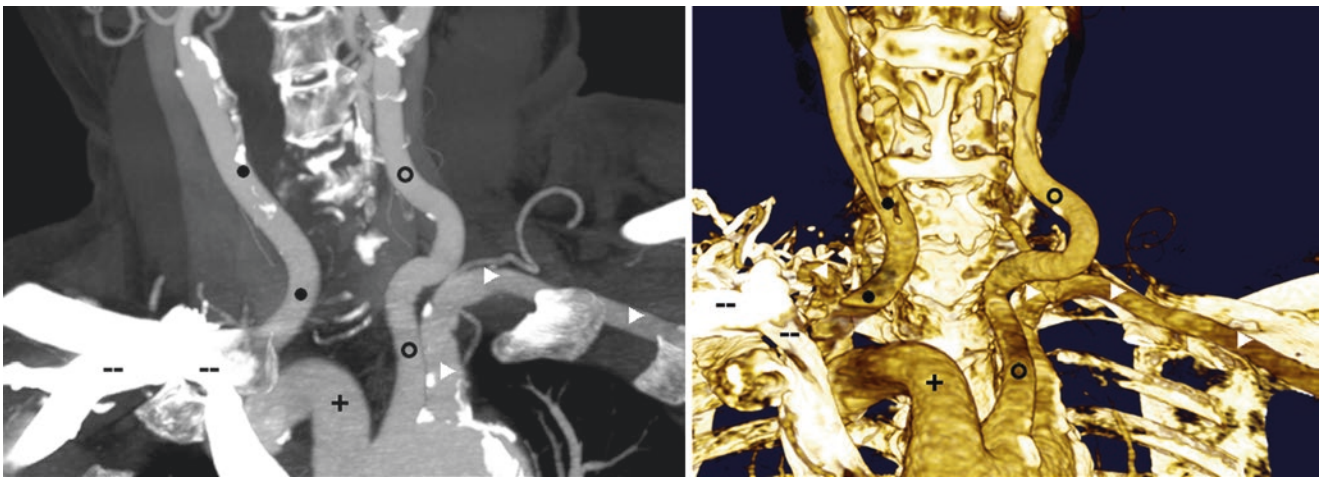

Fig. 34.4 86-year-old with atherosclerotic calcifications of the great vessels' origins on CTA, with a tortuous IA (*plus signs*), as well as RCCA (*black circles*) and LCCA (*open circles*) origins, on a 34 mm-thick MPR coronal-LAO view (*left*), and on a 3D VR AP view (*right*). Extremely hyperdense contrast within the right subclavian vein (*double dashes*) obscures the RSCA. Also note atherosclerosis, but no tortuosity, of the LSCA (*right-facing arrowheads*)

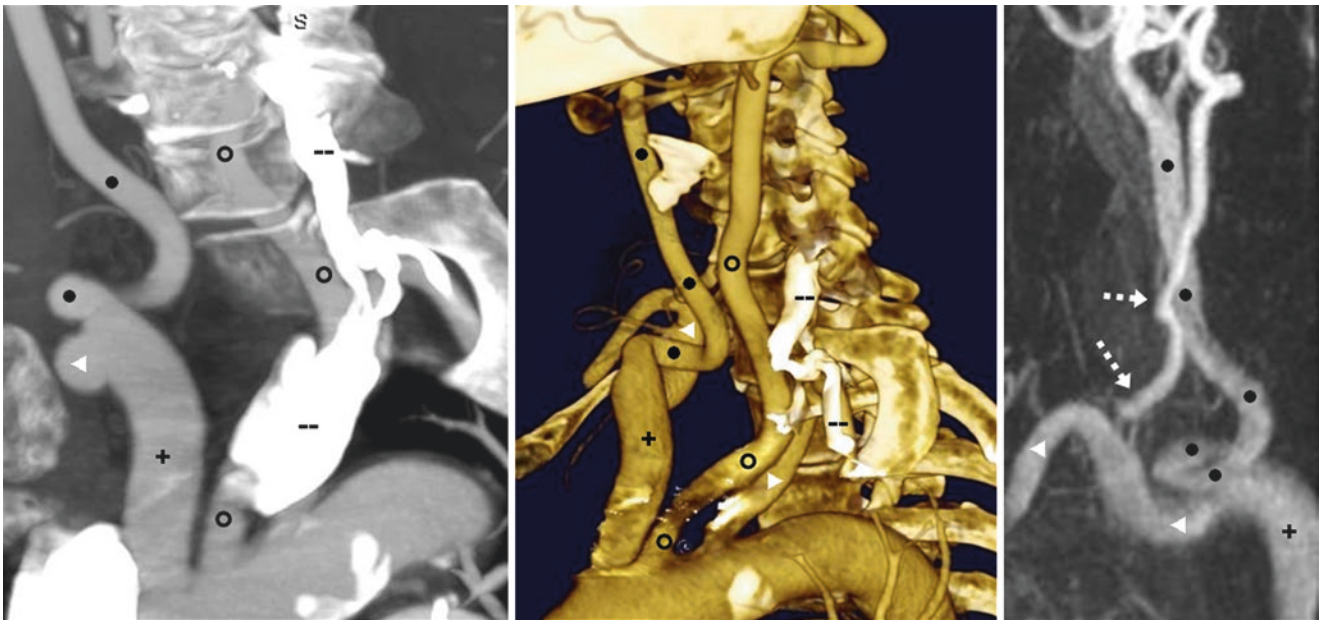

Fig. 34.5 In a 78-year-old, a CTA depicts an elongated aorta (from atherosclerosis), and tortuosity of the IA (*plus signs*), RCCA (*black circles*), and RSCA (*left-facing arrowheads*), as shown on 28 mm-thick MPR (*left*) and 3D VR LAO (*middle*) views, as well as a contrast-enhanced MRA of the right side (*right*). The right vertebral artery (RVA) (*dotted arrows*) is mildly tortuous as well. Note hyperdense internal jugular contrast (*double dashes*) that obscures the LSCA (*right-facing arrowheads*)

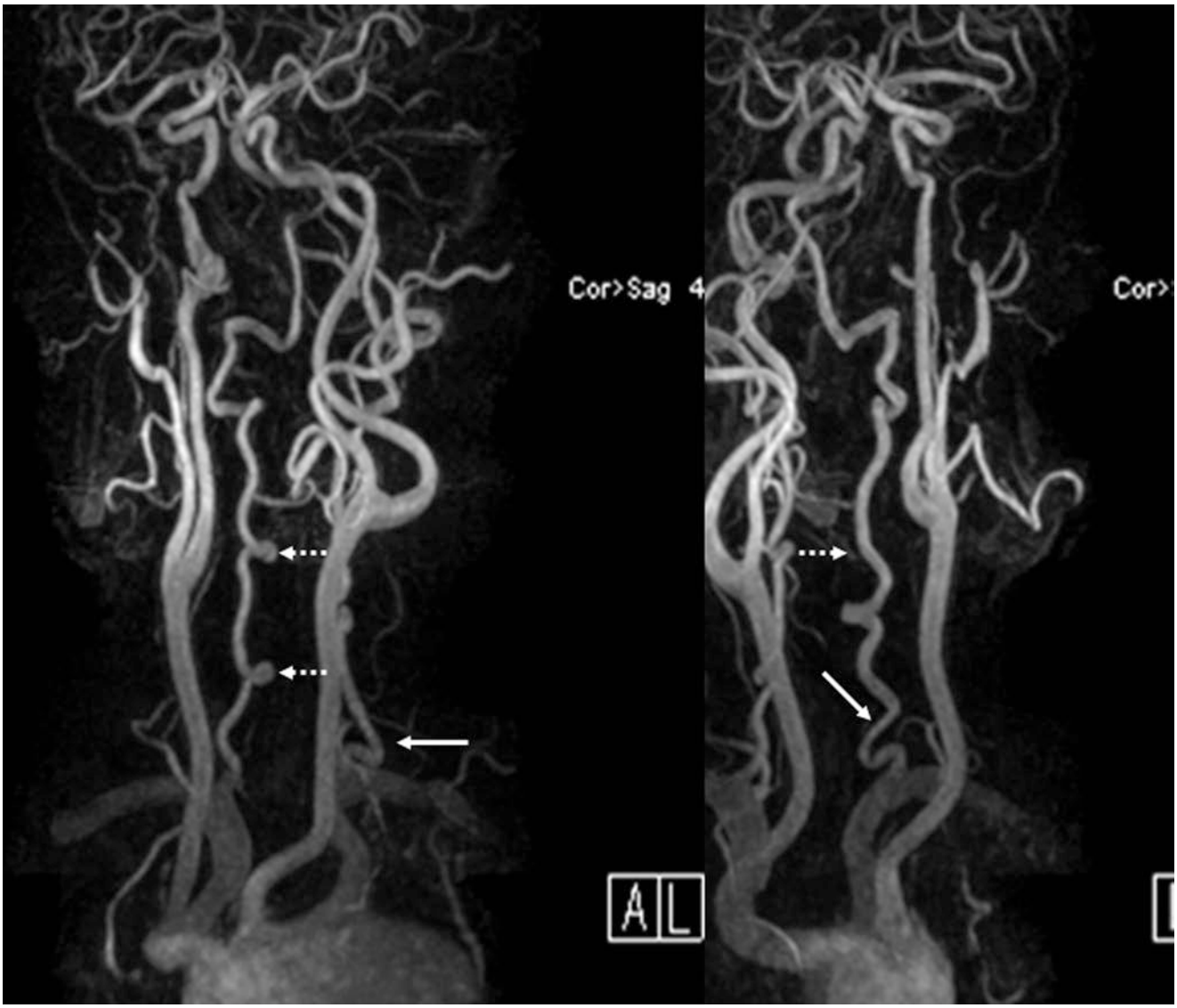

Fig. 34.6 67-year-old with a tortuous left VA origin (*solid arrows*); the VA's courses in the mid-cervical region are also tortuous bilaterally (*dotted arrows*), on bilateral oblique views from a contrast-enhanced MRA. In some patients, such tortuosity (as well as other artifacts) may obscure the VA origins

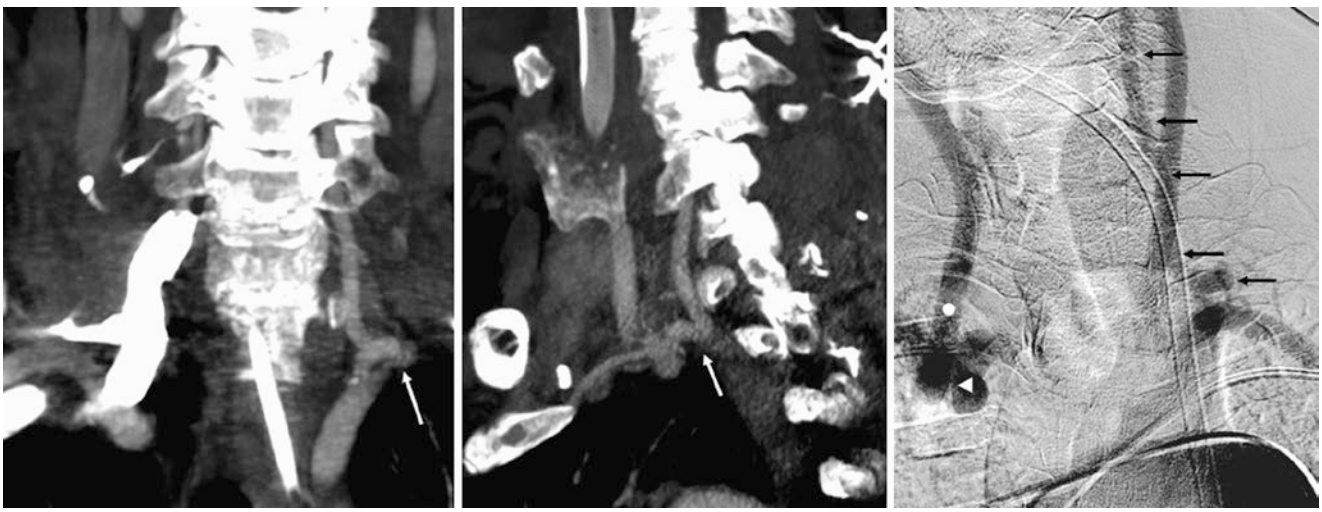

Fig. 34.7 In a 76-year-old, CTA coronal (*left*) and sagittal (*middle*) 10 mm-thick MPRs and a DSA AP view (*right)* show a tortuous LVA (*arrows*), which was hard to catheterize. The right CCA (*white circle*) and RSCA origins (*left-facing arrowheads*) were tortuous, and the aorta was elongated

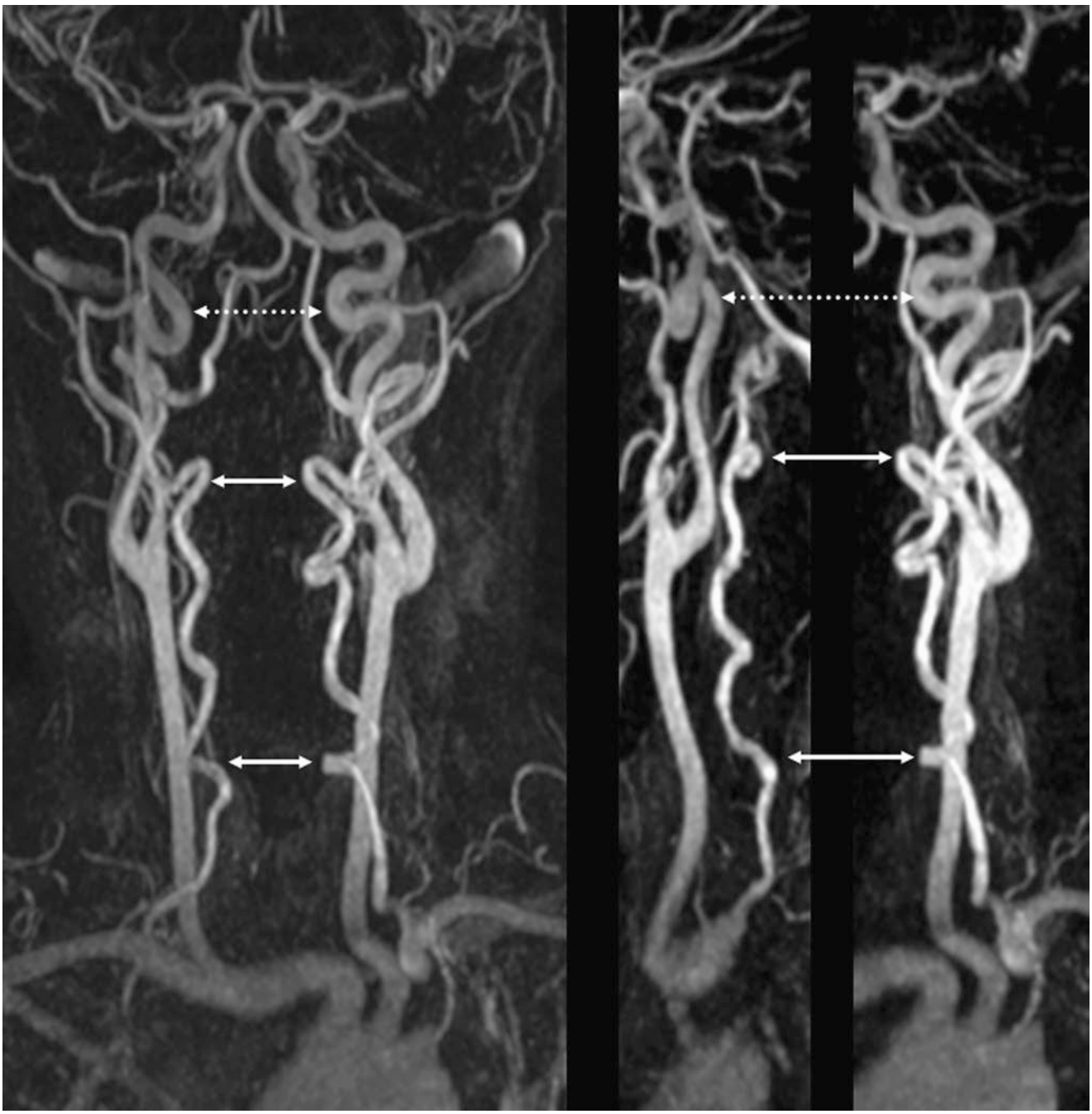

Fig. 34.8 47-year-old with tortuous mid and upper cervical VAs (*arrows*); the tortuosity is only mild at the origins, on AP (*left*), right lateral (*middle*), and left lateral (*right*) views. The upper cervical ICAs are also quite tortuous (*dotted arrows*)

34.2 Vertebral-Basilar Dolichoectasia, Tortuosity, and Carotid Ectasia

Basilar or *vertebrobasilar arterial* (VBA) *dolichoectasia* refers to an elongated and distended artery. The vertebral arteries (VAs) can be tortuous throughout the neck, but by itself, this phenomenon is incidental, unless it occurs bilaterally in the setting of *fibromuscular dysplasia*, when there is an increased risk of dissection and pseudoaneurysm. Typically, the distention is 4.5 mm or greater in size, as 4 mm is the upper limit of normal basilar artery diameter. Although traditional literature suggested that a certain amount of dilatation of the VBA system is normal, more recent evidence suggests that the presence of VBA ectasia or an increased diameter of the basilar artery is associated with vascular events, lacunar infarcts, thrombosis, cerebral microbleeds, and even coronary artery disease; cranial neuropathies can also occur [1–9]. The findings likely relate to an underlying arteriopathy with thinning or "wearing away" of the intima, with or without intraplaque hemorrhage (particularly in the setting of severe atherosclerosis), which can relate to underlying atherosclerotic disease, collagen vascular disease, or other causes of intimal injury. For some reason, it is not uncommon for an ectatic basilar artery to lack calcification relative to the degree of atherosclerotic calcification affecting the internal carotid arteries (ICAs) in the same patient. Overall, atheromatous changes are thought to augment the possibility of thromboembolic infarcts, intraplaque hemorrhage, basilar thrombosis, or spontaneous VBA dissection [1–9].

Thus, while there is no strong evidence as to what is considered "normal" ectasia for aging, the 4.5-mm threshold is most commonly used. Certainly, diameters larger than that are concerning, particularly if enlarging serially over time, as these have been associated with the development of aneurysmal hemorrhage, dissection, and morbidity. In particular, a diameter greater than 8 mm for such "nonsaccular" basilar *fusiform aneurysms* has been associated with poor outcome, owing to a propensity for aneurysmal enlargement [9, 23, 24]. Though catheter angiography is the gold standard, very large or "*giant*" *nonsaccular VBA aneurysms* (>2.5 cm) may actually be better visualized on CTA because of the multipass phenomenon through the vasculature; catheter DSA demonstrates structures on the first arterial pass only, and it may be difficult to deploy a sufficiently large contrast bolus from the catheter.

Also, *neurovascular contact* by the vertebral or basilar arteries on the brainstem at any point—even causing compression to a degree—can be normal and asymptomatic, but any symptoms related to cranial nerves, particularly hemifacial spasm, should be correlated with the imaging findings and side. Limited evidence has not yet confirmed a definite association between compression of cranial nerve X (vagus) near its *root entry/exit zone* (REZ) of the brainstem and hypertension ("neurovascular hypertension"), although the association is still being investigated [25–27].

Finally, *internal carotid artery* (ICA) *ectasia* is less common than VBA ectasia. It can occur with or without basilar ectasia and is most commonly associated with severe atherosclerosis; calcified plaque is usually evident. Thus, it is important to remember that severe atherosclerotic disease of the ICA most commonly presents as stenosis, but it also can become ectatic and even aneurysmal at the other end of the spectrum. Less commonly, ICA ectasia is related to other disorders that can affect the intima, including collagen vascular disease, fibromuscular dysplasia, or homocystinuria.

Figures 34.9, 34.10, 34.11, 34.12, 34.13, 34.14, 34.15, 34.16, 34.17, 34.18, 34.19, and 34.20 aim to demonstrate a spectrum ranging from tortuosity without ectasia in asymptomatic patients, to both tortuosity and dolichoectasia, to fusiform aneurysmal enlargement. Atherosclerosis is present in the more severe examples. 3D volume-rendered (VR) CTA can demonstrate these well, but noncontrast MRA may be compromised by turbulence from the tortuosity.

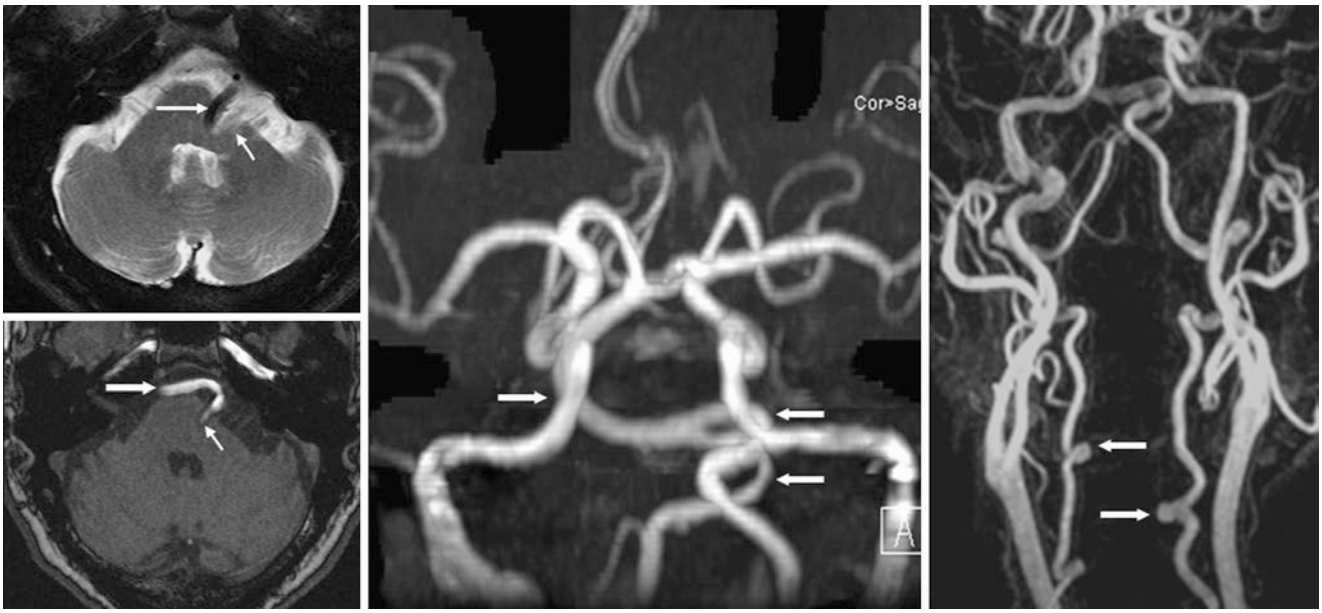

Fig. 34.9 64-year-old with moderate tortuosity and mild ectasia of the vertebrobasilar artery (VBA) (*arrows*), with brainstem indentation on T2WI (*top left*), axial 3DTOF MRA (*bottom left*), and MIP AP (*middle*) images. The cervical VAs were tortuous on a contrast-enhanced MRA AP view (*right*). The VBA compresses the root entry/exit zone (REZ) of the left pontomedullary junction (*thin arrows*)

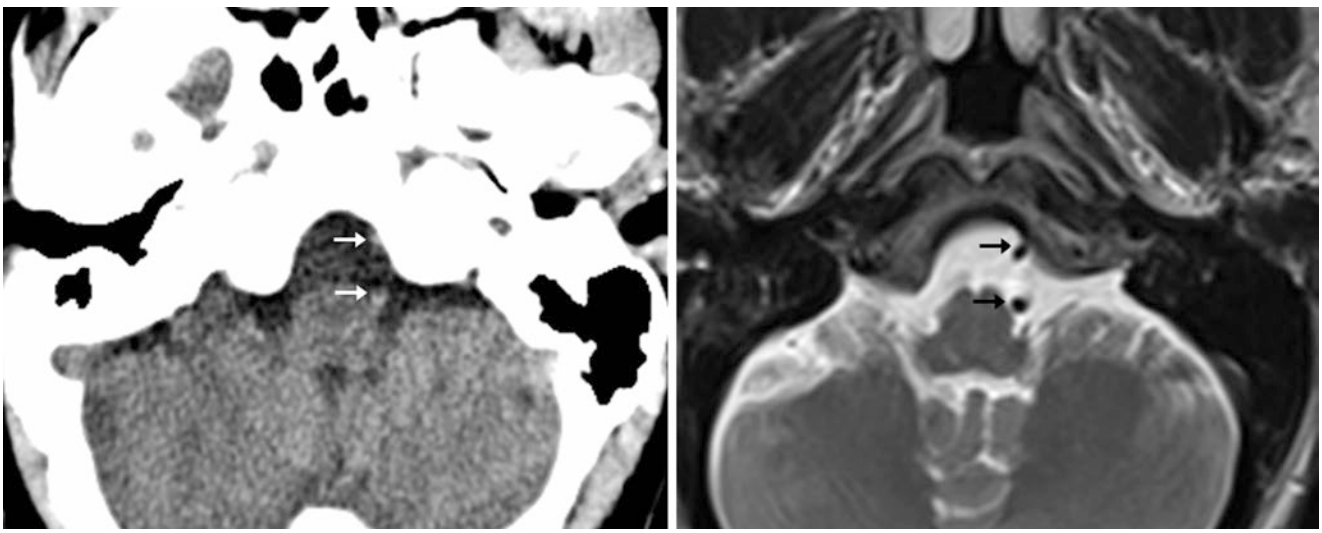

Fig. 34.10 55-year-old with axial nonenhanced CT (*left*) and T2WI MRI (*right*). Both VAs appear on the same side (*arrows*), indicating at least moderate tortuosity, without frank ectasia. This case is an example of how the arteries can be quite tortuous without dilatation. The patient had no associated symptoms

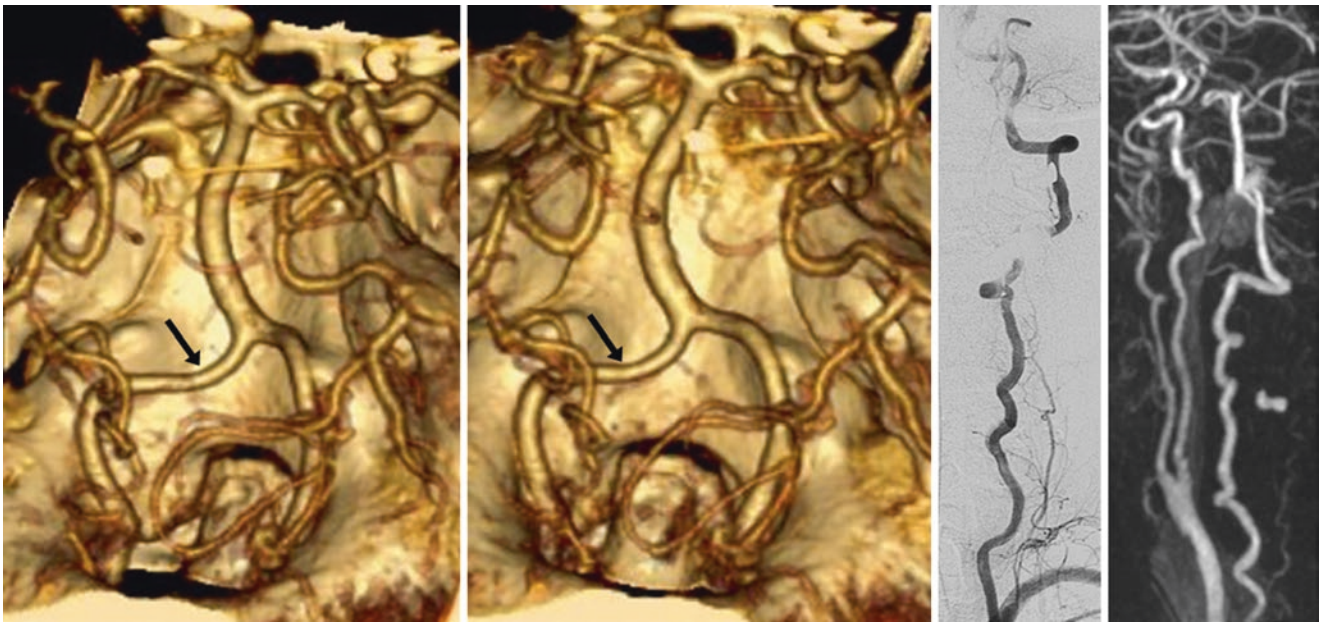

Fig. 34.11 67-year-old having a moderately tortuous left VA intracranially (*arrows*) on CTA 3D VR PA views (*left* and *left middle*), as well as tortuous cervical VAs on catheter DSA AP view (*right middle*) and on a cervical contrast-enhanced MRA lateral view (*far right*). Despite the diffuse degree of tortuosity, there is very little ectasia

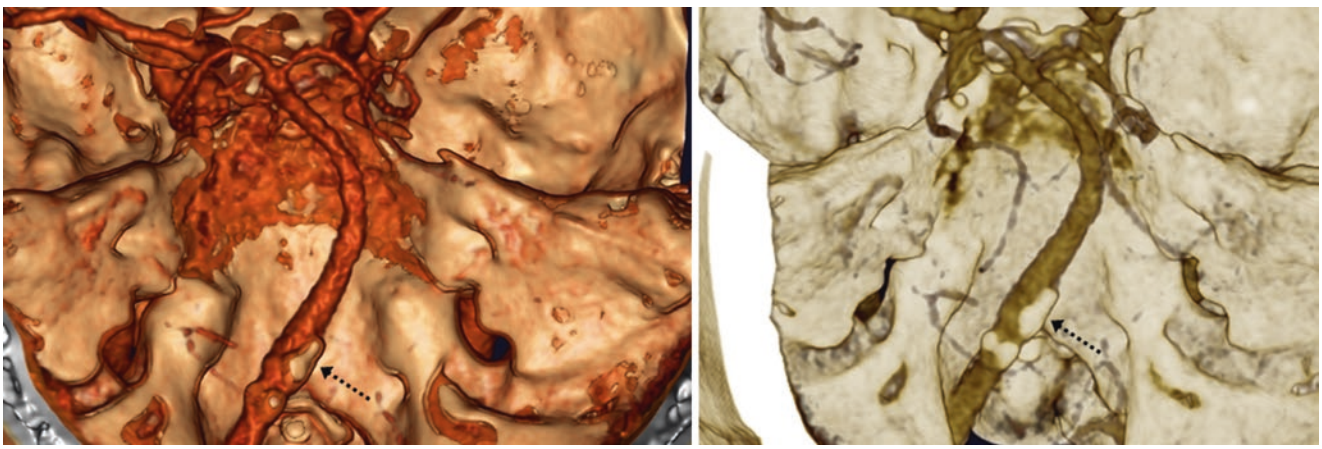

Fig. 34.12 43-year-old diabetic patient with mild-moderate basilar dolichoectasia and calcified plaques (*dotted arrows*) on a CTA with 3D VR reformats (both PA views). The calcified plaques are from atherosclerosis, suggesting the cause of the dolichoectasia. Note that the degree of tortuosity is less than the degree of ectasia (5 mm diameter)

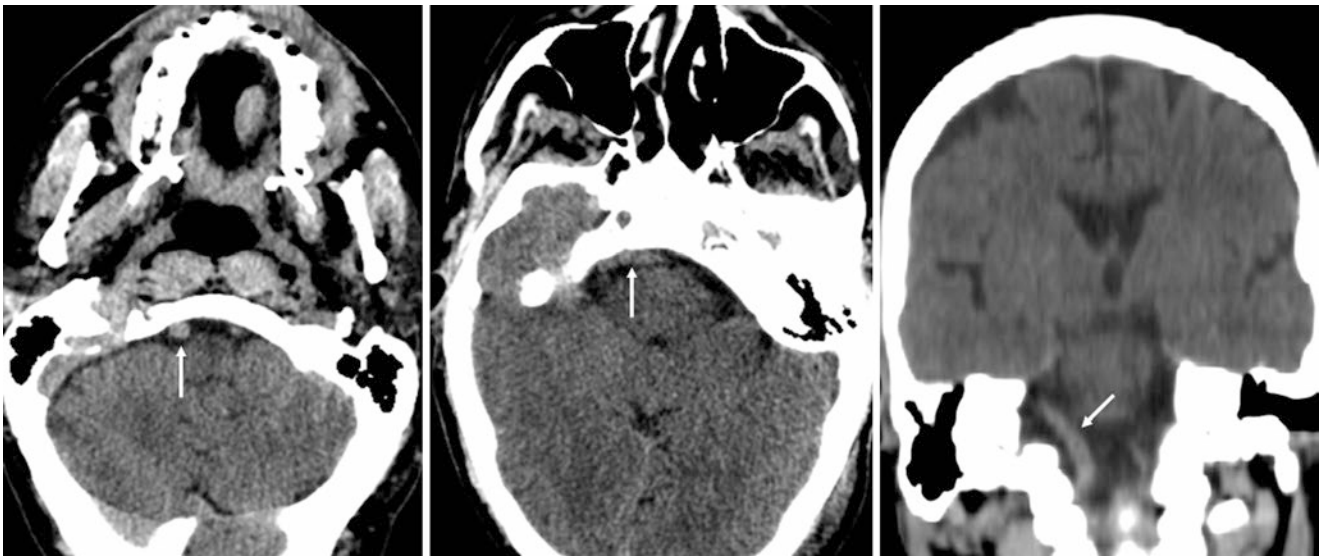

Fig. 34.13 46-year-old with a moderately to severely tortuous, elongated, and mildly ectatic dominant right VA (*arrows*) on nonenhanced CT axial images (*left* and *middle)* and a reconstructed coronal image *(right)*. Initially, the artery seemed focally aneurysmal on the axial images (*arrow*, *left*), but was later confirmed to be simply dolichoectatic on the coronal reconstructions (*right*). This patient was asymptomatic from the dolichoectasia

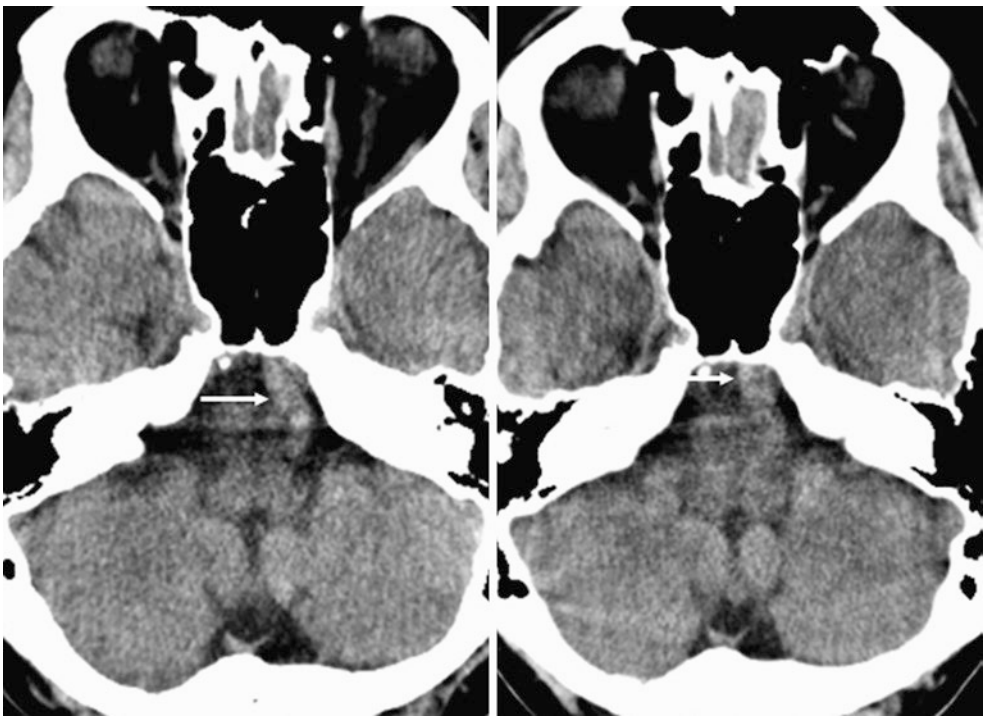

Fig. 34.14 65-year-old with axial nonenhanced CT (*left*) that demonstrates moderate basilar artery dolichoectasia (diameter 7–8 mm). One year later (*right*), this diameter was unchanged (*arrows*). The patient did not have related symptoms

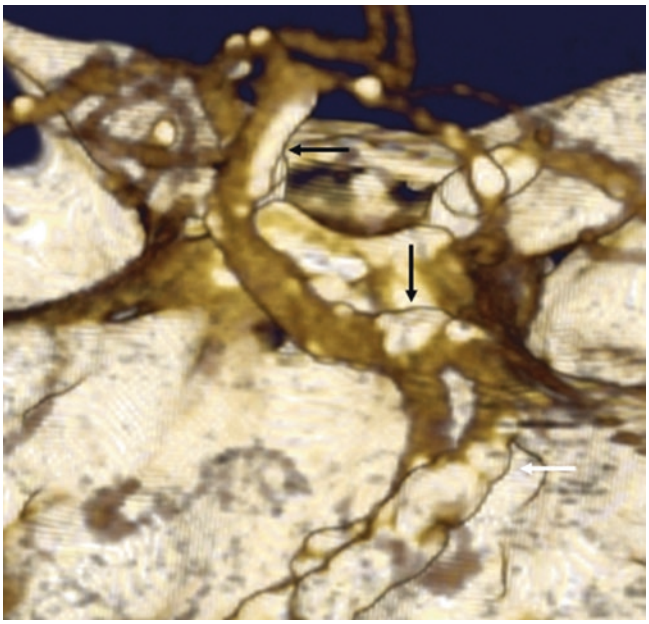

Fig. 34.15 72-year-old with a CTA PA view that depicts moderate basilar artery dolichoectasia, with diffuse atherosclerotic calcifications (*arrows*)

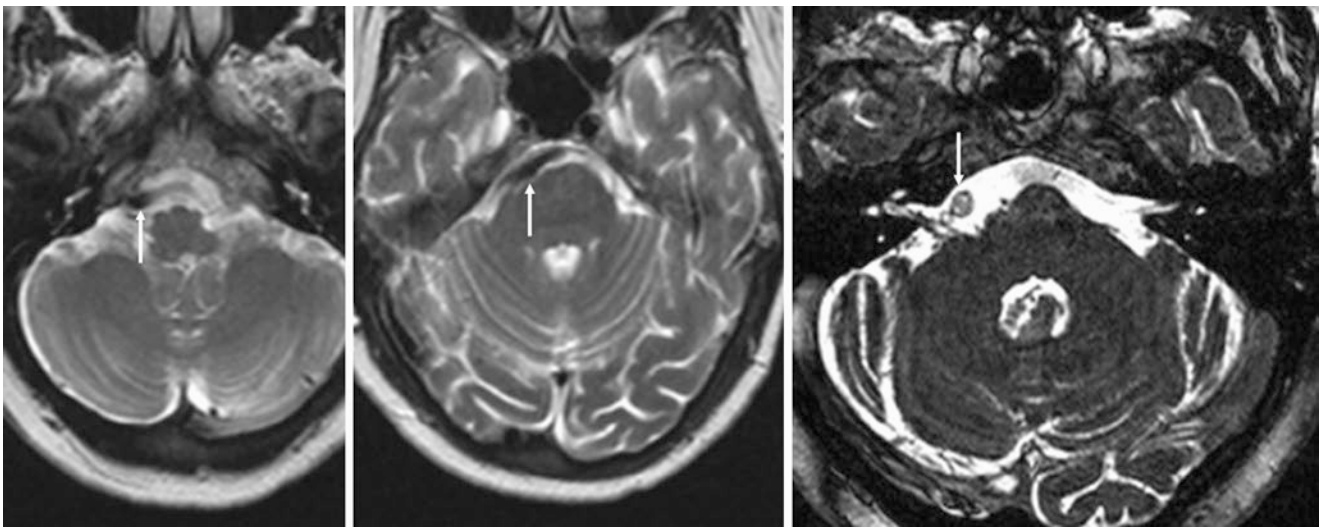

Fig. 34.16 53-year-old with severe tortuosity and mild ectasia of the basilar and right VA on T2WI MRI (*left* and *middle*), causing brainstem indentation (*arrows*). This finding was confirmed on 0.8-mm axial balanced-echo 3D T2WI (*right*), where the basilar artery (*arrow*) was shown to indent cranial nerves VII and VIII. The patient was asymptomatic

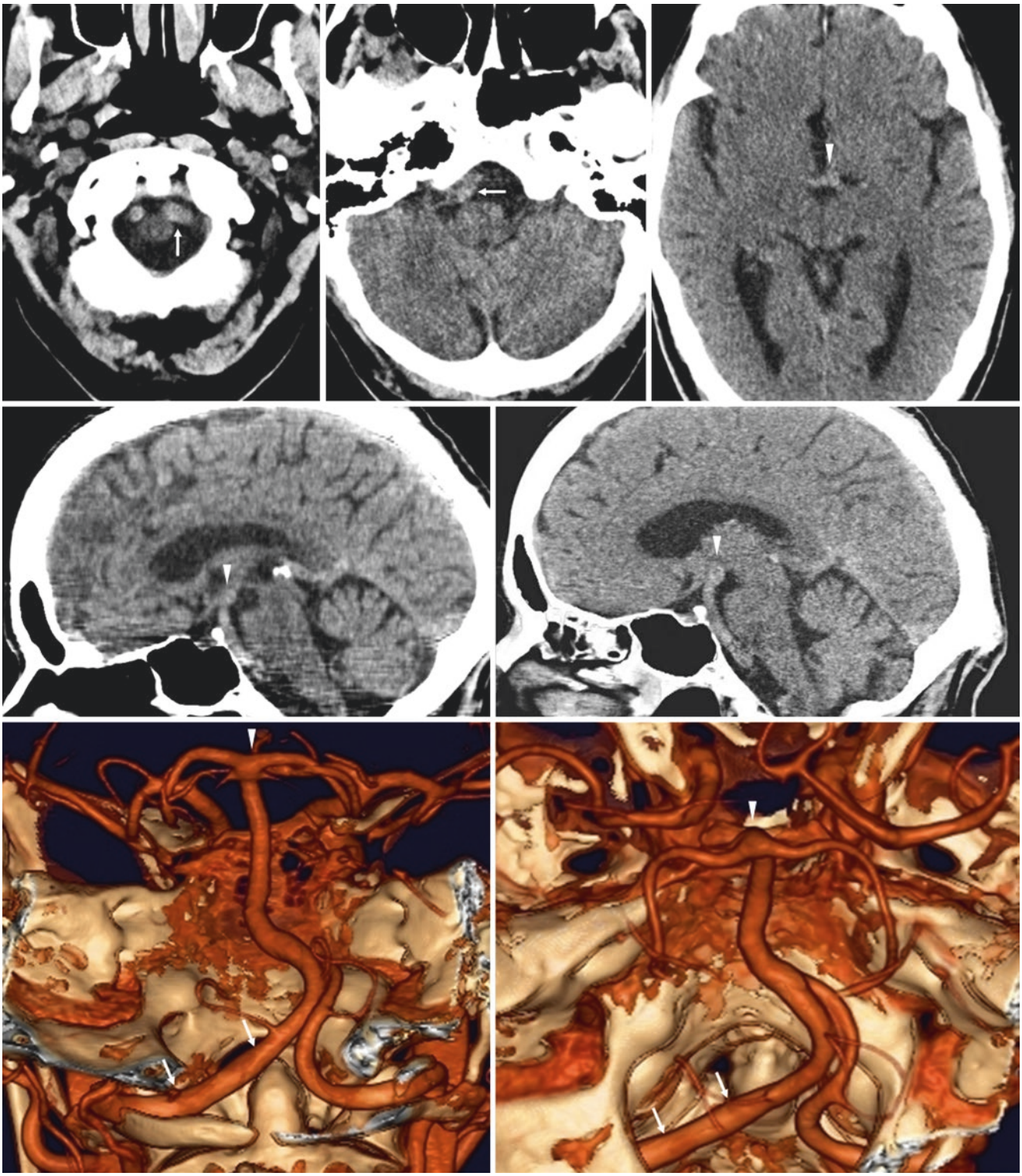

Fig. 34.17 Vertebrobasilar dolichoectasia simulating aneurysm in a 75-year-old man with severe headaches. *Top row*: On axial nonenhanced CT, there is tortuosity and elongation of the left VA (*arrows*), and the basilar tip appears prominent (*arrowhead*); thus, an aneurysm could not be excluded. *Middle row*: Sagittal 2 mm-thick (*left*) and 5 mm-thick (*right*) reconstructions depict prominence of the basilar tip (*arrowheads*) that indented the floor of the third ventricle. *Bottom row*: On CTA 3D VR with both PA (*left*) and superior (*right*) views, the basilar tip (*arrowheads*) seems prominent, likely related to curvature at the tip, and is ectatic, without a defined aneurysm. This scenario, in which volume averaging of dolichoectasia on axial nonenhanced CT simulates an aneurysm, is not uncommon. Note a lack of VBA calcification

Fig. 34.18 Carotid-basilar dolichoectasia bordering on being aneurysmal. *Top row*: In a 68-year-old, axial nonenhanced CT (*left*) and sagittal T1WI MRI (*middle*) show that the basilar artery (*arrowheads*) indents the floor of the third ventricle. On T2WI (*right*), there is also prominence of both ICA flow voids (*arrow*). *Middle row*: SWI (*left*) depicts similar findings; 3D TOF MRA posterior view (*middle*) and LPO view (*right*) show a mildly enlarged right ICA (*arrows*) from dolichoectasia. There is also poor visualization of the left MCA (*thin arrows*), due to combined turbulence and in-plane saturation effect. Similar findings are present for the right MCA (*dotted arrows*, *right*), but the right MCA borders on being aneurysmal. *Bottom row:* Source MRA images (*left*) confirm mild, fusiform dilatation of the right MCA (*dotted arrows*), perhaps being aneurysmal, while the left MCA (*thin arrows*) is poorly visualized along with mild VBA ectasia. The findings are also shown on a 3D VR MRA PA view (*middle*) and right lateral view (*right*)

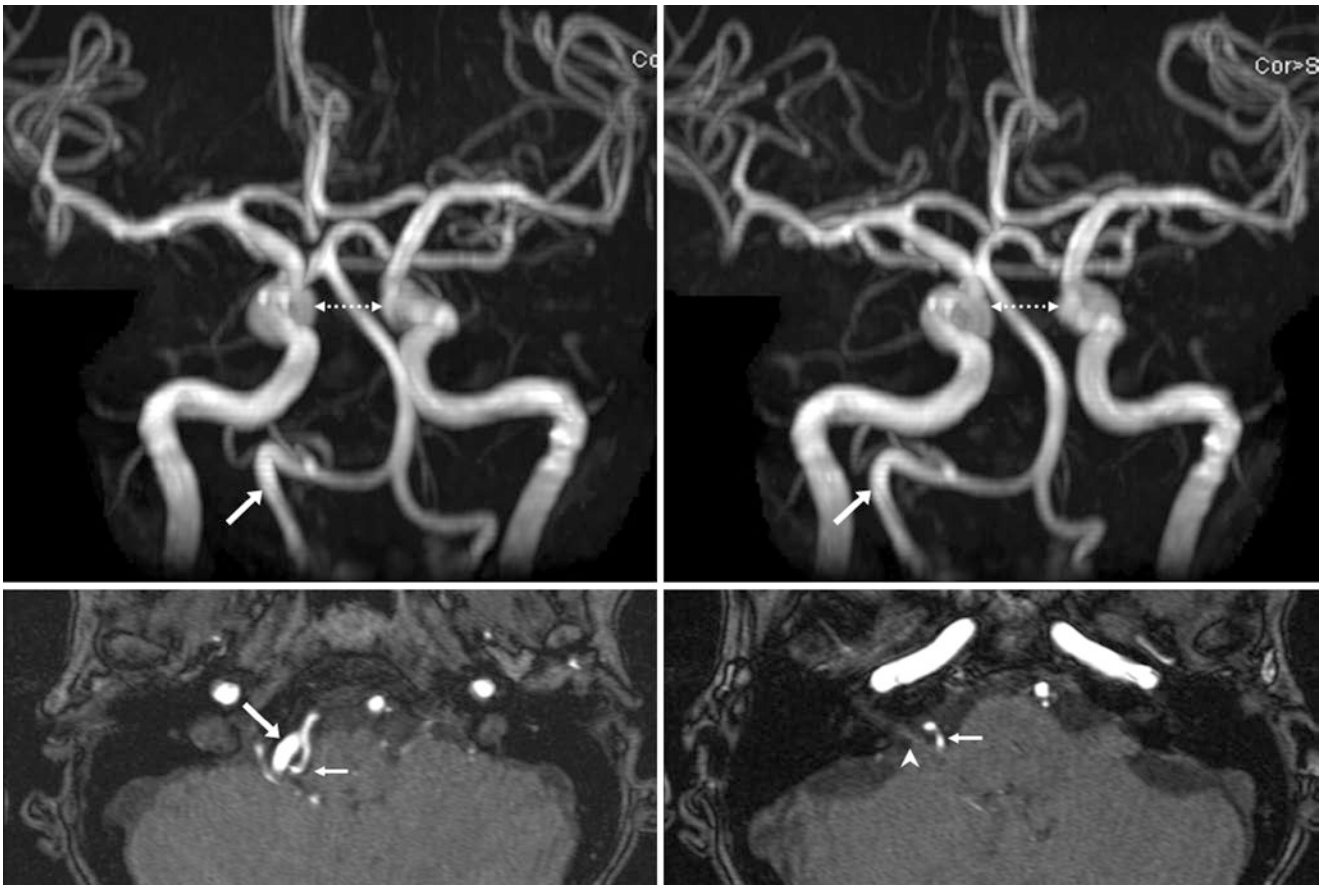

Fig. 34.19 Carotid-basilar dolichoectasia. *Top row*: 42-year-old with a tortuous and high RVA (*arrows*) on 3DTOF MRA AP views, part of a negative stroke workup. Also, both cavernous ICAs (*dotted arrows*) were tortuous and ectatic. *Bottom row*: On source images, the posterior inferior cerebellar artery (*thin arrows*) does contact the root entry zone of CN VII (*arrowhead*), which can cause symptoms, but such symptoms were not present

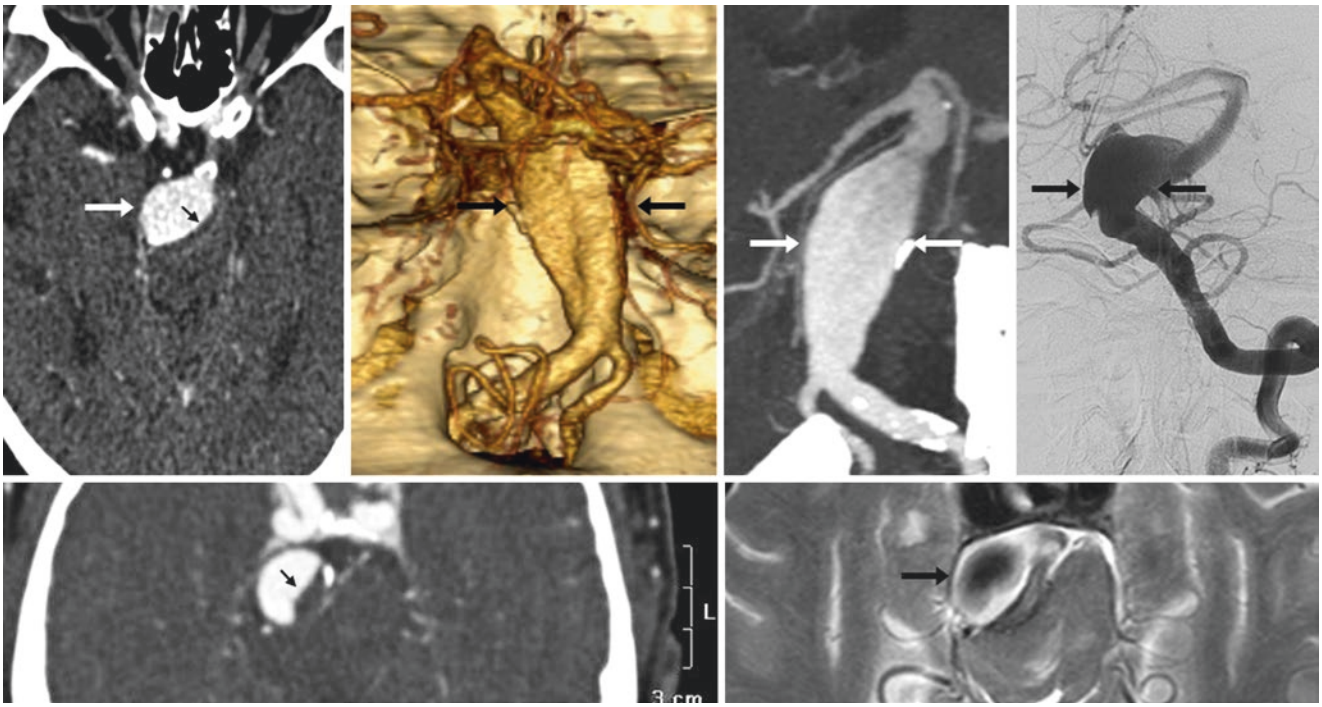

Fig. 34.20 Comparison case of a dissecting VBA aneurysm. *Top row*: A 69-year-old with CN VI symptoms had severe, fusiform VBA enlargement (*large arrows*) with a clot within the lumen of the aneurysm (*thin arrow*) on CTA source images (*left*), 3D VR PA view (*left middle*) and coronal MPR (*right middle*), and on catheter DSA (*right*). *Bottom row*: Three months later, the size of the clot had increased on CTA (*left*); T2WI MRI (*right*) demonstrates a partial flow void

34.3 Upper Cervical Carotid "Kinking" and Tortuous Internal Carotid Arteries

Tortuous cervical ICAs or ICA "*kinking*" not only may cause problems for radiologists in generating adequate 3D images but also can simulate *masses* on nonenhanced CT or MR examinations, particularly at the skull base. Such upper cervical ICA kinking may be present in 3–7 % of the population, and either dolichoectasia, kinking, or tortuosity of the ICAs can be present in 10–20 %, whether in the cervical region or intracranially [10–16]. There is debate as to whether this is a risk factor for cerebrovascular events or the eventual development of stenosis, but it is most commonly noted in asymptomatic patients [10–16].

"Kinking" within the upper cervical region can make measurement of stenoses difficult on ultrasound, CTA, or MRA. Additionally, catheterization and interpretation of catheter DSAs (considered the gold standard in evaluating for stenosis) can become difficult, or a stenosis can be underestimated because of problematic positioning for the projection of the maximum demonstration of a stenosis, particularly if the tortuosity has not previously been noted on noninvasive imaging such as CTA or MRA. Hence, noninvasive imaging by CTA or contrast-enhanced MRA can be quite helpful in evaluating severely tortuous vessels even before the patient undergoes a catheter DSA.

A subset of patients with ICA kinking may also have *dolichoectasia of the ICA* intracranially, but that percentage is unknown. Such kinking is not necessarily related to atherosclerosis, as it is occasionally noted in the upper cervical region in pediatric patients, but the tortuosity does seem to worsen with age and with worsening atherosclerosis. This tortuous or kinked appearance is noted with a higher incidence in pediatric and adult patients who have *fibromuscular dysplasia*, whether in the ICAs or the VAs, where an undulating appearance of a vessel's lumen (also called a "string of beads" appearance) may be present, even prior to the development of stenoses or dissection (Figs. 34.21, 34.22, 34.23, 34.24, 34.25, 34.26, 34.27, 34.28, and 34.29).

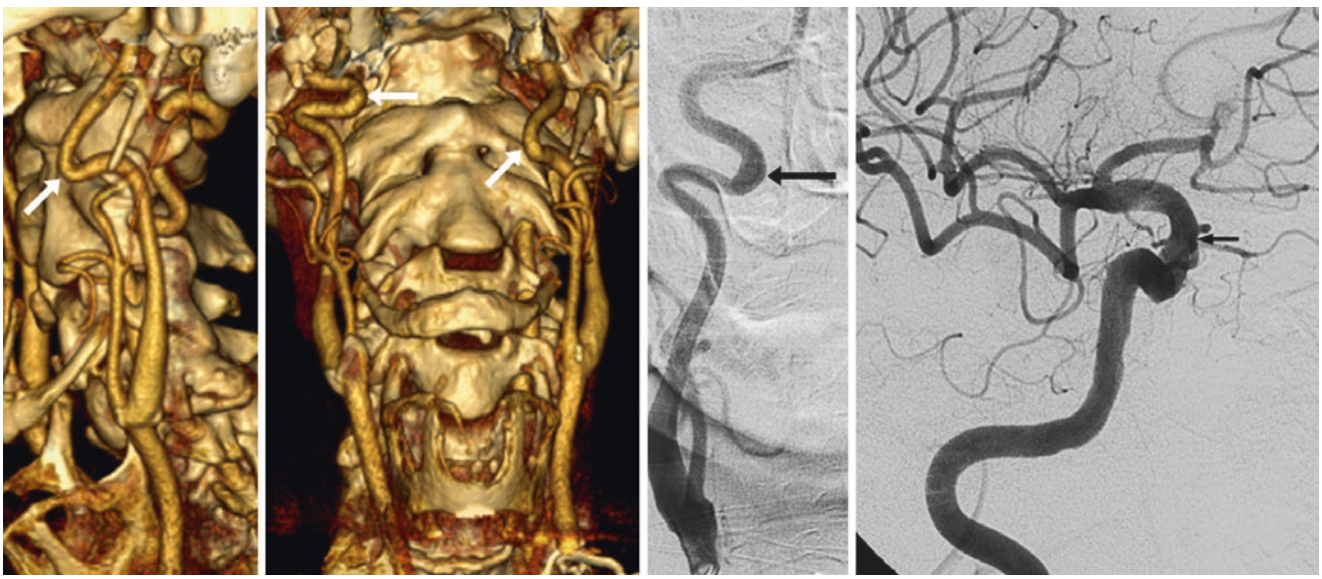

Fig. 34.21 67-year-old with bilateral, tortuous upper cervical ICAs (*arrows*) on CTA 3D VR left lateral (*left*) and AP (*left middle*) views, as well as on catheter DSA lateral (*right middle*) and AP (*right*) views of the right side. Intracranially, the supraclinoid right ICA is also tortuous and mildly to moderately ectatic (*thin arrow, right*)

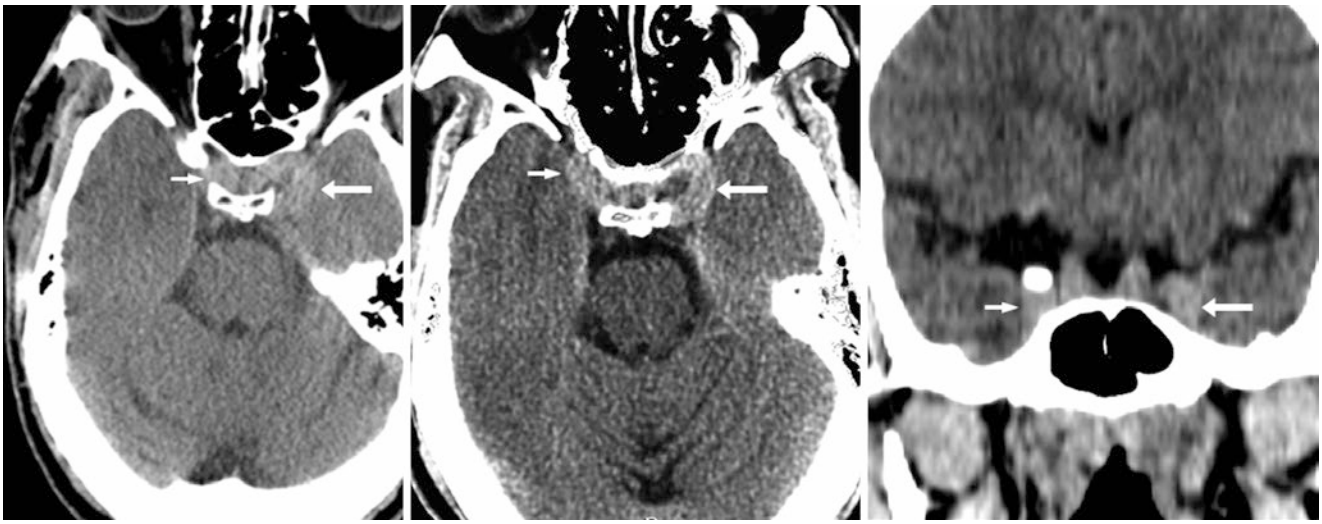

Fig. 34.22 48-year-old with a unilaterally mildly hyperintense left paraclinoid prominence (*large arrow*) on a routine, spiral acquisition 5 mm-thickness nonenhanced CT (*left*), which simulated a parasellar/cavernous aneurysm or mass. Thin reconstructions with "tight" windowing (*middle*), and coronal MPRs (*right*) showed the structure to be a tortuous, mildly ectatic left ICA in the cavernous segment. A more typical ICA is noted on the right side (*thin arrows*)

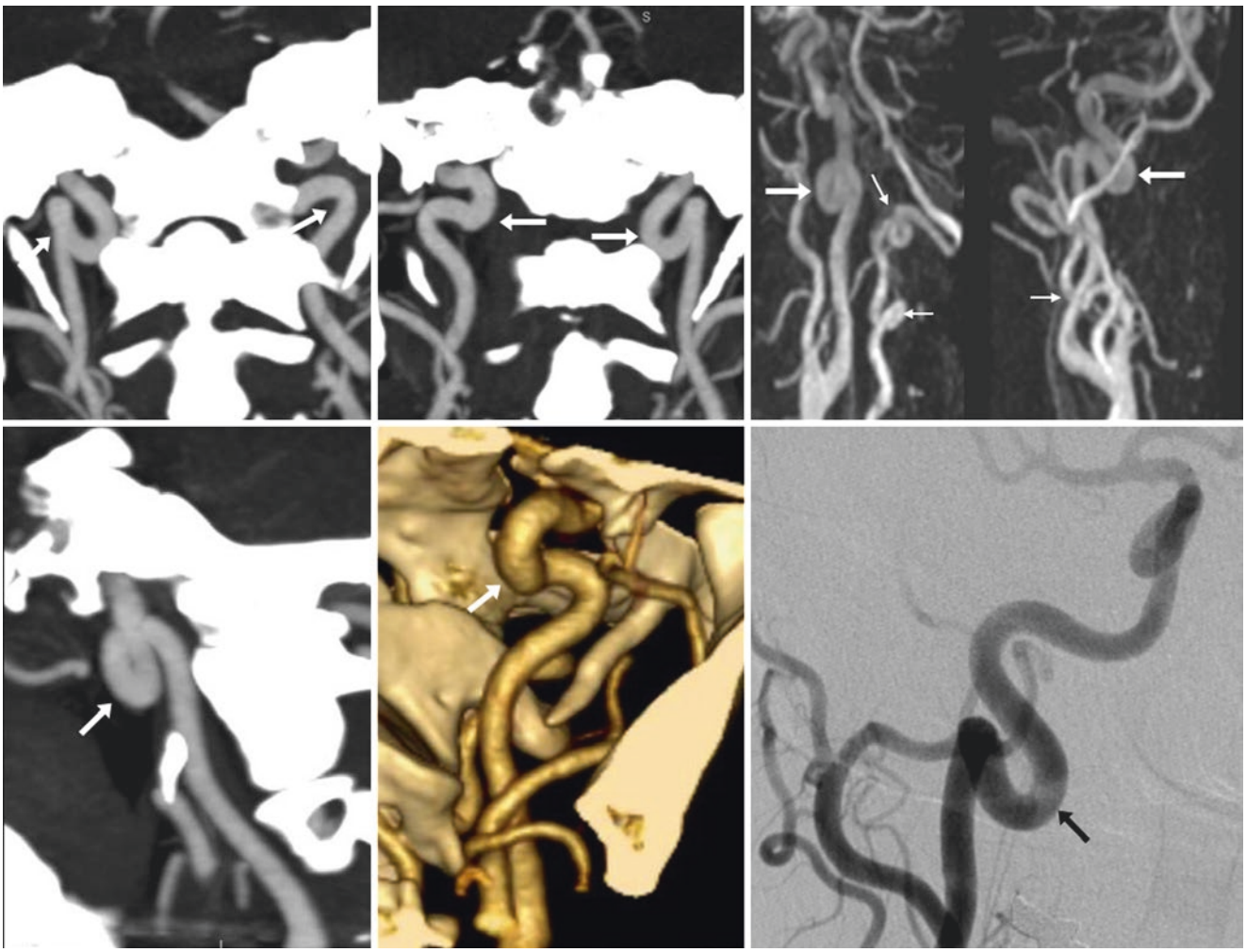

Fig. 34.23 43-year-old with tortuosity and "kinking" of the upper cervical ICAs bilaterally (*arrows*) on CTA MPR AP views (*top left two images*), a sagittal MPR view (*bottom left*), and a 3D VR reconstruction (*bottom middle*). MRA oblique and lateral views (*top right two images*), and a catheter DSA AP view (*bottom right*) demonstrate the tortuous ICAs with mild ectasia. Also note tortuous VAs bilaterally on the contrast-enhanced MRA (*thin arrows, top right*), and the lack of atherosclerosis

Fig. 34.24 48-year-old with bilateral "kinking" of tortuous ICAs (*arrows*) on a CTA 3D VR AP view. This patient had no atherosclerosis

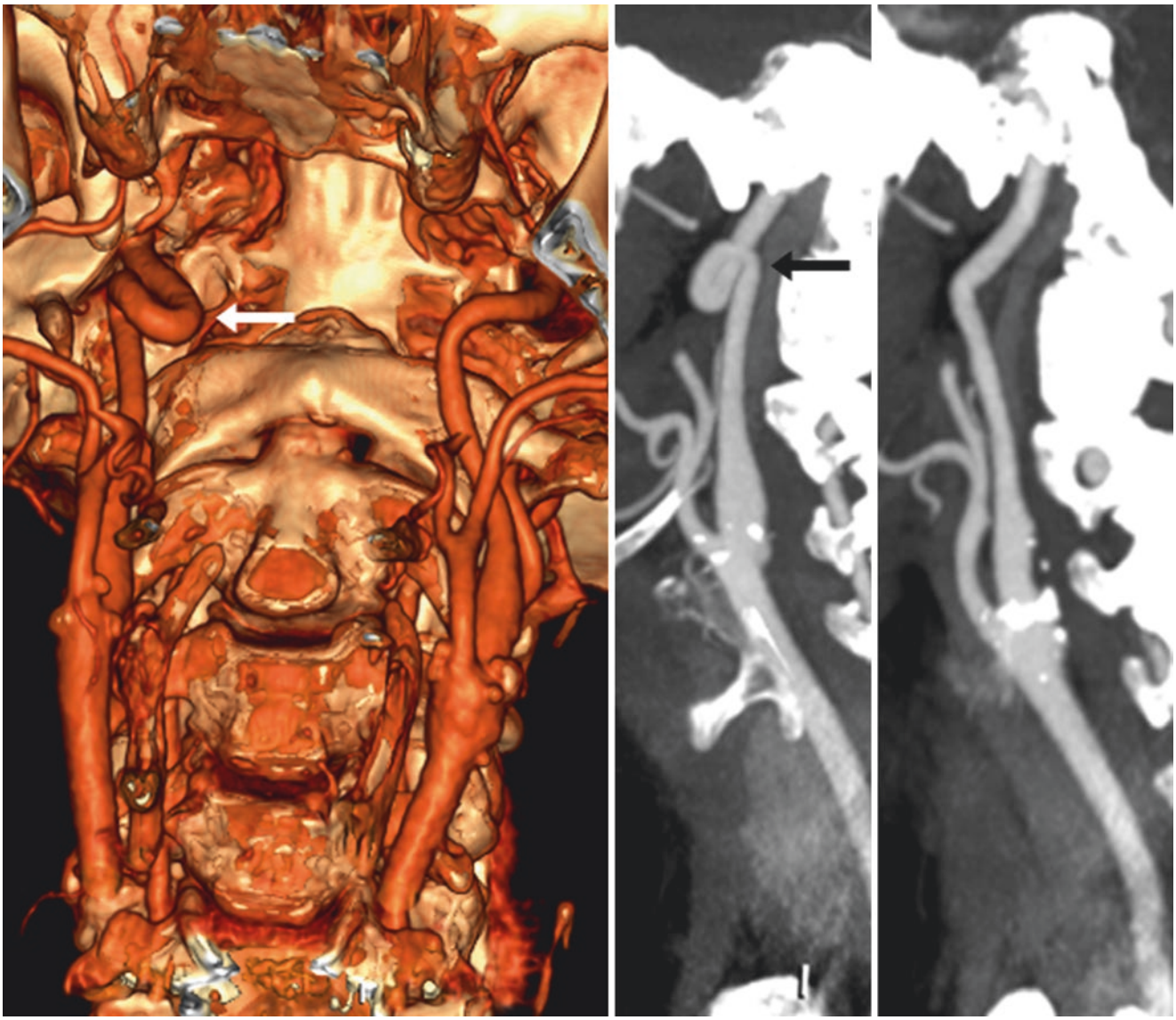

Fig. 34.25 64-year-old with right ICA "kinking" (*arrow*) on a CTA with a 3D VR CTA AP view (*left*). Sagittal 15 mm-thick MPRs of the right (*middle*) and left (*right*) sides are compared side-by-side

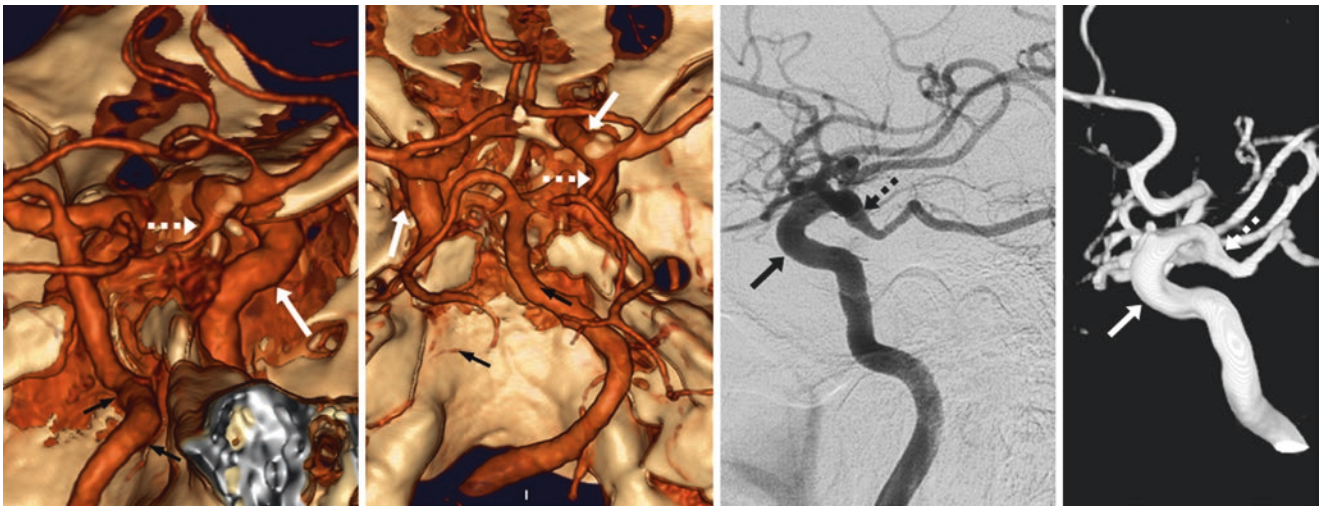

Fig. 34.26 75-year-old with mild bilateral ectasia of the cavernous-supraclinoid ICAs (*arrows*) with vertebrobasilar artery (VBA) tortuosity (*thin arrows*) on 3D VR CTA in RPO (*left, of the right side*) and PA (*left middle*) views. The right posterior communicating artery origin (*dotted arrows*) has infundibular prominence, bordering on being aneurysmal, as noted on catheter DSA (*right middle*) and 3D DSA (*right*) lateral views, with mild ICA atherosclerotic irregularity

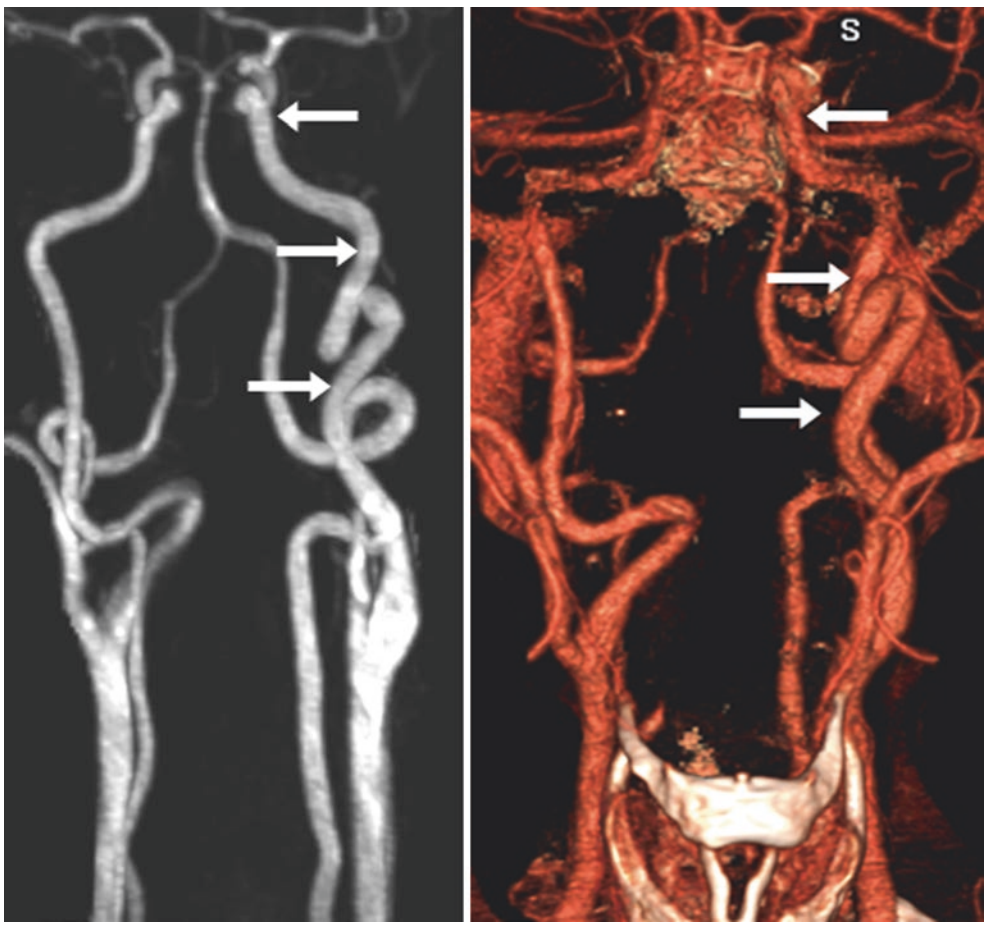

Fig. 34.27 53-year-old with a moderately ectatic and tortuous left ICA diffusely (*arrows*) on AP views from a contrast-enhanced MRA (*left*) and CTA (*right*)

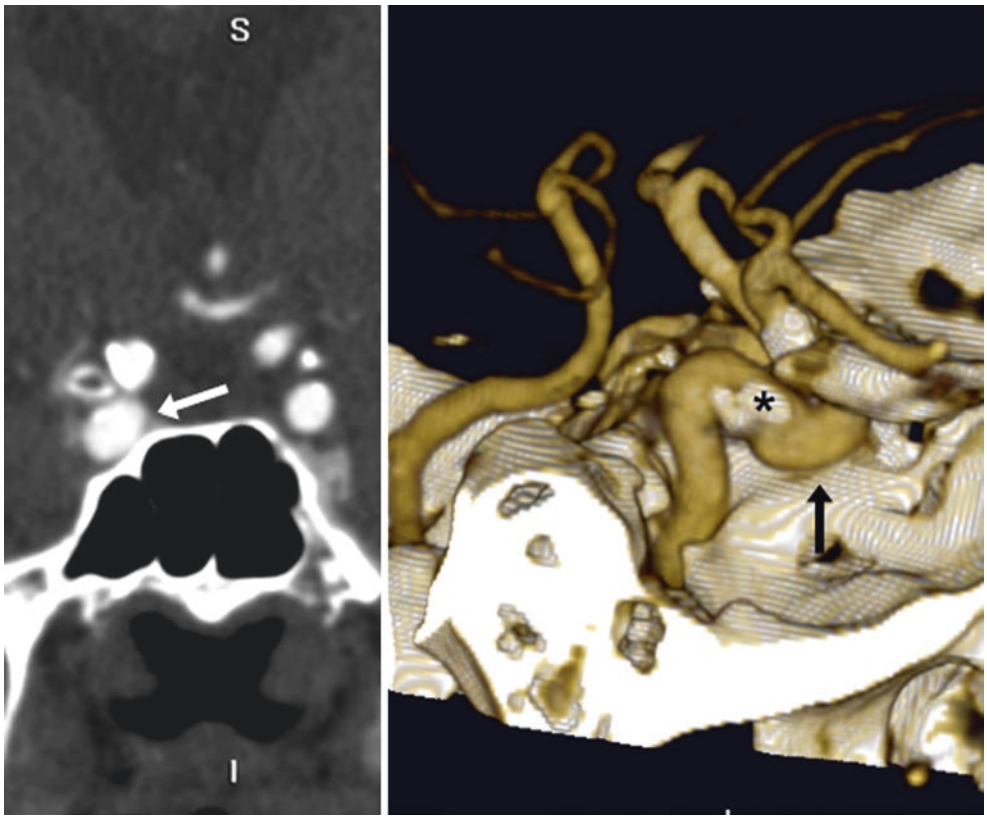

Fig. 34.28 78-year-old with mild cavernous ICA ectasia (*arrows*) on coronal MPR (*left*) and 3D VR lateral view (*right*), due to atherosclerosis, given the calcifications (*asterisk*)

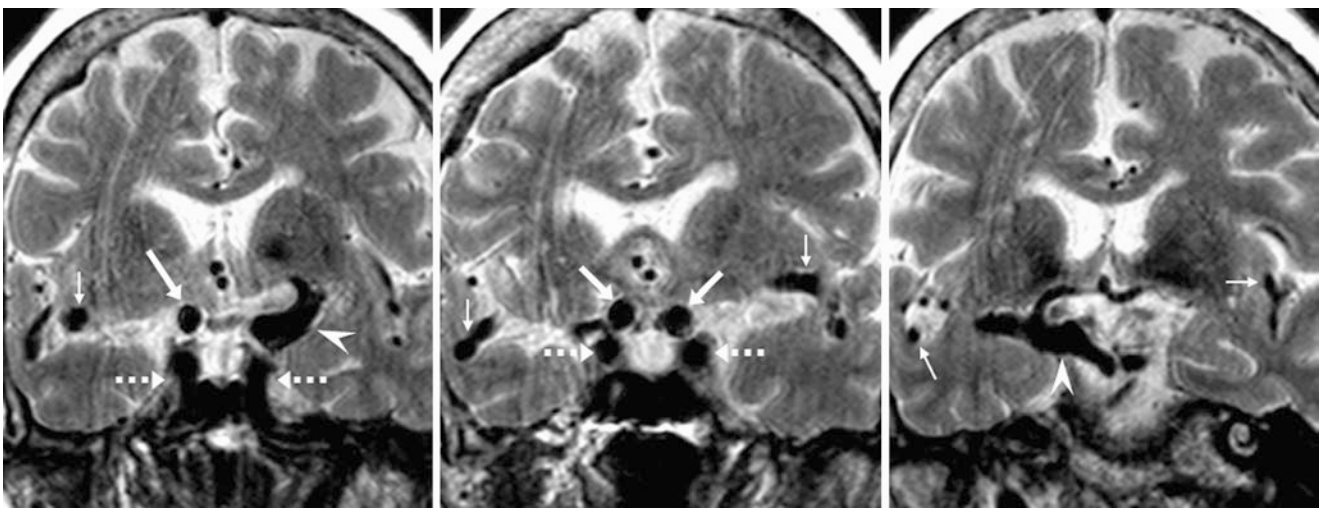

Fig. 34.29 76-year-old with bilateral moderately ectatic supraclinoid ICAs (*arrows*) and MCAs (*thin arrows*) on serial coronal T2WIs. The cavernous ICAs (*dashed arrows*) are not as prominent. Near the termini (*arrowheads*), the supraclinoid ICAs are ectatic to the point that they might be considered fusiform aneurysmal enlargement

34.4 Retropharyngeal Internal Carotid Artery

An *aberrant internal carotid artery* (ICA) posterior to the pharynx ("*retropharyngeal ICA*") is commonly present in elderly patients or those with atherosclerotic or collagen vascular diseases, but it is also not uncommon in otherwise asymptomatic adults. Retropharyngeal ICA often occurs in conjunction with a kinked or tortuous appearance of the ICA, but it is not necessarily associated with ICA kinking. It occurs in about 5 % of the population and is bilateral in most, but it can be seen unilaterally and can be variably stenotic [16–22]. There is debate as to whether this configuration predisposes to symptoms or embolic phenomena.

It is important for radiologists to mention the presence of retropharyngeal ICA, particularly when *mucosal space lesions* are present (such as pharyngeal or tonsillar lesions), in order to assist the surgeons' plan for a biopsy or resection. CT-guided biopsies in such scenarios may also require the use of intravenous contrast to confirm the location of the ICA. The most concerning scenario is when such a patient develops a posterior pharyngeal or *tonsillar mass* and is at risk for carotid injury during a biopsy or an *abscess* drainage [16–22]. Contrast-enhanced CT or even noncontrast T2WI MRI (which can demonstrate the flow voids) best identifies this configuration (Figs. 34.30, 34.31, 34.32, 34.33, 34.34, and 34.35).

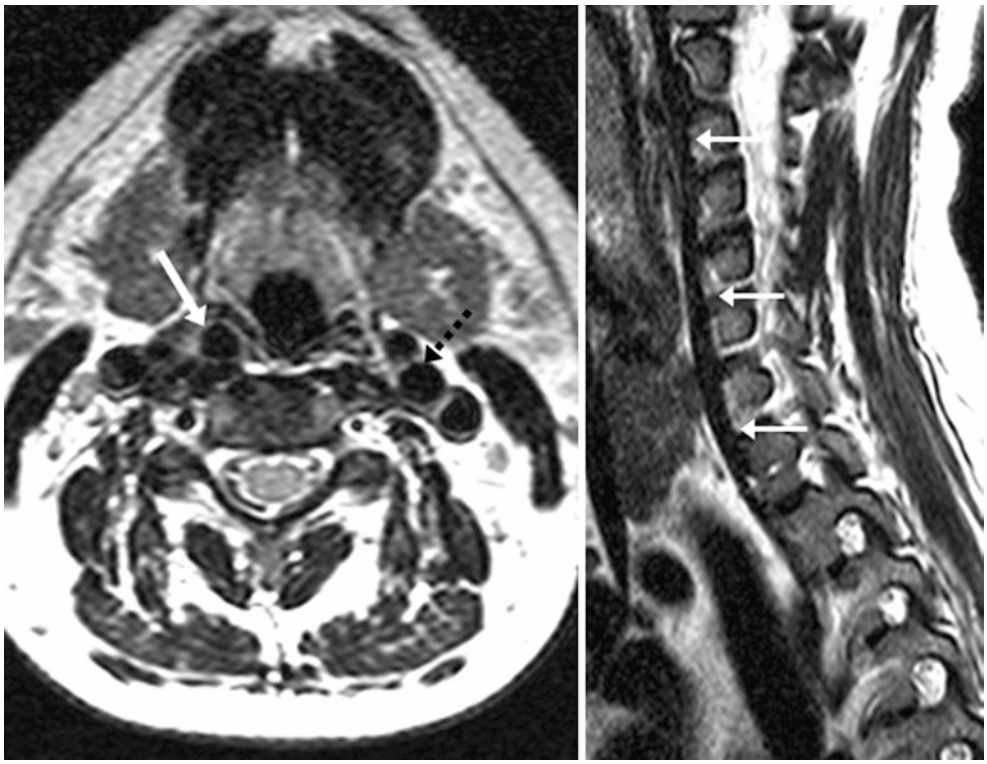

Fig. 34.30 43-year-old with a unilateral right retropharyngeal internal carotid artery (ICA) (*arrows*), just posterior to the pharyngeal mucosa on axial (*left*) and sagittal (*right*) T2WIs from a cervical MRI. Note the typical location of the left ICA (*dotted arrow*)

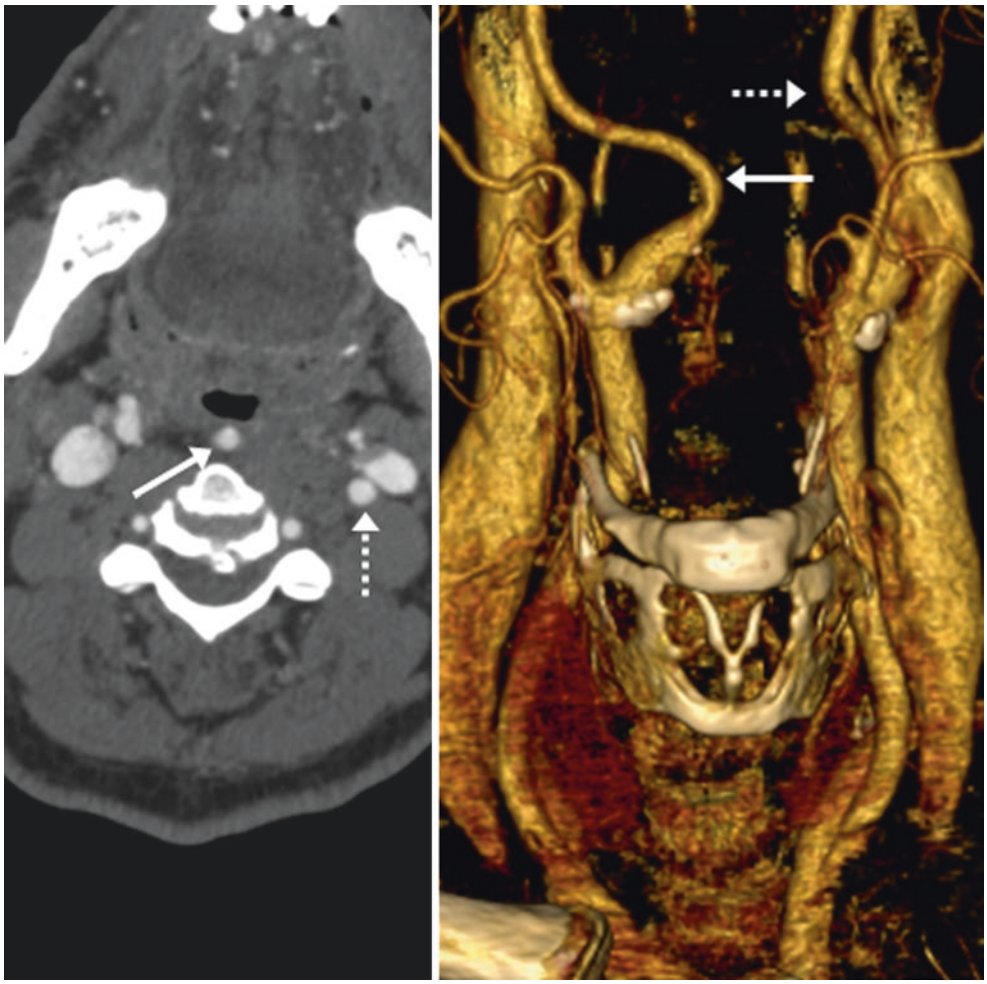

Fig. 34.31 59-year-old with a midline right ICA (*arrows*), just posterior to the pharyngeal mucosa on axial (*left*) and 3D VR AP (*right*) CTA images. Note the typical location of the left ICA (*dotted arrows*)

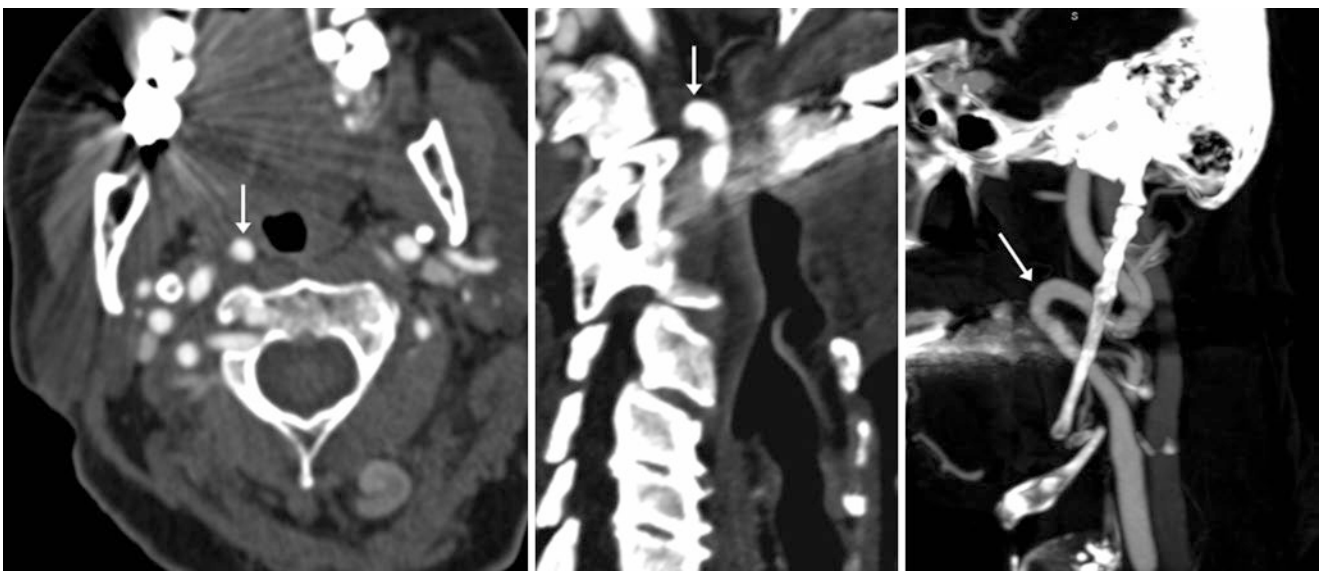

Fig. 34.32 80-year-old with a unilateral right retropharyngeal ICA (*arrows*), located just posterolateral to the pharyngeal mucosa on axial (*left*), right parasagittal (*middle*), and oblique sagittal 17 mm-thick (*right*) CTA reconstructions. In the image on the *right*, note the elongated and calcified/ossified right styloid process, which can cause pain (Eagle's syndrome) in symptomatic patients

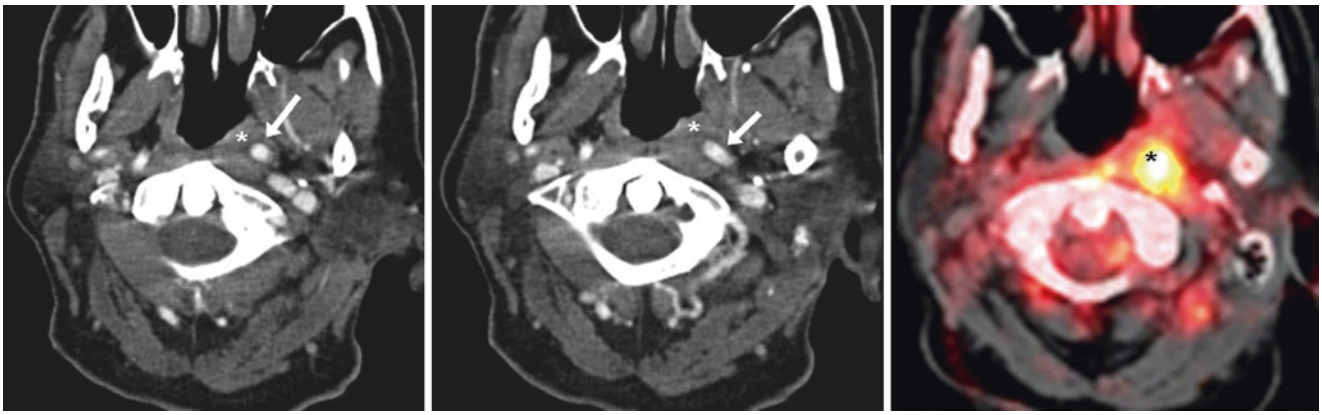

Fig. 34.33 Comparison case of mass and retropharyngeal ICA. A 61-year-old showed a left nasopharyngeal mass (*asterisks*) and a retropharyngeal ICA (*arrows*) on routine contrast-enhanced CT (*left* and *middle*). On a fused ^{18}FDG PET-CT (*right*), the mass had an elevated standardized uptake value (SUV) greater than 7, which was suspicious and later confirmed to be malignancy

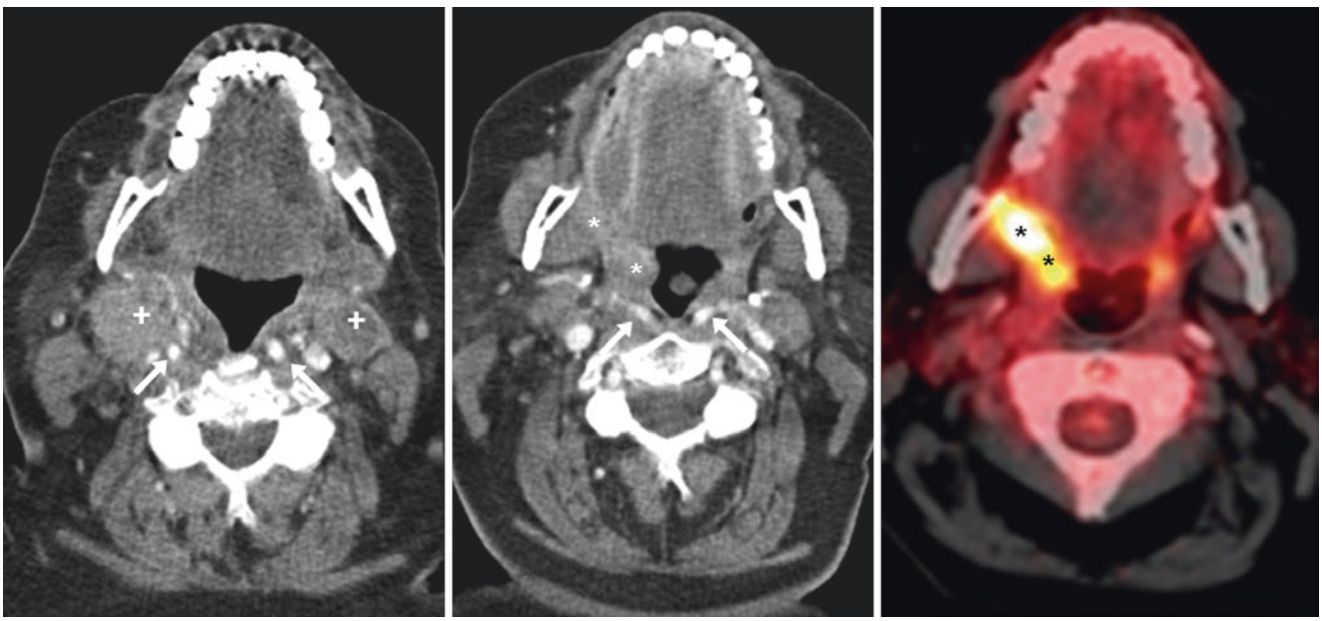

Fig. 34.34 Comparison case of palatine mass and retropharyngeal ICA. A 67-year-old had bilateral level 2A metastatic lymph nodes (*plus signs*) on contrast-enhanced CT (*left*), and a right retromolar trigone lesion (*asterisks*) extending into the palatine tonsil (*middle*). The SUV was greater than 6.0 on fused ^{18}FDG PET-CT (*right*). Bilateral retropharyngeal ICAs (*arrows*) were present, with the right ICA just posterior to both the right level-2A lymph nodes and the palatine tonsil mass

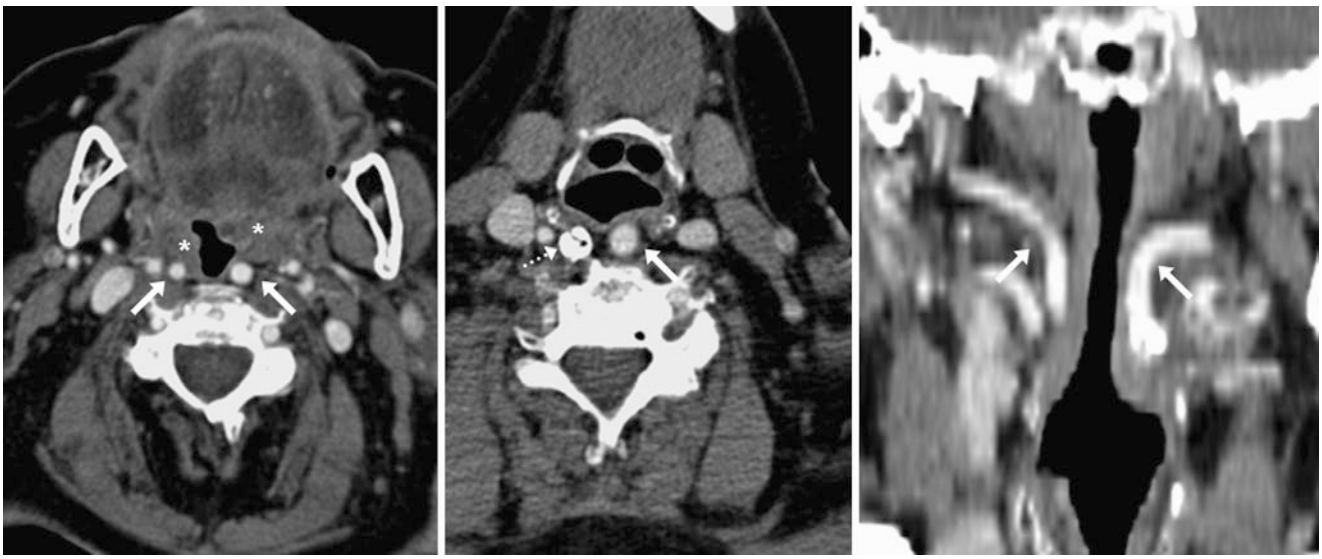

Fig. 34.35 Comparison case of tonsillar lesion and retropharyngeal ICA in an 83-year-old with squamous cell cancer. On contrast-enhanced CT, right palatine and left lingual tonsillar masses (*asterisks*) were noted on axial (*left* and *middle*) and coronal (*right*) reformats, with retropharyngeal ICAs (*arrows*). There was also a focal, severe right ICA stenosis (*dotted arrow*). Together, this combination of findings caused the surgeon to modify the surgical approach

34.5 Aberrant Internal Carotid Artery

An aberrant internal carotid artery (ICA) is thought to be a sort of collateral pathway between the cervical and cranial vascular that develops embryologically due to agenesis/hypogenesis of the ICA's 1st embryonic segment [28–29]. The incidence of this variant is unknown, but it is reliably diagnosed on CT (most commonly), or on MRI/MRA. The findings on imaging include a relative small, hypoplastic ICA with no that extends into the middle ear (entering through an enlarged inferior tympanic canal), and is hardly covered by bone, if at all. This variant may be unilateral (most common) or bilateral. An alternative longer name, based on site of entry, may be the "inferior tympano-caroticotympanic variant of the ICA" [28–29]. This variant is critical to recognize in the setting of planned middle ear surgery so the "exposed" ICA is not injured (Fig. 34.36).

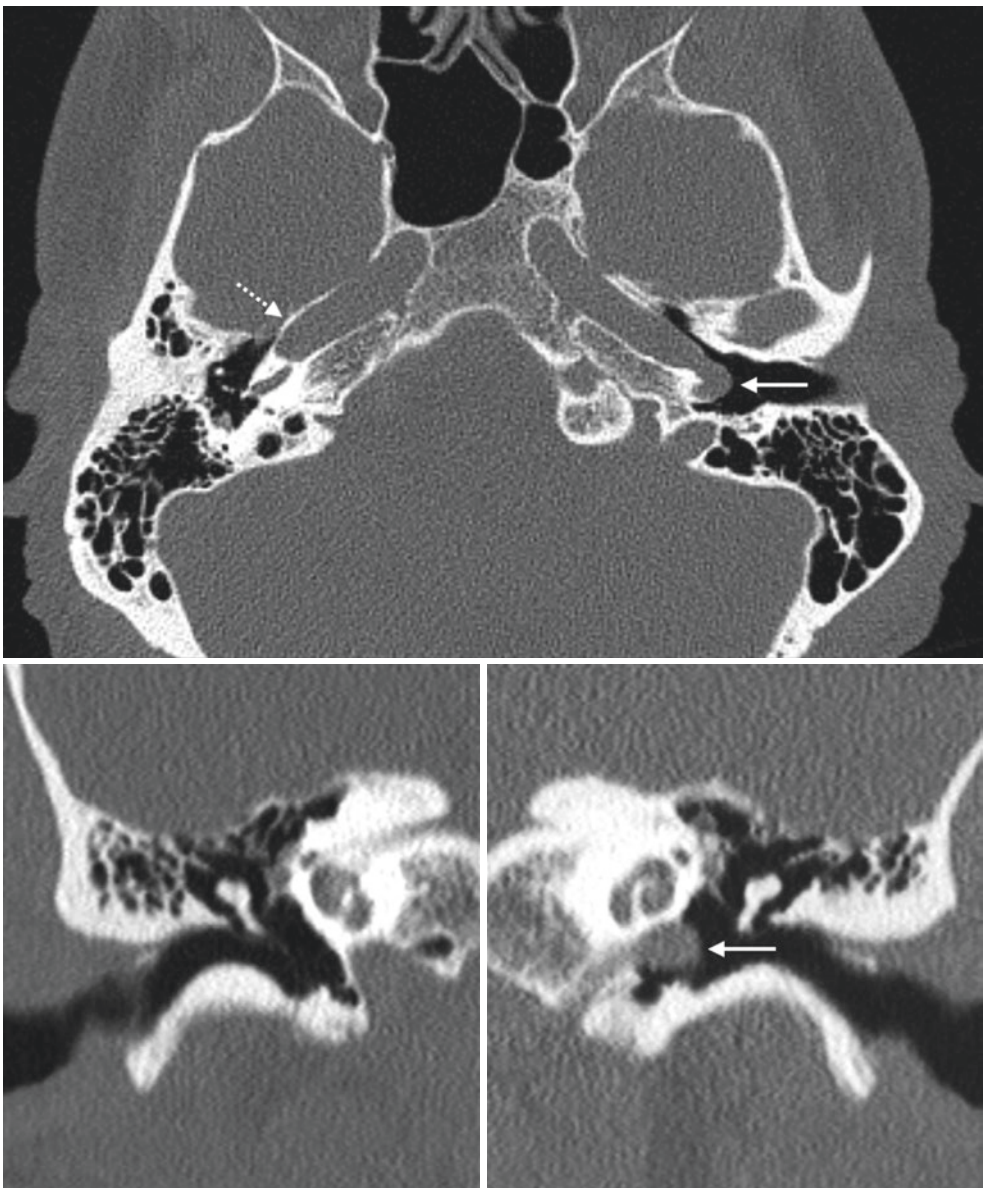

Fig. 34.36 Aberrant ICA. A 48 year old male with left-sided conductive hearing loss underwent a temporal bone CT (*top*), which demonstrated a tortuous course of the small left ICA (*arrows*) overlying the cochlear promontory; this represents an aberrant ICA. Note the right ICA for comparison (*dotted arrows*). Coronal views of the right (*bottom left*) and left (*bottom right*) sides are provided for comparison (Case courtesy of Dr. Zuzan Cayci, University of Minnesota, Minneapolis)

References

1. Songur A, Gonul Y, Ozen OA, Kucuker H, Uzun I, Bas O, Toktas M. Variations in the intracranial vertebrobasilar system. Surg Radiol Anat. 2008;30:257–64.
2. Pico F, Labreuche J, Hauw JJ, Seilhean D, Duyckaerts C, Amarenco P. Coronary and basilar artery ectasia are associated: results from an autopsy case–control study. Stroke. 2016;47:224–7.
3. Matsukawa H, Shinoda M, Fujii M, Uemura A, Takahashi O, Niimi Y. Basilar dolichoectasia and the spontaneous intradural vertebral artery dissection. Brain Inj. 2016;30:90–4.
4. Yuan F, Lin J, Ding L, Chao Y, Wenke L, Heng Z. Hemifacial spasm and recurrent stroke due to vertebrobasilar dolichoectasia coexisting with saccular aneurysm of the basilar artery: a case report. Turk Neurosurg. 2013;23:282–4.
5. Park JM, Koo JS, Kim BK, Kwon O, Lee JJ, Kang K, et al. Vertebrobasilar dolichoectasia as a risk factor for cerebral microbleeds. Eur J Neurol. 2013;20:824–30.
6. Passero SG, Calchetti B, Bartalini S. Intracranial bleeding in patients with vertebrobasilar dolichoectasia. Stroke. 2005;36:1421–5.
7. Takeuchi S, Takasato Y, Masaoka H, Hayakawa T, Otani N, Yoshino Y, et al. Dolichoectasia involving the vertebrobasilar and carotid artery systems. J Clin Neurosci. 2009;16:1344–6.
8. Kumral E, Kisabay A, Ataç C, Kaya C, Calli C. The mechanism of ischemic stroke in patients with dolichoectatic basilar artery. Eur J Neurol. 2005;12:437–44.
9. Tanaka M, Sakaguchi M, Miwa K, Okazaki S, Furukado S, Yagita Y, et al. Basilar artery diameter is an independent predictor of incident cardiovascular events. Arterioscler Thromb Vasc Biol. 2013;33:2240–4.
10. Borioni R, Garofalo M, Actis Dato GM, Pierri MD, Caprara E, Albano P, Chiariello L. Kinking of internal carotid artery: is it a risk factor for cerebro-vascular damage in patients undergoing cardiac surgery? J Cardiovasc Surg (Torino). 1994;35:325–6.
11. Togay-Işikay C, Kim J, Betterman K, Andrews C, Meads D, Tesh P, et al. Carotid artery tortuosity, kinking, coiling: stroke risk factor, marker, or curiosity? Acta Neurol Belg. 2005;105:68–72.
12. Van Damme H, Gillain D, Désiron Q, Detry O, Albert A, Limet R. Kinking of the internal carotid artery: clinical significance and surgical management. Acta Chir Belg. 1996;96:15–22.
13. Ballotta E, Abbruzzese E, Thiene G, Bottio T, Dagiau G, Angelini A, Saladini M. The elongation of the internal carotid artery: early and long-term results of patients having surgery compared with unoperated controls. Ann Vasc Surg. 1997;11:120–8.
14. Pancera P, Ribul M, Presciuttini B, Lechi A. Prevalence of carotid artery kinking in 590 consecutive subjects evaluated by Echo color doppler. Is there a correlation with arterial hypertension? J Intern Med. 2000;248:7–12.
15. Ovchinnikov NA, Rao RT, Rao SR. Unilateral congenital elongation of the cervical part of the internal carotid artery with kinking and looping: two case reports and review of the literature. Head Face Med. 2007;3:29.
16. Paulsen F, Tillmann B, Christofides C, Richter W, Koebke J. Curving and looping of the internal carotid artery in relation to the pharynx: frequency, embryology and clinical implications. J Anat. 2000;197:373–81.
17. Koreckij J, Alvi H, Gibly R, Pang E, Hsu WK. Incidence and risk factors of the retropharyngeal carotid artery on cervical magnetic resonance imaging. Spine (Phila Pa 1976). 2013;38:E109–12.
18. Ozgur Z, Celik S, Govsa F, Aktug H, Ozgur T. A study of the course of the internal carotid artery in the parapharyngeal space and its clinical importance. Eur Arch Otorhinolaryngol. 2007;264:1483–9.
19. Lukins DE, Pilati S, Escott EJ. The moving carotid artery: a retrospective review of the retropharyngeal carotid artery and the incidence of positional changes on serial studies. AJNR Am J Neuroradiol. 2016;37:336–41.
20. Fard SA, Patel AS, Avila MJ, Sattarov KV, Walter CM, Skoch J, Baaj AA. Anatomic considerations of the anterior upper cervical spine during decompression and instrumentation: a cadaveric based study. J Clin Neurosci. 2015;22:1810–5.
21. Muñoz A, Campollo J, Vergas J. Bilateral internal carotid aneurysms presenting as a nonpulsatile parapharyngeal mass: complementary diagnosis by CT, MR imaging, and digital subtraction angiography. AJNR Am J Neuroradiol. 2001;22:864–6.
22. Chan K, Richards PS, Dilkes MG. Internal carotid artery ectasia: the value of imaging studies prior to biopsy of a retropharyngeal mass. J Surg Case Rep. 2010;2010:4.
23. Mangrum WI, Huston 3rd J, Link MJ, Wiebers DO, McClelland RL, Christianson TJ, Flemming KD. Enlarging vertebrobasilar nonsaccular intracranial aneurysms: frequency, predictors, and clinical outcome of growth. J Neurosurg. 2005;102:72–9.
24. Yasui T, Komiyama M, Iwai Y, Yamanaka K, Nishikawa M, Morikawa T. Evolution of incidentally-discovered fusiform aneurysms of the vertebrobasilar arterial system: neuroimaging features suggesting progressive aneurysm growth. Neurol Med Chir (Tokyo). 2001;41:523–7; discussion 528.
25. Savitz SI, Ronthal M, Caplan LR. Vertebral artery compression of the medulla. Arch Neurol. 2006;63:234–41.
26. Ho SL, Cheng PW, Wong WC, Chan FL, Lo SK, Li LS, et al. A case-controlled MRI/MRA study of neurovascular contact in hemifacial spasm. Neurology. 1999;53:2132–9.
27. Levy EI, Scarrow AM, Jannetta PJ. Microvascular decompression in the treatment of hypertension: review and update. Surg Neurol. 2001;55:2–11.
28. Lasjaunias P, Berenstein A, Ter Brugge KG. Surgical Neuroangiography, Clinical Vascular Anatomy and Variations. 2nd ed. New York: Springer-Verlag; 2001.
29. Roll JD, Urban MA, Larson TC, et al. Bilateral aberrant internal carotid arteries with bilateral persistent stapedial arteries and bilateral duplicated internal carotid arteries. AJNR. 2003;24:762–5.

Miscellaneous Cervical Venous Variants

35

The range of cervical venous anatomic variations is vast. The spectrum of minor variations is particularly extensive, but most are not of great import. However, the larger draining veins, such as the internal jugular veins (IJVs) and external jugular veins (EJVs), can be quite asymmetric, and such asymmetry in size or location, or changes in size and appearance in the time between initial and follow-up examinations, can simulate disease. Similarly, posteriorly, the vertebral veins (VVs) and various vertebral venous plexi have myriad appearances. Additionally, reflux of contrast into any of the aforementioned veins from the IJV or subclavian vein after injection of contrast can obscure adjacent anatomic structures, as discussed further in Chap. 44, "Artifacts on Craniocervical CT Angiography."

This chapter does not focus on the multitude of smaller cervical veins and plexi (*e.g.*, the pterygopalatine plexus), as they typically do not simulate anomalies of larger arteries. And though such plexi can simulate enhancing soft tissue masses in certain phases of filling, that situation is more appropriately addressed by a text on head and neck variants. Also, the degree of variation in such smaller vessels is not agreed upon and is quite vast.

This short chapter thus focuses on the larger cervical draining veins, particularly the IJVs, EJVs, and VVs. The goal is to illustrate how differences in size, the presence of a venous plexus (such as with the VVs), and venous contrast timing can affect the appearance of venous structures and simulate pathology. It is important to note that on both CT and MRI, the timing of contrast can be problematic, depending on the vascular structure to be studied: Too early may cause suboptimal visualization, but too late can obscure arterial structures in some regions. This is one of the primary reasons that routine head MRA is obtained without contrast, owing to the very short arterial-to-venous transit intracranially. First-pass contrast-enhanced neck MRA (CEMRA) is obtained with a dynamic bolus of contrast because "venous contamination" can limit visualization of cervical arteries, such as the carotid bifurcation. In particular, the presence of venous contrast or a surrounding plexus within VVs can simulate arterial anomalies, particularly in the setting of trauma or stroke.

A.M. McKinney, *Atlas of Normal Imaging Variations of the Brain, Skull, and Craniocervical Vasculature*,
DOI 10.1007/978-3-319-39790-0_35

35.1 Internal Jugular Vein Asymmetry

Some important observations have been made in the literature regarding IJV asymmetry [1–19]. First, the right IJV (RIJV) has been reported to be dominant (*i.e.*, larger than the left) in 62–80 % of patients [1–19]. Second, the IJVs have been reported to be located immediately lateral and/or anterolateral to the common carotid artery (CCA) in 85–92 % of individuals, versus further laterally (>1 cm) in about 1 %, and medial or posterior in approximately 1 or 2 % apiece. Third, the IJVs may be hypoplastic (<1 cm maximum diameter) unilaterally in about 3–5 %, most commonly aided in drainage by the external jugular vein (EJV); the normal diameter in the vast majority of patients typically ranges from 10 to 20 mm.

IJV asymmetry occasionally may simulate disease by representing a mass palpated by the patient or physician (easily solved by contrast-enhanced CT [CECT] or ultrasound) or a mass suspected by a radiologist on a nonenhanced CT scan in a patient with little cervical fat so the tissues are closely apposed (also easily solved by a CECT or ultrasound). IJV asymmetry may simulate thrombosis when the contrast in the IJV is partially in the venous phase, as the dominant side may be slower to fill because of its caliber (solved by a repeat CECT acquisition at least 20–30 s later in the venous phase). Knowledge of the range of appearances and caliber of the IJV, and the utilization of CECT in the venous phase or ultrasound may helped to resolve questionable cases. Also, although the IJV is usually located anterior to the CCA, it can migrate over time and become located anywhere from lateral to even medial (rare, in <1 %) relative to the CCA; this change can progress with age [3, 17–20]. The relative positions of these vessels can also change with head turning.

Recently, a heated debate has arisen as to whether the presence of "venous stenoses" is a sign of demyelinating disease (versus being entirely normal), and whether the treatment of such stenoses leads to improved white matter lesions [1–7, 10–19]. There are large variations in size of the IJVs (as well as the vertebral veins/plexi) in both patients with multiple sclerosis and controls, and the size also may vary based on a patient's position (sitting *vs* standing *vs* lying), breath-holding/Valsalva, or other factors (size, weight, right-sided dominance) [10–17]. Thus, it has not been clearly demonstrated that the presence of venous stenoses on ultrasound, CT, or MRI correlates with the presence of demyelinating disease, or that one causes the other. In part, there is disagreement as to how to measure a stenosis because of the variability in size along the course of a single IJV; the presence of venous valves can simulate stenoses (*i.e.*, "pseudostenosis"). There are even regional and international differences in the methods used to image the IJVs (Figs. 35.1, 35.2, 35.3, 35.4, 35.5, and 35.6).

Fig. 35.1 This 43-year-old woman felt "swelling" in her lower right neck. Axial contrast-enhanced CT (*top left*) shows that the right IJV (*plus sign*) is dominant at 29 mm diameter, whereas the left IJV (*asterisk*) was normal in size at 15 mm, as also shown on sagittal reformats of the right side (*bottom left*) and left side (*bottom middle*). A coronal reformat (*bottom right*) demonstrates a "bulbous" appearance of the lower right IJV, which appeared similar 5 years earlier on contrast-enhanced CT (*top right*)

Fig. 35.2 **In this** 48-year-old who fell, axial nonenhanced CT (*left*) demonstrates a dominant right IJV (*plus sign*) at 28 mm maximum diameter. The left IJV (*asterisk*) was normal in size at 18 mm maximum axial diameter. Note the CCAs medially (*double arrows*). On a coronal reconstruction (*right*), note the "bulbous" appearance of the inferior right IJV (*plus sign*)

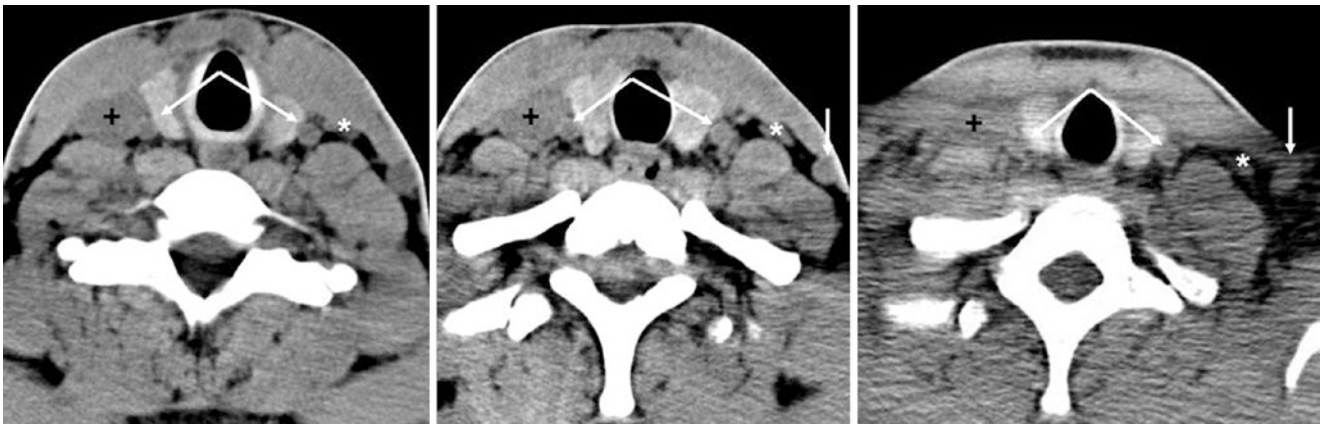

Fig. 35.3 In this 21-year-old who fell, axial nonenhanced CT images (*left two images*) show that the right IJV (*plus sign*) is dominant at 23 mm, whereas the left IJV (*asterisk*) is moderately hypoplastic at 7 to 8 mm maximum axial diameter, unchanged from 4 months earlier (*right*). Note the CCAs medially (*double arrows*). Also note that the left EJV is prominent (*thin arrows*). This case demonstrates how the dominant right IJV can simulate a mass on a poor-quality nonenhanced CT scan (*right*)

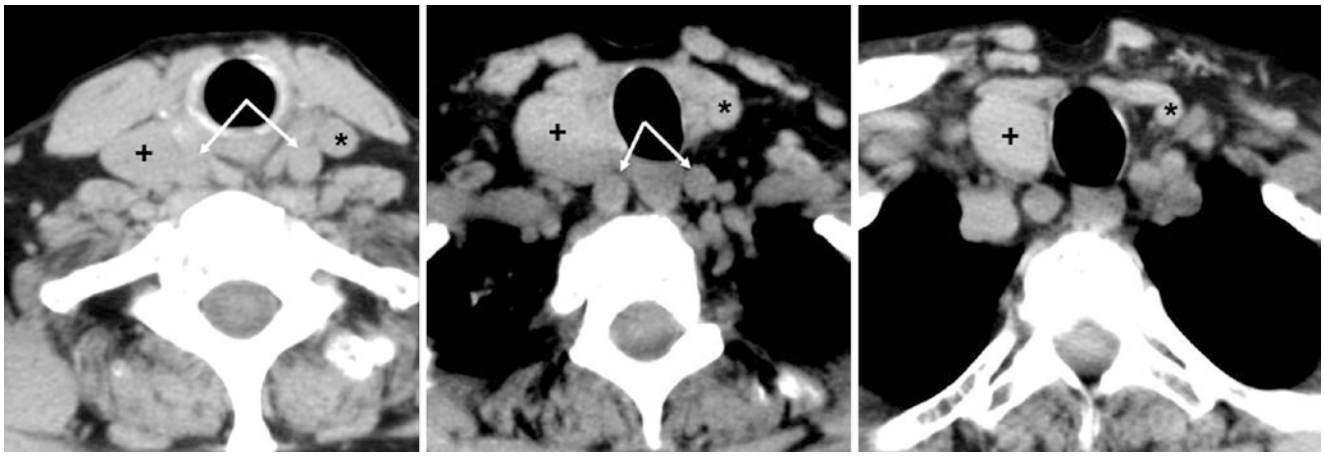

Fig. 35.4 In this 85-year-old, axial nonenhanced CT was performed after a fall. Serial axial images depict that the right IJV (*plus sign*) is dominant at 26 mm diameter, whereas the left IJV (*asterisk*) s borderline hypoplastic at 10–11 mm maximum axial diameter. Note the CCAs medially (*double arrows*)

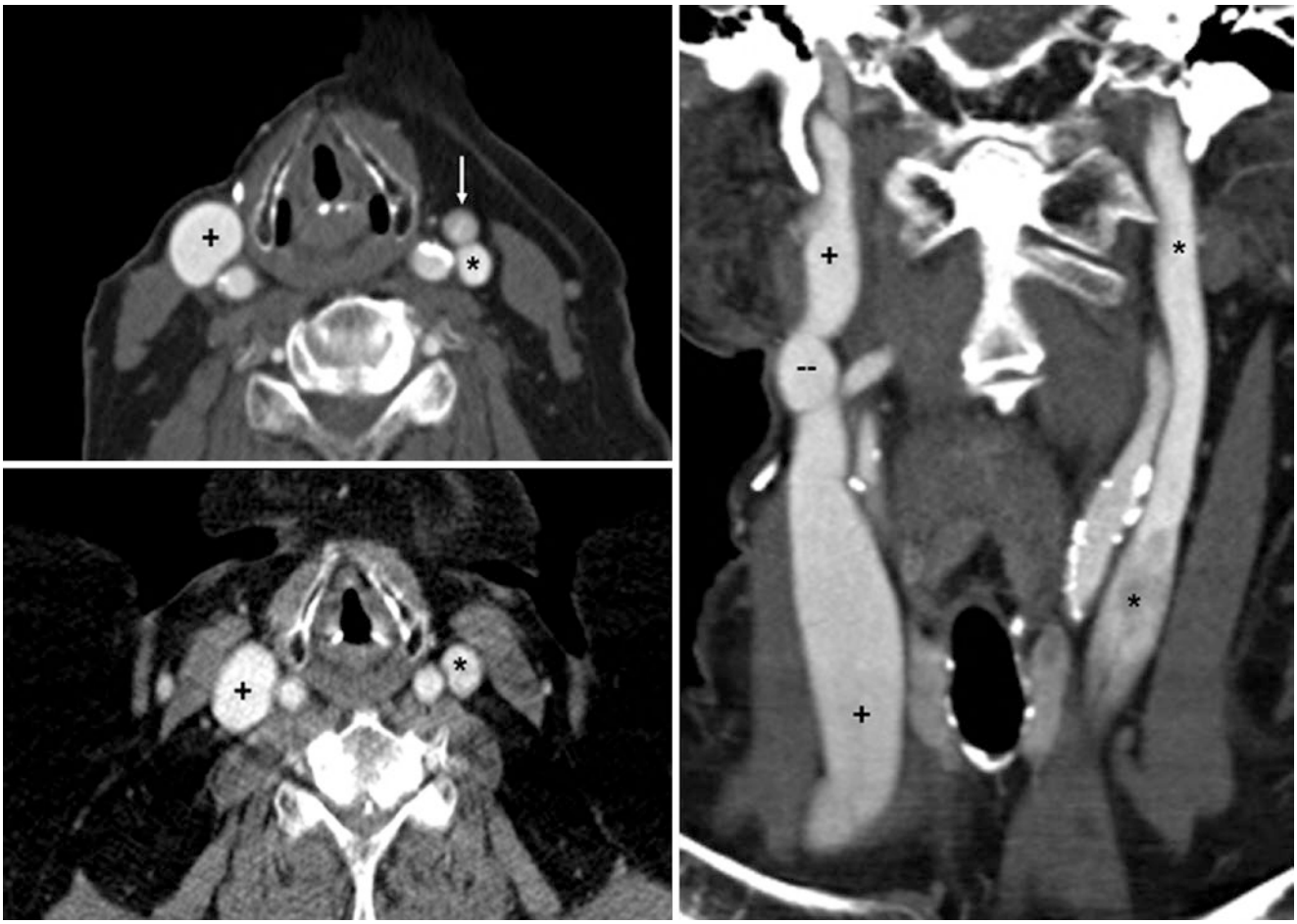

Fig. 35.5 67-year-old with axial contrast-enhanced CT (CECT) to evaluate for metastatic nodes from tongue squamous cell carcinoma. An axial image (*top left*) shows that the right IJV (*plus sign*) is dominant (21 mm diameter), whereas the left IJV (*asterisk*) is borderline hypoplastic (8–10 mm diameter), an asymmetry also shown on coronal reconstructions (*right*). This finding appeared similar to 3 years earlier on axial CECT (*bottom left*). A prominent left facial vein (*thin arrow, top left*) is also seen. Note the irregular and "pseudostenotic" appearance of the midportion of the right IJV (*dashes*) on the coronal reformats

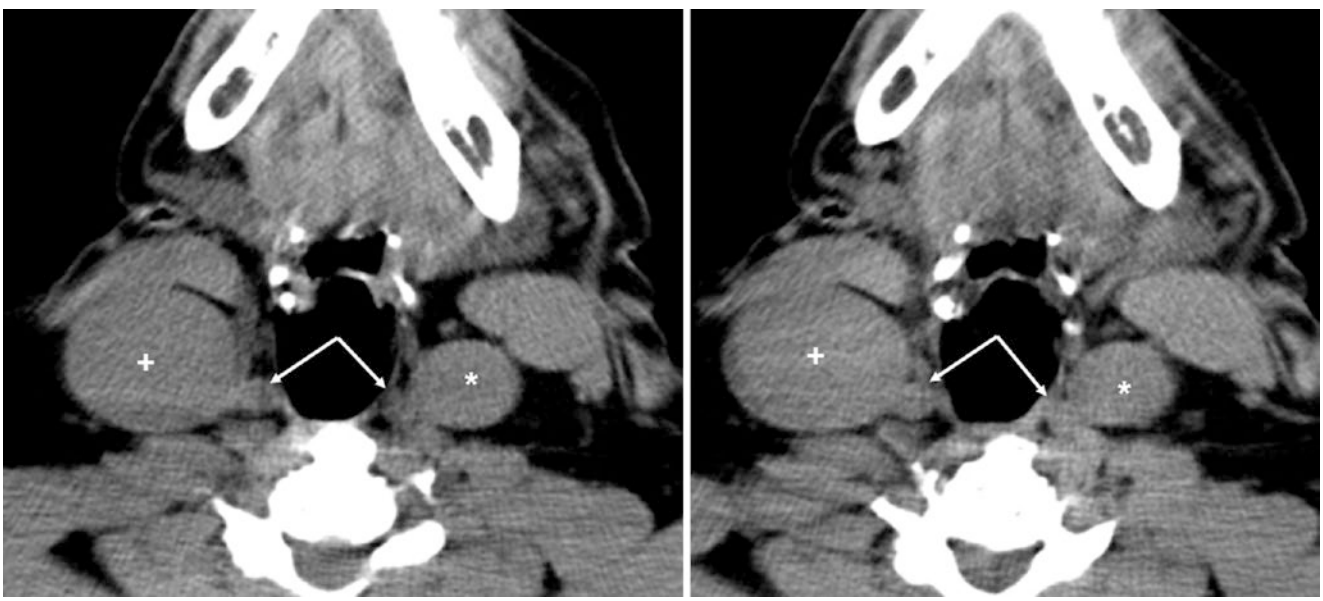

Fig. 35.6 58-year-old with axial nonenhanced CT performed after a fall to evaluate for fracture. Axial images demonstrate that the right IJV (*plus sign*) is dominant at 40–45 mm maximum diameter, whereas the left IJV (*asterisk*) is more normal in size and much smaller but still prominent, measuring 23–25 mm maximum axial diameter. Note the CCAs medially (*double arrows*)

35.2 External Jugular Prominence

As stated previously, the external jugular vein (EJV) can be prominent, most commonly because of hypoplasia of the ipsilateral IJV. However, the EJV can also normally be the dominant source of drainage on that side or can be equivalent in size to a nonhypoplastic ipsilateral IJV [2–4, 10–13]. EJV asymmetry is also not uncommon. This normal finding should be distinguished from chronic IJV thrombosis, in which the EJV (as well as other veins) enlarges in a compensatory fashion because of the IJV occlusion (Figs. 35.7 and 35.8).

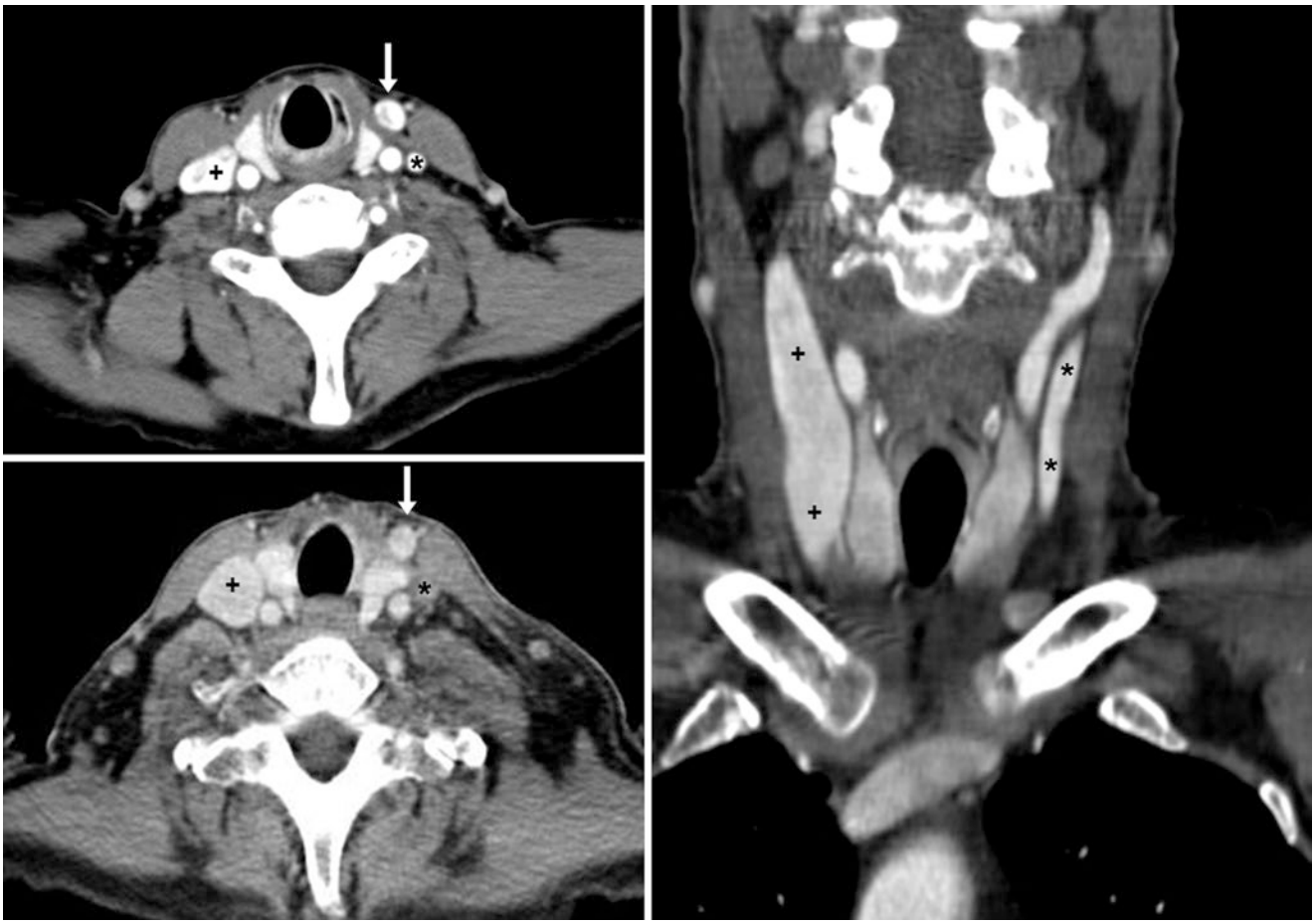

Fig. 35.7 62-year-old who underwent CECT to evaluate for lymphoma (negative neck/chest CT). Axial images (*top left*) show that the left EJV (*arrow*) is prominent, while the left IJV (*asterisk*) is moderately hypoplastic, being smaller than the dominant right IJV (*plus sign*), also shown on a coronal reconstruction (*right*). This asymmetry appeared similar 1 year earlier on axial CECT (*bottom left*), although the left IJV did not opacify well with contrast, probably due to bolus timing

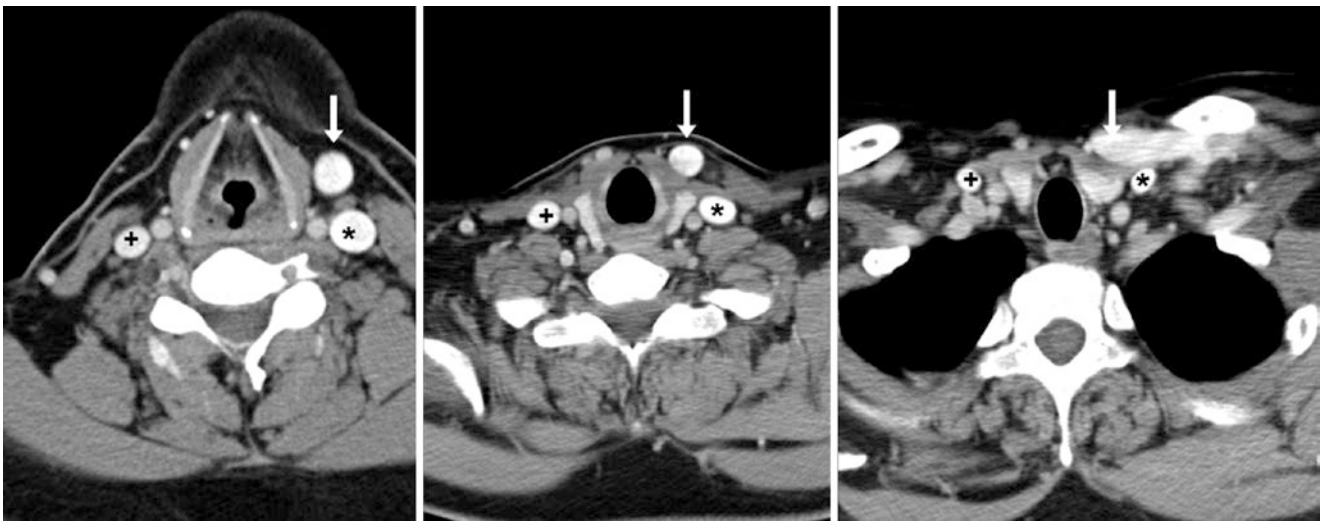

Fig. 35.8 36-year-old who underwent CECT for a small posterior neck lipoma (*not shown*). Serial axial images demonstrate that the left EJV (*arrows*) is prominent, while the left IJV (*asterisk*) is not hypoplastic, being similar in size to the right IJV (*plus sign*). On the most caudal image (*right*), the EJV travels laterally to drain into the subclavian vein

35.3 Vertebral Vein or Plexus Simulating Dissection

MRI is an excellent tool to evaluate for internal carotid artery dissection, typically demonstrating crescentic bright signal on thin, fat-suppressed T1- and T2-weighted images related to the subacute age of intramural hematoma. However, evaluation of the vertebral artery (VA) by MRI is not quite as specific when performing a "carotid dissection" protocol, probably because of the smaller size of the VA, as well as the variable venous anatomy—whether there is an adjacent single vertebral vein (VV) or a vertebral venous plexus (VVP). Indeed, there is an ongoing controversy as to whether there is a single VV versus "dual" VVs (*i.e.*, travelling on both sides of the artery), versus a VVP communicating around the artery.

Recent literature has demonstrated that the vertebral venous anatomy within the transverse foramen is typically a "transversovertebral venous plexus" of communicating, valveless venous structures (rather than a single vein) from the skull base down to C6, although any of the three appearances just mentioned may occur [5–9]. In contrast, the VA has a predictable and well-defined anatomy and a clearly defined arterial vessel contour. Hence, variable flow rates and ambiguous venous anatomy can cause apparent abnormalities (such as T1- and T2-bright slow flow) adjacent to or surrounding the VA, thus simulating intramural hematoma of an arterial dissection on MRI. Also, the size and flow of the VVs/VVPs depend on the status of the IJV, as VVs are potential "valveless" collateral pathways, also allowing greater flow when the body is upright [5–9]. On CT, CTA, or contrast-enhanced MRA, the enhancing VVP communicating around or surrounding the VA also can mimic arterial dissection, particularly if the contrast bolus is in the venous phase. However, one should note the lack of a change in caliber of the VA across such segments, the presence of a patent flow void (on T2-weighted MRI), and the absence of luminal irregularity. Unfortunately, this may be quite difficult to discern in the occasional case of a combination of VA hypoplasia or atherosclerotic disease, which may require catheter angiography for the final determination to exclude a dissection (Figs. 35.9, 35.10, 35.11, and 35.12).

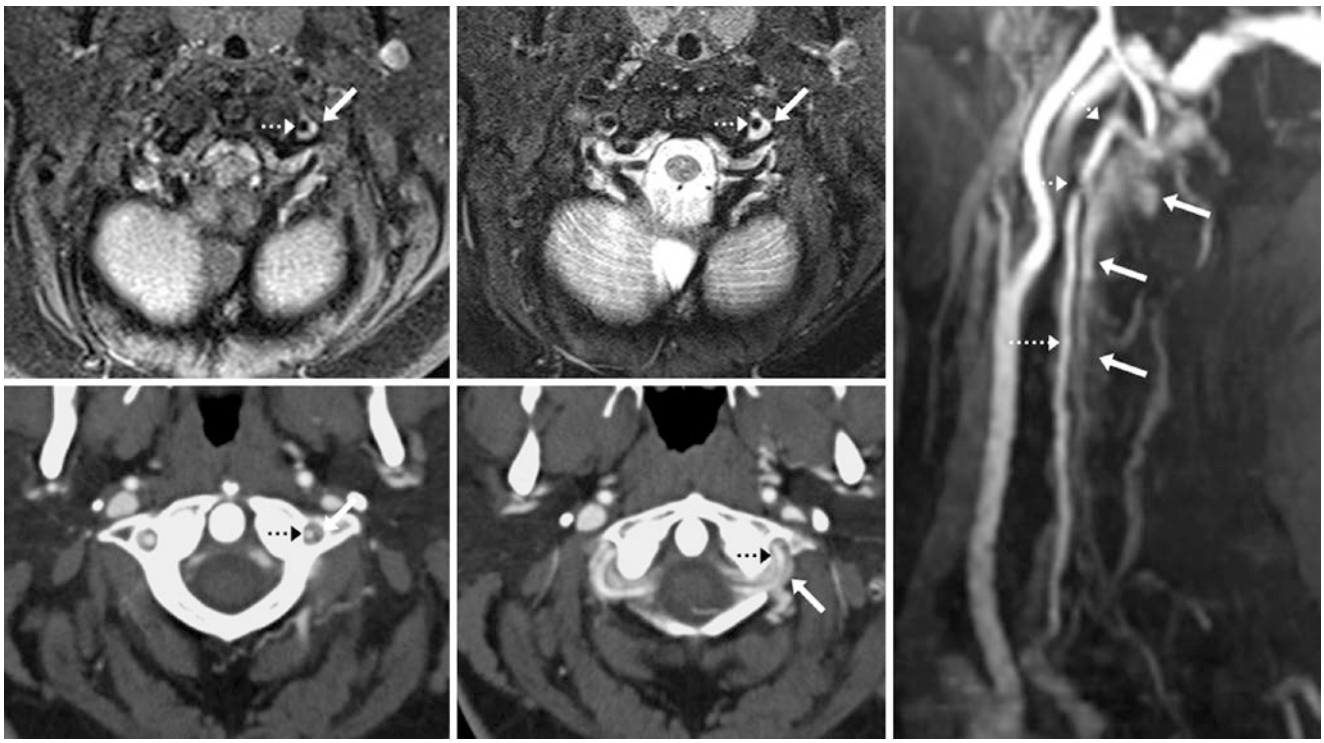

Fig. 35.9 In this 25-year-old, an MRI shows that the left vertebral artery (VA) at the level of C1 (*arrows*) is surrounded by bright signal on fat-suppressed T1WI (*top left*) and T2WI (*top middle*). On a contrast-enhanced MRA lateral view (*right*), ill-defined enhancement surrounds the left VA (*dotted arrows*), as contrast is partially in the venous phase, later confirmed to be the vertebral venous plexus (VVP) on CTA source images (*bottom left* and *middle*). The bright signal on the MRI images was likely due to slow flow within the VVP. Presaturation of caudally travelling venous spins may eliminate venous brightness on noncontrast images, but not on postcontrast images, particularly if the contrast bolus is beyond the arterial phase

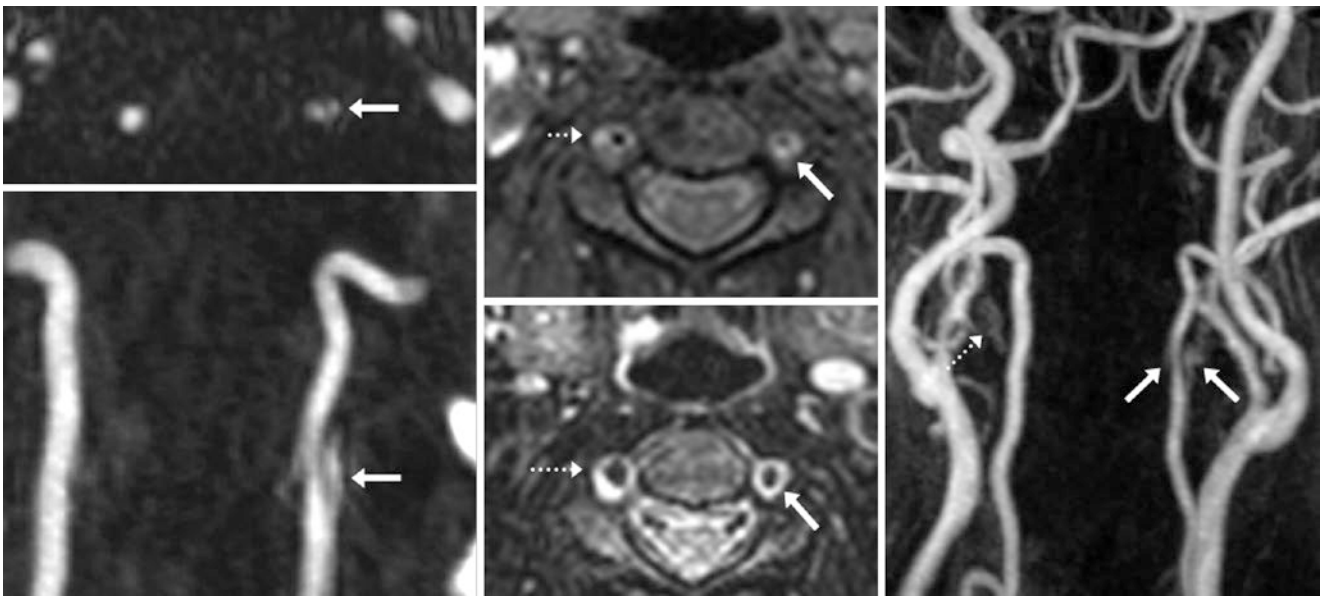

Fig. 35.10 In this 52-year-old, the left VVP (*arrows*) at the level of C3 simulated a VA dissection and pseudoaneurysm on a noncontrast 2DTOF MRA axial view (*top left*) and a 3D MIP AP view (*bottom left*). Noncontrast, fat-saturated axial T1WI (*top middle*) and T2WI (*bottom middle*) showed concentric left VVP brightness, which was also present contralaterally (*dotted arrows*). The bright signal on T1WI and T2WI was likely due to slow flow. The bilateral, ill-defined enhancement of the VVP partially surrounding the left VA on a contrast-enhanced MRA (*right*) confirmed this spurious finding

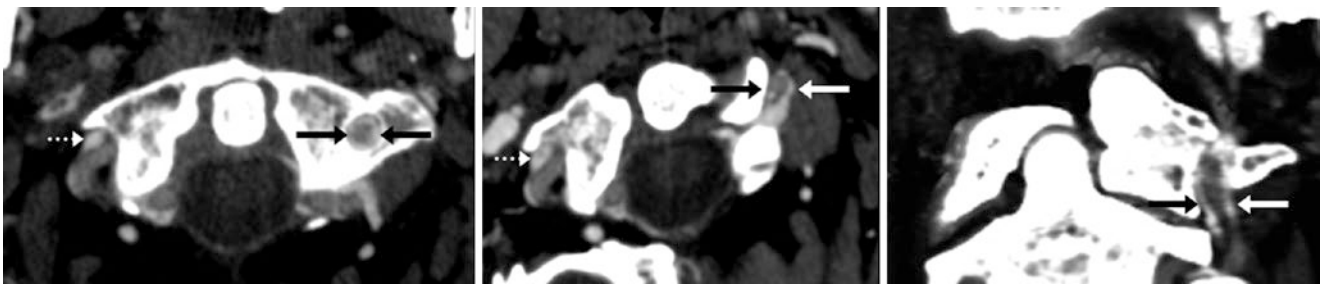

Fig. 35.11 In this 60-year-old, a CTA that was partially in the venous phase demonstrates a left VVP surrounding the VA (*arrows*) on axial (*left* and *middle*) and coronal (*right*) MPRs. The right VVP appears to be a single vein (*dotted arrows*)

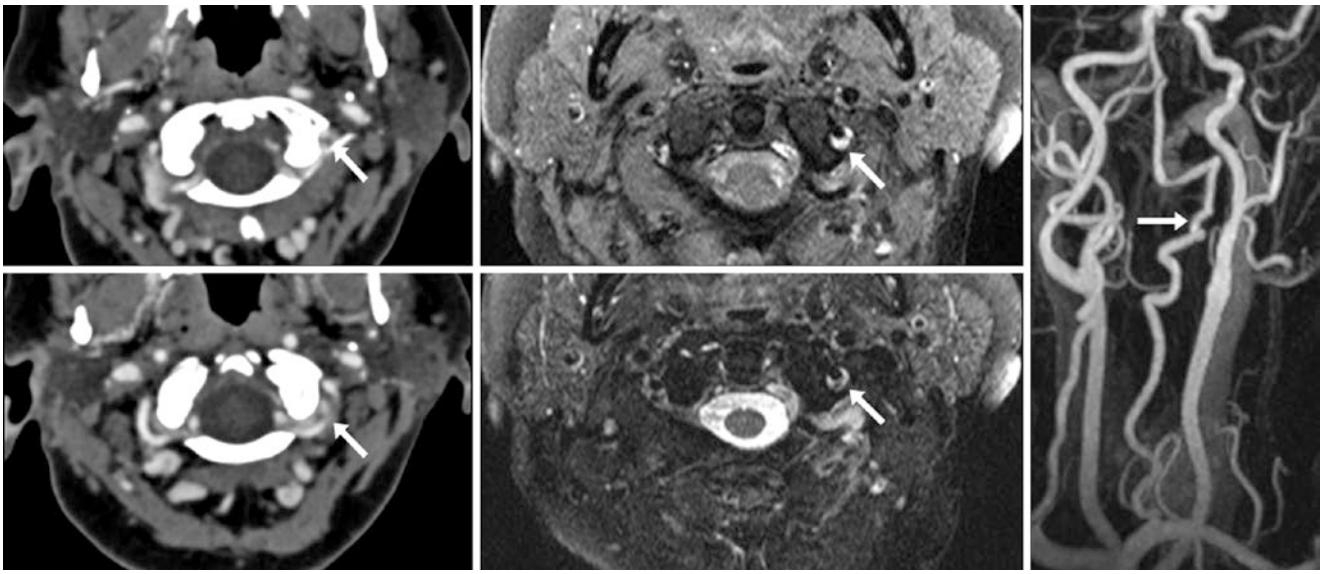

Fig. 35.12 56-year-old with the left VA surrounded by enhancement from the VVP (*arrows*) on CTA axial images (*left, top* and *bottom*), as well as bright signal on fat-suppressed axial T1WI (*top middle*) and T2WI (*bottom middle*). A contrast-enhanced MRA LAO view (*right*) was normal; the VVP was not seen due to the arterial phase of enhancement

35.4 Vertebral Venous Plexus Normal Progressive Enhancement

MRI is an excellent tool to evaluate for internal carotid artery dissection, typically with a sensitivity exceeding 90 % when utilizing fat-suppressed T1WI to image intimal flap hematoma, while contrast-enhanced MRA (CEMRA) is helpful to confirm the degree of stenosis [21–24]. However, CEMRA is subject to poor bolus timing, which affects visualization of the arteries if they are imaged in the venous phase ("venous contamination"). Figure 35.13 illustrates how the vertebral veins (or plexi) progressively enhance over the first few minutes dynamically following intravenous contrast administration.

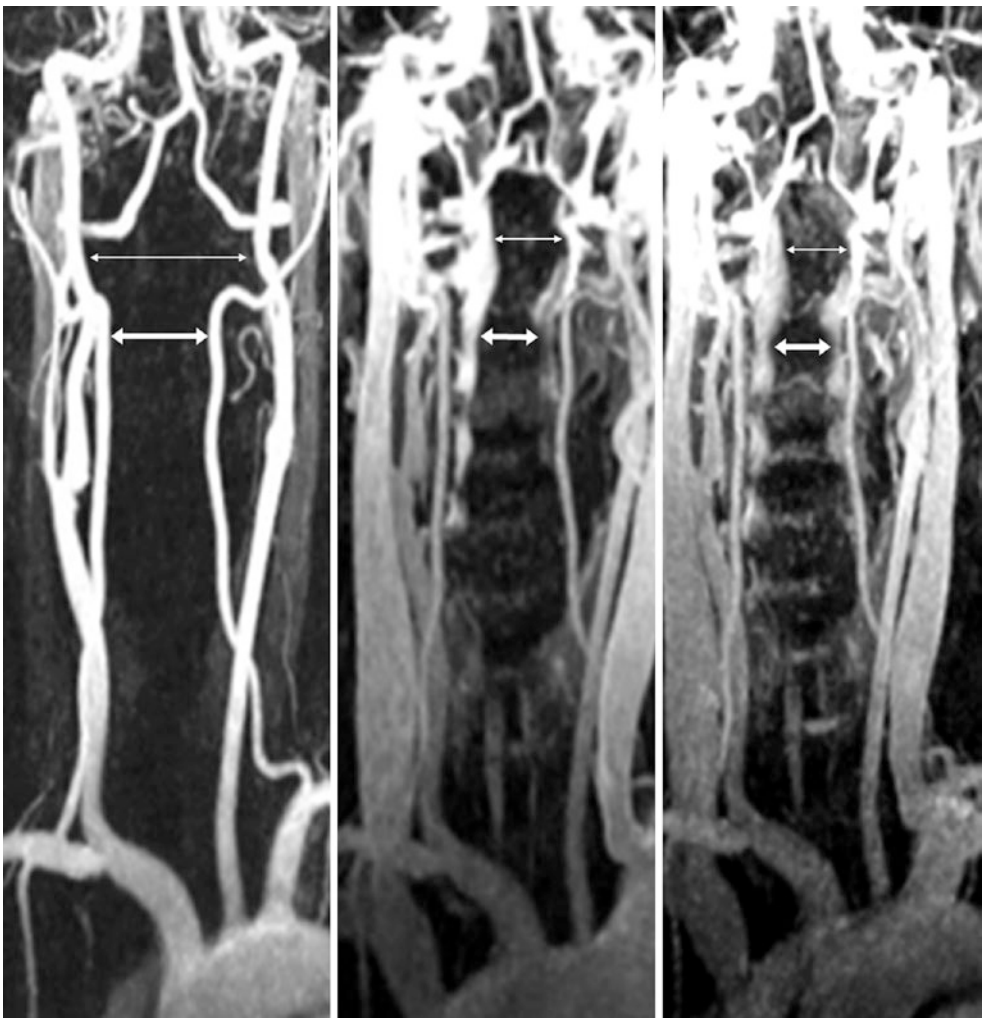

Fig. 35.13 58-year-old with progressive enhancement of the VVP surrounding both VAs (*arrows*) at the level of C2 on a contrast-enhanced MRA, with images obtained at a 15- to 25-s delay (*left*), 3-min delay (*middle*), and at 5 min (*right*) after intravenous gadolinium administration. Note how the VVP enhancement surrounding the VA is most prominent above C2, particularly at the C1 level (*thin arrows*), and at the cervicooccipital junction. These images illustrate how an unintended delay in scanning after the contrast bolus could limit evaluation of the VAs

References

1. Lobato EB, Sulek CA, Moody RL, Morey TE. Cross-sectional area of the right and left internal jugular veins. J Cardiothorac Vasc Anesth. 1999;13:136–8.
2. Lichtenstein D, Saïfi R, Augarde R, Prin S, Schmitt JM, Page B, et al. The internal jugular veins are asymmetric. Usefulness of ultrasound before catheterization. Intensive Care Med. 2001;27:301–5.
3. Lim CL, Keshava SN, Lea M. Anatomical variations of the internal jugular veins and their relationship to the carotid arteries: a CT evaluation. Australas Radiol. 2006;50:314–8.
4. Denys BG, Uretsky BF. Anatomical variations of internal jugular vein location: impact on central venous access. Crit Care Med. 1991;19:1516–9.
5. Palombi O, Fuentes S, Chaffanjon P, Passagia JG, Chirossel JP. Cervical venous organization in the transverse foramen. Surg Radiol Anat. 2006;28:66–70.
6. Lu J, Ebraheim NA, Ouyang J, Yeasting RA. Cervical venous structure in the inter-transverse and intra-transverse foraminal region: an anatomic study. Am J Orthop. 2000;29:196–8.
7. San Millán Ruíz D, Gailloud P, Rüfenacht DA, Delavelle J, Henry F, Fasel JH. The craniocervical venous system in relation to cerebral venous drainage. AJNR Am J Neuroradiol. 2002;23:1500–8.
8. Groen RJ, du Toit DF, Phillips FM, Hoogland PV, Kuizenga K, Coppes MH, et al. Anatomical and pathological considerations in percutaneous vertebroplasty and kyphoplasty: a reappraisal of the vertebral venous system. Spine. 2004;29:1465–71.
9. Magro E, Gentric JC, Talagas M, Alavi Z, Nonent M, Dam-Hieu P, Seizeur R. Venous organization in the transverse foramen: dissection, histology, and magnetic resonance imaging. J Neurosurg. 2015;123:118–25.
10. Torres C, Hogan M, Patro S, Chakraborty S, Nguyen T, Thornhill R, et al. Extracranial venous abnormalities: a true pathological finding in patients with multiple sclerosis or an anatomical variant? Eur Radiol. 2016 [Epub ahead of print].
11. Czyżewska D, Krysiuk K, Dobrzycki K, Ustymowicz A. Ultrasound assessment of the jugular and vertebral veins in healthy individuals: selected physiological aspects and morphological parameters. J Ultrason. 2015;15:267–73.
12. Zivadinov R, Lopez-Soriano A, Weinstock-Guttman B, Schirda CV, Magnano CR, Dolic K, et al. Use of MR venography for characterization of the extracranial venous system in patients with multiple sclerosis and healthy control subjects. Radiology. 2011;258:562–70.
13. Buch K, Groller R, Nadgir RN, Fujita A, Qureshi MM, Sakai O. Variability in the cross-sectional area and narrowing of the internal jugular vein in patients without multiple sclerosis. AJR Am J Roentgenol. 2016;206:1082–6.
14. Chambers B, Chambers J, Churilov L, Cameron H, Macdonell R. Internal jugular and vertebral vein volume flow in patients with clinically isolated syndrome or mild multiple sclerosis and healthy controls: results from a prospective sonographer-blinded study. Phlebology. 2014;29:528–35.
15. Zwischenberger BA, Beasley MM, Davenport DL, Xenos ES. Meta-analysis of the correlation between chronic cerebrospinal venous insufficiency and multiple sclerosis. Vasc Endovascular Surg. 2013;47:620–4.
16. Rodger IW, Dilar D, Dwyer J, Bienenstock J, Coret A, Coret-Simon J, et al. Evidence against the involvement of chronic cerebrospinal venous abnormalities in multiple sclerosis. A case–control study. PLoS One. 2013;8, e72495.
17. Diehn FE, Schwartz KM, Hunt CH, Eckel LJ, Campeau NG, Carter RE, et al. Prevalence of incidental narrowing of the superior segment of the internal jugular vein in patients without multiple sclerosis. Clin Neuroradiol. 2014;24:121–7.
18. Umaña M, García A, Bustamante L, Castillo JL, Sebastián Martínez J. Variations in the anatomical relationship between the common carotid artery and the internal jugular vein: an ultrasonographic study. Colomb Med. 2015;46:54–9.
19. Ozbek S, Apiliogullari S, Kıvrak AS, Kara I, Saltali AO. Relationship between the right internal jugular vein and carotid artery at ipsilateral head rotation. Ren Fail. 2013;35:761–5.
20. Turba UC, Uflacker R, Hannegan C, Selby JB. Anatomic relationship of the internal jugular vein and the common carotid artery applied to percutaneous transjugular procedures. Cardiovasc Intervent Radiol. 2005;28:303–6.
21. Bachmann R, Nassenstein I, Kooijman H, Dittrich R, Kugel H, Niederstadt T, et al. Spontaneous acute dissection of the internal carotid artery: high-resolution magnetic resonance imaging at 3.0 tesla with a dedicated surface coil. Invest Radiol. 2006;41:105–11.
22. Cuvinciuc V, Viallon M, Momjian-Mayor I, Sztajzel R, Pereira VM, Lovblad KO, Vargas MI. 3D fat-saturated T1 SPACE sequence for the diagnosis of cervical artery dissection. Neuroradiology. 2013;55:595–602.
23. Provenzale JM, Sarikaya B. Comparison of test performance characteristics of MRI, MR angiography, and CT angiography in the diagnosis of carotid and vertebral artery dissection: a review of the medical literature. AJR Am J Roentgenol. 2009;193:1167–74.
24. Rizzo L, Crasto SG, Savio D, Veglia S, Davini O, Giraudo M, et al. Dissection of cervicocephalic arteries: early diagnosis and follow-up with magnetic resonance imaging. Emerg Radiol. 2006;12:254–65.

Intracranial Posterior Circulation Variants

36

There are many normal congenital variations of the vessels branching off the *vertebrobasilar system* [1–20]. First, it is important to note whether a vertebral artery is *hypoplastic* or quite small (as opposed to a stenosis or occlusion); a vertebral artery can terminate in the posterior inferior cerebellar artery (PICA) or it can be extremely small distal to the PICA origin. Also, *fenestrations* of the vertebral or basilar arteries or their branches are not uncommon and may involve nearly any vessel in the anterior or posterior circulations.

Vertebral and basilar *fenestrations* are focal duplications of the artery that create a "fenestra" ("window"). They are present in the vertebrobasilar system in approximately 0.5–5 % of the population [1–5]. These are considered normal variants, but are of note clinically because of a debate about whether these focal duplications mildly increase the risk of associated aneurysms at the site of fenestration or the remainder of the Circle of Willis, relative to patients without fenestrations. A risk of 5–8 % has been reported in those with fenestrations, versus 3–5 % in the general population [1–5]. The recent literature suggests that anterior communicating artery fenestrations may have a slightly higher risk of an associated aneurysm, whereas this is probably not true for vertebrobasilar fenestrations. The location and length of the fenestration and its relationship to the posterior inferior cerebellar artery (PICA) and anterior inferior cerebellar artery (AICA) become critical factors to describe when such patients present for aneurysm embolization. A relatively rare duplication or fenestration is of the posterior cerebral artery (PCA).

Another posterior circulation variant at the skull base is an *extradural origin of the PICA*—that is, it arises from the vertebral artery before it pierces the dura of the foramen magnum to travel intracranially. This variant is estimated to occur in 5–20 % of patients [6, 7]. Also, the PICA can rarely arise from the basilar artery, or even more rarely, from the internal carotid artery (ICA).

Duplication of the superior cerebellar artery (SCA) occurs in about 5–25 % of the population, *duplication of the anterior inferior cerebellar artery* (AICA) may be present in up to 10–20 %, and a *common trunk of the SCA and PCA* occurs in about 1–5 %. Another variant is when the AICA may be dominant on one side, with the ipsilateral PICA absent or tiny; there are many variations in how much of the cerebellar parenchyma each of these vessels supplies [8–15]. The reverse can also occur: a large PICA may be dominant on one side, with the ipsilateral AICA absent or tiny. The AICA may also loop into the internal auditory canal and mimic a vascular contact syndrome [15–17].

At the level of the Circle of Willis, the most commonly noted variant is likely the so-called *fetal origin of the PCA*, in which the PCA arises from the posterior communicating segment of the ICA, and the ipsilateral P1 segment arising from the basilar termination is either absent or quite hypoplastic [18–21]. This variant occurs in about 10–20 % of the population; usually the P1 segment from the basilar is present to some degree, although the artery may be very tiny. This variant can be unilateral or bilateral, and occasionally a quite small (or even hypoplastic) basilar can occur with prominent, bilateral "fetal PCAs." Again, duplication or *fenestration of the PCA* does occur but is relatively rare.

It is important to note CTA and MRA are the two most commonly utilized modalities to detect and screen for *aneurysms*. Modern CT scanners of 64 detectors or greater, or 3.0 T MRA can readily resolve aneurysms at least 2 mm in size [22–24]. Thus, conventional catheter DSA is generally reserved either for therapy or to confirm a suspected aneurysm. It is not necessary to confirm any of the normal variations mentioned above, unless there is a question on how they will affect surgery or endovascular treatment.

This chapter is first organized from caudal to cranial regarding each vessel, and thereafter it is organized by the type of anatomic variation.

A.M. McKinney, *Atlas of Normal Imaging Variations of the Brain, Skull, and Craniocervical Vasculature*,
DOI 10.1007/978-3-319-39790-0_36

36.1 Vertebrobasilar Fenestrations

Fenestrations are focal duplications ("fenestra" or "window") of an artery; in the population, vertebrobasilar arterial (VBA) fenestrations are noted incidentally in about 0.5–5 % of the population [1–5]. Hence, these are not rare; they should be considered normal variations and "don't touch" lesions, though most opine that it is important to report them clinically (Figs. 36.1, 36.2, 36.3, 36.4, 36.5, 36.6, 36.7, 36.8, 36.9, 36.10, 36.11, and 36.12).

Debate continues as to whether they have a minimally elevated risk of *aneurysms*, Newer data suggest that there is no elevated risk at the fenestration site, although there could be a slightly higher risk elsewhere intracranially, relative to those who lack fenestrations. (A risk of 5–8 % has been reported in those with fenestrations, versus 3–5 % in the general population [1–5].)

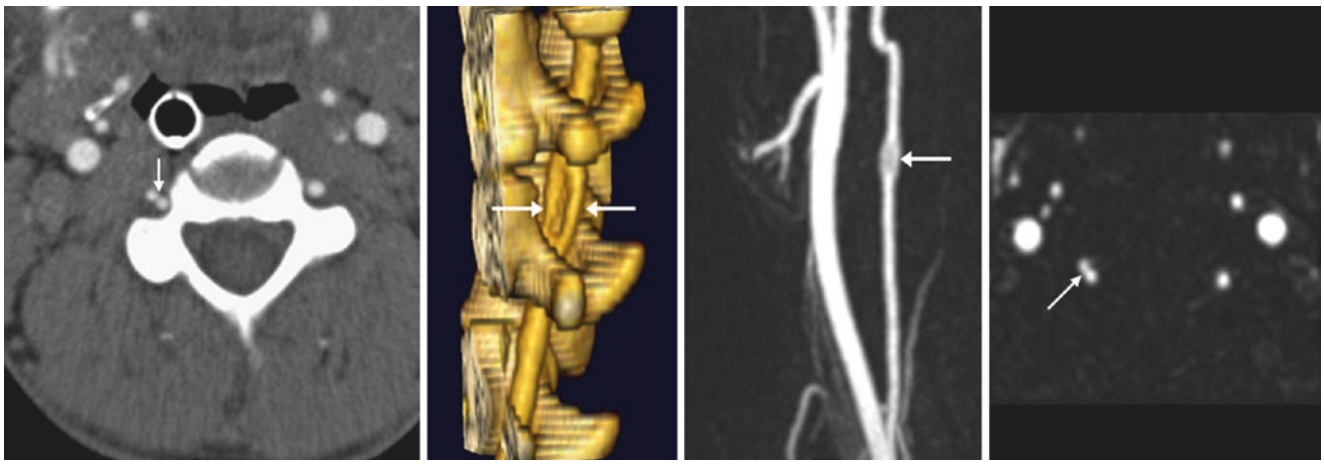

Fig. 36.1 23-year-old with a cervical vertebral artery (VA) fenestration (*arrows*) on 0.8-mm source CTA images (*left*), 3D VR CTA lateral view (*left middle*), and on a contrast-enhanced MRA AP view (*right middle*) with axial source images (*far right*)

Fig. 36.2 40-year-old with a large VA fenestration (*large arrows*) near the craniocervical junction on a 3DTOF MRA AP view (*top left*) and on a source image (*bottom left*). Catheter DSA AP and lateral views (*top middle* and *top right*) and source CTA images (*bottom right*) also depict the fenestration. The right posterior inferior cerebellar artery (PICA) (*tiny arrows*) arises from the superior aspect

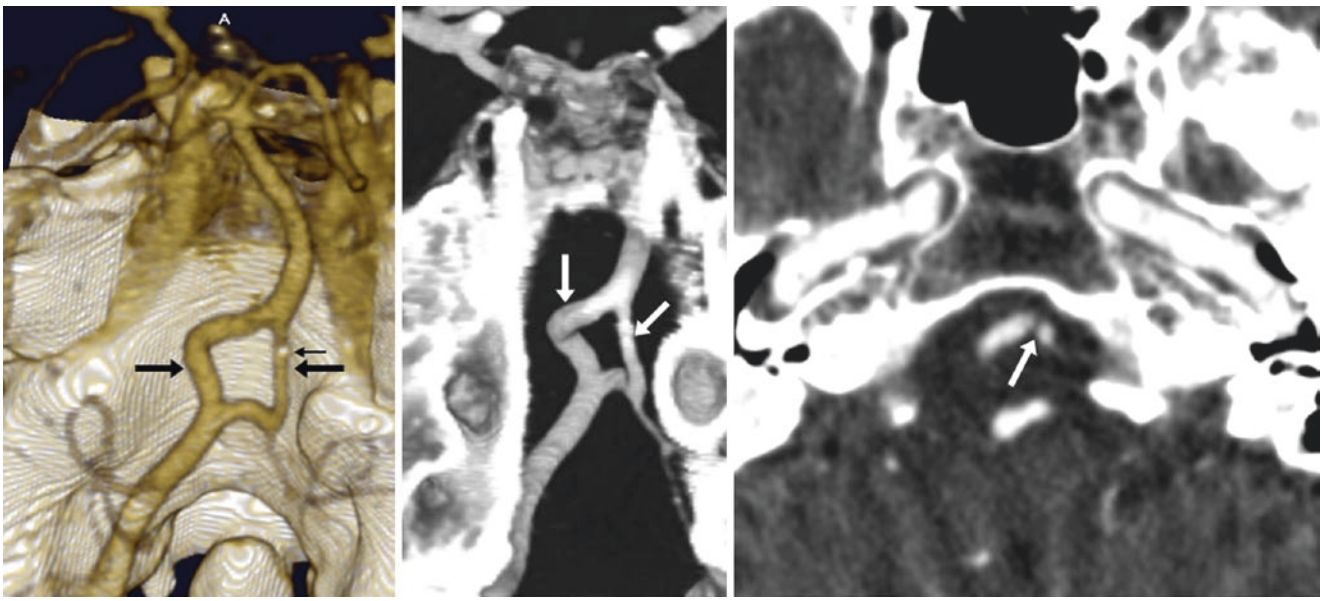

Fig. 36.3 73-year-old with a sizable vertebrobasilar junction fenestration (*large arrows*) on a 3D VR CTA posterior view (*left*), coronal MPR (*middle*), and source axial image, which delineates the cleft (*right, arrow*). Note a tiny atherosclerotic calcification (*left, thin arrow*). The right VA was dominant; the left was quite tiny and hypoplastic

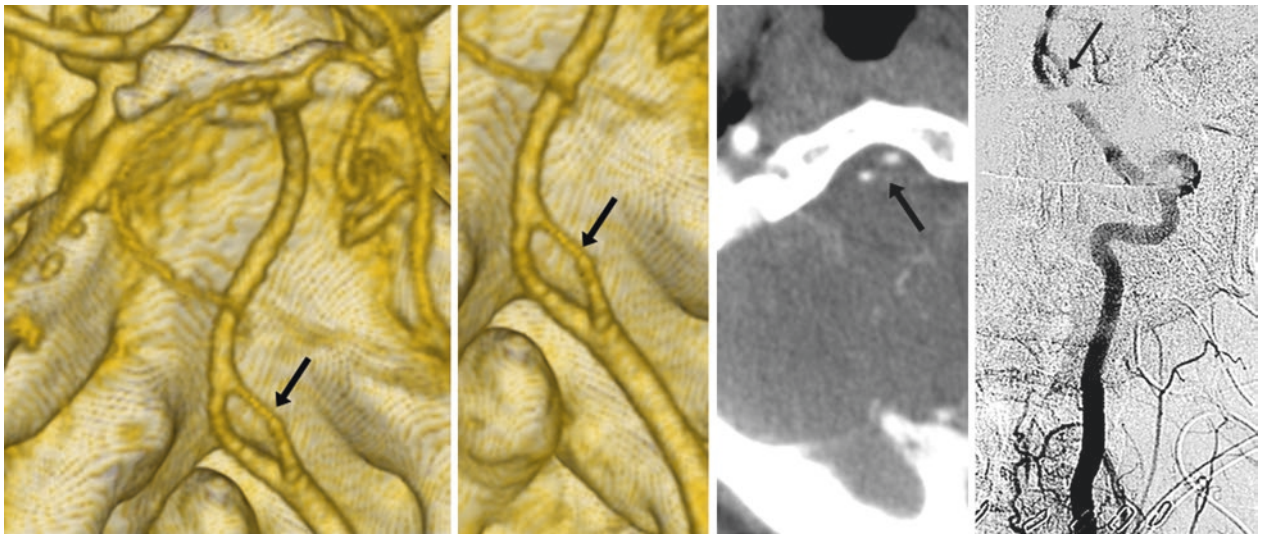

Fig. 36.4 53-year-old with a vertebrobasilar junction fenestration (*arrows*) on posterior views from a 3D VR CTA (*left* and magnified at *left middle*), and on source images (*right middle*). The fenestration also was visualized on a DSA AP view, obtained via a left subclavian artery injection (*right*). The right VA was tiny and hypoplastic

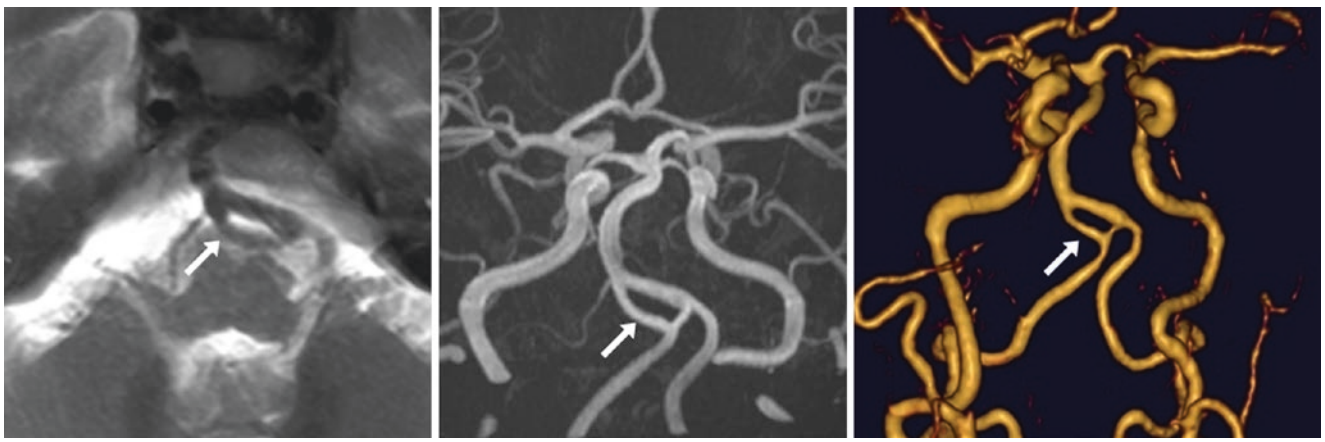

Fig. 36.5 53-year-old with a sizable vertebrobasilar junction fenestration (*arrows*) on an axial T2WI 12-mm MPR (*left*) and on an AP view from a 3DTOF MRA (*middle*), with a color MIP (*right*). The VAs are symmetric in size

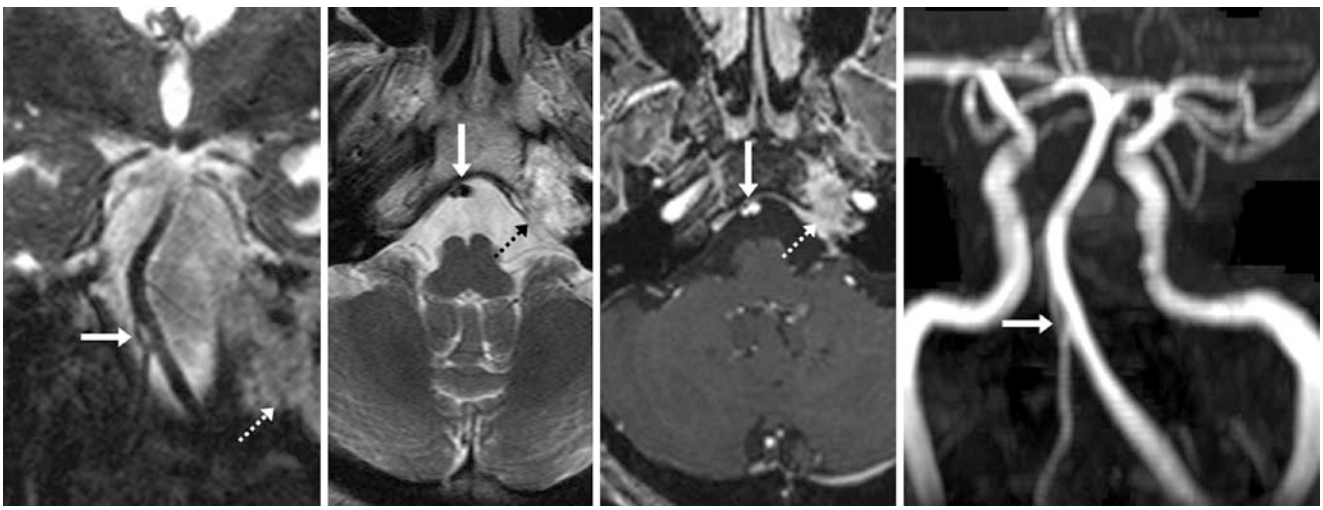

Fig. 36.6 49-year-old with a fenestration at the top of the vertebrobasilar junction (*arrows*) on a coronal T2WI (*left*), axial T2WI (*left middle*), postcontrast T1WI (*right middle*), and on a 3DTOF MRA AP view (*right*), with a hypoplastic right VA. Note a T2-bright, enhancing chondrosarcoma (*dotted arrows*) of the left petrous apex

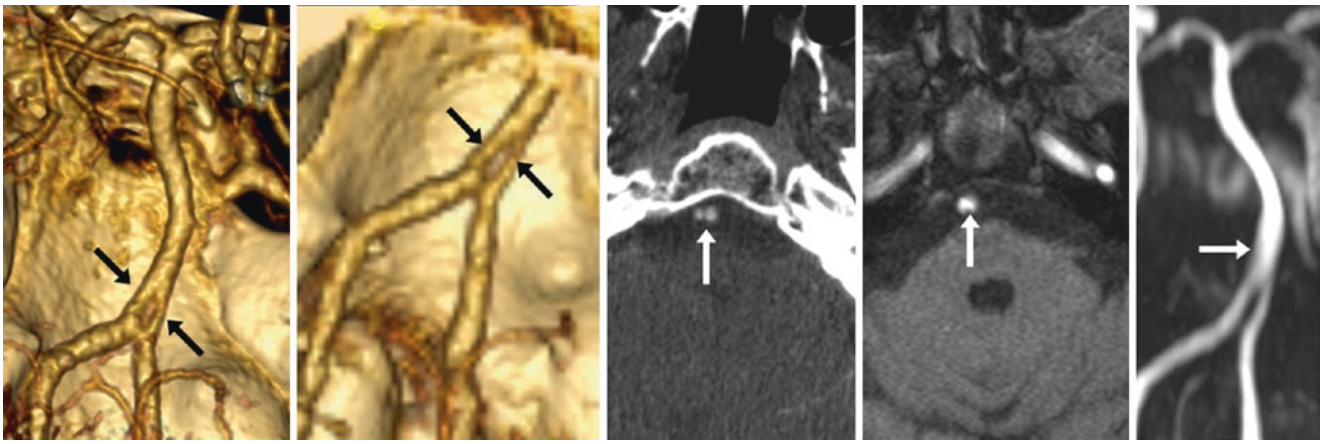

Fig. 36.7 47-year-old with a lower basilar fenestration (*arrows*) just above the vertebrobasilar confluence on a CTA with posterior views (*left* and *left middle*). The cleft was clearly seen on axial source images from the CTA (*middle*), but not on 3DTOF MRA axial source images (*right middle*), or on an MRA MIP AP view (*right*)

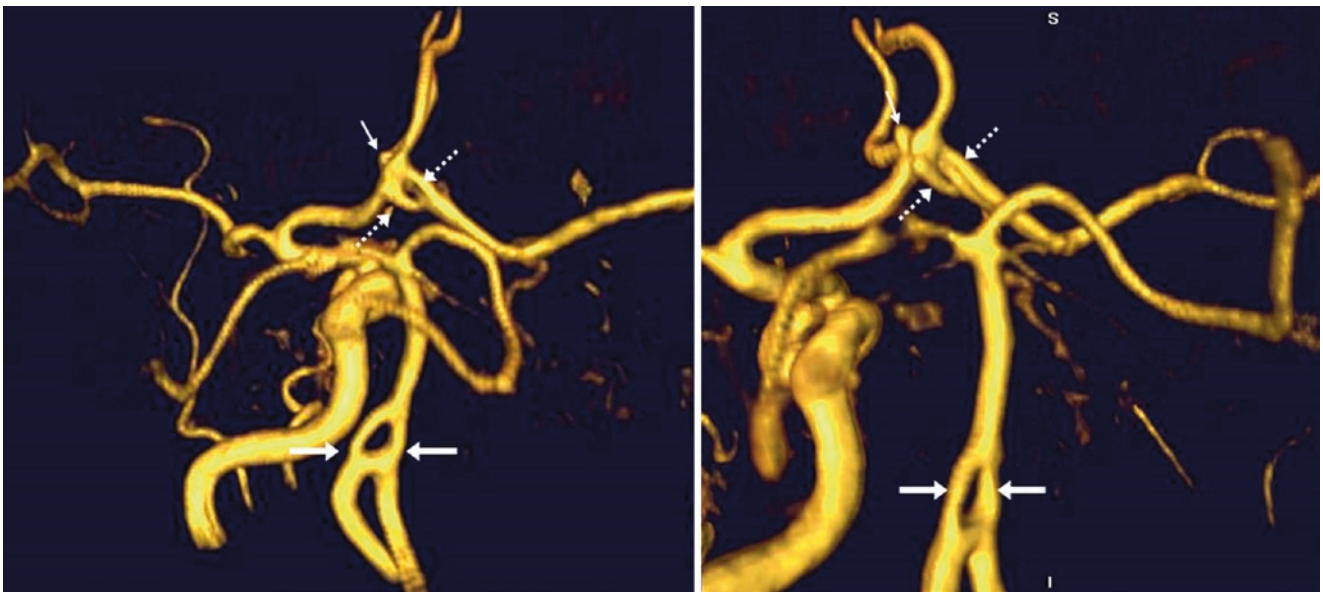

Fig. 36.8 53-year-old with a lower basilar fenestration (*large arrows*) on a 3DTOF MRA posterior view (*left*) and a direct posterior/PA view (*right*), just above the vertebrobasilar junction. Note an anterior communicating artery fenestration as well (*dotted arrows*), with a tiny adjacent aneurysm (*thin arrows*). The right internal carotid artery (ICA) is occluded

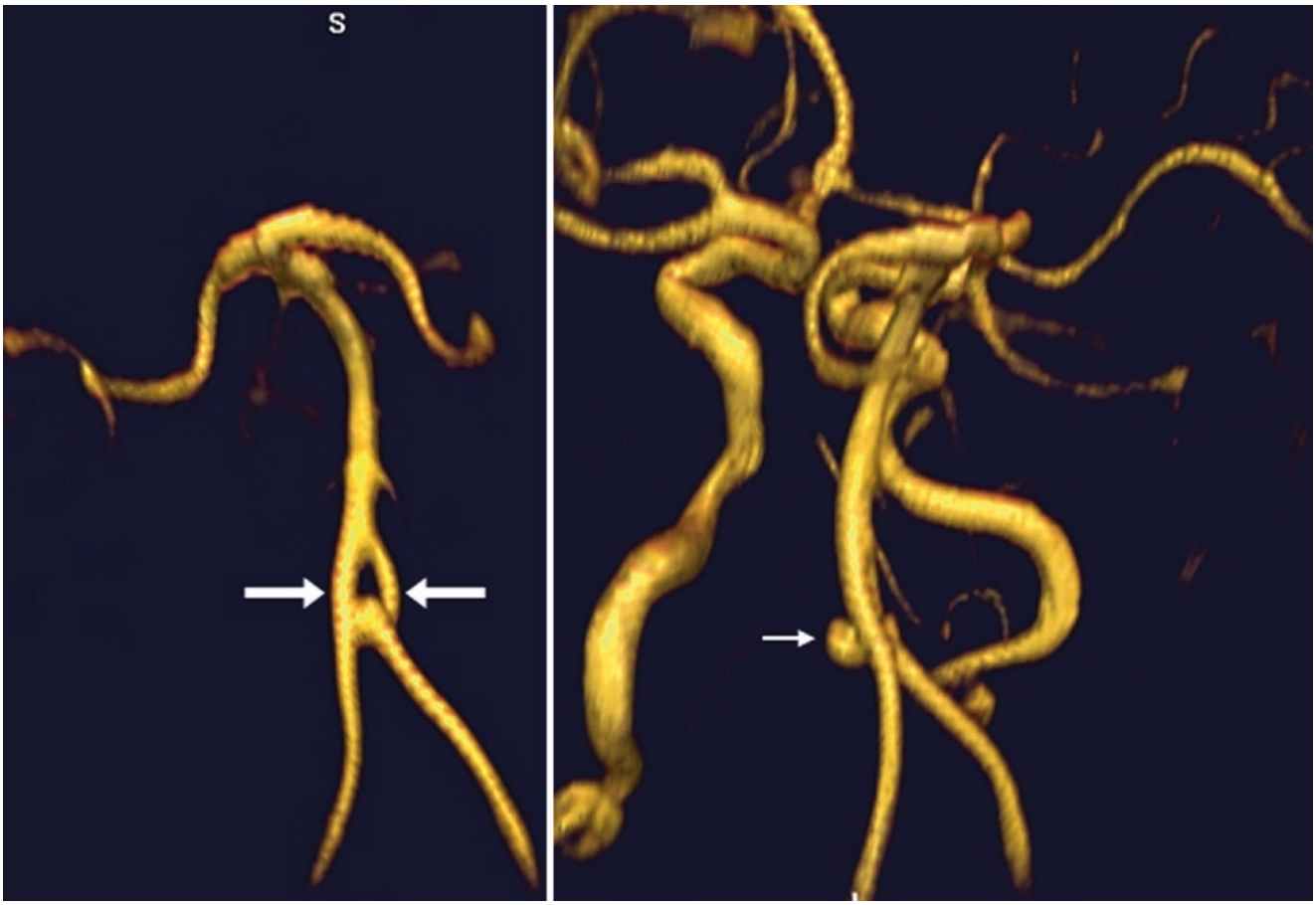

Fig. 36.9 Basilar aneurysm with fenestration in a 61-year-old. A lower basilar fenestration (*large arrows*) is noted on 3DTOF MRA posterior PA (*left*) and oblique (*right*) views, with a small aneurysm (*thin arrow*) protruding from it directly posteriorly

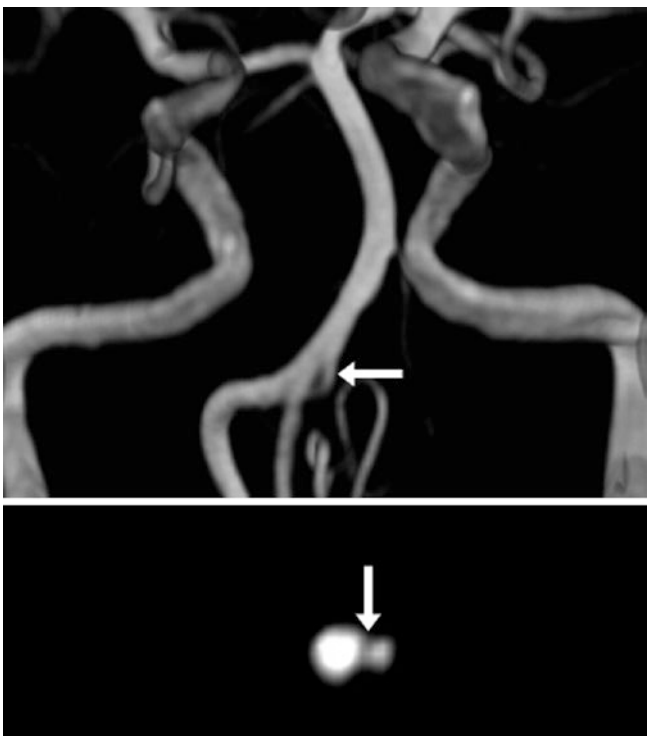

Fig. 36.10 In this 76-year-old, a fenestration (*arrows*) is eccentric to the lumen on 3DTOF MRA AP (*top*) and source (*bottom*) images

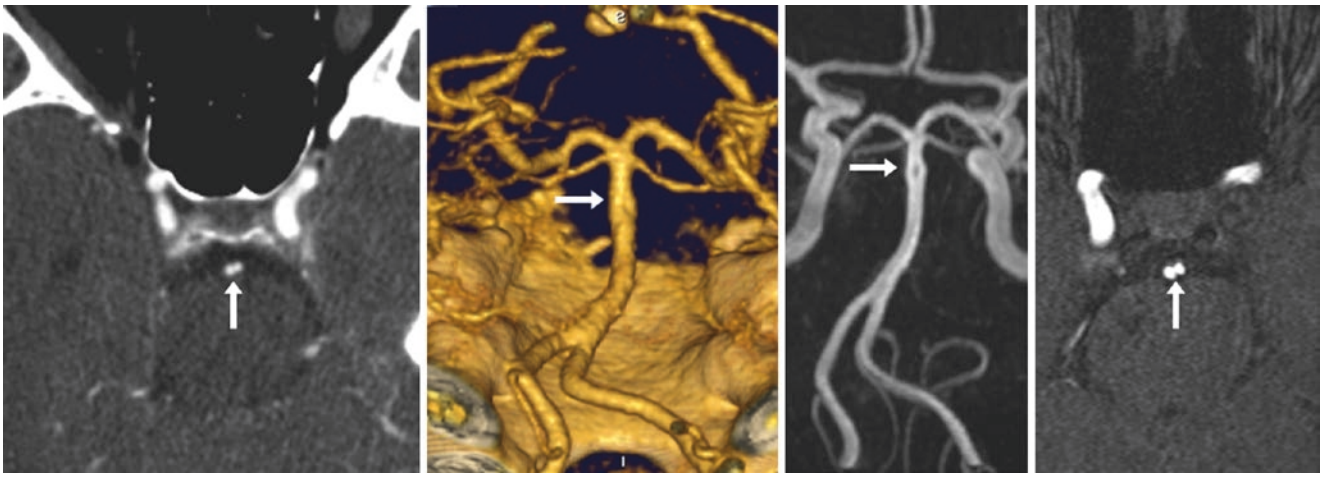

Fig. 36.11 53-year-old with the cleft of a tiny mid-basilar fenestration (*arrows*), questioned on source CTA images (*left*), although not seen on 3D VR images (*posterior view*, *left middle*). The fenestration was better visualized on a 3DTOF MRA posterior view (*right middle*), and the cleft was clearly seen on axial source images (*right*)

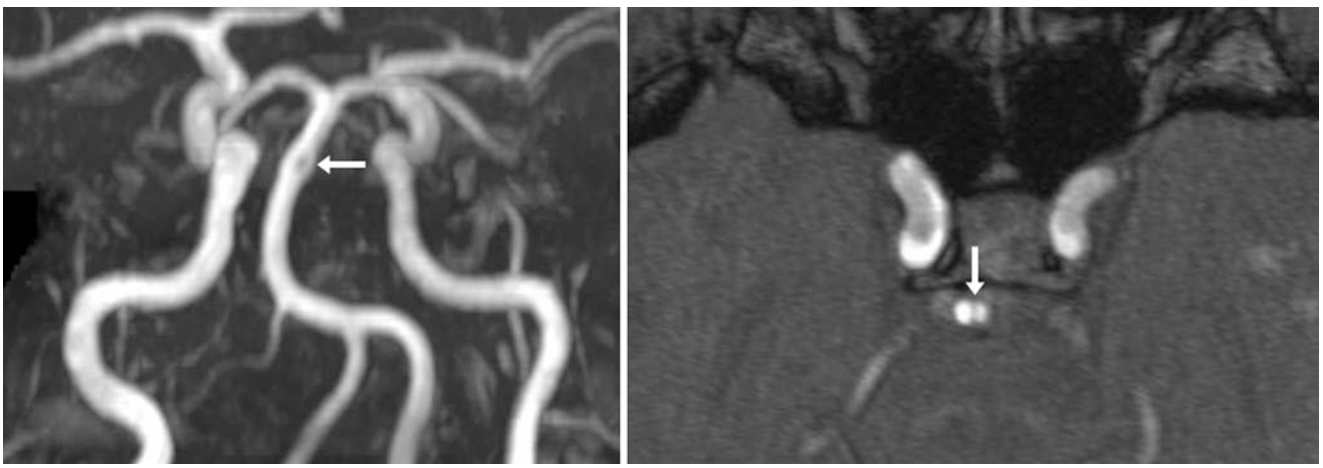

Fig. 36.12 41-year-old with a tiny mid-basilar artery fenestration on a 3DTOF MRA AP view (*left*), with a small cleft (*arrows*) visualized on axial source images (*right*)

36.2 Extradural Origin of the PICA

An *extradural origin of the posterior inferior cerebellar artery* (PICA) arises from the vertebral artery (VA) before it pierces the dura (Fig. 36.13). This variant is thought to occur in 5–20 % of patients [6, 7]. Rarely, the PICA can originate even from the basilar artery or the internal carotid artery (ICA). This variant is likely of import only for surgical purposes.

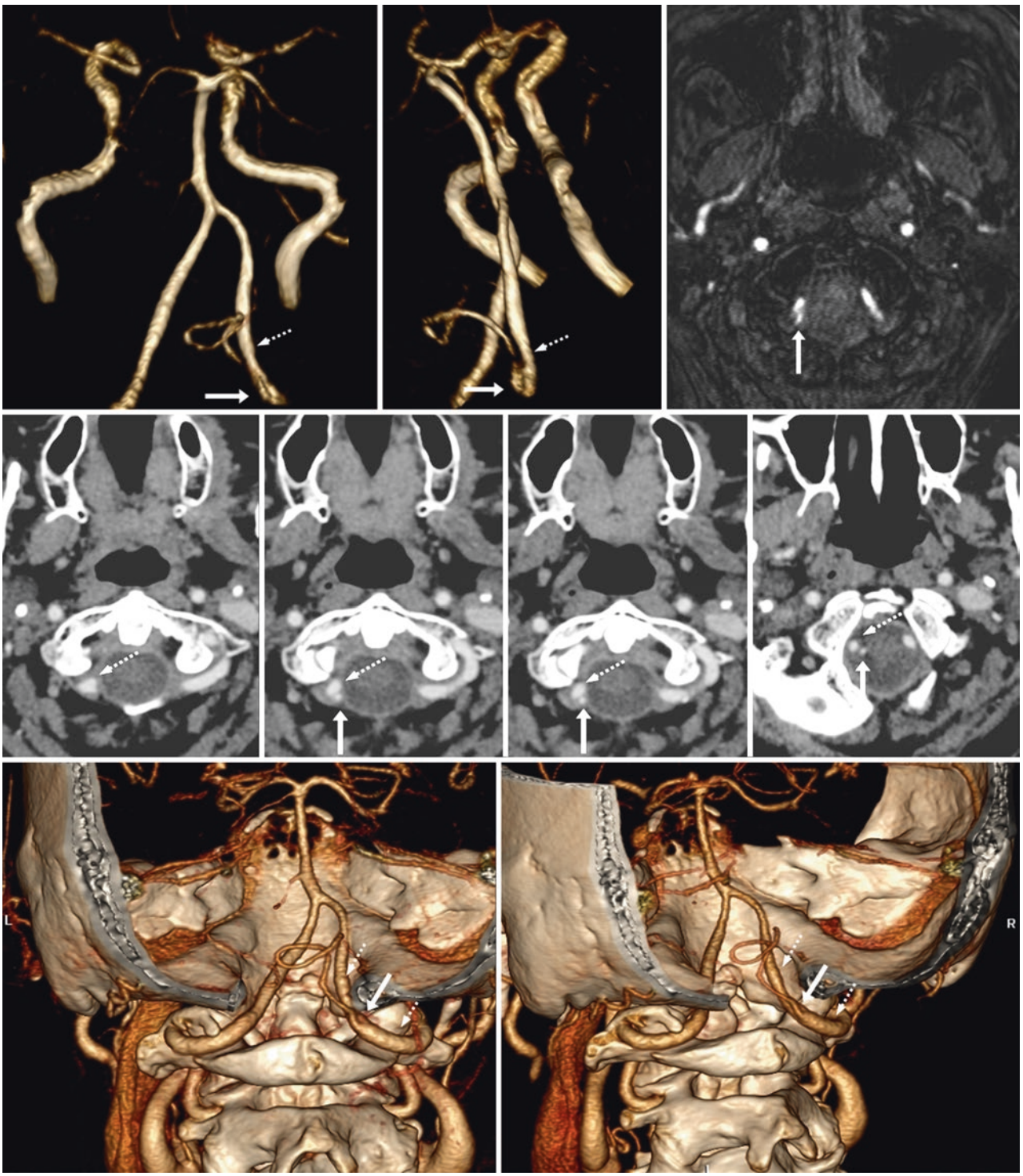

Fig. 36.13 76-year-old with dizziness. *Top row:* 3DTOF MRA PA view (*left*) and right lateral view (*middle*) show a low origin of the right PICA (*arrows*) from the right VA (*dotted arrows*), also visualized on source MRA images (*right*). *Middle row:* CTA source images confirm the extradural origin of the PICA. *Bottom row:* A 3D VR CTA PA view (*left*) and LPO view (*right*) depict the origin of the PICA (*arrows*), along with the course of the right VA (*dotted arrows*)

36.3 AICA-PICA Variations in Size and Supply

The course of the *anterior inferior cerebellar artery* (AICA) is variable, as is the amount of cerebellar parenchyma it supplies. It can be dominant on one side, with the ipsilateral PICA absent or tiny, and often the size of the AICA and PICA are inversely proportional to each other [8–14]. For example, it is not uncommon for a prominent PICA on one side to supply the posteroinferior and anteroinferior cerebellum, with the ipsilateral AICA being absent, while the contralateral AICA is dominant and the contralateral PICA is absent. Other variations include *AICA duplication* (about 30 %), *PICA duplication* (rare), or *AICA-PICA complex* (AICA bifurcates early on one side and supplies both distributions with absent PICA) (Figs. 36.14, 36.15, 36.16, 36.17, 36.18, 36.19, 36.20, 36.21, 36.22, 36.23, 36.24, and 36.25).

Fig. 36.14 64-year-old with AICA-PICA dominance on opposite sides, on PA views from 3D VR CTA (*left*) and TOF MRA (*right*). Only the left posterior inferior cerebellar artery (PICA) (*solid arrows*) and right anterior inferior cerebellar artery (AICA) (*dotted arrows*) are present

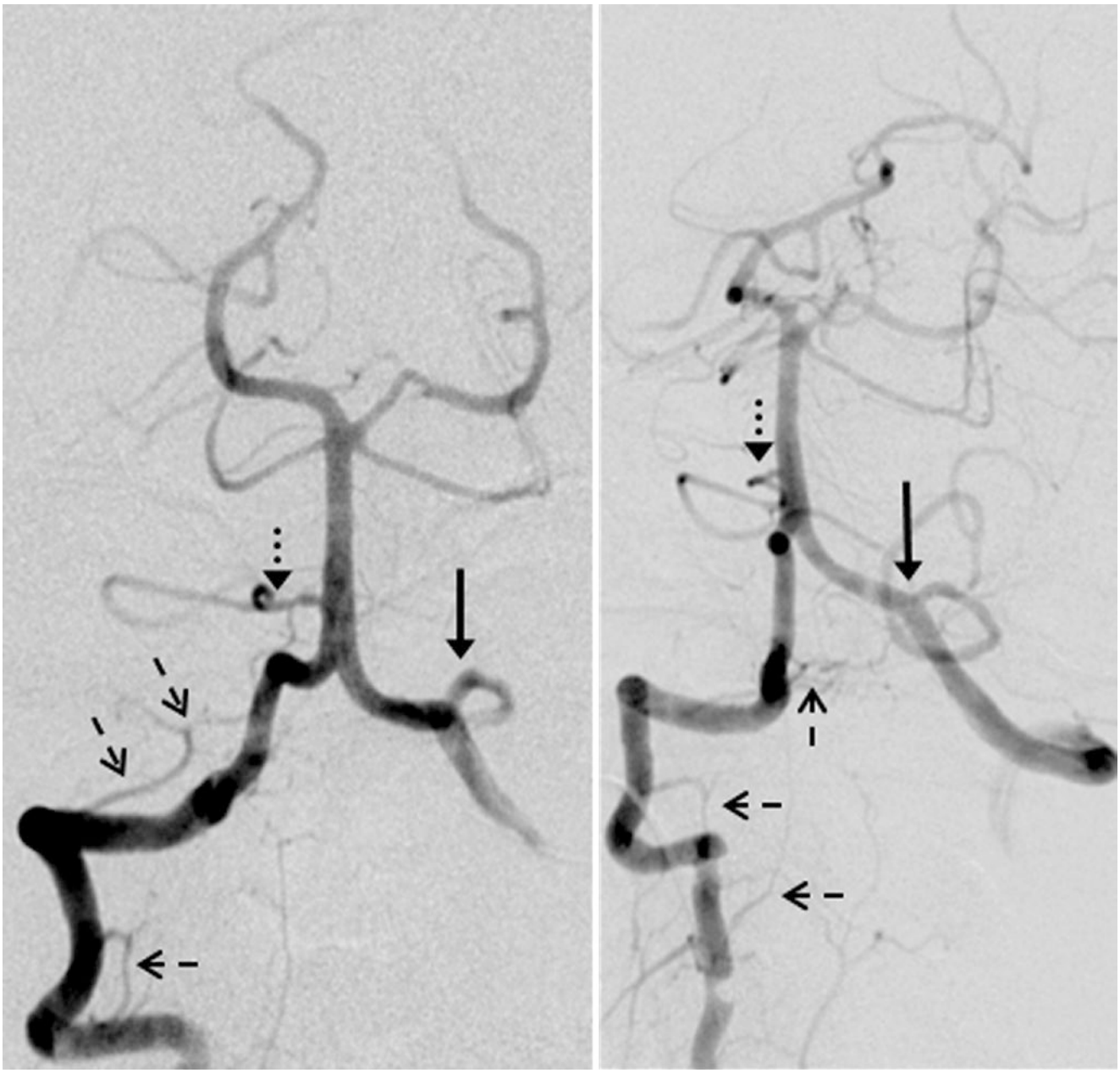

Fig. 36.15 42-year-old with an "AICA-PICA complex" on DSA AP view (*left*) and LAO view (*right*). The right AICA (*dotted arrows*) bifurcates early; the left PICA (*large arrows*) dominates. Note normal VA perforators (*dashed arrows*)

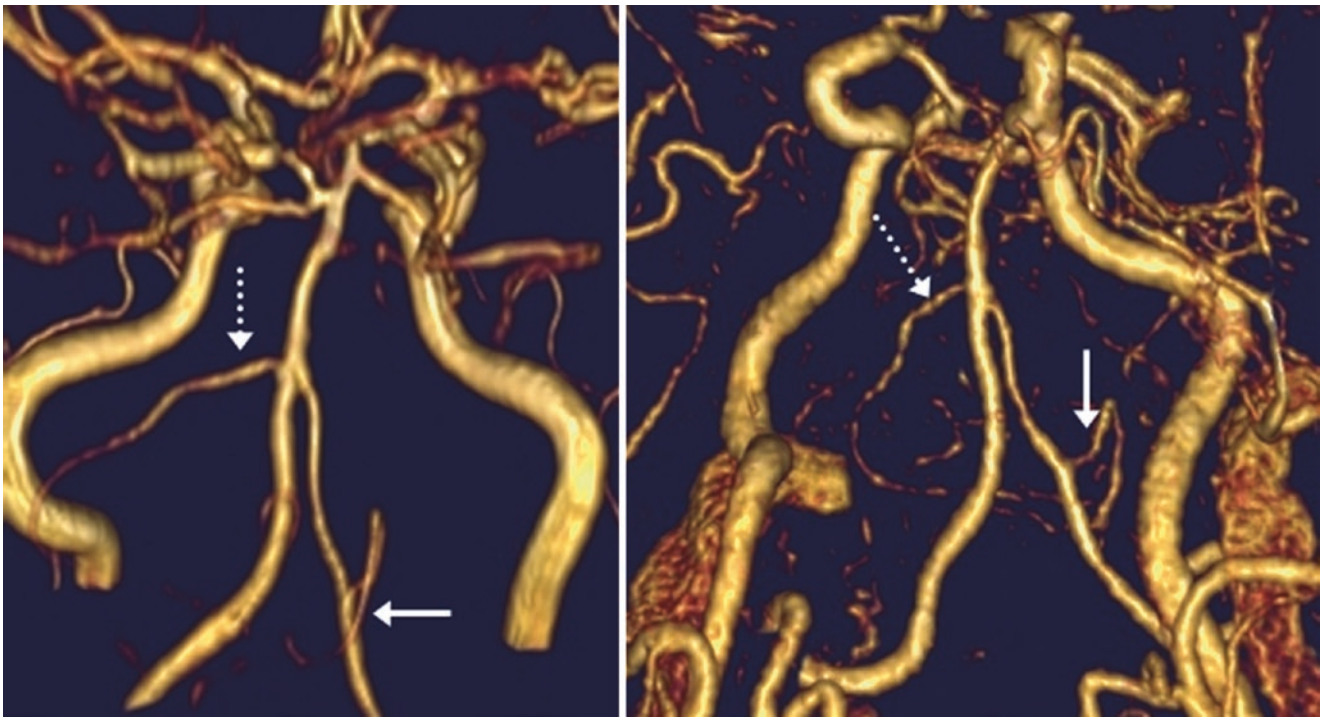

Fig. 36.16 49-year-old with contralateral AICA-PICA (*arrows*) dominance on PA views from 3DTOF MRA (*left)* and contrast-enhanced MRA (*right*). Only the right PICA (*solid arrows*) and left AICA (*dotted arrows*) are visualized in a patient with a small, mildly hypoplastic basilar artery

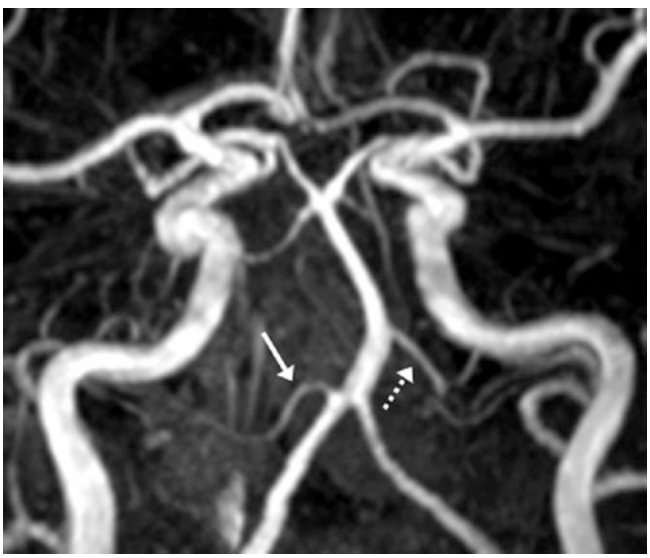

Fig. 36.17 66-year-old with a left AICA-PICA complex on a 3DTOF MRA AP view; the left AICA splits early (*dotted arrow*). Note an atypical high right PICA or low AICA (*arrow*)

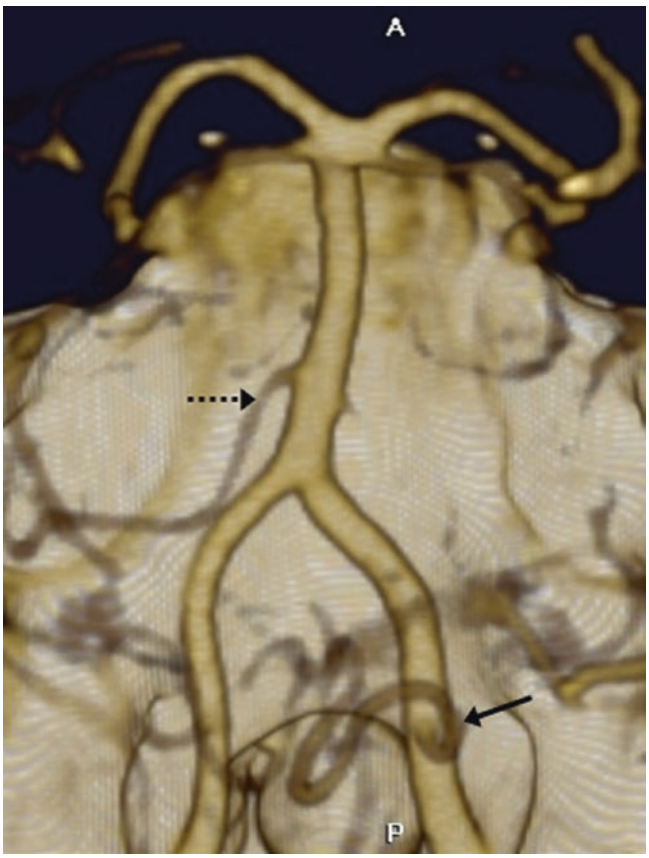

Fig. 36.18 55-year-old with AICA-PICA dominance on opposite sides on 3D VR CTA PA view, with right PICA (*arrow*) and left AICA (*dotted arrow*) dominance

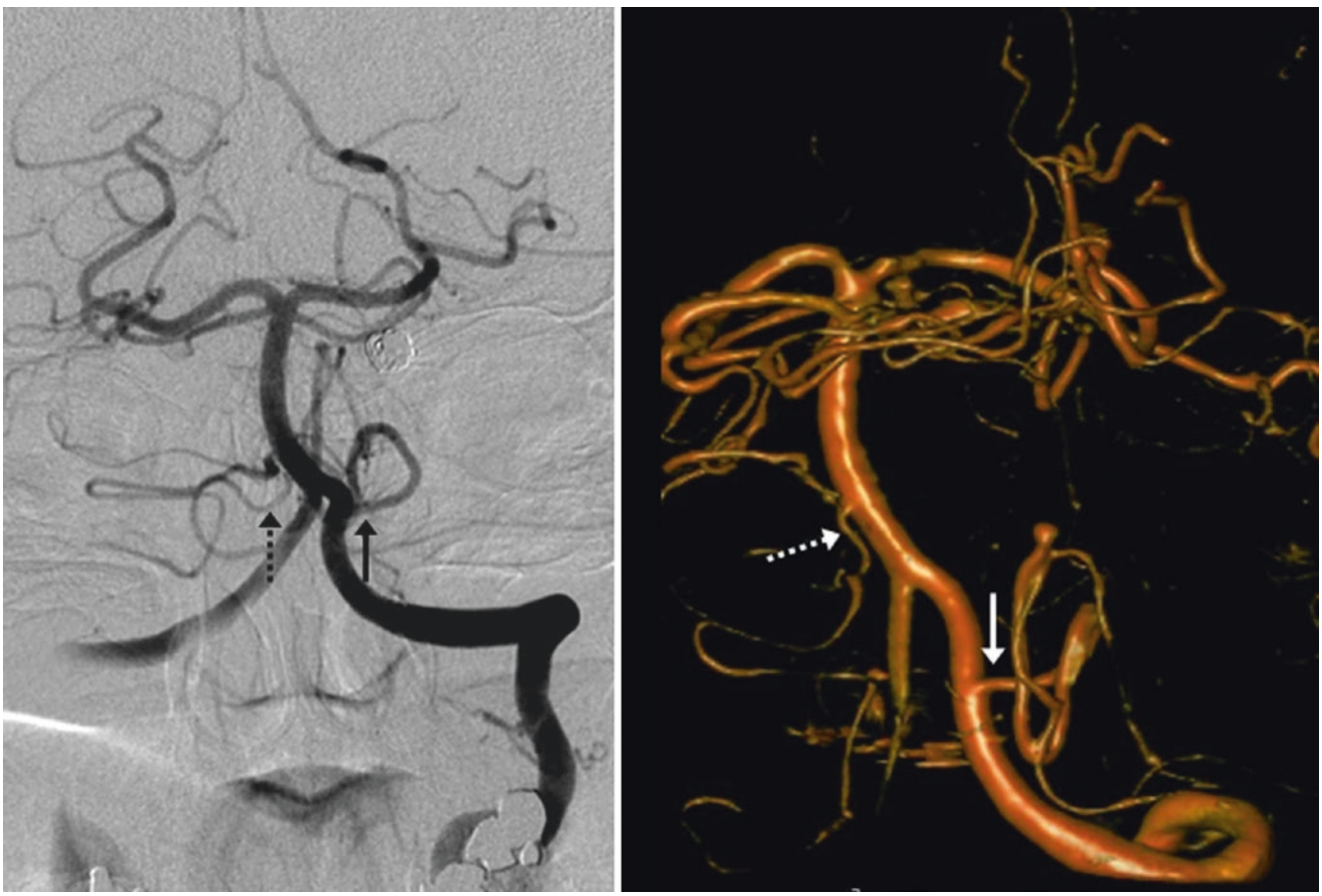

Fig. 36.19 58-year-old with AICA-PICA dominance on contralateral sides, on DSA AP views (*left*), and 3D rotational DSA (*right*), obtained by catheterizing the left VA. There is a dominant left PICA (*arrows*) and right AICA (*dotted arrows*). The right may be an AICA-PICA complex

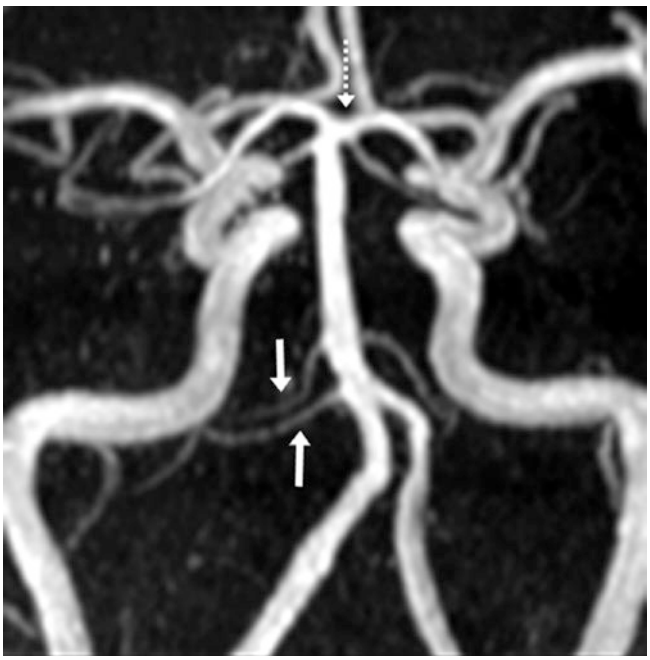

Fig. 36.20 33-year-old with a 3DTOF MRA AP view that shows a duplicated right AICA (*arrows*) and a common origin of the left posterior cerebral artery (PCA) and superior cerebellar artery (SCA) (*dotted arrow*)

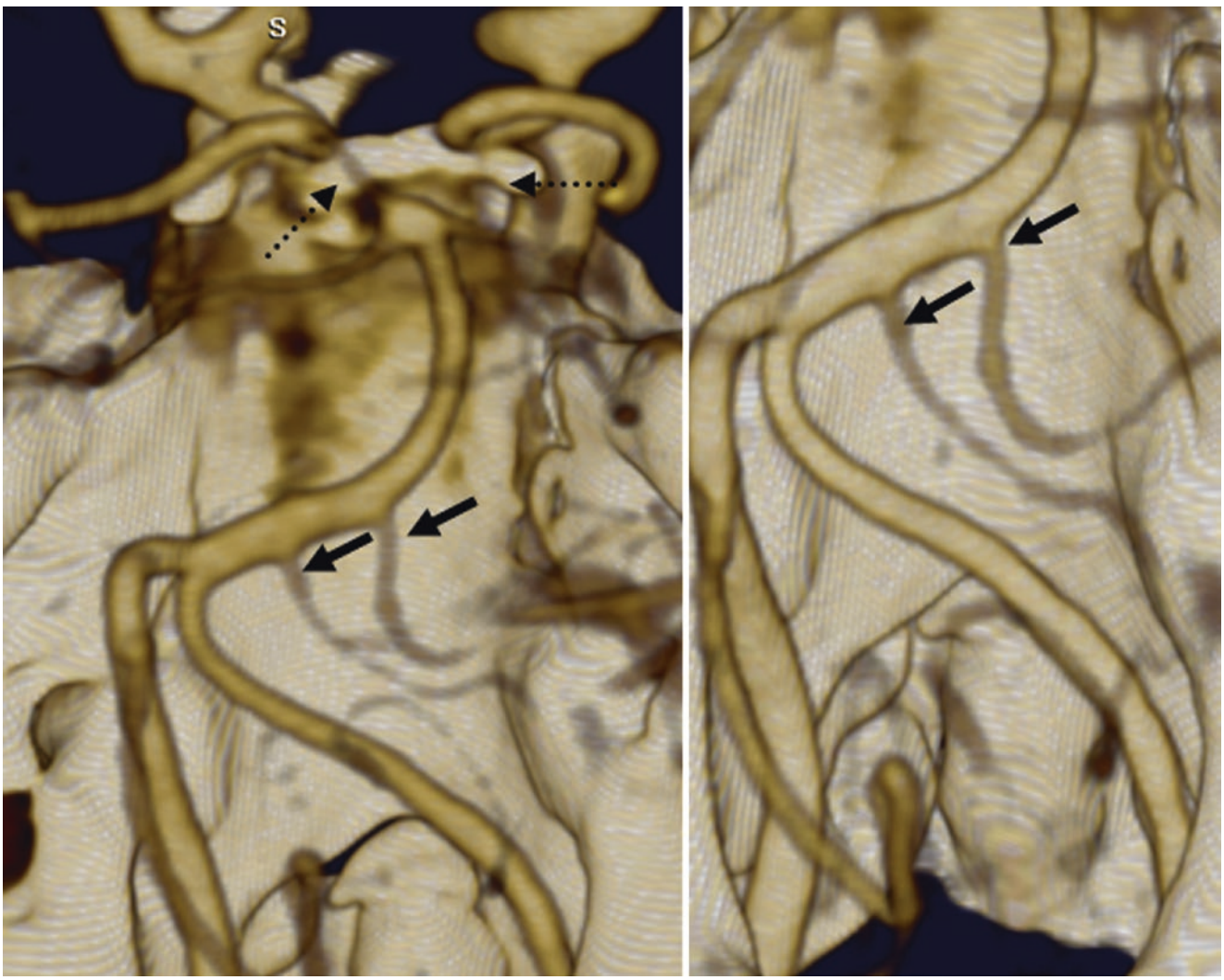

Fig. 36.21 74-year-old with duplicated right AICAs (*arrows*) on 3D VR CTA PA views, and bilateral "fetal PCAs" (*dotted arrows*), which have corresponding hypoplastic P1 segments from the basilar artery

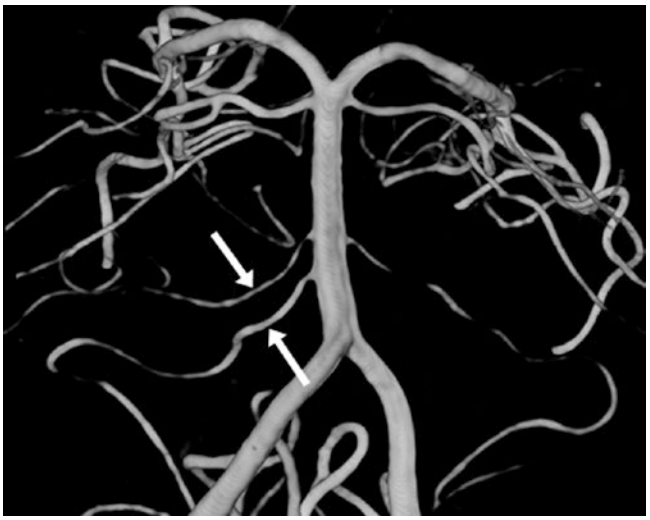

Fig. 36.22 57-year-old with a duplication of the right AICA (*arrows*) on a 3D catheter DSA AP view

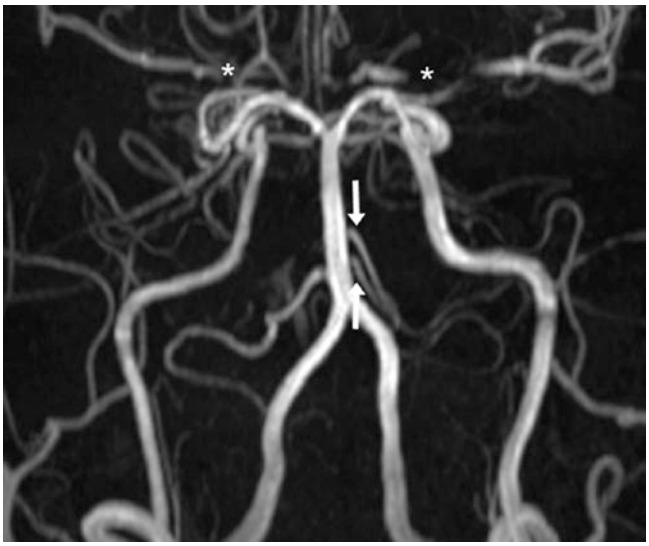

Fig. 36.24 41-year-old with moyamoya syndrome and bilateral internal carotid artery (ICA) occlusion (*asterisks*). There is a left AICA duplication (*arrows*) on a 3DTOF MRA AP view. Vertebrobasilar collaterals supply the distal ICAs. The PICAs are absent

Fig. 36.23 67-year-old with bilateral duplications of the AICAs (*large arrows*) and SCAs (*thin arrows*) on catheter DSA AP views via the left VA

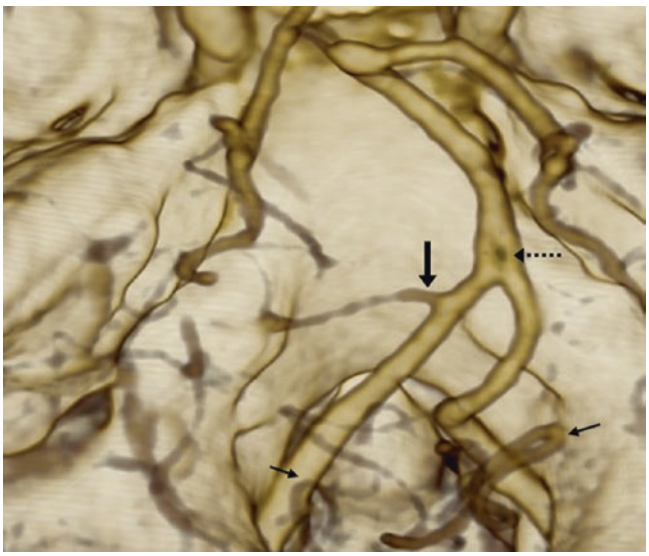

Fig. 36.25 51-year-old with bilateral AICA absence on a 3D CTA PA view. A duplicated PICA arises off the distal left VA (*arrow*), supplying AICA territory. Note bilateral PICAs (*thin arrows*) and a tiny basilar fenestration (*dotted arrow*)

36.4 AICA Looping into the Internal Auditory Canal

The *AICA* or its branches may be visualized *"looping" into the internal auditory canal* (IAC) on CT or MR angiography, or even on routine T2WI MRI as a flow void. The AICA loops into the IAC in approximately 10–20 % of the population [15–17]. Recent evidence suggests that looping of a normal-sized vessel into the IAC is not associated with symptoms of tinnitus. There is also no significant difference in symptoms if cranial nerve VIII is contacted by the AICA, either in the cerebellopontine angle or in the IAC, in patients affected with tinnitus versus controls [15–17]. Additionally, the depth of the loop into the IAC does not relate to the presence or degree of symptoms. This phenomenon and its close proximity to the seventh and eighth cranial nerves can best be seen on 3D volume acquisition, thin-section, heavily T2-weighted or "balanced" images that emphasize the contrast of the cranial nerves to the CSF. MPR views reconstructed along the seventh and eighth cranial nerves can best demonstrate this phenomenon. Notably, although AICA looping into the IAC should be considered a normal variant, other forms of vascular contact or brainstem indentation causing symptoms near the root entry/exit zones (REZs) of cranial nerves V, VII, IX, and X can potentially be symptomatic and are still being debated, so these are not listed here as normal variants (Figs. 36.26, 36.27, 36.28, 36.29, 36.30, 36.31, 36.32, 36.33, and 36.34).

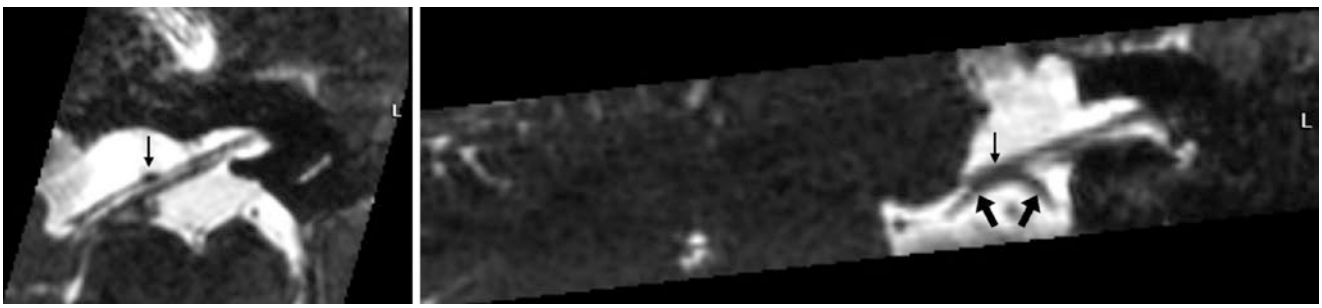

Fig. 36.26 59-year-old in whom the left AICA (*arrows*) abuts the undersurface of the seventh and eighth cranial nerves (*thin arrows*) within the cerebellopontine angle on an axial image from a 3D volumetric acquisition T2WI (*left*). The normal vascular contact with the cranial nerves is also well demonstrated on an oblique paracoronal reconstruction from the same sequence (*right*)

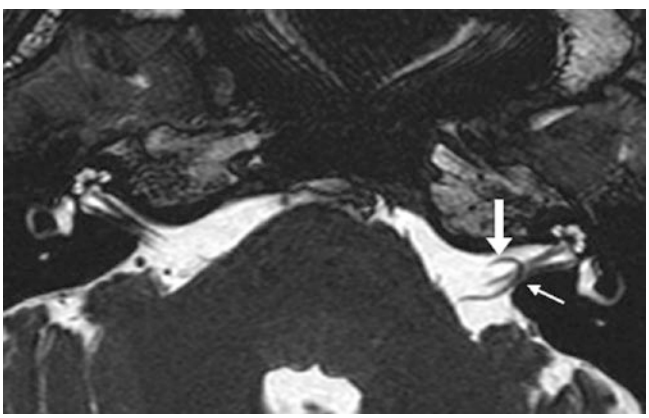

Fig. 36.27 In this 53-year-old, the left AICA (*arrow*) loops into the left internal auditory canal (IAC) on an axial 3D T2WI. Note the site of apparent contact with cranial nerve VIII (*thin arrow*)

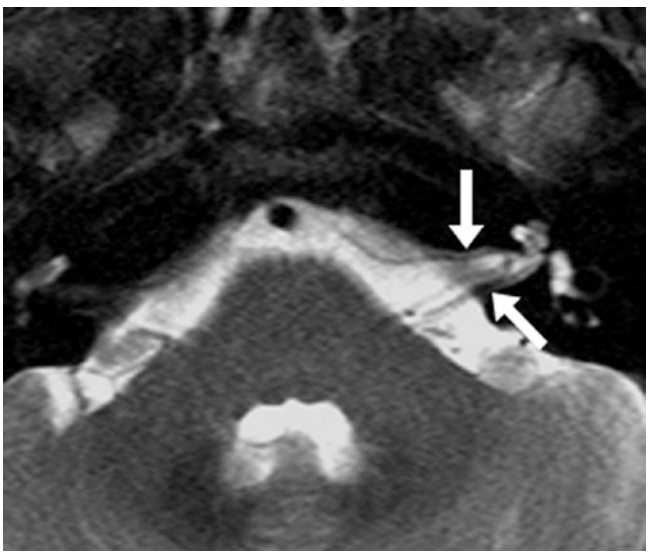

Fig. 36.28 56-year-old with a left AICA that loops far into the IAC (*arrows*) on an axial T2WI

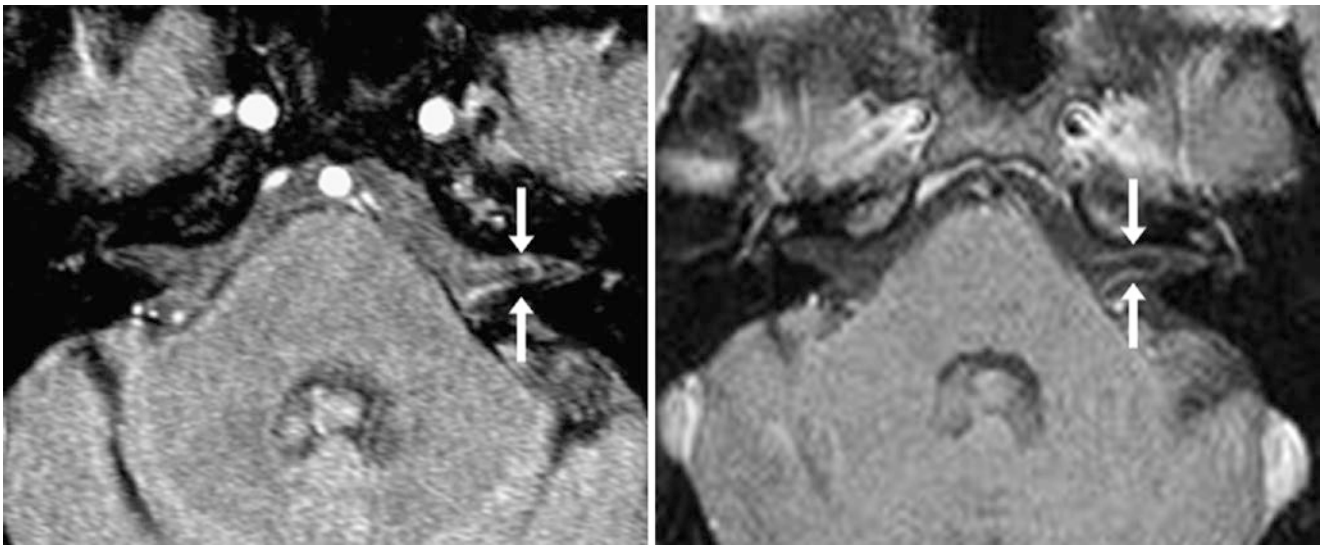

Fig. 36.29 In this 48-year-old with tinnitus, the left AICA (*arrows*) loops into the left IAC on an axial 3DTOF source MRA image (*left*), and on an axial postcontrast T1WI (*right*). This looping is considered unlikely to be the cause of the patient's symptoms

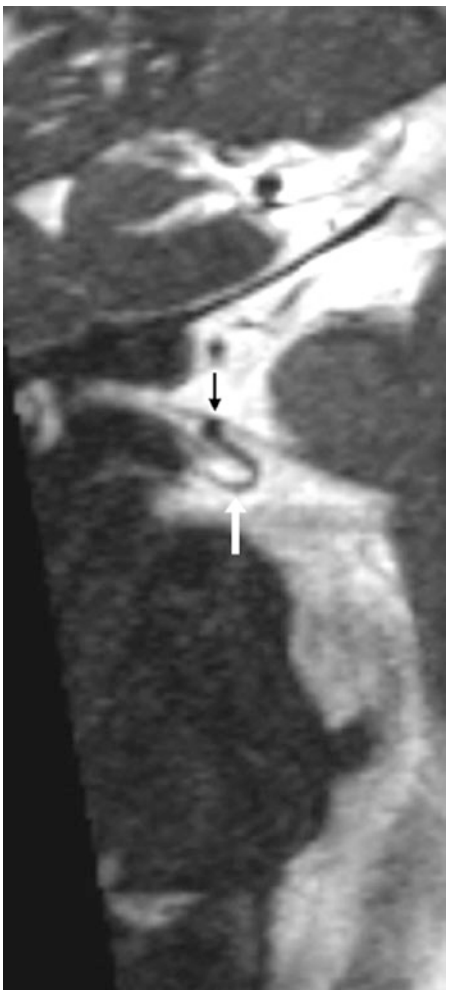

Fig. 36.30 87-year-old with AICA tortuosity (*white arrow*) that abuts cranial nerve VIII (*thin arrow*) adjacent to the IAC on an oblique MPR (paracoronal view) from a 3D T2WI acquisition

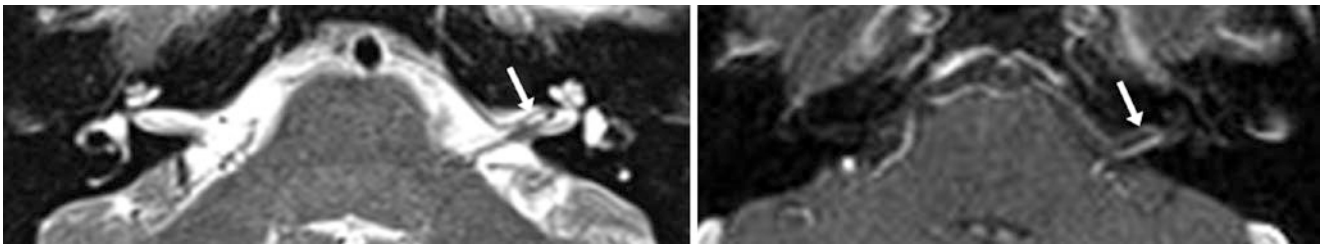

Fig. 36.31 In this 45-year-old, the left AICA (*arrows*) loops two thirds of the way into the IAC, on T2WI (*left*) and postcontrast T1WI (*right*)

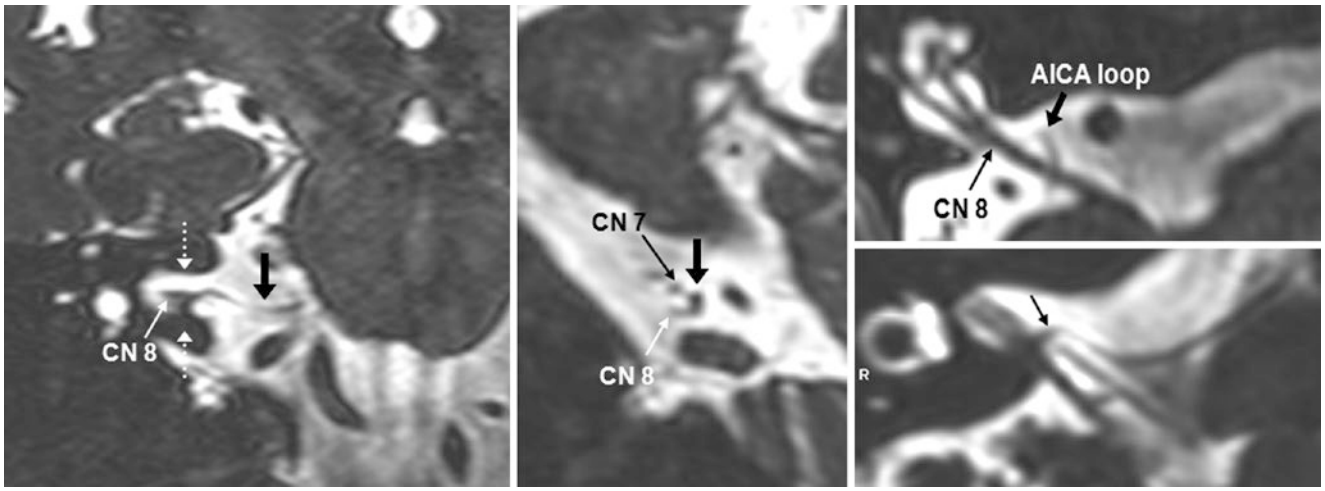

Fig. 36.32 In this 44-year-old, the right AICA (*large arrows*) loops into the IAC *(between dotted arrows)* to abut (*bottom right*) and surround (*top right*) the right cranial nerve VIII (CN 8), as shown on oblique MPRs of a 3D volumetric T2WI. Note points of contact with CN 8 (*thin arrows*)

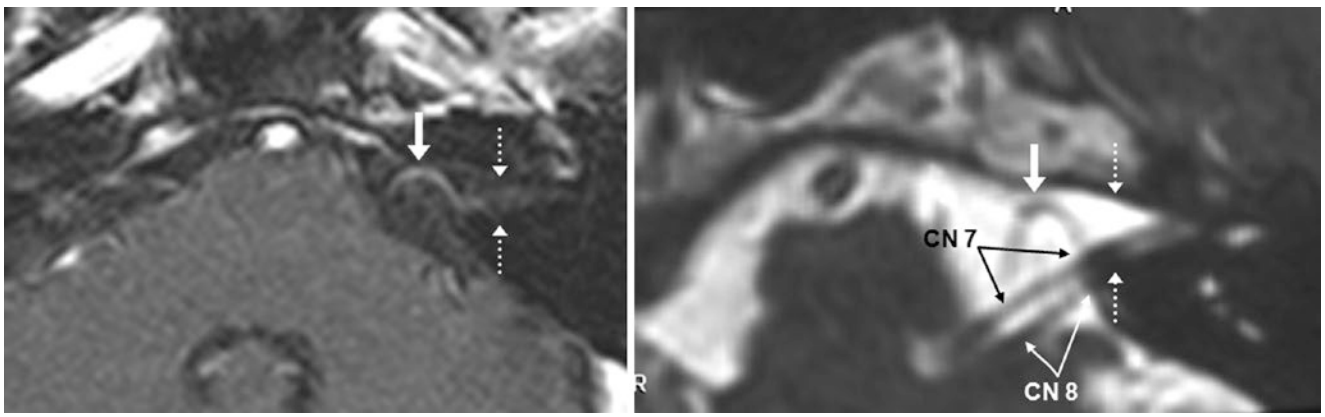

Fig. 36.33 In this 58-year-old, the left AICA (*large arrows*) loops into the IAC (*between dotted arrows*) and contacts the seventh and eighth cranial nerves (CN 7, CN 8) (*thin arrows*), as shown on an axial source 3DTOF MRA image (*left*) and a thin oblique MPR from 3D T2WI (*right*)

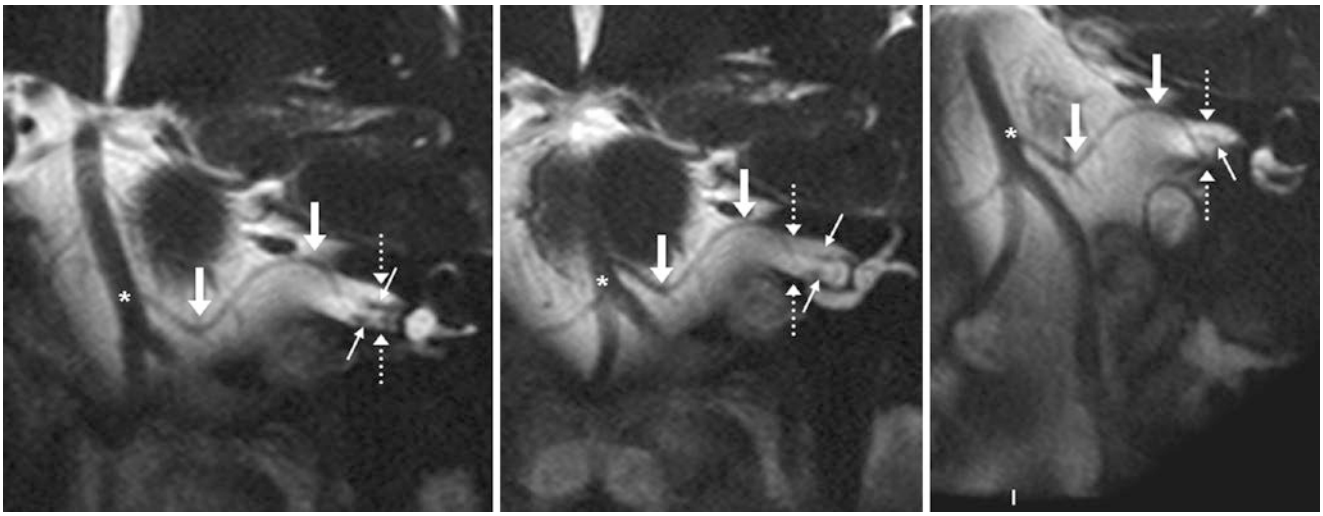

Fig. 36.34 In this 31-year-old, the left AICA (*large arrows*) loops into the IAC (*between dotted arrows*) and touches the seventh and eighth cranial nerves (*thin arrows*), as seen on thin coronal MPRs of a 3D T2WI. Note the origin of the left AICA from the basilar artery (*asterisks*)

36.5 PCA and SCA Duplications, Fenestrations, and Common Origins

The *posterior cerebral artery* (PCA) and *superior cerebellar artery* (SCA) can overlap in supply and distribution. Both vessels can have *duplications* as normal variations, and can share a *common PCA-SCA origin*, which may even appear as an infundibulum. Such *SCA duplication* is fairly common, occurring in about 5–25 % of the population. It is most often unilateral but can be bilateral [8–15]. A common PCA-SCA origin—termed a "common trunk"—occurs in about 1–10 %; the *SCA can also arise from the PCA* in about the same percentage of the population [8–15]. *Fenestrations* can also occur in either vessel or the common origin of the two vessels, but these are estimated to occur in less than 1 % of the population, whether PCA or SCA (Figs. 36.35, 36.36, 36.37, 36.38, 36.39, 36.40, 36.41, 36.42, 36.43, 36.44, and 36.45).

Other variations include *early bifurcation of the PCA* or SCA, and *SCA origin from a persistent trigeminal artery* (a persistent carotid-basilar anastomosis, addressed in Chap. 39). Finally, the "fetal PCA" (discussed in the following Sect. 36.6) is the most common PCA variation.

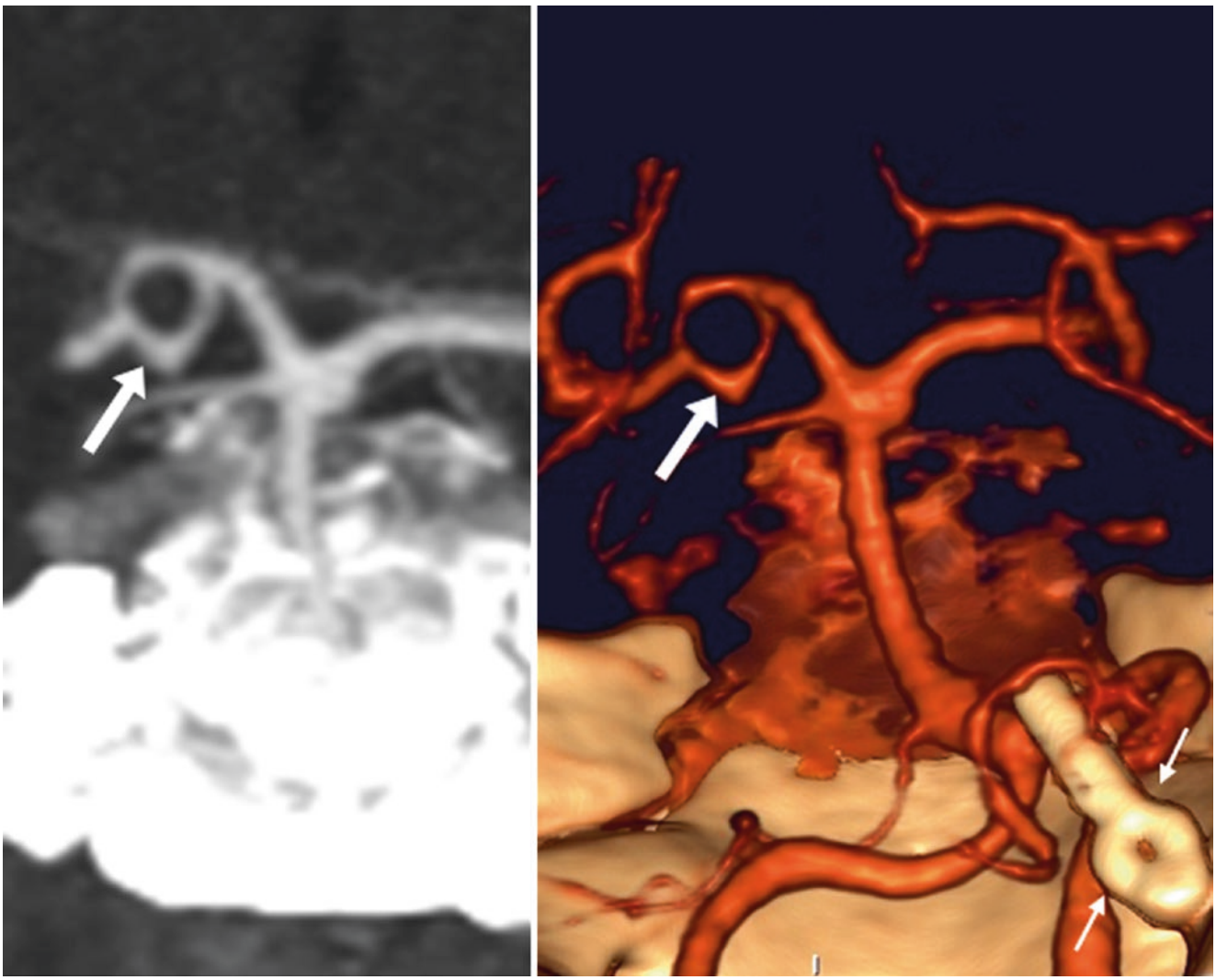

Fig. 36.35 54-year-old with a left P1 segment fenestration (*arrows*) on a coronal MPR (*left*) and 3D VR CTA PA view (*right*). Note clips (*thin arrows*) previously placed for a left PICA aneurysm

Fig. 36.36 25-year-old with right SCA duplication (*large arrow*) on a coronal T2WI. Cranial nerve III (*thin arrows*) is located between the PCAs and SCAs

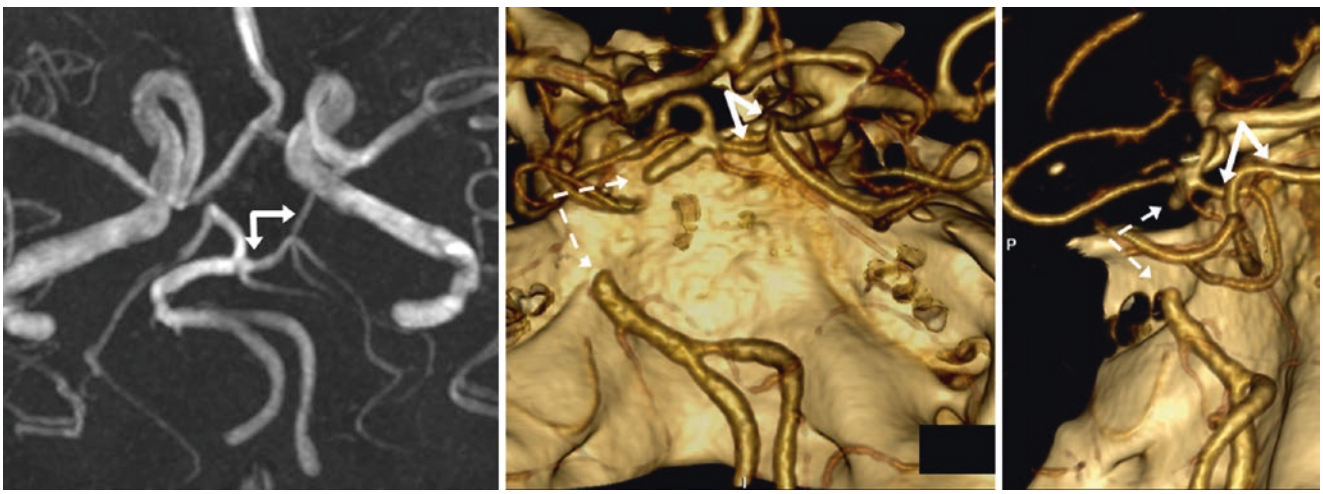

Fig. 36.37 62-year-old with a duplicated right PCA (*solid arrows)* on a 3DTOF MRA superior view (*left*), and on 3D VR CTA PA (*middle)* and lateral (*right*) views, obtained 1 year after the MRA. Equally sized but separate PCAs arise from both the ICA and basilar. In the intervening year, the basilar became occluded (*dashed arrows*)

Fig. 36.38 23-year-old with a duplicated right SCA (*arrows*) on post-contrast coronal T1WI

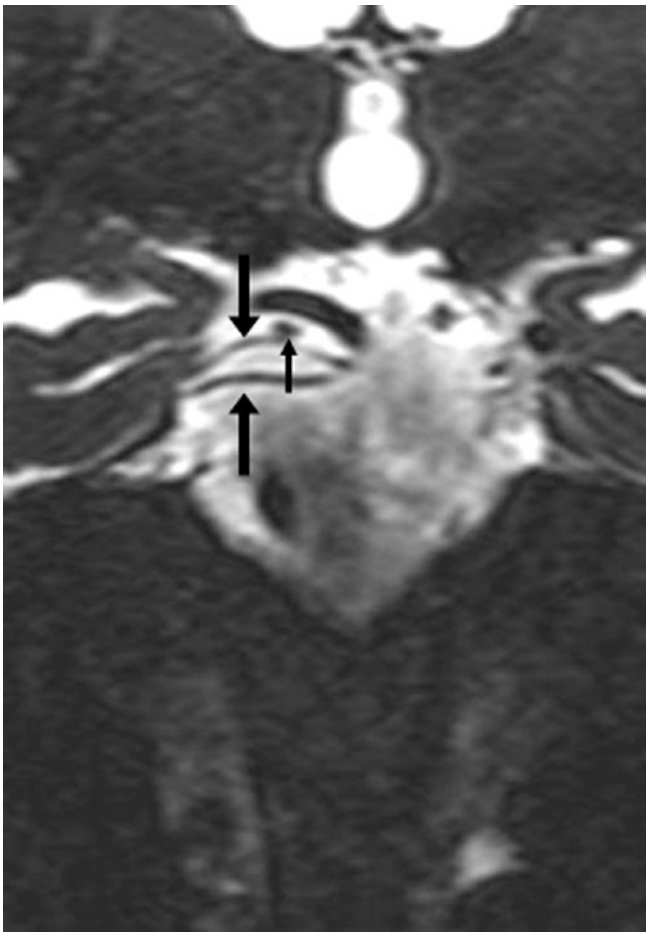

Fig. 36.39 35-year-old with SCA duplication (*arrows*) on 3D coronal T2WI. Note cranial nerve III (*thin arrow*)

Fig. 36.40 85-year-old with left SCA duplication (*arrows*) on a 5 mm-thickness coronal MPR from a CTA

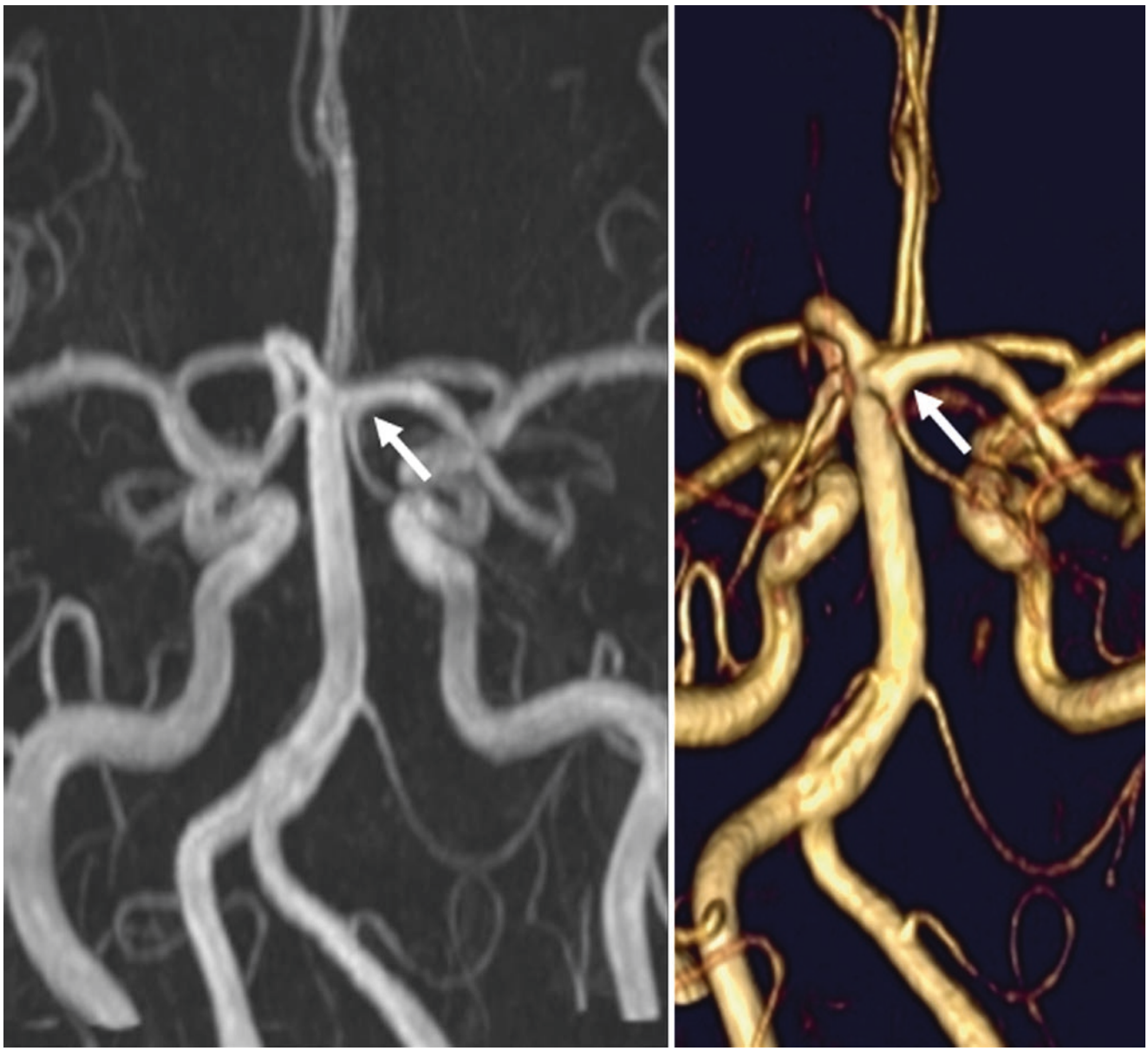

Fig. 36.41 54-year-old with a common infundibular origin of the right PCA and SCA (*arrows*) on two 3DTOF MRA PA views, including MIP (*left*) and 3D VR (*right*) views

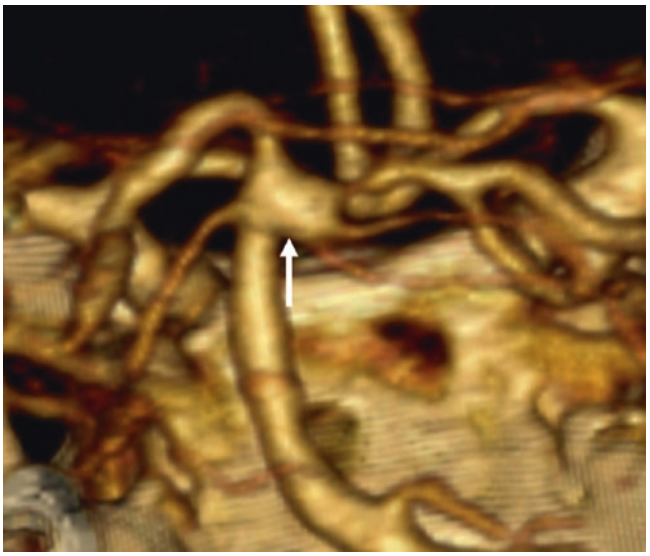

Fig. 36.42 51-year-old with a 3D VR PA view from a CTA, showing an infundibular common origin (*arrow*), which gives rise to three vessels: the right PCA and two duplicated SCAs

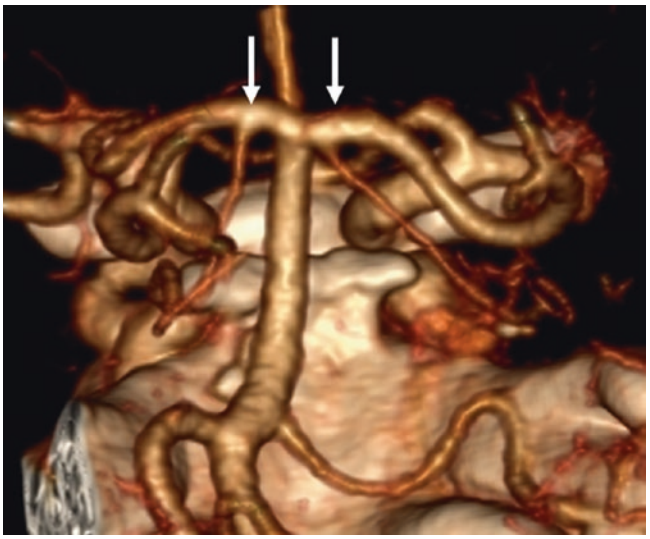

Fig. 36.43 44-year-old with bilateral common origins (*arrows*) of both the SCAs and PCAs on a CTA 3D VR PA view. These could also be termed "SCA origin from the PCA" on both sides

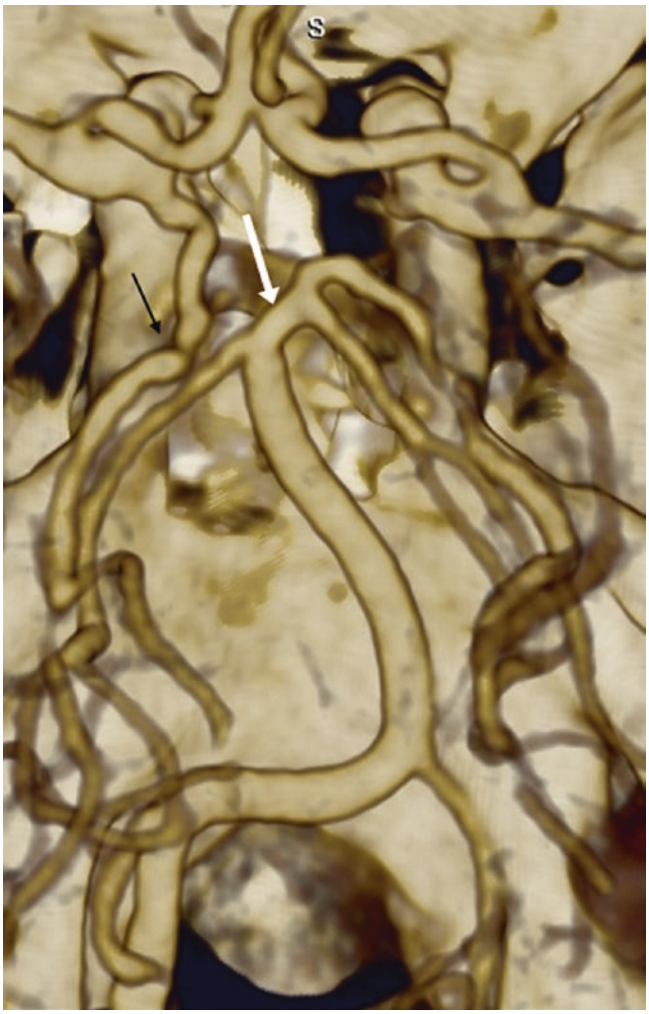

Fig. 36.44 90-year-old with a common origin (*arrow*) of the right PCA and SCA on a CTA 3D VR PA view. Additionally, on the left, there is a fetal PCA (*thin arrow*), with a normal left SCA arising from the basilar

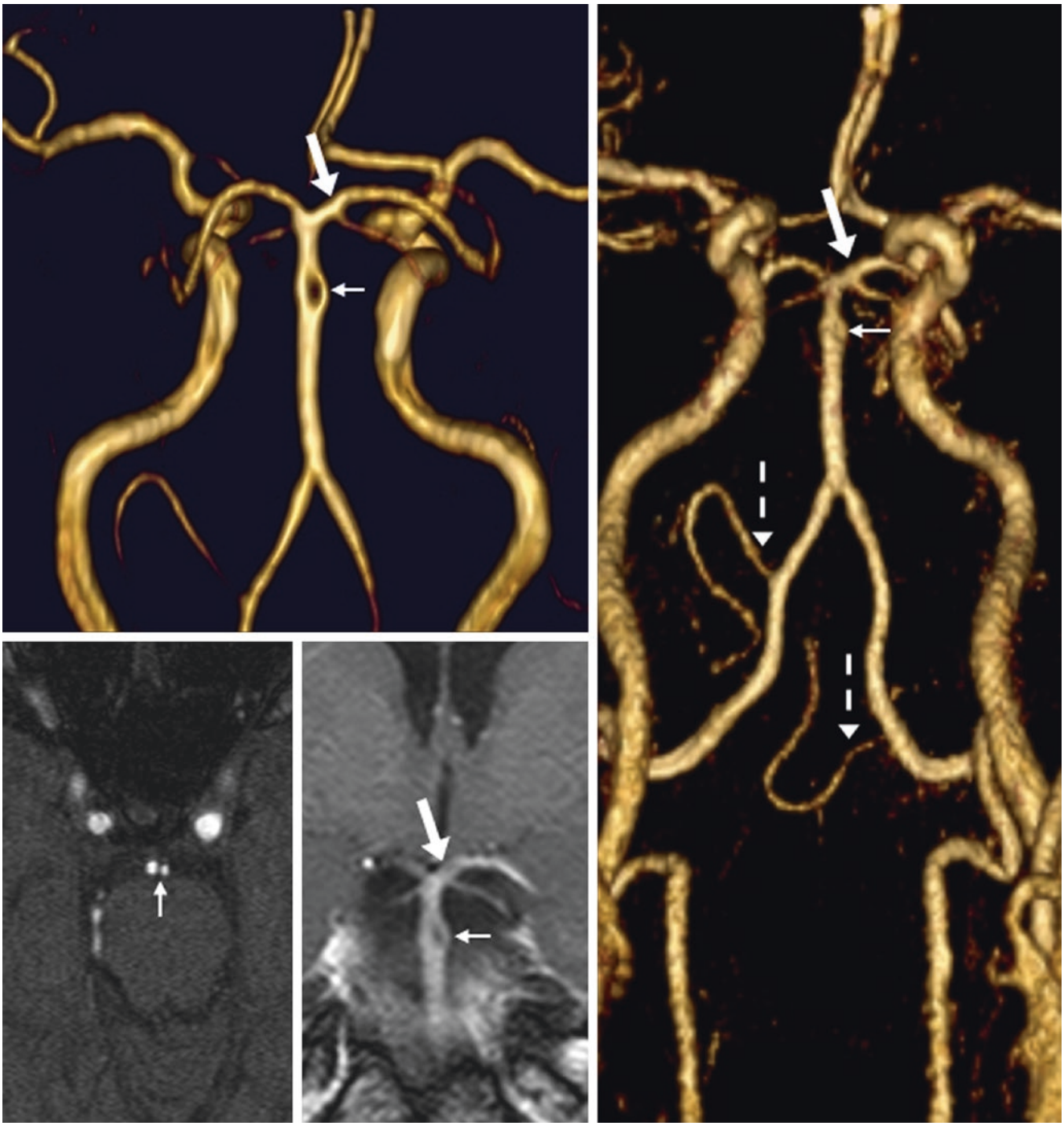

Fig. 36.45 50-year-old with a common origin of the right PCA and SCA (*arrows*) on 3DTOF MRA PA view (*top left*), source images (*bottom left*), coronal postcontrast T1WI (*bottom middle*), and contrast-enhanced MRA (*right*). Note a tiny basilar fenestration (*thin arrows*) and AICA-PICA dominance on opposite sides (*dashed arrows*)

36.6 Hypoplastic PCA and "Fetal PCA"

The most commonly noted variant of the major intracranial arteries is the so-called *fetal origin of the PCA* (also termed a "fetal PCA"), in which the PCA originates from the posterior communicating segment of the internal carotid artery (ICA); the ipsilateral P1 segment arising from the basilar terminus is either absent or hypoplastic [18–21]. This normal variant occurs in about 10–20 % of the population, in contrast to the normal "Circle of Willis" pattern that occurs in only 60 % of brains [25]. Typically, the P1 segment of the PCA arising from the basilar is present on catheter DSA to some degree, but it may be very tiny, and thus may be difficult to visualize on noninvasive imaging such as CTA or MRA. If this variant is bilateral, a small, or even hypoplastic, basilar artery may be present. This variant can be significant in the setting of *ischemia* of the PCA territory, as knowledge of the presence of a fetal PCA may potentially alter the site of endovascular therapy. Both CTA and high-resolution MRA can readily identify this variant with high specificity and sensitivity (Figs. 36.46, 36.47, 36.48, 36.49, 36.50, and 36.51) [18–21].

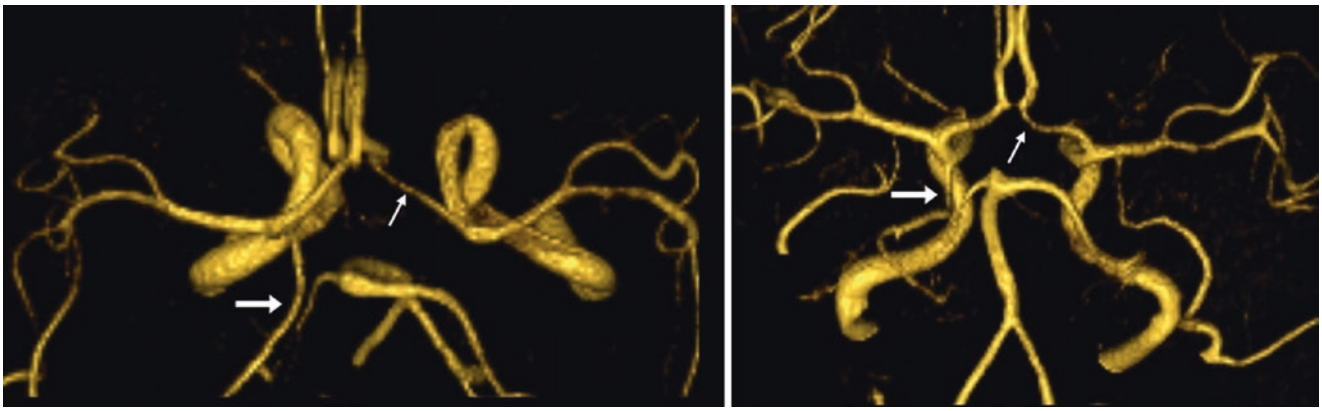

Fig. 36.46 73-year-old with a unilateral left "fetal PCA" (*large arrows*) on 3DTOF MRA superior (*left*) and PA (*right*) views. The left P1 segment is a continuation of the posterior communicating artery. The right PCA arises in the typical configuration from the basilar artery. Also, note a hypoplastic A1 segment of the left anterior cerebral artery (ACA) (*thin arrows*)

Fig. 36.47 In this 42-year-old, two superior views from a CTA show a small basilar artery, an absent right VA (*dotted arrows*), and absent P1 segments of both PCAs (*arrows*), which arise from the internal carotid arteries (ICAs) (*i.e.*, "fetal origins")

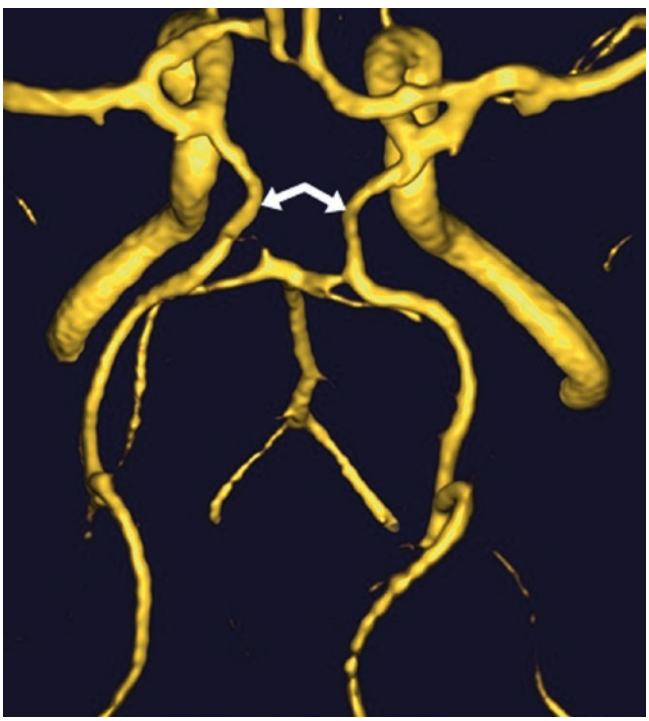

Fig. 36.48 45-year-old with 3DTOF MRA superior view that shows a small basilar, with bilateral "fetal PCAs" (*arrows*), although tiny P1 segments may be present

Fig. 36.49 In this 52-year-old, a 3DTOF MRA superior view (*left*) and AP view (*middle*) depict a "fetal PCA" (*large arrows*) arising from the right ICA. The right P1 segment off the basilar is quite hypoplastic (*thin arrows*). A large artifact (*dotted arrows*) on source images (*right*) is from phase wrap, using sensitivity-encoding (SENSE) gradient coils, as the ears were not included in the field of view. Also, AICA-PICA dominance is present on opposite sides; the left AICA and right PICA are dominant

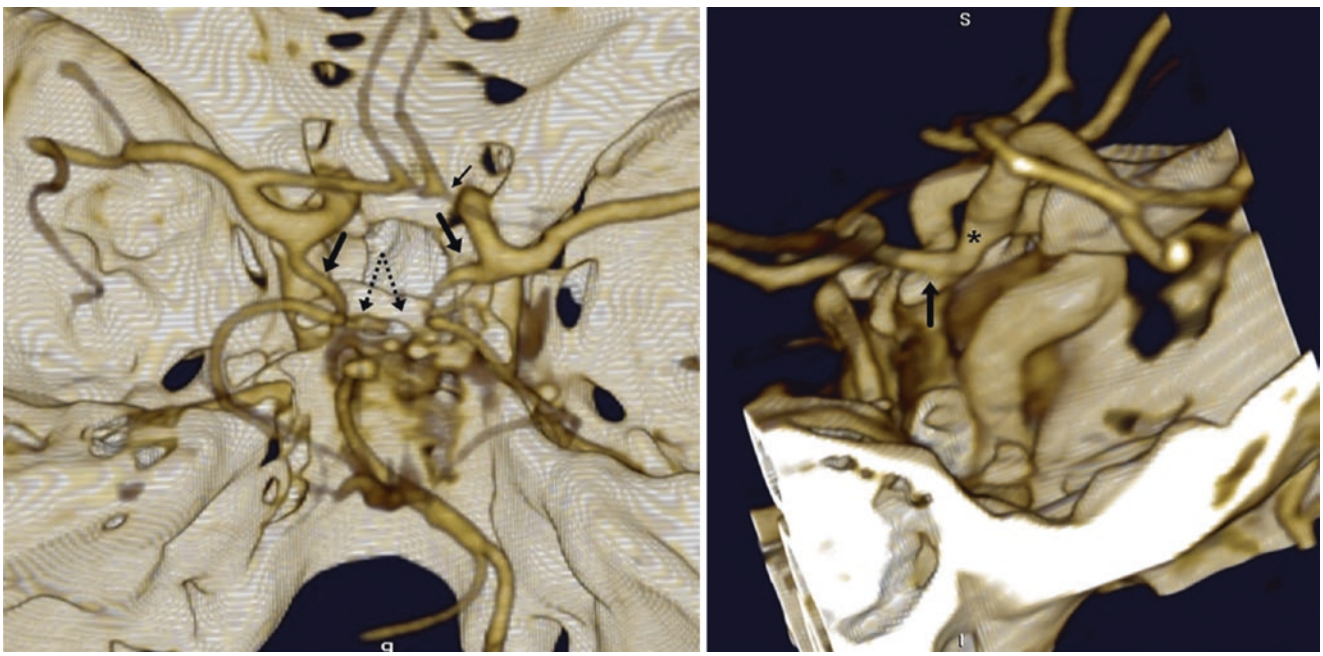

Fig. 36.50 73-year-old with bilateral "fetal PCAs" (*dotted arrows*) arising from the ICAs, with absent P1 segments (*large arrows*) and a normal right PCA infundibular origin (*asterisk*) on 3D VR CTA superior (*left*) and lateral (*right*) views. The basilar artery is hypoplastic; the ICAs are the dominant vascular supply. Also note a hypoplastic right ACA (*thin arrow*)

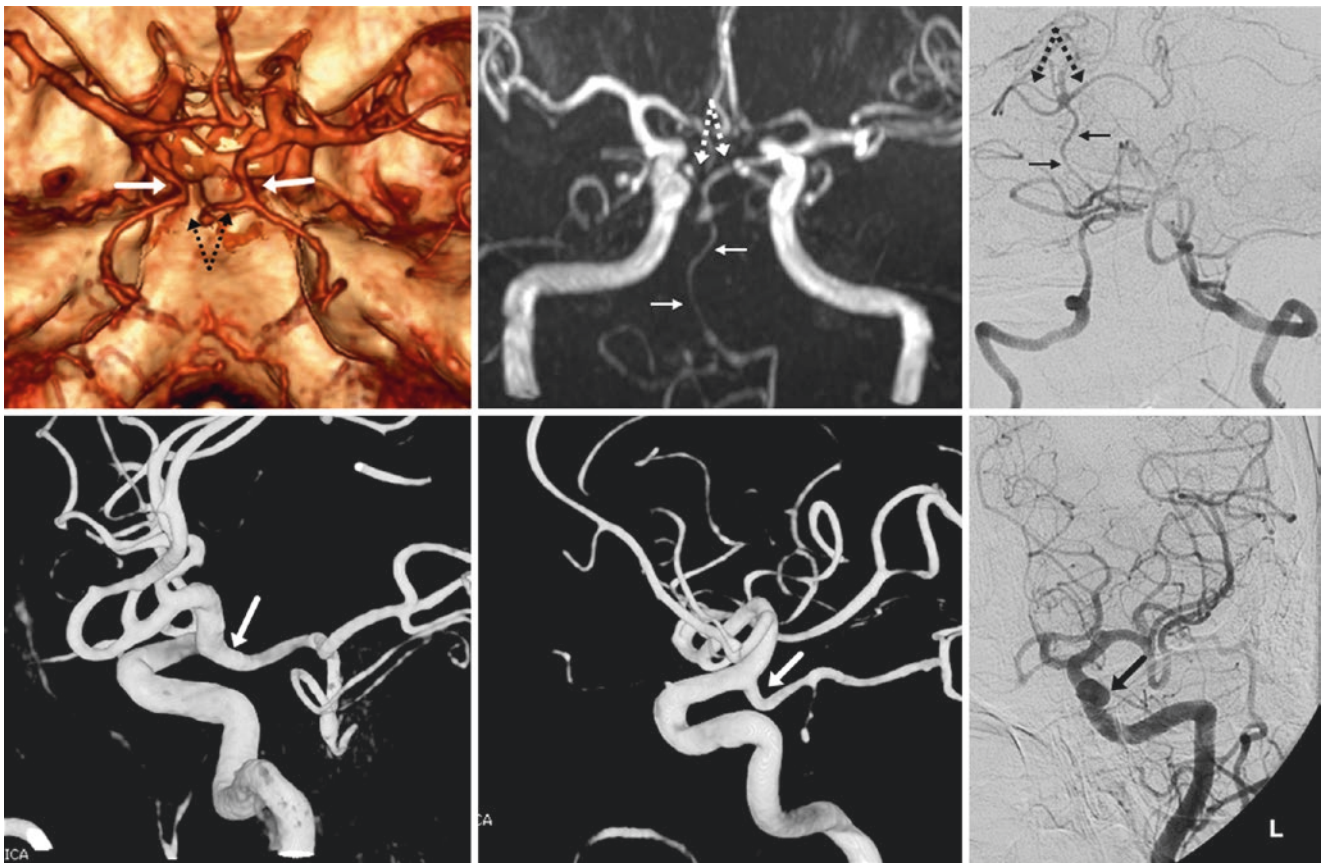

Fig. 36.51 52-year-old with bilateral "fetal PCAs" (*large arrows*) and tiny bilateral P1 segments (*dotted arrows*), on a 3D VR CTA superior view (*top left*). The basilar was initially thought by a referring physician to have a severe stenosis, also seen on a 3DTOF MRA AP view (*top middle*). However, both a catheter DSA AP view (*top right*) and 3D-DSA lateral views (*bottom left* and *middle*) showed the basilar to be hypoplastic (*thin arrows*), not stenotic. Note the fetal left PCA on DSA AP view (*bottom right*)

References

1. Parmar H, Sitoh YY, Hui F. Normal variants of the intracranial circulation demonstrated by MR angiography at 3 T. Eur J Radiol. 2005;56:220–8.
2. Songur A, Gonul Y, Ozen OA, Kucuker H, Uzun I, Bas O, Toktas M. Variations in the intracranial vertebrobasilar system. Surg Radiol Anat. 2008;30:257–64.
3. Cooke DL, Stout CE, Kim WT, Kansagra AP, Yu JP, Gu A, et al. Cerebral arterial fenestrations. Interv Neuroradiol. 2014;20:261–74.
4. Sogawa K, Kikuchi Y, O'uchi T, Tanaka M, Inoue T. Fenestrations of the basilar artery demonstrated on magnetic resonance angiograms: an analysis of 212 cases. Interv Neuroradiol. 2013;19:461–5.
5. Sanders WP, Sorek PA, Mehta BA. Fenestration of intracranial arteries with special attention to associated aneurysms and other anomalies. AJNR Am J Neuroradiol. 1993;14:675–80.
6. Fine AD, Cardoso A, Rhoton Jr AL. Microsurgical anatomy of the extracranial-extradural origin of the posterior inferior cerebellar artery. J Neurosurg. 1999;91:645–52.
7. Uchino A, Saito N, Ishihara S. Double origin of the posterior inferior cerebellar artery diagnosed by MR angiography: A report of two cases. Neuroradiol J. 2015;28:187–9.
8. Matsushima T. Microsurgical anatomy and surgery of the posterior cranial fossa. Tokyo: Springer; 2015. p. 24–6.
9. Uchino A, Saito N, Takahashi M, Okano N, Tanisaka M. Variations of the posterior cerebral artery diagnosed by MR angiography at 3 tesla. Neuroradiology. 2016;58:141–6.
10. Vlajković S, Vasović L, Trandafilović M, Jovanović I, Ugrenović S, Đorđević G. Fenestrations of the human posterior cerebral artery. Childs Nerv Syst. 2015;31:381–7.
11. Uchino A, Sawada A, Takase Y, Kudo S. Variations of the superior cerebellar artery: MR angiographic demonstration. Radiat Med. 2003;21:235–8.
12. Pekcevik Y, Pekcevik R. Variations of the cerebellar arteries at CT angiography. Surg Radiol Anat. 2014;36:455–61.
13. Pekcevik Y. Double origin and early bifurcation of the anterior inferior cerebellar artery diagnosed by CT angiography. Surg Radiol Anat. 2015;37:1141–3.
14. Mazighi M, Porter PJ, Rodesch G, et al. Vascular anomalies and the risk of multiple aneurysms development and bleeding. Interv Neuroradiol. 2002;8:15–20.
15. Kazawa N, Togashi K, Ito J. The anatomical classification of AICA/PICA branching and configurations in the cerebellopontine angle area on 3D-drive thin slice T2WI MRI. Clin Imaging. 2013;37:865–70.
16. Reisser C, Schuknecht HF. The anterior inferior cerebellar artery in the internal auditory canal. Laryngoscope. 1991;101:761–6.
17. Gultekin S, Celik H, Akpek S, Oner Y, Gumus T, Tokgoz N. Vascular loops at the cerebellopontine angle: is there a correlation with tinnitus? AJNR Am J Neuroradiol. 2008;29:1746–9.
18. Gunnal SA, Farooqui MS, Wabale RN. Study of posterior cerebral artery in human cadaveric brain. Anat Res Int. 2015;2015:681903.
19. de Monyé C, Dippel DW, Siepman TA, Dijkshoorn ML, Tanghe HL, van der Lugt A. Is a fetal origin of the posterior cerebral artery a risk factor for TIA or ischemic stroke? A study with 16-multidetector-row CT angiography. J Neurol. 2008;255:239–45.
20. van der Lugt A, Buter TC, Govaere F, Siepman DA, Tanghe HL, Dippel DW. Accuracy of CT angiography in the assessment of a fetal origin of the posterior cerebral artery. Eur Radiol. 2004;14:1627–33.
21. Avci E, Bademci G, Oztürk A. Posterior communicating artery: from microsurgical, endoscopic and radiological perspective. Minim Invasive Neurosurg. 2005;48:218–23.
22. McKinney AM, Palmer CS, Truwit CL, Karagulle A, Teksam M. Detection of aneurysms by 64-section multidetector CT angiography in patients acutely suspected of having an intracranial aneurysm and comparison with digital subtraction and 3D rotational angiography. AJNR Am J Neuroradiol. 2008;29:594–602.
23. Villablanca JP, Jahan R, Hooshi P, Lim S, Duckwiler G, Patel A, et al. Detection and characterization of very small cerebral aneurysms by using 2D and 3D helical CT angiography. AJNR Am J Neuroradiol. 2002;23:1187–98.
24. Teksam M, McKinney A, Casey S, Asis M, Kieffer S, Truwit CL. Multi-section CT angiography for detection of cerebral aneurysms. AJNR Am J Neuroradiol. 2004;25:1485–92.
25. Gunnal SA, Farooqui MS, Wabale RN. Anatomical variations of the circulus arteriosus in cadaveric human brains. Neurol Res Int. 2014;2014:687281.

Intracranial Anterior Circulation Variants

37

This chapter covers anterior circulation variants regionally, from anterior to posterior, including congenital arterial variant absence of first-order segments, branching, duplications, fenestrations, and early origins. Included are variations in the supraclinoid *internal carotid artery* (ICA), *anterior cerebral artery* (ACA), and finally the *middle cerebral artery* (MCA) [1–46]. The *lenticulostriate arteries* (medial and lateral) are also briefly covered, as well as several other uncommon or rare variations of the ACA, MCA, and ICA. Infundibula of the various anterior and posterior circulation vessels are covered separately in Chap. 38. The "fetal PCA" (posterior cerebral artery, where the vascular distribution of a P1 segment arises from the distal ICA rather than the basilar artery) was covered in Chap. 36.

Variants involving the ACA and its branches are mostly related to persistence or lack of regression of an embryologic anterior communicating plexus and the median artery of the corpus callosum (MACC); among such derivatives are *fenestrations* and *duplications, A1 segment hypoplasia, azygous ACA, bihemispheric ACA,* and *MACC* ("triple ACA") [1–25]. Other variations include prominent *orbitofrontal* or *frontopolar branches* arising from the A1 segment, and the *primitive olfactory artery*. There is controversy as to whether the presence of these variants relates to lack of regression of the embryonic arterial plexus and MACC, or whether it is related to development of anomalous arteries; this subject is covered briefly under the topic of anterior communicating artery (AcoA) and ACA fenestrations.

There are many MCA variants in first-order M1 segment branching. The most common are *early branches* arising from the M1 segment (whether inferior or superior "trunk" origins), *duplication of the MCA*, and an *accessory MCA*; a focal *fenestration* is relatively rare [5–8, 11, 26–32]. Though some opine that a fenestration may be a focal duplication embryologically, for the purposes of discussing MCA variations, these are treated separately: a duplication is a double origin that follows the course of the MCA, whereas a fenestration ("window") is a focal hole within the vessel. The topic of *prominent lenticulostriate branches* (typically lateral) is also covered with the MCA variants; although the medial and lateral lenticulostriate branches can vary in site of origin, size, and number, the most common site for their appearance to be prominent and potentially problematic is from the MCA's M1 segment.

It is important to mention that is quite common to encounter such normal variant or "don't touch" vascular anomalies on either routine MRI or CT examinations, with or without contrast. The most common scenarios in which such variants simulate disease or cause a clinical dilemma is when an *aneurysm* or *arteriovenous malformation* (AVM) is suspected, either on the basis of subarachnoid hemorrhage or a potentially prominent vessel on routine, nonvascular MRI or CT imaging. Such variants are typically readily confirmed (and aneurysms excluded) by noncontrast MRA, such as with 3D time-of-flight (3DTOF) acquisition, contrast-enhanced MRA or CTA [47–49]. Knowledge of these vascular variants can also be critical in the setting of guiding endovascular therapy, to initiate more rapid treatment and to avoid unnecessary complications. Ultimately, catheter DSA, optimally with 3D rotational acquisition in questionable cases, is the gold standard for discerning difficult anatomy.

With the advent of newer techniques such as CT perfusion (CTP), MR perfusion (MRP), and arterial spin-labeling (ASL) to measure blood flow, tissue perfusion, and oxygen extraction, interesting data are emerging about the use of such techniques to evaluate disease states, underscoring the importance of recognizing many of these variants. The most interesting is likely to be stroke imaging, as the presence of variations in branching, absence, hypoplasia, or duplication of vasculature can affect the vascular distribution of an *infarct* or *ischemia* and casts light on the importance of assessing collateral flow in the setting of thromboembolic arterial occlusion. The size and presence of such variations is bound to affect the degree of collateral flow in the setting of acute infarction, and may become a subject of future research.

A.M. McKinney, *Atlas of Normal Imaging Variations of the Brain, Skull, and Craniocervical Vasculature*,
DOI 10.1007/978-3-319-39790-0_37

37.1 Internal Carotid Artery Duplication or Fenestration

Duplications or *fenestrations* of the intracranial internal carotid artery (ICA) are far less frequent than those of the vertebrobasilar system, anterior communicating artery (AcoA), or anterior cerebral arteries (ACAs). Notably, this variant is extremely rare, with likely less than 20 cases reported in the literature [1–3]. There is debate whether these have a higher propensity to develop *aneurysm* than normal cerebral vasculature. Most cases reported in the literature have had aneurysms, but there have not been studies in larger populations of asymptomatic patients to perform proper statistics; this association could reflect an expectation or selection bias (Fig. 37.1).

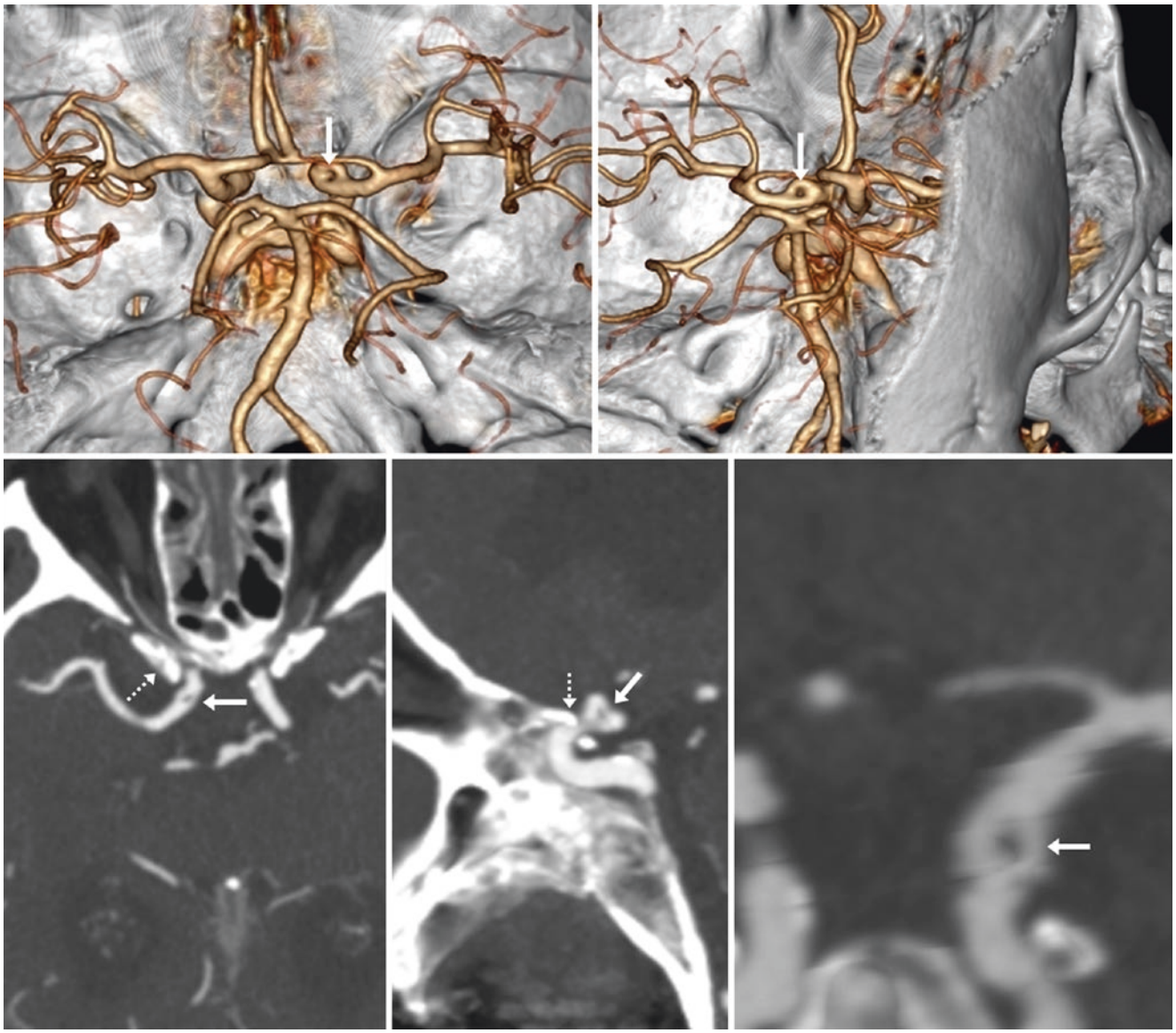

Fig. 37.1 *Top row:* 84-year-old with a fenestration of the supraclinoid right internal carotid artery (ICA) (*arrows*) on 3D VR CTA superior view (*left*) and oblique superior view (*right*). *Bottom row:* Axial (*left*), sagittal (*middle*), and magnified coronal (*right*) MPRs confirm the "hole" in the vessel's center, located just distal to the anterior clinoid process (*dotted arrows*)

37.2 Dorsal Ophthalmic Artery

Persistence of the vestigial/embryonic *dorsal ophthalmic artery* (DOA) into infancy or adulthood is relatively rare, occurring in less than 0.5 % of the population [33–39]. The persistent DOA is located at the site of the inferolateral trunk in the adult or child (which is often not visualized on catheter angiography unless there is an occlusion), and is located along the lateral aspect of the cavernous ICA. Of note is that the exit site into the orbit is not the optic foramen, but rather the *superior orbital fissure*, which also contains cranial nerves III, IV, V_1, VI, and the ophthalmic vein.

This variant can usually be recognized by catheter angiography, MRA, or CTA (Fig. 37.2). It can be important in several scenarios. First, the prominence at its origin can simulate a cavernous ICA *aneurysm* when only 3D MIP data are viewed. Second, it is important to be aware of this variant during endovascular *intervention*, as stenting or coiling across it could cause loss of the patient's vision. Third, it is important to be aware of it in the event of a *carotid occlusion*, not only for the purpose of endovascular intervention but also because knowledge of its normal appearance is necessary to understand collateral supply to the ICA distribution.

Other extremely rare variations include a persistent ventral ophthalmic artery, ophthalmic artery origin from the middle meningeal artery, and even ophthalmic origin from the posterior communicating artery [33–39]. These variants, which can be found in sporadic case reports in the literature, are even rarer than the DOA and are not discussed further here.

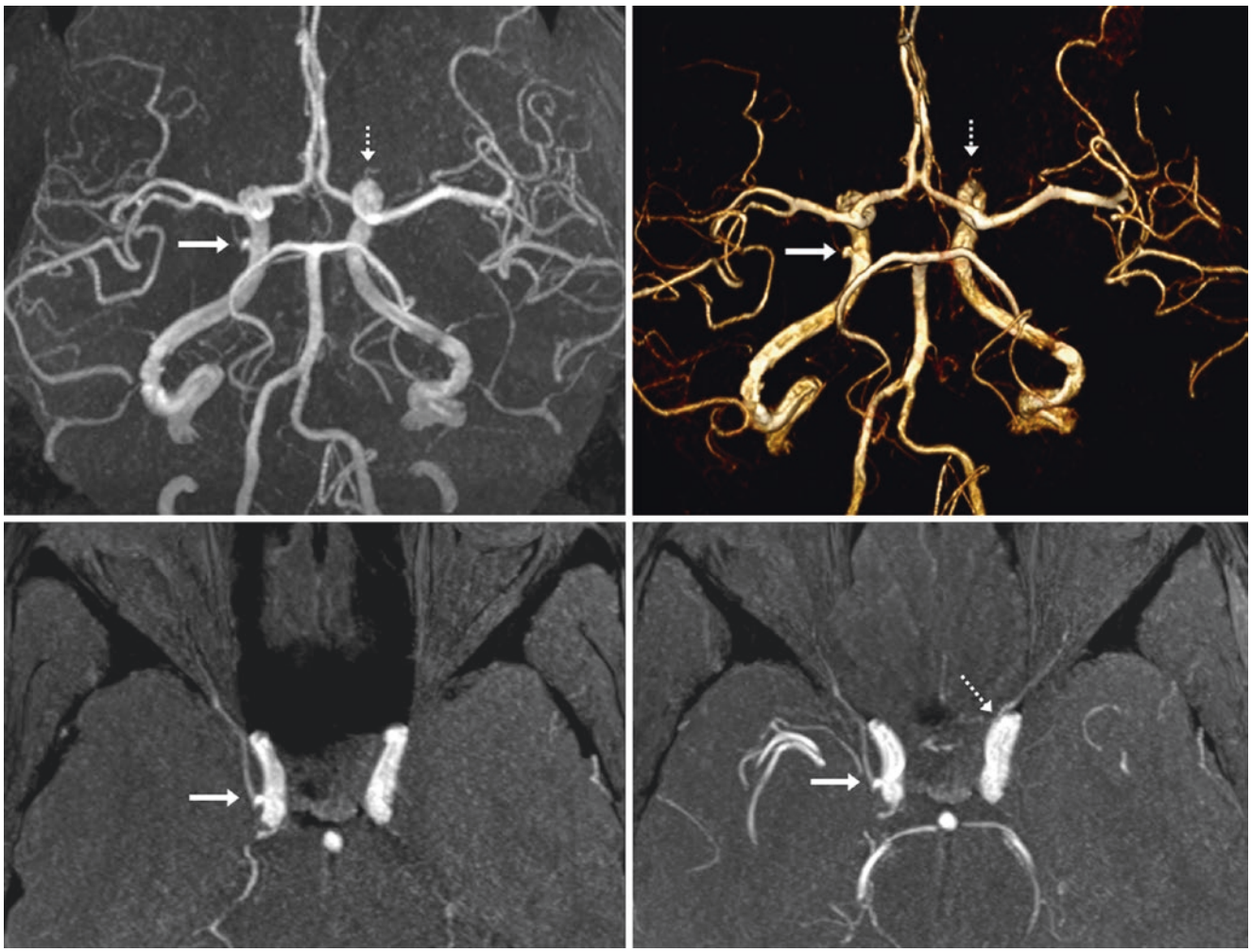

Fig. 37.2 A 52-year-old with delirium had a right dorsal ophthalmic artery (DOA) (*arrows*), as demonstrated on reformats from a 3 T TOF MRA with PA views in MIP (*top left*) and 3D VR (*top right*) reconstructions. The left OA was normal (*dotted arrows*). The DOA initially simulated an aneurysm on the MIP, but axial MPRs at 2-mm (*bottom left*) and 5-mm (*bottom right*) thicknesses confirmed the origin of the DOA and showed that it was not an aneurysm. Note the ventral position of the normal left OA (*dotted arrow*) (*Courtesy of* David Nascene MD, University of Minnesota–Fairview, Minneapolis, MN.)

37.3 Anterior Communicating and Anterior Cerebral Artery Fenestrations

Overall, *fenestrations* or focal *duplications* of the intracranial arteries are not uncommon, having been reported in 1–10 % of the population, depending on modality; those of the AcoA (more common) or proximal A1 segment of the ACA (less common) have been reported in 0.5–5 % of the population on MRA, CTA, or DSA; this number has been reported to be as high as 20–40 % on older studies of cadavers [4–13]. Notably, fenestrations are about two to three times as likely to be found in the posterior circulation (vertebrobasilar) than in the anterior circulation [4–13], perhaps because some fenestrations are too small (in the range of 0.1–0.3 mm) to see on even high-resolution imaging studies. Fenestrations are less common in the A1 segments or proximal A2 segments of the ACAs than in the AcoA [4–13]. A slightly increased chance of *aneurysm* formation, compared with the general population, has been reported, but whether such differences exist is still debated. As the use of noninvasive imaging for screening increases, the incidence of fenestrations could also increase. Notably, such AcoA or ACA A1 segment fenestrations can also be bilateral ("double fenestrations") (Figs. 37.3, 37.4, 37.5, 37.6, 37.7, 37.8, 37.9, 37.10, 37.11, 37.12, 37.13, and 37.14).

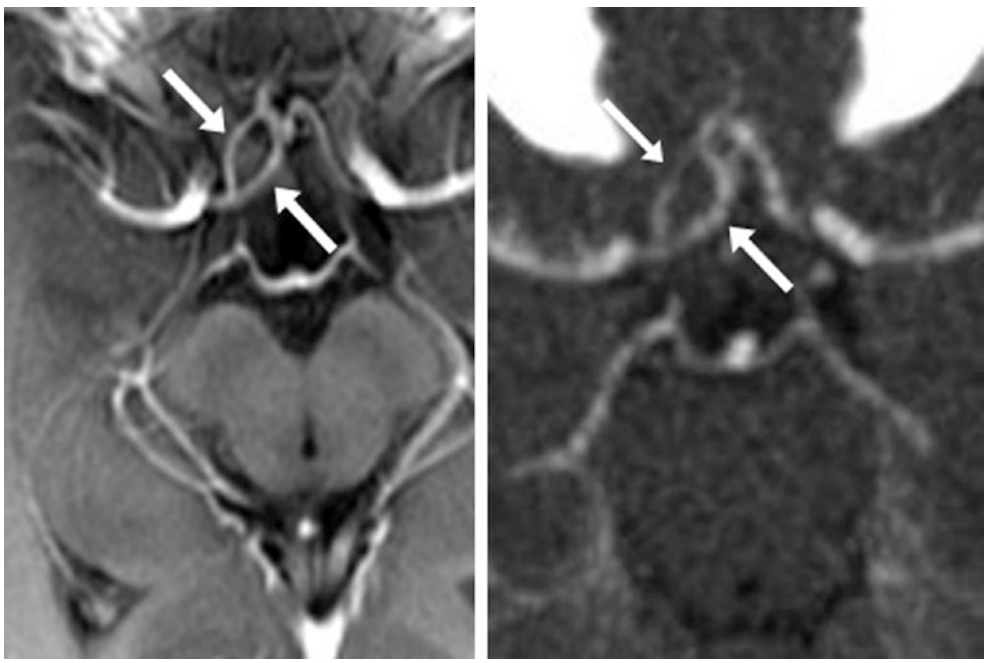

Fig. 37.3 62-year-old with a fenestration of the right anterior cerebral artery (ACA) A1 segment (*between arrows*) on axial postcontrast T1WI (*left*) and on a contrast-enhanced CT (*right*)

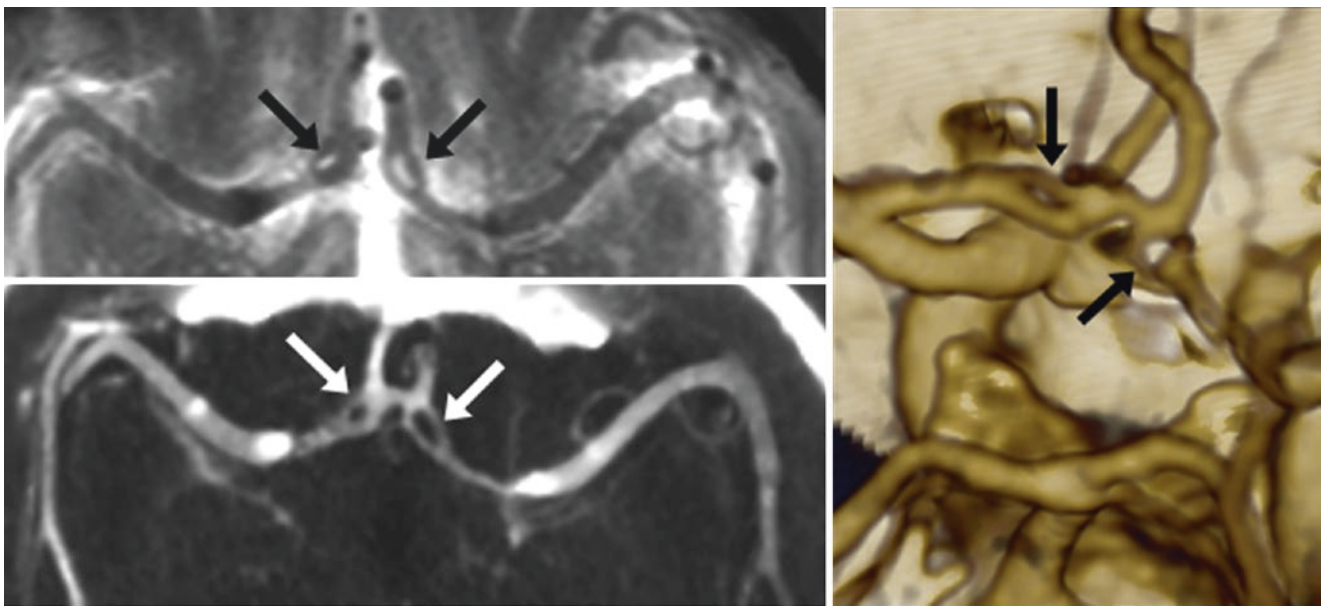

Fig. 37.4 58-year-old with bilateral ACA A1 segment fenestrations (*arrows*), shown on T2WI MRI (*top left*), 3D VR CTA superior view (*right*), and a 20-mm axial MPR from the CTA (*bottom left*)

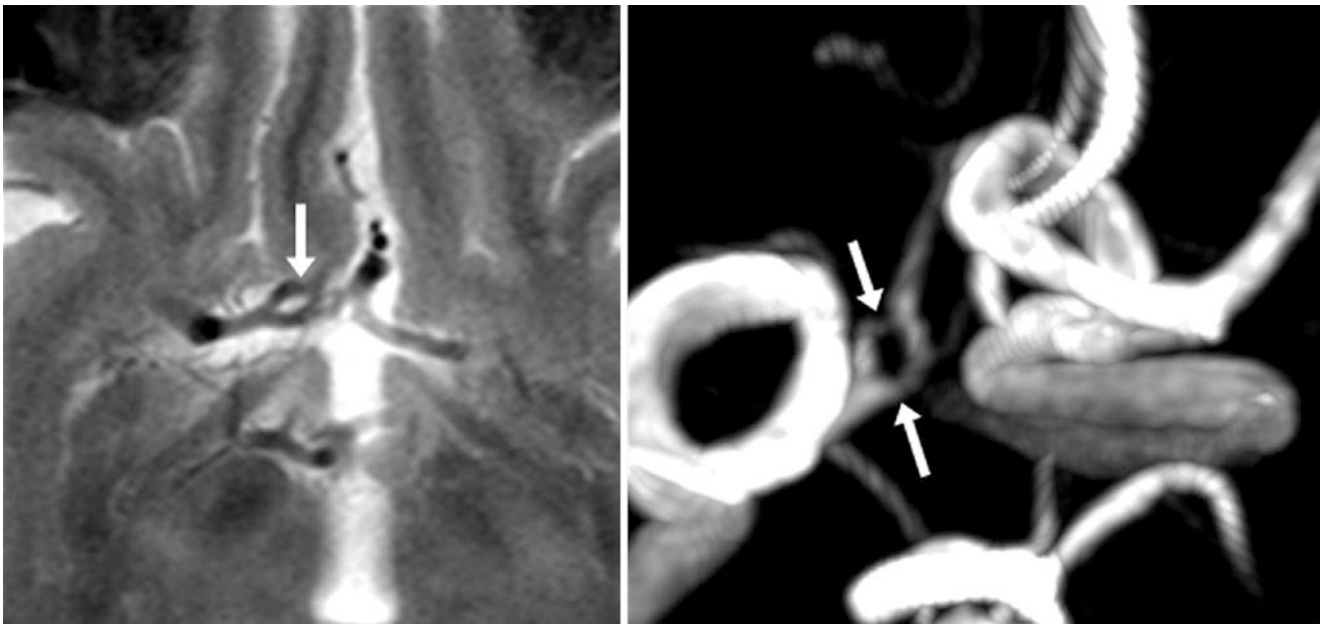

Fig. 37.5 29-year-old with a right ACA A1 segment fenestration (*between arrows*) on axial T2WI MRI (*left*), and 3DTOF MRA superior oblique view (*right*)

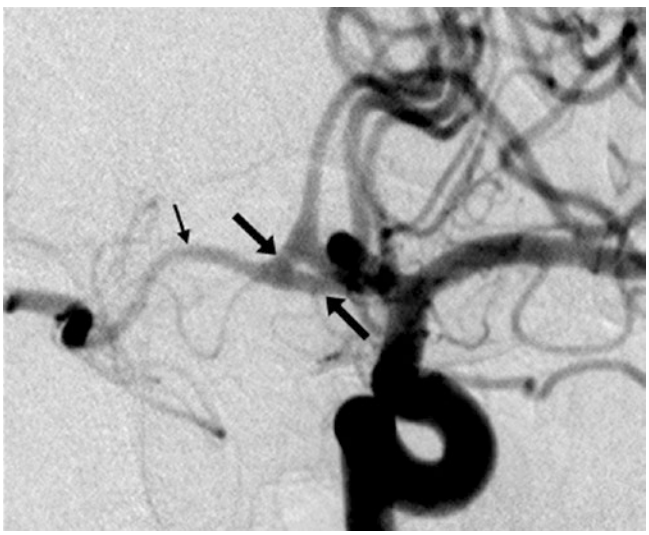

Fig. 37.6 In this 61-year-old, a right A1–anterior communicating artery (AcoA) junction fenestration (*between arrows*) cross-fills on catheter DSA RAO views (via left ICA injection). The right ACA (*thin arrow*) is hypoplastic

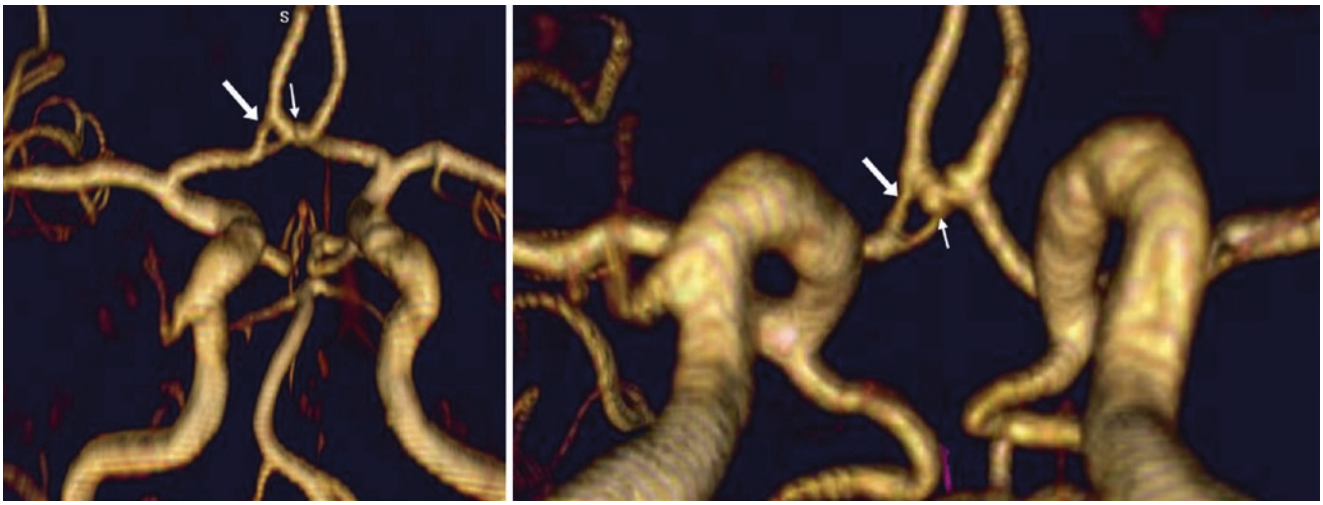

Fig. 37.7 In this 34-year-old, a 3DTOF MRA AP view (*left*) depicts mildly ectatic ICAs bilaterally with a fenestration (*large arrows*) situated at the right A1–AcoA junction. An inferior oblique view (*right*) better depicts the fenestration, as well as a tiny outpouching suspicious for an aneurysm (*thin arrows*), which is protruding from the posteroinferior aspect of the AcoA

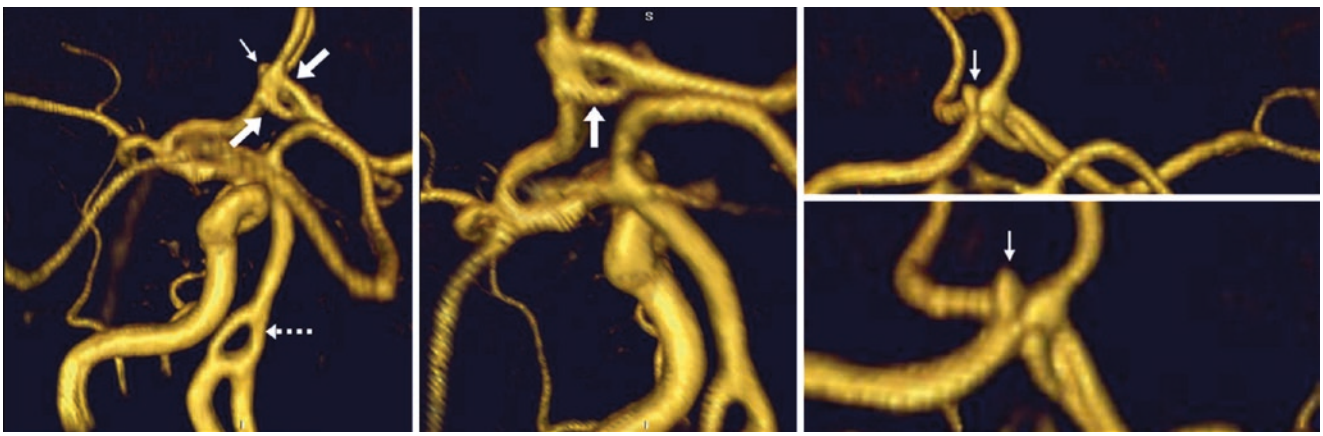

Fig. 37.8 51-year-old with simultaneous AcoA fenestration (*large arrows*) and basilar fenestration (*dashed arrow*), on 3DTOF MRA left anterior oblique (LAO) view (*left*), with a focus on the AcoA fenestration on a magnified LAO view (*middle*). An oblique AP view (*right, top*) with a further magnified image (*right, bottom*) confirms that an aneurysm (*thin arrows*) less than 2 mm in size is present. The aneurysm protrudes superiorly from the AcoA fenestration

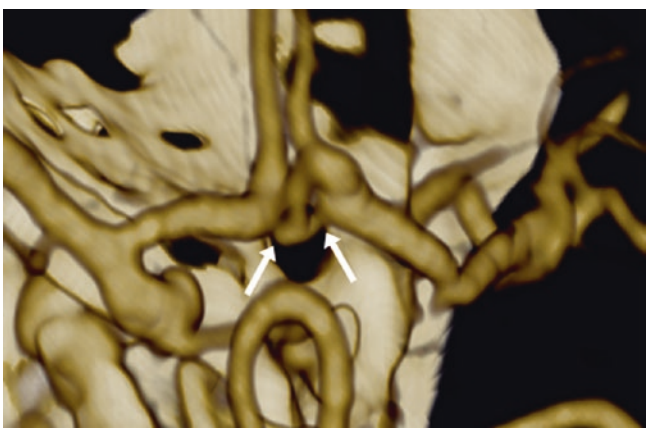

Fig. 37.9 In this 72-year-old, "double fenestrations" of the AcoA (*arrows*) are adjoining each other on a 3D VR CTA PA view

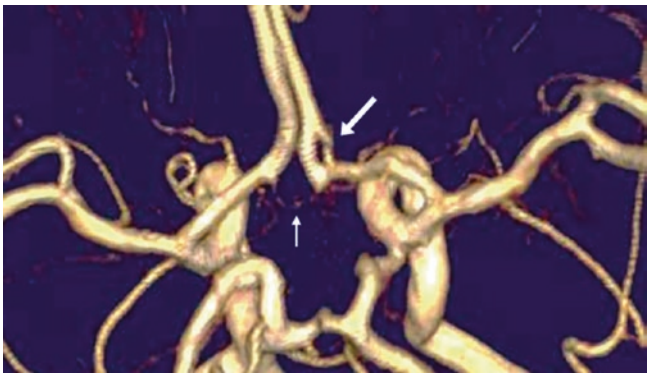

Fig. 37.10 27-year-old with an A2 segment fenestration (*large arrow*) on a 3DTOF MRA superior view. The AcoA is tiny (*thin arrow*)

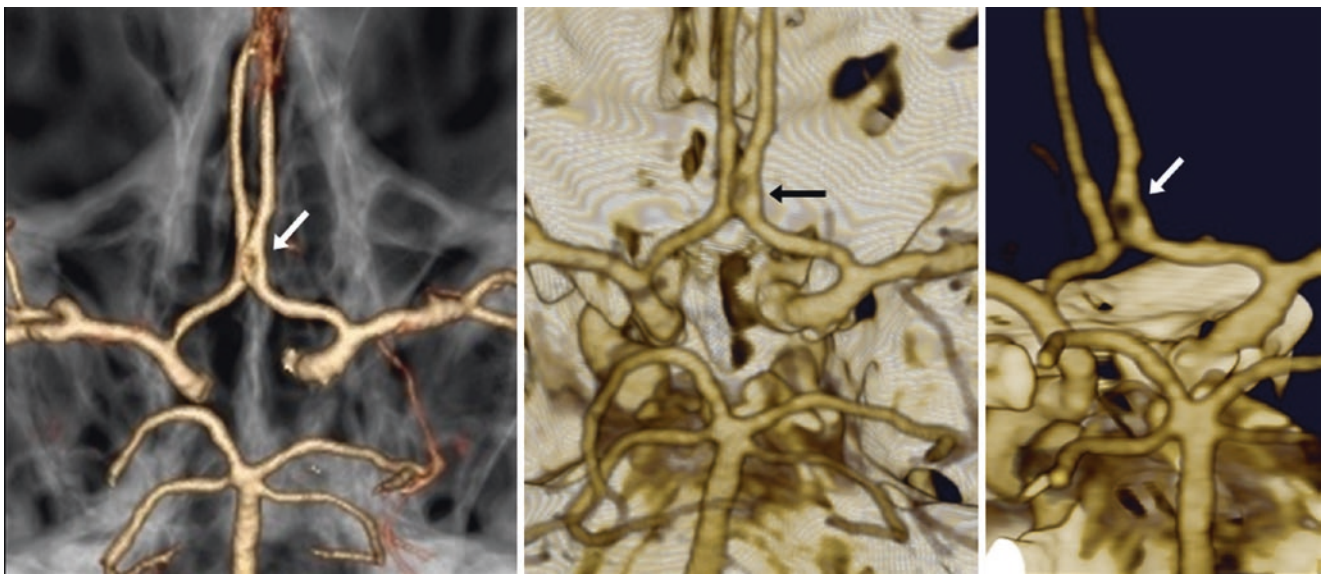

Fig. 37.11 75-year-old with a tiny fenestration (*arrows*) of the proximal A2 segment of an ACA on three different 3D VR CTA PA views, including a transparent bone view (*left*), a bone overlay (*middle*), and a "coned down" view (*right*)

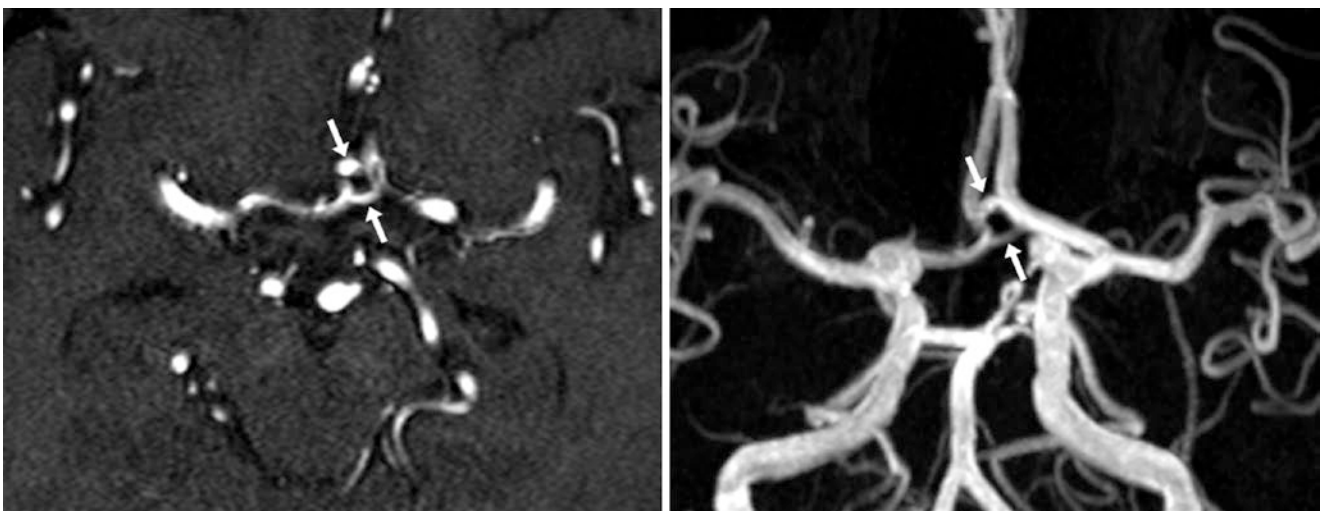

Fig. 37.12 In this 56-year-old, a 3DTOF MRA axial source image (*left*) depicts a duplicated AcoA (*arrows*), with a sizable gap seen between the two vessels, as shown on an MIP AP view (*right*)

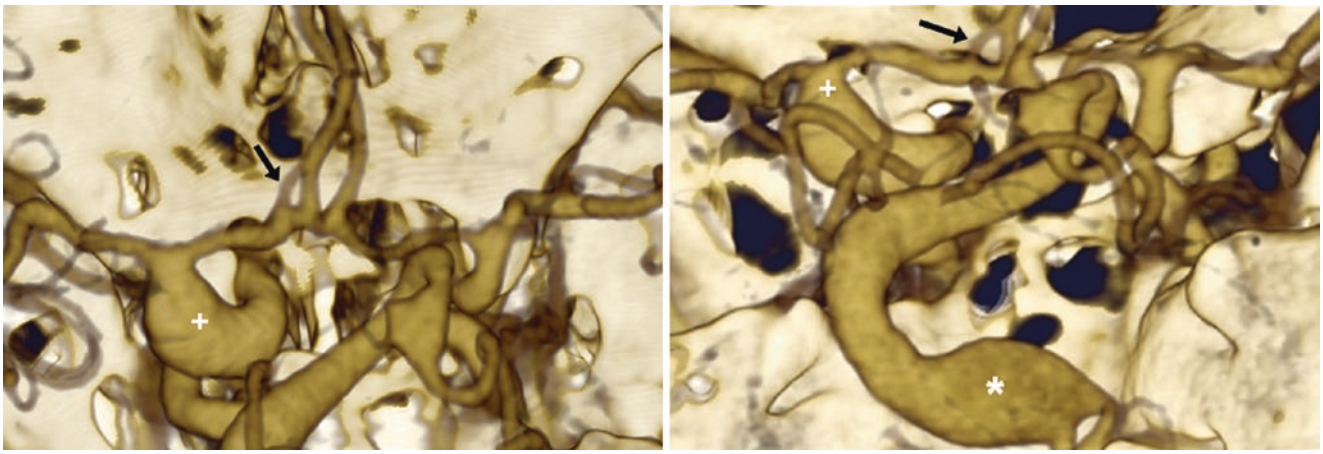

Fig. 37.13 41-year-old with an AcoA–A2 junction fenestration (*arrows*) on 3D VR CTA PA (*left*) and RPO (*right*) views. The patient also has diffuse arterial ectasia, including fusiform aneurysmal enlargement of the ICA (*plus sign*) and lower basilar (*asterisk*)

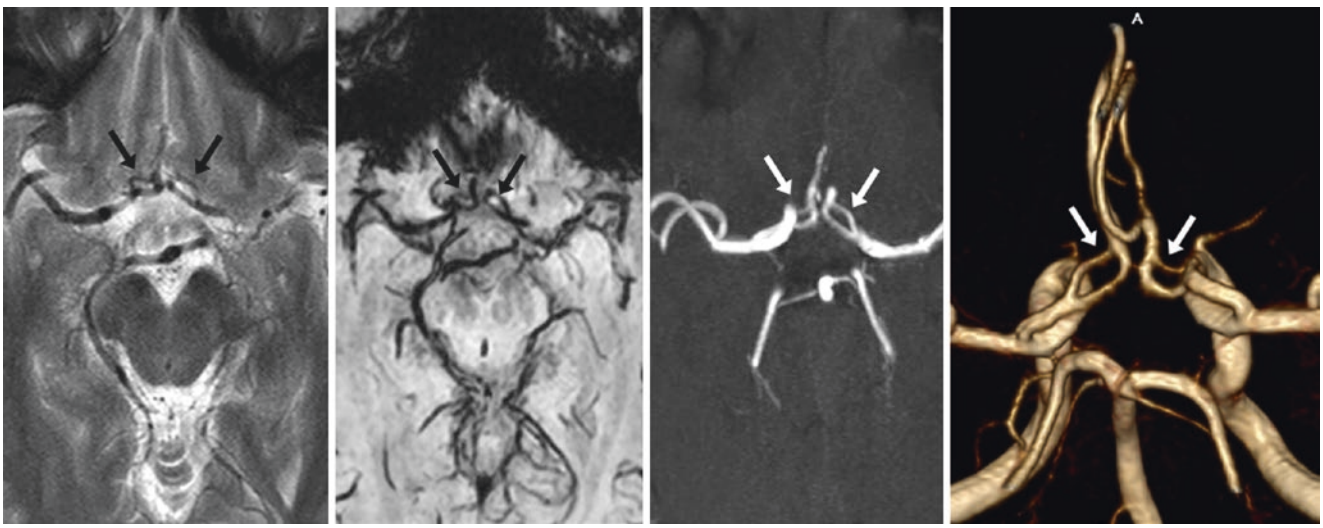

Fig. 37.14 41-year-old with bilateral ACA A1 segment fenestrations (*arrows*) on 3 T MRI axial T2WI (*left*), SWI (*left middle*), 3D TOF MRA 5 mm-thick MPR (*right middle*), and on a 3D VR superior view (*right*) from the 3D TOF MRA

37.4 Hypoplasia or Absence of the Anterior Cerebral Artery A1 segment

An *absent or hypoplastic ACA* (typically referring solely to the A1 segment) is most commonly incidental and asymptomatic, unless a concomitant severe stenosis of the contralateral ACA or distal ICA is present. An absent or hypoplastic ACA occurs in about 5–25 % of the population (Figs. 37.15, 37.16, 37.17, 37.18, 37.19, and 37.20). Most commonly, the ipsilateral A2 segment is supplied predominantly by the contralateral A1 segment via the AcoA [8–14]. The A1 segment may appear totally absent (particularly on T2WI or time-of-flight MRI, in which noncontrast sequences are dependent on refreshing of spins and hence flow rate), but autopsy studies have shown that the A1 segment is usually present to some degree. There has been some debate as to whether A1 segment hypoplasia presents a slightly higher risk of an *aneurysm*, but such an association is doubtful. Notably, a focal *stenosis* should be excluded before calling A1 segment hypoplasia, and patency of the distal vasculature (A2 segments and beyond) should also be assessed, particular if stroke symptoms or infarcts are noted in the distribution of the ACA. A *bihemispheric ACA variant* consisting of severely hypoplastic A1 and A2 segments on one side while the contralateral A1 and A2 segments dominate (discussed in the following Sect. 37.5) is present in just under 1 % of the population [12–15].

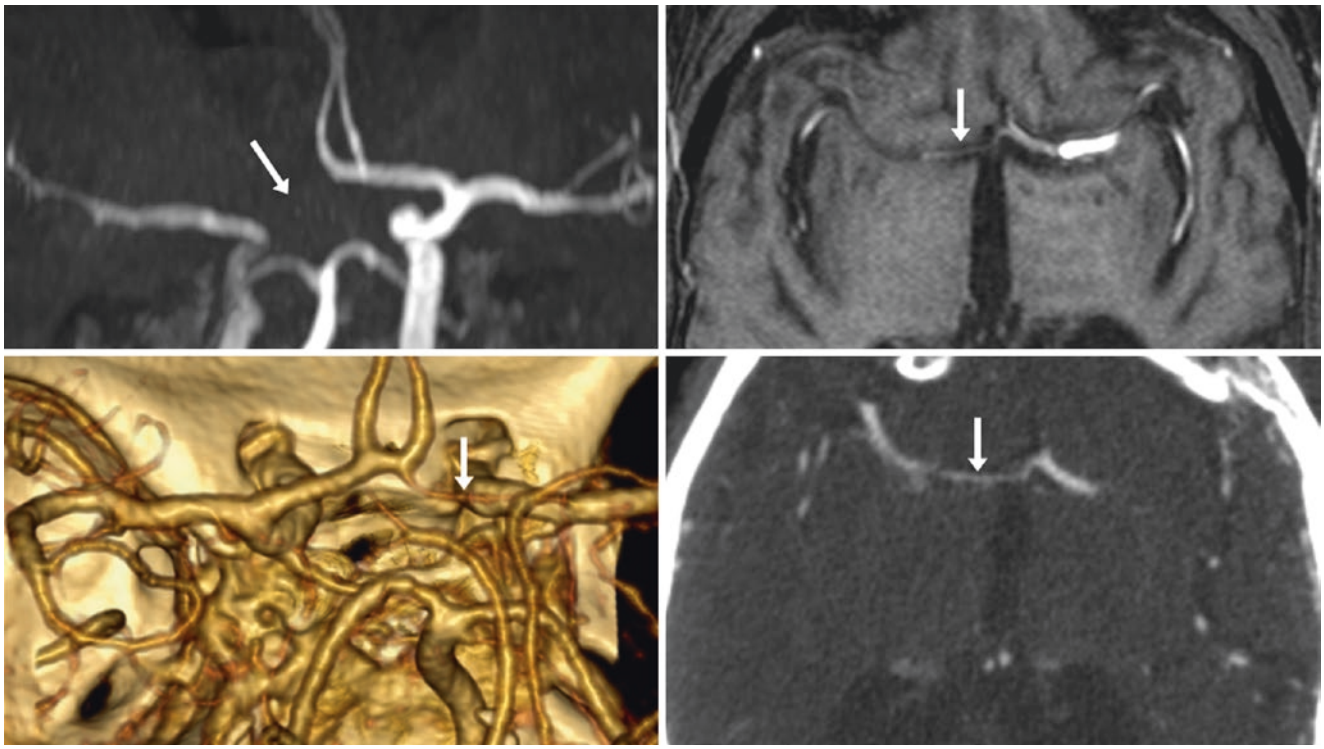

Fig. 37.15 78-year-old with a lack of a visualized right ACA A1 segment on a noncontrast 3D TOF MRA AP view (*top left*); on axial source images (*top right*), the A1 segment was quite tiny, but patent. The A1 segment hypoplasia (*arrows*) was also noted on a 3D VR CTA PA view (*bottom left*) and on the source axial images (*bottom right*)

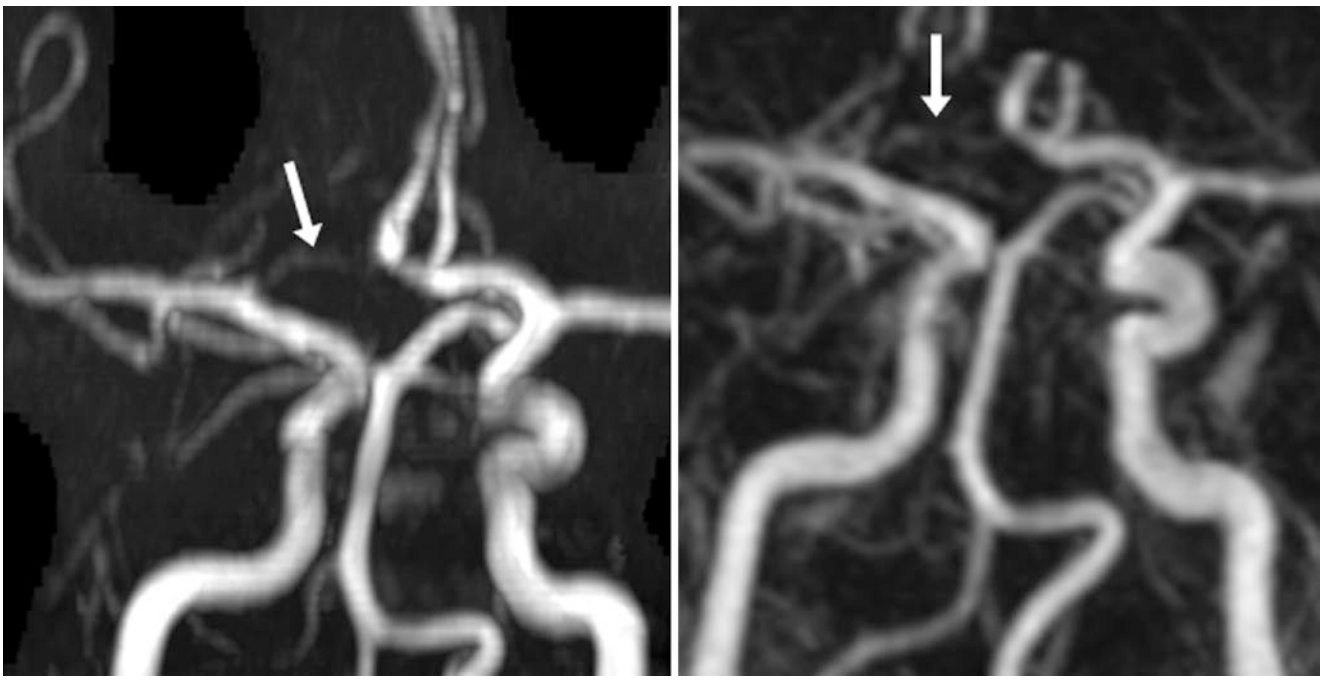

Fig. 37.16 53-year-old with a quite hypoplastic right ACA A1 segment (*arrows*) on a noncontrast 3DTOF head MRA AP view (*left*). It is barely (but better) visualized on a contrast-enhanced MRA AP view (*right*)

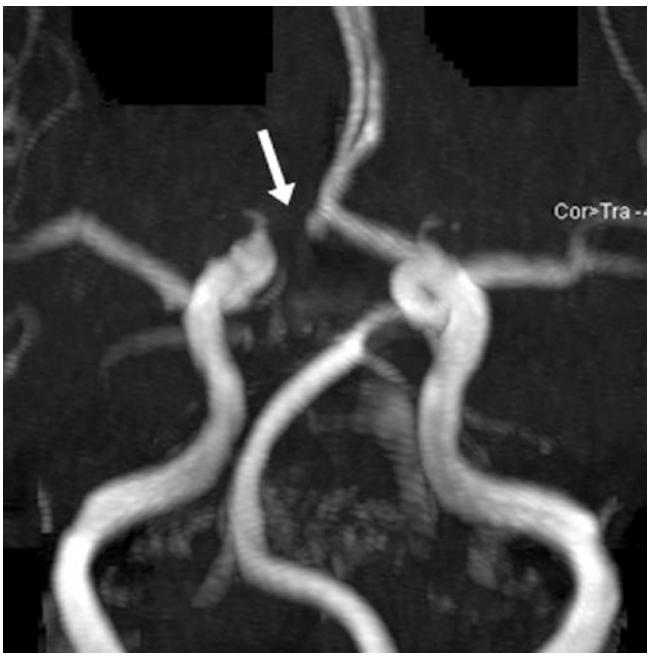

Fig. 37.17 86-year-old with an absent right A1 segment (*arrow*), visualized on a 3DTOF MRA AP view

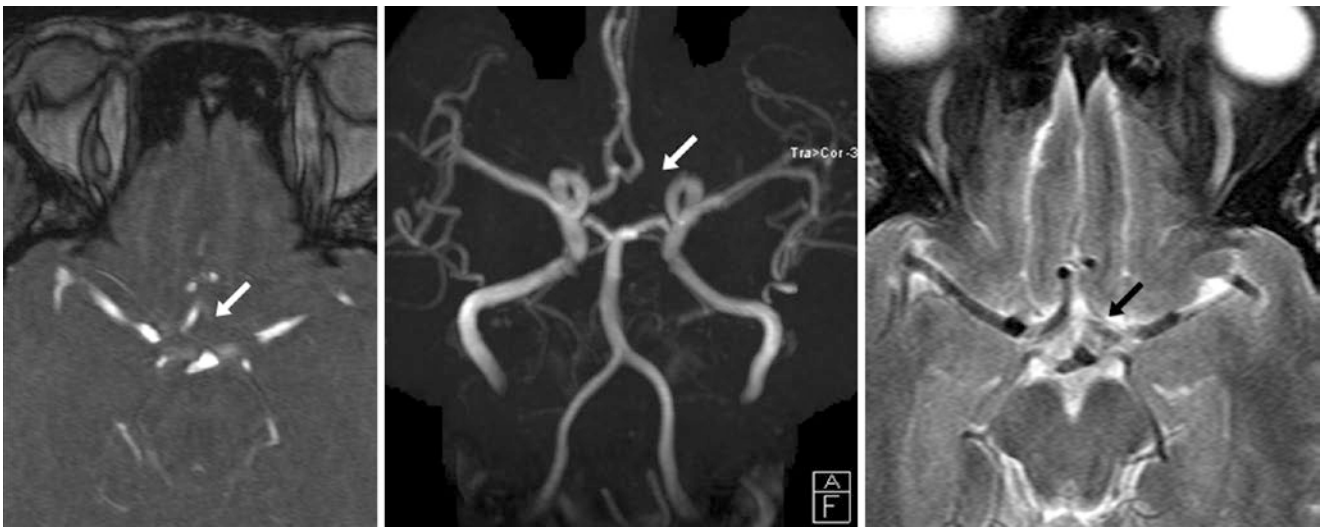

Fig. 37.18 67-year-old with an absent A1 segment (*arrows*) of the left ACA, suspected on source (*left*) and on MIP AP view (*middle*) images from a 3DTOF MRA, with a possible tiny left ACA flow void on an axial T2WI (*right*). As this case illustrates, the A1 segment can be quite tiny; in some cases, it may be visible only by catheter DSA

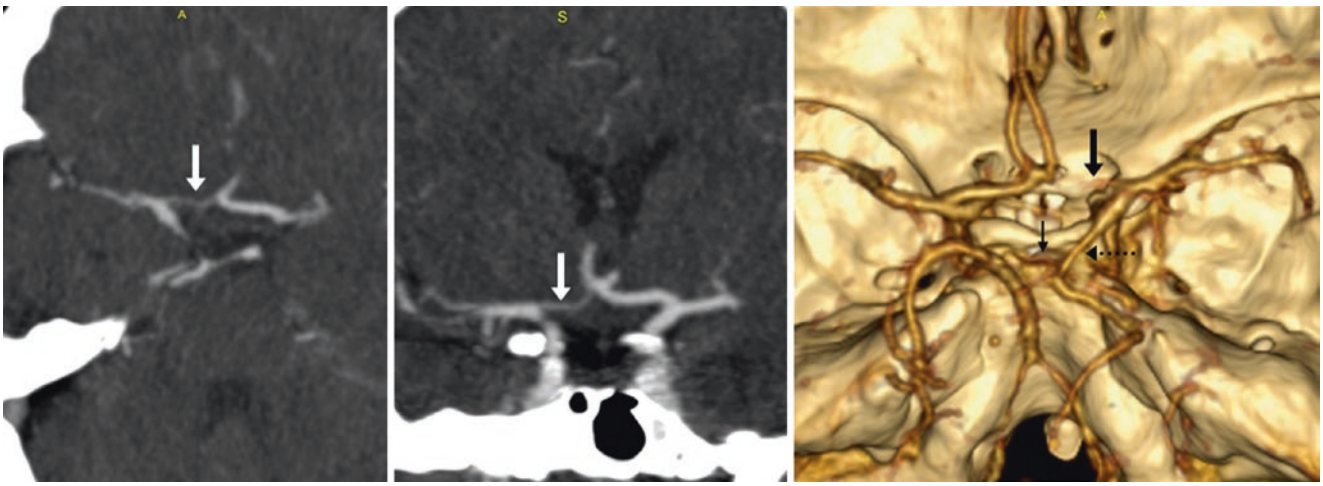

Fig. 37.19 In this 60-year-old, axial (*left*) and coronal (*middle*) 5 mm-thick MPR images from a head CTA depict a hypoplastic right ACA A1 segment (*arrows*), confirmed on a 3D VR CTA PA view (*right*). Note also the severely hypoplastic right P1 segment (*thin arrow*), with a "fetal origin" of the right posterior cerebral artery (PCA) (*dotted arrow*) from the right ICA

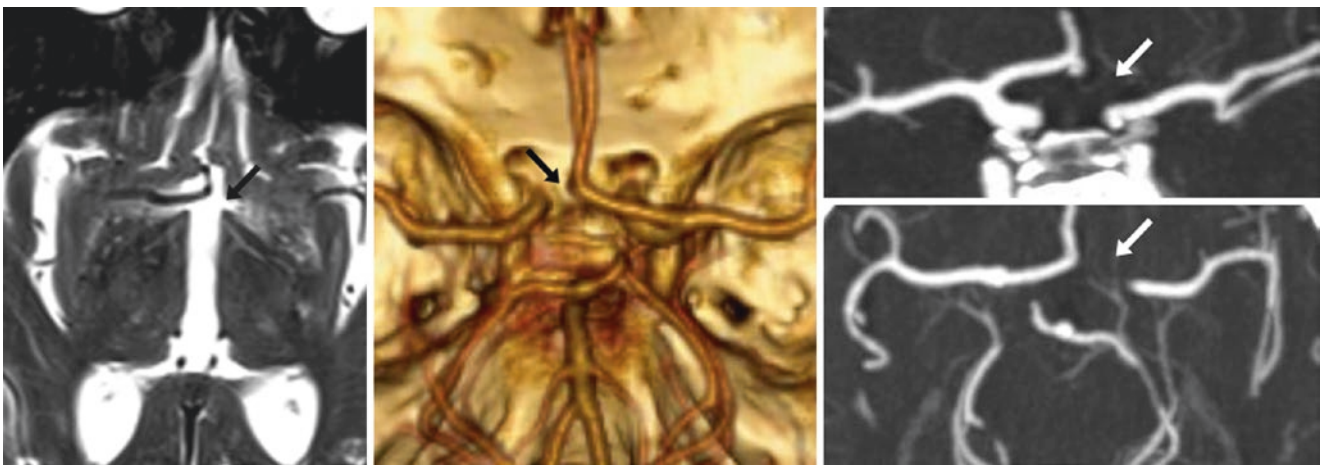

Fig. 37.20 85-year-old with an absent left A1 segment (*arrows*) suspected on an axial T2WI MRI (*left*); this was confirmed on a 3D VR CTA PA view (*middle*), with coronal (*top right*) and axial (*bottom right*) 5-mm MPRs

37.5 "Azygous" ACA and Bihemispheric ACA

An unpaired *"azygous" ACA* is a normal variant present in about 0.1–1.0% of the population [8–15]. This variant consists of a single midline vessel arising from an unpaired A1 segment of the ACA only on one side, although there can be occasional bilateral small A1 segments contributing to the azygous ACA (Figs. 37.21, 37.22, 37.23, 37.24, 37.25, 37.26, 37.27, 37.28, and 37.29). Although most patients with an azygous ACA are asymptomatic, it has classically been associated with certain syndromes and congenital abnormalities, most notably *holoprosencephaly* and neural migration anomalies. This variant arises due to persistence of the embryonic *median artery of the corpus callosum* (MACC, which typically branches off of the AcoA and atrophies during fetal life), in combination with ACA aplasia. The significance is that thromboembolic disease in the setting of an azygous ACA can lead to bilateral medial frontal lobe infarctions. An azygous ACA is readily identified as a single midline A2 vessel by CTA, MRA, or even noncontrast, nonangiographic routine CT or MRI examinations. Persistence of the MACC in combination with normal, bilateral ACAs (the *"triple ACA"* appearance) is discussed later.

The azygous ACA variant is distinct from a "*bihemispheric ACA*," which consists of dominant A1 and A2 segments on one side that ultimately supply both hemispheres, with severe contralateral A1 and A2 hypoplasia. A bihemispheric ACA is about as common as an azygous ACA, also being present in about 0.1–1.0% of the population [8–15]. Usually, these two variants can be distinguished from each other, although at times this distinction may be difficult. Notably, with a bihemispheric ACA, a tiny, proximal A2 segment is found opposite the larger, dominant A2 segment, whereas with an azygous ACA, only a single, midline A2 segment is noted.

Some series have estimated that an azygous ACA may occur in up to 5% of the population, but a retrospective review of these series has led many to believe that a number of those were more likely to have been bihemispheric ACAs, as evident in more recent reports using catheter DSA or higher-resolution CTA or MRA.

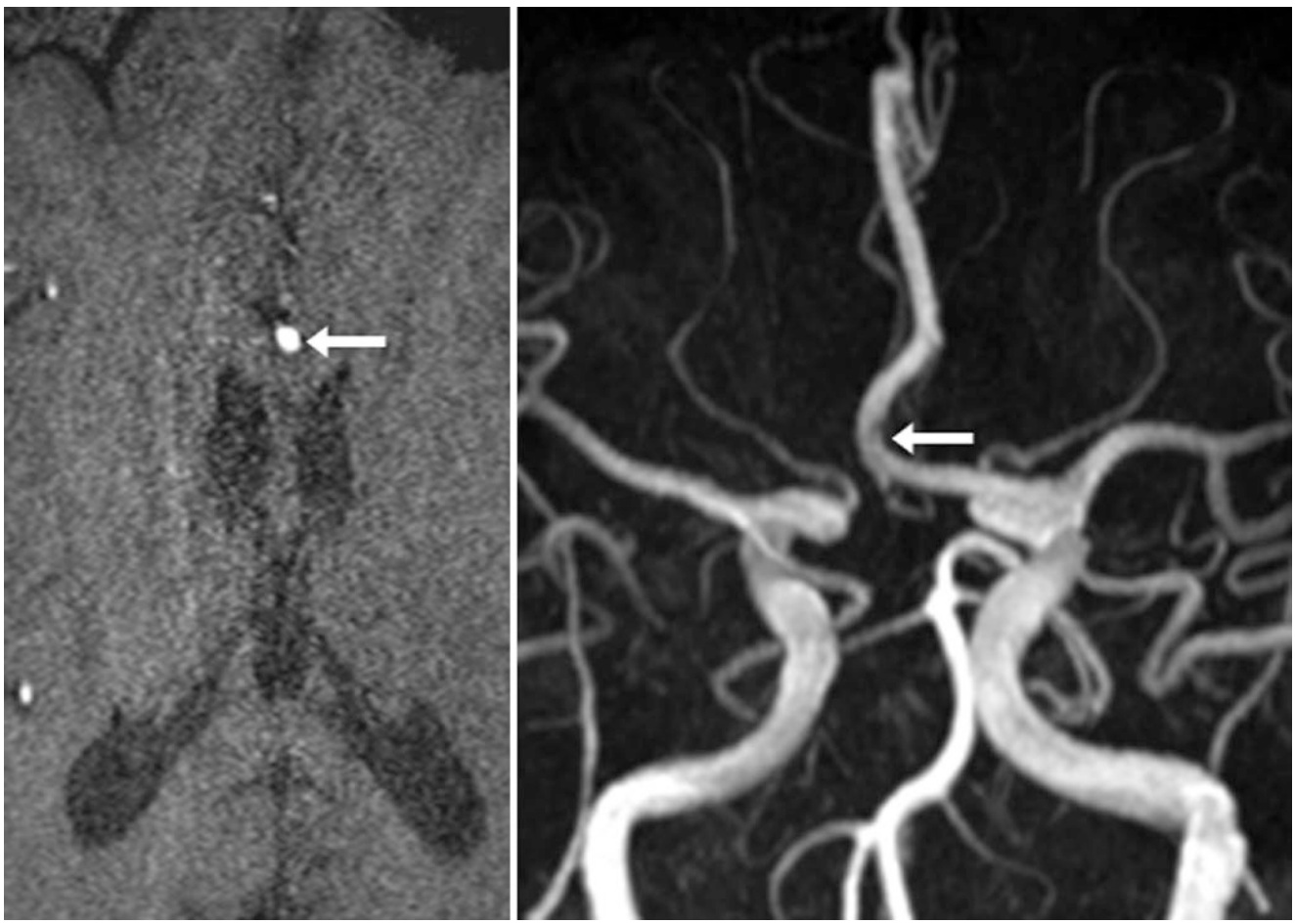

Fig. 37.21 72-year-old with a single midline A2 segment (*arrows*), which is an azygous ACA off the left ICA, on a 3DTOF MRA source image (*left*) and on a MIP AP view (*right*). The right ACA is absent

Fig. 37.22 In this 31-year-old, a 3DTOF MRA AP view shows an azygous ACA (*arrow*) that arises from the right ICA terminus

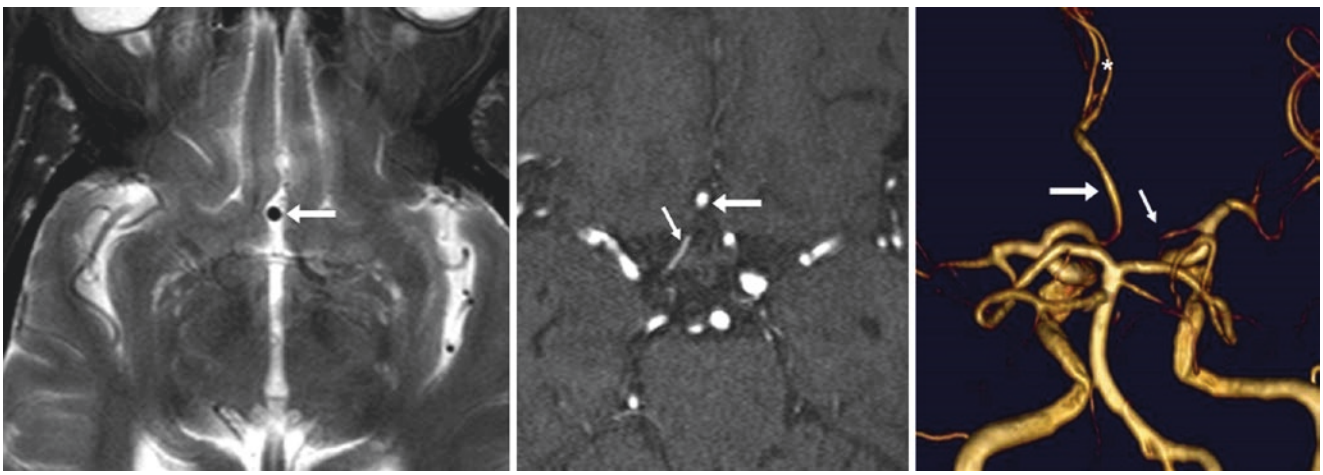

Fig. 37.23 76-year-old with a single midline A2 vessel (*large arrows*) on T2WI (*left*), with a hypoplastic right A1 segment (*thin arrows*) on a 3DTOF MRA source image (*middle*) and on an MIP PA view (*right*). The A2 segment supplying both sides is most consistent with an azygous ACA. Superiorly, it bifurcates (*asterisk*) to supply the ACA distribution to both hemispheres (*Courtesy of* Basar Sarikaya, MD, University of Minnesota, Minneapolis, MN.)

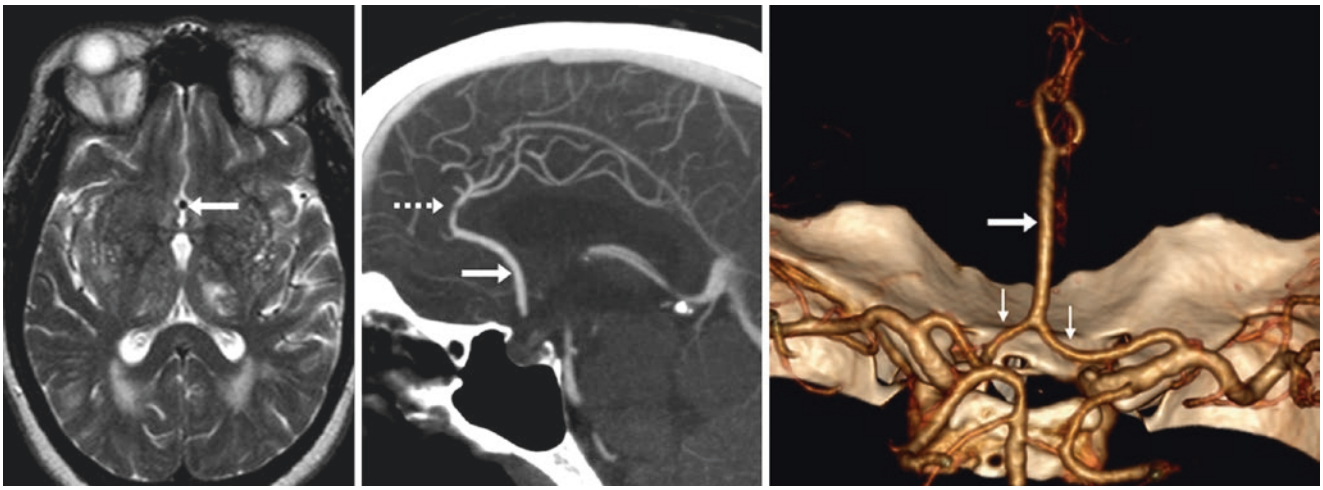

Fig. 37.24 In this 61-year-old vasculopath, a T2WI MRI (*left*; *note diffuse T2-bright lesions*) shows an azygous ACA (*large arrows*), as only one midline A1-A2 segment is seen. A midline MPR (*middle*) from a CTA depicts the azygous ACAs bifurcation (*dotted arrows*); a 3D VR PA view (*right*) confirms two patent A1 segments (*thin arrows*) that merge

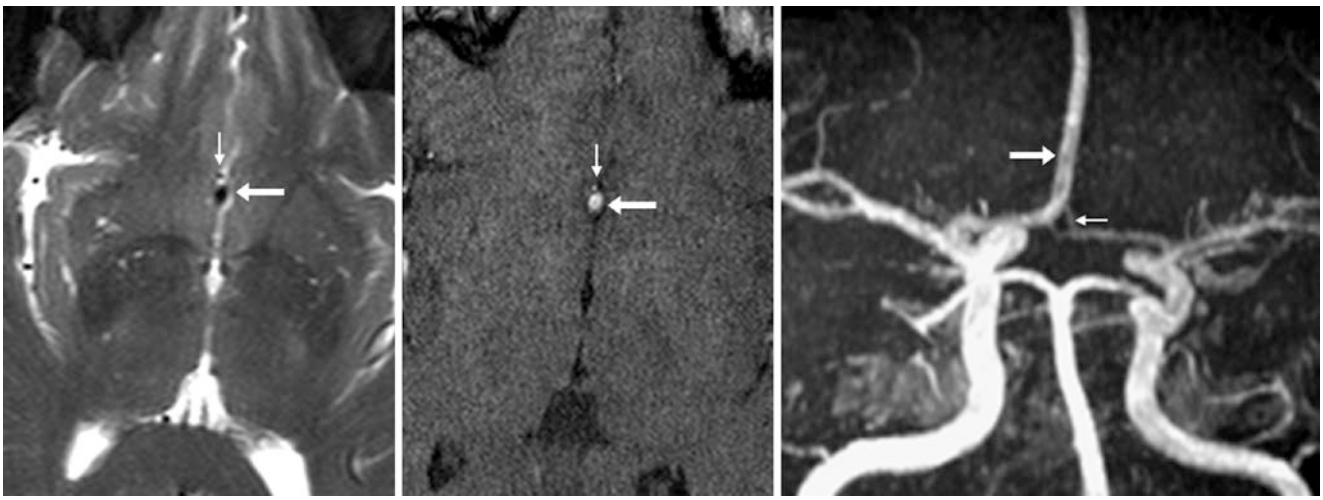

Fig. 37.25 64-year-old with a quite hypoplastic left A2 segment (*thin arrows*) on an axial T2WI MRI (*left*), on a 3DTOF MRA source image (*middle*), and on a 3DTOF MRA MIP AP view (*right*). The dominant right A2 segment (*arrows*), along with the diminutive, hypoplastic (but present) left A2 segment is suggestive of a bihemispheric ACA

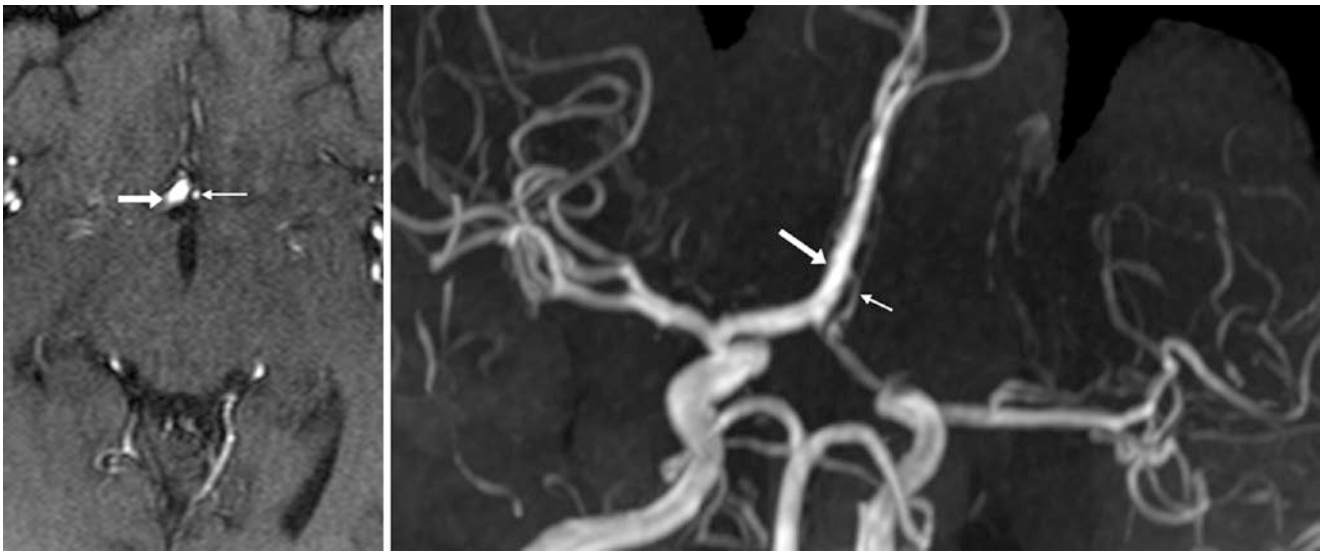

Fig. 37.26 18-year-old with a dominant right A2 segment (*large arrows*) and a hypoplastic left A2 segment (*tiny arrows*) on a 3DTOF MRA source image (*left*) and on an MIP AP view (*right*). These findings indicate a bihemispheric ACA

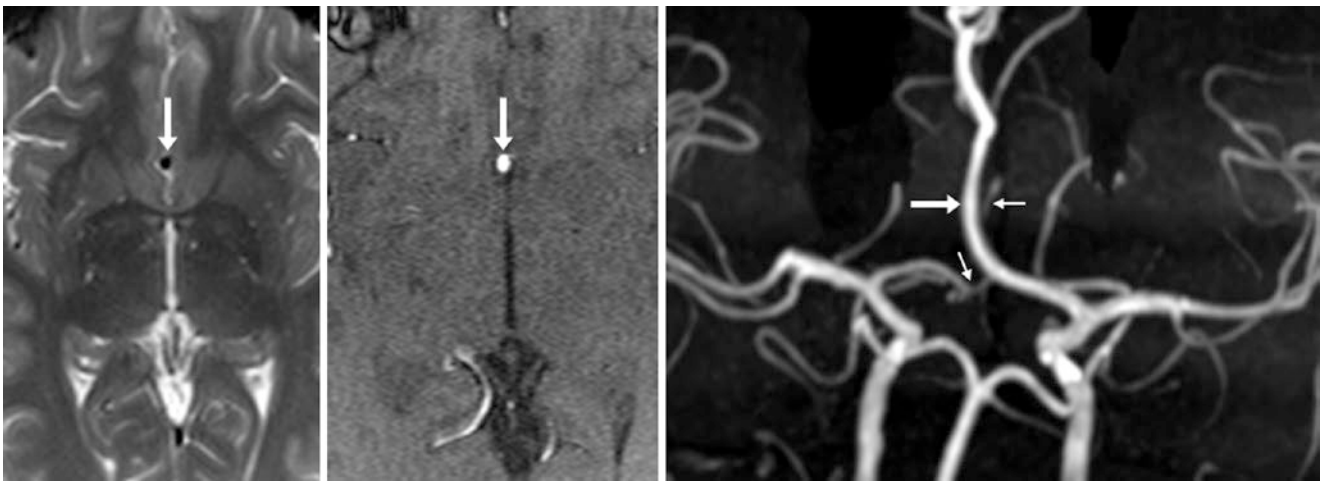

Fig. 37.27 In this 43-year-old, an axial T2WI (*left*) and a source 3DTOF MRA image (*middle*) show what appears to be a single, midline A2 segment (*large arrows*) arising from the left A1 segment. A 3D MIP AP view (*right*), however, depicts what are probably hypoplastic contralateral A1-A2 segments (*tiny arrows*), suggesting a bihemispheric left ACA

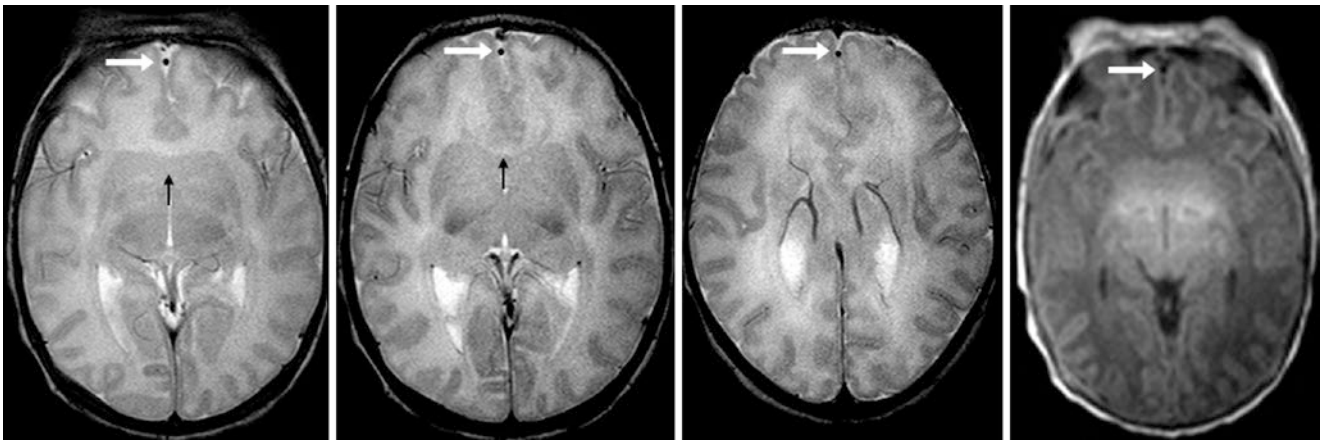

Fig. 37.28 Companion case of lobar holoprosencephaly with an azygous ACA: 2-day-old neonate with an azygous ACA (*arrows*) seen within the anterior interhemispheric fissure on an axial T2WI MRI (*left three images*); note the lack of a falx anteriorly, with interdigitation of the gyri. The axial T2WIs and a T1WI (*right*) confirm abnormal fusion (*thin arrows*) of both gray matter (corpus striatum) and white matter tracts in the orbitofrontal regions

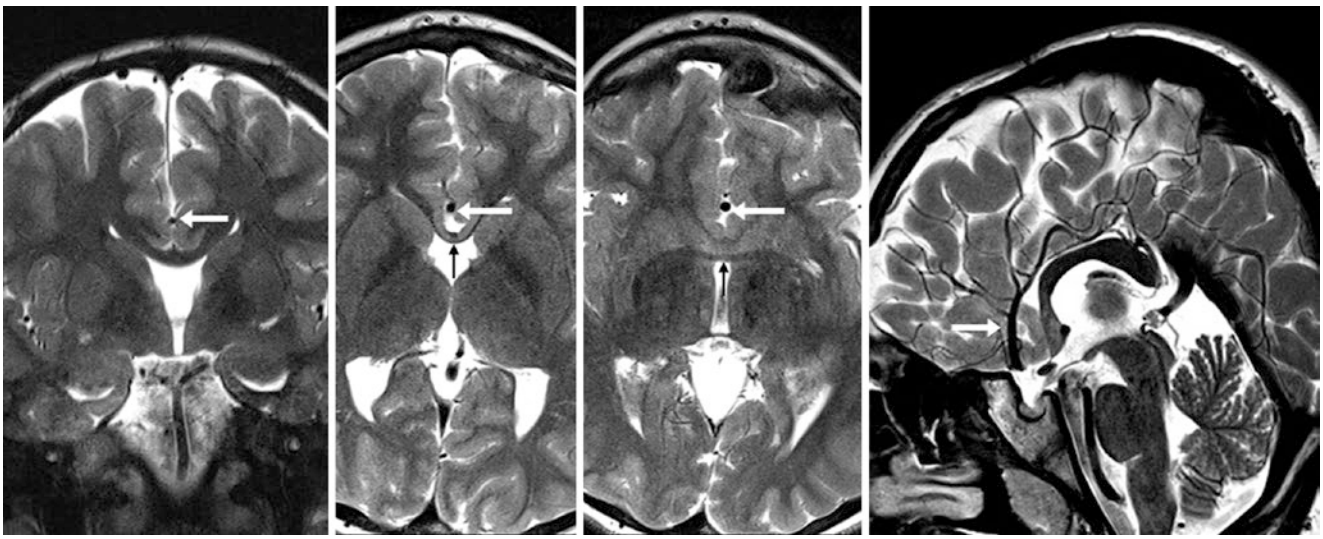

Fig. 37.29 Companion case of septopreoptic holoprosencephaly: 10-year-old with an azygous ACA (*arrows*) in the interhemispheric fissure on coronal (*left*), axial (*middle two images*), and sagittal (*right*) T2WI MRI. Note a partial lack of a falx anteriorly, with interdigitating gyri. The axial images confirm caudate and gray and white matter fusion anterior to the anterior commissure (*thin arrows*) (*Courtesy of* David Nascene, MD, University of Minnesota, Minneapolis, MN.)

37.6 Median Artery of the Corpus Callosum ("Triple ACA")

Persistence of the *median artery of the corpus callosum* (MACC) is an embryonic remnant that normally involutes as the more distal A2 segments of the ACAs develop above the level of the AcoA. This variant has alternatively been referred to as the *median callosal artery*. The term used depends on whether or not this third, middle ACA vessel is considered a vestigial remnant of a normal embryologic plexus. Its appearance is also colloquially referred to as an "*accessory ACA," "third ACA"* or *"triple ACA."*

According to Padget's theory [17], the embryologic anterior cerebral arterial circle consists of three ACAs, connected between each other by a web-like anterior communicating plexus, where the MACC is the middle of the three [16–20]. By this theory, the MACC and the plexus should regress, but persistence of either or both leads to any of a number of anatomic variants. This theory has been refuted to a degree; it has been advanced that the presence of this third vessel actually differs in course from the MACC, better explaining the presence of azygous and bihemispheric ACAs [16–20].

Whatever its source (and whatever the preferred term), the MACC persists in about 1–5 % of the population [16–20]. The typical configuration of the three vessels has the bilateral A2 segments of the ACA with the MACC being the third at the midline (Figs. 37.30, 37.31, 37.32, 37.33, 37.34, and 37.35). This vessel typically lies in the pericallosal sulcus, where it lies in close apposition to gray matter along the superior surface of the corpus callosum, called the *induseum griseum*. The MACC is usually not associated with an increased incidence of aneurysms, congenital anomalies, or syndromes, and is readily identifiable on CTA or MRA, with the midline vessel arising directly from the top of the AcoA. Notably, this normal variant should not be confused with another variant in which the pericallosal artery arises early (*i.e.*, where an A2 segment on one side branches off early into the pericallosal and callosalmarginal arteries), or early branching of other A2 or A3 segments (such as early orbitofrontal or frontopolar branches).

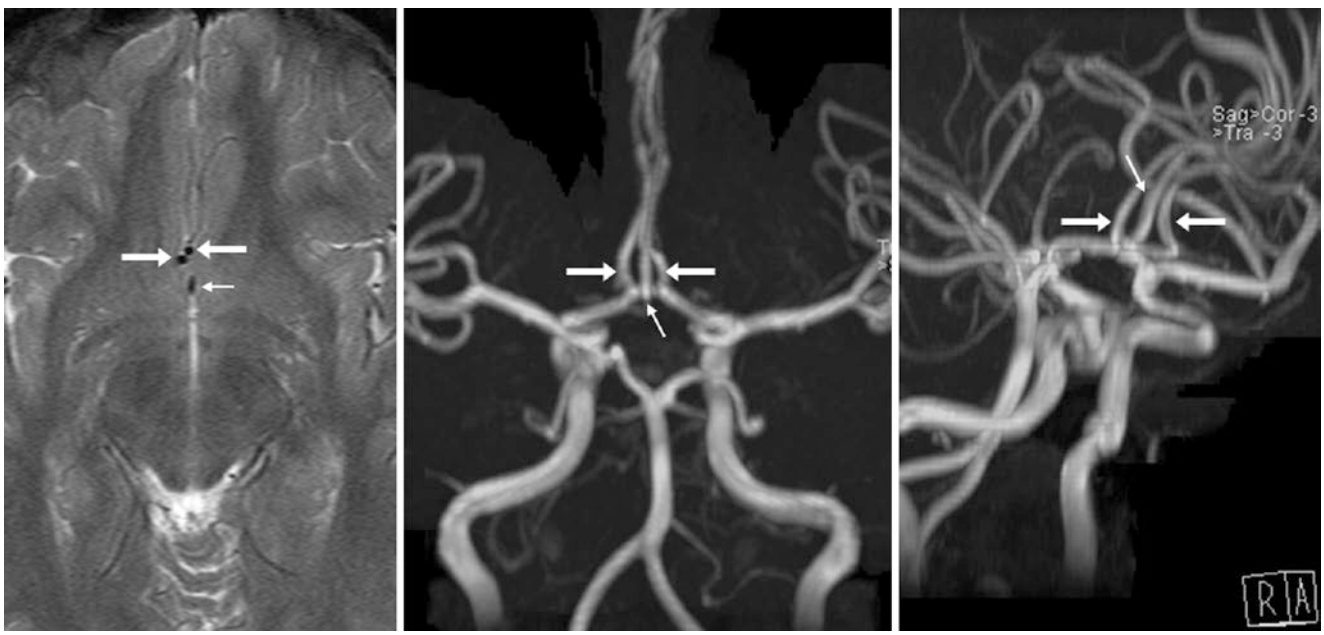

Fig. 37.30 In this 15-year-old, an axial T2WI MRI (*left*) depicts three vessels (*arrows*) just above the AcoA, also seen on 3DTOF MRA AP (*middle*) and oblique (*right*) MIP views, indicating a persistent MACC (*thin arrows*)

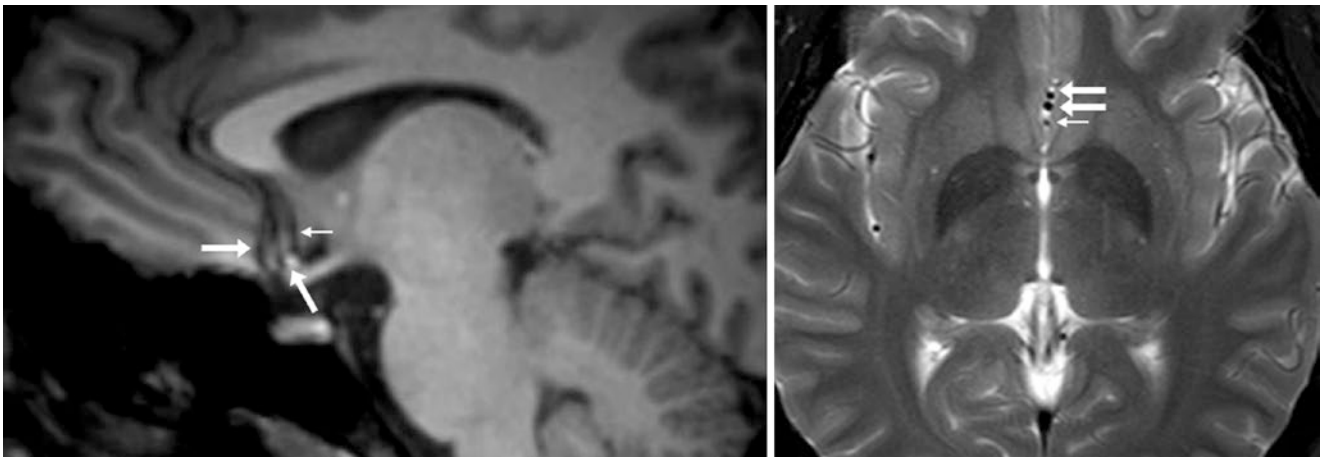

Fig. 37.31 25-year-old with three flow voids (*arrows*) just above the AcoA on a sagittal 3D T1WI MPR (*left*) and on an axial T2WI (*right*). No MRA was performed, but the findings suggest a persistent MACC (*thin arrows*)

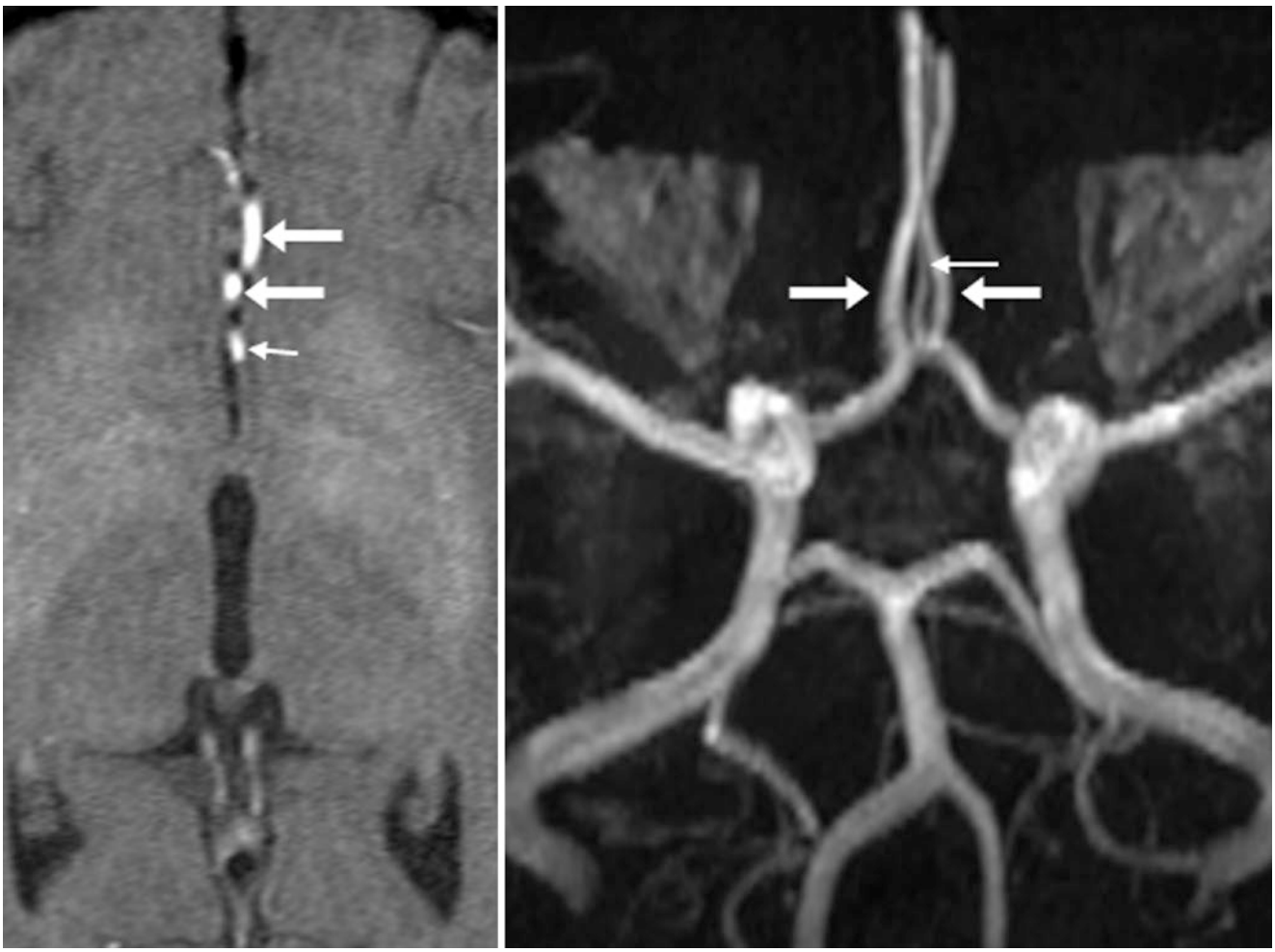

Fig. 37.32 20-year-old with a "triple ACA" appearance (*arrows*) on a source 3DTOF MRA image (*left*) and on an AP-superior view (*right*), due to an MACC (*thin arrows*)

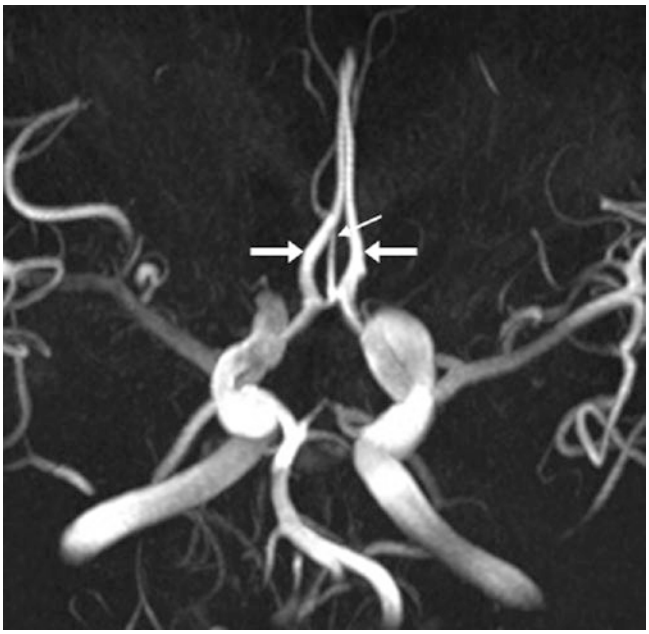

Fig. 37.33 63-year-old with an MACC (*thin arrow*) situated between the typical A2 segments (*arrows*) on a 3DTOF MRA AP-superior view

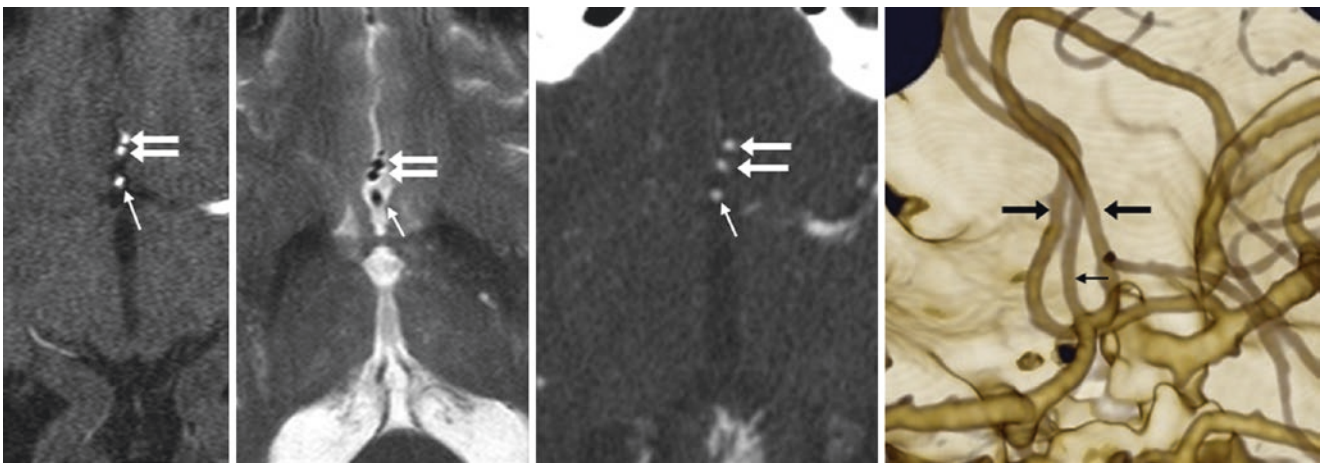

Fig. 37.34 In this 73-year-old, a source 3DTOF MRA image (*left*) demonstrates three vessels (*arrows*) just above the AcoA, also shown on an axial T2WI (*left middle*). Source axial CTA images (*right middle*) and a 3D VR CTA lateral-oblique view (*right*) further depict the persistent MACC (*thin arrows*)

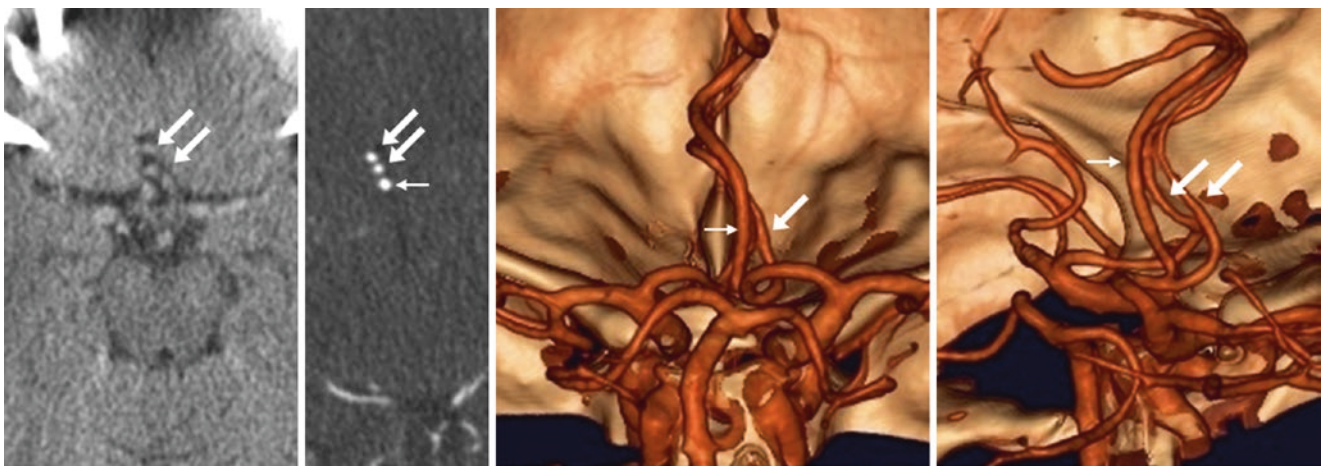

Fig. 37.35 In this 42-year-old, a nonenhanced CT (*left*) was interpreted as having prominent AcoA vessels, suspicious for aneurysm. CTA axial source images (*left middle*) showed three vessels (*arrows*) just above the AcoA, representing a persistent MACC (*thin arrows*). A 3D VR CTA PA view (*right middle*) and right lateral view (*right*) further depicted the MACC

37.7 Primitive Olfactory Artery or Olfactory Course of the Anterior Cerebral Artery

The *primitive olfactory artery* (POA) (also known as an "olfactory course of the ACA") is a rather rare normal variant, with fewer than 20 cases reported in the modern literature [21–23]. In normal development, the POA is the precursor to the ACA; it regresses and persists as the recurrent artery of Heubner. The POA is identified by an anteromedial and inferior course of the proximal A1 segment of the ACA (which is actually the POA at that point), which then makes a characteristic hairpin turn posterosuperiorly to become the normal distal A1 segment just proximal to the AcoA. This course can occur to varying degrees along a spectrum. The vessel typically lies near the olfactory tracts beneath the posterior portion of the orbitofrontal parenchyma and olfactory sulcus. (The olfactory sulcus lies between the gyrus rectus and the medial orbital gyrus.) In contrast to the *recurrent artery of Heubner* (which typically arises from the distal A1 segment or proximal A2 segment), in the setting of a POA, the artery of Heubner is characteristically absent on that side and the AcoA typically has an elongated course. The POA has no definite clinical significance, although aneurysms at the hairpin turn have been demonstrated in about one third of the reported cases [21–23] (Fig. 37.36).

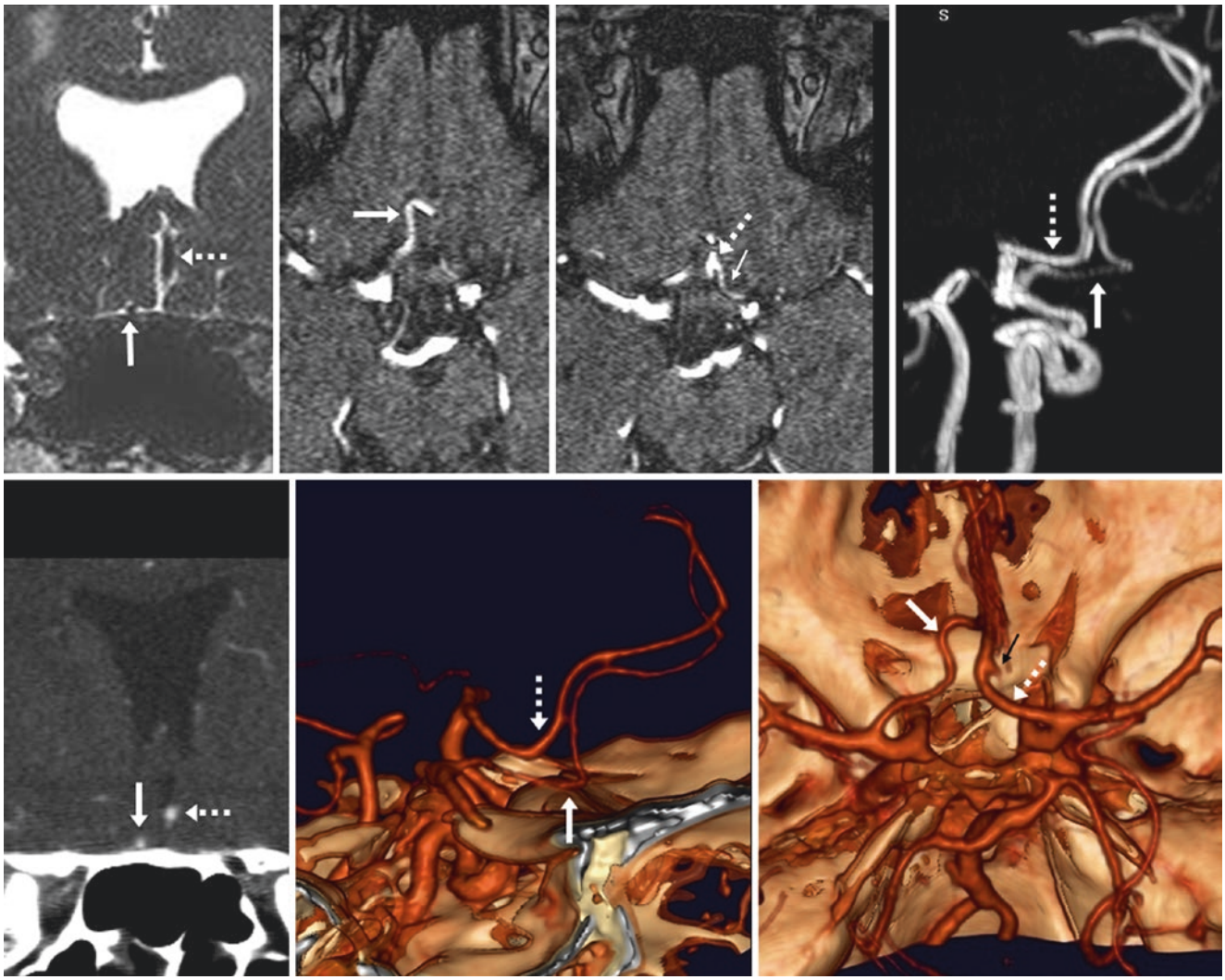

Fig. 37.36 *Top row:* In a 52-year-old, a coronal 3D T2WI (*left*) depicts an olfactory course of the ACA/POA (*arrows*) under the right orbitofrontal parenchyma, with a characteristic "hairpin" posterior turn noted on source 3DTOF MRA source images (*left middle* and *right middle*), and on an MIP lateral view (*right, middle cerebral arteries [MCAs] removed*). The contralateral ACA (*dotted arrows*) and its recurrent artery of Heubner (*thin arrows*) are also denoted. *Bottom row:* A coronal MPR (*left*) from a CTA also depicts the POA. A 3D VR lateral view (*middle, MCAs removed*) and superior view (*right)* further show the POA's abrupt course and contralateral recurrent artery of Heubner. The AcoA was not visualized (*Courtesy of* Basar Sarikaya, MD, University of Minnesota, Minneapolis, MN.)

37.8 Orbitofrontal or Frontopolar Branch Prominence

As previously described, there can be a large amount of congenital and normal variation in the A1 and A2 segments of the ACA. Other variations that can appear perplexing are a prominent *orbitofrontal artery* (OFA, also termed a "frontal-orbital artery") or a prominent *frontopolar artery* (FPA), particularly if these arteries arise from the A1 segments. A prominence of such a branch arising from the A1 segment occurs in about 1–5 % of the population [20–25].

Normally, the OFA is the first cortical branch of the ACA and arises from the proximal, ipsilateral pericallosal artery A2 segment, supplying the orbitofrontal gyri. The FPA is typically the next cortical branch, supplying the cortex slightly more superior to that of the OFA's supply (such as the cortex of the anterior and lower superior frontal gyrus). These two arteries can be in close proximity, can arise from a common branch, or even can arise directly off of an A1 segment. Although the arteries are typically bilateral, they can also rarely supply both sides. If one of these vessels is prominent on CTA or MRA, and particularly if arising from the A1 segment, they may be difficult to name without visualizing the adjacent hypoplastic vessels; that is, the OFA may be prominent and the FPA may be hypoplastic, or vice versa. These can be distinguished by noting their course and supply, and may be easier to properly identify and name on a dedicated catheter angiogram [20–25] (Figs. 37.37 and 37.38).

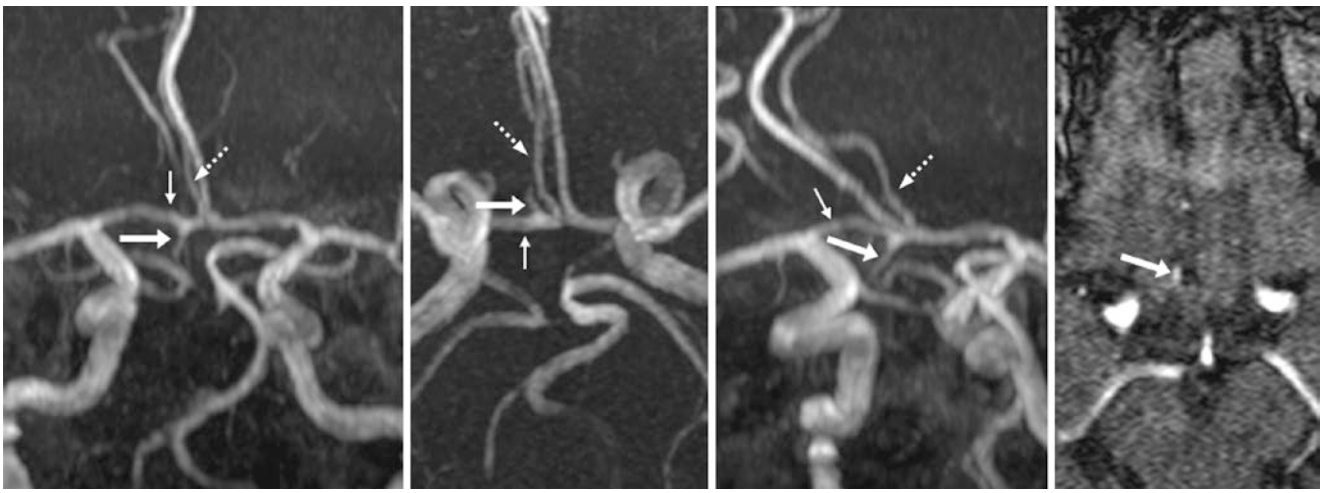

Fig. 37.37 In this 48-year-old, a 3DTOF MRA MIP AP view (*left*), AP-superior view (*left middle*), and LPO view (*right middle*) show a vessel (*large arrows*) arising from the right ACA's A1 segment (*thin arrows*), lateral to the right A2 segment (*dotted arrows*). This prominent vessel is seen to travel below and medial to the orbitofrontal gyri on source MRA images (*right*), suggesting that the branch is a prominent orbitofrontal artery (OFA), which normally arises off the A2 segment. However, the vessel is difficult to see at its distal extent, so alternatively the vessel could represent an anomalous frontopolar artery (FPA)

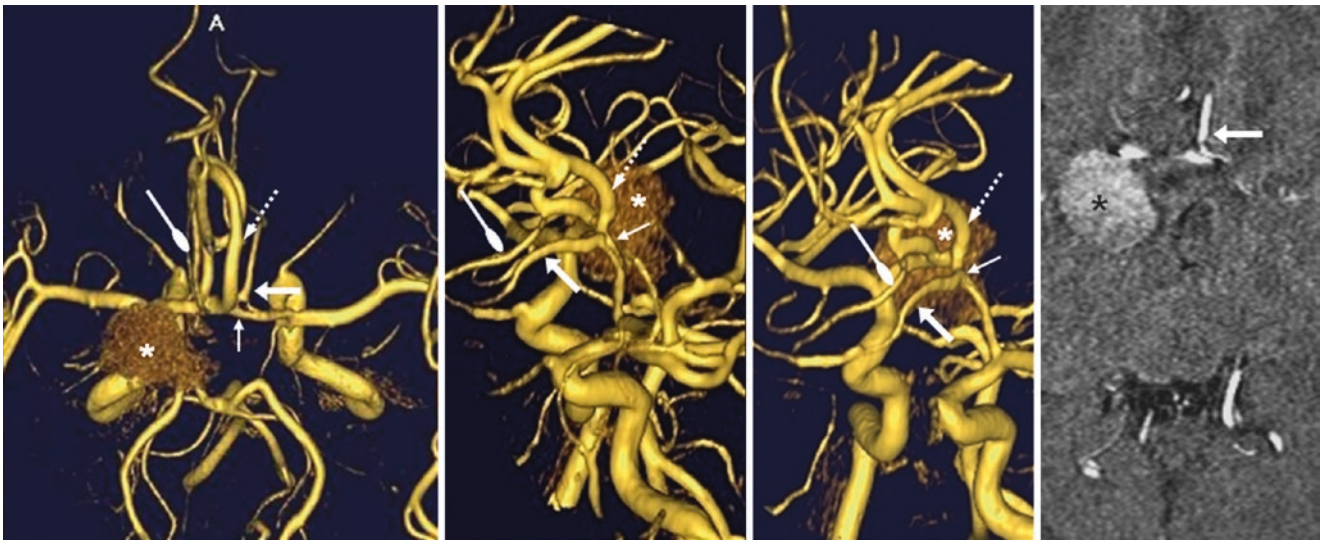

Fig. 37.38 In this 32-year-old, a 3DTOF MRA superior view (*left*), lateral view (*left middle*), and LAO view (*right middle*) show a left A1 segment fenestration (*thin arrows*), from which a vessel (*arrows*) arises just before the A2 segment (*dotted arrows*). This vessel travels medial to, but not under, the orbitofrontal gyri on source images (*right*), suggesting that the branch is a prominent FPA (or less likely, an OFA). A typical contralateral OFA (*oval-tip arrows*) arises off an A2 pericallosal branch. Note "T1 shine-through" effect (*asterisks*) due to T1-shortening effect of subacute hemorrhage

37.9 Middle Cerebral Artery Early Branching

There are many variations in the MCA in first-order M1 segment branching [5–8, 11, 26–32]. The most common are *early branches arising from the M1 segment* (whether inferior or superior "trunk" origins), *duplication of the MCA*, and an *accessory MCA* (the least common of the three). The latter two variants should be distinguished from "early branching," in which the *anterior temporal artery* usually originates prior to the MCA bifurcation and initially travels inferiorly before being oriented towards its destination. Larger *superior* or *inferior trunks* can also arise off of the main M1 segment, which can further bifurcate or trifurcate distally. It should be noted that the MCA "bifurcates" (into superior and inferior divisions) in approximately 70–80 % of people, "trifurcates" (into superior, inferior, and middle divisions) in about 20–30 %, and splits into variable, smaller segmental arteries in <5–10 % [5–8, 11, 26–32] (Figs. 37.39, 37.40, 37.41, 37.42, 37.43, 37.44, and 37.45).

Fig. 37.39 47-year-old with an early anterior temporal branch (*arrows*) that arises from the M1 segment of the left middle cerebral artery (MCA) just proximal to the bifurcation on AP views from a 3DTOF MRA MIP (*left*) and on a catheter DSA (*right*)

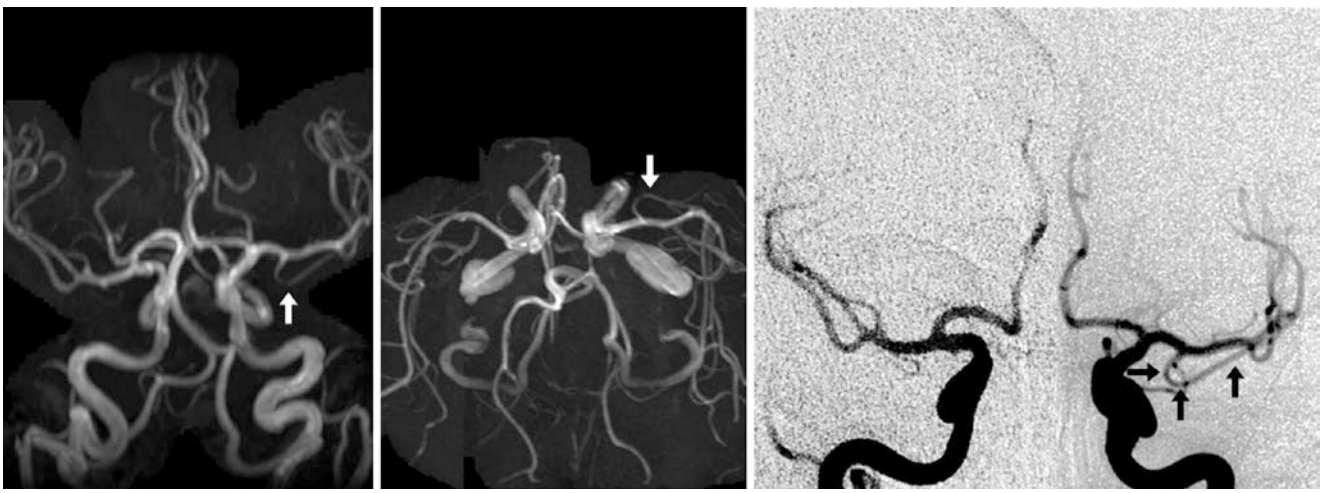

Fig. 37.40 43-year-old with headaches, who has an incidental early anterior temporal branch (*arrows*) that arises from the M1 segment of the left MCA just proximal to the bifurcation on AP (*left*) and superior (*left middle*) views from a 3DTOF MRA MIP. This finding was confirmed on a catheter DSA, with views of the right side (*left middle*) and left side (*right*); the left anterior temporal branch is outlined by *arrows*. Note a normal, typical "trifurcation" appearance of the distal M1 segment on the contralateral right side

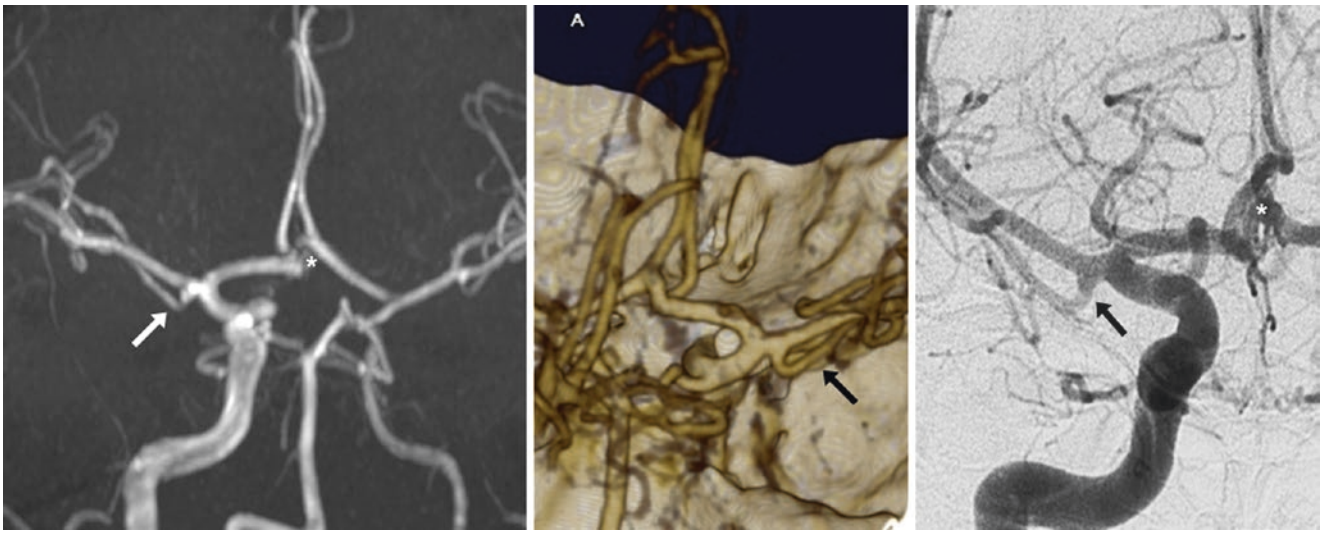

Fig. 37.41 42-year-old with an early bifurcation of the right MCA, likely representing an early anterior temporal branch (*arrows*), on AP view from a 3DTOF MIP MRA (*left*), PA view from a 3D VR CTA (*middle*), and on a catheter DSA (*right*). The early MCA branch originates just after the ICA terminus. Also note an incidental AcoA fenestration (*asterisks*)

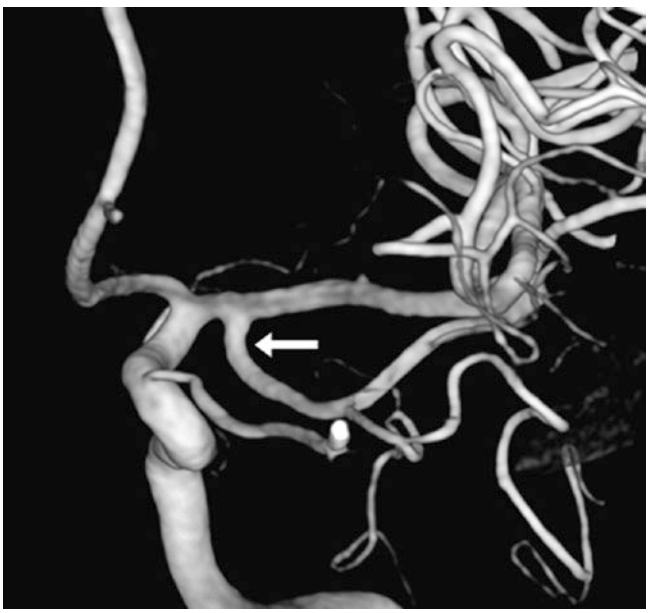

Fig. 37.42 In this 67-year-old, an inferior trunk (*arrow*) represents either an early bifurcation of the MCA or an early origin of the anterior temporal branch on a 3D DSA AP view

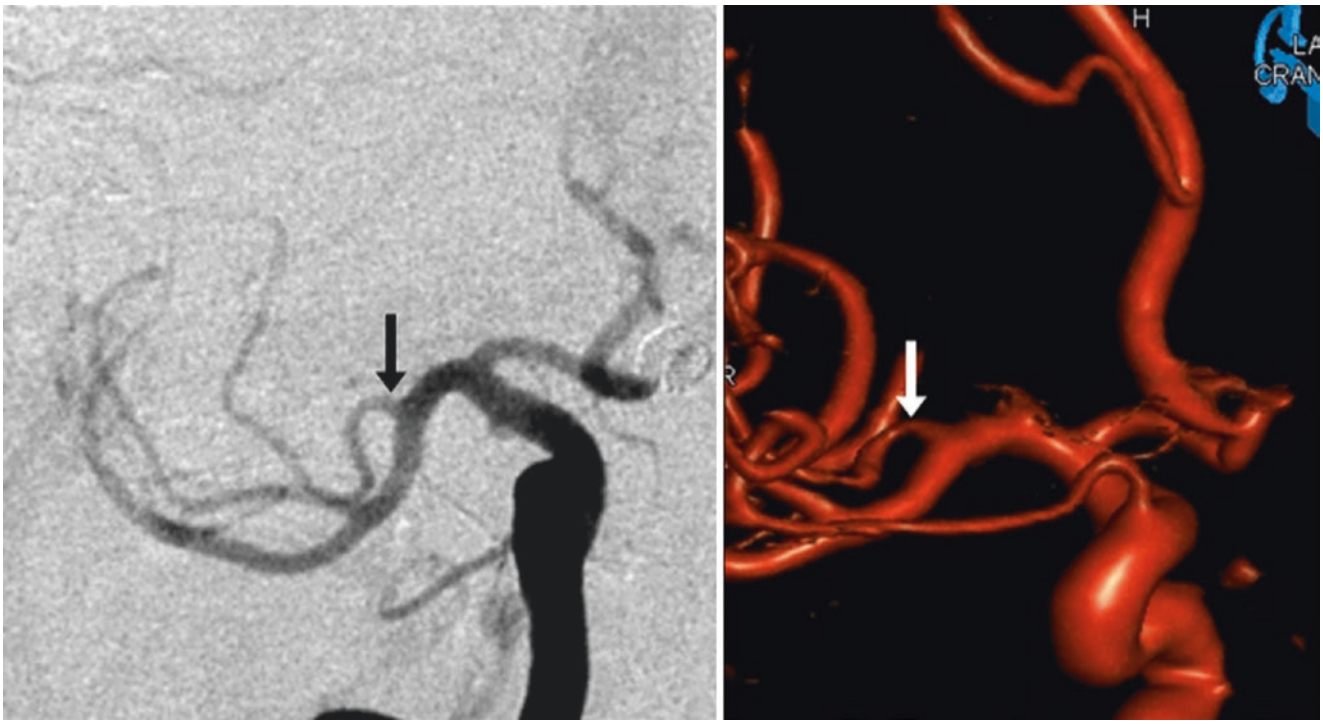

Fig. 37.43 In this 48-year-old, a catheter DSA right ICA injection shows an early superior trunk arising from the M1 segment of the right MCA (*arrow*) on an AP view (*left*) and on a 3D DSA AP view (*right*)

Fig. 37.44 40-year-old with an early left MCA superior trunk shown on a DSA AP view (*arrow*)

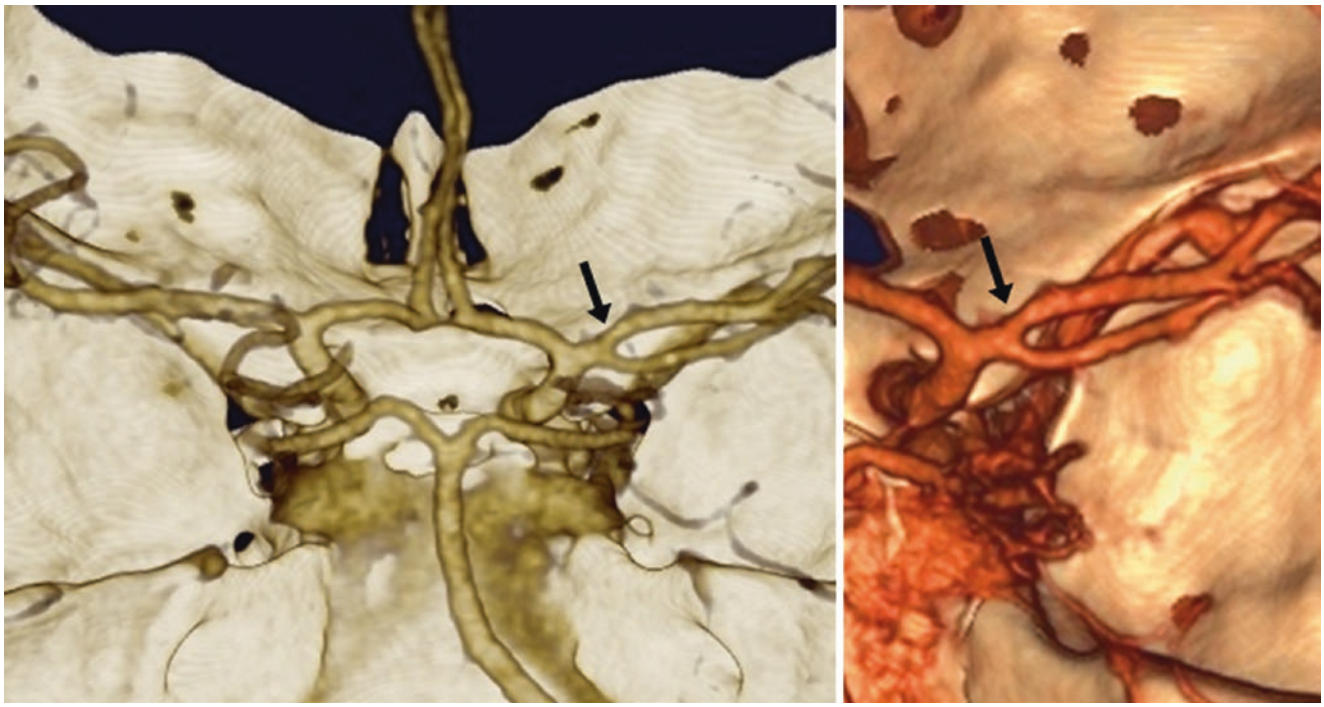

Fig. 37.45 19-year-old with an early bifurcation of the M1 segment of the right MCA (*arrows*) on a 3D VR CTA PA view (*left*), as well as on a magnified PA view (*right*), likely representing both the superior and inferior divisions of the MCA

37.10 Duplicated MCA, Accessory MCA, and Fenestration

A *duplication of the MCA* is when both branches arise from the distal ICA; an accessory MCA is when an MCA branch originates from the ACA; and a *fenestration* ("window") refers to a focal hole within the artery (not duplicated at the M1's origin). Together, such anomalous MCA variants occur in about 2–5 % of the population, with the most common likely being MCA duplication [5–8, 11, 26–32]. Both the MCA duplication and *accessory MCA* variants have been reported to occur in about 0.3–3.0 % of patients, depending on the modality used (less with DSA than with autopsy, CTA, or MRA); the duplicated MCA is almost twice as common as the accessory MCA. Besides the modality used to detect them, variation in their incidence may also occur because these two variants are often confused with one another and with other, more common variants such as early M1 segment bifurcation or trifurcation.

With a *duplicated MCA*, typically one branch travels more anteriorly and inferiorly, and the other more posteriorly and superiorly. Most commonly, the duplicated branches arise together from the ICA terminus, where the "lower branch" arises from the terminus along with the other "proper" MCA branch; the "proper" MCA branch usually arises opposite the ACA. However, the inferior branch may arise from the ICA as low as the anterior choroidal artery (AchoA) segment and travel laterally. This pattern is usually readily noticeable on CTA, MRA, or catheter DSA, unless one of the duplicated branches is occluded while the other M1 segment is patent, so that the images are mistakenly interpreted as normal (Figs. 37.46, 37.47, 37.48, 37.49, 37.50, 37.51, and 37.52).

With an *accessory MCA*, the accessory branch typically arises from A1 segment of the proximal ACA and then travels laterally into the sylvian fissure to parallel the M1 segment that arose from the distal ICA. This accessory branch can occasionally arise from the distal A1 segment, or even from the A2 segment, and it is often smaller than the "proper" MCA branch that arises from the ICA terminus; thus, an accessory branch may be overlooked. However, there can be overlap in the appearances of duplicated and accessory MCAs, and there is not a consensus as to the terminology. Some will refer to an M1 branch arising from the junction of the ICA terminus and the proximal A1 segment as an accessory (rather than a duplicated) MCA. The accessory MCA may also have an increased incidence of *aneurysms* [5–8, 11, 26–32] (Figs. 37.53, 37.54, 37.55, and 37.56).

Even more uncommon is a *fenestration of the MCA* (0.1–0.5 % of the population), a normal variant that probably represents an incomplete duplication; these are occasionally associated with an aneurysm at the proximal end [5–8, 11, 26–32]. Finally, *MCA hypoplasia* or aplasia is extremely rare (<0.1 %). One should note that a *"nonbifurcating" ICA* is not uncommon; in this variant, the ICA continues as the MCA because of ACA hypoplasia or aplasia (as discussed earlier in Chap. 37.4) (Figs. 37.57, 37.58, and 37.59).

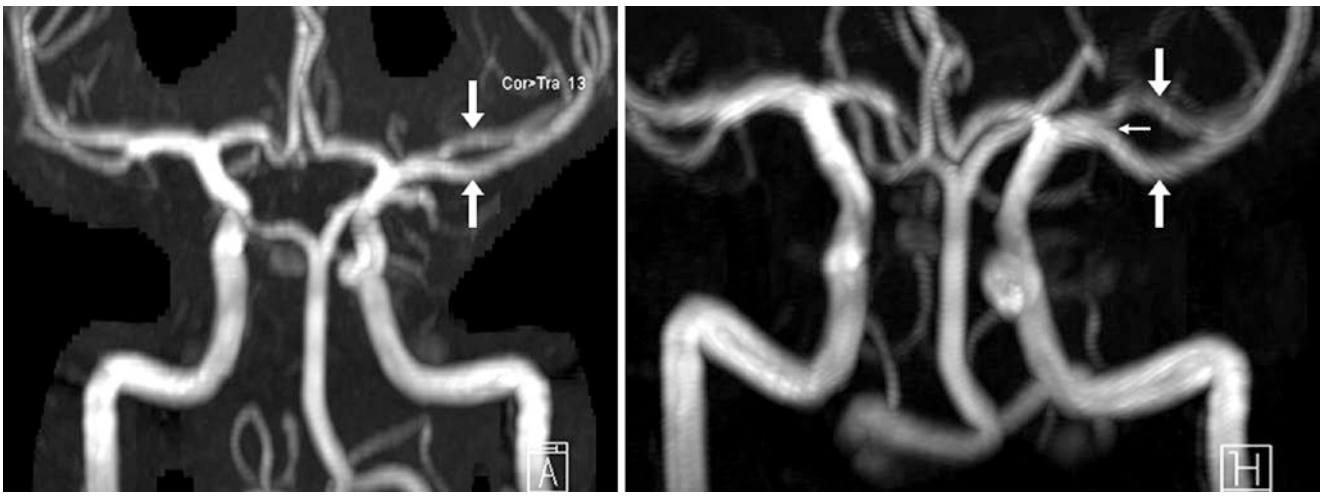

Fig. 37.46 20-year-old with what appeared to be an early bifurcation of the left MCA on an MIP AP view (*left*), obtained from a 3DTOF MRA. However, there was a tiny cleft (*thin arrow*) at the carotid terminus on another AP view with greater cranial-caudal obliquity (*right*), confirming that this was actually a subtle duplication of the MCA (*arrows*)

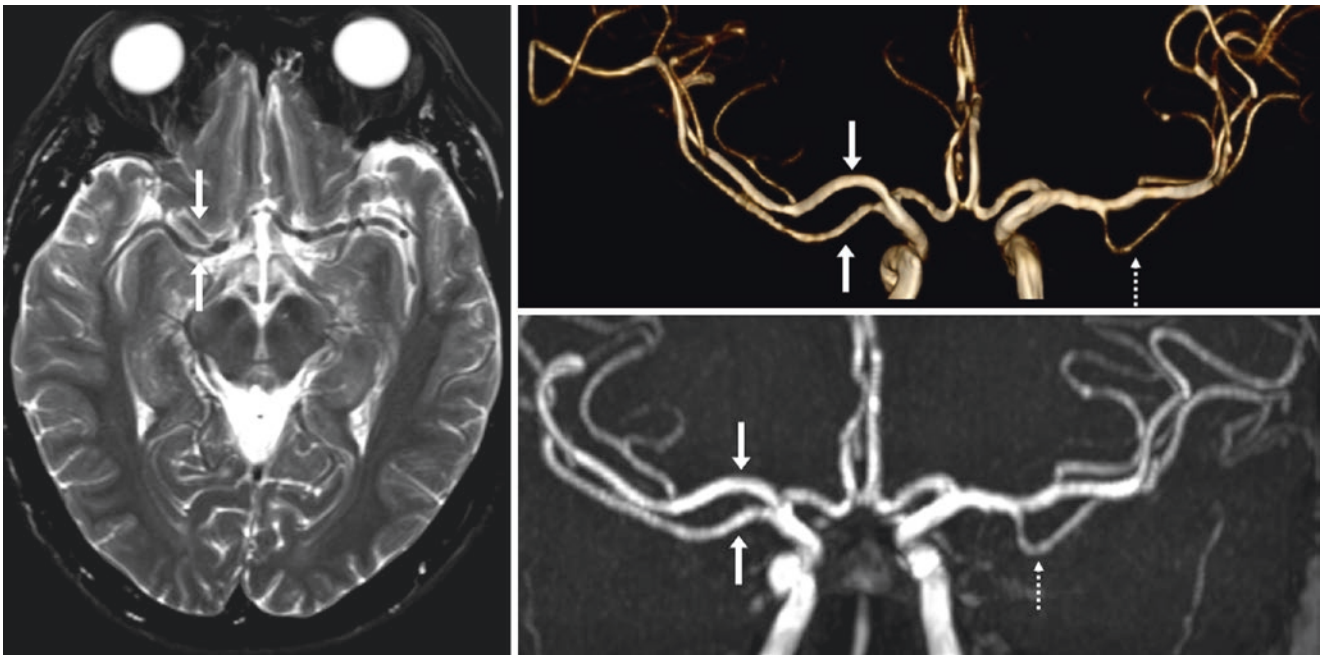

Fig. 37.47 49-year-old with dizziness, lacking related imaging abnormality. A duplicated MCA (*arrows*) is arising from the right ICA terminus on T2WI (*left*) and coronal/AP views from a 3D TOF MRA (*top right*) and 17-mm MIP (*bottom right*), with the basilar removed. Contralaterally, note an early anterior temporal branch off of the M1 segment of the left MCA (*dotted arrows*)

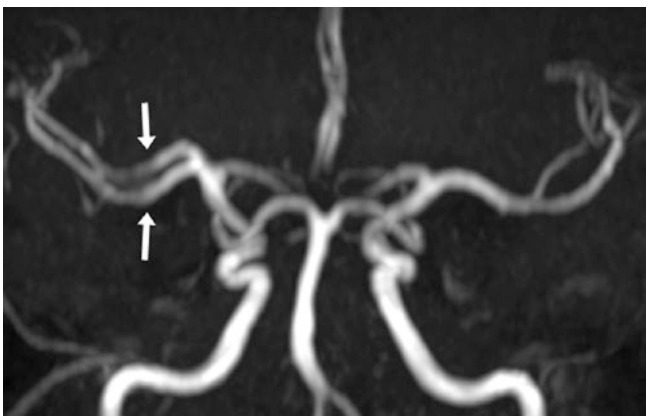

Fig. 37.48 36-year-old with a duplication of the right MCA (*arrows*) on a 3DTOF MRA MIP AP view

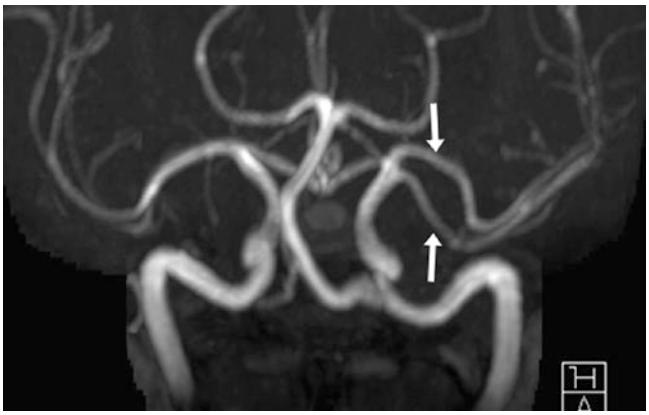

Fig. 37.49 51-year-old with a left MCA duplication (*arrows*) on a 3DTOF MRA AP view, rather than an accessory MCA

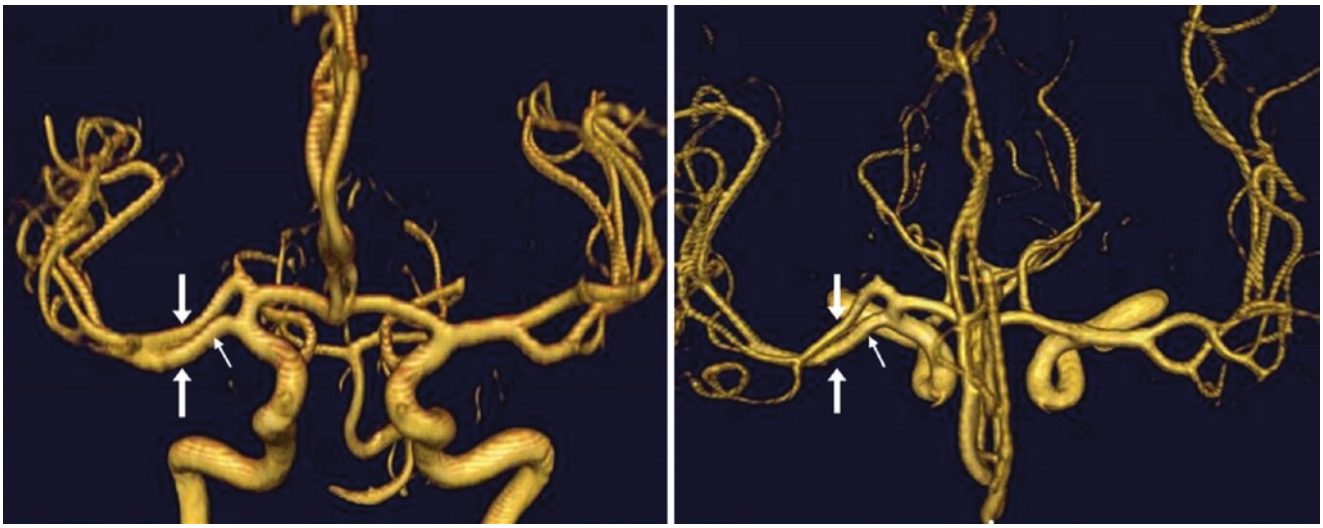

Fig. 37.50 40-year-old with duplicated MCAs (*large arrows*) arising from the right ICA terminus on a 3DTOF MRA AP view (*left*) and superior view (*right*). Note that one branch arises just below the ICA terminus (*thin arrows*). This lower branch arises at the anterior choroidal artery level, separate from the other duplicated vessel

Fig. 37.51 74-year-old with a duplication of the right MCA (*arrows*), as demonstrated on a 3 T MRI acquisition of 3DTOF MRA AP view (*left*), and a minimum intensity projection (MiniP) from a "dark-blood" technique spin-echo T1WI (*right*) (*Courtesy of* David Nascene, MD, University of Minnesota, Minneapolis, MN.)

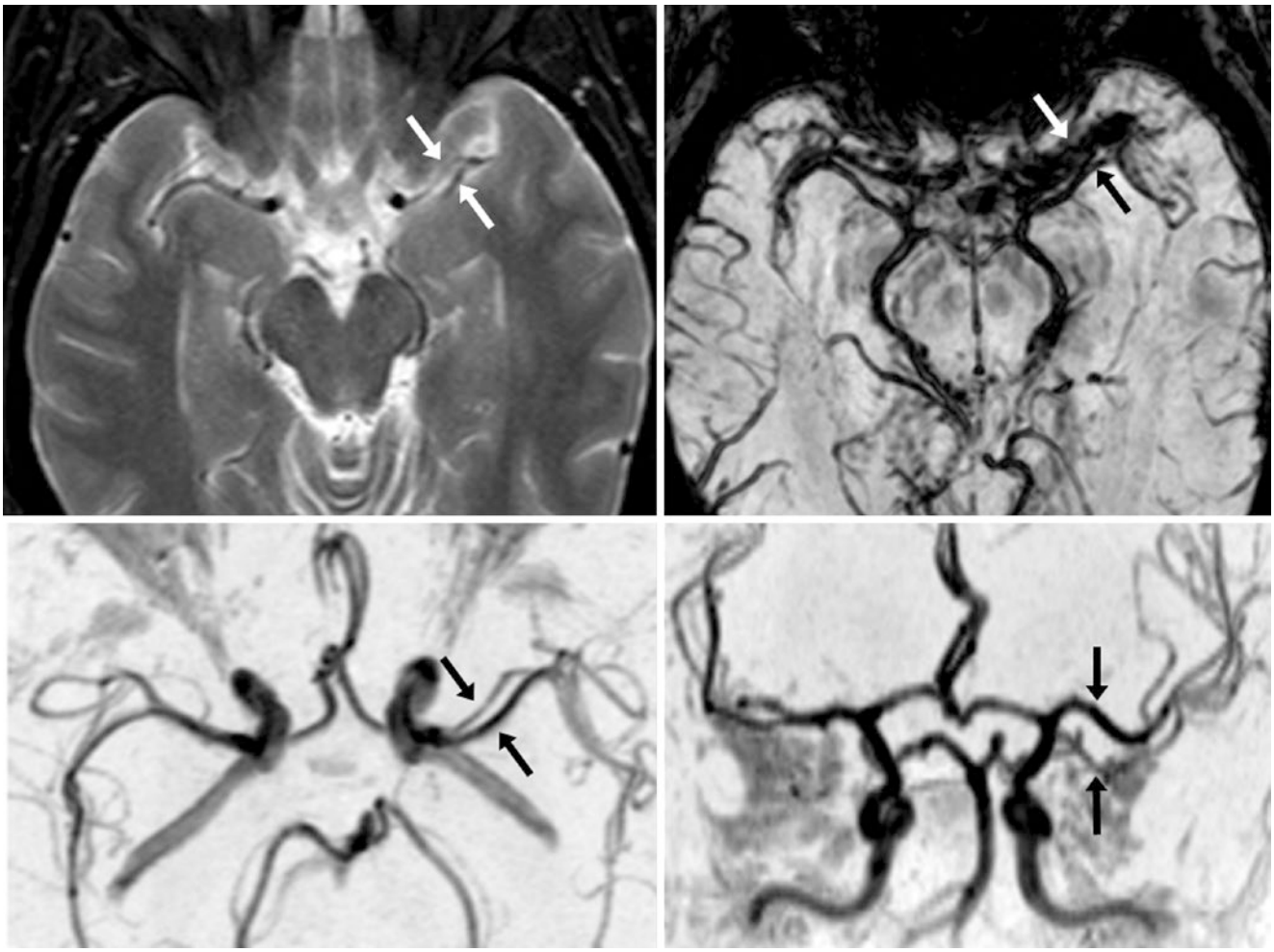

Fig. 37.52 46-year-old with an MCA duplication (*arrows*), depicted on axial T2WI (*top left*), but obscured on SWI (*top right*) because of adjacent flow voids from middle cerebral veins and overlapping of the duplicated arteries. 3DTOF MRA superior (*bottom left*) and AP (*bottom right*) video-inverted MIP views further confirm the duplication

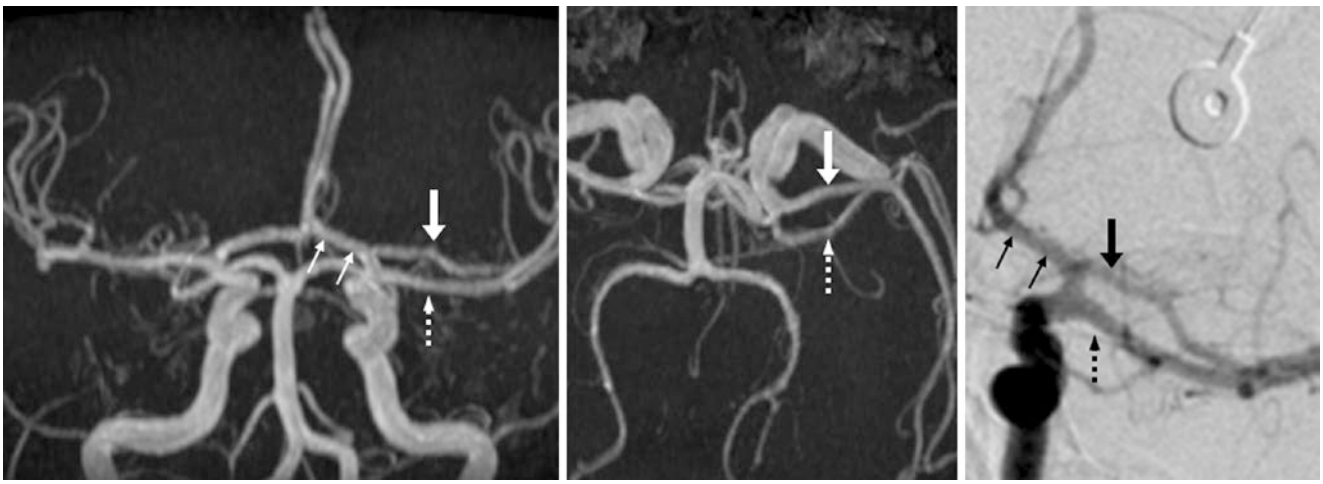

Fig. 37.53 59-year-old woman with what is likely an accessory MCA (*large arrows*), which appears to arise from the A1 segment of the left ACA (*thin arrows*), and parallels the other M1 segment (*dotted arrows*) on a 3DTOF MRA MIP AP view (*left*) and superior view (*middle*), and on a catheter DSA AP view (*right*). Alternatively, one could call this is a duplicated MCA arising from the ICA terminus, illustrating how MCA variants occur along a spectrum

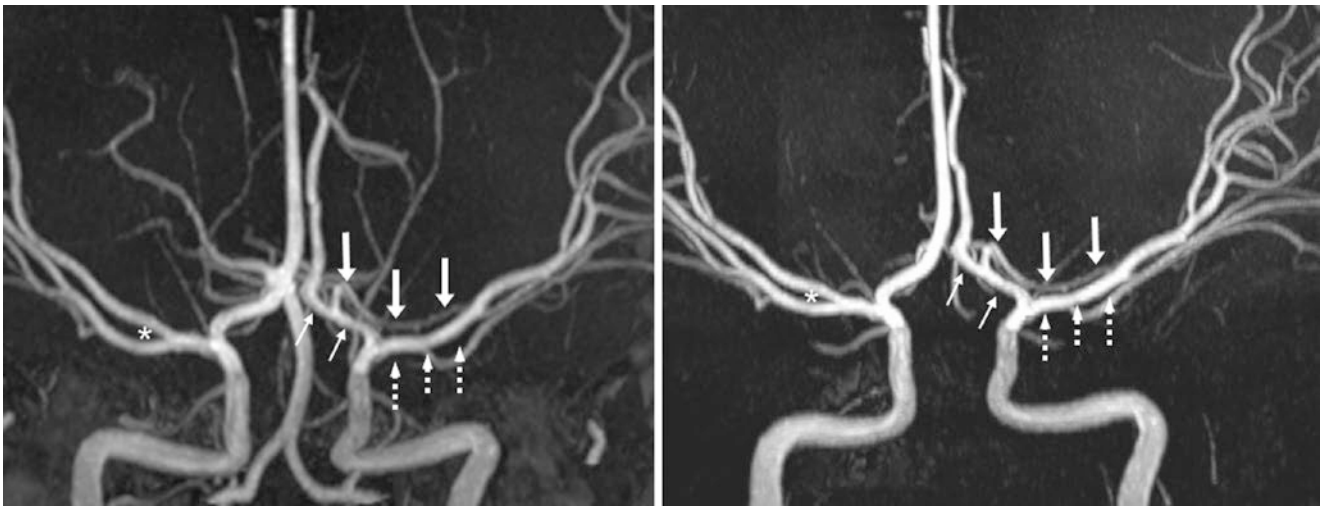

Fig. 37.54 20-year-old with an accessory MCA (*large arrows*) that arises from the proximal A1 segment of the left ACA (*thin arrows*), as seen on AP views from a 3DTOF MRA. (On the right image, the posterior circulation and the ophthalmic arteries have been removed.) The accessory branch parallels the proper left M1 segment (*dotted arrows*) as it travels into the sylvian fissure. Note that there is also an early bifurcation of the right MCA (*asterisks*)

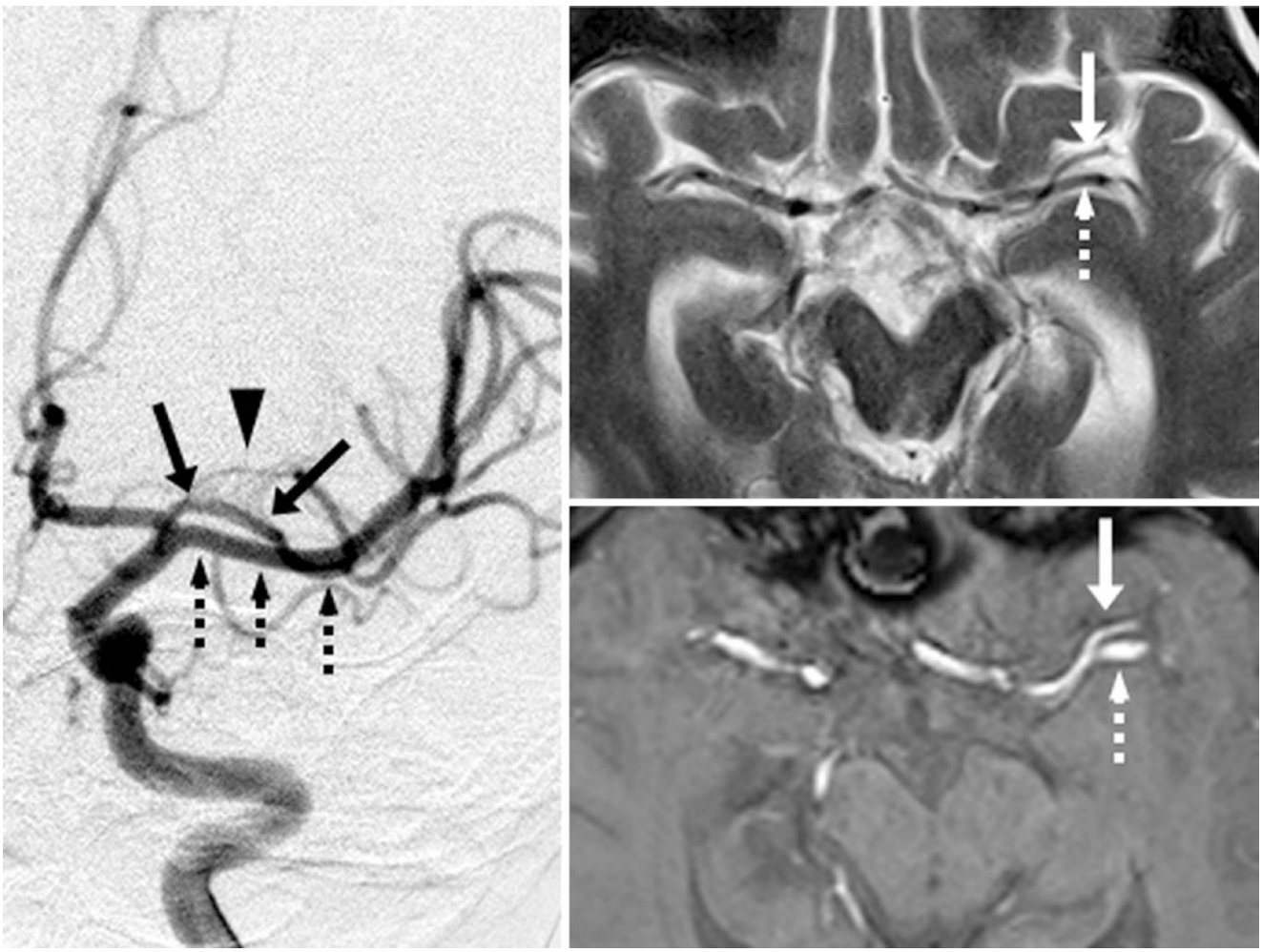

Fig. 37.55 An accessory left MCA (*arrows*) is shown to arise from the left A1 segment on a catheter DSA AP view (*left*) and on 3 T MRI T2WI (*right, top*) and SWI *(right, bottom*). Note (*dotted arrows*) denote the "M1 segment" lenticulostriate arteries (*arrowhead*)

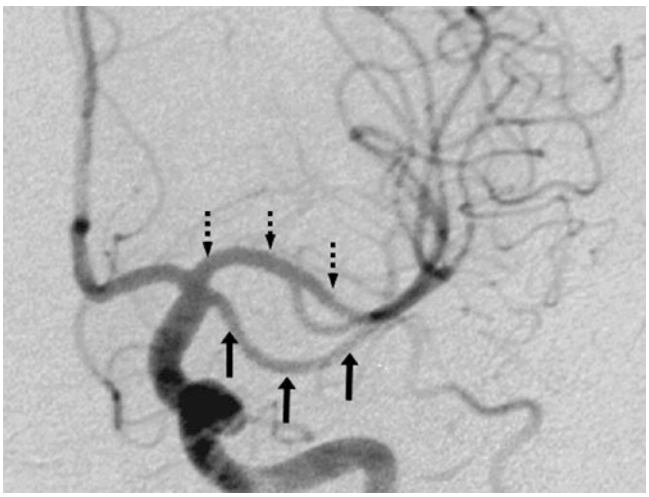

Fig. 37.56 On a catheter DSA, an accessory left MCA (*arrows*) arises from the ICA terminus; it is larger than the other M1 segment (*dotted arrows*) (*Courtesy of* Phillippe Gailloud, MD, Johns Hopkins University, Baltimore, MD.)

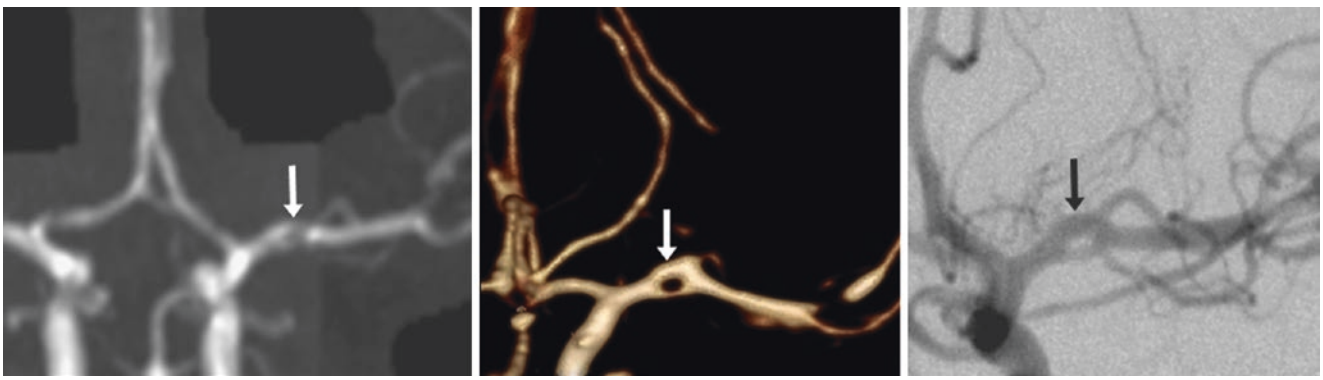

Fig. 37.57 29-year-old with a fenestration of the M1 segment of the left MCA (*arrows*), initially suspected on a 3DTOF MRA AP view (*left*) and later confirmed by similar views from a 3D VR CTA (*middle*) and a catheter DSA (*right*)

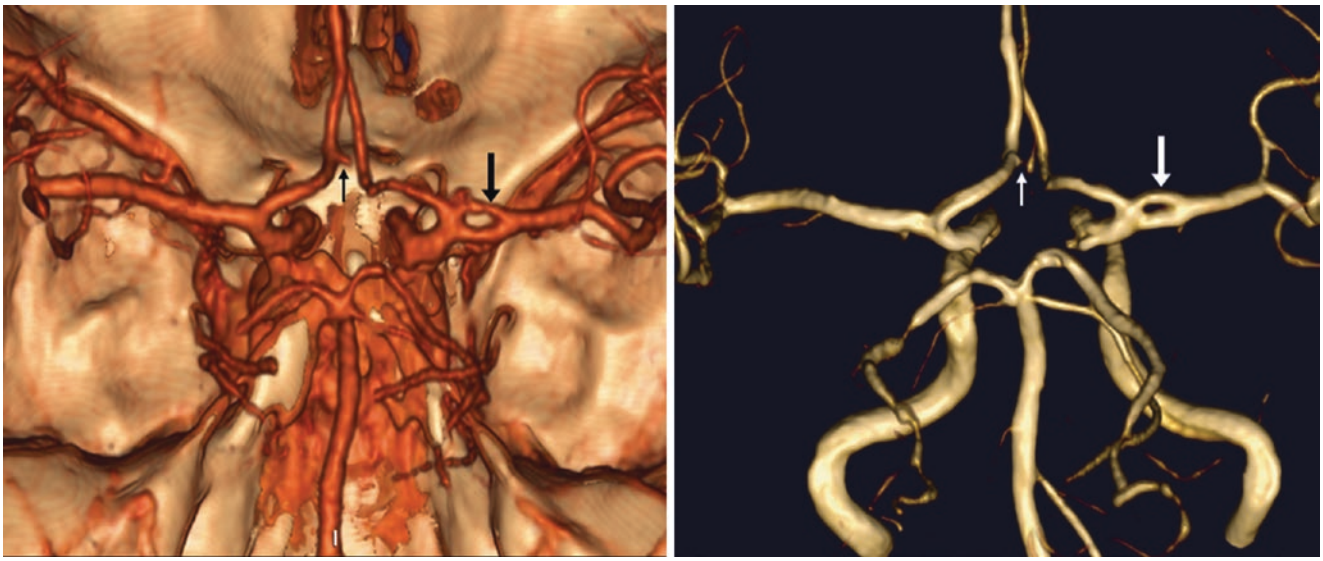

Fig. 37.58 52-year-old with a proximal M1 segment fenestration (*arrows*) on PA views from 3D VR CTA (*left*) and 3 T 3DTOF MRA (*right*). A tiny AcoA infundibulum was also noted (*thin arrows*). There was no associated aneurysm

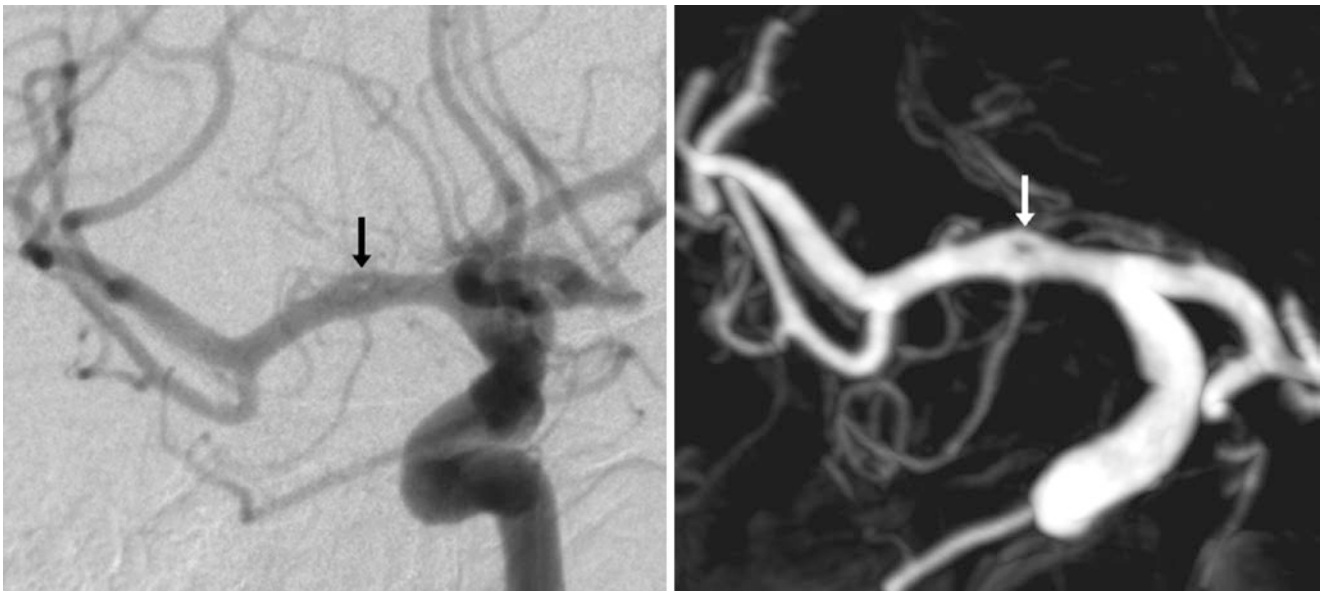

Fig. 37.59 A small right MCA fenestration (*arrows*) is noted on a catheter DSA AP view (*left*) and on a 3D DSA (*right*), without an associated aneurysm (*Courtesy of* Phillippe Gailloud, MD, Johns Hopkins University, Baltimore, MD.)

37.11 Prominent Lenticulostriate Branches

Lenticulostriate branches arising from the proximal MCA or ACA are relatively common on higher-resolution MR or CT angiography, and are normal [40–45]. They are best visualized on conventional catheter DSA. The branches may appear single, multiple, or as a "candelabra"; on histopathologic sectioning, there are usually 3–20 branches. There are many variations in origins of both the *medial* and *lateral lenticulostriates*; in the most common combination, the medial and lateral lenticulostriates are present together, but this variant is seen in only about one third of patients [40–45]. A single medial lenticulostriate vessel is often referred to as a "*recurrent artery of Heubner,*" identified in about 10–20% of patients. This vessel may be unilateral or bilateral, and when present, it may arise from the A1 or A2 segments, or anywhere in between. The medial lenticulostriates are from the ACA in about two thirds of patients; they can arise from the A1 segment (most common), or from the A1-A2 junction, the A2 segment, or the AcoA. The lateral lenticulostriates arise from the M1 segments of the MCA in about two thirds of patients, and from a proximal M2 segment (typically the superior division) in about 15–20% [40–45]. Lenticulostriate branches can also arise from duplicated or accessory MCAs (Figs. 37.60, 37.61, 37.62, 37.63, 37.64, and 37.65).

There may also be *mild infundibular prominence* (<2 mm) at the original of these branches (covered separately in Chapter 38). Lenticulostriate arteries are progressively better visualized with increasing field strength, and may be particularly discernible on MRA at 3.0 T and above [40–45]. Prominence of these vessels on CTA, MRA, or catheter DSA can simulate vascular anomalies.

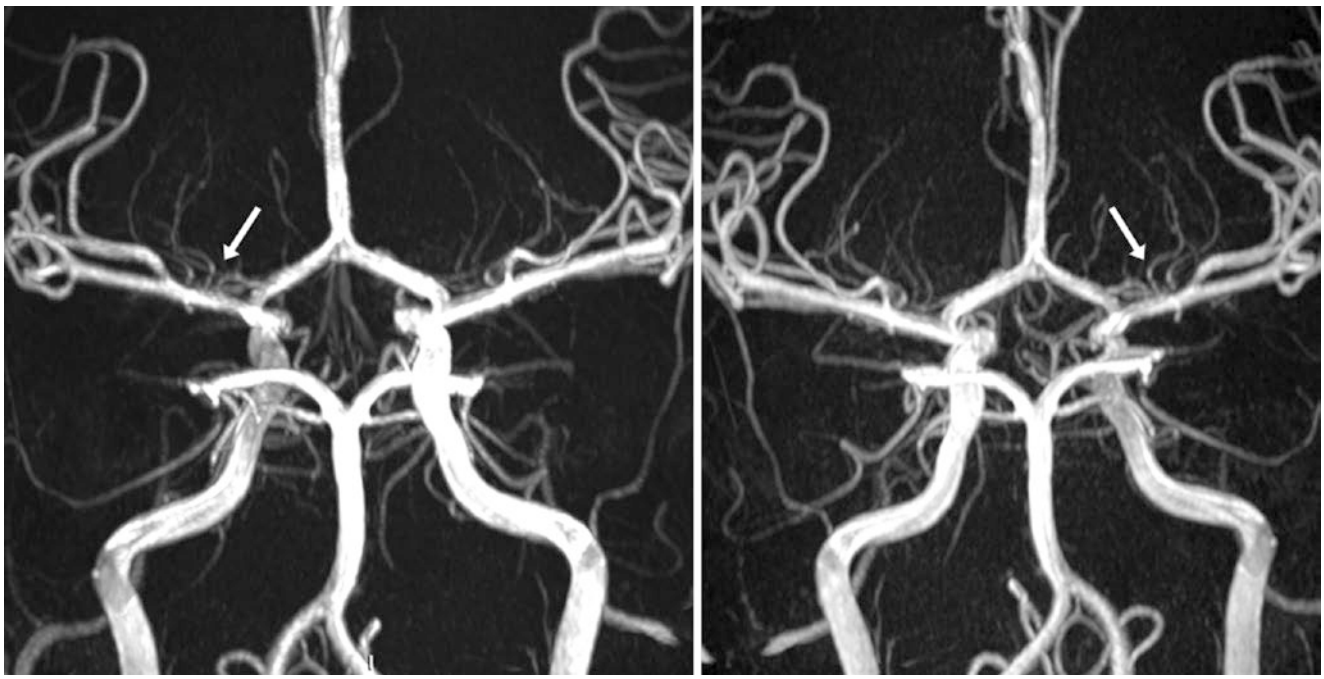

Fig. 37.60 18-year-old with multiple lenticulostriate branches arising from both MCAs on 3 T high-resolution 3DTOF MRA AP views (*arrows*). These branches were not visualized at all on a 64-slice CTA (*not shown*)

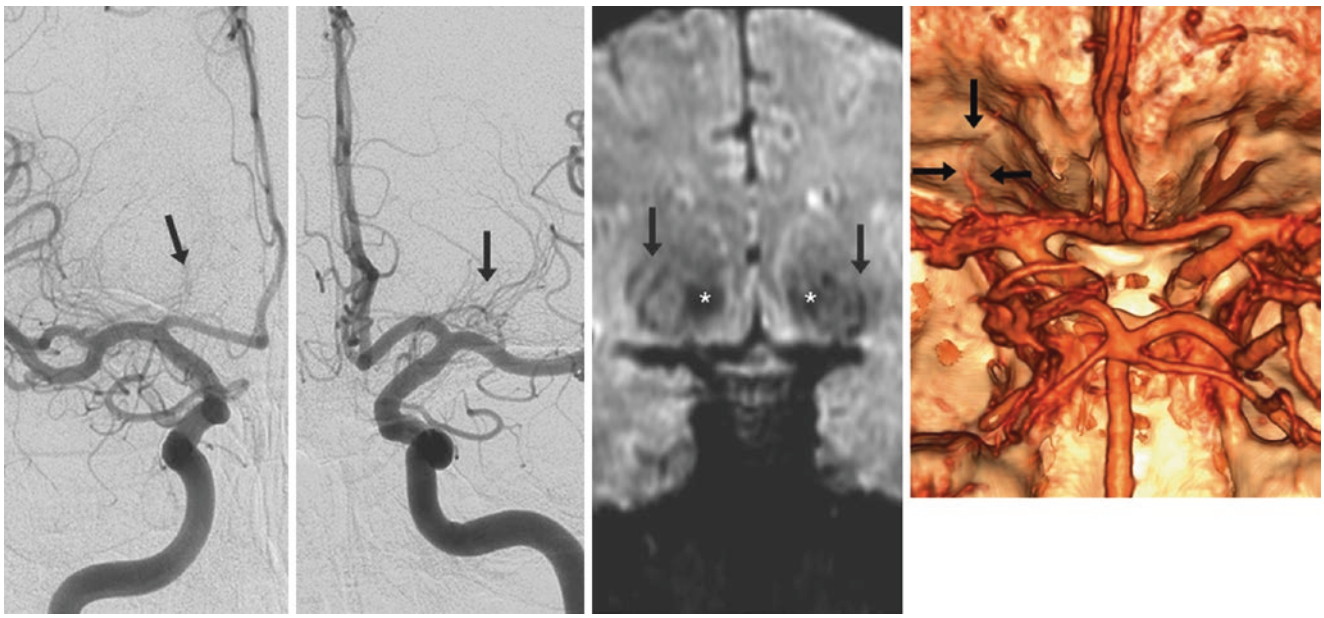

Fig. 37.61 46-year-old with prominent left (but faint right) lenticulostriate branches (*arrows*) from the ICA termini at the proximal ACA and MCA segments, on AP views from catheter DSA (*left* and *left middle*). Coronal SWI MRI (*right middle*) demonstrates left lenticulostriate prominence as tiny flow voids located lateral to the mildly dark globi pallidi (*asterisks*). On CTA (*right*), only the left lenticulostriate branches are partially visualized on a 3D VR PA view

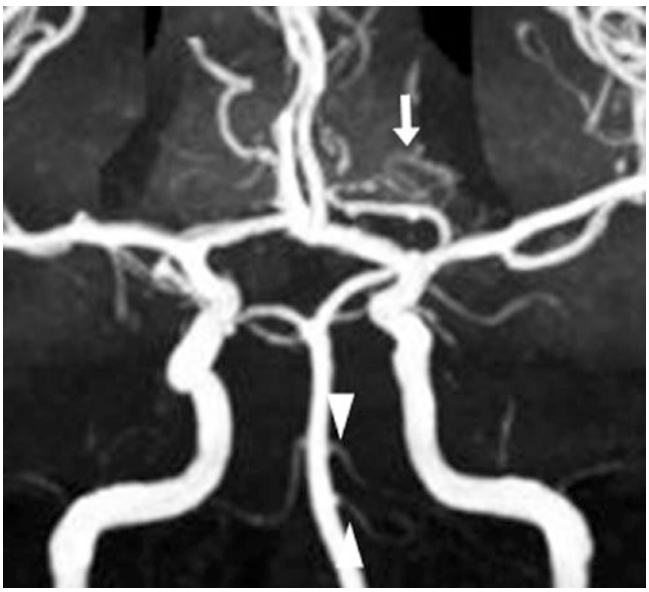

Fig. 37.62 33-year-old with faint lenticulostriate branches arising from the left MCA (*arrow*) on a 3DTOF MRA MIP AP view. Also, note the left anterior inferior cerebellar artery (AICA) duplication (*arrowheads*)

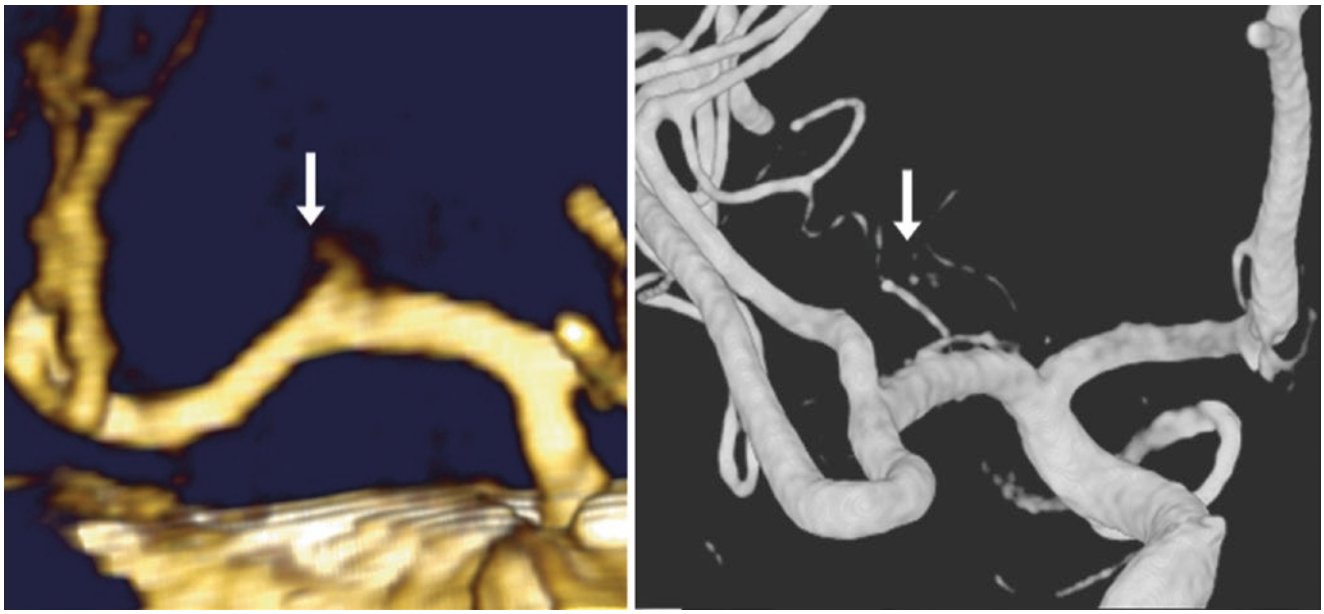

Fig. 37.63 35-year-old with lenticulostriate branches (*arrows*) off the left MCA on AP views from a 3D VR CTA (*left*) and a 3D DSA (*right*)

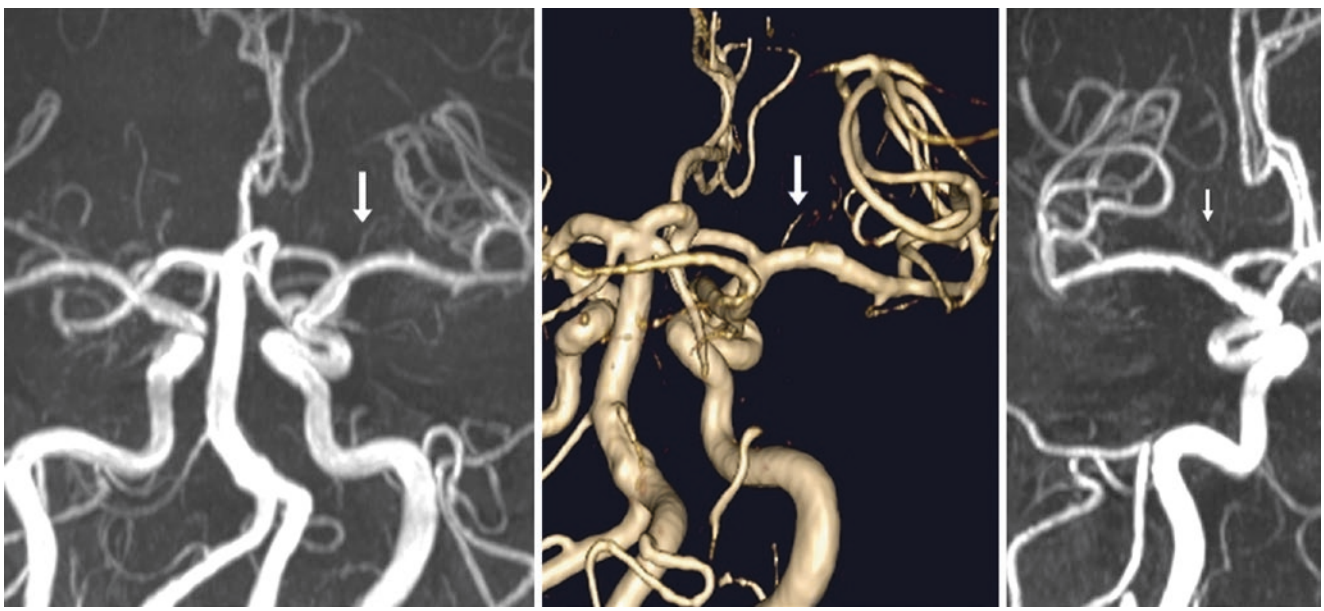

Fig. 37.64 54-year-old with a lenticulostriate branch (*arrow*) arising from the proximal right MCA just distal to the ICA terminus on PA views from a 3DTOF MRA with MIP (*left*) and "tightly windowed" 3D VR images (*middle*). Note smaller, similar branches (*thin arrow*) on the left side (*right*)

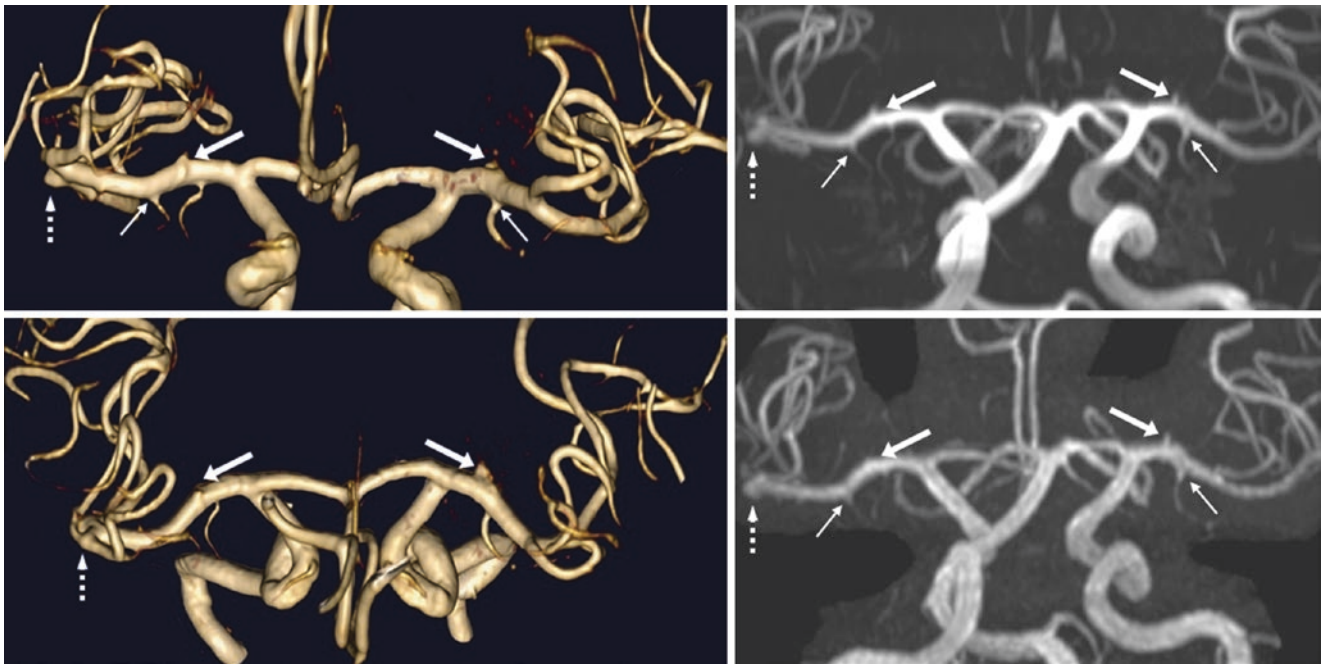

Fig. 37.65 This 74-year-old had a 3D TOF MRA at 3 T to follow a right MCA bifurcation aneurysm (*dashed arrows*). On 3D VR AP (*top left*) and superior (*bottom right*) views with the basilar removed, note prominent lenticulostriate origins with infundibula (*large arrows*) bilaterally, particularly on the left. An MIP AP view (*top right*) depicts these branches, as well as incidental infundibula of bilateral early anterior temporal artery origins (*thin arrows*). The findings were unchanged from 3 years prior (*bottom right*)

References

1. Dey M, Awad IA. Fenestration of supraclinoid internal carotid artery and associated aneurysm: embryogenesis, recognition, and management. World Neurosurg. 2011;76:592.e1–5.
2. Banach MJ, Flamm ES. Supraclinoid internal carotid artery fenestration with an associated aneurysm. Case report. J Neurosurg. 1993;79:438–41.
3. Bharatha A, Fox AJ, Aviv RI, Symons SP. CT angiographic depiction of a supraclinoid ICA fenestration mimicking aneurysm, confirmed with catheter angiography. Surg Radiol Anat. 2007;29:317–21.
4. de Gast AN, van Rooij WJ, Sluzewski M. Fenestrations of the anterior communicating artery: incidence on 3D angiography and relationship to aneurysms. AJNR Am J Neuroradiol. 2008;29:296–8.
5. Cooke DL, Stout CE, Kim WT, Kansagra AP, Yu JP, Gu A, et al. Cerebral arterial fenestrations. Interv Neuroradiol. 2014;20:261–74.
6. Yasargil MG. Microneurosurgery, vol. 1. Stuttgart: Georg Thieme Verlag; 1984. p. 99–107.
7. Busse O. Aneurysmen und Bildungsfehler der Arteri communicans anterior. Virchows Arch Pathol Anat. 1921;229:178–89.
8. Jinkins JR. Internal carotid artery. In: Jinkins JR, editor. Atlas of neuroradiologic embryology, anatomy, and variants. Philadelphia: Lippincott Williams & Wilkins; 2000. p. 299–329.
9. Uchino A, Nomiyama K, Takase Y, Kudo S. Anterior cerebral artery variations detected by MR angiography. Neuroradiology. 2006;48:647–52.
10. Perlmutter D, Rhoton Jr AL. Microsurgical anatomy of the anterior cerebral-anterior communicating-recurrent artery complex. J Neurosurg. 1976;45:259–72.
11. Dimmick SJ, Faulder KC. Normal variants of the cerebral circulation at multidetector CT angiography. Radiographics. 2009;29:1027–43.
12. Krzyżewski RM, Tomaszewski KA, Kochana M, Kopeć M, Klimek-Piotrowska W, Walocha JA. Anatomical variations of the anterior communicating artery complex: gender relationship. Surg Radiol Anat. 2015;37:81–6.
13. Krzyzewski RM, Tomaszewska IM, Lorenc N, Kochana M, Goncerz G, Klimek-Piotrowska W, et al. Variations of the anterior communicating artery complex and occurrence of anterior communicating artery aneurysm: A2 segment consideration. Folia Med Cracov. 2014;54:13–20.
14. Chuang YM, Liu CY, Pan PJ, Lin CP. Anterior cerebral artery A1 segment hypoplasia may contribute to A1 hypoplasia syndrome. Eur Neurol. 2007;57:208–11.
15. LeMay M, Gooding CA. The clinical significance of the azygous anterior cerebral artery (A.C.A.). AJR Am J Roentgenol. 1966;98:602–10.
16. Niederberger E, Gauvrit JY, Morandi X, Carsin-Nicol B, Gauthier T, Ferré JC. Anatomic variants of the anterior part of the cerebral arterial circle at multidetector computed tomography angiography. J Neuroradiol. 2010;37:139–47.
17. Padget DH. The development of the cranial arteries in the human embryo. Contrib Embryol. 1948;32:205–61.
18. Lasjaunias P, Berenstein A, Ter Brugge KG. Intradural arteries. In: Lasjaunias P, Berenstein A, Ter Brugge KG, editors. Clinical vascular anatomy and variations (surgical neuroangiography). Berlin: Springer; 2001. p. 479–631.
19. Baptista AG. Studies on the arteries of the brain II. The anterior cerebral artery: some anatomic features and their clinical implications. Neurology. 1963;13:825–35.
20. Ture U, Yasargil MG, Krisht AF. The arteries of the corpus callosum: a microsurgical anatomic study. Neurosurgery. 1996;39:1075–84.
21. Uchino A, Sawada A, Takase Y, Kudo S. MR angiography of anomalous branches of the internal carotid artery. AJR Am J Roentgenol. 2003;181:1409–14.
22. Uchino A, Sawada A, Takase Y, Kudo S. Persistent primitive olfactory artery: diagnosis with MR angiography. Clin Imaging. 2001;25:258–61.
23. Lee ER, Eastwood JD. An unusual variant of the fronto-orbital artery. AJNR Am J Neuroradiol. 2000;21:939–40.
24. Hong SK. Ruptured proximal anterior cerebral artery (A1) aneurysm located at an anomalous branching of the fronto-orbital artery: a case report. J Korean Med Sci. 1997;12:576–80.
25. Marinkovic S, Milisavljevic M, Kovacevic M. Anatomical bases for surgical approach to the initial segment of the anterior cerebral artery: microanatomy of Heubner's artery and perforating branches of the anterior cerebral artery. Surg Radiol Anat. 1986;8:7–18.
26. Reis CV, Zabramski JM, Safavi-Abbasi S, Hanel RA, Deshmukh P, Preul MC. The accessory middle cerebral artery: anatomic report. Neurosurgery. 2008;63(1 Suppl 1):ONS10–3; discussion ONS13–4.
27. Yamamoto H, Marubayashi T, Soejima T, Matsuoka S, Matsukado Y, Ushio Y. Accessory middle cerebral artery and duplication of middle cerebral artery – terminology, incidence, vascular etiology, and developmental significance. Neurol Med Chir (Tokyo). 1992;32:262–7.
28. Komiyama M, Nakajima H, Nishikawa M, Yasui T. Middle cerebral artery variations: duplicated and accessory arteries. AJNR Am J Neuroradiol. 1998;19:45–9.
29. Uchino A, Kato A, Takase Y, Kudo S. Middle cerebral artery variations detected by magnetic resonance angiography. Eur Radiol. 2000;10:560–3.
30. Uchino A, Takase Y, Nomiyama K, Egashira R, Kudo S. Fenestration of the middle cerebral artery detected by MR angiography. Magn Reson Med Sci. 2006;5:51–5.
31. Gailloud P, Albayram S, Fasel JH, Beauchamp NJ, Murphy KJ. Angiographic and embryologic considerations in five cases of middle cerebral artery fenestration. AJNR Am J Neuroradiol. 2002;23:585–7.
32. Iida Y, Tamase A, Kamide T, Mori K, Seki S, Nomura M. Aneurysm at origin of duplicated middle cerebral artery associated with another aneurysm. Surg Neurol Int. 2015;6:S549–52.
33. Lasjaunias P, Moret J, Mink J. The anatomy of the inferolateral trunk (ILT) of the internal carotid artery. Neuroradiology. 1977;13:215–20.
34. Lasjaunias P, Santoyo-Vazquez A. Segmental agenesis of the internal carotid artery: angiographic aspects with embryological discussion. Anat Clin. 1984;6:133–41.
35. Pretterklieber ML, Schindler A, Krammer EB. Unilateral persistence of the dorsal ophthalmic artery in man. Acta Anat. 1994;149:300–5.
36. Gregg L, San Millán D, Orru E, Tamargo RJ, Gailloud P. Ventral and dorsal persistent primitive ophthalmic arteries. Neurosurgery. 2015 Oct 19 [Epub ahead of print]. PMID: 26485335.
37. Uchino A, Saito N, Takahashi M, Kozawa E, Mizukoshi W, Nakajima R, Okano N. Persistent dorsal ophthalmic artery and ophthalmic artery arising from the middle meningeal artery diagnosed by MR angiography at 3 T. Surg Radiol Anat. 2013;35:775–82.
38. Uchino A, Saito N, Ikeda S, Ishihara S. Ophthalmic artery arising from the anterior cerebral artery diagnosed by MR angiography. Surg Radiol Anat. 2015;37:1009–12.
39. Louw L. Different ophthalmic artery origins: embryology and clinical significance. Clin Anat. 2015;28:576–83.
40. Andersen PE. The lenticulo-striate arteries and their diagnostic value. Acta Radiol. 1958;50:84.
41. Umansky F, Gomes FB, Dujovny M, Diaz FG, Ausman JI, Mirchandani HG, Berman SK. The perforating branches of the middle cerebral artery: a microanatomical study. J Neurosurg. 1985;62:261–8.
42. Marinkovic SV, Kovacevic MS, Marinkovic JM. Perforating branches of the middle cerebral artery: microsurgical anatomy of their extracerebral segments. J Neurosurg. 1985;63:266–71.

43. Kang HS, Han MH, Kwon BJ, Kwon OK, Kim SH, Chang KH. Evaluation of the lenticulostriate arteries with rotational angiography and 3D reconstruction. AJNR Am J Neuroradiol. 2005;26:306–12.
44. Cho ZH, Kang CK, Han JY, Kim SH, Kim KN, Hong SM, et al. Observation of the lenticulostriate arteries in the human brain in vivo using 7.0T MR angiography. Stroke. 2008;39:1604–6.
45. Kang CK, Park CW, Han JY, Kim SH, Park CA, Kim KN, et al. Imaging and analysis of lenticulostriate arteries using 7.0-Tesla magnetic resonance angiography. Magn Reson Med. 2009;61:136–44.
46. Impiombato FA, Baltsavias G, Valavanis A. The recurrent artery of Heubner in routine selective cerebral angiography. Neuroradiology. 2014;56:745–50.
47. McKinney AM, Palmer CS, Truwit CL, Karagulle A, Teksam M. Detection of aneurysms by 64-section multidetector CT angiography in patients acutely suspected of having an intracranial aneurysm and comparison with digital subtraction and 3D rotational angiography. AJNR Am J Neuroradiol. 2008;29:594–602.
48. Villablanca JP, Jahan R, Hooshi P, Lim S, Duckwiler G, Patel A, et al. Detection and characterization of very small cerebral aneurysms by using 2D and 3D helical CT angiography. AJNR Am J Neuroradiol. 2002;23:1187–98.
49. Teksam M, McKinney A, Casey S, Asis M, Kieffer S, Truwit CL. Multi-section CT angiography for detection of cerebral aneurysms. AJNR Am J Neuroradiol. 2004;25:1485–92.

Infundibular Outpouchings of Intracranial Arteries

38

Differentiating "*infundibula*" from true *aneurysms* is a common source of consternation for radiologists. Infundibula are typically considered "don't touch" lesions that are incidental, being most commonly located at the posterior communicating artery (PcoA) origin of the internal carotid artery (ICA) in 7–25 % of the population; the vast majority do not rupture over time [1–12]. Histologically, the findings have varied. Some smaller studies have shown defects similar to aneurysms within the media, and occasionally defects of the internal elastic lamina, but other studies have shown no difference from normal arterial bifurcations. Several criteria can be used to differentiate an infundibulum from an aneurysm, but there can be a slight overlap between the two, particularly at the PcoA origin, and there is still debate as to how commonly aneurysms arise from infundibula, an event that has been shown (rarely) to occur many years later.

An infundibulum is defined as a funnel-shaped bodily passage or opening, and it can be present at any major vessel bifurcation [1–12]. In the cranial vasculature, an infundibulum can occur at any major arterial branch point, but is most common at the PcoA origin, followed by the anterior communicating artery (AcoA), lenticulostriate origins (from the middle cerebral arteries [MCAs], anterior cerebral arteries [ACAs], or ICAs), or hypoplastic posterior cerebral artery (PCA) origins. This author has noticed that these infundibula are particularly common and often can border on being aneurysmal at sites of very small or hypoplastic branching points. For example, infundibula are not uncommon at the origin of a tiny AcoA, or where there is a "fetal PCA" mostly originating from the ICA but connected to a tiny, hypoplastic P1 segment infundibulum arising from the basilar artery.

The criteria proposed to identify infundibula have varied over time and have evolved, but an infundibulum should definitely be less than 3 mm in size, should be symmetrically conical or funnel-shaped without a neck, and a vessel should arise from the apex of the outpouching [1–12]. Regarding size, it is helpful to use 2.5 mm as the maximum size of an infundibulum; if the other characteristics are present and the size is under 2 mm, I believe that it can be definitively considered a normal infundibulum. It is also this author's opinion that symptomatic patients with hemorrhage and outpouchings 2 mm or more in size (even with such characteristics) should be followed for some time to exclude enlargement. We have noted a few rare cases where ruptured aneurysms arose from outpouchings 2 mm or less in size that occurred at branch points and were previously called infundibula; several reports in the literature have also documented this evolution [1–12]. Therefore, infundibula should be distinguished from *saccular* ("berry") *aneurysms*, which usually have a definable neck with either no branch vessel or a branch vessel arising eccentric to the outpouching.

Notably, both infundibula and saccular aneurysms should also be distinguished from *sessile* ("blister-like") *aneurysms*. These uncommon lesions can be identified by several characteristics [13–19]:

- wide neck
- usually located along the dorsal (superior) aspect of the supraclinoid ICA at nonbranching sites
- usually small (<3 mm) at the time of initial presentation
- often increasing in size within days to weeks (particularly when ruptured)
- often occurring in the setting of atherosclerosis

Hence, although infundibular outpouchings are almost always normal, the documented cases of enlargement with aneurysm formation and rupture suggest that they can be predisposed to evolve into an aneurysm, albeit rarely. Indeed, histologic data on infundibula from 20 to 30 years ago has noted that microscopic pathologic changes in the vascular wall (defects in the media) are present in most infundibula, but such histologic findings can be noted even in newborn infants [1–12]! Hence the controversy.

The diagnosis can be made with CTA or MRA (especially at 3 T field strength, which has better background saturation and magnetization transfer effects), or with catheter DSA. 3D

A.M. McKinney, *Atlas of Normal Imaging Variations of the Brain, Skull, and Craniocervical Vasculature*,
DOI 10.1007/978-3-319-39790-0_38

rotational DSA (3DDSA) can be obtained during a traditional catheter DSA, requiring a separate contrast injection, and is considered the gold standard for the diagnosis of aneurysms and for the evaluation of suspicious lesions in the setting of intracranial hemorrhage [13–15, 20, 21]. In the end, a catheter DSA should be used for confirmation if an infundibulum carries some question of being aneurysmal (whether because of its configuration or size). It is not uncommon to follow infundibula yearly or every 6 months if the infundibulum borders on being aneurysmal (for example, if it is 2.5 mm in size or a vessel does not arise from the apex of the outpouching). Also, if a suspect outpouching is poorly visualized owing to technique, a further workup should be carried out (Figs. 38.1, 38.2, 38.3, 38.4, 38.5, 38.6, 38.7, 38.8, 38.9, 38.10, 38.11, 38.12, 38.13, 38.14, 38.15, 38.16, 38.17, 38.18, 38.19, 38.20, 38.21, 38.22, 38.23, 38.24, and 38.25).

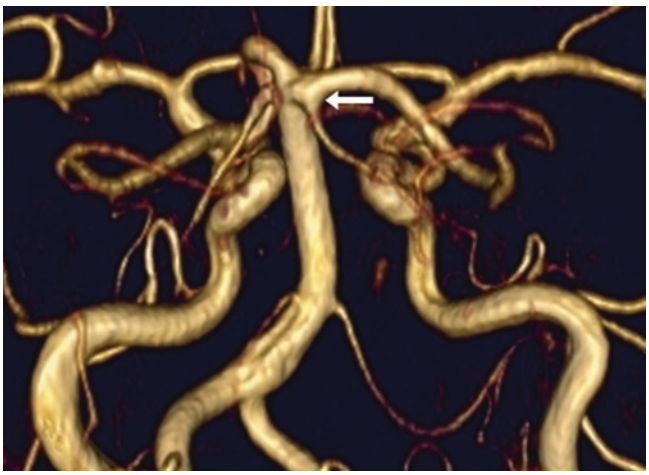

Fig. 38.1 54-year-old with an infundibulum of a common origin (*arrow*) of the right posterior cerebral artery (PCA) and superior cerebellar artery (SCA), noted on a 3DTOF MRA PA view. The size is just under 2.5 mm

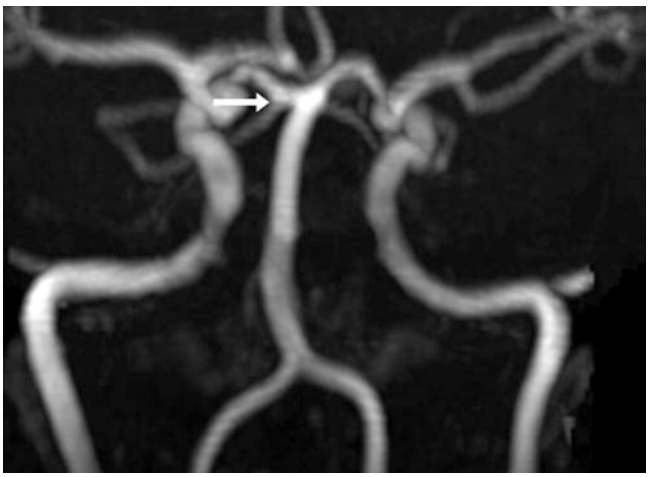

Fig. 38.2 67-year-old with an infundibulum of a common origin of the right PCA and SCA (*arrow*), noted on a 3DTOF MRA AP view. The size measures just under 2.0 mm

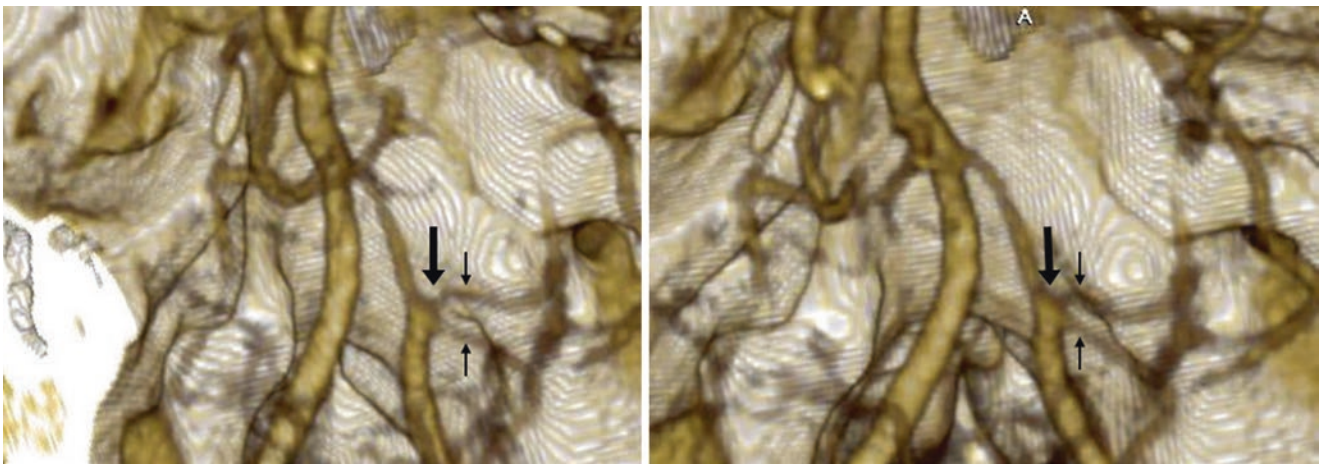

Fig. 38.3 In this 61-year-old, 3D VR CTA PA views demonstrate a small (<1.5 mm) infundibular outpouching (*arrows*) of the right posterior inferior cerebellar artery (PICA) origin at the site of a PICA duplication (*thin arrows*), which arises from the apex of the outpouching

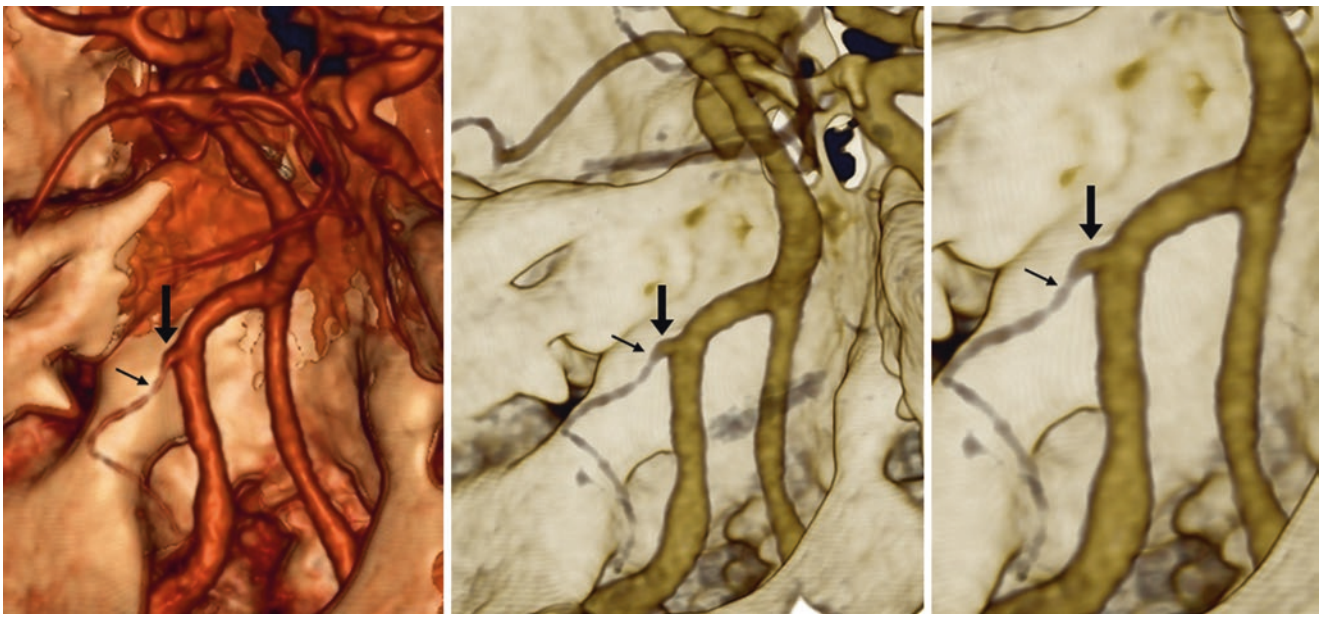

Fig. 38.4 In this 48-year-old, multiple 3D VR CTA images in PA views demonstrate a tiny (<1.5 mm) outpouching (*large arrows*) of left PICA origin. Shown are a high-resolution reconstructed PA view (*left*), a slightly oblique view (*middle*), and a magnified view (*right*). Note how a small vessel (*thin arrows*) arises from the infundibulum's apex

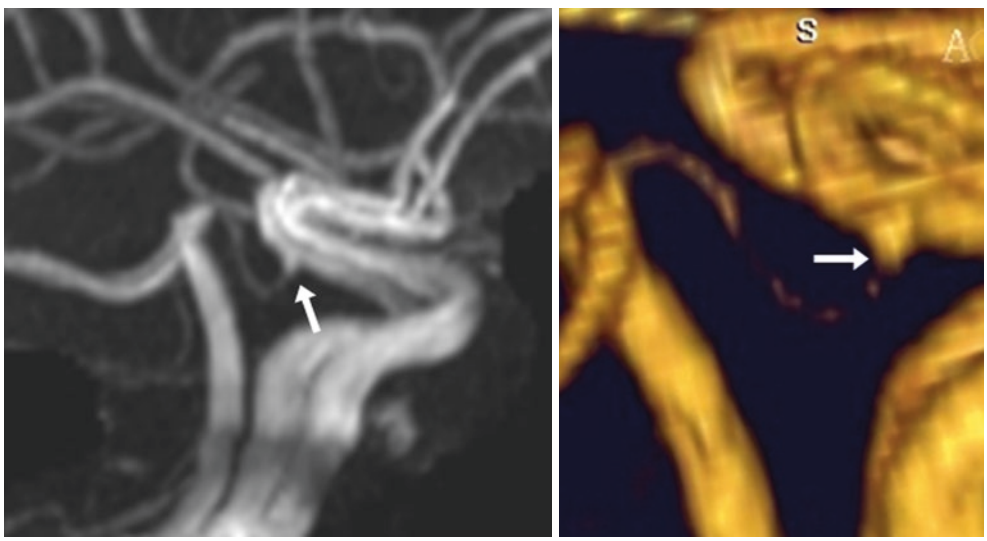

Fig. 38.5 In this 37-year-old, lateral (*left*) and magnified (*right*) 3DTOF MRA views show an infundibulum (<2 mm) (*arrows*) at the origin of the posterior communicating artery (PcoA) from the internal carotid artery (ICA), with a tiny vessel arising from the apex of the outpouching

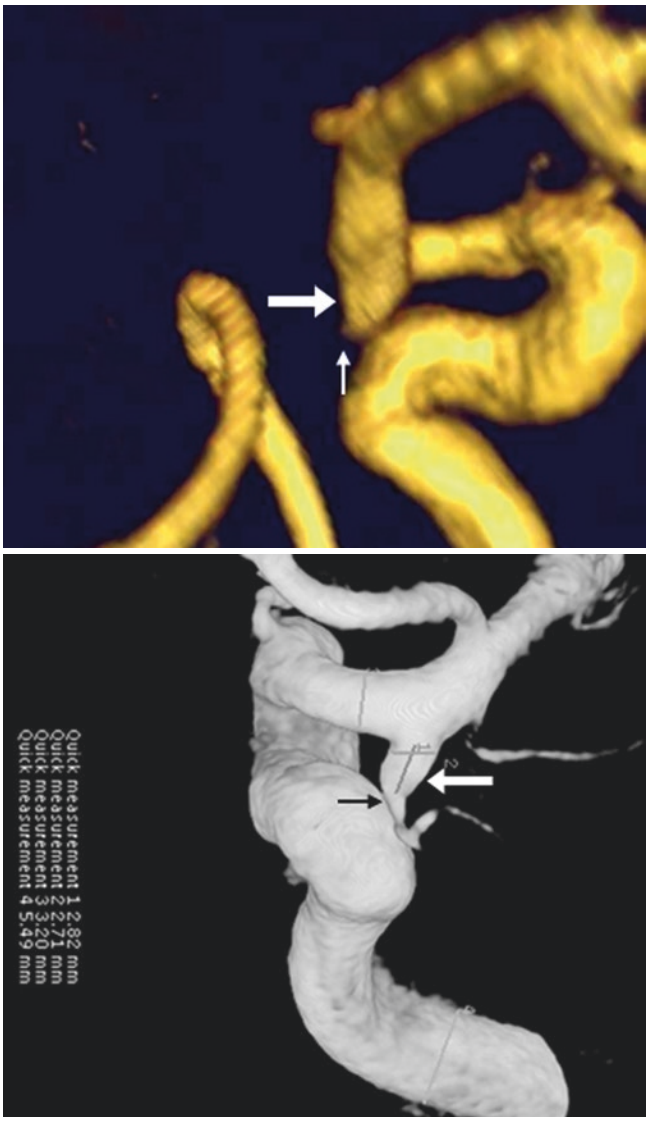

Fig. 38.6 76-year-old with an outpouching (*large arrows*) 2.8 mm in size. The PcoA arises at the apex (*thin arrow*s) on TOF MRA lateral view (*top*) and on 3DDSA (*bottom*). The size favors an aneurysm, but the location favors an infundibulum. This lesion was observed for years without change

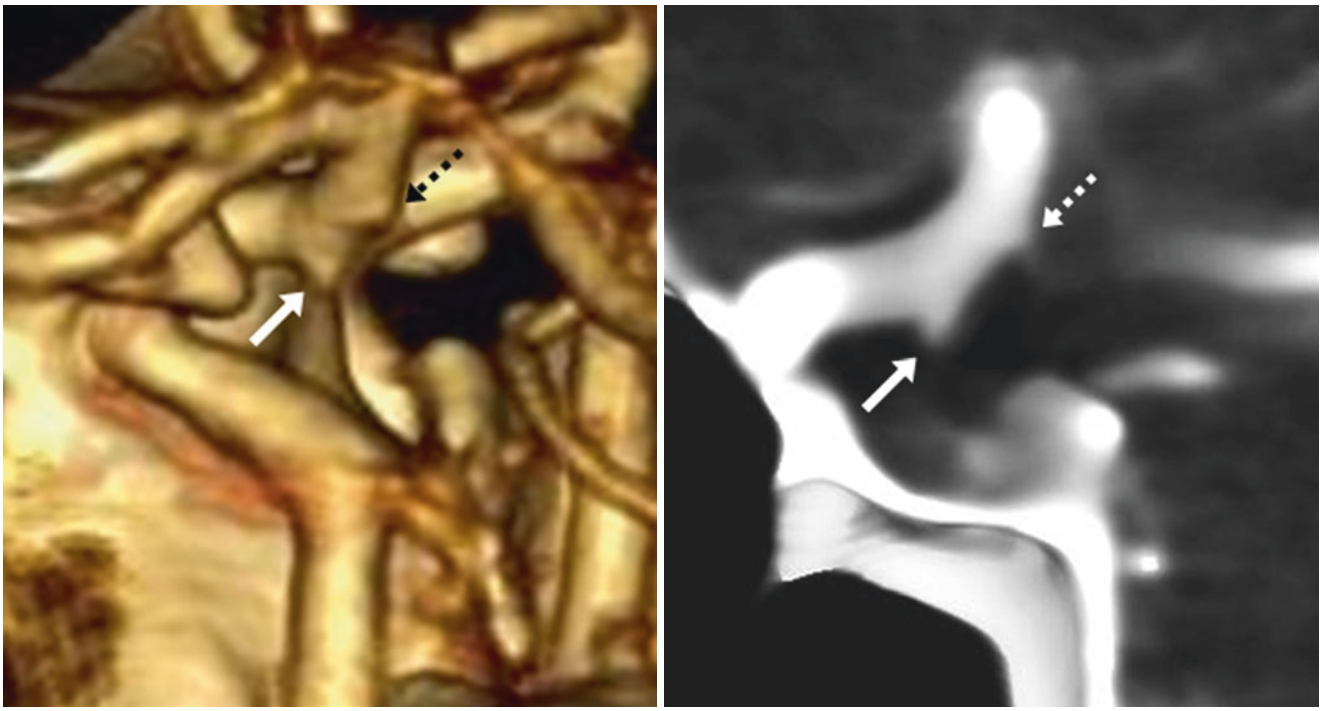

Fig. 38.7 In this 49-year-old, a VR CTA lateral view (*left*) depicts a tiny (<2 mm) infundibular outpouching (*arrows*) arising at the origin of the PcoA. A vessel arises from the apex, as seen on a 4-mm MPR (*arrows, right*). Also note a tiny anterior choroidal-origin infundibulum (*dotted arrows*)

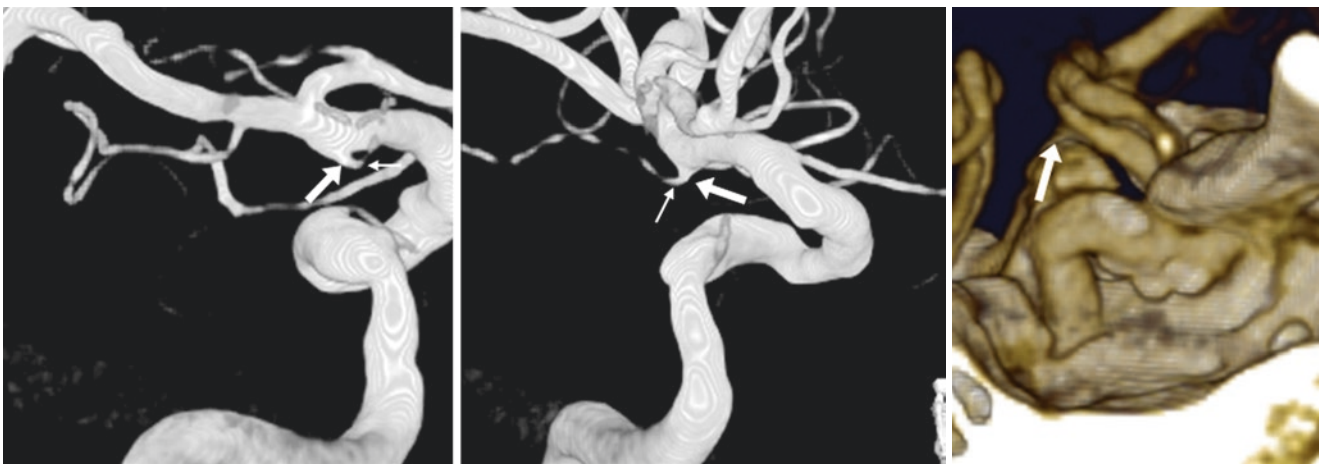

Fig. 38.8 70-year-old with a tiny (<2 mm) PcoA segment infundibulum (*arrows*) seen on a catheter 3DDSA AP view (*left*) and right lateral view (*middle*), but not visualized on a 3D VR CTA right lateral view (*right*), most likely because of the multifocal atherosclerotic calcifications. Note the tiny PcoA arising from the apex of the outpouching (*thin arrows*)

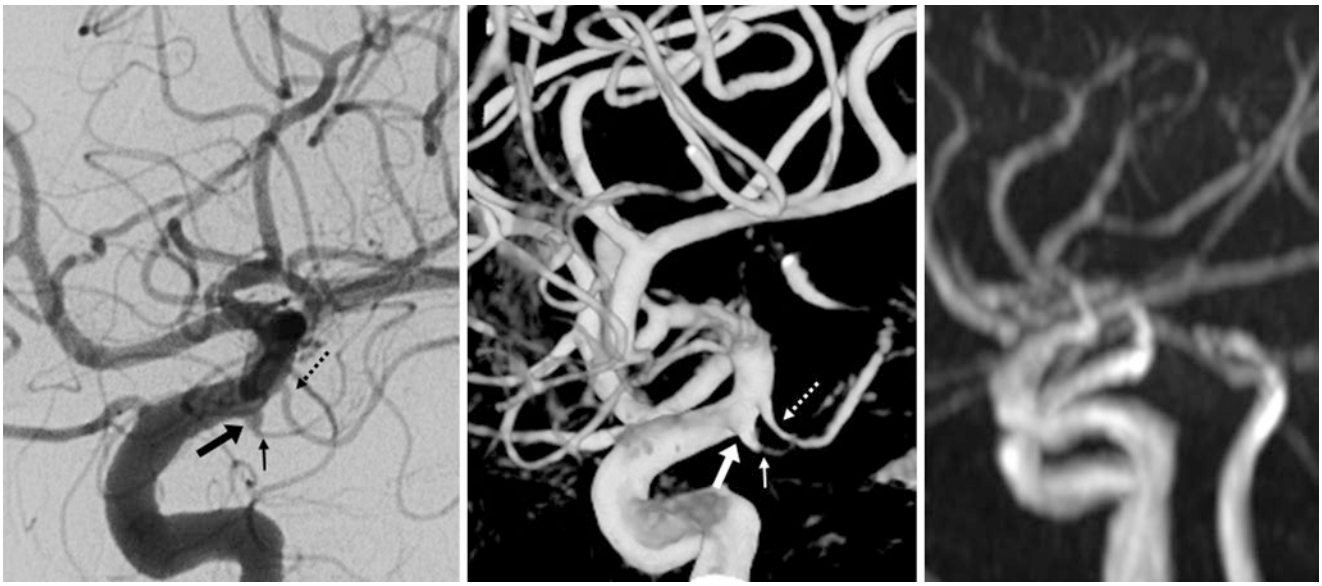

Fig. 38.9 54-year-old with an infundibulum <2 mm in size (*large arrows*) at the PcoA origin, as noted on lateral views of both a catheter DSA (*left*) and 3DDSA (*middle*), with a tiny vessel arising from the apex (*thin arrows*). This lesion was not visualized on a 3DTOF MRA (*right*). Note the normal anterior choroidal artery slightly distally (*dotted arrows*)

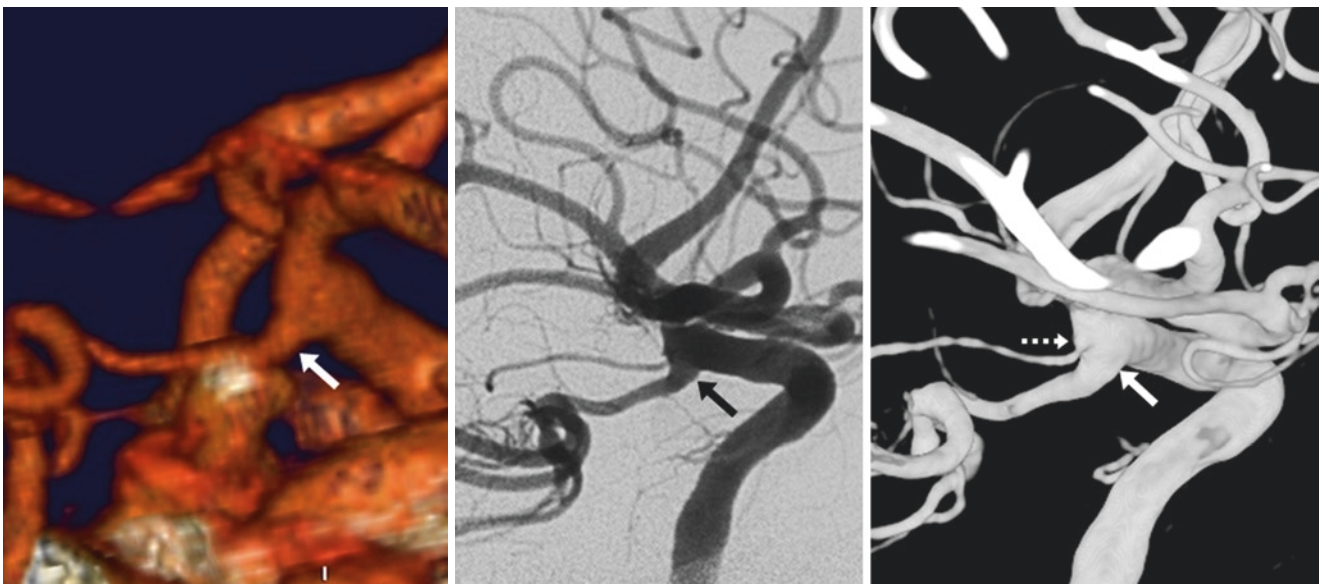

Fig. 38.10 In this 46-year-old, a 3D VR CTA lateral view (*left*) shows an infundibular outpouching (*arrows*) of the PcoA origin, with a prominent PcoA. Lateral views from both DSA (*middle*) and 3DDSA (right) confirm that the vessel arises from the apex. Note a tiny anterior choroidal artery infundibulum (*dotted arrow*) distally on the 3DDSA

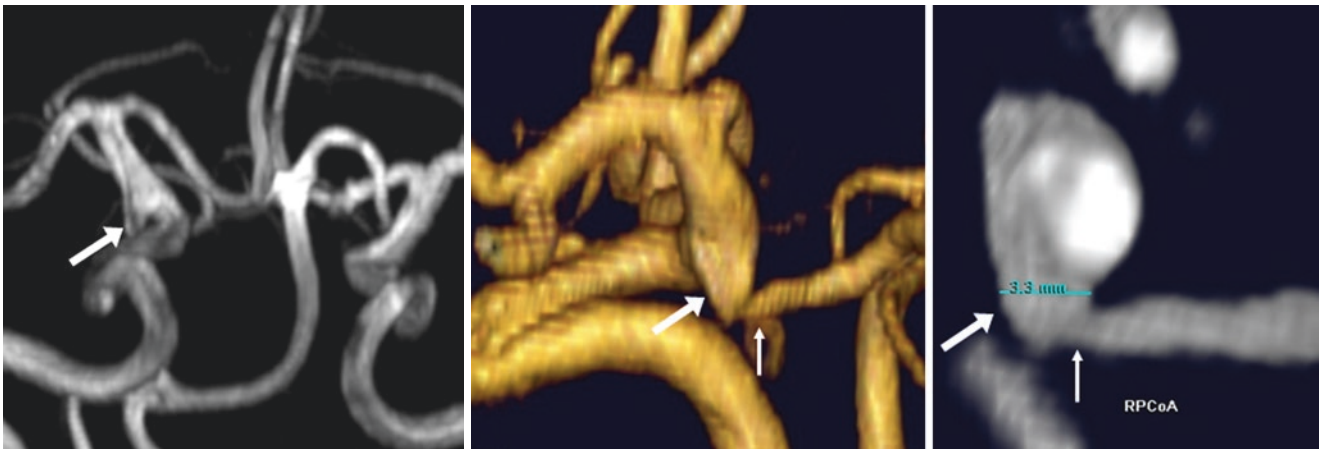

Fig. 38.11 Comparison case of PcoA aneurysm: in a 46-year-old, a 3DTOF MRA AP view (*left*) depicts a 3.3-mm outpouching (*arrows*) of the PcoA origin. A 3D VR lateral view (*middle*) and a 6 mm-thick MPR lateral view (*right*) both confirm that the PcoA vessel (*thin arrows*) arises eccentrically, and not directly, from the apex of the outpouching. This lesion should be considered an aneurysm, as it is too large and bulbous to be an infundibulum

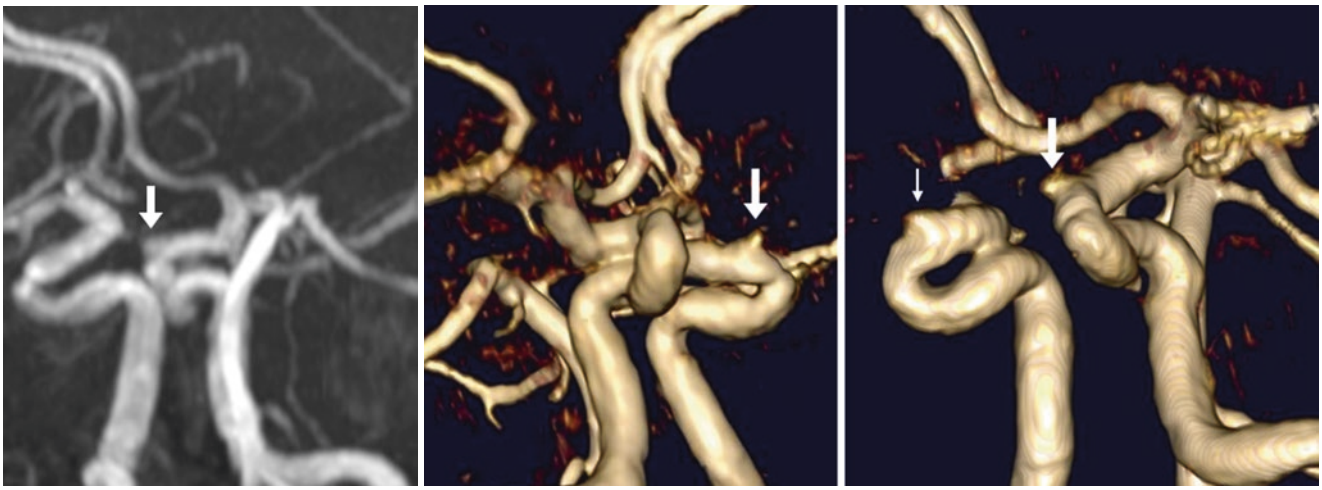

Fig. 38.12 82-year-old with a <2-mm infundibulum (*arrows*) arising from the left ophthalmic artery (OA) origin on multiple 3DTOF MRA oblique views. There may also be a tiny OA origin infundibulum on the right (*thin arrow*)

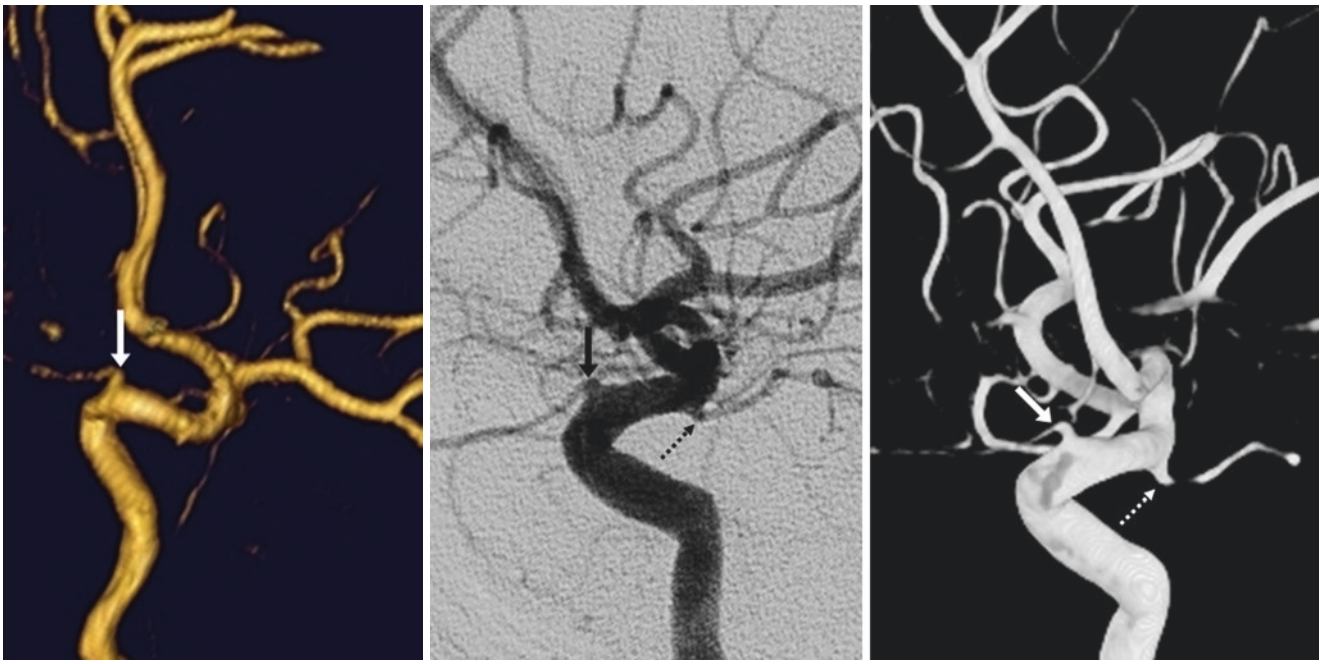

Fig. 38.13 30-year-old with a <2-mm infundibulum (*arrows*) arising from an OA origin on a 3DTOF MRA lateral view (*left*), with a tiny vessel arising from the apex of the outpouching. Catheter DSA (*middle*) and 3DDSA (*right*) lateral views confirm the findings. There may also be a tiny PcoA infundibulum (*dotted arrows*) on the DSA images

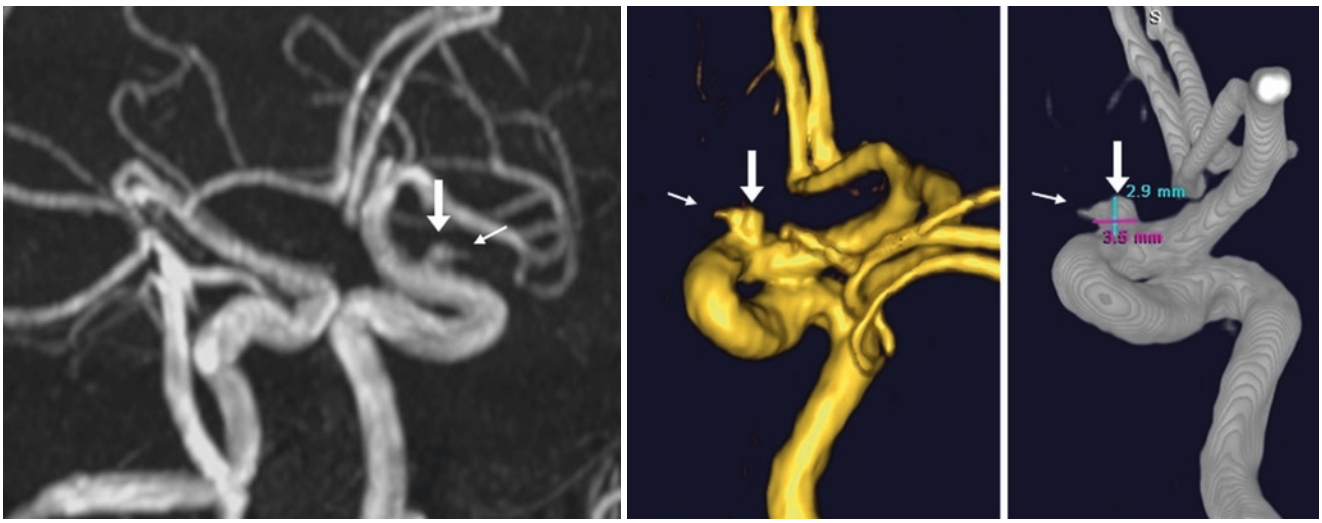

Fig. 38.14 Comparison case of an OA-origin aneurysm: 63-year-old with an OA outpouching (*arrows*) on 3DTOF MRA oblique (*left*) and lateral (*middle*) views. This outpouching likely represents a saccular aneurysm of the left ICA at the OA origin (*thin arrows*), as the OA arises eccentrically from the outpouching's anterior margin, not from the apex. The size measured 2.9–3.5 mm on catheter 3DDSA (*right*), which is too large to simply be an infundibulum

Fig. 38.15 40-year-old with an infundibulum (*arrow*) of early left anterior temporal artery origin on a 3DTOF MRA AP view

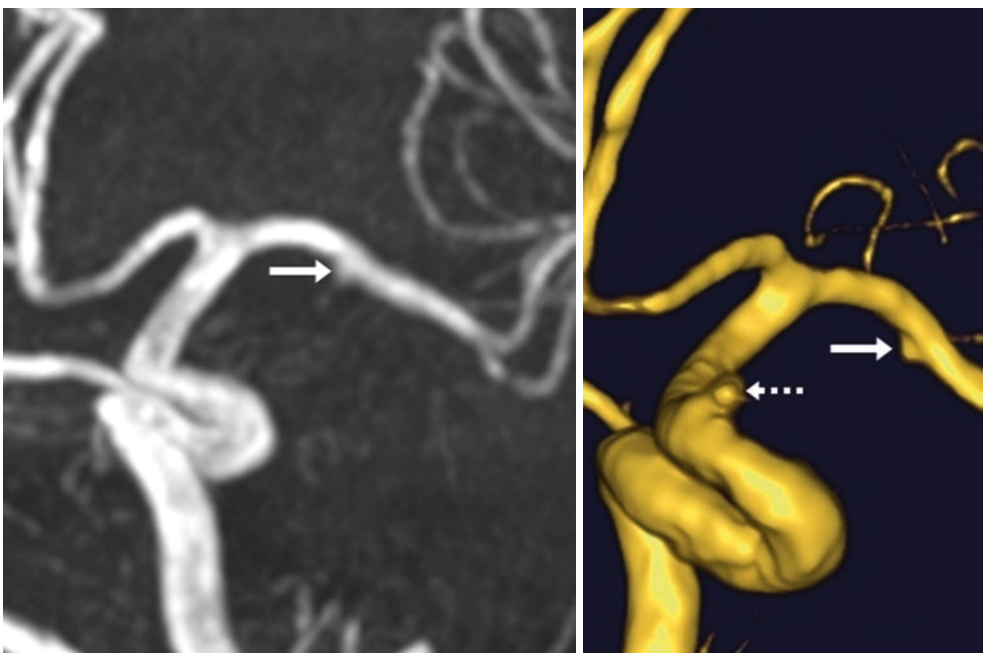

Fig. 38.16 63-year-old with a tiny infundibulum (*arrows*) of early left anterior temporal artery origin on 3DTOF MRA AP views. Also note a small infundibulum of left OA origin (*dotted arrow*)

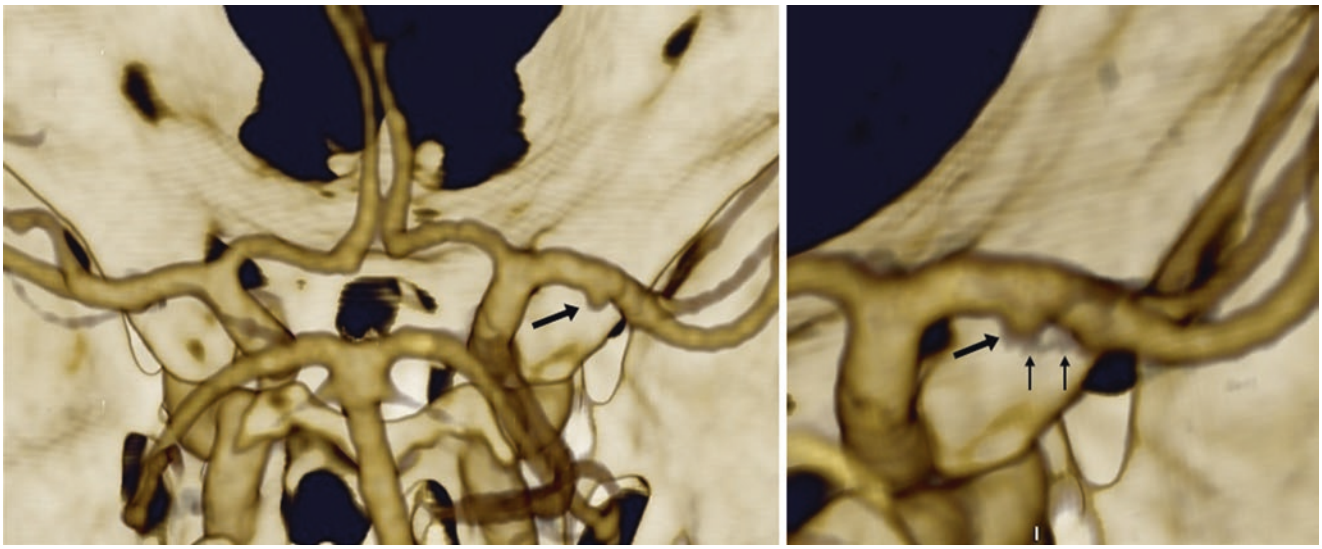

Fig. 38.17 In this 48-year-old, 3D VR CTA PA views show an infundibulum (*arrows*) of an early right anterior temporal branch. Magnified views (*right*) depict a tiny vessel arising from the apex (*thin arrows*)

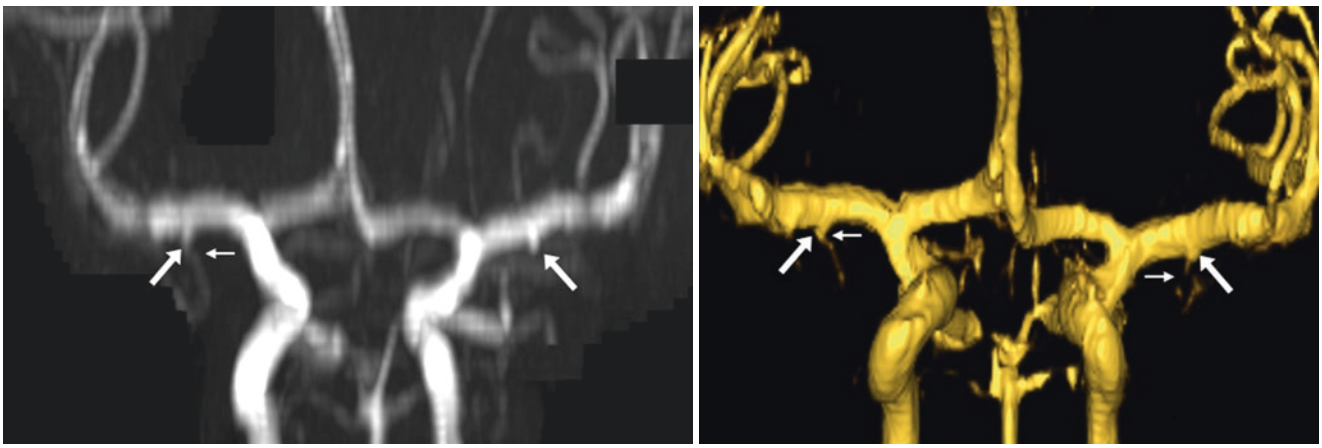

Fig. 38.18 In this 33-year-old, a noncontrast 3DTOF MRA AP view (*left*) shows infundibula (*large arrows*) of early anterior temporal artery origins bilaterally. Contrast-enhanced MRA (*right*) depicts tiny vessels (*thin arrows*) arising from the apices of these outpouchings

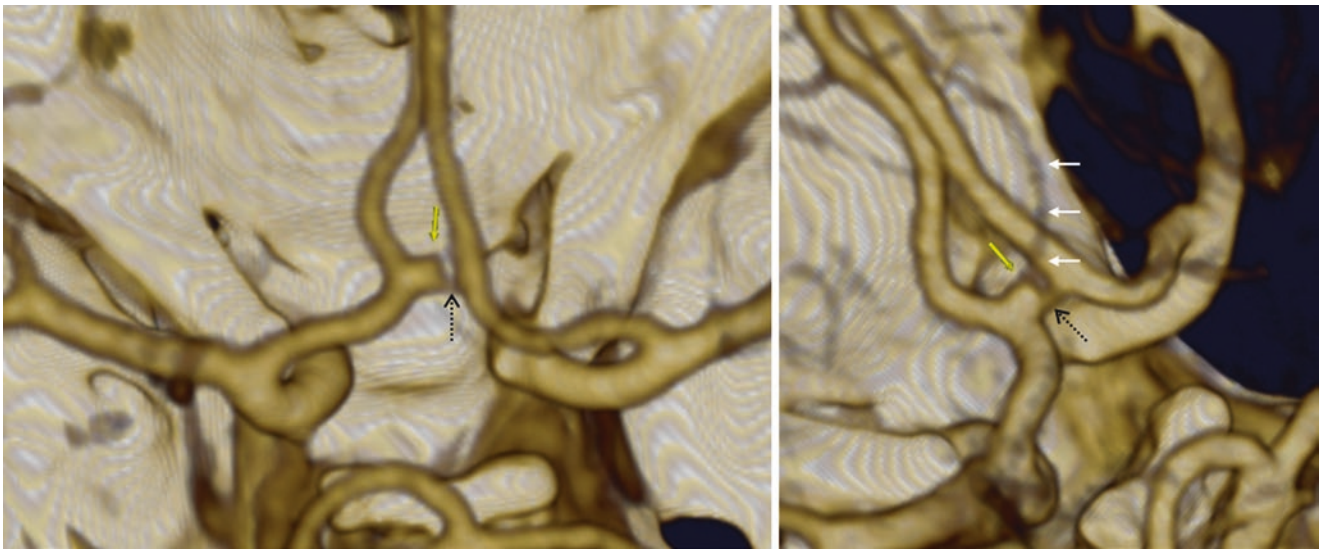

Fig. 38.19 55-year-old with a 2.2-mm infundibulum (*yellow arrows*) of the left side of the AcoA origin on 3D VR CTA PA (*left*) and on superior oblique (*right*) views. The AcoA (*dotted arrows*) is oriented towards the contralateral A1-A2 junction, with a tiny early pericallosal branch also arising from the apex of the infundibulum (*white arrows*)

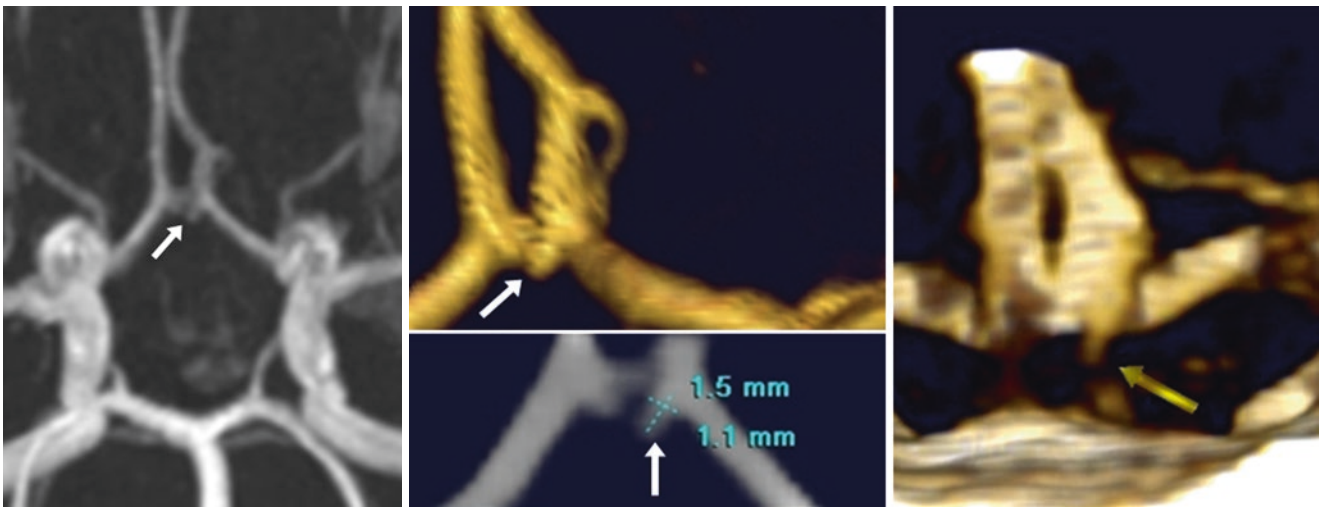

Fig. 38.20 17-year-old with a 1.5-mm outpouching (*white arrows*) from the AcoA on a 3DTOF MRA superior view (*left*) and superior oblique view (*middle*). A tiny vessel was noted to arise from the apex of the outpouching (*yellow arrow*) on a 3D VR CTA performed the next day (*right*), confirming that it was an infundibulum, not an aneurysm

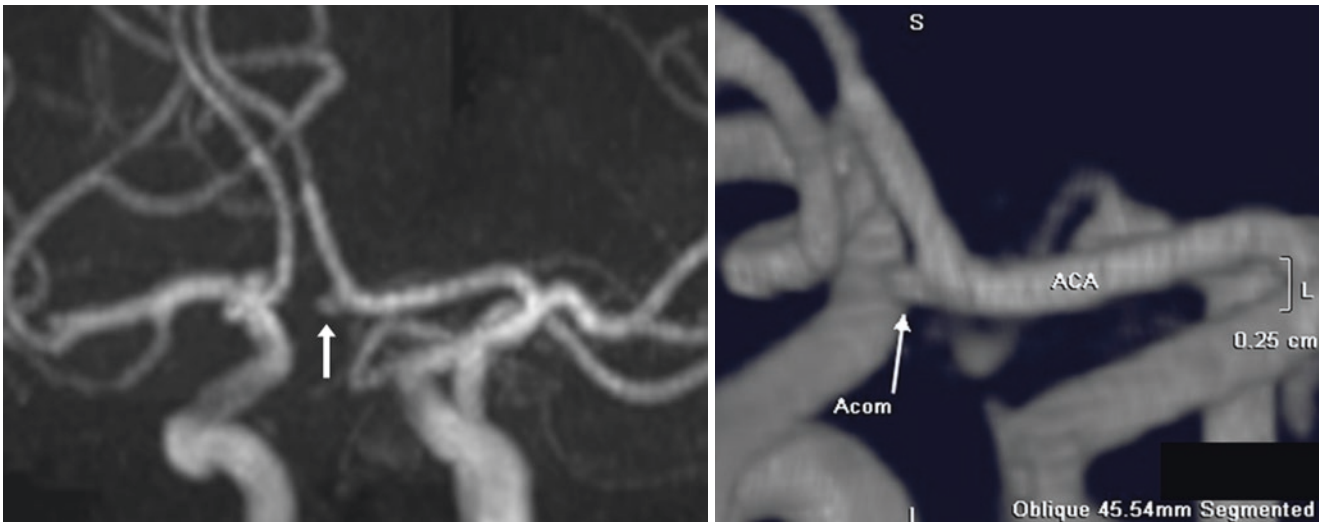

Fig. 38.21 In this 37-year-old, a <2-mm infundibulum (*arrows*) is at the expected location of the AcoA on the left, on a 3DTOF MRA AP view (*left*). The AcoA is not visualized, but one can imagine that it points towards the contralateral A1-A2 junction, as depicted on an oblique MPR (*right*). The lack of a vessel suggests that this is an aneurysm, but the orientation, location, and size favor an infundibulum. This indeterminate lesion was stable for many years

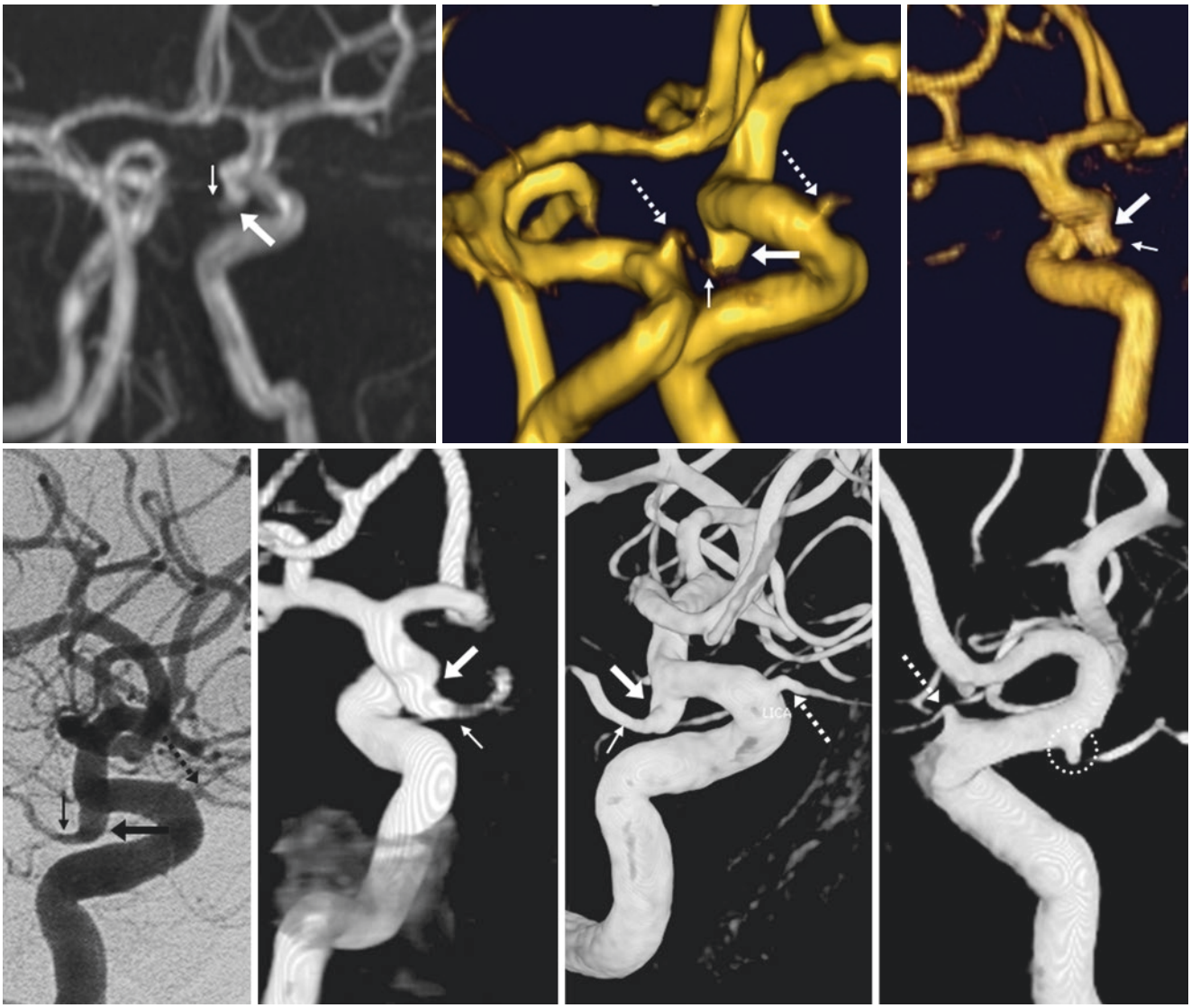

Fig. 38.22 Comparison case of both infundibula and aneurysm: 30-year-old woman with a 2.5-mm left PcoA segment outpouching (*large arrows*) on a 3DTOF MRA, as depicted by multiple oblique AP views (*top row*). The PcoA (*thin arrows*) arises eccentrically from the apex, suggesting aneurysm, as confirmed by lateral views from a left ICA catheter DSA (*bottom left*), with 3DDSA images of the left ICA (*bottom middle images*) and right ICA (*bottom right*). Small (<2 mm) infundibular outpouchings are also noted at the OA origins bilaterally (*dotted arrows*), each with a vessel arising from the apex. Note a tiny right PcoA-origin infundibulum (*dotted circle*)

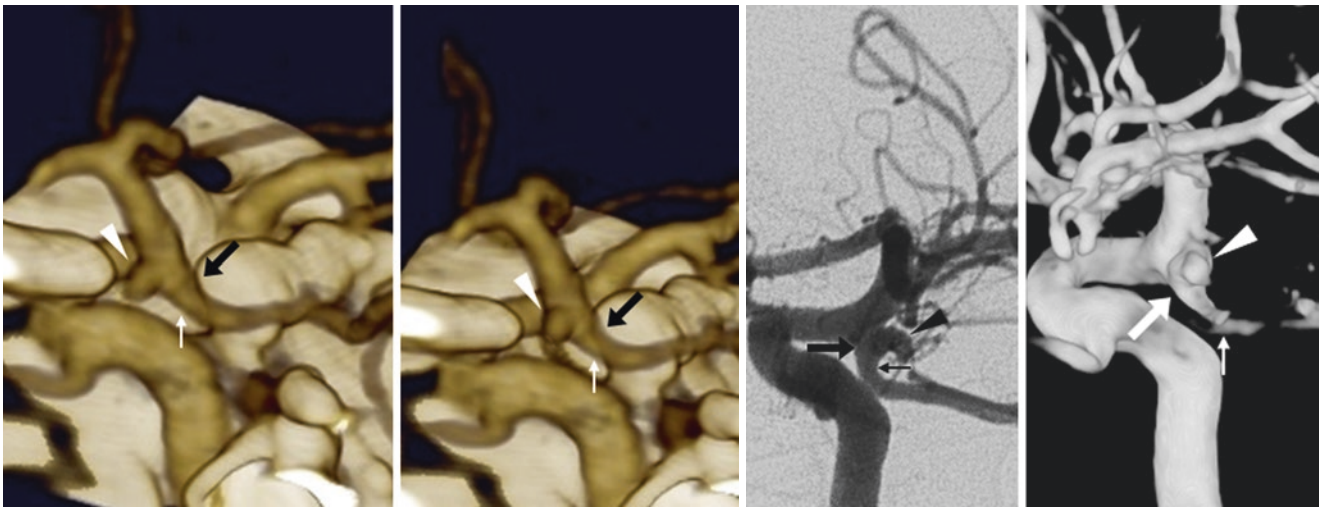

Fig. 38.23 Comparison case of both infundibulum and aneurysm: 23-year-old man with a 2.5-mm PcoA-origin infundibulum (*large arrows*) in a patient with a "fetal PCA" as seen on 3D VR lateral views from a CTA (*left two images*), DSA (*middle right*), and 3DDSA (*far right*). Note a "fetal PCA" arising from the apex (*thin arrows*). However, there is a tiny (1.5–2 mm) aneurysm arising off the lateral aspect of the infundibulum (*arrowheads*)

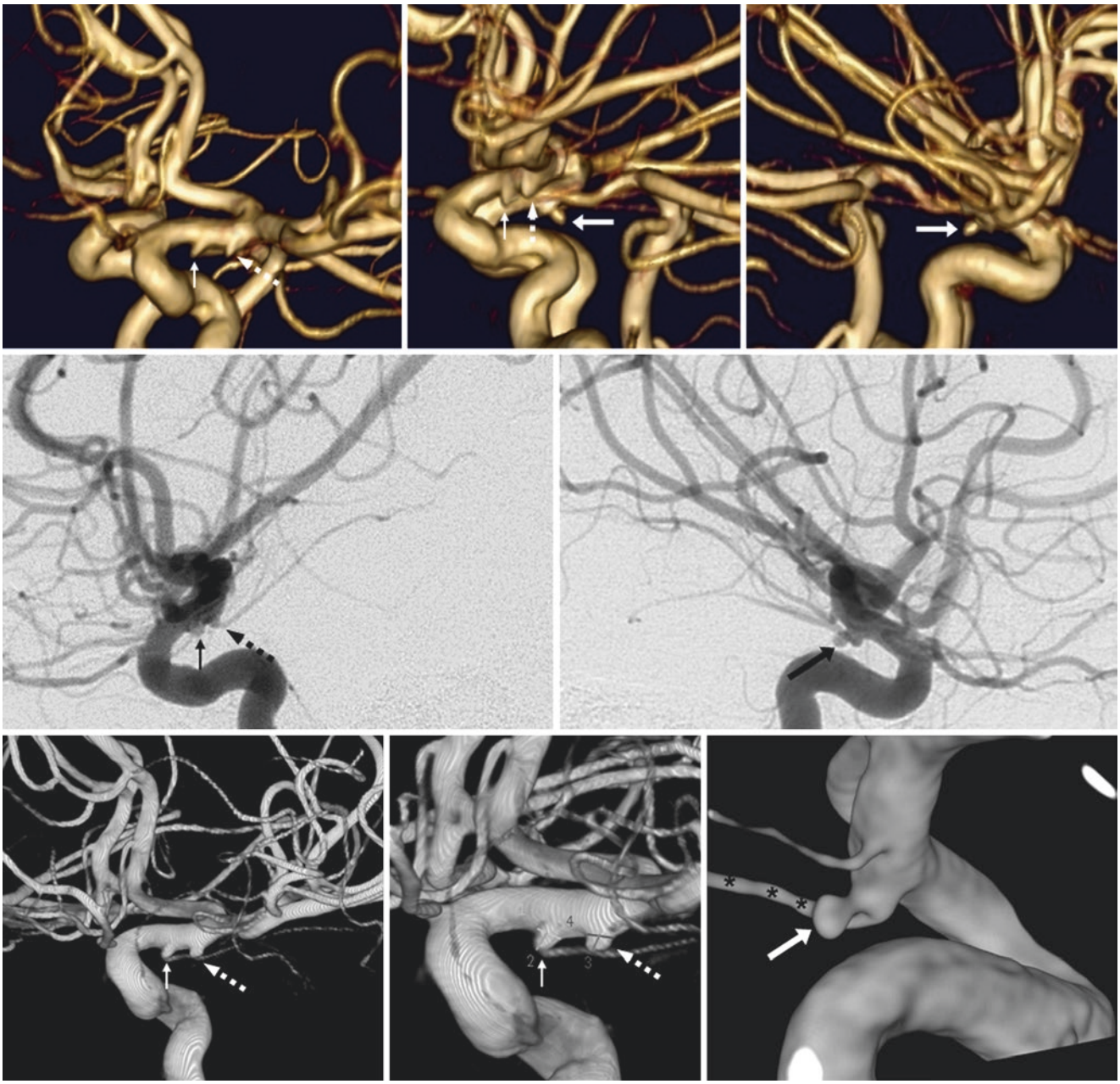

Fig. 38.24 Comparison case of infundibula and aneurysm: *top row:* 18-year-old with <2-mm infundibula of both the left anterior choroidal artery (*dotted arrows*) and PcoA (*thin arrows*) on LAO (*top left*) and left lateral (*top middle*) views from 3DTOF MRA. Note a 3-mm right PcoA aneurysm (*arrows*) on a right lateral view (*top right*). *Middle and Bottom rows*: The infundibula were confirmed on catheter DSA (*middle, left*) and 3DDSA (*bottom left*) lateral views, with a magnified view (*bottom middle*) that confirms their size to be less than 2 mm. The right PcoA aneurysm was confirmed on both catheter DSA (*middle, right*) and 3DDSA (*bottom right*) right lateral views. On 3DDSA, note how the right PcoA (*asterisks*) arises both eccentric to the apex and medial to the aneurysm's base

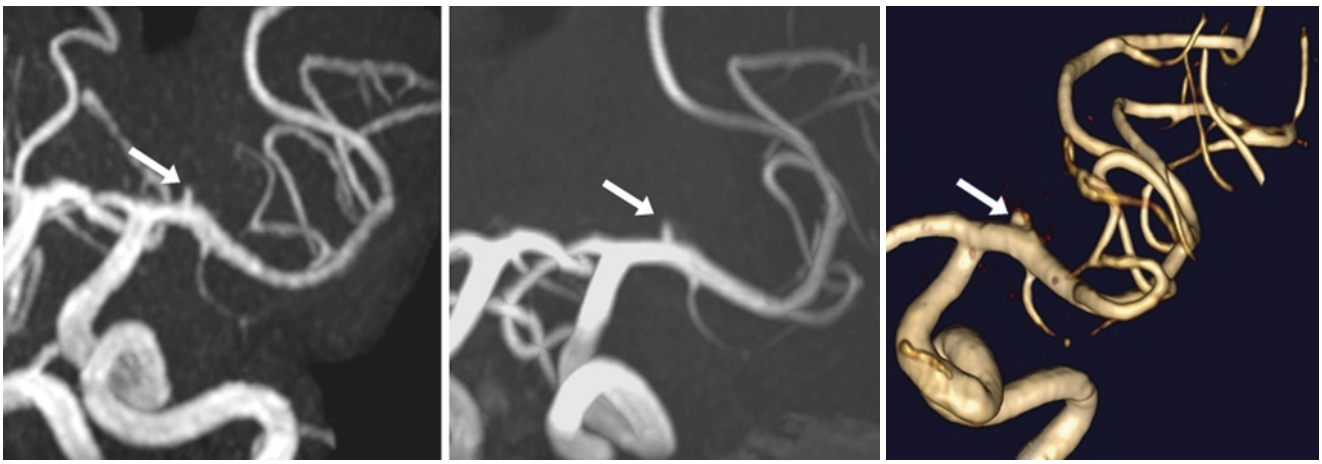

Fig. 38.25 Comparison case of aneurysm, less likely infundibulum: 73-year-old with a 2.1-mm outpouching of the left lenticulostriate artery origin (*arrows*) on 3 T 3DTOF MRA PA views, with MIP (*left*), 10-mm MPR (*middle*), and 3D VR MRA (*right*). No vessels were seen to arise from the apex of the outpouching. This lesion was stable for several years and never bled

References

1. Hassler O, Saltzman GF. Histologic changes in infundibular widening of the posterior communicating artery. A preliminary report. Acta Pathol Microbiol Scand. 1959;46:305–12.
2. Fox JL, Baiz TC, Jakoby RK. Differentiation of aneurism from infundibulum of the posterior communicating artery. J Neurosurg. 1964;21:135–8.
3. Stuntz JT, Ojemann GA, Alvord EC. Radiographic and histologic demonstration of an aneurysm developing of the infundibulum of the posterior communicating artery: case report. J Neurosurg. 1970;33:591–5.
4. Archer CR, Silbert S. Infundibula may be clinically significant. Neuroradiology. 1978;15:247–51.
5. Trasi S, Vincent LM, Zingesser LH. Development of aneurysm from infundibulum of posterior communicating artery with documentation of prior hemorrhage. AJNR Am J Neuroradiol. 1981;2: 368–70.
6. Marshman LAG, Ward PJ, Walter PH, Dossetor RS. The progression of an infundibulum to aneurysm formation and rupture: case report and literature review. Neurosurgery. 1981;43:1445–9.
7. Miyasaka K, Wolpert SM, Prager RJ. The association of cerebral aneurysms, infundibula, and intracranial arteriovenous malformations. Stroke. 1982;13:196–203.
8. Sun ZK, Li YD, Li MH, Chen SW, Tan HQ. Detection of infundibula using three-dimensional time-of-flight magnetic resonance angiography with volume rendering at 3.0 Tesla compared to digital subtraction angiography. J Clin Neurosci. 2011;18:504–8.
9. Fischer S, Hopf N, Henkes H. Evolution from an infundibulum of the posterior communicating artery to a saccular aneurysm. Clin Neuroradiol. 2011;21:87–90.
10. Shi WY, Li YD, Li MH, Gu BX, Gu JP. Differential diagnosis of infundibular dilation versus a small aneurysm of the internal carotid artery: assessment by three-dimensional rotational angiography with volume rendering. Neurol Sci. 2013;34:1065–70.
11. Min KJ, Yoon DY, Kim HC, Lee JY, Cho BM. Infundibular dilation and aneurysm at the origin of the posterior communicating artery: differential diagnosis by CT angiography. Neuroradiology. 2014;56:917–23.
12. Karekezi C, Boutarbouch M, Djoubairou BO, Melhaoui A, Arkha Y, El Ouahabi A. Are infundibular dilatations at risk of further transformation? Ten-year progression of a prior documented infundibulum into a saccular aneurysm and rupture: case report and a review of the literature. Neurochirurgie. 2014;60:307–11.
13. Villablanca JP, Jahan R, Hooshi P, Lim S, Duckwiler G, Patel A, et al. Detection and characterization of very small cerebral aneurysms by using 2D and 3D helical CT angiography. AJNR Am J Neuroradiol. 2002;23:1187–98.
14. Teksam M, McKinney A, Casey S, Asis M, Kieffer S, Truwit CL. Multi-section CT angiography for detection of cerebral aneurysms. AJNR Am J Neuroradiol. 2004;25:1485–92.
15. McKinney AM, Palmer CS, Truwit CL, Karagulle A, Teksam M. Detection of aneurysms by 64-section multidetector CT angiography in patients acutely suspected of having an intracranial aneurysm and comparison with digital subtraction and 3D rotational angiography. AJNR Am J Neuroradiol. 2008;29:594–602.
16. Gaughen Jr JR, Raghavan P, Jensen ME, Hasan D, Pfeffer AN, Evans AJ. Utility of CT angiography in the identification and characterization of supraclinoid internal carotid artery blister aneurysms. AJNR Am J Neuroradiol. 2010;31:640–4.
17. Horie N, Morikawa M, Fukuda S, Hayashi K, Suyama K, Nagata I. Detection of blood blister-like aneurysm and intramural hematoma with high-resolution magnetic resonance imaging. J Neurosurg. 2011;115:1206–9.
18. Gonzalez AM, Narata AP, Yilmaz H, Bijlenga P, Radovanovic I, Schaller K, et al. Blood blister-like aneurysms: single center experience and systematic literature review. Eur J Radiol. 2014; 83:197–205.
19. Yu J, Xu B, Guo Y, Xu K. Direct clipping of a blister-like aneurysm in the supraclinoid segment of the internal carotid artery: a clinical analysis of nine cases. Int J Clin Exp Med. 2015;8:21786–95.
20. McKinney AM, Truwit CL, Palmer CS, Teksam M. Intracranial aneurysms: is the diagnostic accuracy rate of multidetector CT angiography equivalent to that of three-dimensional rotational conventional angiography? Radiology. 2008;246:982.
21. Teksam M, McKinney A, Cakir B, Truwit CL. Multi-slice CT angiography of small cerebral aneurysms: is the direction of aneurysm important in diagnosis? Eur J Radiol. 2005;53:454–62.

Persistent Carotid-Basilar and Carotid-Vertebral Anastomoses

39

Carotid-basilar and *carotid-vertebral anastomoses* are remnants of the early fetal vasculature, in which four paired, presegmental arteries are seen as early as 6 weeks gestational age, when the embryo is 4–5 mm in size. These arteries are the *trigeminal, otic, hypoglossal,* and *proatlantal intersegmental arteries* (in order of anterior-posterior or rostral-caudal location, depending on gestational age and named by adjacent structures). As the bilateral, posteriorly located longitudinal neural arteries regress and join together to form the basilar artery, the lack of regression of these presegmental arteries leads to *carotid-basilar anastomoses* (persistent trigeminal, otic and hypoglossal arteries) or *carotid-vertebral anastomoses* (persistent proatlantal intersegmental artery). Together, these variants have an overall incidence of about 0.1–1.0 % of the population, although carotid-vertebral anastomoses are much rarer, occurring in less than 0.1 % of the population [1–21].

The most common of these variants is the *persistent trigeminal artery* (PTA), representing more than 90 % of the persistent carotid-basilar anastomoses and occurring in 0.1–1.0 % of the population [1–9] (Figs. 39.1, 39.2, 39.3, 39.4, 39.5, 39.6, and 39.7). Typically, the ipsilateral vertebral artery (VA) and posterior communicating artery (PcoA) are hypoplastic, although this varies along a spectrum: even bilateral VA or basilar hypoplasia can occur, with the basilar circulation distal to the anastomosis supplied completely by a PTA. (About two thirds have some degree of basilar hypoplasia.) In another variation, the PTA unites or fills the superior cerebellar arteries (SCAs) below their origin, so the posterior cerebral arterial (PCA) supply can be largely from the internal carotid arteries (ICAs). Of note, traditional data had suggested that the PTA could be associated with intracranial vascular anomalies such as aneurysms in up to 15 % of patients, but further reports have found that the prevalence of aneurysms in PTAs is in the range of 3–4 %, not significantly different than the prevalence in the general population [10–12]. Notably, however, a PTA can uncommonly cause symptoms such as trigeminal neuralgia by direct compression of cranial nerves. There are several different classification mechanisms proposed for PTAs [1–12]. A further point of distinction is regarding whether the PTA passes lateral to the sella (about 67 %) versus medially through the sella (about 33 %); this distinction is important for those undergoing pituitary surgery. PTAs also may be classified according to whether they go lateral (>90 %) or medial (<10 %) to the abducens nerve (CN VI) in the prepontine cistern [1–12].

The second most common carotid-basilar/vertebral anastomosis is the *persistent hypoglossal artery* (PHA), a persistent fetal artery that is estimated to occur in about 0.02–0.10 % of the population [13–17]. The PHA arises between the C1–C2 levels and enters the skull base via an enlarged hypoglossal canal. The ipsilateral vertebral artery is usually hypoplastic, and there are typically absent PcoAs (Figs. 39.8, 39.9, and 39.10).

The third most common is the *proatlantal intersegmental artery* (PIA), reported to occur in less than 0.01 % of the population [1–3, 17–20]. The PIA is a persistent carotid-vertebral anastomosis, originating from the cervical ICA (or occasionally the external carotid artery), and uniting with the vertebral artery at about the level of C2–C3 to course vertically without travelling within the transverse foramina. It enters the skull base through the foramen magnum, from which the ipsilateral VA arises (Fig. 39.11).

Finally, the *otic artery* is an extremely rare carotid-basilar anastomosis, which is probably reportable if actually seen; it is almost never seen in adults [21–25]. Theoretically, it should arise at the lateral portion of the distal petrous ICA, should pass through the internal auditory canal, and should connect to the basilar artery at a caudal point. However, no definitive cases have been demonstrated in recent MRI or CT literature that have clearly fulfilled these criteria, leading some to doubt this variant's existence [21–25].

A.M. McKinney, *Atlas of Normal Imaging Variations of the Brain, Skull, and Craniocervical Vasculature*,
DOI 10.1007/978-3-319-39790-0_39

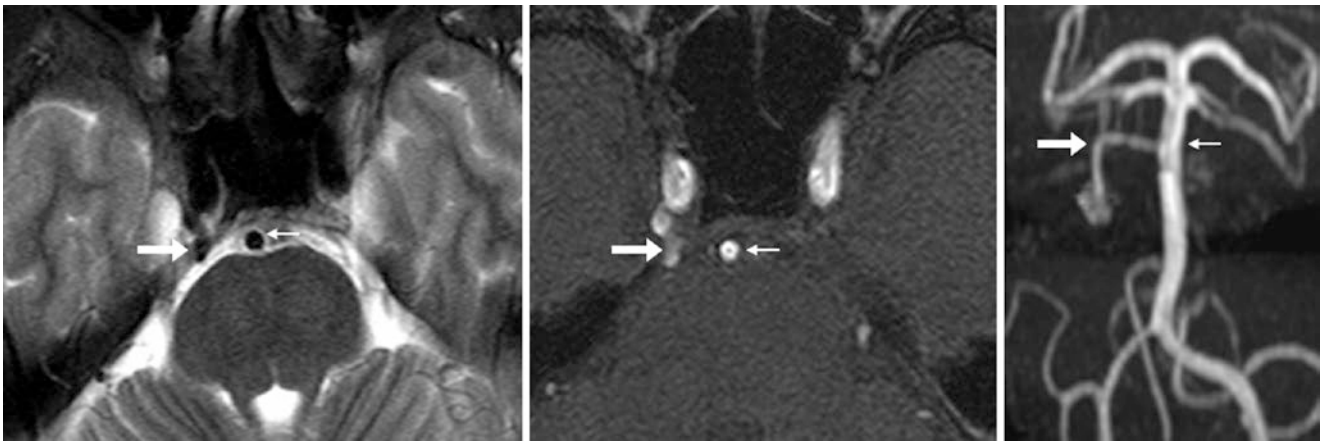

Fig. 39.1 In this 56-year-old, a T2WI MRI (*left*) shows a persistent trigeminal artery (PTA) (*large arrows*) that arises from the cavernous right internal carotid artery (ICA) and travels lateral to the sella, tapering in size as it approaches the mid-basilar (*thin arrows*). This PTA is also demonstrated on axial source MRA images (*middle*), and on a 3DTOF MRA AP view (*right*). Note a fenestrated left superior cerebellar artery (SCA)

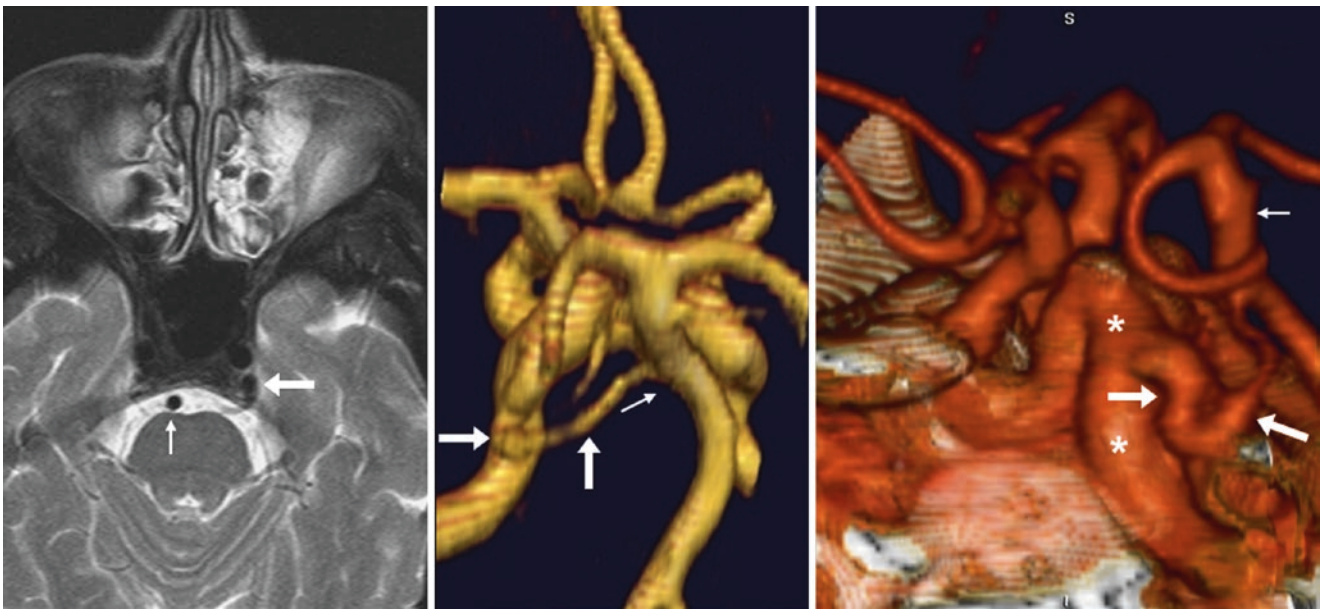

Fig. 39.2 In this 78-year-old, an axial T2WI MRI (*left*) depicts a left PTA (*large arrows*) lateral to the sella, arising from the left ICA and oriented towards the mid-basilar (*thin arrow*). On a 3DTOF MRA PA view (*middle*) and on a 3D VR CTA left lateral view (*right*), the PTA originates from the cavernous left ICA (*asterisks*), with its course depicted

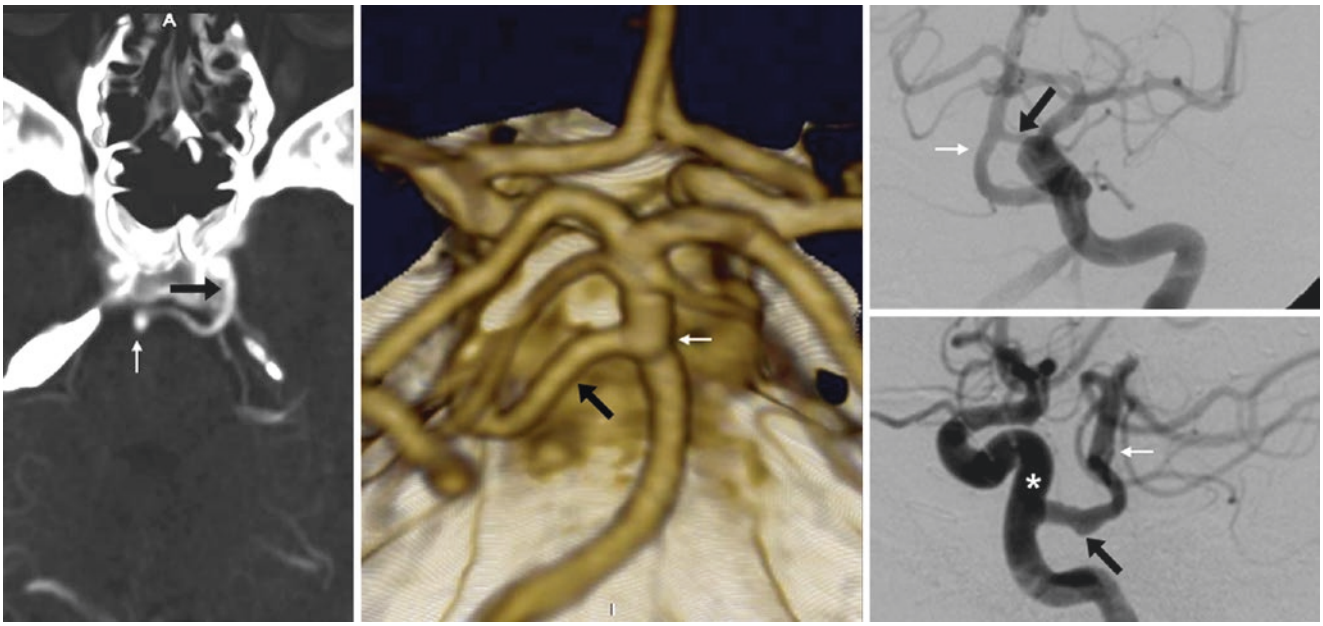

Fig. 39.3 In this 64-year-old, an axial source CTA 9-mm MPR image (*left*) depicts a PTA (*black arrows*) travelling lateral to the sella from the cavernous left ICA and terminating in the mid-basilar (*thin arrows*), as seen on a 3D VR PA view (*middle*). The PTA fills from the left ICA (*asterisk*) on DSA AP (*right*, *top*) and lateral (*right*, *bottom*) runs

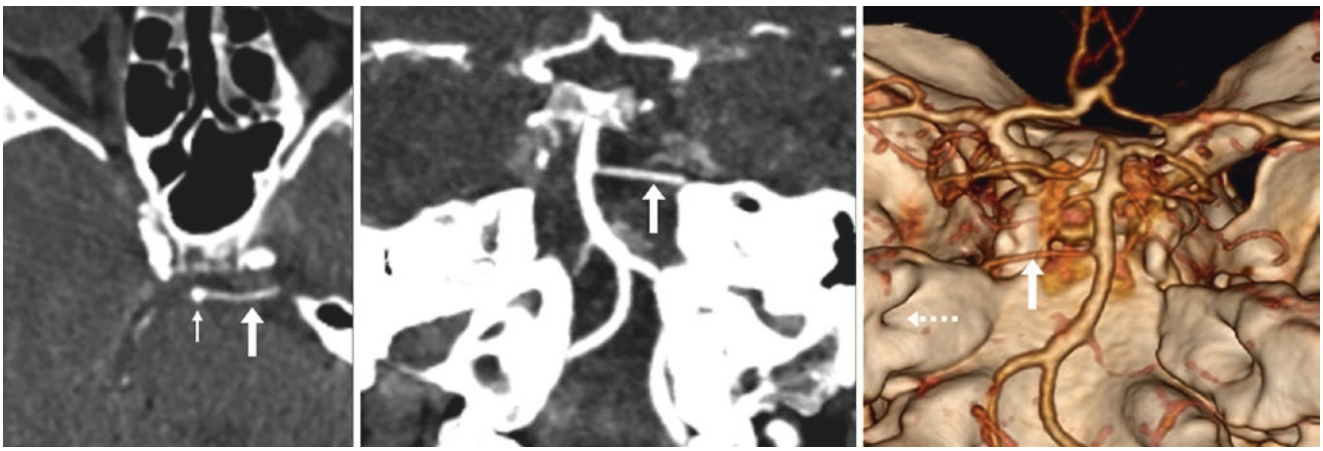

Fig. 39.4 In this 69-year-old, axial 0.8-mm (*left*) and coronal 3-mm (*middle*) MPRs depict a PTA (*large arrows*) between the cavernous left ICA and the mid-basilar (*thin arrow*). This far lateral type of PTA may mimic the otic artery on catheter DSA, but it does not enter the internal auditory canal (*dotted arrow*), shown on a 3D VR PA view (*right*)

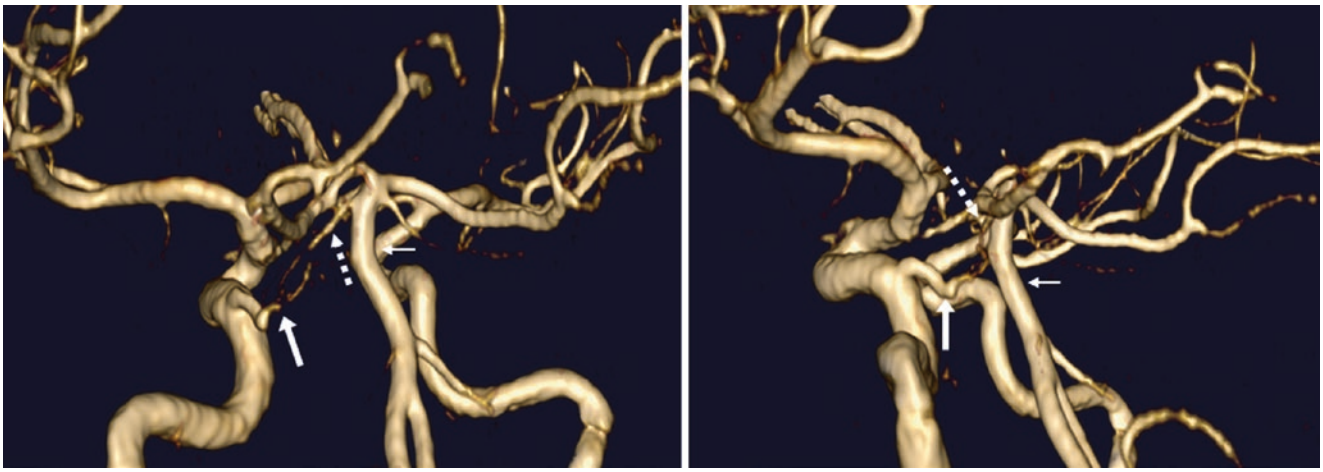

Fig. 39.5 In this 34-year-old, a 3DTOF MRA PA view (*left*) shows a PTA (*large arrow*) that arises from the cavernous left ICA and then travels towards the mid-basilar (*thin arrow*), but actually directly connects to the right SCA (*dotted arrow*). This configuration is also depicted on a left lateral view (*right*)

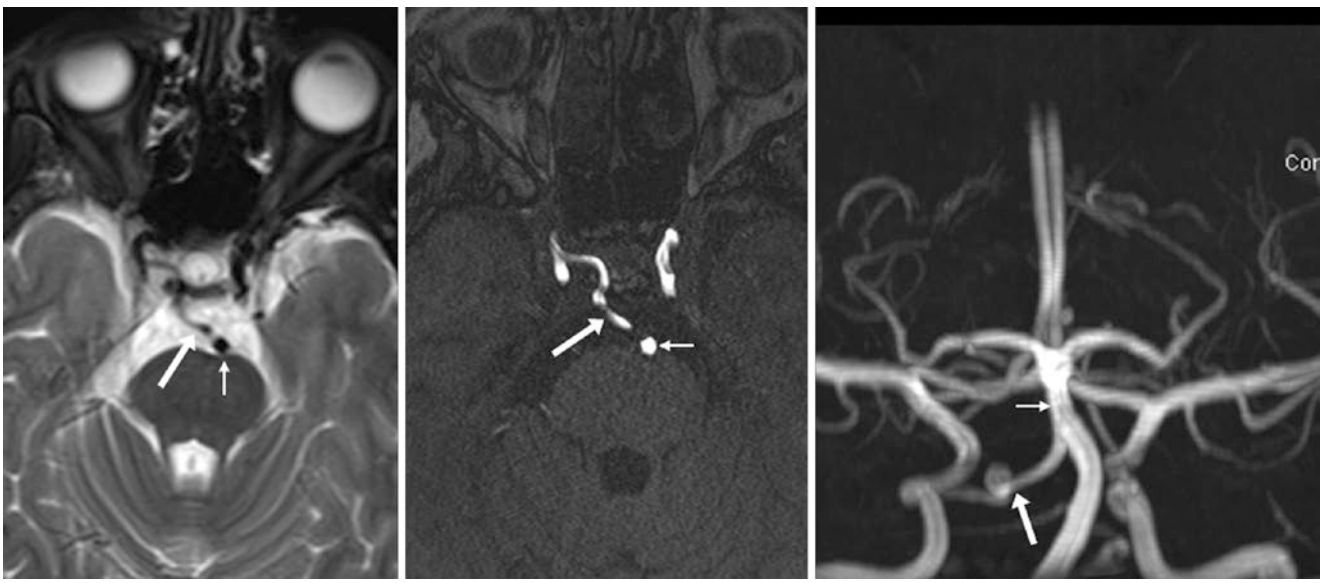

Fig. 39.6 In this 19-year-old, an axial T2WI MRI (*left*) demonstrates a left PTA (*large arrow*) that travels from the cavernous ICA medially through the sella towards the mid-basilar (*thin arrow*). A 3DTOF MRA source image (*middle*) and an MIP AP view (*right*) delineate the PTA's tortuous course from the right ICA through the sella

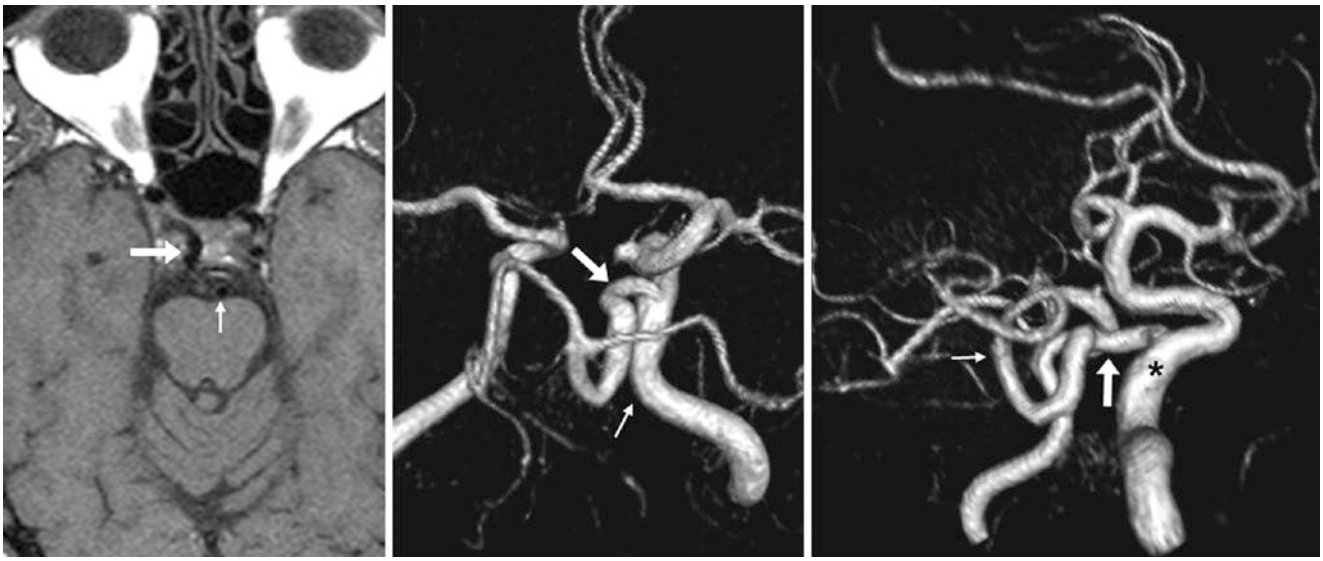

Fig. 39.7 In this 60-year-old, an axial noncontrast T1WI (*left*) demonstrates a right PTA (*large arrow*) that travels medially through the sella to become the mid-basilar (*thin arrow*). A 3DTOF MRA PA view (*middle*) and right lateral view (*right*) illustrate how the PTA arises from the cavernous right ICA (*asterisk*), and comprises the basilar's entire supply

Fig. 39.8 In this 37-year-old, an axial T2WI MRI (*top left*) and a sagittal T1WI (*bottom left*) show a persistent hypoglossal artery (PHA, *arrows*) that connects the right ICA (*dotted arrow*) to the basilar artery (*thin arrows*) via the right hypoglossal canal, as shown on lateral (*middle*) and oblique (*right*) catheter DSA runs that were obtained via right common carotid artery catheterization (*Courtesy of* Chip Truwit, MD, Hennepin County Medical Center, Minneapolis, MN)

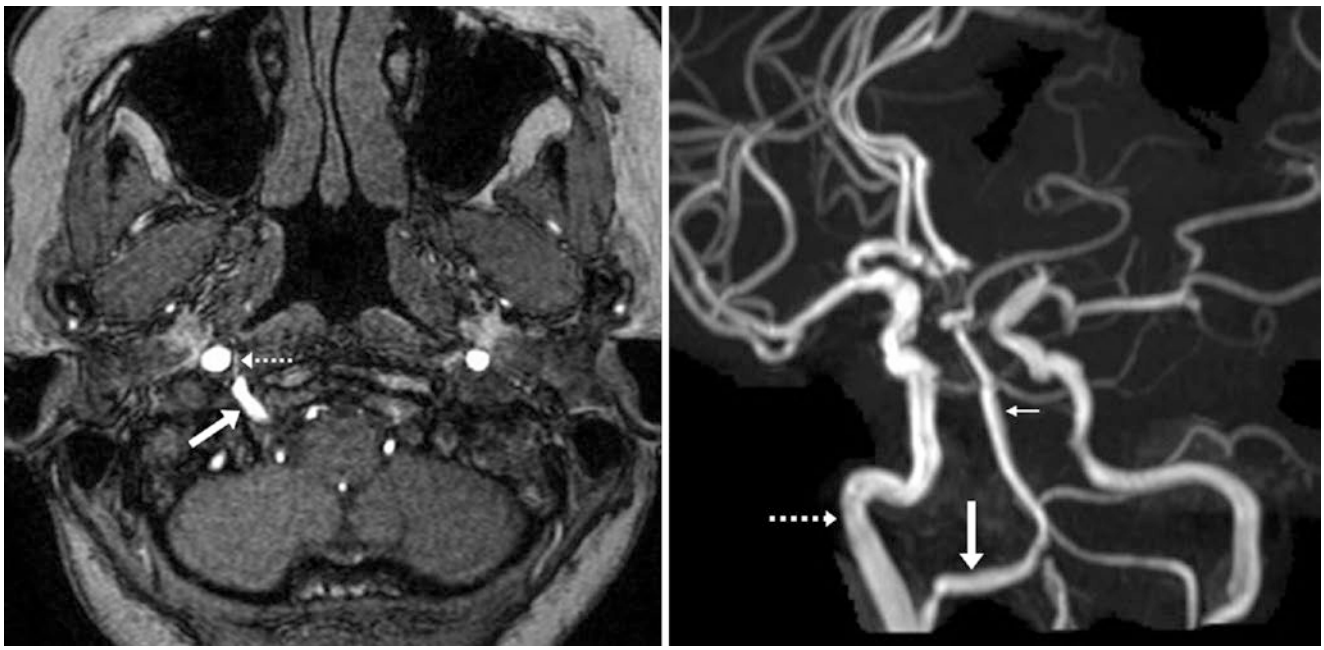

Fig. 39.9 A 3DTOF MRA axial source image (*left*) and an MIP AP view (*right*) demonstrate a PHA (*arrows*) between the right ICA (*dotted arrows*) and basilar (*thin arrow*) (*Courtesy of* H. Parmar, MD, University of Michigan, Ann Arbor, MI)

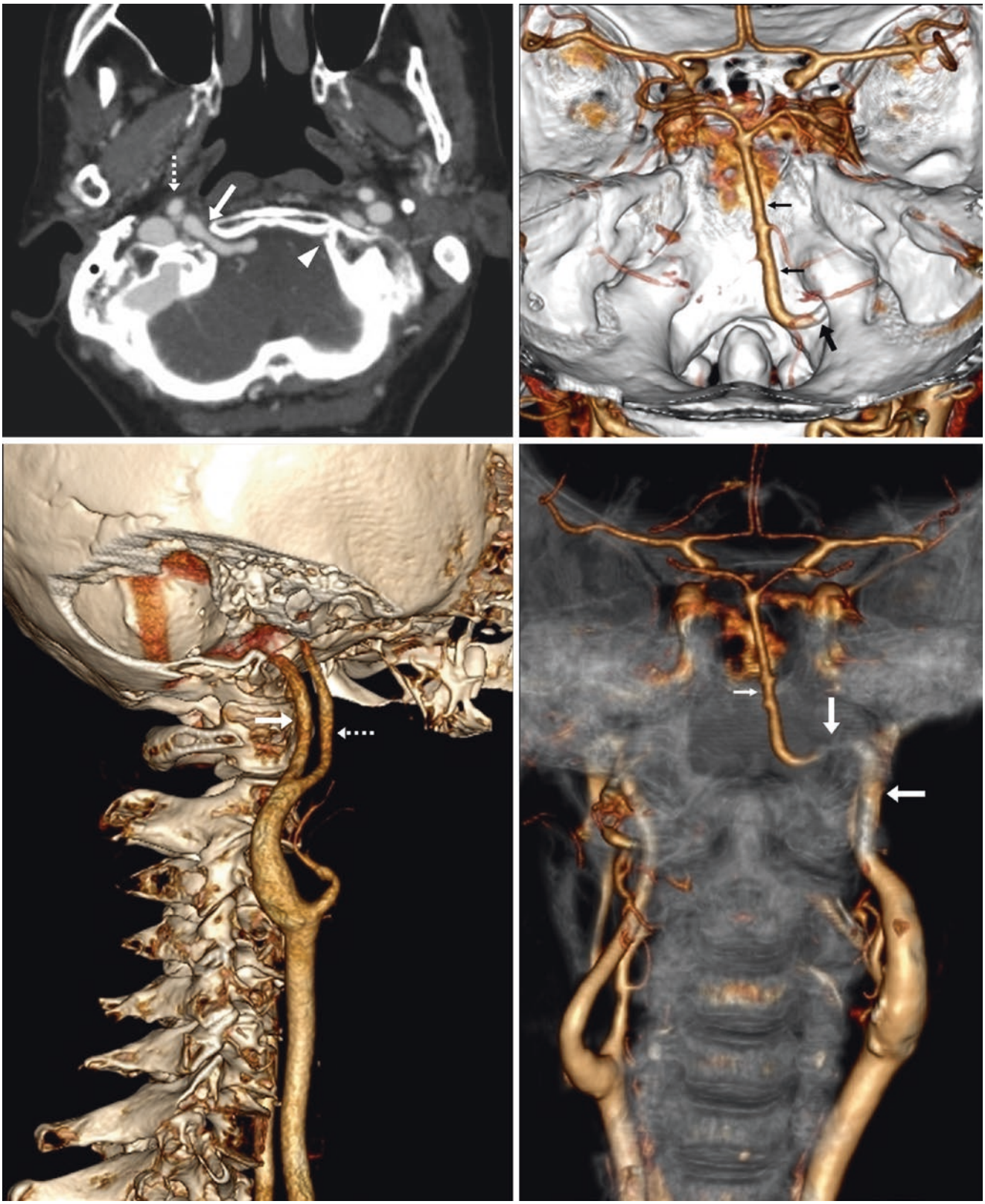

Fig. 39.10 79-year-old with throat pain. The patient had a right PHA (*large arrows*), which was depicted on a CTA's axial source images (*top left*), as well as on a 3D VR PA view (*top right*), a right lateral view (*bottom left*), and on a "transparent bone" 3D PA view (*bottom right*). Note the position of the right ICA anteriorly (*dotted arrows*), and the basilar artery (*thin arrows*). Also, note the normal contralateral hypoglossal canal (*arrowhead*, *top left*)

Fig. 39.11 A persistent proatlantal intersegmental artery (*arrows*) was noted on catheter DSA lateral views (*top* and *bottom left*), and on an AP view (*bottom right*), obtained via a right common carotid artery injection. This vessel supplies the entire basilar circulation. An aneurysm of this artery (*asterisk*s) was noted intracranially. Also note the ICA situated anteriorly (*dotted arrows*) (*Courtesy of* Chip Truwit, MD, Hennepin County Medical Center, Minneapolis, MN)

References

1. Harrison CR, Luttrell C. Persistent carotid-basilar anastomosis; three arteriographically demonstrated cases with one anatomical specimen. J Neurosurg. 1953;10:205–15.
2. Titrud LA. Carotid-basilar anastomosis. A report of two cases. Lancet. 1962;82:150–2.
3. Yilmaz E, Ilgit E, Taner D. Primitive persistent carotid-basilar and carotid-vertebral anastomoses: a report of seven cases and a review of the literature. Clin Anat. 1995;8:36–43.
4. Salas E, Ziyal IM, Sekhar LN, Wright DC. Persistent trigeminal artery: an anatomic study. Neurosurgery. 1998;43:557–61.
5. Tubbs RS, Shoja MM, Salter EG, Oakes WJ. Cadaveric findings of persistent fetal trigeminal arteries. Clin Anat. 2007;20: 367–70.
6. Weon YC, Choi SH, Hwang JC, Shin SH, Kwon WJ, Kang BS. Classification of persistent primitive trigeminal artery (PPTA): a reconsideration based on MRA. Acta Radiol. 2011;52: 1043–51.
7. Arráez-Aybar LA, Fuentes-Redondo T, Millán JM. Persistent trigeminal artery: a cross-sectional study based on over 3 years conventional angiography, CT angiography and MR angiography images. Surg Radiol Anat. 2016;38:445–53.
8. Uchino A, Saito N, Okada Y, Kozawa E, Mizukoshi W, Inoue K, et al. Persistent trigeminal artery and its variants on MR angiography. Surg Radiol Anat. 2012;34:271–6.
9. O'uchi E, O'uchi T. Persistent primitive trigeminal arteries (PTA) and its variant (PTAV): analysis of 103 cases detected in 16,415 cases of MRA over 3 years. Neuroradiology. 2010;52: 1111–9.
10. Cloft HJ, Razack N, Kallmes DF. Prevalence of cerebral aneurysms in patients with persistent primitive trigeminal artery. J Neurosurg. 1999;90:865–7.
11. Tamura Y, Shimano H, Kuroiwa T, Miki Y. Trigeminal neuralgia associated with a primitive trigeminal artery variant: case report. Neurosurgery. 2003;52:1217–9.
12. Kim MJ, Kim MS. Persistent primitive trigeminal artery: analysis of anatomical characteristics and clinical significances. Surg Radiol Anat. 2015;37:69–74.
13. Hahnel S, Hartmann M, Jansen O, Sartor K. Persistent hypoglossal artery: MRI, MRA and digital subtraction angiography. Neuroradiology. 2001;43:767–9.
14. Fujita N, Shimada N, Takimoto H, Satou T. MR appearance of the persistent hypoglossal artery. AJNR Am J Neuroradiol. 1995;16:990–2.
15. Oelerich M, Schuierer G. Primitive hypoglossal artery: demonstration with digital subtraction-, MR- and CT angiography. Eur Radiol. 1997;7:1492–4.
16. Uchino A, Saito N, Okada Y, Kozawa E, Nishi N, Mizukoshi W, et al. Persistent hypoglossal artery and its variants diagnosed by CT and MR angiography. Neuroradiology. 2013;55:17–23.
17. Anderson RA, Sondheimer FK. Rare carotid-vertebrobasilar anastomoses with notes on the differentiation between proatlantal and hypoglossal arteries. Neuroradiology. 1976;11:113–8.
18. Rao TS, Sethi PK. Persistent proatlantal artery with carotid-vertebral anastomosis. Case report. J Neurosurg. 1975;43:499–501.
19. Donmez H, Kahriman G, Serifov E, Mavili E, Ozcan N. Incidental finding of a proatlantal intersegmental artery. A case report. Neuroradiol J. 2011;24:758–61.
20. Uchino A, Saito N, Inoue K. Type 2 proatlantal intersegmental artery associated with persistent trigeminal artery diagnosed by MR angiography. Surg Radiol Anat. 2012;34:773–6.
21. Reynolds Jr AF, Stovring J, Turner PT. Persistent otic artery. Surg Neurol. 1980;13:115–7.
22. Patel AB, Gandhi CD, Bederson JB. Angiographic documentation of a persistent otic artery. AJNR Am J Neuroradiol. 2003;24:124–6.
23. Bhattacharya JJ, Lamin S, Thammaroj J. Otic or mythic? AJNR Am J Neuroradiol. 2004;25:160–2.
24. Croft HJ. Persistent otic artery. AJNR Am J Neuroradiol. 2004;25:162.
25. Tubbs RS, Mortazavi MM, Denardo AJ, Cohen-Gadol AA. Persistence of the otic artery with neurological sequelae: case report. Surg Radiol Anat. 2012;34:191–3.

Variations in the Intracranial Venous System

40

The intention of this chapter is to separate variations of the *dural venous sinuses* from variations of the *deep* and *superficial cerebral veins*, but this distinction can be difficult in some instances because of the close proximity of these two intracranial venous systems in some locations (*e.g.*, the sphenoparietal sinus and superficial middle cerebral vein). It is important to keep in mind that the appearance of the deep and superficial cerebral veins and the dural venous sinuses can vary much more widely than the appearance of the arteries. Therefore, a brief synopsis of the intracranial venous anatomy is provided in the following paragraphs [1–37].

The *dural sinuses* represent venous channels lying between the two layers of *dura mater*. They are composed of two layers: an outer periosteal layer and an inner meningeal layer. These sinuses eventually largely drain into the *internal jugular veins* (IJVs) in the absence of occlusions, but there can be extensive collateral flow between deep and superficial venous systems and the dural sinuses. The larger dural venous sinuses include the *superior sagittal sinus*, the *transverse sinuses*, the *straight sinus*, and the *sigmoid sinuses*. Smaller dural sinuses include the *inferior sagittal sinus*, the *petrosal sinuses* (superior and inferior), the *basilar plexus*, the *cavernous and intercavernous sinuses*, the *occipital sinus* (if present), and other rarer variants (*e.g.*, a persistent falcine sinus). The *sphenoparietal sinus* is another dural sinus that variably occurs and varies in size, usually related to the presence or absence or size of the adjacent superficial and deep draining veins. *Hypoplasia of the transverse or sigmoid sinuses* is the most commonly noted and most obvious cerebral venous variation, which may occur in combination with a small ipsilateral cervical IJV. Notably, a lesser-known connection to the dural sinuses is the *lateral tentorial sinus*, which is often called abnormal and in its prominence can simulate disease, such as arteriovenous fistula.

On the other hand, the *cerebral veins* (such as the basal vein of Rosenthal) do not travel between the two layers of dura. They consist of the deep and superficial systems [1–37]. The major structures in the deep venous system are the paired *internal cerebral veins*, the paired *basal veins of Rosenthal*, and the *vein of Galen*. The *deep middle cerebral* and *anterior cerebral veins* (and other lesser-known veins) are often present but not noted on routine imaging; thus one should be cognizant of their locations. The major superficial veins include various *cortical veins*, which are mostly unnamed because of their variable appearance. The *superficial middle cerebral vein*, the *vein of Trolard* (superior anastomotic vein), and the *vein of Labbé* (inferior anastomotic vein) are the most consistently visualized superficial veins. The extreme variations of the cortical/superficial and deep veins are not covered in great detail within this book except to the degree that they can simulate disease, particularly with regards to their asymmetry or prominence. For example, a notable variant is the *anterior pontomesencephalic vein*, in which prominence can simulate disease (especially subarachnoid hemorrhage) in the interpeduncular fossa.

MR venography (MRV) and CT venography (CTV) are excellent methods to evaluate the patency of the dural venous sinuses [1–37]. CTV has a higher spatial resolution and can delineate the adjacent bony anatomy (but utilizes radiation), whereas MRV typically has higher contrast-to-noise and signal-to-noise ratios. 2D time-of-flight MRV (2DTOF MRV) does not typically utilize intravenous contrast and is quite sensitive in evaluating for thrombi or stenoses, but it has a low specificity, particularly in low-flow states, hypoplastic sinuses, and when hemorrhage is present. Contrast-enhanced MRV (CEMRV) may delineate whether potential abnormalities are actual, particularly in the common situation when it is necessary to differentiate between stenosis/thrombosis and unilaterally hypoplastic

A.M. McKinney, *Atlas of Normal Imaging Variations of the Brain, Skull, and Craniocervical Vasculature*,
DOI 10.1007/978-3-319-39790-0_40

transverse-sigmoid sinuses. Hence, this author considers CTV the technique of choice to work up *cerebral venous thrombosis*, whereas MRV is excellent if the intention is screening, used together with routine brain sequences that can detect *cerebral edema, hemorrhage, or venous infarction*. At times, both CTV and MRV are used in combination, particularly in difficult cases. Also, multiplanar reformats (MPRs) can often distinguish variants, whether the modality of acquisition is CTV or MRV. A rudimentary CTV can be acquired during a CT angiogram (CTA) if the CTA is acquired late in the arterial phase (about 30–40 s after injection), although there may be some venous contamination. Even if a formal MRV is not performed, a 3D acquisition of certain sequences such as postcontrast T1WI, susceptibility-weighted imaging (SWI), or spin-echo T2WI may also be helpful as a substitute to visualize venous structures. On MRI, if a venous anomaly is suspected, an MRV can also be obtained many minutes after the initial contrast bolus, as gadolinium-based contrast persists for some time.

The overall organization of this chapter moves from inferior to superior, with the most inferior veins and petrosal sinuses at the skull base described first, and then progressing generally superiorly. However, the progression of the chapter is also generally related to which veins are adjacent to or closely related to each other or drain each other. Thus, the exception to the inferior-to-superior organization is the larger dural venous sinuses (the transverse/sigmoid, superior/inferior sagittal, occipital, and falcine sinuses), which are shown later. Finally, miscellaneous variants involving the dural sinuses, such as *arachnoid granulations, MRI/MRV artifacts*, and *dense dural sinuses* on nonenhanced CT are discussed near the end.

40.1 Hypoglossal Canal and Other Skull Base Emissary Veins

The *hypoglossal canal* may transit *emissary veins* from the cranial cavity and dura (such as from the basilar venous plexus) to the *internal jugular vein* (IJV, usually from the sigmoid sinus), or less commonly to the *vertebral venous plexus* (VVP). Typically, the IJV is present ipsilaterally, and the presence of emissary veins within the hypoglossal canal does not seem directly related to the size of the IJV. These can be problematic, in that a prominent, focally enlarged vein can simulate a *mass* such as a schwannoma or meningioma, and a prominent plexus can simulate the network of a *dural arteriovenous fistula* (DAVF) or an *arteriovenous malformation* (AVM). These veins can be distinguished from a mass by their connection to the IJV or to the sigmoid sinuses, and they can be distinguished from a DAVF or AVM by the lack of corresponding enlarged arteries or veins, along with the lack of a nidus, although catheter angiography may be necessary to exclude a DAVF in some rare and difficult cases. Variably present and variably sized emissary veins can also be noted passing through the condylar canals, foramen ovale, foramen rotundum, foramen of Vesalius, or parietal foramina, to name a few. The hypoglossal canal is shown in this chapter because of its propensity to appear as an abnormal mass or vasculature; other variants are discussed further elsewhere in this book; emissary veins can pass through any of the variably present foraminal variants. Notably, contrast enhancement within the hypoglossal canal is often not related to a particular, single emissary vein (although it can be); most often it relates to the presence of a normally prominent perineural plexus [1–10] (Figs. 40.1, 40.2, 40.3, 40.4, and 40.5).

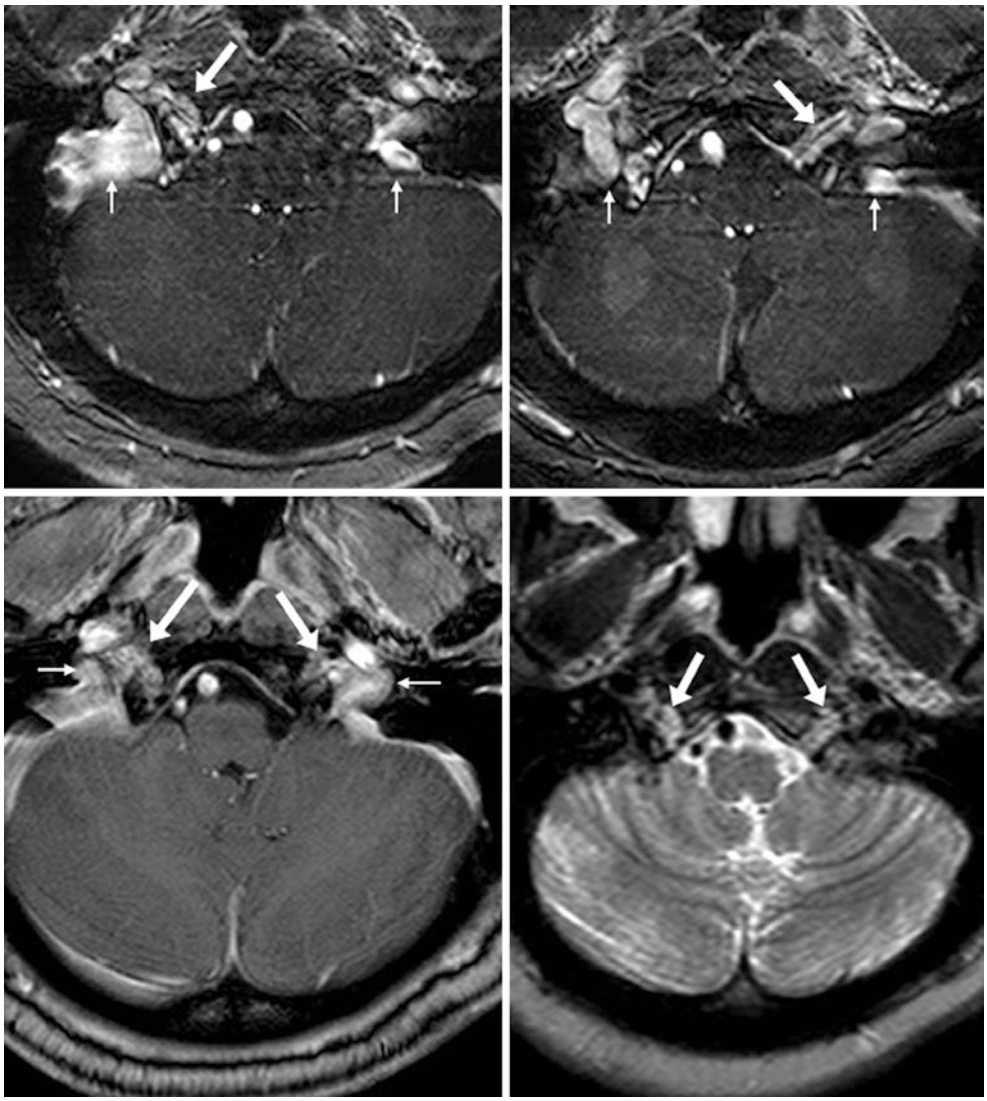

Fig. 40.1 *Top row*: 63-year-old with enhancement within the hypoglossal canals (*large arrows*) on postcontrast T1WI, being anterior to the internal jugular veins (IJVs) within the jugular foramina (*thin arrows*). *Bottom row*: The enhancement is unchanged from 3 years prior on T1WI (*left*). Both the left IJV and sigmoid sinus are small. Note bright signal in both canals on T2WI (*bottom right*)

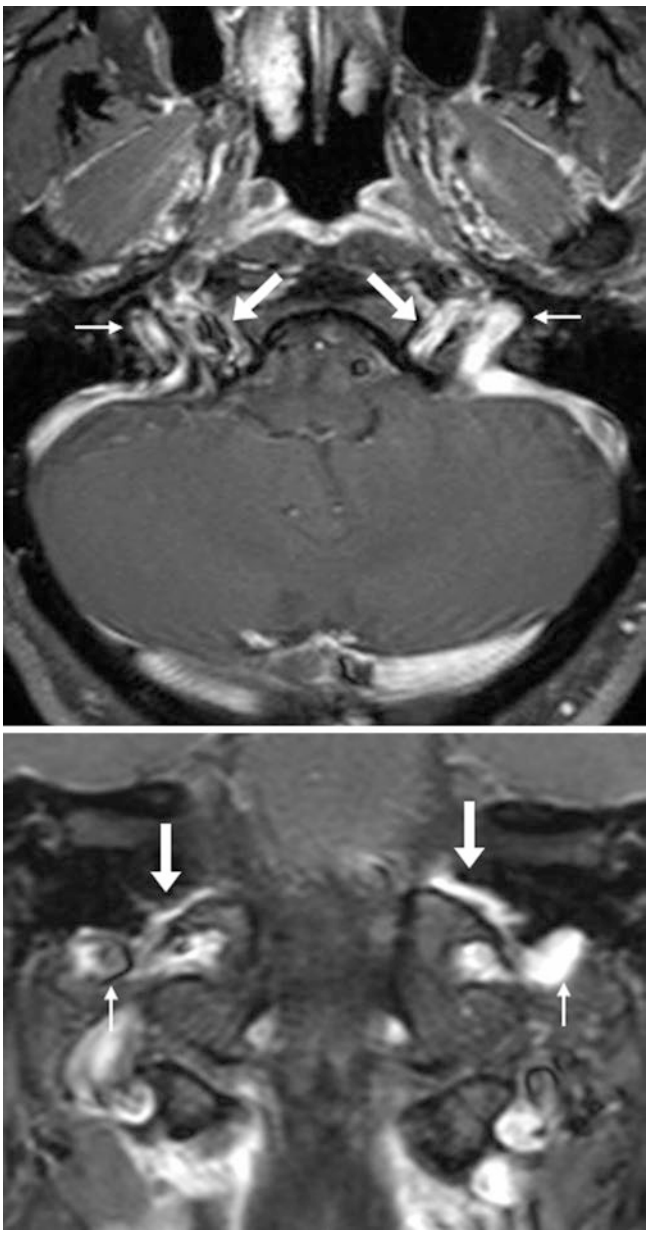

Fig. 40.2 60-year-old with bilateral enhancement within the hypoglossal canals (*large arrows*), anterior to the IJVs within the jugular foramina (*thin arrows*), on postcontrast axial (*top*) and coronal (*bottom*) T1WIs. Also, note that the right sigmoid sinus and IJV are small

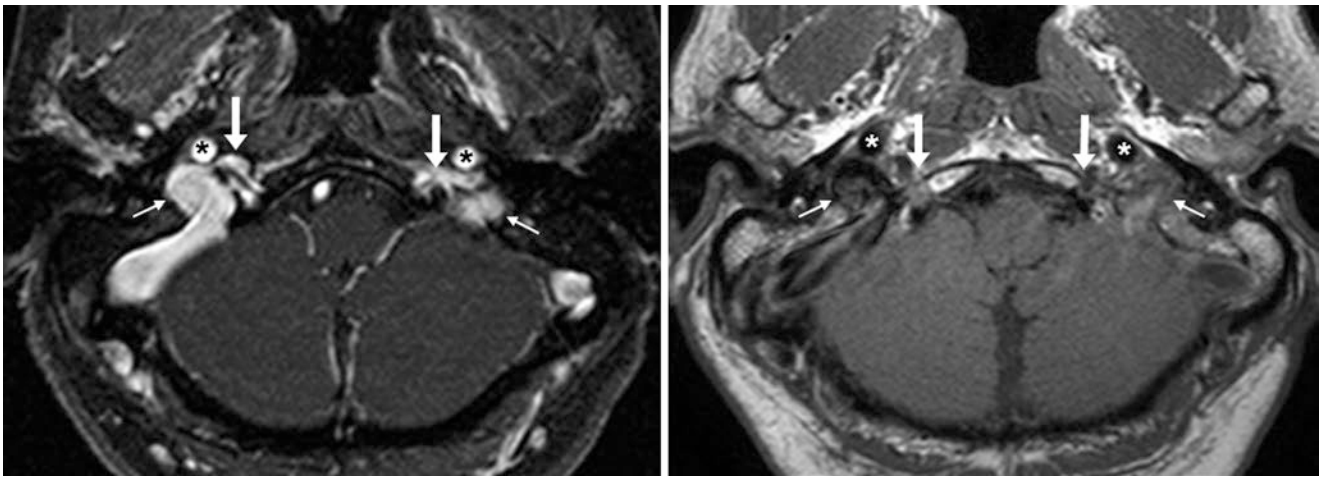

Fig. 40.3 71-year-old with mildly prominent enhancement present bilaterally within the hypoglossal foramina (*large arrows*) on a thin (2 mm) postcontrast axial T1WI (*left*). The IJVs (*thin arrows*) and the internal carotid arteries (ICAs) (*asterisks*) are delineated. A noncontrast T1WI (*right*) shows heterogeneous signal in the venous structures owing to varying or slow flow rates

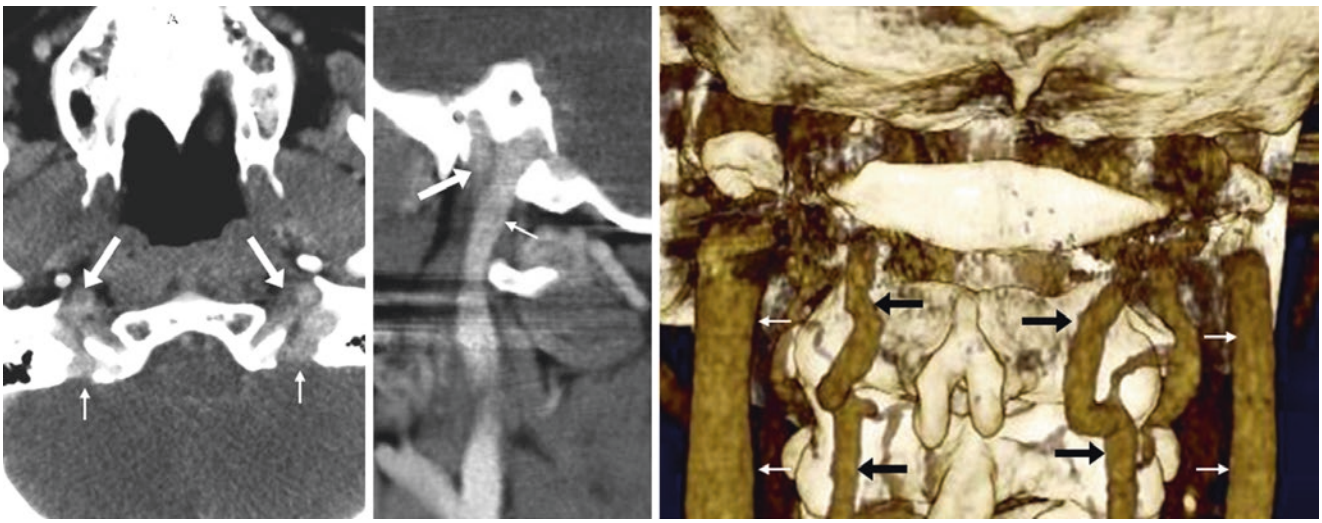

Fig. 40.4 53-year-old with venous phase contrast enhancement bilaterally within the hypoglossal foramina (*arrows*) on postcontrast axial CTV source images (*left*), confirmed to be anterior to the IJVs within the jugular foramina (*thin arrows*) on sagittal MPRs (*middle*). A 3D VR posterior view (*right*) demonstrates that these hypoglossal emissary veins continue caudally as prominent posterior vertebral veins (*black arrows*) within the deep cervical musculature posteriorly

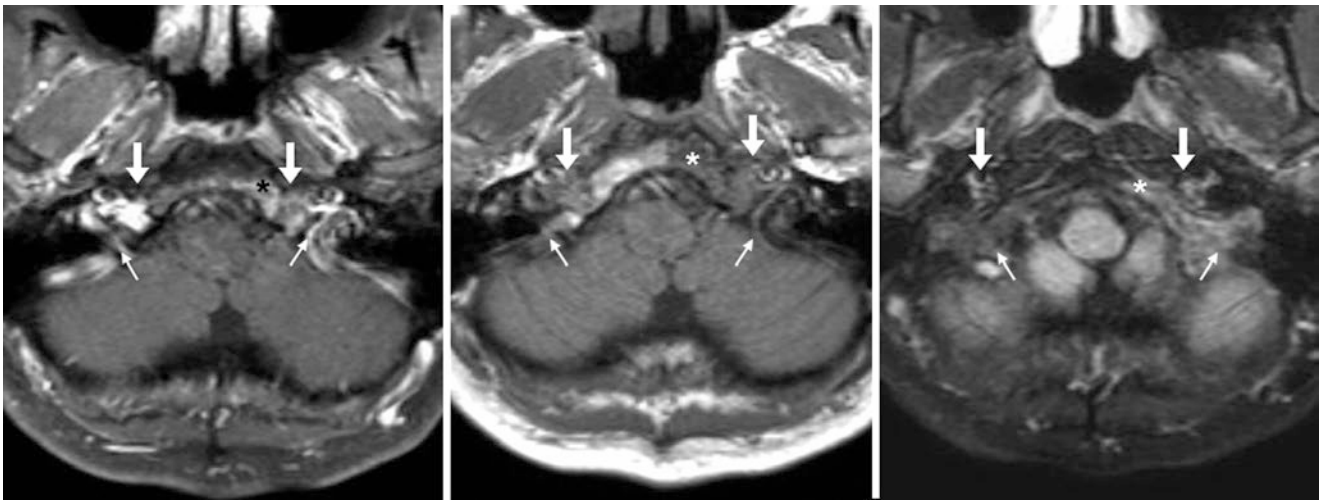

Fig. 40.5 Comparison case of tumor involving the hypoglossal canal. A 62-year-old with lung cancer had enhancement noted on a postcontrast T1WI (*arrows*, *left*) within the right hypoglossal plexus, with heterogeneous IJV signal (*thin arrows bilaterally*) from slow or nonlaminar flow. On a precontrast T1WI (*middle*), there is loss of the normal T1-bright fatty signal within the left hypoglossal foramen and within the clival marrow (*asterisk*). FLAIR MRI with fat saturation (*right*) confirms clival and left hypoglossal foraminal tumor, consistent with metastatic disease

40.2 Asymmetric Prominence of the Internal Jugular Vein and Foramen

Asymmetric prominence of the IJV at the jugular bulb commonly occurs at the skull base on the bottom of brain images. It is one of the most common normal skull base variants to imitate a mass (such as *glomus tumor, schwannoma*, or *metastasis*), particularly on postcontrast T1WI MRI [5–11]. Such asymmetric IJV prominence commonly (although not always) occurs in combination with asymmetry or *hypoplasia of the* contralateral *transverse and sigmoid sinuses*. Additionally, high-riding, aberrant, or "dehiscent" bony jugular foramina adjacent to the middle ear and petrous bone can also simulate masses. There is no good description of the incidence of this asymmetry, as IJV caliber varies significantly between sides and from the skull base down to the chest; even the IJV on the same side can appear to be of various sizes at different levels because of phenomena such as the caliber of draining veins, collateral drainage, venous pulsation throughout the cardiac cycle, and even the respiratory phase! Asymmetry of the jugular bulb or the bony jugular foramen is usually depicted well and confirmed on postcontrast CT or MRI examinations (Figs. 40.6, 40.7, 40.8, 40.9, 40.10, and 40.11).

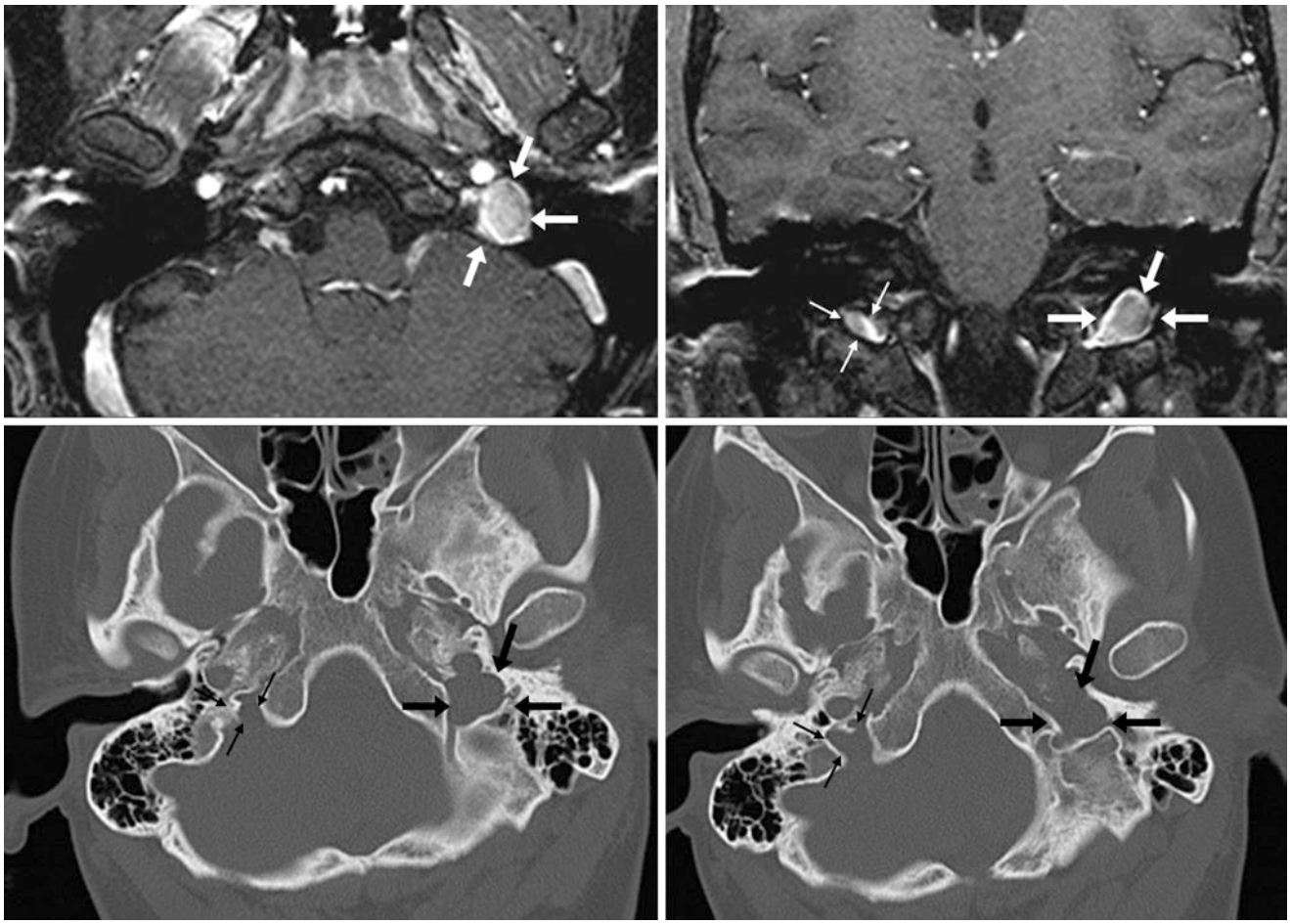

Fig. 40.6 34-year-old with a prominent left jugular bulb/foramen (*outlined by arrows*) simulating a skull base mass with homogeneous enhancement on a postcontrast axial T1WI (*top left*) and coronal T1WI (*top right*). However, the postcontrast T1WIs demonstrate a connection to the sigmoid sinus, indicating that this is the jugular foramen. Axial CT images (*bottom*) depict a prominent left jugular foramen; the right side is smaller (*thin arrows*)

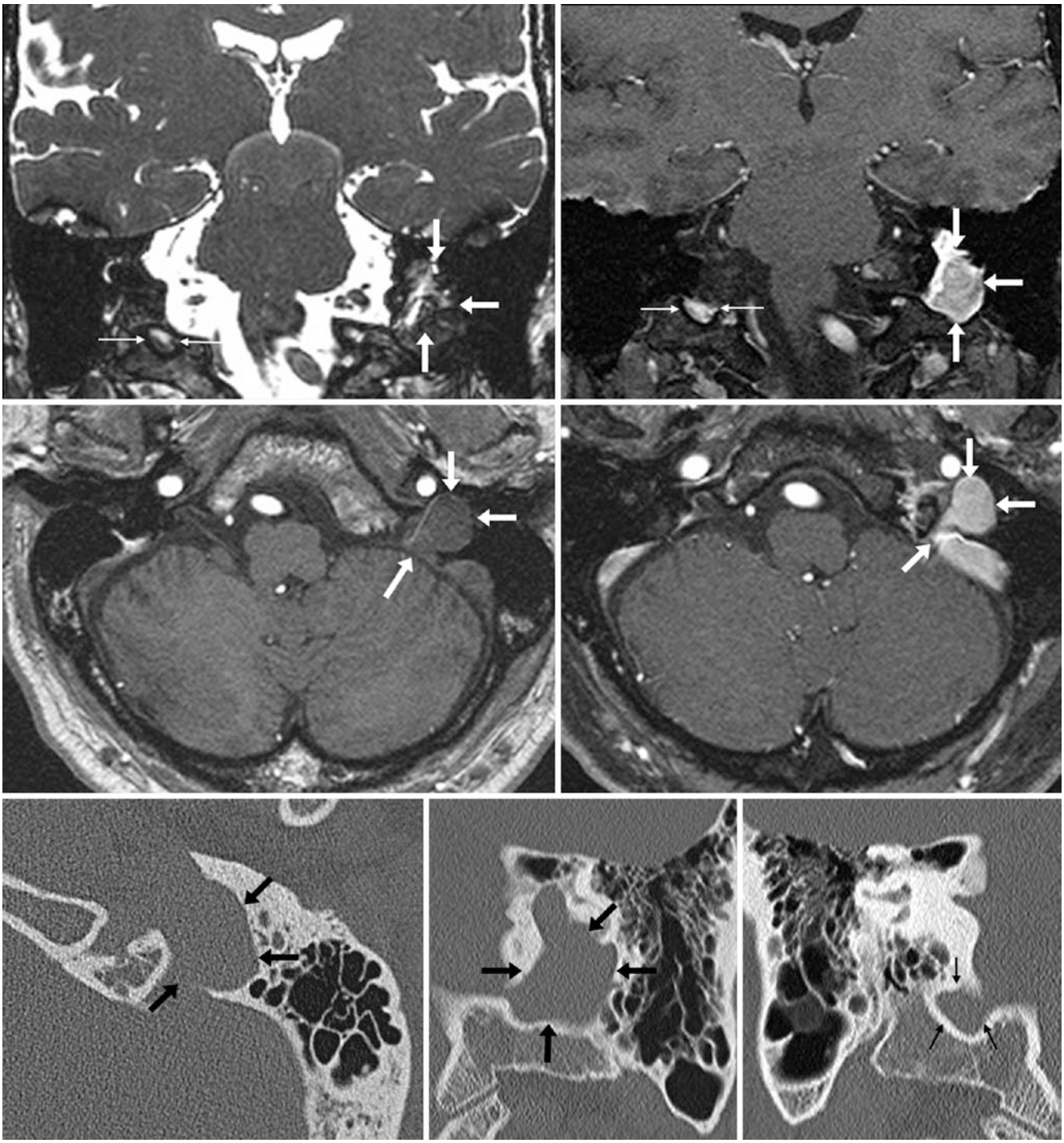

Fig. 40.7 In this 53-year-old, a prominent left jugular foramen (*outlined by arrows*) simulates a skull base mass. *Top row*: There is heterogeneous signal centered on the left jugular bulb/foramen, simulating a skull base mass on coronal T2WI (*left*), with homogeneous enhancement on postcontrast T1WI (*right*). *Middle row:* Axial precontrast (*left*) and postcontrast (*right*) T1WIs depict a connection to the sigmoid sinus. *Bottom row:* Axial (*left*) and coronal (*middle*) CT images depict the prominent bony left jugular foramen. Note the smaller right side (*thin arrows*) on a coronal CT image (*right*)

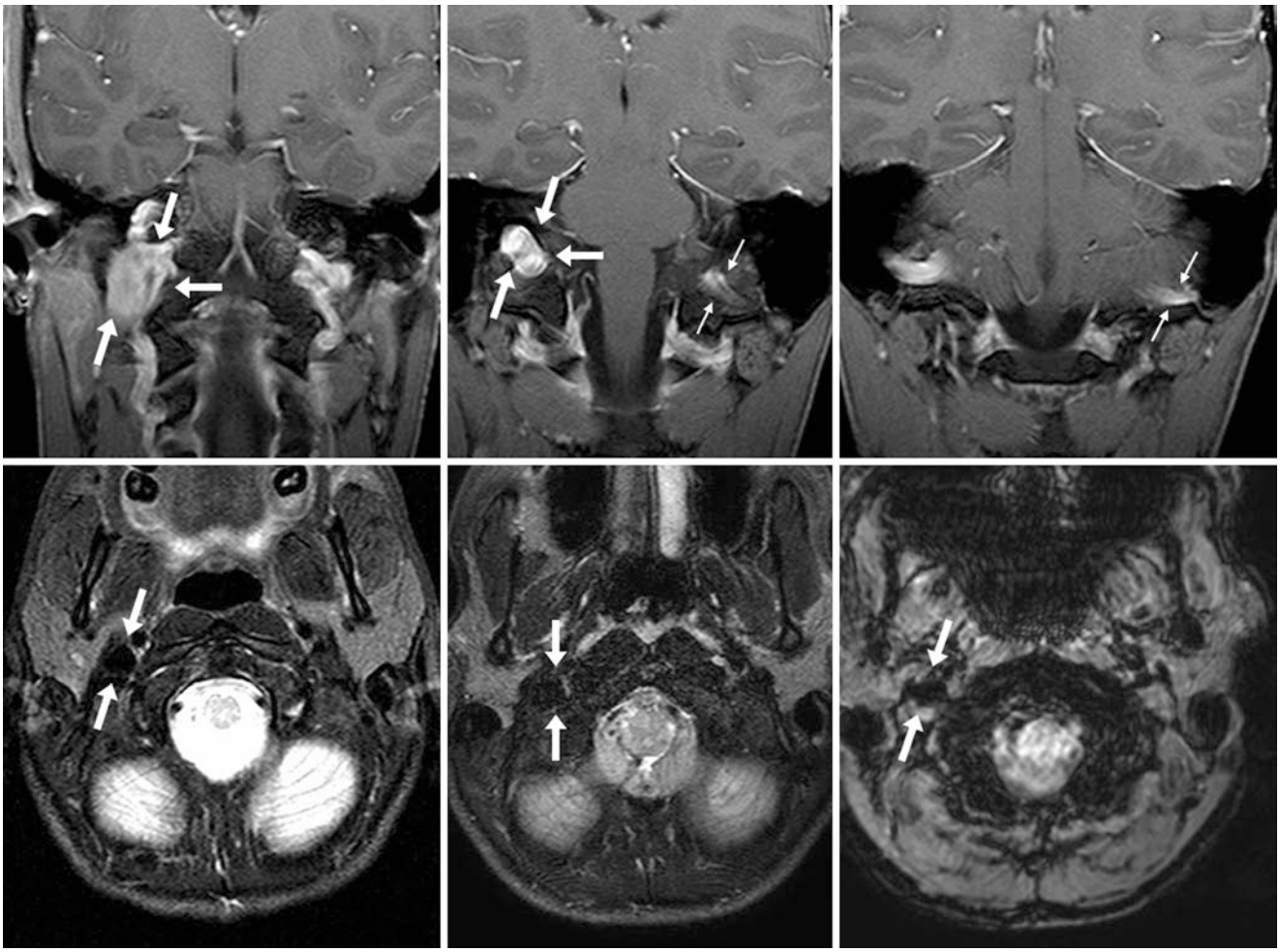

Fig. 40.8 *Top row:* 23-year-old with a prominent right jugular bulb (*outlined by arrows*) on postcontrast coronal T1WIs MRI. *Bottom row:* Axial T2WI (*left*), FLAIR (*middle*), and SWI (*right*) depict right IJV flow voids. Note asymmetry in the size of the dural sinuses, where the right sigmoid sinus is larger than the hypoplastic left sigmoid sinus (*thin arrows*)

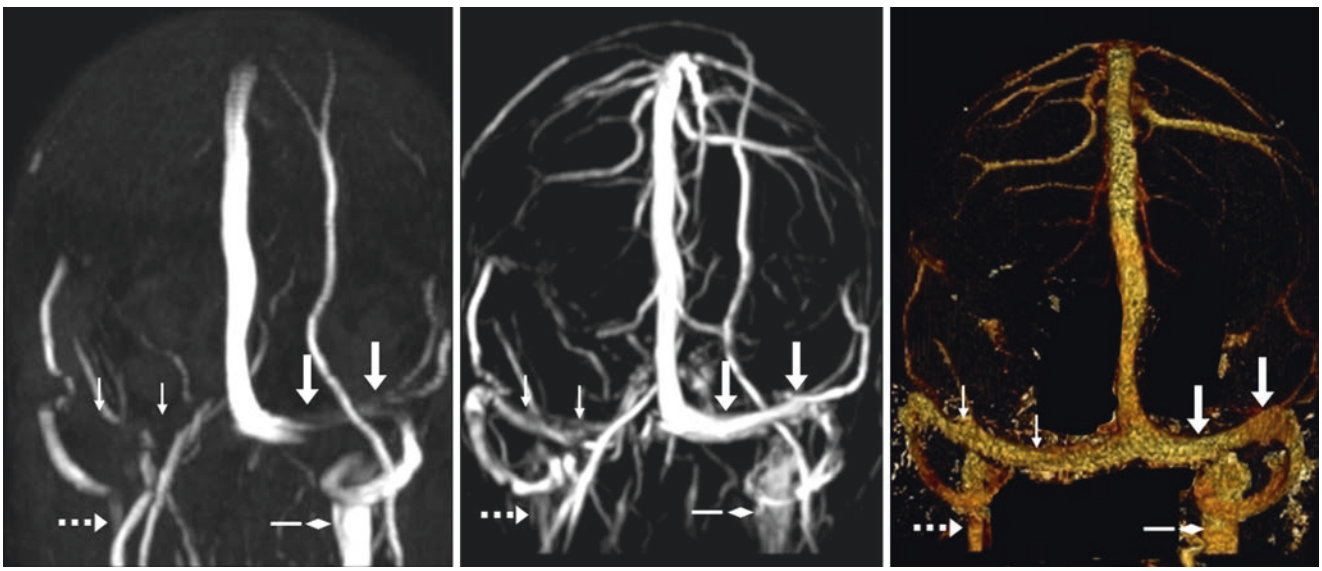

Fig. 40.9 In this 41-year-old, a noncontrast 2DTOF MRV PA view (*left*) fails to visualize the left transverse sinus (*thin arrows*) and IJV; the contralateral transverse sinus (*large arrows*) and IJV are seen. On a CEMRV PA view (*middle*), the left transverse sinus is shown to actually be patent, also confirmed on a CTV PA view (*right*). The CTV also shows that the upper left IJV (*dotted arrows*) is quite small; the right IJV (*diamond arrows*) is dominant

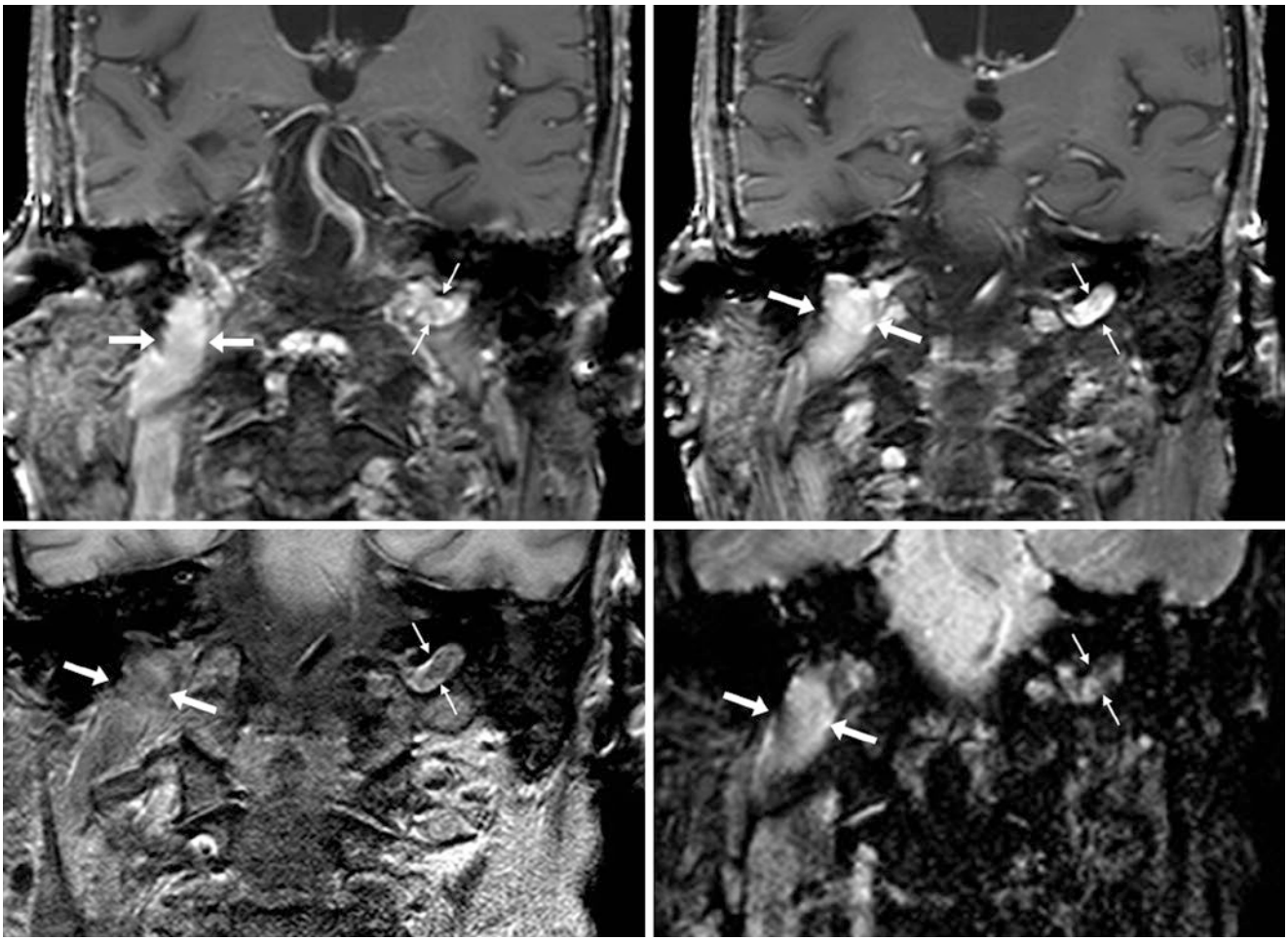

Fig. 40.10 *Top row:* 65-year-old with a prominent right jugular bulb (*outlined by arrows*) on postcontrast coronal T1WIs. *Bottom row:* The right IJV is depicted on a noncontrast T1WI (*left*) and on a coronal T2* image (*right*); note bright signal due to patent flow within the right IJV on the T2*WI. Also note the smaller contralateral left IJV (*thin arrows*)

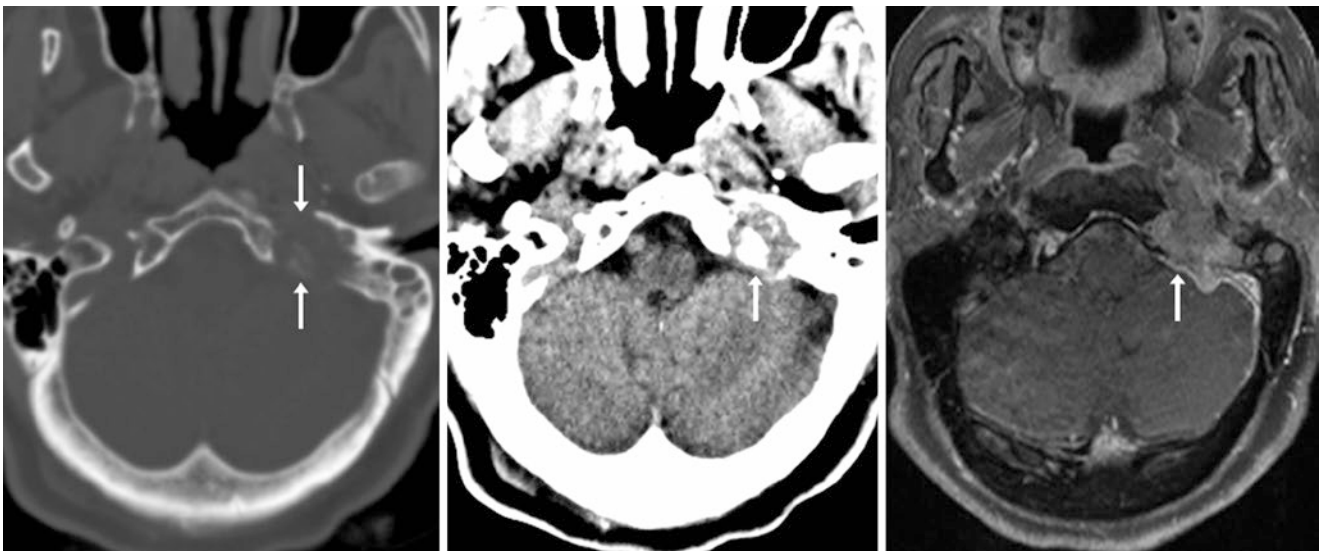

Fig. 40.11 Comparison case of glomus tumor. On NECT bone window (*left*) and soft tissue window (*middle*), a glomus tumor enlarges the left jugular foramen, eroding the surrounding temporal and occipital bones. On T1WI MRI (*right*), it has an irregular border and enhances (*arrows*)

40.3 Basilar Plexus and Petrosal Sinuses Along the Posterior Sphenoid/Clivus

The *basilar plexus* is variably located dorsal or posterior to the clivus at its superior aspect, and is dorsal to the tectorial membrane (the cephalad continuation of the posterior longitudinal ligaments in the cervical region) at its inferior aspect [2–7]. It is usually about 1 mm in thickness, but its thickness can vary. Part of this variation may be due to changes with respiratory inspiration or expiration from many varied connections with the venous system inferiorly. It is important to note that the basilar plexus nearly always communicates directly with the *inferior petrosal sinuses* laterally, and to a lesser degree, it also communicates with the *superior petrosal sinuses*. The superior petrosal sinus typically drains into the junction of the *transverse and sigmoid sinuses*, whereas the inferior petrosal sinus usually drains into the superior bulb of the IJV, just below the inferior portion of the sigmoid sinus at the skull base. Hence, the examples shown include prominence of the basilar plexus and/or the petrosal sinuses, which can simulate a postsphenoidal or postclival/retroclival lesion such as *meningioma* or *lymphoma*, involving the dura (Figs. 40.12, 40.13, 40.14, 40.15, and 40.16).

The *intercavernous sinuses* may also communicate with these venous systems; they are not mentioned further here because after contrast administration the intercavernous sinuses often enhance along with the pituitary and may be indistinguishable from the pituitary gland.

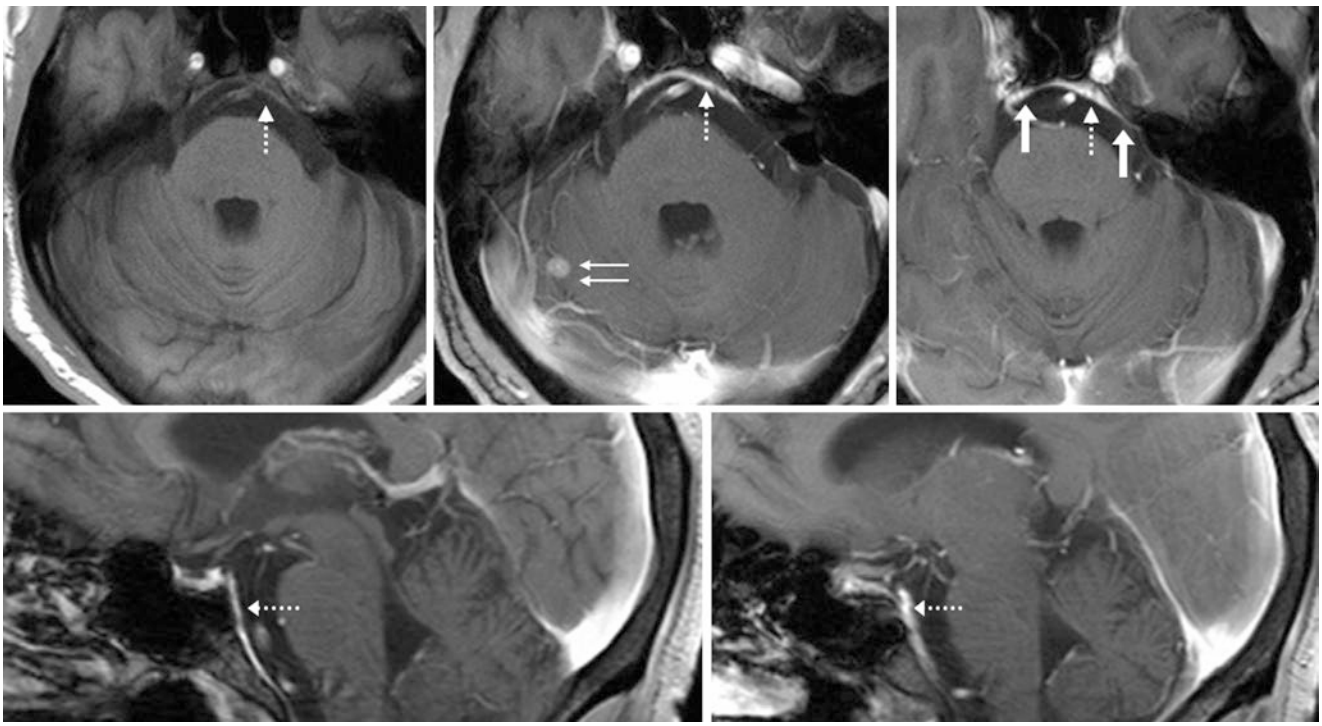

Fig. 40.12 In this 55-year-old, isointense postclival tissue (*dotted arrows*) on noncontrast T1WI (*top left*) enhances on postcontrast T1WIs (*top middle*, *top right*), simulating a dural lesion. This is the basilar plexus, which follows the clivus inferiorly on sagittal T1WIs (*bottom row*). Drainage from that plexus also extends laterally to the transverse-sigmoid junction (*solid arrows*), via the superior petrosal sinus. Note a right cerebellar lung cancer metastasis (*double arrows*, *top middle*)

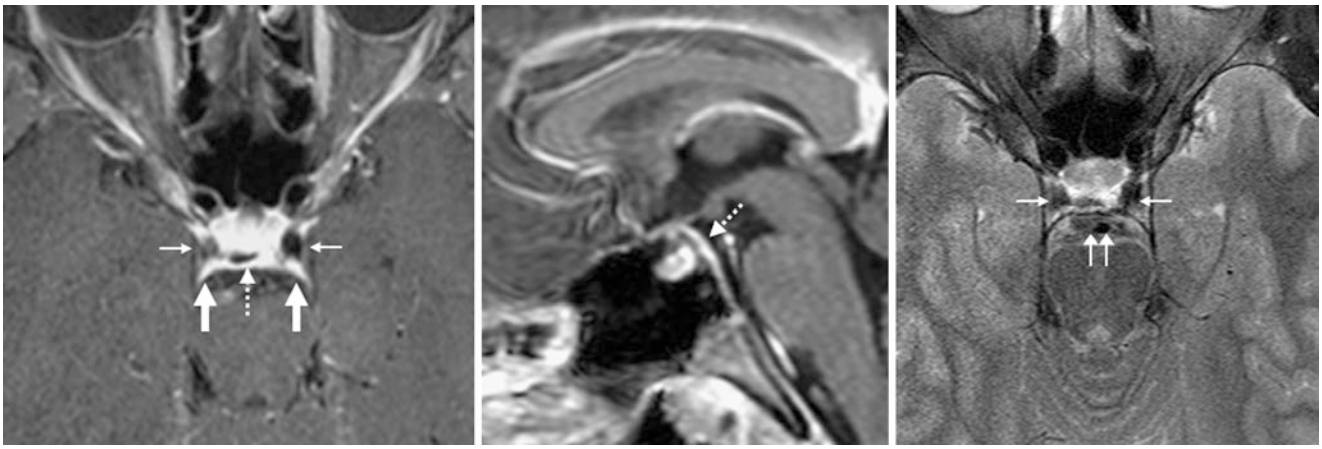

Fig. 40.13 In this 41-year-old, axial (*left*) and sagittal (*middle*) postcontrast T1WIs depict enhancing basilar plexus (*dashed arrows*) along the midline posterior aspect of the sphenoid/sella. The superior petrosal sinus (*large arrows*) enhances bilaterally; these plexi appear isointense on T2WI (*right*). Note the cavernous ICAs anteriorly (*thin arrows*). Also, note artifact from flow voids surrounding the basilar artery (*double arrows*, *right*), related to prominent CSF flow

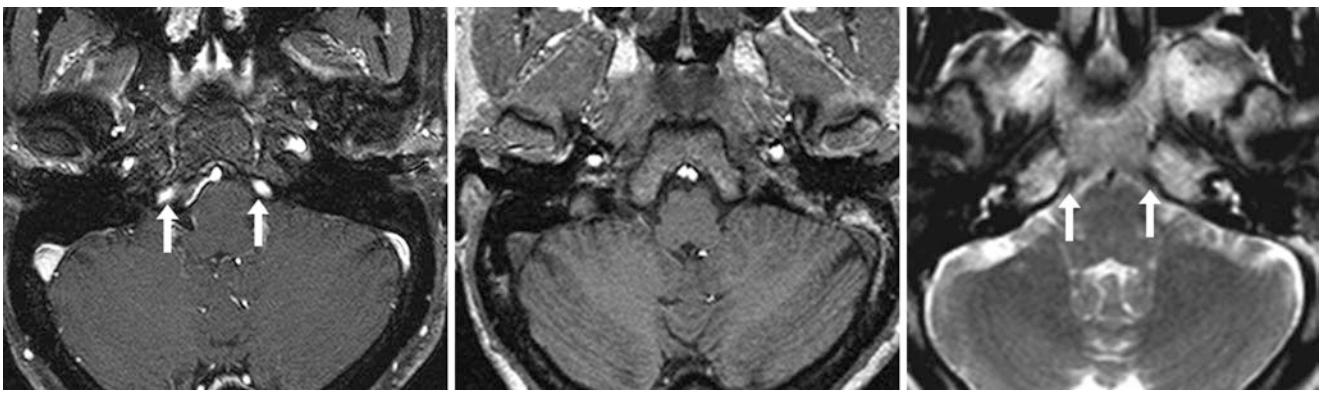

Fig. 40.14 33-year-old with enhancing vessels (*arrows*) bilaterally along the posterolateral aspect of the sphenoid and clivus on a postcontrast T1WI (*left*). These represent inferior petrosal sinuses that drain inferiorly into the jugular-sigmoid junctions. They are invisible on a noncontrast T1WI (*middle*), with subtle flow voids on a T2WI (*right*)

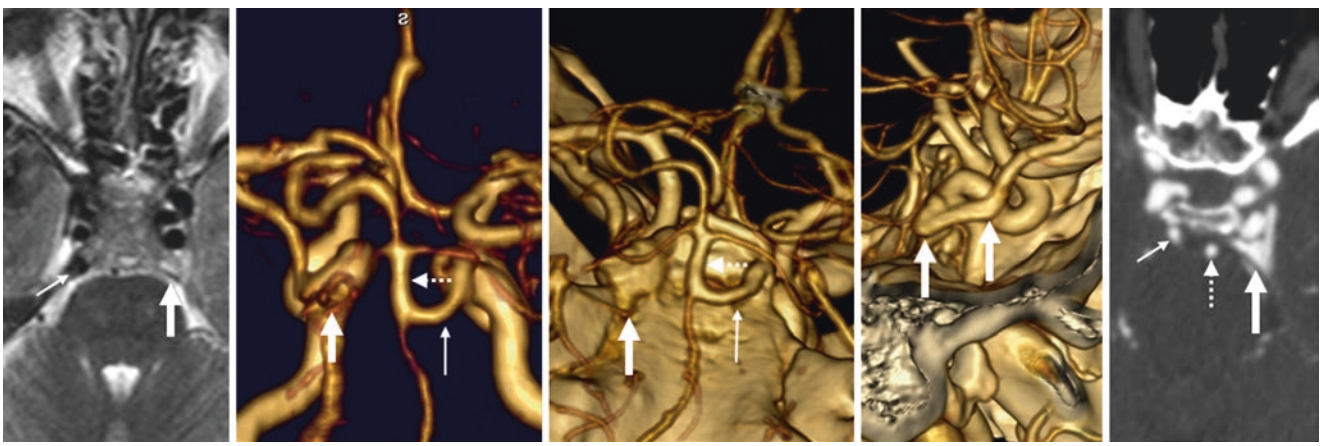

Fig. 40.15 In this 29-year-old, a T2WI (*left*) shows a flow void (*thin arrows*) from a persistent trigeminal artery that connects the cavernous right ICA to the basilar (*dotted arrows*). On PA views from CEMRA (*left middle*) and CTA (*middle*), there is a prominent, left-sided vascular structure (*arrows*) that mimics a left ICA aneurysm but appears separate from the ICA on lateral views (*right middle*). CTA source images (*right*) confirm that this is a petrosal sinus that is visible as the CTA is partially in the venous phase

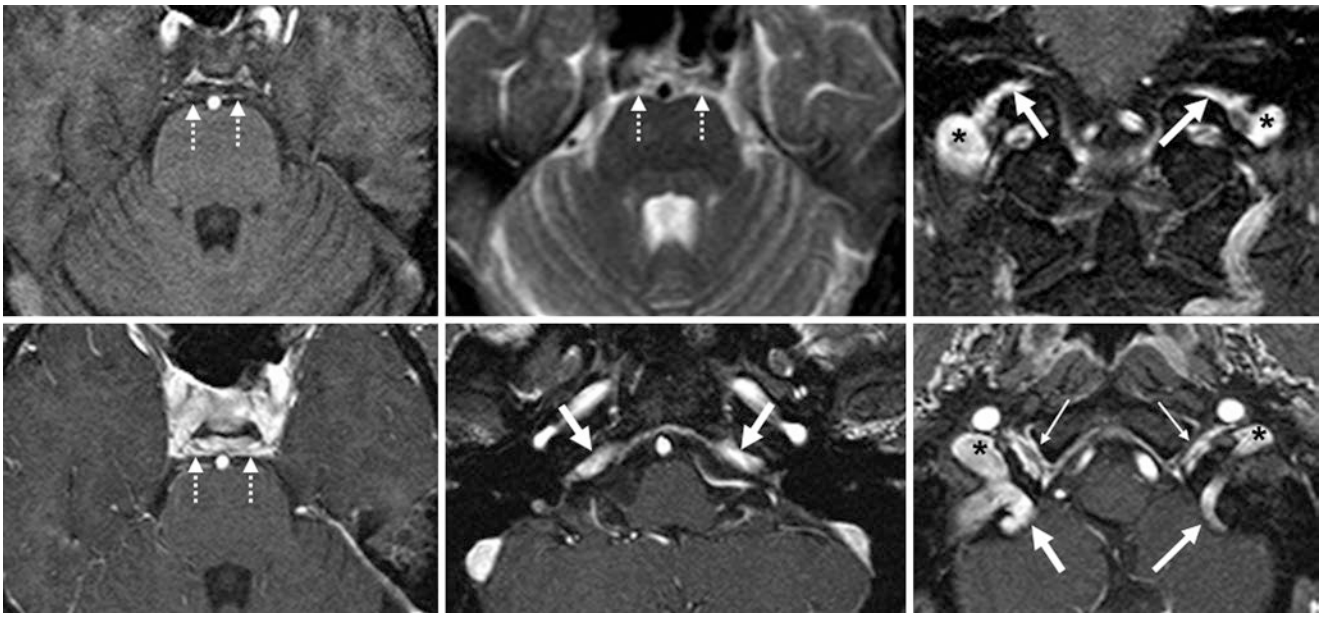

Fig. 40.16 74-year-old with postsphenoidal tissue (*dotted arrows*) on gradient echo T1WI (*top left*) that is bright on T2WI (*top middle*). On postcontrast coronal T1WI (*top right*) and axial T1WI (*bottom row*), it mimics lymphoma or a meningioma. However, if one follows the enhancing structures inferolaterally, they drain into the junctions of the sigmoid sinus and IJV (*asterisks*), indicating that the draining veins are inferior petrosal veins (*large arrows*, *bottom middle and right*), and that the midline enhancing tissue is the basilar plexus. Note venous plexi in both hypoglossal canals (*thin arrows*, *bottom right*)

40.4 Intercavernous Sinuses

Intercavernous sinuses communicate across the midline—thus representing "anastomoses"—and are typically circular, surrounding the pituitary gland and its stalk (hence, the original term used in the 1600s, "circular sinus"). The intercavernous sinus technically consists of two to three separate sinuses named on the basis of their relationship to the hypophysis (pituitary gland): anterior, posterior, and more recently, inferior. In the past (as in *Gray's Anatomy*), these were separated into two: antero-inferior and postero-superior. Recent research has revealed that the *anterior intercavernous sinus* (AIS) is the most likely to be prominent. It is the dominant sinus of the three in most patients, and varies widely in diameter from 0.5 to 5.0 mm. The *posterior intercavernous sinus* (PIS) is far less likely to be dominant (<5% of patients), and varies less in caliber, ranging from 0.7 to 4.0 mm [12–18]. Both the AIS and PIS can be identified to some degree in more than 95% of cadavers, although occasionally either sinus is nonexistent. The *inferior intercavernous sinus* (IIS) is more variably identified between studies. This discrepancy may occur because some authors consider the venous plexus that communicates transversely across the midline at the floor of the sella to be less well defined and perhaps an extension of the AIS, the PIS, or even of the *basilar plexus* (BP), which can also represent a communication between the *cavernous sinuses* dorsal to the clivus, rather than terming it an IIS. Notably, the BP is the most common and the most dominant connection between the cavernous sinuses, being situated along the dorsal aspect of the clivus. It should also be noted that the PIS may be difficult to distinguish from the BP under nonpathologic conditions. Also, as stated previously, the intercavernous sinuses often enhance along with the pituitary after contrast administration, and thus may be indistinguishable from the gland.

The various intercavernous sinuses can be visualized on MRI; this is best done with thin-section imaging (<3 mm). The AIS, PIS, and BP are best visualized in the axial and sagittal planes, but the IIS is best visualized in the coronal plane. These sinuses can simulate disease such as *meningioma, leptomeningeal disease* (carcinomatosis or meningitis), lymphoma, *pituitary lesions*, *pseudotumor* (*i.e.*, Tolosa-Hunt), or *tumor extension* from adjacent, enhancing tumor. The intercavernous sinuses and BP are easily volume-averaged with nearby structures, which is one reason why their appearance can be misleading. One technique for visualizing these sinuses is to utilize subtraction imaging (T1, FLAIR, or even SWI) as the last precontrast sequence and first postcontrast sequence, in order to minimize patient motion and optimize enhancement of adjacent structures (Figs. 40.17, 40.18, 40.19, 40.20, 40.21, 40.22, 40.23, 40.24, 40.25, 40.26, and 40.27).

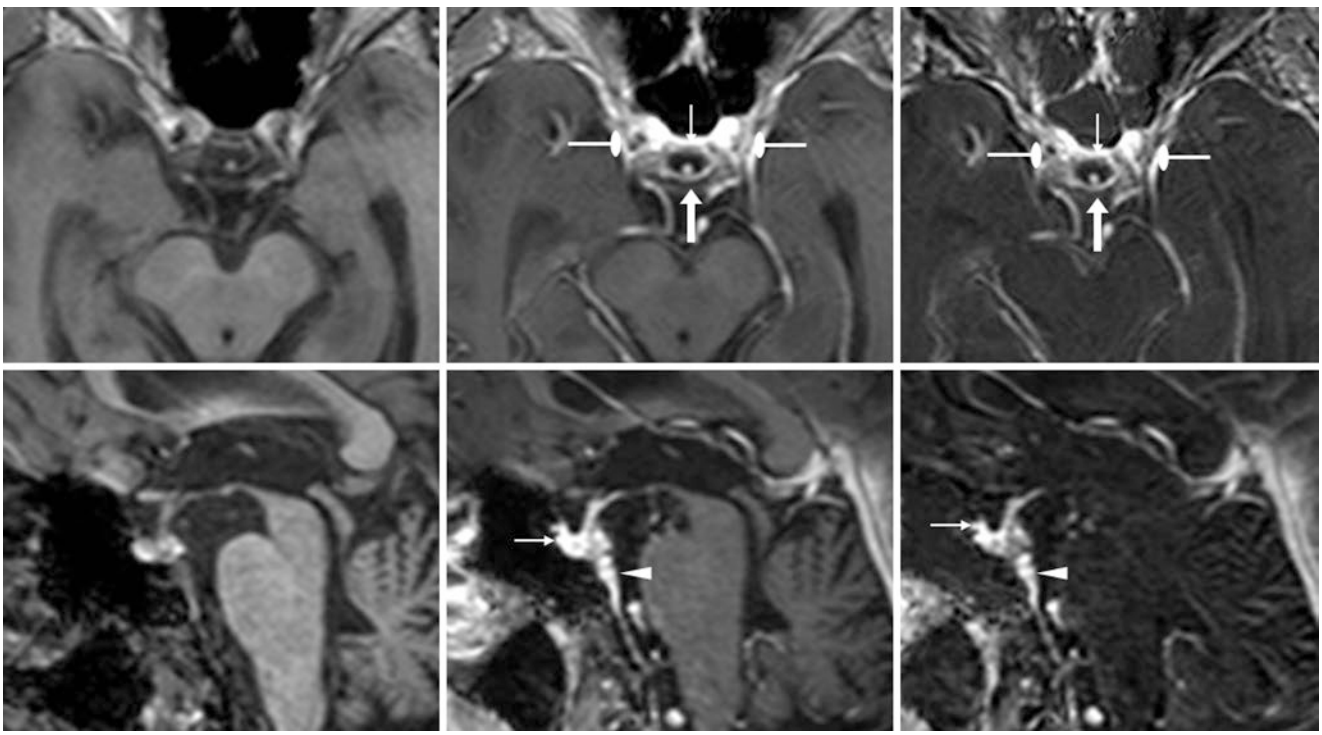

Fig. 40.17 In this 81-year-old, a dominant anterior intercavernous sinus (AIS) enhances (*thin arrows*) on axial precontrast (*top left*) and postcontrast (*top middle*) T1WIs, and on subtracted T1WI (*top right*), as well as on sagittal precontrast (*bottom left*), postcontrast (*bottom middle*), and subtracted T1WIs (*bottom right*). The posterior intercavernous sinus (PIS) enhances (*arrows*), but is small. Also note the enhancement of the basilar plexus (BP, *arrowheads*) and cavernous sinus (*oval-tip arrows*). On sagittal images, enhancing AIS is difficult to separate from the anterior pituitary

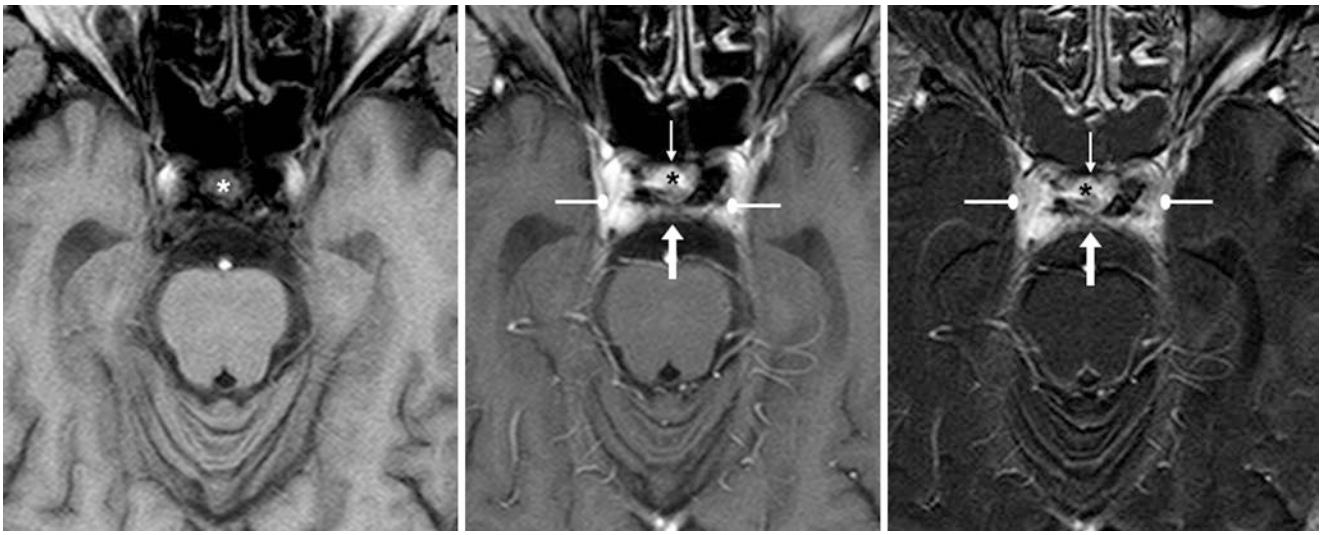

Fig. 40.18 70-year-old with "circular" enhancement of the intercavernous sinuses on axial precontrast (*left*) and postcontrast (*middle*) T1WI, and on subtracted T1WI (*right*). Enhancement of the AIS (*thin arrows*) and PIS (*large arrows*) surrounds the enhancing pituitary (*asterisks*). Note cavernous sinus enhancement (*oval-tip arrows*)

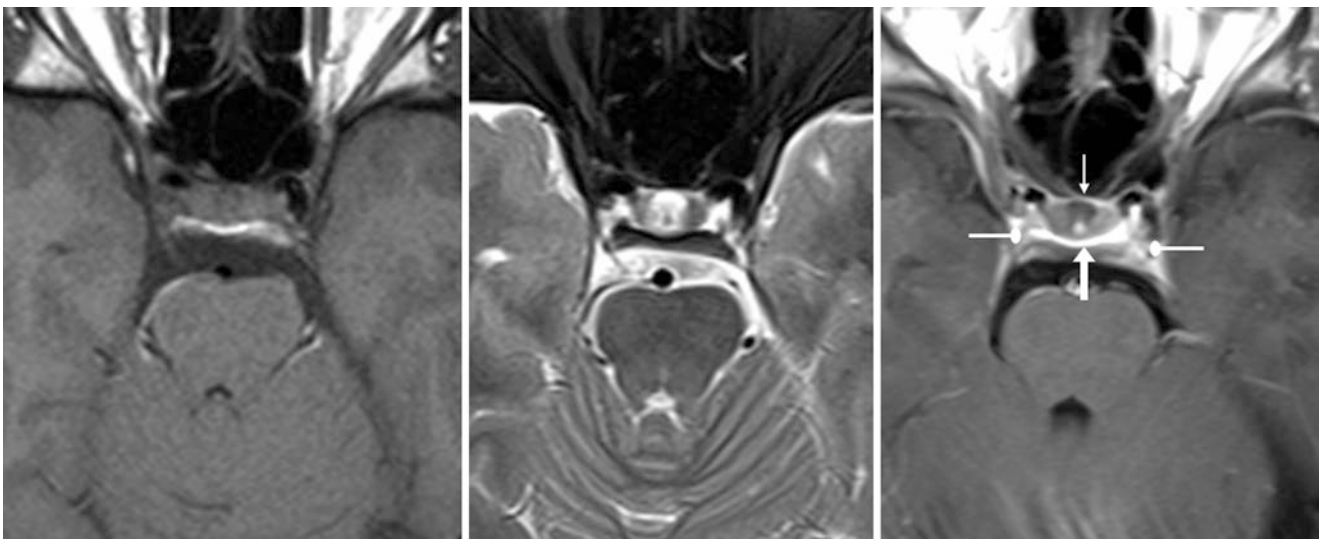

Fig. 40.19 13-year-old with "circular" enhancement of the intercavernous sinuses; axial noncontrast T1WI (*left*), T2WI (*middle*), and postcontrast T1WI (*right*) are provided. There was minimal enhancement of the AIS (*thin arrows*), while the PIS (*large arrows*) was more prominent. Note cavernous sinus enhancement (*oval-tip arrows*)

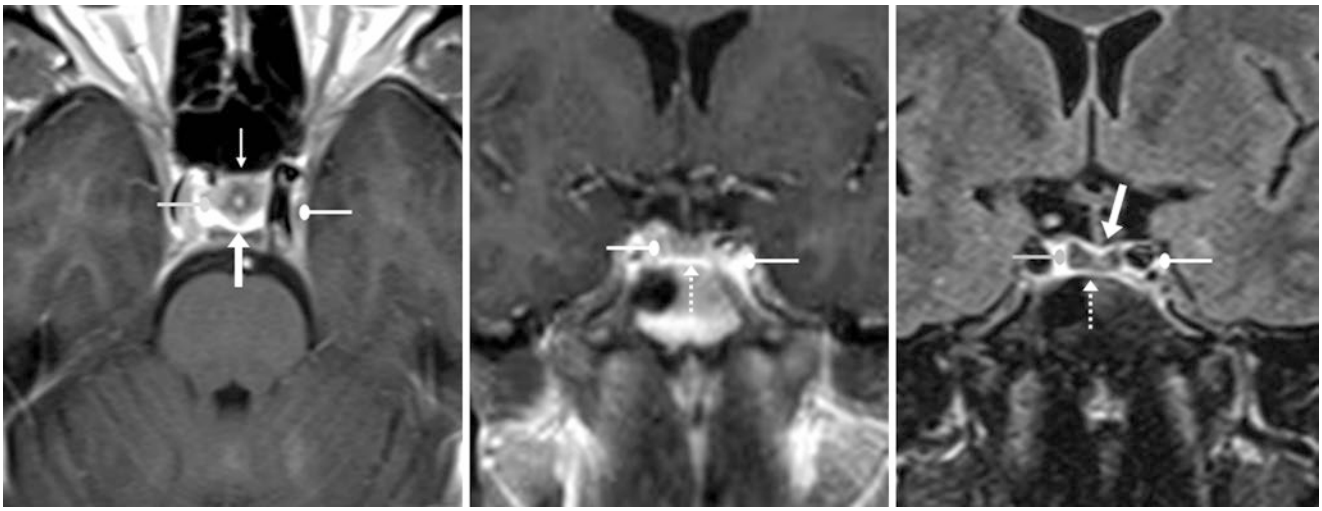

Fig. 40.20 44-year-old with "circular" enhancement of the intercavernous sinuses, having enhancement of the AIS (*thin arrow*), the PIS posteriorly and superiorly (*large arrows*), the inferior intercavernous sinus (IIS) (*dotted arrows*), and the cavernous sinus (*oval-tip arrows*). Provided are postcontrast axial (*left*) and coronal (*middle*) T1WI, and postcontrast coronal FLAIR (*right*)

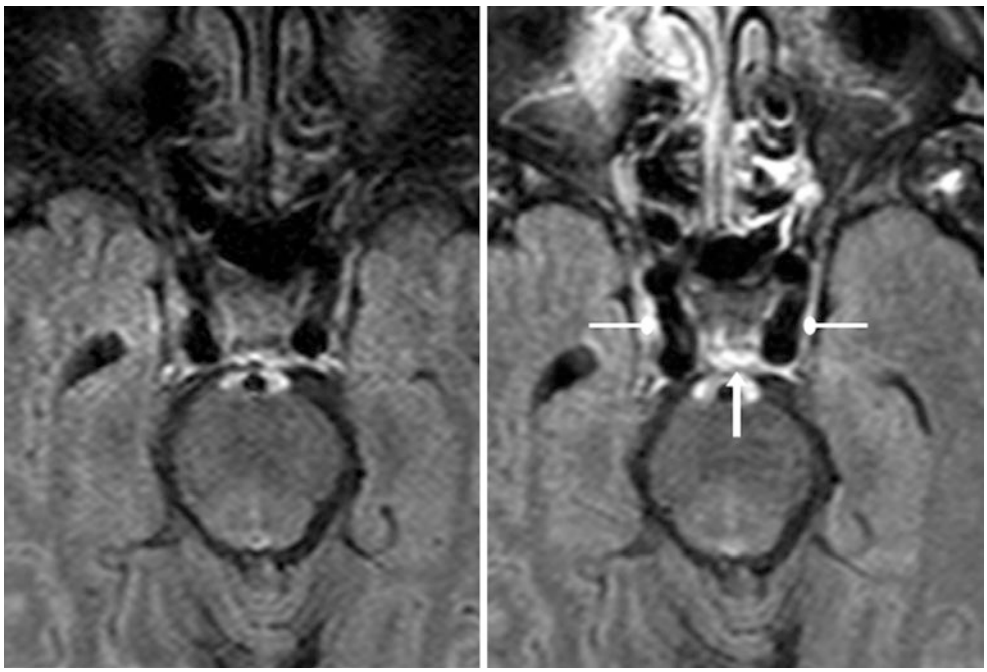

Fig. 40.21 57-year-old with enhancement of the PIS (*arrows*) and cavernous sinus (*oval-tip arrows*), as demonstrated on axial precontrast (*left*) and postcontrast (*right*) FLAIR MRI. The AIS is not visualized

Fig. 40.22 45-year-old with enhancement of the PIS (*arrows*) and cavernous sinus (*oval-tip arrows*) on postcontrast T1WI

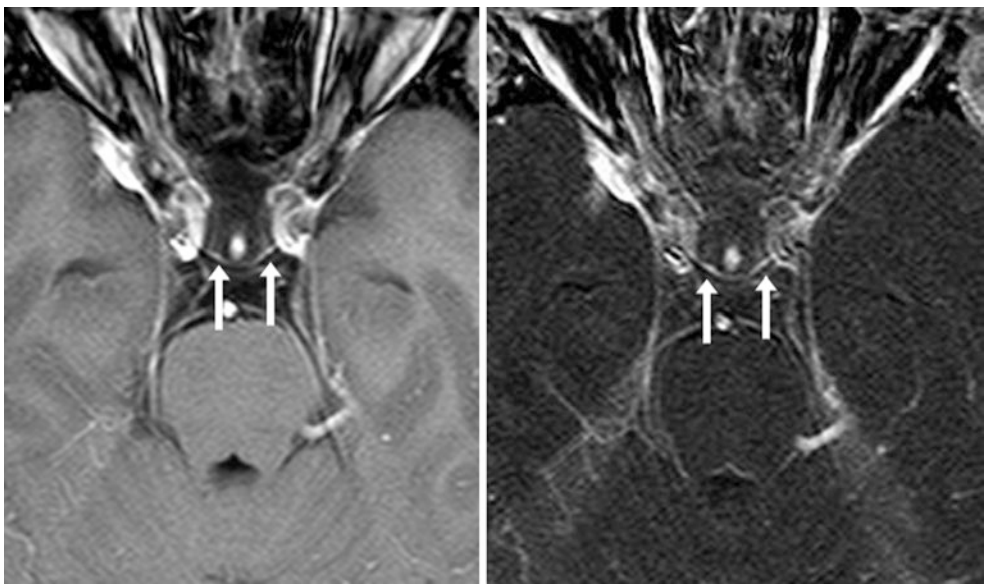

Fig. 40.23 43-year-old with quite thin enhancement of the PIS (*arrows*) on axial postcontrast T1WI (*left*) and subtracted T1WI (*right*). Precontrast images are not shown. The AIS is not visualized

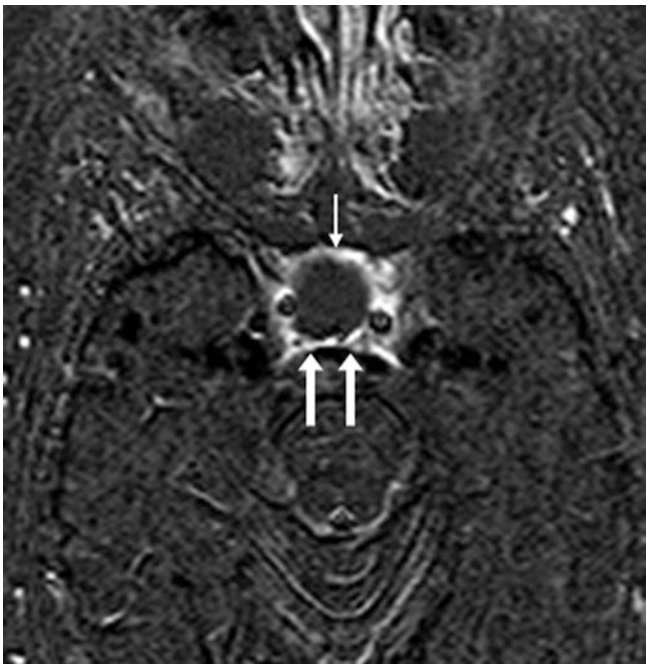

Fig. 40.24 56-year-old with a partially empty sella and a thin PIS (*arrows*) and AIS (*thin arrows*) on an postcontrast axial subtracted T1WI

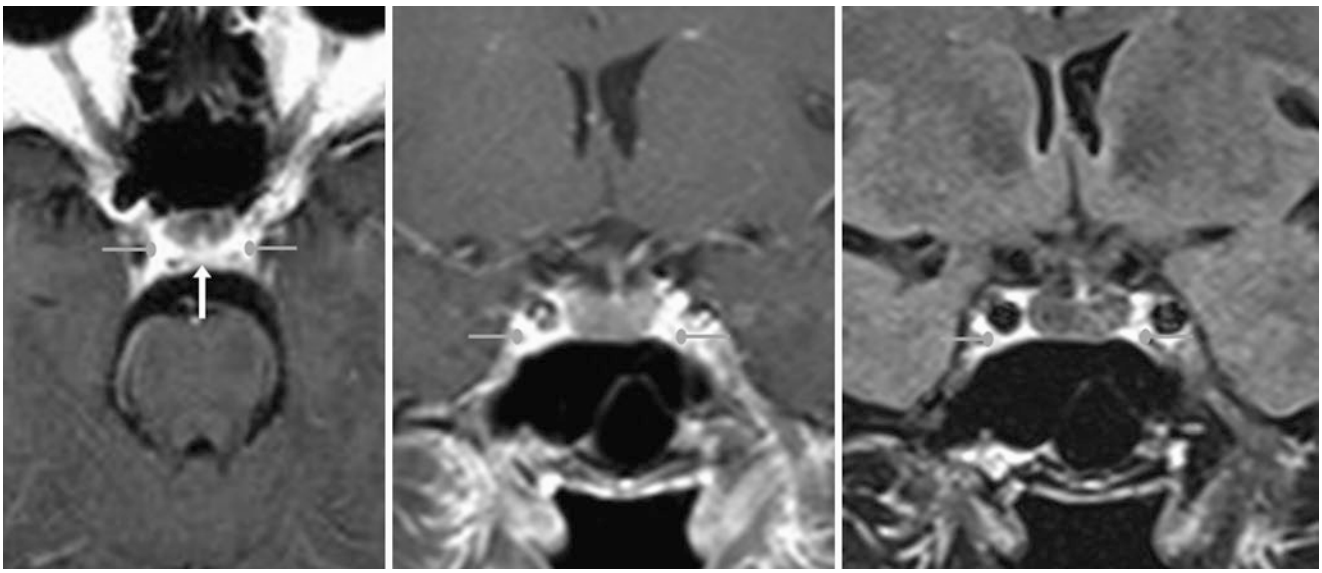

Fig. 40.25 57-year-old with enhancement of the PIS predominantly (*arrow*), without enhancement of the AIS or IIS. Provided are postcontrast axial (*left*) and coronal (*middle*) T1WI, as well as postcontrast coronal FLAIR (*right*). Note cavernous sinus enhancement bilaterally (*gray-colored oval-tip arrows*)

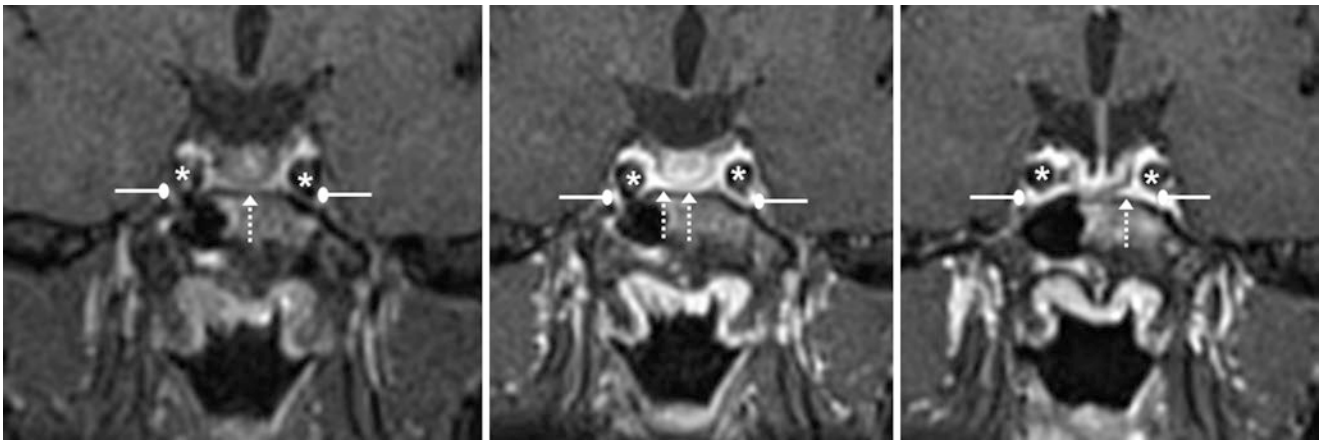

Fig. 40.26 In this 46-year-old, a coronal dynamic postcontrast T1WI obtained at 10 s post-injection (*left*), followed by an image at 50 s (*middle*) and an image more posteriorly (*right*) show progressive enhancement of the IIS (*dotted arrows*) that temporally enhances with the cavernous sinus (*oval-tip arrows*), which surrounds the ICAs (*asterisks*)

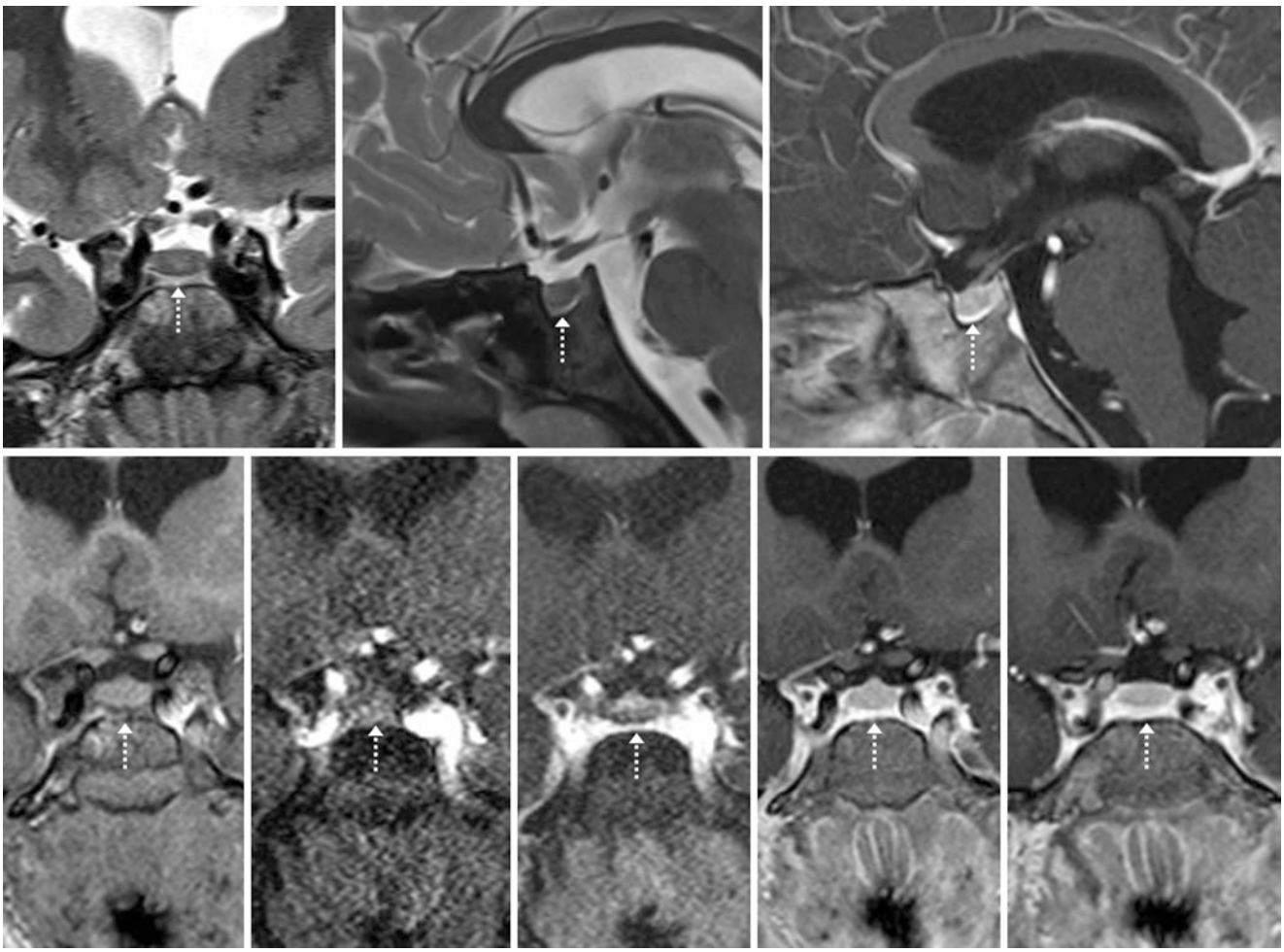

Fig. 40.27 8-year-old with an IIS. *Top row:* Coronal (*left*) and sagittal (*middle*) T2WIs and postcontrast sagittal T1WI (*right*) illustrate a normal, prominent IIS (*dotted arrows*). *Bottom row:* Coronal dynamic enhanced T1WIs show that the IIS progressively enhances from 0 (*left*) to 60 (*right middle*) seconds; a more posterior image is also seen (*right*)

40.5 Anterior Pontomesencephalic Vein

The *anterior pontomesencephalic vein* (APMV) is a vertically oriented vein that is part of a network of mesencephalic and pontine veins that travel on the surface of the brainstem and midbrain. They typically drain into the *basal vein of Rosenthal* posterolaterally [19–23]. The APMV may appear prominent in about 5 % of the population, located just posterior to the *basilar artery* in the interpeduncular fossa/cistern. If a prominent or large APMV is seen on a screening noncontrast head CT and dense vessels (often due to dehydration) are present, the appearance may resemble a tiny amount of *subarachnoid hemorrhage* (SAH) in the interpeduncular fossa. However, a prominent APMV usually can be identified on CTA, CTV, or axial T2WI MRI (on which it is represented by a linear flow void), or on postcontrast T1WI MRI (represented by a linear enhancing vessel) (Figs. 40.28, 40.29, 40.30, 40.31, 40.32, 40.33, and 40.34).

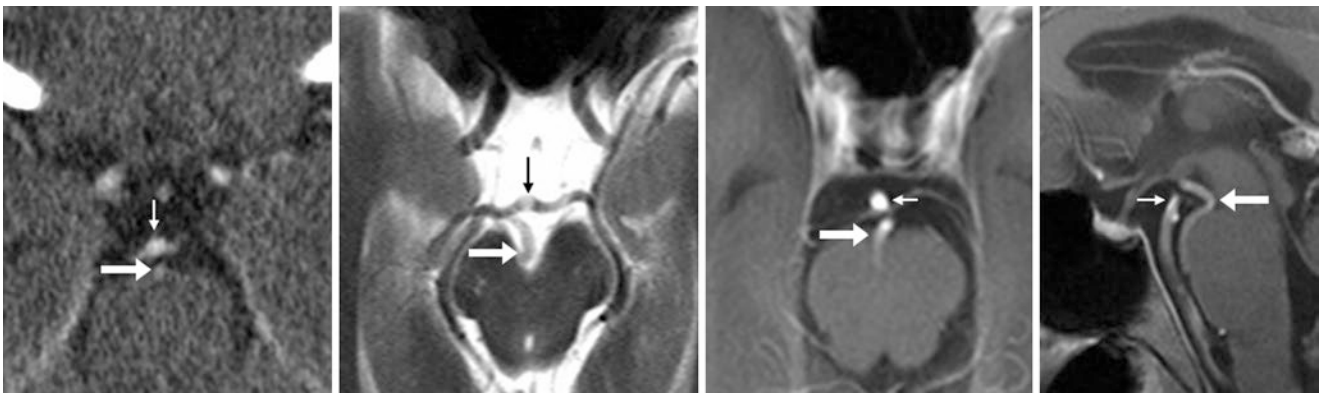

Fig. 40.28 71-year-old with an anterior pontomesencephalic vein (APMV) (*arrows*) within the interpeduncular fossa, just posterior to the basilar (*thin arrows*), on a contrast-enhanced CT (*left*). An MRI with axial T2WI (*left middle*) depicts a corresponding flow void, while postcontrast T1WIs in axial (*right middle*) and sagittal (*right*) planes show that this APMV is closely apposed to the brainstem

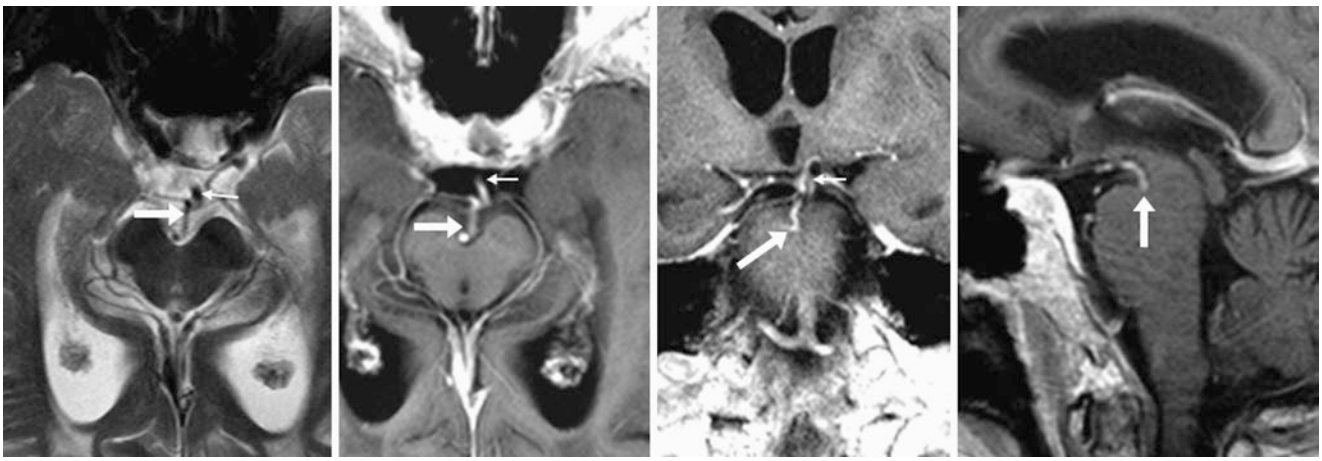

Fig. 40.29 77-year-old with an APMV (*arrows*) within the interpeduncular fossa. The APMV appears inseparable from the basilar artery (*thin arrows*) on axial T2WI MRI (*left*). Postcontrast T1WIs in axial (*left middle*), coronal (*right middle*), and sagittal (*right*) planes depict the APMV within the interpeduncular fossa in various projections

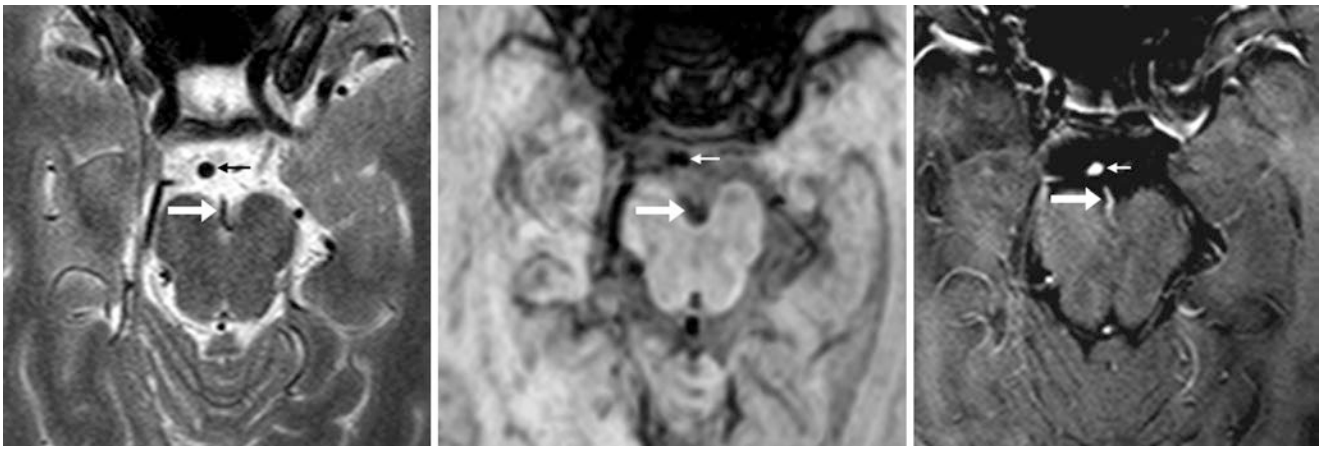

Fig. 40.30 48-year-old with a linear flow void (*arrows*) on an axial T2WI MRI (*left*) within the interpeduncular fossa, situated posterior to the basilar tip (*thin arrows*). On SWI (*middle*), this flow void is only mildly hypointense (perhaps owing to slow flow), but it enhances similar to other veins on postcontrast T1WI MRI (*right*), confirming it to be an APMV

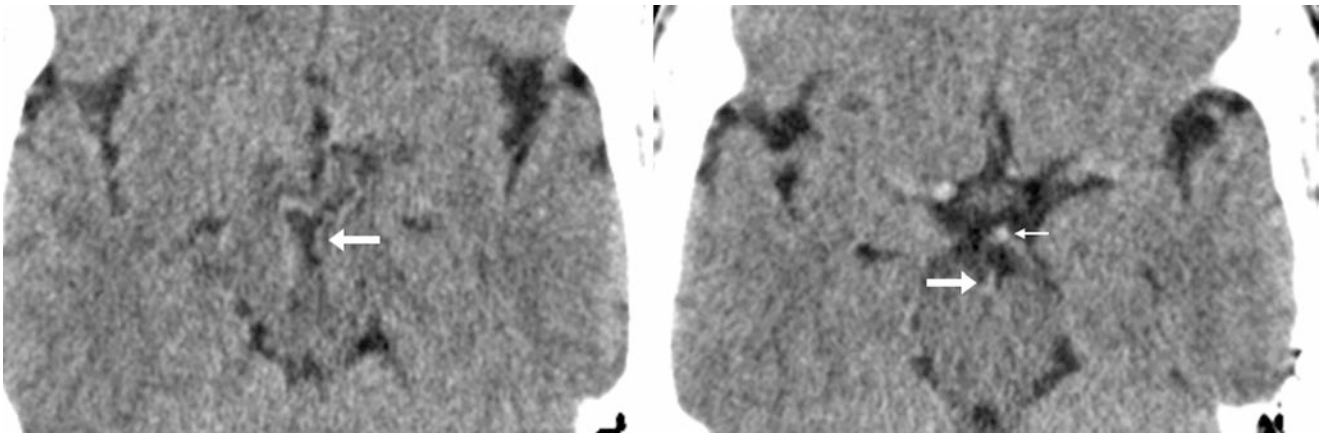

Fig. 40.31 55-year-old with a mild hyperdensity in the interpeduncular fossa on axial nonenhanced CT (*left*), which simulated subarachnoid hemorrhage (SAH) on another image (*right*), but represented the APMV (*arrows*). Note the linear appearance of this structure just posterior to the basilar artery's tip (*thin arrow, right*). No intracranial hemorrhage was found at lumbar puncture

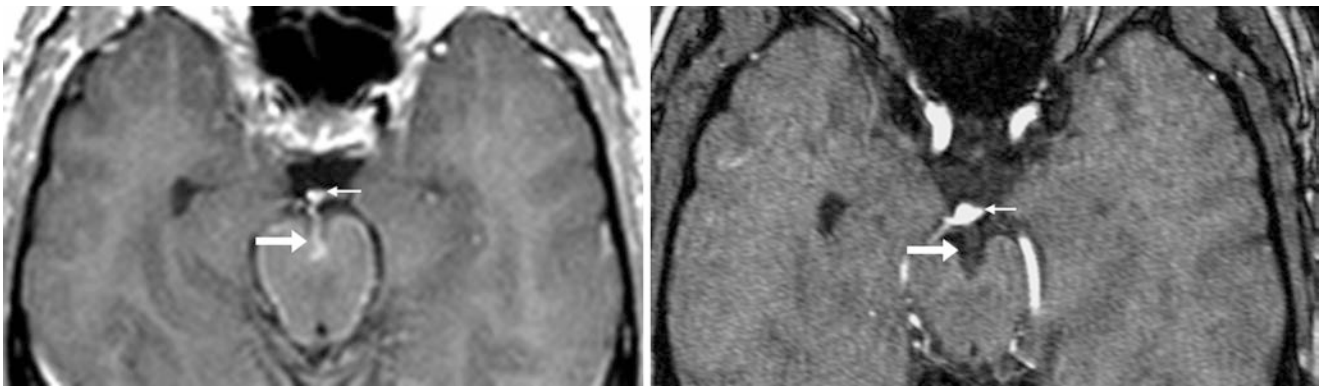

Fig. 40.32 In this 48-year-old, a postcontrast T1WI MRI (*left*) demonstrates the APMV (*large arrows*), situated within the interpeduncular fossa. The APMV appears inseparable from the basilar tip (*thin arrow*). However, on a 3DTOF MRA source image (*right*), flow is not detected within the APMV, related to directionality and the low venous flow rate

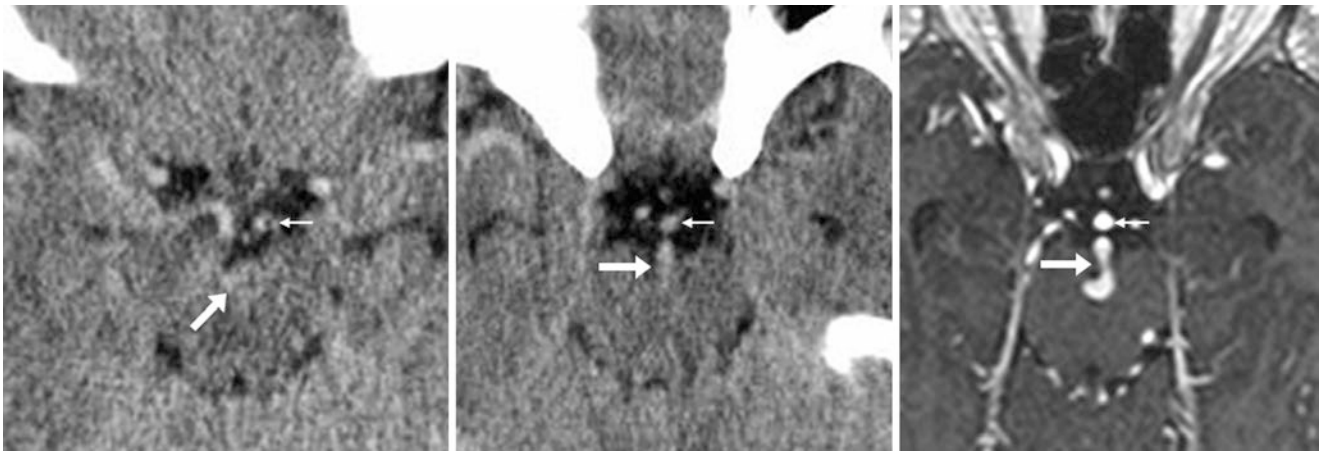

Fig. 40.33 38-year-old with severe headache. On nonenhanced CT (*left*), a subtle hyperdensity within the interpeduncular fossa was called a tiny focus of SAH, but a slightly more caudal image (*middle*) depicted a linear structure (*large arrow*) just posterior to the basilar tip (*thin arrow*). Postcontrast T1WI (*right*) confirmed an APMV in the fossa

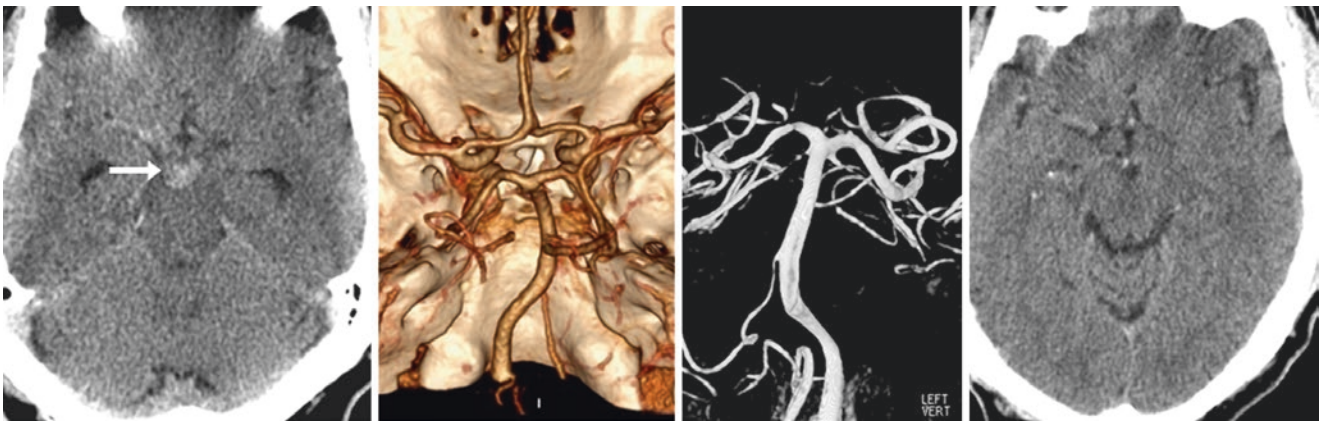

Fig. 40.34 Comparison case of perimesencephalic nonaneurysmal SAH: A 57-year-old with a severe headache had SAH (*arrows*) solely within the interpeduncular fossa on nonenhanced CT (*left*). CTA (*left middle*) and catheter 3DDSA (*right middle*) PA views were negative. Two months later, repeat nonenhanced CT (*right*) and CTA (*not shown*) were also negative

40.6 Susceptibility-Weighted Images: Deep Veins, Transmedullary Veins, and Subventricular Veins

On SWI, *deoxygenated venous vessels* are easily visualized and may simulate microhemorrhage within the parenchyma; however, prominent *deep veins* or *transmedullary veins* may be present, particularly located centrally within the periventricular white matter (PVWM) surrounding the lateral ventricles [23–30]. Such deep veins are typically tributaries to the *internal cerebral vein* (ICV), and include the *anterior caudate veins* (ACVs), *anterior septal veins* (ASVs) (*i.e.*, "septal" veins), *choroidal veins*, *direct lateral veins* (DLVs), *medial atrial veins* (MAVs), *thalamostriate veins* (TSVs, the principal drainage of the transmedullary and subependymal veins), and the *superior thalamic vein* (STV, the largest thalamic vein). The ICVs then drain into the *vein of Galen* (VOG), also known as the great cerebral vein. Notably, there is variation in drainage of these veins, as they may drain directly into the ICVs, or into each other. Essentially, *deep medullary veins* (*i.e.*, "transmedullary veins") may serve as collateral pathways between the superficial and deep venous systems, located along the lateral margin of the lateral ventricles and draining into many of the deep, central veins described above. Such transmedullary veins within the PVWM (having arisen from subcortical veins that traverse the subcortical white matter) are oriented perpendicular to the lateral ventricles, and drain into the *longitudinal caudate veins* followed by the *transverse caudate veins* (collectively called the "longitudinal caudate veins" because they are difficult to distinguish from each other on imaging), which are found immediately adjacent to the lateral angles of the bodies of the lateral ventricles. Notably, the "venous angle" (an angiographic sign) is formed by the joining of the anterior septal vein into the ICV just posterior to the foramen of Monro. The transmedullary (*i.e.*, transcerebral) and subcortical veins are normally visible to some degree. Such prominent deep transmedullary veins may simulate a vascular anomaly of concern such as *arteriovenous fistula* (AVF) or *arteriovenous malformation* (AVM); they may also simulate benign vascular anomalies such as *developmental venous anomalies* (DVAs) or even prominent medullary veins in acute stroke. Knowledge of the normal, variable venous anatomy in this location helps interpretation.

Visualization of medullary and transmedullary veins bilaterally is normal, but in *acute ischemic stroke* these veins can appear abnormally prominent unilaterally on the side of an acute ischemic injury or infarct [31, 32]. This finding is presumably related to abnormal dilatation of small veins corresponding to the arterial distribution of the infarct, and it is thought to be related to elevated oxygen extraction in that territory. Two other findings that may be present within an acute infarct on SWI include a hypointense artery (related to T2*-dark clot within the vessel), and small microhemorrhages ("petechial" hemorrhages). Abnormally dilated medullary/perimedullary veins in acute stroke can be distinguished by their unilateral or asymmetric appearance, by their "radiating" appearance within the affected arterial distribution of the infarct, and by correlation with the location of acute infarct on DWI (Figs. 40.35, 40.36, 40.37, 40.38, 40.39, 40.40, 40.41, 40.42, 40.43, 40.44, 40.45, 40.46, 40.47, 40.48, 40.49, and 40.50).

Another scenario that involves abnormalities of the deep transmedullary veins, and in which SWI can be helpful to detect injury, is *periventricular hemorrhage* (*i.e.*, hemorrhagic periventricular leukomalacia) in premature infants [33, 34]. Such hemorrhage results from diffuse *hypoxic-ischemic injury* to the deep white matter in premature neonates. SWI demonstrates the hemorrhages that may occur in such patients, which range from punctate to large, and also may depict enlargement of such veins due to thrombosis, which may not be visualized on most other MR sequences.

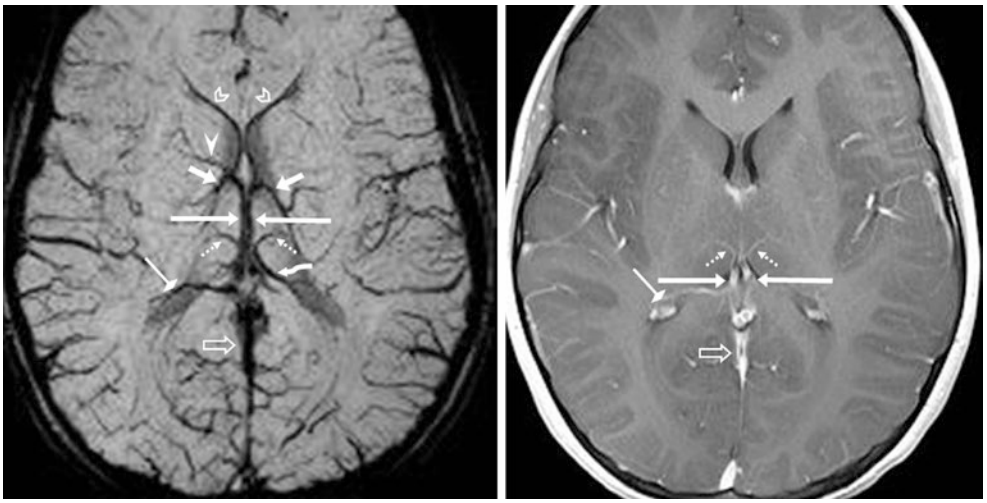

Fig. 40.35 In this 7-year-old, a 3 T MRI was performed to evaluate the pituitary (normal). 15 mm thickness SWI (*left*) illustrates normal venous anatomy. Note normal internal cerebral veins (ICVs) (*long arrows*), asymmetric drainage of the thalamostriate veins (TSVs) (*short arrows*), superior thalamic veins (STVs) (*thin dotted arrows*) and asymmetry of the direct lateral veins (DLVs) (*curved arrows*). Also seen are an anterior caudate vein (ACV) (*arrowhead*), anterior septal veins (ASVs) (*chevrons*), medial atrial veins (MAVs) (*diamond-tip arrows*), and the vein of Galen (VOG) (*open arrows*). On a postcontrast T1WI (*right*), note that the venous anatomy is much more difficult to visualize

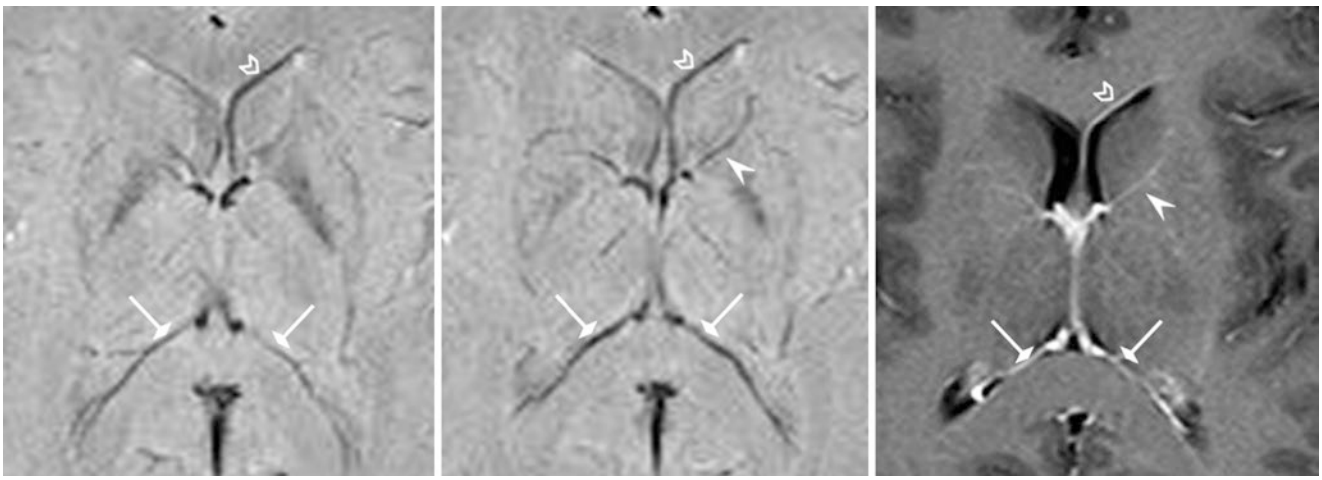

Fig. 40.36 49-year-old with extremity numbness (negative study). 2 mm thickness SWIs (*left* and *middle*) at 1.5 T depict asymmetry of the left ACVs (*arrowheads*) and left ASVs (*chevrons*). Postcontrast T1WI (*right*) often does not depict deep veins as well, but a prominent left ACV and ASV are visible. The prominent left ACV mimics a venous angioma, also known as a developmental venous anomaly (DVA). Also seen are the MAVs (*diamond-tipped arrows*)

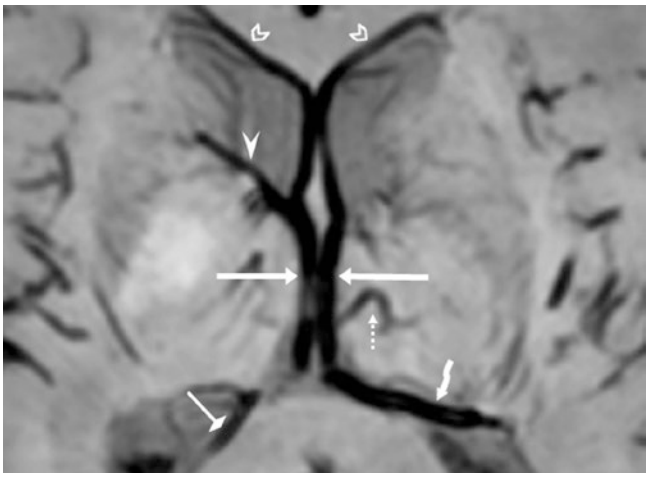

Fig. 40.37 90-year-old with weakness (negative MRI). 3 T 12 mm thickness SWI shows an asymmetric left DLV (*curved arrow*), a right MAV (*diamond-tip arrow*), a right ACV (*arrowhead*), and a left superior thalamic vein (STV) (*thin dotted arrow*). Also seen are the ASVs (*chevrons*) and ICVs (*long arrows*)

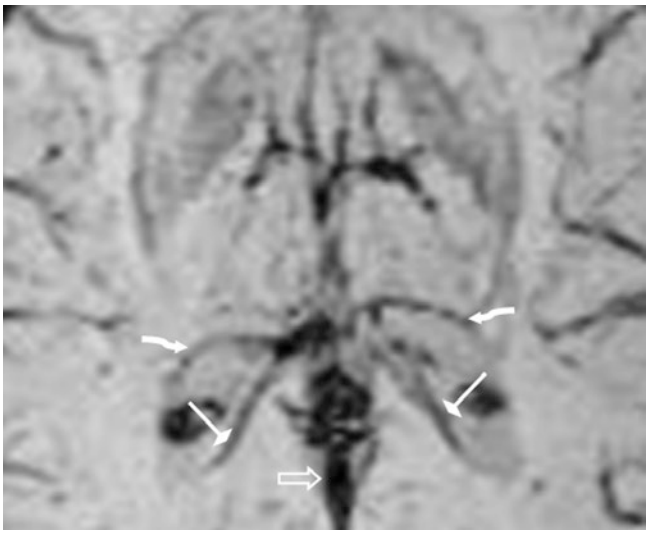

Fig. 40.38 32-year-old with weakness (negative MRI). A 1.5 T 15 mm thickness SWI shows the DLVs (*curved arrows*) and the MAVs (*diamond-tip arrows*) bilaterally, as well as the VOG (*open arrow*)

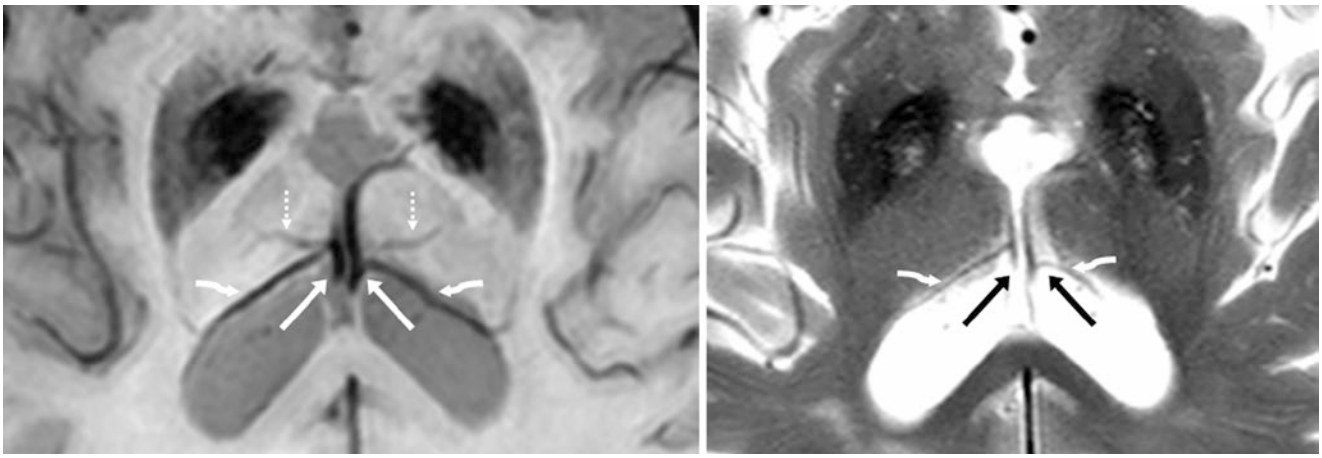

Fig. 40.39 81-year-old with altered mental status (negative examination). 2 mm thickness SWI (*left*) and T2WI (*right*) at 3 T both demonstrate normal DLVs bilaterally (*curved arrows*). However, SWI better depicts the STVs (*thin dotted arrows*). Also seen are the ICVs (*long arrows*)

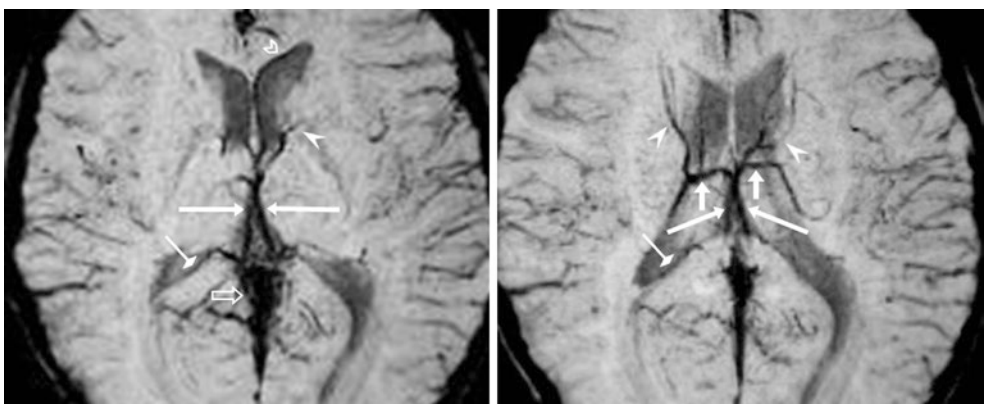

Fig. 40.40 In this 10-year-old, a 3 T MRI was performed after a seizure (negative MRI). 12 mm thickness SWIs depict normal venous anatomy, with the ACVs (*arrowheads*), ASV (*chevron*), ICVs (*long arrows*), MAV (*diamond-tip arrows*), and VOG (*open arrow*) denoted. Note normal, asymmetric drainage of the TSVs (*short arrows*), as well as the asymmetric prominence of the left ASV (*chevron*) and ACV (*arrowheads*)

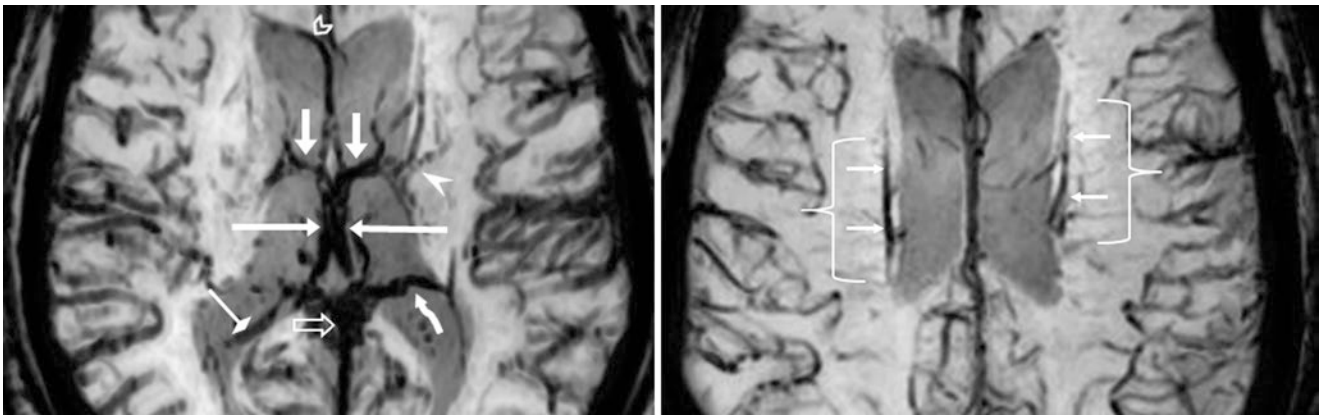

Fig. 40.41 This 51-year-old had a 3 T MRI for multiple sclerosis (negative study), on which 12 mm thickness SWIs show normal veins, including the ACV (*arrowhead*), ASV (*chevron*), ICVs (*long arrows*), MAV (*diamond-tip arrow*), thalamostriate veins (TSVs) (*short arrows*), and VOG (*open arrow*). Note that the transmedullary/deep medullary veins (TMVs) (*brackets*) drain into larger longitudinal caudate veins (*thin arrows*)

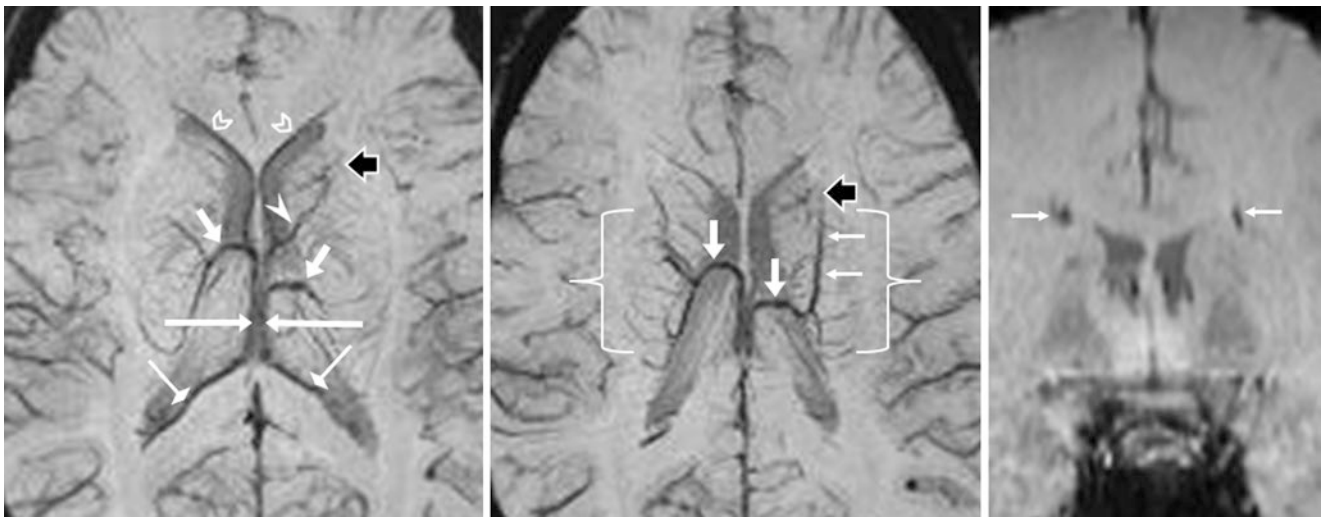

Fig. 40.42 This 15-year-old had a 3 T MRI to follow up an incidental developmental venous anomaly (DVA). 12 mm thickness axial SWIs (*left* and *middle*) and a 2 mm thickness coronal SWI (*right*) depict normal venous anatomy, with a "caput" of the DVA (*wide dark arrows*), perhaps draining via the ACV (*arrowhead*). Note normal, asymmetric drainage of the TSVs (*short arrows*). Also, note that the left-sided transmedullary/transcerebral veins (*brackets*) drain into a larger longitudinal caudate vein (*thin arrows*). Also seen are the ICVs (*long arrows*), ASVs (*chevrons*), and MAVs (*diamond-tip arrows*)

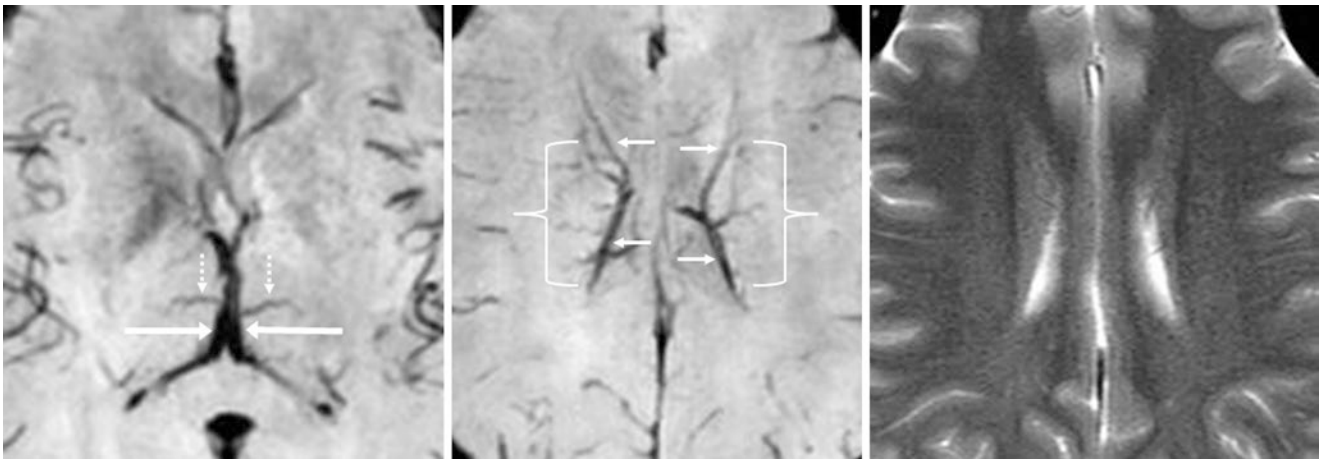

Fig. 40.43 36-year-old with weakness (negative study); 2 mm thickness SWIs at 1.5 T (*left* and *middle*) depict transmedullary veins (*outlined by brackets*) that drain into the transverse/longitudinal caudate veins (*thin arrows*). Note the STVs (*thin dotted arrows*). The STVs and transverse/longitudinal caudate veins eventually drain into the ICVs (*long arrows*). Note that on routine T2WI (*right*), the flow voids of these smaller venous structures are relatively invisible, whereas T2WI typically shows flow voids of larger vasculature with faster flow. This demonstrates the utility of SWI in detecting deoxyhemoglobin in smaller venous structures with slower flow

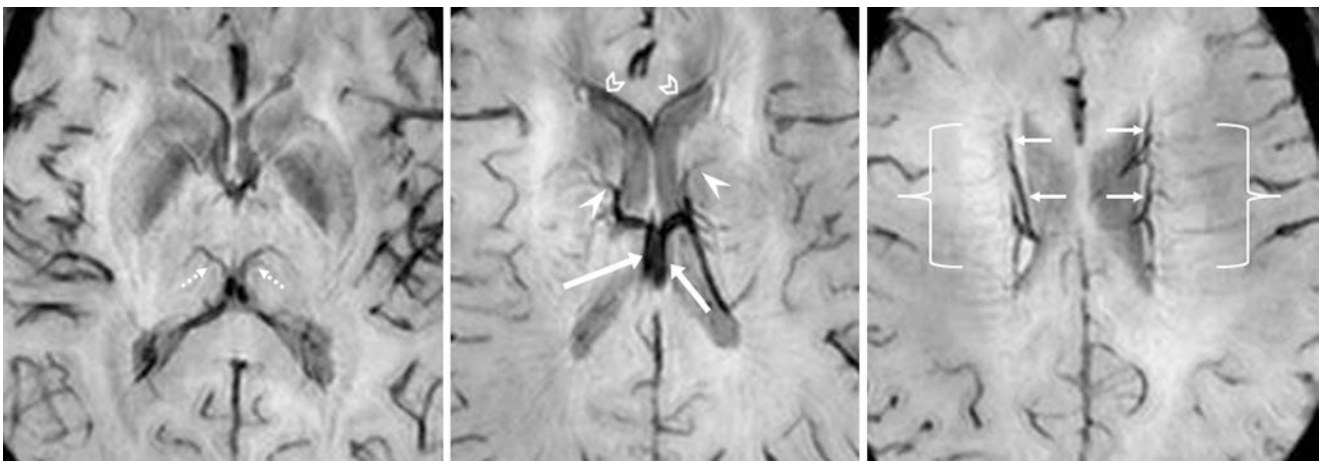

Fig. 40.44 33-year-old with headaches (negative study). Serial 2 mm thickness SWIs at 3 T demonstrate transmedullary veins (*outlined by brackets*) that drain into the transverse/longitudinal caudate veins (*thin arrows*). Note the STVs (*thin dotted arrows*). The ASVs (*chevrons*), ACVs (*arrowheads*), transverse/longitudinal caudate veins, and STVs combine to form the ICVs (*long arrows*)

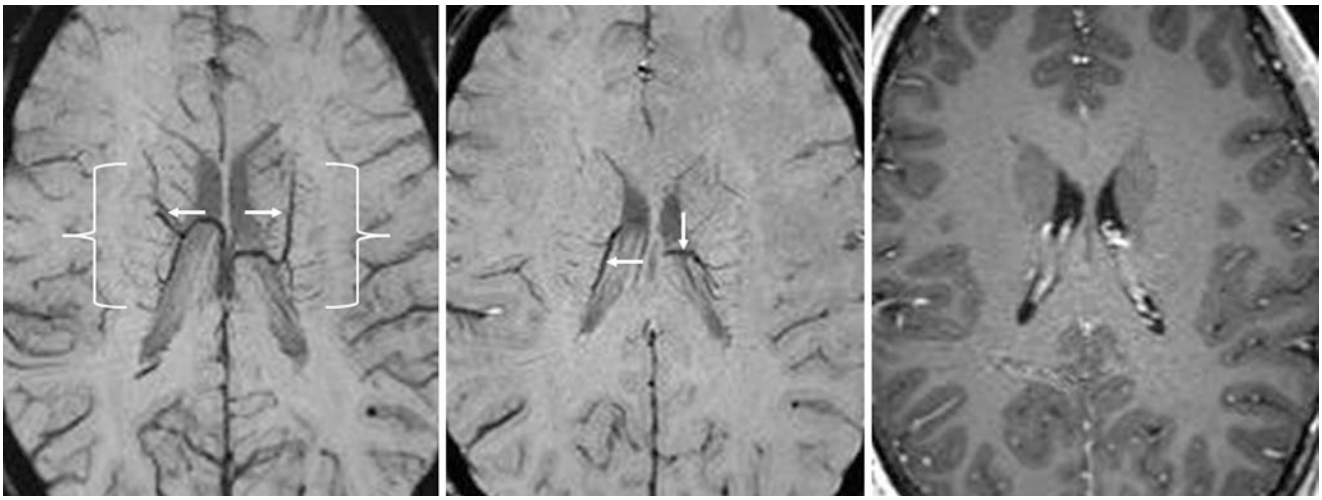

Fig. 40.45 In this 16-year-old, SWI was performed at 3 T. The thicker (12 mm) SWI image (*left*) best depicts the transmedullary/transcerebral veins (*outlined by brackets*) draining into the transverse/longitudinal caudate veins (*thin arrows*), which are not as well seen on 2 mm thickness SWI (*middle*), or on postcontrast T1WI (*right*)

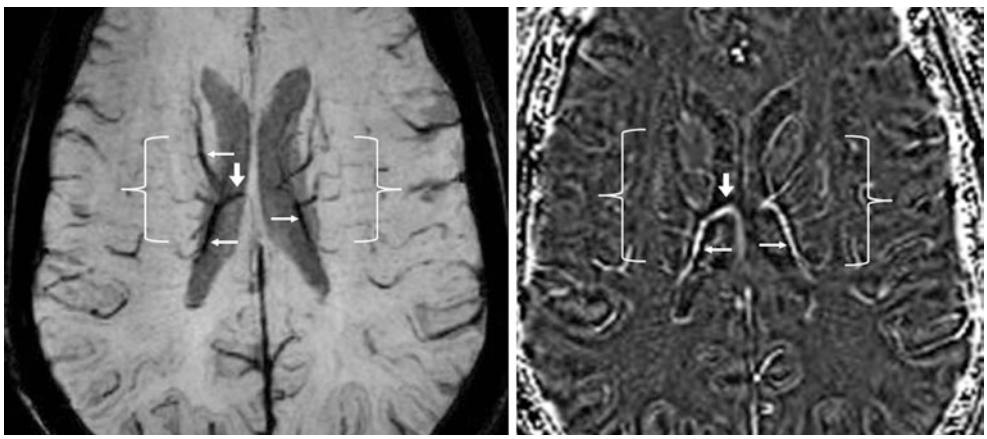

Fig. 40.46 52-year-old with seizures (negative study). At 3 T, an 8 mm thickness SWI image (*left*) shows transcerebral veins (TMVs, *brackets*) bilaterally, which drain medially into the transverse/longitudinal caudate veins (*thin arrows*), and thereafter to the top of the TSVs (*short arrows*). On a similar-thickness "filtered" phase map (*right*), these veins are bright from deoxygenated blood

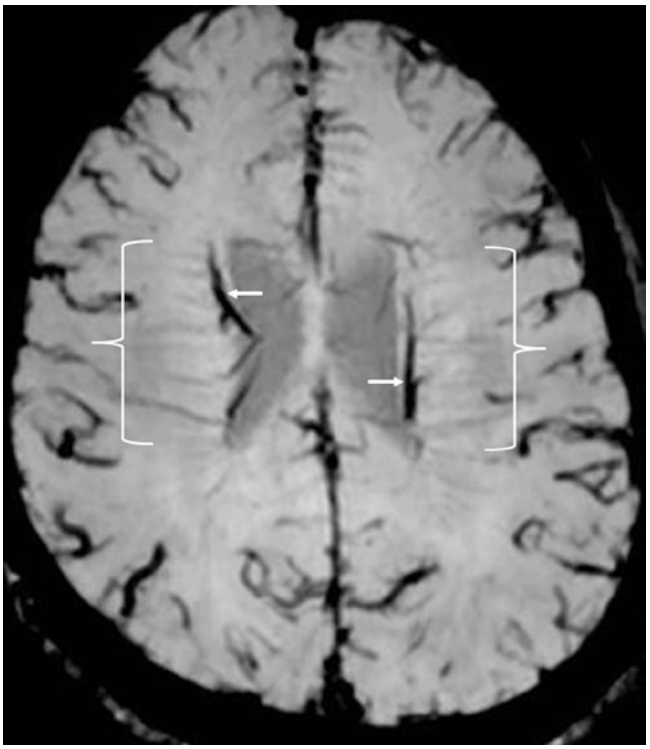

Fig. 40.47 91-year-old with stroke-like symptoms (negative study). At 3 T, 2 mm thickness SWI shows transcerebral veins (TMVs, *brackets*) that drain medially into the transverse (longitudinal) caudate veins (*thin arrows*). In this patient, the resolution is high enough to visualize the TMVs crossing the white matter from the cortex bilaterally

Fig. 40.48 10-year-old with follow-up for an ear lesion, with a negative brain MRI. At 3 T, a 21 mm thickness SWI minimum intensity projection (minIP) image illustrates TMVs (*brackets*) that drain medially into transverse/longitudinal caudate veins (*thin arrows*), and also depicts a duplicated left ACV (*arrowheads*), a right ASV (*chevron*), the ICVs (*long arrows*), MAVs (*diamond-tip arrows*), TSVs (*short arrows*), and the VOG (*open arrow*)

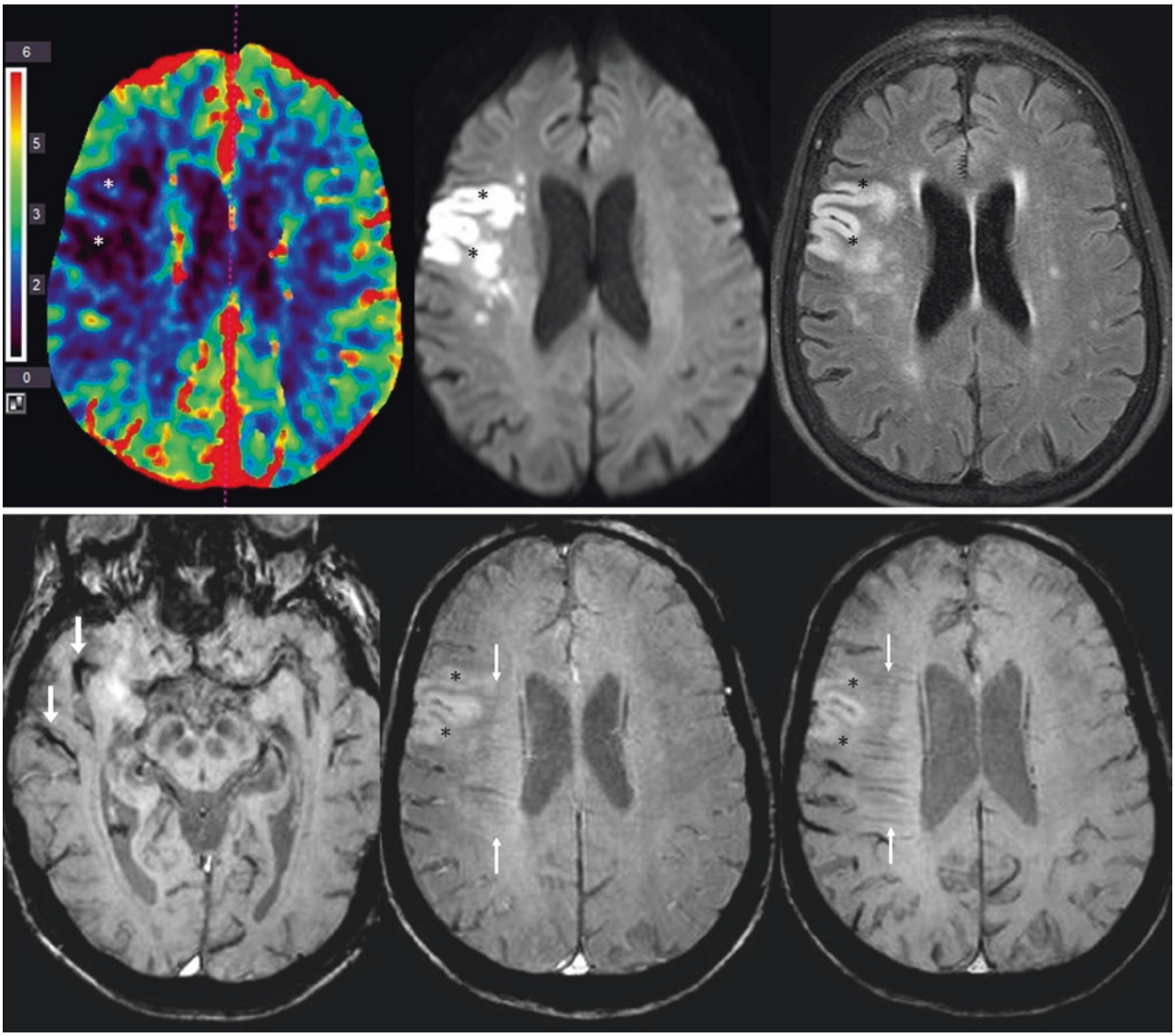

Fig. 40.49 Comparison case of acute ischemic stroke. *Top row*: A 66-year-old with left-sided weakness had an infarct (*asterisks*) on a CT perfusion cerebral blood volume (CBV) map (*left*), and on 3 T MRI DWI (*middle*) and FLAIR (*right*). *Bottom row:* On SWI with a TE of 40 ms (*left*), there was darker signal within the middle cerebral artery (MCA) branches, consistent with acute clot (*arrows*). On SWI images at a higher level, the prominent medullary veins were barely visible (*between thin arrows*) at a lower TE of 20 ms (*middle*), as compared with a TE of 40 ms (*right*), demonstrating the effect of TE on venous visualization

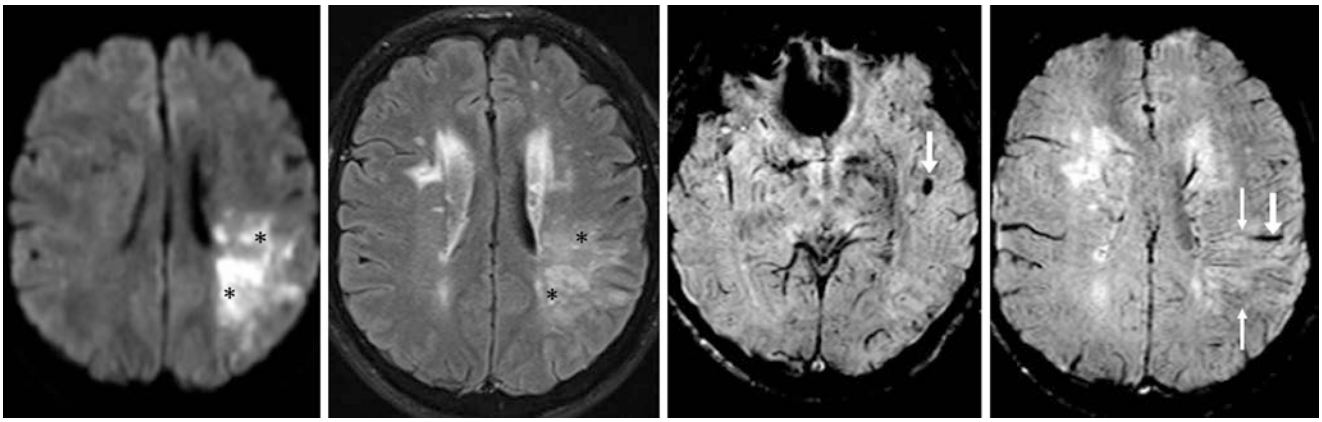

Fig. 40.50 Comparison case of acute ischemic stroke. A 50-year-old with right-sided weakness had an infarct (*asterisks*) on 1.5 T DW MRI (*left*), which was also bright on FLAIR (*left middle*). On SWI (*right middle*), there was focally dark signal within the left MCA's M2 segment in the sylvian fissure, consistent with acute clot (*arrows*). On an SWI image at a higher level (*right*), the prominent medullary veins were visible (*between thin arrows*), most likely related to elevated oxygen extraction from infarcted parenchyma

40.7 Susceptibility-Weighted Images: Cerebellar Veins

Since *deoxygenated venous vessels* are easily visualized on SWI, *veins in the posterior fossa or cerebellum* can appear much more prominent and ubiquitous than on routine T2WI or postcontrast T1WI, or even more prominent than on MRV sequences. Thus, it is helpful to have a general working knowledge of the anatomy of the more notable cerebellar veins, which can be quite prominent on SWI [35–41]. These veins may simulate clinically important abnormalities such as an *AVF*, *AVM*, or *microhemorrhages* (when viewed perpendicularly or transversely through the veins' direction of travel). They also can simulate typically benign vascular anomalies such as *DVAs*, particularly when viewed as thicker, "sliding" maximum or minimum intensity projections (MIPs)—that is, 10 mm thickness or greater with slice overlap.

Although the nomenclature varies slightly between sources, there is generally considered to be somewhat standard nomenclature for cerebellar venous anatomy [35–41]. Near the midline, there are paired *inferior vermian veins* (IVVs), typically along with a dominant *superior vermian vein* (SVV). More laterally, there are variably present *inferior cerebellar veins* (ICVs) *and superior cerebellar veins* (SCVs), which have been variably termed; for the purposes of this text, these are further subclassified as *medial* (MICV and MSCV) and *lateral* (LICV and LSCV) *inferior and superior cerebellar veins*. (In other sources, they may be classified generally as posterior inferior or posterior superior cerebellar veins.) These veins typically anastomose with one another. The *petrosal vein* (PV)—also known as the floccular vein, vein of Dandy, or great anterior cerebellar vein—and the *vein of the lateral recesses* (VLR) typically constitute most of the inferior cerebellar drainage for that side. Notably, the PV (along the lateral aspect of the cerebellar flocculus) and the VLR (along the medial aspect of the flocculus and overlying the foramen of Luschka) can appear quite prominent, so that on "sliding" MIPs they may simulate one of the abovementioned anomalies, such as AVM, AVF, or DVA (Figs. 40.51, 40.52, 40.53, 40.54, 40.55, and 40.56).

The SCVs are less commonly visualized on SWI because there is overlap with the tentorium, where the *tentorial sinuses* (particularly the lateral tentorial sinus [LTS]) may obscure them. (The lateral tentorial sinuses are discussed in more depth later in Chap. 40.10). Thicker sliding MIPs may cause the LTSs to overlap with and obscure the SCVs, which are located posteriorly (Figs. 40.57, 40.58, 40.59, 40.60, 40.61, and 40.62).

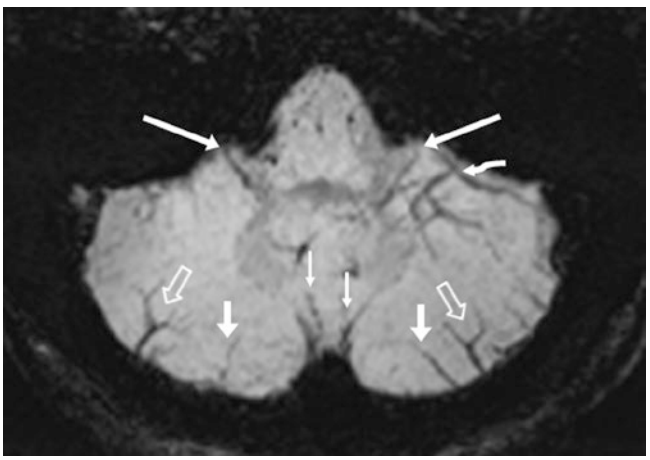

Fig. 40.51 A 12 mm-thick SWI at 3 T, in a 16-year-old. Note the paired inferior vermian veins (IVVs, *thin arrows*), lateral inferior cerebellar veins (LICVs, *open arrows*), veins of the lateral recess of the 4th ventricle (VLRs, *long arrows*), and mildly asymmetric medial inferior cerebellar veins (MICVs, *short arrows*). Note asymmetry of the left petrosal vein (PV, *curved arrow*); the right PV is not seen

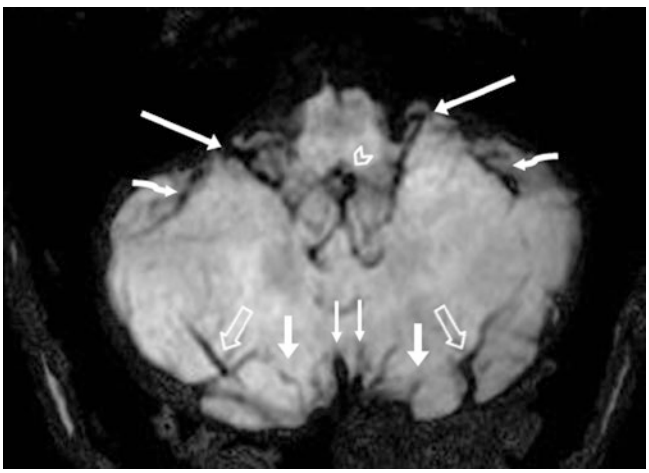

Fig. 40.52 In this 27-year-old, 3 T 10 mm thickness SWI depicts asymmetric IVVs (*thin arrows*), LICVs (*open arrows*), PVs (*curved arrows*), VLRs (*long arrows*), and MICVs (*short arrows*), with a prominent posteromedian medullary vein (*chevron*)

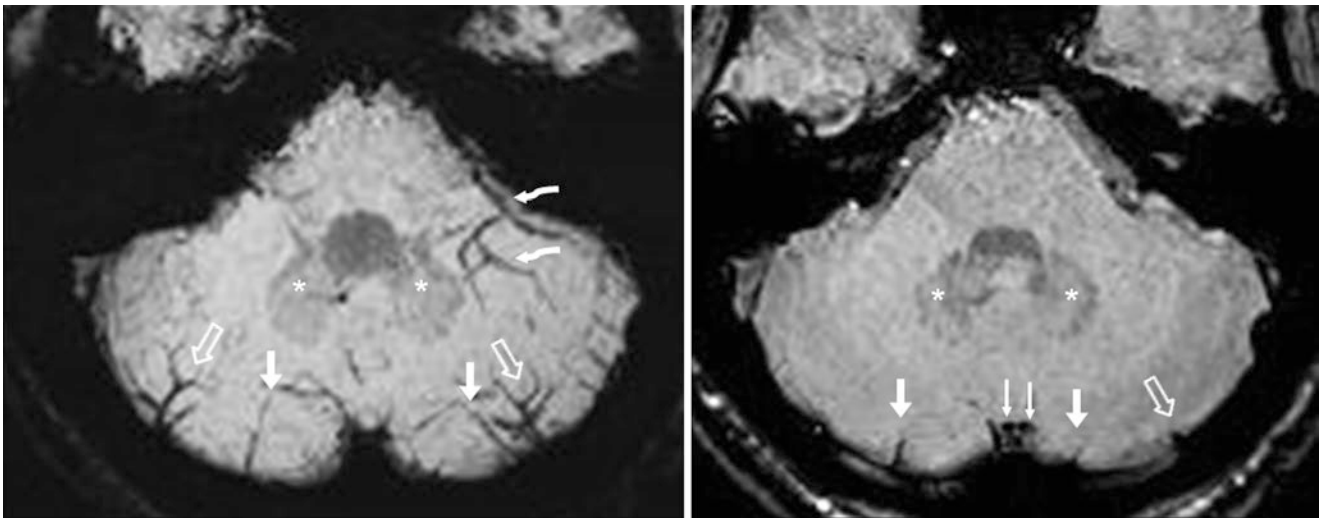

Fig. 40.53 This 17-year-old had a 3 T MRI that implemented SWI at thicknesses of 12 mm (*left*) and 2 mm (*right*). Note that the paired IVVs (*thin arrows*) are difficult to distinguish on the thicker SWI. Also, note the LICVs (*open arrows*), and MICVs (*short arrows*). The left PVs (*curved arrows*) are prominent, and asymmetrically so. On the thinner SWI, the margins of the dentate nuclei (*asterisks*) are better defined

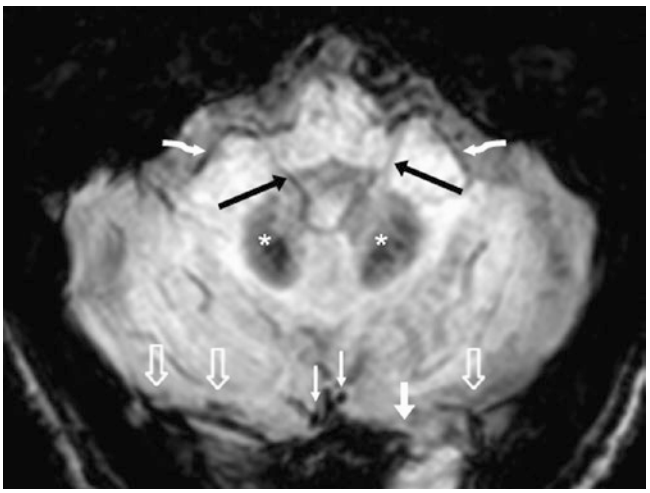

Fig. 40.54 A 12 mm thickness SWI at 3 T in a 91-year-old. Note paired IVVs (*thin arrows*), the LICVs (*open arrows*), PVs (*curved arrows*), and VLRs (*long arrows*). The dark signal of the dentate nuclei (*asterisks*) is not unexpected for this age

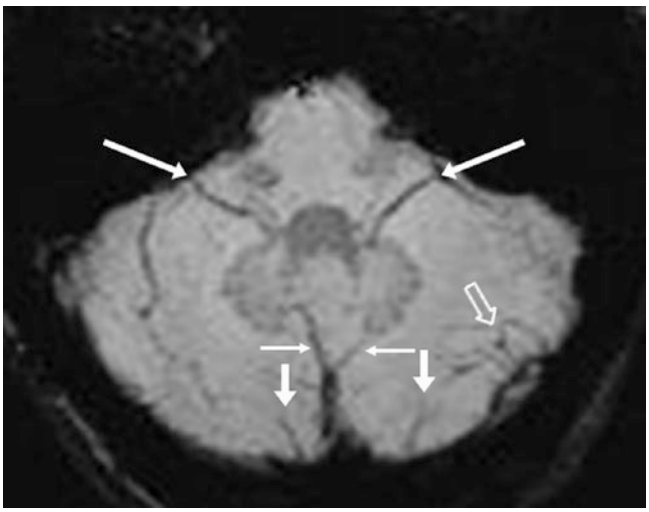

Fig. 40.55 A 14 mm thickness SWI at 3 T in a 35-year-old. Note the paired, but asymmetric, IVVs (*thin arrows*). Also, note the LICV (*open arrow*), VLRs (*long arrows*), and mildly asymmetric MICVs (*short arrows*)

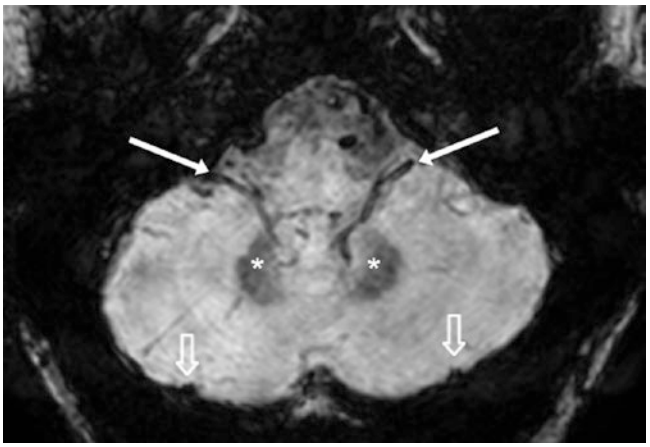

Fig. 40.56 A 2 mm thickness SWI at 3 T in a 40-year-old, with asymmetric prominence of the left VLR (*long arrow*). On such thin images, it is difficult to visualize most of the cerebellar veins, such as the LICVs (*open arrows*). The dentates' dark signal (*asterisks*) is not unexpected for this age

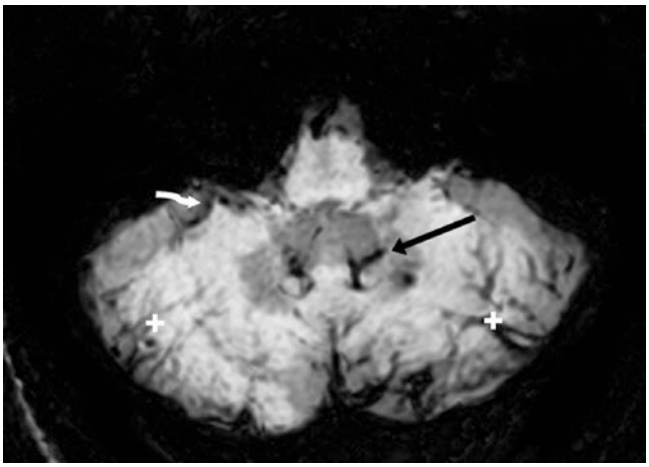

Fig. 40.57 A 12 mm thickness SWI at 3 T in a 50-year-old. The left VLR (*long arrow*) is prominent and asymmetric, whereas the right PV (*curved arrow*) is prominent. There are large lateral tentorial sinuses (LTSs) (*plus sign*s), left greater than right, which make it difficult to visualize most cerebellar veins

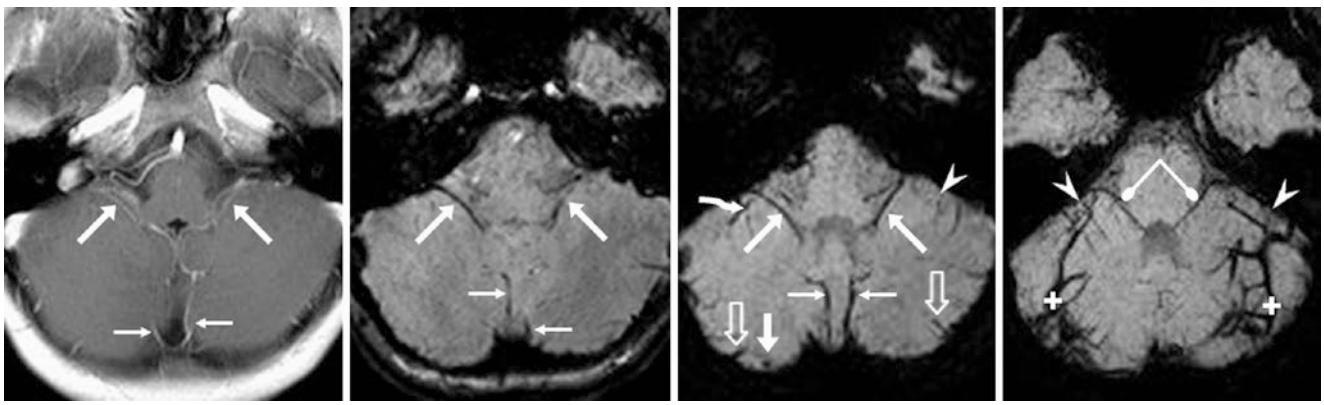

Fig. 40.58 In this 7-year-old, with a 5 mm thickness postcontrast T1WI (*left*) depicts the VLRs (*long arrows*) and the IVVs (*thin arrows*). By comparing 3 T SWIs at both 2 mm (*left middle*) and 12 mm (*right middle*) thicknesses, note that the 12 mm image best delineates the smaller cerebellar veins. Increasing the SWI thickness to 17 mm (*right*) increases the prominence of the LTSs (*plus sign*s) and obscures most cerebellar veins. Note anterior surface veins (ASVs, *arrowheads*) and veins of the middle cerebellar peduncles (*oval-tip arrows*) right MICV (*short arrow*), and right PV (*curved arrow*)

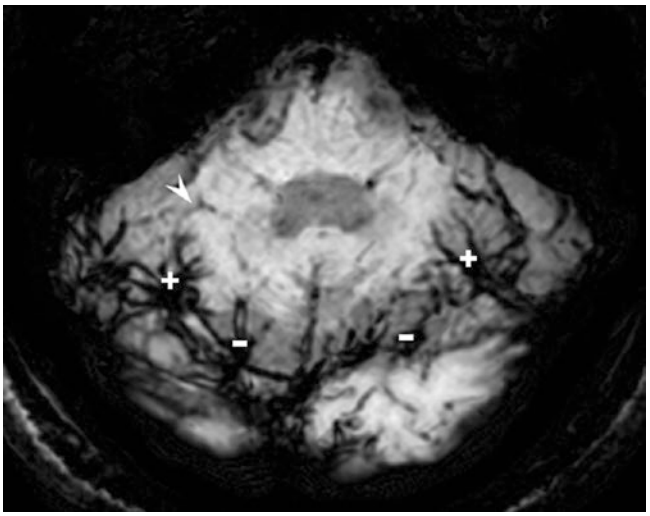

Fig. 40.59 15 mm thickness SWI at 3 T in a 51-year-old. On thicker images such as this, the smaller cerebellar veins, such as the ASVs (*arrowhead*), are obscured by the typically larger tentorial sinuses, in particular the LTSs (*plus signs*). Also note the medial tentorial sinuses (*minus signs*)

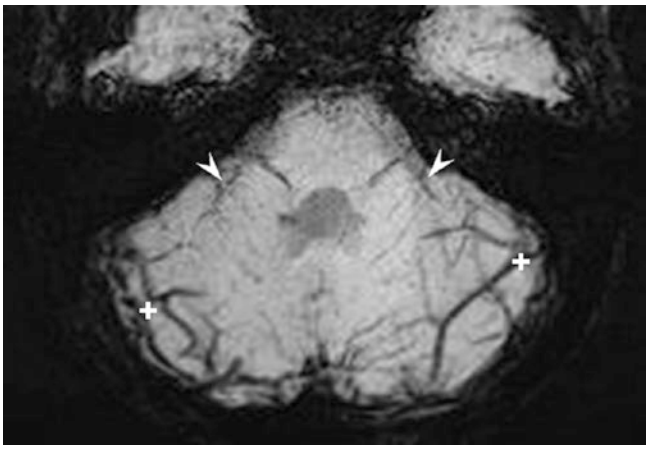

Fig. 40.61 17 mm thickness SWI at 3 T in a 10-year-old. Thicker images such as this may obscure the smaller cerebellar veins, such as the ASVs (*arrowheads*), by both volume averaging with parenchyma and overlap with the LTSs (*plus signs*), which are usually much more visible

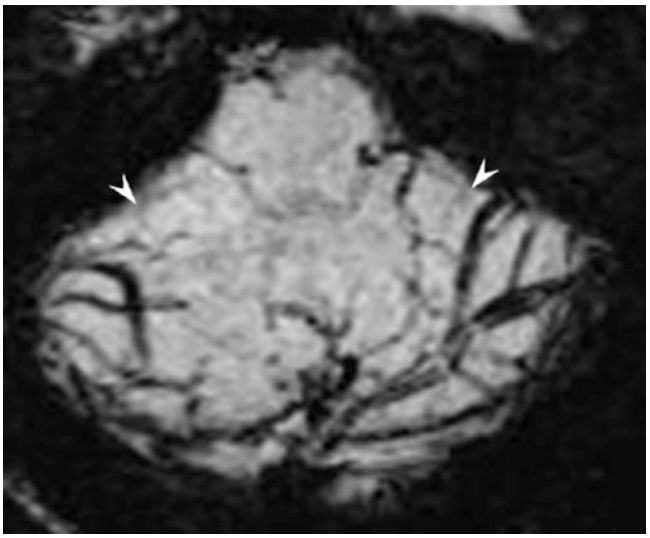

Fig. 40.60 20 mm thickness SWI at 3 T in a 49-year-old. In this patient, the SWIs are reconstructed so thick that the tentorial sinuses appear to cover most of the cerebellum, thus completely obscuring the smaller cerebellar veins, such as the ASVs (*arrowheads*)

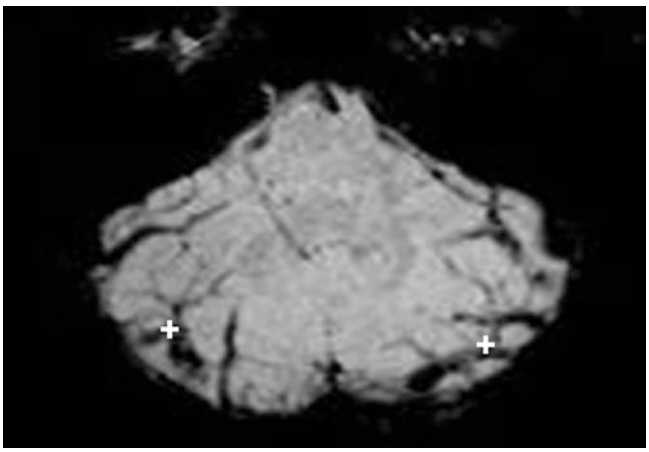

Fig. 40.62 20 mm thickness SWI at 3 T in a 14-year-old. Thicker images may obscure smaller cerebellar and petrosal veins by volume averaging with parenchyma, and by overlap with the typically much larger LTSs (*plus signs*)

40.8 Susceptibility-Weighted Images: Basal Cerebral Venous System

As deoxygenated veins are easily visualized on SWI, an important venous system to be aware of is the *basal cerebral venous system*, which drains via the basal veins (specifically, the *basal vein of Rosenthal* [BVR]). Prominence of such veins (or a plexus of veins) can simulate *SAH, AVM, AVF*, or *aneurysm*. These veins can appear prominent or asymmetric near the brainstem; one reason that basal veins may simulate SAH is that the locations through which the basal venous system travels are prime locations to evaluate for hemorrhage, such as the suprasellar cisterns, interpeduncular fossa, perimesencephalic cisterns, and the medial aspects of the sylvian fissures.

The BVR has been subdivided into three segments [3–6, 21–30, 35–40]:

- *Proximal* (first) segment, from the union of the inferior striate vein, anterior cerebral vein (ACV), and deep middle cerebral vein (MCV) to the point of extending up to the anterior aspect of the cerebral peduncle
- *Middle* (second) segment, from the anterior end of the cerebral peduncle up to the union of the BVR and the lateral mesencephalic vein (LMV), which links the BVR to the superior petrosal sinus
- *Distal* (third) segment, from the peduncle up to the point of drainage into the great vein of Galen (VOG) or into the internal cerebral vein (ICV).

The BVR empties into the VOG about 85–90 % of the time; the remainder drain into lesser-known pathways such as the *lateral mesencephalic vein, sphenoparietal sinus, cavernous sinus, superficial MCV*, or *peduncular veins*. Additionally, it should be noted that on axial SWI at this level, the *internal occipital vein* (IOV), or calcarine vein, may be visualized in most patients, and appears as a vein (sometimes asymmetric) draining the inferomedial occipital lobe into the VOG, just medial to the lateral ventricles.

Following are examples of the spectrum of appearances of the basal venous system on SWI. Notably, as stated elsewhere in this section, thicker SWI sections, or "sliding" (overlapping) maximum-intensity projections (MIPs) or minimum-intensity projections (MinIPs) depict deoxygenated blood within veins better than do thinner sections. Therefore, although it is helpful to view thicker MIPs or MinIPs to screen for AVMs or AVFs, it may be necessary to review thinner sections of SWI (which usually can be reconstructed in thinner slices, as they are typically a 3D acquisition). Postcontrast TOF MRA can also be helpful to exclude an abnormality (Figs. 40.63, 40.64, 40.65, 40.66, 40.67, 40.68, 40.69, and 40.70).

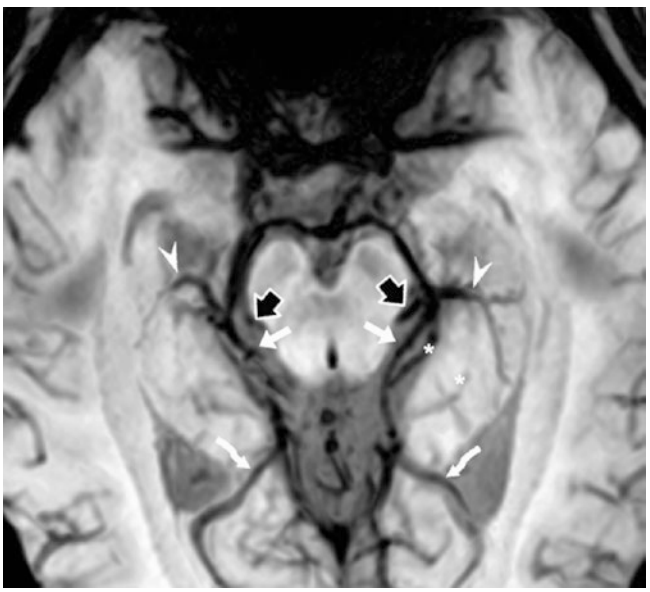

Fig. 40.63 In this 27-year-old, a 3 T MRI with 10 mm thickness SWI shows the basal veins of Rosenthal (BVRs, *short white arrows*) superimposed on the posterior cerebral arteries (PCAs) (*asterisk*). The arteries are dark because of the technique (selected TE). Note the internal occipital/calcarine veins (IOVs, *curved arrows*), inferior choroidal/ventricular veins (IVVs, *arrowheads*), and lateral mesencephalic veins (*wide arrows*)

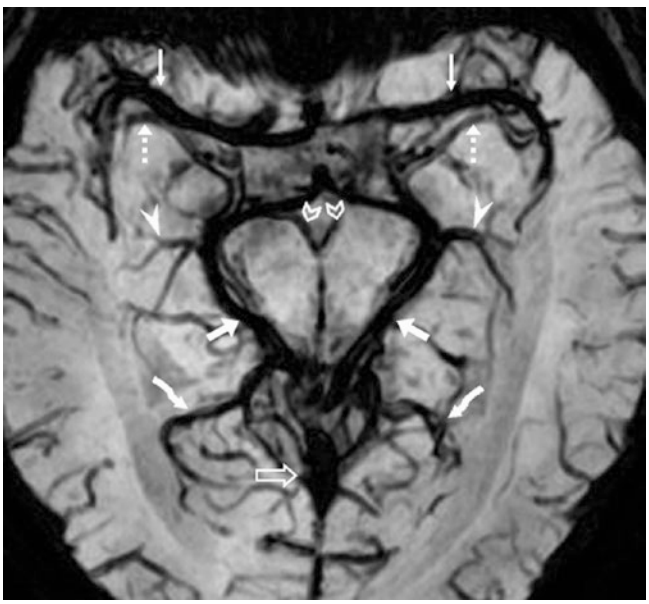

Fig. 40.64 A 3 T MRI with 12 mm thickness SWI in a 13-year-old shows relative symmetry of the BVRs (*short arrows*) and deep MCVs (*dotted arrows*), but there is asymmetry of the IOVs (*curved arrows*) and IVVs (*arrowheads*). Note normal interpeduncular veins (*chevrons*). The MCAs (*thin arrows*) are dark because of technique (selected TE and flip angle)

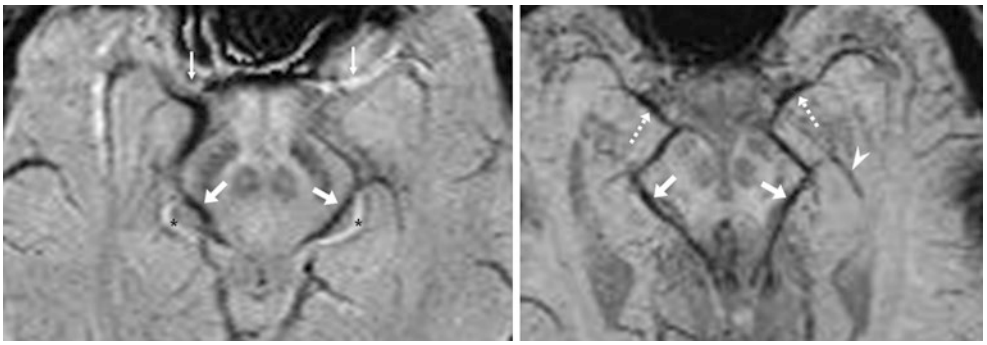

Fig. 40.65 This 25-year-old had a 1.5 T MRI with SWIs at 2 mm thickness (*left*) and 10 mm thickness (*right*) that delineate the BVRs (*short arrows*) draining from the deep MCVs (*dotted arrows*) bilaterally. The arteries are bright on the 2 mm-thick image but disappear on minimum intensity projection (minIP) 10 mm images, owing to volume averaging. Also, note the inferior choroidal/ventricular veins (IVVs, *arrowhead*), MCAs (*thin arrows*), and PCAs (*asterisks*)

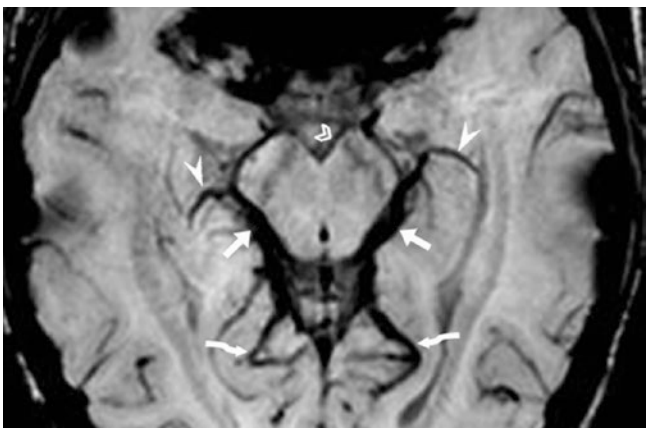

Fig. 40.66 A 3 T MRI in a 14-year-old. 10 mm thickness SWI shows the BVRs (*short arrows*), asymmetry of the IVVs (*arrowheads*), a dominant left IOVs (*curved arrows*), and a small left interpeduncular vein (*chevron*). The deep MCVs are obscured by artifact from gas in the sphenoid sinus

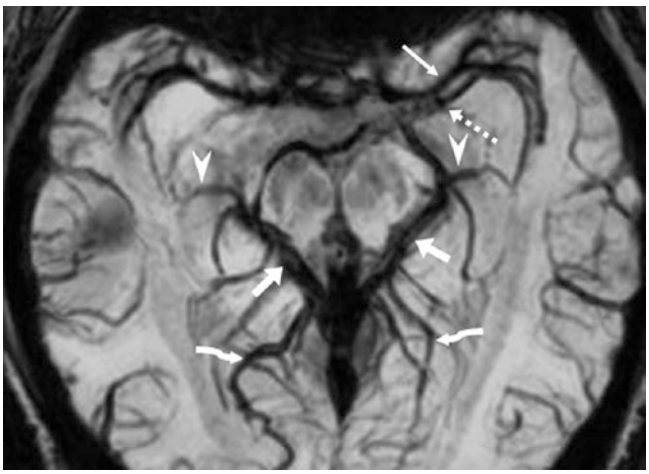

Fig. 40.67 In this 33-year-old with a 3 T MRI, 16 mm thickness SWI shows the BVRs (*short arrows*), IVVs (*arrowheads*), and prominence of both the right IOV (*curved arrows*) and left deep MCV (*dotted arrow*), which is closely apposed to the MCA (*thin arrow*). The arteries are dark owing to technique

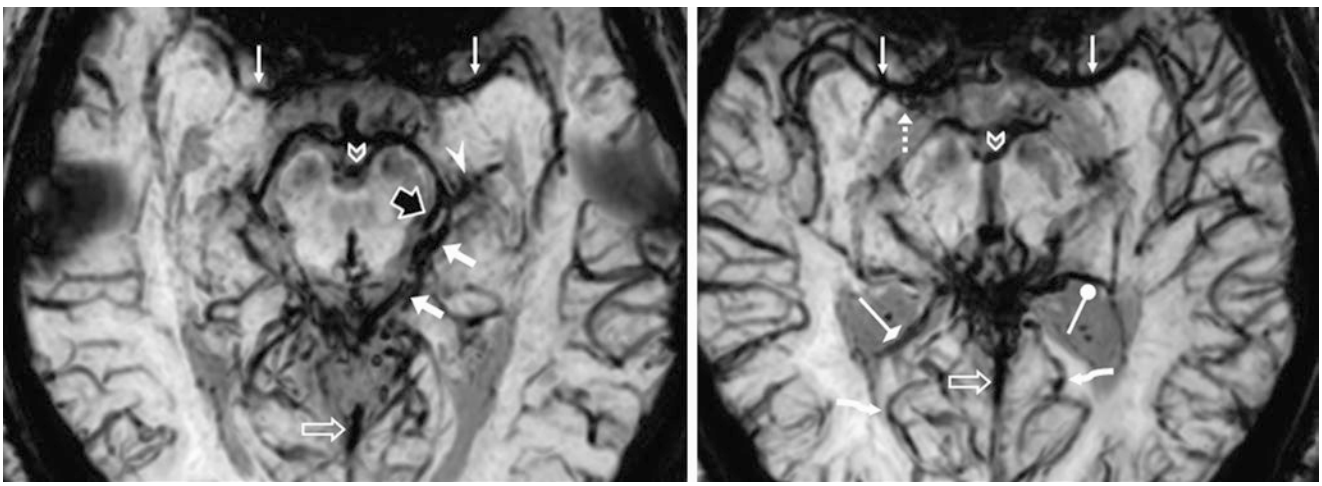

Fig. 40.68 In this 51-year-old, 3 T SWI MRI at 15 mm thickness demonstrates normal veins, with asymmetry of the right deep MCV (*dotted arrow*) and the left BVR (*short white arrows*). (The MCAs [*thin arrows*] are also dark owing to technique.) Note an interpeduncular or anterior ponto-mesencephalic vein (*chevrons*), a left direct lateral vein (*circle-tip arrow*), a left IVV (*arrowhead*), and a right medial atrial vein (*diamond-tip arrow*). Also note that the posterior cerebral artery (*wide arrow*) is in close proximity to the BVR. Note the improved visualization of venous connections with increasing slice thickness

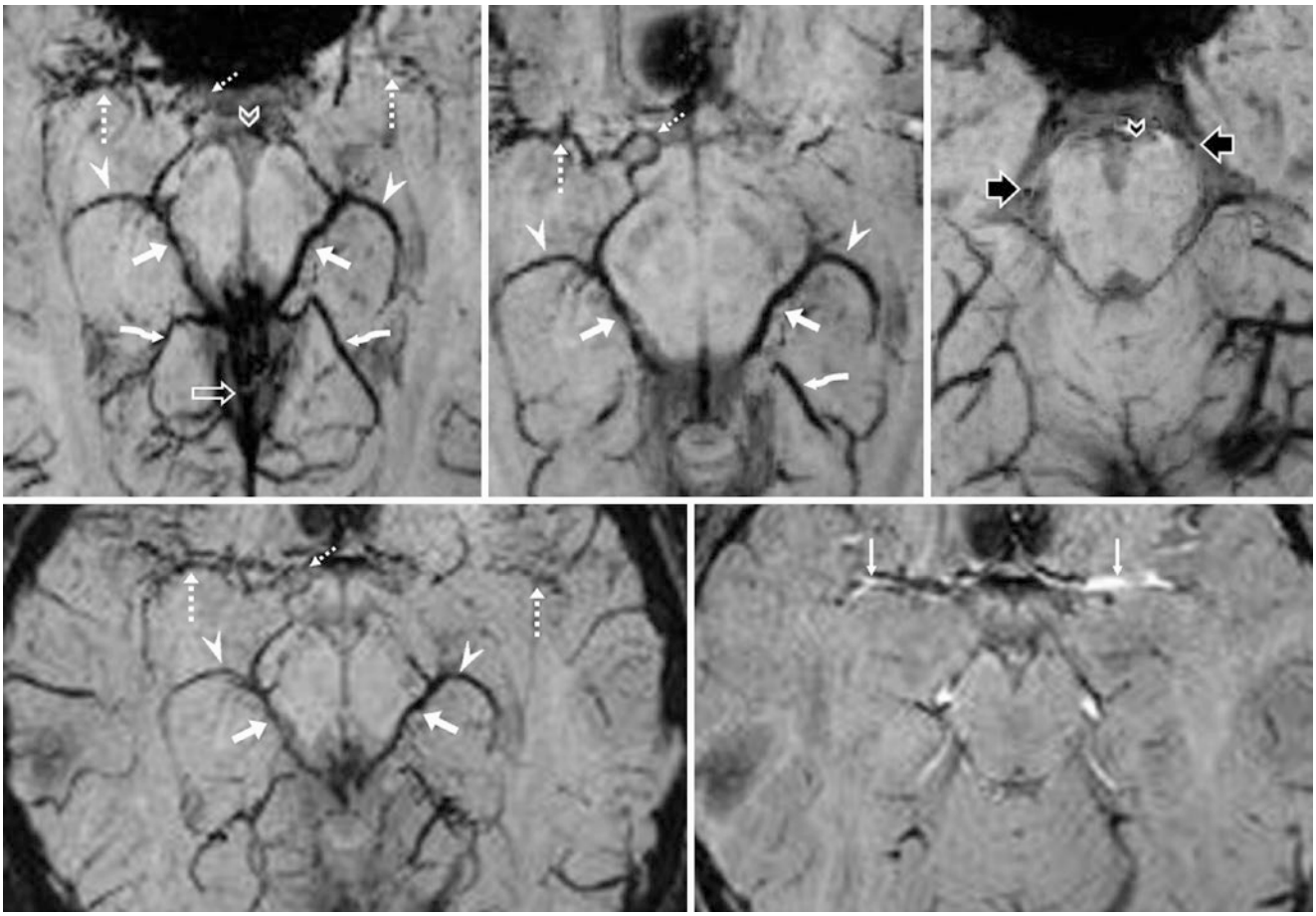

Fig. 40.69 3T MRI in a 7-year-old depicts the BVRs (*short arrows*), deep MCVs (*dotted arrows*), IVVs (*arrowheads*), IOVs (*curved arrows*), uncal veins (*thin dotted arrows*), and VOG (*open arrows*) on SWI at thicknesses of 17 mm (*top left*), 7 mm (*top middle and right*, *bottom left*) and 1.5 mm (*bottom right*). Note the lateral mesencephalic veins (*wide arrows*) and the interpeduncular veins (*chevrons*). The MCAs (*thin arrows*) are bright only on the thin images. These images demonstrate how the appearance of arterial structures can vary with TR, TE, and slice thickness

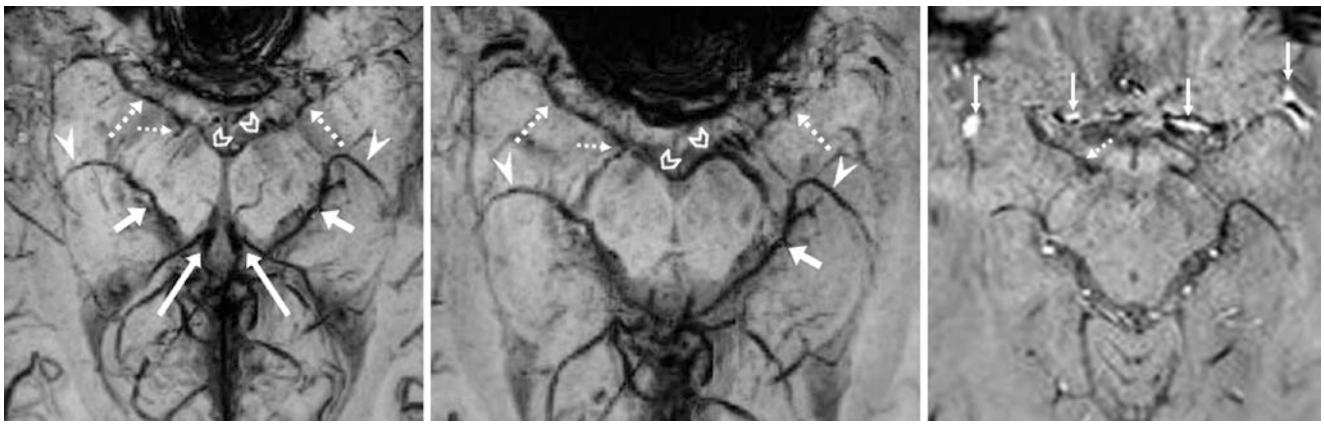

Fig. 40.70 In this 15-year-old, a 3 T SWI MRI at 21 mm thickness (*left*) shows asymmetric basal drainage, with a dominant left BVR (*short arrows*) and a dominant right deep MCV (*dotted arrows*). Note interpeduncular veins (*chevrons*), internal cerebral veins (ICVs, *long arrows*), IVVs (*arrowheads*), and a right uncal vein (*thin dotted arrow*). A magnified view with slightly greater angulation (*middle*) further demonstrates these findings. On thinner images (1 mm, *right*), the MCAs (*thin arrows*) are bright; they are darker on the thicker images because of volume averaging

40.9 Basal Vein of Rosenthal and Deep Middle Cerebral Veins Asymmetry

The *basal veins of Rosenthal* (BVRs) arise bilaterally at the medial aspects of both temporal lobes, typically formed by the joining of the deep *MCVs* laterally from the deep portion of the insula, along with what are most commonly smaller *anterior cerebral veins* [3–6, 21–30, 35–41]. The BVRs course posteromedially along the lateral surface of the cerebral peduncles in the perimesencephalic cisterns to eventually join the *vein of Galen* (VOG) in more than 90 %; occasionally the BVRs drain into a *lateral mesencephalic vein* or into a *tentorial sinus*. The *internal cerebral veins* (ICVs) also typically join the BVRs to form the VOG. Veins or plexi from the cavernous sinus, sphenoparietal sinus, or the superficial MCVs may also contribute to or drain along with the BVRs. Note that the paired BVRs travel in close proximity to, and can be mistaken for, the posterior cerebral arteries (PCAs), particularly when imaging studies using intravenous contrast, such CTA, CTV, or contrast-enhanced MR angiography or venography (CEMRA or CEMRV) are inadvertently obtained in the venous phase, when both arteries and veins are opacified with contrast. If contrast is present in the intracranial arteries and veins simultaneously, asymmetric prominence or a unilateral plexus in the region of the BVR can simulate an *aneurysm, AVM*, or an *AVF* (Figs. 40.71, 40.72, 40.73, and 40.74).

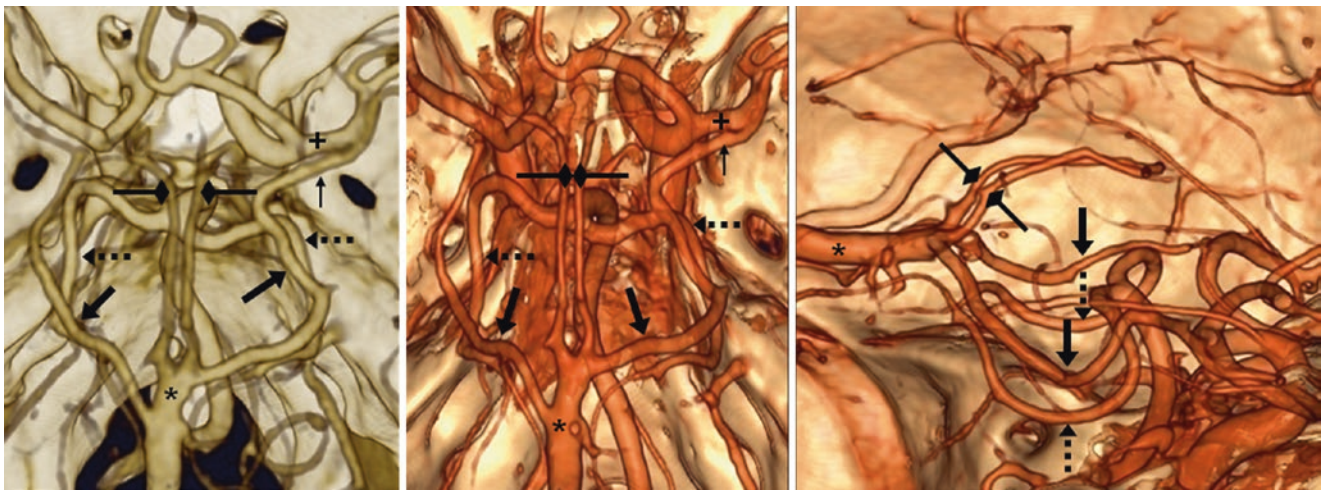

Fig. 40.71 76-year-old with a normal CTA. On superior (*left* and *middle*) and right lateral (*right*) views, the BVRs (*large arrows*) can be distinguished from the PCAs (*dotted arrows*). The right BVR connects to the superficial MCV via a deep MCV (*thin arrows*) closely apposed to the MCA (*plus sign*). The BVRs join the ICVs (*diamond-tip arrows*) to form the VOG (*asterisks*)

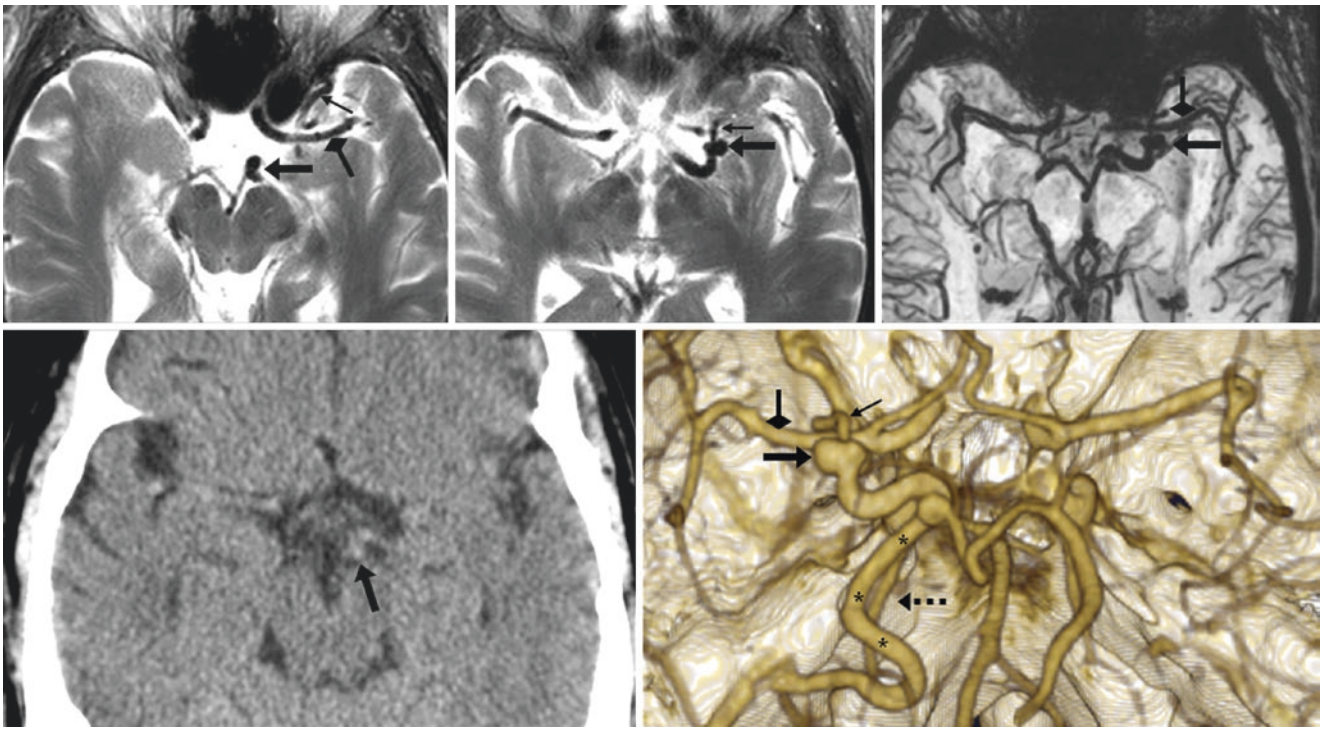

Fig. 40.72 79-year-old evaluated for carotid stenosis. *Top row:* On axial T2WI MRI (*left* and *middle*) and 8 mm-thick SWI (*right*), a bulbous flow void (*arrows*) simulated an aneurysm of the MCA or PCA. *Bottom row:* The structure also appeared suspicious on nonenhanced CT (*left*), but a 3D VR CTA PA view (*right*) showed it to be separate from both the PCA (*dotted arrows*) and MCA (*diamond-tip arrow*). Note a branch (*thin arrow*) that connects to the sphenoparietal sinus anteriorly. This likely represents a plexus at the junction of the deep MCV and the BVR (*asterisks*)

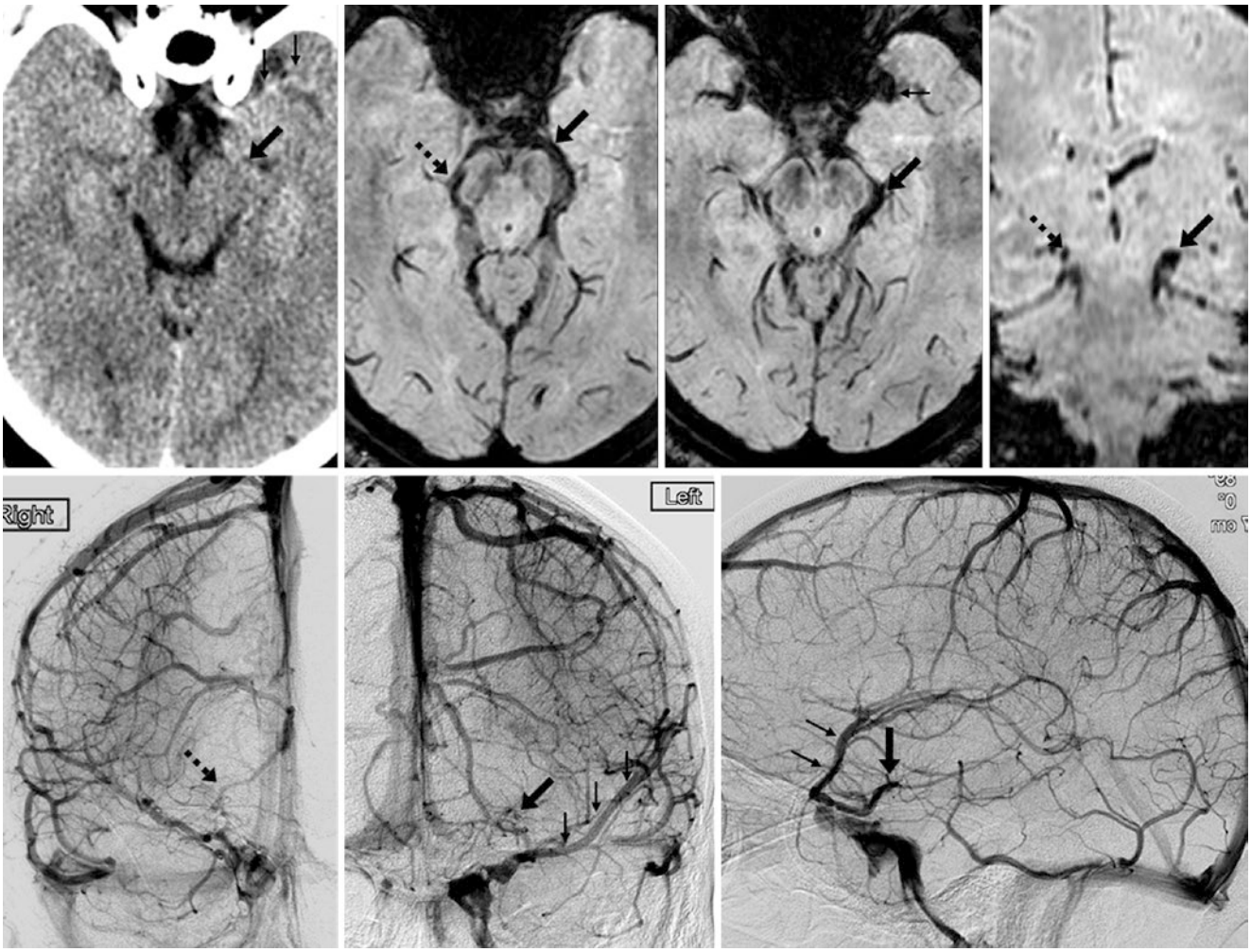

Fig. 40.73 *Top row:* In a 36-year-old, nonenhanced CT (*left*) and 2 mm thickness axial (*middle images*) and coronal (*right*) SWI showed an asymmetrically prominent vessel (*arrows*) within the left perimesencephalic cistern, simulating an enlarged PCA from an AVM or AVF. *Bottom row:* A venous-phase catheter DSA AP view (*left*) via right ICA injection shows a normal right BVR (*dotted arrows*), and a venous-phase left ICA injection (*middle*) reveals a prominent BVR plexus (*arrow*) that largely drains anteriorly into the MCVs (*thin arrows*), rather than into the VOG; a lateral view of the left ICA injection is also provided (*right*)

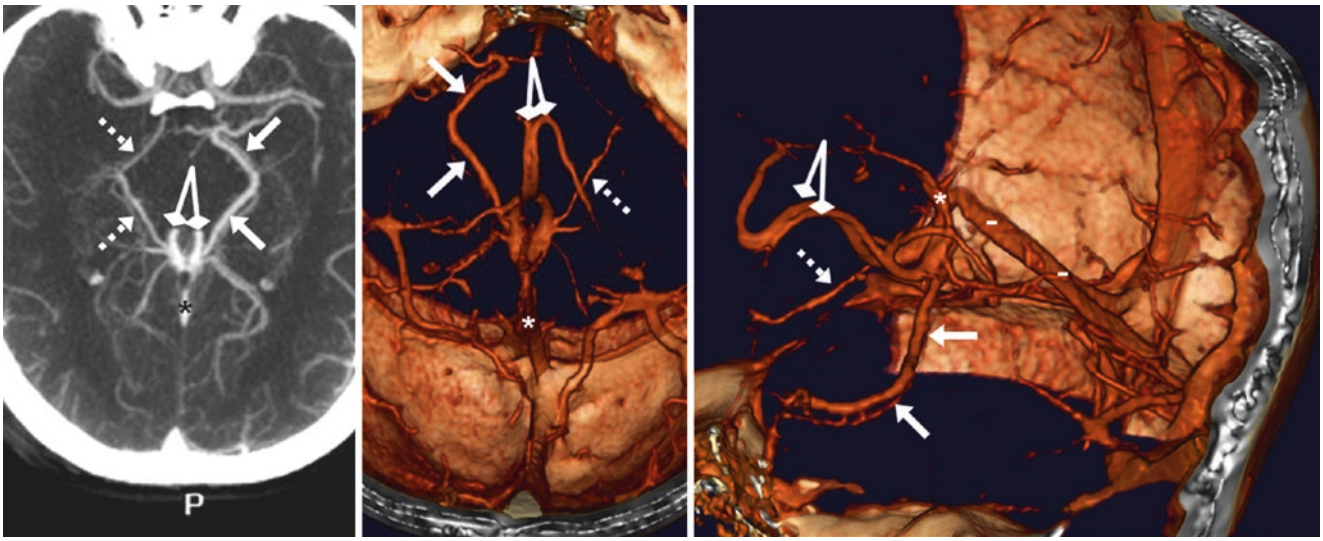

Fig. 40.74 In this 26-year-old, a CTA with a 12 mm thickness axial MPR (*left*), a 3D VR superior view (*middle*), and a 3D VR left lateral view (*right*) depict an asymmetrically prominent left BVR (*arrows*) as compared with the right (*dotted arrows*). This finding simulates an abnormally enlarged PCA, which can be seen with an AVM or AVF. The BVR drains as expected into the VOG (*asterisk*s), along with the ICVs (*double diamond arrows*). Note the normal straight sinus posteriorly (*minus signs*)

40.10 Lateral Tentorial Sinus Prominence

The *tentorial sinuses* consist of both *medial* and *lateral* divisions. The medial divisions that drain the surface of the cerebellum travel superiorly, thereafter draining into the *straight sinus, transverse sinus*, and *torcular*. The lateral divisions drain the surface of the lateral base of the occipital-temporal lobes, and drain into the *transverse-sigmoid junction*. The veins that converge into the lateral tentorial sinus include the *anterior, middle*, and *posterior temporal veins*; the *vein of Labbé; the occipitobasal veins*; and the *anterior, middle*, and *posterior temporobasal veins* [22, 41–43].

It is important to be aware of the presence of the tentorial sinuses because the *lateral tentorial sinus* (LTS) in particular can appear quite prominent on MRI (particularly postcontrast T1WIs), and may simulate prominent arteries or veins that can be seen in *AVFs* or *AVMs*. The tentorial sinuses are best visualized on axial postcontrast images in the plane of the tentorium, and are usually not well seen on coronal or sagittal images. They may appear quite prominent on axial SWI as well, because of the dark, deoxygenated blood within the overlapping veins travelling horizontally in the axial plane. Three different appearances regarding the LTS have been typically identified [22, 41–43]:

- Type I, "candelabra" appearance
- Type II, independent draining veins
- Type III, "venous lake" appearance with a pooling or confluence of draining veins that ultimately drains into the transverse-sigmoid junction

Multiplanar MRI postcontrast images (and sometimes T2WI or SWI) can identify normal LTSs and distinguish the subtypes. Thicker SWI "sliding MIPs" can demonstrate LTSs especially well, particularly with thicknesses of 8–10 mm and 2–4 mm overlap (Figs. 40.75, 40.76, 40.77, 40.78, 40.79, 40.80, 40.81, 40.82, 40.83, 40.84, 40.85, and 40.86).

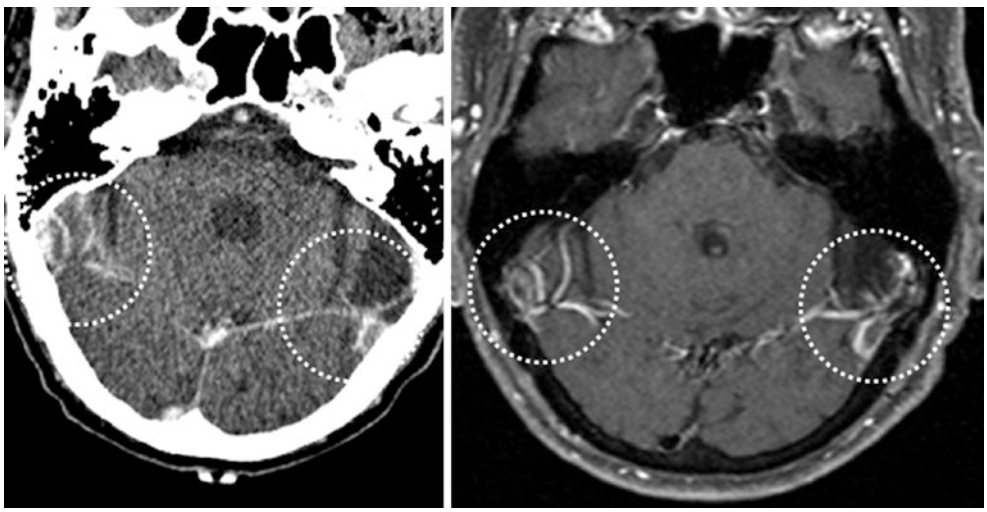

Fig. 40.75 71-year-old with bilateral type I ("candelabra"-type) lateral tentorial sinuses (LTSs) (*dotted circles*) on contrast-enhanced CT (*left*), which are situated on top of the transverse sinuses. On postcontrast axial T1WIs (*right*), these sinuses could mimic enlarged draining veins of an AVM or an AVF. This appearance was unchanged 1 year later (*not shown*)

Fig. 40.76 48-year-old with a right type I LTS that exhibits a "candelabra" appearance (*dotted circle*) on postcontrast T1WI

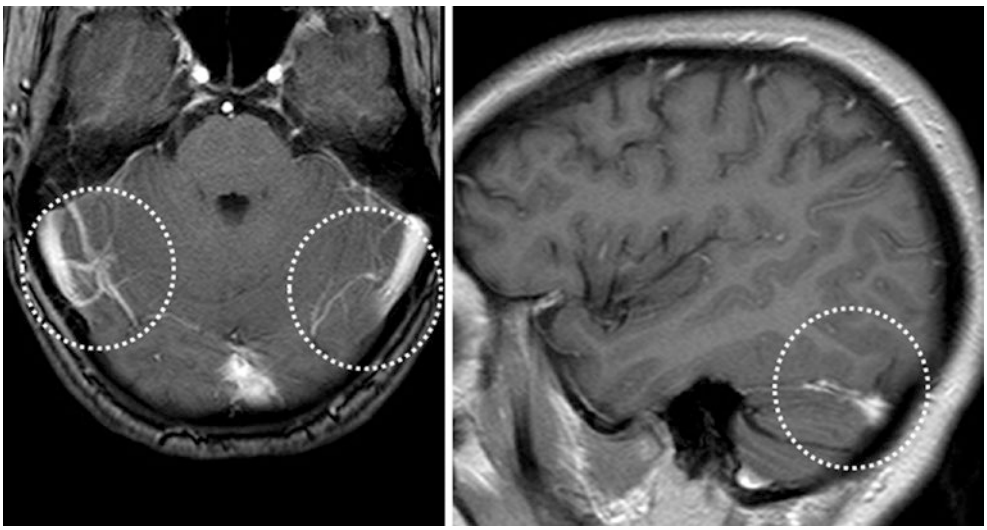

Fig. 40.77 17-year-old with a right type I LTS (*dotted circles*) on an axial postcontrast T1WI (*left*), which was not as apparent as on sagittal T1WI (*right*). The left LTS appears to be type II, multiple independent draining veins

Fig. 40.78 5-year-old with a right type I LTS and a left type II LTS (*dotted circles*) on a postcontrast T1WI

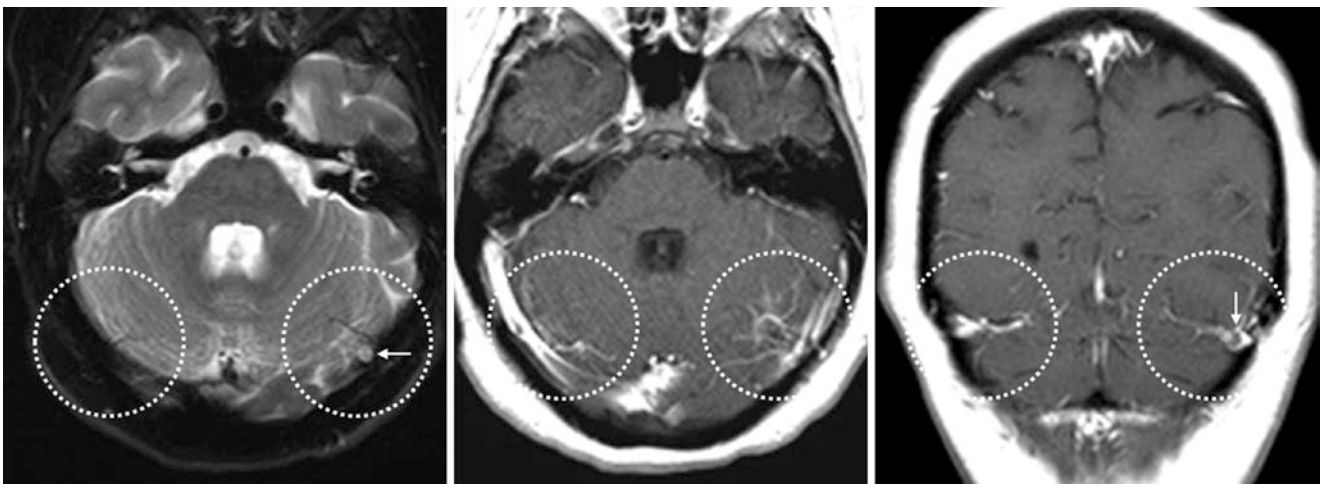

Fig. 40.79 13-year-old with a type II (independent draining veins) LTS (*dashed circles*) on the right, and a type III ("venous lake") LTS on the left, as seen on a T2WI (*left*) and on axial (*middle*) and coronal (*right*) postcontrast T1WIs. Note how the LTSs are best depicted on axial images. Also note an incidental T2-bright arachnoid granulation (*tiny arrows*) within the left transverse sinus–LTS junction, which appears as a filling defect on postcontrast T1WIs

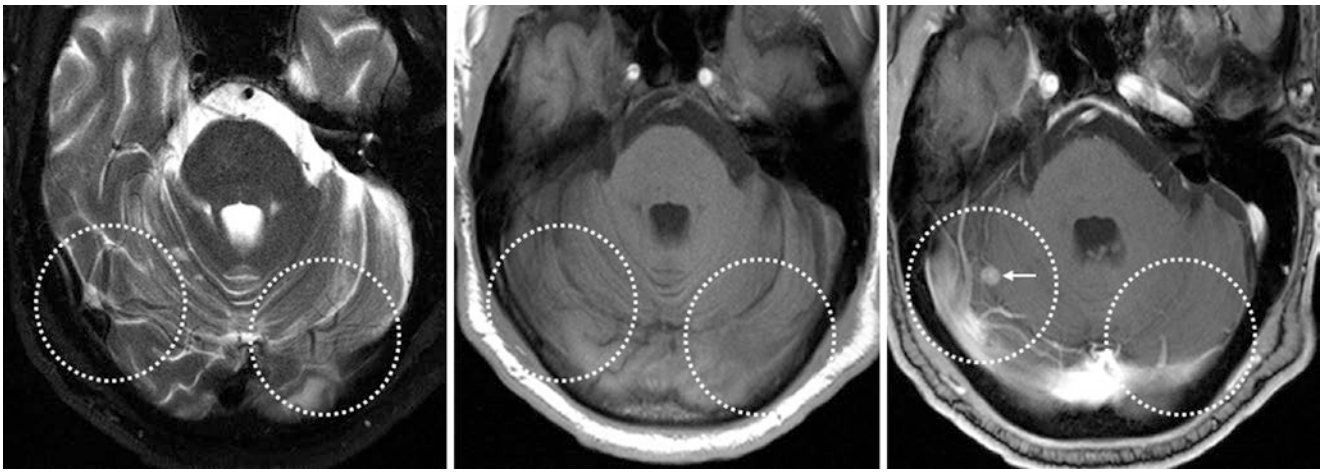

Fig. 40.80 63-year-old with flow voids of a right type III "venous lake" LTS (*dashed circles*) along the superior aspect of the transverse sinus, which could simulate prominent veins of a dural AVF or an AVM on an axial T2WI (*left*). Precontrast (*middle*) and postcontrast (*right*) T1WIs show an enhancement pattern typical of an LTS. The left LTS is less distinct, but is likely a type II. Also note a right cerebellar lung cancer metastasis (*tiny arrow*)

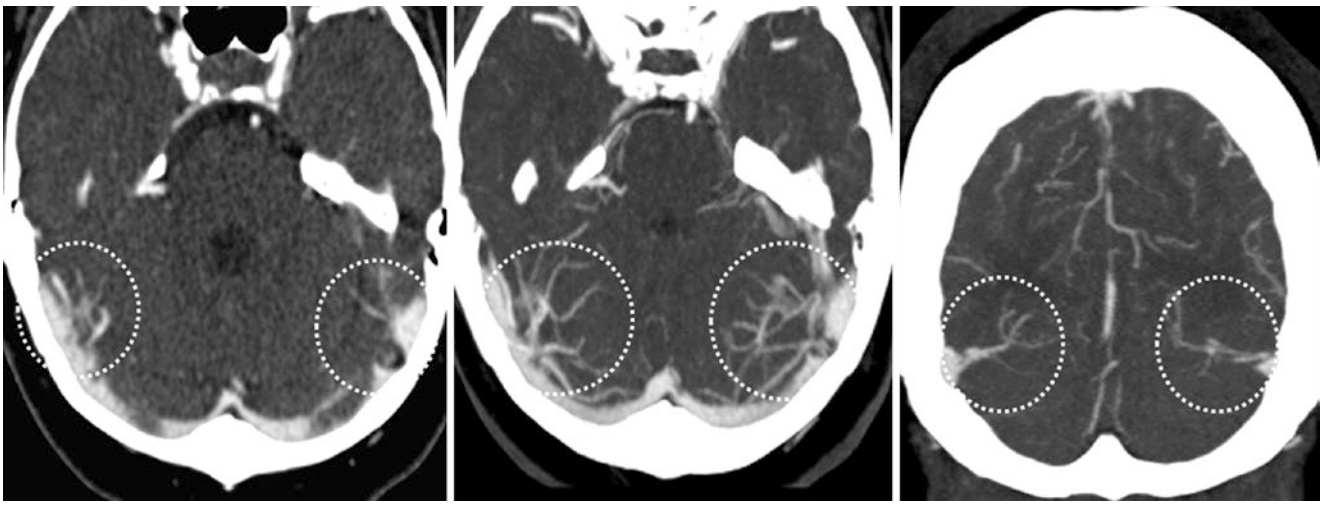

Fig. 40.81 54-year-old with a right type I and a left type I or type II LTS (*dashed circles*) on axial thin (<1 mm) CTA images (*left*), which on thicker (15–20 mm) MPR images (*middle*) appear prominent but well-discerned. Coronal (15–20 mm) thick MPR images (*right*) show that the coronal plane does not demonstrate the LTSs as well as the axial plane

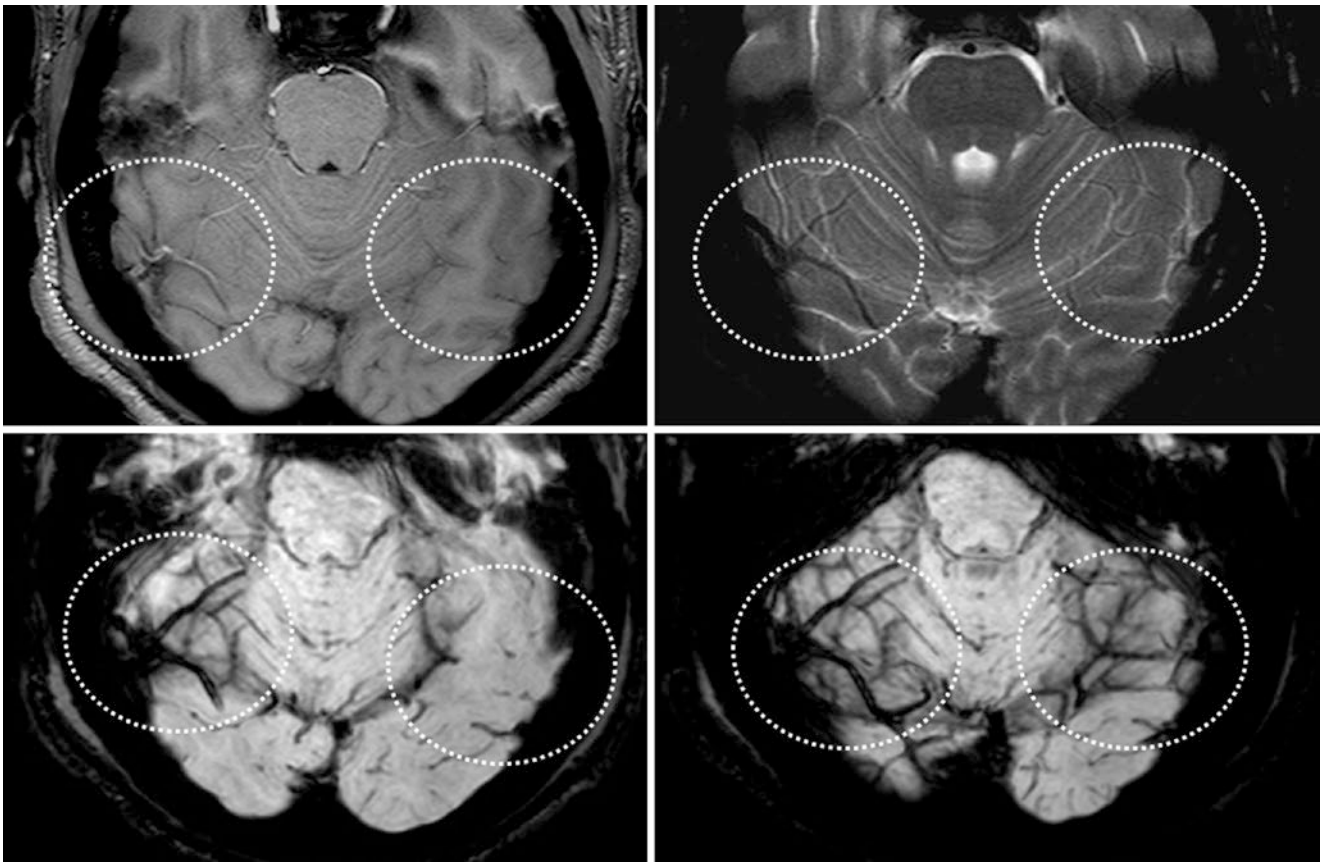

Fig. 40.82 In this 25-year-old, a noncontrast gradient echo T1WI (*top left*) depicts a right type I LTS, also discernible on T2WI (*top right*). The left LTS is type II and is not as well seen. A similar appearance is noted on 2 mm thickness SWI (*bottom left*); 8 mm-thick SWI (*bottom right*) exaggerates and better depicts the type II left LTS

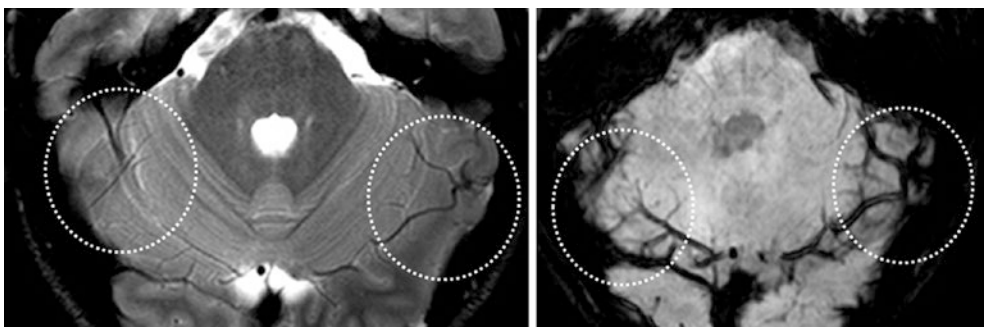

Fig. 40.83 14-year-old with a right type II and left type I LTS (*circles*) on an axial T2WI (*left*). A 10 mm thickness SWI (*right*) better depicts the LTSs. It is important to note that such venous plexi may be exaggerated on thicker (>5 mm) images

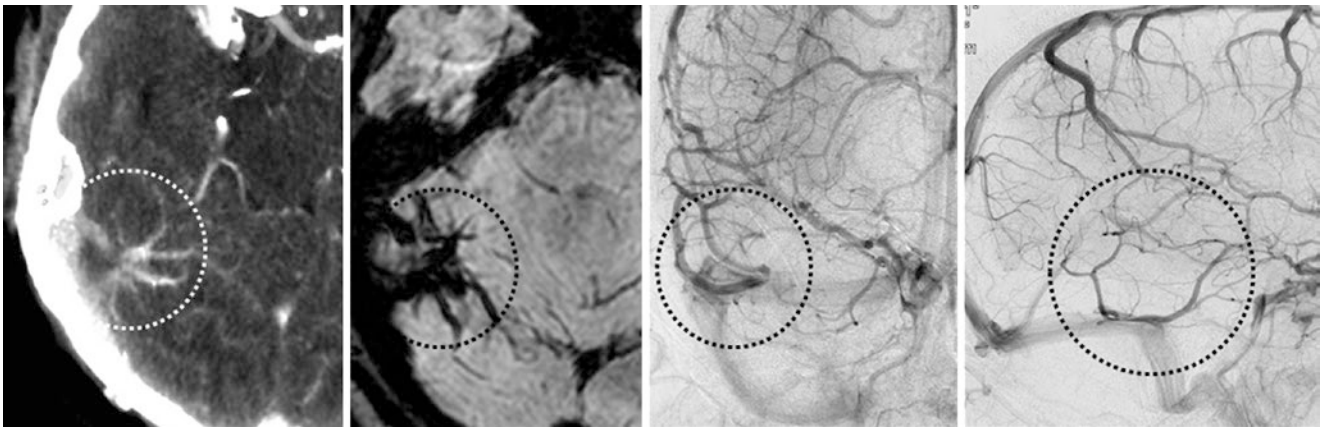

Fig. 40.84 46-year-old with a right type I LTS (*circle*) at the top of the transverse sinus on a CTA (*left*); the LTS simulated prominent veins, and an AVF/AVM was questioned. A 10 mm thickness SWI (*left middle*) and catheter DSA AP (*right middle*) and lateral (*right*) views all confirmed a normal LTS (*Courtesy of* Basar Sarikaya, MD, Minneapolis, MN)

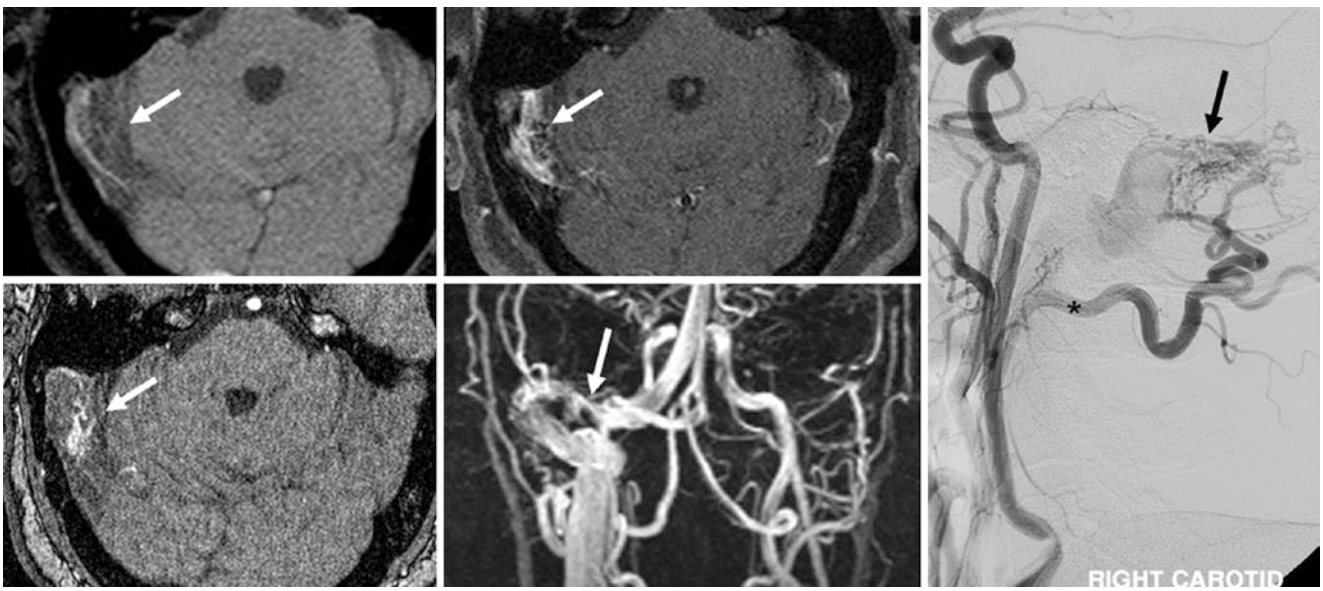

Fig. 40.85 Comparison case of a dural AVF. 55-year-old with pulsatile tinnitus. Suspicious MRI findings included loss of the right transverse sinus flow void on T1WI (*top left*), as well as irregular margins of the transverse-sigmoid junction on postcontrast T1WI (*top middle*), noncontrast 3DTOF MRA (*bottom left*), and CEMRV (*bottom middle*). Catheter DSA (*right*) showed arterial-phase venous filling, indicating a dural AVF (DAVF) (*arrow*) supplied by an enlarged occipital artery (*asterisk*)

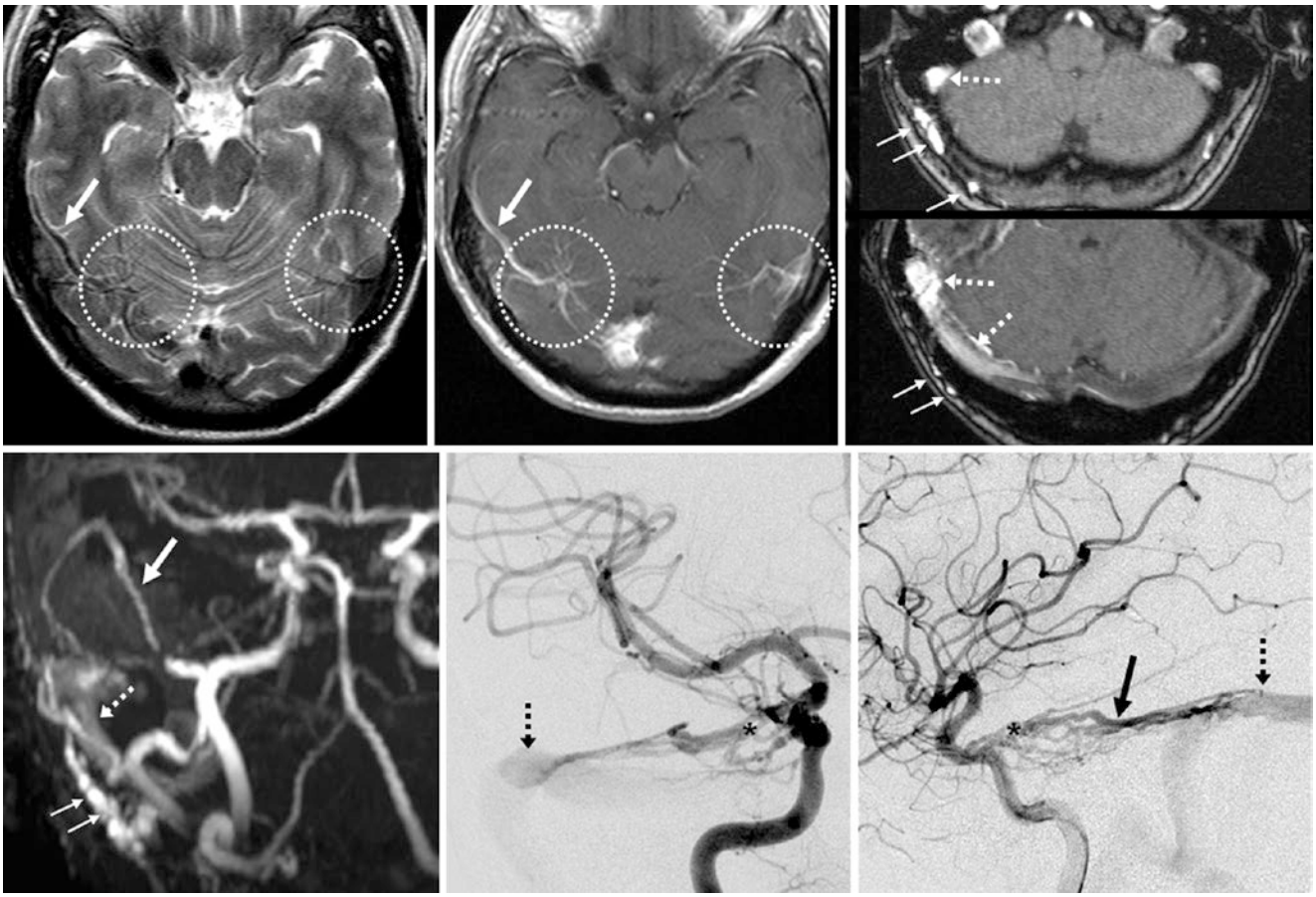

Fig. 40.86 Comparison case of a DAVF. 48-year-old with a right type I LTS and a left type II LTS (*dotted circles*) on T2WI (*top left*) and postcontrast T1WI (*top middle*). There is a prominent vein of Labbé (*arrows*). Source 3DTOF MRA (*top right*) and a 3D MIP AP view (*bottom left*) shows abnormal bright signal at the transverse-sigmoid junction (*dotted arrows*) with parasitized adjacent scalp (occipital artery) feeders (*thin arrows*). A catheter DSA AP view (*bottom middle*) and lateral view (*bottom right*) confirm a DAVF from scalp (external carotid) and meningohypophyseal (*asterisk*, ICA) branches. This case illustrates why abnormal dural sinus signal and prominent vessels should be evaluated further

40.11 Superficial Middle Cerebral Vein or Plexus Simulating Aneurysm or Arteriovenous Malformation

The *superficial middle cerebral vein* (SMCV) has a varied appearance, along a spectrum from totally absent to prominent and focally appearing enlarged, or having a poorly defined venous plexus that ubiquitously surrounds or abuts the *middle cerebral artery* (MCA) [3–6, 21–30, 35–46]. Two types are the most problematic: First, focal enlargement of the SMCV can exist in close proximity to the MCA and simulate an aneurysm on a poorly timed CTA or MRA after intravenous contrast administration. Similarly, a poorly defined SMCV or *sylvian plexus* could simulate an AVM or AVF. This appearance can uncommonly lead to an invasive procedure such as catheter DSA, which readily disproves the existence of an aneurysm, AVM, or AVF.

The SMCV lies within the superficial aspect of the sylvian fissure (which is why some refer to it as the "sylvian vein") and along the lateral surface of the cerebral hemisphere (mostly the temporal lobe). When present, it typically has six possible drainage routes [3–6, 21–30, 35–46]:

- Sphenoparietal type, draining with the sphenoparietal sinus (SPS) along the lesser wing of the sphenoid into the anterior aspect of the cavernous sinus
- Cavernous type, directly into the anterolateral aspect of the cavernous sinus by itself
- Emissary type, inferiorly into the pterygoid plexus via the middle cranial fossa
- Basal type, along the lesser wing of the sphenoid into the superior petrosal or tentorial sinuses and ultimately into the transverse sinus
- Squamosal type, posteriorly to join the transverse sinus (via the lateral tentorial sinus)
- Basal vein type, becoming the basal vein of Rosenthal posteromedially

Note that the SMCV is just posterior to the SPS, where the SPS is directly along the inner surface of the sphenoids' lesser wing. Superiorly, the SMCV often connects with the superior sagittal sinus via the *anastomotic vein of Trolard*, and with the transverse sinus via the posterior *anastomotic vein of Labbé*. The term "superficial" can be misleading, as it can travel into the sylvian fissure and closely appose the MCA (Figs. 40.87, 40.88, 40.89, 40.90, 40.91, and 40.92).

Fig. 40.87 *Top row:* 49-year-old with a prominent vascular structure (*arrow, left*) along the inferior aspect of the right MCA (*dotted arrow, right*) on nonenhanced CT, which raised the question of an MCA aneurysm. *Bottom row:* MRI and MRA were ordered; T2WI (*left*) depicted a small flow void from the SMCV (*arrow*), being anterior to the MCA, with a tiny, normal sphenoparietal sinus (SPS) (*thin arrow*) just anterior to the SMCV. A noncontrast 3DTOF MRA superior view (*right*) showed only a prominent, fast-flowing SMCV plexus (*arrow*). Although this simulated an aneurysm, this plexus also could have been mistaken for an AVM or AVF on T2WI, but there was a lack of accompanying enlarged arteries

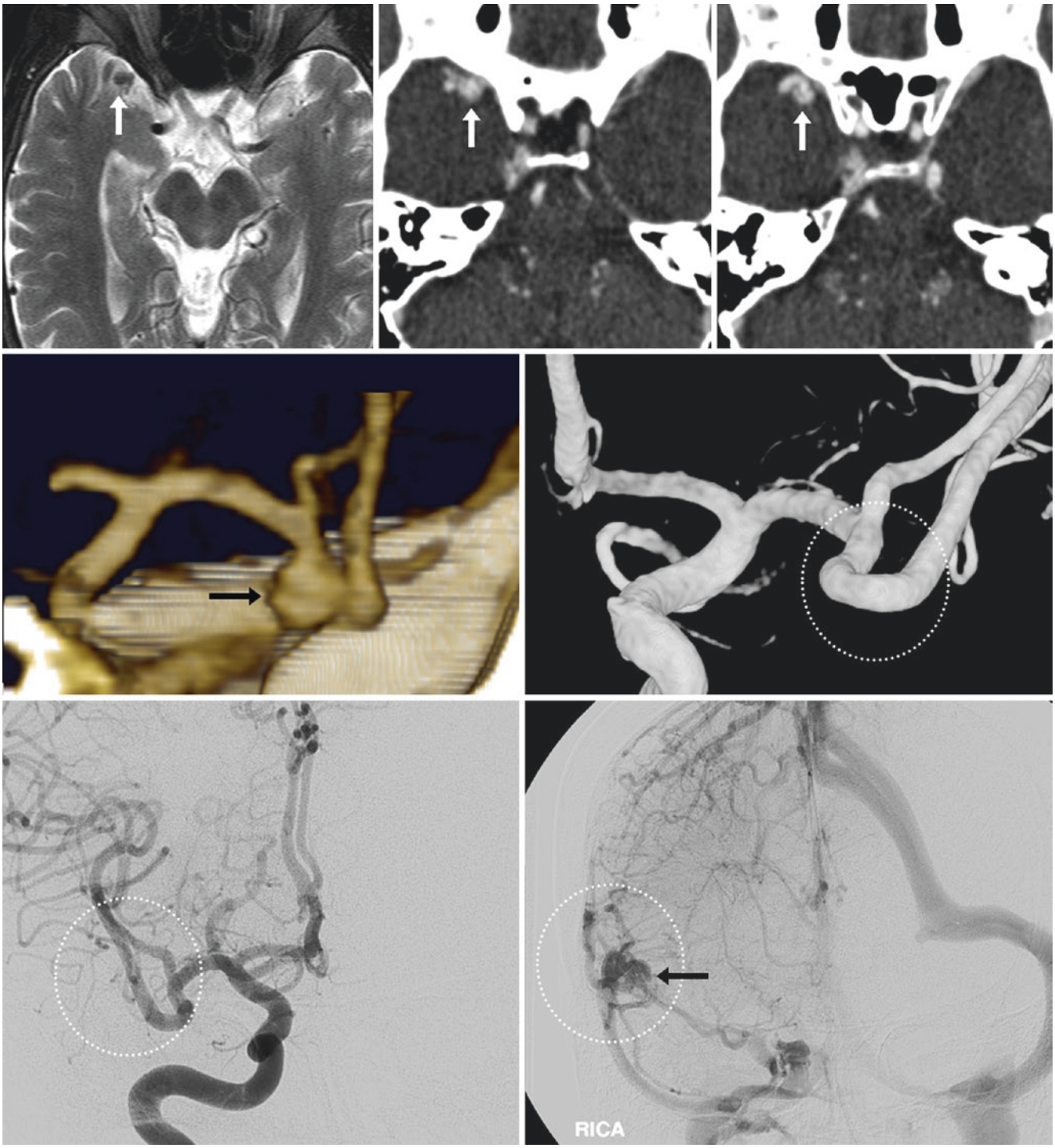

Fig. 40.88 38-year-old with confusion. *Top row:* A focal bulbous vessel (*arrows*) was noted in the vicinity of the right MCA on axial T2WI (*left*) and source CTA images (*middle* and *right*), raising the possibility of an aneurysm. *Middle row:* A 3D VR CTA PA view (*left*) showed that this was adjacent to an inferior division M1-2 branch (*thin arrows*), but at this point it was considered indeterminate whether the bulbous structure was arterial or venous in nature. Catheter 3DDSA images did not find an aneurysm in that location (*dotted circle*, *right*). *Bottom row:* The lack of abnormality was also confirmed on a catheter DSA AP view (*dashed circle, left*). However, in the venous phase, the SMCV appeared quite prominent as a venous plexus immediately adjacent to the right MCA (*arrow, right*). The likely reason that this SMCV venous plexus was visualized was that the CTA was partially contaminated by contrast in the venous phase

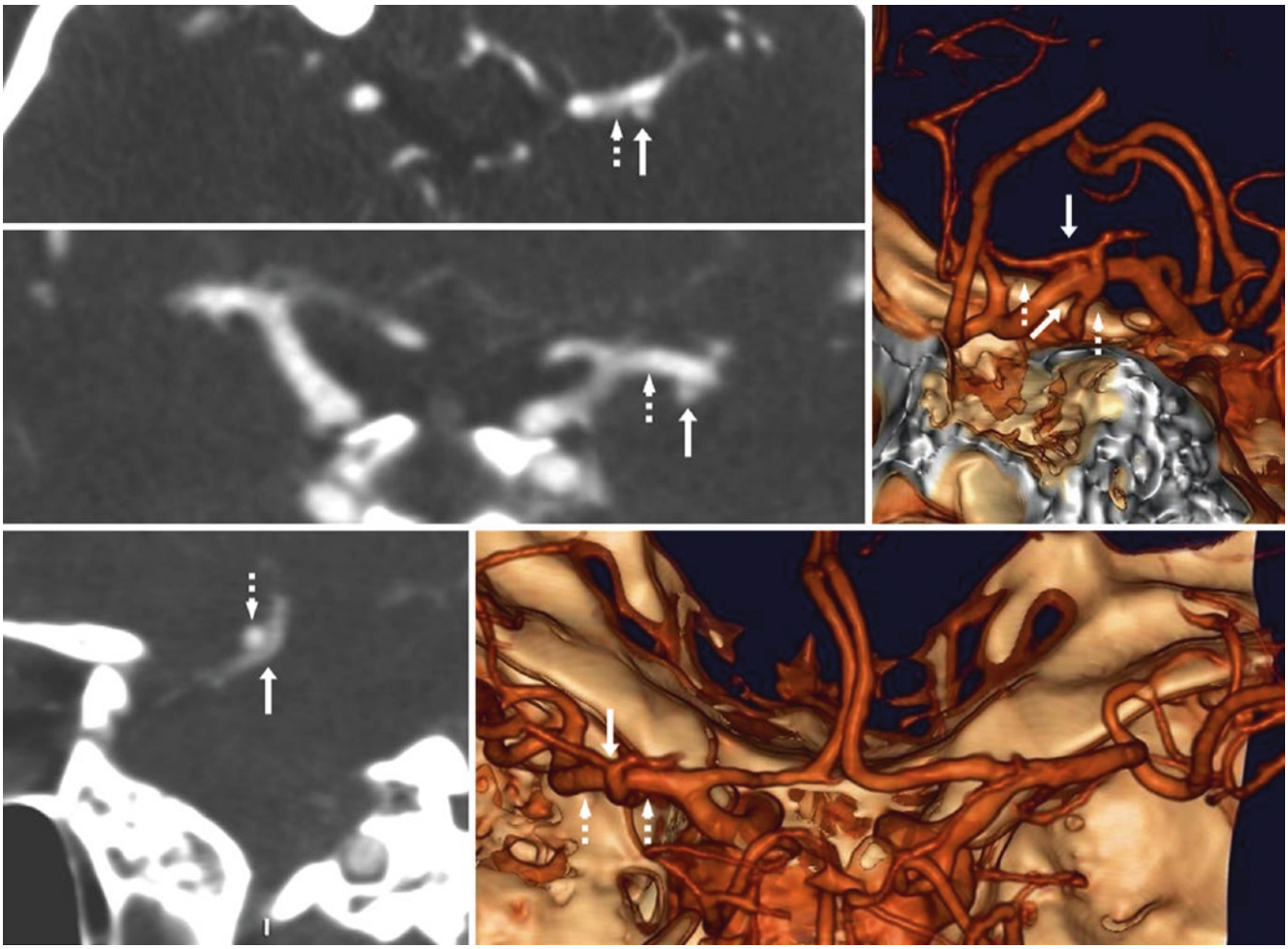

Fig. 40.89 50-year-old with a small outpouching (*arrows*) on axial thin-section source CTA images (*top left*), which abuts the left MCA (*dotted arrows*) and simulates a tiny aneurysm, also seen on a coronal thin image (*middle left*). 3D VR CTA images confirm this structure to be separate from, and travelling just inferior to, the MCA on an LPO view (*top right*) and PA view (*bottom right*). A sagittal MPR (*bottom left*) shows that this structure is indeed a prominent SMCV, as it had a different density of contrast. The SMCV was visualized adjacent to the MCA and simulated aneurysm because the CTA was partially in the venous phase

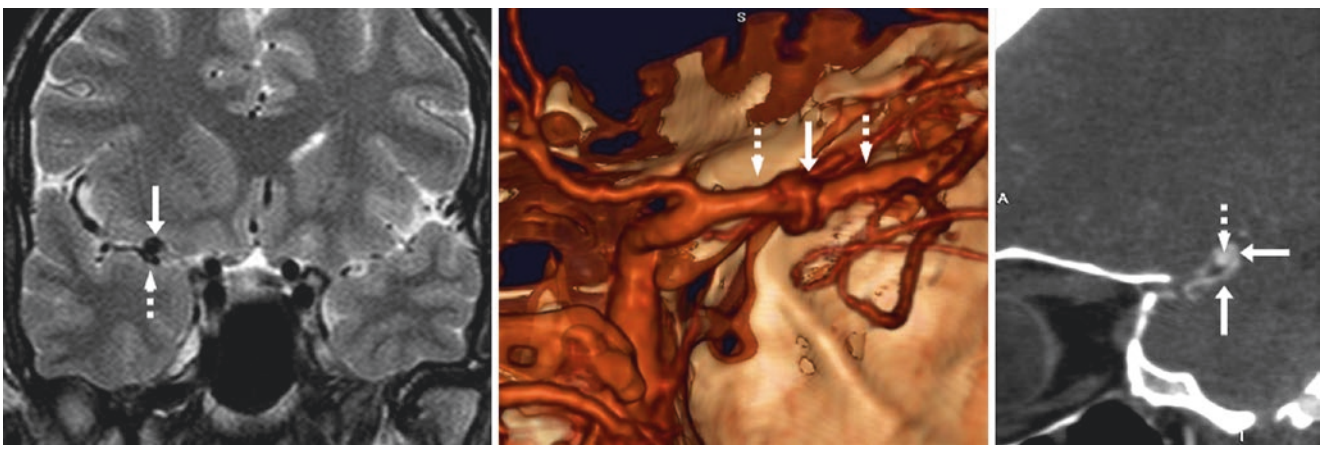

Fig. 40.90 32-year-old with an SMCV (*arrows*) suspected to represent an aneurysm on coronal T2WI MRI (*left*). A CTA later showed that the SMCV wrapped around the right MCA (*dotted arrows*) on a PA view (*middle*), and on a sagittal MPR (*right*). Note the difference in contrast density between the SMCV and the MCA; the CTA was partly into the venous phase (*Courtesy of* Chip Truwit, MD, and Chris Palmer, MD, Hennepin County Medical Center, Minneapolis, MN)

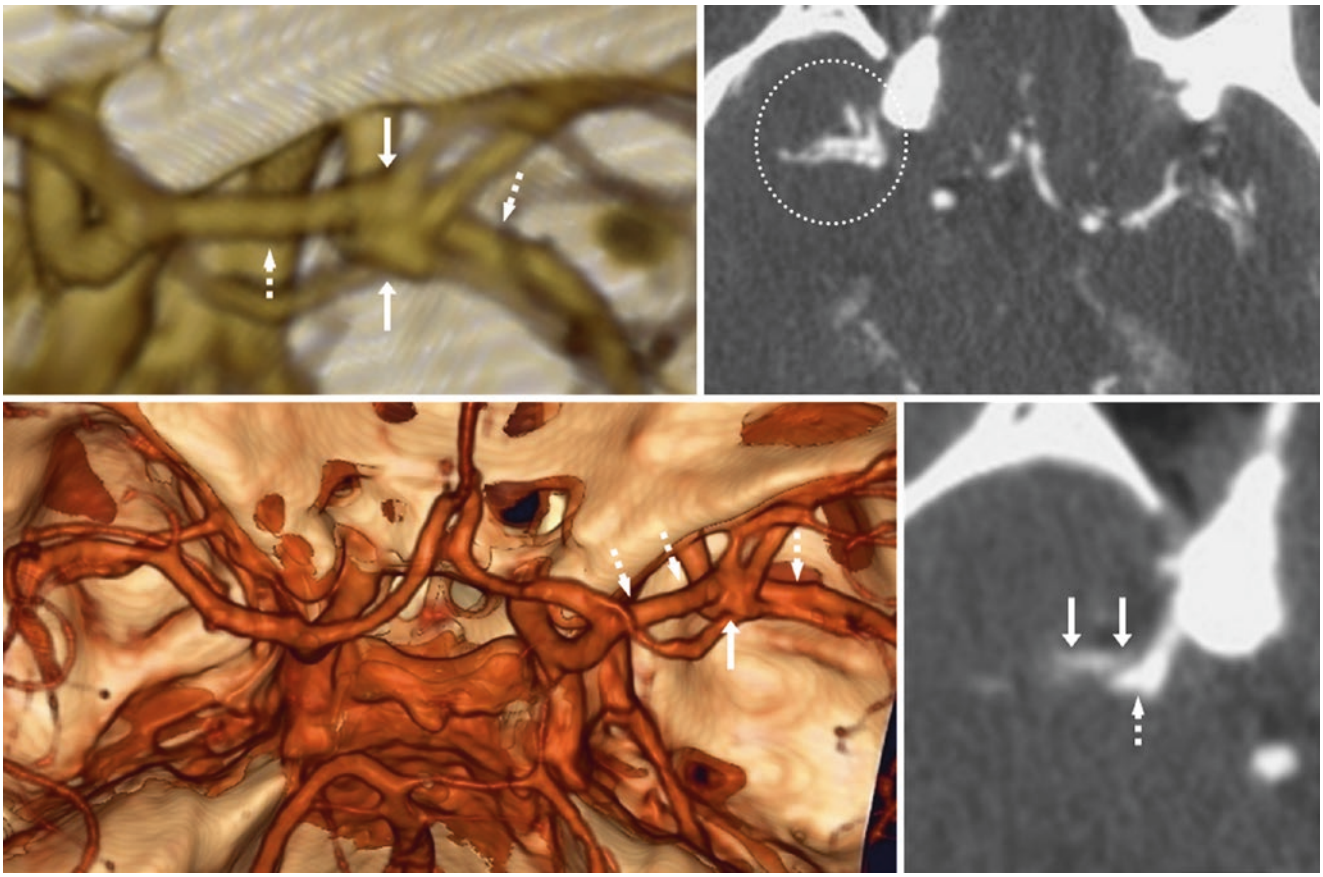

Fig. 40.91 51-year-old with a large outpouching (*arrows*) noted on a 3D VR CTA superior view (*top left*); the outpouching either abuts or surrounds the left MCA (*dashed arrows*), simulating an aneurysm or AVM nidus. This confusing network of vessels was thought to be a combination of both MCA and SMCV on axial images (*top right*). A 3D VR CTA PA-superior view (*bottom left*) showed the arteries and veins to be separate, a finding confirmed by thin axial images (*bottom right*), as the arteries and veins had differing contrast concentrations. Thus, the CTA was partially in the venous phase

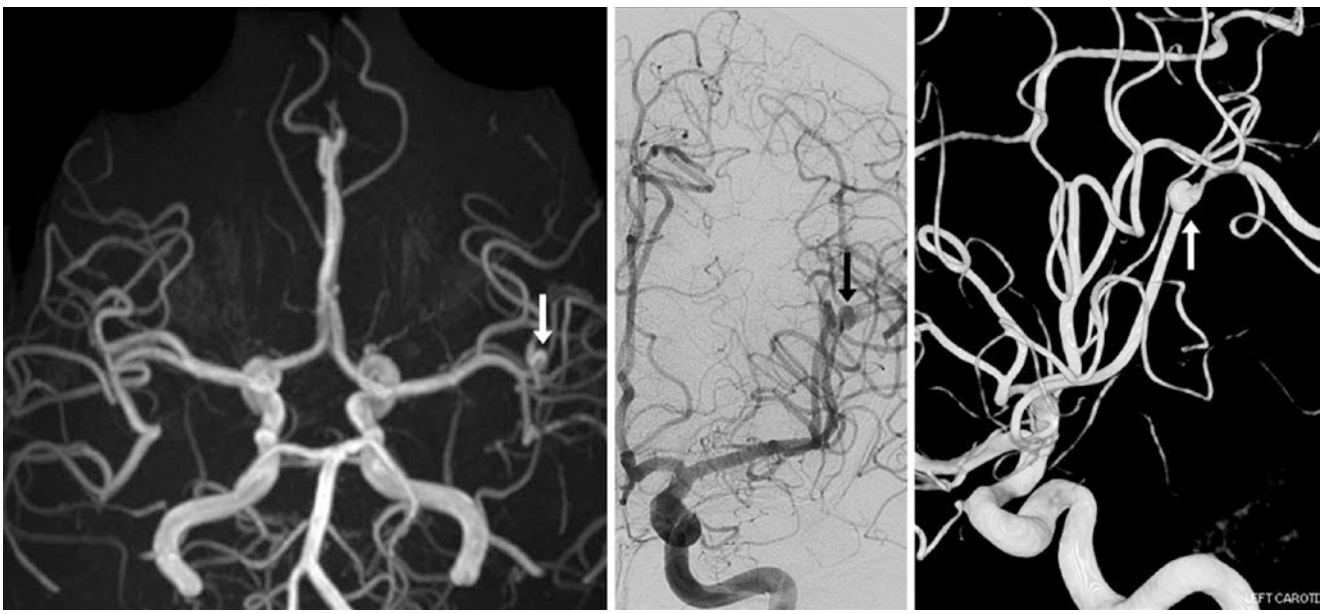

Fig. 40.92 Comparison Case of Mycotic Aneurysm. 26-year-old with a tiny subarachnoid hemorrhage in the left sylvian fissure and an infarct on DWI MRI (*not shown*). A 3DTOF MRA AP view (*left*) found a small left MCA outpouching (*arrow*) of a distal M2 segment, suspicious for an aneurysm. A catheter DSA AP view (*middle*) and a 3DDSA lateral view (*right*) confirmed the aneurysm; the distal location was suspicious for a mycotic aneurysm. A central infectious source was later found to have predisposed the patient to developing a mycotic aneurysm

40.12 Sphenoparietal Sinus Variants

The term "*sphenoparietal sinus*" (SPS) has been used with some ambiguity, traditionally referring to the venous plexus or sinus drainage lining the inner surface of the lesser sphenoid wing, and receiving drainage from veins along the meninges, the greater sphenoid wing, and the temporal bone. This name has caused confusion, as it was thought (and propagated as such) that the *SMCV* ultimately terminated in the SPS under the lesser wing of the sphenoid or drained into the *cavernous sinus* directly; many authors have suggested that the SMCV and the SPS are one and the same or always communicate with each other [21–30, 35–48]. However, recent evidence suggests that the SPS is likely to be separate from the SMCV with separate drainage, and the term "SPS" should be reserved for the vein that drains along the inner aspect of the lesser wing of the sphenoid and that has three types of general appearances and drainage routes [21–30, 35–48]:

- Draining into the anterior portion of the cavernous sinus
- Draining inferiorly into the region of the foramen ovale or *pterygoid plexus*
- A tiny hypoplastic SPS draining into the cavernous sinus anteriorly

Occasionally, the SPS may also drain posteriorly into (or connect with) the *vein of Labbé* (VOL).

The SPS can appear quite prominent in a fashion similar to the SMCV. This appearance can be problematic if it resembles a focal hyperdensity on an emergent nonenhanced CT, thus simulating a focal *parenchymal hemorrhage*, if lobular; a *subdural hemorrhage* (SDH), if appearing as a linear or crescentic hyperdensity; a vascular hyperdensity simulating *aneurysm* (if bulbous) or an *AVM* or *AVF* if linear; or as a plexus/network when poorly defined. Being familiar with the normal and wide variation in anatomy can delineate this appearance, but care is required because a dilated SPS or SMCV can occur in an AVM or AVF, though it typically occurs with enlarged arterial vessels and early (arterial phase) filling of dilated veins, which can be confirmed by catheter DSA if necessary. On postcontrast images, the SPS can also imitate abnormal dural thickening such as from *meningeal tumor* or *meningeal inflammation* (Figs. 40.93, 40.94, 40.95, 40.96, 40.97, and 40.98).

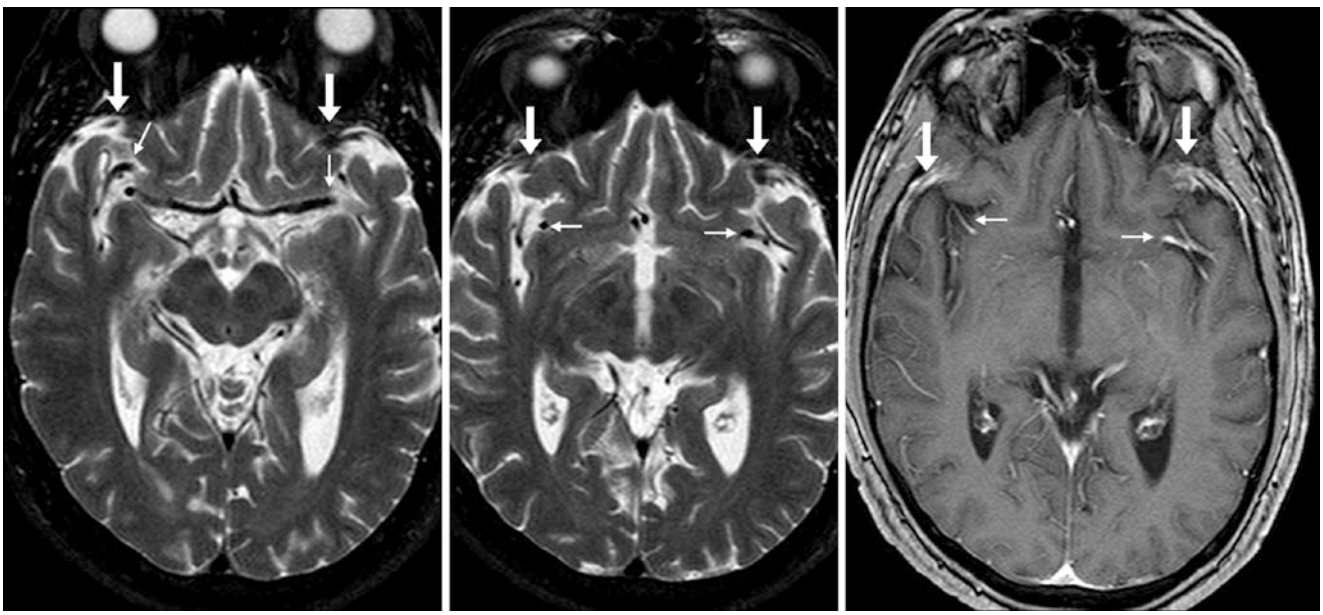

Fig. 40.93 59-year-old with a focal bulbous flow void (*arrows*) on T2WI (*left* and *middle*) anterior to the left MCA (*tiny arrows denote the MCAs*), which could mimic prominent vessels of an AVM, AVF, or aneurysm. Postcontrast T1WI (*right*) confirmed venous enhancement that was typical of an SPS, also present, but not bulbous, on the right side

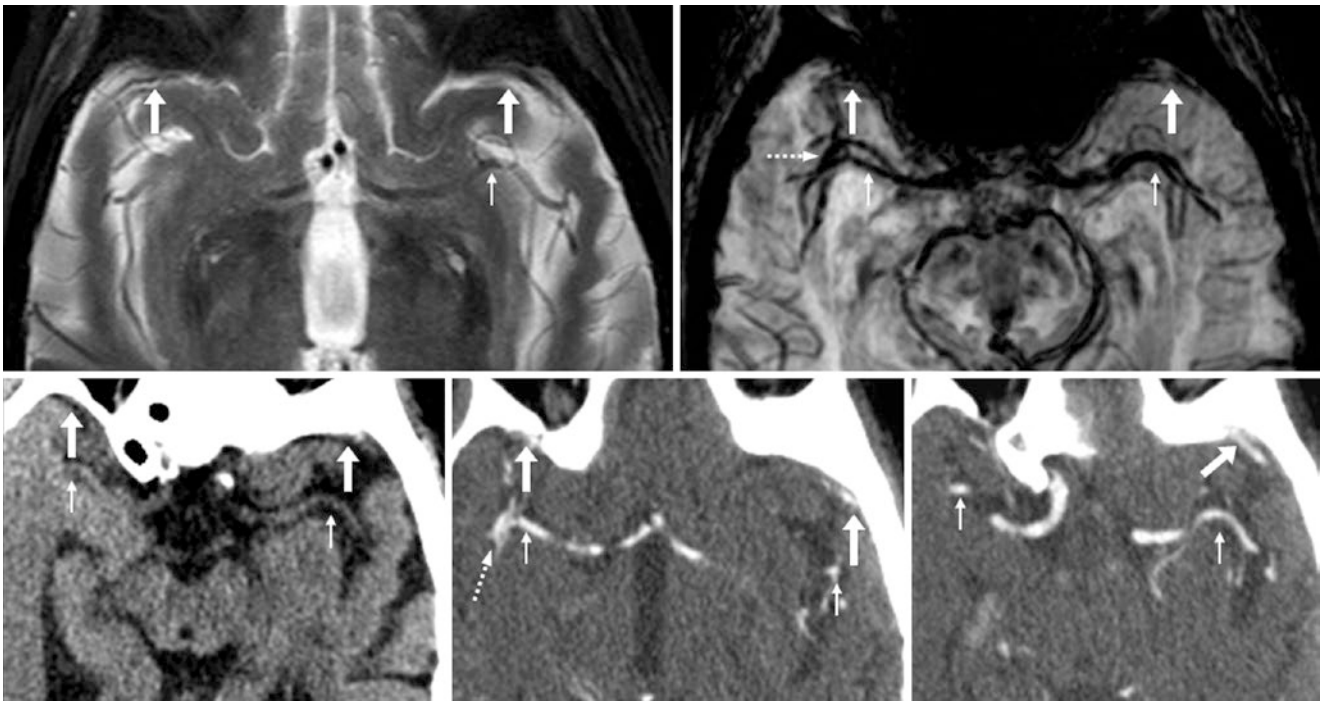

Fig. 40.94 84-year-old with bilateral flow voids from SPSs (*large arrows*) on T2WI (*top left*) and 10 mm thickness SWI (*top right*), with the MCAs (*thin arrows*) located posteriorly. On nonenhanced CT (*bottom left*), the left SPS is hyperdense from beam hardening artifact (which could simulate a subdural hemorrhage), but is patent on axial MPRs from a CTA (*bottom middle, bottom right*). The *dotted arrows* indicate a right SMCV plexus surrounding the right MCA

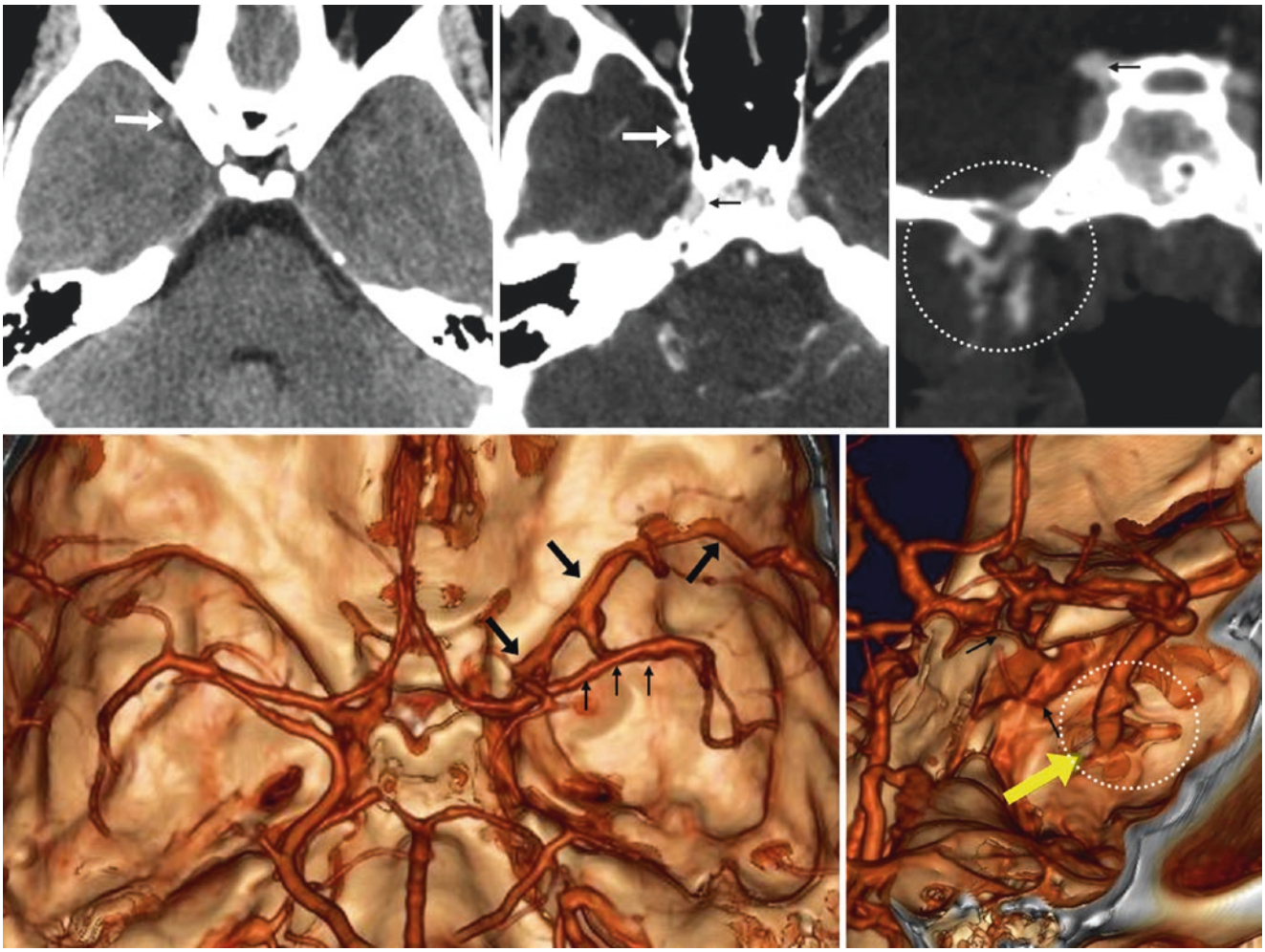

Fig. 40.95 *Top row:* 19-year-old with a focal hyperdensity (*arrows*) from an SPS that mimics an aneurysm on nonenhanced CT (*left*); it drains inferiorly on a CTA in axial (*middle*) and coronal (*right*) MPRs. *Bottom row:* A 3D VR superior view (*left*) delineates the SPS (*arrows*) and the ICA/MCAs (*thin arrows*). An oblique view (*right*) depicts the right SPS (*yellow arrow*) as it passes through a venous plexus (*dotted circle*) that spans the foramen ovale and pterygoid plexus

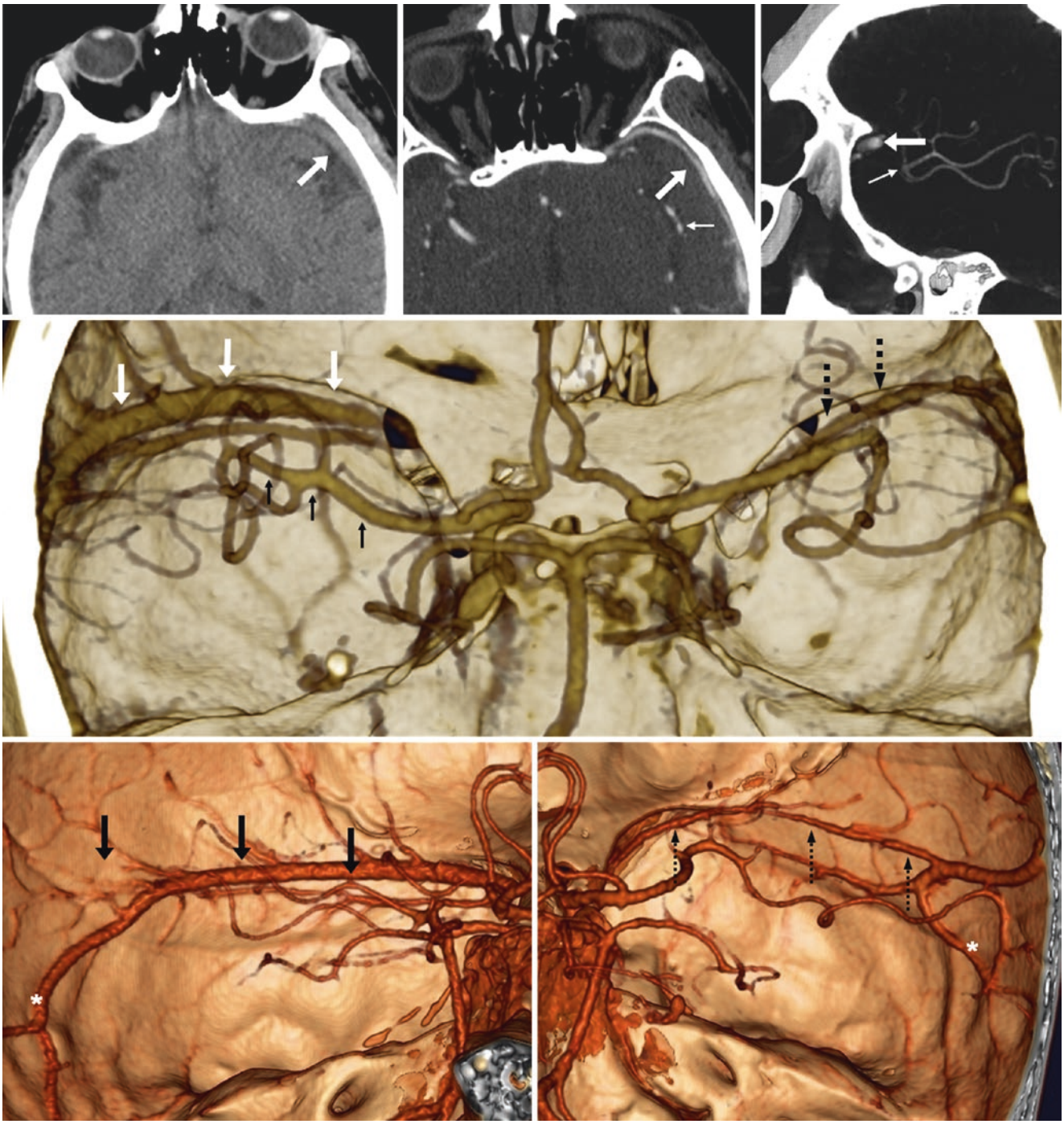

Fig. 40.96 45-year-old after trauma. *Top row:* Nonenhanced CT (*top left*) demonstrated a crescentic density (*arrows*) anterior to the left temporal lobe, which was questioned by a radiology resident physician to be a subdural hematoma (SDH), but later confirmed to be an SPS on a CTA reconstructed with axial (*top middle*) and sagittal (*top right*) MPRs. *Middle row:* A 3D VR PA view delineated the left SPS (*arrows*) and MCA (*thin arrows*), along with a smaller contralateral SPS (*dotted arrows*). *Bottom row:* Bilateral oblique views showed both SPSs connecting to the veins of Labbé (VOLs) (*white asterisks*). This case demonstrates how unilateral SPS prominence can simulate a SDH

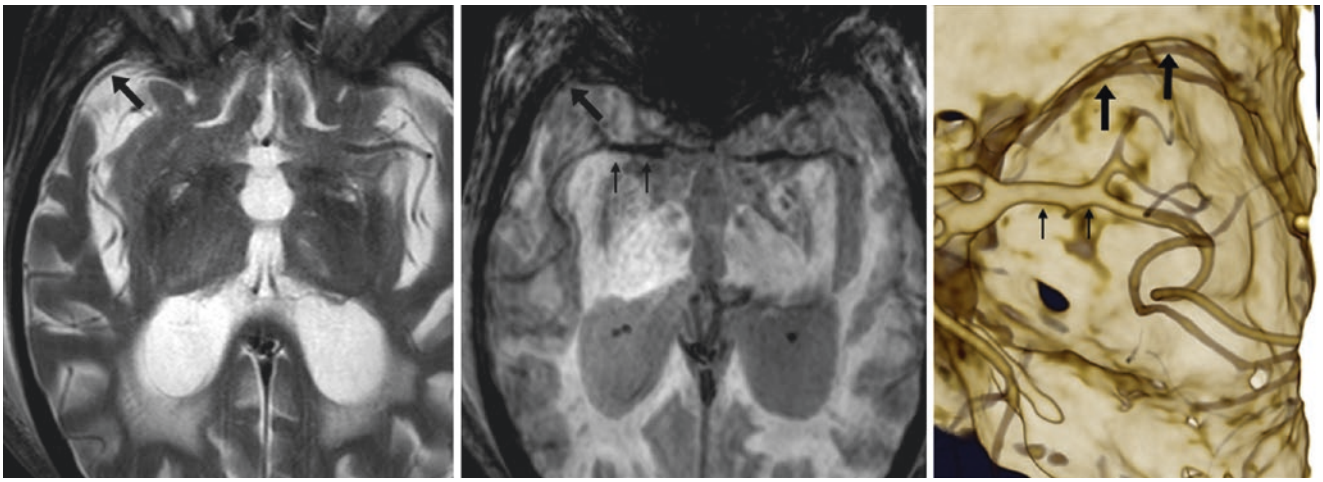

Fig. 40.97 94-year-old with a small right SPS (*large arrows*) depicted by a flow void on an axial T2WI MRI (*left*), an SWI MRI (*middle*), and on a 3D VR CTA superior view (*right*); the two adjacent veins along the inner aspect of the lesser wing of the sphenoid combine to form the SPS. The right MCA (*thin arrows*) is also shown

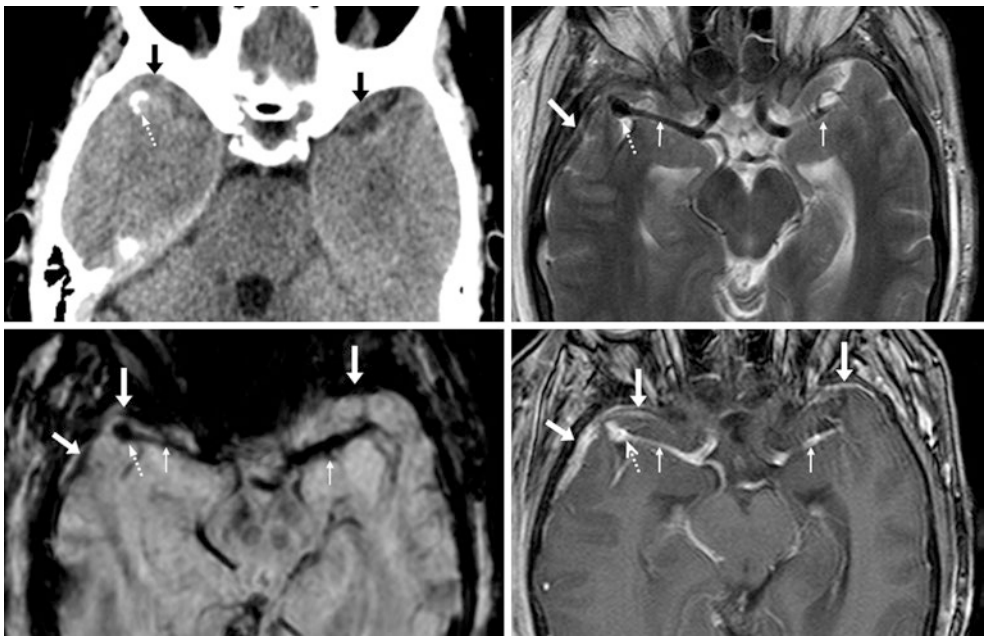

Fig. 40.98 Comparison Case of an MCA Aneurysm. 64-year-old post-trauma, with bilateral crescentic-appearing SPSs (*top right*, *large arrows*), simulating SDHs. A partially calcified lesion is situated just posterior to the right SPS (*dotted arrows*), confirming an MCA aneurysm. On T2WI (*top right*) and SWI (*bottom left*), the flow voids confirm an aneurysm, also shown on postcontrast T1WI (*bottom right*). *Thin arrows* denote the MCA's M1 segments

40.13 Prominence of the Superficial Anastomotic Veins of Trolard or Labbé

To understand the superficial anastomotic veins, it may be best to discuss the drainage of the *superficial middle cerebral vein* (SMCV). As previously discussed, the SMCV may drain into or separately from the *sphenoparietal sinus* (SPS). The SMCV lies within the superficial aspect of the sylvian fissure (which explains why it is also called the sylvian vein), coursing over the surface of the lateral aspect of each temporal lobe. It may connect with the dural sinuses, typically via two anastomotic veins: Superiorly, the great anastomotic *vein of Trolard* (VOT) can connect the SMCV to the *superior sagittal sinus* (SSS); inferiorly, the posterior anastomotic *vein of Labbé* (VOL) can connect the SMCV to the *transverse sinus* [22, 36–48]. The VOL may also connect to the SPS in addition to the SMCV. Though the drainage of the VOL is somewhat variable, it drains through the *lateral tentorial sinus* (LTS) into the transverse sinus in more than 80 % of the population; it drains less often into *petrosal sinuses* [22, 36–48].

The VOT is typically located somewhere between the precentral (frontal lobe) and postcentral (parietal lobe) sulci, although occasionally it may occur further anteriorly or posteriorly. If the VOT is not clearly present, there are usually several prominent cortical veins that may serve as substitutes by draining into the SSS. The VOL and the SMCV are more commonly the dominant superficial veins (each being dominant on that side in about 30–40 % of the population), relative to the VOT (10 %); co-dominance of all three veins occurs in about 10–20 %. Recent literature based on imaging suggests that the VOL may be seen in up to 90 % of the population on routine imaging, whereas the VOT is clearly visualized in about one third [22, 36–48]. A prominent VOL is usually normal, but it can also be seen in *AVMs* or *AVFs*. In this regard, it is important to note that AVMs or AVFs will usually have associated prominent arterial supply (Figs. 40.99, 40.100, 40.101, 40.102, 40.103, 40.104, and 40.105).

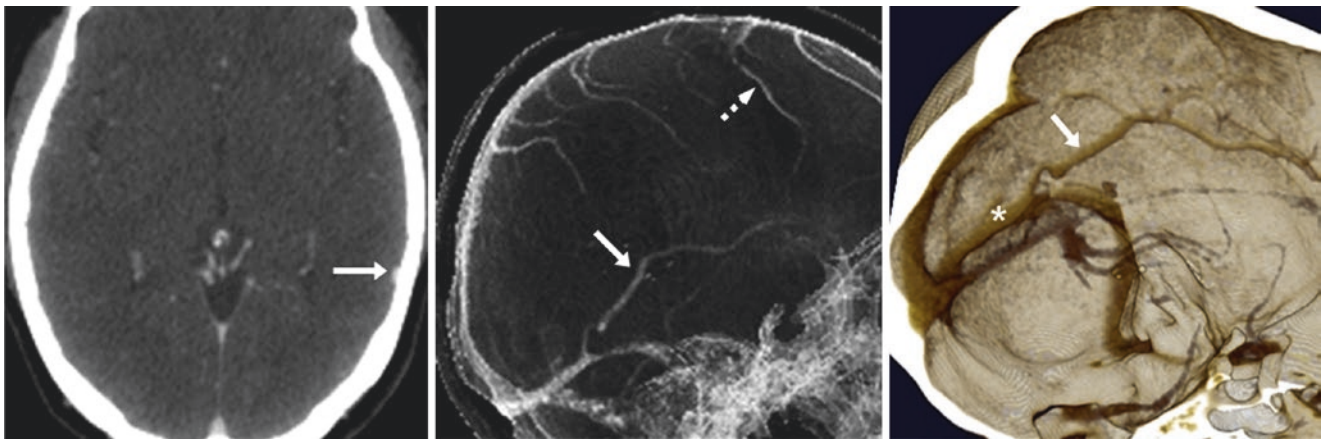

Fig. 40.99 41-year-old with a dominant/prominent left VOL (*arrows*) that connects to the left transverse sinus (*asterisk*) on axial (*left*) CTV images and on 3D "see through" left lateral MIP (*middle*) and "inner" (*right*) views. The vein of Trolard (VOT) (*dashed arrows*) is also depicted, but appears much smaller, as it is not the dominant superficial draining vein

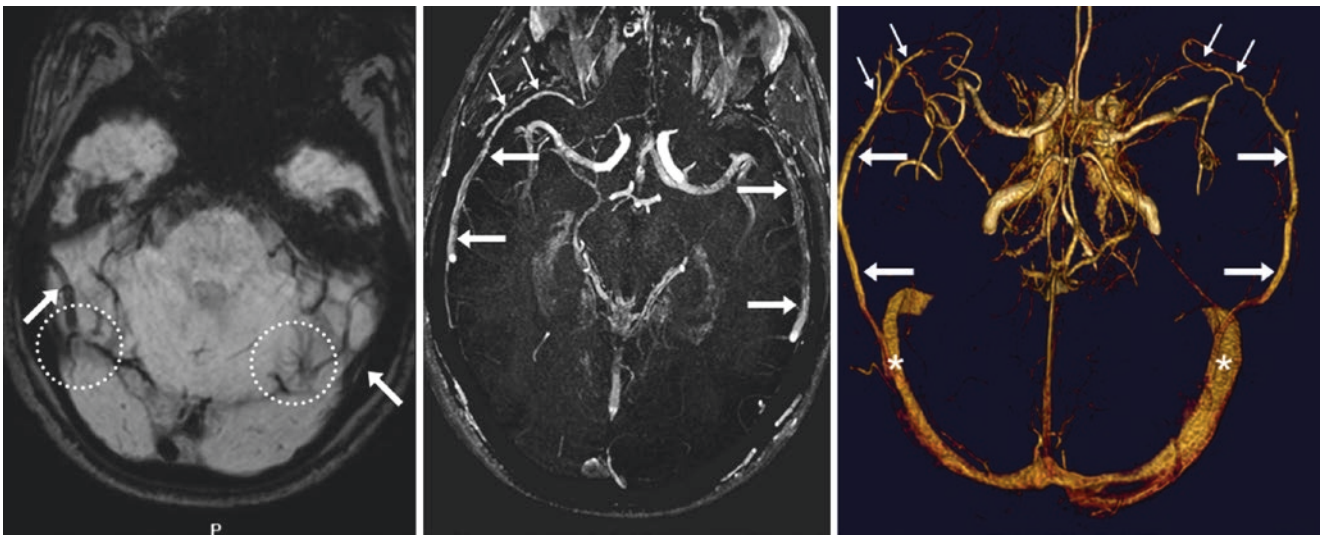

Fig. 40.100 41-year-old with bilaterally prominent VOLs (*arrows*) that drain through the LTSs (*dashed circles*) into the transverse sinuses (*asterisks*) on axial SWI images (*left*), on a 15 mm thick MPR CEMRA superior view (*middle*) and on an MIP 3D superior view (*right*). In this patient, both VOLs also connect anteriorly to the SPSs (*thin arrows*)

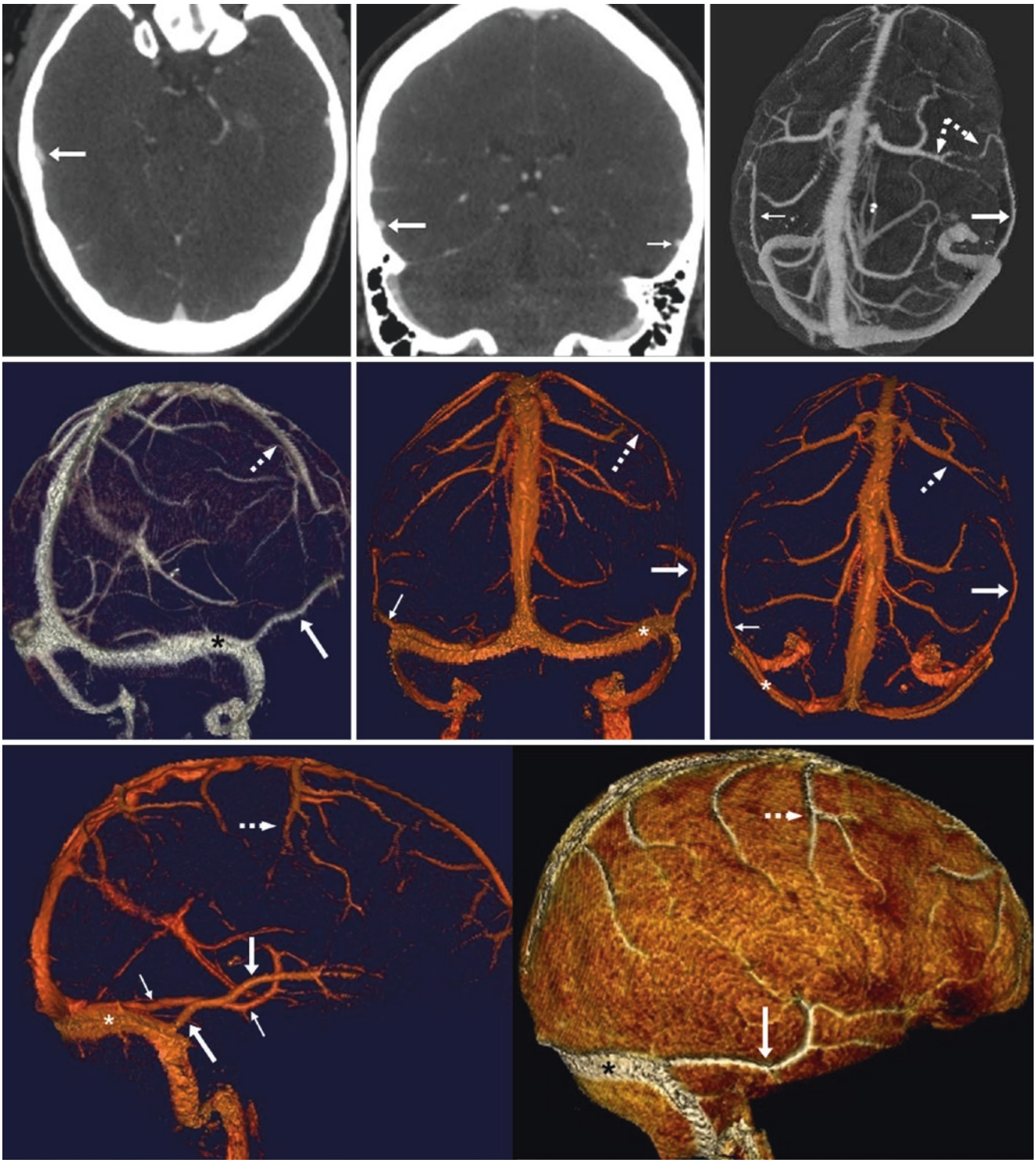

Fig. 40.101 35-year-old with headaches. *Top row:* There is a mildly prominent right VOL (*large arrows*) on CTV axial (*top left*) and coronal (*top middle*) MPRs, with a slightly prominent left VOL as well (*thin arrows*); note the VOT (*dotted arrows*). The right VOL connects to the right transverse sinus on 3D "see through" superior view images with the bones removed (*top right*). *Middle row:* 3D "see through" images including PA oblique (*left*), PA (*middle*), and superior (*right*) views demonstrate the mildly prominent right VOL. *Bottom row:* A right lateral view (*left*) and a surface-rendered lateral view (*right*) demonstrate that the right VOT (*dotted arrows*) is also prominent. Thus, the right VOL and VOT are considered to be "co-dominant"

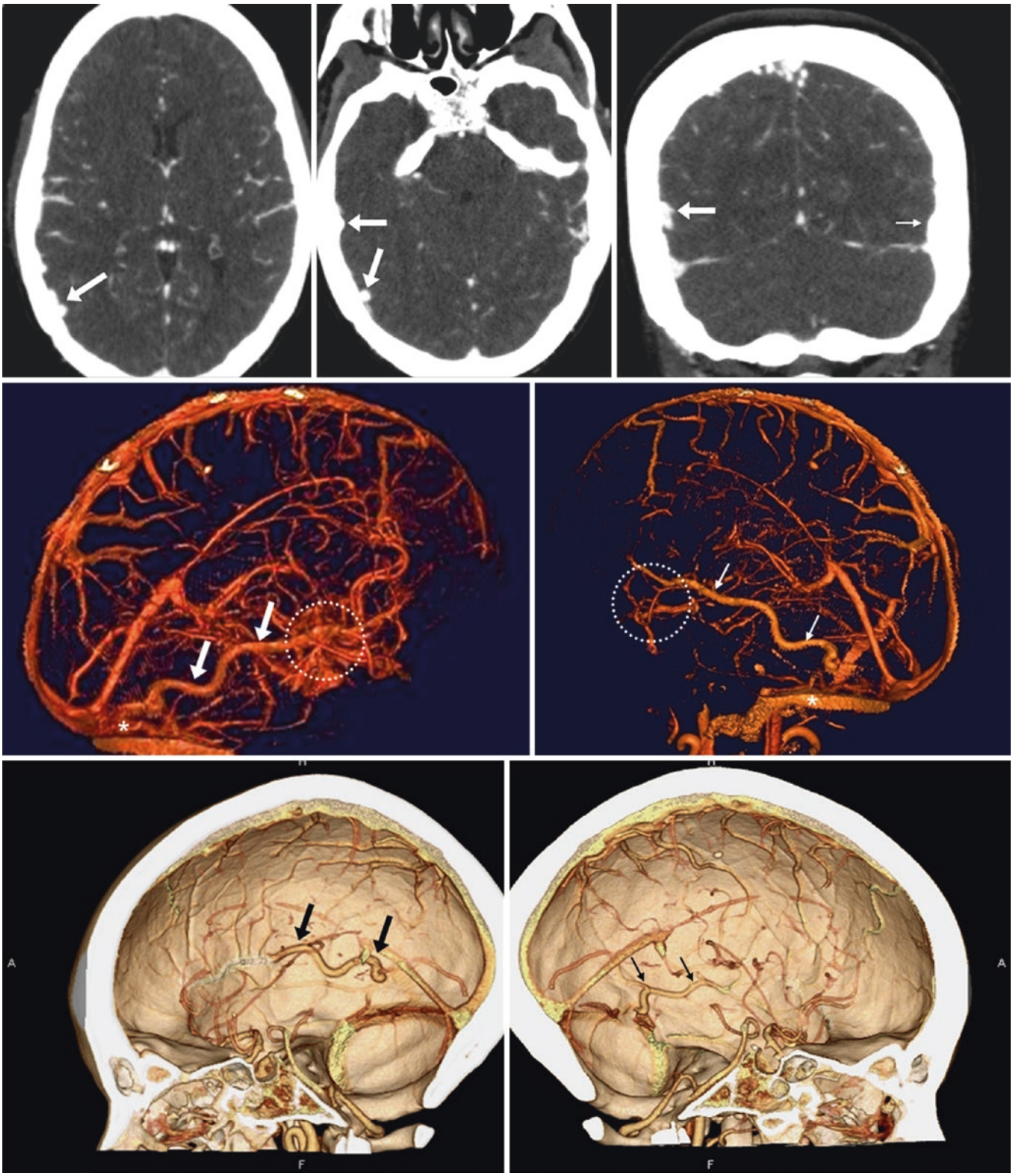

Fig. 40.102 In this 55-year-old, a CTV was obtained to rule out thrombosis (negative study). *Top row:* CTV depicts a dominant right VOL (*arrows*) on axial (*left two images*) and coronal (*right*) MPRs, with a mildly prominent left VOL (*thin arrows*). *Middle row:* 3D VR RPO (*left*) and LPO (*right*) images are shown with the bones removed. The right VOL runs from a plexus in the expected location of the SMCV (*dotted circles*), connecting to the right transverse sinus (*asterisks*). *Bottom row:* "Inner" views of the right (*left*) and left (*right*) sides with most arteries removed confirm that the left VOL (*thin arrows*) is also dominant, and depict its course towards the transverse sinus

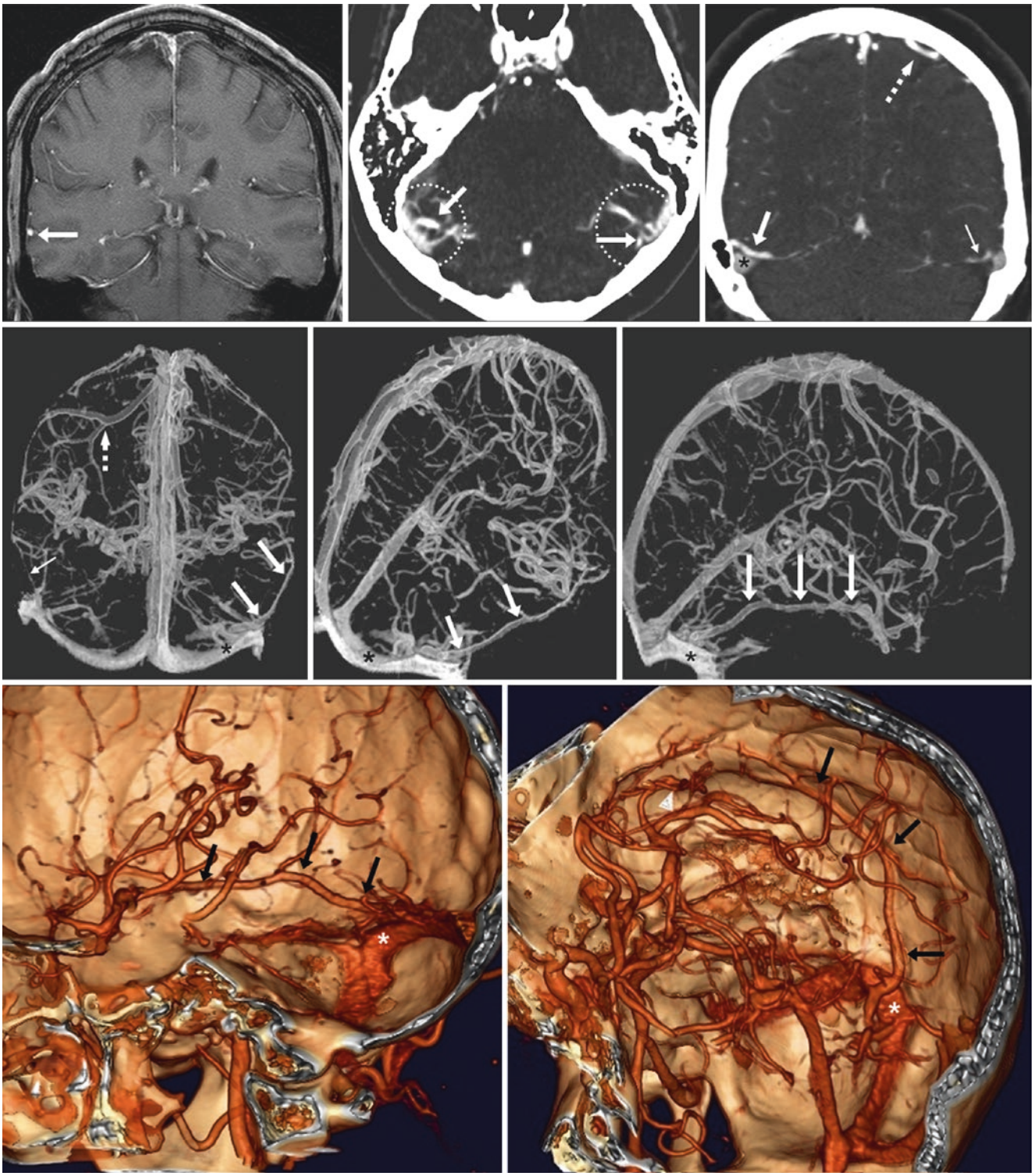

Fig. 40.103 45-year-old with pain (negative study). *Top row:* A prominent right VOL (*arrow*) is seen on coronal postcontrast T1WI MRI (*left*). CTV 7 mm thickness axial (*middle*) and coronal (*right*) MPRs demonstrate that the right VOL courses through the LTS (*bilaterally outlined by dotted circles*) to connect to the transverse sinus (*asterisk*). There is a tiny left VOL (*thin arrow*), with a larger, dominant VOT (*dotted arrows*). *Middle row:* 3D "see through" images in PA-superior (*left*), RPO (*middle*), and right lateral (*right*) views show the course of the right VOL. *Bottom row:* The right VOL is also seen on an "inner view" of the right calvarium, with (*left*) and without (*right*) the arteries removed. Note: On the right side, the VOL is the dominant superficial drainage, whereas on the left side, the VOT (*dotted arrows*) is dominant

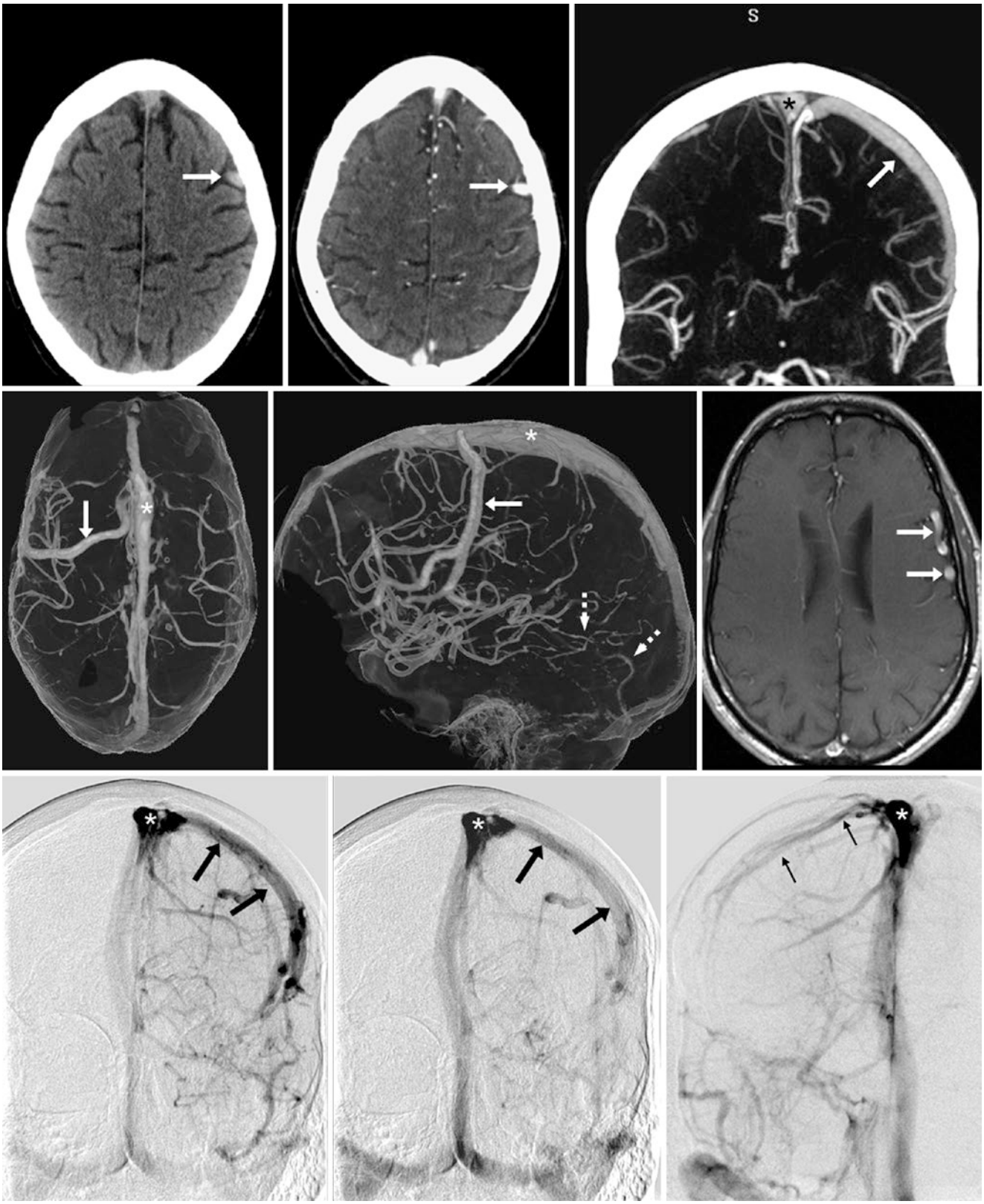

Fig. 40.104 In this 58-year-old, a venous phase CTA was negative. *Top row:* A prominent, dense vein in the left precentral sulcus (*arrows*) on nonenhanced CT (*left*) was shown to be a dominant left VOT on CTV with axial (*middle*) and coronal 20 mm thick (*right*) images. *Middle row:* 3D VR CTV "see through" superior (*left*) and left lateral (*middle*) views and postcontrast T1WI (*right*) confirm left VOT enlargement, which could be mistaken for an enlarged artery from an AVM. Note a tiny left VOL (*dotted arrows*). *Bottom row:* Catheter DSA AP views confirm the connection of the left VOT (*arrows*) to the superior sagittal sinus (SSS) (*asterisks*). Note a small right VOT (*thin arrows*)

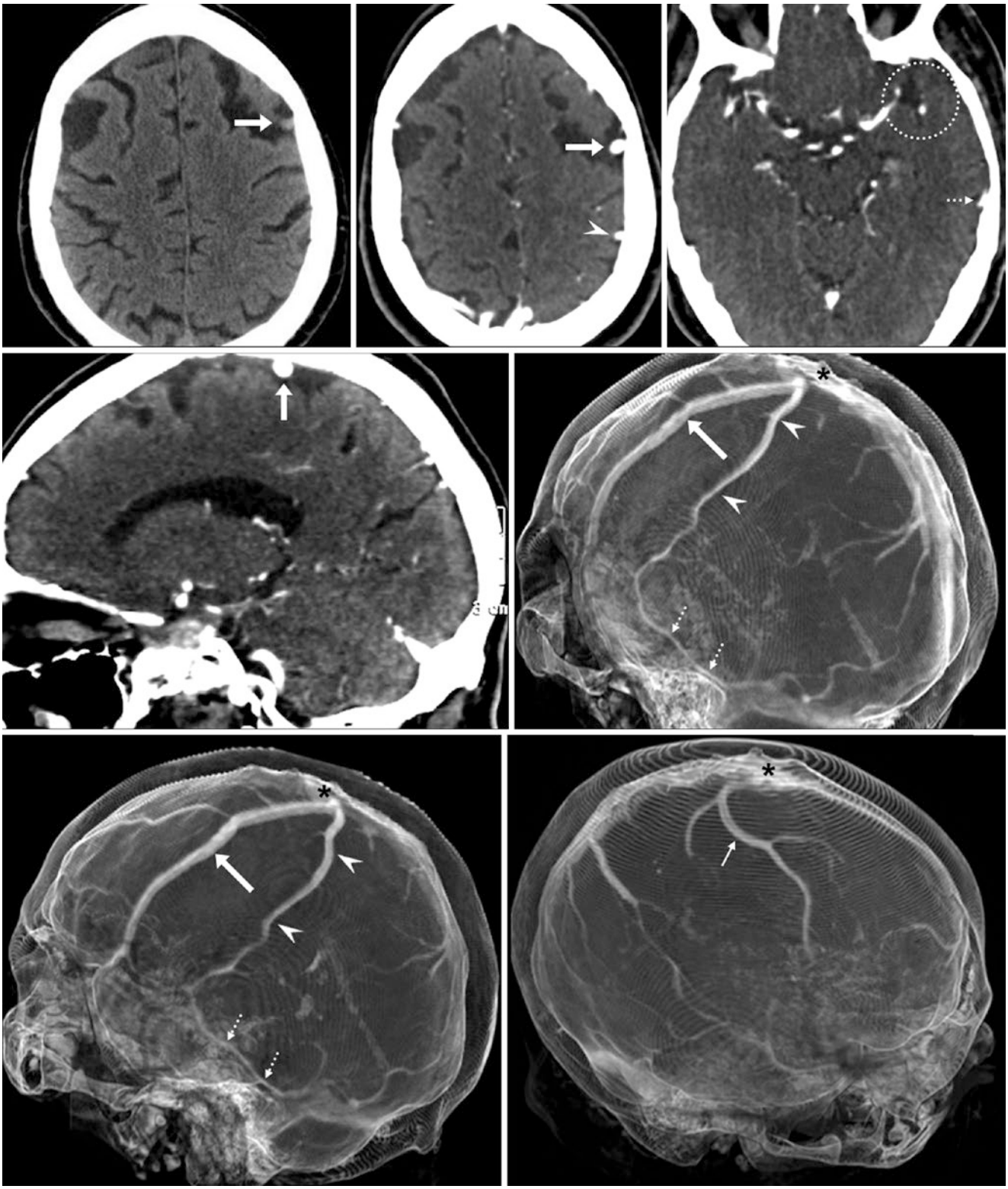

Fig. 40.105 67-year-old with memory loss. *Top row:* A prominent vascular structure (*arrows*) was initially noted within the left superior frontal sulcus on a nonenhanced CT (*left*). A CTV with axial images (*middle* and *right*) confirmed this to be an early bifurcation of a dominant VOT, where an enlarged cortical vein (*arrows*) arose early from the VOT (*arrowheads*). *Middle row:* On a CTV, a sagittal MPR (*left*) and an LPO 3D CTV "see through" image (*right*) delineate the two veins that join to form the left VOT, which drains into the SSS (*asterisk*). *Bottom row:* Left lateral (*left*), and right lateral (*right*) views confirm a small left VOL (*dotted arrows*); the left VOL and VOT do not connect to the tiny left SMCV (*dotted circle, top row*). On the contralateral side, note a less prominent (but dominant) right VOT (*thin arrow*)

40.14 Occipital Sinus

The *occipital sinus* (OS) can be visualized on MRI to varying degrees in roughly 10–35 % of the population [47–57]. Typically, the OS has regressed in most patients by birth, although it can be seen in a majority of cadavers. The OS typically travels directly inferiorly from the *torcular herophili* (*i.e.*, the confluence of the sinuses, simply called the "torcular"), where the torcular essentially represents the confluence of the straight and superior sagittal sinuses and is the point at which both transverse sinuses typically arise. In patients with an OS, the OS typically drains into one or both *internal jugular veins* (IJVs) as the vein(s) exit the skull base, although drainage into the lower *sigmoid sinus* can also be seen; thus, the site of drainage likely varies with the degree of transverse or sigmoid sinus hypoplasia. Preliminary studies suggest that bilateral versus unilateral drainage of OSs may occur with equal frequency, or the bilateral drainage variant may be slightly more common. There is no known association with congenital abnormalities. Some have found OSs to be less common in older children, teenagers, and adults, leading to the theory that it regresses with physiologic changes related to increasing age, such as upright walking, erect posture, or possibly skull changes (Figs. 40.106, 40.107, 40.108, 40.109, 40.110, and 40.111).

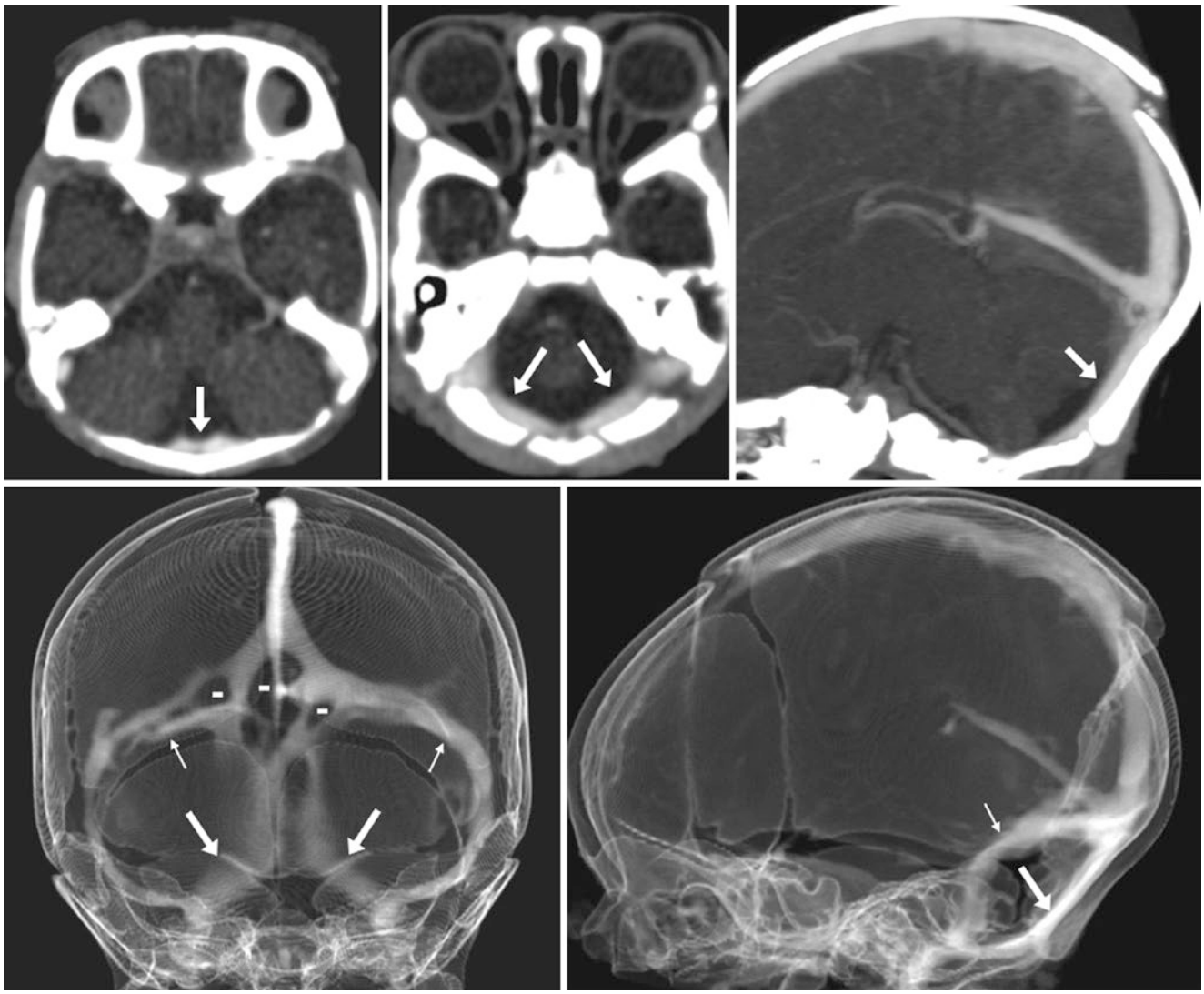

Fig. 40.106 *Top row:* In this 1-day-old neonate, a CTV shows an occipital sinus (OS) (*arrows*) that drains bilaterally into the internal jugular veins (IJVs) on axial (*left two images*) and sagittal (*right*) MPRs. *Bottom row:* The OS is best delineated on a 3D VR "see-through" PA view (*left*) and left lateral view (*right*). Note normal fenestrae/"clefts" (*minus signs*) within the transverse sinuses bilaterally (*thin arrows*)

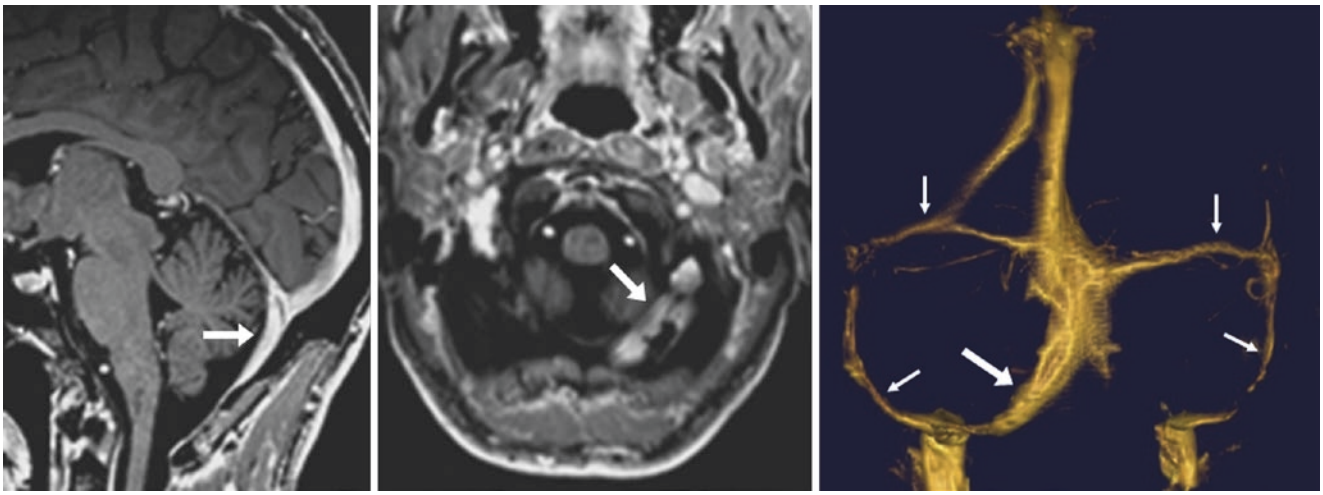

Fig. 40.107 50-year-old with a unilateral left OS (*large arrows*), visualized on sagittal postcontrast 3D T1WI (*left*). The OS drains mostly into the left sigmoid–IJV junction, as noted on an axial T1WI (*middle*), and on an MIP PA view (*right*), both reconstructed from a 3D T1WI dataset. Both the transverse and sigmoid sinuses (*thin arrows*) appear small

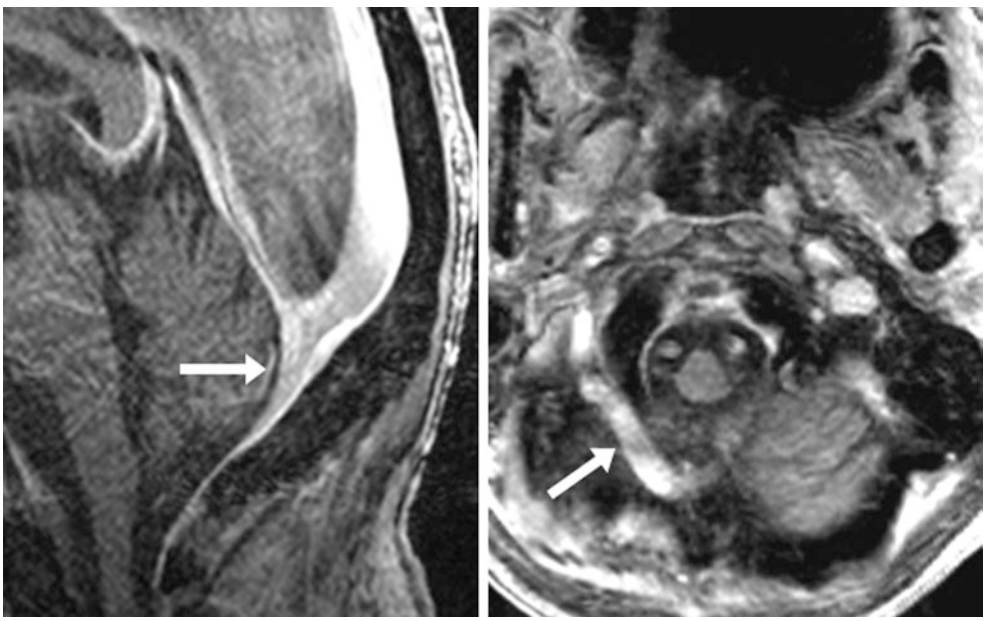

Fig. 40.108 65-year-old with a unilateral right OS on a sagittal postcontrast T1WI (*arrow, left*) that unilaterally drains to the right side, as seen on an axial postcontrast T1WI (*arrow, right*)

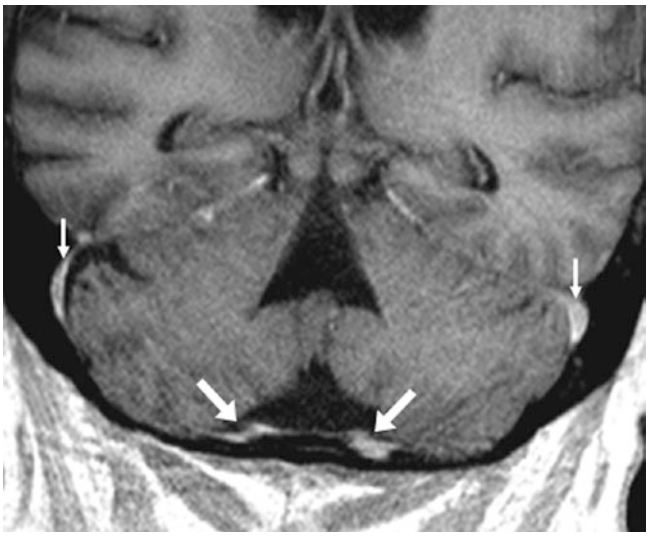

Fig. 40.109 58-year-old with bilateral OSs (*large arrows*) on coronal postcontrast T1WI. Note that there are relatively small transverse sinuses as well (*thin arrows*)

Fig. 40.110 33-year-old with a tiny OS (*arrow*) on a coronal postcontrast T1WI

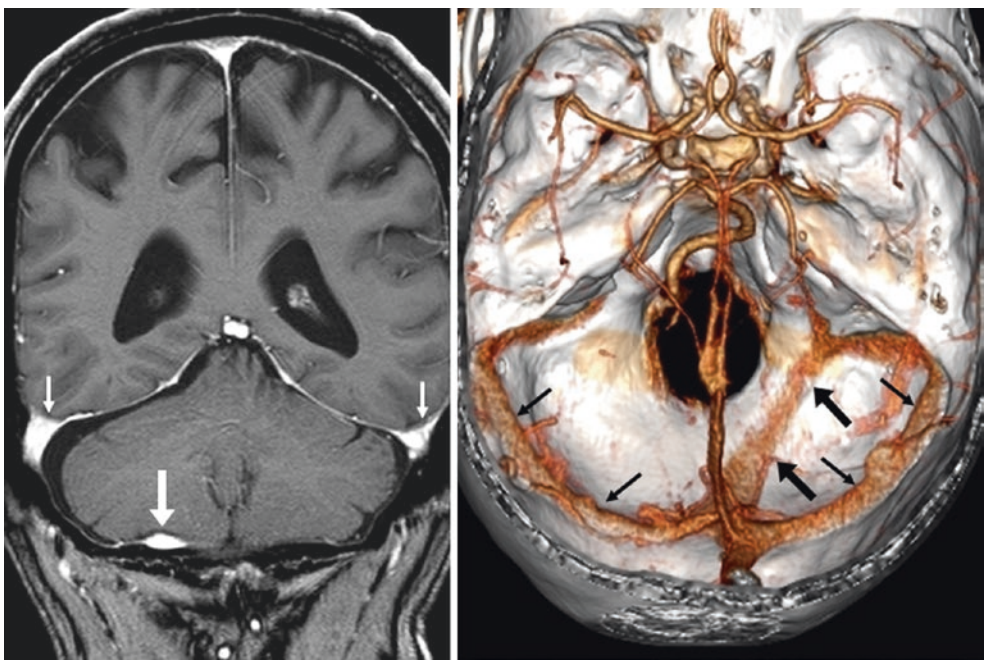

Fig. 40.111 58-year-old with a unilateral, prominent OS (*large arrows*) on a coronal postcontrast T1WI (*left*) and on a CTV "inner" superior view (*right*). Note similar-sized transverse sinuses bilaterally (*thin arrows*)

40.15 Transverse-Sigmoid Sinus Hypoplasia and Normal Asymmetry in Size

The *transverse sinuses* range from being equal in size on both sides (in approximately 30–40 % of the population), to dominance on one side (about 30–50 %), to frank *hypoplasia* on one side (percentage varies, but is estimated to be 20–30 %); the sinus may even be almost completely absent on one side (<10 %) [46–64]. These numbers vary with age, as some evidence suggests that in children there is more equality in size and codominance of the transverse sinuses, whereas in adults there is increasing asymmetry, with the right transverse sinus more commonly being the dominant side (estimated to be in about 40–50 %), with the left dominant in about 15–25 %. *Physiologic changes* with breathing and the cardiac cycle may also affect the apparent size and signal (on MRI) of the transverse sinuses. Note that one should evaluate for *internal jugular vein* (IJV) asymmetry if transverse sinus aplasia is suspected, because those entities often occur in conjunction. In particular, if *thrombus* is suspected and the transverse sinus appears small, it is recommended to evaluate for asymmetry in the cervical segment of the upper IJV, as well as to evaluate for clot in the IJV at the skull base and upper neck, if such images of the cervical region are available.

Both MRV and CTV typically distinguish cases of *hypoplasia* or *absence* quite readily. Difficulties in interpretation can arise in several scenarios. In this author's experience, three problematic situations are the most common: (1) distinguishing mild, focal normal narrowing (sometimes accompanied by a normal arachnoid granulation) from a true stenosis or thrombus; (2) distinguishing chronic narrowing or stenosis (from prior thrombosis with resultant collateral drainage) from normal hypoplasia or aplasia; and (3) distinguishing true occlusion from artifactual nonpatency of a dural sinus that shows no flow on a noncontrast 2DTOF MRV or a phase contrast (PC) MRV. This lack of flow occurs on 2DTOF MRV either because of slow flow or directionality; on PC MRV, artifactual nonvisualization may result from either very slow or very fast flow, if the appropriate encoding velocity ("V_{enc}") is not selected. Hence, it is recommended to perform both noncontrast MRV (which is more sensitive in demonstrating narrowing) and postcontrast MRV (which is more specific and thus eliminates false positive cases) in questionable cases. It is not recommended to perform solely postcontrast MRV because a T1-bright hemorrhage or clot from subacute thrombus may occasionally be obscured by gadolinium contrast. Also, subtraction images (precontrast from postcontrast MRV) may be helpful, if there is not substantial patient motion (Figs. 40.112, 40.113, 40.114, 40.115, 40.116, 40.117, 40.118, 40.119, and 40.120).

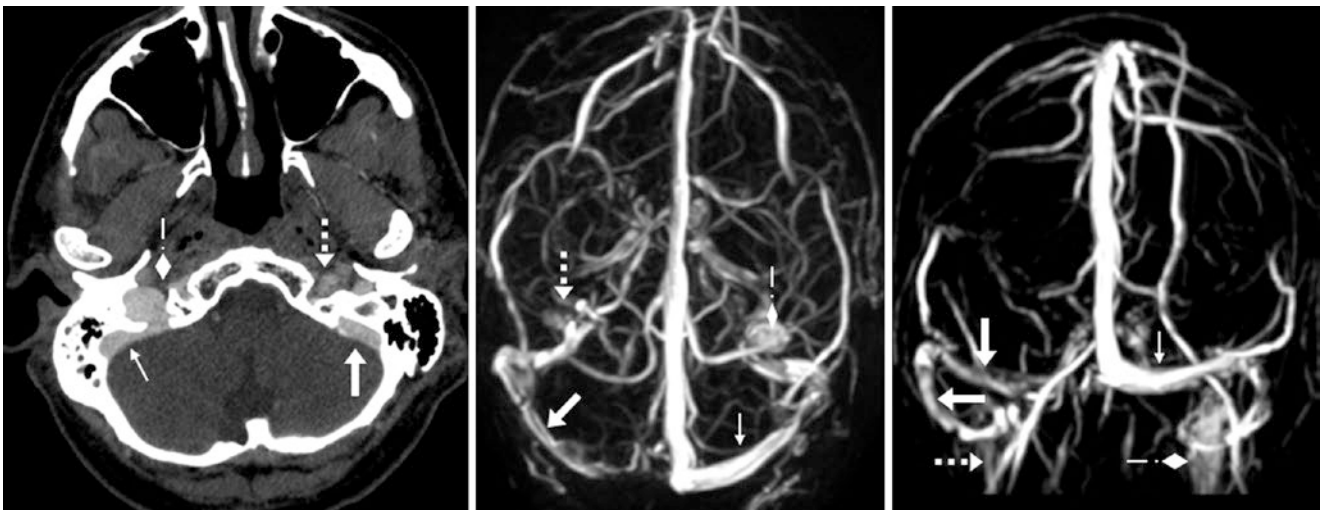

Fig. 40.112 41-year-old with a prominent right jugular bulb (*diamond arrows*) that drains from dominant right transverse-sigmoid sinuses (*thin arrows*) on axial source CTV images (*left*), with a tiny left jugular bulb (*dotted arrows*). On 3D CEMRV superior (*middle*) and PA (*right*) views, the hypoplastic left transverse and sigmoid sinuses (*large arrows*) are better depicted

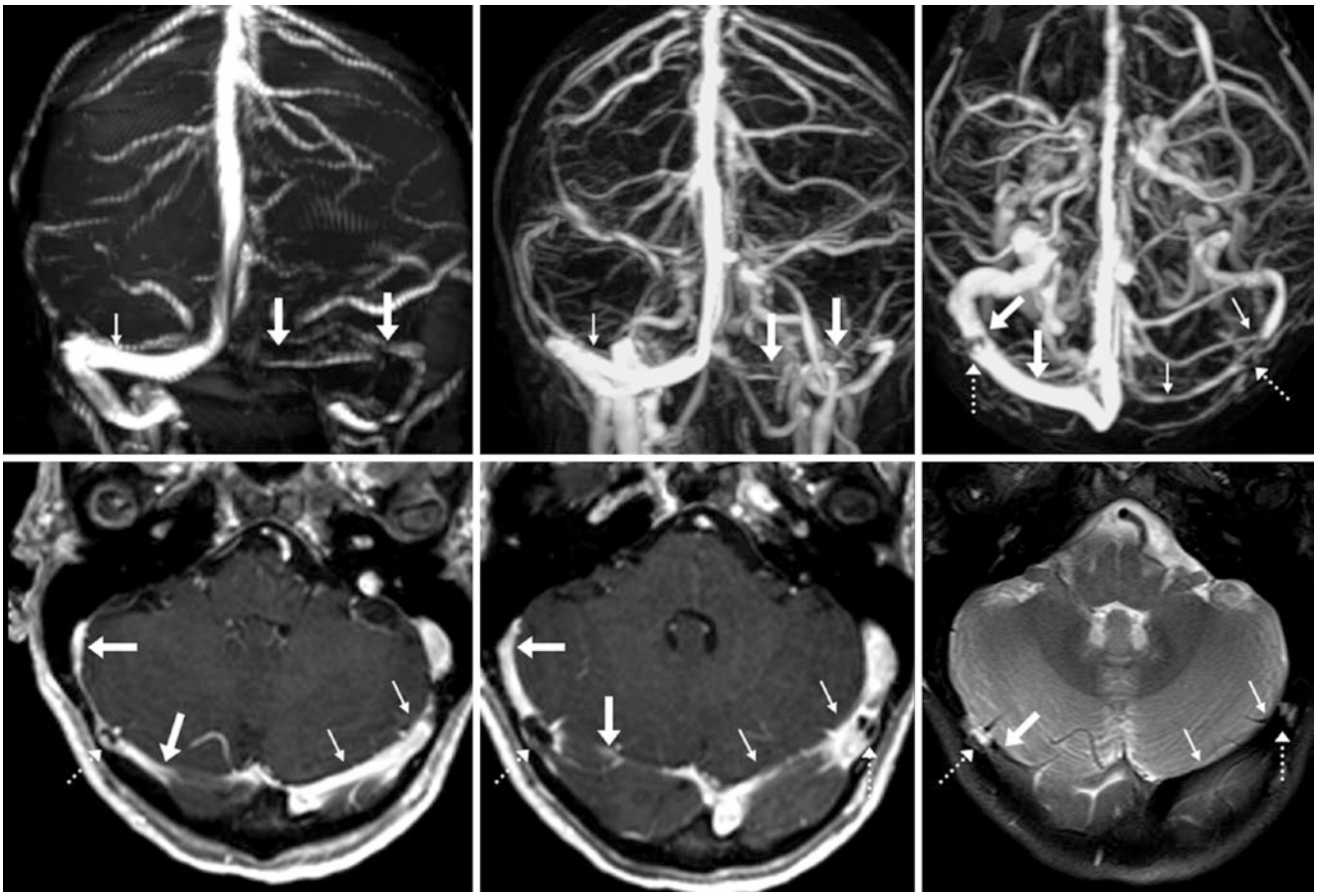

Fig. 40.113 *Top row:* In this 30-year-old, a 2DTOF MRV PA view (*left*) shows a small right transverse sinus (*large arrows*) relative to the left side (*thin arrows*). This mimics thrombus or high-grade stenosis. However, CEMRV PA (*middle*) and superior (*right*) views confirm the right transverse sinus to be hypoplastic. *Bottom row:* These findings are also visualized on postcontrast T1WI (*left* and *middle*) and on T2WI (*right*). Note incidental arachnoid granulations (*dotted arrows*)

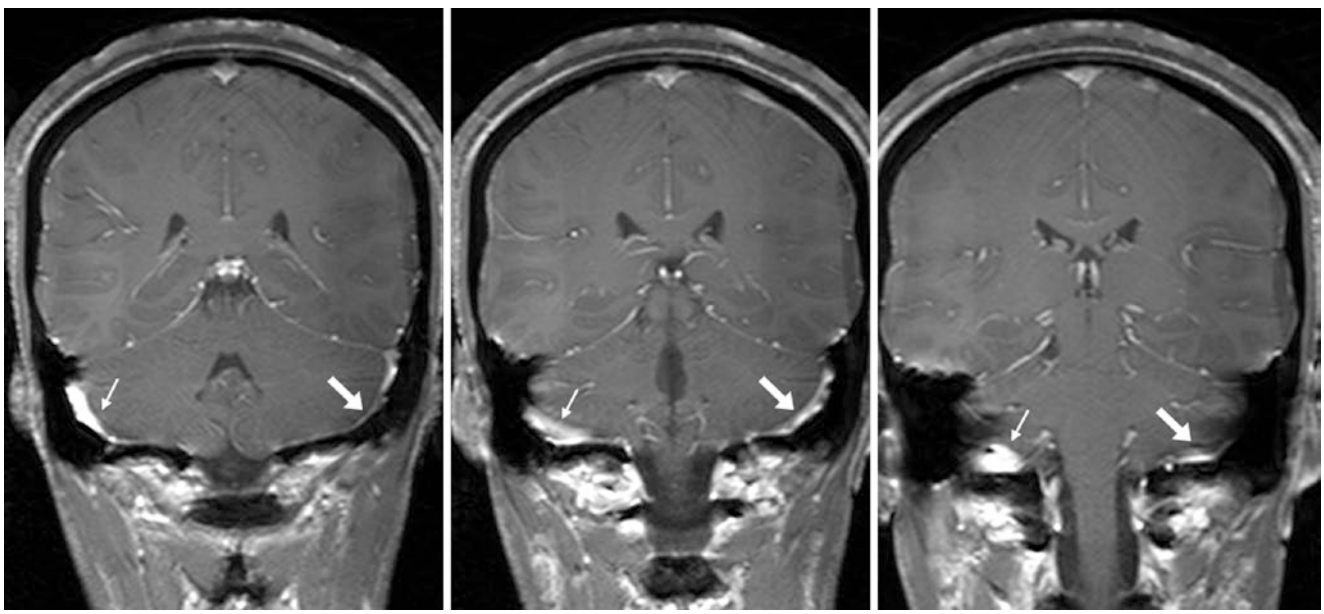

Fig. 40.114 In this 26-year-old, serial, coronal postcontrast T1WIs demonstrate incidental, small left transverse-sigmoid sinuses (*large arrows*) relative to the contralateral right side (*thin arrows*). The left IJV (*not shown*) was also small; the right IJV was dominant. This patient did not have symptoms related to the dural sinuses

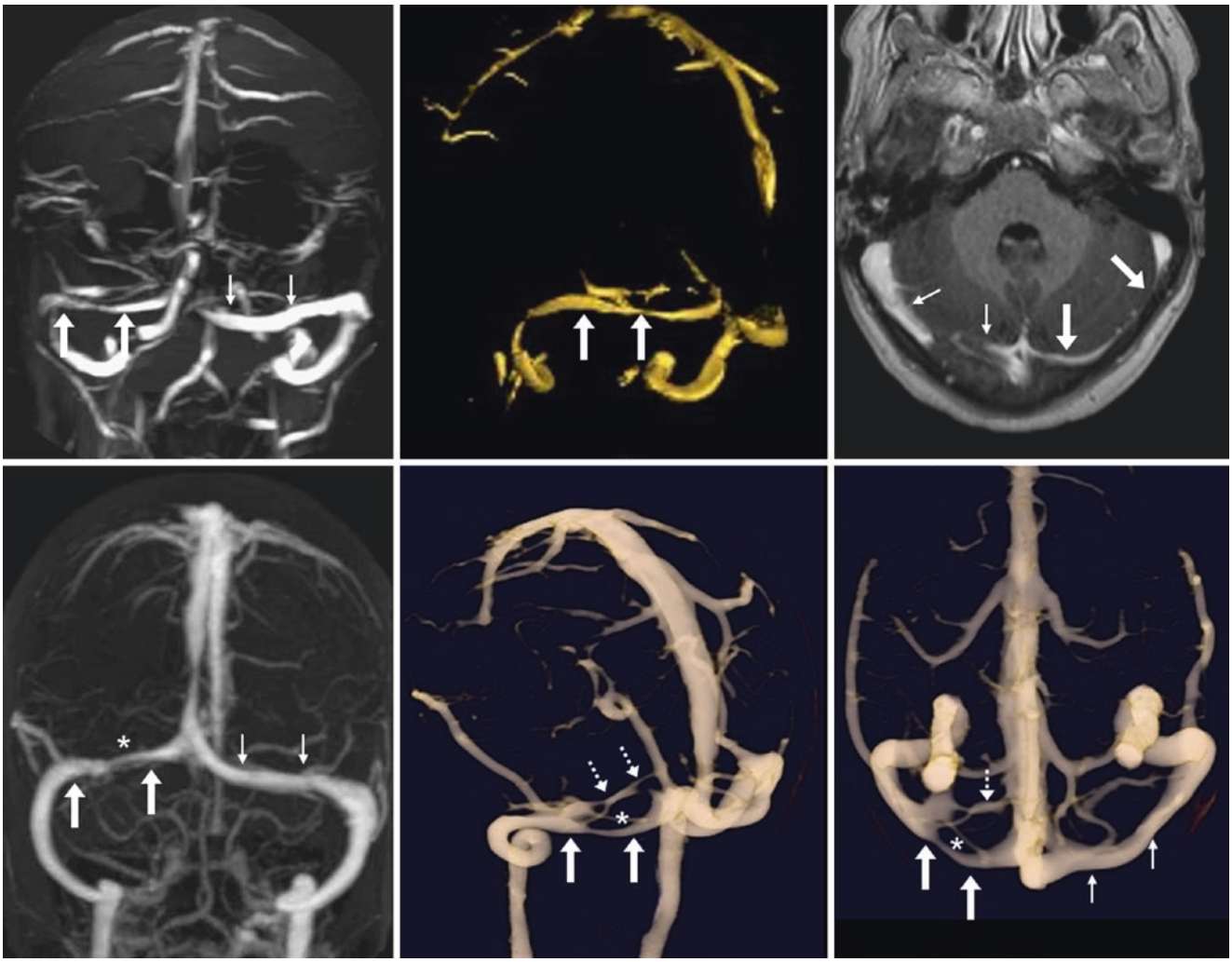

Fig. 40.115 In this 10-year-old, a 2D TOF MRV shows a left transverse sinus (*large arrows*) that appears narrowed on PA (*top left*) and LPO (*top middle*) views, as well as on postcontrast T1WI (*top right*). The right side (*thin arrows*) is dominant. CEMRV PA (*bottom left*), LPO (*bottom middle*), and superior (*bottom right*) views depict focal left transverse sinus hypoplasia (*asterisks*), where an accessory deep vein (*dotted arrows*) travels between the straight sinus and the distal left transverse sinus. The presence of this accessory vein may account for the transverse sinus hypoplasia

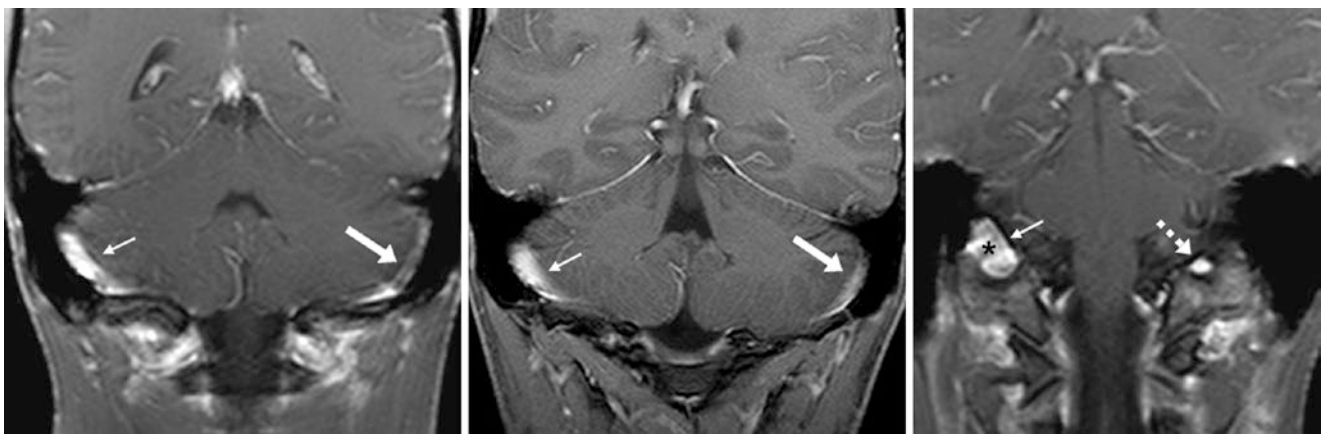

Fig. 40.116 In this 23-year-old, serial coronal postcontrast T1WIs (from posterior to anterior) demonstrate left transverse and sigmoid sinuses (*large arrows*) that are small compared with the contralateral sinuses (*thin arrows*). Note how the left IJV (*dotted arrow*, *right*) is quite small and could be considered hypoplastic, whereas the right IJV (*asterisk*) is dominant

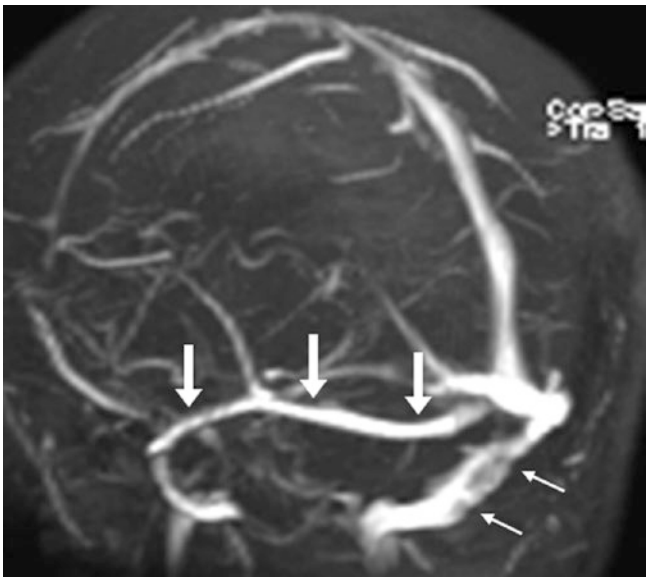

Fig. 40.117 In a 17-year-old, a noncontrast 2DTOF MRV LPO view shows hypoplastic left transverse-sigmoid sinuses (*large arrows*), with right-sided dominance (*thin arrows*)

Fig. 40.118 48-year-old with left transverse sinus aplasia (*large arrows*) on catheter DSA AP views from right (*left*) and left (*right*) ICA runs. Distally, the left sigmoid sinus (*dotted arrow*) fills via the VOL, VOT, and the SPS. Note the right transverse sinus dominance (*thin arrows*)

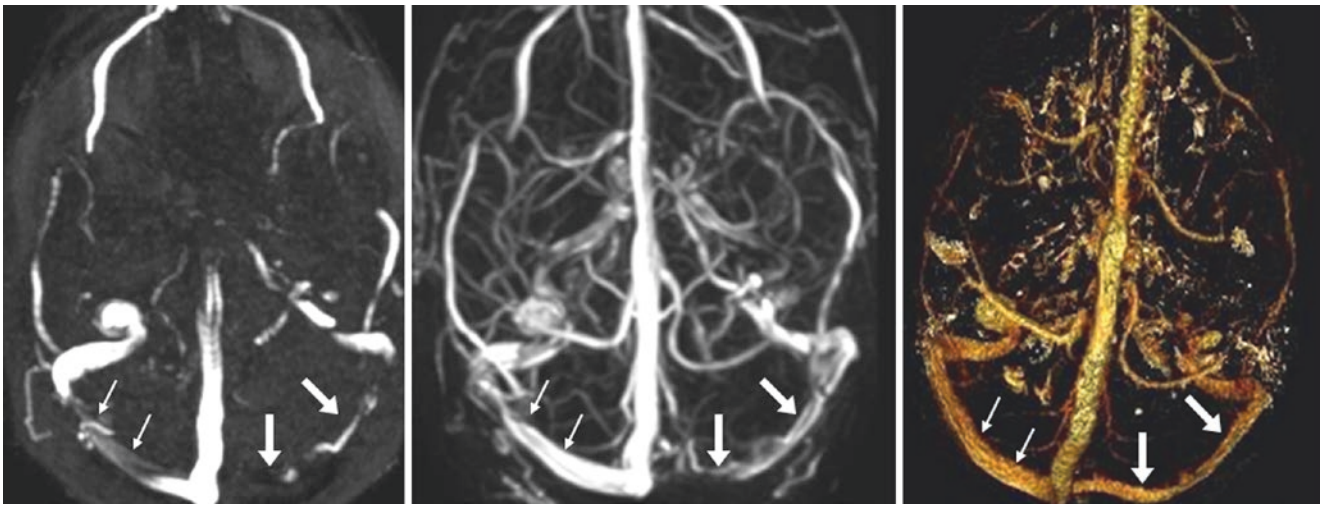

Fig. 40.119 In this 41-year-old, superior views from a 2DTOF MRV (*left*) and a CEMRV (*middle*) did not demonstrate the right transverse sinus (*large arrows*) to be patent, as compared with the left (*thin arrows*). However, it was found patent the next day on a 3D VR CTV superior view (*right*). The initial findings were likely artifact from slow flow within a small sinus

Fig. 40.120 Comparison case of dural sinus thrombosis. In this 18-year-old, a CEMRV MIP PA view (*left*) was initially called negative for thrombosis, with a "hypoplastic" left transverse sinus (*thin arrows*). However, on a CTV with 3D MIP "see through bone" images in a PA view (*middle*), as well as sagittal (*top right*) and coronal (*bottom right*) views, a luminal filling defect (*arrows*) was noted within the left transverse sinus, along with a normal split in the torcular (*asterisk*, *middle*), representing non-occlusive dural sinus clot. Note how MIPs from an MRA or MRV may miss intraluminal defects

40.16 Falcine Plexus

Rarely, a venous plexus is situated within the connective tissue of the falx and is visible on pathologic sectioning; it is generally located along the proximal portion of the *inferior sagittal sinus* [65–67]. This plexus may simulate prominent vasculature, such as seen with an *AVM* or *AVF*. This plexus within the falx has been termed a "*falcine venous plexus*," as it lies immediately adjacent to the falx cerebri anywhere along its extent. If it is located posteriorly, it is typically larger and denser than when located anteriorly. Tubbs et al. [65] report that this plexus communicated with the inferior sagittal sinus in all 27 of their cases, while it communicated with the superior sagittal sinus in only 17 of 27 (63 %); another study found that while the falcine plexus can communicate with either the superior or inferior sagittal sinus, the plexus should not communicate with both sinuses [66]. It is hypothesized that the falcine plexus arises from the embryonic sagittal plexus, and it has been anecdotally reported that venous hemorrhage has been noted in such a location. This appearance may be perplexing initially if it is prominent on nonenhanced CT or on an improperly timed CTA or CTV, but a catheter DSA readily excludes an AVM or AVF. Note that the falcine plexus is a distinct entity from the *persistent falcine sinus*, discussed in the following Sect. 40.17, although one theory has suggested that persistence of the vestigial falcine sinus may be manifest as the falcine plexus later in life [65–67] (Figs. 40.121 and 40.122).

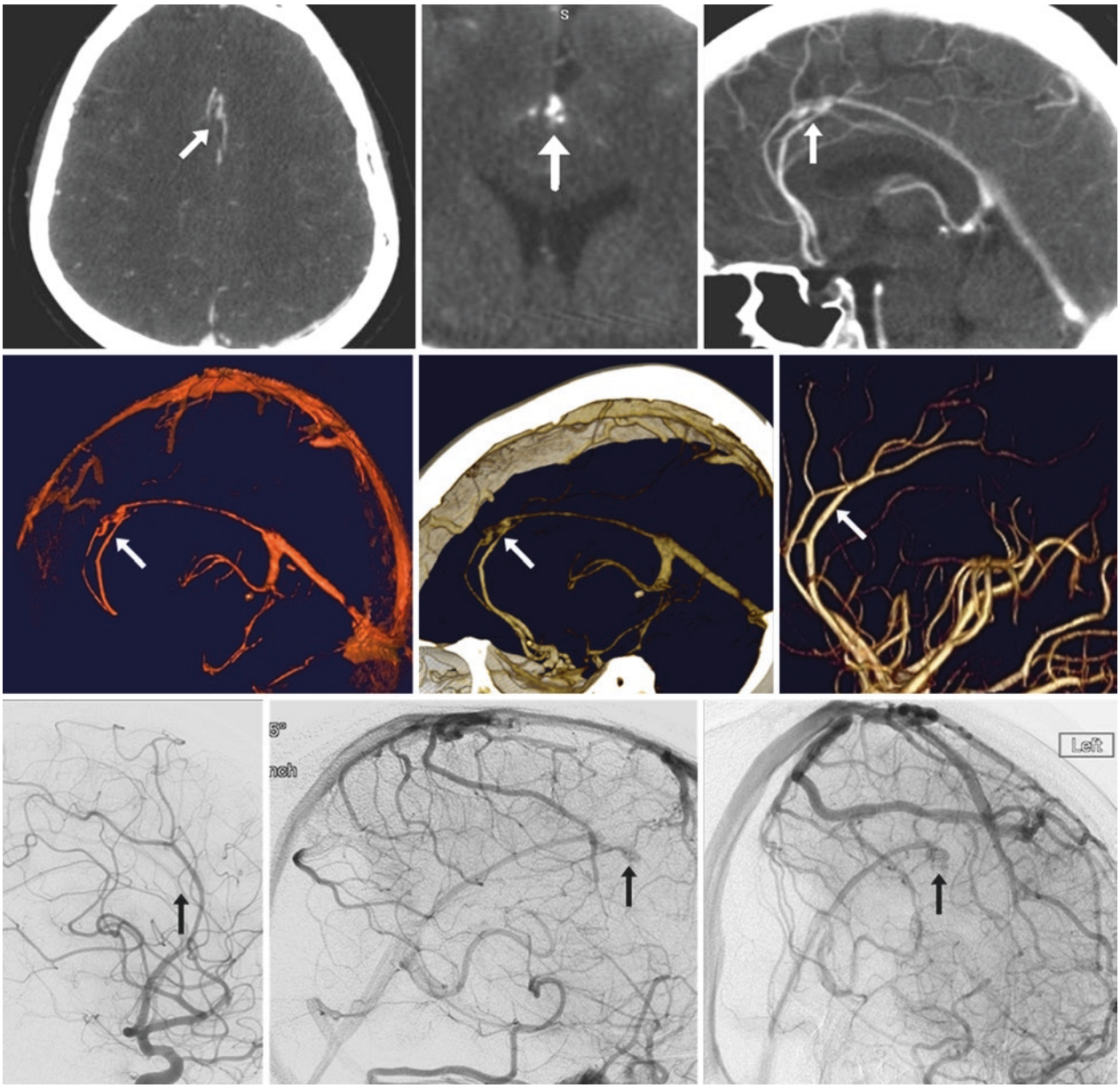

Fig. 40.121 This 50-year-old underwent a CTA for headaches. *Top row:* Axial, coronal, and sagittal MPRs demonstrated an atypical clump of vessels in the cingulate sulcus surrounding the callosomarginal artery (*arrows*), without edema or hemorrhage. Hence, while a normal variant venous plexus was suspected, a small AVM was also a consideration. *Middle row:* 3D VR CTA left lateral views (*left* and *middle*) did not find any dilated artery or AVM nidus; a 3DTOF MRA lateral view (*right*) was also normal. *Bottom row:* Catheter DSA did not demonstrate any abnormality on oblique views in the arterial phase (*left*). The falcine plexus filled later, in the venous phase (*middle* and *right*)

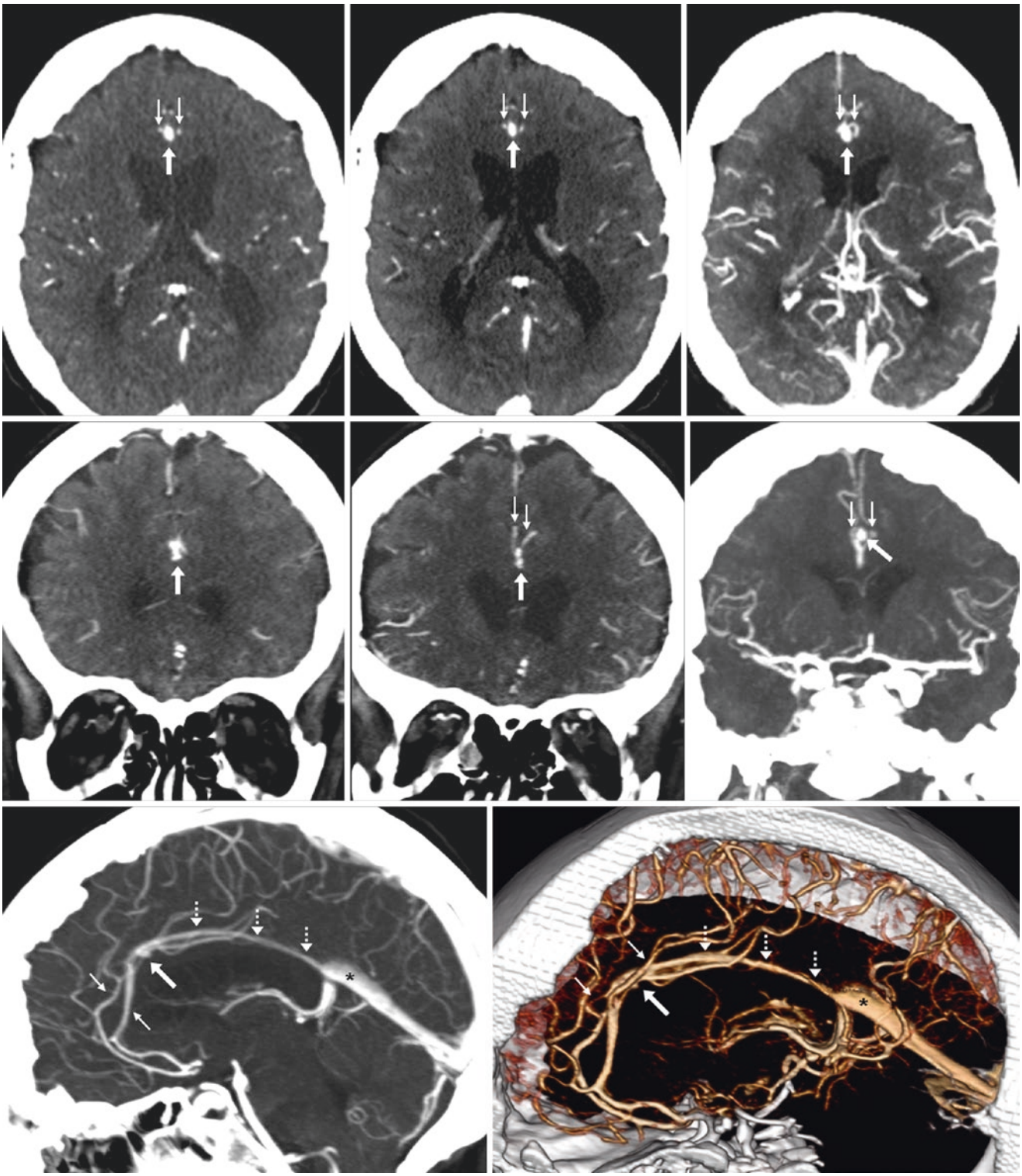

Fig. 40.122 This 50-year-old underwent a CTA for headaches. *Top row:* Axial source images from the CTA at thicknesses of 0.75 mm (*left*), 2 mm (*middle*), and 8 mm (*right*) demonstrated a 2.0-mm focus of contrast (*arrows*) that simulated an outpouching versus being a clump of vessels situated within the pericallosal sulcus and surrounding the pericallosal artery (*thin arrows*). Thus, an aneurysm or AVM (versus a normal falcine plexus) was an initial consideration based solely on axial images. *Middle row:* Coronal MPRs at thicknesses of 2 mm (*left*), 5 mm (*middle*), and 10 mm (*right*) did not depict an AVM nidus. The "outpouching" was found to be in communication with venous, rather than arterial, structures. Also, the "outpouching" had a greater density of contrast than surrounding arterial structures, suggesting it was not arterial, but rather venous, as the CTA was mostly within the venous phase. *Bottom row:* The structure in question was shown to communicate with the inferior sagittal sinus (*dotted arrows*) on a sagittal 3 mm thickness MPR (*left*), and on a 3D VR left lateral view (*right*), confirming that this was a normal falcine plexus. Note the straight sinus (*asterisks*)

40.17 Persistent Falcine Sinus

The *falcine sinus* represents the embryonic caudal, anastomotic loop of the *sagittal plexus* (the *superior sagittal sinus* [SSS] and the *straight sinus* develop from the sagittal plexus); it is normally located within the falx [67–73]. It is termed a "*persistent falcine sinus*" when it does not involute after birth, and the remaining sinus communicates directly between the *vein of Galen* (VOG) and the posterior portion of the SSS. In most cases, some degree of a *straight sinus* (StS) is also present, but the StS may be rudimentary or hypoplastic. Persistence of the falcine sinus has traditionally been reported in the literature as associated with congenital vascular disorders (such as *VOG malformations*). Other reports have described a persistent falcine sinus in association with congenital nonvascular cerebral or skull malformations, such as *callosal dysgenesis*, *craniosynostoses, abnormal tentorium*, or *giant parietal foramina*. More recently, Ryu [67] (and others in case reports) have described likely incidental persistence in about 2 % of adult patients, and other recent studies have found that it is not uncommon in children as well [67–73]. Hence, a persistent falcine sinus is perhaps a normal variation that is probably more common in the general population than previously thought, with most not associated with a congenital brain or vascular anomaly. When a falcine sinus is encountered, however, one should search diligently for those cerebral parenchymal or vascular abnormalities that have been described to occur in conjunction with it (Figs. 40.123, 40.124, 40.125, 40.126, and 40.127).

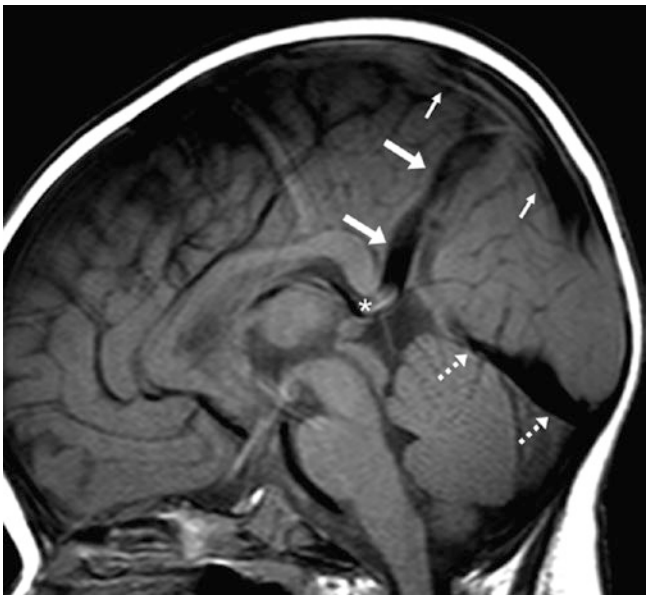

Fig. 40.123 6-month-old with seizures, with an incidental persistent falcine sinus (*large arrows*) on sagittal T1WI. Note the superior sagittal sinus (SSS) (*thin arrows*), straight sinus (StS) (*dotted arrows*), and vein of Galen (VOG) (*asterisk*) (*Courtesy of* Chang-Woo Ryu, MD, Kyunghee University, Seoul, South Korea)

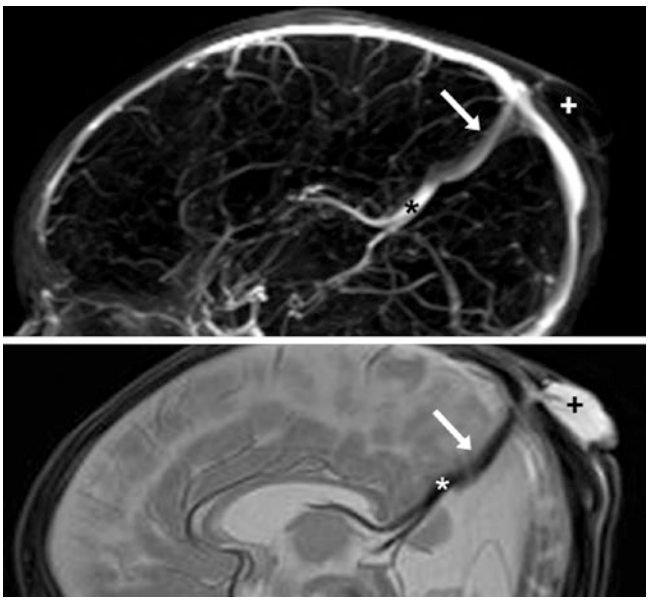

Fig. 40.124 11-day-old with a persistent falcine sinus (*arrows*) and a small meningocele (*plus signs*) on a sagittal CEMRA (*top*) and on a T2WI (*bottom*). Note the VOG (*asterisks*)

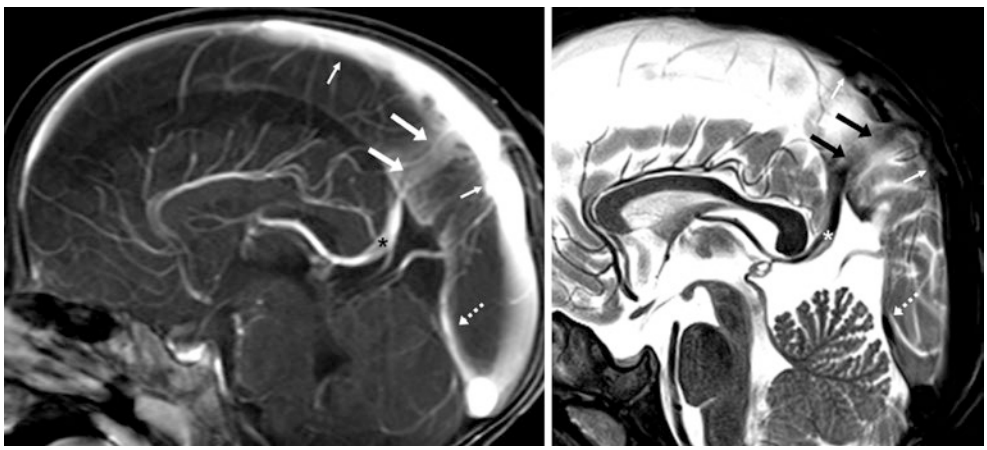

Fig. 40.125 9-month-old with an incidental persistent falcine sinus (*large arrows*), which was depicted on postcontrast sagittal T1WI (*left*) and on sagittal T2WI (*right*). Note the SSS (*thin arrows*), StS (*dotted arrows*), and VOG (*asterisk*)

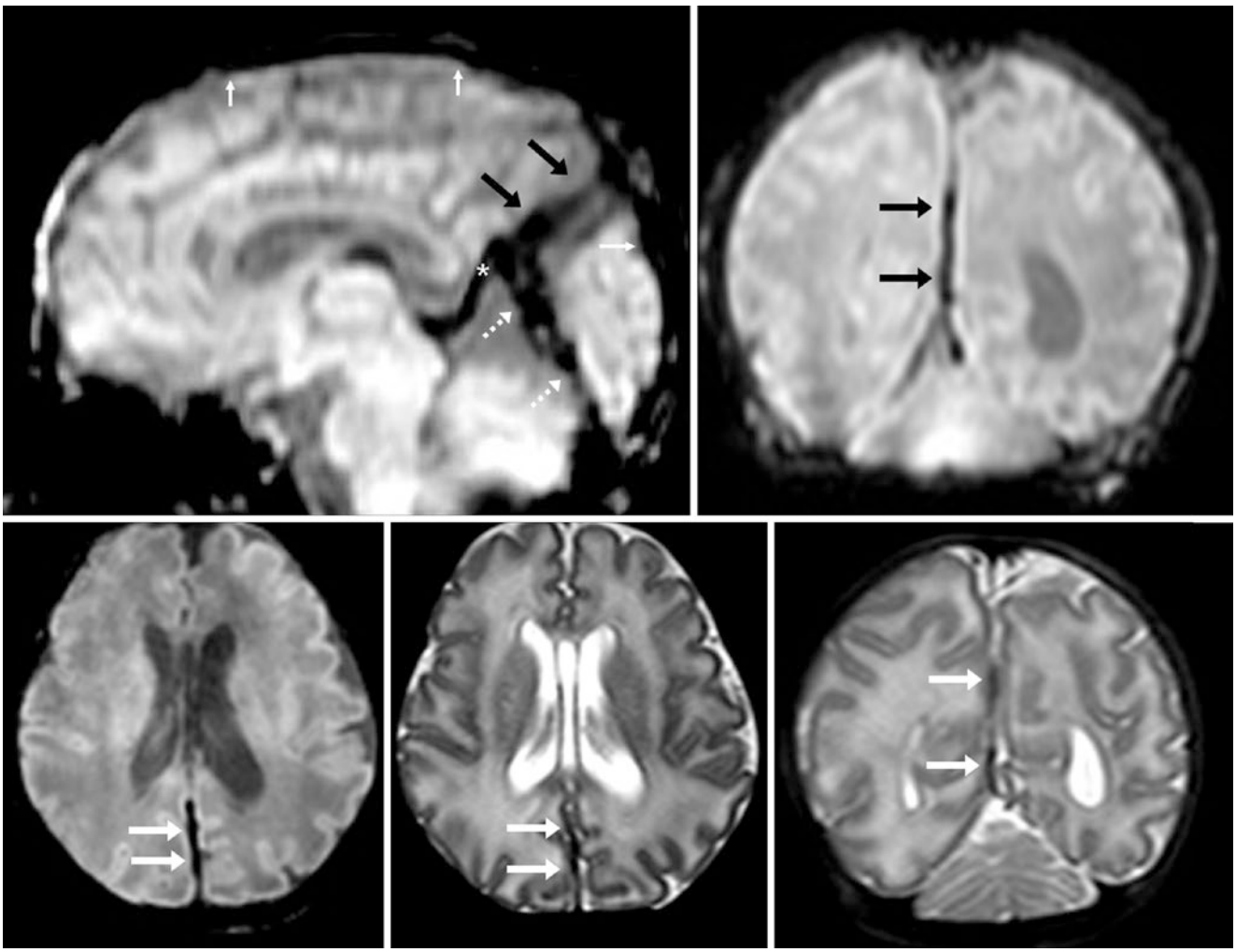

Fig. 40.126 A 2-week-old boy with mandibulofacial dysostosis (Treacher-Collins syndrome) had no cerebral anomalies, but did have an incidental persistent falcine sinus (*large arrows*), as depicted on sagittal (*top left*), coronal (*top right*), and axial (*bottom left*) SWI. Note the SSS (*thin arrows*), StS (*dotted arrows*), and the VOG (*asterisk*). Also, note that patent dural sinuses are better visualized on SWI than on ultrafast axial (*bottom middle*) and coronal (*bottom right*) T2WI

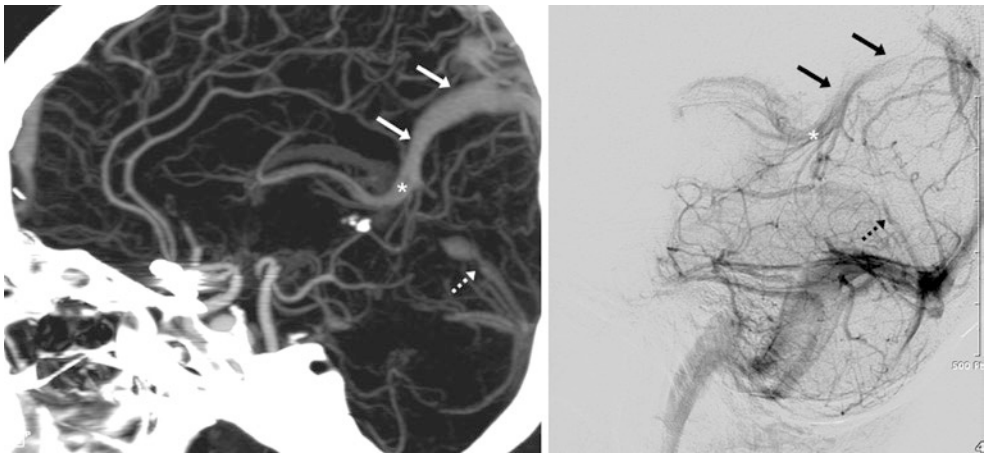

Fig. 40.127 40-year-old with a ruptured aneurysm and hemorrhage on nonenhanced CT (*not shown*). A CTA with sagittal MPR (*left*) and a venous-phase catheter DSA lateral view (*right*) depict a persistent falcine sinus (*arrows*) between the SSS and the VOG (*asterisks*), with a rudimentary StS (*dotted arrows*) (*Courtesy of* Chang-Woo Ryu, MD, Kyunghee University, Seoul, South Korea)

40.18 Superior Sagittal Sinus and Torcular Variants

There are a number of variations of the superior sagittal sinus (SSS), but there should nearly always be a midline sinus within the attached falx that typically extends posteriorly from the foramen cecum (at the anterior extent of the SSS) to the torcular (i.e., the confluence of the sinuses). The foramen cecum and its normal variations are described further in the Skull section of this book. To adhere to proper anatomic description, the anterior/proximal third of the SSS is also referred to within this chapter as "rostral," the middle third as the "midportion," and the posterior/distal third (just before the torcular) as "dorsal" [46–64]. Please note that the *torcular herophili* ("torcular" for short, also known as the "confluence of the sinuses") is included along with the SSS in this chapter, as many of the normal variations of the distal, dorsal SSS also involve the torcular. This discussion of normal variation of the SSS or the torcular is subdivided into *anterior (rostral) variants, midportion (central) variants*, and *posterior (dorsal) variants*.

Regarding the *rostral variants*, a common variation anteriorly of the rostral SSS is incomplete visualization of the SSS because of *SSS atresia or hypoplasia*, or because a tiny sinus is located far anteriorly on CT or MRI and is not visualized owing to its small size [46–64]. In such instances, prominent *cortical (frontal) veins* may serve as accessory venous channels of drainage. Such aplasia or hypoplasia of the rostral SSS may lead to bilaterally prominent cortical veins (an apparent "bifurcation" or joining of the SSS), unilaterally prominent cortical veins, or even a "triplicate" appearance—three veins joining anteriorly to form the SSS at the midportion. These rostral variants do not likely represent true duplications, as they are typically not associated with fenestrations (a window between a bifurcation of the vessel and subsequent rejoining), and because the atretic portion is typically accompanied by enlarged cortical veins located laterally. Other rostral variants are relatively uncommon and poorly documented; to this author's knowledge, most variations that occur anteriorly are related to varying degrees of prominent cortical veins that parallel a relatively small or hypoplastic rostral segment of the SSS (and may even simulate the SSS itself) (Figs. 40.128, 40.129, 40.130, and 40.131).

At the *midportion of the SSS*, variants include true *fenestrations/duplications, prominent cortical veins* (or anastomotic veins) that parallel the SSS, or "*splits*" of the SSS [46–64]. Such splits in the sinus can drain laterally into the transverse or sigmoid sinus directly, thus bypassing the torcular confluence. This phenomenon can be unilateral or bilateral. Occasionally, there can be drainage through the torcular inferiorly into the uncommon occipital sinus.

Another variant of the SSS is a "*bulbous*" or "*patulous*" appearance. This variant can occur within any segment of the SSS, but it typically occurs centrally, within the midportion. This variant simulates an enlarged dural sinus, such as occurs with *chronic thrombosis or recanalization*. However, recanalized thrombosis typically has enlarged, adjacent venous collaterals (Figs. 40.132, 40.133, 40.134, and 40.135).

Regarding the most *posterior (dorsal) segment* of the sinus, the torcular herophili ("torcular") is considered to be the somewhat dilated continuation of the SSS that has a variable appearance [46–64]. Through the torcular, there is typically a small transvenous channel present that travels transversely through the bottom of the torcular to communicate with the opposite side. However, there are varying degrees of *aplasia or hypoplasia* that may occur in the general location of the torcular confluence, as the SSS can *split* and completely favor one transverse sinus (TS), while the opposite TS is hypoplastic or fills predominately via the straight sinus (StS). Recent works have demonstrated that the SSS favors the right TS more commonly then the left, particularly if draining exclusively to one side [46–64]. Such splitting in the SSS or torcular can simulate a filling defect from *dural sinus thrombosis* (Figs. 40.136, 40.137, 40.138, 40.139, 40.140, 40.141, 40.142, 40.143, 40.144, 40.145, 40.146, 40.147, 40.148, 40.149, 40.150, and 40.151).

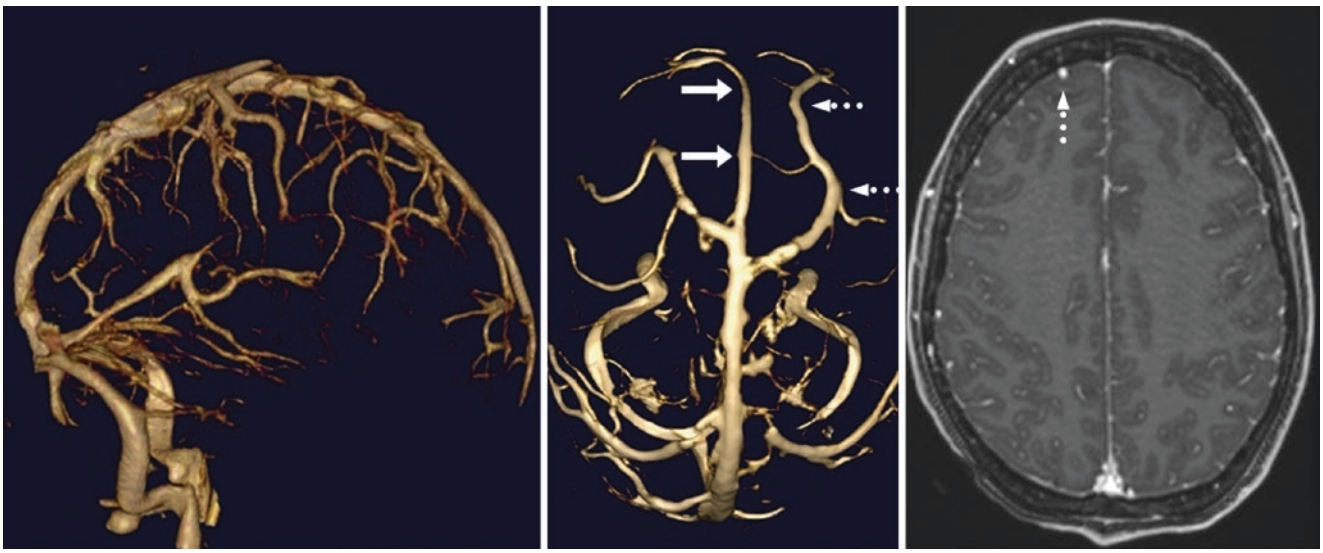

Fig. 40.128 Rostral SSS hypoplasia (mild). An 18-year-old with a CEMRV and 3D reconstructions in right lateral (*left*) and superior (*middle*) views. The rostral SSS (*arrows*) is mildly reduced in caliber, with compensatory enlargement of a right frontal cortical vein (*dotted arrows*). An axial postcontrast T1WI (*right*) confirms this prominent cortical vein

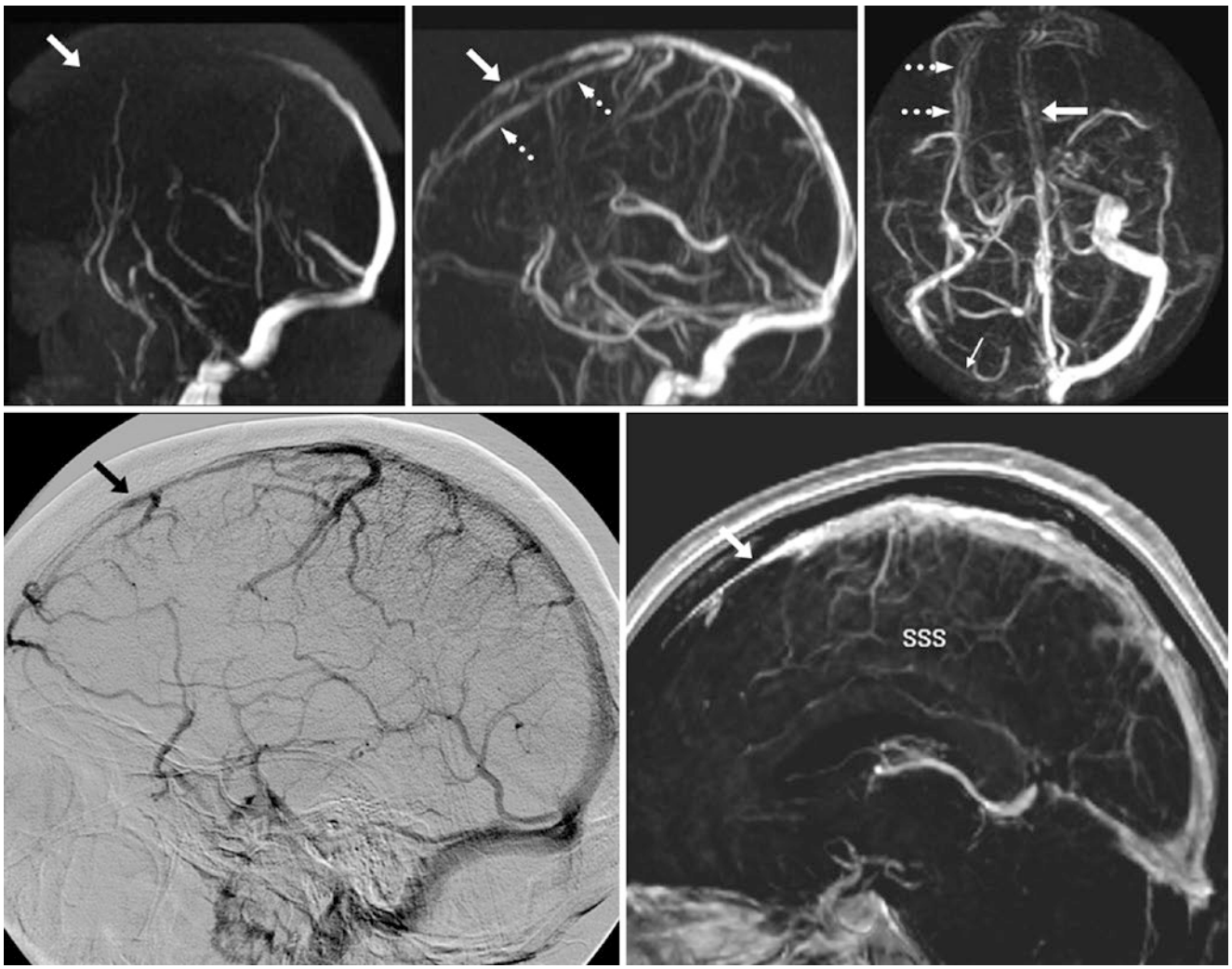

Fig. 40.129 Rostral SSS hypoplasia (moderate). *Top row:* a 61-year-old with an MIP 2DTOF MRV left lateral view (*left*) and CEMRV lateral view (*middle*) and superior view (*right*), which do not show the rostral SSS (*arrows*). *Bottom row:* A DSA lateral view (*left*) and a 3D postcontrast sagittal T1WI MPR (*right*) showed this region to be patent, albeit tiny. A prominent left cortical vein (*dotted arrows*) parallels the SSS. The SSS signal loss on the 2DTOF MRV was likely exacerbated by "in-plane saturation." Also note a hypoplastic left transverse sinus (*thin arrow*)

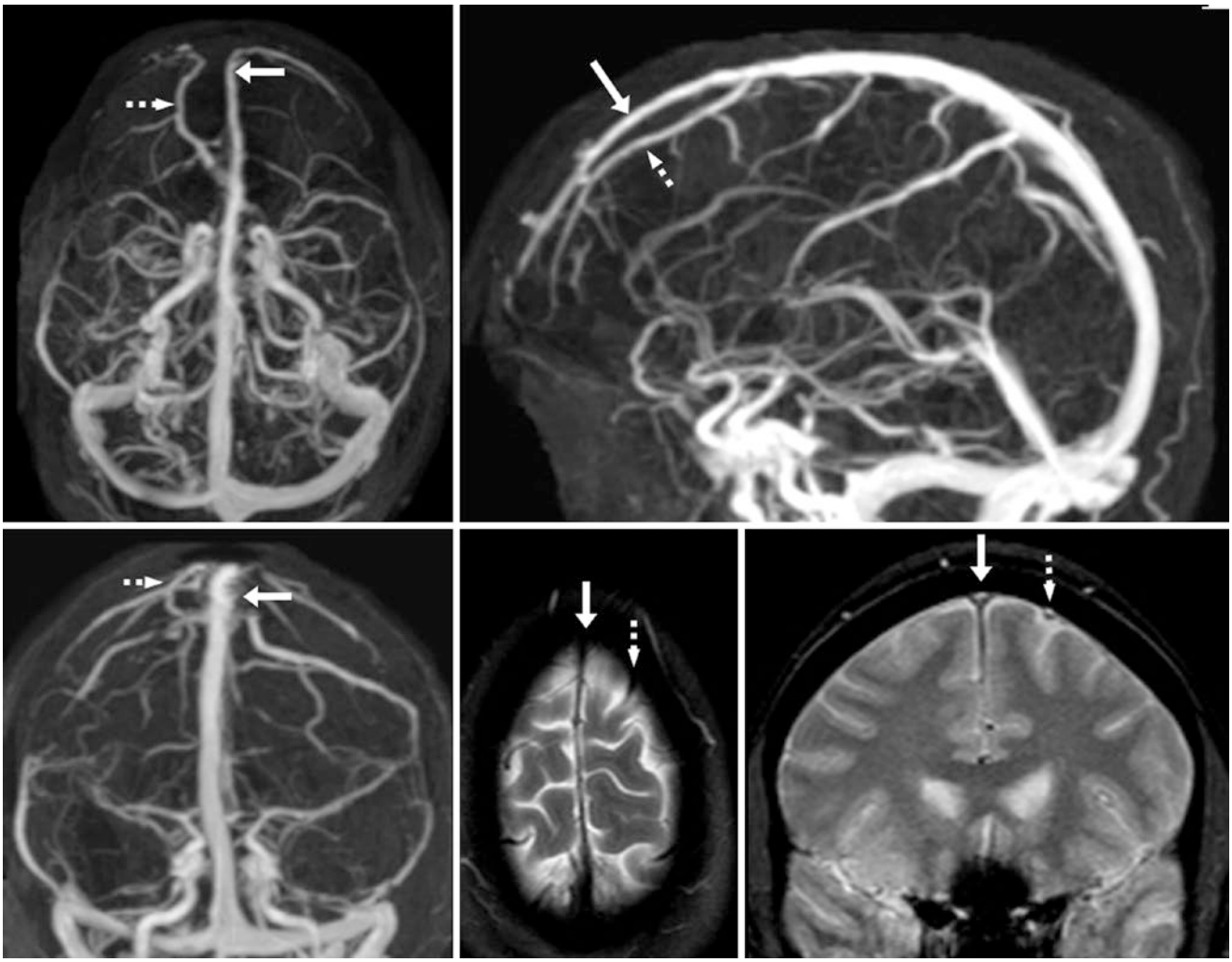

Fig. 40.130 Rostral SSS hypoplasia (moderate). A 38-year-old with a prominent left cortical vein (*dotted arrows*) that parallels the SSS (*arrows*) on CEMRV with superior (*top left*), left lateral (*top right*), and PA (*bottom left*) views. The vein appears to be similar in size to the SSS. Axial T2WI (*bottom middle*) and coronal T2* images (*bottom right*) depict the parallel veins and confirm the SSS to be at midline with the cortical vein situated to the left of midline

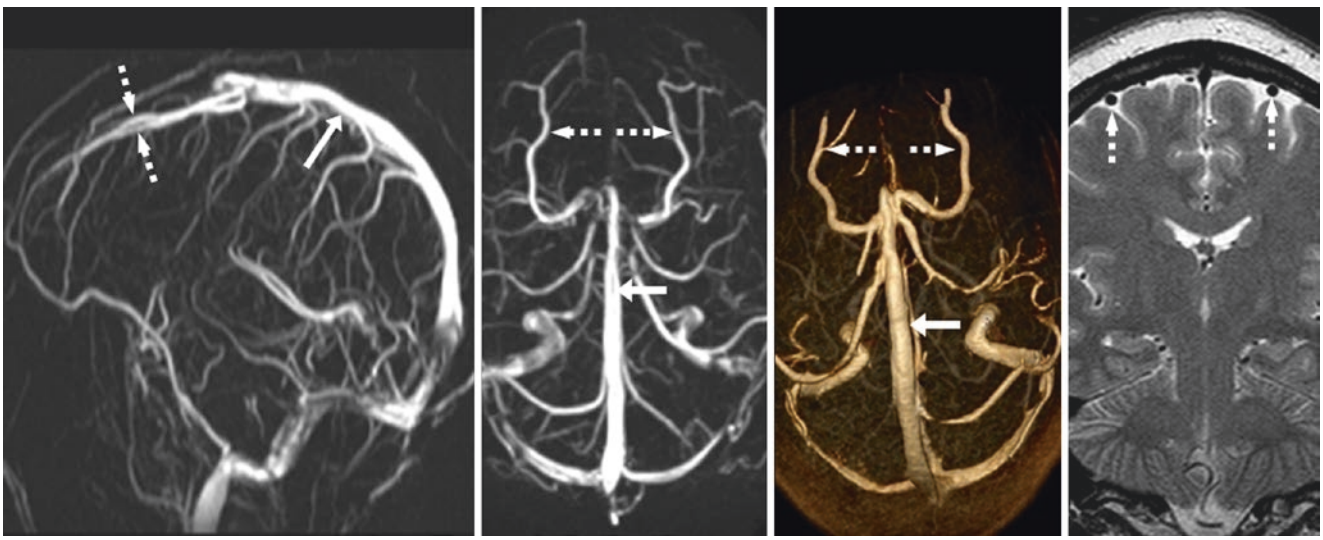

Fig. 40.131 Rostral SSS atresia (severe). A 29-year-old had prominent bilateral cortical (frontal) veins (*dotted arrows*) that parallel an absent SSS at the midline on a CEMRV lateral view (*left*), superior views (*middle two images*), and on a coronal T2WI (*right*). There is aplasia of the rostral one third of the SSS, which is substituted for by the bilateral normal variant cortical veins. Posteriorly, both accessory cortical veins join to form a more typical-appearing SSS (*arrows*)

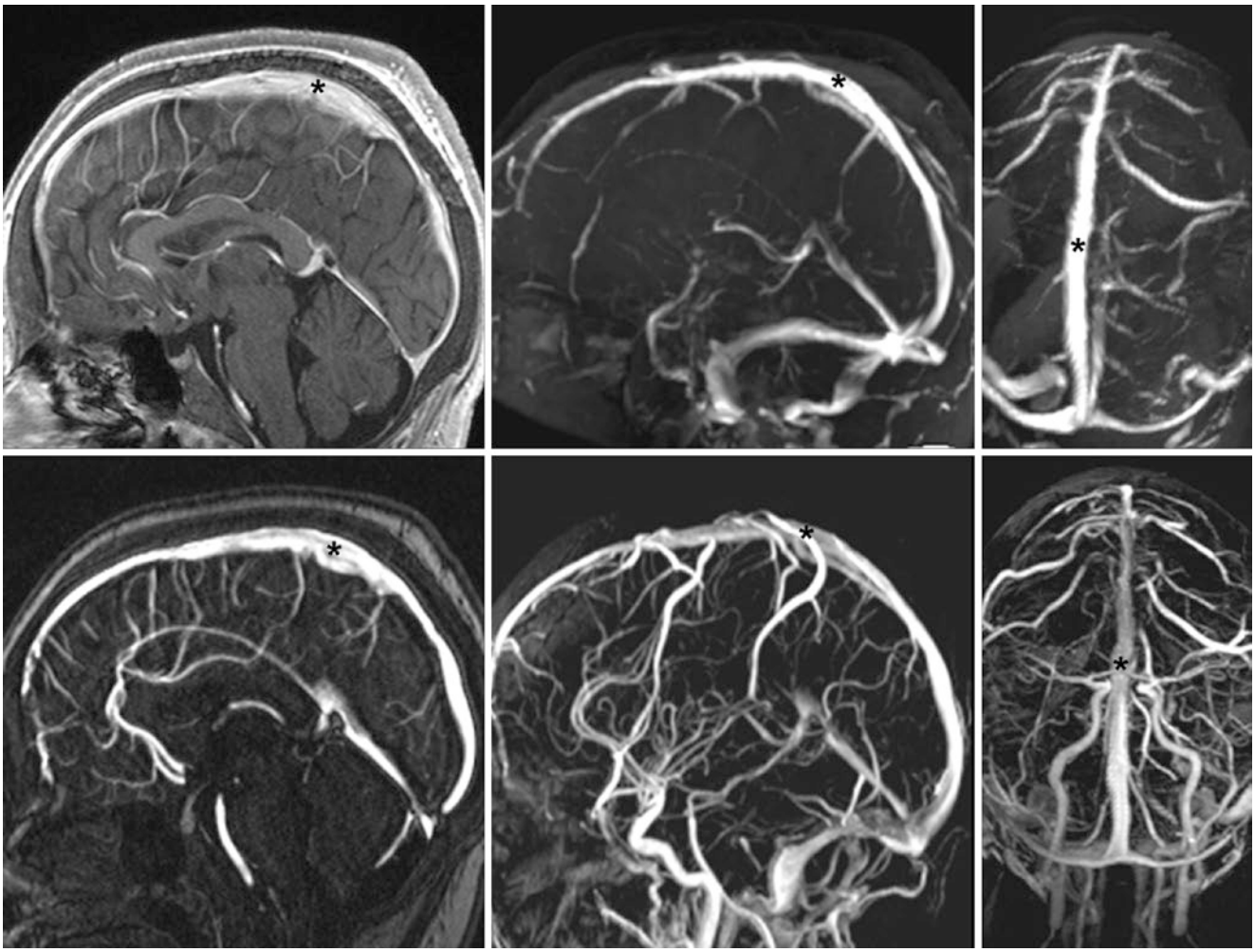

Fig. 40.132 Central SSS "bulbous" enlargement. *Top row*: A 15-year-old had a bulbous-appearing SSS (*asterisks*) on postcontrast T1WI (*left*) and on 2DTOF MRV left lateral (*middle*) and PA (*right*) views. *Bottom row:* The patient also underwent a CEMRV with source sagittal (*left*) and 3D left lateral (*middle*) images, as well as a PA view (*right*), which also depict the bulbous-appearing SSS. This SSS appears less bulbous on the CEMRV PA view and on the noncontrast 2DTOF MRV

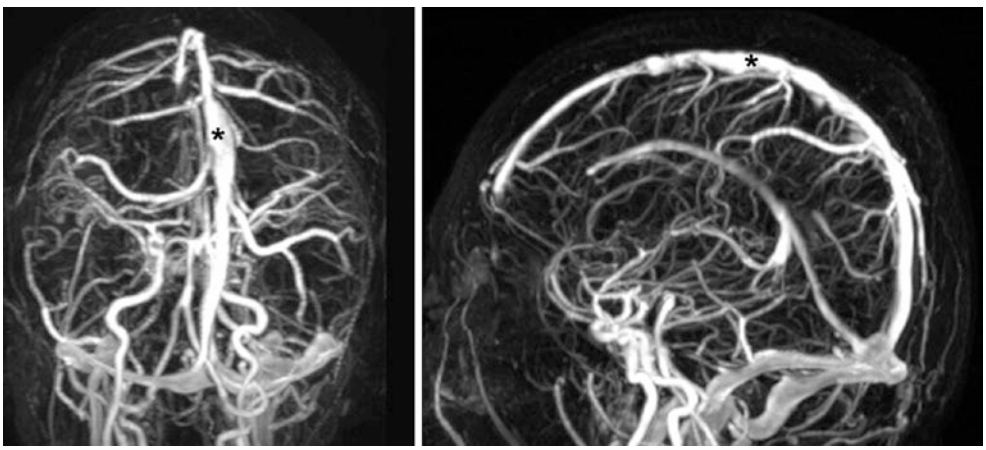

Fig. 40.133 Central SSS "bulbous" enlargement. A 30-year-old had CEMRV PA (*left*) and lateral (*right*) views of a bulbous SSS (*asterisks*), which has an "undulating" appearance, particularly on the lateral view. The prominent, undulating appearance could be mistaken for a sequela of thrombosis, as dilatation may occur following chronic dural sinus thrombosis

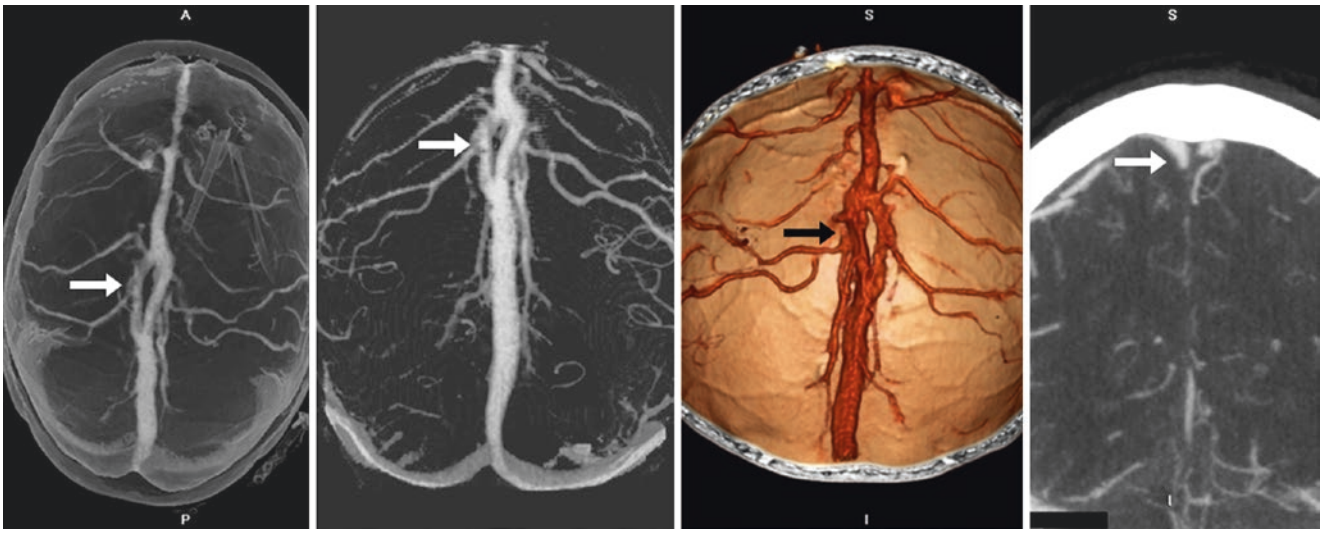

Fig. 40.134 Central SSS fenestration. A 76-year-old had a "split" or fenestration (*arrows*) in the SSS near the vertex, which was demonstrated on a CTV with superior (*left*), PA (*left middle*), and inner (*viewed from inferiorly*, *right middle*) views. It was also confirmed by a coronal MPR (*right*)

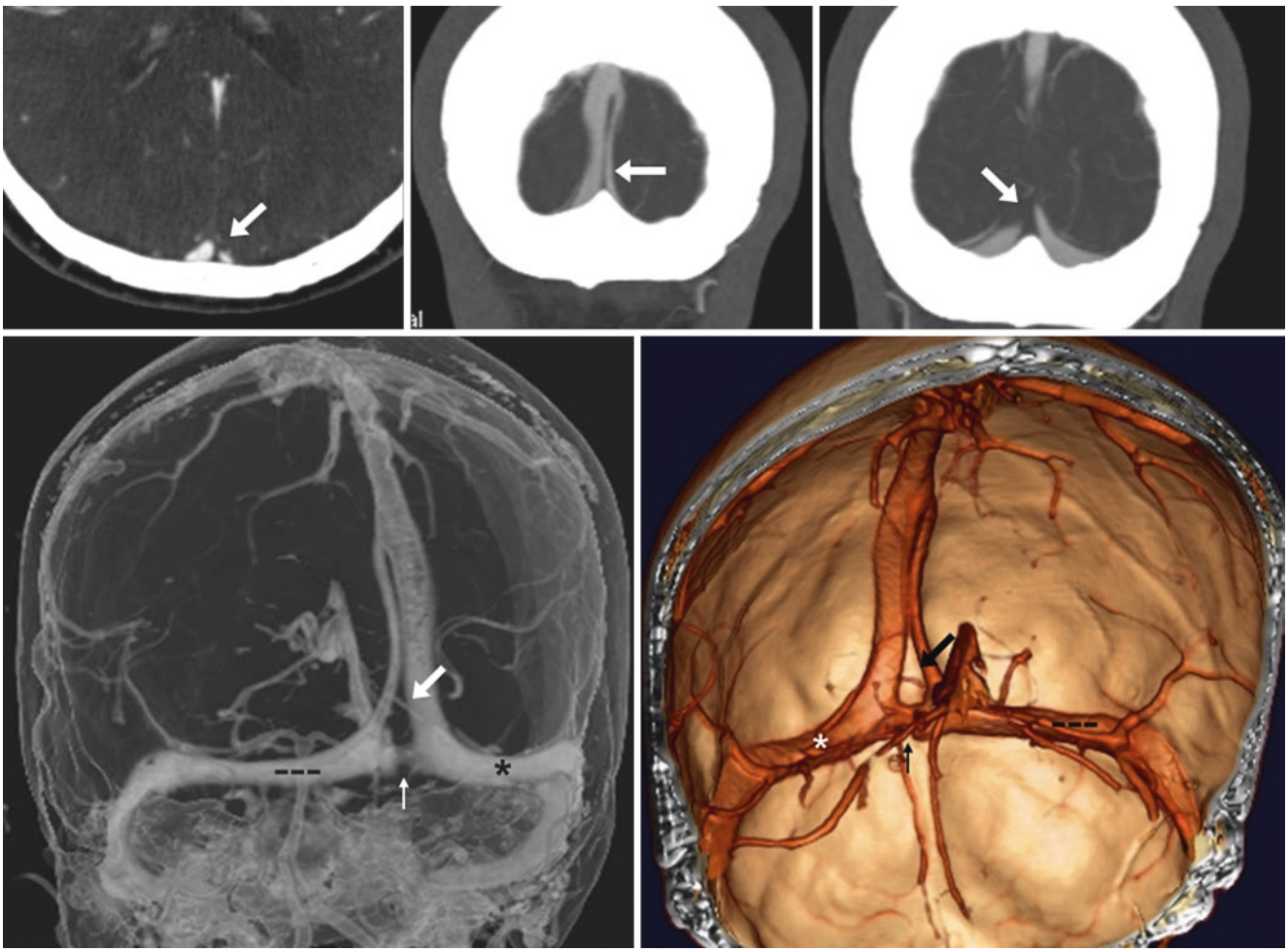

Fig. 40.135 Central SSS "split." *Top row*: A 45-year-old had a SSS "split" (*arrows*) extending down into the torcular on axial (*left*) and coronal (*middle* and *right*) MPRs from a CTV. The split mimics a filling defect from thrombus. *Bottom row:* On a 3D VR PA view (*left, bone removed*) and on an AP inner view (*right*), the SSS drainage favors the right transverse sinus (TS) (*asterisk*), whereas the SSS favors the left TS (*minus signs*). A thin communication (*thin arrows*) travels between the right and left TSs along the floor of the torcular

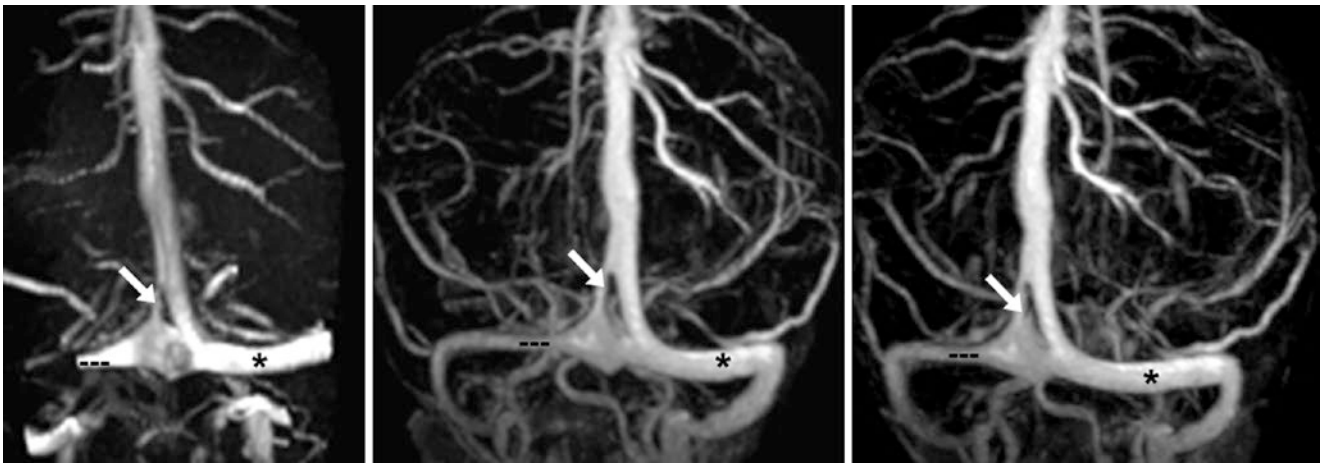

Fig. 40.136 Dorsal SSS "split." In this 9-month-old, PA views using 2DTOF MRA (*left*) and CEMRV (*middle* and *right*) demonstrate a split SSS (*arrows*) just above the torcular, which favors the right TS (*asterisks*). The left TS (*minus signs*) is rather small. In such a case, the split within the torcular could simulate a thrombus on axial reconstructions

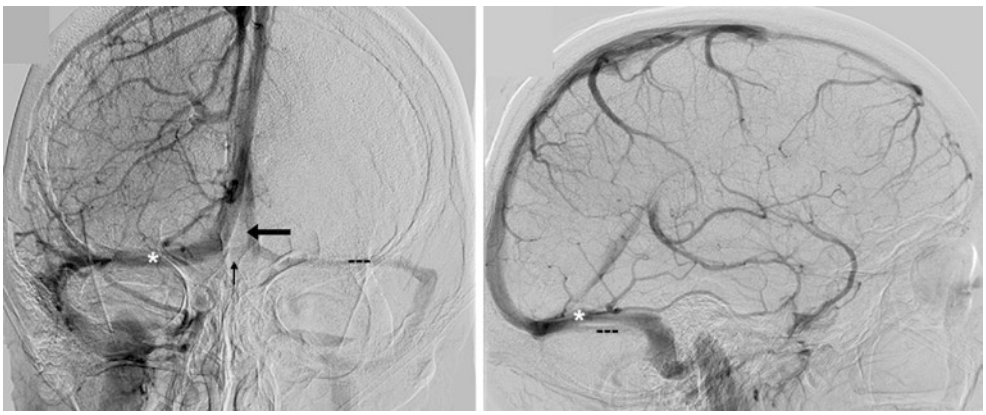

Fig. 40.137 Dorsal SSS "split." A 65-year-old underwent a catheter DSA. In the venous phase, on AP (*left*) and lateral (*right*) views, a split SSS (*arrows*) is demonstrated just above the level of the torcular, favoring the right TS (*asterisks*). The left TS (*minus signs*) is rather tiny. There is a very thin venous communication along the bottom of the torcular (*thin arrows*)

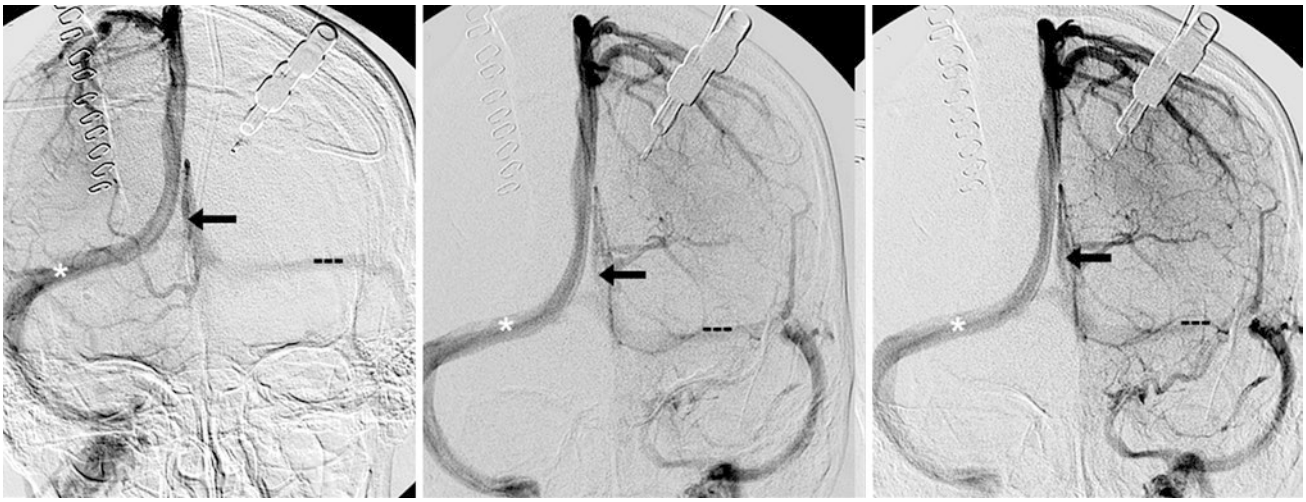

Fig. 40.138 Dorsal SSS "split." A 34-year-old underwent a catheter DSA via right ICA injection after right subdural hemorrhage evacuation. An AP view in the early venous phase (*left*) depicts a split SSS (*arrows*) above the torcular, also visible on left ICA injections in the early (*middle*) and late (*right*) venous phases. The SSS drainage favors the right TS (*asterisks*). Note a hypoplastic left TS (*minus signs*)

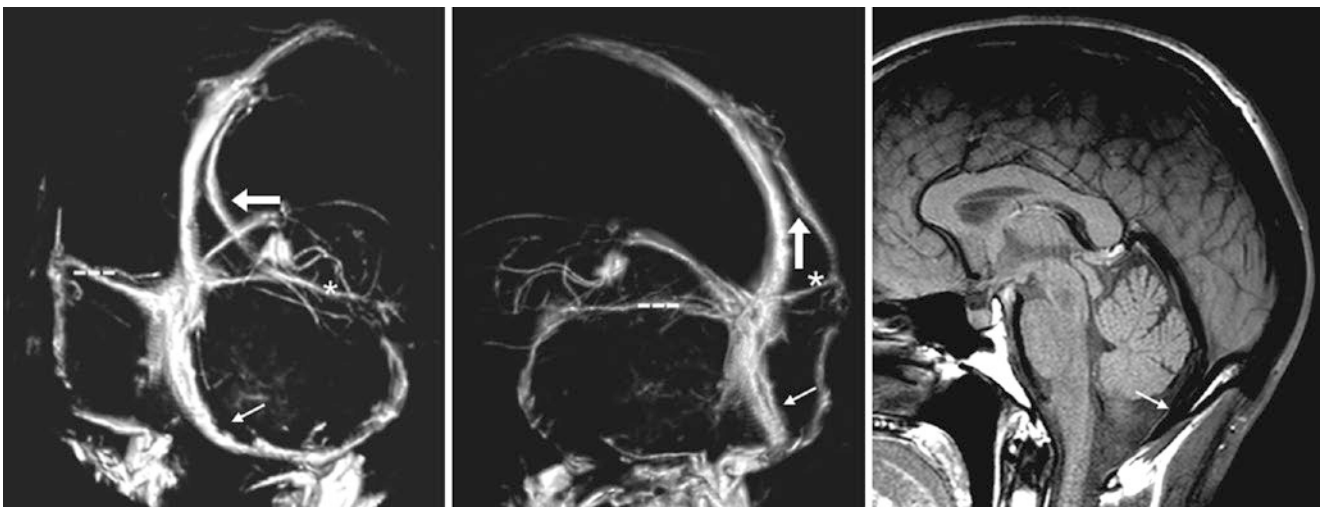

Fig. 40.139 Dorsal SSS "split." In this 50-year-old, CEMRV bilateral PA-oblique views (*left* and *middle*) show a split SSS with a prominent accessory branch (*arrows*) headed towards the proximal segment of a small right TS (*asterisks*); the contralateral TS (*minus signs*) is also small. Note that most drainage is to an occipital sinus (*thin arrows*), which has a patent flow void on T1WI (*right*)

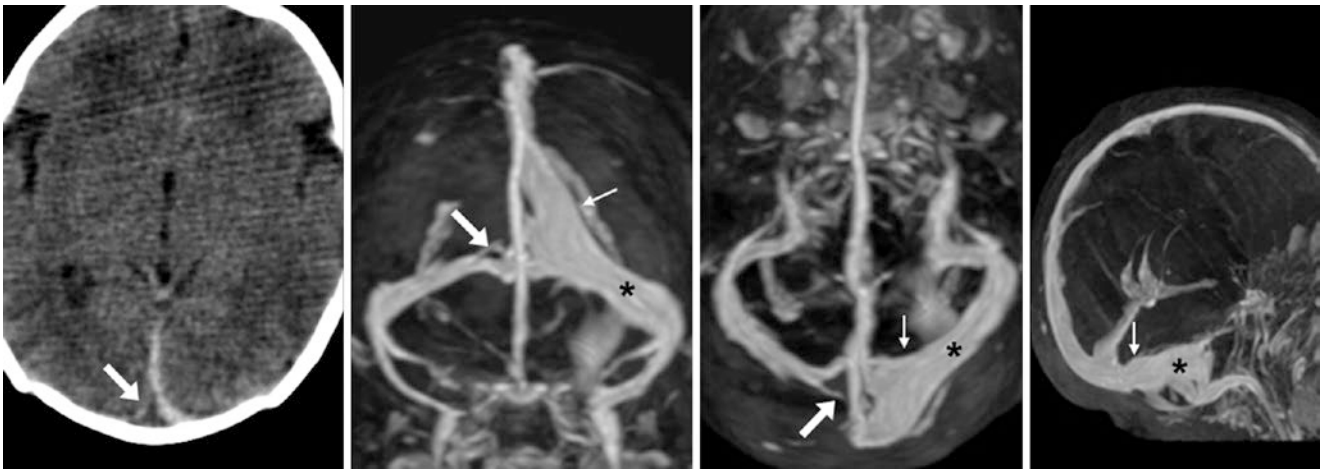

Fig. 40.140 Dorsal SSS "split." A 5-day-old, in whom thrombus was questioned on nonenhanced CT (*left*), owing to a spurious filling defect within a hyperdense SSS (*arrows*). However, CEMRV MIPs in PA (*left middle*), superior (*right middle*), and RPO (*right*) views did not identify intraluminal thrombus, but rather depicted a split of an entirely patent SSS extending into the torcular, with a large accessory vein (*thin arrows*) that drained into the right TS (*asterisks*). The dense SSS was due to dehydration

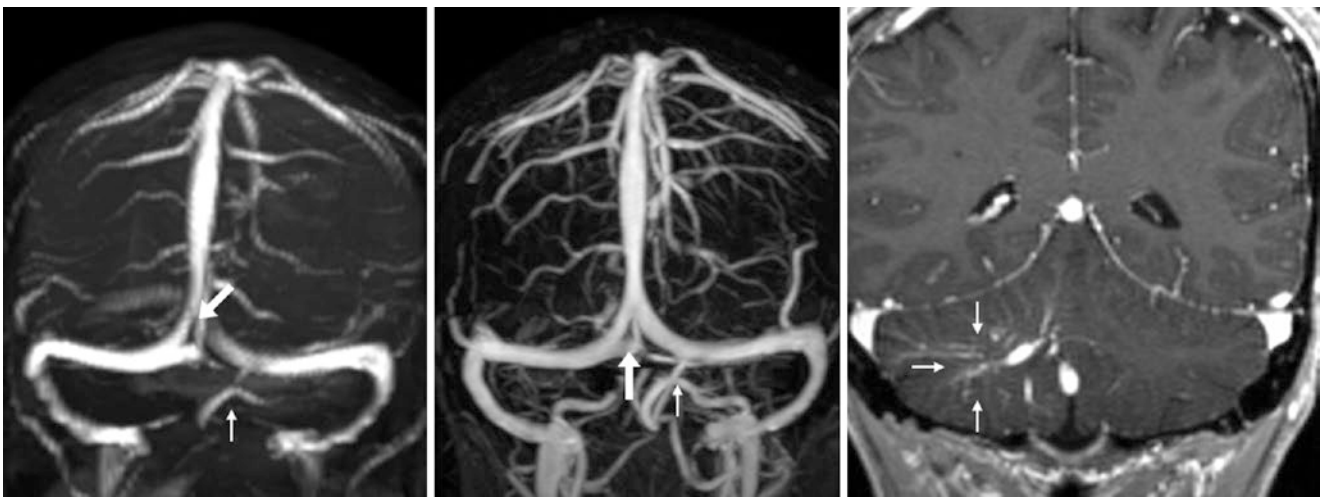

Fig. 40.141 A 24-year-old, in whom a 2DTOF MRV PA view (*left*) showed a split in the distal SSS-torcular (*arrows*) that was better visualized on a CEMRV PA view (*middle*). Also note enlarged draining veins (*thin arrows*) on a postcontrast T1WI (*right*), with a "caput medusa" appearance of a developmental venous anomaly within the right hemicerebellum

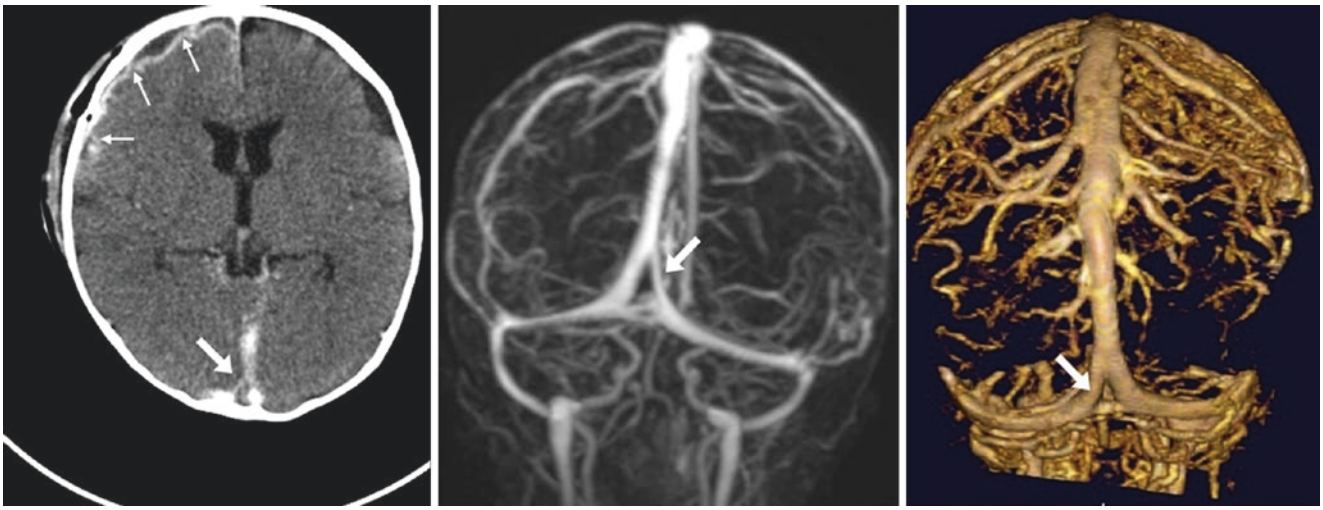

Fig. 40.142 Dorsal SSS "split." A 5-month-old with meningitis had a filling defect on a venous-phase contrast-enhanced CT (*left*), which simulated thrombus within the torcular (*large arrows*). The *thin arrows* denote pial enhancement and a subdural effusion. However, CEMRV PA views (*middle* and *right*) confirmed the defect to be a split SSS/torcular (*arrows*), not an actual thrombus

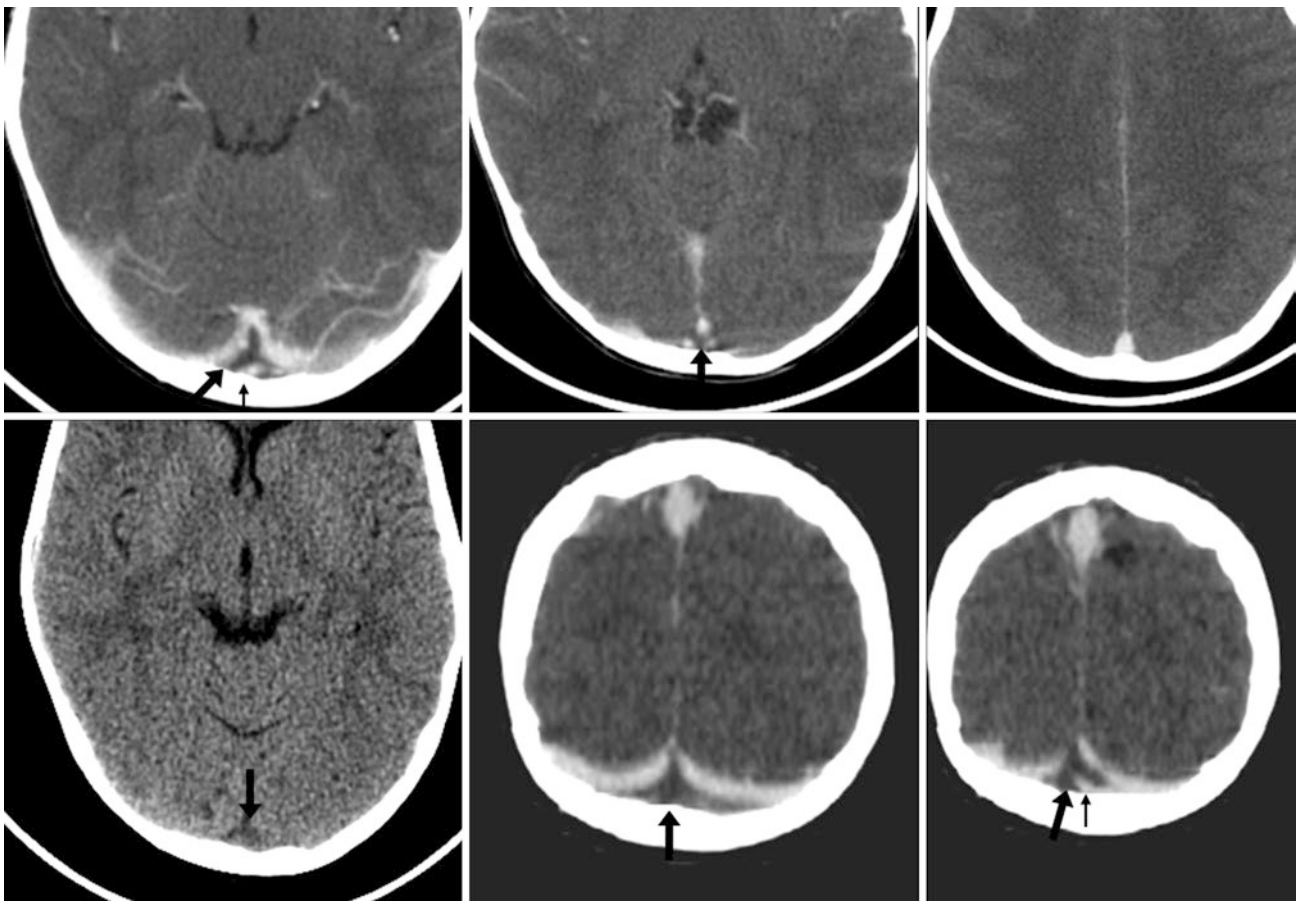

Fig. 40.143 Dorsal SSS "split." *Top row*: In this 3-year-old, axial contrast-enhanced CT images showed a torcular defect (*arrows*) that mimicked thrombus. *Bottom row:* The lack of hyperdensity on nonenhanced CT (*left*) excluded acute thrombus, and coronal MPRs (*middle* and *right*) showed this to be a normal split/fenestration, with a tiny transverse communicating channel (*thin arrows*)

Fig. 40.144 Dorsal SSS "split." A 61-year-old had catheter DSA AP views via right ICA injection (*left*) and left ICA injection (*middle*). The distal SSS is split just above the torcular (*arrows*). A slightly oblique view (*right*), obtained via a left vertebral artery injection, demonstrates the contribution from the StS (*thin arrow*), as well as the VOG

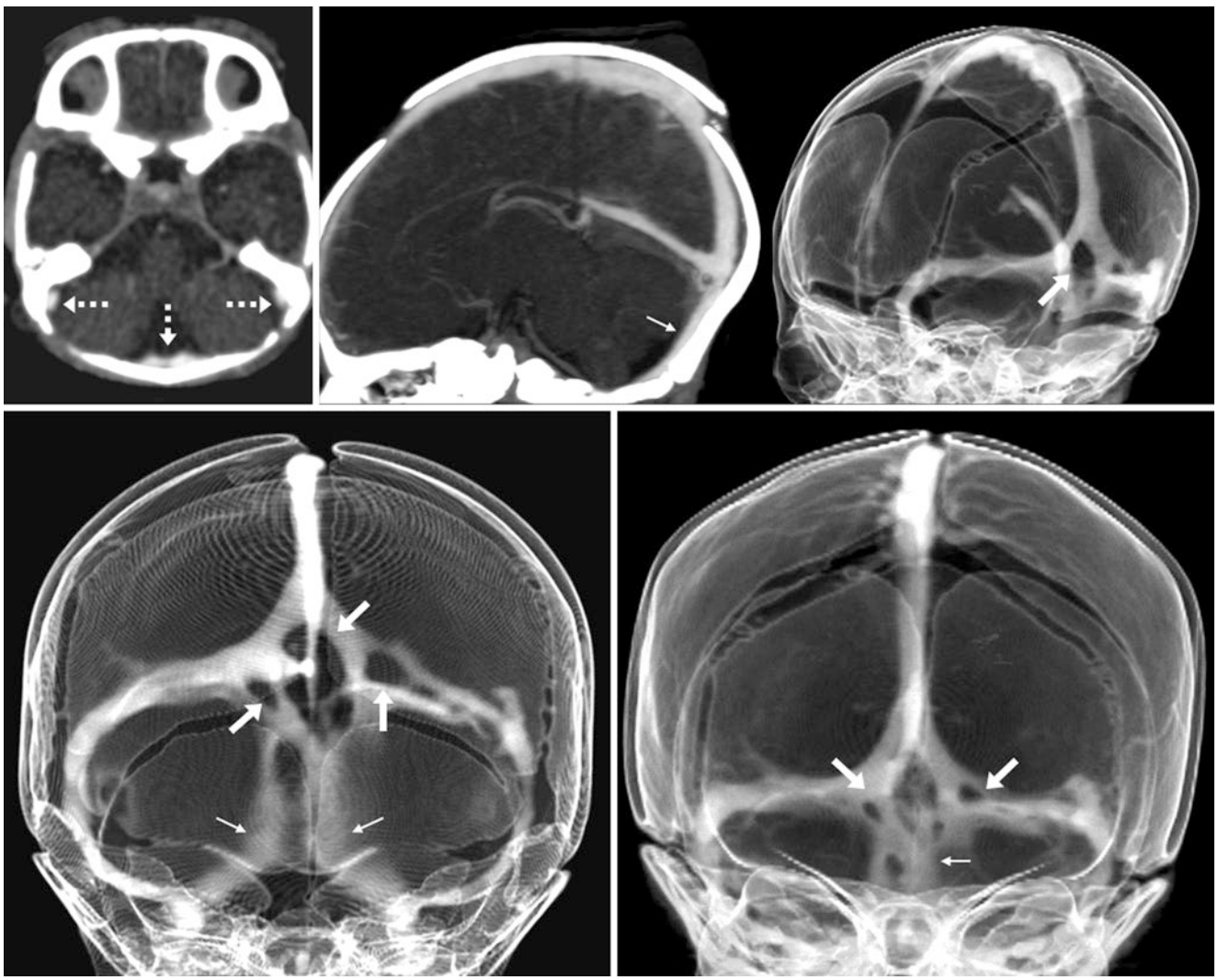

Fig. 40.145 Dorsal SSS multiple fenestrations. A 1-day-old neonate had diffusely dense dural sinuses on nonenhanced CT (*dotted arrows, top left*), raising the question of thrombosis. However, a CTV showed patent sinuses on a sagittal MPR (*top middle*) and on "see through bone" LPO (*top right*) and PA views (*bottom row*). It also showed numerous fenestrations of the torcular (*large arrows*), of the right TS, and of a bilateral occipital sinus (*thin arrows*). The dense sinuses were due to normal fetal hemoglobin

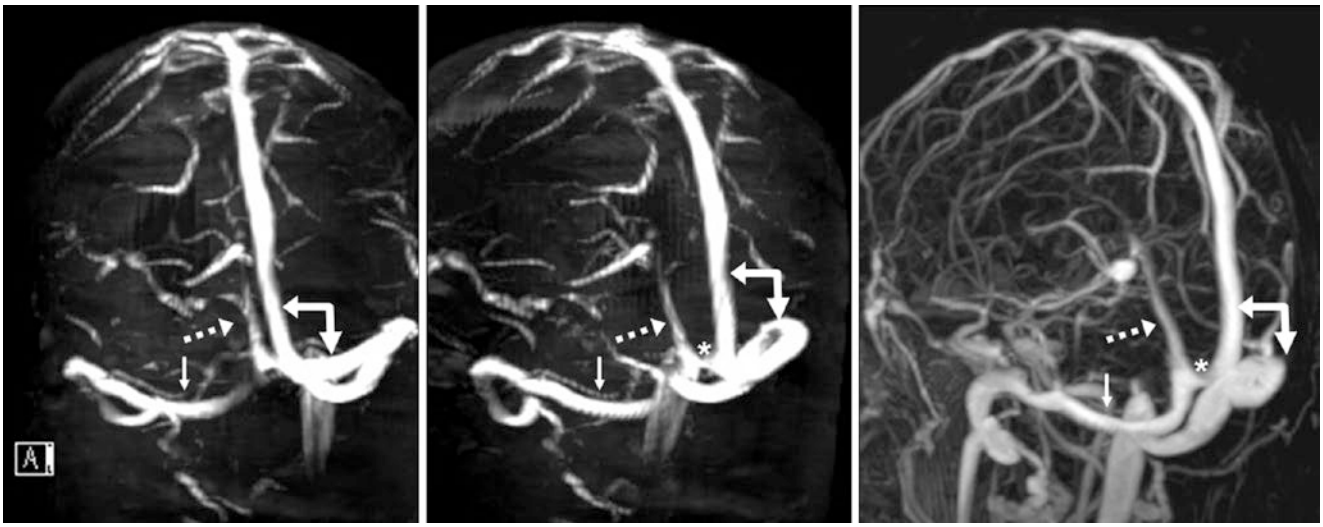

Fig. 40.146 Dorsal SSS unilateral drainage. In a 1-day-old neonate, 2DTOF MRV PA (*left*) and LPO (*middle*) views and a CEMRV LPO view (*right*) demonstrate the SSS draining predominantly to the right TS (*large arrows*). The left TS (*thin arrows*) is small and fills largely via the StS (*dotted arrows*). A tiny communicator (*asterisks*) connects the SSS and StS

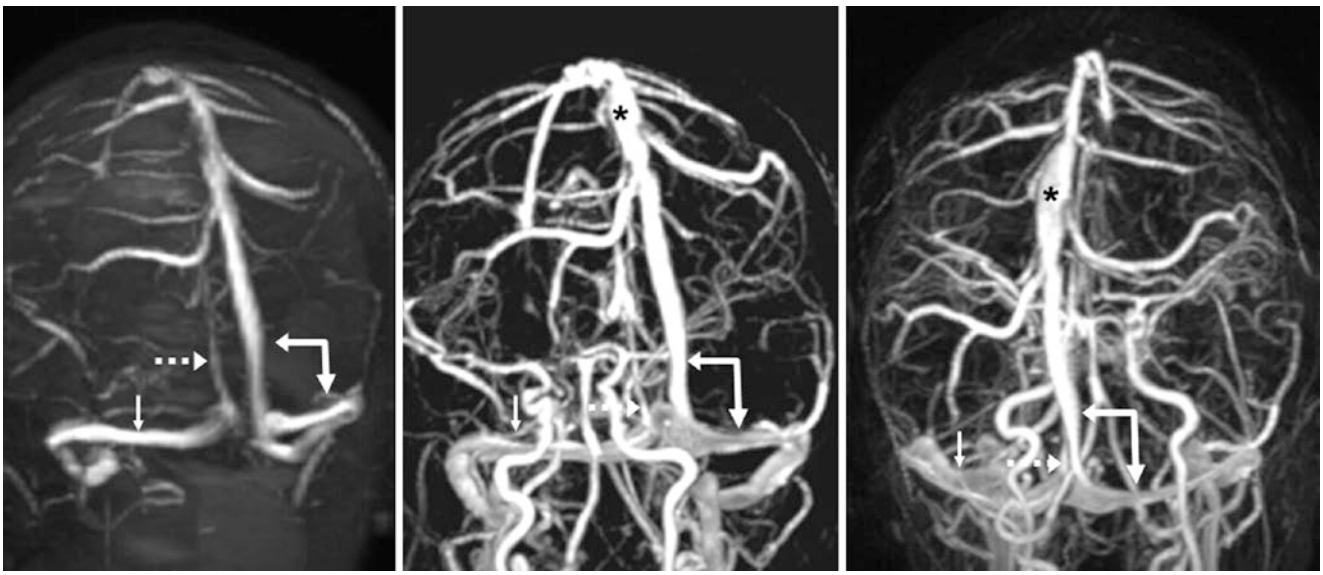

Fig. 40.147 Dorsal SSS unilateral drainage. In this 30-year-old, 2DTOF (*left*) and CEMRV (*middle* and *right*) PA views demonstrate that the SSS drains predominantly into the right TS (*large arrows*). The StS (*dotted arrows*) drains largely into the left TS (*thin arrows*), which is notably not hypoplastic. Also, note a normal variant mildly "bulbous" and "undulating" SSS (*asterisks*)

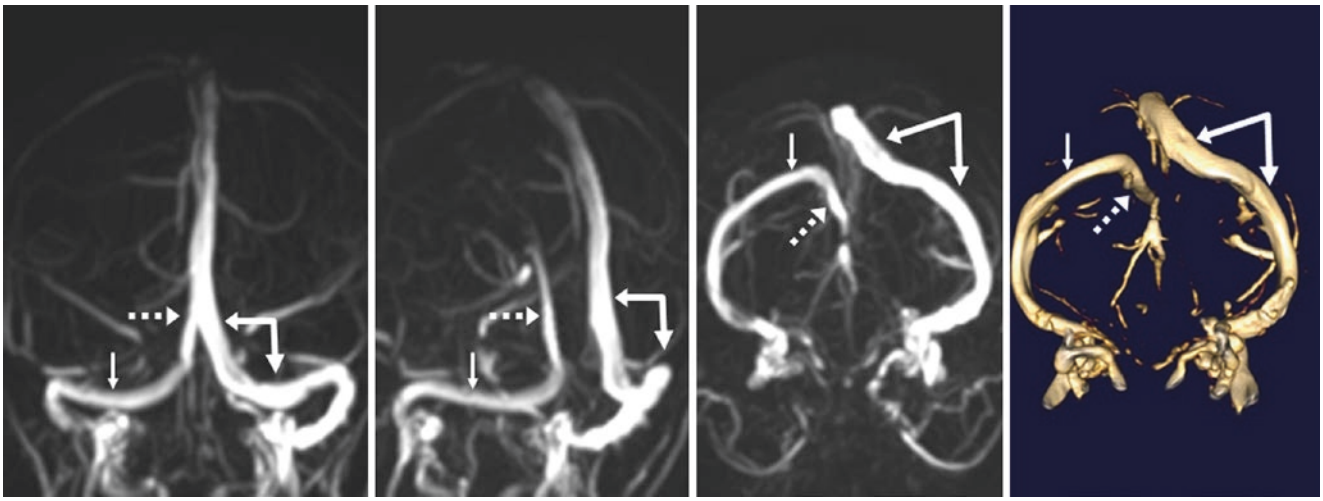

Fig. 40.148 Dorsal SSS unilateral drainage. In this 20-year-old, 2DTOF MRV PA (*left*), LPO (*left middle*), and inferior (*right middle* and *right*) views show that the SSS drains predominantly into the right TS (*large arrows*), whereas the StS (*dotted arrows*) drains into the left TS (*thin arrows*). In this patient, the left TS is slightly smaller than the right, but it is not frankly hypoplastic

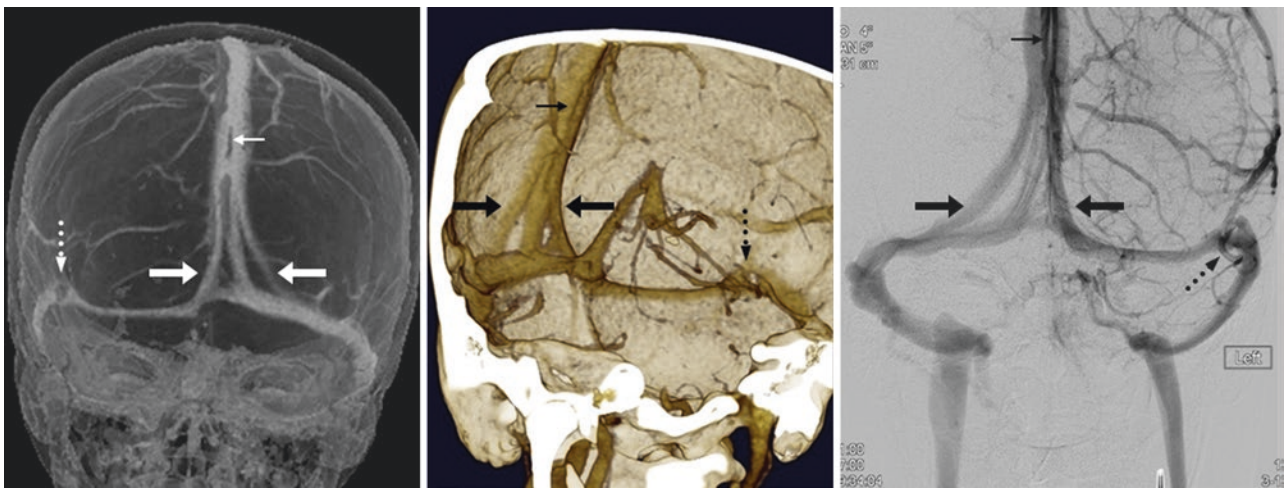

Fig. 40.149 Dorsal SSS multiple fenestrations. In an 18-year-old, CTV "see-through" PA (*left*) and oblique inner (*middle*) views depict two splits in the SSS: an upper split (*thin arrows*) and a lower double split just above the torcular (*large arrows*). These could be considered multiple fenestrations. The findings are confirmed on a venous-phase AP view via catheter DSA, obtained via the left ICA (*right*). Note a filling defect (*dotted arrows*) in the left TS from a normal arachnoid granulation

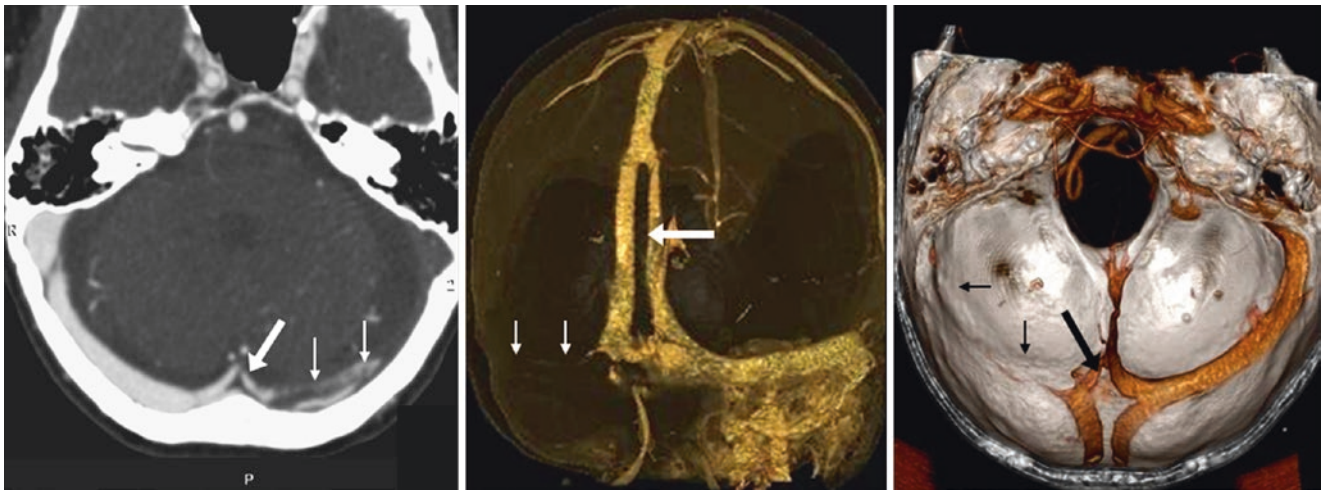

Fig. 40.150 Comparison Case of a Normal Split SSS as well as Actual Thrombus. In an 87-year-old, CTV depicts filling defects within the distal SSS (*large arrows*) and within the left TS (*thin arrows*) on source images (*left*), on a 3D VR PA view (*middle*), and on an "inner view" seen from superiorly (*right*). However, the filling defect within the distal SSS is a normal split/fenestration, whereas the defect within the left TS is from nearly occlusive thrombus

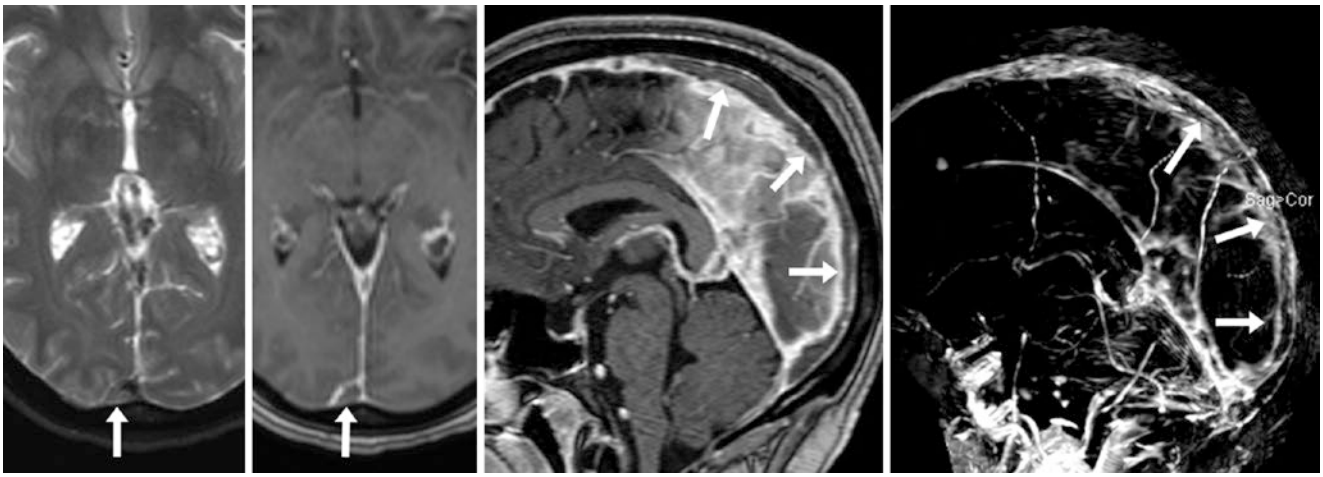

Fig. 40.151 Comparison Case of SSS Thrombosis. In this 44-year-old, an axial T2WI (*left*) and postcontrast axial (*left middle*) and sagittal (*right middle*) T1WIs show diffuse filling defects (*arrows*) throughout the SSS and torcular. A sagittal subtracted T1WI (precontrast from postcontrast T1WI) (*right*) confirms near-occlusive thrombus within the SSS

References

1. Stuckey SL. Dilated venous plexus of the hypoglossal canal mimicking disease. AJNR Am J Neuroradiol. 1999;20:157–8.
2. Tanoue S, Kiyosue H, Sagara Y, Hori Y, Okahara M, Kashiwagi J, Mori H. Venous structures at the craniocervical junction: anatomical variations evaluated by multidetector row CT. Br J Radiol. 2010;83:831–40.
3. Tubbs RS, Hansasuta A, Loukas M, Louis Jr RG, Shoja MM, Salter EG, Oakes WJ. The basilar venous plexus. Clin Anat. 2007;20:755–9.
4. Doppman JL, Krudy AG, Girton ME, Oldfield EH. Basilar venous plexus of the posterior fossa: a potential source of error in petrosal sinus sampling. Radiology. 1985;155:375–8.
5. Gebarski SS, Gebarski KS. Inferior petrosal sinus: imaging-anatomic correlation. Radiology. 1995;194:239–47.
6. Mitsuhashi Y, Nishio A, Kawahara S, Ichinose T, Yamauchi S, Naruse H, et al. Morphologic evaluation of the caudal end of the inferior petrosal sinus using 3D rotational venography. AJNR Am J Neuroradiol. 2007;28:1179–84.
7. Tubbs RS, Ammar K, Liechty P, Wellons 3rd JC, Blount JP, Salter EG, Oakes WJ. The marginal sinus. J Neurosurg. 2006;104:429–31.
8. Katsuta T, Rhoton Jr AL, Matsushima T. The jugular foramen: microsurgical anatomy and operative approaches. Neurosurgery. 1997;41:149–201.
9. Olivier G, Demoulin F. Asymmetry, correlations and sex difference in the descriptive properties of the cranium. Bull Assoc Anat. 1975;59:241–6.
10. Tomura N, Sashi R, Kobayashi M, Hirano H, Hashimoto M, Watarai J. Normal variations of the temporal bone on high-resolution CT: their incidence and clinical significance. Clin Radiol. 1995;50:144–8.
11. Koesling S, Kunkel P, Schul T. Vascular anomalies, sutures and small canals of the temporal bone on axial CT. Eur J Radiol. 2005;54:335–43.
12. Kaplan HA, Browder J, Krieger AJ. Intercavernous connections of the cavernous sinuses. The superior and inferior circular sinuses. J Neurosurg. 1976;45:166–8.
13. Schnitzlein HN, Murtagh FR, Arrington JA, Parkinson D. The sinus of the dorsum sellae. Anat Rec. 1985;213:587–9.
14. Aquini MG, Marrone AC, Schneider FL. Intercavernous venous communications in the human skull base. Skull Base Surg. 1994;4:145–50.
15. Giudicelli G, Resche F, Louis R, Salamon G. Radioanatomie du sinus caverneux. Neurochirurgie. 1972;18:599–612.
16. Renn WH, Rhoton Jr AL. Microsurgical anatomy of the sellar region. J Neurosurg. 1975;43:288–98.
17. Bonneville JF, Cattin F, Tang YS. Radioanatomy of the laterosellar veins. Value of dynamic computerized tomography. J Neuroradiol. 1991;18:240–9.
18. Tubbs RS, Griessenauer C, Loukas M, Cohen-Gadol AA. The circular sinus: an anatomic study with neurosurgical and neurointerventional applications. World Neurosurg. 2014;82:e475–8.
19. Teksam M, Casey S, McKinney A, Michel E, Truwit CL. Anatomy and frequency of large pontomesencephalic veins on 3D CT angiograms of the circle of Willis. AJNR Am J Neuroradiol. 2003;24:1598–601.
20. Tubbs RS, Loukas M, Louis Jr RG, Shoja MM, Askew CS, Phantana-Angkool A, et al. Surgical anatomy and landmarks for the basal vein of Rosenthal. J Neurosurg. 2007;106:900–2.
21. Suzuki Y, Ikeda H, Shimadu M, Ikeda Y, Matsumoto K. Variations of the basal vein: identification using three-dimensional CT angiography. AJNR Am J Neuroradiol. 2001;22:670–6.
22. Chung JI, Weon YC. Anatomic variations of the deep cerebral veins, tributaries of basal vein of Rosenthal: embryologic aspects of the regressed embryonic tentorial sinus. Interv Neuroradiol. 2005;11:123–30.
23. Cai M, Zhang XF, Qiao HH, Lin ZX, Ren CG, Li JC, et al. Susceptibility-weighted imaging of the venous networks around the brain stem. Neuroradiology. 2015;57:163–9.
24. Haacke EM, Tang J, Neelavalli J, Cheng YCN. Susceptibility mapping as a means to visualize veins and quantify oxygen saturation. J Magn Reson Imaging. 2010;32:663–76.
25. Christoforidis GA, Bourekas EC, Baujan M, Abduljalil AM, Kangarlu A, Spigos DG, et al. High resolution MRI of the deep brain vascular anatomy at 8 Tesla: susceptibility-based enhancement of the venous structures. J Comput Assist Tomogr. 1999;23:857–66.
26. Xia XB, Tan CL. A quantitative study of magnetic susceptibility-weighted imaging of deep cerebral veins. J Neuroradiol. 2013;40:355–9.
27. Chen L, Zhang J, Wang QX, Peng L, Luo X, Zhu WZ, et al. Enhanced susceptibility-weighted angiography (ESWAN) of cerebral arteries and veins at 1.5 Tesla. Br J Radiol. 2014;87:20130486.
28. Mahvash M, Pechlivanis I, Charalampaki P, Jansen O, Mehdorn HM. Visualization of small veins with susceptibility-weighted imaging for stereotactic trajectory planning in deep brain stimulation. Clin Neurol Neurosurg. 2014;124:151–5.
29. Zhang XF, Li JC, Wen XD, Ren CG, Cai M, Chen CC. Susceptibility-weighted imaging of the anatomic variation of thalamostriate vein and its tributaries. PLoS One. 2015;10:e0141513.
30. Wang J, Wang J, Sun J, Gong X. Evaluation of the anatomy and variants of internal cerebral veins with phase-sensitive MR imaging. Surg Radiol Anat. 2010;32:669–74.
31. Mucke J, Möhlenbruch M, Kickingereder P, Kieslich PJ, Bäumer P, Gumbinger C, et al. Asymmetry of deep medullary veins on susceptibility weighted MRI in patients with acute MCA stroke is associated with poor outcome. PLoS One. 2015;10:e0120801.
32. Yu X, Yuan L, Jackson A, Sun J, Huang P, Xu X, et al. Prominence of medullary veins on susceptibility-weighted images provides prognostic information in patients with subacute stroke. AJNR Am J Neuroradiol. 2016;37:423–9.
33. Intrapiromkul J, Northington F, Huisman TA, Izbudak I, Meoded A, Tekes A. Accuracy of head ultrasound for the detection of intracranial hemorrhage in preterm neonates: comparison with brain MRI and susceptibility-weighted imaging. J Neuroradiol. 2013;40:81–8.
34. Niwa T, de Vries LS, Benders MJ, Takahara T, Nikkels PG, Groenendaal F. Punctate white matter lesions in infants: new insights using susceptibility-weighted imaging. Neuroradiology. 2011;53:669–79.
35. Kaminogo M, Hayashi H, Ishimaru H, Morikawa M, Kitagawa N, Matsuo Y, et al. Depicting cerebral veins by three-dimensional CT angiography before surgical clipping of aneurysms. AJNR Am J Neuroradiol. 2002;23:85–91.
36. Schuenke M, Schulte E, Schumacher U. Blood vessels of the brain. In: Head and neuroanatomy, Thieme atlas of anatomy. New York: Thieme; 2010.
37. Patel SC, Wagner S. The vasculature of the human brain. In: Conn PM, editor. Neuroscience in medicine. 2nd ed. Totowa: Humana Press; 2003. p. 129–58.
38. Schilling H, Lehmann R. Topographic measurement of the superior vermian vein by lateral vertebral phlebography. Neuroradiology. 1976;11:53–6.
39. Kiliç T, Ozduman K, Cavdar S, Ozek MM, Pamir MN. The galenic venous system: surgical anatomy and its angiographic and magnetic resonance venographic correlations. Eur J Radiol. 2005;56:212–9.
40. Schlesinger B. The venous drainage of the brain, with special reference to the Galenic system. Brain. 1939;62:274–91.
41. Miabi Z, Midia R, Rohrer SE, Hoeffner EG, Vandorpe R, Berk CM, Midia M. Delineation of lateral tentorial sinus with contrast-enhanced MR imaging and its surgical implications. AJNR Am J Neuroradiol. 2004;25:1181–8.
42. Muthukumar N, Palaniappan P. Tentorial venous sinuses: an anatomic study. Neurosurgery. 1998;42:363–71.

43. Silva PS, Vilarinho A, Carvalho B, Vaz R. Anatomical variations of the vein of Labbé: an angiographic study. Surg Radiol Anat. 2014;36:769–73.
44. Tubbs RS, Salter EG, Wellons 3rd JC, Blount JP, Oakes WJ. The sphenoparietal sinus. Neurosurgery. 2007;60:ONS9–12.
45. San Millán Ruíz D, Fasel JH, Rüfenacht DA, Gailloud P. The sphenoparietal sinus of Breschet: does it exist? An anatomic study. AJNR Am J Neuroradiol. 2004;25:112–20.
46. Ikushima I, Korogi Y, Kitajima M, Yamura M, Yamashita Y. Evaluation of drainage patterns of the major anastomotic veins on the lateral surface of the cerebrum using three-dimensional contrast-enhanced MP-RAGE sequence. Eur J Radiol. 2006; 58:96–101.
47. Ayanzen RH, Bird CR, Keller PJ, McCully FJ, Theobald MR, Heiserman JE. Cerebral MR venography: normal anatomy and potential diagnostic pitfalls. AJNR Am J Neuroradiol. 2000; 21:74–8.
48. Wetzel SG, Kirsch E, Stock KW, Kolbe M, Kaim A, Radue EW. Cerebral veins: comparative study of CT venography with intra-arterial digital subtraction angiography. AJNR Am J Neuroradiol. 1999;20:249–55.
49. Gray H. The sinuses of the dura mater. In: Anatomy of the human body. 20th ed. Philadelphia: Lea & Febiger; 1918. http://www.bartleby.com/107/171.html.
50. San Millán Ruíz D, Fasel JH, Gailloud P. Unilateral hypoplasia of the rostral end of the superior sagittal sinus. AJNR Am J Neuroradiol. 2012;33:286–91.
51. Kaplan HA, Browder AA, Browder J. Atresia of the rostral superior sagittal sinus: associated cerebral venous patterns. Neuroradiology. 1972;4:208–11.
52. Browder J, Browder A, Kaplan AH. The venous sinuses of the cerebral dura mater: I. Anatomical structures within the superior sagittal sinus. Arch Neurol. 1972;26:175.
53. Kobayashi K, Suzuki M, Ueda F, Matsui O. Anatomical study of the occipital sinus using contrast-enhanced magnetic resonance venography. Neuroradiology. 2006;48:373–9.
54. Gökçe E, Pınarbaşılı T, Acu B, Fırat MM, Erkorkmaz Ü. Torcular herophili classification and evaluation of dural venous sinus variations using digital subtraction angiography and magnetic resonance venographies. Surg Radiol Anat. 2014;36:527–36.
55. Widjaja E, Shroff M, Blaser S, Laughlin S, Raybaud C. 2D time-of-flight MR venography in neonates: anatomy and pitfalls. AJNR Am J Neuroradiol. 2006;27:1913–8.
56. Rollins N, Ison C, Booth T, Chia J. MR venography in the pediatric patient. AJNR Am J Neuroradiol. 2005;26:50–5.
57. Widjaja E, Griffiths PD. Intracranial MR venography in children: normal anatomy and variations. AJNR Am J Neuroradiol. 2004;25:1557–62.
58. Fukusumi A, Okudera T, Takahashi S, Taoka T, Sakamoto M, Nakagawa H, et al. Anatomical evaluation of the dural sinuses in the region of the torcular herophili using three dimensional CT venography. Acad Radiol. 2010;17:1103–11.
59. Kopuz C, Aydin ME, Kale A, Demir MT, Corumlu U, Kaya AH. The termination of superior sagittal sinus and drainage patterns of the lateral, occipital at confluens sinuum in newborns: clinical and embryological implications. Surg Radiol Anat. 2010;32: 827–33.
60. Tubbs RS, Loukas M. Duplication of the superior sagittal sinus. Clin Anat. 2006;19:728.
61. Brockmann C, Kunze SC, Schmiedek P, Groden C, Scharf J. Variations of the superior sagittal sinus and bridging veins in human dissections and computed tomography venography. Clin Imaging. 2012;36:85–9.
62. Park HK, Bae HG, Choi SK, Chang JC, Cho SJ, Byun BJ, Sim KB. Morphological study of sinus flow in the confluence of sinuses. Clin Anat. 2008;21:294–300.
63. Bisaria KK. Anatomic variations of venous sinuses in the region of the torcular herophili. J Neurosurg. 1985;62:90–5.
64. Kaplan HA, Browder J, Knightly JJ, Rush BF, Browder A. Variations of the cerebral dural sinuses at the torcular herophili: importance in radical neck dissection. Am J Surg. 1972;124:456–61.
65. Tubbs RS, Loukas M, Louis Jr RG, Shoja MM, Acakpo-Satchivi L, Blount JP, et al. Anatomy of the falcine venous plexus. J Neurosurg. 2007;107:155–7.
66. Tatarli N, Ceylan D, Canaz H, Tokmak M, Bay HH, Şeker A, et al. Falcine venous plexus within the falx cerebri: anatomical and scanning electron microscopic findings and clinical significance. Acta Neurochir. 2013;155:2183–9.
67. Ryu CW. Persistent falcine sinus: Is it really rare? AJNR Am J Neuroradiol. 2010;31:367–9.
68. Sener RN. Association of persistent falcine sinus with different clinicoradiologic conditions: MR imaging and MR angiography. Comput Med Imaging Graph. 2000;24:343–8.
69. Strub WM, Leach JL, Tomsick TA. Persistent falcine sinus in an adult: demonstration by MR venography. AJNR Am J Neuroradiol. 2005;26:750–1.
70. Tubbs RS, Loukas M, Shoja M. Two cases of persistent falcine sinus. World J Pediatr. 2009;5:234.
71. Smith A, Choudhary AK. Prevalence of persistent falcine sinus as an incidental finding in the pediatric population. AJR Am J Roentgenol. 2014;203:424–5.
72. Matouk CC, Mandell DM, Krings T, Willinsky RA, Ter Brugge KG. Persistent anterior falcine sinus: demonstration by CT angiography. Can J Neurol Sci. 2011;38:760–1.
73. Manoj KS, Krishnamoorthy T, Thomas B, Kapilamoorthy TR. An incidental persistent falcine sinus with dominant straight sinus and hypoplastic distal superior sagittal sinus. Pediatr Radiol. 2006;36:65–7.

Suggested Reading

Rischall MA, Boegel KH, Palmer CS, Knoll B, McKinney AM. MDCT Venographic patterns of dural venous sinus compromise after acute Skull Fracture. AJR Am J Roentgenol. 2016;19:1–7.
Goyal G, Singh R, Bansal N, Paliwal VK. Anatomical variations of Cerebral MR venography: Is Gender Matter? Neurointervention. 2016;11:92–8.

Arachnoid Granulations Within the Dural Sinuses

41

Arachnoid (pacchionian) *granulations* are enlarged arachnoid villi, being extensions of the subarachnoid space that contain cerebrospinal fluid (CSF) internally. They serve as an important drainage route for CSF into the venous system. These outpouchings extend from the subarachnoid space through the dura mater into the *dural sinuses* (and occasionally into the calvarium). They may simulate dural sinus filling defects such as *thrombus*, *stenosis*, or *occlusion*. Studies have shown that they can be identified in most asymptomatic patients (60–90 %, based on imaging or autopsy) if a thin-section postcontrast MRI or MR venogram (MRV) is thoroughly inspected, and that they are often multiple. On contrast-enhanced CT, the frequency is lower, likely in the range of 25–33 % [1–11].

The majority of arachnoid granulations are present within the superior sagittal sinus (SSS, about 50–60 %) or transverse sinuses (TS, about 25–30 %); they are less common in the sigmoid sinuses and the straight sinus (StS, about 15–20 %) [1–11]. They are also not uncommon in the lateral tentorial sinus (LTS) at the junction with the transverse-sigmoid sinuses. It is quite rare to see them involve a deep vein, although occasionally, if larger, they can extend retrograde from the junction of the StS back into the vein of Galen. They do not occur in the upper internal jugular vein (IJV) or lower sigmoid sinus, which can be an important criterion to distinguish true intraluminal clot from a granulation. Their mean diameter is between 2 mm and 5 mm, and they tend to be larger in the TS than in the SSS.

Arachnoid granulations seem to be more problematic and more likely to mimic clot when located in the TS, even though they are more common in the SSS, perhaps because axial images are the most commonly reviewed plane, and in this plane the TS is more readily visualized than the SSS. Typical granulations can be diagnosed by a characteristic filling defect that appears well circumscribed and akin to CSF density on CT, with CSF signal intensity on T1WI, T2WI, and on FLAIR. Importantly, typical granulations suppress nearly as much as CSF on FLAIR. However, atypical, uncommon granulations (<10 %) lack complete suppression with CSF on FLAIR [1–11]. Postcontrast CT venography (CTV) or MRV can help distinguish these normal structures from intraluminal thrombi, but an arachnoid granulation can resemble a thrombus on noncontrast MRV alone (Figs. 41.1, 41.2, 41.3, 41.4, 41.5, 41.6, 41.7, 41.8, 41.9, 41.10, 41.11, 41.12, 41.13, 41.14, 41.15, 41.16, and 41.17).

Notably, giant granulations can also mimic pathology, particularly if they protrude into the skull. Please note that as arachnoid granulations can also protrude into the calvarium, the variants protruding into the skull are discussed separately in Sect. 30.1 of the *Skull* section of this book.

A.M. McKinney, *Atlas of Normal Imaging Variations of the Brain, Skull, and Craniocervical Vasculature*,
DOI 10.1007/978-3-319-39790-0_41

Fig. 41.1 In this 38-year-old, a nonenhanced CT depicts a focal, hypodense arachnoid granulation within the left transverse sinus (TS) (*arrow*)

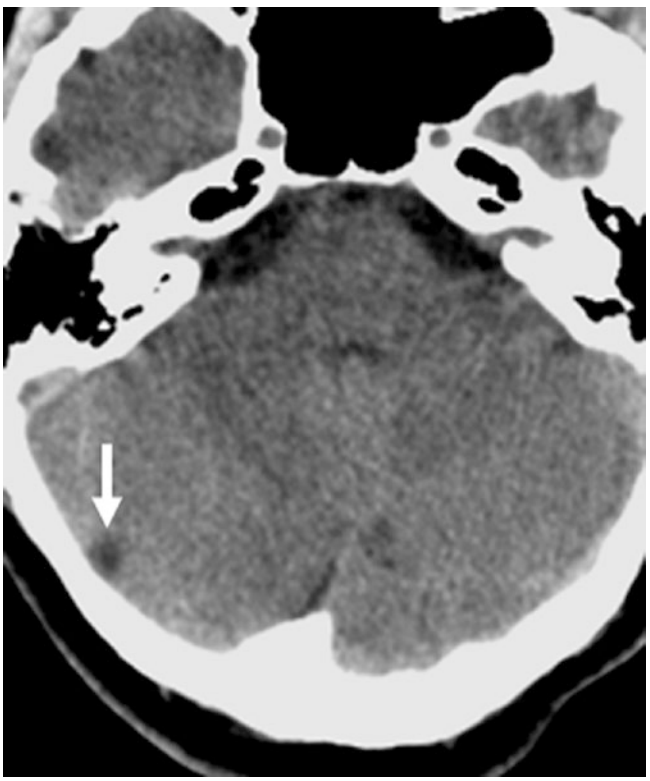

Fig. 41.2 In this 25-year-old, an arachnoid granulation (*arrow*) is seen within the right TS on a nonenhanced CT

Fig. 41.3 In a 35-year-old, contrast-enhanced MR angiography (PA view) shows TS arachnoid granulations bilaterally (*arrows*) that mimic thrombi

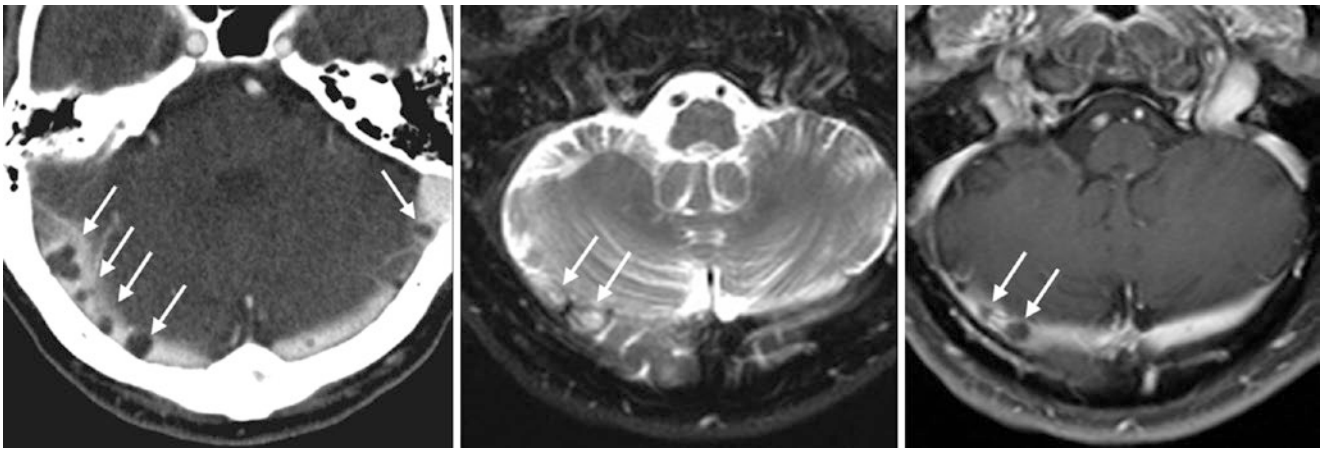

Fig. 41.4 In an 83-year-old, a contrast-enhanced CT (*left*) incidentally noted multiple filling defects within the right TS (*arrows*). On an MRI 3 months later, these followed CSF signal on axial T2WI (*middle*) and postcontrast T1WI (*right*); FLAIR images were not obtained. The well-circumscribed appearance, lack of symptoms, multifocality, nonconfluent nature, and the density/signal intensity of CSF were all factors that were consistent with arachnoid granulations

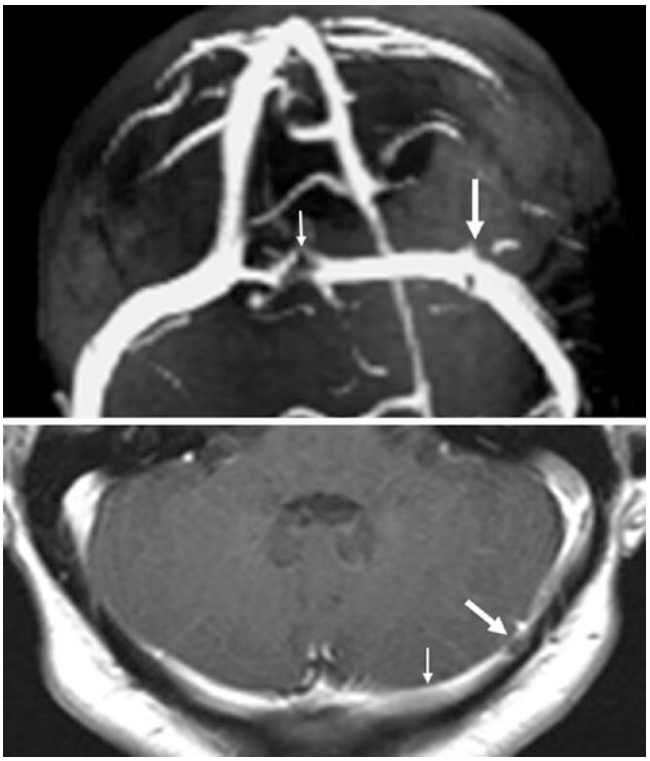

Fig. 41.5 13-year-old with arachnoid granulations (*arrows*) on a 2DTOF MRV AP view (*top*). The medial granulation (*thin arrows*) is not well seen on postcontrast T1WI (*bottom*) because of volume averaging with intravascular contrast

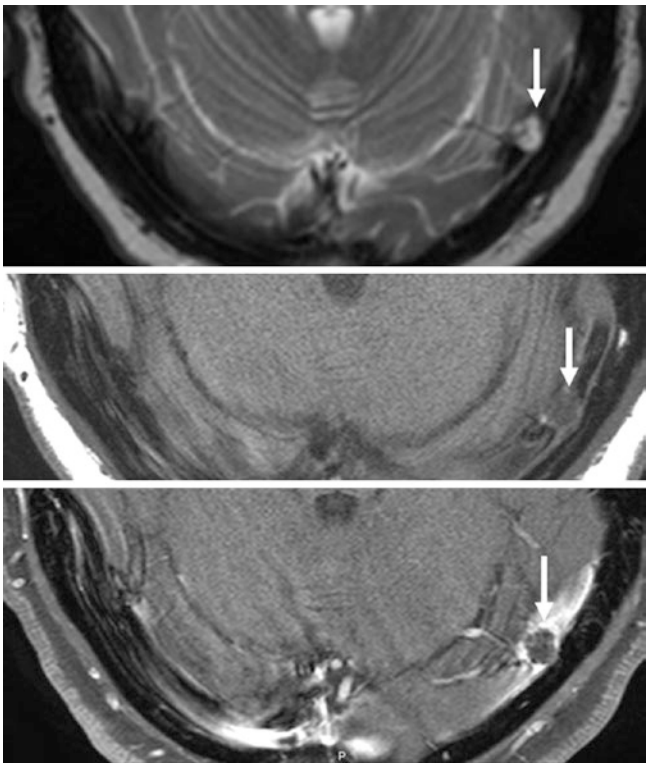

Fig. 41.6 66-year-old with headaches. *Top:* an incidental left TS arachnoid granulation (*arrow*) is seen on T2WI MRI. *Middle and Bottom:* the arachnoid granulation is shown on both precontrast (*middle*) and postcontrast (*bottom*) T1WI

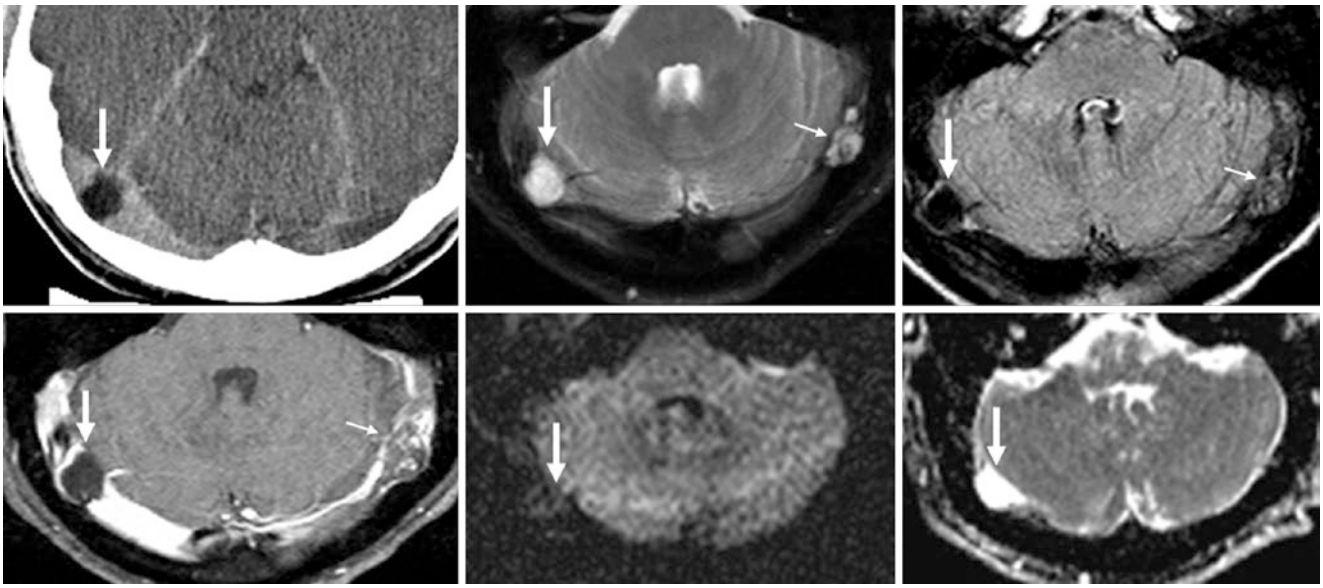

Fig. 41.7 *Top row:* 38-year-old with a well-circumscribed, typical right TS arachnoid granulation (*large arrows*) on contrast-enhanced CT (*left*), with density of CSF, also following CSF on T2WI (*middle*) and FLAIR (*right*). *Bottom row:* this typical granulation did not enhance on postcontrast T1WI (*left*) and exhibited the typical lack of reduced diffusion on DWI (*middle*), with corresponding bright ADC map signal (*right*). However, a left TS granulation (*thin arrows*) is atypical, as it does not entirely suppress with CSF on FLAIR

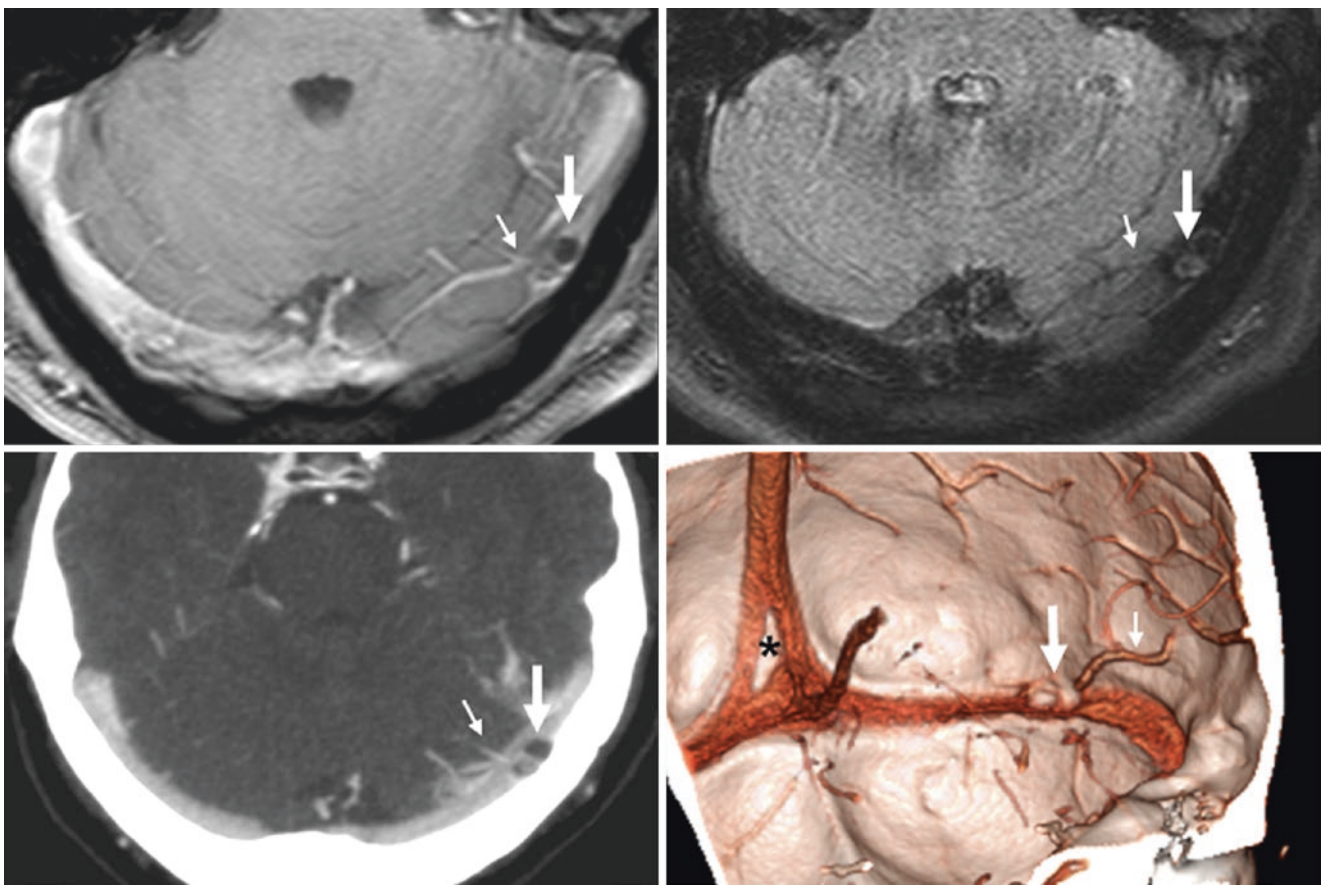

Fig. 41.8 In this 51-year-old, a postcontrast T1WI (*top left*) shows two adjacent filling defects in the left TS (*arrows*), just below the lateral tentorial sinus (LTS) (*thin arrows*); these defects nearly suppress with CSF on FLAIR (*top right*). These granulations are confirmed on a CTV axial image (*bottom left*) and on a 3D VR "inner view" (*bottom right*). Thus, these adjacent arachnoid granulations could simulate an intravascular clot or stenosis. Note a normal split/fenestration (*asterisk*) in the torcular confluence

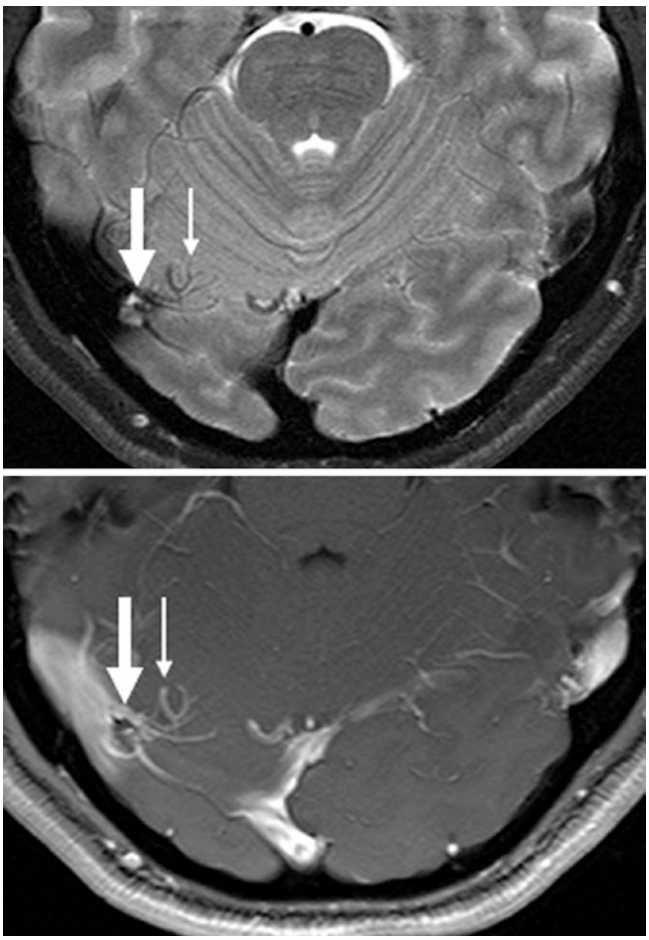

Fig. 41.9 31-year-old with an arachnoid granulation (*large arrows*) within the right LTS (*thin arrows*) on an axial T2WI MRI (*top*) and on a postcontrast T1WI (*bottom*), simulating intraluminal thrombus

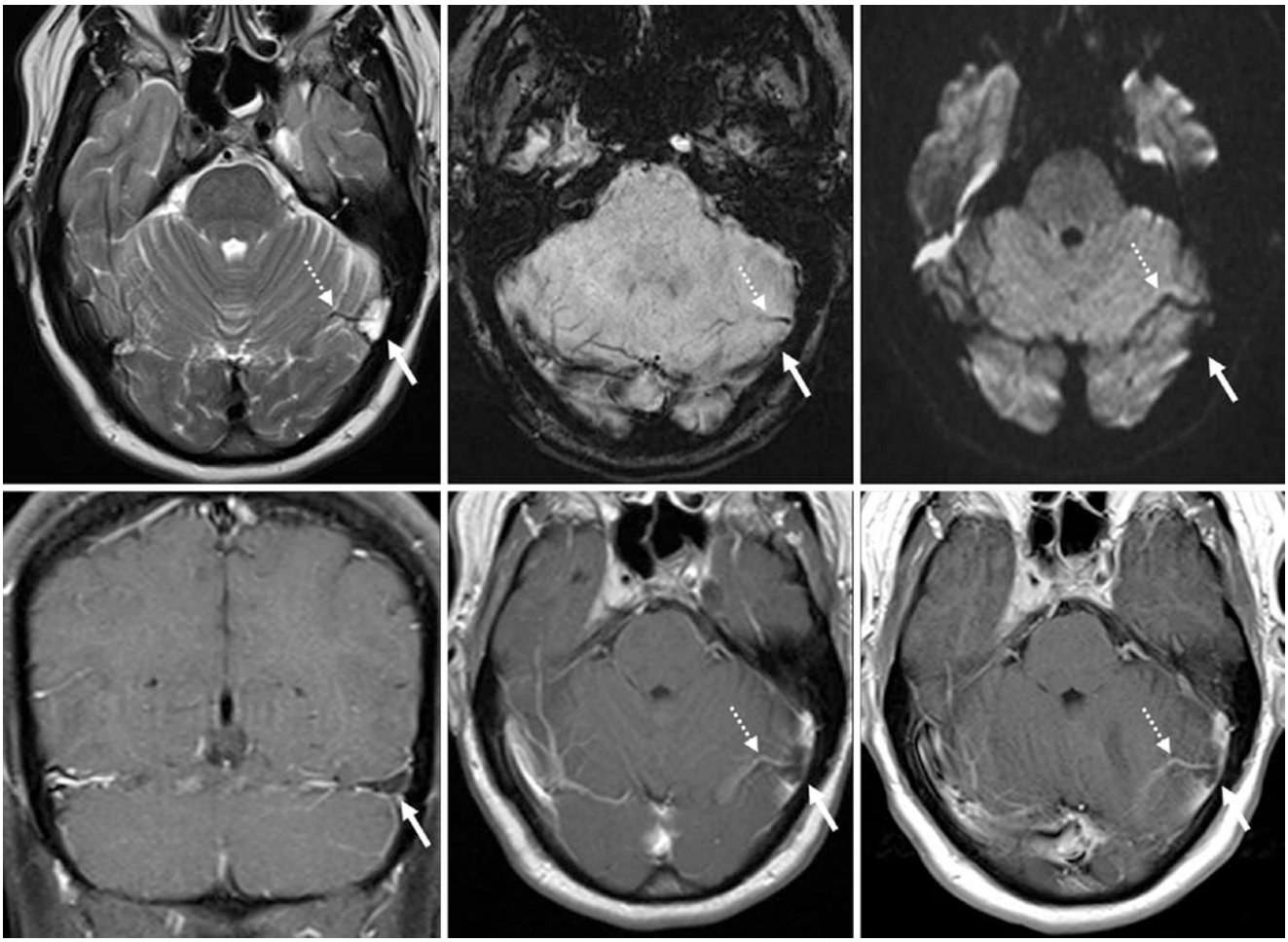

Fig. 41.10 *Top row:* 37-year-old with a normal arachnoid granulation (*arrows*) that filled most of the LTS on a 1.5 T MRI. The granulation was bright akin to CSF on T2WI (*left*), was imperceptible on SWI (*middle*), and was dark on DWI (*right*), and FLAIR (*not shown*). *Bottom row*: on postcontrast coronal (*left*) and axial (*middle*) T1WI, the granulation appears as a filling defect within the LTS; it was not changed 2 years later (*right*). Note a tiny vein draining through the granulation (*dotted arrows*)

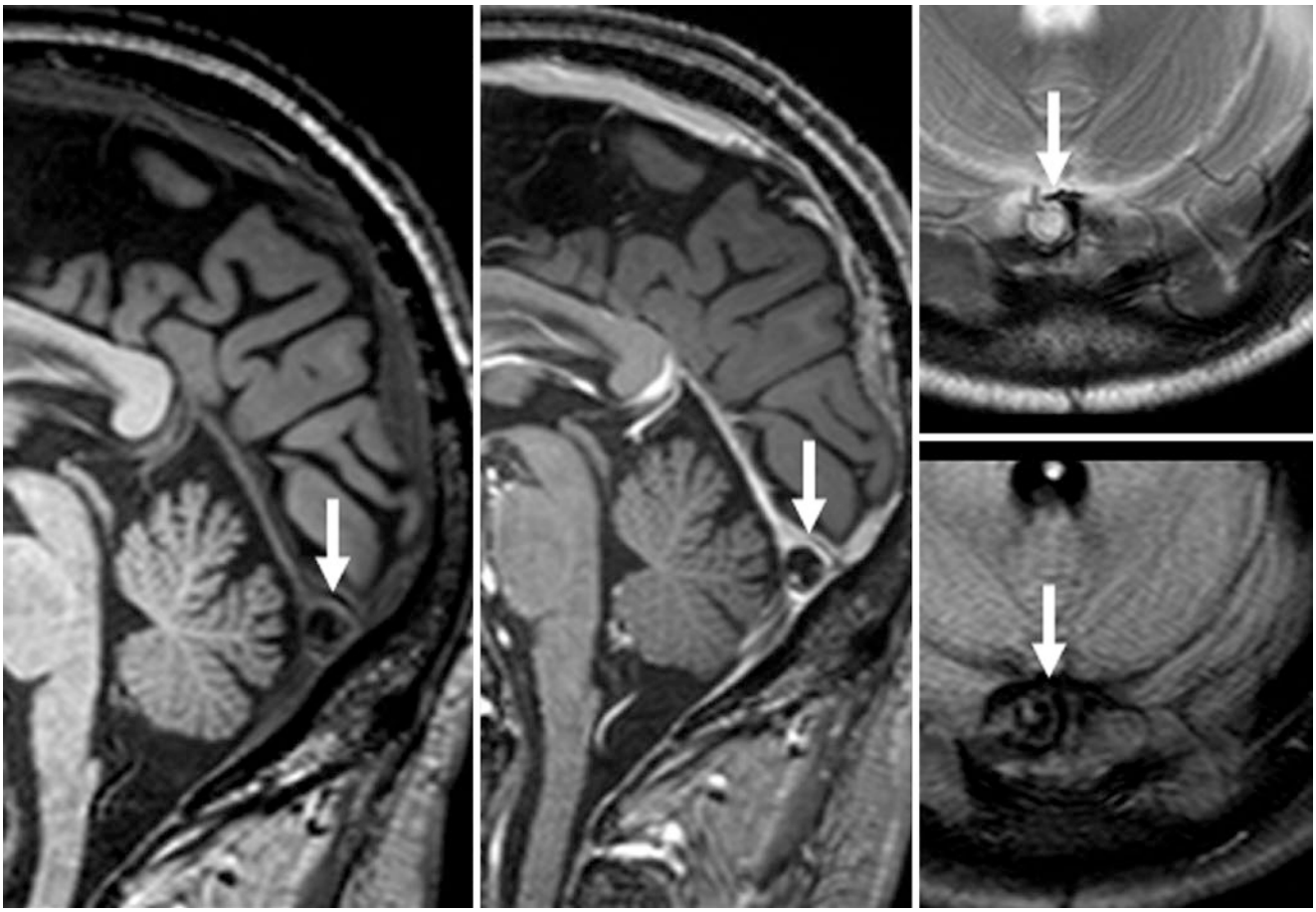

Fig. 41.11 52-year-old with an arachnoid granulation (*arrows*) of the torcular on sagittal precontrast (*left*) and postcontrast (*middle*) T1WI MRI. Note the bright signal intensity on axial T2WI (*top right*) and the suppression similar to CSF on axial FLAIR (*bottom right*)

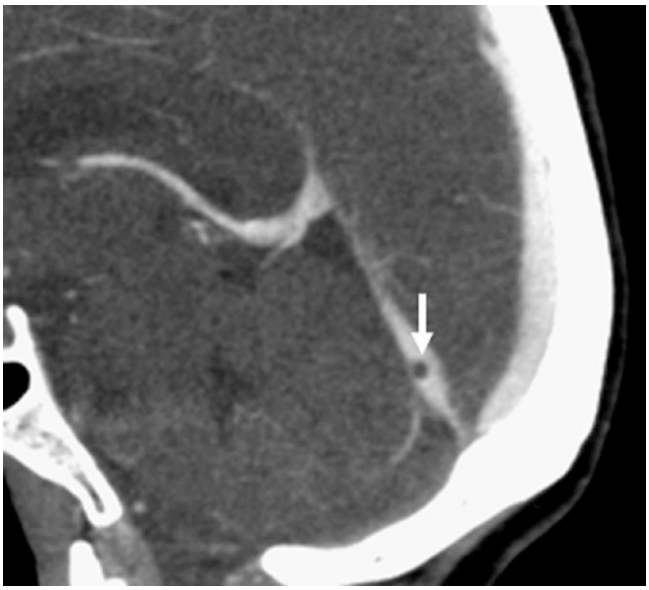

Fig. 41.12 45-year-old with a tiny arachnoid granulation (*arrows*) in the straight sinus (StS) on a sagittal MPR obtained from a CTV. This is a less frequent location for arachnoid granulations

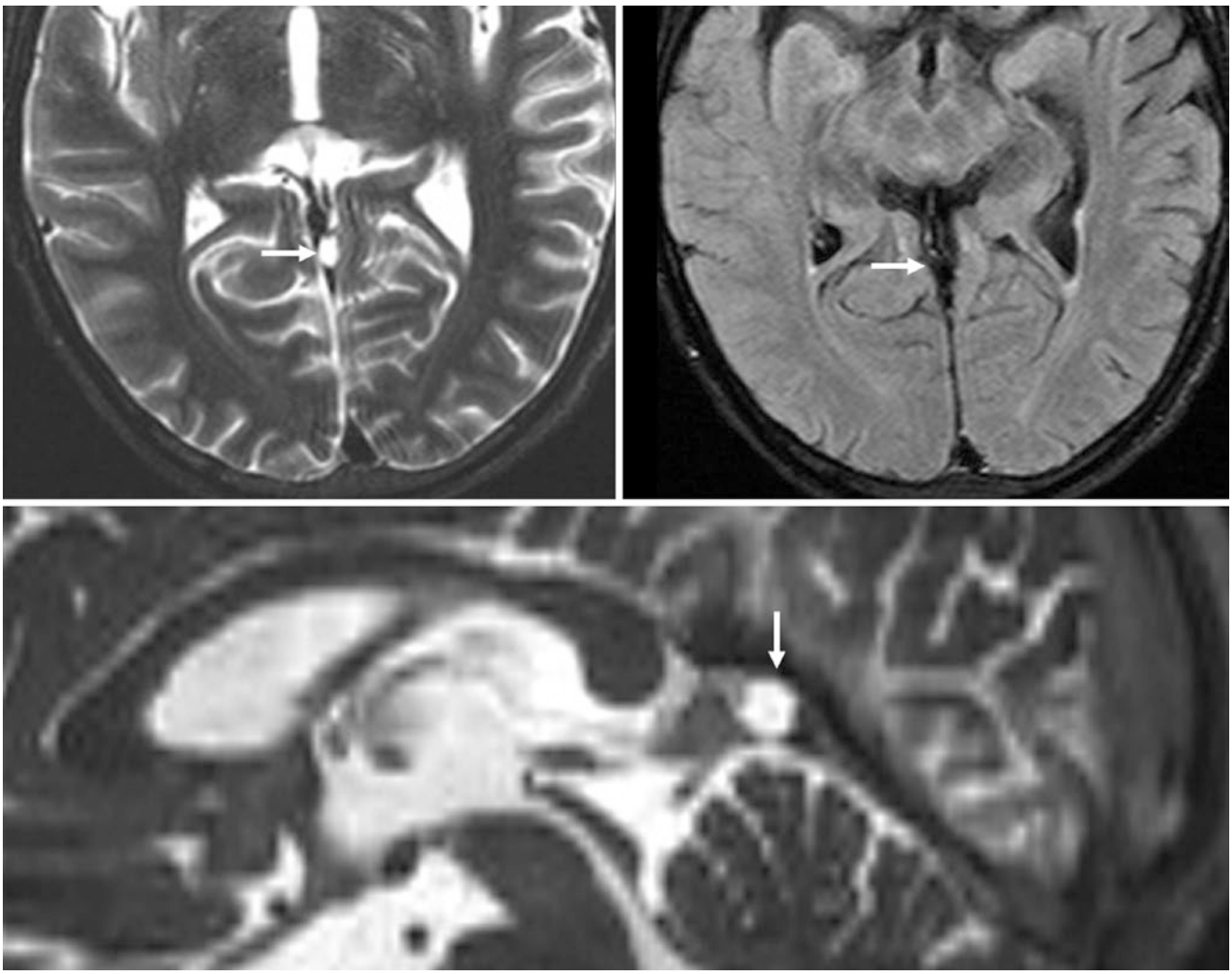

Fig. 41.13 16-year-old with a filling defect (*arrows*) within the StS on axial T2WI MRI (*top left*); the defect is well-circumscribed and suppresses along with CSF on FLAIR (*top right*), indicating an arachnoid granulation. Sagittal MPRs of thin T2WIs (*bottom*) confirm the location of the granulation within the StS

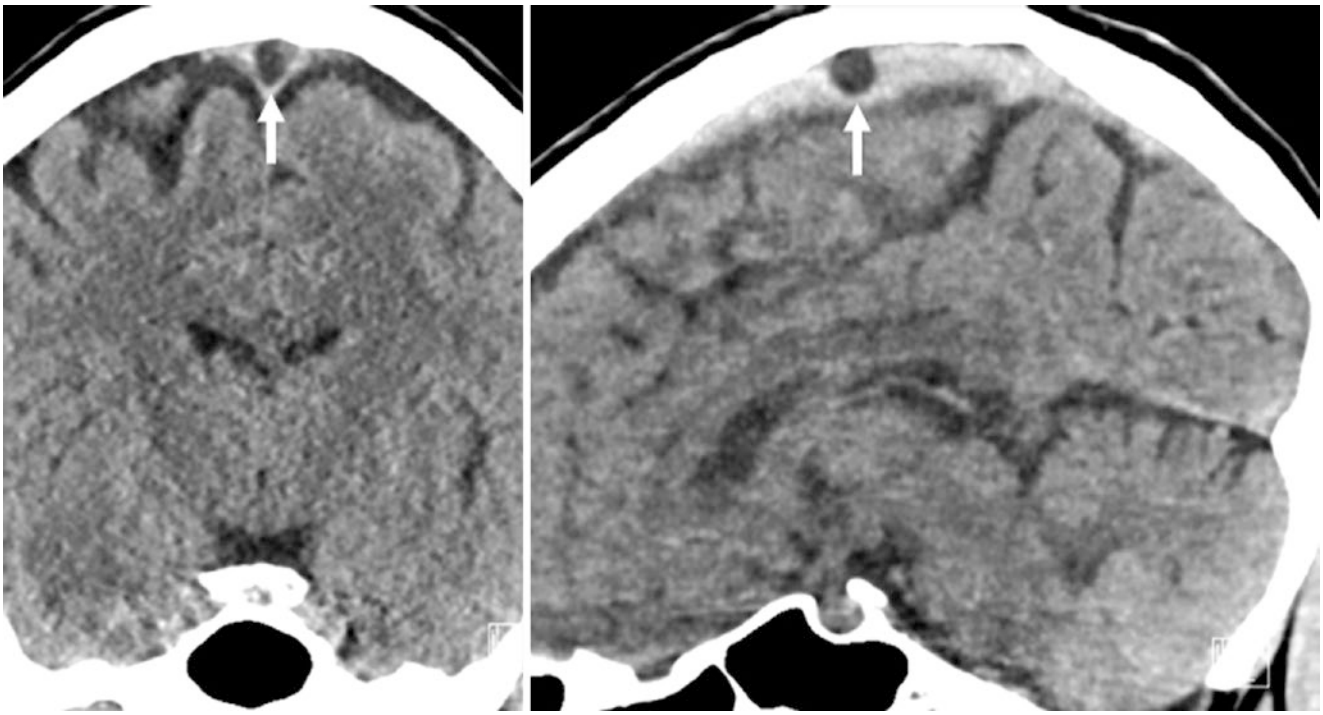

Fig. 41.14 52-year-old with a moderate-sized arachnoid granulation (*arrows*) within the midportion of the SSS on coronal (*left*) and sagittal (*right*) MPRs obtained from an otherwise normal NECT. This is an infrequent location for arachnoid granulations

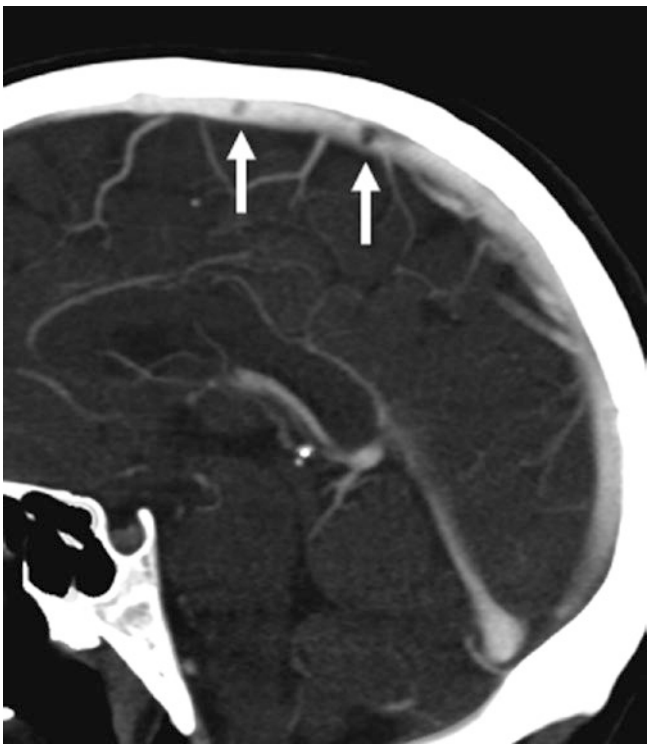

Fig. 41.15 In a 51-year-old, a sagittal MPR from a CTV depicts two superior sagittal sinus (SSS) arachnoid granulations (*arrows*)

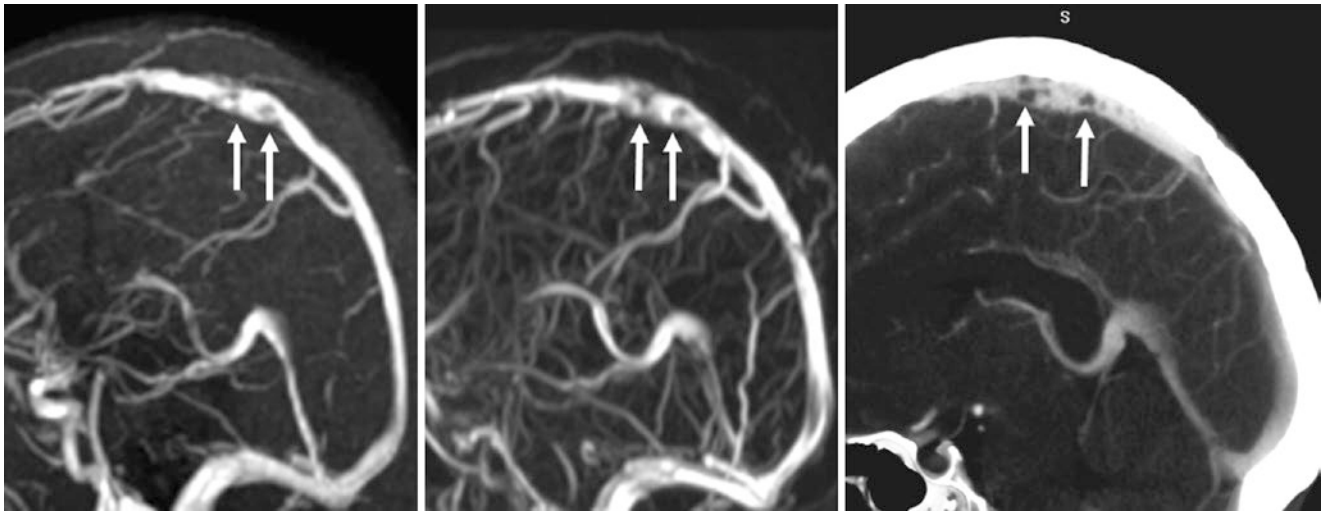

Fig. 41.16 29-year-old with several adjacent filling defects simulating thrombi, centered within the midportion of the SSS (*arrows*) on lateral/sagittal views from a noncontrast 2DTOF MRV (*left*), contrast-enhanced MRV (*middle*), and on a 5-mm MPR from a CTV (*right*). The defects are arachnoid granulations, which did not change over several follow-up CTVs

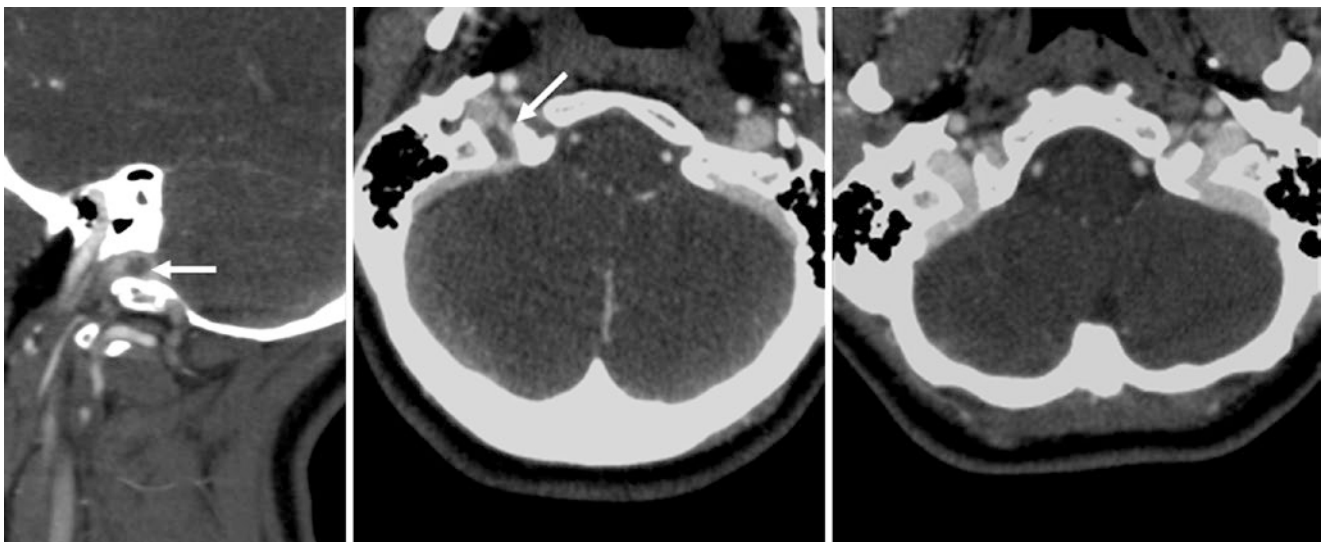

Fig. 41.17 Comparison case of thrombus. This 18-year-old post-trauma patient had a focal filling defect (*arrows*) located in the lower right sigmoid sinus–internal jugular vein (IJV) junction on CTV sagittal (*left*) and axial (*middle*) MPRs. Arachnoid granulations are common in the upper sigmoid or transverse sinuses, but they almost never occur in the lower sigmoid sinus or IJV. After anticoagulation, the clot had resolved on a CTV obtained 1 month later (*right*)

References

1. Liang L, Korogi Y, Sugahara T, Ikushima I, Shigematsu Y, Takahashi M, Provenzale JM. Normal structures in the intracranial dural sinuses: delineation with 3D contrast-enhanced magnetization prepared rapid acquisition gradient-echo imaging sequence. AJNR Am J Neuroradiol. 2002;23:1739–46.
2. Ikushima I, Korogi Y, Makita O, Yamura M, Kawano H, Kohama M, et al. MRI of arachnoid granulations within the sinuses using a FLAIR pulse sequence. Br J Radiol. 1999;72:1046–51.
3. Roche J, Warner D. Arachnoid granulations in the transverse and sigmoid sinuses: CT, MR, and MR angiographic appearance of a normal anatomic variation. AJNR Am J Neuroradiol. 1996;17:677–83.
4. Leach JL, Meyer K, Jones BV, Tomsick TA. Large arachnoid granulations involving the dorsal superior sagittal sinus: findings on MR imaging and MR venography. AJNR Am J Neuroradiol. 2008;29:1335–9.
5. Leach JL, Jones BV, Tomsick TA, Stewart CA, Balko MG. Normal appearance of arachnoid granulations on contrast-enhanced CT and MR of the brain: differentiation from dural sinus disease. AJNR Am J Neuroradiol. 1996;17:1523–32.
6. Mamourian AC, Towfighi J. MR of giant arachnoid granulation, a normal variant presenting as a mass within the dural venous sinus. AJNR Am J Neuroradiol. 1995;16:901–4.
7. Trimble CR, Harnsberger HR, Castillo M, Brant-Zawadzki M, Osborn AG. "Giant" arachnoid granulations just like CSF?: NOT!! AJNR Am J Neuroradiol. 2010;31:1724–8.
8. Choi HJ, Cho CW, Kim YS, Cha JH. Giant arachnoid granulation misdiagnosed as transverse sinus thrombosis. J Korean Neurosurg Soc. 2008;43:48–50.
9. De Keyzer B, Bamps S, Van Calenbergh F, Demaerel P, Wilms G. Giant arachnoid granulations mimicking pathology. A report of three cases. Neuroradiol J. 2014;27:316–21.
10. Rodallec MH, Krainik A, Feydy A, Hélias A, Colombani JM, Jullès MC, et al. Cerebral venous thrombosis and multidetector CT angiography: tips and tricks. Radiographics. 2006;26:S5–18; discussion S42–3.
11. Provenzale JM, Kranz PG. Dural sinus thrombosis: sources of error in image interpretation. AJR Am J Roentgenol. 2011;196:23–31.

Artifacts of the Craniocervical Venous System on MRI

42

A number of venous artifacts on routine craniocervical MRI or MR venography (MRV) can simulate *stenosis* or *thrombosis* [1–19]. Artifacts limiting the evaluation of the cranial venous vasculature can be related to *turbulence* (or fast flow), *slow or reversed flow, in-plane saturation effects*, patient *motion*, or *susceptibility artifact* (adjacent to metal or gas), to name a few. The following pages demonstrate such artifacts on routine T1-weighted images (T1WI) and T2-weighted images (T2WI), as well as on 2D time-of-flight (2DTOF) MRV and contrast enhanced MRV (CEMRV), as well as ways to counter artifacts and to exclude or confirm potential abnormalities. Newer techniques utilizing blood-oxygen level dependent (BOLD) imaging and susceptibility-weighted imaging (SWI) have been used for the purposes of high-resolution MRV, but these are not discussed in detail here [1–19]. It is important to note that the relatively high resolution of postcontrast CT venography (CTV) or dedicated MRV can help distinguish normal structures. In particular, the multiple-pass nature of CTV and its high resolution can be quite helpful in confirming flow abnormalities or normal variations suspected on MRI. MRV is often preferred, however, because of the additional information obtained from evaluation of the brain by MRI, which yields superior information regarding the degree of cerebral edema and infarction, and has higher sensitivity in detecting contrast-enhancing lesions. Also, CTV utilizes radiation, which is not insignificant, particularly in children [1–20].

In brief, MRI with MRV is often a preferred method for the initial evaluation of dural sinus thrombosis or stenosis, but CTV is an excellent choice as an alternative or when MRV is indeterminate. In particular, noninvasive CTV can spare a patient from invasive catheter digital subtraction angiography (DSA), the standard for diagnosis. Regarding MRV, the best approach is to perform noncontrast MRV followed by postcontrast MRV, for reasons that are delineated throughout in this chapter. The following topics provide a slightly more detailed description of the advantages and pitfalls of the techniques used to image the cranial region.

A.M. McKinney, *Atlas of Normal Imaging Variations of the Brain, Skull, and Craniocervical Vasculature*,
DOI 10.1007/978-3-319-39790-0_42

42.1 Fast Flow or Turbulence Artifacts Within the Dural Sinuses on Postcontrast T1-Weighted Images

Very *fast flow*, very *slow flow*, or *nonlaminar* (turbulent) *flow* can simulate *thrombus* in the dural sinuses on postcontrast T1WI, particularly in the transverse sinuses (TSs) or sigmoid sinuses. These artifacts also may occur in the superior sagittal sinus (SSS), although the lack of curvature and angulation relative to the TS and sigmoid sinuses makes this location less common. Any of three findings can easily distinguish these artifacts from cases of true thrombus: (1) a normal flow void in the sinus on noncontrast T1WI or T2WI; (2) a venous sinus that is not enlarged; or (3) a normal MRV (Figs. 42.1, 42.2, 42.3, 42.4, 42.5, and 42.6).

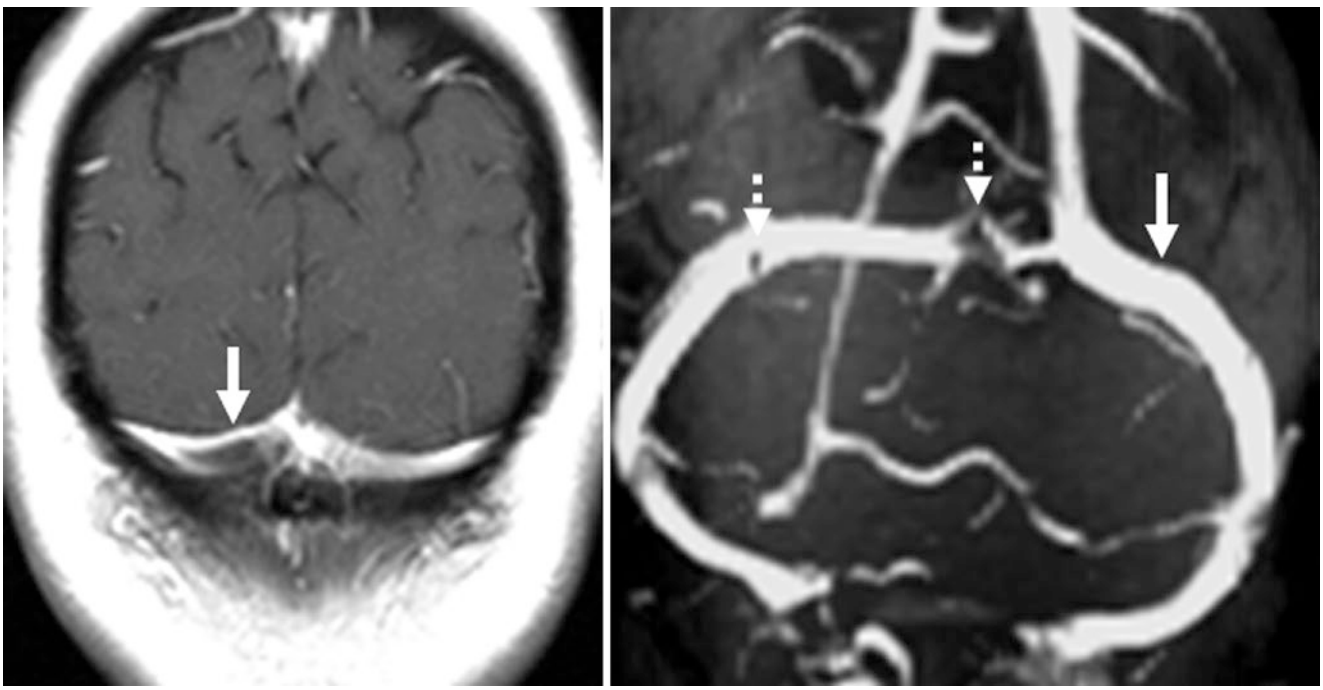

Fig. 42.1 13-year-old with fast flow or turbulence (*arrow*) in the right transverse sinus (TS), which simulates a filling defect (*i.e.*, thrombus) on postcontrast T1WI (*left*). Note that this defect is not present on a 2DTOF MRV PA view (*right*), which shows that the sinus is patent. Note incidental arachnoid granulations within the left TS (*dotted arrows*)

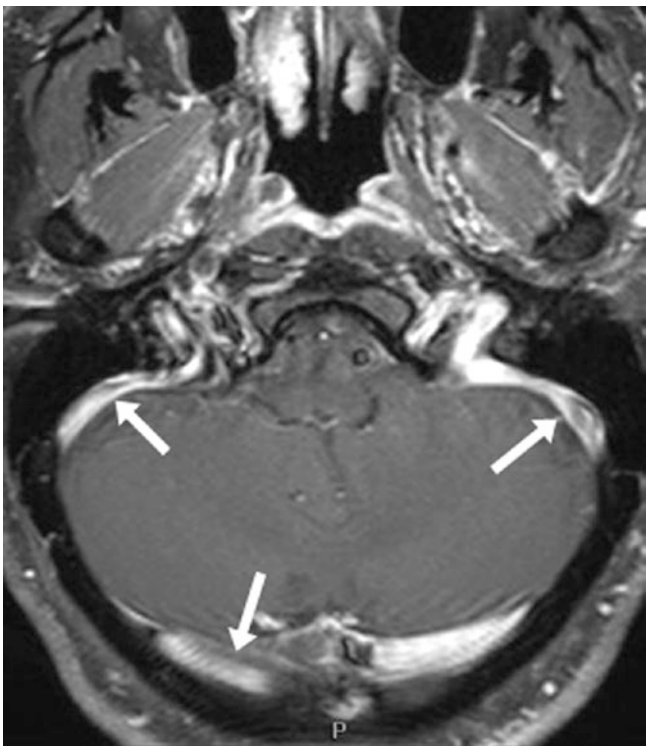

Fig. 42.2 In this 15-year-old, bilateral fast flow or turbulence (*arrows*) within the sigmoid-TSs simulates filling defects on a postcontrast T1WI

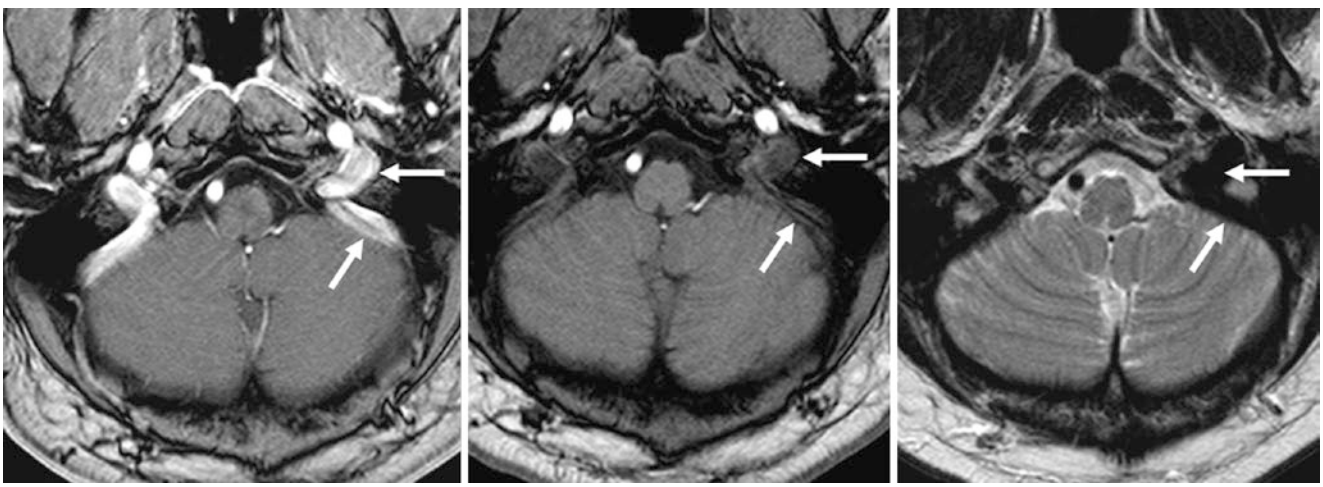

Fig. 42.3 59-year-old with apparent filling defects (*arrows*) from fast flow or turbulence within the junction of the left sigmoid sinus and internal jugular vein (IJV). These filling defects mimic thrombus on postcontrast T1WI (*left*), but the appearance of the flow voids appears normal on precontrast T1WI (*middle*) and T2WI (*right*). Thus, the left sigmoid sinus and upper IJV are both patent without clot. Note the more normal appearance on the opposite side

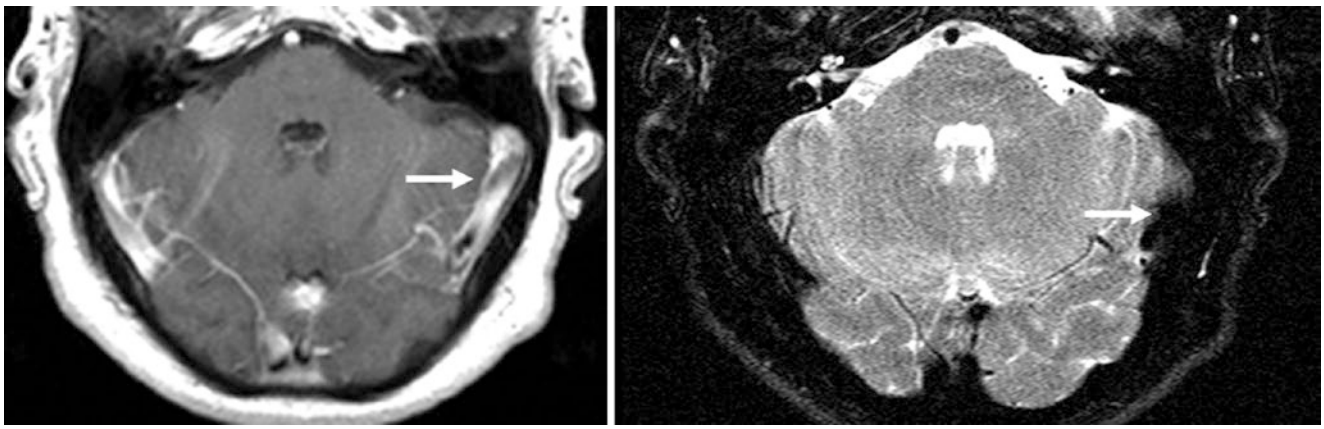

Fig. 42.4 In this 53-year-old, a simulated filling defect on postcontrast T1WI (*left*) arises from fast or turbulent flow within the left TS (*arrows*). A T2WI (*right*) depicts a patent flow void. The left TS was also patent on a follow-up MRI (*not shown*)

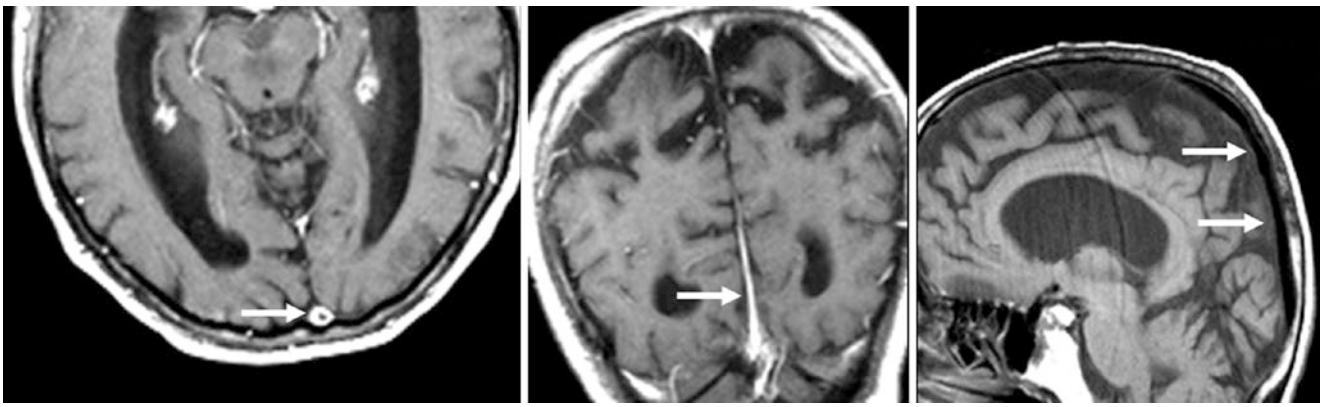

Fig. 42.5 89-year-old with an apparent filling defect (*arrows*) within the superior sagittal sinus (SSS) on a postcontrast axial T1WI (*left*), but with patent flow voids demonstrated on coronal postcontrast T1WI (*middle*) and sagittal precontrast T1WI (*right*)

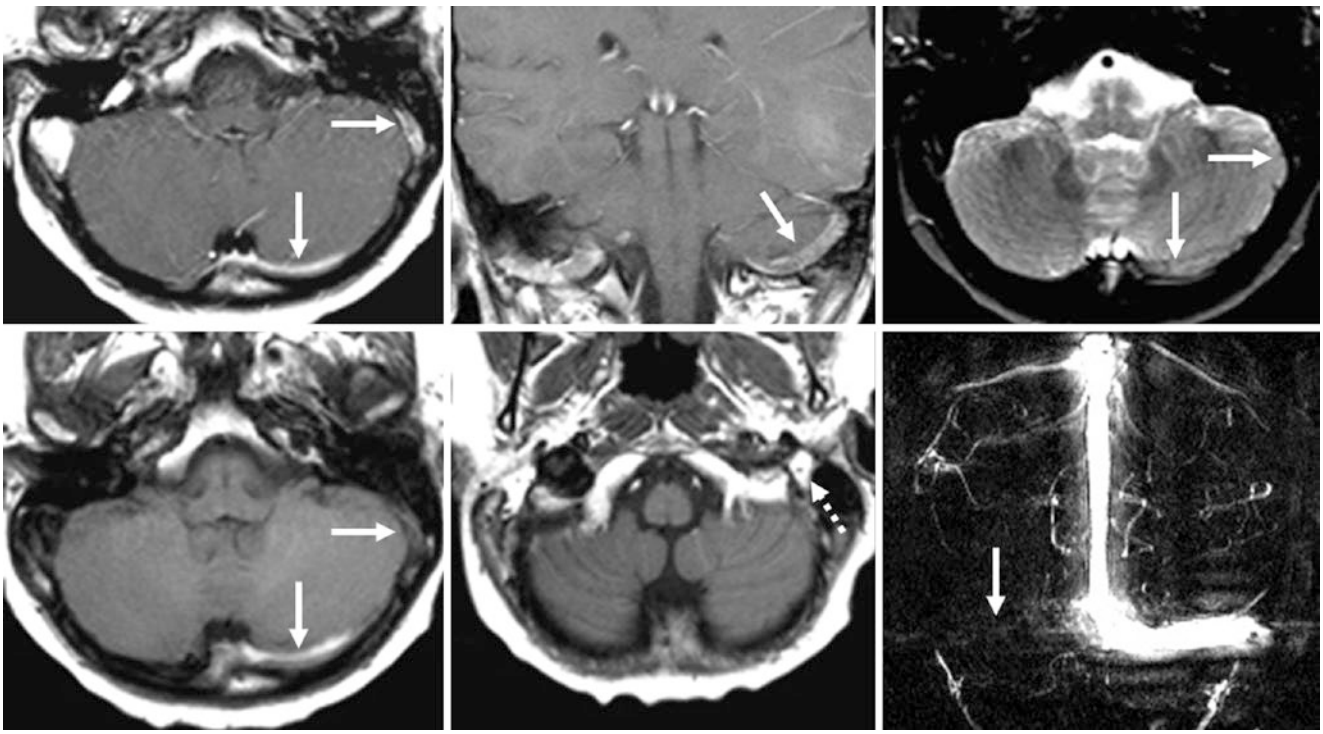

Fig. 42.6 Comparison case of thrombus. *Top row:* in a 13-year-old, postcontrast axial (*left*) and coronal (*middle*) T1WIs showed a filling defect (*arrows*) within the left TS, without a flow void on T2WI (*right*). *Bottom row:* There was corresponding bright signal on a noncontrast T1WI within the left TS–sigmoid sinuses (*left*) and within the IJV (*dotted arrow, middle*). A phase-contrast MRV PA view (*right*) confirmed occlusive thrombus

42.2 Slow Flow Causing Bright Dural Sinus Signal on Noncontrast T1-Weighted Images

On noncontrast spin-echo T1WI, the dural sinuses can appear bright because of *slow flow*, *turbulent flow*, or "*entry-slice phenomenon*." This phenomenon more commonly occurs in arteries, but it can theoretically occur in either arteries or veins. Hence, slow flow in veins may cause bright signal that may mimic *venous thrombosis* [1–5]. This signal typically is most prominent in the TS or SSS, but it can be seen in any dural venous sinus. Its occurrence varies with anatomy, size, and flow rate. Thus, slow or turbulent flow in veins or arteries commonly occurs on T1WI without being frank thrombosis, and the presence of a normally dark flow void on T2WI or SWI (without blooming effect) typically excludes thrombosis. Also, on T2WI, care should be exercised before calling bright signal a normal variant (which less commonly occurs in situations with slow venous flow), as T2-bright (or isointense) vessels are suspicious for thrombosis and should be further evaluated with MRV. CEMRV or CTV are the most sensitive modalities for further venous evaluation [1–20]. Also notable is that vascular structures can appear normally bright on noncontrast *gradient echo* T1WI; thus, this finding should be disregarded if other findings of venous thrombosis (*e.g.*, dural sinus enlargement, lack of flow voids on T2WI, lack of enhancing sinuses) are not present (Figs. 42.7, 42.8, 42.9, 42.10, and 42.11).

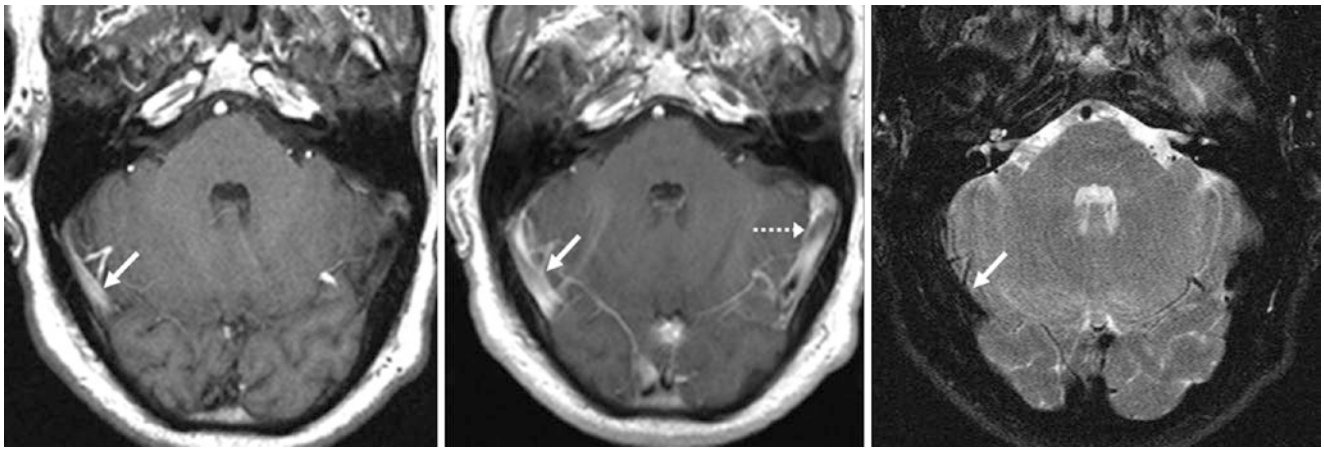

Fig. 42.7 53-year-old with bright signal in the right TS (*arrow*) on noncontrast T1WI (*left*); this finding could simulate dural sinus thrombosis. However, the sinus is patent on postcontrast T1WI (*middle*), with a normally patent flow void on T2WI (*right*). Also note a normal fast flow void or turbulence on postcontrast T1WI within the left TS (*dotted arrows*)

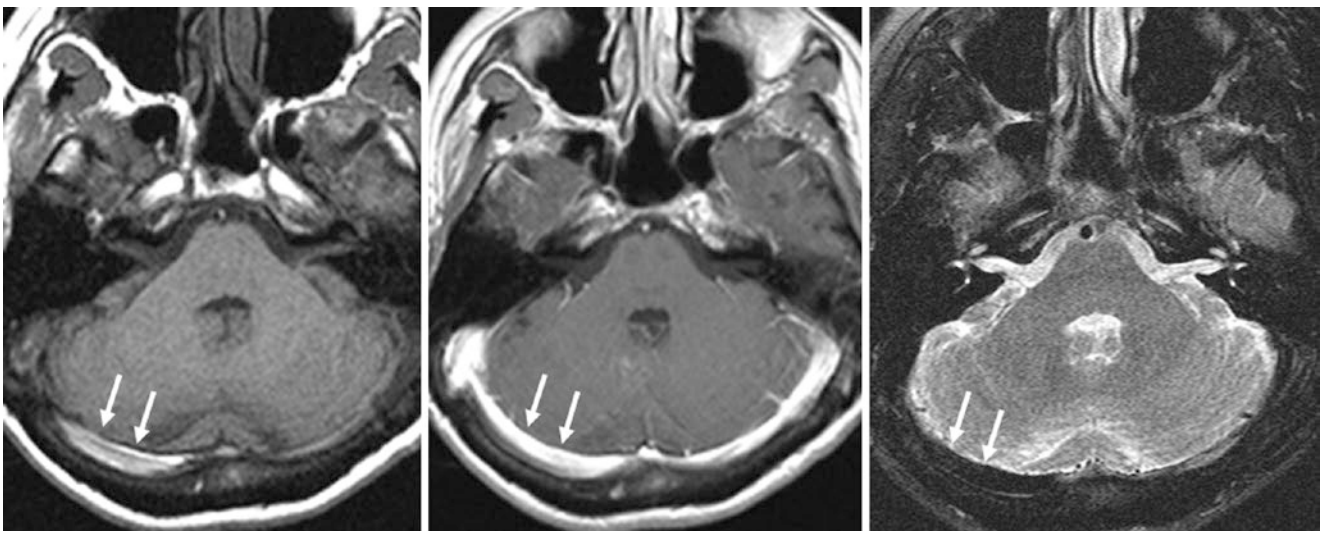

Fig. 42.8 In this 59-year-old, normal, bright signal in the right TS (*arrows*) on noncontrast T1WI (*left*) could simulate dural sinus thrombosis. However, the right TS appears to have normal venous enhancement on postcontrast T1WI (*middle*), as well as a normal flow void on T2WI (*right*), confirming patency

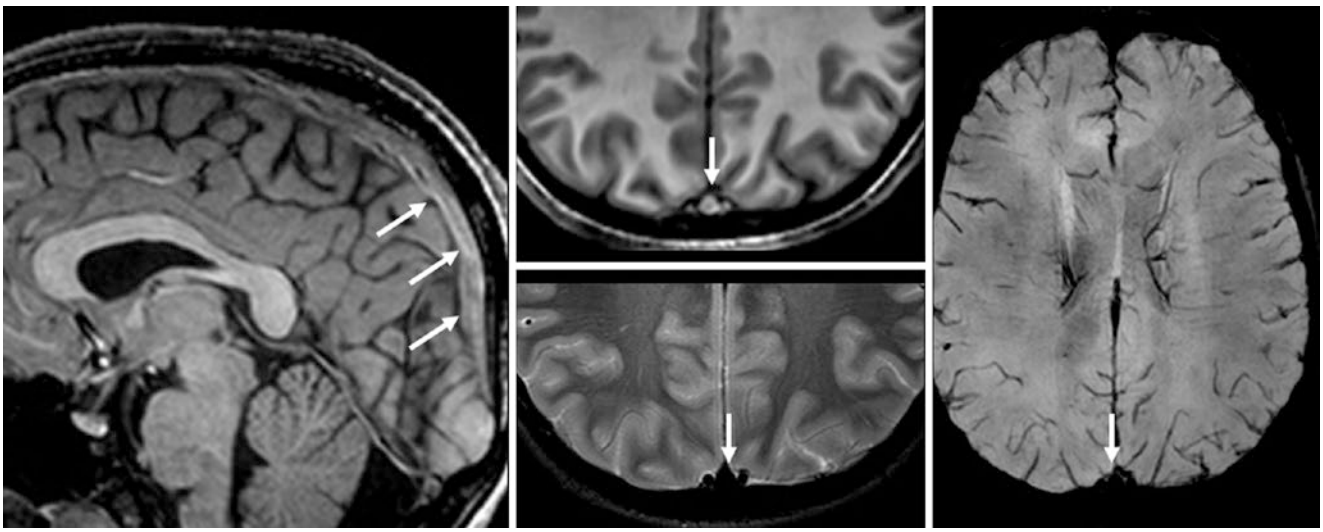

Fig. 42.9 In this 14-year-old, noncontrast sagittal (*left*) and axial (*middle, top*) gradient echo T1WI depicts bright signal within the SSS (*arrows*) that mimics thrombosis. However, there are normal flow voids on T2WI (*middle, bottom*) and SWI (*right*). Note that although hemorrhage may exhibit T2WI and SWI-dark signal in acute/early subacute thrombosis, the lack of parenchymal edema, SSS enlargement, or flow void loss on T2WI makes thrombosis rather unlikely

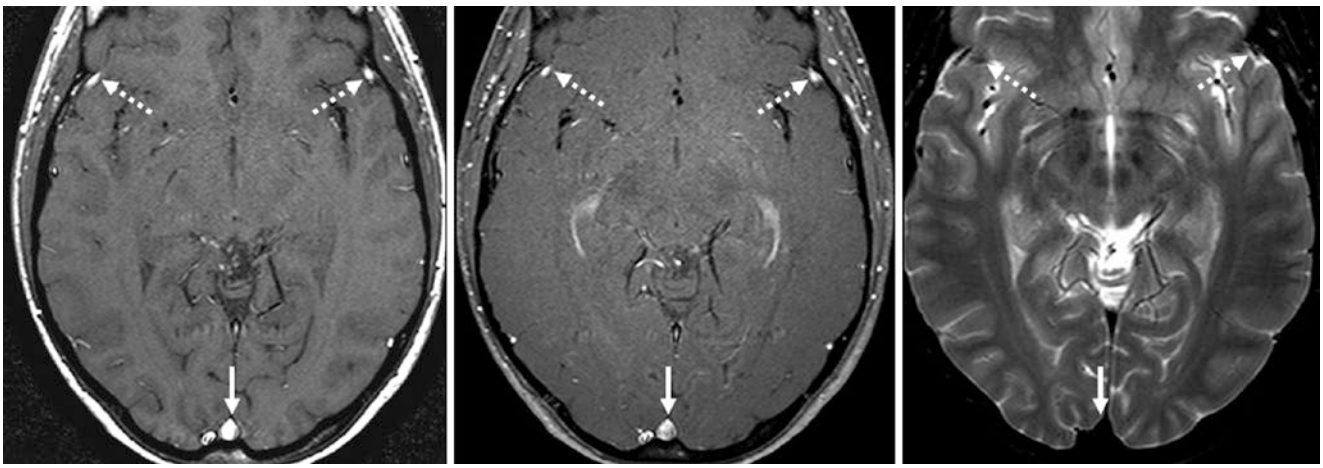

Fig. 42.10 50-year-old with bright signal within the SSS (*solid arrows*) and the superficial middle cerebral veins (*dotted arrows*) on noncontrast T1WI (*left*), but with patent flow voids on postcontrast T1WI (*middle*) and T2WI (*right*). These images illustrate how almost any dural, deep, or superficial veins can potentially appear bright on spin-echo T1WI, owing to slow flow

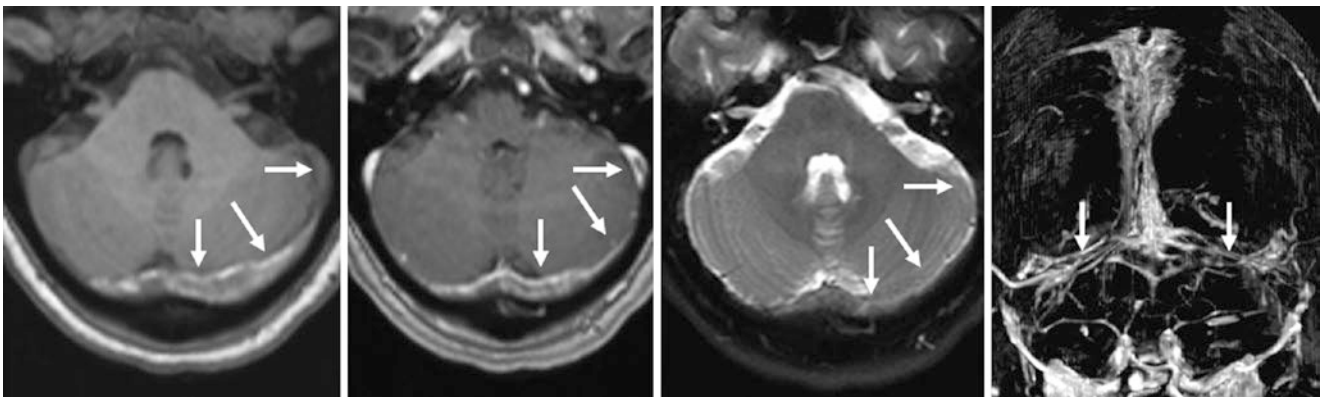

Fig. 42.11 Comparison case of transverse sinus thrombosis. 44-year-old with abnormally heterogeneous, bright signal in mildly enlarged TSs bilaterally (*arrows*) on noncontrast T1WI (*left*), filling defects on postcontrast T1WI (*left middle*), and loss of normal flow voids and hyperintensity on T2WI (*right middle*). A CEMRV PA view (*right*) confirms the filling defects and enlargement of the SSS, with distention due to thrombosis

42.3 Artifacts on 2D Time-of-Flight MR Venography That May Simulate Thrombosis or Stenosis

Several phenomena can attenuate the typically bright appearance of flow within the TSs or sigmoid sinuses on 2DTOF MRV, simulating the appearance of *thrombus* or *stenosis* [1–5]. This effect may also occur in the SSS, albeit less frequently. The most common of these phenomena is *slow flow*, which has a particular predilection to cause this effect in small or hypoplastic sinuses. *In-plane saturation effect* or patient *motion* also can exacerbate this artifactual phenomenon. This phenomenon may also occur, but less frequently, with phase-contrast MRV (PCMRV), which is also velocity-dependent to a degree because it depends on the user to select an encoding velocity. Confirmation of an asymmetrically small or hypoplastic sinus is relatively easy with either postcontrast 3D T1WIs, CEMRV, or CTV, but even on CEMRV, slow flow can make a small sinus difficult to see or can simulate narrowing, such as occurs with nonocclusive or chronic thrombosis. T2WI (dark flow voids) or T2*WI (in which bright signal is present because it is a gradient echo image) can also aid in preventing an incorrect diagnosis (Figs. 42.12, 42.13, 42.14, 42.15, 42.16, 42.17, 42.18, 42.19, 42.20, 42.21, 42.22, and 42.23).

Fig. 42.12 Artifact from slow flow or turbulence. In this 17-year-old, PA (*left*) and superior (*left middle*) views from a 2DTOF MRV were suspicious for proximal right TS stenosis (*arrows*). Axial T2WI MRI lacked an entirely dark flow void in that location (*right middle*). The next day, a 3D VR CTV "see-through bone" PA view (*right*) confirmed these findings to be due to slow flow or turbulence. Note normal bilateral arachnoid granulations located at the upper sigmoid–TS junctions (*dotted arrows*)

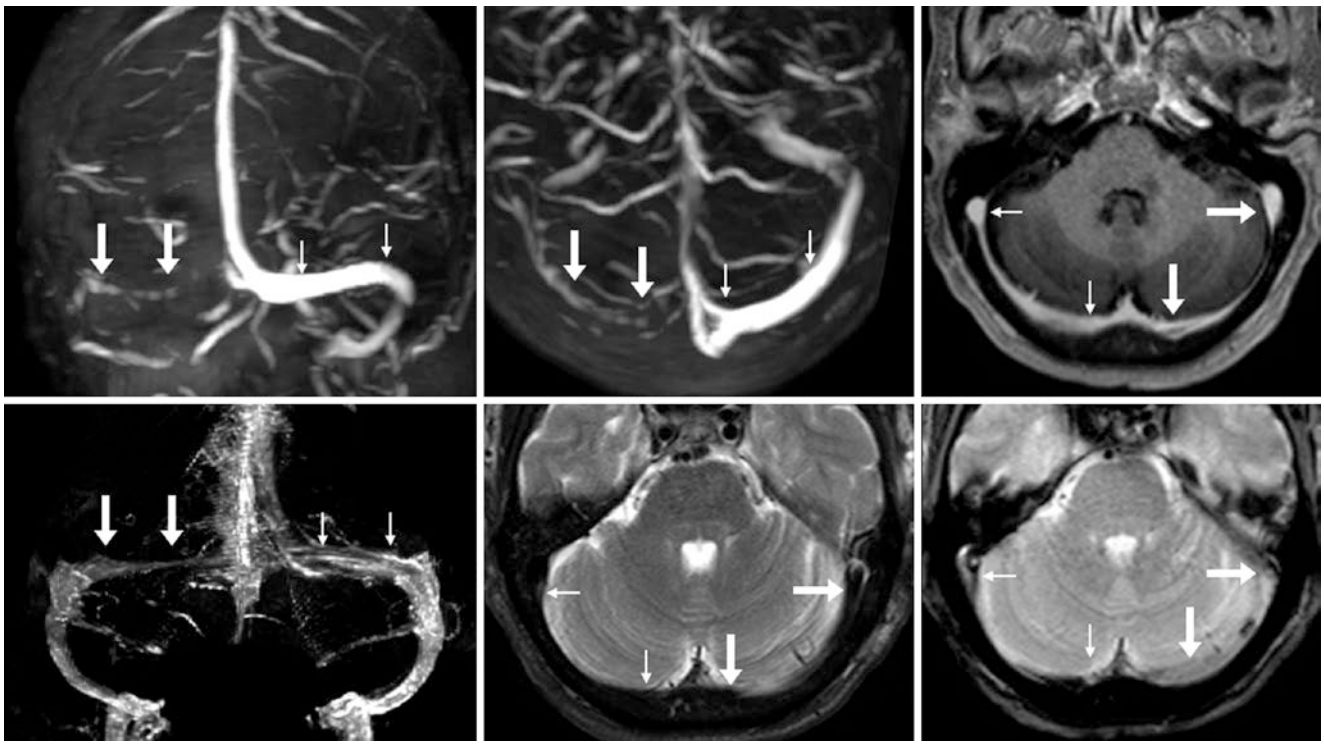

Fig. 42.13 Artifact from slow flow in a hypoplastic sinus. In a 58-year-old, 2DTOF MRV PA (*top left*) and superior (*top middle*) views did not show left TS patency (*large arrows*), as compared with the right (*thin arrows*). However, 3D acquisition postcontrast T1WI (*top right*) confirmed that this finding was from slow flow in a small sinus, also shown on a 3D VR PA view (*bottom left*). Note the patent flow voids on axial T2WI (*bottom middle*), being bright on T2*WI (*bottom right*), as T2*WI is a low flip angle gradient echo sequence

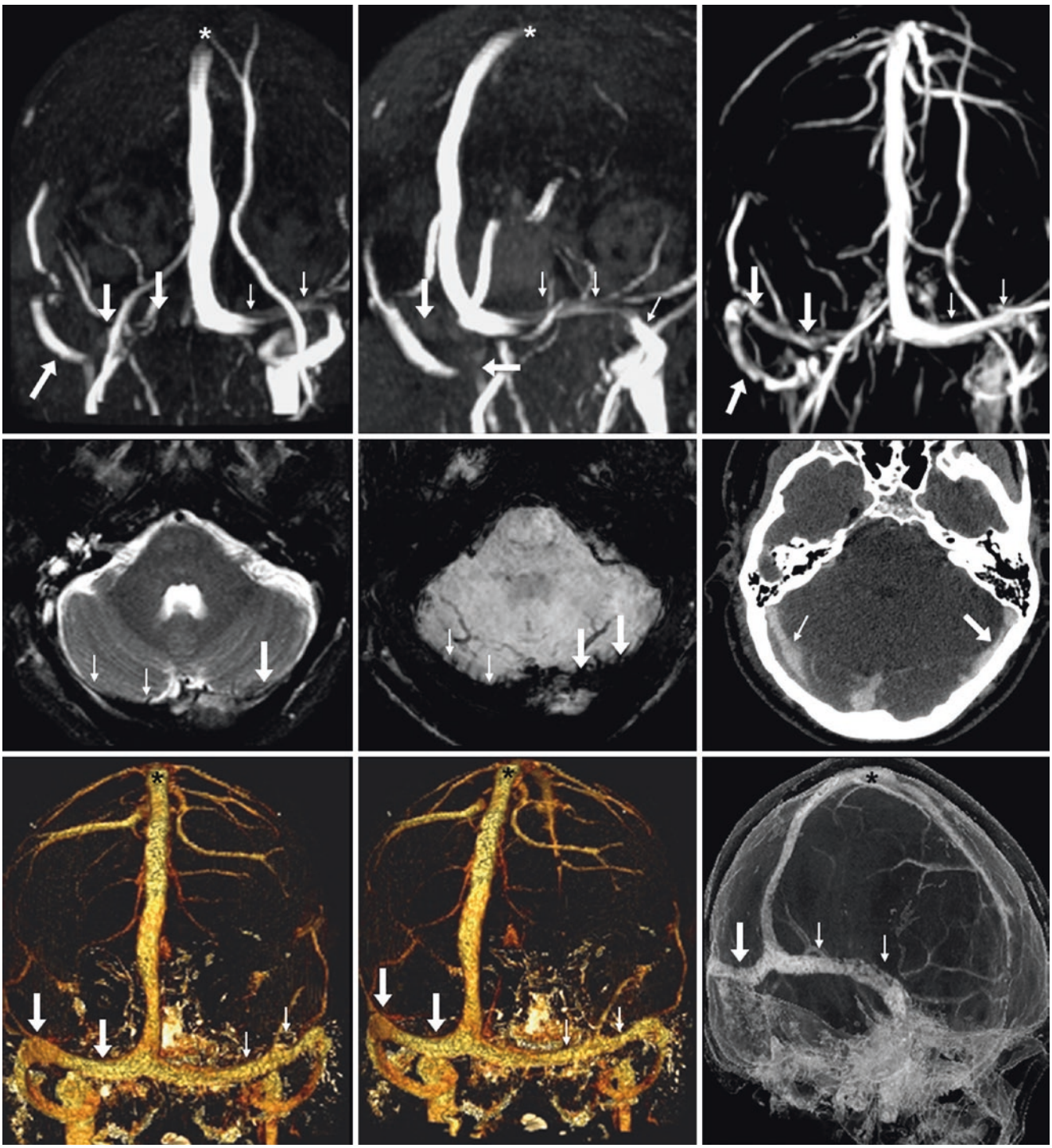

Fig. 42.14 Artifact from slow flow. 41-year-old with headaches. *Top row:* 2DTOF MRV PA (*left*) and RPO (*middle*) views did not depict a patent left TS (*arrows*); however, the left sigmoid (*arrows*) and right TS (*thin arrows*) did exhibit some flow. A CEMRV (*right*) showed gross patency of these sinuses, but the question of intraluminal, nonocclusive thrombus still remained. *Middle row:* an axial T2WI (*left*) and SWI (*middle*) did demonstrate flow voids in these sinuses, suggesting patency. They were also deemed patent on CTV (*right*). *Bottom row:* CTV bone-removed 3D VR PA (*left*), RPO (*middle*), and further RPO (*right*) views were normal. The defects were deemed due to slow flow. Note a similar finding in the SSS (*asterisks*) on the initial 2DTOF MRV

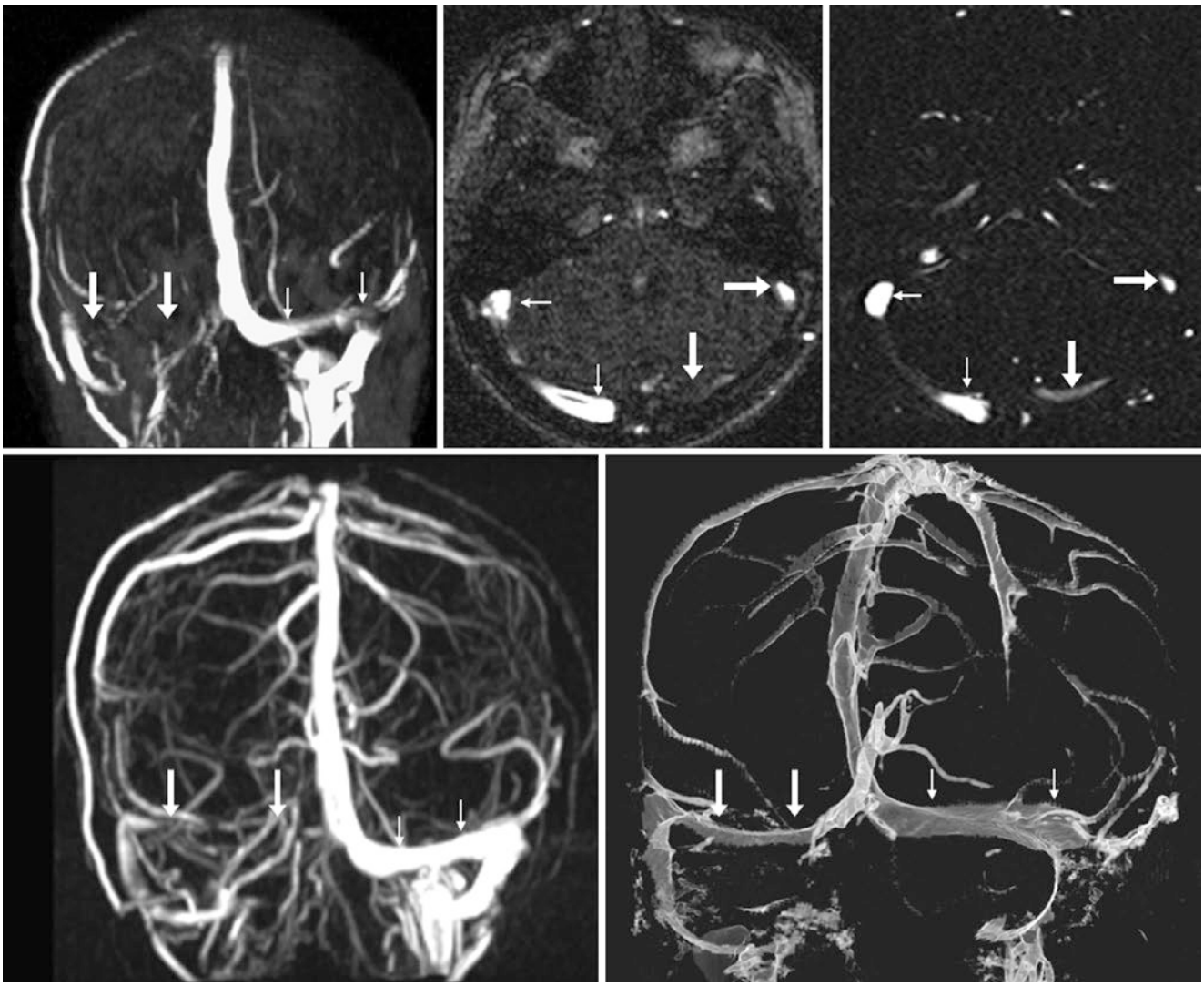

Fig. 42.15 Artifact from slow flow in a hypoplastic sinus. In this 17-year-old, 2DTOF PA view (*top left*) and axial source (*top middle*) images and phase-contrast MRV (PCMRV) axial (*top right*) and PA view (*bottom left*) images did not show the left TS (*arrows*) to be patent, as compared with the larger right TS (*thin arrows*). A CTV was performed, and a PA view (*bottom right*) confirmed left TS patency. The findings were likely due to slow flow within a hypoplastic left TS on PCMRV, along with motion and in-plane saturation on the 2DTOF MRV

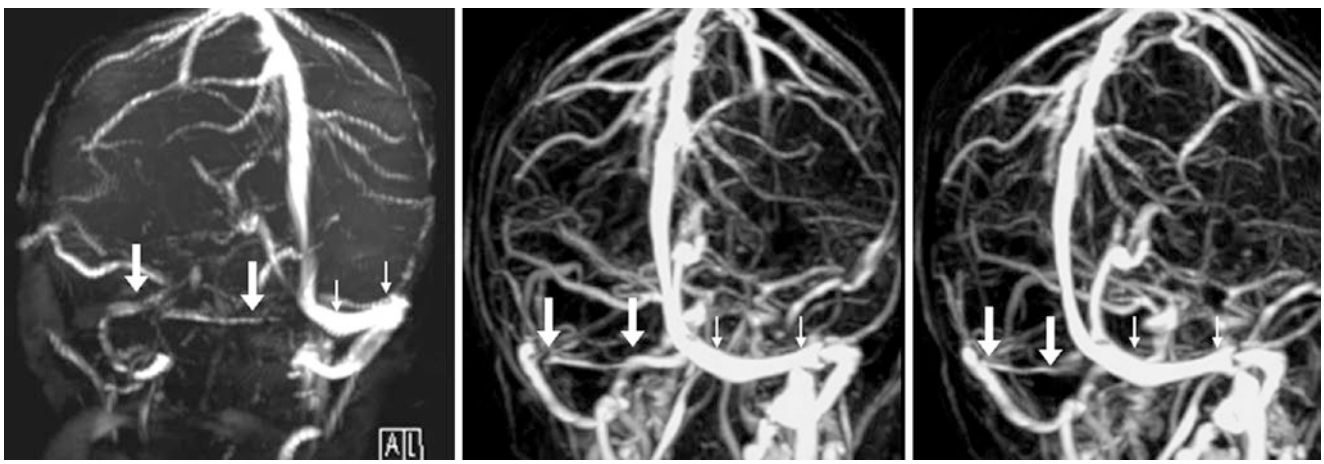

Fig. 42.16 Artifact from slow flow in a hypoplastic sinus. In this 30-year-old, a 2DTOF MRV PA view (*left*) did not clearly show the left TS (*arrows*) to be patent, as compared with the right side (*thin arrows*). However, a CEMRV with a PA view (*middle*) and further oblique view (*right*) confirmed this appearance to be due to slow flow artifact within a hypoplastic TS

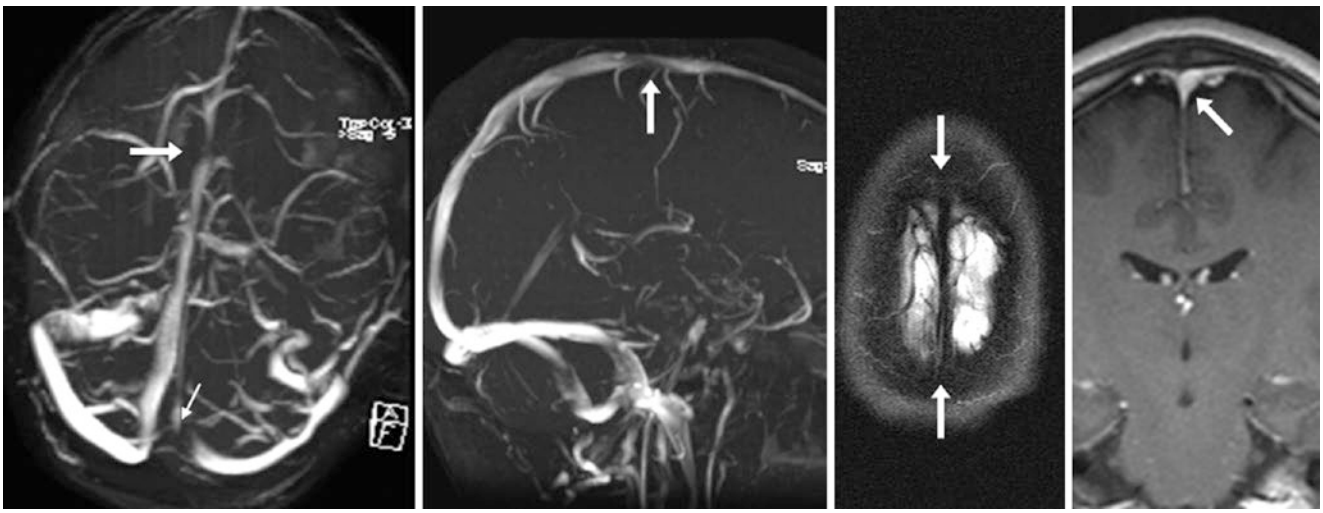

Fig. 42.17 Artifact from slow flow, turbulence, and in-plane saturation effects. In a 38-year-old, 2DTOF MRV superior (*left*) and lateral (*left middle*) views depict a defect in the midportion of the SSS (*arrows*), owing to in-plane saturation artifact (axial acquisition). A T2WI (*right middle*) and a postcontrast T1WI (*right*) confirm the patency of that portion of the SSS. Also, note an incidental, focal in-plane saturation effect versus turbulence causing an artifactual filling defect in the proximal right TS (*thin arrow)*

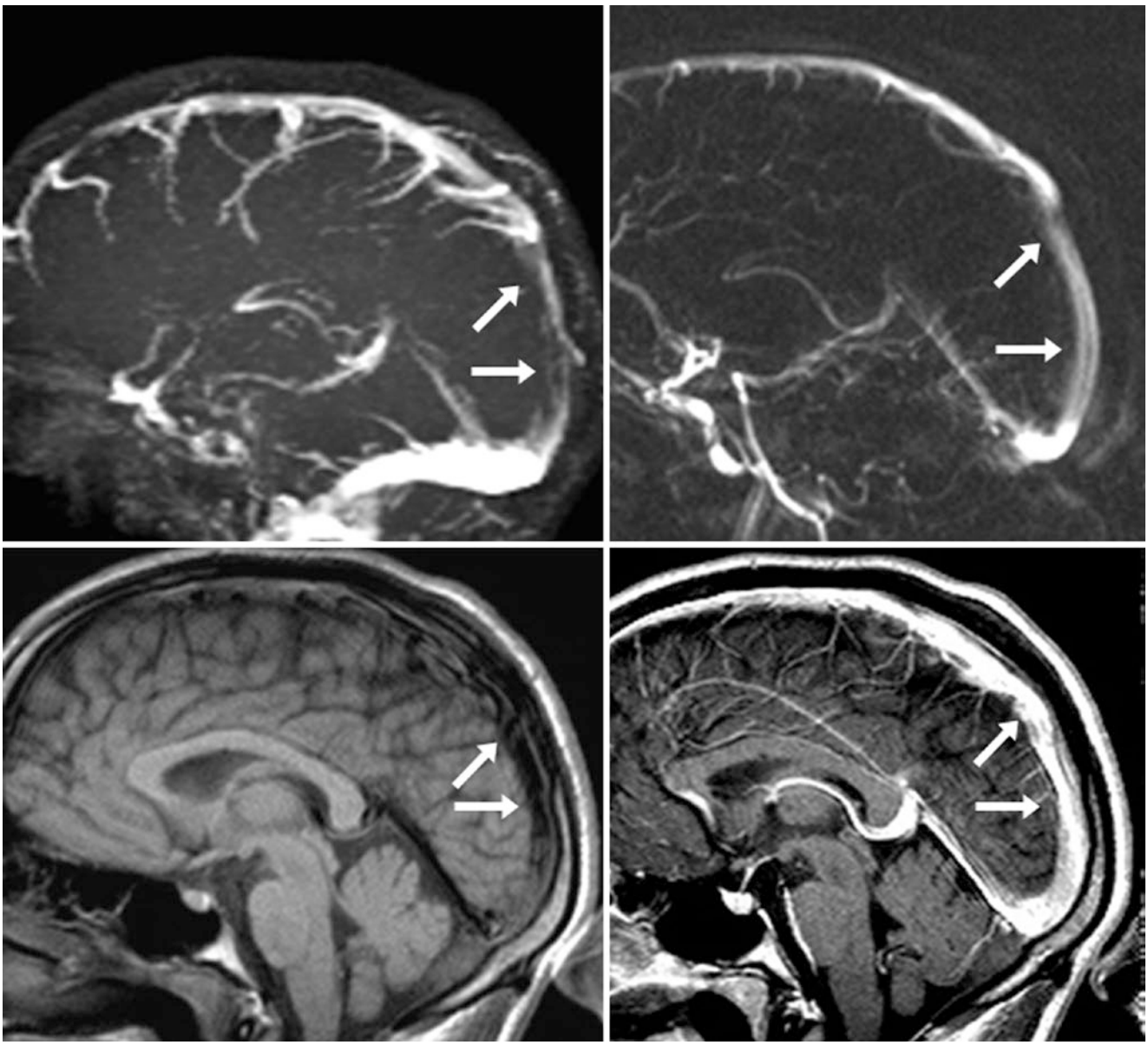

Fig. 42.18 Artifact from in-plane saturation effect. In a 25-year-old, a 2DTOF MRV left lateral view (*top left*) shows a lack of flow in the SSS (*arrows*) from in-plane saturation (sagittal acquisition). PCMRV (*top right*) depends on velocity, not direction, and shows that the SSS is patent, as confirmed by precontrast T1WI (*bottom left*) and postcontrast T1WI (*bottom right*)

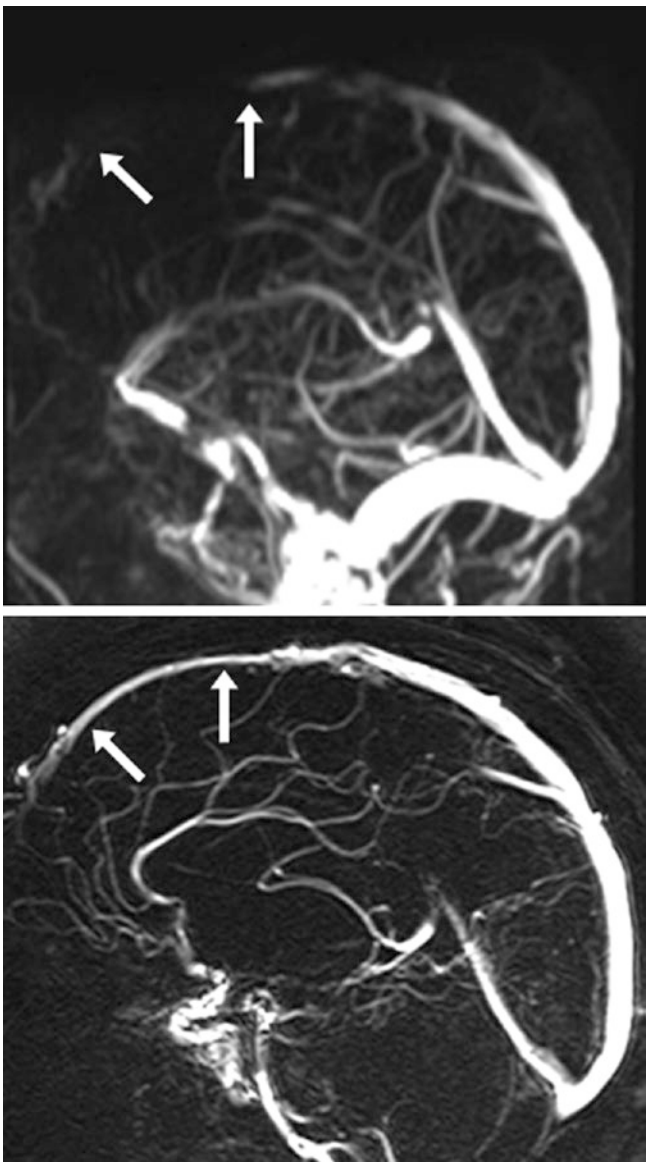

Fig. 42.19 Artifact from in-plane saturation effect. 20-year-old with a lack of flow in the anterior SSS (*arrows*) on a 2DTOF MRV (*top*), from in-plane saturation (sagittal acquisition). However, the SSS is patent on PCMRV (*bottom*)

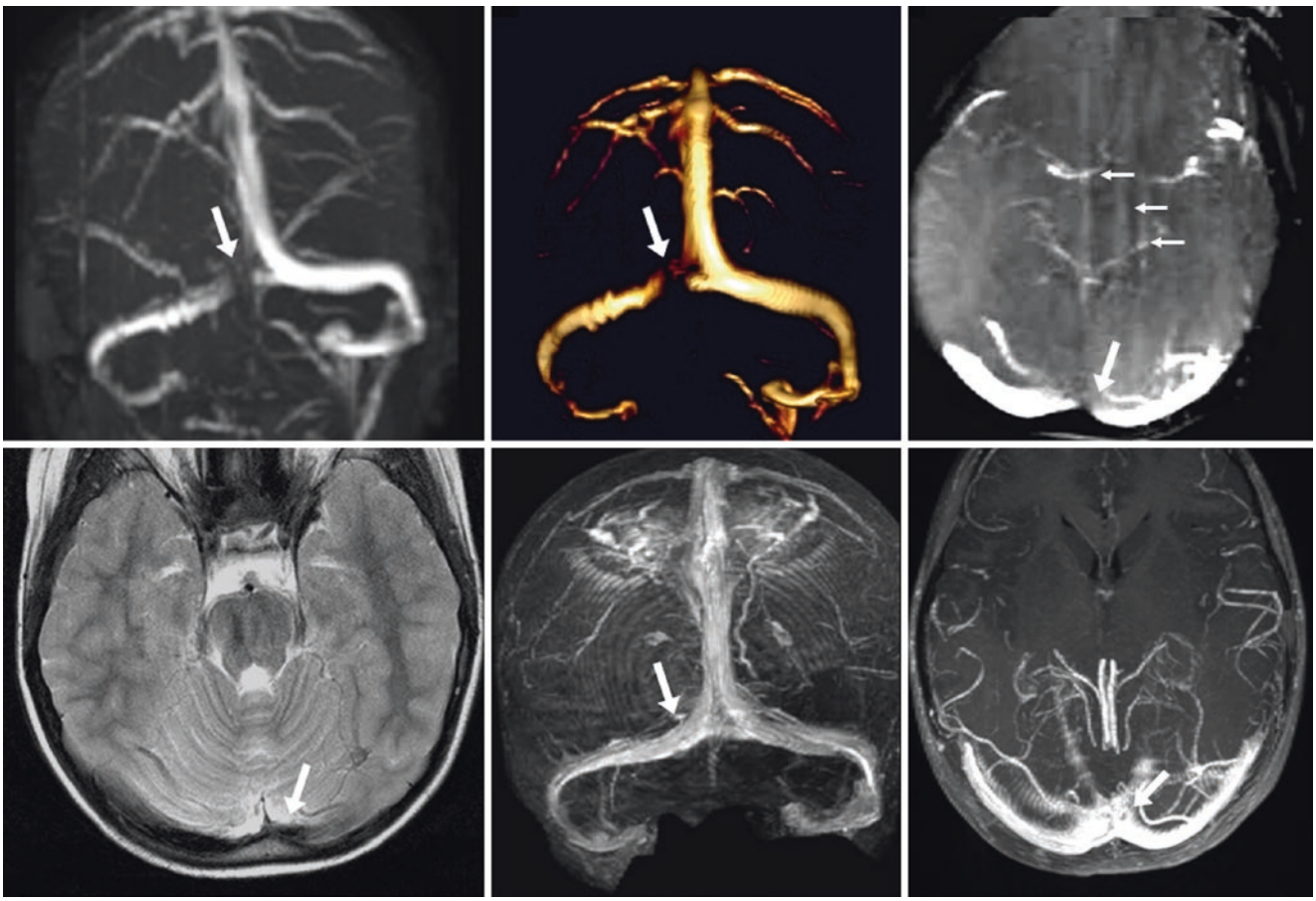

Fig. 42.20 Artifact from patient motion. *Top row*: In this 8-year-old, 2DTOF MRV PA views (*left* and *middle*) show a potential left TS defect near the torcular (*arrows*). However, note the amount of patient motion on a 22 mm-thick axial MPR (*thin arrows, right*), which was reconstructed from the original sagittal plane acquisition. *Bottom row:* T2WI (*left*), an MIP PA view reconstructed from a 3D postcontrast T1WI (*middle*), and an axial 30 mm MPR (*right*) do not confirm this defect

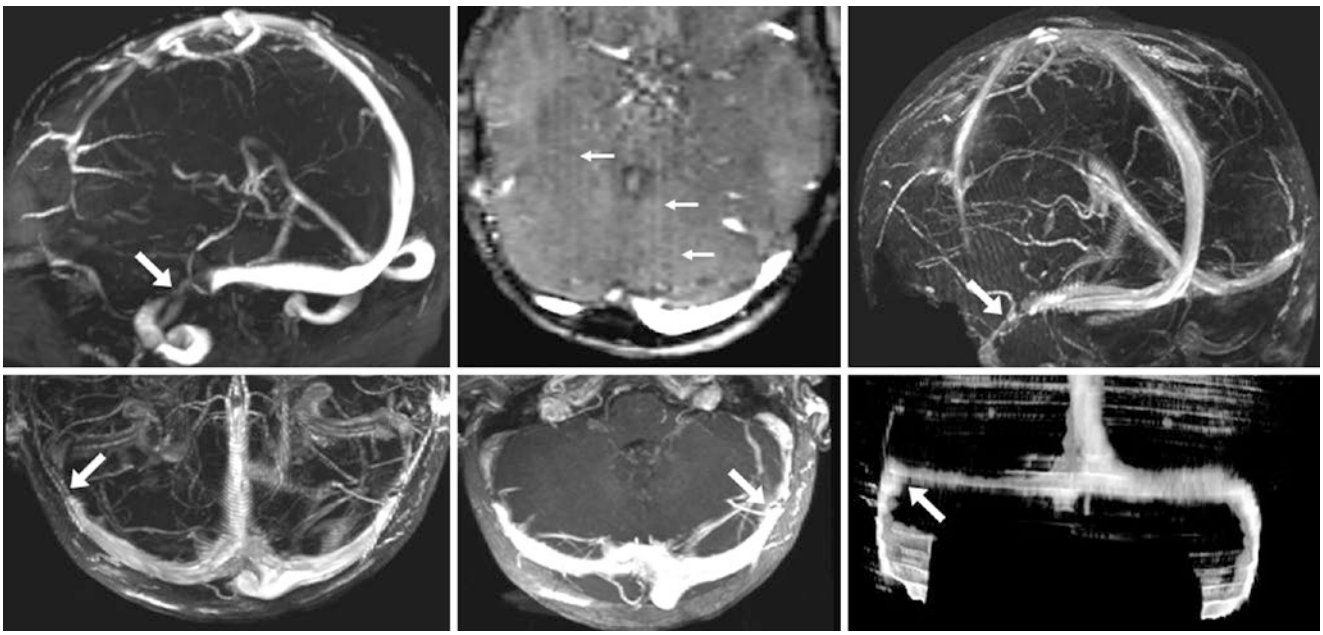

Fig. 42.21 Artifact from patient motion. *Top row*: in this 4-year-old, a 2DTOF MRV LPO view (*left*) and an axial 3 mm MPR (*middle*) show a defect in the distal left TS (*arrows*). However, there is moderate motion (*thin arrows*); the acquisition was acquired in the sagittal plane. A 3D postcontrast T1WI reconstructed in LPO (*right*) excludes thrombus. *Bottom row:* 3D postcontrast T1WIs reconstructed in superior (*left*) and 12 mm-thickness axial MPR (*middle*) confirm patency, but a stenosis-like defect remains. A contrast-enhanced CT MIP PA view (*right*) confirms that the defect fills with contrast, and was thus artifactual

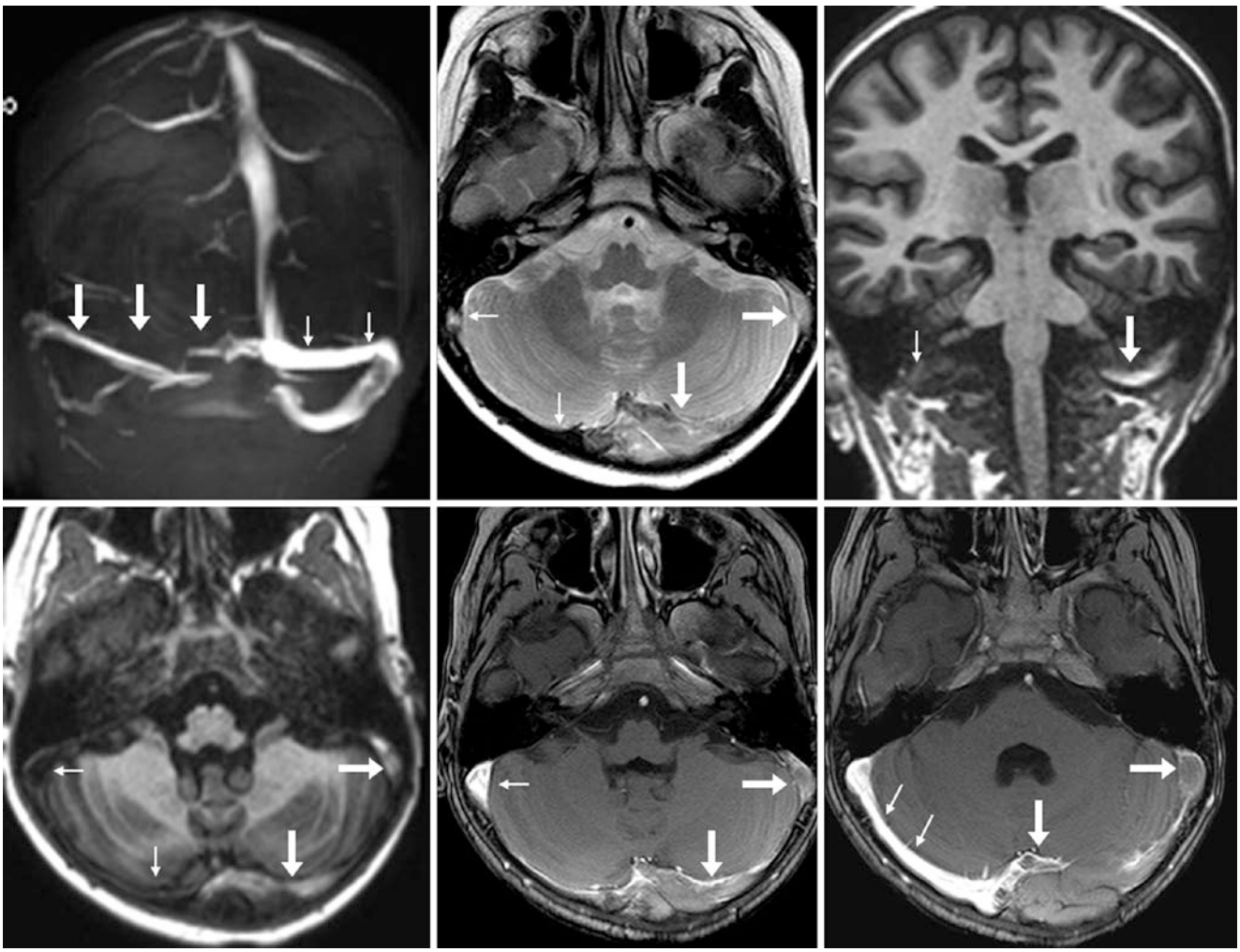

Fig. 42.22 Comparison case of dural sinus thrombosis. In a 4-year-old, a 2DTOF MRV PA view (*top left*) demonstrated incomplete visualization of the left TS (*arrows*), a lack of a dark flow void on T2WI (*top middle*), and bright signal internally on coronal (*top right*) and axial (*bottom left*) noncontrast T1WI. CEMRV was not obtained, but T1WIs after contrast (*bottom middle* and *right*) showed the left TS to be distended and containing thrombus, as compared with the right (*thin arrows*). The mild left TS signal on the 2DTOF MRV indicated that the thrombus was nonocclusive

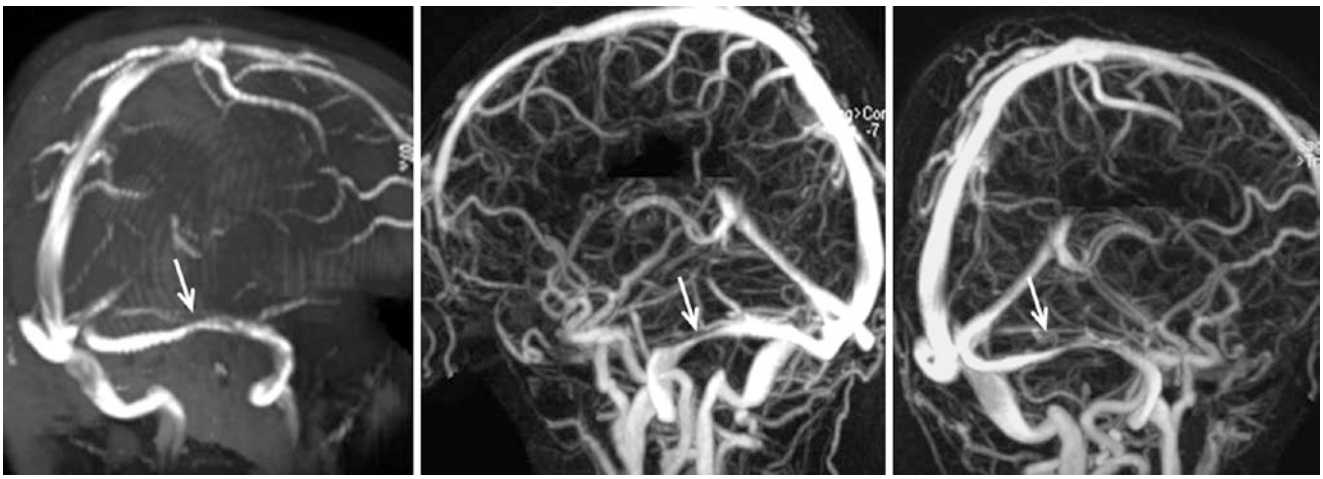

Fig. 42.23 Comparison case of pseudotumor cerebri with transverse sinus stenoses. An 11-year-old morbidly obese patient with headaches underwent a noncontrast 2DTOF MRV (*left*), which showed bilateral narrowed sigmoid-TS junctions (*arrows*), also seen on bilateral oblique CEMRV views (*middle* and *right*). The CSF opening pressure was quite elevated (45–50 cm H_2O), with optic disc cupping on T2WI MRI (*not shown*), consistent with pseudotumor

References

1. Ayanzen RH, Bird CR, Keller PJ, McCully FJ, Theobald MR, Heiserman JE. Cerebral MR venography: normal anatomy and potential diagnostic pitfalls. AJNR Am J Neuroradiol. 2000;21:74–8.
2. Leach JL, Fortuna RB, Jones BV, Gaskill-Shipley MF. Imaging of cerebral venous thrombosis: current techniques, spectrum of findings, and diagnostic pitfalls 1. Radiographics. 2006;26:S19–41.
3. Manara R, Mardari R, Ermani M, Severino MS, Santelli L, Carollo C. Transverse dural sinuses: incidence of anatomical variants and flow artefacts with 2D time-of-flight MR venography at 1 Tesla. Radiol Med. 2010;115:326–8.
4. Provenzale JM, Kranz PG. Dural sinus thrombosis: sources of error in image interpretation. AJR Am J Roentgenol. 2011;196:23–31.
5. White JB, Kaufmann TJ, Kallmes DF. Venous sinus thrombosis: a misdiagnosis using MR angiography. Neurocrit Care. 2008;8:290–2.
6. Erdman WA, Weinreb JC, Cohen JM, Buja LM, Chaney C, Peshock RM. Venous thrombosis: clinical and experimental MR imaging. Radiology. 1986;161:233–8.
7. Huston 3rd J, Ehman RL. Comparison of time-of-flight and phase-contrast MR neuroangiographic techniques. Radiographics. 1993;13:5–19.
8. Curé JK, Van Tassel P, Smith MT. Normal and variant anatomy of the dural venous sinuses. Semin Ultrasound CT MR. 1994;15:499–519.
9. Catalano C, Pavone P, Laghi A, Scipioni A, Fanelli F, Assael FG, et al. Role of MR venography in the evaluation of deep venous thrombosis. Acta Radiol. 1997;38:907–12.
10. Lafitte F, Boukobza M, Guichard JP, Reizine D, Woimant F, Merland JJ. Deep cerebral venous thrombosis: imaging in eight cases. Neuroradiology. 1999;41:410–8.
11. Lin W, Mukherjee P, An H, Yu Y, Wang Y, Vo K, et al. Improving high-resolution MR bold venographic imaging using a T1 reducing contrast agent. J Magn Reson Imaging. 1999;10:118–23.
12. Kudo K, Terae S, Ishii A, Omatsu T, Asano T, Tha KK, Miyasaka K. Physiologic change in flow velocity and direction of dural venous sinuses with respiration: MR venography and flow analysis. AJNR Am J Neuroradiol. 2004;25:551–7.
13. Rollins N, Ison C, Booth T, Chia J. MR venography in the pediatric patient. AJNR Am J Neuroradiol. 2005;26:50–5.
14. Rodallec MH, Krainik A, Feydy A, Hélias A, Colombani JM, Jullès MC, et al. Cerebral venous thrombosis and multidetector CT angiography: tips and tricks. Radiographics. 2006;26:S5–18; discussion S42–3.
15. Widjaja E, Shroff M, Blaser S, Laughlin S, Raybaud C. 2D time-of-flight MR venography in neonates: anatomy and pitfalls. AJNR Am J Neuroradiol. 2006;27:1913–8.
16. Chen HM, Chen CC, Tsai FY, Shy CG, Wu CH, Chen WS, Hung HC. Cerebral sinovenous thrombosis. Neuroimaging diagnosis and clinical management. Interv Neuroradiol. 2008;14 Suppl 2:35–40.
17. Jin Z, Xia L, Du YP. Reduction of artifacts in susceptibility-weighted MR venography of the brain. J Magn Reson Imaging. 2008;28:327–33.
18. Liu S, Mok K, Neelavalli J, Cheng YC, Tang J, Ye Y, Haacke EM. Improved MR venography using quantitative susceptibility-weighted imaging. J Magn Reson Imaging. 2014;40:698–708.
19. Neelavalli J, Mody S, Yeo L, Jella PK, Korzeniewski SJ, Saleem S, et al. MR venography of the fetal brain using susceptibility weighted imaging. J Magn Reson Imaging. 2014;40:949–57.
20. Casey SO, Alberico RA, Patel M, Jimenez JM, Ozsvath RR, Maguire WM, Taylor ML. Cerebral CT venography. Radiology. 1996;198:163–70.

Artifacts of the Craniocervical Arterial System on MRI

43

Three-dimensional time-of-flight (3DTOF) MRA utilizes the concept of *flow-related enhancement* (FRE) to produce bright signal on a gradient echo acquisition, where fresh spins in blood flowing into (and preferentially perpendicular to) the slice are unsaturated and exhibit strong signal prior to being saturated [1–25]. Arteries do not always follow a perpendicular orientation, however. Particular examples include *tortuous internal carotid arteries* (ICAs) in the cervical region, *vertebral arteries* (VAs) near their origin, or the normal horizontal course of the petrous ICAs. When travelling horizontally within a slice, the phenomenon of in-plane saturation may reduce FRE and thus decrease the visualized flow of vasculature. This phenomenon is overcome on contrast-enhanced MRA (CEMRA), as the T1-bright gadolinium usually overpowers the saturation effect. Note that the FRE effect is also useful with 2D or 3DTOF MR venography, most commonly in the transverse sinuses with an axial acquisition, or within the superior sagittal sinus with a sagittal acquisition. It is also important to point out that 3D acquisitions can be susceptible to saturation if a larger volume is obtained, or if the technique of multiple overlapping thin slab acquisition (MOTSA) is not used properly. Hence, most facilities utilize overlapping slabs to decrease *in-plane saturation* effect for noncontrast cranial MRA, but saturation may still occur if flow occurs within the same plane as the plane of acquisition.

Many of the same factors leading to artifacts on cervical MRA cause similar problems at the skull base and intracranially. The in-plane saturation effect is a particular problem, as the ICAs travel transversely in several locations, most notably the horizontal segment of the petrous ICA, the horizontal segment of the cavernous ICA, and possibly even the proximal supraclinoid ICA [1–25]. This effect also is not uncommon in the middle cerebral artery (MCA) distal M1 and proximal segments within the sylvian fissure, where the artery travels horizontally before turning and travelling superiorly along the convexity. Focal apparent loss of an M1 or M2 segment flow may simulate intraluminal thrombus in an acute stroke. The phenomenon is also not uncommon in anterior cerebral artery (ACA) distal A1 or proximal A2 segments, before they travel superiorly. CT angiography (CTA) can be used for confirmation of patency in cases where in-plane saturation has been suspected of simulating a stenosis, whether in the neck or intracranially.

"*Stepladder*" or *"venetian blind"* artifacts occur intracranially, but less commonly than they do with cervical MRA, as the head comprises a smaller field of view, which can be exacerbated by *respiratory motion* [1–25]. In particular, mild respiratory motion may not be readily detected as the source of image compromise when it causes or worsens such artifacts. Also, *tortuosity* or *dolichoectasia* can exacerbate in-plane saturation effects, and can also predispose to turbulence, another factor causing or worsening artifact and diminishing the necessary FRE.

For most of the abovementioned artifacts, CEMRA can improve visualization of the affected/suspected segment [1–25]. In particular, when an MCA segment appears focally thrombosed or is not visualized on a noncontrast 3DTOF head MRA, it is quite helpful to refer to accompanying neck CEMRA source images (if performed) to evaluate whether the artery is truly thrombosed. Contrast is not typically administered for routine 3DTOF head MRA because the low arterial-to-venous time (potentially less than a few seconds) often causes the venous structures to fill, which can obscure the contours of the arteries on 3D maximum intensity projection (MIP) images.

Five other sources of artifacts can independently become problems that are more common in cranial MRA evaluation than in cervical MRA [1–25]:

- *Susceptibility artifacts* (particularly adjacent paranasal sinus air, but also artifacts from adjacent bone, metal, hemorrhage, or other foreign materials)
- *Head motion artifacts* (whether front-to-back or side-to-side)

A.M. McKinney, *Atlas of Normal Imaging Variations of the Brain, Skull, and Craniocervical Vasculature*,
DOI 10.1007/978-3-319-39790-0_43

- *Pulsation artifacts* (whether from CSF or vasculature) (carried along the phase direction)
- *Parallel imaging artifact* (because the head has a larger transverse and anterior-posterior field to cover than does the neck)
- *"T1 shine-through" effects* (arising from orbital/scalp fat, or when there is an adjacent T1-bright hemorrhage).

Again, CEMRA and subtraction imaging (subtracting precontrast from postcontrast) can help exclude the presence of such pseudo-stenoses or pseudo-occlusions.

43.1 Flow-Related Enhancement: Bright Arteries on Spin-Echo T1-Weighted Images

On noncontrast T1-weighted imaging (T1WI), arteries can appear bright because of *FRE* (also known as the "entry-slice phenomenon") [1–25]. FRE is a result of unsaturated protons entering a slice during the time to repeat (TR). These unsaturated protons retain their complete longitudinal magnetization, and this longitudinal magnetization is then flipped into the transverse plane by the initial RF pulse, which results in a higher signal than stationary protons in the slice (*e.g.*, the surrounding soft tissues or vessel wall). Hence, FRE is most prominent within arteries at the skull base and at the beginning slices of an axial sequence, such as at the lower slices of the skull base. It can be seen with either the VA or ICA, whether unilaterally or bilaterally. This artifact is typically seen on routine spin echo T1WI. On most *gradient echo T1WI sequences* (which are increasingly used, particularly at 3.0 T), bright signal within arterial vessels is expected, so this would not be considered an artifact. For example, the FRE phenomenon serves as the basis for providing intra-arterial signal on the gradient echo sequences used to generate TOF MRA or TOF MRV.

Additionally, *slow flow* or *turbulent flow* may also contribute further to unexpected T1 hyperintensity on spin echo T1WI within arteries that do not have evidence of thrombosis [1–25]. MRA or CTA can be used to confirm arterial patency. If either turbulence (due to tortuosity or an enlarged vessel such as an aneurysm, for example) or slow flow (*e.g.*, poststenotic) is suspected, then CTA may be more helpful because of its higher resolution and the contrast recirculation phenomenon (Figs. 43.1, 43.2, and 43.3).

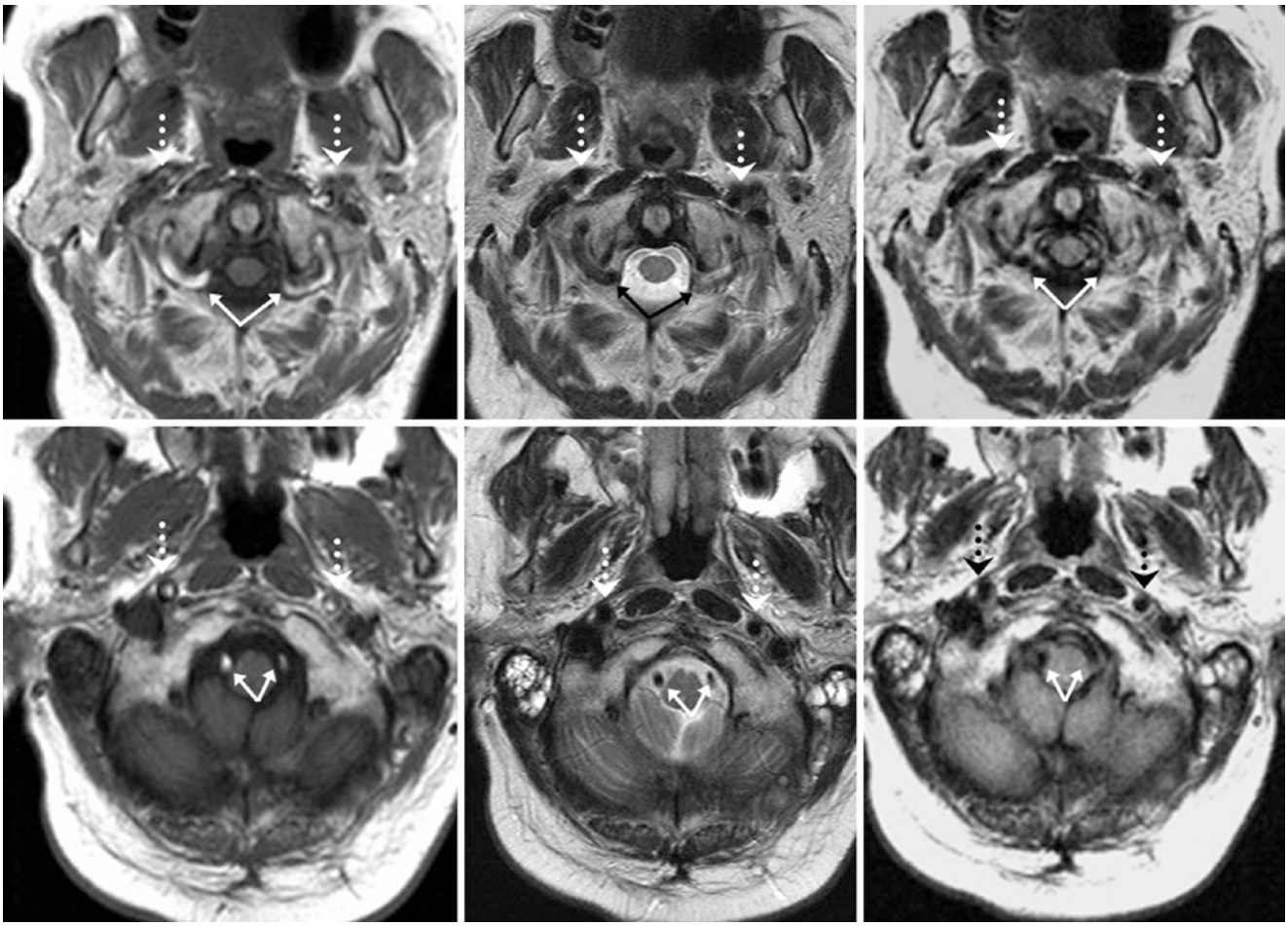

Fig. 43.1 In this 62-year-old, bright signal was noted within both vertebral arteries (VAs) (*solid arrows*) just below the skull base on noncontrast T1WI (*top left* and *bottom left*). However, both VAs are patent with flow voids on T2WI (*top middle* and *bottom middle*) and FLAIR (*top right* and *bottom right*). Similarly, on noncontrast T1WI, bright signal is seen in both internal carotid arteries (ICAs) (*large dotted arrows, best seen on bottom left*), but with patent flow voids in those locations on both T2WI and FLAIR images

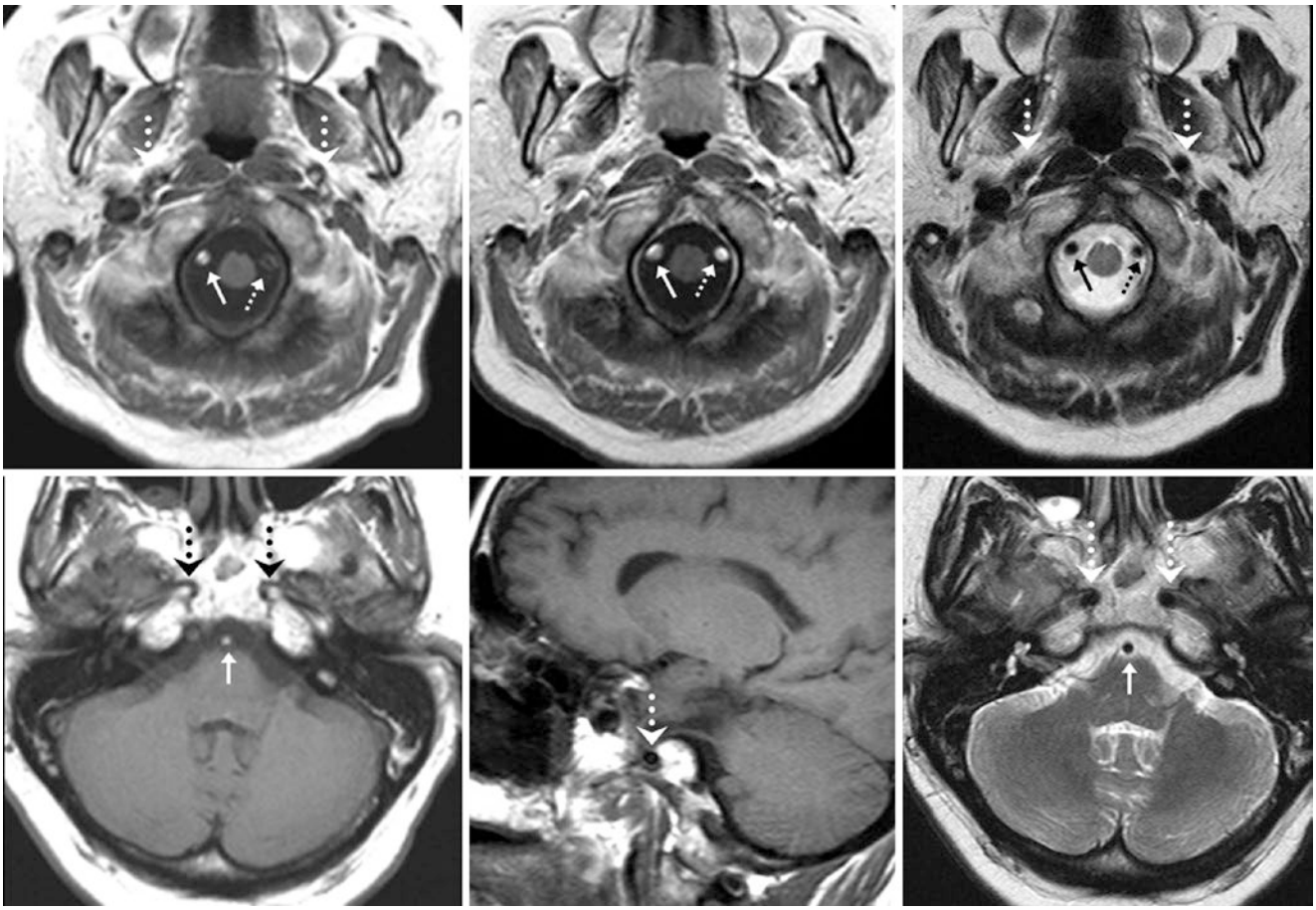

Fig. 43.2 60-year-old with unilateral bright signal within the right VA and basilar (*solid arrows*) on axial noncontrast T1WIs (*top left* and *bottom left*); note a normal left VA flow void (*small dotted arrows)*. Both VAs are patent on postcontrast T1WI (*top middle*), and show flow voids on T2WI (*top right* and *bottom right*). Similarly, bright signal is seen in both ICAs (*large dotted arrows)* on noncontrast axial T1WIs, but with normal, dark flow voids present on the sagittal T1WI (*bottom middle*), as that is not the entry slice. The patent ICA flow voids are confirmed on axial T2WIs

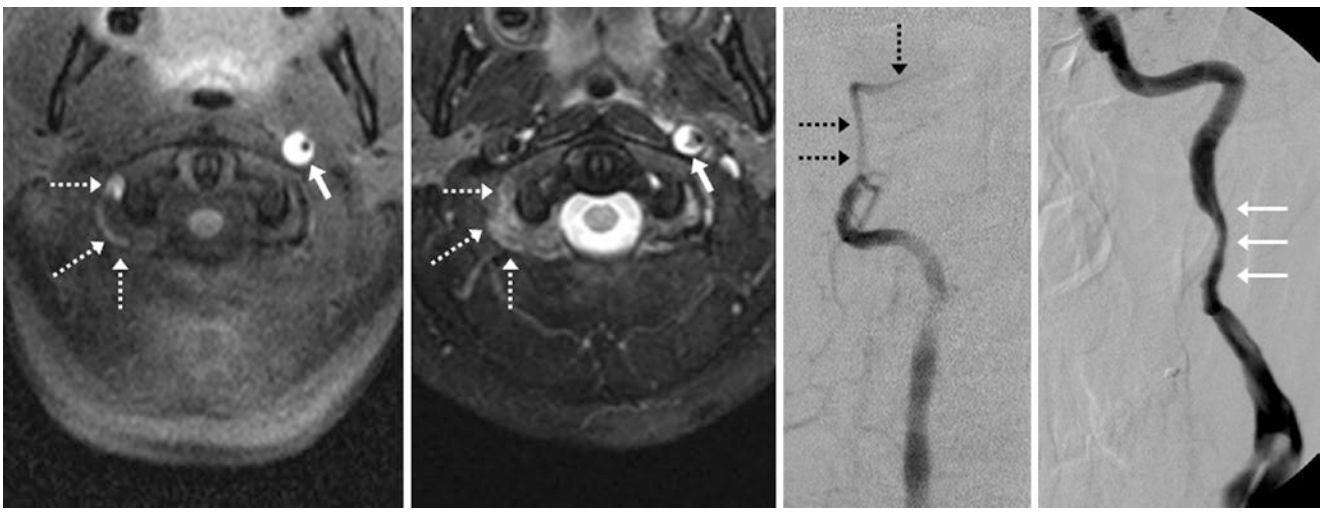

Fig. 43.3 Comparison case of multiple dissections. In this 34-year-old (post–motor vehicle crash), noncontrast fat-suppressed T1WI (*left*) and T2WI (*left middle*) depict crescentic bright signal around the lumen of the left ICA (*solid arrows*) just below the skull base. The lack of a right VA flow void (*dotted arrows*) suggests an occlusion. Catheter DSA AP views of the right VA (*right middle*) and left ICA (*right*) confirm the right VA occlusion and left ICA dissection

43.2 2D Time-of-Flight Neck MRA Artifacts and Turbulent Flow That May Simulate Stenosis (Pseudo-stenosis)

Noncontrast MRA can be used to evaluate the major cervical arteries [1–25]. In brief, the continual entry of "fresh" spins into the slices (*i.e.*, *flow-related enhancement* (FRE)) that have received multiple excitations is the cause of the bright signal in these arteries on TOF MRA, whereas venous signals from the opposite direction are usually saturated by a 90° pulse placed above the region of interest. 2DTOF (multiple thin slices placed together) or 3DTOF (one or multiple thicker slabs) techniques can be used. 3DTOF has a higher signal-to-noise ratio and typically higher resolution, but results in greater saturation of spins with larger volumes of coverage, and usually requires a longer acquisition time. 2DTOF can cover a larger field by combining multiple slices with less saturation, as each slice is obtained independently and the slices are stacked together for a 3D effect. Each 2DTOF thin slice is typically obtained at a thickness of less than 2–3 mm, and, because it is acquired independently, 2DTOF can also contain "directionality" of flow, where saturation of down-flowing spins (venous flow) is usually performed as part of this technique. (The downward flow is also saturated independently for each slice.) This is helpful in evaluating potential *subclavian steal syndrome*, in conjunction with *contrast-enhanced MRA* (CEMRA), where CEMRA demonstrates the severe stenosis, but not the directionality of flow.

A hybrid technique, *multiple overlapping thin slab acquisition* (MOTSA), combines multiple small 3D slabs that overlap to cover a large area, such as the neck, with less saturation of spins [8]. Thus, MOTSA is commonly used to produce noncontrast TOF MRA images, but it has one side effect: Transverse bands of decreased signal can occur at the junctions between slabs. This artifact, known as the *"venetian blind"* or *"stepladder" artifact*, occurs at the junctions of slabs when using 2DTOF and MOTSA techniques and can be problematic by simulating ICA or VA stenoses (pseudo-stenosis). In such cases, CEMRA can aid in the diagnosis. Notably, patient *motion,* whether respiratory or vascular, can also exaggerate such artifacts and cause pseudo-stenoses. *Tortuosity* at the VA origins, another problem that can exacerbate artifacts, is most common in older patients.

CEMRA utilizes a 3D acquisition but generally alleviates some of the 3D acquisition–related artifacts that are seen with a 3DTOF technique, owing to intravenous contrast administration; contrast prevents saturation of spins in the larger 3D volume, which would typically occur on 3DTOF MRA [1–25]. Because CEMRA can cover a larger area in less time than a 3DTOF technique, CEMRA usually has less resolution but higher signal and contrast-noise ratio. CEMRA is also the most specific MRI technique in evaluating for ICA or VA stenosis, but it is not the most sensitive. Thus, in general, 2DTOF MRA or 3DTOF MRA may have higher resolution (but more potential artifacts) than CEMRA.

Not all patients can receive gadolinium, however, and contrast bolus timing may fail, so 2DTOF MRA is far from useless. *Phase-contrast MRA* (PCMRA) can also be helpful in patients who cannot receive intravenous contrast and can also allow quantification of the flow velocity. The disadvantage is that it usually requires much more time than TOF MRA, because PCMRA typically requires acquisition in three separate directions to obtain the 3D images. Also, as with PCMRV, improper selection of the encoding velocity (V_{enc}) may lead to incomplete visualization of the intended vessels of interest (such as in very slow flow or post-stenotic flow). Newer, noncontrast techniques such as 3D turbo field echo (TFE) or other 3D-acquisition gradient echo techniques may also help in such patients, as flowing blood appears bright because of the refreshing of spins/FRE effect, although their range of coverage may be more limited than 2DTOF MRA and CEMRA.

Because the short time from the intracranial arterial circulation to the venous circulation is only a few seconds, noncontrast 3DTOF MRA is typically used initially for brain MRA, as CEMRA can suffer from venous contamination that causes arteries or aneurysms to be obscured, or venous structures to be mistaken for arteries owing to their close proximity. Although 3DTOF MRA can be used in the cervical region, this use is often not feasible, as the large region of coverage predisposes to saturation, which necessitates the acquisition of multiple 3D slabs (possibly requiring >15 min) to cover the same territory [1–25]. Also, even cervical CEMRA may occasionally suffer from artifacts related to turbulence, patient motion (especially respiratory motion), or in-plane saturation effects, Thus, CTA or catheter DSA may be necessary to confirm stenoses in difficult cases, such as when a certainty of diagnosis is needed as part of a preprocedural workup (Figs. 43.4, 43.5, 43.6, 43.7, 43.8, 43.9, 43.10, 43.11, 43.12, 43.13, 43.14, and 43.15).

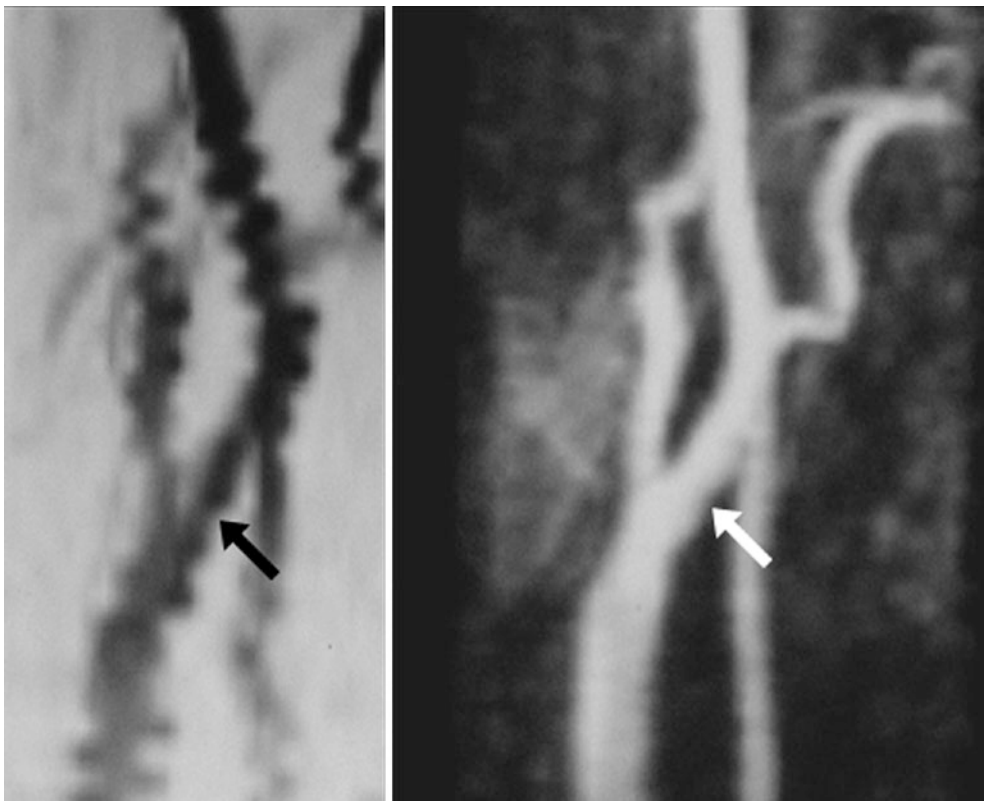

Fig. 43.4 In this 38-year-old, a 2DTOF MRA LAO view from the mid-1990s (*left*) showed severe "venetian blind" artifact, precluding left ICA evaluation (*arrows*). A contrast-enhanced MRA (CEMRA) (*right*) was performed, which was normal

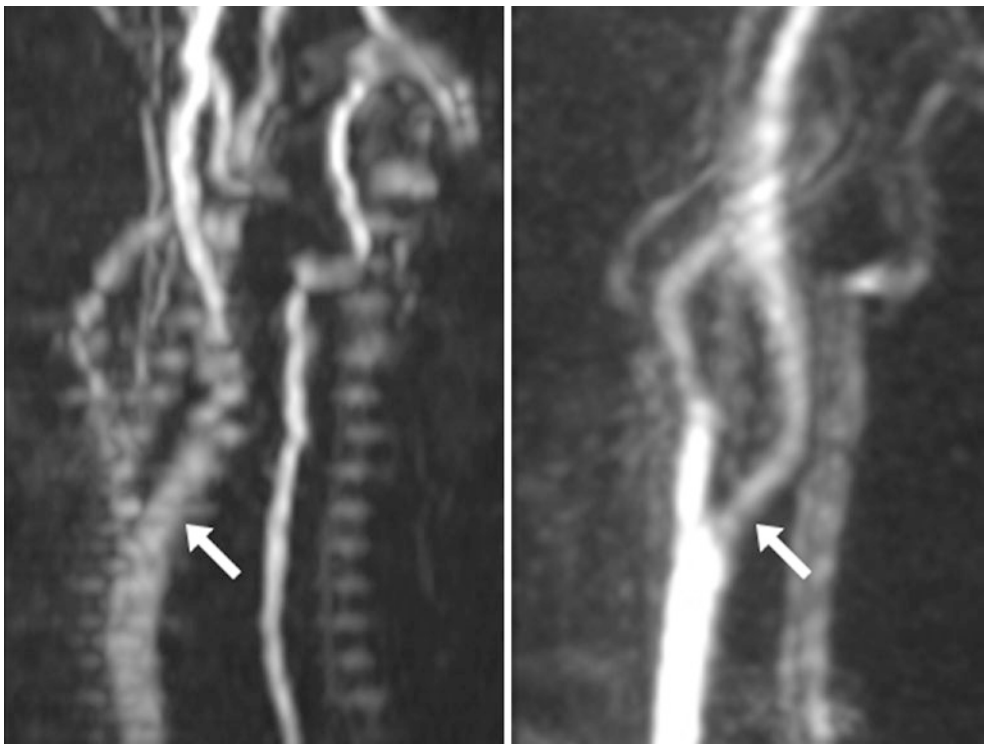

Fig. 43.5 In this 52-year-old, a motion-compromised 2DTOF MRA (*left*) caused severe "venetian blind" artifacts, inhibiting left ICA evaluation (*arrows*). Phase-contrast MRA (PCMRA) (*right*) confirmed ICA patency. The patient could not receive IV gadolinium

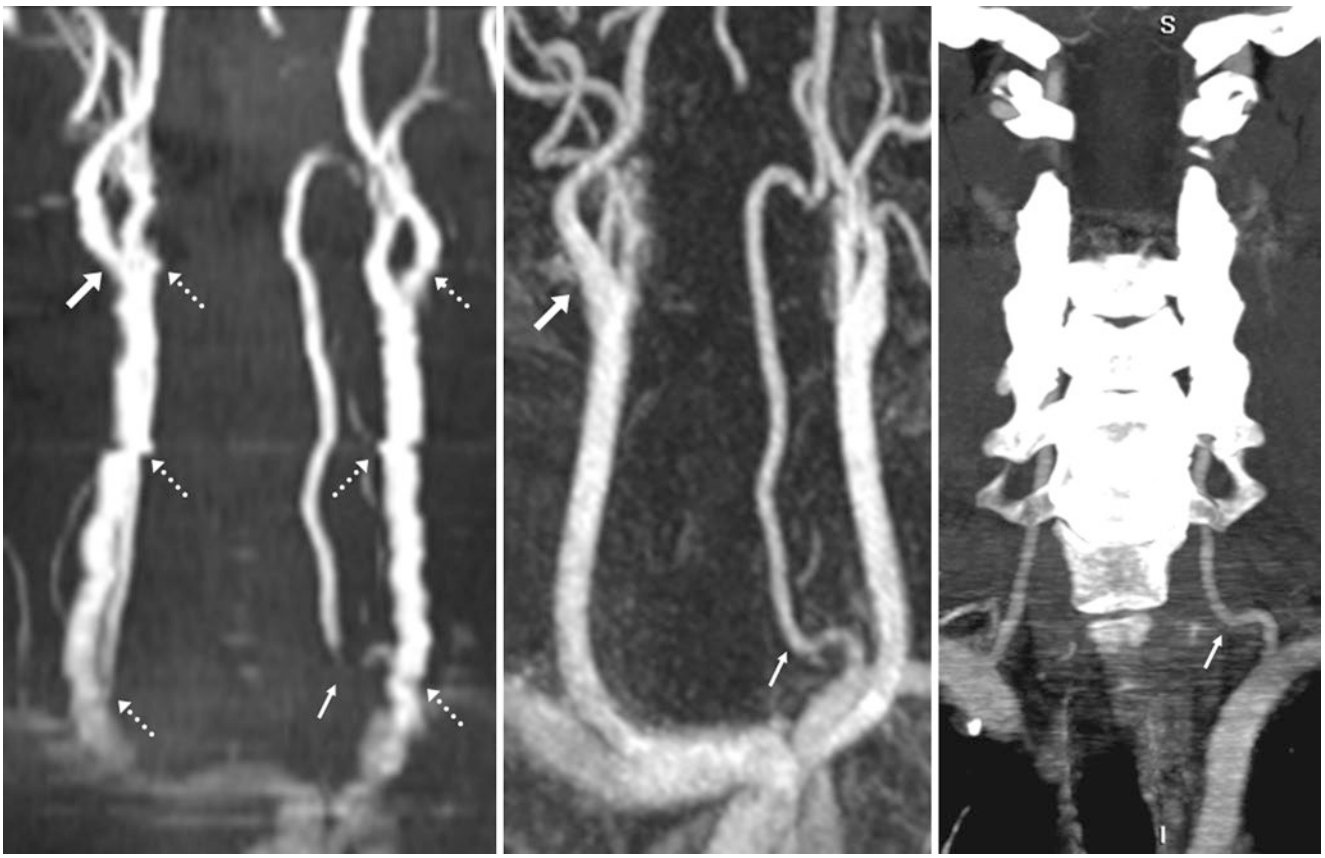

Fig. 43.6 Pseudo-stenosis in this 17-year-old, a 2D TOF AP view (*left*) showed "stepladder" artifacts (*dotted arrows*). The right ICA was called mildly narrowed (*arrows*), and the left VA near the origin was not seen (*thin arrows*), so a stenosis was suspected. However, artifacts were noted from patient motion, turbulence, and in-plane saturation. A CEMRA (*middle*) did not demonstrate either left VA or right ICA stenosis, findings further confirmed by coronal 5 mm MPRs from a CTA (*right*)

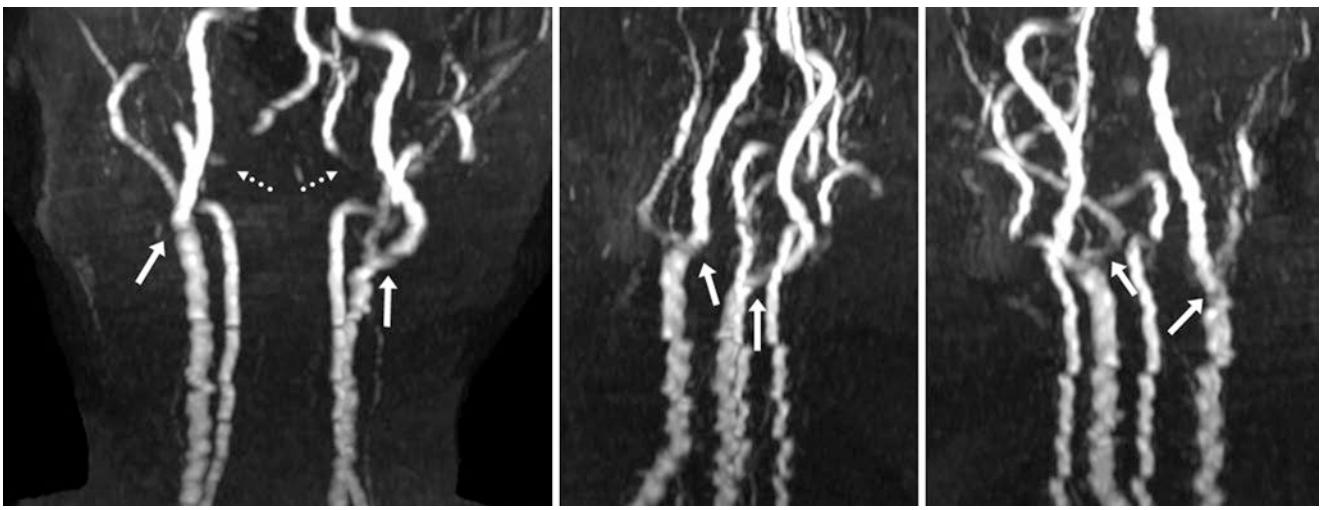

Fig. 43.7 In this 47-year-old, a 2DTOF MRA AP view (*left*) showed severe "venetian blind" artifacts and motion, with numerous transverse defects. A left lateral view (*middle*) and right lateral view (*right*) are also shown. Dark signal is present at the ICA origins (*arrows*), but the presence or absence of a stenosis cannot be determined because of the severe artifacts. The VAs are also obscured at the C1 level owing to in-plane saturation, best seen on the AP view (*dotted arrows*)

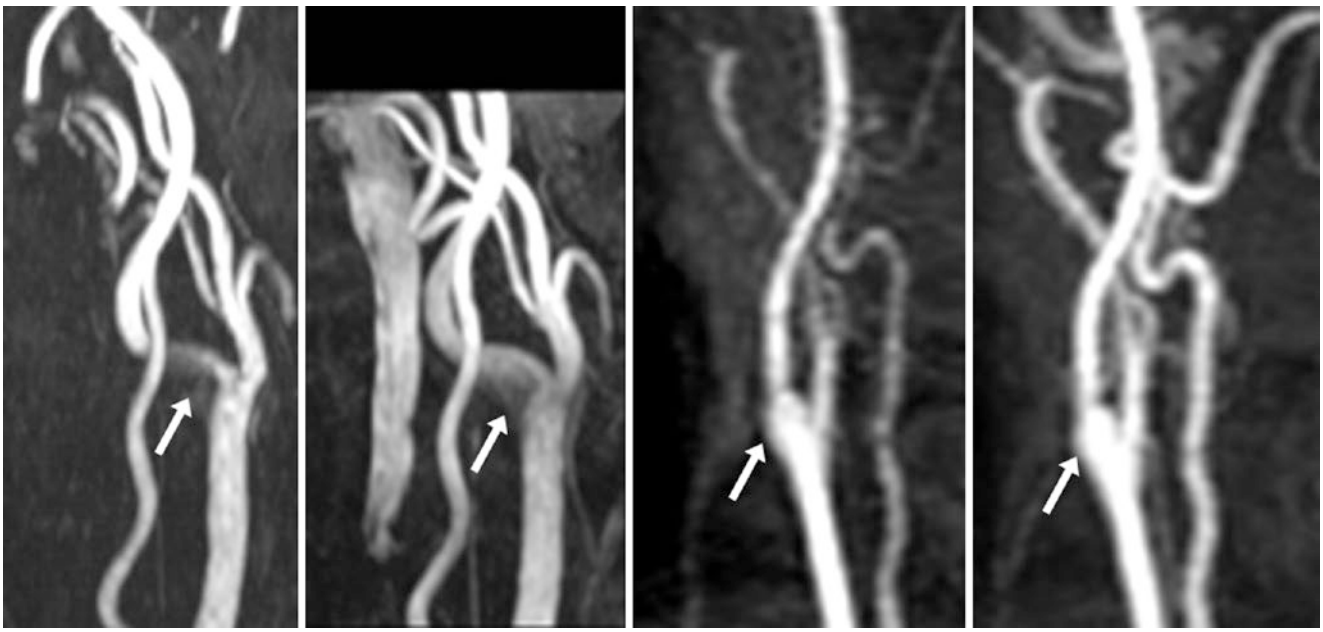

Fig. 43.8 Pseudo-stenosis in this 39-year-old, a 2DTOF MRA lateral view (*left*) showed an apparent stenosis (*arrows*) of the right ICA origin. A 3D turbo field echo sequence (*left middle*) had limited coverage and also suffers from such artifact to a lesser degree. Time-resolved CEMRA in early (*right middle*) and late (*right*) phases confirmed patency of the right ICA origin. Either turbulence or in-plane saturation effect was the cause of this pseudo-stenosis on the noncontrast images

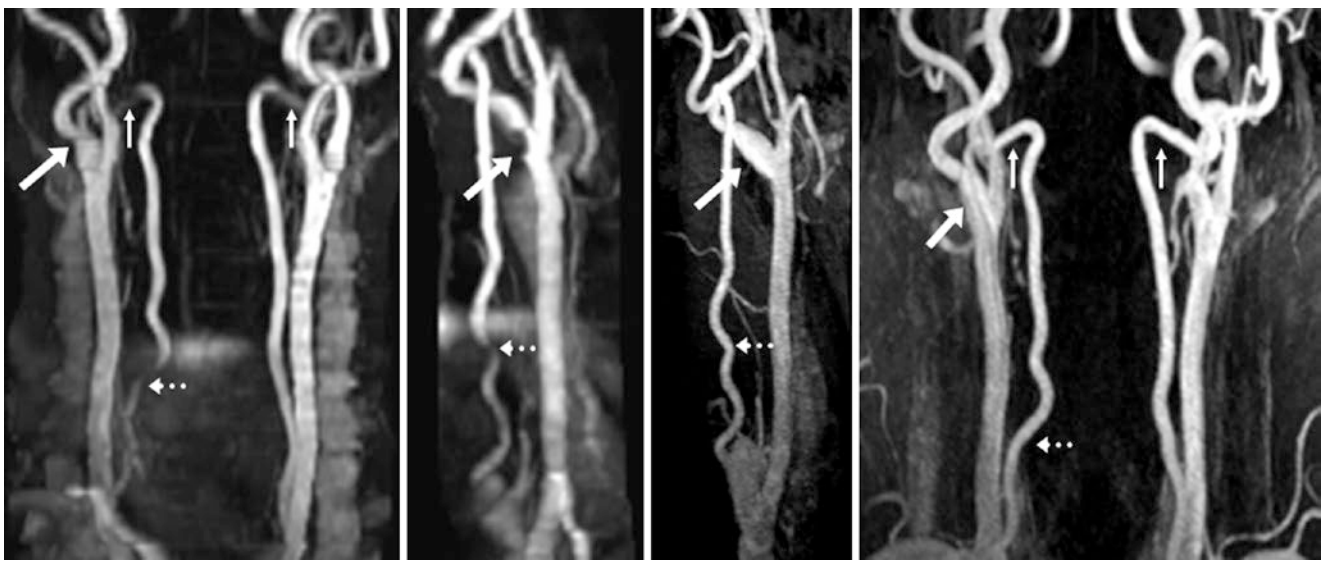

Fig. 43.9 Pseudo-stenosis 52-year-old with mild "stepladder" artifact on a 2DTOF MRA AP view (*left*), along with turbulent flow, simulating a right ICA stenosis (*large arrows*), particularly on lateral views (*left middle*). The lower right VA is also obscured by stepladder artifact (*dotted arrows*), and both upper VAs at the C1 level suffer from in-plane saturation (*thin arrows*). Such artifacts disappear on CEMRA lateral (*right middle*) and AP (*right*) views

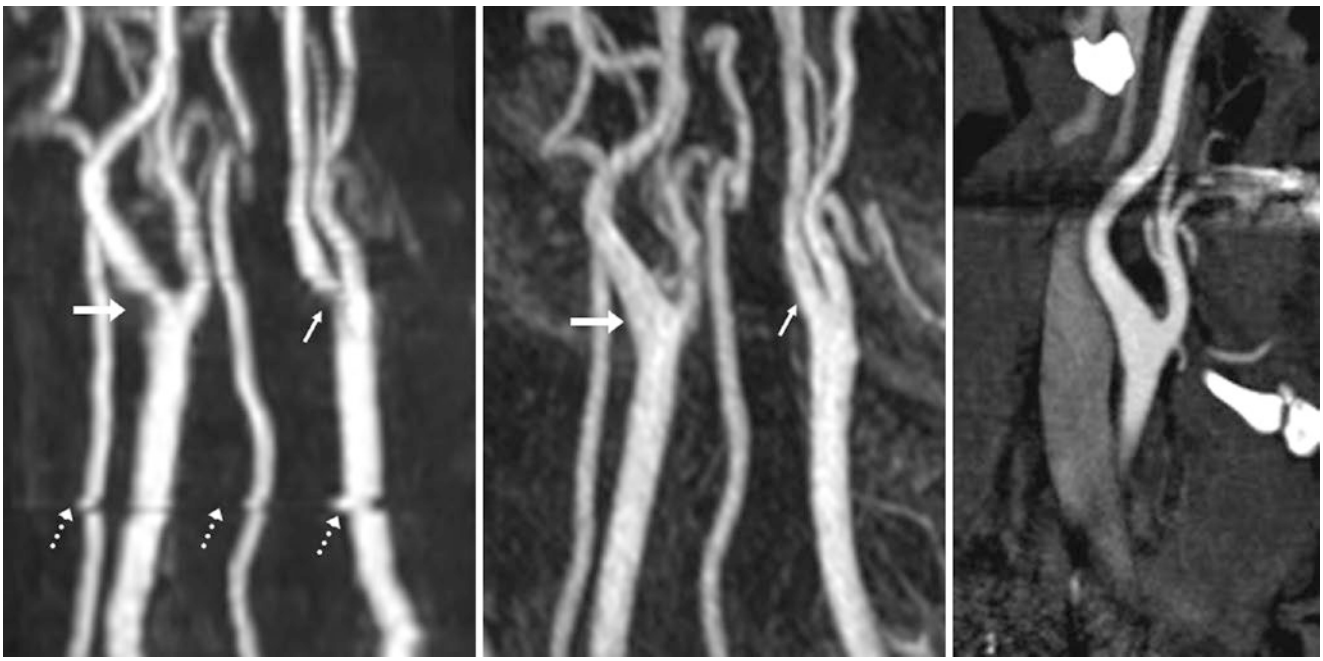

Fig. 43.10 Pseudo-stenosis on this 53-year-old, a 2DTOF MRA LAO view (*left*) contains "stepladder" artifacts (*arrows*), leading to questions of stenoses of the right (*arrows*) and left (*thin arrows*) ICA origins; note such artifacts caudally affecting all arteries (*dotted arrows*). These artifacts disappeared on CEMRA (*middle*). A CTA sagittal 3 mm MPR of the right ICA origin (*right*) is confirmatory. The pseudo-stenoses arose from a combination of turbulent flow and stepladder artifacts

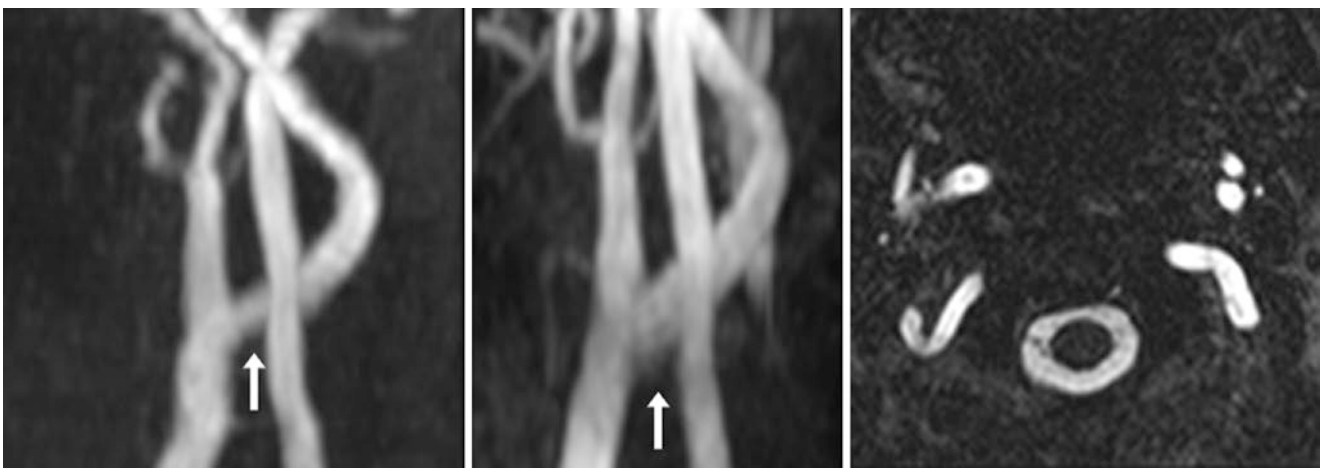

Fig. 43.11 Pseudo-stenosis 78-year-old with severe renal failure, who could not receive intravenous gadolinium. A 2DTOF MRA lateral view (*left*) shows turbulence artifact simulating mild stenosis (*arrows*), but the stenosis is not seen on 3D turbo field echo (TFE) lateral (*middle*) views. The TFE sequence has limited coverage, but may exclude stenoses without utilizing contrast

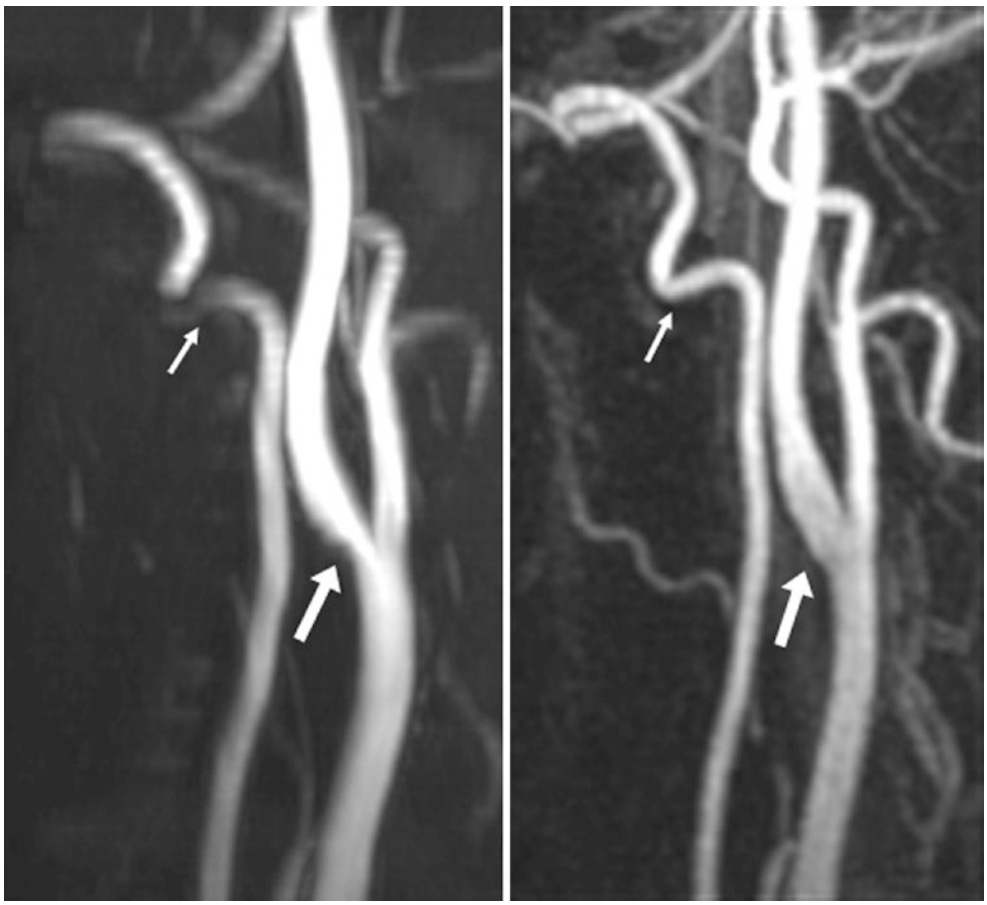

Fig. 43.12 Pseudo-stenosis in this 31-year-old, a 2DTOF MRA (*left*) shows turbulence mimicking a mild ICA stenosis (*arrows*). In-plane saturation artifact affects the VA (*thin arrows*). A CEMRA (*right*) is normal

Fig. 43.13 Pseudo-stenosis in this 29-year-old, a 2DTOF MRA LAO view (*left*) suffers moderate, diffuse "venetian blind" artifact that obscures the ICA origin (*arrows*). A CEMRA (*right*) is normal

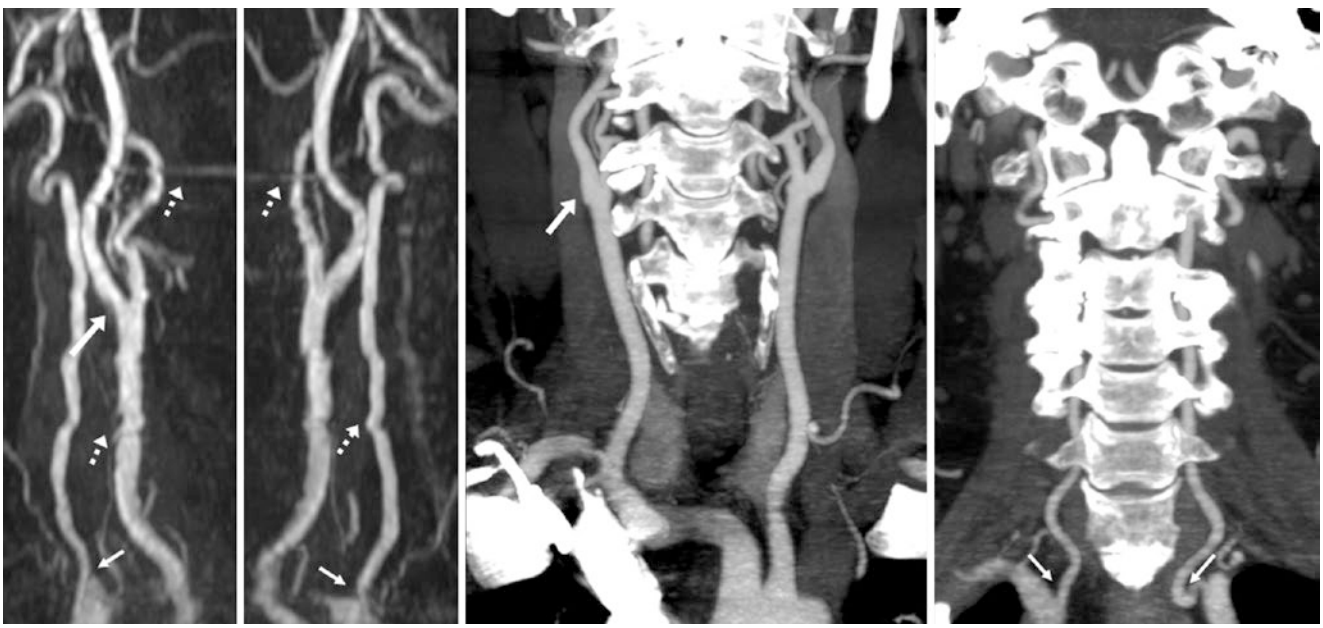

Fig. 43.14 Pseudo-stenosis in this 53-year-old, 2DTOF MRA AP views of the right (*left*) and left (*left middle*) sides suggested a mild right ICA stenosis (*arrows*) and mild bilateral VA stenoses (*thin arrows*). Moderate step-ladder artifact (*dotted arrows*) was present. Such pseudo-stenoses disappeared on a CTA, which showed patency of the ICAs (*right middle*) and VAs (*right*) on coronal MPRs. The artifacts affecting the right ICA and the VAs were likely due to a combination of turbulence and in-plane saturation. The VA tortuosity also made it difficult to find a plane on the MRA to evaluate for stenosis

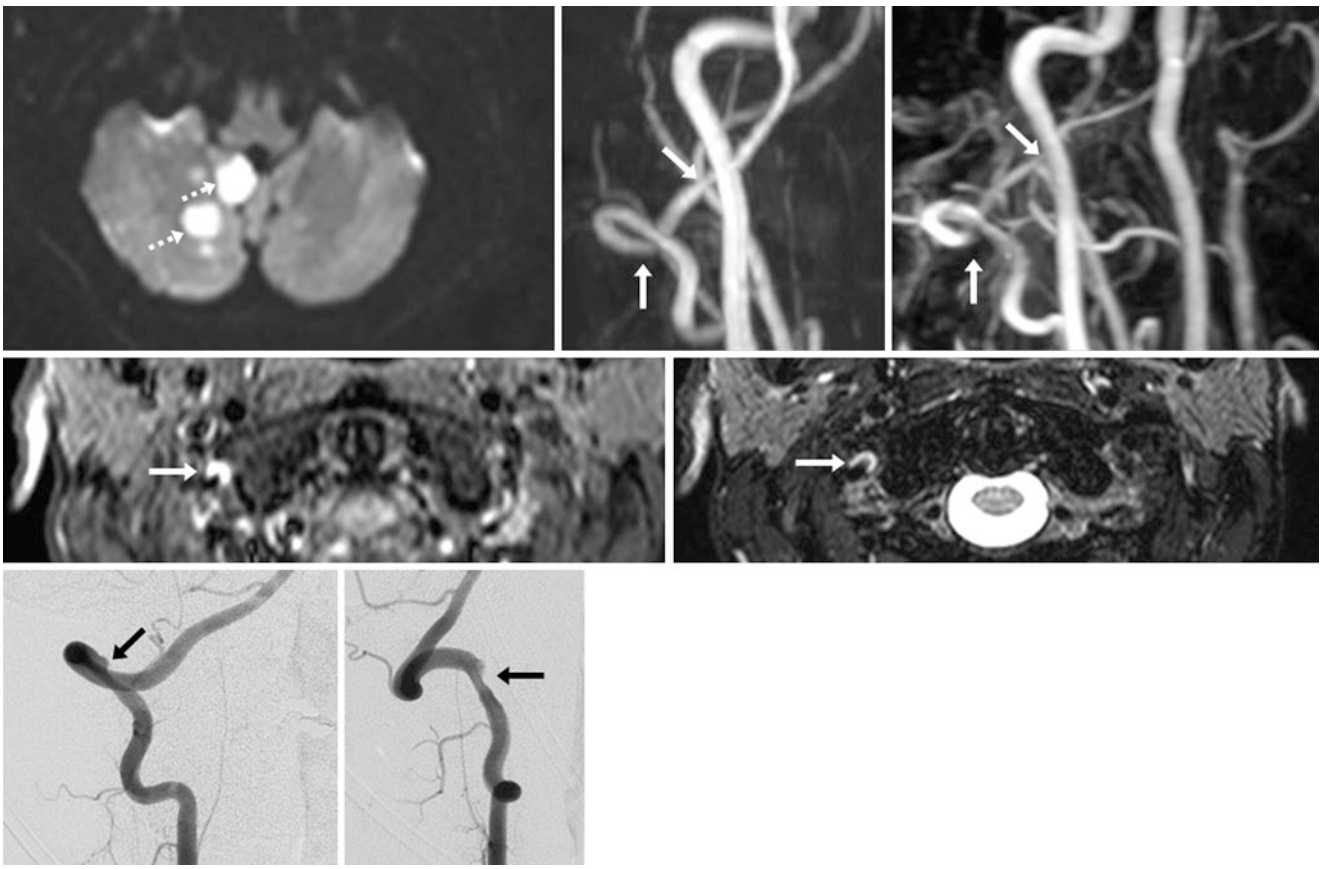

Fig. 43.15 Comparison case of vertebral dissection. *Top row:* 34-year-old with neck pain 10 days after skiing. There are infarcts within the right hemicerebellum and tonsil on DWI (*left*). On 2DTOF MRA (*top*) and on CEMRA (*top*), there was question of a subtle irregularity of the right VA at the C1 level and above (*arrows*). *Middle row:* focal bright, crescentic signal on fat-suppressed T1WIs (*left*) and T2WIs (*middle*) indicated a focal right VA dissection (*arrows*). *Bottom row:* catheter DSA is considered the gold standard, and AP (*left*) and lateral (*right*) views of the right VA confirmed a small, focal Grade 1 injury

43.3 Contrast-Enhanced Neck MRA: Simulated Arterial Stenoses (Pseudo-stenosis)

Arterial stenoses that may be simulated on CEMRA are usually due to turbulent flow but also may be secondary to motion or even a component of in-plane saturation artifacts [1–25]. Although stenoses of the ICA origin are typically easily detected by cervical CEMRA, there are still cases where such artifacts cause consternation. This situation is relatively uncommon with regard to the cervical ICA, as studies have validated the use of CEMRA, compared with catheter DSA. There is less evidence to support the detection by CEMRA of VA stenosis. VA occlusions or near-occlusions are usually readily diagnosed by CEMRA, but characterizing less critical stenoses in the VAs is problematic owing to a combination of the degree of tortuosity at the VA origin (which generally increases with age), which causes spin dephasing from turbulence, as well as saturation effects from larger 3D volume acquisitions, adjacent motion, and other artifacts (such as adjacent artifact from bone and the subclavian veins' filling with contrast). The location of the VA origins, which may be at the edge of the field of view, can also be a problem. Recent studies suggest similar accuracy rates of CTA and CEMRA in detecting VA stenoses, but basically CTA (also affected by lower cervical artifacts) is slightly more specific in detecting VA stenoses greater than 50 %, whereas CEMRA is a bit more sensitive but slightly less specific. Hence, a VA-origin stenosis is readily detected by CEMRA, but may need to be confirmed in questionable cases by CTA or catheter DSA, as the specificity of CEMRA is not nearly as high as its sensitivity in evaluating the VAs.

Regarding the ICA, a perceived ICA-origin stenosis on CEMRA is usually real, but one needs to be aware of potentially misleading artifacts, as pseudo-stenoses may occasionally occur at the ICA origins on CEMRA for the reasons described above. One needs to be aware of such pitfalls and consider catheter DSA in some situations to confirm "critical" stenoses, especially prior to endovascular therapy or surgery (Figs. 43.16, 43.17, 43.18, 43.19, 43.20, 43.21, and 43.22).

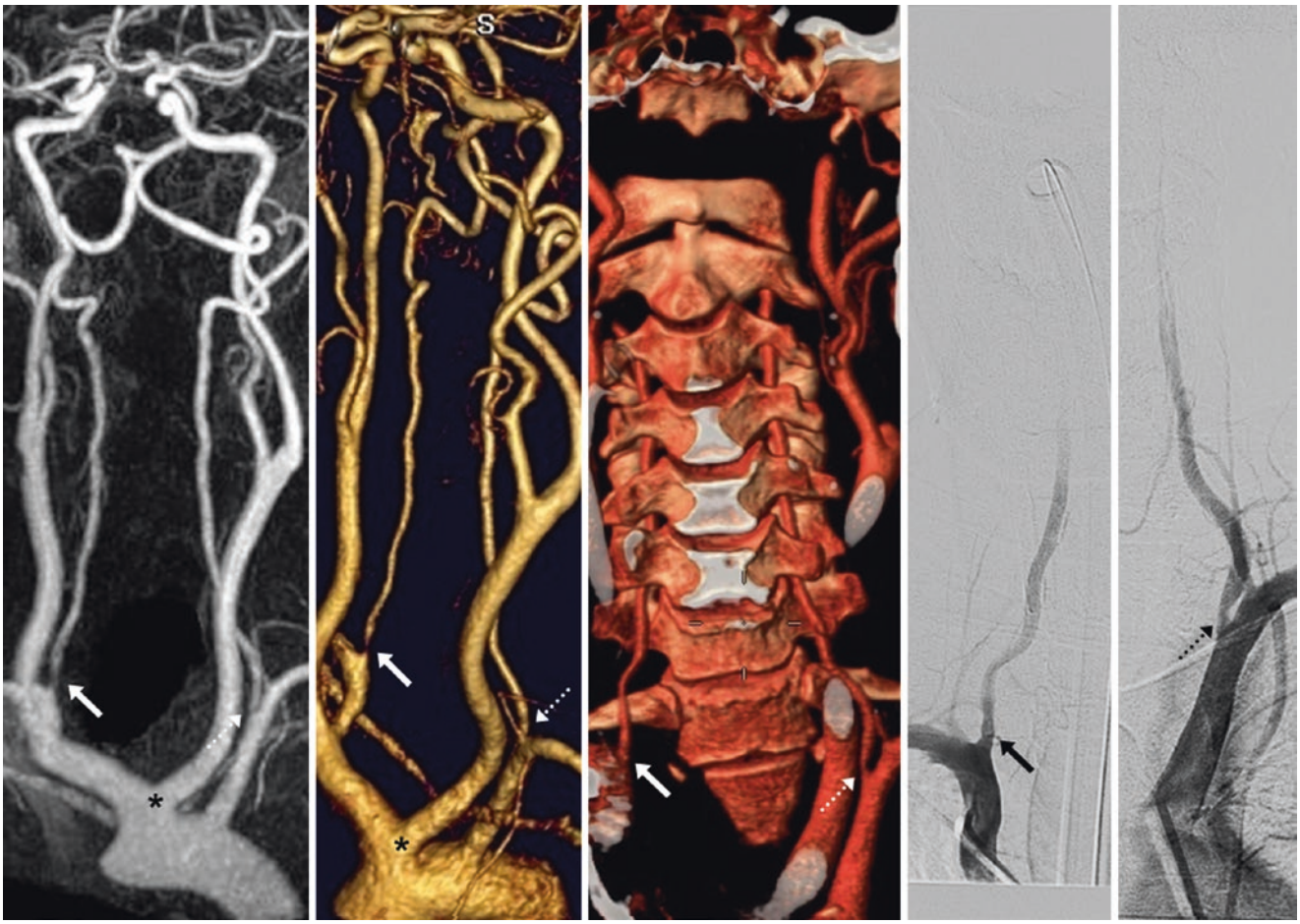

Fig. 43.16 Pseudo-stenosis and true stenosis. In this 62-year-old, a right VA origin stenosis (*arrows*) was suspected on a CEMRA oblique AP view (*left* and *left middle*), but was not apparent on a CTA 3D VR AP view (*middle*). DSA found no stenosis (*right middle*), but a 60% stenosis of the left VA origin was found (*dotted arrow*, *right*). Note a common origin of the left common carotid artery and innominate artery (*asterisks*, *left*)

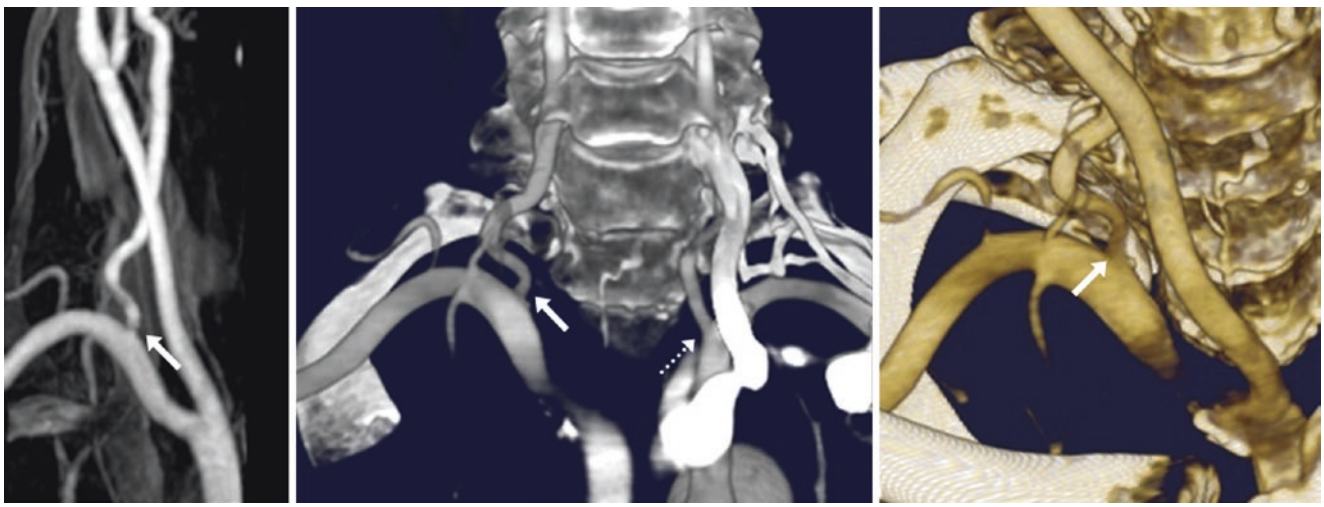

Fig. 43.17 Pseudo-stenosis 72-year-old with a right VA origin stenosis (*arrows*) suspected on a CEMRA AP view (*left*), but not present on a CTA with a 24 mm coronal MPR (*middle*) and a 3D VR AP view (*right*). The left VA (*dotted arrow*) was normal

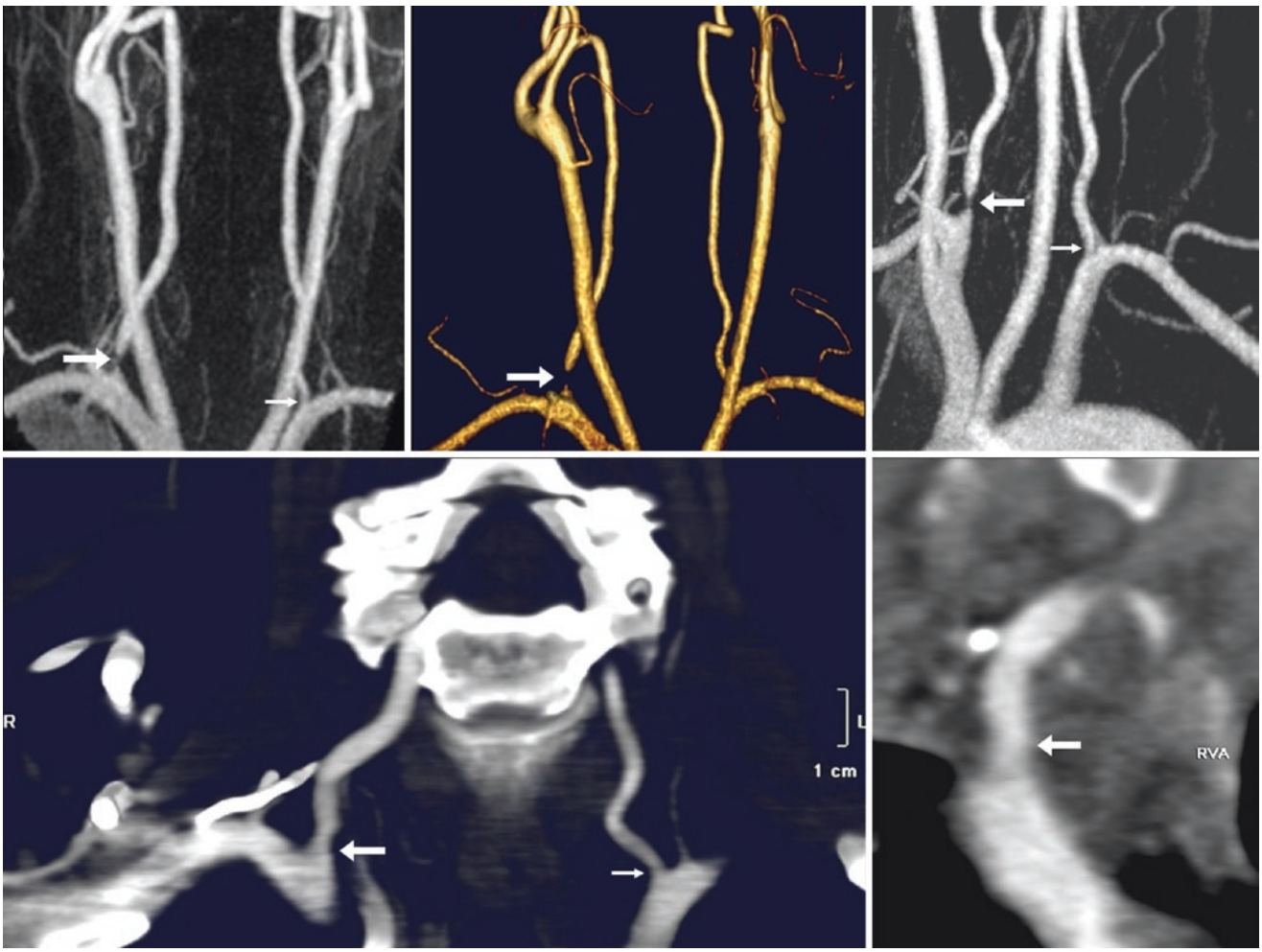

Fig. 43.18 Pseudo-stenosis *top row*: in this 55-year-old, a right VA origin stenosis (*arrows*) was questioned on CEMRA MIP (*left*) and on high-resolution 3D VR (*middle*) AP views, as well as on an LAO view (*right*). *Bottom row*: CTA with coronal 4.5 mm (*left*) and magnified sagittal 4.5 mm (*right*) MPRs confirmed right VA patency. Thus, the pseudo-stenosis was likely from turbulence. The left VA origin (*thin arrows*) was smaller, but appeared patent on the CEMRA

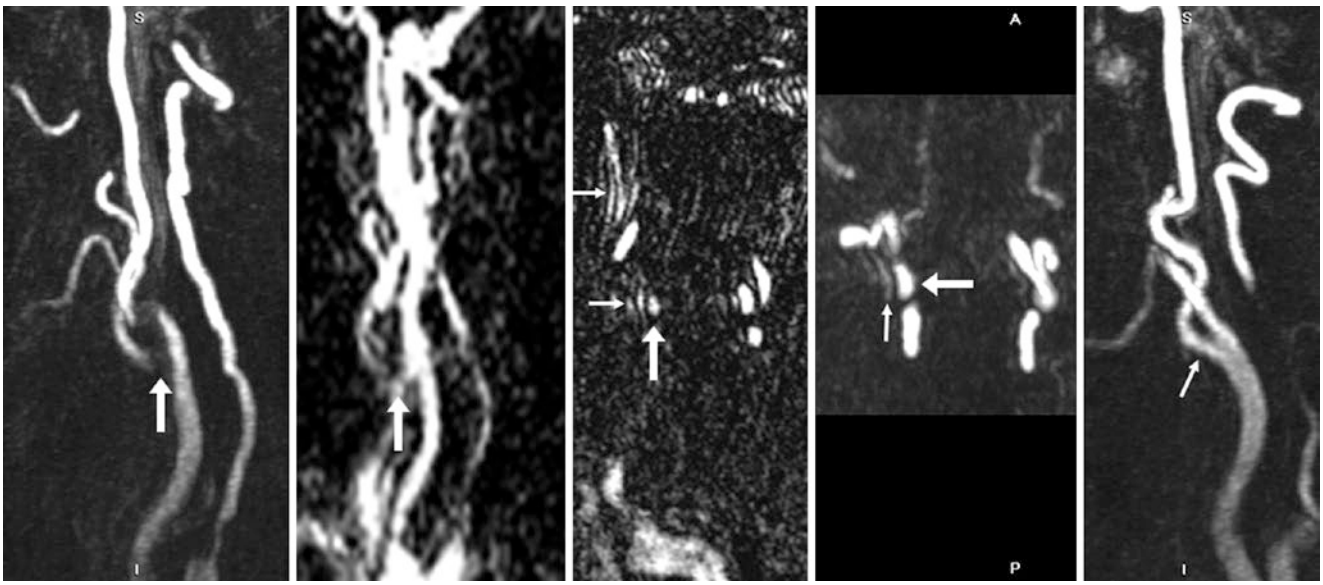

Fig. 43.19 Pseudo-stenosis 69-year-old with a possible stenosis (*arrows*) on a CEMRA lateral view of the right side (*left*). However, dynamic CEMRA scout views (used to "catch" the optimal time to begin the CEMRA acquisition) suggested that the right ICA origin was patent (*left middle*). Review of the coronal source data (*middle*) suggested that either motion or a subtraction artifact (*thin arrows*) was near the right ICA (*arrows*). A 20.5 mm axial MPR (*right middle*) best shows the artifact near the right ICA. The left ICA appeared normal on a CEMRA lateral view (*right*)

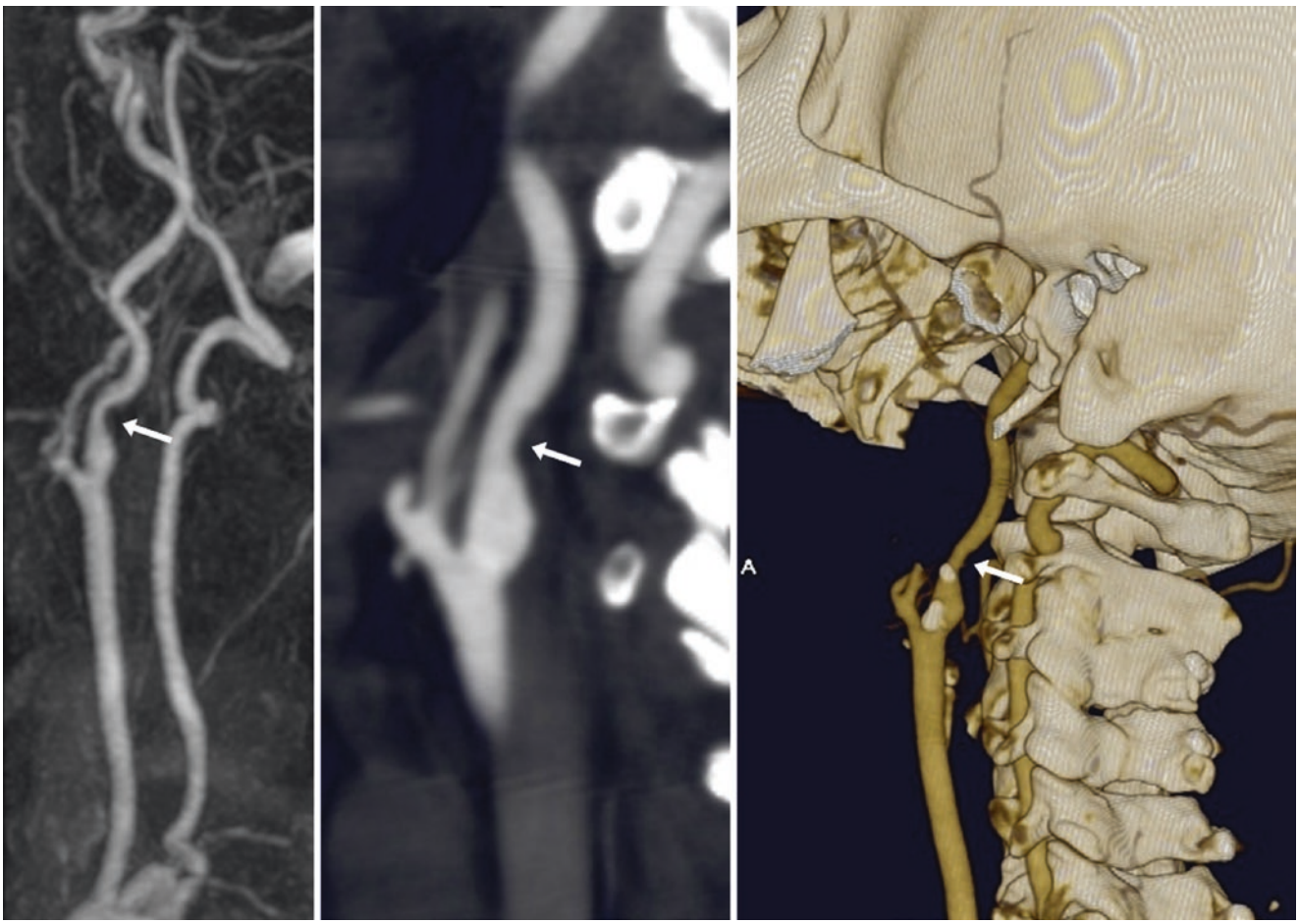

Fig. 43.20 Pseudo-stenosis in this 63-year-old, a CEMRA lateral view of the right ICA (*left*) suggested a mild to moderate stenosis (*arrows*). However, on a CTA, a sagittal MPR (*middle*) and a 3D VR lateral view with the external carotid artery and its branches removed (*right*) detected only minimal stenosis (<20 %) using North American Symptomatic Carotid Endarterectomy Trial (NASCET) criteria. The stenosis may have been exaggerated by turbulence, or it may have appeared worse due to the ICA's tortuosity

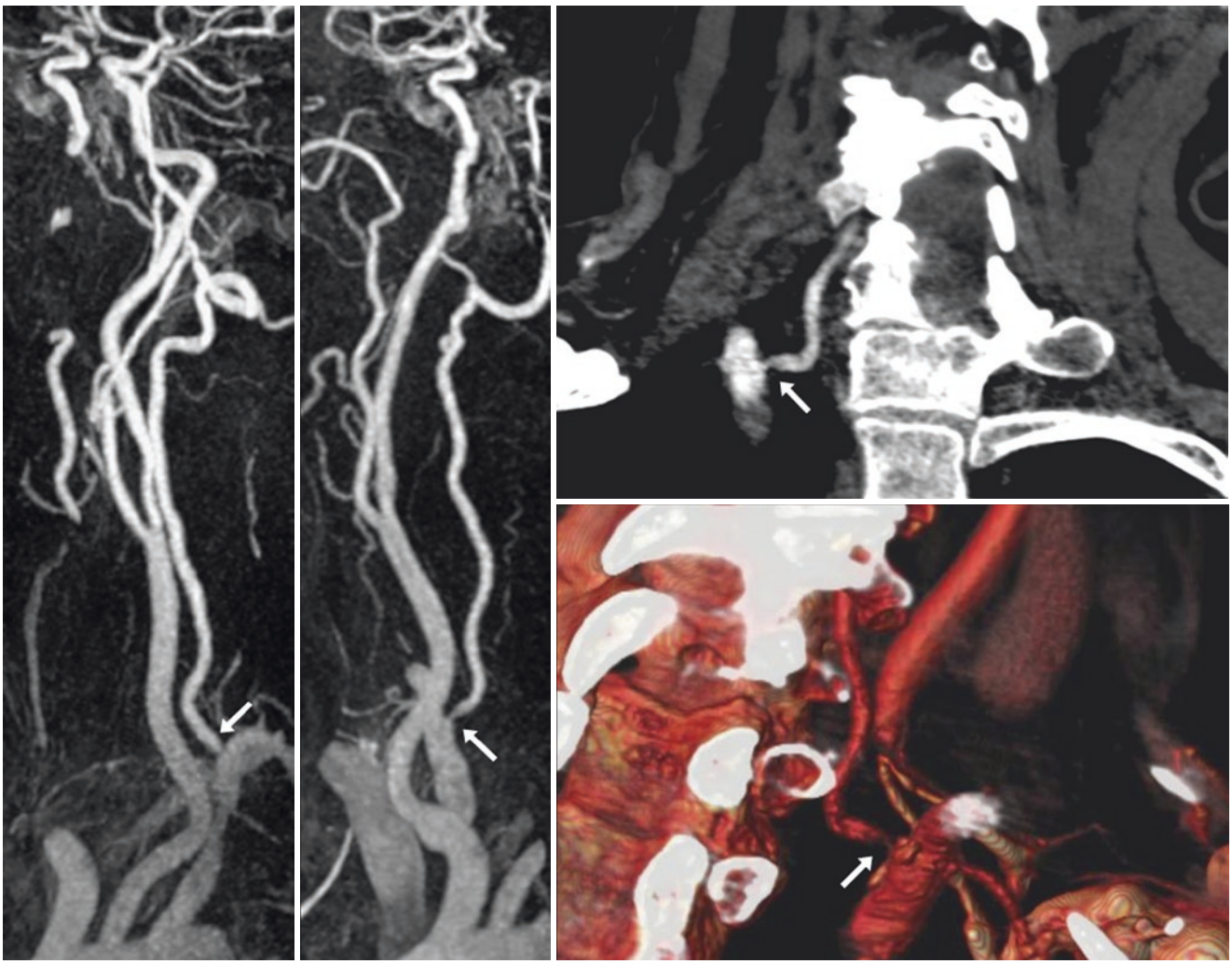

Fig. 43.21 Comparison Case of Actual VA Origin Stenosis on CEMRA. 87-year-old with a right VA stenosis (*arrows*) suspected on CEMRA oblique views (*left* and *middle*). The stenosis is confirmed by a CTA with coronal MPRs (*right, top*) and on a 3D VR RAO view (*right, bottom*)

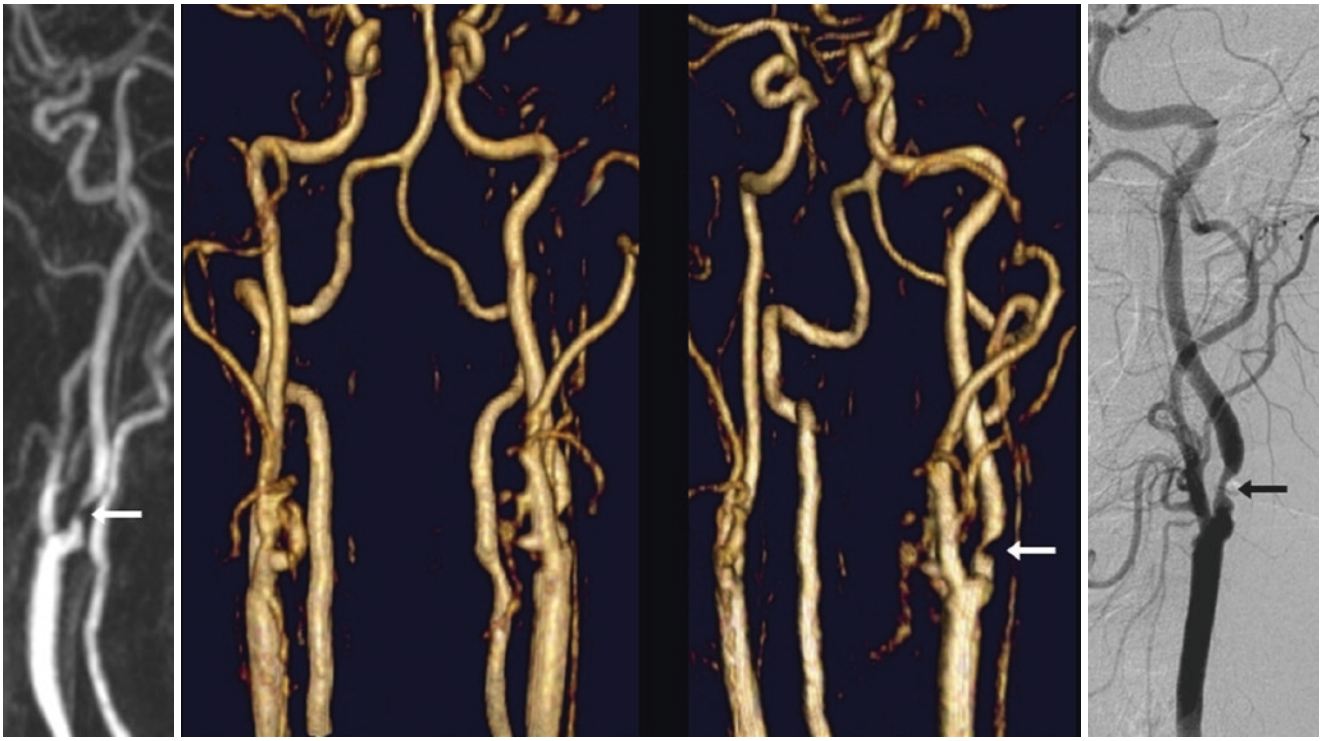

Fig. 43.22 Comparison case of an actual ICA stenosis on CEMRA. In this 62-year-old, a lateral view of the left ICA obtained from a CEMRA (*left*) demonstrated what was suspected to be a high-grade stenosis (*arrow*), which was obscured on an AP view (*left middle*) but better demonstrated on an LAO view (*right middle*). A catheter DSA (*right*) confirmed that the degree of left ICA origin stenosis was indeed "critical."

43.4 "In-Plane Saturation" on Time-of-Flight MR Angiography Simulating Stenosis (Pseudo-stenosis)

In-plane saturation effect relates to signal dropout that occurs in the plane of acquisition as spins traverse that plane. This is why the optimal plane of acquisition for TOF MRA is typically perpendicular to the expected direction of flow, such as axial MRA slices on a cervical MRA because the ICA predominantly flows vertically (cranially). This effect may be exacerbated by motion or turbulence. Turbulence often occurs in areas with very tight angles or multiple turns, such as in the cavernous or petrous ICAs, or with greater tortuosity with increasing patient age. In-plane saturation effects may also be exacerbated by true low-flow states such as in post-stenotic regions, where the segment distal to a stenosis is saturated easily, particularly as that vessel travels horizontally (Figs. 43.23, 43.24, 43.25, 43.26, 43.27, 43.28, 43.29, 43.30, and 43.31).

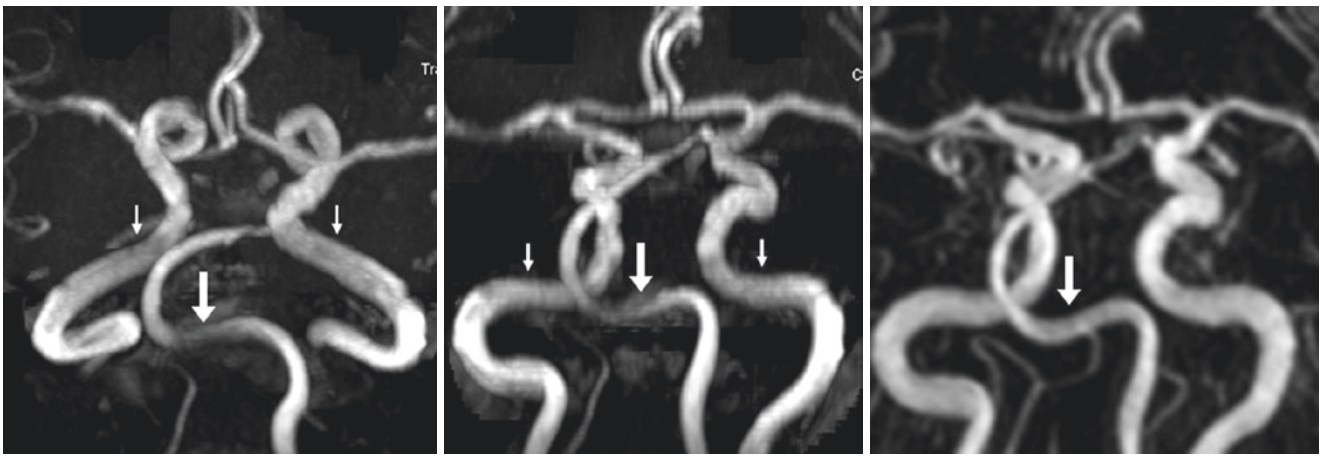

Fig. 43.23 Pseudo-stenosis in this 75-year-old, 3DTOF MRA superior (*left*) and AP (*middle*) views show signal loss from in-plane saturation in a tortuous basilar artery focally travelling horizontally (*large arrows*), simulating a stenosis. This effect is also present to a lesser degree in the petrous ICAs (*thin arrows*). A CEMRA AP view (*right*) appears normal

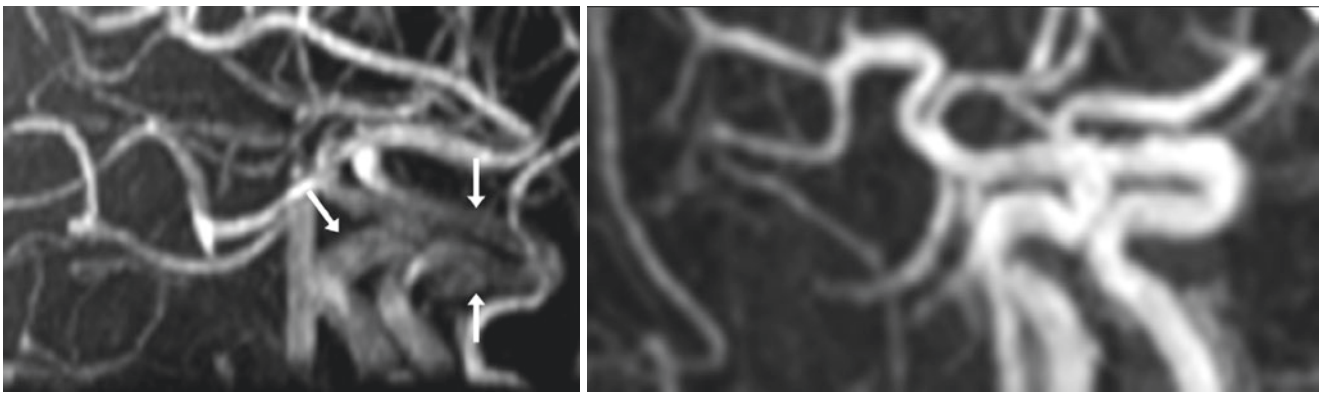

Fig. 43.24 Pseudo-stenosis in this 57-year-old, a 3DTOF MRA slightly oblique, lateral view (*left*) depicts severe signal loss of both ICAs in the distal cavernous/proximal supraclinoid segments (*arrows*), likely owing to tight turns with nearly horizontal, acute ICA angles; such angles predispose to saturation and turbulence. The CEMRA is normal (*right*)

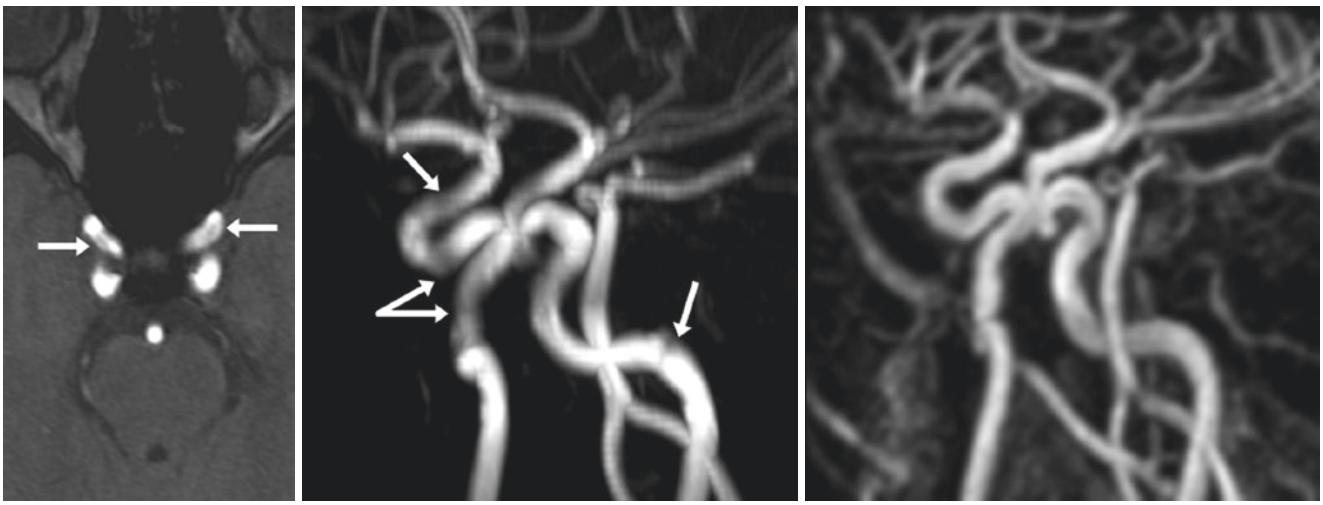

Fig. 43.25 Pseudo-stenosis in an 18-year-old, 3DTOF MRA source images (*left*) show focal, mild loss of flow-related enhancement (FRE) signal (*arrows*), also seen on LPO views (*middle*) in the cavernous and petrous ICAs (*arrows*). The signal loss is likely from in-plane saturation, in combination with turbulence. The ICAs' signal improves on CEMRA (*right*), although the CEMRA has less resolution

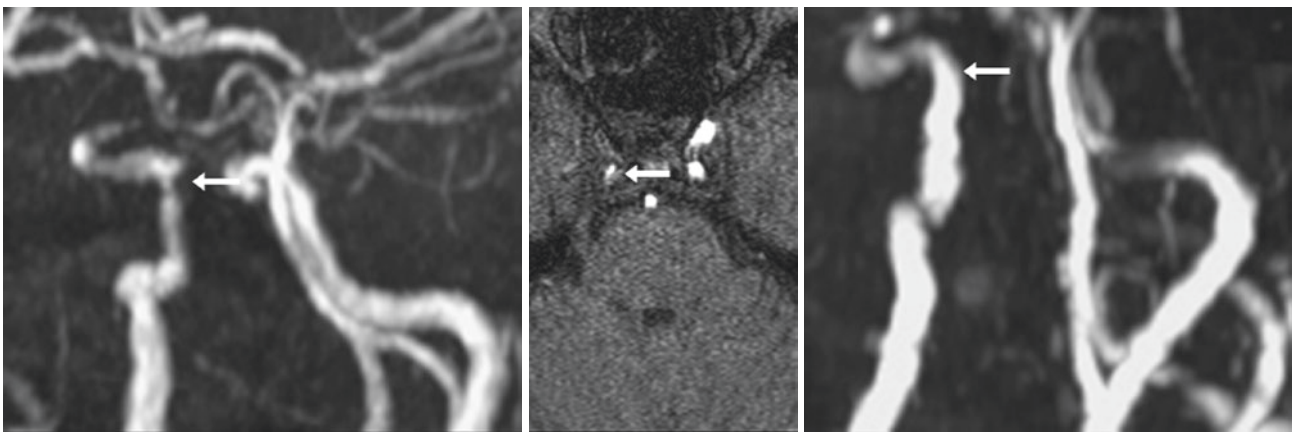

Fig. 43.26 Pseudo-stenosis this 47-year-old with renal failure was not given gadolinium contrast. A 3DTOF MRA oblique view (*left*) shows signal loss in the cavernous right ICA from turbulence (*arrows*), simulating a high-grade stenosis, also confirmed on axial source images (*middle*). A noncontrast upper cervical 2DTOF MRA (*right*) excludes a high-grade stenosis there

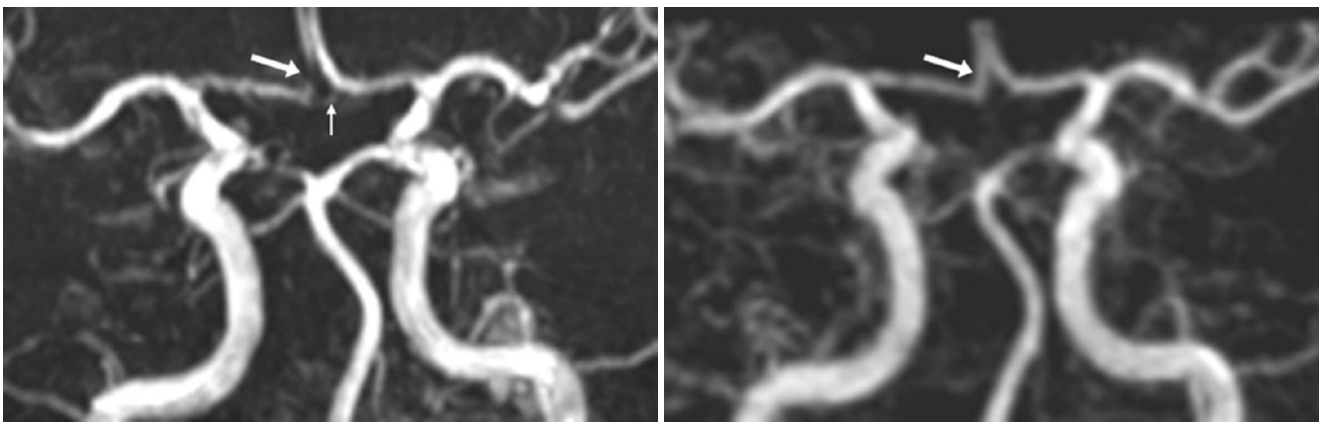

Fig. 43.27 Pseudo-stenosis 68-year-old with focal signal loss in the proximal A2 segment of the right anterior cerebral artery (*arrows*) on 3DTOF MRA AP view (*left*). However, on CEMRA (*right*), this area appears normal. The artifact was likely from turbulence and in-plane saturation. Note that the anterior communicating artery (*thin arrow*) is better depicted on 3DTOF MRA because of higher resolution

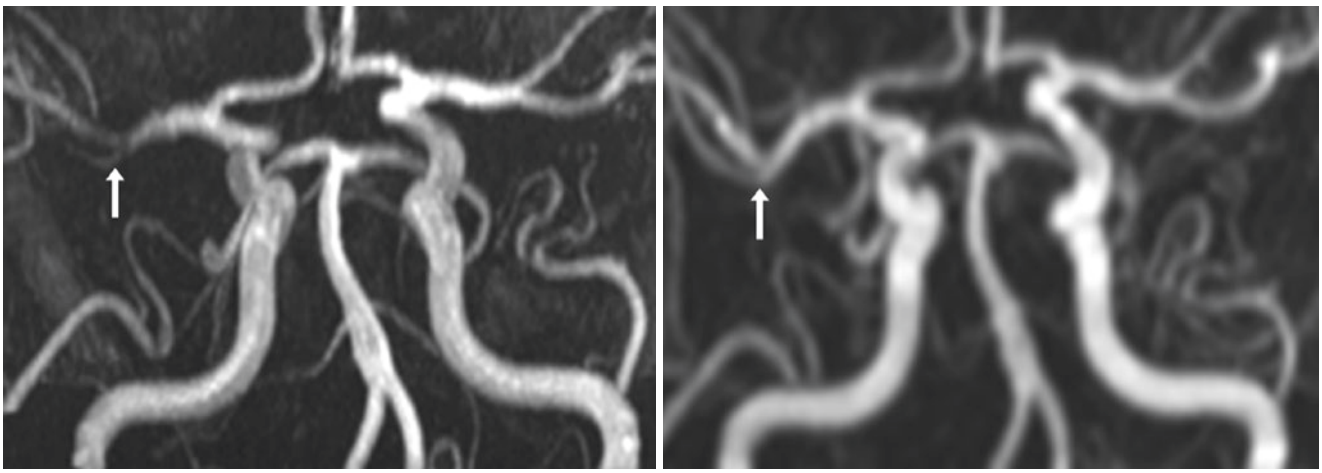

Fig. 43.28 Pseudo-stenosis 85-year-old with a simulated right middle cerebral artery (MCA) defect (*arrows*) on a 3DTOF MRA AP view (*left*). This defect was not seen on a CEMRA (*right*). The artifact was likely related to in-plane saturation effects, perhaps combined with turbulence, where the shorter T1 time of gadolinium contrast increases the contrast-to-noise ratio, even in tortuous or horizontal segments

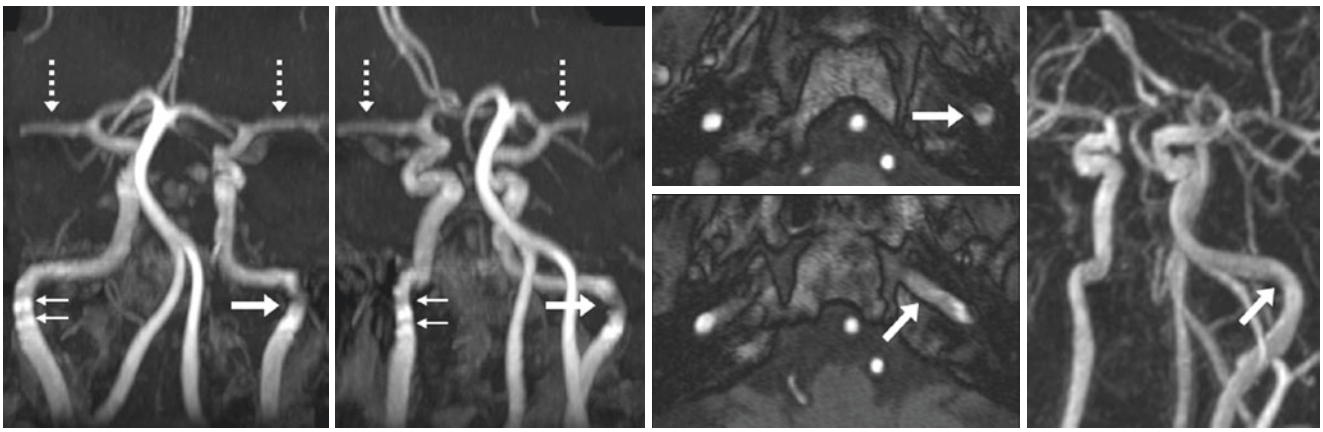

Fig. 43.29 Pseudo-stenosis in this 83-year-old, 3DTOF MRA AP (*left*) and oblique (*left middle*) views show loss of signal in the left petrous ICA as it enters the skull base, simulating a stenosis (*large arrows*). On source images (*right middle*), and on CEMRA (*right*), stenosis is not seen. The artifact is likely related to turbulence. Mild in-plane saturation effect is also noted in both proximal MCAs (*dotted arrows*). Note artifact affecting the right ICA upon skull base entry (*thin arrows*)

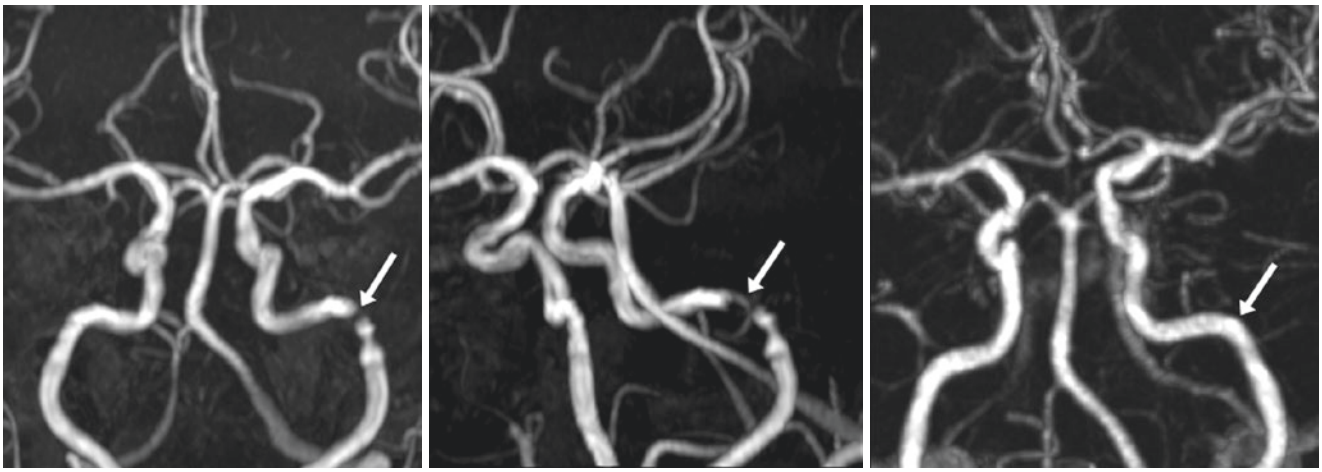

Fig. 43.30 Pseudo-stenosis in this 56-year-old, 3DTOF MRA AP (*left*) and oblique (*middle*) views show unilateral signal loss in the left petrous ICA as it enters the skull base, thus simulating a stenosis (*arrows*). An AP view from a CEMRA (*right*) appears normal. The pseudo-stenosis was likely related to artifacts from a combination of turbulence and in-plane saturation

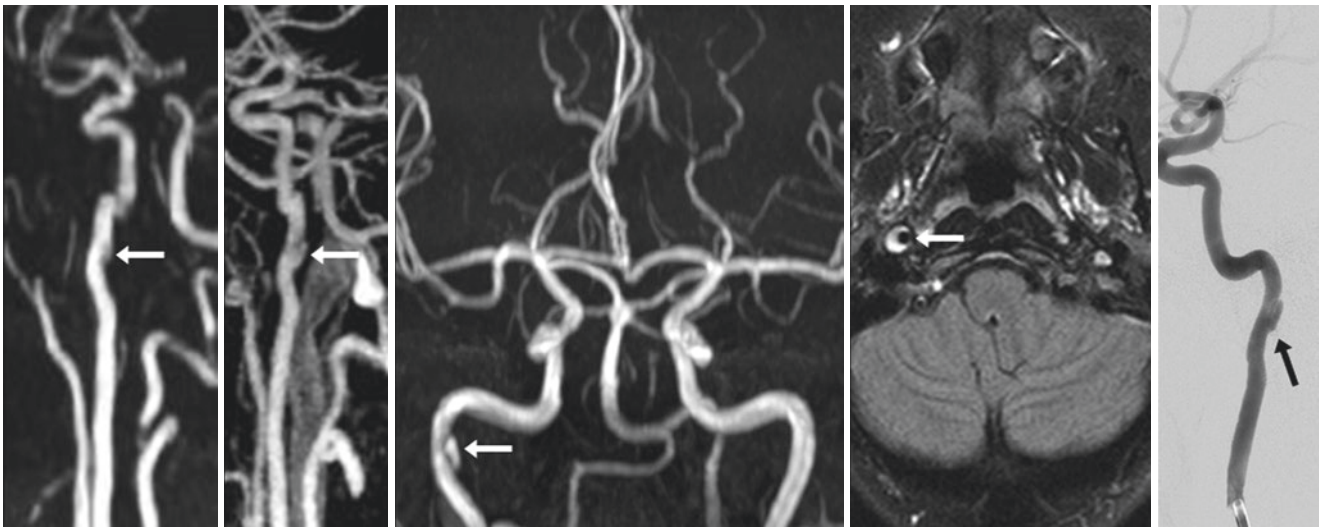

Fig. 43.31 Comparison case of ICA dissection. In this 45-year-old, 2DTOF MRA (*left*) and CEMRA (*left middle*) lateral views of the right ICA are indeterminate for arterial injury, whereas 3DTOF MRA (*middle*) and fat-suppressed FLAIR (*right middle*) suggest a lower petrous ICA outpouching or pseudoaneurysm (PSA, *arrows*). Catheter DSA (*right*) confirmed a PSA

43.5 Susceptibility, Motion, and Pulsation Artifacts Affecting MRA

As previously mentioned, other sources of artifacts quite commonly can cause varying degrees of MRA degradation and difficulty in interpretation, perhaps more often affecting cranial MRA evaluation rather than cervical [1–25]. Susceptibility artifacts can arise from adjacent sphenoid sinus air located medially, for example, and may obscure the cavernous ICAs. Similarly, mastoid aeration extending into the petrous apices can obscure the petrous ICA and simulate a stenosis. Head motion in any direction can cause image degradation; this problem may seem innocuous when only mild motion occurs, but it can simulate a vascular stenosis. Pulsation artifacts (carried along the phase direction) can also disrupt the appearance of flow, and typically occur along the phase direction of the image, most commonly from an ICA. As mentioned previously, CEMRA may reduce the appearance of pseudo-stenoses or pseudo-occlusions (Figs. 43.32, 43.33, 43.34, and 43.35). Parallel imaging artifact (occurring because the head has a larger transverse and anterior-posterior field to cover, compared with the neck), and "T1 shine-through" effects are discussed below.

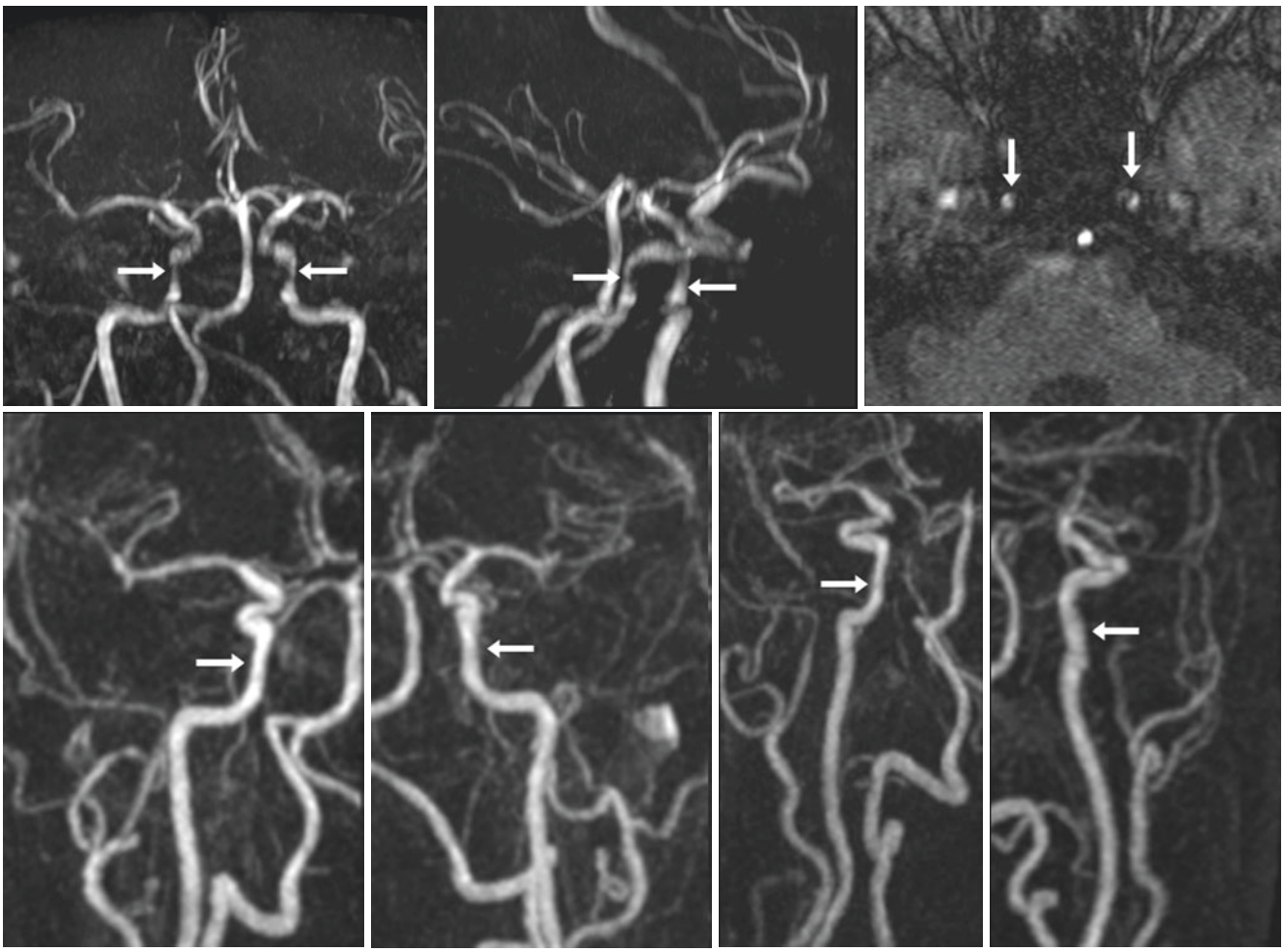

Fig. 43.32 Pseudo-stenosis in this 68-year-old, 3DTOF MRA AP (*top left*) and lateral (*top middle*) views illustrate bilateral cavernous ICA pseudo-stenoses due to signal loss (*arrows*) from motion/pulsation artifact in the phase direction (transverse plane), as confirmed on source data (*top right*). CEMRA AP (*bottom left*) and lateral (*bottom right*) views appear normal

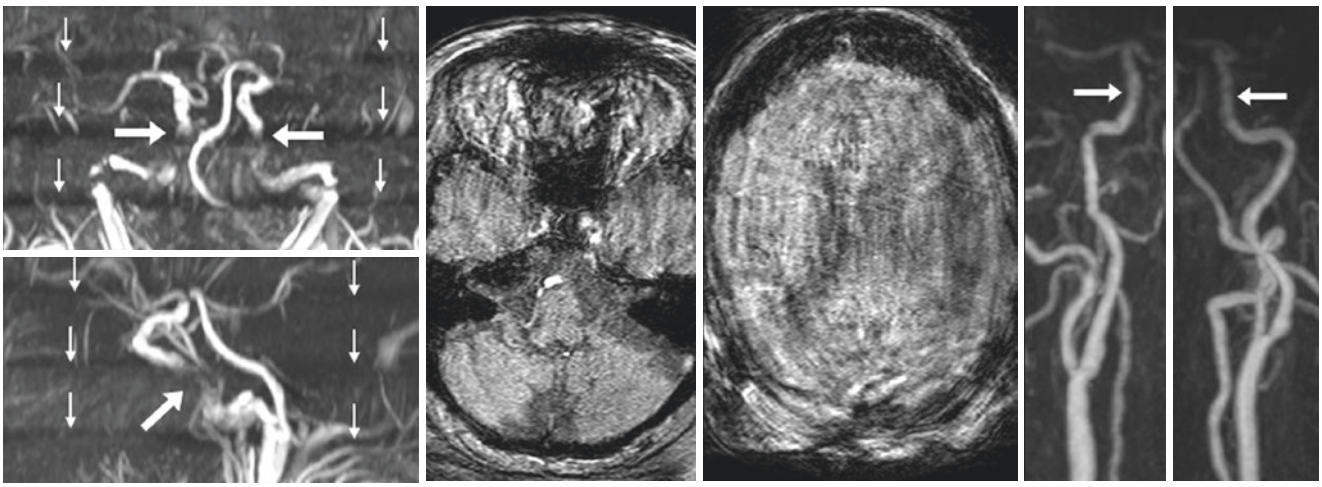

Fig. 43.33 Pseudo-stenosis in this 88-year-old, 3DTOF MRA AP (*top left*) and lateral (*bottom left*) views suffer from severe loss of FRE signal due to motion on source images (*left middle* and *middle*), causing bilateral cavernous ICA pseudo-stenoses (*arrows*). On CEMRA (*right images*), which is less affected by patient motion, these arteries are patent. Bands of motion artifact (*thin arrows*) exist between overlapping 2 cm-thick multiple overlapping thin slab acquisition (MOTSA) slabs, stacked together to construct the 3D MIP images

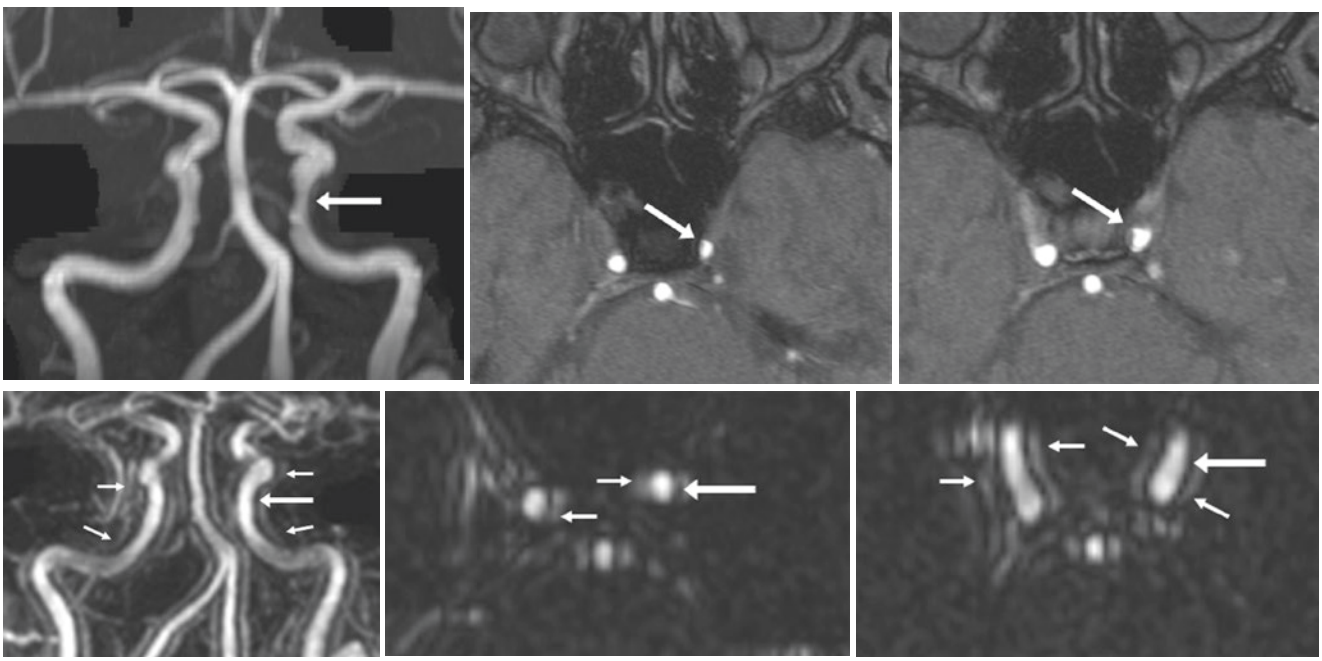

Fig. 43.34 Pseudo-stenosis *top row*: 83-year-old in whom the left cavernous ICA appears moderately narrowed (*arrows*) on a 3DTOF MRA AP view (*left*). An artifact from adjacent sphenoid sinus air and/or ICA pulsation is noted on axial source images (*middle* and *right*). *Bottom row*: CEMRA 3D MIP (*left*) and source images (*middle* and *right*) confirm ICA patency in that segment, but also suffer from motion artifact (*thin arrows*)

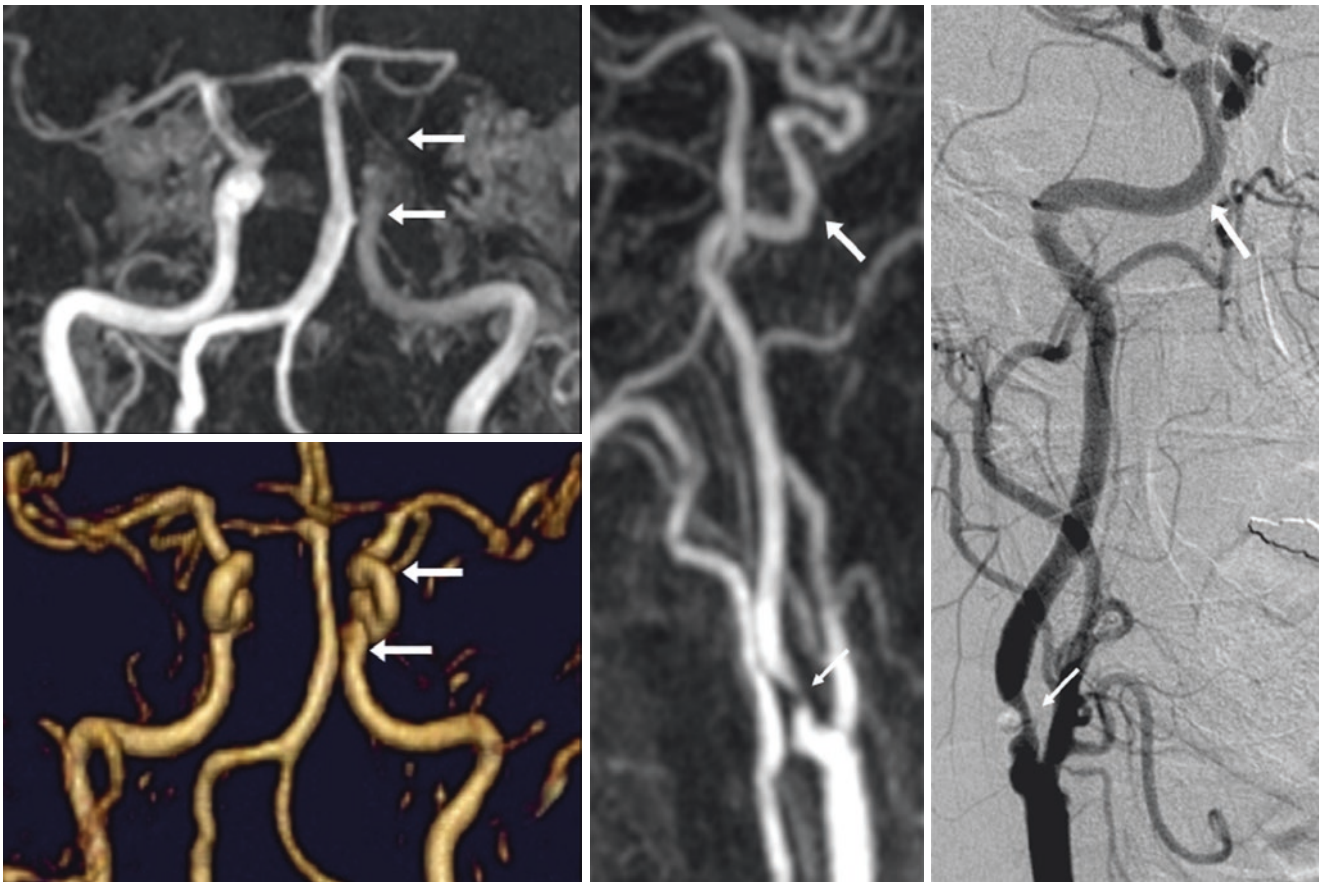

Fig. 43.35 Comparison case of poor visualization on MRA distal to a critical stenosis. On a 3DTOF MRA AP view (*top left*), the cavernous left ICA was not seen (*arrows*), but it was patent on AP (*bottom left*) and lateral (*middle*) views from a CEMRA. Catheter DSA (*right*) confirmed that the cavernous left ICA was patent. Thus, the apparent lack of intracranial flow on the initial MRA was due to the proximal, critical cervical ICA stenosis (*thin arrows, right*)

43.6 Sensitivity Encoding Parallel Imaging Unfolding Artifact on 3D TOF MRA

As parallel imaging is more commonly utilized, along with larger field strengths and improved coil signal-to-noise ratio (SNR) profiles, one should be aware of artifacts related to such. The intricacies of parallel imaging are too complex for the scope of this text, but a basic explanation should suffice for the purposes of discussing artifacts. In short, SENSE (Philips), mSENSE (Siemens), ASSET (GE), RAPID (Hitachi), and SPEEDER (Toshiba) are all acronyms that refer to a type of rapid acquisition of images using parallel imaging, in tandem with reconstruction via sensitivity encoding. Such parallel imaging utilizes two more separate surface coil elements of a phased array coil system (*ie*, a "multicoil multichannel system") to shorten acquisition time. Compared with reception by a single coil, faster imaging of an area of interest is possible by reconstructing the image using the "sensitivity profile." That is, the signal obtained from multiple elements is analyzed and reconstructed based on the signal's distance from the area of interest. The largest contribution to an image's signal from an area of interest is from signal that arises from the nearest coil; the contribution decreases with distance further away. Hence, via sensitivity encoding, each coil receives and contributes a portion of the signal, so the various components of the image can be obtained faster than an acquisition that does not implement SENSE. However, the tradeoff is a reduction in SNR, which is decreased by $1/\sqrt{(R)}$, where R is the "parallel factor." This decreased SNR can be mitigated to a degree by imaging at higher field strengths, such as at 3 T instead of 1.5 T.

Although artifacts related to parallel imaging sensitivity encoding can be noted in any part of the body and at any field strength (as discussed in the Brain section of this book), they are mentioned here because MRA at 3 T typically utilizes such techniques to obtain higher-quality images than at 1.5 T in a shorter amount of time. This artifact may cause the spurious appearance of abnormal vessels, such as from an aneurysm or arteriovenous anomaly, if one does not notice that the artifact occurs in the phase-encoding direction and originates from objects outside of the field of view (FOV). Such subtle or severe artifacts are due to aliasing with an incomplete selection of the FOV, where the selected FOV is significantly smaller than the patient's body part of interest. The artifactual signal that arises outside of the FOV forms signal centrally in the brain that most often arises from ears, face, scalp vessels, etc. This type of artifact, also termed "SENSE ghosting" or "unfolding artifact," can be corrected by either turning off the sensitivity-encoding factor or selecting a FOV larger than the region to be imaged, so that the reconstructive algorithm properly unfolds signals outside of the area of interest (Figs. 43.36, 43.37, and 43.38).

Fig. 43.36 Simulation of parallel imaging "unfolding" artifact. In this 55-year-old, 3DTOF MRA source images were performed at 3 T. The field of view (FOV) and SENSE parallel-imaging (PI) factor was turned "on" and "off" to create spurious artifact within the brainstem (*arrows*). The artifact on the leftmost image arises from the pinna of either ear (*thin arrows, right*), where both ears are located outside the FOV. The artifact is removed by either removing SENSE (*middle*), which doubles the scan time, or by widening the FOV with SENSE turned "on" (*right*). The best combination of scan time and quality is the rightmost image, where the entire FOV is covered with SENSE "on", albeit with a 50% greater scan time than when it is off. This time is faster than for the same quality at 1.5 T (*Images obtained with aid of* Luke Kim and John Saali, Philips Healthcare, Andover, MA, USA)

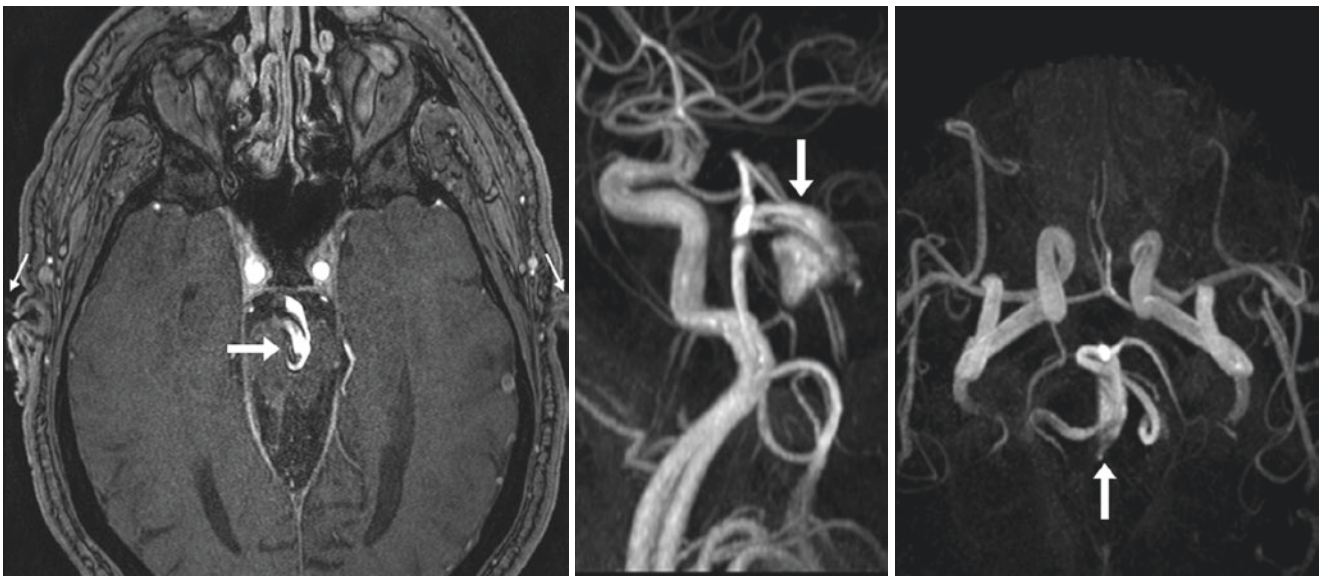

Fig. 43.37 In this 52-year-old, a 3 T 3DTOF MRA source image (*left*) demonstrates spurious signal within the brainstem (*arrows*) that simulates an aneurysm, as shown on 3D MIP lateral (*middle*) and superior (*right*) views. The artifact likely arises from the pinna of the ears, which are partially outside of the FOV (*thin arrows, left*)

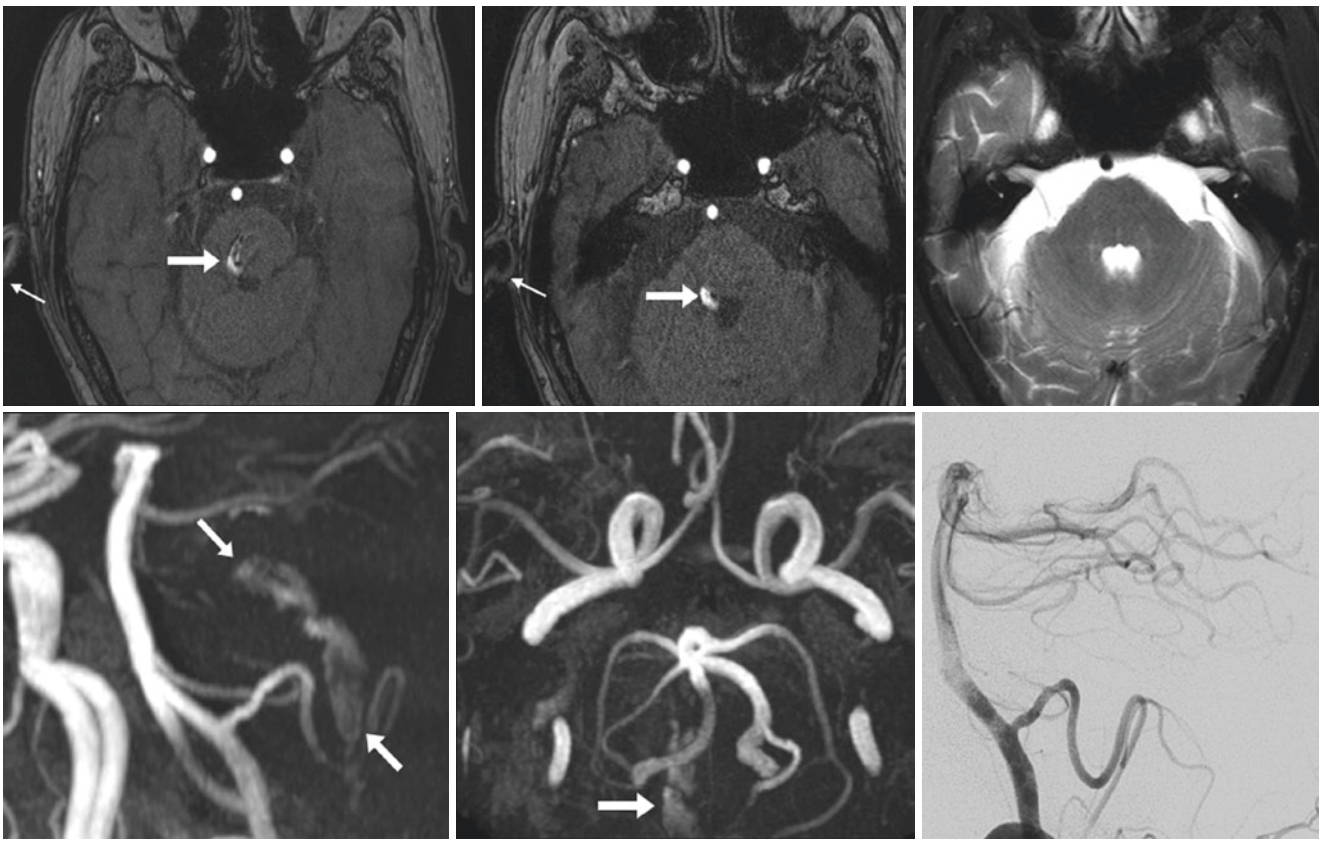

Fig. 43.38 *Top row*: in this 68-year-old, 3DTOF MRA source images (*left* and *middle*) illustrate spurious signal within the brainstem (*arrows*), not visualized on axial T2WI (*right*). *Bottom row:* the artifact was present on 3DTOF MRA MIP lateral (*left*) and superior (*middle*) views, but catheter DSA (*right*) was normal (although performed for a different reason). The artifact arises from the right ear, which is partially outside of the FOV (*thin arrows*)

43.7 "T1 Shine-Through" Effect on 3D Time-of-Flight MR Angiography

The term "T1 shine-through" refers to an appearance in which artifacts, lesions, gadolinium-based contrast, or hemorrhage—having extremely shortened T1 relaxation times—are seen on the 3DTOF MRA or MRV source or MIP images, but are not related to patent, flowing vasculature. Normally, only faster-flowing vessels traveling superiorly on cranial MRA are visualized (with inferiorly traveling spins saturated to appear dark), owing to the constant entry of fresh blood ("fresh spins") into the cranium (*ie*, flow-related enhancement [FRE]). T1 shortening caused by "T1 shine-through" effects can be related to normal findings (such as fatty marrow in the clivus, orbital fat, or the normally bright posterior lobe of the pituitary gland); actual abnormalities (such as subacute age hemorrhages or thrombosed aneurysms that are T1-bright); MRI artifacts (such as aliasing, CSF pulsation, or arterial pulsation); or residual gadolinium contrast. (In a patient with renal failure, for example, contrast may persist within lesions or the vasculature for several days.) Notably, this "T1 shine-through" effect can also occur within vasculature (or enhancing lesions) on SWI (Figs. 43.39, 43.40, 43.41, 43.42, 43.43, and 43.44).

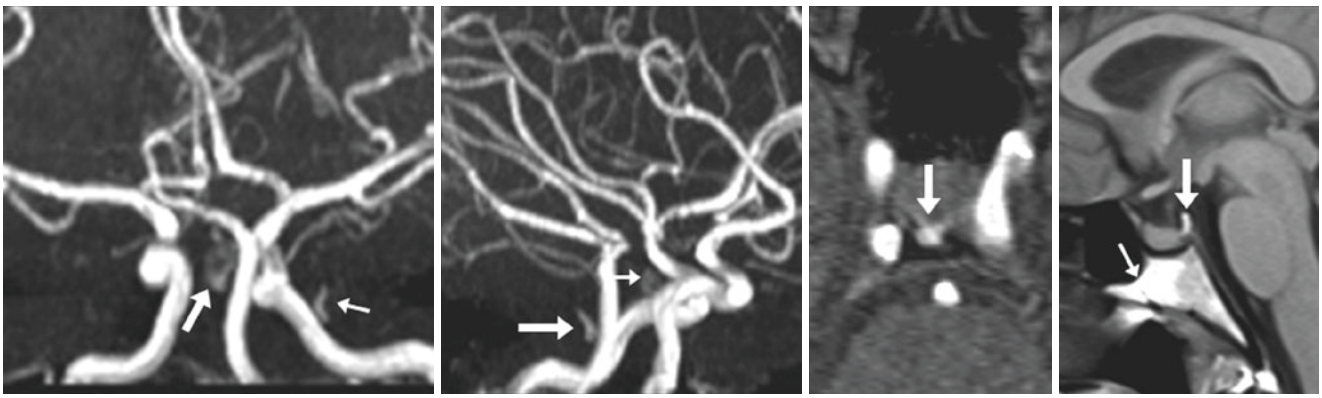

Fig. 43.39 In this 36-year-old, 3DTOF MRA MIP AP (*left*) and lateral (*left middle*) views demonstrate "T1 shine-through" effect from normally T1-bright posterior pituitary lobe (*arrows*) and from T1-bright clival marrow (*thin arrows*). The T1-bright signal in both locations is confirmed on 3DTOF MRA source images (*right middle*) and on sagittal T1WI (*right*)

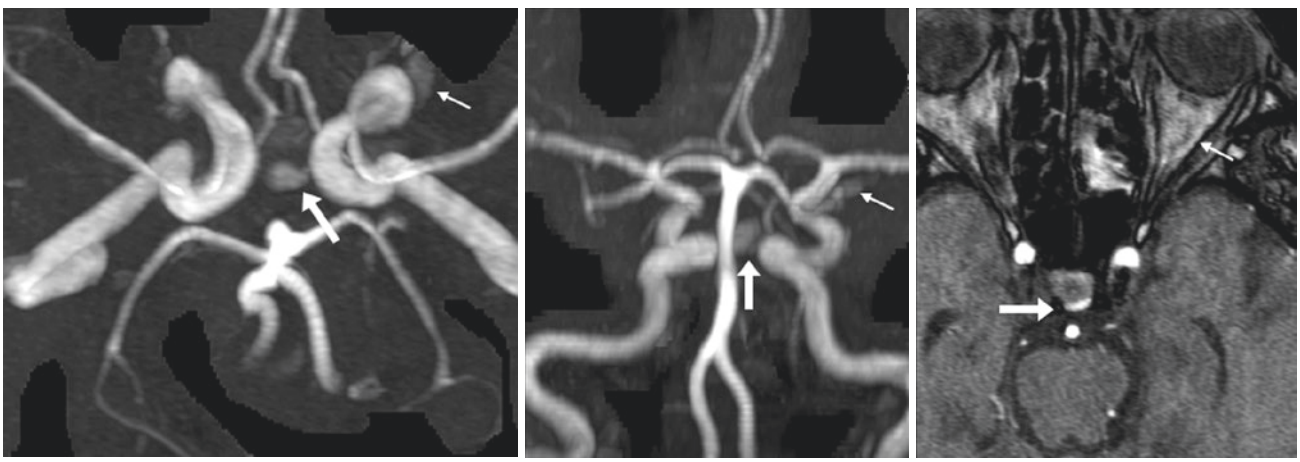

Fig. 43.40 In this 73-year-old, 3DTOF MRA MIP superior (*left*) and AP (*middle*) views illustrate "T1 shine-through" effect from normally T1-bright posterior pituitary lobe (*arrows*), as well as from T1-bright orbital fat (*tiny arrows*). The T1-bright signal in such locations is confirmed on the 3DTOF MRA axial source images (*right*)

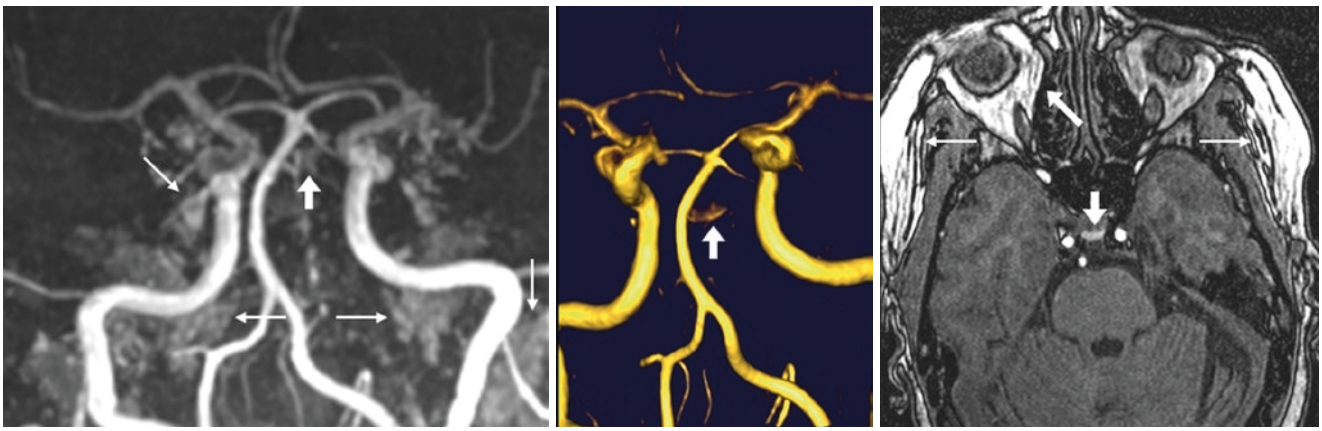

Fig. 43.41 In this 65-year-old, a 3DTOF MRA MIP AP view (*left*) is affected by diffuse "T1 shine-through" due to scalp and orbital fat (*thin arrows*), with a normal T1-bright posterior pituitary lobe (*arrows*), which is better seen after scalp and orbital fat are removed (*middle*). Axial source 3DTOF MRA images (*right*) best illustrate the extent of T1-bright scalp fat

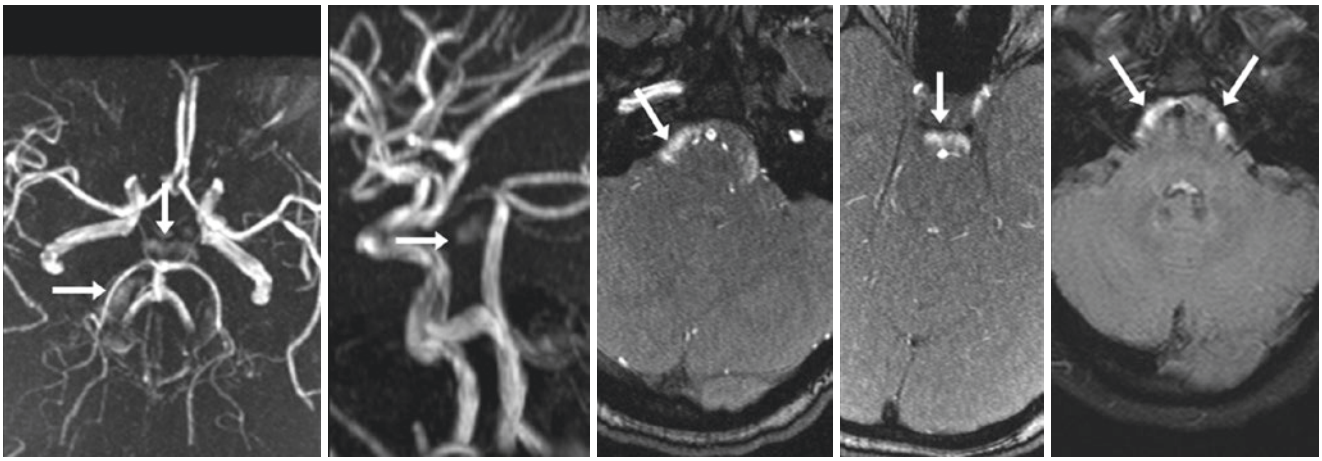

Fig. 43.42 In this 20-year-old, 3DTOF MRA MIP superior (*left*) and lateral (*left middle*) views demonstrate "T1 shine-through" within the basal cisterns (*arrows*), arising from pronounced CSF pulsation artifact surrounding the brainstem. This appearance is confirmed by the axial source images for the MRA (*middle, right middle*), and on FLAIR MRI (*right*)

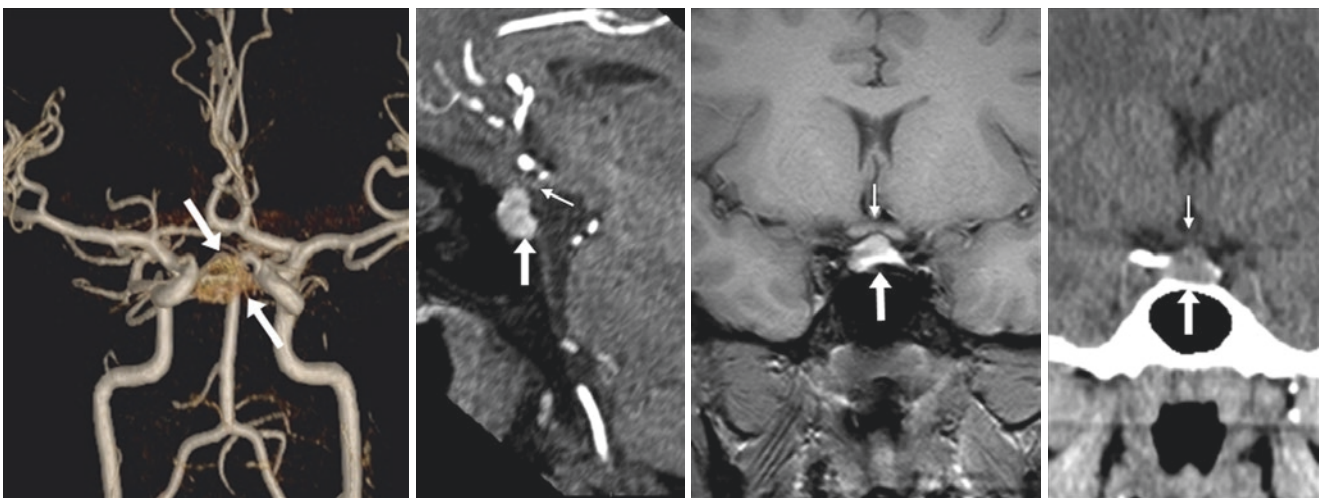

Fig. 43.43 Comparison case of pituitary hemorrhage. 20-year-old woman who was 2 days postpartum with headaches. A 3DTOF MRA MIP AP view (*left*) illustrates "T1 shine-through" obscuring the basilar artery tip (*arrows*); this was confirmed to be hemorrhage on source MRA sagittal reformats (*left middle*), and on coronal T1WIs (*right middle*), with mass effect on the optic chiasm (*thin arrows*). A coronal nonenhanced CT (*right*) also demonstrates the hemorrhage

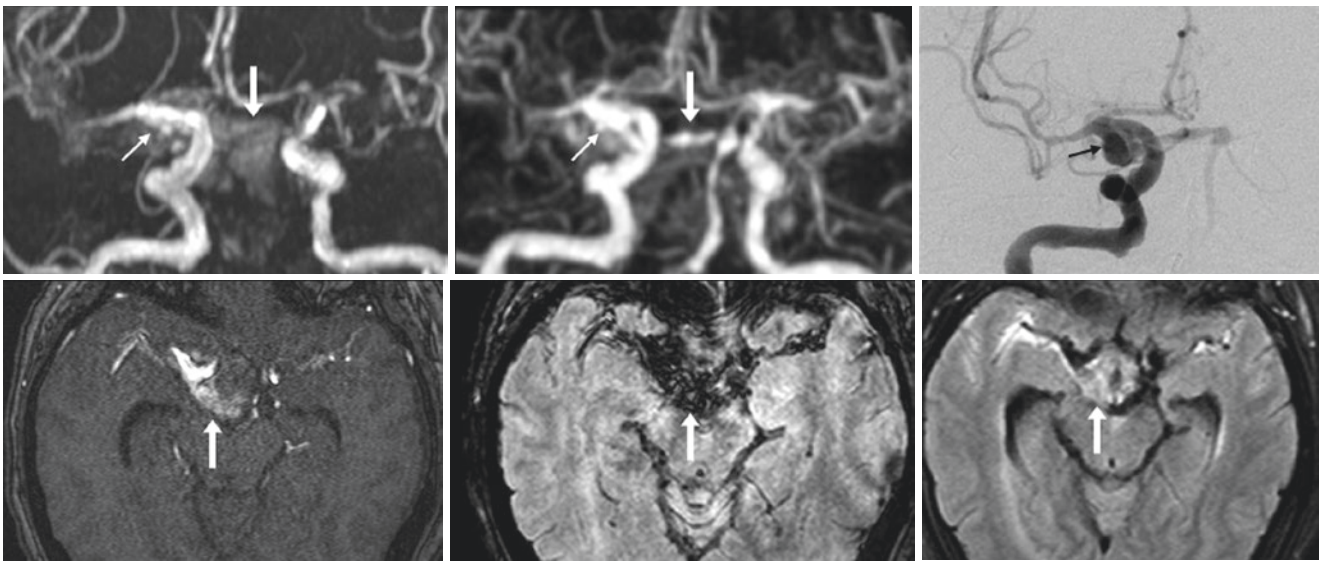

Fig. 43.44 Comparison case of subarachnoid hemorrhage. *Top row*: in this 69-year-old, "T1 shine-through" is seen on a 3DTOF MRA AP view (*left*), arising from subacute subarachnoid hemorrhage (SAH) (*arrows*) within the suprasellar cistern that surrounds and obscures a distal right ICA aneurysm (*thin arrows*). This effect is not as severe on CEMRA (*middle*), but the aneurysm remains obscured due to T1-bright SAH. (Note: SAH is not as bright as contrast, as the T1 time of contrast is shorter.) A DSA AP view (*right*) confirms the aneurysm. *Bottom row*: at the level of the midbrain, the subacute SAH appears bright on 3DTOF MRA source images (*left*), dark on SWI (*middle*), and bright on FLAIR (*right*)

References

1. Gullberg GT, Wehrli FW, Shimakawa A, Simons MA. MR vascular imaging with a fast gradient refocusing pulse sequence and reformatted images from transaxial sections. Radiology. 1987;165:241–6.
2. Needell WM, Maravilla KR. MR flow imaging in vascular malformations using gradient recalled acquisition. AJNR Am J Neuroradiol. 1988;9:637–42.
3. Tsuruda JS, Halbach VV, Higashida RT, Mark AS, Hieshima GB, Norman D. MR evaluation of large intracranial aneurysms using cine low flip angle gradient-refocused imaging. AJR Am J Roentgenol. 1988;151:153–62.
4. Parker DL, Yuan C, Blatter DD. MR angiography by multiple thin slab 3D acquisition. Magn Reson Med. 1991;17:434–51.
5. Hausmann R, Lewin JS, Laub G. Phase-contrast MR angiography with reduced acquisition time: new concepts in sequence design. J Magn Reson Imaging. 1991;1:415–22.
6. Chakeres DW, Schmalbrock P, Brogan M, Yuan C, Cohen L. Normal venous anatomy of the brain: demonstration with gadopentetate dimeglumine in enhanced 3-D MR angiography. AJR Am J Roentgenol. 1991;156:161–72.
7. Anderson CM, Haacke EM. Approaches to diagnostic magnetic resonance carotid angiography. Semin Ultrasound CT MR. 1992;13:246–55.
8. Blatter DD, Bahr AL, Parker DL, Robison RO, Kimball JA, Perry DM, Horn S. Cervical carotid MR angiography with multiple overlapping thin-slab acquisition: comparison with conventional angiography. AJR Am J Roentgenol. 1993;161:1269–77.
9. Ding X, Tkach JA, Ruggieri PR, Masaryk TJ. Sequential three-dimensional time-of-flight MR angiography of the carotid arteries: value of variable excitation and postprocessing in reducing venetian blind artifact. AJR Am J Roentgenol. 1994;163:683–8.
10. Bosmans H, Wilms G, Marchal G, Demaerel P, Baert AL. Characterisation of intracranial aneurysms with MR angiography. Neuroradiology. 1995;37:262–6.
11. Talagala SL, Jungreis CA, Kanal E, Meyers SP, Foo TK, Rubin RA, Applegate GR. Fast three-dimensional time-of-flight MR angiography of the intra-cranial vasculature. J Magn Reson Imaging. 1995;5:317–23.
12. Cloft HJ, Murphy KJ, Prince MR, Brunberg JA. 3D gadolinium-enhanced MR angiography of the carotid arteries. Magn Reson Imaging. 1996;14:593–600.
13. Nesbit GM, DeMarco JK. 2D time-of-flight MR angiography using concatenated saturation bands for determining direction of flow in the intracranial vessels. Neuroradiology. 1997;39:461–8.
14. Alexander AL, Buswell HR, Sun Y, Chapman BE, Tsuruda JS, Parker DL. Intracranial black-blood MR angiography with high-resolution 3D fast spin echo. Magn Reson Med. 1998;40:298–310.
15. Willig DS, Turski PA, Frayne R, Graves VB, Korosec FR, Swan JS, et al. Contrast-enhanced 3D MR DSA of the carotid artery bifurcation: preliminary study of comparison with unenhanced 2D and 3D time-of-flight MR angiography. Radiology. 1998;208:447–51.
16. Slosman F, Stolpen AH, Lexa FJ, Schnall MD, Langlotz CP, Carpenter JP, Goldberg HI. Extracranial atherosclerotic carotid artery disease: evaluation of non-breath-hold three-dimensional gadolinium-enhanced MR angiography. AJR Am J Roentgenol. 1998;170:489–95.
17. Scarabino T, Carriero A, Magarelli N, Florio F, Giannatempo GM, Bonomo L, Salvolini U. MR angiography in carotid stenosis: a comparison of three techniques. Eur J Radiol. 1998;28:117–25.
18. Fellner FA, Fellner C, Wutke R, Lang W, Laub G, Schmidt M, et al. Fluoroscopically triggered contrast-enhanced 3D MR DSA and 3D time-of-flight turbo MRA of the carotid arteries: first clinical experiences in correlation with ultrasound, x-ray angiography, and endarterectomy findings. Magn Reson Imaging. 2000;18:575–85.
19. Al-Kwifi O, Emery DJ, Wilman AH. Vessel contrast at three Tesla in time-of-flight magnetic resonance angiography of the intracranial and carotid arteries. Magn Reson Imaging. 2002;20:181–7.
20. Jeong EK, Parker DL, Tsuruda JS, Won JY. Reduction of flow-related signal loss in flow-compensated 3D TOF MR angiography, using variable echo time (3D TOF-VTE). Magn Reson Med. 2002;48:667–76.

21. Ozsarlak O, Van Goethem JW, Parizel PM. 3D time-of-flight MR angiography of the intracranial vessels: optimization of the technique with water excitation, parallel acquisition, eight-channel phased-array head coil and low-dose contrast administration. Eur Radiol. 2004;14:2067–71.
22. Gibbs GF, Huston 3rd J, Bernstein MA, Riederer SJ, Brown Jr RD. Improved image quality of intracranial aneurysms: 3.0-T versus 1.5-T time-of-flight MR angiography. AJNR Am J Neuroradiol. 2004;25:84–7.
23. Ozsarlak O, Van Goethem JW, Maes M, Parizel PM. MR angiography of the intracranial vessels: technical aspects and clinical applications. Neuroradiology. 2004;46:955–72.
24. DeMarco JK, Willinek WA, Finn JP, Huston 3rd J. Current state-of-the-art 1.5 T and 3 T extracranial carotid contrast-enhanced magnetic resonance angiography. Neuroimaging Clin N Am. 2012;22:235–57.
25. Pandey S, Hakky M, Kwak E, Jara H, Geyer CA, Erbay SH. Application of basic principles of physics to head and neck MR angiography: troubleshooting for artifacts. Radiographics. 2013;33:E113–23.

Artifacts on Craniocervical CT Angiography

44

With the advent in the late 1990s of multichannel, multidetector (also called "multislice") technology for CT, and its subsequent implementation, the performance of CT angiography (CTA) has been augmented in terms of coverage, speed, and dose efficiency. Overall, perhaps more than 95 % of examinations are interpretable and have adequate contrast attenuation (>150 HU), and more than 85 % have adequate difference in contrast density (>50 HU) between arteries and veins for the purpose of CTA [1–5]. However, there are a number of artifacts that can limit CTA evaluation and potentially lead to false interpretation [1–5]. Kim et al. [1] describe these artifacts in detail, but for the purposes of discussion here, these are the most common:

- Streak artifact from reflux of dense contrast material in adjacent veins, such as within a subclavian vein or brachiocephalic vein that may obscure visualization of an adjacent common carotid artery or vertebral artery
- Streak artifact or decreased attenuation horizontally due to the shoulders
- Streak or beam-hardening artifact from metal such as dental amalgam
- Flow-related artifacts due to the high speed of multislice CT acquisition
- Motion artifacts

It is not uncommon for more than one type of artifact to affect a study in various ways. For example, metallic streak or motion artifacts may limit evaluation or simulate stenoses near the carotid bifurcation, and metallic streak artifact or shoulder streak artifact may completely obscure the great vessel origins; in particular, streak artifact from the dense bones (shoulders) may occasionally entirely obscure the vertebral arteries' origins. Overall, the newest versions of 128-section or 256-section scanners are less affected by streak from bone, dental amalgam, or venous pooling or reflux of contrast, in part because of the increased number of detectors, but also through the advent of newer reconstruction algorithms such as iterative reconstruction (a concept discussed further in the Brain section of this book).

The 64-section CT scanners have shown decreased artifacts and increased detection of vascular lesions (such as aneurysms or stenoses) with significantly decreased scan time relative to the 16-slice and 4-slice scanners [6–9]. However, as the newer 64-section, 128-section, and 256-section CT scanners can cover the whole head and neck in a matter of seconds, they may have a greater predisposition to flow-related artifacts than slower scanners (such as 16-slice and lower) because the scanner speed will "outstrip" the contrast bolus, potentially leading to the appearance of a pseudodissection [1] (Figs. 44.1, 44.2, 44.3, 44.4, 44.5, 44.6, 44.7, 44.8, 44.9, 44.10, 44.11, 44.12, 44.13, 44.14, 44.15, and 44.16).

A.M. McKinney, *Atlas of Normal Imaging Variations of the Brain, Skull, and Craniocervical Vasculature*,
DOI 10.1007/978-3-319-39790-0_44

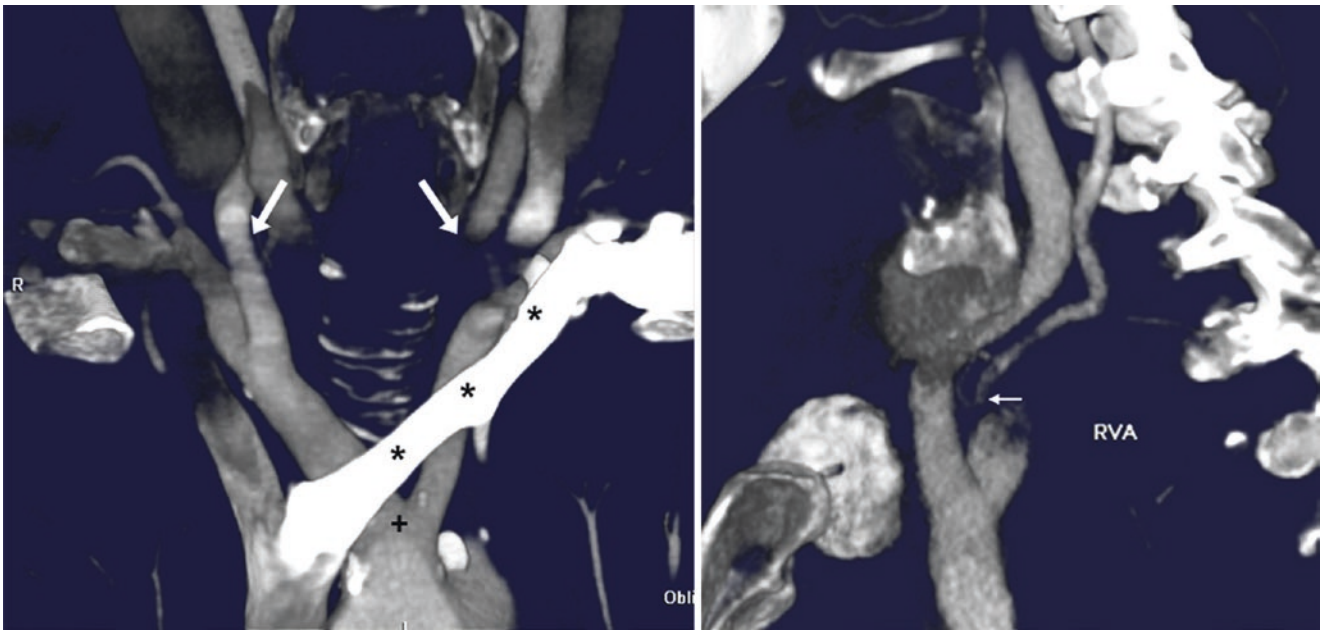

Fig. 44.1 80-year-old with contrast reflux artifact. A neck CTA illustrates contrast reflux into, and severe streak artifact from, the left brachiocephalic vein (BCV) and subclavian vein (SCLV) (*asterisks*). The streak obscures the left common carotid artery (CCA), along with the right CCA to a lesser degree (*arrows*), on a coronal 21 mm MPR (*left*). The right vertebral artery (VA) origin is also obscured (*thin arrow, right*), thus simulating a stenosis

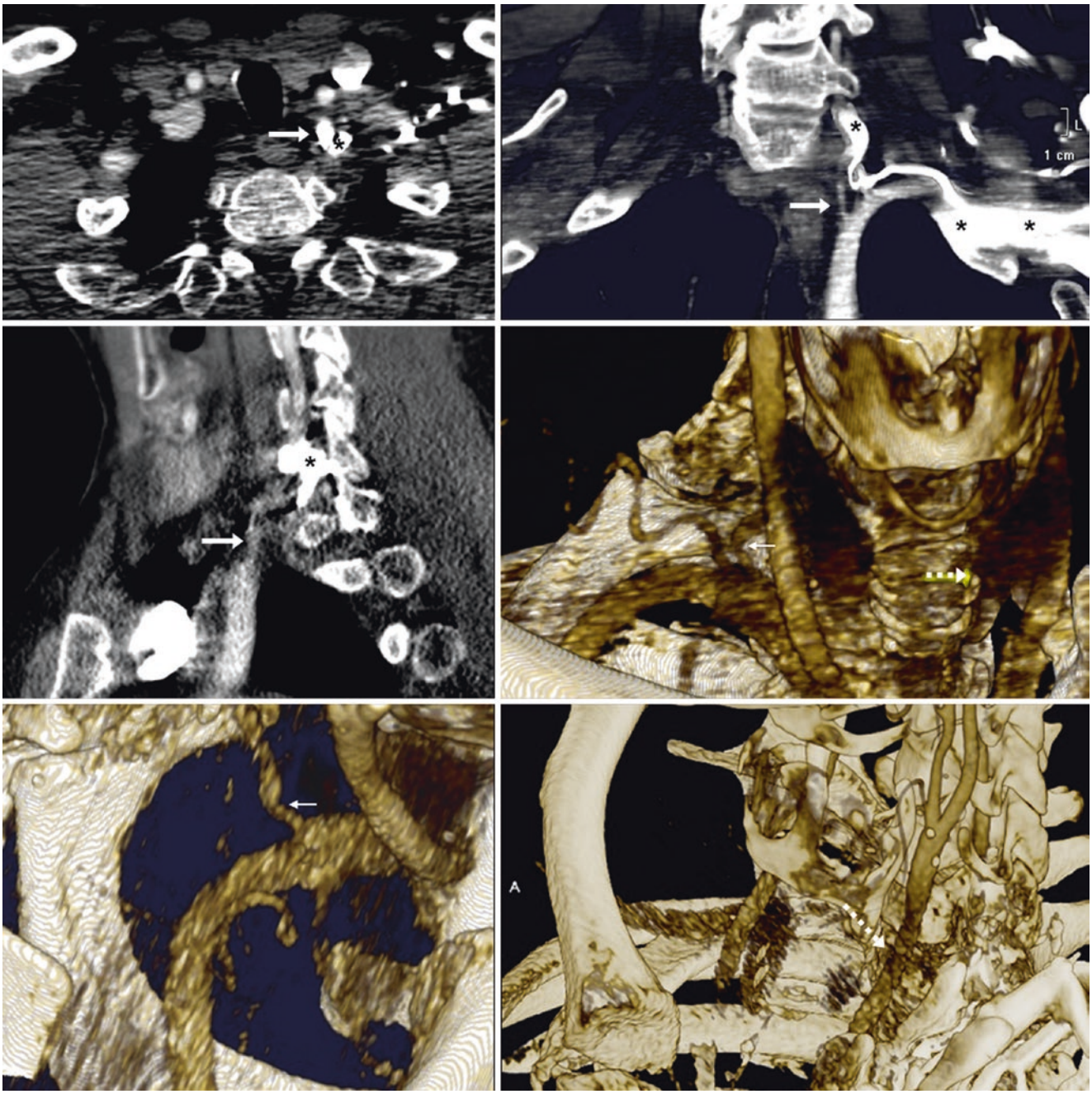

Fig. 44.2 65-year-old with contrast reflux artifact. *top row*: on a neck CTA, there is reflux (*asterisk*) into the left SCLV and vertebral venous plexus (VVP) on axial (*left*) and coronal (*right*) MPRs. *Middle row:* contrast reflux is also visible on sagittal MPR (*left*), and a 3D VR AP view (*right*) demonstrates how the artifact obscures most arterial origins, including the right VA origin (*thin arrows*) and the left CCA (*dotted arrows*). These streak artifacts, along with shoulder streak artifact, obscure the left VA origin (*arrows*) and could simulate a stenosis. *Bottom row:* a 3D VR superior view of the right side (*left*) illustrates the obscured origin of the right VA, and a 3D VR LAO view (*right*) shows that the lower left CCA is obscured as well

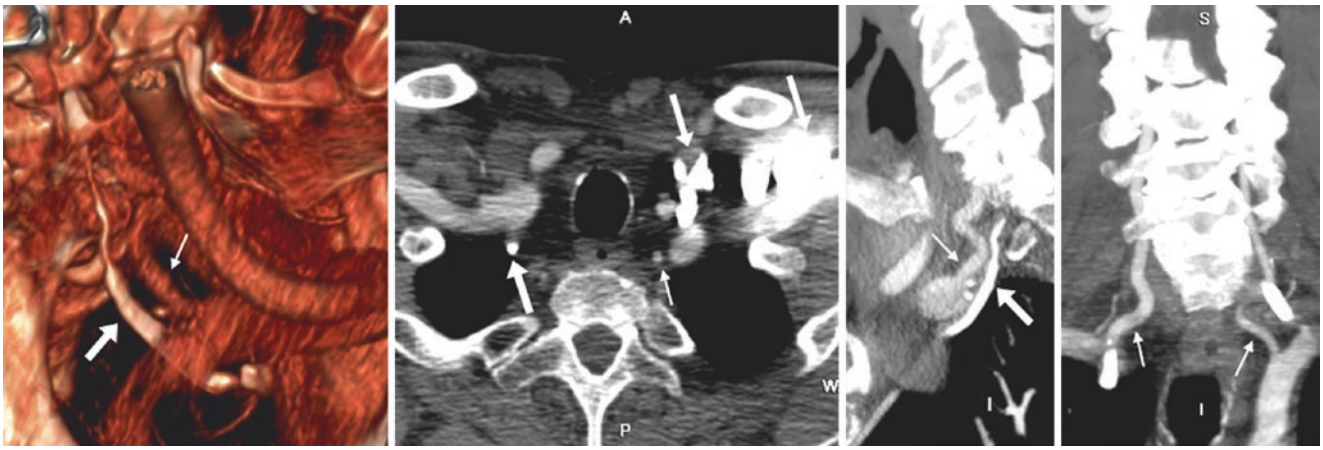

Fig. 44.3 78-year-old with contrast reflux artifact. On a CTA, it was difficult to discern the left VA (*thin arrows*) from the left vertebral vein/plexus (VVP, *arrows*) on a 3D VR LAO view (*left*). Axial images (*left middle*), a 6 mm MPR sagittal view of the right VA (*right middle*), and a coronal view of the VAs (*right*) all demonstrated contrast reflux from the SCLVs into both VVPs, greater on the left than on the right (*arrows*). These images also confirmed that both VA origins were patent (*thin arrows*)

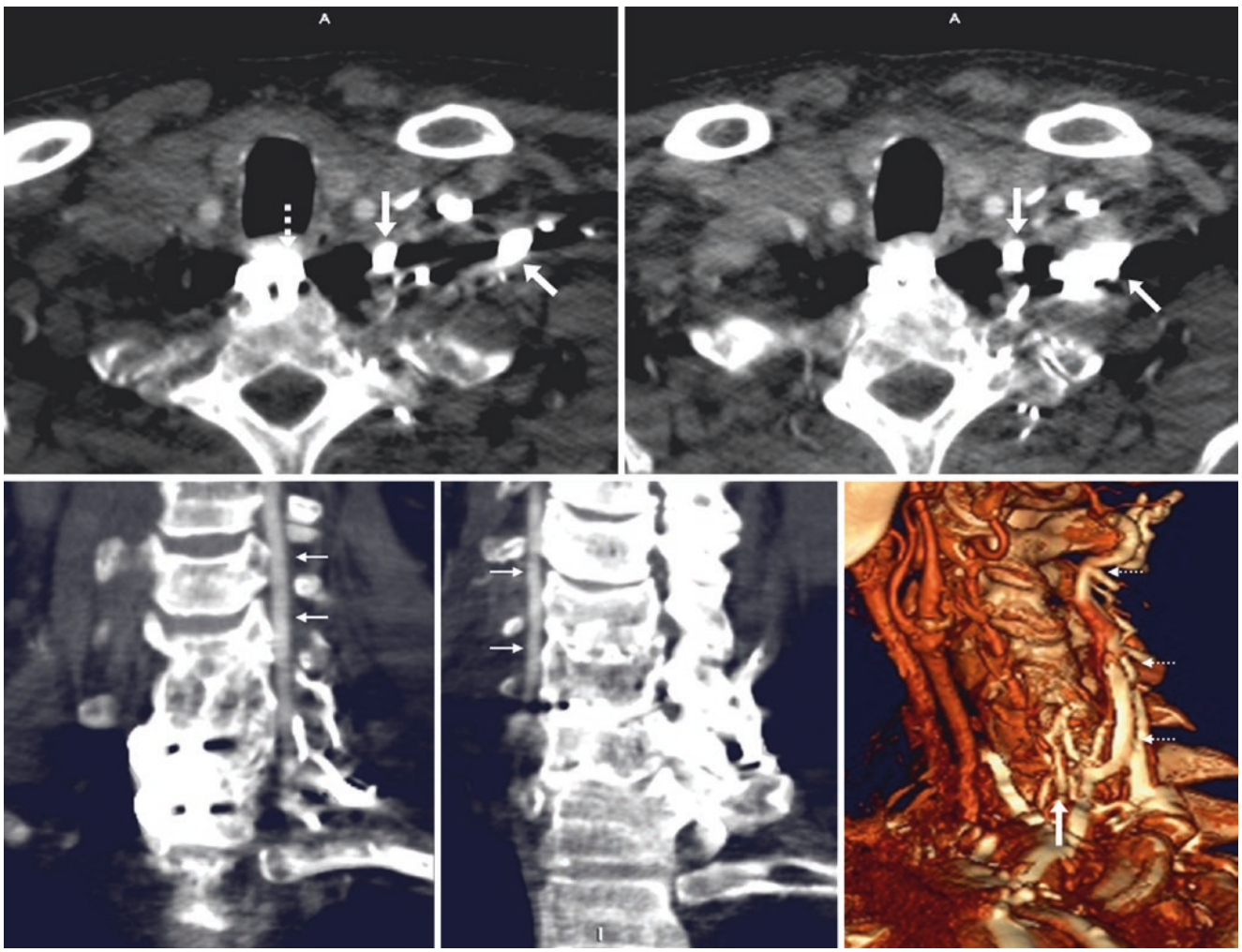

Fig. 44.4 68-year-old with multiple contributors to severe streak artifact. *Top row:* on a CTA, streak artifact is related to contrast reflux into the left SCLV and VVP (*arrows*), which, along with metallic streak artifact from anterior cervical fusion (*dotted arrows*) made it impossible to discern the lower VAs on axial images. *Bottom row:* superiorly, the VAs (*thin arrows*) are patent, as shown on coronal MPRs of the left VA (*left*) and right VA (*middle*). A 3D VR left lateral view (*right*) shows that contrast reflux extends cephalad into posterior cervical veins (*tiny dotted arrows*), and further up to the skull base

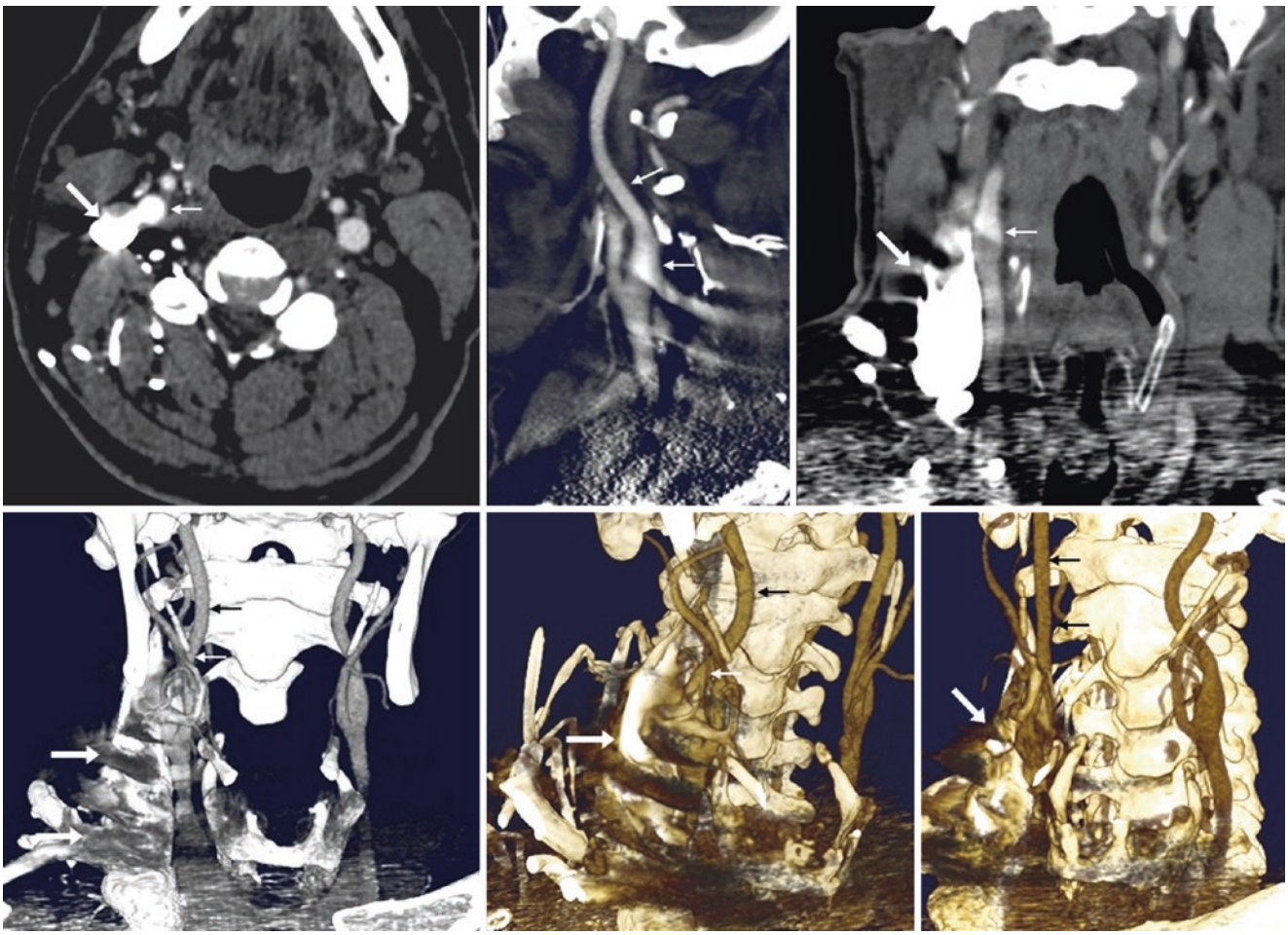

Fig. 44.5 43-year-old with severe contrast reflux artifact. *Top row*: streak artifact arises from contrast reflux that extends cephalad into the right internal jugular vein (*arrows*). It is difficult to assess the right internal carotid artery (ICA) (*thin arrows*) on axial (*left*), sagittal (*middle*), and coronal (*right*) MPRs. *Bottom row:* 30 mm thick coronal MPRs (*left*), as well as RAO (*middle*) and LAO (*right*) 3D VR images, demonstrate how the upwards contrast reflux obscures visualization of the adjacent right ICA near the carotid bifurcation

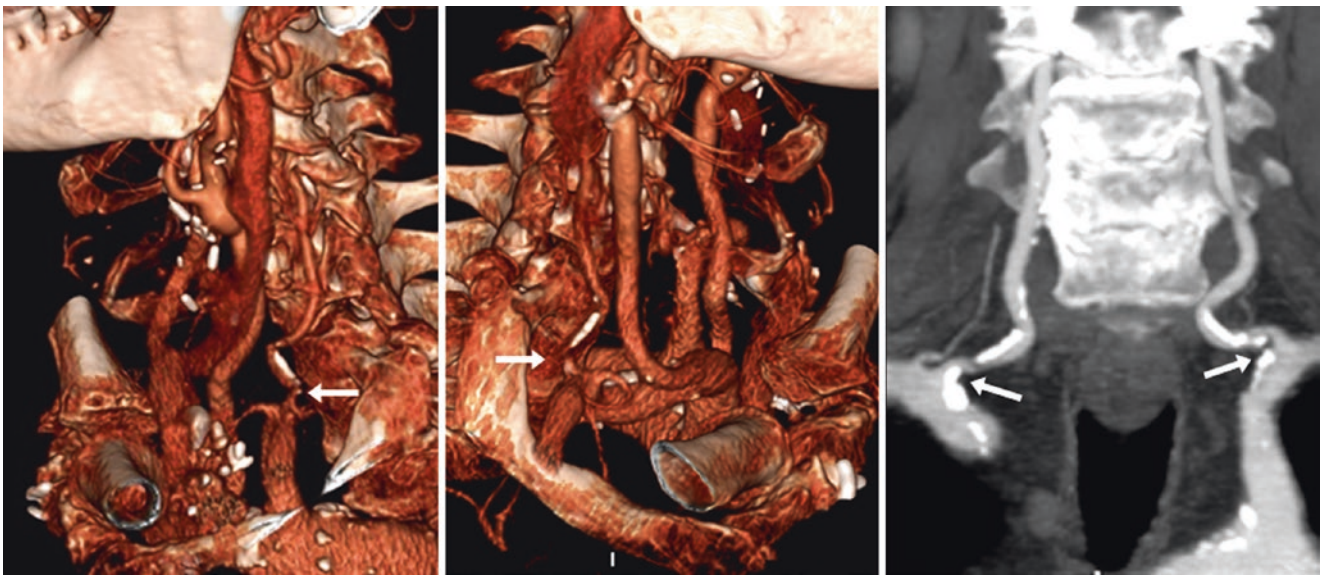

Fig. 44.6 Companion case of vertebral artery stenosis bilaterally with atherosclerotic calcifications. A 75-year-old had severe, heavily calcified VA origins bilaterally (*arrows*), causing moderate stenoses on 3D VR LAO (*left*) and RAO (*middle*) views. The stenoses are confirmed to be real on a coronal 3 mm MPR (*right*)

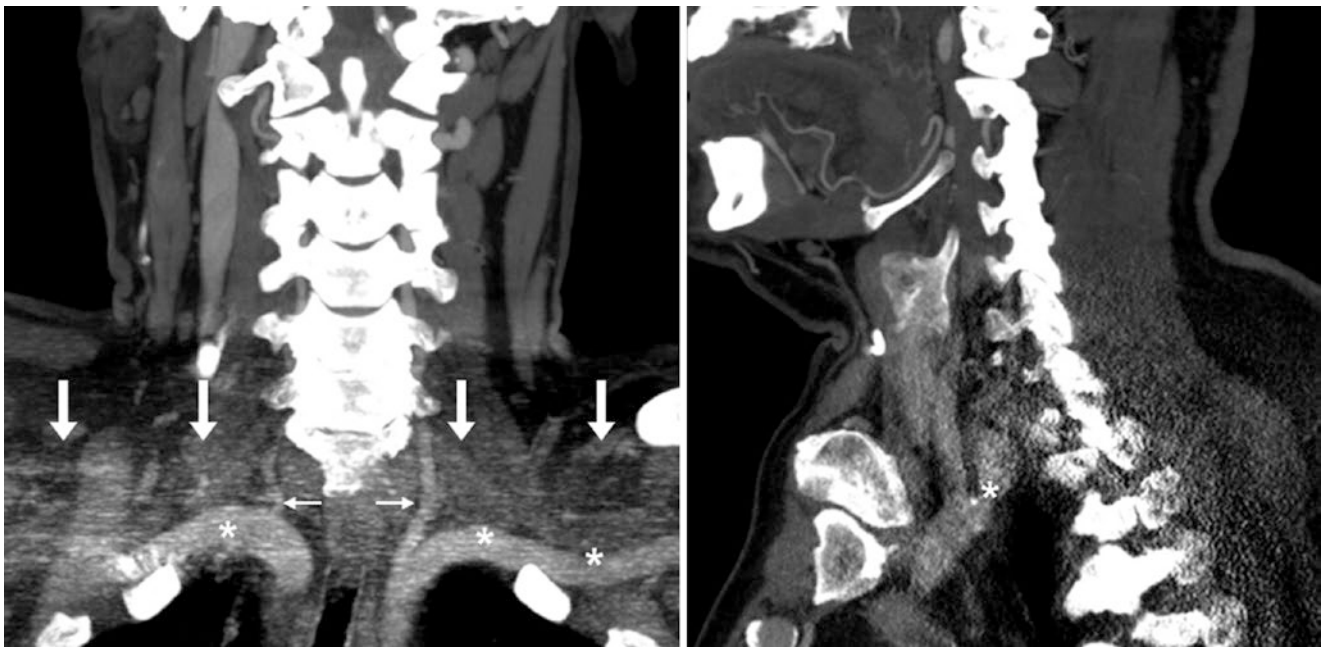

Fig. 44.7 74-year-old with shoulder streak artifact. VA origins (*thin arrows*) and subclavian arteries (SCLAs) (*asterisks*) are bilaterally obscured by shoulder artifact (*arrows*) (but can be seen to be patent) on a neck CTA reconstructed into 6 mm coronal (*left*) and sagittal (*right*) MPRs of the left side

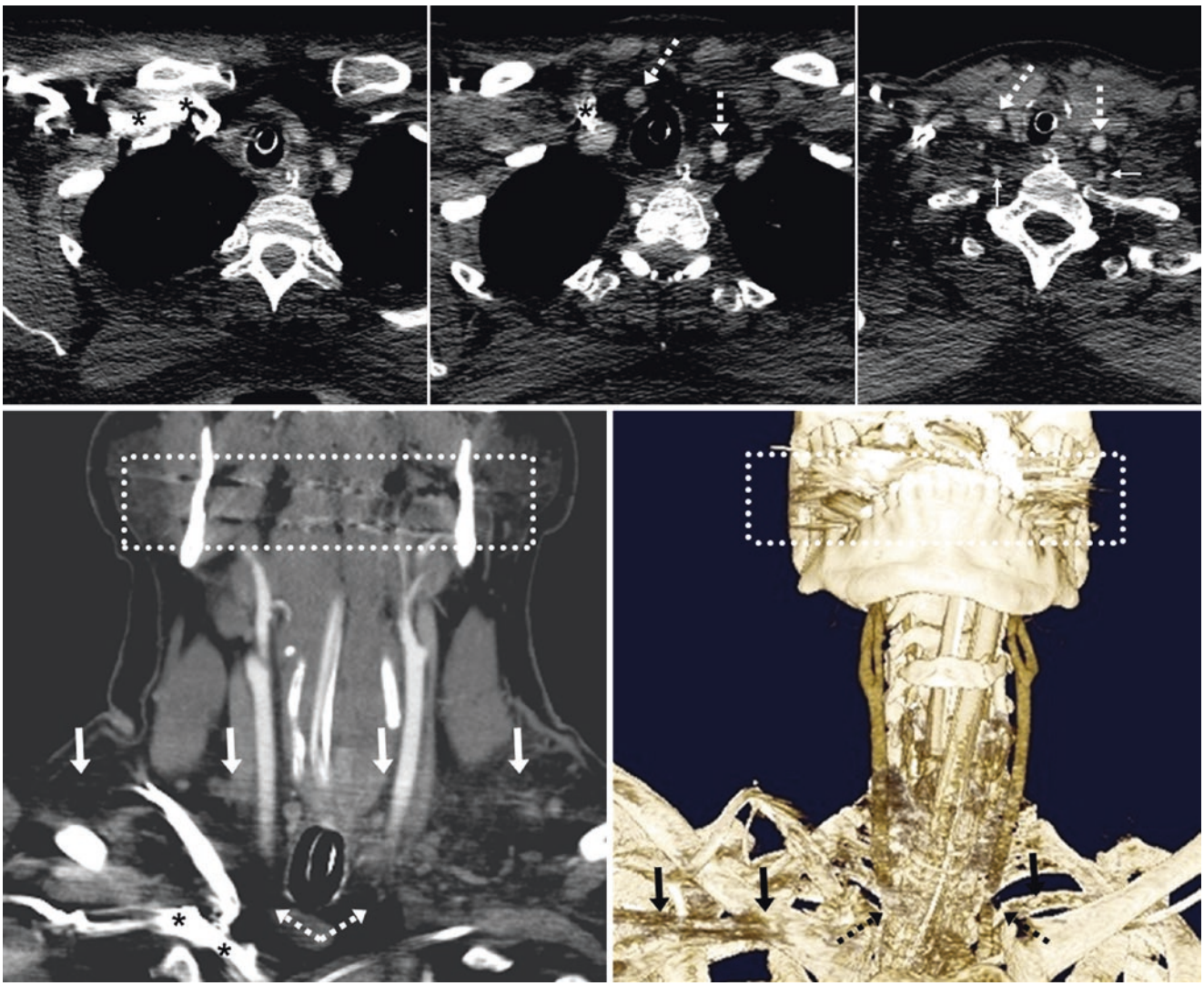

Fig. 44.8 43-year-old with shoulder streak artifact. *Top row:* on neck CTA axial images, severe streak artifact from both shoulders, along with contrast persistence within the right BCV and SCLV (*asterisks*), together combine to completely obscure the lower CCAs (*dotted arrows*) and VAs (*tiny arrows*). *Bottom row:* the image degradation from steak artifact (*arrows*) in the lower neck is also illustrated on a coronal 20 mm MPR (*left*) and on a 3D VR AP view (*right*). Also, note streak artifact from dental amalgam (*dotted boxes*)

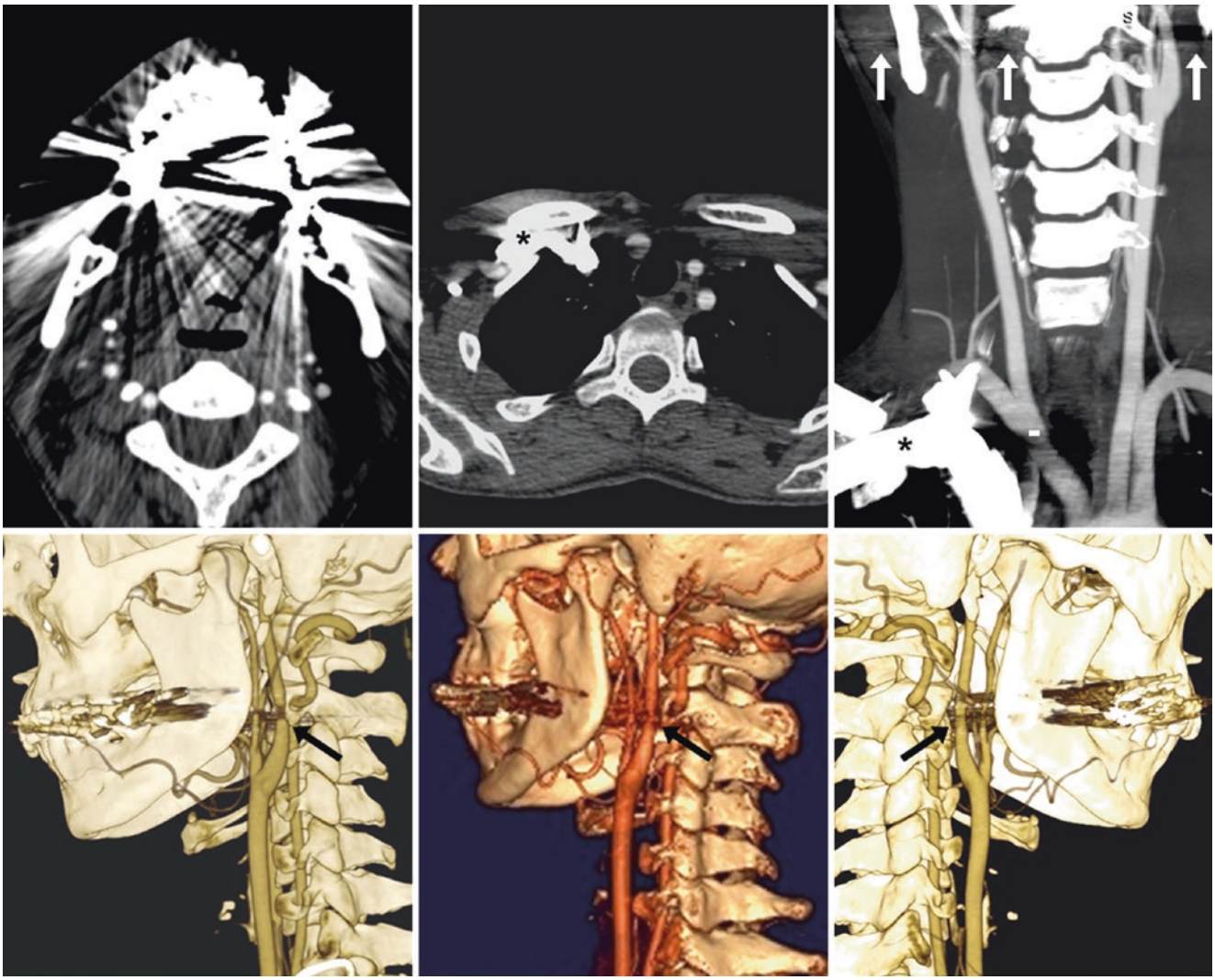

Fig. 44.9 30-year-old with a neck CTA limited by streak artifact from dental amalgam. *Top row*: streak artifact (*arrows*) obscures the ICA origins, as shown on axial images (*left and middle*), and on a coronal MPR (*right*), causing pseudo-stenoses. There is also streak artifact at the thoracic inlet from contrast persistence within the right BCV and SCLV (*asterisk*), obscuring the innominate artery (*minus sign*) on the coronal MPR (*right*). *Bottom row:* 3D VR views further demonstrate how the streak artifact (*arrows*) obscures the ICA origins on right (*left* and *middle*) and left lateral (*right*) views

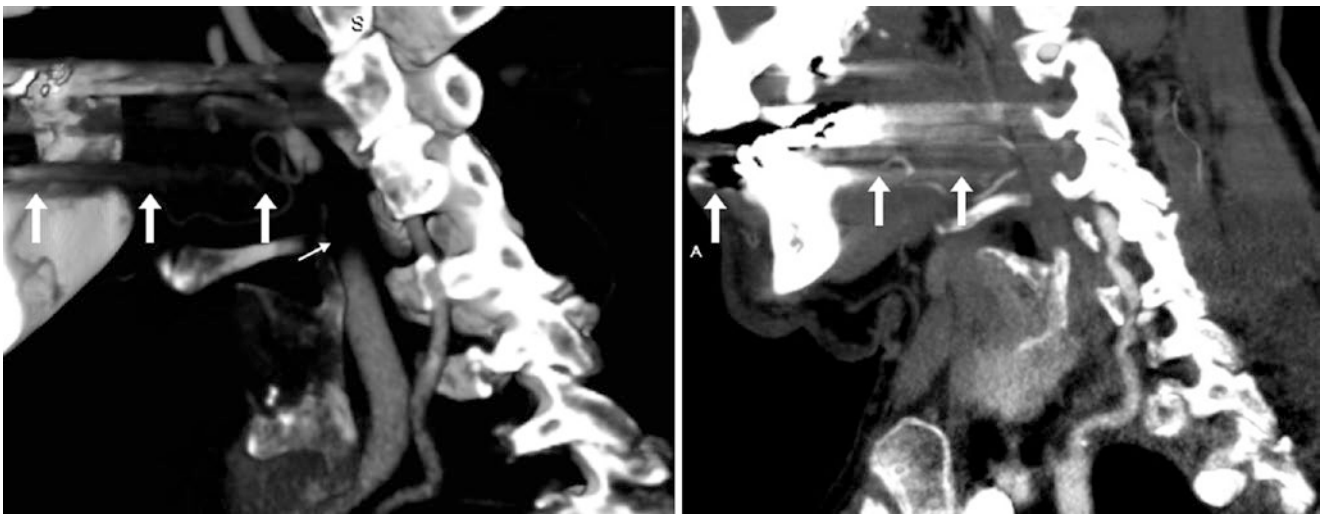

Fig. 44.10 80-year-old with severe streak artifact from dental amalgam. The severe artifact (*arrows*) entirely obscures the left ICA (*thin arrow*) near the bifurcation, on sagittal 7 mm MPRs. (The left image is more medial; the right image is further lateral.) The severe streak artifact precludes evaluation of the left ICA origin

Fig. 44.11 66-year-old with pseudodissection. On a CTA, streak artifact (*thin arrows*) from dental amalgam causes a right ICA "pseudodissection" (*arrow, which shows a simulated intimal flap*) above the carotid bifurcation, on axial (*left*), sagittal (*middle*), and coronal (*right*) MPRs. The right ICA is actually normal. There were no symptoms of stroke or dissection

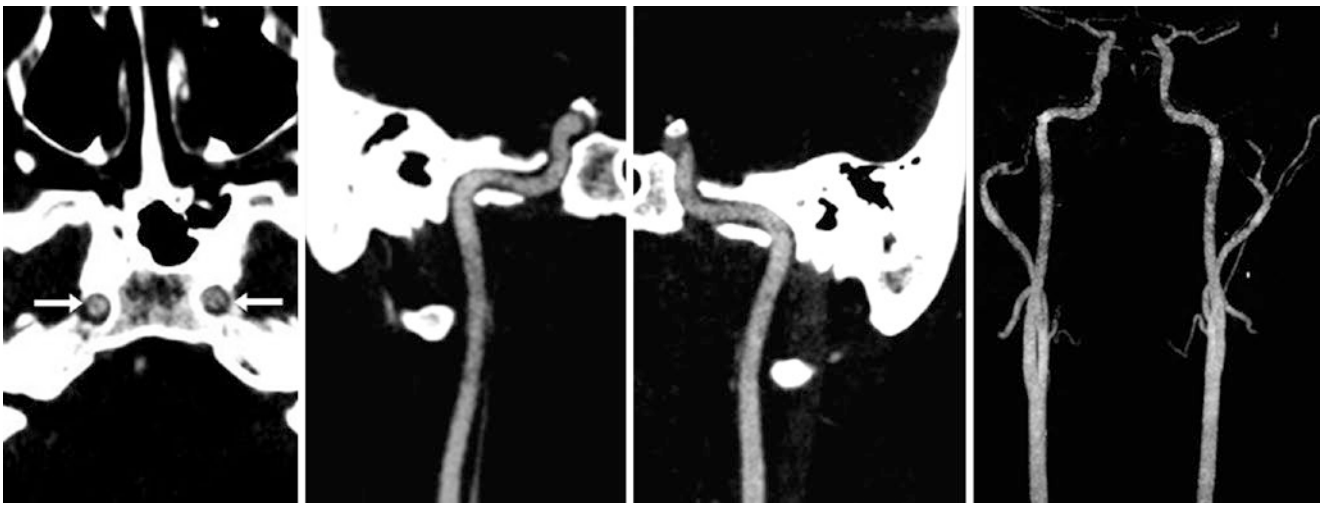

Fig. 44.12 19-year-old with pseudodissection. Axial CTA images depict flow-related "pseudodissections" (*arrows*) in the petrous ICAs bilaterally because a fast 256-slice CT scanner "outpaces" the contrast bolus. Coronal MPRs of the right ICA (*left middle*) and left ICA (*right middle*) show that the bolus becomes less dense (*ie*, "thins") from caudally to cranially, the same direction in which the scan is obtained. This "thinning" of the bolus is shown on a 3D MIP AP view (*right*)

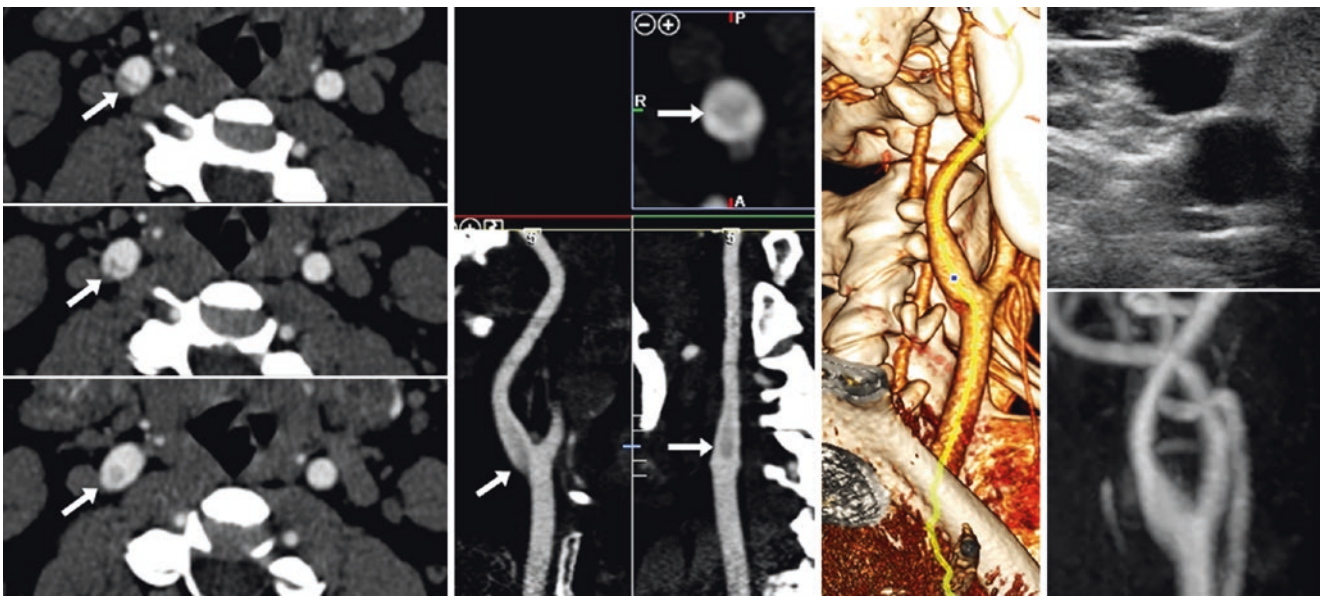

Fig. 44.13 32-year-old with posttraumatic pseudodissection. On a 256-slice neck CTA, a pseudodissection (*arrows*) of the right ICA is noted on serial 0.8 mm axial (*left column*) and MPR reformats with localization cursors (*middle left*), with 3D (*middle right*) images indicative of laminar flow (*the arrows denote a simulated intimal flap*). For confirmation, both a negative ultrasound (*axial view, top right*) and CEMRA with MIP (*bottom right*) were performed. There were no symptoms of dissection

Fig. 44.14 53-year-old with trauma and pseudodissection. The pseudodissection artifact (*arrows*) is located at the left ICA origin on axial (*left*) and coronal (*middle*) MPRs from a 128-slice CTA. An intimal flap was initially suspected (*arrows*). A subsequent catheter DSA (*right*) was negative. The patient had no stroke symptoms. Note the appearance of laminar flow on the sagittal 0.8 mm (*bottom left*) and thicker 5 mm (*bottom middle*) MPRs

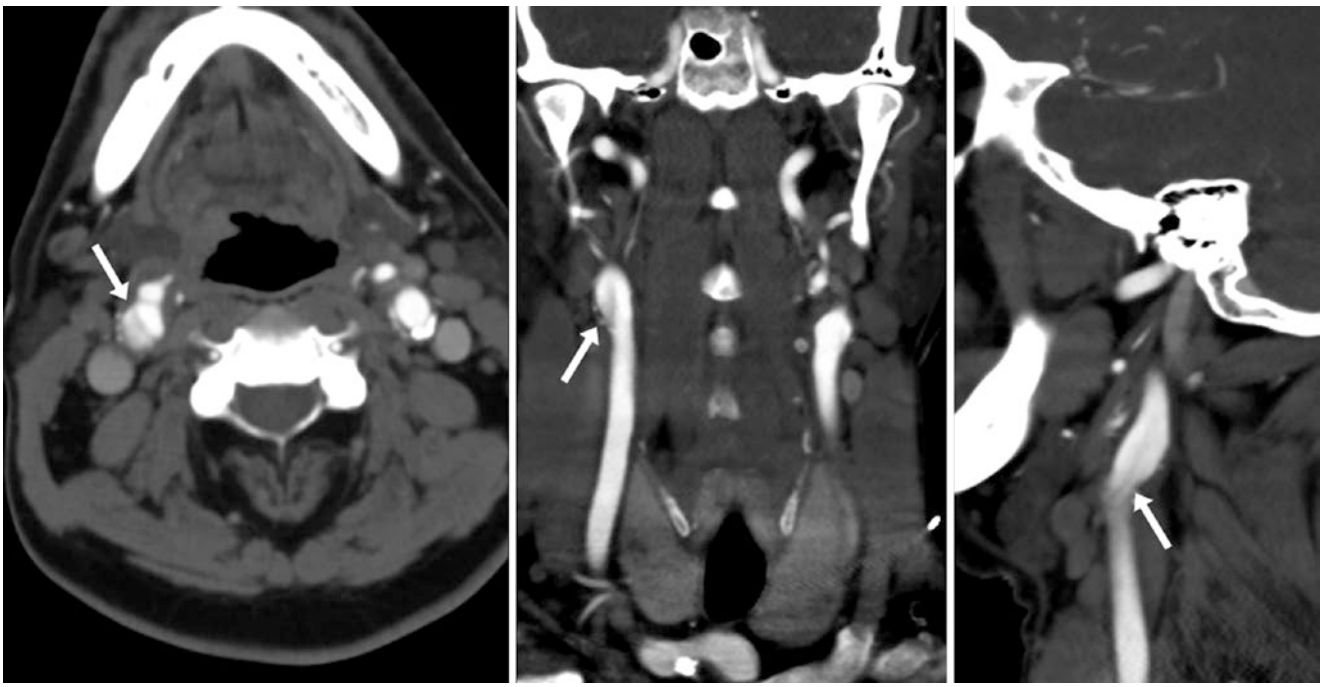

Fig. 44.15 58-year-old with pseudodissection artifact. On a neck CTA, a pseudodissection (*arrows*) was noted at the right ICA origin, likely from CT scanner speed (128-slice CT) relative to flow and pulsation (*the arrow shows a simulated intimal flap*), as shown on axial (*left*), coronal (*middle*), and sagittal (*right*) MPRs. The patient had a right-sided stroke acutely, later found to be due to emboli from the cardiac system. Note the appearance of laminar flow on the sagittal image to confirm pseudodissection

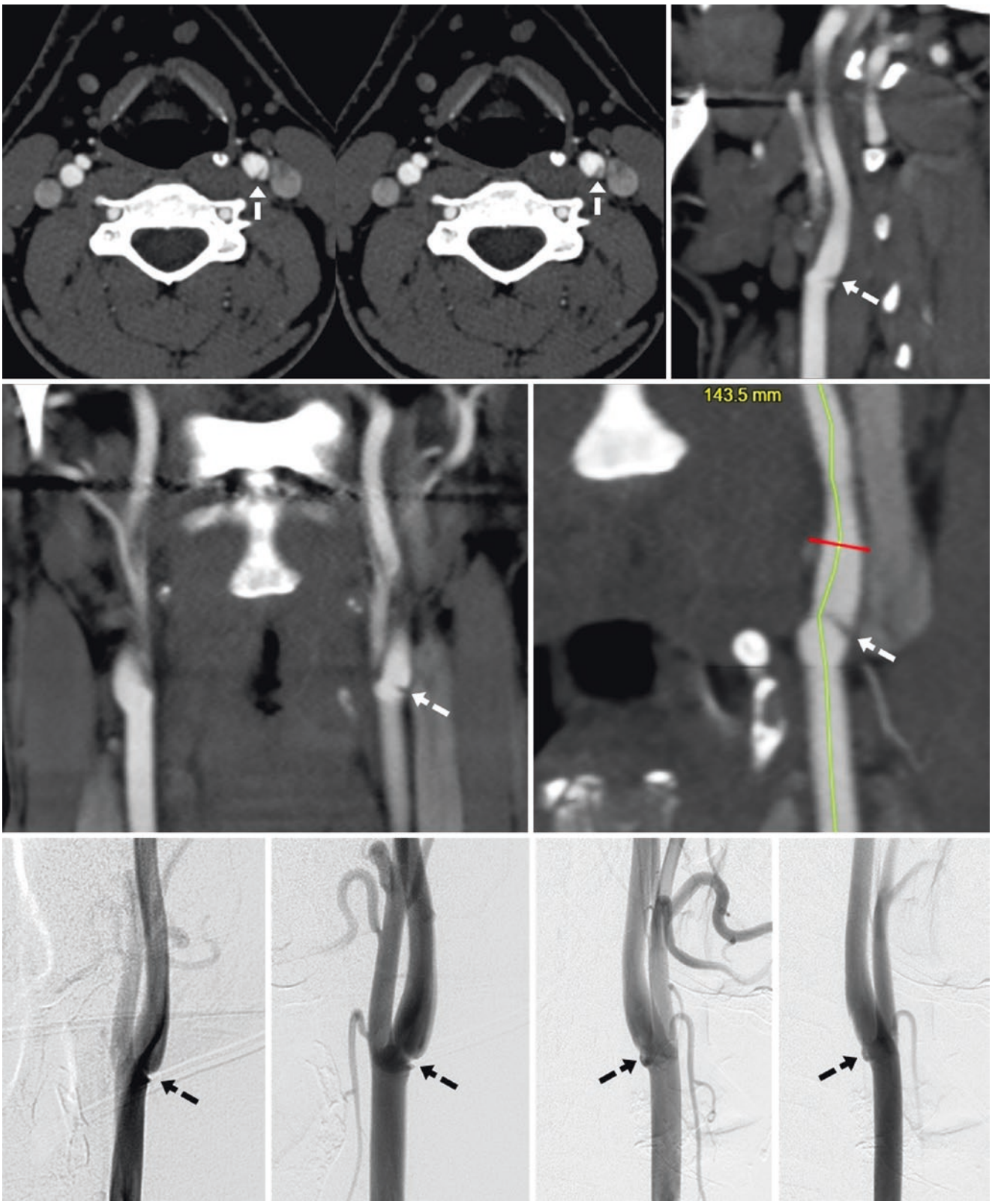

Fig. 44.16 Comparison case of carotid dissection and pseudoaneurysm. 31-year-old with penetrating trauma. *Top row:* axial and sagittal reformats from a 128-slice CTA demonstrate a linear defect (*dashed arrows*) at the left ICA origin. *Middle row:* an intimal flap was confirmed on coronal (*left*) and curved MPR (*right*) views. *Bottom row:* on left ICA catheter DSA, both earlier and later phases in lateral views (*left two images*) and oblique views (*right two images*) confirm the dissection, but also identify a tiny pseudoaneurysm, making this a Grade 3 blunt vascular injury

References

1. Kim JJ, Dillon WP, Glastonbury CM, Provenzale JM, Wintermark M. Sixty-four-section multidetector CT angiography of carotid arteries: a systematic analysis of image quality and artifacts. AJNR Am J Neuroradiol. 2010;31:91–9.
2. Takahashi M, Ashtari M, Papp Z, Patel M, Goldstein J, Maguire WM, et al. CT angiography of carotid bifurcation: artifacts and pitfalls in shaded-surface display. AJR Am J Roentgenol. 1997;168:813–7.
3. Johnson JM, Reed MS, Burbank HN, Filippi CG. Quality of extracranial carotid evaluation with 256-section CT. AJNR Am J Neuroradiol. 2013;34:1626–31.
4. de Monyé C, de Weert TT, Zaalberg W, Cademartiri F, Siepman DA, Dippel DW, van der Lugt A. Optimization of CT angiography of the carotid artery with a 16-MDCT scanner: craniocaudal scan direction reduces contrast material-related perivenous artifacts. AJR Am J Roentgenol. 2006;186:1737–45.
5. Venema HW, Hulsmans FJ, den Heeten GJ. CT angiography of the circle of Willis and intracranial internal carotid arteries: maximum intensity projection with matched mask bone elimination—feasibility study 1. Radiology. 2001;218:893–8.
6. Villablanca JP, Jahan R, Hooshi P, Lim S, Duckwiler G, Patel A, et al. Detection and characterization of very small cerebral aneurysms by using 2D and 3D helical CT angiography. AJNR Am J Neuroradiol. 2002;23:1187–98.
7. Teksam M, McKinney A, Casey S, Asis M, Kieffer S, Truwit CL. Multi-section CT angiography for detection of cerebral aneurysms. AJNR Am J Neuroradiol. 2004;25:1485–92.
8. Tipper G, U-King-Im JM, Price SJ, Trivedi RA, Cross JJ, Higgins NJ, et al. Detection and evaluation of intracranial aneurysms with 16-row multislice CT angiography. Clin Radiol. 2005;60:565–72.
9. McKinney AM, Palmer CS, Truwit CL, Karagulle A, Teksam M. Detection of aneurysms by 64-section multidetector CT angiography in patients acutely suspected of having an intracranial aneurysm and comparison with digital subtraction and 3D rotational angiography. AJNR Am J Neuroradiol. 2008;29:594–602.

Dense Vessels Simulating Thrombosis on Nonenhanced CT

45

A normal appearance of *hyperdense vessels*, whether arterial or venous, can occur on nonenhanced CT (NECT) for several reasons [1–14]. This appearance can represent a true increase in density, or it can be artifactual. Notably, there is a correlation between the *hemoconcentration* of whole blood and the density on NECT. Hence, *higher hemoglobin* and/or *higher hematocrit* levels may lead to relatively hyperdense vessels diffusely on NECT, which is most commonly due to frank *dehydration* in patients without stroke symptoms presenting to the emergency room. Thus, higher hemoconcentrations can lead to a hyperdense appearance of the arteries and dural sinuses, whether due to a relative *polycythemia*, which can occur with decreased fluid intake or fluid loss or with a higher hematocrit, such as that occurring normally in newborns. Because newborns do have some risk for venous thrombosis, it is occasionally necessary to implement contrast-enhanced MR venography (CEMRV) or CT venography (CTV) to exclude venous thrombosis. Also, *artifactual vascular hyperdensity* can occur unilaterally or bilaterally at the skull base as a result of artifacts from *beam hardening* (decreased penetration in areas of dense bones or metal), *patient motion*, or *volume averaging* (such as the middle cerebral artery volume averaged with adjacent cerebrum or subarachnoid space).

On NECT, either unilateral arterial hyperdensity or diffuse venous hyperdensity should be viewed with suspicion if there are other associated imaging findings or if an appropriate clinical history is present, in the absence of associated artifact. Examples of this include a *hyperdense middle cerebral artery* in a patient with stroke-like symptoms (*eg*, acute unilateral weakness), or *dense dural venous sinuses* in a patient with a spontaneous cerebral hemorrhage. Also, *venous thrombosis* will typically have enlarged veins and may have adjacent parenchymal edema; the regional distribution of the parenchymal edema or hemorrhage (such as parasagittal edema/hemorrhage in superior sagittal sinus thrombosis, or temporal edema/hemorrhage in transverse sinus thrombosis) can be useful to discern true thrombosis. Notably, in the setting of trauma, the presence of a calvarial fracture adjacent to a dural sinus on NECT has a high frequency of sinus thrombosis (ranging from 25–40 %, being higher with multiple fractures) as well as compression from extra-axial hemorrhage causing venous stenosis (reported in about 35–45 %) [15–17]. In most of these scenarios, appropriate imaging may include CT angiography (CTA), MR angiography (MRA), CTV, or MRV to confirm the presence or absence of vascular thrombus (Figs. 45.1, 45.2, 45.3, 45.4, 45.5, 45.6, 45.7, 45.8, 45.9, 45.10, 45.11, 45.12, 45.13, 45.14, 45.15, 45.16, 45.17, 45.18, 45.19, 45.20, 45.21, and 45.22).

A.M. McKinney, *Atlas of Normal Imaging Variations of the Brain, Skull, and Craniocervical Vasculature*,
DOI 10.1007/978-3-319-39790-0_45

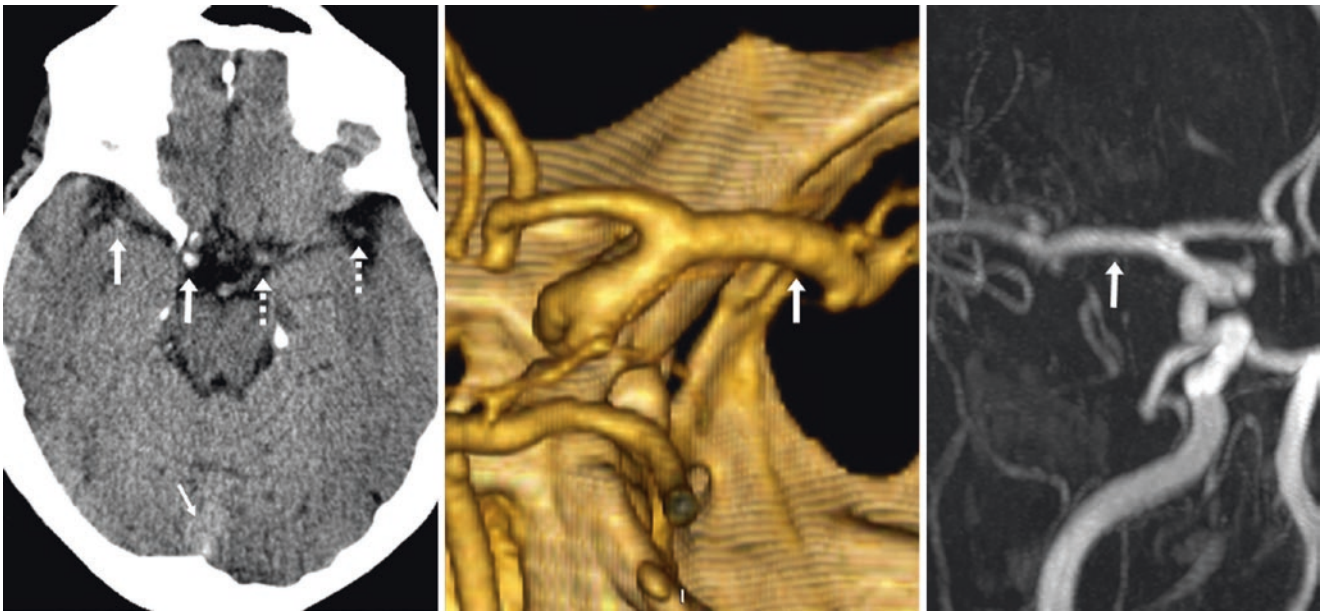

Fig. 45.1 79-year-old with a dense MCA. The patient had stroke-like symptoms, and a dense right middle cerebral artery (MCA) was questioned (*arrows*) on nonenhanced CT (NECT) (*left*), as compared with contralaterally (*dotted arrows*), owing to either beam hardening or volume averaging artifact (or a combination of the two). There was likely mild dehydration, as the venous sinuses were mildly hyperdense (*thin arrow*). On CTA PA (*middle*) and MRA AP (*right*) views later the same day, the right MCA was demonstrated to be patent

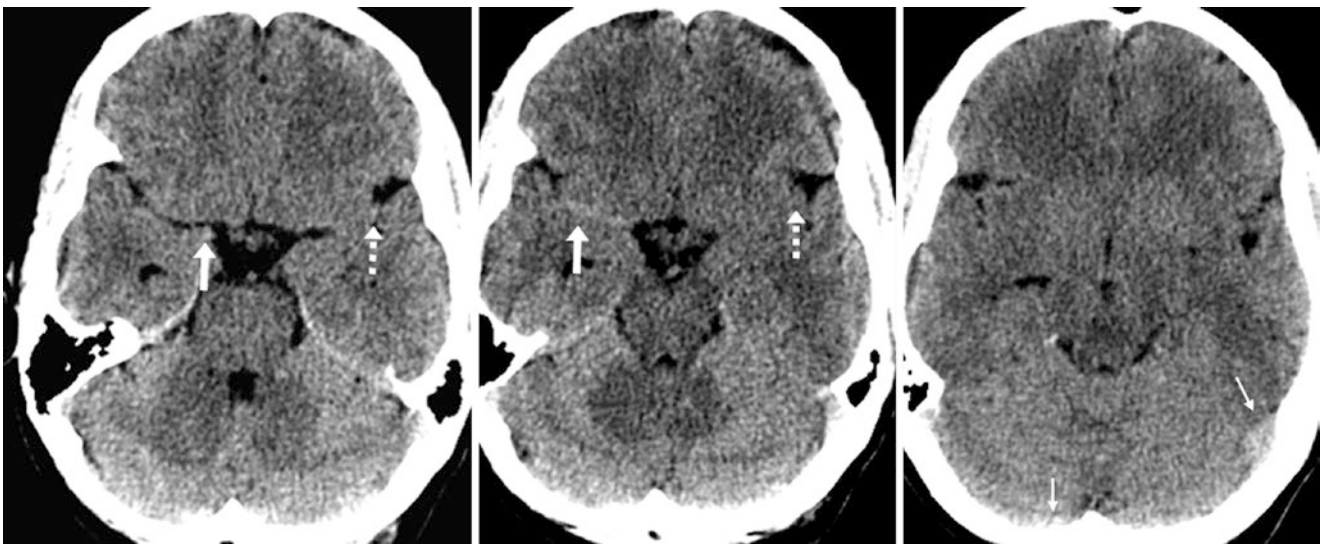

Fig. 45.2 41-year-old with a unilateral dense MCA. A mildly hyperdense right MCA (*arrows*) was noted on axial NECT (*left* and *middle*) in a patient with "psychosis." The left MCA is not hyperdense, but is not well visualized (*dashed arrows*), while the dural sinuses are mildly hyperdense (*thin arrows*), suggesting that the findings are related to dehydration

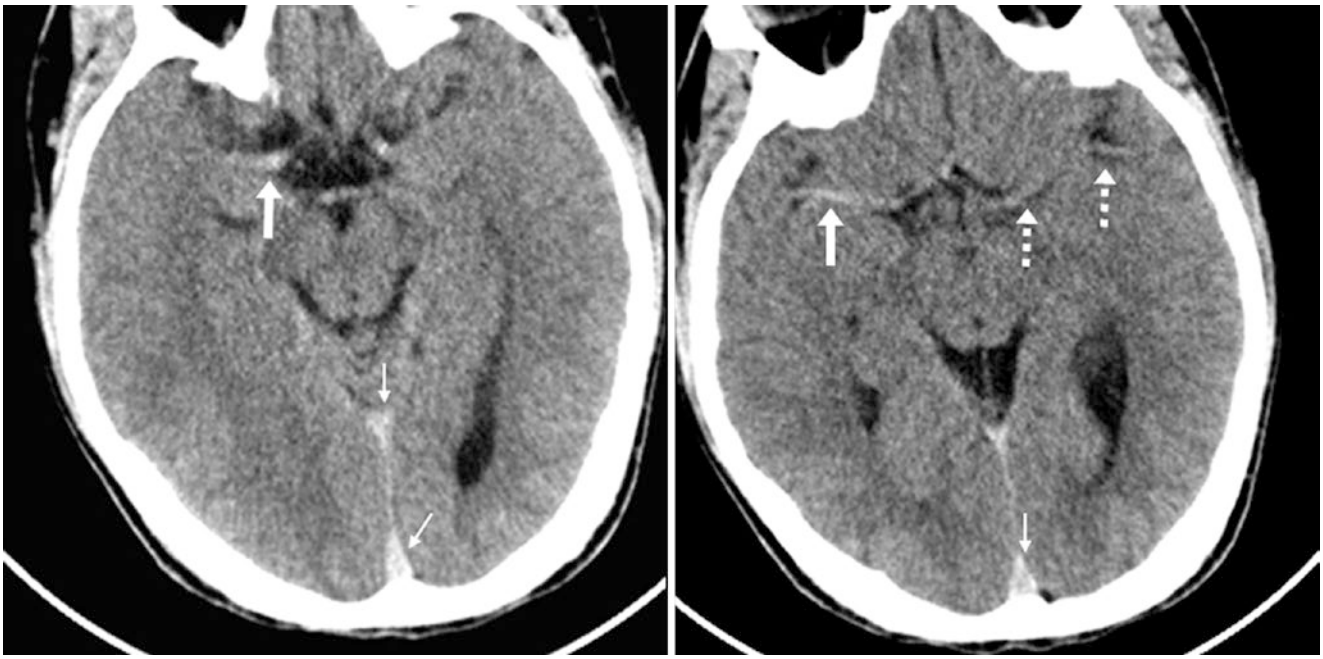

Fig. 45.3 19-year-old with a unilateral dense MCA. The right MCA was moderately focally hyperdense (*arrows*) on NECT. The left MCA was not as dense (*dotted arrows*), and the dural sinuses were also hyperdense (*thin arrows*). These findings were likely from dehydration. The patient's symptoms were generalized headaches, without stroke or stroke-like symptoms

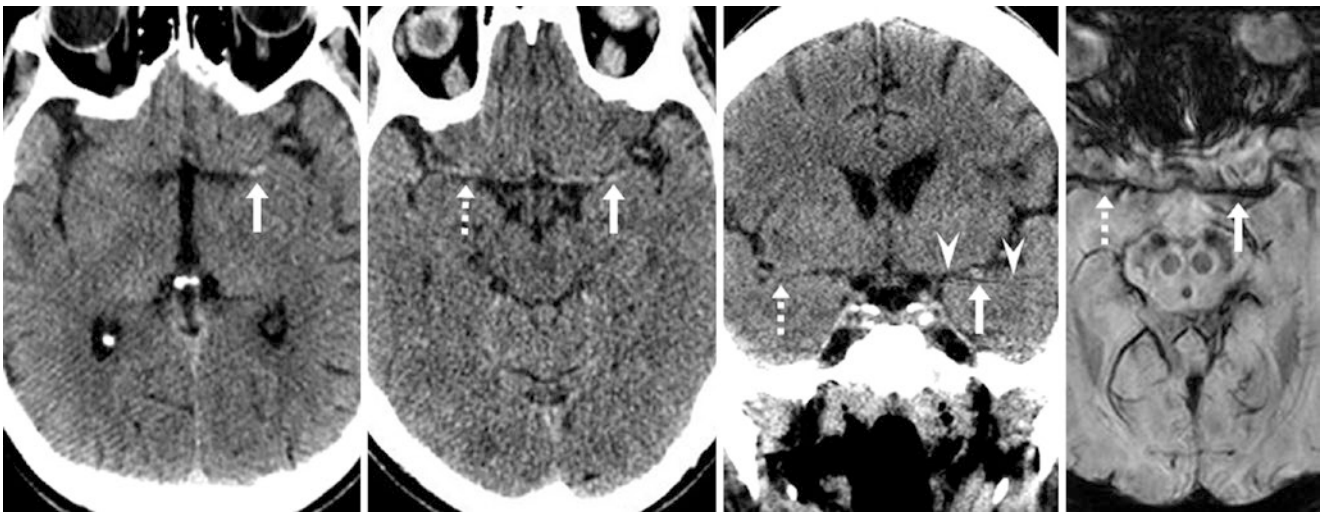

Fig. 45.4 50-year-old with a unilateral dense MCA. The patient suffered a seizure, and had a unilaterally dense left MCA (*arrows*) on axial NECT (*left*), as compared with the right MCA (*dotted arrows*). This difference is less pronounced after reconstruction and re-alignment with thinner images (1.5 mm) in the axial plane (*left middle*). Coronal reformats (*right middle*) demonstrate that the hyperdense MCA was likely due to beam hardening artifact (*arrowheads*). 3 T SWI MRI (*right*) confirmed a patent left MCA

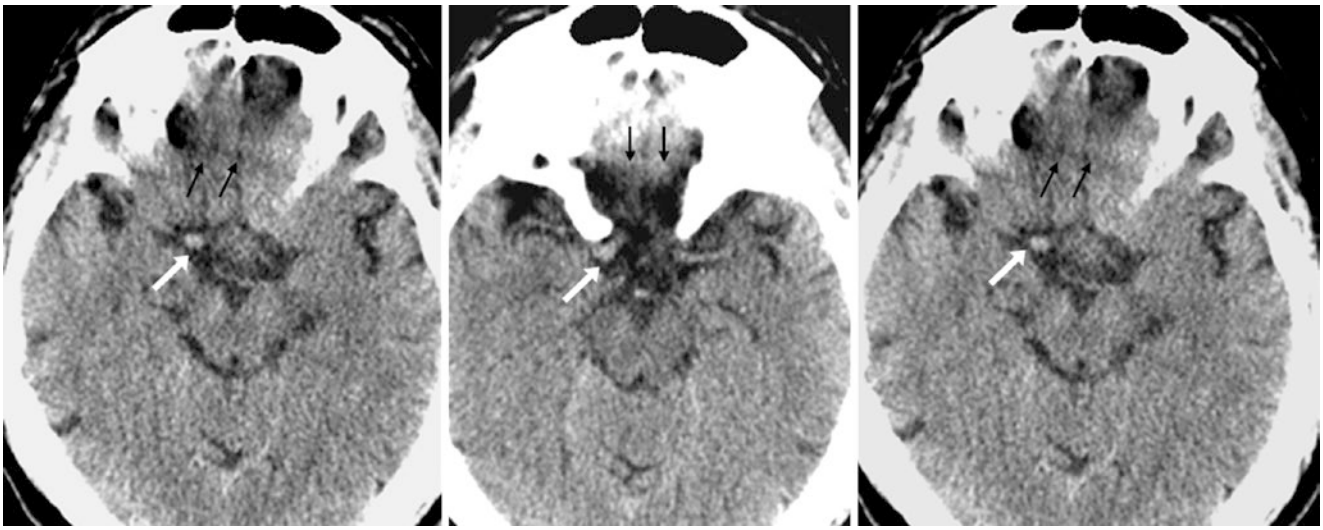

Fig. 45.5 34-year-old with a unilateral dense MCA. The right MCA is hyperdense (*arrows*) on adjacent NECT slices (*left* and *middle*), likely a result of beam hardening artifact anteriorly (*thin arrows*), as other vessels were not dense. This was originally questioned to be an early sign of infarct, but the clinical history that was provided later did not match. The dense right MCA was also present on a NECT 4 years earlier (*right*), with a similar degree of beam hardening artifact

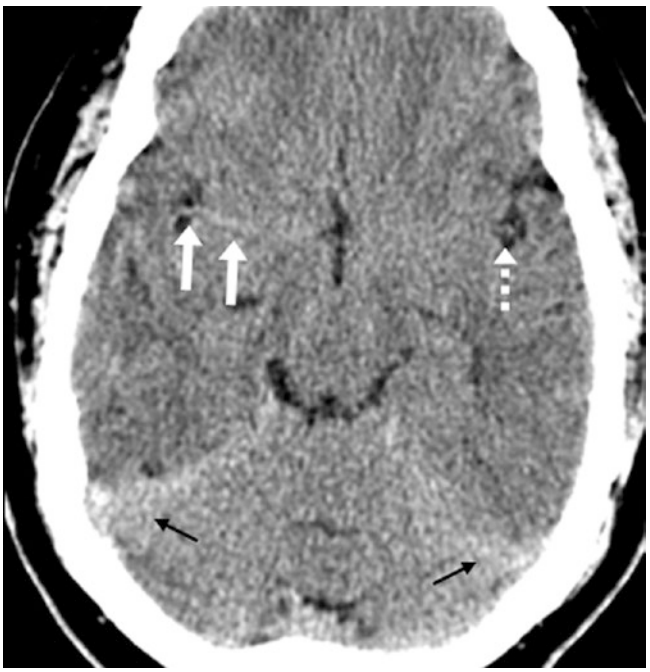

Fig. 45.6 21-year-old with a unilateral dense MCA. Note a dense right MCA (*arrows*), versus the left (*dotted arrow*), with dense dural sinuses (*thin arrows*)

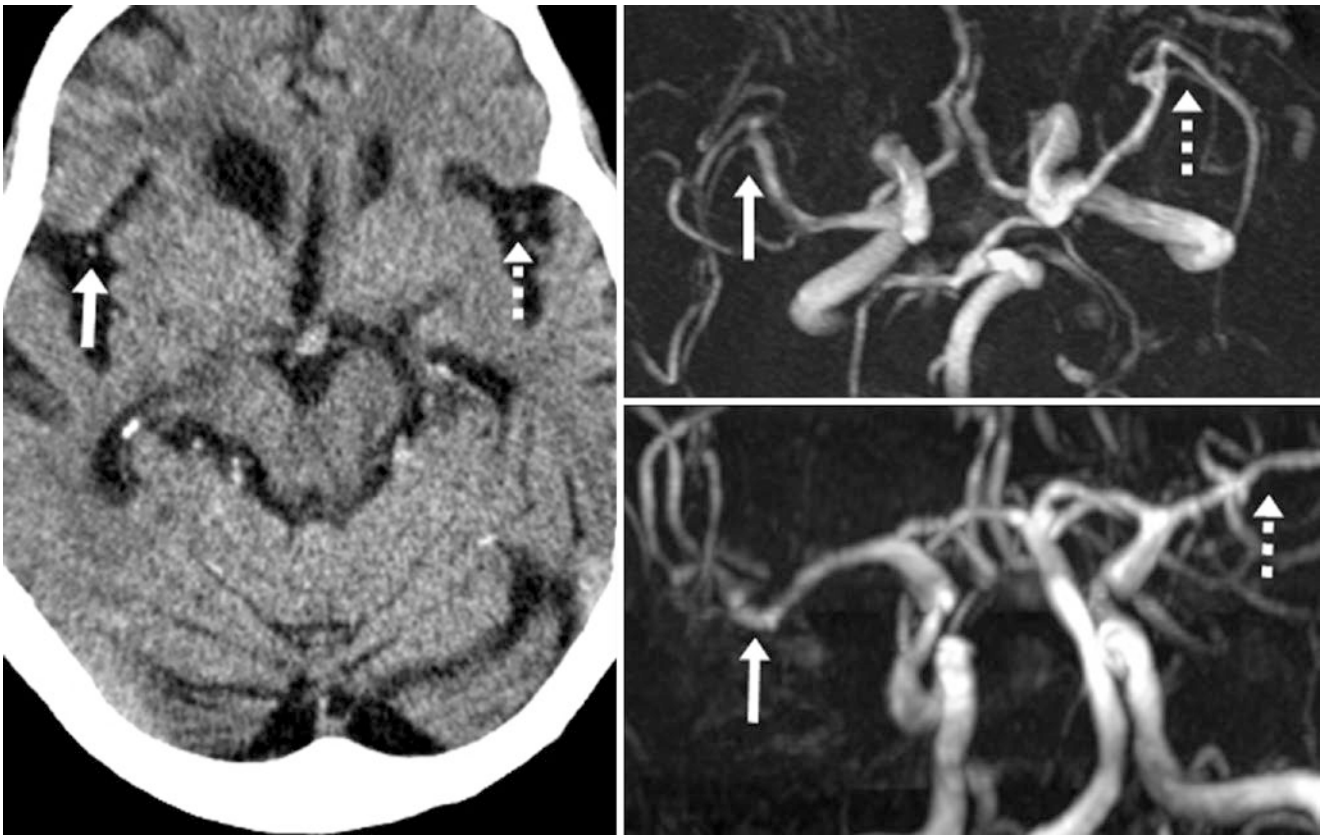

Fig. 45.7 89-year-old with a unilateral dense MCA. Note an apparently dense right M2 branch (*arrows*) on NECT, relative to the left MCA (*dotted arrows*), likely due to beam hardening artifact. MRA superior (*upper right*) and AP (*bottom right*) views were normal

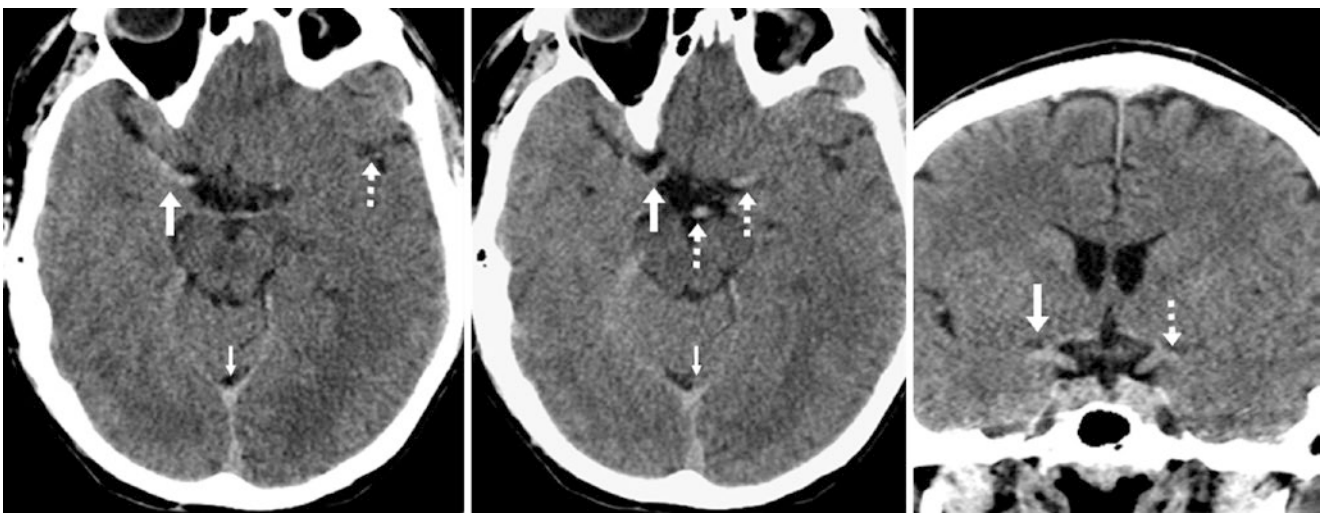

Fig. 45.8 35-year-old with a hyperdense MCA. The right MCA was hyperdense (*arrows*) on NECT (*left*), but the patient lacked stroke symptoms. The vessel was not dense on an adjacent slice (*middle*); the left MCA and basilar (*dotted arrows*) were not as dense. The dural sinuses were only mildly hyperdense (*thin arrows*). A coronal MPR (*right*) confirmed that the right MCA was mildly hyperdense. Thus, this finding was probably related to dehydration combined with beam hardening artifact

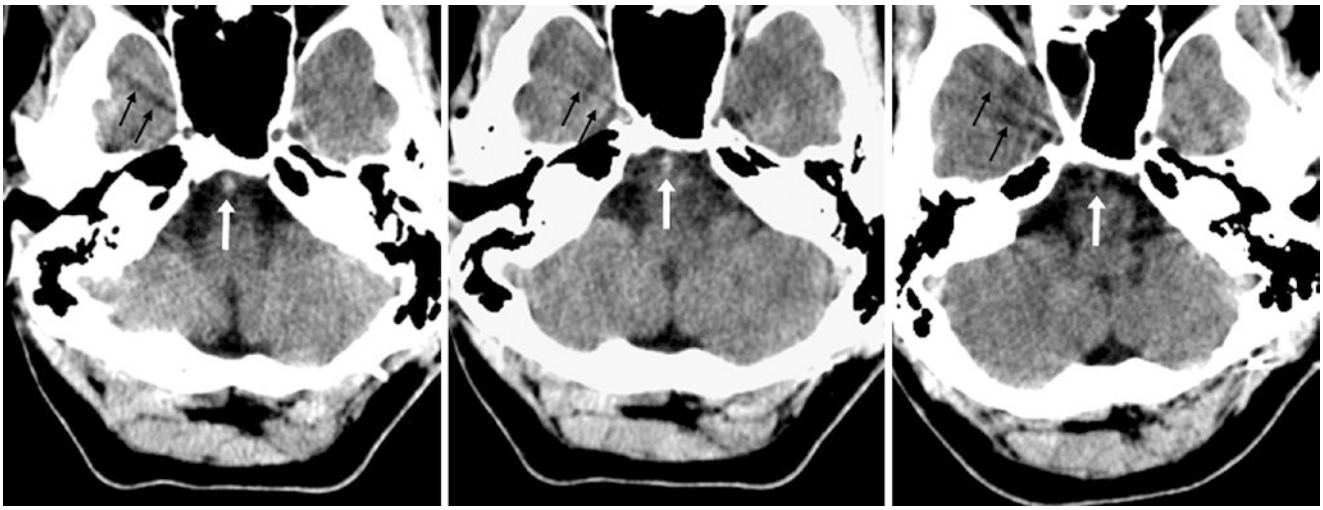

Fig. 45.9 46-year-old with a dense basilar artery. The basilar is dense (*arrows*) on consecutive slices from NECT (*left* and *middle*), likely because of beam hardening artifact, as evident by streak artifact from dense bony clivus and basisphenoid at the skull base (*thin arrows*). The other vessels were not hyperdense. There were no symptoms of stroke. This finding was not present on NECT performed 6 months later (*right*), although beam hardening and streak artifacts were present

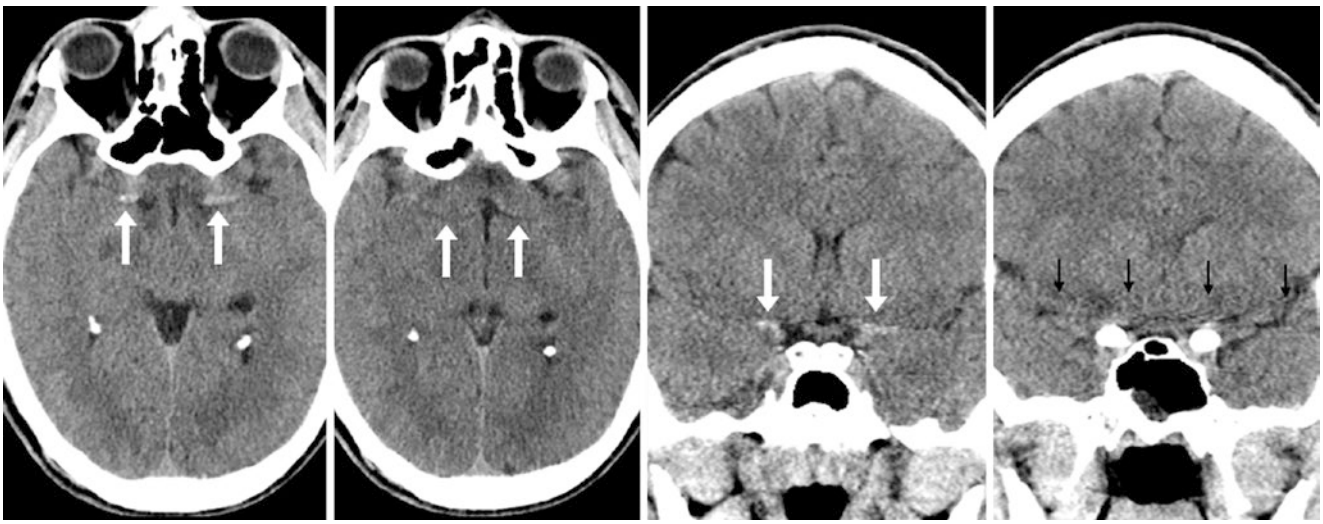

Fig. 45.10 23-year-old with bilaterally dense MCAs. On NECT, there were bilaterally dense MCAs (*arrows*) on axial images (*left*) from beam hardening artifact. The relationship to beam hardening artifact and streak was more apparent (*thin arrows*) on coronal reformats (*right*)

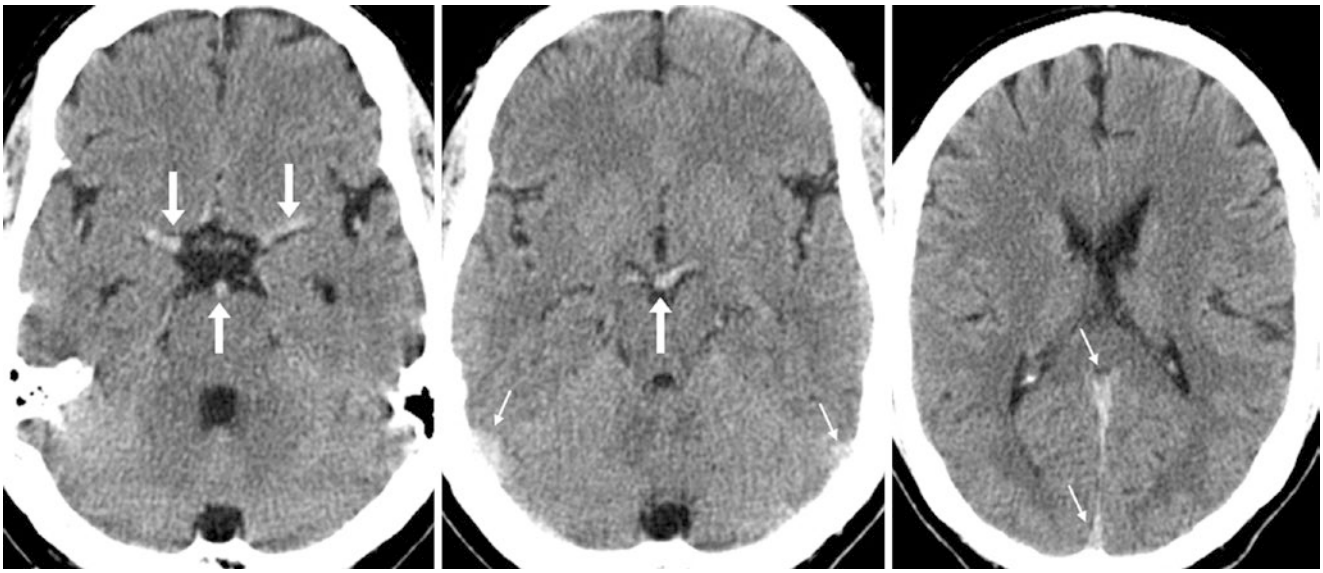

Fig. 45.11 45-year-old with diffusely dense vasculature. NECT demonstrates diffusely hyperdense arteries (*arrows*) as well as diffusely hyperdense dural venous sinuses (*thin arrows*). Clinically, these findings were thought to be related to dehydration. The patient lacked symptoms of stroke

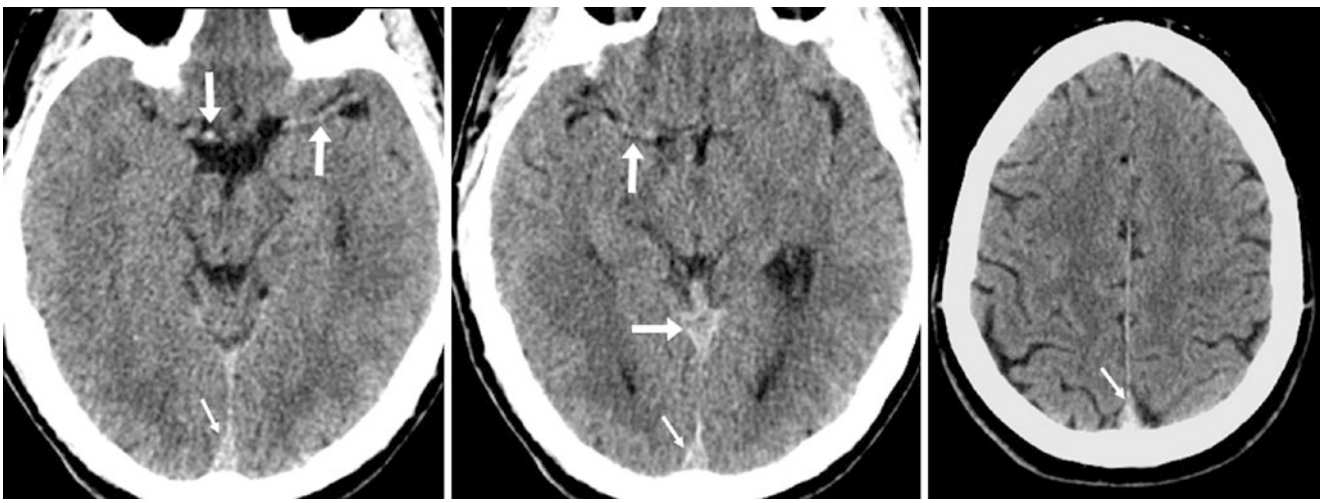

Fig. 45.12 49-year-old with diffusely dense vasculature. Note dense arteries (*arrows*) and veins (*thin arrows*) on NECT, likely from dehydration. The left MCA was initially deemed hyperdense by the radiology resident, as there was a clinical question of stroke, but the arteries and veins appeared equally dense, and the patient's symptoms were transient

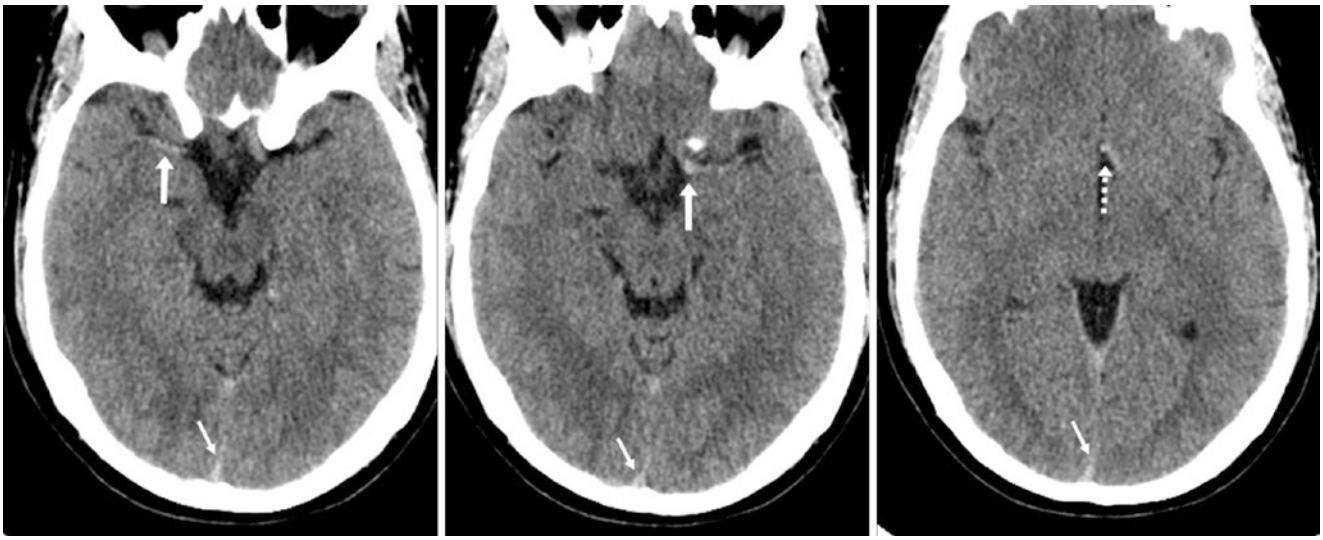

Fig. 45.13 34-year-old with diffusely dense vasculature. On an NECT performed for "psychosis," dense arteries (*large arrows*) were noted diffusely, likely related to dehydration. The MCAs (*arrows, left* and *middle*) and ACAs (*dotted arrow, right*) were bilaterally hyperdense, and the venous sinuses (*thin arrows*) similarly appeared hyperdense

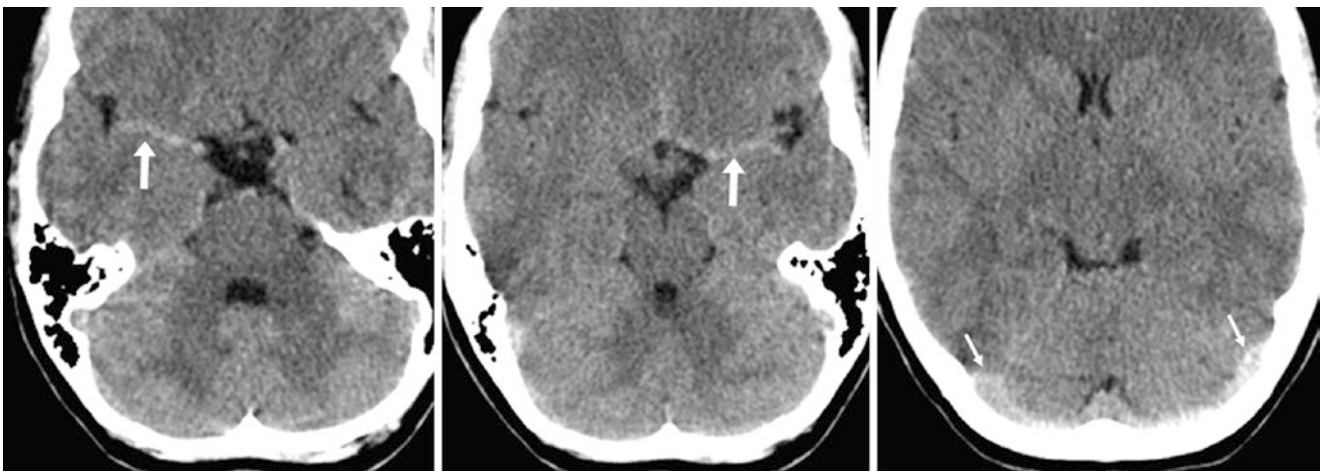

Fig. 45.14 22-year-old with diffusely dense vasculature. On axial NECT, dense MCAs were noted bilaterally (*arrows, left* and *middle*), as well as hyperdense dural venous sinuses diffusely (*thin arrows, right*), in a patient clinically suffering headaches. The hyperdensity was due to dehydration

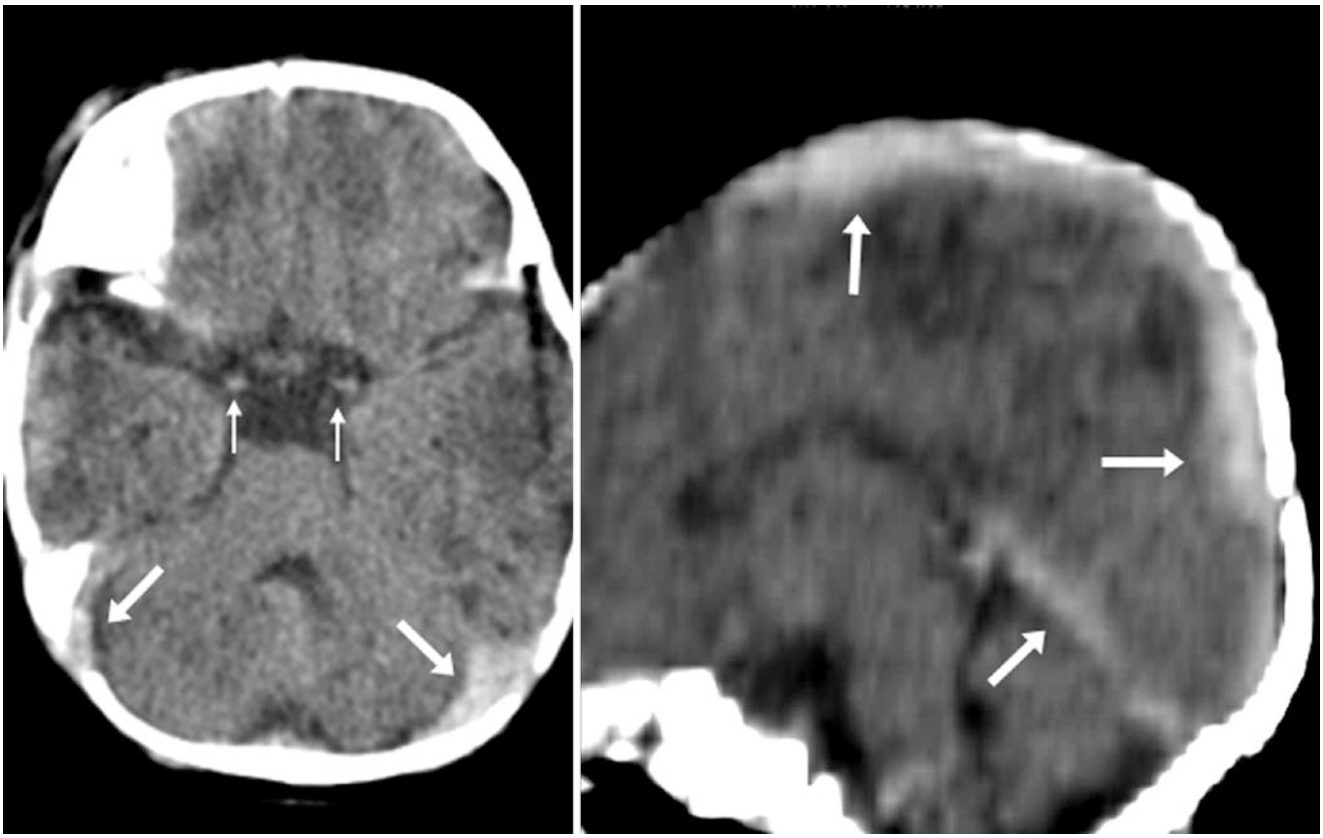

Fig. 45.15 4-day-old with dense dural sinuses. Axial (*left*) and sagittal (*right*) NECT images show dense venous sinuses (*large arrows*) due to fetal hemoglobin and a high hematocrit. There was no venous thrombosis. The arteries are mildly hyperdense (*thin arrows*)

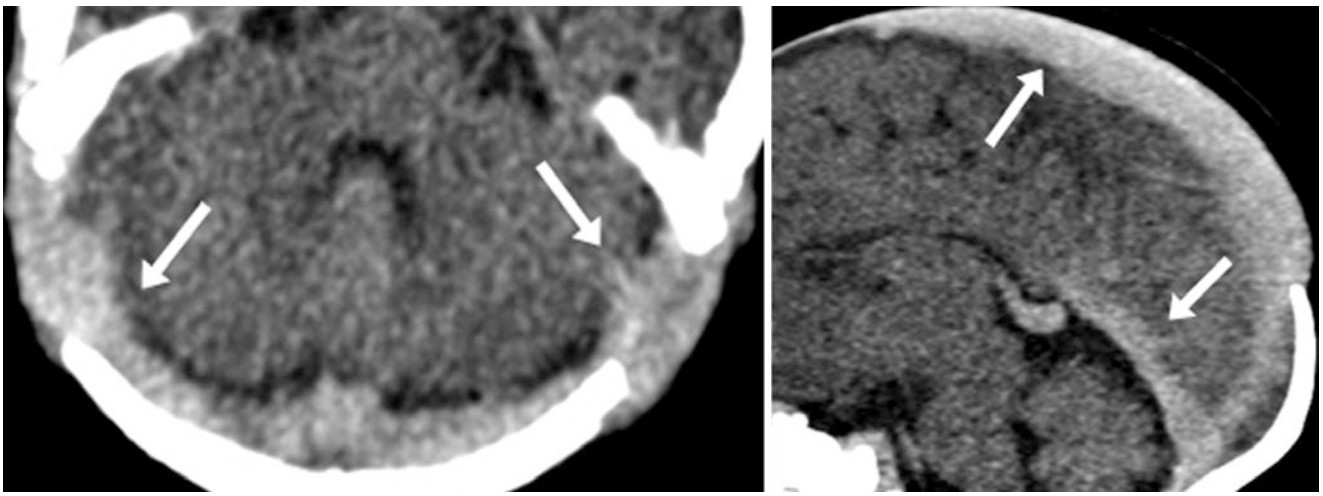

Fig. 45.16 4-day-old with dense dural sinuses. On NECT, hyperdense dural venous sinuses (*arrows*) were noted on axial (*left*) and sagittal (*right*) MPRs

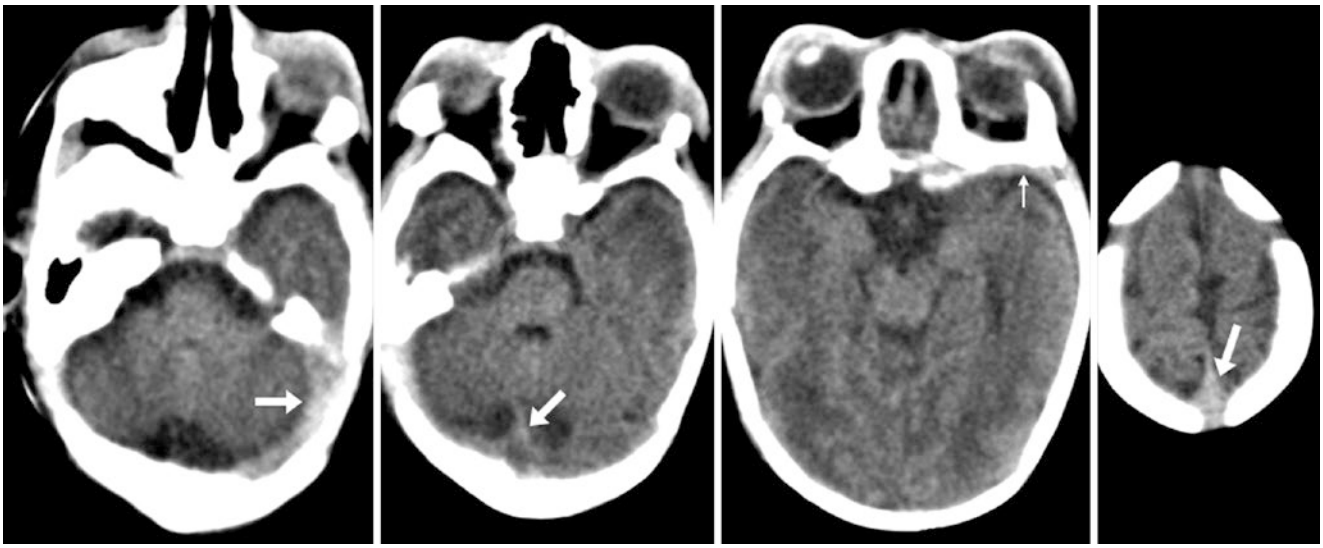

Fig. 45.17 6-day-old with dense dural sinuses. Dense dural venous sinuses (*arrows*) were seen on consecutive slices from NECT, as a result of normal neonatal hemoconcentration. Note the lack of parenchymal hemorrhage or venous distention, which would typically be seen in venous thrombosis. Also, note mild hyperdensity of the left sphenoparietal sinus (*thin arrow*)

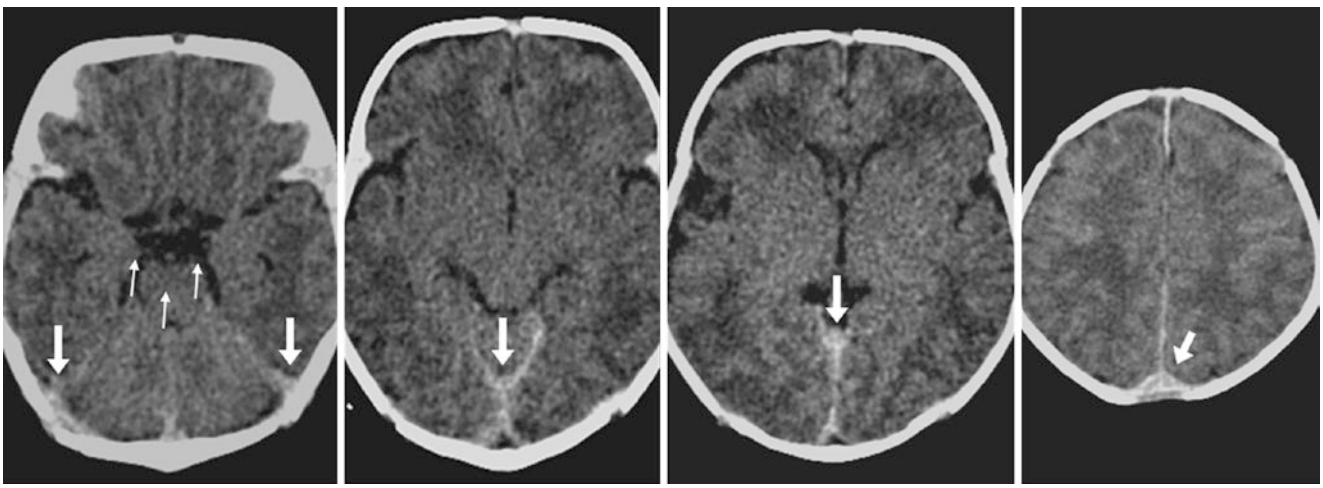

Fig. 45.18 7-day-old with dense dural sinuses. Diffusely dense venous sinuses were noted on serial NECT images (*arrows*), related to normal neonatal high hematocrit. The arteries (*thin arrows*) are not as dense, but the patient had a normal clinical follow-up. These findings raise the question whether this hyperdensity is not only from neonatal hemoconcentration but also from mild posterior fossa hemorrhage, which can be seen in up to 30–40 % of normal, spontaneous, asymptomatic live births

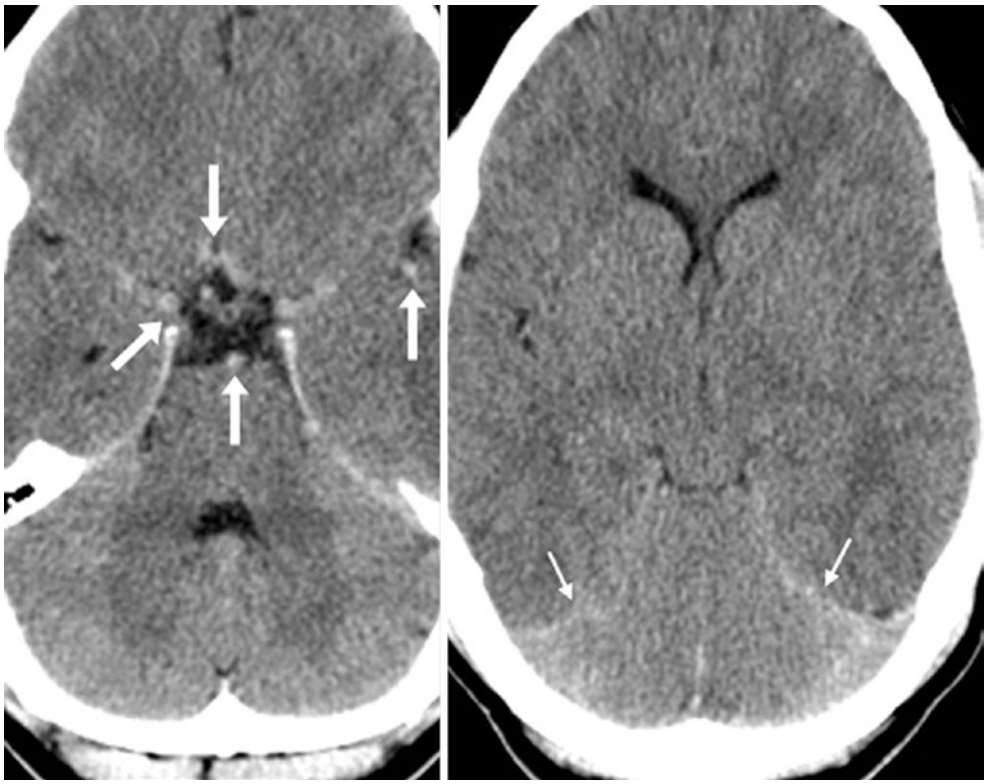

Fig. 45.19 14-year-old with diffusely dense vasculature. On NECT, hyperdense arteries (*arrows*) and dural sinuses along the tentorium (*thin arrows*) are present, presumably secondary to dehydration, in a patient with headaches

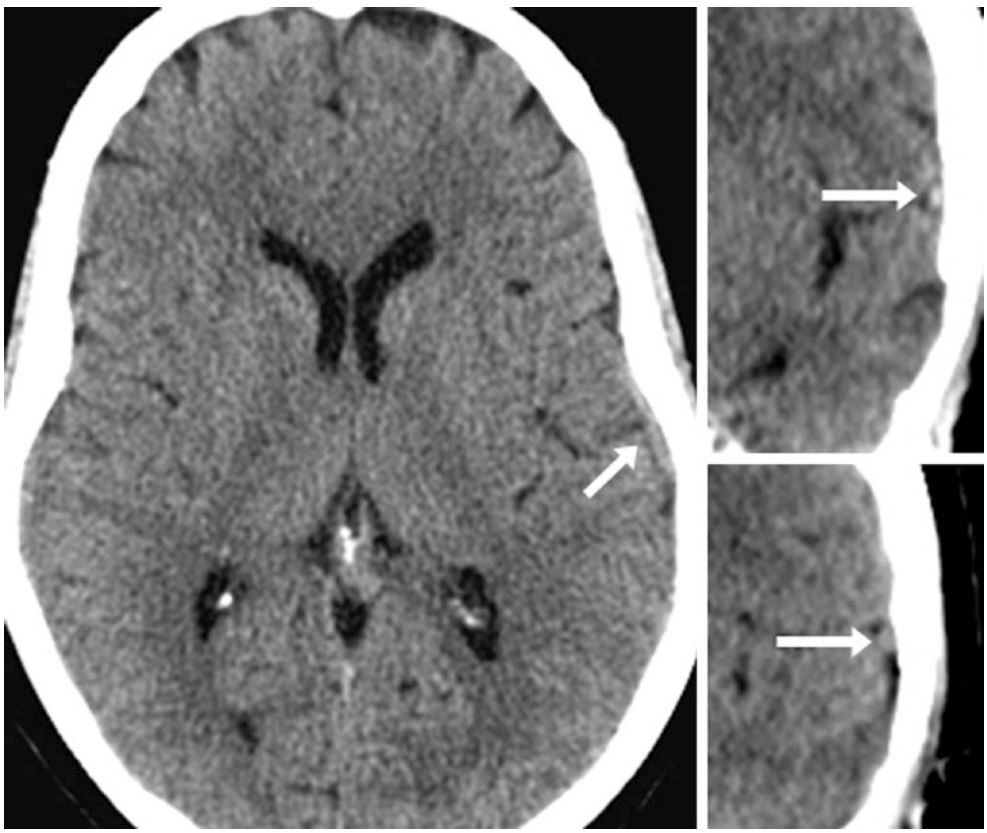

Fig. 45.20 38-year-old with a dense superficial vein. A radiology resident questioned subdural hematoma (*arrow*) on NECT (*left*), which, on coronal MPR (*top right*), was found to be a vein of Labbé that appeared dense owing to beam hardening; it was not dense dorsally (*bottom right*)

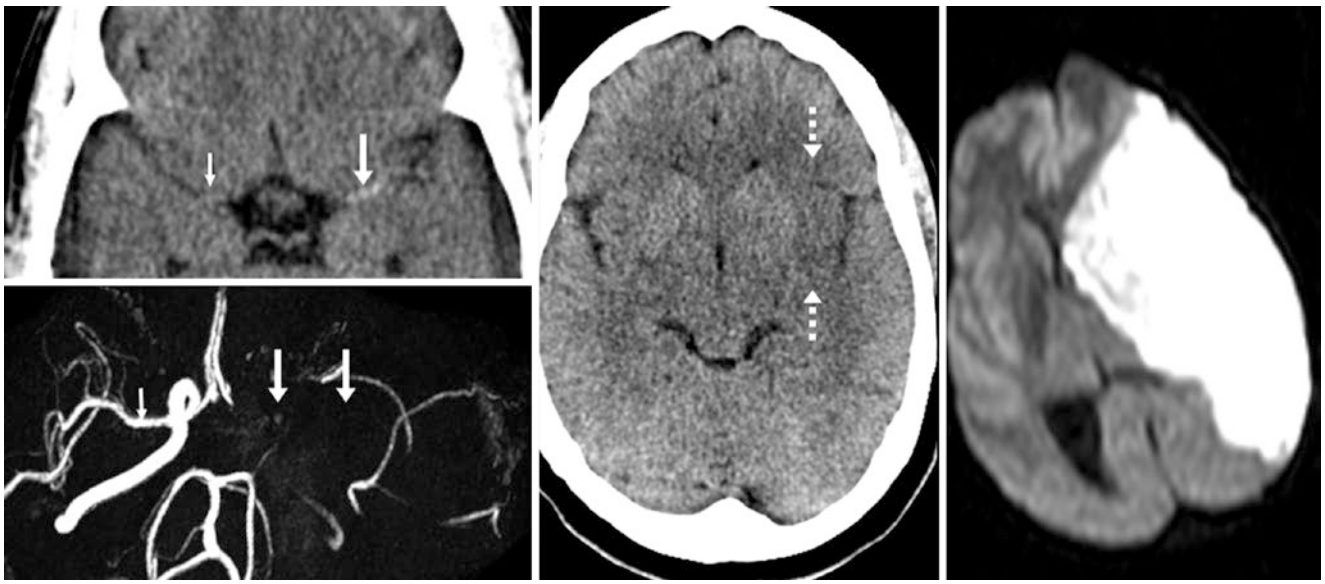

Fig. 45.21 Comparison case of a dense MCA and an acute infarct. In a 41-year-old, NECT (*top left*) found a dense left MCA (*large arrows*), with focal loss of gray-white differentiation ("insular ribbon" sign) (*dotted arrows, middle*). The internal carotid artery (ICA) and MCA were occluded (*arrows*) on a 3DTOF MRA superior view (*bottom left*), with contralateral MCA patency (*thin arrow*). DWI MRI 2 days later (*right*) confirmed the presence of an infarct, which had expanded since the NECT

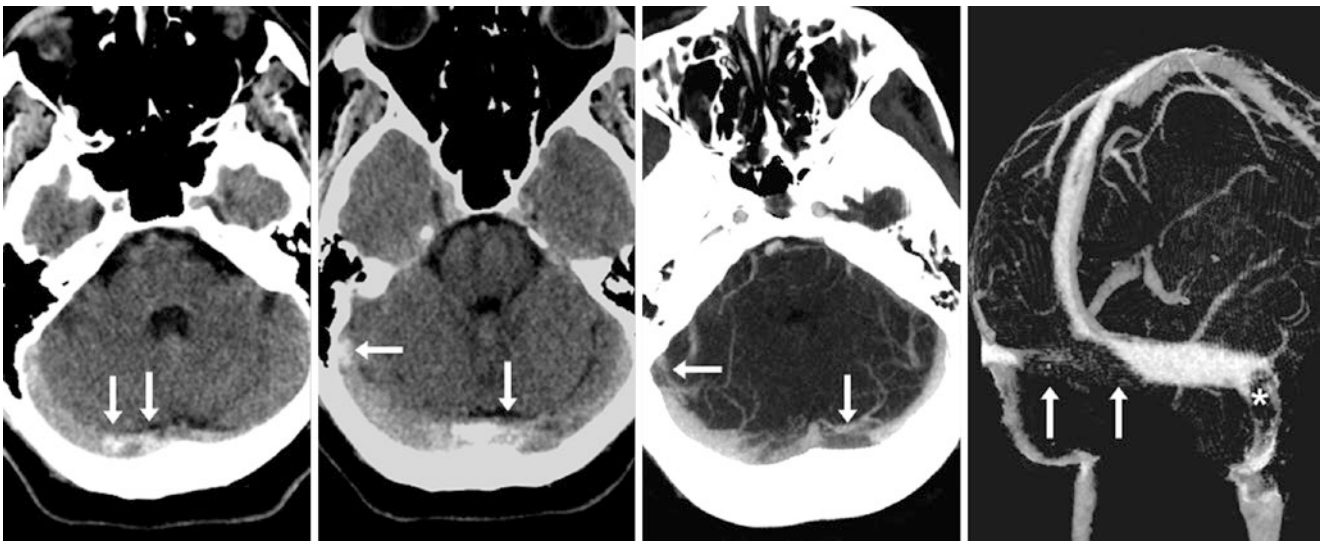

Fig. 45.22 Comparison case of dense dural sinuses from thrombosis. A 35-year-old with dense transverse and sigmoid sinuses (*arrows*) on NECT (*left* and *left middle*). A CTV with 16-mm axial MPR (*right middle*) and a 3D VR RPO view (*right*) showed thrombus (*arrows*) within the torcular, extending into both transverse sinuses, and within the right sigmoid sinus (*asterisk*). Note how the thicker MPR and 3D VR images clearly confirmed the presence of thrombus

References

1. New PF, Aronow S. Attenuation measurements of whole blood and blood fractions in computed tomography. Radiology. 1976;121:635–40.
2. Eick JJ, Miller KD, Bell KA, Tutton RH. Computed tomography of deep cerebral venous thrombosis in children. Radiology. 1981;140:399–402.
3. Nelson Jr MD, Thompson JR, Hinshaw Jr DB, Hasso AN. Radiodense dural sinuses: new CT sign in patients at risk for hypoxemic insult. AJNR Am J Neuroradiol. 1981;2:545–8.
4. Healy JF, Nichols C. Polycythemia mimicking venous sinus thrombosis. AJNR Am J Neuroradiol. 2002;23:1402–3.
5. Ben Salem D, Osseby GV, Rezaizadeh-Bourdariat K, Pastural G, Martin D, Brunotte F, et al. [Spontaneous hyperdense intracranial vessels seen on CT scan in polycythemia cases]. [French]. J Radiol. 2003;84:605–8.
6. Black DF, Rad AE, Gray LA, Campeau NG, Kallmes DF. Cerebral venous sinus density on noncontrast CT correlates with hematocrit. AJNR Am J Neuroradiol. 2011;32:1354–7.
7. Garetier M, Rousset J, Pearson E, Tissot V, Gentric JC, Nowak E, et al. Value of spontaneous hyperdensity of cerebral venous thrombosis on helical CT. Acta Radiol. 2014;55:1245–52.
8. Casey SO, Alberico RA, Patel M, Jimenez JM, Ozsvath RR, Maguire WM, Taylor ML. Cerebral CT venography. Radiology. 1996;198:163–70.
9. Rodallec MH, Krainik A, Feydy A, Hélias A, Colombani JM, Jullès MC, et al. Cerebral venous thrombosis and multidetector CT angiography: tips and tricks. Radiographics. 2006;26:S5–18. discussion S42–3.
10. Provenzale JM, Kranz PG. Dural sinus thrombosis: sources of error in image interpretation. AJR Am J Roentgenol. 2011;196:23–31.
11. Zaheer S, Iancu D, Seppala N, Patro S, Glikstein R, Thornhill RE, Lum C. Quantitative non-contrast measurements improve diagnosing dural venous sinus thrombosis. Neuroradiology. 2016;58(7):657–63.
12. Truwit CL, Barkovich AJ, Gean-Marton A, Hibri N, Norman D. Loss of the insular ribbon: another early CT sign of acute middle cerebral artery infarction. Radiology. 1990;176:801–6.
13. Yock DH Jr. CT demonstration of cerebral emboli. J Comput Assist Tomogr. 1981;5:190–6.
14. Avsenik J, Oblak JP, Popovic KS. Non-contrast computed tomography in the diagnosis of cerebral venous sinus thrombosis. Radiol Oncol. 2016;50:263–8.
15. Rischall MA, Boegel KH, Palmer CS, Knoll B, McKinney AM. MDCT Venographic Patterns of Dural Venous Sinus Compromise After Acute Skull Fracture. AJR Am J Roentgenol. 2016;19:1–7.
16. Delgado Almandoz JE, Kelly HR, Schaefer PW, Lev MH, Gonzalez RG, Romero JM. Prevalence of traumatic dural venous sinus thrombosis in high risk acute blunt head trauma patients evaluated with multidetector CT venography. Radiology. 2010;255:570–577.
17. Rivkin MA, Saraiya PV, Woodrow SI. Sinovenous thrombosis associated with skull fracture in the setting of blunt head trauma. Acta Neurochir (Wien). 2014;156:999–1007.

Index

A.M. McKinney, *Atlas of Normal Imaging Variations of the Brain, Skull, and Craniocervical Vasculature* ,
DOI 10.1007/978-3-319-39790-0

R